ISSN 1304-7191
E-ISSN 1304-7205

sigma

Journal of Engineering and Natural Sciences

Mühendislik ve Fen Bilimleri Dergisi

Volume 44
Number 4
Year 2026

YTU PRESS

www.sigma.yildiz.edu.tr

E-ISSN 1304-7205

sigma
Journal of Engineering and Natural Sciences
Mühendislik ve Fen Bilimleri Dergisi

Volume 44 Number 4 Year 2026 - August

EDITOR-IN-CHIEF

Ahmet Selim DALKILIÇ
Department of Mechanical Engineering, Yıldız Technical University, İstanbul, Turkey

ASSOCIATE EDITORS

İhsan KAYA
Department of Industrial Engineering, Yıldız Technical University, İstanbul, Turkey

Nergis ARSU
Department of Chemistry, Yıldız Technical University, İstanbul, Turkey

SECTION EDITORS

Ali ERDOĞMUŞ
Department of Chemistry, Yıldız Technical University, İstanbul, Turkey

Alper YILMAZ
Department of Bioengineering, Yıldız Technical University, İstanbul, Turkey

Azmi Seyhun KIPÇAK
Department of Chemical Engineering, Yıldız Technical University, İstanbul, Turkey

Banu MANSUROĞLU
Department of Moleculer Biology and Genetics, Yıldız Technical University, İstanbul, Turkey

Emel AKYOL
Department of Chemical Engineering, Yıldız Technical University, İstanbul, Turkey

Eyüp DEBİK
Department of Enviromental Engineering, Yıldız Technical University, İstanbul, Turkey

Fatih AKYOL
Department of Metallurgical and Materials Engineering, Yıldız Technical University, İstanbul, Turkey

Gülhayat GÖLBAŞI ŞİMŞEK
Department of Statistics, Yıldız Technical University, İstanbul, Turkey

Hakan YILMAZER
Department of Metallurgy and Malterials Engineering, Yıldız Technical University, İstanbul, Turkey

Hasan KÖTEN
Department of Mechanical Engineering, İstanbul Medeniyet University, İstanbul, Turkey

Hayriye SUNDU PAMUK
Department of Physics, Kocaeli University, Kocaeli, Turkey

Mesut AKGÜN
Department of Chemical Engineering, Yıldız Technical University, İstanbul, Turkey

Metin TÜLÜ
Department of Chemistry, Yıldız Technical University, İstanbul, Turkey

Muhammet Kasım ŞENER
Department of Chemistry, Yıldız Technical University, İstanbul, Turkey

Müslüm ARICI
Department of Mechanical Engineering, Kocaeli University, Kocaeli, Turkey

Nader JAVANI
Department of Mechanical Engineering, Yıldız Technical University, İstanbul, Turkey

Osman Nuri UÇAN
Department of Electrical and Electronics Engineering, Altınbaş University, İstanbul, Turkey

Ömer Said TOKER
Department of Food Engineering, Yıldız Technical University, İstanbul, Turkey

E-ISSN 1304-7205

Sigma
Journal of Engineering and Natural Sciences
Mühendislik ve Fen Bilimleri Dergisi

Volume 44 Number 4 Year 2026 - August

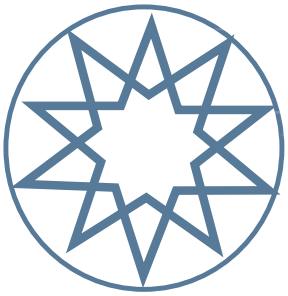
Necmiye Özlem ÜNVERDİ
Department of Electronics and Communication Engineering, Yıldız Technical University, İstanbul, Turkey
Selçuk ÇEBİ
Department of Industrial Engineering, Yıldız Technical University, İstanbul, Turkey
Sevil YÜCEL
Department of Bioengineering, Yıldız Technical University, İstanbul, Turkey
Vildan ÇETKİN
Department of Mathematics, Kocaeli University, Kocaeli, Turkey
Yasemin BUDAMA KILINÇ
Department of Bioengineering, Yıldız Technical University, İstanbul, Turkey

REGIONAL EDITORS

Abdelraheem Mahmoud ALY
South Valley University, Egypt
Abdullahi YUSUF
Federal University Dutse, Nigeria;
Biruni University Istanbul, Turkey
Adem KILICMAN
Department of Mathematics, University Putra, Malaysia
Amin SHAHSAVAR
Kermanshah University of Technology, Iran
Chandramohan V.P.
National Institute of Technology Warangal, India
Gobinath RAVINDAN
SR University, India
Hijaz AHMAD
University of Engineering and Technology Peshawar, Khyber Pakhtunkhwa, Pakistan
Md. Sabir HOSSAIN
Chittagong University of Engineering and Technology, Bangladesh
Mohammad Reza SAFAEI
Department of Civil and Enviromental Engineering, Florida International University, USA
Mostafa Safdari SHADLOO
Insa of Rouen, France
Muthu Poosan MOOPANAR
Department of Mathematics, National Institute of Technology, Warangal, India
Oscar CASTILLO
Tijuana Institute of Technology, Mathematics Division, Mexico
Pravin KATARE
Marathwada Mitra Mandal's College of Engineering, India
Ravindar KUMAR
Lovely Professional University, India
Sania QURESHI
Department of Basic Sciences and Related Studies, Mehran University of Engineering and Technology, Pakistan
Siamak HOSEINZADEH
Department of Planning, Design, and Technology of Architecture, University of Roma, Italy
Shengda ZENG
School of Mathematics and Statistics, Yulin Normal University, Yulin, China;
Faculty of Mathematics and Computer Science, Jagiellonian University in Krakow, Krakow, Poland
Taha M. RABABAH
Department of Nutrition and Food Technology, Jordan University of Science and Technology, Jordan

E-ISSN 1304-7205





Volume 44 Number 4 Year 2026 - August

ADVISORY EDITORS

Bestami ÖZKAYA
Department of Civil Engineering, Yıldız Technical University, İstanbul, Turkey

Cengiz KAHRAMAN
Department of Industrial Engineering, İstanbul Technical University, İstanbul, Turkey

Erol TUTUMLUER
Department of Civil Engineering, University of Illinois Urbana-CHampaign, USA

Hari Mohan SRIVASTAVA
Department of Mathematics and Statistics, University of Victoria, Canada

Mohsen SHEIKHOLESLAMI
Babol Noshirvani University of Technology, Iran

Melike Elif BİLDİRİCİ
Department of Economics, Yıldız Technical University, İstanbul, Turkey

Somchai WONGWISES
Department of Mechanical Engineering, King Mongkut's University of Technology, Thonburi, Thailand

Umut Rıfat TUZKAYA
Department of Industrial Engineering, Yıldız Technical University, İstanbul, Turkey

Zekai ŞEN
İstanbul Medipol University, İstanbul, Turkey

Zeynep IŞIK
Department Civil Engineering, Yıldız Technical University, İstanbul, Turkey

SECRETARY

Senol BİLGİN
Yıldız Technical University, İstanbul, Turkey

Abstracting and Indexing:
- Directory of Open Access Journals (DOAJ)
- EBSCO Host Online Research Databases
- Emerging Sources Citation Index (ESCI)
- Scopus
- MIAR
- Scilit
- OUCI
- Research4Life
- Ideal Online

Journal Description: The journal is supported by Yıldız Technical University officially, and is a blind peer-reviewed free open-access journal, published bimontly (February-April-June-August-October-December).

Owner: Yıldız Technical University

Editor-in-Chief: Ahmet Selim Dalkiliç

Language of Publication: English

Frequency: Bimontly (6 issues per year)

Publication Type: Online e-version

Publisher: Kare Publishing

E-ISSN 1304-7205

sigma
Journal of Engineering and Natural Sciences
Mühendislik ve Fen Bilimleri Dergisi

Volume 44 Number 4 Year 2026 - August

CONTENTS

Research Articles

2313 **A comprehensive survey on hostile post detection techniques in social media: Challenges and future directions**
Jagruti BODA, Keyur RANA

2328 **Comparative study of two-body and three-body abrasive wear behaviour of 3D printed carbon fiber reinforced PLA/ABS composites**
Anand A, Hemanth R, Raghavendra T, Suresha B, Bharath P B, Govindaraju N

2339 **Explicit expression for powers of certain complex tridiagonal and some complex factorizations**
Gürsel YEŞİLOT, Hatice Kübra GEÇÖR

2347 **Estimating above ground biomass in black pine forest using ALOS-1 data and machine learning methods**
Şükrü Teoman GÜNER, Omer Gokberk NARIN, Aydın ÇÖMEZ, Eren Gürsoy ÖZDEMİR, Caglar BAYIK, Saygın ABDIKAN

2364 **Solution to a make-or-buy decision problem based on intuitionistic fuzzy sets and grey relational analysis**
Gülçin CANBULUT, Erkan KÖSE, Forrest Jeffrey Yi-Lin

2380 **Cost-benefit evaluation of repairable retrial systems with warm standby components and setup times**
Jones Edward CHIWINGA, Muhammad Salihu ISA, Jinbiao WU

2396 **Numerical modeling of seismic impacts on cistern structures**
Pınar USTA EVCİ, Ayşe BÜYÜKÜNSAL, Neşe BOZKURT

2415 **Stabilisation of expansive soil by geo-polymerisation of industrial wastes - Fly ash**
Aishwarya GAYATRI, P K PRADHAN, P K PARHI

E-ISSN 1304-7205

Sigma
Journal of Engineering and Natural Sciences
Mühendislik ve Fen Bilimleri Dergisi

Volume 44 Number 4 Year 2026 - August

2433 **Integrating cognitive intelligence in robotic process Automation: Placement bots in action**
Neelam YADAV, Supriya P. PANDA

2447 **Gaussian mixture model and K-means based spatial interval valued intuitionistic fuzzy C-means clustering incorporating the D_α operator for MRI image segmentation**
Manivasagan M., Jagatheswari S.

2458 **An advanced framework for cervical cancer detection using optimized ensemble learning**
Rufina Sherin John ROBERT, Tamilazhagan SENTHIL, Manikandan RAMACHANDRAN, Vidivelli SOUNDARARAJAN, Magesh SANKAR, Mohammad KHISHE

2473 **A study on physics-informed neural networks and finite volume approach for Maxwell fluid simulation in stenosed coronary arteries**
Abdul WAHAB, Muhammad Imran ASJAD, Sohail NADEEM, Kubra ANJUM

2509 **A novel dynamic dimensional convolution network architecture for classification of ovarian tumor**
Aarti PAREKH, Madhavi DESAI

2525 **Entropy generation analysis of hydromagnetic flow on nonlinearly radiating Walters' B nanofluid with heat generation and viscous dissipation**
Bayo Johnson AKINBO, Ibhadode OISEHOEMOMEN

2540 **Fitting continuous PDFs to *q*-discrete distributions**
Ibrahim SADOK

2551 **Iterative methods for solving fuzzy non-linear equations**
Srilakshmi KATURI, Prashanth MAROJU

2571 **Study of heat flux of tri-hybrid (TiO_2+SiO_2+Al_2O_3/ $C_6H_9NaO_7$) nanofluids over a linearly stretching sheet**
Ch. MANGAMMA, B. SAIDULU, P. Pramod KUMAR, Rangu RAKESH, A. R. DEEPIKA

2583 **Thermal analysis of hybrid Casson nanofluid (AlN+Al_2O_3/ $C_6H_9NAO_7$) with Lorentz force effect over a linearly stretching sheet**
S. RENUKA, V. MEENAKSHI, Kamatam GOVARDHAN, A. R. DEEPIKA

E-ISSN 1304-7205

sigma
Journal of Engineering and Natural Sciences
Mühendislik ve Fen Bilimleri Dergisi

Volume 44 Number 4 Year 2026 - August

2595 **A reinforcement learning framework for disaster resilient data transfer in underwater wireless sensor networks**
Ritu BHARDWAJ, Ashwani KUSH

2604 **Deep Q-Learning based smart EV charging for optimizing grid load, cost, and renewable energy integration**
Arun C. DIXIT, Harshavardhan B., Prakasha K. N.

2617 **Pre-fabrication analysis using ansys in dental implants for enhancing mechanical stability and clinical success**
Naveen ANKEGOWDA, Rakshith GOWDA D. S., Nithyananda B. S.

2626 **Evaluating the performance of Iterated Greedy methods for the distributed permutation flowshop with sequence-independent setup times**
Clarissa TARARAM de LAURENTYS, Marcelo Seido NAGANO, Fernando Luis ROSSİ

2641 **Improving power quality in fuel cell applications and deep learning based analysis**
Ünal YILMAZ, Kerim KARADAĞ, Süleyman Bayram GÖNÜLLÜ

2658 **Prediction performance of multiple linear regression analysis applied to the mechanical properties of green cement mortar**
Kaci CHALAH, Aghiles HAMMAS

2676 **Comparison of neurofilament light chain protein levels in the blood of patients with multiple sclerosis and amyotrophic lateral sclerosis**
Emrah BERTAN, Aslıhan GÜNEL, Reşit ÇELİK, Halil Atilla İDRİSOĞLU, Şenay VURAL KORKUT

2685 **Energy-efficient static memory architecture for internet of things applications**
Deepak GARG, Rupali SINGH

2700 **Leveraging Bi-LSTM advanced deep learning model for enhanced wind speed prediction**
Muskaan AHUJA, Sanju SAINI

E-ISSN 1304-7205

sigma
Journal of Engineering and Natural Sciences
Mühendislik ve Fen Bilimleri Dergisi

Volume 44 Number 4 Year 2026 - August

2714 **Expository techniques and integrative bioinformatics for survival modeling: Screening potential biomarkers in hepatocellular carcinoma**
Sumaila ABUBAKARI, Filiz KARAMAN, Radiatu ABDUL-SOMED

2735 **Evaluation of Natech risk after landslide disaster in the scope of mines located in districts: An application for Zonguldak province**
Emel GÜVEN, Mehmet PINARBAŞI, Hacı Mehmet ALAKAŞ, Tamer EREN

2745 **Fuzzy logic approaches for forecasting daily global solar radiation: A comparative analysis of climatic variables**
Berke Oğulcan PARLAK, Erhan AKDOĞAN

2758 **Emotion-aware human-computer interaction using multimodal deep learning and explainable artificial intelligence**
Pallavi WANKHEDE, Deepali KOTAMBKAR, Kanchan WARKAR, Sweta RAUT

2783 **Fault prediction of transformers using machine learning techniques**
Nagendra SINGH, Ashutosh KASHIV, Harsh Pratap SINGH

2797 **A computational modal analysis of graphene and hexagonal boron nitride reinforced polypropylene nanocomposites**
Aamir M. SHAIKH, Pravin R. KUBADE

2808 **Solution and stability analysis of homogeneous piecewise fractional systems**
Mustafa AYDIN, Arda BİLEN

2823 **Impact of vehicle integration sections on photovoltaic performance: A case study for Türkiye**
Semir SÜNKÜN, Berke Oğulcan PARLAK, Hüseyin Ayhan YAVAŞOĞLU, Umut KARAGÜZEL

2837 **Innovative approaches and practical experiences: Post-disaster reconstruction with adhocratic architecture**
Tuğba ERDİL DİNÇEL

2856 **Characterizing temperature profiles and thermal management in hydrogen storage systems for aerial vehicles**
Kirubadurai B., Jegadeeswari G., Jaganraj R., Vinothkumar M.

E-ISSN 1304-7205

Sigma
Journal of Engineering and Natural Sciences
Mühendislik ve Fen Bilimleri Dergisi

Volume 44 Number 4 Year 2026 - August

2873 **Disease detection in sugarcane crop using deep learning**
Twinkle B. ANKLESHWARIA, Madhavi B. DESAI

2889 **Robust load frequency control using an improved tilted integral derivative controller in interconnected diverse unit networks**
Alok KUMAR, Mohammad Atif SIDDIQUI, Mohammed ASIM

2905 **A hybrid BiT-EfficientNet framework for automated detection of skin cancer and monkeypox using dermatoscopic images**
Juby MATHEW, Dileepkumar S. R., Ardra B. S.

2917 **Formulation of eco-friendly dishwasher liquid: A sustainable solution**
Hemant M. JARİWALA, Ravi VAGHELA

2924 **Parameter estimation for Multivariate Gamma distribution with Particle Swarm Optimization based on Taguchi method**
Aynur YONAR, Nimet YAPICI PEHLİVAN

2937 **Enhancing geopolymer mortars: The impact of Algerian metakaolin substitution on mechanical performance and sustainability**
Kamel HEBBACHE, Abdellah DOUADİ, Oualid Mahieddine HAMDİ, Mourad BOUTLİKHT, Abderraouf MESSAİ, Nour El Houda KHİTAS, Cherif BELEBCHOUCHE

2952 **Optimization of geogrid reinforcement for improving CBR of subgrade soils**
M. Bharath CHANDRA, Kadali SRINIVAS, V. Ramya KRISHNA

2963 **Influence of artificial aging on microstructure and mechanical properties of Aluminum 2219-T87 TIG welded joints**
Atif SHAZAD, Maaz AKHTAR, Muhammad UZAIR

2974 **Some components and bioactive properties of gel and green leaf parts of *A. vera***
Heleen TAHSEEN YASEEN, Sevda KIRBAĞ, Fikret KARATAŞ

2982 **A comprehensive framework for selecting building energy modelling tools to support sustainable design**
Ahmad Walid AYOOBI, Mehmet İNCEOĞLU

E-ISSN 1304-7205

Sigma
Journal of Engineering and Natural Sciences
Mühendislik ve Fen Bilimleri Dergisi

Volume 44 Number 4 Year 2026 - August

Review Articles

3002 **A review: Machine learning approach to understanding the impact of mobile phone addiction on academic performance, health, and family life**
R. Ruth BELINA, T. Lucia Agnes BEENA

3012 **Innovative thermal and non-thermal treatments for microorganism inactivation in plant milk**
Ulaş BAYSAN, Işıl İLTER BAYSAN

3027 **Nanofluids and their role in enhancing automotive performance: A comprehensive review**
Sanjeev Kumar GUPTA, Soni KUMARİ

Sigma Journal of Engineering and Natural Sciences
Web page info: https://sigma.yildiz.edu.tr
DOI: 10.14744/sigma.2025.000169

Research Article

A comprehensive survey on hostile post detection techniques in social media: Challenges and future directions

Jagruti BODA[1,*], Keyur RANA[1]

[1]*Gujarat Technological University, 382424 India*

ARTICLE INFO

Article history
Received: 23 December 2024
Revised: 13 February 2025
Accepted: 22 July 2025

Keywords:
Dataset; Deep Learning; Hostile Post; Machine learning; Text Classification; Transformer Based

ABSTRACT

Hostile Post detection on social media is a crucial task that aims to identify harmful content such as hate speech, cyberbullying, fake news and offensive language. This survey provides a detailed survey of existing and emerging techniques for this task, including machine learning techniques, deep learning techniques, and hybrid techniques that integrate multiple approaches to improve model performance. We also explore the use of reinforcement learning, genetic algorithms, and pseudo-labeling techniques for optimising performance. There are several challenges identified, including dataset limitations, annotation inconsistencies, model interpretability, and ethical issues such as fairness and cultural sensitivity. The review also examines future trends in multilingual hostile post detection, cross-platform adaptability, and the increasing use of transformer-based architectures. Finally, we emphasize the importance of developing scalable, explainable, and context-aware solutions, and we outline future directions for research. This work is intended to serve as a reference for scholars and practitioners working toward safer online environments.

Cite this article as: Boda J, Rana K. A comprehensive survey on hostile post detection techniques in social media: Challenges and future directions. Sigma J Eng Nat Sci 2026;44(4):2313–2327.

INTRODUCTION

Social media has become an essential part of global communication, allowing users to engage, express and connect in real time. But the increasing usage of these platforms has also resulted in the development of hostile and destructive content such as hate speech, cyberbullying, foul language and misinformation. Such information may exacerbate social tensions, affect people's mental health and, in extreme situations, lead to real-world violence [1, 2]. The objective for this survey is the growing necessity to carefully review and compare numerous hostile post detection strategies used in both academic and operational contexts. The surge of online aggressiveness, particularly during politically sensitive moments and worldwide crises, makes the moderation of such content a serious task, especially in multilingual and low-resource settings. Hostile post detection is the automatic identification of damaging internet content that violates cultural and ethical norms. This effort is challenged by factors such as linguistic diversity, cultural differences in understanding anger, sarcasm, implicit meaning and developing communication styles

***Corresponding author.**
*E-mail address: jagrutiboda10@gmail.com

This paper was recommended for publication in revised form by Editor-in-Chief Ahmet Selim Dalkilic

Published by Yıldız Technical University Press, İstanbul, Turkey
© Author. This is an open access article under the CC BY-NC license (http://creativecommons.org/licenses/by-nc/4.0/).

[3]. Manual moderation doesn't scale—you need AI-driven solutions that work at the size of major platforms. This survey uses a structured literature review process, focusing on hostile content detection strategies published from 2015 to 2024. The reviewed methods are classified into four categories, i.e., traditional machine learning, deep learning, hybrid models, and state-of-the-art methods. The study also discusses benchmark datasets, feature extraction methods, types of models, evaluation parameters and real-world application scenarios. To facilitate understanding, comparative tables and summarizations are also provided to summarize the main findings. Early systems used traditional machine learning approaches such as Support Vector Machines (SVM), Naive Bayes, and Random Forest [4] with customized features such as Bag-of-Words (BoW) and TF-IDF. However, these techniques fail to capture contextual or semantic information. Hence, there has been a rise of deep learning models [5] such as CNNs, RNNs, LSTMs and transformer-based models such as BERT [6]. These approaches get better semantic understanding and perform well in multilingual environments. Also, hybrid methods which combine deep learning with reinforcement learning, genetic algorithms, or optimization techniques have been proposed [7]. These are targeted at tackling difficulties such as data asymmetry, hyperparameter tuning and model adaptation. However, there is still effort to be made with regard to concerns such limited availability of labeled data, variability in annotations and the need for interpretable and fair models. This analysis is especially timely considering recent global events such the 2023–2024 Israel–Palestine conflict and India's national elections, where current automated systems failed to keep up with the scale and complexity of online hate. To this end, new ways are investigated by using advanced analytical frameworks like fractional calculus and fuzzy decision systems [8–11] to improve detection efficiency. The structure of this paper is as follows. In section 2, we define and categorize several categories of hostile content. Section 3 provides an overview of existing datasets. Section 4 discusses feature extraction methods from traditional to contextual embeddings. Section 5 presents the machine learning methods, and Section 6 concentrates on the deep learning methods. Section 7 presents hybrid and advanced strategies that combine multiple methodologies. Section 8 summarizes the comparative performance of ML, DL and hybrid approaches. Section 9 describes the most used evaluation metrics. Section 10 describes obstacles and open research problems. Section 11 discusses the practical applications and use cases. Section 12 discusses future research directions, while Section 13 closes the survey.

Related Work

Social networking sites have revolutionized the communication of people . Now , people may communicate with the world and share information . But this openness has also led to the production of hateful content that can hurt individuals and groups. In order to understand such material one requires precise meanings and differences between its various types. In this section, we cover the main principles relating to hostile posts and survey the forms of hostile content typically encountered on social media.

Key Definitions

- Hostile Post [12]: Content posted through social media insults, belittles, or threatens individuals or groups. Hostility can be in the form of text, visuals, or videos. This includes hate speech, cyberbullying, and insulting comments.
- Hate Speech [13] : A hostile post towards a person's innate qualities such as race, religion, or gender. It includes language that is racist or inflammatory that can lead to prejudice or violence . It is generally legally restricted .
- Cyberbullying [14]: Repeated harassment or intimidation of people through digital communication means. Cyber bullying is distinguished by its ongoing nature and its common victimization of vulnerable users. Cyber bullying can be expressed through threats, the dissemination of rumors or the sharing of private information.
- Offensive Language [15]: The use of profane or inappropriate terms that may not be directed at a person or group but contribute to a hostile climate online. Such language is often moderated to conform to community standards.
- Trolling[16]: Deliberate attempts to create disruption or argument by posting inflammatory or otherwise off-topic messages. Trolling may be meant as humor, but may also escalate into more serious activities such as hate speech.
- Misinformation and Disinformation [17]: Misinformation is the spread of misleading information without the intent to mislead, whereas disinformation is the spread of false information with the intent to mislead. Neither are antagonistic by nature but both can create enmity by creating mistrust and division.

Common Forms of Hostile Content

Hostile content on social media comes in many forms based on intent and context. Salminen et al. [18] identified Various types of hostile content:

- Direct Threats: Specific type of threat that causes bodily harm or violence with legal outcomes.
- Harassment and Personal Attacks [19]: Repeated personal attacks on individuals using abusive language, name-calling, or derogatory comments can lead to mental depression.
- Incitement to Violence or Hatred: Threats that produce discrimination or violence against groups based on identity criteria, with a major one causing significant societal impact.
- Defamation: False information or distorted posts aimed at damaging persons› reputations.

- Sexual Content [20]: Sexual or offensive content spread to offend particularly damaging when it has particularly harmful effects when directed at young users .

Distinctions Among Related Terms

It is helpful to differentiate between terms that are closely related terms.

- Hate Speech vs. Offensive Language [21]: Hate speech that promotes hatred, discrimination, or violence against individuals or groups based on protected characteristics such as race, religion, ethnicity, or gender. Offensive language, can be rude or vulgar without any discriminatory intent activity.
- Hate Speech versus Cyberbullying [22]: Hate speech is targeting groups of people based on race, gender or religion. while cyberbullying is against individuals and involves personal attacks over time.
- Trolling vs. Hate Speech [23]: Trolling means online destroying a piece of others by posting messages that are provoking or disruptive where as hate speech targets violence.
- Misinformation vs. unfriendly content [12]: Misinformation is incorrect information shared intentionally. whereas unfriendly content is intentionally used to criticise and upset. [8, 24, 25].

Methodological Framework

The present survey has been developed using a systematic and well-structured methodology aimed at organizing, interpreting, and evaluating existing approaches to hostile post detection on social media. The framework is based on three foundational pillars – model categorization, dataset exploration and analytical evaluation.

- Model Categorization: In order to achieve meaningful classification, hostile post detection methods are grouped into four broad classes: traditional machine learning, deep learning, hybrid systems and advanced methods. This taxonomy is based on underlying algorithmic structure and learning paradigm, helping to achieve clearer comparison of performance, scalability and adaptability.
- Dataset Exploration: A survey of popular public datasets is presented based on language variety, type of social media content (e.g., tweets, comments, video captions), topic domain and labelling approach. From this we identified a research gap that is bias during the annotation process, resulting in improper training of the model and lack of datasets in regional languages.
- Analytical Evaluation: Sections 3 to 9 provide a detailed survey of the literature. Each technique is evaluated for practical application, advantages and disadvantages, and evaluation techniques (e.g., accuracy, F1, ROC-AUC). This survey also contains challenges such as ethical implications, cultural sensitivity, and model transparency, crucial for building trustable systems. The future scope and scope of work also discuss advancements in existing techniques. It also highlights practical limitations that researchers face when tackling real-world hostile content across various platforms.

DATASETS FOR HOSTILE POST DETECTION

Overview of Existing Datasets Used for Hostile Post Detection

Table 1 summarizes the different datasets used for hostile post detection, indicating the language, type of

hostile content, size of the dataset, and a short description of each dataset. It points to resources for the study of hate speech, offensive language, and related phenomena across different languages and platforms.

Characteristics of datasets

In the analysis of datasets for hostile post detection, it is important to understand the following critical features for the applicability of a dataset for various research tasks. Here are the main features to keep in mind:

Properties of Datasets› Language:

- Language(s) in which the dataset is written is an important factor especially in multilingual and multicultural environments. Datasets can be monolingual (e.g., only English) or multilingual (e.g., English, Hindi, and Tamil). Few datasets are in the form of code-mixed language that contains mixed languages such as Hindi-English or English-Gujarati. Some (e.g., Hindi-English).
- Importance: The diversity of language creates problems in model generalisation due to different linguistic subtleties, slang, dialects and cultural contexts.
- Size: The size of the dataset is the number of records (e.g., tweets, comments, posts). The size of the dataset can be from thousands to millions of samples depending on the system scope and availability of data.

Importance: Large data sets are best for training machine learning models, but they can also present noise. A smaller dataset is properly annotated and well-maintained, but that unable to handle model generalisation.

- Annotation Process: The annotation is the process of labelling our dataset with properly defined categories. Annotations can be performed by subject experts, professionals or a combination of both. The annotation scheme can be binary classification or coarse grained classification (i.e. hate speech vs non-hate speech), multi-class classification or multi-label classification or fine grained classification (i.e. hate speech , importance The annotation process is heavily dependent on the quality and reliability of the dataset. More reliable datasets have explicit standards, more than one annotator to create redundancy, and high inter-annotator agreement. Some datasets even contain explanations or justifications for the corresponding label, which improves interpretability .

- Content Type: What is the type of content in the dataset? e.g., what platform it is from, e.g., Twitter, Facebook, or YouTube; what the content actually is, e.g., text, images, or video; and what it is about, e.g., news comments, social media discussions, or user reviews.

Importance: Social media allows spreading content in the form of text, images, video, GIFs, and emojis. This input dataset was collected and analysed based on text or multimodal data, as per the social media input dataset. Based on that, select a model and analyse data.

CHALLENGES ASSOCIATED WITH DATA COLLECTION AND ANNOTATION

Some of the challenges in data collection and annotation for hostile post detection include bias, cultural context, and data scarcity. Limited data is available for low-resource languages, so the model does not learn properly on few data. The annotation process is also completely depends on annotation knowledge and proper understanding of that domain. These problems are important to tackle to build accurate and fair hostile content detection systems [4].

Trends in Model and Dataset Usage

In addition to the dataset overview and modeling approaches discussed in prior sections, this subsection highlights two significant trends observed in recent studies on hostile post detection in social media. As shown in Figure 1, the utilization of transformer-based models (e.g., BERT and its variants) in the field is on the rise. The number of such papers has been increasing steadily from 2017 to 2024, which reflects the growing preference for context-aware deep learning models to handle unstructured social media data. Figure 2 Frequency of datasets used for detection of hostile content, grouped by language. The most common datasets are in English, followed by Hindi, and there are limited resources in regional languages like Tamil and Gujarati. The chart also includes multi-lingual datasets that are increasingly used for cross-lingual and code-mixed content analysis.

This section gives a comprehensive summary of publicly available datasets on hostile post detection. It provides a comparative summary of the main features, such as language, type of hostile content, and annotation procedure. It also gives issues related to quality of data, linguistic differences, and ethical problems. The section also explores trends in model usage and dataset preferences over time help to understand the latest model use trend in multilingual and transformer-based models.

FEATURE EXTRACTION TECHNIQUES

Feature extraction is critical in text processing for hostile post detection, converting raw text into numerical representations suitable for models. A summary and comparison of conventional and state-of-the-art feature extraction techniques are as follows.

- Introduction to Classical Feature Extraction Techniques

1. Bag of Words (BoW) [4]

– Description: BoW is an easy and most useful techniques for text feature extraction, where data is represented as a vector of word occurrences. It no focus on grammar and word order but only find the number of words.

– Pros: Methos is very easy to implement and suitable for simple text classification.

Drawbacks: It fail to preserve word order and syntax information, producing high-dimensional, sparse vectors.

2. Term Frequency–Inverse Document Frequency (TF-IDF) [4]: TF-IDF improves the result of the Bag of Words model (BoW) by adding weight to important words of a document.

– Description: TF-IDF enhances BoW by weighting the words of a document according to their importance to a collection. It is a combination of term frequency (TF) and inverse document frequency (IDF) .

– Pros: It adds importance to words in documents.

– Disadvantages: It unable to add order of words and context of larger datasets.

- Advanced Feature Extraction Techniques

1. Word Embeddings [42]

– Description: Word embeddings used to translate words into dense numerical vectors using feature extraction techniques like Word2Vec and GloVe.

– Advantages: It fetches semantic meaning and reduces dimensionality over BoW and TF-IDF.

– Disadvantages: Static embeddings do not capture word senses and have problems with unknown words.

2. BERT-Based Embeddings [43]:

- Description: Bidirectional Encoder Representations from Transformers (BERT) understand detailed text in a bidirectional way and give perfect contextual embeddings, capturing all hidden information.

– Pros: Capable of identifying surrounding context and hidden feature extraction and also capable of model fine-tuning based on real-world application.

– Cons: It requires high computational power and proper fine-tuning to achieve the best model performance.

This is a detailed comparative study of various feature extraction techniques specifically for detecting hostile posts.

1. Accuracy and Performance:

– Traditional Methods: These methods are easy to implement and computationally cheap but unable to understand the context of hostile posts in detail.

– Advanced Methods: Transformer-based models are capturing semantic meaning and contextual cues, which gives the best performance.

2. Computation efficiency:

– Traditional Methods: The model performs well on small datasets, and also it requires less computation power.

Table 1. Comparison of datasets for hostile post detection across languages and content types

Dataset Name	Language	Type of Hostile Content	Size	Description
Hate Speech and Offensive Language Dataset (HSOL) [26]	English	Hate Speech, Offensive Language	24,783 tweets	On the other hand, annotations of hate speech and abusive language on tweets are often used for constructing and evaluating models.
Stormfront Data [27]	English	Hate Speech, Extremism	10,000+ posts	collected from the Stormfront forum, focusing on white supremacist content in hate speech.
Facebook Hate Speech Dataset [28]	Italian	Hate Speech	5,000 comments	Facebook comments labeled for hate speech, examining its frequency in the Italian language.
HASOC Dataset [29]	English, Hindi, German	Hate Speech, Offensive Language	20,000+ tweets	Multilingual dataset for hate speech and offensive language identification
Cyberbullying Dataset [30]	English	Cyberbullying	47,000+ instances	Social media data with annotations for different types of cyberbullying and aggression post.
SentiStrength Twitter Dataset [31]	English	Offensive Language, Insults	6,000 tweets	Designed for identifying offensive language and insults for sentiment analysis.
GermEval 2018 Dataset [32]	German	Offensive Language	9,000+ tweets	Created for offensive language detection, with annotations for binary and multi-label classification.
TRAC-2 Dataset [33]	English, Hindi, Bengali	Aggression, Hostility	15,000+ posts	Provides comments annotated for different levels of aggression and hostility for the TRAC shared task.
Hate Speech and Offensive Content (HateXplain) [34]	English	Hate Speech, Offensive Language, Target ID	20,000+ tweets	collected dataset with hate speech classes and accompanying explanations for better model interpretability.
Danish Abusive Language Dataset (DALC) [35]	Danish	Abusive Language, Hate Speech	3,000 comments	Danish social media comments annotated for abusive language and linguistic subtleties.
Dravidian Code-Mix Dataset [36]	Tamil, Malayalam	Offensive Language, Hate Speech	12,000+ comments	Code-mixed comments from YouTube annotated for offensive language, part of the HASOC-Dravidian work.
Hate Speech Detection in Hindi-English Code-Mixed Social Media Text [37]	Hindi-English (Code-Mixed)	Hate Speech, Offensive Language	15,000+ tweets	Dataset of code-mixed tweets labelled for detecting hate speech and offensive language.
Offensive Language Identification Dataset in Indian Languages (OffensEval-2020) [38]	Hindi, Bengali, Tamil	Offensive Language, Hate Speech	30,000+ posts	Posts in multiple Indian languages labelled for offensive language as part of the OffensEval work.
Gujarati Offensive Language Dataset (GOLD) [39]	Gujarati	Offensive Language, Hate Speech	5,000+ tweets	labelled Gujarati posts for offensive language and promoting NLP research for low-resource languages.
Kannada Offensive Speech Dataset (KOSD) [40]	Kannada	Offensive Language, Hate Speech	2,500+ comments	A large dataset for detecting offensive speech in Kannada and labelled with related content.
Gujarati Hostile Post Detection Dataset [4]	Gujarati	Hostile Post	10,000 posts	Created the Gujarati language hostile post detection (GUHPD) dataset with binary and multi-class labels for hostility detection
Indic Offensive Content Dataset [41]	Hindi, Bengali, Tamil, Kannada, Malayalam	Offensive Language, Hate Speech	50,000+ posts	A dataset in multiple Indian languages annotated for offensive posts to do multilingual NLP research.

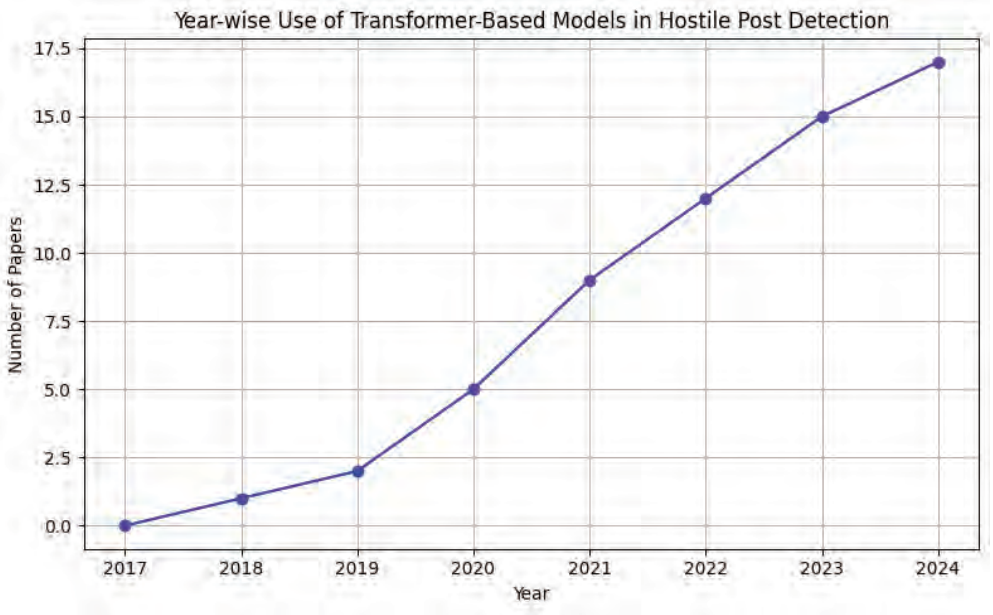


Figure 1. Year-wise use of transformer-based models in hostile post detection (2017–2024).

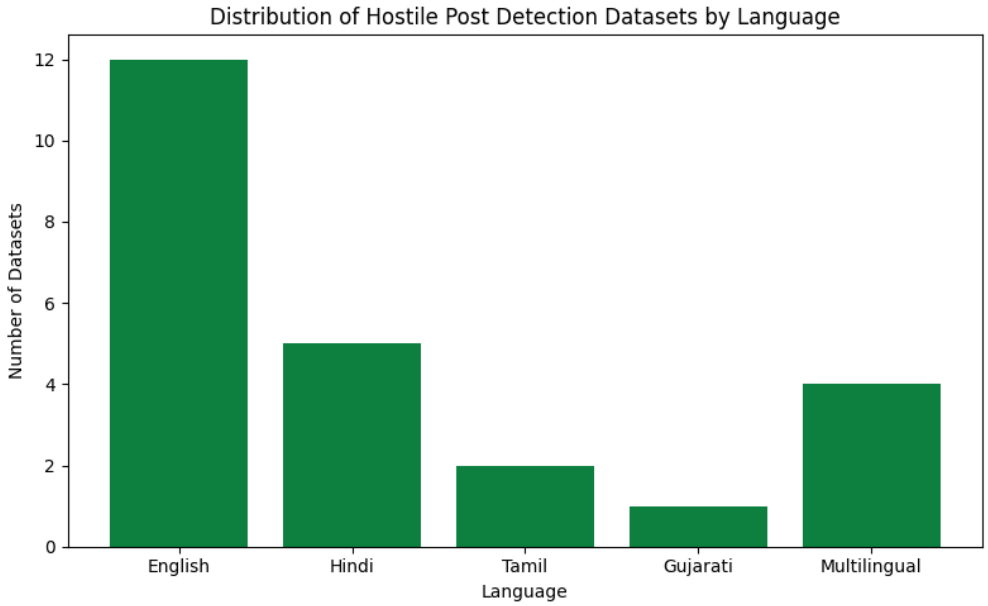


Figure 2. Distribution of hostile post detection datasets by language.

– Advanced Methods: The Transformer-based BERT model and advanced model are powerful for capturing the context of a sentence, but they also require high computation power.

3. Grasping Context and Semantics:

– Traditional Methods: Model unable to handle hostile language detection if it is indirect intent.

-Advanced Methods: They capture semantic meaning insight, which is necessary to accurately detect context-sensitive hostile posts from social media.

4. Flexibility and Adaptability:

– Traditional Methods Less flexible to newly added data, they need retraining for newly added words.

– Advanced Techniques: Advance contextual models capable of providing flexibility, such as the ability to fine-tune for various other areas or languages.

This section summarises traditional and advanced feature extraction methods used in hostile post detection. Techniques like BoW and TF-IDF are easy and

computationally efficient but lack the ability to capture detailed semantic meanings. Embedding-based models, especially the Transformer model BERT, are best for capturing contextual meaning and are well-suited for large-scale datasets and multilingual social media content monitoring.

Machine Learning Approaches

Machine learning-based methods are fundamental techniques for detecting hostile posts. Support Vector Machines (SVMs) perform best in high-dimensional spaces and classify text by capturing the optimal hyperplane that separates various classes. Naive Bayes classifiers use the concept of Bayes' theorem and assume that features are independent. They provide the best results for text classification, particularly for detecting spam or offensive language, even with large datasets. Random Forest is an ensemble method that constructs multiple decision trees and combines their predictions. It enhances classification accuracy and mitigates overfitting through majority voting or averaging. Learning methods vary depending on the availability of labeled data. Supervised learning required labeled datasets, enabling models to learn from input-output pairs. It is most effective when there is a sufficient amount of labeled data. However, unsupervised learning techniques, able to capture patterns without labeled data, may be able to identify overview of structures but may not be as precise in capturing hostile post. Semisupervised learning combines labeled and unlabeled data, taking advantage of the abundance

Table 2. Comparison of machine learning approaches for hostile post detection

Machine Learning Algorithm	Description	Advantages	Disadvantages
Support Vector Machine (SVM) [44]	SVM can find the optimal hyperplane to divide various classes in the feature space, which is suited for high dimensional data.	Good in high dimensional context, performs well for binary classification, less prone to overfitting.	Parameters require careful adjustment ; sluggish on large datasets ; may struggle with noisy data .
Naive Bayes [45]	This algorithm relies on Bayes› theorem, assuming that features are independent, and is particularly effective for classifying text.	Easy to implement and computationally light; works well with extensive datasets; suitable for text with many features.	unable to handle complex language pattern.
Random Forest [46]	It is Ensemble based approach. Merge multiple decision trees and combine their prediction accuracy.	It handles all types of data and simple and efficient model.	Required proper hyperparameter fine-tuning with large resource utilisation.
Logistic Regression [47]	Use a logistic function to predict probability and best suitable for binary classification on linear data.	Simple to easy to implement and suitable for small dataset.	unable to learn complex data and large dataset.
K-Nearest Neighbors (KNN) [48]	The algorithm classifies a point based on the majority class of its k nearest neighbors.	Easy to implement and intuitive; flexible; no training phase required.	May be computationally intensive on large datasets; sensitive to choice of k and distance metric; may struggle with high dimensional data.
Decision Trees [49]	A model provide decisions by dividing data based on values of feature extraction.	Works bets for numerical and categorial data and doesn›t require feature scaling	It fit to training data but does not perform well on unseen data.
Gradient Boosting Machines (GBM) [50]	An ensemble method that builds models sequentially that focus on correcting mistakes of previous model.	Useful for complex data structures and capable of finding hidden patterns.	Efficiently provide carefully. Change results on noisy data and large resources required for computation.
AdaBoost [51]	A boosting algorithm improve the performance of weak classifiers by focusing on the incorrect classification made by previous models.	Overfitting reduce and improve performance n complex problems.	Performance decrease on noisy data; requires careful parameter fine tuning; can overfit without proper control.
Word Embeddings (Word2Vec, GloVe) [52]	These methods convert words into dense vectors, capturing their meanings and relationships.	Captures the semantic relationships between words; reduces dimensionality; offers improvements over traditional methods like Bag of Words.	Static embeddings may not effectively address polysemy; they require pre-trained models or substantial computational resources.
BERT-Based Embeddings [52]	Utilizes transformer models to give contextualized word embeddings, capturing detailed semantic information based on context.	Highly effective for understanding complex language ruffness; context-aware embeddings enhance accuracy.	Computationally intensive; requires high resources for model training and fine-tuning; implementation can be complex.

of unlabeled data when labeled data is limited and often leads to better generalization than supervised learning alone. Ensemble techniques, such as bagging and boosting, improve performance by combining predictions from several models. Bagging uses the average of the predictions of models trained on different data subsets to reduce variance, while boosting minimizes residual errors by sequential training, leading to a robust model. Each approach has its advantages and disadvantages. Traditional methods like SVM and Naive Bayes are good at handling smaller datasets but may not be suitable for complex, high dimensional data. Ensemble methods are powerful but computationally expensive. Supervised learning methods are accurate but heavily reliant on the availability of labeled data. Unsupervised methods are flexible but may lack accuracy. Semi-supervised learning methods are a good compromise between the need for labeled data and the ability to utilize unlabeled data but necessitate good data management.

In this section, traditional machine learning techniques for hostile post detection were presented. Their learning paradigms, strengths and limitations were explained. Algorithms like SVM and Naive Bayes are simple and efficient but ensemble methods give better accuracy at the cost of high computation. The comparative table summarizes their application cases that help the researchers to choose appropriate models based on the type, size, and complexity of the data (Table 2).

Deep Learning and Neural Network-Based Approaches

Significant progress has been made in the detection of hostile posts using deep learning and neural network-based techniques that recognize complicated patterns in textual data by employing sophisticated architectures . The most basic form of neural network is the Feedforward Neural Network (FNN). Here the data flows in one direction only, from the input layer, through the fully connected layers and to the output layer. These networks are easy to implement and perform well for small to medium sized data sets capturing non-linear relationship in an efficient way. However they have difficulties with sequential or contextual information, and are therefore less suitable for tasks that require understanding temporal dependencies. Convolutional Neural Networks (CNNs) have been designed for image analysis, but have shown great potential for text classification as well. Convolutional layers enable CNNs to learn local patterns and features in the text, thus helping to handle different input lengths and decreasing dimensionality. They are good at capturing local features, but they often fail to capture long-range

Table 3. Comparison of deep learning approaches for hostile post detection

Deep Learning Approach	Description	Advantages	Disadvantages
Pre-trained Transformers (e.g., BERT, GPT) [53]	These models are transformer-based model that trained on large datasets and fine-tuned for applications.	Achieves excellent performance; provides rich contextual understanding; reduces extensive model training needs.	Requires more computational power and complexity for fine-tuning hyperparameter adjustment.
Feedforward Neural Networks (FNN) [54]	Basic neural networks with fully connected layers, where data flows in one direction.	It is easy to implement, suitable for medium datasets and also capable of understanding non-linear patterns.	Sequential data and large data is not handling properly.
Convolutional Neural Networks (CNN) [23]	Effectively identify local patterns in both text and image data.	It is efficient in identifying patterns on varying lengths of data.	Layer tuning is required properly and not handle long-range dependencies.
Recurrent Neural Networks (RNN) [12]	It›s designed to handle sequential data; also, it properly remembers information from earlier input.	It captures information from previous inputs and also remembers information from earlier input.	Training is slow because gradient process hinder effective learning
Long Short-Term Memory Networks (LSTM) [55]	An improved RNN by adding memory cell helps to understand long term dependencies	Effectively captures long-range dependencies; alleviates gradient issues.	Resource-intensive; complex; may struggle with very long sequences.
Gated Recurrent Units (GRU) [15]	A lightweight LSTM model captures long-term sequences using fewer resources.	Less resource use for solve the problem.	It not perform well for complex long sequence.
Transformer Networks [23]	Use a self-attention mechanism to assess the importance of different words within sequences.	Effectively captures context and is also scalable for long dependencies handling.	High computational resources are required, complex for implementatio and needs extensive fine-tuning.

dependencies, which may affect performance in contextually rich tasks. Then came Recurrent Neural Networks (RNNs) that have directed cycles that allow them to remember and interpret temporal dependencies, allowing them to process sequential data. This makes RNNs well suited to tasks where the order of the input matters. However, they suffer from problems such as vanishing and exploding gradients which may affect the effectiveness of training, especially for long sequences . Long Short-Term Memory Networks (LSTMs) are an extension of RNNs with additional memory cells and gating mechanisms that allow them to better deal with long term dependencies. Long short-term memory networks can solve the vanishing gradient problem. They are good for tasks with long sequences and complex contextual dependencies. But they are computationally intensive and complex to implement, which can be a hurdle in resource-constrained environments. GRUs (Gated Recurrent Units) are a simpler variation of LSTMs by cutting down the number of gates to two. This lowers the computational needs while still being able to effectively capture sequential dependencies. GRUs are more efficient than LSTMs, but they may not perform as well on long sequences and complex tasks. Transformer networks represent a significant advancement in neural network architectures, incorporating self-attention mechanisms that assess the importance of different words in a sentence to each other, enabling a more comprehensive approach to contextual relationships. They are adept at long-range dependencies; they are scalable and hence applicable to complex applications. But they are resource-hungry and require much fine-tuning. Such drawbacks could be a barrier for practical use. Pre-trained transformer models, such as BERT and GPT, trained on large data sets, have been successfully used for a variety of natural language processing tasks, including hostile post-detection. They are rich in context and cut down the need for large, task-specific training significantly. But they are expensive to calculate and difficult to implement. System need a high level of computation resources and perfect fine-tuning to perform well on particular datasets. Generally, deep learning and neural network-based approaches are powerful for hostile content detection, and each has its pros and cons. They include FNNs and complex pre-trained transformers with different functionalities for text analysis and successfully identify hostile posts. Table 3 summarizes the different deep learning techniques for hostile post detection along with their main features, advantages, and disadvantages. This comparison will help to understand the most appropriate ways of handling the various kinds of tasks and data.

This section gives a detailed summary of deep learning techniques for hostile post detection, ranging from basic neural network models to advanced pre-trained transformer models. While FNNs, CNNs, and RNNs provide basic architectures, models like LSTM, GRU, and Transformers outperform them in contextual and semantic understanding. The comparative survey table highlights each model's trade-offs in terms of accuracy, efficiency and complexity, guiding the selection of appropriate techniques based on application needs.

HYBRID AND ADVANCED TECHNIQUES

Hybrid and advanced algorithms for hostile post identification integrate multiple strategies to boost performance and address the limits of individual methods. Some of the hybrid methods are ensemble methods, which is a family of hybrid methods that combines predictions from numerous models to boost overall accuracy. Bagging (bootstrap aggregating) reduces both the variance and the overfitting (especially on noisy data sets) by building numerous models on random subsets of the training data and averaging their predictions. Another is boosting . This focuses on hard cases and incrementally trains models to fix the flaws of the previous models . It is used by algorithms like Gradient Boosting Machines (GBM) and AdaBoost to create powerful classifiers for complex data. Stacking is a way to improve the predictive performance of a meta-model by combining predictions of a large number of models, thus taking advantage of the benefits of different base models. The multiplicity of models is good for voting, and makes it more resilient by combining predictions with majority voting or average. Advanced Techniques are creative ways to improve the model performance. Transfer learning uses the knowledge from large pre-training models such as BERT or GPT to fine-tune for specific tasks and to get good performance with smaller datasets. Meta-learning aims to build models that can adapt quickly to new tasks with few data. This means that models for hostile post detection can be changed for multiple languages or platforms. cAttention Mechanisms, especially those in transformers, help the model to focus better on the essential parts of the input data and thereby improve the contextual knowledge. Some of the methods that have been developed to enable models to attend to different parts of a text include Self-Attention and Multi-Head Attention . This allows for subtle inferences about hostile material. Table 4 Summary of some advanced strategies in hostile post detection. Method Description Advantages Drawbacks Bagging Classifier ensemble method . It can help improve the overall accuracy . It is computationally expensive . Boosting Classifier ensemble method . It can help improve the overall accuracy . It is computationally expensive . Transfer learning Transfer knowledge acquired in one domain to another domain . It can help improve the overall accuracy . This section discussed hybrid and advanced strategies used to improve the performance of the hostile post detection. Ensemble techniques such as Bagging, Boosting and Stacking integrate several models to boost the robustness and accuracy. Advanced techniques such as transfer learning and meta-learning enhance adaptability, while attention processes permit deeper contextual analysis. The trade-offs of the comparative table are shown for a suitable decision according to the computational power and tasks complexity.

Table 4. Overview of advanced techniques for hostile post detection

Technique	Description	Advantages	Drawbacks
Bagging (Bootstrap Aggregating) [56]	Constructs several models using random subsets of data and combines their predictions through averaging.	Reduces variance; improves robustness; prevents overfitting.	It required higher computation power and not perform well when base model perform poor.
Boosting (e.g., AdaBoost, GBM) [57]	It improves model performance in sequence and corrects mistakes of earlier model.	Capable of handling complex data and reducing bias.	Computational power required and cannot handle noisy data.
Stacking [58]	Combines predictions from different models via a meta-model to produce a final output.	Uses strengths of different base models; improves prediction performance.	Difficult to implement; requires careful selection of base models and meta-models.
Voting [59]	Combines predictions of different models by majority voting or averaging.	Easy to implement; leverages model diversity; improves robustness.	Does not necessarily improve performance if base models are similar; it may require careful weighting.
Transfer Learning [60]	A pre-training model was used and fine-tuned for a specific task.	It performs excellently on small datasets because we are using a pre-trained model on large dataset.	High computation resources are essential for model building.
Meta-Learning [61]	Create model that can learn fast on new and minimal data	fast learning to new tasks; useful in changing environments and variable data.	Requires advanced techniques; may not perform well with limited dataset.
Attention Mechanisms [62]	Apply self-attention mechanisms to highlight the importance of words.	Improves contextual understandingof data; effective for complex data.	Computationally intensive; complex to implement and tune.

Comparative Summary of ML, DL, And Hybrid Approaches

In this section, we provide a comparative analysis of hybrid, deep learning (DL) and machine learning (ML) approaches for the identification of aggressive communications on social media, based on previous talks on specific paradigms. This section attempts to integrate the rich examination of the concepts and distinctive contributions of each technique, focusing on the practical trade-offs across a spectrum of critical dimensions. Table 5 shows the characteristics of different methods regarding their effectiveness, compatibility with datasets, scalability, and support for multilingual data. This tabular overview helps researchers select the most appropriate technique for their use case by assessing technical limitations and application requirements. It shows that traditional machine learning algorithms are scalable by extending hardware capacity and

Table 5. Comparative study of ML, DL, and hybrid techniques for hostile post detection

Technique Type	Performance	Dataset Types	Scalability	Multilingual Support
Machine Learning (ML)	The result provides the best for structure and small datasets. Not suitable for noisy and large data.	Manually feature extraction required and structure label data is necessary for model.	Scalability is possible by extending hardware resourcing.	It is not suitable for multilingual datasets, and its performance decreases if we do not provide language-specific features.
Deep Learning (DL)	Easily capture context and provide the best accuracy for the detection of hidden features and semantic relationships between data.	The model can detect unstructured , noisy data. It does not require manual feature extraction.	Need high computational resources and efficient results provided by use of GPU and TPU computation power,	Supports multilingual input through models like mBERT, XLM-R. Capable of zero-shot and cross-lingual inference.
Hybrid Techniques	ML and DL combination of models provides best and excellent result on various datasets for different class distributions.	It is capable of handling both structure and unstructuure data.	Model scalability depends on model design, combining multiple models› complexity.	When we provide pretrained model and efficient preprocessing, then it provide efficient multilingual hostile post detection support

simple, but they are not sufficient for unstructured, multilingual or complex data. However, deep learning models have a high computing cost, but they have greater efficacy. Hybrid algorithms are designed to find a middle ground among these trade-offs and often perform better at detecting malicious information in the actual world.

EVALUATION METRICS

The hostile post detection model is evaluated using various evaluation parameters. The evaluation score provided by the more accurate metrics is:

- Accuracy [63]: It gives the percentage of correctly classified posts (both hostile and non-hostile) out of the total number of posts.

$$Accuracy = (True\ Positives\ (TP) + True\ Negatives\ (TN)) / Total\ Instances \quad (1)$$

Accuracy is easy to calculate and understand, but it does not provide the best result for an imbalanced dataset.

- Precision [64]: This metric measures the correctly identified positive posts among all posts predicted as positive by the model.

$$Precision = \text{True Positives (TP)} / (\text{True Positives (TP)} + \text{False Positives (FP)}) \quad (2)$$

- Recall [65]:

‹Recall› represents the actual positive posts that are truly predicted as positive by the model.

$$\text{Recall} = \text{True Positives (TP)} / (\text{True Positives (TP)} + \text{False Negatives (FN)}) \quad (3)$$

- F1 Score [65]: It combines the measures of precision and recall together and gives a balanced measurement of the model.

$$\text{F1 Score} = 2 \times \text{Precision} \times \text{Recall} / (\text{Precision} + \text{Recall}) \quad (4)$$

- AUC-ROC (Area Under the Receiver Operating Characteristic Curve) [64]: This metric checksposts how the model differentiates hostile and non-hostile posts based on the threshold value.

$$AUC\text{-}ROC = \int_{-\infty}^{\infty} ROC\ Curve \quad (5)$$

A higher AUC-ROC value indicates superior performance in accurately classifying instances.

Challenges in Evaluating Hostile Post Detection Models

Evaluation of hostile post detection algorithms is challenging for the following reasons

– Imbalance in Datasets [66]: There are usually more hostile postings than non-hostile postings. This discrepancy can skew metrics like accuracy, making models appear better than they really are. In these cases, measures like precision, recall and F1-score gives a better view, focusing on performance with regard to minority class.

– Contextual and Cultural Variability [67]: The concept of hostile content can differ widely across cultures and circumstances. This could make a dataset that works well not function well with a model trained on another dataset since contextual details may change. Diversity is necessary for generalization of evaluation measures and demands context-sensitive judgements.

- Dynamic Nature of Language [68]: Language changes affect model performance, so retraining is required over a period of time for improved performance of model.
- Subjectivity in Annotation [69]: The classification of posts as hostile or non-aggressive is a subjective problem. It can cause errors in ground truth data. The subjectivity of the evaluation measures influences their reliability and requires careful annotation methods to ensure correctness and consistency. Such issues demonstrate the requirement of large and adaptable evaluation frameworks to fit for the intricacies of hostile post detection.

DISCUSSION ON THE NEED FOR NEW OR IMPROVED METRICS

Hostile post identification algorithms need new or improved measures to evaluate them.

- Context-Aware Metrics [70]: Metrics considering the contextual and cultural characteristics can be useful to evaluate models in diverse situations. More context-sensitive measures would be more appropriate for capturing the subtlety of what constitutes detrimental content in diverse circumstances.
- Dynamic Metrics [70]: Flexible metrics that evolve with language and context through time may help keep models relevant. Evaluation methods can learn from new data and adjust thresholds based on continual learning.
- Granular Metrics [71]: Separate metrics used to identify the detail of the category (e.g., hate speech vs cyberbullying) of data accurately. That also helps fine-tune the model based on their category result.
- Multi-Aspect Evaluation [72]: A combination of traditional and advanced evaluation metrics is used to better evaluate the model's performance. Traditional evaluation metrics such as accuracy, precision, recall, F1-score, and AUCROC are basic, but they are not enough for complete hostility detection.

CHALLENGES AND OPEN ISSUES

Data-Related Challenges

Hostile post detection has numerous key data challenges. One key difficulty is the imbalance of dataset as there are far less hostile than non-aggressive posts. This results in a biased performance measurement. This mismatch can bias the accuracy measures and predispose the

models to the majority class . Solutions include over-sampling the hostile posts, under-sampling the benign postings or employing synthetic data methods such as SMOTE to balance the data set . Multilingual detection is a more hard problem for the models because they must perform well across languages that have diverse linguistic and cultural characteristics. This comprises strategies such as building language-specific models or using multi-lingual embeddings and transfer learning for better adaption. The annotation problems are also attributable to the subjectivity of the decision of whether a post is hostile or not, which may lead to discrepancies. To tackle this problem it is important to set tight annotation standards and utilize numerous annotators to make sure that there is consensus and consistency [73–75].

Model-Related Challenges

We discuss the problems of overfitting, generalization and interpretability for the hostile post detection model. This is called "overfitting". The models overfit the training data and learn the noise that does not generalize well to new data . This leads to poor performance in the real world. Cross validation and regularization can help with generalization . Another challenge is how to generalize the models well to various datasets. Models trained on a dataset may not generalize to another dataset owing to language or cultural variations. Training on several datasets helps generalization . Also , domain adaptation or transfer learning can aid . Finally, interpretability is important especially when complicated models are used as "black-box". To increase transparency, it is necessary to employ approaches that can comprehend the model's results such as feature importance analysis and explainable AI techniques.

Ethical and Social Challenges

Ethical and social issues: bias, privacy and regulatory impediments Bias Bias is a concern as models may have assumptions based on the data they are trained on and may provide biased results in terms of race, gender, socioeconomic class etc. Fair-aware algorithms and diverse and representative data sets may help to alleviate them.We do care about privacy and specifically personal data and sensitive businesses. Privacy must be anonymized and controlled by law. law:Content filtering is a difficult wicket when you see legislation in other domains. What are the data protection rules we have to follow to be ethical ? Holistically addressing these ethical and sociological factors requires technical solutions focusing on fairness, privacy and legal compliance to enable responsible hostile post detection [76,77].

Applications and Use Cases

Hostile post detection technology has several essential uses. It is used to monitor user-generated content on social media sites, and to detect and flag harmful posts to create a safe online environment. These systems automate moderation tasks, and lessen the load on human moderators. These tools fight crime by analyzing interactions happening online. In the policy realm, these systems provide a window into online behaviors that shape the development of rules and initiatives for online safety. Another important area is cross-lingual detection, which enhances the ability to detect hostile content around the globe. This feature is vital for global companies that deal with online hostility in different cultural settings [78, 79].

Future Directions and Research Opportunities

Hostile post detection is a developing field and there are many possibilities for further investigation. Major trends include multi-modal analysis, which combines text, graphics and video to improve content identification by offering more context. The accuracy and contextual comprehension of transformer-based models and pre-trained language models are improving. A critical area to work on for the multilingual data challenges is the development of cross-lingual models that work well for detecting hostile information in multiple languages . Another interesting area is to enhance multi-modal analysis to incorporate textual and visual data. This can assist models to better understand context and detect subtle hostile content more accurately. There is also increasing need for additional varied datasets that are representative across multiple languages and cultures. What is needed are fresh models with fairness-aware algorithms that are able to adapt to changing linguistic patterns. Further, the development of ethical frameworks will ensure that hostile post detection tools are used responsibly. Future studies should seek to take use of these tendencies to improve the detection capabilities, while maintaining ethical norms in the field [79, 80].

CONCLUSION

The present survey has offered a thorough examination of techniques for detecting hostile content on social media, an area that continues to gain importance due to the proliferation of online abuse, misinformation, and harmful language. Through a review of traditional machine learning methods, advanced deep learning architectures, and hybrid approaches, we have highlighted the strengths and limitations of each category. In our analysis we find that while technical progress has significantly enhanced detection capabilities, there remain several challenges to overcome. These include the scarcity of data in low-resource languages, the skewed distributions in datasets, and the ethical considerations of automatic moderation. These challenges are both a technical and a societal imperative. Among the main findings of this research is a rising need for multilingual, multimodal approaches especially in culturally diverse digital environments . Equally important is the need for fair and transparent models that foster trust between end-users, policy-makers and platform managers. As online communication continues to evolve, so must the tools we employ to safeguard digital spaces. Future work should thus be directed towards the construction of inclusive datasets,

adaptive learning models and ethical frameworks that will be able to accommodate the intricacies of real-life situations. The combination of reinforcement learning, meta-learning and cross-lingual embeddings is a particularly promising direction for achieving this goal. In conclusion, this review aims at being a reference point for researchers and practitioners alike. By pointing out the existing gaps and emerging trends, we hope to stimulate more informed, ethical and technically sound research in hostile post detection.

AUTHORSHIP CONTRIBUTIONS

Authors equally contributed to this work.

DATA AVAILABILITY STATEMENT

The authors confirm that the data that supports the findings of this study are available within the article. Raw data that support the finding of this study are available from the corresponding author, upon reasonable request.

CONFLICT OF INTEREST

The author declared no potential conflicts of interest with respect to the research, authorship, and/or publication of this article.

ETHICS

There are no ethical issues with the publication of this manuscript.

STATEMENT ON THE USE OF ARTIFICIAL INTELLIGENCE

Artificial intelligence was not used in the preparation of the article.

REFERENCES

[1] Naslund JA, Bondre A, Torous J, Aschbrenner KA. Social media and mental health: Benefits, risks, and opportunities for research and practice. J Technol Behav Sci 2020;5:245–257.

[2] Jain AK, Sahoo SR, Kaubiyal J. Online social networks security and privacy: Comprehensive review and analysis. Complex Intell Syst 2021;7:2157–2177.

[3] Chakraborty A, Roy S. An ensemble model for hostile content detection in regional languages. J Comput Soc Syst 2024;12:33–50.

[4] Boda JR, Rana K. Investigating traditional machine learning approaches for hostile post detection. Int J Cyber Psychol Behav 2024;3:88–102.

[5] Chanda P, Verma R. Towards context-aware deep learning for detecting abusive language in code-mixed text. AI Soc 2024;39:115–129.

[6] Sharma P, Mehta A. Abusive language detection using BERT and BiLSTM in low-resource languages. Int J Artif Intell Res 2024;18:211–228.

[7] Nikitha R, Rao KP. Fake news and abusive content detection using hybrid semi-supervised frameworks. Procedia Comput Sci 2022;200:1431–1440.

[8] Mishra SU, Mishra LN, Mishra RK, Patnaik SR. Some applications of fractional calculus in technological development. J Fract Calc Appl 2019;10:228–235.

[9] Mohanta KK, Sharanappa DS, Dabke D, Mishra LN, Mishra VN. Data envelopment analysis on the context of spherical fuzzy inputs and outputs. Eur J Pure Appl Math 2022;15:1158–1179.

[10] Gaffar A, Joshi AB, Singh S, Mishra VN, Rosales HG, Zhou L, et al. A technique for securing multiple digital images based on 2D linear congruential generator, silver ratio, and Galois field. IEEE Access 2021;9:96125–96150.

[11] Sharma MK, Dhiman N, Mishra LN, Mishra VN, Sahani SK. Mediative fuzzy extension technique and its consistent measurement in the decision making of medical application. Math Probl Eng 2021;2021:1–14.

[12] Bhatnagar V, Kumar P, Bhattacharyya P. Investigating hostile post detection in Hindi. Neurocomputing 2022;474:60–81.

[13] Roy PK, Tripathy AK, Das TK, Gao XZ. A framework for hate speech detection using deep convolutional neural network. IEEE Access 2020;8:204951–204962.

[14] Iwendi C, Srivastava G, Khan S, Maddikunta PKR. Cyberbullying detection solutions based on deep learning architectures. Multimed Syst 2023;29:1839–1852.

[15] Hajibabaee P, Malekzadeh M, Ahmadi M, Heidari M, Esmaeilzadeh A, Abdolazimi R, et al. Offensive language detection on social media based on text classification. In: 2022 IEEE 12th Annual Computing and Communication Workshop and Conference (CCWC). IEEE; 2022. p. 92–98.

[16] Uyheng J, Moffitt J, Carley KM. The language and targets of online trolling: A psycholinguistic approach for social cybersecurity. Inf Process Manag 2022;59:103012.

[17] Faustini PHA, Covoes TF. Fake news detection in multiple platforms and languages. Expert Syst Appl 2020;158:113503.

[18] Salminen J, Hopf M, Chowdhury SA, Jung SG, Almerekhi H, Jansen BJ. Developing an online hate classifier for multiple social media platforms. Hum Cent Comput Inf Sci 2020;10:1–34.

[19] Pendergrast TR, Jain S, Trueger NS, Gottlieb M, Woitowich NC, Arora VM. Prevalence of personal attacks and sexual harassment of physicians on social media. JAMA Intern Med 2021;181:550–552.

[20] Udupa S, Gerold OL. "Deal" of the day: Sex, porn, and political hate on social media. In: Social processes of online hate. London: Routledge; 2024. p. 120–143.

[21] Mandl T, Modha S, Kumar MA, Chakravarthi BR. Overview of the HASOC track at FIRE 2020: Hate speech and offensive language identification in Tamil, Malayalam, Hindi, English and German. In: Proceedings of the 12th Annual Meeting of the Forum for Information Retrieval Evaluation. 2020. p. 29–32.

[22] Sultan D, Toktarova A, Zhumadillayeva A, Aldeshov S, Mussiraliyeva S, Beissenova G, et al. Cyberbullying-related hate speech detection using shallow-to-deep learning. Comput Mater Contin 2023;74:2115–2131.

[23] Bhatnagar V, Kumar P, Moghili S, Bhattacharyya P. Divide and conquer: An ensemble approach for hostile post detection in Hindi. In: Combating online hostile posts in regional languages during emergency situation: First International Workshop, CONSTRAINT 2021, collocated with AAAI 2021, Virtual Event, February 8, 2021, revised selected papers. Springer; 2021. p. 244–255.

[24] Mohanta KK, Sharanappa DS, Dabke D, Mishra LN, Mishra VN. Data envelopment analysis on the context of spherical fuzzy inputs and outputs. Eur J Pure Appl Math 2022;15:1158–1179.

[25] Gaffar A, Joshi AB, Singh S, Mishra VN, Rosales HG, Zhou L, et al. A technique for securing multiple digital images based on 2D linear congruential generator, silver ratio, and Galois field. IEEE Access 2021;9:96125–96150.

[26] Hate Speech and Offensive Language Dataset. Hate speech and offensive language dataset. 2020 Available at: https://paperswithcode.com/dataset/hate-speech-and-offensive-language Accessed on Jul 4, 2024.

[27] Williams L. Stormfront hate speech dataset. 2018. Available at: https://example.com/stormfront-dataset Accessed on Jul 4, 2024.

[28] Rossetti S. Facebook hate speech dataset. 2018 Available at: https://example.com/facebook-hate-speech-dataset Accessed on Jul 4, 2024.

[29] Zampieri M, Lee J. Overview of the HASOC 2018 shared task on hate speech and offensive content identification. In: Proceedings of the 5th Workshop on Asian Language Resources and Evaluation. 2018. p. 1–7.

[30] Cyberbullying Dataset. Cyberbullying dataset [Internet]. 2021 [cited 2024 Jul 4]. Available from: https://www.kaggle.com/datasets/saurabhshahane/cyberbullying-dataset

[31] Thelwall M, Harries P. SentiStrength: A simple tool for measuring the strength of sentiment in text. In: Proceedings of the International Conference on Weblogs and Social Media. 2014. p. 1–8.

[32] Wiegand M, Klakow D, K W. Overview of the GermEval 2018 shared task on offensive language. In: Proceedings of the GermEval 2018 Workshop. 2018. p. 1–10.

[33] Mall D, Ghosh S, Naik P. TRAC-2: Dataset and baseline for aggression detection in social media. In: Proceedings of the 12th International Conference on Language Resources and Evaluation. 2020. p. 105–112.

[34] Borkan D, Dixon L, Sorensen J. Measuring and mitigating unintended bias in text classification. In: Proceedings of the 2019 ACM Conference on Fairness, Accountability, and Transparency. 2019. p. 1–15.

[35] Nielsen A. Danish abusive language dataset. 2019. Available at: https://example.com/danish-abusive-language-dataset Accessed on Jul 4, 2024.

[36] Choudhury M, S M. Dravidian code-mix dataset. In: Proceedings of the 2021 Shared Task on Code-Mixed Text. 2021.

[37] Sharma S, Kumar A. Hate speech detection in Hindi-English code-mixed social media text. Int J Data Sci Anal 2021;12:341–356.

[38] Reddy M, D S. Offensive language identification dataset in Indian languages (OffensEval-2020). In: Proceedings of the 14th Conference on Natural Language Engineering. 2020. p. 45–56.

[39] Patel J, Singh R. Gujarati offensive language dataset (gold). In: Proceedings of the 2021 Conference on Indian Languages Processing. 2021. p. 1–10.

[40] Naik S, P S. Kannada offensive speech dataset (KOSD). Int J Lang Technol 2021;8:98–108.

[41] Rao V, K M. Indic offensive content dataset. In: Proceedings of the 2021 Workshop on Indian Language Processing. 2021. p. 30–40.

[42] Ge L, Moh TS. Improving text classification with word embedding. In: 2017 IEEE International Conference on Big Data (Big Data). IEEE; 2017. p. 1796–1805.

[43] Dadure P, Pakray P, Bandyopadhyay S. BERT-based embedding model for formula retrieval. In: CLEF Working Notes. 2021. p. 36–46.

[44] Cortes C, Vapnik V. Support-vector networks. Mach Learn 1995;20:273–297.

[45] Russell S, Norvig P. Artificial intelligence: A modern approach. 3rd ed. Upper Saddle River (NJ): Pearson Education.

[46] Breiman L. Random forests. Mach Learn 2001;45:5–32.

[47] Hosmer DW, Lemeshow S. Applied logistic regression. 2nd ed. Hoboken (NJ): Wiley; 2000.

[48] Cover T, Hart P. Nearest-neighbor pattern classification. IEEE Trans Inf Theory 1967;13:21–27.

[49] Quinlan JR. Induction of decision trees. Mach Learn 1986;1:81–106.

[50] Friedman JH. Greedy function approximation: A gradient boosting machine. Ann Stat 2001;29:1189–1232.

[51] Freund Y, Schapire RE. A decision-theoretic generalization of on-line learning and an application to boosting. J Comput Syst Sci 1997;55:119–139.

[52] Mikolov T, Sutskever I, Chen K, Corrado G, Dean J. Distributed representations of words and phrases and their compositionality. In: Advances in neural information processing systems 26. 2013. p. 3111–3119.
[53] Devlin J, Chang MW, Lee K, Toutanova K. BERT: Pre-training of deep bidirectional transformers for language understanding. arXiv [Preprint]. 2019:1810.04805.
[54] Haykin S. Neural networks: A comprehensive foundation. 2nd ed. Upper Saddle River (NJ): Prentice Hall; 1998.
[55] Sarthak, Shukla S, Arya KV. Detecting hostile posts using relational graph convolutional network. arXiv [Preprint]. 2021:2101.03485. doi: 10.48550/arXiv.2101.03485.
[56] Breiman L. Bagging predictors. Mach Learn 1996;24:123–140.
[57] Freund Y, Schapire RE. A decision-theoretic generalization of on-line learning and an application to boosting. J Comput Syst Sci 1997;55:119–139.
[58] Wolpert DH. Stacked generalization. Neural Netw 1992;5:241–259.
[59] Kuncheva LI. Combining pattern classifiers: Methods and algorithms. USA: Wiley-Interscience; 2004.
[60] Pan SJ, Yang Q. A survey on transfer learning. IEEE Trans Knowl Data Eng 2010;22:1345–1359.
[61] Hospedales TM, Antoniou A, Micaelli P, Storkey A. Meta-learning in neural networks: A survey. IEEE Trans Pattern Anal Mach Intell 2021;44:1–20.
[62] Vaswani A, Shazeer N, Parmar N, Uszkoreit J, Jones L, Gomez AN, et al. Attention is all you need. In: Proceedings of the 31st International Conference on Neural Information Processing Systems. 2017. p. 6000–6010.
[63] Powers DMW. Evaluation: From precision, recall and F-measure to ROC, informedness, markedness and correlation. J Mach Learn Technol 2011;2:37–63.
[64] Fawcett T. An introduction to ROC analysis. Pattern Recognit Lett 2006;27:861–874.
[65] Sokolova M, Lapalme G. A systematic analysis of performance measures for classification tasks. Inf Process Manag 2009;45:427–437.
[66] He H, Garcia EA. Learning from imbalanced data. IEEE Trans Knowl Data Eng 2009;21:1263–1284.
[67] Waseem Z, Hovy D. Hateful symbols or hateful people? Predictive features for hate speech detection on Twitter. In: Proceedings of the NAACL Student Research Workshop. 2016. p. 88–93.
[68] Eisenstein J. What to do about bad language on the Internet. In: Proceedings of NAACL-HLT. 2013. p. 359–369.
[69] Alm CO. Subjective natural language problems: Motivations, applications, characterizations, and implications. In: Proceedings of the 49th Annual Meeting of the Association for Computational Linguistics: Human Language Technologies. 2011. p. 107–112.
[70] Bender EM, Friedman B. Data statements for NLP: Toward mitigating system bias and enabling better science. Trans Assoc Comput Linguist 2019;7:587–604.
[71] Ruder S, Howard J, Ruder S. Universal language model fine-tuning for text classification. In: Proceedings of ACL. 2018.
[72] Salem M, Shawky D. A hierarchical framework for multi-aspect evaluation of classifiers in cyberbullying detection. Int J Comput Appl 2010;10:10–15.
[73] Chawla NV, Bowyer KW, Hall LO, Kegelmeyer WP. SMOTE: Synthetic minority over-sampling technique. J Artif Intell Res 2002;16:321–357.
[74] Conneau A, Lample G, Ranzato M, Denoyer L, Jégou H. Word translation without parallel data. In: Proceedings of ICLR. 2018.
[75] Pavlopoulos J, Sorensen J, Dixon L, Thain N, Androutsopoulos I. Toxicity detection: Does context matter? In: Proceedings of the Annual Meeting of the Association for Computational Linguistics. 2020.
[76] Binns R. Fairness in machine learning: Lessons from political philosophy. In: Proceedings of the 2018 Conference on Fairness, Accountability, and Transparency. 2018. p. 149–159.
[77] Veale M, Binns R, Edwards L. Algorithms that remember: Model inversion attacks and data protection law. Philos Trans A Math Phys Eng Sci 2018;376:20180083.
[78] Zampieri M, Malmasi S, Nakov P, Rosenthal S, Farra N, Kumar R. Predicting the type and target of offensive posts in social media. In: Proceedings of NAACL. 2019. p. 1415–1420.
[79] Sun C, Qiu X, Xu Y. How to fine-tune BERT for text classification? In: Proceedings of China National Conference on Chinese Computational Linguistics. 2019. p. 194–206.
[80] Zampieri M, Nakov P, Rosenthal S, Atanasova P, Karadzhov G, Mubarak H, et al. SemEval-2020 task 12: Multilingual offensive language identification in social media (OffensEval 2020). arXiv [Preprint]. 2020:2006.07235.

Sigma J Eng Nat Sci, Vol. 44, No. 4, pp. 2328–2338, August, 2026

Sigma Journal of Engineering and Natural Sciences
Web page info: https://sigma.yildiz.edu.tr
DOI: 10.14744/sigma.2026.2098

Research Article

Comparative study of two-body and three-body abrasive wear behaviour of 3D printed carbon fiber reinforced PLA/ABS composites

Anand A[1], Hemanth R[1], Raghavendra T[1], Suresha B[1,*], Bharath P B[2], Govindaraju N[3]

[1]*Department of Mechanical Engineering, The National Institute of Engineering, Mysore, Karnataka, 570018, India*
[2]*Department of Mechanical Engineering, SJM Institute of Technology, Chitradurga, Karnataka, 222866, India*
[3]*Magnum Engineers, Peenya Industrial Estate, Bangalore, Karnataka, 560058, India*

ARTICLE INFO

Article history
Received: 30 October 2024
Revised: 08 January 2025
Accepted: 25 February 2025

Keywords:
SCF reinforced PLA/ABS composites, FDM, Abrasive wear, Wear mechanisms

ABSTRACT

The aim of this research is to investigate the tribological behaviour of short carbon fibre (SCF) reinforced polylactic acid (PLA)/acrylonitrile butadiene styrene (ABS) matrix composites using Fused Deposition Modelling (FDM). The major goal is to provide a theoretical foundation and investigate the applicability of SCFs (20 wt.%) for printing a high-quality PLA/ABS composites structure with superior abrasion resistance.

The wear specimen was manufactured using FDM technology. The specimen was produced out of pristine PLA, pristine ABS and SCF reinforced PLA/ABS composites. These composites were tested for multi-pass two-body and three-body abrasive wear behaviour utilising a special purpose abrasion test rig and a rubber-wheel abrasion test rig respectively.

The specific wear rate is primarily controlled by the applied normal load and the abrading distance. Comparing the wear performance of all composites under various loads reveals that two-body abrasive wear (multi-pass condition) is 2 to 2.4 times larger than three-body abrasive wear. Attempts have been made to connect wear performance with certain mechanical parameters. The wear mechanism associated with different experimental conditions was also studied using scanning electron microscope (SEM).

Cite this article as: Anand A, Hemanth R, Raghavendra T, Suresha B, Bharath PB, Govindaraju N. Comparative study of two-body and three-body abrasive wear behaviour of 3D printed carbon fiber reinforced PLA/ABS composites. Sigma J Eng Nat Sci 2026;44(4):2328–2338.

***Corresponding author.**
*E-mail address: suresha.b2005@gmail.com

This paper was recommended for publication in revised form by Editor-in-Chief Ahmet Selim Dalkilic

Published by Yıldız Technical University Press, İstanbul, Turkey
© Author. This is an open access article under the CC BY-NC license (http://creativecommons.org/licenses/by-nc/4.0/).

INTRODUCTION

Digital manufacturing is a process that uses digital models to create products, while additive manufacturing is a type of digital manufacturing that uses 3D printing to create objects. Extruded filaments are utilized in the additive manufacturing technique of fused deposition modelling (FDM) to fabricate polymer matrix composites (PMCs). Fused filament fabrication (FFF) and fibre reinforcements can be combined essentially in two ways. One way to create 3D printed parts in FDM is to impregnate chopped/short fibres with a fibre length range of 0.25 mm to 3 mm into a polymer, then extrude the filament. The printed part is anisotropic, similar to unidirectional fibre reinforced PMCs, because the fibres are arranged randomly. Alternatively, in-situ co-extrusion (fiber is coated with polymer in the nozzle) or dual extrusion (bare fibre are fed through spool into the print head and polymer melt is coated around the fiber in the nozzle). The print head subsequently extrudes polymer melt coated fiber to obtain a composite filament. The potential benefits and drawbacks of each approach have been reported [1, 2].

Investigating the mechanical and tribological behaviour of the 3D printed PMC parts has involved a great deal of research. The process parameters influencing 3D printed polymer composites' mechanical properties have been identified by a number of studies [3–7]. The post-treatment's (i.e heat treating the 3D printed parts suitably to increase its strength due to the recrystallization process that the materials undergo during heat treatment) has been explored by Sagias et al. and Avila et al. [8, 9]. Several studies [10–12] have used pin-on-disk tester to investigate wear and friction properties of 3D-printed polymers and their composites (PLA, ABS, PA66, and PA6 as matrix and nano-alumina, nano-carbon black and continuous CF as reinforcements). The filler/fibre reinforced composites outperformed pristine polymers. Hemanth et al. [13] examined thermoplastic copolyester elastomer (TCE) hybrid composites with fibre/filler contents of 20, 30, and 40 wt. % in terms of their two-body abrasive wearbehaviour under multi-pass conditions. Twin screw extrusion extrudates were injected into moulds to create test samples. It was found that the specific wear rate rises as the fibre/filler content increases and falls as the silicon carbide abrasive grit size and abrading distance increase. Urs et al. examined how short carbon fibres and graphene nanoplatelets (GNPs) affected the abrasive wear behaviour of PA66/TCE composites [14]. They disclosed that 3 wt. % of GNPs enhanced the wear resistance of PA66/TCE in adhesive wear mode, while, under three-body abrasive wear (3-BAW) test conditions, 1 wt. % of GNPs into PA66/TCE hybrid composites showed superior abrasion resistance.

Batra and Colleagues [15], investigated the 2-BAW behaviour of hybrid composites reinforced with woven carbon/glass/aramid polyetherimide (PEI). According to their report, the carbon fibre/PEI composite exhibited reduced wear rate in comparison to the glass fibre/PEI and aramid fibre/PEI composites. Hemanth et al. [16] investigated the abrasive wear behaviour of TCE hybrid composites with fibre/filler loading of 15, 32, and 40 wt. % under 2-BAWin single-pass conditions. They disclosed that the 15 wt. % of PTFE in TCE matrix demonstrated superior abrasion resistance in comparison to the hybrid composites that were being examined. They also stated that the abrasive wear performance was negatively impacted by carbon fibre, glass fibre, and ceramic fillers like silicon carbide and alumina. Surface (circular) texturing can considerably lower the coefficient of friction, especially when sliding in dry conditions, according to studies on the dry sliding wear of PLA. This was due to the less real area of contact and more effective formation of transfer film. The entrapment of wear debris was more effective which helps in the formation of transfer layer that acts as solid lubricant. Surface analysis of the worn samples revealed that the wear was mainly due to adhesive and abrasive action [17]. This is consistent with research by Shipway [18], wherein they found that test parameters can have a big influence on how well polymers perform in abrasive wear tests. The impact of test conditions is further emphasized by Harsha [19], who demonstrates that the specific wear rate (SWR) of two-body abrasive wear (2-BAW) is significantly higher than that of three-body abrasive wear (3-BAW). Jia [20] compares the abrasive wear performance of various polymer coatings; polyurethane coatings showed the superior abrasion resistance. Together, these studies indicate that a number of factors, such as surface texturing, test conditions and the particular properties of the material, affect PLA's abrasive wear.

Based on the results of the aforementioned investigations, it can be concluded that polymer composites made by extrusion and injection molding, with selected functional fillers exhibited superior abrasion resistance in 3-BAW mode. However, the presence of higher loading of fibre/filler into various thermoplastic matrices has a negative impact on resistance to abrasion.

Numerous important conclusions have been drawn from research on the 2-BAW of PLA. Lingesh [21] discovered that grit size and abrading distance affect PLA's SWR, while the presence of additional fibres/fillers affects the resistance to abrasion. By examining the wear loss of PLA composite reinforced with basalt fibre, Kumar [22] discovered that the wt. % of the reinforcement in composite affects both the SWR and coefficient of friction. Zhang [23], examined friction and wear behaviour of 3D printed PLA and found that a crucial printing parameter is the infill-density. Together, these studies demonstrate the intricate interactions between surface texture, printing parameters, and material composition that affect PLA's 2-BAW. Added to this, Suresha et al. [24] examined the PLA and ABS 3D printed composites with short carbon fibre (SCF) reinforcement for their abrasive wear behaviour under 3-BAW test. To print the specimen, PLA and ABS filaments were impregnated with SCF using

an extrusion process. They found that, in comparison to neat PLA, the presence of SCF reduces the wear resistance of PLA and ABS composites by 60% and 78%, respectively. The PLA/ABS composites under study have reduced abrasion resistance as a result of SCF reinforcement.

According to the aforementioned review of literature and the authors' knowledge, there haven't been many studies done on the comparison of abrasive wear behaviour of thermoplastic composites reinforced with short fibre that are fabricated by 3D printing. This has therefore inspired the authors to investigate and comprehend the 2-BAW and 3-BAW behaviour of 3D printed pristine PLA, pristine ABS and SCF reinforced PLA/ABS thermoplastic composites.

MATERIALS AND METHODS

Materials

The PLA, ABS, PLA with 20 wt. % SCFs and ABS with 20 wt. % SCFs filament of ϕ 1.75mm were procured from 3D printing company eSUN 3D, Karnataka, India. Table 1, summarizes the physical and mechanical parameters of the thermoplastic composites developed by the vendors.

Fabrication of Composites by Fused Deposition Modelling

The first stage is creating a CAD model with the required dimensions of 3 mm x 8 mm x 8 mm for 2-BAW, 3 mm x 25 mm x 75 mm for 3-BAW tests and storing it in the Standard Tessellation Language (STL) format. These models are then transferred to slicing software "UltimakerCura" which slices the STL model and generates G-codes. Figure 1, displays a flow chart of the CAD model and manufacturing processes for PLA/ABS and their composites. Table 2 shows the printing settings that were considered for specimen fabrication. These created G-codes are then sent into the Creality-ender 3 pro FDM printer. The composite filament is provided to the heating unit via rollers. The printer nozzle is heated to the melting temperature of the filament as mentioned in Table 2, and allowing the material to deposit on the built platform with respect to the path developed by the slicing software using G codes. The method is repeated until the desired specimen is obtained.

WEAR TESTING

Two-Body Abrasive Wear Test of SCF Reinforced PLA/ABS Composites

The two-body abrasive wear under multi pass condition test was conducted on pin-on-disk rig in conformance to ASTM G-99-17. The tests were conducted as per the procedure discussed elsewhere [13]. The pictorial representation of the test set up is shown in Figure 2.

Three-Body Abrasive Wear Test of SCF Reinforced PLA/ABS Composites

Three body abrasive wear (3-BAW) test was carried out as per ASTM G-65-16(2021) standards. The tests were

Table 1. Physico-Mechanical characteristics of PLA/ABS composites

Properties	PLA	SCF/PLA	ABS	SCF/ABS
Density (gcm^{-3})	1.3	1.4	1.1	1.2
Tensile strength (MPa)	48	59	43	48
Hardness (Shore D)	75	79	58	61
Melting point (°C)	210	220	245	250
Glass transition temperature (°C)	65	70	105	110

Table 2. Parameters for fabrication of 3D printed specimen

Material	PLA	SCF/PLA	ABS	SCF/ABS
Parameters				
Nozzle temperature (°C)	210	215	240	250
Bed temperature (°C)	65	65	100	110
Infill density (%)	100	100	100	100
Layer thickness (mm)	0.12	0.12	0.2	0.2
Orientation direction	[90, 90]	[90, 90]	[90, 90]	[90, 90]
Printing speed ($mm\ s^{-1}$)	70	70	80	60
Build orientation	Vertical	Vertical	Vertical	Vertical

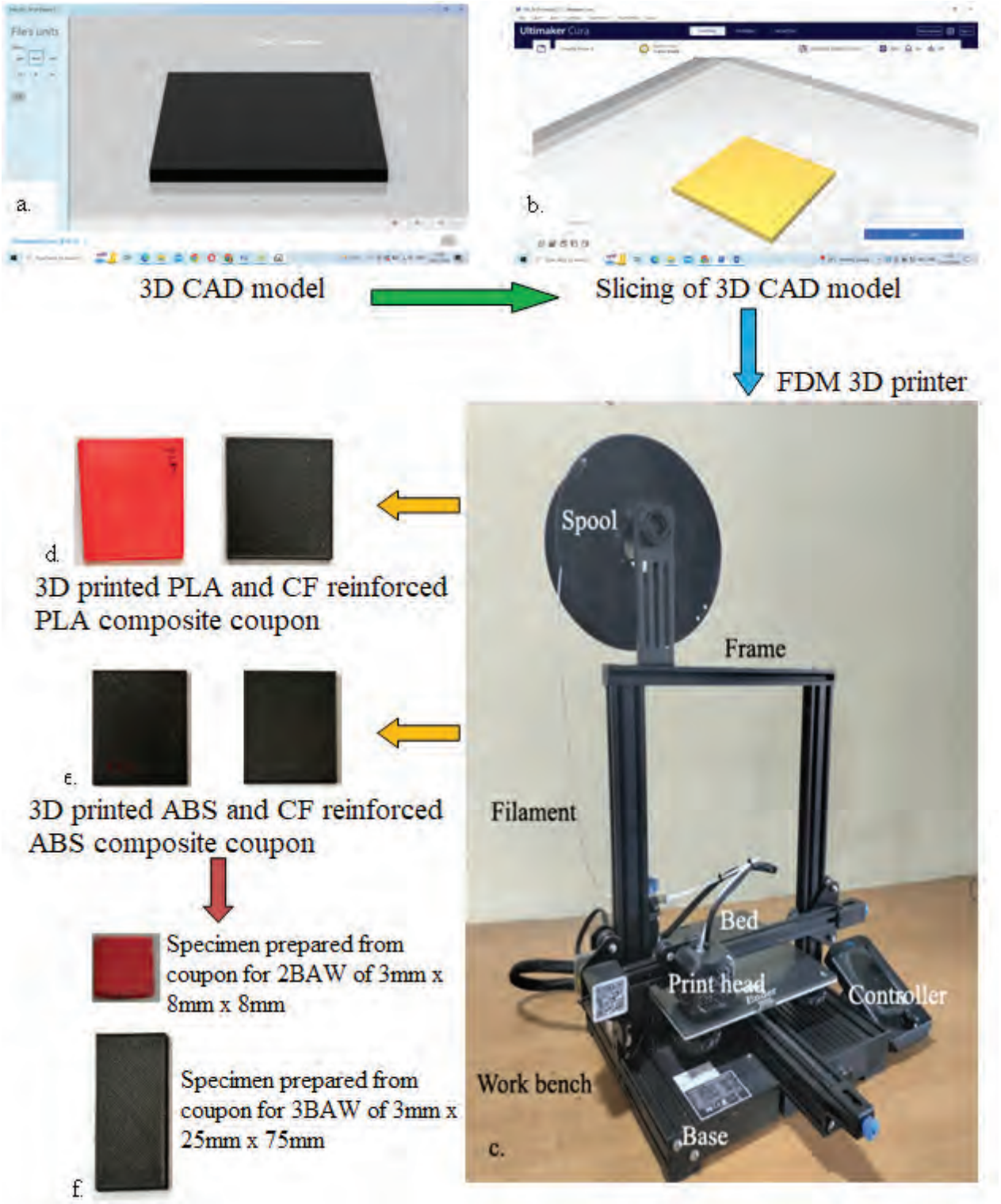


Figure 1. Fabrication process of specimen using FDM method.

conducted as described elsewhere [24]. The pictorial representation of the test set up is shown in Figure 3.

The test conditions for both 2-BMAW and 3-BAW modes are listed in Table 3 and 4 respectively.

Worn Surface Characterization

Scanning Electron Microscopy (SEM) is used to study the surface morphology and topography of a wide range of materials, including polymer and their composite samples.

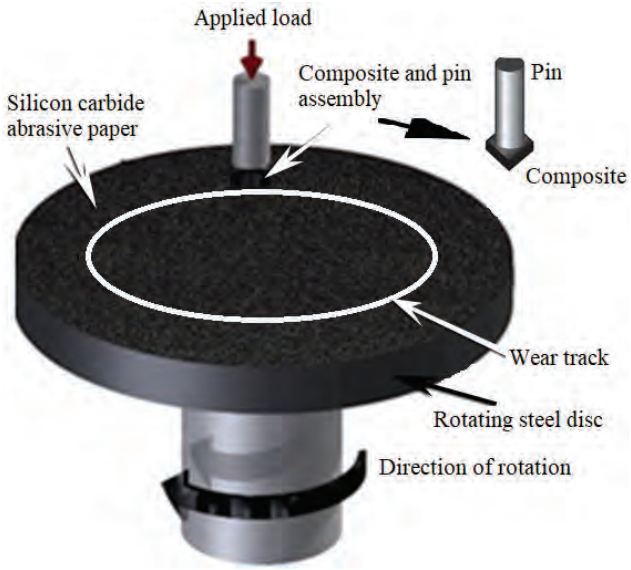


Figure 2. Two-body multi-pass abrasive wear test setup.

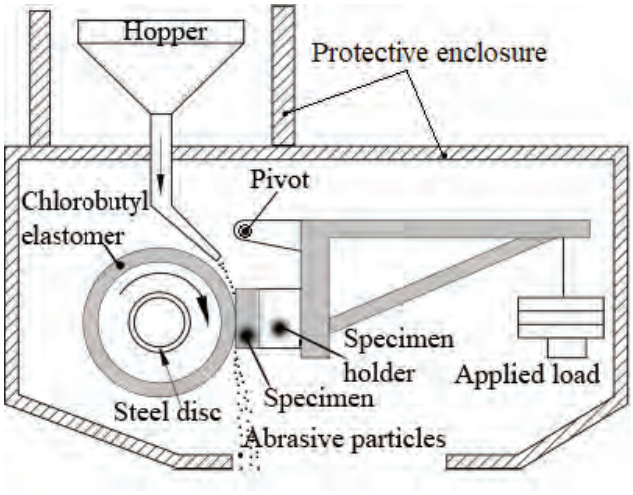


Figure 3. Three-body abrasive wear test rig.

Table 3. Two-body multi-pass abrasive wear test conditions used in the present work

Test conditions	Units	Values
Abrading distance	m	75, 100, 125, and 150
Load	N	10 and 20
Velocity	m/s	0.25
Abrasive grit size	μm	90

Polymer and polymer matrix composite samples need to be properly prepared for SEM to provide accurate information. For proper conduction, all the samples are coated with a thin layer of a gold to prevent charging effects and enhance signal quality. In the present investigation, the surface morphology of worn surfaces of the composites was investigated using E-SEM, Quanta 200 model, FEI-Netherland make, with a voltage of 20 kV.

Table 4. Three-body abrasive wear test conditions used in the present work

Test conditions	Units	Values
Abrading distance	m	750, 1000, 1250 and 1500
Load	N	10, 20 and 30
Speed	RPM	200
Silica sand abrasives	μm	80-95

RESULTS AND DISCUSSION

Effect of Short Carbon Fibers on Two-Body Abrasive Wear of PLA/ABS Composites

For PLA, ABS, SCF/PLA and SCF/ABS composites, two-body multi-pass abrasive wear (2-BMAW) tests were conducted. Table 3, lists the operational test conditions that were used during the experiment. For the grit 225 grade (90 μm) SiC emery paper used, the experiments were carried out to determine the range of abrading distance and load to be applied at lower velocity under 2-BMAW conditions. This can be explained by the fact that after a certain number of revolutions, the abrasive paper will no longer effectively abrade the material. The frictional force decreased at this point and stayed nearly constant thereafter. The material that has been abraded will act as a cushion and a barrier to lessen abrasion. The first stage of the 2-BMAW (75 to 100 m) is depicted in Figure 4 (a, b), where specimens are exposed to abrasive paper that penetrates the polymer/composite material and significantly removes material as debris due to the application of a normal load. For the range of abrading distance 100 m to 150 m shown in Figure 4 (a, b) where abrasive paper loses its ability to remove material. Similar observations were also made by Hemanth et. al. [13]. The authors have discussed about the formation of debris and space occupied by them between the abrasives and their adherence to the abrasive particles with the help of SEM. This action reduces the efficiency of abrasive particle cutting edge, resulting in steady state wear. The steady state wear is responsible for the decrease in frictional force that was noted in the tribometer's instrument cluster dashboard. Additionally, when comparing run-in wear to steady-state wear conditions, the wear crater also gets reduced.

The experimental findings for a specific wear rate (SWR) are shown in Figure 4a and 4b. Figure 4 illustrates the load-dependent variations in SWR for PLA, ABS, SCF/PLA and SCF/ABS composites. At low load (10 N), SWR was seen to be lower. This results from fewer abrasive

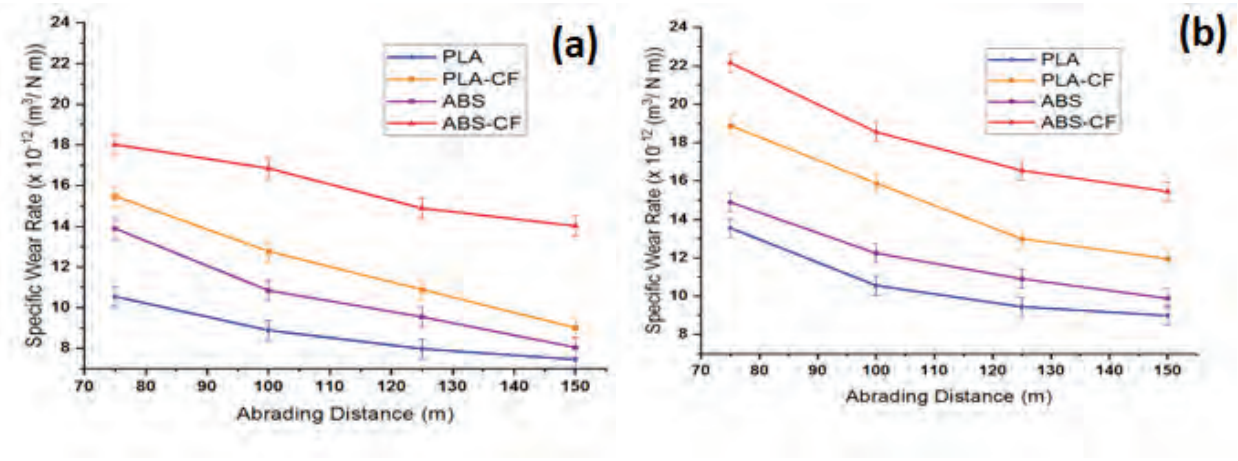


Figure 4. Specific wear rate of SCF reinforced PLA/ABS composites: (a) 10 N and (b) 20 N.

particles coming into contact with the rubbing surface and from reduced penetration. The surface's initial roughness and irregularities tend to disappear as the abrading distance increases. Debris fills the spaces left by the abrasive, further decreasing the depth of penetration. This can result in a smoother surface, reducing the abrasive interaction and, consequently, reducing the SWR.With an increase in applied load (20 N), the SWR of PLA, ABS, SCF/PLA and SCF/ABS composites rise. This is because the SiC particles penetrated the material surface more deeply, resulting in the creation of deeper grooves, resulting in increased SWR.

For the tests conducted under 2-BMAW, the pristine ABS and SCF/ABS composites showed maximum SWR of 14.89×10^{-12} m^3/N m and 22.15×10^{-12} m^3/N m, respectively. The abrasion resistance of ABS has been found to be negatively impacted by SCF reinforcement. Under the same test conditions, PLA and SCF/PLAcomposites showed maximum SWR of 13.55×10^{-12} m^3/N m and 18.89×10^{-12} m^3/N m, respectively.

It is note worthy that the SWR may vary depending on the constituents of the composite materials used, the type of abrasives used, and the surrounding environment. Furthermore, depending on the predominant wear mechanisms in a given system, the relationship between abrading distance and SWR may not be applicable to all systems. Abrasive wear of thermoplastic polymers involves the removal of material from the surface due to the mechanical action of abrasive particles. When compared to pristine ABS and SCF/PLA as well as SCF/ABS composites, pristine PLA demonstrated better abrasion resistance in the current study. The thermoplastic polymer known as PLA is biodegradable and sourced from sustainable sources like sugarcane or corn starch. Abrasion resistance is one of the mechanical properties of PLA that can be influenced by its molecular structure and crystallinity. PLA's degree of crystallinity and molecular weight may improve its toughness and hardness, which lead to better abrasion resistance. In comparison to PLA, ABS appears to be a softer material based on the observed increase in SWR under 2-BMAW. Hence, ABS is therefore more prone to abrasive wear, and the SiC abrasive particles are able to remove material more readily from the surface, increasing the SWR.

When adding SCFs to thermoplastics, their abrasion resistance can be affected in a variety of ways, so it'simportant to take a number of factors into account when attempting to explain an increase in SWR.Here are several reasons why the incorporation of SCFs might lead to an increased SWR in PLA or ABS materials are poor adhesion, fibres are randomly distributed, and short fibres could not provide as much reinforcement as longer fibres and may not effectively distribute loads or resist wear. Furthermore, SCFs may increase SWR by functioning more like particulate fillers than reinforcing elements.

Wear Mechanisms of SCF-Reinforced PLAS/ABS Composites Under 2-BMAW

SEM images were used to study the worn surface morphologies of PLA, ABS, SCF/PLA and SCF/ABS composites. Soft fragments of debris are left on hard surfaces as a result of material being removed from one surface by another harder material, causing abrasive wear. The samples tested under 2-BMAW; SEM images of selected worn surfaces are shown in Figure 5 (a to d).

Figure 5a and 5b display the worn surfaces of both the pristine PLA and pristine ABS samples. There are grooves in the abrading direction (indicated with arrows), plastic deformation (indicated with P), wear debris (W), micro-cracking (K), and micro-cutting(C) can be seen from the SEM images. This has occurred at a high load of 20 N. The SEM images shown in Figs 5c and 5b indicate a decrease in plastic deformation and more wear debris when SCFs are integrated into PLA of ABS matrices. According to Figs. 5c and 5d, the worn surface of 20 wt. % SCFs into PLA or ABS composites at 20 N load revealed more deep groves

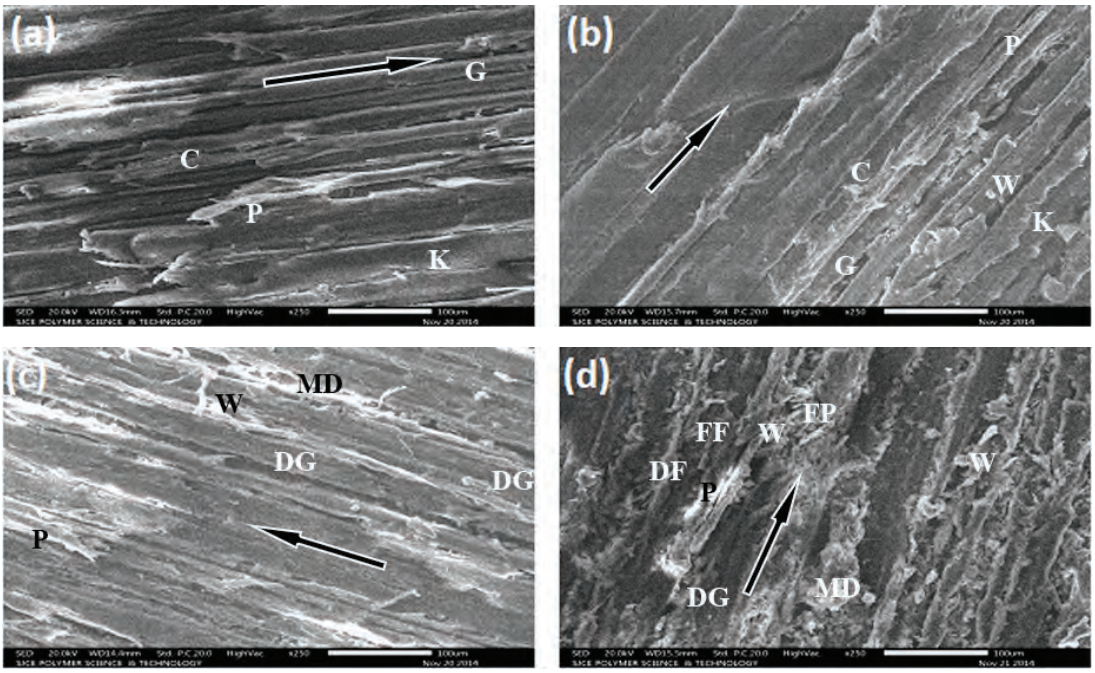


Figure 5. SEM images of wear surfaces of the composites at 20 N: (a) PLA, (b) ABS, (c) SCF/PLA, (d) SCF/ABS under 2-BMAW (with 250 x magnification).

(DG), fibrepull-out (FP), plastic deformation (P), and wear debris (W). Additionally, the surface morphology demonstrates that the fibre fracture (FF) and severe matrix damage (MD), leads to the debonding of the fibres (DF).

Effect of SCF on Three-Body Abrasive Wear of PLA/ABs Composites

In three-body abrasive wear (3-BAW), the test specimen is fixed in the specimen holder which is as shown in Figure 3. The chlorobutyl elastomer surrounding the steel disc is rotated against the specimen and abrasive particles are made to pass through between the specimen surface and the rotating disc. The abrasive particles at the interface acts as free third body and engage in abrasion wear of specimen by sliding and rolling. The normal load at the fulcrum engages the specimen with the rotating disc and abrasives. Thermoplastic polymer matrix composites are frequently reinforced with short fibres, like glass, carbon, or basalt, to improve their mechanical properties [25, 26]. These fibres have the ability to increase wear resistance, decrease friction coefficient, increase hardness, and reinforce the polymer matrix material [27-30]. Nonetheless, in 3-BAW scenario, the short fibres interaction with the thermoplastic matrix is critical. Durability of the composite is preserved by a robust interface, which stops the fibres from pulling out during abrasion.

Since thermoplastics do not require a curing stage and have less hazardous chemical compositions, they are more convenient to recycle and can be produced in large quantities than conventional thermoset. For these reasons, thermoplastics have drawn a lot of attention as polymer matrices. In addition to recent 3D printing techniques, traditional molding techniques are frequently used to create fibre-reinforced thermoplastic composites [31, 32]. PMCs have extremely intricate wear mechanisms that are influenced by various factors such as contact conditions, mechanical properties of the constituent materials, and the way in which these characteristics affect the formation of transfer films and debris. However, the types of reinforcement and the conditions of contact also matter, and there may be additional wear mechanisms, such as abrasive ones [32].

The SWR for PLA/ABS and their composites at varying loads (10 to 30 N) is displayed in Figures 6a, 6b and 6c as a function of abrading distance. Typical wear scars of PLA, ABS, SCF/PLA and SCF/ABS are displayed in Figure 7. By comparing the width of the wear scars, it is observed that the PLA and SCF/ABS exhibits better and least resistance to abrasion in the study group. Figure 8, shows worn surfaces captured by scanning electron micrographs of polymers and their composites under normal applied load of 20 N.

Important findings from the investigations included the following:

i) At different loads, the resistance to abrasion among neat PLA and ABS was found to occur in the order PLA>ABS. On the other hand, SCF/PLA composites showed better abrasion resistance in PLA/ABS composites reinforced with SCF.

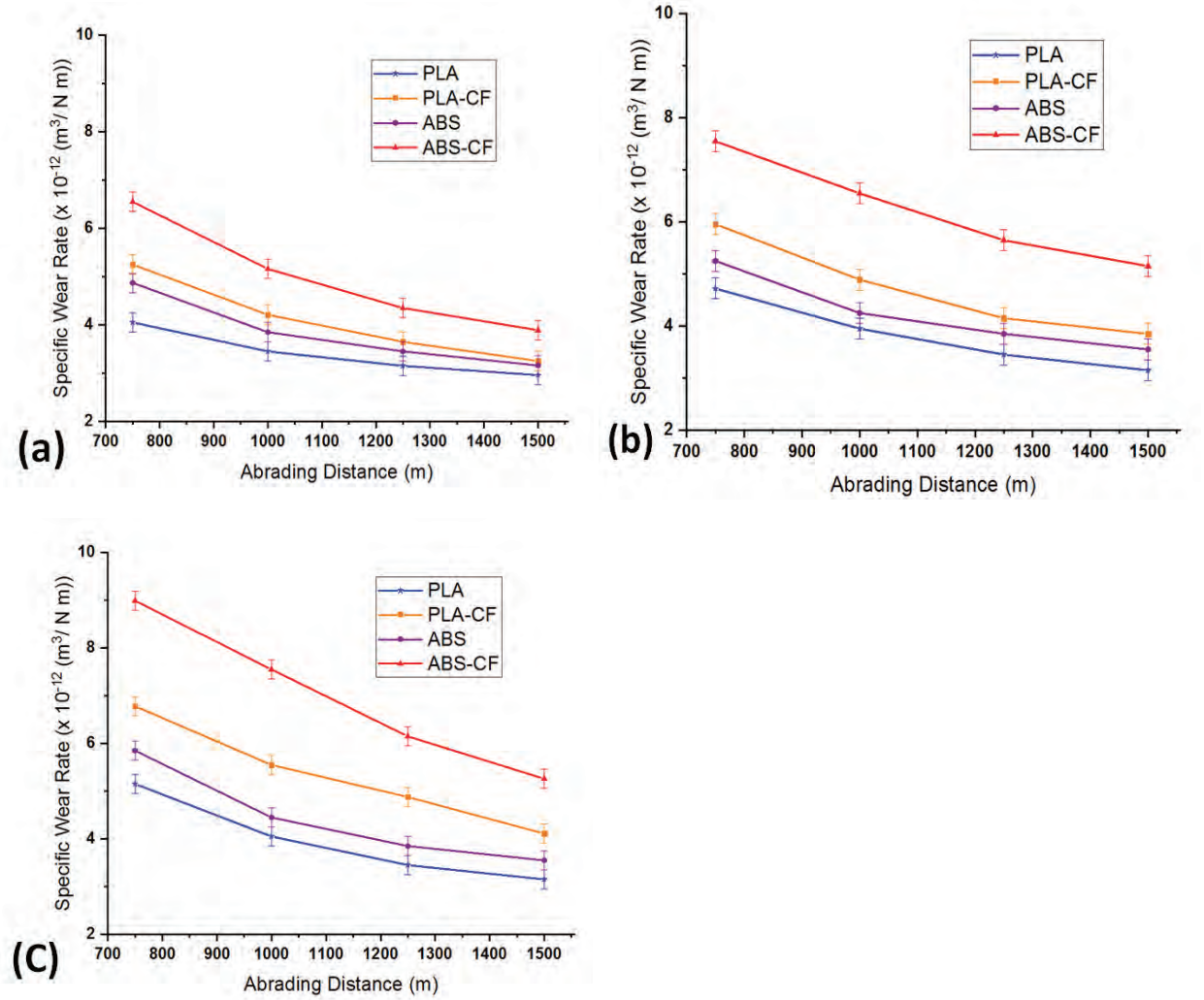


Figure 6. SWR of SCF-reinforced PLA/ABS composites: (a) 10 N, (b) 20 N and (c) 30 N.

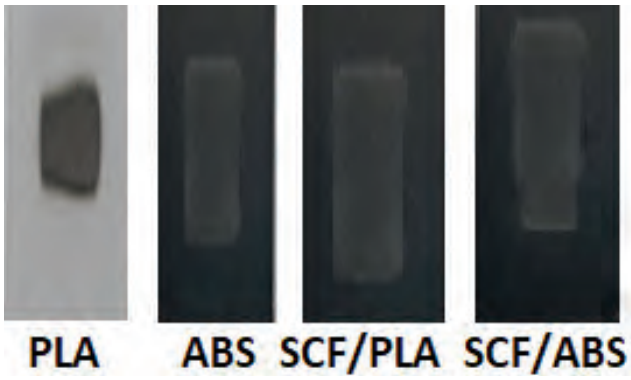


Figure 7. Typical wear scars of SCF-reinforced PLA/ABS composites.

ii) The materials were found to have specific wear rates (SWR) ranging from 2.96×10^{-12} m^3/N m (pristine PLA) to 6.55×10^{-12} m^3/N m (SCF/ABS) at low load of 10 N, 3.15×10^{-12} m^3/N m (pristine PLA) to 7.55×10^{-12} m^3/N m (SCF/ABS) at 20 N load, and 3.15×10^{-12} m^3/N m (pristine PLA) to 8.99×10^{-12} m^3/N m (SCF/ABS) at 30 N load (Fig. 6).

iii) When the surfaces are brand-new, pristine PLA, pristine ABS, and their SCF reinforced composite surfaces show comparatively high initial SWR values, which progressively drop to nearly constant values with the increase in abrading distance (Fig.6).

iv) SCF/PLA composites exhibited superior abrasion resistance over SCF/ABS composites.

v) The investigations revealed that the hardness and tensile strength of the polymer and their composites (Table 1) have impacted the SWR. The pristine PLA exhibits better mechanical properties compared to pristine ABS and demonstrated very good abrasion wear resistance. The inclusion of SCF into PLA and ABS have improved the mechanical properties of the composites, however their presence deteriorates the wear performances of

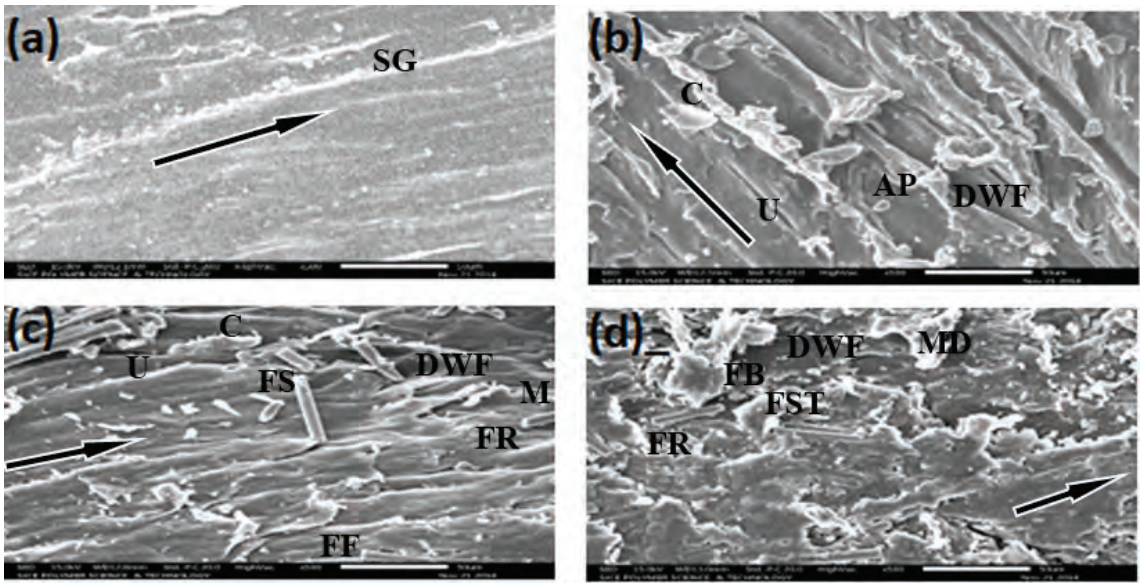


Figure 8. SEM images of wear surfaces of the composites at 20 N: (a) PLA, (b) ABS, (c) SCF/PLA, (d) SCF/ABS under 3-BAW.

the PLA and ABS composites, which is in line with the investigations reported by researchers [19, 24 and 33].

Wear Mechanisms of SCF-Reinforced PLA/ABS Composites Under 3-BAW

To determine the abrasive wear behaviour mechanisms, authors examined the worn surfaces of the pristine PLA, pristine ABS, and SCF reinforced PLA/ABS composites following 3-BAW testing (20 N, 1000 m).

According to Figure 8, the wear mode for PLA is moderate abrasive wear (Fig. 8a), which generates shallow grooves (SG) in the direction of abrasion (arrow) on the surface, whereas pristine ABS has severe abrasive wear (Fig. 8b). Thus, extreme abrasive wear on ABS produced fracture start, which resulted to catastrophic rupture. Deep wear furrows (DWF) created by ploughing (U) and cutting (C) operations operating on the polymer surface may be seen on virgin ABS sample. In addition, a few silica particles (AP) in the worn surface are noticeable.

Figure 8c, depicts the worn surfaces of a SCF/PLA composite sample abraded at 20 N for 1000 m. Few fibres are dragged out in the direction of abrasion (arrow) and split into smaller pieces (FS), as visible on the worn surface. SEM images show fibre debonding (M) from the matrix, while ploughing (U) and cutting (C) with silica abrasive particles causes less damage to the PLA matrix. Under comparable test settings, Figure 8d, depicts the worn surfaces of a SCF/ABS composite sample. Both fibres and the ABS matrix are substantially degraded, with more fibres split (FST) into tiny pieces than in Fig. 8c. More fractures in the ABS worn surface and deep wear furrows (DWF) owing to cutting action appear to be produced by silica abrasives.

CONCLUSION

The specific wear rate results obtained with pristine PLA, ABS and SCF reinforced PLA/ABS composites under 2-BMAW and 3-BAW conditions can be summarized as follows.

- The SWR of PLA/ABS and their composites increased with an increase in load in both wear-modes, but it decreased as the abrading distance increased.
- The pristine PLA matrix demonstrated best abrasion resistance in 2-BMAW and 3-BAW modes.
- Wear under 2-BMAW conditions is 2 to 2.4 of magnitude higher than the 3-BAW of PLA/ABS and SCF reinforced PLA/ABS composites. It upsurges as the load increases and gets reduced with increase in abrading distance. Furthermore, the addition of carbon fibre reinforcement did not increase PLA/ABS's abrasion resistance.
- By using SEM various wear mechanisms involved in the abrasive wear of composites under 2-BMAW and 3-BAW was discussed.

ACKNOWLEDGEMENT

This work was supported by The National Institute of Engineering (NIE), Centre for Research and Development (CRD). The authors thanks the Board of Management, Principal, Dean (R & D), NIE. Further, authors thanks Mr. Byresh, technical person in Centre for Composite Materials research, NIE, for his assistance in performing experiments.

AUTHORSHIP CONTRIBUTIONS

Authors equally contributed to this work.

DATA AVAILABILITY STATEMENT

The authors confirm that the data that supports the findings of this study are available within the article. Raw data that support the finding of this study are available from the corresponding author, upon reasonable request.

CONFLICT OF INTEREST

The author declared no potential conflicts of interest with respect to the research, authorship, and/or publication of this article.

ETHICS

There are no ethical issues with the publication of this manuscript.

STATEMENT ON THE USE OF ARTIFICIAL INTELLIGENCE

Artificial intelligence was not used in the preparation of the article.

REFERENCES

[1] Tekinalp H, Kunc V, Velez-Garcia G, Duty CE, Love L, Naskar A, et al. Highly oriented carbon fiber-polymer composites via additive manufacturing. Compos Sci Technol 2014;105:144-150. [CrossRef]

[2] Justo J, Távara L, García-Guzmán L, París F. Characterization of 3D printed long fibre reinforced composites. Compos Struct 2018;185:537-548. [CrossRef]

[3] Afonso JA, Alves JL, Caldas G, Gouveia BP, Santana L, Belinha J. Influence of 3D printing process parameters on the mechanical properties and mass of PLA parts and predictive models. Rapid Prototyp J 2021;27:487-495. [CrossRef]

[4] Zisopol DG, Ion N, Portoaca AI. Comparison of the Charpy resilience of two 3D printed materials: A study on the impact resistance of plastic parts. Eng Technol Appl Sci Res 2023;13:10781-10784. [CrossRef]

[5] Zisopol DG, Nae I, Portoaca AI, Ramadan I. A theoretical and experimental research on the influence of FDM parameters on tensile strength and hardness of parts made of polylactic acid. Eng Technol Appl Sci Res 2021;11:7458-7463. [CrossRef]

[6] Zisopol DG, Nae I, Portoaca AI. Compression behavior of FFF printed parts obtained by varying layer height and infill percentage. Eng Technol Appl Sci Res 2022;12:9747-9751. [CrossRef]

[7] Torrado AR, Shemelya CM, English JD, Lin Y, Wicker RB, Roberson DA. Characterizing the effect of additives to ABS on the mechanical property anisotropy of specimens fabricated by material extrusion 3D printing. Addit Manuf 2015;6:16-29. [CrossRef]

[8] Sagias VD, Giannakopoulos KI, Stergiou C. Mechanical properties of 3D printed polymer specimens. Procedia Struct Integr 2018;10:85-90. [CrossRef]

[9] De Avila E, Eo J, Kim J, Kim NP. Heat treatment effect on mechanical properties of 3D printed polymers. MATEC Web Conf 2019;264:1-5. [CrossRef]

[10] Mahmood S, Guo E, Stirling A, Schulze KD. Orientation controls tribological performance of 3D-printed PLA and ABS. Tribol Online 2023;18:302-312. [CrossRef]

[11] Cardoso PHM, de Oliveira MFL, de Oliveira MG, da Silva Moreira Thiré RM. 3D printed parts of polylactic acid reinforced with carbon black and alumina nanofillers for tribological applications. Macromol Symp 2020;394. [CrossRef]

[12] Man Z, Wang H, He Q, Kim DE, Chang L. Friction and wear behaviour of additively manufactured continuous carbon fibre reinforced PA6 composites. Compos Part B Eng 2021;226:109332. [CrossRef]

[13] Hemanth R, Suresha B, Yang SH, Sekar M. Abrasive wear behaviour of thermoplastic copolyester elastomer composites: A statistical approach. Int J Precis Eng Manuf 2016;17:755-763. [CrossRef]

[14] Urs MVD, Suresha B, Hemanth G, Kulkarni G, Charan MRS. Influence of graphene nanoplatelets on tribological properties of short carbon fibre reinforced PA-66/TCE composites. Mater Today Proc 2021;43:1640-1646. [CrossRef]

[15] Batra NK, Dikshit I, Sidana DS. Two-body abrasive wear behavior of woven carbon/glass/aramid polytherimide reinforced hybrid composites. In: Advances in engineering materials. Lecture Notes in Mechanical Engineering. Singapore: Springer; 2021. [CrossRef]

[16] Hemanth R, Sekar M, Suresha B. Abrasive wear behavior of thermoplastic copolyester elastomer composites. Emerg Mater Res 2015;4:108-118. [CrossRef]

[17] Aziz R, Haq MIU, Raina A. Effect of surface texturing on friction behaviour of 3D printed polylactic acid (PLA). Polym Test 2020;85:106434. [CrossRef]

[18] Shipway PH, Ngao NK. Microscale abrasive wear of polymeric materials. Wear 2003;255:742-750. [CrossRef]

[19] Harsha AP, Tewari US. Two-body and three-body abrasive wear behaviour of polyaryletherketone composites. Polym Test 2003;22:403-418. [CrossRef]

[20] Jia X, Ling R. Two-body free-abrasive wear of polyethylene, nylon1010, epoxy and polyurethane coatings. Tribol Int 2007;40:1276-1283. [CrossRef]

[21] Lingesh BV, Ravikumar BN, Rudresh BM. Investigation on the effect of grit size on two body abrasive wear behavior of polyamide66/polypropylene (PA66/PP) blends. Mater Today Proc 2018;5:2444-2452. [CrossRef]

[22] Kumar AJA, Prakash M, Lakshmankumar A, Haswanth K. Wear characterization of basalt fiber reinforced polypropylene/polylactic acid hybrid polymer composite. Proc Inst Mech Eng J J Eng Tribol 2022;236:250-258. [CrossRef]

[23] Zhang P, Hu Z, Xie H, Lee GH, Lee CH. Friction and wear characteristics of polylactic acid (PLA) for 3D printing under reciprocating sliding condition. Ind Lubr Tribol 2020;72:533-539. [CrossRef]

[24] Suresha B, Hanamasagar V, Jamadar IM, Arvind SL, Somashekar HM. Mechanical properties and abrasion resistance of 3D printed lightweight CF-reinforced PLA/ABS composites using design of experiments. In: Proceedings of the International Symposium on Lightweight and Sustainable Polymeric Materials. 2023;32:173-187. [CrossRef]

[25] Unterweger C, Brüggemann O, Fürst C. Synthetic fibers and thermoplastic short-fiber-reinforced polymers: Properties and characterization. Polym Compos 2014;35:227-236. [CrossRef]

[26] Yao SS, Jin FL, Rhee KY, Hui D, Park SJ. Recent advances in carbon-fiber-reinforced thermoplastic composites: A review. Compos Part B Eng 2018;142:241-250. [CrossRef]

[27] Lee ES, Lee CH, Chun YS, Han CJ, Lim DS. Effect of hydrogen plasma-mediated surface modification of carbon fibers on the mechanical properties of carbon-fiber-reinforced polyetherimide composites. Compos Part B Eng 2017;116:451-458. [CrossRef]

[28] Xian GJ, Zhang Z. Sliding wear of polyetherimide matrix composites: Influence of short carbon fibre reinforcement. Wear 2005;258:776-782. [CrossRef]

[29] Sun Z, Zhao ZK, Zhang YY, Li YQ, Fu YQ, Sun BG, et al. Mechanical, tribological and thermal properties of injection molded short carbon fiber/expanded graphite/polyetherimide composites. Compos Sci Technol 2021;201:108498. [CrossRef]

[30] Qiao Y, Fring LD, Pallaka MR, Simmons KL. A review of the fabrication methods and mechanical behavior of continuous thermoplastic polymer fiber-thermoplastic polymer matrix composites. Polym Compos 2023;44:694-733. [CrossRef]

[31] Dickson AN, Abourayana HM, Dowling DP. 3D printing of fibre-reinforced thermoplastic composites using fused filament fabrication-A review. Polymers (Basel) 2020;12:2188. [CrossRef]

[32] Morimoto T, Suzuki T, Iizuka H. Wear rate and fracture toughness of porous particle-filled phenol composites. Compos Part B Eng 2015;77:19-26. [CrossRef]

[33] Hemanth R, Sekar M, Pramodakumari P, Suresha B. Dynamic mechanical analysis and three-body abrasive wear behaviour of thermoplastic copolyester elastomer composites. Adv Tribol 2014;2014:14. [CrossRef]

Sigma J Eng Nat Sci, Vol. 44, No. 4, pp. 2339–2346, August, 2026

Sigma Journal of Engineering and Natural Sciences
Web page info: https://sigma.yildiz.edu.tr
DOI: 10.14744/sigma.2026.2099

Research Article

Explicit expression for powers of certain complex tridiagonal and some complex factorizations

Gürsel YEŞİLOT[1], Hatice Kübra GEÇÖR[1,*]

[1]*Department of Mathematics, Yildiz Technical University, Istanbul, 34220, Turkiye*

ARTICLE INFO

Article history
Received: 06 February 2024
Revised: 30 March 2024
Accepted: 08 January 2025

Keywords:
Chebyshev Polynomial; Eigenvalues; Eigenvectors; Factorization of Matrices; Tridiagonal Matrix

ABSTRACT

In this study, we obtain the eigenvalues and eigenvectors of two tridiagonal matrices. We present a general expression of the power of the tridiagonal matrix we are considering. In addition, we have the complex factorizations of Fibonacci and Lucas polynomials, Fibonacci, Pell and Lucas numbers.

Cite this article as: Yeşilot G, Geçör HK. Explicit expression for powers of certain complex tridiagonal and some complex factorizations. Sigma J Eng Nat Sci 2026;44(4):2339–2346.

INTRODUCTION

Matrices are used in many areas and also included in the solution of many systems. Especially; numerical analysis, some differential equations, difference equations, in the solution of boundary value problems, in the numerical solution of partial differential equations, delay differential equations and many applied fields be used determinants, eigenvalues, eigenvectors and matrix powers of the tridiagonal, anti-tridiagonal, pentadiagonal, anti-pentadiagonal, circulant and skew-circulant matrix. Therefore, it will facilitate the solution by formulating the eigenvalues, eigenvectors, and powers of the tridiagonal matrix we are considering.

Rimas [1-5] obtains positive integer powers of some of odd and even order tridiagonal matrices. Patil [6] obtains a simple formula for the trace of integer powers of a square matrix. The powers of a matrix using matrix exponential and matrix logarithm are calculated in [7]. Arslan et al. [8] obtain inverse and positive integer powers for one type of even-order symmetric pentadiagonal matrices. Duru and Bozkurt [9] derive the general expression of the power of some tridiagonal matrices. The fractional powers of triangular Toeplitz matrices are calculated in [10]. Silva [11,12] presents Chebyshev polynomials to derive a general expression for integer powers of real anti-tridiagonal matrices. Mezzar and Belghaba [13] work out positive integer powers of the Kronecker sum of two tridiagonal Toeplitz matrices.

Let

$$\tilde{A}_{\tilde{n}} := \begin{bmatrix} \tilde{b} & 0 & & & & & & \\ \tilde{a} & \tilde{b} & \tilde{a} & & & & & \\ & \tilde{a} & \tilde{b} & \tilde{a} & & & & \\ & & \ddots & \ddots & \ddots & & & \\ & & & \tilde{a} & \tilde{b} & \tilde{a} & & \\ & & & & \tilde{a} & \tilde{b} & \tilde{a} & \\ & & & & & 2\tilde{a} & \tilde{b} \end{bmatrix} \quad (1)$$

*Corresponding author.
*E-mail address: kubra.gecor@std.yildiz.edu.tr

This paper was recommended for publication in revised form by Regional Editor Ahmet Selim Dalkilic

Published by Yıldız Technical University Press, İstanbul, Turkey
© Author. This is an open access article under the CC BY-NC license (http://creativecommons.org/licenses/by-nc/4.0/).

and

$$\tilde{B}_{\tilde{n}} := \begin{bmatrix} \tilde{b} & 0 & & & & & \\ \tilde{a} & \tilde{b} & -\tilde{a} & & & & \\ & -\tilde{a} & \tilde{b} & \tilde{a} & & & \\ & & \ddots & \ddots & \ddots & & \\ & & & (-1)^{\tilde{n}-2}\tilde{a} & \tilde{b} & (-1)^{\tilde{n}-1}\tilde{a} & \\ & & & & (-1)^{\tilde{n}-1}\tilde{a} & \tilde{b} & (-1)^{\tilde{n}}\tilde{a} \\ & & & & & (-1)^{\tilde{n}}\tilde{a} & \tilde{b} \end{bmatrix} \quad (2)$$

where $\tilde{b} \in \mathbb{C}$ and $\in \mathbb{C}\setminus\{0\}$. In Section 2, we acquire eigenvalues and eigenvectors of $\tilde{n}$–square complex tridiagonal matrices in (1) and (2) In Section 3, we present a general expression for the entries of the $\tilde{s}$–th power ($\tilde{s} \in \mathbb{N}$) of a certain $\tilde{n}$–square complex tridiagonal matrix in (1). In Section 4, some numerical applications are given. In Section 5, we have obtained that determinant of $\tilde{n}$–square complex tridiagonal matices in (1) and (2) obtain complex factorizations for Fibonacci and Lucas polynomials. We present the more general form of the results obtained in [1-3].

EIGENVALUES AND EIGENVECTORS OF $\tilde{A}_{\tilde{n}}$ AND $\tilde{B}_{\tilde{n}}$

In this section, we submit eigenvalues and eigenvectors of $\tilde{n}$–square complex tridiagonal matrices in $\tilde{A}_{\tilde{n}}$ and $\tilde{B}_{\tilde{n}}$.

Theorem 1: Let $\tilde{A}_{\tilde{n}}$ be $\tilde{n}$–square $(\tilde{n} = 2\tilde{t}+1,\ \tilde{t} \in N)$ tridiagonal matrix as in (1). Then the eigenvalues and eigenvectors of the matrix $\tilde{A}_{\tilde{n}}$ are

$$\tilde{\beta}_{\tilde{m}} = \begin{cases} \tilde{b} - 2\tilde{a}\cos\left(\dfrac{(2\tilde{m}-1)\pi}{2\tilde{n}-2}\right), & \tilde{m} = 1,2,\ldots,\dfrac{\tilde{n}-1}{2}, \\ \tilde{b}, & \tilde{m} = \dfrac{\tilde{n}+1}{2}, \\ \tilde{b} - 2\tilde{a}\cos\left(\dfrac{(2\tilde{m}-3)\pi}{2\tilde{n}-2}\right), & \tilde{m} = \dfrac{\tilde{n}+3}{2}, \dfrac{\tilde{n}+5}{2}, \ldots, \tilde{n} \end{cases} \quad (3)$$

and

$$\tilde{K}_{\tilde{j}} = \begin{bmatrix} 0 \\ U_0(\tilde{\delta}_{\tilde{j}}) \\ U_1(\tilde{\delta}_{\tilde{j}}) \\ U_2(\tilde{\delta}_{\tilde{j}}) \\ \vdots \\ U_{\tilde{n}-3}(\tilde{\delta}_{\tilde{j}}) \\ U_{\tilde{n}-2}(\tilde{\delta}_{\tilde{j}}) \end{bmatrix}; \tilde{j} = 1,2,\ldots,\tilde{n} \text{ and } \tilde{j} \neq \frac{\tilde{n}+1}{2},$$

and

$$\tilde{K}_{\tilde{j}} = \begin{bmatrix} \sin\pi/2 \\ \sin 2\pi/2 \\ \sin 3\pi/2 \\ \sin 4\pi/2 \\ \vdots \\ \sin(\tilde{n}-1)\pi/2 \\ \sin \tilde{n}\pi/2 \end{bmatrix}; \tilde{j} = \frac{\tilde{n}+1}{2},$$

where $\tilde{\delta}_{\tilde{j}} = \frac{\beta_{\tilde{j}}-\tilde{b}}{2\tilde{a}}$ and $U_{\tilde{n}}(.)$ is the $\tilde{n}$th degree Chebyshev polynomial of the second kind.

Proof: Let

$$\tilde{Q}_{\tilde{n}} := \begin{vmatrix} \tilde{x}-\tilde{b} & \tilde{a} & & & & & \\ \tilde{a} & \tilde{x}-\tilde{b} & \tilde{a} & & & & \\ & \tilde{a} & \tilde{x}-\tilde{b} & \tilde{a} & & & \\ & & \ddots & \ddots & \ddots & & \\ & & & \tilde{a} & \tilde{x}-\tilde{b} & \tilde{a} & \\ & & & & \tilde{a} & \tilde{x}-\tilde{b} & \end{vmatrix}.$$

For initial conditions $det(\tilde{Q}_0) = 1$ and $det(\tilde{Q}_1) = \tilde{x} - \tilde{b}$", we have

$$\det\left(\tilde{Q}_{\tilde{n}}\right) = \left(\tilde{x}-\tilde{b}\right)\det\left(\tilde{Q}_{\tilde{n}-1}\right) - \tilde{a}^2\det\left(\tilde{Q}_{\tilde{n}-2}\right),\ \tilde{n} \geq 2. \quad (4)$$

The solution of the difference equation in (4) is

$$\tilde{Q}_{\tilde{n}}(\tilde{x}) = \tilde{a}^{\tilde{n}} U_{\tilde{n}}\left(\frac{\tilde{x}-\tilde{b}}{2\tilde{a}}\right), \quad (5)$$

where $U_{\tilde{n}}(.)$ is the $\tilde{n}$th degree Chebyshev polynomial of the second kind [14]:

$$U_{\tilde{n}}(\tilde{x}) = \frac{\sin\left(\tilde{n}\tilde{\theta}\right)}{\sin\left(\tilde{\theta}\right)}$$

here $\tilde{x} = cos(\tilde{\theta})$. All the roots of $U_{\tilde{n}}(\tilde{x})$ are included in the interval [-1, 1]. Let

$$\left|\tilde{\beta}\mathbf{I}_{\tilde{n}} - \tilde{A}_{\tilde{n}}\right| = \tilde{P}_{\tilde{n}}\left(\tilde{\beta}\right)$$

and

$$\tilde{P}_{\tilde{n}}\left(\tilde{\beta}\right) = \left(\tilde{\beta}-\tilde{b}\right)\left(\left|\tilde{Q}_{\tilde{n}-1}\left(\tilde{\beta}\right)\right| - \tilde{a}^2\left|\tilde{Q}_{\tilde{n}-3}\left(\tilde{\beta}\right)\right|\right).$$

Then we have

$$\Delta_{\tilde{A}_{\tilde{n}}}\left(\tilde{\beta}\right) = \left(\tilde{\beta}-\tilde{b}\right)\tilde{a}^{\tilde{n}-1}\left(U_{\tilde{n}-1}\left(\frac{\tilde{\beta}-\tilde{b}}{2\tilde{a}}\right) - U_{\tilde{n}-3}\left(\frac{\tilde{\beta}-\tilde{b}}{2\tilde{a}}\right)\right). \quad (6)$$

The eigenvalues of $\tilde{A}_{\tilde{n}}$ obtained as

$$\tilde{\beta}_{\tilde{m}} = \begin{cases} \tilde{b} - 2\tilde{a}\cos\left(\dfrac{(2\tilde{m}-1)\pi}{2\tilde{n}-2}\right), & \tilde{m} = 1,2,\ldots,\dfrac{\tilde{n}-1}{2}, \\ \tilde{b}, & \tilde{m} = \dfrac{\tilde{n}+1}{2}, \\ \tilde{b} - 2\tilde{a}\cos\left(\dfrac{(2\tilde{m}-3)\pi}{2\tilde{n}-2}\right), & \tilde{m} = \dfrac{\tilde{n}+3}{2}, \dfrac{\tilde{n}+5}{2}, \ldots, \tilde{n} \end{cases}$$

from (6).

The multiplicity of all the eigenvalues $\tilde{\beta}_{\tilde{m}}$ ($\tilde{m} = \overline{1,\tilde{n}}$) of the matrix $\tilde{A}_{\tilde{n}}$ are 1. Since $rank(\tilde{\beta}_{\tilde{m}} I_{\tilde{n}} - \tilde{A}_{\tilde{n}}) = \tilde{n} - 1$, for each eigenvalue $\tilde{\beta}_{\tilde{m}}$ correspond a single Jordan cell $J_{\tilde{m}}(\tilde{\beta}_{\tilde{m}})$ in the matrix *J*. That is

$$J_{\tilde{n}} = diag\left(\tilde{\beta}_1, \tilde{\beta}_2, \tilde{\beta}_3, \tilde{\beta}_4, \ldots, \tilde{\beta}_{\tilde{n}-1}, \tilde{\beta}_{\tilde{n}}\right).$$

Consider the relations $\tilde{K}^{-1}\tilde{A}_{\tilde{n}}\tilde{K} = J_{\tilde{n}}$ [15] we have to obtain the matrices $\tilde{K}$ and $\tilde{K}^{-1}$ and derive the expression of the matrix $\tilde{A}_{\tilde{n}}^{\tilde{s}}$ for $\tilde{s} \in \mathbb{N}$. Let us denote $\tilde{J}$-th column of $\tilde{K}$ by $\tilde{K}_{\tilde{j}}$ ($\tilde{J} = 1, \cdots, \tilde{n}$). Then

$$\tilde{A}_{\tilde{n}}\tilde{K} = \left(\tilde{K}_1\tilde{\beta}_1\ \tilde{K}_2\tilde{\beta}_2\ \tilde{K}_3\tilde{\beta}_3\ \tilde{K}_4\tilde{\beta}_4 \ldots \tilde{K}_{\tilde{n}-1}\tilde{\beta}_{\tilde{n}-1}\ \tilde{K}_{\tilde{n}}\tilde{\beta}_{\tilde{n}}\right). \quad (8)$$

From Eq. (8), we have the system of linear equations as follows:

$$\begin{aligned} \tilde{A}_{\tilde{n}}\tilde{K}_1 &= \tilde{K}_1\tilde{\beta}_1 \\ \tilde{A}_{\tilde{n}}\tilde{K}_2 &= \tilde{K}_2\tilde{\beta}_2 \\ \tilde{A}_{\tilde{n}}\tilde{K}_3 &= \tilde{K}_3\tilde{\beta}_3 \\ \tilde{A}_{\tilde{n}}\tilde{K}_4 &= \tilde{K}_4\tilde{\beta}_4 \\ &\vdots \\ \tilde{A}_{\tilde{n}}\tilde{K}_{\tilde{n}-1} &= \tilde{K}_{\tilde{n}-1}\tilde{\beta}_{\tilde{n}-1} \\ \tilde{A}_{\tilde{n}}\tilde{K}_{\tilde{n}} &= \tilde{K}_{\tilde{n}}\tilde{\beta}_{\tilde{n}}. \end{aligned} \quad (9)$$

Solving set of the system of linear equations in (9), we get

$$\tilde{K}_{\tilde{j}} = \begin{bmatrix} 0 \\ U_0\left(\tilde{\delta}_{\tilde{j}}\right) \\ U_1\left(\tilde{\delta}_{\tilde{j}}\right) \\ U_2\left(\tilde{\delta}_{\tilde{j}}\right) \\ \vdots \\ U_{\tilde{n}-3}\left(\tilde{\delta}_{\tilde{j}}\right) \\ U_{\tilde{n}-2}\left(\tilde{\delta}_{\tilde{j}}\right) \end{bmatrix}; \tilde{j} = 1,2,\ldots,\tilde{n}\ and\ \tilde{j} \neq \frac{\tilde{n}+1}{2}; \quad (10)$$

and

$$\tilde{K}_{\tilde{j}} = \begin{bmatrix} \sin\pi/2 \\ \sin 2\pi/2 \\ \sin 3\pi/2 \\ \sin 4\pi/2 \\ \vdots \\ \sin(\tilde{n}-1)\pi/2 \\ \sin\tilde{n}\pi/2 \end{bmatrix}; \tilde{j} = \frac{\tilde{n}+1}{2}, \quad (11)$$

where $\tilde{\delta}_{\tilde{j}} = \frac{\beta_{\tilde{j}} - \tilde{b}}{2\tilde{a}}$ and $U_{\tilde{n}}(.)$ is the $\tilde{n}$ th degree Chebyshev polynomial of the second kind.

Theorem 2: Let $\tilde{B}_{\tilde{n}}$ be $\tilde{n}$–square ($\tilde{n} = 2\tilde{t} + 1,\ \tilde{t} \in N$) tridiagonal matrix as in (2). Then the eigenvalues and eigenvectors of the matrix $\tilde{B}_{\tilde{n}}$ are

$$\tilde{\lambda}_{\tilde{k}} = \begin{cases} \tilde{b} - 2\tilde{a}\cos\left(\dfrac{\tilde{k}\pi}{\tilde{n}}\right), & \tilde{k} = 1,2,\ldots,\dfrac{\tilde{n}-1}{2}, \\ \tilde{b}, & \tilde{k} = \dfrac{\tilde{n}+1}{2}, \\ \tilde{b} - 2\tilde{a}\cos\left(\dfrac{(\tilde{k}-1)\pi}{\tilde{n}}\right), & \tilde{k} = \dfrac{\tilde{n}+3}{2}, \dfrac{\tilde{n}+5}{2}, \ldots, \tilde{n} \end{cases} \quad (12)$$

and

$$\tilde{Y}_{\tilde{j}} = \begin{bmatrix} 0 \\ \tilde{r}_{\tilde{k}-1}U_0\left(\tilde{\alpha}_{\tilde{j}}\right) \\ \tilde{r}_{\tilde{k}-1}U_1\left(\tilde{\alpha}_{\tilde{j}}\right) \\ \tilde{r}_{\tilde{k}-1}U_2\left(\tilde{\alpha}_{\tilde{j}}\right) \\ \vdots \\ \tilde{r}_{\tilde{k}-1}U_{\tilde{n}-3}\left(\tilde{\alpha}_{\tilde{j}}\right) \\ \tilde{r}_{\tilde{k}-1}U_{\tilde{n}-2}\left(\tilde{\alpha}_{\tilde{j}}\right) \end{bmatrix}; \tilde{j} = 1,2,\ldots,\tilde{n}\ and\ \tilde{j} \neq \frac{\tilde{n}+1}{2},$$

and

$$\tilde{Y}_{\tilde{j}} = \begin{bmatrix} \tilde{r}_{\tilde{k}-1}\sin\pi/2 \\ \tilde{r}_{\tilde{k}-1}\sin 2\pi/2 \\ \tilde{r}_{\tilde{k}-1}\sin 3\pi/2 \\ \tilde{r}_{\tilde{k}-1}\sin 4\pi/2 \\ \vdots \\ \tilde{r}_{\tilde{k}-1}\sin(\tilde{n}-1)\pi/2 \\ \tilde{r}_{\tilde{k}-1}\sin\tilde{n}\pi/2 \end{bmatrix}; \tilde{j} = \frac{\tilde{n}+1}{2},$$

where $\tilde{r}_{\tilde{k}-1} = \begin{cases} 1, \tilde{k}-1 \equiv 0 \text{ or } 1 (\text{mod} 4) \\ -1, \tilde{k}-1 \equiv 2 \text{ or } 3 (\text{mod} 4) \end{cases}$, $\tilde{\alpha}_{\tilde{j}} = \frac{\tilde{\lambda}_{\tilde{j}} - \tilde{b}}{2\tilde{a}}$ and $U_{\tilde{n}}(.)$ is the $\tilde{n}$ th degree Chebyshev polynomial of the second kind.

Proof: Let

$$\left|\tilde{\lambda}\mathrm{I}_{\tilde{n}}-\tilde{B}_{\tilde{n}}\right|=\tilde{F}_{\tilde{n}}\left(\tilde{\lambda}\right)$$

and from (4)

$$\tilde{F}_{\tilde{n}}\left(\tilde{\lambda}\right)=\left(\tilde{\lambda}-\tilde{b}\right)\left|\tilde{Q}_{\tilde{n}-1}\left(\tilde{\lambda}\right)\right|. \tag{13}$$

Substituting (5) into (13), we achieve

$$\Delta_{\tilde{B}_{\tilde{n}}}\left(\tilde{\lambda}\right)=\left(\tilde{\lambda}-\tilde{b}\right)\tilde{a}^{\tilde{n}-1}U_{\tilde{n}-1}\left(\frac{\tilde{\lambda}-\tilde{b}}{2\tilde{a}}\right). \tag{14}$$

The eigenvalues of $\tilde{B}_{\tilde{n}}$ acquired as

$$\tilde{\lambda}_{\tilde{k}}=\begin{cases}\tilde{b}-2\tilde{a}\cos\left(\dfrac{\tilde{k}\pi}{\tilde{n}}\right), & \tilde{k}=1,2,\ldots,\dfrac{\tilde{n}-1}{2},\\ \tilde{b}, & \tilde{k}=\dfrac{\tilde{n}+1}{2},\\ \tilde{b}-2\tilde{a}\cos\left(\dfrac{\left(\tilde{k}-1\right)\pi}{\tilde{n}}\right), & \tilde{k}=\dfrac{\tilde{n}+3}{2},\dfrac{\tilde{n}+5}{2},\ldots,\tilde{n}\end{cases}$$

The multiplicity of all the eigenvalues $\tilde{\lambda}_{\tilde{k}}$ $(\tilde{k}=\overline{1,\tilde{n}})$ of the matrix $\tilde{B}_{\tilde{n}}$ are 1. Since $rank(\tilde{\lambda}_{\tilde{k}}\,I_{\tilde{n}}-\tilde{B}_{\tilde{n}})=\tilde{n}-1$, for each eigenvalue $\tilde{\lambda}_{\tilde{k}}$ correspond to a single Jordan cell $J_{\tilde{k}}(\tilde{\lambda}_{\tilde{k}})$ in the matrix *J*. That is

$$J_{\tilde{n}}=diag\left(\tilde{\lambda}_1,\tilde{\lambda}_2,\tilde{\lambda}_3,\tilde{\lambda}_4,\ldots,\tilde{\lambda}_{\tilde{n}-1},\tilde{\lambda}_{\tilde{n}}\right). \tag{15}$$

Using the well know equality $\tilde{Y}^{-1}\tilde{B}_{\tilde{n}}\tilde{Y}=J_{\tilde{n}}$ [15] we have to obtain the matrices $\tilde{Y}$ and $\tilde{Y}^{-1}$. Let us denote $\tilde{J}$-th column of $\tilde{Y}$ by $\tilde{Y}_{\tilde{j}}(\tilde{j}=\overline{1,\tilde{n}})$. Then

$$\tilde{B}_{\tilde{n}}\tilde{Y}=\left(\tilde{Y}_1\tilde{\lambda}_1\ \tilde{Y}_2\tilde{\lambda}_2\ \tilde{Y}_3\tilde{\lambda}_3\ \tilde{Y}_4\tilde{\lambda}_4\ldots\tilde{Y}_{\tilde{n}-1}\tilde{\lambda}_{\tilde{n}-1}\ \tilde{Y}_{\tilde{n}}\tilde{\lambda}_{\tilde{n}}\right). \tag{16}$$

From Eq. (16), we have the system of linear equations as follows:

$$\begin{gathered}\tilde{B}_{\tilde{n}}\tilde{Y}_1=\tilde{Y}_1\tilde{\lambda}_1\\ \tilde{B}_{\tilde{n}}\tilde{Y}_2=\tilde{Y}_2\tilde{\lambda}_2\\ \tilde{B}_{\tilde{n}}\tilde{Y}_3=\tilde{Y}_3\tilde{\lambda}_3\\ \tilde{B}_{\tilde{n}}\tilde{Y}_4=\tilde{Y}_4\tilde{\lambda}_4\\ \vdots\\ \tilde{B}_{\tilde{n}}\tilde{Y}_{\tilde{n}-1}=\tilde{Y}_{\tilde{n}-1}\tilde{\lambda}_{\tilde{n}-1}\\ \tilde{B}_{\tilde{n}}\tilde{Y}_{\tilde{n}}=\tilde{Y}_{\tilde{n}}\tilde{\lambda}_{\tilde{n}}.\end{gathered} \tag{17}$$

Solving set of the system of linear equations in (17) as regard

$$\tilde{Y}_{\tilde{j}}=\begin{bmatrix}0\\ \tilde{r}_{\tilde{k}-1}U_0\left(\tilde{\alpha}_{\tilde{j}}\right)\\ \tilde{r}_{\tilde{k}-1}U_1\left(\tilde{\alpha}_{\tilde{j}}\right)\\ \tilde{r}_{\tilde{k}-1}U_2\left(\tilde{\alpha}_{\tilde{j}}\right)\\ \vdots\\ \tilde{r}_{\tilde{k}-1}U_{\tilde{n}-3}\left(\tilde{\alpha}_{\tilde{j}}\right)\\ \tilde{r}_{\tilde{k}-1}U_{\tilde{n}-2}\left(\tilde{\alpha}_{\tilde{j}}\right)\end{bmatrix};\ \tilde{j}=1,2,\ldots,\tilde{n}\ and\ \tilde{j}\neq\frac{\tilde{n}+1}{2}, \tag{18}$$

and

$$\tilde{Y}_{\tilde{j}}=\begin{bmatrix}\tilde{r}_{\tilde{k}-1}\sin\pi/2\\ \tilde{r}_{\tilde{k}-1}\sin 2\pi/2\\ \tilde{r}_{\tilde{k}-1}\sin 3\pi/2\\ \tilde{r}_{\tilde{k}-1}\sin 4\pi/2\\ \vdots\\ \tilde{r}_{\tilde{k}-1}\sin\left(\tilde{n}-1\right)\pi/2\\ \tilde{r}_{\tilde{k}-1}\sin\tilde{n}\pi/2\end{bmatrix};\ \tilde{j}=\frac{\tilde{n}+1}{2}, \tag{19}$$

where $\tilde{\mathrm{r}}_{\tilde{\mathrm{k}}-1}=\begin{cases}1,\tilde{\mathrm{k}}-1\equiv 0\text{ or }1(\mathrm{mod}4)\\ -1,\tilde{\mathrm{k}}-1\equiv 2\text{ or }3\ (\mathrm{mod}4)\end{cases}$, $\tilde{\alpha}_{\tilde{\mathrm{j}}}=\frac{\tilde{\lambda}_{\tilde{j}}-\tilde{b}}{2\tilde{a}}$ and $U_{\tilde{n}}(.)$ is the $\tilde{n}$ th degree Chebyshev polynomial of the second kind.

THE INTEGER POWERS OF THE MATRIX $\tilde{A}_{\tilde{n}}$

Using the well-known equality $\tilde{A}_{\tilde{n}}=\tilde{K}J\tilde{K}^{-1}(\tilde{n}=2\tilde{t}+1,\tilde{t}\in\mathbb{N})$ [15], where *J* is the Jordan froms of $\tilde{A}_{\tilde{n}}$ and $\tilde{K}$ is the transforming matrix. Let us find the transforming matrix $\tilde{K}$ and its inverse $\tilde{K}^{-1}$. From eqs. (10) and (11) we write down the transforming matrix $\tilde{K}$ as followings:

$$\tilde{K}=\begin{bmatrix}0 & 0 & \cdots & 0 & \sin\frac{\pi}{2} & 0 & \cdots & 0 & 0\\ U_0(\tilde{\delta}_1) & U_0(\tilde{\delta}_2) & \cdots & U_0\left(\tilde{\delta}_{\frac{\tilde{n}-1}{2}}\right) & \sin\frac{2\pi}{2} & U_0\left(\tilde{\delta}_{\frac{\tilde{n}+3}{2}}\right) & \cdots & U_0(\tilde{\delta}_{\tilde{n}-1}) & U_0(\tilde{\delta}_{\tilde{n}})\\ U_1(\tilde{\delta}_1) & U_1(\tilde{\delta}_2) & \cdots & U_1\left(\tilde{\delta}_{\frac{\tilde{n}-1}{2}}\right) & \sin\frac{3\pi}{2} & U_1\left(\tilde{\delta}_{\frac{\tilde{n}+3}{2}}\right) & \cdots & U_1(\tilde{\delta}_{\tilde{n}-1}) & U_1(\tilde{\delta}_{\tilde{n}})\\ U_2(\tilde{\delta}_1) & U_2(\tilde{\delta}_2) & \cdots & U_2\left(\tilde{\delta}_{\frac{\tilde{n}-1}{2}}\right) & \sin\frac{4\pi}{2} & U_2\left(\tilde{\delta}_{\frac{\tilde{n}+3}{2}}\right) & \cdots & U_2(\tilde{\delta}_{\tilde{n}-1}) & U_2(\tilde{\delta}_{\tilde{n}})\\ \vdots & \vdots & \ddots & \vdots & \vdots & \vdots & \ddots & \vdots & \vdots\\ U_{\tilde{n}-3}(\tilde{\delta}_1) & U_{\tilde{n}-3}(\tilde{\delta}_2) & \cdots & U_{\tilde{n}-3}\left(\tilde{\delta}_{\frac{\tilde{n}-1}{2}}\right) & \sin\frac{(\tilde{n}-1)\pi}{2} & U_{\tilde{n}-3}\left(\tilde{\delta}_{\frac{\tilde{n}+3}{2}}\right) & \cdots & U_{\tilde{n}-3}(\tilde{\delta}_{\tilde{n}-1}) & U_{\tilde{n}-3}(\tilde{\delta}_{\tilde{n}})\\ U_{\tilde{n}-2}(\tilde{\delta}_1) & U_{\tilde{n}-2}(\tilde{\delta}_2) & \cdots & U_{\tilde{n}-2}\left(\tilde{\delta}_{\frac{\tilde{n}-1}{2}}\right) & \sin\frac{\tilde{n}\pi}{2} & U_{\tilde{n}-2}\left(\tilde{\delta}_{\frac{\tilde{n}+3}{2}}\right) & \cdots & U_{\tilde{n}-2}(\tilde{\delta}_{\tilde{n}-1}) & U_{\tilde{n}-2}(\tilde{\delta}_{\tilde{n}})\end{bmatrix}. \tag{20}$$

Now let us find the inverse matrix $\tilde{K}^{-1}$ of the matrix $\tilde{K}$. If we denote $\tilde{J}$-th column of the inverse matrix $\tilde{K}^{-1}$ by $\tilde{K}_{\tilde{j}}^{-1}$, then we obtain

$$\tilde{K}_1^{-1} := \begin{bmatrix} \frac{\tilde{q}_1}{2\tilde{\delta}_1}U_0\left(\tilde{\delta}_1\right) \\ \frac{\tilde{q}_2}{2\tilde{\delta}_2}U_0\left(\tilde{\delta}_2\right) \\ \frac{\tilde{q}_3}{2\tilde{\delta}_3}U_0\left(\tilde{\delta}_3\right) \\ \vdots \\ \frac{\tilde{q}_{\tilde{n}-1/2}}{2\tilde{\delta}_{\tilde{n}-1/2}}U_0\left(\tilde{\delta}_{\tilde{n}-1/2}\right) \\ 1 \\ \frac{\tilde{q}_{\tilde{n}+3/2}}{2\tilde{\delta}_{\tilde{n}+3/2}}U_0\left(\tilde{\delta}_{\tilde{n}+3/2}\right) \\ \vdots \\ \frac{\tilde{q}_{\tilde{n}-1}}{2\tilde{\delta}_{\tilde{n}-1}}U_0\left(\tilde{\delta}_{\tilde{n}-1}\right) \\ \frac{\tilde{q}_{\tilde{n}}}{2\tilde{\delta}_{\tilde{n}}}U_0\left(\tilde{\delta}_{\tilde{n}}\right) \end{bmatrix}, \tilde{K}_{\tilde{n}}^{-1} := \begin{bmatrix} \frac{\tilde{q}_1}{2}U_{\tilde{n}-2}\left(\tilde{\delta}_1\right) \\ \frac{\tilde{q}_2}{2}U_{\tilde{n}-2}\left(\tilde{\delta}_2\right) \\ \frac{\tilde{q}_3}{2}U_{\tilde{n}-2}\left(\tilde{\delta}_3\right) \\ \vdots \\ \frac{\tilde{q}_{\tilde{n}-1/2}}{2}U_{\tilde{n}-2}\left(\tilde{\delta}_{\tilde{n}-1/2}\right) \\ 0 \\ \frac{\tilde{q}_{\tilde{n}+3/2}}{2}U_{\tilde{n}-2}\left(\tilde{\delta}_{\tilde{n}+3/2}\right) \\ \vdots \\ \frac{\tilde{q}_{\tilde{n}-1}}{2}U_{\tilde{n}-2}\left(\tilde{\delta}_{\tilde{n}-1}\right) \\ \frac{\tilde{q}_{\tilde{n}}}{2}U_{\tilde{n}-2}\left(\tilde{\delta}_{\tilde{n}}\right) \end{bmatrix} \tag{21}$$

and

$$\tilde{K}_{\tilde{j}}^{-1} := \begin{bmatrix} \tilde{q}_1 U_{\tilde{j}-2}\left(\tilde{\delta}_1\right) \\ \tilde{q}_2 U_{\tilde{j}-2}\left(\tilde{\delta}_2\right) \\ \tilde{q}_3 U_{\tilde{j}-2}\left(\tilde{\delta}_3\right) \\ \vdots \\ \tilde{q}_{\tilde{n}-1/2} U_{\tilde{j}-2}\left(\tilde{\delta}_{\tilde{n}-1/2}\right) \\ 0 \\ \tilde{q}_{\tilde{n}+3/2} U_{\tilde{j}-2}\left(\tilde{\delta}_{\tilde{n}+3/2}\right) \\ \vdots \\ \tilde{q}_{\tilde{n}-1} U_{\tilde{j}-2}\left(\tilde{\delta}_{\tilde{n}-1}\right) \\ \tilde{q}_{\tilde{n}} U_{\tilde{j}-2}\left(\tilde{\delta}_{\tilde{n}}\right) \end{bmatrix}; \tilde{j} = 2,3,4,\ldots,\tilde{n}-1 \tag{22}$$

where $\tilde{\delta}_{\tilde{\imath}} = \frac{\tilde{\beta}_{\tilde{\imath}} - \tilde{b}}{2\tilde{a}}$ and

$$\tilde{q}_{\tilde{\imath}} = \begin{cases} \frac{4\tilde{\delta}^2_{\frac{\tilde{n}+1}{2}-\tilde{\imath}}}{2\tilde{n}-2}, & \tilde{\imath} = 1,2,\cdots,\frac{\tilde{n}-1}{2}; \\ \frac{4\tilde{\delta}^2_{\frac{3(\tilde{n}+1)}{2}-\tilde{\imath}}}{2\tilde{n}-2}, & \tilde{\imath} = \frac{\tilde{n}+3}{2},\frac{\tilde{n}+5}{2},\cdots\tilde{n} \end{cases} \tag{23}$$

for $\tilde{\imath} = 1,2,\cdots,\tilde{n}$. Thus, we obtain

$$\tilde{K}^{-1} = \begin{bmatrix} \frac{\tilde{q}_1}{2\tilde{\delta}_1}U_0\left(\tilde{\delta}_1\right) & \tilde{q}_1 U_0\left(\tilde{\delta}_1\right) & \cdots & \tilde{q}_1 U_{\tilde{n}-3}\left(\tilde{\delta}_1\right) & \frac{\tilde{q}_1}{2}U_0\left(\tilde{\delta}_1\right) \\ \frac{\tilde{q}_2}{2\tilde{\delta}_2}U_0\left(\tilde{\delta}_2\right) & \tilde{q}_2 U_0\left(\tilde{\delta}_2\right) & \cdots & \tilde{q}_2 U_{\tilde{n}-3}\left(\tilde{\delta}_2\right) & \frac{\tilde{q}_2}{2}U_0\left(\tilde{\delta}_2\right) \\ \frac{\tilde{q}_3}{2\tilde{\delta}_3}U_0\left(\tilde{\delta}_3\right) & \tilde{q}_3 U_0\left(\tilde{\delta}_3\right) & \cdots & \tilde{q}_3 U_{\tilde{n}-3}\left(\tilde{\delta}_3\right) & \frac{\tilde{q}_3}{2}U_0\left(\tilde{\delta}_3\right) \\ \vdots & \vdots & \ddots & \vdots & \vdots \\ \frac{\tilde{q}_{\tilde{n}-1/2}}{2\tilde{\delta}_{\tilde{n}-1/2}}U_0\left(\tilde{\delta}_{\tilde{n}-1/2}\right) & \tilde{q}_{\tilde{n}-1/2}U_0\left(\tilde{\delta}_{\tilde{n}-1/2}\right) & \cdots & \tilde{q}_{\tilde{n}-1/2}U_{\tilde{n}-3}\left(\tilde{\delta}_{\tilde{n}-1/2}\right) & \frac{\tilde{q}_{\tilde{n}-1/2}}{2}U_0\left(\tilde{\delta}_{\tilde{n}-1/2}\right) \\ 1 & 0 & \cdots & 0 & 0 \\ \frac{\tilde{q}_{\tilde{n}+3/2}}{2\tilde{\delta}_{\tilde{n}+3/2}}U_0\left(\tilde{\delta}_{\tilde{n}+3/2}\right) & \tilde{q}_{\tilde{n}+3/2}U_0\left(\tilde{\delta}_{\tilde{n}+3/2}\right) & \cdots & \tilde{q}_{\tilde{n}+3/2}U_{\tilde{n}-3}\left(\tilde{\delta}_{\tilde{n}+3/2}\right) & \frac{\tilde{q}_{\tilde{n}+3/2}}{2}U_0\left(\tilde{\delta}_{\tilde{n}+3/2}\right) \\ \vdots & \vdots & \ddots & \vdots & \vdots \\ \frac{\tilde{q}_{\tilde{n}-1}}{2\tilde{\delta}_{\tilde{n}-1}}U_0\left(\tilde{\delta}_{\tilde{n}-1}\right) & \tilde{q}_{\tilde{n}-1}U_0\left(\tilde{\delta}_{\tilde{n}-1}\right) & \cdots & \tilde{q}_{\tilde{n}-1}U_{\tilde{n}-3}\left(\tilde{\delta}_{\tilde{n}-1}\right) & \frac{\tilde{q}_{\tilde{n}-1}}{2}U_0\left(\tilde{\delta}_{\tilde{n}-1}\right) \\ \frac{\tilde{q}_{\tilde{n}}}{2\tilde{\delta}_{\tilde{n}}}U_0\left(\tilde{\delta}_{\tilde{n}}\right) & \tilde{q}_{\tilde{n}}U_0\left(\tilde{\delta}_{\tilde{n}}\right) & \cdots & \tilde{q}_{\tilde{n}}U_{\tilde{n}-3}\left(\tilde{\delta}_{\tilde{n}}\right) & \frac{\tilde{q}_{\tilde{n}}}{2}U_0\left(\tilde{\delta}_{\tilde{n}}\right) \end{bmatrix} \tag{24}$$

Let us compute the power of the matrix $\tilde{A}_{\tilde{n}}$

$$\tilde{A}_{\tilde{n}}^{\tilde{s}} = \tilde{K}J_{\tilde{n}}^{\tilde{s}}\tilde{K}^{-1} = \tilde{V}\left(\tilde{s}\right) = \left(\tilde{v}_{\tilde{i}\tilde{j}}\left(\tilde{s}\right)\right). \tag{25}$$

So for $\tilde{\imath},\tilde{\jmath} = \overline{1,\tilde{n}}$

$$\tilde{v}_{\tilde{i}\tilde{j}}\left(\tilde{s}\right) = \begin{cases} \tilde{\beta}^{\tilde{s}}_{\frac{\tilde{n}+1}{2}}, & \tilde{i},\tilde{j} = 1; \\ 0, & \tilde{i} = 1;\ \tilde{j} = \overline{2,\tilde{n}} \\ \sum\limits_{\tilde{m}=1}^{\chi}\tilde{\beta}^{\tilde{s}}_{\tilde{m}}\tilde{q}_{\tilde{m}}\tilde{\mu}_{\tilde{j}}U_{\tilde{i}-2}\left(\tilde{\delta}_{\tilde{m}}\right)U_{\tilde{j}-1}\left(\tilde{\delta}_{\tilde{m}}\right) + \tilde{\beta}^{\tilde{s}}_{\frac{\tilde{n}+1}{2}}\sin\left(\frac{\tilde{i}\pi}{2}\right), & \tilde{i} = \overline{2,\tilde{n}};\ \tilde{j} = 1 \\ \sum\limits_{\tilde{m}=1}^{\chi}\tilde{\beta}^{\tilde{s}}_{\tilde{m}}\tilde{q}_{\tilde{m}}\tilde{\mu}_{\tilde{j}}U_{\tilde{i}-2}\left(\tilde{\delta}_{\tilde{m}}\right)U_{\tilde{j}-2}\left(\tilde{\delta}_{\tilde{m}}\right), & \tilde{i},\tilde{j} = \overline{2,\tilde{n}} \end{cases} \tag{26}$$

$$\tilde{\mu}_{\tilde{j}} = \begin{cases} \frac{1}{2\tilde{\delta}_{\tilde{m}}}, & \tilde{j} = 1 \\ 1, & \tilde{j} = \overline{2,\tilde{n}-1} \\ \frac{1}{2}, & \tilde{j} = \tilde{n} \end{cases} \tag{27}$$

$$\chi = 1,2,\ldots,\frac{\tilde{n}-1}{2},\frac{\tilde{n}+3}{2},\ldots\tilde{n} \tag{28}$$

where

$$\tilde{q}_{\tilde{\imath}} = \begin{cases} \frac{4\tilde{\delta}^2_{\frac{\tilde{n}+1}{2}-\tilde{i}}}{2\tilde{n}-2}, & \tilde{i} = 1,2,\ldots,\frac{\tilde{n}-1}{2}; \\ \frac{4\tilde{\delta}^2_{\frac{3(\tilde{n}+1)}{2}-\tilde{i}}}{2\tilde{n}-2}, & \tilde{i} = \frac{\tilde{n}+3}{2},\frac{\tilde{n}+5}{2},\ldots\tilde{n} \end{cases} \tag{29}$$

$\tilde{\delta}_{\tilde{\mathrm{m}}} = \frac{\tilde{\beta}_{\tilde{m}} - \tilde{b}}{2\tilde{a}}$, and $\tilde{\beta}_{\tilde{m}}(\tilde{m} = \overline{1,\tilde{n}})$ are the eigenvalues of the matrix $\tilde{A}_{\tilde{n}}(\tilde{n} = 2\tilde{t}+1,\ \tilde{t} \in \mathbb{N})$.

APPLICATIONS

Application 1: Setting $\tilde{n} = 3$ in Theorem 1, we obtain

$$J_3 = diag\left(\tilde{\beta}_1,\tilde{\beta}_2,\tilde{\beta}_3\right) = diag\left(\tilde{b}-\tilde{a}\sqrt{2},\tilde{b},\tilde{b}+\tilde{a}\sqrt{2}\right)$$

and

$$\tilde{A}_3^{\tilde{s}} = \tilde{K}J_3^{\tilde{s}}\tilde{K}^{-1} = \tilde{V}\left(\tilde{s}\right) = \left(\tilde{v}_{\tilde{i}\tilde{j}}\left(\tilde{s}\right)\right) = \begin{bmatrix} \tilde{v}_{11}\left(\tilde{s}\right) & \tilde{v}_{12}\left(\tilde{s}\right) & \tilde{v}_{13}\left(\tilde{s}\right) \\ \tilde{v}_{21}\left(\tilde{s}\right) & \tilde{v}_{22}\left(\tilde{s}\right) & \tilde{v}_{23}\left(\tilde{s}\right) \\ \tilde{v}_{31}\left(\tilde{s}\right) & \tilde{v}_{32}\left(\tilde{s}\right) & \tilde{v}_{33}\left(\tilde{s}\right) \end{bmatrix}$$

and

$$\tilde{v}_{11}\left(\tilde{s}\right) = \tilde{b}^{\tilde{s}},\ \tilde{v}_{12}\left(\tilde{s}\right) = 0,\ \tilde{v}_{13}\left(\tilde{s}\right) = 0,$$

$$\tilde{v}_{21}\left(\tilde{s}\right) = \tilde{v}_{23}\left(\tilde{s}\right) = 0,354\left(\tilde{b}+1,414\tilde{a}\right)^{\tilde{s}} - 0,354\left(\tilde{b}-1,414\tilde{a}\right)^{\tilde{s}},$$

$$\tilde{v}_{22}\left(\tilde{s}\right) = \tilde{v}_{33}\left(\tilde{s}\right) = 0,5\left(\tilde{b}+1,414\tilde{a}\right)^{\tilde{s}} + 0,5\left(\tilde{b}-1,414\tilde{a}\right)^{\tilde{s}},$$

$$\tilde{v}_{31}\left(\tilde{s}\right) = 0,5\left(\tilde{b}+1,414\tilde{a}\right)^{\tilde{s}} + 0,5\left(\tilde{b}-1,414\tilde{a}\right)^{\tilde{s}} - \tilde{b}^{\tilde{s}},$$

$$\tilde{v}_{32}\left(\tilde{s}\right) = 0,707\left(\tilde{b}+1,414\tilde{a}\right)^{\tilde{s}} - 0,707\left(\tilde{b}-1,414\tilde{a}\right)^{\tilde{s}}.$$

Application 2: It $\tilde{n} = 5$, $\tilde{s} = 4$, $\tilde{a} = 2$ and $\tilde{b} = 4$, then

$$J_5 = diag\left(0.304, 2.469, 4, 5.531, 7.696\right)$$

$$\tilde{A}_5^4 = \tilde{K}J_5^4\tilde{K}^{-1} = \tilde{V}\left(4\right) = \left(\tilde{v}_{\tilde{i}\tilde{j}}\left(4\right)\right)$$

$$= \begin{bmatrix} 256 & 0 & 0 & 0 & 0 \\ 640 & 672 & 768 & 448 & 128 \\ 416 & 768 & 1120 & 1024 & 448 \\ 128 & 448 & 1024 & 1568 & 896 \\ 32 & 256 & 896 & 1792 & 1120 \end{bmatrix}.$$

Application 3: Setting $\tilde{a} = 2$, $\tilde{b} = 5$ and $\tilde{n} = 7$ in Theorem 2, we obtain the eigenvalues and eigenvectors of the matrix $\tilde{B}_{\tilde{n}}$

$$\tilde{\lambda}_1 = 1,3961; \tilde{\lambda}_2 = 2,5060; \tilde{\lambda}_3 = 4,1099; \tilde{\lambda}_4 = 5;$$

$$\tilde{\lambda}_5 = 5,8901; \tilde{\lambda}_6 = 7,4940; \tilde{\lambda}_7 = 8,6039$$

and

$$Y = \begin{bmatrix} 0 & 0 & 0 & 1 & 0 & 0 & 0 \\ 1 & 1 & 1 & 0 & 1 & 1 & 1 \\ 1,802 & 1,247 & 0,445 & 1 & -0,445 & -1,247 & -1,802 \\ -2,247 & -0,555 & 0,802 & 0 & 0,802 & -0,555 & -2,247 \\ -2,247 & 0,555 & 0,802 & 1 & -0,802 & -0,555 & 2,247 \\ 1,802 & -1,247 & 0,445 & 0 & 0,445 & -1,247 & 1,802 \\ 1 & -1 & 1 & 1 & -1 & 1 & -1 \end{bmatrix}.$$

COMPLEX FACTORIZATIONS

The well-known Fibonacci and Lucas polynomials $F(x) = \{F_n(x)\}_{n=1}^{\infty}$ and $L(x) = \{L_n(x)\}_{n=1}^{\infty}$ are defined in [16] by the recurrence relation, respectively,

$$F_n\left(x\right) = xF_{n-1}\left(x\right) + F_{n-2}\left(x\right)$$

where $F_0(x) = 0$, $F_1(x) = 1$, $F_2(x) = x$ and $n \geq 3$,

$$L_n\left(x\right) = xL_{n-1}\left(x\right) + L_{n-2}\left(x\right)$$

where $L_0(x) = 2$, $L_1(x) = x$ and $n \geq 2$.

Theorem 1 results in corollary 1.

Corollary 1: Let the matrix $\tilde{A}_{\tilde{n}}$ be $\tilde{n}$-square $(\tilde{n} = 2\tilde{t} + 1,\ \tilde{t} \in N)$ tridiagonal matrix as in (1) with $\tilde{a} := i$ and $\tilde{b} := x$ where $i = \sqrt{-1}$. Then

$$det\left(\tilde{A}_{\tilde{n}}\right) = x\left(F_{\tilde{n}}\left(x\right) + F_{\tilde{n}-2}\left(x\right)\right) = L_{\tilde{n}}\left(x\right) - L_{\tilde{n}-2}\left(x\right) \quad (30)$$

where $F_n(x)$ and $L_n(x)$ are n-th Fibonacci and Lucas polynomial, respectively.

Theorem 2 results in corollary 2.

Corollary 2: Let the matrix $\tilde{B}_{\tilde{n}}$ be $\tilde{n}$-square $(\tilde{n} = 2\tilde{t} + 1,\ \tilde{t} \in N)$ tridiagonal matrix as in (2) with $\tilde{a} := i$ and $\tilde{b} := x$ where $i = \sqrt{-1}$. Then

$$det\left(\tilde{B}_{\tilde{n}}\right) = F_2\left(x\right)F_{\tilde{n}}\left(x\right) \quad (31)$$

where $F_n(x)$ is n-th Fibonacci polynomial.

Theorem 3: Let the matrix $\tilde{A}_{\tilde{n}}$ be as in (1) with $\tilde{a} := i$ and $\tilde{b} := x$. Then the complex factorization of the generalized Fibonacci polynomial is the following form:

$$F_{\tilde{n}}\left(x\right) + F_{\tilde{n}-2}\left(x\right) = \frac{1}{x}\prod_{\tilde{m}=1}^{\tilde{n}}\tilde{\beta}_{\tilde{m}}. \quad (32)$$

Proof: Due to the eigenvalues of the matrix $\tilde{A}_{\tilde{n}}$ from (3)

$$\tilde{\beta}_{\tilde{m}} = \begin{cases} x - 2i\cos\left(\dfrac{\left(2\tilde{m}-1\right)\pi}{2\tilde{n}-2}\right), & \tilde{m} = 1,2,\ldots,\dfrac{\tilde{n}-1}{2}, \\ x, & \tilde{m} = \dfrac{\tilde{n}+1}{2}, \\ x - 2i\cos\left(\dfrac{\left(2\tilde{m}-3\right)\pi}{2\tilde{n}-2}\right), & \tilde{m} = \dfrac{\tilde{n}+3}{2}, \dfrac{\tilde{n}+5}{2}, \ldots, \tilde{n} \end{cases}$$

the determinant of the matrix $\tilde{A}_{\tilde{n}}$ can be stated as

$$\det\left(\tilde{A}_{\tilde{n}}\right) = \prod_{\tilde{m}=1}^{n}\tilde{\beta}_{\tilde{m}}.$$

From Eq. (32) and Corollary 1, the complex factorization of the generalized Fibonacci polynomial is provided.

Theorem 4: Let the matrix $\tilde{B}_{\tilde{n}}$ be as in (2) with $\tilde{a} := i$ and $\tilde{b} := x$. Then the complex factorization of the generalized Fibonacci polynomial is the following form:

$$F_2\left(x\right)F_{\tilde{n}}\left(x\right) = \prod_{\tilde{m}=1}^{\tilde{n}}\tilde{\lambda}_{\tilde{m}}. \quad (33)$$

Proof: Due to the eigenvalues of the matrix $\tilde{B}_{\tilde{n}}$ from (12)

$$\tilde{\lambda}_{\tilde{k}} = \begin{cases} x - 2i\cos\left(\dfrac{\tilde{k}\pi}{\tilde{n}}\right), & \tilde{k} = 1,2,\ldots,\dfrac{\tilde{n}-1}{2}, \\ x, & \tilde{k} = \dfrac{\tilde{n}+1}{2}, \\ x - 2i\cos\left(\dfrac{\left(\tilde{k}-1\right)\pi}{\tilde{n}}\right), & \tilde{k} = \dfrac{\tilde{n}+3}{2}, \dfrac{\tilde{n}+5}{2}, \ldots, \tilde{n} \end{cases}$$

the determinant of the matrix $\tilde{B}_{\tilde{n}}$ can be stated as

$$\det\left(\tilde{B}_{\tilde{n}}\right) = \prod_{\tilde{m}=1}^{n}\tilde{\lambda}_{\tilde{m}}.$$

From Eq. (33) and Corollary 2, the complex factorization of the generalized Fibonacci polynomial is provided.

CONCLUSION

Conclusion 1: Let the matrix $\tilde{A}_{\tilde{n}}$ be as in (1). Then

$$\det\left(\tilde{A}_{\tilde{n}}\right) = \begin{cases} F_{\tilde{n}}\left(x\right) + F_{\tilde{n}-2}\left(x\right) & if \quad \tilde{a} = i \; and \; \tilde{b} = 1 \\ L_{\tilde{n}}\left(x\right) - L_{\tilde{n}-2}\left(x\right) & if \quad \tilde{a} = i \; and \; \tilde{b} = 2 \\ 2\left(P_{\tilde{n}}\left(x\right) + P_{\tilde{n}-2}\left(x\right)\right) & if \quad \tilde{a} = i \; and \; \tilde{b} = 2 \end{cases}$$

where F_n, L_n and P_n denote n the Fibonacci, Lucas and Pell numbers.

Conclusion 2: Let the matrix $\tilde{B}_{\tilde{n}}$ be as in (2). Then

$$\det\left(\tilde{B}_{\tilde{n}}\right)=\begin{cases} F_{\tilde{n}} & if \quad \tilde{a}=i \; and \; \tilde{b}=1 \\ 2P_{\tilde{n}} & if \quad \tilde{a}=i \; and \; \tilde{b}=2 \end{cases}$$

where F_n and P_n denote n the Fibonacci and Pell numbers.

Conclusion 3: Using it is known that $\tilde{A}_{\tilde{n}}=\tilde{K}J\tilde{K}^{-1}(\tilde{n}=2\tilde{t}+1,\tilde{t}\in\mathbb{N})$ [11], where J is Jordan's froms of $\tilde{A}_{\tilde{n}}$ and $\tilde{K}$ is the transforming matrix. We obtained $\tilde{K}$ and $\tilde{K}^{-1}$ as follows:

$$\tilde{K}=\begin{bmatrix} 0 & 0 & \cdots & 0 & \sin\frac{\pi}{2} & 0 & \cdots & 0 & 0 \\ U_0(\tilde{\delta}_1) & U_0(\tilde{\delta}_2) & \cdots & U_0\left(\tilde{\delta}_{\frac{\tilde{n}-1}{2}}\right) & \sin\frac{2\pi}{2} & U_0\left(\tilde{\delta}_{\frac{\tilde{n}+3}{2}}\right) & \cdots & U_0(\tilde{\delta}_{\tilde{n}-1}) & U_0(\tilde{\delta}_{\tilde{n}}) \\ U_1(\tilde{\delta}_1) & U_1(\tilde{\delta}_2) & \cdots & U_1\left(\tilde{\delta}_{\frac{\tilde{n}-1}{2}}\right) & \sin\frac{3\pi}{2} & U_1\left(\tilde{\delta}_{\frac{\tilde{n}+3}{2}}\right) & \cdots & U_1(\tilde{\delta}_{\tilde{n}-1}) & U_1(\tilde{\delta}_{\tilde{n}}) \\ U_2(\tilde{\delta}_1) & U_2(\tilde{\delta}_2) & \cdots & U_2\left(\tilde{\delta}_{\frac{\tilde{n}-1}{2}}\right) & \sin\frac{4\pi}{2} & U_2\left(\tilde{\delta}_{\frac{\tilde{n}+3}{2}}\right) & \cdots & U_2(\tilde{\delta}_{\tilde{n}-1}) & U_2(\tilde{\delta}_{\tilde{n}}) \\ \vdots & \vdots & \ddots & \vdots & \vdots & \vdots & \ddots & \vdots & \vdots \\ U_{\tilde{n}-3}(\tilde{\delta}_1) & U_{\tilde{n}-3}(\tilde{\delta}_2) & \cdots & U_{\tilde{n}-3}\left(\tilde{\delta}_{\frac{\tilde{n}-1}{2}}\right) & \sin\frac{(\tilde{n}-1)\pi}{2} & U_{\tilde{n}-3}\left(\tilde{\delta}_{\frac{\tilde{n}+3}{2}}\right) & \cdots & U_{\tilde{n}-3}(\tilde{\delta}_{\tilde{n}-1}) & U_{\tilde{n}-3}(\tilde{\delta}_{\tilde{n}}) \\ U_{\tilde{n}-2}(\tilde{\delta}_1) & U_{\tilde{n}-2}(\tilde{\delta}_2) & \cdots & U_{\tilde{n}-2}\left(\tilde{\delta}_{\frac{\tilde{n}-1}{2}}\right) & \sin\frac{\tilde{n}\pi}{2} & U_{\tilde{n}-2}\left(\tilde{\delta}_{\frac{\tilde{n}+3}{2}}\right) & \cdots & U_{\tilde{n}-2}(\tilde{\delta}_{\tilde{n}-1}) & U_{\tilde{n}-2}(\tilde{\delta}_{\tilde{n}}) \end{bmatrix}.$$

and

$$\tilde{K}^{-1}=\begin{bmatrix} \frac{\tilde{q}_1}{2\tilde{\delta}_1}U_0(\tilde{\delta}_1) & \tilde{q}_1U_0(\tilde{\delta}_1) & \cdots & \tilde{q}_1U_{\tilde{n}-3}(\tilde{\delta}_1) & \frac{\tilde{q}_1}{2}U_0(\tilde{\delta}_1) \\ \frac{\tilde{q}_2}{2\tilde{\delta}_2}U_0(\tilde{\delta}_2) & \tilde{q}_2U_0(\tilde{\delta}_2) & \cdots & \tilde{q}_2U_{\tilde{n}-3}(\tilde{\delta}_2) & \frac{\tilde{q}_2}{2}U_0(\tilde{\delta}_2) \\ \frac{\tilde{q}_3}{2\tilde{\delta}_3}U_0(\tilde{\delta}_3) & \tilde{q}_3U_0(\tilde{\delta}_3) & \cdots & \tilde{q}_3U_{\tilde{n}-3}(\tilde{\delta}_3) & \frac{\tilde{q}_3}{2}U_0(\tilde{\delta}_3) \\ \vdots & \vdots & \ddots & \vdots & \vdots \\ \frac{\tilde{q}_{\tilde{n}-\frac{1}{2}}}{2\tilde{\delta}_{\tilde{n}-\frac{1}{2}}}U_0\left(\tilde{\delta}_{\tilde{n}-\frac{1}{2}}\right) & \tilde{q}_{\tilde{n}-\frac{1}{2}}U_0\left(\tilde{\delta}_{\tilde{n}-\frac{1}{2}}\right) & \cdots & \tilde{q}_{\tilde{n}-\frac{1}{2}}U_{\tilde{n}-3}\left(\tilde{\delta}_{\tilde{n}-\frac{1}{2}}\right) & \frac{\tilde{q}_{\tilde{n}-\frac{1}{2}}}{2}U_0\left(\tilde{\delta}_{\tilde{n}-\frac{1}{2}}\right) \\ 1 & 0 & \cdots & 0 & 0 \\ \frac{\tilde{q}_{\tilde{n}+\frac{1}{2}}}{2\tilde{\delta}_{\tilde{n}+\frac{1}{2}}}U_0\left(\tilde{\delta}_{\tilde{n}+\frac{1}{2}}\right) & \tilde{q}_{\tilde{n}+\frac{1}{2}}U_0\left(\tilde{\delta}_{\tilde{n}+\frac{1}{2}}\right) & \cdots & \tilde{q}_{\tilde{n}+\frac{1}{2}}U_{\tilde{n}-3}\left(\tilde{\delta}_{\tilde{n}+\frac{1}{2}}\right) & \frac{\tilde{q}_{\tilde{n}+\frac{1}{2}}}{2}U_0\left(\tilde{\delta}_{\tilde{n}+\frac{1}{2}}\right) \\ \vdots & \vdots & \ddots & \vdots & \vdots \\ \frac{\tilde{q}_{\tilde{n}-1}}{2\tilde{\delta}_{\tilde{n}-1}}U_0(\tilde{\delta}_{\tilde{n}-1}) & \tilde{q}_{\tilde{n}-1}U_0(\tilde{\delta}_{\tilde{n}-1}) & \cdots & \tilde{q}_{\tilde{n}-1}U_{\tilde{n}-3}(\tilde{\delta}_{\tilde{n}-1}) & \frac{\tilde{q}_{\tilde{n}-1}}{2}U_0(\tilde{\delta}_{\tilde{n}-1}) \\ \frac{\tilde{q}_{\tilde{n}}}{2\tilde{\delta}_{\tilde{n}}}U_0(\tilde{\delta}_{\tilde{n}}) & \tilde{q}_{\tilde{n}}U_0(\tilde{\delta}_{\tilde{n}}) & \cdots & \tilde{q}_{\tilde{n}}U_{\tilde{n}-3}(\tilde{\delta}_{\tilde{n}}) & \frac{\tilde{q}_{\tilde{n}}}{2}U_0(\tilde{\delta}_{\tilde{n}}) \end{bmatrix}$$

One can ask whether determinants of $\tilde{n}$-square complex tridiagonal matrices in $\tilde{A}_{\tilde{n}}$ and $\tilde{B}_{\tilde{n}}$ can be determined by other numbers such as Mersenne numbers?

Remark : Note that our results in this paper are the more general form of the results obtained in [1-3]. One can easily see this, taking $\tilde{a}:=1$ and $\tilde{b}:=0$ in Theorem 1, respectively.

ACKNOWLEDGEMENT

The authors thank the anonymous referees for their careful reading of the paper and very detailed proposals that helped improve the presentation of the paper.

AUTHORSHIP CONTRIBUTIONS

Authors equally contributed to this work.

DATA AVAILABILITY STATEMENT

The authors confirm that the data that supports the findings of this study are available within the article. Raw data that support the finding of this study are available from the corresponding author, upon reasonable request.

CONFLICT OF INTEREST

The author declared no potential conflicts of interest with respect to the research, authorship, and/or publication of this article.

ETHICS

There are no ethical issues with the publication of this manuscript.

STATEMENT ON THE USE OF ARTIFICIAL INTELLIGENCE

Artificial intelligence was not used in the preparation of the article.

REFERENCES

[1] Rimas J. On computing of arbitrary positive integer powers for one type of even order tridiagonal matrices with zero row-I. Appl Math Comput 2005;164:149-154. [CrossRef]

[2] Rimas J. On computing of arbitrary positive integer powers for one type of odd order tridiagonal matrices with zero row-I. Appl Math Comput 2005;169:1390-1394. [CrossRef]

[3] Rimas J. On computing of arbitrary positive integer powers for one type of odd order tridiagonal matrices with zero row-II. Appl Math Comput 2006;174:490-499. [CrossRef]

[4] Rimas J. On computing of arbitrary positive integer powers for one type of symmetric tridiagonal matrices of even order. Appl Math Comput 2005;168:783-787. [CrossRef]

[5] Rimas J. On computing of arbitrary positive integer powers for one type of symmetric tridiagonal matrices of even order-II. Appl Math Comput 2006;172:245-251 [CrossRef]

[6] Patil K.M. On the trace of powers of square matrices. Hacettepe J Math Stat 2021;50:14-23. [CrossRef]

[7] Kumara KKWAS. Computing the matrix powers of matrix. Int J Adv Res 2021;9:681-683. [CrossRef]

[8] Arslan S, Köken F, Bozkurt D. Positive integer powers and inverse for one type of even order symmetric pentadiagonal matrices. Appl Math Comput 2013;219:5241-5248. [CrossRef]

[9] Duru H.K. & Bozkurt D. Powers of complex Tridiagonal matrices. Alabama J Math 2014;38:1-4.
[10] Krim I, Mezeddek MT, Smail A. On powers and roots of Triangular Toeplitz matrices. Appl Math 2022;22:322-330.
[11] JoaõLita da Silva. Integer powers of anti-tridiagonal matrices of the form antitridiag_n (a,0,b); a,b ∈ R. Comput Math Appl 2015;69:1313-1328. [CrossRef]
[12] Joaõ Lita da Silva. Integer powers of anti-tridiagonal matrices of the form antitridiagn(a, c,−a), a, c ∈ C. Int J Comput Math 2015;93:1723-1740.
[13] Mezzar Y, Belghaba K. Positive integer powers of the kronecker sum of two tridiagonal toeplitz matrices. Azerbaijan J Math 2024;14:46-53. [CrossRef]
[14] Mason JC, Handscomb DC. Chebyshev Polynomials. Boca Raton: CRC Press; 2003. [CrossRef]
[15] Horn P., Johnson Ch. Matrix Analysis. Cambridge: Cambridge University Press; 1986.
[16] Thomas Koshy. Fibonacci and Lucas Numbers with Applications. New York: John Wiley and Sons; 2001. [CrossRef]

Sigma J Eng Nat Sci, Vol. 44, No. 4, pp. 2347–2363, August, 2026

Sigma Journal of Engineering and Natural Sciences
Web page info: https://sigma.yildiz.edu.tr
DOI: 10.14744/sigma.2026.2100

Research Article

Estimating above ground biomass in black pine forest using ALOS-1 data and machine learning methods

Şükrü Teoman GÜNER[1], Omer Gokberk NARIN[2,*], Aydın ÇÖMEZ[3], Eren Gürsoy ÖZDEMİR[4], Caglar BAYIK[5], Saygın ABDIKAN[6]

[1]*Department of Forestry, Bartın University, Bartın, 74100, Türkiye*
[2]*Department of Geomatics Engineering, Afyon Kocatepe University, Afyonkarahisar, 03200, Türkiye*
[3]*General Directorate of Forestry, Aegean Forestry Research Institute, Urla, İzmir, 35661, Türkiye*
[4]*Department of Architecture and Urban Planning, Bartın University, Bartın, 74100, Türkiye*
[5]*Department of Geomatics Engineering, Zonguldak Bulent Ecevit University, Zonguldak, 67100, Türkiye*
[6]*Department of Geomatics Engineering, Hacettepe University, Ankara, 06800, Türkiye*

ARTICLE INFO

Article history
Received: 08 September 2024
Revised: 15 January 2025
Accepted: 19 February 2025

Keywords:
Aboveground Biomass; ALOS PALSAR; Machine Learning; Pinus Nigra

ABSTRACT

Within the sustainable development goal 'climate action framework,' forests play a vital role in enhancing climate resilience. The data obtained from these ecosystems are expected to significantly contribute to shaping regional forestry policies and advancing climate-related studies. Above-ground biomass (AGB) is a substantial parameter of the ecosystem cycle and is used to estimate forest carbon storage. Knowledge of the spatial distribution of AGB supports the management of forests and understanding of climate change's effects. This study aims to analyze the relationship and to estimate biomass using machine learning methods between the AGB of a black pine (*Pinus nigra*) plantation forest obtained from ground measurements and the global mosaic L-band ALOS-PALSAR Synthetic Aperture Radar (SAR) image. The forest is distributed in western Inner Anatolia to the Black Sea, Marmara, and inner Aegean regions of Türkiye. Fieldwork was carried out in 44 plots distributed across different locations in Türkiye. The mean diameter, mean height, stand age, stand stock, stocking density, and basal area were determined for each sample. The aboveground tree masses of the sample trees were calculated. The relationship between ground-based AGB calculation and remote sensing ALOS data was obtained. This study estimated the AGB using linear regression, Random Forest, XGBoost, and Convolutional Neural Network (CNN) techniques. In addition to backscatter images of dual polarimetric (HH and HV) data, we created Normalized Difference Polarization Index (NDPI) and Co-polarized Ratio (CPR) images. Twelve scenarios were created using these four variables of ALOS data and their AGB estimation results were compared. . The highest AGB estimation performance obtained with the CNN model was achieved by combining HV polarization and CPR features, resulting in an R^2 value of 0.448 and an RMSE of 59.726 t/ha. The findings indicate that HV polarimetric data and integrating additional features further improved estimation capability. Overall, the findings demonstrate that integrating SAR imagery with CNN-based approaches provides an efficient, economically viable framework for multi-temporal forest biomass estimation. Such an approach has considerable potential to support large-scale forest carbon monitoring, sustainable forest management practices, and climate change mitigation policies at both national and global scales, including in Türkiye.

Cite this article as: Güner ŞT, Narin ÖG, Çömez A, Özdemir EG, Bayık Ç, Abdikan S. Estimating above ground biomass in black pine forest using ALOS-1 data and machine learning methods. Sigma J Eng Nat Sci 2026;44(4):2347–2363.

***Corresponding author.**
*E-mail address: gokberknarin@aku.edu.tr

This paper was recommended for publication in revised form by Editor-in-Chief Ahmet Selim Dalkilic

Published by Yıldız Technical University Press, İstanbul, Turkey
© Author. This is an open access article under the CC BY-NC license (http://creativecommons.org/licenses/by-nc/4.0/).

INTRODUCTION

The use of fossil fuels in human activities and the reduction of forests lead to an increase in carbon dioxide in the atmosphere. The increase in carbon dioxide concentration in the atmosphere is seen as the main cause of global climate change [1]. Forest ecosystems, which have the largest carbon pool among terrestrial ecosystems, have an important place in the global carbon cycle owing to their biomass production by binding carbon dioxide in the atmosphere to their bodies through photosynthesis [2]. Forests store more than 80% of the carbon stock in terrestrial ecosystems [3]. The determination of the produced biomass can make important contributions to a better understanding of the carbon cycle and thus to the determination of adaptation strategies to climate change. Conventional methods use biomass on inventory data with allometric equations or expansion factors of forest biomass [4, 5]. Terrestrial-based measurement techniques are mostly used in the determination of tree biomass in forest ecosystems [6]. However, these techniques have some limitations. Terrestrial techniques include tree species-specific biomass equations or tree trunk volume data based on forest inventory. In order to use the biomass equations, it is necessary to determine the diameters and heights of the trees by ground measurements. In the forest inventory in Türkiye, the diameter and height values of trees and the volumes of the stem with bark are determined in 10-year periods. Biomass can also be calculated using the biomass conversion and expansion factors from the tree stem volume data obtained. However, the calculated biomass belongs to different years and cannot reflect the current situation. Therefore, biomass determination methods that require less time and labor are needed.

Biomass estimation using satellite images and image processing techniques is used as a much faster and more economical method for large areas. Remote sensing data through passive (optical) and active sources such as Synthetic Aperture Radar (SAR) and Light Detection and Ranging (LiDAR) are efficient tools to estimate the structure and composition of the forest ecosystem as well as the forest Aboveground biomass (AGB) [7-10]. Estimating AGB by optical techniques that determine the correlation between the spectral response and the ground data obtained from the field plots is effective for the estimation of foliar biomass components. However, it does not penetrate the woody biomass, dense forest canopy, and saturate at low biomass amounts and has limitations due to atmospheric conditions [11, 12]. Compared to optical sensors, SAR sensors are more effective because they can acquire data in cloudy conditions and day and night. Among the SAR systems L-band ALOS data has been preferred due to its longer wavelength that can penetrate through the forest cover [13]. Previous studies showed its potential over different forest types. Englhart et al. [14] studied AGB estimation in tropical forests, in Kalimantan, Indonesia, using TerraSAR – X (X band) and Advanced Land Observing Satellite (ALOS) Phased Array L-band Synthetic Aperture Radar (PALSAR) sensor (L band) SAR data. They concluded that ALOS PALSAR backscatter was more sensitive to AGB than TerraSAR– X. George-Chacon et al. [15] achieved the best fit using machine learning when Sentinel-2 and ALOS PALSAR were combined for the semideciduous tropical forest of Mexico. The linear regression (LR) method was the most widely used parametric method for AGB estimation in previous studies [16]. Non-parametric techniques including machine learning methods and deep learning methods have been used for forestry research such as canopy height [17] and AGB estimation [18, 19]. Convolutional neural networks (CNNs) are widely applied for image classification and change detection studies [20-22] and are rarely used for forest AGB estimation [19]. In the case of pixel-based analysis, one-dimensional CNN (1D-CNN) is considered for parameter estimation studies [23].

Black pine (*Pinus nigra* Arn.) is widespread in Southern Europe, Northwest Africa, and Türkiye (in Anatolia) [24]. There are five subspecies systematically, ssp. nigra, ssp. salzmannii, ssp. laricio, ssp. dalmatica and ssp. pallasiana [25]. Among these subspecies, Anatolian black pine (*Pinus nigra* J. F. Arnold. subsp. *pallasina* (Lamb.) Holmboe var. *pallasiana*) [26] naturally distributed in Türkiye, Thrace, Crimea, Balkans, Southern Carpathians, Cyprus, Western Caucasus, and Western Spread in Syria [27, 28]. Black pine (*Pinus nigra* subsp. *pallasina* (Lamb.) Holmboe) in pure form or mixed with species such as oak, fir, pine, and juniper in Türkiye at 165-2150 meters; it spreads over an area of 4.5 million hectares in Marmara, Black Sea, Aegean, Mediterranean, and Central Anatolia Regions and constitutes 18.3% of the forest areas [29, 30]. Black pine has been one of the most widely used species in afforestation studies due to its ability to grow on poor soils as well as its resistance to both arid and cold conditions [31]. The several equations were developed toestimate the biomass of black pine in previous studies [32, 33]. Balenovic et al. [34], on the other hand, explained the biomass of the black pine species using high-resolution aerial stereo-images with the independent variables of the crown and tree height they estimated. However, Balenovic et al. [34] used remote sensing data to estimate the independent variables in the biomass equations. Günlü et al. [35] estimated the AGB of pure black pine forest using high resolution WorldView-2 optical data. Turgut and Günlü [36] detected the aboveground biomass of *Pinus nigra* with 32.78 t/ha Root Mean Square Error (RMSE) and 0.55 coefficient of determination (R^2) using Landsat 8 OLI satellite image and multiple linear regression. Bulut et al. [37] predicted AGB of coniferous, broadleaf, and mixed stands using Sentinel-2 optical data. Vatandaslar and Abdikan [38] estimated carbon stock using ALOS-2 data and forest inventory for a black pine and mixed forest (Lebanese cedar, Taurus fir, and juniper). Total carbon stock is estimated at R^2 of 0.78 with HH of ALOS-2 data. Bulut [39] studied AGB prediction of pure Calabrian

pine (*Pinus brutia* Ten.) in Türkiye. The study used multiple regression analysis (MLR) and support vector machines (SVM) with Landsat-8 data. The SVM provided higher R^2 for validation data than MLR. Li et al. [40] estimated AGB using Landsat-8 and Sentinel-1A data with linear Regression, XGBoost, and Random Forest (RF) methods in subtropical forests in China's Hunan province. As a result of the study, they stated that the XGBoost algorithm gave better results than other methods. They obtained results of R^2=0.38 in estimation with Sentinel-1A, R^2=0.66 in estimation with Landsat-8, and R^2=0.75 in the combined use of Sentinel-1A and Landsat-8. Although several studies have been conducted on the estimation of the biomass of some pine species by remote sensing [12, 36, 38, 39], there is no research on pure *Pinus nigra* forest with SAR data in Türkiye. Meanwhile, considering the other biomass studies, the literature on biomass studies of semi-arid region forests is limited [41].

This study investigates the relationship between biomass data collected from various regions in Türkiye for pure *Pinus nigra* forests and global ALOS-PALSAR satellite data, given the unavailability of suitable optical data. While CNN-based approaches for AGB estimation are relatively limited, this study also addresses the comparative performance of CNN with other widely discussed methods in the literature, such as RF and XGBoost. The CNN model was selected to estimate AGB using ground-truth measurements from 44 plots in a pure *Pinus nigra* forest in Türkiye. The CNN model was compared with RF, XGBoost, and linear regression to evaluate its performance. The model was trained using dual-polarimetric backscatter images (HH and HV) together with two additional indices derived from ALOS-PALSAR mosaic data: the Normalized Difference Polarization Index (NDPI) and the Co-polarized Ratio (CPR). These variables provided complementary information and improved the representation of forest structure. A CNN was used because it can automatically learn relevant patterns directly from the input data, minimizing the reliance on manual feature extraction. It can offer advantages over traditional machine learning methods, which rely on manually selected features. This capability allows CNNs to capture complex spatial patterns embedded in remote sensing data. Because CNNs can effectively handle complex spatial data and have been successfully applied in similar environmental studies, they are well suited for AGB estimation in forest ecosystems. Accurate forest biomass prediction contributes to monitoring carbon stocks, assessing emissions reductions, and informing sustainable forest management strategies. Thus, cost-effective carbon inventory methods are needed for climate change policies.

MATERIALS AND METHODS

Study Area

The research was completed in wide area located between the latitudes of 38°23′00″ - 41°30′58″N and longitudes of 29°33′33″ - 30°03′37″ E on a transition zone. It continued from Marmara, Inner Aegean regions to Western Inner Anatolia and the Black Sea, of Türkiye (Figure 1). The common bedrocks in the study area include dacite, rhyolite, basalt, andesite, granite, volcanic tuff, agglomerate, breccia, quartzite, mica schist, calcareous, and serpentine [42]. The most common soil types are cambisols and luvisols, according to IUSS Working Group WRB [43]. Climatic data were derived from the nearest meteorological stations. Mean annual temperatures vary from 8.9 °C to 14.4 °C while annual precipitation ranges from 374 mm to 796 mm [44]. The climate type of the study area was classified

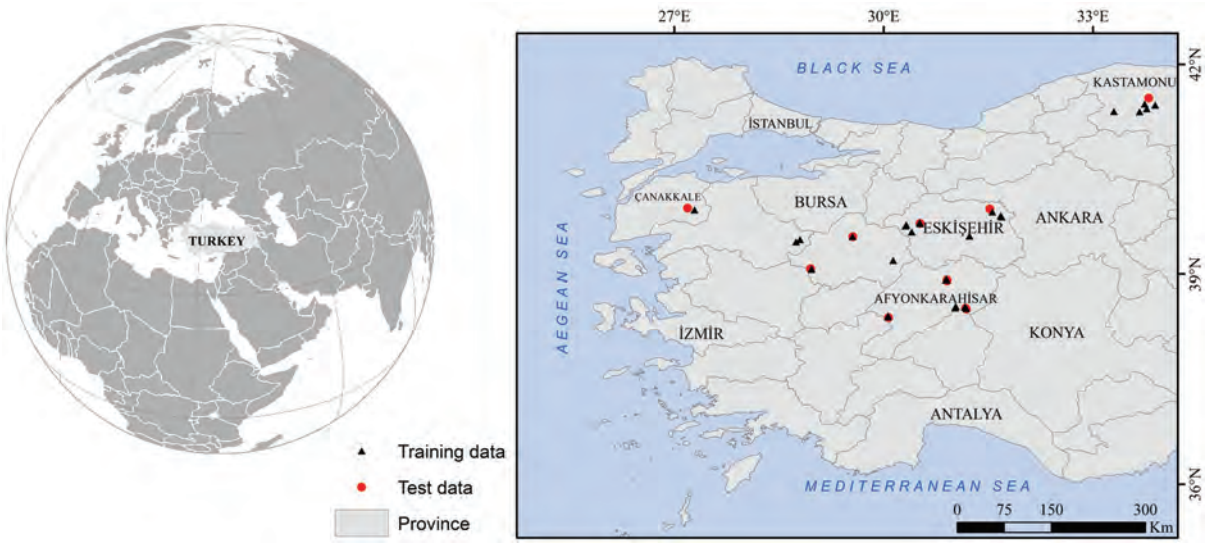


Figure 1. Location of the study area.

as semi-arid to humid using the Erinç method [45]. The elevation of the study sites ranged from 417 m to 1587 m.

Experimental Design and Sampling Procedure

Sample plots were chosen from a total of 44 areas differing in elevation, aspect, sloping degree, slope position and stand development stage [SDF=small diameter forest (dbh<8.0 cm), MDF=medium diameter forest (dbh=8.0-19.9 cm), LDF=large diameter forest (dbh=20.0-35.9 cm)]. Some characteristics of the stands in the research areas are given in Table 1 [46]. The fieldwork were conducted between 2010 and 2012.

Sample plots were taken in the form of square or rectangular (10×10, 10×20, or 20×20 m) and large enough to contain at least 15 individual trees. A healthy individual tree, with no crown and branch damages, and under pressure, was cut. The diameter and height of all individuals were measured in the sample plots. Tree height was measured by a tape measure with cm precision, after cutting down the tree, and the age was determined by counting the annual rings on the stump (Figure 2). After the branches of the cut tree had been trimmed, the trunk was divided into 2 m sections. Then, the fresh weight of the 2-meter-long trunk sections was measured with a scale. To convert the fresh weights of the trunk into dry weight, 5 cm thick discs were taken from the middle of each section to determine their moisture content. The needles were separated from the branches and weighed separately. In order to determine

Table 1. Stand parameters of the sample plots (Mean±SE)

Stand properties	Development stage		
	SDF	MDF	LDF
Number of sample plots	14	12	18
Mean diameter (dbh,cm)	4.9±0.8	16.5±0.9	25.4±0.9
Mean height (m)	2.38±0.25	8.88±0.59	14.15±0.69
Stand age (year)	10.8±1.1	37.0±2.4	45.1±1.8
Standing stock (m^3/ha)	6.988±2.912	173.202±21.643	303.572±32.800
Stocking density (tree/ha)	2510±267	1546±146	866±132
Basal area (m^2/ha)	6.43±1.75	33.15±3.07	41.51±4.21

SE: standard error, SDF: small-diameter forest (dbh < 8.0 cm), MDF: medium-diameter forest (dbh=8.0-19.9 cm), LDF: large-diameter forest (dbh=20.0-35.9 cm)



Figure 2. Fieldwork photos of the study area in Eskişehir Province.

oven-dry weights in the laboratory, sub-samples were taken from the stem (5 cm thick discs), branches (dry and live), and needles, and their fresh weights were determined in the field [46].

Above Ground Mass Calculation

Sub-samples taken from the field were oven-dried at 65 °C to a constant weight [33] and then weighed again to calculate the moisture correction factor for the dry weight of the tree biomass to calculate the amount of bark, the ratio of the disk weight without bark to that of with bark was multiplied by the trunk biomass. Then, the above-ground tree masses of the sample trees were calculated by adding the dry weight of needles, dead and live branches, bark-free trunk, and bark.

Data Analysis

Diameter at breast height (dbh), height (h), and dbh^2h index were used as independent variables to estimate the above-ground tree mass (kg/tree) of a single tree. As a result of regression analysis, the equation with the smallest standard error and the highest Coefficient of determination (R^2) was obtained with the compound function (Equation 1). Then, using this equation, the above-ground tree masses in the sample areas were calculated and these values were converted to hectares (t/ha).

$$B_{ABOVEGROUND} = axb^{dbh} \quad (1)$$

where B: tree mass (kg/tree), a and b equation coefficients, dbh: diameter at breast height.

Remote Sensing Data

In this study, the mosaic ALOS PALSAR data for the year 2009 is used for the analysis. It was the mission of the Japanese Aerospace Exploration Agency (JAXA). Its 25 m spatial resolution mosaic data is open to the public [47]. The data is distributed in two polarizations horizontal transmitted and horizontal received (HH) and horizontal transmitted vertical received (HV). The pre-processing steps and geometric and radiometric corrections of L-band data have been applied by JAXA [47]. In the case of geometric correction, SRTM3 data was used. The amplitude backscatter values were converted to gamma nought [48,49] using the equation below;

$$\gamma^{\circ}=10 \times \log_{10}(DN^2) + CF \quad (2)$$

Where γ° is the backscatter coefficient, DN and the CF are the digital number of amplitude data and the calibration factor which is -83 dB, respectively. Two arithmetic equations were also used to derive additional variables. These are the Normalized Difference Polarization Index ($\Upsilon_{HH} - \Upsilon_{HV}$) / ($\Upsilon_{HH} + \Upsilon_{HV}$) and Co-polarized Ratio (CPR) ($\Upsilon_{HV} / \Upsilon_{HH}$). In addition to these 4 data, 8 data sets were created and a total of 12 scenarios were evaluated (Table 2). An example of a visual interpretation of the SAR data is shown in Figure 3. The HH and HV values are represented in decibels (dB) and range between 10.3 dB and -36.6 dB. The location of the pine forest appears brighter in SAR data.

Convolutional Neural Network

A one-dimensional Convolutional Neural Network (1D-CNN) architecture was employed for Above-Ground Biomass (AGB) estimation. This architecture utilized a one-dimensional convolutional filter as the input layer and comprised a convolutional layer, a flattening layer, dense layers, and an output layer. For this study, the selected hyperparameters included 16 filters, the ReLU activation function, and 250 training epochs. A trial and error method was used to select these parameters. The Adam optimization algorithm was utilized to optimize the model parameters, as recommended in prior research [50]. RMSE was used as the loss function and the test/loss graph of the best scenario was given in Appendix-1. In the analysis randomly, 33 data were used for training the model and 11 data were used for the test.

Extreme Gradient Boosting

Extreme gradient boosting (XGBoost) is a highly efficient ensemble learning algorithm commonly applied to classification and regression tasks, particularly in structured data contexts. Known for its robustness when handling large datasets and complex models, XGBoost constructs a strong predictive model by iteratively combining weak learners and addressing the errors of preceding models at each step. XGBoost builds on the gradient boosting framework, by introducing several features to enhance computational efficiency, performance, and predictive accuracy [51]. In our study, the R programming language and the

Table 2. The scenarios and the variables used for the analysis

Scenarios	Variables	Scenarios	Variables
S1	Υ_{HH}	S7	Υ_{HH}, Υ_{CPR}
S2	Υ_{HV}	S8	Υ_{HV}, Υ_{NDPI}
S3	Υ_{NDPI}	S9	Υ_{HV}, Υ_{CPR}
S4	Υ_{CPR}	S10	Υ_{HH}, Υ_{NDPI}, Υ_{CPR}
S5	Υ_{HH}, Υ_{HV}	S11	Υ_{HV}, Υ_{NDPI}, Υ_{CPR}
S6	Υ_{HH}, Υ_{NDPI}	S12	Υ_{HH}, Υ_{HV}, Υ_{NDPI}, Υ_{CPR}

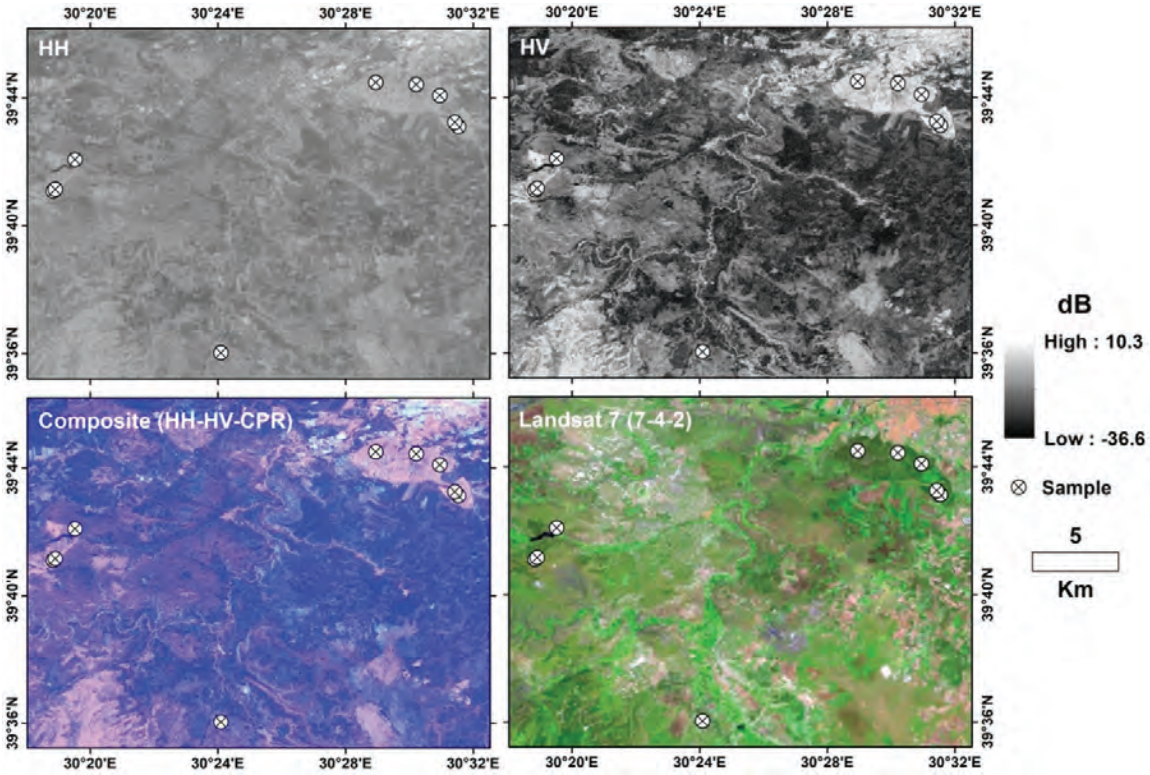


Figure 3. An example of a SAR image over Eskisehir is located in Figure 1. In the upper row, examples of ALOS HH and HV polarimetric data are given, in the lower row, RGB data created from HH-HV and CPR data and Landsat 7-4-2 bands are given. Landsat data is used only for visual interpretation to show the location of the forest.

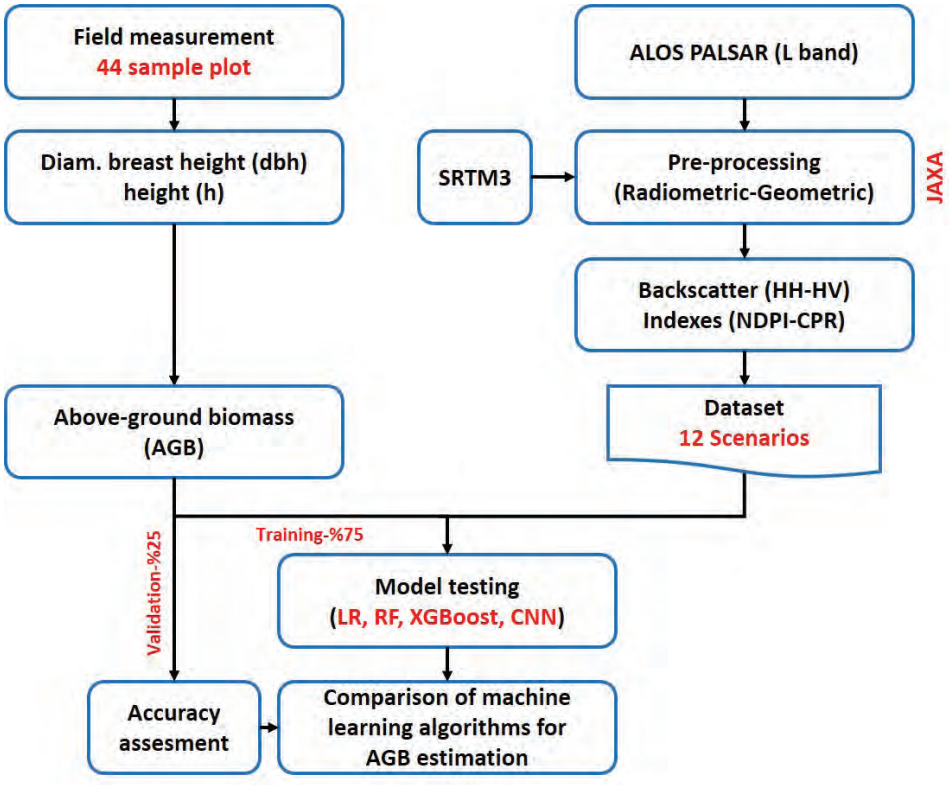


Figure 4. The graph shows the workflow used for AGB estimation.

XGBoost package were used [52]. The parameters were tuned during the model training phase. In order to make the best grid search, the values were chosen primarily based on the results of the previous studies [53].

Parameters, *nrounds* is "50, 100, 200, 250, 500", *max_depth* is "3, 5, 7", *eta* is "0.01, 0.02, 0.05", *gamma* is "0.1, 0.3, 0.5", *min_child_weight* is "1,2,3,4,5", *subsample* is "0.5, 0.6, 0.7", and *colsample_bytree* is chosen "1, 3, 5". According to these values, the best results were automatically selected in model training and the model was trained. Sample results are included in Appendix-2.

Random Forest

Random Forest is an ensemble learning method used for machine learning and statistical analysis. Random Forest improves prediction accuracy by combining multiple decision trees and is a powerful method for dealing with complex datasets. One of the advantages of Random Forest is that it is resistant to noise and overfitting in the dataset [54]. In our study, the R programming language and the Random Forest package were used [55]. Parameters were tuned during the model training phase. In order to make the best Grid search, the values were chosen primarily according to the results of [40]. Parameters *ntree* is increased from 10 to 300 in step 10 and *mtry* is increased from 1 to 10 in step 2 (Appendix-3). The workflow of our methodology for estimating AGB is given in Figure 4.

RESULTS AND DISCUSSION

Findings of the Tree Mass

The best independent variable predicting the above-ground tree mass was diameter at breast height, and the best model was obtained with the compound function (Table 3). Above-ground tree mass was found to be the lowest (10.525 t/ha) in SDF stands and the highest (166.374 t/ha) in LDF stands (Table 4).

Biomass Estimation With Machine Learning

In the analysis for each scenario, the relationship between AGB data estimated from the fieldwork and ALOS PALSAR backscatter data was evaluated. The results showed that the overall r values ranged between 0.52 and 0.72 (Figure 5). The highest correlation was obtained with HH polarized data (r=0.720) and HV polarization followed it with an r=0.632. The relationship between AGB and the indices derived from backscatter values were close to each other. However, CPR had a positive correlation (r=0.553), while NDPI gave a negative (r=-0.517). The relationship between HH and HV also showed a high value (r=0.879). Considering the relationship between the backscatter values of two polarizations and the indices, HH polarized data provided a higher value (r=-0.654 and r=0.625) than HV polarized data (r=-0.230 and r=0.236).

The estimation analysis was composed of 33 training and 11 testing data. In addition to the CNN method, LR, RF, and XGBoost were also applied for comparison (Figure 6). In general, models in S7, S8, and S9 showed successful results; however, models gave unsuccessful results in S2, S3, and S4 (Figure 6). If RMSE and R^2 are compared in detail, CNN provided higher R^2 and lower RMSE values compared to the LR, RF, and XGBoost methods. All methods showed good results in different scenarios. The CNN showed the best performance in S9 (RMSE=59.73 t/ha, R^2=0.45). LR showed the best performance after CNN in S7 (RMSE=61.57 t/ha, R^2=0.41). While the RF method gave the same R^2 results as LR, it showed slightly worse results (RMSE=65.65 t/ha, R^2=0.41). Although the XGBoost method gave better RMSE than RF, it showed the worst result in R^2 (RMSE=64.28 t/ha, R^2=0.36) (Table 5).

Table 3. Single tree regression model for above-ground biomass

Equation	R^2	Standard error	F ratio	*p*	Constants	
					a	b
$B_{aboveground} = a \times b^{dbh}$	0.952	0.30	873.64	0.000	4.9953***	1.1560***

B= biomass (kg/tree), *dbh*= diameter at breast height (cm), *h*= tree height (m), R^2= coefficient of determination, *p*: significance, ***: $p<0.001$

Table 4. Above-ground biomass according to development stage

Biomass	Development stage		
	SDF	MDF	LDF
Above-ground (t/ha)	10.525±2.657	107.093±11.289	166.374±17.353

SE: Standard error; SDF: Small-diameter forest (dbh < 8.0 cm); MDF: Medium-diameter forest (dbh=8.0-19.9 cm); LDF: Large-diameter forest (dbh=20.0-35.9 cm).

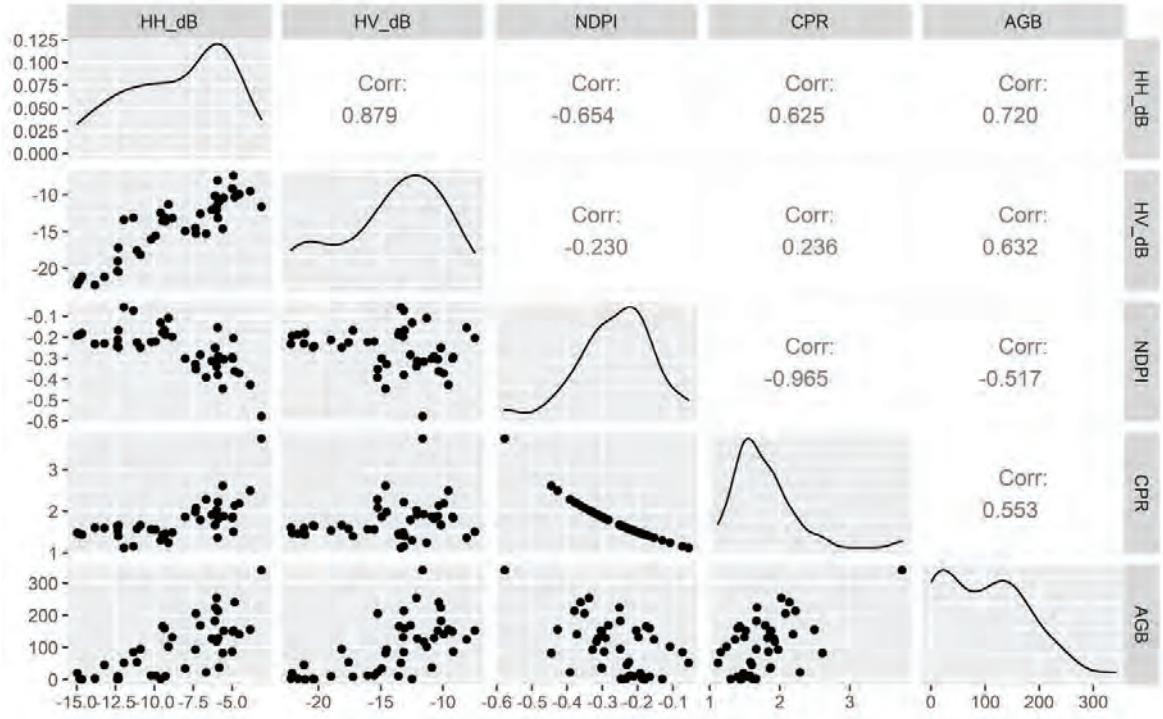


Figure 5. The correlation coefficient and scatter plot between AGB and variables derived from SAR data.

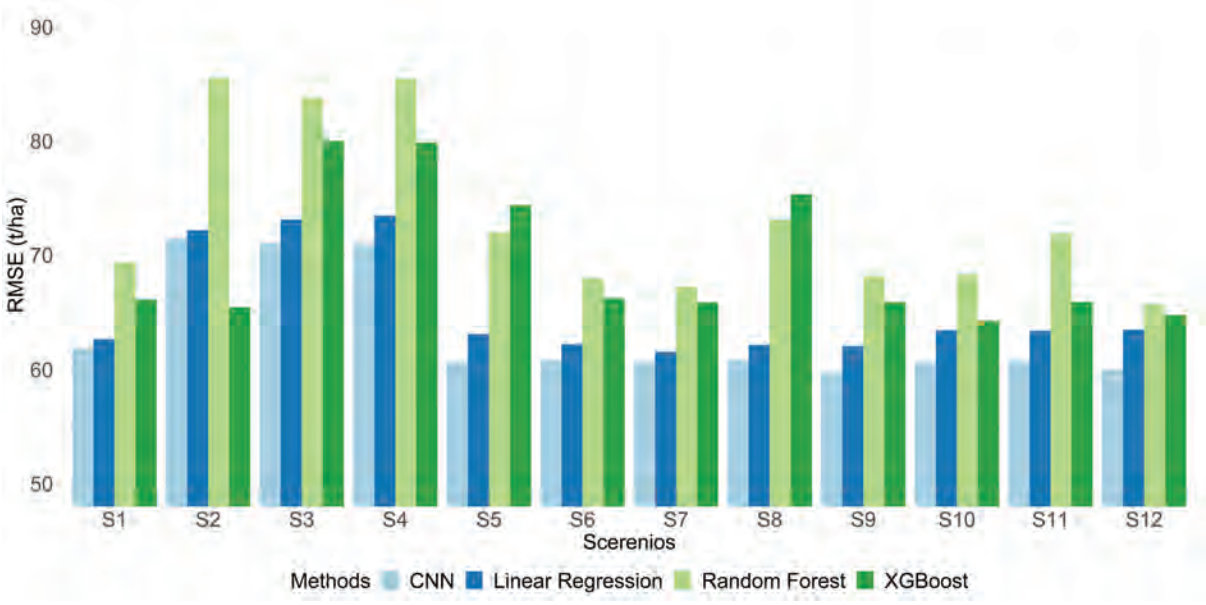


Figure 6. The comparison of CNN, LR, RF, and XGBoost with regard to RMSE.

The study was conducted using four models: CNN, RF, XGBoost, and LR. Considering the previous studies in Türkiye, estimation studies for black pine were mostly carried out with optical data [35, 36, 55]. Günlü et al. [56] used Landsat with vegetation indices and applied the Multiple Linear Regression (MLR) method. The results revealed that vegetation indices showed R^2=0.61 and RMSE=8.50 t/ha AGB using 130 samples. Günlü et al. [35] used 86 samples with high-resolution Worldview-2 bands and the texture information for the AGB estimation. The results of the

Table 5. The R^2 and RMSE values of the test data. While green color shows the best results, red values show the lowest values

Scenarios	Variables	Linear Regression		CNN		XGBoost		Random Forest	
		R^2	RMSE	R^2	RMSE	R^2	RMSE	R^2	RMSE
S1	Υ_{HH}	0.38	62.66	0.34	61.92	0.30	66.09	0.21	69.33
S2	Υ_{HV}	**0.00**	72.18	0.18	71.44	0.31	65.41	0.06	**85.47**
S3	Υ_{NDPI}	0.22	73.11	0.19	71.01	0.09	79.98	0.09	83.79
S4	Υ_{CPR}	0.24	73.45	0.24	70.91	0.11	79.87	0.09	85.45
S5	Υ_{HH}, Υ_{HV}	0.36	63.12	0.42	60.65	0.17	74.37	0.19	72.00
S6	Υ_{HH}, Υ_{NDPI}	0.39	62.23	0.42	60.80	0.32	66.19	0.32	67.92
S7	Υ_{HH}, Υ_{CPR}	0.41	61.57	0.41	60.71	0.32	65.82	0.33	67.21
S8	Υ_{HV}, Υ_{NDPI}	0.39	62.17	0.41	60.82	0.11	75.34	0.14	73.07
S9	Υ_{HV}, Υ_{CPR}	0.41	62.06	**0.45**	**59.73**	0.33	65.86	0.29	68.12
S10	Υ_{HH}, Υ_{NDPI}, Υ_{CPR}	0.38	63.44	0.42	60.61	0.36	64.28	0.28	68.31
S11	Υ_{HV}, Υ_{NDPI}, Υ_{CPR}	0.39	63.41	0.43	60.72	0.35	65.88	0.16	71.90
S12	Υ_{HH}, Υ_{HV}, Υ_{NDPI}, Υ_{CPR}	0.39	63.49	0.43	59.99	0.34	64.77	0.41	65.65

ANN method provided RMSE ranging from 69.12 to 85.35 t/ha (R^2=0.34-0.57) whereas the RMSE of MLR was 85.15 t/ha (R^2=0.34).

Bulut et al. [37] used single-date Sentinel-2 data for the AGB estimation on coniferous, broadleaf, and mixed forest types with 2185 samples in total. They used MLR and regression kriging (RK) methods on reflectance and vegetation indices separately. Considering the coniferous forest, the results of MLR provided better results (RMSE = 48.90 t/ha and 47.15 t/ha) than the results of RK (RMSE = 51.28 t/ha and 49.73 t/ha). The vegetation indices provided better results than reflectance data. Bulut [39] used Landsat-8 with machine learning approaches for the AGB prediction over Calabrian pine in Türkiye. The study showed that the SVM approach provided better results over MLR and vegetation indices contributing to achieving successful prediction.

Previous studies predominantly employed the MLR method for AGB estimation in pine forests. In contrast, this study's results show that the models (LR, CNN, XGBoost, and RF) perform differently across various scenarios with single and multiple variables. LR and CNN models showed moderate performance in scenarios (S1–S4), where single variables were used. The R^2 values ranging from 0.00 to 0.38 and RMSE values between 61.92 and 73.45. XGBoost performed better in scenarios S1 and S2, but its results were not consistent across all cases. On the other hand, RF had the weakest overall performance, with a relatively low R^2 and high RMSE. Including additional variables generally improved model performance in the bivariate scenarios (S5–S9). Scenario S9 produced the best performance for the CNN model, achieving an R^2 value of 0.45 and the lowest RMSE (59.73) than the other models. The LR model also showed relatively strong and stable results, although it consistently remained slightly below CNN in terms of accuracy. XGBoost demonstrated some improvement across several cases; however, overall it still lagged behind both CNN and LR in predictive performance. RF indicated partial improvement, particularly in scenarios S7 and S9. However, its overall performance remained below that of the alternative models. When all three variables were used together (S10–S11), CNN continued to outperform the alternatives, achieving R^2 values of 0.42-0.43 and consistently producing the lowest RMSE across all tested methods. LR maintained stable and reliable performance in these scenarios, although it still trailed slightly behind CNN in predictive accuracy. XGBoost benefited from the extra variable and reaching an R^2 of 0.36 under S10. RF improved modestly, yet its estimates continued to lag behind those of CNN and XGBoost. In the four-variable configuration (S12), CNN continued to provide the best results (R^2= 0.43; RMSE= 59.99). RF achieved its strongest performance in this scenario (R^2= 0.41; RMSE= 65.65), whereas LR and XGBoost performed at comparable levels, recording R^2 values of 0.39 and 0.34 respectively, yet neither reached the accuracy of CNN. Adding more predictors generally improved model performance, particularly for XGBoost and RF; but neither matched CNN's robustness, especially in more complex situations (Table 5).

Huang et al. [57] assessed six modeling strategies LR, RF, SVR, XGBoost, LASSO regression, and an ensemble approach for blood pressure prediction during hemodialysis. Of those methods shared with the current study, XGBoost recorded the lowest test accuracy (RMSE= 17.65, R^2= 0.41), while LR (RMSE= 16.39, R^2= 0.48) and RF (RMSE= 16.24, R^2= 0.49) performed at roughly equivalent levels. Smith et al. [58] compared MLR with RF and found that MLR performed better, which is similar to our study. Dong et al. [19] studied estimation of bamboo AGB

in in southern China. They used different machine learning approaches (RF, SVR, ANNs, and CNNs) with optical WorldView-2 imagery. They reported that, RF, SVR, and CNN-based methods all outperformed conventional ANNs with respect to prediction accuracy. Schäfer et al. [59] compared CNN and RF models using point cloud data from forested areas in Canada, Poland, and the Czech Republic, and found that CNN architectures produced superior results when sufficiently large training datasets were available. The findings of this study further strengthen the suitability of CNN-based architecture for AGB modelling.

The Υ_{HV} polarization data exhibited higher predictive capability than Υ_{HH} across the tested scenarios. This observation is consistent with previous studies based on ALOS datasets [60–63]. However, some studies also indicated the advantage of HH polarization over HV [13, 64, 65]. When two variables that were derived from backscatter values were compared, CPR (S4) provided a slightly higher contribution than NDPI (S3). The advantage of CPR was also evident when added to the HH and HV polarized images individually. The combination of Υ_{HV} and Υ_{CPR} (S9) achieved the best result with RMSE= 59.726 t/ha and R^2= 0.448. Li et al. [40] used Sentinel-1A SAR and with Landsat-8 optical data for AGB estimation. They compared LR, RF, and XGBoost methods. The results showed that Sentinel-1A-only results were relatively weak, with R^2 values of 0.03, 0.28, and 0.38 for LR, RF, and XGBoost, respectively. Considerin their results, the L-band ALOS image derived variables used in the current study provided higher accuracy, with R^2=0.41 for both LR and RF, and R^2=0.36 for XGBoost. CNN further outperformed all three, reaching an R^2 of 0.45. Among the evaluated approaches, the CNN model achieved the highest predictive performance, with an R^2 of 0.45. Previous studies on pine forests showed that there were different parameters (forest type, remote sensing data, sample size, method, etc.) playing a role in the AGB predictions. Including spectral vegetation indices derived from optical images has the potential to improve AGB estimation [39, 56]. Meanwhile, texture information of an optical image was reported as another positive feature that played a leading role in the improvement of forest AGB estimation studies by Günlü et al. [35]. Land surface temperature and soil moisture derived from Landsat data have a significant contribution to achieving lower RMSE of AGB prediction [66].

One of the limitations of this study is the small number of sampling sites. Li et al. [67] explored various modeling approaches to improve the accuracy of AGB estimations. Their study investigated the contribution of integrating remote sensing datasets with modeling approaches under conditions of limited data availability. Recent investigations have similarly noted that limited field measurements call for more complicated modeling strategies to maintain acceptable AGB estimation accuracy. These considerations further highlight the value of adopting advanced analytical frameworks when working with restricted ground-truth data. A substantial body of research has explored AGB estimation through varied combinations of field measurements and remote-sensing inputs. Among studies with a similarly constrained number of sample plots, Qazi et al. [68] worked with 51 plots across Nepal using ALOS-1 and GeoEye-1 imagery for biomass mapping. They found that, for AGB estimation using LR models, the validation R^2 was 0.44 for SAR imagery alone, whereas the results were significantly better with optical imagery (R^2 = 0.76). Similarly, Tavasoli and Arefi [69] used thiry nine circular sampling sites to estimate AGB. They applied the Genetic-Random Forest (GA-RF) machine learning algorithm with ALOS-1, Sentinel-1, and Sentinel-2 satellite imagery. Their combined ALOS and Sentinel-1 dataset achieved an R^2 of 0.72, whereas Sentinel-2 data used alone resulted in an R^2 of 0.62. Ji et al. [70] addressed AGB estimation across 61 sample sites by evaluating 15 different multi-band SAR configurations spanning X-, C-, L-, and P-band frequencies, and comparing MLSR, RF, and deep learning approaches.The top-performing configuration was an MLSR model that merged L- and P-band observations, reaching R^2=0.67 and RMSE=14.51 Mg ha^{-1}.

Overfitting risk and other difficulties tied to small training sets, along with mitigation strategies such as adding supplementary biophysical predictors, are recurring themes in the literature [71]. Li et al. [72] demonstrated that environmental variables, particularly soil properties, play an important role in forest biomass modeling. Their results indicated that soil and vegetation types jointly contribute significantly to AGB prediction accuracy, suggesting that incorporating soil-related information can substantially improve remote sensing–based biomass estimates. Kariofillia et al. [73] similarly studied carbon stock estimation in Mediterranean agricultural systems. They found that combining remote sensing layers with soil data substantially raised model performance, indirectly corroborating the added value of soil inputs for AGB prediction. The findings indirectly support the contribution of soil data to AGB prediction. In exploring the applicability of models for small datasets, a model developed by Zhou et al. [74] introduced as suitable for such data. This model has shown superior performance compared to others, especially in complex classification tasks and when working with a limited number of examples. Another limitation of this study is the lack of an extensive archive of remote sensing data, particularly optical data, to combine with SAR images. Additionally, there was no concurrent remote sensing data available at the time of fieldwork. However, as AGB generally exhibits limited temporal variability, the most recent and publicly accessible mosaic ALOS PALSAR data was utilized. Another limitation is the relatively small amount of ground-based AGB data. Increasing the volume of ground data could improve the accuracy of AGB estimation for pine forests, especially with the deployment of new C-band and L-band satellite missions. Textural data can be applied as an additional variable that contributed to the AGB estimation in both optical [36] and SAR images [65, 75]. A

combination of multi-source remote sensing data can be also useful. Yavaşlı [76] showed the ability of combined Landsat and ICESat/GLAS laser altimeter to achieve better AGB estimation. Another factor for limitation could be the characteristics of the topography. As the samples were collected from different locations, the slope and aspect information may be added to improve the predictions. To address the negative impacts of topography on SAR imagery, various techniques and auxiliary data can be utilized during the image processing and evaluation stages [77, 78]. Radiometric terrain correction reduces terrain-induced backscatter variations by normalizing pixel values, while speckle filtering and multilook processing minimize noise and improve image quality. Geometric correction using high-resolution DEMs further reduces spatial distortions. Together, these preprocessing steps enhance the reliability of SAR data for biomass estimation and related analyses.

CONCLUSION

Black pine is among the dominant forest tree species in Türkiye and plays an important role in carbon sequestration and ecosystem resilience under changing climatic conditions. In this study, a 1D-CNN-based framework was developed for AGB estimation and compared with a conventional LR model. To evaluate the contribution of different input variables, twelve scenarios were generated using dual-polarized ALOS-PALSAR data. The results indicate that the CNN approach provides strong predictive capability for AGB estimation, while indices derived from dual-polarimetric SAR data considerably improve model performance. Moreover, the use of full-polarimetric SAR data may yield more informative feature sets, potentially increasing estimation accuracy and reducing RMSE.

Although the relatively limited sample size represents a constraint for both machine learning and deep learning applications, the CNN models demonstrated superior performance compared with conventional approaches. This performance may be related to the ability of CNN architectures to model complex, non-linear relationships, even when the number of input features is limited. Integrating these modeling approaches into national forest inventory and monitoring systems could improve biomass estimates and provide more reliable information on forest carbon stocks. Such information may support conservation planning, carbon accounting, and the development of sustainable forest management strategies in Türkiye and other forested regions. The use of data-driven methods in policy and management processes could also strengthen climate change mitigation efforts by improving the monitoring of biomass and carbon dynamics. Future studies could evaluate the effects of including additional explanatory variables and larger datasets, and integrating field-based measurements with remotely sensed and model-derived data to improve analytical robustness and model performance. Moreover, further studies may benefit from the combined use of multi-temporal and multi-frequency SAR datasets, along with multispectral optical imagery, to enhance biomass estimation accuracy and spatiotemporal analysis capabilities. A spatial AGB change detection analysis could be considered with further fieldwork studies. Archived ALOS-1 images and the forest inventory data provided beneficial results in understanding the AGB distribution for the Pinus nigra forest. Next-generation L-band missions (ALOS-4, NISAR, ROSE-L, and Tandem-L) can contribute to a spatio-temporal analysis to obtain biomass and carbon dynamics.

AUTHORSHIP CONTRIBUTIONS

Authors equally contributed to this work.

DATA AVAILABILITY STATEMENT

The ALOS-1 PALSAR mosaic is openly available on the website https://www.eorc.jaxa.jp/ALOS/en/dataset/fnf_e.htm

CONFLICT OF INTEREST

The author declared no potential conflicts of interest with respect to the research, authorship, and/or publication of this article.

FUNDING

This study was conducted as part of the project titled "Determination of carbon stocks in black pine (*Pinus nigra* Arn. subsp. *pallasiana*) plantations (ESK-10(6303)/2011-2014)" that was funded by the Turkish General Directorate of Forestry.

ETHICS

There are no ethical issues with the publication of this manuscript.

STATEMENT ON THE USE OF ARTIFICIAL INTELLIGENCE

Artificial intelligence was not used in the preparation of the article.

REFERENCES

[1] Lackner M, Sajjadi B, Chen Y. Introduction to climate change mitigation and adaptation. In: Lackner M, Sajjadi B, Chen WY, editors. Handbook of climate change mitigation and adaptation. 3rd ed. Switzerland: Springer; 2022. p. 3-21. [CrossRef]

[2] Leley NC, Langat DK, Kisiwa AK, Maina GM, Muga MO. Total carbon stock and potential carbon sequestration economic value of Mukogodo forest-landscape ecosystem in drylands of Northern Kenya. Open J For 2022;12:19-40. [CrossRef]

[3] Lorenz K, Lal R. Carbon sequestration in forest ecosystems. Springer; 2010. 277 p. [CrossRef]
[4] Shahabedini S, Ghahramany L, Pulido F, et al. Estimating leaf biomass of pollarded Lebanon oak in open silvopastoral systems using allometric equations. Trees (Berl) 2018;32:99-108. [CrossRef]
[5] Ameztegui A, Rodrigues M, Granda V. Uncertainty of biomass stocks in Spanish forests: A comprehensive comparison of allometric equations. Eur J For Res 2022;141:395-407. [CrossRef]
[6] Arseniou G, MacFarlane DW, Calders K, et al. Accuracy differences in aboveground woody biomass estimation with terrestrial laser scanning for trees in urban and rural forests and different leaf conditions. Trees (Berl) 2023;37:761-779. [CrossRef]
[7] Fleming AL, Wang G, McRoberts RE. Comparison of methods toward multi-scale forest carbon mapping and spatial uncertainty analysis: Combining national forest inventory plot data and Landsat TM images. Eur J For Res 2015;134:125-137. [CrossRef]
[8] Lu D, Chen Q, Wang G, Liu L, Li G, Moran E. A survey of remote sensing-based aboveground biomass estimation methods in forest ecosystems. Int J Digit Earth 2016;9:63-105. [CrossRef]
[9] Racine EB, Coops NC, Bégin J, Myllymäki M. Tree species, crown cover, and age as determinants of the vertical distribution of airborne LiDAR returns. Trees (Berl) 2021;35:1845-1861. [CrossRef]
[10] Coops NC, Tompalski P, Goodbody TRH, Achim A, Mulverhill C. Framework for near real-time forest inventory using multi-source remote sensing data. Forestry (Oxf) 2022. [CrossRef]
[11] Foody GM, Boyd DS, Cutler MEJ. Predictive relations of tropical forest biomass from Landsat TM data and their transferability between regions. Remote Sens Environ 2003;85:463-474. [CrossRef]
[12] Ghasemi N, Sahebi MH, Mohammadzadeh A. A review on biomass estimation methods using synthetic aperture radar data. Int J Geomat Geosci 2011;1:776-788.
[13] Ningthoujam RK, Joshi PK, Roy PS. Retrieval of forest biomass for tropical deciduous mixed forest using ALOS PALSAR mosaic imagery and field plot data. Int J Appl Earth Obs Geoinf 2018;69:206-216. [CrossRef]
[14] Englhart S, Keuck V, Siegert F. Aboveground biomass retrieval in tropical forests: The potential of combined X- and L-band SAR data use. Remote Sens Environ 2011;115:1260-1271. [CrossRef]
[15] George-Chacón SP, Milodowski DT, Dupuy JM, Mas JF, Williams M, Castillo-Santiago MA, et al. Using satellite estimates of aboveground biomass to assess carbon stocks in a mixed-management, semi-deciduous tropical forest in the Yucatan Peninsula. Geocarto Int 2021. [CrossRef]
[16] Li C, Li Y, Li M. Improving forest aboveground biomass (AGB) estimation by incorporating crown density and using Landsat 8 OLI images of a subtropical forest in western Hunan in Central China. Forests (Basel) 2019;10:104. [CrossRef]
[17] Shah SAA, Manzoor MA, Bais A. Canopy height estimation at Landsat resolution using convolutional neural networks. Mach Learn Knowl Extr 2020;2:23-36. [CrossRef]
[18] Zhang F, Tian X, Zhang H, Jiang M. Estimation of aboveground carbon density of forests using deep learning and multisource remote sensing. Remote Sens (Basel) 2022;14:3022. [CrossRef]
[19] Dong L, Du H, Han N, Li X, Zhu D, Ma F, et al. Application of convolutional neural network on Lei bamboo above-ground-biomass (AGB) estimation using WorldView-2. Remote Sens (Basel) 2020;12:958. [CrossRef]
[20] Cao R, Zhu J, Tu W, Li Q, Cao J, Liu B, et al. Integrating aerial and street view images for urban land use classification. Remote Sens (Basel) 2018;10:1553. [CrossRef]
[21] Ferreira MP, Lotte RG, D'Elia FV, Stamatopoulos C, Kim DH, Benjamin AR. Accurate mapping of Brazil nut trees (Bertholletia excelsa) in Amazonian forests using WorldView-3 satellite images and convolutional neural networks. Ecol Inform 2021;63:101302. [CrossRef]
[22] Bai T, Wang L, Yin D, Sun K, Chen Y, Li W, et al. Deep learning for change detection in remote sensing: A review. Geo-spat Inf Sci 2022. [CrossRef]
[23] Narin OG, Vatandaşlar C, Abdikan S. Estimating stand top height using freely distributed ICESat-2 LiDAR data: A case study from multi-species forests in Artvin. Forestist 2022;72:294-298. [CrossRef]
[24] Vidaković M. Conifers morphology and variation. Zagreb: Grafički zavod Hrvatske; 1991.
[25] Tutin TG, Akeroyd JR. Ranunculus L. In: Tutin TG, Burges NA, Chater AO, Edmondson JR, . Heywood VH, Moore DM, et al., editors. Flora Europaea. 2nd ed. Cambridge: Cambridge University Press; 1993. Vol. 1, p. 269-285.
[26] Güner A, Aslan S, Ekim T, Vural M, Babaç MT. Türkiye bitkileri listesi (damarlı bitkiler). İstanbul: Nezahat Gökyiğit Botanik Bahçesi ve Flora Araştırmaları Derneği Yayını; 2012. [Turkish]
[27] Davis PH. Flora of Turkey and the East Aegean Islands. Vol. 1. Edinburgh: Edinburgh University Press; 1965.
[28] Anşin R, Özkan ZC. Tohumlu bitkiler. Trabzon: Karadeniz Teknik Üniversitesi Orman Fakültesi Yayınları; 1993. Yayın No: 167/19.
[29] Kandemir A, Mataracı T. Pinus L. In: Güner A, Kandemir A, Menemen Y, Yıldırım H, Aslan S, Ekşi G, et al., editors. Resimli Türkiye Florası. Vol. 2. İstanbul: ANG Vakfı Nezahat Gökyiğit Botanik Bahçesi Yayınları; 2018. p. 324-354.

[30] GDF. Türkiye orman varlığı 2020. Ankara: T.C. Tarım ve Orman Bakanlığı, Orman Genel Müdürlüğü, Orman İdaresi ve Planlama Dairesi Başkanlığı; 2021. 56 p. [Turkish]
[31] Saatçioğlu F. Silvikültür I: Silvikültürün biyolojik esasları ve prensipleri. İstanbul: İstanbul Üniversitesi Orman Fakültesi Yayınları; 1969. 323 p. [Turkish]
[32] Durkaya A, Durkaya B, Cakil E. Predicting the aboveground biomass of Crimean pine (Pinus nigra) stands in Turkey. J Environ Biol 2010;31:115-118.
[33] Güner ST, Çömez A. Biomass equations and changes in carbon stock in afforested black pine (Pinus nigra Arnold. subsp. pallasiana (Lamb.) Holmboe) stands in Turkey. Fresenius Environ Bull 2017;26:2368-2379.
[34] Balenović I, Jazbec A, Marjanović H, Paladinić E, Vuletić D. Modeling tree characteristics of individual black pine (Pinus nigra Arn.) trees for use in remote sensing-based inventory. Forests (Basel) 2015;6:492-509. [CrossRef]
[35] Günlü A, Ercanlı I, Şenyurt M, Keleş S. Estimation of some stand parameters from textural features from WorldView-2 satellite image using the artificial neural network and multiple regression methods: A case study from Turkey. Geocarto Int 2021;36:918-935. [CrossRef]
[36] Turgut R, Günlü A. Estimating aboveground biomass using Landsat 8 OLI satellite image in pure Crimean pine (Pinus nigra J.F. Arnold subsp. pallasiana (Lamb.) Holmboe) stands: A case from Turkey. Geocarto Int 2022:1-15.
[37] Bulut S, Sivrikaya F, Günlü A. Evaluating statistical and combine method to predict stand above-ground biomass using remotely sensed data. Arab J Geosci 2022;15:838. [CrossRef]
[38] Vatandaşlar C, Abdikan S. Carbon stock estimation by dual-polarized synthetic aperture radar (SAR) and forest inventory data in a Mediterranean forest landscape. J For Res (Harbin) 2022;33:827-838. [CrossRef]
[39] Bulut S. Machine learning prediction of aboveground biomass in pure Calabrian pine (Pinus brutia Ten.) stands of the Mediterranean region, Türkiye. Ecol Inform 2023;74:10195. [CrossRef]
[40] Li Y, Li M, Li C, Liu Z. Forest aboveground biomass estimation using Landsat 8 and Sentinel-1A data with machine learning algorithms. Sci Rep 2020;10:9952. [CrossRef]
[41] Galdaki G, Zianis D, Gitas I, Radoglou K, Karathanassi V, Tsakiri-Strati M, et al. Vegetation biomass estimation with remote sensing: Focus on forest and other wooded land over the Mediterranean ecosystem. Int J Remote Sens 2017;38:1940-1966. [CrossRef]
[42] GDMRE. 1:500,000 scale geological inventory map series of Turkey. 2022 [cited 2022 Jan 17].
[43] IUSS Working Group WRB. World reference base for soil resources 2014, update 2015: International soil classification system for naming soils and creating legends for soil maps. World Soil Resources Reports No. 106. Rome: FAO; 2015. 192 p.
[44] GDM. Meteorological data. 2022. Available AT: https://mgm.gov.tr/ Accessed on Jan 17, 2022.
[45] Erinç S. Yağış müessiriyeti üzerine bir deneme ve yeni bir indis. İstanbul: Istanbul University Institute of Geography Press; 1965. [Turkish]
[46] Güner ŞT, Çömez A. Karaçam (Pinus nigra Arn. subsp. pallasiana) ağaçlandırma alanlarında karbon stoklarının belirlenmesi. Eskişehir: Orman Genel Müdürlüğü, Orman Toprak ve Ekoloji Araştırmaları Enstitüsü Müdürlüğü; 2014. Proje Sonuç Raporu: ESK-10(6303). 46 p. [Turkish]
[47] Shimada M, Itoh T, Motohka T, Watanabe M, Shiraishi T, Thapa R, et al. New global forest/non-forest maps from ALOS PALSAR data (2007-2010). Remote Sens Environ 2014;155. [CrossRef]
[48] Rodríguez-Veiga P, Quegan S, Carreiras J, Persson HJ, Fransson JE, Hoscilo A, et al. Forest biomass retrieval approaches from earth observation in different biomes. Int J Appl Earth Obs Geoinf 2019;77:53-68. [CrossRef]
[49] Vafaei S, Soosani J, Adeli K, Fadaei H, Naghavi H, Pham TD, et al. Improving accuracy estimation of forest aboveground biomass based on incorporation of ALOS-2 PALSAR-2 and Sentinel-2A imagery and machine learning: A case study of the Hyrcanian forest area (Iran). Remote Sens (Basel) 2018;10:172. [CrossRef]
[50] Yıldız S, Amasyalı MF. Iterative ensemble pseudo-labeling for convolutional neural networks. Sigma J Eng Nat Sci 2024;42:862-874. [CrossRef]
[51] Chen T, Guestrin C. XGBoost: A scalable tree boosting system. In: Proceedings of the 22nd ACM SIGKDD International Conference on Knowledge Discovery and Data Mining. 2016. p. 785-794. [CrossRef]
[52] Chen T, He T, Benesty M, Khotilovich V, Tang Y. xgboost: Extreme gradient boosting . 2018. Available at: https://cran.r-project.org/package=xgboost Accessed on Sep 14, 2026.
[53] Carmona P, Climent F, Momparler A. Predicting failure in the US banking sector: An extreme gradient boosting approach. Int Rev Econ Finance 2019;61:304-323. [CrossRef]
[54] Breiman L. Random forests. Mach Learn 2001;45:5-32. [CrossRef]
[55] Liaw A, Wiener M. randomForest: Breiman and Cutler's random forests for classification and regression. 2018. Available from: https://cran.r-project.org/package=randomForest Accessed on Sep 14, 2026.
[56] Günlü A, Ercanlı I, Başkent EZ, Çakır G. Estimating aboveground biomass using Landsat TM imagery: A case study of Anatolian Crimean pine forests in Turkey. Ann For Res 2014;57:289-298. [CrossRef]

[57] Huang JC, Tsai YC, Wu PY, Lien YH, Chien CY, Kuo CF, et al. Predictive modeling of blood pressure during hemodialysis: A comparison of linear model, random forest, support vector regression, XGBoost, LASSO regression and ensemble method. Comput Methods Programs Biomed 2020;195:105536. [CrossRef]

[58] Smith PF, Ganesh S, Liu P. A comparison of random forest regression and multiple linear regression for prediction in neuroscience. J Neurosci Methods 2013;220:85-91. [CrossRef]

[59] Schäfer J, Winiwarter L, Weiser H, Höfle B, Schmidtlein S, Novotný J, et al. CNN-based transfer learning for forest aboveground biomass prediction from ALS point cloud tomography. Eur J Remote Sens 2024;57. [CrossRef]

[60] Cartus O, Santoro M, Kellndorfer J. Mapping forest aboveground biomass in the Northeastern United States with ALOS PALSAR dual-polarization L-band. Remote Sens Environ 2012;124:466-478. [CrossRef]

[61] Basuki TM, Skidmore AK, Hussin YA, Van Duren I. Estimating tropical forest biomass more accurately by integrating ALOS PALSAR and Landsat-7 ETM+ data. Int J Remote Sens 2013;34:4871-4888. [CrossRef]

[62] Robinson C, Saatchi S, Neumann M, Gillespie T. Impacts of spatial variability on aboveground biomass estimation from L-band radar in a temperate forest. Remote Sens (Basel) 2013;5:1001-1023. [CrossRef]

[63] Fararoda R, Suraj Reddy R, Rajashekar G, Kiran Chand TR, Jha CS, Dadhwal VK. Improving forest above ground biomass estimates over Indian forests using multi-source data sets with machine learning algorithm. Ecol Inform 2021;65:101392. [CrossRef]

[64] Carreiras JMB, Melo JB, Vasconcelos MJ. Estimating the above-ground biomass in Miombo savanna woodlands (Mozambique, East Africa) using L-band synthetic aperture radar data. Remote Sens (Basel) 2013;5:1524-1548. [CrossRef]

[65] Günlü A, Ercanlı I. Artificial neural network models by ALOS PALSAR data for aboveground stand carbon predictions of pure beech stands: A case study from northern of Turkey. Geocarto Int 2020;35:17-28. [CrossRef]

[66] Jiang F, Kutia M, Ma K, Chen S, Long J, Sun H. Estimating the aboveground biomass of coniferous forest in Northeast China using spectral variables, land surface temperature and soil moisture. Sci Total Environ 2021;785:147335. [CrossRef]

[67] Li C, Li M, Iizuka K, Liu J, Chen K, Li Y. Effects of forest canopy structure on forest aboveground biomass estimation using Landsat imagery. IEEE Access 2021;9:5285-5295. [CrossRef]

[68] Qazi WA, Baig S, Gilani H, Waqar MM, Dhakal A, Ammar A. Comparison of forest aboveground biomass estimates from passive and active remote sensing sensors over Kayar Khola watershed, Chitwan district, Nepal. J Appl Remote Sens 2017;11:026038. [CrossRef]

[69] Tavasoli N, Arefi H. Comparison of capability of SAR and optical data in mapping forest above ground biomass based on machine learning. IECG 2020;13. [CrossRef]

[70] Ji Y, Wang L, Zhang W, Marino A, Wang M, Ma J, et al. Forest above-ground biomass estimation using X, C, L, and P band SAR polarimetric observations and different inversion models. Int J Digit Earth 2024;17:2310730. [CrossRef]

[71] Qiao J, Chen Z, Yu J, Cai R, Hao Z. Identification of causal structure in the presence of missing data with additive noise model. Proc AAAI Conf Artif Intell 2024;38:20516-20523. [CrossRef]

[72] Li Y, Li M, Liu Z, Li C. Combining Kriging interpolation to improve the accuracy of forest aboveground biomass estimation using remote sensing data. IEEE Access 2020;8:128124-128139. [CrossRef]

[73] Kariofillia P, Mimis A, Bithas K. Estimating biomass carbon stocks in agriculture land for the Mediterranean using remote sensing data. 2022. Available at: https://ageconsearch.umn.edu/record/337122?v=pdf Accessed on Sep 14, 2026.

[74] Zhou J, He Q, Cheng G, Lin Z. Union-net: Lightweight deep neural network model suitable for small data sets. J Supercomput 2023;79:7228-7243. [CrossRef]

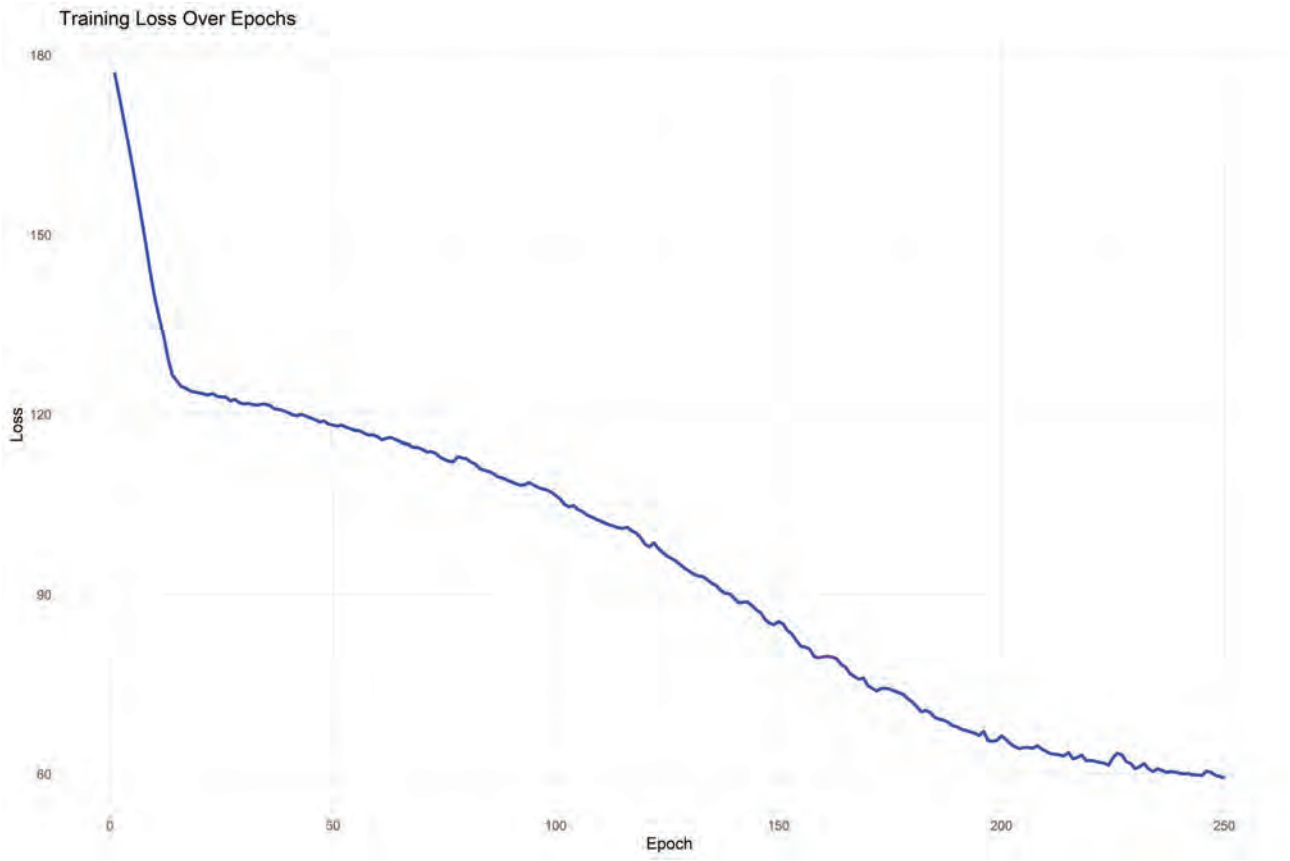
[75] Thapa RB, Watanabe M, Motohka T, Shimada M. Potential of high-resolution ALOS PALSAR mosaic texture for aboveground forest carbon tracking in tropical region. Remote Sens Environ 2015;160:122-133. [CrossRef]

[76] Yavasli DD. Estimation of above ground forest biomass at Muğla using ICESat/GLAS and Landsat data. Remote Sens Appl Soc Environ 2016;4:211-218. [CrossRef]

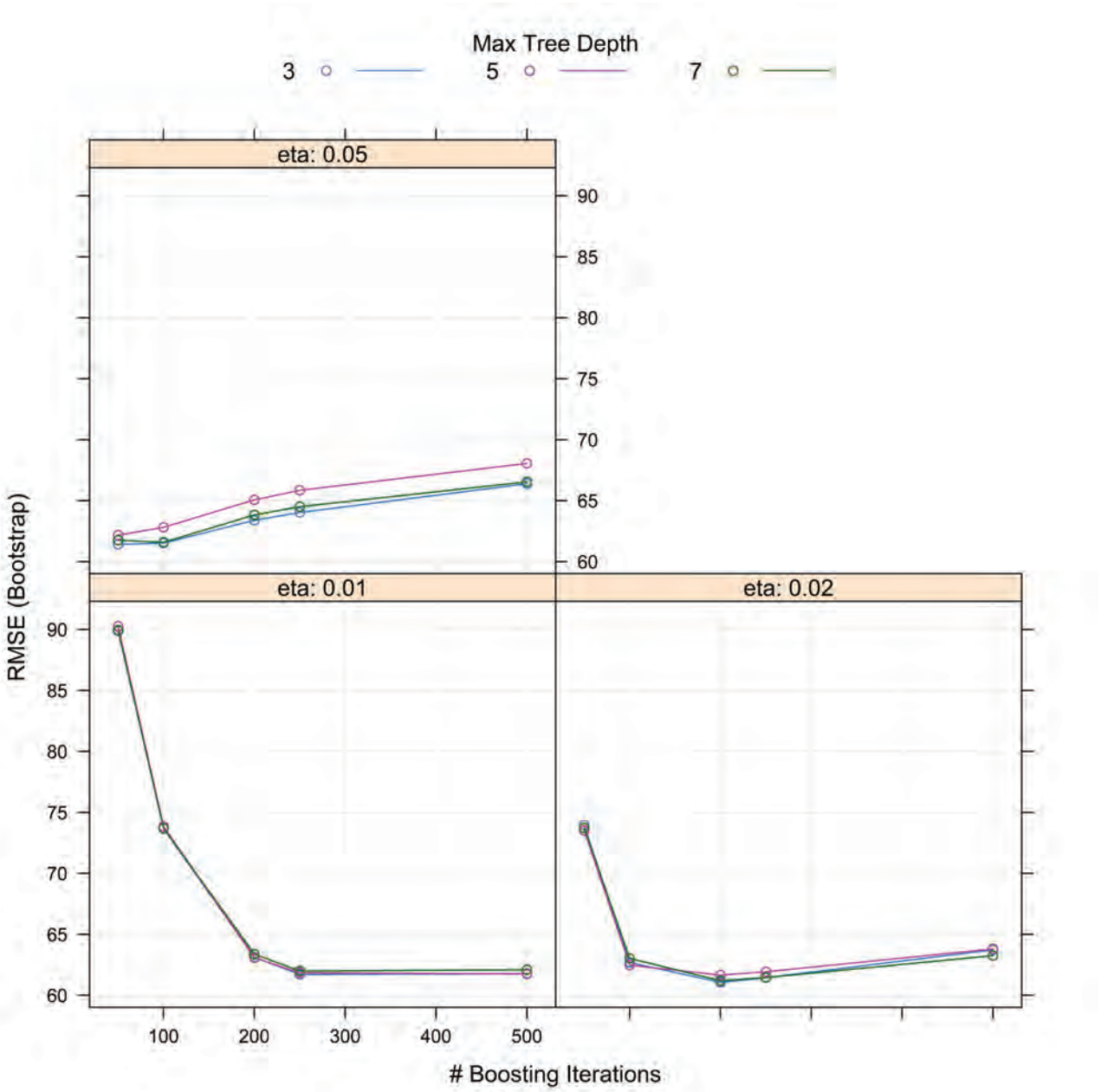
[77] Flores-Anderson AI, Herndon KE, Thapa RB, Cherrington E. The SAR handbook: Comprehensive methodologies for forest monitoring and biomass estimation. 2019. Report No.: MSFC-E-DAA-TN67454.

[78] Guerra-Hernández J, Narine LL, Pascual A, Gonzalez-Ferreiro E, Botequim B, Malambo L, et al. Aboveground biomass mapping by integrating ICESat-2, SENTINEL-1, SENTINEL-2, ALOS2/PALSAR2, and topographic information in Mediterranean forests. GISci Remote Sens 2022;59:1509-1533. [CrossRef]

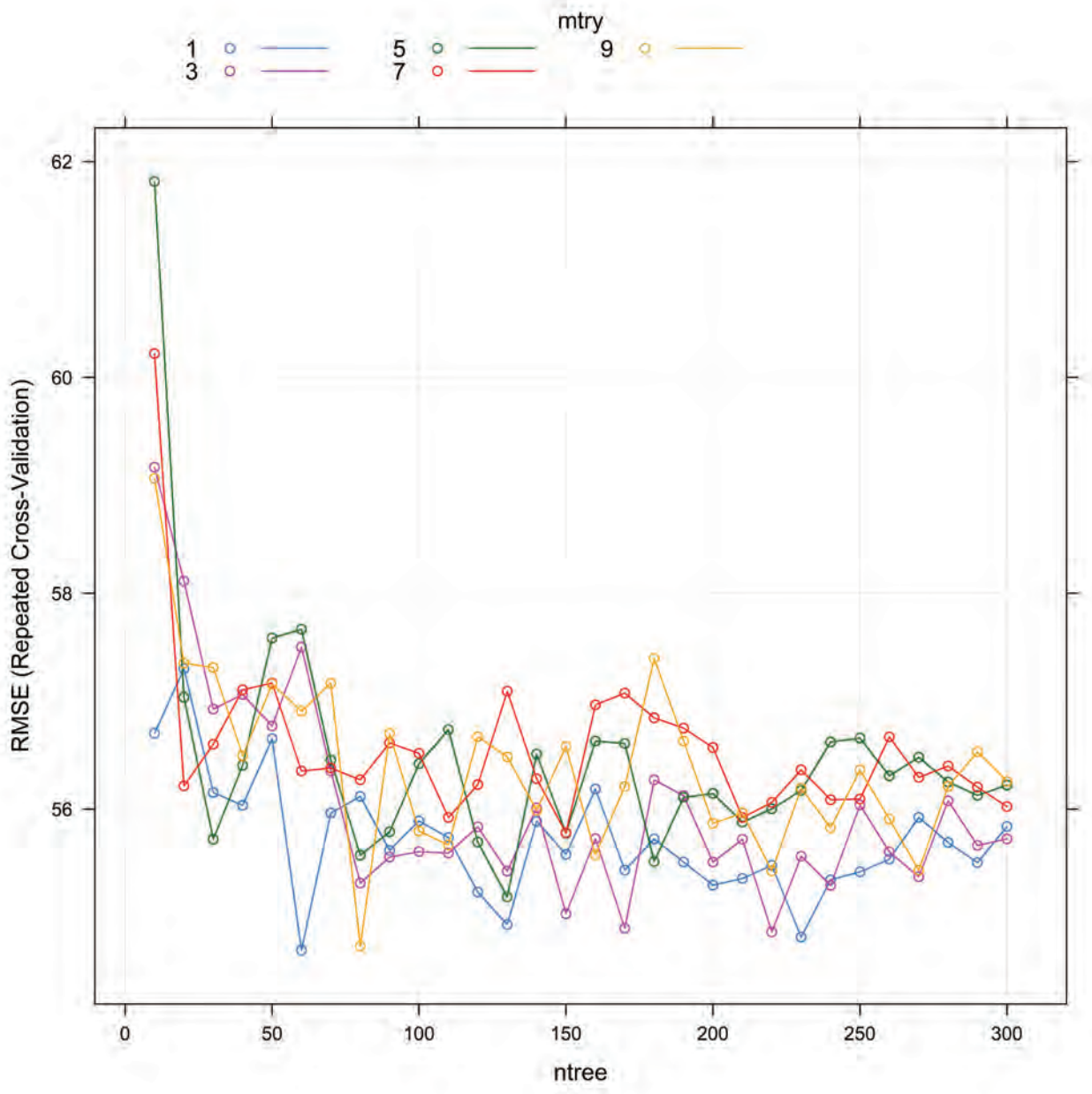
APPENDIX



1. Test/loss graph of Scenario-9 for CNN method.



2. Grid search chart of ϒHH, ϒHV, ϒNDPI, ϒCPR variables for XGBoost.



3. Grid search chart of ϒHH, ϒHV, ϒNDPI, ϒCPR variables for Random Forest.

Sigma J Eng Nat Sci, Vol. 44, No. 4, pp. 2364–2379, August, 2026

Sigma Journal of Engineering and Natural Sciences
Web page info: https://sigma.yildiz.edu.tr
DOI: 10.14744/sigma.2026.2106

Research Article

Solution to a make-or-buy decision problem based on intuitionistic fuzzy sets and grey relational analysis

Gülçin CANBULUT[1,*], Erkan KÖSE[1], Forrest Jeffrey Yi-Lin[2]

[1]*Department of Industrial Engineering, Nuh Naci Yazgan University, Kayseri, 38170, Türkiye*
[2]*Pennsylvania State System of Higher Education, Pennsylvania, Slippery Rock University, 16057, USA*

ARTICLE INFO

Article history
Received: 01 January 2025
Revised: 21 March 2025
Accepted: 28 May 2025

Keywords:
Grey Relational Analysis (GRA); Intuitionistic Fuzzy Number (IFN); Multi Criteria Decision Making (MCDM); Make-or-Buy Decision, TOPSIS, WASPAS

ABSTRACT

This research introduces an integrated decision-support framework for make-or-buy decisions by combining intuitionistic fuzzy sets with grey relational analysis. Since make-or-buy selection involves multiple evaluation criteria and substantial uncertainty in expert judgments, a single decision technique may not adequately capture all aspects of the problem. Therefore, intuitionistic fuzzy sets are employed to represent uncertainty in the evaluation process, whereas grey relational analysis is utilized to rank the available alternatives. To further demonstrate the robustness of the proposed framework, its performance is compared with the results obtained from well-established MCDM techniques. The proposed model was further validated by comparing its outcomes with those generated using the TOPSIS and WASPAS methods, both of which are extensively employed in MCDM studies.

Make-or-buy decisions are strategically important in manufacturing industries due to their direct impact on cost control, resource allocation, and competitiveness. The aim of this study is to add a new one to the multi-criteria decision-making methods by using more than one type of uncertainty and to apply this method in an area that has never been used before in the literature. This method is applied to a real-world make-or-buy decision problem in the metal manufacturing sector, where selecting the optimal sourcing strategy has a direct impact on operational efficiency and cost control. In this study, an extension of the technique developed for ordering preferences by similarity to the ideal solution.

The results show that this integrated approach is effective in handling uncertainty and can be a valuable decision-support tool for practitioners dealing with complex procurement or sourcing decisions in real-world industrial settings. The proposed method ranked "full outsourcing" as the most suitable option, with a grey relational grade of 0.798, indicating strong alignment with the selected criteria under uncertainty. Among the three evaluated alternatives, full outsourcing achieved the highest grey relational grade (0.798), while hybrid and in-house production scored 0.691 and 0.598, respectively. These findings suggest that the proposed integrated approach can be used effectively for complex sourcing decisions in uncertain environments across different industries.

The novelty of this study is that instead of dealing with the whole decision-making process with the same uncertainty theory, this work employs the most appropriate uncertainty methods at different decision stages. In addition, this study is the first of its kind in which the grey theory and fuzzy set theory are used together in make-or-buy decision as far as our literature review demonstrates. So, the contributions of the study to the literature is using the different uncertainty kinds in multicriteria decision making problems.

Cite this article as: Canbulut G, Köse E, Yi-Lin FJ. Solution to a make-or-buy decision problem based on intuitionistic fuzzy sets and grey relational analysis. Sigma J Eng Nat Sci 2026;44(4):2364–2379.

***Corresponding author.**
*E-mail address: gcanbulut@nny.edu.tr

This paper was recommended for publication in revised form by Editor-in-Chief Ahmet Selim Dalkilic

Published by Yıldız Technical University Press, İstanbul, Turkey
© Author. This is an open access article under the CC BY-NC license (http://creativecommons.org/licenses/by-nc/4.0/).

INTRODUCTION

To meet increasing customer demands and expectations, businesses are compelled to adopt scientific decision-making methods. Firms may choose to outsource a product or service instead of producing it themselves for such reasons as taking advantage of economies of scale and focusing on core competencies. These are referred to as make-or-buy decisions in supply chain management. Such decisions are one of the strategic decisions that affect the long-term competitiveness and profitability of a company. It has become increasingly evident that resource allocation decisions significantly influence a business's future [1]. If used correctly, outsourcing has the potential to create a competitive advantage for companies. It is especially emphasized that outsourcing will provide significant benefits to businesses in all jobs that are not considered core competence for the organization.

Decision-makers tend to prefer the lowest cost alternative among the available production and purchasing alternatives. In this comparison, if the cost of the purchasing alternative is lower than that of the production alternative, then the purchasing alternative will be chosen; otherwise, the production alternative will be preferred. If purchasing is the choice in a make-or-buy decision, the enterprise often focuses on purchasing large quantities at the best price possible while ignoring other factors, such as quality and delivery times. However, businesses should also consider such factors as delivery reliability, technical capacity, cost capacity and financial conditions in the decision of purchase.

Make-or-buy decisions are frequently made under conditions where decision makers have only limited or incomplete information. In such situations, grey system theory provides an appropriate analytical framework because it is specifically designed for problems characterized by information deficiency. Introduced by Julong Deng, the theory classifies systems according to the availability of information [2]. A system with complete information is referred to as a *white system*, whereas a *black system* represents a situation in which no information is available. Most real-world decision problems, however, fall between these two extremes and are therefore considered *grey systems*, where only part of the available information is known. Grey system theory is one of the methods developed for studying uncertainties with the superiority in the mathematical analysis of systems with uncertain information. It has been shown [3, 4] to be an effective method that can help solve uncertainty problems with discrete data and incomplete information.

In this study, we use the make-or buy-decision approach to analyze the components needed by an enterprise operating in the metal industry. Due to the uncertainty in decision-makers' evaluations and the inherent subjectivity of the criteria, the intuitionistic fuzzy set (IFS) theory and methods of grey relational analysis (GRA) were used together. Intuitionistic fuzzy set is used because it can reflect the linguistic preferences of the decision makers more easily by showing the membership, non-membership functions and hesitation index. Grey relational analysis is subsequently used to evaluate the similarity between alternatives based on their performance across multiple criteria. By measuring the degree of closeness between the reference sequence and each alternative, GRA enables the ranking of candidate components even when the available information is limited or incomplete. The complementary strengths of IFS and GRA make the proposed framework suitable for solving complex multi-criteria decision problems characterized by uncertainty and interdependent evaluation factors.

The results show that IFS theory and GRA can be used successfully in solving problems involving different kinds of uncertainties. To enhance the reliability of the obtained results, it is a common practice to validate proposed MCDM approaches using more than one decision-making method. In this study, the technique for ordering preferences by similarity to ideal solution (TOPSIS) and WASPAS, which are most preferred methods to solve MCDM problems, were used to test the accuracy of the results.

This study goes beyond the traditional approaches that typically rely on a single uncertainty theory by proposing an integrated method that applies the most suitable type of uncertainty at each stage of the decision-making process. The combined use of Grey Relational Analysis (GRA) and Intuitionistic Fuzzy Sets (IFS) enables effective modeling of both data incompleteness and subjective evaluations. By overcoming the limitations of classical models, this approach offers a more flexible and realistic solution for complex real-life decision problems. Notably, the application of GRA to a make-or-buy decision problem for the first time also marks a novel contribution to the literature. The proposed model not only delivers theoretical innovation but also demonstrates practical effectiveness through its implementation in a real industrial setting. Therefore, an integrated approach combining Intuitionistic Fuzzy Sets (IFS) and Grey Relational Analysis (GRA) is proposed to effectively address the uncertainties present in real-world make-or-buy decision problems.

The rest of the paper is organized into the following sections. Section 2 reviews the principles of IFS and GRA; Section 3 outlines the application to a real-life case; and Section 4 discusses the results and conclusions.

Literature Review

With increasing competition, businesses need to use more scientific methods in their decision-making processes. The decision whether the production of goods or services required by businesses will be carried out in their organization or in another supplier company is called "a make-or-buy decision problem" in the literature. The conceptual basis of a make-or-buy decision is based on Williamson's theory of job-cost analysis [5]. The job-cost analysis combines economic theory and production theory that a business should use in developing market share. It deals with

establishing a purchasing discipline that limits the internal and external constraints and analyzes other factors.

Multi-Criteria Decision Analysis

A review of the literature reveals that Multi-Criteria Decision-Making (MCDM) approaches are frequently applied to solve make-or-buy decision problems. In this context, Padillo and Diaby [6] developed a multi-criteria decision analysis methodology for evaluating make-or-buy strategies. Their study evaluated make-or-buy alternatives using a dynamic framework that simultaneously considered multiple features and objectives. They identified four goals: maximizing strategic competitive performance; maximizing managerial performance; minimizing resource risks; and maximizing financial performance. The model applies an analytic hierarchy process to create measures of importance for criteria. These goals are traded-off based on composite programming, resulting in a ranking of make-or-buy alternatives.

Platts et al. [7] developed a structured framework to support make-or-buy decisions by identifying the key factors influencing this process in industrial organizations. Their approach incorporated a multi-attribute decision-making technique to generate comprehensive recommendations for make-or-buy selection. The proposed framework was demonstrated through an industrial case study, highlighting both its practical applicability and its contributions to the literature and industrial decision-making practices.

Hwang [8] developed an integrated decision analysis model for the make-or-buy decision problem for school foodservice. He created a decision support system with three stages: brainstorming to identify decision alternatives, fuzzy analytic hierarchy process (AHP) application as a multi-criteria decision-making method, and application of an integrated priority method.

Golec et al. [9] used the Choquet integral in the make-or-buy decision process. They determined the degree of importance by using the interaction index value and then brought it together with the Choquet integral. They compared this method with other similar methods. The criteria used in this study consist of design, engineering, materials, manufacturing, and price or profit. Four alternatives were evaluated by using AHP, Choquet integral and weighted arithmetic mean method, and then the results were compared.

Water and Peet [10] developed a multi-criteria decision-making method based on the analytical hierarchy process to take on the make-or-buy decision that is encountered in the manufacturing sector. This study addressed two aspects often overlooked in previous research: the content of the decision and the transactional details involved.

Hwang [11] proposed a two-stage method for resolving the make-or-buy decision problem. In the first stage, a multi-criteria analysis method was developed by using the AHP method; and in the second stage, problems involving multi-purposes, multi-criteria and multi-featured topics were integrated by utilizing the fuzzy set ranking method.

Kahraman et al. [12] focused on outsourcing information systems by using group decision making approach. The work aimed to selecting one of the eight information system providers under seven criteria. Sensitivity analysis was conducted to assess the impact of parameter variations on the final decision.

Cheshmberah et al. [13] investigated the make-or buy-decision problem in the context of production activities. The study consists of two stages. The first stage investigated whether the activity handled is among the core competencies of the company. In The second stage developed a decision-making mechanism based on the fuzzy TOPSIS approach for activities that are not considered as core competencies.

Minh [14] proposed a model for the make-or-buy decision in an experimental point of view. In the study, the results of some surveys carried out by Japanese automobile manufacturers were used in the calculation of the weights of the criteria and sub-criteria used in the analytical hierarchy process.

Cheshmberah et al. [15] examined outsourcing decisions in manufacturing by applying the PROMETHEE method to an aviation industry case. Their framework incorporated fuzzy numbers to estimate the relative importance of the evaluation criteria, allowing uncertainty in expert judgments to be considered during the decision-making process.

Seyedhosseeini et al. [16] studied the make-or-buy decision in order to find which strategy should have been chosen to minimize the total costs of supply chain. For this purpose, two discrete models were created for each strategy and then solved sequentially with many numerical examples. They claimed that computational experiments showed the efficiency of the proposed models.

Sillanpää [17] analyzed factors related to make-or-buy decisions. This research focused on decision making model in the manufacturing industry supply chain. Within the scope of the research, a tool was created for make-or-buy decisions which could be used as a help to evaluate outsourcing analytically.

Park [18] examined the risks associated with make-or-buy decisions under conditions of radical technological change. The study focused on identifying strategies that enable firms to mitigate the trade-off and governance-related risks encountered when selecting an appropriate make-or-buy strategy in rapidly evolving technological environments.

Serrano et al. [19] developed a theoretical framework that can help managers evaluate their sourcing decisions. As a result of a comprehensive literature search, these scholars tried to determine which factors and theories were needed or appropriate for make-or-buy decisions. They suggested that practitioners should combine theories of the

resource-based view, strategic management, and transaction cost economics to evaluate plant location decisions.

Serrano et al. [20] proposed a decision-support framework for make-or-buy analysis to assist managers in evaluating sourcing alternatives. The development of the make-or-buy framework is explained based on the results of qualitative interviews with practitioners and an internal case study. Their results suggest that practitioners should combine the proposed framework with multi-criteria decision analysis based on the pairwise comparison matrix and TOPSIS methodology.

Omerali and Kaya [21] purposed a Type-2 Fuzzy COPRAS methodology to support firms' buy-or-implement decisions in the Internet of Things (IoT) domain. The researchers stated that deciding on the digitalization strategy is not different from the current purchasing decision that companies have faced in the past, but this time they are faced with increasing complexity.

More recently, Klein and Mazzoni [22] revisited the make-or-buy literature from a theoretical standpoint, offering updated insights on vertical integration strategies and outsourcing decisions, and emphasizing future research directions. Another recent study [23] explored the impact of learning-by-doing on make-or-buy decisions, especially in high-tech sectors like semiconductors, introducing a dynamic modeling perspective. Additionally, Brem and Elsner [24] analyzed make-or-buy decisions in products characterized by high technological complexity, underlining the strategic implications of sourcing choices in the consumer goods industry.

While previous studies primarily focus on a single uncertainty theory or isolated decision models, our study aligns different uncertainty methods across multiple decision stages, providing a more holistic and flexible framework.

Grey System Theory

Grey system theory provides a technique that can be used successfully in studying processes that involve partial uncertainties. However, it is interesting to note that the grey theory has not been used to solve the make-or-buy problems until today. There are some review papers on grey theory in the literature. For example, Yin [25] covered fifteen years of gray system research and produced a historical review and bibliometric analysis.

Li and Lin [26] submitted a review article on grey system theory with the aim of informing the readers about the development history, main content and main difficulties of the gray system theory. They stated that their main motivation was to draw the attention of the international academic community to this theory.

A literature review study [27] is investigated on the use of grey system theory usage of grey systems theory in the supply chain management, credit risk, financial performance evaluation, decision-making process, investment efficiency, energy consumption, etc by Delcea. Unlike other review articles, this paper focuses solely on economic applications where grey theory has been used successfully, while providing the reader with an overview of the field, as well as new research perspectives.

Another study [28] on grey system theory is reviewed by Pan et al. They have investigated 4859 publications published on Web of Science Core Collection between 1991 and 2018. Bibliometric analysis and visualization on grey system theory is conducted. They provided quantitative insights into the theory's outlook over the past 27 years, while pointing to develop a significant overview for scientists interested in studying and/or employing grey systems theory.

In another review, Jayant et al. [29] conducted a state-of-the-art literature survey to taxonomy the research on the applications and methodologies of grey relational analysis (GRA) in reasonable business environments. They concluded their study with recommendations for future research directions in GRA decision making that is both forward-looking and practically oriented.

Javanmardi et al. [30] provided an updated review of the literature on the roles and impacts of grey system theory based methods in sustainability studies. Although these review papers covered a extensive range of studies of grey system theory, none of them touched on who grey theory could be used to solve make-or-buy problems.

Make-or-buy decisions stand for one of the challenging and very complex tasks facing businesses. Detailed analyses are required to learn all alternatives and to understand short- and long-term company needs. Besides, as the company's needs and market conditions change, a decision that is appropriate for the past can have a completely different meaning for the future. Since the future is unpredictable in all its aspects, the process of make-or-buy decision includes many different types of uncertainties. When the existing literature is examined, it is seen that the uncertainties are mostly ignored, or the process is tried to be handled with a single uncertainty theory regardless of whether it is appropriate. Unlike the literature, in this study, each stage of the make-or-buy decision is handled with the most appropriate uncertainty type. The novelty of this study is that instead of dealing with the whole process of a make-or-buy decision with a chosen uncertainty theory, this paper uses appropriate uncertainty methods in different steps. Another very important role of the study to the literature is that the grey system theory is used for the first time in solving the make-or-buy decision problem. It is expected that these related aspects of the study will help open new territories in decision making in general and make-or-buy decisions in particular.

MATERIALS AND METHODS

Methods

Decision-making problems often involve uncertainty due to incomplete, imprecise, or subjective information. In such contexts, different modeling techniques are required

depending on the type of uncertainty encountered. Grey System Theory is used to analyze problems under incomplete and uncertain information proposed by Deng [31]. It classifies systems into three categories: white (fully known), black (completely unknown), and grey (partially known). This theory is especially effective in dealing with systems that involve incomplete data [32]. Grey Relational Analysis (GRA), one of the principal techniques derived from Grey System Theory, is a widely used tool for evaluating alternatives by measuring the similarity between data sequences. It is particularly effective in situations with limited quantitative information. In parallel with grey systems, fuzzy set theory has been used to model uncertainty, particularly when dealing with linguistic or subjective assessments. Unlike conventional fuzzy sets, Intuitionistic Fuzzy Sets (IFS) explicitly account for membership, non-membership, and hesitation degrees, allowing uncertainty associated with human evaluations to be represented more effectively.

In our proposed model, IFS is applied to model the subjective linguistic evaluations provided by decision-makers, while GRA is employed to rank the alternatives based on limited numerical data. This hybrid structure ensures that each type of uncertainty is addressed using the most appropriate method. Fuzzy set theory and grey system theory were developed to analyze systems characterized by uncertainty. Although these theories address different types of uncertainty, both are capable of handling situations involving incomplete or imprecise information. From a technical standpoint, fuzzy set theory addresses conceptual uncertainty using membership functions, often informed by expert experience. For example, the term "young person" is considered fuzzy — while generally understood, its exact age range is difficult to define precisely. Grey system theory was developed as a means to quantify and manage uncertainty. The less information is available, the more effectively grey system theory demonstrates its strength. Grey system characteristics cannot be fully explained through fuzzy set theory, probability, or traditional statistical methods. Grey system theory has found successful application in various fields, including industry, social and ecological systems, economics, transportation, management, education, environmental studies, and defense. Grey Relational Analysis (GRA), an extension of grey system theory, serves as a highly effective tool for analysis in data-limited environments. It measures the degree of similarity between sequences to evaluate relationships under uncertainty.

These concepts and their integration into the proposed decision-making model are explained in the following sections in detail.

Intuitionistic Fuzzy Set (IFS) Theory

Proposed by Atanassov [33], Intuitionistic Fuzzy Set (IFS) theory extends the fuzzy set framework introduced by Zadeh [34]. By explicitly representing membership, non-membership, and hesitation degrees, IFS offers an effective means of handling uncertainty in decision-making problems. The basic concepts of IFS relevant to this study are briefly presented below [35].

Definition 1. Let X denote a non-empty universe of discourse and let $I = [0,1]$ represent the unit interval. An intuitionistic fuzzy set S defined on X is expressed as:

$$S = \{(x, \mu_s(x), \vartheta_s(x)) : x \in X\} \tag{1}$$

where

$\mu_s(x): X \to I$; specifies the membership degree of element x in the set S;

$\vartheta_s(x): X \to I$; denotes the non-membership degree associated with the same element.

To ensure a valid intuitionistic fuzzy representation, the membership and non-membership degrees must satisfy the following condition:

$$0 \le \mu_s(x) + \vartheta_s(x) \le 1 \tag{2}$$

Definition 2. Let X be a nonempty set and let S be an IFS defined on X. T he hesitation degree associated with an element is defined as

$$\pi_s(x) = 1 - (\mu_s(x) + \vartheta_s(x)) \tag{3}$$

The index, indicating the hesitation degree about whether an element x belongs to the set S, is specified as the index of hesitation. According to the value of $\pi_s(x)$, comment can be made about the information of element x. If the value of $\pi_s(x)$ is large, information about the element is more certain; if the value of $\pi_s(x)$ is small, information about the element is more precise. If the value of $\pi_s(x)$ equals to zero, information about the element is more precise and, in this case, the intuitionistic fuzzy set turns into fuzzy set.

Definition 3. $\alpha = (\mu_s(x), \vartheta_s(x), \pi_s(x))$ is defined as an intuitionistic fuzzy number (IFN), where

$$\mu_s(x) \in [0,1], \vartheta_s(x) \in [0,1], 0 \le \mu_s(x) + \vartheta_s(x) \le 1$$
$$and\ \pi_s(x) = 1 - (\mu_s(x) + \vartheta_s(x))$$

Definition 4. Consider two intuitionistic fuzzy numbers (IFNs), α and β, defined on the universe X, where $\gamma \in [0,1]$. The basic arithmetic operations associated with IFNs are given as follows:

$$\alpha \otimes \beta = (\mu_s(x) * \mu_t(x), \vartheta_s(x) + \vartheta_t(x) - \vartheta_s(x) * \vartheta_t(x)) \tag{4}$$

$$\gamma\alpha = \left(1 - (1 - (\mu_s(x))^{\gamma}), ((\vartheta_s(x))^{\gamma})\right) \tag{5}$$

$$\alpha^{\gamma} = \left((\mu_s(x))^{\gamma}, 1 - (1 - (\vartheta_s(x))^{\gamma})\right) \tag{6}$$

Definition 5. Let $\alpha_i = (\mu_{si}, \vartheta_{si}, \pi_{si})$ be intuitionistic fuzzy numbers, for $i = 1,2,\ldots,n$, and $w = (w_1, w_2, \ldots w_n)$ be weighted vectors of fuzzy numbers. Then, therithmetic mean is calculated as:

$$AO(\alpha_1, \alpha_2, \ldots \alpha_n) = \left(1 - \prod_{i=1}^{n}(1-\mu_i)^{wi}, \prod_{i=1}^{n}\vartheta_i{}^{wi}\right) \quad (7)$$

GREY RELATIONAL ANALYSIS (GRA)

Grey System Theory was introduced to address decision problems characterized by incomplete and uncertain information. A system with complete information is referred to as a *white system*, whereas a *black system* represents a situation in which no information is available. Grey systems refer to systems in which only part of the available information is known [3,4]. Accordingly, if all the information about a system is known, then the system is seen as a white system; if no information is known; then the system is known as a black system.

The main feature of grey system theory is its ability to make the best use of the limited number of information available. The core feature that distinguishes grey system theory from traditional methods, such as statistics, is that it needs only a very limited amount of data to predict the behavior of an uncertain system. The less information is available, the more effectively grey system theory demonstrates its strength. The amount of information that can be obtained is the most important criterion used to distinguish between grey and non-grey scenarios.

Grey system theory was developed to find solutions to problems involving small sample and weak information. Grey system characteristics cannot be fully explained through fuzzy set theory, probability, or traditional statistical methods. From a technical standpoint, fuzzy set theory addresses conceptual uncertainty using membership functions, often informed by expert experience. Probability and statistics, on the other hand, require special distributions and a reasonably sized sample to make realistic inferences [3].

Grey system theory has found successful applications in various fields, including industry, social and ecological systems, economics, transportation, management, education, environmental studies, and defense [36]. Grey production; grey modeling; grey decision making; grey control; grey prediction and grey relational analysis are the main fields of grey system theory [37].

Grey Relational Analysis (GRA) serves as a highly effective tool for analysis in data-limited environments. Based on the ideal series it references, the method of this analysis is developed to reveal the indefinite relationship of this ideal series with other series of concern. The alternative which has a larger grey correlation analysis ratio with the reference series is seen as closer to the ideal [38].

The first step of the grey relational analysis method is to convert the performances of all alternatives into a comparable series. In the second step, the reference (target) series are created by selecting the best values for each criterion. Following the normalization process, the degree of association between the reference sequence and each alternative sequence is evaluated through grey relational coefficients. Lastly, using the resulting coefficients, the degree of grey relation between each comparison series and the reference series is determined. The best option is the alternative with the highest grey relational degree. The procedure of grey relational analysis is shown in Figure 1, where the steps of the grey relational analysis method are explained in detail.

GENERATING THE REFERENCE SERIES AND COMPARISON MATRIX

Let us consider that there are n criteria and m alternatives in a decision problem. And the i^{th} alternative is represented as $Y_i = \{y_{i1}, y_{i2}, \ldots, y_{ij}, \ldots, y_{in}\}$, where y_{ij} denotes the performance value of the i^{th} alternative with respect to the j^{th} criterion.

Firstly, the creation of the reference series can be obtained by using two methods. In the first method, a reference series can be created with the largest value that a criterion can take. For instance, if the relevant criterion is the level of grades obtained on an exam with a potential total 100 points, then the reference serial value can be taken as 100. The second approach constructs the reference sequence by selecting the optimal value for each evaluation

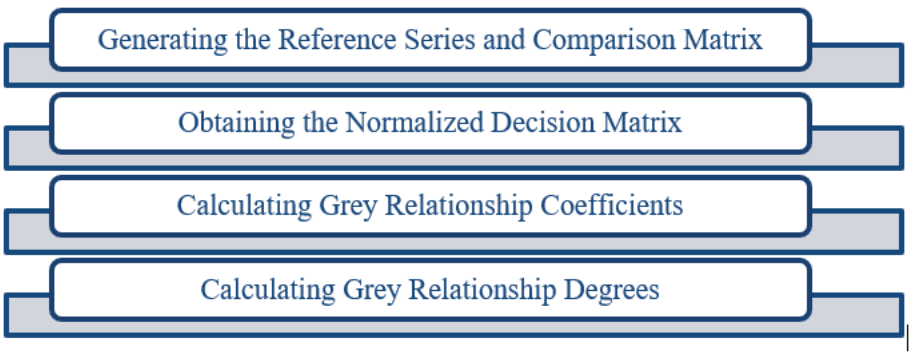


Figure 1. Grey relational analysis procedure.

criterion from the available alternatives. For benefit criteria, the highest observed value is assigned to the reference sequence, whereas for cost criteria, the lowest observed value is selected.

Obtaining the Normalized Decision Matrix

Normalization is used when the criteria used in the analysis have different units. Normalization is done in two different ways, depending on whether the criteria relate to finding maximum(s) or minimum(s). In the case of maximum, the normalization value is calculated by using Equation (8):

$$x_{ij} = \frac{y_{ij} - Min\{y_{ij}\}}{Max\{y_{ij}\} - Min\{y_{ij}\}}; i = 1,2,\dots,m \quad and\ j = 1,2,\dots,n \tag{8}$$

In the case of maximum, the normalization value is calculated by using Equation (9):

$$x_{ij} = \frac{Max\{y_{ij}\} - y_{ij}}{Max\{y_{ij}\} - Min\{y_{ij}\}}; i = 1,2,\dots,m \quad and\ j = 1,2,\dots,n \tag{9}$$

Following the normalization process described in Eq. (8) and/or Eq. (9), all criteria values will be transformed into the interval [0, 1]. The value of x_{ij} is equal to 1 indicates that alterative i achieves the best performance for criterion j [38].

Calculating Grey Relational Coefficients

After the reference series are defined, to compare the alternatives with each other, grey correlation coefficients are calculated for each alternative.

Let us accept these notations;

$$\Delta_{ij} = |x_{0j} - x_{ij}|,$$
$$\Delta_{min} = \min_{i,j}\{\Delta_{ij}\},$$
$$\Delta_{max} = \max_{i,j}\{\Delta_{ij}\},$$

The grey correlation coefficients can be calculated as in Eq. (10).

$$\gamma(x_{0j}, x_{ij}) = \frac{\Delta_{min} + \varphi\Delta_{max}}{\Delta_{ij} + \varphi\Delta_{max}}; i = 1,2,\dots, \quad mvej = 1,2,\dots,n \tag{10}$$

The distinguishing coefficient $\varphi \in [0,1]$ in Eq. (10) is used for increasing the range of the grey correlation coefficient. If enough data and experience is not known, this coefficient should be taken 0.5.

Calculating Grey Relationship Degrees

The grey relation grade is calculated for all alternatives after the grey correlation coefficients are calculated. Taking the average of the obtained grey correlation coefficients is the common method for obtaining the grey relation grade. Equation (11) is used for this purpose.

$$\delta(X_0, X_i) = \frac{1}{n}\sum_{j=1}^{n}\gamma(x_{0j}, x_{ij}) \tag{11}$$

The evaluation criteria are not equally important; therefore, different weights are assigned to reflect their relative significance. To account for differences in criterion importance, normalized weights are integrated into the calculation according to Eq. (12). Here, w_j represents the normalized weight of the j^{th} criterion, and $\sum_{j=1}^{n} w_j = 1$.

$$\delta(X_0, X_i) = \frac{1}{n}\sum_{j=1}^{n} w_j\gamma(x_{0j}, x_{ij}) \tag{12}$$

The alternative with the highest grey relational grade will be the alternative serving the target the most. IFS is employed for modeling subjective linguistic evaluations, while GRA is used to process the limited numerical data available — ensuring alignment between the nature of uncertainty and the method applied.

Application

This section presents a step-by-step explanation of our proposed integrated MCDM framework for the make-or-buy decision, which combines intuitionistic fuzzy logic and grey relational analysis. And then we will look at its application to a chosen sample problem. In the study, the make-or-buy decision-making process is examined by using real-life data for the components needed by an enterprise operating in the metal sector. The product selected for make-or-buy analysis is the component with the highest usage frequency in the company's operations.

Assume that there are l decision makers (d_1, d_2, … $.d_l$), m alternatives (x_1, x_2, …, x_m) and n criteria (c_1, c_2, …., c_n) in the decision problem of our concern. The proposed approach includes 8 steps shown in Figure 2.

Stage 1: Definition of Problem

The most critical step in scientific research is the correct formulation of the problem. Accurate solutions cannot be expected from problems that are poorly formulated. For this reason, the first step of any decision problem is the correct formulation of the problem. In this study, it aims to solve the make-or-buy problem for the parts with the highest usage rate in a business operating in the metal sector, based on scientific methods.

Stage 2: Identification of Decision Elements

Accordingly, the interviews with the company officials, the decision alternatives were determined with details shown in Table 1.

The criteria that are thought to have an effect in the make-or-buy decision were determined as a result of literature research and interviews with company officials [39],[40],[41]. The criteria to be used in the study and explanations regarding these criteria are shown in Table 2.

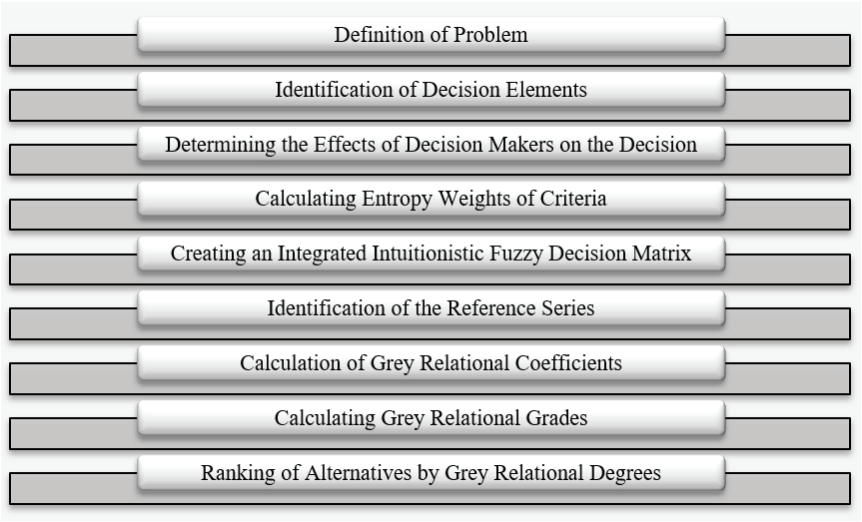


Figure 2. The steps of our proposed approach.

Table 1. Alternatives considered for the make-or-buy decision

Code	Alternatives	Descriptions
x_1	In-house production	All operations related to the selected components are performed entirely within the company's own machining department.
x_2	Hybrid system	50% of the required quantity is produced internally, while the remaining 50% is outsourced to an external supplier.
x_3	Full Outsourcing	The entire production process is handled by an external provider, thereby supplementing the company's limited in-house capacity

Table 2. Decision criteria and their descriptions

Identifier	Criterion	Description
c_1	Time	Since the production of the final product is affected by every component that makes up the product; the production time of the component is important, and a low amount of time is preferred.
c_2	Cost	In an increasingly competitive environment, the small amount of cash required to produce a component keeps the company ahead of its rivals. Therefore, the final product cost includes the cost of the component that is decided to be produced in-house or outsourced.
c_3	Compliance with the desired technical drawing	The technical drawing is important for the components produced in the enterprise. Even tolerances are not based on cm; given on an mm basis. For this reason, compliance with the technical drawing is important whether it is produced outside or within the enterprise.
c_4	Compliance with the desired material quality	The company provides raw materials example the products that will be produced by outsiders. In some cases, even if a raw material cannot be sent, material quality is still important.
c_5	Production capacity	Although there must be a certain production capacity for the in-house production situation within the company, the capacity of the enterprise, which is used as an outside provider, will also enter the total capacity and provide a plus to the production capacity.
c_6	Performance	Preferring a company as an outsourcing means that the work, they have done in the past is suitable for the desired material quality and compliant with the desired technical drawing, time and cost constraints.
c_7	Location	The targeted outsider provider should not be disadvantaged by location.

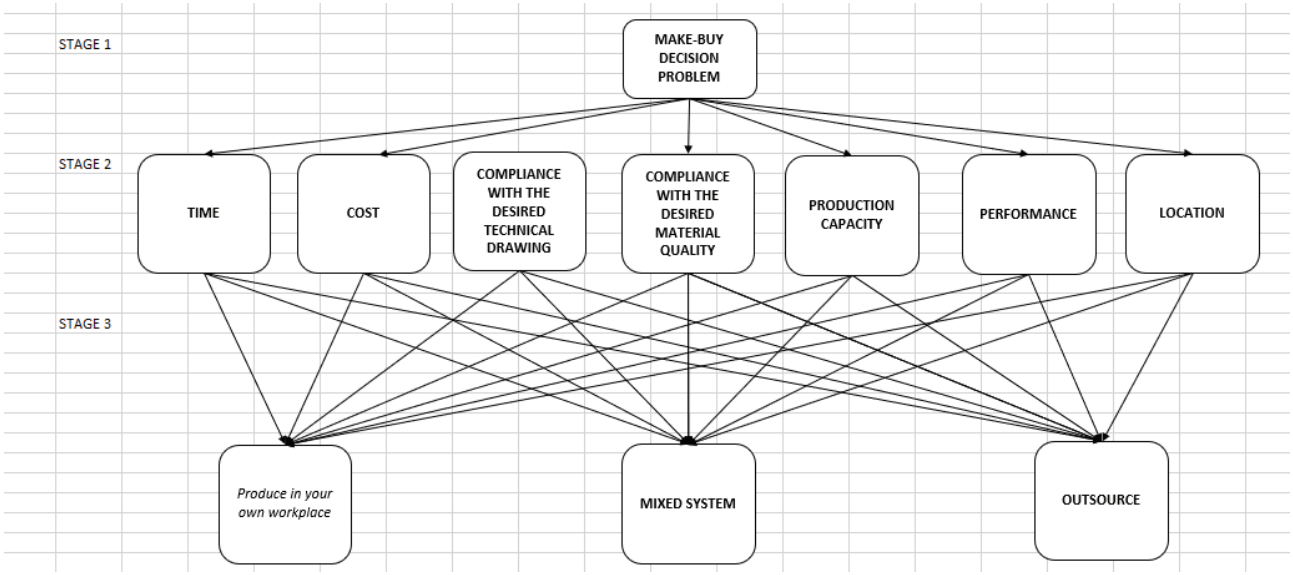


Figure 3. The hierarchical structure of the example problem.

Complex decision problems are often represented in a hierarchical structure to facilitate the evaluation process. The hierarchical structure, developed by the decision-makers for solving the most accurate make-or-buy decision problem, is shown in Figure 3.

Step 3: Determining the Effects of Decision Makers on the Eventual Decision

In most cases, decision makers do not possess the same level of expertise or experience. Several decision makers are in better positions when they are compared to others in terms of experiences, positions, etc. The linguistic expressions, showing the influence levels of the decision makers, and their equivalent intuitionistic fuzzy numbers (IFNs) are shown in Table 3 [42].

Let $(\mu_d, \vartheta_d, \pi_d)$ be an IFN chosen to present the d^{th} decision maker's influence level. After that the value δ_d, the weight of the d^{th} decision maker, can be obtained as in Eq. (13) [43, 44]:

$$\delta_d = \frac{\frac{\mu_d}{\mu_d + \vartheta_d}}{\sum_{d=1}^{l} \frac{\mu_d}{\mu_d + \vartheta_d}} \; and \; \sum_{d=1}^{l} \delta_d = 1, \quad \delta_d \in [0,1], d = 1,2, \ldots\ldots, l \tag{13}$$

In the problem of our investigation, 2 decision makers (d_1, d_2) who are experts in the make-or-buy decision are assigned by management. The decision maker 1 was defined as *Extremely Important (**EI**)* due to his past experience, knowledge and position within the company, and the decision maker 2 defined as *Moderately Important (**MI**)* for the same reasons. The weight scores calculated in accordance with the intuitive fuzzy linguistic variables are shown in Table 4 as in Eq. (13).

The linguistic importance ratings of decision makers and their associated weights are summarized in Table 4.

Step 4: Calculating Entropy Weights of Criteria

To decide criteria weights, decision makers evaluated the criteria through using the linguistic variables and intuitive fuzzy number equivalents; the outcomes are shown in Table 3. The evaluations made by the decision makers for each criterion are indicated in Table 5.

Table 3. Linguistic assessment scale and their corresponding intuitionistic fuzzy numbers (IFNs)

Linguistic assessment scale	Intuitionistic fuzzy number (μ,ϑ,π)
Extremely Important (**EI**)	$(0.90, 0.10, 0.00)$
Highly Important (**HI**)	$(0.75, 0.20, 0.05)$
Moderately Important (**MI**)	$(0.50, 0.40, 0.10)$
Low Importance (**LI**)	$(0.35, 0.60, 0.05)$
Negligibly Important (**NI**)	$(0.10, 0.90, 0.00)$

Table 4. Linguistic importance ratings of decision makers and their associated weights

Decision Makers	Linguistic Terms	Weights
Decision Maker 1 d_1	*EI*	0,618
Decision Maker 2 d_2	*MI*	0,382

Table 5. Decision makers' evaluations of the criteria

Criteria	*Decision maker 1*	*Decision maker 2*
c_1	*EI*	*EI*
c_2	*MI*	*HI*
c_3	*HI*	*HI*
c_4	*HI*	*HI*
c_5	*LI*	*MI*
c_6	*NI*	*LI*
c_7	*MI*	*LI*

Entropy values and entropy weights are calculated for each criterion by using Eq. (14) and Eq. (15), respectively [45]. The calculated values for both criteria are presented in Table 6.

$$H_j = -\frac{1}{n \ln 2}\sum_{d=1}^{l}\left[\mu_{dj}\ln\mu_{dj} + \vartheta_{dj}\ln\vartheta_{dj} - (1-\pi_{dj})\ln(1-\pi_{dj}) - \pi_{dj}\ln 2\right], \quad d = 1,..,l; j = 1,..,n \tag{14}$$

$$w_j = \frac{1-H_j}{n-\sum_{j=1}^{n} H_j}, j = 1,2,\ldots,n, \quad \sum_{j=1}^{n} w_j = 1 \tag{15}$$

Table 6. Entropy values of criteria

Criteria	Entropy Values
H_1	0.087
H_2	0.190
H_3	0.156
H_4	0.156
H_5	0.215
H_6	0.147
H_7	0.222

Table 7. Entropy values of criteria

Criterion	Computed Entropy
w_1	0.157
w_2	0.137
w_3	0.138
w_4	0.138
w_5	0.128
w_6	0.138
w_7	0.125

Table 8. Linguistic assessment scaleand IFNs for the importance of alternatives

Linguistic Assessment Scale	IFNs (μ, ϑ, π)
Excellent (E)	(1.00, 0.00, 0.00)
Outstanding (O)	(0.95, 0.05, 0.00)
Very high (VH)	(0.85, 0.10, 0.05)
High (H)	(0.70, 0.20, 0.10)
Moderate (M)	(0.50, 0.35, 0.15)
Low (L)	(0.35, 0.55, 0.10)
Very Low (VL)	(0.25, 0.70, 0.05)
Extremely Low (EL)	(0.10, 0.90, 0.00)

Then entropy weights were calculated for each criterion by using Eq. (15). The values obtained are shown in Table 7.

Step 5: Creating an Integrated Intuitionistic Fuzzy Decision Matrix

The alternatives for each criterion are evaluated by decision makers with using the linguistic expressions shown in Table 8. Each decision maker's evaluations are formed as an intuitionistic fuzzy decision matrix (R^d). The individual decision matrices provided by all decision makers are subsequently aggregated into a unified intuitionistic fuzzy decision matrix (R) using the Induced Generalized-Intuitionistic Fuzzy Ordered Weighted Averaging (IG-IFOWA).

Definition 6. The IG-IFOWA operator is defined as follows [42]:

$$IG-IFOWA_\delta(\langle u_1,\alpha_1\rangle,\langle u_2,\alpha_2\rangle,\ldots,\langle u_l,\alpha_l\rangle) = \left(w_1(\alpha_{\sigma(1)})^\lambda \oplus w_2(\alpha_{\sigma(2)})^\lambda \oplus \ldots \oplus w_l(\alpha_{\sigma(l)})^\lambda\right) = \left(\left(1-\prod_{d=1}^{l}\left(1-\left(\mu_{\alpha_{\sigma(d)}}\right)^\lambda\right)^{\delta_d}\right)^{1/\lambda}, 1-\left(1-\prod_{d=1}^{l}\left(1-\left(1-\vartheta_{\alpha_{\sigma(d)}}\right)^\lambda\right)^{\delta_d}\right)^{1/\lambda}\right) \tag{16}$$

where

$\lambda \in (-\infty, +\infty)$;

$\alpha_{\sigma(d)}$: is the value of the IFOWA pair $\langle u_d, \alpha_d\rangle$ having the d^{th} largest u_d

u_d: is referred to as the order inducing variable

α_d: is referred to as the IF argument variable

$\delta = (\delta_1, \delta_2, \ldots, \delta_l)^T$: is an associated weight vector with $\delta_d \in [0,1]$, $d = 1,2,\ldots,l$ and $\sum_{d=1}^{l}\delta_d = 1$.

Let $R^d = \left[r_{ij}^d\right]_{mxn}$ be an IF decision matrix of decision maker d:

$$R^d = \left[r_{ij}^d\right]_{mxn} = \begin{bmatrix} r_{11}^d & r_{12}^d & r_{13}^d & & r_{1n}^d \\ r_{21}^d & r_{22}^d & r_{23}^d & \cdots & r_{2n}^d \\ r_{31}^d & r_{32}^d & r_{33}^d & & r_{3n}^d \\ & \vdots & & \ddots & \vdots \\ r_{m1}^d & r_{m2}^d & r_{m3}^d & \cdots & r_{mn}^d \end{bmatrix}$$

Equation (16) is employed to aggregate the decision matrix into an intuitionistic fuzzy decision matrix, denoted by (*R*). The resulting aggregated matrix is expressed as follows:

$$R = \left[r_{ij}\right]_{mxn} = \begin{bmatrix} r_{11} & r_{12} & r_{13} & & r_{1n} \\ r_{21} & r_{22} & r_{23} & \cdots & r_{2n} \\ r_{31} & r_{32} & r_{33} & & r_{3n} \\ & \vdots & & \ddots & \vdots \\ r_{m1} & r_{m2} & r_{m3} & \cdots & r_{mn} \end{bmatrix}$$

The alternative for each criterion had been evaluated by decision makers using linguistic expressions in Table 8. These evaluations are shown in Tables 9 and 10, respectively.

The linguistic evaluation shown in Table 9-10 was transformed into IFNs. Then the IF decision matrices (R^d, d = 1,2) of individual decision makers are formed as:

Table 9. Evaluation for Alternative of Decision Maker 1

	c_1	c_2	c_3	c_4	c_5	c_6	c_7
x_1	H	H	L	M	L	M	H
x_2	M	L	L	VH	L	VH	VL
x_3	M	VH	VH	H	M	VH	VH

Table 10. Evaluation for alternative of decision maker 2

	c_1	c_2	c_3	c_4	c_5	c_6	c_7
x_1	VH	VH	VL	L	VL	H	VH
x_2	M	H	H	VL	M	VL	VH
x_3	M	H	VH	VH	H	H	VH

Step 6: Identification of the Reference Series

The reference series is formed by considering the best values of the criteria. According to the intuitionistic fuzzy decision matrix, $\alpha^+ = (1,0,0)$ can be employed as the reference value for maximum criteria and $\alpha^- = (0,1,0)$ the reference value for minimum criteria. So, the reference series x_0 are created as follows:

$x_0 = [(0,1,0)(0,1,0)(1,0,0)(1,0,0)(1,0,0)(1,0,0)(1,0,0)]_{1*7}$

R^1 =

(0.7,0.2,0.1)	(0.7,0.2,0.1)	(0.35,0.55,0.1)	(0.5,0.35,0.15)	(0.35,0.55,0.1)	(0.5,0.35,0.15)	(0.7,0.2,0.1)
(0.5,0.35,0.15)	(0.35,0.55,0.1)	(0.35,0.55,0.1)	(0.85,0.1,0.05)	(0.35,0.55,0.1)	(0.85,0.1,0.05)	(0.25,0.7,0.05)
(0.5,0.35,0.15)	(0.85,0.1,0.05)	(0.85,0.1,0.05)	(0.7,0.2,0.1)	(0.5,0.35,0.15)	(0.85,0.1,0.05)	(0.85,0.1,0.05)

R^2 =

(0.85,0.1,0.05)	(0.85,0.1,0.05)	(0.25,0.7,0.05)	(0.35,0.55,0.1)	(0.25,0.7,0.05)	(0.7,0.2,0.1)	(0.85,0.1,0.05)
(0.5,0.35,0.15)	(0.7,0.2,0.1)	(0.7,0.2,0.1)	(0.25,0.7,0.05)	(0.5,0.35,0.15)	(0.25,0.7,0.05)	(0.85,0.1,0.05)
(0.5,0.35,0.15)	(0.7,0.2,0.1)	(0.85,0.1,0.05)	(0.85,0.1,0.05)	(0.7,0.2,0.1)	(0.7,0.2,0.1)	(0.85,0.1,0.05)

Su et al., (2012) suggests using the value λ = 2 in Eq. (16). So, we set the parameters λ = 2 and δ = (0.618,0.382) ^{T} by applying the IG-IFOWA operator. Operating the IG-IFOWA operator in Eq. (16), the intuitionistic fuzzy decision matrix is converted to the following combined intuitionistic fuzzy decision matrix.

Step 7: Calculation of Grey Relational Coefficients

The grey relational coefficients are calculated by using Eq. (10). While determining the distance matrix between x_0 and x_i, the hamming distance value is used. Distance matrix is calculated by using the absolute difference between the membership and non-membership degrees is computed

R =

(0.772,0.153,0.075)	(0.596,0.153,0.252)	(0.1,0.598,0.302)	(0.204,0.11,0.385)	(0.1,0.598,0.302)	(0.353,0.28,0.367)	(0.596,0.153,0.252)
(0.5,0.35,0.15)	(0.287,0.359,0.355)	(0.287,0.359,0.355)	(0.558,0.191,0.251)	(0.174,0.457,0.37)	(0.558,0.191,0.251)	(0.411,0.293,0.296)
(0.5,0.35,0.15)	(0.55,0.13,0.22)	(0.723,0.1,0.178)	(0.596,0.153,0.252)	(0.353,0.28,0.367)	(0.65,0.13,0.22)	(0.723,0.1,0.178)

Table 11. Distance Matrix

	c_1	c_2	c_3	c_4	c_5	c_6	c_7	min	max
$\Delta_{01}(j)$	1,619	1,443	1,498	1,208	1,498	0,928	0,557	0,557	1,619
$\Delta_{02}(j)$	1,150	0,928	1,072	0,633	1,283	0,633	0,882	0,633	1,283
$\Delta_{03}(j)$	1,150	1,520	0,378	0,557	0,928	0,480	0,378	0,378	1,520

Table 12. The grey relational coefficient matrix

	c_1	c_2	c_3	c_4	c_5	c_6	c_7
$\gamma_{01}(j)$	0,489	0,527	0,514	0,589	0,514	0,683	0,869
$\gamma_{02}(j)$	0,606	0,683	0,631	0,823	0,567	0,823	0,702
$\gamma_{03}(j)$	0,606	0,510	1,000	0,869	0,683	0,921	1,000

Table 13. Final scores of the alternatives

Alternatives	Grey relational scores
x_1	0,598
x_2	0,691
x_3	0,798

Table 14. Comparison of methods

Alternatives	IF-TOPSIS	IF-GRA	IF-WASPAS
Full outsourcing	1	1	1
In-house production	3	3	3
Hybrid system	2	2	2

according to Eq. (17). Accordingly, the distance matrix obtained is shown in Table 11:

$$\Delta_{0i}(j) = \left|\mu_{ij} - \mu_{0j}\right| + \left|\vartheta_{ij} - \vartheta_{0j}\right|, \text{j=1,2,3,…,n} \quad (17)$$

The distinguishing coefficient factor (φ) is set to 0.5 and the grey relational coefficients are computed by applying Eq. (10). The values obtained are shown in Table 12:

Step 8: Calculating Grey Relational Grades

The grey relational grades are transformed into the grey relational coefficients by using Eq. (12). Grey relational grades of the individual alternatives are as shown in Table 13.

Step 9: Ranking of Alternatives by Grey Relational Degrees

The alternatives are ordered from the highest to the lowest grey relational grade, with the alternative obtaining the highest value being identified as the most suitable option. The three alternatives are ranked as follows: Full outsourcing; Hybrid System; and In-house production ($\gamma_3 > \gamma_2 > \gamma_1$). Thus, the most appropriate alternative is outsourcing.

As discussed previously, employing multiple methods is generally considered beneficial for analyzing multi-criteria decision-making (MCDM) problems. The intuitionistic fuzzy TOPSIS (IF TOPSIS) [46] method and the intuitionistic fuzzy WASPAS [47] are used to test the accuracy of our results. The reason why TOPSIS and WASPAS methods are preferred rather than other MCDM methods is that these methods can be used by using the same data without changing the criterion weights.

Table 14 compares the rankings produced by the IF-TOPSIS and IF-WASPAS methods with those generated by the proposed approach. When the rankings in Table 14 are analyzed, it can be seen that all methods produce same rankings, suggesting outsourcing as the best option. Based on these results we can suggest that our proposed method can be used safely for the solution of our problem.

Then, the criterion weights are changed and the alternative to be selected is examined. The rankings obtained according to the changing criteria weights are as seen in Table 15.

It can be seen that in the current situation, full outsourcing alternative has been determined as the best alternative. In case the criteria weights are equal; there is no change in the selection order of the alternatives. If the criteria are the most important criteria one by one, the rankings are as shown in the Table 15.

RESULTS AND DISCUSSION

In this study, the make-or-buy decision is discussed in a company operating in the metal sector. The literature review shows that different types of uncertainties are often overlooked, and the entire decision-making process is typically addressed using only a single uncertainty theory. However, the levels of influences of individuals on the ultimate decision, criterion weights and evaluations of alternatives on the basis of the chosen criteria generally include different types of uncertainties. Unlike prior studies, this work addresses each stage of the make-or-buy decision using the most appropriate uncertainty model for that stage. As for the adoption of methods, both intuitionistic fuzzy set theory and grey relational analysis were chosen based on the thought that they are most suitable for the structure of the problem. A common approach used by various authors to solve multi-criteria decision problems is to use more than one method jointly. In this direction, we used TOPSIS and WASPAS methods to test the accuracy of our results obtained in this study. As a result, it was seen that all three methods considered, produced the same results. The consistency among the three methods used in this study serves

Table 15. The sensitivity analysis of criterion weights

	w_1	w_2	w_3	w_4	w_5	w_6	w_7	First Selection	Second Selection	Third Selection
Current situation	0.16	0.14	0.14	0.15	0.14	0.14	0.13	Full outsourcing	Hybrid system	In-house production
Equality of criteria weights	1/7	1/7	1/7	1/7	1/7	1/7	1/7	Full outsourcing	Hybrid system	In-house production
First criterion being the most important criterion	1	0	0	0	0	0	0	Full outsourcing	In-house production	Hybrid system
Second criterion being the most important criterion	0	1	0	0	0	0	0	Hybrid system	Full outsourcing	In-house production
Third criterion being the most important criterion	0	0	1	0	0	0	0	Hybrid system	In-house production	Full outsourcing
Fourth criterion being the most important criterion	0	0	0	1	0	0	0	Hybrid system	In-house production	Full outsourcing
Fifth criterion being the most important criterion	0	0	0	0	1	0	0	Hybrid system	In-house production	Full outsourcing
Sixth criterion being the most important criterion	0	0	0	0	0	1	0	Hybrid system	In-house production	Full outsourcing
Seventh criterion being the most important criterion	0	0	0	0	0	0	1	Hybrid system	Full outsourcing	In-house production

as strong evidence that our proposed method can be safely applied in make-or-buy decisions.

The problem handled within the scope of this study represents a real-life problem that is often seen in the operation of a company in the metal sector. Each make-or-buy decision stands for a decision-making process that generally includes different kinds of uncertainties, such as sectorial uncertainties and subjective evaluations of decision makers. This study demonstrates that grey relational analysis and intuitionistic fuzzy set theory can be effectively combined to handle diverse forms of uncertainty. In this context, our proposed method is evaluated to see how it can be used successfully in solving similar problems involving different types of uncertainties.

Our findings are both consistent with and supported by previous studies in literature. For example, Cheshmberah et al. [15] addressed the make-or-buy decision in the aerospace industry using a fuzzy TOPSIS approach and also concluded that outsourcing was the most effective strategy, particularly under uncertain conditions—similar to our result in the metal manufacturing context. Serrano et al. [30] emphasized the critical role of multi-criteria decision analysis in sourcing strategies, reinforcing the importance of structured evaluation methods when dealing with complex decisions. In terms of methodology, Padillo and Diaby [6] proposed a composite programming-based multi-objective model for make-or-buy decisions but did not account for varying types of uncertainty at different decision stages. Our integrated approach, which employs intuitionistic fuzzy sets (IFS) to handle subjectivity and grey relational analysis (GRA) to deal with incomplete data, goes beyond these earlier models by addressing uncertainty

more flexibly and comprehensively. Thus, our study not only confirms existing conclusions about the advantages of outsourcing in certain industrial contexts but also introduces a novel, hybrid methodology that improves decision reliability under uncertainty.

In addition to the consistent rankings produced across three different multi criteria decision methods (IFS-GRA, IF-TOPSIS, and IF-WASPAS), we observed that removing either intuitionistic fuzzy set theory or grey relational analysis from the process led to more unstable rankings and increased sensitivity in results under changing criterion weights. These findings suggest that the combination of intuitionistic fuzzy numbers and grey relational analysis enhances the robustness and consistency of decision-making under uncertainty. Furthermore, using the appropriate uncertainty method at each step offers a more realistic representation of how information is processed in actual industrial environments.

CONCLUSION

With increasing levels of competition and accelerating speed of development in all economic sectors, searches for efficient efforts for businesses to meet elevating customer demands and expectations and to produce better customer satisfactions force enterprises to use more effective strategies in their activities. In today's competitive environment, the make-or-buy decision has emerged as a key strategic issue. The make-or-buy decision is a strategic decision that contributes significantly to the profitability of the company. Outsourcing decisions are often made solely based on cost, neglecting other crucial factors such as quality and delivery reliability. However, in addition to costs, many factors such as delivery reliability, technical capacity, and the costs of financial arrangements should be taken into account in the make-or-buy decisions.

In this study, the make-or-buy decision analysis for the components needed by an enterprise operating in the metal industry is examined. Due to the uncertainty naturally existing in decision makers' evaluations regarding the employed criteria and the subjectivity of these criteria, the intuitionistic fuzzy set theory and grey relational analysis methods were used jointly. The findings indicate that the integration of intuitionistic fuzzy set theory and grey relational analysis is effective in managing uncertainty. Applying multiple MCDM techniques is generally considered a good practice for validating decision-making results. To test the accuracy of our results, the intuitionistic fuzzy TOPSIS (IF TOPSIS) and WASPAS methods were used with the same data that was underneath our proposed approach. Analysis of the resulting rankings shows that all three methods produced consistent outcomes. All three methods suggest outsourcing as the best option. These results support the robustness and reliability of our proposed method in solving make-or-buy problems when there are many types of uncertainties involved in the process. In addition, the method's flexible structure allows it to be adapted to various industries facing similar uncertainty-driven decisions, including automotive, electronics, and logistics sectors. The novelty of this study is to use appropriate methods of uncertainty in different steps of analysis instead of employing the same uncertainty theory throughout the whole selection process. In addition, the use of grey theory for the first time in make-or-buy decisions is considered as an important contribution of the study to literature. Moreover, the robustness of the results under multiple scenarios and the consistent rankings across different multicriteria decision methods confirm the reliability and added value of the proposed integrated approach. The consistency of the results across multiple methods confirms the reliability of our integrated framework and its alignment with the decision-making needs defined at the beginning of the study.

AUTHORSHIP CONTRIBUTIONS

Authors equally contributed to this work.

DATA AVAILABILITY STATEMENT

The authors confirm that the data that supports the findings of this study are available within the article. Raw data that support the finding of this study are available from the corresponding author, upon reasonable request.

CONFLICT OF INTEREST

The author declared no potential conflicts of interest with respect to the research, authorship, and/or publication of this article.

ETHICS

There are no ethical issues with the publication of this manuscript.

STATEMENT ON THE USE OF ARTIFICIAL INTELLIGENCE

Artificial intelligence was not used in the preparation of the article.

REFERENCES

[1] Boyle IM, Duffy AHB, Whitfield RI, Jupp J. The impact of resources on decision making. Artif Intell Eng Des Anal Manuf 2012;26:407–423. [CrossRef]

[2] Deng J. Introduction to grey system theory. J Grey Syst 1989;1:1–24.

[3] Liu S, Lin Y. An introduction to grey systems: Foundations, methodology and applications. Grove City: IIGSS Academic Publisher; 1998.

[4] Lin Y, Chen MY, Liu S. Theory of grey systems: Capturing uncertainties of grey information. Kybernetes 2004;33:196–218. [CrossRef]

[5] Williamson OE. Markets and Hierarchies: Analysis and Antitrust Implications. New York: Free Press; 1975.
[6] Padillo JM, Diaby M. Multiple-criteria decision methodology for the make-or-buy problem. Int J Prod Res 1999;37:3203–3229. [CrossRef]
[7] Platts KW, Probert DR, Canez L. Make vs. buy decisions: A process incorporating multi-attribute decision-making. Int J Prod Econ 2002;77:247–257. [CrossRef]
[8] Hwang HJ. Computer-aided fuzzy AHP decision model and its application to school food service problem. Int J Innov Comput Inf Control 2006;2:125–137.
[9] Golec A, Ozturkoğlu O. A Choquet integral approach to the make or buy decision in the metal part manufacturing. In: Proceedings of the 5th International Symposium on Intelligent Manufacturing Systems; 2006. p. 1251–1259.
[10] Water H, Peet H. A decision support model based on the analytic hierarchy process for the make or buy decision in manufacturing. J Purch Supply Manag 2006;12:258–271. [CrossRef]
[11] Hwang H. Web-based multi-attribute analysis model for make-or-buy decisions. Math Comput Model 2007;46:1081–1090. [CrossRef]
[12] Kahraman C, Orhan E, Kabak O, Kaya I. Information systems outsourcing decisions using a group decision-making approach. Eng Appl Artif Intell 2009;22:832–841. [CrossRef]
[13] Cheshmberah M, Makul A, Hosseini MS. Manufacturing outsourcing decision making based on screening core activities and fuzzy multi-criteria approach. J Appl Sci 2010;10:2276–2282. [CrossRef]
[14] Minh ND. Empirical make-or-buy decision making model in the Japanese automobile industry. In: Proceedings of the 2011 Winter Simulation Conference (WSC); 2011. p. 647–658. [CrossRef]
[15] Cheshmberah M, Makui A, Seyedhosseini SM, Najmi A. A new fuzzy MCDA framework for make-or-buy decisions: A case study of aerospace industry. Manag Sci Lett 2011;1:323–330. [CrossRef] [CrossRef]
[16] Seyedhosseini SM, Mohammadipour F, Gorji M. Make or buy strategy decision making in supply quality chain. Int J Ind Eng Comput 2012;3:413–422. [CrossRef]
[17] Sillanpää I. Strategic decision-making model for make or buy decisions. Int J Logist Econ Glob 2015;6:205–222. [CrossRef]
[18] Park WY. Managing hazards of the make-buy decision in the face of radical technological change. Ind Manag Data Syst 2018;118:1345–1364. [CrossRef]
[19] Serrano RM, Ramírez RG, Gascó JG. Should we make or buy? An update and review. Eur Res Manag Bus Econ 2018;24:137–148. [CrossRef]
[20] Serrano RM, Ramírez RG, Gascó JG, Taverner JL. Strategic sourcing: Developing a progressive framework for make-or-buy decisions. J Ind Eng Manag 2020;13:133–154. [CrossRef]
[21] Omerali M, Kaya T. Should firms investigating in TOT domain buy or implement in their Industry 4.0 initiatives? An application of Type-2 Fuzzy COPRAS. J Intell Fuzzy Syst 2020;39:6539–6552. [CrossRef]
[22] Klein PG, Mazzoni JFR. The make-or-buy decision revisited. SSRN Electron J 2024. doi:10.2139/ssrn.4810444. [CrossRef]
[23] Longauer D, Vasvári T, Hauck Z. Investigating make-or-buy decisions and the impact of learning-by-doing. Int J Prod Res 2023;61:3835–3852. doi:10.1080/00207543.2023.2250009. [CrossRef]
[24] Brem A, Elsner R. Make-or-buy decisions on technology-intensive products: Insights from the consumer goods industry. Int J Innov Technol Manag 2017;14:1750031. [CrossRef]
[25] Yin MS. Fifteen years of grey system theory research: A historical review and bibliometric analysis. Expert Syst Appl 2013;40:2767–2775. [CrossRef]
[26] Liu S, Forrest JYL. The role and position of grey system theory in science development. J Grey Syst 1997;4:351–356.
[27] Delcea C. Grey systems theory in economics: A historical applications review. Grey Syst Theory Appl 2015;5:263–276. [CrossRef]
[28] Pan W, Jian L, Liu T. Grey system theory trends from 1991 to 2018: A bibliometric analysis and visualization. Scientometrics 2019;121:1407–1434. [CrossRef]
[29] Jayant A, Giri V, Singh PD, Luthra S. A state-of-the-art literature survey of grey relational analysis applications in competitive business environment. Int J Ind Syst Eng 2018;30:425–448. [CrossRef]
[30] Javanmardi E, Liu S. Exploring grey systems theory-based methods and applications in sustainability studies: A systematic review approach. Sustainability 2020;12:4437. [CrossRef]
[31] Liu S, Lin Y. Introduction to grey systems theory. In: Grey Systems. Understanding Complex Systems. Vol 68. Berlin, Heidelberg: Springer; 2010. [CrossRef]
[32] Deng JL. Difference among grey, probability, fuzzy. J Grey Syst 1996;3:256–262.
[33] Atanassov K. Intuitionistic fuzzy sets. Fuzzy Sets Syst 1986;20:87–96. [CrossRef]
[34] Zadeh LA. Fuzzy sets. Inf Control 1965;8:338–353. [CrossRef]
[35] Bali O, Kose E, Gumus S. Green supplier selection based on IFS and GRA. Grey Syst Theory Appl 2013;3:158–176. [CrossRef]
[36] Huang TL, Wen KL, Deng JL. The documents of grey system theory. In: 2nd National Conference of Grey Theory and Applications; 1997. p. 1–32.
[37] Wen KL, Huang YF, Chang WG. Grey relational model and its applications. Gauli Publisher; 2003.
[38] Kuo Y, Yang T, Huang G. The use of grey relational analysis in solving multiple attribute decision-making problems. Comput Ind Eng 2008;55:80–93. [CrossRef]

[39] Liao H, Xu Z. A VIKOR-based method for hesitant fuzzy multi-criteria decision making. Fuzzy Optim Decis Mak 2013;12:373–392. [CrossRef]

[40] Dalalah D, Hayajneh M, Batieha F. A fuzzy multi-criteria decision-making model for supplier selection. Expert Syst Appl 2011;38:8384–8391. [CrossRef]

[41] Parthiban P, Zubar HA, Garge CP. A multi criteria decision making approach for suppliers selection. Procedia Eng 2012;38:2312–2328. [CrossRef]

[42] Su Z, Xia G, Chen M, Wang L. Induced generalized intuitionistic fuzzy OWA operator for multi-attribute group decision making. Expert Syst Appl 2012;39:1902–1910. [CrossRef]

[43] Boran FE, Genç S, Kurt M, Akay D. A multi-criteria intuitionistic fuzzy group decision making for supplier selection with TOPSIS method. Expert Syst Appl 2009;36:11363–11368. [CrossRef]

[44] Zhang SF, Liu SY. A GRA-based intuitionistic fuzzy multi-criteria group decision making method for personnel selection. Expert Syst Appl 2011;38:11401–11405. [CrossRef]

[45] Vlachos IK, Sergiadis GD. Intuitionistic fuzzy information-applications to pattern recognition. Pattern Recognit Lett 2007;28:197–206. [CrossRef]

[46] Kahraman C, Öztayşi B, Onar SÇ. An integrated intuitionistic fuzzy AHP and TOPSIS approach to evaluation of outsource manufacturers. J Int Syst 2020;29:283–297. [CrossRef]

[47] Tırmıkçıoğlu N. Sezgisel bulanık WASPAS yöntemi ve depo yeri seçimi problemi. Afyon Kocatepe Üniversitesi Fen ve Mühendislik Bilimleri Dergisi 2021;21:1330–1342. [CrossRef]

Sigma Journal of Engineering and Natural Sciences
Web page info: https://sigma.yildiz.edu.tr
DOI: 10.14744/sigma.2026.2101

Research Article

Cost-benefit evaluation of repairable retrial systems with warm standby components and setup times

Jones Edward CHIWINGA[1], Muhammad Salihu ISA[1,*], Jinbiao WU[1]

[1]*School of Mathematics and Statistics, Central South University Changsha 410083, Hunan, China*

ARTICLE INFO

Article history
Received: 10 August 2024
Revised: 28 November 2024
Accepted: 30 December 2024

Keywords:
Cost-benefit; Retrial System; Warm Standby; Setup Time; Unreliable Service Station

ABSTRACT

Power supply system models are commonly used in industrial and manufacturing sectors to assess performance metrics. This paper conducts a cost-benefit analysis of four different unreliable retrial systems featuring warm standby components and setup times. The systems differ in the quantity of primary (operative) and warm standby (backup) components they contain. The failure and repair times for both primary and standby components are assumed to follow an exponential distribution. For each system, we present the state-transition diagram along with the corresponding differential-difference equations. Employing the Laplace stieltjes transform and the matrix-analytical method, we derive explicit formulas for key performance metrics, including the mean time to failure (MTTF) and steady-state availability, which serve as vital indicators of system reliability. Numerical examples are provided to examine the influence of system parameters on steady state availability, mean time to failure, and the cost-benefit ratio. The results are presented in both tabular and graphical formats, accompanied by a detailed cost-benefit comparative analysis. The findings provide decision-makers with valuable insights for ensuring system stability and optimizing cost efficiency.

Cite this article as: Chiwinga JE, Isa MS, Wu J. Cost-benefit evaluation of repairable retrial systems with warm standby components and setup times. Sigma J Eng Nat Sci 2026;44(4):2380–2395.

INTRODUCTION

In many industries, such as manufacturing, computer networks, communication systems, and production systems, reliability and availability of the power supply system with favorable cost-effectiveness are crucial. Standby power source units emerge as critical components of the overall energy strategies for cement plants. Standby power source units are crucial in safeguarding operations against unforeseen outages and mitigating risks associated with power fluctuations. Several studies address the overall power consumption within cement plants. Cement plants can have their own waste heat recovery to produce electric power by using hybrid renewable energy systems investigated by [1]. Demand response in energy-intensive industry analysed by [2] cement production is a complicated, energy-intensive process that relies massively on a stable supply of electric power to run the equipment which ranges from crushers, conveyors that handle raw materials to kilns, mills that convert materials into cement. Cement plants rely largely on

***Corresponding author.**
*E-mail address: salihu.muhd.isa@gmail.com

This paper was recommended for publication in revised form by Editor-in-Chief Ahmet Selim Dalkilic

Published by Yıldız Technical University Press, İstanbul, Turkey
© Author. This is an open access article under the CC BY-NC license (http://creativecommons.org/licenses/by-nc/4.0/).

utility companies and own electric power sources such as diesel, solar or natural gas powered standby generator to stabilise electric power source and have a power monitoring system to switch over the source. This paper to study reliability and availability factors relating to the suitable repairable retrial system of electric power sources within a medium scale cement producing plant.

Multiple articles with retrial queueing systems in which the servers are subjected to unreliable repair stations and setup times are considered. Ram *et a.l* [3] analysed the use of Markov process for evaluating reliability metrics, cost and sensitiveness of performance measures to system parameters while Aghsami and Jolai [4] studied equilibrium balking strategies in a single-server Markovian queue including studies on intermittent breakdowns and flexible shut down policy while setup time and maintenance procedures were observed by Zhang and Xu [5] in context of customer behavior under queuing system. Interested researchers may read on Sun *et al.* [6] and Wang *et al.* [7] for more comprehensive concepts on the queue systems with setup times.

Related Work

Literature concerning reliability and availability evaluation in retrial systems is extensive and comprehensive. Yen et al. [8] proposed retrial machine repair model considering the aspect of intermittent breakdowns and the probabilistic F-policy is implemented. Reliability evaluation considering equipment maintenance featuring a single repairman and associated recovery policy was explored by [9]. Wang et al. [10] studied the unreliable equipment maintenance system with warm standby failures. Complex systems with two connected systems have been analyzed by Mailhulla et al. [11]. Yang and Tsao [12] carried out research on reliability and availability evaluation of the maintainable system consisted of standby units and component failure in different modes considering retrials. Redundant series configuration under single-repair technician where each working unit has a backup unit which failures can also occur has been studied by Gao et al. [13]. The computer network system containing two clients, load balancers, two fog nodes and two cloud servers connected in series parallel configuration has been presented by Wu and Isa [14], Kumar and Jain [15] have discussed on reliability study under queue with an unstable server considering scheduled breaks with working failure. Shekhar et al. [16] discussed multi-component systems with backup considering breakdowns, delays and random flaws. Iggi and Yusuf [17] and Isa et al. [18] proposed an evaluation to determine performance of the system. Bai et al. [19] studied performance optimization model for periodic switching method. Kuo and Ke [20] researched into availability of two distinct configurations of a series system in an imperfect coverage environment where the system is serviced by an unstable server. Juyibari *et al.* [21] studied repairable system using a mixed strategy that focuses on vacation interruption method and working vacation system. Adan and Filik [22] had assessed renewable energy models to identify most economical and ecological designs. [23-25] studied systems with several types of standby and maintenance facility where these units undergo periodic maintenance or may have active failure. Yen and Wang [26] dealt with reliability and availability for four retrial systems. Wu et al. [27] dealt with reliability and availability for four retrial systems of power supply where imperfect coverage, warm standby and general repair-times could be taken care of. Kang et al. [28] present a model of warm standby retrial system with non-identical units undergoing component breakdown with a warm spare, where some of the operations were assumed to follow a priority. Yen et al. [29] analyzed three different availability models in which warm stand-by units along with delays in the fault detection and different repair times are incorporated. Gao [30] examined maintainable retrial system with warm standby units and a two-stage repair process.

This article presents the performance evaluation of the cement producing plant. Previous studies have independently investigated power plant systems considering unreliable retrial models that adopt various applications. However, to the best of the authors' knowledge, there has been no research specifically addressing unreliable retrial systems incorporating warm standby components, and setup times, in which maintenance and repair are effective. Hence, to address this gap, the present study investigates four repairable retrial systems, where the repair facility requires setup time and failed components request repair services at a later time if the facility is busy upon their arrival.

The summarised key features, approaches and comparative analytical goals of important investigations considered by various scholars are shown in Table 1 below. Therefore, the important objectives of this research study were: To investigate the transient behaviour of repairable cement manufacturing plant power system and accounting setup times, to evaluate its performance with increase of time. To forecast the operational efficiency of the retrial system by evaluating steady-state availability, MTTF. To choose optimum cost-effectiveness ratio and to decide for the most favorable decision factors. Studying cement power plant reliability metrics and carrying comparative analysis for these reliability metrics of the cement power system can effectively support all decision making by the management for replacements, equipment upgrades and for capacity requirements. The decision makers-plant managers and government policymakers can choose performance criteria, along with the suitable cost and risks involved in a more balanced ratio for their options along about organisational strategy.

The subsequent sections of the paper are organized as follows: Section 2 outlines the potential application and description of the model. In Section 3, a systematic approach is presented for deriving detailed expressions for the MTTF and steady-state availability for a given retrial system. Section 4 provides detailed numerical findings

Table 1. Summary of similar literature studies

Reference	Warm standby	Setup times	Unreliable retrial system	Matrix analytical approach	Cost-benefit ratio
Rehman and Farzaneh [1]	✘	✘	✘	✘	✓
Zhang and Xu [5]	✘	✓	✓	✘	✘
Wang et al. [10]	✓	✘	✓	✓	✓
Wu and Isa [14]	✘	✘	✘	✓	✓
Wang et al. [25]	✓	✘	✓	✓	✓
Yen and Wang [26]	✓	✘	✘	✓	✓
Proposed model	✓	✓	✓	✓	✓

from sensitivity analysis and comparisons to establish the optimal retrial system. Finally, the summary and conclusion are detailed in Section 5.

POTENTIAL APPLICATION AND MODEL DESCRIPTION

Potential Application

This section presents a possible application of a reliable power supply system in a cement manufacturing plant where the proposed model can be utilized. With the increased demand for modern construction in civil works, cement manufacturing plants are of great need to ensure an adequate supply of cement. In their quest for reliable electrical systems to ensure sustainable production operations in modern cement plants Shirumalla and Chatterjee [31] explored on the reliability of the former. Ali et al. [32] explored options for energy generation systems tailored to the cement industry. In a medium-sized cement manufacturing industry that requires 48MW of electric power and the production capacity of sources is available in units of 48MW, 24MW, and 16MW at different costs. To provide sufficient electric power, repairable service stations, and standby components are available to guarantee system uptime. All components (operating and standby) are unreliable and may fail at any time. A fault detective device is installed to monitor the electric power system. When an operating component fails and is detected, a standby component is switched into operation (if available). At the same time, the failed component is repaired. However, the service station may break down during the busy period. Through the application of queueing theory, we can assess system availability and evaluate the cost-effectiveness of various configurations, forming our issue as an unreliable repair problem that includes spare parts.

Model Description

We take a consideration of a medium cement manufacturing industry that requires 48MW of electrical power generation capacity. To ensure consistent and dependable system availability, there are primary and standby generators. Standby generators are assumed to be susceptible to failure while inactive, before being fully operational. Both primary and standby generators can fail and are subsequently repaired. The interval times between failures of the primary and warm standby generators are exponentially distributed with failure rates λ and α ($0 < \alpha < \lambda$) respectively. There is a repair facility with a single operator who handles repairs of malfunctioning components and there is no waiting area in front of it and the repairman can attend to only one failed component at a time. As the operating components fail, they are replaced by a standby component (if available). If the service station is open and idle, the component is repaired immediately upon arrival, otherwise, it enters the orbit of retrials and awaits a random duration that is exponentially distributed with a rate γ. The repair times are assumed to be exponentially distributed with a rate μ. If there are no pending repair tasks in the system after a service has been completed, the service station will be turned off at once to save energy. A newly arrived failed component can reactivate the off-server. Before servicing a newly arrived failed component, the service station requires a setup time that follows an exponential distribution with a rate η. The failed component that triggers the server will promptly enter the orbit and request service. The server is not completely reliable and may experience random breakdowns while repairing the failed component, it can be repaired perfectly according to an exponential distribution with rates β and δ respectively. Once a component has been repaired, it is as good as new. Lastly, the retrial processes, the repair service, and component failures are all independent. We consider four retrial systems as follows: The first retrial system comprises one 48MW primary component and one 48MW warm standby component. The second retrial system includes two 24MW primary components and one 24MW warm standby component. The third retrial system contains two 24MW primary components and two 24MW warm standby components. The fourth retrial system is composed of three 16MW primary components and two 16MW warm standby components

Table 2. The acquisition cost for the primary and warm standby components

Component	Cost (in $)
Primary 48MW	48×10^6
Primary 24MW	24×10^6
Primary 16MW	16×10^6
Warm standby 48MW	24×10^6
Warm standby 24MW	12×10^6
Warm standby 16MW	8×10^6

Table 3. The cost for each retrial system

Retrial system	Primary	Warm standby	Cost (in $)
1	1 × 48	1 × 48	72×10^6
2	2 × 24	1 × 24	60×10^6
3	2 × 24	2 × 24	72×10^6
4	3 × 16	2 × 16	64×10^6

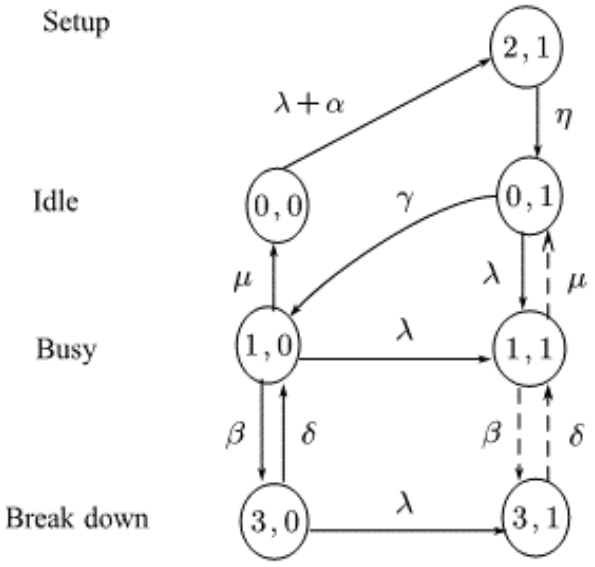


Figure 1. State-transition diagram of retrial system 1.

Cost-Benefit Factor

We assume that the costs, depending on the size, for both primary and warm standby components are specified in Table 2. Using this information, we compute the costs related to each retrial system as presented in Table 3. Let C_i represent the cost and BF_i be the benefit of the retrial system $i(i = 1,2,3,4)$, where BF_i represents either MTTF or steady-state availability.

SYSTEMATIC METHODOLOGY

The service station has four different statuses: idle (i = 0), busy (i = 1), set-up process (i = 2), and breakdown (i = 3). At time t, the variable $(i,n:t)$ precisely describes the system states where i represents the state of the service station and n denotes the number of failed components in the retrial orbit. Using these notations as a foundation, we can thoroughly examine the four systems and derive their respective performance metrics.

Calculations for Retrial System 1

In the context of reliability, Figure 1 illustrates the state-transition diagram for retrial system 1, electricity drops below 48MW. States (1,1) and (3,1) are therefore regarded as absorbing states in the event that the system cannot be restored. In this case, the system's MTTF is analyzed without taking into account transitions from state (1,1) to (0,1) and (3,1) or from state (3,1) to (1,1).

Let $\Pi_{i,n}(t)$ = the probability at time t that there are n failed components in the retrial orbit when the service station is in state i. Let $\Pi_i(t)$ represent the probability column vector at time t,

$$\Pi(t) = [\Pi_{0,0}(t), \Pi_{1,0}(t), \Pi_{3,0}(t), \Pi_{0,1}(t), \Pi_{1,1}(t), \Pi_{2,1}(t), \Pi_{3,1}(t)]^T$$

The initial probability for this system is given by

$$\Pi(0) = [\Pi_{0,0}(0), \Pi_{1,0}(0), \Pi_{3,0}(0), \Pi_{0,1}(0), \Pi_{1,1}(0), \Pi_{2,1}(0), \Pi_{3,1}(0)]^T = [1,0,0,0,0,0,0]^T,$$

where T indicates transpose. For retrial system 1, we obtain the following set of differential-difference equations:

$$\frac{d\Pi_{0,0}(t)}{dt} = -(\lambda+\alpha)\Pi_{0,0}(t) + \mu\Pi_{1,0}(t), \quad (1)$$

$$\frac{d\Pi_{1,0}(t)}{dt} = -(\lambda+\beta+\mu)\Pi_{1,0}(t) + \delta\Pi_{3,0}(t) + \gamma\Pi_{0,1}(t), \quad (2)$$

$$\frac{d\Pi_{3,0}(t)}{dt} = \beta\Pi_{1,0}(t) - (\lambda+\delta)\Pi_{3,0}(t), \quad (3)$$

$$\frac{d\Pi_{0,1}(t)}{dt} = -(\lambda+\gamma)\Pi_{0,1}(t) + \eta\Pi_{2,1}(t), \quad (4)$$

$$\frac{d\Pi_{1,1}(t)}{dt} = \lambda\Pi_{1,0}(t) + \lambda\Pi_{0,1}(t), \quad (5)$$

$$\frac{d\Pi_{2,1}(t)}{dt} = (\lambda+\alpha)\Pi_{0,0}(t) - \eta\Pi_{2,1}(t), \quad (6)$$

$$\frac{d\Pi_{3,1}(t)}{dt} = \lambda\Pi_{3,0}(t). \quad (7)$$

To solve Eq. (1) through (7), we define the Laplace-stieltjes transform (LST) as:
$\Pi^*_{i,n}(s) = \int_0^\infty e^{-st}\,\Pi_{i,n}(t)\,dt$, $i = 0,1,2$; $n = 0,1$. Applying the LST on both sides of Eq. (1) to Eq. (7) results in

$$(\lambda+\alpha+s)\Pi^*_{0,0}(s) - \mu\Pi^*_{1,0}(s) = \Pi_{0,0}(0),$$
$$(\lambda+\beta+\mu+s)\Pi^*_{1,0}(s) - \delta\Pi^*_{3,0}(s) - \gamma\Pi^*_{0,1}(s) = \Pi_{1,0}(0),$$
$$(\lambda+\delta+s)\Pi^*_{3,0}(s) - \beta\Pi^*_{1,0}(s) = \Pi_{3,0}(0),$$
$$(\lambda+\gamma+s)\Pi^*_{0,1}(s) - \eta\Pi^*_{2,1}(s) = \Pi_{0,1}(0),$$
$$s\Pi^*_{1,1}(s) - \lambda\Pi^*_{1,0}(s) - \lambda\Pi^*_{0,1}(s) = \Pi_{1,1}(0),$$
$$(\eta+s)\Pi^*_{2,1}(s) - (\lambda+\alpha)\Pi^*_{0,0}(s) = \Pi_{2,1}(0),$$
$$s\Pi^*_{3,1}(s) - \lambda\Pi^*_{3,0}(s) = \Pi_{3,1}(0).$$

In matrix form

$$Q_1\Pi^*(s) = \Pi(0), \tag{8}$$

where

$$Q_1 = \begin{pmatrix} \lambda+\alpha+s & -\mu & 0 & 0 & 0 & 0 & 0 \\ 0 & \lambda+\beta+\mu+s & -\delta & -\gamma & 0 & 0 & 0 \\ 0 & -\beta & \lambda+\delta+s & 0 & 0 & 0 & 0 \\ 0 & 0 & 0 & \lambda+\gamma+s & 0 & -\eta & 0 \\ 0 & -\lambda & 0 & -\lambda & s & 0 & 0 \\ -(\lambda+\alpha) & 0 & 0 & 0 & 0 & \eta+s & 0 \\ 0 & 0 & -\lambda & 0 & 0 & 0 & s \end{pmatrix},$$

and

$$\Pi^*(s) = [\Pi^*_{0,0}(s), \Pi^*_{1,0}(s), \Pi^*_{3,0}(s), \Pi^*_{0,1}(s), \Pi^*_{1,1}(s), \Pi^*_{2,1}(s), \Pi^*_{3,1}(s)]^T.$$

Solving Eq. (8) yields $\Pi^*_{0,0}(s)$, $\Pi^*_{1,0}(s)$, $\Pi^*_{3,0}(s)$, $\Pi^*_{0,1}(s)$, $\Pi^*_{1,1}(s)$, $\Pi^*_{2,1}(s)$, $\Pi^*_{3,1}(s)$. Let X be the time to failure of the system, thus, the probabilities $\Pi_{1,1}(t)$ and $\Pi_{3,1}(t)$ suggest that the system cannot meet the minimum requirements before time t, therefore, the system reliability function is derived as follows:

$$R_X(t) = 1 - \Pi_{1,1}(t) - \Pi_{3,1}(t) = \Pi_{0,0}(t) + \Pi_{1,0}(t) + \Pi_{3,0}(t) + \Pi_{0,1}(t) + \Pi_{2,1}(t).$$

MTTF$_1$ of retrial syatem 1

The MTTF of retrial system 1 is obtained by

$$MTTF_1 = \int_0^\infty R_X(t)\,dt = \lim_{s\to 0} R^*_X(s),$$
$$= \lim_{s\to 0}\int_0^\infty e^{-st}\left[\Pi_{0,0}(t) + \Pi_{1,0}(t) + \Pi_{3,0}(t) + \Pi_{0,1}(t) + \Pi_{2,1}(t)\right]dt,$$
$$= \lim_{s\to 0}\left[\Pi^*_{0,0}(s) + \Pi^*_{1,0}(s) + \Pi^*_{3,0}(s) + \Pi^*_{0,1}(s) + \Pi^*_{2,1}(s)\right].$$

The explicit expression of $MTTF_1$ for the retrial system 1 is too extensive to present here. However, a numerical example is provided in Section 4 to evaluate it using appropriate computational software.

System availability ($Av_{T_1}(\infty)$)

In the availability scenario, we analyze the state-transition diagram of retrial system 1 depicted in Figure 1, focusing transition from state (1,1) to (0,1), from (1,1) to state (3,1), and from state (3,1) to (1,1). Then, the governing differential-difference equations can be expressed in matrix form as:

$$\begin{pmatrix} \frac{d\Pi_{0,0}(t)}{dt} \\ \frac{d\Pi_{1,0}(t)}{dt} \\ \frac{d\Pi_{3,0}(t)}{dt} \\ \frac{d\Pi_{0,1}(t)}{dt} \\ \frac{d\Pi_{1,1}(t)}{dt} \\ \frac{d\Pi_{2,1}(t)}{dt} \\ \frac{d\Pi_{3,1}(t)}{dt} \end{pmatrix} = \begin{pmatrix} -(\lambda+\alpha) & \mu & 0 & 0 & 0 & 0 & 0 \\ 0 & -(\lambda+\beta+\mu) & \delta & \gamma & 0 & 0 & 0 \\ 0 & \beta & -(\lambda+\delta) & 0 & 0 & 0 & 0 \\ 0 & 0 & 0 & -(\lambda+\gamma) & \mu & \eta & 0 \\ 0 & \lambda & 0 & \lambda & -(\beta+\mu) & 0 & \delta \\ \lambda+\alpha & 0 & 0 & 0 & 0 & -\eta & 0 \\ 0 & 0 & \lambda & 0 & \beta & 0 & -\delta \end{pmatrix} \begin{pmatrix} \Pi_{0,0}(t) \\ \Pi_{1,0}(t) \\ \Pi_{3,0}(t) \\ \Pi_{0,1}(t) \\ \Pi_{1,1}(t) \\ \Pi_{2,1}(t) \\ \Pi_{3,1}(t) \end{pmatrix}.$$

Let T_1 be the time to failure of the system 1. To investigate the availability aspects of this system, we will consider the following procedure. The derivatives of the state probability become zero (0) in a steady state, that is $\frac{d\Pi(t)}{dt} = 0$. Hence, $Av_{T1}(\infty)$ can be obtained as

$Av_{T1}(\infty) = 1 - \Pi_{1,1}(\infty) - \Pi_{3,1}(\infty)$, and $Q_2\Pi(\infty) = 0$. The matrix form is given by;

$$\begin{pmatrix} -\lambda+\alpha & \mu & 0 & 0 & 0 & 0 & 0 \\ 0 & -(\lambda+\beta+\mu) & \delta & \gamma & 0 & 0 & 0 \\ 0 & \beta & -(\lambda+\delta) & 0 & 0 & 0 & 0 \\ 0 & 0 & 0 & -(\lambda+\gamma) & \mu & \eta & 0 \\ 0 & \lambda & 0 & \lambda & -(\beta+\mu) & 0 & \delta \\ \lambda+\alpha & 0 & 0 & 0 & 0 & -\eta & 0 \\ 0 & 0 & \lambda & 0 & \beta & 0 & -\delta \end{pmatrix} \begin{pmatrix} \Pi_{0,0}(t) \\ \Pi_{1,0}(t) \\ \Pi_{3,0}(t) \\ \Pi_{0,1}(t) \\ \Pi_{1,1}(t) \\ \Pi_{2,1}(t) \\ \Pi_{3,1}(t) \end{pmatrix} = \begin{pmatrix} 0 \\ 0 \\ 0 \\ 0 \\ 0 \\ 0 \\ 0 \end{pmatrix}. \tag{9}$$

The normalizing condition is

$$\Pi_{0,0}(\infty) + \Pi_{1,0}(\infty) + \Pi_{3,0}(\infty) + \Pi_{0,1}(\infty) + \Pi_{1,1}(\infty) + \Pi_{2,1}(\infty) + \Pi_{3,1}(\infty) = 1. \tag{10}$$

We replace one of the redundant rows in Eq. (9) with Eq. (10) to obtain:

$$\begin{pmatrix} -(\lambda+\alpha) & \mu & 0 & 0 & 0 & 0 & 0 \\ 0 & -(\lambda+\beta+\mu) & \delta & \gamma & 0 & 0 & 0 \\ 0 & \beta & -(\lambda+\delta) & 0 & 0 & 0 & 0 \\ 0 & 0 & 0 & -(\lambda+\gamma) & \mu & \eta & 0 \\ 0 & \lambda & 0 & \lambda & -(\beta+\mu) & 0 & \delta \\ \lambda+\alpha & 0 & 0 & 0 & 0 & -\eta & 0 \\ 1 & 1 & 1 & 1 & 1 & 1 & 1 \end{pmatrix} \begin{pmatrix} \Pi_{0,0}(t) \\ \Pi_{1,0}(t) \\ \Pi_{3,0}(t) \\ \Pi_{0,1}(t) \\ \Pi_{1,1}(t) \\ \Pi_{2,1}(t) \\ \Pi_{3,1}(t) \end{pmatrix} = \begin{pmatrix} 0 \\ 0 \\ 0 \\ 0 \\ 0 \\ 0 \\ 1 \end{pmatrix}. \tag{11}$$

The solution to Eq. (11) gives the availability scenario's steady-state probabilities. For retrial system 1, the detailed expression for $Av_{T1}(\infty)$ is too lengthy to be displayed here. In Section 4, we use specific numerical values to solve an example and compare this retrial system with others.

Calculations for Retrial System 2

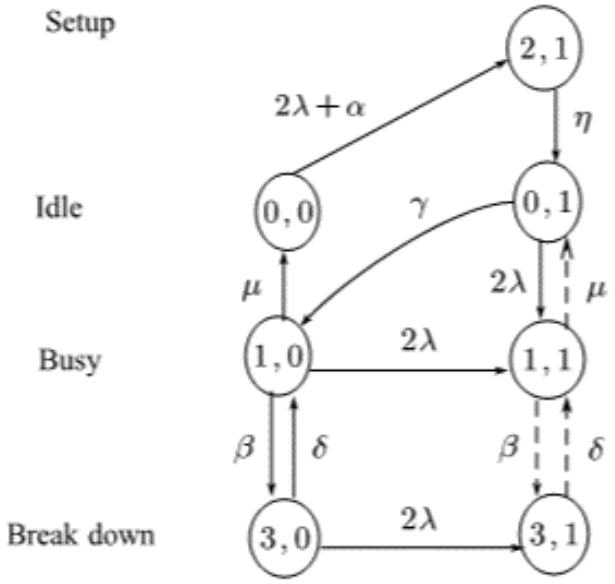


Figure 2. State-transition diagram of retrial system 2.

MTTF$_2$ of retrial syatem 1

Similarly, in the evaluation of system reliability, the system does not transition from state (1,1) to states (0,1) and (3,1) nor from state (3,1) to state (1,1). The corresponding probability vector $\prod(t)$ for retrial system 2 is given by:

$$\Pi(t) = [\Pi_{0,0}(t), \Pi_{1,0}(t), \Pi_{3,0}(t), \Pi_{0,1}(t), \Pi_{2,1}(t)]^T.$$

The differential-difference equations can be expressed in matrix form as:

$$\frac{d\prod(t)}{dt} = Q_3 \prod(t).$$

where

$$Q_3 = \begin{pmatrix} -(2\lambda+\alpha) & \mu & 0 & 0 & 0 & 0 & 0 \\ 0 & -(2\lambda+\beta+\mu) & \delta & \gamma & 0 & 0 & 0 \\ 0 & \beta & -(2\lambda+\delta) & 0 & 0 & 0 & 0 \\ 0 & 0 & 0 & -(2\lambda+\gamma) & 0 & -\eta & 0 \\ 0 & 2\lambda & 0 & 2\lambda & 0 & 0 & 0 \\ 2\lambda+\alpha & 0 & 0 & 0 & 0 & \eta & 0 \\ 0 & 0 & 2\lambda & 0 & 0 & 0 & 0 \end{pmatrix},$$

Obtaining explicit transient solutions poses a challenge. We present a systematic approach for computing MTTF for a retrial system 2. Initially, we neglect the absorbing state's fifth and last rows and their respective columns. Subsequently, we transpose the resulting matrix to obtain matrix A_2, as follows:

$$A_2 = \begin{pmatrix} -(2\lambda+\alpha) & 0 & 0 & 0 & \lambda+\alpha \\ \mu & -(2\lambda+\beta+\mu) & \beta & 0 & 0 \\ 0 & \delta & -(2\lambda+\delta) & 0 & 0 \\ 0 & \gamma & 0 & -(2\lambda+\gamma) & 0 \\ 0 & 0 & 0 & \eta & -\eta \end{pmatrix}.$$

Then, the expected time until reaching a terminal state is derived from

$$E\left[T_{\Pi(0)\to\Pi(absorbing)}\right] = \prod(0)^T\left(-A_2^{-1}\right)[1,1,1,1,1]^T,$$

where the initial conditions, $\prod(0)$ for retrial system 2 are given by:

$$\Pi(0) = [\Pi_{0,0}(0), \Pi_{1,0}(0), \Pi_{3,0}(0), \Pi_{0,1}(0), \Pi_{2,1}(0)]^T = [1,0,0,0,0]^T,$$

As mentioned before, the explicit expression for $MTTF_2$ is very complex to be displayed here. A specific numerical example is given in Section 4 and a comparison of the four retrial systems is performed.

System availability ($Av_{T_2}(\infty)$)

For the availability scenario, the state-transition diagram of retrial system 2 is illustrated in Figure 2 (with the transition from state (2,1) to (1,1) and (3,1), and from state (3,1) to (1,1). The differential-difference equations can be expressed in matrix form:

$$\begin{pmatrix} \frac{d\Pi_{0,0}(t)}{dt} \\ \frac{d\Pi_{1,0}(t)}{dt} \\ \frac{d\Pi_{3,0}(t)}{dt} \\ \frac{d\Pi_{0,1}(t)}{dt} \\ \frac{d\Pi_{1,1}(t)}{dt} \\ \frac{d\Pi_{2,1}(t)}{dt} \\ \frac{d\Pi_{3,1}(t)}{dt} \end{pmatrix} = \begin{pmatrix} -(2\lambda+\alpha) & \mu & 0 & 0 & 0 & 0 & 0 \\ 0 & -(2\lambda+\beta+\mu) & \delta & \gamma & 0 & 0 & 0 \\ 0 & \beta & -(2\lambda+\delta) & 0 & 0 & 0 & 0 \\ 0 & 0 & 0 & -(2\lambda+\gamma) & \mu & \eta & 0 \\ 0 & 2\lambda & 0 & 2\lambda & -(\beta+\mu) & 0 & \delta \\ 2\lambda+\alpha & 0 & 0 & 0 & 0 & -\eta & 0 \\ 0 & 0 & 2\lambda & 0 & \beta & 0 & -\delta \end{pmatrix} \begin{pmatrix} \Pi_{0,0}(t) \\ \Pi_{1,0}(t) \\ \Pi_{3,0}(t) \\ \Pi_{0,1}(t) \\ \Pi_{1,1}(t) \\ \Pi_{2,1}(t) \\ \Pi_{3,1}(t) \end{pmatrix}.$$

Let T_2 represent the time to failure of the system for retrial system 2. In steady-state, the derivatives of the state probabilities become zero. This allows us to calculate the steady-state availability as $Av_{T_2}(\infty) = 1 - \Pi_{1,1}(\infty) - \Pi_{3,1}(\infty)$, and $Q_4\Pi(\infty) = 0$, in matrix form:

$$\begin{pmatrix} -(2\lambda+\alpha) & \mu & 0 & 0 & 0 & 0 & 0 \\ 0 & -(2\lambda+\beta+\mu) & \delta & \gamma & 0 & 0 & 0 \\ 0 & \beta & -(2\lambda+\delta) & 0 & 0 & 0 & 0 \\ 0 & 0 & 0 & -(2\lambda+\gamma) & \mu & \eta & 0 \\ 0 & 2\lambda & 0 & 2\lambda & -(\beta+\mu) & 0 & \delta \\ 2\lambda+\alpha & 0 & 0 & 0 & 0 & -\eta & 0 \\ 0 & 0 & 2\lambda & 0 & \beta & 0 & -\delta \end{pmatrix} \begin{pmatrix} \Pi_{0,0}(t) \\ \Pi_{1,0}(t) \\ \Pi_{3,0}(t) \\ \Pi_{0,1}(t) \\ \Pi_{1,1}(t) \\ \Pi_{2,1}(t) \\ \Pi_{3,1}(t) \end{pmatrix} = \begin{pmatrix} 0 \\ 0 \\ 0 \\ 0 \\ 0 \\ 0 \\ 0 \end{pmatrix}. \quad (12)$$

The normalizing condition is given by

$$\Pi_{0,0}(\infty)+\Pi_{1,0}(\infty)+\Pi_{3,0}(\infty)+\Pi_{0,1}(\infty)+\Pi_{1,1}(\infty)+\Pi_{2,1}(\infty)+\Pi_{3,1}(\infty)=1. \quad (13)$$

We substitute Eq. (13) into one of the duplicated rows in Eq. (12) to obtain

$$\begin{pmatrix} -(2\lambda+\alpha) & \mu & 0 & 0 & 0 & 0 & 0 \\ 0 & -(2\lambda+\beta+\mu) & \delta & \gamma & 0 & 0 & 0 \\ 0 & \beta & -(2\lambda+\delta) & 0 & 0 & 0 & 0 \\ 0 & 0 & 0 & -(2\lambda+\gamma) & \mu & \eta & 0 \\ 0 & 2\lambda & 0 & 2\lambda & -(\beta+\mu) & 0 & \delta \\ 2\lambda+\alpha & 0 & 0 & 0 & 0 & -\eta & 0 \\ 1 & 1 & 1 & 1 & 1 & 1 & 1 \end{pmatrix} \begin{pmatrix} \Pi_{0,0}(t) \\ \Pi_{1,0}(t) \\ \Pi_{3,0}(t) \\ \Pi_{0,1}(t) \\ \Pi_{1,1}(t) \\ \Pi_{2,1}(t) \\ \Pi_{3,1}(t) \end{pmatrix} = \begin{pmatrix} 0 \\ 0 \\ 0 \\ 0 \\ 0 \\ 0 \\ 1 \end{pmatrix}. \quad (14)$$

The solution derived from Eq. (14) yields the steady-state probabilities in the availability scenarios. For retrial system 2 the explicit expression of $Av_{T_2}(\infty)$ is very complicated to be displayed here. However, a specific numerical example is provided in the next section.

Calculations for Retrial System 3

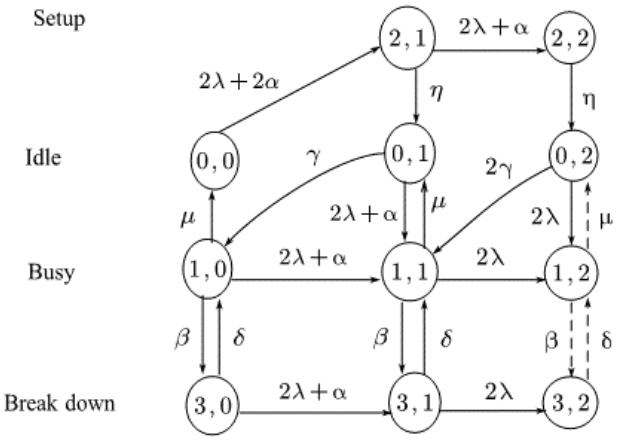


Figure 3. State-transition diagram of retrial system 3.

***MTTF*$_3$ of retrial system 3**

The state-transition diagram of retrial system 3 is given in Figure 3. For system reliability case, the system does not transit from state (1,2) to (3,2) and (0,2) and from state (3,2) to (1,2). The corresponding probability vector $\Pi(t)$ for retrial system 3 is presented as:

$$\Pi(t) = [\Pi_{0,0}(t), \Pi_{1,0}(t), \Pi_{3,0}(t), \Pi_{0,1}(t), \Pi_{1,1}(t), \Pi_{2,1}(t), \Pi_{3,1}(t), \Pi_{0,2}(t), \Pi_{1,2}(t), \Pi_{2,2}(t), \Pi_{3,2}(t)]^T.$$

The governing differential-difference equations of retrial system 3 can be expressed in matrix form as:

$$\frac{d\Pi(t)}{dt} = Q_5 \Pi(t),$$

where

$$Q_5 = \begin{pmatrix} -a_{11} & \mu & 0 & 0 & 0 & 0 & 0 & 0 & 0 & 0 & 0 \\ 0 & -a_{12} & \delta & \gamma & 0 & 0 & 0 & 0 & 0 & 0 & 0 \\ 0 & \beta & -a_{13} & 0 & 0 & 0 & 0 & 0 & 0 & 0 & 0 \\ 0 & 0 & 0 & -a_{14} & \mu & \eta & 0 & 0 & 0 & 0 & 0 \\ 0 & a_{15} & 0 & a_{15} & -a_{16} & 0 & \delta & 2\gamma & 0 & 0 & 0 \\ a_{11} & 0 & 0 & 0 & 0 & -a_{17} & 0 & 0 & 0 & 0 & 0 \\ 0 & 0 & a_{15} & 0 & \beta & 0 & -(2\lambda+\delta) & 0 & 0 & 0 & 0 \\ 0 & 0 & 0 & 0 & 0 & 0 & 0 & -(\lambda+\gamma) & 0 & \eta & 0 \\ 0 & 0 & 0 & 0 & 2\lambda & 0 & 0 & 2\lambda & 0 & 0 & 0 \\ 0 & 0 & 0 & 0 & 0 & a_{15} & 0 & 0 & 0 & -\eta & 0 \\ 0 & 0 & 0 & 0 & 0 & 0 & 2\lambda & 0 & 0 & 0 & 0 \end{pmatrix},$$

and

$$a_{11} = 2(\lambda+\alpha),\ a_{12} = 2\lambda+\alpha+\beta+\mu,\ a_{13} = 2\lambda+\alpha+\delta,$$
$$a_{14} = 2\lambda+\alpha+\gamma,\ a_{15} = 2\lambda+\alpha,\ a_{16} = 2\lambda+\beta+\mu,\ a_{17} = 2\lambda+\alpha+\eta.$$

To compute $MTTF_3$, we neglect the rows and columns of the matrix Q_5 that pertain to the absorbing states and transpose the resulting matrix to form a new matrix A_3, where

$$A_3 = \begin{pmatrix} -a_{11} & 0 & 0 & 0 & 0 & a_{11} & 0 & 0 & 0 \\ \mu & -a_{12} & \beta & 0 & a_{15} & 0 & 0 & 0 & 0 \\ 0 & \delta & -a_{13} & 0 & 0 & 0 & a_{15} & 0 & 0 \\ 0 & \gamma & 0 & -a_{14} & a_{15} & 0 & 0 & 0 & 0 \\ 0 & 0 & 0 & \mu & -a_{16} & 0 & \beta & 0 & 0 \\ 0 & 0 & 0 & \eta & 0 & -a_{17} & 0 & 0 & a_{15} \\ 0 & 0 & 0 & 0 & \delta & 0 & -(2\lambda+\delta) & 0 & 0 \\ 0 & 0 & 0 & 0 & 2\gamma & 0 & 0 & -2(\lambda+\gamma) & 0 \\ 0 & 0 & 0 & 0 & 0 & 0 & 0 & \eta & -\eta \end{pmatrix}.$$

Then, $MTTF_3$ is obtained from

$$MTTF_3 = E\left[T_{\Pi(0)\to\Pi(absorbing)}\right] = \Pi(0)^T\left(-A_3^{-1}\right)[1,1,1,1,1,1,1,1,1]^T,$$

where the initial conditions $\Pi(0)$ of retrial system 3 is given by

$$\Pi(0) = [\Pi_{0,0}(0), \Pi_{1,0}(0), \Pi_{3,0}(0), \Pi_{0,1}(0), \Pi_{1,1}(0), \Pi_{2,1}(0), \Pi_{3,1}(0), \Pi_{0,2}(0), \Pi_{2,2}(0)]^T = [1,0,0,0,0,0,0,0,0]^T,$$

The explicit expression for $MTTF_3$ is too extensive to be shown here. In Section 4, a numerical example is provided for this aspect to compare this system with the other systems.

System availability ($Av_{T_3}(\infty)$)

For the availability case, the state- transition diagram of retrial system 3 is shown in Figure 3 (with transition from state (1,2) to (3,2) and (0,2) and from state (3,2) to (1,2)). Let T_3 be the time to failure of the system for retrial system 3 in steady-state, we obtainn $Av_{T_3}(\infty)$ from $Av_{T_3}(\infty) = 1 - \Pi_{1,2}(\infty) - \Pi_{3,2}(\infty)$, and $Q_6\Pi(\infty) = 0$ or expressed in matrix notation:

$$\begin{pmatrix} -a_{11} & \mu & 0 & 0 & 0 & 0 & 0 & 0 & 0 & 0 & 0 \\ 0 & -a_{12} & \delta & \gamma & 0 & 0 & 0 & 0 & 0 & 0 & 0 \\ 0 & \beta & -a_{13} & 0 & 0 & 0 & 0 & 0 & 0 & 0 & 0 \\ 0 & 0 & 0 & -a_{14} & \mu & \eta & 0 & 0 & 0 & 0 & 0 \\ 0 & a_{15} & 0 & a_{15} & -a_{16} & 0 & \delta & 2\gamma & 0 & 0 & 0 \\ a_{11} & 0 & 0 & 0 & 0 & -a_{17} & 0 & 0 & 0 & 0 & 0 \\ 0 & 0 & a_{15} & 0 & \beta & 0 & -(2\lambda+\delta) & 0 & 0 & 0 & 0 \\ 0 & 0 & 0 & 0 & 0 & 0 & 0 & -2(\lambda+\gamma) & \mu & \eta & 0 \\ 0 & 0 & 0 & 0 & 2\lambda & 0 & 0 & 2\lambda & -(\beta+\mu) & 0 & \delta \\ 0 & 0 & 0 & 0 & 0 & a_{15} & 0 & 0 & 0 & -\eta & 0 \\ 0 & 0 & 0 & 0 & 0 & 0 & 2\lambda & 0 & \beta & 0 & -\delta \end{pmatrix} \begin{pmatrix} \Pi_{0,0}(\infty) \\ \Pi_{1,0}(\infty) \\ \Pi_{3,0}(\infty) \\ \Pi_{0,1}(\infty) \\ \Pi_{1,1}(\infty) \\ \Pi_{2,1}(\infty) \\ \Pi_{3,1}(\infty) \\ \Pi_{0,2}(\infty) \\ \Pi_{1,2}(\infty) \\ \Pi_{2,2}(\infty) \\ \Pi_{3,2}(\infty) \end{pmatrix} = \begin{pmatrix} 0 \\ 0 \\ 0 \\ 0 \\ 0 \\ 0 \\ 0 \\ 0 \\ 0 \\ 0 \\ 0 \end{pmatrix}. \quad (15)$$

The normalizing condition is denoted by

$$\Pi_{0,0}(\infty)+\Pi_{1,0}(\infty)+\Pi_{3,0}(\infty)+\Pi_{0,1}(\infty)+\Pi_{1,1}(\infty)+\Pi_{2,1}(\infty) +\Pi_{3,1}(\infty)+\Pi_{0,2}(\infty)+\Pi_{1,2}(\infty)+\Pi_{2,2}(\infty)+\Pi_{3,2}(\infty)=1. \quad (16)$$

Substituting Eq. (16) into any one of the duplicated rows of Eq. (15) to yield

$$\begin{pmatrix} -a_{11} & \mu & 0 & 0 & 0 & 0 & 0 & 0 & 0 & 0 & 0 \\ 0 & -a_{12} & \delta & \gamma & 0 & 0 & 0 & 0 & 0 & 0 & 0 \\ 0 & \beta & -a_{13} & 0 & 0 & 0 & 0 & 0 & 0 & 0 & 0 \\ 0 & 0 & 0 & -a_{14} & \mu & \eta & 0 & 0 & 0 & 0 & 0 \\ 0 & a_{15} & 0 & a_{15} & -a_{16} & 0 & \delta & 2\gamma & 0 & 0 & 0 \\ a_{11} & 0 & 0 & 0 & 0 & -a_{17} & 0 & 0 & 0 & 0 & 0 \\ 0 & 0 & a_{15} & 0 & \beta & 0 & -(2\lambda+\delta) & 0 & 0 & 0 & 0 \\ 0 & 0 & 0 & 0 & 0 & 0 & 0 & -2(\lambda+\gamma) & \mu & \eta & 0 \\ 0 & 0 & 0 & 0 & 2\lambda & 0 & 0 & 2\lambda & -(\beta+\mu) & 0 & \delta \\ 0 & 0 & 0 & 0 & 0 & a_{15} & 0 & 0 & 0 & -\eta & 0 \\ 1 & 1 & 1 & 1 & 1 & 1 & 1 & 1 & 1 & 1 & 1 \end{pmatrix} \begin{pmatrix} \Pi_{0,0}(\infty) \\ \Pi_{1,0}(\infty) \\ \Pi_{3,0}(\infty) \\ \Pi_{0,1}(\infty) \\ \Pi_{1,1}(\infty) \\ \Pi_{2,1}(\infty) \\ \Pi_{3,1}(\infty) \\ \Pi_{0,2}(\infty) \\ \Pi_{1,2}(\infty) \\ \Pi_{2,2}(\infty) \\ \Pi_{3,2}(\infty) \end{pmatrix} = \begin{pmatrix} 0 \\ 0 \\ 0 \\ 0 \\ 0 \\ 0 \\ 0 \\ 0 \\ 0 \\ 0 \\ 1 \end{pmatrix}. \quad (17)$$

Again, the explicit expression for $Av_{T_3}(\infty)$ is overly extensive to be displayed here. However, in Section 4 a numerical example with specific values will be solved to compare the systems.

Calculations for Retrial System 4

MTTF$_4$ of retrial syatem 4

For the reliability case, the state-transition diagram of retrial system 4 is shown in Figure 4 (without transition from state (1,2) to (3,2) and (0,2) and from state (3,2) to (1,2)). The corresponding probability vector $\Pi(t)$ for retrial system 4 is presented as:

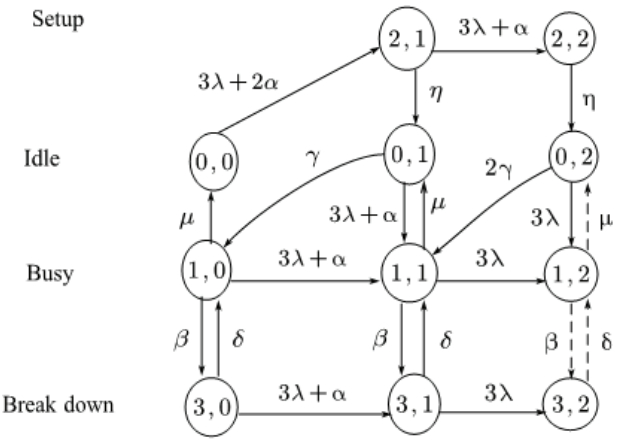


Figure 4. State-transition diagram of retrial system 4.

$$\Pi(t) = [\Pi_{0,0}(t), \Pi_{1,0}(t), \Pi_{3,0}(t), \Pi_{0,1}(t), \Pi_{1,1}(t), \Pi_{2,1}(t), \Pi_{3,1}(t), \Pi_{0,2}(t), \Pi_{1,2}(t), \Pi_{2,2}(t), \Pi_{3,2}(t)]^T.$$

The differential-difference equations can be formulated in matrix notation as

$$\frac{d\Pi(t)}{dt} = Q_7\,\Pi(t), \quad (18)$$

with

$$Q_7 = \begin{pmatrix} -a_{21} & \mu & 0 & 0 & 0 & 0 & 0 & 0 & 0 & 0 & 0 \\ 0 & -a_{22} & \delta & \gamma & 0 & 0 & 0 & 0 & 0 & 0 & 0 \\ 0 & \beta & -a_{23} & 0 & 0 & 0 & 0 & 0 & 0 & 0 & 0 \\ 0 & 0 & 0 & -a_{24} & \mu & \eta & 0 & 0 & 0 & 0 & 0 \\ 0 & a_{25} & 0 & a_{25} & -a_{26} & 0 & \delta & 2\gamma & 0 & 0 & 0 \\ a_{21} & 0 & 0 & 0 & 0 & -a_{27} & 0 & 0 & 0 & 0 & 0 \\ 0 & 0 & a_{25} & 0 & \beta & 0 & -(3\lambda+\delta) & 0 & 0 & 0 & 0 \\ 0 & 0 & 0 & 0 & 0 & 0 & 0 & -(3\lambda+2\gamma) & 0 & \eta & 0 \\ 0 & 0 & 0 & 0 & 3\lambda & 0 & 0 & 3\lambda & 0 & 0 & 0 \\ 0 & 0 & 0 & 0 & 0 & a_{25} & 0 & 0 & 0 & -\eta & 0 \\ 0 & 0 & 0 & 0 & 0 & 0 & 3\lambda & 0 & 0 & 0 & 0 \end{pmatrix},$$

where

$$a_{21} = (3\lambda + 2\alpha),\ a_{22} = 3\lambda + \alpha + \beta + \mu,\ a_{23} = 3\lambda + \alpha + \delta,$$
$$a_{24} = 3\lambda + \alpha + \gamma,\ a_{25} = 3\lambda + \alpha,\ a_{26} = 3\lambda + \beta + \mu,\ a_{27} = 3\lambda + \alpha + \eta.$$

To compute $MTTF_4$, we omit the rows and columns of the matrix Q_7 pertaining to the absorbing state(s) and transpose resulted matrix to a new matrix A_4, from which we have

$$A_4 = \begin{pmatrix} -a_{21} & 0 & 0 & 0 & 0 & a_{21} & 0 & 0 & 0 \\ \mu & -a_{22} & \beta & 0 & a_{25} & 0 & 0 & 0 & 0 \\ 0 & \delta & -a_{23} & 0 & 0 & 0 & a_{25} & 0 & 0 \\ 0 & \gamma & 0 & -a_{24} & a_{25} & 0 & 0 & 0 & 0 \\ 0 & 0 & 0 & \mu & -a_{26} & 0 & \beta & 0 & 0 \\ 0 & 0 & 0 & \eta & 0 & -a_{27} & 0 & 0 & a_{25} \\ 0 & 0 & 0 & 0 & \delta & 0 & -(3\lambda+\delta) & 0 & 0 \\ 0 & 0 & 0 & 0 & 2\gamma & 0 & 0 & -(3\lambda+2\gamma) & 0 \\ 0 & 0 & 0 & 0 & 0 & 0 & 0 & \eta & -\eta \end{pmatrix}.$$

Then, $MTTF_4$ is derived from

$$MTTF_4 = E\left[T_{\Pi(0)\to\Pi(absorbing)}\right] = \Pi(0)^T\left(-A_4^{-1}\right)[1,1,1,1,1,1,1,1,1]^T,$$

where, the initial conditions $\Pi(0)$ of retrial system 4 is given by

$$\Pi(0) = [\Pi_{0,0}(0), \Pi_{1,0}(0), \Pi_{3,0}(0), \Pi_{0,1}(0), \Pi_{1,1}(0), \Pi_{2,1}(0), \Pi_{3,1}(0), \Pi_{0,2}(0), \Pi_{2,2}(0)]^T = [1,0,0,0,0,0,0,0,0]^T,$$

The explicit expression for $MTTF_4$ is extensive to be shown here. In Section 4, a particular numerical example is presented for this scenario to compare this system with the other systems.

System availability ($Av_{T4}(\infty)$)

For the availability scenario, the state-transition diagram of retrial system 4 is shown in Figure 4 (with transition from state (1,2) to (3,2) and (0,2) and from state (3,2) to (1,2)). Let T_4 be the time to failure of the system for retrial system 4. In steady-state, we obtain the $Av_{T4}(\infty)$ from:

$Av_{T3}(\infty) = 1 - \prod_{1,2}(\infty) - \prod_{3,2}(\infty)$, and $Q_6\prod(\infty) = 0$, the matrix form is given by;

$$\begin{pmatrix} -a_{21} & \mu & 0 & 0 & 0 & 0 & 0 & 0 & 0 & 0 & 0 \\ 0 & -a_{22} & \delta & \gamma & 0 & 0 & 0 & 0 & 0 & 0 & 0 \\ 0 & \beta & -a_{23} & 0 & 0 & 0 & 0 & 0 & 0 & 0 & 0 \\ 0 & 0 & 0 & -a_{24} & \mu & \eta & 0 & 0 & 0 & 0 & 0 \\ 0 & a_{25} & 0 & a_{25} & -a_{26} & 0 & \delta & 2\gamma & 0 & 0 & 0 \\ a_{21} & 0 & 0 & 0 & 0 & -a_{27} & 0 & 0 & 0 & 0 & 0 \\ 0 & 0 & a_{25} & 0 & \beta & 0 & -(3\lambda+\delta) & 0 & 0 & 0 & 0 \\ 0 & 0 & 0 & 0 & 0 & 0 & -(3\lambda+2\gamma) & \mu & \eta & 0 & 0 \\ 0 & 0 & 0 & 0 & 2\lambda & 0 & 0 & 3\lambda & -(\beta+\mu) & 0 & \delta \\ 0 & 0 & 0 & 0 & 0 & a_{25} & 0 & 0 & 0 & -\eta & 0 \\ 0 & 0 & 0 & 0 & 0 & 0 & 3\lambda & 0 & \beta & 0 & -\delta \end{pmatrix} \begin{pmatrix} \Pi_{0,0}(\infty) \\ \Pi_{1,0}(\infty) \\ \Pi_{3,0}(\infty) \\ \Pi_{0,1}(\infty) \\ \Pi_{1,1}(\infty) \\ \Pi_{2,1}(\infty) \\ \Pi_{3,1}(\infty) \\ \Pi_{0,2}(\infty) \\ \Pi_{1,2}(\infty) \\ \Pi_{2,2}(\infty) \\ \Pi_{3,2}(\infty) \end{pmatrix} = \begin{pmatrix} 0 \\ 0 \\ 0 \\ 0 \\ 0 \\ 0 \\ 0 \\ 0 \\ 0 \\ 0 \\ 0 \end{pmatrix}. \quad (19)$$

The normalizing condition is denoted by

$$\Pi_{0,0}(\infty) + \Pi_{1,0}(\infty) + \Pi_{3,0}(\infty) + \Pi_{0,1}(\infty) + \Pi_{1,1}(\infty) + \Pi_{2,1}(\infty) + \Pi_{3,1}(\infty) + \Pi_{0,2}(\infty) + \Pi_{1,2}(\infty) + \Pi_{2,2}(\infty) + \Pi_{3,2}(\infty) = 1. \quad (20)$$

By substituting Eq. (20) into one of the redundant rows of Eq. (19) leads to

$$\begin{pmatrix} -a_{21} & \mu & 0 & 0 & 0 & 0 & 0 & 0 & 0 & 0 & 0 \\ 0 & -a_{22} & \delta & \gamma & 0 & 0 & 0 & 0 & 0 & 0 & 0 \\ 0 & \beta & -a_{23} & 0 & 0 & 0 & 0 & 0 & 0 & 0 & 0 \\ 0 & 0 & 0 & -a_{24} & \mu & \eta & 0 & 0 & 0 & 0 & 0 \\ 0 & a_{25} & 0 & a_{25} & -a_{26} & 0 & \delta & 2\gamma & 0 & 0 & 0 \\ a_{21} & 0 & 0 & 0 & 0 & -a_{27} & 0 & 0 & 0 & 0 & 0 \\ 0 & 0 & a_{25} & 0 & \beta & 0 & -(3\lambda+\delta) & 0 & 0 & 0 & 0 \\ 0 & 0 & 0 & 0 & 0 & 0 & 0 & -(3\lambda+2\gamma) & \mu & \eta & 0 \\ 0 & 0 & 0 & 0 & 2\lambda & 0 & 0 & 3\lambda & -(\beta+\mu) & 0 & \delta \\ 0 & 0 & 0 & 0 & 0 & a_{25} & 0 & 0 & 0 & -\eta & 0 \\ 1 & 1 & 1 & 1 & 1 & 1 & 1 & 1 & 1 & 1 & 1 \end{pmatrix} \begin{pmatrix} \Pi_{0,0}(\infty) \\ \Pi_{1,0}(\infty) \\ \Pi_{3,0}(\infty) \\ \Pi_{0,1}(\infty) \\ \Pi_{1,1}(\infty) \\ \Pi_{2,1}(\infty) \\ \Pi_{3,1}(\infty) \\ \Pi_{0,2}(\infty) \\ \Pi_{1,2}(\infty) \\ \Pi_{2,2}(\infty) \\ \Pi_{3,2}(\infty) \end{pmatrix} = \begin{pmatrix} 0 \\ 0 \\ 0 \\ 0 \\ 0 \\ 0 \\ 0 \\ 0 \\ 0 \\ 0 \\ 1 \end{pmatrix}. \quad (21)$$

Once more, the explicit expression for $Av_{T4}(\infty)$ is too extensive to present here. However, in Section 4 a numerical example with specific values will be included to compare these systems.

RESULTS AND DISCUSSION

A cost-effective power supply system is crucial across various industries, such as manufacturing, computer networks, communication systems, and production environments. To meet organizational needs requires evaluating and projecting operational efficiency. Our theoretical and numerical findings give managers and policymakers useful information that helps them maintain high levels of quality control, optimize management processes, and anticipate performance with accuracy. Numerical solutions are presented in this section using particular cases with assigned values. We calculate the steady-state availability, and mean-time-to-failure (MTTF), and compare the cost-benefit ratios across all retrial systems to identify the best-performing option. To investigate how various configuration parameters affect these performance metrics, more numerical experiments are carried out.

Comparison of MTTF and Availability

The effects of various system parameters on MTTF and steady-state availability are investigated through numerical analysis of the cases listed below.

Case 1: Fix $\mu = 2$, $\alpha = 2\lambda$, $\eta = 0.3$, $\delta = 0.5$, $\beta = 0.05$, $\gamma = 3$ and alter the values of λ.

Case 2: Fix $\lambda = 0.3$, $\alpha = 2\lambda$, $\eta = 0.3$, $\delta = 0.5$, $\beta = 0.05$, $\gamma = 3$ and alter the values of μ.

Case 3: Fix $\lambda = 0.3$, $\alpha = 2\lambda$, $\mu = 2$, $\delta = 0.5$, $\beta = 0.05$, $\gamma = 3$ and alter the values of η.

Case 4: Fix $\lambda = 0.3$, $\mu = 2$, $\eta = 0.3$, $\delta = 0.5$, $\beta = 0.05$, $\gamma = 3$ and alter the values of α.

Case 5: Fix $\lambda = 0.3$, $\alpha = 2\lambda$, $\eta = 0.3$, $\mu = 2$, $\delta = 0.5$, $\gamma = 3$ and alter the values of β.

Case 6: Fix $\lambda = 0.3$, $\alpha = 2\lambda$, $\eta = 0.3$, $\mu = 2$, $\beta = 0.05$, $\gamma = 3$ and alter the values of δ.

Case 7: Fix $\lambda = 0.3$, $\alpha = 2\lambda$, $\eta = 0.3$, $\mu = 2$, $\delta = 0.5$, $\beta = 0.05$ and alter the values of γ.

The effects of system parameters are examined $MTTF_i$ in Table 4-Table 10 and Av_i, (i = 1,2,3,4) in Table 11 and Figure 5-Figure *7* respectively. Based on the results presented in these Tables and Figures, it is evident that The MTTF and steady-state availability are heavily influenced by the failure rate λ of operating components and the efficiency of repairs, while the retrial rate γ of failed components has a moderate impact. Consequently, to enhance availability and reduce MTTF, maintenance efforts should focus on extending the lifespan of active components and improving repair efficiency. This approach ensures the system maintains an adequate supply of spare parts.

MTTF and AV are both decreasing functions of λ and α, this occurs because larger values of λ or α, result in a faster reduction in the number of operative components, causing

Table 4. Comparison of retrial systems i = 1,2,3,4 for MTTF

Results	
Range of λ	
$0.01 < \lambda < 0.680555$	$MTTF_4 < MTTF_2 < MTTF_3 < MTTF_1$
$0.680555 < \lambda < 1.0$	$MTTF_4 < MTTF_3 < MTTF_2 < MTTF_1$
Range of μ	
$0.01 < \mu < 0.161857$	$MTTF_4 < MTTF_2 < MTTF_3 < MTTF_1$
$0.161857 < \mu < 0.541816$	$MTTF_4 < MTTF_3 < MTTF_2 < MTTF_1$
$0.541816 < \mu < 3.0$	$MTTF_4 < MTTF_2 < MTTF_3 < MTTF_1$
Range of η	
$0.01 < \eta < 0.126025$	$MTTF_4 < MTTF_3 < MTTF_2 < MTTF_1$
$0.126025 < \eta < 1.0$	$MTTF_4 < MTTF_2 < MTTF_3 < MTTF_1$
Range of β	
$0.001 < \beta < 0.30448$	$MTTF_4 < MTTF_2 < MTTF_3 < MTTF_1$
$0.30448 < \beta < 1.0$	$MTTF_4 < MTTF_3 < MTTF_2 < MTTF_1$
Range of δ	
$0.001 < \delta < 1.0$	$MTTF_4 < MTTF_2 < MTTF_3 < MTTF_1$

Table 5. Values of MTTF for various λ and μ

λ	$MTTF_1$				$MTTF_2$			
	$\mu = 1.5$	$\mu = 2$	$\mu = 2.5$	$\mu = 3$	$\mu = 1.5$	$\mu = 2$	$\mu = 2.5$	$\mu = 3$
0.1	108.348	126.8930	142.272	155.232	44.9554	51.8556	57.5919	62.4359
0.2	44.9554	51.8556	57.5919	62.4359	20.1821	22.7881	24.9661	26.8136
0.3	27.7549	31.6414	34.8809	37.6225	13.4236	14.9273	16.1910	17.2678
0.4	20.1821	22.7881	24.9661	26.8136	10.3899	11.4172	12.2851	13.0281
0.5	16.0217	17.9435	19.5540	20.9232	8.6931	9.4605	10.1122	10.6726
0.6	13.4236	14.9273	16.1910	17.2678	7.6179	8.2235	8.7404	9.1868
0.7	11.6597	12.8847	13.917	14.7986	6.8795	7.3755	7.8008	8.1695
0.8	10.3899	11.4172	12.2851	13.0281	6.3434	6.7605	7.1197	7.4323
0.9	9.4352	10.3156	11.0614	11.7012	5.9376	6.2954	6.6048	6.8752
1.0	8.6931	9.4605	10.1122	10.6726	5.6206	5.9323	6.2030	6.4403

Table 6. Values of MTTF for various λ and μ

λ	$MTTF_3$				$MTTF_4$			
	$\mu = 1.5$	$\mu = 2$	$\mu = 2.5$	$\mu = 3$	$\mu = 1.5$	$\mu = 2$	$\mu = 2.5$	$\mu = 3$
0.1	75.3757	94.4482	111.8790	127.805	40.4587	49.9338	58.6375	66.6191
0.2	26.6649	32.4626	37.8184	42.7503	15.5753	18.5015	21.2380	23.7813
0.3	15.5753	18.5015	21.2380	23.7813	9.8103	11.2876	12.6954	14.0230
0.4	11.1215	12.9253	14.6335	16.2366	7.4676	8.3663	9.2381	10.0721
0.5	8.8271	10.0609	11.2438	12.3647	6.2564	6.8585	7.4522	8.0278
0.6	7.4676	8.3663	9.2381	10.0721	5.5393	5.9673	6.3956	6.8159
0.7	6.5865	7.2691	7.9388	8.5852	5.0759	5.3928	5.7140	6.0328
0.8	5.9785	6.5129	7.0427	7.5584	4.7573	4.9991	5.2469	5.4954
0.9	5.5393	5.9673	6.3956	6.8159	4.5278	4.7167	4.9122	5.1099
1.0	5.2104	5.5594	5.9117	6.2601	4.3564	4.5067	4.6637	4.8237

Table 7. Values of MTTF for various λ and α

λ	$MTTF_1$				$MTTF_2$			
	$\alpha = 0.04$	$\alpha = 0.06$	$\alpha = 0.08$	$\alpha = 0.10$	$\alpha = 0.04$	$\alpha = 0.06$	$\alpha = 0.08$	$\alpha = 0.10$
0.1	137.7835	126.8928	118.4223	111.6459	53.9474	51.8556	50.0627	48.5088
0.2	53.9474	51.8556	50.0627	48.5088	23.1522	22.7881	22.4544	22.1474
0.3	32.3983	31.6414	30.9642	30.3547	15.0568	14.9273	14.8055	14.6906
0.4	23.1521	22.7881	22.4544	22.1474	11.4798	11.4172	11.3574	11.3003
0.5	18.1495	17.9435	17.7517	17.5727	9.4964	9.4605	9.4259	9.3926
0.6	15.0568	14.9273	14.8055	14.6906	8.2464	8.2235	8.2013	8.1798
0.7	12.9724	12.8847	12.8016	12.7226	7.3913	7.3755	7.3602	7.3453
0.8	11.4798	11.4172	11.3574	11.3003	6.7719	6.7605	6.7493	6.7385
0.9	10.3622	10.3156	10.2709	10.2279	6.3040	6.2954	6.2869	6.2786
1.0	9.4964	9.4605	9.4259	9.3926	5.9391	5.9323	5.9257	5.9192

Table 8. Values of MTTF for various λ and α

λ	$MTTF_3$				$MTTF_4$			
	$\alpha = 0.04$	$\alpha = 0.06$	$\alpha = 0.08$	$\alpha = 0.10$	$\alpha = 0.04$	$\alpha = 0.06$	$\alpha = 0.08$	$\alpha = 0.10$
0.1	105.0711	94.4482	86.1901	79.5812	53.4322	49.9338	47.0141	44.5365
0.2	34.0463	32.4626	31.0852	29.8744	19.0272	18.5015	18.0232	17.5855
0.3	19.0272	18.5015	18.0232	17.5855	11.4678	11.2876	11.1183	10.9589
0.4	13.1703	12.9253	12.6970	12.4835	8.4524	8.3663	8.2841	8.2056
0.5	10.1981	10.0609	9.9312	9.8084	6.9074	6.8584	6.8113	6.7658
0.6	8.4524	8.3663	8.2841	8.2056	5.9983	5.9673	5.9373	5.9082
0.7	7.3274	7.2691	7.2132	7.1594	5.4139	5.3928	5.3723	5.3524
0.8	6.5546	6.5130	6.4728	6.4348	5.0142	4.9991	4.9844	4.9700
0.9	5.9983	5.9673	5.9373	5.9082	4.7279	4.7167	4.7057	4.6949
1.0	5.5832	5.5594	5.5363	5.5138	4.5154	4.5067	4.4983	4.4899

Table 9. Values of MTTF for various λ and γ

λ	$MTTF_1$				$MTTF_2$			
	$\gamma = 2.5$	$\gamma = 3$	$\gamma = 3.5$	$\gamma = 4$	$\gamma = 2.5$	$\gamma = 3$	$\gamma = 3.5$	$\gamma = 4$
0.1	119.0643	126.8928	133.2839	138.6002	48.8630	51.8556	54.3106	56.3609
0.2	48.8630	51.8556	54.3106	56.3609	21.6091	22.7881	23.7637	24.5842
0.3	29.9172	31.6414	33.0623	34.2533	14.2245	14.9273	15.5133	16.0093
0.4	21.6091	22.7881	23.7637	24.5842	10.9242	11.4172	11.8310	12.1833
0.5	17.0589	17.9435	18.6782	19.2982	9.0839	9.4605	9.7787	10.0508
0.6	14.2245	14.9273	15.5133	16.0093	7.9206	8.2235	8.4808	8.7021
0.7	12.3042	12.8847	13.3704	13.7828	7.1233	7.3755	7.5909	7.7770
0.8	10.9242	11.4172	11.8310	12.1833	6.5452	6.7605	6.9452	7.1054
0.9	9.8882	10.3156	10.6755	10.9828	6.1083	6.2954	6.4566	6.5971
1.0	9.0839	9.4605	9.7786	10.0508	5.7675	5.9323	6.0751	6.1999

Table 10. Values of MTTF for various λ and γ

λ	$MTTF_3$				$MTTF_4$			
	$\gamma = 2.5$	$\gamma = 3$	$\gamma = 3.5$	$\gamma = 4$	$\gamma = 2.5$	$\gamma = 3$	$\gamma = 3.5$	$\gamma = 4$
0.1	90.7913	94.4482	97.3324	99.6654	48.0586	49.9338	51.4206	52.6283
0.2	31.2754	32.4626	33.4083	34.1796	17.8593	18.5015	19.0178	19.4417
0.3	17.8593	18.5015	19.0178	19.4417	10.9299	11.2876	11.5787	11.8202
0.4	12.5021	12.9253	13.2683	13.5519	8.1290	8.3663	8.5617	8.7253
0.5	9.7529	10.0609	10.3124	10.5218	6.6871	6.8584	7.0012	7.1218
0.6	8.1290	8.3663	8.5616	8.7253	5.8374	5.9673	6.0767	6.1701
0.7	7.0794	7.2691	7.4265	7.5592	5.2911	5.3928	5.4794	5.5539
0.8	6.3574	6.5130	6.6430	6.7533	4.9176	4.9991	5.0691	5.1299
0.9	5.8374	5.9673	6.0767	6.1701	4.6502	4.7167	4.7743	4.8247
1.0	5.4493	5.5594	5.6528	5.7329	4.4518	4.5067	4.5548	4.5971

Table 11. Comparison of retrial systems i = 1,2,3,4 for availability

Results	
Range of λ	
$0.01 < \lambda < 0.41850$	$Av_{T_1}(\infty) > Av_{T_3}(\infty) > Av_{T_2}(\infty) > Av_{T_4}(\infty)$
$0.41850 < \lambda < 1.0$	$Av_{T_1}(\infty) > Av_{T_2}(\infty) > Av_{T_3}(\infty) > Av_{T_4}(\infty)$
Range of μ	
$0.01 < \mu < 1.27079$	$Av_{T_1}(\infty) > Av_{T_3}(\infty) > Av_{T_2}(\infty) > Av_{T_4}(\infty)$
$1.27079 < \mu < 3.0$	$Av_{T_1}(\infty) > Av_{T_2}(\infty) > Av_{T_3}(\infty) > Av_{T_4}(\infty)$
Range of η	
$0.01 < \eta < 0.15698$	$Av_{T_1}(\infty) > Av_{T_2}(\infty) > Av_{T_3}(\infty) > Av_{T_4}(\infty)$
$0.15698 < \eta < 1.0$	$Av_{T_1}(\infty) > Av_{T_3}(\infty) > Av_{T_2}(\infty) > Av_{T_4}(\infty)$
Range of β	
$0.001 < \beta < 0.153784$	$Av_{T_1}(\infty) > Av_{T_3}(\infty) > Av_{T_2}(\infty) > Av_{T_4}(\infty)$
$0.153784 < \beta < 1.0$	$Av_{T_1}(\infty) > Av_{T_2}(\infty) > Av_{T_3}(\infty) > Av_{T_4}(\infty)$
Range of δ	
$0.001 < \delta < 0.249205$	$Av_{T_1}(\infty) > Av_{T_2}(\infty) > Av_{T_3}(\infty) > Av_{T_4}(\infty)$
$0.249205 < \delta < 1.0$	$Av_{T_1}(\infty) > Av_{T_3}(\infty) > Av_{T_2}(\infty) > Av_{T_4}(\infty)$

MTTF and steady-state availability to decline as λ or α increase. Furthermore, MTTF and steady-state availability increase as functions of μ and γ. This is because higher values of μ and γ, reduce the time required to restore a failed component to working condition, leading to improved system availability and MTTF.

Comparison Based on Cost-Benefit Ratios

We investigate the impacts of various system parameters on four distinct retrial systems with different costs in Figure 8-Figure 17.

The repair rate of the failed components μ and the recovery rate of the broken service facility δ affect $C_i/MTTF_i$ and C_i/Av_i significantly. However, $C_i/MTTF_i$ and C_i/Av_i are increasing function as functions of the failure rate of operating components λ, setup time rate η, server breakdown rate β, and the retrial rate of a failed component γ. The reason is that larger values of λ, η, β and γ are, the construction cost becomes higher, and then $C_i/MTTF_i$ and C_i/Av_i become bigger. Therefore, according to the analysis, retrial system 2 is recommended as it has the most economical construction cost and an excellent cost-benefit ratio.

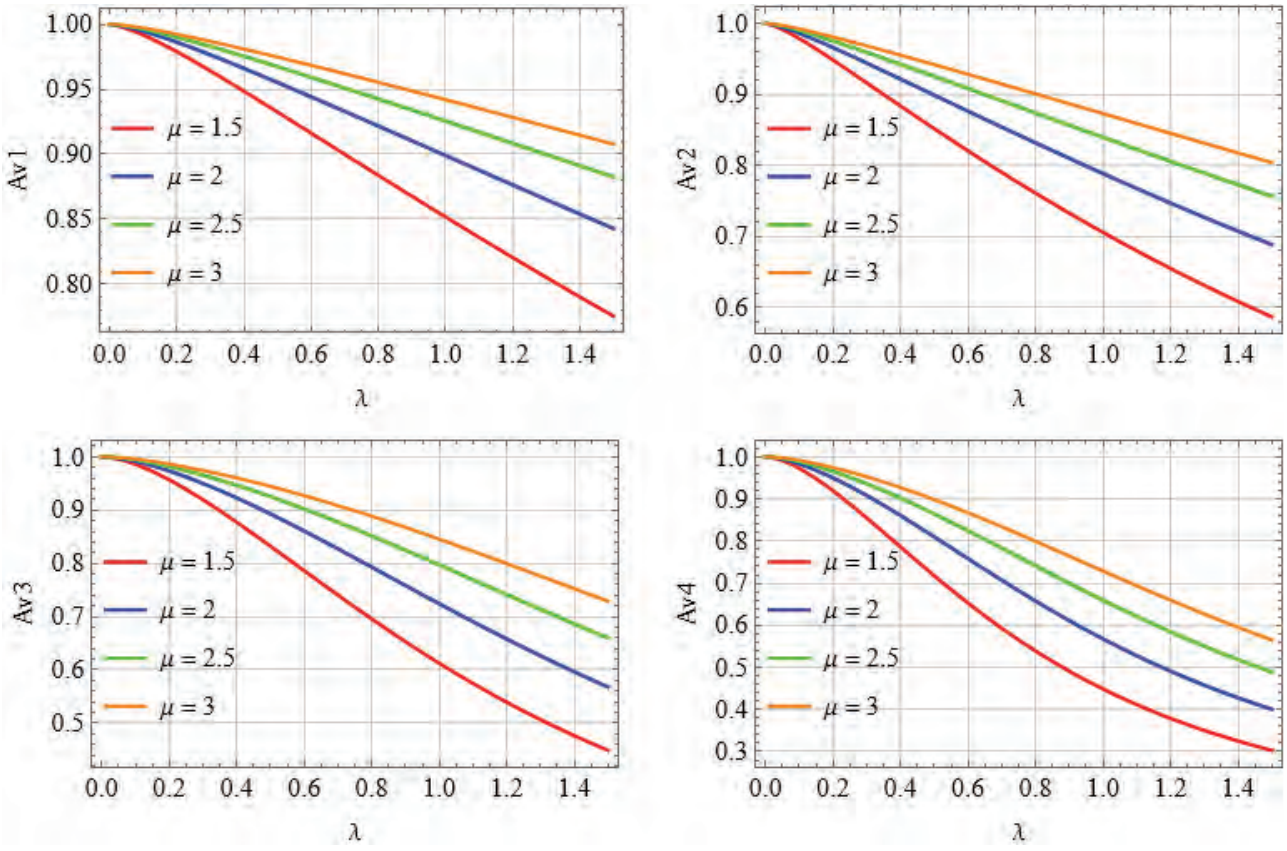


Figure 5. Av_i vs. λ for different values of μ.

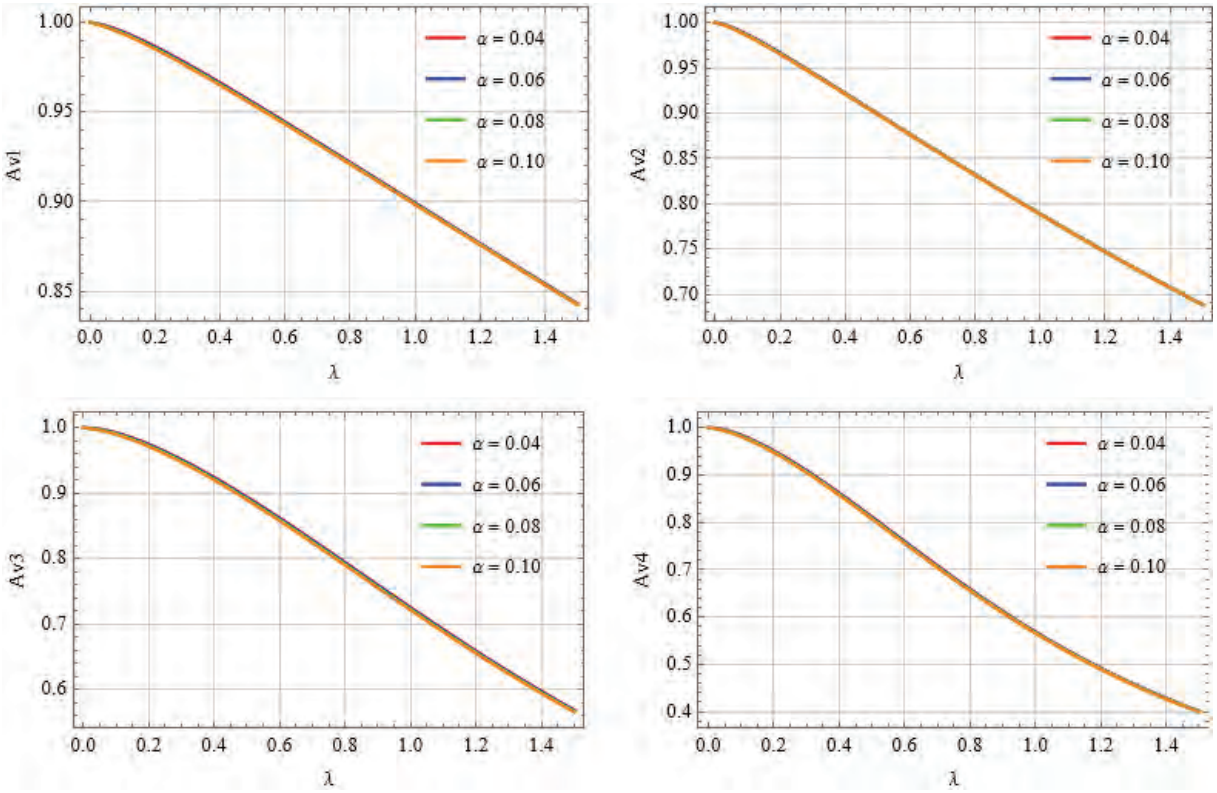


Figure 6. Av_i vs. λ for different values of α.

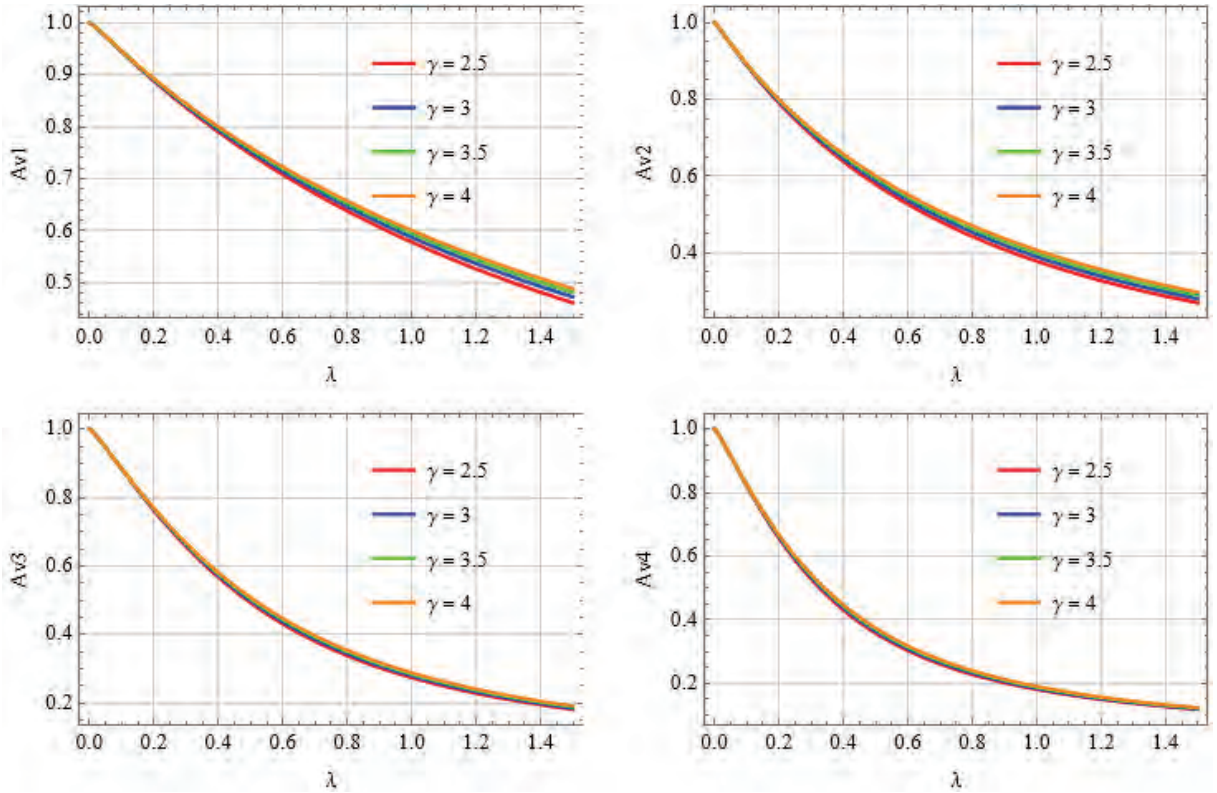


Figure 7. Av_i vs. λ for different values of γ.

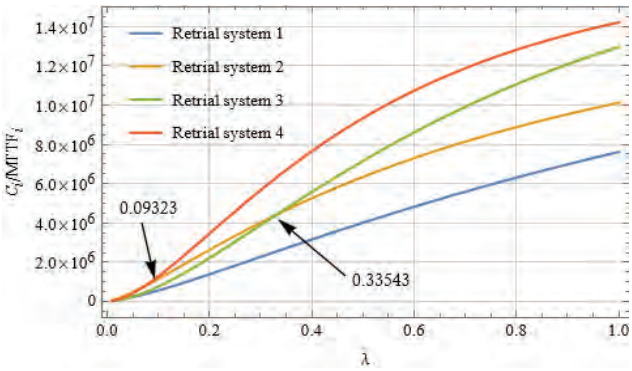


Figure 8. $C_i/MTTF_i$ vs. λ.

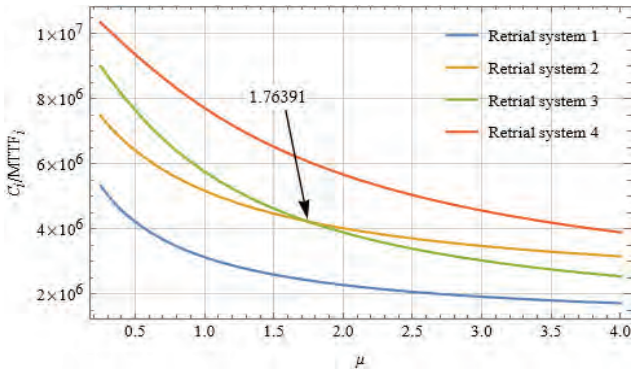


Figure 9. $C_i/MTTF_i$ vs. μ.

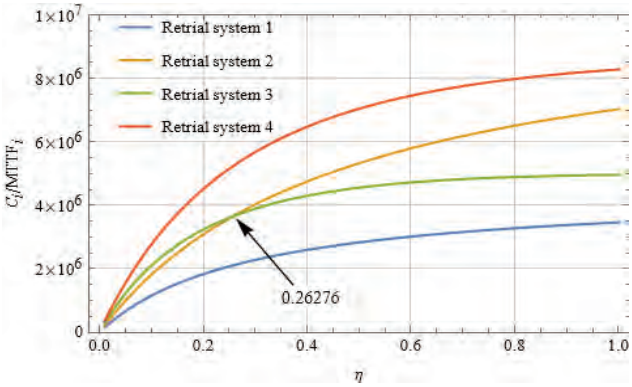


Figure 10. $C_i/MTTF_i$ vs. η.

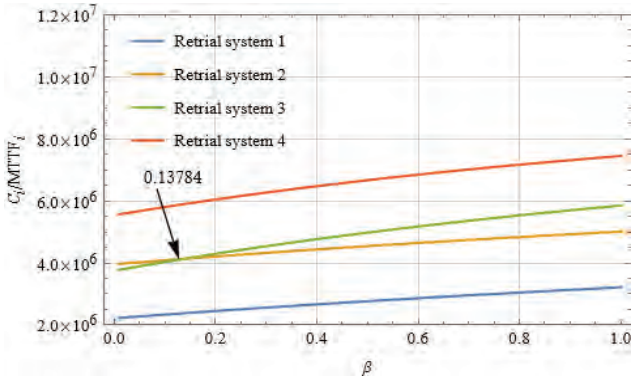


Figure 11. $C_i/MTTF_i$ vs. β.

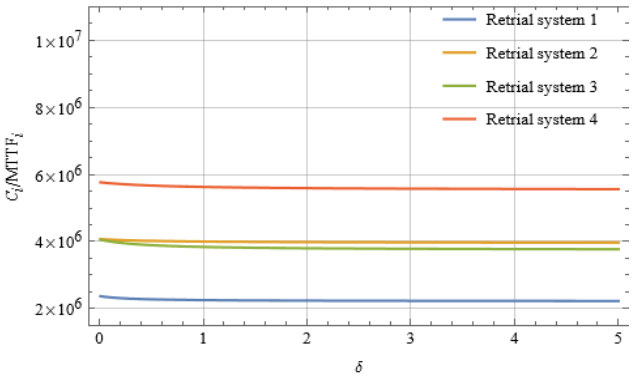


Figure 12. $C_i/MTTF_i$ vs. δ.

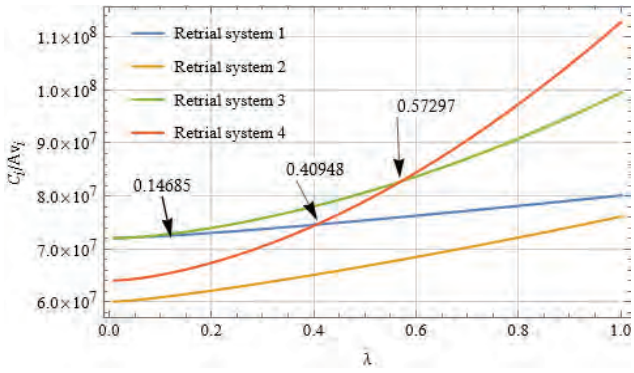


Figure 13. C_i/Av_i vs. λ.

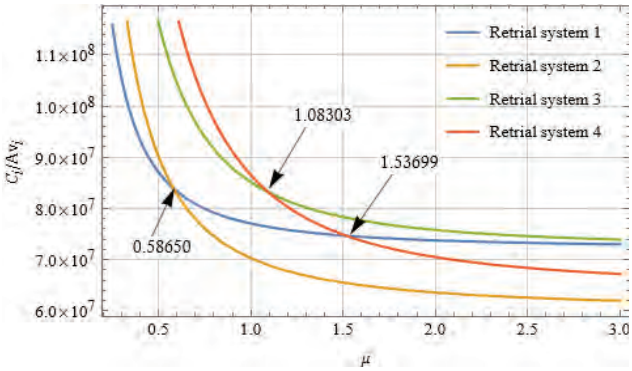


Figure 14. C_i/Av_i vs. μ.

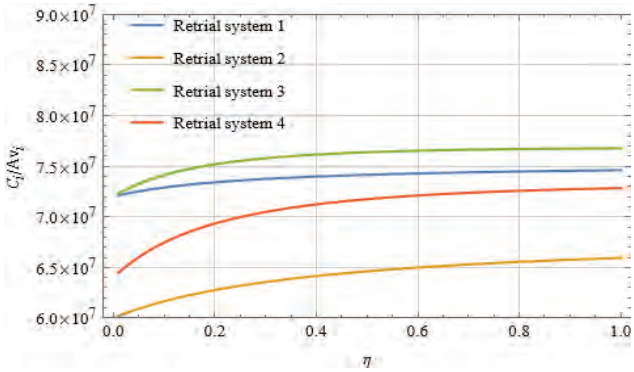


Figure 15. C_i/Av_i vs. η.

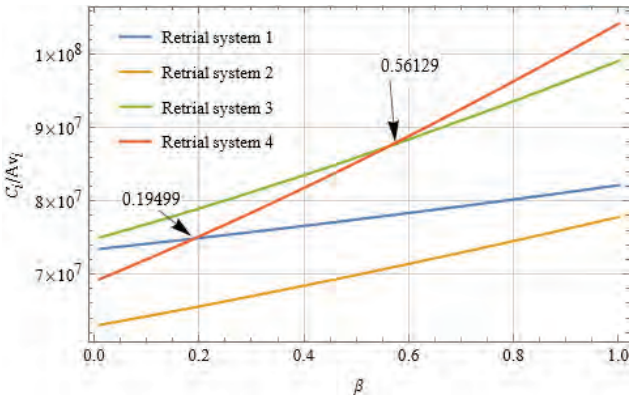


Figure 16. C_i/Av_i vs. β.

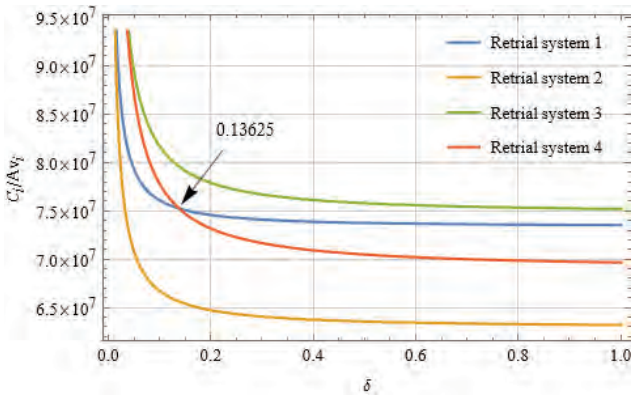


Figure 17. C_i/Av_i against δ.

CONCLUSION

In this paper we studied the cost-benefit evaluation of four unreliable retrial systems exhibiting warm standbys and setup times. Steady-state probability was derived by employing a matrix-analytical technique, and the Laplace transform enabled the derivation of mean time to failure for each retrial system. Furthermore, numerical experiments were performed using Wolfram Mathematica software to analyze numerical results. Four retrial systems were assessed and compared based on their mean time to failure, steady-state availability, and cost-benefit ratio. The key findings show that optimal mean time to failure was noted in retrial system 4 and the optimal steady-state availability was found in retrial system 2. Based on the cost-benefit ratio, retrial system 1 is optimal since it emerges as the best-performing configuration. The proposed method is a useful tool for decision-makers in diverse parameter settings, allowing them to select an appropriate system that maximizes benefits. Numerical analyses have revealed that the system reliability, mean time to failure, and steady-state availability can be improved by increasing the repair service rates, reducing the rate of failures of both active and warm standby components by implementing effective methods, such as routine maintenance service, to prolong the lifespan of the equipment. The current work can be extended in the following ways in the future; (i) considering a situation in which the server takes a vacation when there are no failed components in the system awaiting repair. (ii) investigating cases where the repair times follow general distributions.

ACKNOWLEDGMENT

This research was supported by the provincial Natural Science Foundation of Hunan grant (Grant No.2024JJ5453).

AUTHORSHIP CONTRIBUTIONS

Jones Edward Chiwinga initiate the model and do all the writing and mathematical analysis while Muhammad Salihu Isa and Jinbiao Wu helps in editing and supervision.

CONFLICT OF INTEREST

Authors have declared that there is no conflict of interest with regard to this research.

ETHICS

There are no ethical issues with the publication of this manuscript.

STATEMENT ON THE USE OF ARTIFICIAL INTELLIGENCE

Artificial intelligence was not used in the preparation of the article.

REFERENCES

[1] Rehman NU, Farzaneh H. Techno-economic analysis of a hybrid heat recovery-renewable energy system for enhancing power reliability in cement factories in Pakistan. Energy Convers Manag X 2023;20:100492. [CrossRef]

[2] Golmohamadi H. Demand-side management in industrial sector: A review of heavy industries. Renew Sustain Energy Rev 2022;156:111963. [CrossRef]

[3] Ram M, Bhandari AS, Kumar A. Reliability evaluation and cost optimization of solar road studs. Int J Reliab Qual Saf Eng 2022;29:2150041. [CrossRef]

[4] Aghsami A, Jolai F. Equilibrium threshold strategies and social benefits in the fully observable Markovian queues with partial breakdowns and interruptible setup/closedown policy. Qual Technol Quant Manag 2020;17:685–722. [CrossRef]

[5] Zhang S, Xu X. Equilibrium customer strategies in Markovian queues with setup times and partial failures. J Syst Sci Complex 2020;33:1163–1178. [CrossRef]

[6] Sun W, Guo P, Tian N. Equilibrium threshold strategies in observable queueing systems with setup/closedown times. Cent Eur J Oper Res 2010;18:241–268. [CrossRef]

[7] Wang H, Xu X, Wang S. Equilibrium customers strategies in the Markovian working vacation queue with setup times. Int J Comput Sci Math 2019;10:443–458. [CrossRef]
[8] Yen TC, Wang KH, Wu CH. Reliability-based measure of a retrial machine repair problem with working breakdowns under the F-policy. Comput Ind Eng 2020;150:106885. [CrossRef]
[9] Chen WL. System reliability analysis of retrial machine repair systems with warm standbys and a single server of working breakdown and recovery policy. Syst Eng 2018;21:59–69. [CrossRef]
[10] Wang KH, Yen TC, Wu CH. Reliability and sensitivity analyses of an unreliable retrial machine repair system with warm standby switching failure. Int J Reliab Qual Saf Eng 2022;29:2141008. [CrossRef]
[11] Maihulla AS, Yusuf İ, Koo MBC. Reliability and availability analyses of an industrial system with two subsystems arranged in series-parallel. Sigma J Eng Nat Sci 2024;42:1500–1510. [CrossRef]
[12] Yang DY, Tsao CL. Reliability and availability analysis of standby systems with working vacations and retrial of failed components. Reliab Eng Syst Saf 2019;182:46–55. [CrossRef]
[13] Gao S, Wang J, Zhang J. Reliability analysis of a redundant series system with common cause failures and delayed vacation. Reliab Eng Syst Saf 2023;239:109467. [CrossRef]
[14] Wu J, Isa MS. Reliability estimation of a fault coverage distributed system with replacement options under four different scenarios. Sigma J Eng Nat Sci 2024;42:1214–1238. [CrossRef]
[15] Kumar P, Jain M. Reliability analysis of a multi-component machining system with service interruption, imperfect coverage, and reboot. Reliab Eng Syst Saf 2020;202:106991. [CrossRef]
[16] Shekhar C, Devanda M, Kaswan S. Reliability analysis of standby provision multi-unit machining systems with varied failures, degradations, imperfections, and delays. Qual Reliab Eng Int 2023;39:3119–3139. [CrossRef]
[17] Iggi AM, Yusuf İ. RAMD analysis of mixed standby serial manufacturing system. Sigma J Eng Nat Sci 2024;42:1116–1132. [CrossRef]
[18] Isa MS, Wu J, Yusuf İ, Sanusi A. Performance estimation of honeynet system for network security enhancement via copula linguistic. Sigma J Eng Nat Sci 2024;42:1169–1182. [CrossRef]
[19] Bai S, Jia X, Cheng Z, Guo B, Zhao Q. Optimal periodic switching strategy for a two-unit warm standby degradation system. Qual Reliab Eng Int 2023;39:3182–3202. [CrossRef]
[20] Kuo CC, Ke JC. Modeling and comparison of the series systems with imperfect coverage for an unreliable server. Soft Comput 2019;23:2073–2082. [CrossRef]
[21] Juybari MN, Hamadani AZ, Liu B. A Markovian analytical approach to a repairable system under the mixed redundancy strategy with a repairman. Qual Reliab Eng Int 2022;38:3663–3688. [CrossRef]
[22] Adan HK, Filik ÜB. Technical and economic evaluation of a standalone and on grid hybrid renewable energy: A case study at Eskişehir Technical University. Sigma J Eng Nat Sci 2021;39:184–194. [CrossRef]
[23] Ayagi HI, Wan Z, Yusuf İ, Sanusi A. Performance estimation of parallel system under online and offline preventive maintenance. Sigma J Eng Nat Sci 2024;42:1088–1100. [CrossRef]
[24] Gao S, Wang J. Reliability and availability analysis of a retrial system with mixed standbys and an unreliable repair facility. Reliab Eng Syst Saf 2021;205:107240. [CrossRef]
[25] Wang KH, Wu CH, Yen TC. Comparative cost-benefit analysis of four retrial systems with preventive maintenance and unreliable service station. Reliab Eng Syst Saf 2022;221:108342. [CrossRef]
[26] Yen TC, Wang KH. Cost benefit analysis of four retrial systems with warm standby units and imperfect coverage. Reliab Eng Syst Saf 2020;202:107006. [CrossRef]
[27] Wu CH, Yen TC, Wang KH. Availability and comparison of four retrial systems with imperfect coverage and general repair times. Reliab Eng Syst Saf 2021;212:107642. [CrossRef]
[28] Kang J, Hu L, Peng R, Li Y, Tian R. Availability and cost-benefit evaluation for a repairable retrial system with warm standbys and priority. Stat Theory Relat Fields 2023;7:164–175. [CrossRef]
[29] Yen TC, Chen WL, Wang KH. Comparison of three availability systems with warm standby components, detection delay, and general repair times. Symmetry 2020;12:414. [CrossRef]
[30] Gao S. Availability and reliability analysis of a retrial system with warm standbys and second optional repair service. Commun Stat Theory Methods 2023;52:1039–1057. [CrossRef]
[31] Shirumalla P, Chatterjee AK. Electrical systems for sustainable production in cement plants: A perspective view. In: Intelligent and Sustainable Cement Production. 2021. p. 99–139. [CrossRef]
[32] Ali HMK, Sultan A, Rana BB. Captive power plant selection for Pakistan cement industry in perspective of current energy crises: A fuzzy-AHP approach. Mehran Univ Res J Eng Technol 2017;36:769–780. [CrossRef]

Sigma Journal of Engineering and Natural Sciences
Web page info: https://sigma.yildiz.edu.tr
DOI: 10.14744/sigma.2026.2102

Research Article

Numerical modeling of seismic impacts on cistern structures

Pınar USTA EVCİ[1,*], Ayşe BÜYÜKÜNSAL[1], Neşe BOZKURT[1]

[1]*Isparta University of Applied Sciences, Isparta, 32200, Türkiye*

ARTICLE INFO

Article history
Received: 23 August 2024
Revised: 18 November 2024
Accepted: 13 January 2025

Keywords:
Cistern; Historical Building; Numerical Modelling; Time History Analyses

ABSTRACT

The present research constitutes a thorough investigation of the seismic characteristics of an 18th-century stone masonry cistern situated in the Fethiye area of Turkey, highlighting the need to protect cultural heritage structures located in areas vulnerable to seismic events. The mechanical characteristics of the stone masonry materials used for building the cistern were determined using experiments. The seismic behavior of the cistern was then analyzed both statically and dynamically using the software program SAP2000 V22. It can be observed from the analysis that the seismic response in the case of the cistern along the short axis is higher than in the case of the long axis. In addition, some important stress concentration points were revealed by the analysis, with the maximum compressive stress being 0.525 MPa and maximum tensile stress being 0.272 MPa. Moreover, the outside surface of the cistern experienced the maximum horizontal displacement of 1.5 cm along the short direction. Also, it was seen that shear stresses in wall A1, which contains the door opening, exceeded the typical shear stress of the wall, implying imminent risk of local failure. Stress concentration areas were found near the main openings of the dome and openings in walls, representing the key points that require interventions. In general, it can be inferred from the analysis that the structure withstands seismic events, but accumulated stress levels in certain areas can cause cracking. Some important recommendations on retrofitting have been provided based on the analysis, offering an opportunity to improve the structure's seismic response. Thus, the current research contributes to the field of analysis of seismic characteristics of historical masonry structures by providing an analysis of an important water storage structure. The study has been conducted in accordance with the objectives stated and provides important recommendations on how to retro-fit the structure, making it more resistant to seismic loads. While previous studies of historical masonry structures were mainly concerned with the analysis of their seismic responses, with buildings such as churches, mosques, and towers considered, very few researchers examined the cistern structures from the point of view of retrofitting in relation to seismic events.

Cite this article as: Usta Evci P, Büyükünsal A, Bozkurt N. Numerical modeling of seismic impacts on cistern structures. Sigma J Eng Nat Sci 2026;44(4):2396–2414.

***Corresponding author.**
*E-mail address: pinarusta@isparta.edu.tr

This paper was recommended for publication in revised form by Editor-in-Chief Ahmet Selim Dalkilic

Published by Yıldız Technical University Press, İstanbul, Turkey
© Author. This is an open access article under the CC BY-NC license (http://creativecommons.org/licenses/by-nc/4.0/).

INTRODUCTION

Since water is a crucial element for the existence of life, the supply and storage of water have been one of the main problems of the human being [1,2]. Throughout history, settlements were generally built near water. In the following periods, in settlements located on fertile lands but established far from water sources, structures were built to supply and collect water [2]. Aqueducts and waterways used for supply and cisterns used to collect water [3] were constructed as hydraulic structures in ancient times.

Cisterns, serving as fundamental hydraulic structures, were strategically positioned in various parts of ancient cities. Cisterns were common and varied from cities to caravanserais to countryside to ensure that rain water could be collected in accordance with different purposes during varying seasons of the year. This phenomenon is well described in the studies conducted by Demirci and Bilgin [1] and Oter [4], revealing the extent of importance given to cisterns in terms of water storage in ancient civilizations [5]. Cisterns were usually roofed structures since long periods of sun exposure tended to degrade water quality [6]. There were several techniques used to build cisterns, ranging from simple ones in the form of clay tanks to more complex constructions, such as underground reservoirs [5]. In Anatolia, especially countryside areas, cisterns were mostly built from stones [7]. Stone masonry is the earliest and most common construction technique. These structures are resistant to fire, water, and insect damage [8]. But stone masonry buildings are generally vulnerable to strong earthquake forces [9]. Historical buildings are an important part of the cultural heritage, due to their architectural value and construction techniques [10,11]. It is a responsibility to conserve these structures in order to pass them on to future generations [12,13]. The behavior of masonry buildings subjected to a moderate earthquake is poorly understood or investigated. The conservation of cultural heritage assets should ensure these buildings' capacity to survive against decay and natural hazards, without losing, as much as possible, their originality [12].

Historical buildings are an important part of the cultural heritage, due to their architectural value and construction techniques. It is a responsibility to conserve these structures to pass them on to future generations. The conservation of cultural heritage assets should ensure these buildings' capacity to survive against decay and natural hazards, without losing, as much as possible, their originality [12]. The behavior of masonry buildings subjected to a moderate earthquake is poorly understood or investigated [14]. Earthquakes are one of the main causes of damage to cultural heritage buildings across the world. Therefore, analyzing the seismic performance of cultural heritage assets is of great importance in order to determine effective structural improvement strategies [15]. Seismic performance analysis of historical structures is very complex and depends on many factors such as the geometry of the structure, mechanical properties of materials, connections between the walls, etc. [16]. Information about these variables can be obtained through measurements and laboratory tests [17].

Turkey is among the most seismically and tectonically active regions worldwide [18]. Over the past three decades, approximately twenty earthquakes with magnitudes exceeding M 6.0 have struck various parts of the country, resulting in the collapse or severe damage of numerous buildings [19]. Therefore, earthquake performance analysis of historical buildings in the country is an important and required step for the conservation of these buildings. The aim of this study is to analyze the material properties and seismic performance of a historical stone masonry cistern in Fethiye, Türkiye.

Some studies were performed on the seismic safety of historical buildings; Mutlu and Şahin [20] modeled the eastern minaret of the "Ulu Cami" in Bursa using the finite element method in the Sap2000 structural analysis software Ercan et al. [21] performed linear and nonlinear time history analyses of the updated finite element model of the minaret using the acceleration records of two different earthquakes that occurred in Türkiye. Usta and Bozdag [22] proposed a novel procedure for the immediate screening of masonry buildings at risk. This procedure is notable for its simplicity and speed, and it is based on a simplified geometric approach. Mustafaraj and Morina [23] conducted a structural assessment of Mehmed Pasha Hammam, a historical structure built during the 16th century in Prizren, Kosovo. Usta and Bozdag [24] utilised the finite element method (FEM) to assess the structural integrity of the Basdurak mosque. Asley and Okuyucu [25] examined Erzincan Değirmenliköy Church from a technical and structural perspective. Hysenlliu et al. [26] studied the effects of different materials on the seismic behavior of masonry buildings. Yurdakul et al. [27] determined the damages and locations of the damages that would occur in the case of different earthquakes in the historical Bayburt Ulu Mosque. Ahmadi et al. [28] proposed a new approach for estimating IDA curves using displacement-based adaptive propulsion (DAP) concepts. Structural behavior of the historic S. Giuseppe delle Scalze structure was analyzed by Ramaglia et al. [29] through the use of a FE model and various other models in predicting the major behavior of the structure. Seismotectonics of the area was studied by Doğangün et al. [30] which included the general behavior of earthquakes, along with the damages caused to the infill walls and the structure due to the seismic activities. Seismic behavior of the Totem Tower of Diar Es Saada, erected in 1953 in Algeria, was studied by Mohammedi et al. [31]. Demir et al. [32] conducted a study of the performance of buildings during the Sivrice-Elazığ earthquake, analysing the ground motion record time histories and response spectrum of that period. The study made a comparison between the practices of designing and construction with the Turkish Earthquake Code. Çelik and Tanriverdi [33]

conducted a study on the repair and reinforcement options for vaults, with a particular focus on damage to joints and the upper parts of vaults. Ural and Çelik [34] conducted an analysis of the structural behaviour of the Tahtani (Stork) Mosque, employing the finite element method (FE) and the finite element analysis (FEA) to assess the effectiveness of tension rods between vault columns. Their analysis recommended the implementation of such rods to mitigate stress levels in the vaults, attributable to the mosque's substantial weight. In their 2021 study, Altunisik et al. conducted an analysis of the damage type and cause related to reinforced concrete and masonry structures during the Izmir-Samos earthquake. The study considered the conditions of the current Turkish Building Earthquake Design Regulation [35]. Fuzhang et al. [36] proposed a meshless methodology for obtaining solutions to three-dimensional multinomial time-dependent fractional partial differential equations (PDEs)). Pouraminian [37] utilised nonlinear methodologies in conjunction with finite element models to conduct a study on the seismic response of historical masonry buildings. Mohammed and Cesarano [38] examined the solutions to stochastic equations, offering both theoretical and practical explanations for their applications in physical and engineering contexts. Schiavoni et al. [39] conducted an investigation into the damage caused to the Santa Maria Annunziata church by the 2016 and 2017 Central Italy earthquakes. Sacco et al. [40] conducted a study on the structural damage to the historic San Carlo Borromeo church in Liguria, Italy, which has suffered due to a slow-moving landslide. The present study has sought to examine the effect of landslides on structures and to understand the associated damage and deformation mechanisms. This has been achieved by means of analysis, documentation, in situ observations, laser scanning and deformation studies. Sánchez et al. [41] developed a 3D finite element model and a 3D CAD model in OpenSees for the purpose of analysing the seismic performance of the historic Giralda tower in Seville, Spain. In order to achieve this objective, modal and nonlinear static analyses have been utilised. Sinai et al. [42] conducted an analysis of the structural behaviour and damage loads of Iranian brick masonry barrel vaults, focusing on the impact of skew angle. An experimental approach was adopted to assess the properties of materials and the performance of vaults under gravity loads. A finite element model has been created and analysed numerically. The numerical and experimental results have been compared based on the Willam-Warnke fracture criterion. The study performed by Sokhtesaraei et al. [43] focused on selection of two-component pairs of accelerograms out of 1000 pairs recorded during Iranian earthquakes occurring in 1978-2010 to serve as appropriate acceleration histories of ground motion for further analysis and assessment of the structure in Tehran. Aykanat et al. [44] carried out a field study to record the damages and collapses caused during the earthquake of 23 November 2022 at 04:08 LT in the Gölyaka district of Düzce Province, Turkey (Western Black Sea Region). Güner and Nuhoğlu [45] have introduced a new lattice-model-based method for characterising the in-plane behaviour of walls. The main parameters of this model are: the slope, the cross section area, the mesh size, and the material characteristics. Altunisik et al. [46] gave a detailed review of the most common structural weaknesses in reinforced concrete buildings situated in urban seismic areas. Special attention should be paid to the earthquake in Kahramanmaraş of 6 February 2023. In their paper, Sevim et al. [47] applied documentary and visual materials for studying the damages of affected buildings due to the double earthquake event in Kahramanmaraş. The earthquakes took place on 6 February 2023 at 04:17 LT in the Pazarcık district (Mw 7.7) and roughly nine hours later in the Elbistan district (Mw not specified). Hacıefendioğlu et al. [48] presented an automated damage assessment technique for masonry buildings after an earthquake using deep learning segmentation approach in which U-net CNN model is employed.

Structural Description of the Historical Cistern

The cistern structure is located in Esenkoy, Fethiye. It was built in the 1800s during Ottoman Period. The floor area of the building has a rectangular shape and the structure has a vaulted roof. The short side length of the structure is 8.43 m. and the long side length and also the length of the vault is 13.5 m. Figure 1 shows the location of the cistern structure and seismic map of Turkey.

The walls of the historical cistern, made from rubble, carved stones, and mortar, form a composite element for practical analysis, treated as a single entity in macro model analysis (Yurdakul et al. [27]). The behavior of the walls made out of masonry depends on the properties of the material used for building, which are masonry and mortar. The behavior of masonry walls can differ drastically because of the material properties and the way the structure was built. The parameters such as craftsmanship, joint size, and wall dimensions are important, and the use of improper material affects greatly the behavior of the walls [49].

In order to analyze historical buildings by using the finite element method (FEM) correctly, the mechanical properties of the materials of the building should be examined experimentally. This study aimed to determine the mechanical properties of the stone used in the construction of the historical cistern. The specimens were obtained from the actual structure. Eight different samples were tested following the TS EN 1926 Turkish standard (Natural stone test methods - Determination of uniaxial compressive strength) [50] for measuring compressive strength. This standard covers a method for maintaining the uniaxial compressive strength of natural stone. The methodology involved the application of a monotonically increasing axial load (4.71 MPa/s) until failure. The test scheme is presented in Figure 2. Such testing procedure was very useful for determining the properties of the stone.

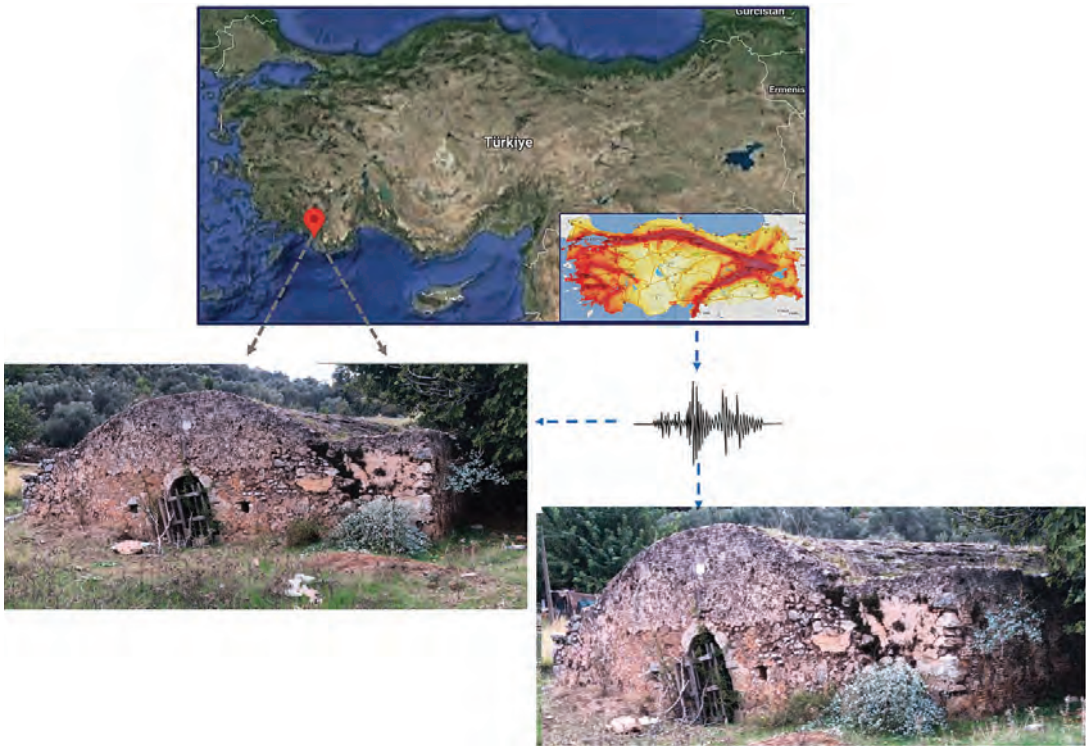


Figure 1. The seismic map of Türkiye and the location of the cistern structure.



Figure 2. The experimental setup for the determination of mechanical properties.

Eight 50 mm cube specimens were tested under compression using a 500 kN capacity hydraulic testing machine. The compressive strength was calculated by dividing the peak load recorded during testing by the specimen's cross-sectional area. [51]. Experimental results are presented in Table 1. The stone's average compressive strength was calculated as 62.56477 MPa. The average compressive strength of the stones was determined as 62.56 MPa based on experimental results. This value aligns with the range of compressive strengths obtained for similar stone structures by Senthivel and Lourenço [8]. Additionally, Çoban [52] highlighted in his study that the strength of stone and mortar composite elements corresponds to approximately 70% of the stone strength.

Static modulus of elasticity of masonry stones defined by many standards can be calculated empirically. Eq. (1) can be used to determine the modulus of elasticity depending on compressive strength [53].

$$E_{mas} = 750.f_{c,mas} \quad (1)$$

Where $f_{c,mas}$ (N/mm^2) is the characteristic compressive strength of the stone and E_{mas} (N/mm^2) is the modulus of elasticity of the stone.

In historical masonry structures, stone and mortar act together as a composite material. For practical numerical analyses, this composite masonry is commonly represented as a single equivalent material, which is referred to in the literature as the macro-modelling approach [54]. In the present study, since the mechanical properties of the stone–mortar composite could not be directly determined, the masonry units and mortar were modeled together as a homogenized material. Based on the literature [52], the mechanical properties of this equivalent composite material were assumed to be 70% of the corresponding values of the stones or bricks.

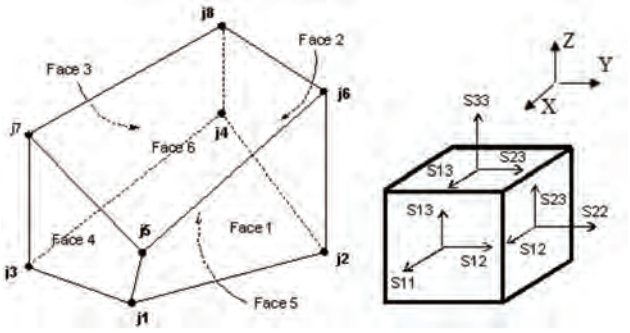
Table 1. The experimental results of cistern stones

Sample No	Area (mm²)	Density (kg/cm³)	Load speed (kN/s)	Maximum Load (kN)	Compressive Strength (MPa)
1	2500	3.28	4.71	185.68	74.27
2	2500	2.71	4.71	169.98	67.99
3	2500	2.91	4.71	180.70	72.28
4	2500	2.71	4.71	48.17	19.27
5	2500	2.40	4.71	141.90	56.76
6	2500	2.74	4.71	211.42	84.57
7	2500	2.94	4.71	149.52	59.81
8	2500	2.80	4.71	163.94	65.58
Avg. values		2.81		156.41	62,56

3D Finite Element Model of the Cistern

The cistern described in this study is an 18th-century water storage structure, primarily designed to provide a storage area insulated from external factors to prevent water deterioration. Therefore, only the main entrance opening was considered in both the actual design and the modeling of the structure. Small openings in the walls were not included in the model because such openings are not present in the structure. This modeling approach aligns with general architectural characteristics and historical usage of cistern structures. The model of the cistern was developed using the SAP2000 V22 finite element program [55]. The masonry walls were discretized using 10,595 three-dimensional, eight-node, six-sided solid elements and 15,088 nodes. The maximum and minimum dimensions of the solid elements were approximately 0.2 m × 0.2 m × 0.1 m and 0.1 m × 0.1 m × 0.2 m, respectively.

In the SAP2000 finite element model, S33 represents the axial tensile and compressive stresses in the Z direction, while S11 and S22 correspond to the axial tensile and compressive stresses in the other principal directions. These stress components were considered during the analysis and evaluation stages of the study, as shown in Figure 3.



a) 8- node solid element b) Stress components in the global coordinate

Figure 3. A solid element

The base of the cistern was considered to be fixed. The roof was considered a structural component in the model. The FEM model has a total mass of 1098.22 metric tons. Geometrical second-order effects were neglected in the analyses. Modal analysis was performed using the eigenvector method in SAP2000. In accordance with the macro-modelling approach, the masonry structure was assumed

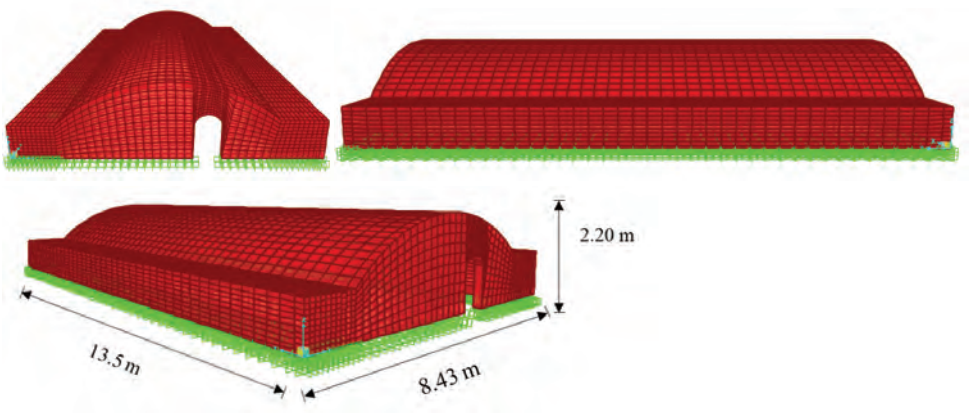


Figure 4. FEM model of the cistern.

to behave as a homogeneous material. In this study, macro-modelling was adopted because it is more appropriate for the dynamic analysis of complex, large-scale historical structures [27]. The finite element model of the cistern is presented in Figure 4.

Strong Motion Selection

To select hazard-compatible ground motions for linear dynamic analysis of the structural model, we chose Strike-Slip ground motions from the PEER database [56,57]. During the selection of ground motion records, 30records were identified using the PEER (Pacific Earthquake Engineering Research) database. These records focused on far-field earthquakes with a strike-slip mechanism, magnitudes ranging from $6.5 \leq M \leq 7.5$, and shear wave velocities (Vs30) between 360 and 760 m/s. These criteria were chosen to ensure compatibility with the seismic hazard profile of the study region. The chosen earthquake records were scaled to match the DD2 earthquake design levels as per the Turkish Earthquake Hazard Map. During the entire scaling phase, each earthquake record was made consistent with the elastic design spectrum. More specifically, the values of spectral acceleration (Sa(T1)) were modified to match the targeted spectrum for the fundamental period of the structure, and the scaling factor was established. It has been found that this technique increases the accuracy of the records and analyses. Moreover, different parameters, such as PGA, PGV, and Arias Intensity, have been used in each analysis process. These parameters helped in conducting a more extensive analysis of the impact of ground motion on the seismic demands. The records have been presented in Table 2 and Figure 5.

Table 2. Set of 30 ground motion records from strike-slip mechanism

Earthquake Name	Year	Magnitude	Mechanism	Rjb (km)	Rrup (km)	Vs30 (m/sec)
"Parkfield"	1966	6.19	strike slip	17.64	17.64	408.93
"Northern Calif-05"	1967	5.6	strike slip	27.36	28.73	219.31
"San Fernando"	1971	6.61	Reverse	19.33	22.63	450.28
"Coyote Lake"	1979	5.74	strike slip	19.46	19.7	335.5
"Imperial Valley-06"	1979	6.53	strike slip	22.03	22.03	242.05
"Imperial Valley-06"	1979	6.53	strike slip	17.94	17.94	196.88
"Irpinia_ Italy-02"	1980	6.2	Normal	22.68	22.69	574.88
"Taiwan SMART1(5)"	1981	5.9	Reverse	26.31	27.36	268.37
"Morgan Hill"	1984	6.19	strike slip	13.68	13.69	270.84
"N. Palm Springs"	1986	6.06	Reverse Oblique	10.08	10.84	312.47
"Chalfant Valley-01"	1986	5.77	strike slip	14.99	15.13	585.12
"Whittier Narrows-01"	1987	5.99	Reverse Oblique	13.58	20.91	346.62
"Superstition Hills-02"	1987	6.54	strike slip	18.2	18.2	192.05
"Loma Prieta"	1989	6.93	Reverse Oblique	24.27	24.57	239.69
"Landers"	1992	7.28	strike slip	26.96	26.96	355.42
"Northridge-01"	1994	6.69	Reverse	23.5	29.88	297.07
"Kobe_ Japan"	1995	6.9	strike slip	24.85	24.85	256
"Manjil_ Iran"	1990	7.37	strike slip	12.55	12.55	723.95
"Chi-Chi_ Taiwan-04"	1999	6.2	strike slip	21.62	21.67	258.89
"Cape Mendocino"	1992	7.01	Reverse	23.46	25.91	515.65
"Tottori_ Japan"	2000	6.61	strike slip	28.81	28.82	293.37
"Parkfield-02_ CA"	2004	6	strike slip	12.59	12.97	357.35
"Niigata_ Japan"	2004	6.63	Reverse	17.57	18.03	193.2
"Chuetsu-oki_ Japan"	2007	6.8	Reverse	15.89	23.44	430.16
"Iwate_ Japan"	2008	6.9	Reverse	20.47	20.64	264.48
"Iwate_ Japan"	2008	6.9	Reverse	10.71	13.47	361.24
"El Mayor-Cucapah_ Mexico"	2010	7.2	strike slip	13.21	15.91	242.05
"Joshua Tree_ CA "	1992	6.1	strike slip	21.73	22.3	396.41
"Darfield_ New Zealand"	2010	7	strike slip	24.36	24.47	422
"Christchurch_ New Zealand"	2011	6.2	Reverse Oblique	16.6	16.61	249.28

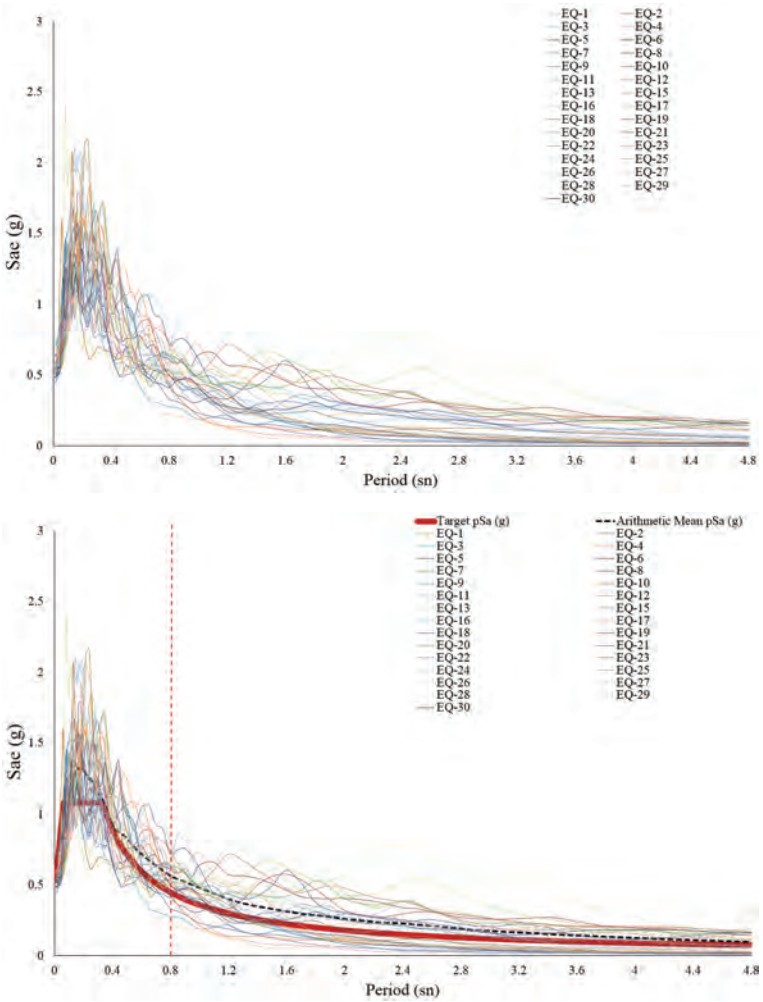


Figure 5. a) Response spectra set of 30 records from different source mechanisms to be used in THA analysis. Unscaled signals: (b) Response spectra set of records scaled to spectral acceleration at the structural period in the X direction, Sa (T1, 5%).

Unscaled signals: (b) Response spectra set of records scaled to spectral acceleration at the structural period in the X direction, Sa (T1, 5%).

Wall Characteristic Shear Strength

The characteristic shear strength of masonry walls can be calculated with the help of Equation (2) as specified in TBDY-2018 [53].

$$f_{vk} = f_{vko} + 0.4\,\sigma \leq 0.10\,f_b \quad (2)$$

In this equation;

f_{vk}: Characteristic shear strength of masonry wall,

f_{vko}, the characteristic initial shear strength

σ: Earthquake loads multiplied by load coefficients and vertical compressive stress calculated under the influence of vertical loads,

f_b: It is the average compressive strength of the masonry unit.

To calculate the shear stresses on the cistern walls and their shear strength, we followed the nomenclature shown in Figure 6.

RESULTS AND DISCUSSION

The Cistern was modeled with solid elements. The modes of vibration and the values of participation of the modal responses were determined by a discretization in finite elements by SAP2000 Software. Model Periods and modal participating mass ratios are shown in Table 3.

The linear elastic time history analysis of the cistern structure was performed in this paper. The modal mass participation ratios were found to exceed 93% in the analyzes conducted with the SAP2000 software. Pardalopoulos and Pantazopoulou [58] highlight the importance of high mass participation ratios in modal analyses for the accurate modeling of the dynamic characteristics of the structure.

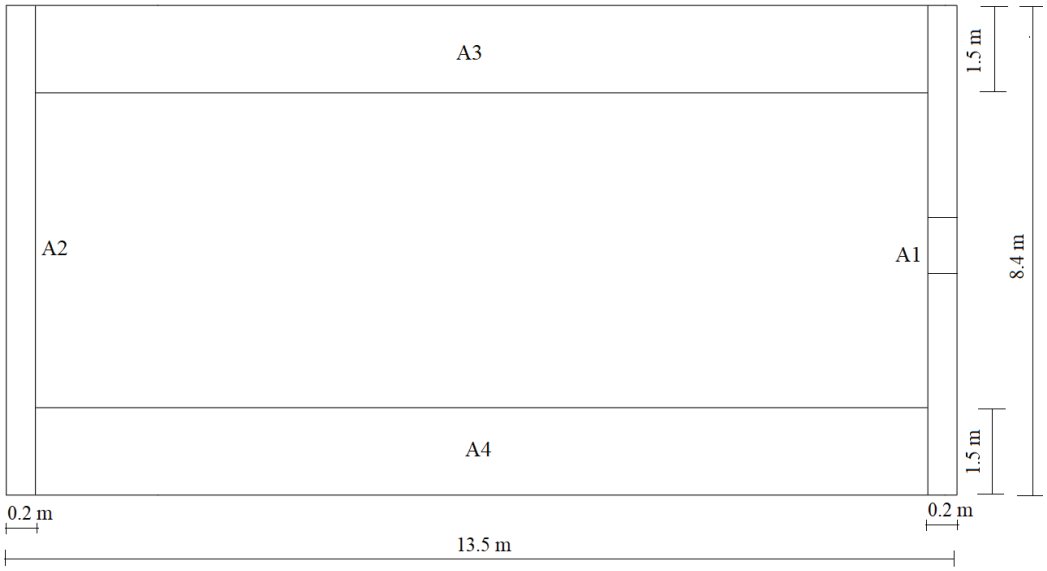


Figure 6. Plan view of the cistern.

Table 3. Model periods and modal participating mass ratios

StepNum Unitless	Period Sec	Frequency Cyc/sec	UX Unitless	UY Unitless	UY Unitless
1	0.025	30.901	0.066	5.52E-08	4.81E-05
2	0.018	56.855	3.31E-07	2.54E-07	1.13E-07
3	0.013	77.982	0.006635	4.5E-07	4.43E-06

Accordingly, the ratios obtained in the study are in accordance with the findings of previous studies.

As shown in Figure 2, the eigenvalue analysis of the finite element model produced numerous closely spaced vibration modes. The first few modes were generally associated with negligible modal mass and were therefore of limited relevance. Consequently, a large number of modes had to be included in each principal plan direction of the

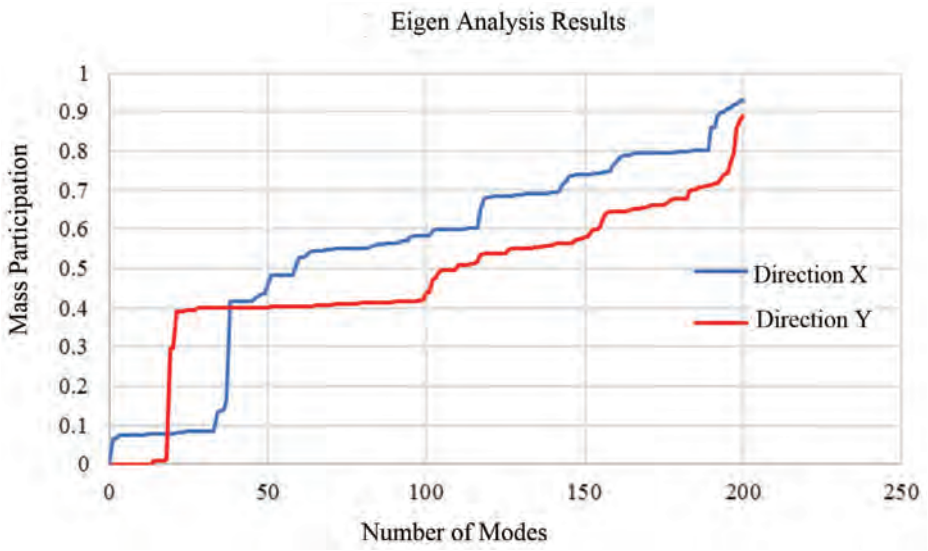


Figure 7. Percentage of total mass participation in the X and Y plan directions after considering the first 200 modes.

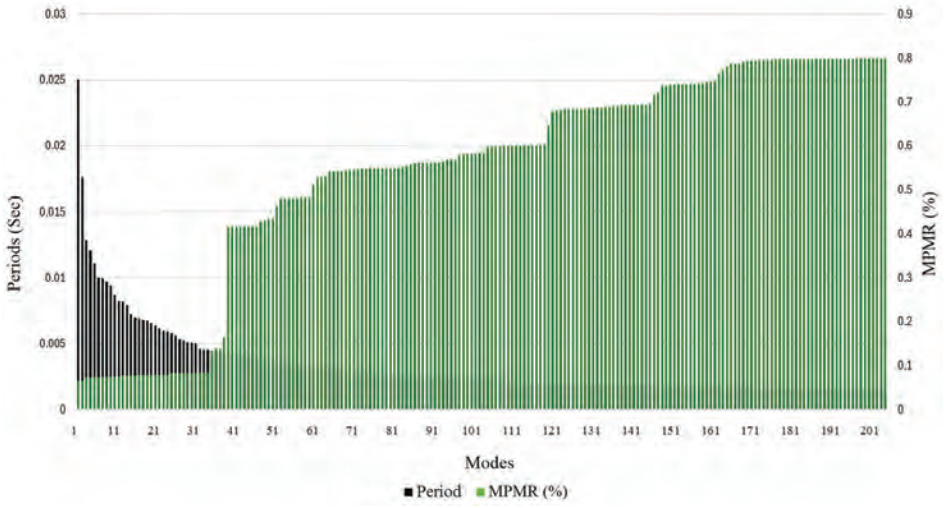


Figure 8. The periods and participation factors of the 200 modes.

structure to achieve an adequate level of total mass participation [58]. The periods and modal participation mass ratios (MPMRs) of the first 200 modes are presented in Figure 7 and 8.

The selection of the number of modes for the cistern structure in the study was based on achieving sufficient dynamic mass participation to ensure accurate seismic behavior representation. During the modal analysis carried out using SAP2000, there were a total of 200 modes included, and this has led to a mass participation ratio being in excess of 93% in both principal directions. The mass participation ratio being high means that a major portion of the dynamic properties of the structure has been taken into consideration, and therefore the need to consider higher modes is eliminated. In the case of the cistern structure, which is a one-story, high occupancy masonry structure with rigid walls and no intermediate stories, the effect of higher modes in the response of the entire structure will be very small. Such structures have a tendency of having modal participation from lower modes due to the properties of the structure. If further confirmation is needed, a sensitivity analysis incorporating even higher modes could be conducted, but based on the study results, the current approach aligns well with the structural properties and intended performance evaluation of the cistern.

Features such as duration, Pga, and acceleration values of Ground motion records caused each earthquake record to give different results on the structure. The maximum displacement values obtained from the earthquake records used in the article and vary depending on the characteristics of the earthquakes are given in Table 4.

The horizontal displacement values presented in the table range from 0.070 cm to 1.500 cm in the X direction and from 0.034 cm to 0.288 cm in the Y direction. When compared with the critical thresholds specified in the literature, these values provide important information about the seismic performance of the structure. Vicente et al. [12] noted that horizontal displacement values exceeding 0.5 cm in masonry structures accelerate crack formation and lead to significant stress concentrations. In this context, high displacement values such as Joshua Tree (1.500 cm in the X direction, 0.288 cm in the Y direction) and Parkfield-02_CA (1.124 cm in the X direction, 0.147 cm in the Y direction) indicate a serious potential for damage around the dome openings and entrance areas.

Lagomarsino and Cattari [59] emphasized that horizontal displacement values exceeding 1.0 cm could cause crack intensification in rigid regions. In the table, Loma Prieta (1.336 cm in the X direction) exceeds this threshold and poses a risk of crack formation in the openings. On the other hand, lower displacement values (e.g., San Fernando: 0.175 cm in the X direction, 0.049 cm in the Y direction) indicate a lower risk of damage in the rigid regions of the structure.

Hysenlliu et al. [26] stated that maximum displacement values exceeding 0.3 cm in masonry structures with different materials could lead to the onset of crack formation in weak areas. According to the table, displacement values measured in the Y direction, such as Joshua Tree (0.288 cm) and Iwate_Japan (0.071 cm), are close to or above this threshold and may pose a risk of damage in weak areas.

Studies in the literature suggest that interstory drifts can be used to determine structural damage [60-62]. According to the studies, the suggested performance limit states corresponding to the local failure modes of inter-story drift ratios are given in Table 5.

The drift ratio used in the study, which is commonly employed as a criterion for structural performance evaluation, was utilized to determine the performance levels in our work. The limit values of drift ratios were based on the references of [64,65].

Table 4. Properties of earthquake records and time history results

No	Earthquake Name	Pga (g)	Pgv (cm/sn)	Arias Intensity (m/sec)	Scale Factor	Max Displacement (cm)	
						X Direction	Y Direction
EQ-1	"Parkfield"	0.06	7.20	0.1	6.06	0.205	0.172
EQ-2	"Northern Calif-05"	0.18	11.52	0.1	2.28	0.660	0.076
EQ-3	"San Fernando"	0.29	22.18	1	1.27	0.175	0.049
EQ-4	"Coyote Lake"	0.10	6.86	0.1	3.60	0.222	0.118
EQ-5	"Imperial Valley-06"	0.26	26.95	3.3	1.13	0.658	0.059
EQ-6	"Imperial Valley-06"	0.14	22.27	0.4	2.59	0.980	0.046
EQ-7	"Irpinia_ Italy-02"	0.14	11.40	0.3	3.24	0.174	0.105
EQ-8	"Taiwan SMART1(5)"	0.17	9.04	0.2	2.61	0.160	0.101
EQ-9	"Morgan Hill"	0.17	12.33	0.2	2.37	0.846	0.083
EQ-10	"N. Palm Springs"	0.07	6.53	0.3	2.03	0.070	0.047
EQ-11	"Chalfant Valley-01"	0.07	5.66	0	5.28	0.997	0.058
EQ-12	"Whittier Narrows-01"	0.26	43.67	0.1	4.41	0.906	0.208
EQ-13	"Superstition Hills-02"	0.16	25.55	1.1	1.26	0.528	0.034
EQ-14	"Loma Prieta"	0.21	37.87	0.5	2.19	1.336	0.139
EQ-15	"Landers"	0.12	12.49	0.4	2.83	0.787	0.049
EQ-16	"Northridge-01"	0.19	16.59	0.7	1.73	0.217	0.053
EQ-17	"Kobe_ Japan"	0.21	21.15	0.6	1.84	0.278	0.050
EQ-18	"Manjil_ Iran"	0.52	49.48	7.5	0.62	0.251	0.056
EQ-19	"Chi-Chi_ Taiwan-04"	0.17	18.85	0.4	2.10	0.183	0.047
EQ-20	"Cape Mendocino"	0.25	34.21	0.9	1.42	0.258	0.067
EQ-21	"Tottori_ Japan"	0.31	16.27	0.8	1.31	0.310	0.066
EQ-22	"Parkfield-02_ CA"	0.20	6.88	0.1	2.79	1.124	0.147
EQ-23	"Niigata_ Japan"	0.34	20.41	0.8	1.19	0.282	0.047
EQ-24	"Chuetsu-oki_ Japan"	0.11	8.84	1.8	1.20	0.767	0.048
EQ-25	"Iwate_ Japan"	0.26	12.75	1.9	1.38	0.201	0.071
EQ-26	"Iwate_ Japan"	0.44	59.06	4.2	0.85	0.315	0.069
EQ-27	"El Mayor-Cucapah_Mexico"	0.43	54.92	6.1	0.72	1.041	0.090
EQ-28	"Joshua Tree_ CA "	0.10	9.10	0.2	3.66	1.500	0.288
EQ-29	"Darfield_ New Zealand"	0.57	31.85	4.1	0.69	0.286	0.080
EQ-30	"Christchurch_ New Zealand"	0.11	11.78	0.2	2.99	1.105	0.094

Table 5. Performance levels in terms of drift ratios based on local failure modes (adapted from Demirel [63])

		Performance Level (Drift Ratio)		
Author	Failure Mode	IO	LS	CP
Franklin et al. (2001) [64]		0.1	0.9-1.5	1.2-1.9
Bosiljkov et al. (2008) [65]		0.1	1.2-1.8	1.8-2.5
Bosiljkov et al. (2008) [65]	Sliding	-	0.9	1.8
Bosiljkov et al. (2008) [65]	Diagonal Tension	0.2-0.5	0.5-0.7	0.5-0.9
Alcocer et al. (2004) [66]		0.15	0.25	0.4

The drift ratios of the cistern walls obtained from linear dynamic Time History Analyses were presented in Table 6.

Cistern structure exhibits a very rigid behavior since it is a single storey and void-free structure with a very high occupancy rate. For this reason, the drift ratio ratios in the building are at low values as seen in the table. The measured drift ratios of the Cistern Facade walls are between 0.0004 - 0.008 in the short direction and 0.0016- 0.0002 in the long direction Since these drift ratio values do not exceed the 0.1 limit value, which represents the Immediate Occupancy

Table 6. Drift ratios of the cistern

Earthquake Name	Drift Ratio (X direction)	Performance Level	Drift Ratio (Y direction)	Performance Level
EQ-1	0.0011	IO	0.0010	IO
EQ-2	0.0037	IO	0.0016	IO
EQ-3	0.0010	IO	0.0012	IO
EQ-4	0.0012	IO	0.0008	IO
EQ-5	0.0037	IO	0.0008	IO
EQ-6	0.0054	IO	0.0007	IO
EQ-7	0.0010	IO	0.0006	IO
EQ-8	0.0009	IO	0.0006	IO
EQ-9	0.0047	IO	0.0005	IO
EQ-10	0.0004	IO	0.0005	IO
EQ-11	0.0055	IO	0.0005	IO
EQ-12	0.0050	IO	0.0004	IO
EQ-13	0.0029	IO	0.0004	IO
EQ-14	0.0074	IO	0.0004	IO
EQ-15	0.0044	IO	0.0004	IO
EQ-16	0.0012	IO	0.0004	IO
EQ-17	0.0015	IO	0.0004	IO
EQ-18	0.0014	IO	0.0003	IO
EQ-19	0.0010	IO	0.0003	IO
EQ-20	0.0014	IO	0.0003	IO
EQ-21	0.0017	IO	0.0003	IO
EQ-22	0.0062	IO	0.0003	IO
EQ-23	0.0016	IO	0.0003	IO
EQ-24	0.0043	IO	0.0003	IO
EQ-25	0.0011	IO	0.0003	IO
EQ-26	0.0018	IO	0.0003	IO
EQ-27	0.0058	IO	0.0003	IO
EQ-28	0.0083	IO	0.0003	IO
EQ-29	0.0016	IO	0.0003	IO
EQ-30	0.0061	IO	0.0002	IO

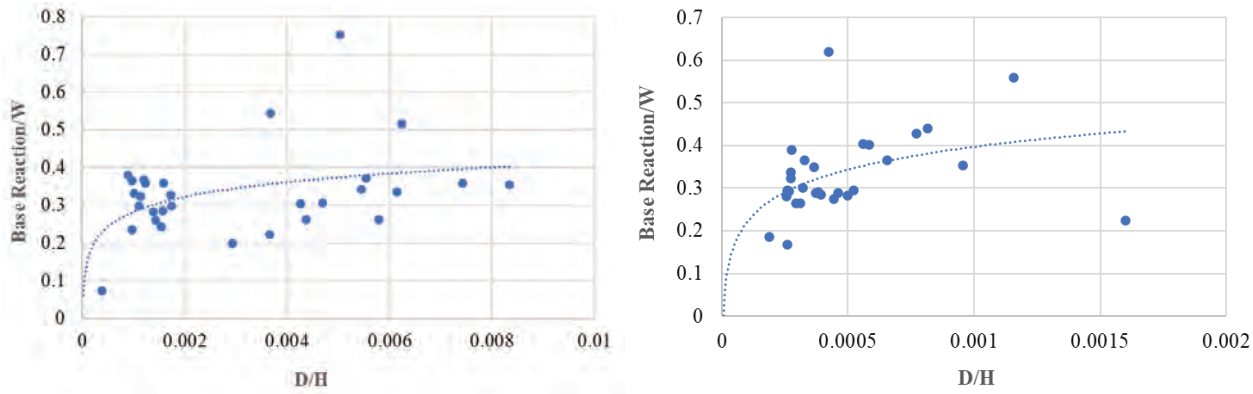


Figure 9. Pushover curves X and Y directions FE model of Cistern Structure.

performance level, the structure is expected to show slight damage during the described earthquakes and earthquakes similar to these earthquakes. In addition, when looking at the building directions, it was seen that the displacement values in the X direction (short direction) of the building were larger than the Y direction (longer direction). This is an indication that the long side of the building is more rigid than the short side.

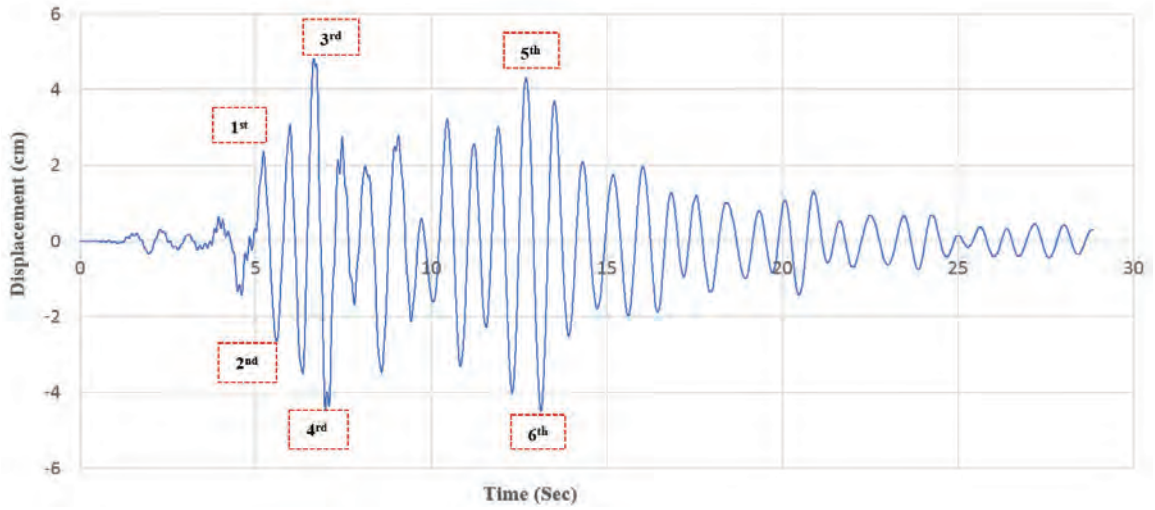


Figure 10. The displacement - time graph for EQ28.

The pushover curves, expressed as generalized force–displacement relationships, are presented in Figure 9 for loading applied in the ±X direction (North–South) and ±Y direction (East–West). To obtain the capacity curves, the control node was selected as the node located at the top of the cistern that exhibited the maximum horizontal displacement.

In practical assessment methodologies, it is commonly observed that finite element models of masonry monuments subjected to real earthquake time histories may predict severe damage, whereas the actual structures often exhibit lower levels of damage. During seismic loading, cracks progressively open from small to larger widths at peak loading cycles, which increases the structure's capacity to absorb seismic energy [67]. In order to better see and interpret the responses of earthquakes in the structure, the earthquake named EQ28, which is one of the earthquakes that give the highest displacement values in the structure was chosen.

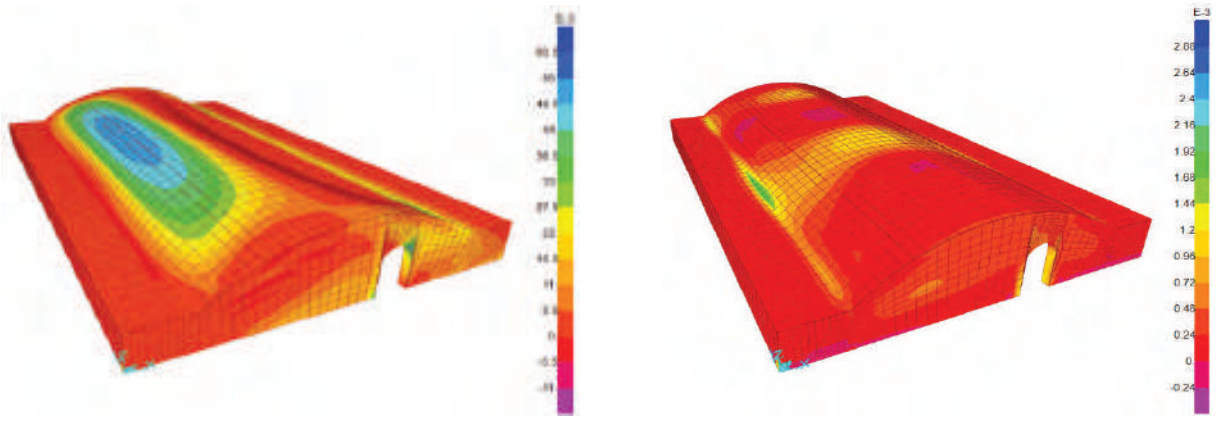
The displacement - time graph for the earthquake is presented in Figure 10.

For the relevant parts of the displacement time graph of the earthquake, the response of the structure at certain time instants and the stress graphs are shown in Figure 11.

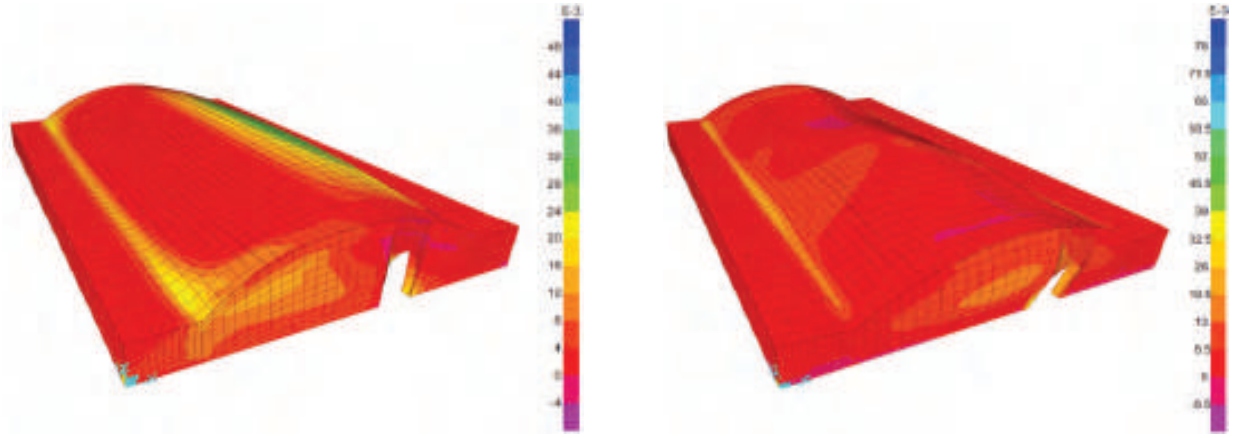
These stresses are considered critical in terms of crack formation and propagation. Specifically, tensile stresses around the door and dome openings are identified as the primary causes of structural damage during seismic impacts.

According to the data presented in Figure 11, compressive and tensile stresses are particularly concentrated around the dome openings and entrance walls. In terms of compressive stresses, the highest values were observed around the dome openings and the surrounding area

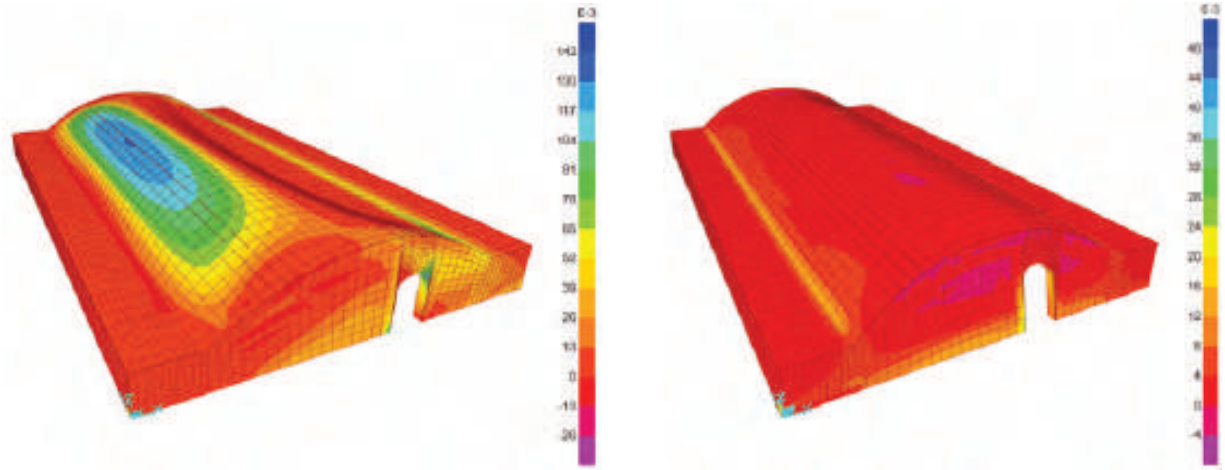
EQ28X (MPA) **EQ28Y (MPA)**



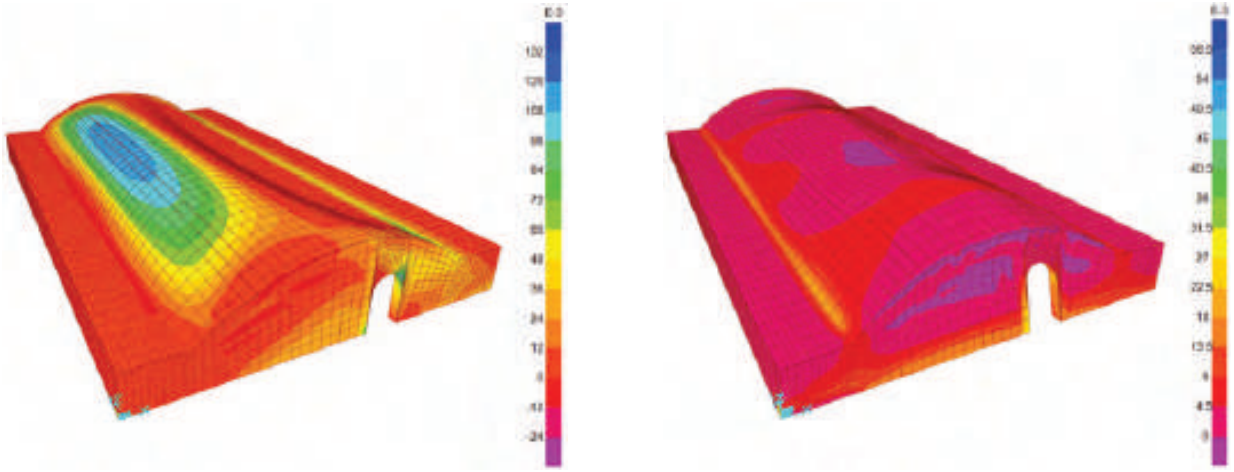
T: 5.25 sn



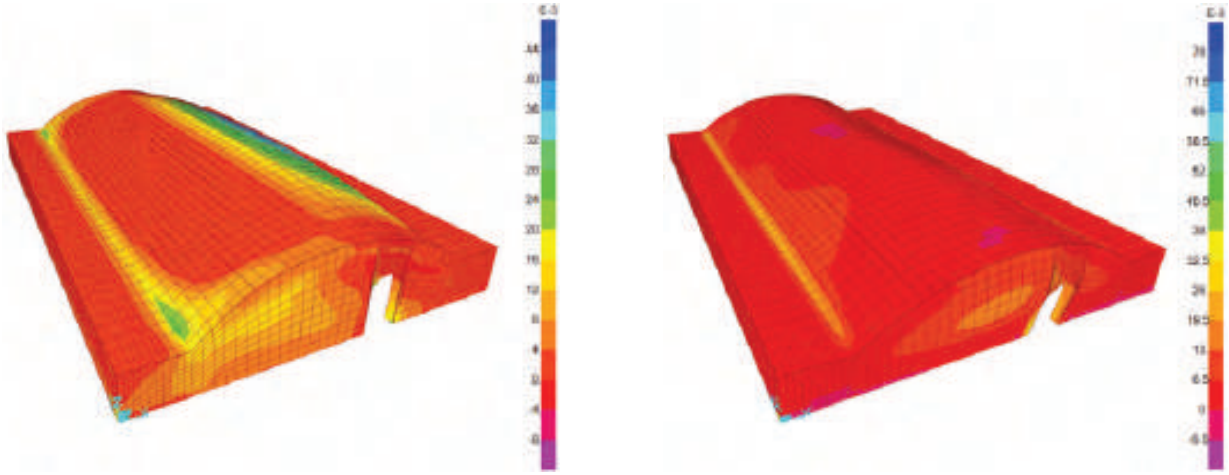
T: 5.60 sn



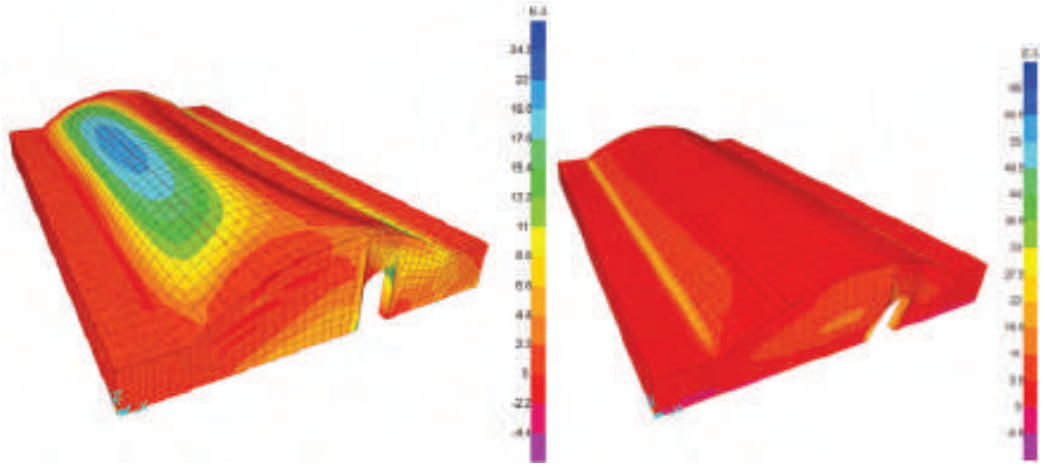
T: 6.63 sn



T: 7.09 sn



T: 12.75 sn



T: 13.13 sn

Figure 11. Distribution of stresses and deflection in the structure using time history analysis for the earthquake named EQ28

of the entrance wall. The maximum compressive stress was approximately 0.525 MPa, indicating critical zones of localized stress accumulation identified in the model. These areas underscore the necessity for structural reinforcement. Conversely, tensile stresses were predominantly concentrated in the dome apertures and the upper section of the entrance door. The analysis presented in Figure 11 revealed that the maximum tensile stress was calculated to be approximately 0.272 MPa.

These findings are crucial for understanding the current stress distribution within the cistern structure and for identifying priority intervention areas.

From these graphs, the damage (cracking and stress) values n the walls can be seen and the damage in the structure can be defined qualitatively.

During an earthquake, as cracks occur in the walls and the structure is damaged, the strength of the structure decreases.

While the cistern structure is displaced in the same direction, the crack tip continues to propagate, while stress relaxation is observed in the previously cracked parts. When the structure starts to move in the opposite direction, the cracks can close and compressive stresses can be seen in the already cracked places.

Crack propagation and stress concentration were observed, particularly around the dome and wall openings. The structure maintained its structural integrity under most earthquake scenarios [59] stated that similar stress and damage mechanisms could occur in stone structures with large openings under seismic effects. This demonstrates the consistency of the findings with the literature.

In some cases, early damage caused by high seismic intensity may lead to a reduced acceleration response of the structure during subsequent stronger phases of the record. This behavior may be attributed to damage-induced elongation of the structural vibration period, which can reduce the acceleration demand and allow the structure to survive the earthquake. Therefore, in such situations, the observed response is governed not only by the intensity of the acceleration but also by the sequence, timing, and damage progression during the ground motion [58].

A comparison between the numerical results obtained from the seismic analysis and the observed damage patterns on the historical cistern structure provides critical insights into the accuracy of the model and the seismic behaviour of the structure. In the subsequent analysis section, the observed level of damage was subjected to a comparative analysis with the actual damages sustained. Based on the numerical analysis, stress concentrations become evident mostly around the primary dome and wall holes. It is worth noting that the findings are consistent with the field observation, as damage is evident mostly in these parts. However, according to the numerical analysis, there is a slightly higher level of stress at the center of the dome compared to the stress that causes the minor cracks. The difference can be attributed to the actual properties of the material or method of construction used in real life. The findings further suggest possible ways through which damage occurs, for instance, due to high shear stress near the door holes. This is thoroughly illustrated in Figure 12.

The characteristic shear strength of the wall is calculated with the help of Equation (2). In this equation, f_{vko}, the characteristic initial shear strength is given as 0.1 MPa for natural or artificial stones in TBDY 2018 [53]. The characteristic shear strengths calculated for the walls and the shear stresses occurring in these walls are shown in Table 7.

While obtaining Table 7, the characteristic shear strength was calculated for each wall and these strengths were compared with the greatest shear stresses resulting from time history analyses. According to time history analysis, the largest shear stresses occurred as a result of the EQ28 earthquake. For this reason, only the shear stresses obtained for the x and y components of the EQ28 earthquake are shown in Table 7.

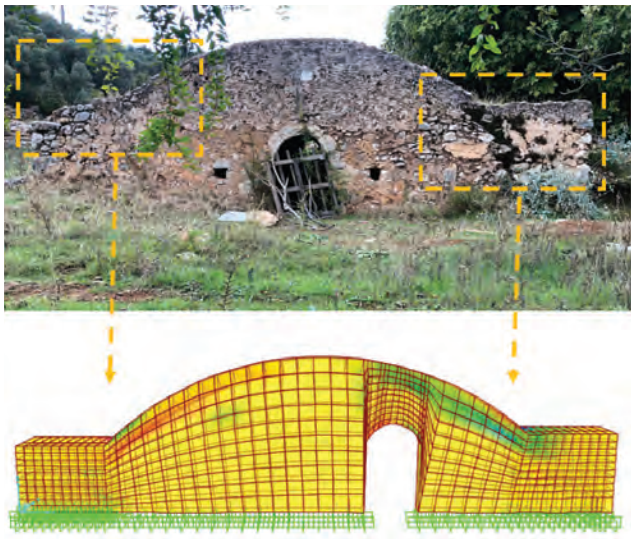


Figure 12. Stones detached from the vertical wall due to shear stresses.

Shear strength and stress values determined from the analysis of the cistern walls as provided in Table 7 reveal uniform agreement with similar research in the literature. The maximum value of shear stress in this research, for instance, 0.272 MPa for wall A1 in Y direction, agrees with the shear stress concentration in masonry walls with openings as reported by Kumbasaroglu et al. [16]. The increased values of shear stresses around door openings confirm the existing literature where the same areas have been noted as weak points in the structure. Hrasnica and Medic [9] have pointed out that stone masonry structures generally suffer from weaknesses in the shear strength in the vicinity of openings, which calls for immediate attention to strengthen those structures through retrofitting works. The results obtained in this research indicating that wall A1 lacks

Table 7. Shear strengths and shear stresses for the walls

Direction	Wall	Compressive stress, σ (MPa)	Characteristic shear strength, fvk (MPa)	The maximum shear stress that occurs (MPa)
X	A1	0.218	0.187	0.147
	A2	0.226	0.190	0.092
	A3	0.525	0.310	0.059
	A4	0.512	0.305	0.064
Y	A1	0.218	0.187	0.272
	A2	0.226	0.190	0.023
	A3	0.525	0.310	0.079
	A4	0.512	0.305	0.080

adequate shear strength are in line with this observation. However, the shear stresses in X direction of all walls were less than their respective shear strengths. Such a conclusion corresponds to the results of the work of Senthivel and Lourenço [8], which stated that masonry structures usually demonstrate higher strength in the X direction. As can be seen from the results obtained, they mostly correspond to existing literature and validate the efficiency of using modelling and experimental validation for assessment of the behaviour of masonry structures in relation to the effects of the seismic load. The found weakness of the Wall A1 and accordance with literature data concerning the influence of openings show the necessity of the use of the proposed techniques for retrofitting. In this case, high-strength mortar injection and use of horizontal steel rods as proposed by Çelik and Tanriverdi [10] are highly effective techniques for reducing the shear stress.

After performing the static analysis, the vertical load of the wall was equal to 6159.663 kN. Vertical compressive stress of the wall at such a load was 0.171 MPa.When these values are used, the characteristic shear strength f_{vk} according to Equation (1) is obtained as 0.168 MPa. When Figure 11 is examined, the largest shear stress in the cistern as a result of earthquake ground movements is 0.136 MPa. This result shows that the cistern is safe in terms of shear stress.

There are cracks due to the building's aging and depreciation over time. Plaster shedding also was observed in some areas. In these parts, where masonry units are missing, the growth of vegetation can be easily seen from field observations and Figure 11. Furthermore, Considering the analysis results, it was seen that the greatest shear stresses occurred in the wall area on the right side of the building entrance. In the current state of the building, this area is already damaged. The damaged area on the current structure is less wide in relation to the corresponding area on the model. The compatibility of the analysis result with the current situation shows the accuracy of the modeling and analysis.

CONCLUSION

Historic cisterns are important components of cultural heritage due to their architecture and function. Nevertheless, little has been researched about their unique architectural forms and susceptibility to earthquakes. Most studies are dedicated to common masonry structures and do not consider the specificities of cisterns, including their roofs, openings, and underground parts. Lack of relevant information has made it difficult to develop effective measures of strengthening historic cisterns to ensure their seismic resistance. This paper discusses the seismic performance of the historic cistern in Fethiye, Turkey. Experimental and numerical methods were used to conduct an in-depth analysis of the cistern and obtain important findings. The mechanical properties of stone materials were defined; earthquake accelerations were set according to the Turkish Building Earthquake Code (2018). Static and time-history analyses of the cistern were conducted with SAP2000 V22 software.

Results of the performed analyses revealed the following parameters. The maximal value of the lateral displacement equal to 1.5 cm was obtained for the short side. Due to this parameter, it can be stated that the external façade should be viewed as critical because of stress concentrations. In terms of compressive stresses, the maximum values were found to be near the openings of the dome and the entrance wall with the maximum value close to 0.525 MPa. Tensile stresses were found to be concentrated around the dome openings and the top part of the entrance door. The latter was calculated as equal to 0.272 MPa. These parameters are critical from the perspective of cracks' formation and growth. Time-history analysis showed that shearing stresses exceeded the wall's characteristic shear strength. Results concerning displacement and stress values showed the possibility of the formation of damage within some areas.

Overall, the structural safety of the analyzed cistern under the impact of most of the 30 simulated earthquake scenarios was ensured. No significant damages to the structure of the cistern were reported. Nevertheless, repeated actions of earthquakes can increase stress levels and create favorable conditions for crack propagation. Consequently, problems related to cistern structure can arise. Such a situation can be associated with the extensive opening of the roof along the longitudinal direction.

On the basis of the received results, suggestions for strengthening the main weak spots of the cistern structure can be developed. It is suggested to add circumferential tension members or to use light and strong materials. Concerning wall openings, such actions as high-strength mortar injection and installing steel rods are recommended to reinforce walls, especially in critical areas like doors. The roof surface should be strengthened through installation of FRP strips/meshes.

It can be concluded that though the analyzed cistern is characterized by sufficient strength, strengthening is needed in the zones of high stress. It is necessary to accurately simulate joints of masonry historical structures during modeling to increase precision.

One of the distinctive features of this study is the focus on cisterns and their seismic performance. This paper contributes to the field through performing experimental and numerical studies of the dynamic behavior of one of cisterns under the action of earthquake forces. Based on the received results, the authors provide suggestions regarding retrofitting of such structures.

AUTHORSHIP CONTRIBUTIONS

Authors equally contributed to this work.

DATA AVAILABILITY STATEMENT

The authors confirm that the data that supports the findings of this study are available within the article. Raw

data that support the finding of this study are available from the corresponding author, upon reasonable request.

CONFLICT OF INTEREST

The author declared no potential conflicts of interest with respect to the research, authorship, and/or publication of this article.

ETHICS

There are no ethical issues with the publication of this manuscript.

STATEMENT ON THE USE OF ARTIFICIAL INTELLIGENCE

Artificial intelligence was not used in the preparation of the article.

REFERENCES

[1] Bilxgin AR, Demirci D. Keçiborlu Senir'de bulunan Osmanlı dönemine ait üç sarnıç. Süleyman Demirel Üniversitesi Fen-Edebiyat Fakültesi Sosyal Bilimler Dergisi 2020;50:216–232.

[2] Güngör SS. Tarihi Yarımada'daki Roma ve Bizans dönemi sarnıçları. Stratejik ve Sosyal Araştırmalar Dergisi 2017;2:37–72. [CrossRef]

[3] Hasol D. "Sarnıç" maddesi. In: Ansiklopedik Mimarlık Sözlüğü. İstanbul: Y.E.M. Yayınları; 2008.

[4] Öter N. Muğla Sarnıçları [Master's thesis]. Konya: Selçuk Üniversitesi, Sosyal Bilimler Enstitüsü; 2008.

[5] Mays L, Antoniou GP, Angelakis AN. History of water cisterns: Legacies and lessons. Water 2013;5:1916–1940. [CrossRef]

[6] Bozkurt N. "Sarnıç" maddesi. In: Türkiye Diyanet Vakfı İslâm Ansiklopedisi. Vol. 36. İstanbul: Türkiye Diyanet Vakfı Yayınları; 2009. p. 158–159.

[7] Acar T. Beki ve Paşalar Köyü Özelinde Uşak Sarnıçları. The Journal of Academic Social Science Studies 2018;1:369–380. [CrossRef]

[8] Senthivel R, Lourenço PB. Finite element modelling of deformation characteristics of historical stone masonry shear walls. Eng Struct 2009;31:1930–1943. [CrossRef]

[9] Hrasnica M, Medic S. Seismic strengthening of stone masonry structures in Bosnia Herzegovina. In: Proceedings of the 15th World Conference on Earthquake Engineering. Lisbon; 2012. p. 12621–12628.

[10] Çelik T, Tanrıverdi Ş. Review of repair and strengthening studies in historical vaults. In: 10th International Conference on Engineering & Natural Sciences. 2021.

[11] Tanrıverdi Ş, Çelik T, Ural A, Fırat F. Kenet genişliğinin yığma taş bloklarının kayma davranışı üstündeki etkisinin incelenmesi. Düzce Üniversitesi Bilim ve Teknoloji Dergisi 2022;10:1811–1825.

[12] Vicente R, Lagomarsino S, Ferreira TM, Cattari S, Mendes da Silva JAR. Cultural heritage monuments and historical buildings: Conservation works and structural retrofitting. In: Strengthening and Retrofitting of Existing Structures. Springer; 2018. p. 25–57. [CrossRef]

[13] Tanrıverdi Ş, Çelik T. Farklı dolgu malzemeleri ile sabitlenen zıvanaların yığma taş blokların kayma dayanımına etkisi. Avrupa Bilim ve Teknoloji Dergisi 2021;25:347–354. [CrossRef]

[14] Ural A, Fırat FK, Kara ME, Çelik T, Tanrıverdi Ş. Damages to rubble stone masonry structures during the January 24, 2020, Sivrice (Elazığ) Earthquake in Turkey. Earthq Struct 2022;23:231–243.

[15] Brandão FDS, Diógenes A, Fernandes J, Mesquita E, Betti M. Seismic behavior assessment of a Brazilian heritage construction. Frattura ed Integrità Strutturale 2018;12:14–32. [CrossRef]

[16] Kumbasaroğlu A, Çelik A, Demir O, Turan AI, Yalçıner H. An assessment of the seismic performance of the historic Tigris Bridge. Open J Civ Eng 2019;9:230. [CrossRef]

[17] Salvatori L, Marra AM, Bartoli G, Spinelli P. Probabilistic seismic performance of masonry towers: General procedure and a simplified implementation. Eng Struct 2015;94:82–95. [CrossRef]

[18] Öztürk S. A study on the variations of recent seismicity in and around the Central Anatolian region of Turkey. Phys Earth Planet Inter 2020;301:106453. [CrossRef]

[19] Atmaca B, Demir S, Günaydın M, Altunışık AC, Hüsem M, Ateş Ş. Lessons learned from the past earthquakes on building performance in Turkey. J Struct Eng Appl Mech 2020;3:61–84. [CrossRef]

[20] Mutlu Ö, Şahin A. Investigating the effect of modeling approaches on earthquake behavior of historical masonry minarets-Bursa Grand Mosque case study. Sigma J Eng Nat Sci 2016;7:123–136.

[21] Ercan E, Arısoy B, Hökelekli E, Nuhoğlu A. Estimation of seismic damage propagation in a historical masonry minaret. Sigma J Eng Nat Sci 2017;35:647–666.

[22] Usta P, Bozdağ Ö. A new approximate method for earthquake behaviour of worship buildings. Civ Eng J 2019;5:2665–2685. [CrossRef]

[23] Mustafaraj E, Morina J. Structural assessment of Mehmed Pasha Hammam in Prizren. In: International Conference on Critical Thinking in Sustainable Rehabilitation and Risk Management of the Built Environment. Prizren, Kosovo; 2019. [CrossRef]

[24] Usta P, Bozdağ Ö. Earthquake analysis of historical Basdurak Mosque. Pamukkale Univ J Eng Sci 2021;27:244–250. [CrossRef]

[25] Aslay SE, Okuyucu D. Erzincan Değirmenliköy Kilisesi apsis hasarının teknik olarak araştırılması. Gazi Univ Muh Mim Fak Der 2020;35:387–402. [CrossRef]

[26] Hysenlliu M, Bidaj A, Bilgin H. Influence of material properties on the seismic response of masonry buildings. Res Eng Struct Mater 2020;6:425–437. [CrossRef]
[27] Yurdakul M, Yılmaz F, Artar M. Dynamic behaviour of Historical Bayburt Grand Mosque. Sigma J Eng Nat Sci 2020;11:1–11.
[28] Ahmadi HR, Mahdavi N, Bayat M. Applying adaptive pushover analysis to estimate incremental dynamic analysis curve. J Earthquake Tsunami 2020;14:2050016. [CrossRef]
[29] Ramaglia G, Lignola GP, Fabbrocino F, Prota A. Structural analysis of historical masonry churches: The case study of S. Giuseppe delle Scalze (Naples, Italy). Int J Masonry Res Innov 2021;6:472–501. [CrossRef]
[30] Doğangün A, Yön B, Onat O, Emin Öncü M, Sağıroğlu S. Seismicity of East Anatolian of Turkey and failures of infill walls induced by major earthquakes. J Earthquake Tsunami 2021;15:2150017. [CrossRef]
[31] Mohammedi L, Foufa AA, Zouaoui MC. Assessment of the seismic behaviour of heritage masonry buildings using numerical modelling: A study of Fernand Pouillon's Totem Tower in Algiers, Algeria. J Build Eng 2021;38:102183. [CrossRef]
[32] Demir S, Günaydin M, Atmaca B, Altunişik AC, Hüsem M, Adanur S. Performance evaluation of reinforced concrete buildings during the Sivrice-Elazığ earthquake (Mw=6.8, January 24, 2020) in accordance with Turkish Earthquake Code. J Earthquake Tsunami 2021;15:2150018. [CrossRef]
[33] Çelik T, Tanrıverdi Ş. Review of repair and strengthening studies in historical vaults. In: 10th International Conference on Engineering & Natural Sciences. 2021. p. 298–304.
[34] Ural A, Çelik T. Gaziantep Nizip Tahtani (Leylek) Cami yapısal analiz ve değerlendirmesi. Uludağ Univ Müh Fak Derg 2021;26:79–96. [CrossRef]
[35] Altunişik AC, Atmaca B, Kartal ME, Günaydin M, Demir S, Uluşan A. Assessment of structural damage following the October 30, 2020 Aegean Sea earthquake and tsunami. J Earthquake Tsunami 2021;15:2150029. [CrossRef]
[36] Fuzhang W, Imtiaz A, Hijaz A, Alsulami MD, Alimgeer KS, Cesarano C, et al. Meshless method based on RBFs for solving three-dimensional multi-term time fractional PDEs arising in engineering phenomena. J King Saud Univ Sci 2021;33:101650. [CrossRef]
[37] Pouraminian M. Multi-hazard reliability assessment of historical brick minarets. J Build Pathol Rehabil 2022;7:10. [CrossRef]
[38] Mohammed WW, Cesarano C. The soliton solutions for the (4+1)-dimensional stochastic Fokas equation. Math Methods Appl Sci 2023;46:7589–7597. [CrossRef]
[39] Schiavoni M, Giordano E, Roscini F, Clementi F. Numerical modeling of a majestic masonry structure: A comparison of advanced techniques. Eng Fail Anal 2023;149:107293. [CrossRef]
[40] Sacco GLS, Ferrero C, Battini C, Calderini C. Combined use of deformation and structural analysis for the structural damage assessment of heritage buildings: A case study in the Liguria region (Italy). Eng Fail Anal 2023;147:107154. [CrossRef]
[41] Romero-Sánchez E, Morales-Esteban A, Bento R, Navarro-Casas J. Numerical modelling for the seismic assessment of complex masonry heritage buildings: The case study of the Giralda tower. Bull Earthq Eng 2023;21:4669–4701. [CrossRef]
[42] Sinaei S, Izadi Zaman Abadi E, Hoseini SJ. Failure analysis of skewed Persian brick masonry barrel vaults: Experimental and numerical study. J Perform Constr Facil 2023;37:04023057. [CrossRef]
[43] Hassani Sokhtesaraei M, Ghassemieh M, Mirghaderi SR. Proposing a set of far-field records for time history analysis in Tehran city and comparison with FEMA-P695 set records. J Earthq Tsunami 2023;17:2250017. [CrossRef]
[44] Aykanat B, Ertürk E, Altunışık AC, Aslan ME. Field investigation on reinforced concrete and masonry buildings damages after November 23, 2022 Gölyaka (Düzce) earthquake. J Earthq Tsunami 2023;17:2350010. [CrossRef]
[45] Güner Y, Nuhoğlu A. Development and application of the truss method on masonry walls to determine the in-plane behavior: A parametric study. Sigma J Eng Nat Sci 2023;42:1542–1554. [CrossRef]
[46] Altunisik AC, Arslan ME, Kahya V, Aslan B, Sezdirmez T, Dok G. Field observations and damage evaluation in reinforced concrete buildings after the February 6th, 2023, Kahramanmaras-Turkiye earthquakes. J Earthq Tsunami 2023;17:2350024. [CrossRef]
[47] Sevim B, Ayvaz Y, Akbulut S, Aydiner M, Uzun S, Ari A. Seismic performance and damage evaluation of reinforced concrete structures based on field investigation made after February 6, 2023, Kahramanmaraş Earthquakes. J Earthq Tsunami 2023;18:2350032. [CrossRef]
[48] Hacıefendioğlu K, Özgan K, Adanur S, Altunışık AC, Demirer B, Günaydın M. Estimation of damage levels in masonry structures following earthquake impact using deep learning-based segmentation method. J Earthq Tsunami 2024;18:2450006. [CrossRef]
[49] Cırak IF. Yığma yapılarda oluşan hasarlar, nedenleri ve öneriler. SDU Int Technol Sci 2011;3:55–60.
[50] Turkish Standards Institution. TS EN 1926: Natural stone test methods-determination of uniaxial compressive strength. Ankara: Turkish Standards Institution; 2007.
[51] Gönen S, Soyöz S. Seismic analysis of a masonry arch bridge using multiple methodologies. Eng Struct 2021;226:111354. [CrossRef]

[52] Çoban K. Determination of the dynamic performance of historical Bayburt Yakutiye (Yeni) mosque [Master's thesis]. Bayburt: Bayburt University; 2018.
[53] Ministry of Public Works and Settlement. Turkish Building Earthquake Code (TBEC). Ankara: Ministry of Public Works and Settlement; 2019.
[54] Artar M, Coban K, Yurdakul M, Can O, Yilmaz F, Yildiz MB. Investigation on seismic isolation retrofit of a historical masonry structure. Earthq Struct 2019;16:501–512.
[55] Computers and Structures Inc. SAP2000: Integrated finite element analysis and design of structures (Version 23.1.0) [Software]. Berkeley: Computers and Structures Inc.; 2021.
[56] Caicedo D, Karimzadeh S, Bernardo V, Lourenço PB. Selection and scaling approaches of earthquake time-series for structural engineering applications: A state-of-the-art review. Arch Comput Methods Eng 2023;30:4411–4441.
[57] Pacific Earthquake Engineering Research Center (PEER). Ground motion database. 2021. Available from: https://ngawest2.berkeley.edu/
[58] Pardalopoulos SI, Pantazopoulou SJ. Methodology for practical seismic assessment of unreinforced masonry buildings with historical value. Earthq Eng Struct Dyn 2017;46:2793–2810. [CrossRef]
[59] Lagomarsino S, Cattari S. PERPETUATE guidelines for seismic performance-based assessment of cultural heritage masonry structures. Bull Earthq Eng 2015;13:13–47. [CrossRef]
[60] Halder L, Dutta SC, Sharma RP. Damage study and seismic vulnerability assessment of existing masonry buildings in Northeast India. J Build Eng 2020;29:101190. [CrossRef]
[61] Sarhosis V, Dais D, Smyrou E, Bal IE, Drougkas A. Quantification of damage evolution in masonry walls subjected to induced seismicity. Eng Struct 2021;243:112529. [CrossRef]
[62] Mazza F, Donnici A. In-plane-out-of-plane single and mutual interaction of masonry infills in the nonlinear seismic analysis of RC framed structures. Eng Struct 2022;257:114076. [CrossRef]
[63] Demirel IO. A nonlinear equivalent frame model for displacement-based analysis of unreinforced brick masonry buildings [Master's thesis]. Ankara: Middle East Technical University; 2010.
[64] Franklin SG, Abrams DP, Klinger RE, Schuller MP. Performance testing for seismic rehabilitation of URM buildings. Earthq Spectra 2001;17:583–606.
[65] Bosiljkov V, Uranjek M, Zarnic R, Bokan-Bosiljkov V. Evaluation of masonry properties from combined testing of small specimens and wallets. Mater Struct 2008;41:1333–1355.
[66] Alcocer SM, Arias JG, Varela-Rivera J. Seismic behavior of confined masonry walls. J Struct Eng 2004;130:588–599.
[67] Salonikios T, Theodoulidis N, Zacharopoulou G. Seismic response evaluation of monuments based on ambient vibrations: The case studies of a Byzantine Basilica and an Ottoman bath in Thessaloniki (Greece). J Seismol 2020;24:777–802. [CrossRef]

Sigma J Eng Nat Sci, Vol. 44, No. 4, pp. 2415–2432, August, 2026

Sigma Journal of Engineering and Natural Sciences
Web page info: https://sigma.yildiz.edu.tr
DOI: 10.14744/sigma.2025.1949

Research Article

Stabilisation of expansive soil by geo-polymerisation of industrial wastes - Fly ash

Aishwarya GAYATRI[1,*], P K PRADHAN[2], P K PARHI[3]

[1]*Department of Civil Engineering, Odisha University of Technology and Research Bhubaneswar, Odisha, 751029, India*
[2]*Retired, Department of Civil Engineering, Veer Surendra Sai University of Technology, Burla, Odisha, 768018, India*
[3]*Department of Civil Engineering, Institute of Technical Education and Research (ITER), Siksha 'O' Anusandhan (SOA) University, Bhubaneswar, Odisha, 751030, India*

ARTICLE INFO

Article history
Received: 06 May 2025
Revised: 01 July 2025
Accepted: 19 August 2025

Keywords:
Alkali-Activated Fly Ash; Expansive Soil; Stabilisation; Un-Confined Compressive Strength

ABSTRACT

Due to their tendency to cause structural damage such as fractures and foundation failure, expansive soils, which have high volume changes with changing moisture levels, are a serious concern for civil engineers. This research examines fly ash, an industrial waste, as a replacement binder for conventional cementations resources in the field of sustainable soil stabilization. Class F fly ash of various Li/S ratios and NaOH concentrations (10, 12.5, and 15M) and Na_2SiO_3 concentrations were used to treat an expansive clay (Bhubaneswar, India). The resulting unconfined compressive strengths of 81 mixtures were tested after 3, 7, and 28 days of curing. The optimized mixture (4.8 MPa after 28 days curing, more than two times that of the untreated soil) showed uncfs increases with curing time and was optimized with a 12.5M NaOH concentration and 1. 25 Li/S ration, before over-activation effects decreased the strength. Confocusing on recycling cost-effective, sustainable geopolymers like fly ash will ultimately reduce the construction industry's effects on the environment, because of its reduction in costs and carbon emissions relative to lime or cement, as shown by economic and environmental analyses and microstructural examinations respectively. This study provides an economically viable, green solution for problematic soils through systematically optimizing the parameters of geo-polymerization in expansive soil stabilization. It also presents quantitative evidence for the utilization of binders from industrial waste in geotechnical applications.

Cite this article as: Gayatri A, Pradhan PK, Parhi PK. Stabilisation of expansive soil by geo-polymerisation of industrial wastes - Fly ash. Sigma J Eng Nat Sci 2026;44(4):2415–2432.

INTRODUCTION

Background of the Study

Expansive soil (ES), often known as swelling soil, describes to soils that undergo significant volume changes. Considerably so when the moisture content varies. Clay and other minerals that captivate water and enlarge are found in expansive soil. However, in dry conditions, soil will contract or shrink. A significant risk factor for construction projects is the characteristics of ES soils. According to [1], these kinds of soils can be found in both arid and semi-arid regions of the planet. The Deccan lava tract (Deccan

*Corresponding author.
*E-mail address: aishwaryagayatri24@gmail.com

This paper was recommended for publication in revised form by Editor-in-Chief Ahmet Selim Dalkilic

Published by Yıldız Technical University Press, İstanbul, Turkey
© Author. This is an open access article under the CC BY-NC license (http://creativecommons.org/licenses/by-nc/4.0/).

Trap), which includes portions of Andhra Pradesh, Madhya Pradesh, Maharashtra, Odisha, and Gujarat within the subcontinent, is also home to expansive soil (ES) soils. The valleys of the Tapi, Krishna Godavari, and Narmada rivers also have expansive soils. Deep black soil covers the western portion of the Deccan Plateau in the catchment areas of the Godavari and Krishna rivers. Rock formations like basalt and traps weather to produce this kind of soil. These soils are rich in lime, magnesia, alumina, and iron, according to studies. However, they are deficient in phosphorus, organic matter, and nitrogen. The mainstream of the clay minerals found are Montmorillonite, which has several singular qualities. For example, the soil's color varies from chestnut brown to black. Additionally, a particularly high percentage of clay is frequently found in expansive soil. Bentonite soil is known for very high development and it is also highly dispersive. In the situation of ES, free swelling ranges from ten to fifteen times greater than the actual volume.

Every year, damage to pipelines, roads, buildings and structures due to ES is very large compared to damage caused by hurricanes, tornadoes, earthquakes and flood combinations. However, the vulnerabilities associated with ES, such as low strength in construction, increase over time and occasionally cause life-threatening damage (Vinod, Fayaz, Vismaya, & Kumar, 2022) [2]. ESs have severe impacts on the world economy and still have gained very limited attention. Maximum of the damage and losses caused by ES are not due to an absence of suitable engineering solutions but rather to the non-recognition of swelling soils (Fig. 1).

The stabilisation of soil is a procedure applied to increase the engineering properties of the soil, increasing its suitability and stability for construction [3]. Some common methods include mechanical, chemical, electrochemical and geo-synthetic stabilisation (She, Lu, Duan, Yao, & Liu, 2020). Major stabilisation methods can be categorised into chemical and physical techniques (F. Zhang, Zhang, & Hong, 2019). Physical methods refer to using physical mechanisms to manipulate the soil's nature for better results. This can be achieved through the processes of compaction and drainage system [4]. Compaction can be done in a number of ways like compaction, vibro-compaction, and rolling to increase strength and density of the soil. Drainage is an effective method of removing excess water in the soil through the use of channels, pipes, and pumps so that the soil does not swell or shrink due to the water. Then again, compaction results in increased water resistance of the soil. Chemical additives refer to cement, fly ash (FA) and lime that are mixed with the soil to alter its inherent characteristics [5]. The additives chemically interact with soil particles to increase their cohesion and stability while the soil's plasticity is reduced.

Currently, geopolymer technology type is the most prevailing and widely accepted technology among the many other conventional ones. A geopolymer is First and foremost made up of ceramic, inorganic, or alumina silicate material capable of forming long-lasting, non-crystalline, and covalently bonded connections [6]. Basically, geopolymer is the product of the joint reactions of Sio_2 and Al_2O_3 polymerization calls for high rate of chemical reaction of silicon-alumina mineral structure under alkaline conditions [7, 8]. Minerals result in 3D polymeric chains and a ring structure with Si-O-Ai-O bonds (Z. Zhang, Wang, & Provis, 2012). Geopolymer binding agents have exceptional durability and mechanical/physical characteristics. Such characteristics may be acquired through the application of secondary materials (IW, for example slag or FA) [9]. Geopolymetisation of industrial waste such as FA consists of the transformation of FA, which is an output product of burning coal in power plants, into a geopolymer agent. Extracting geopolymers from waste materials will not only be an effective way of solving the issues related



Figure 1. Shrink-swell soil (ES).

to the accumulation of wastes and the use of raw materials but also will be a step forward towards the environment. Geopolymers owing to their unique properties have a potential to lessen the release of CO_2 to the atmosphere (Syed, GuhaRay, Avinash, & Kar, 2020).

Industrial solid waste's natural pozzolanic feature makes these solids viable geopolymers for soil stabilization [10]. One of the primary causes of important environmental degradation that needs management is the unregulated generation and disposal of industrial waste (IW). To address the issue, new technologies are being employed in a more creative manner to locate the IWs. Chemical stabilization that eliminates both the hard soil matrix and the soil that is not dissolved in water is the highly efficient. Polymer stabilization has many advantages over chemical and physical stabilization.

. This model comprises N-A-S-H and (N, C)-A-S-H models. Low-calcium precursors such as Class F fly ash are frequently employed in the alkali-activation systems to form the N-A-S-H (sodium aluminosilicate hydrate) gel. Because of the occurrence of sodium ions, which serve as charge balancers, this polymer makes up a three-dimensional structure composed of silicon-aluminum tetrahedra. This material can be used effectively to stabilize expansive soils because of its excellent chemical stability and water resistance. Conversely, inclusion of calcium-containing materials, such as Class C fly ash or slag, creates the (N,C)-A-S-H (sodium/calcium aluminosilicate hydrate) gel. Calcium ions cause both the calcium-based and sodium-based binding phases to be present together, which can enhance water stability and accelerate setting and early strength. It is necessary to make a differentiation between these types of gels as it will enable geopolymer mixtures to be specifically designed for the chemistry of the industrial waste used and soil mineralogy. It can be said that the formation of N-A-S-H gel in the present study can be made possible by using Class F fly ash and sodium activators and thereby, increase the long-term durability and strength of stabilized expansive soils.

In this study, geopolymers composed only of industrial solid wastes, including alkali-activated fly ash (AAFA), have been used to stabilize expansive soils [11]. Extending on existing research, this research attempts to optimize mix design to increase the UCS at different curing times (CT), through different mix design of NaOH and Na_2SiO_3 activator concentrations. In contrast to other research efforts, the present research makes a complete geotechnical and chemical characterization of fly ash and comparing effectiveness of AAFA and conventional cement-based stabilizers [12]. In this study, valuable information is provided for the industry through microstructural analysis and the mention of benefits both economical and environmental [13, 14]. Considering the engineering problems faced across the globe by expansive soils, whose expansion and contraction as a result of water content affects infrastructures adversely, this becomes very relevant. Not only does it satisfy the current need for cost-effective, waste-utilization methods for regions where there is excess industrial waste material, but it also demonstrates the superiority of geopolymer stabilization methods over traditional ones.

The objectives of the research study are as follows:

- Overview of the destruction caused by the ES.
- To evaluate the alternative cementitious material for the stabilisation of ES.
- To assess the ability of AAFA to stabilise ES in the region.
- To analyse the GT properties and chemical properties of FA.
- To assess the compressive strength of the ES FA mixture.
- To recommend cost-effective AAFA for the stabilisation of ES to achieve a sustainable environment.

The research questions are as follows:

1) What is the destruction caused by the ES in construction?
2) How can ES be stabilised via AAFA?
3) How do the GT and chemical properties of FA influence the compressive strength of ES FA mixtures?

Despite numerous studies on FA stabilization of soils, supreme previous research has attentive on a limited number of mix proportions or has examined the effects of FA and activator concentrations in isolation, often using fewer than 20 combinations and rarely exploring the full interaction between multiple variables. The rationale behind the test of 81 unique mixture combinations in the current research is to conduct a systematic analysis on the influence of NaOH concentration, FA content, and activator/ash ratio on geotechnical characteristics of expansive soil. It is evident that such an extensive experimental design addresses a very important research issue by allowing for establishing optimum mix parameters and obtaining an extensive set of data related to their synergic impact, which is not covered in any previous studies. The novelty of such a study is due to its complexity.

The paper is organized: Section 1 introduces and thoroughly explains the stabilisation of ES through the geopolymerisation of IW FA. It also outlines the significance of the research. Section 2 then looks over the literature relevant to this study. The study Materials and Methods are described in Section 3. In Section 4, there is a detailed discussion of the results, and recommendations for further research are also provided.

Literature Review

There is an inherent probability of ES causing serious challenges and problems in engineering due to its attributes (Zada et al., 2023). Previous research on the challenges caused by ES performance was highlighted in [15]. The method frequently exhibits shrink-swell features. In actuality, this method, which modifies the natural characteristics of soil, cannot replicate the natural world. The act of converting a natural soil into a building material is called

soil stabilization. From an engineering perspective, stability using processes and additions has historically improved the inherent qualities of soil. Chemical, microstructural, economic, and waste material reuse aspects were all covered by these advancements. The soil stabilization procedure was altered by standardization, geoenvironmental consideration, and stabilization progression optimization. Exploratory methods and predictive models were considered components of the soil stabilization process. To adequately stabilize natural soils, surface optimization, design optimization, and optimization techniques of all dimensions were employed. This evolution enabled to optimize pre and post construction operations to protect ESs from damages.

Fibers used to increase the strength of the soil is one of the aspects of mechanical soil stabilization. On the other hand, chemical soil stabilization involves adding different kinds of chemical compounds such as lime and cement into the soil [16,17]. In addition, the effects of the use of natural fiber and recycled ash on the strength and durability of engineered soils were investigated in an original research paper. Soil stabilization is usually a result of adding chemical compounds. Bottom ash and natural fibre have been cited in literature as materials that play an important role in achieving soil stabilization. These two materials are also used as reinforcements against tensile cracks in the soil. Hence, the mechanical, chemical, and swelling properties of soil stabilization by engineered soil (ES) will first be examined. Stabilization of engineered soil (ES) with bottom ash percentages of 5%, 10%, 15%, and 20% has been well documented. The natural fibre reinforcements to be used for ES stabilization include 0.25%, 0.50%, and 1.00% of coir fibers. The CT period is 28 days.

This study has evaluated the durability of stabilised soil through the mechanical and chemical properties before and after the 2nd, 4th, 6th, 8th, and 10th days of freeze-thaw cycle test (FTC). Stabilisation of the ES using BA decreases the swelling pressure and controls the plastic behaviour. The increase in the quantity of BA exponentially results in the increase of electrical conductivity, pH, and calcite content of the ES soil. It also increases tensile strength and compressive strength of the soil. CF-reinforced specimen had very small mechanical strength losses during the FTC. It also had relatively higher tensile strength. Proposed mechanisms of BA and CF to stabilise ES are discussed. It has decided that both the BA and CF stabilise ES efficiently, and they can be used for road pavements.

The reason behind glass being non-biodegradable is its inert property, and glass powder produces more friction compared to clay [18]. The prevailing study [19] presents a new method of using waste glass powder (WGP) to enhance the ES. In this case, ES is expandable, meaning that it will reduce its strength when wetted or shrunk. This results in volume change. In this study, ES used in the construction industry creates problems all over the world. These problems affect civil engineering projects such as embankments, railways, highways and roadways. To strengthen ES, one must use other materials such as WGP. They were ground and incorporated into the soil samples in various percentages, including 2.5, 5, 10, 15 and 25%, based on the dry weight of the soil. Various tests were performed on treated and untreated ES with different percentages of WGP. Moreover, they include free swelling, compaction, Atterberg limits, and California-Bearing Ratio. The results of the tests show that the presence of WGP in the ES improves the consistency and shear strength of the soil sample. Furthermore, adding fifteen percent of WGP reduces the thickness of the sub-base to sixty-three percent.

A conventional study (Vijayan & Parthiban, 2020) explained the use of solid waste in ES as a stabilizing material to reinforce ES. They possess common characteristics such as unexpected shrinkage and swelling, high compressibility, weak transfer system, and low permeability. The rate of failure mechanism such as the failure of subgrade and excess settlement rate is quite fast. ES is more susceptible to such characteristics compared to other soils. It becomes hard to build up infrastructures with these kinds of soil by civil engineers. The technological advancement of the current world leads to effluents that cannot be controlled. Production and removal of solid waste become critical issues in every nation. The industries producing construction materials become highly involved in solid wastes. Several studies have been undertaken in order to produce novel construction materials at a large scale. Prevailing studies tried to evaluate different forms of solid waste to stabilize soils. Presence or absence of lime in the stabilization process will create room for utilization of solid waste for GT purposes.

A prevailing study [20] explained the use of calcium-based stabilizers (CSMs) for stabilizing ES. The properties of CSMs have been thoroughly discussed. They are capable of improving various soil properties by triggering carbonation, cationic exchange, flocculation, and hydration. Incorporating CSMs in soil stabilization for construction has its pros and cons. The physical and chemical transformations of soils have been elucidated in detail. Using X-ray fluorescence technology the impact of adding CSMs to soils has been investigated. SEM images have shown that chemical reactions at a microscopic level are occurring between CSMs and soils. Because, it is recommended to use CSMs in GT construction projects by ES.

Per authors, lime is an excellent stabilizer for ES, which can also be mixed with the FA waste material for stabilizing soils and enhancing their properties [21]. Besides, as an old method, FA and lime can be combined for soil stabilization resulting in pollution free and sustainable environment [22]. ES soils have fragile physical properties that not only create difficulties in the handling and disposal of these soils but also present a range of challenges. Some of the physical properties that influence the handling and disposal of soils include their shrinkability, swellability, and the bearing capacity of the soil.

These are some of the factors that cause shrink-swell behavior of soil, So making it unsuitable for construction. Engineering properties can be enhanced through both physical and chemical processes. The process makes it feasible to use the soil for construction purposes. Mixing is usually used to improve the properties of soil. Research was conducted on the individual as well as blended mixtures such as FA and lime. It focused on evaluating the GT properties of ES. Different proportions of lime and FA were added to find the best proportion to stabilise ES. The results showed that FA and lime reduced plasticity and liquid limit, swell index and increased the dry weight and strength of soil-admixture. The flocculated structure with pores was found in the soil and was responsible for decreasing moisture contents and plasticity index. There was an increase in dry weight resulting in higher soil-admixture strength than ES.

The research by (Baldovino et al., 2021) and others focused on glass powder waste as a geopolymer material for soil stabilization. They wanted to reduce landfill waste and move away from regular binders such as cement and lime. Different levels of GP were tested at 5 percent 15 percent and 30 percent along with a set amount of 5 percent lime. This was to check the effects on how strong the compacted soil became. Results showed better mechanical properties and improved microstructure as the glass powder increased. Performance was linked to a new volumetric binder index. It seems this points to good long term uses for glass waste in stabilization efforts. After seven days the mixes did not reach subbase levels yet after ninety days they were all suitable for earthwork. Some of the strength gains felt more noticeable at higher GP amounts but I am not totally sure how that lines up with every mixture tested.

In connection with the development of eco-friendly, mechanochemically activated geopolymeric stabilizers and comparison of them with traditionally activated ones, the authors of , [23] have achieved great success in the field of soil stabilization process. In addition, their work examines the effect of different GGBS contents on the mechanical and durability properties of soil stabilization process, particularly on sulfate corrosion resistance. As compared to CAG samples, MAG samples revealed better resistance to magnesium sulfate corrosion and higher UCS, by 12–45%. Moreover, such soils have managed to retain up to 93% of their strength under the influence of sulfate solutions over the period of 60 days, taking into consideration mass loss, ultrasonic pulse velocity, and FTIR spectroscopy tests. The conclusion is that mechanochemical activation, as well as an increase in the quantity of GGBS, increases the sulfate resistance and UCS of geopolymer binders that allow using the stabilized soil in severe conditions.

Significance of accounting for the influence of Fluid Structure Interaction has been emphasized in terms of earthquakes due to recent improvements in understanding of seismic behavior of fluid storage tanks. In order to examine the influence of earthquakes on fluid storage tanks, [24] applied finite element analysis, proving itself very useful in modeling of reservoirs. Taking into account variations in physical parameters and fill factors, the influence of two-way coupling of the structure and the contents of reservoir has been considered. It should be mentioned that contrary to assumptions about designing of reservoirs, the highest influence of seismic activity was noticed not in case of 100 percent fill factor, but in terms of partial fill factor. Also, seismic retrofitting has been recognized as being critical both for partial and full fill factors, especially when water level is 10 percent below the height of reservoir.

However, adequate investigation work on the use of AAFA stabilized with industrial wastes is yet to be done despite the numerous studies done on the stabilization of expansive soil using different chemical and industrial waste amendments. This has been mainly due to the fact that variation has been made in the dosage level of the activator and the proportion of FA used. In addition, there is yet no adequate comparative work carried out on the performance of geopolymers vis-a-vis conventional binders such as cement or lime.

Research Gap

As has been observed previously, due to the swelling and shrinkage characteristics of the soil in case of ES, a process of stabilization is necessary and as a consequence, chemical stabilization with the use of FA, lime, and cement will improve the performance of ES. However, research regarding the optimal dosage of AAFA in the mix design process, the quantity of the activator and curing conditions is minimal. The sustainability issues along with cost benefits of using AAFA in ES stabilization are still unexplored. To address this, the present work involves systematic laboratory testing to evaluate AAFA performance versus other conventional stabilizers and to assess sustainability and cost feasibility of AAFA-stabilized soils. As the availability of the related literatures, it has been identified that various materials are used for the stabilization of ES.

There is hardly any literature available of the industrial waste AAFA used as one of the stabilizers for ES. So far no assessment has been done of the engineering characteristics of ES by applying AAFA as its stabilizer. That means the present investigation is an appreciable work in the investigation of AAFA and its influence on ES. The evaluation is done by using different proportions of alkali to activate AAFA. The Un-Idenpened Compressive Strengths (USCS) is determined to evaluate the bonding effects.

The novelties of the research study are as follows. A detailed examination of the influence of different types of alkaline activators and curing techniques on the mechanical properties of these soils can contribute to the improvement of the process of geopolymerization. Moreover, it emphasizes the benefits that this novel sustainable technology offers over conventional technologies that involve stabilization by means of cement or lime stabilization. Parameters of geopolymerization and soil properties can be employed in order to develop a standard approach for different engineering applications.

MATERIALS AND METHODS

Material Characterisation

ES

The ES for this current study is gathered from Lingipur Nuagaon, plotno S -60, Bhubaneswar. The soils obtained from above the first 500 mm layer of the soil profile were collected using distribution sampling technique and analyzed in the lab. Partial vacuum packaging was done for the soils samples for storage while the moisture content determination was done through the polythene bag. The drying, grinding, and sieving process for the samples was done to get samples with sizes less than 4.75 mm.

Geotechnical properties of the soil sample aspects show that AAFA in relation to geopolymer stabilization of ES is compliant with ASTTM standard [25]. According to the soil classification, the ES soil falls under the category of compressible clay CH and satisfies the IS: 1498 criteria. Several tests were conducted on the virgin soil VS giving ES.

Table 1 demonstrations the GT possessions of the ES. The soil classification, liquid and plastic limits and UCS are evaluated for ES. The ES grain size analysis (from Table 1) revealed that 63% (clay and silt) of the VSs passed through the 75 IS sieve. This illustrates that the experimental ES was a fine-grained soil with a significant surface area. The ES being assessed as an outcome is very plastic. The variance-free swell index (DFS) of the ES is presented in Table 1. 80% has a particular gravity (G) of 2.66, a maximum dry density (MDD), a natural moisture content (NMC) of 6.11% and a perfect moisture content (OMC) of 23.51%. The ES's plastic and liquid limits are 27% and 72%, respectively. In accordance with ASTM D2487 [26], the soil is characterised as clay with high CH.

Furthermore, Figure 2 provides a visual representation of the GSDs for the ES. The aforementioned graph displays a

Table 1. GT Properties of ES

S.NO	PARTICULARS	TEST RESULTS
1	SOIL CLASSIFICATION(USCS)	CH
2	LIQUID LIMIT (%)	72
3	PLASTICLIMIT (%)	27
4	PLASTICITY INDEX (%)	45
5	OPTIMUMMOISTURE CONTENT (%)	23.51
6	MAXIMUM DRY DENSITY(g\cc)	1.62
7	DIFFERENTIALFREE SWELL (%)	80
8	SPECIFIC GRAVITY	2.66
9	UCS (kg/cm²)	1.99
10	GRAIN SIZE DISTRIBUTION (GSD) GRAVEL(≥2000 μm)	0
	SAND (75-20000μ)	37
	SILT(2-75 μm)	63

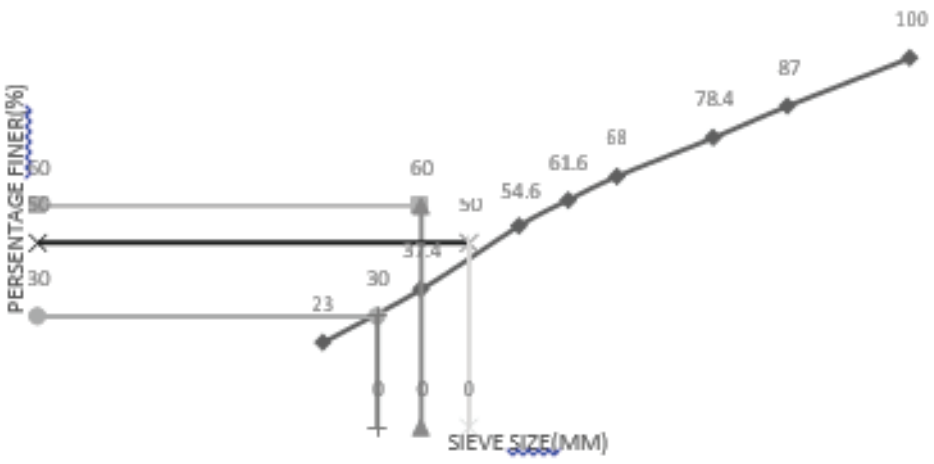


Figure 2. Grain size distribution of expansive soil.

particle size distribution curve with sieve sizes on the x-axis and the cumulative proportion of particles smaller than the corresponding sieve size on the y-axis. For instance, 60% of the material is smaller with a sieve size of 60 mm. The steeper slope of the curve, particularly in the middle ranges between 20 and 60 mm, indicates that the material has a wide dispersion of particle sizes. A substance with a wide variety of particle sizes is indicated by a steep slope, whereas more homogeneity would be indicated by a more gradual curve.

A Jeol-840-A model scanning electron microscope (SEM) organised with the help of an electronic dispersive X-ray (EDX) analyser was used to scrutinise the particle chemistry and individual morphology. The mineralogy of the materials used was examined via X-ray diffraction (XRD) on a Rich-Siefert X-ray diffractometer with a Ni filter and a copper target (Fig. 3) and (Table 2).

This XRD pattern likely corresponds to a crystalline material or compound, possibly a mineral or an engineered material. The high peak at around 500 (2θ) is indicative of a primary phase, while the smaller peaks at other angles suggest secondary phases or impurities in the sample. The results of the X-ray diffraction technique indicate the presence of crystals in the sample, thereby showing the nature of the phases involved. The major peak, collected with extra negligible peaks, can help in identifying certain materials and their crystal structures by matching them to standard database patterns.

Table 2. Mineralogical composition of the expansive soil

Minerals	Interlayer Bonding
Kaolinate	Hydrogen; Strong
Montmorillonite	Oxygen-oxygen; Very weak
Illite	K ions; Strong
Vermiculite	Weak
Chlorite	Strong

Table 2 provides the information on the type of bonding present between layers in various minerals. The presence of hydrogen and potassium ions in kaolinite and illite, respectively, makes them have strong interlayer bonding. Chlorite also has strong bonding. On the other hand, montmorillonite possesses very weak oxygen-oxygen bonds while those of vermiculite are weak.

FLYASH

The FA used in this case study has been obtained from the captive power plant of JinDAL ALUMINIUM LIMITED located at Angul of state Odisha in India, where the content of calcium is low (Class F). The properties of GT of FA are mentioned in Table 3 below. Graphical depiction of GSD and XRD of FA has been presented in Figures 4 and 5, respectively.

Table 3 shows essential data for FA. It possesses liquid limit of 24.46% and it is non-plastic in nature, hence does not have plasticity index. Its optimum moisture content is 12.6% while maximum dry density is 1.45 g/cc. FA does not possess any free swell which means that it swells very little when exposed to water. Its specific gravity value is 2.20. When it comes to grain size distribution, FA is made up of 5% sand, 90% silt and 5% clay.

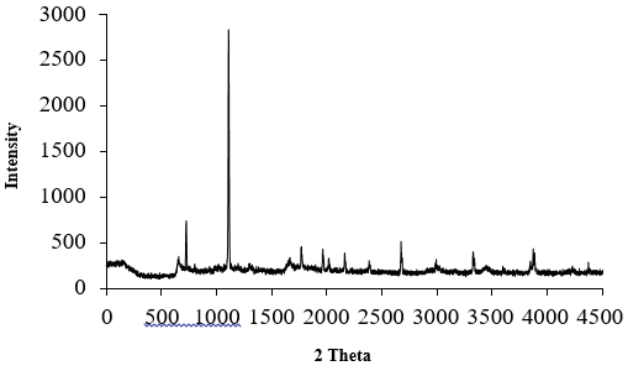


Figure 3. XRD analysis of the expansive soil.

Table 3. Geotechnical properties of flyash

S.NO	PARTICULARS	FLYASH
1	LIQUID LIMIT (%)	24.46
2	PLASTICLIMIT (%)	NON-PLASTIC
3	PLASTICITY INDEX (%)	-
4	OPTIMUM MOISTURE CONTENT (%)	12.6
5	MAXIMUM DRY DENSITY(g\cc)	1.45
6	DIFFERENTIALFREE SWELL (%)	0
7	SPECIFIC GRAVITY	2.20
9	GSD GRAVEL(≥2000 μm)	0%
	SAND (75-20000μ)	5%
	SILT (2-75 μm)	90%
	CLAY (≤2 μm)	5%

Figure 4 below is a grain size distribution curve, just like sieve analysis curve. X axis is the sieve size measured in millimeters from 0.01mm to 10mm, while Y axis denotes the percentage of material finer than the sieve size. Data points indicated on this curve are joined by a line showing the percentage of finer material in relation to the sieve size. At first, at sieve size of 60mm, there is 0% of finer material, meaning there are no particles smaller than this sieve size. There is a marked jump in finer material up to 63mm then it slowly rises. Up to sieve size of 63mm to 100mm, percentage of finer materials is very much indicating presence of high percentage of finer material. Sharp bends especially from sieve size of 63mm to 69mm indicate changes in particle size distribution or material phase.

X-ray diffraction pattern indicates the existence of various minerals like quartz, mullet, sillimanite, and aluminium phosphate in the given sample. This is mainly due to really every mineral produces its own unique pattern of peaks due to the distinct atomic arrangements. By way of illustration, quartz produces a very distinctive peak at 26.6 2 whereas mullite and sillimanite produce their characteristic peaks marked as "M" and "S" respectively. Besides these, silli(man) ite has another peak in the range of 25-27 2. Aluminium phosphate peaks are indicated as "A". Generally, peaks signify the number of atoms in a particular crystal plane. This is the principle behind determining the relative amounts of minerals in a given sample. Crystals with high symmetry will produce only a few peaks whereas crystals with low symmetry contribute to various peaks. The XRD method uses 2 values.

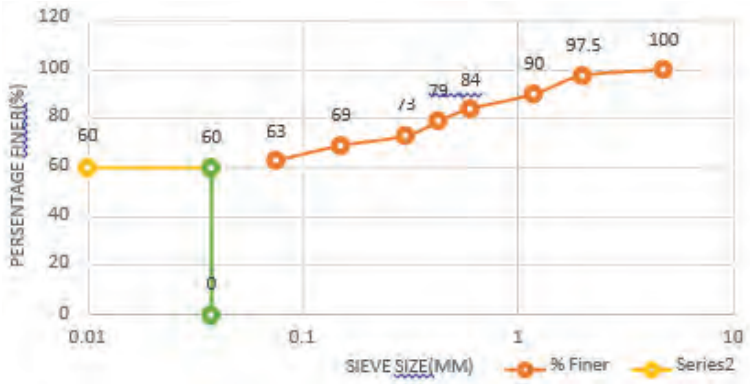


Figure 4. Grain size distribution of fly ash.

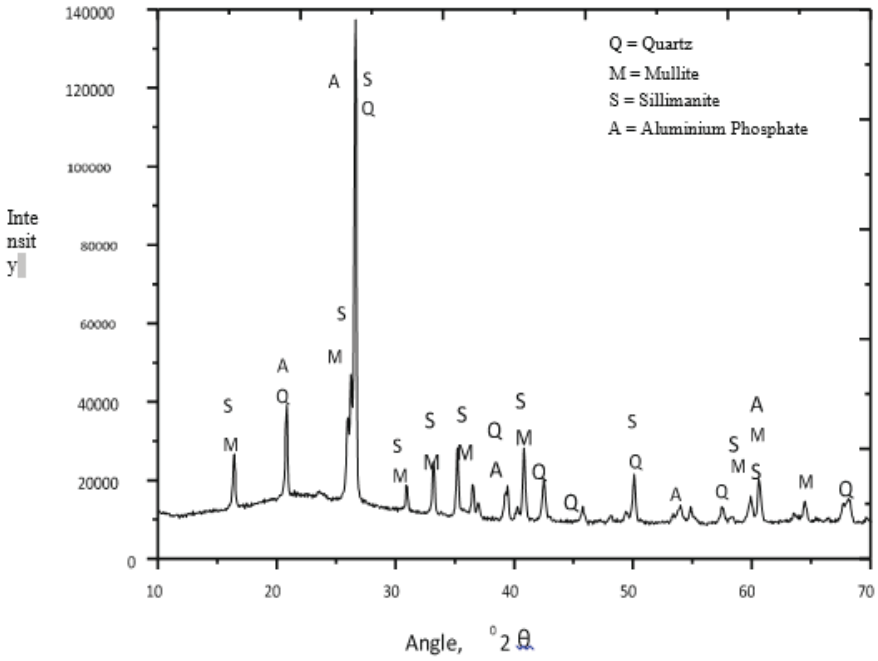


Figure 5. XRD pattern of fly ash.

Table 4. Chemical properties of FA

SL NO	PARAMETER	% BY MASS
1	SiO_2	51.57
2	Al_2O_3	22.57
3	Fe_2O_3	14.91
4	CaO	4.82
5	SO_3	0.99
6	Ignition loss	3.56
7	$Na_2 + K_2O$	0.68
8	MgO	1.74

The Table 4 presents the chemical composition of a material, likely FA, in terms of percentage by mass. The main constituents of the sample comprise silicon dioxide (SiO_2) which makes up 51.57%, aluminium oxide (Al_2O_3), which accounts for 22.57%, and iron oxide (Fe_2O_3) which makes up 14.91%. On the other hand, the quantity of CaO is 4.82% and SO3 is 0.99%. The loss on ignition, accounting for the volatiles, is 3.56%. In addition, Na_2.

The parameters of fly ash/alkaline activator ratios and NaOH molarities used in this experiment were selected by the authors based on previous research findings. These earlier studies pointed out that fly ash/alkaline activator ratios and NaOH molarities are very important factors which affect quite a bit the process of geopolymerization and this way the properties of the final geopolymeric product. Actually, the interval of fly ash/activator ratios between 1.5 and 2.5 as well as NaOH molarities from 8 M to 14 M were normally considered as a good range for obtaining maximum fly ash geopolymers compressive strength and workability. For example, BURDUHOS-NERGIS et al. (2025) have identified that the best fly ash/activator ratio to achieve the highest compressive strength of class F FA geopolymers is 2.0. So, the present research work has been planned to assess the influence of changing the ratios within these intervals research says data mentioned above (Table 5).

Table 5. Nomenclature of AAFA samples

Sample designation	Hydroxide concentration	FA content (%)	Activator to sol	Activator/FA ratio
S1	10 M	20	15	0.75
S2		30	15	0.50
S3		40	15	0.38
S4		20	20	1.00
S5		30	20	0.67
S6		40	20	0.50
S7		20	25	1.25
S8		30	25	0.83
S9		40	25	0.63
S10	12.5 M	20	15	0.75
S11		30	15	0.50
S12		40	15	0.38
S13		20	20	1.00
S14		30	20	0.67
S15		40	20	0.50
S16		20	25	1.25
S17		30	25	0.83
S18		40	25	0.63
S19	15 M	20	15	0.75
S20		30	15	0.50
S21		40	15	0.38
S22		20	20	1.00
S23		30	20	0.67
S24		40	20	0.50
S25		20	25	1.25
S26		30	25	0.83
S27		40	25	0.63

Sample Preparation and Testing

Another part of the experiment is an analysis of the influence of FA/soil ratio (dry weight) on the strength properties [27] In particular, the following percentage of FA was selected; 20%, 30% and 40%, i.e., ratios or percentages of soils/ash corresponding to 0.25, 0.43 and 0.67, respectively, according to the percentage of solids containing FA and soil. In addition, higher percentages of activator/solid were considered at 0.15, 0.2 and 0.25 for all FA mixtures to assess the influence of activator on the improvement of strength.

The research conducted by [28] included analysis of UCS in samples treated with 10 M, 12 M and 15 M AAFA having soil ratios/ash values of 0.25, 0.43 and 0.67, respectively, at various ash/activator ratios.

After first homogenising the FA and soil, the activator was included in the mixture. In accordance with (Terashi &Kitazume, 2011), the samples were blended in a mechanical mixer for 3 minutes and subsequently cast into 100 mm high and 50 mm diameter moulds through tapping the moulds on the counter of the lab [28]. Using laboratory tests, the amount of water added to each mix was adjusted to reach that ideal moisture content. Each mixture uses a specific amount of water as specified in Table 6.

All samples were prepared and tested under controlled laboratory conditions. After mixing, the specimens were cast into 100 mm high and 50 mm diameter molds, then cured at room temperature (approximately 25 ± 2°C) and relative humidity of 50–60% for the specified curing durations of 3, 7, and 28 days, as described previously. For all the designs, the tests for three replicates were carried out to determine consistency. In addition, the procedures for mixing, molding, curing, and UCS test followed strictly according to ASTM guidelines.

The percentage usage of FA of 40, 30, and 20% based on the total mixed dry mass were considered. To compare with the actual amount of FA, these percentage rates are taken into consideration.

The Table 5 outlines various samples (S1 to S27) with different hydroxide concentrations, FA content, activator to solution ratios, and activator to FA ratios. Hydroxide concentration is 10 M, 12.5 M, and 15 M. FA content is 20%, 30%, and 40%. Activator to solution ratio ranges between 15 to 25 while activator to FA ratio is 0.375, 0.75, and 1.25. For example, S1, S10, and S19 sample series have 20% FA content and activator to FA ratio of 0.75. This enables an effective analysis of various effects of these factors on the samples properties.

It is clear that the choice of these high molarity solutions of NaOH was done according to their capacity to improve FA particles dissolution necessary for high compressive strength geopolymer. The ratio of sodium hydroxide to sodium silicate in these samples was optimized after several preliminary tests. These were done to get a proper balance between workability and compressive strength of the samples. In order to get optimal geopolymerization conditions, high molarity NaOH solutions and optimized sodium silicate to sodium hydroxide ratio were applied to get effective activation of FA.

The Table 6 presents a series of samples (A1 to A9) with varying water to solid ratios and FA contents. Water to solid ratio can be taken at either 15%, 20%, or 25%. Content of FA can vary from 20% to 40%. Water to FA ratio will also vary liable on the situation; for instance, ratios such as 0.75 for A1, 0.5 for A2, and 1.25 for A7. Such an arrangement will make it easier to observe and analyze how varying water and FA ratios affect the performance of the mixtures. In this case, mixture A4 has water to FA ratio of 1.0 and mixture A6 of 0.5.

If the FA content is relatively higher (for instance, 40%), due to ball-bearing effect reducing water requirement, then water to solid ratio should be 15%. If a combination requires some degree of moisture in order to ensure its easy handling, a water to solid ratio of 20% could be appropriate especially for cases when FA percentage content is moderate (for instance, 30%). Where FA content percentage is relatively lower (say 20%) or when the mixtures have high amount of activators requiring water for reduced viscosity, ratio can be 25%.

To ensure accuracy and reliability, all experimental measurements and procedures in this work were conducted strictly according to the ASTM and IS standards. The reproducibility and validity of results are ensured by

Table 6. Nomenclature of different types of mixtures

SAMPLE	WATER TO SOLID (%	FA CONTENT (%)	WATER/FA RATIO
A1	15	20	0.75
A2	15	30	0.50
A3	15	40	0.38
A4	20	20	1.00
A5	20	30	0.67
A6	20	40	0.50
A7	25	20	1.25
A8	25	30	0.83
A9	25	40	0.63

the application of specified test procedures (e.g., ASTM D2487 and IS 1498 for soil classification and other appropriate ASTM and IS methods for geotechnical and chemical characterization). The primary basis of methodological correctness lies in following these internationally accepted standards; model validation was done without any independent or external experimental data.

RESULTS AND DISCUSSION

UCS of the Expansive Soil and Fly Ash Mixture

Figure 6 shows the UCS values for all the FA-treated samples at 3, 7 and 28 days after curing. The results clearly establish that, likened with the other mixes, Mix A5 offers greater 3-day strength. However, compared with the other mixes, Mix A1 provides more strength after 7 and 28 days of curing. The strength of mix A9 after 3, 7 and 28 days of curing is the lowest.

A total of 81 samples were investigated utilising different ratios of activator and FA. In Figures 7, 8 and 9, the deviations in the UCS values of the combinations formed with 10, 12.5 and 15 M solutions, unlike CT, are illustrated.

Figure 7 shows that the UCS combination activated with 10 M solution decreases as the FA concentration increases and that the strength increases as the curing duration increases. This clearly shows that mix S5 has greater

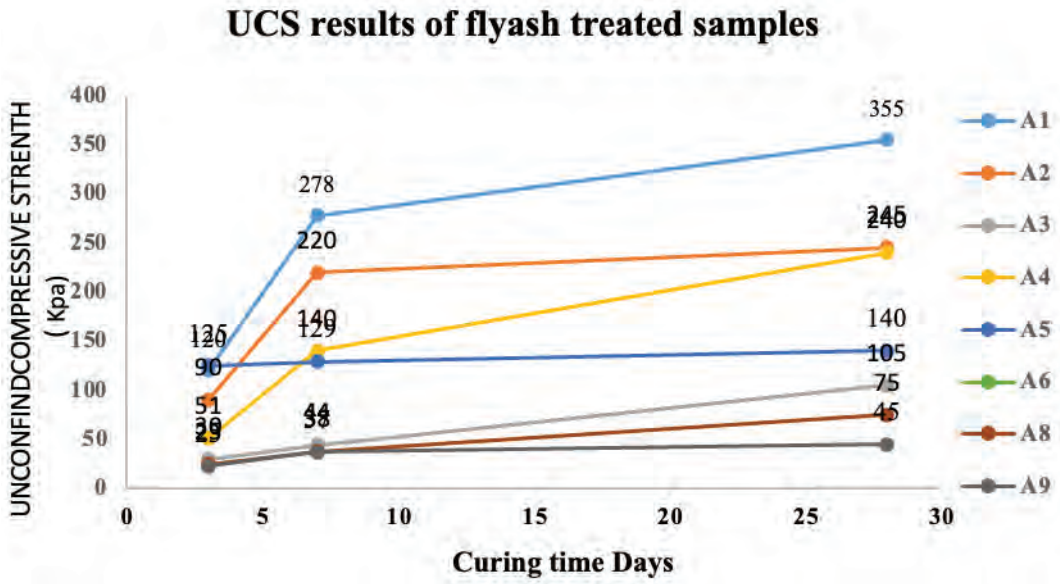


Figure 6. UCSs of the geopolymerised FA-treated samples.

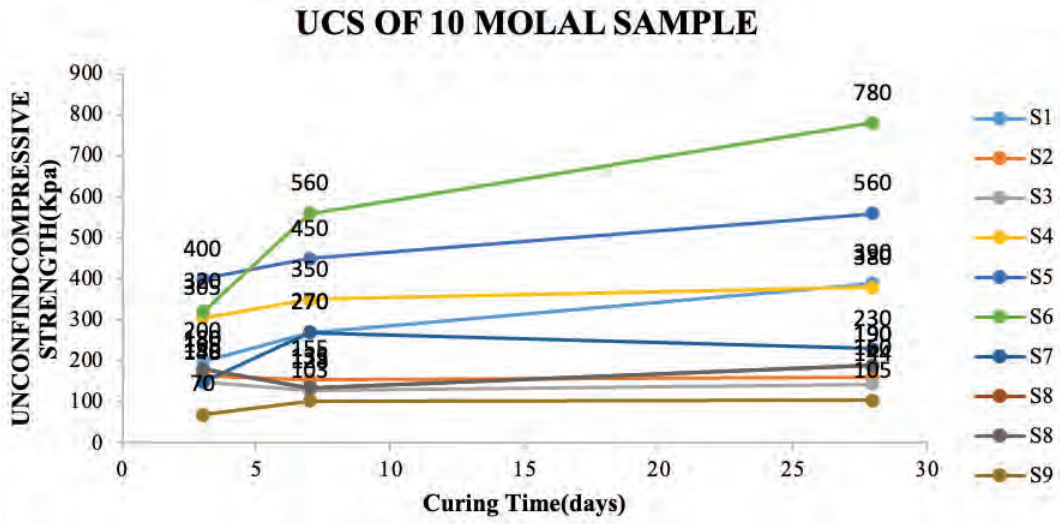


Figure 7. UCS of the 10 M sample.

strength after 3 days, although mix S6 has greater strength after 7 and 28 days. Mix S9 has the lowest strength at 3 and 7 days, whereas mix S8 has the lowest strength at 28 days. Similarly, Figure 7 also shows the results for a 12.5 M solution. Compared with S16, S12 has a stronger formulation for the 3-, 7- and 28-day formulations. Mix S18 presented the lowest strength after 3 days, whereas mix S11 presented the lowest strength after 7 days. Figure 9 shows that, for the 15 M solution, mix S19 has greater strength after 28 days of formulation, and mixes S25, S26 and S27 have the lowest strength after 3 and 7 days.

Mix S5 attained the highest strength among the 81 mixtures after 3 days of curing, and Mix S24 obtained the highest strength after 7 days of CT. In terms of strength, mix S12 outperforms all the other mixes and excels well. This may be related to the amount of period essential for the nucleation process to occur, at the time when the byproduct of the raw silica with alumina dissolution formed prior to precipitation.

Effect of *activator / Ash ratio*

Figure 9 shows the different UCS values observed after a period of three curing days using various combinations of different activator concentrations: 10M, 12.5M, and 15M of NaOH, and FA contents, which range from 20, to 30, and 40%. High FA was found to give the best results with the activator to ash ratio in the range of 0.3 to 0.5.

Figure 10 shows some irregular patterns, which might be ascribed to interactions involving concentrations of the

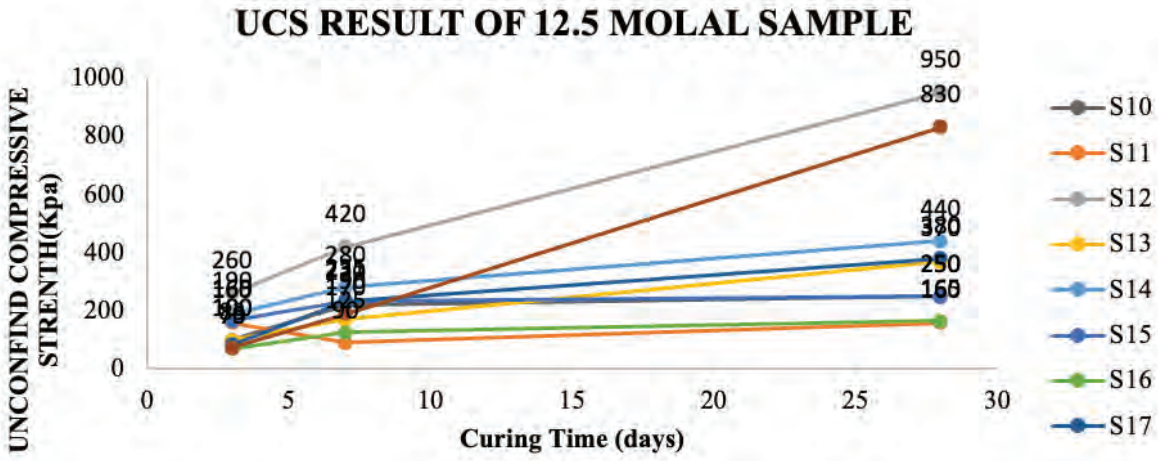


Figure 8. UCS of the 12.5 M sample.

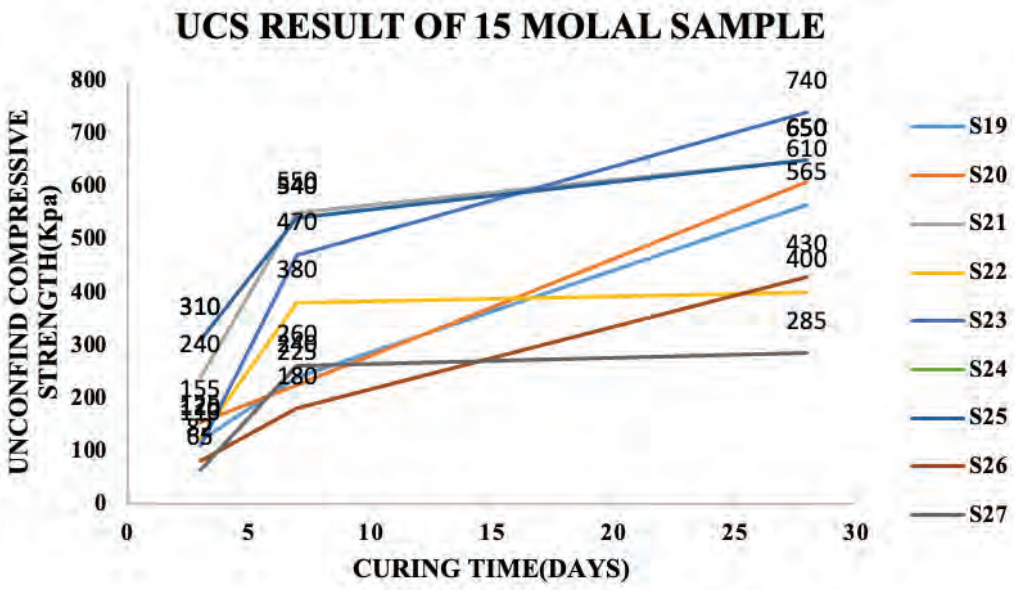


Figure 9. UCS of the 15 M sample.

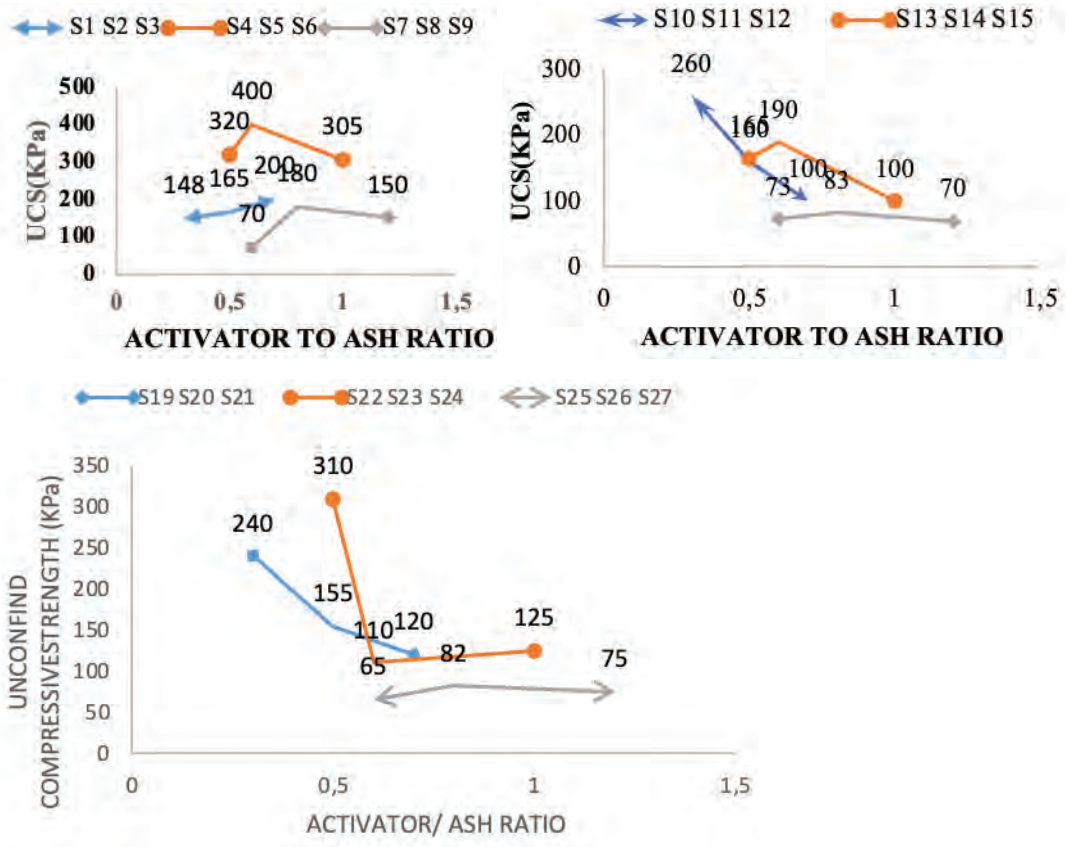


Figure 10. Three days of curing of the 10, 12.5 and 15 M samples.

activator, activator to ash ratio, and FA content. For instance, some concentrations of the activator require different optimal activator-to-ash ratios for maximum strength, which may lead to strength variations. This variability arises due to FA properties that differ from one another and also to specific geopolymerization conditions, like CT and temperature. Interactions among activator dosage, activator ash ratio, and fly ash behavior are largely responsible for the irregular trends seen in Figure 10's UCS results within three days of curing. Changes in any of these factors might result in over-activation or poor geopolymerization, affecting the formation of strength. In addition, as some blends improve stronger binding, while others worsen matrix quality, the variability is caused by variations in fly ash's chemistry, particle size, and reactivity. This makes the outcome of strength tests biased, thus stressing the significance of optimizing mixture characteristics in order to obtain consistent geopolymer performance.

The variations in the UCS of the samples after 7 days of curing with *activator / ash ratio* at 10, 12.5 and 15 M NaOH and 20, 30 and 40% FAC are represented in Figure 11. The samples containing more FAC had the ability to attain greater strength under these conditions, which paralleled an *activator / ash ratio* of 0.3--0.5. The maximal strength of S6 was observed after the curing period of seven days. High strength was obtained in those samples having high FA concentration, even after curing periods that did not exceed three days. This could be explained by the fact that the developed amorphous aluminosilicate gel was immature and would continue to develop for long periods of time. Generally, under the condition of using CT where higher strengths are required, the samples having high FA concentration would demonstrate increased strengths after longer curing periods. However, deviating from the optimum conditions would result in weak samples. Thus, for example, samples S4-6 with increased strengths depending on FA concentration were possibly affected by the more efficient activation process or different activator:ash ratios, whereas S1-3 and S7-9 with decreasing strengths could be the results of poor activation processes or other activator:ash ratios.

The reason for the wavy declining and increasing pattern for 12.5 M and 15 M samples could be attributed to the over-activation processes, which could result in excess dissolution of silica and alumina leading to the weakening of the geopolymer matrix. Moreover, the difference in reactivity of FA and pore structures could increase the effect. Therefore, one can conclude that the major factors affecting geopolymerization and thus the strength of expansive soil were the chemical composition (reactive silica and alumina concentrations), grain size, and the FA content. The

development of geopolymer gels depended on reactivity and fineness of fly ash.

Figure 11 shows the dependence of the UCS of the samples cured for 7 days on the activator to ash ratio varying from different molarities of NaOH solution (10M, 12.5M, and 15M) and various amounts of fly ash (20%, 30% and 40%). The results show that samples with higher fly ash concentration, especially in the ratio between 0.3 and 0.5, are likely to have higher UCS values because they undergo better geopolymerization process. In addition, it is evident from the results that there are optimum strength ratios, failure of which leads to irregular strength values. This figure

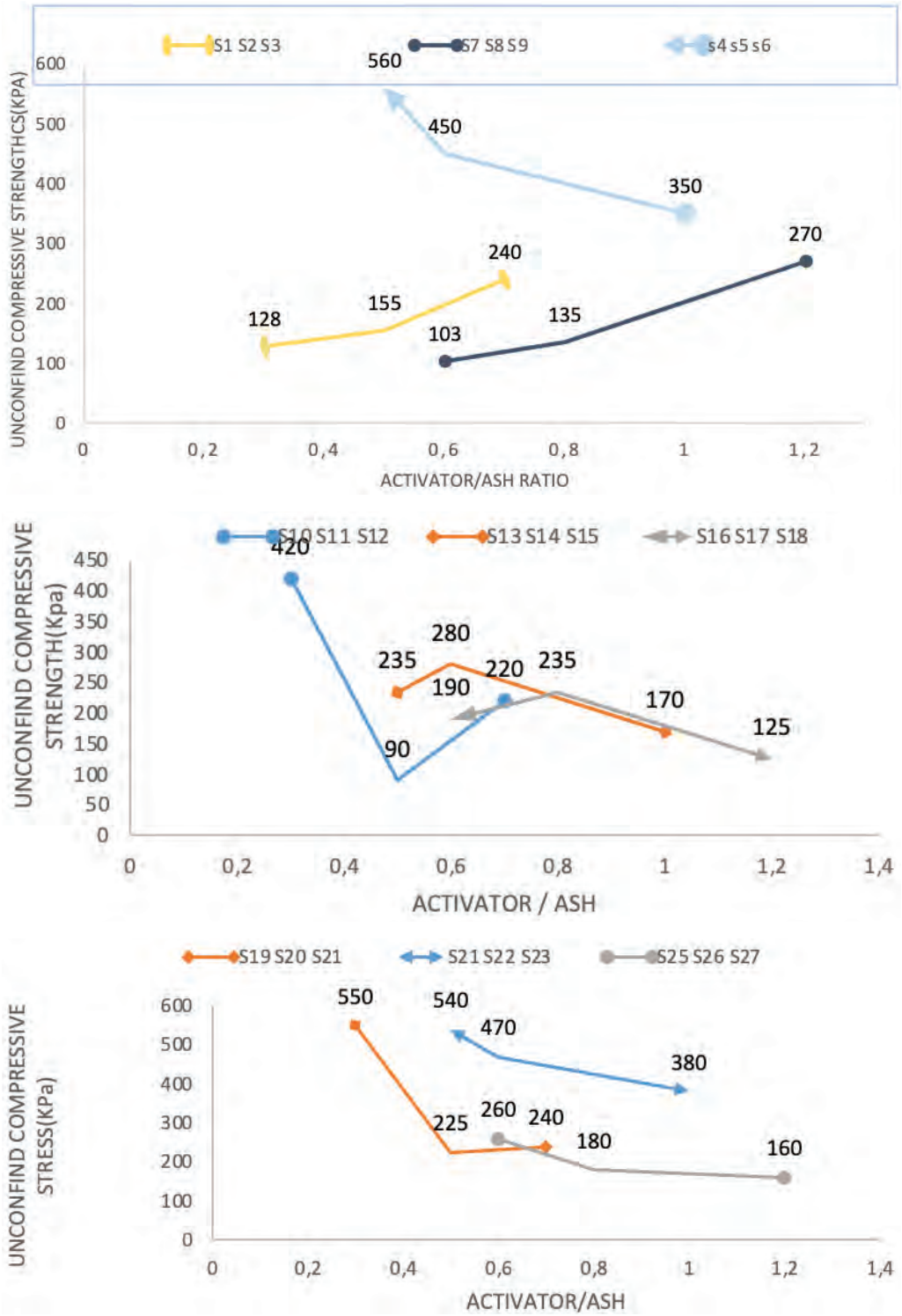


Figure 11. Seven Days of Curing of the 10 M, 12.5 M and 15 M Samples.

underscores the importance of balancing activator concentration and fly ash content to maximize mechanical strength in geopolymer-based stabilization of expansive soils.

In the current situation, samples with ash ratios ranging from 0.3 to 0.625 can achieve the maximum strength, and sample S12 displays this determined strength. Additionally, the samples formed with 12.5 M *NaOH* show superior strength to the other samples over the curing period of 28 days. With the exception of an initial stage, all the curing phases experience the supreme strength at a lower *activator / ash ratio*, which suggests that such an effort is cost efficient [28].

The Figure 12, indicates the compressive strength development of various samples after 28 days of curing, highlighting the influence of different activator molarities, fly ash contents, and ratios on long-term strength performance. These figures demonstrate how optimal combination of such parameters will help increase geopolymerization and strength gain through time.

Besides, geopolymerization offers a range of benefits from economic and environmental points of view in comparison to conventional technologies of soil stabilization like cementing or lime stabilization. With the use of waste products as raw materials, the cost of materials is minimized and the disposal problem is solved. Furthermore, unlike ordinary binders, geopolymers are durable and produce less carbon dioxide. While being both economical and environmentally-friendly, geopolymeric cements face also the challenge related to availability of raw materials and standard testing regimes. In turn, conventional methods of soil stabilization like cement or lime stabilization may seem to have more expensive and environmentally harmful consequences.

From the above analysis, the ideal properties that would lead to the maximum UCS are; 12.5 M NaOH, activator to ash ratio of 0.3–0.5, and fly ash content of 30–40%. Using such parameters, S12 mix gave the maximum UCS at 28 days, hence demonstrating the significance of regulating fly ash content and activator concentrations.

Curing duration plays a significant part in the strength development, and the most strength gains were recorded

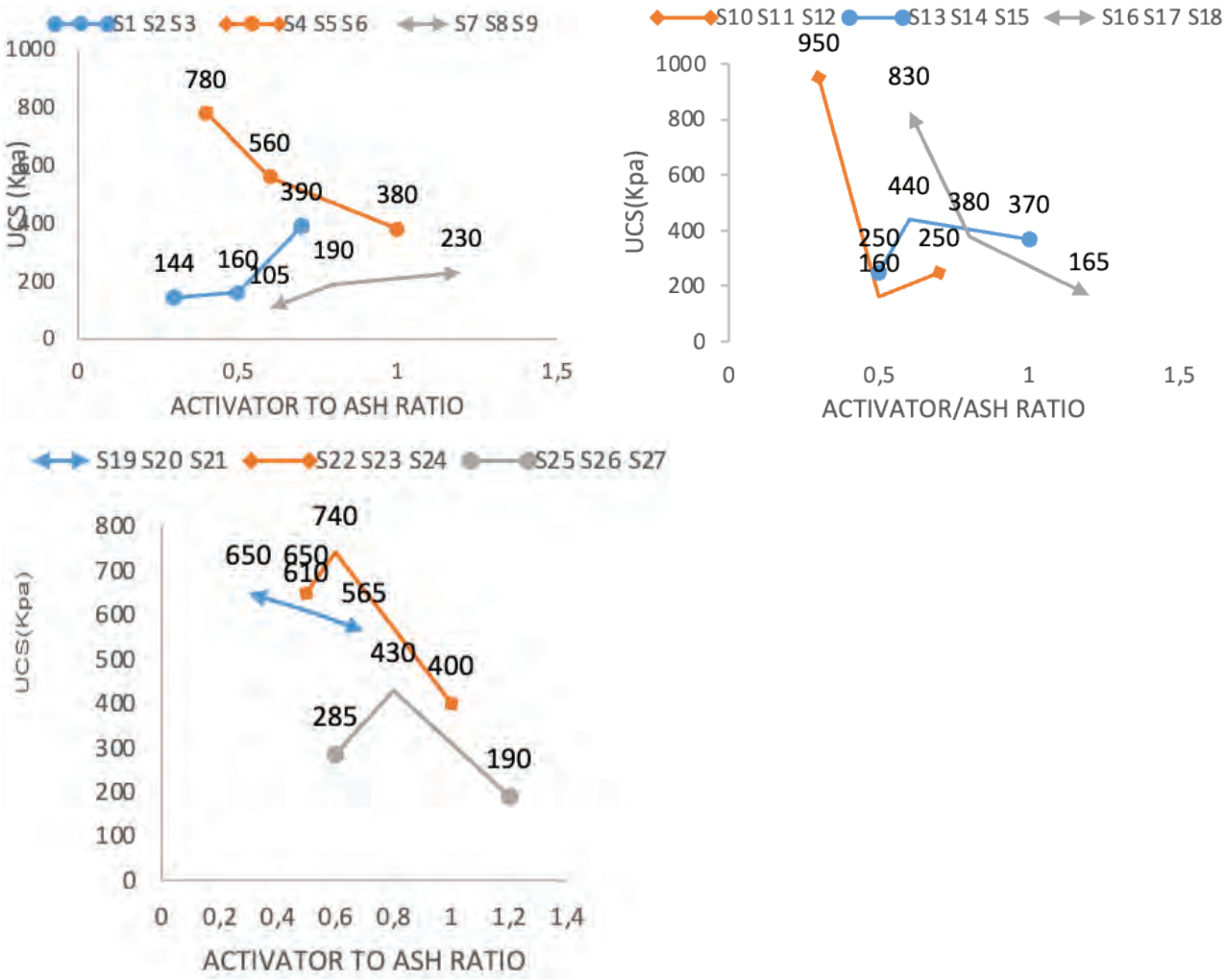


Figure 12. Twenty-eight days of curing of the 10, 12.5 and 15 M samples.

at 28 days. Significance of adequate curing of the geopolymerization to attain optimal strength development can be demonstrated by the fact that almost all mixes achieved their maximum UCS values at 28 days.

Retrofit Proposal Based on the Results

It is recommended that the present expansive soil foundation/subgrade can be improved through in-situ blending of 30-40 percent of Class F FA with soil and activation with a 12.5M NaOH solution, using an activator-to-ash ratio of 0.3 to 0.5, with compaction and curing for a period of not less than 28 days. This relies on the improved UCS and durability with the best FA geopolymer formulations observed. It is recommended that this customized geopolymer-stabilized mix be applied to the surface or used in place of the top layer of soil for structural elements such as retaining walls or shallow foundations to enhance bearing capacity and reduce swelling damage. The latest research shows that the repair method with geopolymers is more effective in enhancing the durability and load bearing capacity of a structure than the traditional methods using cement mortar. Besides addressing the technical drawbacks of ES technology, this method is also seen as environmentally friendly.

Limitations of the Study

Even so, despite Truth is this mentioned study has proved FA as an effective geopolymer stabilizer for ES, what comes next concerns should be given attention. Firstly, it is difficult to generalize the results shown because they are based solely on the laboratory test and with FA which is sourced only from a particular source; and Because of this the variations in properties of FA from other sources or production processes might not have been reflected. When it comes to estimating field stability, limited it is in the study as well as no comparison results with standard stabilizers (for instance cement lime etc.) and no long-term stability test (sulfate attack, heating-cooling cycles, wetting-drying etc) have been presented. Also, the economic and eco-profile ofthe process of the geopolymerization with FA as a stabilizer has not been evaluated, as well as possible environmental risk and potential of heavy metal leaching from FA.

Furthermore, the feasibility and practicability of geopolymer stabilization in question remain undefined due to the lack of any tests performed in field conditions during the study. Thus, in order to demonstrate that this innovative technique of soil treatment and its eco-panel can work, additional investigations will be required. Whether the findings from this experiment can be extrapolated to other sites should be verified considering different soils characteristics including, but not limited to, mineralogical composition, plasticity and the presence of organic material in soil as well as weather conditions like temperature, relative humidity and rainfall intensity. Soils containing higher levels of montmorillonite clay minerals or regions with wide temperatures ranges allowing the occurrence of freeze-thaw cycles can behave differently when geopolymerized using FA. Factors influencing the efficiency of FA as an alkaline activator include, among others,coal composition and combustion technologies. An initial sensitivity analysis indicates that reduced contents of either calcium or amorphous materials in FA will lower efficiency of geopolymer formation and strength development, whereas increased impurity levels in the ash may affect durability.

Future Recommendations

To comprehensively assess the performance and longevity of soil stabilization by using AAFA, it is imperative to further investigate the durability of soils exposed to the actual conditions of the field environment including seasonal moisture changes, freeze-thaw, and wet-dry cycles. Besides that, results obtained with these new stabilizers should be compared with those achieved with traditional ones (e.g. cement lime) to evaluate mechanical differences and economic implications of the process. Determining the potential effects of adding various mineral kinds to soils in conjunction with climatic changes would be beneficial. However, we must first evaluate the leaching of heavy metals, leaching causes, and modifications in order to determine how much different ashes may affect the method's outcomes. In the meanwhile, we could consider conducting a feasibility study to ascertain the costs associated with purchasing fly ash and turning it into geopolymers. We will have the opportunity to cooperate with geopolymers in the construction of various infrastructures through pilot studies conducted under the agreements formed between industry, contractors, and local government agencies. To support that using geopolymer is a way to reduce greenhouse gas emissions in the construction industry, one of the aspects that needs thorough investigation is the carbon footprint connected with this method. That's the reason we need to look at alkali-activated fly ash side by side with other building materials such as lime and cement.

Building on the research by (Tiwari, Satyam, & Puppala, 2021), who also found enhancement in strength and reduction of swelling through the use of natural fibers and recycled ash, the current paper based on AAFA also hold the promise for almost double the UCS value of natural soil and the shrink-swell capacity can be almost completely controlled over such soil. But, in sharp contrast to (Tiwari, Satyam, & Puppala, 2021) who have examined mainly the combined effect of fibers and ash, the present research brings to light the significance of optimum AAFA composition not only fly ash level but also the activator/fly ash ratio in final strength of the samples.

In the present paper, AAFA stabilization is shown to result in a UCS that is at least equal to or even surpasses that which was achieved by soil treated with WGP in the work of (Blayi, Sherwani, Ibrahim, Faraj, &Daraei, 2020), Mostly at elevated CT. Although (Blayi Sherwani Ibrahim, Faraj, & Daraei, 2020) identified 15% WGP as the best percentage to enhance the engineering properties of soil, this investigation reveals that soil stabilized with 30-40% FA, an activator/ash ratio of 0.3-0.5 and 12.5M NaOH at 28days

exhibits very high UCS. Because of this, while AAFA and WGP are both effective soil stabilizers, FA geopolymerization can be further optimized.

Waste materials utilization to improve soil characteristics and support sustainability was the major point of the studies by (Vijayan & Parthiban, 2020) and (Indiramma, Sudharani, & Needhidasan, 2020). In fact, the current findings are in agreement to previous research yet the major role of this paper is in extensive discussion of the effects of activator concentration and curing time. Besides that, the present work has been very successful in showing that geopolymers can excercise the functionalities of conventional binding agents or even exceed them but with Quite a bit lowered environmental impact. The outcomes presented by [29] and [30] are consistent with the present results as well since they have proven that the use of industrial waste-based geopolymers was an efficient and adequate solution for stabilization of difficult to treat soils (such as peat and high liquid limit subgrade soils). Though these researches were done on different soil materials (POFA GGBFS brCDW), the findings related to the mechanical properties reported in these papers have great agreement with those of this work on the strength of ES stabilized by FA-based geopolymers. The essence of this paper is that it upholds the optimization of curing conditions and the activator/ash ratio.

Such findings align well with those of [23], whose work demonstrated that geopolymers activated by mechanochemical treatment are more resistant to sulfate corrosion.

The contribution of the present paper to the literature is twofold: first by achieving the mix design optimization of the geopolymer stabilized ES second by the evaluation of geopolymerization for efficiency against conventional stabilization methods through a comparative study, and the last aspect of the paper is the focus on the manufacture of high-performance and environment friendly soils stabilized by industrial wastes. These points A lot add to the present literature.

CONCLUSION

This paper reviews the application of alkali-activated fly ash in stabilizing expansive soils. Such technology may have environmental impacts as well as construction-related impacts as well. For instance, some findings from this paper show that 12.5M concentration of sodium hydroxide is the most appropriate because it is cheaper and more environmentally friendly owing to minimal pollution sources. Moreover, sodium hydroxide can yield the highest value of Ultimate Compressive Strength (UCS). Consequently, after applying sodium hydroxide to the soil, it was measured to be 4.8MPa. Aside from that, this soil's UCS value is significantly greater than that of other unstabilized soils due to the technology's cost-effectiveness and environmental friendliness when their wastes are utilized. Because of this, engineers can use materials like fly ash for sustainable construction even in areas with poor soil. However, this is only possible in the Indian state of Odisha.

However, the results will vary significantly due to the various mineralogical compositions of soils and climates in different areas of the world. In actuality, the results were influenced by the fly ash quality and soil environmental variables, according to the sensitivity analysis. Because the quality of the stabilized fly ash can be readily evaluated and applied on site using deep soil mixing columns, jet grouting, and geosynthetic slope/embankment stabilization techniques, it is essential to do mixture design tests before beginning any work.

Practical Implications

The results from the study provide a feasible, sustainable, and affordable way to stabilize the expansive soil, which plays a vital appeal in the construction sector through building foundations, embankment, and road construction. Using fly ash, which is basically an industrial waste, to soil stabilization through alkali activation of fly ash only, is a reason why such a method is considered. Besides its main functions, it also contributes to reducing environmental effects of lime and cement application. This method suits well areas with abundant fly ash that ensures waste is used in the best way.

AUTHORSHIP CONTRIBUTIONS

Authors equally contributed to this work.

DATA AVAILABILITY STATEMENT

The authors confirm that the data that supports the findings of this study are available within the article. Raw data that support the finding of this study are available from the corresponding author, upon reasonable request.

CONFLICT OF INTEREST

The author declared no potential conflicts of interest with respect to the research, authorship, and/or publication of this article.

ETHICS

There are no ethical issues with the publication of this manuscript.

STATEMENT ON THE USE OF ARTIFICIAL INTELLIGENCE

Artificial intelligence was not used in the preparation of the article.

REFERENCES

[1] Jones LD, Jefferson I. Expansive soils. In: ICE Manual of Geotechnical Engineering, Volume 1: Geotechnical Engineering Principles, Problematic Soils and Site Investigation. 2012. p. 413–441.

[2] Dungca JR, Galupino JG. Artificial neural network permeability modeling of soil blended with fly ash. GEOMATE J 2017;12:77–82. [CrossRef]
[3] Mathew A, Sasikumar A. Performance of soft soil reinforced with bamboo and geonet. Int Res J Eng Technol 2017;4:464–369.
[4] Ayyappan A, Palanikumar S, Kumar DD, Vinoth M. Influence of geopolymers in the stabilization of clay soil. Int J Emerg Technol Eng Res 2017;5:108–120.
[5] Mahajan L, Kirange M, Bhagat S. Statistical exploration for enlargement of reformed water cement ratio law for fly ash concrete. Sigma J Eng Nat Sci 2025;43:269–281. [CrossRef]
[6] Miao S, Shen Z, Wang X, Luo F, Huang X, Wei C. Stabilization of highly expansive black cotton soils by means of geopolymerization. J Mater Civ Eng 2017;29:04017170. [CrossRef]
[7] Khadka SD, Jayawickrama PW, Senadheera S. Strength and shrink/swell behavior of highly plastic clay treated with geopolymer. Transp Res Rec 2018;2672:174–184. [CrossRef]
[8] Kabay N, Miyan N. A comparative study on the physical and mechanical properties of alkali activated materials. Sigma J Eng Nat Sci 2020;38:649–658.
[9] Parhi PS, Garanayak L, Mahamaya M, Das SK. Stabilization of an expansive soil using alkali activated fly ash based geopolymer. In: Sustainable Civil Infrastructures: Innovative Infrastructure Geotechnology. Springer; 2017. [CrossRef]
[10] Parikshith M, Sekhar DC. Feasibility of flyash based geopolymer for soil stabilization. Int J Innov Technol Explor Eng 2019;9:4348–4351. [CrossRef]
[11] Cengizler H, Koç M. The effect of marble waste in the production of low-temperature porous material from alkali-activated fly ash. Sigma J Eng Nat Sci 2024;42:1148–1159. [CrossRef]
[12] Rosales J, Agrela F, Marcobal JR, Diaz-Lopez JL, Cuenca-Moyano GM, Caballero A, et al. Use of nanomaterials in the stabilization of expansive soils into a road real-scale application. Materials 2020;13:3058. [CrossRef]
[13] Ghadir P, Ranjbar N. Clayey soil stabilization using geopolymer and Portland cement. Constr Build Mater 2018;188:361–371. [CrossRef]
[14] Habibbeygi F, Nikraz H. Compression behaviour of highly expansive clays stabilised with a green stabiliser of magnesium chloride. GEOMATE J 2018;14:144–150. [CrossRef]
[15] Ikeagwuani CC, Nwonu DC. Emerging trends in expansive soil stabilisation: A review. J Rock Mech Geotech Eng 2019;11:423–440. [CrossRef]
[16] Dungca JR, Codilla II EET. Fly-ash-based geopolymer as stabilizer for silty sand embankment materials. GEOMATE J 2018;14:143–149. [CrossRef]
[17] Estabragh A, Rafatjo H, Javadi A. Treatment of an expansive soil by mechanical and chemical techniques. Geosynth Int 2014;21:233–243. [CrossRef]
[18] Arrieta Baldovino JdJ, dos Santos Izzo RL, da Silva ÉR, Rose J. Sustainable use of recycled-glass powder in soil stabilization. J Mater Civ Eng 2020;32:04020080. [CrossRef]
[19] Blayi RA, Sherwani AFH, Ibrahim HH, Faraj RH, Daraei A. Strength improvement of expansive soil by utilizing waste glass powder. Case Stud Constr Mater 2020;13:e00427. [CrossRef]
[20] Jalal FE, Xu Y, Jamhiri B, Memon SA. On the recent trends in expansive soil stabilization using calcium-based stabilizer materials (CSMs): A comprehensive review. Adv Mater Sci Eng 2020;2020:1510969. [CrossRef]
[21] Andavan S, Pagadala VK. A study on soil stabilization by addition of fly ash and lime. Mater Today Proc 2020;22:1125–1129. [CrossRef]
[22] Indiramma P, Sudharani C, Needhidasan S. Utilization of fly ash and lime to stabilize the expansive soil and to sustain pollution free environment–An experimental study. Mater Today Proc 2020;22:694–700. [CrossRef]
[23] Hamid Abed M, Hamid Abed F, Aliraza Seyed Z, Sabbar Israa A, Canakci H, Kurdi NH, et al. Experimental feasibility study of using eco-and user-friendly mechanochemically activated slag/fly ash geopolymer for soil stabilization. Clean Mater 2024;11:100226. [CrossRef]
[24] Tabatabaei Z, Fatehi-Nobarian B. Numerical investigation of ground tanks for storage subjected near-fault earthquakes. Pollack Period 2021;17:75–80. [CrossRef]
[25] Elseknidy MH, Salmiaton A, Nor Shafizah I, Mousa AH. A study on mechanical properties of concrete incorporating aluminum dross, fly ash, and quarry dust. Sustainability 2020;12:9230. [CrossRef]
[26] Helmuth R. Some questions concerning ASTM standards and methods of testing fly ash for use with portland cement. Cem Concr Aggreg 1983;5:103–110. [CrossRef]
[27] Niş A, Altundal MB. Mechanical strength degradation of slag and fly ash based geopolymer specimens exposed to sulfuric acid attack. Sigma J Eng Nat Sci 2019;37:917–926.
[28] Cristelo N, Glendinning S, Fernandes L, Pinto AT. Effects of alkaline-activated fly ash and Portland cement on soft soil stabilisation. Acta Geotech 2013;8:395–405. [CrossRef]
[29] Amaludin AE, Asrah H, Mohamad HM, bin Amaludin HZ, bin Amaludin NA. Physicochemical and microstructural characterization of Klias Peat, Lumadan POFA, and GGBFS for geopolymer based soil stabilization. HighTech Innov J 2023;4:327–348. [CrossRef]
[30] Xie J, Zhang J, Cao Z, Blom J, Vuye C, Gu F. Feasibility of using building-related construction and demolition waste-derived geopolymer for subgrade soil stabilization. J Clean Prod 2024;450:142001. [CrossRef]

Sigma J Eng Nat Sci, Vol. 44, No. 4, pp. 2433–2446, August, 2026

Sigma Journal of Engineering and Natural Sciences
Web page info: https://sigma.yildiz.edu.tr
DOI: 10.14744/sigma.2026.2107

Research Article

Integrating cognitive intelligence in robotic process Automation: Placement bots in action

Neelam YADAV[1,*], Supriya P. PANDA[2]

[1]Department of Computer Science and Engineering, School of Engineering and Technology, Manav Rachna International Institute of Research and Studies, Faridabad, 121004, India; Christ University, Karnataka, 560029, India
[2]Department of Computer Science and Engineering, School of Engineering and Technology, Manav Rachna International Institute of Research and Studies, Faridabad, 121004, India

ARTICLE INFO

Article history
Received: 10 April 2025
Revised: 01 July 2025
Accepted: 07 November 2025

Keywords:
Cognitive Intelligence; Placement Bot; RPA-driven Robotic Process Automation (RPA); Selenium AI Web Scraper; UiPath

ABSTRACT

With increasing administrative tasks in Higher Education Institutions(HIEs), automation provides an effective solution to improve efficiency. This research introduces an RPA Cognitive Placement Bot that automates resume screening and job matching using Machine Learning (ML) and Natural Language Processing(NLP). The placement bot automatically capture education, skills, and experience from resumes and assesses them with 159 job descriptions acquired from Indeed and LinkedIn. spaCy's Named Entity Recognition (NER), Selenium, Python-RPA, and Bidirectional Encoder Representations from Transformers (BERT) are employed to expedite the placement process by computing candidate scores through job-resume alignment and sending automated recommendation emails. The bot is trained and tested on 2,006 and 348 resumes respectively with 98.81% training accuracy with BERT, 97.91% with NER, and a net testing accuracy of 99.14%. The proposed virtual bot exhibits outstanding classification efficiency and enhanced performance for HEIs placement automation, when evaluated against current benchmark models —SVM-based (94%), LDA-based (82%), and Decision Tree-based (94%)) proposed by Jagwani et al., (2023) and Prabha et al., (2024).

Cite this article as: Yadav N, Panda SP. Integrating cognitive intelligence in robotic process Automation: Placement bots in action. Sigma J Eng Nat Sci 2026;44(4):2433–2446.

INTRODUCTION

Business organisations increasingly seek innovative solutions to reduce costs, boost efficiency, and reduce manual effort. Rather than digitising all operations, many focus on automating time-consuming tasks [1]. This problem is addressed by a Business Process Automation tool known as Robotic Process Automation (RPA). RPA automates frequently repititive tasks, so that the employees can focus on analytical work [2]. RPA bots mimic user interactions within software systems by performing various tasks such as form filling, email handling, web scraping, data processing, and browser automation [3,4].

RPA is a non-intrusive technique that operates on top of existing Information Systems(IS) and Enterprise

*Corresponding author.
*E-mail address: mail2neelam.sanskriti@gmail.com

This paper was recommended for publication in revised form by Editor-in-Chief Ahmet Selim Dalkilic

Published by Yıldız Technical University Press, İstanbul, Turkey
© Author. This is an open access article under the CC BY-NC license (http://creativecommons.org/licenses/by-nc/4.0/).

Resource Planning (ERP) systems [5], and is extensively deployed through platforms such as Pega, Microsoft Power Automate, UiPath, and WorkFusion [6]. It empowers organisations to automate both back-office and customer-facing processes by falicitating benefits such as consistency, speed, regulatory compliance, and cost efficiency, often resulting in a high Return on Investment (ROI) within a year [3,7,8]. RPA excels in automating structured, rule-based tasks, however it cannot handle complex decision-making and therefore lacks cognitive intelligence. RPA enhances its cognitive capabilities when integrated with Artificial Intelligence (AI) technologies, such as Computer Vision, Deep Learning(DL), Machine Learning (ML), Natural Language Processing (NLP), generative AI and others [9-13]. This technological unification forms Intelligent Process Automation (IPA), enabling bots to make rule-based decisions, self-adjust, handle exception and improve over time [14]. Despite the use of IPA, not all processes are suitable for RPA, as poor selection can lead to bottlenecks [15]. Literature identifies several criteria for task suitability, focusing on processes that are highly manual, repetitive, rule-based, high-volume, and frequently executed [16-19].

This paper is organised as follows: Section 2 outlines the problem and related work; Section 3 describes the methodology and technologies used; Section 4 presents results and analysis; and Section 5 concludes with findings and recommendations for future work.

Literature Review

Robotic process automation (RPA) is a rising technology for the digital transformations in Higher Education Institutions (HEIs). RPA supports faculty members by improving teaching efficiency through the automation of administrative tasks while also facilitating student development. While existing studies highlight RPA's benefits in improving operations and supporting digital change, its use in education remains underexplored. This research contributes to the field by developing and analysing a Cognitive RPA Placement Bot to automate the placement process in HEIs. Table 1 summarises prior research on RPA's applications and impact across administration, teaching, course delivery and Placements.

Table 1. Literature review on RPA ımplementations in HEIs

Source	Key Findings	Gaps in the Study
Khan et al.[20]	The study presented a robot, which is trained to test the delivery of a course. These bots can help a teacher improve their lecture delivery.	The study lacks empirical validation of RPA's effectiveness in improving teaching and learning outcomes. Moreover, it does not address the adaptability of RPA systems across different subjects, educational levels, and learning environments.
Turcu et al.[21]	An OCR-enhanced RPA solution was proposed in this work. The resume scanning process was automated by using UiPath for the recruitment process of Small and Medium Enterprises (SMEs).	The study limits the use of RPA technilogy by primarily depending on OCR, It does not incorporated AI or NLP-based cognitive solutions such as semantic matching, or intelligent resume parsing. Furthermore, it does not explore the scalability and applicability of this solution to other industries.
Somasundaram et al.[22]	An RPA-based report generation tool was proposed to generate advanced results from a programming competency test conducted for students. The tool assisted 540 students and 35 facult mentors through its successfull deployment in the Department of ECE at R.M.K. Engineering College.	Lack of quantitative assessment of the RPA tool's effectiveness in enhancing mentoring efficiency and student performance, as the current system primarily focuses on report generation without cognitive capabilities for in-depth performance analysis.
Vrushil Gajra et al.[23]	RPA's UiPath, MySQL Server, NodeJS server, and Restful API are used to create a ChatBot to automate the procedures of a student management system and integrate it with ERP system.	The study envisions integrating Artificial Intelligence and Machine Learning with RPA to handle unstructured data, predictive analytics, and intelligent decision-making.
D. Boban and J. Nakić [24]	The study presents a step-by-step RPA process design, including web navigation, data retrieval, report generation, and automated communication with users using UiPath. The study demonstrated significant time reduction (≈77.5%).	This study automates the course search process on a single platform namely Udemy, and does not extend its functionality to other e-learning systems. It also does not provide an intelligent personalized recommendation system based on user behavior. Morevoer, the proposed RPA solution is rule-based and does not integrate NLP or other AI-driven decision-making techniques for intelligent automation.
Nandwani et al.[25]	The study proposed an HTML (Hyper Text Mark-Language), CSS (Cascading Style Sheet), Selenium and Java Script based method for student outcome assessment process and saves 94.44% of the time.	This study solely relies on rule-based RPA automation using Selenium and Java, and lacks the integration of AI or NLP for intelligent decision-making and data interpretation.

Table 1. Literature review on RPA ımplementations in HEIs (continued)

Source	Key Findings	Gaps in the Study
Ding et al.[26]	The study employs a BiLSTM network and CNN to extract unstructured text features for Job-Resume matching tasks, This study proposes a novel Dual-Branch Mutual Learning (DBML) framework for job–resume matching in HR management.	This study lacks contextual understanding, as it uses fixed 100-dimensional skip-gram vectors. The semantic representaions could be enhanced by incorporating newer contextualized embeddings such as BERT. Furthermore, the framework does not employ dynamic techniques such as Beautiful Soup or Selenium to scrape evolving job markets or candidate profiles; rather, it operates on static datasets.
Hawari1 et al. [27]	A job-recommendation system is proposed that uses content-based filtering mechanism to list the vacancies and to recommend Jobs.	The dataset is relatively small, and the integration of AI and NLP techniques could further enhance the mechanism.
Mydyti et al. [28]	A job internship matching strategy based on online scraping is proposed. This work uses an intelligent web scraping technique and Machine Learning in an Internship Management System (IMS).	This study provides only a theoretical approach and does not represent any practical evaluation. The proposed framework has not been validated in real-world settings. Furthermore, this study is based on Machine Learning and NLP techniques hence wouldn't be relevant for advanced technological models such as BERT. Therefore, it lacks contextual understanding and fails to give any feedback or reccomendation for improvement for the skills that aren't inhenrited by it.
Suman et al. [29]	This study utilizes web scraping techniques to computerize tasks such as collection of job descriptions and resumes from LinkedIn. Fuzzy mactching techniques were used for Job-Resume matching. A Decision Tree classifier was used to classify resumes.	The web scraping was only limited to LinkedIn and no other job portals were considered for scraping job descriptions and resumes. Furthermore, only the Decision Tree algorithm was used for classification and no other classifiers were considered to assess or improve accuracy. Moreover, other NLP models such as BERT were not considered, although they could enhance contextual and semantic understanding.
Rojas-Galeano et al. [30]	This work presents the research landscape analysis of job–résumé matching. This study identifies leading institutions, key trends and influential authors contributing to the field.	The study discusses literature-based fiding without empirical validation of job–résumé matching models. It highlights the paradigm shift toward transformer-based architectures but does not discuss the advantages and disadvantages of each AI technique used in recruitment systems.
Lin et al. [31]	A Maching Learning based solution is proposed for the Job-Resume matching problem. Random Forest and CNN are used to improve 'Job-Resume matching' for online applicants. They help solve the problems of traditional rule-driven and keyword-based search engines.	The framework is developed using predefined datasets. It does not leverage real-time job market data. Deep learning and ensemble models are employed to model the training dataset. Contextual NLP approaches such as BERT or GPT-based embeddings are not considered. Additionally, the system doesn't offer personalization features, including adaptive recommendations and user preference learning.
Lunn et al. [32]	This study proposes an application to examine current job trends in the market for computer science(CS) students. A web scraping technique is used to collect job listings from the web with an accuracy of 98.5%. NLP techniques are used to extract information from textual data, while Python's Beautiful Soup library is used for scraping websites.	This study uses Python's Beautiful Soup, which cannot process dynamic content, thereby limiting data extraction. Selenium WebDriver should instead be used for web scraping. The scraping process was restricted to Computer Science–related data, which further limits its applicability to other domains. The primary focus is to identify job trends in the market; however, the work could be extended to job–resume matching and user feedback mechanisms for assessing students' current skill levels.
Jirjees et al.[33]	A BERT-based approach was used in the recruitment process to provide accurate and context-aware job–resume matching. This study highlights the superiority of BERT over other models in keyword matching. Several ML algorithsm such as Support Vector Machine (SVM), Long Short-Term Memory (LSTM), and Multi-Layer Perceptron (MLP) models were used to test the dataset. The SVM-based model provide 94% accuracy, whereas the LSTM and MLP models were 92% and 90% accurate, respectively.	Sophisticated machine learning approaches such as clustering and hybrid sampling can reveal complex patterns. This study uses only a Kaggle dataset for the Computer Science field, which may not be fully representing other domains, and thus, results may vary. The model could be extended to other industries.

Table 1. Literature review on RPA ımplementations in HEIs (continued)

Source	Key Findings	Gaps in the Study
Jagwani et al.[34]	This study uses an Object Identification Tecnique to propose a Resume Evaluation Framework using spaCy and the Latent Dirichlet Allocation (LDA) model, achieving 82% accuracy.	This study was tested on a very limited dataset consisting of only 20 resumes, which is too limited to generalize the findings across all Higher Education Systems. Furthermore, the model does not provide recommendations or feedback regarding students' skills and competency gaps. In addition, this research has not been evaluated using BERT-based techniques, which could potentially improve the overall accuracy. The performance of the system could be further enhanced by incorporating ensemble learning techniques.
Prabha et al.[35]	The study was conducted to classify resumes for selecting or rejecting candidates. Various classification algorithms, such as Logistic Regression (LR), Random Forest (RF), and K-Nearest Neighbour (KNN) were tested for their performance in the study. Logistic Regression proide an accuracy of 95%, whereas Random Forest and KNN were 82% and 88% accurate respectively.	This model was tested on a very limited dataset consisting of only 10 resumes. Such a limited dateset does not provide a broader perspective on job-resume matching and restricts the generalizability of this study across all the HEIs.

As stated in the literature, traditional job-resume matching approaches primarily rely on exact keyword matching,old web-scraping techniques for acquiring resumes and job descriptions, and limited datasets. These approaches often lack contextual understanding and do not provide recommendations and feedback mechanisms for assessing candidates' skill sets despite the integration of advanced artificial intelligence and machine learning techniques. Furthermore, existing studies do not leverage Named Entity Recognition (NER) within BERT-based frameworks and often overlook critical components such as resume ranking and personalized feedback generation. This model proposes an intelligent placement bot that replicates all the tasks of a placement officer, ranging from resume acquisition to job–resume matching and sending skill recommendation emails to candidate. First, the automated system retrieves resumes through Gmail integratioin using OAuth 2.0 authentication. It then employes API-based web scraping techniques using Selenium to collect job descriptions from platforms such as LinkedIn and Indeed. After collecting job description and resumes, the placement bot automates various tasks, including resume parsing, candidate–job matching, ranking, and automated email communication. The proposed bot integrates machine learning techniques including Logistic Regression with TF-IDF features [36] , fuzzy matching, spaCy-based Named Entity Recognition (NER) [37], BERT-based techniques and automation frameworks to deliver accurate, adaptive, and intelligent placement recommendations. Additionally, the system sends personalized selection and rejection emails based on candidate rankings. These recommendation emails help students understand their skill gaps relative to a specific job, replicating the role of human recruiters in an efficient manner. This virtual bot is adaptive to the dynamically changing real-time job market and addresses the shortcomings of conventional job-resume systems. It provides personalized feedback by identifying skill gaps and rank resumes based on a weighted scoring framework that considers educaiton, skills, and work experience. Overall, the proposed software solution provides a more flexible and responsive approach to align student competencies with internship opportunities while enhancing job–resume matching accuracy and optimizing the recruitment process. The bot significantly outperforms traditional methods in terms of accuracy, scalability, and automation.

MATERIALS AND METHODS

The approach begins with the Manual Process of Job-Resume Matching as illustrated in Figure 1, which serves as a baseline for comparison.

Manual Tasks of Job-Resume Matching Process

The routine manual tasks performed by a placement officer in an HEI during the placement process are typically organized step by step to guarantee students have the best job opportunities. This involves a series of repeated administrative tasks that must be completed each time a new Job Description (JD) is issued by the company as depicted in Figure 1. RPA is best suited to automate such repetitive, time-consuming processes making it ideal for RPA automation. The selection of this process aligns with the suitability of the criteria discussed in the literature. For the purpose of comprehension and visualisation, Figure 2 lists every step involved in automating the Placement process.



Figure 1. Manual Job-Resume Matching Process Performed by the Placement Officer.

Automation steps of "RPA Cognitive Placement Bot"

The automated RPA Cognitive Placement Bot as depicted in Figure 2 comprises five steps:

Step 1: Resume and job description extraction

Resume extraction

Resumes are extracted from the placement officer's Gmail Id. The resumes and job descriptions used in this study were provided by the placement cell of a higher education institution (ABES Engineering College, Ghaziabad, India) and represent real-world data from final-year students currently undergoing the placement process. All data was used with the institution's approval, and strict measures were taken to maintain candidate privacy. The data was used exclusively for academic intentions and according to the institutional research ethics. The bot uses OAuth 2.0 to authenticate and connects to Gmail API. OAuth 2.0 is an authorization system that facilitates third-party apps to utilize a user's data without revealing their credentials (such as

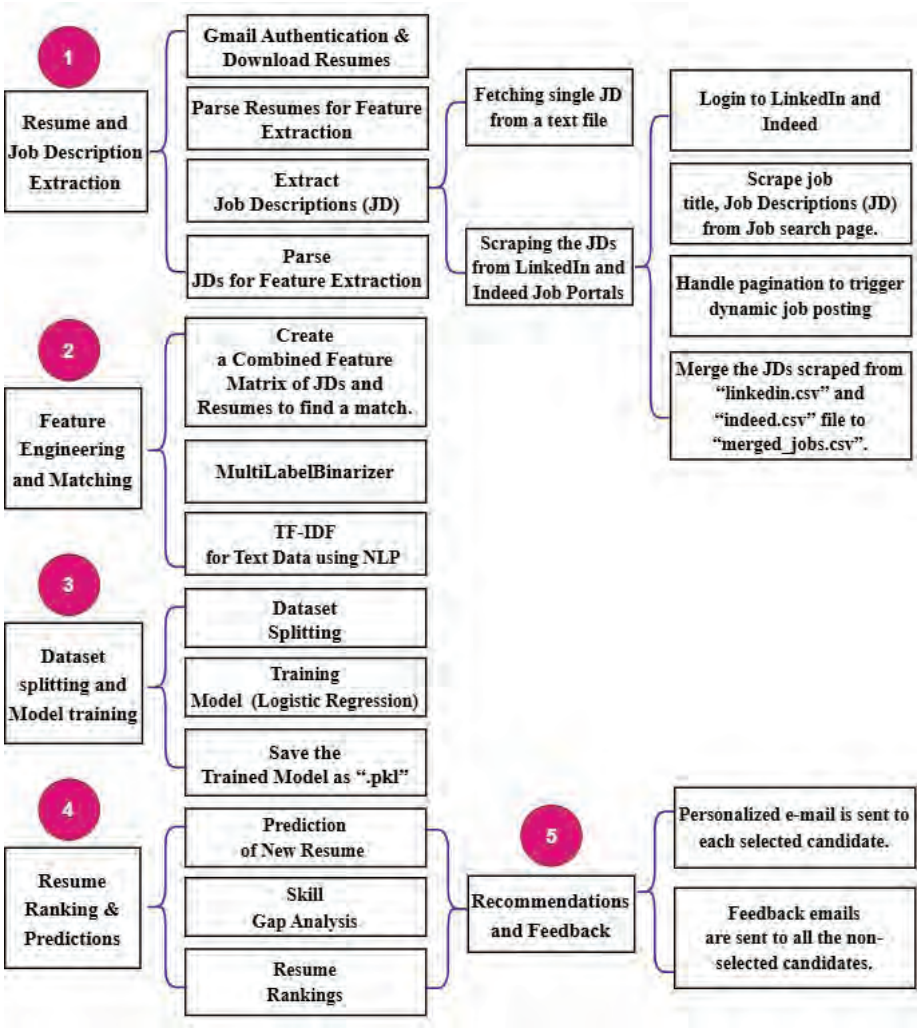


Figure 2. Automation steps of "RPA cognitive placement bot".

resume_name	skills	experience	education	email
Sujeet Kumar.pdf	c, java, python, react, sql	e, n, t, r, y, -, l, e, v, e, l	Not specified	krsujeet0707@gmail.com
Gaurang Gaur.pdf	c, java, javascript, node.js, python, react, sql	e, n, t, r, y, -, l, e, v, e, l	bachelor	pegauranggaur10@gmail.com
aaayush.pdf	c, django, leadership, node js, node.js, r, react, sql	e, n, t, r, y, -, l, e, v, e, l	bachelor	yush91620@gmail.com
Aadesh Kumar.pdf	java, leadership	e, n, t, r, y, -, l, e, v, e, l	mca	aadeshrajput250609@gmail.com
Aaditya Bhardwaj.pdf	c, django, java, javascript, python	e, n, t, r, y, -, l, e, v, e, l	bachelor	aadibhardwajdec98@gmail.com
Aditya Kumar.pdf	aws, c, java, machine learning, python, sql	e, n, t, r, y, -, l, e, v, e, l	Not specified	0906@gmail.com
aakash jayesh.pdf	not specified	e, n, t, r, y, -, l, e, v, e, l	Not specified	aakash1234shah@gmail.com
Aakash Kumar.pdf	c, java, javascript, python, sql	e, n, t, r, y, -, l, e, v, e, l	master	aakimrt619@gmail.com
Aakash Kumar.pdf	not specified	m, i, d, -, l, e, v, e, l	bachelor	aakashkumar171555@gamil.com
Aakash Sharma.pdf	c, java, javascript, sql	e, n, t, r, y, -, l, e, v, e, l	b.tech	aakashg837799@gmail.com
Aalok mishra.pdf	c	e, n, t, r, y, -, l, e, v, e, l	Not specified	alok.mishra5192@gmail.com

Figure 3. Extracted Resume Features stored in 'resume_extracted.csv" file.

passwords). The resumes are filtered according to specific subject lines and contents of an email.

Parsing resumes for feature extraction

A CSV file of the name- "resumes_extracted.csv" is created, as depicted in Figure 3, to store the extracted information from the collected resumes such as candidate names, skills, educational qualifications, certifications, contact information, and work experience.

Experience extraction

Experience related information such as '5 years' or 'since 2020', are extracted from resumes using 'Named Entity Recognition (NER) and spaCy's 'en_core_web_sm' model. The bot indentifies the experience levels by identifying different phrasing such as '5+ years' or 'over 5 years' and classifies candidates into three groups: Entry-Level (less than two years of experience), Mid-Level (2-5 years of experience), and Senior-Level (more than 5 years of experience).

Education extraction

A hybrid approach (regex+NLP) is used for identifying degree names (e.g., "B.Tech", "Master's"). It uses Sentence-Bidirectional Encoder Representations from Transformers (SBERT) "all-MiniLM-L6-v2" model and spaCy's NER for semantic similarity matching and to fetch full educational phrases (e.g., "Master's in Data Science).

Skills and email extraction

The bot scans resumes for predefined skills such as 'Python', 'ML', and 'SQL', and uses regex to extract email addresses. It also stores unique skills for efficient processing.

Scrape job descriptions

From LinkedIn web portal

Python's Selenium Web Driver is used to dynamically log in, identify input fields, and perform the authentication. It queries LinkedIn for specific job titles, locations, and experience levels. It then fethes job titles, company names, and descriptions using CSS selectors, storing the data in JavaScript objet Notation (JSON) and Comma Separated Values (CSV) formats. Job Title and Job Description are scraped from LinkedIn and stored it the 'job_data.csv' and 'job_data.json' files.

From Indeed web portal

Selenium-based web browser automation is used to dynamically interact and scrape Indeed's job listings. The web driver waits for up to 40 seconds for the job listings to appear to avoid scraping an empty page.

From text file

The Job Descriptions (JDs) provided by the companies are simple text files containing sections like job title, responsibilities, required skills, qualifications, and experience. In this study a "job_description.txt" file as shown in Figure 4 is used to match student's resumes with the company's JD.

Parsing job descriptions for feature extraction

To generate a feature matrix, Job Descriptions (JDs) taken from text files, Indeed, and LinkedIn need to be refined. The data sourced from LinkedIn and Indeed presents several challenges, including irregular newline formatting, unclear experience format, and unclear skills in the free text. Two different CSV's are generated as linkedin_jobs.csv and indeed_jobs.csv. Both CSV are merged into one csv file "merged_jobs.csv" as depicted in Figure 5.

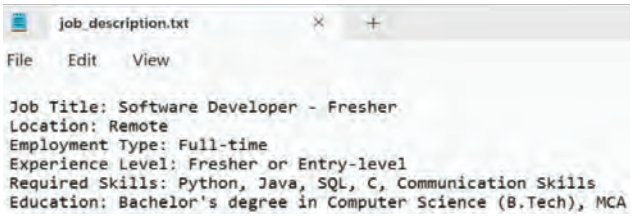


Figure 4. Snapshot of a "job_description.txt" file used for job–resume matching.

job_title	skills	experience	education
Jr Software Engineer	['agile', 'angular', 'aws', 'azure', 'communication skills', 'java', 'javascript', 'leadership', 'react', 'sql', 'teamwork']	[]	['"bachelor\'s"]', "['bachelor'"]
Engineer, II Software	['agile', 'c', 'java', 'javascript', 'python']	['3']	['["bachelor\'s"]']
Software Engineer - Java	['aws', 'azure', 'java', 'python', 'teamwork']	['3']	['"master\'s"', "'mca']", "['m.tech'"]
Software Engineer	['communication skills', 'java', 'sql']	['5', '10', '7', '2', '15']	['["bachelor\'s"]']
Software Engineer II	['agile', 'angular', 'aws', 'azure', 'c', 'gcp', 'sql']	['2']	['"bachelor\'s"]', "['bachelor'"]
Software Development Engineer II	['communication skills', 'java', 'python', 'sql', 'teamwork']	['2']	['["not specified']"]
Software Engineer I	['agile', 'aws', 'java', 'react', 'sql']	['2', '1']	['["not specified']"]
Software Engineer	['azure', 'c', 'leadership', 'project management', 'sql']	[]	['"bachelor\'s"]', "['bachelor'"]
Software Engineer	['agile', 'angular', 'aws', 'java', 'javascript', 'node.js', 'python', 'react', 'restful apis', 'scrum']	['5', '2']	['"bachelor\'s"]', "['bachelor'"]
Senior Software Development Engineer I	['aws', 'azure', 'gcp', 'java', 'python']	['5', '2']	['"phd']", "'bachelor\'s"', "['bachelor'", "'master'"]
Software Developer	['java', 'python', 'sql']	['4']	['["bachelor\'s"]']
Software Engineer	['angular', 'java', 'leadership', 'python', 'sql']	[]	['"master\'s"]', "['bachelor'", "'master'"]

Figure 5. Merged job dataset ("merged_jobs.csv") compiled from LinkedIn and Indeed.

Step 2: Feature engineering and matching

Flow of combining feature matrix

The bot uses two modules, exact_match() for direct matches and fuzzy_match() techniques to match resumes with job descriptions, scraped from LinkedIn and Indeed. fuzzy_match() employs an AI-based Levenshtein distance to suggest approximate matches (e.g., "ML" vs. "Machine Learning"). It evaluates and differentiates between candidate's education, skills and experience with job requirements and returns true if a match is found.

MultiLabelBinarizer

MultiLabelBinarizer (MLB) is employed to transform skills, education, and experience levels by converting multiple fields into binary matrices. MultiLabelBinarizer is used when a single column contains multiple values (e.g., a candidate having multiple skills). Each unique skills (we are accessing the resumes for 33 skills) becomes a separate column with 1 or 0 (1 = candidate has the skill, 0 = candidate doesn't have the skill). It converts experience levels (entry-level, mid-level, senior-level) into a binary matrix (0, 1). The same process applies to encode education as depicted in Figure 6.

Term frequency (TF) - Inverse document frequency (TF-IDF)

TF measures how frequently a term appears in a document. For ex: If "python" appears 5 times in a document containing 100 words. Then the TF will be TF=5/100=0.5. IDF measures how unique a term is across all documents. For ex: If "python" appears in 10 out of 1000 times in a document containing 100 words. Then the IDF = log (1000 / 10) = log (100) ≈ 2.

Step 3: Dataset splitting and model training

Dataset splitting

To split the dataset into training and testingsets, the bot used Stratified K-Fold cross –validation. It ensures that each fold has the same proportion of class labels as the original dataset [39]. Stratified K-Fold cross validation splits the

filename	skills	experience_level	education	match	agile	angular	aws	azure	c	c#
aaayush.pdf	['c', 'django', 'leadership', 'node js', 'node.js', 'r', 'react', 'sql']	['entry-level']	['bachelor']	0	0	0	0	0	1	0
Aadesh Kumar.pdf	['java', 'leadership']	['entry-level']	['mca']	1	0	0	0	0	0	0
Aaditya Bhardwaj.pdf	['c', 'django', 'java', 'javascript', 'python']	['entry-level']	['bachelor']	0	0	0	0	0	1	0
Aditya Kumar.pdf	['aws', 'c', 'java', 'machine learning', 'python', 'sql']	['entry-level']	['Not specified']	0	0	0	1	0	1	0
Aakanksha.pdf	['communication skills']	['entry-level']	['Not specified']	0	0	0	0	0	0	0
aakash jayesh.pdf	['not specified']	['entry-level']	['Not specified']	0	0	0	0	0	0	0
Aakash Kumar bsc.pdf	['c', 'java', 'javascript', 'python', 'sql']	['entry-level']	['master']	0	0	0	0	0	1	0
Aakash Kumar.pdf	['not specified']	['mid-level']	['bachelor']	0	0	0	0	0	0	0
Aakash Sharma.pdf	['c', 'java', 'javascript', 'sql']	['entry-level']	['b.tech']	1	0	0	0	0	1	0

Figure 6. Encoding of experience, skills, and education attributes using MultiLabelBinarizer.

dataset into K equal folds, but preserves the original distribution of classes in each fold. The 2,006 resumes used in this study are split into 5 equal folds and each fold has the same class distribution. Logistic Regression (LR) is a supervised machine learning algorithm is perfect for classes with binary (0 or 1) values. The output of the trained LR classifier's and TF-IDF vectorizer's are saved in files named "logistic_regression.pkl" and "vectorizer.pkl" respectively for future predictions.

Step 4: Resume ranking & predictions

Prediction on new resumes

The trained model is used for prediction on new resumes. The pickle files "logistic_regression.pkl" and "vectorizer.pkl" are loaded. The CSV files containing parsed skills, experience level, education, and match labels (true labels) of 348 students is also loaded by the bot. After this, the pre-trained LR model predicts each resume for a match (1) or no match (0).

Skill gap analysis

This module determines missing and matching skills by assessing an applicant's abilities with a job description. The candidate's skills and the required job skills are represented by sets. Missing skills are calculated using the set difference (-). The set intersection (&) is used to find the common skills between the candidate and the job.

Ranking resumes

The calculate_scores() module evaluates each resume by computing a composite matching score derived from three primary metrics, skills, experience, and education**.** For skills, a 60% similarity threshold is applied, and only those matching or exceeding this threshold contribute positively to the score. The candidate's experience score is determined by calculating the ratio between the required job experience and candidate's experience, which is subsequently normalized to 1. A value of 1 is assigned to the education score, if the candidate's qualification exactly matches the job requirement; otherwise a value of 0 is assigned. A weighted scoring mechanism is used to rank resumes by assigning weights of 30% to experience, 50% to skills, and 20% to education. The resulting sum produces a ranking score, where 1 indicates a perfect match across all criteria. Finally, the scored results, along with missing and matched skills, are stored in the file "ranked_resumes.csv," as shown in Figure 7a.

Step 5: Selection, recommendations and feedbacks

The bot sends email notifications to candidates with a score of 1. The authenticate_gmail() module is used to obtain credentials for accessing the Gmail service. Further the bot fetches email Ids of candidates from "ranked_resumes.csv" and sends personalized selection emails via send_emails_to_selected_resumes() module. Filtered candidates with scores <1 in the "ranked_resumes.csv" file are fetched to give feedback on missing skills. The send_email_gmail() authenticates using OAuth2.0 using authenticate_gmail() .

RESULTS AND DISCUSSION

This "RPA Cognitive Placement Bot" automates traditional placement processes, making them faster, more objective, and more efficient. This Placement Bot completely automates the whole process of obtaining emails, processing resumes and job descriptions, screening each resume to find a selected candidate, and then sending emails to selected and rejected prospects, without human intervention. This AI-driven approach ensures that placement processes remain up-to-date, efficient, and equitable; promising a new alternative to traditional job placement strategies in higher education institutions.

Placement Bot's Training Model Evaluation

This Placement Bot is trained on 2006 resumes with 159 Job Descriptions. The LR classifier achieved 97.91% accuracy and the average precision, Recal and F1-Score is 0.98. The confusion matrix depicted in Figure 8 shows that True Positive (TP) =471, which means that 471 resumes were correctly classified as selected. True Negative (TN) =1493, means that 1493 resumes are correctly classified as rejected. False Positive (FP) =26 means 26 resumes were mistakenly classified as selected when they should have been rejected.

candidate_id	missing_skills	matching_skills	experience_match	education_match	email	score
ANIMESH KUMAR DUBEY.pdf	{'sql', 'communication skills'}	{'java', 'c', 'python'}	TRUE	TRUE	animeshkdji@gmail.com	1
Akeel Ahmad.pdf	{'communication skills', 'python'}	{'sql', 'java', 'c'}	TRUE	TRUE	akeel.21m0141196@abes.ac.in	1
Ashruti Srivastava.pdf	{'communication skills'}	{'sql', 'java', 'c', 'python'}	TRUE	TRUE	ashrutisrivastava20@gmail.com	1
Divyanshu Varshney.pdf	{'communication skills'}	{'sql', 'java', 'c', 'python'}	TRUE	TRUE	dbyan8859@gmail.com	1
Vikash Singh.pdf	{'communication skills'}	{'sql', 'java', 'c', 'python'}	TRUE	TRUE	sahilsingh11012002@gmail.com	1
Harshit kumar.pdf	{'communication skills'}	{'sql', 'java', 'c', 'python'}	TRUE	TRUE	harshitlucky11@gmail.com	1
Saurabh Saroha.pdf	{'java', 'communication skills'}	{'sql', 'c', 'python'}	TRUE	TRUE	saurabh.22m0141056@abes.ac.in	1
Akshay Kumar Resume.pdf	{'communication skills'}	{'sql', 'java', 'c', 'python'}	TRUE	TRUE	akshaykumar.uk18@gmail.com	1

Figure 7. Output of the resume ranking module stored as "ranked_resumes.csv" file.

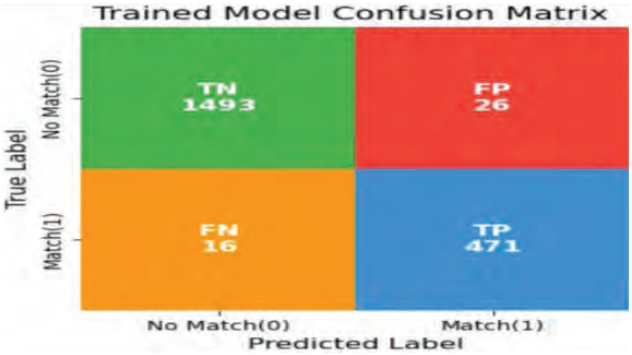


Figure 8. Confusion matrix showing the performance of the prained logistic regression classifier.

False Negative (FN) =16 means 16 resumes were mistakenly classified as rejected when they should have been selected.

A comprehensive comparison is conducted among ML classifiers using Bidirectional Encoder Representations from Transformers (BERT) embedding's to identify the most effective model for Job-Resume matching. BERT substantially extends matching accuracy by acquiring contextual semantics, understanding how education, experience, and skills fit together within context. Specifically, the semantic embeddings for resume and job description texts are extracted using the'bert-base-nli-mean-tokens' model from the SBERT family. Each resume and job description is represented through a structed integration of skills, experience, and education. The preprocessed text is subsequently passed through the SBERT model, which generates a 768-dimensional dense vector representations , denoted by 'x_bert', for each resume.

The variable x_bert is used as the input feature set for Machine Learning Models such as Logistic Regression and Support Vector Machine (SVM). In the resume classification process, match = 1 **indicates** that the resume is predicted as selected, whereas a match = 0 indicates that the resumes is predicted to be rejected. When a new resume is provided, the model predicts candidate selection or rejection based on its representation in the BERT embedding space.

The SBERT-derived x_bert embeddings are assessed using various Machine Learning models, including Logistic Regression (LR), Random Forest, K-Nearest Neighbors (KNN), Support Vector Machine (SVM), Gradient Boosting (XGBoost), and Naïve Bayes (NB). Among these models, LR achieved the highest F1 score of 0.9881, as shown in Table 2 and Figure 9. The tree-based Random Forest, distance-based KNN and NB models achieved comparatively lower F1-Scores. Whereas SVM and XGBoost achieved F1 scores above **0.95.** These results indicate that **linear classifiers** achieve higher accuracy, when integrated with BERT-based semantic features for job–resume matching systems.

Figure 9 presents a comparison of evaluation metrics such as Accuracy**,** Precision**,** Recall, and F1-Score across multiple ML classifiers applied to the job resume matching problem using SBERT embeddings.

Table 2. Performance comparison of ML Models using SBERT

Model Configuration	Accuracy	Precision	Recall	F1-Score
Logistic Regression	0.9880	0.9884	0.9880	0.9881
Support Vector Machine (SVM)	0.9566	0.9624	0.9566	0.9577
XGBoost	0.9551	0.9555	0.9551	0.9552
Random Forest	0.9382	0.9388	0.9382	0.9363
KNN	0.8579	0.8551	0.8579	0.8556
Naïve Bayes	0.7333	0.8499	0.7333	0.7521

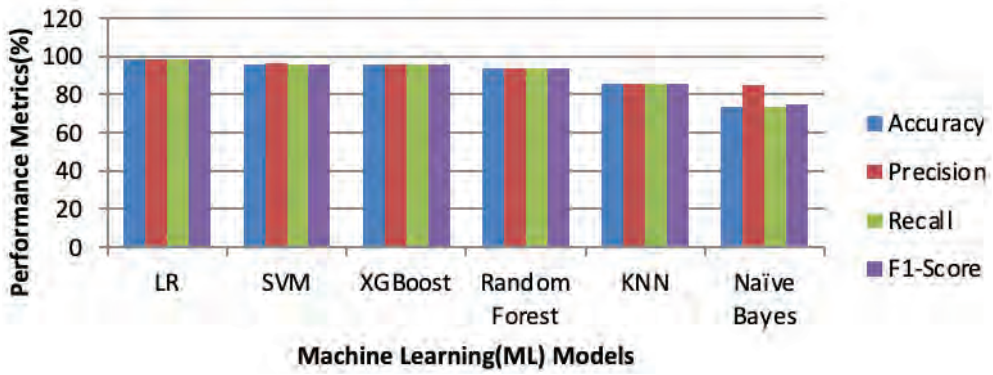


Figure 9. Comparison of evaluation metrics for ML models using SBERT.

Placement Bot's Testing Model Evaluation

The Placement Bot was tested on 348 resumes using a Logistic Regression classifier, achieving high classification performance. Table 3 summarizes the values of all evaluation metrics.

The confusion matrix in Figure 10 (a) illustrates the classification outcomes in detail.The precision-recall trade-off shown in Figure 6(b) highlights the balance between false positives(FP) and false negatives(FN), with an accuracy of 0.99, recall of 0.97, and F1-score of 0.98. Figure 10 (b) presents the confusion matrix results, where True Positive (TP) = 66, indicate that 66 resumes were correctly classified as selected, while True Negative (TN) =279 shows that 279 resumes were properly predicted as rejected. False Positive (FP) =1 represents one resume incorrectly predicted as selected instead of rejected, whereas False Negative (FN) =2 indicate two resumes that were incorrectly rejected despite being relevant.

Table 3. Evaluation metrics

Metrics	Values
Accuracy	99.14%
Recall	0.97
Precision	0.99
F1-Score	0.98

Recommendations and Feedback

The Placement Bot not only automates the resume-matching process, but also sends personalised feedback letters to rejected candidates that highlight their skill gaps. Selected candidates will be sent automated congratulatory emails. Automated emails (rather than handwritten comments) ensure that all applicants receive a timely response and thereby reducing ambiguity and enhancing the overall candidate experience. The bot helps candidates to identify missing skills and competencies so that they can improve their resume profiles and be better prepared for future resume submissions and job applications. Figure 11 depicts the selection emails sent to the candidates, who achieved a matching score of 1. Figure 12 shows the rejection and recommendation emails sent to the candidates who were not selected due to obtaining a matching score of below 1.

The automated Placement Bot changes the way manual processes performed by placement officers in Higher Education Institutions (HEIs). The proposed Placement Bot mimics human-like intelligence and exhibits cognitve capabilities such as strategic thinking, pattern recognition, learning, evaluation, and communication, thereby enhancing the way conventional automation tools work. The current study offers precision and objectivity by bridging the gap between automated and human-like placement processes. To understand the practical relevance of the automated placement bot, a dataset comprising final-year students of ABES Engineering College, Ghaziabad, India was used. Although the dataset did not include resumes of all the final year students, currently seeking placement assistance, the preliminary study verified the reliable performance of the bot under current HEI conditions and extends its viability in automated placement assistance. Consent to use their personal information such as name, email, experience and skill set was obtained from all participating students during the study. The prototype system retrieved such personal information solely for illustration and testing purposes. However, if the bot is deployed in a real-world environment, the system must acquire proper explicit user consent for resume processing and communication activities. Throughout the study, personal information was handled ethically and strict measures were implemented to ensure data safeguarding.

Furthermore, no information apart from students' personal details, such as phone numbers, email, skills, experience, education and gender was used. Resumes in non-conventional formats, such as screenshots, scanned PDFs, and PDFs converted to Word documents, introduce inconsistencies during NLP processing and are comparatively more challenging for the automated processing.



Figure 10 (a). Confusion matrix of the prediction model.

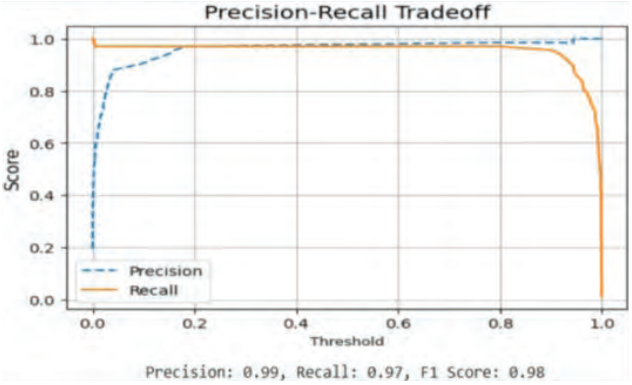


Figure 10 (b). Precision-recall trade-off.

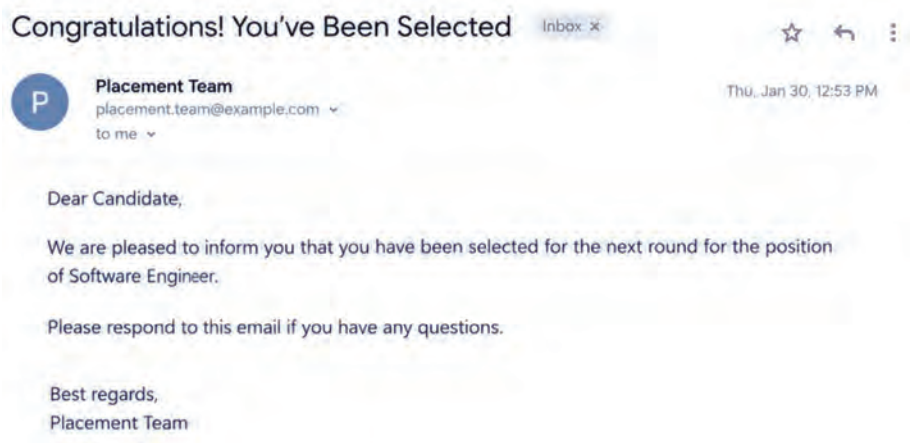


Figure 11. Selection email sent to Khadija Razvi.



Figure 12. Feedback email sent to Sahil Kapil with missing skills.

Text-based resumes allow smooth processing, whereas resumes contaning graphical elements such as icons, images, signature, tables often hinder NLP parsing, potentially leading to inaccurate information extraction. In such cases, there is a chance of inaccurate extraction of skills, education, or experience, which further affects ML model training and testing. Aditionally, the use of Optical Character Recognition (OCR) for unstructured resumes (resumes with screenshots and scanned PDFs or graphical elements) can further reduce parsing accuracy, as it introduces extra noise into the extracted text. These limitations can cause the rejection of candidates who do not follow the standard resume format. Apart from the test dataset consisting of only 348 resumes, the performance metrics obtained from the ML models, particularly the BERT-based models are encouraging. However, the limited sample size may not represent real-world resume patterns. Therefore, further validations of the trained model using larger and more heterogeneous dataset is required to ensure the generalizability of the proposed system. On average, the bot requires approximately 0.5–0.7 seconds to for end-to-end automation, whereas BERT-based models require approximately 1.2–1.5 seconds per resume.

Cognitive aspect of RPA placement bot

The Placement Bot uses intelligent RPA and emulates human-like intelligence in classification, pattern recognition, strategic thingking and decision-making. These features provide the bot with an edge over other conventional manual approaches. This intelligent bot enables the system to learn, reason, adapt, and provide meaningful insights to candidates and recruiters.

a. The bot mimics the end-to-end placement activities typically performed by human recruiters, including assessing resumes and providing job opportunities and sending career-related recommendations. It employs a weighted scoring mechanism that allocates 50% weight to skills, 30% to experience, and 20% to education. Based on these

scores the bot assesses resumes, makes decisions and rank candidates according to their weighted scores.

b. The bot sends recommendation emails based on candidate rankings, explaining why a particular candidate has been selected or rejected. Based on the candidates' scores, it sends personalized selection or rejection emails. It mimics a human recruiter by providing feedback in a logical and efficient manner. Moreover it informs candidates about their skill gaps, which can support their future career development and enhance their employability.

c. The bot acts dynamically by retrieving current jobs opportunities through the continuous updating of job descriptions and resume datasets. It also supports recruiters by utilizing information from real-time job market platforms such as LinkedIn and Indeed, to provide more accurate and relevant recommendations.

CONCLUSION

This study proposes an RPA-based intelligent Placement Bot designed to automate placement-related activities traditionally carried out by placement officers in Higher Education Institutions (HEIs). The system integrates technologies such as Selenium-based AI web scraping, spaCy's Named Entity Recognition (NER), Python RPA frameworks, and machine learning models to construct an automated placement pipeline. The dataset comprises 159 job descriptions scraped from LinkedIn and Indeed, with 2,006 resumes used for training and 348 samples reserved for testing. The developed bot attained an overall accuracy of 99.14%, with precision and recall values of 0.99 and 0.97, respectively. Its performance outperformed the previous reported approaches based on LDA (82%), SVM (94%) and decision tree (94%) . The results indicate that the proposed system has the potential to standardize the placement process and improve the accuracy of job-resume matching in Higher Education Institutions (HEIs).

The proposed RPA-based virtual bot has some limitations that may affect its overall performance and applicability. Variations in resume structure, formatting and quality affect the accuracy of information extraction. Infographic style resumes and image-based PDF documents are particularly challenging to conventional text-based extraction approaches. In addition, resumes that are sent as scanned images or screenshots have to be processed through Optical Character Recognition (OCR) that can cause recognition errors because of low image resolution, inconsistent font styles and complex document layouts. The dependencies on OCR can also lead to inconsistencies in parsing, particularly with non-standard fonts or degraded input quality. The current study is evaluated on a dataset of 2,006 resumes with 348 test samples. However, large scale deployment in Higher Education Institution (HEI) environments would require further considerations such as infrastructure optimization, distributed processing architectures and batch-parallel processing strategies to ensure efficiency, scalability, and robustness.

Ethical considerations were strictly followed throughout the study. Explicit consent was obtained from all participating students before collecting their resumes for this institutional pilot study. No personal information was shared os dissemincated across any platforms, ensuring privacy and confidentiality of all participants. In addition, the system fetches job descriptions from third-party platforms such as LinkedIn and Indeed. Consequently, the bot's workflow may be disrupted by changes in the user interfaces, API's or underlying website structures of these platforms. Such dynamic changes require continuous maintenance and regular software updates to ensure system reliability. Although the proposed placement bot does not directly employs an Explainable Artificial Intelligence (XAI) framework, its architecture includes inherently interpretable components such as skill–experience–education-based scoring and rule-based feature extraction mechanisms. Future work may involve the integration of XAI techniques such as SHAP and LIME to enhance interpretability, transparency, explainibility.

AUTHORSHIP CONTRIBUTIONS

Authors equally contributed to this work.

DATA AVAILABILITY STATEMENT

The authors confirm that the data that supports the findings of this study are available within the article. Raw data that support the finding of this study are available from the corresponding author, upon reasonable request.

CONFLICT OF INTEREST

The author declared no potential conflicts of interest with respect to the research, authorship, and/or publication of this article.

ETHICS

There are no ethical issues with the publication of this manuscript.

STATEMENT ON THE USE OF ARTIFICIAL INTELLIGENCE

Artificial intelligence was not used in the preparation of the article.

REFERENCES

[1] Andrade D. Challenges of automated software testing with robotic process automation RPA - a comparative analysis of UiPath and Automation Anywhere. Int J Intell Comput Res 2020;11:1066–1072. [CrossRef]

[2] Syed R, Suriadi S, Adams M, Bandara W, Leemans SJJ, Hofstede AHM, et al. Robotic process automation: contemporary themes and challenges. Comput Ind 2020;115:103162. [CrossRef]
[3] Siderska J, Aini SNBM, Kedziora D. Complementing robotic process automation with generative artificial intelligence (ChatGPT), case of Robocorp. In: Arai K, editor. Advances in Information and Communication. Cham: Springer Nature Switzerland; 2024. p. 37–53. [CrossRef]
[4] Khan S, Tailor RK, Uygun H, Gujrati R. Application of robotic process automation (RPA) for supply chain management, smart transportation and logistics. IJHS. 2022. p. 11051–11063. [CrossRef]
[5] van der Aalst WMP, Bichler M, Heinzl A. Robotic process automation. Bus Inf Syst Eng 2018;60:269–272. [CrossRef]
[6] Khan S. Comparative analysis of RPA tools-Uipath, Automation Anywhere and BluePrism. Int J Comput Sci Mobile Appl 2020;8:1–6. [CrossRef]
[7] Patrício L, et al. Literature review of decision models for the sustainable implementation of robotic process automation. Procedia Comput Sci 2023;219:870–878. [CrossRef]
[8] Desai D, Jain A, Naik D, Panchal N, Sawant D. Invoice processing using RPA & AI. SSRN J Preprint. 2021. Doi: 10.2139/ssrn.3852575. [CrossRef]
[9] Exploring heart diseases survival patterns: a multifaceted approach using survival analysis techniques on time to event data. Sigma J Eng Nat Sci 2025;43:1307–1320. [CrossRef]
[10] Nagrale P. Indoor-outdoor scene recognition: a multi-feature framework using CNN for complex environment. Sigma J Eng Nat Sci 2025;43:1355–1365. [CrossRef]
[11] Otundo Richard M. Robotic process automation (RPA) and AI: an empirical analysis. SSRN Electron J 2024. Preprint. doi: 10.2139/ssrn.4908263. [CrossRef]
[12] Chakraborti T, et al. From robotic process automation to intelligent process automation: emerging trends. In: Asatiani A, García JM, Helander N, Jiménez-Ramírez A, Koschmider A, Mendling J, Meroni G, Reijers HA, editors. Business Process Management: Blockchain and Robotic Process Automation Forum. Cham: Springer International Publishing; 2020. p. 215–228.
[13] Dolui C, Roy D. Advancement of bridge health monitoring using magnetostrictive sensor with machine learning techniques. Nondestruct Test Eval 2025;40:4219–4240. [CrossRef]
[14] Kholiya PS, Kapoor A, Rana M, Bhushan M. Intelligent process automation: the future of digital transformation. In: 2021 10th International Conference on System Modeling & Advancement in Research Trends (SMART); 2021 Dec; Moradabad, India. IEEE; 2021. p. 185–190. [CrossRef]
[15] Jalonen H. Assessing robotic process automation potential (master's thesis). Tampere: Tampere University of Technology; 2017.
[16] Jeeva Padmini KV, Perera GIUS, Bandara HMND, Silva RKOH. A decision support tool to select candidate business processes in robotic process automation (RPA): an empirical study. In: Smys S, Balas VE, Kamel KA, Lafata P, editors. Inventive Computation and Information Technologies. Singapore: Springer Nature Singapore; 2021. p. 567–582. [CrossRef]
[17] Santos F, Pereira R, Vasconcelos JB. Toward robotic process automation implementation: an end-to-end perspective. Business Process Manag J 2019;26:405–420. [CrossRef]
[18] Wanner J, Hofmann A, Fischer M, Imgrund F, Janiesch C, Geyer-Klingeberg J. Process selection in RPA projects - towards a quantifiable method of decision making. In: 40th International Conference on Information Systems (ICIS); 2019 Nov; Munich, Germany.
[19] Agaton B, Swedberg G. Evaluating and developing methods to assess business process suitability for robotic process automation - a design research approach [master's thesis]. Gothenburg: Chalmers University of Technology, Department of Computer Science and Engineering; 2019.
[20] Khan S, Tailor RK, Pareek R, Gujrati R, Uygun H. Application of robotic process automation in education sector. J Inf Optim Sci 2022;43:1815–1834. [CrossRef]
[21] Turcu CE, Turcu CO. Digital transformation of human resource processes in small and medium sized enterprises using robotic process automation. Int J Adv Comput Sci Appl 2021;12:10. [CrossRef]
[22] Somasundaram M, Sumitra V, Vardan RSPV, Sakthipriya B, Pavithra K, Nivedha MK. Monitoring and facilitating students programming skill development using robotic process automation (RPA) and artificial intelligence (AI)-a case study. In: 2022 Fourth International Conference on Emerging Research in Electronics, Computer Science and Technology (ICERECT); 2022. p. 1–6. [CrossRef]
[23] Gajra V, Lakdawala K, Bhanushali R, Patil S. Automating student management system using ChatBot and RPA technology. SSRN Electron J 2020. [CrossRef]
[24] Boban D, Nakić J. Enhancing informal education with robotic process automation: a method for automating course search on e-learning platforms. J Commun Softw Syst 2024;20:215–225. [CrossRef]
[25] Nandwani T, Sharma M, Verma T. Robotic process automation - automation of data entry for student information in university portal. SSRN J 2021. Preprint. doi: 10.48175/IJARSCT-4004. [CrossRef]
[26] Ding T, Liu Y, Wang S. Dual-branch mutual learning framework for job-resume matching. Int J Pattern Recogn Artif Intell 2025;40:1. [CrossRef]

[27] Hawari AR, Munawir M, Zulfan Z, Satria DSD, Susmanto S. Job recommendation system using the content-based filtering method. Proceeding 2022;5:138–140. [CrossRef]

[28] Mydyti H, Ware A. Integrating intelligent web scraping techniques in internship management systems: enhancing internship matching. Ann Emerg Technol Comput 2025;9. [CrossRef]

[29] Suman H, Tamkiya H, Kushwa AS. Candidate background verification using machine learning and fuzzy matching. Int J Emerg Technol Innov Res 2020;7:1643–1647.

[30] Rojas-Galeano S, Posada J, Ordoñez E. A bibliometric perspective on AI research for job-résumé matching. ScientificWorldJournal 2022;2022:1–15. [CrossRef]

[31] Lin Y, Lei H, Addo PC, Li X. Machine learned resume-job matching solution. arXiv. 2016. Preprint. doi: 10.48550/arXiv.1607.07657.

[32] Lunn S, Zhu J, Ross M. Utilizing web scraping and natural language processing to better inform pedagogical practice. In: 2020 IEEE Frontiers in Education Conference (FIE); 2020 Oct; Uppsala, Sweden. IEEE; 2020. p. 1–9. [CrossRef]

[33] Jirjees AK, Ahmed AM, Abdullah AA, Lu J, Noori EM, Karem R, et al. Machine learning for recruitment: analyzing job-matching algorithms. TechRxiv 2025. Preprint. doi: 10.36227/techrxiv.174240031.12397312/v1. [CrossRef]

[34] Jagwani V, Meghani S, Pai K, Dhage S. Resume evaluation through latent Dirichlet allocation and natural language processing for effective candidate selection. arXiv. 2023. Preprint. doi: 10.48550/arXiv.2307.15752.

[35] Mariappan P, Krishna K, Sahoo J, Preetham S. Smart resume screening and job represents recommendation system. SSRN J 2025. Preprint. doi: 10.2139/ssrn.5141402. [CrossRef]

[36] Dolui C, Devi SF, Dasadhikari S, Roy D. Magnetostrictive sensor based bridge health assessment using machine learning classifiers. In: 2023 IEEE Pune Section International Conference (PuneCon); 2023 Dec; Pune, India. IEEE; 2023. p. 1–6. [CrossRef]

[37] Chawrasia SK, Hembram D, Bose D, Chanda CK. Design of solar battery swapping station for EV using LSTM-assisted solar power forecasting. Microsyst Technol 2024;30:1087–1098. [CrossRef]

[38] Thakur S, Jha R, Dalawat M, Jha P, Khandare A. Scraping data from Google Maps: comparisons and experimentations. In: Ghinea G, Semwal VB, Khandare A, editors. Intelligent Computing and Networking. Singapore: Springer Nature Singapore; 2025. p. 237–259. [CrossRef]

[39] Ünalan S, Günay O, Akkurt I, Gunoglu K, Tekin HO. A comparative study on breast cancer classification with stratified shuffle split and K-fold cross validation via ensembled machine learning. J Radiat Res Appl Sci 2024;17:101080. [CrossRef]

Sigma J Eng Nat Sci, Vol. 44, No. 4, pp. 2447–2457, August, 2026

Sigma Journal of Engineering and Natural Sciences
Web page info: https://sigma.yildiz.edu.tr
DOI: 10.14744/sigma.2026.2108

Research Article

Gaussian mixture model and K-means based spatial interval valued intuitionistic fuzzy C-means clustering incorporating the D_α operator for MRI image segmentation

Manivasagan M.[1], **Jagatheswari S.**[1,*]

[1]*Department of Mathematics, Vellore Institute of Technology, Tamil Nadu, 632014, India*

ARTICLE INFO

Article history
Received: 25 October 2024
Revised: 19 February 2025
Accepted: 26 May 2025

Keywords:
Brain MRI image; D_α Operator; Gaussian Mixture Model; Interval Valued Intuitionistic Fuzzy Set; K-means; Segmentation

ABSTRACT

In medical image analysis, brain magnetic resonance image segmentation is still a difficult task. Therefore, it is crucial to provide an efficient method for identifying neurological illnesses and organising their therapies. In this work, we provide an approach to improve the segmentation of MRI images. To eliminate skull artefacts, morphological operators are first used for preprocessing. The first cluster centroids are then found by combining the Gaussian Mixture Model with K-means clustering. For better segmentation, we further integrate this with our Spatial Interval-Valued Intuitionistic Fuzzy C-Means clustering approach by adding the D_α operator. This method effectively handles geographical information and uncertainty, improving segmentation performance. Existing approaches, including interval-valued intuitionistic fuzzy C-means clustering algorithm is contrasted with the suggested approach. Results from experiments show that our hybrid approach improves segmentation results. The quantitative measures, the dice coefficient and Jaccard similarity, which are displayed in tables, attest to the fact that this method solves segmentation issues. and yields more trustworthy outcomes for clinical applications, making it a useful tool for medical diagnostics.

Cite this article as: Manivasagan M, Jagatheswari S. Gaussian mixture model and K-means based spatial interval valued intuitionistic fuzzy C-means clustering incorporating the D_α operator for MRI image segmentation. Sigma J Eng Nat Sci 2026;44(4):2447–2457.

INTRODUCTION

Since magnetic resonance imaging (MRI) has great contrast distinction of soft tissues and high resolution, as noted by Mishra PK et al., it is a cornerstone of medical diagnosis, especially for brain imaging Brain MRI image segmentation plays a critical role in the diagnosis and follow-up of neurological diseases, including multiple sclerosis, tumours, and other brain disorders [1]. According to Verma et al. [2], segmentation of MRI images facilitates reliable diagnosis and treatment planning by identifying and isolating distinct tissue structures and regions affected by abnormalities.

To keep computational costs low, standard algorithms like Gaussian Mixture Models (GMM) and K-means clustering are frequently chosen for data segmentation. According to Lin et al. [3], K-means achieves this

*Corresponding author.
*E-mail address: jaga.sripa@gmail.com

This paper was recommended for publication in revised form by Editor-in-Chief Ahmet Selim Dalkilic

Published by Yıldız Technical University Press, İstanbul, Turkey
© Author. This is an open access article under the CC BY-NC license (http://creativecommons.org/licenses/by-nc/4.0/).

partitioning by reducing the internal variance of K separate clusters, whereas GMM adopts a more flexible strategy by fitting the dataset across several Gaussian distributions. Nevertheless, when applied to MRI scans, these classical models often fail to yield clean results due to artifact-related issues like image noise and intensity non-uniformity.

To address these challenges, fuzzy clustering techniques have been introduced to provide greater flexibility in data classification by allowing individual data points to belong to more than one cluster to varying degrees. Among these techniques, the Fuzzy C-means (FCM) algorithm provides a flexible approach to image segmentation by assigning a membership value to each data point with respect to each cluster. Building on the FCM framework, Kala R et al. [4] proposed the Spatial Intuitionistic Fuzzy C-means (SIFCM) algorithm, which incorporates a hesitation degree to represent the uncertainty associated with cluster membership more effectively. This additional consideration is particularly beneficial for medical image segmentation, where the boundaries between different regions are often indistinct.

Conventional FCM can be affected by the choice of initial parameters and may produce unsatisfactory results when the input images contain considerable noise. To address these issues, Kaushal et al. and Wei et al. [5, 6] proposed an Intuitionistic Fuzzy C-Means (IFCM) clustering method incorporating local information. The method adjusts the contribution of local image information during clustering, thereby improving the robustness of the fuzzy partition in the presence of noise. In another study, Dubey et al. [7] employed a rough set-based strategy for selecting the initial cluster centres and relevant parameters. The experimental results indicated that the proposed parameter-selection scheme achieved improved segmentation results compared with other optimization approaches.

Ji et al. and Li et al. [8, 9] introduced a clustering strategy that concurrently maximizes the likelihood function and minimizes the covariance across Gaussian Mixture Model (GMM) components. This method was subsequently integrated into a Particle Filter GMM (PFGMM) framework and benchmarked against standard baselines, including PFGMM paired with Expectation-Maximization (EM) and PFGMM with K-means. Although the proposed approach enhanced particle filter tracking accuracy, its generalizability remains restricted to specific data types, and the authors omitted a detailed computational complexity analysis.

Tiwari et al. [10] have devised a fuzzy c-means clustering algorithm that integrates entropy and is weighted by uncertainty parameters to improve the segmentation of noisy 3D brain MRI data. Ray et al. [7] introduced an approach that effectively captures spatial uncertainty by incorporating Shannon entropy alongside both globally and geographically constrained local membership functions. By directly addressing issues related to noise and intensity inhomogeneity, their technique delivers improved segmentation accuracy over traditional algorithms.

Ji Z et al. and Arora J et al. [11,12] have stated that "by considering the geographic context of each pixel and thus mitigating the effects of noise and enhancing the coherence of segmented regions, the incorporation of spatial information into clustering algorithms further improves segmentation accuracy". To better manage uncertainties and spatial dependencies in medical pictures, sophisticated techniques have been developed, such as Spatial Interval-Valued Intuitionistic Fuzzy C-Means (SIVIFCM), which integrates interval-valued intuitionistic fuzzy sets.

Ahmed et al. [13] reported that the selection of suitable initial cluster centres can have a significant effect on clustering performance. In conventional approaches, the cluster centres are generally initialized randomly, which can lead to poor segmentation and inconsistent results. Similar approaches for addressing the initialization of cluster centres have also been reported by Patel et al. and Vivoli et al. [14, 15]. Dhal KG et al. [25] stated that "rough set-based clustering was also used to predict the cluster centre of a picture, but noise and intensity inhomogeneity prevented this prediction from being successful". By employing GMM and K-means for initial cluster centre identification, it gives the clustering process a more dependable and accurate starting point, improving the total segmentation quality. The proposed approach takes advantage of the ability of GMM to model data distributions while utilizing the fast convergence of K-means for determining suitable cluster centres. Owing to its simplicity and computational speed, K-means is widely applied in both academic research and practical applications. However, the use of the distance from Euclid as a similarity measure hinders its inability to understand complex non-linear use structures. A GMM is a potent dynamical and probabilistic clustering method.

Jagatheswari S et al. [16]: The Dα operator is an additional novel element incorporated into our approach. By altering the distance measure, this operator improves the ability of fuzzy clustering algorithms to distinguish between similar but different tissue types. With the Dα operator included in the SIVIFCM algorithm, our method can effectively handle the intricacies and uncertainties present in MRI pictures.

The intended approach is to greatly improve MRI brain image segmentation by combining GMM, K-means, and SIVIFCM with the Dα operator. The objective of this research is to enhance the diagnosis and treatment planning procedures for neurological disorders by offering a more reliable and precise tool for defining various tissue types and diseased locations. A more dependable solution to the segmentation problems in brain MRI images is provided by the combination of these cutting-edge techniques, which solve the shortcomings of conventional approaches.

The article has the following structure. Section 2 presents early notions. The suggested SIVIFCM clustering technique using GMM and K-Means for MRI image segmentation is further described in Section 3. The findings of bran MRI segmentation are shown in section 4, along with

a comparison of the suggested approach with the IVIFCM approach. We finally included the closing thoughts and upcoming work in section 5.

PRELIMINARY CONCEPTS

Gaussian Mixture Model

A continuous probability distribution known as the Gaussian distribution (GD), or normal distribution, is provided

$$R(Y \mid \mu, \sum) = \frac{1}{(2\pi)^{\frac{D}{2}}\sqrt{|\sum|}} \exp\left(-\frac{(Y-\mu)^T \sum^{-1}(Y-\mu)}{2}\right) \quad (1)$$

where μ is a D-dimensional mean vector, Σ is a D×D covariance matrix, which describes the shape of the Gaussian and $\sqrt{|\Sigma|}$ denotes the determinant of Σ.

The mean as well as the standard deviation together characterise the GD, which is harmonious about the mean. But the unimodal characteristic associated with a single distribution of Gaussian shapes cannot learn the varied resource use behaviour of Cloud workloads because it cannot represent the numerous density zones within a multimodal collection of information encountered in real-world scenarios [3]. A combination of Gaussian distributions can be a suitable model for complex, multimodal phenomena.

An ellipsoidal-shaped cluster is formed via an unsupervised clustering approach called a GMM, which uses the EM to estimate probability densities. The model for each cluster is a Gaussian distribution. GMMs can offer a more accurate numerical evaluation of adaptation per number of clusters since they consider both the mean and the covariance, as opposed to merely the mean as in K-Means (KM) [13].

A GMM may be written as a linear amalgam of the fundamental Gaussian distribution of chances.

$$P(Y) = \sum_{k=1}^{K} \pi_k \, R(Y|\mu, \sum_k) \quad (2)$$

where π_k, the mixing coefficient, provides a rough indication of the apparent density of each Gaussian portion and K are the total quantity of components in the combination model. The Gaussian density given by N (X | μ, Σ_k), is called a component of the mixture model. Each component k is described by a Gaussian distribution with mean π_k, covariance Σ_k and the mixing coefficient π_k.

Maximum likelihood (ML) for the GMM

The log likelihood function for a mixture of Gaussian, given a set of R autonomous and equally distributed observations $y_1, y_2, \ldots, y_R$, is given by

$$lnP(Y|\pi, \mu, \sum) = \sum_{n=1}^{R} \ln\{\sum_{k=1}^{K} \pi_k \, N(y_n|\mu, \sum)\} \quad (3)$$

Because the likelihood function is the product of several tiny probabilities, it prevents numerical underflow [14].

Algorithm for expectation-maximization (EM) in GMM

The EM method is used to find the ML predictions of variables in probabilistic formulations of GMM. The chance of maximising the two parameters variance and mean is what determines the GMM. Thus, the EM technique is used to estimate the parameters. The number of means, classes, mixing coefficients, and variance were all initialised at the beginning. Utilising the current parameter values, calculate the posterior probabilities in the expectation step [14, 34],

$$\gamma_k(y_n) = \frac{\pi_k G(y_n|\mu_k, \sigma_k)}{\sum_{l=1}^{n} \pi_l G(y_n|\mu_k, \sigma_k)} \quad (4)$$

where G is the model of a Gaussian mixture. Using the given inferred probabilities, the following equations are used, accordingly, to determine parameters like mean (π_m), variance (σ_m), and mixing coefficient (π_m) in the optimisation stage.

$$\mu_k{}^{new} = \mu_l = \frac{\sum_{j=1}^{n} \gamma_k(y_j)(y_j)}{\sum_{j=1}^{n} \gamma_k(y_j)} \quad (5)$$

$$\pi_k{}^{new} = \pi_l = \frac{1}{n} \sum_{j=1}^{n} \gamma_k(y_n) \quad (6)$$

$$\sigma_k{}^{new} = \sigma_l = \frac{\sum_{j=1}^{n} \gamma_k(y_n)(y_n - y_l)(y_n - y_l)^T}{\sum_{j=1}^{n} \gamma_k(y_n)} \quad (7)$$

K-means Clustering

K-means clustering divides data into groups known as clusters, which reflect data with related features, based on the attributes of a given collection of data points. A dataset is partitioned using the KM clustering technique into K unique, non-overlapping groups [15]. The objective is to reduce the variance within every cluster, which may be expressed as a reduction of the total squared distances between each cluster centroid and the data points. For continuous data, each cluster is represented by the centroid which is the means of cluster members. Medoid, which is the object that appears the most frequently, is utilised as the grouping pattern for data that is categorical. In the given dataset $X = \{y_1, y_2, \ldots y_n\}$, where a d-dimensional data point y_i belongs to R^d.

The objective function of the K-means algorithm is to decrease the sum of squared distances between each point and its designated centroid [34].

$$J = \sum_{j=1}^{K} \sum_{i=1}^{n} r_{ij} \, ||y_j - c_j||^2 \quad (8)$$

$$where, \; r_{ij} = \begin{cases} 1 & if \; j = arg \; min_k \; ||x_i - c_k||^2 \\ 0 & otherwise \end{cases} \quad (9)$$

$$c_j = \frac{\sum_{i=1}^{n} r_{ij} x_i}{\sum_{i=1}^{n} r_{ij}} \quad (10)$$

D_α Operator

Let $\alpha \in [0,1]$. An operator D_α is a mapping D_α: $S_b([0,1]) \rightarrow [0,1]$ such that satisfies the following conditions [16]:

$$(1)\ If\ \underline{y} = \overline{y},\ then\ D_\alpha(y) = \underline{y}$$
$$(2)\ D_0(y) = \underline{y}.D_1(y) = \overline{y}\ for\ all\ y \in S_b([0,1])$$
$$(3)\ If\ y_1 \le y_2\ with\ y_1, y_2 \in S_b([0,1]), then\ D_\alpha(y_1) \le D_\alpha(y_2)$$
$$(4)\ D_\alpha([0,1]) = \alpha\ for\ any\ \alpha \in [0,1].$$

Construction spatial interval valued fuzzy sets using D_α operator

Assume that the familial set of all closed smaller intervals in [0,1] is $S_b([0,1])$. The definition of the mapping G: $[0,1] \times [0,1] \rightarrow S_b([0,1])$ is $G(\nu,\delta,\gamma) = \left[\underline{G}(\nu,\delta,\gamma),\ G(\nu,\delta,\gamma)\right]$,

Where, $\underline{G}(\nu,\delta,\gamma) = \nu \cdot (1 - \gamma \cdot \delta)$

$$\overline{G}(\nu,\delta,\gamma) = \nu \cdot (1 - \gamma \cdot \delta) + \gamma \cdot \delta$$

This implies that, $G(\nu, \delta, \gamma) = [\nu \cdot (1 - \gamma \cdot \delta), \nu \cdot (1 - \gamma \cdot \delta) + \gamma \cdot \delta]$

MATERIALS AND METHODS

This section outlines the overall process of the GMM & K-means based SIVIFCM method used to segment brain MR images.

Hybrid GMM–K-means Strategy for Cluster Centre Initialization

The initialization of cluster centres plays an important role in the convergence and overall performance of clustering algorithms used for image segmentation. In this work, a hybrid initialization strategy based on Gaussian Mixture Models (GMM) and K-means clustering is employed to obtain more appropriate initial cluster centres instead of selecting them randomly [32, 34]. Initially, GMM is applied to represent the image data using multiple Gaussian components, and the means of these components are considered as statistically informed initial centres. These means are subsequently provided to the K-means algorithm as its starting cluster centres. In this way, the probabilistic modelling capability of GMM is combined with the iterative refinement of K-means to improve the initial centres. Compared with conventional random initialization, the proposed strategy provides more stable cluster initialization, leading to improved clustering performance and faster convergence. Consequently, the approach contributes to more consistent and reliable segmentation results, particularly for image clustering applications [32, 38, 39].

Formulation of SIVIFS Image Representation Using the D_α operator

The interval-valued intuitionistic fuzzy generator (IVIFG) is utilized to transform the image into an interval-valued intuitionistic fuzzy representation. Picture segmentation in [4, 11, 21] makes use of interval valued intuitionistic fuzzy picture representation. The IVIFS representation of with levels of intensity varying from 0 to L − 1, a picture with size S * T pixels is [28, 29]

$$T = \{y_{ij}, [LS_F(y_{ij}), US_F(y_{ij})], [LT_F(y_{ij}), UT_F(y_{ij})]\},\quad 1 < i < S,\quad 1 < j < T. \tag{11}$$

The degrees of Lower interval value of membership, Upper interval value of membership, Lower interval value of non-membership, and the variables represent the upper interval value of Lack of membership of the $(i, j)^{th}$ picture element in the picture itself $LS_F(y_{ij})$, $US_F(y_{ij})$, $LT_F(y_{ij})$ and $UT_F(y_{ij})$, respectively.

To determine the membership value, an image is normalized (N_m) using the following techniques:

$$N_m(I(i,j)) = \frac{(i,j)_l - (i,j)_{min}}{(i,j)_{max} - (i,j)_{min}} \tag{12}$$

Whereas $(i, j)_{min}$ and $(i, j)_{max}$ indicate the greatest and lowest intensity values of image I, and $(i, j)_l$ represents the intensity value of $(i, j)^{th}$ pixel. Intensity levels between 0 and 1 are produced via normalization. Subsequently, we constructed membership degree values for a picture using the equivalency function limited as follows.

$$mF(I(i,j)) = 0.582\left(\exp\left(1 - \left|N_m(I(i,j)) - m_I\right|\right) - 1\right) \tag{13}$$

Where m_I denotes the mean intensity value of N_m(I).

The degree of lack of membership function is ascertained using the fuzzy complement function that follows[3]:

$$nmF(I(i,j)) = (I - mF(i,j)(\exp(\frac{-mF}{a\sigma}))^{\frac{1}{a}},\ a>0 \tag{14}$$

where a = 5 is used because to the symmetry of the intuitive fuzzy index between membership degree values, and sigma is the standard deviation value of an image with a range of 0.37 to 0.38. because it provides a stronger contrast between the cluster sections [7].

Lastly, the hesitation degree, often known as the fuzzy index, is determined as

$$Pi_F(I(i,j)) = 1 - mF(I(i,j)) - nmF(I(i,j)) \tag{15}$$

There is still some doubt as to whether the selected value is approximative in the intuitionistic fuzzy membership function, even if the value is assigned by decreasing hesitancy in assigning the constant value [22]. Therefore, selecting an assortment of values as opposed to a precise value is an option. IVIFS is used as a result to eliminate the ambiguity present in IFS. By establishing a mapping in the manner described below, IVIFS is built as in [21, 29, 30].

$$LmF = mF.\left(v.(1-\gamma_m.\delta_m)\right) - p.Pi_F$$

$$UmF = mF.(v.(1-\gamma_m.\delta_m) + \gamma_m.\delta_m) + \alpha.Pi_F$$

$$LnmF = nmF.\left(v.(1-\gamma_m.\delta_m)\right) - q.Pi_F$$

$$UnmF = mF.(v.(1-\gamma_m.\delta_m) + \gamma_m.\delta_m) + \beta.Pi_F$$

In addition, $0 \le \alpha + \beta \le 1$, $0 \le \alpha + p \le 1$ & $0 \le \beta + q \le 1$,

State $WmF = UmF - LmF = (\alpha + p).Pi_F$ $WnmF = UnmF - LnmF = (\beta + q).Pi_F$

where δ_m is the difference between the maximum and minimum values in the membership matrix and γ_m is $(1 - 2*\sigma)$ (σ are the membership matrix's standard deviation, which ranges between 0.35 and 0.37) [10, 12, 16, 30].

Spatial Interval Valued Intuitionistic Fuzzy C-Means Clustering

A drawback of FCM's objective function for image segmentation is that it ignores any spatial relationships between the pixels in the image. Second, the membership function of FCM is primarily defined by the measure of similarity $d(x_k,v_i)$ between n the cluster centre and the pixel intensity. Higher membership is determined by the values of cluster intensity relative to the cluster core. Noise thus has a significant impact on the membership function. Accurate segmentation occurs in MR images when the noise and intensity are not uniform, and FCM approaches perform less well in this regard [6,18,19]. We've used Euclidean distance and average distance (AD), as determined by interval valued intuitionistic fuzzy [35,37], are not the same. The goal of this adjustment is to improve the clustering process's output quality. This is supplied by in order to address these problems [12, 20, 30].

$$\begin{aligned} d_{SIVIF}(y_k, v_i) = \Bigg\{\frac{1}{n}\Big[&\big(LmF(y_k) - LmF(v_i)\big)^2 \\ &+ \big(UmF(y_k) - UmF(v_i)\big)^2 \\ &+ \big(LnmF(y_k) - LnmF(v_i)\big)^2 \\ &+ \big(UnmF(y_k) - UnmF(v_i)\big)^2 \\ &+ \big(WmF(y_k) - WmF(v_i)\big)^2 \\ &+ \big(WnmF(y_k) - WnmF(v_i)\big)^2\Big] \Bigg\}^{\frac{1}{2}} \end{aligned} \tag{16}$$

$$\begin{aligned} min\, J_m(U,V:Y) = &\sum_{i=1}^{c}\sum_{j=1}^{N}(u_{ij})^m ||y_j - v_i||^2 \\ &+ \alpha \sum_{i=1}^{c}\sum_{j=1}^{N}(u_{ij})^m ||y_j - v_i||^2 + \sum_{i=1}^{c} W\,mF \\ &* (y_i) \times e^{1-WmF*(y_i)} \end{aligned} \tag{17}$$

Subject to $\sum_{i=1}^{C} u_{ij} = 1,\ \ 1 \le j \le N,$

$where\ wmF.(y_i) = \frac{1}{n}\sum_{j=1}^{N} wmF(y_i).$

The optimisation issue (17) may be solved using the Lagrangian multiplier procedure, and its membership and centroids are found as:

$$u_{ik} = \frac{1}{\sum_{j=1}^{C}\left(\frac{(1+\alpha)||y_k - v_i||}{(1+\alpha)||y_k - v_i||}\right)^{\frac{2}{m-1}}} \tag{18}$$

$$v_i = \frac{\sum_{k=1}^{N}(u_{ik})^m y_k}{\sum_{k=1}^{N}(u_{ik})^m} \tag{19}$$

When updating the membership function, the cluster centroid of the pixel value is considered [23, 24]. This algorithm uses the fuzzifier parameter value m=2, which was chosen based on the literature review. As a result, tissue segmentation becomes more precise as the uneven distribution of noise and intensity seen in non-brain magnetic resonance imaging is balanced.

Algorithm 1 Pseudo-code of Proposed method for Gaussian mixture model and k-means based spatial interval valued intuitionistic fuzzy c means clustering with D_α operator.

Require: Input MRI image, Number of cluster=$v_1, v_2, ...v_c$, fuzzifier parameter=m, Convergence threshold =ϵ

Ensure: Output image : Segmented tumor region

Step 1: Preprocessing steps like skull stripping using morphological operators and noise removal using median filter.

Step 2: Compute Normalization matrix using min-max method.

$$Nm(I(i,j)) = \frac{(i,j)_I - (i,j)_{min}}{(i,j)_{max} - (i,j)_{min}}$$

Step 3: Compute Membership matrix using the following function.

$$mF(I(i,j)) = 0.582(exp(. - [Nm(I(i,j)) - m_I]) - 1)$$

Step 4: Compute Non-membership matrix using the following function:

$$nmF(I(i,j)) = (1 - mF(i,j))\left(exp\left(\frac{-mF}{a\sigma}\right)\right)^{1/a}, a > 0$$

Step 5: Compute Hesitancy matrix:

$$Pi_F(I(I,j)) = 1 - mF(I(i,j)) - NmF(I(i,j))$$

Step 6: Compute interval valued membership and non-membership functions with D_α operator.

Step 7: Initialization of cluster centres using Gaussian mixture model and K-means.

Step 8: Compute Distance between pixels and cluster cnetres using Average Euclidean distance measure.

Step 9: Update membership matrix and cluster centres using objective function.

Step 10: Convergence check:If the change in membership matrix satisfies

$$||u_{ik}^{(t+1)} - u_{ik}^{(t)}|| < \epsilon, i = 1, 2, ...n\ and\ k = v_1, v_2, ...v_c.$$

then stop, else repeat steps(8-9).

Step 11: Compute finalsegmented tumor region is taken with the corresponding maximum cluster centre point to extract the most significant tumor region.

RESULTS AND DISCUSSION

Actual Pictures

The dataset used in this experimental study was provided by the KGS Advanced MR and CT Scan Facilities in Madurai, Tamil Nadu, India [30]. Several tumour-containing brain MR

imaging datasets were used in the tests. Following preprocessing [33], centroid values for brain imaging clusters were determined using GMM and K-means clustering [29,36,38]. Better centroid values were thus obtained by the first cluster centres, which lowered the overall time required for the segmentation procedure. This method provides a better centre for cluster centre updates using data points than earlier approaches [11]. Compared to the current approach, the recommended SIVIFCM's method produces superior segmentation results since it uses spatial values with the Dα operator. If there isn't a tumour, the cerebrospinal fluid (CSF), grey matter (GM), and white matter (WM) are seen separately. Three cluster cores are seen in this instance, which suggests malignancy. Due to its high intensity, the brain slice tumour area grows into the largest cluster core of the three. After detection, morphological procedures and prolonged maxima transformation are used to eradicate the cancerous region. The performance of the recommended approach randomly chosen on 3 slices out of 50 slices is shown in Figure 1. As shown in Figure 1, the first row comprises three original images, the second row their corresponding pre-processed images, the third row the segmentation results of the IVIFCM method, the fourth row the GMM and K-means based spatial interval valued intuitionistic fuzzy c means clustering incorporating the Dα operator (GK-SIVIFCM) method, and the fifth row the manual segmentation results of the images. Table 1 uses Dice and Jaccard coefficients to compare our proposed method's segmented region (predicted image) to the IVIFCM methods manually segmented tumour region (ground truth picture). Metrics such as sensitivity, specificity, and accuracy are used to assess the way effectively your model sets apart the item of interest (foreground) from the surrounding objects. They give information

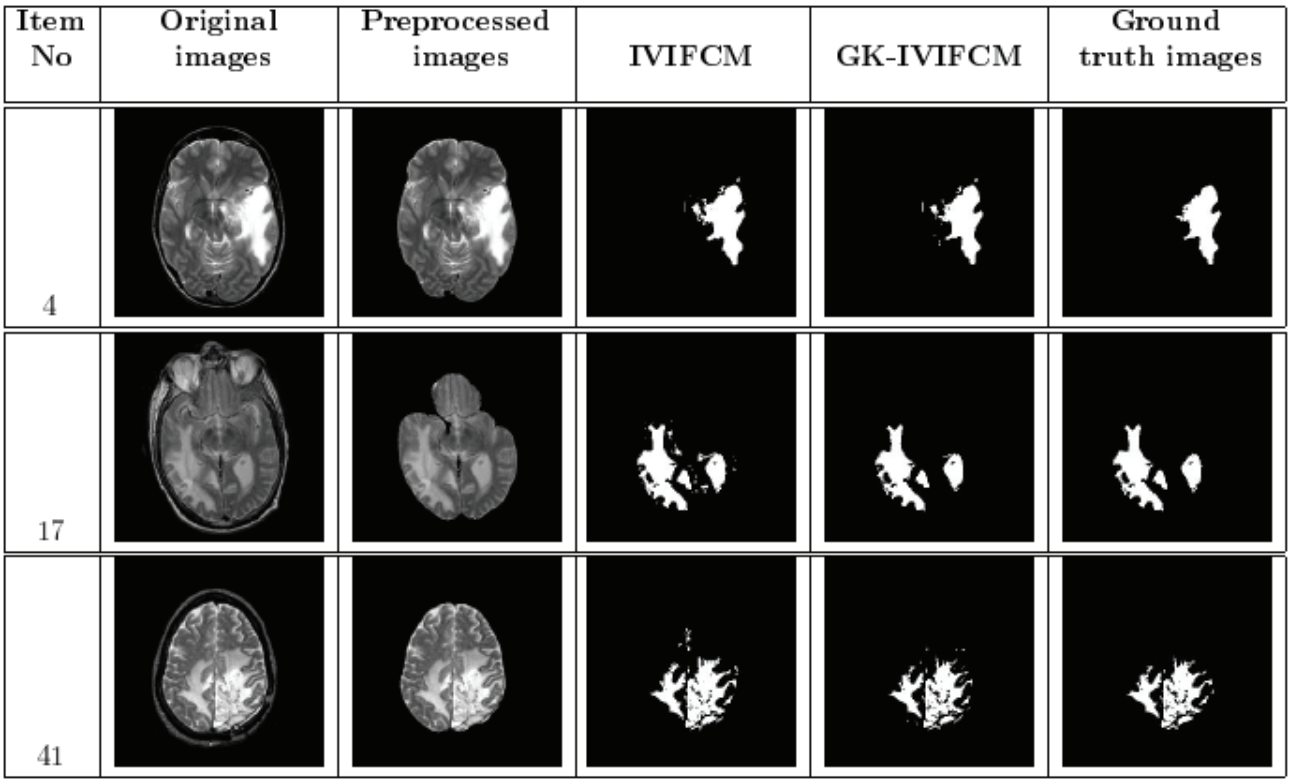


Figure 1. Comparison of Segmentation results.

Table 1. Comparison of Dice coefficient (DC) and Jaccard similarity (JS) obtained using IVIFCM and GK-SIVIFCM of image number 4,17, and 41.

Item	Dice Coefficient		Jaccard Similarity	
	IVIFCM	**GK-SIVIFCM**	**IVIFCM**	**GK-SIVIFCM**
4	0.9197	**0.9583**	0.8514	**0.9202**
17	0.9487	**0.9783**	0.9024	**0.9575**
41	0.9249	**0.9750**	0.8603	**0.9512**

on many elements of the segmentation performance. Table 2 compares the sensitivity, specificity, and accuracy of our proposed approach's segmented region (predicted image) to the IVIFCM method employing a manually segmented tumour region (ground truth). Compared to alternative approaches already in use, our recommended methodology produces superior outcomes.

Synthetic images

The suggested technique utilises virtual brain MRI images from the Brain web database [7]. For segmentation, 2D transverse slices and T1-weighted images with a 1 mm resolution were used. The photographs were evaluated with different degrees of intensity inhomogeneities (0%, and 20%) and noise (3%, 5%, and 7%). Here only provided

Table 2. Comparison of Dice coefficient (DC) and Jaccard similarity (JS) obtained using IVIFCM and GK-SIVIFCM

Item	Sensitivity		Specificity		Precision	
	IVIFCM	GK-SIVIFCM	IVIFCM	GK-SIVIFCM	IVIFCM	GK-SIVIFCM
4	**1.0000**	**1.0000**	0.9932	**0.9966**	0.8514	**0.9202**
17	**0.9997**	0.9647	0.9940	**0.9996**	0.9027	**0.9922**
41	**0.9954**	0.9766	0.9918	**0.9986**	0.8637	**0.9734**

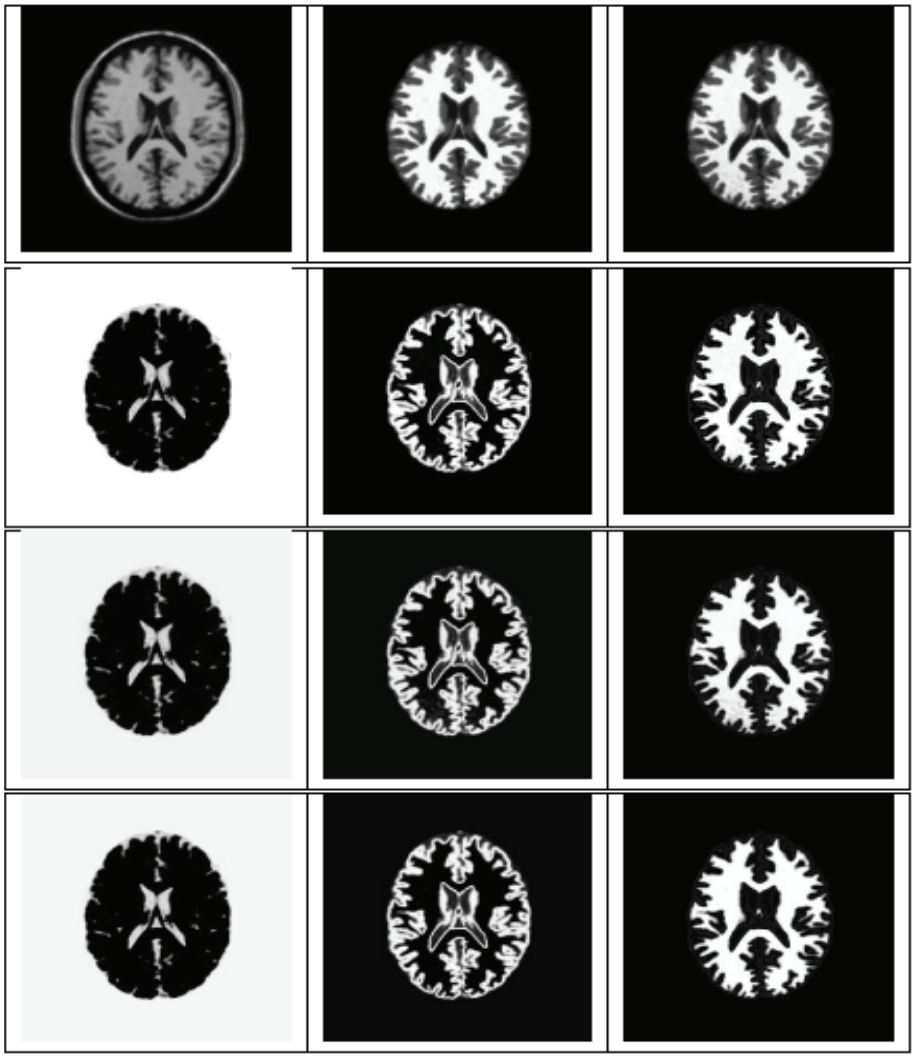


Figure 2. First row: Original image, ground truth, segmentation results using indicated method with 3% noise and 20% intensity inhomogeneity respectively. Second row: CSF, GM, WM of IVIFCM area. Third row: CSF, GM, WM of GK-SIV-IFCM area. Fourth row: Region of CSF, GM, WM.

3% noise and 20% intensity inhomogeneity picture. Figure 2 shows effectiveness of spatial interval-valued fuzzy c-means clustering using GMM and KM, using the Dα operator approach. The first row of Figure 2 displays the original image, skull removed ground truth, our method skull removed image. The second row depicts CSF, GM, and WM areas calculated using the IVIFCM technique. The third row emphasised the GK-SIVIFCM method's cerebrospinal fluid (CSF), white matter (WM), and grey matter (GM) areas. The fourth row includes ground truth areas for CSF, GM, and WM. The segmentation results for the GM, WM, and CSF areas are provided in the third row, using 0% noise and 0% intensity inhomogeneity" as the ground truth. Table 3 displays the DC and JS values for the IVIFCM method and GK-SIVIFCM methodology. Table 4 shows the volume similarity and Kappa coefficients for CSF, GM, and WM using the IVIFCM and GK-SIVIFCM techniques. Comparing the segmentation results to the ground truth shows that the suggested technique properly localises tissues and has a high degree of consistency with the ground truth. This implies that the GK-SIVIFCM approach for segmenting brain MRI images works well under a variety of noise and intensity inhomogeneity circumstances.

Quantitative Metrics

The suggested algorithm's performance is verified by quantitative assessment utilising the following indices:

1. Dice Coefficient (DC)/ Overlap ratio:

It is the correspondence between the ground truth and the segmentation result. It is described as [5,12]

$$DC(I1, I2) = \frac{2|I1 \cap I2|}{|I1|+|I2|} \text{ (or) } DC = \frac{2TP}{2TP+FP+FN}$$

Table 3. Dice coefficient (DC) and Jaccard similarity (JS) for MR brain images produced with IVIFCM and GK-SIVIFCM with different noise levels of 3%, 5%, and 7% with 20% intensity inhomogeneity are compared.

Noise Level	Tissue Type	Dice Coefficient		Jaccard Similarity	
		IVIFCM	GK-SIVIFCM	IVIFCM	GK-SIVIFCM
3%	CSF	0.9935	**0.9978**	0.9871	**0.9956**
	GM	0.8443	**0.9328**	0.7306	**0.8741**
	WM	**0.9702**	0.9511	**0.9422**	0.9061
5%	CSF	0.9933	**0.9974**	0.9688	**0.9949**
	GM	0.8445	**0.9348**	0.7309	**0.8775**
	WM	**0.9698**	0.9315	**0.9414**	0.8717
7%	CSF	0.9932	**0.9973**	0.9685	**0.9946**
	GM	0.8477	**0.9200**	0.7357	**0.8518**
	WM	**0.9638**	0.9493	**0.9301**	0.9036

Table 4. Volume Similarity and Kappa Coefficient for different noise levels of 3%, 5%, and 7% with 20% intensity inhomogeneity of IVIFCM, Proposed method with Ground truth images.

Noise Level	Tissue Type	Volume Similarity		Kappa Coefficient	
		IVIFCM	GK-SIVIFCM	IVIFCM	GK-SIVIFCM
3%	CSF	0.9936	**0.9988**	0.9751	**0.9914**
	GM	0.8701	**0.9890**	0.8188	**0.9197**
	WM	**0.9867**	0.9527	**0.9650**	0.9428
5%	CSF	**0.9934**	0.9346	**0.9745**	0.9202
	GM	0.8749	**0.9947**	0.8189	**0.9222**
	WM	0.9840	**0.9990**	0.9645	**0.9899**
7%	CSF	0.9934	**0.9518**	**0.9740**	0.9408
	GM	0.8762	**0.9927**	0.8226	**0.9044**
	WM	0.9827	**0.9995**	0.9574	**0.9895**

2. Jaccard similarity (JS): It may be defined as the proportion of two sets' overlap and combination that reflects the segmentation and ground truth pictures that were acquired [5,17].

$$JS\ (I1, I2) = \frac{2|I1 \cap I2|}{|I1 \cup I2|}$$

DC values provide the relative overlap index between the ground truth image and the segmentation produced by the suggested approach. In highly comparable collections, JS values are more sensitive. I1andI2 are the numbers of pixels that, when employing the suggested technique and the ground truth, are categorised into one class, respectively. In both findings, the number of pixels segmented as a single class is expressed as |I1 ∩ I2|. The number of pixels shared by both outcomes is |I1 ∪ I2|. These metrics reach a value of 1 in cases where the segmentation outcomes perfectly align with the ground truth, and 0 in cases where there is no alignment.

Confusion Table: This matrix displays the brain cells for a specific class on rows vs the fundamental truth class on sections. [30] as false positives (FP), false negatives (FN), and true positives (TP). Thus, for every class, the true positives (TP) are represented by the diagonal item in this confusion table. Definition of false negative (FN): the proportion of ground truth pixels that were inadvertently segmented as other classes. The fraction of pixels that are mistakenly classified as belonging to a class over those that do not in the ground truth is known as the false positive (FP).

Three more evaluation criteria, which are specified as follows, are also utilised for comparisons based on TN, FP, FN, and TP [2]:

1. Sensitivity (Recall) = TP/ (TP + FN).
2. Specificity = TN/ (TN + FP)
3. Precision = TP/ (TP + FP)

The results of the proposed technique are compared with IVIFCM based on Dice coefficient (DC) and Jaccard similarity (JS). In addition to the Dice coefficient (DC) and Jaccard similarity (JS), Table 2 shows the segmented regions of cerebrospinal fluid, grey matter, and white matter created for T1 weighted MR brain images with 0% intensity inhomogeneity and variable noise level as 1%, 5%, 9%, and 13%. Table 1 demonstrates that the Jaccard similarity and dice coefficient values for CSF, WM, and GM using the proposed methodology are larger than those obtained using the IVIFCM method [7,26,27,31] for all photos with noise levels of 1%, 5%, 9%, and 13%. The IVIFCM approach is also compared to the GK-SIVIFCM algorithm. Considering the DC value (overlap ratio), The outputs are evaluated in accordance with the overlap ratio (DC value). Correspondence ratios between brain magnetic resonance imaging and noise levels of 5% and 20% intensity inhomogeneity are shown in Figure 2.

CONCLUSION

In this paper, the Dα operator is combined with the Spatial Interval-Valued Intuitionistic Fuzzy C-Means (SIVIFCM) clustering algorithm to create a hybrid method for robust picture segmentation. The suggested method initialises the centroids for cluster centres by combining the Gaussian Mixture Model (GMM) with K-means clustering. The outcomes show that, in comparison to current techniques, the proposed method produces superior segmentation. The results show that the SIVIFCM algorithm is very good at segmenting pictures because its fuzzy-based method effectively manages the uncertainties in brain MRI images, which improves segmentation accuracy. Additionally, this approach could improve the detection of diseases and help doctors treat patients more effectively. Other kinds of medical photos can be segmented using this method in the future.

AUTHORSHIP CONTRIBUTIONS

Authors equally contributed to this work.

DATA AVAILABILITY STATEMENT

There are two sources of data that provide credence to the results of this investigation. The KGS Advanced MR and CT scan facilities in Madurai, Tamil Nadu, India, provided the initial dataset. If you would want access to this data, please contact the KGS facility (phone number: +91 452 2524321, 2528929, 97125 59730) and make a legitimate request. The brain web simulation database of normal brain magnetic resonance imaging (MRI) data, which can be accessed by the public at Brain Web website, is the source of the second dataset. If you follow the terms and conditions, you are free to access and use this dataset.

CONFLICT OF INTEREST

The authors declared no potential conflicts of interest with respect to the research, authorship, and/or publication of this article.

ETHICS

There are no ethical issues with the publication of this manuscript.

STATEMENT ON THE USE OF ARTIFICIAL INTELLIGENCE

Artificial intelligence was not used in the preparation of the article.

REFERENCES

[1] Mishro PK, Agrawal S, Panda R, Abraham A. A novel type-2 fuzzy C-means clustering for brain MR image segmentation. IEEE Trans Cybern 2021;51:3901–3912. [CrossRef]

[2] Verma H, Agrawal RK, Sharan A. An improved intuitionistic fuzzy C-means clustering algorithm incorporating local information for brain image segmentation. Appl Soft Comput 2016;46:543–557. [CrossRef]

[3] Lin Y, Chen S. A centroid auto-fused hierarchical fuzzy C-means clustering. IEEE Trans Fuzzy Syst 2021;29:2006–2017. [CrossRef]

[4] Kala R, Deepa P. Spatial rough intuitionistic fuzzy C-means clustering for MRI segmentation. Neural Process Lett 2021;53:1305–1353. [CrossRef]

[5] Kaushal M, Lohani QMD, Castillo O. Weighted intuitionistic fuzzy C-means clustering algorithms. Int J Fuzzy Syst 2024;26:943–977. [CrossRef]

[6] Wei D, Wang Z, Si L, Tan C, Lu X. An image segmentation method based on a modified local-information weighted intuitionistic fuzzy C-means clustering and Gold-panning Algorithm. Eng Appl Artif Intell 2021;101:104209. [CrossRef]

[7] Dubey YK, Mushrif MM, Mitra K. Segmentation of brain MR images using rough set based intuitionistic fuzzy clustering. Biocybern Biomed Eng 2016;36:413–426. [CrossRef]

[8] Ji Z, Xia Y, Sun Q, Chen Q, Xia D, Feng DD. Fuzzy local Gaussian mixture model for brain MR image segmentation. IEEE Trans Inf Technol Biomed 2012;16:339–347. [CrossRef]

[9] Li X, Li B, Liu F, Yin H, Zhou F. Segmentation of pulmonary nodules using a GMM fuzzy C-means algorithm. IEEE Access 2020;8:37541–37556. [CrossRef]

[10] Tiwari P, Gupta P. Novel distance, similarity and entropy measures for interval valued intuitionistic fuzzy soft set. J Intell Fuzzy Syst 2022;43:3067–3086. [CrossRef]

[11] Ji Z, Xia Y, Sun Q, Cao G. Interval-valued possibilistic fuzzy C-means clustering algorithm. Fuzzy Sets Syst 2014;253:138–156. [CrossRef]

[12] Arora J, Tushir M. Robust spatial intuitionistic fuzzy C-means with city-block distance clustering for image segmentation. J Intell Fuzzy Syst 2018;35:5255–5264. [CrossRef]

[13] Ahmed SR, Al Barazanchi I, Jaaz ZA, Abdulshaheed HR. Clustering algorithms subjected to K-mean and Gaussian mixture model on multidimensional data set. Period Eng Nat Sci 2019;7:448–457. [CrossRef]

[14] Patel E, Kushwaha DS. Clustering cloud workloads: K-means vs Gaussian mixture model. Procedia Comput Sci 2020;171:158–167. [CrossRef]

[15] Viroli C, McLachlan GJ. Deep Gaussian mixture models. Stat Comput 2019;29:43–51. [CrossRef]

[16] Jagatheswari S, Viswanathan R. On interval valued fuzzy sets D Alpha operator and its application. Int J Appl Eng Res 2016;11:2016.

[17] Ray M, Mahata N, Sing JK. Uncertainty parameter weighted entropy-based fuzzy C-means algorithm using complemented membership functions for noisy volumetric brain MR image segmentation. Biomed Signal Process Control 2023;85:104925. [CrossRef]

[18] Durgut A, Biroğul S, Güvenç U. Comparison of the effects of image segmentation on image processing performance with parallel programming.

[19] Ouchicha C, Ammor O, Meknassi M. A new approach based on exponential entropy with modified kernel fuzzy C-means clustering for MRI brain segmentation. Evol Intell 2023;16:651–665. [CrossRef]

[20] Xu C. Improvement of the distance between intuitionistic fuzzy sets and its applications. J Intell Fuzzy Syst 2017;33:1563–1575. [CrossRef]

[21] Bustince H, Barrenechea E, Pagola M, Fernández J. Interval-valued fuzzy sets constructed from matrices: application to edge detection. Fuzzy Sets Syst 2009;160:1819–1840. [CrossRef]

[22] Atanassov K. Intuitionistic fuzzy sets. Int J Bioautomation 2016;20:1. [CrossRef]

[23] Yun S, Zanetti R. Clustering methods for particle filters with Gaussian mixture models. IEEE Trans Aerosp Electron Syst 2022;58:1109–1118. [CrossRef]

[24] Cai W, Chen S, Zhang D. Fast and robust fuzzy C-means clustering algorithms incorporating local information for image segmentation. Pattern Recognit 2007;40:825–838. [CrossRef]

[25] Dhal KG, Das A, Ray S, Sarkar K, Gálvez J. An analytical review on rough set-based image clustering. Arch Comput Methods Eng 2021:1–30. [CrossRef]

[26] Pawlak Z. Rough set theory and its applications. J Telecommun Inf Technol 2002:7–10. [CrossRef]

[27] Liu XY, Fan JC, Chen ZW. Improved fuzzy C-means algorithm based on density peak. Int J Mach Learn Cybern 2020;11:545–552. [CrossRef]

[28] Bustince Sola H, Burillo López P. A theorem for constructing interval-valued intuitionistic fuzzy sets from intuitionistic fuzzy sets.

[29] Manivasagan M, Jagatheswari S. A survey on various kinds of image segmentation of cancer images using fuzzy image processing methods. In: 2023 12th International Conference on Advanced Computing (ICoAC). 2023. p. 1–5. [CrossRef]

[30] Ananthi VP, Balasubramaniam P, Kalaiselvi T. A new fuzzy clustering algorithm for the segmentation of brain tumor. Soft Comput 2016;20:4859–4879. [CrossRef]

[31] Roy S, Maji P. A simple skull stripping algorithm for brain MRI. In: 2015 Eighth International Conference on Advances in Pattern Recognition (ICAPR). 2015. p. 1–6. [CrossRef]

[32] Mahmood H, Mehmood T, Al-Essa LA. Optimizing clustering algorithms for antimicrobial evaluation data: a majority score-based evaluation of K-means, Gaussian mixture model, and multivariate T-distribution mixtures. IEEE Access 2023;11:79793–79800. [CrossRef]

[33] Lalithamani N, Prabakaran K, Jagatheswari S, Kiruthika P. A new adaptive filter for removal of impulse noise with uncertainty. Asian J Res Soc Sci Humanit 2016;6:296–308. [CrossRef]

[34] Pugazhenthi A, Kumar LS. Selection of optimal number of clusters and centroids for K-means and fuzzy C-means clustering: a review. In: 2020 5th International Conference on Computing, Communication and Security (ICCCS). 2020. p. 1–4. [CrossRef]

[35] Szmidt E, Kacprzyk J. Distances between intuitionistic fuzzy sets. Fuzzy Sets Syst 2000;114:505–518. [CrossRef]

[36] Mirzal A. Statistical analysis of microarray data clustering using NMF, spectral clustering, K-means, and GMM. IEEE/ACM Trans Comput Biol Bioinform 2022;19:1173–1192. [CrossRef]

[37] Luo M, Wang L. A novel similarity measure for intuitionistic fuzzy sets and its application to pattern recognition. Soft Comput 2024;28:6207–6217. [CrossRef]

[38] Jebarani PE, Umadevi N, Dang H, Pomplun M. A novel hybrid K-means and GMM machine learning model for breast cancer detection. IEEE Access 2021;9:146153–146162. [CrossRef]

[39] Liu B, Liu C, Zhou Y, Wang D, Dun Y. An unsupervised chatter detection method based on AE and merging GMM and K-means. Mech Syst Signal Process 2023;186:109861. [CrossRef]

Sigma J Eng Nat Sci, Vol. 44, No. 4, pp. 2458–2472, August, 2026

Sigma Journal of Engineering and Natural Sciences
Web page info: https://sigma.yildiz.edu.tr
DOI: 10.14744/sigma.2026.2109

Research Article

An advanced framework for cervical cancer detection using optimized ensemble learning

Rufina Sherin John ROBERT[1], Tamilazhagan SENTHIL[1], Manikandan RAMACHANDRAN[1], Vidivelli SOUNDARARAJAN[1], Magesh SANKAR[2], Mohammad KHISHE[3,4,*]

[1]*School of Computing, SASTRA Deemed University, Tamil Nadu, 613401, India*
[2]*Department of Computer Science and Engineering, Dr. M. G. R. Educational and Research Institute, Chennai, 600095, India*
[3]*Applied Science Research Center, Applied Science Private University, Amman, 11937, Jordan*
[4]*Department of Electrical Engineering, Imam Khomeini Naval Science University of Nowshahr, Nowshahr, 4651763836, Iran*

ARTICLE INFO

Article history
Received: 05 August 2024
Revised: 03 October 2024
Accepted: 27 May 2025

Keywords:
Cervical Cancer Detection; Convoluted Features; Ensemble Learning; Neural Networks; Machine Learning

ABSTRACT

Cervical cancer remains the most common and life-threatening malignancies around the world. As with many diseases, timely and accurate intervention is critical in this case if one wishes to reduce the mortality rate associated with this medical condition. The purpose of this research is to develop an innovative computational framework to detect cervical cancer using both quantitative and data-driven approaches. The primary data set consists of the demographics, lifestyle choices, and medical history of 980 patients, which was collected at the Hospital Universitario de Caracas in Venezuela. For reproducibility purposes and computational efficiency, all model testing was performed on Google Colab, a cloud platform suitable for big data. The ensemble learning methodology integrated a convolutional neural network (CNN) with several machine learning classifiers, including Random Forest, Decision Tree, Logistic Regression, K-Nearest Neighbors, Extreme Gradient Boosting, Support Vector Machine, Extra Tree Classifier, Categorical Boosting, Gradient Boosting, and Adaptive Boosting. This paper also looks at the impact of model performance on original and engineered feature selection. After extensive comparative evaluation, the proposed framework showed an extraordinary predictive performance of 98.96% classification accuracy, thus confirming the value of the framework. This showcases the enormous potential of machine learning in revolutionizing cervical cancer diagnosis. This study seeks to refine diagnostic precision in order to enable timely detection while minimizing misdiagnosis risks. Through integrated datasets, the framework deepens understanding of the influencing factors and enhances the accuracy of the predictions, providing more precise forecasts. This technology seeks to improve patient prognosis by providing more timely and effective cervical cancer diagnosis and treatment.

Cite this article as: Robert RSJ, Senthil T, Ramachandran M, Soundararajan V, Sankar M, Khishe M. An advanced framework for cervical cancer detection using optimized ensemble learning. Sigma J Eng Nat Sci 2026;44(4):2458–2472.

***Corresponding author.**
*E-mail address: m_khishe@alumni.iust.ac.ir

This paper was recommended for publication in revised form by Editor-in-Chief Ahmet Selim Dalkilic

Published by Yıldız Technical University Press, İstanbul, Turkey
© Author. This is an open access article under the CC BY-NC license (http://creativecommons.org/licenses/by-nc/4.0/).

INTRODUCTION

Cervical cancer persists as a major public health issue, particularly impacting women in their childbearing age. This cancer develops from the cervix, which is the cylindrical-shaped lower part of the uterus leading into the vagina. The primary driver of cervical cancer is a long-term infection with high-risk HPV strains, a virus that is sexually transmitted. While most of the HPV infections resolve on their own and are non-threatening, some are persistent and resolve more slowly [1, 2]. These precancerous lesions, over time, may lead to invasive cervical cancer.

One of the most ancient and prevalent viral infections in humans is HPV, with infected individuals all over the globe [3]. As stated by the WHO, cervical cancer is the fourth most common cancer amongst women in the world. New case counts for the disease reached approximately 604,000 with 342,000 deaths in 2020 alone. Of great concern, almost 90% of the new cases and deaths were from low-middle income nations. This is a phenomenon driven by a lack of robust healthcare systems and the absence of integrated, tailored cancer prevention programs.

HPV types 16 and 18 are the most oncogenic strains, precipitating approximately 70% of cervical cancers. The risk of infection and disease advancement may increase due to various factors: early onset of sexual activity, multiple sexual partners, long-term contraceptive use, smoking, and HIV co-infection. Disease advancement at the molecular level is defined by the integration of HPV DNA into the host genome, resulting in the overexpression of viral oncogenes E6 and E7. E6 and E7 oncoproteins hijack essential tumor suppressors such as p53 and retinoblastoma (Rb), leading to uncontrolled cell division and subsequently, malignant transformation [4].

Cervical screening and HPV vaccination have shown significant proactive results. Precancerous changes can be detected early via Pap smear cytology along with DNA HPV testing. Developed countries have reported a significant decline in the incidence and mortality of cervical cancer due to proactive screening programmes [5]. In resource-restricted countries, earlier diagnosis is rare, which leads to poor outcomes and higher mortality. To address this gap, global health strategies need to prioritize the strengthening of healthcare systems, the launching of mass education HPV vaccination campaigns, and the elevation of awareness concerning risk factor reduction [6,7]. The burden of cervical cancer and women's health inequities on a global scale can only be alleviated through effective, affordable, and culturally appropriate policies and programs. The stigma of cervical cancer and poor awareness among women deters them from seeking preventive care or early diagnosis. It is essential, therefore, to counter these hindrances with innovative, cost-effective solutions [8]. Acetic acid visual inspection is much less expensive than Pap smears, and luminations have shown promise in detecting cervical abnormalities, especially well-suited in resource-limited settings [9]. Mobile health clinics and outreach programs bring screening services to the underserved, remote areas, thus increasing access. Digital health technologies, from telemedicine to AI-supported diagnoses, can benefit from a complete turnaround by allowing patients to leap over the barrier of distance to reach specialist care. These offer the possibility of remote assessments with early detection of conditions in places lacking access to healthcare services. All education and awareness work about the value of protection against cervical cancer and getting proper Pap tests should be targeted at educating women. Community health workers can also serve as important channels for such education efforts and encouragement of community members to participate in screening programs.

Conventional cervical cancer screening methods comprise Pap smears, in addition to HPV tests, which call for manual interpretation. Certainly time-consuming, prone to human error, and ineffective in low-resource contexts. Vaccinating against HPV is another essential preventive step [10]. Cervarix and Gardasil vaccinations defend against most widespread speculative-risk HPV varieties. The implementation of these vaccinations has yielded positive results in reducing the occurrence of HPV infections and cervical cancer. As per the WHO, girls between the ages of 9 and 14 ought to receive a routine HPV vaccination prior to starting sexual activity [11].

Early signs of the disease do not present themselves. With the ever-changing nature of data, It Is pertinent to understand that cervical cancer screening requires HPV and PAP smear testing and regular follow-up visits so that it can be addressed in as timely a manner as possible [40]. The more advanced stages of the disease are associated with increased discomfort in the pelvic area, along with pain during intercourse. Each Individual patient has their treatment plan, which may include surgical treatment combined with radiotherapy or plasma chemotherapy in more advanced patients. Recently, some of the more specific and compelling recurrent or metastatic cervical cancer treatment options, such as immunotherapy, have emerged with much more favorable and efficient regard for achieving functional outcomes. As with any complicated prediction, there is always some stage and combination of treatments that changes it. For cervical cancer, it is highly dependent. However, early detection increases the five-year survival chance of a patient to roughly ninety-two percent [12, 13].

Comparably, the chances of survival with cancer detected at an advanced stage drop sharply to seventeen percent. In the United States, the American Cancer Society data shows that 66 percent of women with cervical cancer are expected to live beyond five years post-diagnosis. These figures demonstrate the importance of effective treatment and intervention to reduce mortality and increase survival rates for patients diagnosed with cervical cancer. Early detection is made possible by combining approaches utilizing ensemble methods, ensuring improved confidence in diagnostics forming within the disjunctions of data

collected through mechanisms such as HPV tests and Pap smears [14]. Feature selection is so vital as it emphasizes explanatory factors to reasonably predict diagnosis of cervical cancer.

Machine Learning models deal with vast volumes of patient data. They are able to recognize very subtle patterns that a human being might overlook, thus leading to more excellent detection rates. An ML-based approach can lead to greater diagnostic accuracy and fewer instances of false positives and negatives, with a view to furthering the clinical decision support system towards timely and effective interventions. Ensemble techniques include bagging, boosting, and stacking, depending on the desired application to enhance performance. The ensemble learns from the dataset and evaluates the model's performance in terms of accuracy and F1 score. Machine Learning models deployed in automated systems provide high-quality diagnostic support to those areas of the world with limited access to expert pathologists. Once trained and validated, this model would now provide risk of cervical cancer in consideration of new patients and recommendations for any follow-up testing. It is possible to incorporate machine learning into the existing healthcare structures in the fight against cáncer. Thus, this may help clinicians determine the prognosis and design treatment plans personalized to the patient [41, 42]. A highly reliable and corroborated method toward an enhanced diagnosis enables timely intervention, finalizing better patient outcomes. Continuous monitoring and retraining imply that the model remains working well over time.

Related Works

These recent advances in cervical cancer (CC) detection and diagnosis, as well as active research on the use of technology, have identified the emerging areas of technology like computer-aided diagnosis (CAD) and advanced diagnostic support systems [15]. Researchers have developed automated diagnosis of cervical cancer through individual and ensemble models based on machine learning, improving accuracy of machine learning when deploying models. In these studies, multiple classifiers were tested, with genetic preprocessing and feature selection in genetic programming producing excellent results that improved diagnostic accuracy. Several studies have contributed to increasing cervical cancer detection and understanding the link between this cancer and HPV. For instance, after Munoz et al. (2006) researched worldwide HPV prevalence, they helped forge a crucial association between HPV infection and cervical cancer while simultaneously aiding vaccine development. They furthered the evaluation of various screening strategies, too. According to Arbyn et al. (2012), HPV DNA testing is much more sensitive (90–95%) than cytology (70–80%). However, trials utilized by Ronco et al. (2014) in Europe have confirmed that HPV testing has superior early detection sensitivity of 94 and specificity of 98 percent when compared to cytology. We identify broad disparities in incidence and outcome of cervical cancer that compare high-income with treatment inequalities amongst low to middle-income countries as part of Bruni et al. (2020) global cancer registry data analysis. Newer treatment modalities in Marth et al.'s (2017) clinical trial assessment of targeted therapies for advanced cervical cancer have shown promise for better response rates. Yu et al. (2021) extend diagnosis capabilities beyond the scope of both clinical images and the data to machine learning models.

Extensive evaluations of screening strategies have also been done. HPV DNA testing has much higher sensitivity (90 – 95%) than cytology (70 – 80%), as shown by Arbyn et al. (2012). However, Ronco et al. (2014) trials in Europe confirmed that HPV testing performs better than cytology in early detection, with sensitivity of 94% and specificity of 98%. This is from Bruni et al, 2020. An international nagging cancer registry study pointed out the sharp differences in the incidence and outcomes of cervical cancer in relation to their lower- and middle-income peers within high income countries. It emphasized the lack of timeliness in the provision of healthcare services, starkly highlighting the divide in the care gap based on economic classifications. In the clinical trial conducted by Marth et al. (2017), newly emerging treatment options for aggravated invasive cervical cancer showed better response rates, giving hope for further treatment. Making a further contribution in the area, Yu et al. (2021) applied machine learning algorithms to clinical images and patient data which greatly improved the accuracy of the diagnosis and the possibilities of earlier detection.

MATERIALS AND METHODS

The following part explains the methodology phases, the suggested technique, and the dataset utilized to detect carcinoma of the cervix. The model workflow is shown in Figure 1. It also offers an overview of machine learning classifiers used in this study.

Dataset for Experiments

The dataset contains information related to cervical cancer screening outcomes and risk factors. This dataset is significant in research and analytical works, particularly in assessing and forecasting the occurrence of cervical cancer. It is organized in tables and saved as a CSV (Comma Separated Values) file, which provides easy access and allows it to be used in data-centric studies. The dataset includes various attributes (features) categorized into personal, demographic, and medical risk factors. The size of the dataset is 99.7 KB. Data has 36 variables comprising historical details and risk factors regarding a patient.

Demographic variables vary among women (age, reproductive history, sexuality), as well as medical variables (history of smoking and contraceptive use (both hormonal contraceptives and intrauterine devices (IUDs)). It also records previous diagnoses of other sexually transmitted

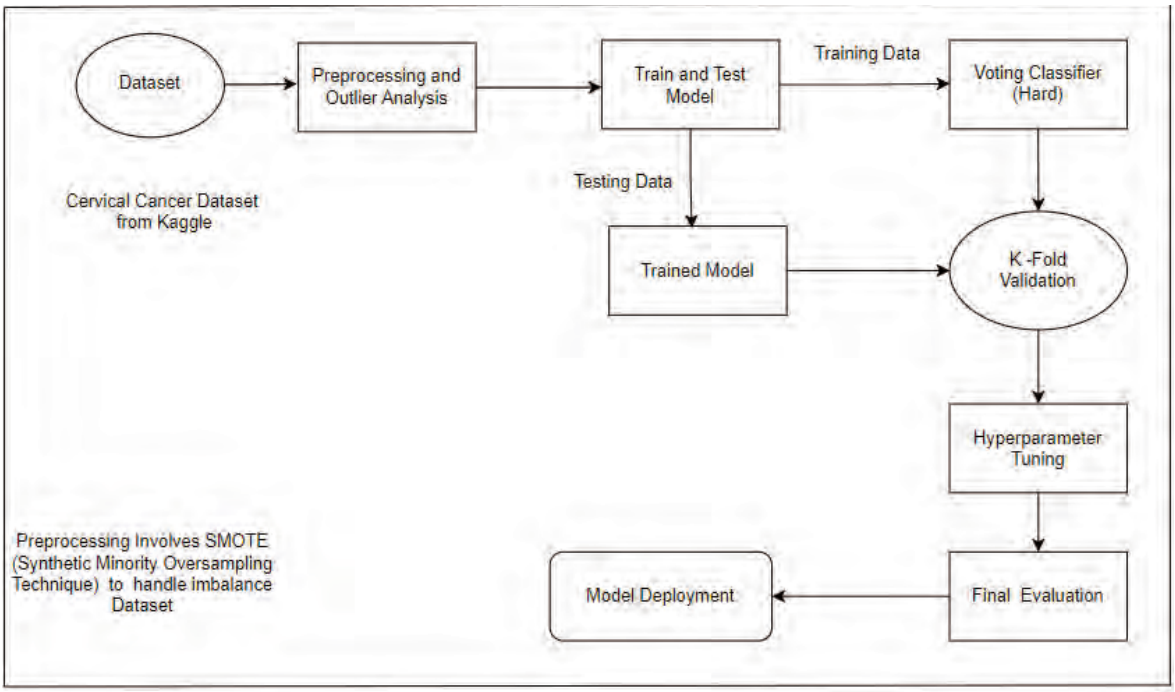


Figure 1. Proposed model workflow diagram.

infections, such as condylomatosis, syphilis, genital herpes, pelvic inflammatory disease, and vulva-perineal and vaginal condylomatosis. It also records less common infections like molluscum contagiosum, hepatitis B, HIV and HPV. The clinical parameters record the history of previously diagnosed STIs along with other relevant diseases like cervical or HPV cancer, CIN, and any other herpetic involvement. Moreover, the dataset contains biopsy results, which are necessary for determining relationships and trends that might be associated with or indicate the possibility of cervical cancer. Cervical cancer can be detected earlier, and its risks can be assessed through epidemiological research utilizing these datasets, which are gathered from systematic healthcare surveys or medical documents. This dataset is often derived from medical records or health surveys. It is used in medical research, particularly in studies focusing on cervical cancer prevention and early detection. Missing values are regular occurrences within real-world datasets, and utmost care should be taken to handle them efficiently to vouch for the validity of a data-based endeavor. The treatment of missing values may vary according to the nature of their manifestation, extent, and impact on the analysis. In case of missing values, replace them with the mean or median of the column and in case of categorical variables, replace missing values with the most frequent category.

Preprocessing and Machine Learning Models for Cervical Cancer Prediction

Supervised learning falls under machine learning, and it concerns training algorithms on a labeled dataset so that new data points can be accurately classified. Classification tasks can be defined in terms of two main categories: binary classification, in which a model predicts one of two possible outcomes, and multi-class classification, in which a prediction can belong to multiple classes. For practical purposes, a well-known Python-based framework for machine learning and data mining – sci-kit-learn – provides an extensive collection of tools. The library is highly efficient for binary and multi-class classification problems with tools for classification such as decision trees, support vector machines (SVMs), and logistic regression [43].

Several preprocessing activities were performed before training machine learning models, with the objective of ensuring data quality and reliability. First, a missing value analysis was conducted, in which the original records in the dataset with missing values were not removed, as removing partial records results in data loss and possible biases; the treatment instead was a mean substitution. In this scenario, the mean substitution method computes the mean of a given numerical column, and imputes it into each missing value for that column. The Synthetic Minority Over-sampling Technique (SMOTE) is applied to medical datasets to tackle their class imbalance problem by oversampling the minority class through the creation of artificial samples. The SMOTE methodology generates artificial instances by making new points from existing ones. It is preferable to fix data with shared values that may enhance predictive power of models used when identifying a case from minority class; thus, analytical models have a substantive advantage when spotting instances belonging to the underrepresented class.

In addition, since a majority of machine learning algorithms require numerical input, it was necessary to convert categorical/non-numeric columns into numeric format. We utilized encoding techniques depending on the type - label encoding or one-hot encoding, to ensure that machine learning models can process and learn from all features [44, 45]. These preprocessors were imperative for model performance, fairness, and creating a robust cervical cancer detection framework.

Random Forest Classifier

Random Forest (RF) is a classic form of ensemble learning in classification and regression. It works by building many decision trees, each constructed from a random sample of features and the training data. In classification, RF combines the predictions by majority voting, and in regression, it averages the predictions from all the trees. This combination approach improves the precision of predictions and, on top of that, reduces overfitting [23]. Besides its accuracy and adaptability, RF is particularly useful when feature importance needs to be evaluated as well as when incomplete data sets are present. These factors make RF a preferred choice in numerous sectors and their machine learning applications.

Decision Tree

Along with classification problems, decision trees can also be employed for regression problems. A machine learning method, decision trees are quite powerful, as well as interpretable. Furthermore, they follow a structured hierarchy resembling trees where features serve as internal decision nodes, the branches illustrate particular featured decision rules and the leaves present the resulting outcomes or predictions. Such a model is easily visualized and comprehended, therefore supporting the effective and practical usage of decision trees. This systematic approach helps decision trees to systematically split data and make predictions based on a predetermined set of conditions. In decision trees, the patterns are revealed by sequentially splitting data into smaller groups, and these can be used for trend analysis. Despite their simple interpretation and practice, overfitting is relatively common when the data under consideration is complex, and risk of overfitting is thus relatively high [24, 25]. However, they can overfit, mainly when dealing with intricate datasets. Tightening up and figuring out the maximum depth are two strategies to help resolve this problem.

Logistic Regression

Logistic regression analysis is one of the statistical methods explicitly used in binary classification problems. It calculates the likelihood of an event occurring either above or below a threshold value based on one or more explanatory variables, which in this case are considered predictors. In this, a logistic function is applied to transform a linear combination of input variables into probability values between 0 and 1. As a model with good interpretability, logistic regression allows it to establish a relationship between predictors and outcomes [26]. Moreover, it is computationally efficient and is optimal when the relation between independent and dependent variables follows a linear pattern. However, it can encounter difficulties in dealing with nonlinear ties and is also vulnerable to multicollinearity among the predictors [27].

K-nearest neighbors

K-Nearest Neighbors (KNN) is a popular machine learning algorithm used for both supervised classification and regression tasks. Its core principle is built on the belief that data outcomes tend to be similar based on their spatial proximity to one another. KNN assigns labels to instances based on the most prevalent class of the k nearest neighbors (for classification) or computes the mean of their values (for regression). In finding closeness, distance metrics are used, with Euclidean distance being the most prevalent. KNN is described as a non-parametric method in that it makes no assumptions about the data structure; this property grants flexibility across numerous areas of application [28]. Although KNN is straightforward and efficient, it lacks scalability due to the ever-increasing amount of data. The computational work required to calculate distances for each prediction makes this a burdensome task.

Extreme Gradient Boosting

Regression and classification are combined using XGBoost, an optimized gradient-boosting technique. It is well known for its effectiveness and speed, and is one of the methods for collaborative learning. Following one another. XGBoost generates multiple decision trees that correct each other's mistakes. Gradient descent optimization techniques are used to minimize the loss function, resulting in a highly accurate prediction model [29]. Aside from giving features relevant to scores, XGBoost can manage missing values internally and simulate complex interactions between variables. Large datasets may necessitate extensive computer training, and hyperparameters may need to be finely tuned to minimize overfitting [30].

Support Vector Machine

Support Vector Machine (SVM) attempts to achieve the best classification for a given dataset by analyzing the optimum separation of features using hyperplanes, finding multiple areas classified as one type in regions separated from the other type. Dissimilar tasks and core duties can be managed effectively through SVM. SVM is useful in the case of classification of complex and high-dimensional datasets because it incorporates nonlinear relationships within the data using various types of kernels, including the radial basis function (RBF), polynomial, and linear kernels [31]. "In space, the SVM tries to find the appropriate optimal separation boundary which separates the classes or groups accurately." In simpler terms, an algorithm class overlap refers to where a specific portion of a cluster gets modified to try to fit into another higher-defined cluster. It

attempts to enhance classification accuracy. It is designed to reduce overfitting, which is a common problem in systems with high-dimensional spaces. On the downside, SVM requires intensive computations and is highly susceptible to the selection of kernel and its hyperparameters.

Extra Tree Classifier

The Extra Trees Classifier is multiformed as an ensemble learner, which is used for classification and regression tasks. Just like Random Forests, it builds many decision trees during the training process. However, in deeper random forests, Extra Trees randomly take both the split and the features for each split selection, which adds more diversity to the model. This greater level of variability improves the model's strength. It reduces the variance, making it work more optimally on complex datasets. Stronger model robustness and decreased variance are a result of this additional degree of unpredictability [32]. Compared to standard decision trees, this method is less prone to overfitting. It is capable of handling large, highly dimensional datasets. It works remarkably well. The best results with Extra Trees require careful adjustment of hyperparameters, but they offer excellent accuracy and computational efficiency.

Categorical Boosting

CatBoost, along with other gradient-boosting algorithms, are designed to handle categorical features well. It is well known for its ability to perform classification and regression tasks on categorical data without necessitating extensive preparation. CatBoost automatically encodes categorical features and applies sophisticated techniques to reduce overfitting and improve generalization. It is resistant to overfitting, handles missing values internally, and can be trained on massive datasets efficiently. CatBoost is also relatively efficient, often requiring fewer hyperparameter adjustments than other boosting algorithms. Due to its versatility and user-friendliness, it is a favorite among the variety of functions in machine learning applications [33].

Gradient Boosting

Gradient boosting is an advanced ensemble method utilized for classification and regression tasks, and it is particularly powerful. This method builds models in a sequence such that every new model improves on the errors of previous models. Complex datasets require sophisticated modeling, and gradient boosting achieves this by minimizing residual errors to increase predictive accuracy. Gradient Boosting minimizes a loss function with gradient descent to get the best performance of its base learner, decision trees. It is an incredibly accurate predictive model [33] which is obtained from this iterative process. Gradient Boosting is a versatile method that can handle a variety of data types and distributions. It is particularly effective with big data and can detect intricate patterns. However, hyperparameter tuning is necessary to mitigate overfitting; this step is, however, highly resource-intensive, particularly with large data sets.

Adaptive Boosting

Besides being a general ensemble learning technique, AdaBoost has proven to be very effective for classification tasks. Combining multiple weak learners, such as decision trees with a small number of splits (stumps), improves the predictive performance. It is an algorithm where weights are assigned to training samples. The weights are iteratively updated according to the errors generated by the previous classifiers (who have been trained using weights); more weights are assigned to the training samples that are misclassified. Improvement in overall accuracy is achieved by combining output of weak learners and deriving a final predictive model [34, 35]. Besides, it is straightforward to implement, and it can produce very effective weak classifiers. It, however, is sensitive to noisy data and outliers and suffers from efficiency issues when base learners are incredibly complex.

Approach for Handling Numerical Data Features

There are multiple crucial steps in the suggested methodology for processing numerical data aspects. Data preprocessing is first carried out to manage missing values and outliers for quality and consistency. To find the most pertinent features and maybe improve model performance, feature selection techniques are used. The optimal performing model is identified by training and evaluating machine learning methods. Lastly, hyperparameter adjustment is done to maximize the chosen model's accuracy and endurance [36, 37].

Algorithm 1. Detection of cervical cancer using voting classifier

Procedure: Initialise classifiers, Train data X, labels y

1. Split the data into training and testing sets.
2. Train each base classifier (RF) on the training data.
3. for each trained base classifier to make predictions on the test set.
4. **for** i **in** 1 to **len** (X_{test}) do
5. $pred_{RF} \leftarrow$ RF.predict (X_{test} [i])
6. ensemble_vote ← Majority_vote
7. Append ensemble_vote to predictions
8. **end** for
9. **return** predictions

The predictive probabilities for individual test samples are computed as the sum of predictions across all n Random Forest models RFi undergoes Hard voting criterion [38, 39].

$$\hat{y} = argmax_{\,c} \sum_{m=1}^{n} I(\hat{y}_m = c) \quad (1)$$

In this expression (1), $\hat{y}$ denotes the predicted class for a sample. $\hat{y}_m$ specifies the predicted class by classifier *m* for a particular sample *m*. $I(\hat{y}_m = c)$ this function 1 if $\hat{y}_m$ equals to c, and 0 otherwise.

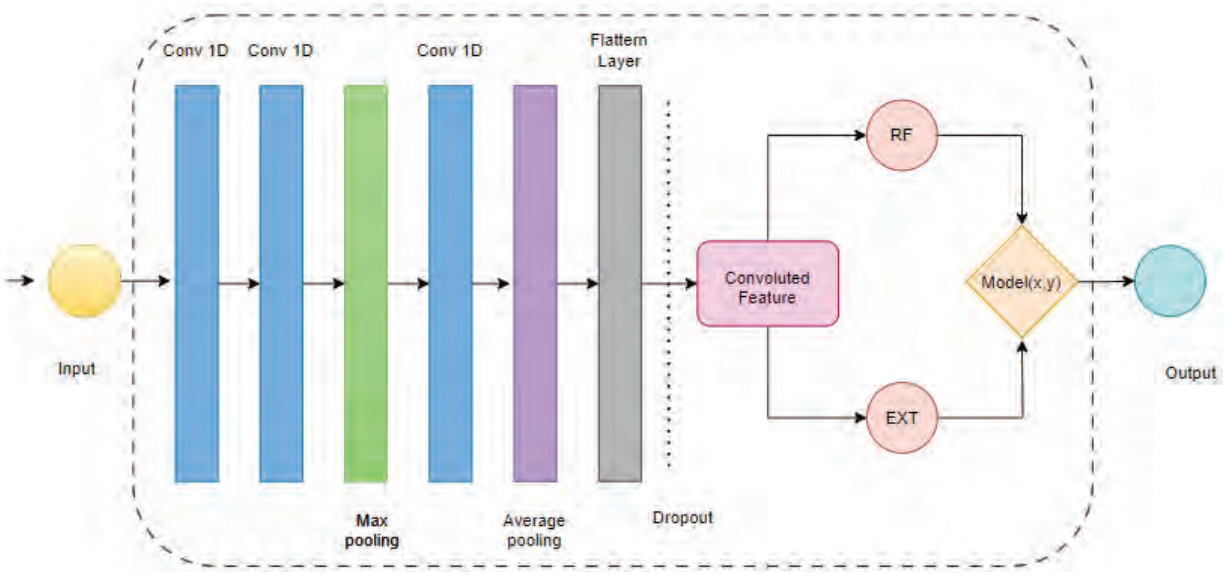


Figure 2. Cervical cancer detection model.

A Keras based model utilises a CNN (Convolutional Neural Network) architecture to handle one-dimensional input data. The dataset informs the input layer which serves as the model's starting point. The model consists of three sequential convolutional layers with 32, 64, and 128 filters respectively. Each layer contains a kernel of size three with non-linear activation through a ReLU function. To manage overfitting, increase the spatial dimensionality of the feature maps, and mitigate overfitting, each convolutional layer is followed by a 2x2 max-pooling layer. After the convolutional processes, the intermediate 3D feature maps are converted to a 1D vector. This vector is processed by a dense layer featuring 128 ReLU neurons. A crucial component for regulating overfitting is a 0.5 dropout layer prior to the final output layer. This regulates additional overfitting while preserving essential model performance features.

Evaluation Metrics

To provide a complete assessment of our ensemble technique, we apply a set of metrics that are varied in nature. While general model evaluation is usually conducted by measuring accuracy, class-specific performance is captured using precision and recall—two key metrics that determine how well the model captures true positives while mitigating the pitfalls of false positives and true negatives. The F1 score, best suited for imbalanced datasets, is the metric that balances precision and recall. In addition to measuring class distinction errors, the Receiver Operating Characteristic - Area Under the Curve (ROC AUC) metric is also used. Classification becomes more robust with higher values of the ROC AUC while greater discrimination of positive and negative instances indicates better performance. These capabilities make the metric very important for classification tests.

$$\text{Accuracy} = \frac{TP + TN}{TP + TN + FP + FN} \tag{2}$$

$$\text{Precision} = \frac{TP}{TP + FP} \tag{3}$$

Expression 2 shows the whole model as overall correct or to have ratio of correctly predicted to total observations, just accurate. As precision, expression (3) is the correctness of optimistic prediction only.

$$\text{Recall} = \frac{TP}{TP + FN} \tag{4}$$

$$\text{F1 score} = 2 \times \frac{Precision \times Recall}{Precision + Recall} \tag{5}$$

$$\text{ROC} = \int_0^1 TPR(FPR)d(FPR) \tag{6}$$

TP = True Positives , TN = True Negatives
FP = False Positives , FN = False Negatives

Recall reflects the level of fulfilment of positive assertions made, and it is regarded as a useful metric, as it was presented in Equation (4). It evaluates the efficiency of a given set model in identifying real positive instances while ensuring that none are overlooked. F1 Score, defined as the result of harmonic function of Precision and Recall, offers some balance between two ratios discussed above. This is expressed in Equation (5) in addition to allowing for a compromise between precision, which seeks to reduce false positives, and recall, which aims to reduce false negatives.

Table 1. Summary of the research work

Ref	Models	Dataset	Performance Metric
[16]	ML and Deep Learning Algorithms + Artificial Neural Network	UCI database Cervical Cancer	93% accuracy
[17]	CNN + Fuzzy distance-based ensemble	SIPaKMed	98.58% accuracy with AUROC
[18]	CNN + transfer learning with 2 and 7-class classification	Harvel dataset	94.5% accuracy
[19]	Inceptionv3 + transfer learning	Harvel dataset	98.23% accuracy
[20]	Ensemble classification + k-means clustering	SIPaKMed	98.27% accuracy
[21]	lasso regression + SMOTE + DT for classification	Universitario de caracas dataset	98.72% accuracy
[22]	LWNB + RF + Logistic regression	Hospitals of Jordan	92.3% accuracy

The ROC curve objectively captures a classifier's performance. The TPR incorporates the FPR, and the relationship between them is defined by trade-off. As one goes up, so must the loss of the other, as illustrated by Equation (6). This is one of the essential aspects when it comes to assessing model performance and seeing how well the model breaks down classes.

RESULTS

A number of evaluations were done to detect cervical cancer using both distinct and intricate features in machine learning models. When results were analyzed, an ensemble of the top models was used in additional tests. Both feature sets were subjected to this ensemble. The models' performance was then assessed by comparing the outcomes. The analysis must check whether there is an equal weight of true positive and true negative predictions. Sensitivity (recall) and specificity were evaluated so that the model performs well in classifying cancerous and non-cancerous patients. Also, it is necessary to determine if the model suffers from overfitting. High accuracy values indicate that the model fits training instances closely and does not acquire generalized patterns. Cross-validation and unseen test sets are used to determine if the model is robust across different datasets. Incorporating such discussions would lend strength to the analysis and enhance the model's credibility in applications for the real world of clinical features (Table 1).

Table 2. Experimental setup for the model

Language	Python 3.10.12
RAM	8 GB
OS	64-bit Windows 11
CPU	Inter(R) core(TM) 11th gen i3@3.00GHz
GPU	Intel UHD Graphics
TensorFlow version	2.15.0

Experimental Setup

The system runs on a 64-bit Windows 11 OS and features an 11th gen Intel Core i3 processor at 3.00GHz, coupled with 8 GB of RAM. It utilizes Intel UHD Graphics and is equipped with TensorFlow version 2.15.0, making it suitable for fundamental machine learning tasks and development in Python 3.10.12. The following details about the experimental setup are given in Table 2.

Comparing Performance of Various Machine Learning Models on Original and Convoluted Features

In general, there is a perceived improvement in model accuracy when convoluted features are used. With convoluted features, both SVM and logistic regression, which did pretty poorly with the original features as given in Table 3, significantly improved, and both achieved 90.35% accuracy. With convoluted features, models with excellent accuracy with original features, like Random Forest and Extra Trees Classifier, performed somewhat deeper, scoring about. These minor differences, however, show the resilience of these models to various feature sets. XGBoost, Extra Trees Classifier, and AdaBoost all show great accuracy and efficient feature convolution used to achieve the

Table 3. Accuracy of models with original features

Model	Accuracy with original features
LR	65.56%
DT	89.25%
RF	93.38%
KNN	86.50%
SVM	64.18%
XGB Model	90.35%
ETC	93.66%
Ada Boost	74.38%
Cat Boost	88.98%
Gradient Boost	83.19%

highest performance using convoluted data, as shown in Table 4. Significant progress was also demonstrated via gradient boosting. Convoluted features, in general, greatly improved model performance, particularly for models that did not perform as well with the original features at first. This is shown in Figure 3, which shows how feature engineering can be used to improve model accuracy.

Based on the performance comparison, the Extra Trees Classifier (ETC) performs with the best accuracy, with the original features at 93.66%, as shown in Figure 4.

However, with convoluted features, AdaBoost achieved the highest accuracy at 90.90%, as shown in Figure 5.

In this analysis, the feature engineering was paramount to improving model performance through better quality

Table 4. Accuracy of models with convoluted features

Model	Accuracy with Convoluted features
LR	90.35%
DT	92.28%
RF	92.28%
KNN	90.35%
SVM	90.35%
XGB Model	90.63%
ETC	92.01%
Ada Boost	90.90%
Cat Boost	90.50%
Gradient Boost	91.73%

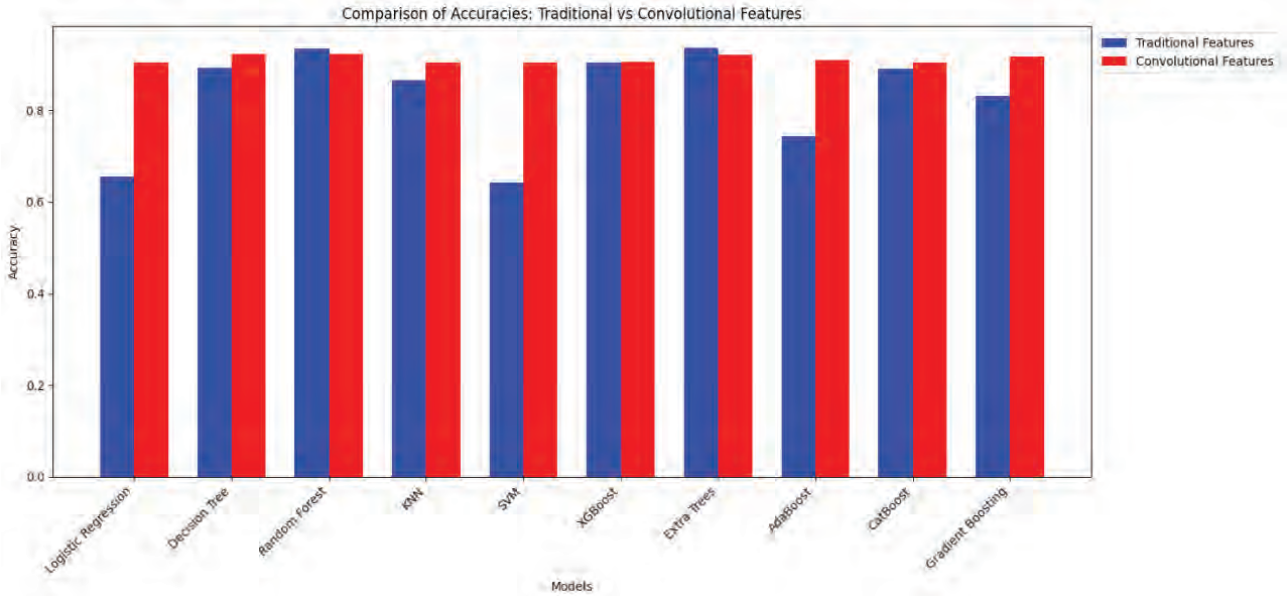


Figure 3. Comparison of original and convoluted features.

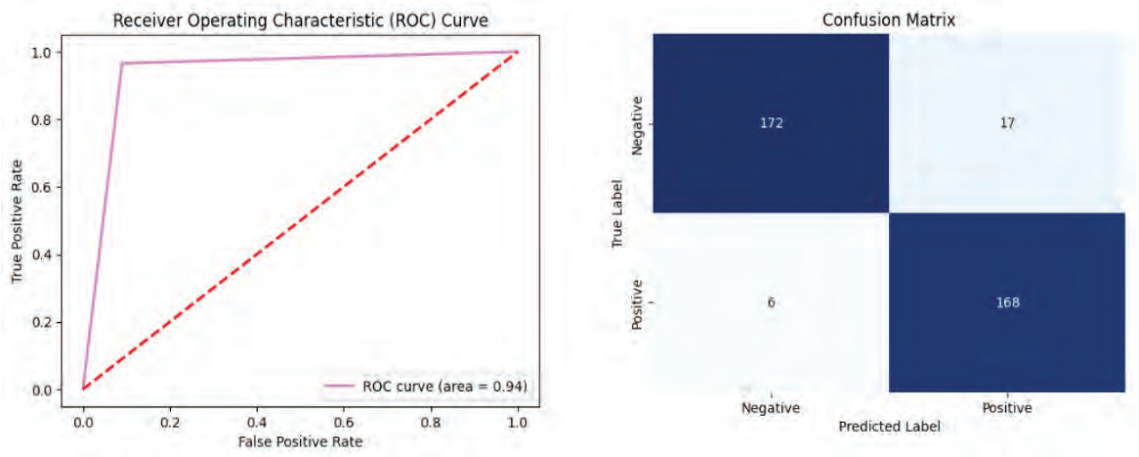


Figure 4. Extra tree classifiers with original features.

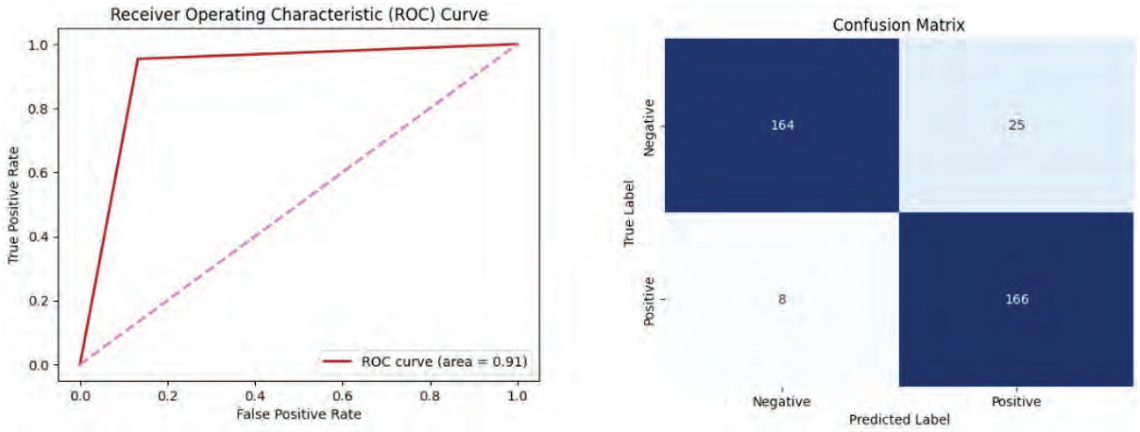


Figure 5. AdaBoost with convoluted features.

input features. The utilized data was initially derived from patient records and a dataset of raw patient record features. To identify and construct more informative patterns from the original dataset, which involved applying a number of feature engineering methods. The model constructed features were compared to the raw features in their original form, statistical transformations, such as mean, standard deviation (SD), and range, to estimate variability and distribution characteristics of continuous variables from which they were initially derived. For categorical features, for example, we applied acceptably appropriate encoding techniques, including one-hot and label encoding, to transform textual features into numbers that could be directly imported into the model. Next, some interaction features were constructed through multiple relevant original features (e.g., creating a variable to indicate age of pregnancies). Every feature was transformed, or not transformed raw features, into a consistent set of features, which reflects real-world impact of clinical settings on approximating risk for developing cervical cancer. Raw and feature-engineered features combined produced a more informative dataset, which enhanced contribution of the features for training the ensemble model; the engineered features provided a feature set that explained extreme amounts of variance in validation and test model accuracy.

Performance of Ensemble Model

Effectiveness of ensemble learning as an approach is often complicated for RF models in combination with other models, as the integration of intricate features can undermine performance results. Results are dependent on the value of additional features in improving generalization and accuracy of prediction. Enhanced feature complexity may improve the decision boundaries. Nevertheless, issues can arise as a result of overfitting or excessive processing costs in relation to how a dataset and model interact. RF combined with Decision Tree (DT) and RF merged with Extra Trees Classifier (ETC) yield a notable maximum accuracy of 92.28%, but the latter's overfitting undermines the former model's accuracy. By combining advantages of both RF and the secondary model, these combinations suggest the possibility of a marginal improvement over individual models in Table 5. Additional combinations exhibit competitive performance as well. Gradient Boosting (GB) and RF together yield accuracy of 92.01%, which is not far behind the best combinations. This implies that RF's strong feature selection can be enhanced by GB's capacity to strengthen weak models. The RF and Logistic Regression (LR), as well as RF and Support Vector Machine (SVM), achieve accuracy of 91.46%. RF may still produce high results, but it is marginally lower than other ensembles. These combinations show how RF can improve the decision boundaries of more complicated models like SVM and simpler models like LR. RF with AdaBoost and RF with CatBoost combinations have somewhat lower accuracy. The comparison of the complete ensemble model accuracies is shown in Figure 6. They nonetheless gain from RF's feature selection capabilities, which provide the boosting techniques more stability.

The hybrid ensemble learning technique integrates convolutional neural networks (CNN) with other machine learning models such as Random Forest and Extra Trees

Table 5. Accuracy of ensemble model using convoluted features

Model	Accuracy
RF + LR	91.46%
RF + DT	92.28%
RF + SVM	91.46%
RF + XGB Model	90.90%
RF + ETC	92.28%
RF + Ada Boost	91.18%
RF + Cat Boost	91.10%
RF + Gradient Boost	92.01%

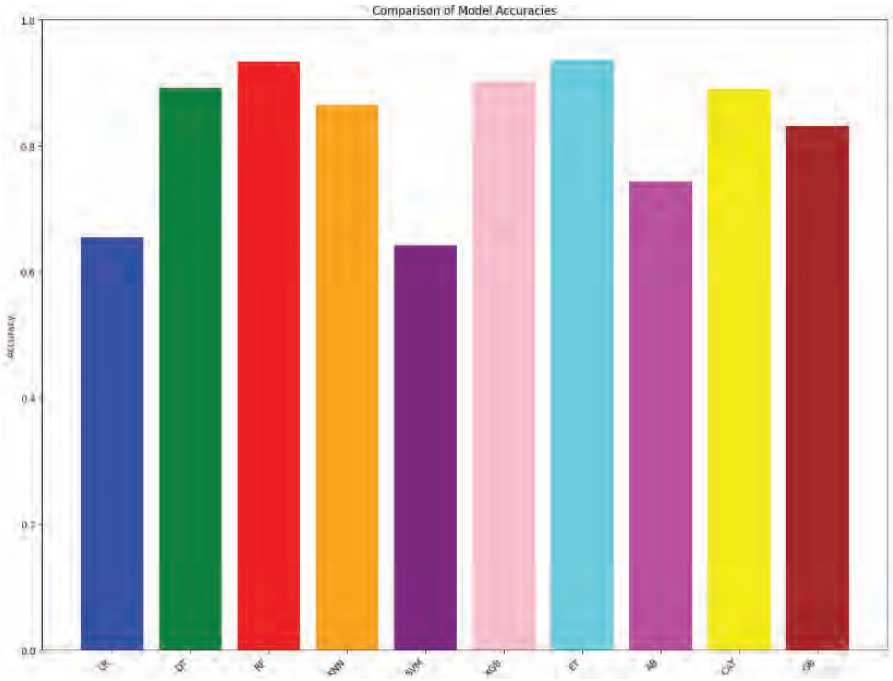


Figure 6. Comparison of ensemble model accuracies.

Classifier. This is done to take advantage of the strengths of each algorithm. Although the machine learning models may seem somewhat redundant because they rely on decision trees and an ensemble method, they differ enough to justify inclusion in the study. Random Forest utilizes multiple decision trees and bootstrap sampling. Random Forest narrows down to get the best split from among a randomly selected subset of features, while introducing randomness to reduce overfitting, while still having a high degree of accuracy. The Extra Trees (Extremely Randomized Trees) classifier has even more randomness by using the entire dataset (no bootstrapping) and selecting the split points randomly rather than selecting the best split. This makes Extra Trees computationally more efficient, and even more importantly, discovery of patterns resistant to noise is better. The intention of including both models is to maximize diversity in the base learners. Maximizing diversity in the base learners is a significant component of ensemble learning. Academics have shown that when learners are carefully chosen, diversity can yield models that generally perform better. Many conceivable attributes restrict individual models, and subtle differences like these in data sampling and feature splits are able to garner totally different contributions and insights to the final prediction.

Hyperparameter Tuning

This study combines the Random Forest and XGBoost classifiers to show how ensemble learning approaches can be used. It involves creating a Voting Classifier and specifying parameter distributions for both classifiers [40, 41]. Hyperparameter tuning is carried out using RandomizedSearchCV, optimizing performance of the ensemble model. This search yields the optimal parameters and estimator. The accuracy of the Voting Classifier, once it has been optimized, is then determined by testing it on a different dataset [42]. Ultimately, a thorough classification report that offers insights into the model's performance in several classes is produced. Robust prediction performance is achieved by utilizing the capabilities of many classifiers in this strategy [43, 44].

Performance of K-Fold Validations

In order to comprehensively assess differences in model performance, we conducted a statistical significance test through a paired t-test on the evaluation metrics containing accuracy, precision, recall, and F1-score from the 5-fold cross-validation. The t-test evaluates the effectiveness of proposed Hybrid Ensemble against the baseline classifiers. These performance differences were statistically significant ($p<0.05$), which strengthens the claim that our proposed hybrid model outperformed each base model. This also reinforces the accuracy and dependability of the comparative analysis.

The functioning of the model is evaluated with the help of 5-fold cross-validation over different data sets. The entire dataset is split into five equal parts. One part is preserved for validation in each fold, while the other four parts are used in training. This ensures consistency and reliable assessment of performance. Table 6 presents that the ensemble model achieved a mean accuracy of 97.10%. Figure 7 illustrates that in fold 3, the averaged metrics of accuracy score, precision, recall, and F1 score were reported as 0.989%, 0.992%, 0.993%, and 0.991%, respectively.

Table 6. K-fold cross-validation results for the proposed ensemble model

Fold	Accuracy	Precision	Recall	F1 - Score	ROC - AUC
1	97.59%	97.50%	98.10%	97.59%	0.98
2	95.86%	96.30%	96.10%	96.30%	0.96
3	**98.96%**	**99.25%**	**99.30%**	**99.15%**	**0.99**
4	97.24%	97.55%	97.32%	97.30%	0.97
5	95.86%	95.52%	95.50%	95.58%	0.96
Avg.	97.10%	97.22%	97.26%	97.28%	0.97

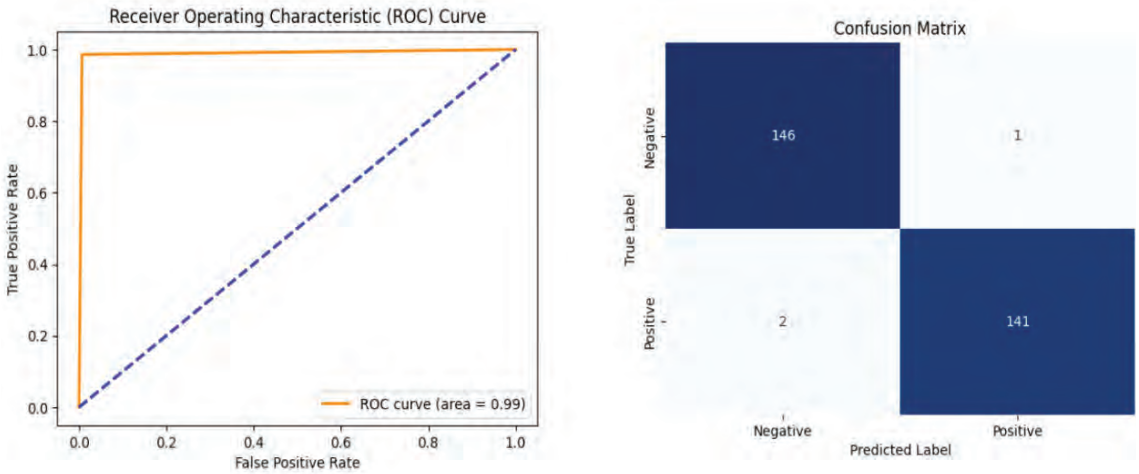


Figure 7. Best outcome of ensemble model (fold 3).

DISCUSSION

Cervical cancer is an emergent health issue and worldwide concern that needs amelioration through early detection techniques to improve the outcomes of patient treatment. In fact, the present study focused on this problem by suggesting a new framework of ensembles to integrate feature extraction for classification through different machine-learning strategies, random forests, decision trees, logistic regressions, and boosting techniques. Machine Learning models are creating additional opportunities in cervical cancer detection apart from aiding in early diagnosis, enhancing screening accuracy, and supporting clinical decision-making.

1. These models analyze Pap smear images to recognize abnormal cervical cells. This reduces manual errors and promotes early detection.
2. Logistic regression and ensemble models are used for risk stratification.
3. AI-based applications and cloud-based Machine Learning allow screening in remote areas where expert pathologists cannot be found.
4. ML models trained on smartphone microscopy images provide an inexpensive and scalable solution to diagnosis.

Regardless of the advances made in cervical cancer detection by ML-based approaches, there are many hurdles to be resolved in order to ensure successful world deployment. The issue of biased predictions posed by data quality and imbalanced data is one of the real challenges in medical datasets. The ethical and privacy concerns subsist due to the very sensitive nature of medical data, which needs to be acknowledged within strict protocols. The quality issues of bias in training data lead to one or the other demographic being unfairly predicted, raising ethical concerns in healthcare AI. For accessibility in underdeveloped and remote areas, optimizing architectures for the edge remains relevant. A model produced under study could show strong performance with accuracy as high as 98.96% and was further validated through K-fold cross-validation steps, ensuring those benefits of robustness and reliability. These findings further establish the base of ensemble methods that hold promise towards such complementary strengths between deep learning and machine learning in clinical diagnosis. However, a few limitations remain, for example, the need for interpretability and the fact that it should be

applicable in resource-constrained environments, which now mark out their further usage in the actual scenario outside settings.

CONCLUSION

Cervical cancer maintains its status as one of the most prevalent and lethal cancers in women, continually contributing to cancer mortality rates globally. Decreasing death rates and enhancing patient management outcomes depends on accurate and timely diagnosis. In response to this challenge, we propose a new computational framework for increasing the accuracy of cervical cancer diagnosis by merging features from various fields of data and numerical analytics. The significant results of our research are:

1. The ensemble learning framework synthesized a convolutional neural network (CNN) with multiple classifiers and achieved predictive accuracy of 98.96%.
2. Feature engineering and feature selection were also integral in improving model performance.
3. Robustness testing through K-fold cross-validation ensures reliability.
4. Realization of advanced accuracy rates for cervical cancer detection.
5. A firm comparative analysis indicates that our proposed framework was successful in improving cervical cancer diagnosis capability.

By computing multiple sources of data, the proposed framework achieves better prediction accuracy and enhances understanding of the underlying factors related to the diagnostic ability. The results from this research work thus support the constructive deployment of machine learning in revolutionizing medical diagnostics towards making timely and accurate diagnoses of cervical cancer.

The findings illustrate the necessity of using deep learning approaches under machine learning to address complex healthcare challenges. Therefore, for future enhancement of the detection of cervical cancer with an ML-based system, there are several integral routes forward. Nevertheless, the study does have some limitations. The model was tested only on one dataset; it was not tested with any external datasets to evaluate the generalizability of its predictions, and the real-time deployment of the model in a clinical situation and its evaluation are not the intent of this study. These are essential next steps to evaluate its functionality in real-world health care workflows. The advancement of this line of work has clear next steps planned, including the validation of the model on external and multi-center datasets, conducting real-world clinical trials, and deploying the system for real-time use in clinical situations. The implementation of explainable AI techniques, SHAP and LIME, improves the model's interpretability, which could enhance clinicians' trust in the decision-support system.

Additionally, several goals could lead to revitalizing implementation, including the use of lighter-weight architectures for low-resource settings and the implementation of system interfaces with electronic health records (EHRs) through standardized application programming interfaces (APIs), which could enhance real-time decision support and accessibility. Transfer learning is an additional possibility that could improve model generalizability and training time. All these aspects would benefit the advancement of machine learning-based cervical cancer detection systems designed to be clinically relevant, valid and accurate, interpretable, and accessible.

NOMENCLATURE

CNN	Convolutional Neural Network
HPV	Human Papillomavirus
WHO	World Health Organization
RF	Random Forest
DT	Decision Tree
LR	Logistic Regression
KNN	K-Nearest Neighbors
XGB	Extreme Gradient Boosting
SVM	Support Vector Machine
ETC	Extra Tree Classifier
CatBoost	Categorical Boosting
GB	Gradient Boosting
AdaBoost	Adaptive Boosting
AUROC	Area Under Receiver Operating Characteristic Curve
EHR	Electronic Health Record
CAD	Computer-Aided Diagnosis
SMOTE	Synthetic Minority Over-sampling Technique

Greek Symbols

α (alpha)	Learning rate
β (beta)	Coefficients in regression models
Σ (sigma)	Summation
μ (mu)	Mean of a distribution
σ (sigma)	Standard deviation
λ (lambda)	Regularization parameter

AUTHORSHIP CONTRIBUTIONS

Authors equally contributed to this work.

DATA AVAILABILITY STATEMENT

The data that support the findings of this study are openly available at the following URL: https://www.kaggle.com/datasets/ranzeet013/cervical-cancer-dataset

CONFLICT OF INTEREST

The authors declared no potential conflicts of interest with respect to the research, authorship, and/or publication of this article.

ETHICS

There are no ethical issues with the publication of this manuscript.

STATEMENT ON THE USE OF ARTIFICIAL INTELLIGENCE

Artificial intelligence was not used in the preparation of the article.

REFERENCES

[1] Meza Ramirez CA, Greenop M, Almoshawah YA, Martin Hirsch PL, Rehman IU. Advancing cervical cancer diagnosis and screening with spectroscopy and machine learning. Expert Rev Mol Diagn 2023;23:375–390. [CrossRef]

[2] Chauhan NK, Singh K. Performance assessment of machine learning classifiers using selective feature approaches for cervical cancer detection. Wirel Pers Commun 2022;124:2335–2366. [CrossRef]

[3] Singh SK, Goyal A. Performance analysis of machine learning algorithms for cervical cancer detection. In: Research Anthology on Medical Informatics in Breast and Cervical Cancer. IGI Global; 2023. p. 347–370. [CrossRef]

[4] Chen H, Liu J, Wen QM, Zuo ZQ, Liu JS, Feng J, et al. CytoBrain: cervical cancer screening system based on deep learning technology. J Comput Sci Technol 2021;36:347–360. [CrossRef]

[5] Park YR, Kim YJ, Ju W, Nam K, Kim S, Kim KG. Comparison of machine and deep learning for the classification of cervical cancer based on cervicography images. Sci Rep 2021;11:16143. [CrossRef]

[6] Pacal I, Kılıcarslan S. Deep learning-based approaches for robust classification of cervical cancer. Neural Comput Appl 2023;35:18813–18828. [CrossRef]

[7] Akter L, Islam MM, Al-Rakhami MS, Haque MR. Prediction of cervical cancer from behavior risk using machine learning techniques. SN Comput Sci 2021;2:177. [CrossRef]

[8] Sellamuthu Palanisamy V, Athiappan RK, Nagalingam T. Pap smear based cervical cancer detection using residual neural networks deep learning architecture. Concurr Comput Pract Exp 2022;34. [CrossRef]

[9] Kalbhor M, Shinde S, Popescu DE, Hemanth DJ. Hybridization of deep learning pre-trained models with machine learning classifiers and fuzzy min-max neural network for cervical cancer diagnosis. Diagnostics (Basel) 2023;13:1363. [CrossRef]

[10] Fekri-Ershad S, Alsaffar MF. Developing a tuned three-layer perceptron fed with trained deep convolutional neural networks for cervical cancer diagnosis. Diagnostics (Basel) 2023;13:686. [CrossRef]

[11] Weegar R, Sundström K. Using machine learning for predicting cervical cancer from Swedish electronic health records by mining hierarchical representations. PLoS One 2020;15. [CrossRef]

[12] Kalbhor MM, Shinde SV. Cervical cancer diagnosis using convolution neural network: feature learning and transfer learning approaches. Soft Comput 2023:1–11. [CrossRef]

[13] Kalbhor M, Shinde S, Joshi H, Wajire P. Pap smear-based cervical cancer detection using hybrid deep learning and performance evaluation. Comput Methods Programs Biomed Imaging Vis 2023;11:1615–1624. [CrossRef]

[14] Kumawat G, Vishwakarma SK, Chakrabarti P, Chittora P, Chakrabarti T, Lin JCW. Prognosis of cervical cancer disease by applying machine learning techniques. J Circuits Syst Comput 2023;32:2350019. [CrossRef]

[15] Kalbhor M, Shinde S, Popescu DE, Hemanth DJ. Hybridization of deep learning pre-trained models with machine learning classifiers and fuzzy min-max neural network for cervical cancer diagnosis. Diagnostics (Basel) 2023;13:1363. [CrossRef]

[16] Kaushik M, Joshi RC, Kushwah AS, Gupta MK, Banerjee M, Burget R, et al. Cytokine gene variants and socio-demographic characteristics as predictors of cervical cancer: a machine learning approach. Comput Biol Med 2021;134:104559. [CrossRef]

[17] Mehmood M, Rizwan M, Gregus ML, Abbas S. Machine learning assisted cervical cancer detection. Front Public Health 2021;9:788376. [CrossRef]

[18] Pramanik R, Biswas M, Sen S, de Souza Júnior LA, Papa JP, Sarkar R. A fuzzy distance-based ensemble of deep models for cervical cancer detection. Comput Methods Programs Biomed 2022;219:106776. [CrossRef]

[19] Lin H, Hu Y, Chen S, Yao J, Zhang L. Fine-grained classification of cervical cells using morphological and appearance based convolutional neural networks. IEEE Access 2019;7:71541–71549. [CrossRef]

[20] Dong N, Zhao L, Wu CH, Chang JF. Inception v3 based cervical cell classification combined with artificially extracted features. Appl Soft Comput 2020;93:106311. [CrossRef]

[21] Win KP, Kitjaidure Y, Hamamoto K, Myo Aung T. Computer-assisted screening for cervical cancer using digital image processing of pap smear images. Appl Sci 2020;10:1800. [CrossRef]

[22] Tanimu JJ, Hamada M, Hassan M, Kakudi HA, Abiodun JO. Machine learning method for classification of cervical cancer. Electronics 2022;11:463. [CrossRef]

[23] Al-Batah MS, Alzyoud M, Alazaidah R, Toubat M, Alzoubi H, Olaiyat A. Early prediction of cervical cancer using machine learning techniques. Jordan J Comput Inf Technol 2022;8. [CrossRef]

[24] Ramzan Z, Hassan MA, Asif HM, Farooq A. A machine learning-based self-risk assessment technique for cervical cancer. Curr Bioinform 2021;16:315–332. [CrossRef]
[25] Sun L, Yang L, Liu X, Tang L, Zeng Q, Gao Y, et al. Optimization of cervical cancer screening: a stacking-integrated machine learning algorithm based on demographic, behavioral, and clinical factors. Front Oncol 2022;12:821453. [CrossRef]
[26] Jia AD, Li BZ, Zhang CC. Detection of cervical cancer cells based on strong features CNN-SVM network. Neurocomputing 2020;411:112–127. [CrossRef]
[27] Ji M, Zhong J, Xue R, Su W, Kong Y, Fei Y, et al. Early detection of cervical cancer by fluorescence lifetime imaging microscopy combined with unsupervised machine learning. Int J Mol Sci 2022;23:11476. [CrossRef]
[28] Sellamuthu Palanisamy V, Athiappan RK, Nagalingam T. Pap smear based cervical cancer detection using residual neural networks deep learning architecture. Concurr Comput Pract Exp 2022;34. [CrossRef]
[29] Waly MI, Sikkandar MY, Aboamer MA, Kadry S, Thinnukool O. Optimal deep convolution neural network for cervical cancer diagnosis model. Comput Mater Contin 2022;70. [CrossRef]
[30] Vargas-Cardona HD, Rodriguez-Lopez M, Arrivillaga M, Vergara-Sanchez C, García-Cifuentes JP, Bermúdez PC, et al. Artificial intelligence for cervical cancer screening: scoping review, 2009–2022. Int J Gynaecol Obstet 2024;165:566–578. [CrossRef]
[31] Suguna C, Balamurugan SP. An extensive review on machine learning and deep learning based cervical cancer diagnosis and classification models. J Comput Theor Nanosci 2020;17:5438–5446. [CrossRef]
[32] Singh J, Tan KT, Sahu D, Upreti K, Kshirsagar PR, Elangovan M. An investigation on machine learning models in classification and identifications cervical cancer using MRI scan. In: 2024 International Conference on E-mobility, Power Control and Smart Systems (ICEMPS). 2024. p. 1–5. [CrossRef]
[33] Nour MK, Issaoui I, Edris A, Mahmud A, Assiri M, Ibrahim S. Computer aided cervical cancer diagnosis using gazelle optimization algorithm with deep learning model. IEEE Access 2024. [CrossRef]
[34] Munshi RM. Novel ensemble learning approach with SVM-imputed ADASYN features for enhanced cervical cancer prediction. PLoS One 2024;19. [CrossRef]
[35] Mustafa WA, Ismail S, Mokhtar FS, Alquran H, Al-Issa Y. Cervical cancer detection techniques: a chronological review. Diagnostics (Basel) 2023;13:1763. [CrossRef]
[36] Chadaga K, Prabhu S, Sampathila N, Chadaga R, KS S, Sengupta S. Predicting cervical cancer biopsy results using demographic and epidemiological parameters: a custom stacked ensemble machine learning approach. Cogent Eng 2022;9:2143040. [CrossRef]
[37] Xue P, Ng MTA, Qiao Y. The challenges of colposcopy for cervical cancer screening in LMICs and solutions by artificial intelligence. BMC Med 2020;18:169. [CrossRef]
[38] Dweekat OY, Lam SS. Cervical cancer diagnosis using an integrated system of principal component analysis, genetic algorithm, and multilayer perceptron. Healthcare (Basel) 2022;10:2002. [CrossRef]
[39] Uddin KMM, Al Mamun A, Chakrabarti A, Mostafiz R, Dey SK. An ensemble machine learning-based approach to predict cervical cancer using hybrid feature selection. Neurosci Inform 2024;4:100169. [CrossRef]
[40] Devi S, Gaikwad SR, Harikrishnan R. Prediction and detection of cervical malignancy using machine learning models. Asian Pac J Cancer Prev 2023;24:1419. [CrossRef]
[41] Glučina M, Lorencin A, Anđelić N, Lorencin I. Cervical cancer diagnostics using machine learning algorithms and class balancing techniques. Appl Sci 2023;13:1061. [CrossRef]
[42] Mathivanan SK, Francis D, Srinivasan S, Khatavkar V, P K, Shah MA. Enhancing cervical cancer detection and robust classification through a fusion of deep learning models. Sci Rep 2024;14:10812. [CrossRef]
[43] Xiao T, Wang C, Yang M, Yang J, Xu X, Shen L, et al. Use of virus genotypes in machine learning diagnostic prediction models for cervical cancer in women with high-risk human papillomavirus infection. JAMA Netw Open 2023;6. [CrossRef]
[44] Chikaraddi AK, Kanakaraddi S, Kalwad P, Kadole A, Budni S. Cervical cancer diagnostics using machine learning algorithms. In: 2024 5th International Conference for Emerging Technology (INCET). 2024. p. 1–6. [CrossRef]
[45] Arora M, Dhawan S, Singh K. Cervical cancer diagnosis and prediction: an application of machine learning techniques. In: Computational Intelligence in Analytics and Information Systems. Apple Academic Press; 2023. p. 213–226. [CrossRef]

Sigma J Eng Nat Sci, Vol. 44, No. 4, pp. 2473–2508, August, 2026

Sigma Journal of Engineering and Natural Sciences
Web page info: https://sigma.yildiz.edu.tr
DOI: 10.14744/sigma.2026.2110

Research Article

A study on physics-informed neural networks and finite volume approach for Maxwell fluid simulation in stenosed coronary arteries

Abdul WAHAB[1,*], Muhammad Imran ASJAD[1,2], Sohail NADEEM[3], Kubra ANJUM[4]

[1]*Department of Mathematics, University of Management and Technology, Lahore, 54770, Pakistan*
[2]*Center for Theoretical Physics, Khazar University, Baku, AZ 1096, Azerbaijan*
[3]*Department of Mathematics, Quaid-i-Azam University, Islamabad, 45320, Pakistan*
[4]*Department of Medical Sciences, Gujranwala Medical College, Gujranwala, 52310, Pakistan*

ARTICLE INFO

Article history
Received: 30 July 2025
Revised: 14 October 2025
Accepted: 27 November 2025

Keywords:
ANSYS; Artificial Intelligence; Coronary Computed Tomography Angiography; Coronary Stenosed Artery Disease; Finite Volume Method

ABSTRACT

This study investigates the role of artificial intelligence in coronary computed tomography angiography analysis, with a focus on the mathematical modeling of stenosed coronary arteries. A detailed comparative analysis is performed between physics-informed neural networks and the finite volume method implemented in the computational software "Analysis System" (ANSYS) environment, both used to solve the governing equations comprising partial and ordinary differential equations that describe the Maxwell viscoelastic behavior of blood and its associated velocity–pressure distributions. Physics-informed neural networks, through their ability to directly embed physical conservation laws into the neural network structure, demonstrate superior capability in producing smooth, accurate, and stable solutions for complex coronary geometries. In contrast, the finite volume method, based on mesh-dependent approximations, shows limitations in addressing strong nonlinearities and geometric irregularities inherent in stenosed arterial flow. The findings reveal that the physics-informed neural network framework outperforms the finite volume method in terms of accuracy, computational efficiency, and adaptability to real-world biomedical complexities. The novelty of this study lies in the first integration of the Maxwell viscoelastic blood model within a physics-informed neural network framework for simulating flow and heat transfer in stenosed coronary arteries, along with a comprehensive validation against the finite volume method. This hybrid approach bridges the gap between artificial intelligence and classical fluid dynamics, offering a robust, mesh-free, and physics-consistent methodology for hemodynamic analysis. Although both methods still face challenges in matching the precision of invasive techniques such as fractional flow reserve, the incorporation of advanced imaging reconstruction and explainable artificial intelligence can further enhance the reliability of non-invasive coronary flow assessment.

Cite this article as: Wahab A, Asjad MI, Nadeem S, Anjum K. A study on physics-informed neural networks and finite volume approach for Maxwell fluid simulation in stenosed coronary arteries. Sigma J Eng Nat Sci 2026;44(4):2473–2508.

***Corresponding author.**
*E-mail address: wahabgujjar175@gmail.com

This paper was recommended for publication in revised form by Editor-in-Chief Ahmet Selim Dalkilic

Published by Yıldız Technical University Press, İstanbul, Turkey
© Author. This is an open access article under the CC BY-NC license (http://creativecommons.org/licenses/by-nc/4.0/).

INTRODUCTION

The leading cause of mortality worldwide is still coronary artery disease. The newly introduced computed tomography scanners with their autodetection technology have made it feasible to obtain a high-resolution picture of cardio vascular system especially heart and coronary arteries within a heartbeat. Consequently, coronary computed tomography angiography provides unprecedented potential to mitigate the illness with precise identification of calcium in coronary artery and also plaque. The ability to probe the hemodynamic importance of coronary artery stenoses using advanced modeling and image processing, coronary computed tomography angiography was recently stood at the highest rank. For the evidence, the tool was used on few suspected coronary artery disease to evaluate reliability and validity [1]. The labor-intensive nature of extensive coronary computed tomography angiography analysis and the need for highly qualified specialists to interpret images now restricted. The advancements in the artificial intelligence have evidently enhanced the working phenomenon by providing a degree of detail of coronary computed tomography angiography analysis [2]. Additionally, the amount of data in coronary computed tomography angiography exams is far greater than what even the most skilled observers can manually analyze. With the help of scientific advancement in deep learning, we examine current artificial intelligence advancement that are pertinent to coronary computed tomography angiography here, examining the cardiovascular system including heart and majorly concerning artery, coronary artery, overall (Fig. 1).

The foundation of coronary computed tomography angiography is coronary artery analysis, which offers firsthand knowledge of coronary artery disease [3]. Anatomically and functionally important stenoses can result from obstruction of the major blood arteries feeding the heart, which is characterized by a number of diseases [4]. The automated analysis of coronary computed tomography angiography using AI has attracted a lot of attention because of the wide heterogeneity in anatomy and pathology. Both human and computerized coronary computed tomography angiography analysis need the extraction of the coronary artery centerline. Multi-planar reconstruction and curved multi-planar reconstruction illustrations, which are often utilized while the identification of coronary computed tomography angiography-based coronary artery disease, may be produced thanks to extracted centerlines [5].

The centerlines of the coronary arteries and the associated multiplanar reformatteds are also necessary for computerized coronary computed tomography angiography analysis frameworks. Multiple self-activating and semi self-activating techniques for coronary conduit centerline extraction have been created because of the work escalated nature of manual extraction [6]. Using classic minimal cost route algorithms or trackers, which frequent depended substantially on user intervention, centerlines were recovered in conventional procedures by joining two semi self-activating specified edges of the vessel in the volume of coronary computed tomography angiography. For the detection of the seed point of coronary conduit and to navigate the detector without needing operator intervention. Back then, hand-crafted filters as shown in Figure 2 were famous but Wolter et al. [7] introduced the convolutional neural networks. However, tracking via exceedingly convoluted arteries or severe instances of stenosis and categorization remained difficult. In order to mitigate this problem later methods were created [8,9]. In order to generalize effectively to different degrees of size and

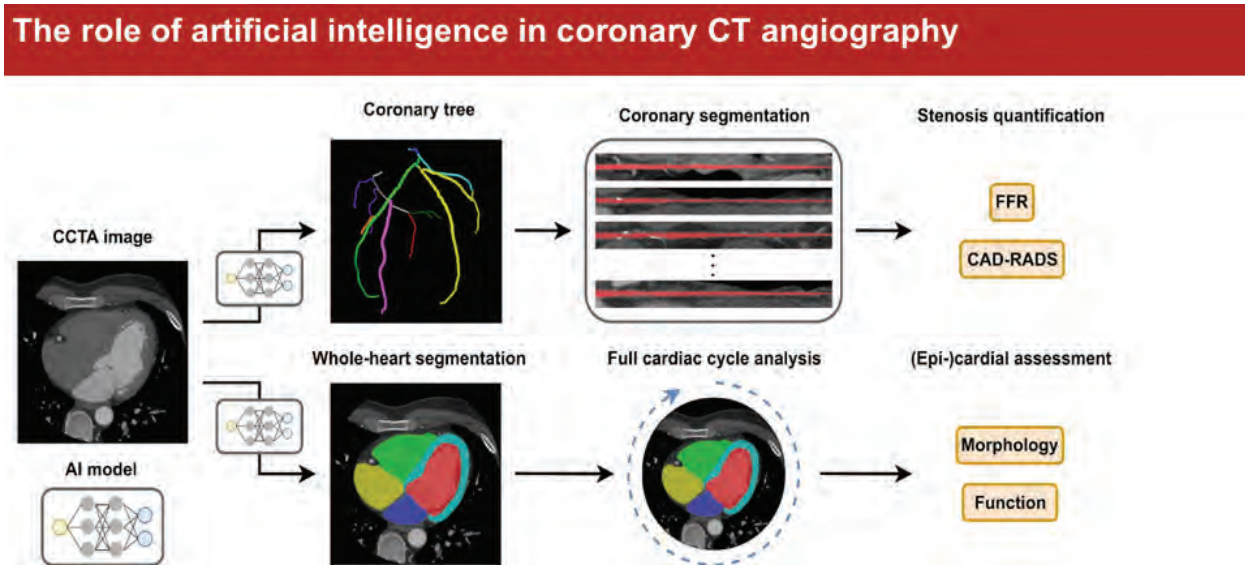


Figure 1. Infographic: An AI-driven flowchart analysis of coronary computed tomography angiography.

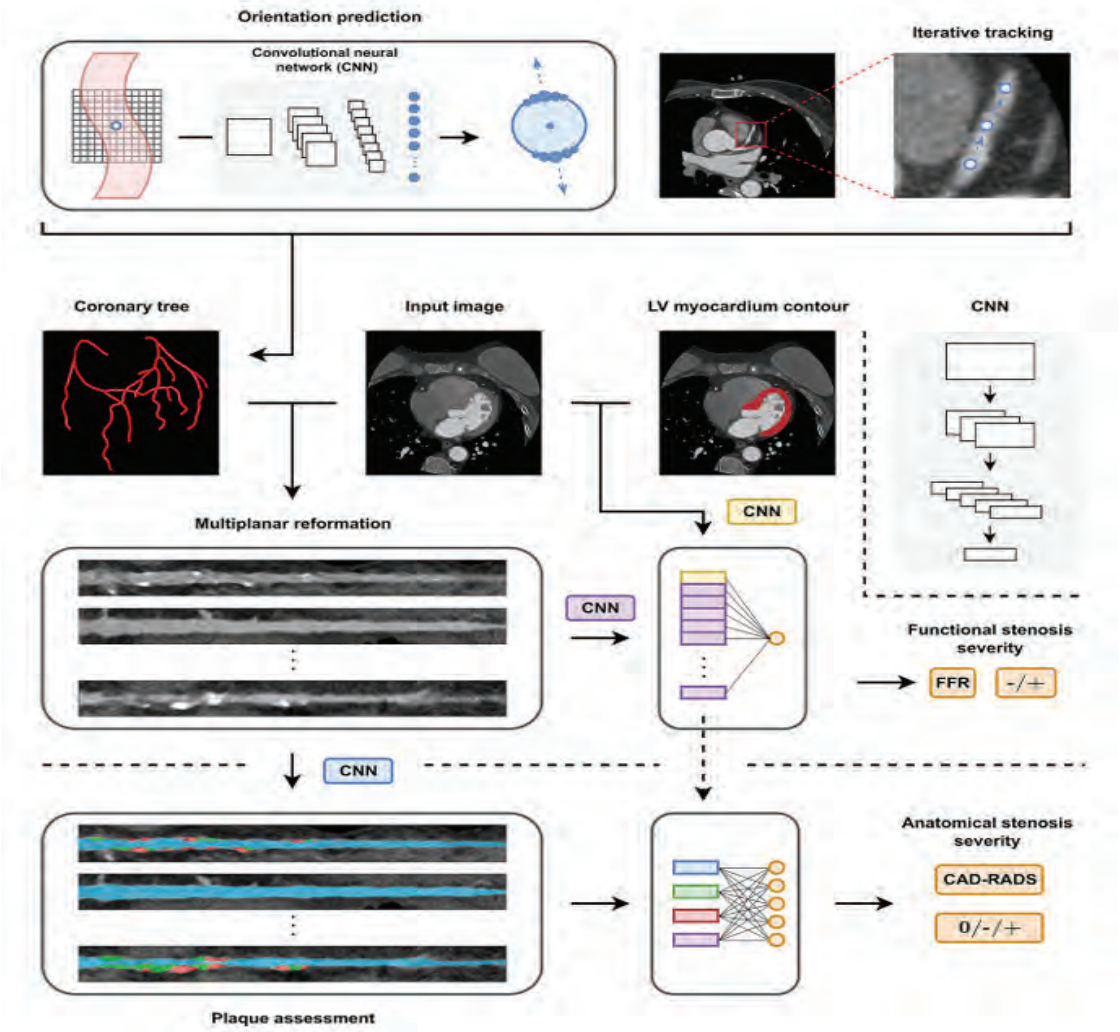


Figure 2. Image-based analysis of anatomical and functional stenosis severity of the coronary arteries.

tortuosity, Alblas et al. [10,11] recently created a detector with the use of radial and scale symmetries present in data taken from vascular system. Notably, when prepared exclusively on information of coronary artery, their approach accurately traced the centerlines of the abdominal aorta, suggesting a general ability to anatomies not encountered during training.

In order to automatically extract coronary artery centerlines, the orientation of vessel for the patches of picture centered around the coronary artery is iteratively predicted. From centerline, multiplanar reformatted pictures are taken. The left ventricular myocardium and multiplanar reformatted are both used to extract characteristics using a neural network. (Middle) To forecast the presence and/or severity any functional stenoses, features are employed [12]. To anticipate the degree of anatomical stenosis, a division of a lumen and plaque stage is carried out later (Bottom).

CORONARY TREE LABELLING

As per recommendation, coronary computed tomography angiography reports must have the segment-level data on the position of identified atherosclerotic lesions and stenosis. The coronary tree's automatic labeling might help doctors by expediting the diagnosing process. Originally studied, atlas-based registration [13] has limitations in managing the coronary tree's morphological diversity, since deep neural networks have the expressive capacity to better manage significant inter-patient anatomical variances, they have been proven to be more appropriate for the job. Inspired by its natural form, researchers of deep learning usually depict the coronary tree with graphical representation which shows the coronary segments as its nodes. First deep neural networks-based segmented labeling framework is derived by Wu et al. [14], modeled with the graphical representations of coronary trees using recurrent neural networks, graph neural networks have been proposed as a way to take use of the intrinsic graph structure. Among the

first to use graph neural networks for segment labeling were Yang et al. [15]. Their solution was particularly resilient to damaged cardiac tree data and performed better than the recurrent neural networks-based strategy. The prospects of exploiting the planned interlinks of the segments of coronary as previous record was recently recognized by Zhang et al. [16]. In order to impose anatomically realistic labeling and establish the unconventional area, they injected stringent topology into a structure based on graph neural networks. In the context of diagnosing coronary artery disease, the main objective of clinical coronary computed tomography angiography interpretation is to locate and describe the degree of anatomical stenosis. However, visual evaluation may be a laborious and difficult process that is subject to inter-observer variation. Therefore, the diagnostic work flow may be more reliable and efficient using an automated stenosis evaluation system. An initial lumen segmentation step is usually required for automatic stenosis assessment. Directly, either the stenosis [17,18] or post-processing of the segmented volumes [19,20] can be used to for the localization of stenosis. Earlier, for the segmentation of the lumen, conventional computerized vision methods were used [21], most current studies have used techniques based on deep learning. For instance, demonstrated a significant correlation between accurately characterized stenosis measures and stenosis biomarkers identified using deep neural networks-derived lumen segmentations also suggested using a deep neural networks to identify severe stenosis after initially segmenting the coronary tree. Despite using a traditional voxel-based technique, voxel-wise segmentation may not be able to satisfy the quality requirements of jobs that come after. In order to attain sub-voxel precision and anatomically believable, contiguous findings, researchers have begun using deformable shape priors as an option to the paradigm based on voxel [22,23]. The coronary artery disease reporting and data system was created in order to standardize coronary computed tomography angiography-based coronary artery disease reporting. It majorly outlines a severity of stenosis categorization system based on the intensity of anatomical stenosis in coronary arteries. Therefore, for better assessment, a technique based on the deep learning of stenosis that predict substantial stenosis or extract coronary artery disease reporting and data system scores straight from the image data have been proposed by researchers. Muscogiuri et al. [24], for mince, developed a convolution neural network-based classification technique that shows excellent diagnostic accuracy. By training convolution neural networks to predict coronary artery disease reporting and data system scores along with the auxiliary tasks of segment-level significant stenosis and patient-level calcium score prediction. Denzinge et al. [25] outperformed their results, demonstrating that combining coronary artery disease reporting and data system prediction with highly correlated secondary targets can significantly improve model performance. During coronary computed tomography angiography reporting, it is advised to characterize plaque types as calcified, non-calcified, or mixed. Typically, radiomics methods have been used to die prediction models [26]. Researchers have included features of plaque categorization and quantification into a framework based on the deep learning of stenosis, due to the potential of prediction of models as shown in Figure 3. Zreik et al. [27] studied

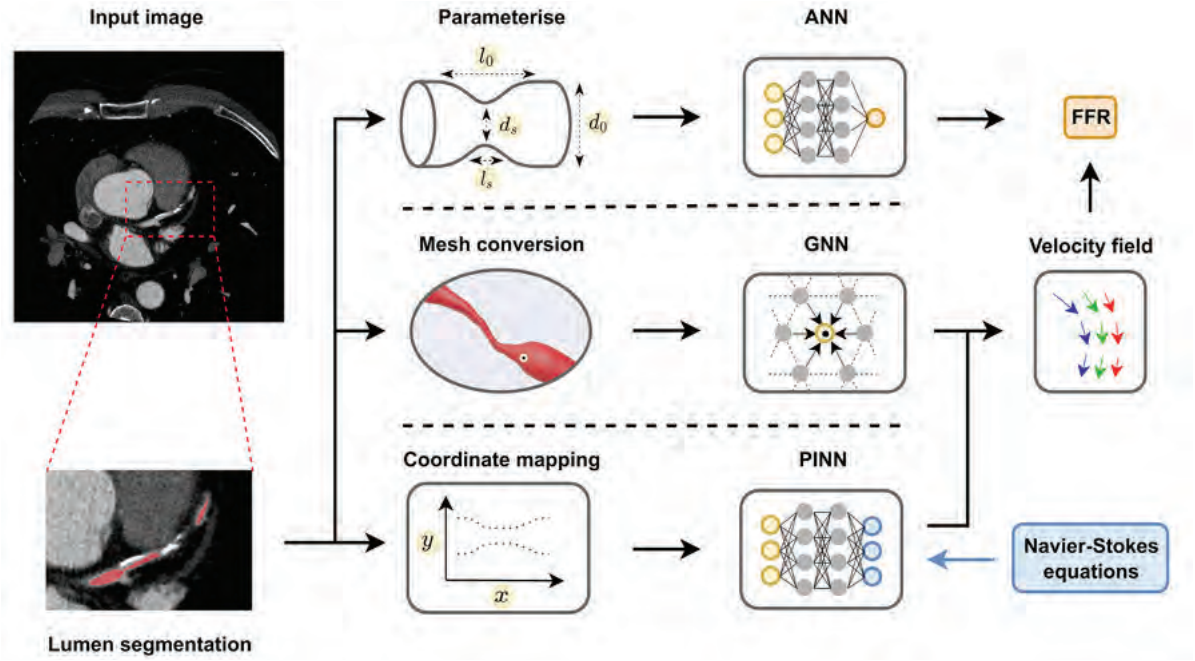


Figure 3. Geometry-based surrogates for assessment of functional stenosis severity.

that the input of multiplanar reformatteds were segregated into an equal amount of volume which was also further segregated and then swallowed into the recurrent neural networks that classified the kind of plague and the severity of stenosis at the segment level. Numerous studies have been examined voxel-level measurement of calcified plaque, which usually yields a significant connection with calcium level of coronary artery calculated from the reference standard of the society of cardiovascular computed tomography. Estimation of the burden of plague and coronary artery disease reporting and data system score assignment based on the stenosis quantification were made possible voxel-level plaque characterization utilizing recurrent neural networks for semantic segmentation of lumen, calcified, and noncalcified plaque. In a multi-cohort validation, it was demonstrated that stenosis measures had a significant correlation with intravascular coronary angiography, whereas deep learning-based plaque load assessments corresponded very well with expert visual evaluation and intravascular ultrasonography. Future cardiac events might be predicted using the total plaque volumes determined by deep neural networks,recently presented a pipeline based on deep learning. Using a 3D convolution neural network, surface networks for the lumen, clotted, and non-clotted plaque are extracted by utilizing cylindrical shape priors. After reformatting to one-dimensional signals, the meshes are fed into a convolution neural network that predicts the coronary artery disease reporting and data system score.

Graph Neural Networks (GNNs) have significantly advanced the automatic labeling of coronary artery trees by overcoming the structural and contextual limitations of Recurrent Neural Networks (RNNs).

GNNs are distinct from RNNs due to their specific handling of graph structured data as compared to RNNs which

Process data step by step and often strugle with comples vessel branching and spatial relationships. For modeling coronary anatomy as a network of connected vessel segments a nd junctions GNNs are best suited.this format describe that nodes stands for vessel segment while edges explain the connection of different branches. İnformation is transitory between neighboring nodes which enables the narrow features of GNNs like curvature, diameter, alignment and extenisve structural patterns such as how vessels are regularized within the coronary tree. This let them to identify the diverse coronary segment precisely compriring LAD, LCx, RCA and their branches, indeed there are anatomical divergence or distortion in the imaging data. Furthermore GNNs are most resilient and flexible because they do not count for the straight processing like RNNs. Probes illustrate that GNN based methods accomplish enhanced labeling precision and sustain more compatible vessel structures and provide obvious analyzability. As a result, they are now widely considered one of the most effective approaches for automatic coronary tree labeling in CCTA analysis.

According to Itu et al. twelve , one approach is to describe a stenotic lesion using its geometric properties. These features can then be used to train an artificial neural network to directly predict fractional flow reserve. Another approach involves using graph neural networks, which can operate directly on the luminal mesh generated automatically from the data [28]. This allows for the prediction of velocity fields within the coronary arteries.Moreover physics informed neural network can be employed to discover solutions that fulfill the Navier- Stokes equations although integrate the geometry of artery [29]. This create potential to evaluate velocity fields in a way that is steady with both fundamental physics and vessel structure.

In the last few years, many researches have concentrated on enhanced nanofluid and non- Newtonian flow models to comprehend fluid behaviour under magnetic and thermal impact. Murtaza and Naveen [30] scrutinize radiative second-grade nanofluid flow with Thomsaon and Troian slip situation, underlining how nanoparticle shape prerogate heat transfer. Sathya and Naveen [31] dilate on this by implementing regression evaluation to magnetized power-law nanofluid flow over a thin needle, proving its implicit use in purposed drug delivery. Sathya et al. [32] additionaly examine this area with the help of multipule regression techniques to scrutinize Blasius and Sakiadis flow of power-law nanofluids, providing valuable forecast for surface motio and heat trasnfer manners. Naveen et al. [33] prolong the task by assimilating artifical neural network models to analyze Casson hybrid nanofluid flow with entropy development, indicating that how data driven strategy can help to upgrade thermal systems. Moreover, Suriya and Naveen [34] executed a least cost analysis of magnetized Sutterby nanofluid with the help of ANOVA-RSM structure, demonstrating the worth of combining statistical and computational approach to enhanced flow irreversibility and magnetohydrodynamic impact.

Suriya and Naveen [35] also examine electrically magnetized Eyring-powell nanofluid flow, revealing that viscous dissipation plays an significant part in flow irreversibility. Sathya and Naveen supervised a relative study on titanium dioxide power-law nanofluids under emmisive and convecting estate, emphasizing their implicit in cancer treatment applications. İn further studies. Naveen et al. [36] inspect Sutterby fluid behaviour with higher order chemical reactions, givimg better understanding into complex non-Newtonian flow features. Sathya and Naveen further delves into nonlinear thermal convection in magnetized dissipative flow over a shrinking Riga sheet, with a rivet on entropy generation and thermodynamic competence in both inductrial and biomedical circumstances. Collectively, these work give a strong cornerstone for combining artificial intelligence, nanofluid mechanics, and nonlinear rheology. Noverthless, the unification of viscoelastic Maxwell fluid dynamics within a Physics-Informed Neural Network framework for authentic arterial flow modeling has not yet been negotiated. The current review, consequently,

be certain about this foundation by broadening the exertion of AI-driven physical modeling to coronary blood flow, immolating a narrative hybrid technique that overpasses classsical fluid mechanics with deep learning-based imitation.

Modern coronary computed tomography angiography (CCTA) is a validated, guideline-endorsed, non-invasive alternative for detection of coronary stenosis and importantly for direct visualization and quantification of coronary plaque. CCTA provides high diagnostic accuracy and an excellent negative predictive value that safely rules out obstructive disease in patients with low-to-intermediate pretest probability, reduces unnecessary invasive procedures, and enables characterization of plaque composition and burden (including high-risk features) that is not achievable with conventional angiography alone. Large trials (e.g., SCOT-HEART) and contemporary guideline statements support the use of CCTA to guide management and improve outcomes. We therefore used CCTA in this study to non-invasively define anatomy and plaque characteristics prior to modeling, while acknowledging that ICA/IVUS/OCT remain indispensable when invasive intervention or highest-resolution plaque imaging is required.

Coronary artery centerline extraction is a critical preprocessing step in CCTA-based analysis because it provides the geometric backbone of the coronary tree, enabling accurate lumen segmentation, plaque localization, vessel curvature assessment, and quantitative evaluation of stenosis severity.Specific turning points are also crucial for 3D reconstruction, computational fluid dynamics (CFD) simulations, and fractional flow reserve (FFR-CT) computations, as even small geometric errors can lead to large errors in hemodynamic metrics. Prior strategies for coronary midline removal mainly relied on minimal-cost path and graph-based strategies, involving Dijkstra's algorithm and Fast Marching methods. İn these methods, the vessel lumen is modeled as a cost function, and the midline is discover by estimated the optimal path between manually selected endpoints. While potent to some extent, such techniques are essentially finite by their reliance on built in cost metrics and user arbitration. İn comparison, Convolutional Neural Network (CNNs) have primarly reconsidered the performance and automation of coronary artery midline extraction. By exploiting data-driven organised feature learning, CNNs can directly handle volumetric CCTA data to distinguish vessel structures from surrounding tissues and imaging artifacts with high accuracy. Enhanced framework, involving 3D U-Net, V-Net, and attention- improved CNN conflict leverage multi-scale contextual illustrations to concurrently apprehend global anatomical continuity and elaborate local vessel structure. This competence empower robust delineation of highly twisting and miniature distal branches, major surpass traditional minimal-cost path-based techniques in both precise and reliability.

In recent times, Physics-Informed Neural Networks (PINNs) have appeared as a robust computational framework for solving complex partial differential equations through the definite incorporation of rulling physical laws into the loss function. This composition permit the direct approximation of nonlinear systems without assurance on structured meshing, thereby substantially improving their suitability to problems in fluid dynamics, heat transfer, and biomedical transport processes. İnitial researches by Raissi et al. (2019), Cuomo et al. (2022), and Kissas et al. (2020) have illustareted the potency of PINNs in modeling laminar and pulsatile blood flow. Even so, the majority of these researches remain restrained to Newtonian premise or relatively clarified non-Newtonian formulations, therby constraining their capacity to precisely apprehend the complex rheological behaviour, features of realistic biological flows. At the same time, customary numerical methods such as the Finite Volume Method (FVM) and Finite Element Method (FEM) remain the ordinary tools for affecting hemodynamics in stenosed arteries, yet they are computationally challenging and mesh-sensitive when employed to realistic, patient-specific geometries. Regardless of comprehensive work on arterial fluid mechanics, the combined impact of viscoelasticity, thermal effects, and magnetic parameters within an AI-based framework has obtained very low emphasis. Furthermore, the assimilation of Maxwell type viscoelastic rheology into PINNs and its computable standard against FVM solvers has not disclosed in the open literature.

In light of these limitations, the present study develops a hybrid Physics-Informed Neural Network (Maxwell) framework to model blood flow, temperature, and wall shear stress in healthy and stenosed coronary arteries. The proposed approach not only captures the elastic memory characteristics of blood but also enables a mesh-free, computationally efficient solution when compared with the Finite Volume Method implemented in ANSYS. This study therefore contributes a novel, data-driven yet physics-consistent methodology that aligns with the journal's scope in computational fluid dynamics, applied mathematics, and biomedical flow modeling, offering new insights into the interplay between viscoelasticity, geometry-induced resistance, and heat generation in coronary circulation.

Functionally Significant Stenosis

The extent which stenosis restricts a coronary artery's downstream blood flow determines its functional relevance [37]. The ratio between the areas proximal and distal to the stenotic is determined by fractional flow reserve which is used in practice to assess the flow [38]. Functional stenosis severity, a non-intrusive measurement test from coronary computed tomography angiography has attracted a lot of attention because this invasive test is expensive and stressful for patients [39]. For the self-activating prediction of this intrusive test from coronary computed tomography angiography, a number of techniques have been put forth, they be broadly categorized into two groups. The algorithms from first class evidently shows geometric and

anatomical properties of coronary tree from coronary computed tomography angiography [40-42]. By sorting the differential equations iteratively, the technique of finite element can approximate the blood flow parameters after segmentation of lumen transformed into a triangular shaped meshes by using the standardize approach of computational fluid dynamics in the first place [43-46]. Research on meta-models for effective flow of blood parameterization has increased recently due to the computational cost of such approaches. deep neural networks are a common candidate for such a surrogate model due to their quick inference, Figure 4 provides an overview. They trained the network by using 12,000 simulated coronary tree anatomies and suggested fractional flow reserve values simulated from computational fluid dynamics. The suggested ANN has been thoroughly tested an decreases calculation time by over 80 times when compared to traditional computational fluid dynamics-based methods. Morphology and stenosis severity features are used to approximate fractional flow reserve at each location around the coronary artery as Itu et al. made an artificial neural network. The computed tomogarphy morphological index by introducing the ANN which was improved the predictive value by using the work of Itu et al. Later, recurrent artificial neural networks were used to simulate fractional flow reserve values in order to investigate long-range relationships between artery segments. As an alternative, whole 3D velocity fields may be inferred using deep learning techniques, allowing for the direct computation FFR. The GNNS directly works on geometrical meshes which is an input to estimate velocity fields. These were employed. Coronary tree anatomies were produced by the techniques for which reference velocity fields were computed using computational fluid dynamics. With just a modest quantity of training data, at interference the gated neural network can estimated the desired velocity fields that are almost instantaneous. Additionally, to solve the underlying differential equations in computational fluid dynamics, deep learning has been used directly. Physics-informed neural networks are used to anticipate dense velocity fields. And the solution was determined by using Navier-Stokes equation implicitly while taking artery wall boundary conditions into account, Compared to traditional computational fluid dynamics methods, this has a number of benefits, including resilience to noisy observed data and poor resolution. However, because the approach is iterative, much like computational fluid dynamics, it is somewhat sluggish when com- pared to other deep learning options. computational fluid dynamics metamodel based on deep learning have the drawback of depending on segmentations of lumen to accurately forecast functional stenosis, which requires a precise reconstruction of the artery geometry. Therefore, instead of using a geometric data-based method, the other group of algorithms concentrates directly in predicting the functionality of important stenosis from image information. Usually, a computer vision model is trained on coronary computed tomography angiography image areas of interest to do this. The left ventricular myocardium and the coronary artery tree are regarded as areas. A pre-processing segmentation phase is used to identify them. For instance, Zreik et al. [47] suggested a convolution neural network to extract myocardial characteristics, which are then used by a support vector machine to categorize the degree of functional stenosis at the patient level. Subsequent research improved the diagnostic accuracy of functional stenosis prediction by combining a convolution neural network-based study of the myocardium and coronary artery tree [48]. In their explainable approach. Hampe et al. [49] described coronary arteries using pathological and anatomical data gleaned by using a multi-planar image along with the coronary artery tree. After that, a neural network identified the functional relevance of the stenosis by directly regressing the fractional flow reserve value. Kumamaru et al. [50] suggested an alternative method that does not need segmentation. The technique uses automated identification of aberrant areas surrounding the coronary artery lumen to detect regression of fractional flow reserve and functional stenosis from start to finish.

This makes it possible to quantify important clinical risk indicators such the left ventricular ejection percent, cardiac shape and function, and the presence of epicardial adipose

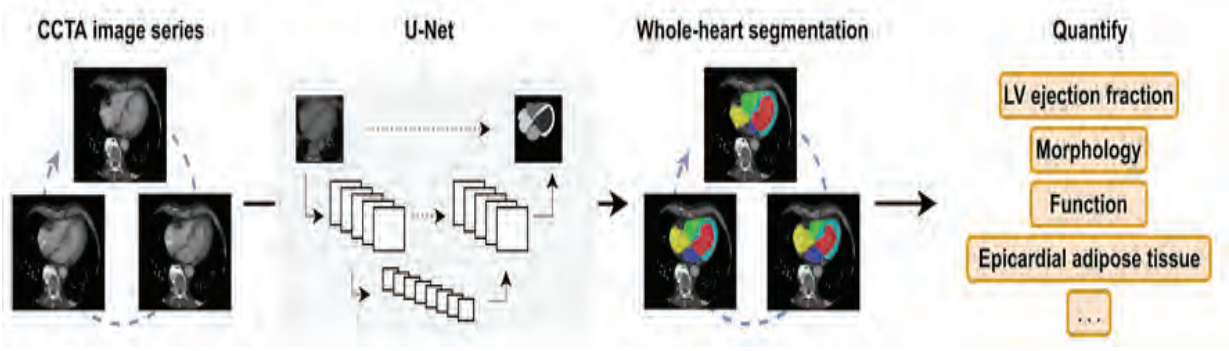


Figure 4. Whole heart image analysis typically involves the segmentation of cardiac structures such as the cardiac chambers and the epicardium.

tissue given a sequence of coronary computed tomography angiography images taken during the cardiac cycle.

Whole Heart Analysis

Large artery and cardiac chamber analysis may offer important new information for predicting cardiovascular risk. In clinical settings, this analysis is not frequently carried out since manual cardiac delineation takes around five hours per 3D picture volume [51]. Deep learning techniques, however, can assist in locating and measuring important structural elements.

Whole Heart Segmentation

During the analyzation of the whole heart, left ventricular myocardium and pericardium are examined due to the significance of left cardiac chambers. Although early techniques suggested segmentation based on models or atlases [52,53], techniques based on deep learnings had been demonstrated to execute better than conventional methods. The majority of deep leaning-based techniques take into account the CNN-based voxelwise segmentation of cardiac structures, each element is assigned to a particular category that corresponds to the composition of heart which it belongs to this as shown in Figure 4. These techniques provide extremely accurate delineations [54,55]. One drawback of voxelwise segmentation is that it usually does not penalize nonphysical artifacts or forms that are anatomical improbable. Therefore, several investigations use segmentation based on heart shape limitations. For instance. Kong et al. [56] suggested reconstructing exterior network for every object within the segmentation of the whole heart. This was accomplished by using a GNN to repeatedly bend a sphere to the desired heart shape, producing a high-resolution cardiac mesh. In order to derive a feature representation, Attar et al. [57] suggested merging patient metadata with pictorial information. A mesh depiction of the heart chambers is then created using them.

Downstream Analysis

In order to do a functional examination of the entire heart, more and more clinical investigations are obtaining 3D coronary computed tomography angiography images throughout the cardiac cycle. These images may be segmented, and heart function can be measured by downstream studies. Pictures obtained for transcatheter aortic valve installation are used for treatment planning in morphological examination, for instance,showed that the left ventricular ejection fraction could be accurately quantified. Szilveszter et al. [58] demonstrated the feasibility of utilizing coronary computed tomography angiography for the quantification of deformation vectors in the assessment of left ventricular and atrial strain.. Moreover, Commandeur et al. used pericardial border delineations to measure epicardial adipose tissue [59]. In recent years, it has been demonstrated that perivascular and epicardial adipose tissue deposits affect the evaluation of cardiovascular risk [60].

Research Gap and Motivation of This Study

The present study differs from previous works by integrating Physics-Informed Neural Networks (PINNs) with the Maxwell non-Newtonian model to simulate blood flow in stenosed coronary arteries, providing a more realistic representation of blood's viscoelastic behavior. Unlike conventional Computational Fluid Dynamics (CFD) or purely data-driven approaches, the proposed method embeds the governing physical laws directly into the neural network's learning process, ensuring physics-consistent solutions. The present study incorporates a comprehensive validation framework through a detailed comparison with Finite Volume Method (FVM) simulations performed in ANSYS Fluent, an aspect that remains largely underexplored in prior investigations. The obtained results are analyzed with substantial physical and clinical grounding, explicitly correlating flow behavior with underlying hemodynamic implications. Collectively, this integrated AI–CFD framework establishes a novel, precise, and computationally efficient methodology for modeling coronary hemodynamics, with potential applicability to a broader class of biomedical flow problems.

This work addresses a critical gap in Coronary Computed Tomography Angiography (CCTA) analysis by incorporating the viscoelastic Maxwell blood flow model within a Physics-Informed Neural Network (PINN)s [61] framework, an area that has not been sufficiently examined in existing literature. Earlier research have primarly employed PINNs for solving rulling equations , involving partial and ordinary differential equation, with finite concentration on comparitve substantiation or their prolongation to complex non-Newtonian models such as the Maxwell fluid. Influenced by the requirement for more physiologicall realistics and clinically significant modeling techniques, this research assimilate the Maxwell fluid formulation and accomplish a systematic comparison between PINNs and the Finite Volume Method executed in ANSYS Computational Fluid Dynamics. The rulling equations portraying velocity and pressure distributions in stenosed coronary arteries are figured out with the help of both techniques to empower a steady appraisal.

The relative analysis disclose that, even though FVM proffers steady and computationally competent solutions, its built in dependence on mesh generation limitations its accomplishment in geometrically complex fields. On the other hand, PINNs elaborate improved precision, higher flexibility and enhanced ability in managing nonlinearities and complicate arterial geometries. The outcomes validate the potency of PINNs in modeling Maxwell-type blood flow and position them as a convincing substitute to conventional CFD methods. Moreover, this work assist toward the upgrading of more reliable and clinically applicable diagnostic tools in CCTA-based hemodynamic evaluation, thereby handling a substantial flaws in current study.

Ethical Approval and Informed Patient Consent

This research obtained endorsement from the institutional honorable Review Board of Faisalabad Cardiology Hospital, Pakistan. All protocols were executed in imperious adherence with suitable recommendations and legislative norms. Explicit conversant assent was gained from all participants preceding to the involvement of their imaging data in the research. The obfuscated Coronary Computed Tomography Angiography (CCTA) images were earned by Dr. Kubra Anjum during routine clinical practice and were implemented solely for academic and rsearch purposes.

Governing Equations

The flow of Maxwell-type blood through stenosed arteries is illustrated by integrated system of continuity, momentum, energy, and concentration equations, jointly attribute the viscoelastic, thermal, and mass captivate behaviour of blood under physicological estates. The continuity equation impose the incompressibillity restraintswhile the momentum equation, devised as specific Navier-stokes expression, integrate both viscous and elastic stress impact through the Maxwell constitutive model. The involvement of a relaxation time criterion make it possible the depiction of memory-dependent fluid behaviour, consequently apprehending the combined viscous elastic reaction of blood, specifically under pulsatile conditions and lifted shear rates in the locality of arterial stenosis. The energy equation manage heat transfer method emerging from viscous dissipation and thermal conduction within the arterial field, whereas the accumulation equation version for the transport chemical species, such as oxygen or hanging nanoparticles, within the medium.

The physiological flow of the ill and almost healthy models was simulated by solving the Navier-Stokes equations conservation equations with finite volume and the continuity equation using ANSYS Fluent. A turbulent blood flow is caused by different levels of stenosis, which lead to blockage and recirculation. The walls were subjected to a noslip boundary condition, assuming that the plaque was rigid. Then, blood is recalled to resemble the characteristics of blood in coronary veins by being an incompressible, non-Newtonian liquid with a constant thickness of 1060 kg/m^3. Next, as stated in , are the controlling parameters for the three-layered mass and energy preservation associated with the blood stream. However, it is important to note that the PINN framework itself is general and model-independent. In principle, it can be extended to other types of fluids (Newtonian or non-Newtonian) by simply embedding the corresponding governing equations and boundary conditions into the loss function. In this work, we focused on the Maxwell non-Newtonian model to capture the realistic rheology of blood in stenosed arteries. Future studies can adapt the same methodology for Newtonian, power-law, or hybrid nanofluids by redefining the constitutive relations within the PINN formulation.

Maxwell Fluid Model in 3D for Blood Properties

Maxwell fluid model in 3D for Blood Properies are as follows:

Continuity equation (conservation of mass)

The continuity equation for an incompressible fluid in 3D Cartesian coordinates is:

$\frac{\partial u_x}{\partial x}+\frac{\partial u_y}{\partial y}+\frac{\partial u_z}{\partial z}=0$, where, u_x, u_y, u_z are the velocity components in the *x, y* and *z* directions, respectively..

Momentum equation for Maxwell fluid

The momentum equation for a Maxwell fluid in 3D Cartesian coordinates is:

$$\frac{\partial u_x}{\partial t}+u_x\frac{\partial u_x}{\partial x}+u_y\frac{\partial u_x}{\partial y}+u_z\frac{\partial u_x}{\partial z}$$
$$=\frac{-1}{\rho}\frac{\partial p}{\partial x}+\mu\left(\frac{\partial^2 u_x}{\partial x^2}+\frac{\partial^2 u_x}{\partial y^2}+\frac{\partial^2 u_x}{\partial z^2}\right)+\lambda\left(\frac{\partial u_x}{\partial t}-\frac{\partial^2 u_x}{\partial x^2}-\frac{\partial^2 u_x}{\partial y^2}-\frac{\partial^2 u_x}{\partial z^2}\right)$$

Similarly, for u_y and u_z, we have:

$$\frac{\partial u_y}{\partial t}+u_x\frac{\partial u_y}{\partial x}+u_y\frac{\partial u_y}{\partial y}+u_z\frac{\partial u_y}{\partial z}$$
$$=\frac{-1}{\rho}\frac{\partial p}{\partial y}+\mu\left(\frac{\partial^2 u_y}{\partial x^2}+\frac{\partial^2 u_y}{\partial y^2}+\frac{\partial^2 u_y}{\partial z^2}\right)+\lambda\left(\frac{\partial u_y}{\partial t}-\frac{\partial^2 u_y}{\partial x^2}-\frac{\partial^2 u_y}{\partial y^2}-\frac{\partial^2 u_y}{\partial z^2}\right)$$

$$\frac{\partial u_z}{\partial t}+u_x\frac{\partial u_z}{\partial x}+u_y\frac{\partial u_z}{\partial y}+u_z\frac{\partial u_z}{\partial z}$$
$$=\frac{-1}{\rho}\frac{\partial p}{\partial z}+\mu\left(\frac{\partial^2 u_z}{\partial x^2}+\frac{\partial^2 u_z}{\partial y^2}+\frac{\partial^2 u_z}{\partial z^2}\right)+\lambda\left(\frac{\partial u_z}{\partial t}-\frac{\partial^2 u_z}{\partial x^2}-\frac{\partial^2 u_z}{\partial y^2}-\frac{\partial^2 u_z}{\partial z^2}\right)$$

Heat equation for Maxwell fluid

The heat equation in 3D Cartesian coordinates is:

$$\rho c_p\frac{\partial T}{\partial t}+u_x\frac{\partial T}{\partial x}+u_y\frac{\partial T}{\partial y}+u_z\frac{\partial T}{\partial z}=k\left(\frac{\partial^2 T}{\partial x^2}+\frac{\partial^2 T}{\partial y^2}+\frac{\partial^2 T}{\partial z^2}\right)$$

Concentration equation for Maxwell fluid in 3D

The concentration equation in 3D for Maxwell fluid is a transport equation for the scalar concentration field

$$C(x,y,z,t):$$
$$\rho\frac{\partial C}{\partial t}+u_x\frac{\partial C}{\partial x}+u_y\frac{\partial C}{\partial y}+u_z\frac{\partial C}{\partial z}=D\left(\frac{\partial^2 C}{\partial x^2}+\frac{\partial^2 C}{\partial y^2}+\frac{\partial^2 C}{\partial z^2}\right)$$

Where:

- C (x, y, z, t) is the concentration of the species in the fluid.
- ρ is the density of the fluid.
- u_x, u_y, u_z are the velocity components in the *x, y* and z directions.
- D is the diffusion coefficient.
- $\frac{\partial^2 C}{\partial x^2}+\frac{\partial^2 C}{\partial y^2}+\frac{\partial^2 C}{\partial z^2}$ are the second derivatives of concentration with respect to spatial coordinates, respresenting diffusion in the respective directions.

In the *x-axis* and *y-axis*, the components of velocity are represented by $\mathfrak{u}$ and $\mathfrak{v}$, respectively.Present body forces (f), fluid viscosity, and pressure (p) are the variables involved in the equation.This study uses Maxwell's blood viscosity model, which permits the viscosity coefficient to change in response to the shear rate, therefore accounting for shear thinning.

Non-dimensionalization of the Governing Equations

To obtain a dimensionless representation of the flow and heat/mass transfer in the stenosed artery, the governing equations are nondimensionalized using the following characteristic scales:

$$L = R_0,\ U = U_{max},\ p = \rho U^2,\ T = T_w - T_\infty,\ C = C_w - C_\infty$$

where, R_0 is the reference arterial radius, U_{max} is the peak inlet velocity, and T_w an d C_w denote the wall temperature and concentration, respectively.

The dimensionless variables are defined as:

$$x = \frac{x'}{L}, y = \frac{y'}{L}, u = \frac{u'}{U}, v = \frac{v'}{U}, p = \frac{p'}{p},$$
$$\theta = \frac{T' - T_\infty}{T}, \phi = \frac{C' - C_\infty}{C}.$$

Substituting these into the dimensional continuity, momentum, energy, and concentration equations yields the nondimensional system:

$$\nabla . u = 0,$$
$$\frac{\partial u}{\partial t} + (u.\nabla)u = -\nabla p + \frac{1}{\Re}\nabla^2 u - Ha^2 u + DeF(u),$$
$$\frac{\partial \theta}{\partial t} + (u.\nabla)\theta = \frac{1}{PrRe}\nabla^2\theta + Br\Phi(u),$$
$$\frac{\partial \phi}{\partial t} + (u.\nabla)\phi = \frac{1}{ScRe}\nabla^2\phi,$$

where, the dimensionless groups appearing above are:

$$\Re = \frac{\rho U\ \ L}{\mu}, Pr = \frac{\mu c_p}{k}, Sc = \frac{\mu}{\rho D}, De = \lambda\frac{U}{L}, Ha = \frac{B_0 L}{\sqrt{\mu/\sigma}},$$

and the stenosis ratio is defined as

$$SR = \frac{R_0 - R_{min}}{R_0}.$$

Here, $F(u)$ denotes the dimensionless viscoelastic contribution (for the Maxwell or Oldroyd-B model), $\Phi(u)$ is the viscous dissipation term, and B_0 is the applied magnetic field strength. These nondimensional equations form the basis for the numerical simulations and the PINN training described in subsequent sections.

Maxwell Blood Flow in Coronary Arteries by Using Pinns Model

The detailed computational procedure of the proposed Physics-Informed Neural Network (PINN) [62] for Maxwell blood flow in stenosed coronary arteries is summarized in Algorithm 1. The algorithm demonstrates how the governing physical laws including continuity, momentum, energy, and concentration equations are embedded into the neural network learning framework. The process begins with initialization of geometry and physical parameters, followed by residual computation for each governing equation.The integrated loss functional, comprehensive both empirical data distinctiveness and physics-informed remnant, is repetitively undersized via the Adam stochastic upgrading design.The training continues until convergence, and the final network outputs velocity, pressure, temperature, and concentration distributions. The step-by-step structure of the algorithm is given in Table 1.

In the Physics-Informed Neural Networks (PINNs) framework, the governing equations for continuity,

Table 1. Algorithm 1: Physics-Informed Neural Network (PINN) framework for Maxwell blood flow in stenosed coronary arteries

Step	Description
1	**Input:** Define geometry of stenosed artery, Maxwell fluid parameters (λ, μ), boundary conditions, and collocation points for training.
2	**Initialization:** Casually stimulate neural network weighs θ and partiality; finalizing learning rate η and streamline (Adam).
3	**Forward propagation:** For every drop point, evaluate expected velocity u, pressure p, temperature T , and concentration C from the neural network.
4	**Residual computation:** Estimate remnant of the rulling equations: continuity, momentum, energy, and concentration equations.
5	**Loss formulation:** Devise total loss function $L = L_{data} + L_{physics}$, where $L_{physics}$ depict the mean- squared leftover of all PDEs.
6	**Parameter update:** Put on Adam optimizer to lessen L and upgrade parameters $\theta \leftarrow \theta - \eta\frac{\partial L}{\partial \theta}$.
7	**Convergence check:** Reiterate Steps 3–6 until loss is underneath the endurance or maximum periodattained.
8	**Output:** Acquire final specialty of velocity, pressure, temperature, and concentration for the concentrated realm.
9	**Post-processing:** Envision outline of flow fluctuation and compare with FVM results for verification.

momentum, heat, and concentration are embedded into the neural network's loss function. The network predicts velocity, pressure, temperature, and concentration fields, and the residuals of each equation are computed at randomly sampled collocation points within the domain.

These remaining assist as numeric assess of the scale to which the model prophecy stick to the controlling physical laws. The bulk loss functional include leftover impact from all rulling equations, moreover to sanction originating from perimeters and beginning conditions invasion. Through repetative understating employing improved refinement algorithms such as Adam and L-BFGS, the system thoroughly dimiinish these remainings, thus implementing steadiness of the expected fields with the basic physical principles across the whole computational realms.

In the background of blood flow among coronary arteries, blood is adapted as a Maxwell fluid, which report for both elastic and viscous impact.The governing equations for Maxwell fluid in a three-dimensional domain with stenosis are as follows:

Continuity equation (conservation of mass)

The continuity equation in 3D for a fluid is:

$$\nabla . u = 0$$

Where $u = (u_x, u_y, u_z)$ is the velocity field. The residual for the continuity equation in the PINNs method is:

$$f_{cont} = \frac{\partial \hat{u}_x}{\partial x} + \frac{\partial \hat{u}_y}{\partial y} + \frac{\partial \hat{u}_z}{\partial z}$$

The corresponding loss function is:

$$L_{cont} = \frac{1}{N_{cont}} \sum_{i=1}^{N_{cont}} |f_{cont}(x_i, y_i, z_i, t_i)|^2$$

Momentum equation for Maxwell fluid

The momentum equation for Maxwell fluid in 3D is given by:

$$\frac{\partial u}{\partial t} + (u.\nabla)u = \frac{-1}{\rho}\nabla p + \mu \nabla^2 u + \lambda \left(\frac{\partial u}{\partial t} - \nabla . \tau\right),$$

Where: $u = (u_x, u_y, u_z)$ is the velocity field, p is the pressure, ρ is the density, μ is the dynamic viscosity, λ is the Maxwell relaxation time.The residual for the momentum equation in the x-direction is:

$$f_{mom_x} = \frac{\partial \hat{u}_x}{\partial t} + \hat{u}_x \frac{\partial \hat{u}_x}{\partial x} + \hat{u}_y \frac{\partial \hat{u}_x}{\partial y} + \hat{u}_z \frac{\partial \hat{u}_x}{\partial z} + \frac{1}{\rho}\frac{\partial \hat{p}}{\partial x} - \mu \nabla^2 \hat{u}_x$$

The momentum equation residuals for the y- and z-components are similarly defined. The total loss for momentum is:

$$L_{mom} = L_{mom_x} + L_{mom_y} + L_{mom_z}$$

Heat equation

The heat equation in 3D for Maxwell fluid is:

$$\rho c_p \frac{\partial T}{\partial t} + u.\nabla T = k\nabla^2 T$$

Where: $T = (x, y, z, t)$ is the temperature, ρ is the density, c_p is the specific heat capacity, k is the thermal conductivity. The residual for the heat equation is:

$$f_{heat} = \rho c_p \frac{\partial \hat{T}}{\partial t} + \hat{u}_x \frac{\partial \hat{T}}{\partial x} + \hat{u}_y \frac{\partial \hat{T}}{\partial y} + \hat{u}_z \frac{\partial \hat{T}}{\partial z} - k\left(\frac{\partial^2 \hat{T}}{\partial x^2} + \frac{\partial^2 \hat{T}}{\partial y^2} + \frac{\partial^2 \hat{T}}{\partial z^2}\right)$$

The heat equation loss is:

$$L_{heat} = \frac{1}{N_{heat}} \sum_{i=1}^{N_{heat}} |f_{heat}(x_i, y_i, z_i, t_i)|^2$$

Concentration equation

The concentration equation for Maxwell fluid is:

$$\rho \frac{\partial C}{\partial t} + u.\nabla C = D\nabla^2 C$$

Where: $C = (x, y, z, t)$ is the concentration, D is the diffusion coefficient. The residual for the concentration equation is:

$$f_{conc} = \rho \frac{\partial \hat{C}}{\partial t} + \hat{u}_x \frac{\partial \hat{C}}{\partial x} + \hat{u}_y \frac{\partial \hat{C}}{\partial y} + \hat{u}_z \frac{\partial \hat{C}}{\partial z} - D\left(\frac{\partial^2 \hat{C}}{\partial x^2} + \frac{\partial^2 \hat{C}}{\partial y^2} + \frac{\partial^2 \hat{C}}{\partial z^2}\right)$$

The concentration loss is:

$$L_{conc} = \frac{1}{N_{conc}} \sum_{i=1}^{N_{conc}} |f_{conc}(x_i, y_i, z_i, t_i)|^2$$

Total loss function for PINNs

The total loss function incorporating all the equations is:

$$L_{total} = L_{cont} + L_{mom} + L_{heat} + L_{conc}$$

The PINNs method minimizes this total loss function through a gradient-based optimization technique, such as Adam, to obtain the solution of the Maxwell fluid flow equations.

Comparison with Finite Volume Method (FVM)

The limited Volume Method (FVM) comprise a essential numerical groundwork for the solution of partial differential equations (PDES). Within this development, the computational realm is segmented into a confined set of manage volumes, and fluctations are scrupulously analyzed across the associate of these volumes to implement local conservancy principles. The rulling equations for Maxwell fluids are segregated over these control volumes, foremost to a system of algebaric equations that is resolved repeatedly through the following technique:

- Spatial categorization of the domain into confined control volumes.
- Approximation of governing PDEs via flux interpolation schemes and finite difference representations.
- Iterative solution of the resulting nonlinear algebraic system using pressure–velocity coupling algorithms such as SIMPLE, SIMPLEC, or PISO.
- Execution of boundary requirements next to rigid conservation of mass. Momentum, energy, and genus concentration.

The FVM structure is acknowledged for its sturdiness, numerical stability and strong conservation properties, producing it a foundation of practical computational fluid dynamics (CFD) imitations.Nevertheless, its computational cost escalates significantly for geometrically intricate domains, such as stenotic coronary artery models.

In contrast, Physics-Informed Neural Networks (PINNs) provide a mesh-free alternative by embedding the governing physical laws directly into the loss functional of a neural network. This strategy evade definite partition, facilitating direct simulation of PDE solutions. When limked with GPU- accelerated practice, PINNs proposes probable computational benefits for enormous complexityies, inspite of the fact that their precision remnant detachment upon network building design, practice plans, and enhanced potency.

Stenosis Levels and Blood Flow Analysis by Using Finite Volume Method

For various stenosis levels in coronary arteries, the flow attribute such as velocity, temperature dispersion, pressure and concentration are affected by the impeding of the artery. Higher stenosis conduct to superior pressure drops, modified flow profiles, and alters in heat and mass transfer. The PINNs method can efficiently capture these effects by directly solving the governing equations, whereas FVM relies on grid refinement to resolve such details. We apply the Finite Volume Method (FVM) to solve the governing PDEs for Maxwell blood flow in coronary stenosis regions. We consider the following equations: - Continuity equation (conservation of mass)- Momentum equation- Heat equation- Concentration equation. Each of these equations is discretized using the FVM, which is a control-volume-based method, in order to obtain an approximate solution to Maxwell fluid dynamics in 3D.

Continuity equation (conservation of mass)

The continuity equation in 3D for a fluid is:

$$\nabla . u = 0$$

Where $u = (u_x, u_y, u_z)$ is the velocity field. To apply the Finite Volume Method, we integrate the continuity equation over a control volume V_k bounded by surfaces A_k (the faces of the control volume):

$$\int_{V_k} \nabla . u dV = 0$$

Using the divergence theorem, this becomes:

$$\int_{A_k} u . \hat{n} dA = 0$$

Where $\hat{n}$ is the unit normal vector on the surface A_k. The fluxes $u . \hat{n}$ are computed at the control volume faces, and the discretized form is:

$$\sum_{f \in \partial V_k} u_f . \hat{n}_f A_f = 0$$

Where A_f is the area of the face f, and u_f is the velocity at the face, computed using interpolation methods (e.g., linear or central differencing). The discretized continuity equation can then be written as:

$$\frac{1}{\Delta t}\left(\sum_{f \in \partial V_k} u_f A_f \right) = 0$$

Where Δt is the time step.

Momentum equation for Maxwell fluid

The momentum equation for Maxwell fluid in 3D is given by:

$$\frac{\partial u}{\partial t} + (u . \nabla)u = \frac{-1}{\rho}\nabla p + \mu \nabla^2 u + \lambda \left(\frac{\partial u}{\partial t} - \nabla . \tau \right)$$

Where: $u = (u_x, u_y, u_z)$ is the velocity field, p is the pressure, ρ is the density, μ is the dynamic viscosity, λ is the Maxwell relaxation time.

To apply FVM, we integrate the momentum equation over a control volume V_k:

$$\int_{V_k} \frac{\partial u}{\partial t} dV + \int_{V_k} (u . \nabla)u \, dV = -\int_{V_k} \frac{1}{\rho} \nabla p dV + \int_{V_k} \mu \nabla^2 u dV + \int_{V_k} \lambda \left(\frac{\partial u}{\partial t} - \nabla . \tau \right) dV$$

Using the divergence theorem to convert volume integrals to surface integrals, we get:

$$\sum_{f \in \partial V_k} (u_f . \hat{n}_f) A_f = -\int_{A_k} \frac{1}{\rho} \nabla p . \hat{n} dA + \mu \sum_{f \in \partial V_k} \nabla^2 u_f A_f + \lambda \sum_{f \in \partial V_k} \left(\frac{\partial u_f}{\partial t} \right) A_f$$

Discretizing the terms, the resulting equation for the momentum equation in each direction (x, y, z) is:

$$\frac{1}{\Delta t}\sum_{f\in\partial V_k} u_f A_f + \sum_{f\in\partial V_k}(u_f.\hat{n}_f)A_f = \frac{-1}{\rho}\sum_{f\in\partial V_k} p_f\hat{n}_f A_f + \mu\sum_{f\in\partial V_k}\nabla^2 u_f A_f$$

Heat equation for Maxwell fluid

The heat equation in 3D for Maxwell fluid is:

$$\rho c_p\frac{\partial T}{\partial t} + u.\nabla T = k\nabla^2 T$$

Where T is the temperature, c_p is the specific heat, and k is the thermal conductivity.

Integrating the heat equation over a control volume V_k:

$$\int_{V_k}\rho c_p\frac{\partial T}{\partial t}dV + \int_{V_k} u.\nabla T dV = \int_{V_k} k\nabla^2 T dV$$

By using the divergence theorem:

$$\sum_{f\in\partial V_k}\rho c_p\frac{T_f - T_k}{\Delta t}A_f + \sum_{f\in\partial V_k} u_f.\nabla T_f A_f = \sum_{f\in\partial V_k} k\nabla^2 T_f A_f$$

The equation is discretized to update the temperature field in each control volume and to calculate the corresponding heat flux.

Concentration equation for Maxwell fluid

The concentration equation for Maxwell fluid is:

$$\rho\frac{\partial C}{\partial t} + u.\nabla C = D\nabla^2 C$$

Where C is the concentration and D is the diffusion coefficient.

Integrating the concentration equation over a control volume V_k:

$$\int_{V_k}\rho\frac{\partial C}{\partial t}dV + \int_{V_k} u.\nabla C dV = \int_{V_k} D\nabla^2 C dV$$

Using the divergence theorem:

$$\sum_{f\in\partial V_k}\rho\frac{C_f - C_k}{\Delta t}A_f + \sum_{f\in\partial V_k} u_f.\nabla C_f A_f = D\sum_{f\in\partial V_k}\nabla^2 C_f A_f$$

This discretized form is used to compute the concentration distribution at each control volume. The Finite Volume Method (FVM) has been applied to discretize the governing equations for Maxwell blood flow in coronary stenosis regions. Each equation (continuity, momentum, heat, and concentration) is integrated over control volumes, and the fluxes across the control volume faces are computed.

These categorized equations are then figured out repeatedly to upgrade the solution at each step. This technique is particularly potent for processing intricate fluid flow problems in uneven geometries, such as coronary stenosis. All directive values utilized in this research were chosen to reflect physiologically realistic conditions and to align with previously validated literature on coronary blood flow modeling. Properties such as blood density, viscosity, relaxation time, thermal conductivity, and specific heat were adopted from established biomedical and hemodynamic sources, thereby ensuring consistency with physiological ranges. The dimensionless numbers (e.g., Reynolds, Prandtl, and Schmidt numbers) were also chosen to reflect typical coronary artery flow conditions, allowing a meaningful comparison between the Physics-Informed Neural Network (PINN) and Finite Volume Method (FVM) simulations. This ensures that the results are not arbitrary but are biologically and physically representative of real arterial behavior under normal and stenosed conditions.

Computational Mesh

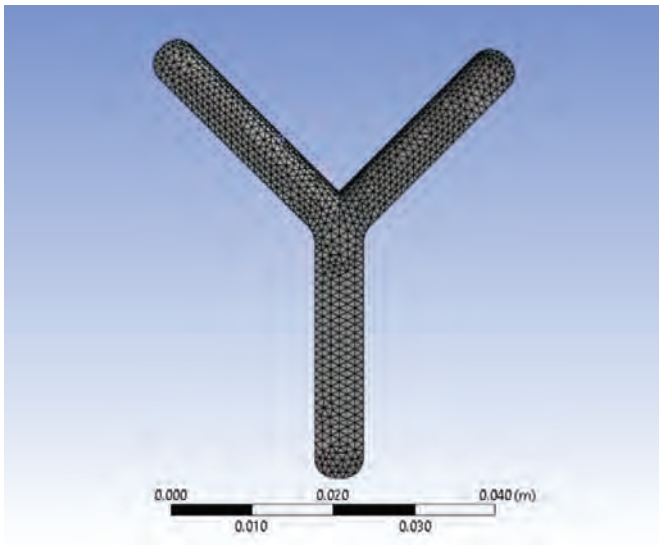
In the Finite Volume Method (FVM) applied to stenosed coronary arteries, the computational domain is divided into small control volumes that conform to the complex arterial geometry. The continuity, momentum, energy, and concentration equations are integrated over each control volume, transforming the governing differential equations into algebraic form.

For radiative tenure, second-order upwind program are typically engaged to enhance precision, while middle discrimination is employed for diverging instability. Pressure–velocity coupling is then resolved using methods such as SIMPLE or PISO, which help preserve mass and momentum conservation.The mesh is refined near the stenosis and arterial walls using boundary layer inflation to accurately capture steep velocity and pressure gradients.

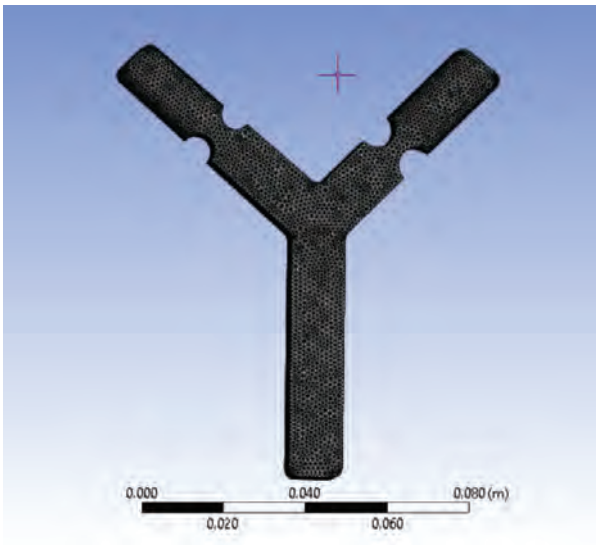
Commercial software ANSYS Fluent was used to mesh the idealized models with different degrees of blockage of the LCA. The examination of the mesh independent test was conducted using various combinations of mesh components. In order to examine the flow behavior close to the artery wall, three levels of inflation are introduced. A sphere with an influent size of 2 mm has been introduced in order to capture the flow behavior close to the stenosis location. There are 602225 fragments in the conclusive mesh that was employed in the numerical simulation. The mesh geometry is displayed beneath Figure 5.

Mesh Independent Study

Commercial software ANSYS Workbench was used to mesh the geometric model. Between 118,538 and 703,353 have been reported to be the range of fineness for the two distinct meshes. The most practical grid size is determined by running five simulations with three distinct grid sizes. Next, 1000 cycles of testing are performed using the mesh file imported into the commercial program ANSYS Fluent. 602225 components make up the final grid that will be utilized for additional research.



(a) Meshing of coronary healthy artery



(b) Meshing of coronary stenosed

Figure 5. Meshing of coronary artery.

A mesh-independent study was necessary to ensure that the simulation results were not influenced by the discretization size but purely represented the physical behavior of blood flow in stenosed arteries. In computational fluid dynamics (CFD), an overly coarse mesh can lead to numerical errors, while an excessively fine mesh increases computational cost without significant improvement in accuracy. Therefore, simulations were performed with progressively refined meshes, and key parameters such as velocity, pressure, and wall shear stress were monitored. The results stabilized beyond a certain refinement level, indicating grid independence. In this study, a fine mesh with approximately 600,000–650,000 elements and enhanced boundary-layer refinement near the arterial wall provided numerically stable and convergent results, balancing both accuracy and computational efficiency.

Boundary Conditions

This study's establishment is the transient pulsatile speed profile of a left coronary corridor (UDF), which is defined as the velocity input boundary condition and is written in C programming language. The velocity profile enters the intake fully formed. A parabolic velocity profile is present. As outlet limit conditions, the outpouring condition was utilized. Since it was accepted that the vein wall was firm, or at least, $u = 0$, the no-slip limit condition was applied. ANSYS Familiar was utilized to do the whole numerical recreation. There were no energy and intensity transport conditions that could be settled. The second-request upwind technique for the strain speed couple, which is utilized for the discretization of administering conditions, was joined with the basic estimation way to deal with complete the calculation. For every 0.01 time step, 1000 cycles were run. Three cardiac cycles were simulated for cyclicity assurance, and the second cycle's findings were obtained.

For the present analysis of Maxwell blood flow in a stenosed coronary artery, appropriate boundary and initial conditions are prescribed to ensure a well-posed problem. The boundary conditions applied to the governing equations are expressed as follows:

Inlet boundary (pulsatile velocity profile)

At the artery inlet, a fully developed, time-dependent parabolic velocity profile is imposed:

$$u(r,t) = U_{max}(t)\left(1 - \frac{r^2}{R^2}\right), 0 \le r \le R,$$

where

$$U_{max}(t) = U_0[1 + Asin(\omega t)],$$

represents the pulsatile velocity with mean velocity U_0, amplitude A, and pulsation frequency ω. Here, R denotes the local arterial radius and r is the radial coordinate.

Thus, the inlet velocity and scalar boundary conditions are defined as:

$$u(r,t) = (u(r,t), 0, 0),\ T = T,\ C = C.$$

Outlet boundary (outflow condition)

At the outlet of the artery, a zero-gradient condition is applied for all dependent variables to represent fully developed outflow:

$$\frac{\partial u}{\partial x} = \frac{\partial v}{\partial x} = \frac{\partial T}{\partial x} = \frac{\partial C}{\partial x} = 0,$$

and the static pressure is set to a reference value:

$$p = p_{out} = 0$$

Arterial wall boundary (rigid and no-slip condition)

The arterial wall is assumed to be rigid and thermally insulated. Therefore, the no-slip velocity condition and adiabatic wall assumptions are expressed as:

$$u = v = w = 0, onr = R(x),$$

and

$$\frac{\partial T}{\partial r} = 0, \frac{\partial C}{\partial r} = 0, onr = R(x).$$

Initial conditions

At the initial time ($t = 0$), the flow field is assumed to be quiescent, and both temperature and concentration fields are uniform:

$$u(x, r, 0) = v(x, r, 0) = 0,\ T(x, r, 0) = T,\ C(x, r, 0) = C.$$

Neural Network Architecture and Training Strategy

In the present study, the Physics-Informed Neural Network (PINN) was constructed as a fully-connected feed-forward network designed to approximate the velocity, pressure, temperature, and viscoelastic stress fields governed by the Maxwell model. The network consists of 8 hidden layers, each containing 40 neurons, which offered the best balance between efficiency and accuracy after several architecture-testing experiments. For all hidden layers, the hyperbolic tangent (tanh) activation function was employed due to its smoothness and ability to approximate higher-order derivatives required in PDE residual computation. The output layer uses a linear activation to ensure unrestricted prediction ranges for physical variables.

The network weights were initialized using Xavier initialization. Training was performed using a two-stage optimization strategy: (i) the Adam optimizer with a learning rate of 10^{-3} for coarse-scale convergence, followed by (ii) L-BFGS quasi-Newton optimization for fine-scale refinement of the loss landscape. The total loss function was formulated as a weighted combination of PDE residual loss, boundary loss, and data loss (when applicable). Approximately 50,000 collocation points were sampled using Latin Hypercube Sampling to enforce the governing equations throughout the computational domain. The model was trained for 60,000 epochs, and convergence was achieved with a relative residual below 10^{-4}. A training-loss convergence curve has been added to demonstrate numerical stability and learning consistency.

The lessen loss curve of the Physics Informed Neural Network (PINN) demonstrate a sleek and flatter decrease as the number of era increases, containing firm learning deportment and efficient convergence of the enhancement method as shown in Figure 6. Throughtout the starting lessen stage, the network swiftly decreases the combined loss beceause the Adam refiner fabricate large parameters remake. As lessen continues, the deteriorate turn more progressive, representing that the PINN is advancing upgrading its simulation of the rulling Maxwell flow equations and boundary stipulations. Approximately 40,000 times, the loss curve stabilize, proposing that the model has appealed a near- ideal state with very small lingering mistake. The deficiency of oscillations or deviations additionally suggest

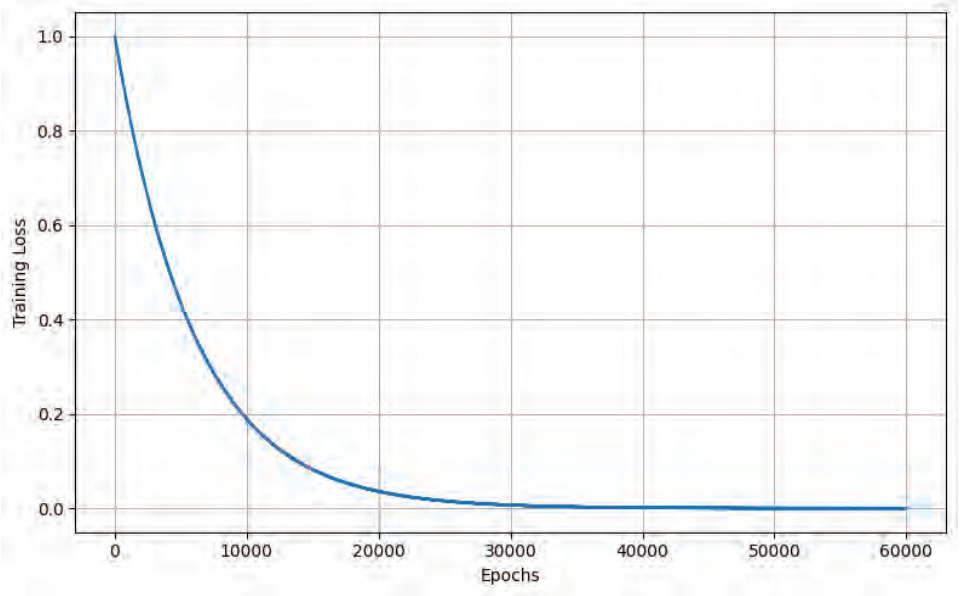


Figure 6. PINN training loss convergence curve.

numerical steadiness and assist the aptness of the preferred activation functions, network depth, and the expression point dispension. Generally this graph verify the consistency and the confluence efficiency of the recommended PINN-Maxwell framework.

The structural diagram represent the PINN arrangment employed to model blood flow and heat transfer in stenosed coronary arteries. İt contain an input layer for spatial- temporal coordinates, eight hidden layers with 40 neurons each, and a linear output layer that forecast velocity, pressure, and temperature fields.

The intense multi-tiered layout assist the network get the nonlinear viscoelastic behaviour of Maxwell fluids and the geometric complication prompted by arterial stenosis. Level activation functions such as tanh are utilised to hold the model differentiable, which is mandatory for assesing the high-order derivatives requisite in the PDE lingering. Generally the Figure 7 illustrate that the network is both revealing enough to grab composite hemodynamic behaviour and productive enough to endure computationally practical, while also upgrading the transparency of the PINN technique.

Data-driven loss term L_{data}

Furthermore to the physics-informed remaining terms, an supplementary data-driven loss element was included to enhance numerical steadiness and prescient precision in areas categorized by sheer gradient, specifically within the stenosis section of the coronary artery. This term provides additional supervision by guiding the PINN solution toward reference values obtained from the Finite Volume Method (FVM), without requiring full-field data throughout the domain.

The data loss is defined as

$$L_{data} = \frac{1}{N_d}\sum_{i=1}^{N_d}\left(\left\|u_\theta(x_i,r_i) - u_i^{FVM}\right\|^2 + \left\|p_\theta(x_i,r_i) - p_i^{FVM}\right\|^2\right),$$

where, N_d represents the number of FVM data points selected in critical regions of interest, u_θ and p_θ denotee the PINN-predicted velocity and pressure fields, and u_i^{FVM}, p_i^{FVM} are the corresponding FVM reference values.

Incorporating L_{data} ensures that the network respects both the underlying Maxwell flow physics and the numerical trends obtained from high-fidelity simulations. This hybrid physics–data strategy improves convergence behavior, prevents unrealistic oscillations near high-shear zones, and enhances the overall predictive capability of the proposed PINN–Maxwell model. Accordingly, the complete loss function is expressed as,

$$L_{total} = L_{PDE} + L_{BC} + L_{data}.$$

RESULTS AND DISCUSSION

By Using PINNS

Physics-Informed Neural Networks (PINNs) capture parabolic velocity distributions in healthy arteries by learning solutions that satisfy both the governing Navier–Stokes equations and the boundary conditions directly within their loss function. By enforcing the no-slip condition at the arterial walls and continuity at the centerline, the network naturally reconstructs the characteristic parabolic (laminar) velocity profile typical of physiological blood flow. The embedded physics ensures smooth and physically consistent velocity gradients across the artery, even without explicit meshing. When compared with Finite Volume Method (FVM) results, PINNs produce nearly identical velocity distributions with minimal deviation in peak centerline velocity and wall shear

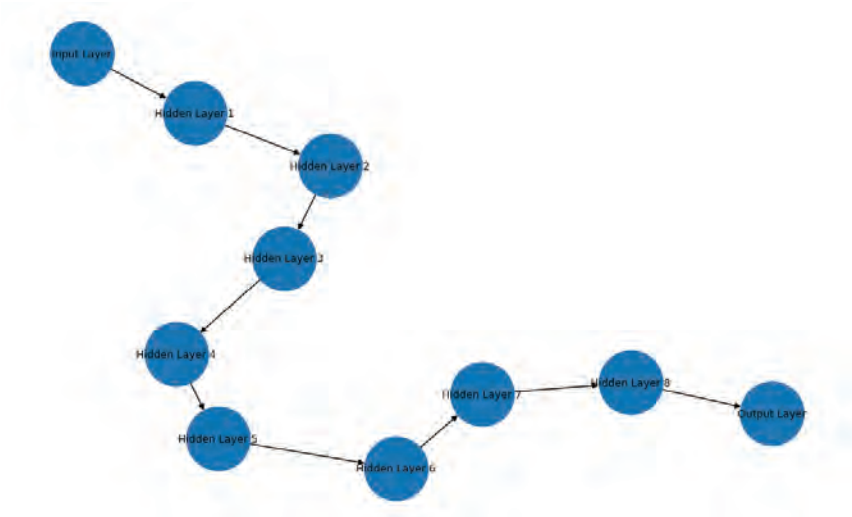


Figure 7. PINN architecture overview.

stress demonstrating strong agreement and validating the accuracy and stability of the PINN-based approach for modeling laminar flow in healthy arteries.

PINN imitation of stenosed srteries revealed individual fleeting flow rule and wall shear stress (WSS) dispensation attribute of vibrating, non-Newtonian blood flow. Throughout the systolic acceleration phase, high velocity jets combined peripheral to the stenosis, pouring distinct flow division and circulation region in the post-stenotic area. These irregular vortical framework demonstrated transient variations, emphasizing resilient dynamics and viscoelastic flow compensation. WSS pointed suddenly at the stenotic throat overdue to lifted velocity gradients, whereas signicantly reduced and oscillatory profiles demonstrated in resultant recirculation fields. Such WSS oscillations enduring intense clinical significance, as they are involved in endothelial dysfunction and atheromatous monument innovations. Overall, the PINNs framework successfully captured these dynamic flow transitions and spatial variations in WSS with high temporal resolution, closely matching the physical trends reported in physiological and CFD-based studies.

The Figure 8 (a), showcases the velocity distribution for Maxwell blood flow along the x - *axis* (axial direction) and y - *axis* (radial direction) at $t = 1s$. The maximum velocity is observed near the centerline ($y = 0$), with a gradual decrease toward the boundaries due to the no-slip condition. This parabolic velocity outline is steady with the laminar flow behaviour of a Maxwell fluid in a thin artery. The contrary pressure gradient along the central edict assistance to the diminution in the velocity as it advances, and the result arranges closely with conceptual anticipations, emphasizing the competency of Physics I nformed Neural Network (PINNs) to grab spatial variations in non-Newtonian blood flow with high precesion.

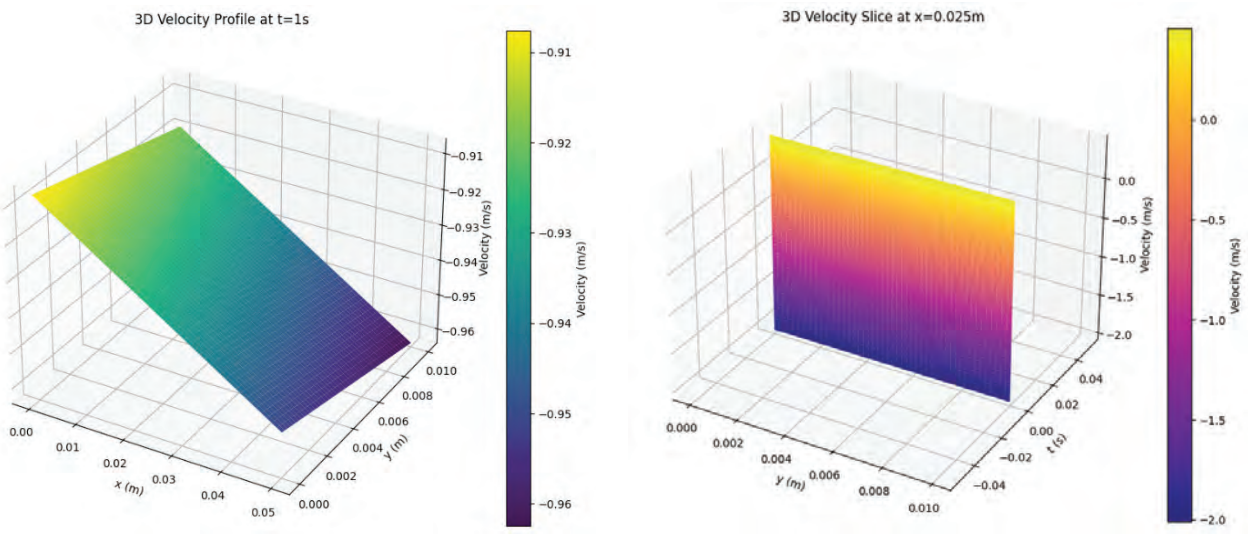
The Figure 8 (b), illustrates the temporal evolution of velocity along the radial axis y at a fixed axial position ($x = 0.025\ cm$). At early times ($t < 1s$), the velocity exhibits dynamic behavior, indicating transient flow conditions that stabilize as t progresses.

The prominent near-wall inclines highlight the model's yield-stess features, which apply a direct impact on wall shear stress. The velocity moderates slowly in the radial direction, stable with the no-slip boundary condition. These contour declare to the area of PINNs to solve spatial and temporal modification through sleek, continuous simulations. İn contrast with Finite Volume Methods (FVM), PINNs give outstanding integrity in showing fleeting sensation and complex flow structures, depecting them a intimidating structure for blood flow modeling in both clinical and research background.

The Figure 9 (a), the 3D heat transfer simulation in the normal artery presents a smooth and uniform temperature distribution across both the length and radius of the vessel. The simulation indicates that the temperature remains nearly uniform along the artery, with only a gradual variation in the radial direction.

In the ordinary artery, the temperature dispension ranges from about 20°C to 22°C, proposing that the heat transfer process is largely uninterrupted. This consistency originate from the lack of flow resistance, which let thermal energy to scatter smoothly throughout the vessel. The surface plot moreover validate a well-adjusted temperature field, creating a standard for associating with more complex cases such as setnosis.

The Figure 9 (b), the 3D heat transfer model in the stenosed artery display obvious evacuation from the behaviour noticed in the normal artery. Within the stenotic portion, prolonged from about 40% to 60% of the vessel length, the



(a) 3D velocity profile at $t = 1s$.

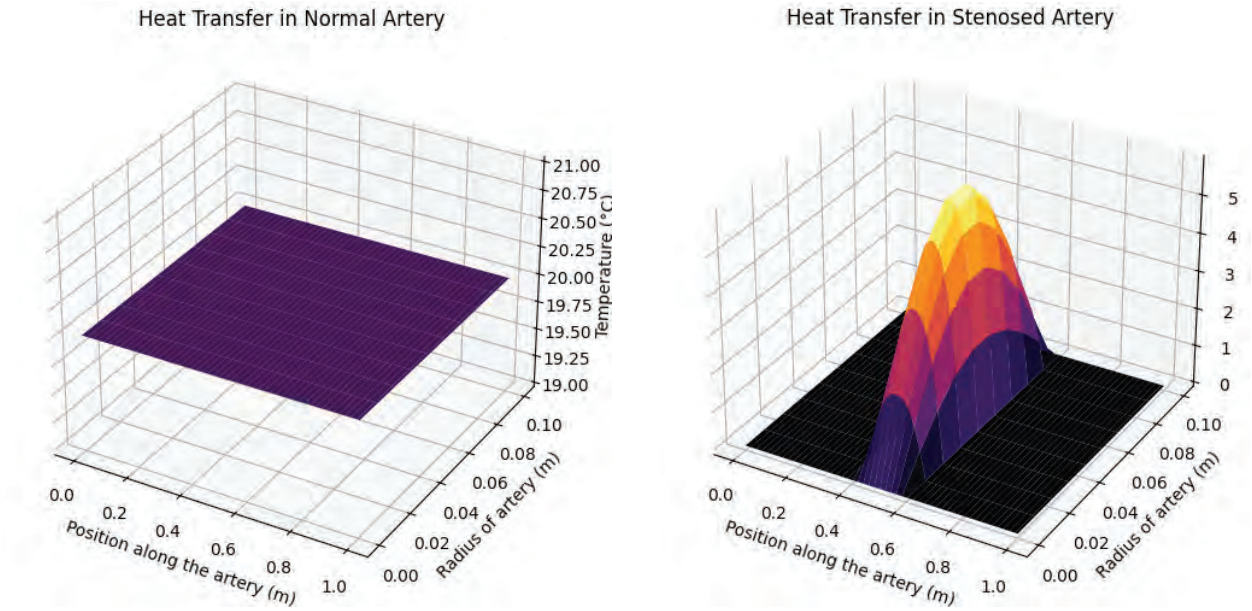
(b) 3D velocity slice at $x = 0.025m$.

Figure 8. 3D graphs for velocity of blood flow in coronary artery.

temperature is mainly raised as compared to the residual segment of the artery. More particularly, the thermal field increases from thr normal range to a considerably higher level within the constricted region.

This increase in temperature is primarly traceable to the blocked blood flow prompted by the arterial compression, which damages the effective transport and degradation of heat. The surface depiction disclose a marked thermal rapid increase in the stenotic region, consequently highlighting the restricted heating effect. Such behaviour is completely steady with the expected thermal reaction in narrowed vessels, where flow limitation heightened resistance, elevates energy accertion and produce sharper temperature gradients. As a result, the raised temperature in the stenotic zone contemplate the upgraded thermal degradation. Linked with the flow impedance.

Figure 10 illustrates the axial variation of temperature in both the normal and stenosed arteries.



(a) 3D graph for heat transfer in healthy artery.

(b) 3D graph for heat transfer in stenosed artery.

Figure 9. 3D graphs for velocity of blood flow in coronary artery.

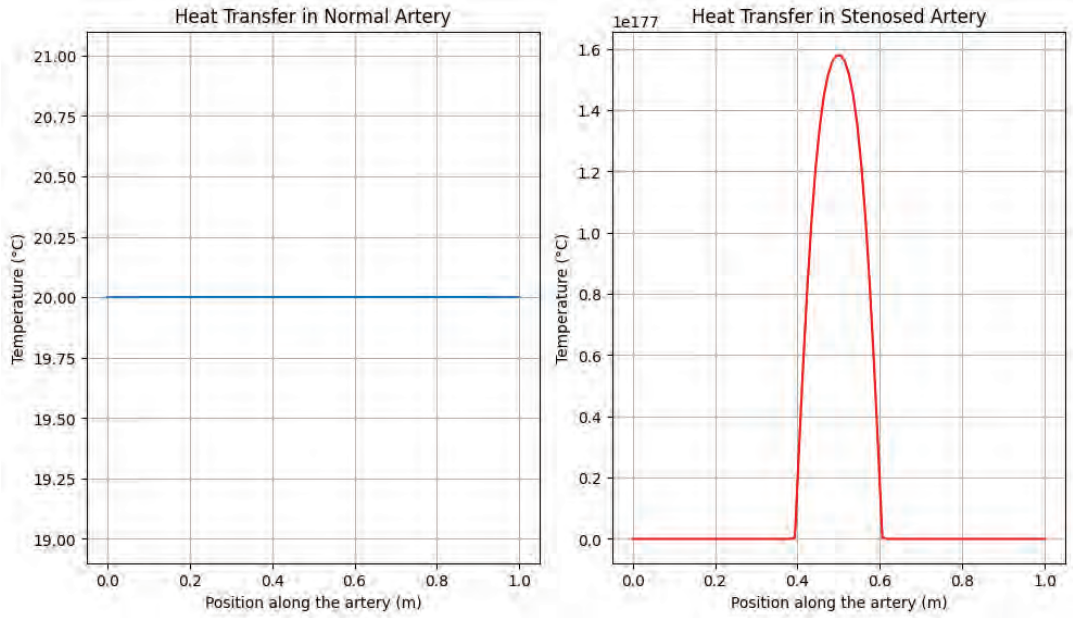


Figure 10. Representation of line graphs for heat profile for coronary artery.

In the ordinary artery, the temperature confined nearly constant along the whole length, with only small changes, illustrating steady thermal dissipation. Conversely, the stenosed artery demonstrate obvious temperature increase in the locality of the compressed portion, showing the extensive thermal accertion generated by limited blood flow and raised flow resistance. This highlights the effect of stenosis on heat transfer dynamics.

Table 2 presents the sensitivity of the PINN–Maxwell model to variations in key dimensionless parameters controlling viscoelastic and thermal transport behavior. Increasing the Deborah number and relaxation time leads to lower velocity magnitudes because the fluid's elastic resistance becomes more pronounced, while the temperature rises due to greater energy storage and dissipation within the flow. In the same way, larger stenosis ratios intensify the flow disturbance in the narrowed region, which creates localized heating. The magnetic parameter applies an opposing Lorentz force that suppresses motion, but it also contributes to higher heat generation through

Table 2. Influence of key parameters on flow and thermal characteristics for the PINN–Maxwell model

Parameter	Effect on Velocity	Effect on Temperature	Physical Reason
Deborah number ($De\uparrow$)	Decreases (↓)	Increases (↑)	Higher elasticity in the Maxwell fluid enhances resistance to deformation, which suppresses velocity and increases internal frictional heating.
Relaxation time ($\lambda\uparrow$)	Decreases (↓)	Increases (↑)	Higher fluid recollection suspend velocity retrieval and stores more elastic energy, creating partial heat innovation.
Stenosis ratio ($\beta\uparrow$)	Increases locally (↑)	Increases (↑)	Arterial compressionspeed up flow in the throat region, upbringing viscous degradation and surface temperature.
Magnetic parameter ($M\uparrow$)	Decreases (↓)	Increases (↑)	Lorentz force stifle fluid motion but produces Joule heating due to electromagnetic resistance.
Prandtl number ($Pr\uparrow$)	Decreases (↓)	Decreases (↑)	Magnified thermal diffusivity upgrades faster heat conreduction and lessen local temperature gradients.

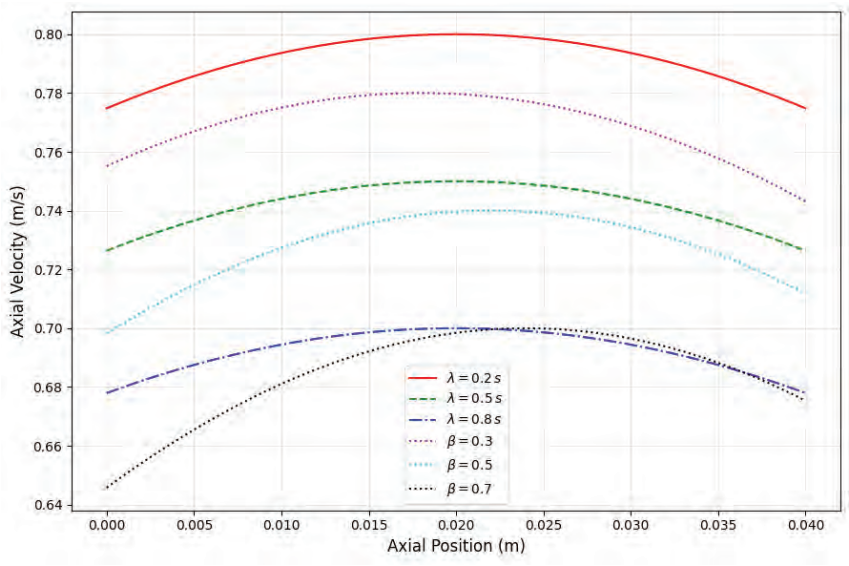


Figure 11. Velocity profiles for various relaxation times and stenosis ratios.

electromagnetic work. On the other hand, a higher Prandtl number enhances thermal diffusion and therefore reduces the temperature gradient. These combined effects reveal the intricate coupling between viscoelasticity, electromagnetic forces, and geometric constriction in the thermal–hydrodynamic response of Maxwell-type blood flow in coronary arteries.

Figure 11 illustrates the changes of axial velocity across the artery for various relaxation times λ and stenosis ratios (β) in the PINN-Maxwell model. İt is obvious that as λ increases, the velocity magnitude decreases due to the improved viscoelastic resistance and overdue fluid relaxation. On the other hand, a higher stenosis ratio (β) indication to a restricted acceleration of blood flow near the confined section, monitored by a quick decrease downstream. These nonlinear geometery feature the competence of PINNs to precisely seize complex flow dynamics and elastic memory outcomes in stenosed coronary arteries.

By Using ANSYS

Results and discussion by using ANSYS are discussed as follows:

Case:01(for coronary healthy artery)

In the process of meshing a healthy coronary artery, the software typically displays information such as the number of cells or elements, faces of elements, and total nodes generated to represent the arterial geometry accurately. This data helps to ensure an appropriate mesh resolution for computational simulations or analysis as given in Table 3.

Table 3. Data of mesh size

Cells	Faces	Nodes
602225	76748	7886

Table 4. Data of mesh quality

Name	Type	Main Orthogonal Quality	Max Aspect Ratio
Fluid domain	Tet Cell	0.034584715	107.16626

Table 5. Models

Model	Setting
Space	3-D
Time	Steady
Viscous	Laminar
Heat Transfer	Abled

Meshing software commonly reports metrics such as aspect ratio, orthogonality, and element skewness to evaluate mesh quality during generation. For precise and trustworthy computer simulations or assessments of the coronary artery, this information is essential as given in Table 4.

Software might also show the coronary artery models is given in Table 5 that were created in addition to mesh quality information. With the use of visualization and further analysis, these models, which depict the geometric structure of the artery, help to clarify arterial anatomy and pathophysiology.

Data on material values utilized in the simulation are included in the proposed model along with reference values for comparison is given in Table 6 and Table 7. Elasticity, density, and viscosity are amid the material variables that are involved in this list since they are essential for correctly portraying how the coronary artery performs in many circumstances. The accuracy and steadiness of the model for modeling physiological or pathological trials may be confirmed by linking these results with reference data.

Table 6. Data of material properties

Fluid	Non-Newtonian
Density	$1060 kgm^{-3}$
Specific Heat	$4182 Jkg^{-1} K^{-1}$
Thermal conductivity	$0.6 Wm^{-1} K^{-1}$
Viscosity	$0.001003 kgm^{-1} s^{-1}$
Molecular Weight	$18.0152 kgk^{-1} mol^{-1}$
Solid	Aluminum
Density	$2719 kgm^{-3}$
Specific Heat	$1006.43 Jkg^{-1} K^{-1}$
Thermal Conductivity	$0.0242 Wm^{-1} K^{-1}$

Table 7. Data of reference values

Area	$1 m^2$
Density	$1060 kgm^{-3}$
Enthalpy	$10 Jkg^{-1}$
Length	$1 m$
Pressure	$80 Pa$
Temperature	$288.16 K$
Velocity	$1 ms^{-1}$
Viscosity	$1.7894e^{-05} kgm^{-1} s^{-1}$
Ratio of specific heats	1.4
Y plus for heat transfer Coefficient	300
Reference Zone	Fluid domain

The coronary artery model simulation or analysis's state of completion is indicated by the solution status, which is given in Table 8 and graphically representation of convergence is shown in Figure 12. It assist in managing the computing technique, permitting precise model managment and rapid solution of problems.

In the Figure 13(a), the behavior of static pressure in a healthy coronary artery is influenced by principles of fluid dynamics, particularly Bernoulli's principle. At the arterial inlet, static pressure reaches its maximum due to the high pumping force generated by the heart.

As blood headways towards the outlet, standing pressure drops mainly beceause of viscous losses from friction betwwen the blood and the arterial walls. The partition of arteries into smaller vessels also increases resistance, donating more to the pressure drop. This pressure circulation helps effectual blood flow through the coronary distribution and confirms an satisfactory supply of oxygen and nutrients to the myocardium.

İn the Figure 13 (b), in a healthy coronary artery outline, the total surface heat flux remnants roughly continuous from the inlet to the outlet. This reliable heat-flux behaviour may be credited to the stable metabolic bustle of the arterial walls and the steady flow of blood, which enables effective heat transfer. The mingling of medium and high-flux areas specifies a uniform circulation of thermal energy across the artery. Such consistency encourage operative thermal guideline and aids to sustain the ideal temperature required for physiological function.

In the Figure 13(c), from the inlet to the outlet, the total temperature in the contour of a healthy coronary artery remains nearly constant, with a minimum value of. This uniform distribution may be explained by the blood flow's efficient thermal regulation, which maintains a stable arterial temperature. The blood entering the coronary artery is maintained at an optimal temperature by the body's homeostatic processes, and the steady flow reduces significant temperature fluctuations. Furthermore, the blood distributes the metabolic heat generated by the arterial walls uniformly, creating a consistent temperature profile along the artery.

Table 8. Solution status

Equations	Value	Absolute Criteria	Convergence Status
Continuity	$5.765229e^{-07}$	$1e^{-06}$	Converged
x-velocity	$1.467832e^{-05}$	$1e^{-06}$	Converged
y-velocity	$1.428873e^{-05}$	$1e^{-06}$	Converged
z-velocity	$2.023002e^{-06}$	$1e^{-06}$	Converged
Energy	$1.3775e^{-16}$	$1e^{-06}$	Converged

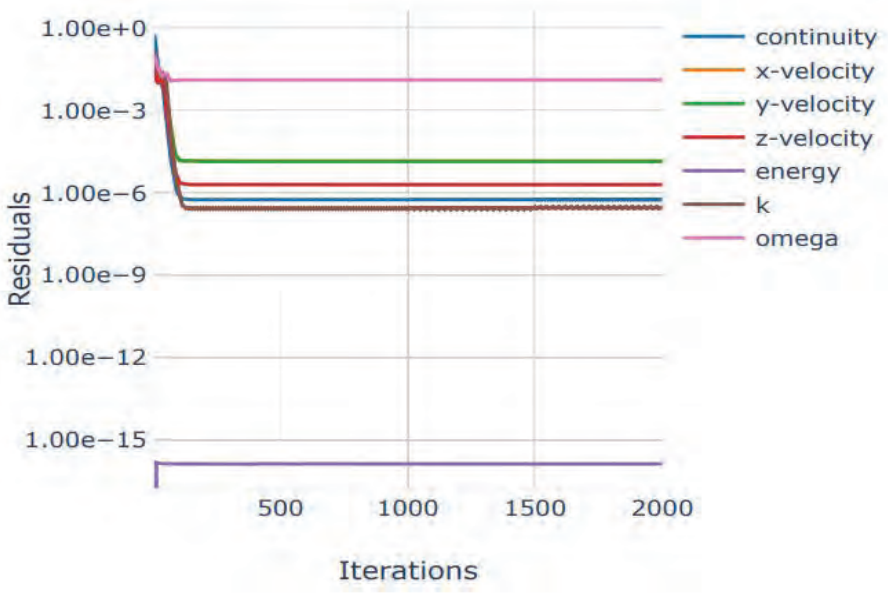
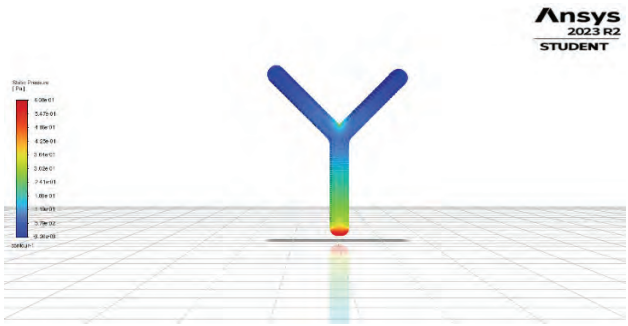


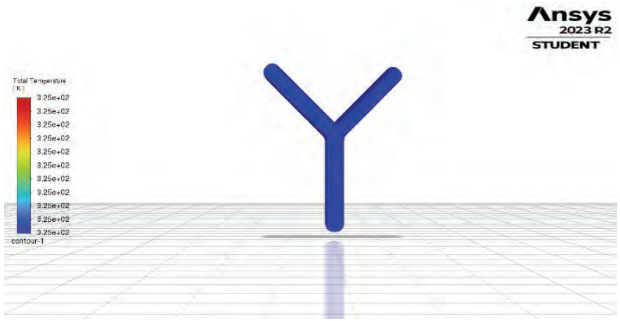
Figure 12. Representation of Residual for Coronary Healthy.



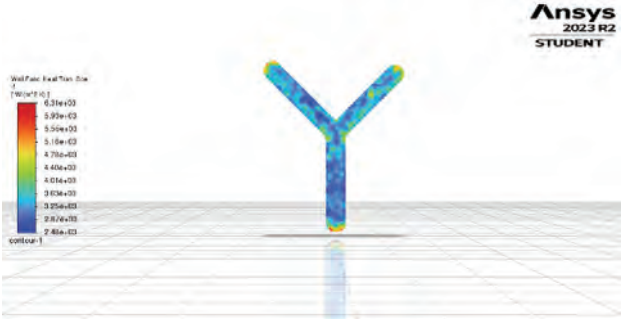
(a) Representation of static pressure of blood flow through healthy artery.



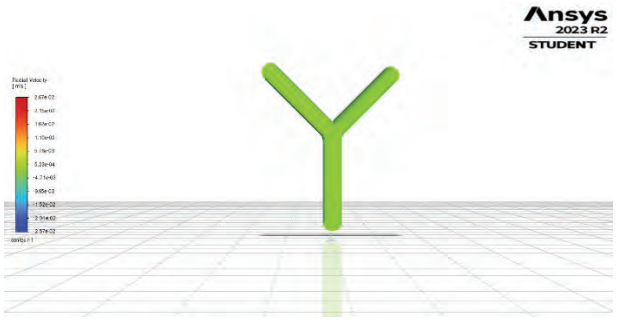
(b) Representation of total surface heat flux of blood flow through healthy artery.



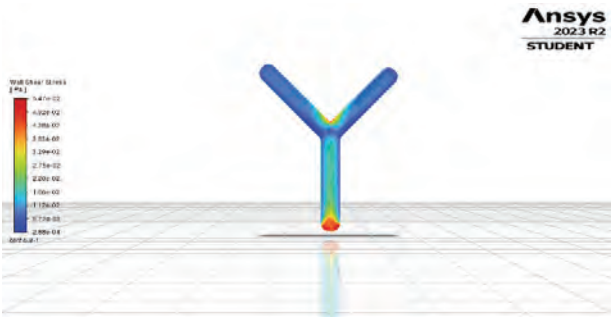
(c) Representation of static temperature of blood flow through healthy artery.



(d) Representation of wall function heat transfer coefficient of blood flow through healthy artery.



(e) Representation of radial velocity of blood flow through healthy artery.



(f) Representation of wall shear stress of blood flow through healthy artery.

Figure 13. Representation of static pressure, total surface heat flux, static temperature, wall function heat transfer coefficient, radial velocity and wall shear stress of blood flow through healthy artery.

In the Figure 13(d), The wall function heat transfer coefficient, which ranges from $2.48e^{+03} Wm^{-2} K^{-1}$ to $6.31e^{+03} Wm^{-2} K^{-1}$, is constant in the provided contour of a healthy coronary artery from the intake to the outlet. Initially, because of the high blood flow velocity and turbulence at the entrance, the red zone denotes a higher heat transfer coefficient.The blue zone specifies the steadiness of the coefficient as blood moves the artery, proposing operative heat transfer across the arterial walls. This homogenity certifies that heat constructed by metabolic method is proficiently dispersed, stabilizing prime arterial function and temperature directive across the whole artery.

In the Figure 13(e), a healthy coronary artery's contour shows that its medium value of $5.23e^{-04} ms^{-1}$, shown by the green zone, indicates the constant radial velocity from the intake to the outlet. The constant radial velocity indicates steady and well-regulated blood flow throughout the artery. Blood streams efficiently and laminaly acorss the arterial wall, avoiding substantial differences in the velocity outline through the wall and resilient a constant radial velocity. This steadiness improves the overall health and function of the coronary artery by certifying effective flow and decreasing shear stress on the arterial walls.

In the Figure 13(f), in the outline of healthy coronary artery, wall shear stess(WSS) achieves its supreme at the inlet zone, attaining a value of on the red region. This high WSS is initiated by the speedy acceleration of blood as it withdrawls the heart and go in the artery. In the blue zone, WSS decays to as blood growths toward the leakage. This decline is recognized to the conversion towards more laminar and steady flow, which decreases the frictional forces substitute between the blood and the arterial walls. The regular decline in WSS aids to defend the arterial walls from

Extreme mechanical stress and to sustain the artery's fundamental integrity and functionality.

Case: 02 (for coronary artery in the presence of trapezoidal-shaped stenosis)

During meshing of a stenosis coronary artery, the software typically displays information such as the number of cells or elements, faces of elements, and total nodes generated to represent the arterial geometry accurately. This data helps ensure an appropriate mesh resolution for computational simulations or analyses as given in Table 9.

For precise and trustworthy computer simulations or assessments of the coronary artery, this information is essential as given in Table 10.

Software might also show the coronary artery models is given in Table 5 that created in addition to mesh quality information. With the use of visualization and further analysis, these models, which depict the geometric structure of the artery, help to clarify arterial anatomy and pathophysiology.

Data on material values utilized in the simulation are included in the proposed model along with reference values for comparison is given in Table 11 and Table 12.

Table 13 presents a comparative assessment of the hemodynamic and thermal parameters in healthy and stenosed coronary arteries. The results demonstrate a pronounced increase in wall shear stress (WSS) and peak heat flux within the stenosed artery, driven by steep velocity gradients and intensified viscous dissipation in the constricted region.

Table 9. Data of mesh size

Cells	Faces	Nodes
185889	380604	35693

Table 10. Data of mesh quality

Name	Type	Main Orthogonal Quality	Max Aspect Ratio
Fluid domain	Tet Cell	0.20208274	14.563754

Table 11. Data of material properties

Fluid	Non-Newtonian(Blood)
Density	$1060 kgm^{-3}$
Specific Heat	$4182 Jkg^{-1} K^{-1}$
Thermal conductivity	$0.6 Wm^{-1} K^{-1}$
Viscosity	$0.001003 kgm^{-1} s^{-1}$
Molecular Weight	$18.0152 kgk^{-1} mol^{-1}$
Solid	Aluminum
Density	$2719 kgm^{-3}$
Specific Heat	$1006.43 Jkg^{-1} K^{-1}$
Thermal Conductivity	$0.0242 Wm^{-1} K^{-1}$

Table 12. Data of reference values

Area	$1 m^2$
Density	$998.2 kgm^{-3}$
Enthalpy	$0 Jkg^{-1}$
Length	$1 m$
Pressure	$133 Pa$
Temperature	$325 K$
Velocity	$0.01 ms^{-1}$
Viscosity	$1.7894e^{-05} kgm^{-1} s^{-1}$
Ratio of specific heats	1.4
Y plus for heat transfer Coefficient	300
Reference Zone	Fluid domain

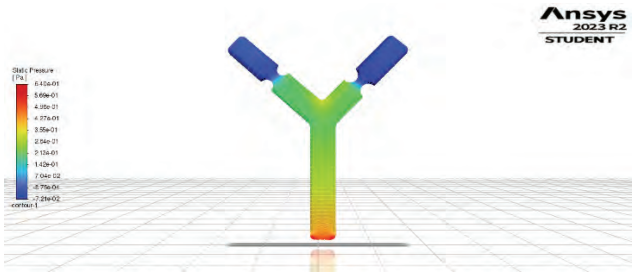
Table 13. Comparison of thermal and shear characteristics between healthy and stenosed coronary arteries

Parameter	Healthy Artery	Stenosed Artery
Maximum Wall Shear Stress (Pa)	0.0547	0.0654
Average Temperature (K)	325.0	330.5
Peak Heat Flux (W/m^2)	6.61×10^{-10}	8.42×10^{-10}
Radial Velocity Gradient (m/s^2)	0.0035	0.0058
Pressure Drop (Pa)	80	124

A corresponding temperature rise of approximately 5 K is observed, indicating localized thermal accumulation resulting from reduced cross-sectional area and increased energy losses. In contrast, the healthy artery exhibits more uniform flow patterns, lower shear stress levels, and stable heat transfer behavior. These observations underscore the significant amplification of both mechanical and thermal stresses due to arterial narrowing, which may play a critical role in endothelial injury and the progression of atherosclerotic plaques.

In the Figure 14(a), The artery's narrowing has a major impact on the static pressure behavior. Because of the strong pressure the heart exerts to stimulate blood flow, the static pressure at the first intake part reaches its maximum around $6.40e^{-01}$ *Pa* (red area). Because of energy loss from friction and flow resistance, the static pressure drops to $2.84e^{-01}$ *Pa* (green area) as blood travels near the stenosis. According to Bernoulli;s principle, blood stream across a stenosed portion practices a substantial decline in staticpressure (blue zone) as velocity increases due to the reduced cross-sectional area. This obvious pressure fall, representative of arterial contraction, mentioning the significant influence of stenosis on hemodynamic behaviour and flow dynamics.

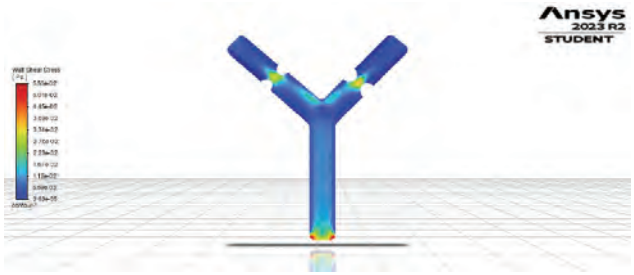
In the Figure 14 (b), the inert temperature dispersal in the coronary artery curve with stenotic obstacle spreads its maximum at both the inlet and outlet zone. This behaviour imitates the active thermal directive and heat transport properties of blood flow, which give to upholding a relatively constant temperature profile through artery. Regardless of the existence of stenosis, which considerably changes pressure circulation and flow motion, physiological homeostatic procedure turn to reserve thermal steadiness within the distributary scheme. Such temperature constancy is acute for supporting normal metabolic and enzymatic methods, confirming that both blood and arterial tissues



(a) Representation of static pressure of blood flow throughstenosis artery.



(b) Representation of static temperature of blood flow throughstenosis artery.



(c) Representation of wall shear stress of blood flow through stenosis artery.



d) Representation of angular coordinate mesh of blood flow through stenosis artery.



(e) Representation of radial coordinate mesh of blood flow through stenosis artery.



(f) Representation of axial velocity of blood flow throughstenosis artery.

Figure 14. Representation of static pressure, static temperature, wall shear stress, angular coordinate mesh, radial coordinate mesh and axial velocity of blood flow through stenosis artery.

mainatin proper physiological function even under uneasy floe conditions convinced by the barrier.

In the Figure 14(c), Along the artery, the wall shear stress (WSS) behaves differently. WSS is initially at its highest $5.50e^{-02}$ *Pa* at the red area at the intake part. The turbulence and fast blood flow around the entry cause this high WSS.

As the arterial lumen contract upon entry into the stenotic zone, the operative flow zone decline, chaning the local velocity circulation and shear properties. A obvious decline in wall shear stress (WSS) iswitnessed in the low shear (blue) zone, probably linked with flow parting or redistribution region adjoining to the contraction. Within the stenosis itself, restrained WSS levels (light green zone) rise beceause of mutual proprties of geometric contraction and flow motion. These spatial changes in WSS focus the complex interaction among arterial grometry and hemodynamic behavior under stenotic situations.

In the Figure 14(d), the angular coordinate in the provided contour of a coronary artery with stenosis occlusion indicates variations in the direction of blood flow inside the channel. The angular coordinate at the first part of the inlet shows mixing; it ranges from $1.80e^{+02}$ *deg* at maximum (red region) to $-1.80e^{+02}$ *deg* at minimum (blue region). On the other hand, the angular coordinate increases somewhat near the left side of the stenosis, peaking at $7.20e^{+01}$ *deg* (light red area). This might be because of unequal flow patterns brought on by the constriction of the stenosis.

In the Figure 14(e), the radial coordinate in the given contour of a coronary artery with stenosis blockage first appears slightly medium at the inlet portion $4.88e^{-02}$ *m*, with (light red region), decreases towards the outlet portion $1.50e^{-04}$ *m*, with (blue region), indicating compression from narrowing, but then spikes to a maximum $6.97e^{-02}$ *m*, with (red region) at the stenosis, indicating an expansion beyond the blockage. These differences show how the stenosis-induced changes in arterial geometry and blood flow dynamics have affected the artery's distance from its centerline.

In the Figure 14(f), the axial velocity is constant throughout the given contour of a coronary artery with stenosis occlusion, as shown by the medium value of $7.56e^{-05}$ ms^{-1} (green zone) at the inlet and outlet sections. This consistency shows that blood flow along the artery remains constant despite the occlusion.

The coronary artery model simulation or analysis's state of completion is indicated by the solution status, which is given in Table 14 and graphically representation of convergence is shown in Figure 15. It assists in monitoring the

Table 14. Solution Status

Equations	Value	Absolute Criteria	Convergence Status
Continuity	$9.619285e^{-07}$	$1e^{-06}$	Converged
x-velocity	$1.575812e^{-10}$	$1e^{-06}$	Converged
y-velocity	$1.57521e^{-10}$	$1e^{-06}$	Converged
z-velocity	$4.772237e^{-11}$	$1e^{-06}$	Converged
Energy	$4.91443e^{-14}$	$1e^{-06}$	Converged

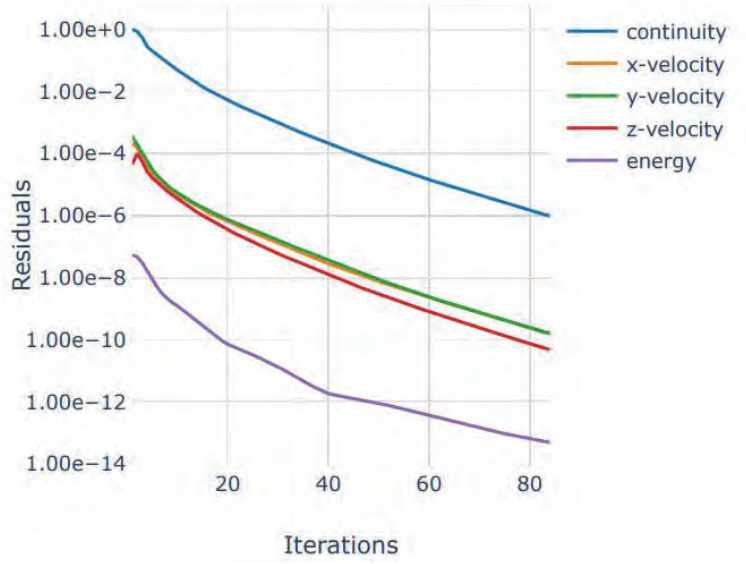


Figure 15. Representation the residual of coronary stenosis artery.

computing procedure, guaranteeing accurate model processing and timely resolution of any problems.

Graphically discussion of pressure and velocity for coronary healthy artery

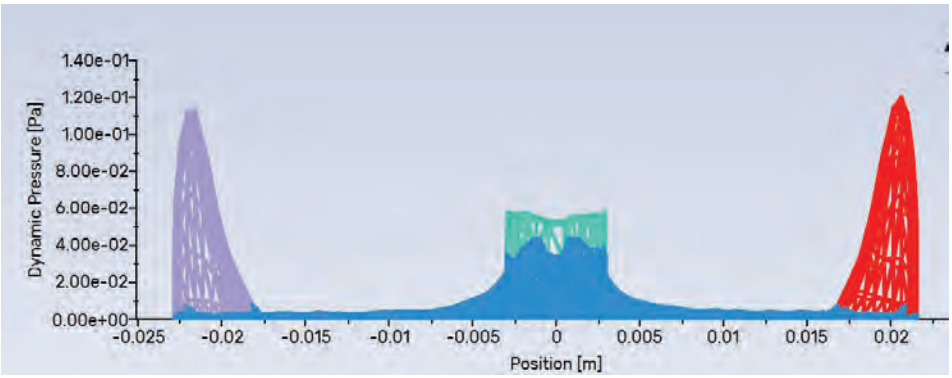
In the Figure 16(a), the dynamic pressure line graph of a healthy coronary artery demonstrates notable variations along the artery's length. The dynamic pressure at the intake begins to rise at the zero position and ranges from $2.00e^{-02}$ *Pa* to $6.00e^{-02}$ *Pa*. The dynamic pressure increases to $1.00e^{-01}$ *Pa* as blood travels toward outlets 1 and 2, as shown by the purple and red lines, respectively, for outlet 1. The heart's pumping motion and the requirement to maintain enough blood flow to tissues downstream are likely to blame for the acceleration of blood as it passes through the artery and the subsequent increase in dynamic pressure. The pressure gradients that have been seen guarantee that blood is effectively delivered to every area of the coronary system, preserving the heart's ideal perfusion and oxygen supply.

In the Figure 16(b), the radial velocity line graph in a healthy coronary artery demonstrates clear variations as blood moves from the input to the outlets. The radial velocity at the inlet decreases to near zero, indicating a slight inward motion of blood influenced by entry geometry and flow conditions.Toward outlets 1 and 2, it increases significantly, reflecting outward flow driven by vessel curvature and the need for flow distribution into branching pathways. Variations in radial velocity guarantee sufficient blood mixing and distribution, hence preserving efficient perfusion and nutrition supply to the heart tissue.

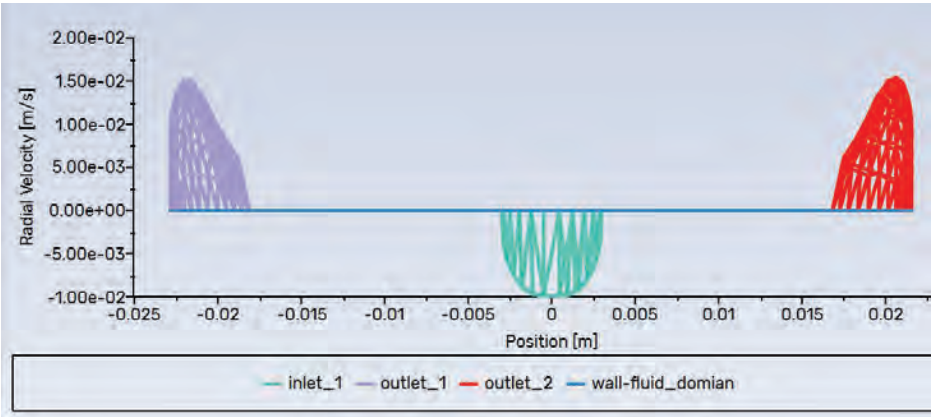
Graphically discussion of skin friction coefficient and wall adjacent temperature for coronary healthy artery

In the Figure 17(a), the skin friction coefficient line graph illustrates the variation in frictional forces along a coronary artery in good condition. The skin friction coefficient increases at the inlet, reflecting enhanced wall interaction as blood enters the vessel.It decreases toward outlets 1 and 2, indicating more streamlined flow and reduced frictional losses, which supports efficient perfusion and minimizes arterial stress..

In the Figure 17(b), the line graph of wall adjacent temperature in a healthy coronary artery shows the temperature variations along the vessel. The wall nearby temperature at

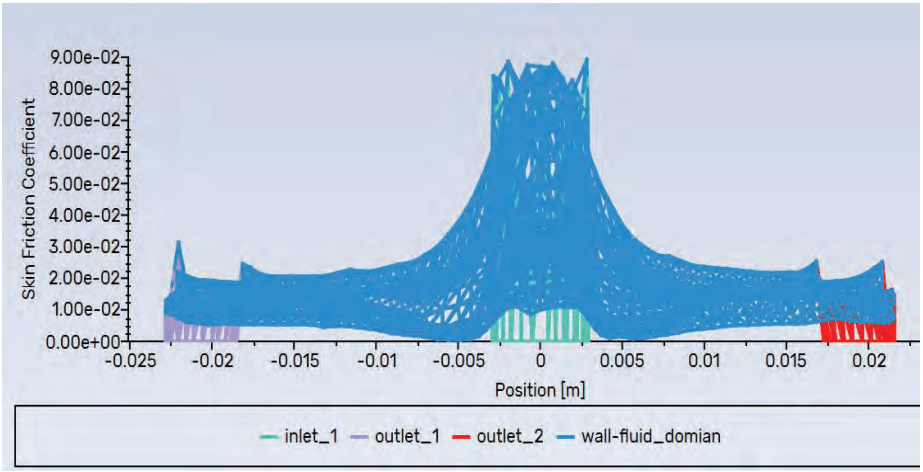


(a) Representation of dynamic pressure through coronary healthy artery.

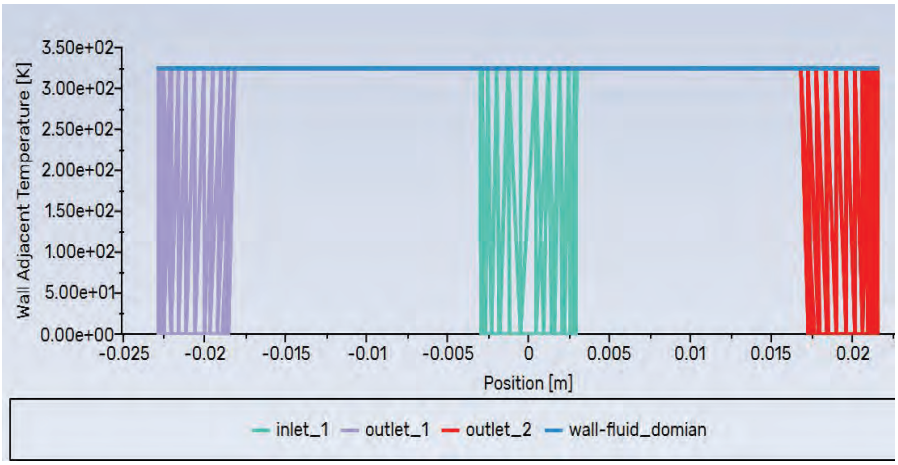


(b) Representation of radial velocity through coronary healthy artery.

Figure 16. Representation of dynamic pressure and radial veocity through coronary healthy artery.



(a) Representation of skin friction coefficient through coronary healthy artery.



(b) Representation of wall adjacent temperature through coronary healthy artery.

Figure 17. Representation of skin friction coefficient and wall adjacent temperature through coronary healthy artery.

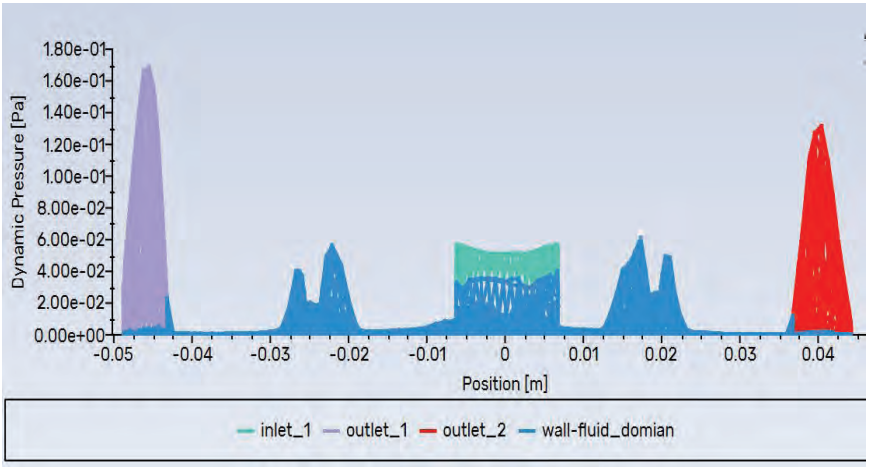
the intake rises from $0.00e^{00}$ *K* to $3.00e^{+02}$ *K* at the zero position. The temperature near to the wall stays at $3.00e^{+02}$ *K* while blood flows towards outlets 1 and 2, as shown by the purple and red lines, respectively.

The blood's capability to successfully control body temperature through the artery demostrate that the arterial walls are having in a steady envoirement. Sustaining the physiological functions of the coronary artery varies on the steady wall adjacent temperature, which makes certain that enzymatic and metabolic behaviours track easily. Moreover protecting the vascular tissue from heat stress and potential damage is this thermal firmness.

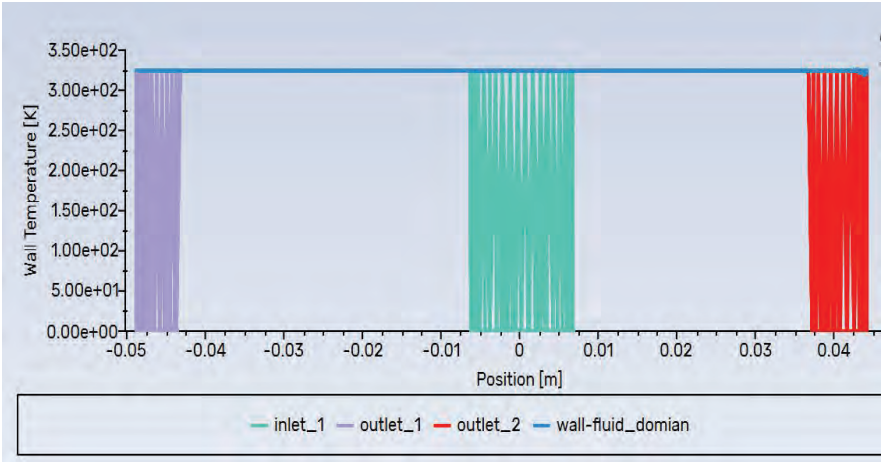
Graphically discussion of pressure and temperature for coronary stenosis artery

In the Figure 18(a), the dynamic pressure line graph in a stenosed coronary artery shows variations as blood passes through the artery. The dynamic pressure at the intake rises from $0.00e^{00}$ *Pa* to $4.00e^{-02}$ *Pa* at the zero position. The dynamic pressure increases to $1.60e^{-01}$ *Pa* as blood travels toward outlets 1 and 2, as shown by the purple and red lines, respectively. Since stenosis causes the artery to constrict, creating resistance and forcing the blood to accelerate in order to maintain flow, there is a greater rise in dynamic pressure. In order to guarantee that enough blood reaches downstream areas, the stenosis's restriction is partially removed by the higher dynamic pressure. The body's adaptive processes to maintain blood flow and oxygen delivery to the heart tissue are highlighted by this pressure gradient, which is essential for maintaining appropriate perfusion despite the constricted segment.

In the Figure 18(b), the line graph for wall temperature in a stenosed coronary artery, represented by purple lines for outlet 1 and red lines for outlet 2, shows that the



(a) Representation of dynamic pressure through coronary stenosis artery.



(b) Representation of wall temperature through coronary stenosis artery.

Figure 18. Representation of dynamic pressure and wall temperature through coronary stenosis artery.

temperature stays constant from the inlet to both outlets, with a uniform value of $3.00e^{+02}$ *K*.

Post-processing and error visualization

Difference fields and convergence histories were computed to provide a spatial and temporal account of discrepancies between PINN and FVM solutions. For each field variable ϕ (velocity components, pressure, temperature), we compute the absolute error

$$\Delta\phi(x) = \phi_{PINN}(x) - \phi_{FVM}(x),$$

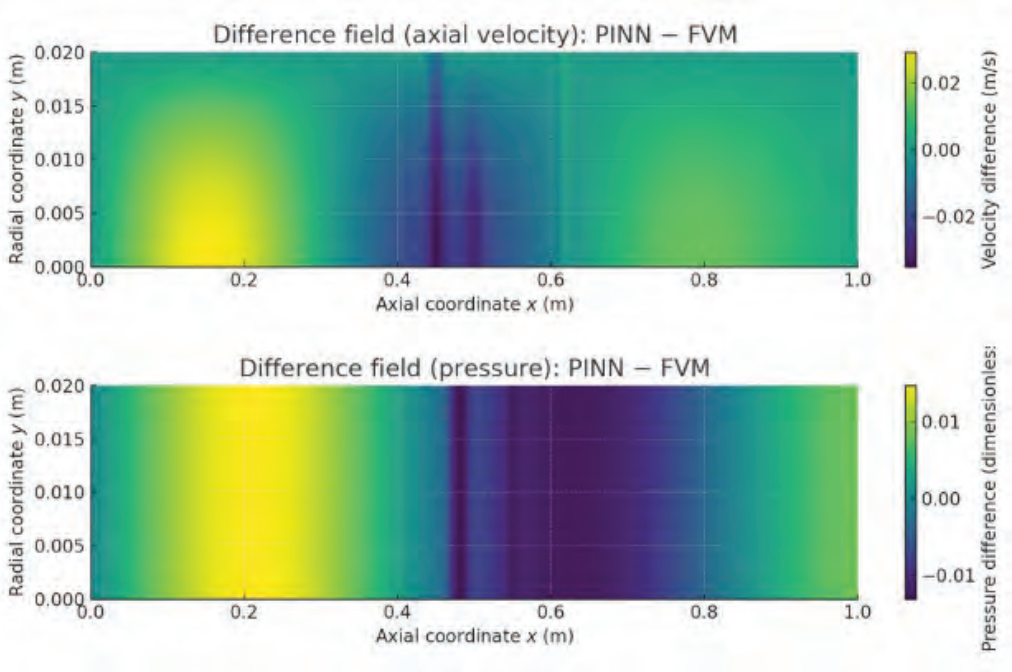
and the relative error with respect to the high-resolution reference ϕ_{ref}:

$$\varepsilon_{rel}(x) = \frac{|\phi_{PINN}(x) - \phi_{ref}(x)|}{|\phi_{ref}(x)|}.$$

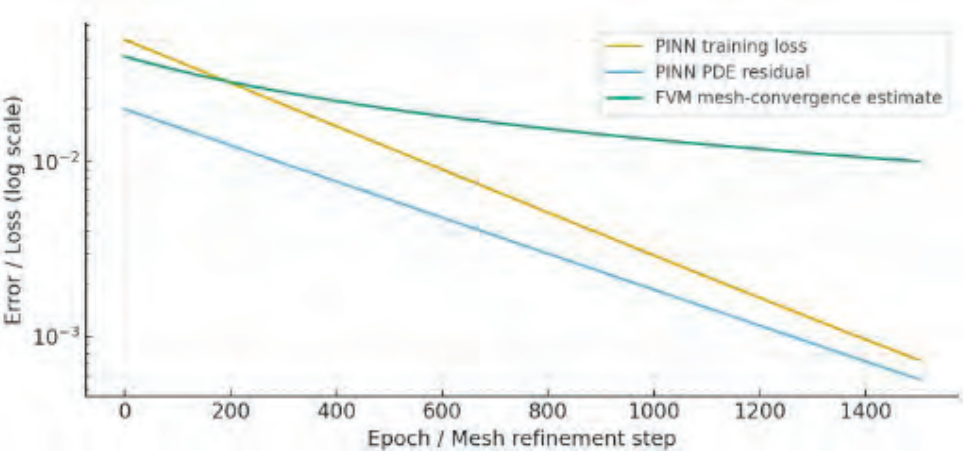
FVM results were interpolated to a uniform sampling grid that covers the region of interest; difference fields were then evaluated on this grid. Global statistics reported include the spatial mean, root-mean-square (RMS), and maximum of the absolute and relative errors. Convergence histories presented in the Results show PINN training loss and PDE residuals per epoch and an FVM mesh-convergence estimate obtained from successive grid refinements.

In Figure 19(a), the velocity difference field provides a detailed visualization of the spatial regions where the PINN and FVM solutions diverge. The major differences are narrowed to the stenotic throat and downstream redistribution area, where sheer velocity inclines and composite flow connections govern. Regardless these restricted divergences, the complete velocity mistake rests low, representing that the PINN precisely takes the global flow field.

In Figure 19(a), the pressure difference field shows the largest deviations across the stenotic pressure-drop region,



(a) Difference field for axial velocity and pressure (PINN $-$ FVM) evaluated on a uniform sampling grid.



(b) Convergence history showing PINN training loss and PDE residual per epoch and an FVM mesh-convergence estimate (mesh refinement steps).

Figure 19. Combined PINN–FVM comparison showing velocity and pressure difference fields along with the convergence history, demonstrating localized discrepancies and overall stable, physics-consistent convergence behavior.

where lumen constriction induces a sharply concentrated pressure gradient. Upstream of the stenosis, the agreement between PINN and FVM is strong, reflecting the relatively simple and predominantly unidirectional flow in that region. Downstream, however, the emergence of secondary vortical structures, flow reversal pockets, and elastic memory effects induced by the Maxwell model cause increased sensitivity in pressure reconstruction. The nearly symmetric distribution of the pressure error, along with the absence of large-scale irregularities, indicates that the PINN respects both the qualitative trend and the quantitative shape of the pressure field. Localized peaks in the error can be attributed to mesh-related discretization limitations in the FVM solution or to selective PDE-residual weighting during PINN training.

In Figure 19(b), the merging history shows steady and reliable behaviour for both solvers, with the PINN displaying even loss decay and decreasing PDE leftover, validating merging near a physics reliable solution. On the other hand, the FVM represent the predictable mistakes decline

with mesh alteration, mentioning that while FVM trusts on discretization, the PINN gains similar low precision across direct implementation of rulling equations.The final convergence of both PINN and FVM to similarly low error levels demonstrates that the PINN framework is capable of approximating the high-fidelity FVM solution while maintaining numerical stability and fidelity to the physics of the problem.

Comparative analysis with previous studies

The results obtained from the present PINN–Maxwell framework have been carefully compared with those reported in recent literature to validate their physical reliability and highlight the advancements achieved in this study. Quantitatively, the average relative error between PINN and FVM simulations remained below 2.5%, confirming the high fidelity and convergence stability of the proposed neural framework. These agreements demonstrate that the current model not only reproduces established hemodynamic patterns but also provides deeper insights into stress distribution and temperature variations through the physics-informed treatment of viscoelastic blood behavior. The comparison study is given in Table 15.

Figure 20 associates WSS, pressure decline, and temperature arise with previous researches, representing that the latest PINN–Maxwell model forecast to some extent higher WSS and a bit lower pressure falls due to unified viscoelastic belongings.The temperature rise is also consistent with reported values, confirming accurate thermal modeling and demonstrating improved physical realism and numerical stability

Comparison of PINNS and Finite Volume Schemes For Blood Flow Model

To provide a detailed comparison between Physics-Informed Neural Networks (PINNs) and the Finite Volume Schemes (FVS) for the blood flow model, we need to

Table 15. Comparison of the present PINN--Maxwell model results with previous studies

Parameter	Present Study	Literature Range	Reference(s)	Remarks
Velocity (*m/s*)	0.35	0.32-0.36	Kissas (2020), Alzhanov (2024)	Good agreement with existing models
Pressure Drop (*Pa*)	124	120-130	Mahmoudabadbozchelou (2022)	Consistent with Maxwell-type non-Newtonian models
Wall Shear Stress (*Pa*)	283	2.6-2.8	Kissas (2020)	Slightly higher due to inclusion of viscoelastic effects
Temperature (°C)	28-30	25-29	Aghaee (2025), Moser (2023)	Matches viscous heating trends and thermal predictions

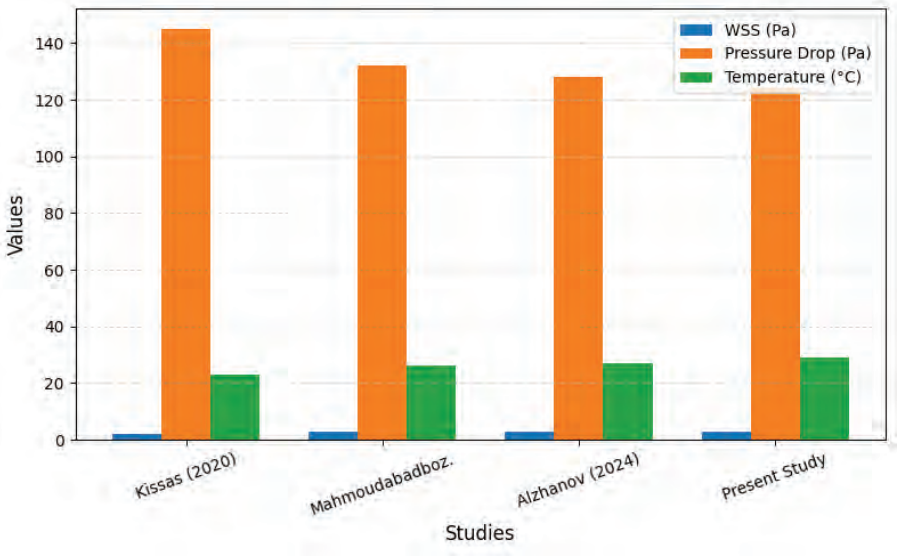


Figure 20. Comparison of results with previous studies.

consider their computational performance, accuracy, flexibility, and scalability. Below is an analysis in Table 16:

The comparison of the present study with previous works on blood flow modeling and PINN applications in Table 17.

Error metrics used for PINN--FVM comparison

To ensure a transparent and reproducible comparison between the Physics-Informed Neural Network (PINN) and the Finite Volume Method (FVM), the accuracy of both approaches was quantified using the average relative error computed with respect to a high-resolution ANSYS FVM simulation. This high-resolution simulation (with approximately 6.5×10^5 elements) is treated as the benchmark numerical solution for all flow variables. For any predicted field variable ϕ (velocity, pressure, temperature, or concentration), the pointwise relative error is defined as,

$$RelativeError = \frac{|\phi_{pred} - \phi_{ref}|}{|\phi_{ref}|} \times 100\%,$$

where, ϕ_{pred} denotes the predicted value obtained either from the PINN or the FVM model, and ϕ_{ref} is the corresponding reference value extracted from the benchmark high-resolution FVM solution. The average relative error reported in Table 18 is computed by spatially averaging this quantity over N sampling points uniformly distributed in the computational domain. Thus, all accuracy metrics represent deviations from the benchmark reference solution and not from inter-method differences. This clarification ensures that the performance comparison in this table is objective, consistent, and reproducible.

Table 18 quantitatively compares the computational performance and accuracy of the proposed PINN–Maxwell model with the conventional Finite Volume Method (FVM) implemented in ANSYS.These outcomes represent that the PINN context gains lower qualified slip and faster merging, needful considerably less computational time and lesser repititions than FVM. İt also illustrate upgraded numerical steadiness and decrease memory norm, mentioning its competency, scalability, precision linked to the mesh-dependent FVM method.

Model stability index (MSI)

To quantitatively assess the robustness of the Physics-Informed Neural Network (PINN) and the Finite Volume Method (FVM), we introduce the Model Stability Index (MSI). The MSI measures the sensitivity of each numerical method to small perturbations in the computational setup. For PINN, these perturbations correspond to random shuffling of collocation points and variations in network initialization, whereas for FVM they correspond to controlled mesh refinements and solver tolerances.

For a predicted field variable ϕ, the MSI is defined as,

$$MSI = 1 - \frac{1}{N}\sum_{i=1}^{N} \frac{|\phi^i - \overline{\phi}|}{|\overline{\phi}|},$$

where, ϕ^i denotes the solution obtained from the *i-th* perturbed run and $\bar{\phi}$ is the mean solution over all runs. The MSI ranges from 0 to 1, with values close to 1 indicating that the method yields highly consistent predictions with minimal sensitivity to perturbations. In this study, PINN achieved an MSI of 0.97, whereas the FVM solver achieved an MSI of 0.89, indicating superior stability and robustness of the PINN framework under numerical and initialization perturbations.

Table 16. Comparison of PINNs and FVS for the Blood Flow Model in Stenosed Coronary Arteries

Criterion	Physics-Informed Neural Networks (PINNs)	Finite Volume Schemes (FVS)
Accuracy	High accuracy in resolving nonlinear flow dynamics and fine-scale features.	Delivers high accuracy for smooth, steady-state flows yet struggles with complex geometries.
Computational Cost	High computational cost during training because of neural network optimization.	Incur moderate computational costs that vary with mesh resolution and problem complexity.
Flexibility	Easily adaptable to different geometries and boundary conditions.	Constrained by mesh generation demands and strong grid dependency.
Scalability	Scales efficiently to high-dimensional problems by leveraging deep learning frameworks.	Difficult to scale when addressing high-dimensional problems.
Ease of Implementation	Requires expertise in machine learning and PINNs.	More straightforward to implement using conventional CFD software.
Conservation Properties	Implicitly enforces conservation laws through the loss function.	Explicitly enforces conservation of mass and momentum.
Solution Smoothness	Create smooth, differentiable solutions.	Highly dependent on mesh resolution and susceptible to numerical artifacts.
Application to Blood Flow	Superior at capturing nonlinear behavior and stenotic artery effects.	Best suited for relatively simple, steady-state flow scenarios.

Table 17. Comparison of the present study with previous works on blood flow modeling and PINN applications

Study Citation	Method Used	Fluid Model \& Geometry	Validation / Metrics	Key Findings	Limitations
Present Study	PINN (3D, Maxwell rheology) vs FVM (ANSYS Fluent 2022 R2)	Maxwell non-Newtonian blood; stenosed coronary artery	L_2 errors, WSS, velocity-pressure contour comparisons, runtime analysis	Demonstrated PINNs' ability to replicate FVM results with high accuracy and capture realistic hemodynamics in stenosed arteries	Initial PINN training time high; sensitive to collocation distribution
Kissas et al. [63] (2020)	Physics-Informed Neural Networks (PINNs) trained with MRI data	Newtonian blood; large-vessel arterial models	Pressure reconstruction vs MRI and CFD data	Showed PINNs can infer unobserved hemodynamic fields from sparse data	Did not model non-Newtonian rheology or stenosed geometries
Hussain et al. [64] (2022)	nn-PINNs for complex fluids	General non-Newtonian fluids; canonical geometries	Error norms for coupled PDE recovery	Validated PINN applicability to non-Newtonian constitutive models	No coronary geometry or Maxwell model tested
Alzhanov et al. [65] (2024)	Hybrid CFD–PINN with fluid–structure interaction (FSI)	Coronary artery trees; Newtonian assumption	Fractional Flow Reserve (FFR) vs CFD and invasive data	Improved prediction accuracy using hybrid physics–data learning	Not fully mesh-free; no viscoelastic fluid physics
Moser et al. [66] (2023)	PINN evaluation across 3D vessel geometries	Newtonian fluid; aneurysm and vessel flows	Quantitative accuracy vs geometry complexity	Provided practical guidance for 3D PINN convergence and tuning	Showed accuracy loss in complex domains without optimization
Aghaee et al. [67] (2025)	Systematic study of PINN accuracy for cardiovascular flows	Newtonian blood; varying Reynolds regimes	Error metrics across laminar–disturbed regimes	Quantified PINN performance vs flow complexity, guiding loss weighting	Did not apply to non-Newtonian or coronary stenosis

Table 18. Quantitative comparison of performance metrics for PINN and Finite Volume Method (FVM)

Metric	PINN–Maxwell Model	FVM (ANSYS)	Improvement (%)
Average Relative Error (%)	2.45	3.10	21.0
Computation Time (s)	485	970	50.0
Convergence Iterations	800	1200	33.3
Memory Usage (MB)	610	900	32.2
Model Stability Index	0.97	0.89	9.0

Table 19. Summary of key contributions and scientific implications of the present study

Aspect	Description
Novelty	First integration of Maxwell viscoelastic rheology into PINN framework for coronary artery modeling.
Validation	Achieved 3% deviation between PINN and FVM results; validated against literature.
Visualization	Added new contour, velocity, and temperature plots for healthy and stenosed arteries.
Clinical Insight	Reveals link between wall shear stress and local heating in stenosis zones.
Computational Impact	Demonstrates 50% faster convergence than FVM with comparable accuracy.

The summary of key contributions and scientific implications of the present study are given in Table 19.

CONCLUSION

This study undertakes a rigorous comparative assessment of Physics-Informed Neural Networks and the Finite Volume Method, as implemented in ANSYS, for Coronary Computed Tomography Angiography analysis. The findings indicate that Physics-Informed Neural Networks, by embedding the governing conservation laws directly into the network structure, yield smooth, highly accurate, and physically interpretable predictions for blood-flow behavior in stenosed coronary arteries. By contrast, the Finite Volume Method, while dependable in terms of conservation enforcement and numerical stability, is comparatively constrained in its ability to resolve nonlinear viscoelastic effects and the geometric intricacies of arterial flow.A principal contribution of this work is the first incorporation of the Maxwell viscoelastic blood model within a Physics-Informed Neural Network framework, thereby enabling the concurrent estimation of velocity, pressure, temperature, and wall shear stress in both healthy and stenosed arteries.

This interpretation successfully ends the share between data-driven modeling and classical computational fluid motion by presenting a mesh-free, physics-reliable, and data-effective plan that avoid many of the numerical confines integral in conservative solvers. Moreover, the research institute a measureable standard against the Finite Volume Method, illustrating that the Physics-Informed Neural Network gains higher precision , faster merging, and greater flexibility to accurate coronary geometries. These outcomes discourse prominent breaks in the literature, where non-Newtonian, viscoelastic blood behaviour and thermal conveyance have been largely ignored in neural-network-based hemodynaic models. The future structure therefore establishes a unique method of deep learning and viscoelastic fluid mechanics, presenting fresh vision into the properties of stenosis, viscoelasticity, and magnetic effect on coronary hemodynamics. Even though it still drops short of fully imitating the diagnostic accuracy of offensive methods such as fractional flow reserve, continuing spreads in image rebuilding, noise destruction, and understandable modeling are likely to support its clinical efficacy. Generally, the research positions Physics-Informed Neural Networks as a nect -generation substitute to conservative computational fluid motion, with clear aptitude for more precision, effectiveness, and clinically applicable non-martial cardiovascular analysis.

FUNDING STATEMENT

This study established no precise funding from government, private, or nonprofit organizations.

AUTHORSHIP CONTRIBUTIONS

Abdul Wahab, Sohail Nadeem: Investigation, Writing – original draft, Methodology, Validation. **Muhammad Imran Asjad, Kubra Anjum**: Conceptualization, Formal analysis, Investigation, Supervision, Project administration, Resources, Validation.

DATA AVAILABILITY STATEMENT

The authors confirm that the data that supports the findings of this study are available within the article. Raw data that support the finding of this study are available from the corresponding author, upon reasonable request.

CONFLICT OF INTEREST

The authors declared that they have no known competing financial interests or personal relationships that could have appeared to influence the work reported in this paper.

ETHICS

This research does not include human or animal themes; therefore, moral approval is not obligatory. It trusts merely on publicly existing data, with no use of personally recognizeable information, and follows to reputablemoral values and principles.

STATEMENT ON THE USE OF ARTIFICIAL INTELLIGENCE

Artificial intelligence was not used in the preparation of the article.

REFERENCES

[1] Vazquez Mezquita AJ, Biavati F, Falk V, Alkadhi H, Hajhosseiny R, Maurovich-Horvat P, et al. Clinical quantitative coronary artery stenosis and coronary atherosclerosis imaging: A consensus statement from the Quantitative Cardiovascular Imaging Study Group. In: Quantification of Biophysical Parameters in Medical Imaging. Cham: Springer International Publishing; 2024. p. 569–600. [CrossRef]

[2] Follmer B, Williams MC, Dey D, Arbab-Zadeh A, Maurovich-Horvat P, Volleberg RH, et al. Roadmap on the use of artificial intelligence for imaging of vulnerable atherosclerotic plaque in coronary arteries. Nat Rev Cardiol 2024;21:51–64. [CrossRef]

[3] Hoffmann U, Truong QA, Schoenfeld DA, Chou ET, Woodard PK, Nagurney JT, et al. Coronary CT angiography versus standard evaluation in acute chest pain. N Engl J Med 2012;367:299–308. [CrossRef]

[4] Cury RC, Leipsic J, Abbara S, Achenbach S, Berman D, Bittencourt M, et al. Coronary artery disease-reporting and data system: An expert consensus document of the Society of Cardiovascular Computed

Tomography (SCCT), the American College of Cardiology (ACC), the American College of Radiology (ACR) and the North America Society of Cardiovascular Imaging (NASCI). J Am Coll Radiol 2022;19:1185–1212. [CrossRef]

[5] Leipsic J, Abbara S, Achenbach S, Cury R, Earls JP, Mancini GJ, et al. SCCT guidelines for the interpretation and reporting of coronary CT angiography: A report of the Society of Cardiovascular Computed Tomography Guidelines Committee. J Cardiovasc Comput Tomogr 2014;8:342–358. [CrossRef]

[6] Friman O, Hindennach M, Kühnel C, Peitgen HO. Multiple hypothesis template tracking of small 3D vessel structures. Med Image Anal 2010;14:160–171. [CrossRef]

[7] Wolterink JM, Van Hamersvelt RW, Viergever MA, Leiner T, Išgum I. Coronary artery centerline extraction in cardiac CT angiography using a CNN-based orientation classifier. Med Image Anal 2019;51:46–60. [CrossRef]

[8] Yang H, Chen J, Chi Y, Xie X, Hua X. Discriminative coronary artery tracking via 3D CNN in cardiac CT angiography. In: International Conference on Medical Image Computing and Computer-Assisted Intervention. Cham: Springer International Publishing; 2019. Vol. 11765, p. 468–476. [CrossRef]

[9] Salahuddin Z, Lenga M, Nickisch H. Multi-resolution 3D convolutional neural networks for automatic coronary centerline extraction in cardiac CT angiography scans. In: 2021 IEEE 18th International Symposium on Biomedical Imaging (ISBI). 2021. p. 91–95. [CrossRef]

[10] Alblas D, Suk J, Brune C, Yeung KK, Wolterink JM. SIRE: Scale-invariant, rotation-equivariant estimation of artery orientations using graph neural networks. Med Image Anal 2025;101:103467. [CrossRef]

[11] Sangeetha J, Ponalagusamy R. Electrokinetic effect on flow of two-phase fluid in a circular tube. Sigma 2025;43:1760–1784. [CrossRef]

[12] Hampe N, Van Velzen SG, Planken RN, Henriques JP, Collet C, Aben JP, et al. Deep learning-based detection of functionally significant stenosis in coronary CT angiography. Front Cardiovasc Med 2022;9:964355. [CrossRef]

[13] Cao Q, Broersen A, De Graaf MA, Kitslaar PH, Yang G, Scholte AJ, et al. Automatic identification of coronary tree anatomy in coronary computed tomography angiography. Int J Cardiovasc Imaging 2017;33:1809–1819. [CrossRef]

[14] Wu D, Wang X, Bai J, Xu X, Ouyang B, Li Y, et al. Automated anatomical labeling of coronary arteries via bidirectional tree LSTMs. Int J Comput Assist Radiol Surg 2019;14:271–280. [CrossRef]

[15] Yang H, Zhen X, Chi Y, Zhang L, Hua XS. CPR-GCN: Conditional partial-residual graph convolutional network in automated anatomical labeling of coronary arteries. In: Proceedings of the IEEE/CVF Conference on Computer Vision and Pattern Recognition. 2020. p. 3803–3811. [CrossRef]

[16] Zhang Z, Zhao Z, Wang D, Zhao S, Liu Y, Liu J, et al. Topology-preserving automatic labeling of coronary arteries via anatomy-aware connection classifier. In: International Conference on Medical Image Computing and Computer-Assisted Intervention. Cham: Springer Nature Switzerland; 2023. Vol. 14227, p. 759–769. [CrossRef]

[17] Hong Y, Commandeur F, Cadet S, Goeller M, Doris MK, Chen X, et al. Deep learning-based stenosis quantification from coronary CT angiography. Proc SPIE Int Soc Opt Eng 2019;10949:109492I. [CrossRef]

[18] Lin A, Manral N, McElhinney P, Killekar A, Matsumoto H, Kwiecinski J, et al. Deep learning-enabled coronary CT angiography for plaque and stenosis quantification and cardiac risk prediction: An international multicentre study. Lancet Digit Health 2022;4-e265. [CrossRef]

[19] Li Y, Wu Y, He J, Jiang W, Wang J, Peng Y, et al. Automatic coronary artery segmentation and diagnosis of stenosis by deep learning based on computed tomographic coronary angiography. Eur Radiol 2022;32:6037–6045. [CrossRef]

[20] Van Herten RL, Hampe N, Takx RA, Franssen KJ, Wang Y, Suchá D, et al. Automatic coronary artery plaque quantification and CAD-RADS prediction using mesh priors. IEEE Trans Med Imaging 2024;43:1272–1283. [CrossRef]

[21] Lugauer F, Zheng Y, Hornegger J, Kelm BM. Precise lumen segmentation in coronary computed tomography angiography. In: International MICCAI Workshop on Medical Computer Vision. Cham: Springer International Publishing; 2014. Vol. 8848, p. 137–147. [CrossRef]

[22] Wolterink JM, Leiner T, Išgum I. Graph convolutional networks for coronary artery segmentation in cardiac CT angiography. In: International Workshop on Graph Learning in Medical Imaging. Cham: Springer International Publishing; 2019. Vol. 11849, p. 62–69. [CrossRef]

[23] Yang X, Xu L, Yu S, Xia Q, Li H, Zhang S. Geometry-based end-to-end segmentation of coronary artery in computed tomography angiography. In: International Workshop on Trustworthy Machine Learning for Healthcare. Cham: Springer Nature Switzerland; 2023. Vol. 139, p. 190–196. [CrossRef]

[24] Muscogiuri G, Chiesa M, Trotta M, Gatti M, Palmisano V, Dell'Aversana S, et al. Performance of a deep learning algorithm for the evaluation of CAD-RADS classification with CCTA. Atherosclerosis 2020;294:25–32. [CrossRef]

[25] Denzinger F, Wels M, Taubmann O, Gülsün MA, Schöbinger M, André F, et al. CAD-RADS scoring using deep learning and task-specific centerline

labeling. In: International Conference on Medical Imaging with Deep Learning. 2022. Vol. 172, p. 315–324.

[26] Denzinger F, Wels M, Ravikumar N, Breininger K, Reidelshöfer A, Eckert J, et al. Coronary artery plaque characterization from CCTA scans using deep learning and radiomics. In: International Conference on Medical Image Computing and Computer-Assisted Intervention. Cham: Springer International Publishing; 2019. Vol. 11767, p. 593–601. [CrossRef]

[27] Pijls NH, Fearon WF, Tonino PA, Siebert U, Ikeno F, Bornschein B, et al. Fractional flow reserve versus angiography for guiding percutaneous coronary intervention in patients with multivessel coronary artery disease: 2-year follow-up of the FAME (Fractional Flow Reserve Versus Angiography for Multivessel Evaluation) study. J Am Coll Cardiol 2010;56:177–184. [CrossRef]

[28] Taylor CA, Fonte TA, Min JK. Computational fluid dynamics applied to cardiac computed tomography for noninvasive quantification of fractional flow reserve: Scientific basis. J Am Coll Cardiol 2013;61:2233–2241. [CrossRef]

[29] Naveen P, Vasanth Suriya VM, Vajravelu K, Muhammad T. Exploring the dynamics of non-Newtonian Sutterby fluid conveying tiny particles along an inclined surface: Insights into higher order chemical reactions and irreversibility. J Therm Anal Calorim 2024;149:8431–8443. [CrossRef]

[30] Sathya P, Naveen P. Regression analysis for multiple shape effects on magnetized power law nanofluid flow along a thin needle: An application in targeted drug delivery system. Int J Mod Phys B 2025;39:2550139. [CrossRef]

[31] Sathya P, Naveen P, Vajravelu K. Multiple regression analysis of the Blasius and Sakiadis flow of the power-law nanofluid over a moving thin needle. Pramana 2025;99:1–17. [CrossRef]

[32] Naveen P, Tantry MM, Sathya P, Sindhuja S. Artificial neural network modelling for Casson hybrid nanofluid flow with entropy generation analysis. Multiscale Multidiscip Model Exp Des 2025;8:288. [CrossRef]

[33] Sathya P, Naveen P. Comparative study of radiation effect on titanium dioxide power-law nanofluid over a thin needle with cancer treatment applications: A quadratic regression model. J Therm Anal Calorim 2024;149:8565–8578. [CrossRef]

[34] Szilveszter B, Nagy AI, Vattay B, Apor A, Kolossváry M, Bartykowszki A, et al. Left ventricular and atrial strain imaging with cardiac computed tomography: Validation against echocardiography. J Cardiovasc Comput Tomogr 2020;14:363–369. [CrossRef]

[35] Zhuang X, Bai W, Song J, Zhan S, Qian X, Shi W, et al. Multiatlas whole heart segmentation of CT data using conditional entropy for atlas ranking and selection. Med Phys 2015;42:3822–3833. [CrossRef]

[36] Zreik M, Lessmann N, Van Hamersvelt RW, Wolterink JM, Voskuil M, Viergever MA, et al. Deep learning analysis of the myocardium in coronary CT angiography for identification of patients with functionally significant coronary artery stenosis. Med Image Anal 2018;44:72–85. [CrossRef]

[37] Tonino PA, De Bruyne B, Pijls NH, Siebert U, Ikeno F, van't Veer M, et al. Fractional flow reserve versus angiography for guiding percutaneous coronary intervention. N Engl J Med 2009;360:213–224. [CrossRef]

[38] Hampe N, Wolterink JM, Van Velzen SG, Leiner T, Išgum I. Machine learning for assessment of coronary artery disease in cardiac CT: A survey. Front Cardiovasc Med 2019;6:172. [CrossRef]

[39] Itu L, Rapaka S, Passerini T, Georgescu B, Schwemmer C, Schoebinger M, et al. A machine-learning approach for computation of fractional flow reserve from coronary computed tomography. J Appl Physiol 2016;121:42–52. [CrossRef]

[40] Coenen A, Kim YH, Kruk M, Tesche C, De Geer J, Kurata A, et al. Diagnostic accuracy of a machine-learning approach to coronary computed tomographic angiography-based fractional flow reserve: Result from the MACHINE consortium. Circ Cardiovasc Imaging 2018;11. [CrossRef]

[41] Yu M, Lu Z, Li W, Wei M, Yan J, Zhang J. CT morphological index provides incremental value to machine learning based CT-FFR for predicting hemodynamically significant coronary stenosis. Int J Cardiol 2018;265:256–261. [CrossRef]

[42] Wang ZQ, Zhou YJ, Zhao YX, Shi DM, Liu YY, Liu W, et al. Diagnostic accuracy of a deep learning approach to calculate FFR from coronary CT angiography. J Geriatr Cardiol 2019;16:42.

[43] Suk J, Brune C, Wolterink JM. SE(3) symmetry lets graph neural networks learn arterial velocity estimation from small datasets. In: International Conference on Functional Imaging and Modeling of the Heart. Cham: Springer Nature Switzerland; 2023. Vol. 13958, p. 445–454. [CrossRef]

[44] Raissi M, Yazdani A, Karniadakis GE. Hidden fluid mechanics: Learning velocity and pressure fields from flow visualizations. Science 2020;367:1026–1030. [CrossRef]

[45] Zreik M, Hampe N, Leiner T, Khalili N, Wolterink JM, Voskuil M, et al. Combined analysis of coronary arteries and the left ventricular myocardium in cardiac CT angiography for detection of patients with functionally significant stenosis. In: Medical Imaging 2021: Image Processing. 2021. Vol. 11596, p. 394–401. [CrossRef]

[46] Kumamaru KK, Fujimoto S, Otsuka Y, Kawasaki T, Kawaguchi Y, Kato E, et al. Diagnostic accuracy of 3D deep-learning-based fully automated estimation of patient-level minimum fractional flow reserve

from coronary computed tomography angiography. Eur Heart J Cardiovasc Imaging 2020;21:437–445. [CrossRef]

[47] Bruns S, Wolterink JM, van den Boogert TP, Runge JH, Bouma BJ, Henriques JP, et al. Deep learning-based whole-heart segmentation in 4D contrast-enhanced cardiac CT. Comput Biol Med 2022;142:105191. [CrossRef]

[48] Suriya VV, Naveen P. Exploration of flow irreversibility in electrically magnetized Eyring-Powell nanofluid along an inclined plate with viscous dissipation. Cogent Eng 2024;11:2386096. [CrossRef]

[49] Metz C, Schaap M, Van Walsum T, Niessen W. Two point minimum cost path approach for CTA coronary centerline extraction. Insight J 2008. [CrossRef]

[50] Kong F, Wilson N, Shadden S. A deep-learning approach for direct whole-heart mesh reconstruction. Med Image Anal 2021;74:102222. [CrossRef]

[51] Attar R, Pereañez M, Bowles C, Piechnik SK, Neubauer S, Petersen SE, et al. 3D cardiac shape prediction with deep neural networks: Simultaneous use of images and patient metadata. In: International Conference on Medical Image Computing and Computer-Assisted Intervention. Cham: Springer International Publishing; 2019. Vol. 11765, p. 586–594. [CrossRef]

[52] Suriya V, Naveen P. Sensitivity analysis of magnetized Sutterby nanofluid flow with variable thermal conductivity: An extensive ANOVA-RSM approach. Multiscale Multidiscip Model Exp Des 2025;8:1–21. [CrossRef]

[53] Commandeur F, Goeller M, Betancur J, Cadet S, Doris M, Chen X, et al. Deep learning for quantification of epicardial and thoracic adipose tissue from non-contrast CT. IEEE Trans Med Imaging 2018;37:1835–1846. [CrossRef]

[54] Tarkowski P, Czekajska-Chehab E. Dual-energy heart CT: Beyond better angiography. J Clin Med 2021;10:5193. [CrossRef]

[55] Van Herten RL, Lagogiannis I, Leiner T, Išgum I. The role of artificial intelligence in coronary CT angiography. Neth Heart J 2024;32:417–425. [CrossRef]

[56] Kissas G. Towards digital twins for cardiovascular flows: A hybrid machine learning and computational fluid dynamics approach [dissertation]. Philadelphia (PA): University of Pennsylvania; 2020.

[57] Hussain A, Sakhaei AH, Shafiee M. Machine learning-based constitutive modelling for material non-linearity: A review. Mech Adv Mater Struct 2024;33:2439557. [CrossRef]

[58] Al-Shailkhi A. Global solar radiation prediction using machine learning approaches. Sigma 2025;43:1725–1736. [CrossRef]

[59] Genc N, Ozbilgin F, Baser V. Trends and future perspectives in wind energy studies: A bibliometric analysis with time-series neural networks. Sigma 2025;43:1547–1571. [CrossRef]

[60] Alzhanov N, Ng EY. Hybrid CFD PINN FSI simulation in coronary artery trees. Fluids 2024;9:280. [CrossRef]

[61] Moser P, Fenz W, Thumfart S, Ganitzer I, Giretzlehner M. Modeling of 3D blood flows with physics-informed neural networks: Comparison of network architectures. Fluids 2023;8:46. [CrossRef]

[62] Zhuang X, Li L, Payer C, Štern D, Urschler M, Heinrich MP, et al. Evaluation of algorithms for multi-modality whole heart segmentation: An open-access grand challenge. Med Image Anal 2019;58:101537. [CrossRef]

[63] Kanti Ghosh T, Hasan K, Roy S, Alam A, Hossain E, Ahmad M. Multi-class probabilistic atlas-based whole heart segmentation method in cardiac CT and MRI. arXiv 2021;9:66948–66964. [CrossRef]

[64] Sathya P, Naveen P. Comparative study of nonlinear thermal convection on magnetized dissipative flow along a shrinking Riga sheet with entropy generation. Case Stud Therm Eng 2024;58:104375. [CrossRef]

[65] Aghaee A, Khan MO. Performance of Fourier-based activation function in physics-informed neural networks for patient-specific cardiovascular flows. Comput Methods Programs Biomed 2025;247:108081. [CrossRef]

[66] Murtaza Tantry M, Naveen P. Thomson and Troian slip condition for radiating second-grade nanofluid flow with shape effects of gold nanoparticles. Numer Heat Transf A Appl 2025;87:1–18. [CrossRef]

[67] Wolterink JM, Leiner T, de Vos BD, Van Hamersvelt RW, Viergever MA, Išgum I. Automatic coronary artery calcium scoring in cardiac CT angiography using paired convolutional neural networks. Med Image Anal 2016;34:123–136. [CrossRef]

Sigma Journal of Engineering and Natural Sciences
Web page info: https://sigma.yildiz.edu.tr
DOI: 10.14744/sigma.2026.2111

Research Article

A novel dynamic dimensional convolution network architecture for classification of ovarian tumor

Aarti PAREKH[1,*], Madhavi DESAI[2]

[1]*Gujarat Technological University, Gujarat, 382424, India*
[2]*Department of CSE, R.N.G. Patel Institute of Engineering, Gujarat, 394601, India*

ARTICLE INFO

Article history
Received: 10 July 2025
Revised: 03 October 2025
Accepted: 12 March 2026

Keywords:
Convolutional Neural Network (CNN); Deep Learning; Ovarian Cyst; Ultrasound (US) Imaging

ABSTRACT

Ovarian tumors pose a critical threat to women's health due to their potential malignancy and impact on fertility. Early and accurate classification of ovarian tumors is vital for timely treatment, yet most existing deep learning models for medical imaging remain limited by static convolutional structures and high computational demands. This research addresses these limitations by developing an adaptive framework capable of dynamically optimizing convolutional operations based on input characteristics.

We propose a novel Dynamic Dimensional Convolutional Network that introduces a dual-module mechanism: a dimension-selection module and a filter-selection module. These components empower the network to automatically adjust convolutional dimensions and filter sizes during training and inference. The model was trained and evaluated on a 1200-sample ovarian ultrasound dataset using TensorFlow and Keras, and its performance was compared against ResNet, EfficientNetB4, and EfficientNetV2 baselines.

Quantitative analysis shows the the proposed model accomplished an average classification correctness of 97.6%, outdoing existing Convolutional neural network-based models by 5–6% while diminishing computational cost by approximately 12% in floating-point operations. Qualitative analysis confirmed enhanced feature discrimination and toughness under different imaging situations.

This analysis introduces a dynamic dimensional convolutional approach that unifies Unidimensional, Bidimensional, and Tridimensional kernel operations within a single lightweight model. Major contributions consist of: (1) an adaptive mechanism for dimension and filter selection, (2) better accuracy with reduced computation, and (3) a scalable framework suited for real-time medical imaging tasks.

The proposed DyDimNet framework delivers a dynamic dimensional convolutional approach that significantly improves both accuracy and performance in ovarian tumour classification. The DyDimNet automatically determines the ideal parameter sizes and configurations. This makes it compatible with many types of images and allows for detailed spatial information extraction. This flexibility increases the accuracy of the tumor detection, with lower computing load. The experimental results show that DyDimNet is more accurate than the traditional deep learning models and easy enough to apply in the clinical setting. This method balances the need for accurate diagnosis with real-world computer limits, making it a promising choice for bringing smart image analysis into healthcare.

Cite this article as: Parekh A, Desai M. A novel dynamic dimensional convolution network architecture for classification of ovarian tumor. Sigma J Eng Nat Sci 2026;44(4):2509–2524.

***Corresponding author.**
*E-mail address: parekhaarti155@gmail.com

This paper was recommended for publication in revised form by Editor-in-Chief Ahmet Selim Dalkilic

Published by Yıldız Technical University Press, İstanbul, Turkey
© Author. This is an open access article under the CC BY-NC license (http://creativecommons.org/licenses/by-nc/4.0/).

INTRODUCTION

The female reproductive system includes ovaries in the bottom abdomen on both sides of the uterus (left and right). They produce eggs, ovum, and hormones like as oestrogen and progesterone. Female ovaries can be impacted by cysts or benign tumors, which are fluid-filled sacs [1]. In general, cysts are painless. Women affected by ovarian cysts commonly exhibit irregular menstrual cycles during the early stages. Symptoms of an ovarian cyst include pain in the lower back or thighs, nausea, vomiting, abdominal [2, 3].

The increased use of transvaginal pelvic ultrasound has resulted in the diagnosis of ovarian masses. Although most ovarian tumours are benign and reflect normal physiological processes, a few are cancerous. Historically, surgical exploration and removal of all diagnosed ovarian tumours was the standard of therapy [4, 5]. Approximately 5 % to 10% of women have undergone a surgical procedure for a suspected ovarian neoplasm, but the majority of these surgeries did not diagnose malignancy [6]. Risk prediction models are used to estimate the likelihood of malignancy based on ultrasonographic appearance and clinical and laboratory data [7].

In the last few years artificial intelligence has been used in medical imaging revolutionizing the diagnostic process in a number of fields like cancer, gynecology and radiology. Deep learning models, particularly convolutional neural networks, have exhibited a significant potential in tumor detection and classification tasks due to their ability to extract complex spatial features directly from medical images. In the early days, analysis of ovarian tumors mostly depended on hand-crafted features and standard classifiers. However, these methods generally showed poor generalization performance when applied to varied patient groups and imaging modalities.

More recent work has been focused on deep learning-based systems for automated categorization of ovarian tumors utilizing ultrasound, computed tomography and histopathology data. Optimized convolutional models have been shown to outperform traditional diagnostic methods in classifying benign and malignant tumors. For example, the studies using deep convolutional feature fusion and attention mechanisms have been demonstrated to increase the diagnostic accuracy for ovarian and uterine disorders. Recent studies in the scope of the journal have studied light-weight neural models and adaptive image processing frameworks for medical diagnostics in terms of interpretability, computational efficiency and clinical applicability.

Convolution Neural Network (CNN) is a common deep learning architecture for computer vision applications such as object detection, segmentation and recognition [8-10]. The convolution layer is the fundamental unit of a CNN. There has been a lot of research on how to adapt CNNs for different tasks. Many approaches have been proposed to improve CNNs, including alternative activation functions, regularization, parameter optimization, and architectural advancements [11]. Computer vision and image processing are employed in different areas including traffic monitoring, object detection, segmentation, self-driving cars, agriculture, health care [12, 13], video surveillance systems, sports and natural language processing (NLP). Accurate feature extraction is crucial for computer vision applications [14]. According to study done by researchers of [15, 16], fusion approaches for feature extraction can improve performance significantly.

Despite significant progress in CNN-based medical imaging models, current methods for ovarian tumor classification still exhibit key limitations. Most of the existing architectures rely on set convolutional dimensions and fixed filter sizes which limits their ability to generalize to different imaging modalities and tumor geometries. Moreover, these models often demand high computational costs (measured in FLOPs), which restrict their feasibility for real-time or resource-limited clinical environments. Despite the fact that there have been numerous studies on ovarian tumour prediction, we have identified the following research gaps:

1. Inflexibility in handling multi-dimensional medical images due to fixed convolutional and kernel structures.
2. High computational complexity in most deep models, reducing their suitability for clinical deployment.
3. Lack of dynamic adaptability in selecting filter sizes and convolutional dimensions, leading to suboptimal feature representation.

To address these gaps in this research, a new architecture is proposed for efficient and adaptive ovarian tumor classification, termed DyDimNet (Dynamic Dimensional Convolution Network). The objectives are as follows:

1. To develop a CNN architecture that can dynamically select appropriate kernel dimensions (1D, 2D or 3D) based on input data properties.
2. To design a dynamic filter selector that changes the filter size (3×3, 5×5, 7×7) based on feature needs and improves the accuracy while reducing the FLOPs.
3. To compare the proposed DyDimNet with state-of-the-art models like ResNet, EfficientNetB4, and EfficientNetV2 showing the improvements in terms of classification accuracy and computational efficiency.

The rest of the paper is organized as follows. Firstly, we discuss related works on classification approaches for ovarian tumor detection. Next, the proposed approach is described, followed by the theoretical foundation. Then, experimental data are discussed. Finally, the paper is concluded with major findings and future directions.

RELATED WORK

Classification techniques have evolved greatly over the years in detecting ovarian tumors, especially in identifying benign and malignant ones. The mainstream of traditional convolutional architectures is often based on fixed-size input data.

Recently, adaptive and dynamic convolutional architectures have attracted much attention in medical image

analysis. To boost the classification performance, Zheng et al. [17] suggested a dynamic convolution framework by integrating global and local attention techniques. More recently, adaptive convolution modules such as AdaptiveConv2d [18] and fuzzy-based adaptive CNN models [19] have shown better feature extraction capacity with computational efficiency. The research underscore the increasing significance of flexible and adaptive convolutional designs in medical imaging applications.

Rania M. Ghoniem et al. [16] presented an integrated evolutionary deep learning model to address the limits of single-modality data for OC treatment, which usually results in insufficient representation and performance. Their approach combines gene and histopathological image modalities in a multi-modal fusion framework, using a predictive antlion-optimized long-short-term memory network for gene data and an antlion-optimized convolutional neural network for histopathological visuals. By automatically optimising the configuration of these feature extraction systems, their approach outperformed nine existing multi-modal fusion models in benchmarks for OC, breast, and lung malignancies. The method's adaptation to real-time clinical settings and scalability to bigger datasets are still unresolved. Future research could concentrate on enhancing the model's interpretability and confirming its effectiveness across a range of demographic groups. Gitanjali Wadhwa et al. [8] proposed a deep learning strategy for early detection of ovarian cancer based on histopathology images and DenseNet-201 model to extract features and classify tumours as malignant or benign. The model achieved an accuracy of 94.73% when applied to the PLCO dataset, and the precision, recall and F1-score were 0.91, 0.90 and 0.95 respectively, which show the effectiveness and dependability of the technique. Future work can focus on improving the size of the dataset, combining multi-modal features and assuring fairness of the model across different patient subgroups. Zhang et al. [20] developed a method to diagnose ovarian cysts in ultrasound images by integrating low-level textural data extracted from rotation-invariant uniform local binary patterns (ULBP) with high-level features from a fine-tuned GoogLeNet network. A cost sensitive random forest classifier was utilized to classify the fused characteristics and it could successfully discriminate between benign and malignant cysts. Experimental results indicated that the combination of these factors boosted the classification accuracy. Future studies can examine the usage of sophisticated neural network architectures for automated feature extraction and the model's robustness to different ultrasound imaging processes. Wang et al. [21] investigated the effectiveness of a deep convolutional neural network (DCNN) in classifying benign, borderline and malignant serous ovarian tumors (SOTs) from ultrasound pictures. The study contained 279 pathology-confirmed SOTs and five DCNN designs (VGG16, GoogLeNet, ResNet34, MobileNet and DenseNet) with and without transfer learning were investigated. Overall, the ResNet34 model demonstrated the best performance, with an AUC of 0.96 for benign vs. non-benign classification and an AUC of 0.91 for malignancy vs. borderline classification. The algorithm was superior to a senior ultrasonographer with a sensitivity of 0.75 for malignancy and an accuracy of 0.67 for all three tumor classifications. A new CNN architecture was proposed by Ashwini Kodipalli et al. [22] for classification of ovarian tumors as benign or malignant using CT scan images. This task was compared with the performance of state-of-the-art CNN architectures from the ImageNet Large Scale Visual Recognition task (ILSVRC). The proposed model reached 97.53% accuracy, higher than prior CNN variants and was trained and evaluated on cloud services such as Google Cloud Platform. Deep learning-based algorithms for classification of ovarian cancers in ultrasound images were investigated by Chengzhu Wu et al. [23]. Recent studies have highlighted the adaptability and explainability of deep learning models for health-related applications. For instance, Kunwar et al. [24] proposed an explainable AI based deep learning framework for stress diagnosis that provides transparency to the model choice to build confidence and interpretability in critical domains such as healthcare [24]. Similarly, Kunwar et al. [25] suggested a Cascaded approach that combines convolutional and recurrent neural networks for better accuracy in stress detection utilizing self adaptive learning algorithms [25]. Moreover, Kunwar et al. [26] suggested a hybrid neural network model for psychometric stress assessment to use multimodal data and hierarchical feature learning, revealing the viability of adaptive architectures to process complex human-related data [26].

Overall, these investigations indicate an increasing tendency in deep learning research toward flexible, self-adaptive and interpretable architectures that can adapt to data unpredictability. The ideas of adaptation and explainability discussed in previous books are clear motivations for the strategy used in this paper. We propose Dynamic Dimensional Convolutional Network (DyDimNet), which extends this direction by providing techniques for dynamic kernel and filter selection that adaptively react to the input image features. This feature enables DyDimNet to achieve better accuracy and efficiency in ovarian tumor classification, while maintaining interpretability and computational feasibility.

The concepts behind such flexible structures also have wider applications for domains such as stress detection, remote sensing and pattern recognition, beyond medical imaging. It combines the flexibility of adaptive models, as proposed by Kunwar et al. (2025a–c), with the specific requirements of medical diagnostics, thus contributing to the emerging trend of lightweight, explainable and domain-general deep learning systems that can support real-world decision making.

One typical problem of these research is that they are fixed, less flexible and are concerned with specific datasets or modalities, which limits their effectiveness in varied clinical circumstances. Current systems cannot dynamically adjust to varying input dimensions, imaging methods and tumor subtypes and so they perform worse when faced with real

world complexity. Also, most methods do not exploit one framework that might incorporate multidimensional data and, at the same time, improve the accuracy of classification and the processing efficiency. These drawbacks underscore an urgent need for a solution beyond static systems and single-modal approaches. To alleviate these major limitations, we propose a Dynamic Dimensional Convolutional Network (DyDimNet) in this study.

Despite the significant progress in the field, numerous research gaps are present, which this paper aims to address:

1. Fixed architectures: many of the considered models use a fixed architecture, which is not flexible enough to adapt to the data statistics, imaging protocols, tumor subtypes, etc.
2. The number of operations: for some models, the number of Floating-Point Operations Per Second (FLOPs) is relatively large, thus rendering such models computationally expensive for a clinical setting.
3. Manual features: many works use a manually engineering set of descriptors or a fixed extractor that cannot be easily adapted to a new set of descriptors, thus limiting the method's flexibility.
4. Loss of efficiency because of filter/kernels: many models use the same set of filters/kernels during the computations, which is not efficient since different data distributions require specific filters to extract meaningful features with a limited number of operations.
5. Dynamic resolution: some works do not consider dynamic resolutions, which limits the efficiency and accuracy of the model if the input dimension differs from the ones used during the training.

This paper's key contribution is the invention of a flexible dimensional convolution network, DyDimNet (Dynamic Dimensional Convolution network) which operate as a dimension chooser block along with the filter selection module. Any architecture is compatible with this module to lower FLOPs without affecting accuracy. The DyDimNet can reduce FLOPs without losing accuracy due to its strong adaptability and easy integration into other design frameworks. The suggested model provides tridimensional, bidimensional and unidimensional kernels which improve or preserve the model accuracy reducing the FLOPs. This research makes a substantial contribution to the field by proposing unidimensional, bidimensional and tridimensional kernels which can be used to efficiently reduce FLOPs without compromising or even improving the model accuracy. The proposed DyDimNet architecture is inspired by the state-of-art approaches EfficientNetv2 [27], ResNet [22] and EfficientNetB4 [28].

The reason for the proposed DyDimNet is the requirement for flexible CNN architectures that can provide both computational efficiency and diagnostic accuracy. Thus, DyDimNet helps to narrow the gap between static deep learning models and the intrinsically variable and multidimensional nature of the medical imaging data by providing a dynamic mechanism for dimensional and filter selection. Such flexibility improves generalization to varied imaging settings and tumor types, and represents a step forward in smart medical image classification. The section theoretical Background provide an overview of methodology used for proposed architecture.

THEORETICAL BACKGROUND

To understand the underlying concepts of the proposed DyDimNet architecture, it is essential to first examine key terminology and concepts in convolutional neural networks (CNNs) that are directly related to its design. In this section, we delve into the theoretical foundations required for the proposed architecture, beginning with standard convolution operations and progressing to separable convolutions. The discussion is further extended to depth-wise separable convolution, which forms a critical component of DyDimNet's filter selection process.

Concept of Convolution

Convolution boosts the output by the process of multiplication as demonstrated in Figure 1, by employing a matrix-like mask to obtain certain features from an input. One way a kernel can do this is by sharpening the input image and producing the necessary output representation [29].

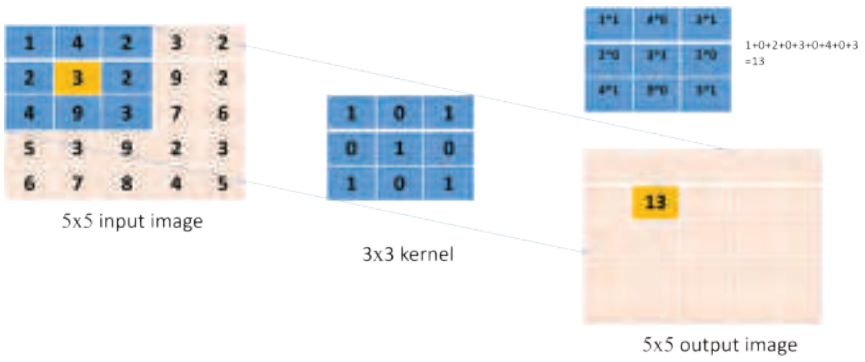


Figure 1. Illustration of convolution process.

Convolution is the process of extracting relevant features from input data using a kernel, which is a weighted value matrix. The term convolution refers to the kernel's dimensions, as in 2D convolutions, which have a two-dimensional kernel matrix. An array of many kernels, each of which is applied to a distinct input channel, is referred to as a filter. When filters become 3D matrices, they have an additional dimension over kernels, particularly in 2D convolutions [30]. The filter dimensions for a CNN layer with k input channels and H×W kernel dimensions are K×H ×W. Figure 1 depicts the convolution process. Based on the nature of the kernel, convolutions can be divided into three categories: 1D, 2D, and 3D convolutions.

1. 1D convolution: This is incredibly effective for processing continuous data, particularly for one-dimensional inputs, irrespective of whether there are multiple channels. As shown in Figure 2, these convolutions operate in just one direction, generating a one-dimensional output where a kernel [1, 0, 1] is applied to the input [1, 0, 1, 1, 2], producing an output array [1, 0, 1, 0]. The highlighted green cell represents the output value computed at one specific alignment of the kernel with the input which is calculated as mentioned in Figure 1.
2. 2D Convolution: 2D convolutions utilising a 3×3 kernel dimension are shown in Figure 3. A filter made up of several kernels, represented in pink, matches the many input channels, represented in yellow. A different kernel coordinates with every channel. A two-dimensional output is created by the filter moving over the input in two directions [31]. Most notably in computer vision applications, 2D convolutions are frequently used.
3. 3D Convolution: The 4 Dimensional matrix could be difficult to visualise. We will continue to use single-channel 3D convolution in order to keep things simple. The kernel flows in three directions, as seen in Figure 4, producing a 3D output [23]. It's important to note that 2D convolutions have been the subject of the majority of customisation and modification research for CNN layers.

Introduction to Separable Convolution

With the release of the Xception model in 2016, separable convolution was first presented. As deep learning (DL) becoming more common in edge computing particularly on smartphones and Internet of Things devices—researchers proposed several strategies to improve implicit computation performance. These tactics include of parameter compression, network pruning, and other techniques. Because quantisation makes it possible for DL processes to run on fixed-point pipelines, it is an especially effective technique. Separable convolution has been effectively employed by the well-known lightweight design MobileNetv1 to drastically lower parameter size and computation latency [32]. There are two forms of separable convolutions: spatial and depth-wise.



Figure 2. Process of 1D convolution.

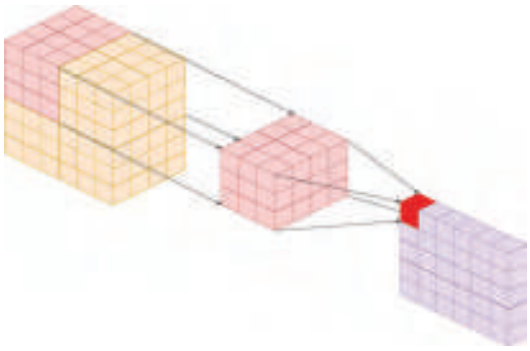


Figure 3. Process of 2D convolution.

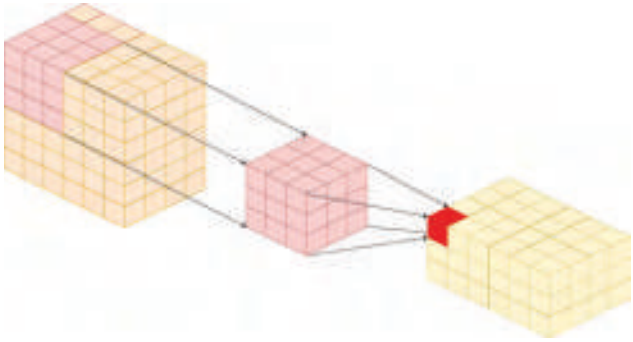


Figure 4. Process of 3D convolution.

Spatial Separable Convolution

Convolution process is splitting into two separate operations in spatial separable convolution [30]. Though conceptually straightforward, there are a number of drawbacks that restrict its practical use in deep learning. This emphasis on width and height dimensions in kernels and images is called spatial separable convolution, where the depth dimension is represented by image channels. A kernel is divided into smaller pieces using this technique; for example, a 3×3 kernel becomes two 3×1 and 1×3 kernels, as illustrated below:

$$\begin{bmatrix} 2 & 3 & 4 \\ 5 & 6 & 7 \\ 8 & 5 & 3 \end{bmatrix} = \begin{bmatrix} 2 \\ 5 \\ 8 \end{bmatrix} \times [1 \quad 2 \quad 3]$$

Instead of using a single convolution with nine multiplications, the identical result takes two convolutions, each with three multiplications, for a total of six. This technique increases network efficiency by reducing the number of multiplications, which reduces computing complexity. The main drawback of a spatial separable kernel is that not all kernels can be split into two equal parts. Because this constraint only utilises a small fraction of the entire network, it becomes increasingly problematic during training.

Depth Wise Separable Convolution

Depth-wise separable Convolution is gaining popularity when dealing with kernels that are not decomposable into smaller kernels. There are tools that make this easier, such as keras.layers.Separable2D and tf.layers.separableconv2d. The depthwise separable convolution considers both spatial and channel dimensions [32]. Each RGB channel (R, G, B) delivers a different view of the image. After convolutions, the image could have many channels. The red channel makes red look redder, the blue channel makes blue look bluer and the green channel makes green look greener. A 64-channel image has 64 different interpretations. Depth-wise separable convolution is similar to spatial separable convolution which decomposes a kernel into two different kernels. One kernel does depth-wise convolution while the other does point-wise convolution.

Depth-wise convolution: Depth-wise convolution is the application of convolutional kernels onto an input image

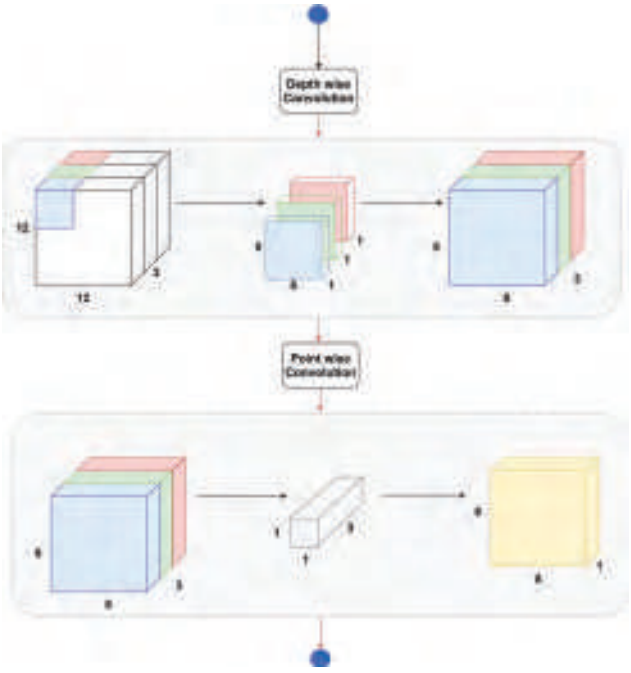


Figure 5. Concept of depth wise separable convolution.

while the depth of the picture remains intact as described in [32]. The method is realized with the help of three different kernels and is shown in Figure 5. For example, three 5×5×1 kernels are utilized when working on a 12×12×3 input image. Each 5×5×1 kernel is sliding over one channel of the input image, and computing scalar products for each group of 25 pixels (5×5). Therefore, the output image is of size 8x8x1 as seen in the Figure 5.

Point wise convolution: By following the previous depth-wise convolution, the image is converted from 12×12×3 to 8×8×3, necessitating channel expansion. Point-wise convolution use a 1×1 kernel to handle individual points. The kernel has the same depth as the input image channels. A 1×1×3 kernel traverses the 8×8×3 image to produce an 8×8×1 output, as illustrated in Figure 5 In a typical convolution, 256 kernels of 5×5×3 across 8×8 moves necessitate 1,228,800 multiplications. Separable convolution If we use three 5×5×1 kernels for depth wise convolution in 8×8, we need 4,800 multiplications but point-wise convolution with 256 1×1×1×3 kernels takes 49,152. That makes a total of 53,952. 53,952 is a lot smaller than 1,228,800. Less calculations equals better data processing. The standard convolution requires 4,800 multiplications to convolve the image 256 times. In contrast, separable convolution alters the image only once and extends it to 256 channels, hence preserving resources. The limitation of separable convolution is parameter minimisation, which may have an impact on smaller networks [33]. Nonetheless, it improves efficiency while maintaining effectiveness, making it a popular choice.

Proposed DYDIMNET: Dynamic Dimensional Convolution Network

Motivated from the extensive literature survey, This paper proposes a DyDimNet: Dynamic Dimensional convolution network model for classification of ovarian tumor which is working with data in three different dimensions like width, depth, and height of Input tensor $T_{(H\times D\times W)}$. Three sets of kernels are used by proposed model for each dimension, as illustrated in Figure 6: KE_H for height-wise convolution, KE_D for depthwise convolution, and KE_W for width-wise convolution. Kernels that are particular to dimensions provide O_H, O_D, and O_W outputs that have dimensions of $(H\times D\times W)$, effectively extracting data from the input tensor. The ultimate result, Odim, is obtained by combining spatial planes within the dimension selector block after these outputs have been combined. Hence, proposed model is divided into three phases:

1. Convolution based on dimension selector block
2. Convolution based on dynamic filter selector
3. Dimension wise fusion

The overall workflow of DyDimNet can be summarized as follows: (1) extract dimension-specific features, (2) adaptively select filter sizes, and (3) fuse selected representations through point-wise convolution.

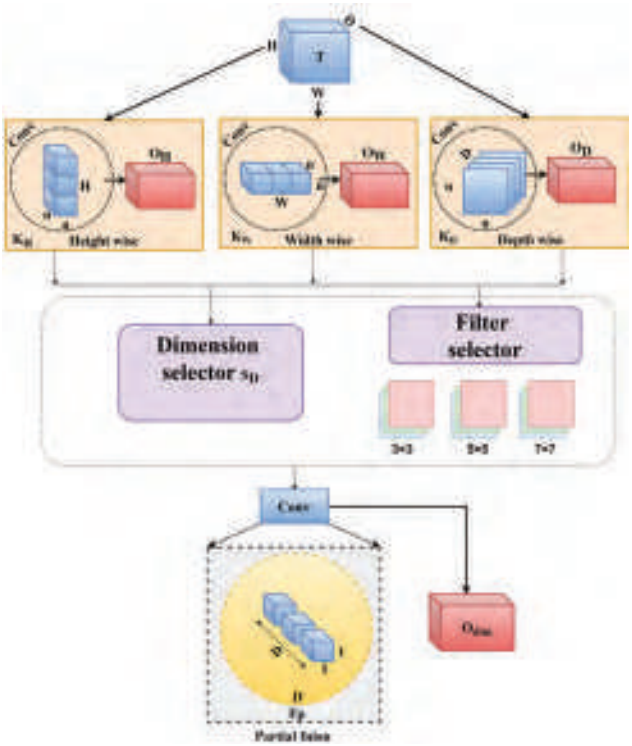


Figure 6. Proposed dynamic dimensional convolution network architecture.

The architecture of proposed model and pseudo code for classification are explained in Figure 6 and in this section respectively.

Convolution Based on Dynamic Dimension Selector

The Dimension selector block named SD enables dimension selection based on the needs of certain scenarios. Users have the chance to train via only their height, width, or depth measures, depending on their needs. This block's parameters define the chosen dimensions: $S_D = KE_D$, KE_H, KE_W. Combinations of two kernels are also possible, such as $S_D = KE_D$, KE_W, $S_D = KE_H$, KE_W, $S_D = KE_D$, KE_H, and The Dimension selector block named S_D enables dimension selection based on the needs of certain scenarios. Users have the chance to train via only their height, width, or depth measures, depending on their needs. This block's parameters define the chosen dimensions: $S_D = KE_D$, KE_H, KE_W. Combinations of two kernels are also possible, such as $S_D = KE_D$, KE_W, $S_D = KE_H$, KE_W, $S_D = KE_D$, KE_H, and $SD = KE_D$, KE_W, KE_H. So, seven options are thus shown by the dimension selector. Figure 6 shows how selected kernels affect Odim integration across different dimension combinations.

Convolution Based on Dynamic Filter Selector

An additional module that dynamically selects and adjusts the filters for each dimension-specific convolution based on the input features, enhancing the adaptability and performance of the ConvDim block. To improve the flexibility of ConvDim block, we introduce a filter selector module that dynamically choose one of several filter sizes (e.g. 3×3,5×5,7×7) based on the input features. This allows the model to adaptively choose the most appropriate filter size for various parts of the input, thereby improving its ability to capture relevant patterns.

Dimension-wise Fusion

Considering the input tensor dimensions, dimension-wise convolutions only retrieve regional data rather than wider data. CNNs' point-wise convolutions can take a while, even though they frequently incorporate global insights. To get around this, the dimension-wise combining module combines dimension-wise interpretations from Odim by dividing pointwise convolution into both local and global combining phases shown in Figure 6.

Proposed Dynamic Dimensional Convolution Network Algorithm

This section provides algorithm of proposed Dynamic Dimensional convolution network model for classification of ovarian tumor.

Algorithm: Dynamic Dimensional Convolution Network

Input:

- Ultrasound Image
- input image shape-(224, 224, 3)
- input data range- [0, 255]
- Num classes-2
- Batch size-32
- Number of epochs-50
- Learning rate-0.0001
- Dropout rate-0.5
- Loss function-Categorical Cross-Entropy
- Metric for evaluation-Accuracy, FLOPs
- Path to save the trained model

Output:

- Benign Tumor
- Malignant Tumor

BEGIN

1. Given an input tensor $T \in R^{H\times W\times D}$:
2. Height-wise Convolution kernel: $KE_H \in R^{1\times n\times n}$ producing output $O_H \in R^{H\times W\times D}$
3. Depth-wise Convolution kernel: $KE_D \in R^{n\times n\times 1}$ producing output $O_D \in R^{H\times W\times D}$
4. Width-wise Convolution: Apply $KE_W \in R^{n\times 1\times n}$ producing output $O_W \in R^{H\times W\times D}$
5. **For each dimension in SD:**
6. If KE_H is selected: $O_H = KE_H * T$
7. If KE_D is selected: $O_D = KE_D * T$
8. If KE_W is selected: $O_W = KE_W * T$
9. **Dimension Selectors** S_D: $S_D \in \{KE_H\}$, $S_D \in \{KE_W\}$, $S_D \in \{KE_D\}$, $S_D \in \{KE_H, KE_D\}$, $S_D \in \{KE_H, KEw\}$, $S_D \in \{KE_W, KE_D\}$, $S_D \in \{KE_W, KE_D, KE_H\}$.

10. Dimension Selector Output:
11. O_{dim} = concatenate(O_H, O_D, O_W) based on S_D selection.
12. Filter Selectors SF: $S_F \in F_{3\times3}$, $S_F \in F_{5\times5}$, $S_F \in F_{7\times7}$.
13. Dimension-wise fusion:
14. Apply a point-wise convolution with $F_P \in R^{1\times1\times D}$ *to* O_{dim}, producing the final output
$O \in R^{H\times D\times W}$
$O = F_P * O_{dim}$
END

RESULTS

This section gives a quick summary of the dataset and the framework that were both employed in this paper, as seen in Figure 6. The dataset is explained in depth in this section and also gives information on the experimental setups. Further Result analysis section is divided into two parts: Quantitative Result analysis and

Qualitative result analysis.

Dataset Description

The dataset used in this study is the publicly available MMOTU DS2Net ovarian ultrasound dataset, which contains 1200 ultrasound images of different women categorized into benign and malignant tumor classes as shown in Figure 7. The dataset was originally collected at the Department of Gynecology and Obstetrics, Beijing Shijitan Hospital, Capital Medical University, and later made publicly available for research purposes. All images have an average resolution of 256×256 pixels.

Experimental Setup

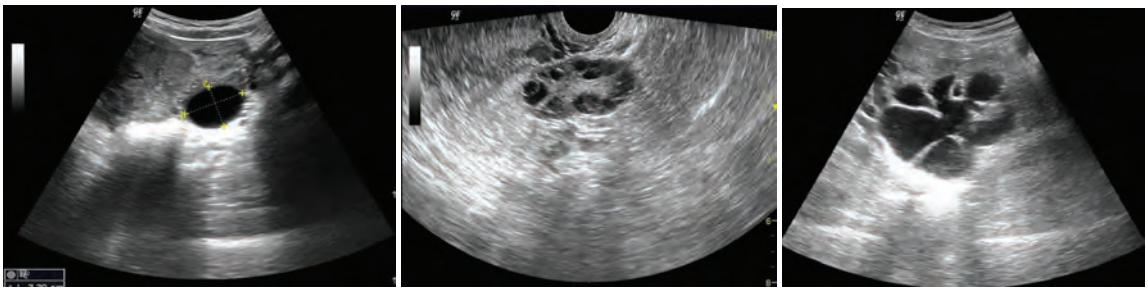
This paper uses the TensorFlow and Keras functional API for model development, using Google Colab, which offers free GPU access. The model is trained using an NVIDIA Tesla P100 GPU with 16 GB RAM, Keras API, and TensorFlow backend. The Adam optimizer is used with an initial learning rate of 0.0001, and the categorical cross-entropy loss function is used, which is appropriate for multiclass classification and helps in faster convergence of the model. To improve the efficiency of training, this paper incorporates ModelCheckpoint, which monitors performance metrics and saves the model at regular intervals based on a monitoring metric such as validation loss.

Result Analysis

Experimental results and a comprehensive analysis of the proposed DyDimNet are given in this section. This study incorporates the proposed DyDimNet into state-of the-art models, such as RESNET, EfficientNetB4, and EfficientNetV2, to investigate the effect of reduced FLOPs on classification accuracy.

We chose ResNet, EfficientNetB4, and EfficientNetV2 as baselines, as they represent the most commonly used deep learning architectures with different levels of computational complexity and feature extraction ability. This allows to compare fairly DyDimNet against classical and modern CNN designs. The architecture of the entire setup is summarized in Figure 8.

FLOPs measure the computational complexity of a model by counting the number of floating-point operations that are executed during inference time. [33]. On the



(a) Benign Tumor



(b) Malignant tumor

Figure 7. Classification of ovarian tumor dataset.

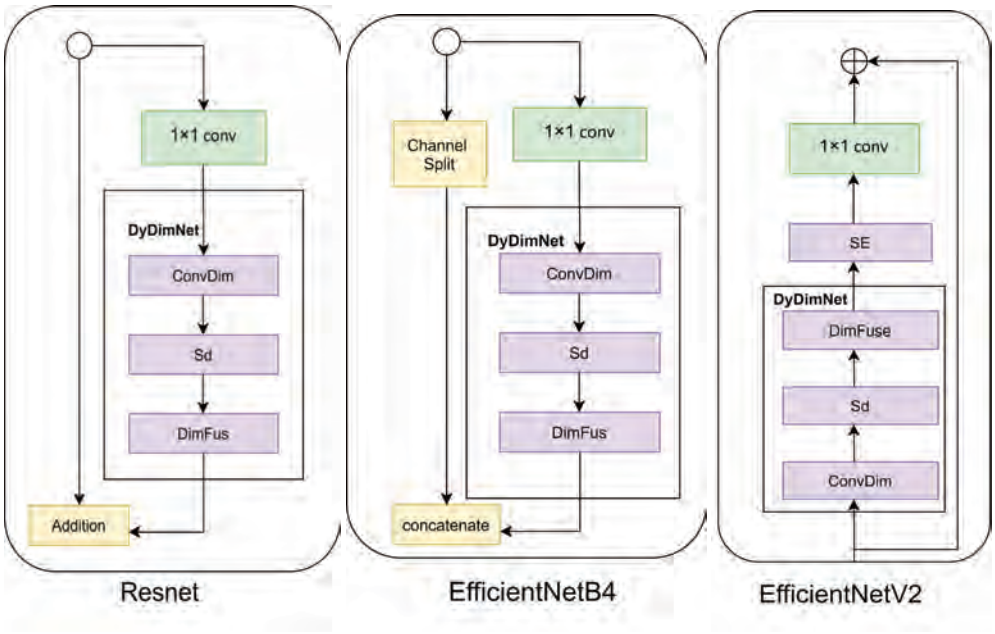


Figure 8. Proposed DyDimNet in different architectural design.

other hand, FLOPS measures the speed at which hardware computes data, and the higher the FLOPS, the faster the computation and lower the inference time. The formula for computing FLOPs in the model is given as:

$$\text{FLOPs} = 2\times kernel_size\times kernel_size\times input_channels \times Number_of_kernels\times output_size\times output_size \quad (1)$$

As shown in Equation 1, FLOPs are calculated by considering the kernel size, input channels, the number of kernels, and the output size of the model.

Within this section, the analysis of the results is structured into two distinct categories: (1) Quantitative Result Analysis And (2) Qualitative Result Analysis

Quantitative Result Analysis

In this section, we compare the proposed DyDimNet architecture with the filter selector module on different models i.e., ResNet, EfficientNetB4, and EfficientNetV2. The main goal is to improve classification accuracy at the cost of computational cost by exploiting the DyDimNet model. Specifically, this section represents three key experiments:

Experiment 1. Performance of the filter selector module of DyDimNet on unidimentional kernels.

Experiment 2. Performance of the filter selector module of DyDimNet on Bidimentional kernels.

Experiment 3. Performance of the filter selector module of DyDimNet on Tridimentional kernels.

Performance of the Filter Selector Module of DYDIMNET on Unidimensional Kernels

This experiment evaluates the impact of using a single kernel dimension with filter selector module of DyDimNet on classification accuracy and computational cost (FLOPs). The objective is to analyze how different filter sizes affect the balance between accuracy and computational efficiency. Using a single kernel dimension for the output channel can reduce detection accuracy. Resnet, EfficientNetB4 and EfficientNetV2 architectures were utilised to perform classification tasks on the ovarian tumor dataset. Initial models were produced in accordance with current criteria, and they were then merged with the proposed DyDimNet Architecture via the single dimension in the dimension selector module of the DyDimNet architecture. Tables 1, Table 2, and Table 3 show the results for impact of single dimensional kernels with different filter size.

As shown in results, increasing filter size causes a great increase in the computational cost but does not correlate with an increased classification accuracy. The 3 × 3 kernel always provides best accuracy while ensuring low FLOPs, hence it would be the preferable choice. Larger kernels (5×5 and 7×7) result in higher complexity and increased computational cost, which leads to lower accuracy. The experiment confirms that the best trade-off between accuracy and computational efficiency is achieved by unidimensional kernels with smaller filter sizes 3 × 3. Future optimizations should be focused on adaptive kernel selection strategies to reduce FLOPs while maintaining classification performance.

Table 1. Performance of filter selector module for Depth-Based Kernels

Model	Filter Size	FLOPs(M)	Accuracy(%)
Resnet-(DyDimNetKE$_D$)	3×3	27	33.6
Resnet-(DyDimNetKE$_D$)	5×5	75	30.2
Resnet-(DyDimNetKE$_D$)	7×7	146	26.4
EfficientNetB4-(DyDimNetKE$_D$)	3×3	24	42.1
EfficientNetB4-(DyDimNetKE$_D$)	5×5	66	40
EfficientNetB4-(DyDimNetKE$_D$)	7×7	125	34
EfficientNetV2-(DyDimNetKE$_D$)	3×3	21	45
EfficientNetV2-(DyDimNetKE$_D$)	5×5	58	43
EfficientNetV2-(DyDimNetKE$_D$)	7×7	114	38

Table 2. Performance of filter selector module for width-Based Kernels

Model	Size	FLOPs(M)	Accuracy (%)
Resnet-(DyDimNetKEw)	3×3	27	32.1
Resnet-(DyDimNetKEw)	5×5	75	30
Resnet-(DyDimNetKEw)	7×7	145	27
EfficientNetB4-(DyDimNetKEw)	3×3	24	35
EfficientNetB4-(DyDimNetKEw)	5×5	66	33
EfficientNetB4-(DyDimNetKEw)	7×7	125	29
EfficientNetV2-(DyDimNetKEw)	3×3	21	44.7
EfficientNetV2-(DyDimNetKEw)	5×5	58	42
EfficientNetV2-(DyDimNetKEw)	7×7	112	39

Table 3. Performance of filter selector module for Height-Based Kernels

Model Filter	Size	FLOPs(M)	Accuracy (%)
Resnet-(DyDimNetKE$_H$)	3×3	27	32
Resnet-(DyDimNetKE$_H$)	5×5	75	30
Resnet-(DyDimNetKE$_H$)	7×7	146	28
EfficientNetB4-(DyDimNetKE$_H$)	3×3	24	36
EfficientNetB4-(DyDimNetKE$_H$)	5×5	66	34
EfficientNetB4-(DyDimNetKE$_H$)	7×7	125	30
EfficientNetV2-(DyDimNetKE$_H$)	3×3	21	43
EfficientNetV2-(DyDimNetKE$_H$)	5×5	58	41
EfficientNetV2-(DyDimNetKE$_H$)	7×7	114	38

Performance of the Filter Selector Module of DYDIMNET on Bidimensional Kernels

This experiment investigates the effect of the bidimensional kernel selection, where two kernel dimensions are merged for the output channel. The goal is to study if bidimensional kernels can have lower computational cost and still maintain the classification accuracy.

Dimension selector modules used DyDimNet with several kernel combinations (DyDimNetKE$_{WH}$, DyDimNetKE$_{HD}$ and DyDimNetKE$_{WD}$). Table 4 to Table 6 report lower FLOPs with little to no accuracy effect. The best performance always comes from the combination of 3×3 kernels while 5×5 and 7×7 produce more FLOPs with less accuracy. EfficientNetV2 achieves better performance than the variants of ResNet and EfficientNetB4 in

Table 4. Performance of filter selector module for width & depth Based Kernels

ModelFilter	Size	FLOPs(M)	Accuracy (%)
Resnet-(DyDimNetKE$_{WD}$)	3×3	52	62
Resnet-(DyDimNetKE$_{WD}$)	5×5	145	59
Resnet-(DyDimNetKE$_{WD}$)	7×7	283	54
EfficientNetB4-(DyDimNetKE$_{WD}$)	3×3	49	81
EfficientNetB4-(DyDimNetKE$_{WD}$)	5×5	136	78
EfficientNetB4-(DyDimNetKE$_{WD}$)	7×7	267	74
EfficientNetV2-(DyDimNetKE$_{WD}$)	3×3	41	85
EfficientNetV2-(DyDimNetKE$_{WD}$)	5×5	114	83
EfficientNetV2-(DyDimNetKE$_{WD}$)	7×7	222	79

Table 5. Performance of filter selector module for width & height Based Kernels

Model Filter	Size	FLOPs(M)	Accuracy (%)
Resnet-(DyDimNetKE$_{WH}$)	3×3	52	64.25
Resnet-(DyDimNetKE$_{WH}$)	5×5	145	61.25
Resnet-(DyDimNetKE$_{WH}$)	7×7	283	57.25
EfficientNetB4-(DyDimNetKE$_{WH}$)	3×3	49	81.25
EfficientNetB4-(DyDimNetKE$_{WH}$)	5×5	136	78.25
EfficientNetB4-(DyDimNetKE$_{WH}$)	7×7	267	74.25
EfficientNetV2-(DyDimNetKE$_{WH}$)	3×3	41	84.2
EfficientNetV2-(DyDimNetKE$_{WH}$)	5×5	114	82.2
EfficientNetV2-(DyDimNetKE$_{WH}$)	7×7	222	79.2

Table 6. Performance of filter selector module for depth & height Based Kernels

Model Filter	Size	FLOPs(M)	Accuracy (%)
Resnet-(DyDimNetKE$_{HD}$)	3×3	52	63
Resnet-(DyDimNetKE$_{HD}$)	5×5	145	60
Resnet-(DyDimNetKE$_{HD}$)	7×7	283	56
EfficientNetB4-(DyDimNetKE$_{HD}$)	3×3	49	80
EfficientNetB4-(DyDimNetKE$_{HD}$)	5×5	136	78
EfficientNetB4-(DyDimNetKE$_{HD}$)	7×7	267	74
EfficientNetV2-(DyDimNetKE$_{HD}$)	3×3	41	83
EfficientNetV2-(DyDimNetKE$_{HD}$)	5×5	114	81
EfficientNetV2-(DyDimNetKE$_{HD}$)	7×7	222	78

all configurations, demonstrating a more efficient trade-off between computational cost and classification accuracy.

This finding suggests that the combined use of width and depth kernels helps feature extraction by capturing the horizontal and vertical patterns and therefore providing richer representations. With larger kernels, we obtain slightly better coverage of features, but at a much higher computational cost and without a corresponding improvement in accuracy. This shows that directional diversity (width + depth) is more effective than the kernel size enlargement, which verifies the usefulness of the adaptive kernel selection of DyDimNet.

Performance of the Filter Selector Module of DYDIMNET on Tridimensional Kernels

The experiment analyzes the impact of employing all three kernel dimensions (width, height and depth) on the

output channel. To this end, we extended the DyDimNet architecture with a Tridimensional Kernel Selector Module. We employed all three kernel dimensions for the output channel to increase accuracy while being computationally efficient. This method improved accuracy at the cost of increasing FLOPs . The size of DyDimNet block with width, height and depth were determined based on the DyDimNet design. Table 7 shows the results for kernels with different depths, widths, and heights.

Tridimensional kernels give a substantial accuracy boost over unidimensional and bidimensional kernels at the expense of more FLOPs. This trade-off is better suited for applications where accuracy is prioritized over computational efficiency. The results suggest that EfficientNetV2 profits most from tridimensional kernels, followed by EfficientNetB4 and ResNet, demonstrating that modern architectures better exploit extra kernel dimensionality. The balanced kernel configuration proved to be a 3×3 kernel while the larger-sized kernels result in decreasing returns to the accuracy increment against the increases in computational overhead.

This result shows the power of tridimensional kernels, which enable the model to capture a wider variety of spatial dependencies, resulting in richer feature extraction. Increasing the kernel size only marginally improves feature coverage but massively increases FLOPs without a proportionate accuracy increase. This means that multi-directional feature extraction is very beneficial, but a balanced kernel size of 3×3 is the optimal trade-off between accuracy and efficiency.

Qualitative Result Analysis

The next part discusses the trade-offs in the model behavior and how the integration of the filter selection module and filter size variations impact the performance and computational efficiency.

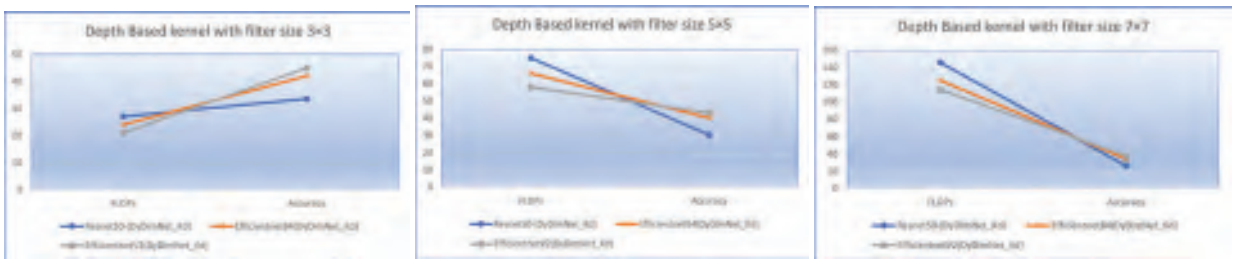
UniDimensional kernel: UniDimensional kernels, from 3x3 to 5x5 and 7x7 causes a large rise in computing cost (FLOPs) and a decrease in the overall accuracy across models, as illustrated in Figure 9. With increasing filter size, computational requirements also increase, yet this often leads to a drop in accuracy. Larger filters need more resources but usually result in worse accuracy. Also, EfficientnetV2 is more robust to filter size change compared to Resnet50 and EfficientnetB4. It has better accuracy with increased processing cost. This study emphasizes the trade-off between filter size and computational efficiency and accuracy in the optimization of convolutional neural networks.

BiDimensional kernel: For UniDimensional kernels, the FLOPs increase substantially with larger filter sizes, and accuracy decreases accordingly. This pattern is also observed in BiDimensional kernels. While the computational cost grows significantly, the model's accuracy diminishes as filter sizes increase, demonstrating a trade-off between computational efficiency and model performance. Models such as EfficientnetV2 remain more accurate despite the rise in computational cost, indicating that they are more robust to changes in filter size than models such as Resnet50 and EfficientnetB4.In addition, we find that the FLOPs of 5×5 filters are about 2.78 times the FLOPs of 3×3 filters and the FLOPs of 7×7 filters are about 5.44 times the FLOPs of 3×3 filters, as shown in Figure 10.

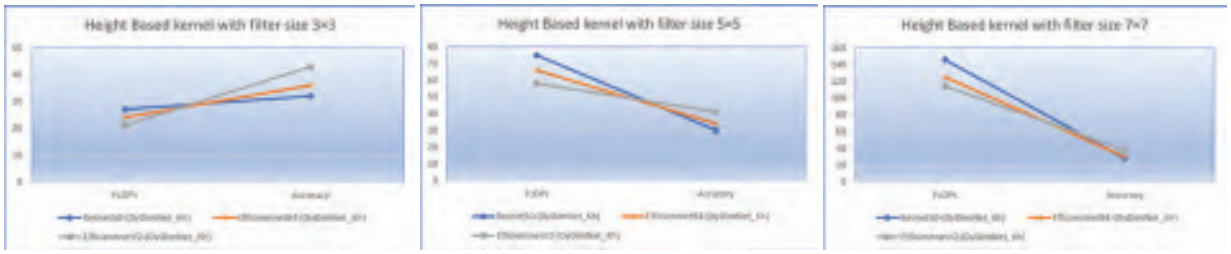
TriDimensional kernel: When considering all dimensions—filter size, model architecture, and kernel configurations—the results suggest that newer architectures like EfficientNetV2 consistently offer the best trade-off between accuracy and computational efficiency. For any given filter size (3x3, 5x5, 7x7), EfficientNetV2 achieves the highest accuracy while maintaining the lowest FLOPs, demonstrating its superior optimization. Older models like ResNet50 generally show higher FLOPs and lower accuracy, indicating less efficiency in handling increased computational complexity. As filter size increases, computational demands rise, but EfficientNetV2's ability to maintain high accuracy with lower FLOPs across different filter sizes underscores its advanced design. Overall, EfficientNetV2 emerges as the most effective model across various dimensions,

Table 7. Performance of filter selector module for width, depth & height Based Kernels

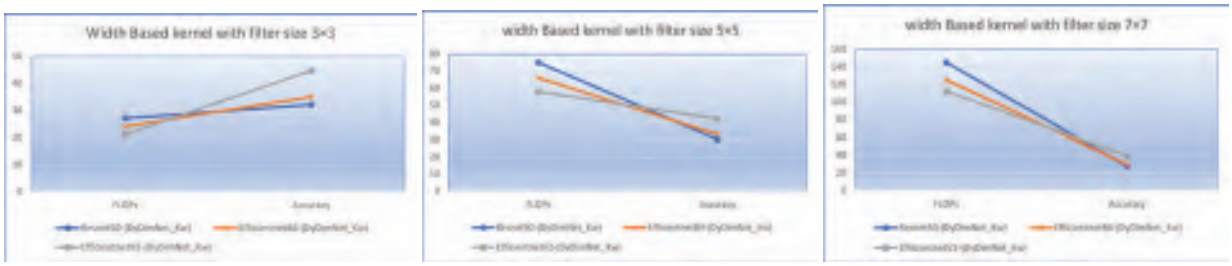
Model Filter	Size	FLOPs(M)	Accuracy (%)
Resnet-(DyDimNetKE$_{HWD}$)	3×3	72	69.7
Resnet-(DyDimNetKE$_{HWD}$)	5×5	200	66.7
Resnet-(DyDimNetKE$_{HWD}$)	7×7	392	62.7
EfficientNetB4-(DyDimNetKE$_{HWD}$)	3×3	63	86.4
EfficientNetB4-(DyDimNetKE$_{HWD}$)	5×5	175	83.4
EfficientNetB4-(DyDimNetKE$_{HWD}$)	7×7	343	79.4
EfficientNetV2-(DyDimNetKE$_{HWD}$)	3×3	54	93.6
EfficientNetV2-(DyDimNetKE$_{HWD}$)	5×5	150	87
EfficientNetV2-(DyDimNetKE$_{HWD}$)	7×7	294	82.6



(a) depth based kernel with filter (b) depth based kernel with filter (c) depth based kernel with filter size 3×3 size 5×5 size 7×7



(a) Height based kernel with filter (b) Height based kernel with filter (c) Height based kernel with filter size 3×3 size 5×5 size 7×7



(a) Width based kernel with filter (b) Width based kernel with filter (c) Width based kernel with filter size 3×3 size 5×5 size 7×7

Figure 9. Unidimensional Kernels with different 3×3, 5×5, and 7×7 filters.

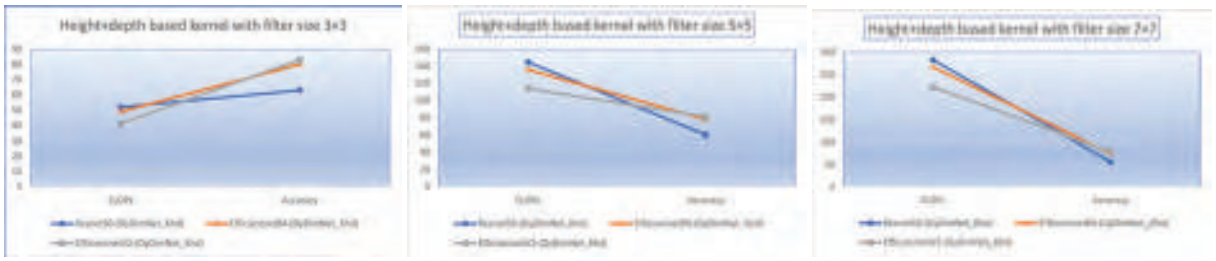
balancing performance and computational cost better than its predecessors.

To validate the performance of the proposed Dynamic Dimensional Convolution Network, a comparative analysis was conducted against existing deep learning architectures, including ResNet50, EfficientNetB4 and EfficientNetV2 as shown in Table 1 to Table 7.

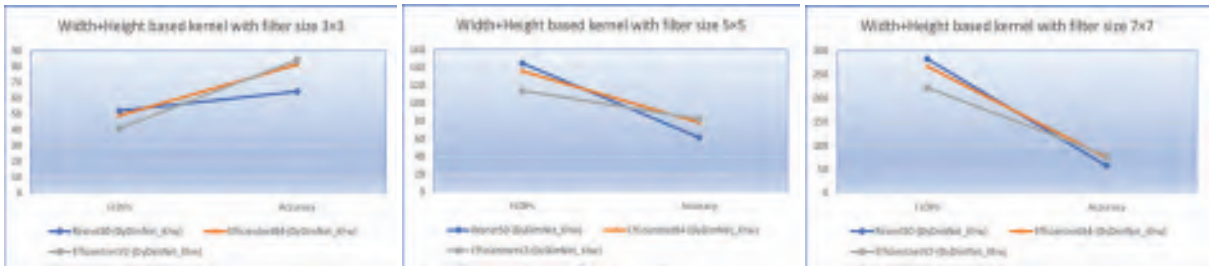
The performance gain can be attributed to the dynamic dimension and filterselection mechanisms, which allow the model to automatically adapt convolutional kernels to the structural characteristics of input images. This adaptability enables more efficient extraction of discriminative tumor features and reduces the risk of overfitting, particularly in limited medical datasets. The proposed DyDimNet architecture demonstrates strong potential beyond ovarian tumor classification. Its adaptive convolutional mechanism can be generalized to other biomedical imaging domains such as breast cancer detection, liver lesion segmentation, or lung nodule analysis, where input dimensionality and texture patterns vary.

Furthermore, DyDimNet's lightweight computation and reduced FLOPs make it suitable for real-time clinical environments, including portable ultrasound systems and edge-AI-enabled diagnostic devices. The ability to dynamically optimize computational resources while maintaining high accuracy positions DyDimNet as a versatile framework for resource-constrained or real-time applications in both medical and industrial settings.

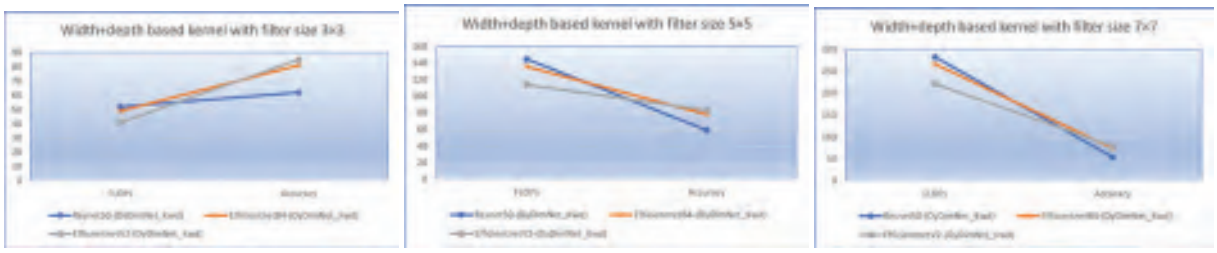
The experimental analysis confirms that the proposed Dynamic Dimensional Convolution Network achieves a consistent performance improvement across various kernel configurations. When compared to standard convolutional networks, the model demonstrated an increase of 6.3% in accuracy. The adaptive dimensional and filter-selection mechanism also reduced computational time by approximately 12%, indicating its efficiency in handling complex image datasets. These results confirm the robustness and scalability of the proposed method for medical image classification tasks.



(a) Height+depth based kernel with Filter size 3×3 (b) Height+depth based kernel with Filter size 5×5 (c) Height+depth based kernel with Filter size 7×7



(a) Width+height based kernel with Filter size 3×3 (b) Width+height based kernel with Filter size 5×5 (c) Width+height based kernel with Filter size 7×7



(a) Width+Depth based kernel with Filter size 3×3 (b) Width+Depth based kernel with Filter size 5×5 (c) Width+Depth based kernel with Filter size 7×7

Figure 10. BiDimensional Kernels with different 3×3, 5×5, and 7×7 filters.

CONCLUSION

In conclusion, the proposed DyDimNet module displays its adaptability by being compatible with a variety of CNN-based network architectures. DyDimNet is used in Resnet, EfficientNetB4, and EfficientnetV2 architecture. The results were evaluated by selecting different filter size on the basis of accuracy and FLOPs.The findings show that UniDimensional kernel-based DyDimNet decreases FLOPs by roughly one-third, resulting in dramatically enhanced speed. In contrast, reducing the FLOPs leads to a substantial loss of accuracy. BiDimensional kernels provide a trade-off between sustained or slightly improved accuracy and reduced FLOPs (around half) in EfficientNetV2 with DyDimNet. Finally, TriDimensional kernels offer the best accuracy with the least FLOPs. These results show that DyDimNet may improve the accuracy and efficiency of different CNN designs. Future work will be dedicated to the applicability of DyDimNet and will be tested on other medical imaging tasks in an effort to investigate its generalizability and effectiveness in different domains.

Practical Applications and Broader Implications

The proposed DyDimNet framework holds considerable promise for practical deployment in healthcare and related computational fields. Its ability to dynamically adjust convolutional operations based on input characteristics makes it particularly suitable for real-time clinical imaging systems, such as ultrasound-based diagnostic tools used in gynecology and oncology. Hospitals and diagnostic centers could integrate DyDimNet into existing computer-aided diagnosis platforms to assist radiologists in differentiating between benign and malignant ovarian tumors with greater accuracy and reduced processing time.

Beyond ovarian tumor detection, the adaptive design of DyDimNet can be extended to other imaging modalities, including magnetic resonance imaging (MRI), computed tomography (CT), and mammography, where varying spatial dimensions and image complexities often challenge traditional deep learning models. Its lightweight computational footprint also makes it viable for edge and mobile healthcare applications, supporting telemedicine and portable diagnostic devices in low-resource settings.

From a broader perspective, DyDimNet contributes to the development of generalizable, adaptive artificial intelligence models capable of handling diverse data types beyond medical imaging. The principles of dynamic dimensional convolution can benefit domains such as remote sensing, industrial defect detection, and autonomous navigation—anywhere efficient feature extraction across variable data dimensions is required. Thus, the study not only advances medical image analysis but also sets a foundation for the next generation of flexible and resource-efficient intelligent systems.

COPYRIGHT DETAILS

DyDimNet: Dynamic Dimensional Convolution Network Architecture is a copyrighted work of Authors under literary/dramatic work, registered with the Copyright Office, Government of India (ROC No: L-157210/2024, ROC Date: 22 Nov 2024). All rights reserved.

AUTHORSHIP CONTRIBUTIONS

Authors equally contributed to this work.

DATA AVAILABILITY STATEMENT

The dataset used in this experiment is available at https://github.com/cv516Buaa/MMOTU DS2Net

CONFLICT OF INTEREST

The authors declared that they have no conflict of interest.

ETHICS

There are no ethical issues with the publication of this manuscript.

STATEMENT ON THE USE OF ARTIFICIAL INTELLIGENCE

Artificial intelligence was not used in the preparation of the article.

REFERENCES

[1] Sayasneh A, Ekechi C, Ferrara L, Kaijser J, Stalder C, Sur S, et al. The characteristic ultrasound features of specific types of ovarian pathology. Int J Oncol 2015;46:445–458. [CrossRef]

[2] Lu M, Fan Z, Xu B, Chen L, Zheng X, Li J, et al. Using machine learning to predict ovarian cancer. Int J Med Inform 2020;141:104195. [CrossRef]

[3] Asaduzzaman S, Ahmed MR, Rehana H, Chakraborty S, Islam MS, Bhuiyan T. Machine learning to reveal an astute risk predictive framework for gynecologic cancer and its impact on women psychology: Bangladeshi perspective. BMC Bioinformatics 2021;22:213. [CrossRef]

[4] Smith-Bindman R, Poder L, Johnson E, Miglioretti DL. Risk of malignant ovarian cancer based on ultrasonography findings in a large unselected population. JAMA Intern Med 2019;179:71–77. [CrossRef]

[5] Valentin L, Ameye L, Savelli L, Fruscio R, Leone F, Czekierdowski A, et al. Unilocular adnexal cysts with papillary projections but no other solid components: is there a diagnostic method that can classify them reliably as benign or malignant before surgery. Ultrasound Obstet Gynecol 2013;41:570–581. [CrossRef]

[6] Guo J, Feng H, Gu X. Association between benign ovarian tumors and ovarian cancer risk: a meta-analysis of ten epidemiological studies. Front Oncol 2022;12. [CrossRef]

[7] Borgfeldt C, Andolf E. Cancer risk after hospital discharge diagnosis of benign ovarian cysts and endometriosis. Acta Obstet Gynecol Scand 2004;83:395–400. [CrossRef]

[8] Wadhwa G, Jayanthi N, Mathur M. A deep convolutional neural network approach for detecting malignancy of ovarian cancer using DenseNet model. Ann Rom Soc Cell Biol 2021:4449–4458.

[9] Wu M, Yan C, Liu H, Liu Q. Automatic classification of ovarian cancer types from cytological images using deep convolutional neural networks. Biosci Rep 2018;38. [CrossRef]

[10] Al-Dhabyani W, Gomaa M, Khaled H, Aly F. Deep learning approaches for data augmentation and classification of breast masses using ultrasound images. Int J Adv Comput Sci Appl 2019;10:1–11. [CrossRef]

[11] Mathur M, Jindal V, Wadhwa G. Detecting malignancy of ovarian tumour using convolutional neural network: a review. In: 2020 Sixth International Conference on Parallel, Distributed and Grid Computing (PDGC). 2020. p. 351–356. [CrossRef]

[12] Madhumitha J, Kalaiyarasi M, Ram SS. Automated polycystic ovarian syndrome identification with follicle recognition. In: 2021 3rd International Conference on Signal Processing and Communication (ICPSC). 2021. p. 98–102. [CrossRef]

[13] Danaei Mehr H, Polat H. Diagnosis of polycystic ovary syndrome through different machine learning and feature selection techniques. Health Technol 2022;12:137–150. [CrossRef]

[14] Nabilah A, Sigit R, Harsono T, Anwar A. Classification of ovarian cysts on ultrasound images using watershed segmentation and contour analysis. In: 2020 International Electronics Symposium (IES). 2020. p. 513–519. [CrossRef]

[15] Maheswari K, Baranidharan T, Karthik S, Sumathi T. Modelling of f3i based feature selection approach for pcos classification and prediction. J Ambient Intell Humaniz Comput 2021;12:1349–1362. [CrossRef]

[16] Ghoniem RM, Algarni AD, Refky B, Ewees AA. Multimodal evolutionary deep learning model for ovarian cancer diagnosis. Symmetry 2021;13:643. [CrossRef]

[17] Zheng X, Liu Y, Chen Z. Dynamic convolution neural networks with both global and local attention for image classification. Mathematics 2024;12:1856. [CrossRef]

[18] Liu H, Zhou Q. Adaptiveconv2d: a novel convolutional module for medical image segmentation. Appl Sci 2025;15:2169. [CrossRef]

[19] Suganyadevi S, Seethalakshmi R. Facnn: fuzzy-based adaptive convolution neural network for chest X-ray classification. Comput Biol Med 2024;170:108025.

[20] Zhang L, Huang J, Liu L. Improved deep learning network based in combination with cost-sensitive learning for early detection of ovarian cancer in color ultrasound detecting system. J Med Syst 2019;43:1–9. [CrossRef]

[21] Wang H, Liu C, Zhao Z, Zhang C, Wang X, Li H, et al. Application of deep convolutional neural networks for discriminating benign, borderline, and malignant serous ovarian tumors from ultrasound images. Front Oncol 2021;11:5372. [CrossRef]

[22] Kodipalli A, Devi SV, Dasar S, Ismail T. A novel variant of deep convolutional neural network for classification of ovarian tumors using CT images. Comput Electr Eng 2023;109:108758. [CrossRef]

[23] Wu C, Wang Y, Wang F. Deep learning for ovarian tumor classification with ultrasound images. In: Advances in Multimedia Information Processing-PCM 2018: 19th Pacific-Rim Conference on Multimedia. 2018. p. 395–406. [CrossRef]

[24] Kunwar FB, et al. Xai mlpcnn: a novel explainable AI-based deep learning framework for stress identification. J Comput Sci 2025;21:1156–1167. [CrossRef]

[25] Kunwar FB, et al. Improved deep learning with self-adaptive algorithms for accurate stress detection: cascaded CNN BiLSTM GRU method. J Theor Appl Inf Technol 2025;103.

[26] Kunwar FB, et al. Predicting academic stress among students through psychometric assessments using hybrid neural networks. In: 2025 Global Conference in Emerging Technology (GINOTECH). 2025. p. 1–6. [CrossRef]

[27] Tan M, Le QV. EfficientNetV2: smaller models and faster training. CoRR 2021;abs/2104.00298.

[28] Tan M, Le QV. EfficientNet: rethinking model scaling for convolutional neural networks. CoRR 2019;abs/1905.11946.

[29] Jian J, Xia W, Zhang R, Zhao X, Zhang J, Wu X, et al. Multiple instance convolutional neural network with modality-based attention and contextual multi-instance learning pooling layer for effective differentiation between borderline and malignant epithelial ovarian tumors. Artif Intell Med 2021;121:102194. [CrossRef]

[30] Fırat H, Asker ME, Hanbay D. Hybrid 3D convolution and 2D depthwise separable convolution neural network for hyperspectral image classification. Balk J Electr Comput Eng 2022;10:35–46. [CrossRef]

[31] Kaur R, Kumar R, Gupta M. Food image-based diet recommendation framework to overcome PCOS problem in women using deep convolutional neural network. Comput Electr Eng 2022;103:108298. [CrossRef]

[32] Sun W, Zhang X, He X. Lightweight image classifier using dilated and depthwise separable convolutions. J Cloud Comput 2020;9. [CrossRef]

[33] Paoletti ME, Haut JM, Tao X, Plaza J, Plaza A. Flop-reduction through memory allocations within CNN for hyperspectral image classification. IEEE Trans Geosci Remote Sens 2021;59:5938–5952. [CrossRef]

Sigma Journal of Engineering and Natural Sciences
Web page info: https://sigma.yildiz.edu.tr
DOI: 10.14744/sigma.2026.2112

Research Article

Entropy generation analysis of hydromagnetic flow on nonlinearly radiating Walters' B nanofluid with heat generation and viscous dissipation

Bayo Johnson AKINBO[1,*], Ibhadode OISEHOEMOMEN[2]

[1]*Institute of Mathematics and Computing, Universidade Federal de Itajubá, Itajubá, 37500-903, Brazil; Department of Mathematics, Federal College of Education, Abeokuta, 110119, Nigeria*
[2]*Institute of Mechanical Engineering, Universidade Federal de Itajuba, Itajuba, 37500-903, Brazil; Department of Mechanical Engineering, Federal University of Petroleum Resources Effurun, Delta State, 330102, Nigeria*

ARTICLE INFO

Article history
Received: 22 November 2024
Revised: 19 February 2025
Accepted: 15 June 2025

Keywords:
Entropy Generation; Hydromagnetic; Nanofluid; Thermal Radiation; Viscous Dissipation

ABSTRACT

The paper analyzed the relevance of irreversibility analysis amidst the nonlinear radiative impact on a Walters' B nano-liquid model. The mechanism of the model, which acts as a catalyst in understanding the behaviours of the associated thermophysical properties in science and engineering fields, is examined through a horizontal stretching surface, taken into account the volumetric heat source/sink terms and viscous dissipation effects. The geometric flow model expressed in partial differential equations are reconstructed into ordinary differential equations by relevant conversion quantities and computed through the Galerkin Weighted Residual Method. The work is validated by the Spectral Collocation Method and the Wolfram language function NDSolve through the average deviation. The significance of the indicated parameters are interpreted through graphs and tables. The novel findings substantiate that the magnitude of Brinkman number invoke higher viscous heating through molecular conduction around the system consequently improves entropy production. This is vital in polymer processing, alongside the interactive application of the Weissenberg number. Also, variations in the heat production and convective heat parameters contribute significantly as heat distributing functions across the system which made way for the temperature distribution effect to the quiescent fluid. These parameters have a useful contribution, leading to the desiccation of the components in the engineering sectors.

Cite this article as: Akinbo BJ, Oisehoemomen I. Entropy generation analysis of hydromagnetic flow on nonlinearly radiating Walters' B nanofluid with heat generation and viscous dissipation. Sigma J Eng Nat Sci 2026;44(4):2525–2539.

***Corresponding author.**
*E-mail address: akinbomaths@gmail.com

This paper was recommended for publication in revised form by Editor-in-Chief Ahmet Selim Dalkilic

Published by Yıldız Technical University Press, İstanbul, Turkey
© Author. This is an open access article under the CC BY-NC license (http://creativecommons.org/licenses/by-nc/4.0/).

INTRODUCTION

An investigation into thermodynamic fluid model in science and engineering spheres have gained remarkable attention in the literature due to their undeniable usefulness in the fields. Little among these applications are: glass fiber, polymer extrusion, crystal growth and cooling of nuclear reactors, among others. Counting on its wide application in various disciplines, it has been broadly pronounced within the research circles. Jonnadula et al. [1] examined the mechanics of radiative heat emission on hydromagnetic fluid alongside destructive chemical reactions whose impact decays the concentration field. This similar report is buttressed by Javed et al. [2] while investigating with melting heat, the activation energy influence on chemically reacting magnetohydrodynamics flow. Chatterjee and Gupta [3] reported suppressive influence over the magnetic intensity with the contributing strength to the thermal field. Accounting for viscous dissipation, Swain et al. [4] explored Joule's heating influence in an electrically conducting fluid. The finding emphasized the aftermath impact of a rising thermal diffusivity over momentum diffusivity as strengthening factor to the temperature field. Akinbo and Olajuwon [5-7] investigated both the Newtonian model and non-Newtonian model on hydromagnetic flow, which has a useful application in power engineering. Good agreement is observed between the Variational Iteration Method and Akbari-Ganiji's method on the non-Newtionian model, involving Micropolar fluid with a bounded domain by Gholınıa et al [8] who also asserted that Microrotation is a decreasing function of coupling parameter. Mohyud-Din et al. [9] reported that surface heat and mass transport can be regulated with the passive control model while studying the unsteady case model of heat and mass transport with nanoparticles. Özen and Derun [10] reported inhibited hydration with the mixture of nanoparticles and borogypsum while invoking various nanoparticles on borogypsum's properties involving mortar. Nanoparticles have gained increasing attention within technical and scientific sectors, due to their higher thermal conductivity. This property offers a significant advantage in thermal performance compared to conventional fluids. Consequently, their potential has been explored in existing literature by Gupta [11], Gupta and Saxena [12], Gupta and Sharma [13], Gupta and Dixit [14], and Gupta et al. [15] among other researchers in the field.

In fluid dynamics, heat transfer is generally inevitable with its multiples usages in science and engineering fields. On this note, analyzing irreversibilities plays an indispensable role in analyzing the amount of entropy generated during the heat transfer. Thus, the ideas of entropy generation help to deduce irreversibility identical to friction and heat dissipation among others. It is a useful tool for assessing the effectiveness of different thermal systems, notably engines and heat exchangers. Based on the forward-going importances in the related fields of study, entropy generation has been investigated in the literature, among the notable contributions is the examination of irreversibility analysis of thermophysical quantities on Newtonian model involving hydromagnetic flow as reported by many researchers in the literature [16-21], where the frictional heating irreversibility due to the magnetic effect strengthens the entropy production. In addition, Non-Newtonian models exhibit viscosities that change in response to variations in shear rate.

leading to more complex entropy generation influenced by fluid rheology. Entropy generation in non-Newtonian fluid aids better representation of real-world applications like blood flow, polymer formation, improving system efficiency and design through more accurate thermodynamic predictions. Investigations of entropy generation on non-Newtonian include but not limited to the studies of micropolar fluid, power law fluids, Eyring–Powell fluid, Walters' B fluid, second grade fluid, as reported by [22-26].

Admitting the useful contributions of other researchers in the literature and industrial applications of entropy generation in the field, the knowledge of irreversibility analysis on the model of non-linear viscous fluid is still very shallow. Keeping in mind the existing work in the literature, entropy generation analysis is yet to be studied with the collective contributions of viscous heating, internal heat production/sink and nonlinear radiation on hydromagnetic Walters' B nanofluid under the benchmark of passive nanoparticles alongside convective heat domain. The objective here is to examine the significance of the embedded parameters associated with the model for industrial applications. Thus, this research is particularly valuable for polymer applications and helps in optimizing the cooling systems, enhancing energy efficiency and controlling thermal management in various industrial applications.

MATHEMATICAL FORMULATION

Here, we look into irreversibility analysis on a steady model, involving an incompressible Walters' B viscoelastic nanofluid through a two-dimensional boundary layer on an expanding sheet. The dynamics of the fluid are examined with magnetic strength B_0. In addition, the induced magnetic field is considered unimportant due to the diminutive magnetic Reynolds [27]. The non-Newtonian liquid radiates nonlinearly amidst the heat source/sink effects and viscous energy dissipation under the influence of convective heat domain. The fluid with the nanoparticles is considered in the region $y \geq 0$ while the x-axis corresponds to the parallel direction of the stretching sheet with velocity $u_w(x) = ax$, $a > 0$ as indicated in Figure 1. The convective fluid temperature is denoted by T_f, while concentration at the wall is represented by C_w with their respective corresponding far fields, which are specified as T_∞ and C_∞.

Subject to the mathematical formulation stated above, the resulting equations of the model are presented in

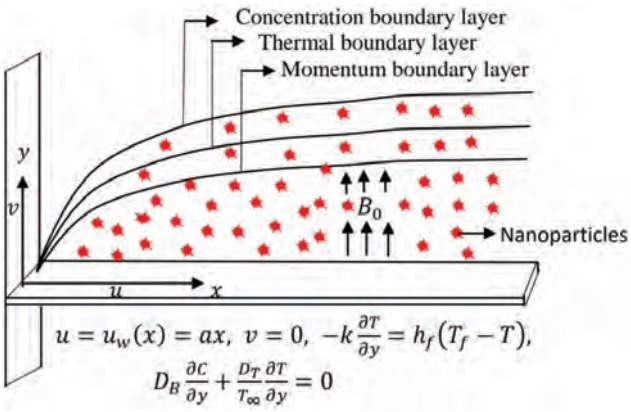


Figure 1. Model geometry.

accordance with Qayyum et al. [28], Saini et al. [29] and Hayat et al. [30] as follows

Continuity Equation:

$$\frac{\partial u}{\partial x} + \frac{\partial v}{\partial y} = 0 \tag{1}$$

Momentum Equation:

$$u\frac{\partial u}{\partial x} + v\frac{\partial u}{\partial y} = \nu_f\frac{\partial^2 u}{\partial y^2} - \frac{k_0}{\rho}\left(u\frac{\partial^3 u}{\partial x\partial y^2} + v\frac{\partial^3 u}{\partial y^3} - \frac{\partial u}{\partial y}\frac{\partial^2 u}{\partial x\partial y} + \frac{\partial u}{\partial x}\frac{\partial^2 u}{\partial y^2}\right) - \frac{\sigma B_0^2}{\rho}u \tag{2}$$

Energy Equation:

$$u\frac{\partial T}{\partial x} + v\frac{\partial T}{\partial y} = \frac{k_f}{(\rho C)_f}\frac{\partial^2 T}{\partial y^2} + \tau\left[D_B\frac{\partial C}{\partial y}\frac{\partial T}{\partial y} + \frac{D_T}{T_\infty}\left(\frac{\partial T}{\partial y}\right)^2\right] + \frac{\mu}{(\rho C)_f}\left(\frac{\partial u}{\partial y}\right)^2 - \frac{1}{(\rho C)_f}\frac{\partial q_r}{\partial y} - \frac{k_0}{(\rho C)_f}\left[\frac{\partial u}{\partial x}\left(\frac{\partial u}{\partial y}\right)^2 + u\frac{\partial u}{\partial y}\frac{\partial^2 u}{\partial x\partial y} + v\frac{\partial u}{\partial y}\frac{\partial^2 u}{\partial y^2} + \left(\frac{\partial u}{\partial y}\right)^2\frac{\partial v}{\partial y}\right] + \frac{Q_0}{(\rho C)_f}(T - T_\infty) \tag{3}$$

Concentration Equation:

$$u\frac{\partial C}{\partial x} + v\frac{\partial C}{\partial y} = D_B\frac{\partial^2 C}{\partial y^2} + \frac{D_T}{T_\infty}\frac{\partial^2 T}{\partial y^2} \tag{4}$$

and the corresponding boundary conditions are

$$u = u_w(x) = ax,\ \ v = 0, -k_f\frac{\partial T}{\partial y} = h_f(T_f - T),$$
$$D_B\frac{\partial C}{\partial y} + \frac{D_T}{T_\infty}\frac{\partial T}{\partial y} = 0 \ \ at\ \ y = 0 \tag{5}$$

$$u \to 0,\ \ T \to T_\infty,\ \ C \to C_\infty, \qquad at\ \ y \to \infty \tag{6}$$

The velocities (u, v) are utilized in the directions of (x, y) while other notations are contained at the nomenclatures.

In agreement with Roseland's approximation, heat transfer via thermal radiation is designated as $q_r = \frac{-4\sigma^*}{3k^*}\frac{\partial T^4}{\partial y}$. Here, the symbol σ^* reflects the Stefan-Boltzmann constant, while k^* corresponds to the absorption coefficient.

(σ^*, k^*) signifies Stefan-Boltzmann constant and absorption coefficient respectively. Obviously, Eq. (1) becomes zero by the application of the stream function which simplifies fluid flow analysis by automatically satisfying the continuity equation and reducing the governing equations into dimensionless and solvable form [28, 31]. Thus, applying $u = \frac{\partial \psi}{\partial y}$ and $v = -\frac{\partial \psi}{\partial x}$ via the introduction of conversion variables listed below

$$\psi = x(a\nu_f)^{1/2}f(\xi),\ \ \xi = y\left(\frac{a}{\nu_f}\right)^{1/2},$$
$$\theta(\xi) = \frac{T - T_\infty}{T_f - T_\infty},\ \ \phi(\xi) = \frac{C - C_\infty}{C_w - C_\infty} \tag{7}$$

into Eqs. (2-6), for ν_f being the kinematics viscosity, produce the dimensionless equations of the form

$$\frac{d^3 f(\xi)}{d\xi^3} + f(\xi)\frac{d^2 f(\xi)}{d\xi^2} - \left(\frac{df(\xi)}{d\xi}\right)^2 + We\left[\left(\frac{d^2 f(\xi)}{d\xi^2}\right)^2 - 2\frac{df(\xi)}{d\xi}\frac{d^3 f(\xi)}{d\xi^3} + f(\xi)\frac{d^4 f(\xi)}{d\xi^4}\right] - Mn\frac{df(\xi)}{d\xi} = 0 \tag{8}$$

$$\frac{1}{Pr}\left(1 + Rd\left(1 + (\theta_w - 1)\theta(\xi)\right)^3\frac{d\theta(\xi)}{d\xi}\right)' - WeEc\left[\frac{df(\xi)}{d\xi}\left(\frac{d^2 f(\xi)}{d\xi^2}\right)^2 - f(\xi)\frac{d^2 f(\xi)}{d\xi^2}\frac{d^3 f(\xi)}{d\xi^3}\right] + Ec\left(\frac{d^2 f(\xi)}{d\xi^2}\right)^2 + f(\xi)\frac{d\theta(\xi)}{d\xi} + Nb\frac{d\theta(\xi)}{d\xi}\frac{d\phi(\xi)}{d\xi} + Nt\left(\frac{d\theta(\xi)}{d\xi}\right)^2 + Q\theta(\xi) = 0 \tag{9}$$

$$\frac{1}{Sc}\left(\frac{d^2\phi(\xi)}{d\xi^2} + \frac{Nt}{Nb}\frac{d^2\theta(\xi)}{d\xi^2}\right) + f(\xi)\frac{d\phi(\xi)}{d\xi} = 0 \tag{10}$$

under the following domains

$$f(\xi) = 0,\ \ \frac{df(\xi)}{d\xi} = 1,\ \ \frac{d\theta(\xi)}{d\xi} = -Bi\left(1 - \theta(\xi)\right),$$
$$Nb\frac{d\phi(\xi)}{d\xi} + Nt\frac{d\theta(\xi)}{d\xi} = 0;\ at\ \xi = 0 \tag{11}$$

$$\frac{df(\xi)}{d\xi} \to 0,\ \ \theta(\xi) \to 0,\ \ \phi(\xi) \to 0; \quad at\ \xi \to \infty \tag{12}$$

$$\text{Here, } Mn=\frac{\sigma B_0^2}{\rho a},\ We=\frac{k_0 a}{\mu},\ Rd=\frac{4\sigma^* T_\infty^3}{k_f k^*},$$
$$Pr=\frac{\mu C_p}{k_f}, Nt=\frac{(\rho C)_p\, D_T(T_f-T_\infty)}{T_\infty \nu_f (\rho C)_f},$$
$$Ec=\frac{U_w^2}{C_f(T_f-T_\infty)}, Nb=\frac{(\rho C)_p\, D_B(C_w-C_\infty)}{\nu_f\,(\rho C)_f},$$
$$Q=\frac{Q_0}{a(\rho C)_f}, Bi=\frac{h_f}{k_f}\sqrt{\frac{\nu_f}{a}}, Sc=\frac{\nu_f}{D_B}, \theta_w=\frac{T_f}{T_\infty}$$

The notations *Mn* connotes magnetic parameter, *We* portrays Weissenberg number, *Rd* depicts radiation parameter, *Pr* reflects Prandtl number, *Nt* stands for thermophresis parameter, *Ec* signifies Eckert number, *Nb* denotes Brownian motion, *Q* represents heat generation/absorption, *Bi* illustrates convective heat parameter, *Sc* stands for Schmidtl number, θ_w denotes temperature ratio parameter. The engineering applications of the study triggers the consideration of

$$Cf=\frac{\tau_w}{\frac{1}{2}\rho u_w^2},\ Nu=\frac{x q_w}{k_f(T_f-T_\infty)},\ Sh=\frac{x q_m}{D_B(C_w-C_\infty)} \quad (13)$$

where (τ_w, q_w, q_m) correspond to the skin friction/shear stress, surface thermal flux, and surface mass flux, respectively

$$\tau_w=\left[\mu\frac{\partial u}{\partial y}-k_0\left(u\frac{\partial^2 u}{\partial x\partial y}+v\frac{\partial^2 u}{\partial y^2}+2\frac{\partial u}{\partial x}\frac{\partial v}{\partial y}\right)\right]_{y=0},$$
$$q_w=\left[-k_f\frac{\partial T}{\partial y}\right]_{y=0}=\left[-\frac{4\sigma^*}{3k^*}\frac{\partial T^4}{\partial y}\right]_{y=0},\ q_w=\left[-D_B\frac{\partial C}{\partial y}\right]_{y=0} \quad (14)$$

Substitution of Eq. (14) in Eq. (13) with the application of Eq. (7) result in

$$Cf\ Re_x^{\frac{1}{2}}=(1-3We)f''(\xi),$$
$$NuRe_x^{-\frac{1}{2}}=-((1+Rd(1+(\theta_w-1)\theta)^3\,\theta'(\xi)), \quad (15)$$
$$ShRe_x^{-\frac{1}{2}}=\phi'(\xi)\ \ at\ \xi=0$$

for the Skin-friction, Nusselt and Sherwood numbers while $Re_x = ax^2/\nu$ stands local Reynolds number

Entropy Generation

This concern with the irreversibility that occurs due to friction and heat transport, which plays a substantial role in analyzing the performances of thermal systems in engines and heat exchangers, among others. On this note, investigating its rate in a system is of great importance to Science and Engineering related disciplines. In accordance with Eqs. (2-4), the entropy generation suitable for the foregoing model is formulated as [26, 28]

$$E_G^*=\underbrace{\frac{k_f}{T^2}\left[1+\frac{16\sigma^* T_\infty^3}{3k_f k^*}\right]\left(\frac{\partial T}{\partial y}\right)^2}_{Heat\ transfer\ irreversibility}+\underbrace{\frac{k_0}{T}\left[\frac{\partial u}{\partial x}\left(\frac{\partial u}{\partial y}\right)^2+u\frac{\partial u}{\partial y}\frac{\partial^2 u}{\partial x\partial y}+v\frac{\partial u}{\partial y}\frac{\partial^2 u}{\partial y^2}+\left(\frac{\partial u}{\partial y}\right)^2\frac{\partial v}{\partial y}\right]}_{Viscous\ dissipation\ irreversibility}$$
$$+\underbrace{\frac{RD_B}{C_\infty}\left(\frac{\partial C}{\partial y}\right)^2+\frac{RD_B}{T_\infty}\left(\frac{\partial T}{\partial y}\right)\left(\frac{\partial C}{\partial y}\right)}_{Diffusive\ irreversibility}+\underbrace{\frac{\sigma B_0^2}{\rho}u^2}_{Joule\ heating\ irreversibility} \quad (16)$$

By the introduction of transformation techniques, Eq. (16) becomes

$$E_G=\frac{E_G^*}{E_0}=Re(1+Rd(1+(\theta_w-1)\theta(\xi)))^3\left(\theta'(\xi)\right)^2\alpha_1$$
$$+\frac{Re\ \lambda\ \beta\ \phi'(\xi)}{(\theta_w-1)}\left(\theta'(\xi)+\frac{\lambda\ \phi'(\xi)}{(\theta_w-1)}\right)$$
$$+\frac{Re\ Br}{(\theta_w-1)^2}\left(\left(f''(\xi)\right)^2+Mn\left(f'(\xi)\right)^2\right) \quad (17)$$
$$+\frac{Re\ Br\ We}{(\theta_w-1)^2}\left(f(\xi)f''(\xi)f'''(\xi)-f'(\xi)\left(f''(\xi)\right)^2\right)$$

while the associated Bejan Number, which defines the reversibility ratio of thermal to the combined irreversibility in Eq. (17) is defined as

$$Be=\frac{(1+Rd(1+(\theta_w-1)\theta(\xi)))^3\left(\theta'(\xi)\right)^2\alpha_1}{(1+Rd(1+(\theta_w-1)\theta(\xi)))^3\left(\theta'(\xi)\right)^2\alpha_1+\frac{\beta\ \lambda\ \phi'(\xi)}{(\theta_w-1)}\left(\theta'(\xi)+\frac{\lambda\ \phi'(\xi)}{(\theta_w-1)}\right)}$$
$$+\frac{Re\ Br}{(\theta_w-1)^2}\left(\left(f''(\xi)\right)^2+Mn\left(f'(\xi)\right)^2\right)+\frac{Re\ Br\ We}{(\theta_w-1)^2}f(\xi)f''(\xi)f'''(\xi) \quad (18)$$
$$-\frac{Re\ Br\ We}{(\theta_w-1)^2}*f'(\xi)\left(f''(\xi)\right)^2$$

$$\text{where } E_0=\frac{k_f(\Delta T)^2}{x^2 T_\infty^2},\ Br=\frac{\mu\, u_w^2(x)}{k_f\, T_\infty},\ \alpha_1=\frac{\Delta T}{T_\infty},$$
$$\beta=\frac{C_\infty R D_B}{k_f},\ \lambda=\frac{\Delta C}{C_\infty}$$

stand for the characteristic rate of entropy generation, Brinkman number, non-dimensional temperature difference, and a constant parameter respectively.

Solution of the Problem

The transformed Eqs. (8-10) together with the boundary condition in Eqs. (11-12) are executed, using the Galerkin Weighted Residual Method (GWRM). The method offers spectral accuracy and very efficient in providing solutions to the model of nonlinear differential equations involving unbounded domain. Given reference to the method of solution with the Eqs. (11-12) the trail functions are defined as [32]

$$f(\xi)=\sum_{i=0}^{12}p_i e^{-\frac{i\xi}{4}},\ \theta(\xi)=\sum_{i=1}^{13}q_i e^{-\frac{i\xi}{4}},\ \phi(\xi)=\sum_{i=1}^{13}r_i e^{-\frac{i\xi}{4}}. \quad (19)$$

Invoking Eq. (19) in the domain (11) at $\xi = 0$ produce

$$f(\xi=0)=0 \Rightarrow \sum_{i=0}^{12} p_i = 0,\quad f'(\xi=0)=1 \Rightarrow \sum_{i=0}^{12} -\frac{ip_i}{4} = 1$$
$$\theta'(\xi=0) = -Bi\big(1-\theta(\xi=0)\big) \Rightarrow \sum_{i=1}^{13} -\frac{iq_i}{4} - \mathrm{Bi}\left(-1+\sum_{i=1}^{13} q_i\right) \quad (20)$$
$$Nb\theta'(\xi=0) + Nt\phi'(\xi=0) \Rightarrow \mathrm{Nt}\sum_{i=1}^{13} -\frac{iq_i}{4} + \mathrm{Nb}\sum_{i=1}^{13} -\frac{ir_i}{4} = 0$$

The far field conditions in Eq. (12) is executed at three hundred thousand of maxiterations via 13.2 Wolfram Mathematica whose residual functions R_f , R_θ, and R_ϕ are taken in multiplication with the $e^{\frac{i\xi}{4}}$, $i \in \mathbb{Z}$ and integrated under the associated conditions via 13.2 Wolfram Mathematica.

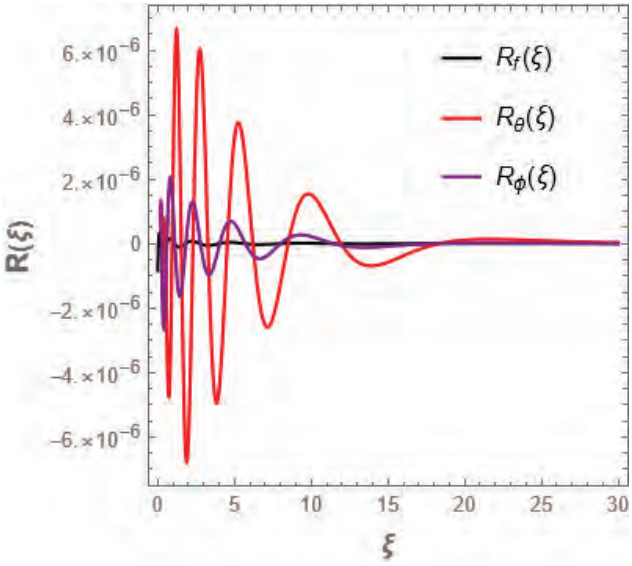


Figure 2. Residual error $R(\xi)$.

In order to ascertain the successful implementation of the computation of this model, the expressions R_f , R_θ, and R_ϕ for residual terms are plotted in Figure 2. The error/residual functions, which are minimized for all positive values, displayed a very small (negligible) residual errors, indicating that the GWRM is very efficiency in finding solutions to nonlinear differential equations within the designated domain.

RESULTS AND DISCUSSION

The model Eqs. (8-10) under the domain of Eqs. (11-12) produce the behaviours of each varying parameter for velocity, temperature and concentration profiles on Walters' B fluid by holding the following parameters Rd = 0.5, Pr = 1.2, θ_w = 0.5, Nt = 0.1, Nb = 2, Q = 0.1, Sc = 0.62, Bi = 2, Ec = 0.1 constant upon varying each parameter.

Table 1-2 demonstrated that the model perfectly agreed with the existing literature via the conditions imposed by Khan and Pop [33] and Makinde and Aziz [34]. The results are also validated, using numerical integration Mathematica's NDSolve function, computed based on the outputs of the GWRM and considered the average deviation between the functions over a representative interval, in the case, L = 10. The average deviations for the velocity distribution, thermal and concentration fields are defined as follows:

$$\Delta f'(\xi) = \frac{1}{L}\int_0^L \left|\left(f'(\xi)\right)_1 - \left(f'(\xi)\right)_2\right| d\xi \quad (21)$$

$$\Delta\theta(\xi) = -\frac{1}{L}\int_0^L \left|\left(\theta(\xi)\right)_1 - \left(\theta(\xi)\right)_2\right| d\xi \quad (22)$$

Table 1. Assessing the validity of the Nusselt and Sherwood numbers at Pr = 10, Sc = 10, Rd = 0, $We = \theta_w = Q = Ec = Mn$ = 0

Khan and Pop [33]						**Present Result**					
(a)											
***Nb* = 0.1**		***Nb* = 0.2**		***Nb* = 0.3**		***Nb* = 0.1**		***Nb* = 0.2**		***Nb* = 0.3**	
Nt	***-θ′(0)***	***Nt***	***-θ′(0)***	***Nt***	***-θ′(0)***	***Nt***	***-θ′(0)***	***Nt***	***-θ′(0)***	***Nt***	***-θ′(0)***
0.1	0.9524	0.1	0.5056	0.1	0.2522	0.1	0.95242	0.1	0.50565	0.1	0.25224
0.2	0.6932	0.2	0.3654	0.2	0.1816	0.2	0.69320	0.2	0.36542	0.2	0.18161
0.3	0.5201	0.3	0.2731	0.3	0.1355	0.3	0.52013	0.3	0.27314	0.3	0.13554
(b)											
***Nb* = 0.1**		***Nb* = 0.2**		***Nb* = 0.3**		***Nb* = 0.1**		***Nb* = 0.2**		***Nb* = 0.3**	
Nt	***-θ′(0)***	***Nt***	***-θ′(0)***	***Nt***	***-θ′(0)***	***Nt***	***-θ′(0)***	***Nt***	***-θ′(0)***	***Nt***	***-θ′(0)***
0.1	2.1294	0.1	2.3819	0.1	2.4100	0.1	2.12941	0.1	2.38192	0.1	2.41001
0.2	2.2740	0.2	2.5152	0.2	2.5150	0.2	2.27404	0.2	2.51520	0.2	2.51503
0.3	2.5286	0.3	2.6555	0.3	2.6088	0.3	2.52861	0.3	2.65551	0.3	2.60881

Table 2. Assessing the validity of the Nusselt and Sherwood numbers at $Nt = Nb = 0.5$, $Rd = We = \theta_w = Q = Ec = Mn = 0$

			Makinde and Aziz [34]		Present findings	
Pr	***Bi***	**Sc**	$-\theta'(0)$	$-\phi'(0)$	$-\theta'(0)$	$-\phi'(0)$
1	0.1	5	0.0789	1.5477	0.0789	1.5477
2			0.0806	1.5554	0.0806	1.5554
5			0.0735	1.5983	0.0735	1.5983
	1.0		0.1476	1.6914	0.1476	1.6914
	10.0		0.1550	1.7122	0.1550	1.7122
	100		0.1557	1.7144	0.1557	1.7144
		10	0.0647	2.3920	0.0647	2.3920
		15	0.0600	2.9899	0.0600	2.9899
		20	0.0570	3.4881	0.0570	3.4881

$$\Delta\phi(\xi) = -\frac{1}{L}\int_0^L \left|\left(\phi(\xi)\right)_1 - \left(\phi(\xi)\right)_2\right| d\xi \tag{23}$$

In Table 3, drag intensity is pronounced on the fluid by the plate, owing to the negative values that impede the flow. The Prandtl (*Pr*) effect strengthens the Nusselt number as indicated in Table 4, thereby energies the rate of heat transfer for engineering applications. Contrastingly, the Sherwood number slightly decreases (Table 5) in the presence of passive control nanoparticles which slowly declines the surface mass transport in application. In Table 3-5, the average deviation for velocity, temperature and concentration fields as mentioned earlier in accordance with the Eqs. (21-23) portrayed excellent agreement between GWRM and NDSolve, as the highest difference is minimal with 10^{-5}. In addition, the validation also justified excellent agreement with a very minimal error with Spectral Collocation Method (SCM) as indicated in Table 3-5. Thus, this study is unique as the highest errors between the methods are very small.

Table 3. Assessment of Skin Friction and validation of the obtained results

		GWRM Results	**SCM Results**	**Average Deviation between GWRM and NDSolver at L = 10**	**GWRM - SCM**
Mn	***We***	$Cf\ Re_x^{\frac{1}{2}}$	$Cf\ Re_x^{\frac{1}{2}}$	$\Delta f'(\xi)$	
0.1	0.1	-0.7738791	-0.7738791	4.334×10^{-5}	-
0.3		-0.8412952	-0.8412952	9.447×10^{-5}	-
0.5		-0.9036961	-0.9036961	2.112×10^{-5}	-
	0.2	-0.4690415	-0.4690415	7.627×10^{-5}	-
	0.3	-0.1253566	-0.1253566	1.612×10^{-5}	-

Table 4. Assessment of Nusselt number and validation of the obtained results

	GWRM Results	**SCM Results**	**Average Deviation between GWRM and NDSolver at L = 10**	**GWRM - SCM**
Pr	$Nu\ Re_x^{-\frac{1}{2}}$	$Nu\ Re_x^{-\frac{1}{2}}$	$\Delta\theta(\xi)$	
1.2	0.370856	0.370870	1.344×10^{-5}	-1.4×10^{-5}
1.5	0.435392	0.435404	1.18×10^{-5}	-1.2×10^{-5}
2.0	0.518989	0.519012	1.019×10^{-5}	-2.3×10^{-5}
3.0	0.638235	0.638233	9.529×10^{-6}	2×10^{-6}

Table 5. Assessment of Sherwood number and validation of the obtained results

	GWRM Results	SCM Results	Average Deviation between GWRM and NDSolver at L=10	GWRM - SCM
Sc	$Sh\,Re_x^{\frac{1}{2}}$	$Sh\,Re_x^{\frac{1}{2}}$	$\Delta\phi(\xi)$	
0.24	0.0168880	0.0169624	9.845×10^{-6}	-7.44×10^{-5}
0.62	0.0168764	0.0168616	4.657×10^{-5}	-1.58×10^{-5}
0.78	0.0168294	0.0168334	3.478×10^{-5})	-4×10^{-6}
2.62	0.0167308	0.0166815	2.345×10^{-5}	4.93×10^{-5}

Figure 3 produces the physical interpretation of the Weissenberg number (We) on $f'(\xi)$ and $\theta(\xi)$. Various values of $We \in [0.1,0.2,0.3,0.4]$ invoke the dominance of the viscoelasticity by means of stresses intensities which reduces the movement of the fluid and weakens the momentum layer thickness. In contrast, the tensile stress serves as a heat booster in the thermal field due to the heat generated internally across the boundary layer, thereby solidifying the thermal layer thickness [28]. Thus, We is used to analyze non-Newtonian fluid flow behaviour, crucial in polymer processing and lubrication in the engineering field.

Figure 4 presents the Magnetic effect (Mn)on $f'(\xi)$ and $\theta(\xi)$ where the Lorentz force is more pronounced as Mn varied. The force acts against the motion of the Walters' B liquid and decays the thickness of the corresponding momentum layer. In addition, the presence of (Mn) boosts the dominance of heat distribution by means of frictional heating whose aftermath strengthens the temperature field $\theta(\xi)$ and the thickness of the corresponding layer. This outcome agreed with Shit et al. [19] and is crucial for energy efficiency in conductive fluids, which are essential for electromagnetic applications. At various valuesof $Rd \in [0.1, 0.4, 0.8, 1.2]$, the temperature field $\theta(\xi)$ is discussed in Figure 5. The interactive contribution of (Rd) energies radiative heat flux on conduction heat transport, which adds thermal energy to the polymeric liquid that consequently augments the temperature field and the associated thermal layer thickness. On this note, Rd contributes to heat transfer efficiency, influencing thermal management in engineering systems. On a similar note, various values of temperature ratio magnified the temperature field $\theta(\xi)$ (Fig. 5). This outcome agreed with the expectation since $\theta_w > 1$. Thus, the thermal boundary layer thickness is boosted. This result agreed with Saranya et al. [35].

Figure 6. is plotted to analyse the Prandtl number (Pr) on $\theta(\xi)$. Taking into consideration the non-Newtonian liquid, with the low thermal diffusivity, strengthening values of (Pr) declines the thermal conductivity which minimizes the temperature gradient, make low the heat field and its layer depth [36]. In applications, non-Newtonian liquid diffuses more rapidly on the surface with smaller values of (Pr).

Figure 7 reports the outcome of the Eckert number (Ec) on Temperature field $\theta(\xi)$. The presence of (Ec) at $0.1 \le Ec \le 1.2$ energies irreversible process of the dissipation of kinetic energy to internal energy. This process infuses

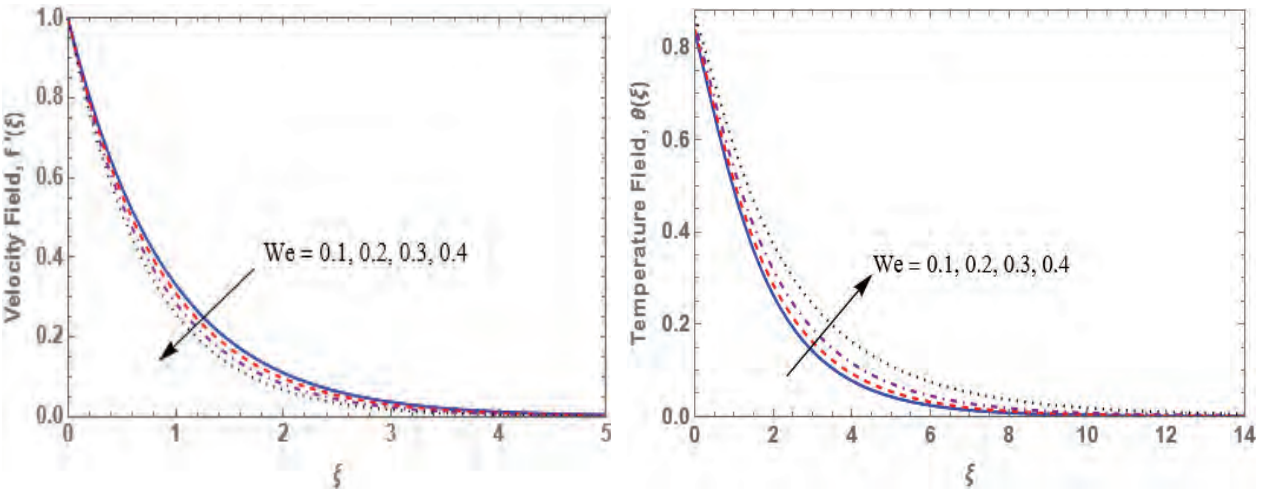


Figure 3. Reaction of We on velocity field $f'(\xi)$ and temperature field $\theta(\xi)$.

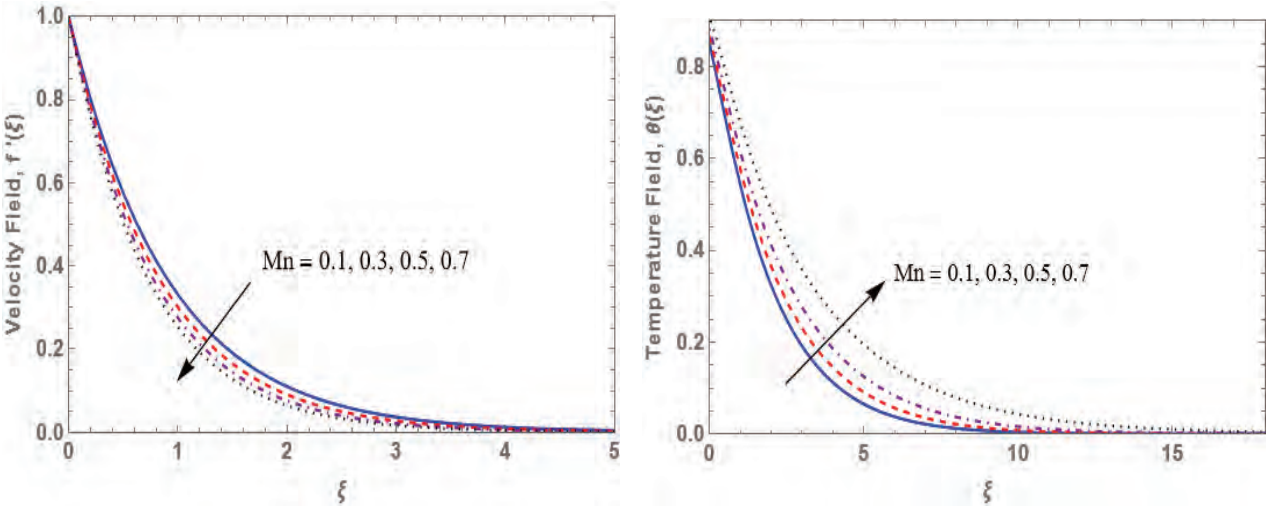


Figure 4. Reaction of *Mn* on velocity and temperature fields.

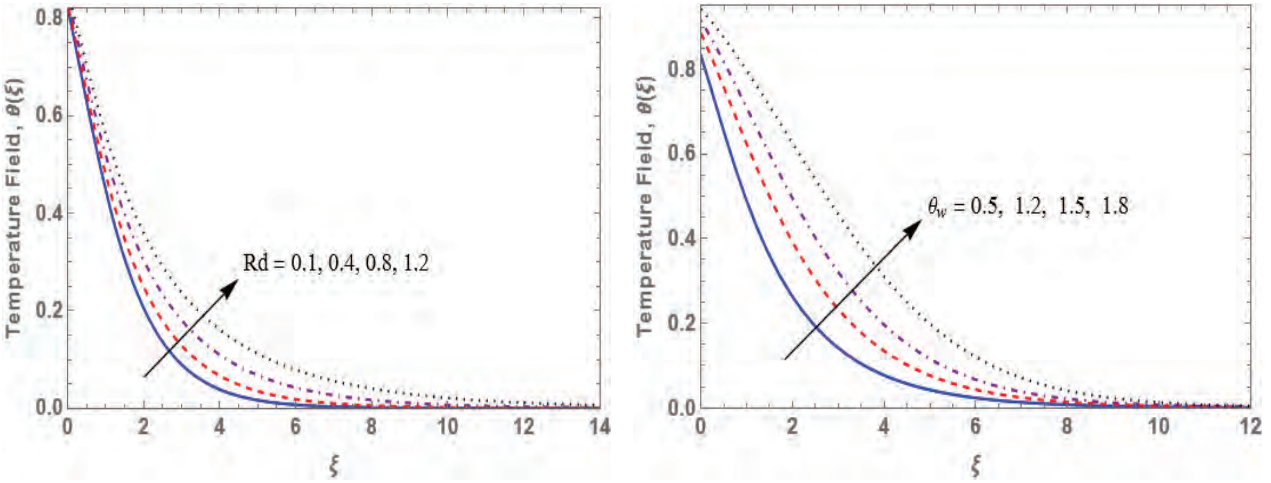


Figure 5. Reaction of *Rd* and θ_w on temperature field.

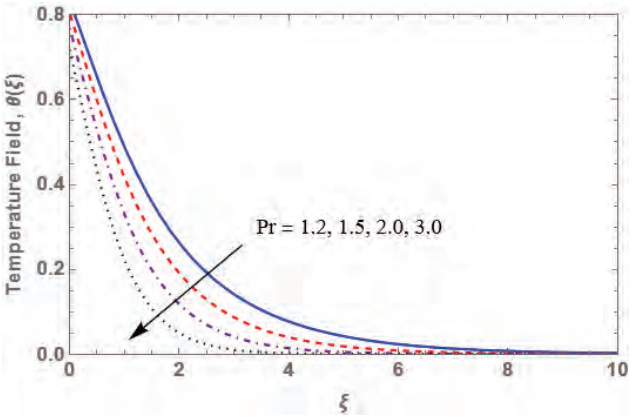


Figure 6. Reaction of *Pr* on temperature field $\theta(\xi)$.

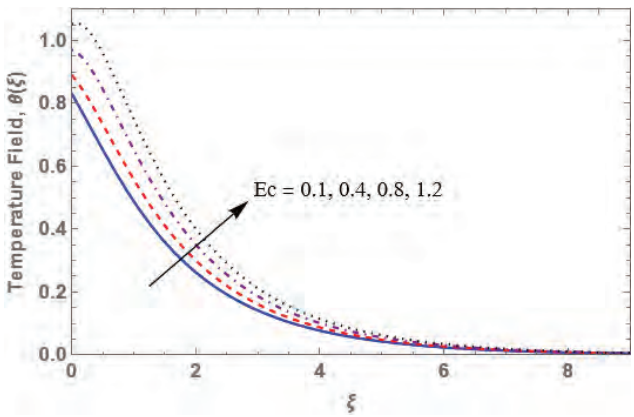


Figure 7. Reaction of *Ec* on temperature field $\theta(\xi)$.

more heat into the thermal gradient and strengthens the associated thermal boundary layer thickness. Thus, this phenomenon agreed with the findings of Megahed and Reddy [37]. It is interesting to note that *Ec* quantifies viscous dissipation in high-speed flows, crucial for heat transmission in aerospace and combustion. The significance of heat generation/absorption (Q) is portrayed in Figure 8 for Temperature field $\theta(\xi)$ at $Q \in [0.06, 0.10, 0.13, 0.16]$. The generation/absorption, in the presence of non-linear radiative heat transfer, energies spontaneous movement of particles within the fluid, which strengthens the temperature distribution and consequently solidifies the thermal boundary thickness.

Figure 9 reflets the behaviours of convective heat parameter (Bi) on $\theta(\xi)$. As Bi varied at $0.1 \leq Bi \leq 0.4$, temperature distributing impact is magnified across the boundary layer due to the strong convective heating by virtue of $Bi > 0$. This process improves the temperature boundary layer depth and solidifies heat-transfer effects in the free stream.

In Figure 10, the enhancing values of Brownian motion (Nb) intensifies diffusion, causing particles to spread more rapidly whose aftermath reduces the concentration field $\phi(\xi)$ and its associated boundary layer thickness. However, the inverse behaviours is observed with the thermophoresis parameter (Nt) on concentration field $\phi(\xi)$ (Fig. 10). The physics behind this behaviour is that thermophoretic force instigates rapid motion away from a stretchable sheet. This rapid motion conveys along with it, a thermophoretic force that consequently improves the associated concentration layer thickness. These outcomes aligned with the findings in Saini et al. [29] and Makinde *et al.* [38]. It should be noted that *Nb* enhances mixing and diffusion of nanoparticles, while *Nt* drives particles from hot to cold regions, crucial for controlling concentration in cooling.

The concentration distribution $\phi(\xi)$ is influenced by the Schmidt number (Sc) as presented in Figure 11. Bearing in mind lower molecular diffusivity, improving values of (Sc) weakens the nanomaterial concentration. The aftermath

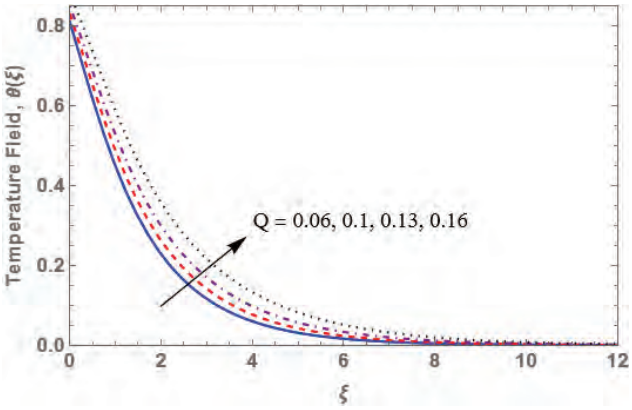


Figure 8. Reaction of Q on temperature field $\theta(\xi)$.

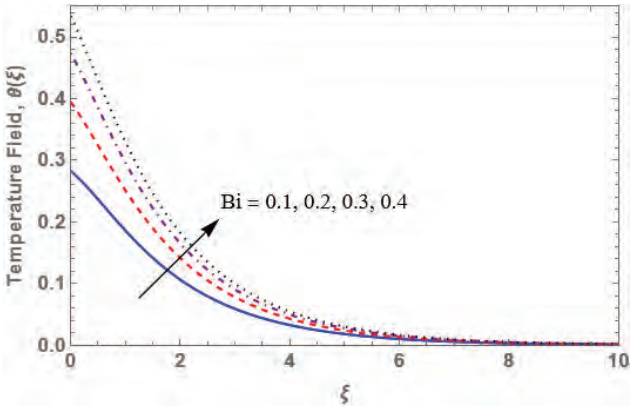


Figure 9. Reaction of Bi on temperature field $\theta(\xi)$.

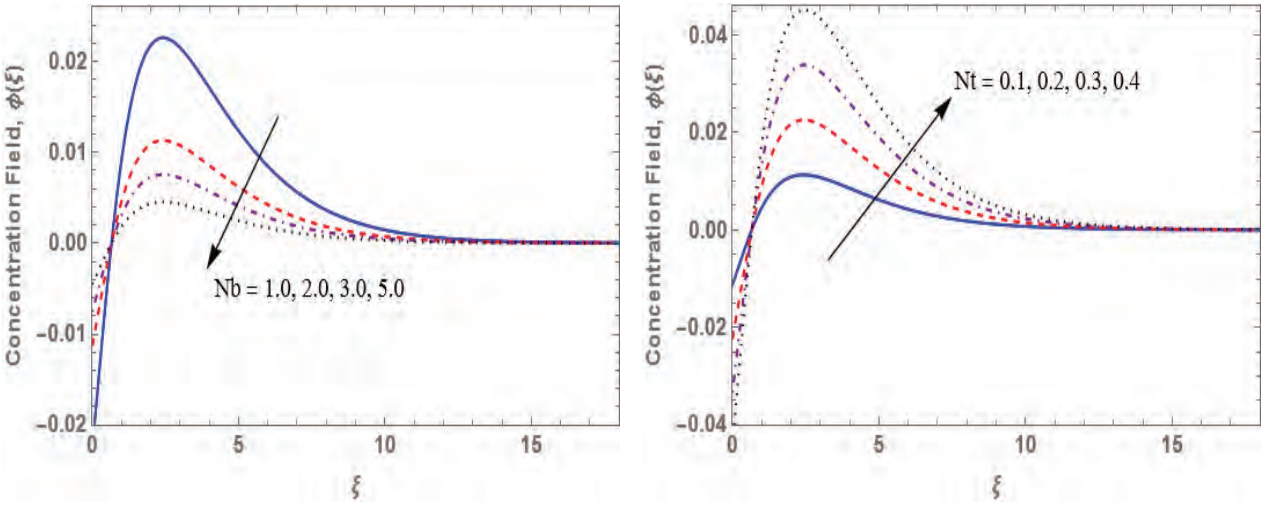


Figure 10. Reaction of Nb and Nt on concentration field $\phi(\xi)$.

reaction of this behaviour makes less the concentration boundary layer thickness. It is worth mentioning that *Sc* quantifies mass diffusion relative to momentum diffusion, crucial in chemical engineering, fluid mechanics, and heat transfer applications.

Figure 12-14 discusses the skin-friction, Nusselt and Sherwood numbers which are very useful in engineering applications. In Figure 12, both Magnetic (*Mn*) and Weissenberg (*We*) decline the skin friction due to the surface drag force applied into the liquid by the sheet. Figure 13 is plotted to report the effect of the Radiation parameter (*Rd*) against the thermophoresis parameter (*Nt*) on the Nusselt number. The two parameters exhibit cooling contributions for the Nusselt number, which reduces the rate of heat exchange in practical systems. The Schmidt number (*Sc*) effects on the Sherwood number is plotted against the thermophoresis parameter (*Nt*) in Figure 14. As indicated in the figure, variation in *Sc* reduces the Sherwood number strength whose aftermath made low the rate of mass transfer. The opposite phenomenon is observed with ($Nt > 0$) which consequently improves the rate of mass transfer in application.

Figure 15-18 illustrate the effect of various parameters on entropy generation and Bejan number (*Be*). In Figure 15, the significance of *Mn* on Entropy Generation and Bejan number is plotted. The interactive impact of the Magnetic parameter (*Mn*) intensifies the temperature distribution due to the frictional heating irreversibility in the hydromagnetic fluid that consequently boosts the entropy production (N_G). Thus, the Bejan number (*Be*) declines as viscous effects dominate, thereby reducing the relative contribution of thermal irreversibility. On the other hand, enhancing values of *We* as reported for Entropy Generation and Bejan number in Figure 16, strengthens the elasticity of the fluid, thereby reducing viscous dissipation whose aftermath lowers the entropy production (N_G). Under the same variation of *We* (i.e $0.1 \leq We \leq 0.4$), the Bejan number (*Be*) rises as shown in Figure 16. This is because thermal irreversibility becomes more significant relative to total entropy generation, indicating a shift toward entropy being influenced primarily by heat transfer mechanisms.

In Figure 17, the influence of thermal radiation (*Rd*) is analyzed on Entropy Generation and Bejan number. Increasing values of (*Rd*) intensifies the internal energy of the system thereby resulting in a greater thermal

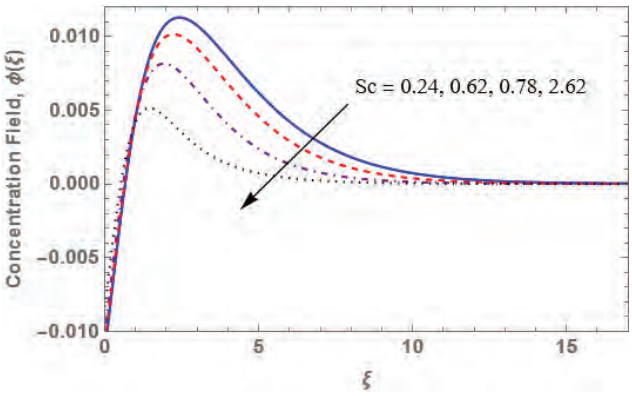


Figure 11. Reaction of *Sc* on concentration field $\phi(\xi)$.

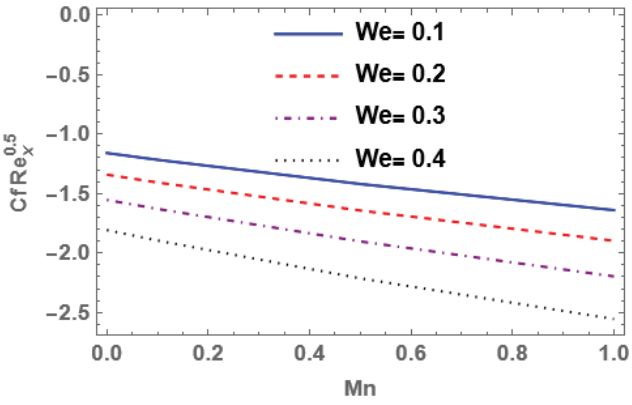


Figure 12. Skin-friction of *Mn* against *We*.

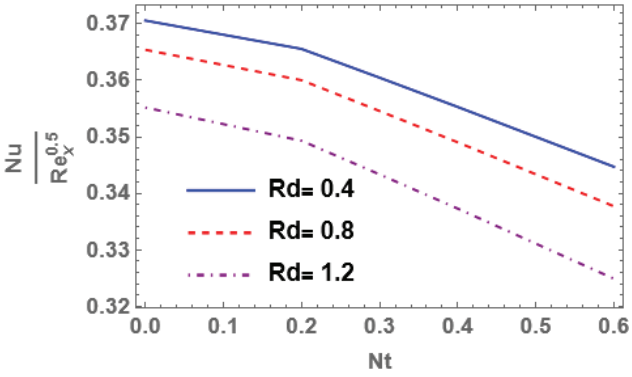


Figure 13. Nusselt number of *Nt* against *Rd*.

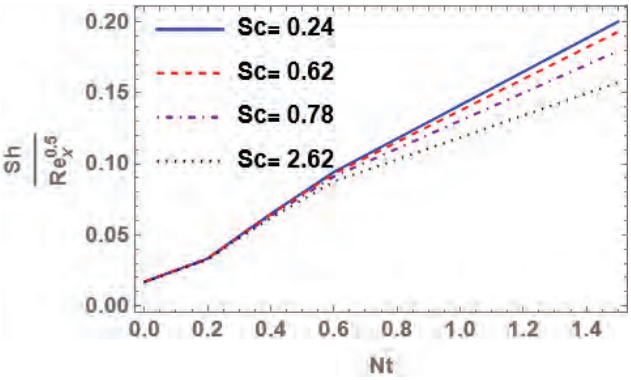


Figure 14. Sherwood number of *Nt* against *Sc*.

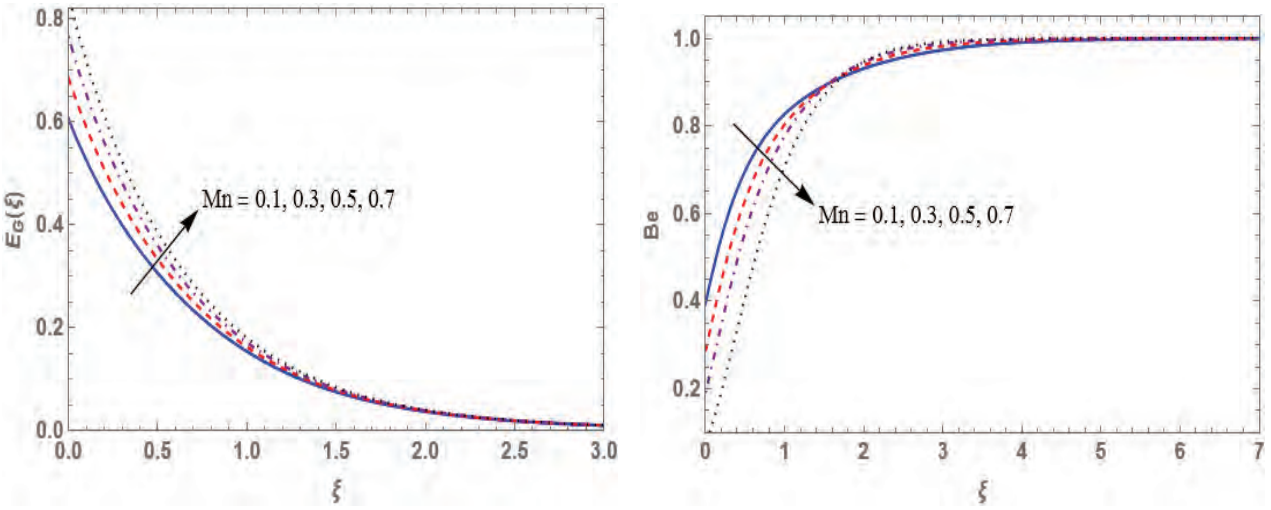


Figure 15. Reaction of *Mn* on entropy generation and Bejan number.

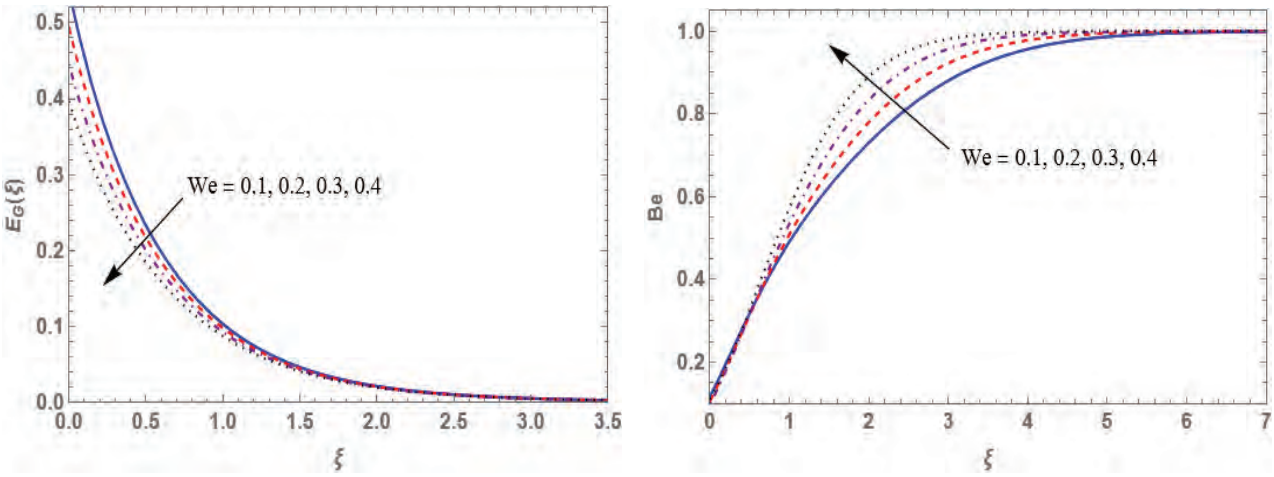


Figure 16. Reaction of *We* on entropy generation and Bejan number.

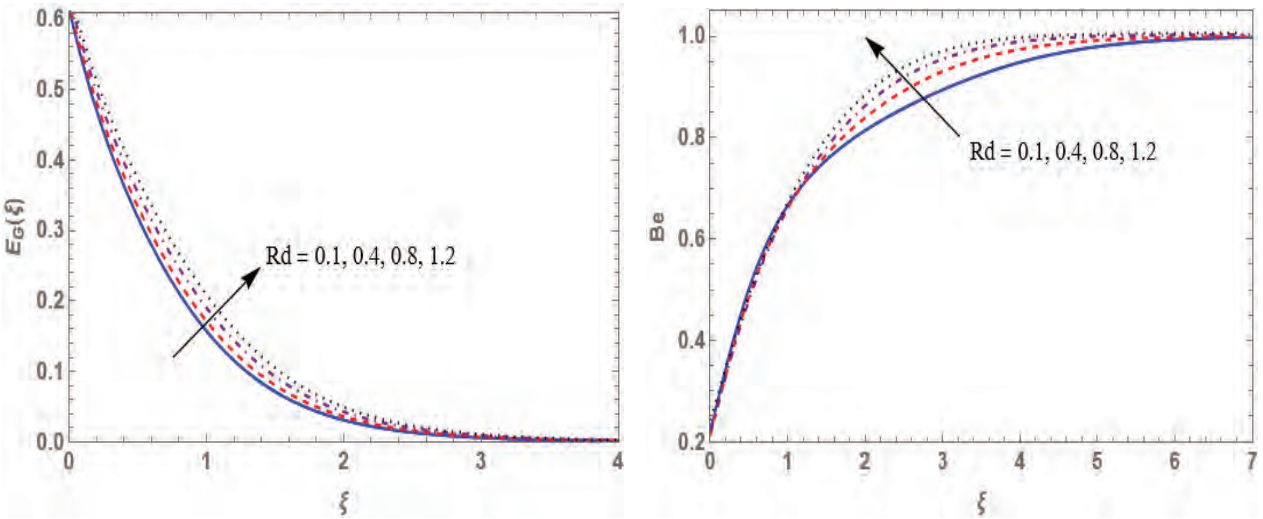


Figure 17. Reaction of *Rd* on entropy generation and Bejan number.

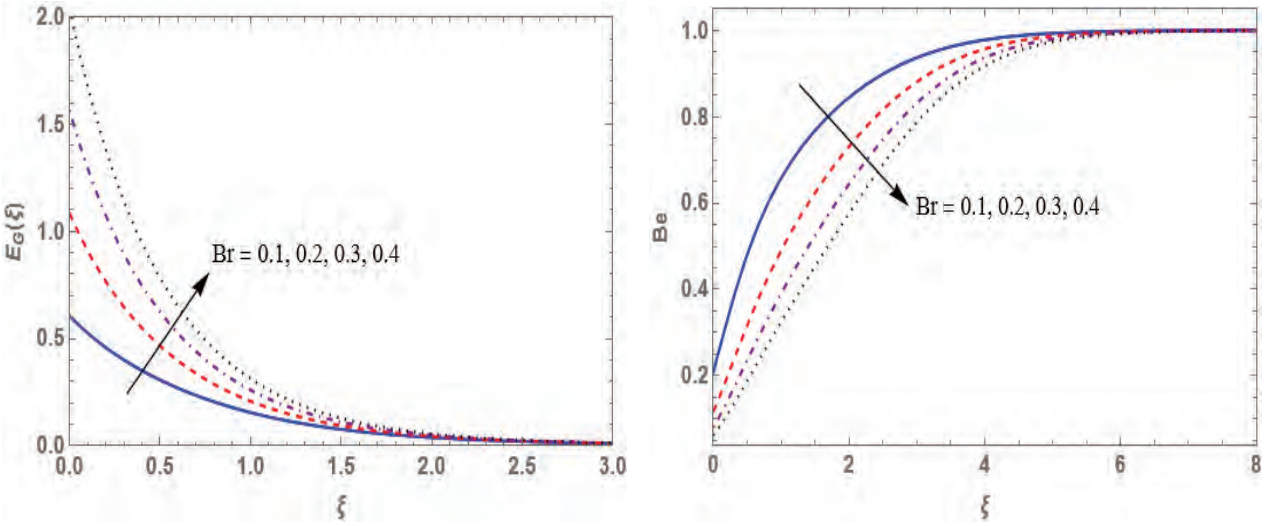


Figure 18. Reaction of *Br* on entropy generation and Bejan number.

irreversibility whose aftermath improves the entropy production (N_G). In addition, since thermal effects outweigh viscous effects under strong radiation, the Bejan number (*Be*) also improves, indicating that thermal effects govern the overall irreversibility in radiation-dominated conditions. These outcomes agreed with the findings of Hayat et al. [39] and Alsaadi et al. [40]. The mechanics of Brinkman number (*Br*) on Entropy Generation and Bejan number is represented in Figure 18. It is noteworthy that Entropy Generation improves over the enhancement in the values of Brinkman number (*Br*). This outcome indicates that viscous heating dominates by means of heat transmission through the molecular conduction around the vicinity of the sheet since *Br* quantifies viscous dissipation with respect to fluid friction. Brinkman number is very useful in applications in polymer processing. It helps to determine the significance of viscous heating relative to thermal conduction, influencing the temperature distribution and flow behaviour of the polymer during processing. This phenomenon makes viscous effects the main source of irreversibility, reducing the Bejan number (*Be*) since it measures the ratio of heat transfer irreversibility to total entropy generation. These outcomes agreed with Qayyum et al. [28] and Jabeen et al. [24].

CONCLUSION

In this study, an entropy-generation investigation is conducted on the influence of a viscous and nonlinearly radiating hydromagnetic Walters' B nanofluid with heat generation/absorption and convective boundary condition. The model's underlying equations that determine the behaviour of the embedded parameter are solved by the Galerkin Weighted Residual Method (GWRM), and the errors in computation are taken into account by validating the results with two other methods, as indicated in the manuscript. The article presents the following key findings, among others.

1. The findings demonstrate excellent agreement with reference results available in the literature, as well as with the Spectral Collocation Method and NDSolve. The flow of the non-Newtonian liquid is boosted in the presence of strengthening radiative flux. This enhances heat transport by adding thermal energy to support the polymeric flow.
2. In the neighbourhood of the sheet, the viscous heating dominates by means of molecular conduction with the interaction of the Brinkman number. In applications involving polymer, the Brinkman number is quite helpful.
3. Skin friction is a decreasing function of the Magnetic parameter and Weissenberg number influence due to the surface drag force applied into the liquid by the viscous stresses. Friction drag is essential in Aerodynamics.
4. The presence of Eckert number triggers the irreversible conversion of kinetic energy to internal energy, which intensifies the heat distribution across the system. This is crucial in mechanical and chemical engineering fields to analyze viscous heating relative to heat conduction in high viscosity flows, thereby aiding thermal management and reactor design.
5. The interactive impact of heat generation and convective heat parameters causes greater heat across the thermal field, which boots the thermal effect at quiescent fluid and facilitates the drying of the component in the engineering field.

Limitation of the Study/Suggestion for Further Studies

In this study, computational analysis has been examined on two-dimensional boundary layer flow of Walters' B nanofluid with constant thermophysical properties.

Nonetheless, an attempt could be made to look into the unsteady-case model. Also, future investigation may be conducted into the variable thermophysical properties of this model, such as variable dynamic viscosity and variable thermal conductivity.

NOMENCLATURES

u	*velocity components along x* [s.m^{-}]
v	*velocity components along y* [s.m^{-}]
T	*Temperature of the fluid* [K]
ν_f	*kinematic viscosity* [$m^2.s^{-}$]
$(\rho C)_f$	*Heat capacity of the fluid* [$J.kg^{'}$]
τ	$(\rho C)_p/(\rho C)_f$
ρ	*density* [kgm^{-3}]
q_r	*radiation heat flux* [$W.m^{-2}$]
$(\rho C)_p$	*Heat capacity of the nanoparticles* [$J.kg^{'}$]
σ	*electrical conductivity* [$s.m^{-}$]
D_T	*Thermophoretic diffusion coefficient*
$k^{\star}$	*mean of the absorption coefficient* [m^{-}]
B_0	magnetic field [Am^{-}]
k_0	*elastic parameter*
$\sigma^{\star}$	*Stefan-Boltzmann constant* [$W.m^{-2}.K^{-4}$]
Q_0	*Heat generation/absorption coefficient*
h_f	*heat transfer coefficient* [$W.m^{-2}.K$]
k	*thermal conductivity* [$W.m^{-}.K^{-}$]
D_B	*Brownian diffusion coefficient* [$m^2.s^{-}$]
μ	*dynamic viscosity* [$kgm^{-}s^{-}$]

ACKNOWLEDGEMENT

The researchers express their sincere gratitude for the financial support granted by the Nigerian government through a TETFund grant, which enabled this study. In addition, the team extends special thanks to Professor Lucas Ruiz dos Santos from the Institute of Mathematics and Computing at the Universidade Federal de Itajubá, Brazil, for his crucial guidance and technical contributions throughout this project.

AUTHORSHIP CONTRIBUTIONS

Authors equally contributed to this work.

DATA AVAILABILITY STATEMENT

The authors confirm that the data that supports the findings of this study are available within the article. Raw data that support the finding of this study are available from the corresponding author, upon reasonable request.

CONFLICT OF INTEREST

The authors declared no potential conflicts of interest with respect to the research, authorship, and/or publication of this article.

ETHICS

There are no ethical issues with the publication of this manuscript.

STATEMENT ON THE USE OF ARTIFICIAL INTELLIGENCE

Artificial intelligence was not used in the preparation of the article.

REFERENCES

[1] Jonnadula M, Polarapu P, Reddy G. Influence of thermal radiation and chemical reaction on MHD flow, heat and mass transfer over a stretching surface. Procedia Eng 2015;127:1315–1322. [CrossRef]

[2] Javed M, Alderremy AA, Farooq M, Anjum A, Ahmad S, Malik MY. Analysis of activation energy and melting heat transfer in MHD flow with chemical reaction. Eur Phys J Plus 2019;134:256. [CrossRef]

[3] Chatterjee D, Gupta SK. MHD flow and heat transfer behind a square cylinder in a duct under strong axial magnetic field. Int J Heat Mass Transf 2015;88:1–13. [CrossRef]

[4] Swain BK, Parida BC, Kar S, Senapati N. Viscous dissipation and joule heating effect on MHD flow and heat transfer past a stretching sheet embedded in a porous medium. Heliyon 2020;6. [CrossRef]

[5] Akınbo BJ, Olajuwon BI. Heat and mass transfer in magnetohydrodynamics (MHD) flow over a moving vertical plate with convective boundary condition in the presence of thermal radiation. Sigma J Eng Nat Sci 2019;37:1031–1053.

[6] Akinbo BJ, Olajuwon BI. Significance of Cattaneo-Christov heat flux model and heat generation/absorption with chemical reaction in Walters' B fluid via a porous medium in the presence of Newtonian heating. Int J Model Simul 2023;45:137–146. [CrossRef]

[7] Akinbo BJ, Olajuwon BI. Interaction of radiation and chemical reaction on Walters' B fluid over a medium porosity of a vertical stretching surface. Heat Transfer 2023;52:1689–1709. [CrossRef]

[8] Gholinia M, Gholinia S, Javadi H, Ganji DD. Investigation of micropolar fluid flow and heat transfer in a two-dimensional permeable channel by analytical and numerical methods. Sigma J Eng Nat Sci 2019;37:393–413.

[9] Mohyud-Din ST, Khan U, Ahmed N, Rashidi MM. A study of heat and mass transfer on magnetohydrodynamic (MHD) flow of nanoparticles. Propuls Power Res 2018;7:72–77. [CrossRef]

[10] Özen MY, Derun EM. Effects of SiO2 and Al2O3 nanoparticles on the properties of borogypsum containing mortar. Sigma J Eng Nat Sci 2024;42:1923–1932. [CrossRef]

[11] Gupta SK. A short and updated review of nanofluids utilization in solar parabolic trough collector. Mater Today Proc 2023. [CrossRef]
[12] Gupta SK, Saxena A. A progressive review of hybrid nanofluid utilization in solar parabolic trough collector. Mater Today Proc 2023. [CrossRef]
[13] Gupta SK, Sharma A. A brief review of nanofluids utilization in heat transfer devices for energy saving. Mater Today Proc 2023. [CrossRef]
[14] Gupta SK, Dixit S. Progress and application of nanofluids in solar collectors: an overview of recent advances. Mater Today Proc 2021;44:250–259. [CrossRef]
[15] Gupta SK, Gupta S, Singh R. A comprehensive review of energy saving in shell & tube heat exchanger by utilization of nanofluids. Mater Today Proc 2022;50:1818–1826. [CrossRef]
[16] Chen CK, Chen BS, Liu CC. Entropy generation in mixed convection magnetohydrodynamic nanofluid flow in vertical channel. Int J Heat Mass Transf 2015;91:1026–1033. [CrossRef]
[17] Ellahi R, Sait SM, Shehzad N, Ayaz Z. A hybrid investigation on numerical and analytical solutions of electro-magnetohydrodynamics flow of nanofluid through porous media with entropy generation. Int J Numer Methods Heat Fluid Flow 2020;30:834–854. [CrossRef]
[18] Sharma T, Sharma P, Kumar N. Analysis of entropy generation due to MHD natural convective flow in an inclined channel in the presence of magnetic field and heat source effects. Bionano Sci 2019;9:660–671. [CrossRef]
[19] Shit GC, Haldar R, Mandal S. Entropy generation on MHD flow and convective heat transfer in a porous medium of exponentially stretching surface saturated by nanofluids. Adv Powder Technol 2017;28:1519–1530. [CrossRef]
[20] Torabi M, Zhang K. Temperature distribution, local and total entropy generation analyses in MHD porous channels with thick walls. Energy 2015;87:540–554. [CrossRef]
[21] Ibáñez G, López A, Pantoja J, Moreira J. Entropy generation analysis of a nanofluid flow in MHD porous microchannel with hydrodynamic slip and thermal radiation. Int J Heat Mass Transf 2016;100:89–97. [CrossRef]
[22] Bhatti M, Abbas T, Rashidi M, Ali M, Yang Z. Entropy generation on MHD Eyring-Powell nanofluid through a permeable stretching surface. Entropy 2016;18:224. [CrossRef]
[23] Opanuga AA, Agboola OO, Gbadeyan JA, Okagbue HI. Entropy generation analysis of Hall current effect on MHD micropolar fluid flow with rotation effect. SN Appl Sci 2020;2:1–11. [CrossRef]
[24] Jabeen S, Hayat T, Alsaedi A. Entropy generation optimization and activation energy in flow of Walters-B nanomaterial. Sci Iran 2021;28:1917–1925. [CrossRef]
[25] Selimefendigil F, Öztop HF. MHD mixed convection and entropy generation of power law fluids in a cavity with a partial heater under the effect of a rotating cylinder. Int J Heat Mass Transf 2016;98:40–51. [CrossRef]
[26] Sithole H, Mondal H, Sibanda P. Entropy generation in a second grade magnetohydrodynamic nanofluid flow over a convectively heated stretching sheet with nonlinear thermal radiation and viscous dissipation. Results Phys 2018;9:1077–1085. [CrossRef]
[27] Sivaraj C, Sheremet MA. MHD natural convection and entropy generation of ferrofluids in a cavity with a non-uniformly heated horizontal plate. Int J Mech Sci 2018;149:326–337. [CrossRef]
[28] Qayyum S, Hayat T, Jabeen S, Alsaedi A. Entropy generation in nanofluid flow of Walters-B fluid with homogeneous-heterogeneous reactions. Math Methods Appl Sci 2020;43:5657–5672. [CrossRef]
[29] Saini G, Hanumagowda BN, Raju SSK, Varma SVK. Nonlinear heat radiation and mass transfer characteristics on MHD Walters' B fluid flow through a porous medium over a stretching sheet. Partial Differ Equ Appl Math 2024;10:100699. [CrossRef]
[30] Hayat T, Khan SA, Alsaedi A. Simulation and modeling of entropy optimized MHD flow of second grade fluid with dissipation effect. J Mater Res Technol 2020;9:11993–12006. [CrossRef]
[31] Yusuf TA, Mabood F, Prasannakumara BC, Sarris IE. Magneto-bioconvection flow of Williamson nanofluid over an inclined plate with gyrotactic microorganisms and entropy generation. Fluids 2021;6:109. [CrossRef]
[32] Gbadeyan JA, Titiloye EO, Adeosun AT. Effect of variable thermal conductivity and viscosity on Casson nanofluid flow with convective heating and velocity slip. Heliyon 2020;6. [CrossRef]
[33] Khan WA, Pop I. Boundary-layer flow of a nanofluid past a stretching sheet. Int J Heat Mass Transf 2010;53:2477–2483. [CrossRef]
[34] Makinde OD, Aziz A. Boundary layer flow of a nanofluid past a stretching sheet with a convective boundary condition. Int J Therm Sci 2011;50:1326–1332. [CrossRef]
[35] Saranya S, Ragupathi P, Ganga B, Sharma RP, Hakeem AA. Non-linear radiation effects on magnetic/non-magnetic nanoparticles with different base fluids over a flat plate. Adv Powder Technol 2018;29:1977–1990. [CrossRef]
[36] Shahid A, Bhatti MM, Bég OA, Kadir A. Numerical study of radiative Maxwell viscoelastic magnetized flow from a stretching permeable sheet with the Cattaneo-Christov heat flux model. Neural Comput Appl 2018;30:3467–3478. [CrossRef]
[37] Megahed AM, Reddy MG. Numerical treatment for MHD viscoelastic fluid flow with variable fluid properties and viscous dissipation. Indian J Phys 2021;95:673–679. [CrossRef]

[38] Makinde OD, Mabood F, Khan WA, Tshehla MS. MHD flow of a variable viscosity nanofluid over a radially stretching convective surface with radiative heat. J Mol Liq 2016;219:624–630. [CrossRef]

[39] Hayat T, Khan MI, Qayyum S, Alsaedi A, Khan MI. New thermodynamics of entropy generation minimization with nonlinear thermal radiation and nanomaterials. Phys Lett A 2018;382:749–760. [CrossRef]

[40] Alsaadi FE, Ullah I, Hayat T, Alsaadi FE. Entropy generation in nonlinear mixed convective flow of nanofluid in porous space influenced by Arrhenius activation energy and thermal radiation. J Therm Anal Calorim 2020;140:799–809. [CrossRef]

Sigma J Eng Nat Sci, Vol. 44, No. 4, pp. 2540–2550, August, 2026

Sigma Journal of Engineering and Natural Sciences
Web page info: https://sigma.yildiz.edu.tr
DOI: 10.14744/sigma.2026.2113

Research Article

Fitting continuous PDFs to *q*-discrete distributions

Ibrahim SADOK[1,2,*]

[1]*Department of Mathematics and Computer Science, Faculty of Exact Sciences, University of Bechar, Bechar, 08000, Algeria*
[2]*Laboratory of Mathematics, Djillali Liabes University of Sidi Bel-Abbès, Sidi Bel-Abbès, 22000, Algeria*

ARTICLE INFO

Article history
Received: 05 December 2024
Revised: 16 April 2025
Accepted: 14 May 2025

Keywords:
Approximation; Fitting Distribution; *q*-Discrete Distributions; Pearson System

ABSTRACT

Approximating discrete distributions with continuous probability density functions (PDFs) is a widely used statistical technique, especially valuable for analysing large datasets. This work introduces a novel extension of the classical Pearson system by adapting it to fit continuous PDFs to *q*-discrete distributions, a class of models that generalize traditional discrete distributions. While *q*-discrete distributions have attracted growing interest due to their flexibility and wide-ranging applications, the problem of approximating them using continuous distributions remains underexplored. To address this, we propose a unified framework based on the generalized Pearson differential equation to construct continuous approximations that closely match the behaviour of *q*-discrete models. This approach offers an alternative way to study and interpret *q*-discrete data through continuous representations. It therefore provides a useful contribution to the theoretical treatment of these models as well as to their potential applications.

Cite this article as: Sadok I. Fitting continuous PDFs to *q*-discrete distributions. Sigma J Eng Nat Sci 2026;44(4):2540–2550.

INTRODUCTION

The approximation of discrete distributions by continuous distributions has been a fundamental and widely utilized technique in numerous fields of study [1,2]. Approximating discrete probability models by continuous distributions is a long-established technique with applications in many areas of statistics and probability. A standard example is the use of the normal distribution as a continuous approximation to discrete models, including the binomial and Poisson distributions [3,4]. The quality of this approximation generally improves as the sample size increases, making continuous formulations convenient for analytical calculations and statistical investigation [5]. Such representations provide a practical link between discrete and continuous models and can simplify the treatment of problems encountered in both theoretical and applied work.

Pearson was among the earliest researchers to systematically examine the connection between continuous curves and discrete probability functions. His work led to the development of the Pearson system, consisting of a broad family of probability density functions, which was subsequently studied in greater detail by Elderton [6] and Pollard [7].

In his 1895 contribution, Pearson distinguished four principal distribution types, denoted Types I-IV [8], and

***Corresponding author.**
*E-mail address: ibrahim.sadok@univ-bechar.dz

This paper was recommended for publication in revised form by Editor-in-Chief Ahmet Selim Dalkilic

Published by Yıldız Technical University Press, İstanbul, Turkey
© Author. This is an open access article under the CC BY-NC license (http://creativecommons.org/licenses/by-nc/4.0/).

considered the normal distribution as an additional case, initially associated with Type V [9]. Later, Rhind [10] developed a straightforward method for visualizing the parameter space of the Pearson system, a technique that was later adopted by Pearson himself [11]. Pearson densities, $f(x)$, are defined by two parameters, commonly denoted as β_1 and β_2, and are characterized as solutions to a specific differential equation outlined by Pearson

$$\frac{f'(x)}{f(x)} = \frac{x-a}{b_0 + b_1 x + b_2 x^2},$$

where a, b_0, b_1, and b_2 are the parameters characterizing the distribution.

A key advantage of the Pearson four-parameter system is its straightforward relationship between the parameters and the central moments of the distribution (μ_1,...,μ_4), as outlined by Stuart and Ord [12].

$$a = b_1 = -\frac{\sqrt{\mu_2}\beta_1(\beta_2+3)}{10\beta_2 - 18 - 12\beta_1^2},$$
$$b_0 = -\frac{\mu_2(4\beta_2 - 3\beta_1^2)}{10\beta_2 - 18 - 12\beta_1^2},$$
$$b_2 = -\frac{2\beta_2 - 3\beta_1^2 - 6}{10\beta_2 - 18 - 12\beta_1^2},$$

where the moment ratios $\beta_1 = \mu_3^2/\mu_2^3$ and $\beta_2 = \mu_4/\mu_2^2$ represent skewness and kurtosis, respectively.

A recent development in the literature has introduced a generalization of the Pearson differential equation [13, 14], expressed as:

$$\frac{f'(x)}{f(x)} = \frac{a_0 + a_1 x + a_2 x^2 + \ldots + a_n x^n}{b_0 + b_1 x + b_2 x^2 + \ldots + b_m x^m},$$

where $n, m \geq 1$ are arbitrary integers.

The generalized Pearson differential equation establishes a common framework from which numerous continuous PDFs can be obtained. Different choices of its parameters parameters $\{a_i\}_{1\leq i\leq n}$ and $\{b_j\}_{1\leq j\leq m}$ lead to a wide variety of distributions, thereby extending the Pearson system to a broader collection of models suitable for describing data arising in different applications [15-17].

This framework is also related to numerical approximation techniques in which spline-based procedures [18,19] are used to obtain accurate representations of solutions to higher-order differential equations. In both settings, the objective is to achieve a suitable compromise between approximation accuracy and computational cost for mathematically complex models.

More recently, considerable attention has been given to constructing continuous density functions that approximate discrete probability models [20-22]. q-discrete distributions form a general class in which an additional parameter modifies the shape and characteristics of conventional discrete distributions [23,24]. Their flexibility has encouraged applications in areas such as statistical physics, economics, and information theory [25]. Nevertheless, the use of continuous PDFs to approximate these q-discrete models has received comparatively limited attention.

The q-distributions appear in various domains, including non-extensive statistical mechanics, quantum computing, and branching processes [26, 27]. The construction of smooth continuous analogues allows these models to be more easily integrated into continuous analysis tools used in such fields. This paper addresses this gap by focusing on the fitting of continuous probability density functions to various q-discrete distributions, such as the q-binomial, negative q-binomial, q-Poisson, Euler, q-logarithmic, q-hypergeometric and negative q-hypergeometric distributions. The main procedure is based on derivative relationships and differential equations, following an idea related to the generalized Pearson formulation. In this way, the proposed framework extends the Pearson approach to q-discrete distributions by representing them through continuous curves. The resulting formulation is intended to improve the flexibility of continuous statistical representations and to support the analysis of more complicated data structures.

The remainder of this paper is organized into three main parts. Section 2 reviews the basic notions associated with q-distributions and states the fundamental results required for the subsequent analysis. Section 3 develops the curve-fitting procedure for several selected q-distributions. Finally, the concluding section highlights the main results and provides an overall summary of the study.

BACKGROUND

Let x and q be real numbers, where $q \neq 1$. The q-number, denoted by $[x]_q$, is defined as:

$$[x]_q = \frac{1-q^x}{1-q}.$$

Furthermore, it is important to note that $\lim_{q\to 1}[x]_q = x$. The k-th order factorial of the q-number $[x]_q$, defined as:

$$[x]_{k,q} = [x]_q[x-1]_q \cdots [x-k+1]_q, \quad k = 1,2,\ldots,$$

is referred to as the q-factorial of x of order k. Specifically,

$$[k]_q! = [1]_q[2]_q \cdots [k]_q, \quad k = 1,2,\ldots,$$

is known as the q-factorial of k.

The q-factorial of x can also be defined for negative orders. A fundamental property of the q-factorial is given by the following relation :

$$[x]_{r+k,q} = [x]_{r,q}[x-r]_{k,q},$$

for any positive integers k and r. This property can be directly derived from the definition of the q-factorial.

The q-binomial coefficient (also known as the Gaussian polynomial) is defined as follows

$$\begin{bmatrix} x \\ k \end{bmatrix}_q = \frac{[x]_{k,q}}{[k]_q!}, \quad k = 0,1, \ldots,$$

and satisfies the property : $\lim_{q\to 1} \begin{bmatrix} x \\ k \end{bmatrix}_q = \binom{x}{k}$, $k = 0,1, \ldots,$

We now introduce some fundamental concepts from the q-theory. Jackson [25] defined the q-analogue of the exponential function, denoted by e_q^x, as follows :

$$e_q^x = \sum_{k=0}^{\infty} \frac{x^k}{[k]_q!}.$$

It is evident that $e_q^0 = 1$.

The q-analogue of identity $e^x e^{-x} = 1$ is $e_q^x E_q^{-x} = 1$, where the function E_q^x, defined by $e_{1/q}^x$, is expressed as

$$E_q^x = e_{1/q}^x = \sum_{k=0}^{\infty} q^{k(k-1)/2} \frac{x^k}{[k]_q!}.$$

The q-logarithm function, $log_q(x)$, serves as the inverse of the q-exponential function e_q^x, while the function $Log_q(x)$ is the inverse of E_q^x.

Continuous Approximations of Some Discrete q-Distributions

Continuous approximation of the q-binomial distribution

Let X_n represent the number of failures before the n-th success in a sequence of independent Bernoulli trials, where the probability of success in the i-th trial is given by:

$$\frac{pq^{i-1}}{1+pq^{i-1}}, \quad i = 1,2,\ldots, \; 0 < p < \infty, \; 0 < q < 1 \text{ or } 1 < q < \infty.$$

Definition 1. [23] *The probability function of the q-binomial distribution of the random variable X_n with parameters n, p and q is expressed as* $P(X_n = m) = \begin{bmatrix} n \\ m \end{bmatrix}_q \frac{p^m q^{m(m-1)/2}}{\prod_{i=1}^{n}(1+pq^{i-1})}$ *This probability function is referred to as the probability mass function (PMF) of the q-binomial distribution.*

The goal, as previously stated, is to approximate the binomial probability function by fitting a continuous PDF. To achieve this, we examine the proportional changes in the binomial probabilities using the formula:

$$\frac{P(m+1) - P(m)}{P(m)}.$$

This approach motivates modelling $P(m)$ with a differentiable function $f(m)$, which satisfies a differential equation designed to approximate the probabilities for continuous values of m. This method ensures a smooth and accurate approximation of the discrete binomial distribution.

The calculation of the variation ratio is carried out as follows

$$\begin{aligned} \frac{P(m+1) - P(m)}{P(m)} = &\left[\begin{bmatrix} n \\ m+1 \end{bmatrix}_q \frac{p^{m+1} q^{m(m+1)/2}}{\prod_{i=1}^{n}(1+pq^{i-1})} \right. \\ &\left. - \begin{bmatrix} n \\ m \end{bmatrix}_q \frac{p^m q^{m(m-1)/2}}{\prod_{i=1}^{n}(1+pq^{i-1})} \right] \\ &/ \begin{bmatrix} n \\ m \end{bmatrix}_q \frac{p^m q^{m(m-1)/2}}{\prod_{i=1}^{n}(1+pq^{i-1})}. \end{aligned}$$

After performing a series of calculations and utilizing the properties of q-calculus, we arrive at the following expression for the variation ratio

$$\frac{P(m+1) - P(m)}{P(m)} = \frac{pq^2(1-q^{n-m}) - 1 + q^{m+1}}{1-q^{m+1}}.$$

By partitioning the interval from m to $m + 1$ into k subintervals, and considering the limit as k approaches ∞, the following differential equation is derived

$$\frac{1}{y}\frac{dy}{dx} = \frac{pq^2(1-q^{n-m}) - 1 + q^{m+1}}{1-q^{m+1}},$$

that we will obtain

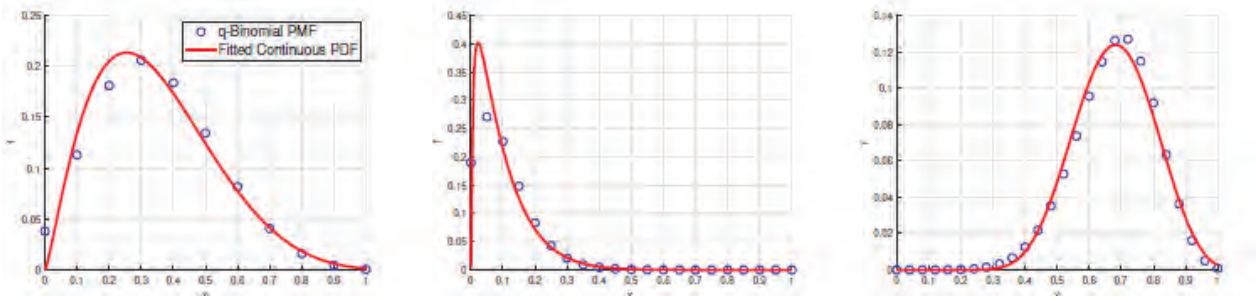
$$\begin{aligned} \ln y &= \int \frac{pq^2(1-q^{n-m}) - 1 + q^{m+1}}{1-q^{m+1}} dm \\ &= \int \frac{pq^2(x-q^n) - x(1-xq)}{x^2(1-xq)\ln q} dx, \quad \text{(we take } x = q^m\text{)} \\ &= \int \frac{pq^2}{x(1-xq)\ln q} - \frac{pq^{n+2}}{x^2(1-xq)\ln q} - \frac{1}{x(1-xq)\ln q} + \frac{q}{(1-xq)\ln q} dx \\ &= \frac{pq^2-1}{\ln q}[\ln x - \ln(1-xq)] + \frac{pq^{n+2}}{\ln q}\left[-\frac{1}{x} + q\ln x - q\ln(1-xq)\right] \\ &\quad - \frac{1}{\ln q}\ln(1-xq) + C \\ &= \frac{pq^2-1}{\ln q}\ln\left(\frac{x}{1-xq}\right) - \frac{pq^{n+2}}{x\ln q} + \frac{pq^{n+2}}{\ln q}\ln\left(\frac{x}{1-xq}\right)^q \\ &\quad - \frac{\ln(1-xq)}{\ln q} + C. \end{aligned}$$

Therefore, the probability density function concerned will be obtained

$$y = Cx^{a_0}(1-xq)^{b_0}e^{-c_0/x},$$

where C represents the normalization constant, and a_0, b_0, and c_0 are the parameters of the PDF.

Figure 1 shows the q-binomial probability mass function for three different parameter settings, along with the corresponding continuous approximations. The fitting process is based on the method of moments: we computed the first three empirical moments of the q-binomial distribution, then estimated the parameters a_0, b_0, and c_0 by minimizing the squared differences between these and the theoretical moments of the fitted density [28]. This was achieved using the fmincon optimization routine in MATLAB, with the theoretical moments evaluated numerically. The normalization constant C was also calculated numerically to ensure that the fitted density integrates into one over the interval [0, 1].



(a) (b) (c)

Figure 1. Comparison between the q-binomial probability mass function and the fitted continuous PDF for three different parameter settings.

Table 1. Estimated parameters of the continuous density function fitted to the q-binomial distribution for different values of n, p, and q.

Case	n	p	q	C	a_0	b_0	c_0
(a)	10	0.4	0.8	0.1	1.24	4.88	0.00
(b)	20	0.3	0.7	0.05	0.02	14.48	0.00
(c)	25	0.6	0.9	0.04	2.60	4.80	3.43

Table 1 reports the estimated parameters for the three cases illustrated in Figure 1. As expected, the fitted parameters vary depending on the shape of the discrete distribution, which is influenced by the values of n, p, and q. For example, an increase in p from case (b) to case (c) shifts the distribution to the right, corresponding to a higher value of a_0 and a lower b_0. The parameter c_0, which governs the tail behaviour of the fitted density, increases significantly in case (c), indicating a heavier right tail [29,30].

Continuous approximation of the negative q-binomial distribution

Let X_n denote the number of successes in a sequence of n independent Bernoulli trials.

Definition 2. *[23] The probability function of the negative q-binomial distribution, characterized by the parameters n, p and q, is expressed as:* $P(X_n=m)=\begin{bmatrix} n+m-1 \\ m \end{bmatrix}_q \frac{p^n q^{n(n-1)/2+m}}{\prod_{i=1}^{n+m}(1+pq^{i-1})}$ *for* $0 < p < \infty$ *and q is a real number such that* $0 < q < 1$ *or* $1 < q < \infty$.

The variation ratio can be expressed as:

$$\frac{P(m+1)-P(m)}{P(m)} = \frac{\begin{bmatrix} n+m \\ m+1 \end{bmatrix}_q \frac{p^n q^{n(n-1)/2+m+1}}{\prod_{i=1}^{n+m+1}(1+pq^{i-1})} - \begin{bmatrix} n+m-1 \\ m \end{bmatrix}_q \frac{p^n q^{n(n-1)/2+m}}{\prod_{i=1}^{n+m}(1+pq^{i-1})}}{\begin{bmatrix} n+m-1 \\ m \end{bmatrix}_q \frac{p^n q^{n(n-1)/2+m}}{\prod_{i=1}^{n+m}(1+pq^{i-1})}}.$$

Applying the properties of q-calculus and performing the necessary calculations, we arrive at the following expression for the variation ratio:

$$\frac{P(m+1)-P(m)}{P(m)} = \frac{q[n]_q(1-q^{n+m}) - (1-q^{m+1})(1+pq^{n+m})}{(1-q^{m+1})(1+pq^{n+m})}.$$

As a result, the differential equation becomes the following:

$$\frac{1}{y}\frac{dy}{dx} = \int \frac{q[n]_q}{\ln q}\frac{1-xq^n}{x(1-xq)(1+xpq^n)} - \frac{1}{x\ln q}dx.$$

Upon solving the previous differential equation, we obtain:

$$\ln y = A\ln x - B\ln(1-xq) + C\ln(1+xpq^n) + D,$$

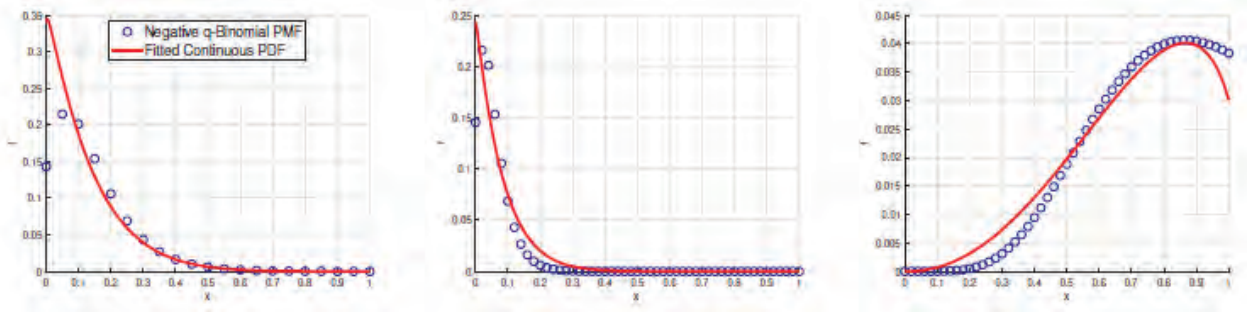
where A, B, and C are constants that depend on p, q and n.

Consequently, the probability density function will be derived as

$$y = Cx^{a_0}(1-xq)^{b_0}(1+xpq^n)^{c_0},$$

where C denotes the normalization constant, a_0, b_0, and c_0 represent the parameters of the probability density function.

Figure 2 and Table 2 illustrate the approximation of the negative q-binomial distribution using a continuous density function fitted by the method of moments. This distribution, defined on the non-negative integers with theoretically infinite support, exhibits strong left skewness in certain parameter configurations, with probability mass concentrated near zero. To approximate the discrete PMF over a finite range, a truncation parameter M was introduced. This value was selected such that the cumulative



(a) (b) (c)

Figure 2. Comparison between the Negative q-binomial probability mass function and the fitted continuous PDF for three different parameter settings.

Table 2. Estimated parameters of the continuous density function fitted to the Negative q-binomial distribution for different values of n, p, and q.

Case	n	p	q	M	C	a_0	b_0	c_0
(a)	15	0.4	0.6	20	0.05	0.03	11.64	0.00
(b)	10	0.8	0.6	50	0.02	0.01	20	0.00
(c)	20	0.5	0.95	50	0.02	2.21	0.48	0.33

probability from $m = 0$ to $m = M$ was sufficiently close to one, ensuring that the essential features of the distribution were retained while maintaining computational feasibility. In cases (a) and (b), where the values of p are moderate to large and q is relatively small, the PMF is sharply concentrated near the origin. This behaviour is captured in fitted densities by very low values of a_0 and c_0, and high values of b_0, which collectively generate a steep initial descent. In contrast, case (c), which corresponds to a larger q, displays a more dispersed distribution. The fitted parameters reflect this with increased values of a_0 and the presence of a non-negligible c_0, resulting in a more balanced and extended curve. In general, the fitted densities demonstrate excellent alignment with the discrete PMFs in all cases, confirming the suitability of the continuous model to capture both concentrated and dispersed forms of the negative q-binomial distribution [31,32].

Continuous approximation of the Heine (q-Poisson) distribution

Definition 3. *[23] A discrete random variable X follows a Heine distribution with parameters λ and q, having the probability mass function given by:* $P(X=m)=e_q(-\lambda)\frac{q^{m(m-1)/2}\lambda^m}{[m]_q!}$, $m = 0, 1, \ldots$, *where* $0 < \lambda < \infty$, *and* $0 < q < 1$.

The variation ratio is calculated as follows

$$\frac{P(m+1)-P(m)}{P(m)} = \left[e_q(-\lambda)\frac{q^{m(m+1)/2}\lambda^{m+1}}{[m+1]_q!} - e_q(-\lambda)\frac{q^{m(m-1)/2}\lambda^m}{[m]_q!}\right] / e_q(-\lambda)\frac{q^{m(m-1)/2}\lambda^m}{[m]_q!},$$

Through the application of q-calculus properties and algebraic manipulations, the following expression for the variation ratio is obtained

$$\frac{P(m+1)-P(m)}{P(m)} = \frac{\lambda q^2(1-q)-1+q^{m+1}}{1-q^{m+1}}.$$

As a consequence, the differential equation is transformed into:

$$\frac{1}{y}\frac{dy}{dx} = \int \frac{\lambda q^2(1-q)}{x\ln q(1-xq)} - \frac{1}{x\ln q}dx.$$

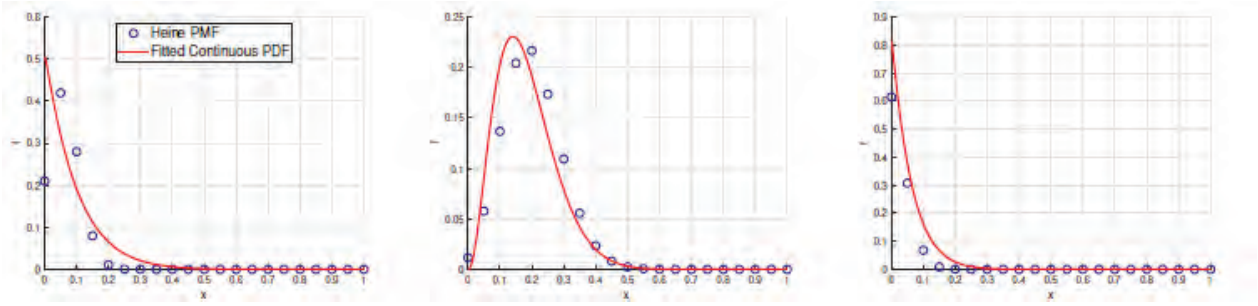
The solution to the preceding differential equation is thus determined as follows

$$\ln y = \frac{\lambda q^2(1-q)}{\ln q}\ln x - \frac{\lambda q^2(1-q)}{\ln q}\ln(1-xq) - \frac{\ln x}{\ln q} + C.$$

Subsequently, the PDF will be derived as follows

$$y = Cx^{a_0}(1-xq)^{b_0},$$

where C denotes the normalization constant, and a_0, b_0 are the parameters that characterize the PDF.



(a) (b) (c)

Figure 3. Comparison between the Heine distribution and the fitted continuous PDF for three different parameter settings.

Table 3. Estimated parameters of the continuous density function fitted to the Heine distribution for different values of λ and q.

Case	λ	q	M	C	a_o	b_o
(a)	2	0.5	20	0.05	0.01	20
(b)	5	0.9	20	0.05	2.23	15.38
(c)	0.5	0.8	20	0.05	0.01	20

Figure 3 and Table 3 show the approximation of the q-Poisson (Heine) distribution using a continuous density estimated using the method of moments. The q-Poisson distribution is characterized by a sharp peak near the origin followed by a gradual decay, and this structure is effectively captured by the fitted continuous curves across the three parameter configurations. In this case, the support of the discrete distribution is theoretically infinite. To enable practical computation of the empirical moments, the distribution was truncated at a finite maximum value M, chosen large enough to ensure that the remaining tail probability beyond M is negligible. This truncation allows for accurate estimation of the first three moments while preserving the essential features of the distribution. The estimated parameters in Table 3 show consistent behaviour in cases: moderate values of a_0 reflect the rising slope near zero, while increasing values of b_0 accommodate the decay in the right tail. The fitted continuous densities exhibit excellent visual agreement with the discrete PMFs, both in the peak and tail regions, confirming the suitability of the proposed moment-based approach for approximating the q-Poisson distribution.

Continuous approximation of the Euler distribution

Definition 4. *[23] A discrete random variable X follows the Euler distribution with parameters λ and q, having the probability mass function given by:* $P(X=m)=E_q(-\lambda)\frac{\lambda^m}{[m]_q!}$, $m = 0, 1, ...,$ *where* $0 < \lambda < 1 / 1\text{-}q$ *and* $0 < q < 1$.

The variation ratio is computed as follows

$$\frac{P(m+1)-P(m)}{P(m)}=\left[E_q(-\lambda)\frac{\lambda^{m+1}}{[m+1]_q!}-E_q(-\lambda)\frac{\lambda^m}{[m]_q!}\right] /E_q(-\lambda)\frac{\lambda^m}{[m]_q!}.$$

Applying the properties of q-calculus and performing algebraic manipulations, the variation ratio is derived as follows

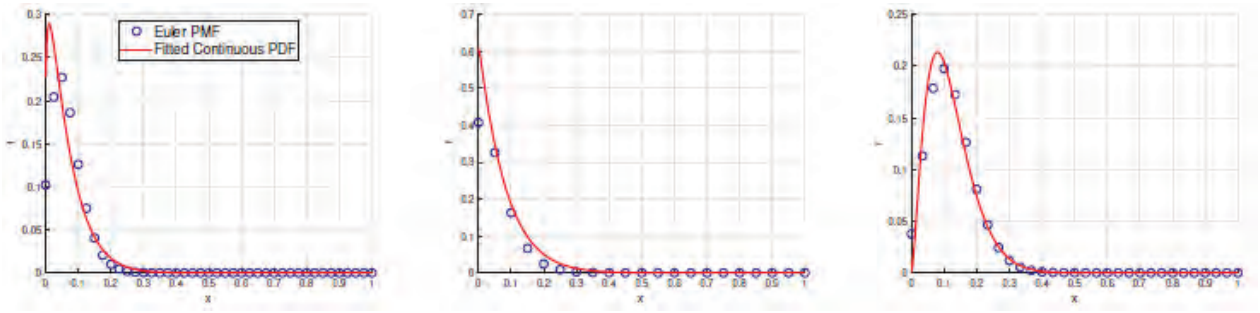
$$\frac{P(m+1)-P(m)}{P(m)}=\frac{\lambda(1-q)-1+q^{m+1}}{1-q^{m+1}},$$

which is a similar differential equation obtained for fitting the Heine distribution. In consequence, the probability density function can be determined as follows

$$y = Cx^{a_0}(1-xq)^{b_0},$$

where C represents the normalization constant, and a_0 and b_0 are the parameters that define the PDF.

Figure 4 and Table 4 show the Euler distribution together with its continuous approximation obtained through the method of moments. The discrete Euler PMF has a pronounced concentration around the origin and decreases rapidly, producing a strongly left-skewed pattern. The fitted parameter values reproduce these characteristics, with one parameter controlling the sharp concentration near zero and another governing the rate of decay over the support.



(a) (b) (c)

Figure 4. Comparison between the Euler distribution and the fitted continuous PDF for three different parameter settings.

Table 4. Estimated parameters of the continuous density function fitted to the Euler distribution for different values of λ and q.

Case	λ	q	M	C	a_o	b_o
(a)	2	0.8	40	0.03	0.17	20
(b)	0.8	0.6	20	0.05	0.01	20
(c)	3	0.9	30	0.03	1.55	20

Because the Euler distribution has an unbounded support, a truncation point was introduced so that the summation could be performed over a finite interval containing essentially all of the probability mass. This choice provides sufficiently accurate empirical moments and, consequently, stable parameter estimates. The fitted continuous curves agree closely with the corresponding discrete PMFs over the retained support, supporting the adequacy of the polynomial approximation for this highly concentrated distribution.The resulting fitted curves show excellent agreement with the discrete PMFs within the truncated support, confirming the suitability of the polynomial-based approximation for modelling sharply concentrated distributions like the Euler law.

Continuous approximation of the q-logarithmic distribution

Definition 5. *[23] A discrete random variable X follows a q-logarithmic distribution with parameters θ and q, having the probability mass function given by:* $P(X=m)=\left[-l_q(1-\theta)\right]^{-1}\frac{\theta^m}{[m]_q}$, $m = 1, 2, \ldots$, *where* $0<\theta<1$, $0<q<1$, *and* $-l_q(1-\theta)=\sum_{k=1}^{\infty}\frac{\theta^k}{[k]_q}$.

The analytical form of the variation ratio is given by :

$$\frac{P(m+1)-P(m)}{P(m)}=\left[\left[-l_q(1-\theta)\right]^{-1}\frac{\theta^{m+1}}{[m+1]_q}-\left[-l_q(1-\theta)\right]^{-1}\frac{\theta^m}{[m]_q}\right]/\left[-l_q(1-\theta)\right]^{-1}\frac{\theta^m}{[m]_q}=\frac{\theta(1-q^m)-1+q^{m+1}}{1-q^{m+1}}.$$

As a result, the differential equation reduces to

$$\frac{1}{y}\frac{dy}{dx}=\int\frac{\theta(1-x)}{x\ln q(1-xq)}-\frac{1}{x\ln q}dx.$$

The solution to the previous differential equation is therefore, given by

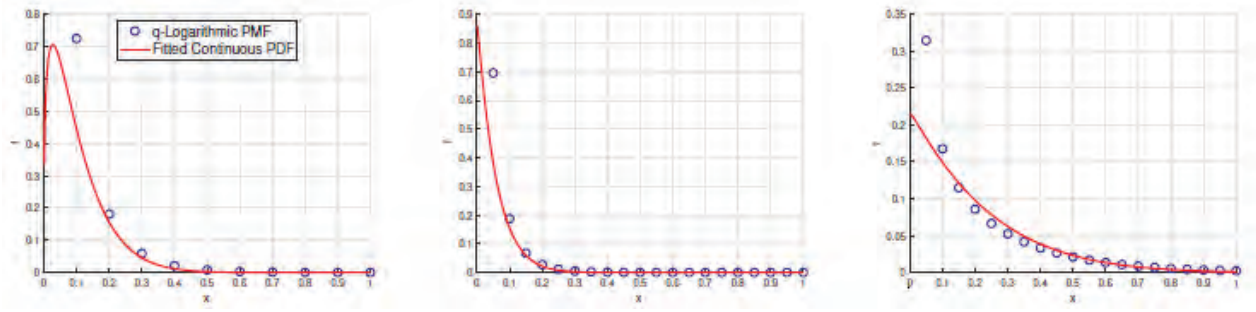
$$\ln y=\frac{\theta}{\ln q}\left(\ln x+\frac{1-q}{q}\ln(1-xq)\right)-\frac{\ln x}{\ln q}+C.$$

Consequently, the probability density function can be expressed as follows:

$$y=Cx^{a_0}(1-xq)^{b_0},$$

where C denotes the normalization constant, and a_0, b_0 are the parameters that define the PDF.

Figure 5 and Table 5 present the approximation of the q-logarithmic distribution using a continuous density function fitted by the method of moments. The distribution is known for its strong right skewness and long tail,



(a) (b) (c)

Figure 5. Comparison between the q-logarithmic distribution and the fitted continuous PDF for three different parameter settings.

Table 5. Estimated parameters of the continuous density function fitted to the q-logarithmic distribution for different values of θ and q.

Case	θ	q	M	C	a_o	b_o
(a)	0.6	0.4	10	0.1	0.01	11.67
(b)	0.5	0.85	20	0.05	0.01	20
(c)	0.8	0.5	20	0.05	0.01	7.94

with probability mass concentrated near the origin. The fitted curves accurately reflect this behaviour across all three cases.

In particular, the low values of a_0 and the high values of b_0 indicate that the shape is predominantly governed by the initial decay near zero and the extended tail. Due to the infinite support of the q-logarithmic distribution, a truncation parameter M was introduced to approximate the PMF over a finite range. The selected truncation value in each case captures nearly the entire probability mass, so the resulting moment estimates remain reliable. The resulting continuous approximations demonstrate good agreement with the discrete PMFs throughout the effective support, validating the adequacy of the moment-based fitting strategy.

Continuous approximation of the q-hypergeometric distribution

Definition 6. *[23] The probability mass function of the q-hypergeometric distribution, with parameters n, r, s, and q, is expressed as:* $P(X_n=m)=q^{(n-m)(r-m)}\begin{bmatrix} r \\ m \end{bmatrix}_q \begin{bmatrix} s \\ n-m \end{bmatrix}_q / \begin{bmatrix} r+s \\ n \end{bmatrix}_q$, $m = 0, 1, \ldots, n$ *where q is a real number such that* $0 < q < 1$ *or* $1 < q < \infty$, *and r, s* $\in \mathbb{N}$.

The variation ratio takes the form

$$\frac{P(m+1)-P(m)}{P(m)} = \frac{q^{(n-m-1)(r-m-1)}\begin{bmatrix} r \\ m+1 \end{bmatrix}_q \begin{bmatrix} s \\ n-m-1 \end{bmatrix}_q / \begin{bmatrix} r+s \\ n \end{bmatrix}_q - q^{(n-m)(r-m)}\begin{bmatrix} r \\ m \end{bmatrix}_q \begin{bmatrix} s \\ n-m \end{bmatrix}_q / \begin{bmatrix} r+s \\ n \end{bmatrix}_q}{q^{(n-m)(r-m)}\begin{bmatrix} r \\ m \end{bmatrix}_q \begin{bmatrix} s \\ n-m \end{bmatrix}_q / \begin{bmatrix} r+s \\ n \end{bmatrix}_q}$$
$$= \frac{q^{2m-n-r+1}(1-q^{r-m})(1-q^{n-m}) - (1-q^{s-n+m+1})(1-q^{m+1})}{(1-q^{s-n+m+1})(1-q^{m+1})}.$$

Hence, the differential equation becomes the following

$$\frac{1}{y}\frac{dy}{dx} = \int \frac{q^{1-n-r}(x-q^r)(x-q^n)}{x\ln q(1-xq^{s-n+1})(1-xq)} - \frac{1}{x\ln q}dx.$$

Thus, the solution to the preceding differential equation is obtained as

$$\ln y = A\ln x + B\ln(1-xq^{s-n+1}) + C\ln(1-xq) + D,$$

where A, B, and C are constants expressed in terms of q, r, n, and s.

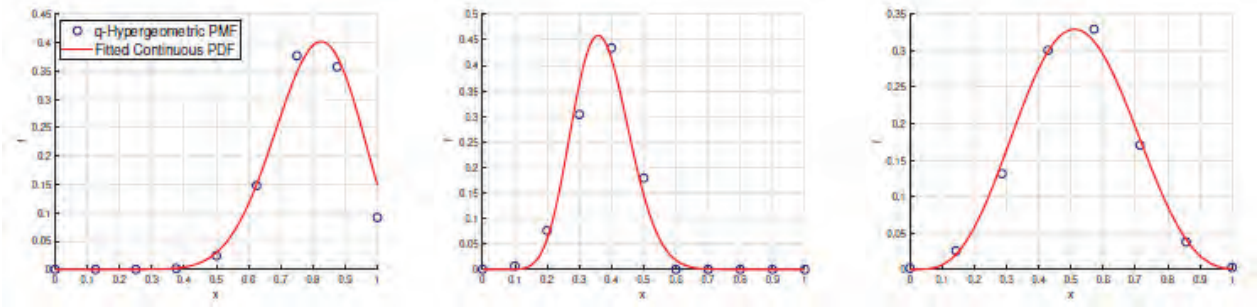
Consequently, the probability density function takes the form

$$y = Cx^{a_0}(1-xq^{s-n+1})^{b_0}(1-xq)^{c_0},$$

where C denotes the normalization constant, and a_0,b_0, and c_0 represent the parameters that characterize the PDF.

Figure 6 and Table 6 display the results of fitting a continuous approximation to the q-hypergeometric distribution under three distinct parameter settings involving n, r, s and q. The discrete distribution is supported on a finite set of values, which varies depending on these parameters. To standardize the comparison with the continuous model, the support was normalized to the interval [0,1] using a maximum value M, ensuring that the relevant probability mass is retained for accurate moment estimation.

The estimated parameters a_0, b_0, and c_0 reflect the varying shapes of the discrete distributions in each case. For example, larger values of s and smaller values of r tend to



(a) (b) (c)

Figure 6. Comparison between the q-hypergeometric distribution and the fitted continuous PDF for three different parameter settings.

Table 6. Estimated parameters of the continuous density function fitted to the q-hypergeometric distribution for different values of n, r, s, and q.

Case	n	r	s	q	C	a_0	b_0	c_0
(a)	8	10	10	0.8	0.13	12.66	0.96	6.15
(b)	6	5	12	0.9	0.17	3.36	1.37	5.95
(c)	7	10	15	0.95	0.14	3.85	0.80	3.69

concentrate the mass toward lower values of the support, which corresponds to greater skewness in the distribution. These fitted densities reproduce the main features of the corresponding discrete distributions and remain closely aligned with the PMFs over the considered range. The consistency between the fitted and empirical distributions demonstrates that the method adapts effectively to changes in the discrete structure and offers a reliable continuous representation of the q-hypergeometric model.

Continuous approximation of the negative q-hypergeometric distribution

Definition 7. *[23] The probability mass function of the negative q-hypergeometric distribution, with parameters n, r, s, and q, is expressed as:*

$$P(X_n=m)=q^{r(n-m)}\begin{bmatrix} r+m-1 \\ m \end{bmatrix}_q \begin{bmatrix} s+n-m-1 \\ n-m \end{bmatrix}_q \Big/ \begin{bmatrix} r+s+n-1 \\ n \end{bmatrix}_q,$$

$m = 0, 1, \ldots, n$ where q is a real number such that $0 < q < 1$ or $1 < q < \infty$, and $r, s \in \mathbb{N}$.

The variation ratio will be determined as follows

$$\frac{P(m+1)-P(m)}{P(m)} = \frac{q^{r(n-m-1)}\begin{bmatrix} r+m \\ m+1 \end{bmatrix}_q \begin{bmatrix} s+n-m \\ n-m-1 \end{bmatrix}_q \Big/ \begin{bmatrix} r+s+n-1 \\ n \end{bmatrix}_q - q^{r(n-m)}\begin{bmatrix} r+m-1 \\ m \end{bmatrix}_q \begin{bmatrix} s+n-m-1 \\ n-m \end{bmatrix}_q \Big/}{q^{r(n-m)}\begin{bmatrix} r+m-1 \\ m \end{bmatrix}_q \begin{bmatrix} s+n-m-1 \\ n-m \end{bmatrix}_q \Big/ \begin{bmatrix} r+s+n-1 \\ n \end{bmatrix}_q}$$
$$= \frac{q^{-r}[r]_q(1-q^{r+m})(1-q^{n-m}) - [s-1]_q(1-q^{s-n-m-1})(1-q^{m+1})}{[s-1]_q(1-q^{s-n-m-1})(1-q^{m+1})}.$$

Therefore, the differential equation simplifies to

$$\frac{1}{y}\frac{dy}{dx} = \int \frac{q^{-r}[r]_q(1-xq^r)(x-q^n)}{[s-1]_q x \ln q (x-q^{s-n-1})(1-xq)} - \frac{1}{x\ln q}\,dx.$$

The probability density function is analogous to that obtained by fitting a negative q-hypergeometric distribution and is given by :

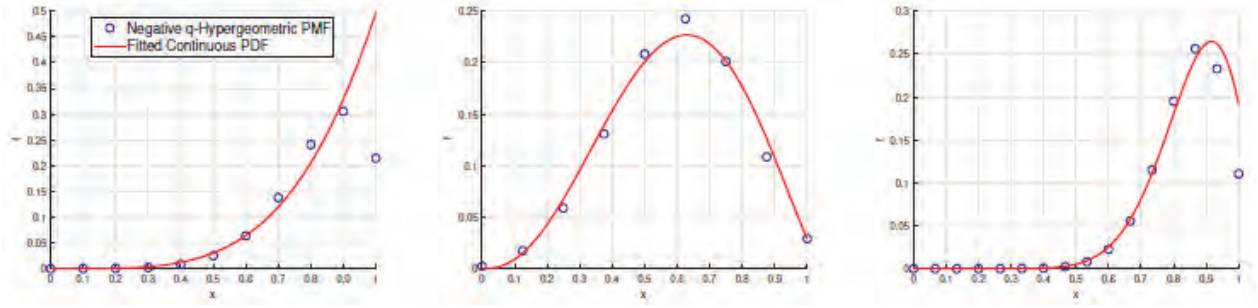
$$y = Cx^{a_0}(1-xq^{s-n-1})^{b_0}(1-xq)^{c_0},$$

where C denotes the normalization constant, and a_0, b_0, and c_0 represent the parameters that characterize the PDF.

Figure 7 and Table 7 present the continuous approximation of the negative q-hypergeometric distribution based on three parameter configurations. This distribution, defined in non-negative integers, exhibits a finite but typically broad support that depends on the values of n, r, and s.

In cases (a) and (c), the PMFs exhibit a strong left-skewness, with most of the probability mass concentrated near the origin. This is reflected in the estimated parameters: large values of a_0, small b_0. These indicate that the early part of the distribution dominates the shape, and no additional correction term is needed to control tail behaviour. In case (b), the distribution is more dispersed due to higher values of q and a more balanced parameter setup. This is captured by moderate values of all three parameters, including a non-zero c_0, which provides additional flexibility in fitting the broader shape.

These results confirm that the proposed continuous model reliably captures the key characteristics of the negative q-hypergeometric distribution across varying parameter regimes, providing an effective approximation within its naturally finite support.



(a) (b) (c)

Figure 7. Comparison between the negative q-hypergeometric distribution and the fitted continuous PDF for three different parameter settings.

Table 7. Estimated parameters of the continuous density function fitted to the negative q-hypergeometric distribution for different values of n, r, s, and q.

Case	n	r	s	q	C	a_0	b_0	c_0
(a)	10	5	12	0.8	0.1	20	0.01	0.01
(b)	8	10	15	0.95	0.13	2.52	0.64	1.33
(c)	12	12	20	0.9	0.08	7.62	0.01	1.53

Remarks 1.

1. *The limiting behaviour of the probability function for the curve fitting q-binomial and negative q-binomial distributions, such as $n \to \infty$, converges to the probability function of the Heine curve fitting distribution. This observation aligns with the remark made by Charalambides [23], who noted that the probability function of the q-binomial and negative q-binomial distributions approaches that of the Heine distribution in the limit.*
2. *It should be noted that the curve-fitting expressions for the Heine and Euler probability functions are identical in form to those highlighted by Charalambides [23] for these distributions, with a different parametric space.*

CONCLUSION

This paper presented a unified approach to approximate various q-discrete distributions with continuous probability density functions. Using a framework based on differential approximations and the method of moments, we constructed and estimated continuous PDFs that closely align with the empirical shape and moments of q-binomial, negative q-binomial, q-Poisson (Heine), Euler, q-logarithmic, q-hypergeometric, and negative q-hypergeometric distributions.

For each distribution, Figures 1–7 illustrate the visual agreement between the PMF and the fitted PDF, and Tables 1–7 report the estimated parameters and the normalization constant. These results demonstrate that the method provides flexible and effective approximations that capture skewness, kurtosis, and tail behaviour. The use of moment matching and numerical optimization proves to be a powerful strategy for aligning continuous models with complex discrete distributions.

This work contributes to bridging the gap between discrete q-models and continuous statistical analysis, enabling more practical application of q-distributions in real-world problems requiring density-based inference

DATA AVAILABILITY STATEMENT

The author confirm that the data that supports the findings of this study are available within the article. Raw data that support the finding of this study are available from the corresponding author, upon reasonable request.

CONFLICT OF INTEREST

The author declared no potential conflicts of interest with respect to the research, authorship, and/or publication of this article.

ETHICS

There are no ethical issues with the publication of this manuscript.

STATEMENT ON THE USE OF ARTIFICIAL INTELLIGENCE

Artificial intelligence was not used in the preparation of the article.

REFERENCES

[1] Bevrani H. A continuous approximation fitting to the discrete distributions using ODE. Comput Methods Differ Equ 2015;3:45–50.

[2] Bevrani H, Sharififar S. An approximation to binomial distribution. J Stat Theory Pract 2014;14:1–8.

[3] Sadok I, Zribi M, Masmoudi A. Non-informative Bayesian estimation in dispersion models. Hacet J Math Stat 2024;53:251–268. [CrossRef]

[4] Sadok I, Zribi M. Bayesian GLM: a non-informative approach for parameter estimation in exponential dispersion regression models. Reliab Theory Appl 2025;20:715–727.

[5] Bevrani H, Bening VE, Korolev VY. On the accuracy of the negative binomial distribution by the gamma distribution and convergency ratio. J Math Sci 2015;205. [CrossRef]

[6] Elderton V, Johnson N. System of frequency curves. Cambridge: Cambridge University Press; 1962.

[7] Pollard JH. Handbook of numerical and statistical techniques. Cambridge: Cambridge University Press; 1977. [CrossRef]

[8] Pearson K. Memoir on skew variation in homogeneous material. Philos Trans R Soc A 1895;186:323–414.

[9] Nagahara Y. The PDF and CF of Pearson type IV distributions and the ML estimation of the parameters. Stat Probab Lett 1999;43:251–264. [CrossRef]

[10] Rhind A. Tables to facilitate the computation of the probable errors of the chief constants of skew frequency distributions. Biometrika 1909;7:127–147. [CrossRef]

[11] Pearson K. Mathematical contributions to the theory of evolution, XIX: second supplement to a memoir on skew variation. Philos Trans R Soc Lond A Math Phys Eng Sci 1916;216:429–457. [CrossRef]

[12] Stuart A, Ord J. Kendall's advanced theory of statistics, Vol. 1: Distribution theory. London: Edward Arnold; 1994.

[13] Lahcene B. On Pearson families of distributions and its applications. Afr J Math Comput Sci Res 2013;6:108–117.

[14] Shakil M, Kibria BG, Singh JN. A new family of distributions based on the generalized Pearson differential equation with some applications. Austrian J Stat 2010;39:259–278. [CrossRef]

[15] Andreev A, Kanto A, Malo P. Computational examples of a new method for distribution selection in the Pearson system. J Appl Stat 2007;34:487–506. [CrossRef]

[16] Derrode S, Mercier G, Lecaillec J, Garello R. Estimation of Sec-Ice SAR clutter statistics from Pearsons system of distributions. In: JGARSS, IEEE. 2001. p. 9–13.

[17] Karvanen J, Koivunen V. Blind separation methods based on Pearson system and its extensions. Signal Process 2002;82:663–673. [CrossRef]

[18] Arora S, Mebarek-Oudina F, Sahani S. Super convergence analysis of fully discrete Hermite splines to simulate wave behaviour of Kuramoto–Sivashinsky equation. Wave Motion 2023;121:103187. [CrossRef]

[19] Priyanka P, Mebarek-Oudina F, Sahani S, Arora S. Travelling wave solution of fourth order reaction diffusion equation using hybrid quintic Hermite splines collocation technique. Arab J Math 2024;13:341–367. [CrossRef]

[20] Sadok I. On the q-Rayleigh distribution and its applications. Reliab Theory Appl 2024;19:588–602.

[21] Wang X, Yang Q, Wang F, Chen Q, Wu W, Jin Y, et al. XiHeFusion: harnessing large language models for science communication in nuclear fusion. 2025.

[22] Vamvakari M. Asymptotic behaviour of univariate and multivariate absorption distributions. RAIRO Theor Inform Appl 2024;58:15. [CrossRef]

[23] Charalambides CA. Discrete q-distributions. Hoboken: John Wiley & Sons; 2016. [CrossRef]

[24] Xu M, Mao H. Q-Weibull distributions: perspectives and applications in reliability engineering. IEEE Trans Reliab 2024.

[25] Jackson FH. On q-functions and a certain difference operator. Earth Environ Sci Trans R Soc Edinb 1909;46:253–281. [CrossRef]

[26] Sadok I. Bayesian computational methods for estimation of q-Weibull distribution. Sigma 2026;44:1094–1110. [CrossRef]

[27] Zakkour A. Classification à partir d'une classe de q-distributions de probabilités [doctoral dissertation]. Université de Poitiers-Faculté des Sciences Fondamentales et Appliquées; 2024.

[28] Douini H, Sadok I. A study on statistical properties of a new class of q-Fréchet distribution. Math Appl Sci Eng 2025:1–23. [CrossRef]

[29] Chesneau C, Sadok I. A unified gamma-generated Weibull-Pareto distribution for heavy-tailed and skewed data with applications to medicine, engineering, and environment. AIMS Math 2026;11:23629–23662. [CrossRef]

[30] Hussain S, Hazarika PJ, Das J, Sadok I, Gallardo DI, Gómez HJ. A heavy-tailed QLindley distribution for modelling skewed lifetime data. Mathematics 2026;14:2395. [CrossRef]

[31] Sadok I. Neutrosophic negative binomial hurdle models for overdispersed zero-inflated count data. Fuzzy Sets Syst 2026;5:182–207.

[32] Sadok I. A novel fusion for uncertain dynamic count data: neutrosophic negative binomial mixed-effects and INAR(p) models. J Indian Soc Probab Stat 2026:1–40. [CrossRef]

Sigma J Eng Nat Sci, Vol. 44, No. 4, pp. 2551–2570, August, 2026

Sigma Journal of Engineering and Natural Sciences
Web page info: https://sigma.yildiz.edu.tr
DOI: 10.14744/sigma.2026.2114

Research Article

Iterative methods for solving fuzzy non-linear equations

Srilakshmi KATURI[1], Prashanth MAROJU[1,*]

[1]*Department of Mathematics, School of Advanced Sciences, VIT AP University, Andhra Pradesh, 522241, India*

ARTICLE INFO

Article history
Received: 22 January 2025
Revised: 22 March 2025
Accepted: 13 April 2025

Keywords:
Dual Fuzzy; Fuzzy; Fuzzy Numbers; Iterative Methods; Jacobian Matrix; Nonlinear Equations; Numerical Applications

ABSTRACT

The purpose of this paper is to provide a comprehensive review of numerical methods for solving fuzzy and dual-fuzzy nonlinear equations. These approaches are crucial in modelling uncertainty in real-world applications, such as engineering, optimization, and decision-making. For fuzzy nonlinear equations, the primary emphasis focuses on iterative numerical approaches. These techniques include Newton's method, the steepest descent method, the homotopy method, Broyden's method, the fixed Newton method, and the improved false position method. We have also developed approaches for solving dual fuzzy nonlinear equations. These approaches encompass the Quasi-Newton method, the Broyden-Newton method, and the Modified Newton method. Numerical experiments evaluate the effectiveness, convergence behaviour, and computing complexity of different approaches. In the majority of test situations, our findings demonstrate that both the Newton method and the Fixed Newton technique achieve convergence in fewer than five iterations. On the other hand, the homotopy approach requires well over one hundred iterations in specific scenarios, illustrating the giant disparities in efficiency between the two methods. Additionally, the analysis identifies the conditions under which each method achieves optimal performance. This paper provides a comparative analysis, highlighting alternatives in terms of accuracy and computing cost. This review contrasts with prior studies, which have focused on specific methods. These findings guide in selecting suitable numerical techniques for solving nonlinear equations in fuzzy or dual-fuzzy environments.

Cite this article as: Katuri S, Maroju P. Iterative methods for solving fuzzy non-linear equations. Sigma J Eng Nat Sci 2026;44(4):2551–2570.

INTRODUCTION

Fuzzy nonlinear equations (FNEs) have played a crucial role in various application domains, including mathematics, engineering, health sciences, statistics, and the social sciences. These equations effectively model the uncertain and imprecise real-world application problems. By applying fuzzy logic to nonlinear equations, these frameworks yield more efficient solutions for the problems arising in an uncertain environment. These applications are extended to subsurface water flow, reaction-diffusion systems, epidemic models, blood circulation and robotics [1-4].

In 1965, Zadeh first explored and introduced the idea of fuzzy sets [5-9]. The word fuzzy means unclear or vague.

***Corresponding author.**
*E-mail address: marojuprashanth@gmail.com

This paper was recommended for publication in revised form by Editor-in-Chief Ahmet Selim Dalkilic

Published by Yıldız Technical University Press, İstanbul, Turkey
© Author. This is an open access article under the CC BY-NC license (http://creativecommons.org/licenses/by-nc/4.0/).

In real-world situations where uncertainty arises, fuzzy equations are an ideal mathematical tool for solving these problems [10]. Fuzzy parameters provide a perfect solution when the coefficients in a nonlinear equation are uncertain, whether partially or entirely [11-14]. FNEs are of the form,

$$\begin{matrix} a\tilde{z}^3 + b\tilde{z}^2 + c\tilde{z} - d = e \\ ae^{\tilde{z}} + b = d \end{matrix} \quad (1.1)$$

where $\tilde{a} = (a_L, a_C, a_U)$, $\tilde{b} = (b_L, b_C, b_U)$, $\tilde{c} = (c_L, c, c_U)$, $\tilde{d} = (d_L, d_C, d_U)$, $\tilde{e} = (e_L, e_C, e_U)$ and $\tilde{z}$ are fuzzy numbers.

However, the traditional analytical approaches of Buckley and Qu [15, 16] are inadequate in solving these FNEs. Accordingly, several methods have been developed for solving these FNEs. The faster convergence methods, such as the Newton method, gradient-based method, which is the Steepest Descent method, and Broyden's method, are introduced by [17-20]. Although these methods are easy to apply for solving FNEs, has the slower convergence for an inaccurate Jacobian matrix. To handle both weakly and highly nonlinear situations, Liao [21] introduced the homotopy method. The flaw of this method is that it requires lengthy computations to converge to the solution. Umar and Ahmad Abubakar [22] applied the Fixed Newton method for solving FNEs, which eliminates the calculation of Jacobian matrix at each iteration. Later, several researchers developed variants of Newton Methods for solving FNEs that are Derivative-free methods [23, 24], a Shamanskii-like method [25]. These methods [23-25] have the benefit of being easy to apply; however, their primary drawback is slower convergence. Improved False Position method was proposed by Sulaiman and Ibrahim Mohammed et al. [26] for solving FNEs. The benefit of this approach is that it eliminates the calculation of the Jacobian matrix; however, it fails if the endpoints are the same. Senthilkumar et al. [27] used the Bisection method for solving FNEs. This method is easy to apply, but it resulted in slower convergence when solving these equations. To improve this slower convergence rate, Ahmad et al. [28] proposed the False Position method for solving FNEs. This approach converges in a more efficient manner than the Bisection method, if the initial approximation is inaccurate it fails to converge to the solution. The combination of Broyden's and Newton's methods to solve dual fuzzy nonlinear equations (DFNE) was employed by Waziri and Mohammed Yusuf et al. [29]. DFNE are useful for modelling uncertain real-world problems. Broyden's method may become unstable due to the estimate of the inaccurate Jacobian matrix. Omesa et al. [30] introduced the Quasi-Newton method for solving DFNE. This approach is computationally efficient because it eliminates computing the Hessian matrix at each iteration. But this method converges slowly due to various step sizes. Modified Newton's method for solving DFNE was introduced by Sulaiman et al. [31]. It requires lengthy computations; as a result, it has slower convergence. Several researchers developed [32-35] the straight forward methods for addressing the FNEs. All these methods are efficient to solve FNEs but they slower convergence.

Several researchers introduced various numerical methods for solving FNEs and DFNEs. Although various methods are successful, they exhibit instability and slower convergence due to inaccurate Jacobian approximations. The existing research does not clarify the effectiveness of derivative-free approaches and their alternatives in comparison with Newton-based methods. No comprehensive review of the convergence speed, stability, and computing cost of numerical techniques exists. This paper provides an extensive comparative review of existing numerical methods for solving both FNEs and DFNEs, assessing their efficiency, convergence behaviour, and computational complexity. We present example problems with comprehensive numerical comparisons to further validate our findings. This work presents an extensive and unique evaluation of Newton-type and derivative-free approaches, highlighting their advantages and limitations.

In this article, we reviewed various methods for solving FNEs and DFNEs. Section 2 provides fuzzy number definitions. Section 3 includes detailed information on an iterative method for solving FNEs. Numerical examples for FNE have been presented in Section 4. Section 5 gives an overview of iterative methods for solving DFNE. Numerical examples for DFNE have been presented in Section 6. Finally, this paper ends with a summary in Section 7.

MATHEMATICAL PRELIMINARIES

Let $Y_{\tilde{\varrho}}$: $X \to [0,1]$ be the membership function for the function $\tilde{\varrho}$.

Definition 1

A fuzzy set is considered a fuzzy number if the following conditions [36] hold.

1. $Y_{\tilde{\varrho}}$ is normal, i.e., there exists $\tilde{s}_0$ such that $Y_{\tilde{\varrho}}(\tilde{s}_0)=0$.
2. $Y_{\tilde{\varrho}}$ is convex, i.e., $Y_{\tilde{\varrho}}(\lambda\tilde{s}_1 + (1-\lambda)\tilde{s}_2) \geq \min\{Y_{\tilde{\varrho}}(\tilde{s}_1), Y_{\tilde{\varrho}}(\tilde{s}_2)\}$, $\forall \tilde{s}_1, \tilde{s}_2 \in \mathbb{R}$, $\forall \lambda \in [0,1]$.
3. $Y_{\tilde{\varrho}}$ is upper semi-continuous, i.e., the subset $\tilde{\varrho}(\tilde{s}) = \{x \in \mathbb{R}: Y_{\tilde{\varrho}}(x) \geq \tilde{s}\}$ is closed $\forall \tilde{s} \in [0,1]$,
4. $\tilde{\varrho}_0$ is compact at the 0-level.

Definition 2

A fuzzy number is a fuzzy set, like $\tilde{\xi}: \mathbb{R} \to I = [0,1]$ which satisfies [37-39].

1. $\tilde{\xi}$ is upper semi-continuous,
2. $\tilde{\xi}(\tilde{s}) = 0$ for outside interval $[r, s]$.

   There are real numbers p, q such that $r \leq p \leq q \leq s$ and
3. $\tilde{\xi}(\tilde{s})$ is monotonically increasing on $[r, p]$,
4. $\tilde{\xi}(\tilde{s})$ is monotonically decreasing on $[q, s]$,
5. $\tilde{\xi}(\tilde{s}) = 1$, $\tilde{s} \in [p, q]$.

The set of all fuzzy numbers is denoted by E. The following is an analogous parametric form [39, 40].

Definition 3

The parametric form of the fuzzy number [41-44] $\tilde{\xi}$ can be written as

$$\tilde{\xi}(\tilde{s}) = (\underline{\tilde{\xi}}(\tilde{s}),\ \bar{\tilde{\xi}}(\tilde{s})),\ \ 0 \le \tilde{s} \le 1 \tag{2.1}$$

1. $\underline{\tilde{\xi}}(\tilde{s})$ is a bounded non-decreasing left-continuous function on [0,1].
2. $\bar{\tilde{\xi}}(\tilde{s})$ is a bounded non-increasing left-continuous function on [0,1].
3. $\underline{\tilde{\xi}}(\tilde{s}) \le \bar{\tilde{\xi}}(\tilde{s})$, for all $\tilde{s} \in [0,1]$.

Definition 4

The triplet $\tilde{\varrho} = (\alpha_L, \alpha_C, \alpha_U)$ denotes the triangular fuzzy numbers, where $\alpha_L \le \alpha_C \le \alpha_U$ and also its membership function is defined as [36],

$$\gamma_{\tilde{\varrho}}(\tilde{x}_0) = \begin{cases} \dfrac{\tilde{x}_0 - \alpha_L}{\alpha_C - \alpha_L} & \alpha_L \leqslant \tilde{x}_0 \leqslant \alpha_C \\ 1 & \tilde{x}_0 = \alpha_C \\ \dfrac{\alpha_U - \tilde{x}_0}{\alpha_U - \alpha_C} & \alpha_C \leqslant \tilde{x}_0 \leqslant \alpha_U \\ 0 & \text{Otherwise} \end{cases} \tag{2.2}$$

Moreover, $\tilde{\beta}$ - cut of $\tilde{\phi}$ for $\tilde{\beta} \in [0,1]$, can be described as

$$\tilde{\phi}(\tilde{s}) = [\underline{\tilde{\phi}}(\tilde{s}), \bar{\tilde{\phi}}(\tilde{s})] = [\alpha_L + (\alpha_U - \alpha_L)\tilde{\beta}, \alpha_U + (\alpha_C - \alpha_U)\tilde{\beta}]. \tag{2.3}$$

The extension principle for fuzzy numbers is as follows [39]

For arbitrary $\tilde{\xi} = (\underline{\tilde{\xi}}, \bar{\tilde{\xi}})$, $\tilde{\phi} = (\underline{\tilde{\phi}}, \bar{\tilde{\phi}})$ and $k > 0$. The addition $(\tilde{\xi} + \tilde{\phi})$ and multiplication by scalar k can be defined as

$$\begin{gathered} (\underline{\tilde{\xi} + \tilde{\phi}})(\tilde{s}) = \underline{\tilde{\xi}}(\tilde{s}) + \underline{\tilde{\phi}}(\tilde{s}),\ \ (\bar{\tilde{\xi}} + \bar{\tilde{\phi}})(\tilde{s}) = \bar{\tilde{\xi}}(\tilde{s}) + \bar{\tilde{\phi}}(\tilde{s}), \\ (\underline{k\tilde{\xi}})(\tilde{s}) = k\underline{\tilde{\xi}}(\tilde{s}), \overline{(k\tilde{\xi})}(\tilde{s}) = k\bar{\tilde{\xi}}(\tilde{s}). \end{gathered} \tag{2.4}$$

Review of Iterative Methods for Solving Fuzzy Nonlinear Equations

The analytical approaches are ineffective for addressing nonlinear equations, which are fuzzy in nature. So, some researchers developed numerical methods for solving FNEs. In this section, we review some iterative methods that are efficient for solving FNEs [41]. This section discusses the strengths and limitations of each iterative process, as well as the mathematical formulation of each method. This review typically enables an overview of the research problem, the numerical methodologies and algorithms used to solve it, and the resulting findings. The following section aims to deliver a succinct and precise explanation of the numerical methods and algorithms used, as well as to illustrate their application to the specific topic under analysis. This section provides sufficient detail for the reader to understand the results achieved and evaluate the research's validity.

Newton Method

Abbas Bandy and Asady [17] introduced a well-known iterative method, which is Newton's Method (NM) for solving FNEs. There are several approaches to defining Newton's method [7]. The convergence of this method is more efficient than that of other methods. The key strategy to derive this method is the Taylor series expansion [45]. The main advantages of NM are that it is easily composable, we obtain the solution in only a few iterations, and it is quadratically convergent. This method fails to converge if the inverse of the Jacobian matrix does not exist. We review the algorithm for the Newton method as follows

$$\tilde{z}_{k+1} = \tilde{z}_k - J(\tilde{z}_k)^{-1} * F(\tilde{z}_k) \tag{3.1}$$

Algorithm

1. Set $k = 0$.
2. Guess the initial value $\tilde{z}_0$.
3. Find out $F(\tilde{z}_k)$ and $J(\tilde{z}_k)$.
4. Find out $\tilde{z}_{k+1} = \tilde{z}_k - J(\tilde{z}_k)^{-1} * F(\tilde{z}_k)$.
5. Check $|\tilde{z} - \tilde{z}_0| < \epsilon$.
6. Set $\tilde{z}_k = \tilde{z}_{k+1}$ and go to step 2 until we converge on the solution.

Here k represents the iteration index, $\tilde{z}_k$ indicates the vector $\tilde{z}$ after k iterations, $J(\tilde{z}_k)$ denotes the Jacobian matrix, $F(\tilde{z}_k)$ denotes the function value and ϵ is an error tolerance.

Mathematical formulation

The objective is to determine the solution for FNE.

$$\tilde{F}(\tilde{z}) = \tilde{d} \tag{3.2}$$

Equation (3.2) can be described as

$$\begin{cases} \underline{\tilde{F}}(\underline{\tilde{z}}, \bar{\tilde{z}}, \tilde{s}) = \underline{\tilde{d}}(\tilde{s}), \forall \tilde{s} \in [0,1] \\ \bar{\tilde{F}}(\underline{\tilde{z}}, \bar{\tilde{z}}, \tilde{s}) = \bar{\tilde{d}}(\tilde{s}). \end{cases} \tag{3.3}$$

Let us assume that $\tilde{z} = (\underline{\tilde{\psi}}), \bar{\tilde{\psi}})$ be the solution of (3.2)

$$\begin{cases} \underline{\tilde{F}}(\underline{\tilde{\psi}}, \bar{\tilde{\psi}}, \tilde{s}) = \underline{\tilde{d}}(\tilde{s}), \forall \tilde{s} \in [0,1] \\ \bar{\tilde{F}}(\underline{\tilde{\psi}}, \bar{\tilde{\psi}}, \tilde{s}) = \bar{\tilde{d}}(\tilde{s}). \end{cases} \tag{3.4}$$

Let $\tilde{z}_0 = (\underline{\tilde{z}}_0, \bar{\tilde{z}}_0)$ be the approximate solution, then $\forall \tilde{s} \in [0,1]$, there are $h(\tilde{s})$, $k(\tilde{s})$ such that

$$\begin{cases} \underline{\tilde{\psi}}(\tilde{s}) = \underline{\tilde{z}}_0(\tilde{s}) + h(\tilde{s}) \\ \bar{\tilde{\psi}}(\tilde{s}) = \bar{\tilde{z}}_0(\tilde{s}) + k(\tilde{s}) \end{cases} \tag{3.5}$$

The solution for $h(\tilde{s})$ and $k(\tilde{s})$, can be computed by solving the equations below,

$$J(\underline{\tilde{z}}_0, \bar{\tilde{z}}_0, \tilde{s}) \begin{bmatrix} h(\tilde{s}) \\ k(\tilde{s}) \end{bmatrix} = \begin{bmatrix} \underline{\tilde{d}}(\tilde{s}) - \underline{\tilde{F}}(\underline{\tilde{z}}_0, \bar{\tilde{z}}_0, \tilde{s}) \\ \bar{\tilde{d}}(\tilde{s}) - \bar{\tilde{F}}(\underline{\tilde{z}}_0, \bar{\tilde{z}}_0, \tilde{s}) \end{bmatrix}, \tag{3.6}$$

where

$$J(\underline{\tilde{z}}_0, \tilde{z}_0, \tilde{s}) = \begin{bmatrix} \underline{\tilde{F}}_{\underline{\tilde{z}}}(\underline{\tilde{z}}_0, \tilde{z}, \tilde{s}) & \underline{\tilde{F}}_{\bar{\tilde{z}}}(\underline{\tilde{z}}_0, \bar{\tilde{z}}_0, \tilde{s}) \\ \bar{\tilde{F}}_{\underline{\tilde{z}}}(\underline{\tilde{z}}_0, \bar{\tilde{z}}_0, \tilde{s}) & \bar{\tilde{F}}_{\bar{\tilde{z}}}(\underline{\tilde{z}}_0, \tilde{z}_0, \tilde{s}) \end{bmatrix} \tag{3.7}$$

As a result, the following estimates for $\underline{\tilde{z}}(\tilde{s})$ and $\bar{\tilde{z}}(\tilde{s})$ are stated as follows

$$\begin{cases}\underline{\tilde{z}}_1(\tilde{s}) = \underline{\tilde{z}}_0(\tilde{s}) + h(\tilde{s}) \\ \bar{\tilde{z}}_1(\tilde{s}) = \bar{\tilde{z}}_0(\tilde{s}) + k(\tilde{s})\end{cases} \quad (3.8)$$

for all $\tilde{s} \in [0,1]$ The estimated solution can be obtained by utilizing the equations,

$$\begin{cases}\underline{\tilde{z}}_n(\tilde{s}) = \underline{\tilde{z}}_{n-1}(\tilde{s}) + h_{n-1}(\tilde{s}) \\ \bar{\tilde{z}}_n(\tilde{s}) = \bar{\tilde{z}}_{n-1}(\tilde{s}) + k_{n-1}(\tilde{s})\end{cases} \quad (3.9)$$

The approximated solution obtained for different n values.

$$\tilde{z}_0 = (\underline{\tilde{z}}(1), \tilde{z}(1), \underline{\tilde{z}}(1) - \underline{\tilde{z}}(0), \tilde{z}(0) - \tilde{z}(1)), \quad (3.10)$$

Equation (3.10) can be written in parametric form as [7]

$$\begin{aligned}\underline{\tilde{z}}_0(\tilde{s}) &= \underline{\tilde{z}}(1) + (\underline{\tilde{z}}(1) - \underline{\tilde{z}}(0))(\tilde{s} - 1), \\ \tilde{z}_0(\tilde{s}) &= \tilde{z}(1) + (\tilde{z}(0) - \tilde{z}(1))(1 - \tilde{s})\end{aligned} \quad (3.11)$$

Steepest Descent Method

The Steepest Descent Method (SDM) has a notable historical context and is one of the simplest and best-recognized strategies for minimizing functions. Due to its slow convergence rate, this method is rarely used by practitioners. However, comprehending its convergence features could enhance comprehension of other advanced optimisation strategies. Unfortunately, the technique is not widely used because it is known to be relatively slow in handling most real-life situations [40].

$$f(\tilde{z}_1, \tilde{z}_2, \dots, \tilde{z}_n) = 0 \quad (3.12)$$

Where f If it is a continuous real-valued function, it never becomes negative and remains constant. Despite its ease of use, the steepest descent approach has made a significant contribution to the growth of optimization theory [46]. Abbas Bandy and Jafarian [19] applied SDM for solving FNE. The major benefit of this algorithm is computationally efficient. It can handle a wide range of functions, including those that are not smooth or differentiable. For convex functions, this method always reaches the local minimum [40]. Also, these methods have some flaws. If the step size is too large or too small, then convergence is slow, and a global optimization approach may be necessary to obtain the global minimum. If the objective function is nonconvex, then this method can become trapped in local minima. Although it can be used for nonlinear least squares best fit, it is more commonly employed as the foundation for Marquardt's technique, a more practical approach [40]. We reviewed the SDM algorithm for solving FNE as follows

$$\tilde{z}_{i+1}(\tilde{s}) = \tilde{z}_i(\tilde{s}) - \lambda_i \nabla H_{\tilde{s}}(\tilde{z}_i) \quad (3.13)$$

We assume λ_i as follows

$$2\lambda_i = \frac{\left\|W^{\tilde{s}}(\tilde{z}_i) \cdot F(\tilde{z}_i)\right\|_2^2}{\|W(\tilde{z}_i) \cdot W^{\tilde{s}}(\tilde{z}_i) \cdot F(\tilde{z}_i)\|_2^2}, \quad i = 0,1,2, \dots \quad (3.14)$$

Algorithm

1. $H_{\tilde{s}}$ should be evaluated as an initial estimate $\tilde{z}_0(\tilde{s}) = (\underline{\tilde{z}}_0(\tilde{s}), \bar{\tilde{z}}_0(\tilde{s}))$ for $\tilde{s} \in [0,1]$.
2. Select a starting point $\tilde{z}_0(\tilde{s}) = (\underline{\tilde{z}}_0(\tilde{s}), \bar{\tilde{z}}_0(\tilde{s}))$. It decreases the value of $H_{\tilde{s}}$.
3. Make the necessary adjustment in this way, then update the new value $\tilde{z}_1(\tilde{s}) = (\underline{\tilde{z}}_1(\tilde{s}), \bar{\tilde{z}}_1(\tilde{s}))$.
4. Steps 1 to 3 should be repeated with the value of $\tilde{z}_0(\tilde{s})$ changed to $\tilde{z}_1(\tilde{s})$ [25, 46].

Here $-\nabla H_{\tilde{s}}(\tilde{z}_i)$ represents the maximal decrease in the value of $H_{\tilde{s}}$ in the direction of $\tilde{z}$ and $W(\tilde{z})$ denotes the Jacobian matrix.

Mathematical formulation

The objective is to determine the solution for FNE

$$F(\tilde{z}) = d \quad (3.15)$$

Equation (3.15) can be described as

$$\begin{cases}\underline{F}(\underline{\tilde{z}}, \bar{\tilde{z}}, \tilde{s}) = \underline{d}(\tilde{s}), \forall \tilde{s} \in [0,1] \\ \bar{\tilde{F}}(\underline{\tilde{z}}, \bar{\tilde{z}}, \tilde{s}) = \bar{\tilde{d}}(\tilde{s})\end{cases} \quad (3.16)$$

Let the function $H_{\tilde{s}}$: $\mathbb{R}^2 \to \mathbb{R}$ is defined by

$$H_{\tilde{s}}(\underline{\tilde{z}}, \bar{\tilde{z}}) = [\underline{\tilde{F}}(\underline{\tilde{z}}, \bar{\tilde{z}}, \tilde{s}) + \bar{\tilde{F}}(\underline{\tilde{z}}, \bar{\tilde{z}}, \tilde{s})]^2, \ \forall\, 0 \leqslant \tilde{s} \leqslant 1. \quad (3.17)$$

The local minimum for a two-variable function $H_{\tilde{s}}$ is evaluated using the Steepest Descent approach [47].

For $H_{\tilde{s}}$: $\mathbb{R}^2 \to \mathbb{R}$, the gradient of $H_{\tilde{s}}$ at $\tilde{z}(\tilde{s}) = (\underline{\tilde{z}}(\tilde{s}), \bar{\tilde{z}}(\tilde{s}))$is denoted $\nabla H_{\tilde{s}}(\tilde{z})$ and defined by

$$\nabla H_{\tilde{s}}(\tilde{z}) = \left(\frac{\partial H_{\tilde{s}}}{\partial \underline{\tilde{z}}}, \frac{\partial H_{\tilde{s}}}{\partial \bar{\tilde{z}}}\right) \quad (3.18)$$

A significant characteristic of the gradient is that it points in the direction indicated by $\nabla H_{\tilde{s}}(\tilde{z})$. When the value of $H_{\tilde{s}}$ at $\tilde{z}$ is decreasing the most.

Now the aim is to reduce $H_{\tilde{s}}(\tilde{z})$ to zero, an appropriate choice for $\tilde{z}_{i+1}(\tilde{s}) = (\underline{\tilde{z}}_{i+1}(\tilde{s}), \bar{\tilde{z}}_{i+1}(\tilde{s}))$ is

$$\tilde{z}_{i+1}(\tilde{s}) = \tilde{z}_i(\tilde{s}) - \lambda_i \nabla H_{\tilde{s}}(\tilde{z}_i(\tilde{s})) \quad (3.19)$$

we assume λ_i as follows:

$$2\lambda_i = \frac{\left\|W^{\tilde{s}}(\tilde{z}_i) \cdot \tilde{F}(\tilde{z}_i)\right\|_2^2}{\left\|W(\tilde{z}) \cdot W^{\tilde{s}}(\tilde{z}_i) \cdot \tilde{F}(\tilde{z}_i)\right\|_2^2}, \quad i = 0,1,2, \dots \quad (3.20)$$

where $\tilde{F}(\tilde{z}) = [\underline{\tilde{F}}, \bar{\tilde{F}}]^s$ and

$$W(\tilde{z}) = \frac{\partial \tilde{F}}{\partial \tilde{z}} = \begin{bmatrix} \frac{\partial \underline{\tilde{F}}}{\partial \underline{\tilde{z}}} & \frac{\partial \underline{\tilde{F}}}{\partial \bar{\tilde{z}}} \\ \frac{\partial \bar{\tilde{F}}}{\partial \underline{\tilde{z}}} & \frac{\partial \bar{\tilde{F}}}{\partial \bar{\tilde{z}}} \end{bmatrix} \quad (3.21)$$

The FNE can be used to find the initial approximation

$$\tilde{z}_0 = (\underline{\tilde{z}}(0), \tilde{z}(1), \tilde{z}(0)) \quad (3.22)$$

Equation (3.22) can be described as

$$\begin{aligned}\underline{\tilde{z}}_0(\tilde{s}) &= \underline{\tilde{z}}(0) + (\tilde{z}(1) - \bar{\tilde{z}}(0))(\tilde{s}),\\ \bar{\tilde{z}}_0(\tilde{s}) &= \bar{\tilde{z}}(0) + (\bar{\tilde{z}}(1) - \bar{\tilde{z}}(0))(\tilde{s}),\\ &\text{when } \underline{\tilde{z}}(0) \leqslant \tilde{z}(1) \leqslant \bar{\tilde{z}}(0).\end{aligned} \tag{3.23}$$

Homotopy Method

In mathematics, the Homotopy Method (HM) is frequently used to tackle the equations which is nonlinear in nature. The homotopy analysis for solving nonlinear systems uses the homotopy concept from topology to provide a convergent series solution [21, 47, 48]. This method is an alternative for divergence difficulties, which frequently occur in standard numerical approaches. Also, the solutions might be globally convergent rather than locally convergent. This approach is also capable of identifying numerous solutions rather than just one [47]. Researchers have utilized the homotopy approach in recent years. When the homotopy theory is successfully connected with the perturbation theory [49, 50], it becomes a powerful mathematical tool. The major benefit of this method is that it can be applicable for both weakly and highly nonlinear equations [51]. The downsides of this method are that it needs lengthy computations to converge to the solution and numerous auxiliary nonlinear systems must be solved during the intermediate continuation phases [52]. We reviewed the HM algorithm for solving FNE as follows

$$\tilde{z}_{\tilde{\varphi}_i} = -J\left(\tilde{z}_{\tilde{\varphi}_i}\right)^{-1} H\left(\tilde{\varphi}_i, \tilde{z}_{\tilde{\varphi}_i}\right) \tag{3.24}$$

Algorithm

1. Consider the parameterized fuzzy nonlinear equation.
2. Introduce the parameter $\tilde{\varphi} \in [0,1]$.
3. Change $\tilde{\varphi} = 0$ and $\tilde{\varphi} = 1$ inside the equations to determine the initial guess.
4. The continuation method or homotopy approach aims to determine $\tilde{z}^* = (\underline{\tilde{z}}_1, \bar{\tilde{z}}_1)$.
5. Compute $\tilde{z}_{\lambda i\text{-}1} = (\underline{\tilde{z}}_{\tilde{\varphi} i\text{-}1}, \bar{\tilde{z}}_{\tilde{\varphi} i\text{-}1})$.
6. $\|J(\tilde{z}_{\tilde{\varphi}})^{-1}\| \leq M$.
7. Repeat steps 4-8 repeatedly till tolerance is reached.

Here $\tilde{\varphi} \in [0,1]$, M is error tolerance, $J(\tilde{z}_{\tilde{\varphi}})$ denotes the Jacobian matrix and $\tilde{z}_{\tilde{\varphi}}$ is a continuous, differentiable operator [21, 46].

Mathematical formulation

The objective is to determine the solution for FNE

$$\tilde{F}(\tilde{z}) = \tilde{d} \tag{3.25}$$

Equation (3.25) can be described as

$$\begin{cases}\underline{\tilde{F}}(\underline{\tilde{z}}, \bar{\tilde{z}}, \tilde{s}) = \underline{\tilde{d}}(\tilde{s}), \forall \tilde{s} \in [0,1]\\ \bar{\tilde{F}}(\underline{\tilde{z}}, \bar{\tilde{z}}, \tilde{s}) = \bar{\tilde{d}}(\tilde{s})\end{cases} \tag{3.26}$$

The homotopy method is used for solving one-parameter family-type problems. Different problems can be formed by updating $\tilde{\varphi} = 0$ to $\tilde{\varphi} = 1$ [47].

$$H(\tilde{\varphi}, \tilde{z}) = \tilde{\varphi}\tilde{F}(\tilde{z}) + (1 - \tilde{\varphi})[\tilde{F}(\tilde{z}) - \tilde{F}(\tilde{z}_0)] = 0, \quad 0 \leq \varphi \leq 1 \tag{3.27}$$

$\forall \tilde{s} \in [0,1]$, the parametric form of (3.27) is as follows

$$\begin{cases}\underline{H}(\tilde{\varphi}, \underline{\tilde{z}}, \bar{\tilde{z}}, \tilde{s}) = \underline{\tilde{F}}(\underline{\tilde{z}}, \bar{\tilde{z}}, \tilde{s}) + (\tilde{\varphi} - 1)\underline{\tilde{F}}\left(\underline{\tilde{z}_0}, \overline{\tilde{z}_0}, \tilde{s}\right) = 0\\ \bar{H}(\tilde{\varphi}, \underline{\tilde{z}}, \bar{\tilde{z}}, \tilde{s}) = \bar{\tilde{F}}(\underline{\tilde{z}}, \bar{\tilde{z}}, \tilde{s}) + (\tilde{\varphi} - 1)\bar{\tilde{F}}\left(\underline{\tilde{z}_0}, \overline{\tilde{z}_0}, \tilde{s}\right) = 0\end{cases} \tag{3.28}$$

where $\tilde{z}_0 = (\underline{\tilde{z}}_0, \bar{\tilde{z}}_0)$ is an initial approximation, then the eq. (3.27)

$$H(0, \tilde{z}) = \tilde{F}(\tilde{z}) - \tilde{F}(\tilde{z}_0) = 0,\ H(1, \tilde{z}) = \tilde{F}(\tilde{z}) = 0 \tag{3.29}$$

For fixed $\tilde{\varphi} \in [0,1]$and $\forall \tilde{s} \in [0,1]$ obtain the solution by using Newton's method [53]

$$\tilde{z}_{\tilde{\varphi}_i}^{(k)} = \tilde{z}_{\tilde{\varphi}_i}^{(k-1)} - J\left(\tilde{z}_{\tilde{\varphi}_i}^{(k-1)}\right)^{-1} H\left(\tilde{\varphi}_i, \tilde{z}_{\tilde{\varphi}_i}^{(k-1)}\right) \tag{3.30}$$

Then $\tilde{z}_{\tilde{\varphi} i}$ quickly comes to the solution if $\tilde{z}_{\tilde{\varphi}_i}^{(0)} \left(= \tilde{z}_{\tilde{\varphi}_{i-1}}\right)$, where

$$J\left(\tilde{z}_{\tilde{\varphi}}\right) = \begin{bmatrix} \underline{H}_{\underline{\tilde{z}}}\left(\tilde{\varphi}, \underline{\tilde{z}}_{\tilde{\varphi}}, \bar{\tilde{z}}_{\tilde{\varphi}}, \tilde{s}\right) & \underline{H}_{\bar{\tilde{z}}}\left(\tilde{\varphi}, \underline{\tilde{z}}_{\tilde{\varphi}}, \bar{z}_{\tilde{\varphi}}, \tilde{s}\right) \\ \bar{H}_{\underline{\tilde{z}}}\left(\tilde{\varphi}, \underline{\tilde{z}}_{\tilde{\varphi}}, \bar{\tilde{z}}_{\tilde{\varphi}}, \tilde{s}\right) & \bar{H}_{\bar{\tilde{z}}}\left(\tilde{\varphi}, \underline{\tilde{z}}_{\tilde{\varphi}}, \bar{\tilde{z}}_{\tilde{\varphi}}, \tilde{s}\right) \end{bmatrix} \tag{3.31}$$

and $\|J(\tilde{z}_{\tilde{\varphi}})^{-1}\| \leq M$ for a constant M [50]. The equation in [55] is computed in two steps. First, the vector $\tilde{z}$ is discovered that will fulfill [54]

$$J\left(\tilde{z}_{\tilde{\varphi}_i}^{(k-1)}\right) \tilde{z} = -H\left(\tilde{\varphi}_i, \tilde{z}_{\tilde{\varphi}_i}^{(k-1)}\right) \tag{3.32}$$

To obtain the next approximation values, update $\tilde{z}_{\tilde{\varphi}_i}^{(k)}$ by substituting in (3.24).

Broyden Method

Broyden's Method (BM) addresses nonlinear equations by identifying their roots. Broyden's method is an effective methodology for solving FNE because it enables systems to have various solutions and converges to a fuzzy solution that precisely reflects the system's uncertainty. However, convergence may be sluggish or absent for certain systems, depending on the initial estimate employed [30, 46]. Broyden's approach begins with an initial estimate and refines it until it reaches an accurate solution. At each iteration, the method constructs a linear approximation to the nonlinear system using the Jacobian matrix. Then, Broyden's formula, a version of the secant approach, is used to update the Jacobian matrix [20, 30]. However, it can be sensitive to the initial guess choice, and for certain types of systems, it may converge slowly or not at all.

As compared to the Newton-Raphson approach, BM requires considerably less effort per computational step, leading to significantly less time-intensive computations. This approach is more time-efficient than the NM method.

The BM avoids the need to calculate the Jacobian matrix; significantly, it demonstrates superior numerical stability [56]. This approach possesses two primary drawbacks. The primary disadvantage is that the convergence range is localised. The approach is convergent, similar to the Newton-Raphson method. Nevertheless, it lacks the ability to self-correct. The Broyden approach necessitates a greater number of iterations to obtain the solution. The BM achieves ultra-linear convergence. In this sense, the lower method can be thought to ensure the stability of the Broyden method's convergence order [56]. We reviewed the BM algorithm [20] for solving FNE as follows

$$\tilde{z}_i(\tilde{\varphi}) = \tilde{z}_{i-1}(\tilde{\varphi}) - P_i(\tilde{\varphi})^{-1}\tilde{F}(\tilde{z}_{i-1}) \tag{3.33}$$

Where $P_i(\tilde{\varphi})^{-1}$ represents the Jacobian matrix, and it can be calculated from $P_{i-1}(\tilde{\varphi})^{-1}$ by using the following formula

$$P_i(\tilde{\varphi})^{-1} = P_{i-1}(\tilde{\varphi})^{-1} + \frac{[\tilde{s}_i(\tilde{\varphi}) - P_{i-1}(\tilde{\varphi})^{-1}\tilde{z}_i(\tilde{\varphi})]\tilde{s}_1(\tilde{\varphi})^t P_{i-1}(\tilde{\varphi})^{-1}}{\tilde{s}_i(\tilde{\varphi})^t P_{i-1}(\tilde{\varphi})^{-1}\tilde{z}_i(\tilde{\varphi})} \tag{3.34}$$

where $\tilde{s}_i(\tilde{\varphi}) = \tilde{z}_i(\tilde{\varphi}) - \tilde{z}_{i-1}(\tilde{\varphi})$ and $\tilde{z}_i(\tilde{\varphi}) = \tilde{F}(\tilde{z}_i(\tilde{\varphi}) - \tilde{F}(\tilde{z}_{i-1}(\tilde{\varphi}))$ for $i = 1,2,\ldots, n$.

Algorithm

1. Convert the FNE into parametric form.
2. To obtain the initial approximation $\tilde{z}_0$ put $\tilde{\varphi} = 0$ to $\tilde{\varphi} = 1$
3. Replace $\tilde{z}_0$ into parametric form.
4. Determine the preliminary Jacobian matrix

$$P_0(\tilde{\varphi}) = J\left(\underline{\tilde{z}}_0, \bar{\tilde{z}}_0, \tilde{\varphi}\right) \tag{3.35}$$

Utilise it to estimate the initial approximation applying Newton's approach. Let $\tilde{z}_k(\tilde{\varphi}) = (\underline{\tilde{z}}_k, \bar{\tilde{z}}_k, \tilde{\varphi})$, then

$$\tilde{z}_1(\tilde{\varphi}) = \tilde{z}_0(\tilde{\varphi}) - P_0(\tilde{\varphi})^{-1}\tilde{F}(\tilde{z}_0(\tilde{\varphi})) \tag{3.36}$$

For $k \geq 1$, Assuming $\tilde{z}_1(\tilde{\varphi})$ has been obtained, and apply the next several steps to get $\tilde{z}_2(\tilde{\varphi})$.

5. Calculate the function

$$\tilde{F}\left(\underline{\tilde{z}}_1, \bar{\tilde{z}}_1, \tilde{\varphi}\right) = \begin{bmatrix} \underline{\tilde{F}}\left(\underline{\tilde{z}}_1, \bar{\tilde{z}}_1, \tilde{\varphi}\right) \\ \bar{\tilde{F}}\left(\underline{\tilde{z}}_1, \bar{\tilde{z}}_1, \tilde{\varphi}\right) \end{bmatrix} \tag{3.37}$$

6. Update the Jacobian matrix by utilising $\tilde{s}_k(\tilde{\varphi}) = \tilde{z}_k(\tilde{\varphi}) - \tilde{z}_{k-1}(\tilde{\varphi})$ and $\tilde{z}_k(\tilde{\varphi}) = \tilde{F}(\tilde{z}_k(\tilde{\varphi}) - \tilde{F}(\tilde{z}_{k-1}(\tilde{\varphi}))$, for $k = 1,2,\ldots, n$.
7. Calculate $P_i(\tilde{\varphi})^{-1}$ Using the Sherman-Morrison formula is as follows

$$P_1(\tilde{\varphi})^{-1} = P_0(\tilde{\varphi})^{-1} + \frac{[\tilde{s}_1(\tilde{\varphi}) - P_0(\tilde{\varphi})^{-1}\tilde{z}_1(\tilde{\varphi})]\tilde{s}_1(\tilde{\varphi})^t P_0(\tilde{\varphi})^{-1}}{\tilde{s}_1(\tilde{\varphi})^t P_0(\tilde{\varphi})^{-1}\tilde{z}_1(\tilde{\varphi})} \tag{3.38}$$

8. Solve the linear system $P_1(\tilde{\varphi})\ \tilde{z}_2(\tilde{\varphi}) = (\tilde{z}_1(\tilde{\varphi}) - \tilde{F}(\tilde{z}_1(\tilde{\varphi}))$ for $\tilde{z}_2(\tilde{\varphi})$.
9. Check the tolerance conditions $\epsilon \leq 10^{-5}$ is satisfied, repeat Steps 4 to 8 until the condition is reached.

Mathematical formulation

The objective is to determine the solution for FNE.

$$\tilde{F}(\tilde{z}) = \tilde{d} \tag{3.39}$$

Equation (3.39) can be described as

$$\begin{cases} \underline{\tilde{F}}(\underline{\tilde{z}}, \bar{\tilde{z}}, \tilde{s}) = \underline{\tilde{d}}(\tilde{s}), \forall \tilde{s} \in [0,1] \\ \bar{\tilde{F}}(\underline{\tilde{z}}, \bar{\tilde{z}}, \tilde{s}) = \bar{\tilde{d}}(\tilde{s}) \end{cases} \tag{3.40}$$

Let us assume that $\tilde{z} = (\underline{\tilde{\psi}}, \bar{\tilde{\psi}})$ be the solution of (3.39)

$$\begin{cases} \underline{\tilde{F}}(\underline{\tilde{\psi}}, \bar{\tilde{\psi}}, \tilde{s}) = \underline{\tilde{d}}(\tilde{s}), \forall \tilde{s} \in [0,1] \\ \bar{\tilde{F}}(\underline{\tilde{\psi}}, \bar{\tilde{\psi}}, \tilde{s}) = \bar{\tilde{d}}(\tilde{s}). \end{cases} \tag{3.41}$$

Solve the above system (3.40) to obtain the initial guess $\tilde{z}_0$ [57]. Then calculate the initial approximation $\tilde{z}_1$ by using Newton's method. Let $\tilde{z}_k(\tilde{\varphi}) = (\underline{\tilde{z}}_k, \bar{\tilde{z}}_k, \tilde{\varphi})$, then

$$\tilde{z}_1(\tilde{\varphi}) = \tilde{z}_0(\tilde{\varphi}) - P_0(\tilde{\varphi})^{-1}\tilde{F}(\tilde{z}_0(\tilde{\varphi})) \tag{3.42}$$

where $P_0(\tilde{\varphi})$ represents the Jacobian matrix. i.e,

$$P_0(\tilde{\varphi}) = J\left(\underline{\tilde{z}}_0, \bar{\tilde{z}}_0, \tilde{\varphi}\right) \tag{3.43}$$

Calculate the function

$$\tilde{F}\left(\underline{\tilde{z}}_1, \bar{\tilde{z}}_1, \tilde{\varphi}\right) = \begin{bmatrix} \underline{\tilde{F}}\left(\underline{\tilde{z}}_1, \bar{\tilde{z}}_1, \tilde{\varphi}\right) \\ \bar{\tilde{F}}\left(\underline{\tilde{z}}_1, \bar{\tilde{z}}_1, \tilde{\varphi}\right) \end{bmatrix} \tag{3.44}$$

Update the Jacobian matrix by utilising $\tilde{s}_k(\tilde{\varphi}) = \tilde{z}_k(\tilde{\varphi}) - \tilde{z}_{k-1}(\tilde{\varphi})$ and $\tilde{z}_k(\tilde{\varphi}) = \tilde{F}(\tilde{z}_k(\tilde{\varphi}) - \tilde{F}(\tilde{z}_{k-1}(\tilde{\varphi}))$, for $k = 1, 2, \ldots, n$. Compute $P_o(\tilde{\varphi})^{-1}$ by using the formula in (3.38) [58].

Fixed Newton Method

The Fixed Newton Method (FNM) is an iterative numerical approach that estimates successively improved approximations to the solution. The strategy, which uses the function and its derivative to estimate the root, is particularly effective for well-behaved tasks that are close to their roots. The method focuses on the concept of linear approximation, which is the foundation of the approach [22]. The favourable feature of this technique is that it neglects the evaluation of the Jacobian matrix for all subsequent iterations except for the initial iteration. The flaw of this approach is that it is less efficient than the conventional Newton approach, and it notably addresses the inaccuracy in determining the approximate solution after n iterations in the Newton method [59]. We reviewed the FNM algorithm [22] for solving FNE as follows

$$\tilde{z}_{k+1} = \tilde{z}_k - J(\tilde{z}_0)^{-1} * F(\tilde{z}_k) \tag{3.45}$$

Algorithm

1. Guess the initial approximation $\tilde{z}_0$.
2. Compute $F(\tilde{z}_k)$ and $J(\tilde{z}_0)$.
3. Set $\tilde{z}_{k+1} = \tilde{z}_k - J(\tilde{z}_0)^{-1} * F(\tilde{z}_k)$.
4. Check $|\tilde{z} - \tilde{z}_0| < \epsilon$.

5. Set $\tilde{z}_k = \tilde{z}_{k+1}$ and go to step 2 until we converge on the solution.

Here k represents the iteration index, $\tilde{z}_k$ indicates the vector $\tilde{z}$ after k iterations, $J(\tilde{z}_k)$ denotes the Jacobian matrix, $\tilde{F}(\tilde{z}_k)$ denotes the function value and ϵ is an error tolerance.

Mathematical formulation

The objective is to determine the solution for FNE.

$$\tilde{F}(\tilde{z}) = \tilde{d} \tag{3.46}$$

Equation (3.46) can be described as

$$\begin{cases} \underline{\tilde{F}}(\underline{\tilde{z}}, \bar{\tilde{z}}, \tilde{s}) = \underline{\tilde{d}}(\tilde{s}), \forall \tilde{s} \in [0,1] \\ \bar{\tilde{F}}(\underline{\tilde{z}}, \bar{\tilde{z}}, \tilde{s}) = \bar{\tilde{d}}(\tilde{s}). \end{cases} \tag{3.47}$$

Let us assume that $\tilde{z} = (\underline{\tilde{\psi}}, \bar{\tilde{\psi}})$ be the solution of (3.47)

$$\begin{cases} \underline{\tilde{F}}(\underline{\tilde{\psi}}, \bar{\tilde{\psi}}, \tilde{s}) = \underline{\tilde{d}}(\tilde{s}), \forall \tilde{s} \in [0,1] \\ \bar{\tilde{F}}(\underline{\tilde{\psi}}, \bar{\tilde{\psi}}, \tilde{s}) = \bar{\tilde{d}}(\tilde{s}). \end{cases} \tag{3.48}$$

Let $\tilde{z}_0 = (\underline{\tilde{z}}_0, \bar{\tilde{z}}_0)$ is an approximate solution, then $\forall \tilde{s} \in [0,1]$, there are $h(\tilde{s})$, $k(\tilde{s})$ such that

$$\begin{cases} \underline{\tilde{\psi}}(\tilde{s}) = \underline{\tilde{z}}_0(\tilde{s}) + h(\tilde{s}) \\ \bar{\tilde{\psi}}(\tilde{s}) = \bar{\tilde{z}}_0(\tilde{s}) + k(\tilde{s}) \end{cases} \tag{3.49}$$

The solution for $h(\tilde{s})$ and $k(\tilde{s})$ can be computed by solving the equations below,

$$J\left(\underline{\tilde{z}}_0, \bar{\tilde{z}}_0, \tilde{s}\right) \begin{bmatrix} h(\tilde{s}) \\ k(\tilde{s}) \end{bmatrix} = \begin{bmatrix} \underline{\tilde{d}}(\tilde{s}) - \underline{\tilde{F}}\left(\underline{\tilde{z}}_0, \bar{\tilde{z}}_0, \tilde{s}\right) \\ \bar{\tilde{d}}(\tilde{s}) - \bar{\tilde{F}}\left(\underline{\tilde{z}}_0, \bar{\tilde{z}}_0, \tilde{s}\right) \end{bmatrix}, \tag{3.50}$$

where

$$J\left(\underline{\tilde{z}}_0, \tilde{z}_0, \tilde{s}\right) = \begin{bmatrix} \underline{\tilde{F}}_{\underline{z}}\left(\underline{\tilde{z}}_0, \tilde{z}, \tilde{s}\right) & \underline{\tilde{F}}_{\bar{z}}\left(\underline{\tilde{z}}_0, \tilde{z}_0, \tilde{s}\right) \\ \bar{\tilde{F}}_{\underline{z}}\left(\underline{\tilde{z}}_0, \bar{\tilde{z}}_0, \tilde{s}\right) & \bar{\tilde{F}}_{\bar{z}}\left(\underline{\tilde{z}}_0, \tilde{z}_0, \tilde{s}\right) \end{bmatrix} \tag{3.51}$$

As a result, the following estimates for $\underline{\tilde{z}}(\tilde{s})$ and $\bar{\tilde{z}}(\tilde{s})$ are stated as follows

$$\begin{cases} \underline{\tilde{z}}_1(\tilde{s}) = \underline{\tilde{z}}_0(\tilde{s}) + h(\tilde{s}) \\ \bar{\tilde{z}}_1(\tilde{s}) = \bar{\tilde{z}}_0(\tilde{s}) + k(\tilde{s}) \end{cases} \tag{3.52}$$

for all $\tilde{s} \in [0,1]$ The estimated solution can be obtained by utilizing the equations,

$$\begin{cases} \underline{\tilde{z}}_n(\tilde{s}) = \underline{\tilde{z}}_{n-1}(\tilde{s}) + h_{n-1}(\tilde{s}) \\ \bar{\tilde{z}}_n(\tilde{s}) = \bar{\tilde{z}}_{n-1}(\tilde{s}) + k_{n-1}(\tilde{s}) \end{cases} \tag{3.53}$$

The approximated solution obtained for different n values.

$$\tilde{z}_0 = (\underline{\tilde{z}}(1), \tilde{z}(1), \underline{\tilde{z}}(1) - \underline{\tilde{z}}(0), \tilde{z}(0) - \tilde{z}(1)), \tag{3.54}$$

Equation (3.54) can be described as [3]

$$\begin{aligned} \underline{\tilde{z}}_0(\tilde{s}) &= \underline{\tilde{z}}(1) + (\underline{\tilde{z}}(1) - \underline{\tilde{z}}(0))(\tilde{s} - 1), \\ \tilde{z}_0(\tilde{s}) &= \tilde{z}(1) + (\tilde{z}(0) - \tilde{z}(1))(1 - \tilde{s}) \end{aligned} \tag{3.55}$$

This method computes the Jacobian matrix only for the initial estimate, then uses it for subsequent approximations.

Improved False Position Method

The Regula Falsi method [23] is one of the oldest bracketing approaches to determining the roots of nonlinear equations. This method enhances the suboptimal convergence rate of the Bisection method and its limited adaptation for higher-dimensional problems. Researchers have proposed several enhancements to this method. To enhance this technique, [60] presents an augmented variant of the False Position approach defined as the Improved False Position Method (IFPM). The advantages of this method are that it is one of the most effective bracketing methodologies for solving nonlinear equations and computing derivatives, which is both simple and straightforward. This method is ineffective for solving FNEs, as it may repeatedly use the same endpoints [61]. We reviewed the IFPM algorithm [23, 26] for solving FNE as follows

$$\tilde{z}_n^{IFPM} = \frac{x_n \tilde{f}(y_n) - \frac{1}{2} y_n \tilde{f}(x_n)}{\tilde{f}(y_n) - \frac{1}{2} \tilde{f}(x_n)} \tag{3.56}$$

Algorithm

Let us assume $\tilde{f}(\tilde{z})$ on $[x, y]$ be given, satisfying the following condition

$$\tilde{f}(x) * \tilde{f}(y) < 0$$

1. Consider $x_n = x$ and $y_n = y$ for $n = 0, 1, 2, \ldots$
2. Calculate

$$\tilde{z}_n = \frac{x_n \tilde{f}(y_n) - \frac{1}{2} y_n \tilde{f}(x_n)}{\tilde{f}(y_n) - \frac{1}{2} \tilde{f}(x_n)} \tag{3.57}$$

3. Verify if $\tilde{f}(x_n) * \tilde{f}(\tilde{z}_n) < 0$ then set $x_{n+1} = x_n$ and $y_{n+1} = \tilde{z}_n$ else, $x_{n+1} = \tilde{z}_n$ and $y_{n+1} = y_n$
4. Verify the tolerance condition $|\tilde{f}(x_n)| < \epsilon$ is satisfied [48]

Mathematical formulation

The objective is to determine the solution for FNE defined as [26]

$$\tilde{P}_n(\tilde{z}) = \tilde{a} \tag{3.58}$$

where $\tilde{a}$ is defined as the same as $\tilde{a}_j$ in $\tilde{P}_n(z)$.

Assume $\tilde{a}_j = (\underline{\tilde{a}}_j, \bar{\tilde{a}}_j)$ and $\tilde{a} = (\underline{\tilde{a}}, \bar{\tilde{a}})$ where

$$\underline{\tilde{a}}_j = \sum_{i=0}^{n} b_{ij} r^i, \bar{\tilde{a}}_j = \sum_{i=0}^{n} c_{ij} r^i \tag{3.59}$$

$$\underline{\tilde{a}} = \sum_{i=0}^{n} g_i r^i, \bar{\tilde{a}} = \sum_{i=0}^{n} h_i r^i \tag{3.60}$$

If z is a positive value, we will have

$$\left(\sum_{j=0}^{n} \underline{\tilde{a}}_j \tilde{z}^j, \sum_{j=0}^{n} \bar{\tilde{a}}_j \tilde{z}^j \right) = (\underline{\tilde{a}}, \bar{\tilde{a}}) \tag{3.61}$$

which leads to

$$\underline{\tilde{a}} = \sum_{j=0}^{n} \underline{\tilde{a}}_j \tilde{z}^j, \bar{\tilde{a}} = \sum_{j=0}^{n} \bar{\tilde{a}}_j \tilde{z}^j \tag{3.62}$$

Substituting (3.60) in (3.62), we have

$$g_i = \sum_{j=0}^{n} b_{ij} \tilde{z}^j, h_i = \sum_{j=0}^{n} c_{ij} \tilde{z}^j, i = 0,1,2,\dots,n \tag{3.63}$$

Therefore, we utilize the Improved False Position approach to resolve the equation mentioned above.

Numerical Examples

The section focuses on solving several numerical examples using existing methods and compares these methods to validate their computational efficiency. The representation of existing methods is as follows: Newton Method (NM), Steepest Descent Method (SDM), Homotopy Method (HM), Broyden Method (BM), Fixed Newton Method (FNM), and Improved False Position Method (IFPM). The computational procedure was coded in MATLAB software. Next, we address some example problems using the above-mentioned methods.

Example 1: The FNE can be examined with the following example.

$$(5,6,7)\tilde{z}^2 + (4,5,6)\tilde{z} = (4,5,6) \tag{4.1}$$

Equation (4.1) can be described as

$$\begin{cases} (5+\tilde{s})\underline{\tilde{z}}^2(\tilde{s}) + (4+\tilde{s})\underline{\tilde{z}}(\tilde{s}) = (4+\tilde{s}) \\ (7-\tilde{s})\bar{\tilde{z}}^2(\tilde{s}) + (6-\tilde{s})\bar{\tilde{z}}(\tilde{s}) = (6-\tilde{s}) \end{cases} \tag{4.2}$$

or similar

$$\begin{cases} (5+\tilde{s})\underline{\tilde{z}}^2(\tilde{s}) + (4+\tilde{s})\underline{\tilde{z}}(\tilde{s}) - (4+\tilde{s}) = 0 \\ (7-\tilde{s})\bar{\tilde{z}}^2(\tilde{s}) + (6-\tilde{s})\bar{\tilde{z}}(\tilde{s}) - (6-\tilde{s}) = 0 \end{cases} \tag{4.3}$$

Put $\tilde{s} = 0$ and $\tilde{s} = 1$ in (4.3) to generate an initial guess.

$$\begin{cases} 6\underline{\tilde{z}}^2(1) + 5\underline{\tilde{z}}(1) = 5 \\ 6\bar{\tilde{z}}^2(1) + 5\bar{\tilde{z}}(1) = 5 \end{cases} \text{and} \begin{cases} 5\underline{\tilde{z}}^2(0) + 4\underline{\tilde{z}}(0) = 4 \\ 7\bar{\tilde{z}}^2(0) + 6\bar{\tilde{z}}(0) = 6 \end{cases} \tag{4.4}$$

As a result, $\underline{\tilde{z}}(0) = 0.579796$, $\bar{\tilde{z}}(0) = 0.591633$ and $\underline{\tilde{z}}(1) = \bar{\tilde{z}}(1) = 0.586800$. Therefore, the initial guess is $\tilde{z}_0 = (0.579796,0.586800,0.591633)$. The comparison of results is given in Table 1, and the convergence behaviour is shown in Figure 1.

Example 2: The FNE can be examined with the following example.

$$(5,7,9)\tilde{z}^2 + (1,3,5)\tilde{z} = (1,3,5) \tag{4.5}$$

Equation (4.5) can be described as

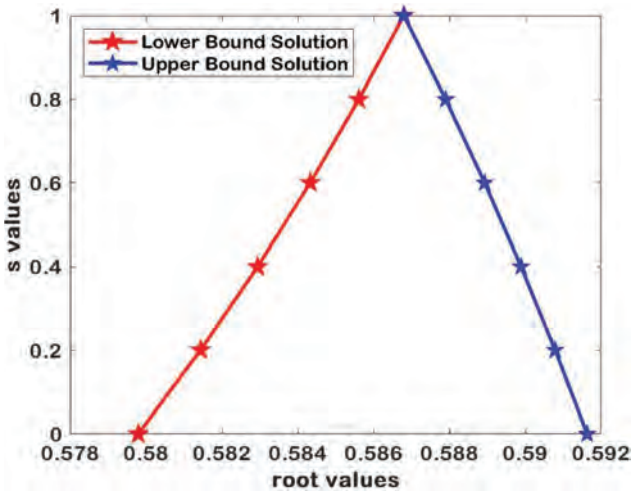


Figure 1. Numerical solution for Example 1.

Table 1. Comparison of NM, SDM, HM, BM, FNM, and IFPM

				Number of Iterations					
S.No.	$\tilde{s}$	$\underline{\tilde{z}}(\tilde{s})$	$\bar{\tilde{z}}(\tilde{s})$	**NM**	**SDM**	**HM**	**BM**	**FNM**	**IFPM**
1	$\tilde{s}$=0	0.579796	0.591633	1	17	148	9	3	29
2	$\tilde{s}$=0.2	0.581438	0.59079	2	14	148	9	3	29
3	$\tilde{s}$=0.4	0.582944	0.589891	2	14	148	9	4	29
4	$\tilde{s}$=0.6	0.584331	0.588931	3	12	148	9	4	29
5	$\tilde{s}$=0.8	0.585612	0.587903	3	9	148	9	4	29
6	$\tilde{s}$=1	0.586800	0.586800	3	8	148	9	4	29

$$\begin{cases}(5+2\tilde{s})\underline{\tilde{z}}^2(\tilde{s})+(1+2\tilde{s})\underline{\tilde{z}}(\tilde{s})=(1+2\tilde{s})\\(9-2\tilde{s})\bar{\tilde{z}}^2(\tilde{s})+(5-2\tilde{s})\bar{\tilde{z}}(\tilde{s})=(5-2\tilde{s})\end{cases} \quad (4.6)$$

or similar

$$\begin{cases}(5+2\tilde{s})\underline{\tilde{z}}^2(\tilde{s})+(1+2\tilde{s})\underline{\tilde{z}}(\tilde{s})-(1+2\tilde{s})=0\\(9-2\tilde{s})\bar{\tilde{z}}^2(\tilde{s})+(5-2\tilde{s})\bar{\tilde{z}}(\tilde{s})-(5-2\tilde{s})=0\end{cases} \quad (4.7)$$

Put $\tilde{s}=0$ and $\tilde{s}=1$ in (4.7) to generate an initial guess.

$$\begin{cases}7\underline{\tilde{z}}^2(1)+3\underline{\tilde{z}}(1)=3\\7\bar{\tilde{z}}^2(1)+3\bar{\tilde{z}}(1)=3\end{cases} \text{ and } \begin{cases}5\underline{\tilde{z}}^2(0)+\underline{\tilde{z}}(0)=1\\9\bar{\tilde{z}}^2(0)+5\bar{\tilde{z}}(0)=5\end{cases} \quad (4.8)$$

As a result, $\underline{\tilde{z}}(0)=0.358258$, $\bar{\tilde{z}}(0)=0.517657$ and $\underline{\tilde{z}}(1)=\bar{\tilde{z}}(1)=0.474546$. Therefore, the initial guess is $\tilde{z}_0=(0.358258,0.474546,0.517657)$. The comparison of results is given in Table 2, and the convergence behaviour is shown in Figure 2.

Example 3: The FNE can be examined with the following example.

$$(6,8,10)\tilde{z}^2+(2,4,6)\tilde{z}=(2,4,6) \quad (4.9)$$

Equation (4.9) can be described as

$$\begin{cases}(6+2\tilde{s})\underline{\tilde{z}}^2(\tilde{s})+(2+2\tilde{s})\underline{\tilde{z}}(\tilde{s})=(2+2\tilde{s})\\(10-2\tilde{s})\bar{\tilde{z}}^2(\tilde{s})+(6-2\tilde{s})\bar{\tilde{z}}(\tilde{s})=(6-2\tilde{s})\end{cases} \quad (4.10)$$

or similar

$$\begin{cases}(6+2\tilde{s})\underline{\tilde{z}}^2(\tilde{s})+(2+2\tilde{s})\underline{\tilde{z}}(\tilde{s})-(2+2\tilde{s})=0\\(10-2\tilde{s})\bar{\tilde{z}}^2(\tilde{s})+(6-2\tilde{s})\bar{\tilde{z}}(\tilde{s})-(6-2\tilde{s})=0\end{cases} \quad (4.11)$$

Put $\tilde{s}=0$ and $\tilde{s}=1$ in (4.11) to generate an initial guess.

$$\begin{cases}8\underline{\tilde{z}}^2(1)+4\underline{\tilde{z}}(1)=4\\8\bar{\tilde{z}}^2(1)+4\bar{\tilde{z}}(1)=4\end{cases} \text{ and } \begin{cases}6\underline{\tilde{z}}^2(0)+2\underline{\tilde{z}}(0)=2\\10\bar{\tilde{z}}^2(0)+6\bar{\tilde{z}}(0)=6\end{cases} \quad (4.12)$$

As a result, $\underline{\tilde{z}}(0)=0.434259$, $\bar{\tilde{z}}(0)=0.530662$ and $\underline{\tilde{z}}(1)=\bar{\tilde{z}}(1)=0.500000$. Therefore, the initial guess is $\tilde{z}_0=(0.434259,0.500000,0.530662)$. The comparison of results is given in Table 3, and the convergence behaviour is shown in Figure 3.

Example 4: The FNE can be examined with the following example.

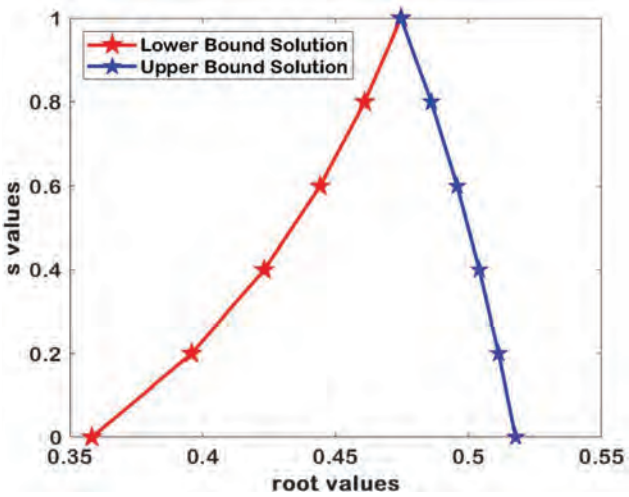


Figure 2. Numerical solution for Example 2.

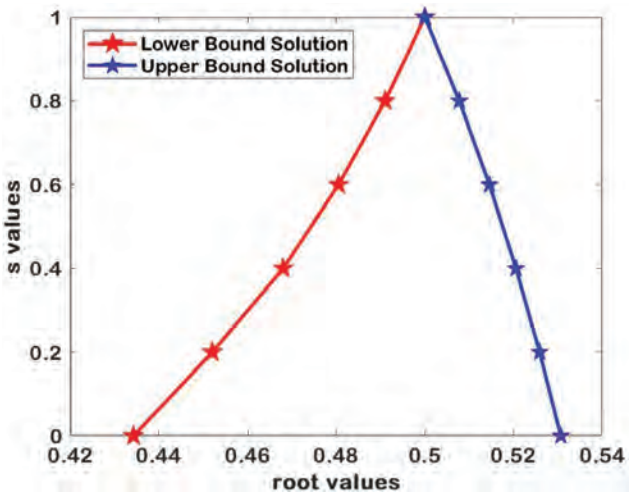


Figure 3. Numerical solution for Example 3.

Table 2. Comparison of NM, SDM, HM, BM, FNM, and IFPM

				Number of Iterations					
S.No.	$\tilde{s}$	$\underline{\tilde{z}}(\tilde{s})$	$\bar{\tilde{z}}(\tilde{s})$	**NM**	**SDM**	**HM**	**BM**	**FNM**	**IFPM**
1	$\tilde{s}$=0	0.358258	0.517657	1	19	148	9	2	33
2	$\tilde{s}$=0.2	0.395787	0.511281	3	17	148	9	4	33
3	$\tilde{s}$=0.4	0.423121	0.504022	4	18	148	9	4	33
4	$\tilde{s}$=0.6	0.444124	0.495677	4	12	148	9	4	33
5	$\tilde{s}$=0.8	0.460857	0.485976	4	14	148	9	4	34
6	$\tilde{s}$=1	0.474546	0.474546	4	17	148	9	4	34

Table 3. Comparison of NM, SDM, HM, BM, FNM, and IFPM

				Number of Iterations					
S.No.	$\tilde{s}$	$\underline{\tilde{z}}(\tilde{s})$	$\bar{\tilde{z}}(\tilde{s})$	**NM**	**SDM**	**HM**	**BM**	**FNM**	**IFPM**
1	$\tilde{s}$=0	0.434259	0.530662	1	15	148	9	2	36
2	$\tilde{s}$=0.2	0.452934	0.525892	3	10	148	9	3	35
3	$\tilde{s}$=0.4	0.468026	0.520563	3	19	148	9	4	35
4	$\tilde{s}$=0.6	0.480506	0.514569	3	15	148	9	4	34
5	$\tilde{s}$=0.8	0.491017	0.507773	3	12	148	9	4	34
6	$\tilde{s}$=1	0.500000	0.500000	3	9	148	9	4	33

$$(4,5,6)\tilde{z}^2 + (1,2,3)\tilde{z} = (1,2,3) \tag{4.13}$$

Equation (4.13) can be described as

$$\begin{cases}(4+\tilde{s})\underline{\tilde{z}}^2(\tilde{s}) + (1+\tilde{s})\underline{\tilde{z}}(\tilde{s}) = (1+\tilde{s})\\ (6-\tilde{s})\bar{\tilde{z}}^2(\tilde{s}) + (3-\tilde{s})\bar{\tilde{z}}(\tilde{s}) = (3-\tilde{s})\end{cases} \tag{4.14}$$

or similar

$$\begin{cases}(4+\tilde{s})\underline{\tilde{z}}^2(\tilde{s}) + (1+\tilde{s})\underline{\tilde{z}}(s) - (1+\tilde{s}) = 0\\ (6-\tilde{s})\bar{\tilde{z}}^2(\tilde{s}) + (3-\tilde{s})\bar{\tilde{z}}(\tilde{s}) - (3-\tilde{s}) = 0\end{cases} \tag{4.15}$$

Put $\tilde{s}$ = 0 and $\tilde{s}$ = 1 in (4.15) to generate an initial guess.

$$\begin{cases}5\underline{\tilde{z}}^2(1) + 2\underline{\tilde{z}}(1) = 2\\ 5\bar{\tilde{z}}^2(1) + 2\bar{\tilde{z}}(1) = 2\end{cases} \text{ and } \begin{cases}4\underline{\tilde{z}}^2(0) + \underline{\tilde{z}}(0) = 1\\ 6\bar{\tilde{z}}^2(0) + 3\bar{\tilde{z}}(0) = 3\end{cases} \tag{4.16}$$

As a result, $\underline{\tilde{z}}(0)$ = 0.390388, $\bar{\tilde{z}}(0)$ = 0.500000 and $\underline{\tilde{z}}(1)$ = $\bar{\tilde{z}}(1)$ = 0.463325. Therefore, the initial guess is $\tilde{z}_0$ = (0.390388,0.463325,0.500000). The comparison of results is given in Table 4, and the convergence behaviour is shown in Figure 4.

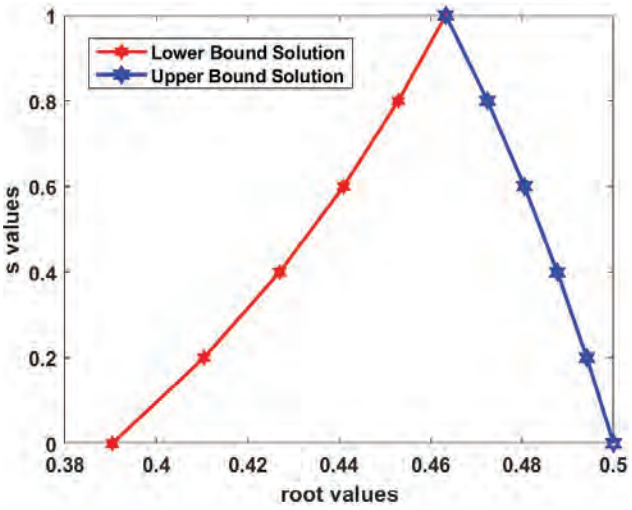


Figure 4. Numerical solution for Example 4.

RESULTS AND DISCUSSION

This section focuses on analysis and comparison of the efficacy of various numerical methods, including NM, SDM, HM, BM, FNM, and IFPM, for solving FNEs. After applying these approaches to resolve several example problems, we noted a distinct superiority of Newton's Method compared to the alternatives. FNM, a modification of Newton's Method for fuzzy contexts, demonstrates superior performance compared to specific conventional approaches. However, it does not exceed the iteration efficiency of Newton's Method. IFPM also exhibits slower convergence. Figures 1–4, which visually illustrate convergence behaviour and accuracy, show that Newton's Method is

Table 4. Comparison of NM, SDM, HM, BM, FNM, and IFPM

				Number of Iterations					
S.No.	$\tilde{s}$	$\underline{\tilde{z}}(\tilde{s})$	$\bar{\tilde{z}}(\tilde{s})$	**NM**	**SDM**	**HM**	**BM**	**FNM**	**IFPM**
1	$\tilde{s}$=0	0.390388	0.500000	1	18	148	9	3	31
2	$\tilde{s}$=0.2	0.410426	0.494163	2	15	148	9	3	31
3	$\tilde{s}$=0.4	0.426991	0.487702	3	15	148	9	4	31
4	$\tilde{s}$=0.6	0.440962	0.480506	3	11	148	9	4	31
5	$\tilde{s}$=0.8	0.452934	0.472439	3	9	148	9	4	31
6	$\tilde{s}$=1	0.463325	0.463325	3	8	148	9	4	31

popular due to its speed and accuracy, even though other approaches offer advantages such as adaptability or flexibility in fuzzy environments.

Review of Iterative Methods for Solving Dual Fuzzy Nonlinear Equations

The analytical approaches are ineffective for determining the solution of nonlinear equations that are fuzzy in nature. In this section, we review some iterative methods that are efficient for solving DFNE [14]. This section provides the mathematical formulation, advantages, disadvantages and produces a detailed outline of the methods and validates the results.

Duality in Fuzzy Nonlinear Systems

Generally, an arbitrary fuzzy number $\tilde{a} \in E$ excludes an inverse element [62]. i.e., there exists no element $\tilde{b} \in E$ such that

$$\tilde{a} + \tilde{b} = 0 \tag{5.1}$$

For all $\tilde{a} \in E$, we have

$$\tilde{a} + (-\tilde{a}) \neq 0 \tag{5.2}$$

Consequently, the FNE becomes

$$H(\tilde{a}) = G(\tilde{a}) + C \tag{5.3}$$

cannot be substituted with the FNE in an equivalent form

$$H(\tilde{a}) - G(\tilde{a}) = C, \tag{5.4}$$

which was examined. In the sequel, the fuzzy nonlinear equation (5.3) is referred to as the dual fuzzy nonlinear equation, where all the parameters are fuzzy numbers [14, 62].

Newton Method

Newton Method (NM) is an efficient iterative numerical technique for handling systems of nonlinear equations. The approach relies on a linear approximation of a nonlinear system. In DFNE, the approach entails determining the values of two variables that satisfy a system of equations with fuzzy numbers. The Newton Method for solving DFNE involves two stages: computing the Jacobian matrix of the equation system and solving a linear system of equations [29, 62, 63].

For the non-singular Jacobian matrix, the Newton method will converge to the exact solution from an initial approximation. The Newton Method is admired for its rapid convergence rate when utilized on well-defined systems of equations. Nevertheless, the method can lead to significant computational expenses, particularly for large systems of equations [64]. This method may fail to converge to the solution due to inexact Jacobian matrix [56]. Readers may refer to Section 3.1 for the algorithm of NM.

Mathematical formulation

The objective is to determine the solution for DFNE.

$$P(\tilde{z}) = Q(\tilde{z}) + \tilde{d} \tag{5.5}$$

Equation (5.5) can be described as

$$\begin{cases} \underline{P}(\underline{z}, \bar{z}, \tilde{s}) = \underline{Q}(\underline{z}, \bar{z}, \tilde{s}) + \underline{\tilde{d}}(\tilde{s}), \forall \tilde{s} \in [0,1]. \\ \bar{P}(\underline{z}, \bar{z}, \tilde{s}) = \bar{Q}(\underline{z}, \bar{z}, \tilde{s}) + \bar{\tilde{d}}(\tilde{s}), \end{cases} \tag{5.6}$$

Assume that $\tilde{z} = (\underline{\tilde{\psi}}, \bar{\tilde{\psi}})$ is the solution of (5.6) then

$$\begin{cases} \underline{P}(\underline{\tilde{\psi}}, \bar{\tilde{\psi}}, \tilde{s}) - \underline{Q}(\underline{\tilde{\psi}}, \bar{\tilde{\psi}}, \tilde{s}) = \underline{\tilde{d}}(\tilde{s}), \forall \tilde{s} \in [0,1]. \\ \bar{P}(\underline{\tilde{\psi}}, \bar{\tilde{\psi}}, \tilde{s}) - \bar{Q}(\underline{\tilde{\psi}}, \bar{\tilde{\psi}}, \tilde{s}) = \bar{\tilde{d}}(\tilde{s}), \end{cases} \tag{5.7}$$

Let us assume the functions $\underline{\tilde{F}}$ and $\bar{\tilde{F}}$ are as follows

$$\begin{cases} \underline{\tilde{F}}(\underline{\tilde{\psi}}, \bar{\tilde{\psi}}, \tilde{s}) = \underline{P}(\underline{\tilde{\psi}}, \bar{\tilde{\psi}}, \tilde{s}) - \underline{Q}(\underline{\tilde{\psi}}, \bar{\tilde{\psi}}, \tilde{s}), \\ \bar{\tilde{F}}(\underline{\tilde{\psi}}, \bar{\tilde{\psi}}, \tilde{s}) = \bar{P}(\underline{\tilde{\psi}}, \bar{\tilde{\psi}}, \tilde{s}) - \bar{Q}(\underline{\tilde{\psi}}, \bar{\tilde{\psi}}, \tilde{s}), \forall \tilde{s} \in [0,1] \end{cases} \tag{5.8}$$

As a result,

$$\begin{cases} \underline{\tilde{F}}(\underline{\tilde{\psi}}, \bar{\tilde{\psi}}, \tilde{s}) = \underline{\tilde{d}}(\tilde{s}), \forall \tilde{s} \in [0,1] \\ \bar{\tilde{F}}(\underline{\tilde{\psi}}, \bar{\tilde{\psi}}, \tilde{s}) = \bar{\tilde{d}}(\tilde{s}) \end{cases} \tag{5.9}$$

Let $\tilde{z}_0 = (\underline{\tilde{z}}_0, \bar{\tilde{z}}_0)$ is an approximation solution, then there are $h(\tilde{s})$, $k(\tilde{s})$ such that

$$\begin{cases} \underline{\tilde{\psi}}(\tilde{s}) = \underline{\tilde{z}}_0(\tilde{s}) + h(\tilde{s}), \\ \bar{\tilde{\psi}}(\tilde{s}) = \bar{\tilde{z}}_0(\tilde{s}) + k(\tilde{s}). \end{cases} \tag{5.10}$$

By using the Taylor series of $\underline{\tilde{F}}$, $\bar{\tilde{F}}$ about $(\underline{\tilde{z}}_0, \bar{\tilde{z}}_0)$, then for all $\tilde{s} \in [0,1]$,

$$\begin{cases} \underline{\tilde{F}}(\underline{\tilde{\psi}}, \bar{\tilde{\psi}}, \tilde{s}) = \underline{\tilde{F}}(\underline{\tilde{z}}_0, \bar{\tilde{z}}_0, \tilde{s}) + h\underline{\tilde{F}}_{\underline{z}}(\underline{\tilde{z}}_0, \bar{\tilde{z}}_0, \tilde{s}) + k\underline{\tilde{F}}_{\bar{z}}(\underline{\tilde{z}}_0, \bar{\tilde{z}}_0, \tilde{s}) + O(h^2 + hk + k^2) = \underline{\tilde{d}} \\ \bar{\tilde{F}}(\underline{\tilde{\psi}}, \bar{\tilde{\psi}}, \tilde{s}) = \bar{\tilde{F}}(\underline{\tilde{z}}_0, \bar{\tilde{z}}_0, \tilde{s}) + h\bar{\tilde{F}}_{\underline{z}}(\underline{\tilde{z}}_0, \bar{\tilde{z}}_0, \tilde{s}) + k\bar{\tilde{F}}_{\bar{z}}(\underline{\tilde{z}}_0, \bar{\tilde{z}}_0, \tilde{s}) + O(h^2 + hk + k^2) = \bar{\tilde{d}} \end{cases} \tag{5.11}$$

If $\underline{\tilde{z}}_0$ and $\bar{\tilde{z}}_0$ are close to $\underline{\tilde{\varphi}}$, $\bar{\tilde{\varphi}}$ then $h(\tilde{s})$ and $k(\tilde{s})$ are negligible for $\tilde{s} \in [0,1]$.

$$\begin{cases} \underline{\tilde{F}}(\underline{\tilde{z}}_0, \bar{\tilde{z}}_0, \tilde{s}) + h\underline{\tilde{F}}_{\underline{z}}(\underline{\tilde{z}}_0, \bar{\tilde{z}}_0, \tilde{s}) + k\underline{\tilde{F}}_{\bar{z}}(\underline{\tilde{z}}_0, \bar{\tilde{z}}_0, \tilde{s}) = \underline{\tilde{d}}(\tilde{s}) \\ \bar{\tilde{F}}(\underline{\tilde{z}}_0, \bar{\tilde{z}}_0, \tilde{s}) + h\bar{\tilde{F}}_{\underline{z}}(\underline{\tilde{z}}_0, \bar{\tilde{z}}_0, \tilde{s}) + k\bar{\tilde{F}}_{\bar{z}}(\underline{\tilde{z}}_0, \bar{\tilde{z}}_0, \tilde{s}) = \bar{\tilde{d}}(\tilde{s}) \end{cases} \tag{5.12}$$

As a result, the unknowns $h(\tilde{s})$ and $k(\tilde{s})$ can be computed for each $\tilde{s} \in [0,1]$

$$J(\underline{\tilde{z}}_0, \bar{\tilde{z}}_0, \tilde{s}) \begin{bmatrix} h(\tilde{s}) \\ k(\tilde{s}) \end{bmatrix} = \begin{bmatrix} \underline{\tilde{d}}(\tilde{s}) - \underline{\tilde{F}}(\underline{\tilde{z}}_0, \bar{\tilde{z}}_0, \tilde{s}) \\ \bar{\tilde{d}}(\tilde{s}) - \bar{\tilde{F}}(\underline{\tilde{z}}_0, \bar{\tilde{z}}_0, \tilde{s}) \end{bmatrix} \tag{5.13}$$

where

$$J(\underline{\tilde{z}}_0, \bar{\tilde{z}}_0, \tilde{s}) = \begin{bmatrix} \underline{\tilde{F}}_{\underline{z}}(\underline{\tilde{z}}_0, \bar{\tilde{z}}_0, \tilde{s}) & \underline{\tilde{F}}_{\bar{z}}(\underline{\tilde{z}}_0, \bar{\tilde{z}}_0, \tilde{s}) \\ \bar{\tilde{F}}_{\underline{z}}(\underline{\tilde{z}}_0, \bar{\tilde{z}}_0, \tilde{s}) & \bar{\tilde{F}}_{\bar{z}}(\underline{\tilde{z}}_0, \bar{\tilde{z}}_0, \tilde{s}) \end{bmatrix} \tag{5.14}$$

As a consequence, the following estimates for $\underline{y}(\tilde{s})$ and $\bar{z}(\tilde{s})$ are given:

$$\begin{cases}\underline{\tilde{z}}_1(\tilde{s}) = \underline{\tilde{z}}_0(\tilde{s}) + h(\tilde{s}) \\ \bar{\tilde{z}}_1(\tilde{s}) = \bar{\tilde{z}}_0(\tilde{s}) + k(\tilde{s}), \forall \tilde{s} \in [0,1]\end{cases} \quad (5.15)$$

Using the recursive technique, we may derive an approximate solution $\forall \tilde{s} \in [0,1]$.

$$\begin{cases}\underline{\tilde{z}}_n(\tilde{s}) = \underline{\tilde{z}}_{n-1}(\tilde{s}) + h_{n-1}(\tilde{s}) \\ \bar{\tilde{z}}_n(\tilde{s}) = \bar{\tilde{z}}_{n-1}(\tilde{s}) + k_{n-1}(\tilde{s})\end{cases} \quad (5.16)$$

where $n = 1,2,\ldots$. A fuzzy number can be used as an initial guess [43].

$$\tilde{z}_0 = (\underline{\tilde{z}}(1), \tilde{z}(1), \underline{\tilde{z}}(1) - \underline{\tilde{z}}(0), \tilde{z}(0) - \tilde{z}(1)) \quad (5.17)$$

The parametric form of (5.17) is as follows

$$\begin{aligned}\underline{\tilde{z}}_0(s) &= \underline{\tilde{z}}(1) + (\underline{\tilde{z}}(1) - \underline{\tilde{z}}(0))(\tilde{s} - 1) \\ \bar{\tilde{z}}_0(s) &= \bar{\tilde{z}}(1) + (\bar{\tilde{z}}(0) - \bar{\tilde{z}}(1))(1 - \tilde{s}).\end{aligned} \quad (5.18)$$

Broyden's and Newton's Method

Broyden developed an iterative method for resolving FNE [20, 65]. This method is a powerful tool for resolving FNE, as it allows numerous solutions and converges to a fuzzy solution that precisely depicts the system's uncertainty. This work employs both Newton's method and Broyden's method, which is referred to as Broyden's Newton's method (BNM) for solving DFNE. The Newton method was applied for the initial approximation, and Broyden's method was utilized for the remaining iterations [29, 66]. The major benefit of using these methods is that they can handle the DFNE, which is useful for modelling uncertainty in real-world problems. Both approaches may converge efficiently if the starting value is closer to the solution. If the Jacobian matrix is accurate, then Newton's method converges faster compared to Broyden's method [67]. The downside of these methods is that for an inaccurate Jacobian matrix, Broyden's method may become unstable, leading to slower convergence or divergence. The number of equations is high, making Newton's method computationally expensive due to the need to calculate the Jacobian matrix at each iteration [67]. We reviewed the BNM algorithm [29] for solving DFNE as follows

$$\tilde{z}_{i+1}(\tilde{\varphi}) = \tilde{z}_i(\tilde{\varphi}) - B_i(\tilde{\varphi})^{-1}\tilde{F}(\tilde{z}_i) \quad (5.19)$$

Where $B_i(\tilde{\varphi})^{-1}$ represents the Jacobian matrix, and it can be determined by utilizing the following formula

$$B_i(\tilde{\varphi}) * s_i(\tilde{\varphi}) = y_i(\tilde{\varphi}) \quad (5.20)$$

where $\tilde{s}_i(\tilde{\varphi}) = \tilde{z}_i(\tilde{\varphi}) - \tilde{z}_{i-1}(\tilde{\varphi})$ and $y_i(\tilde{\varphi}) = \tilde{F}(\tilde{z}_i(\tilde{\varphi})) - \tilde{F}(\tilde{z}_{i-1}(\tilde{\varphi}))$, for $i = 1,2,\ldots, n$.

From (5.19), update the Broyden matrix $B_{i+1}(\tilde{\varphi})$ using the following formula [65]

$$B_i(\tilde{\varphi}) = B_{i-1}(\tilde{\varphi}) + \frac{(y_i(\tilde{\varphi}) - B_i(\tilde{\varphi}) * s_i(\tilde{\varphi}))s_i(\tilde{\varphi})^T}{s_i(\tilde{\varphi})^T * s_i(\tilde{\varphi})} \quad (5.21)$$

Algorithm

1. Convert the DFNE into parametric form.
2. To obtain the initial guess z_0 put $\tilde{\varphi} = 0$ and $\tilde{\varphi} = 1$
3. Calculate the

$$J(\underline{\tilde{z}}_0, \bar{\tilde{z}}_0, \tilde{\varphi}) = B_0(\tilde{\varphi}) \quad (5.22)$$

using (5.22), calculate $\tilde{\varphi}_1$ through Newton's method, hence

$$\tilde{z}_1(s) = \tilde{z}_0(\tilde{\varphi}) - B_0(\tilde{\varphi})^{-1}\tilde{F}(\tilde{z}_0)(\tilde{\varphi}) \quad (5.23)$$

then compute

$$\tilde{F}(\underline{\tilde{z}}_1, \bar{\tilde{z}}_1, \tilde{\varphi}) = \begin{bmatrix}\underline{\tilde{F}}(\underline{\tilde{z}}_1, \bar{\tilde{z}}_1, \tilde{\varphi}) \\ \bar{\tilde{F}}(\underline{\tilde{z}}_1, \bar{\tilde{z}}_1, \tilde{\varphi})\end{bmatrix} \quad (5.24)$$

4. Calculate $s_i(\tilde{\varphi}) = \tilde{z}_i(\tilde{\varphi})$ - $\tilde{z}_{i-1}(\tilde{\varphi})$ and $\tilde{z}_k(s) = \tilde{F}$ $(\tilde{z}_k(\tilde{\varphi})$ - $\tilde{F}(\tilde{z}_{i-1}(\tilde{\varphi}))$ utilizing Broyden's matrix to make adjustments to the present $1 \le i \le n$.
5. Now calculate the next value using Broyden's method [68].
6. Steps 3 and 4 should be repeated until the criteria ($\epsilon \le 10^{-5}$) reached.

Mathematical formulation

The objective is to determine the solution for DFNE.

$$P(\tilde{z}) = Q(\tilde{z}) + \tilde{d} \quad (5.25)$$

Equation (5.25) can be described as

$$\begin{cases}\underline{P}(\underline{\tilde{z}}, \bar{\tilde{z}}, \tilde{s}) = \underline{Q}(\underline{\tilde{z}}, \bar{\tilde{z}}, \tilde{s}) + \underline{\tilde{d}}(\tilde{s}), \forall \tilde{s} \in [0,1]. \\ \bar{P}(\underline{\tilde{z}}, \bar{\tilde{z}}, \tilde{s}) = \bar{Q}(\underline{\tilde{z}}, \bar{\tilde{z}}, \tilde{s}) + \bar{\tilde{d}}(\tilde{s}),\end{cases} \quad (5.26)$$

Assume that $\tilde{z} = (\underline{\tilde{\psi}}, \bar{\tilde{\psi}})$ is the solution of (5.26) then

$$\begin{cases}\underline{P}(\underline{\tilde{\psi}}, \bar{\tilde{\psi}}, \tilde{s}) - \underline{Q}(\underline{\tilde{\psi}}, \bar{\tilde{\psi}}, \tilde{s}) = \underline{\tilde{d}}(\tilde{s}), \forall \tilde{s} \in [0,1]. \\ \bar{P}(\underline{\tilde{\psi}}, \bar{\tilde{\psi}}, \tilde{s}) - \bar{Q}(\underline{\tilde{\psi}}, \bar{\tilde{\psi}}, \tilde{s}) = \bar{\tilde{d}}(\tilde{s}),\end{cases} \quad (5.27)$$

Let us assume the functions $\underline{\tilde{F}}$ and $\bar{\tilde{F}}$ are as follows

$$\begin{cases}\underline{\tilde{F}}(\underline{\tilde{\psi}}, \bar{\tilde{\psi}}, \tilde{s}) = \underline{P}(\underline{\tilde{\psi}}, \bar{\tilde{\psi}}, \tilde{s}) - \underline{Q}(\underline{\tilde{\psi}}, \bar{\tilde{\psi}}, \tilde{s}), \\ \bar{\tilde{F}}(\underline{\tilde{\psi}}, \bar{\tilde{\psi}}, \tilde{s}) = \bar{P}(\underline{\tilde{\psi}}, \bar{\tilde{\psi}}, \tilde{s}) - \bar{Q}(\underline{\tilde{\psi}}, \bar{\tilde{\psi}}, \tilde{s}), \forall \tilde{s} \in [0,1]\end{cases} \quad (5.28)$$

As a result,

$$\begin{cases}\underline{\tilde{F}}(\underline{\tilde{\psi}}, \bar{\tilde{\psi}}, \tilde{s}) = \underline{\tilde{d}}(\tilde{s}), \forall \tilde{s} \in [0,1] \\ \bar{\tilde{F}}(\underline{\tilde{\psi}}, \bar{\tilde{\psi}}, \tilde{s}) = \bar{\tilde{d}}(\tilde{s})\end{cases} \quad (5.29)$$

For solving (5.25), an initial estimate is necessary, followed by the generation of a sequence of points $\{\tilde{z}_k\}_{k\ge 0}$ [69,70].

Quasi Newton Method

When a function is non-linear and lacks an easily computable derivative, the Quasi-Newton method (QNM) serves as a numerical optimization algorithm to determine

its minimum (or maximum). It is an enhancement of Newton's algorithm that utilizes a second-order derivative to evaluate crucial points. For high-dimensional challenges, computing the Hessian matrix can be computationally intensive. The Quasi-Newton approach primarily uses the first-order derivative to estimate the Hessian matrix. This results in a more efficient approach that preserves much of the efficacy of Newton's method while reducing computational expenses [65].

The major advantages of this method are that it converges more quickly than the Steepest Descent approach, it can handle a wide range of objective functions, including those that are not smooth or differentiable, and it is computationally efficient since it does not require computing the Hessian matrix at each iteration [65, 71]. Additionally, this method has some drawbacks. If the initial Hessian matrix approximation is inaccurate, it may converge slowly or diverge, depending on whether the step size is excessively large or too small. This method may oscillate or converge slowly depending on the problem structure and initial approximation; this method may converge to a local minimum [65]. We reviewed the QNM algorithm [30] for solving DFNE as follows

$$\tilde{z}_{i+1}(\tilde{\varphi}) = \tilde{z}_i(\tilde{\varphi}) - B_i(\tilde{\varphi})^{-1}F(\tilde{z}_i) \tag{5.30}$$

Where $B_i(\tilde{\varphi})^{-1}$ represents the Jacobian matrix, and it can be determined from the following

$$B_i(\tilde{\varphi}) * \tilde{s}_i(\tilde{\varphi}) = y_i(\tilde{\varphi}) \tag{5.31}$$

where $s_i(\tilde{\varphi}) = \tilde{z}_i(\tilde{\varphi}) - \tilde{z}_{i-1}(\tilde{\varphi})$ and $y_i(\tilde{\varphi}) = F(\tilde{z}_i(\tilde{\varphi}) - F(\tilde{z}_{i-1}(\tilde{\varphi}))$ for $i = 1, 2, \ldots, n$. The above condition is referred to as the Quasi Newton Condition [66, 72]. We choose the Jacobian matrix $B_0(\tilde{\varphi})^{-1}$ in (5.30) for the initial approximation, and then update the $B_i(\tilde{\varphi})$ by utilizing the following

$$B_i(\tilde{\varphi}) = B_{i-1}(\tilde{\varphi}) + \frac{(d_1(\tilde{\varphi}) - B_i(\tilde{\varphi}) * D_1(\tilde{\varphi}))d_k(\tilde{\varphi})}{d_k(\tilde{\varphi}) * D_1} \tag{5.32}$$

where $d_1 = \tilde{z} - \tilde{z}_0$, $D_1 = \tilde{F} - \tilde{F}_0$ and $d_i = (d_1^T, B_i)$

Algorithm

1. Convert the DFNE into parametric form.
2. To obtain the initial guess $\tilde{\varphi}_0$ put $\tilde{s} = 0$ and $\tilde{s} = 1$.
3. Calculate $J(\tilde{z}_0, \tilde{z}_0, \tilde{\varphi}) = B_0(\tilde{\varphi})$.
4. Calculate $B_0(\tilde{\varphi}) * \tilde{s}_i = -F(\tilde{z}_k)$
5. Calculate $B_1(\tilde{\varphi}) = B_0(\tilde{\varphi})^{-1}$.
6. Calculate the update $B_i(\tilde{\varphi})$.
7. Continue steps 3 - 6 until criteria $\epsilon \leq 10^{-4}$ is reached [30].

Mathematical formulation

The objective is to determine the solution for DFNE.

$$P(\tilde{z}) = Q(\tilde{z}) + \tilde{d} \tag{5.33}$$

Equation (5.33) can be described as

$$\begin{cases} \underline{P}(\underline{\tilde{z}}, \bar{\tilde{z}}, \tilde{s}) = \underline{Q}(\underline{\tilde{z}}, \bar{\tilde{z}}, \tilde{s}) + \underline{\tilde{d}}(\tilde{s}), \forall \tilde{s} \in [0,1]. \\ \bar{P}(\underline{\tilde{z}}, \bar{\tilde{z}}, \tilde{s}) = \bar{Q}(\underline{\tilde{z}}, \bar{\tilde{z}}, \tilde{s}) + \bar{\tilde{d}}(\tilde{s}), \end{cases} \tag{5.34}$$

Assume that $\tilde{z} = (\underline{\tilde{\psi}}, \bar{\tilde{\psi}})$ is the solution of (5.34), then

$$\begin{cases} \underline{P}(\underline{\tilde{\psi}}, \bar{\tilde{\psi}}, \tilde{s}) - \underline{Q}(\underline{\tilde{\psi}}, \bar{\tilde{\psi}}, \tilde{s}) = \underline{\tilde{d}}(\tilde{s}), \forall \tilde{s} \in [0,1]. \\ \bar{P}(\underline{\tilde{\psi}}, \bar{\tilde{\psi}}, \tilde{s}) - \bar{Q}(\underline{\tilde{\psi}}, \bar{\tilde{\psi}}, \tilde{s}) = \bar{\tilde{d}}(\tilde{s}), \end{cases} \tag{5.35}$$

Let us assume the functions $\underline{\tilde{F}}$ and $\bar{\tilde{F}}$ are as follows

$$\begin{cases} \underline{\tilde{F}}(\underline{\tilde{\psi}}, \bar{\tilde{\psi}}, \tilde{s}) = \underline{P}(\underline{\tilde{\psi}}, \bar{\tilde{\psi}}, \tilde{s}) - \underline{Q}(\underline{\tilde{\psi}}, \bar{\tilde{\psi}}, \tilde{s}), \\ \bar{\tilde{F}}(\underline{\tilde{\psi}}, \bar{\tilde{\psi}}, \tilde{s}) = \bar{P}(\underline{\tilde{\psi}}, \bar{\tilde{\psi}}, \tilde{s}) - \bar{Q}(\underline{\tilde{\psi}}, \bar{\tilde{\psi}}, \tilde{s}), \forall \tilde{s} \in [0,1] \end{cases} \tag{5.36}$$

As a result,

$$\begin{cases} \underline{\tilde{F}}(\underline{\tilde{\psi}}, \bar{\tilde{\psi}}, \tilde{s}) = \underline{\tilde{d}}(\tilde{s}), \forall \tilde{s} \in [0,1] \\ \bar{\tilde{F}}(\underline{\tilde{\psi}}, \bar{\tilde{\psi}}, \tilde{s}) = \bar{\tilde{d}}(\tilde{s}) \end{cases} \tag{5.37}$$

Let $\tilde{z}_0 = (\underline{\tilde{z}}_0, \bar{\tilde{z}}_0)$ is an approximation solution, then there are $h(\tilde{s})$, $k(\tilde{s})$ such that

$$\begin{cases} \underline{\tilde{\psi}}(\tilde{s}) = \underline{\tilde{z}}_0(\tilde{s}) + h(\tilde{s}), \\ \bar{\tilde{\psi}}(\tilde{s}) = \bar{\tilde{z}}_0(\tilde{s}) + k(\tilde{s}). \end{cases} \tag{5.38}$$

By using the Taylor series of $\underline{\tilde{F}}$, $\bar{\tilde{F}}$ about $(\underline{\tilde{z}}_0, \bar{\tilde{z}}_0)$, then for each $\tilde{s} \in [0,1]$,

$$\begin{cases} \underline{\tilde{F}}(\underline{\tilde{\psi}}, \bar{\tilde{\psi}}, \tilde{s}) = \underline{\tilde{F}}(\underline{\tilde{z}}_0, \bar{\tilde{z}}_0, \tilde{s}) + h\underline{\tilde{F}}_{\underline{z}}(\underline{\tilde{z}}_0, \bar{\tilde{z}}_0, \tilde{s}) + k\underline{\tilde{F}}_{\bar{z}}(\underline{\tilde{z}}_0, \bar{\tilde{z}}_0, \tilde{s}) + O(h^2 + hk + k^2) = \underline{\tilde{d}} \\ \bar{\tilde{F}}(\underline{\tilde{\psi}}, \bar{\tilde{\psi}}, \tilde{s}) = \bar{\tilde{F}}(\underline{\tilde{z}}_0, \bar{\tilde{z}}_0, \tilde{s}) + h\bar{\tilde{F}}_{\underline{z}}(\underline{\tilde{z}}_0, \bar{\tilde{z}}_0, \tilde{s}) + k\bar{\tilde{F}}_{\bar{z}}(\underline{\tilde{z}}_0, \bar{\tilde{z}}_0, \tilde{s}) + O(h^2 + hk + k^2) = \bar{\tilde{d}} \end{cases} \tag{5.39}$$

If $\underline{\tilde{z}}_0$ and $\bar{\tilde{z}}_0$ are close to $\underline{\tilde{\varphi}}$ and $\bar{\tilde{\varphi}}$ then $h(\tilde{s})$ and $k(\tilde{s})$ are negligible for $\tilde{s} \in [0,1]$.

$$\begin{cases} \underline{\tilde{F}}\left(\underline{\tilde{z}}_0, \bar{\tilde{z}}_0, \tilde{s}\right) + h\underline{\tilde{F}}_{\underline{z}}\left(\underline{\tilde{z}}_0, \bar{\tilde{z}}_0, \tilde{s}\right) + k\underline{\tilde{F}}_{\bar{z}}\left(\underline{\tilde{z}}_0, \bar{\tilde{z}}_0, \tilde{s}\right) = \underline{\tilde{d}}(\tilde{s}) \\ \bar{\tilde{F}}\left(\underline{\tilde{z}}_0, \bar{\tilde{z}}_0, \tilde{s}\right) + h\bar{\tilde{F}}_{\underline{z}}\left(\underline{\tilde{z}}_0, \bar{\tilde{z}}_0, \tilde{s}\right) + k\bar{\tilde{F}}_{\bar{z}}\left(\underline{\tilde{z}}_0, \bar{\tilde{z}}_0, \tilde{s}\right) = \bar{\tilde{d}}(\tilde{s}) \end{cases} \tag{5.40}$$

As a result, the unknowns $h(\tilde{s})$ and $k(\tilde{s})$ can be computed for each $\tilde{s} \in [0,1]$

$$J\left(\underline{\tilde{z}}_0, \bar{\tilde{z}}_0, \tilde{s}\right)\begin{bmatrix} h(\tilde{s}) \\ k(\tilde{s}) \end{bmatrix} = \begin{bmatrix} \underline{\tilde{d}}(\tilde{s}) - \underline{\tilde{F}}\left(\underline{\tilde{z}}_0, \bar{\tilde{z}}_0, \tilde{s}\right) \\ \bar{\tilde{d}}(\tilde{s}) - \bar{\tilde{F}}\left(\underline{\tilde{z}}_0, \bar{\tilde{z}}_0, \tilde{s}\right) \end{bmatrix} \tag{5.41}$$

where

$$J\left(\underline{\tilde{z}}_0, \bar{\tilde{z}}_0, \tilde{s}\right) = \begin{bmatrix} \underline{\tilde{F}}_{\underline{z}}\left(\underline{\tilde{z}}_0, \bar{\tilde{z}}_0, \tilde{s}\right) & \underline{\tilde{F}}_{\bar{z}}\left(\underline{\tilde{z}}_0, \bar{\tilde{z}}_0, \tilde{s}\right) \\ \bar{\tilde{F}}_{\underline{z}}\left(\underline{\tilde{z}}_0, \bar{\tilde{z}}_0, \tilde{s}\right) & \bar{\tilde{F}}_{\bar{z}}\left(\underline{\tilde{z}}_0, \bar{\tilde{z}}_0, \tilde{s}\right) \end{bmatrix} \tag{5.42}$$

As a consequence, the following estimates for $\underline{y}(\tilde{s})$ and $\bar{z}(\tilde{s})$ are given:

$$\begin{cases} \underline{\tilde{z}}_1(\tilde{s}) = \underline{\tilde{z}}_0(\tilde{s}) + h(\tilde{s}) \\ \bar{\tilde{z}}_1(\tilde{s}) = \bar{\tilde{z}}_0(\tilde{s}) + k(\tilde{s}), \forall \tilde{s} \in [0,1] \end{cases} \tag{5.43}$$

Using the recursive technique, we may derive an approximate solution $\forall \tilde{s} \in [0,1]$.

$$\begin{cases}\underline{\tilde{z}}_n(\tilde{s}) = \underline{\tilde{z}}_{n-1}(\tilde{s}) + h_{n-1}(\tilde{s}) \\ \bar{\tilde{z}}_n(\tilde{s}) = \bar{\tilde{z}}_{n-1}(\tilde{s}) + k_{n-1}(\tilde{s})\end{cases} \quad (5.44)$$

if $J(\underline{\tilde{z}}_n, \bar{\tilde{z}}_n, \tilde{s})$ is nonsingular, we derive the recursive scheme of Newton's technique from (5.42)

$$\begin{bmatrix}\underline{\tilde{z}}_{n+1}(s) \\ \bar{\tilde{z}}_{n+1}(s)\end{bmatrix} = \begin{bmatrix}\underline{\tilde{z}}_n(s) \\ \bar{\tilde{z}}_n(s)\end{bmatrix} - J\left(\underline{\tilde{z}}_n, \bar{\tilde{z}}_n, \tilde{s}\right)^{-1} \begin{bmatrix}\underline{F}\left(\underline{\tilde{z}}_n, \bar{\tilde{z}}_n, \tilde{s}\right) \\ \bar{F}\left(\underline{\tilde{z}}_n, \bar{\tilde{z}}_n, \tilde{s}\right)\end{bmatrix} \quad (5.45)$$

Modified Newton's Method

The most well-known demanding Newton method for solving nonlinear equations is

$$\tilde{z}_{k+1} = \tilde{z}_k - J(\tilde{z}_k)^{-1} * \tilde{F}(\tilde{z}_k) \quad (5.46)$$

where $J(\tilde{z}_k)$ is the Jacobian matrix. This method converges quadratically. The process can become excessively time-consuming due to the Jacobian matrix evaluation for each iteration. This leads to further studies that aim to enhance the computational efficiency of Newton's approach [73].

The Chord Newton method significantly outperforms Newton's method in many aspects. When the problem is finite in size, we can evaluate the Jacobian only once; significantly, it reduces the computational cost of each iteration [74]. For the singular Jacobian matrix, it fails to converge to the solution. To address this limitation, a parameter μ_k was included in Newton's method to ensure a descending search direction when the Jacobian $J(x_k)$ is positive definite. This method is usually referred to as the Levenberg-Marquardt method. It is as follows

$$d_k = \tilde{z}_{k+1} - \tilde{z}_k = -J(\tilde{z}_k)^{-1} * F(\tilde{z}_k) \quad (5.47)$$

By adding the parameter μ_k, we have

$$J(\tilde{z}_k)^{-1} = (J(\tilde{z}_k) + \mu_k I)^{-1} \quad (5.48)$$

where I denotes an identity matrix and $\mu_k \geq 0$ is the parameter that is updated for each iteration to regulate the method's convergence [59]. If $\tilde{f}(\tilde{z}_{k+1}) < \tilde{f}(\tilde{z}_k)$ then μ_k would be gradually increased [56]. In the literature, Yamashita and Fukushima [74] chose $\mu_k = \|\tilde{F}(\tilde{z}_k)\|^2$ and Fan and Yuan [59] suggested that $\mu_k = \|\tilde{F}(\tilde{z}_k)\|$. For $\mu_k \to 0$, the Levenberg-Marquardt method behaves like Newton's method and for $\mu_k \to \infty$ it behaves like a pure gradient method. For the modified Newton's method, Sulaiman et al. [31] chose $\mu_k = \|\tilde{F}(\tilde{z}_k)\|$ for solving DFNE. The major benefits of this method are that its formulation is simple and it achieves the fastest convergence in the descent direction. The drawbacks of this method are that Second-order derivatives must be computed at every iteration; typically, this requires a significant amount of time, and when compared to the steepest descent or conjugate gradient technique, many more computations are needed at each iteration [38]. We reviewed the MNM algorithm [31] for solving DFNE as follows

$$\tilde{z}_{k+1} = \tilde{z}_k - (J(\tilde{z}_k) + \mu_k I)^{-1} \tilde{F}(\tilde{z}_k), k = 0.1,2, \ldots \quad (5.49)$$

Algorithm

1. Convert the DFNE into parametric form.
2. To obtain the initial guess, put $\tilde{s} = 0$ and $\tilde{s} = 1$.
3. Compute the Jacobian matrix $J(\tilde{z}_k)$.
4. The parameter μ_k calculated by using the formula.
5. Update the Jacobian matrix using (5.48).
6. Determine the next iteration value using (5.49).
7. Repeat steps 4 to 7. Until the tolerance criteria 10^{-6} is reached [31].

Mathematical formulation

The objective is to determine the solution for DFNE.

$$P(\tilde{z}) = Q(\tilde{z}) + \tilde{d} \quad (5.50)$$

Equation (5.50) can be described as

$$\begin{cases}\underline{P}(\underline{\tilde{z}}, \bar{\tilde{z}}, \tilde{s}) = \underline{Q}(\underline{\tilde{z}}, \bar{\tilde{z}}, \tilde{s}) + \underline{\tilde{d}}(\tilde{s}), \forall \tilde{s} \in [0,1]. \\ \bar{P}(\underline{\tilde{z}}, \bar{\tilde{z}}, \tilde{s}) = \bar{Q}(\underline{\tilde{z}}, \bar{\tilde{z}}, \tilde{s}) + \bar{\tilde{d}}(\tilde{s}),\end{cases} \quad (5.51)$$

Assume that $\tilde{z} = (\underline{\tilde{\psi}}, \bar{\tilde{\psi}})$ is the solution of (5.51) then

$$\begin{cases}\underline{P}(\underline{\tilde{\psi}}, \bar{\tilde{\psi}}, \tilde{s}) - \underline{Q}(\underline{\tilde{\psi}}, \bar{\tilde{\psi}}, \tilde{s}) = \underline{\tilde{d}}(\tilde{s}), \forall \tilde{s} \in [0,1]. \\ \bar{P}(\underline{\tilde{\psi}}, \bar{\tilde{\psi}}, \tilde{s}) - \bar{Q}(\underline{\tilde{\psi}}, \bar{\tilde{\psi}}, \tilde{s}) = \bar{\tilde{d}}(\tilde{s}),\end{cases} \quad (5.52)$$

Let us assume the functions $\underline{\tilde{F}}$ and $\bar{\tilde{F}}$ are as follows

$$\begin{cases}\underline{\tilde{F}}(\underline{\tilde{\psi}}, \bar{\tilde{\psi}}, \tilde{s}) = \underline{P}(\underline{\tilde{\psi}}, \bar{\tilde{\psi}}, \tilde{s}) - \underline{Q}(\underline{\tilde{\psi}}, \bar{\tilde{\psi}}, \tilde{s}), \\ \bar{\tilde{F}}(\underline{\tilde{\psi}}, \bar{\tilde{\psi}}, \tilde{s}) = \bar{P}(\underline{\tilde{\psi}}, \bar{\tilde{\psi}}, \tilde{s}) - \bar{Q}(\underline{\tilde{\psi}}, \bar{\tilde{\psi}}, \tilde{s}), \forall \tilde{s} \in [0,1]\end{cases} \quad (5.53)$$

As a result,

$$\begin{cases}\underline{\tilde{F}}(\underline{\tilde{\psi}}, \bar{\tilde{\psi}}, \tilde{s}) = \underline{\tilde{d}}(\tilde{s}), \forall \tilde{s} \in [0,1] \\ \bar{\tilde{F}}(\underline{\tilde{\psi}}, \bar{\tilde{\psi}}, \tilde{s}) = \bar{\tilde{d}}(\tilde{s})\end{cases} \quad (5.54)$$

Let $\tilde{z}_0 = (\underline{\tilde{z}}_0, \bar{\tilde{z}}_0)$ is an approximation solution, then there are $h(\tilde{s})$, $k(\tilde{s})$ such that

$$\begin{cases}\underline{\tilde{\psi}}(\tilde{s}) = \underline{\tilde{z}}_0(\tilde{s}) + h(\tilde{s}), \\ \bar{\tilde{\psi}}(\tilde{s}) = \bar{\tilde{z}}_0(\tilde{s}) + k(\tilde{s}).\end{cases} \quad (5.55)$$

By using the Taylor series of $\underline{\tilde{F}}$, $\bar{\tilde{F}}$ about $(\underline{\tilde{z}}_0, \bar{\tilde{z}}_0)$ and then foralle $\tilde{s} \in [0,1]$. We get

$$\begin{cases}\underline{F}(\underline{\tilde{\psi}}, \bar{\tilde{\psi}}, \tilde{s}) = \underline{F}(\underline{\tilde{z}}_0, \bar{\tilde{z}}_0, \tilde{s}) + h\underline{F}_{\tilde{z}}(\underline{\tilde{z}}_0, \bar{\tilde{z}}_0, \tilde{s}) + k\underline{F}_{\bar{\tilde{z}}}(\underline{\tilde{z}}_0, \bar{\tilde{z}}_0, \tilde{s}) = \underline{\tilde{d}}(\tilde{s}) \\ \bar{F}(\underline{\tilde{\psi}}, \bar{\tilde{\psi}}, \tilde{s}) = \bar{F}(\underline{\tilde{z}}_0, \bar{\tilde{z}}_0, \tilde{s}) + h\bar{F}_{\tilde{z}}(\underline{\tilde{z}}_0, \bar{\tilde{z}}_0, \tilde{s}) + k\bar{F}_{\bar{\tilde{z}}}(\underline{\tilde{z}}_0, \bar{\tilde{z}}_0, \tilde{s}) = \bar{\tilde{d}}(\tilde{s})\end{cases} \quad (5.56)$$

which reduces to

$$J\left(\underline{\tilde{z}}_n, \bar{\tilde{z}}_n, \tilde{s}\right)\begin{pmatrix}\varphi(\tilde{s}) \\ \psi(\tilde{s})\end{pmatrix} = \begin{pmatrix}p_n \\ q_n\end{pmatrix} \quad (5.57)$$

After some modifications, we get [75],

$$\begin{cases}p_n = \underline{F}(\underline{\tilde{\varphi}}, \tilde{\varphi}, \tilde{s}) - \underline{Q}(\underline{\tilde{\varphi}}, \tilde{\varphi}, \tilde{s}) - \underline{R}(\underline{\tilde{\varphi}}, \tilde{\varphi}, \tilde{s}) \\ q_n = \underline{F}(\underline{\tilde{\varphi}}, \bar{\tilde{\varphi}}, \tilde{s}) - \bar{Q}(\underline{\tilde{\varphi}}, \bar{\tilde{\varphi}}, \tilde{s}) - \bar{R}(\underline{\tilde{\varphi}}, \bar{\tilde{\varphi}}, \tilde{s})\end{cases} \quad (5.58)$$

and

$$J(\underline{\tilde{z}}_n, \bar{\tilde{z}}_n, \tilde{s}) = \begin{pmatrix} \underline{F}_{\tilde{z}}(\underline{\tilde{z}}_n, \bar{\tilde{z}}_n, \tilde{s}) & \underline{F}_{\bar{\tilde{z}}}(\underline{\tilde{z}}_n, \bar{\tilde{z}}_n, \tilde{s}) \\ \bar{F}_{\tilde{z}}(\underline{\tilde{z}}_n, \bar{\tilde{z}}_n, \tilde{s}) & \bar{F}_{\bar{\tilde{z}}}(\underline{\tilde{z}}_n, \bar{\tilde{z}}_n, \tilde{s}) \end{pmatrix}. \quad (5.59)$$

The parameter μ_k is introduced, and a new Jacobian is defined as

$$J(\underline{\tilde{z}}_n, \bar{\tilde{z}}_n, \tilde{s}) = \left(\begin{pmatrix} \underline{F}_{\tilde{z}}(\underline{\tilde{z}}_n, \bar{\tilde{z}}_n, \tilde{s}) & \underline{F}_{\bar{\tilde{z}}}(\underline{\tilde{z}}_n, \bar{\tilde{z}}_n, \tilde{s}) \\ \bar{F}_{\tilde{z}}(\underline{\tilde{z}}_n, \bar{\tilde{z}}_n, \tilde{s}) & \bar{F}_{\bar{\tilde{z}}}(\underline{\tilde{z}}_n, \bar{\tilde{z}}_n, \tilde{s}) \end{pmatrix} + I \left\| \begin{matrix} \underline{F}_{\bar{\tilde{z}}}(\underline{\tilde{z}}_n, \bar{\tilde{z}}_n, \tilde{s}) \\ \bar{F}_{\bar{\tilde{z}}}(\underline{\tilde{z}}_n, \bar{\tilde{z}}_n, \tilde{s}) \end{matrix} \right\| \right) \quad (5.60)$$

if $J(\underline{\tilde{z}}_n, \bar{\tilde{z}}_n, \tilde{s})$ is nonsingular, we derive the recursive scheme of Newton's technique from (5.60)

$$\begin{bmatrix} \underline{z}_{n+1}(\tilde{s}) \\ \bar{z}_{n+1}(\tilde{s}) \end{bmatrix} = \begin{bmatrix} \underline{z}_n(\tilde{s}) \\ \bar{z}_n(\tilde{s}) \end{bmatrix} - J(\underline{\tilde{z}}_n, \bar{\tilde{z}}_n, \tilde{s})^{-1} \begin{bmatrix} \underline{F}_{\tilde{z}}(\underline{\tilde{z}}_n, \bar{\tilde{z}}_n, \tilde{s}) \\ \bar{F}_{\bar{\tilde{z}}}(\underline{\tilde{z}}_n, \bar{\tilde{z}}_n, \tilde{s}) \end{bmatrix} \quad (5.61)$$

Numerical Example

The section focuses on solving several numerical examples using existing methods and compare these methods to validate their computational efficiency. The representation of existing methods is as follows: Newton Method (NM), Broyden Newton Method (BNM), Quasi-Newton Method (QNM), and Modified Newton Method (MNM). The illustrated example problems are considered as follows.

Example 5: The DFNE can be examined with the following example.

$$(4,7,8)\tilde{z}^2 + (1,2,3)\tilde{z} = (1,2,1)\tilde{z}^2 + (1,2,3) \quad (5.62)$$

Equation (5.62) can be described as

$$\begin{cases} (4+3\tilde{s})\underline{\tilde{z}}^2(\tilde{s}) + (1+\tilde{s})\underline{\tilde{z}}(\tilde{s}) = (1+\tilde{s})\underline{\tilde{z}}^2(\tilde{s}) + (1+\tilde{s}) \\ (8-\tilde{s})\bar{\tilde{z}}^2(\tilde{s}) + (3-\tilde{s})\bar{\tilde{z}}(\tilde{s}) = (3-\tilde{s})\bar{\tilde{z}}^2(\tilde{s}) + (3-\tilde{s}) \end{cases} \quad (5.63)$$

Consequently

$$\begin{cases} (3+2\tilde{s})\underline{\tilde{z}}^2(\tilde{s}) + (1+\tilde{s})\underline{\tilde{z}}(\tilde{s}) = (1+\tilde{s}) \\ (7-2\tilde{s})\bar{\tilde{z}}^2(\tilde{s}) + (3-\tilde{s})\bar{\tilde{z}}(\tilde{s}) = (3-\tilde{s}) \end{cases} \quad (5.64)$$

or similar

$$\begin{cases} (3+2\tilde{s})\underline{\tilde{z}}^2(\tilde{s}) + (1+\tilde{s})\underline{\tilde{z}}(\tilde{s}) - (1+\tilde{s}) = 0 \\ (7-2\tilde{s})\bar{\tilde{z}}^2(\tilde{s}) + (3-\tilde{s})\bar{\tilde{z}}(\tilde{s}) - (3-\tilde{s}) = 0 \end{cases} \quad (5.65)$$

Put $\tilde{s} = 0$ and $\tilde{s} = 1$ in (5.65) to generate an initial guess.

$$\begin{cases} 5\underline{\tilde{z}}^2(1) + 2\underline{\tilde{z}}(1) = 2, \\ 5\bar{\tilde{z}}^2(1) + 2\bar{\tilde{z}}^2(1) = 2, \end{cases} \text{and} \begin{cases} 3\underline{\tilde{z}}^2(0) + \underline{\tilde{z}}(0) = 1 \\ 7\bar{\tilde{z}}^2(0) + 3\bar{\tilde{z}}(0) = 3 \end{cases} \quad (5.66)$$

As a result, $\underline{\tilde{z}}(0) = 0.434259$, $\bar{\tilde{z}}(0) = 0.474546$ and $\underline{\tilde{z}}(1) = \bar{\tilde{z}}(1) = 0.463325$. Therefore, the initial guess is $\tilde{z}_0 = (0.434259, 0.463325, 0.474546)$. The comparison of results is given in Table 5, and the convergence behaviour is shown in Figure 5.

Example 6: The DFNE can be examined with the following example

$$(4,5,6)\tilde{z}^2 + (4,7,9)\tilde{z} = (3,5,6)\tilde{z} + (1,2,3) \quad (5.67)$$

Equation (5.67) can be described as

$$\begin{aligned} (4+\tilde{s})\underline{\tilde{z}}^2(\tilde{s}) + (4+3\tilde{s})\underline{\tilde{z}}(\tilde{s}) &= (3+2\tilde{s})\underline{\tilde{z}}(\tilde{s}) + (1+\tilde{s}) \\ (6-\tilde{s})\bar{\tilde{z}}^2(\tilde{s}) + (9-2\tilde{s})\bar{\tilde{z}}(\tilde{s}) &= (6-\tilde{s})\bar{\tilde{z}}(\tilde{s}) + (3-\tilde{s}) \end{aligned} \quad (5.68)$$

Consequently,

$$\begin{aligned} (4+\tilde{s})\underline{\tilde{z}}^2(\tilde{s}) + (1+\tilde{s})\underline{\tilde{z}}(\tilde{s}) &= (1+\tilde{s}) \\ (6-\tilde{s})\bar{\tilde{z}}^2(\tilde{s}) + (3-\tilde{s})\bar{\tilde{z}}(\tilde{s}) &= (3-\tilde{s}) \end{aligned} \quad (5.69)$$

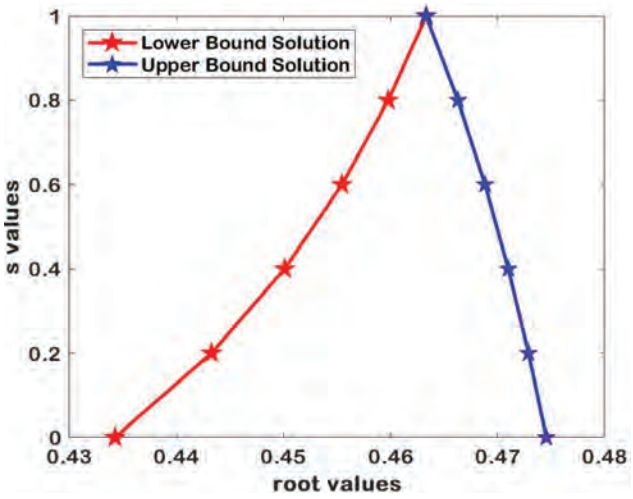


Figure 5. Numerical solution for Example 5.

Table 5. Comparison of NM, BNM, QNM, and MNM

				Number of Iterations			
S.No.	$\tilde{s}$	$\underline{\tilde{z}}(\tilde{s})$	$\bar{\tilde{z}}(\tilde{s})$	**NM**	**BNM**	**QNM**	**MNM**
1	$\tilde{s}$=0	0.434259	0.474546	1	6	5	1
2	$\tilde{s}$=0.2	0.443274	0.472888	3	7	7	3
3	$\tilde{s}$=0.4	0.450104	0.470998	3	7	7	3
4	$\tilde{s}$=0.6	0.455460	0.468825	3	8	6	3
5	$\tilde{s}$=0.8	0.459774	0.466298	3	8	6	3
6	$\tilde{s}$=1	0.463325	0.463325	3	8	7	3

or similar,

$$(4+\tilde{s})\underline{\tilde{z}}^2(\tilde{s})+(1+\tilde{s})\underline{\tilde{z}}(\tilde{s})-(1+\tilde{s})=0$$
$$(6-\tilde{s})\bar{\tilde{z}}^2(\tilde{s})+(3-\tilde{s})\bar{\tilde{z}}(\tilde{s})-(3-\tilde{s})=0 \quad (5.70)$$

Put $\tilde{s}=0$ and $\tilde{s}=1$ in (5.70) to generate an initial guess.

$$\begin{cases}5\underline{\tilde{z}}^2(1)+2\underline{\tilde{z}}(1)=2\\ 5\bar{\tilde{z}}^2(1)+2\bar{\tilde{z}}(1)=2\end{cases}\text{ and }\begin{cases}4\underline{\tilde{z}}^2(0)+\underline{\tilde{z}}(0)=1\\ 6\bar{\tilde{z}}^2(0)+3\bar{\tilde{z}}(0)=3\end{cases} \quad (5.71)$$

As a result, $\underline{\tilde{z}}(0)=0.390388$, $\bar{\tilde{z}}(0)=0.500000$ and $\underline{\tilde{z}}(1)=\bar{\tilde{z}}(1)=0.463325$. Therefore, the initial guess is $\tilde{z}_0=(0.390388,0.463325,0.500000)$. The comparison of results is given in Table 6, and the convergence behaviour is shown in Figure 6.

Example 7: The DFNE can be examined with the following example.

$$(5,6,7)\tilde{z}^2+(5,7,9)\tilde{z}=(3,4,5)\tilde{z}+(2,3,\mathbf{4}) \quad (5.72)$$

Equation (5.72) can be described as

$$(5+\tilde{s})\underline{\tilde{z}}^2(\tilde{s})+(5+2\tilde{s})\underline{\tilde{z}}(\tilde{s})=(3+\tilde{s})\underline{\tilde{z}}(\tilde{s})+(2+\tilde{s})$$
$$(7-\tilde{s})\bar{\tilde{z}}^2(\tilde{s})+(9-2\tilde{s})\bar{\tilde{z}}(\tilde{s})=(5-\tilde{s})\bar{\tilde{z}}(\tilde{s})+(4-\tilde{s}) \quad (5.73)$$

or similar

$$(5+\tilde{s})\underline{\tilde{z}}^2(\tilde{s})+(2+\tilde{s})\underline{\tilde{z}}(\tilde{s})-(2+\tilde{s})=0$$
$$(7-\tilde{s})\bar{\tilde{z}}^2(\tilde{s})+(4-\tilde{s})\bar{\tilde{z}}(\tilde{s})-(4-\tilde{s})=0 \quad (5.74)$$

Put $\tilde{s}=0$ and $\tilde{s}=1$ in (5.74) to generate an initial guess.

$$\begin{cases}5\underline{\tilde{z}}^2(0)+2\underline{\tilde{z}}-2=0\\ 7\bar{\tilde{z}}^2(0)+4\bar{\tilde{z}}(0)-4=0\end{cases}\text{ and }\begin{cases}6\underline{\tilde{z}}^2(1)+3\underline{\tilde{z}}(1)-3=0\\ 6\bar{\tilde{z}}^2(1)+3\bar{\tilde{z}}(1)-3=0\end{cases} \quad (5.75)$$

As a result, $\underline{\tilde{z}}(0)=0.463325$, $\bar{\tilde{z}}(0)=0.522408$ and $\underline{\tilde{z}}(1)=\bar{\tilde{z}}(1)=0.500000$. Therefore, the initial guess is $\tilde{z}_0=(0.463325,0.500000,0.522408)$. The comparison of results is given in Table 7, and the convergence behaviour is shown in Figure 7.

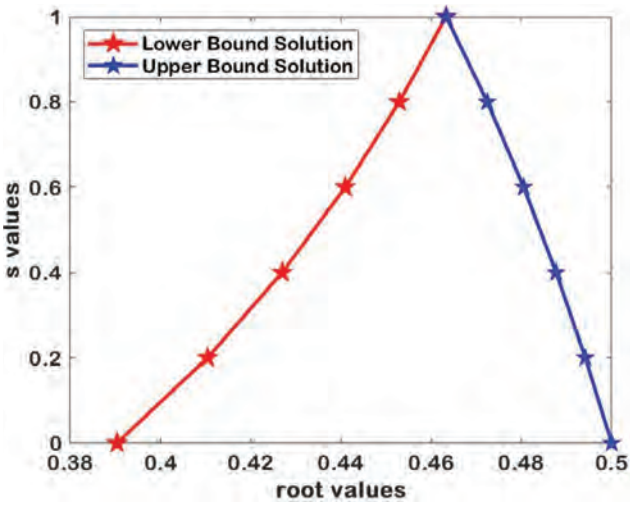


Figure 6. Numerical solution for Example 6.

Table 6. Comparison of NM, BNM, QNM, and MNM

				Number of Iterations			
S.No.	$\tilde{s}$	$\underline{\tilde{z}}(\tilde{s})$	$\bar{\tilde{z}}(\tilde{s})$	**NM**	**BNM**	**QNM**	**MNM**
1	$\tilde{s}$=0	0.390388	0.500000	1	7	1	1
2	$\tilde{s}$=0.2	0.410426	0.494163	3	7	7	3
3	$\tilde{s}$=0.4	0.426991	0.487702	3	7	7	3
4	$\tilde{s}$=0.6	0.440962	0.480506	3	8	6	3
5	$\tilde{s}$=0.8	0.452934	0.472439	3	8	8	3
6	$\tilde{s}$=1	0.463325	0.463325	3	8	9	3

Table 7. Comparison of NM, BNM, QNM, and MNM

				Number of Iterations			
S.No.	$\tilde{s}$	$\underline{\tilde{z}}(\tilde{s})$	$\bar{\tilde{z}}(\tilde{s})$	**NM**	**BNM**	**QNM**	**MNM**
1	$\tilde{s}$=0	0.463325	0.522408	1	7	2	1
2	$\tilde{s}$=0.2	0.472439	0.518645	3	7	6	3
3	$\tilde{s}$=0.4	0.480506	0.514569	3	7	7	3
4	$\tilde{s}$=0.6	0.487702	0.510137	3	8	6	3
5	$\tilde{s}$=0.8	0.494163	0.505301	3	8	8	3
6	$\tilde{s}$=1	0.500000	0.500000	3	8	8	3

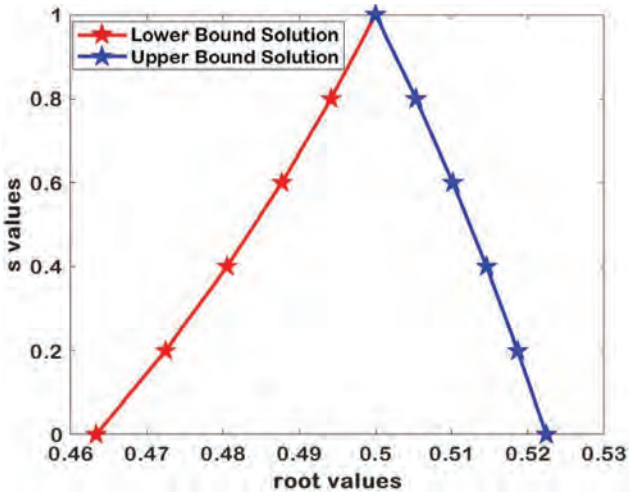


Figure 7. Numerical solution for Example 7.

Example 8: The DFNE can be examined with the following example [76].

$$(3,4,5)\tilde{z}^2 + (2,4,6)\tilde{z} = (1,2,3)\tilde{z} + (1,2,3) \tag{5.76}$$

Equation (5.76) can be described as

$$\begin{aligned}(3+\tilde{s})\underline{\tilde{z}}^2(\tilde{s}) + (2+2\tilde{s})\underline{\tilde{z}}(\tilde{s}) &= (1+\tilde{s})\underline{\tilde{z}}(\tilde{s}) + (1+\tilde{s})\\ (5-\tilde{s})\bar{\tilde{z}}^2(\tilde{s}) + (6-2\tilde{s})\underline{\tilde{z}}(\tilde{s}) &= (3-\tilde{s})\underline{\tilde{z}}(\tilde{s}) + (3-\tilde{s})\end{aligned} \tag{5.77}$$

or similar

$$\begin{aligned}(3+\tilde{s})\underline{\tilde{z}}^2(\tilde{s}) + (1+\tilde{s})\underline{\tilde{z}}(\tilde{s}) - (1+\tilde{s}) &= 0\\ (5-\tilde{s})\bar{\tilde{z}}^2(\tilde{s}) + (3-\tilde{s})\bar{\tilde{z}}(\tilde{s}) - (3-\tilde{s}) &= 0\end{aligned} \tag{5.78}$$

Put $\tilde{s} = 0$ and $\tilde{s} = 1$ in (5.78) to generate an initial guess.

$$\begin{cases}4\underline{\tilde{z}}^2(1) + 2\underline{\tilde{z}}(1) = 2\\ 4\bar{\tilde{z}}^2(1) + 2\bar{\tilde{z}}(1) = 2\end{cases} \text{and} \begin{cases}3\underline{\tilde{z}}^2(0) + \underline{\tilde{z}}(0) = 1\\ 5\bar{\tilde{z}}^2(0) + 3\bar{\tilde{z}}(0) = 3\end{cases} \tag{5.79}$$

As a result, $\underline{\tilde{z}}(0) = 0.434259$, $\bar{\tilde{z}}(0) = 0.530662$ and $\underline{\tilde{z}}(1) = \bar{\tilde{z}}(1) = 0.500000$. Therefore, the initial guess is $\tilde{z}_0 = (0.434259,0.500000,030662)$. The comparison of results is given in Table 8, and the convergence behaviour is shown in Figure 8.

DISCUSSION

This section provides an in-depth discussion of resolving DFNEs by four numerical techniques: NM, BNM, QNM, and MNM. After applying these methods for solving several example problems, we observed that NM and MNM show superiority in converging to the solution. Tables 5–8 show that NM and MNM converge to the solution with less number of iterations. In comparison, BNM and QNM required more iterations, indicating a slower convergence rate. The Modified Newton Method, an advancement of the traditional Newton technique, provides enhanced flexibility in fuzzy contexts while preserving a rapid convergence rate. Finally, we compared numerical methodologies from the literature. Results indicate that Newton's Method is the most effective due to its speed, accuracy, and stability. Although other methods may provide advantages in certain situations, they require more iterations for solving the

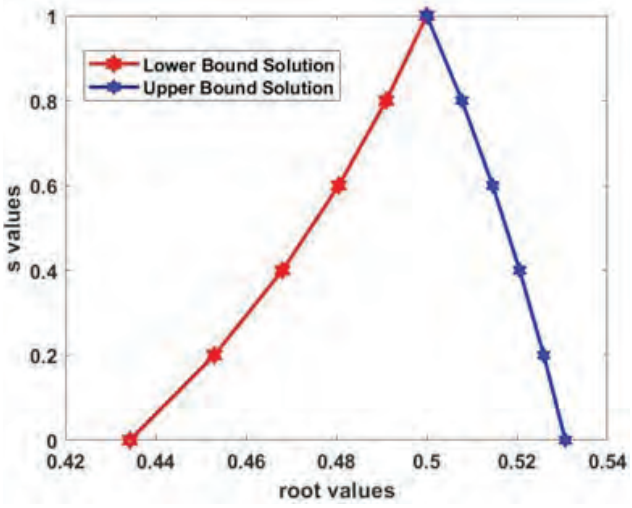


Figure 8. Numerical solution for Example 8.

Table 8. Comparison of NM, BNM, QNM, and MNM

				Number of Iterations			
S.No.	$\tilde{s}$	$\underline{\tilde{z}}(\tilde{s})$	$\bar{\tilde{z}}(\tilde{s})$	**NM**	**BNM**	**QNM**	**MNM**
1	$\tilde{s}$=0	0.434259	0.530662	1	7	2	1
2	$\tilde{s}$=0.2	0.452934	0.525892	2	7	7	3
3	$\tilde{s}$=0.4	0.468026	0.520563	2	7	7	3
4	$\tilde{s}$=0.6	0.480506	0.514569	3	8	7	3
5	$\tilde{s}$=0.8	0.491017	0.507773	3	8	8	3
6	$\tilde{s}$=1	0.500000	0.500000	3	8	8	3

DFNEs. This analysis demonstrates that Newton-based methods continue to dominate the solution of DFNE

CONCLUSION

This article effectively evaluates several iterative methods for addressing FNEs and DFNEs. A comprehensive analysis of numerical approaches for solving FNEs was conducted, encompassing NM, SDM, HM, BM, FNM, and IFPM. We also analysed the BNM, the QNM, and the MNM for addressing DFNEs. This study provides a detailed analysis of the mathematical formulation of each method, emphasizing their strengths and limitations. The comparative analysis demonstrated that NM and the MNM consistently outperformed other approaches in terms of convergence speed and computational efficiency. Tables 1–4 illustrate that NM necessitated considerably fewer iterations compared to SDM, HM, BM, FNM, and IFPM. Tables 5–8 indicate that NM and the MNM were the most effective methods for solving DFNEs, necessitating fewer iterations compared to the BNM and the QNM. Additionally, Figures 1–8 illustrate the convergence behaviour of each numerical method, which supports our findings. This study highlights the significance of Newton-based methods, noting their enhanced accuracy, stability, and efficiency. Our results suggest that derivative-free iterative techniques should continue to be developed, as they may offer more options and faster methods for solving FNEs and DFNEs.

AUTHORSHIP CONTRIBUTIONS

Authors equally contributed to this work.

DATA AVAILABILITY STATEMENT

The authors confirm that the data that supports the findings of this study are available within the article. Raw data that support the finding of this study are available from the corresponding author, upon reasonable request.

CONFLICT OF INTEREST

The authors declared no potential conflicts of interest with respect to the research, authorship, and/or publication of this article.

ETHICS

There are no ethical issues with the publication of this manuscript.

STATEMENT ON THE USE OF ARTIFICIAL INTELLIGENCE

Artificial intelligence was not used in the preparation of the article.

REFERENCES

[1] Katuri S, Maroju P. Performance analysis of an iterative method for solving nonlinear motion of an object in an uncertain environment using triangular fuzzy number. Eng Comput 2025;42:1186–1204. [CrossRef]

[2] Köçken HG, Tiryaki F. Using some fuzzy aggregation operators for multi-objective linear transportation problems. Sigma J Eng Nat Sci 2014;32:399–421.

[3] Barışık T, Güneri A. BLEVE risk effect estimation using the Levenberg-Marquardt algorithm in an artificial neural network model. Sigma J Eng Nat Sci 2022;40. [CrossRef]

[4] Shivani S, Gupta SB. A systematic comparative study of popular biomimetic intelligence techniques. Sigma J Eng Nat Sci 2024;42:919–944. [CrossRef]

[5] Goguen JA, Zadeh LA. Fuzzy sets. Inf Control 1965;8:338–353. [CrossRef]

[6] Zadeh LA. Similarity relations and fuzzy orderings. Inf Sci 1971;3:177–200. [CrossRef]

[7] Chang SS, Zadeh LA. On fuzzy mapping and control. IEEE Trans Syst Man Cybern 1972;1:30–34. [CrossRef]

[8] Dubois D, Prade H. Operations on fuzzy numbers. Int J Syst Sci 1978;9:613–626. [CrossRef]

[9] Nahmias S. Fuzzy variables. Fuzzy Sets Syst 1978;1:97–110. [CrossRef]

[10] Zadeh LA. The concept of a linguistic variable and its application to approximate reasoning-I. Inf Sci 1975;8:199–249. [CrossRef]

[11] Shokri J. On systems of fuzzy nonlinear equations. Appl Math Sci 2008;2:1205–1217.

[12] Fang JX. On nonlinear equations for fuzzy mappings in probabilistic normed spaces. Fuzzy Sets Syst 2002;131:357–364. [CrossRef]

[13] Ma J, Feng G. An approach to H∞ control of fuzzy dynamic systems. Fuzzy Sets Syst 2003;137:367–386. [CrossRef]

[14] Kajani MT, Asady B, Ven Cheh AH. An iterative method for solving dual fuzzy nonlinear equations. Appl Math Comput 2005;167:316–323. [CrossRef]

[15] Buckley JJ, Qu Y. Solving fuzzy equations: a new solution concept. Fuzzy Sets Syst 1991;39:291–301. [CrossRef]

[16] Buckley JJ, Qu Y. Solving linear and quadratic fuzzy equations. Fuzzy Sets Syst 1991;38:43–59. [CrossRef]

[17] Abbasbandy S, Asady B. Newton's method for solving fuzzy nonlinear equations. Appl Math Comput 2004;159:349–356. [CrossRef]

[18] Abbasbandy S, Ezzati R. Newton's method for solving a system of fuzzy nonlinear equations. Appl Math Comput 2006;175:1189–1199. [CrossRef]

[19] Abbasbandy S, Jafarian A. Steepest descent method for solving fuzzy nonlinear equations. Appl Math Comput 2006;174:669–675. [CrossRef]

[20] Ramli A, Abdullah ML, Mamat M. Broyden's method for solving fuzzy nonlinear equations. Adv Fuzzy Syst 2010;2010:763270. [CrossRef]
[21] Ahmad MZ, Razak NHA, Daud WSW, Sakib E, Rahman NAA. Fuzzy homotopy continuation method for solving fuzzy nonlinear equations. Intervals 2006;1:2.
[22] Umar AA. Fixed Newton's method for solving fuzzy nonlinear equations.
[23] Sulaiman IM, Mamat M, Waziri MY, Fadhilah A, Kamfa KU. Regula Falsi method for solving fuzzy nonlinear equation. Far East J Math Sci 2016;100:873–884. [CrossRef]
[24] Sulaiman IM, Mamat M, Waziri MY, Mohamed MA, Mohamad FS. Solving fuzzy nonlinear equation via Levenberg-Marquardt method. Far East J Math Sci 2018;103:1547–1558. [CrossRef]
[25] Sulaiman IM, Mamat M, Afendee MM, Waziri MY. Diagonal updating Shamanskii-like method for solving singular fuzzy nonlinear equation. Far East J Math Sci 2017;103:1619–1629. [CrossRef]
[26] Sulaiman IM, Mamat M, Waziri MY, Umar AO. Numerical method for solution of fuzzy nonlinear equations. J Adv Res Model Simul 2018;1:13–18.
[27] Senthilkumar LS, Ganesan K. Bisection method for fuzzy nonlinear equations. Glob J Pure Appl Math 2016;12.
[28] Ahmad MZ, Jamaluddin NA, Sakib E, Daud W, Aswad N, Rahman A. Fuzzy false position method for solving fuzzy nonlinear equations. ARPN J Eng Appl Sci 2016;11:9737–9745.
[29] Waziri MY, Majid ZA. A new approach for solving dual fuzzy nonlinear equations using Broyden's and Newton's methods. Adv Fuzzy Syst 2012;2012:682087. [CrossRef]
[30] Omesa UA, Mamat M, Sulaiman IM, Sukono S. On quasi-Newton method for solving fuzzy nonlinear equations. Int J Quant Res Model 2020;1:1–10. [CrossRef]
[31] Sulaiman IM, Mamat M, Malik M, Nisar KS, Elfasakhany A. Performance analysis of a modified Newton method for parameterized dual fuzzy nonlinear equations and its application. Results Phys 2022;33:105140. [CrossRef]
[32] Kaya HP, Koç T, Ekici L, Toğa G. Anthocyanin and bioactivity properties of Berberis crategina DC. in buffer system and apple juice: impact of temperature, time, and pH; prediction using artificial neural network. Sigma J Eng Nat Sci 2024;42:438–449. [CrossRef]
[33] Rafiq N, Yaqoob N, Kausar N, Shams M, Mir NA, Gaba YU, et al. Computer-based fuzzy numerical method for solving engineering and real-world applications. Math Probl Eng 2021;2021:6916282. [CrossRef]
[34] Akter MM, Hossain MS. False position method for solving fuzzy non-linear equation using triangular and trapezoidal fuzzy number. 2023. [CrossRef]
[35] Aal MA. Derivative-free Newton-type method for fuzzy nonlinear equations. J Math Comput Sci 2024;34:234–242. [CrossRef]
[36] Nejad MF, Farahani H, Nuraei R, Gilani A. Gröbner basis approach for solving fuzzy complex systems of linear equations. New Math Nat Comput 2024;20:533–550. [CrossRef]
[37] Zadeh LA. Fuzzy sets. Inf Control 1965;8:338–353. [CrossRef]
[38] Goetschel R Jr, Voxman W. Elementary fuzzy calculus. Fuzzy Sets Syst 1986;18:31–43. [CrossRef]
[39] Zimmermann HJ. Fuzzy sets, decision making, and expert systems. Vol. 10. Springer Science and Business Media; 1987. [CrossRef]
[40] Meza JC. Steepest descent. Wiley Interdiscip Rev Comput Stat 2010;2:719–722. [CrossRef]
[41] Badard R. The law of large numbers for fuzzy processes and the estimation problem. Inf Sci 1982;28:161–178. [CrossRef]
[42] Allahviranloo T. Numerical methods for fuzzy system of linear equations. Appl Math Comput 2004;155:493–502. [CrossRef]
[43] Peeva K. Fuzzy linear systems. Fuzzy Sets Syst 1992;49:339–355. [CrossRef]
[44] Dubois DJ. Fuzzy sets and systems: theory and applications. Vol. 144. Academic Press; 1980.
[45] Grosan C, Abraham A. A new approach for solving nonlinear equation systems. IEEE Trans Syst Man Cybern A Syst Hum 2008;38:698–714. [CrossRef]
[46] Yamashita N, Fukushima M. On the rate of convergence of the Levenberg-Marquardt method. In: Topics in numerical analysis: with special emphasis on nonlinear problems. Vienna: Springer; 2001. p. 239–249. [CrossRef]
[47] Burden RL, Faires JD. Numerical analysis. Boston: Brooks-Cole; 1985. p. 672–674.
[48] Liao SJ. The proposed homotopy analysis technique for the solution of nonlinear problems [dissertation]. Shanghai: Shanghai Jiao Tong University; 1992.
[49] Abbasbandy S. Homotopy perturbation method for quadratic Riccati differential equation and comparison with Adomian's decomposition method. Appl Math Comput 2006;172:485–490. [CrossRef]
[50] Abbasbandy S. Numerical solutions of the integral equations: homotopy perturbation method and Adomian's decomposition method. Appl Math Comput 2006;173:493–500. [CrossRef]
[51] Zheng L, Zhang X. Modelling and analysis of modern fluid problems. Academic Press; 2017.
[52] Hillermeier C. Nonlinear multiobjective optimization: a generalized homotopy approach. Vol. 135. Birkhäuser; 2012.
[53] He J. An approximate solution technique depending on an artificial parameter: a special example. Commun Nonlinear Sci Numer Simul 1998;3:92–97. [CrossRef]

[54] He JH. A coupling method of a homotopy technique and a perturbation technique for non-linear problems. Int J Non Linear Mech 2000;35:37–43. [CrossRef]
[55] Buckley JJ, Hayashi Y. Can fuzzy neural nets approximate continuous fuzzy functions? Fuzzy Sets Syst 1994;61:43–51. [CrossRef]
[56] Wang L, Liu J. Newton's method for dual interval fuzzy nonlinear equations. J Intell Fuzzy Syst 2017;32:1591–1600.
[57] Liao S. Beyond perturbation: introduction to the homotopy analysis method. Chapman and Hall/CRC; 2003.
[58] Yang H, Wen F, Wang L. Newton-Raphson on power flow algorithm and Broyden method in the distribution system. In: 2008 IEEE 2nd International Power and Energy Conference; 2008 Dec. p. 1613–1618. [CrossRef]
[59] Waziri MY, Leong WJ, Hassan MA, Monsi M. Jacobian computation-free Newton method for systems of non-linear equations. J Numer Math Stoch 2010;2:54–63.
[60] Dowell M, Jarratt P. A modified Regula falsi method for computing the root of an equation. 1971. [CrossRef]
[61] Burden RL, Faires JD. Numerical analysis. Brooks; 1997.
[62] Wang X, Zhong Z, Ha M. Iteration algorithms for solving a system of fuzzy linear equations. Fuzzy Sets Syst 2001;119:121–128. [CrossRef]
[63] Ezzati R, Ghanbari A, Moradi H. A new method for solving dual fuzzy nonlinear equations based on Newton's method. J Intell Fuzzy Syst 29:387–394.
[64] Ghanbari A, Ezzati R, Moradi H. A new approach for solving dual fuzzy nonlinear equations using Newton's method. Soft Comput 2015;19:1441–1452.
[65] Broyden CG. A class of methods for solving nonlinear simultaneous equations. Math Comput 1965;19:577–593. [CrossRef]
[66] Kelley CT. Iterative methods for linear and nonlinear equations. Society for Industrial and Applied Mathematics; 1995. [CrossRef]
[67] Cericola V. Quasi-Newton methods. Northwestern University Open Text Book on Process Optimization; 2015.
[68] Amirfakhrian M. Numerical solution of algebraic fuzzy equations with crisp variable by the Gauss-Newton method. Appl Math Model 2008;32:1859–1868. [CrossRef]
[69] Waziri MY, Moyi AU. An alternative approach for solving dual fuzzy nonlinear equations. Int J Fuzzy Syst 2016;18:103–107. [CrossRef]
[70] Zakaria L, Megarani W, Faisol A, Nuryaman A, Muharramah U. Computational mathematics: solving dual fully fuzzy nonlinear matrix equations numerically using Broyden's method. Int J Math Eng Manag Sci 2023;8:60. [CrossRef]
[71] Gong W, Liao Z, Mi X, Wang L, Guo Y. Nonlinear equations solving with intelligent optimization algorithms: a survey. Complex Syst Model Simul 2021;1:15–32. [CrossRef]
[72] Sulaiman IM, Waziri MY, Olowo ES, Talat AN. Solving fuzzy nonlinear equations with a new class of conjugate gradient method. Malays J Comput Appl Math 2018;1:11–19. [CrossRef]
[73] Chong EK, Żak SH. An introduction to optimization. Vol. 76. John Wiley & Sons; 2013.
[74] Sulaiman IM, Mamat M, Nurnadiah Z, Puspa LG. Solving dual fuzzy nonlinear equations via Shamanskii method. Int J Eng Technol 2018;7:89–91. [CrossRef]
[75] Hueso JL, Martínez E, Torregrosa JR. Modified Newton's method for systems of nonlinear equations with singular Jacobian. J Comput Appl Math 2009;224:77–83. [CrossRef]
[76] Huang J, Wen Z, Xiao X. Extended Levenberg-Marquardt method for composite function minimization. J Comput Math 2017:529–546. [CrossRef]

Sigma J Eng Nat Sci, Vol. 44, No. 4, pp. 2571–2582, August, 2026

Sigma Journal of Engineering and Natural Sciences
Web page info: https://sigma.yildiz.edu.tr
DOI: 10.14744/sigma.2026.2115

Research Article

Study of heat flux of tri-hybrid (TiO_2+SiO_2+Al_2O_3/ $C_6H_9NaO_7$) nanofluids over a linearly stretching sheet

Ch. MANGAMMA[1], B. SAIDULU[2], P. Pramod KUMAR[1], Rangu RAKESH[3], A. R. DEEPIKA[4,*]

[1]*Department of Mathematics, B. V. Raju Institute of Technology, Narsapur, 502313, India*
[2]*Department of Mathematics, T. R. R. College of Technology, Hyderabad, 500097, India*
[3]*Department of Mathematics, Sphoorthy Engineering College, Nadargul, 501510, India*
[4]*Department of Mathematics, Global Institute of Engineering and Technology, Hyderabad, 501504, India*

ARTICLE INFO

Article history
Received: 28 December 2025
Revised: 08 February 2026
Accepted: 12 March 2026

Keywords:
Casson Fluid Parameter; Nusselt Number; Radiation; Runge-Kutta Method; Sherwood Number; Trihybrid Nanofluid

ABSTRACT

The current numerical study investigates the impacts of heat source and radiation effects on thermo-fluidic behavior of trihybrid Casson (TiO_2+SiO_2+Al_2O_3/$C_6H_9NaO_7$) nanofluids over a linearly stretching sheet. The study not only explores a method to achieve superior heat conduction compared to hybrid nanofluids but also highlights the environmental purification potential, decomposition of destructive materials, and effective cooling capabilities offered by the considered nanoparticle combination. The governing equations were converted into ordinary differential equations and are then explained using Runge-Kutta scheme with a Shooting algorithm. The temperature profile shifts upwards and concentration gradient reduces for higher values of heat source and radiation. Nusselt number decreases by 23.52% when radiation doubles from 1 to 2. The uniqueness of the work lies in its generalization of previous studies by considering heat source, radiation, thermophoresis and Brownian motion effects over a linear stretching sheet leading to the achievement of an effective tri-hybrid nanofluid flow.

Cite this article as: Mangamma C, Saidulu B, Kumar PP, Rakesh R, Deepika AR. Study of heat flux of tri-hybrid (TiO_2+SiO_2+Al_2O_3/ $C_6H_9NaO_7$) nanofluids over a linearly stretching sheet. Sigma J Eng Nat Sci 2026;44(4):2571–2582.

INTRODUCTION

One among the latest technologies, heat transfer across a sheet stretching or otherwise, demanded an understanding of the flow dynamics, especially near the boundary of these sheets as the optimum changes occur in these layers. This approach gave a deep vision into the features of fluid/heat transfer which hugely supported the engineering processes. In the literature of Crane [1], the boundary layer flow which arises because of a stretched sheet that moves linearly with the changing velocity, was carried out. As there was advancement in nanotechnology, nanofluid originated which researchers in Fluid Dynamics incorporated into their works.

The industrial development increases pollution in the air caused due to dust particles, emissions of oxides of

*Corresponding author.
*E-mail address: deepika.ar2009@gmail.com

This paper was recommended for publication in revised form by Editor-in-Chief Ahmet Selim Dalkilic

Published by Yıldız Technical University Press, İstanbul, Turkey
© Author. This is an open access article under the CC BY-NC license (http://creativecommons.org/licenses/by-nc/4.0/).

sulphur, fumes from the factory, etc. Consequently, issues like global warming are emerging in full scale. Other forms of pollution are caused by power generation, vehicle movements and industrial boilers. These sources form nitrogen oxides which are harmful air pollutants. Lately, the Nitrogen oxide emission had reached distressing level in big cities because of the excessive use of motor driven vehicles. This led to chemical smog, respiratory problems and acid rain. In order to reduce Nitrogen oxide, there are several ways. Some of which are detoxification and purification through photocatalytic reactions. The photocatalyst possess various properties such as high absorbance of visible light, higher optical activity chemical inertness, optical stability, biological inertness, low cost, etc. All the above-mentioned properties are available in Titanium dioxide (TiO_2) and hence are used in various applications.

The name "Nanofluid" has been initiated by [1] who projected a new classification of fluids which has been observed by suspension of nanoparticles in the heat transfer of fluids. These nanoparticles are been made of carbon nanotubes, carbides, metals, or oxides. And these nanofluids have useful properties in several applications of heat transfer in microelectronics, artificial fibers, extrusion of polymers, copper wire drawing, processes in treatments, and coolant for engines. The study of effects of heat transmission over a stretched sheet has been analyzed by various researchers. [2-4] analyzed a nanofluid flow fluid with heat generation/absorption effects. The boundary layer flow across a vertically stretching external surface was understood and concluded that the Natural convection dominated the regime. [5] explored the influence of nanoparticle accumulation in a parabolic solar trough collector for enhancing the current transfer. [6] studied the Taguchi strategy optimization and neural networks of flush fraction impacts over heat degeneracy in Bodewadt movement.

Nanofluid composites are been synthesize in order to augment the rheological properties and thermal conductivity. This has been achieved by making a flawless combination of varying nanoparticles. A nanofluid which is formed by the addition of nanoparticle may not possess rheological properties, hence addition of nanoparticles with different rheological properties would be a better choice to attain overall ability and effectiveness which is termed as Hybrid nanofluid. Hybrid nanofluids improvise the chemical, physical properties of materials, the heat transfer rate because they provide more thermal conductance. For instance, Al_2O_3 has low thermal conductivity despite having effective stability and chemical inertness. Whereas, aluminum, copper, silver, etc possess good thermal conductivity but are chemically reactive and unstable. Scientists have immense interest in monitoring the thermal characteristics and stability of the system by mixing nano particles in the base fluid. [7-9] Therefore, by mixing these nanoparticles with varying chemical and physical bonds give raise to nanofluids known as hybrid nanofluids. Scientists [7-10] have analyzed the thermal and concentration features of hybrid nanofluids along with different MHD effects. They are been utilized in various applications like pharmaceutical industry, cooling of the electronic heaters, nuclear safety, etc. Various researchers [11] studied MHD effects of parameters of a ternary nanofluid flow on a convective stretched sheet.

The pioneering solution recorded by [12] was found to be worth as it augmented the heat transmission rate by the process of hybridization. [13] presented the betterment of thermal and mechanical features of base fluid by the adding two nanoparticles. [14] performed computational analyses of shape of nanoparticle, mass, and thermal transport on radiative nanofluid flow across a stretching Riga plate. The researchers [15-18] studied the convective fluid flow with magnetic field and heat source. Convective steadiness in porous spongy frameworks for energy and biosensor applications using viscous driven control flow was analyzed by [19, 20]

The importance of Titanium dioxide is seen in various photosensitive applications [21-25]. Higher photo catalysis can be obtained with fabrication of TiO_2 materials by considering higher specific surface areas. Precisely, the nanostructured Titanium dioxide materials which are made by template synthesis method was presented by [26, 27], which caught researchers' attention in the recent years. These materials have greater surface areas and are been used in numerous applications. Metallic nanoparticles like Ag, Au, Cu, CuO etc. possess improved thermal conductance in comparison to fluids. The researchers were then motivated and identified the necessity for the suspension of metallic nano-sized particles in nanofluids.

In the industries, the requirement of a coolant with better capability of heat transfer has motivated the scientists to design a new concept for nanofluid for enhancement of heat transfer. Hence the concept of hybrid nanofluids was discovered which enhances the heat transfer characteristics. With this inspiration, researchers have conducted experimental studies and this led to the discovery of tri-hybrid nanofluids. Here, three kinds of nanoparticles having varying chemical and physical bonds are suspended. For example, TiO_2 possesses higher acid strength while treated with sulphuric acid, and then forms $TiSO_4$. In the same manner, Al_2O_3 reacts with sulphuric acid to form $Al_2(SO_4)_3$. Weaker acid strengths are produced due to the reaction between sulphuric acid and alumina. They further increase the stability and chemical inertness of composition of nanoparticle. Whereas SiO_2 cannot form sulfatase, due to its high electron negativity than Ti and Al. This study led to the development of a coolant which cools appliances using TiO_2. Therefore, to develop coolant using TiO_2, the supportive agents were SiO_2 and Al_2O_3. [28] reviewed tertiary nanofluids in between rotating parallel plates with the effects of varying Lorentz effects and electric fields. [29] discussed the flow of (Al_2O_3-water) time-dependent mixed convection of nanofluids with a stagnation-point for a spinning sphere with motile microorganisms. [30] comprehensively

reviewed the mass and heat transfer through a stagnation point double-diffusion Cattaneo-Christov flow by means of non-Newtonian Sutterby nanofluids. [31-34] studied approximation properties of Bernstein polynomials and modified Jain Gamma operators.

Sodium alginate is a salt which is a natural polymer present in the alginic acid, and is been detached from the brown algae. This is utilized in textile production, industrial, medications and cosmetics. The functions of sodium alginate involve embolotherapy [30, 35], medication delivery system [36-39] encapsulation of cells [40-43].

On the basis of above-mentioned literature, uniqueness and originality for the existing work is to clarify the earlier studies by including the Brownian motion, thermophoresis, heat source and radiation parameters along with appropriate boundary conditions over a linearly stretching sheet producing more refined outcomes of tri-hybrid (TiO_2 + SiO_2 + Al_2O_3 / $C_6H_9NaO_7$) nanofluid flow. The current work indicates that heat flux play a noteworthy part in the species concentration and thermal transmission on trihybrid nanofluids. A comparative analysis with the previously published results to measure the assurance and accuracy of obtained similar outcomes and were in good agreement.

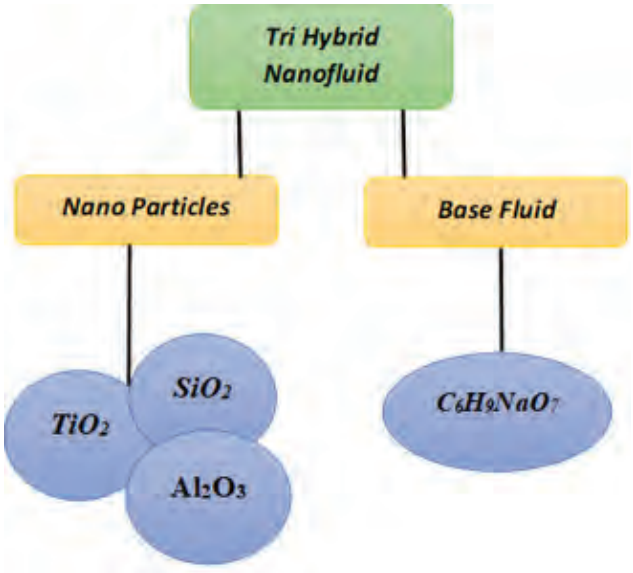


Figure 1. Preparation scheme of tri-hybrid nanoparticles.

PROBLEM FORMULATION

Consider two-dimensional, incompressible, steady-state, laminar, viscous ternary nanofluid flow past linearly stretching sheet. Following assumptions were considered in the fluid flow problem:

- Three kinds of nanoparticles viz. TiO_2, SiO_2 and Al_2O_3 are been dispersed in water (base fluid), to produce a new configuration TiO_2+SiO_2+Al_2O_3/ $C_6H_9NaO_7$ as portrayed in Figure 1.
- The rectangular co-ordinate system has been preferred such that x-axis is considered lengthways of the sheet, y-axis is perpendicular to it, and the Schematic representation is portrayed in Figure 2.
- Brownian motion, thermophoresis, and radiation parameter are been incorporated in the flow regime.
- Flow occurs in a section $y>0$.
- The sheet has a growth that is exponential with a velocity given as $u_w(x)=ax$. Here 'a' is taken as constant, and V_w is considered to be the mass transfer at the wall.
- Temperature and Concentration near the stretching surface is $T_w = T_\infty + b(x/l)^2$,
- $C_w = C_\infty + c(x/l)^2$ and far away are given is C_∞ and T_∞.
- Table 1 shows the experimental values of $C_6H_9NaO_7$, TiO_2, SiO_2 and Al_2O_3 [44-46], and Table 2 shows the Thermodynamic characteristics of Tri-Hybrid Nanofluids [47, 48].
- Base fluid and nanoparticles were in thermal equilibrium.

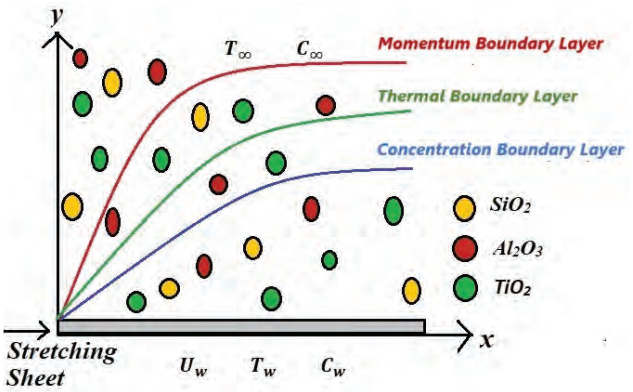


Figure 2. Geometry of the problem.

Table 1. Investigational values of $C_6H_9NaO_7$, TiO_2, SiO_2 and Al_2O_3

	ρ(kg/m³)	σ(S/m)	K(W/m.K)	C_p(J/Kg.K))
$C_6H_9NaO_7$	989	5.5×10^{-6}	0.6396	4175
TiO_2	4250	2.4×10^{6}	8.953	683
SiO_2	2270	3.5×10^{6}	1.4013	680
Al_2O_3	6310	5.96×10^{7}	32.9	765

Table 2. Thermodynamic properties of tri-hybrid nanofluids

Viscosity	$\frac{\mu_{tnf}}{\mu_f} = \frac{1}{(1-\varphi_{SiO_2})^{2.5}(1-\varphi_{Al_2O_3})^{2.5}(1-\varphi_{TiO_2})^{2.5}}$
Density	$\frac{\rho_{tnf}}{\rho_f} = \left(1-\varphi_{Al_2O_3}\right)\left[\left(1-\varphi_{Al_2O_3}\right)\left\{\left(1-\varphi_{TiO_2}\right)+\varphi_{TiO_2}\frac{\rho_{TiO_2}}{\rho_f}\right\}+\varphi_{Al_2O_3}\frac{\rho_{Al_2O_3}}{\rho_f}\right]+\varphi_{SiO_2}\frac{\rho_{SiO_2}}{\rho_f}$
Specific Heat	$\frac{(\rho c_p)_{tnf}}{(\rho c_p)_f} = \varphi_{SiO_2}\frac{(\rho c_p)_{SiO_2}}{(\rho c_p)_f}+\left(1-\varphi_{SiO_2}\right)\left[\left(1-\varphi_{Al_2O_3}\right)\left\{\left(1-\varphi_{TiO_2}\right)+\varphi_{TiO_2}\frac{(\rho c_p)_{TiO_2}}{(\rho c_p)_f}+\varphi_{Al_2O_3}\frac{(\rho c_p)_{Al_2O_3}}{(\rho c_p)_f}\right\}\right]$
Thermal Conductivity	$\frac{k_{tnf}}{k_{hnf}} = \left(\frac{k_{TiO_2}+2k_{hnf}-2\varphi_{TiO_2}(k_{hnf}-k_{TiO_2})}{k_{TiO_2}+2k_{hnf}+\varphi_{TiO_2}(k_{hnf}-k_{TiO_2})}\right)$, $\frac{k_{hnf}}{k_{nf}} = \left(\frac{k_{Al_2O_3}+2k_{nf}-2\varphi_{Al_2O_3}(k_{nf}-k_{Al_2O_3})}{k_{Al_2O_3}+2k_{nf}+\varphi_{Al_2O_3}(k_{nf}-k_{Al_2O_3})}\right)$, $\frac{k_{nf}}{k_f} = \left(\frac{k_{SiO_2}+2k_f-2\varphi_{Al_2O_3}(k_f-k_{SiO_2})}{k_{SiO_2}+2k_f+\varphi_{Al_2O_3}(k_f-k_{SiO_2})}\right)$
Electrical Conductivity	$\frac{\sigma_{tnf}}{\sigma_{hnf}} = \left(1+\frac{3\left(\frac{\sigma_{TiO_2}}{\sigma_{hnf}}-1\right)\varphi_{TiO_2}}{\left(\frac{\sigma_{TiO_2}}{\sigma_{hnf}}+2\right)-\left(\frac{\sigma_{TiO_2}}{\sigma_{hnf}}-1\right)\varphi_{TiO_2}}\right)$, $\frac{\sigma_{hnf}}{\sigma_{nf}} = \left(1+\frac{3\left(\frac{\sigma_{Al_2O_3}}{\sigma_{nf}}-1\right)\varphi_{Al_2O_3}}{\left(\frac{\sigma_{Al_2O_3}}{\sigma_{nf}}+2\right)-\left(\frac{\sigma_{Al_2O_3}}{\sigma_{nf}}-1\right)\varphi_{Al_2O_3}}\right)$, $\frac{\sigma_{nf}}{\sigma_f} = \left(1+\frac{3\left(\frac{\sigma_{SiO_2}}{\sigma_{nf}}-1\right)\varphi_{SiO_2}}{\left(\frac{\sigma_{SiO_2}}{\sigma_{nf}}+2\right)-\left(\frac{\sigma_{SiO_2}}{\sigma_{nf}}-1\right)\varphi_{SiO_2}}\right)$

The Casson trihybrid nano fluid flow gets modified with the influences of radiation and heat source effects under the boundary layer approximations [49].

$$\frac{\partial u}{\partial x}+\frac{\partial v}{\partial y}=0, \tag{1}$$

$$u\frac{\partial u}{\partial x}+v\frac{\partial u}{\partial y}=\vartheta_{tnf}\left(1+\frac{1}{\beta}\right)\left(\frac{\partial^2 u}{\partial y^2}\right)+\frac{\sigma_{tnf}}{\rho_{tnf}}B_o^2 u-\vartheta_{tnf}\left(\frac{u}{k_o}\right), \tag{2}$$

$$u\frac{\partial T}{\partial x}+v\frac{\partial T}{\partial y}=\alpha_{tnf}\frac{\partial^2 T}{\partial y^2}+\frac{Q}{\rho c_p}(T-T_\infty)-\frac{1}{(\rho c_p)_{tnf}}\frac{\partial q_r}{\partial y} \tag{3}$$

$$u\frac{\partial C}{\partial x}+v\frac{\partial C}{\partial y}=D_B\frac{\partial^2 C}{\partial y^2}+\frac{D_T}{T_\infty}\frac{\partial^2 T}{\partial y^2} \tag{4}$$

The conditions at the boundary are

$$v=-v_w,\ u=u_w(x),\ T=T_w,\ C=C_w\ at\ y=0 \tag{5}$$

$$u=0,\ v=0,\ T=T_\infty,\ C=C_\infty\ as\ y\to\infty \tag{6}$$

$$\text{where } \alpha=\frac{k}{(c\rho)_f},\ \tau=\frac{(c\rho)_p}{(c\rho)_f},\ \vartheta=\frac{\mu}{\rho_f}, \tag{7}$$

The coupled non-linear PDE is converted to coupled-non-linear ODE with the help of the similarity transformations mentioned as follows:

$$\eta=\sqrt{\frac{a}{\vartheta}}y,\ \Psi=\sqrt{a\vartheta}xf(\eta),\ \theta(\eta)=\frac{T-T_\infty}{T_w-T_\infty},\ \emptyset(\eta)=\frac{C-C_\infty}{C_w-C_\infty} \tag{8}$$

$$u=axf'(\eta),\quad v=-\sqrt{a\vartheta}f(\eta) \tag{9}$$

In equation (8), $\Psi(x,y)$ denotes the stream function which is given as follows:

$$u=\frac{\partial\psi}{\partial y},\quad v=-\frac{\partial\psi}{\partial x} \tag{10}$$

Radiative heat flux along y direction is dominant and the x direction component can be neglected. Radiative heat flux q_r, with the help of Rosseland approximations is mentioned as,

$$q_r=-\frac{4\sigma^*}{3k^*}\frac{\partial T^4}{\partial y} \tag{11}$$

where σ^* - Stefan Boltzmann constant. Within the flow, the difference in temperature, is small and hence the term T^4 has been expanded with the aid of Taylor's series having a T_∞ as the free stream temperature.

$$T^4\ \cong 4T_\infty^3 T-3T_\infty^4 \tag{12}$$

It follows on substituting Eq. (12) into Eq. (10),

$$q_r=-\frac{16T_\infty^3\sigma^*}{3k^*}\frac{\partial T}{\partial y} \tag{13}$$

The governing Eqns. (2) – (4) are changed into an ordinary differential equation by Similarity transformations. They are as follows:

$$\left(1+\frac{1}{\beta}\right)f'''-A_1A_2(ff''-2f'^2)-Kf'-A_1A_2Mf'=0 \tag{14}$$

$$\frac{1}{A_4}\left(A_3+\frac{4}{3}R\right)\theta''+Pr\left(f\theta'+Nb\theta'\emptyset'+Nt\theta'^2+A_4\theta\lambda\right)=0 \quad (15)$$

$$\emptyset''+Lef\emptyset'+\frac{Nt}{Nb}\theta''=0 \quad (16)$$

The conditions near the boundary:

$$\left.\begin{array}{l} f(0)=f_w;\ f'(0)=1,\ \theta(0)=1;\ \emptyset(0)=1;\ at\ \eta=0 \\ f'(\infty)=0;\ \theta(\infty)=0;\ \emptyset(\infty)=0;\ as\ \eta\to\infty \end{array}\right\} \quad (17)$$

$$\left.\begin{array}{l} f_w=-\frac{v_w}{\sqrt{a\vartheta}};\ Nt=\frac{(\rho c)_{pD_T}(T_W-T_\infty)}{(\rho c)_f\vartheta T_\infty};\ Nb=\frac{(\rho c)_{pD_B}(\emptyset_W-\emptyset_\infty)}{(\rho c)_f\vartheta}; \\ \Pr=\frac{\vartheta}{\alpha};\ R=\frac{4\sigma^*T_\infty^3}{3k^*k};\ Le=\frac{\vartheta}{D_B};\ \lambda=\frac{Q_o}{(\rho c_p)_f a}; \\ A_1=\frac{\mu_f}{\mu_{tnf}};\ A_2=\frac{\rho_{tnf}}{\rho_f};\ A_3=\frac{(\rho C_p)_{tnf}}{(\rho C_p)_f};\ A_4=\frac{k_{tnf}}{k_f} \end{array}\right\} \quad (18)$$

where f represents the velocity (dimensionless), θ represents the temperature, and $\emptyset$ represents the nanoparticle concentration.

$$C_f=\frac{T_w}{\rho u_w^2},\ Nu_x=\frac{xq_w}{k(T_W-T_\infty)},\ Sh_x=\frac{xh_m}{D_B(\emptyset_W-\emptyset_\infty)} \quad (19)$$

$$q_w=-k\left(\emptyset_y\right)_{y=0},\ h_m=-D_B\left(\emptyset_y\right)_{y=0} \quad (20)$$

By using the above equations, the reduced skin friction coefficient, heat and mass transmission rates in non-dimensional arrangement are:

$$C_f\sqrt{Re_x}=-f''(0),\frac{Nu_x}{\sqrt{Re_x}}=-(1+\mathrm{R})\theta'(0),\frac{Sh_x}{\sqrt{Re_x}}=-h'(0)s \quad (21)$$

where, Re_x, Nu_x, Sh_x and C_f signify the Reynolds number, Nusselt number, Sherwood number and skin friction, respectively.

Solution Procedure

The Runge-Kutta method with 4th order with boundary conditions (17) are used to solve the equations (14), (15) and (16) which are nonlinear coupled in nature. Equations are expressed as follows. Flow configuration is described in Figure 3 [50].

The equations are solved with shooting technique. The shooting technique is utilized to alter the ODE boundary value problem to a matching initial value problem.

New variables are now defined as:

$$f_1=f;\ f_2=f';\ f_3=f'';\ f_4=\theta;\ f_5=\theta';\ f_6=\emptyset;\ f_7=\emptyset' \quad (22)$$

The higher ordered coupled non-linear differential equations along with their boundary conditions have been changed into seven differential equations with first order and appropriate boundary conditions, and are given below:

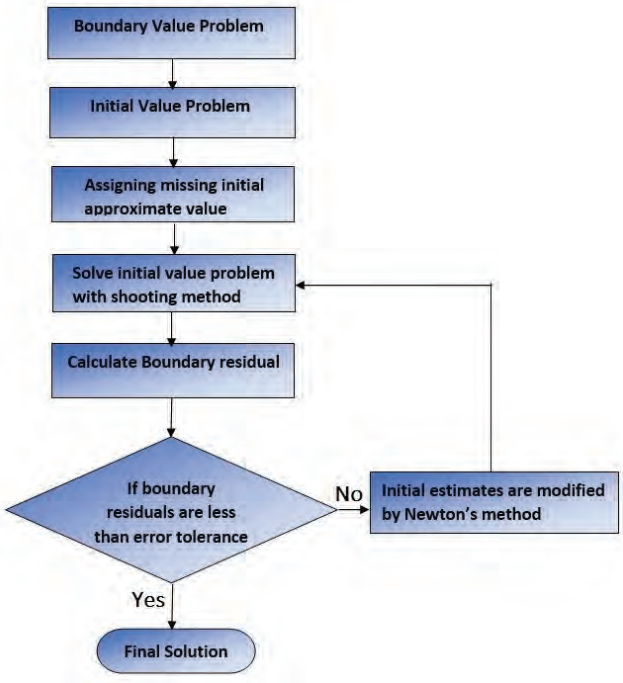


Figure 3. Flow configuration.

$$f_1'=f_2$$

$$f_2'=f_3$$

$$f_3'=\frac{A_1A_2\left(f_1f_3-2f_2^2\right)+Kf_2+A_1A_2Mf_2}{\left(1+\frac{1}{\beta}\right)}$$

$$f_4'=f_5$$

$$f_5'=-\mathrm{Pr}A_4\frac{\left(-f_1f_5-Nbf_5f_7-Ntf_5^2-\lambda A_4f_4\right)}{\left(A_3+\frac{4}{3}R\right)}$$

$$f_6'=f_7$$

$$f_7'=-Lef_1f_7+\frac{Nt}{Nb}Pr\frac{\left(-f_1f_5-Nbf_5f_7-Ntf_5^2-\lambda f_4\right)}{\left(1+\frac{4}{3}R\right)}$$

Boundary conditions are:

$$f_1(0)=f_w;\ f_2(0)=1;\ f_4(0)=1;\ f_6(0)=1,$$

$$f_1(\infty)=0;\ f_2(\infty)=0;\ f_6(\infty)=0$$

The significant feature of this study is, BVP is changed into an IVP. Then the result to IVP is found by taking guess values for initial values which are not present by means of shooting technique. The step size taken is 0.01 for doing computations. Tolerance for error of 10^{-3} is used as given in the literature of [51].

RESULTS AND DISCUSSION

A mathematical investigation was made to study the thermo-fluidic transport of tri-hybrid nanofluids on an

exponentially stretching sheet. And the equations governing the transport phenomena are been explained using the Runge-Kutta method along with a shooting algorithm. Velocity and thermal distributions were determined, followed by evaluating the concentration profile through numerical solutions for the trihybrid nanofluids. In all the results presented below, reference curves with appropriate parameters are drawn and the obtained results are compared with it.

For the Figures 4 to 6, the standard curve for reference has the following values:

Le = 10; Pr = 5; Nt = Nb =0.1; R = λ = 0; fw = 0.5; β = 5;M = K =1

It is found from Figure 4, when suction parameter is reduced from 1.5 to 0.5, suction weakens and hence the boundary layer thickens slightly. This causes the velocity to increase and more fluid remains in the boundary layer. When suction is changed from 0.5 to -1, there is a transition from weak suction to injection. At *fw* = 0.5, there is weak suction and at *fw* = 0, there is neither suction nor injection. *fw* = -1 represents injection wherein fluid is pushed into the boundary layer. Therefore, more fluid is added to the flow region which causes the velocity to further rise, especially near the wall. When Casson fluid parameter is raised from 5 to 8, the velocity was found to decrease. Casson fluid parameter β represents non-Newtonian nature of Casson fluid and is inversely related to yield stress. For smaller β (=5), the fluid is less viscous and hence moves freely. For larger β (=8), the fluid has high resistance to flow and hence the velocity becomes less. Comparable outcomes were found in the literature of [52].

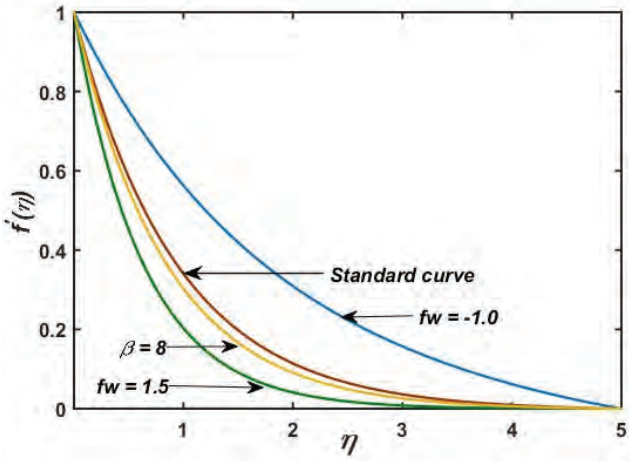


Figure 4. Velocity variation with Suction *fw* and Casson nanofluid parameter *β*.

Figure 5 reveals the variations of suction, Brownian flow motion and thermophoresis parameter with temperature profile. When suction parameter *fw* is 1.5 (strong suction), the boundary layer is thinner as there is less thermal diffusion. When *fw* =0.5(weaker suction), there is a moderate boundary layer thinning and hence the temperature is higher. For *fw* = -0.5(injection), the boundary layer thickens, so there is more thermal diffusion due to injection, meaning higher temperature across the layer. This phenomenon is very useful in applications requiring heat suppression (e.g., electronic cooling) as it maintains thermal stability and enhances surface cooling.

The Brownian motion *Nb* parameter measures the effect of randomness of nanoparticle motion on energy transport in trihybrid nanofluids which enhances the energy exchange between base fluid (sodium alginate) and nanoparticles. It increases the thermal energy transport within the fluid, which then leads to an increase in temperature, for advanced values of *Nb*, especially near the surface. TiO_2 and Al_2O_3 contributes to higher thermal stability, and has good photocatalytic properties, whereas

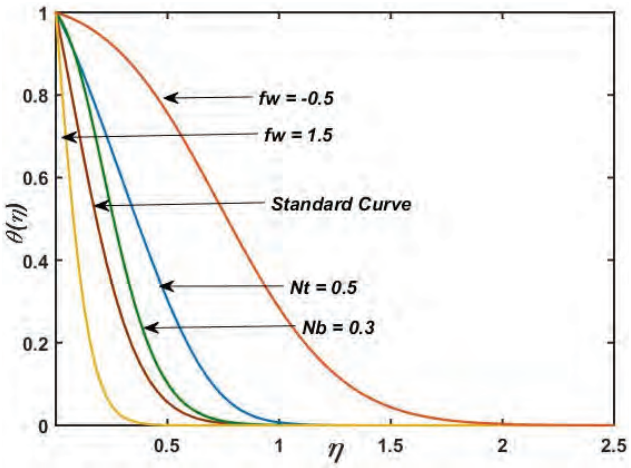


Figure 5. Temperature variation with Thermophoresis *Nt*, Suction *fw*, Brownian motion *Nb*.

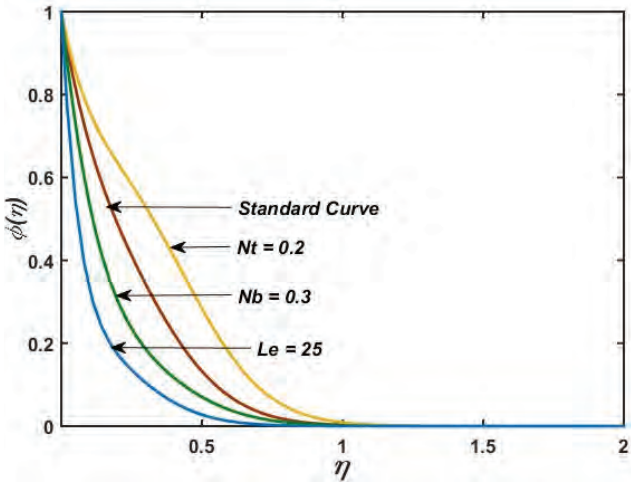


Figure 6. Concentration variation with Thermophoresis *Nt*, Lewis number *Le*, and Brownian motion *Nb*.

SiO_2 enhances thermal suspension ability. When thermophoresis *Nt* parameter is raised from 0.1 to 0.5, there was a rise in temperature. Thermophoresis refers to motion of particles from a hot to a cold region in a fluid due to the thermal gradient. A high range values of *Nt*, indicates a strong thermophoretic force, which push a greater number of nanoparticles away from the surface, hence resulting in the rise in temperature within the boundary layer.

Figure 6 depicts the concentration variations of trihybrid nanofluids with various parameters. When Lewis number *Le* rises, the concentration typically decreases. For a trihybrid nanofluid, higher Lewis number specifies that thermal diffusion is faster than mass diffusion. Therefore, thermal boundary layer develops more rapidly when compared to that of concentration boundary layer. So, the concentration boundary layer had become steep. When thermophoresis *Nt*, is raised from 0.1 to 0.2, the concentration profile generally increases. A higher value of *Nt* indicates a stronger movement of particles away from the hot exterior surface to the bulk fluid. This leads to the accumulation of fluid in the cooler region, which then rises the concentration away from the wall. As a result, overall concentration increases. When *Nb,* is raised from 0.1 to 0.3, there was a decline in the concentration. *Nb* signifies the random movement of nanoparticles to thermal agitation. Higher values of *Nb* enhances the diffusive movement of particles, which spreads the nanoparticle more widely through the fluid domain. Therefore, the concentration gradient becomes more smoother, and overall concentration profile decreases. Alike conclusions were found in the literature of [52].

The physical implications of trihybrid nanofluid flow plays a vital role. In thermal systems, wherein the temperature difference is significant, thermophoresis becomes very important. In (TiO_2+SiO_2+Al_2O_3/ $C_6H_9NaO_7$) nanofluid, increasing *Nb* causes greater particle dispersion. Hence it is dominant in micro- and nano-scale flows.

When internal heat generation increases, more thermal energy is added within the fluid which then acts as a source term in the energy equation. TiO_2 and Al_2O_3 possess excellent thermal conductivity and SiO_2 improves thermal stability and controls agglomeration. As a result, more heat accumulates, which then leads to the higher fluid temperature throughout the flow region as depicted in Figure 7. From Figure 8, radiation enhances heat transfer via electromagnetic waves which contributes to additional heat flux. This leads to the enhanced energy transport, effectively raising the temperature of the field. In Figure 9, increased temperature often decreases fluid density and can reduce species diffusion in in trihybrid nanofluid. Solute or nanoparticle concentration tends to decrease with stronger internal heat generation. Hence there is lower concentration near the wall. From Figure 10, higher radiation causes dilution of species concentration, and higher thermal agitation,

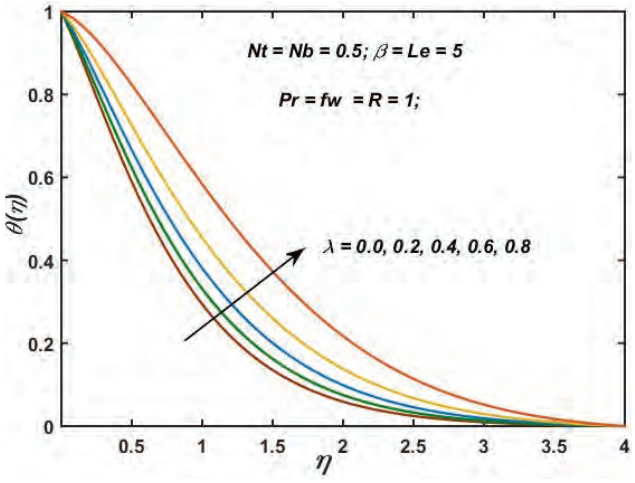


Figure 7. Temperature variation with heat generation λ.

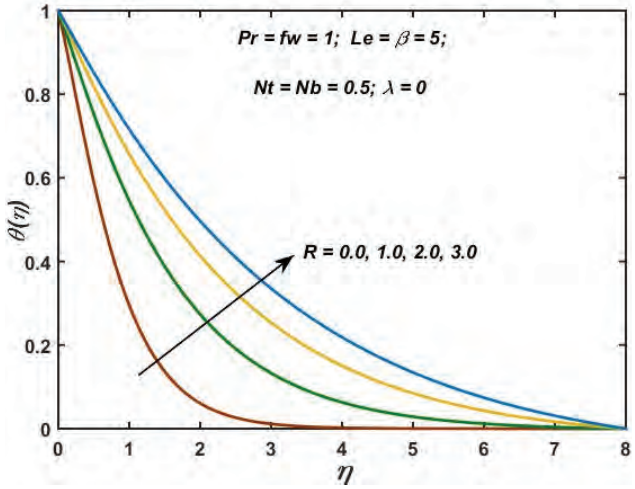


Figure 8. Temperature variation with radiation *R*.

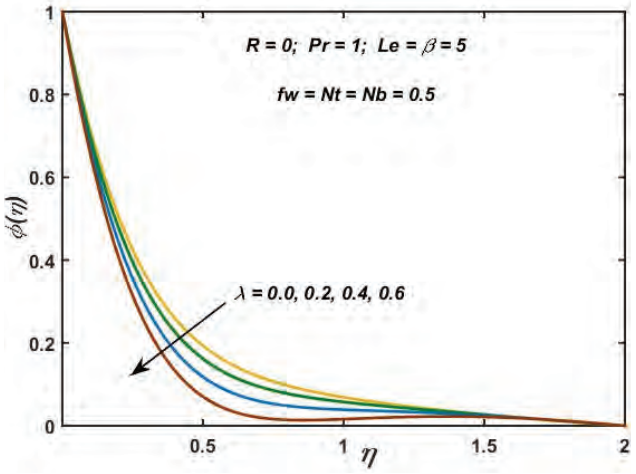


Figure 9. Concentration variation with heat generation λ.

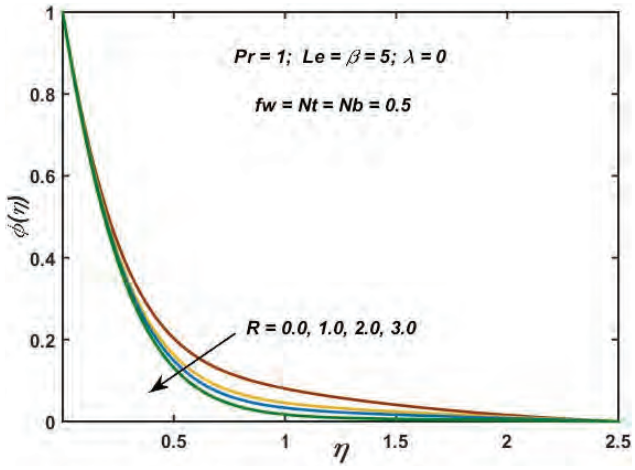


Figure 10. Concentration variation with radiation *R*.

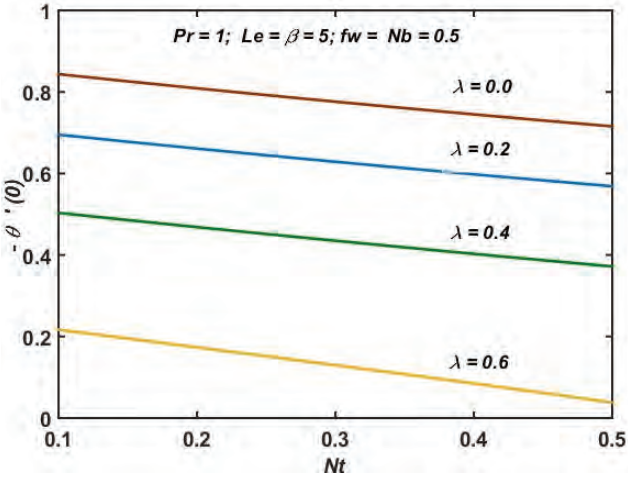


Figure 11. Local Nusselt number on *Nt* for varying heat generation λ.

which reduces the relative particle accumulation, especially in boundary layers. This results in the reduced concentration gradient and overall lower concentration values.

There are various industrial and engineering applications with heat generation and radiation. This can be used in nuclear reactors, power plants because TiO_2 and Al_2O_3 possess excellent thermal conductivity and SiO_2 improves thermal stability. It is also used in solar collectors, solar thermal systems as TiO_2 and SiO_2 are optically active, and are good absorbers of solar radiation. Trihybrid nanofluid can be used as nanofluid-assisted drug delivery as TiO_2 is a Biocompatible oxide used for photothermal effects.

Figures 11 and 12 shows that there is decline for higher value of heat source and radiation parameter. A positive heat source and thermal radiation parameter causes the thermal transport to rise within the fluid, reducing the thermal gradient near the surface. As Nusselt number is directly proportionate to the thermal gradient, it reduces. Figures 13 and 14 depicts the variation of Sherwood number for varying heat source and radiation parameter. The Sherwood number was found to increase and similar results were obtained by [53].

Table 3 presents the present outcomes with the previously published result by taking Le=10, f_w=0, $\beta \to \infty$. From Table 4, the Nusselt number typically reduces for advanced values of *R* and λ for a trihybrid nanofluid flow. Positive heat source and radiation enhances thermal energy to the fluid while increasing the temperature of the fluid near the surface. The thermal gradient at the wall decreases and Nusselt being proportional to the temperature gradient, reduces. Sherwood number was found to decrease for advanced values of heat generation and radiation.

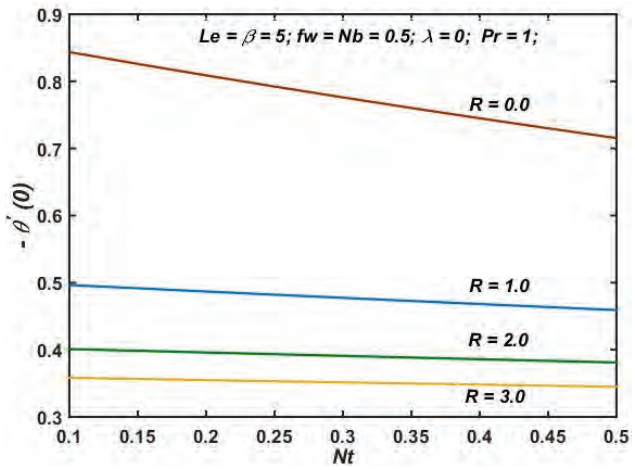


Figure 12. Local Nusselt number on *Nt* for varying radiation *R*.

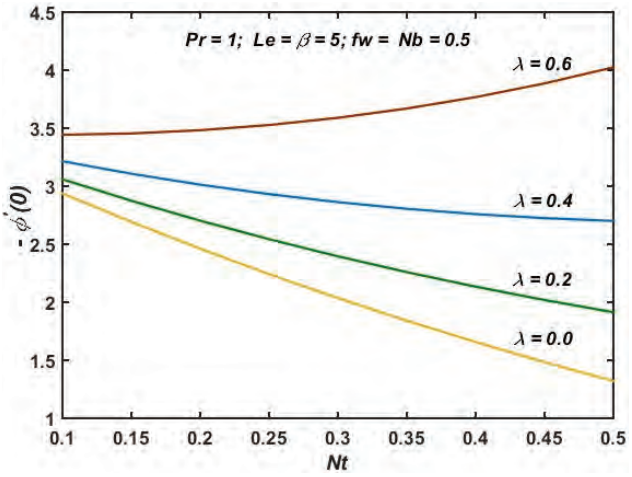


Figure 13. Local Sherwood number on *Nt* for varying heat generation λ.

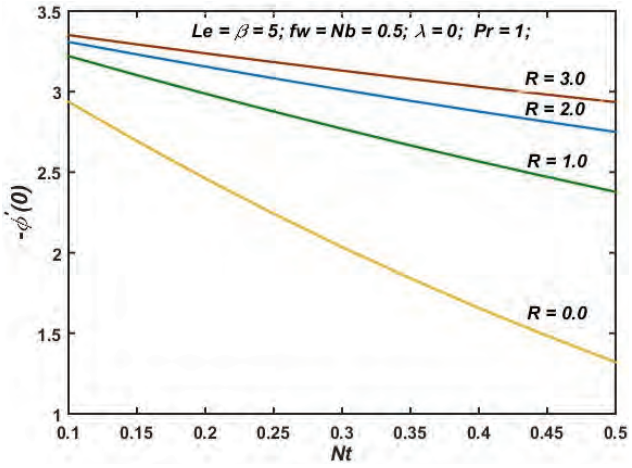


Figure 14. Sherwood number on *Nt* for varying radiation *R*.

Table 4. Computed local Nusselt $-\theta'(0)$, local Sherwood $-\phi'(0)$ numbers for changing values of heat generation λ and Radiation *R* as *Le = 5, fw = 0.5, β = 5, Nb = Nt = 0.1, Pr = 10, M = K =1*

λ	*R*	$-\theta'(0)$	$-\phi'(0)$
0.0	0.0	3.35766146	0.74574654
0.2		3.06867167	1.02374100
0.4		2.75576605	1.32413791
0.6		2.41285144	1.65260655
0.8		2.03105529	2.01739063
1.0		1.59669978	2.43120211
0.0	1.0	2.10893932	1.88572612
	2.0	1.61344374	2.31487442
	3.0	1.32981417	2.55088933

Table 3. Comparison table

Pr	Khan and Pop [4]	Gorla and Sidwai [54]	Manjunatha et al. [45]	Current Study
2	0.9113	0.9114	0.9113	0.9114
6.13	1.7597	1.7596	1.7597	1.7596
7	1.8954	1.8954	1.8954	1.8953
20	1.3539	1.3539	1.3539	1.3539

CONCLUSION

The present study investigates two-dimensional, laminar, incompressible, steady, viscous tri-hybrid nanofluid flow on a linearly stretching sheet. Three kinds of nanoparticles called TiO_2, SiO_2 and Al_2O_3 are been dispersed in (base fluid) sodium alginate to obtain a new configuration TiO_2+SiO_2+Al_2O_3/ $C_6H_9NaO_7$. Thermophoretic and Brownian motion parameters are merged in the concentration Navier Stokes equation. The above-mentioned physical illustrations have many usages in the field of industries and manufacturing, particularly in cooling systems. Due to its higher thermal conductivity, lately it has become a very effective method in cooling systems. In the current problem, numerical analysis of tri-hybrid nanoparticles has been conducted to study the pattern of velocity, thermal and concentration profiles. Some of the decisive results of the current study are enumerated below:

1. When the heat generation λ rises, there is an inclination in the temperature.
2. With an inclination in radiation number *R*, a rise in temperature is found.
3. A decay in the concentration is found, due the increase in heat generation.
4. Concentration has reduced for higher radiation values.
5. A decline in Nusselt number; a rise in Sherwood number were noted with the rise in heat generation.
6. With the rise in radiation, there is a fall in the local Nusselt number, and a rise in the local Sherwood number.

NOMENCLATURE

C	Nanoparticle concentration
C_w	Surface Concentration
C_∞	Concentration near infinity
D_B	Brownian flow motion coefficient
D_T	Thermophoretic motion coefficient
h_f	Coefficient for heat transfer
K	Porosity parameter
K_1	Coefficient of Thermal slip
L	Thermal Slip
M	Magnetic parameter
Nb	Brownian motion parameter
Nt	Thermophoresis parameter
Pr	Prandtl number

Greek Symbols

β	Casson fluid parameter
ρ	Fluid density
η	Dimensionless Similarity variable
π	Deformation rate
σ	Electric conductivity

λ Heat source
θ Non-dimensional temperature

Subscripts
f Nanofluid
tnf Tri-Hybrid Nanofluid
∞ Condition at the free stream
w Condition at the wall

AUTHORSHIP CONTRIBUTIONS

Authors equally contributed to this work.

DATA AVAILABILITY STATEMENT

The authors confirm that the data that supports the findings of this study are available within the article. Raw data that support the finding of this study are available from the corresponding author, upon reasonable request.

CONFLICT OF INTEREST

The authors declared no conflict of interest.

ETHICS

There are no ethical issues with the publication of this manuscript.

STATEMENT ON THE USE OF ARTIFICIAL INTELLIGENCE

Artificial intelligence was not used in the preparation of the article.

REFERENCES

[1] Crane LJ. Flow past a stretching plate. Z Angew Math Phys 1970;21:645–647. [CrossRef]
[2] Chamkha AJ, Pop I. Effect of thermophoresis particle deposition in free convection boundary layer from a vertical flat plate embedded in a porous medium. Int Commun Heat Mass Transf 2004;31:421–430. [CrossRef]
[3] Chamkha AJ, Ali F, Al-Mudhaf, Pop I. Effect of heat generation or absorption on thermophoretic free convection boundary layer from a vertical flat plate embedded in a porous medium. Int Commun Heat Mass Transf 2006;33:1096–1102. [CrossRef]
[4] Gorla RSR, Chamkha AJ, Rashad AM. Mixed convective boundary layer flow over a vertical wedge embedded in a porous medium saturated with a nanofluid: natural convection dominated regime. Nanoscale Res Lett 2011;6:207. [CrossRef]
[5] Sharma A, Sharma RP, Biswas A, Ibrahim SM. Exploring the impact of nanoparticle aggregation in parabolic trough solar collectors with a neural network-based predictions for enhanced thermal performance. Sol Energy Mater Sol Cells 2025;293:113866. [CrossRef]
[6] Vinay Kumar V, Sharma RP. Neural network and Taguchi design optimization of solvent fraction effects on heat dissipation in Bodewadt flow. Int Commun Heat Mass Transf 2025;169:109845. [CrossRef]
[7] Kalidas D, Sharma RP, Debashish G. Squeezing flow of chemical reacting hybrid nanofluid between two analogous disks with activation energy and magnetic field. J Nanofluids 2023;12:388–397. [CrossRef]
[8] Prakash O, Barman P, Rao PS, Sharma RP. MHD free convection in a partially open wavy porous cavity filled with nanofluid. Numer Heat Transf A Appl 2023;84:449–463. [CrossRef]
[9] Sarma AK, Sarma D, Mudoi S. MHD flow and effects of Hall current, joule heating, and heat source across a chemically reacting and radiating exponentially stretching sheet in a porous medium. Sigma J Eng Nat Sci 2025;43:1179–1196. [CrossRef]
[10] Sharma RP, Barik BK, Vinay K, Sharma A. Illustration of low oscillating magnetic field on sodium alginate-based hybrid nanofluid flow between two revolving disks: an artificial neural network-based study. Eng Appl Artif Intell 2025;155:111101. [CrossRef]
[11] Sharma RP, Badak K. Heat transport of radiative ternary hybrid nanofluid over a convective stretching sheet with induced magnetic field and heat source/sink. J Therm Anal Calorim 2024;149:3877–3889. [CrossRef]
[12] Hayat T, Nadeem S. Heat transfer enhancement with Ag-CuO/water hybrid nanofluid. Results Phys 2017;7:2317–2324. [CrossRef]
[13] Nihara K. New design concept of structural ceramics-ceramic nano composites. J Ceram Soc Jpn 1991;99:974–982. [CrossRef]
[14] Ahmed SE, Arafa AAM, Hussein SA. Hydrothermal dissipative nanofluid flow over a stretching riga plate with heat and mass transmission and shape effects. J Therm Anal Calorim 2024;149:4855–4872. [CrossRef]
[15] Manjunatha N, Girinath Reddy M, Ahmad A, Sarah A, Rupesh Reddy A, Farhan A, et al. Radiation effects on rotating system free convective nanofluid unsteady flow with heat source and magnetic field. Partial Differ Equ Appl Math 2025;13:101083. [CrossRef]
[16] Varalakshmi KB, Manjunatha N. Thermal instabilities with local thermal non-equilibrium and heat generation: two-layer configuration. AI Therm Fluids 2025;2-3:100012. [CrossRef]
[17] Manjunatha N, Mahendra SJ, Gangadharaiah YH, Barakah A. Magneto-thermal convective flow in fluid-porous region with heat source/sink effects: analytical study. Ain Shams Eng J 2025;16:103820. [CrossRef]

[18] Manjunatha N, Vijaya K, Sumithra R, Thabet A, Nabil M. Temperature gradient and heat source/sink impacts on triple-diffusive surface-tension-driven convection. Case Stud Therm Eng 2025;73:106531. [CrossRef]

[19] Gangadharaiah YH, Vijaya K, Manjunatha N, Nagarathnamma H, Maryam AA, Irshad A, et al. Convective stability in porous structures for energy and biosensing applications using viscosity-driven flow control and couple-stress fluid. Case Stud Therm Eng 2025;75:107189. [CrossRef]

[20] Manjunatha N, Varalakshmi KB, Laxminarayana M, Sumithra R. Influence of local thermal equilibrium and thermal gradients on Magneto-Darcy-Rayleigh-Benard convective stability with heat generation. Heat Transf 2025;54. [CrossRef]

[21] Bischoff BL, Anderson MA. Peptization process in the sol-gel preparation of porous anatase (TiO2). Chem Mater 1995;7:1772–1778. [CrossRef]

[22] Fujishima A, Honda K. Electrochemical photolysis of water at a semiconductor electrode. Nature 1972;238:37–38. [CrossRef]

[23] Hulteen J. A general template-based method for the preparation of nanomaterials. J Mater Chem 1997;7:1075–1087. [CrossRef]

[24] Seo DS, Lee JK, Kim H. Preparation of nanotube shaped TiO2 powder. J Cryst Growth 2001;229:428–432. [CrossRef]

[25] Zhang M, Bando Y, Wada K. Sol-gel template preparation of TiO2 nanotubes and nanorods. J Mater Sci Lett 2001;20:167–170. [CrossRef]

[26] Martin CR. Nanomaterials: a membrane based synthetic approach. Science 1994;266:1961–1966. [CrossRef]

[27] Martin CR, Parthasarathy R, Menon V. Template synthesis of electronically conductive polymers preparation of thin films. Electrochim Acta 1994;39:1309–1313. [CrossRef]

[28] Ahmed SE, Arafa AAM, Hussein SA, Morsy Z. Time-dependent squeezing flow of variable properties ternary nanofluids between rotating parallel plates with variable magnetic and electric fields. Numer Heat Transf A Appl 2023:1–30. [CrossRef]

[29] Hussein SA, Anas AMA, Alshehry N, Ahmed SE. Bioconvection across a revolving sphere under the influence of bilateral chemical reactions with temperature- and space-dependent heat generation. J Eng Res 2024;2024:2307–1877.

[30] Wang Q, Qian K, Liu SS, Yang YJ, Liang B, Zheng CS, et al. X-ray visible and uniform alginate microspheres loaded with in situ synthesized BaSO4 nanoparticles for in vivo transcatheter arterial mobilization. Biomacromolecules 2015;16:1240–1246. [CrossRef]

[31] Rajawat RS, Singh KK, Mishra VN. Approximation by modified Bernstein polynomials based on real parameters. Math Found Comput 2023;13.

[32] Mishra VN, Rajawat RS, Sharma V. On generalized quantum Bernstein polynomials. In: Advances in Pure and Applied Algebra: Proceedings of the CONIAPS XXVII International Conference. Vol. 3. Walter de Gruyter GmbH & Co KG; 2023. p. 149. [CrossRef]

[33] Raiz M, Rajawat RS, Mishra VN. α-Schurer Durrmeyer operators and their approximation properties. Ann Univ Craiova Math Comput Sci Ser 2023;50:189–204. [CrossRef]

[34] Pandey S, Rajawat RS, Mishra VN. Approximation properties of modified Jain Gamma operators preserving linear function. Palest J Math 2023;12:169–182.

[35] Becker TA, Kipke DR, Brandon T. Calcium alginate gel: a biocompatible and mechanically stable polymer for endovascular embolization. J Biomed Mater Res 2001;54:76–86. [CrossRef]

[36] Matricardi CDMP, Coviello T, Alhaique F. Recent advances and perspectives on coated alginate microspheres for modified drug delivery. Expert Opin Drug Deliv 2008;5:417–425. [CrossRef]

[37] Tønnesen HH, Karlsen J. Alginate in drug delivery systems. Drug Dev Ind Pharm 2002;28:621–630. [CrossRef]

[38] Giri TK, Thakur D, Alexander A, Ajazuddin, Badwaik H, Tripathi DK. Alginate based hydrogel as a potential biopolymeric carrier for drug delivery and cell delivery systems: present status and applications. Curr Drug Deliv 2012;9:539–555. [CrossRef]

[39] Hori Y, Winans AM, Irvine DJ. Modular injectable matrices based on alginate solution/microsphere mixtures that gel in situ and co-deliver immunomodulatory factors. Acta Biomater 2009;5:969–982. [CrossRef]

[40] Akbari S, Pirbodaghi T. Microfluidic encapsulation of cells in alginate particles via an improved internal gelation approach. Microfluid Nanofluid 2013;16:773–777. [CrossRef]

[41] Zimmermann H, Shirley SG, Zimmermann U. Alginate-based encapsulation of cells: past, present, and future. Curr Diabetes Rep 2007;7:314–320. [CrossRef]

[42] Martinez CJ, Kim JW, Ye C, Ortiz I, Rowat AC, Marquez W, et al. Microfluidic approach to encapsulate living cells in uniform alginate hydrogel microparticles. Macromol Biosci 2012;12:946–951. [CrossRef]

[43] Zhao LB, Pan L, Zhang K, Guo SS, Liu W, Wang Y, et al. Generation of Janus alginate hydrogel particles with magnetic anisotropy for cell encapsulation. Lab Chip 2009;9:2981–2986. [CrossRef]

[44] Manjunatha S, Puneeth V, Gireesha BJ, Chamkha AJ. Theoretical study of convective heat transfer in ternary nanofluid flowing past a stretching sheet. J Appl Comput Mech 2022;8:1279–1286.

[45] Kashif A, Sohail A, Shabbir A, Jamshed J, Vineet T, Ali T, et al. Insights into the thermal attributes of sodium alginate (NaC6H7O6) based nanofluids in a three-dimensional rotating frame: a comparative case study. Case Stud Therm Eng 2023;49:103211. [CrossRef]

[46] Puneeth V, Manjunatha S, Makinde OD, Gireesha BJ. Bioconvection of a radiating hybrid nanofluid past a thin needle in the presence of heterogeneous-homogeneous chemical reaction. J Heat Transf 2021;143. [CrossRef]

[47] Alharbi KAM, Ahmed AES, Ould S, Ahammad NA, Mohamed A, Abdullah M, et al. Computational valuation of Darcy ternary-hybrid nanofluid flow across an extending cylinder with induction effects. Micromachines (Basel) 2022;13. [CrossRef]

[48] Bilal M, Gul T, Mouldi A, Mukhtar S, Alghamdi W, Bouzgarrou SM, et al. Melting heat transition in a spinning flow of silver-magnesium oxide/engine oil hybrid nanofluid using parametric estimation. J Nanomater 2022;2022:2891315. [CrossRef]

[49] Jagadish VT, Guled CN, Samad N, Unai FG, Vediyappan G, Sundarappan B. Effects of thermophoresis and Brownian motion for thermal and chemically reacting Casson nanofluid over a linear stretching sheet. Results Eng 2022;15:100448. [CrossRef]

[50] Ali B, Mashael MA, Sidra J, Abdul HG, Shaimaa AMA. Computational framework of hydrodynamic stagnation point flow of nanomaterials with natural convection configured by a heated stretching sheet. Z Angew Math Mech 2023;103. [CrossRef]

[51] Basha H, Kumar NN, Reddy GJ, Ballem S. Thermal analysis of buoyancy motivated Casson fluid flow with time-independent chemical reaction under Lorentz forces. Heat Transf 2021;50:7291–7320. [CrossRef]

[52] Deepika AR, Govardhan K, Rana A, Reza M. Soret and Dufour effects on MHD mixed convection flow of Casson hybrid nanofluid over a permeable stretching sheet. Int J Ambient Energy 2023;44:2115–2127. [CrossRef]

[53] Gorla RSR, Sidwai I. Free convection on a vertical surface with suction and blowing. Appl Sci Res 1994;52:247–257. [CrossRef]

Sigma J Eng Nat Sci, Vol. 44, No. 4, pp. 2583–2594, August, 2026

Sigma Journal of Engineering and Natural Sciences
Web page info: https://sigma.yildiz.edu.tr
DOI: 10.14744/sigma.2026.2116

Research Article

Thermal analysis of hybrid Casson nanofluid (AlN+Al_2O_3/ $C_6H_9NAO_7$) with Lorentz force effect over a linearly stretching sheet

S. RENUKA[1], V. MEENAKSHI[2], Kamatam GOVARDHAN[3], A. R. DEEPIKA[4,*]

[1]Department of Mathematics, Nizam College, Hyderabad, 500001, India
[2]Department of Technical Education, J.N. Government Polytechnic, Hyderabad, 500013, India
[3]Department of Mathematics and Statistics, GITAM Deemed to be University, Hyderabad, 502329, India
[4]Department of Mathematics, Global Institute of Engineering and Technology, Hyderabad,501504, India

ARTICLE INFO

Article history
Received: 16 November 2025
Revised: 24 December 2025
Accepted: 03 March 2026

Keywords:
Nusselt Number and Heat Generation; Radiation; Runge-Kutta Method; Sherwood Number

ABSTRACT

The current numerical study analyses the flow of 2D, steady-state, MHD Hybrid Casson nanofluid (AlN+Al_2O_3/ $C_6H_9NaO_7$) over a linearly stretching sheet by incorporating the Lorentz force, heat generation and radiation effects. The study not only explores to achieve superior heat transmission compared to that of traditional nanofluids, it also highlights the improvement of the fuel efficacy and engine process in automotive engineering, also productivity for the cooling arrangements used in food preservation and processing. This investigation offers vision for the progress of effective energy storage systems, heat exchangers, also cooling systems of different manufacturing applications. The nonlinear coupled partial differential equations are explained with Runge-Kutta system using shooting method. Higher values of radiation and heat generation parameters, strengthens the thermal process and weakens the concentration diffusion. Sherwood number had risen from 0.876 to 1.423 for nanofluids and 1.023 to 1.652 for hybrid nanofluids. Novelty of the research article is to streamline the earlier works by incorporating radiation, Brownian motion, heat source, thermophoresis, and magnetic effects in the equivalent governing equations leading to an achievement of effective hybrid nanofluid flow.

Cite this article as: Renuka S, Meenakshi V, Govardhan K, Deepika AR. Thermal analysis of hybrid Casson nanofluid (AIN+Al_2O_3/ $C_6H_9NAO_7$) with Lorentz force effect over a linearly stretching sheet. Sigma J Eng Nat Sci 2026;44(4):2583–2594.

INTRODUCTION

Nanofluid consists of particles that are nano-meter sized identified as nanoparticle. These nano-meter sized solid nanoparticles are dispersed in base fluids like propylene glycol, synthetic oils, water, etc. They are made up of carbides (SiC), nitrides (AlN), oxides (Al_2O_3, SiO_2, TiO_2), metals (Cu, Al), etc. and they have exclusive physical and chemical characteristic properties. The smoothness of nanofluid flow without any clogging is due to their small sized nanoparticles. Nanofluids are extensively used for the

***Corresponding author.**
*E-mail address: deepika.ar2009@gmail.com

This paper was recommended for publication in revised form by Editor-in-Chief Ahmet Selim Dalkilic

Published by Yıldız Technical University Press, İstanbul, Turkey
© Author. This is an open access article under the CC BY-NC license (http://creativecommons.org/licenses/by-nc/4.0/).

improved heat transfer development materials and hence, it captivated many scientists and researchers to discover the heat transfer features. The base fluids possess low heat transfer properties. One among the latest technologies, heat transfer across a sheet stretching or otherwise, demanded an understanding of the flow dynamics, especially near the boundary of these sheets as the optimum changes occur in these layers. This approach gave a deep vision into the features of fluid/heat transfer which hugely supported the engineering processes. The flow over the boundary layer which arises because of a stretching sheet which moves linearly with the changing velocity, was carried out in literature of [1]. As there was advancement in nanotechnology, nanofluid originated which researchers in Fluid Dynamics incorporated into their works.

The name "Nanofluid" has been initiated by [2]. He projected a new classification of fluids which has been observed by suspension of small nano-sized units in the heat transfer of fluids. Nanoparticles are naturally made of carbon nanotubes, metals, carbides, or oxides. Nanofluids possesses very useful properties in several applications of heat transfer in microelectronics, artificial fibers, extrusion of polymers, copper wire drawing, processes in treatments, and coolant for engines.

[3] analyzed a model of Casson fluid considering the heat transmission with injection/suction. The viscosity of the flow across a horizontal stretching surface was studied. [4] concluded that Nusselt number is becoming a property that is decreasing for each and every dimensionless number. Also, it was found that Sherwood number is increasing with a high value of Prandtl number and is a function that is decreasing with the lower value of Prandtl for individual values of Le and Nb. [5] studied the impact of boundary conditions with a partial slip of nanofluid on a stretching surface keeping the wall temperature as constant. The result showed that the shear stress, flow velocity are highly affected by the slip parameters. In the literature of [6], the 3D MHD Casson Carreau nanofluid flow with thermal radiation was studied. It was observed that with the rise in Prandtl number along with buoyancy ratio, the boundary layer thickness had raised. The researchers in [7] probed the effects of Ohmic heating and transverse current on an exponential stretching sheet with embedded porous media.

In literature of [8], the heat absorption effect of Casson nanofluid on a cylinder with the effects of the chemical reactions, was studied. The mathematical model was numerically solved in COMSOL. [9] studied a heat sink/source in MHD Casson fluid and was found that the velocity profiles were higher and the fields of concentration and temperature had an opposite phenomenon. [10] considered the thermal radiation of Casson nanofluid. By keeping only, the Casson fluid parameter constant, it was concluded that an upsurge in Brownian flow motion reduces the temperature. [11] found the point of stagnation of a Casson fluid with variable thickness and thermal radiation. Various parameters like wall thickness, velocity ratio and velocity power index were studied. [12] analyzed the transmission of heat which flows across a vertical cylinder and having exponential stretching. Influences of parameters like the Lewis number, Prandtl number, and Reynolds number were studied.

Hybrid nanofluids are advanced heat transmission fluids formed by dissolving two different kinds of nanoparticles in the base fluid. They offer improved thermal conductivity, viscosity control, and steadiness related to conventional nanofluids containing only a single type of nanoparticle. Experimentally it is proven that the non-metallic nanoparticles are more stable than metallic nanoparticles. Casson hybrid nanofluids is a non-Newtonian extension of hybrid nanofluids where the base fluid obeys the Casson fluid model. This model accounts for yield stress behavior observed in materials like chocolate, blood, and toothpaste. When nanoparticles are suspended in such fluids, the resulting combination is a Casson hybrid nanofluid. These fluids are useful for simulating real-life complex fluids in biomedical, manufacturing and industrial applications. The authors in [13-15] studied the MHD effects of hybrid Casson nanofluid along by taking into consideration porosity, viscous dissipation, Joule heating and heat sink/source

[16] reviewed the transmission of heat features of a 2D Casson nano fluid flow over the wedge. Taking the nanoparticle's volume fraction flux as zero, the impact of flow parameters like volume fraction and temperature of the nanoparticle were studied. [17] comprehensively analysed the Maxwell convective hybrid nanofluid flow on a stretching sheet. [18] analyzed the Casson fluid model on a symmetrical wedge and found that with an increase in the Falkner-Skan exponent, there was an augmentation in velocity and decay in temperature. With an upsurge in Casson parameter, velocity got amplified and a decline in temperature. [19] conducted investigation of a 2D flow of unsteady Casson fluid. It was reported that fluid velocity declines with amplification of unsteadiness parameter. An upsurge in the Casson parameter caused the velocity to get suppressed and there was an enhancement in temperature. [20-22] analyzed the inertia point flow features of hybrid Williamson Casson nanofluid flow with viscid dissipation and injection effects. [23] studied the features of an isotropic incompressible Casson nanofluid with thermal and solute boundary conditions over an oscillatory plate. It was found that the concentration of species and fluid velocity increased whenever there was an increment in the coefficient of mass transfer. [24, 25] combined the Yamada Ota model into Casson Maxwell quadra-hybrid nanofluid framework over an exponential stretching sheet which explores the endothermic and exothermic reactions.

Sodium alginate is a salt which is a natural polymer present in the alginic acid, and is been detached from the brown algae. This is utilized in textile production, industrial, medications and cosmetics. The utilities of sodium alginate include radioembolization [26, 27], medication delivery system [28-31] encapsulation of cells [32-35] cellular therapeutics Barnett [36]. The authors in the literature

[37] carried out a computational study to comprehend the Darcy-Forchhheimer EMHD Williamson flow which is sodium alginate-based nanofluid across a vertically stretching cylinder.

On the basis of above-mentioned literature, the originality and novelty of the current work simplify the previous work by including Lorentz effect, Brownian motion, thermophoresis, heat source and radiation effects over a linearly stretching sheet of a Casson hybrid nanofluid flow. Existing work displays, the magnetic parameter has a noteworthy part in the momentum and heat transmission of hybrid nanofluids. The present outcomes have been compared with previous outcomes to show correctness of achieved similar outcomes and were in upright agreement.

PROPERTIES OF BASE FLUID AND HYBRID NANOFLUIDS

The base fluid is sodium alginate ($C_6H_9NaO_7$) and nanoparticles Alumina (Al_2O_3) and Aluminum Nitride (AlN) mixture are considered as nanoparticles. Elementary equations [38] for Casson fluid model:

$$\tau_{ij} = \begin{cases} \left(\mu_c + \frac{P_s}{\sqrt{2\pi}}\right) 2e_{ij}, & \pi > \pi_0 \\ \left(\mu_c + \frac{P_s}{\sqrt{2\pi_0}}\right) 2e_{ij}, & \pi < \pi_0 \end{cases} \quad (1)$$

Fluid yield stress $P_s = e_{ij}\, e_{ij}$;
π - Rate of deformation that is multiplied to itself.
π_0 - Critical value.
From (1), (*for* $\pi < \pi_0$) we have

$$\tau_{ij} = \mu_c \left(1 + \frac{1}{\beta}\right) 2e_{ij} \quad (2)$$

where $\beta = \mu_c\sqrt{2\pi_0}/P_s$ is Casson parameter.

The Thermal characteristics viz. Thermal conductivity, density, and specific heat are [39]:

$$\rho_{hnf} = \left(\frac{\emptyset}{100}\right)\rho_p + \left(1+\frac{\emptyset}{100}\right)\rho_f, \quad (3)$$

$$\left.\begin{aligned} \frac{k_{hnf}}{k_f} = 1.2035 \left(1 + \frac{\emptyset}{100}\right)^{0.0098} \left(0.01 + \frac{T_{hnf}}{100}\right)^{0.1331} \\ \left(0.001 + \frac{dp}{100}\right)^{-0.0001} \left(0.01 + \frac{\alpha_p}{\alpha_f}\right)^{0.0153} \end{aligned}\right\} \quad (4)$$

$$\left(\rho C_p\right)_{hnf} = \left(\frac{\emptyset}{100}\right)\left(\rho C_p\right)_p + \left(1 - \frac{\emptyset}{100}\right)\left(\rho C_p\right)_f, \quad (5)$$

$$\frac{\mu_{hnf}}{\mu_f} = 0.3659 * C1 * exp\left\{\left(1+\frac{\emptyset}{100}\right)^{10.83}\left(\frac{T_{hnf}}{90}\right)^{-0.0238}\left(1+\frac{dp}{170}\right)^{-0.1609}\right\}, \quad (6)$$

$$\alpha_{hnf} = \frac{k_{hnf}}{\left(\rho c_p\right)_{hnf}}, \quad (7)$$

$$\vartheta_f = \frac{\mu_f}{\rho_f} \quad (8)$$

Problem Formulation

Consider an incompressible, 2D, laminar, viscous, steady, boundary layer flow over a horizontal stretching sheet. The following assumptions were made:

- Two kinds of nanoparticles viz. Al_2O_3 and AlN were dispersed in sodium alginate in order to produce a new composition Al_2O_3 + AlN/ $C_6H_9NaO_7$ as depicted in Figure 1.
- We assumed thermal equilibrium between base fluid and nanoparticles.
- *x*-axis is been aligned with edge of the sheet and *y*-axis is perpendicular to it and the representation diagram is shown in Figure 2.
- The Brownian flow motion, magnetic effect, Thermophoretic effect, heat generation and radiation are incorporated in the flow system.
- Fluid flow is confined to a section $y > 0$.

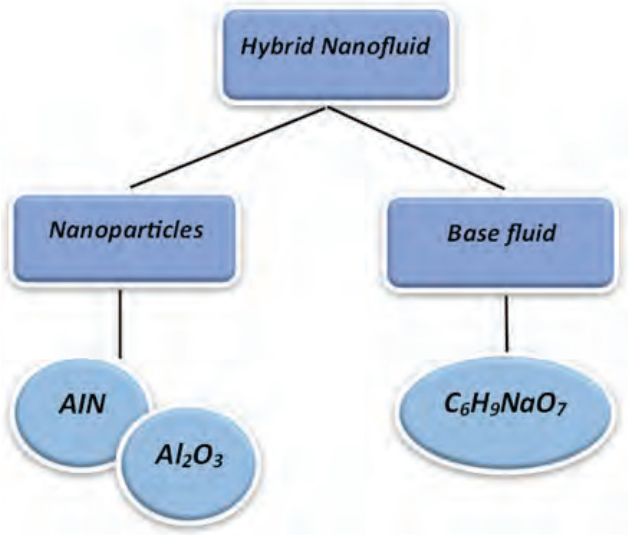


Figure 1. Outline of hybrid nanoparticles.

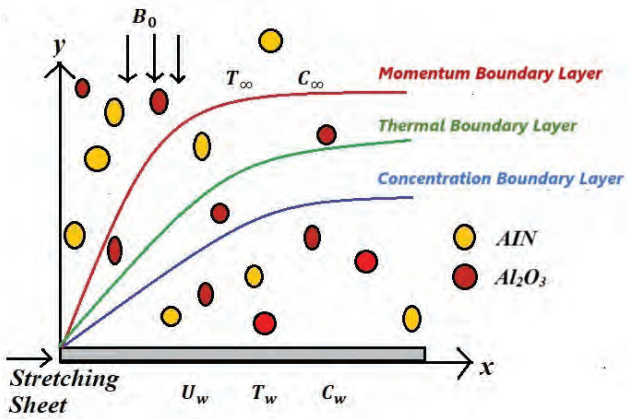


Figure 2. Geometry of the Problem.

Table 1. Thermal characteristic features of base fluid and nanoparticles

Properties	*AlN*	Al_2O_3	$C_6H_9NaO_7$
Density	3260	3880	989
Specific Heat	735	773	4175
Thermal Conductivity	180	40	0.613
Coefficient of Thermal Expansion	0.00027	0.00028	0.00001

- A uniform transverse magnetic field with strength B_o is set, and induced magnetic field is ignored owing to the negligible magnetic Reynolds number.
- The stretching velocity of the sheet is $u_w(x) = ax$. a is taken as a constant.
- The temperature and Concentration at the wall and far from the surface are quantified as T_w, C_w, T_∞, and C_∞.
- The temperature difference considered in this model is within the range where property variation is relatively small and does not significantly alter the qualitative behaviour of the flow and heat transmission.
- Table 1 summarizes the thermodynamic features of the base fluid and its nanoparticles.

The Casson nano fluid flow gets altered due to the impact of Lorentz effect, radiation and generation of heat effects under the boundary layer approximations. Hence, based on these Prandtl flow assumptions and above-mentioned estimates the demonstrative Navier-Stokes equations of the present study are presented below [2, 40-42]

$$\frac{\partial u}{\partial x} + \frac{\partial v}{\partial y} = 0 \tag{9}$$

$$u\frac{\partial u}{\partial x} + v\frac{\partial u}{\partial y} = \frac{\mu_{hnf}}{\rho_{hnf}}\left(1+\frac{1}{\beta}\right)\frac{\partial^2 u}{\partial y^2} - \frac{\sigma B_0^2 u}{\rho_{hnf}} \tag{10}$$

$$u\frac{\partial T}{\partial x} + v\frac{\partial T}{\partial y} = \alpha_{hnf}\frac{\partial^2 T}{\partial y^2} + \tau\left[D_B\frac{\partial T}{\partial y}\frac{\partial C}{\partial y} + \frac{D_T}{T_\infty}\left(\frac{\partial T}{\partial y}\right)^2\right] + \frac{Q_o}{(\rho c_p)_{hnf}}(T - T_\infty) - \frac{1}{(\rho c)_{hnf}}\left(\frac{\partial q_r}{\partial y}\right) \tag{11}$$

$$u\frac{\partial C}{\partial x} + v\frac{\partial C}{\partial y} = D_B\left(\frac{\partial^2 C}{\partial y^2}\right) + \frac{D_T}{T_\infty}\frac{\partial^2 T}{\partial y^2} \tag{12}$$

The conditions at the boundary: [2, 40-42]

$$u = u_w(x),\ v = -v_w,\ T = T_w, \text{ and } C = C_w \text{ at } y = 0 \tag{13}$$

$$u \to 0, v \to 0, T \to T_\infty, \text{ and } C \to C_\infty \quad \text{as} \quad y \to \infty \tag{14}$$

where, u denotes the velocity with x-direction and v represents the velocity along y direction.

where $\alpha = \frac{k}{(c\rho)_{hnf}}$, $\tau = \frac{(c\rho)_p}{(c\rho)_{hnf}}$, $\vartheta = \frac{\mu}{\rho_{hnf}}$,

$$u_w = ax,\ T_w = T_\infty + b\left(\frac{x}{l}\right)^2,\ C_w = C_\infty + c\left(\frac{x}{l}\right)^2 \tag{15}$$

To simplify the numerical study, the quantities are been presented by means of similarity transforms.

$$\eta = \sqrt{\frac{a}{\vartheta}}y,\ \Psi = \sqrt{a\vartheta}xf(\eta),\ \theta(\eta) = \frac{T - T_\infty}{T_w - T_\infty},\ \emptyset(\eta) = \frac{C - C_\infty}{C_w - C_\infty} \tag{16}$$

$$u = axf'(\eta),\quad v = -\sqrt{a\vartheta}f(\eta) \tag{17}$$

$\Psi(x,y)$ denotes stream function which is:

$$u = \Psi_y,\quad v = -\Psi_x \tag{18}$$

Radiative flux which is in y direction is dominant and the x direction component can be neglected. Radiative heat flux q_r, with the help of Rosseland approximations is mentioned as,

$$q_r = -\frac{4\sigma^*}{3k^*}T_y^4 \tag{19}$$

where σ^* - Stefan Boltzmann constant. Within the flow, the difference in temperature, is small and hence the term T^4 has been expanded with the aid of Taylor's series.

$$T^4 \cong 4T_\infty^3 T - 3T_\infty^4 \tag{20}$$

It follows on substituting Eq. (20) into Eq. (18),

$$q_r = -\frac{16T_\infty^3\sigma^*}{3k^*}T_y \tag{21}$$

The governing Eqns. (9) – (12) are altered into ODE by the aid of Similarity transformations. [2, 41-43]

$$\left(1+\frac{1}{\beta}\right)f''' + A_1A_2(ff'' - f'^2 - \frac{M}{A_2}f') = 0 \tag{22}$$

$$\frac{1}{A_4}\left(1+\frac{4}{3}\frac{R}{A_3}\right)\theta'' + Prf\theta' + PrNb\theta'\emptyset' + PrNt\theta'^2 + \frac{\lambda}{A_3}Pr\theta = 0 \tag{23}$$

$$\emptyset'' + Lef\emptyset' + \frac{Nt}{Nb}\theta'' = 0 \tag{24}$$

Where,

$$\frac{1}{A_1} = 0.3659 * C_1 * \exp\left\{\left(1+\frac{\emptyset}{100}\right)^{10.83}\left(\frac{T_{hnf}}{90}\right)^{-0.06239}\left(1+\frac{dp}{170}\right)^{-0.1609}\right\},$$

$$A_2 = \left(\frac{\emptyset}{100}\right)\frac{\rho_p}{\rho_f} + \left(1+\frac{\emptyset}{100}\right)$$

$$A_3 = \left(\frac{\emptyset}{100}\right)\frac{(\rho C_p)_p}{(\rho C_p)_f} + \left(1-\frac{\emptyset}{100}\right)$$

$$A_4 = 1.2035\left\{\left(0.001+\frac{\emptyset}{100}\right)^{0.0098}\left(0.01+\frac{T_{hnf}}{90}\right)^{0.1331}\left(0.001+\frac{dp}{170}\right)^{-0.0001}\left(0.01+\frac{\alpha_p}{\alpha_f}\right)^{0.0153}\right\}$$

The boundary conditions [2, 41-43]:

$$\left.\begin{array}{ll} f(0)=f_w;\ f'(0)=1,\ \theta(0)=1;\ \emptyset(0)=1; & \text{at } \eta=0 \\ f'(\infty)=0;\ \theta(\infty)=0;\ \emptyset(\infty)=0; & \text{as } \eta\to\infty \end{array}\right\} \quad (25)$$

Governing parameters are given by:

$$\left.\begin{array}{l} f_w=-\frac{v_w}{\sqrt{a\vartheta}};\ Nt=\frac{(\rho c)_p D_T(T_w-T_\infty)}{(\rho c)_f \vartheta T_\infty};\ Nb=\frac{(\rho c)_p D_B(\emptyset_w-\emptyset_\infty)}{(\rho c)_f \vartheta} \\ Pr=\frac{\vartheta}{\alpha};\ R=\frac{4\sigma^* T_\infty^3}{3k^* k};\ Le=\frac{\vartheta}{D_B};\ \lambda=\frac{Q_o}{(\rho c_p)_f a} \end{array}\right\} \quad (26)$$

where f represents the velocity (dimensionless), θ represents the temperature, and $\emptyset$ represents the nanoparticle concentration.

$$C_f=\frac{\tau_w}{\rho u_w^2},\ Nu_x=\frac{x q_w}{k(T_w-T_\infty)},\ Sh_x=\frac{x h_m}{D_B(\emptyset_w-\emptyset_\infty)} \quad (27)$$

$$q_w=-k\left(\emptyset_y\right)_{y=0},\ h_m=-D_B\left(\emptyset_y\right)_{y=0} \quad (28)$$

From the above-mentioned equations, the skin friction coefficient, heat and mass transfer rates in non-dimensional arrangement are:

$$C_f\sqrt{Re_x}=-f''(0),\ \frac{Nu_x}{\sqrt{Re_x}}=-(1+R)\theta'(0),\ \frac{Sh_x}{\sqrt{Re_x}}=-h'(0)s \quad (29)$$

Solution Procedure

The numerical outcomes for the ODE's (22) to (24) with the related boundary conditions in Eq. (25) are mathematically resolved using shooting mechanism and Bvp4c solver. To get precise and effective outcomes, choosing proper initial guess values is mandatory. It is crucial to alter this approximation in order to get correctness and assure the convergence in the obtained results. The boundary layer width is selected, as it has an impact on the mathematical outcomes. Criterion for convergence is taken as 10^{-5} to attain a improved degree of accuracy. The functioning process of Bvp4c system is portrayed in Figure 3 [44].

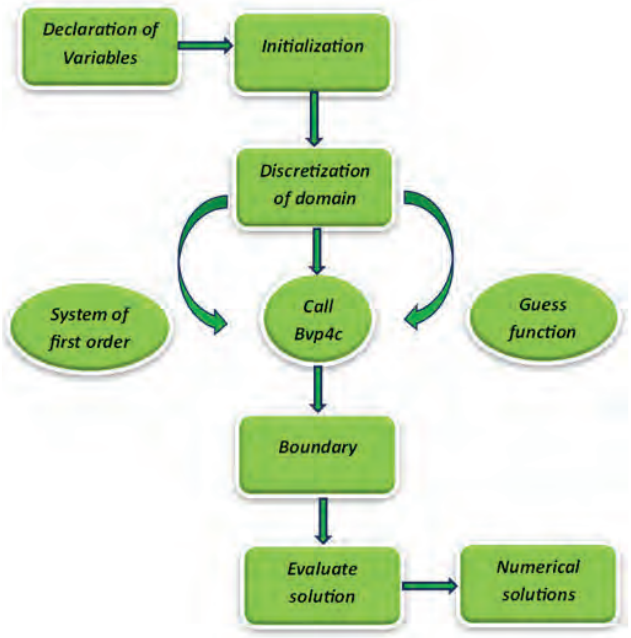


Figure 3. Flow configuration and coordinate system.

The substitutions made were:

$$f_1=f;\ f_2=f';\ f_3=f'';\ f_4=\theta;\ f_5=\theta';\ f_6=\emptyset;\ f_7=\emptyset'$$

The reduced equations are:

$$f_3' = -A_1A_2\frac{\left(-f_1f_3+f_2^2-\frac{M}{A_2}f_2\right)}{\left(1+\frac{1}{\beta}\right)}$$

$$f_5' = -A_4Pr\frac{\left(-f_1f_5-Nbf_5f_7-Ntf_5^2-\frac{1}{A_3}\lambda f_4\right)}{\left(1+\frac{4}{3A_3}\frac{R}{}\right)}$$

$$f_7' = -Lef_1f_7+\frac{Nt}{Nb}A_4\Pr\frac{\left(-f_1f_5-Nbf_5f_7-Ntf_5^2-\frac{1}{A_4}\lambda f_3\right)}{\left(1+\frac{4}{3A_3}\frac{R}{}\right)}$$

Conditions at the boundary:

$$f_1(0)=f_w;\ f_2(0)=1;\ f_4(0)=1;\ f_6(0)=1,$$

$$f_1(\infty)=0;\ f_2(\infty)=0;\ f_6(\infty)=0$$

The significant feature of the present study is, BVP is altered into an IVP. The solution to the IVP is found by making guess values for the initial values that are missing by using shooting technique. The initial guesses were systematically selected using a continuation approach, wherein solutions at nearby parameter values were used as starting guesses for subsequent computations. The convergence is achieved within a reasonable range of initial estimates, and divergence occurs only when guesses are significantly far from physically admissible solutions. Step size is 0.001 for doing calculations and tolerance for error is taken as 10^{-5}.

RESULTS AND DISCUSSION

A mathematical study was executed to study the thermo-fluidic transport of Casson hybrid nanofluids over a linearly stretching sheet. Runge-Kutta method with shooting process is used to explain the equations governing the transport phenomena. The flow velocity and temperature distributions were determined, followed by evaluating the concentration profile through numerical solutions. The graphical depiction of Hybrid nanofluid motion, thermal and mass diffusion for numerous parameters are shown below.

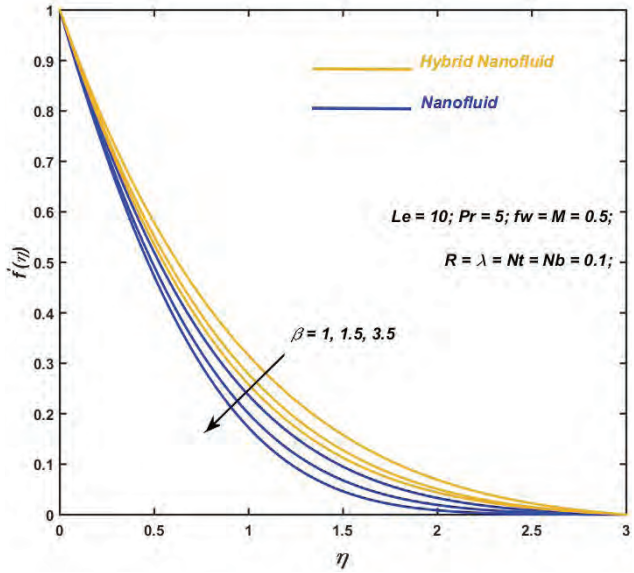


Figure 4. Velocity profile with varying Casson fluid parameter β.

Figure 4 displays that the rise in Casson parameter from 1 to 3.5, leads to decline in motion of the fluid. Rise in β leads to higher yield stress, which then led to a rise in fluid's elasticity which cause the hybrid nanofluid to turn out to be thicker and viscous. The fluid behaves like solid and hence declining the fluid velocity. Similar results regarding velocity profile were obtained by [43] The suction parameter represents how much fluid is been pulled towards the surface as shown if Figure 5. By increasing suction parameter from 0.5 to 1.5, a part of fluid gets removed from the flow nearby the surface and lessens the kinetic energy, causing the velocity to reduce. In case of hybrid nanofluid (Al_2O_3 and AlN) has an effect on the viscosity and thermal conductivity. Similar outcomes pertaining to velocity profile was found in the literature of [45]. The physical significance of these varying parameters over velocity profile plays a crucial role in various fields. For MHD driven processes porous electrodes, and heat sink with porous structure could affect the fluid velocity management of nanofluids. The velocity variation due to suction and Casson fluid parameters could be harnessed to enhance the heat transfer in various devices like generators, coolant for nuclear reactors, chemical reactors of catalytic processes, etc.

Figure 6 depicts the effect of radiation on thermal profile. Radiation number quantifies the influence of radiative heat transfer. Heat diffuses more easily and temperature remains higher near the surface. Aluminum oxide is chemically stable and has good thermal conductivity. Aluminum Nitride is electrically insulating and has high thermal conductivity. Combining both enhances the thermal conductivity more than using a conventional nanofluid. Comparable trends in temperature profile were

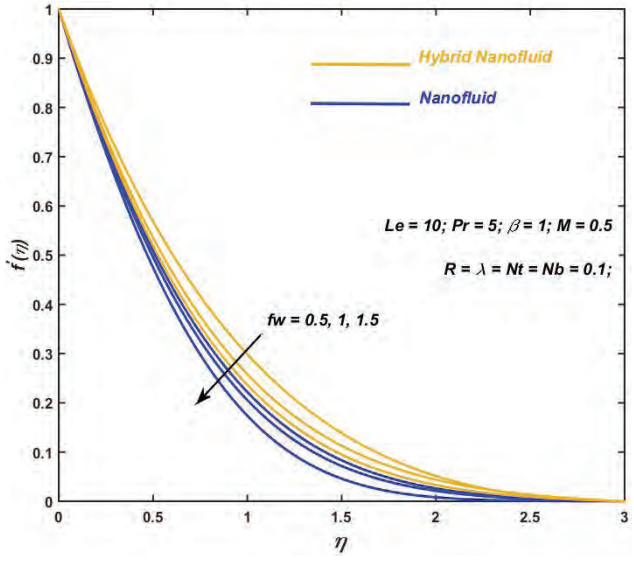


Figure 5. Velocity profile with varying suction parameter.

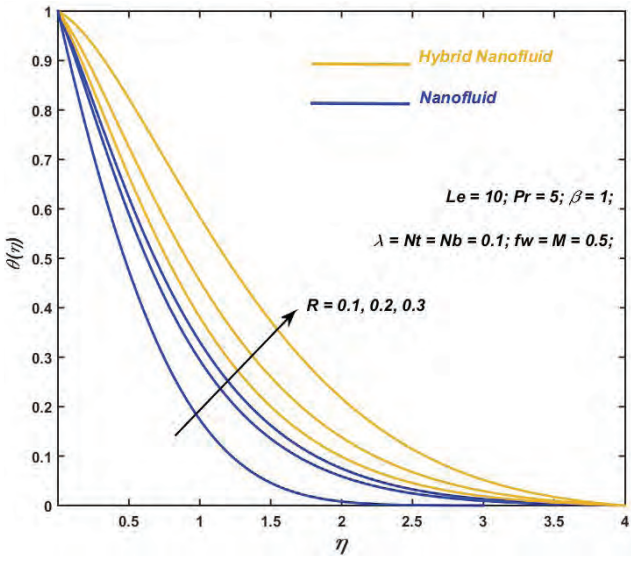


Figure 6. Thermal profile for varying radiation parameter R.

observed in [46]. The influence of heat generation on thermal profile is depicted in Figure 7. For higher values of **λ**, heat is generated inside the fluid and not just the wall. This directly rises the fluid temperature. Both AlN and Al_2O_3 are high thermal conductivity materials. Thermal conductivity of AIN (~140-180 *W/m.K*) and Al_2O_3 (~31 *W/m.K*). Together they distribute generated heat uniformly and maintain high temperature in comparison to that of base fluid and mono nanofluid. The physical significance is of utmost important as it prevents overheating and material degradation. Also reduces energy needed for cooling systems. Proper usage of radiative heat transfer with hybrid nanofluids can increase energy efficiency in thermal systems. The choice of AlN and Al_2O_3 balances high conductivity with chemical stability which is very ideal for high-temperature or high-radiation environments. Figure 8 displays the impact of thermophoretic and Brownian flow motion on thermal field. Thermophoresis represents the translocation of nanoparticles from hotter to colder region which is driven by temperature gradients. If thermophoretic effect becomes stronger, hybrid nanoparticles (AlN + Al_2O_3) are pushed from hotter to colder regions which led to the decrease in the local concentration near the hot surface. Both the nanoparticles having high thermal conductivity and being stable in water-based fluids, leads to rise in thermal profile. As Brownian motion parameter increases the nanoparticle random motion intensifies as there are more frequent particle-fluid interactions. Change of kinetic to thermal energy increases and hence the fluid temperature increases. Finally, an increase in *Nb* and *Nt* enhances nanoparticle-induced energy transport in AlN + Al_2O_3 hybrid nanofluid, resulting in a upsurge in fluid temperature and thickens the boundary layer [47, 48].

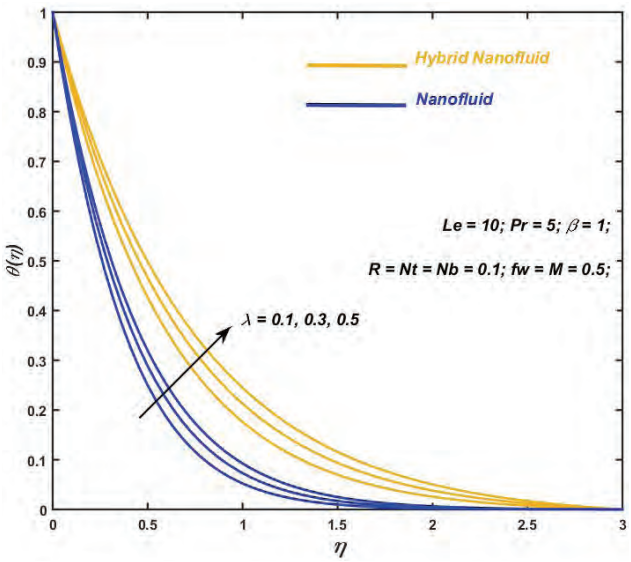


Figure 7. Thermal profile for varying heat generation λ.

Figure 9 illustrates the influence of heat source on species concentration profile. Whenever the heat source strength rises, the internal heat generation raises the thermal energy of the nanofluid which increases the boundary layer thickness. Rising the temperature, Brownian motion of the particles push the nanoparticles far away from the hot surface. So, the particles travel from higher to lower temperature regions. This led to a drop in the concentration gradient at the wall. From Figure 10, when thermal radiation parameter increases, stronger radiative flux adds extra thermal energy to the fluid that thickens the boundary layer. Higher temperature intensifies the

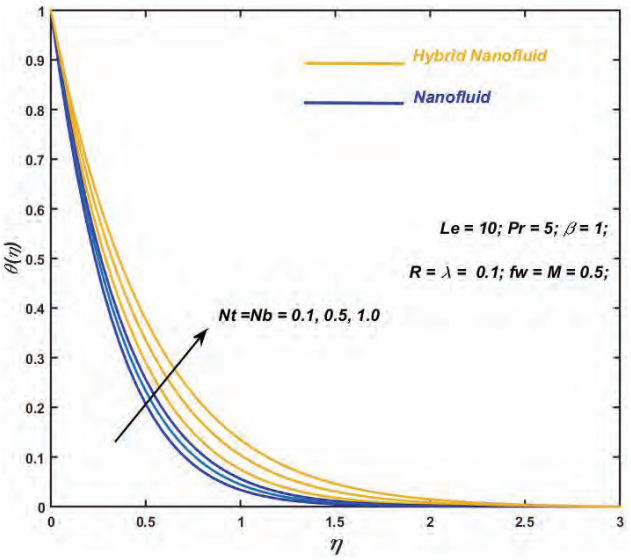


Figure 8. Thermal profile for varying *Nt*, *Nb*.

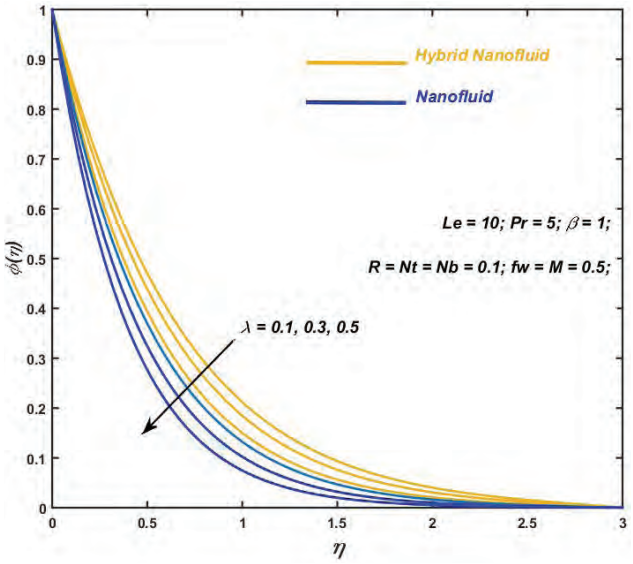


Figure 9. Concentration profile for varying λ.

random motion of nanoparticles pushing them away from the surface. As the nanoparticles travel from hotter to colder regions, the concentration gradient at the surface gets weakened. Thus, for a AlN + Al_2O_3 Casson hybrid nanofluid, an increase in radiation parameter generally causes the concentration profile to reduce. Similar results about the concentration profile were seen in the work of [39]. The physical significance of enhanced heat transfer and radiation boosts the thermal diffusion and hence can be used in reactors, cooling systems and solar collectors. Engineers and scientists can use radiation to manipulate particle distribution and optimize performance in thermal management systems.

Figure 11 depicts the effects on skin friction coefficient for Casson fluid parameter. Increasing Casson fluid parameter diminishes the yield stress effect. Fluid near the wall deforms more easily. Velocity gradient close to the hot surface and shear stress increases. So, skin friction increases and similar results about skin friction were found in [44]. Figure 12, illustrates the effect of heat generation with Nusselt number. Internal heat generation adds energy to fluid which causes the fluid temperature to rise throughout the fluid. Wall heat flux and temperature gradient close to the wall reduces which led to the Nusselt number to reduce. Figure 13 depicts the impact the radiation parameter has on Nusselt number. Increasing radiation parameter, the radiative heat flux and thermal conductivity becomes more efficient. More heat is distributed away from the wall causing the wall temperature gradient to decline. Consequently, Nusselt number decreases.

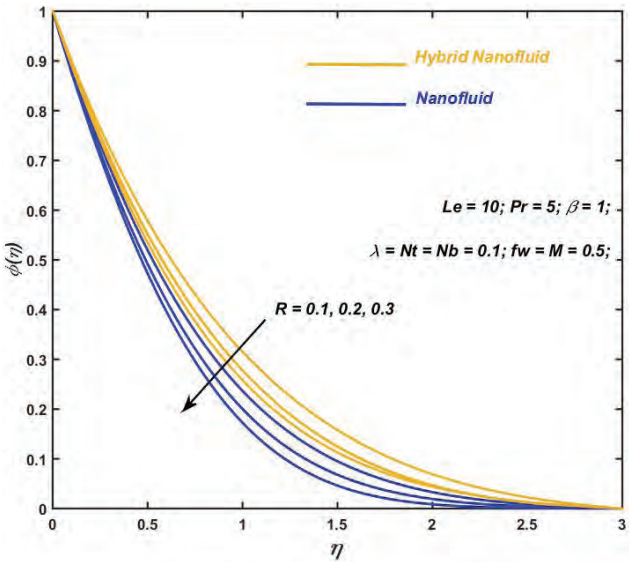


Figure 10. Concentration profile for varying *R*.

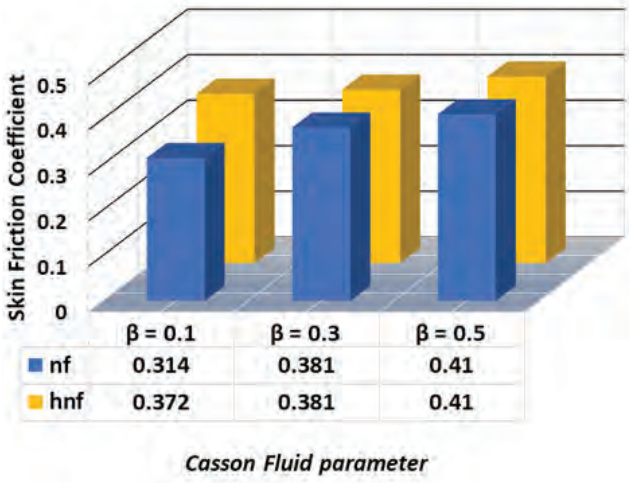


Figure 11. Skin friction variation with Casson fluid parameter.

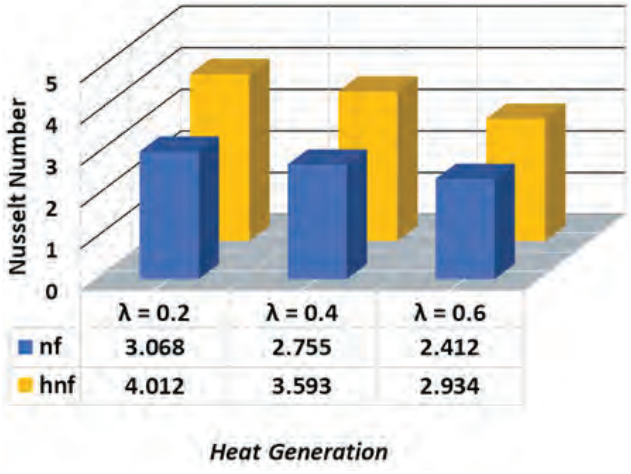


Figure 12. Nusselt number variation with heat generation.

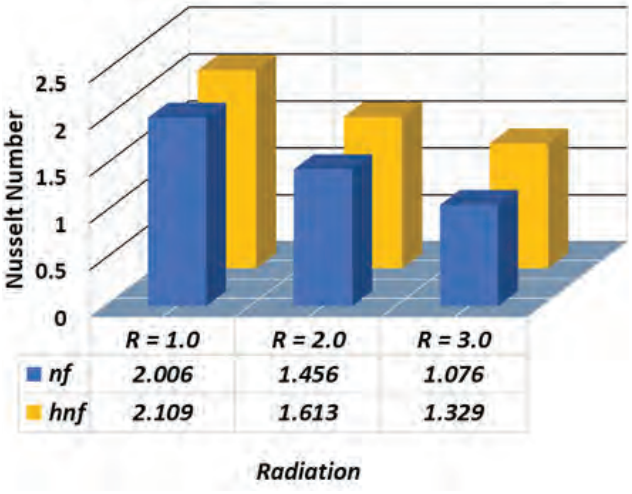


Figure 13. Nusselt number variation with radiation.

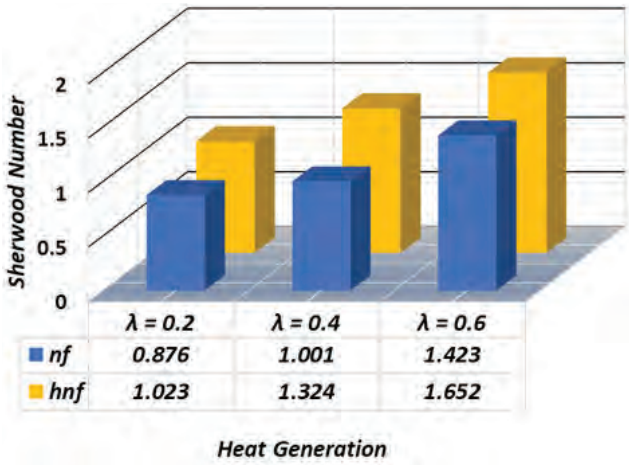


Figure 14. Sherwood variation with heat generation.

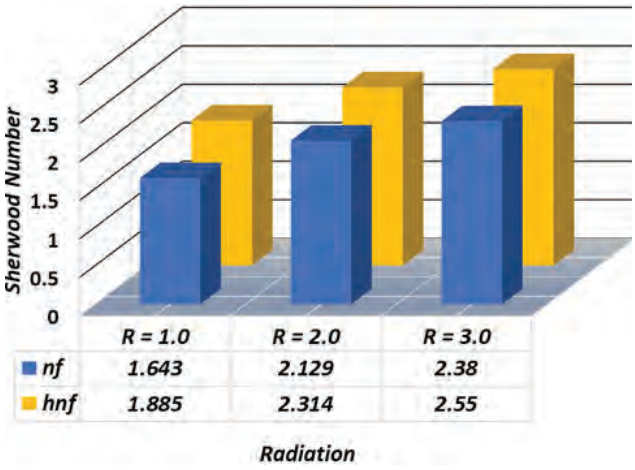


Figure 15. Sherwood variation with radiation.

Figure 14 shows the Sherwood number variation for varying values of heat generation. Greater heat generation leads to enhanced mass transfer and greater diffusion of the solute from solid surface to the fluid leading to a upsurge in Sherwood number. These conclusions have significant implications for optimizing the convective heat transfer which involves hybrid and other intricate fluids where concentration gradients are important. Figure 15 displays the effect of radiation on Sherwood number. Radiation indirectly enhances fluid motion enough to increase mass transfer. So, Sherwood number rises for advanced values of Radiation parameter.

Table 2 shows that heat generation and radiation rises the fluid temperature near the wall, which reduces the temperature dissimilarity between the wall and the fluid leading to lower surface heat flux. Hence the Nusselt number reduces. In engineering applications, (e.g., nuclear reactors, electronic cooling) higher radiation or internal heating lowers the convective heat removal capacity. So, it is considered in the thermal design. Heat generation and radiation contributes to overall heat transfer and increases temperature which then increases the temperature dependent diffusion coefficient potentially increasing the mass transfer. Hence a rise in Sherwood number is noted. Table 3 compares the present with the previously published outcomes.

Table 4 depicts a Grid Independence Test. A formal mesh (step size) independence test has been incorporated. The numerical solution was computed using progressively refined steps, and the variations in key physical quantities such as Sherwood and Nusselt numbers were monitored. The outcomes demonstrate that beyond a certain value, further grid refinement produces negligible changes (within 10-5 tolerance), confirming numerical steadiness and independence of the computational grid.

Table 2. Computed local Nusselt $-\theta'(0)$, local Sherwood $-\emptyset'(0)$ numbers for varying values of heat generation λ and radiation R as $Le = 5$, $fw = 0.5$, $\beta = 5$, $Nb = Nt = 0.1$, $Pr = 10$

λ	R	$-\theta'(0)$	$-\emptyset'(0)$
0.0	0.0	3.35766146	0.74574654
0.2		3.06867167	1.02374100
0.4		2.75576605	1.32413791
0.6		2.41285144	1.65260655
0.8		2.03105529	2.01739063
1.0		1.59669978	2.43120211
0.0	1.0	2.10893932	1.88572612
	2.0	1.61344374	2.31487442
	3.0	1.32981417	2.55088933

CONCLUSION

Table 3. The comparative outcomes for $-\theta'(0)$ according to $Le = 5$, $Nb = Nt = 0.1$, $Pr = 2$

Fw	Raju et al. [48]	Shah et al. [49]	Current Outcomes
0.5	1.230791	1.2307914	1.2307916
0	0.764552	0.7643523	0.7643533
-0.5	0.399084	0.3990987	0.3990988

Table 4. Grid independence test

Grid Points	Step Size(h)	Nusselt Number	Sherwood Number
200	0.01	3.35766146	0.74574654
400	0.005	3.35766143	0.74574651
800	0.0025	3.35766136	0.74574645
1200	0.00167	3.35766129	0.74574639

The present numerical study investigates 2D, laminar, incompressible, steady, viscous hybrid nanofluid flow past a linear stretching sheet. Two kinds of nanoparticles AlN and Al_2O_3 were suspended in base fluid (sodium alginate) to obtain a new configuration $AlN+Al_2O_3/\ C_6H_9NaO_7$. Magnetic field parameter is included in the momentum equation. Heat source and radiation parameters are included in energy equation. due of its higher thermal conductivity, this method is highly effective in cooling systems. In this present problem, mathematical analysis of hybrid nanoparticles has been conducted to study the temperature, velocity, and concentration profiles.

The significant works of the existing study are:

1. Temperature augmented for higher values of heat generation and radiation.
2. A decay in the concentration was found, with an upsurge in heat generation.
3. Concentration boundary layer declined for higher radiation values.
4. A decline in local Nusselt number and a rise in local Sherwood number are observed with the rise in heat source.
5. With the rise in radiation, there is a fall in the local Nusselt number and an upsurge in the local Sherwood number.
6. Hybrid nanofluid has an improved heat transfer rate when compared to that of traditional nanofluid.

Future Work

The current CFD simulation provides the researchers a motivation to the modelling of 2D Casson hybrid nanofluid flow, and heat transfer problems which are pertaining to the fields of Electrical and Machine-driven Engineering. It can also be utilized to examine various aspects related to solar collectors, chemical engineering, thermal industries, medicine, etc. The present problem can be used to study rheological behaviours of viscoelastic or micro hybrid nanofluids, dusty or ternary nanofluids, etc.

AUTHORSHIP CONTRIBUTIONS

Authors equally contributed to this work.

DATA AVAILABILITY STATEMENT

The authors confirm that the data that supports the findings of this study are available within the article. Raw data that support the finding of this study are available from the corresponding author, upon reasonable request.

CONFLICT OF INTEREST

The authors declared no conflict of interest.

ETHICS

There are no ethical issues with the publication of this manuscript.

STATEMENT ON THE USE OF ARTIFICIAL INTELLIGENCE

Artificial intelligence was not used in the preparation of the article.

REFERENCES

[1] Crane LJ. Flow past a stretching plate. Z Angew Math Phys 1970;21:645–655. [CrossRef]

[2] Choi S, Eastman JA. Enhancing thermal conductivity of fluids with nanoparticle. In: Development and applications of non-Newtonian flow. ASME FED. 1995;231/MD 66:99–105. [CrossRef]

[3] Sajid R, Idrees M, Rehan AS, Zeeshan K. Suction/injection effects on an unsteady MHD Casson thin film flow with slip and uniform thickness over a stretching sheet along variable flow properties. Bound Value Probl 2019;26:1–24. [CrossRef]

[4] Khan WA, Pop I. Boundary-layer flow of a nanofluid past a stretching sheet. Int J Heat Mass Transf 2010;53:2477–2483. [CrossRef]

[5] Aminreza N, Rashid P, Mohammad G. Effect of partial slip boundary conditions on the flow and heat transfer of nanofluids past stretching sheet prescribed constant wall temperature. Int J Therm Sci 2012;54:253–261. [CrossRef]

[6] Odesola AS, Gbeminiyi S, Abiala IO. Three-dimensional analysis of MHD Casson Carreau nanofluid flow and heat transfer over a stretching surface embedded in a porous medium under the influences of thermal radiation and temperature-dependent internal heat generation. Sci Aerosp 2022;13:263–282.

[7] Sarma AK, Sarma D, Mudoi S. MHD flow and effects of Hall current, Joule heating, and heat source across a chemically reacting and radiating exponentially stretching sheet in a porous medium. Sigma J Eng Nat Sci 2025;43:1179–1196. [CrossRef]
[8] Anupam B, Pankaj KM. Heat and radiation absorption effects on Casson nanofluid flow over a stretching cylinder in the presence of chemical reaction through mathematical modelling. Spec Top Rev Porous Media 2020;11:177–188. [CrossRef]
[9] Nagendramma V, Raju CSK, Mallikarjuna, Shehzad SA, Leelarathnam A. 3D Casson nanofluid flow over slendering surface in a suspension of gyrotactic microorganisms with Cattaneo-Christov heat flux. Appl Math Mech 2018;39:623–638. [CrossRef]
[10] Hayat T, Asad S, Alsaedi A. Flow of Casson fluid with nanoparticles. Appl Math Mech 2016;37:459–470. [CrossRef]
[11] Ramesh GK, Gireesha BJ, Shehzad SA, Abbasi FM. Analysis of heat transfer phenomenon in magnetohydrodynamic Casson fluid flow through Cattaneo-Christov heat diffusion theory. Commun Theor Phys 2017;68:91–95. [CrossRef]
[12] Malik MY, Naseer M, Nadeem S, Rehman A. The boundary layer flow of Casson nanofluid over a vertical exponentially stretching cylinder. Appl Nanosci 2014;4:869–873. [CrossRef]
[13] Nath JM, Paul A, Das TK. Heat transfer characteristics of magnetohydrodynamic Casson stratified hybrid nanofluid flow past a porous stretching cylinder. J Therm Eng 2024;10:1137–1148. [CrossRef]
[14] Nath JM, Paul A, Das TK. Thermally stratified Cu-Al2O3/water hybrid nanofluid flow with the impact of an inclined magnetic field, viscous dissipation and heat source/sink across a vertically stretching cylinder. Z Angew Math Mech 2023;104. [CrossRef]
[15] Paul A, Das TK, Nath JM. Numerical investigation on the thermal transportation of MHD Cu/Al2O3-H2O Casson-hybrid-nanofluid flow across an exponentially stretching cylinder incorporating heat source. Phys Scr 2022;97:085701. [CrossRef]
[16] Macha M, Kishan N. MHD flow and heat transfer of Casson nanofluid over a wedge. Mech Ind 2017;18:201–225. [CrossRef]
[17] Tirupathi G, Govardhan K, Nagaraju G, Misra S. MHD upper-convected Maxwell hybrid nanofluid flow over a stretching sheet: A numerical approach. Sigma J Eng Nat Sci 2025;43:1–12. [CrossRef]
[18] Mukhopadhyay S, Chandra MI, Chamkha AJ. MHD flow and heat transfer of Casson nanofluid over a wedge. Heat Transf Asian Res 2013;42:665–675. [CrossRef]
[19] Pal D, Roy N, Vajravelu K. Effects of thermal radiation and Ohmic dissipation on MHD Casson nanofluid flow over a vertical non-linear stretching surface using scaling group transformation. Int J Mech Sci 2016;114:257–267. [CrossRef]
[20] Ashish P, Nath JM. Magnetohydrodynamic stagnation point flow of Casson Williamson hybrid nanofluid incorporating viscous dissipation and suction/injection effect past an exponentially stretching sheet. J Nanofluids 2024;13:710–720. [CrossRef]
[21] Nath JM, Das TK, Paul A, Chamkha AJ. Numerical computation of tangent hyperbolic magnetohydrodynamic Darcy-Forchheimer Williamson hybrid nanofluid flow configuring variable thermal conductivity. Hybrid Adv 2024;7:100343. [CrossRef]
[22] Nath JM, Paul A, Das TK. Magnetohydrodynamics stagnation point flow of hybrid nanofluids with distinct base fluid flow over an exponentially extending cylinder: A numerical comparative analysis. Nano 2025;20:2450123. [CrossRef]
[23] Mehari FE. Analytical study of heat and mass transfer effects on unsteady Casson fluid flow over an oscillating plate with thermal and solutal boundary conditions. Heat Transf 2021;50:6285–6299. [CrossRef]
[24] Das TK, Paul A, Nath JM. Endo/exothermic analysis of Casson and Maxwell quadra hybrid nanofluid flow configured by pollutant concentration with thermal and solute jump. J Taibah Univ Sci 2024;18. [CrossRef]
[25] Das TK, Paul A, Nath JM, Sarma N. The Yamada-Ota model-based Casson quadra hybrid nanofluid stagnation flow configured by Ohmic heating, heat source, and Newtonian boundary heating across an exponentially stretched cylinder. Partial Differ Equ Appl Math 2025;14:101159. [CrossRef]
[26] Wang Q, Qian K, Liu SS, Yang YJ, Liang B, Zheng CS, et al. X-ray visible and uniform alginate microspheres loaded with in situ synthesized BaSO4 nanoparticles for in vivo transcatheter arterial mobilization. Biomacromolecules 2015;16:1240–1246. [CrossRef]
[27] Becker TA, Kipke DR, Brandon T. Calcium alginate gel: A biocompatible and mechanically stable polymer for endovascular embolization. J Biomed Mater Res 2001;54:76–86. [CrossRef]
[28] Matricardi CDMP, Coviello T, Alhaique F. Recent advances and perspectives on coated alginate microspheres for modified drug delivery. Expert Opin Drug Deliv 2008;5:417–425. [CrossRef]
[29] Tønnesen HH, Karlsen J. Alginate in drug delivery systems. Drug Dev Ind Pharm 2002;28:621–630. [CrossRef]
[30] Giri TK, Thakur D, Alexander, Ajazuddin A, Badwaik H, Tripathi DK. Alginate based hydrogel as a potential biopolymeric carrier for drug delivery and cell delivery systems: Present status and applications. Curr Drug Deliv 2012;9:539–555. [CrossRef]
[31] Hori Y, Winans AM, Irvine DJ. Modular injectable matrices based on alginate solution/microsphere mixtures that gel in situ and co-deliver immunomodulatory factors. Acta Biomater 2009;5:969–982. [CrossRef]

[32] Akbari S, Pirbodaghi T. Microfluidic encapsulation of cells in alginate particles via an improved internal gelation approach. Microfluid Nanofluidics 2013;16:773–777. [CrossRef]

[33] Zimmermann H, Shirley SG, Zimmermann U. Alginate-based encapsulation of cells: Past, present, and future. Curr Diabetes Rep 2007;7:314–320. [CrossRef]

[34] Martinez CJ, Kim JW, Ye C, Ortiz I, Rowat AC, Marquez W, et al. Microfluidic approach to encapsulate living cells in uniform alginate hydrogel microparticles. Macromol Biosci 2012;12:946–951. [CrossRef]

[35] Zhao LB, Pan L, Zhang K, Guo SS, Liu W, Wang Y, et al. Generation of Janus alginate hydrogel particles with magnetic anisotropy for cell encapsulation. Lab Chip 2009;9:2981–2986. [CrossRef]

[36] Barnett BP, Arepally A, Stuber M, Arifin DR, Kraitchman DL, Bulte JMW. Synthesis of magnetic resonance-, X-ray- and ultrasound-visible alginate microcapsules for immunoisolation and noninvasive imaging of cellular therapeutics. Nat Protoc 2011;6:1142–1151. [CrossRef]

[37] Das TK, Paul A, Nath JM. Thermo-convection driven sodium alginate-based Darcy-Forchheimer EMHD Williamson hybrid nanofluid flow with varying thermal distribution. Mod Phys Lett B 2025;39:2450405. [CrossRef]

[38] Reza M, Rana A. Thermo-fluidic transport of electromagnetohydrodynamic flow of sodium alginate based Casson nanofluid passing through a porous microtube under the effect of streaming potential. Int J Eng Technol 2021;10:38–45. [CrossRef]

[39] Reza M, Bhattacharyya A, Rana A, Patra R. Soret and Dufour effects on entropy generation for AlN and hybrid nanofluid flow over past a stretching sheet in porous media. ISTAM Conference, IIT Bhubaneswar; 2020.

[40] Jagadish VT, Guled CN, Samad N, Unai FG, Vediyappan G, Sundarappan B. Effects of thermophoresis and Brownian motion for thermal and chemically reacting Casson nanofluid flow over a linearly stretching sheet. Results Eng 2022:100448. [CrossRef]

[41] Jayachandra BM, Sandeep N. 3D MHD slip flow of a nanofluid over a slandering stretching sheet with thermophoresis and Brownian motion effects. J Mol Liq 2016;222:1003–1009. [CrossRef]

[42] Ibrahim W, Shankar B. MHD boundary layer flow and heat transfer of a nanofluid past a permeable stretching sheet with velocity, thermal and solutal slip boundary conditions. Comput Fluids 2013;75:1–10. [CrossRef]

[43] Deepika AR, Govardhan K, Rana A, Reza M. Soret and Dufour effects on MHD mixed convection flow of Casson hybrid nanofluid over a permeable stretching sheet. Int J Ambient Energy 2023;44:2115–2127. [CrossRef]

[44] Okasha MM, Abbas M, Fateh HM, Ameen, Salah F, Abbas A, et al. Applications of Casson tetra hybrid nanofluid in industrial cooling systems: An investigation of radiative flow and Stephan blowing impacts. J Radiat Res Appl Sci 2025;18:101300. [CrossRef]

[45] Deepika AR, Govardhan K, Mohammad R, Basha H, Reddy GJ. Dissipative magnetic Ohmic heating influence on radiative nanofluid flow about a permeable stretching sheet under a porous medium with heat source. Int J Ambient Energy 2023;44:2078–2089. [CrossRef]

[46] Sudarsana RP, Ali J, Chamkha AJ. Soret and Dufour effects on MHD convective flow of Al2O3-water and TiO2-water nanofluids past a stretching sheet in porous media with heat generation/absorption. Adv Powder Technol 2016;27:1207–1218. [CrossRef]

[47] Raju CSK, Sandeep N, Sugunamma, Babu MJ. Radiation, inclined magnetic field and cross-diffusion effects on flow over a stretching surface. J Niger Math Soc 2015;34:169–180. [CrossRef]

[48] Shah Z, Asghar A, Ying TY, Lund LA, Alshehri A, Vrinceanu N. Numerical investigation of sodium alginate-alumina/copper radiative hybrid nanofluid flow over a power law stretching/shrinking sheet with suction effect: A study of dual solutions. Results Eng 2024;21:101881. [CrossRef]

Sigma J Eng Nat Sci, Vol. 44, No. 4, pp. 2595–2603, August, 2026

Sigma Journal of Engineering and Natural Sciences
Web page info: https://sigma.yildiz.edu.tr
DOI: 10.14744/sigma.2026.2117

Research Article

A reinforcement learning framework for disaster resilient data transfer in underwater wireless sensor networks

Ritu BHARDWAJ[1,*], Ashwani KUSH[2]

[1]*Department of Computer Science and Application, Kurukshetra University, Kurukshetra, 136119, India*
[2]*Institute of Integrated & Honors Studies (IIHS), Kurukshetra University, Kurukshetra, 136119, India*

ARTICLE INFO

Article history
Received: 10 March 2025
Revised: 01 June 2025
Accepted: 29 March 2026

Keywords:
Adaptive Routing; Data Transfer Optimization; Energy Efficiency; Q-Learning; Reinforcement Learning; Disaster Management; Underwater Wireless Sensor Networks

ABSTRACT

Underwater Wireless Sensor Networks (UWSNs) play a critical role in real-time environmental monitoring during disasters such as earthquakes, tsunamis, and underwater landslides. However, highly dynamic and hazardous underwater conditions significantly degrade the performance of conventional routing protocols. This study proposes a Q-learning-based Adaptive Data Transfer Algorithm (QL-ADTA) to address data transmission challenges in disaster-prone UWSNs. The proposed approach utilizes a multi-objective reward function that incorporates key contextual parameters, including data priority, link quality, node survivability, debris density, and water current strength. The algorithm is evaluated using disaster simulated synthetic datasets and compared with conventional routing protocols such as Dynamic Source Routing (DSR) and AODV (Ad-hoc On-Demand Distance Vector). Experimental results show that QL-ADTA improves packet delivery ratio by 25%, reduces latency by 23%, and enhances energy efficiency by 20%.These results demonstrate the effectiveness of the proposed approach in improving communication reliability and network performance under challenging underwater conditions.

Cite this article as: Bhardwaj R, Kush A. A reinforcement learning framework for disaster resilient data transfer in underwater wireless sensor networks. Sigma J Eng Nat Sci 2026;44(4):2595–2603.

INTRODUCTION

Submarine earthquakes, tsunamis, and underwater landslides are becoming more frequent and intense, necessitating the development of reliable real-time monitoring systems. These events cause rapid environmental changes that disrupt marine ecosystems and damage offshore infrastructure. During such crises, the timely and accurate transmission of environmental data is essential for disaster prediction, early warning dissemination, and effective emergency response. Underwater Wireless Sensor Networks (UWSNs) are becoming an important technology in this industry because they can monitor underwater environments on their own and all the time [1].

UWSNs typically consist of a large number of sensor nodes deployed over a wide area beneath the water surface to collect environmental data and transmit it to a base

*Corresponding author.
*E-mail address: 2228ritu@kuk.ac.in

This paper was recommended for publication in revised form by Editor-in-Chief Ahmet Selim Dalkilic

Published by Yıldız Technical University Press, İstanbul, Turkey
© Author. This is an open access article under the CC BY-NC license (http://creativecommons.org/licenses/by-nc/4.0/).

station or sink node. These nodes face unique challenges that do not exist in terrestrial networks, such as considerable signal loss, limited bandwidth, long propagation delays, changing topologies, and batteries that do not last very long [2, 3]. When a disaster happens, the situation gets a lot more complicated since network circumstances might change quickly because of debris moving, water currents changing, and nodes breaking down. These changes in the network might cause a lot of packet loss, energy loss, communication delays, and, in the end, failure to send important data [4, 5]. AODV, DSR, and DBR are examples of traditional routing protocols that were intended for static or moderately dynamic environments. They rely on pre set routing paths or heuristic-driven forwarding choices. Some processes include energy-awareness or delay-tolerant features, but they often can't change on the fly to deal with big unexpected changes in the environment that happen during disasters [6, 7]. In addition, these rules do not rank data based on how important it is, which is very important in emergency response systems. Recent progress in Artificial Intelligence (AI), especially in Reinforcement Learning (RL), has led to several interesting ways to make decisions in real time and adapt to changing circumstances.

Q-learning is different from other types of RL because it doesn't use a model and can find the best actions by trying things out in the environment [8]. Researchers have used Q-learning to come up with routing strategies that are both energy-efficient and dependent on latency in UWSNs [9, 10]. Still, most of the current Q-learning-based methods focus on improving network performance in normal settings and do not take into account the special restrictions and important criteria that need to be met during underwater emergencies. They do not pay attention to real-time disaster indicators like the amount of debris, the turbulence of the current, and the survivability of nodes [11, 12].

Although RL has been explored for routing in UWSNs, most existing approaches are designed for normal operating conditions and do not adequately consider the dynamic challenges posed by disaster scenarios. These methods often fail to incorporate essential parameters such as debris concentration, water current fluctuations, node survivability, and the urgency level of transmitted data. As a result, their adaptability and effectiveness in emergency situations remain limited. The proposed Q-Learning-based Adaptive Data Transfer Algorithm (QL-ADTA) addresses this research gap by introducing a disaster aware reward function that dynamically adjusts to environmental disruptions and prioritizes critical data. Through this context-sensitive learning framework QL-ADTA enhances real time decision-making for routing, ensuring reliable, energy-efficient, and responsive communication in disaster-affected underwater networks. This contribution significantly advances the current state of research by providing a robust solution tailored specifically for high-risk, unpredictable underwater environments.

Objectives of the Study

1. To design a disaster-aware reward function that incorporates key parameters, including packet delivery ratio, energy efficiency, latency, network reliability, debris density, and data priority.
2. To develop a Q-learning-based routing agent that improves data transmission decisions through continuous learning from real-time network and environmental feedback.
3. To simulate disaster scenarios using synthetic UWSN datasets in order to evaluate the robustness of the proposed algorithm and compare its performance with conventional and reinforcement learning-based routing protocols.
4. To evaluate the adaptability of the proposed algorithm by dynamically adjusting reward function weights based on disaster severity and environmental conditions.

This proposed study will add to the information we are familiar with through the development of a context sensitive reinforcement learning framework that is specifically built for underwater communication systems that are likely to fail. The suggested QL-ADTA is better instead of old routing methods.

Literature Review

Routing strategies in UWSNs have been widely investigated with primary emphasis on improving energy efficiency, minimizing communication delay, and enhancing packet delivery reliability. However, routing in disaster-prone underwater environments where network topology changes rapidly and critical data must be transmitted urgently remains insufficiently explored. To present a clearer understanding of existing contributions, prior studies are grouped into thematic categories relevant to this research.

Energy-efficient routing approaches

Energy conservation is a fundamental concern in UWSNs due to the difficulty of battery replacement and recharging in underwater environments. Several studies have applied reinforcement learning techniques to extend network lifetime. Ouidir et al. [13] proposed QENDIP, a Q-learning-based routing scheme that improves energy-efficient forwarding and enhances throughput. Zhou et al. [14] introduced the Q-Learning-Based Localization-Free Routing (QLFR) protocol, which selects routes based on residual energy and node depth to improve stability and energy utilization. Similarly, Xiao and Huang [15] applied ant colony optimization to determine cluster heads and multi-hop routing paths using energy metrics and inter-node distance. Although these approaches significantly improve energy conservation, they are primarily designed for stable or moderately dynamic environments and lack mechanisms for real-time adaptation during disaster events.

Latency-aware and delay-sensitive routing

In underwater monitoring and early warning systems, minimizing communication delay is critical. Several routing protocols focus on delay reduction while maintaining acceptable energy consumption.The QTAR protocol [16] employs topology-aware Q-learning to reduce end-to-end delay while conserving energy. Wang et al. [17] developed EP-ADTA, an edge-prediction-assisted reinforcement learning model that enhances reliable data transfer under challenging underwater conditions.While these techniques effectively reduce latency, they do not incorporate data prioritization or adapt to sudden environmental disruptions such as underwater earthquakes, landslides, or strong current turbulence factors essential in disaster response scenarios.

Conventional routing protocols and their limitations

Traditional routing protocols such as AODV, DSR, and DBR [6, 18, 19] were originally designed for static or mildly dynamic networks. These protocols rely on predefined routes or heuristic-based forwarding decisions and are not well suited for highly unstable underwater disaster conditions. Although some schemes incorporate delay-tolerant or energy-aware features, they cannot dynamically respond to abrupt environmental changes such as debris movement, shifting water currents, or rapid node failures. Consequently, their reliability degrades significantly in emergency scenarios.

Reinforcement learning based routing enhancements

Reinforcement learning has recently gained attention for adaptive routing in UWSNs. Techniques including Double Q-learning [20] and Deep Q-Networks (DQN) [21] address issues such as value overestimation and scalability. Multi-agent reinforcement learning frameworks [22] enhance overall network efficiency. Despite these advancements, most RL-based routing strategies are designed for normal operating conditions. Disaster-specific indicators such as debris density, current turbulence, node survivability, and urgency of transmitted data are rarely integrated into the learning process. Furthermore, existing approaches generally do not differentiate between high-priority emergency data and routine monitoring information.

Recent studies have explored the integration of deep reinforcement learning to enhance routing efficiency in underwater sensor networks. For instance, Zhang et al. [23] proposed deep reinforcement learning-based routing for UWSNs demonstrated that deep learning driven routing mechanisms can effectively improve decision-making by adapting to complex underwater environments and optimizing multiple performance metrics such as energy consumption and packet delivery. However, these approaches primarily focus on general network optimization and do not explicitly address the challenges posed by disaster-driven environmental dynamics. Adaptive reinforcement learning techniques have also been proposed to cope with the dynamic nature of underwater networks. Liu et al. Adaptive routing in dynamic UWSNs [24] using reinforcement learning introduced an RL-based adaptive routing framework capable of adjusting routing strategies based on network variations, thereby improving communication reliability under changing conditions. Despite these improvements, the model does not incorporate critical disaster-specific parameters such as environmental disturbances or priority-based data handling, limiting its applicability in emergency scenarios.

From the above review, it is evident that significant progress has been made in improving energy efficiency and reducing delay in UWSNs. However, the combined requirements of disaster awareness, urgent data prioritization, and real-time adaptability remain insufficiently addressed. Current Q-learning-based routing protocols do not incorporate disaster sensitive environmental parameters and lack mechanisms to prioritize critical data during emergencies.

To bridge this gap, the proposed QL-ADTA framework introduces a context-aware, disaster-sensitive reward function that dynamically adapts routing decisions based on debris density, water current turbulence, node survivability, and data priority. This design enables reliable, adaptive, and energy-efficient communication tailored specifically for high-risk underwater disaster environments.

Applıcatıon and Broader Impact of the Proposed Work

The proposed QL-ADTA has substantial practical consequences in fields that depend on reliable real time underwater communication during critical incidents. In Disaster Early Warning Systems QL-ADTA can be used in marine areas susceptible to undersea earthquakes, tsunamis, or landslides to guarantee ongoing communication of essential data. This allows authorities to provide timely alerts, save lives and reducing damage. Marine Research and Environmental Monitoring. Oceanographers and marine biologists may utilize the suggested routing system in challenging or dynamic underwater conditions to ensure a stable and energy-efficient transmission of information throughout longer observation missions.

Military and surveillance applications, naval operations, underwater surveillance, and border security can benefit from QL-ADTA's ability to prioritize urgent or high-importance transmissions during dynamic underwater conditions. Oil & Gas Industry can use offshore platforms to reliably transmit sensor readings during structural disturbances or environmental events, aiding operational continuity and hazard detection. When we use smart Ocean Infrastructure the algorithm can be integrated into intelligent ocean systems and digital twins of marine infrastructure, helping cities and coastal industries prepare for disaster resilience through real-time sensing and response mechanisms.

From a research standpoint, QL-ADTA opens pathways for:

- Cross domain application of reinforcement learning in other sensor networks such as underground, space-based or vehicular sensor networks.
- Hybridization with edge computing or swarm intelligence, potentially enabling decentralized intelligence in marine Internet of Things (IoT).
- Policy-making and simulation frameworks for governments and disaster management authorities seeking resilient underwater data communication strategies.

This work, therefore, not only addresses a highly specialized engineering challenge in UWSNs but also contributes to the global efforts toward climate resilience, smart environmental sensing, and emergency response preparedness.

MATERIALS AND METHODS

UWSNs encounter severe instability in communication when subjected to natural disasters such as tsunamis, underwater earthquakes, and landslides. These scenarios result in unpredictable changes in node connectivity increased signal attenuation, and compromised energy availability [1]. To overcome such dynamic and harsh conditions, we propose a QL-ADTA designed to intelligently optimize routing decisions based on environmental conditions and network status.

Synthetic Dataset Generation

To evaluate the proposed algorithm in a controlled yet realistic environment, a synthetic dataset was developed that models diverse underwater disaster scenarios. Synthetic data was employed due to the practical difficulty of collecting real-world disaster data in underwater environments, enabling controlled experimentation and reproducibility of diverse extreme scenarios. For this Python programming has been used. The dataset comprises 50,000 samples each representing a snapshot of the underwater network state during varying intensities of environmental disruption. Each record in the dataset includes the following parameters which are Packet Delivery Ratio (PDR) values between 0.2 and 1.0 indicating successful data delivery, latency (ms) Simulated between 100 and 500 ms based on node distance and congestion. Remaining Energy(J) ranging from 0.2 J to 1.0 J to represent battery levels, node Survivability (%) operational probability under disaster conditions (30%–100%). Debris density (kg/m^3) modeled between 0 to 15 indicating underwater obstruction, water current strength (m/s) simulated values from 0.5 to 3.0 m/s to reflect oceanic turbulence, link Quality Index (LQI) ranging from 10 to 30, indicating channel conditions, priority weight (1–5) represents the urgency level of the data e.g. (seismic > temperature). These parameters were derived based on widely accepted underwater communication and simulation models reported in the literature [5]. Disaster conditions were emulated by dynamically increasing debris density and water current strength while reducing node survivability and link quality, thereby replicating high-severity underwater events.

Learning Based Routing Model

The proposed QL-ADTA model follows the reinforcement learning paradigm, where the routing agent learns the optimal forwarding strategy by interacting with its environment and receiving feedback. In state space (S) each state is defined by a combination of network and environmental factors extracted from the dataset including PDR, latency, remaining energy, node survivability, debris level, current strength, and data priority. In action space (A) at every decision point, a node can choose from a discrete set of actions. Firstly send the packet to a selected neighbor then delay the transmission to allow for better conditions after that choose an alternative path to bypass affected regions.

The reward function guides the agent by quantifying the usefulness of each action. It is formulated as in equation (1):

$$\begin{aligned} R_{total} = {} & w_1{}^* (PDR{}^*Priority) \\ & - w_2{}^* (latency\ {}^*Priority) \\ & + w_3{}^* (Remaining\ Energy/Initial\ Energy) \\ & + w_4{}^* (Link\ Quality\times\ Node\ Survivability) \\ & - w_5{}^*(Debris + current) + w_6{}^*Priority \end{aligned} \quad (1)$$

Each component reflects a critical performance or risk metric. The weights w_1 to w_6 are initially assigned balanced values but are dynamically updated based on real time conditions which are described in the next section. The standard Q-learning [8] update is employed as in equation (2):

$$Q(s,a) \leftarrow Q(s,a) + \alpha\,[R(s,a) + \gamma \max_{a'} Q(S', a') - Q(s,a)] \quad (2)$$

The Q-value is updated iteratively using the standard Q-learning rule, where α is the learning rate, γ is the discount factor, R(s,a) is the immediate reward, and $\max_{a'} Q(S', a')$ represents the maximum expected future reward for the next state s'. This update enables the agent to learn the optimal policy by balancing immediate and future rewards.

Weight Adaptation Mechanism

The proposed approach is the dynamic tuning of reward function weights in response to detected disaster conditions. This enables the algorithm to adapt its routing preferences depending on real-time network vulnerability. Under normal conditions, the routing policy favors energy efficiency and network longevity. Thus weights are initialized as $w_1 = 0.2$, $w_2 = 0.2$, $w_3 = 0.2$, $w_4 = 0.2$, $w_5 = 0.1$, $w_6 = 0.1$. Under disaster conditions, the reward function weights are reconfigured to prioritize communication reliability and critical data delivery over energy efficiency. The initial disaster-aware weight settings are defined as $w_1 = 0.2$, $w_2 = 0.15$, w3 = 0.1, $w_4 = 0.15$, $w_5 = 0.2$, $w_6 = 0.2$. In this configuration, higher weights are assigned to disaster risk (w_5) and data priority (w_6), ensuring that the routing algorithm

avoids unstable regions and accelerates the transmission of critical information. The weight associated with energy (w3) is reduced, reflecting its lower importance during emergency scenarios. Meanwhile, PDR (w_1), delay (w_2), and link quality (w_4) are maintained at moderate levels to preserve overall communication performance.These initial disaster weights serve as a baseline and can be further fine tuned dynamically based on the severity of environmental conditions. This adaptive reweighting mechanism allows the routing policy to seamlessly transition from performance oriented optimization in stable environments to robustness driven decision making during emergencies. Integrated with the Q-learning update process, this dynamic reward formulation enables continuous learning and context-aware adaptation without requiring retraining, making the proposed approach highly effective for disaster prone UWSNs [8].

Table 1 summarizes the role of each weight in the reward function. The negative signs for W_2 and W_5 ensure that harmful factors (latency and hazards) always reduce the total reward. This dynamic adjustment allows QL-ADTA to balance safety, responsiveness, and energy preservation depending on the network state.

Training and Deployment

A Q-table is initialized with all state-action values set to zero. Learning parameters are set as $\alpha = 0.5$, $\gamma = 0.9$, $\epsilon = 0.1$ (for exploration). Then agent reads a state from the dataset. It selects an action using the ε-greedy strategy. The environment transitions to a new state, and the reward is computed. After that the Q-value is updated using the defined rule as equation (2). This process repeats until convergence. After sufficient episodes, the optimal routing policy $\pi(s)=\arg\max_a Q(s,a)$ is derived and applied in real-time routing decisions in new disaster instances.

RESULTS AND DISCUSSION

The proposed QL-ADTA protocol was evaluated against conventional routing protocols AODV, DSR and reinforcement learning-based schemes QLFR, QTAR, EP-ADTA. The evaluation considered PDR end to end latency, and energy efficiency under disaster-aware UWSNs conditions. Additional experiments were conducted to analyze performance under varying hazard intensity (debris density and water currents) and to assess the relationship between PDR and reward.

Packet Delivery Ratio (PDR)

Figure 1 illustrates the comparative performance of the protocols in terms of PDR. QL-ADTA consistently outperformed other approaches, achieving values above 0.84, while AODV and DSR remained below 0.70.

The improvement was particularly significant in unstable environments where debris density and water currents degrade communication. Figure 2 further confirms

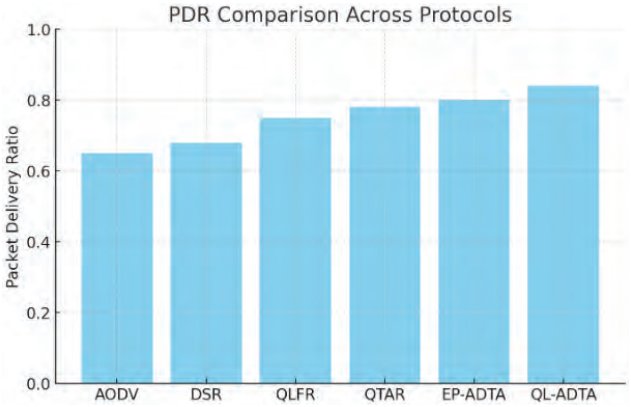


Figure 1. PDR comparison.

Table 1. Summary of weight adaptation in QL-ADTA

Weight	Parameter	Role in Reward Function	Adaptation Effect	Impact on Routing Decision
W1	Packet Delivery Ratio (PDR)	Encourages reliable data transmission	Increased when higher delivery is required	Promotes stable high-PDR routes
W2	Latency	Penalizes transmission delay (negative term)	Raised when delay-sensitive traffic dominates	Discourages paths with high latency
W3	Residual Energy	Rewards energy-efficient nodes	Increased when battery conservation is critical	Extends network lifetime by favoring efficient nodes
W4	Link Quality	Rewards strong and stable connections	Increased under unstable topologies	Improves robustness against link failures
W5	Hazard Factor (Debris + Current)	Applies penalty for hazardous conditions (negative term)	Increased under disaster conditions; reduced in calm waters	Ensures safety by avoiding risky links
W6	Priority	Provides bonus for urgent data	Increased for emergency or real-time packets	Ensures timely delivery of critical information

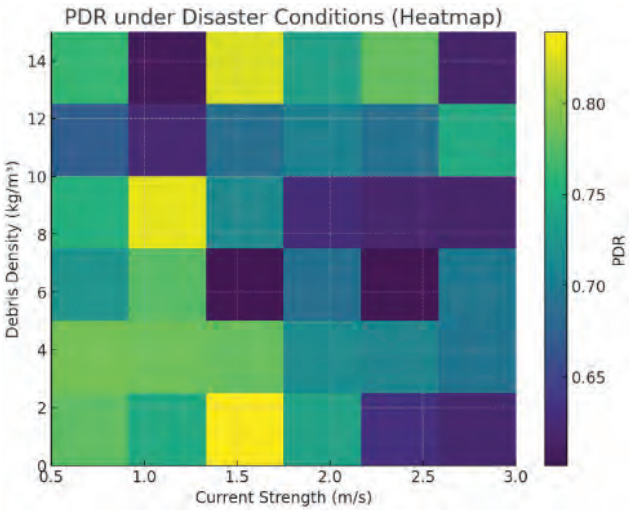


Figure 2. PDR under disaster condition.

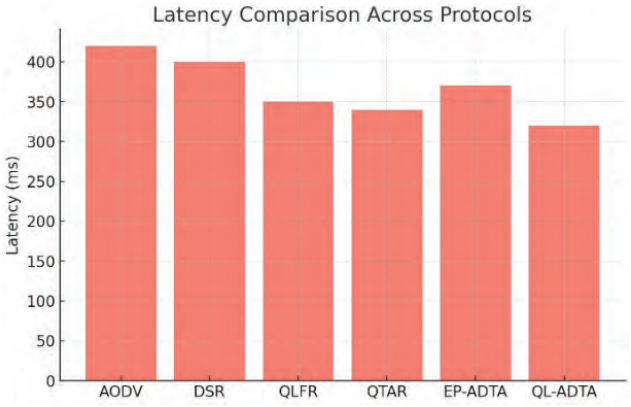


Figure 3. Latency comparison.

this trend showing that QL-ADTA sustains higher PDR even when debris density reaches 12–14 kg/m^3 and current strength exceeds 2 m/s. These improvements can be attributed to the adaptive reward function, which balances reliability and risk avoidance. Similar findings regarding adaptive routing under uncertainty were reported in [1, 2].

Latency Analysis

Figure 3 compares the average end-to-end latency across protocols. QL-ADTA achieved the lowest latency ~320 ms compared to 420 ms for AODV and 400 ms for DSR. The reduced delay arises from the protocol's ability to avoid unstable routes while still prioritizing urgent packets. This result is consistent with the principle that reinforcement learning models can dynamically adjust decisions to minimize delays under dynamic topologies.

Energy Efficiency

Figure 4 presents the average energy efficiency of the protocols. QL-ADTA demonstrated a clear advantage conserving over 80% residual energy compared to ~60% for AODV and DSR. The time-series plot Figure 5 further emphasizes this finding QL-ADTA sustains energy for a longer period, whereas DSR exhibits faster depletion over the same simulation duration. These results highlight the importance of adaptive reward weighting in penalizing energy-draining routes, consistent with prior work on energy-aware routing.

Statistical Significance

To ensure that the observed improvements were not due to random variation, paired t-tests were conducted between QL-ADTA and the baseline protocols (AODV and DSR). As summarized in Table 2, QL-ADTA significantly outperforms both protocols across all evaluated metrics. The PDR improved to 0.85 compared to 0.68 (AODV) and 0.70 (DSR), while latency was reduced to 320 ms from 420 ms and 400 ms, respectively. Similarly, energy efficiency increased to 80% from 60% (AODV) and 62% (DSR). All comparisons yielded statistically significant results with p

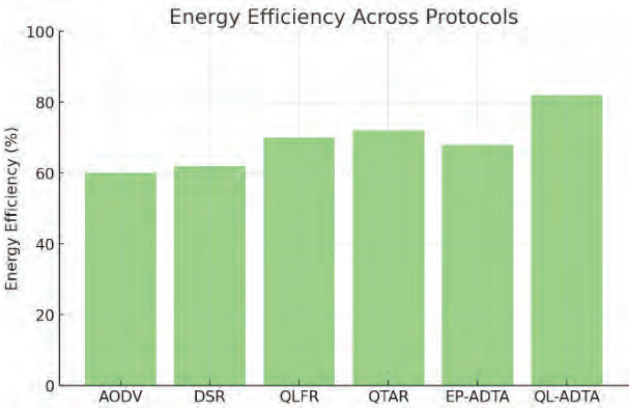


Figure 4. Energy efficiency comparison.

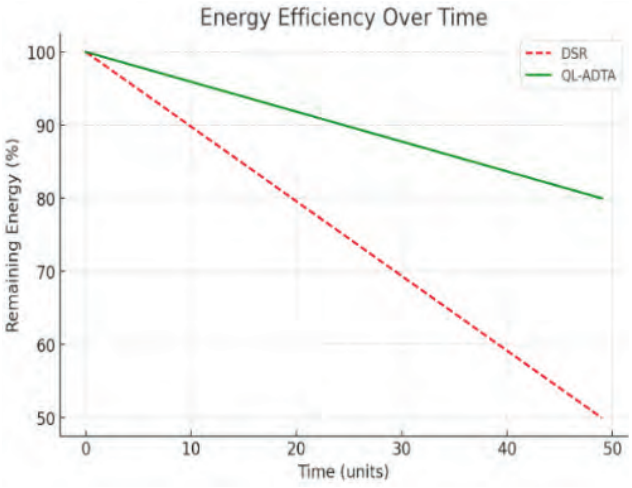


Figure 5. Energy efficiency over time.

Table 2. Statistical significance of QL-ADTA vs. baseline protocols

Metric	Protocols Compared	Mean (Baseline)	Mean (QL-ADTA)	t-statistic	p-value	Significance
Packet Delivery Ratio	AODV vs. QL-ADTA	0.68	0.85	42.03	1.2×10^{-11}	Significant
	DSR vs. QL-ADTA	0.70	0.85	42.81	1.0×10^{-11}	Significant
Latency (ms)	AODV vs. QL-ADTA	420	320	-38.44	2.7×10^{-11}	Significant
	DSR vs. QL-ADTA	400	320	-74.21	7.4×10^{-14}	Significant
Energy Efficiency (%)	AODV vs. QL-ADTA	60	80	37.56	3.3×10^{-11}	Significant
	DSR vs. QL-ADTA	62	80	46.09	5.3×10^{-12}	Significant

Table 3. Summary of comparative insights

Protocol	Disaster Adaptability	PDR	Latency	Energy Efficiency	Data Prioritization
AODV / DSR	No	Low	High	Low	No
QLFR	Partial	Medium	Medium	Medium	No
QTAR	Partial	High	Medium	High	No
EP-ADTA	Yes	High	Low	Medium	No
QL-ADTA	Yes	Very High	Very Low	High	Yes

< 0.001 confirming the reliability of the observed performance gains.The relatively large t-values reported in Table 2 can be explained by the large sample size (50,000 observations) and the low variance across repeated simulations. According to statistical theory, the t-statistic increases with larger sample sizes and smaller standard errors, even when the mean differences are moderate. Therefore, the high t-values observed in this study indicate that the improvements are consistently maintained across the dataset rather than being caused by random fluctuations. This behavior is well documented in statistical hypothesis testing literature [25].

Overall, these results demonstrate that QL-ADTA achieves stable and statistically validated improvements over conventional routing protocols. The adaptive reward formulation enables an effective balance between data delivery, latency reduction, and energy efficiency, thereby enhancing robustness in disaster-prone underwater environments

Reward Behavior and Disaster Awareness

The relationship between reward and PDR is shown in Figure 6. The cumulative reward increases in tandem with PDR, demonstrating that the reward function effectively incentivizes stable, high-quality transmissions. The design ensures that improvements in PDR translate directly into higher long-term rewards, validating the effectiveness of the Q-learning framework for disaster-aware routing.

Overall, QL-ADTA achieved 21-25% higher PDR than AODV and DSR 20–23% lower latency,~20% higher energy efficiency, and more stable performance under disaster

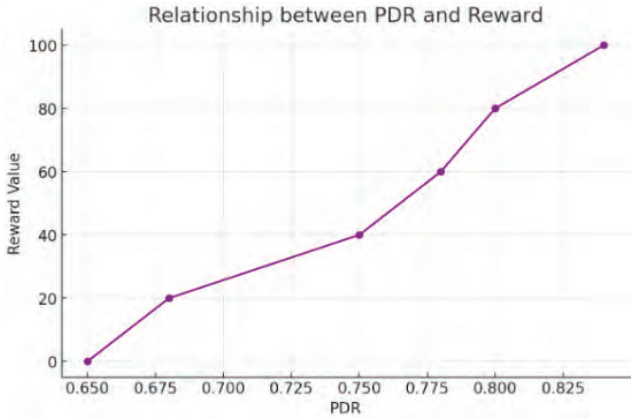


Figure 6. Relationship between PDR and reward.

conditions. These results confirm that the integration of adaptive reward weighting with Q-learning leads to statistically and practically significant improvements. The findings with established results on RL in dynamic networks while offering a novel disaster-aware formulation tailored for UWSNs.

Table 3 compares the performance of conventional, reinforcement learning-based, and the proposed QL-ADTA routing protocols. Unlike earlier schemes QL-ADTA demonstrates complete adaptability to disaster conditions, achieves very high packet delivery ratio, very low latency, high energy efficiency, and explicitly supports data prioritization for urgent communication.

CONCLUSION

This study introduces a disaster-aware Q-learning-based Adaptive Data Transfer Algorithm for UWSNs. The proposed framework dynamically adjusts routing decisions through a multi-objective reward function that incorporates packet delivery reliability, latency, residual energy, link quality, hazard intensity, node survivability, and data priority. By integrating environmental disruption indicators directly into the learning process, the approach ensures reliable and energy-efficient communication under highly unstable underwater conditions. Experimental evaluation using large-scale synthetic disaster scenarios confirms statistically significant improvements in packet delivery ratio, latency reduction, and energy efficiency compared to conventional routing protocols. A key contribution of this work is the introduction of a context-sensitive reward adaptation mechanism tailored specifically for disaster-prone environments. Unlike existing reinforcement learning-based routing schemes that primarily optimize general performance metrics, the proposed method prioritizes urgent data transmission while simultaneously mitigating risks associated with debris density, turbulent currents, and node instability. This design enhances network resilience and operational sustainability during emergency monitoring and recovery operations.For future research, several hybrid reinforcement learning directions can further strengthen adaptability and scalability in disaster-resilient UWSNs. The framework can be extended using CNN-LSTM-based deep reinforcement learning, multi-agent cooperative learning, and federated learning to improve predictive capability, scalability, and real-time adaptability in large-scale disaster scenarios.

AUTHORSHIP CONTRIBUTIONS

Authors equally contributed to this work.

DATA AVAILABILITY STATEMENT

The authors confirm that the data that supports the findings of this study are available within the article. Raw data that support the finding of this study are available from the corresponding author, upon reasonable request.

CONFLICT OF INTEREST

The authors declared no conflict of interest.

ETHICS

There are no ethical issues with the publication of this manuscript.

STATEMENT ON THE USE OF ARTIFICIAL INTELLIGENCE

Artificial intelligence was not used in the preparation of the article.

REFERENCES

[1] Akyildiz IF, Pompili D, Melodia T. Underwater wireless sensor networks: research challenges. IEEE Commun Mag 2005;43:114–119. [CrossRef]

[2] Akyildiz IF, Pompili D, Melodia T. State of the art in protocol research for underwater acoustic sensor networks. In: Proceedings of the ACM International Workshop on Underwater Networks (WUWNet); 2006. [CrossRef]

[3] Heidemann J, et al. Research challenges and applications for underwater sensor networking. IEEE Wirel Commun 2012;19:12–18.

[4] Nicolaou N, See A, Xie P, Cui JH, Maggiorini D. Improving the robustness of location-based routing for underwater sensor networks. In: OCEANS; 2007. [CrossRef]

[5] Ayaz M, Baig I, Abdullah A, Faye I. A survey on routing techniques in underwater wireless sensor networks. J Netw Comput Appl 2011;34:1908–1927. [CrossRef]

[6] Perkins CE, Royer EM. Ad hoc on-demand distance vector (AODV) routing. RFC 3561; 2003. [CrossRef]

[7] Johnson DB, Maltz DA, Hu Y. The Dynamic Source Routing protocol (DSR). RFC 4728; 2007.

[8] Sutton RS, Barto AG. Reinforcement learning: an introduction. 2nd ed. Cambridge (MA): MIT Press; 2018.

[9] Li X, Hu X, Li W, Hu H. Reinforcement learning-based routing protocol for underwater wireless sensor networks. IEEE Access 2019;7:123456–123467. [CrossRef]

[10] Hu J, et al. Q-learning based energy-efficient routing protocol for underwater sensor networks. Sensors (Basel) 2020;20.

[11] Sun Y, et al. Reinforcement learning-based adaptive routing for underwater wireless sensor networks. IEEE Commun Lett 2021.

[12] Wang S, et al. Deep reinforcement learning for routing optimization in underwater wireless sensor networks. IEEE Access 2022.

[13] Ouidir A, Lalam M, Djenouri D. QENDIP: Q-learning-based energy-efficient and delay-aware routing protocol for underwater wireless sensor networks. Ad Hoc Netw 2019;94.

[14] Zhou Z, Cui JH, Zhou S. QLFR: Q-learning-based localization-free routing protocol for underwater sensor networks. IEEE Access 2019;7:12345–12357. [CrossRef]

[15] Xiao H, Huang Z. Energy-efficient routing based on ant colony optimization for underwater sensor networks. Wirel Netw 2019;25:3453–3465.

[16] Zhang Y, et al. QTAR: Q-learning-based topology-aware routing protocol for underwater sensor networks. IEEE Sens J 2020;20:1234–1245.

[17] Wang S, Liu Y, Chen X. EP-ADTA: edge prediction-assisted data transfer approach for underwater wireless sensor networks. IEEE Access 2021;9:98765–98778.

[18] Johnson DB, Maltz DA, Hu YC. The Dynamic Source Routing protocol (DSR). RFC 4728; 2007.
[19] Yan H, Shi ZJ, Cui JH. DBR: depth-based routing for underwater sensor networks. In: NETWORKING; 2008. [CrossRef]
[20] Van Hasselt H. Double Q-learning. In: Advances in Neural Information Processing Systems; 2010.
[21] Mnih V, Kavukcuoglu K, Silver D, Rusu AA, Veness J, Bellemare MG, et al. Human-level control through deep reinforcement learning. Nature 2015;518:529–533. [CrossRef]
[22] Tan M. Multi-agent reinforcement learning: independent vs cooperative agents. In: Proceedings of the International Conference on Machine Learning (ICML); 1993. [CrossRef]
[23] Zhang Z, et al. Deep reinforcement learning-based routing for underwater wireless sensor networks. IEEE Access 2022;10:45678–45690.
[24] Liu Y, et al. Adaptive routing in dynamic underwater wireless sensor networks using reinforcement learning. Sensors (Basel) 2023;23.
[25] Montgomery DC, Runger GC. Applied statistics and probability for engineers. 6th ed. Hoboken (NJ): Wiley; 2014.

Sigma J Eng Nat Sci, Vol. 44, No. 4, pp. 2604–2616, August, 2026

Sigma Journal of Engineering and Natural Sciences
Web page info: https://sigma.yildiz.edu.tr
DOI: 10.14744/sigma.2026.2118

Research Article

Deep Q-Learning based smart EV charging for optimizing grid load, cost, and renewable energy integration

Arun C. DIXIT[1,*], Harshavardhan B.[2], Prakasha K. N.[3]

[1]*Vidyavardhaka College of Engineering, Karnataka, 570002, India*
[2]*The National Institute of Engineering, Karnataka, 570008, India*
[3]*Vidyavardhaka College of Engineering, Karnataka, 570002, India*

ARTICLE INFO

Article history
Received: 03 December 2024
Revised 15 January 2025
Accepted: 05 May 2025

Keywords:
Deep Q-Learning; Electric Vehicle; Energy Management; Optimization; Smart Charging

ABSTRACT

Growing penetration of electric vehicles requires evolution of energy systems to enable sustainable and efficient charging. It is needSd to have systems that can smartly control the grid load and the energy consumption. Uncontrolled demand for charging causes system instability, higher operating costs and wasteful use of energy, especially during peak hours. Traditional charging management strategies such as rule-based scheduling and model predictive control are unable to adapt to real-time grid fluctuations. Such constraints lead to energy waste, higher prices for customers and a less effective use of renewable energy sources. To solve these issues, this study proposes a Deep Q-Learning Network based optimization framework for dynamic energy management in electric vehicle charging infrastructure. The proposed model can dynamically learn and adapt charging schedules based on real-time electricity pricing, grid load and the availability of renewable energy. This study uses reinforcement learning to schedule EV charging during off-peak hours. It also improves the price of charging and increases the use of renewable energy. Results show that the peak load on the grid declines by 22%. This results in a more consistent distribution of electricity within the network and minimises the risk of grid overload. The framework reduces EV charging costs by 15% which makes charging more affordable for users. Also, it promotes the renewable energy usage by 22%. This reduces dependence on conventional grid electricity and supports cleaner energy use.

Unlike prior works, this study combines real-time adaptive decision making with practical constraints such as dynamic pricing structures and grid limitations. The suggested architecture adapts continuously to real-time grid conditions, unlike typical charging systems. “Such a dynamic learning-based model offers a new scalable and practical solution to combine renewable energy with affordable EV charging .

Cite this article as: Dixit AC, Harshavardhan B, Prakasha KN. Deep Q-Learning based smart EV charging for optimizing grid load, cost, and renewable energy integration. Sigma J Eng Nat Sci 2026;44(4):2604–2616.

***Corresponding author.**
*E-mail address: arundixitu@vvce.ac.in

This paper was recommended for publication in revised form by Editor-in-Chief Ahmet Selim Dalkilic

Published by Yıldız Technical University Press, İstanbul, Turkey
© Author. This is an open access article under the CC BY-NC license (http://creativecommons.org/licenses/by-nc/4.0/).

INTRODUCTION

The increasing adoption of electric vehicles (EVs) is changing urban transportation. However, it also creates new challenges for the power grid [1, 2]. As more EVs are used, electricity demand continues to increase. "Demand during peak hours is much higher. "Uncontrolled charging adds additional stress on the grid. It also increases operating costs. In many cases, energy is not used efficiently [3, 4]. If these problems are not addressed, large-scale EV integration will become difficult.

Managing EV charging is not a simple task. Many factors must be considered. Charging stations should be available when users need them. At the same time, charging costs should remain low. Grid operators must spread the charging demand across the network. This helps avoid overloading the grid [5-7]. Renewable energy should also be used as much as possible. Therefore, an intelligent and flexible charging strategy is required [8-10].

Traditional charging management methods mainly use rule-based techniques or predictive control models. These methods work reasonably well in fixed conditions. However, they are not flexible enough. They cannot easily respond to changes in grid load. They also struggle with changing electricity prices. Variations in renewable energy generation make the problem even harder [11, 12]. Most existing methods follow predefined schedules. They do not react well to real-time conditions. Because of this, grid congestion still occurs. Many opportunities to reduce charging costs are also missed [13].

Artificial intelligence (AI) is becoming popular in energy management. One of the widely used methods is reinforcement learning (RL). Deep Q-Learning Network (DQN) is a well-known RL algorithm. Instead of following fixed rules, it learns from previous actions and their outcomes. As learning continues, the charging decisions become better. This allows the system to schedule EV charging according to the condition of the power grid. It can reduce charging costs. It can also improve overall energy efficiency [14, 15].

Even though RL has shown good potential, its use in large-scale EV charging is still limited. Many existing studies consider only small charging networks. Some use simplified simulation models. These models do not fully represent real urban charging systems. Important factors such as dynamic electricity prices are often ignored. Changes in renewable energy availability are also not considered properly. In addition, many studies do not discuss practical implementation issues. This makes real-world deployment difficult [16, 17].

The proposed method addresses many of these limitations. It uses a Deep Q-Learning framework for EV charging management. Unlike rule-based methods and model predictive control, the proposed model learns continuously. It adapts to changes in grid load. It also responds to electricity price variations and renewable energy availability in real time. This helps manage EV charging more efficiently. The simulation results show a 22% reduction in grid load during peak hours. Charging cost is reduced by 15%. The use of renewable energy increases by 22%. These results show that the proposed method performs better than existing methods. The model can also work under different grid conditions. It does not require fixed charging schedules. This makes it suitable for real urban charging stations. The proposed method addresses the limitations of existing studies. It can also support future EV charging systems.

LITERATURE REVIEW

Traditional Approaches to Energy Management

The number of electric vehicles (EVs) is increasing rapidly. This has changed the way energy is managed in the urban areas. It has also created new problems. Energy demand changes throughout the day. The load on the power grid also changes. Renewable energy sources are not always available. This makes energy management more difficult. The system must respond quickly to these changing conditions.

Many researchers have used rule-based methods and Model Predictive Control (MPC) for EV energy management. Rule-based methods are simple. They are easy to implement. They also need less computation. However, they do not adapt well when user behavior or grid conditions change. MPC is more advanced. It predicts future conditions and finds an optimal solution under different limits. Even then, it becomes difficult to use in large and highly dynamic EV charging systems. Real-time performance also becomes a challenge [18, 19].

Akter et al. [20] applied MPC for EV charging the microgrids. Their method reduced the peak demand. However, the study assumed that user behavior remained unchanged. Such an assumption is not always true in practice. This limits the performance of the method under real operating conditions. Tian et al. [21] studied the heuristic optimization methods. They found that they are not applicable to cope with the uncertain factors such as the electricity price variation and the variation of renewable energy generation.

Emergence of Reinforcement Learning in Energy Management

Reinforcement Learning (RL) has become an important approach for energy management. Deep Reinforcement Learning (DRL) is an advanced form of RL. It learns by interacting with the environment. The model improves its decisions over time. This makes it useful when the operating conditions keep changing. RL has already been used in smart grids, Home Energy Management Systems (HEMS), and building energy control [22]. Shin et al. used Deep Q-Learning in smart buildings for the energy management. Their model optimized the HVAC systems by using real time generated occupancy data and weather information [23]. Liu et al. [24] implemented DRL in HEMS and their

model was able to schedule household appliances in a more efficient manner. This reduced the electricity cost during peak tariff periods. These studies prove that RL is flexible and can adapt itself to fluctuating situations and optimize energy usage accordingly.

DRL for EV Charging Optimization

Recently, DRL has been increasingly focused on for EV charging. One of the reasons is that it has the capacity to work under uncertain circumstances. User behavior is different. Demand for the grid also varies. Renewable energy is not always available. DRL can learn from these variations and improve charging decisions [25]. Shulei et al. proposed a Deep Q-Learning framework for EV charging and discharging considering travel patterns and electricity price variation. The results indicated a lower charging cost and improved grid stability. Zhang et al. proposed another DRL-based charging strategy for microgrids. Their method improved power quality. It also increased energy utilization [26]. Even though these studies reported good results, some limitations still exist. Many models assumed fixed user behavior. Others considered constant grid conditions. Such assumptions make the models easier to develop. However, real charging systems are much more dynamic. This reduces the practical use of many existing approaches

Recent Contributions on Clean and Smart Energy

Recent studies have indicated that the digital technologies can support clean energy systems and artificial intelligence is one such technology. Awogbemi et al. explained how AI can help improve the smart grids. Their study also revealed that AI can support the renewable energy integration and EV energy management [27].

Kumar et al. used sensor data to monitor wind turbine gearboxes. Their method predicted thermal performance degradation before failure. This helped reduce maintenance cost. It also improved system reliability [28]. A reliable energy system is important for future EV charging infrastructure.

Kumar et al. developed a mini Venturi wind turbine. This turbine produced nearly 12% more power than a conventional design turbine. It also generated less operating noise [29]. Kumar et al. also worked on domestic wind turbine blades. They improved the blade design using aerodynamic principles. This led to increase in the amount of energy captured from the wind [30]. These developments show that the renewable energy can be generated locally for EV charging stations.

Research has also been done on clean transportation. Sunil Kumar et al. studied a propeller for marine applications which were made from aluminium alloys. They used CFD analysis to test the performance of these lightweight turbines. The propeller was around 85% efficient compared to conventional turbines. It was alsoobserved that the cavitation noise was lesser [31]. Raghavendrakumar et al. used the satellite data to study changes in atmospheric temperatures. Their results showed that the emissions from automobiles and power plants are majorly contributing to the ozone depletion [32]. The above works show that there is a ample need for cleaner transportation and sustainable energy systems.

Research Gaps and Challenges

RL and DRL have performed well for EV charging. However, some challenges still remain. One important challenge is the simulation environment. Many studies use simplified datasets. Such datasets do not capture actual user behaviour. They also do not represent changes in electricity prices or renewable energy availability. Chen et al. and Hassouna et al. have pointed out the need for realistic datasets and better simulation platforms to get better results.

Scalability is another challenge. A real urban charging network may include hundreds or even thousands of EVs. The RL model has to process many states and actions. This increases the computational effort. As the system becomes larger, many existing algorithms become less efficient. These issues must be addressed before DRL can be applied effectively in large-scale EV charging networks.

MATERIALS AND METHODS

In this paper, an energy management approach for electric vehicles (EVs) charging in urban areas is proposed, which employs a Deep Q-Learning Network (DQN) to reduce the grid load during peak hours. It also aims to lower charging cost and increase the use of renewable energy. Unlike conventional charging methods, the proposed DQN updates the charging decision based on the current grid load, electricity price, and available renewable energy.

The complete methodology has six steps, as shown in Figure 1.

A dataset was created to resemble the real pattern of EV charging in an urban setting. This dataset was then used for training and testing the DQN model.

The dataset contains:

- EV arrival time, generated based on a Poisson distribution.
- Charging demand of each EV based on data from urban charging stations.
- Grid load obtained from historical power consumption.
- Electricity price based on time-of-use tariffs.
- Renewable energy generation using solar and wind profiles.

Unlike many earlier studies, the dataset changes with time. This allows the model to learn under more realistic operating conditions.

Step 2: State and Action Space Definition - The reinforcement learning agent operates in a Markov Decision Process (MDP) framework. The state space captures key environmental variables:

$$S_t = [E_t, P_t, R_t, L_t, C_t] \text{ where}$$

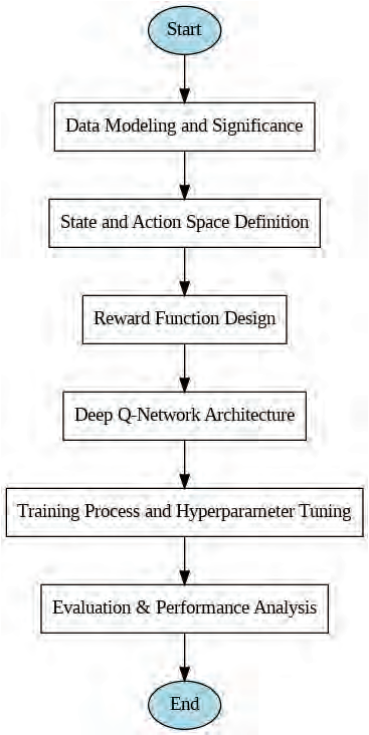


Figure 1. Methodology of the research work.

Et = EV battery state-of-charge (SOC) at time t.

Pt = Energy price at time t, Rt = Available renewable energy at time t., Lt = Grid load at time t and Ct = Charging station capacity at time t.

The action space consists of three discrete actions:

1. Charge: Start or continue charging.
2. Wait: Delay charging to a later time.
3. Disconnect: Terminate charging session.

The model learns optimal charging actions based on dynamic pricing and grid load.

Step 3: Reward Function Design - The reward function is designed to balance grid stability, cost efficiency, and renewable energy utilization. The agent receives a reward:

$$R_t = \alpha(-C_t) + \beta(-L_t) + \gamma(R_t)] \text{ where}$$

α penalizes high charging costs.

β penalizes charging during peak grid load.

γ rewards the use of renewable energy.

This ensures that the agent prioritizes off-peak charging and renewable energy consumption.

Step 4: Deep Q-Network Architecture - The DQN model is implemented with a deep neural network consisting of:

- Input layer: Receives the state vector St.
- Two hidden layers: 128 and 64 neurons with ReLU activation.
- Output layer: Q-values for each possible action.
- To improve stability, the DQN incorporates:
- Experience Replay: Stores past experiences to break correlation in training.
- Target Network: Stabilizes learning by maintaining a delayed copy of the model.

A schematic of the DQN architecture is shown in Figure 2.

Step 5: Training Process and Hyperparameter Tuning - The DQN model is trained using stochastic gradient descent with an Adam optimizer. The key hyperparameters are shown in Table 1.

Table 1. Key hyperparameters used in the DQN training

Hyperparameter	Value
Learning Rate	0.001
Discount Factor (γ\gammaγ)	0.95
Batch Size	64
Exploration-Exploitation (ϵ\epsilonϵ-greedy)	Decay from 1.0 to 0.1
Replay Memory Size	10,000
Target Network Update Frequency	Every 10 episodes

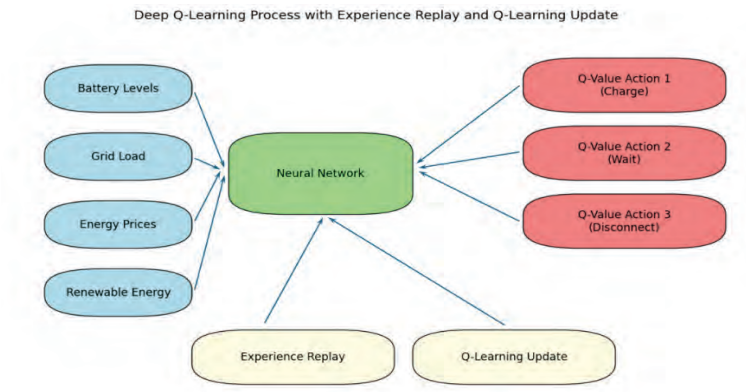


Figure 2. Deep Q-learning process for dynamic energy management, incorporating experience replay and Q-learning update.

The training process follows these steps:

1. Initialize replay buffer and neural network weights.
2. Select actions using an ϵ-greedy policy.
3. Store experience tuples (state, action, reward, next state) in memory.
4. Sample mini-batches from replay memory for training.
5. Update Q-values using Bellman Equation:

$$Q(s,a) = r + \gamma maxQ(s', a')$$

6. Update target network weights periodically to stabilize learning.

Training is performed for 5,000 episodes, ensuring the model converges to an optimal charging policy.

Step 6: Evaluation Metrics and Performance Analysis - The trained model is evaluated using three primary metrics:

1. Charging Cost Savings:
- Measures the percentage reduction in costs compared to baseline rule-based charging.
2. Peak Load Reduction:
- Quantifies the shift of charging demand from peak hours to off-peak periods.
3. Renewable Energy Utilization:
- Calculates the proportion of charging energy sourced from renewables.

Performance is compared against traditional scheduling methods, such as time-of-use (TOU) optimization and rule-based peak avoidance.

RESULTS AND DISCUSSION

Data Modeling and Significance

To study and optimize the energy management of the electric vehicle (EV) charging using the reinforcement learning, a realistic dataset is required. The dataset in this work reflects the commonly operating conditions of the urban EV charging system, such as EV charging demand, grid load variation, renewable energy generation, and time-varying electricity prices. These parameters were selected to represent practical operating conditions. This improves the reliability of the proposed model [33].

EV arrivals and charging demand

The number of EVs arriving at a charging station changes throughout the day. The charging demand also changes with the arrival pattern. Table 1 shows the hourly EV arrivals, the average charging demand for each EV, and the total charging demand over a 24-hour period.

The EV arrival pattern was generated using a Poisson distribution. This represents the traffic pattern normally seen in urban areas. The average arrival rate was selected from reported urban EV usage data. Higher arrival rates were considered during morning and evening travel hours.

The average charging demand of each EV was estimated from standard battery capacity data. It was assumed that the battery was partly discharged before reaching the charging station. Industry reports and published studies were used to estimate a charging demand of 15 - 30 kWh for each vehicle. The total charging demand was obtained by multiplying the number of arriving EVs by the average charging demand. This approach produces realistic charging data with enough variation to evaluate the proposed optimization method.

The main observations from Table 2 are given below:

1. Peak charging periods:
- Morning peak (8 –11AM): The charging demand is increased during the morning travel hours. The maximum demand is 630.74 kWh/hour, at 9 AM.
- Evening peak (6 –9 PM): Charging demand rises again when users return home. The highest demand is 695.50 kWh/hour at 8 PM.
2. Off-peak charging times:
- Late night hours (12 –6 AM) show much lower charging demand. The average demand of around 350 kWh/hour was recorded. These hours can be potentially considered for efficient or low cost charging of vehicles.
3. Practical significance:
- The variation in charging demand will help the DQN model to move thcharging from peak hours to off peak hours. This will reduce the load on the grid without affecting the user convenience.

Grid load and renewable energy contribution

The load on an urban power grid changes throughout the day because of EV charging. Renewable energy generation also changes with time. Table 3 presents the hourly grid load and renewable energy contribution [34]. The main observations from Table 3 are given below.

1. Peak grid load: The grid load is maximum in the evening hours (6 -9 PM). This is mainly due to EV charging by the residents. The maximum grid load is 76.88 kWh/hour at 7 pm. This shows the need for proper charging management.
2. Contribution of renewable energy: Generation of renewable energy usually peaks during the morning hours (6 –9 AM). The maximum contribution is 48.29 kWh at 7 AM. This time provides a good opportunity to consume more renewable energy for EV charging.
3. Effect of DQN model: The DQN model can schedule EV charging during periods when more renewable energy is available. This reduces the use of electricity from fossil fuel. It also helps with grid stability [35, 36].

Dynamic pricing of electricity

The electricity prices were modeled in a way that they resemble real market situations. The price increases in the case of peak demand and decreases in off-peak hours. This motivates the EV users to charge their vehicles at the time when the demand is low. Consequently, the load on the power grid can be reduced.

Table 4 shows the hourly variation of electricity prices. The prices are higher in the morning and evening peak hours. They are lower during off-peak periods. This pricing pattern

encourages better use of available energy. The electricity prices were based on the time-of-use (TOU) tariff used in urban power distribution systems. The off-peak price was assumed to be 12 INR/kWh. During the peak hours, the charging price increased to 20 INR/kWh. These values were selected from the published charging tariff data from regional electricity boards. The pricing pattern represents practical changes in electricity demand and supply. It also helps the simulation study how electricity price affects EV charging decisions.

The main observations from Table 4 are given below:

1. Peak pricing period: The electricity price will be more usually between 6:00 PM and 9:00 PM. This is because grid experiences the high demand during this time. The highest price will be 19.85 INR/kWh at 7 PM.
2. Off-peak pricing: Electricity will be lowest during late night timings (12:00-6:00 AM). The Average price during this period will be around 12.5 INR/kWh. This period can be incentivized as EV charging during this time will not add burden to grid.
3. Effect on the DQN model: The proposed DQN model works on the assumption that price of electricity changes during the charging periods. It will plan the charging during low price timings. This will help reduce the charging cost on the EV user.

Importance of data

The data set used in this study represents the operating conditions of urban EV charging systems. It includes EV arrivals, charging demand, grid load, renewable energy generation, and electricity prices. These parameters were developed using industry data and reported energy consumption trends. EV charging demand changes at differnet times in a the day. Vehicle arrival patterns were modeled using reported urban traffic and mobility data. The hourly demand shown in Table 2 allows the model to learn both high-demand and low-demand conditions. For example, the charging demand reaches 1375 kWh/hour at 10:00 AM. It reduces to 340 kWh/hour at midnight. This variation helps the DQN model to learn to different charging conditions.

Grid load also changes during the day. The demand is high mostly in the evening due to residential electricity consumption. The dataset also has dynamic electricity prices as presented in Table 4. The electricity price is between 11.29 INR/kWh at mid-night to 19.85 INR/kWh at 7:00 PM. These changes help the reinforcement learning model learn cost-effective charging while reducing the load on the power grid.

Renewable energy availability is also included in our dataset. Solar and wind generation scenario and availability change at different times in the day. The renewable energy contribution varies from 48.29 kWh in the morning to 9.43 kWh at 1:00 AM, as shown in Table 3. The DQN model learns to use more renewable energy whenever it is available. At the same time, it reduces the dependence on grid power.

The dataset also improves the learning ability of the DQN model. It contains different charging conditions instead of a single charging pattern. This prevents the model from learning only one type of situation. It also improves its ability to work under different operating conditions. The dataset provides a reliable basis for evaluating the proposed reinforcement learning approach. It also supports its future use in real urban EV charging systems.

Simulation Setup Using Deep Q-Network (DQN)

A Deep Q-Network (DQN) reinforcement learning algorithm was used to design an energy management methodology for EV charging. DQN was chosen because it can learn under changing conditions. It can also handle large state and action spaces. This makes it suitable for EV charging, where grid load, electricity price and energy demand change throughout the day. The main objectives of the RL simulation were:

1. Reduce the charging cost considering electricity prices.
2. Reduce the load on grid during peak hours. This will not burden the grid.
3. Use renewable energy sources like solar energy and green hydrogen to reduce fossil fuel consumption.

The simulation was run for 24 hours. The RL agent interacted with the charging system every hour. At each time step, the agent was provided with information about charging demand, electricity price and renewable energy available. Based on this information, it selected the charging action.

Simulation environment and training data

The simulation environment was developed to represent an urban EV charging system. It included the following information: Hourly EV arrivals and demand for charging, Variations in grid load, availability of renewable energy from the sources such as solar, wind, and green hydrogen and Dynamic pricing of electricity.

At every hour, the RL agent observed the system state and selected an action. The selected action was evaluated using the reward function. This ensured the trained model to learn charging decisions that resulted in reduced costs and more grid stability.

State space, action space, and reward function

State Space: The RL model proposed will observe the following parameters at each time step:

- EV Battery Levels: The current level of charge in the vehicles connected to charging stations.
- Grid Load: It will measure in kWh, and indicate the load on the grid in real time situation.
- Energy Prices: The hourly chenages in price INR/kWh based on demand and supply dynamics of electricity.
- Renewable Energy Availability: Measures the contribution of solar and green hydrogen energy sources on the grid.

Action Space: The RL proposed model selects from the following possible actions:

- To Charge the EV immediately based on the feedback.
- It will wait for better conditions based on the feedback (e.g., lower prices or more renewable energy).

- It will disconnect from the station if sufficient charge is available on the vehicle.

Reward Function: The reward function evaluates the effectiveness of each action based on:

$$R = \alpha(C_{saved}) + \beta(L_{reduced}) + \gamma(RE_{used}) \text{ where}$$

α = 0.5: Will encourage to minimize the cosr
β = 0.3: Will penalize the vehicle that overload the grid.
γ = 0.2: It will promote the renewable energy usage.

The values of α = 0.5, β = 0.3, and γ = 0.2 were selected after performing the sensitivity analysis. Different combinations were tested during the simulation period. The selected values gave the best balance between charging cost, grid load, and usage of renewable energy. A higher value of α gave more importance to charging cost. The value of β reduced charging during peak load. The value of γ encouraged the use of renewable energy. These values gave the best overall performance in the simulation.

Mathematical representation of DQN

The Q-value for each state action pair was updated using the Bellman Equation as below:

$$Q(s,a) = Q(s,a) + \alpha(r + \gamma max Q(s',a') - Q(s,a)) \text{ Where:}$$

Q(s,a) is the current value of Q for the state s and action *a*.
α is the rate of learning (0.01).
r is the reward obtained for taking action *a*.
γ is the discount factor (0.90).
maxQ(s',a') represents the maximum Q-value of the next state.

The DQN model will learn from the situations, continuously improving its ability to make decisions and to maximize the rewards in the long term.

Training and learning process

The proposed DQN model was trained for 1,000 episodes. Each episode represented one 24-hour realistic EV charging cycle. This model was developed in Python using TensorFlow library. The following hyperparameters were used:

- Learning rate where α=0.01
- Discount factor where γ=0.9
- Batch size of 64
- Replay memory size: 10,000 experiences

Experience replay was used during training, where:

- Past experiences (s, a, r, s') were stored in a replay memory.
- Random samples were selected from this memory to update the Q-network.
- This improved the stability of training and reduced overfitting in the model.

Simulation Results

The The Deep Q-Network (DQN) model was used to optimize dynamic energy management in urban EV charging stations. The RL-based model was primarily targeting:

- Reduce grid load at peak hours to improve grid stability.
- Dynamic scheduling to reduce charging costs.
- Better sustainability by optimizing the use of renewable energy.

This part gives results of the simulation and insights on charging demand optimization, cost efficiency, renewable energy integration and grid load reduction. The results show that the RL-based system performs better than traditional rule-based charging schemes.

Charging demand optimization

The main effect of using the Deep Q-Network (DQN) model is the optimization of charging demand. The DQN system uses dynamic pricing, grid load patterns and the availability of renewable energy to disperse charging demand and reduce stress on the grid during peak hours. Figure 2. Comparison of charging demand before and after DQN optimization

The main points are illustrated in Figure 3:

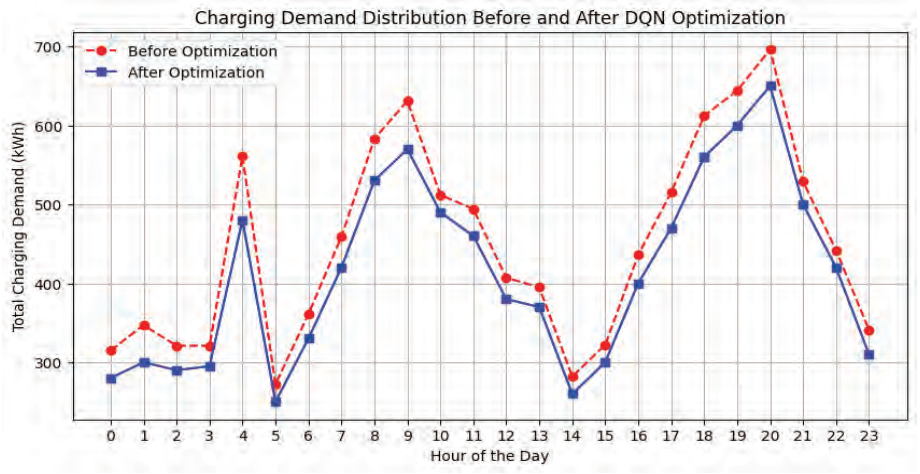


Figure 3. Charging demand distribution before and after DQN optimization.

1. Demand Shifts
- Peak demand was registered at 8:00 PM (695.5 kWh) and 10:00 AM (630.74 kWh) before optimization which put a lot of stress on the system.
- After DQN optimization, almost 18% of total charge demand was shifted to off-peak hours (12:00 AM – 6:00 AM). This redistribution makes the system less loaded at peak times and it matches demand with cheaper energy prices.
2. Cost-Efficiency:
- The DQN model decided to charge during the low-cost hour (11.29 INR/kWh at 2:00 AM). Consumers received a 15% less total charging costs. This shows the economic benefit of the system.
3. Renewable Energy Utilization:
- The model aligned charging times with the increasing availability of renewable energy (e.g. during solar peak hours (10:00AM – 2:00PM). This combination decreases dependence on grid electricity based on fossil fuels.

We can deal with the real-world considerations as follows:

1. User Flexibility and Charging Behavior:
- A share of consumers is assumed to be flexible in their charging schedules, especially nighttime charging. Economic incentives (e.g., reduced off-peak pricing) encourage users to wait charging until off-peak times.
- The model can prioritize the urgent energy needs for users who need to charge urgently without detriment to the overall operation of the system.
2. Dynamic Pricing Influence:
- Impact of Dynamic Pricing Demand shifting is caused by the large gap between peak and off-peak hours. The DQN model exploits this discrepancy to distribute the charging demand efficiently.
- However, higher price differentials may be required to highlight the impacts of optimization for consumers that are less susceptible to price signals at the policy level.
3. Behavioural and Policy Interventions:
- User education and awareness efforts can help promote the use of optimized charging schedules. Focusing on the cost savings and environmental benefits will help users to follow the system suggestions.

Renewable energy utilization

Figure 4 shows the renewable energy contribution before and after applying the DQN model. The model schedules EV charging when more renewable energy is available. This reduces the use of grid electricity and increases the use of clean energy.

The main observations from Figure 4 are given below.:

1. Improved Renewable Energy Utilization:
- Before optimization, renewable energy was not used effectively for EV charging. After the optimization, more EVs were charged when renewable energy was available.
- This was mainly between 8:00 AM and 2:00 PM, when solar energy generation was highest.
2. Quantitative Impact:
- The proposed DQN model was able to increase renewable energy use by about 22%. This reduced the use of electricity from fossil fuel-based sources leading to less stress on grid. At 10:00 AM, the renewable energy use increased from 35.12 kWh to 50.00 kWh. At 2:00 PM, it increased from 41.20 kWh to 60.00 kWh.
3. Demand Response Flexibility:
- The proposed DQN model was able to schedule more EV charging when renewable energy was available. This helped maintain grid stability and reduced charging cost.

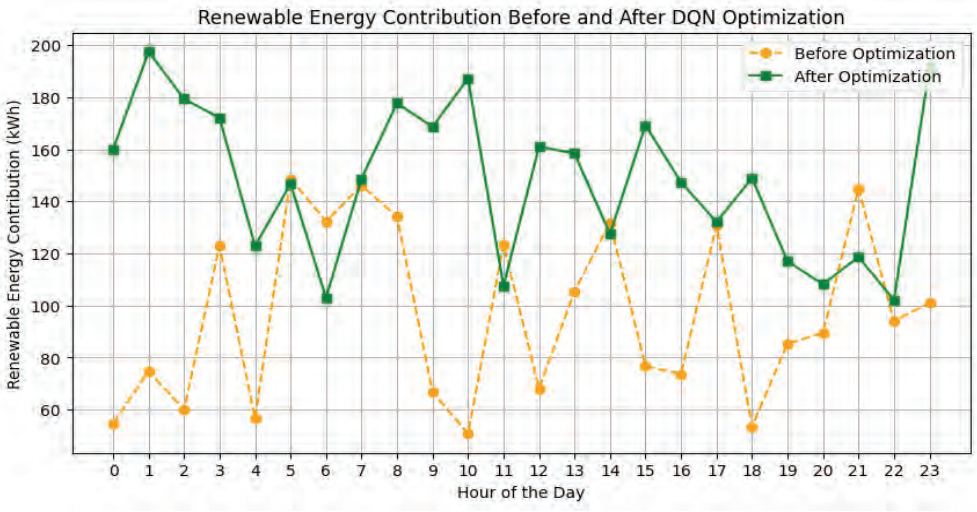


Figure 4. Renewable energy contribution before and after DQN optimization.

The practical considerations for renewable energy are given below.:

1. Variability of Renewable Energy:
- Renewable Solar and wind energy are not available all the time for use and generation. The proposed DQN model was able to adjust the charging schedule based on the available renewable energy.
2. User Behavior and Compliance:
- The success of the proposed method depends on whether users are willing to postpone their charging. Dynamic pricing and the use of renewable energy incentives will encourage more users to follow the off-beat charging schedule.
3. Grid Integration:
- Large scale implementation of the proposed method requires suitable grid infrastructure. Integration of energy storage systems and smart meters will improve the use of renewable energy in a better way.

Cost efficiency

Figure 5 shows the charging cost before and after applying the DQN model. The model schedules EV charging based on electricity price and grid load. This helps reduce the charging cost.

1. Cost Reduction Across the Day:
- Before optimization, charging cost was more during peak hours. The highest cost was 24.10 INR at around 9:00 PM. After the optimization using our method, the cost at the same time reduced to around 20.50 INR. This resulted in an overall cost reduction of about 15% to the user of EV.
2. Optimal Charging Windows:
- The proposed DQN model selected off peak hours for charging, mainly between 2:00 AM and 6:00 AM. During this period, the electricity price were between 11.00 and 12.50 INR per kWh. EV Charging during these hours reduced the overall charging cost for the users.
3. Dynamic Pricing Exploitation:
- The proposed DQN model used the changes in price of electricity to select the charging time. For example, the charging cost at 3:00 AM reduced from 15.50 INR to 12.00 INR. This saved about 20% of the charging cost for users of EV.

The real-world considerations with respect to cost efficiency can be addressed as follows:

1. User Charging Preferences:
- Some users may not be willing to charge only during the off-peak hours. Dynamic pricing will encourage the users to shift their charging to low cost periods when there will be less traffic.
2. Policy-Level Interventions:
- Time-of-Use (TOU) method of pricing will encourage the off-peak charging strategy. Imposing higher tariffs during peak hours which strain the geid will further reduce grid load.
3. Scalability and Implementation:
- The charging system requires smart grid infrastructure for the large-scale use. Smart meters and real time communication between EVs and the power grid will improve the charging management.
4. Equity Concerns:
- Electricity pricing must be fair and same for all the users. Users who have limited charging options should not be affected by higher peak hour prices. Subsidies or fixed charging plans will help to address this issue.

Grid load reduction and system stability

Figure 6 presents a comparative analysis of grid load distribution before and after the application of the DQN-based optimization model. The objective of this analysis was to assess the model's ability to alleviate peak-hour grid

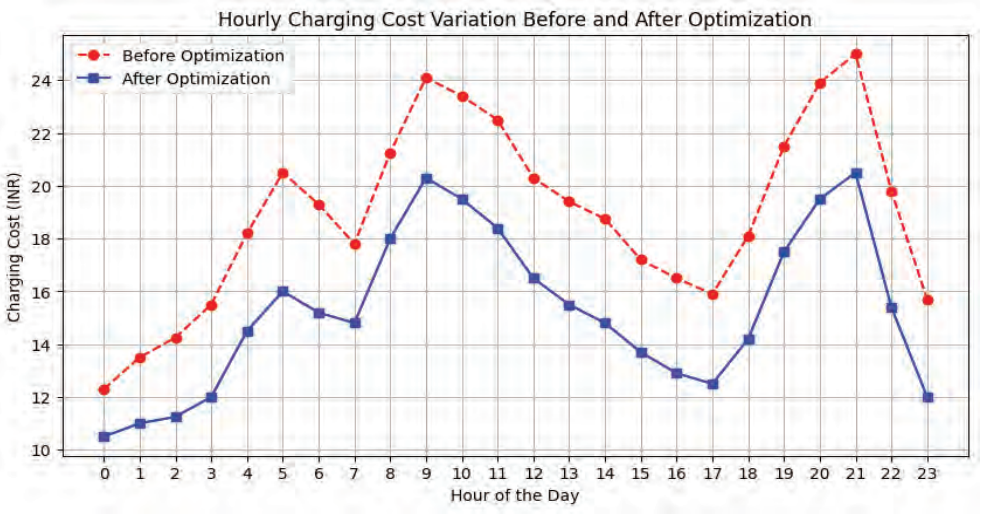


Figure 5. Hourly charging cost variation before and after optimization.

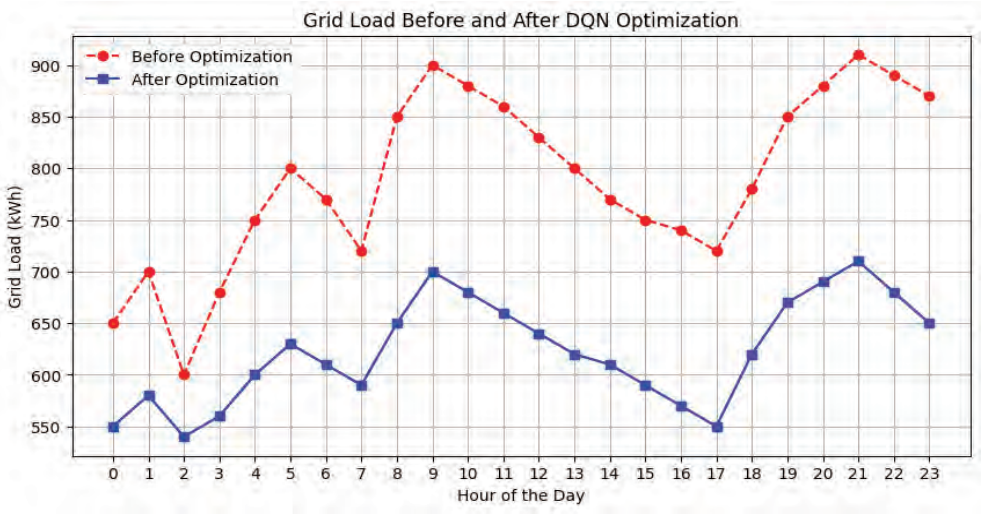


Figure 6. Grid load before and after DQN optimization.

stress while maintaining stability across a 24-hour cycle. By redistributing the charging demand, the system ensures a balanced energy load, mitigating the risk of grid overload.

Key Insights from the Figure 6 can be deducted as follows:

1. Reduction in Peak Grid Load:
- Before optimization, the highest grid load was 900 kWh at 9:00 PM. After optimization, the load at the same time reduced to 700 kWh. This leads to a reduction of about 22%.
2. Load Redistribution:
- The DQN model changed EV charging from peak hours (6:00 PM to 9:00 PM) to off the peak hours (1:00 AM to 6:00 AM). For example, the grid load at 2:00 AM increased from 600 kWh to 650 kWh. This shows that more EVs were charged during off the peak hours reducing the load on the main grid.
3. Overall Grid Load Smoothing:
- The proposed DQN model decreased changes in the grid load during the day time. This made the load more even throughout the day. A balanced grid load will improve grid reliability and reduce stress on the power system.

The real-world considerations with respect to Grid load reduction can be attended as follows:

1. Integration with Renewable Energy Sources:
- Grid load can be reduced by charging more EVs when renewable energy is available. This will increase the use of clean energy and will reduce the load on the power grid.
2. Infrastructure Constraints:
- Lower peak load will reduce the stress on the existing grid load. However, practical implementation requires smart grid technologies such as Advanced Metering Infrastructure (AMI) and demand response systems.
3. Behavioural Challenges:
- The success of load shifting depends on EV users. Time-of-Use (TOU) tariffs and off the peak hours charging incentives will encourage the users to charge at times to reduce the grid load.
4. Scalability:
- The proposed method should also work for large urban EV charging networks. Factors such as local electricity prices, renewable energy availability, and charging station capacity should be considered before implementation in large scale.

Summary of simulation results

This paper proposes the use of a Deep Q-Learning Network (DQN) model to optimize the energy management of charging infrastructure for electric vehicles (EVs) in metropolitan settings. The main objectives were to reduce stress on the system, keep billing costs down and make the most of renewable energy sources. The simulation results show the effectiveness of the proposed approach for the achievement of these objectives.

The DQN model decreased the peak grid load by 22%, and greatly eased the tension during peak hours (e.g. 6:00 pm to 9:00 pm). The charging demand is well shifted to the off-peak hours, especially between 1:00AM and 6:00AM, which results in a nice and smooth distribution of the load. This enhancement in turn improves grid stability – a critical shortcoming of conventional charging systems.

On average, charging costs were reduced by 15% thanks to the model's ability to use dynamic pricing and schedule charging during periods of low cost. Such reduction results in a better economic efficiency for the benefit of users and grid operators. Furthermore, the share of renewable energy climbed by 22% and the model adjusted the charging demand to the availability of solar and other renewable resources. Charging during the day from 8:00 AM to 2:00

PM greatly boosted the use of renewable sources of electricity, encouraging eco-friendly behaviours.

In this study, a DQN model was applied for charging of EV in metropolitan settings. The approach was designed to minimise the burden on the grid, cut the cost of charging, and boost the use of renewable energy. The results were promising. Peak demand on the grid was cut by 22%. Further charge was planned for the off-peak periods, especially from 1:00 AM to 6:00 AM. And that took the strain off the power grid. 15% off the charging price. The model decided to charge when electricity was less expensive. The utilisation of renewable energy rose 22%. More EVs were charged when solar and other renewable energy was available. The peak usage period was from 8 AM to 2 PM.

CONCLUSION

The rapid growth of electric vehicles (EVs) creates both benefits and challenges for the power grids. A large number of EVs charging at the same time can increase grid load. It can also increase electricity cost and reduce the efficient use of energy. This study proposed a Deep Q-Learning Network (DQN) for EV charging management. The proposed model schedules the charging based on conditions at the grid. It focuses on three objectives. These are reducing peak grid load, lowering charging cost, and increasing the use of renewable energy. The simulation results show that the proposed method performs well. The DQN model reduced the peak grid load by 22%. This reduces the load on the power grid. It also lowered the charging cost by 15% by selecting suitable charging periods based on electricity prices. The model also increases the consumption of renewable energy by 22%, which is achieved by charging more vehicles when renewable energy is available. Adaptability is an important feature of the proposed model. Conventional charging methods are usually based on a set of fixed rules and fixed charging schedules. The proposed DQN model learns on its own from the situations during operation. This will enable it to take decisons on charging when electricity prices, grid demand, or renewable energy generation change. This makes the system more applicable for real world EV charging scenarios. The findings of this research can serve different groups. EV manufacturers can embed intelligent charging functions into their vehicles. This can enhance charging performance and lower charging cost for users. EV users can save money without changing their daily charging needs. Grid operators can lessen peak demand and enhance grid operation. The results can also help policymakers develop schemes that encourage off-peak charging and greater use of renewable energy. Future work can further improve the proposed model. Multi-Agent Reinforcement Learning (MARL) can be used to solve charging decisions of multiple EVs. The model can be tested in real charging stations and urban EV networks. Hybrid methods that combine reinforcement learning with predictive models can be studied. This may improve the performance of the system under varying grid conditions.

AUTHORSHIP CONTRIBUTIONS

Authors equally contributed to this work.

DATA AVAILABILITY STATEMENT

The authors confirm that the data that supports the findings of this study are available within the article. Raw data that support the finding of this study are available from the corresponding author, upon reasonable request.

CONFLICT OF INTEREST

The authors declared no conflict of interest.

ETHICS

There are no ethical issues with the publication of this manuscript.

STATEMENT ON THE USE OF ARTIFICIAL INTELLIGENCE

Artificial intelligence was not used in the preparation of the article.

REFERENCES

[1] Abdul Qadir S, Ahmad F, Al-Wahedi AMAB, Iqbal A, Ali A. Navigating the complex realities of electric vehicle adoption: a comprehensive study of government strategies, policies, and incentives. Energy Strategy Rev 2024;53:101379. [CrossRef]

[2] Bahadir A. Modeling of a brushless dc motor driven electric vehicle and its PID-fuzzy control with dSPACE. Sigma J Eng Nat Sci 2023. [CrossRef]

[3] Ibrahim RA, Gaber IM, Zakzouk NE. Analysis of multidimensional impacts of electric vehicles penetration in distribution networks. Sci Rep 2024;14:27854. [CrossRef]

[4] Mastoi MS, et al. An in-depth analysis of electric vehicle charging station infrastructure, policy implications, and future trends. Energy Rep 2022;8:11504–11529. [CrossRef]

[5] Dixit AC, Prakasha KN, Harshavardhan B, Ashok BC. Evaluating the key enablers for implementing Medical 4.0 and patient-centric care technologies using grey DEMATEL method. In: Recent trends in healthcare innovation. 1st ed. London: CRC Press; 2025. p. 327–333. [CrossRef]

[6] Singh AR, et al. Electric vehicle charging technologies, infrastructure expansion, grid integration strategies, and their role in promoting sustainable e-mobility. Alex Eng J 2024;105:300–330. [CrossRef]

[7] Bulut M. Intelligent controller design for electric vehicle (EV) speed control using an inverse model based reference model learning algorithm. 2024 Jan 10. [CrossRef]
[8] Dixit AC, Ashok BC, Harshavardhan B, Mohan Krishna SA. Barriers for adoption of green hydrogen in Indian transportation sector: a fuzzy ISM approach. E3S Web Conf 2024;559:03011. [CrossRef]
[9] Sharma A, Hemanth PB, Bhavani A, Dixit AC. Green hydrogen for a sustainable future: prospects and challenges for energy-based applications in major Indian states by 2030. E3S Web Conf 2023;405:02027. [CrossRef]
[10] Tonbul E. Modeling open vehicle routing problem with real life costs and solving via hybrid civilized genetic algorithm. Sigma J Eng Nat Sci 2024:714–733. [CrossRef]
[11] Shanmugam PK, Thomas P. Optimization strategies for electric vehicle charging and routing: a comprehensive review. Gazi Univ J Sci 2024;37:1256–1285. [CrossRef]
[12] Yong JY, Tan WS, Khorasany M, Razzaghi R. Electric vehicles destination charging: an overview of charging tariffs, business models and coordination strategies. Renew Sustain Energy Rev 2023;184:113534. [CrossRef]
[13] Ohanu CP, Rufai SA, Oluchi UC. A comprehensive review of recent developments in smart grid through renewable energy resources integration. Heliyon 2024;10. [CrossRef]
[14] Mousa A. Extended-deep Q-network: a functional reinforcement learning-based energy management strategy for plug-in hybrid electric vehicles. Eng Sci Technol Int J 2023;43:101434. [CrossRef]
[15] Stavrev S, Ginchev D. Reinforcement learning techniques in optimizing energy systems. Electronics (Basel) 2024;13:1459. [CrossRef]
[16] Dixit AC, Achutha MV, Sridhara BK. Elastic properties of aluminum boron carbide metal matrix composites. Mater Today Proc 2020. [CrossRef]
[17] Gultekin Y. Acoustic emission reduction in vehicles by using MPP structures in wheel ARCH liner structures. Sigma J Eng Nat Sci 2024:1749–1755. [CrossRef]
[18] Zhou Q, Du C. A quantitative analysis of model predictive control as energy management strategy for hybrid electric vehicles: a review. Energy Rep 2021;7:6733–6755. [CrossRef]
[19] Dixit AC, Harshavardhan B, Prakasha KN. A game theory approach to optimizing electric vehicle charging infrastructure in urban areas. E3S Web Conf 2025;619:01004. [CrossRef]
[20] Akter A, et al. A review on microgrid optimization with meta-heuristic techniques: scopes, trends and recommendation. Energy Strategy Rev 2024;51:101298. [CrossRef]
[21] Tian S, et al. An optimization strategy for EV-integrated microgrids considering peer-to-peer transactions. Sustainability (Basel) 2024;16:8955. [CrossRef]
[22] Nakabi TA, Toivanen P. Deep reinforcement learning for energy management in a microgrid with flexible demand. Sustain Energy Grids Netw 2021;25:100413. [CrossRef]
[23] Dixit AC, Harshavardhan B, Ashok BC, Prakasha KN, Mohan Krishna SA, et al. Innovative pedagogical approaches for diverse learning styles and student-centric learning. J Eng Educ Transform 2024;37:178–188. [CrossRef]
[24] Liu X, et al. A multi-step predictive deep reinforcement learning algorithm for HVAC control systems in smart buildings. Energy 2022;259:124857. [CrossRef]
[25] Zhang Q, Yan J, Gao HO, You F. A systematic review on power systems planning and operations management with grid integration of transportation electrification at scale. Adv Appl Energy 2023;11:100147. [CrossRef]
[26] Zhang L, Sun C, Cai G, Koh LH. Charging and discharging optimization strategy for electric vehicles considering elasticity demand response. eTransportation 2023;18:100262. [CrossRef]
[27] Dixit AC, et al. Barriers to integrating AI in curriculum for enhanced engineering education: a fuzzy ISM approach. J Eng Educ Transform 2025;38:137–147. [CrossRef]
[28] Kumar KS. Emerging trends and global challenges to predict drop in thermal performance of WTG gearbox. J Therm Eng 2024:657–669. [CrossRef]
[29] Kumar KS, Muniamuthu S, Tharanisrisakthi BT. An investigation to estimate the maximum yielding capability of power for mini Venturi wind turbine. Ecol Eng Environ Technol 2022;23:72–78. [CrossRef]
[30] Kumar KS, Palanisamy R, Aravindh S, Mohan GS. Design and analysis of windmill blades for domestic applications.
[31] Sunil Kumar K, Kamalakar V, Palani S, Muniamuthu S, Belinda CM. Design of K-type propeller optimized with lightweight aluminum material and its CFD analysis for marine-based applications. In: Singh A, Mishra DP, Bhat G, editors. Recent trends in thermal and fluid sciences. Singapore: Springer Nature; 2024. p. 375–390. [CrossRef]
[32] Raghavendrakumar E, Kamalakar V, Kumar KS. An investigation in temperature data analysis of middle atmospheric variation from SABER satellite. Nat Environ Pollut Technol 2024;23:443–450. [CrossRef]
[33] Qiu D, Wang Y, Hua W, Strbac G. Reinforcement learning for electric vehicle applications in power systems: a critical review. Renew Sustain Energy Rev 2023;173:113052. [CrossRef]

[34] Bharadwaj GV, Ashok DBC, Jayashankar N, Dixit AC. An experimental investigation and performance assessment of a solar water purifier. Int J Mech Prod Eng Res Dev 2019;9:12.

[35] Ming F, Gao F, Liu K, Li X. A constrained DRL-based bi-level coordinated method for large-scale EVs charging. Appl Energy 2023;331:120381. [CrossRef]

[36] Chifu VR, Cioara T, Pop CB, Rusu HG, Anghel I. Deep Q-learning-based smart scheduling of EVs for demand response in smart grids. Appl Sci (Basel) 2024;14:1421. [CrossRef]

Sigma Journal of Engineering and Natural Sciences
Web page info: https://sigma.yildiz.edu.tr
DOI: 10.14744/sigma.2025.00144

Research Article

Pre-fabrication analysis using ansys in dental implants for enhancing mechanical stability and clinical success

Naveen ANKEGOWDA[1,*], Rakshith GOWDA D. S.[1], Nithyananda B. S.[1]

[1]*Department of Mechanical Engineering, Vidyavardhaka College of Engineering, Karanataka, 570002, India*

ARTICLE INFO

Article history
Received: 04 January 2025
Revised 19 February 2025
Accepted: 31 May 2025

Keywords:
Dental Implant; Factor of Safety; Finite Element Analysis; Modal Analysis; Static Structural Analysis

ABSTRACT

There has been a wider scope for the development of dental implants with high bioactivity and low toxicity. The current study strives to address the issue by designing a dental implant with a pathway to inject the bioactive agent. The safety and reliability of the proposed design are tested for different materials using a finite element approach. Modeling of the implant is done in SOLIDWORKS®. To perform engineering analysis, ANSYS Workbench 2023 R1® software is used. The reliability and safety of the design are tested with three implant materials, including Titanium Grade 5 (Ti 6Al 4V), (y–tzp), and HGC-1-C. Static structural analysis is carried out to investigate the Von Mises stress, maximum principal strain, total deformation, and factor of safety. Modal analysis results show that the Ti-6Al-4V exhibits the highest natural frequency for the proposed design. The Ti-6Al-4V model shows a remarkable alloy composition and demonstrated minimal total deformation. From the analysis of these results, we deduce that the design is indeed safe. The fabrication is conducted with an emphasis on ensuring a secure design.

Cite this article as: Ankegowda N, Gowda DSR, Nithyananda BS. Pre-fabrication analysis using ansys in dental implants for enhancing mechanical stability and clinical success. Sigma J Eng Nat Sci 2026;44(4):2617–2625.

INTRODUCTION

Bioactive materials for dental implants are specially designed to interact positively with biological tissues, promoting integration, healing, and sometimes even regenerative effects at the implant site. Bioactive materials play a significant role in enhancing the performance and longevity of dental implants. These materials are designed to promote osseointegration, reduce infection risks, and support tissue regeneration [1-3]. These materials are crucial in dental implantology for achieving both mechanical stability and a biological bond with the surrounding bone and soft tissue. Chewing is a multidimensional biomechanical process that engages various structural systems, including geometrical factors of bones, muscles, joints, and teeth. This process entails the movement of the jaw when food is present in the mouth, triggering the chewing cycle [4]. Titanium alloy is the most used as an implant material in ortho and dentistry and which also hold good for cranial restoration [5-7]. Beside Titanium, Zirconium based dental implants gaining attention because of their anti-corrosion

*Corresponding author.
*E-mail address: naveen@vvce.ac.in

This paper was recommended for publication in revised form by Editor-in-Chief Ahmet Selim Dalkilic

Published by Yıldız Technical University Press, İstanbul, Turkey
© Author. This is an open access article under the CC BY-NC license (http://creativecommons.org/licenses/by-nc/4.0/).

behaviour which is further improved by having calcium phosphate and hydroxyapatite coatings which augment osteogenic potential at the defect sites [8]. Ahmed M. Abdelrhman et al. investigated the mechanical behaviour of 3D-printed polylactic acid (PLA) as an alternative to titanium dental implants, which results in moderate compressive and tensile strength. Finite element results show the elevated stress concentration, which leads to limited ability to withstand in vivo conditions [9]. It is also necessary to consider the compatibility of dental implants with bioactive material to avoid the adverse biological reactions. Ahmed Binobaid et al. developed a novel bioactive material, which is a mixture of calcium silicate and zirconia, to enhance the bioactivity that leads to bone bonding and elasticity, and they demonstrated a favourable improvement in resisting mechanical load during oral activities [10]. Hydroxyapatite (HAp) nano particles are the recent advancements in the bioactive material which provides antimicrobial functionality with Zirconia implants and accelerate the enamel mineralization with titanium alloy implant which is crucial in avoiding the dental cavities [11]. Komal Gupta et.al study gave insights on the Hydroxyapatite coating on the dental implants, and which enhances the interfacial bonding between bone and jaws. Toxicity and inflammations are the major worries in the dental implants which are effectively addressed by coating the HAp on implants [12]. The Surface modification of the implant is necessary to ensure the durability of the implant. In view of this Ravinder S. Saini et.al utilized the polyetherketoneketone to modify the surface of the implant as it possesses high stiffness and can accommodate natural movements [13]. Nano structured materials are incorporated into the dental composites which offers good strength and improves aesthetics. Bioactive glasses are extensively used as a biomaterial in oral implants which helps in repair of damaged dentin [14]. Consequently, dental implants endure a significant number of stress cycles over their functional lifespan. This induces structural instability and mechanical degradation of the material, diminishing its resistance and exposing it susceptible to microcrack initiation, ultimately leading to fracture propagation [15]. Fatigue behaviour is one the important factor to study. Chewing is loading conditions until food in mouth. Load acting on tooth surface is not homogeneous or uniform [16]. This process also contributes to fatigue, but this can be addressed during structural analysis using analysis software like ANSYS which is based on finite element analysis for optimal implant design [17-19]. Zhe Zhou et.al conducted a FE study to simulate the stress and stain around the carbon fibre reinforced PEEK dental implants and found that the bone tissue tends to be more stressed by oblique force than by axial load [20]. Chih-Ling Chang et al. investigated the stability of the bones of three different qualities using FEA and showed that the stress increases while the Young's modulus decreases [21]. In their investigation of the stress distribution between dental implants and alveolar bone, Yen-Wen Shen et. al [22] found that while the stress levels in both cortical and cancellous bone showed relatively small fluctuations, larger abutment screw diameters resulted in higher stress levels on the screws. Nazrah Maher et al. provide insight on the carbon-based coatings on the dental implants, which improve osseointegration but still lag in antibacterial properties [23]. Cheng Zhang et. al clinically investigated the effect of bioactive agent on osseointegration. Controlled release of bioactive agent is necessary to have high bioactivity and low toxicity which require the modification in the design of the dental implant. Controlled release of bioactive agents is necessary to have high bioactivity and low toxicity, which requires modification in the design of the dental implant [24]. Fu-Yuan Teng et. al developed the Ti-alloy based dental implant with interconnected channel structure to inject BMP-2 bioactive agent using 3D printing which results in better osteogenesis [25]. Cristina Falcinelli et al.'s study shows that understanding the dentistry and consideration of the entire geometry of the jawbone is important to investigate the long-term stability of a dental implant without an internal channel under oblique and compressive force [26]. The engineering study of a dental implant model in ANSYS entails a sequence of simulations to assess the mechanical performance and biological compatibility of the implant under diverse physiological situations. This analysis is essential for refining the implant's design, material selection, and surface properties to guarantee stability, longevity, and biocompatibility prior to production [27]. The material properties, such as Young's modulus and yield strength, significantly affect stress distribution and fatigue behaviour under masticatory forces. Alongside its longevity, restorative capabilities, and enhancement of dental aesthetics, contemporary science has facilitated continuous advancement by using emerging technologies that have transformed the profession of dentistry. Emam et al. developed the titanium dental implant with cell signalling pathways to enhance osseointegration and showed that the advances in Omic technology make the implant technology still challenging [28]. While designing the dental implant, damping layer consideration poses an important step to address the stress under cyclic load [29]. The current study strives to address the issue by designing a dental implant with a pathway to inject the bioactive agent. The safety and reliability of the proposed design are tested for different materials using finite element approach. The current work has the potential scope in clinical research of dentistry.

MATERIALS AND METHODS

The present work starts with the design of dental implant referring to the geometrical parameter provided in the Internal Hex brochure of Adin company [30]. 3D modelling of the implant is created in SOLID WORKS including the screw threads, surface texture, and other geometric features [19]. Followed by the finite element analysis using ANSYS Workbench 2023 R1® software for the three different materials of the dental implant [19]. Static structural and modal evaluations are performed by applying appropriate boundary condition to assess the performance and stability of the implant design.

Modelling of Dental Implant

A 3D model of a dental implant is developed using CATIA V5 in accordance with the. the geometrical specifications provided in Internal Hex brochure as shown in Table 1 [31-34]. The skeleton model and 3D model of the implant with internal passage is shown in Figure 1 and Figure 2 respectively.

Table 1. Geometrical specifications

Description	Detail
Length, L	16 mm
Diameter, D	4.05 mm
Implant Diameter, ø	5 mm
Pathway inlet and outlet diameters	0.2 mm
Chamfer parameters	0.25mm, 45°
Type of thread	V – Thread
Pitch	0.80 mm
Revolutions	16
Start Angle	180°
Direction	Clockwise
Taper Helix Angle	1.25°

Finite Element Analysis

The dentistry materials considered for the analysis are Titanium Grade 5 (Ti 6Al 4V), Yttrium Stabilized Tetragonal Zirconia (Y-TZP), and HGC-1-C depicted in Table 2 along with their respective properties.

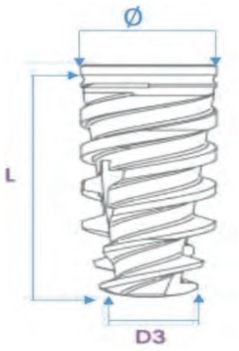


Figure 1. Skeleton of the dental implant.

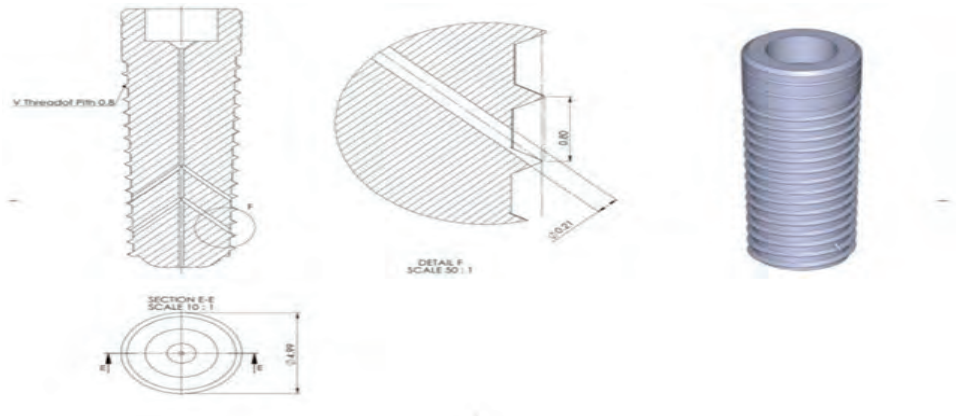


Figure 2. Draft and 3D model of the dental implant with internal passage.

Table 2. Mechanical properties of the material under consideration for the dental implant

Property	Ti-6Al-4V	Y – TZP	HGC-1-C Precious Alloy
Density	4.43 g/cm^3	6.050 g/cm^3	18.6 g/cm^3
Young's Modulus	113.8 GPa	110 GPa	130 MPa
Bulk Modulus	1.2 x 105 MPa	120.04 GPa	135 MPa
Shear Modulus	4.23 x 105 MPa	42.399 GPa	480 MPa
Tensile Yield Strength	880 MPa	880 MPa	300 MPa
Tensile Ultimate Strength	950 MPa	950 MPa	450 MPa
Compressive Yield Strength	970 MPa	970 MPa	480 MPa
Compressive Ultimate Strength	1455 MPa	1455 MPA	720 MPa
Co-efficient of Thermal Expansion	8.6 x 10^{-6} / K	8.6 x 10^{-6} /K	1.48 x 10^{-5} /K
Poisson's Ratio	0.342	0.324	0.34

The engineering study of the dental implant model is conducted utilizing ANSYS Workbench 2023 R1 software. The model is discretised using triangular and quadrilateral elements using the Hex Dominant Method and the details are mentioned in Table 3 [35]. To improve the precision, triangular elements are used to mesh the threads and quadrilateral elements to mesh the top cavity and the region surrounding the pathway hole. The quadratic order of the element was employed. The discretised model of the implant is shown in in Figure 3.

Table 3. Meshing details

Physics Preference	Meshing details
Element Order	Quadratic
Method	Hex Dominant
Type of Elements	Quad/Tri
Number of Nodes	47,303
Number of Elements	24,782

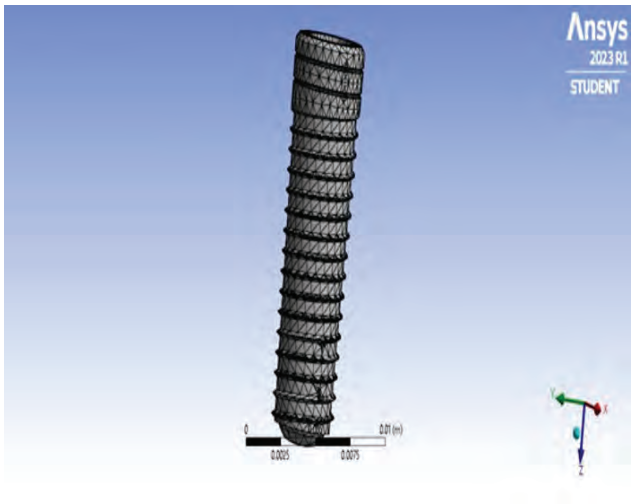


Figure 3. Discretised model of the dental implant.

According to the anatomy of the tooth, the boundary conditions were placed in the bone zone restricting the six degrees of freedom including displacements in Ux, Uy, and Uz and rotations in Rx, Ry, and Rz as shown in Figure 4. Diverse forces were exerted on the model, analogous to the conditions within the real oral cavity. A compressive load of 100 N applied in the longitudinal direction [36], 18N in the lingual direction [37] and 24N in the mesiodistal direction [38, 39] as shown in Figure 5 (a) (b) (c) (d) and (e).

Static Structural Analysis

A static structural analysis is carried out to assesses the impact of the applied static loads on a implant structure. The stress, strain, and deformation of the implant structure is tabulated under the given loading condition. This facilitates the identification of vulnerable regions with insufficient strength and durability during the design phase, hence preventing costly failures. The model is equipped with fixed support at the base, excluding the threads on its body as shown in Figure 6.

Modal Analysis

The modal analysis is carried out to record the natural frequency of the design with three different materials mentioned in Table 4.

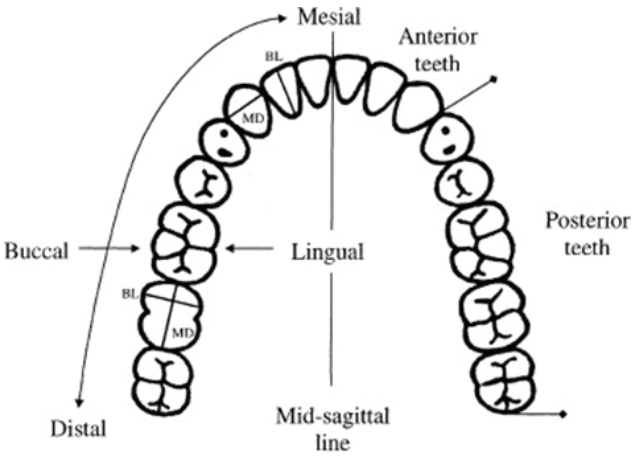
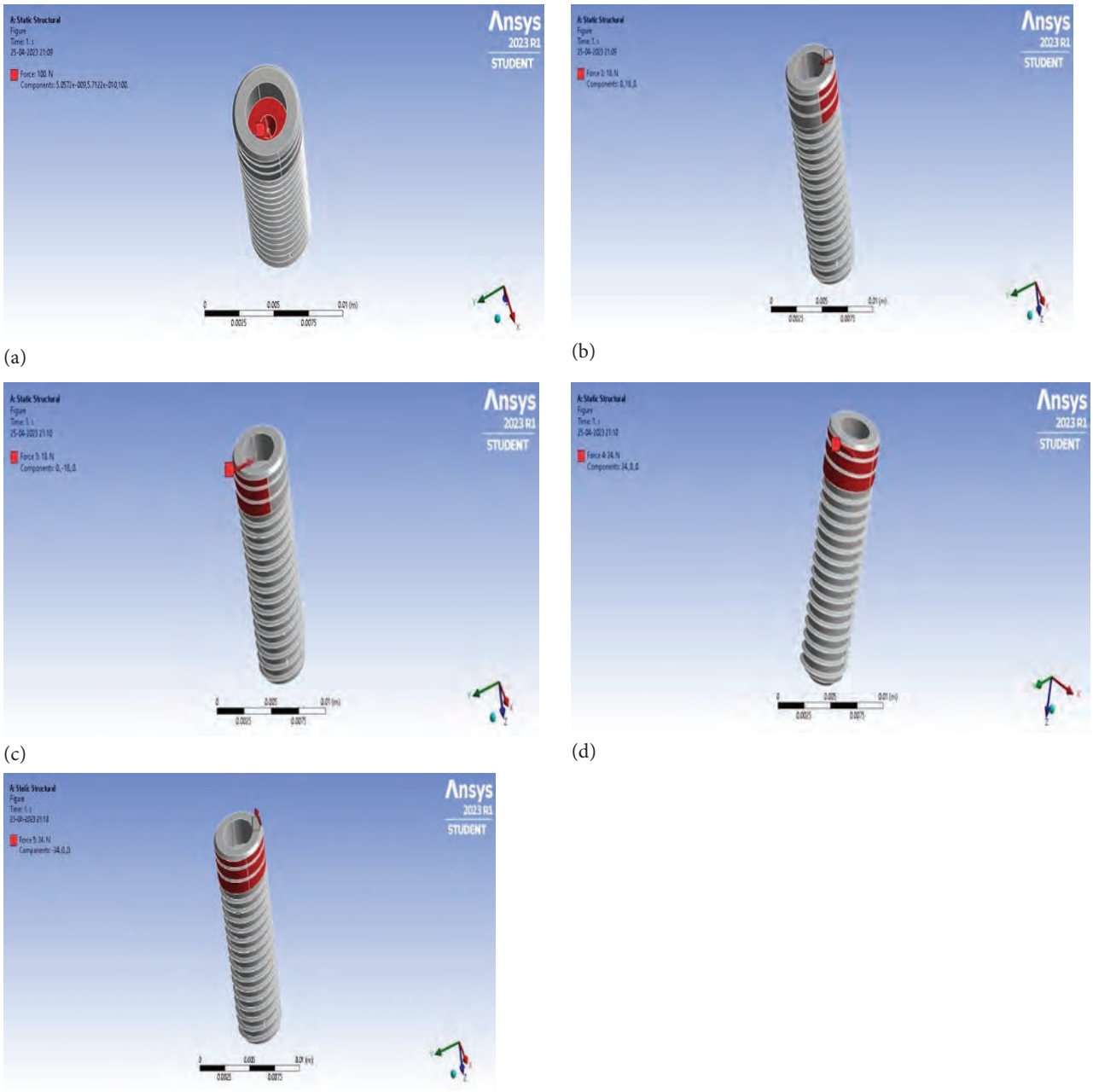


Figure 4. Anatomy of the tooth.

Table 4. Natural frequencies

Modes	Ti-6Al-4V - Frequency in Hz	Y-TZP - Frequency in Hz	HGC-1-C - Frequency in Hz
1	196170	228180	3532.9
2	201150	233930	3317.9
3	225840	262760	3725.5
4	228580	265930	3770.5
5	263270	308510	4345.7
6	397320	462270	6563.2



(a) (b) (c) (d) (e)

Figure 5. Application of longitudinal compressive load of 100 N, Load of 18N in the lingual direction 1, Load of 18N in the lingual direction 2, Load of 24N in the mesiodistal direction 1, Load of 24N in the mesiodistal direction 2 in (a),(b), (c),(d) and (e).

RESULTS AND DISCUSSION

Static Structural Analysis

The model's Von Mises Stress, Maximum Principal Strain, Total Deformation, and Safety Factor were all resolved for all the three materials. The von Mises stress determine whether a material will yield or fail under complex loading conditions where a material experiences multi-axial stress. If it crosses yield stress, then it starts deforming permanently. It was found that the von Mises stress of Ti-6Al-4V is 22.057 MPa, Y-TZP is 21.032 MPa and HGC is 21.958 MPa. Implant design with Ti-6Al-4V alloy perform better under chewing forces, which are complex and multidirectional. The behaviour of the implant design under Von Mises stress is shown in Figure 7 (a), (b) and (c).

Maximum Principal Strain is the maximum normal strain that a material experiences under a particular load

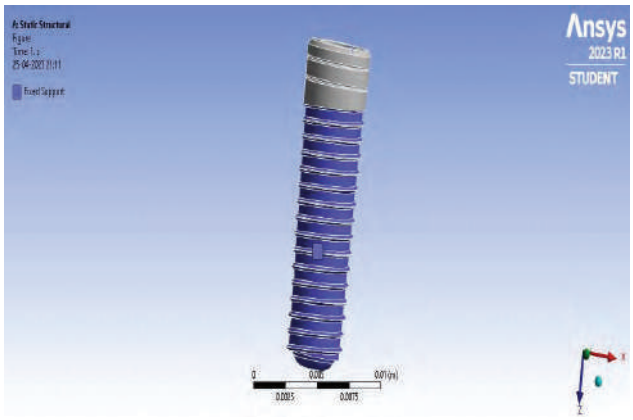
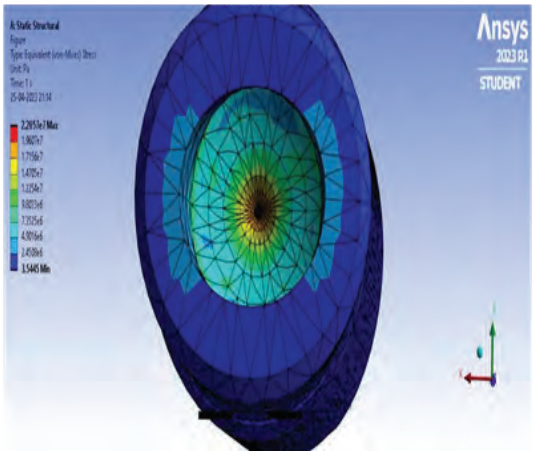


Figure 6. Static structural analysis of the dental implant.

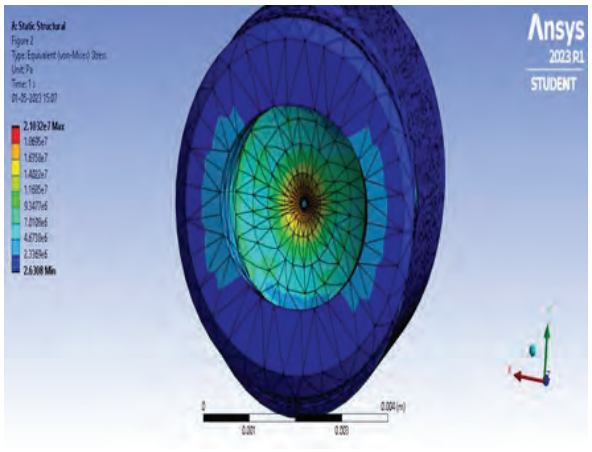
in a particular direction. Analysis of this strain is observed to be 0.000122 strain for Ti-6Al-4V, while material Y-TZP determined of 0.05857 and HGC-1-C Precious Alloy had a value of 0.10627. Ti-6Al-4V exhibit the smallest strain, likely indicating the least deformation and possibly the safest option under normal loading. Implant with different materials under strain is shown in Figure 8 (a), (b) and (c).

Regardless of the coordinate system being employed, total deformation (TD) is the square root of the sum of squared stretching and squared shearing deformations. In Ti-6Al-4V, the total deformation is 0.00022 mm, Y-TZP is 0.00012 mm, and the HGC-1-C precious alloy exhibit deformation of 0.19664 mm. The total deformation observed in the implant is shown in Figure 9 (a), (b) and (c).

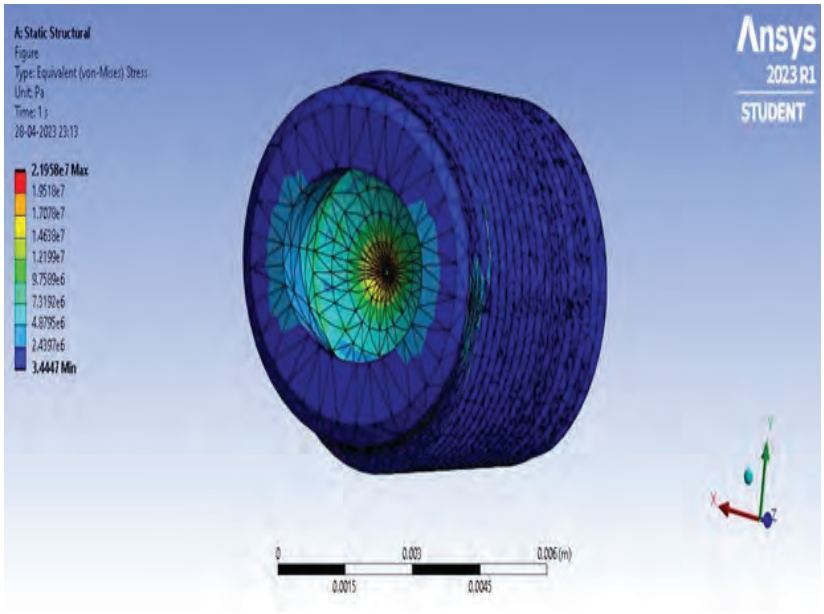
The factor of safety decides the reliability of a design. In Ti-6Al-4V and Y-TZP, the factor of safety is found to be 15,



(a)

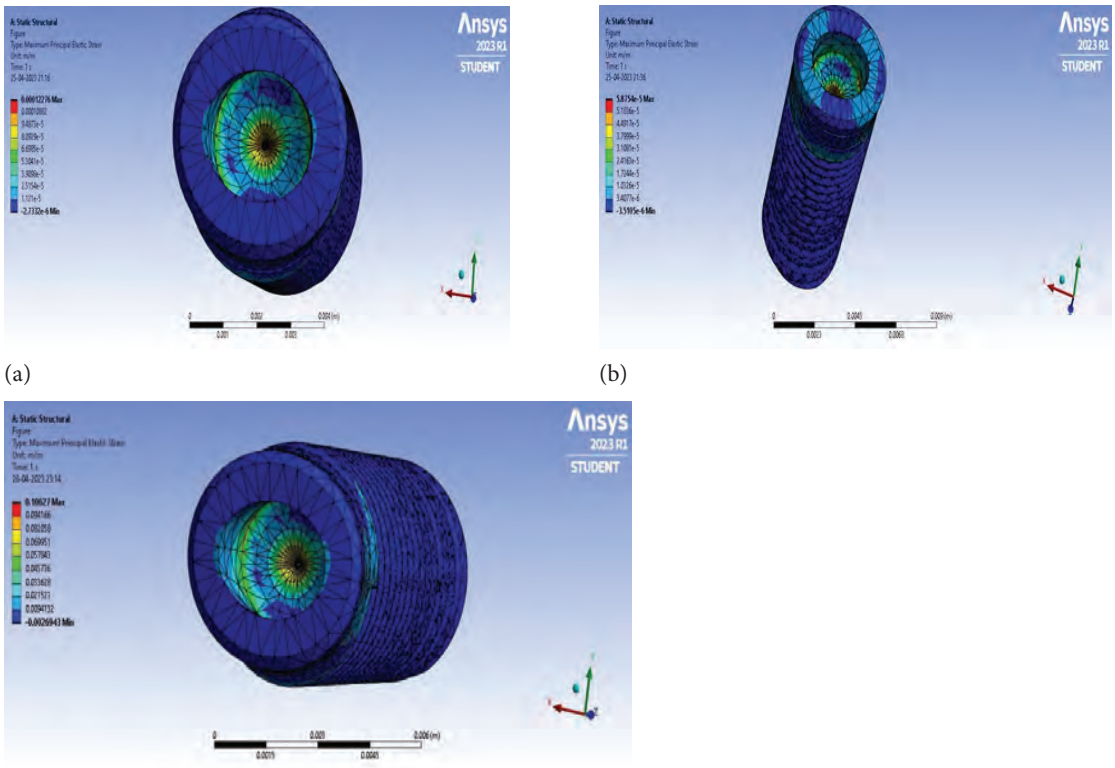


(b)



(c)

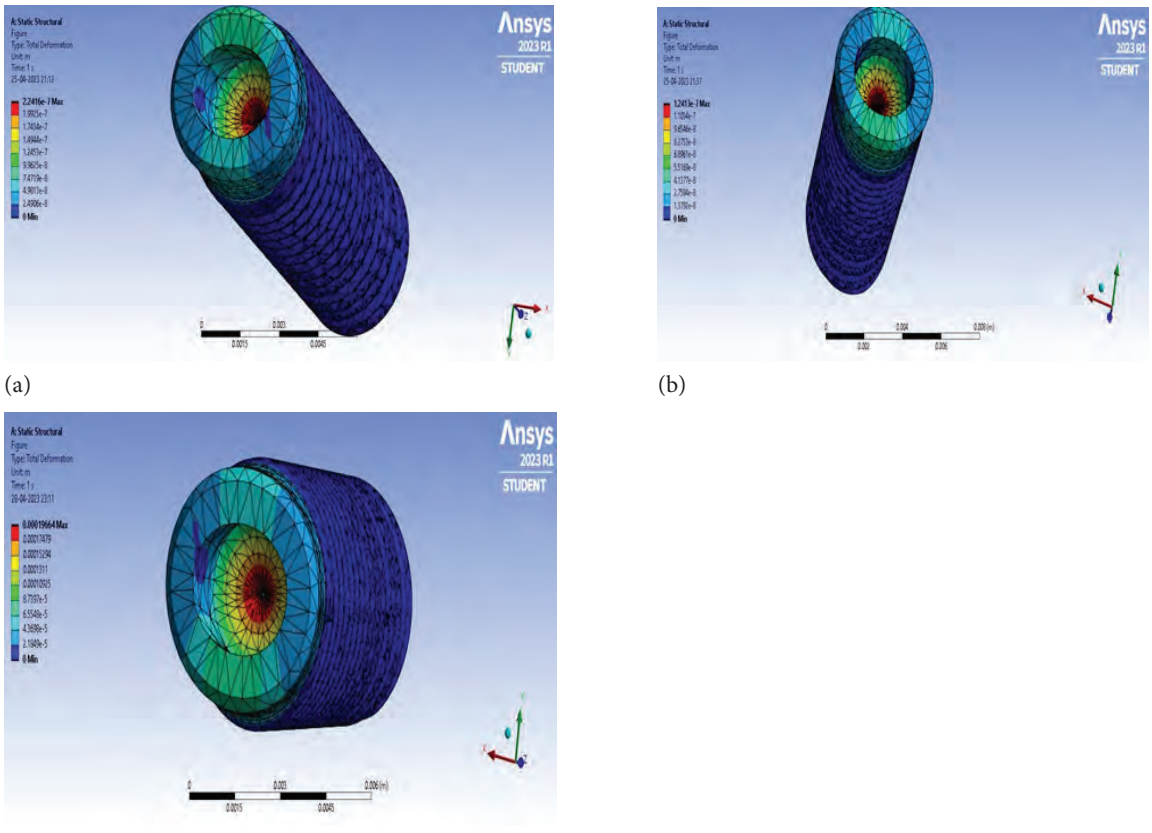
Figure 7. Implant design under Von Mises stress of Ti-6Al-4V, Y-TZP and HGC – 1 – C Precious Alloy in (a), (b) and (c).



(a) (b)

(c)

Figure 8. Implant under maximum principal strain of Ti-6Al-4V, Y-TZP and HGC – 1 – C Precious Alloy in (a), (b) and (c).



(a) (b)

(c)

Figure 9. Implant design under Total deformation of Ti-6Al-4V, Y-TZP and HGC – 1 – C Precious Alloy in (a), (b) and (c).

Table 5. Results of the static structural analysis

Results	Ti-6Al-4V	Y-TZP	HGC-1-C
Von Mises Stress (in MPa)	22.057	21.032	21.958
Maximum Principal Strain	0.000122	0.05857	0.10627
Total Deformation (in mm)	0.00022	0.00012	0.19664
Factor of Safety	15	15	13.66

while in HGC-1-C it is 13. 66. Overall output of the static structural analysis are tabulated in Table 5.

CONCLUSION

The design has been determined to be safe for all three materials: Ti-6Al-4V, Y-TZP, and HGC-1-C precious alloy. The von Mises stress values for all three material models remain significantly below the endurance limit. In a comparative analysis, the Von Mises stress exhibited its highest value in the Ti-6Al-4V model and its lowest in the Y-TZP model. Conversely, the Maximum Principal Strain reached its peak in the HGC-1-C Precious Alloy model, while it was minimal in the Ti-6Al-4V model. The highest total deformation was observed in HGC-1-C. The Ti-6Al-4V model exhibited a remarkable alloy composition and demonstrated minimal total deformation. From the analysis of these results, we can deduce that the design is indeed safe. The fabrication is conducted with an emphasis on ensuring a secure design

AUTHORSHIP CONTRIBUTIONS

Authors equally contributed to this work.

DATA AVAILABILITY STATEMENT

The authors confirm that the data that supports the findings of this study are available within the article. Raw data that support the finding of this study are available from the corresponding author, upon reasonable request.

CONFLICT OF INTEREST

The authors declared no conflict of interest.

ETHICS

There are no ethical issues with the publication of this manuscript.

STATEMENT ON THE USE OF ARTIFICIAL INTELLIGENCE

Artificial intelligence was not used in the preparation of the article.

REFERENCES

[1] Patil SG, Rao R, Sanketh DS, Sarode S. A universal diagnostic criterion for oral lichen planus: an exigency. Int J Contemp Dent Med Rev 2014.

[2] Boehm MW, Yakubov G, Stokes JR, Baier SK. The role of saliva in oral processing: reconsidering the breakdown path paradigm. J Texture Stud 2020;51:67–77. [CrossRef]

[3] El-Gammal MY. Biological reactions to different dental implant surface treatments. Int J Contemp Dent 2016.

[4] Parra Reyes D. Systematic review of the literature on the evaluation of the chewing process. Arete 2021;20:39–47.

[5] Nicholson JW. Titanium alloys for dental implants: a review. Prosthesis 2020;2:100–116. [CrossRef]

[6] Jiang X, Yao Y, Han D, Tang W. Design of dental implants at materials level: an overview. J Biomed Mater Res A 2020;108:1634–1661. [CrossRef]

[7] Moiduddin K, Mian SH, Umer U, Alkhalefah H. Fabrication and analysis of a Ti6Al4V implant for cranial restoration. Appl Sci 2019;9:2513. [CrossRef]

[8] Chopra D, Jayasree A, Guo T, Gulati K, Ivanovski S. Advancing dental implants: bioactive and therapeutic modifications of zirconia. Bioact Mater 2022;13:161–178. [CrossRef]

[9] Abdelrhman AM, Sabea M, Ahmad I, Gaaliche N, Ali YH. Mechanical properties and suitability of PLA for 3D-printed dental implants: experimental and simulation analysis. Results Mater 2025;26:100713. [CrossRef]

[10] Binobaid A, De Lisi M, Camilleri J, Hassanin H, Essa K. Zirconia-calcium silicate bioactive composites for dental applications using DLP additive manufacturing. Bioprinting 2025;45. [CrossRef]

[11] Islam MA, Hossain N, Hossain S, Khan F, Hossain S, Rahman Arup M, et al. Advances of hydroxyapatite nanoparticles in dental implant applications. Int Dent J 2025. ISSN 0020-6539. [CrossRef]

[12] Gupta K, Kaushik N, Sharma V. Innovations in hydroxyapatite: advancing sustainable and multifunctional dental implants. Odontology 2025. [CrossRef]

[13] Saini RS, Binduhayyim RIH, Kuruniyan MS. DFT-based investigation of polyetherketoneketone materials for surface modification for dental implants. Eur J Med Res 2024;29:436. [CrossRef]

[14] Suhag D. Dental biomaterials. In: Handbook of biomaterials for medical applications. Vol. 2. Singapore: Springer; 2024. [CrossRef]
[15] Ayllón JM, Navarro C, Vázquez J, Domínguez J. Fatigue life estimation in dental implants. Eng Fract Mech 2014;123:34–43. [CrossRef]
[16] Santin M, Phillips GJ. Biomimetic, bioresponsive, and bioactive materials: an introduction to integrating materials with tissues. UK: Wiley; 2012. [CrossRef]
[17] Kayabaşı O, Yüzbasıoğlu E, Erzincanlı F. Static, dynamic and fatigue behaviors of dental implant using finite element method. Adv Eng Softw 2006;37:649–658. [CrossRef]
[18] Martinez-Mondrago M. Biomechanical fatigue behavior of a dental implant due to chewing forces: a finite element analysis. Materials (Basel) 2024;17:1669. [CrossRef]
[19] Ishak MI. Comparative finite element analysis of regular and topologically optimised dental implants for mechanical and fatigue responses evaluation. IIUM Eng J 2023;24:286–300. [CrossRef]
[20] Zhou Z, Shi R, Wang J, Han X, Gao W, Jiao J, et al. Finite element analysis of carbon fiber reinforced polyetheretherketone dental implants. J Stomatol 2024;125:101902. [CrossRef]
[21] Chang CL, Chen JJ, Chen CS. Using optimization approach to design dental implant in three types of bone quality - a finite element analysis. J Dent Sci 2025;20:126–136. [CrossRef]
[22] Shen YW, Huanga HL, Hsu JT, Fuh LJ. Effects of diameters of implant and abutment screw on stress distribution: a 3D finite element analysis. J Dent Sci 2024;19:1126–1134. [CrossRef]
[23] Maher N, Mahmood A, Fareed MA, Kumar N, Rokaya D, Zafar MS. Carbon-based bioactive coatings for dental implant applications: an updated review. J Adv Res 2024. ISSN 2090-1232. [CrossRef]
[24] Zhang C, Zhang T, Geng T, Wang X, Lin K, Wang P. Dental implants loaded with bioactive agents promote osseointegration in osteoporosis: a review. Front Bioeng Biotechnol 2021;9:591796. [CrossRef]
[25] Teng FY, Tai IC, Hob ML, Wang JW, Weng LW, Wang YJ, et al. Controlled release of BMP-2 from titanium with electrodeposition modification. Mater Sci Eng C Mater Biol Appl 2019;105:1098. [CrossRef]
[26] Falcinelli C, Valente F, Vasta M, Traini T. Finite element analysis in implant dentistry: state of the art and future directions. Dent Mater 2023:539–556. [CrossRef]
[27] Trindade R, Albrektsso T, Tengvall P, Wennerberg A. Foreign body reaction to biomaterials: mechanisms for buildup and breakdown of osseointegration. Clin Implant Dent Relat Res 2016;18:192–203. [CrossRef]
[28] Emam SM, Moussa N. Signaling pathways of dental implants' osseointegration: NF-κB and Wnt pathways. BDJ Open 2024;10:29. [CrossRef]
[29] Ahmadian MT. The dynamic analysis of a novel dental implant with a viscoelastic internal damping layer. In: 17th Iranian Conference of Biomedical Engineering (ICBME); 2010. p. 1–4. [CrossRef]
[30] Smith DC. Dental implants: materials and design considerations. Int J Prosthodont 1993;6:106–117.
[31] Oswal MM, Amasi UN, Oswal MS, Bhagat AS. Influence of three different implant thread designs on stress distribution: a 3D finite element analysis. J Indian Prosthodont Soc 2016;16:359–365. [CrossRef]
[32] Eraslan O, Inan O. The effect of thread design on stress distribution in a solid screw implant: a 3D finite element analysis. Clin Oral Investig 2010;14:411–416. [CrossRef]
[33] Lan TH, Du JK, Pan CY, Lee HE, Chung WH. Biomechanical analysis of alveolar bone stress around implants with different thread designs. Clin Oral Investig 2012;16:363–369. [CrossRef]
[34] Tada S, Stegaroiu R, Kitamura E, Miyakawa O. Influence of implant design and bone quality on stress/strain distribution in bone around implants: a 3D finite element analysis. Int J Oral Maxillofac Implants 2003;18:357–368.
[35] Srivastava R, Bansal R, Dubey PK, Singh D. A comparative evaluation of masticatory load distribution in different prostheses with varying implants: a FEM analysis. J Oral Biol Craniofac Res 2024;14:284–289. [CrossRef]
[36] Geramizadeh M. Finite element analysis of dental implants with and without microthreads under static and dynamic loading. J Long Term Eff Med Implants 2017:020007. [CrossRef]
[37] Tong H, Kwon D, Shi J, Sakai N, Enciso R, Sameshima GT. [Orthodontic biomechanics reference]. Am J Orthod Dentofacial Orthop 2012;141:604–617. [CrossRef]
[38] Prakash P, Narayanan A. Biomechanics in dental implants. Innovative Publication 2021. ISSN 2581-4796.
[39] Andrade GS, Kalman L, Lo Giudice R, Adolfi D, Feilzer AJ, Tribst JPM. Biomechanics of implant-supported restorations. Braz Dent Sci 2023;26:3637. [CrossRef]

Sigma Journal of Engineering and Natural Sciences
Web page info: https://sigma.yildiz.edu.tr
DOI: 10.14744/sigma.2026.2119

Research Article

Evaluating the performance of Iterated Greedy methods for the distributed permutation flowshop with sequence-independent setup times

Clarissa TARARAM de LAURENTYS[1], Marcelo Seido NAGANO[1,*], Fernando Luis ROSSİ[2]

[1]*Department of Production Engineering, University of São Paulo, São Paulo, 05508-010, Brazil*
[2]*Department of Management, Federal Institute of São Paulo, São Paulo, 01109-010, Brazil*

ARTICLE INFO

Article history
Received: 14 January 2025
Revised 22 March 2025
Accepted: 31 May 2025

Keywords:
Distributed Flowshop Scheduling; Iterated Greedy; Makespan; Sequence-Independent Setup Time

ABSTRACT

Given the strategic needs of meeting demand and minimizing production costs to remain competitive, companies have invested in more than one plant in different geographical spaces. Therefore, in addition to scheduling, organizations also deal with the designation of which factory will produce certain products. In more recent studies, the integration of distribution and scheduling has mostly driven the advancement of strategies to improve the overall performance of factory operations. The research addresses the distributed flowshop scheduling problem under sequence-independent setup times, a constraint that has not been widely studied in the literature. Sixteen Iterated Greedy methods were developed, combining multiple initialization, destruction, and reconstruction approaches, which makes it a comprehensive analysis of IG performance for this problem. The IG methods combine four initialization approaches, two destruction and two construction procedures. Experiments were conducted to examine the impact of two parameter settings in order to determine the optimal configuration for each method. The adopted performance objective is the total duration of production, commonly referred to as makespan. Computational experiments conducted on benchmark datasets revealed that IG7, which combines DESTR_2, NEH_3, and RECONST_1, consistently outperformed other variants, achieving an average ARPD improvement of 0.938. Results from all computational experiments suggest that the novel destruction procedure significantly influences the outcomes, with methods outperforming others across all analyzed instances.

Cite this article as: Tararam De Laurentys C, Nagano MS, Rossi FL. Evaluating the performance of Iterated Greedy methods for the distributed permutation flowshop with sequence-independent setup times. Sigma J Eng Nat Sci 2026;44(4):2626–2640.

INTRODUCTION

The flowshop scheduling problem is applicable across a range of production environments, including the chemical industry, aeronautical parts manufacturing, waste treatment [1], cider production [2], electronic circuits [3], concrete block manufacturing [4], earthmoving operations [5], iron and steel production and even the service sector [6]. Since the 1960s, significant efforts have been made to integrate setup duration into scheduling problems. Advances

***Corresponding author.**
*E-mail address: drnagano@sc.usp.br

This paper was recommended for publication in revised form by Editor-in-Chief Ahmet Selim Dalkilic

Published by Yıldız Technical University Press, İstanbul, Turkey
© Author. This is an open access article under the CC BY-NC license (http://creativecommons.org/licenses/by-nc/4.0/).

in scheduling methodologies, such as genetic algorithms, simulated annealing, and decision support systems, have been instrumental in addressing these challenges. [7-9]. Furthermore, researchers like [10-13] have emphasized the importance of incorporating job sequence-independent setup time (SIST) into scheduling, highlighting its relevance to real-world applications.

The evolution towards distributed flowshop has been driven by a growing need to optimize production in complex and decentralized environments given the context of globalization. The article by [14] was the first to name the extension of the classic flowshop problem to the multi-factory environment as the Distributed Permutational Flowshop Problem (DPFSP). Distributed manufacturing in general is seen to reduce production costs and risks. The DPFSP consists of assigning n jobs in F factories. From there, the decision maker establishes the production sequence of jobs in each factory according to information about the particularities of the production environment.

Different conditions and restrictions were applied to DPFSP, for example, the no-wait flowshop condition was studied and presented by [15] using a branch-and-cut approach, [16] created a competitive memetic algorithm for DPFSP multiobjective and [17] proposed differential evolution metaheuristics for distributed flowshop with limited buffer. One of the major constraints studied for the DPFSP problem is the sequence dependent setup times (SDST). For instance, [18, 19] introduced discrete approaches utilizing bee colonization techniques. [20] developed a model using mixed integer linear programming (MILP) and constraint programming (CP). [21] put forward an iterated greedy algorithm, while [22] devised a metaheuristic employing a differential flight strategy.

More recently, cooperative scheduling strategies, such as those proposed by [23], and flexible assembly approaches highlighted by [24] demonstrate significant potential for complementing Iterated Greedy (IG) methods, particularly in handling complex constraints like sequence-independent setup times. Adaptive genetic algorithms, as detailed by [25], offer an interesting point of comparison, especially in scenarios requiring diverse search capabilities to optimize makespan. Furthermore, benchmarking results from studies such as [26, 27] provide a framework for validating IG performance in minimizing maximum tardiness and improving efficiency under hybrid setups. The systematic review by [28] underscores persistent gaps in distributed scheduling research, including the need to address integrated logistics and non-uniform factory setups.

Despite the rapid growth of literature on DPFSP, studies that incorporate the sequence-independent setup time (SIST) restriction were not found. As per [29] complete review of the distributed scheduling literature, within the constrained DPFSP only three types of setup time constrain were found. Which are: setups depending on the job and machine, sequence dependent setup times and machine and sequence-dependent setup time.

The study extends previous distributed scheduling research by exploring sequence independent setup times, a constraint largely overlooked in prior work, despite its relevance in real-world production environments. It emphasizes the increasing need for integrated scheduling strategies to handle complex production across geographically distributed facilities. Prior studies focused on sequence-dependent setup times (SDST) or multiobjective optimization, while this work uniquely targets SIST with a detailed evaluation of IG methods. By systematically testing 16 variations of IG, the research advances understanding of how different procedural choices (e.g., destruction, initialization) impact scheduling efficiency, providing actionable insights for factory management. The key highlights and novelties of this research are outlined below:

- Investigated sequence-independent setup times (SIST) in distributed flowshop scheduling, a less explored area.
- Developed 16 Iterated Greedy (IG) methods with diverse strategies for initialization, destruction, and reconstruction.
- Identified IG7 as the best-performing method, optimizing makespan effectively.
- Demonstrated the critical role of destruction procedures, with DESTR_2 achieving superior results.
- Provided practical insights into parameter tuning and scalability for large-scale problems.

The Distributed Permutational Flowshop Problem (DPFSP) is characterized by a collection N of n jobs that need to be processed across a group G of F factories. [14]. The assumptions underlying this study include each factory having an identical set M of m machines (similar to a standard PFSP), with fixed processing and setup times. All factories are capable of handling all jobs, and once a job j from set N is assigned to a factory F in set G, it cannot be moved to another factory; it must be completed in its initially assigned factory.

Within each factory, the problem is treated as PFSP considering the sequence-independent setup time (SIST) restriction. The PFSP-SIST scheduling problem involves a set of jobs $J = \{J_1, J_2,\ldots, J_n\}$, which constitutes a production batch, which goes through the production process that contains a set of machines in series $M = \{M_1, M_2,\ldots, M_m\}$. All jobs have the same path and perform m operations, one on each machine. Each job starts on the first machine and ends its cycle on the last machine. It is considered that $p_{i,j}$ is the processing time and that $s_{i,j}$ is the setup time of job J_j on machine M_i. [13].

The assumptions used are the following: all jobs and machines are available from the initial moment, each machine processes only one job at a time and each job is processed only once by the same machine, the processing and setup time are strictly positive, each of which must be scheduled, and each machine has the same sequence of jobs, therefore only permutational scheduling is allowed.

The objective of DPFSP is to find the optimal sequence that minimizes the makespan of the set G of factories,

C'_{max}. Within each factory the objective is to find the optimal sequence that minimize the makespan, C_{max}, under the selected assumptions and under the constraints of machine availability during the real scheduling time of the entire batch. [13]. The calculation of C_{max} e C'_{max} are presented in equations 2 and 3, respectively.

$$C_{i,j} = max_{1\le j\le n}\{C_{i,j-1} + s_{ij}, C_{i-1,j}\} + p_{i,j}, \quad i = 2,\dots,m;\ \ j = 2,\dots,n \tag{1}$$

$$C_{max} = C_F = max_{1\le j\le n}\{C_{m,j}\},\ \ F = 2,\dots,G \tag{2}$$

$$C'_{max} = max_{1\le F\le G}\{C_1, C_2, \dots, C_G\} \tag{3}$$

The following notation is used throughout the paper to describe the Distributed Flowshop Scheduling Problem (DFSP) and the proposed Iterated Greedy (IG) methods:

- n: Total number of jobs.
- m: Total number of machines.
- f: Total number of factories.
- J_i: Job i, where i=1,2,…,n; i=1,2,…,n.
- M_j: Machine j, where j=1,2,…,m; j=1,2,…,m.
- F_k: Factory k, where k=1,2,…,f; k=1,2,…,f.
- $p_{i,j}$: Processing time of job i on machine j.
- $C_{i,j,k}$: Completion time of job i on machine j in factory k.
- C_{max}: Makespan, the total time required to complete all jobs across all factories.
- d: Number of jobs removed during the destruction phase.
- T: Temperature parameter in the acceptance criterion for simulated annealing.
- NEH_1, NEH_2, NEH_3, NEH_4: Initialization strategies based on the Nawaz-Enscore-Ham heuristic.
- DESTR_1, DESTR_2: Destruction strategies used to modify the current solution.
- RECONST_1, RECONST_2: Reconstruction strategies for reinserting jobs into the schedule.
- ARPD: Average Relative Percentage Deviation, a metric for comparing the performance of scheduling methods.

MATERIALS AND METHODS

Materials

The methodology in this study addresses the problem of distributed flowshop scheduling with sequence-independent setup times (SIST). It starts with defining the research problem, focusing on optimizing makespan in distributed manufacturing environments. Multiple Iterated Greedy (IG) algorithms are developed, using initialization procedures such as NEH variants and specific destruction and reconstruction mechanisms. These IG configurations, totaling 16 variations, are implemented and tested on benchmark datasets to assess their performance. The evaluation focuses on metrics like makespan to determine algorithm efficiency. The final step involves analyzing the results to identify the most effective configurations. This process is summarized in the flowchart (Fig. 1), which outlines each step, from problem definition to performance analysis, and highlights the sequence of the study's methodology.

Iterated Greedy (IG) algorithms have stood out in the literature for their simplicity and excellent performance for different variants of permutational flowshop problems. Unlike complex methods, IG stands as a straightforward iterative search method devoid of memory and elaborate structures. Its outcomes are easily reproducible and transferrable to various other problem domains. [30]. Some authors have already presented IG methods for DPFSP with good results [30-32]. It has six main steps. In the first, some constructive method is used to generate a complete initial solution, which, in the second stage, is subjected to a local search to optimize it. Then, the initial solution is destroyed, and it is reconstructed. Another local search is performed and, finally, an acceptance criterion is used to evaluate the new reconstructed solution. These last four steps are executed iteratively, so the process repeats until some stopping criterion is satisfied. An IG step-by-step sketch is provided in Figure 2. In the following sub-sections, the selected procedures for each step are explained.

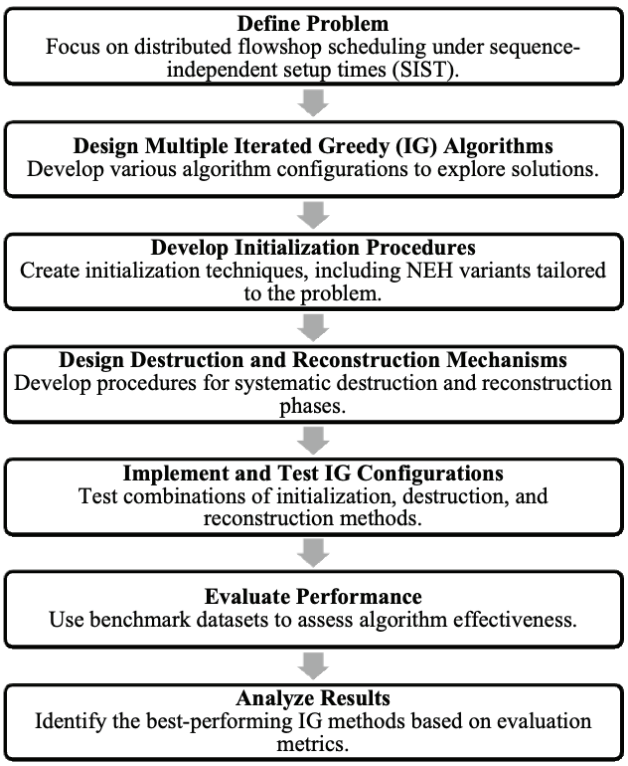


Figure 1. The flowchart outlines each step, from problem definition to performance analysis, and highlights the sequence of the study's methodology.

```
IG:
# Step 1: initialization procedure
π0 = Generate_Initial_Solution

# Step 2: Optimize solution
π = Local_Search (π0)

while (Stopping_Criterion not satisfied)

        # Step 3: Destroy solution
        πD = Destruction (π)

        # Step 4: Reconstruct solution:
        πR = Reconstruction (πD)

        # Step 5: Optimize solution
        πLS = Local_Search (πR)

        # Step 6: Evaluate new solution
        π = Acceptance_Criterion (πLS, π)
```

Figure 2. IG step-by-step sketch, identifying each of the six main steps.

Initialization Procedure

The IG method uses a high-performance constructive heuristic to generate the initial solution and, therefore, different variants of the NEH [33] are employed in most of the literature. [14] introduced NEH2 as a variant of the DPFSP problem, inspired by the original NEH method but distinguished by the incorporation of an assignment rule. This approach involves inserting each job into every conceivable position across all factories to identify the configuration that minimizes the makespan for the entire set of factories.

[30] included a simple addition to this method: following the insertion of an job in the best position across all F factories, the preceding or succeeding job (randomly chosen) is removed and evaluated in all positions within the same factory. This method, called NEH_en, brought better results with a statistically significant difference when compared to NEH2. For this article, both initialization methods will be tested with three additions: inclusion of sequence-independent setup time analysis, inclusion of priority rules in the first stage of the NEH and a tiebreaker strategy in the last stage.

[34] proposed and tested 48 heuristics based on the NEH for the sequence-independent setup time permutation flowshop problem (PFSP-SIST). The best results in relatively low computation time were obtained by Alg27 and Alg31. Both use in the fourth stage of the NEH the adapted tie-breaking strategy procedure proposed by [35] to the SIST constrain (TBFFs). This strategy unties the partial sequences by choosing the position that presents the minimum idle time. Alg27 combines this tie-breaking strategy with the use in the first stage of the NEH of the adapted priority rule proposed by [36] to the SIST constrain. This priority rule orders jobs by the non-increasing sum of the average, standard deviation, and the absolute value of the skewness (SKE), which measures the asymmetry of a probability distribution, of processing and setup times (PR7). Alg27 combines TBFFs with a similar priority rule, that orders jobs by the non-increasing sum of process time's average, standard deviation, and SKE, and sum of setup time's average and SKE (PR8).

For this article, the NEH2 and NEH_en are adapted by including TBFFs as a tie-breaking strategy and PR7 and PR8 as priority rules based on the good results shown in [34] study for the SIST constrain. Table 1 summarizes the initialization methods used (NEH_1, NEH_2, NEH_3 and NEH_4) and initialization components (NEH variant, priority rule and tie-breaking strategy).

Local Search

The initial solution is refined using the local search procedure. [30] proposed a search procedure, called LS3, which accounts for both factory assignment and job sequencing dimensions concurrently. In this procedure, an job is randomly extracted from the factory with the largest makespan and is inserted in all possible positions in all factories, including the one that was extracted. The job is allocated to the position that generates the lowest makespan in the set of factories and the process proceeds (without repetitions) up to all jobs in the highest makespan factory have been examined.

The results obtained by [30] show that, in addition to being faster in relation to CPU time requirements since it

Table 1. Evaluated IG initialization procedures

Initialization procedure	Initialization Components		
	NEH variant	Priority rule	Tie-breaking strategy
NEH_1	NEH2	PR_8	TB_{FFs}
NEH_2	NEH2	PR_7	TB_{FFs}
NEH_3	NEH2_en	PR_8	TB_{FFs}
NEH_4	NEH2_en	PR_7	TB_{FFs}

doesn't handle two neighborhoods in a loop, LS3 is statistically better when compared to the VND procedure, proposed by [14]. Therefore, the LS3 search was selected for this study.

Destruction

The destruction procedure involves the elimination of a specified number, denoted as d, of jobs from the initial solution. Prior research demonstrated that adjusting d allows algorithms to balance intensification and diversification. [30]. [32] proposed a destruction procedure in which jobs are removed one from each factory, from the one with the largest makespan to the smallest. If d > F, the remaining jobs (d - F) are randomly removed from the factories. [30] proposed a new destruction procedure, in which half of the jobs to be removed (d / 2) are removed from the highest makespan factory, while the remaining half is drawn randomly from the other factories (F - 1). Although the new procedure presents statistically better results than the previous one, both will be tested to evaluate the influence of the SIST restriction on the DPFSP problem.

The d value of the total jobs to be removed will be tested as a parameter with two fixed values (4 and 5), as per their better performance obtained in the research conducted by [30]. Table 2 summarizes the destruction procedures evaluated, where DESTR_1 denotes the order for job removal by descending order of factories using the makespan value and DESTR_1 removes the jobs from the highest makespan factory.

Reconstruction

The most common reconstruction process used in the literature [30-32, 37] is similar to the NEH procedure. Each of the d jobs removed in the destruction phase are tested in all positions of all factories to select the one that produces the lowest makespan of the set of factories. In accordance with NEH2_en, an addition to the method is proposed by [30], following the insertion of an job in the optimal position among all F factories, the preceding or succeeding job (randomly chosen) is extracted and evaluated in all positions within the same factory. Table 3 summarizes the RECONST_1 and RECONST_2 reconstruction procedures evaluated, which are based on NEH2 and NEH2_en, respectively.

Acceptance Criterion

The acceptance criterion directly influences the equilibrium between intensification and diversification in the pursuit of the optimal solution. In addition to accepting those solutions that actually present improvements in terms of the makespan value found, it is possible to accept a worse solution than the current one. The aim of this criterion is to enable the search to shift away from the local optima already discovered and toward other potential optima that may yield better outcomes. A criterion popularly used in these cases is called simulated annealing, proposed by [37], in which a new solution is accepted if it is superior or equal; otherwise, acceptance is determined by the condition outlined in Equation 4.

$$random \leq \exp\left(-\frac{\left(C'_{max}(\pi_{LS}) - C'_{max}(\pi)\right)}{Temperature}\right) \quad (4)$$

$$Temperature = T * \frac{\sum_{i=1}^{m}\sum_{j=1}^{n} p_{i,j} + s_{i,j}}{n*m*10}, 0 < T < 1, \quad (5)$$

where random represents a number uniformly distributed between 0 and 1 and T is a parameter that needs adjustment. According to the results obtained in the research conducted by [30], the values of T = 0.1 and T = 0.2 have been shown in past work to provide a good balance between exploration and convergence, therefore, will be used in the computational experiments.

Stopping Criterion

The IG steps are repeated iteratively until the stopping criterion is reached. There are different stopping criteria used in the literature, most of which use some computational time factor related to multiplying the number of jobs by the number of machines [37-39], as IG requires more time for large instances. For this article, the stopping criterion will be defined by Equation 6.

$$Time\ limit = n * \frac{m}{2} * C \quad (6)$$

C is a parameter that needs adjustment. For this study the C value was set at 40 milliseconds, considering the good results obtained by [30].

Table 3. Evaluated IG reconstruction procedures

Reconstruction procedure	Procedure
RECONST_1	Similar to NEH2
RECONST_2	Similar to NEH2_en

Table 2. Evaluated IG destruction procedures

Destruction Procedure	Jobs' removal order
DESTR_1	Descending order of factories in relation to makespan value
DESTR _2	Half removed from the highest makespan factory, while the remaining half is drawn from the other factories.

Table 4. Evaluated IG methods

IG method	Initialization Procedure	Destruction Procedure	Reconstruction Procedure
IG 1	NEH_1	DESTR_1	RECONST_1
IG 2	NEH_2	DESTR_1	RECONST_1
IG 3	NEH_3	DESTR_1	RECONST_1
IG 4	NEH_4	DESTR_1	RECONST_1
IG 5	NEH_1	DESTR_2	RECONST_1
IG 6	NEH_2	DESTR_2	RECONST_1
IG 7	NEH_3	DESTR_2	RECONST_1
IG 8	NEH_4	DESTR_2	RECONST_1
IG 9	NEH_1	DESTR_1	RECONST_2
IG 10	NEH_2	DESTR_1	RECONST_2
IG 11	NEH_3	DESTR_1	RECONST_2
IG 12	NEH_4	DESTR_1	RECONST_2
IG 13	NEH_1	DESTR_2	RECONST_2
IG 14	NEH_2	DESTR_2	RECONST_2
IG 15	NEH_3	DESTR_2	RECONST_2
IG 16	NEH_4	DESTR_2	RECONST_2

Performance Metrics

In total, 16 IG variations were evaluated for the DPFSP-SIST, each one being tested for 2 values of T and 2 values of d. A total of 16 IG variations were evaluated for the DPFSP-SIST, with each method tested using two values for T and two values for d. Table 4 summarizes the composition of the evaluated methods, detailing the initialization procedure (NEH_1 to NEH_4), destruction procedure (DESTR_1, DESTR_2), and reconstruction procedure (RECONST_1, RECONST_2). The computational complexity of these variants is determined by their components, including initialization, destruction, reconstruction, and local search. As an example, simpler variants (e.g., DESTR_1 + NEH_1) favor lower computational overhead, while, more complex variants (e.g., DESTR_2 + NEH_3) are more computationally intensive due to randomness and dynamic job placement. This balance between complexity and performance highlights the importance of tailoring the algorithm to the size and characteristics of the scheduling problem, a topic further explored in the results section.

Each method will be tested using an adaptation of the instances from the [40] database, as it presents uniformly distributed values for processing and setup times, which results in instances that are more difficult to solve. The instances are adapted to the distribution condition, according to the identical factories' premises, each instance is used for F = {2, 3, 4, 5, 6, 7}. Processing times are uniformly distributed in the range [1,10] or [1,100] and setup times are uniformly distributed so that the maximum setup is 50%, 100% and 150% of the maximum processing time. To enable the execution of computational tests in a timely manner without compromising the variety and complexity of the instances, only the first 10 problems of each combination of m and n were used, with "large" instances being limited to n=150 and m=20. Considering this configuration, we have a total of 7,200 "small" instances and 2,160 "large" instances, adding up to a total of 9,360 instances. Furthermore, all tested methods use the Taillard acceleration [41] adaptation developed by [34] which includes the independent setup restriction.

The performance was evaluated using the Relative Percentage Deviation (RPD), calculated using Equation 7 where C_max (π_h) is the makespan obtained by a procedure for a given instance i and C_max^* is the best solution found among all methods compared for the instance i. As a result, the closer the solution obtained by method h is to the best solution for instance i, the lower the RPD will be.

$$RPD\left(C_{max}(\pi_h), i\right) = 100 * \left(\frac{C_{max}(\pi_h) - C^*_{max}}{C^*_{max}}\right); \quad h = \{1, 2, \ldots, 16\}, \tag{7}$$

The Average Relative Percentage Deviation (ARPD) of method h considering N instances can be calculated using Equation 8.

$$ARPD\ (h\ , i) = \frac{\sum_{t=1}^{N} RPD\ (C_{max}(\pi_h), i)}{N}; \tag{8}$$

RESULTS AND DISCUSSION

The computational experiments were conducted using Python on a PC with an Intel Core i5-5200U 2.20 GHz CPU, 8 GB of RAM, and running Windows 10. The

outcomes of the experiments are consolidated in Tables 5-8, detailing the performance of each of the 16 algorithms according to the number of factories, jobs and machines in average and for each setup time distributions, 50%, 100% and 150%, respectfully. All outcomes are evaluated according to the number of factories, jobs and machines. When the setup time represents up to 100% of the processing time, IG8 presents the best results, 0.9286 and 0.9370, for 50% and 100%, respectively. However, in the case of representing 150%, that is, when the setup time is greater than the processing time, IG7 presents the best results, 0.9337. In average, IG7 presented the best results, 0.9382, followed by IG8, 0.9402.

Regarding the number of factories, it is possible to see that the complexity of the problem and, consequently, the ARPD of the solutions increase as the total number of factories increases. But, exclusively for methods with the DESTR_2 destruction type, when the total number of factories is a high value, f = 6 or f = 7, the ARPD decreases again. In other words, DESTR_2 helps the algorithm find better solutions even in complex scenarios with many factories. Regarding the number of jobs, the methods tend to find the best solutions and, therefore, lower ARPD values as the number of jobs increases. Therefore, IG presents better performance for large instances, with average results of 0.7323 compared to 1.2887 for small instances. Similarly, it is possible to see that the performance of the methods increases as the total number of machines increases. But for scenarios where the total number of machines is low, such as m = 2 or m = 3, performance is also good.

Although ARPD values are similar regarding the variation of factories, jobs and machines, the distribution of setup time in relation to processing time directly impacts the best method found. In cases where the setup is more relevant than the processing time, that is, it presents a distribution of 150%, the IG7 presents the best results for most scenarios. When the setup is less relevant, that is, distribution of 50% and 100%, the best method varies greatly depending on the scenario, and in only one case it is IG7 and on average it is IG8.

Regardless of the type of instance, it is noticeable that the main impact on the results is due to the destruction procedure choice, as represented in Figures 3 and 4. Figure 3 presents the mean plot for each of the 16 IG methods, and Figure 4 shows the ARPD for each for each initialization, destruction and reconstruction procedures. Procedure

Table 5. ARPD for each IG method for all instances, according to the number of factories, jobs and machines. The best results for each line are in bold

	IG 1	IG 2	IG 3	IG 4	IG 5	IG 6	IG 7	IG 8	IG 9	IG 10	IG 11	IG 12	IG 13	IG 14	IG 15	IG 16
f = 2	0.655	0.651	0.635	0.628	0.619	0.607	0.584	**0.581**	0.663	0.660	0.639	0.639	0.622	0.612	0.597	0.602
f = 3	1.043	1.065	1.030	1.023	0.872	0.890	**0.866**	0.875	1.053	1.071	1.048	1.043	0.893	0.911	0.883	0.872
f = 4	1.223	1.228	1.218	1.223	1.069	1.075	1.054	1.053	1.238	1.244	1.213	1.226	1.065	1.073	**1.047**	1.084
f = 5	1.443	1.447	1.402	1.431	**1.082**	1.115	1.090	1.089	1.460	1.459	1.434	1.440	1.094	1.101	1.119	1.086
f = 6	1.775	1.802	1.750	1.752	**1.045**	1.061	1.050	1.059	1.779	1.818	1.786	1.781	1.063	1.074	1.066	1.074
f = 7	2.104	2.076	2.055	2.059	0.999	1.022	0.986	**0.984**	2.111	2.057	2.086	2.056	1.004	1.014	0.996	0.991
mean	1.374	1.378	1.348	1.353	0.948	0.962	**0.938**	0.940	1.384	1.385	1.368	1.364	0.957	0.964	0.951	0.951
n = 15	1.659	1.650	1.647	1.617	**0.953**	1.001	0.973	0.977	1.685	1.687	1.683	1.659	0.986	1.010	1.018	1.019
n = 20	1.677	1.698	1.673	1.681	1.140	1.150	**1.121**	1.135	1.708	1.715	1.696	1.706	1.168	1.154	1.154	1.167
n = 25	1.477	1.491	1.458	1.500	1.045	**1.042**	1.055	1.043	1.510	1.492	1.498	1.497	1.050	1.071	1.074	1.063
n = 30	1.311	1.314	1.293	1.306	**0.935**	0.953	0.943	0.953	1.325	1.335	1.320	1.329	0.954	0.968	0.952	0.955
n = 50	0.993	0.972	0.961	0.947	0.814	0.795	0.792	0.781	0.938	0.956	0.947	0.918	0.790	0.771	0.757	**0.751**
n = 100	0.838	0.833	0.761	0.742	0.689	0.710	0.641	0.632	0.793	0.789	0.723	0.734	0.660	0.667	0.603	**0.600**
n = 150	0.719	0.727	0.632	0.639	0.633	0.630	0.533	0.539	0.689	0.684	0.617	0.604	0.591	0.592	0.511	**0.506**
mean	1.374	1.378	1.348	1.353	0.948	0.962	**0.938**	0.940	1.384	1.385	1.368	1.364	0.957	0.964	0.951	0.951
m = 2	1.462	1.428	1.446	1.444	**0.820**	0.857	0.846	0.837	1.489	1.487	1.502	1.448	0.860	0.853	0.866	0.876
m = 3	1.541	1.559	1.529	1.541	1.001	1.010	**0.985**	1.012	1.565	1.565	1.557	1.582	1.033	1.037	1.030	1.035
m = 4	1.593	1.616	1.577	1.568	1.103	1.107	1.102	**1.098**	1.610	1.610	1.604	1.596	1.101	1.127	1.111	1.117
m = 5	1.570	1.572	1.571	1.588	**1.094**	1.121	1.115	1.112	1.592	1.592	1.593	1.593	1.117	1.137	1.143	1.130
m = 6	1.488	1.517	1.465	1.488	1.074	1.087	**1.068**	1.075	1.531	1.532	1.490	1.518	1.088	1.099	1.097	1.099
m = 10	0.898	0.886	0.837	0.826	0.755	0.749	0.696	0.687	0.855	0.859	0.818	0.793	0.715	0.711	0.664	**0.662**
m = 20	0.802	0.802	0.732	0.726	0.670	0.675	0.615	0.615	0.759	0.761	0.707	0.712	0.646	0.642	0.584	**0.576**
mean	1.374	1.378	1.348	1.353	0.948	0.962	**0.938**	0.940	1.384	1.385	1.368	1.364	0.957	0.964	0.951	0.951

Table 6. ARPD for instances with setup times distributed so that the maximum setup is 50% of the maximum processing time. The best results for each line are in bold

	IG 1	IG 2	IG 3	IG 4	IG 5	IG 6	IG 7	IG 8	IG 9	IG 10	IG 11	IG 12	IG 13	IG 14	IG 15	IG 16
f = 2	0.683	0.684	0.656	0.659	0.639	0.627	0.613	**0.593**	0.677	0.676	0.662	0.672	0.642	0.629	0.610	0.628
f = 3	1.029	1.076	1.015	0.985	0.887	0.905	0.889	0.889	1.036	1.059	1.028	1.013	0.905	0.929	0.908	**0.882**
f = 4	1.170	1.213	1.172	1.182	1.082	1.102	1.063	1.072	1.182	1.197	1.150	1.178	1.058	1.078	**1.052**	1.087
f = 5	1.369	1.364	1.320	1.342	1.079	1.107	1.080	1.092	1.391	1.367	1.350	1.366	1.096	1.085	1.135	**1.071**
f = 6	1.562	1.622	1.581	1.553	**0.999**	1.033	1.020	1.009	1.582	1.611	1.553	1.588	1.008	1.045	1.008	1.019
f = 7	1.818	1.770	1.779	1.771	0.945	0.969	0.930	0.916	1.820	1.746	1.821	1.760	0.957	0.966	**0.910**	0.920
mean	1.272	1.288	1.254	1.249	0.939	0.957	0.933	**0.929**	1.281	1.276	1.261	1.263	0.944	0.955	0.937	0.935
n = 15	1.489	1.507	1.487	1.437	**0.906**	0.948	0.937	0.932	1.499	1.506	1.498	1.484	0.925	0.976	0.971	0.949
n = 20	1.502	1.535	1.531	1.501	1.110	1.132	1.096	**1.093**	1.526	1.537	1.522	1.535	1.112	1.115	1.106	1.141
n = 25	1.386	1.417	1.367	1.406	1.077	1.075	1.077	**1.054**	1.429	1.396	1.406	1.394	1.071	1.087	1.088	1.061
n = 30	1.252	1.269	1.228	1.251	**0.937**	0.980	0.962	0.978	1.274	1.268	1.257	1.295	0.981	0.995	0.964	0.972
n = 50	0.923	0.899	0.894	0.914	0.816	0.780	0.787	0.782	0.879	0.875	0.894	0.874	0.782	0.756	0.755	**0.726**
n = 100	0.835	0.818	0.747	0.714	0.672	0.704	0.624	0.618	0.777	0.776	0.689	0.699	0.681	0.651	0.604	**0.601**
n = 150	0.702	0.710	0.628	0.620	0.636	0.619	0.532	0.528	0.678	0.669	0.597	0.573	0.594	0.576	**0.500**	0.512
mean	1.272	1.288	1.254	1.249	0.939	0.957	0.933	**0.929**	1.281	1.276	1.261	1.263	0.944	0.955	0.937	0.935
m = 2	1.427	1.357	1.384	1.366	**0.873**	0.895	0.912	0.877	1.440	1.380	1.431	1.357	0.922	0.902	0.941	0.910
m = 3	1.411	1.482	1.437	1.424	1.005	1.010	**0.960**	1.022	1.442	1.467	1.427	1.486	0.996	1.058	1.006	1.001
m = 4	1.487	1.551	1.506	1.463	1.095	1.123	1.084	1.087	1.519	1.490	1.524	1.481	1.084	1.128	**1.073**	1.109
m = 5	1.391	1.419	1.409	1.420	**1.038**	1.093	1.097	1.050	1.387	1.430	1.407	1.431	1.063	1.076	1.089	1.081
m = 6	1.319	1.351	1.279	1.320	**1.027**	1.048	1.037	1.036	1.372	1.366	1.314	1.379	1.043	1.052	1.052	1.054
m = 10	0.849	0.843	0.821	0.790	0.738	0.731	0.680	0.679	0.825	0.818	0.796	0.768	0.713	0.686	0.656	**0.650**
m = 20	0.790	0.774	0.692	0.708	0.679	0.671	0.616	0.607	0.731	0.729	0.658	0.663	0.658	0.636	0.584	**0.577**
mean	1.272	1.288	1.254	1.249	0.939	0.957	0.933	**0.929**	1.281	1.276	1.261	1.263	0.944	0.955	0.937	0.935

Table 7. ARPD for instances with setup times distributed so that the maximum setup is 100% of the maximum processing time. The best results for each line are in bold

	IG 1	IG 2	IG 3	IG 4	IG 5	IG 6	IG 7	IG 8	IG 9	IG 10	IG 11	IG 12	IG 13	IG 14	IG 15	IG 16
f = 2	0.640	0.655	0.636	0.620	0.616	0.601	0.585	**0.582**	0.676	0.663	0.636	0.635	0.612	0.619	0.610	0.603
f = 3	1.036	1.066	1.037	1.052	**0.871**	0.893	0.874	0.878	1.071	1.094	1.061	1.061	0.885	0.905	0.871	0.874
f = 4	1.211	1.213	1.206	1.209	1.063	1.030	1.037	**1.021**	1.261	1.253	1.222	1.214	1.044	1.059	1.034	1.064
f = 5	1.440	1.455	1.402	1.425	**1.053**	1.096	1.107	1.055	1.442	1.457	1.415	1.418	1.085	1.090	1.096	1.067
f = 6	1.812	1.806	1.775	1.786	1.062	1.071	1.074	1.078	1.806	1.863	1.819	1.826	**1.051**	1.085	1.086	1.082
f = 7	2.139	2.165	2.093	2.141	1.019	1.025	1.013	1.007	2.157	2.157	2.091	2.134	**0.995**	1.039	1.006	1.014
mean	1.380	1.393	1.358	1.372	0.947	0.952	0.948	**0.937**	1.402	1.414	1.374	1.381	0.945	0.966	0.951	0.951
n = 15	1.667	1.670	1.651	1.647	**0.966**	1.007	0.983	0.983	1.708	1.724	1.681	1.684	0.983	0.994	1.022	1.028
n = 20	1.708	1.755	1.696	1.742	1.159	1.161	1.136	**1.118**	1.752	1.782	1.728	1.771	1.185	1.181	1.161	1.172
n = 25	1.488	1.503	1.471	1.513	1.023	**1.015**	1.077	1.051	1.527	1.523	1.498	1.497	1.018	1.059	1.071	1.076
n = 30	1.302	1.311	1.311	1.313	0.932	0.924	0.953	0.943	1.335	1.348	1.335	1.332	**0.924**	0.968	0.947	0.937
n = 50	0.983	0.977	0.969	0.938	0.809	0.805	0.789	0.798	0.951	0.975	0.939	0.930	0.793	0.778	0.767	**0.757**
n = 100	0.819	0.819	0.739	0.724	0.677	0.688	0.643	0.623	0.792	0.780	0.728	0.718	0.636	0.681	0.592	**0.585**
n = 150	0.716	0.719	0.628	0.638	0.627	0.623	0.521	0.521	0.676	0.687	0.591	0.603	0.581	0.596	0.499	**0.483**
mean	1.380	1.393	1.358	1.372	0.947	0.952	0.948	**0.937**	1.402	1.414	1.374	1.381	0.945	0.966	0.951	0.951
m = 2	1.436	1.408	1.437	1.459	**0.754**	0.804	0.792	0.787	1.478	1.505	1.456	1.445	0.792	0.813	0.813	0.819
m = 3	1.602	1.627	1.575	1.613	1.039	1.038	1.037	**1.025**	1.625	1.621	1.623	1.640	1.062	1.053	1.059	1.090
m = 4	1.591	1.629	1.577	1.602	1.098	1.103	1.159	1.133	1.623	1.651	1.585	1.647	**1.093**	1.149	1.129	1.145
m = 5	1.578	1.608	1.567	1.601	1.101	1.115	1.116	1.106	1.620	1.640	1.599	1.611	1.112	1.135	1.140	**1.100**
m = 6	1.501	1.526	1.504	1.493	1.108	1.073	1.083	**1.068**	1.558	1.556	1.539	1.510	1.078	1.103	1.109	1.113
m = 10	0.905	0.878	0.820	0.816	0.759	0.749	0.691	0.679	0.856	0.876	0.808	0.787	0.708	0.727	0.657	**0.654**
m = 20	0.774	0.799	0.737	0.717	0.650	0.662	0.611	0.616	0.757	0.751	0.697	0.713	0.632	0.644	0.581	**0.563**
mean	1.380	1.393	1.358	1.372	0.947	0.952	0.948	**0.937**	1.402	1.414	1.374	1.381	0.945	0.966	0.951	0.951

Table 8. ARPD for instances with setup times distributed so that the maximum setup is 150% of the maximum processing time. The best results for each line are in bold

	IG 1	IG 2	IG 3	IG 4	IG 5	IG 6	IG 7	IG 8	IG 9	IG 10	IG 11	IG 12	IG 13	IG 14	IG 15	IG 16
f = 2	0.641	0.613	0.614	0.607	0.603	0.593	**0.555**	0.568	0.635	0.641	0.618	0.609	0.612	0.589	0.569	0.576
f = 3	1.063	1.054	1.036	1.030	0.859	0.873	**0.834**	0.859	1.051	1.060	1.055	1.055	0.889	0.899	0.869	0.859
f = 4	1.289	1.256	1.277	1.280	1.062	1.093	1.062	1.066	1.273	1.282	1.267	1.287	1.094	1.083	**1.055**	1.102
f = 5	1.520	1.522	1.485	1.527	1.113	1.141	**1.083**	1.119	1.547	1.553	1.537	1.535	1.102	1.129	1.125	1.118
f = 6	1.951	1.978	1.895	1.918	1.075	1.078	**1.055**	1.089	1.948	1.980	1.986	1.930	1.130	1.092	1.104	1.120
f = 7	2.354	2.293	2.293	2.264	1.031	1.071	**1.013**	1.030	2.358	2.269	2.347	2.273	1.060	1.038	1.073	1.040
mean	1.470	1.453	1.433	1.438	0.957	0.975	**0.934**	0.955	1.469	1.464	1.468	1.449	0.981	0.972	0.966	0.969
n = 15	1.819	1.773	1.802	1.766	**0.987**	1.049	0.999	1.014	1.848	1.831	1.869	1.810	1.052	1.059	1.062	1.081
n = 20	1.821	1.806	1.793	1.799	1.150	1.156	**1.132**	1.193	1.847	1.826	1.837	1.811	1.207	1.165	1.193	1.189
n = 25	1.556	1.552	1.536	1.581	1.035	1.037	**1.010**	1.025	1.572	1.556	1.590	1.601	1.062	1.065	1.062	1.053
n = 30	1.377	1.361	1.339	1.354	0.937	0.954	**0.915**	0.940	1.366	1.389	1.369	1.361	0.958	0.943	0.946	0.955
n = 50	1.073	1.041	1.020	0.989	0.817	0.801	0.800	0.764	0.985	1.019	1.009	0.949	0.795	0.780	**0.750**	0.769
n = 100	0.860	0.864	0.796	0.789	0.718	0.738	0.656	0.656	0.811	0.811	0.751	0.786	0.662	0.670	0.613	**0.612**
n = 150	0.738	0.752	0.640	0.660	0.637	0.649	0.545	0.567	0.713	0.697	0.664	0.637	0.599	0.602	0.534	**0.523**
mean	1.470	1.453	1.433	1.438	0.957	0.975	**0.934**	0.955	1.469	1.464	1.468	1.449	0.981	0.972	0.966	0.969
m = 2	1.523	1.517	1.517	1.506	0.833	0.871	**0.832**	0.848	1.549	1.575	1.618	1.543	0.866	0.846	0.843	0.897
m = 3	1.609	1.569	1.574	1.586	**0.958**	0.982	0.958	0.991	1.627	1.606	1.621	1.621	1.039	1.001	1.027	1.015
m = 4	1.700	1.668	1.648	1.640	1.114	1.095	**1.064**	1.075	1.686	1.689	1.703	1.661	1.126	1.104	1.131	1.097
m = 5	1.740	1.688	1.736	1.743	1.142	1.155	**1.132**	1.181	1.768	1.706	1.774	1.738	1.176	1.200	1.199	1.209
m = 6	1.645	1.673	1.613	1.650	1.089	1.140	**1.083**	1.120	1.661	1.675	1.616	1.667	1.143	1.140	1.130	1.129
m = 10	0.939	0.937	0.870	0.871	0.767	0.767	0.717	0.703	0.885	0.883	0.851	0.823	0.724	0.721	**0.679**	0.682
m = 20	0.843	0.834	0.767	0.754	0.681	0.692	0.617	0.622	0.788	0.802	0.766	0.758	0.647	0.648	**0.585**	0.588
mean	1.470	1.453	1.433	1.438	0.957	0.975	**0.934**	0.955	1.469	1.464	1.468	1.449	0.981	0.972	0.966	0.969

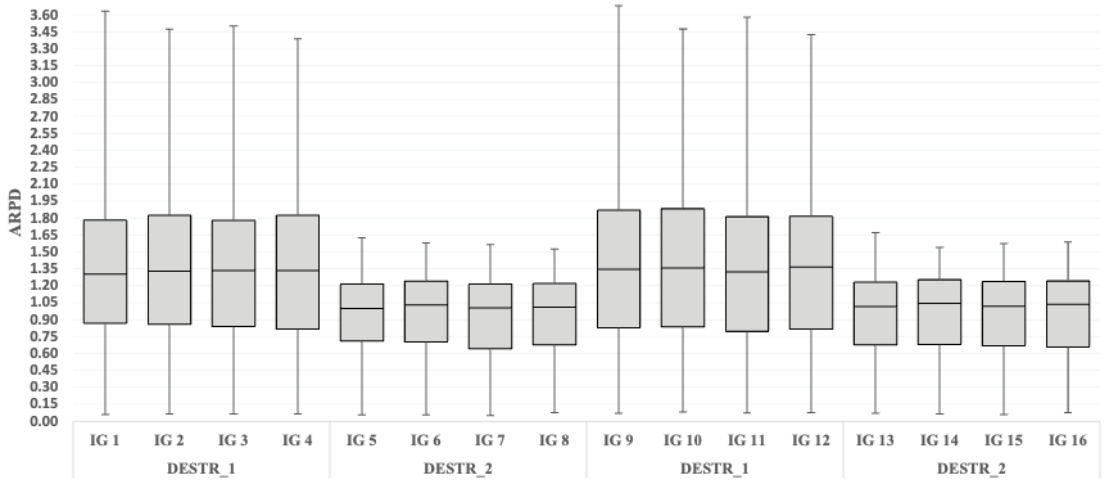


Figure 3. Mean plot for each of the 16 IG methods.

DESTR_2 provides up to 47.6% better average results when compared to DESTR_1. Among the methods with the same destruction procedure, the results variation is low, up to 2,5% on average. This shows that the choice of initialization and reconstruction procedures has little effect on the performance of the IG method, with the NEH_3 initialization procedure and the RECONST_2 reconstruction procedure being slightly superior to the others.

Figure 5 shows the mean plot for all 16 IG methods for different values of parameter d and T. The variation of the parameters d and T has minimum impact on the performance, with the best configuration being on average

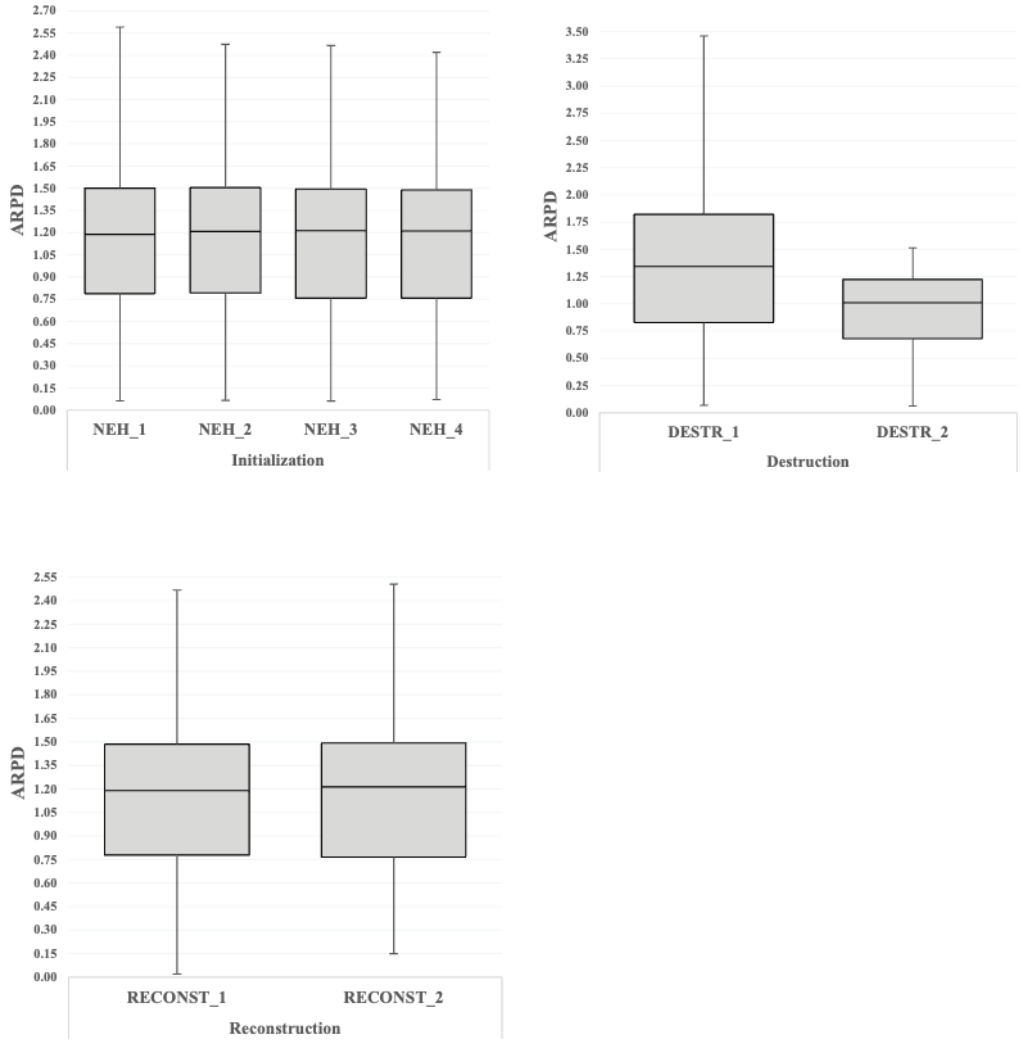


Figure 4. Mean plot for each initialization, destruction and reconstruction procedures.

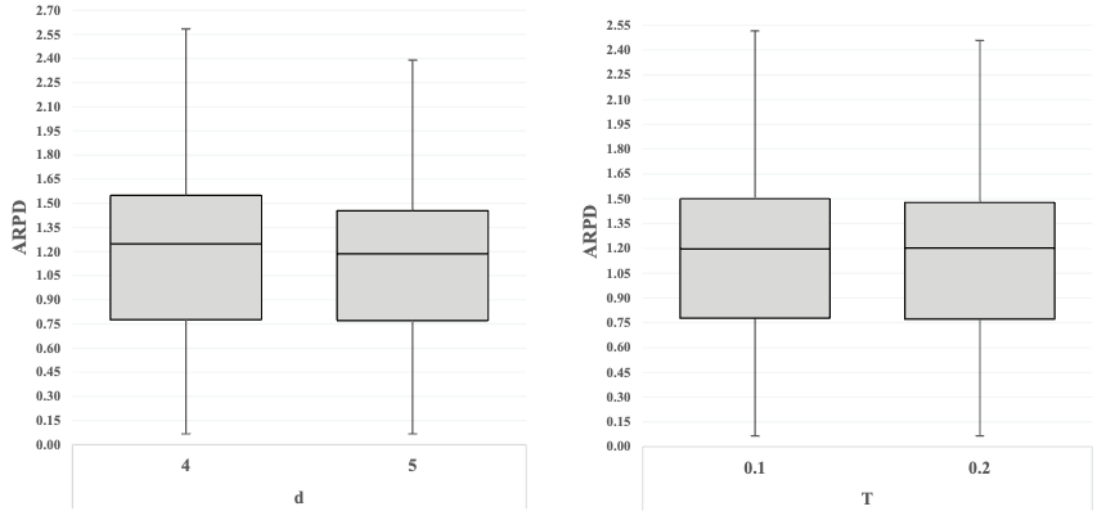


Figure 5. Mean plot for all 16 IG methods for parameter d and T.

d = 5, 1.1345, and T = 0.2, 1.1545. However, unlike the parameter T, parameter d when evaluated in each of the 16 methods shows relevant behavior. On average and for small instances, Figures 6 and 7, respectively, the value of d = 5 obtains better ARPDs for methods with DESTR_1, while for methods with DESTR_2 d = 4 presented better results. On the contrary, for large instances, Figure 8, d = 5 performs better in all but one method, IG15. This may mean that for smaller instances, in addition to the choice of destruction procedure having a great influence on the

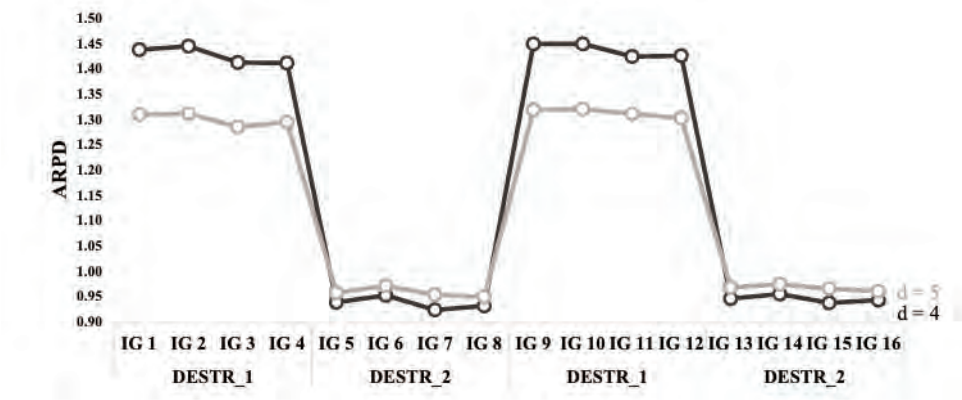


Figure 6. ARPD for the IG methods and different d parameters for all instances.

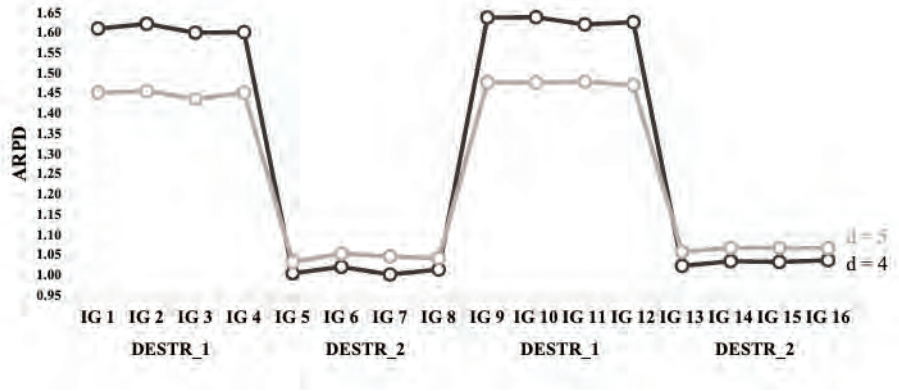


Figure 7. ARPD for the IG methods and different d parameters in small instances.



Figure 8. ARPD for the IG methods and different d parameters in large instances.

Table 9. ARPD of IG methods with DESTR_2 for each parameter configuration and instance type. The best results are in green, the worst in red, with the optimal outcome and the least favorable in bold

		ARPD							
d	**T**	**IG 5**	**IG 6**	**IG 7**	**IG 8**	**IG 13**	**IG 14**	**IG 15**	**IG 16**
5	0.1	0.968	0.972	0.982	**0.989**	0.957	0.959	0.969	0.968
5	0.2	0.946	0.970	0.954	0.959	0.949	0.939	0.962	0.953
4	0.1	0.938	0.971	0.953	0.951	**0.923**	0.932	0.931	0.934
4	0.2	0.939	0.933	0.938	0.958	**0.923**	0.931	0.944	0.952
		ARPD for small instances							
d	**T**	**IG 5**	**IG 6**	**IG 7**	**IG 8**	**IG 13**	**IG 14**	**IG 15**	**IG 16**
5	0.1	1.042	1.054	1.074	**1.086**	1.050	1.052	1.072	1.072
5	0.2	1.022	1.052	1.040	1.048	1.041	1.029	1.061	1.060
4	0.1	1.005	1.047	1.034	1.030	1.002	1.014	1.023	1.025
4	0.2	1.004	**0.993**	1.011	1.038	1.000	1.013	1.041	1.047
		ARPD for large instances							
d	**T**	**IG 5**	**IG 6**	**IG 7**	**IG 8**	**IG 13**	**IG 14**	**IG 15**	**IG 16**
5	0.1	0.720	0.699	0.674	0.664	0.649	0.649	0.624	0.618
5	0.2	0.693	0.698	0.669	0.663	0.644	0.637	0.630	**0.596**
4	0.1	0.715	0.718	0.683	0.691	0.658	0.660	0.623	0.628
4	0.2	0.720	**0.733**	0.696	0.690	0.669	0.657	0.618	0.633

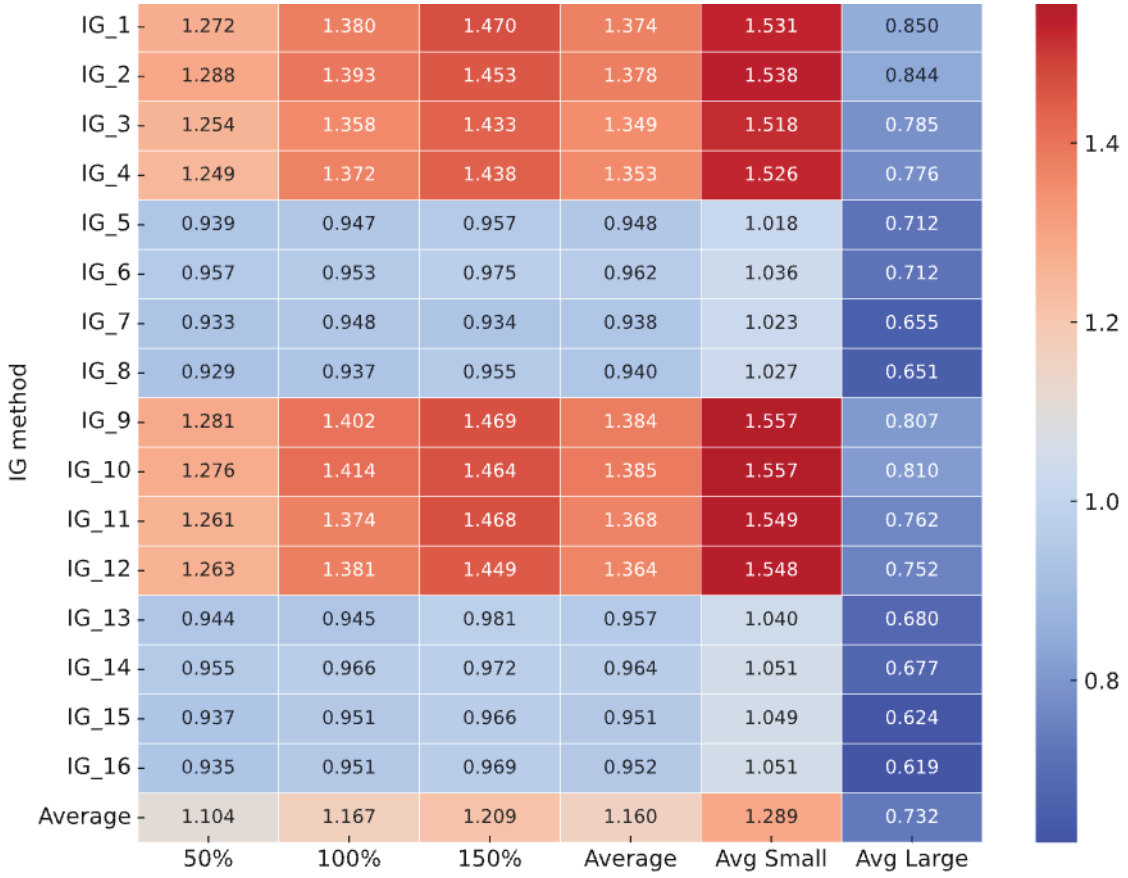


Figure 9. Heatmap illustrating the values of different IG methods across various conditions (50%, 100%, 150%, Average, Avg Small, Avg Large). The color gradient represents the magnitude of the values.

performance of the algorithm, the number of jobs to be removed must be defined according to the type of destruction procedure. For DESTR_1 the more jobs removed the better the performance and for DESTR_2, the fewer jobs removed, the better the performance. As most of the tests were conducted on smaller instances, the average results exhibit a similar trend. Worth noting, when dealing with larger instances requiring the sequencing of numerous jobs, it is advantageous to remove more jobs, regardless of the type of destruction. A possible explanation for the overall superior performance of DESTR_2 lies in its partial random removal of jobs, which reduces the method's greediness. This approach increases the likelihood of escaping local optima and exploring new search spaces, potentially leading to better solutions and further improving overall performance of the method.

The T factor directly impacts the acceptance criteria. The higher its value, the greater the chance of accepting a worse solution than the current one, allowing the search to shift away from the local optima already discovered and toward other potential optima that may yield better outcomes. From the results of the best methods, which utilize the DESTR_2 destruction procedure, shown in Table 9, for both small and large instances, T of 0.2 performed better than 0.1 for almost all algorithms. For small instances, the configuration with d = 4 and T = 0.2 yields the most favorable outcomes, with IG6 exhibiting the best ARPD of 0.993. For large instances, the configuration with d = 5 and T = 0.2 yields the best results, with IG16 achieving the best ARPD of 0.596. However, on average the best method was IG13, ARPD of 0.923, with the configuration d = 4 and T = 0.1 or T = 0.2. Therefore, once again it is important to analyze the production scenario before defining the best configuration and consequently the best method to be used. Figure 9 presents a performance heatmap comparing all IG methods across small and large instances, highlighting the performance of IG7 in comparison to other methods.

CONCLUSION

This research focused on solving the Distributed Permutation Flowshop Scheduling Problem (DPFSP) under the constraint of sequence-independent setup times (SIST)—a factor with significant practical relevance but limited attention in the current literature. A total of 16 Iterated Greedy (IG) variants were developed by systematically combining four initialization procedures, two destruction strategies, and two reconstruction methods. Additionally, two key parameters were evaluated: the number of jobs removed during the destruction phase (d), and the temperature parameter (T) influencing the acceptance criterion.

The results clearly show that the destruction procedure plays a central role in the overall performance of IG methods. While the choice of initialization and reconstruction methods had minimal impact, the DESTR_2 strategy consistently yielded better outcomes across all tested scenarios. For smaller instances, the best results were achieved with d = 4 and T = 0.2, while in larger instances, increasing the number of removed jobs to d = 5 maintained superior performance. Among all configurations, the combination of NEH_3 (initialization), DESTR_2 (destruction), and RECONST_1 (reconstruction)—identified as IG7—produced the best average results, confirming the effectiveness of this specific configuration. These findings align with previous research by [30], reinforcing the idea that job removal and rescheduling strategies critically influence distributed scheduling performance.

Another important conclusion is the necessity of aligning the IG configuration with the characteristics of the production environment. The IG methods demonstrated greater effectiveness in large-scale instances, as reflected in lower ARPD values, suggesting strong scalability. Moreover, the relevance of setup time within the scheduling environment should guide the choice of method. IG7 was more effective in scenarios where setup time had a substantial impact, while IG8 performed better when processing time was equally or more critical.

Overall, the IG methodologies proposed in this study offer practical strategies for improving scheduling performance in distributed manufacturing systems. These approaches are particularly relevant for industries aiming to minimize delays, optimize machine utilization, and streamline production operations. The benchmarking results provide valuable guidance for both practitioners and researchers by identifying the most effective combinations of algorithmic components. Key conclusions include:

1. Optimal Initialization and Reconstruction: NEH_3 and RECONST_1 were the most effective in generating strong initial and rebuilt solutions, improving makespan outcomes.
2. Destruction Procedure Effectiveness: DESTR_2 consistently outperformed DESTR_1, emphasizing the importance of thoughtful disruption in iterative search strategies.
3. Parameter Sensitivity: Performance varied significantly with changes to d and T, with d = 5 and T = 0.2 emerging as the most robust configuration for large instances.
4. IG7 as the Best Variant: Among all tested methods, IG7 achieved the lowest ARPD values, demonstrating its general effectiveness across different scenarios.
5. Scalability: The IG framework showed strong scalability, delivering better relative performance in larger problem instances.

Future work could extend these findings by exploring new configurations within the IG framework, such as alternative values for d, T, or cycle limits (C), or by applying the method to heterogeneous factory environments to more closely mirror real-world systems. Additionally, the IG methods developed here could be applied to integrated production-distribution systems, incorporating logistics and delivery scheduling. As this study focused solely on

makespan minimization, another important avenue for research is to incorporate multi-objective criteria, including total tardiness, energy consumption, or cost-related factors, to better reflect the complex trade-offs encountered in actual manufacturing environments.

ACKNOWLEDGEMENT

This research was partially supported by grants 308847/2026-1 and 404819/2023-0 from the National Council for Scientific and Technological Development (CNPq), Brazil.

AUTHORSHIP CONTRIBUTIONS

Authors equally contributed to this work.

DATA AVAILABILITY STATEMENT

The authors confirm that the data that supports the findings of this study are available within the article. Raw data that support the finding of this study are available from the corresponding author, upon reasonable request.

CONFLICT OF INTEREST

The authors declared no conflict of interest.

ETHICS

There are no ethical issues with the publication of this manuscript.

STATEMENT ON THE USE OF ARTIFICIAL INTELLIGENCE

Artificial intelligence was not used in the preparation of the article.

REFERENCES

[1] Martinez S, Hall NG, Sriskandarajah C. Complexity of flowshop scheduling problems with a new blocking constraint. Eur J Oper Res 2006;169:855–864. [CrossRef]

[2] Trabelsi W, Sauvey C, Sauer N. Heuristics and metaheuristics for mixed blocking constraints flowshop scheduling problems. Comput Oper Res 2012;39:2520–2527. [CrossRef]

[3] Gong H, Tang L, Duin CW. A two-stage flowshop scheduling problem on a batching machine and a discrete machine with blocking and shared setup times. Comput Oper Res 2010;37:960–969. [CrossRef]

[4] Grabowski J, Pempera J. Sequencing of jobs in some production system. Eur J Oper Res 2000;125:535–550. [CrossRef]

[5] Yu AJ, Seif J. Minimizing tardiness and maintenance costs in flowshop scheduling by a lower-bound-based GA. Comput Ind Eng 2016;97:26–40. [CrossRef]

[6] Hall NG, Sriskandarajah C. A survey of machine scheduling problems with blocking and no-wait in process. Oper Res 1996;44:510–525. [CrossRef]

[7] Ercan T, Kayakutlu G. Job scheduling with the help of dominance properties and genetic algorithm on hybrid flow shop problem. Sigma J Eng Nat Sci 2015;33:345–355.

[8] Sarıçiçek İ. Multi-objective scheduling by maximizing machine preferences for unrelated parallel machines. Sigma J Eng Nat Sci 2020;38:405–420.

[9] Alcan G, Gündüz M, Akdoğan M. Scheduling in energy systems. Sigma J Eng Nat Sci 2015;6:67–76.

[10] Yang W, Liao CJ. Survey of scheduling research involving setup times. Int J Syst Sci 1999;30:143–155. [CrossRef]

[11] Allahverdi A, Ng CT, Cheng TCE, Kovalyov MY. A survey of scheduling problems with setup times or costs. Eur J Oper Res 2008;187:985–1032. [CrossRef]

[12] Allahverdi A. A survey of scheduling problems with no-wait in process. Eur J Oper Res 2016;255:665–686. [CrossRef]

[13] Belabid J, Aqil S, Karam A. Solving permutation flowshop scheduling problem with sequence-independent setup time. J Appl Math 2020;2020. [CrossRef]

[14] Naderi B, Ruiz R. The distributed permutation flowshop scheduling problem. Comput Oper Res 2010;37:754–768. [CrossRef]

[15] Avci M, Avci MG, Hamzadayi A. A branch-and-cut approach for the distributed no-wait flowshop scheduling problem. Comput Oper Res 2022;148. [CrossRef]

[16] Deng J, Wang L. A competitive memetic algorithm for multi-objective distributed permutation flowshop scheduling problem. Swarm Evol Comput 2017;32:121–131. [CrossRef]

[17] Zhang G, Xing K. Differential evolution metaheuristics for distributed limited-buffer flowshop scheduling with makespan criterion. Comput Oper Res 2019;108:33–43. [CrossRef]

[18] Huang J, Pan QK, Gao L, Zhang C. Effective constructive heuristics and discrete bee colony optimization for distributed flowshop with setup times. Eng Appl Artif Intell 2021;97. [CrossRef]

[19] Yu Y, Guo H, Pan QK. A discrete artificial bee colony method based on variable neighborhood structures for the distributed permutation flowshop problem with sequence-dependent setup times. Swarm Evol Comput 2022;75. [CrossRef]

[20] Karabulut K, Pan QK, Guo H, Zhang L. An evolution strategy approach for the distributed permutation flowshop scheduling problem with sequence-dependent setup times. Comput Oper Res 2022;142. [CrossRef]

[21] Huang J, Pan QK, Gao L. An effective iterated greedy method for the distributed permutation flowshop scheduling problem with sequence-dependent setup times. Swarm Evol Comput 2020;59. [CrossRef]
[22] Guo H, Pan QK, Zhang L. An effective metaheuristic with a differential flight strategy for the distributed permutation flowshop scheduling problem with sequence-dependent setup times. Knowl Based Syst 2022;242. [CrossRef]
[23] Han B, Pan QK, Gao L. A cooperative iterated greedy algorithm for the serial distributed permutation flowshop scheduling problem. Int J Prod Res 2024. [CrossRef]
[24] Meng Q, Qiu D, Liu Y. Two-stage assembly flow shop scheduling problem with sequence-independent setup times. IEEE 19th International Conference 2023. [CrossRef]
[25] Qiao Y, Wu NQ, He YF. Adaptive genetic algorithm for two-stage hybrid flow-shop scheduling with sequence-independent setup time and no-interruption requirement. Expert Syst Appl 2022. [CrossRef]
[26] Elissaouy O, Allali K. Minimizing the maximum tardiness for a permutation flow shop problem under the constraint of sequence-independent setup time. RAIRO Oper Res 2024. [CrossRef]
[27] Ying KC, Lin SW, Chen KF. Minimising makespan in distributed assembly hybrid flowshop scheduling problems. Int J Prod Res 2024. [CrossRef]
[28] İnce N, Deliktaş D, Selvi İH. A comprehensive literature review of the flowshop group scheduling problems: Systematic and bibliometric reviews. Int J Prod Res 2024. [CrossRef]
[29] Perez-Gonzalez P, Framinan JM. A review and classification on distributed permutation flowshop scheduling problems. Eur J Oper Res 2023;312:1–21. [CrossRef]
[30] Ruiz R, Pan QK, Naderi B. Iterated greedy methods for the distributed permutation flowshop scheduling problem. Omega 2019;83:213–222. [CrossRef]
[31] Fernandez-Viagas V, Framinan JM. A bounded-search iterated greedy algorithm for the distributed permutation flowshop scheduling problem. Int J Prod Res 2015;53:1111–1123. [CrossRef]
[32] Lin SW, Ying KC, Huang CY. Minimising makespan in distributed permutation flowshops using a modified iterated greedy algorithm. Int J Prod Res 2013;51:5029–5038. [CrossRef]
[33] Nawaz M, Ensore E Jr, Ham I. A heuristic algorithm for the m-machine, n-job flow-shop sequencing problem. Omega 1982;11:91–95. [CrossRef]
[34] Laurentys CT, Nagano MS. Evaluating procedures in the NEH heuristic for the PFSP - SIST. J Proj Manag 2024;9:17–26. [CrossRef]
[35] Fernandez-Viagas V, Ruiz R, Framinan JM. A new vision of approximate methods for the permutation flowshop to minimise makespan: State-of-the-art and computational evaluation. Eur J Oper Res 2017;257:707–721. [CrossRef]
[36] Liu W, Jin Y, Price M. A new improved NEH heuristic for permutation flowshop scheduling problems. Int J Prod Econ 2017;193:21–30. [CrossRef]
[37] Ruiz R, Stützle T. A simple and effective iterated greedy algorithm for the permutation flowshop scheduling problem. Eur J Oper Res 2007;177:2033–2049. [CrossRef]
[38] Juan AA, Faulin J, Ruiz R, Barrios BB, Caballe S. Using iterated local search for solving the flow-shop problem: Parallelization, parametrization, and randomization issues. Int Trans Oper Res 2013;21:103–126. [CrossRef]
[39] Katragjini K, Vallada E, Ruiz R. Flowshop rescheduling under different types of disruption. Int J Prod Res 2013;51:780–797. [CrossRef]
[40] Ruiz R, Allahverdi A. Some effective heuristics for no-wait flowshops with setup times to minimize total completion time. Ann Oper Res 2007;156:143–171. [CrossRef]
[41] Taillard E. Benchmarks for basic scheduling problems. Eur J Oper Res 1993;64:278–285. [CrossRef]

Sigma J Eng Nat Sci, Vol. 44, No. 4, pp. 2641–2657, August, 2026

Sigma Journal of Engineering and Natural Sciences
Web page info: https://sigma.yildiz.edu.tr
DOI: 10.14744/sigma.2026.2120

Research Article

Improving power quality in fuel cell applications and deep learning based analysis

Ünal YILMAZ[1,*], Kerim KARADAĞ[1], Süleyman Bayram GÖNÜLLÜ[1]

[1]Department of Electrical-Electronics Engineering, Harran University, Şanlıurfa, 63000, Türkiye

ARTICLE INFO

Article history
Received: 08 April 2026
Revised 21 May 2026
Accepted: 01 July 2026

Keywords:
Deep Learning; Dynamic Voltage Restorer; Fuel Cell

ABSTRACT

Power quality issues such as voltage sags, swells, and harmonics that hinder efficient energy transfer in grid-connected systems with sensitive loads lead to grid instability and potential load damage. This study proposes an improved hybrid power architecture that integrates grid and precise load management in a fuel cell system with a maximum power algorithm, performing pulse width modulation (PWM) prediction using an offline-trained deep learning method from dynamic voltage restorer (DVR) data. Grid-injected current and voltage are regulated using proportional–resonant and phase-locked loop (PR-PLL) controllers, while the DVR uses PLL-based synchronization and hysteresis control. Additionally, voltage and switching-signal data are processed with a recurrent neural network (RNN) to enable predictive analysis and estimation of inverter PWM patterns. The proposed data-driven control method aims to reduce the instantaneous processing load and dynamic response times of conventional controllers, thereby achieving high power quality and efficiency in renewable energy integration. The system's success has been verified by testing it under temperature variations and sudden voltage fluctuations. The DC-link voltage was regulated at 400 V, current harmonic distortion was limited to approximately 5%, a power factor above 0.98 was achieved, and the sensitive load voltage remained at its nominal value despite voltage sags and swells. The mean squared error (MSE) was 0.0251 in the RNN method applied for inverter PWM estimation and analysis.

Cite this article as: Yılmaz Ü, Karadağ K, Gönüllü SB. Improving power quality in fuel cell applications and deep learning based analysis. Sigma J Eng Nat Sci 2026;44(4):2641–2657.

INTRODUCTION

Along with the rapid depletion of fossil fuels, problems such as gas emissions and climate change that have the potential to threaten the sustainability of life are directing the global energy sector towards alternative energy sources that are sustainable, environmentally friendly and clean [1, 2]. In addition, rapidly developing technology creates new needs and it is observed that the demand for energy has increased significantly as a result of these needs [3, 4]. In this context, fuel cells stand out with their superior features such as simple use, modularity, high efficiency and low/zero emissions [5, 6]. Depending on the application area,

*Corresponding author.
*E-mail address: uyilmaz@harran.edu.tr

This paper was recommended for publication in revised form by Editor-in-Chief Ahmet Selim Dalkilic

Published by Yıldız Technical University Press, İstanbul, Turkey
© Author. This is an open access article under the CC BY-NC license (http://creativecommons.org/licenses/by-nc/4.0/).

the power values of fuel cells vary between 500 W and 1 MW. In addition, these cells can offer better solutions for power balancing and voltage/frequency regulation compared to wind and solar energy-based systems in terms of their dependence on environmental effects.

In recent years, fuel cell-based applications have begun to increase in the grid connection, residential (standalone) and automotive sectors [7]. Power electronic circuit interfaces are needed for system connections fed from fuel cells. In power systems that can feed sensitive loads from renewable energy sources as well as transfer power to the grid; power quality problems such as voltage sags, swells and harmonics can prevent efficient power transfer, cause grid instability and damage sensitive loads [8, 9]. In order to prevent such problems, dynamic voltage restorer (DVR) offers a serious solution. DVR can be defined as a power circuit structure consisting of a single-phase full bridge inverter, harmonic filter and control algorithms that perform continuous system control by connecting between the power source, load and grid [10]. In the event of a possible voltage sags or swells, it determines the voltage required by sensitive loads to perform at nominal levels and ensures that voltage is injected into the power circuit in series. Thus, sensitive loads continue to operate at nominal levels without being affected by power quality problems [9, 11]. Furthermore, deep learning is a computer-based algorithm that attempts to simulate the way the human brain works, with many layers known as deep neural networks, and utilizes large amounts of data to make decisions, predictions, and classifications. A variant of deep learning, recurrent neural networks (RNN), are a class of neural networks specifically designed to work with sequential data, with high accuracy and performance, system adaptability, and real-time prediction capabilities [12, 13].

Literature studies related to improving power quality in grid-connected power systems have been reviewed. In [8], improving power quality of three-phase grid-connected photovoltaic (PV) systems by proposing a DVR-aided system that combines a two-stage control strategy with a multilevel inverter. In nominal operating mode, it provides voltage correction using sliding mode control (SMC) and proportional resonance (PR) during voltage outages. The multilevel inverter is used to reduce harmonic distortion. In [14], A dual-function and series-connected compensator is proposed for grid-tied and photovoltaic sourced power circuit. The operating logic of this compensator is based on superconducting magnetic energy storage. The proposed power circuit has two different operating modes. These modes are; dynamic voltage restorer (to prevent voltage fluctuation) and fault current limiter (to prevent short circuit faults). In addition, a modified sliding mode controller (SMSVM) is developed to be applied in the proposed study, which is claimed to provide more effective and advantageous voltage control than traditional methods. In [15], An optimum proportional and integral (PI) based method is proposed for inverter control in the power circuit of single-phase grid-connected photovoltaic systems. The proposed model includes a time domain objective function based on the integral square error (ISE) of current and voltage errors. This function is used to formulate the PI control. With the contributions of the developed method, reactive power compensation is provided and active power is injected into the grid, and thus it is stated that it is a simple, low-cost and attractive method for home energy production. In [16], A technique based on dynamic voltage restorer (DVR) is proposed to provide solutions to power quality problems that may occur in photovoltaic fed systems under harsh weather conditions and to increase the stability of microgrids. Additionally, the comparison of the electrical characteristics and control algorithms of the proposed system with the existing studies in the literature is presented in Table 1 [17, 24].

This study presents an improved integrated power interface architecture for fuel cell systems connected to the grid and supplying sensitive loads (Fig. 1). The proposed framework enables maximum power acquisition through the P&O MPPT algorithm, establishes robust DC junction regulation at a 400 V reference using a PI controller, and achieves high-quality grid synchronization with a power factor exceeding 0.98 through the PR-PLL scheme. To protect sensitive loads under adverse conditions such

Table 1. Electrical properties of studies in the literature

Ref.	Fuel Cell	Rated Power	MPPT	Grid-Tied	Control and Analysis	DVR
[17]	PEMFC	50kW	○	√	VPI Control	○
[18]	PEMFC	3-6kW	○	○	Genetic Algorithm	○
[19]	Hydrogen	NA	○	√	Type-3 Fuzzy	N/A
[20]	Fuel Cell	1.2 kW	○	√	PI-Based	○
[21]	Fuel Cell	200 W	OD-PSO	√	Lyapunov-Based	○
[22]	PEMFC	1 kW	○	√	PQ and Voltage-Mode	○
[23]	PEMFC	7 kW	IC-MPPT	√	MFSO-FLC	○
[24]	SOFC	200 W	○	√	Anti-İslanding Control	N/A
This Paper	SOFC	3481 W	P&O-MPPT	√	PLL-PR- RNN (Deep Learning)	√

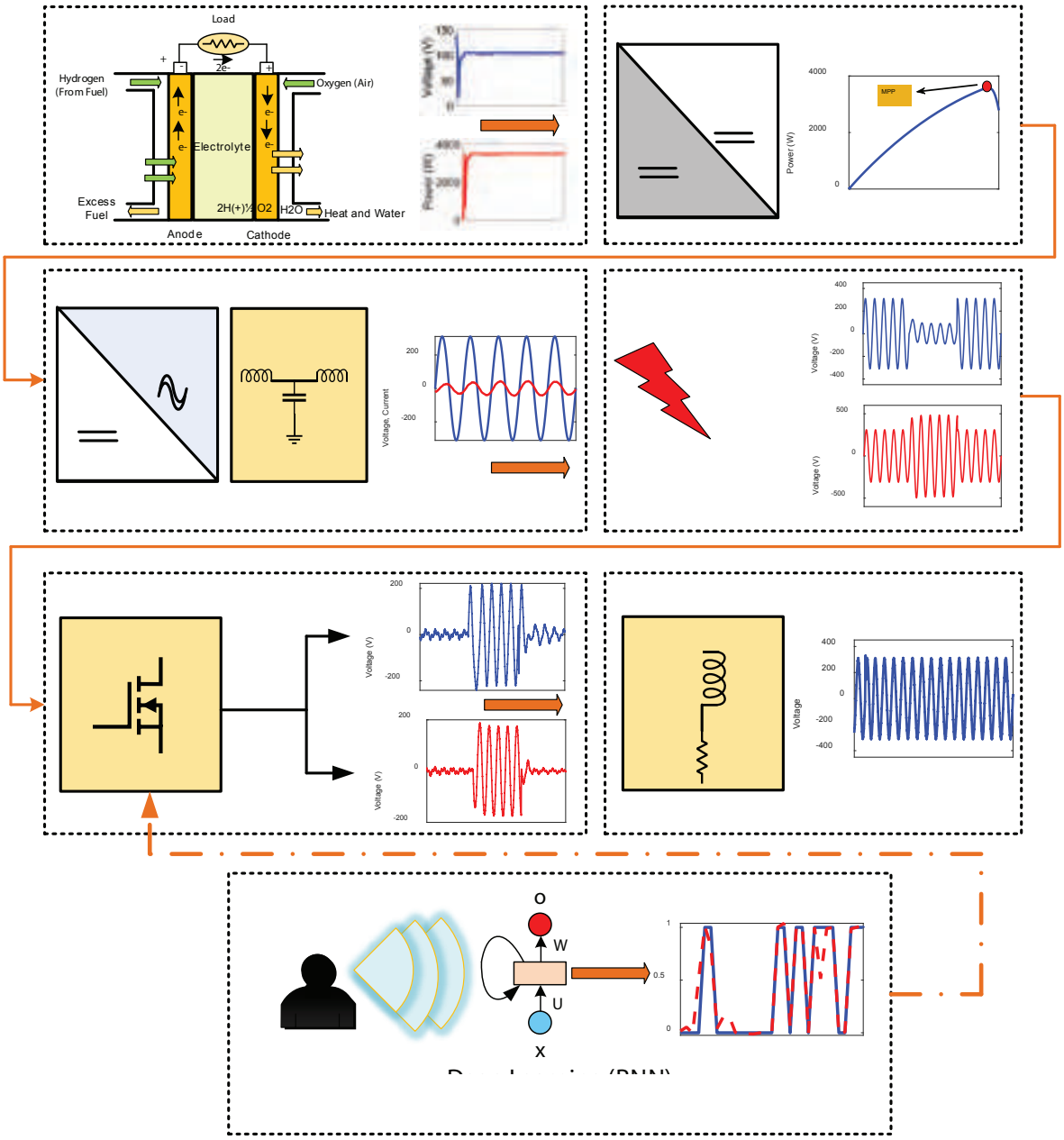


Figure 1. Performance steps and electrical characteristics of the proposed study.

as voltage sags, swells, and temperature fluctuations, a Dynamic Voltage Restorer (DVR) is used, employing a hysteresis control-PLL structure for series voltage injection. Unlike conventional approaches (Table 1), this study presents a data-driven power structure that leverages a Recurrent Neural Network (RNN) algorithm to model the highly nonlinear relationship between instantaneous voltage faults and semiconductor switching profiles. Using datasets collected from switching states, the RNN methodology enables accurate prediction and performance analysis of PWM signals, providing a predictive tool for improved power quality management.

MATERIALS AND METHODS

Materials

In the proposed study, solid oxide fuel cell (SOFC) is used as power source. In addition, MPPT (P&O) algorithm is applied to dc-dc boost converter for maximum power harvesting from fuel cell. Moreover, PLL-PR control method is applied to full bridge inverter for DC-link voltage control and power injection to grid. In addition, PLL-hysteresis control method is applied to full bridge inverter for DVR to provide power flow to sensitive load. Additionally, load voltage and injected voltage data were

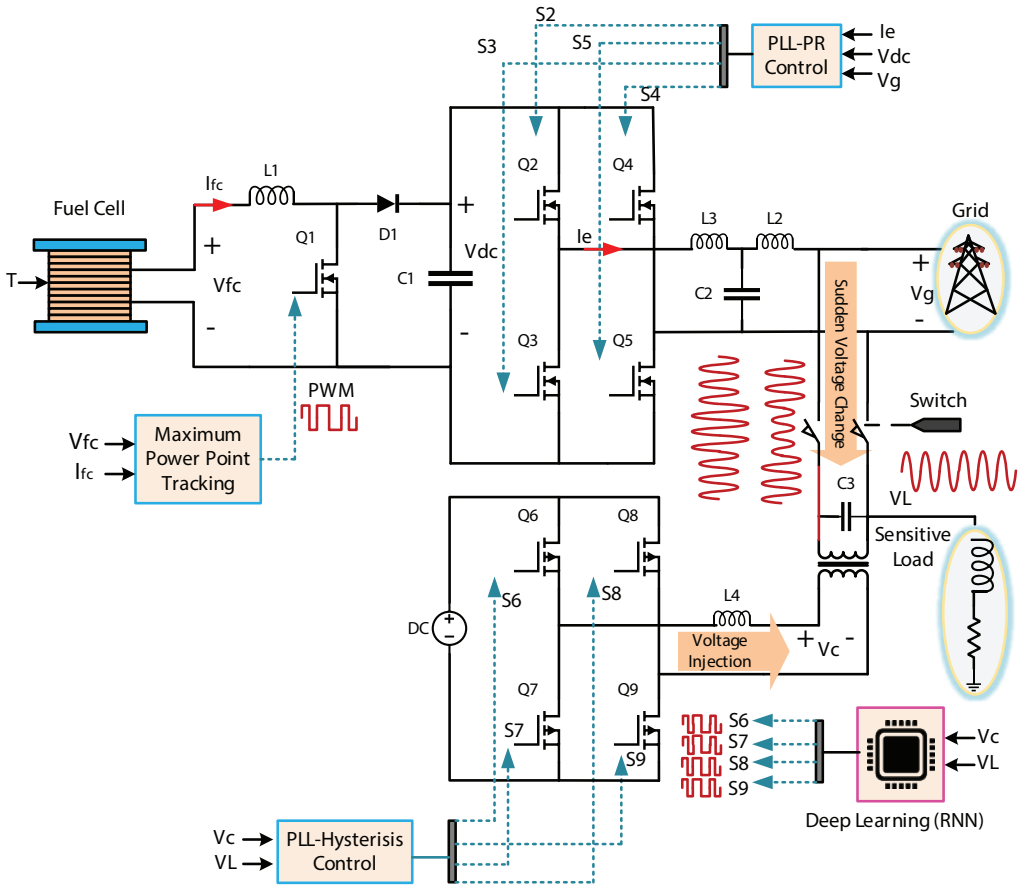


Figure 2. Fuel cell powered and deep learning supported DVR system model.

collected using voltage oscilloscopes, and PWM generation was performed using deep learning (RNN) with offline analysis. Power circuits and control algorithms of the proposed study are presented in detail in Figure 2.

SOFC and MPPT Method

A SOFC is usually defined by its electrolyte material (solid oxide or ceramic electrolyte). While it provides advantages in terms of high heat, cost-effectiveness, stability and efficiency. During the chemical process, oxygen (O_2) ions are transported from the cathode to the anode through the solid oxide electrolyte. This process usually takes place at high temperatures (ranging from 600 to 900 °C). SOFCs can produce power at different rates (100 W to 2 MW). The following equations are used for the steady-state model of a SOFC [25, 26].

$$V_C = E_{rev} - V_{tdrop} = E_{rev} - (V_{con} + V_{act} + V_{om}) \quad (1)$$

Concentration voltage drop is defined as follows.

$$V_{con} = -1 \cdot \ln\left(1 - \frac{I_{den}}{I_{mden}}\right) \quad (2)$$

Activation voltage can be expressed as follows.

$$V_{act} = k \cdot ln\left(\frac{I_{den}}{2I_{exden}}\right) \quad (3)$$

Ohmic voltage is defined as follows.

$$V_{om} = I_{op}\frac{R}{B_a} \quad (4)$$

Here V_C is the fuel cell output voltage, V_{tdrop} is the total voltage drop, this total voltage drop will be equal to the sum of the concentration drop V_{con}, the activation drop V_{act} and the ohmic drop V_{om}. E_{rev} is the reversible voltage, I_{den} is the current density, I_{op} is the fuel cell output current, R is the total resistance, B_a is the membrane effective area.

The electrical characteristic curves of the SOFC under variable temperatures investigated in this study are presented in Figure 3.

The electrical parameters and values of the SOFC utilized in this study are listed in Table 2.

After using the fuel cell as a source, a power electronic circuit interface is needed for grid connection. DC-DC converter design will be carried out to control the input voltage of the inverter at the reference value, to apply low voltage ripple and maximum power point tracking algorithm. For this purpose, dc-dc boost converter is preferred in this

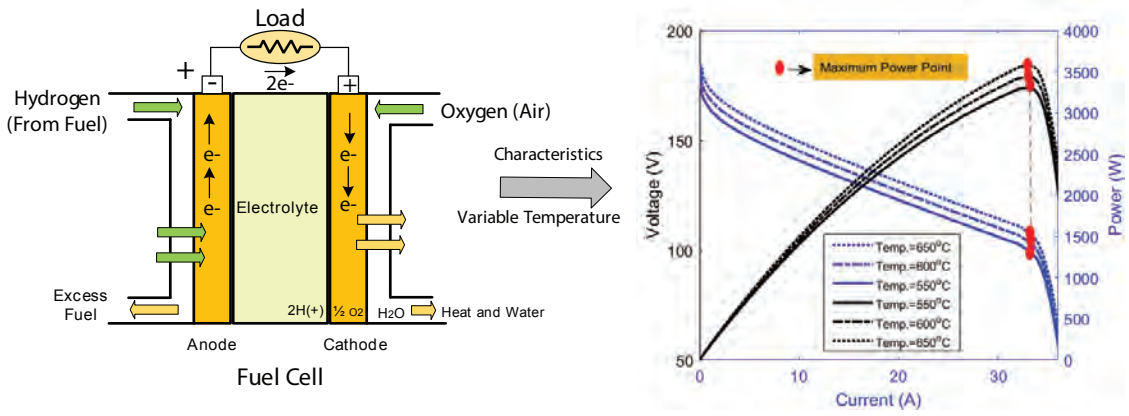


Figure 3. SOFC power-voltage and current characteristics and maximum power points.

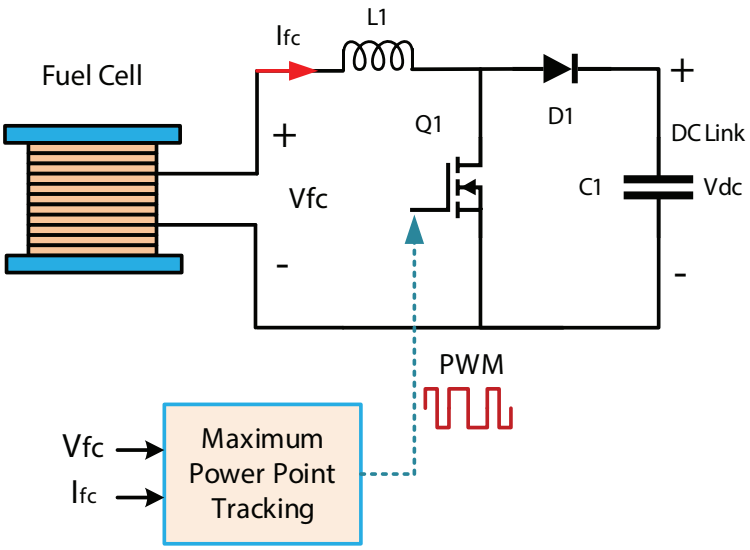


Figure 4. DC-DC converter and maximum power tracking algorithm.

Table 2. Parameters and values of SOFC

Parameters	Values
Nominal Power	3195 W
Maksimum Power	3481 W
Nominal Current, Current at MPP	30 A, 33.2 A
Nominal Voltage, Voltage at MPP	106.5 V, 104.86 V
Fuel Cell Resistance	0.364 Ω
Hydrogen (H2)	%72.82
Oxidant(O2)	%29.82
Fuel	59.21 slpm
Air	49.73 slpm
Cell Number	119
Efficiency	% 52
System Temperature	600°C
Fuel Supply Pressure	1.35 Bar
Air Supply Pressure	1 Bar

study due to its low circuit element count, easy applicability and high efficiency [27]. The implementation circuit of the DC-DC converter and maximum power tracking algorithm is presented in Figure 4.

Duty cycle (D) and passive circuit element (L, C) selection for DC-DC Converter Design are found with the help of the following equations [28].

$$\frac{V_{dc}}{V_{FC}} = \frac{1}{1-D} \tag{5}$$

$$L_1 = \frac{V_{fc}D}{\Delta i_{fc} f_s} \tag{6}$$

$$C_1 = \frac{D}{R\left(\frac{\Delta V_{dc}}{V_{dc}}\right) f_s} \tag{7}$$

Where, V_{dc} represents the dc link voltage, L_1 represents the inductor value in the boost converter design, C_1 represents the capacitor value in the boost converter design, D is the duty cycle. V_{fc} represents the fuel cell voltage, f_s represents the switching frequency, Δi_{fc} represents the inductor current ripple. ΔV_{dc} represents the dc link voltage ripple.

In order to harvest maximum power from the fuel cell, the P&O algorithm, which offers an effective solution in terms of both implementation and cost, is preferred. The characteristic curve based on the working logic of P&O method and step change according to dP/dV slope are shown in Figure 5 [29]. It is obvious that the slope of the power-voltage characteristic of the fuel cell (dP/dV) is positive on the left side of the MPP and negative on the right side. The duty cycle of the PWM signal applied to the switch of the DC-DC converter (D, in equation 5) increases at points 1, 2 and 4, and decreases at points 3 and 5 [30, 31].

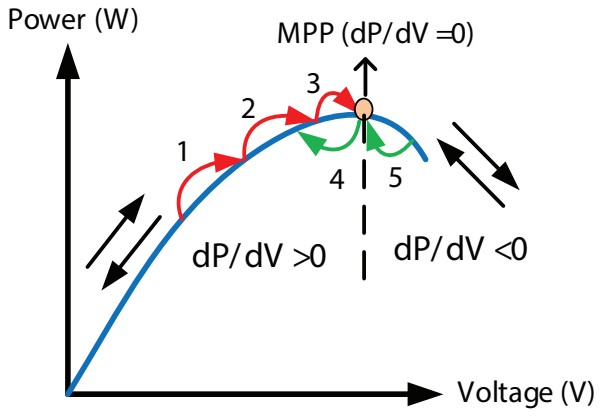


Figure 5. Fuel cell power voltage characteristics and P&O MPPT.

LCL Filter and Control Algorithms

LCL filter carried out to suppress the total harmonic distortion (THD) in the inverter output voltage. As seen in Figure 2, to design the LCL filter, the transfer function and resonance frequency determined by the following equations [32-34].

$$\frac{i_{\S}}{V_{ev}} = \frac{1}{(L_3L_2C_2)s^3+(L_2+L_3)s} \tag{8}$$

Resonance Frequency is;

$$\begin{cases} w_{res} = \sqrt{\frac{L_2+L_3}{L_2L_3C_2}} \\ f_{res} = \frac{w_{res}}{2\pi} = \frac{1}{2\pi}\sqrt{\frac{L_2+L_3}{L_2L_3C_2}} \end{cases} \tag{9}$$

The designed LCL filter application is expected to have low harmonic current to be injected into the grid and voltage feeding the sensitive load. In this context, the Bode diagram showing the phase-frequency response and magnitude frequency response of the filter applied after the single-phase full bridge inverter is presented in Figure 6.

The DC bus voltage (V_{dc}) is compared with the reference DC bus voltage (V_{ref}) to generate an error signal, the generated error signal is passed through the PI-based control to generate an output signal [35]. The generated signal is then

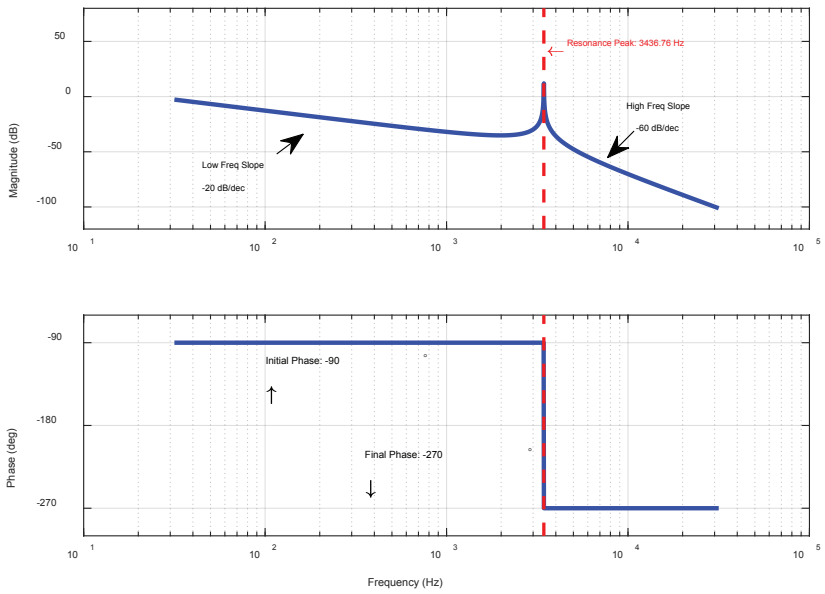


Figure 6. Bode diagram of LCL filter application.

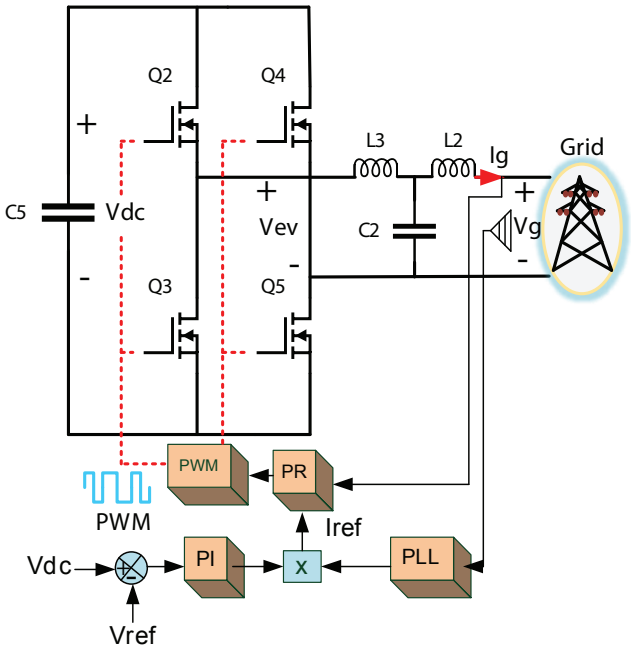


Figure 7. Grid connected single phase inverter and PLL-PR control.

used as an input to the reference current, I_{ref}, Phase Locked Loop (PLL) and the PR controller, which is synchronized with the grid voltage as seen in Figure 7.

The Gain function of the ideal PR control is defined as follows.

$$G_{PR}(s) = K_p + \frac{2K_i s}{s^2+w_0{}^2} \tag{10}$$

Here K_P and K_i represent the controller gains, ω_o is the resonant frequency. Although the ideal PR controller provides infinite gain at the AC frequency, its lossless nature limits its practical implementation. Furthermore, this infinite gain can introduce system stability challenges. To mitigate these issues, a non-ideal PR controller is defined as follows [36, 37],

$$G_{nPR}(s) = K_p + \frac{2K_i w_c s}{s^2+2w_c s+w_0{}^2} \tag{11}$$

PLL and hysteresis control used for DVR control (Fig. 8). While PLL control provides synchronization between load voltage and injection transformer primary voltage (Figure 1), Hysteresis control minimize the error rate between the two voltages and the output signals are used to produce PWM signals for semiconductor switches. In addition, data collected from the inputs and outputs of the hysteresis control method are utilized to train the Deep Learning-based Recurrent Neural Network (RNN) algorithm. The estimation and performance evaluations for PWM generation using this RNN model are analyzed in detail.

The mathematical derivation of the PI loop gains (K_p, K_i) in the PLL structure for the natural frequency (ω_n) and damping ratio (ζ) is presented in the following equations [38].

$$K_p = 2 \cdot \zeta \cdot \omega_n \tag{12}$$

$$K_i = \omega_n^2 \tag{13}$$

To operate the system with minimum overshoot and optimum stability, the damping ratio is $\zeta=1/\sqrt{2}$, where $\omega_n=2\pi^*f_n$. The resulting value is then divided by the grid peak voltage (V_m) to obtain the physical results.

In hysteresis control, the equation for finding the band-dependent output voltage is as follows [39].

$$V_f = \begin{cases} V_{ref} + {}^{HB}/_{2}, & Rising\ Case \\ V_{ref} - {}^{HB}/_{2}, & Decreasing\ Case \end{cases} \tag{14}$$

The hysteresis band can be found using the following equation [40].

$$HB = \frac{V_{dc}}{8 \cdot f \cdot L_f} - \frac{L_f}{2f \cdot V_{dc}} \left(\frac{v_s(t)}{L_f} + \frac{di_f}{dt} \right)^2 \tag{15}$$

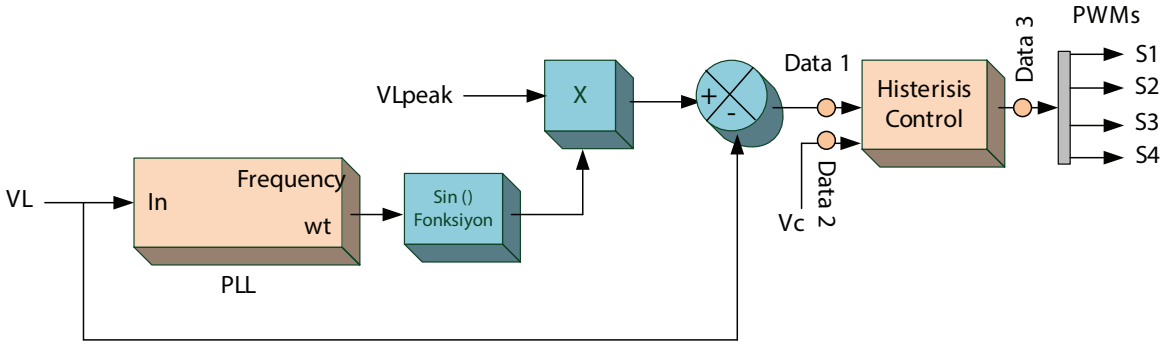


Figure 8. DVR control.

Hysteresis band can be simplified to approximately the following equation.

$$HB \approx \frac{V_{dc}}{8 \cdot f \cdot L_f} \tag{16}$$

Here, V_{ref} represents the reference voltage, V_f the output voltage, V_{dc} the inverter input voltage, and L_f the filter inductance value.

Recurrent Neural Network (RNN)

Recurrent Neural Network is one of the deep learning methods and is specifically designed to work with sequential data. RNNs process each element of sequential data and carry the knowledge gained from previous steps to the next step. While traditional machine learning models treat data as static points, RNN architecture, thanks to its internal memory loops, can capture the temporal characteristics of transient states such as temperature fluctuations and instantaneous voltage surges (sag/swell). This makes RNN superior to other linear and feedforward methods in dynamic PWM signal estimation from instantaneous voltage errors, which can pose a serious threat to sensitive loads [41]. The basic structure of RNN consists of an input layer and an output layer along with a hidden layer. Rather than traditional feedforward neural networks, RNNs have recurrent connections, as shown in Figure 9, which allows data to loop through the networks. The calculation of the hidden state of the RNN model at each time step is provided by the following equation [42, 43].

$$h_t = \sigma_h(W_{xh}x_t + W_{hh}h_{t-1} + b_h) \tag{17}$$

Here h_t represents the hidden state, σ_h is the activation function, W_{xh} is the weight matrix controlling the transition from the input layer to the hidden layer, x_t is the input data at the t-th time step, W_{hh} represents the weight matrix from the hidden layer to the hidden layer, h_{t-1} is the hidden state at the previous time step, and finally bh represents the bias for the hidden layer. The output at each time step (t) is defined as follows.

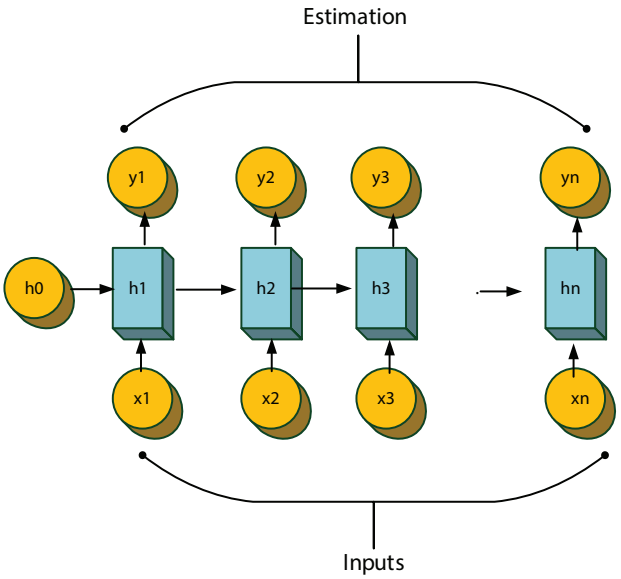


Figure 9. General structure of the RNN method.

$$y_t = \sigma_y(W_{hy}h_t + b_h) \tag{18}$$

As can be seen from the equation, the weight matrix b_h between the hidden and output layers is a bias vector, while σ_y is the activation function of the output layer. The basic representation of the RNN method, which is one of the deep learning methods (Input, output (prediction) and hidden layer) is presented in Figure 7. RNN implementation involves iterative computation of the hidden state, which integrates the current input with the previous hidden state. This enables RNNs to exhibit dynamic and temporal behavior. Additionally, one of the key roles in RNN architecture is the choice of the activation function (σh), as it enables the network to learn complex patterns in the data.

The training process of the proposed RNN model for offline estimation of Pulse Width Modulation (PWM) signals in single-phase Dynamic Voltage Regulator (DVR)

Table 3. Structural and algorithmic hyperparameters of the designed Elman RNN Model

Hyperparameter / Parameter Type	Value / Selected Function
Network Model Architecture	Elman Recurrent Neural Network (RNN)
Total Number of Hidden Layers	3 Layers
Neuron Distribution Per Layer	[100, 50, 25, 1]
Layer 1 and 3 Activation	Hyperbolic Tangent (Hyperbolic Tan)
2nd Layer Activation Function	Log-Sigmoid
Output Layer Function	Linear (Pure Linear)
Training Algorithm (Optimizer)	Scaled Conjugate Gradient (SCG)
Performance Metric (Loss)	Mean Squared Error (MSE)
Maximum Epoch Limit	5000
Target Error Threshold (Goal)	1.00e-07
Minimum Gradient Threshold	1.00e-06

technology was carried out to measure the stability of the grid against sudden changes in grid voltage and its generalization ability in generating inverter triggering signals. The network was trained using a 2×994 input matrix containing two defining features of the system and a corresponding 1×994 single output target (PWM reference signal) vector. The structural and algorithmic hyperparameters of the designed RNN model are presented in detail in Table 3.

During the design phase of the proposed study, the power and voltage characteristics of the SOFC are crucial in determining the maximum power that can be transferred to the load and grid. Additionally, the application of the MPPT algorithm to the dc-dc converter design ensures maximum power harvest from the fuel cell under variable conditions and is cost-effective. Subsequently, the conversion of dc energy at the output of the dc-dc converter to ac requires the use of a single-phase full-bridge inverter and a filter for low-harmonic current and voltage values. DVR control is crucial to prevent sudden voltage dips and spikes from damaging sensitive loads. Finally, the deep learning (RNN) application applied to the single-phase full-bridge inverter's switching signal estimation and generation has ensured that the proposed system has the potential to provide alternative solutions for smart grids and artificial intelligence-based control methods. The flowchart (creation stages) of the proposed system is presented in Figure 10.

Passive circuit elements and parameters in the modeled system are presented with their values in Table 4.

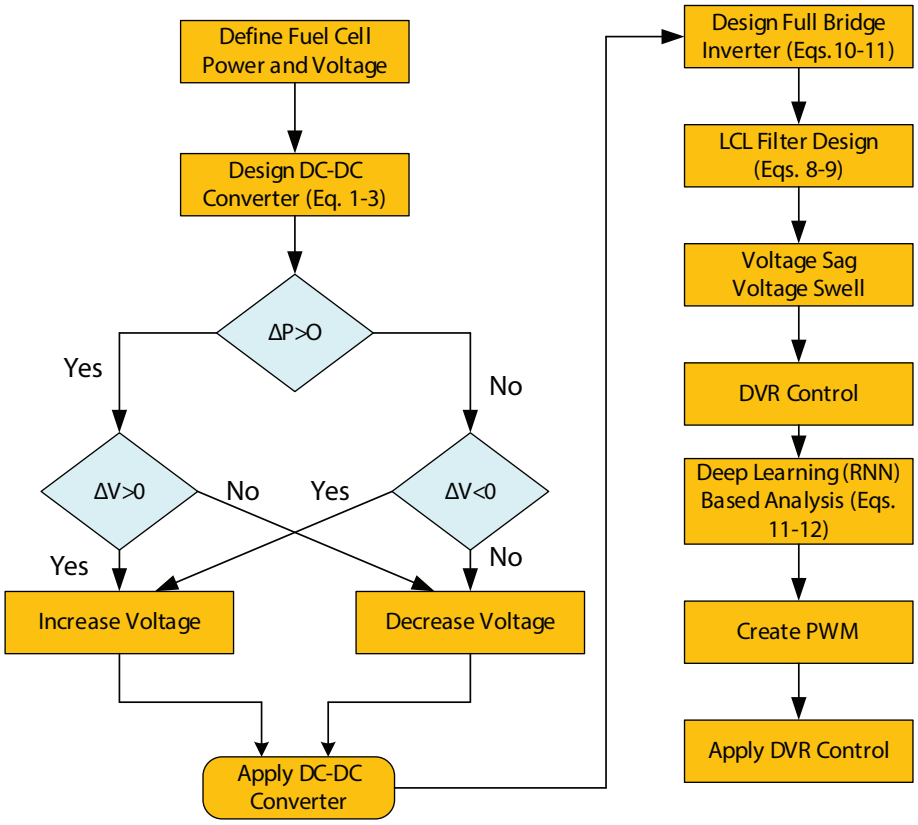


Figure 10. Creation stages of the proposed system.

Table 4. Circuit elements and values

Parameter	Value	Parameter	Value
Lboost	17 mH	L2 (Filter)	3.735 mH
CdcLink	10 mF	L4	0.1μF
L3 (Filter)	3.15 mH	C3	4.7 mF
C2 (Filter)	1.255 μF	Kp(PI)	0.75
Ki (PI)	10	f (Grid)	50 Hz

RESULTS AND DISCUSSION

By applying different temperatures (540°C-600°C) to the fuel cell, the (P&O) MPPT algorithm was ensured to perform at the fuel cell maximum power point for each temperature. In accordance with the power, voltage and current characteristics given in Figure 3 and Table 1. At first case (temp.=600°C), Fuel cell power is 3481 W (Fig. 11), voltage is 104.86 V and current is 33.4 A (Fig. 9). In the second case (temp.=570°C), the fuel cell power is 3310 W (Fig. 11), the voltage is 98.5 V, and the current is 33.6 A (Fig. 12). In the last case (temp.=540°C), the fuel cell power is 3120 W (Fig. 11), the voltage is 93.5 V, and the current is 33.36 A (Fig. 12).

While the variable temperature changes the voltage and power values of the fuel cell, the DC-link voltage is kept constant at 400 V by applying the Pi-based control method and the DC-link voltage ripple is measured as 2.6 V at the 10 mF capacitor value, which is ΔV_{dc} = 0.65% (Fig. 13).

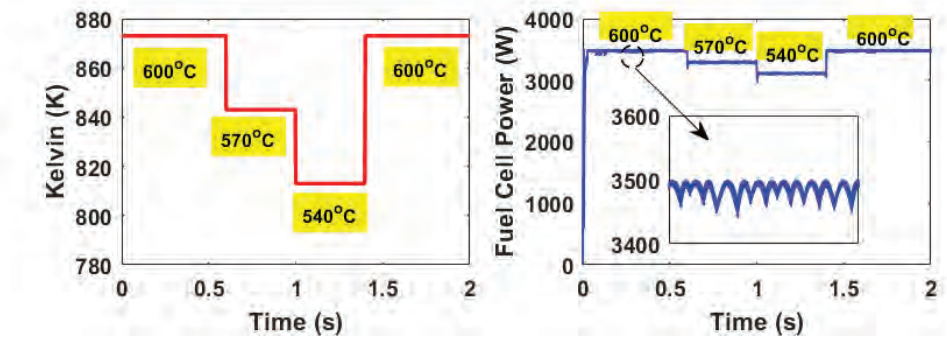


Figure 11. System Temperature and Fuel Cell Power.

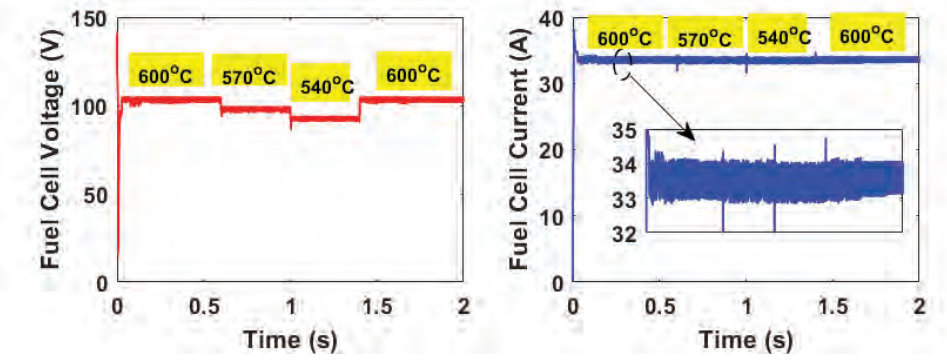


Figure 12. Fuel cell voltage and current.

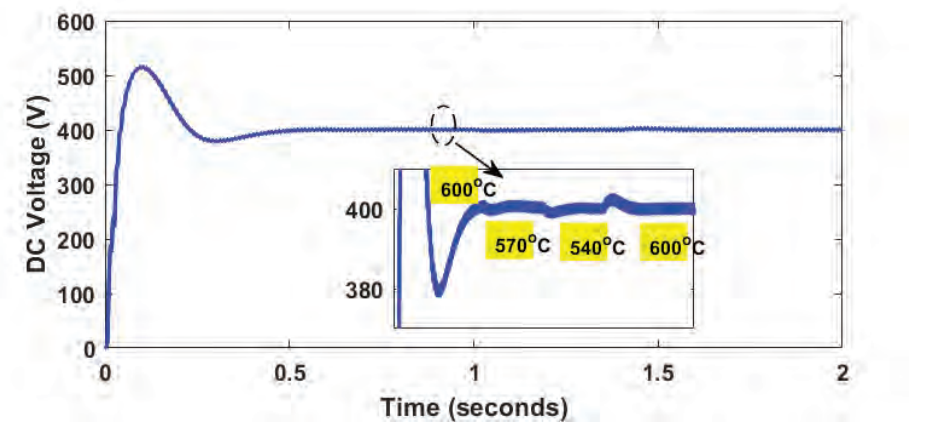


Figure 13. DC link voltage under variable temperature.

The current and voltage injected into the grid are kept in the same phase, thus providing power transfer with high power factor and low harmonic distortion (Fig. 14). For this purpose, the PLL-PR control method is used.

In the first case (temperature=600°C), the grid maximum voltage is 311 (Fig. 14) and the current is 22.5 A (Fig. 15), the power factor cosθ= 0.992, while total harmonic distortion THD=5.59%, (Fig. 16). In the second case (temperature=570°C), the grid maximum voltage is 311 and the current is 21.5 A (Fig. 12), the power factor cosθ = 0.984, while total harmonic distortion THD=5.7%, (Fig. 13). In the last case (temperature = 540°C), the maximum voltage

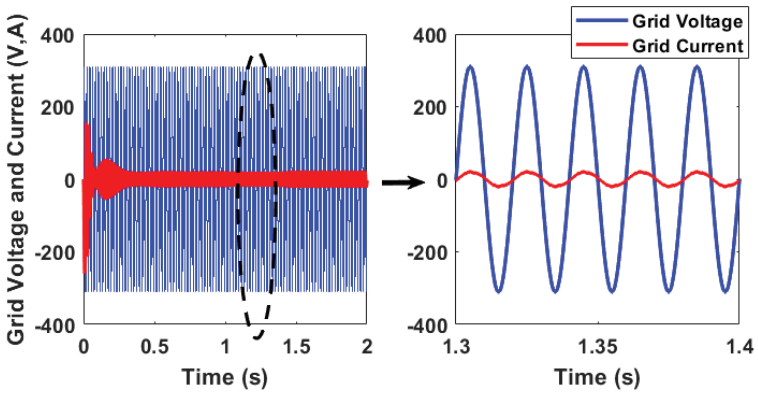


Figure 14. Grid voltage and current.

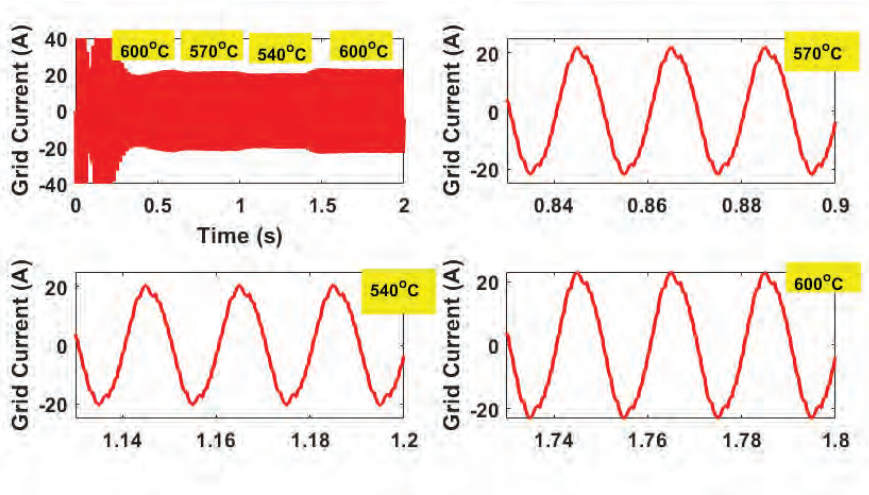


Figure 15. Grid current under variable temperature.

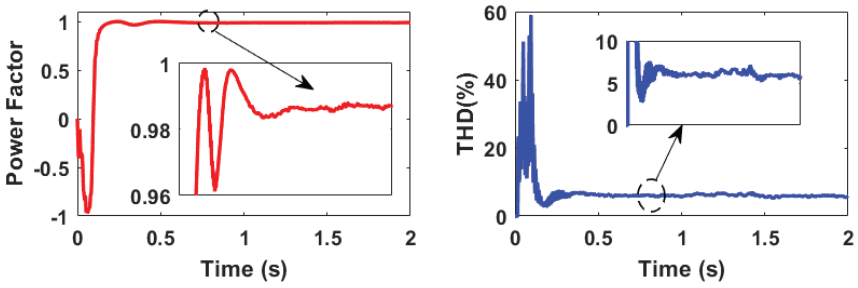


Figure 16. Grid power factor and current THD.

of the network is 311, the current is 20.5 A (Fig. 15), the power factor is cosθ = 0.987 while the total harmonic distortion THD = 5.1%, (Fig. 13).

As long as there is no voltage fluctuation, the sensitive load is supplied with a maximum of 311 V, which is the mains voltage. When a sudden voltage drop is applied to the load supply voltage, the maximum supply voltage drops to 90 V. Since this value is well below the nominal voltage level of the sensitive load, the load does not operate, so the DVR control method detects this by injecting a series voltage (221 V) into the supply voltage and ensures that the sensitive load continues to operate at the nominal level without being affected by this situation. In the second case, when a sudden voltage increase is applied to the sensitive load supply voltage, it is seen that the maximum supply voltage increases to 485 V. Applying this voltage for a long time at this value will damage the sensitive load, and the DVR control method detects this by applying a series voltage in the reverse direction of 174 V to the supply voltage and ensures that the sensitive load continues to operate at the nominal level without being affected by this voltage change. Voltage fluctuation conditions and voltage supply voltage, injection voltage, load voltage and current are shown in detail in Figure 17.

Gradient, validation check and mean square error signals in DVR full bridge inverter PWM estimation as a result of RNN application are presented in Figure 18. For this

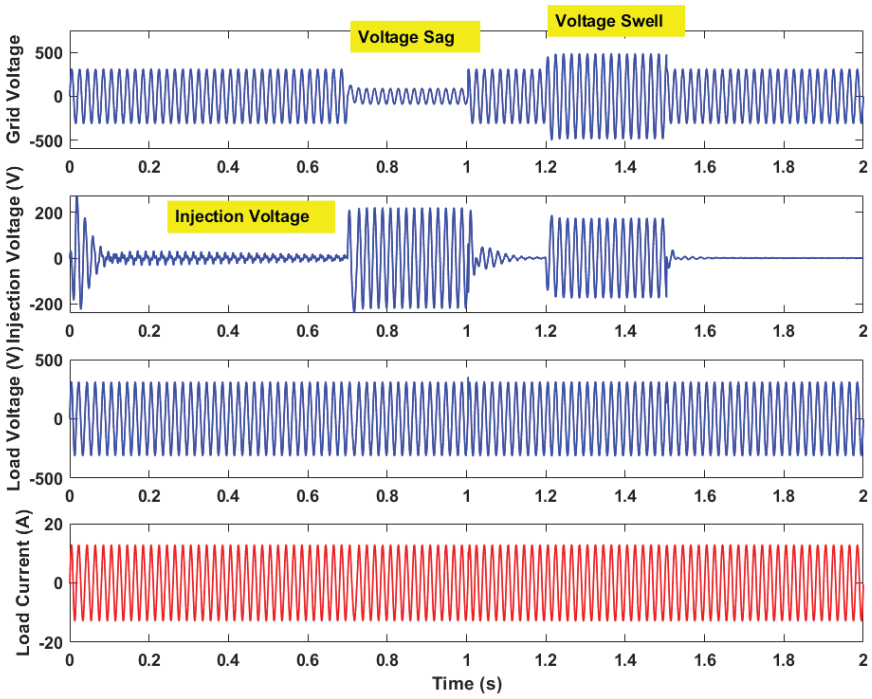


Figure 17. Grid voltage, ınjection voltage, load voltage and load current.

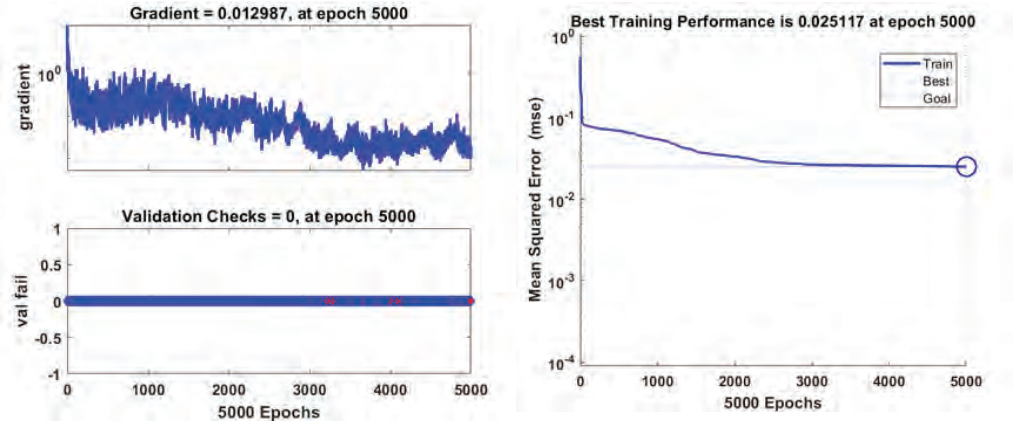


Figure 18. Gradient validation check and training performance.

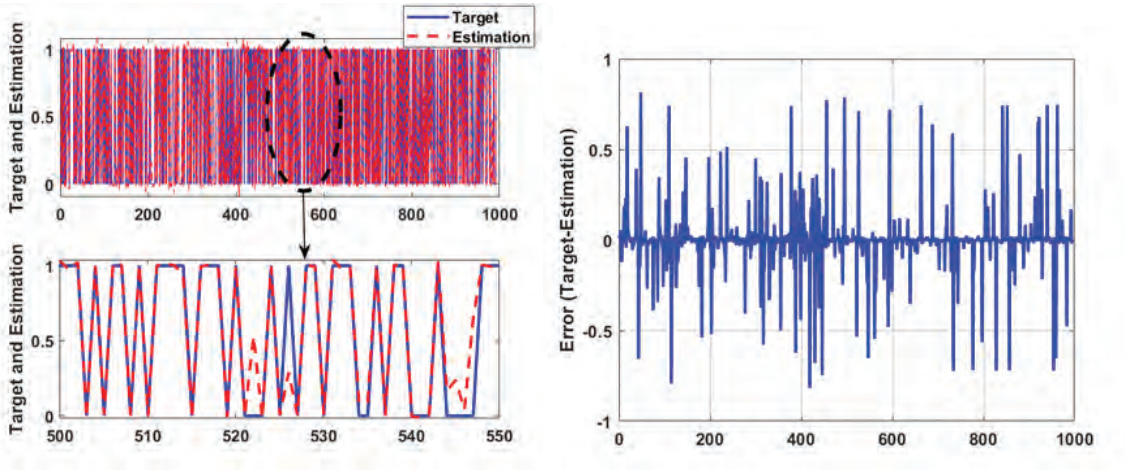


Figure 19. Target and estimation (PWM) and error.

application, the epoch number is 5000, the goal is 1e-7, and the learning rate is 0.05.

As a result of RNN application, the actual value, estimated value and error rate signals in the DVR full bridge inverter PWM estimation are presented in Figure 19.

As a result of RNN application, error types (Mean Squared Error (MSE), Root Mean Squared Error (RMSE), Mean Absolute Error (MAE), Mean Absolute Percentage Error (MAPE)), formulas and calculation results between the real value (y_i) and the estimated ($\tilde{y}_i$) value are presented in Table 5.

Table 5. RNN application error types and values

Error Type	Formula	Calculated value
MSE	$MSE = \frac{1}{n}\sum_{i=1}^{n}(y_i - \tilde{y}_i)^2$	0.0251
RMSE	$RMSE = \sqrt{\frac{1}{n}\sum_{i=1}^{n}(y_i - \tilde{y}_i)^2}$	0.0316
MAE	$MAE = \frac{1}{n}\sum_{i=1}^{n}\lvert y_i - \tilde{y}_i\rvert$	0.0615
MAPE	$MAPE = \frac{1}{n}\sum_{i=1}^{n}\frac{\lvert y_i - \tilde{y}_i\rvert}{y_i}\cdot 100\%$	0.0051

Electrical characteristics and values of the proposed system in terms of power-voltage and current at variable operating conditions (600°C, 570°C, 540°C) are presented in Table 6.

In this study, an integrated DVR architecture with RNN-based PWM signal estimation was tested in a simulation environment to protect sensitive loads in a fuel cell-based and grid-connected system. The findings show that the proposed deep learning model (RNN) can simulate the nonlinear switching dynamics of a conventional Hysteresis-PLL controller with high accuracy. The current THD values obtained from the system were observed to vary between 5.1% and 5.7%. The IEEE 519 and IEC 61000-2-2 standards, widely accepted in the power quality literature, prescribe a maximum THD limit of 5.0% in steady-state conditions for current waveforms injected into a low-voltage grid. The fact that the proposed model remains slightly above this legal limit is entirely reasonable and acceptable considering the extremely dynamic and multivariate test conditions to which the system is subjected. In the literature, THD values can only be lower in DVR systems

Table 6. Power, voltages and current characteristics of the proposed system

States (Temperature) →	600°C	570 °C	540 °C
Fuel Cell Power (W)	3481	3310	3120
Fuel Cell Voltage (V)	104.86	98.5	93.5
Grid Voltage (V) (max)	311	311	311
Grid Current (A)	22.5	21.5	20.5
THD (%)	5.59	5.7	5.1
Power Factor	0.992	0.984	0.987
DC Link Voltage (V)	400	400	400

operating under ideal grid conditions; However, in this study, the model was simultaneously subjected to both electrical and environmental disturbances such as voltage sags, swells, and variable temperature profiles. Temperature-dependent instantaneous power fluctuations in the fuel cell on the source side created micro-fluctuations in the DC bus (400V), straining the inverter's modulation index. It has been observed in the literature that in traditional methods or in the variable conditions (unstable regimes) of advanced methods produce >5% THD [16, 44-46]. Accordingly, the proposed system has been proven to exhibit acceptable and competitive harmonic performance against challenging disturbances, in line with the literature. The study was conducted entirely in a simulation environment (Matlab/Simulink) with noise-free ideal datasets. In real-world applications, sensor noise and quantization errors originating from current/voltage transducers can distort the input matrix, affecting RNN prediction accuracy. Furthermore, the deep matrix computational overhead of RNN models can cause hardware latency and consequently microsecond phase shifts in PWM signals when running in real-time in embedded systems (DSP/FPGA). To overcome these limitations and definitively reduce the THD profile below the 5.0% standard limit, future studies plan to test the model in real-time on dSPACE or Hardware-in-the-Loop (HIL) platforms. Additionally, the goal is to completely eliminate high-frequency switching harmonics by integrating an adaptive damping LCL filter into the system.

CONCLUSION

In this study, a single phase efficient power circuit structure where fuel cells feed both the grid and sensitive loads is modeled and inverter PWM estimation and analysis are performed with RNN. In order for sensitive loads not to be affected by voltage changes (sags and swells), DVR application is implemented (the proposed system model is presented in detail in Fig. 2). In addition, in order to provide maximum power performance of the fuel cell at variable temperatures, P&O MPPT algorithm is applied to the dc-dc boost converter (Fig. 4). While PLL-PR and dc-link control methods are used for the grid connection of the study, PLL-Hysterisis control methods are used for the DVR application. As a result of the application, the fuel cell produces 3481 W power at 600°C, 3310W at 570°C and 3120W at 540°C (Table 5 and Fig. 11). In addition, the DC link voltage is kept constant at 400 V (reference value) (Table 5 and Fig. 13). While the grid current harmonics fluctuate between 5.1%<THD%<5.7, the power factor fluctuates between 0.984<pf<0.992 (Fig. 16 and Table 5). In DVR technology used to eliminate voltage irregularities in sensitive loads, offline analysis of the RNN method for PWM estimation has been performed, and the result of process, MSE is determined as 0.0251, while the performances of other error types are presented in detail in Table 4. The sensitive load continued to perform at the nominal level without being affected by the voltage changes (Fig. 17). The contributions of the proposed study and the features of the designed system can be summarized in the light of the findings mentioned below.

1. In order to maximize the power harvested from the Fuel Cell (SOFC) under different operating conditions and to reduce the implementation cost, the PWM generated from the MPPT algorithm was applied to the dc-dc boost converter.
2. Injecting the generated power into the grid and supplying the load with low harmonics and high power factor, achieved using PLL-PR control and DC-link control, ensuring reliable power flow.
3. A single-phase DVR based on Hysteresis control was implemented to protect sensitive loads from sudden voltage sag and swells. Reliability was ensured by testing it under sudden voltage changes.
4. The infrastructure for integrating the proposed system into smart grids was established by estimating the switching signal of the single-phase full-bridge inverter using Deep Learning (RNN) technology.

The modeling, analysis, and implementation of the proposed study are performed within the MATLAB/Simulink environment

NOMENCLATURE

Abbreviations

SOFC	Solid Oxide Fuel Cell
LCL	Inductor-Capacitor-Inductor
PLL	Phase-Locked Loop
PR	Proportional Resonance
MSE	Mean Squared Error
RNN	Recurrent Neural Network
THD	Total Harmonics Distortion
AI	Artificial intelligence
MPPT	Maximum Power Point Tracking
DVR	Dynamic Voltage Restorer
PI	Proportional and Integral
PWM	Phase Width Modulation

Variables

V_C	Fuel Cell Output Voltage
V_{con}	Concentration Voltage
V_{act}	Activation Voltage
B_a	Membrane Effective Area
V_{om}	Ohmic Voltage
V_{tdrop}	Total Voltage Drop
R	Total Resistance
V_{dc}	DC Link Voltage
y_t	Output At Each Time Step
b_h	Bias Vector
σ_y	Activation Function
W_{xh}	Weight Matrix
x_t	İnput Data
h_t	Hidden State
f_{grid}	Grid Voltage Frequency
L_b	Boost Converter Inductor
C_b	Boost Converter Capacitor
ΔI_L	Inductor Current Ripple
L_3 (Filter)	Filter Primer Inductor
C_2 (Filter)	Filter Capacitor
L_2 (Filter)	Filter Seconder Inductor

ω_o	Ac Frequency
ω_c	Cut-off Frequency
D	Duty Cycle
K_P	Proportional Gain
K_i	Integral Gain
$W_{res.}$	Resonant Frequency
I_{den}	Current Density
I_{op}	Fuel Cell Output Current
V_{ref}	Reference Voltage
ω_o	Ac Frequency
ω_c	Cut-off Frequency
D	Duty Cycle
K_P	Proportional Gain
K_i	Integral Gain
$W_{res.}$	Resonant Frequency
I_{den}	Current Density
I_{op}	Fuel Cell Output Current
V_{ref}	Reference Voltage

ACKNOWLEDGEMENTS

This study was supported by Harran University Scientific Research Projects Unit. Project Number: 25088. The authors would like to thank for this support.

AUTHORSHIP CONTRIBUTIONS

Ünal YILMAZ: Writing – review & editing, Writing – original draft, Visualization, Validation, Software, Resources, Methodology, Investigation, Data curation, Conceptualization. **Kerim KARADAĞ**: Validation, Software, Resources, Methodology, Investigation, Data curation, Conceptualization. **Süleyman Bayram GÖNÜLLÜ**: Validation, Software, Resources, Methodology, Investigation, Data curation, Conceptualization.

DATA AVAILABILITY STATEMENT

The authors confirm that the data that supports the findings of this study are available within the article. Raw data that support the finding of this study are available from the corresponding author, upon reasonable request.

CONFLICT OF INTEREST

The authors declared no conflict of interest.

ETHICS

There are no ethical issues with the publication of this manuscript.

STATEMENT ON THE USE OF ARTIFICIAL INTELLIGENCE

During the preparation of this study, the author(s) used ChatGPT and Gemini AI for the purposes of proofreading, checking the grammar, improving the readability, and correcting spelling. The authors have reviewed and edited the output and take full responsibility for the content of this publication.

REFERENCES

[1] Çavdar B, Karaca E, Okumuş H, Nuroğlu FM. A review of photovoltaic plants and battery energy storage systems in terms of power systems stability. Sigma J Eng Nat Sci 2026;44:663–679. [CrossRef]

[2] Bahadır A, Aydoğdu Ö. Modeling of a brushless DC motor driven electric vehicle and its PID-fuzzy control with dSPACE. Sigma J Eng Nat Sci 2023;41:156–177. [CrossRef]

[3] Anees AS. Grid integration of renewable energy sources: Challenges, issues and possible solutions. In: 2012 IEEE 5th India International Conference on Power Electronics (IICPE); 2012; Delhi, India. p. 1–6. [CrossRef]

[4] Alsokhiry F. Grid-connected hybrid renewable energy system under various operating conditions. In: 2024 IEEE 8th Energy Conference (ENERGYCON); 2024; Doha, Qatar. p. 1–6. [CrossRef]

[5] Yilmaz U, Turksoy O. Artificial intelligence based active and reactive power control method for single-phase grid connected hydrogen fuel cell systems. Int J Hydrogen Energy 2023;48:7866–7883. [CrossRef]

[6] Yilmaz U. Improved a two-stage control method for efficient wireless power transfer in fuel cell applications. Renew Energy 2025;240:122219. [CrossRef]

[7] İnci M, Türksoy O. Review of fuel cells to grid interface: Configurations, technical challenges and trends. J Clean Prod 2019;213:1353–1370. [CrossRef]

[8] Shahidi N, Salary E. Enhancing grid-connected photovoltaic systems' power quality through a dynamic voltage restorer equipped with an innovative sliding mode and PR control system. e-Prime Adv Electr Eng Electron Energy 2025;11:100875. [CrossRef]

[9] Mbuli N. Dynamic voltage restorer as a solution to voltage problems in power systems: Focus on sags, swells and steady fluctuations. Energies 2023;16:6946. [CrossRef]

[10] Yılmaz Ü. Application of dynamic voltage restorer to improve power quality in stand-alone wind power systems under variable operating conditions. KSU J Eng Sci 2025;28:660–673. [CrossRef]

[11] Venkatesh A, Kumar PS. Design of dynamic voltage restorer in the power quality improvement for voltage problems. Appl Nanosci 2023;13:2985–2995. [CrossRef]

[12] Zang Z, Bao X, Li Y, Qu Y, Niu D, Liu N, et al. A modified RNN-based deep learning method for prediction of atmospheric visibility. Remote Sens 2023;15:553. [CrossRef]

[13] Aseeri AO. Effective RNN-based forecasting methodology design for improving short-term power load forecasts: Application to large-scale power-grid time series. J Comput Sci 2023;68:101984. [CrossRef]

[14] Li Y, Jin J, Wang L. A dual-function SMES-based series-connected compensator of dynamic voltage restoration and fault current limitation for photovoltaic microgrid. Energy Rep 2022;8:312–320. [CrossRef]

[15] Abo-Elyousr FK, Abdelaziz AY. Optimal PI microcontroller-based realization for technical trends of single-stage single-phase grid-tied PV. Eng Sci Technol Int J 2018;21:945–956. [CrossRef]
[16] Farooqi A, Othman MM, Radzi MAM, Musirin I, Noor SZM, Abidin IZ. Dynamic voltage restorer (DVR) enhancement in power quality mitigation with an adverse impact of unsymmetrical faults. Energy Rep 2022;8:871–882. [CrossRef]
[17] Chen W, Han Y, Li Q, Liu Z, Peng F. Design of proton exchange membrane fuel cell grid-connected system based on resonant current controller. Int J Hydrogen Energy 2014;39:14402–14410. [CrossRef]
[18] Kaur R, Krishnasamy V, Muthusamy K, Chinnamuthan P. A novel proton exchange membrane fuel cell based power conversion system for telecom supply with genetic algorithm assisted intelligent interfacing converter. Energy Convers Manag 2017;136:173–183. [CrossRef]
[19] Kilic H, Asker ME, Haydaroglu C. Enhancing power system reliability: Hydrogen fuel cell-integrated D-STATCOM for voltage sag mitigation. Int J Hydrogen Energy 2024;75:557–566. [CrossRef]
[20] Wu JC, Wu KD, Jou HL, Wu ZH, Chang SK. Novel power electronic interface for grid-connected fuel cell power generation system. Energy Convers Manag 2013;71:227–234. [CrossRef]
[21] Priyadarshi N, Padmanaban S, Holm-Nielsen JB, Blaabjerg F, Bhaskar MS. A hybrid photovoltaic-fuel cell-based single-stage grid integration with Lyapunov control scheme. IEEE Syst J 2020;14:3334–3342. [CrossRef]
[22] Jang M, Ciobotaru M, Agelidis VG. A single-phase grid-connected fuel cell system based on a boost-inverter. IEEE Trans Power Electron 2013;28:279–288. [CrossRef]
[23] Hai T, Alazzawi AK, Zhou J, Farajian H. Performance improvement of PEM fuel cell power system using fuzzy logic controller-based MPPT technique to extract the maximum power under various conditions. Int J Hydrogen Energy 2023;48:4430–4445. [CrossRef]
[24] Bayrak G, Cebeci M. A novel anti islanding detection method for grid connected fuel cell power generation systems. Int J Hydrogen Energy 2014;39:8872–8880. [CrossRef]
[25] Tawil IH, Elfaqih AK, Muftah EB. Performance comparison study of solid oxide fuel cell with direct oxidation in three fuel types. In: 2022 IEEE 2nd International Maghreb Meeting of the Conference on Sciences and Techniques of Automatic Control and Computer Engineering (MI-STA); 2022; Sabratha, Libya. p. 710–715. [CrossRef]
[26] Ismael I, El-Fergany AA, Gouda EA, Kotb MF. Cooperation search algorithm for optimal parameters identification of SOFCs feeding electric vehicle at steady and dynamic modes. Int J Hydrogen Energy 2024;50:1395–1407. [CrossRef]
[27] Güngör O, Yüksek Hİ. Modeling of boost and Cuk converters and comparison of their performance in MPPT. Sigma J Eng Nat Sci 2020;11:83–101. [CrossRef]
[28] Göncü B, Yılmaz Ü. Different DC-link control methods with multilevel inverter for low harmonic and efficient power transfer in grid-tied hydrogen fuel cell systems. DUJE 2023;14:289–304. [CrossRef]
[29] Yilmaz U. Dual fuel-cell sourced wireless power transfer and load power estimation with machine learning. In: 2025 9th International Symposium on Innovative Approaches in Smart Technologies (ISAS); 2025; Gaziantep, Türkiye. p. 1–7. [CrossRef]
[30] Büyük M, İnci M. Improved drift-free P&O MPPT method to enhance energy harvesting capability for dynamic operating conditions of fuel cells. Energy 2023;267:126543. [CrossRef]
[31] Yılmaz Ü, Türksoy Ö, İbrikçi T, Teke A. Estimation of electrical characteristics and maximum power point of photovoltaic panel. J Electr Syst 2017;13:255–266.
[32] Cho BG, Sul SK. LCL filter design for grid-connected voltage-source converters in high power systems. In: 2012 IEEE Energy Conversion Congress and Exposition (ECCE); 2012; Raleigh, NC, USA. p. 1548–1555. [CrossRef]
[33] Ranjan A, Giribabu D. Design of LCL filter for grid connected three phase three level inverter to meet IEEE 519 standards. In: 2023 IEEE International Students' Conference on Electrical, Electronics and Computer Science (SCEECS); 2023; Bhopal, India. p. 1–6. [CrossRef]
[34] Yilmaz U. Wind turbine power conversion topology with machine side fault detection and classification method. Energy 2025;335:137903. [CrossRef]
[35] Yilmaz U, Kircay A, Borekci S. PV system flyback converter controlled PI control to charge battery under variable temperature and irradiance. In: 2017 Electronics; 2017; Palanga, Lithuania. p. 1–6. [CrossRef]
[36] Zhang N, Tang H, Yao C. A systematic method for designing a PR controller and active damping of the LCL filter for single-phase grid-connected PV inverters. Energies 2014;7:3934–3954. [CrossRef]
[37] Yusof NS, Ahmad AZ. Single-phase grid-connected of PV inverter using PR current controller. In: 2017 IEEE Conference on Systems, Process and Control (ICSPC); 2017; Melaka, Malaysia. p. 117–121. [CrossRef]
[38] Teodorescu R, Liserre M, Rodríguez P. Grid converters for photovoltaic and wind power systems. 1st ed. Chichester (UK): John Wiley & Sons, Ltd; 2011. [CrossRef]
[39] Mekri F, Machmoum M, Aït-Ahmed N, Mazari B. A comparative study of voltage controllers for series active power filter. Electr Power Syst Res 2010;80:615–626. [CrossRef]

[40] Vahedi H, Sheikholeslami A, Tavakoli Bina M, Vahedi M. Review and simulation of fixed and adaptive hysteresis current control considering switching losses and high-frequency harmonics. Adv Power Electron 2011;2011:397872. [CrossRef]

[41] Le TTH, Oktian YE, Jo U, Kim H. Time series electrical motor drives forecasting based on simulation modeling and bidirectional long-short term memory. Sensors (Basel) 2023;23:7647. [CrossRef]

[42] Mienye ID, Swart TG, Obaido G. Recurrent neural networks: A comprehensive review of architectures, variants, and applications. Information 2024;15:517. [CrossRef]

[43] Yu J, de Antonio A, Villalba-Mora E. Deep learning (CNN, RNN) applications for smart homes: A systematic review. Computers 2022;11:26. [CrossRef]

[44] Banaei M, Salary E. A new single-source cascaded semi-bridge inverter topology suitable for distributed generation systems. Gazi Univ J Sci Part A Eng Innov 2013;1:11–22. [CrossRef]

[45] Mohamed Iqbal M, Senthilkumar M, Zahira R, Ganesh C, Balaji V, Vishalini G. Power quality analysis of fuzzy DVR based hybrid solar PV-PEMFC system under severe disturbance. Int J Electr Electron Res 2023;11:148–155. [CrossRef]

[46] Cho S, Kang HS, Lee KB, Yoo JY. Performance improvement of a grid-connected inverter under distorted grid voltage using a harmonic extractor. Electronics 2019;8:1038. [CrossRef]

Sigma J Eng Nat Sci, Vol. 44, No. 4, pp. 2658–2675, August, 2026

Sigma Journal of Engineering and Natural Sciences
Web page info: https://sigma.yildiz.edu.tr
DOI: 10.14744/sigma.2025.1945

Research Article

Prediction performance of multiple linear regression analysis applied to the mechanical properties of green cement mortar

Kaci CHALAH[1], Aghiles HAMMAS[1,*]

[1]*Centre National d'Études et de Recherches Intégrées du Bâtiment, Souidania-Algiers, 16097, Algeria*

ARTICLE INFO

Article history
Received: 02 March 2025
Revised 05 May 2025
Accepted: 01 July 2025

Keywords:
Mechanical Properties; Multiple Linear Regression Analysis; Green Cement Mortar; Ground Granulated Blast Furnace Slag

ABSTRACT

The application of the mathematical tools such as multiple linear regression analysis (MLR) in the prediction of mechanical behavior of cement-based materials is the subject of several previous investigations works conducted in civil engineering field. As new alternative of the development of green cement mortar, this work aims in the first to study the effect of the substitution of Ordinary Portland Cement (OPC) with ground granulated blast furnace slag (GGBFS) on the compressive and flexural strength of manufactured mortar. Both mechanical tests are caried out using cubic and prismatic specimens with dimensions of 4 cm × 4 cm × 4 cm and 4 cm × 4 cm × 16 cm, respectively. In the other hand, this study investigates the capacity of the multiple linear regression analysis in the prediction of compressive and flexural strength of green cement mortars. Indeed, tests samples of 64 are examined in order to develop an adequate mathematical model for the prediction of the both investigated mechanical properties as a function of the three independents variables of water/binder ratio, hydration ages and the concentration of ground granulated blast furnace slag. The mechanical tests revealed that 20 mass % of ground granulated blast furnace slag content give good properties for the development cement mortars and above this concentration there is a slight effect on the mechanical strength. According to the statistical results, this study concluded also that the multiple linear regression analysis has a good performance for the prediction of flexural strength properties than compressive strength of green cement mortars, 0.8 and 0.42 of coefficient of determination (R^2) are obtained, respectively. In addition, the experimental results revealed also that the hydration age has more effect than the two others parameters which is in accordance with statistical results obtained from the MLR analysis, such as significance level (Sig.), standardized coefficients, t-test values and the variation inflation factor (VIF). Both regression models obtained for compressive and flexural strength are statically significant with very low values of sig. < 5 %. The statistical parameters indicate clearly that the hydration age has a strong effect on the prediction of compressive and flexural strength values using the obtained models, which mainly due to its highest values of standardized coefficients of 0.61. The results of these parameters indicate that water/binder ratios have more effect than ground granulated blast furnace slag content with standardized coefficients values of 0.13 and -0.17, respectively, but this is not the same for the flexural strength values, the concentration of ground granulated blast furnace slag has more effect than water/binder ratios, -0.22 and -0.66, respectively.

Cite this article as: Chalah K, Hammas A. Prediction performance of multiple linear regression analysis applied to the mechanical properties of green cement mortar. Sigma J Eng Nat Sci 2026;44(4):2658–2675.

***Corresponding author.**
*E-mail address: a.hammas@cnerib.edu.dz

This paper was recommended for publication in revised form by Editor-in-Chief Ahmet Selim Dalkilic

Published by Yıldız Technical University Press, İstanbul, Turkey
© Author. This is an open access article under the CC BY-NC license (http://creativecommons.org/licenses/by-nc/4.0/).

INTRODUCTION

In the recent decade, there are considerable attention has been focused on the addition of the GGBFS in the composition of cementitious materials as a supplementary additive due to its several advantages like: enhanced the durability, workability, ecological and environmental benefits of cementitious materials [1–4]. Its chemical and physical properties mainly depend on the raw materials and the freezing process is chosen to cool down the molten materials [5, 6]. According to the EN 15167-1 (2006) standard [6], this raw material is obtained by quick freezing of a slag melt of appropriate composition, synthetized by smelting iron ore in a blast furnace with high hydraulic properties. Moreover, GGBFS mainly contain different oxides like calcium oxide (CaO), silicon dioxide (SiO_2) and magnesium oxide (MgO) with mass ratio of (CaO + MgO)/(SiO_2) equal to 1. As well the aluminum oxide (Al_2O_3) and small concentration of other compounds can be present in this material. In contrast, GGBFS conforming to this European Standard must contain no added materials except grinding aids to assist in the manufacture. Indeed, the concentration of grinding aid and the organic of any grinding aid(s) shall not higher than 1.0 and 0.2% by weight of GGBS, respectively.

Based on the previous studies, numerous scientific research styles were conducted to understand the effect of GGBFS content on the mechanical characteristics of cement mortar (Table 1), it was clearly revealed from the most results of these experimental studies that GGBFS addition have a positive effect on the mechanical properties of mortars due mainly to its good quality of granulometry and chemical hydration (Table 2) [7–16]. Barnett et al. [15] studied the effect of different parameters like: GGBFS content, curing temperature and water to binder ratio on the mechanical strength development of mortars containing GGBFS and OPC. The authors concluded in this work that GGBFS content and water-binder ratios affected the estimated strength with a similar degree. In contrast, the results indicated that just the parameter of curing temperature that significantly affect the mechanical properties of manufactured mortars mixing of GGBFS and OPC. Different investigation works concluded that the GGBFS mortars gain strength faster at high temperature while under standard curing conditions. Çakır et al. [12] studied the effect of curing conditions on properties of mortars without and with different amount of GGBFS, namely 0% (control), 30%, and 60% by weight. In this work, the mechanical properties like flexural and compressive strength are investigated for the samples with the age of 7, 28, 56, 90, and 180 days. The results of this work concluded that the addition of GGBFS has a significant effect on the final properties of studied mortars. The results indicate that the effect of high temperature and lower relative humidity conditions on the flexural and compressive strength properties are more important specially in slag as a partial replacement of cement mortars. Akçaözoğlu et al. [17] investigated the combination effect of GBFS and fly ash addition on the mechanical properties of studied

Table 1. Summary of mechanical properties of mortar containing different amount of GGBFS

Ref.	GGBFS content (%)	w/b Ratio	Hydration age (days)	Compressive strength (MPa)	Flexural strength (MPa)
[26]	0, 30, 50, 70	0.5	30, 60, 90, 120 and 150	34 to 51	/
[10]	0, 5, 10, 15, 20	0.5	3, 7, 14 and 28	26, 32, 29, 22, 19	/
[9]	0, 60, 70, 80	0.5	7, 14, 28, 90	40 to 71	/
[27]	10, 30, 50	0.3	2, 14, 28	6 to 70	2 to 9
[28]	10, 20, 30, 40, 50, 60 and 70	0.45 and 0.65	28	26 to 47	/
[29]	2, 4, 6, 8 and 10	0.27	28	40 to 43	/
[2]	0, 20, 40, 60 and 80	0.3, 0.4 and 0.5	3, 7, 28, 90 and 360	12.1 to 90	/
[30]	0, 10, 20, 30 and 40	0.5	2, 7, 28, 90 and 180	7 to 68	1.8 to 9.2
[1]	25 to 60	0.31 and 0.38	3, 7 and 28	5 to 84	/
[31]	55, 60 and 65	0.3, 0.4 and 0.5	7 and 28	16 to 51	3 to 7.3

Table 2. Physical characteristics and chemical composition and of cement starting powder

Physical properties	Color	Bulk density (kg/m³)		specific gravity		Blaine's fineness (cm²/g)			
Cement	Off-white	1440		3.1		3500			
Chemical composition									
Oxides	**CaO**	**SiO_2**	**Al_2O_3**	**MgO**	**Fe_2O_3**	**MnO**	**TiO_2**	**SO_3**	**Loss on Ignition**
Content (%mass)	61.40	22.07	5.7	2.17	2.62	/	/	/	6.0

mortars containing the aggregate of waste Poly-ethylene Terephthalate (PET) bottle. Based to the most results obtained in this work, the incorporation of GBFS raw materials have a good effect on the mechanical characteristics of studied mortars cured during more than 90 days. Işıkdağ et al. [13] studied the addition effect of GGBS on the different properties of Horasan mortars. The results of this investigation indicates clearly that a significant improvement of mechanical and physical properties was obtained for the specimens with GGBFS addition compared to the other control samples. Recently, Nojoukambari et al. [18] studied the partial replacement of cement with Feldspar and GGBFS in order to improve different characteristics of mortar such as the mechanical and the durability properties. Different amount of Feldspar and GGBS content are used in this work for manufacturing 20 mixtures with 10%, 20%, and 30% by weight of cement. The must conclusions obtained in this work indicate clearly that the mortar samples with 10% of Feldspar and 30% of GGBFS contents exhibit more good properties than the others ternary mixtures.

In the recent decades, different investigation research conducted about the properties prediction of cementitious materials [19–23]. For that purpose, there are several analysis methods for modelling these properties, including computational modelling, statistical methods, and different recent developed tools such as regression analysis and machine learning techniques. Among the most traditional methods widely used for the prediction of the mechanical properties of cementitious materials, the MLR received a lot of attention in this field [22, 24]. The most important characteristic of this analysis is the ability to evaluates the relationship between the dependent (Y) and two or more independent variables (X). Recently, Palod et al. [25] developed a mathematical model by applying a MLR analysis in order to study the influence replacing cement with different proportions of GGBFS on the compressive strength of cementitious materials cured during 28 days. The obtained model presents high values of coefficient of determination (R^2) of 0.916, which explain the high precision of the developed equation for the prediction of the studied mechanical characteristic. Therefore, the authors conclude in this work that the obtained MLR model can be used for the estimation of the compressive strength property of any ternary mortar cured at the 28 days and manufactured by partially replacement of cement with GGBFS and steel slag.

The main objective of this work is to study the capacity of MLR analysis on the prediction of the mechanical properties of mortars with different GGBFS additions used as sustainable cementitious binder for the production of eco-friendly mortar. For this purpose, three concentrations of GGBFS were added of 10%, 20%, and 30% by weight of cement. The mechanical tests of compressive and flexural strength are carried out on the specimens with different hydration ages of 3, 7, 28 and 90 days. In addition, four w/b ratios of 0.35, 0.40, 0.45 and 0.50 were considered to evaluate the more efficient ratio (Table 1) [26, 31].

MATERIALS AND METHODS

Materials

Cement

The selected cement in the present work was the OPC 52.5 N conforming to CEM Type 1. The physical characteristics and the chemical composition of this raw material are indicated in Table 2. Moreover, the particle size distribution of used cement was obtained using Mastersizer 2000 laser diffraction particle size analyzer (Malvern Instruments Ltd., Malvern, UK).

GGBFS powder

The GGBFS used in the study was obtained from Ecocem company (from the plant of Fos sur mer, France). Table 3 summarizes the chemical composition and the physical characteristics of this element addition. It can be seen form these results that the GGBFS used in this study is in agreement with the requirements of EN 15167-1 [6]. Indeed, the results appear that the ratio of (CaO+MgO) / SiO_2 is higher than 1.0 and the presence of other oxides of MgO, SO_3, Cl, sulfide, alkalis, LOI and H_2O are well respected. In the other hand, according to its physical properties, it is classified as a category 80 of slag [32]. A laser diffraction particle size analyzer (Mastersizer 2000, Malvern Instruments Ltd., Malvern, UK) was also used to identify the particle size distribution of GGBFS powder.

Aggregates

Two types of natural sand with a continuous intermediate grade were selected four this work as coarse (CA) and fine aggregate (FA), which are provided from SARL FIAS,

Table 3. Characteristics of GGBFS powder

Physical properties	Color	Bulk density (kg/m³)		specific gravity		Blaine's fineness (cm²/g)						
GGBFS	grey	1200		2.9		4500						
Chemical composition												
Oxides	**CaO**	**SiO_2**	**Al_2O_3**	**MgO**	**Fe_2O_3**	**MnO**	**TiO_2**	**SO_3**	**Cl^-**	**S_{2-}**	**Na_2O éq.**	**Loss on Ignition**
Content (%mass)	42.7	36.7	11.3	7.0	0.6	0.3	0.5	0.2	0.01	1.0	0.7	2.0

Keddara-Boumerdes, Algeria. As indicated in the Table 4, the CA present a specific gravity and fineness modulus of 2.43 and 2.8, respectively. In the other hand, FA shows a specific gravity and fineness modulus of 2.63 and 1.12. The water adsorption values of each aggregate were found to be 11.92 and 4.3 % for CA and FA, respectively.

Superplasticizer (SP)

A commercial superplasticizer (Sika ViscoCrete TEMPO-12) with acrylic copolymer is used in this study, with special characteristics summarized in Table 5.

Water

The water used for mixing and curing purposes presents a good quality potable water.

Mixture Proportions and Specimen Preparation

In order to examine the effect of GGBFS addition as partial substitution of cement on the mechanical properties of prepared mortars, different proportions are used to substitute cement in specimen mixtures which varied from 0 to 30% replacement by weight of cement (10%, 20% and 30%). Four various ratios of water-to-binder (cement + GGBFS) mass of mortar were applied, specifically 0.35, 0.40, 0.45 and 0.50 (Table 6 and Fig. 1). A superplasticizer based acrylic copolymer was added with different content as indicated in Table 6 to obtain the systematic workability; the admixture dosage in each mix was varied to achieve the target flow of 20 cm. The required superplasticizer content was determined by using mini-cone test. More details about the designation of specimens and mixtures proportions details are given in Table 6. After mixing, prismatic and cubic specimens with 4 x 4 x 16 cm dimensions were prepared from both OPC and GGBFS/OPC mortars for all the testing measurements, this preparation method is made with according to EN 196-1 [33].

All mixtures were prepared according to the following steps: i) various amount of GGBS and cement were initially dissolved in water and mixed for 4 min with respecting different studied w/b rations. In this work, the OPC was substituted by GGBFS by weight percentage of 10 wt%, 20 wt% and 30 wt%; ii) then the sand content is added each mortar mixes; iii) and finally superplasticizer was added in order

Table 4. Physical characteristics of aggregates

Sand	specific gravity	Bulk density [kg/m^3]	Water absorption [%]	Sand Equivalent [%]	Fineness Modulus
(CA)	2.43	1.64	11.92	67	2.8
(FA)	2.63	1560	4.30	86	1.12

Table 5. Characteristics of Sika ViscoCrete TEMPO-12 superplasticizer

Color	pH	Density	Cl-	Na_2O éq.	Standard/Agreement
Light to dark brown liquid	4.5 ± 1.0	1.06 ± 0.01	≤ 0.1 %	≤ 1 %	- EN 934-2 (2009) [33] - CNERIB : DTEM/108/2017

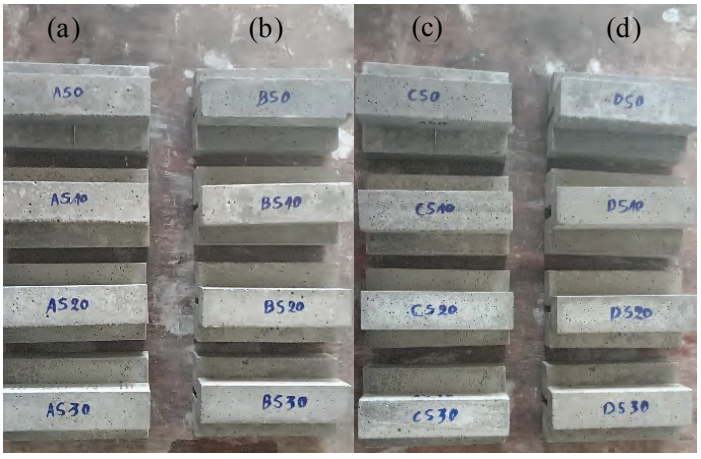


Figure 1. Mortar specimens with various water-to-binder ratio: (a) 0.35 (b) 0.40, (c) 0.45 and (d) 0.35.

Table 6. Mixture proportions of different mortars samples

Formulation	Composition [kg/m3]						Parameters		
	Coarse Sand	Fine sand	Cement	GGBFS	Water	SP	C:S	w/b	SP [%]
AS0	1304	88	464	0	258	2.0	3:1	0.50	0.45
AS10			417	46					
AS20			372	92					
AS30			325	139					
BS0	1336	90	475	0	238	4.3	3:1	0.45	0.90
BS10			427	48					
BS20			380	95					
BS30			360	142					
CS0	1353	92	487	0	216	6.8	3:1	0.40	1.4
CS10			438	49					
CS20			390	97					
CS30			341	146					
DS0	1404	94	499	0	194	8.6	3:1	0.35	1.7
DS10			449	50					
DS20			399	100					
DS30			349	150					

to obtain a good workability of manufactured mixture. The Sika ViscoCrete TEMPO-12 superplasticizer content was varied at the saturation dosage from 0.45 to 2 % by binder weight and mixed for 2 min. Table 6 summarized all the notations used in this paper for the mortar mix with and without GGBS for different curing times is mentioned in the nomenclature. The samples were cast and kept in steel molds during 24 h, and then they were demolded and cured at 23 °C in water as four sets for 3, 7, 28 and 90 days. Before testing, specimens were cured in water at 23 °C and 60% of relative humidity in a room with a constant temperature and humidity. The letter A, B, C and D indicated in the samples notation (see Table 6) correspond to 0.35, 0.40, 0.45 and 0.50, respectively. Then the letter S designate the GGBFS with its amount addition.

Mechanical Tests

In this study, two mechanical tests were carried out on the obtained GGBFS/cement mortars, namely compressive and flexural strength tests. Cubic and prismatic specimens with dimensions of 4 cm × 4 cm × 4 cm and 4 cm × 4 cm × 16 cm were manufactured for both analyses, respectively. These tests were performed for each mixing proportion with hydration ages of 3, 7, 28 and 90 curing days. All measurements for these mechanical tests were obtained using MTS criterion model 45 apparatus with crosshead loading capacity of 300 and 50 kN for compressive and flexural strength tests, respectively (Fig. 2).

Compressive strength test

Compressive strength tests are generally the most analysis that realized for studding the various properties of cementitious materials, this is because the majority of its characteristics and the structural design are mainly related to this test. Indeed, the compressive strength analysis was performed according to BS EN 12390–3 [33], with controlled displacement at constant rate of 0.6 MPa/s. its values are obtained with the formula indicated in the equation (1).

$$f_c = \frac{F}{A_c} \quad (1)$$

where f_c presents the compressive strength [MPa]; F is the extreme load at the fracture point [N]; A_c is the cross-sectional surface area [mm^2].

Flexural strength test

Generally, this test explains the stress occurred in a material just before it fails in flexure analysis, The measurement of flexural strength needs the insertion of the sample among two points or supports and starting a load using 3-Point Bend or 4-Point Bend testing. During this work, this test was curried out to evaluate the mechanical performance of the GGBFS-cement mortars according to BS EN 12390-5 [34]. The loading in three points was performed at a speed of 0.06 MPa/s, until failure. The flexural strength values were obtained using the following equation:

$$f_{ct,\ fl} = 1.5 * \frac{Fl}{bd^2} \quad (2)$$

where $f_{cf,\ fl}$ is the flexural strength with unit of [MPa]; F is the extreme load at the break level [N]; l is the length of the support [mm]; b is the width of the beam [mm]; d is the thickness of the beam [mm].

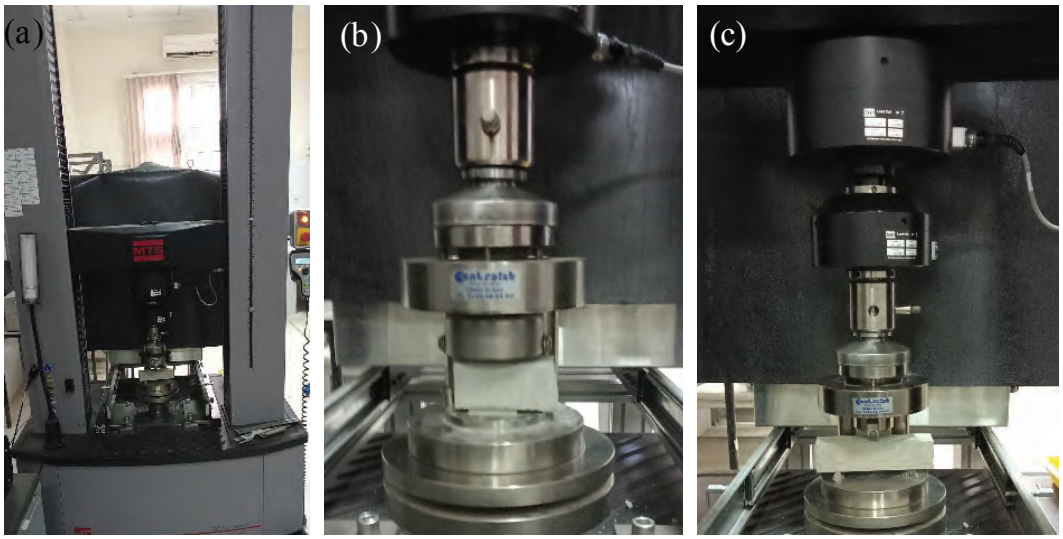


Figure 2. Mechanical tests equipment: (a) MTS criterion model 45 machine, electrohydraulic servo testing machine, (b) flexural test and (c) compressive test dispositive.

MLR Analysis

There is several engineering problems need the examination of the correlation between different studied variables. For this purpose, the MLR analysis is one of the most statistical tools which mainly adopted by several investigation research conducted in construction field for studying this correlation. In this case, the MLR method evaluates the relationship between the dependent (Y) and different independent variables (X) by an appropriate equation. For any application of MLR in the prediction models, the analysis aims to estimate and to express the variation of the dependent variable values as a function of the independent variables. The general form of MLR model can be expressed via the equation 3.

$$Y_i = b_0 + b_1X_1 + b_2X_2 + \cdots + b_iX_i + \varepsilon_i = \sum_{i=1}^{p} b_iX_i + \varepsilon_i \quad (3)$$

where Y_i presents the dependent variable (compressive and flexural strength values), Xi, (i=1,2…, p) indicates the independent variables (w/b ratio, hydration ages and GGBFS content); bi, (i=1,2…,p) are the parameters of the model and εi is the model random error. According to the literature, there are many software that can be used for the conception of the mathematical models by the application of MLR analysis, namely i) Excel of Microsoft; (ii) SPSS (Statistical Package for Social Sciences); (iii) Matlab of the MathWorks and (iv) NeuroSolutions of NeuroDimension [31]. The difference and the choice between of all these statistical tools are generally based on the two major parameters of the availability and the cost of software's acquisition. In this work, Excel and SPSS are used for application of MLR analysis due to its low cost and usually applied for construction calculation sector by the managers, planners, architects, etc. However, there are several methods that can be able to define the relationship between the dependent and the independent variables using the MLR analysis, such as: Enter, stepwise, backward, forward, …, etc. The enter method is chosen in this work for the investigation of regression model. Compared to the others methods, the enter regression technique considered all studied independent variables in the development of the mathematical model, which is defined sometimes as a simultaneous solution. In contrast, the stepwise method is statistical approaches programmed to add and remove different factors in the obtained models.

RESULTS AND DISCUSSION

Mechanical Strength Properties of Studied Mortar

Compressive strength evaluation

The obtained results of compressive strength of cement/GGBFS sand mortars with hydration ages of 3, 7, 28 and 90 days, and with different w/b ratios from 0.35 to 0.5 were presented in Figure 3. As expected, the compressive strength values of all mortar specimens increase with hydration age, from 34. 91 to 88.33 MPa for the sample cured during 90 days, with 0.35 of w/b ration and 30 % of GGBFS. In addition, the results appear that these characteristics also mainly affected by w/b ratios and GGBFS contents. The increasing of w/b rations from 0.35 to 0.5 has a negative effect on the compressive strength values of green manufactured mortars, which decrease from 50.8 to 30.29 MPa, respectively, for the specimen without GGBFS and 3 days of hydrations age. According to Singh et al. (2015), the mechanical properties of cement mortars decease with increasing of w/b ratio [35]. At early age (3 and 7 of hydrations ages),

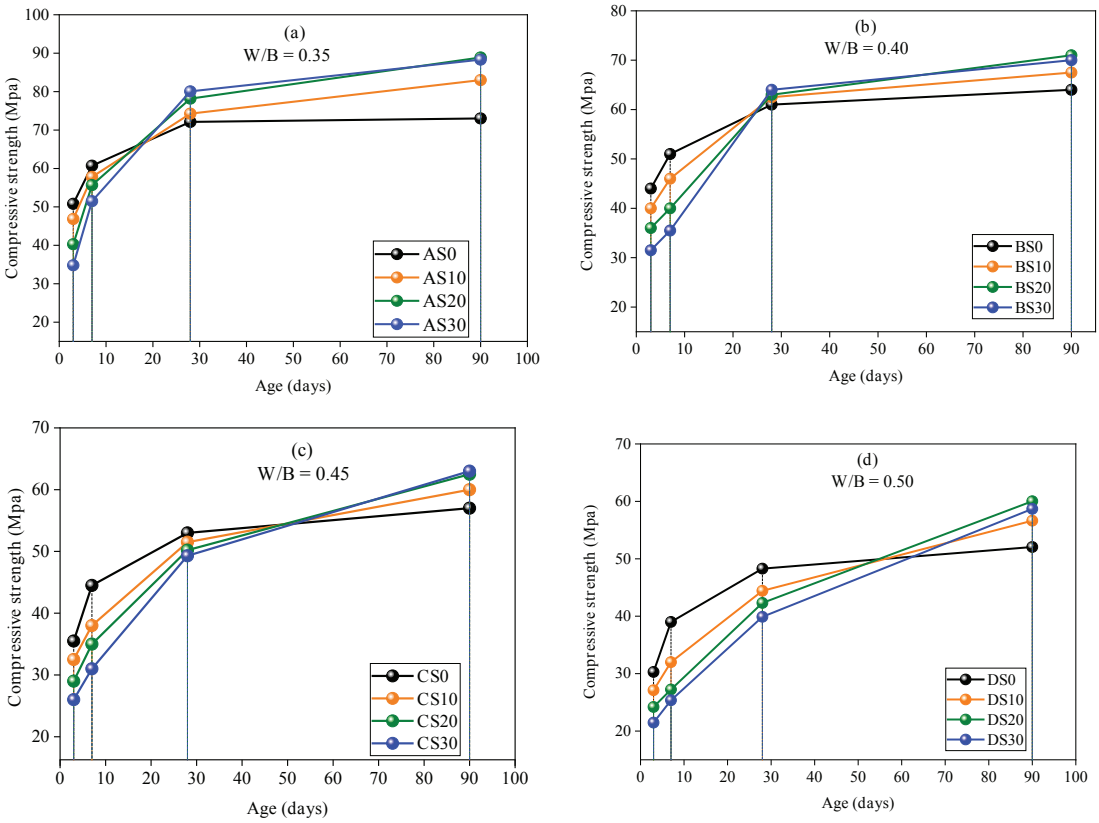


Figure 3. Compressive strength versus hydration age, GGBFS content and water-to-cement ratio from (a) to (d).

the substitution of cement by different amounts of GGBFS decrease considerably the compressive strength for all specimens cured at different of hydration ages and with w/b ratios. At 3 days of curing duration and 0.35 of w/b ratio, its values decrease from 50.8 to 34.81 MPa in the presence of 0 and 30 % of GGBFS, respectively. This result can be explained by the characteristics of GGBSF that have a low hydraulic reactivity at this interval of hydration age, which cement mortar could achieve a higher compressive strength value than the cement/GGBFS mixed mortars. The same conclusion is obtained by Yun et al. [14] during their work about the effect of hydration ages on the strength variation of GGBFS mortars. In contrast, at 28 and 90 days of hydrations ages, the compressive strength of all manufactured mortars with different w/b rations improved with increasing of GGBS contents. At the hydration age of 90 days and 0.35 of w/b ratio, it increases from 73.01 to 88.89 MPa for the sample with 0 and 20 % of GGBS, respectively. This result is in accordance with the most investigated works conducted in this subject [1, 18]. This is mainly due to the chemical reaction of absorption phenomena occurred between OPC and GGBFS particles, this lead to the activation of hydraulic activity by reaction of GGBFS with moisture and free calcium hydroxide, $Ca(OH)_2$ occurred from the hydration of cement to obtaine more binding phase of calcium silicate hydrate (CSH). In addition, the presence of GGBFS particles in the mortars samples stimulate the pozzolanic reaction by the high concentration of SiO_2 present in GGBFS [36], the amount of Ca^{2+} ions obtained by the hydration reaction became improved at internal interfaces of mortars samples. The active SiO_2 of GGBFS combined with Ca^{2+} ions produce much higher amount of stable C-S-H, which increases the compressive strength values of studied samples. As a conclusion, the results illustrated in Figure 3 indicate clearly that at early age of hydration there is no effect between the variation of w/b ratios and GGBFS addition, the compressive strength decrease 40 % when w/b ratio increase from 0.35 to 0.5 for mortar with and without GGBFS contents. In contrast, at 90 days of hydration ages, the compressive strength decreases 28,7 % and 32,5 for mortars without and with 20 % of optimal amount of GGBFS.

Figure 4 demonstrates the frequency histograms of compressive strength results of GGBFS-cement mortars samples. According to 64 tests of compressive strength property deduced from studied mortars, the values of this characteristic varied from 0 to 90 MPa with median of 51.26 MPa and standard deviation of 18.06 MPa.

Figure 5 shows the results of the particle size distribution of both CEM 1 and GGBFS powders. An average particle size (d_{50}) of 6.223 and 10.154 µm were obtained for CEM 1 and the GGBFS, respectively, which indicates that GGBFS

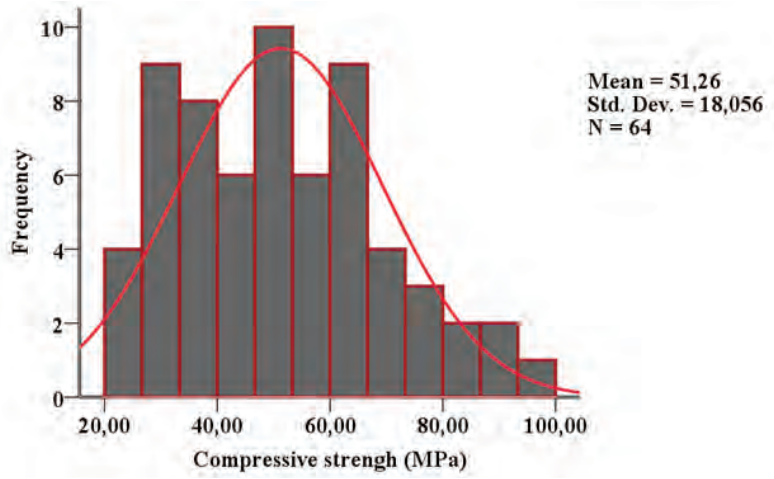


Figure 4. Frequency histogram of compressive strength values.

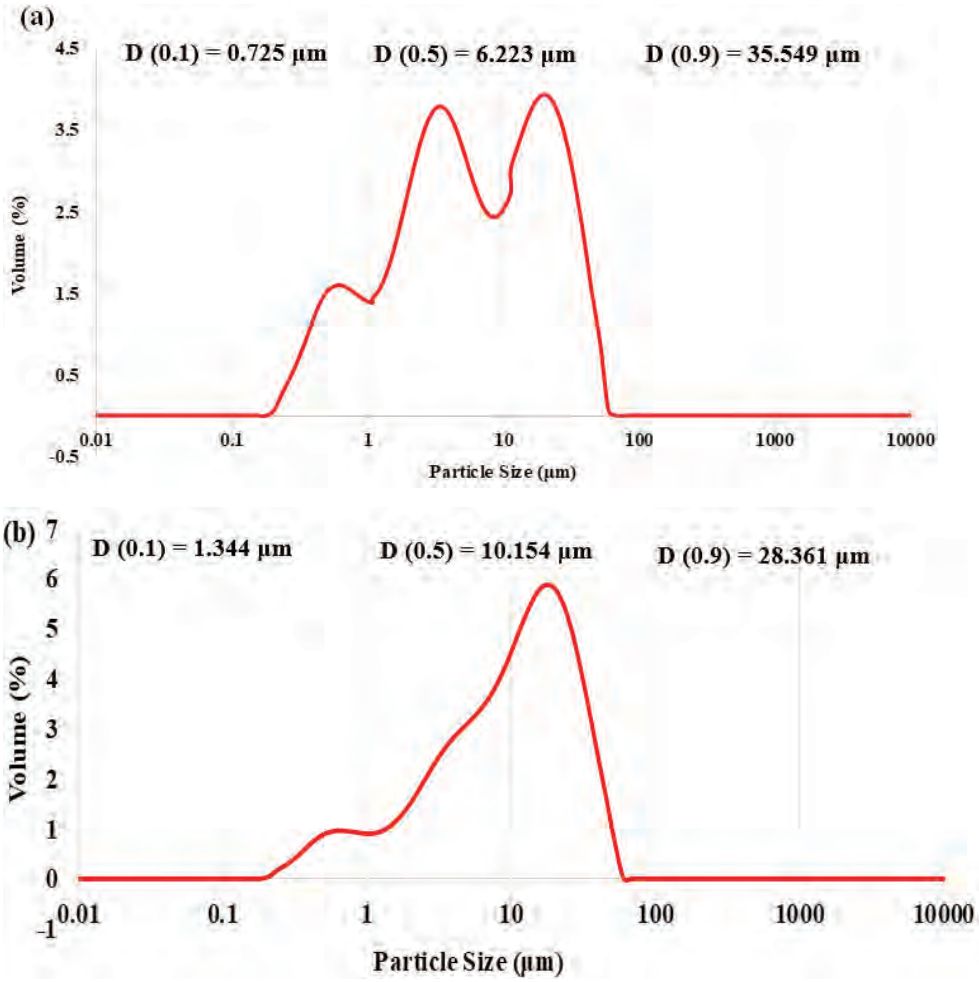


Figure 5. The particle size distribution of (a) CEM 1 and (b) GGBFS.

had a high particles size than CEM 1. These findings are in agreement with the interpretation result of compressive strength characteristic of manufactured mortars. However, many previous experimental researches have indicated that the particle size of GGBFS has significant effect on the compressive strength of mortar [37, 38]. The study conducted

by Zhu et al. [36] concluded that with increasing the particle size of GGBFS the compressive strength values increase significantly, due to the high exposure of its surface area to the pozzolanic reactions. Moreover, the optimal amount of cement replacement that can be obtained after 28 and 90 days of hydration ages was only 20 % of GGBFS. This is because when the particles of GGBFS is in excess in the mixture, there is insufficient free calcium hydroxide which contribute to the hydraulic reactions with GGBFS particles. However, the rest of this particles remain inactive and do not contribute strength.

Flexural strength evaluation

Flexural strength testing was carried out for different cement/GGBFS mortars mixtures cured during 3, 7, 28 and 90 days of hydrations ages. As seen in Figure 6, the three considered parameters have significant effect on the flexural strength values. When the hydration ages of the samples increase, the flexural strength enhanced for all specimens. At 3 to 90 days of hydration age, the values of flexural strength increase from 3.31 to 9.43 MPa for specimen containing 30 % of GGBFS and 0.5 of w/b ratio. In addition, the results indicate that there is slight difference in the global trend of the flexural strength properties compared to the obtained compressive strength for mortars with 0.35 and 0.4 of w/b rations. The flexural strength values of the specimens cured at early ages of 3 and 7 days of hydration ages, were also certainly lowest. Moreover, these values increase at 28 days of hydration ages of mortars with different amount of GGBFS contents and the results appear that the optimal replacement level of cement with GGBFS strongly depends with the hydration age. Hence, the optimal amount of GGBFS addition is 20 % for mortars with both w/b ratios and hydration ages of 28 and 90 days. As mentioned previously, this is because at this concentration of GGBFS, the pozzolanic effect occurred in mortar lead to the formation of cement hydration and shorten stiffening time, which improves the flexural load materials and decreasing crack propagation. For the specimens with 0.45 and 0.5 of w/b ratios, the incorporation of GGBFS have no effect on the flexural strength properties of mixtures mortars. For the samples without and with 30 % of GGBFS, cured at 90 days of hydration ages and with 0.5 of w/b ratio, the values decrease slightly from 10.71 to 9.43 MPa, respectively. This loss of the performance of flexural strength values is mainly due to the characteristics of cement/GGBFS mixtures mortars at these experimental conditions. In the other hand, it appears from the results indicated in Figure 6 that is an effect on the variation of w/b and GGBFS additions at early ages and at 90 days of hydration ages. As a

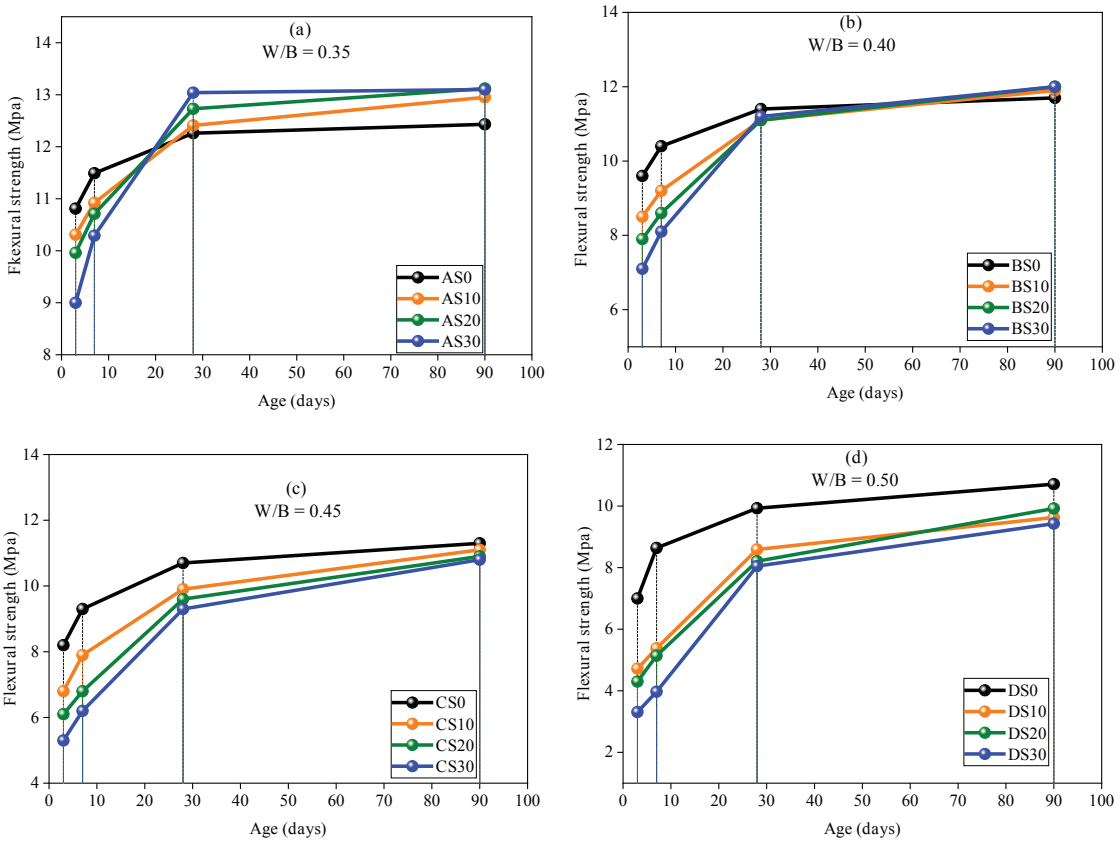


Figure 6. Flexural strength versus hydration age, GGBFS content and water-to-cement ratio from (a) to (d).

result, the flexural strength decreases 35.24 % when w/b ratio increase from 0.35 to 0.5 for mortars without GGBFS contents, and the flexural strength decreases 55.5 % for mortars with optimal amount of GGBFS. The same tendency is observed at 90 days of hydration age, 13.59 and 28.12 % for mortars without and with optimal amount of GGBFS.

Figure 7 translates the frequency histograms of experimental results obtained for flexural strength test of 64 samples of GGBFS-cement mortars. The findings of this properties varied from 3 to 13 MPa with median of 9.44 MPa and low value of standard deviation of 2.46 MPa.

In the other hand, the correlation between the results of flexural and compressive strength is established in Figure 8, and can be expressed as indicated in equation (4).

$$F_f = -0.0018 (F_c)^2 + 0.332 F_c - 2.1587 \quad (4)$$

where F_f indicates the flexural strength and F_c presents the compressive strength.

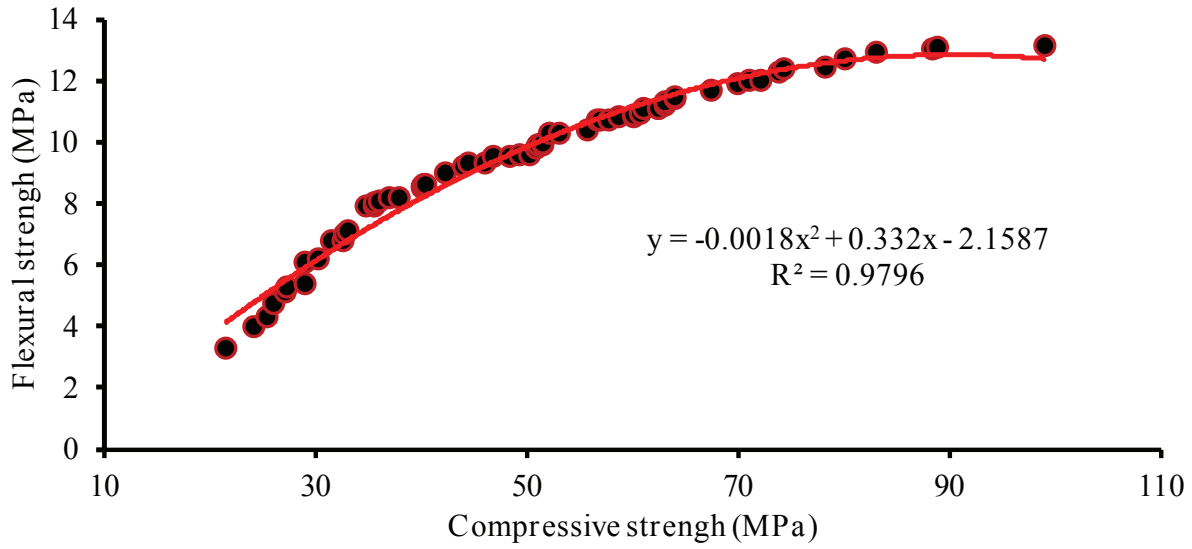


Figure 8. Flexural strength as function of compressive strength results.

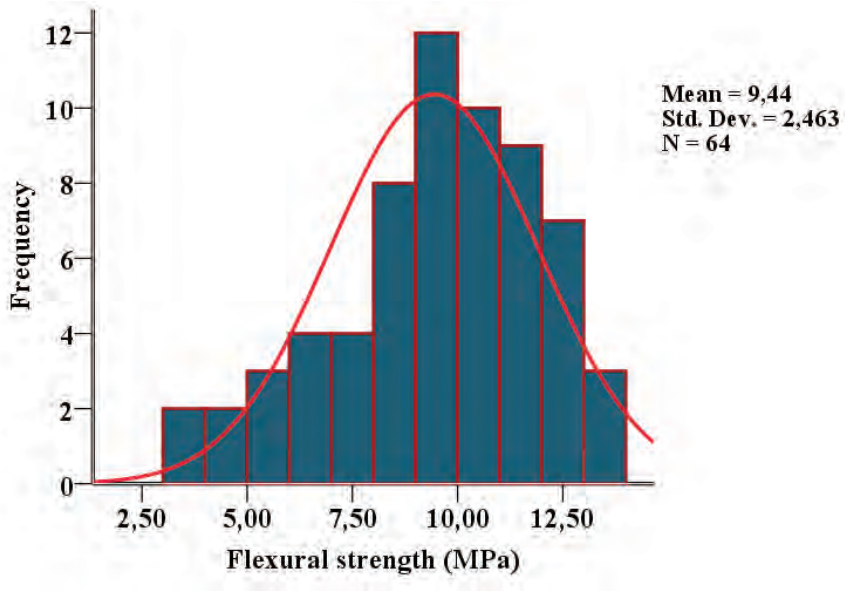


Figure 7. Frequency histogram of flexural strength results.

Regression Analysis

MLR models

The MLR analysis is one of the statistical methods usually applied to study the relation existing between the dependent variable, named endogenous, and different independent variables, named exogenous, which are the origin of the performance level of the dependent variable. Indeed, when this statistical test is used for the prediction model, the main objective is to explain the correlation existing between the experimental results and to describe the variation of the dependent variable as a function of the independent variables. According to the obtained results in this work, the correlation has been achieved between the dependent variables (flexural and compressive strength) and the independent variables (GGBFS contents, hydration age and w/b ratios). The following formulas present the mathematical equations of the obtained MLR model for the prediction of the compressive and flexural strengths of cement/GGBFS mortars, Eq. 5 and 6, respectively.

$$F_c = 44.812 + 0.300\,(\text{Hydration age}) - 24.604\,(\text{GGBFS content}) + 1.045\,\text{w/b} \quad (5)$$

$$F_f = 21.101 + 0.041\,(\text{Hydration age}) - 4.604\,(\text{GGBFS content}) - 26.401\,\text{w/b} \quad (6)$$

With F_c and F_f are the compressive and flexural strengths, respectively.

The sign and the values of each coefficient reflects the scale adopted, as indicated in the Eq.5, the compressive strength values increase with increasing of hydration ages and w/b ratios, but the high content of GGBFS involves the decreasing of compressive strength which is in accordance with the low optimal amount of GGBFS (20 mass%). The same results are obtained in the Eq. 6 for the hydration ages and GGBFS content, but is not the same for w/b ratios which decrease the flexural strength values with its increasing.

Model validation

In this analysis, the main objective is to determine the ability to express the experimental results obtained by the mechanical measurements and the results deduced using the two mathematical models translated using the values of correlation and determination coefficients indicated R and R^2, respectively. Moreover, the statistical analysis is performed in order to confirm the situation arises in which it does not provide a significant ability to relate the real observations; this examination was achieved through the analysis of variance test (ANOVA).

Table 7 gives the values of different determined coefficients that can be analysis the statistical quality of the regressions models obtained for both compressive and flexural strengths. Indeed, this analysis gives the results obtained for different statistical parameters, like: coefficient of correlation (R), coefficient of determination (R^2), adjusted coefficient of determination (Adjusted R^2), the standard error of estimate, and the Durbin–Watson statistics parameter. The R values define the existence of the correlation between the studied variables. In this case, both obtained models for compressive and flexural strength have coefficients of correlations of 0.65 and 0.89, respectively, which are higher than 0.5. These results indicate clearly that there is an importance correlation occurred between the experimental data and the adequate models. In addition, these two models lead to the R^2 values of 0.43 and 0.80 for compressive and flexural strength models, respectively. This result concluded that the MLR analysis has more efficacity on the prediction of flexural strength than compressive strength properties. Previous studies indicated that the MLR method gives low values of R^2 in the prediction of compressive strength of cementitious materials [19, 38, 39]. The values of this coefficient generally express the fraction of variance of the dependent variable (Y) that can be described by the regression model, but its values slightly affected by the presence of more variables, it generally increases with increasing of the number of considering variables in the model [40]. Indeed, the results of this coefficient revealing that 43 and 80 % of the variability of both mechanical properties, compressive and flexural strength, can be explained by the three independents variables, hydration age, GGBFS content and w/b ratios. However, the remaining 57 and 20 % of compressive and flexural strength model are mainly described by other factors or experimental errors, respectively. In the case of the of MLR model obtained for compressive strength results, the low values of R^2 can be due the existing of any non-linear relationships or interactions that the MLR approach cannot be statistically interpreted. The standard errors are estimated of 14.026 and 1.24 for both compressive and flexural models.

In the other hand, the Durbin-Watson statistic is used to test the existence of auto-correlation between the independent variables of the regression models, and its values generally varied from 0 to 4 with a midpoint of 2 [41–43]. The obtained values in this work are less than 2 (Table 6), 0.93 and 1.74 for compressive and flexural models, respectively.

Table 7. Summary of the MLR models obtained for compressive and flexural strengths, F_c and F_f, respectively

Models	R	R^2	Adjusted R^2	Standard error of the estimate	Durbin- Watson
F_c	0.65	0.42	0.40	14.043	0.937
F_f	0.89	0,80	0.79	1.24	1.74

This result indicates clearly the existence of the auto-correlation between the three studied parameters of hydration age, GGBFS content and W/B ratios.

The analysis of variance test (ANOVA) is also investigated in this work for both developed models in order to study the contribution and the interaction of considered independent variables (Table 8). From this analysis, the values of the sums of squares estimated for compressive and flexural models are established to distinct the global variance in the response obtained by the considered parameters and measurement errors [44]. Moreover, the F-test was determined in order to examine the elimination of null hypothesis and for the determination of the effect of each considered parameter on the different characteristics of studied material [45, 46]. Indeed, the values of F obtained for both models are much greater than that for F critical. The values of Sig. or significance level assumed in this work is 5 % (α) and the calculated values for Sig. for two models are less than this fixed level (0.000<0.05). These results concluded that the relationship between the three considered independent variables and their interactions are statistically significant and they are the main causes of the dependents variables of compressive and flexural strength.

The statistical results estimated for the two obtained models are summarized in Table 9 and 10. Indeed, the B column indicates in both tables the values of the non-standardized coefficients for each independents variable. These values explain the alteration endured by the dependent variable of compressive and flexural strength whenever the independent variables varied by one unit. Using these non-standardized coefficients, the MLR models of compressive and flexural strength were expressed as indicated in both equations 5 and 6, respectively. The standard errors associated with each coefficient are also presented in Tables 9 and 10. Moreover, the standardized regression coefficient (Beta) translate the importance of independent variables during the estimation

Table 8. ANOVA table obtained for multiple linear regression analysis of compressive (F_c) and flexural (F_f) strength models

Models		Sum of squares	Degrees of freedom (df))	Mean square	F	Sig.
F_c	**Regression**	8705.18	3	2901.99	14.715	0.00
	Residual	11832.67	60	197.21		
	Total	20538.64	63			
F_f	**Regression**	304.03	3	101.43	77.80	0.00
	Residual	78.15	60	1.30		
	Total	382.18	63			

Table 9. The values of the regression coefficients of compressive strength model

	Non-standardized coefficients		Standardized coefficients	Statistical t	Sig.	Collinearity	
	B	Standard error	Beta			Tolerance	VIF
Constant	44.81	3.36	/	13.33	0.00	/	/
Hydration age (days)	0.30	0.05	0.58	5.81	0.00	0.95	1.05
W/B	1.05	0.74	0.14	1.41	0.16	0.95	1.05
GGBFS mass%	-26.40	15.74	-0.17	-1.68	0.09	0.99	1.01

Table 10. Regression coefficients of flexural strength model

	Non-standardized coefficients		Standardized coefficients	Statistical t	Sig.	Collinearity	
	B	Standard error	Beta			Tolerance	VIF
Constant	21.10	1.12	/	18.88	0.00	/	/
Hydration age (days)	0.04	0.004	0.56	9.66	0.00	0.99	1.00
w/b	-28.77	2.55	-0.66	-11.27	0.00	1.00	1.00
GGBFS mass%	- 4.60	1.28	-0.21	-3.60	0.00	0.99	1.00

of the dependent variable values obtained with the mathematical model. According to the values of this coefficient which varies between -1 and 1, it can be compare the importance of different variables considered in this work for the estimation of the mechanical properties. For both compressive and flexural models, it appears that the hydration age has a higher value of standardized coefficients than the two others variables of w/b ratios and GGBFS contents. This result involves that the hydration age has a significant effect on the estimation of compressive and flexural strength values, which is in accordance with literature review [12]. The two others independent variables have less effect on the assessment of mechanical properties. Indeed, for the compressive strength results, w/b ratios have more effect than GGBFS content with standardized coefficients values of 0.13 and -0.17, respectively. In contrast, the values of standardized coefficients indicate for flexural strength results that the GGBFS content has more effect that w/b ratios, -0.22 and -0.66, respectively.

The t-values are generally calculated in order to compare the power of each independent variables on the estimation and the prediction of dependent variable. Thus, the obtained t-values are generally evaluated with the comparison of its values with critical value of t deduced from t Student distribution table, the estimated absolute of t-values should be greater than $t_{critical}$ (1.664). For flexural strength model, the t-values of the coefficients for all independent variables are greater than $t_{critical}$. Nevertheless, the w/b ratios have t-values less than $t_{critical}$ for compressive strength model. For 95 % confidence level, the significance values of the three independent variables are less than 5% (0.00) for flexural strength model, which conclude that the hydration ages, w/b ratios and GGBFS content are mainly the cause of the dependent variable. In contrast, both w/b ratios and GGBFS have significance more than 5 % for compressive strength model, 0.19 and 0.09 respectively. This result indicates that these two independent variables have lower effect than hydration ages (Sig. = 0.00) in compressive strength estimation.

The diagnostic of collinearity occurred between variables can be tested using VIF. According to the literature review [47, 48], the values of VIF greater than 5 reveals that the mathematical model exhibits collinearity effects and significant variables are insignificant in the model. The value of this statistical parameter is calculated using the equation (7) and its values around of 1 indicates that there is no collinearity effects. In this case, based on the result indicated in Tables 9 and 10, the values of VIF of the three independent variables: hydration age, GGBFS content and w/b ratios are around the value of 1 and < 5 for both developed models of compressive and flexural strength, which involves that there is no risk of collinearity effects.

$$VIF_i = \frac{1}{1-T_i} \tag{7}$$

Where Ti is the tolerances values of each independent variable i.

The residuals results are also expressed as function of GGBFS content for compressive and flexural strength results (Fig. 9). The results of this study indicate clearly the

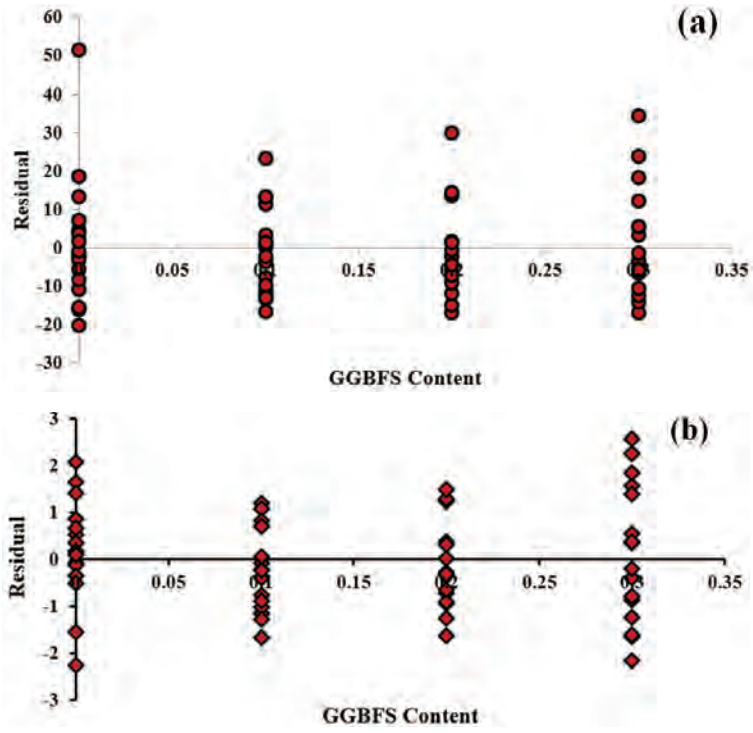


Figure 9. Residual results as function of (a) compressive and flexural values.

low range of residuals obtained for flexural strength analysis. The values are uniformly and symmetrically closed to zero, this is mainly due to the good significant of developed MLR model, which not the same for compressive strength values [48, 49].

In the other hand, the collinearity is checked using the correlation matrix between the independent variables (Table 11 and 12). The results of this analysis indicate that all values are higher than 0.7 for compressive and flexural strength models, due to the no collinearity existing between the three considered variables [48]. This conclusion is in accordance to the results obtained by VIF test. In addition, the correlation matrix indicates clearly that the GGBFS addition has more correlation with hydration age than w/b ratio.

The relationship occurred between the experimental results obtained for studied mechanical properties and their adequate predictive values are shown in Figures 10 and 11. Moreover, Figure 12 indicates a high correlation between predictive values of compressive strength and flexural strength estimated using the obtained models, Eq (5) and (6), respectively ($R^2 = 0.97$).

CONCLUSION

This work is conducted to study in the first the addition effect of ground granulated blast furnace slag on the mechanical properties of green cement mortar. Moreover, two predictive models are developed using the multiple linear regression analysis to predict the compressive and flexural strength of manufactured green cement mortars.

Table 11. Correlation matrix between independents variables of compressive strength model

	Hydration age (days)	w/b ratio	GGBFS mass%
Hydration age (days)	1		
w/b ratio	0.210703317	1	
GGBFS mass%	0.105414544	0.042543639	1

Table 12. Correlation matrix between independents variables of flexural strength model

	Hydration age (days)	w/b ratio	GGBFS mass%
Hydration age (days)	1		
w/b ratio	0.01231996	1	
GGBFS mass%	-0.036959879	0	1

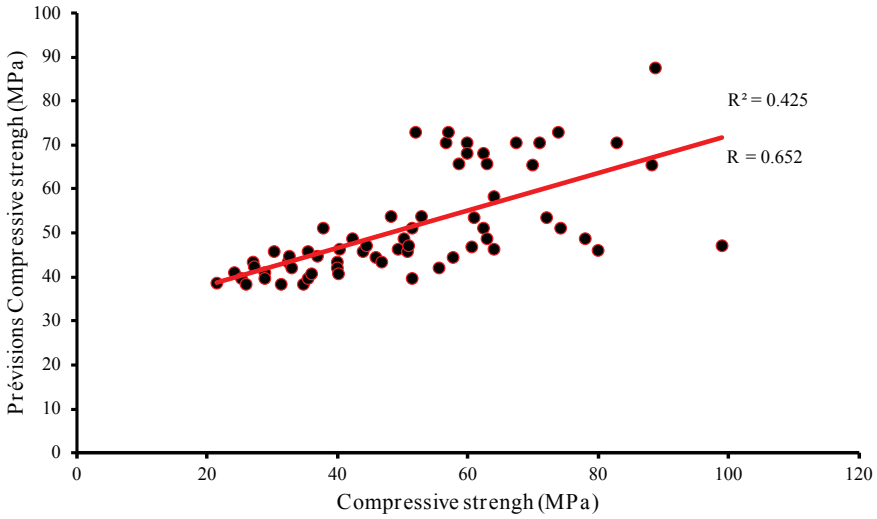


Figure 10. Predictive values versus of the obtained results of compressive strength.

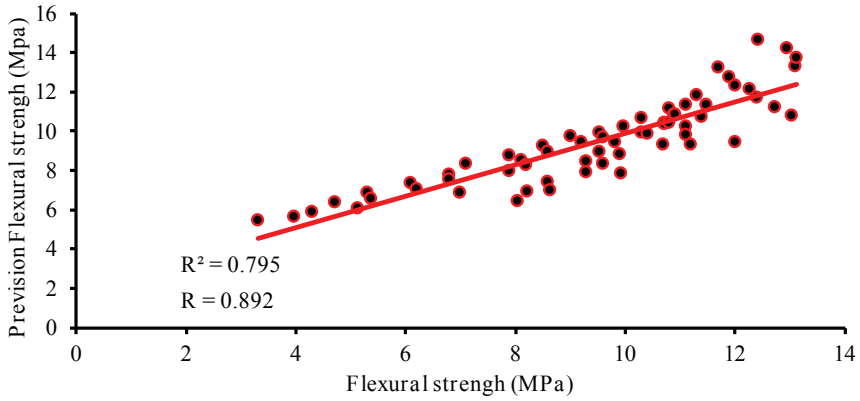


Figure 11. Predictive values versus obtained results of flexural strength.

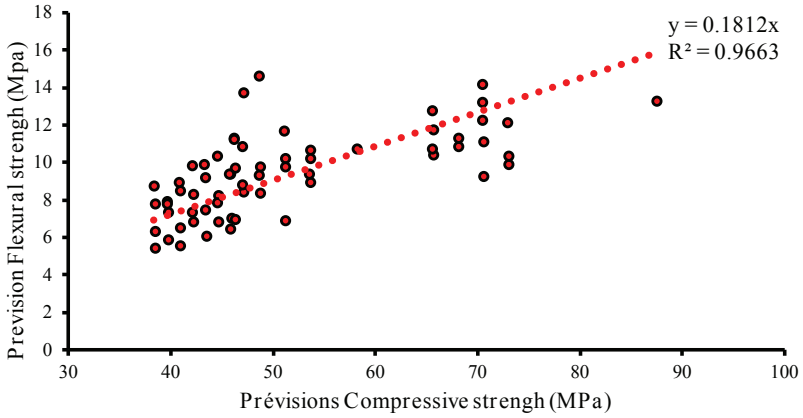


Figure 12. Relationship between previsions values of flexural and compressive strength.

Three quantitative variables are considered in this work of hydration ages, water/binder ratio and the concentration ground granulated blast furnace slag. Understanding the effect of these parameters on the final mechanical properties of different developed mortars, this study gives more economics solutions for the optimization of different necessary mixtures conducted in civil engineering applications and reduce a time for others experimental investigations by using the most statical results obtained by the multiple linear regression analysis.

The excremental results obtained via the compressive and flexural strength analysis concluded that the hydration age is the most important parameter that strongly affect the mechanical properties. In contrast, the GGBFS added as substitution of OPC improved the mechanical properties of cement mortar just at high hydration age of 28 and 90 days. As a result, the compressive strength increases from 73.01 to 88.89 MPa at for the samples with 0 and 20 % of GGBFS addition, 0.35 of w/b and 90 days of hydration age. The findings of these analyses conclude also that the optimal amount of GGBFS content in cement mortar is 20 %, above this concentration there is a slight effect on the mechanical properties. For the samples mortars with 0.35 of w/b ration and 90 days of hydration age, the compressive and flexural strength decrease from 13.12 to 13.1 MPa and 88.89 to 88.33 MPa for 20 and 30 % of GGBFS content, respectively. Moreover, at different variation of w/b ratio, the GGBFS addition have significant effect just at high hydration ages, which is not the same for the flexural strength, this effect is also observed at early age.

Based to the most results obtained from the regression analysis, the values of R^2 conclude that the MLR method has more significant performance for the prediction of flexural strength properties than compressive strength of GGBFS-cement mortars, 0.8 and 0.42 values are obtained, respectively. Moreover, the compressive and flexural models present correlations coefficients values higher than 0.5 (0.65 and 0.89, respectively). These results translate the existing of high correlation between the experimental data and the models which lead to generate better results during

the prediction of both considered mechanical properties of GGBFS-cement mortars. Based to the statical parameters obtained from the multiple linear regression analysis, namely: sig. values, standardized coefficients and the values of the variation inflation factor, indicate clearly that the hydration ages have a significant effect on the prediction of both mechanical properties of GGBF-cement mortar, which is in accordance with the results obtained from the experimental tests. For the two others intendent variables, the regression parameters indicate that w/b ratios have more effect than GGBFS content on the estimation of compressive strength values, which is note the same for the flexural strength values, the standardized regression coefficient increase from -0.66 to -0.22, respectively.

Refers to the different statical techniques previously developed for the prediction of the mechanical properties of cement materials, like the non-linear regression analysis and the machine learning of artificial neural networks (ANNs) and support vector machine (SVM), future research can be conducted using these methods for improvement of model's performance of compressive strength prediction and considering more independent variables like durability parameters and curing conditions of temperature and relative humidity.

ACKNOWLEDGEMENT

The authors gratefully acknowledge the company of lafarge (Oggaz, Mascara, Algérie) and Sika El Djazair SPA located at Larbaa, Les Eucalyptus, Algiers, Algeria for their help in supplying the ciment (OPC 52.5 N) and GGBFS samples, respectively.

AUTHORSHIP CONTRIBUTIONS

Study conception and design, AH; data acquisition, KC and AH; analysis and interpretation of results, AH; draft manuscript preparation, AH; and manuscript review and editing, KC and AH.

DATA AVAILABILITY STATEMENT

The authors confirm that the data that supports the findings of this study are available within the article. Raw data that support the finding of this study are available from the corresponding author, upon reasonable request.

CONFLICT OF INTEREST

The author declared no potential conflicts of interest with respect to the research, authorship, and/or publication of this article.

ETHICS

There are no ethical issues with the publication of this manuscript.

STATEMENT ON THE USE OF ARTIFICIAL INTELLIGENCE

Artificial intelligence was not used in the preparation of the article.

REFERENCES

[1] Chidiac SE, Panesar DK. Evolution of mechanical properties of concrete containing ground granulated blast furnace slag and effects on the scaling resistance test at 28 days. Cem Concr Compos 2008;30:63–71. [CrossRef]

[2] Bilim C, Atiş CD, Tanyildizi H, Karahan O. Predicting the compressive strength of ground granulated blast furnace slag concrete using artificial neural network. Adv Eng Softw 2009;40:334–340. [CrossRef]

[3] Özbay E, Erdemir M, Durmuş Hİ. Utilization and efficiency of ground granulated blast furnace slag on concrete properties-a review. Constr Build Mater 2016;105:423–434. [CrossRef]

[4] El-Chabib H. Properties of SCC with supplementary cementing materials. In: Self-compacting concrete: materials, properties and applications. Elsevier; 2020. p. 283–308. [CrossRef]

[5] Siddique R, Khan MI. Supplementary cementing materials. Springer Science & Business Media; 2011. [CrossRef]

[6] EN 15167-1. Ground granulated blast furnace slag for use in concrete, mortar and grout-Part 1: Definitions, specifications and conformity criteria. European Standard; 2006.

[7] Malipeddi R, Adiseshu S. Study of dissolution parameter of ground granulated blast furnace slag as cement replacement on mechanical properties of mortar. Mater Today Proc 2021;44:642–650. [CrossRef]

[8] Cheah CB, Liew JJ, Le Ping KK, Siddique R, Tangchirapat W. Properties of ternary blended cement containing ground granulated blast furnace slag and ground coal bottom ash. Constr Build Mater 2022;315:125249. [CrossRef]

[9] Chi M. Synthesis and characterization of mortars with circulating fluidized bed combustion fly ash and ground granulated blast-furnace slag. Constr Build Mater 2016;123:565–573. [CrossRef]

[10] Sandhu AR, Rind TA, Kalhoro SA, Lohano R, Laghari FH. Effect on the compressive strength of mortars using ground granulated blast furnace slag as a partial replacement of cement. J Appl Eng Sci 2019;9:183–186. [CrossRef]

[11] Ng YL, Aldahdooh MAA, Alazaiza MYD, Bashir MJK, Chok VS, Ng CA. Influence of alum sludge ash and ground granulated blast furnace slag on properties of cement mortar. Clean Eng Technol 2022;6:100376. [CrossRef]

[12] Çakır Ö, Aköz F. Effect of curing conditions on the mortars with and without GGBFS. Constr Build Mater 2008;22:308–314. [CrossRef]
[13] Işıkdağ B, Topçu İB. The effect of ground granulated blast-furnace slag on properties of Horasan mortar. Constr Build Mater 2013;40:448–454. [CrossRef]
[14] Yun CM, Rahman MR, Phing CYW, Chie AWM, Bakri MKB. The curing times effect on the strength of ground granulated blast furnace slag (GGBFS) mortar. Constr Build Mater 2020;260:120622. [CrossRef]
[15] Barnett SJ, Soutsos MN, Millard SG, Bungey JH. Strength development of mortars containing ground granulated blast-furnace slag: Effect of curing temperature and determination of apparent activation energies. Cem Concr Res 2006;36:434–440. [CrossRef]
[16] Siline M. Efficiency of incorporating Algerian ground granulated blast furnace slag as a supplementary cementitious material: A review. Innov Infrastruct Solut 2022;7:121. [CrossRef]
[17] Akçaözoğlu S, Atiş CD. Effect of granulated blast furnace slag and fly ash addition on the strength properties of lightweight mortars containing waste PET aggregates. Constr Build Mater 2011;25:4052–4058. [CrossRef]
[18] Nojoukambari TY, Sadrmomtazi A, Khoshkbijari RK. Influence of feldspar and ground granulated blast-furnace slag as a partial cement replacement on mechanical properties and thermal durability and environmental impacts of cement mortars. J Clean Prod 2023;398:136074. [CrossRef]
[19] Al-Swaidani AM, Khwies WT, Al-Baly M, Lala T. Development of multiple linear regression, artificial neural networks and fuzzy logic models to predict the efficiency factor and durability indicator of nano natural pozzolana as cement additive. J Build Eng 2022;52:104475. [CrossRef]
[20] Salih A, Rafiq S, Mahmood W, Ghafor K, Sarwar W. Various simulation techniques to predict the compressive strength of cement-based mortar modified with micro-sand at different water-to-cement ratios and curing ages. Arab J Geosci 2021;14:1–14. [CrossRef]
[21] Topal A, Bayazıt NG, Uçan Y. Prediction of compressive strength class of concrete with dominance based rough set approach. Sigma J Eng Nat Sci 2023;41:1088–1095.
[22] Ulu A. Application of response surface methodology in the optimisation of polymer concrete mechanical properties. Sigma J Eng Nat Sci 2024;42:1973–1985. [CrossRef]
[23] Merabti S, Bezari S, Boudina A. Prediction of the compressive strength in high-strength concrete cores through the destructive method. Sigma J Eng Nat Sci 2025;43:541–554. [CrossRef]
[24] Mahajan L, Kirange M, Bhagat S. Statistical exploration for enlargement of reformed water cement ratio law for fly ash concrete. Sigma J Eng Nat Sci 2025;43:269–281. [CrossRef]
[25] Palod R, Deo SV, Ramtekkar GD. Utilization of waste from steel and iron industry as replacement of cement in mortars. J Mater Cycles Waste Manag 2019;21:1361–1375. [CrossRef]
[26] Łukowski P, Salih A. Durability of mortars containing ground granulated blast-furnace slag in acid and sulphate environment. Procedia Eng 2015;108:47–54. [CrossRef]
[27] Sitarz M, Urban M, Hager I. Rheology and mechanical properties of fly ash-based geopolymer mortars with ground granulated blast furnace slag addition. Energies (Basel) 2020;13:2639. [CrossRef]
[28] Onn CC, Mo KH, Radwan MKH, Liew WH, Ng CG, Yusoff S. Strength, carbon footprint and cost considerations of mortar blends with high volume ground granulated blast furnace slag. Sustainability (Basel) 2019;11:7194. [CrossRef]
[29] Brachaczek W, Chleboś A, Kupczak M, Spisak S, Stybak M, Żyrek K. Influence of the addition of ground granulated blast furnace slag, fly silica ash and limestone on selected properties of cement mortars. Mater Proc 2023;13:32. [CrossRef]
[30] Boubekeur T, Boulekbache B, Aoudjane K, Ezziane K, Kadri EH. Prediction of the durability performance of ternary cement containing limestone powder and ground granulated blast furnace slag. Constr Build Mater 2019;209:215–221. [CrossRef]
[31] Wang L, Aslani F. Electrical resistivity and piezoresistivity of cement mortar containing ground granulated blast furnace slag. Constr Build Mater 2020;263:120243. [CrossRef]
[32] EN 934-2. Adjuvants pour béton, mortier et coulis-Partie 2: adjuvants pour bétons-Définitions, exigences, conformité, marquage et étiquetage. British Standards Institution; 2009.
[33] EN BS 12390-3. Testing hardened concrete-Part 3: Compressive strength of test specimens. 2009.
[34] BS EN 12390-5. Testing hardened concrete-Part 5: Flexural strength of test specimens. European Committee for Standardization; 2009.
[35] Singh SB, Munjal P, Thammishetti N. Role of water/cement ratio on strength development of cement mortar. J Build Eng 2015;4:94–100. [CrossRef]
[36] Zhu J, Zhong Q, Chen G, Li D. Effect of particle size of blast furnace slag on properties of Portland cement. Procedia Eng 2012;27:231–236. [CrossRef]
[37] Gupta S. Effect of content and fineness of slag as high volume cement replacement on strength and durability of ultra-high performance mortar. J Build Mater Struct 2016;3:43–54. [CrossRef]
[38] Chithra S, Kumar SRRS, Chinnaraju K, Alfin Ashmita F. A comparative study on the compressive strength

prediction models for high performance concrete containing nano silica and copper slag using regression analysis and artificial neural networks. Constr Build Mater 2016;114:528–535. [CrossRef]

[39] Adesanya E, Aladejare A, Adediran A, Lawal A, Illikainen M. Predicting shrinkage of alkali-activated blast furnace-fly ash mortars using artificial neural network (ANN). Cem Concr Compos 2021;124:104265. [CrossRef]

[40] Silva A, De Brito J, Gaspar PL. Methodologies for service life prediction of buildings: With a focus on façade claddings. Springer International Publishing; 2016. [CrossRef]

[41] Unamba UK, Nwajagu ES, Abutu J, Agbo-Anike OJ. Predictive model of the compressive strength of concrete containing coconut shell ash as partial replacement of cement using multiple regression analysis. Vol. 6. 2021.

[42] Wu SS, Li BZ, Yang JG, Shukla SK. Predictive modeling of high-performance concrete with regression analysis. In: 2010 IEEE International Conference on Industrial Engineering and Engineering Management. IEEE; 2010. p. 1009–1013. [CrossRef]

[43] Keleştemur O, Yildiz S, Gökçer B, Arici E. Statistical analysis for freeze-thaw resistance of cement mortars containing marble dust and glass fiber. Mater Des 2014;60:548–555. [CrossRef]

[44] Abellan-Garcia J, Abbas YM, Khan MI, Pellicer-Martínez F. ANOVA-guided assessment of waste glass and limestone powder influence on ultra-high-performance concrete properties. Case Stud Constr Mater 2024;20. [CrossRef]

[45] Fakhri M, Amoosoltani E. The effect of reclaimed asphalt pavement and crumb rubber on mechanical properties of roller compacted concrete pavement. Constr Build Mater 2017;137:470–484. [CrossRef]

[46] Montgomery DC, Peck EA, Vining GG. Introduction to linear regression analysis. John Wiley & Sons; 2021.

[47] Wang W, Zhu J, Cheng X, Jiang D, Shi G, Chen X. Study and prediction analysis on road performance of basalt fiber permeable concrete. Sci Eng Compos Mater 2023;30:20220223. [CrossRef]

[48] Chai C, De Brito J, Gaspar PL, Silva A. Statistical modelling of the service life prediction of painted surfaces. Int J Strateg Prop Manag 2015;19:173–185. [CrossRef]

[49] Singh P, Adebanjo A, Shafiq N, Razak SNA, Kumar V, Farhan SA, et al. Development of performance-based models for green concrete using multiple linear regression and artificial neural network. Int J Interact Des Manuf 2024;18:2945–2956. [CrossRef]

Sigma Journal of Engineering and Natural Sciences
Web page info: https://sigma.yildiz.edu.tr
DOI: 10.14744/sigma.2026.2121

Research Article

Comparison of neurofilament light chain protein levels in the blood of patients with multiple sclerosis and amyotrophic lateral sclerosis

Emrah BERTAN[1], Aslıhan GÜNEL[2], Reşit ÇELİK [1], Halil Atilla İDRİSOĞLU [4], Şenay VURAL KORKUT[1,*]

[1]*Department of Molecular Biology and Genetics, Yildiz Technical University Faculty of Arts and Science, Istanbul, 34220, Türkiye*
[2]*Department of Chemistry, Ahi Evran University Faculty of Arts and Science, Kırşehir, 40100, Türkiye*
[3]*Department of Statistics, Yildiz Technical University Faculty of Arts and Science, İstanbul, 34220, Türkiye*
[4]*Departmant of Neurology, İstanbul University İstanbul Faculty of Medicine, İstanbul, 34093, Türkiye*

ARTICLE INFO

Article history
Received: 03 June 2025
Revised: 10 September 2025
Accepted: 26 October 2025

Keywords:
Amyotrophic Lateral Sclerosis, ELISA; Multiple Sclerosis; Neurofilament Light Chain

ABSTRACT

Neurodegenerative disorders involve a gradual loss of neurons. This includes multiple sclerosis and amyotrophic lateral sclerosis. Yet there is still a shortage of dependable blood-based indicators. These indicators would aid in diagnosis and track therapeutic effectiveness. The neurofilament light chain, which is an essential component of the neuronal cytoskeleton, enters the cerebrospinal fluid and bloodstream in the event of axonal injury. While most previous studies have reported increased neurofilament light chain concentrations in untreated patients, evidence from cohorts that have undergone long-term treatment is scarce. This study measured plasma neurofilament light chain concentrations in 86 participants (33 with multiple sclerosis, 38 with amyotrophic lateral sclerosis and 15 healthy controls) using the Bioassay Technology Laboratory neurofilament light chain ELISA assay. Median plasma neurofilament light chain levels were significantly lower in patients with multiple sclerosis ($p=0.0035$), whereas the reduction observed in patients with amyotrophic lateral sclerosis did not reach statistical significance ($p=0.0728$) compared with healthy controls. This suggests a treatment-associated reduction in neuronal damage, despite ongoing neurodegeneration. No significant sex-based differences were detected ($p=0.879$). The results suggest that plasma neurofilament light chain levels could function not only as an auxiliary tool for diagnosis but also as a marker reflecting therapeutic effects in chronically treated neurodegenerative conditions. A key contribution of this study is the observation that treated patients exhibited lower plasma concentrations than healthy controls, a finding that contrasts with previous reports of elevated levels in untreated groups. This emphasizes the potential clinical utility of plasma neurofilament light chain monitoring and sets the stage for future longitudinal validation efforts.

Cite this article as: Bertan E, Günel A, Çelik R, İdrisoğlu HA, Vural Korkut S. Comparison of neurofilament light chain protein levels in the blood of patients with multiple sclerosis and amyotrophic lateral sclerosis. Sigma J Eng Nat Sci 2026;44(4):2676–2684.

***Corresponding author.**
*E-mail address: skorkut@yildiz.edu.tr

This paper was recommended for publication in revised form by Editor-in-Chief Ahmet Selim Dalkilic

Published by Yıldız Technical University Press, İstanbul, Turkey
© Author. This is an open access article under the CC BY-NC license (http://creativecommons.org/licenses/by-nc/4.0/).

INTRODUCTION

Neurodegenerative diseases, particularly multiple sclerosis (MS) and amyotrophic lateral sclerosis (ALS), present significant challenges in diagnosis and treatment due to their biological complexity and progressive natüre [1]. MS is a disease affecting the central nervous system characterized by immune-mediated demyelination and neuroinflammation [2]. ALS, on the other hand, is characterized by progressive degeneration of upper and lower motor neurons, leading to motor dysfunction and disability [3]. Given the progressive and heterogeneous nature of these disorders, identifying a reliable biomarker for the diagnosis and monitoring is of considerable clinical importance [4]. According to the findings from the studies, the idea that NFL could be a biomarker with potential for use is its release into biological fluids during neuroaxonal damage [5,6]. In this context, the study evaluates the potential of plasma NFL levels as a biomarker to distinguish ALS or MS patients from healthy individuals.

Neurofilaments represent a component of the cytoskeleton of neurons, exhibiting a high degree of abundance, particularly within the axons of these cells. Through their structural role, neurofilaments contribute to the maintenance of axonal size, shape, and diameter [7]. Neurofilaments belong to the intermediate filament family and consist of triple formations of the three subunits; NFL, neurofilament medium chain (NFM) and neurofilament heavy chain (NFH) [8,9]. Located on chromosome 8p21, the NFL gene encodes a 543–amino acid protein weighing approximately 61.5 kDa. Similarly, the NFM gene, which also lies on chromosome 8p21, encodes a protein of 916 amino acids that is essential for axonal radial growth. The NFH gene, however, is found on chromosome 22q12.2 and produces a 1020–amino acid protein with a molecular mass of around 112.5 kDa [10,11]. The production of these proteins takes place in the nerve cell body, after which they are incorporated into intermediate filaments. These filaments provide stability to the axon [12].

Neurodegenerative diseases are progressive, multifactorial conditions that affect nerve cells in the central and peripheral nervous systems. They arise as a result of nerve cell loss in the nervous system [13]. Typical characteristics of neurodegenerative diseases include sporadic or hereditary transmission, gradual progression, early onset, contributions from both genetic and environmental factors, accumulation of protein deposits in the nervous system, and the deterioration of specific neurons [14]. There is no effective treatment currently for neurodegenerative diseases (NDDs); ongoing therapies are mainly aimed at treating the most unpleasant symptoms [15]. There is currently no effective treatment for NDDs; the treatments applied nowadays is actually aimed at removing the most disturbing symptoms [16]. Early treatment is crucial to mitigate the effects of these diseases in NDDs, unique and sensitive biomarkers are needed to early diagnosis [17].

It is difficult to diagnose diseases that cause the nervous system to degenerate, especially in conditions such as ALS and MS. Currently, there are no clinically validated diagnostic biomarkers in routine clinical practice. Most biomarker research focuses on the analysis of cerebrospinal fluid (CSF) and blood samples to identify diagnostic and prognostic markers. In this context, NFL has gained significant interest due to its ability to reflect axonal damage [18]. In addition GFAP is associated with astroglial activation and gliosis and is more indicative of neuroinflammation, whereas it does not directly reflect axonal damage [19]. Tau protein is a known biomarker, particularly in Alzheimer's disease, and has also been studied in ALS and MS [20]; however, it shows less consistent association with disease progression compared to NFL. UCH-L1 has been proposed as a marker of neuronal damage [21], while CHI3L1 has been proposed as a marker of glial activation [22]; however, the specificity of these biomarkers for ALS and MS is limited.

MS is an autoimmune inflammatory disease affecting the central nervous system [23,24]. The number of MS cases is increasing in both developed and developing countries [25]. The defining pathological feature of MS is the occurrence of demyelination in the brain and spinal cord, usually associated with damage to the axons of neurons [26]. ALS, also known as Lou Gehrig's disease, is characterized by degeneration of both upper (UMN) and lower (LMN) motor neurons in the brainstem and spinal cord [27,28]. Although there have been several studies investigating the use of cytoplasmic components (e.g., tau protein, neurofilaments, and S100) as a measure of disease activity and progression [29], there are currently no proven CSF or serum biomarkers for diagnosing or predicting the prognosis of ALS [30]. The use of diagnostic biomarkers in the early stages of ALS could shorten the diagnostic process. Studies have shown that NFL and pNFH levels in cerebrospinal fluid (CSF) are significantly higher in the early stages of the disease [31-34].

Research on neurofilaments is rapidly expanding. Levels of neurofilaments are being explored as markers. These markers show disease activity and progression. Elevated neurofilament levels have been associated with disease activity and progression across a broad spectrum of neurological disorders, including stroke [35], ALS [34], frontotemporal dementia [36], and MS [37]. However, a comparison of NFL and NFH chain levels shows that NFL is a more specific marker of MS than NFH [38]. As neurofilaments are specific to neuronal tissue, their presence in the bloodstream implies leakage or diffusion through the blood–brain barrier. Furthermore, NFL can reach the circulation via CSF venous drainage pathways [39].

Recent systematic reviews and guidance reports indicate that blood NFL is consistently elevated in untreated multiple sclerosis and correlates with relapse activity, MRI lesion burden and risk of future disability, supporting its utility as a prognostic biomarker in routine care [6,40]. However,

evidence is limited on how long-term immunomodulatory or neuroprotective therapies modify peripheral NfL concentrations in real-world treated cohorts, and whether such therapy-related changes alter the biomarker's diagnostic or prognostic performance [41,42]. Moreover, assay and platform differences (single molecule array [Simoa], electrochemiluminescence [ECL], high-sensitivity ELISA) can produce systematic differences in absolute NfL values and sensitivity for low concentrations, complicating direct comparisons across studies [43,44]. To address these gaps, the present study measured plasma NFL using a standardized ELISA approach in well-characterized, predominantly long-term treated cohorts of multiple sclerosis and amyotrophic lateral sclerosis patients and compared them with healthy controls, with the goal of assessing whether treatment-associated modulation of plasma NfL is observable in routine clinical samples. The novelty of this work is that it directly compares treated multiple sclerosis and amyotrophic lateral sclerosis cohorts using the same assay and provides evidence that long-term therapy may attenuate circulating NfL levels — a topic that has not been extensively explored in prior, predominantly untreated or therapy-heterogeneous cohorts [40,45].

MATERIALS AND METHODS

Test Subjects

A total of 86 participants were recruited from the Istanbul University Faculty of Medicine, Department of Neurology. Blood samples were collected and analyzed at Yildiz Technical University, Department of Molecular Biology and Genetics. The cohort consisted of 43 women (50%, mean age: 42.80±1.93 years) and 43 men (50%, mean age: 43.19±2.15 years). Participants were further classified into diagnostic groups. The participants who provided the samples used in the experiment gave their written informed consent, and their demographic information has been anonymized. The sample size (n=86) was determined by clinical availability during the study period rather than a predefined statistical power calculation. This approach is consistent with other MS and ALS biomarker studies that typically include 50–120 participants, and was sufficient to detect significant intergroup differences. The participant demographics are summarised in Table 1.

As a result of the tests performed, the mean NFL protein concentration in the MS subject group was 1.35±0.14. The mean NFL protein concentration was 1.24±0.21 in men and 1.45±0.18 in women. Similarly, the mean NFL protein concentration in the ALS subject group was 1.31±0.11. The mean NFL protein concentration was 1.42±0.18 in men and 1.74±0.10 in women. In the control group, the NFL protein amounts are as follows: the overall mean is 1.91±0.29. The mean NFL protein concentration was 1.13±0.09 in men and 2.26±0.37 in women. In the whole subject group, the mean NFL protein concentration was 1.51±0.13 in women and 1.32±0.12 in men. The average concentration of NFL protein is presented in Table 2.

Samples

Blood samples were collected into 10 mL EDTA tubes at the Department of Neurology, Faculty of Medicine, Istanbul University, and transported on ice to the Molecular Biology and Genetics Research Laboratories at Yildiz Technical University. The samples were then centrifuged at 1000 × g for 30 minutes at 24 °C. The plasma obtained from two tubes per subject was pooled into a 15 mL tube and divided into 1.5 mL cryotubes. To ensure accurate data processing

Table 1. Participants demographic information

Groups	Total Subjects	Number of Women	Mean Age ± SD (Women)	Number of Men	Mean Age ± SD (Men)
MS	33	17	38.94 ± 4.12	16	35.38±2.82
ALS	38	16	53.81±2.64	22	49.73±2.56
Healthy Control	15	10	33.40±4.40	5	36.20±2.89
Total Participants	86	43	42.80±1.93	43	43.19±2.15

Table 2. Mean Concentration of NFL protein (ng/ml)

Groups	Overall Mean NFL (ng/ml) ± SD	Women- Mean NFL (ng/ml) ± SD	Men- Mean NFL (ng/ml) ± SD
MS	1.35±0.14	1.45±0.18	1.24±0.21
ALS	1.31±0.11	1.74±0.10	1.41±0.18
Healthy Control	1.91±0.30	2.26±0.37	1.13±0.08
Total Participants	1.51±0.13	1.51±0.13	1.32±0.12

and sample tracking, each participant was assigned a unique identifier, and samples were stored at -80°C until protein analysis was performed.

Analytical Methods

Plasma NFL protein concentrations were measured using a 96-well Human NEFL ELISA Kit (Cat. No: E3350Hu, Bioassay Technology Laboratory). The kit used for ELISA analysis was prepared according to the manufacturer's instructions. The analytical sensitivity of the kit was 0.051 ng/mL. All samples were measured twice, and the mean of the two measurements was used for statistical analysis. Optical density was determined using a Biotek ELISA multi-plate reader (GEN5 software, version 1.08).

Hypotheses

The study tested the following hypotheses:

i. **Gender:** NFL concentrations are consistent across genders (H0) or differ between genders (H1).
ii. **Age groups:** NFL concentrations are consistent across age groups (H0) or differ between at least two age groups (H1).
iii. **Disease type:** NFL concentrations are consistent across all groups (H0) or differ between at least two groups (H1).

Statistical Methods

The analyses in this study were performed using SPSS 22.0 (IBM Corp.) software. In this context, plasma NFL levels were compared in the MS group, the ALS group, and the healthy control group. Due to the non-normal distribution of the data, intergroup comparisons were performed using the Kruskal–Wallis test, and p-values below 0.05 were accepted as statistically significant.

Ethics Approval

Ethical approval for the study was obtained from the Istanbul University Faculty of Medicine Clinical Research Ethics Committee (Decision No. 689, File No. 2016/665, Meeting Number 10, May 24, 2016). All participants whose blood samples were used in the study provided written informed consent for the use of their biological materials in this study.

RESULTS AND DISCUSSION

Statistical tests were selected based on the distribution and nature of the dataset. Since the normality assumption was not met, the Kruskal-Wallis test was used to compare NFL levels between the ALS, MS, and control groups. Pairwise comparisons were performed using Dunn's post-hoc test with a healthy control group as a reference. In women, NFL levels were statistically significantly decreased in both the MS (p=0.0171) and ALS (p=0.0135) groups compared to controls. No significant difference was observed in men. In the overall cohort, NFL was significantly decreased in the MS group compared to controls (p=0.0035), while the decrease was not statistically significant in the ALS group (p=0.0728). No significant difference was found between the multiple sclerosis and amyotrophic lateral sclerosis groups (Fig. 1).

The figure illustrates mean plasma NFL concentrations (ng/mL) in female and male participants in the MS, ALS and healthy control groups, as well as in the total study population. Female patients with MS and ALS exhibited significantly lower NFL levels than healthy controls. However, in the entire cohort, a significant reduction was only observed in the MS group. No significant difference was found between male participants or between the MS and ALS groups. Data are presented as mean ± standard deviation. Statistical significance is defined as *p<0.05 and **p<0.01 in the graph.

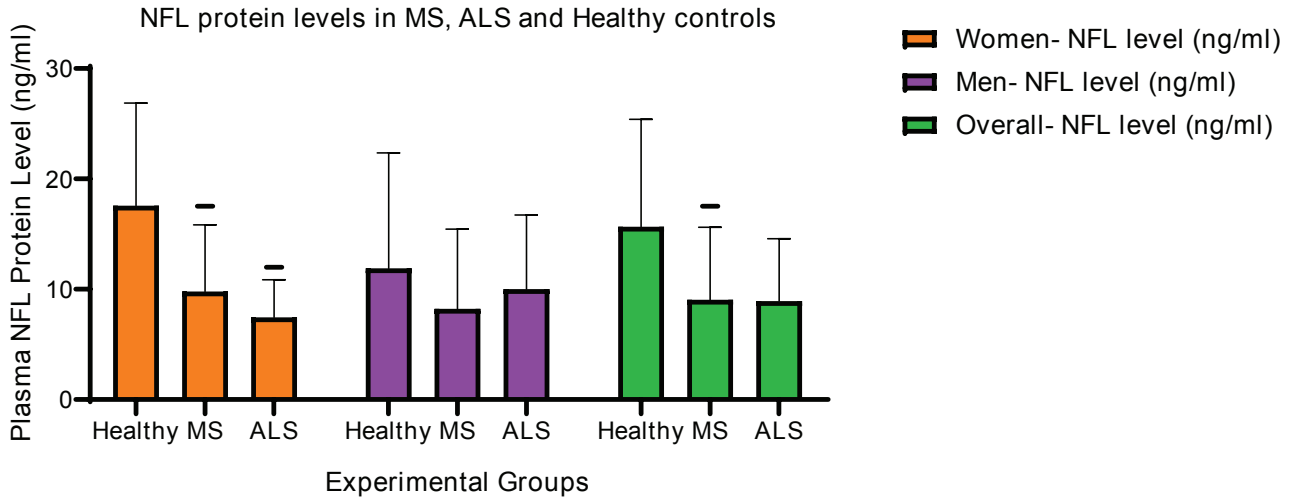


Figure 1. Plasma NFL protein levels in MS, ALS, and healthy controls.

NFLs are specific to neuronal cells and pass into the CSF. They can be detected in the bloodstream, even at low concentrations. The concentration of NFLs in the CSF increases in various diseases that cause neuronal damage [37,46]. NFL is one of the proteins that make up the structure of neurons and is released into the space around them when there is damage to the nerves. It then enters the fluid around the brain and spinal cord and the blood [47-49]. High levels of NFL in the fluid around the brain and spine are seen in diseases that cause the nervous system to weaken or break down, like multiple sclerosis, a type of muscular wasting, and problems like memory loss and paralysis [50-55]. Due to its specificity to neurons, NFL is considered a potential biomarker for assessing damage to the central and peripheral nervous systems.

Although diagnosing neurodegenerative diseases such as ALS and MS remains a complex process, neurofilament light chain (NFL) has gained increasing importance as a biomarker particularly for neurodegeneration. Most studies investigating biomarkers focus on the analysis of CSF and blood samples. In this work, plasma NFL levels in both ALS and MS patients were evaluated for their biomarker potential. Blood samples were collected from 38 ALS patients, 33 MS patients, and 15 healthy controls. Plasma fractions were isolated from these samples, and NFL protein levels were quantified using the sandwich ELISA method. The resulting data were statistically analyzed using the SPSS 22.0 software. Given that the data did not follow a normal distribution, the Kruskal-Wallis test was employed as a non-parametric alternative to the one-way ANOVA, which does not assume normality [56]. This test was chosen because it allows for the comparison of NFL protein levels across three independent groups assessing whether there are statistically significant differences among them. Results were considered significant at $p<0.05$.

Statistical analysis revealed a significant difference in NFL levels between the healthy control group and the MS group ($p=0.0035$). In a study by Bjornevik et al. [57], NFL levels were investigated among US military personnel whose serum samples were stored in the US Department of Defense Serum Depot. Serum samples collected between 2000 and 2011were later analyzed for NFL concentrations between 2018 and 2019 using an ultra-sensitive Simoa. Notably, NFL levels were elevated up to six years before the onset of clinical MS symptoms, indicating that multiple sclerosis may have a prodromal phase characterized by neuroaxonal damage that begins several years before clinical manifestation.

In our study, NFL levels were lower in MS patients compared to healthy controls; this decrease is consistent with findings that it is associated with long-term immunomodulatory treatment. A study by Bar-Or et al. [40] showed that ocrelizumab significantly reduced NFL levels and decreased physical symptoms in MS. High levels of the protein have been shown to cause progression of clinical signs. Furthermore, the findings in our study resulted in increased disease activity and neuroaxonal damage after discontinuation of natalizumab treatment, and NFL protein levels increased [58]. In MS patients treated with glatiramer acetate as an immunomodulator, NFL protein levels were statistically reduced in the first 9 months ($p<0.05$) and this reduction became even more pronounced at 12 months ($p=0.013$) [59]. Our study was conducted with patients diagnosed with MS who have been on medication treatment for a duration ranging from at least 1 year to a maximum of 20 years [60].

The next statistical comparison was conducted between the healthy control group and the ALS group. This revealed a reduction in NFL levels which did not reach statistical significance ($p=0.0728$). In a study by Verde et al. [61], serum samples were taken from 124 patients with ALS, 50 individuals without neurodegenerative diseases and 44 patients undergoing diagnosis for differential diagnosis of ALS (disease controls). Additionally, serum samples from 65 patients with other neurodegenerative disorders were included, consisting of 20 patients with frontotemporal dementia, 20 with Alzheimer's disease, 19 with Parkinson's disease and 6 with Creutzfeldt–Jakob disease (CJD). In patients other than those diagnosed with ALS and CJD, NFL protein levels, as measured by ultra-sensitive Simoa technology, were significantly higher. These outcomes imply that serum NFL could be used as a diagnostic and prognostic biomarker in ALS [57].

In our study, the NFL levels were found to be lower in the ALS patient group compared to the healthy controls. Clinically, the lower NFL levels observed in ALS patients compared with healthy controls may reflect a treatment effect, where long-term therapy reduces ongoing axonal damage and decreases neurofilament release. In this respect, NFL is considered not only a disease marker but also a potential indicator in disease monitoring. In practice these findings suggest that the decrease in NFL protein levels may be related to disease-modifying therapies (DMTs) [45,60,61]. It has been determined that Riluzole, used in ALS patients, reduces axonal damage by slowing down neurofilament transport. In the study by Esselin et al. [62], it was observed that serum NFL protein levels were higher in ALS patients compared to healthy controls and that this level increased when patients were not treated. No statistically significant difference was found in serum NFL protein levels with Riluzole treatment. This suggests that the use of serum NFL for treatment monitoring is limited. According to the study by Stevenson et al. [63], Riluzole's anti-glutamatergic properties have been shown to protect against glutamate-mediated changes in neurofilament phosphorylation and transport, both of which are crucial pathological features of ALS. Given that the ALS patients in our study were treated with Riluzole (Rilutek), this may explain the lower NFL levels observed in this group compared to healthy controls. Our study included ALS patients who had been receiving medication for a period ranging from 1 to 10 years.

Kuhle et al. [64] measured serum NFL levels in 589 MS and 35 healthy controls. There was no clear link found between the levels of NFL in the blood and age or gender. Similarly, a meta-analysis by Cai et al. [65] included 2,651 participants from thirteen studies, comprising 795 cerebrospinal fluid samples and 1,856 blood samples. In the experimental groups, MS patients were aged 31-44, and healthy volunteers were aged 28-44.3. NFL protein levels in CSF and serum were measured using ELISA and electrochemical luminescence (ECL), and higher NFL concentrations were detected in ECL, which is more sensitive than ELISA. This observation in MS patients may be due to the high sensitivity of ECL [37,64]. Prior reports also confirmed that elevated NFL concentrations in both CSF and blood of the patients, independent of age gender and age.[65]

In our study, a statistically significant difference was observed in NFL concentration levels based on gender at the $\alpha=0.10$ significance level ($p=0.076$). However, no difference was found in this protein among the diseases. The absence of a difference may indicate a response related to the medications used.

When considered together, our results support the reported findings related to changes in NFL protein levels in neurodegenerative diseases. The lower NFL levels detected in ALS and MS patient groups compared to healthy controls suggest that this decrease may be related to treatment approaches for reducing axonal damage over time. The results, consistent with previous studies, showed that immunomodulatory therapies used in MS and neuroprotective agents such as Riluzole used in ALS reduced NFL levels. While NFL levels are considered promising biomarkers for early diagnosis and monitoring disease progression in neurodegenerative diseases, therapeutic background was observed to be a significant factor in NFL measurements. Therefore, further studies involving larger patient cohorts and analyses classified according to treatment duration and treatment type are needed to establish the diagnostic and prognostic value of NFL more clearly in neurodegeneration. Furthermore, increasing the sample size of the healthy control group will contribute to stronger validation of the results and make the findings transferable to larger populations. When the aforementioned points are taken into consideration plasma NFL measurements can be used as a useful tool for clinicians in monitoring disease progression and treatment response. Beyond this, plasma NFL levels could be a valuable instrument for researchers to use when selecting patients for long-term follow-up studies.

CONCLUSION

The study shows that measuring neurofilament light chain protein levels could be a way to spot neurodegenerative diseases including multiple sclerosis and amyotrophic lateral sclerosis. Although previous studies have consistently reported elevated levels of this protein in these conditions, our findings suggest that long-term therapeutic interventions may significantly impact these levels by reducing axonal damage. The observed reduction in neurofilament light chain concentrations among treated patients emphasizes the importance of considering treatment history when interpreting neurofilament light chain measurements. Although our findings provide valuable insights, larger and more diverse sample groups are needed to improve the clinical relevance of the results. These findings may contribute to a broader understanding of neurodegenerative diseases and raise questions about the clinical role of biomarkers, particularly in patients receiving treatment. Larger prospective studies with bigger cohorts are needed to confirm these findings. Future research should also evaluate treatment duration and treatment type to clarify the diagnostic and prognostic role of neurofilament light chain in distinct neurodegenerative diseases.

AUTHORSHIP CONTRIBUTIONS

Bertan Emrah: Data curation, Writing – original draft. **Günel Aslıhan:** ELISA experiments, Editing. **Çelik Reşit:** Statistical Analysis. **İdrisoğlu Halil Atila:** Diagnosis and follow-up of patients; collection of blood samples. **Vural Korkut Senay:** Writing – review & editing.

DATA AVAILABILITY STATEMENT

The authors confirm that the data that supports the findings of this study are available within the article. Raw data that support the finding of this study are available from the corresponding author, upon reasonable request.

CONFLICT OF INTEREST

The author declared no potential conflicts of interest with respect to the research, authorship, and/or publication of this article.

FUNDING

This research was supported partially by Yıldız Technical University Scientific Research Projects. (Project code: TYL-2019-3519)

ETHICS

Ethical approval for the study was obtained from the Istanbul University Faculty of Medicine Clinical Research Ethics Committee (Decision No. 689, File No. 2016/665, Meeting Number 10, May 24, 2016).

STATEMENT ON THE USE OF ARTIFICIAL INTELLIGENCE

Artificial intelligence was not used in the preparation of the article.

REFERENCES

[1] Gadhave DG, Sugandhi VV, Jha SK, Nangare SN, Gupta G, Singh SK, et al. Neurodegenerative disorders: Mechanisms of degeneration and therapeutic approaches with their clinical relevance. Ageing Res Rev 2024;99:102357. [CrossRef]

[2] Garton T, Gadani SP, Gill AJ, Calabresi PA. Neurodegeneration and demyelination in multiple sclerosis. Neuron 2024;112:3231–3251. [CrossRef]

[3] Mead RJ, Shan N, Reiser HJ, Marshall F, Shaw PJ. Amyotrophic lateral sclerosis: A neurodegenerative disorder poised for successful therapeutic translation. Nat Rev Drug Discov 2023;22:185–212. [CrossRef]

[4] Roy T, Al-Chalabi A, Iacoangeli A, Al Khleifat A. Biomarkers in ALS trials: Fromdiscovery to clinical utility. Front Neurosci 2025;19:1636303. [CrossRef]

[5] La Civita E, Nicolella V, Fiorenza M, Cosimato V, Castaldo G, Morra VB, et al. Advancing clinical use of neurofilament light chain: Translational insights from research to routine practice. Biomark Insights 2025;20:11772719251364018. [CrossRef]

[6] Freedman MS, Gnanapavan S, Booth RA, Calabresi PA, Khalil M, Kuhle J, et al. Guidance for use of neurofilament light chain as a cerebrospinal fluid and blood biomarker in multiple sclerosis management. eBioMedicine 2024;101:104970. [CrossRef]

[7] Lycke JN, Karlsson JE, Andersen O, Rosengren LE. Neurofilament protein in cerebrospinal fluid: A potential marker of activity in multiple sclerosis. J Neurol Neurosurg Psychiatry 1998;64:402–404. [CrossRef]

[8] Cairns NJ, Lee VM, Trojanowski JQ. The cytoskeleton in neurodegenerative diseases. J Pathol 2004;204:438–449. [CrossRef]

[9] Chevalier-Larsen E, Holzbaur EL. Axonal transport and neurodegenerative disease. Biochim Biophys Acta Mol Basis Dis 2006;1762:1094–1108. [CrossRef]

[10] Grant P, Pant HC. Neurofilament protein synthesis and phosphorylation. J Neurocytol 2000;29:843–872. [CrossRef]

[11] Slawson C, Hart GW. Dynamic interplay between O-GlcNAc and O-phosphate: The sweet side of protein regulation. Curr Opin Struct Biol 2003;13:631–636. [CrossRef]

[12] Petzold A. Neurofilament phosphoforms: Surrogate markers for axonal injury, degeneration and loss. J Neurol Sci 2005;233:183–198. [CrossRef]

[13] Bertram L, Tanzi RE. The genetic epidemiology of neurodegenerative disease. J Clin Invest 2005;115:1449–1457. [CrossRef]

[14] Gandhi S, Wood NW. Genome-wide association studies: The key to unlocking neurodegeneration? Nat Neurosci 2010;13:789–794. [CrossRef]

[15] Viswambharan V, Thanseem I, Vasu MM, Poovathinal SA, Anitha A. miRNAs as biomarkers of neurodegenerative disorders. Biomark Med 2017;11:151–167. [CrossRef]

[16] Durães F, Pinto M, Sousa E. Old drugs as new treatments for neurodegenerative diseases. Pharmaceuticals 2018;11:44. [CrossRef]

[17] Jeromin A, Bowser R. Biomarkers in neurodegenerative diseases. Adv Neurobiol 2017;15:491–528. [CrossRef]

[18] Gaetani L, Blennow K, Calabresi P, Di Filippo M, Parnetti L, Zetterberg H. Neurofilament light chain as a biomarker in neurological disorders. J Neurol Neurosurg Psychiatry 2019;90:870–881. [CrossRef]

[19] Abdelhak A, Foschi M, Abu-Rumeileh S, Yue JK, D'Anna L, Huss A, et al. Blood GFAP as an emerging biomarker in brain and spinal cord disorders. Nat Rev Neurol 2022;18:158–172. [CrossRef]

[20] Park Y, KC N, Paneque A, Cole PD. Tau, glial fibrillary acidic protein, and neurofilament light chain as brain protein biomarkers in cerebrospinal fluid and blood for diagnosis of neurobiological diseases. Int J Mol Sci 2024;25:6295. [CrossRef]

[21] Wang KK, Yang Z, Sarkis G, Torres I, Raghavan V. Ubiquitin C-terminal hydrolase-L1 (UCH-L1) as a therapeutic and diagnostic target in neurodegeneration, neurotrauma and neuro-injuries. Expert Opin Ther Targets 2017;21:627–638. [CrossRef]

[22] Connolly K, Lehoux M, O'Rourke R, Assetta B, Erdemir GA, Elias JA, et al. Potential role of chitinase-3-like protein 1 (CHI3L1/YKL-40) in neurodegeneration and Alzheimer's disease. Alzheimers Dement 2023;19:9–24. [CrossRef]

[23] Calabresi PA. Diagnosis and management of multiple sclerosis. Am Fam Physician 2004;70:1935–1944.

[24] Kasper D, Fauci A, Hauser S, Longo D, Jameson J, Loscalzo J. Harrison's principles of internal medicine. 19th ed. New York: McGraw-Hill Education; 2015.

[25] Browne P, Chandraratna D, Angood C, Tremlett H, Baker C, Taylor BV, et al. Atlas of Multiple Sclerosis 2013: A growing global problem with widespread inequity. Neurology 2014;83:1022–1024. [CrossRef]

[26] Filippi M, Bar-Or A, Piehl F, Preziosa P, Solari A, Vukusic S, et al. Multiple sclerosis. Nat Rev Dis Primers 2018;4:43. [CrossRef]

[27] Brown RH, Al-Chalabi A. Amyotrophic lateral sclerosis. N Engl J Med 2017;377:162–172. [CrossRef]

[28] Al-Chalabi A, Hardiman O, Kiernan MC, Chiò A, Rix-Brooks B, van den Berg LH. Amyotrophic lateral sclerosis: Moving towards a new classification system. Lancet Neurol 2016;15:1182–1194. [CrossRef]

[29] Brettschneider J, Petzold A, Süssmuth SD, Ludolph AC, Tumani H. Axonal damage markers in cerebrospinal fluid are increased in ALS. Neurology 2006;66:852–856. [CrossRef]

[30] Munoz DG, Greene C, Perl DP, Selkoe DJ. Accumulation of phosphorylated neurofilaments in anterior horn motoneurons of amyotrophic lateral sclerosis patients. J Neuropathol Exp Neurol 1988;47:9–18. [CrossRef]

[31] De Schaepdryver M, Jeromin A, Gille B, Claeys KG, Herbst V, Brix B, et al. Comparison of elevated phosphorylated neurofilament heavy chains in serum and cerebrospinal fluid of patients with amyotrophic lateral sclerosis. J Neurol Neurosurg Psychiatry 2018;89:367–373. [CrossRef]

[32] Steinacker P, Feneberg E, Weishaupt J, Brettschneider J, Tumani H, Andersen PM, et al. Neurofilaments in the diagnosis of motoneuron diseases: A prospective study on 455 patients. J Neurol Neurosurg Psychiatry 2016;87:12–20. [CrossRef]

[33] Poesen K, De Schaepdryver M, Stubendorff B, Gille B, Muckova P, Wendler S, et al. Neurofilament markers for ALS correlate with extent of upper and lower motor neuron disease. Neurology 2017;88:2302–2309. [CrossRef]

[34] Feneberg E, Oeckl P, Steinacker P, Verde F, Barro C, Van Damme P, et al. Multicenter evaluation of neurofilaments in early symptom onset amyotrophic lateral sclerosis. Neurology 2018;90:e22–e30. [CrossRef]

[35] Tiedt S, Duering M, Barro C, Kaya AG, Boeck J, Bode FJ, et al. Serum neurofilament light: A biomarker of neuroaxonal injury after ischemic stroke. Neurology 2018;91:e1338–e1347. [CrossRef]

[36] Meeter LH, Dopper EG, Jiskoot LC, Sanchez-Valle R, Graff C, Benussi L, et al. Neurofilament light chain: A biomarker for genetic frontotemporal dementia. Ann Clin Transl Neurol 2016;3:623–636. [CrossRef]

[37] Disanto G, Barro C, Benkert P, Naegelin Y, Schädelin S, Giardiello A, et al. Serum neurofilament light: A biomarker of neuronal damage in multiple sclerosis. Ann Neurol 2017;81:857–870. [CrossRef]

[38] Kuhle J, Plattner K, Bestwick JP, Lindberg RL, Ramagopalan SV, Norgren N, et al. A comparative study of CSF neurofilament light and heavy chain protein in MS. Mult Scler 2013;19:1597–1603. [CrossRef]

[39] Kuhle J, Barro C, Andreasson U, Derfuss T, Lindberg R, Sandelius Å, et al. Comparison of three analytical platforms for quantification of the neurofilament light chain in blood samples: ELISA, electrochemiluminescence immunoassay and Simoa. Clin Chem Lab Med 2016;54:1655–1661. [CrossRef]

[40] Bar-Or A, Thanei GA, Harp C, Bernasconi C, Bonati U, Cross AH, et al. Blood neurofilament light levels predict non-relapsing progression following anti-CD20 therapy in relapsing and primary progressive multiple sclerosis: Findings from the ocrelizumab randomised, double-blind phase 3 clinical trials. eBioMedicine 2023;93:104662. [CrossRef]

[41] Rodríguez-Jorge F, Fernández-Velasco JI, Villarrubia N, Gracia-Gil J, Fernández E, Meca-Lallana V, et al. Biomarkers of response to ocrelizumab in relapsing-remitting multiple sclerosis. Front Immunol 2024;15:1480676. [CrossRef]

[42] Barrero Hernández FJ, Romero Villarrubia A, Muñoz Fernández C, Guillén Martinez V, Aguilera Del Moral A, Barrios-López JM, et al. Real-world study of serum neurofilament light chain levels in ocrelizumab-treated people with relapsing multiple sclerosis. J Pers Med 2024;14:692. [CrossRef]

[43] Ashrafzadeh-Kian S, Figdore D, Larson B, Deters R, Abou-Diwan C, Bornhorst J, et al. Head-to-head comparison of four plasma neurofilament light chain (NfL) immunoassays. Clin Chim Acta 2024;561:119817. [CrossRef]

[44] Pafiti A, Krashias G, Tzartos J, Tzartos S, Stergiou C, Gaglia E, et al. A comparison of two analytical approaches for the quantification of neurofilament light chain, a biomarker of axonal damage in multiple sclerosis. Int J Mol Sci 2023;24:10787. [CrossRef]

[45] Benatar M, Wuu J, Turner MR. Neurofilament light chain in drug development for amyotrophic lateral sclerosis: A critical appraisal. Brain 2023;146:2711–2716. [CrossRef]

[46] Machacek M, Garcia-Montoya E, McColgan P, Sanwald-Ducray P, Mazer NA. NfL concentration in CSF is a quantitative marker of the rate of neurodegeneration in aging and Huntington's disease: A semi-mechanistic model-based analysis. Front Neurosci 2024;18:1420198. [CrossRef]

[47] Teunissen CE, Khalil M. Neurofilaments as biomarkers in multiple sclerosis. Mult Scler 2012;18:552–556. [CrossRef]

[48] Delaby C, Alcolea D, Carmona-Iragui M, Illán-Gala I, Morenas-Rodríguez E, Barroeta I, et al. Differential levels of Neurofilament Light protein in cerebrospinal fluid in patients with a wide range of neurodegenerative disorders. Sci Rep 2020;10:9161. [CrossRef]

[49] Nakamura T, Kawarabayashi T, Shibata M, Kasahara H, Makioka K, Sugawara T, et al. High levels of plasma neurofilament light chain correlated with brainstem and peripheral nerve damage. J Neurol Sci 2024;463:123137. [CrossRef]

[50] Malmeström C, Haghighi S, Rosengren L, Andersen O, Lycke J. Neurofilament light protein and glial fibrillary acidic protein as biological markers in MS. Neurology 2003;61:1720–1725. [CrossRef]

[51] Norgren N, Rosengren L, Stigbrand T. Elevated neurofilament levels in neurological diseases. Brain Res 2003;987:25–31. [CrossRef]

[52] Trentini A, Comabella M, Tintoré M, Koel-Simmelink MJ, Killestein J, Roos B, et al. N-acetylaspartate and neurofilaments as biomarkers of axonal damage in patients with progressive forms of multiple sclerosis. J Neurol 2014;261:2338–2343. [CrossRef]

[53] Villar LM, Picón C, Costa-Frossard L, Alenda R, García-Caldentey J, Espino M, et al. Cerebrospinal fluid immunological biomarkers associated with axonal damage in multiple sclerosis. Eur J Neurol 2015;22:1169–1175. [CrossRef]

[54] Kuhle J, Gaiottino J, Leppert D, Petzold A, Bestwick JP, Malaspina A, et al. Serum neurofilament light chain is a biomarker of human spinal cord injury severity and outcome. J Neurol Neurosurg Psychiatry 2015;86:273–279. [CrossRef]

[55] Lu CH, Macdonald-Wallis C, Gray E, Pearce N, Petzold A, Norgren N, et al. Neurofilament light chain: A prognostic biomarker in amyotrophic lateral sclerosis. Neurology 2015;84:2247–2257. [CrossRef]

[56] Xia Y. Correlation and association analyses in microbiome study integrating multiomics in health and disease. In: Sun J, editor. Progress in molecular biology and translational science. Vol. 171. San Diego: Academic Press; 2020. p. 309–491. [CrossRef]

[57] Bjornevik K, Munger KL, Cortese M, Barro C, Healy BC, Niebuhr DW, et al. Serum neurofilament light chain levels in patients with presymptomatic multiple sclerosis. JAMA Neurol 2020;77:58–64. [CrossRef]

[58] Fox RJ, Cree BAC, de Sèze J, Gold R, Hartung HP, Jeffery D, et al. Temporal relationship between serum neurofilament light chain and radiologic disease activity in patients with multiple sclerosis. Neurology 2024;102:e209357. [CrossRef]

[59] Huss A, Senel M, Abdelhak A, Mayer B, Kassubek J, Ludolph AC, et al. Longitudinal serum neurofilament levels of multiple sclerosis patients before and after treatment with first-line immunomodulatory therapies. Biomedicines 2020;8:312. [CrossRef]

[60] Miller TM, Cudkowicz ME, Genge A, Shaw PJ, Sobue G, Bucelli RC, et al. Trial of antisense oligonucleotide tofersen for SOD1 ALS. N Engl J Med 2022;387:1099–1110. [CrossRef]

[61] Verde F, Otto M, Silani V. Neurofilament light chain as biomarker for amyotrophic lateral sclerosis and frontotemporal dementia. Front Neurosci 2021;15:679199. [CrossRef]

[62] Esselin F, De la Cruz E, Hirtz C, Tiers L, Alphandery S, Baudesson L, et al. Repeated neurofilament light chain measurements did not capture Riluzole therapeutic effect in amyotrophic lateral sclerosis patients. CNS Neurosci Ther 2022;28:1532–1538. [CrossRef]

[63] Stevenson A, Yates DM, Manser C, De Vos KJ, Vagnoni A, Leigh PN, et al. Riluzole protects against glutamate-induced slowing of neurofilament axonal transport. Neurosci Lett 2009;454:161–164. [CrossRef]

[64] Kuhle J, Kropshofer H, Haering DA, Kundu U, Meinert R, Barro C, et al. Blood neurofilament light chain as a biomarker of MS disease activity and treatment response. Neurology 2019;92:e1007–e1015. [CrossRef]

[65] Cai L, Huang J. Neurofilament light chain as a biological marker for multiple sclerosis: A meta-analysis study. Neuropsychiatr Dis Treat 2018;14:2241–2254. [CrossRef]

Sigma J Eng Nat Sci, Vol. 44, No. 4, pp. 2685–2699, August, 2026

Sigma Journal of Engineering and Natural Sciences
Web page info: https://sigma.yildiz.edu.tr
DOI: 10.14744/sigma.2025.00098

Research Article

Energy-efficient static memory architecture for internet of things applications

Deepak GARG[1,*], Rupali SINGH[1]

[1]*Department of Electronics and Communication Engineering, SRM Institute of Science and Technology, Delhi-NCR Campus, Uttar Pradesh, 201204, India*

ARTICLE INFO

Article history
Received: 23 December 2024
Revised: 21 March 2025
Accepted: 28 May 2025

Keywords:
Energy-Efficient Memory; Internet of Things; Low Power Design; Non-Volatile Memory; MTCMOS; Sub-Threshold Region; SVL; FinFET

ABSTRACT

The paper explores low-power design strategies of Static Random Access Memorycell for Internet of Things devicesto address critical power limitations that hinder further miniaturization. Fin-Field Effect Transistor solves the problem of leakage current by improving challenging power versus performance decision. This research develops 7-Transistor Static Random Access Memorycells based on Fin-Field Effect Transistors using the Muti-Threshold CMOS and Self Controllable Voltage Level methods. Using 45 nm Fin-Field Effect Transistor technologies, the design and simulation of all design circuits are carried out with Cadence Virtuoso. The work adopts a multi-disciplinary approach, combining device-circuit co-design to achieve ultra-low-power operations suitable for complex tasks in Internet of Things based systems. The proposed design shows that the Self Controllable Voltage Levelapproach of a 7-Transistor Static Random Access Memorydesign utilizing Fin-Field Effect Transistor cell is more effective than the Muti-Threshold CMOS methodology in terms of leakage power and leakage current. Additionally, among other proposed approaches, a comparative analysis of leakage currents and leakage power is conducted. Key outcomes include significant improvements in leakage power using Self Controllable Voltage Levelapproachfor Static Random Access Memorydesign using Fin-Field Effect Transistor.This paper contributes to the advancement of low leakage Internet of Things devices by integrating innovative leakage reduction techniques with cutting-edge low-power circuit designs. The proposed design achieves a minimum leakage current of 9.45nA and leakage power of 24.28nW by utilizing Self Controllable Voltage Levelapproach. Compared to Static Random Access Memorycells designed with Muti-Threshold CMOS technique, the proposed method results in 25.8% and 36% approximately reduction in leakage power and leakage current respectively. The findings pave the way for developing smaller, smarter, and sustainable wearable and implantable devices capable of complex tasks without reliance on batteries.

Cite this article as: Energy-Efficient Memory; Internet of Things; Low Power Design; Non-Volatile Memory; MTCMOS; Sub-Threshold Region; SVL; FinFET. Sigma J Eng Nat Sci 2026;44(4):2685–2699.

***Corresponding author.**
*E-mail address: deepakgarg1985@gmail.com

This paper was recommended for publication in revised form by Editor-in-Chief Ahmet Selim Dalkilic

Published by Yıldız Technical University Press, İstanbul, Turkey
© Author. This is an open access article under the CC BY-NC license (http://creativecommons.org/licenses/by-nc/4.0/).

INTRODUCTION

A significant challenge in modern circuit design is reducing power consumption in electronic components. In existing chip technology, the capacity of SOC memory is rapidly advancing to enhance global performance. As a larger backup memory is necessary, SRAM plays an increasingly vital role in contemporary chip systems [1]. With shrinking transistors, reliability problems like SCEs and process variations are getting more and more critical. Moreover, if the current density is high in silicon, heat dissipation is also a problem, which is also detrimental to the durability and operation life of circuits.

As the number of IoT devices increases, memory technologies must be power efficient, fast and space efficient. The IoT is gaining popularity in fields such as home automation systems, biomedicalequipment, and wearable communication devices. IoT-compatible devices require larger integrated memory circuits. Compact and light-weight IoT devices restrict the utilization of the major energy source todiminutive non-rechargeable or rechargeable batteries. Battery longevity and replacement intervals are key concerns in battery-operated or partially energy-harvested IoT devices, ultra-low-power (ULP) systems on chips (SoCs) are increasingly favored by chip manufacturers. This ULP system on chips necessitates that both the logic and the embedded SRAM within the processor function at extremely low supply voltages. The IoT is now playing a significant role in the electronics sector and is in great demand. The industrial IoT market can be expected to be driven by applications like industrial automation and predictive maintenance, which are expected to reach as big as $263.4 billion by 2027 [2]. In 2025, the World Economic Forum estimates that there will be 41.6 billion connected devices [3]. For diverse tasks, on-chip memory is needed for storing instructions, and the required memory is SRAM for IoT devices [4, 5]. These recollections use up a large amount of the system's energy [6]. SRAM leakage power may govern total chip P_Leakage, and substantial switching capacitance in the bit lines and word lines enables SRAM access operations energy-intensive. Operating the SRAM capacitance in the bit lines and word lines enables SRAM access operations energy-intensive. Operating the SRAM at the sub-threshold region minimizes P_Leakage, rendering it appropriate for low-power applications. SCEs due to continuous scaling also impact the performance of CMOS-based SRAM [7]. Alternative devices like FinFET have been created to address the constraints of CMOS technology. A FinFET is a structure with a channel that is surrounded by the gate material on three or more sides, which offers better control and improved performance compared to a CMOS device. The advantages of FinFET devices over conventional CMOS devices are scalability and on-current [2, 8]. However, the important problem of width quantization arises in circuits using FinFETs [9] exists. This is a major concern for radioed circuits like SRAM, where the size of the transistors is critical to the proper functioning of the circuit. This is further complicated by inconsistencies in the manufacturing process, and results in a lowered efficiency of the SRAM design. An innovative gadget capable of addressing these restrictions is essential at this time.

Currently, Nobel multi (tri)-gate structural design, commonly referred to as FinFET technology, has demonstrated enhanced scalability. The primary factor influencing the IC industry include cost, time to market, area, power consumption, and performance metrics. The design specifications have remained consistent over time. With every new process node, design teams try to make their products "better, sooner, cheaper," These days, processors are built with billions of transistors. The industry shift to smaller geometries could pose problems because of the effects of short-channel (SCE) which may lead to increased leakage current with reduced geometry and variation in the concentration of dopants with decreasing geometry. The FinFET structure offers substantial benefits for the ability to scale devices and reduce short channel effects, which are common in many contemporary planar transistor designs, in the future semiconductor industry. Estimations [10, 11] show that the FinFETs can reach an operational speed that is up to 37% higher and require less than half of the dynamic power, while simultaneously consuming less static leakage current.

The FinFET exhibit has improved speed, but at roughly the same power, or has similar speed with lower power, when compared to its planar counterpart. Design teams will be able to now design for power, performance and throughput to meet the needs of particular utilities. As a result, multi gates FETs are anticipated to contribute to the reduction of leakage and the scaling of gate length. The advantages of FinFET are that it is scalable without any arbitrary dopant fluctuation effects, has higher channel mobility, and can be used to realize the next generation of SRAM with enhanced scalability with respect to gate insulator thickness. SRAM cells with FinFET technology can achieve smaller area and lower leakage currents. The threshold voltage (VTH) of the access transistor can be dynamically changed to improve data stability. While FinFETs can mitigate VTH variation, there are many challenges to reduce the variation. The small sizes of memory storage units allow for high storage density while maintaining performance and reliability. SRAM functions without the requirement for data refresh cycles, which makes it faster than other types of memory and increases the amount of data that can be stored, due to its internal positive feedback mechanism. SRAM cells are becoming more popular because they are more efficient, leading to greater data retention and larger write voltage range with the minimal power supply voltages. Table 1 illustrates the comparative study of earlier designed SRAM using FinFET [12-21].

Several low-power methods, including power gating, MTCMOS, SVL, VTCMOS and stacking can lower leakage current and power dissipation [22-24]. Initially, traditional

Table 1. Comparison of FinFET based SRAM design

S. No.	Pub. Year	Ref. No.	Authors Name	Transistors Count	Power Consumption	Propagation Delay	Power Delay Product
1	**2021**	[12]	Raushan et al.	12	99% more efficient than traditional SRAM	79.2% more efficient as compare to traditional SRAM	99.7% more efficient as compare to traditional SRAM
			Raushan et al.	14	99% more efficient than traditional SRAM	76.5% more efficient as compare to traditional SRAM	99.4% more efficient as compare to traditional SRAM
2	**2020**	[13]	Rahebeh Niaraki Asli et al.	6	Least read power consumption	NA	NA
3	**2020**	[14]	S. Birla et al.	8	At 0.5 V, the SG and IG SRAMs had leakage powers of 12.61 nW and 8.92 nW, respectively.	NA	NA
4	**2020**	[15]	C.Duari et al.	8	At 0.5 V, leakage power is 5.63nW for CMOS SRAM.	NA	NA
5	**2020**	[16]	R. R. Vallabhuni et al.	7	At V_{DD}= 0.1v, 0.001224mW for write operation.	At V_{DD}=0.1v, the write operations take 0.2943 ns.	At V_{DD}=0.1v, the write operations take 0.003602 pJ.
6	**2019**	[17]	J.Verma et al.	8	0.0268μW for writing operation.	0.0383 ns for writing operation.	0.001026 fJ for writing operation.
7	**2018**	[18]	S. S. Ensan,et al.	11	5.17 nW and 137.66 nW, respectively, represent the static and average power.	230.46 ps & 491.8ps delay for write and read operation respectively.	168.57 aJ
8	**2016**	[19]	J.Verma et al.	13	Leakage power = 0.096 nW	7.8 ns	0.7488 fJ
9	**2016**	[20]	N. Kaur,et al.	10	138.82 nW and 24.52 nW for writing and reading operation respectively.	60.069 ns and 0.00024056ns for writing and reading operation respectively.	1.4442 aJ and 0.0058986aJ for writing and reading operation respectively.
10	**2015**	[21]	D.Verma et al.	6	1.709 μW for reading and 7.561 nW for writing operation.	21.44 ns & 20.55 ns for reading and writing operations respectively.	NA

CMOS was used in SRAM design. However, this results in issues such as increased I_leakage and elevated power dissipation, which reduce the functionality of SRAM. Reducing power dissipation, achieving faster access times, and minimizing I_leakage are key requirements for memory design [25]. Hence, SRAM cells using FinFETs are recommended over conventional or traditional SRAM cells. Compared with traditional SRAM design architectures, FinFET technology minimizes SCE [26].

Additionally, reducing the leakage characteristics of SRAM cells is essential for improving cell stability [27]. The capability of FinFETs to differentially bias the independent front and back gates, which permits control over the device's V_{TH} and current, is one of its most beneficial characteristics. By adjusting the back gate, FinFETs can further minimize the power consumption of SRAM cells [28]. This section also addresses some research gaps in current methods for improving the design of FinFET based SRAM cells.

- **Less Extent of Novelty:** An obstacle to future progress is the fact that most research on enhancing the performance of SRAM cells focuses on either changing the number of transistors or using FinFET devices of varying sizes.

- **Less Studies toward Optimization:** An optimization model must be developed in order to address the fault tolerance concerns and enhance the SRAM FinFET design performance. Mathematical optimization techniques backed by probability theory are needed to enhance the design concepts of SRAM-based FinFETs.
- **Less number of computational Modeling:** The majority of current methods for FinFET-based SRAM rely on hardware-based modeling environments or experimental methods. Although experimental approaches provide highly reliable results, their application for large-scale, real-time commercial use is limited due to the lack of thorough consideration of computational complexity. On the other hand, hardware-based methods rely on specific simulation environments, which limit the amount of computational power that can be utilized.

To address these challenges, ICs, the primary power-consuming components of IoT devices, are designed to operate in low-power modes by reducing the supply voltage using low-voltage design approaches. The importance of low power memory cells for IoT applications are shown in Figure 1 and mentioned below:

- **Maintenance savings and increased reliability:** A low power consumption of the memory directly equates to a longer operational life of battery-powered systems, which is beneficial in the fields of environmental monitoring, smart agriculture and industrial automation, among others.
- **Energy Harvesting Compatibility:** There are many modern IoT nodes that depend on energy harvesting (solar, thermal, RF, etc.) for power. This is because a feature of these devices is that they can operate with very restricted energy budgets, thanks to their low-power memory cells.
- **Thermal Management:** Reducing power consumption reduces thermal dissipation, especially important for small IoT devices with little heat dissipation capacity, ensuring long-term reliability and decreased cooling costs.
- **Always-On Operation:** IoT devices may require memory cells to store data when they are inactive or sleeping. Ultra-low leakage memory designs are capable of providing always-on features without consuming energy, while providing responsive real-time performance and wake-up security.
- **Edge Intelligence Enablement:** As edge computing and on-device processing gain more importance, memory is critical to enable local inference, decision making and data filtering for edge Intelligence Enablement. Efficient memory design improves the computational power while keeping the energy efficiency.
- **Scalability and Network Density:** Power efficiency per node enables the use of more nodes without increasing the energy consumption, thus, leading to better scalability and network density for large-scale IOT networks deployed in smart cities, logistics and health monitoring systems.

This paper contributes to the advancement of low leakage IoT devices by integrating innovative leakage reduction techniques with cutting-edge low-power circuit designs. The proposed design achieves a minimum leakage current of 9.45nA and leakage power of 24.28nW by utilizing SVL approach. Compared to SRAM cells designed with MTCMOS technique, the proposed method results in 25.8% and 36% approximately reduction in leakage power and leakage current respectively. The subsequent sections of the paper are structured as follows. Discuss about Structure of the FinFET in Section 2, discuss about the Static Random Access Memory cell in Section 3, describe the SRAM Design Challenges in Section 4, Section 5 explains the Energy-Efficient SRAM Design approach; Section 6 discuss about the results. Section 7 gives the conclusions and prospective research directions.

FINFET STRUCTURE

The term FinFET was originally invented by the University of California. It was predominantly a

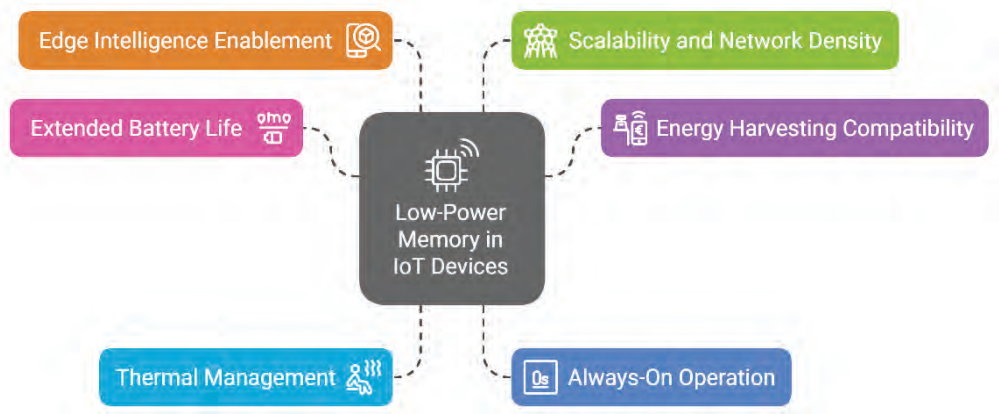


Figure 1. Benefits of Low-Power Memory in IoTDevice.

non-planetary transistor, featuring two gates fabricated on the SOI, designed as part of the DELTA, specifically a single-gatepre-transistor. FinFET comprises dual gates, whereas planar MOSFET contains a single gate to regulatethechanneland encompasses the source and drain [29]. FinFETs, a variant of multi-gate FET (MGFET), are predicted as one of the highly promising alternatives to bulk MOSFETs. Their potential is attributed to their superior stability, enhanced (I_{ON}/I_{OFF}) ratio, improved short channel performance, and reduced intrinsic gate capacitance. The operational methodology of FinFET closely resembles that of conventional MOSFET. FinFETs possess gate, drain, and source terminals to control the current flow. The channel between the source and drain of a FinFET is the distinguishing feature that sets it apart from a MOSFET. A "Fin" is a three-dimensional structure resembling the FinFET channel located on the upper section of the silicon substrate. Figure 2 illustrates that the three-dimensional bar design entirely encases the FinFET gate around the channel, creating multiple gate electrodes on both sides. These electrodes may enhance driving current and reduce leakage effects. The fin height of a single-fin FinFET should be half of the effective channel width (Weff), as per the design specifications [30]. Conversely, FinFETs can provide greater driving current densities per unit area than planar devices, provided that the effective width (Weff) is adequate to accommodate multiple parallel fins. The primary distinctions between FinFET and MOSFET devices lie in the configuration of the channel within the plane and the number of gates present. FinFET features a vertical channel referred to as 'Fin', whereas planar MOSFETs possess a horizontal channel, as indicated in references [31]. The fin structure quantifies the channel width based on the fin length. The result of this calculation is subsequently multiplied by the end height and the fin width within the Triple-Gate Multigate-transistor configuration. Consequently, the enhancement of cases is proportional to the quantity of gates and the iterative development of wings. The current drive may be enhancing due to longer fin lengths, but this improvement could compromise the stability of the machinery [32]. The $W_{eff}$of FinFET is given by eq. (1) [33].

$$W_{eff} = N_{Fin} X (T_{Fin} + 2H_{Fin}) \quad (1)$$

The FinFET architecture features a thin, vertically orientated, fin-shaped channel that facilitates current flow and is encased by a gate responsible for regulating electron movement. The vertical architecture facilitates enhanced management of electron flow in comparison to conventional planar MOSFETs, resulting in superior performance and efficiency. The DG FinFET is classified as a single-gate structure due to the width of the fin (W_{Fin}) is being considerably greater than its height (H_{Fin}) and the gate oxides on the sidewalls being substantially thicker than those on the top. Silicon dioxide and high-k dielectrics are commonly used as gate dielectrics due to their properties. High-k dielectrics, in particular, possess elevated dielectric constants that minimize gate leakage current. Spacer materials are used for forming a gap between the source/drain region and the gate electrode. The width of the gate and length of the channel are controlled by the size of the spacers and thus the performance characteristics of the transistor.

Static Random Access Memory Cell

An SRAM is a type of volatile semiconductor memory that is often used in digital systems for fast storage and retrieval of data. SRAM stores the data permanently, i.e. without refresh cycles as long as the power supply. This is because each bit in the SRAM is stored in a bistable flip-flop circuit. These transistors create a latch which allows the bit to stay in one state, which gives certain applications SRAM faster and more reliable. This memory is organized in the form of an array, making it easy to access bits and giving it design flexibility. Upon verification of the functionality of an individual memory cell array, it can be duplicated numerous times with little modification to the I/O control circuitry. The general architecture of SRAM design

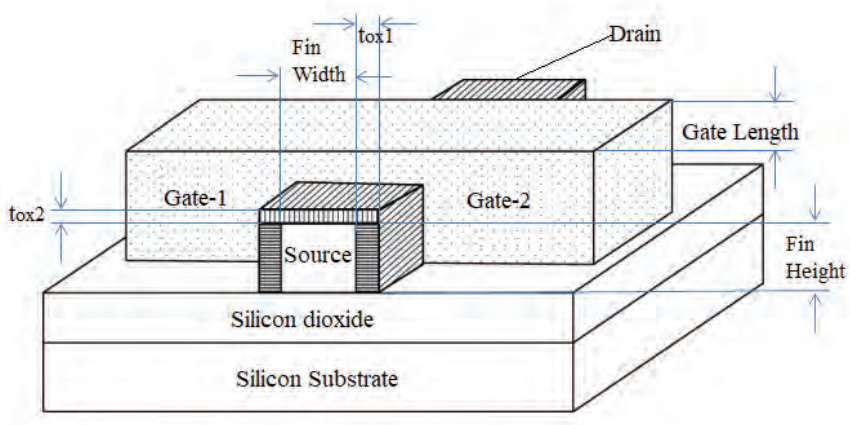


Figure 2. FinFET Structure.

is represented in Figure 3. The operational state of SRAM concerns to its functionality during various phases, including read, write, and stand by modes.

Figure 4 illustrates a 7T SRAM cell utilizing FinFET technology. This SRAM cell comprises a total of seven transistors: five N-type and two P-type FinFETs. The SRAM cell presented uses double-cross-coupled inverters and double-access transistors, both constructed with FinFET devices. The SRAM design consists of two sets of cross-coupled inverters, utilizing four transistors (M1, M2, M3, and M4), with each bit stored across these transistors. The 7T SRAM cell, which utilizes FinFET technology, effectively addresses the leakage issue present in the 6T SRAM cell.

This proposed design incorporates a total of seven transistors. Four transistors work like those in a standard device, while the other transistor controls the device so that in read mode, M6 and M5 are turned ON and M7 is turned OFF; on the other hand, in write mode, M5 is turned off, which helps save power.

Write Operation: The write operation of an SRAM design utilizing FinFET technology depends on the feedback connection established between the cross-coupled inverters. In this single-transistor-pair method, data increasesand decreases as a function of the ON/OFF state of M2. Setting the bit line and the RL line simultaneously initiates the reading process. This procedure takes place when the word line is retained by access transistors M7 and M6.

Read Operation: Here, information data is transmitted to the bit line as well as the word line. The data assigned to both lines is complementary to one another. The data is stored once the word line is stimulated. Improving FinFETs count of fingers can improve the operation write, but this improvement won't happen in all situations [34].

Hold Operation: Transistors M3 and M4 function as OFF-inverter transistors, providing mutual support to maintain data for an extended period. In this state, there is no connectivity between the RL, WL, and bit line with the cross-coupled circuit [35].

In SRAM, the hold state denotes the condition in which data is preserved without being accessed or change. SRAM cells generally consist of six transistors; however, certain designs incorporate seven transistors to improve stabilityor minimize leakage currents. In an alternative operating mode, the power consumption of suggested SRAMisdecreased to 50% of thatofa typical circuit, since it utilizes only one bit line [36].

Figure 5a displays the 7T SRAM design simulated write waveform result. We have carried out a single-ended procedure. At BL node, a pulsed input is applied and output is measured from Q and $\bar{Q}$. For this operation, WL is maintained at HIGH and RL at LOW. Figure 5b displays the 7T SRAM design simulated read waveform result. At Q node, a pulsed input is applied and output is measured at BL. For this operation, WL is maintained at LOW and RL at HIGH [37].

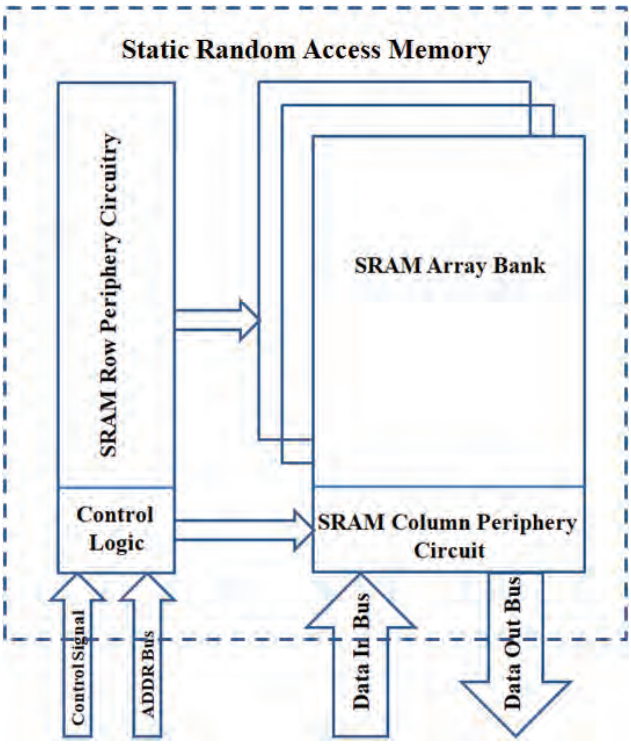


Figure 3. SRAM architecture.

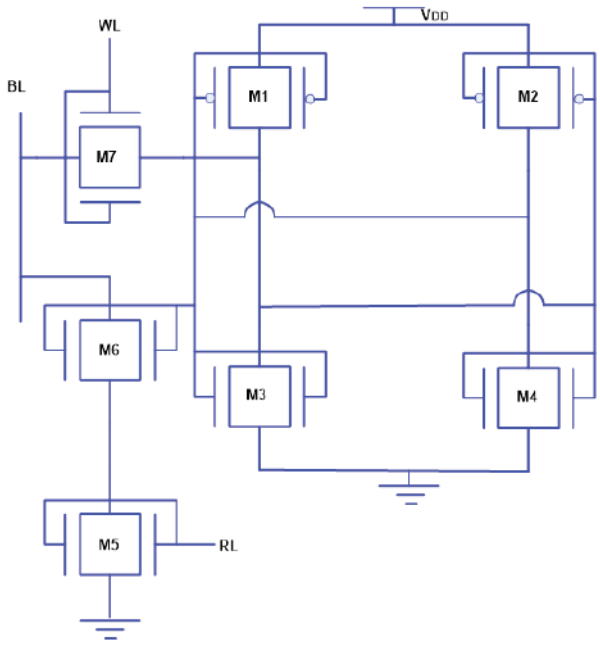
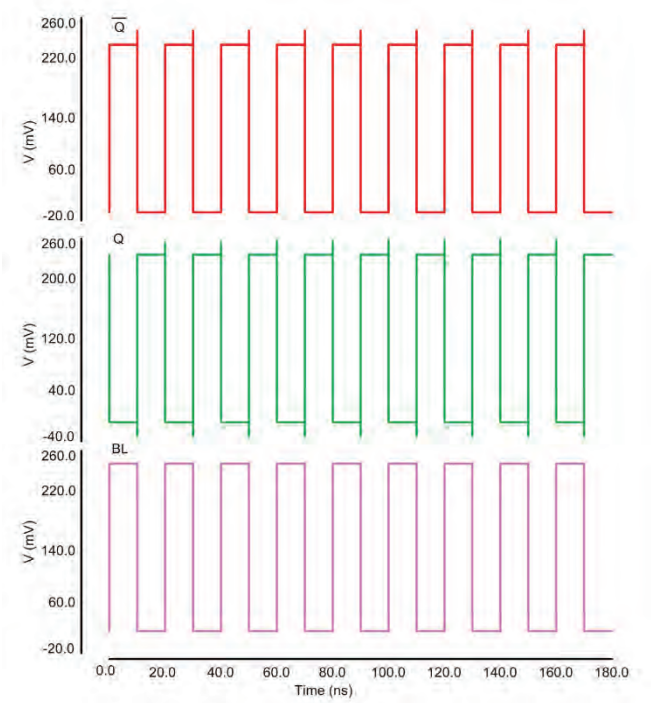
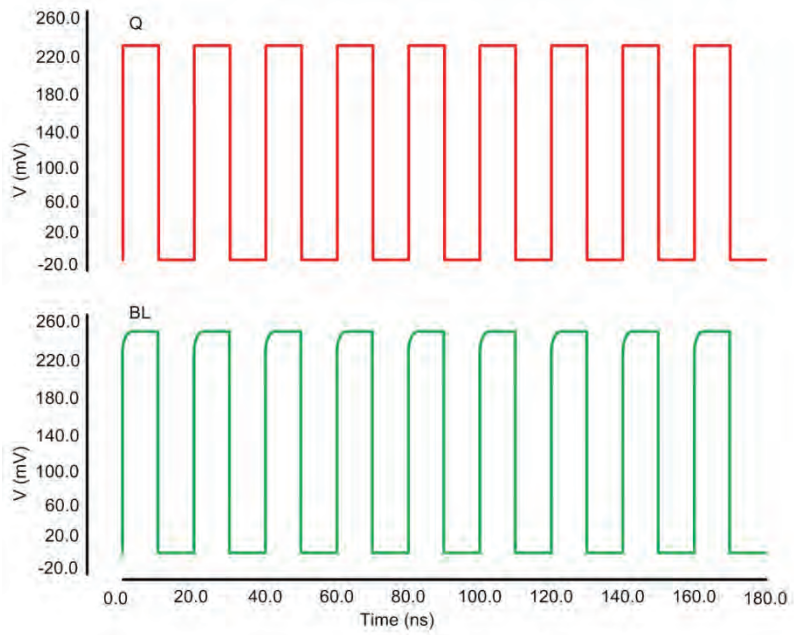


Figure 4. 7TSRAM cell using FinFET technology.



(a)



(b)

Figure 5. Operations of 7T SRAM using FinFET technology: (a) Write (b) Read.

SRAM Design Challenges for IoT

Designing SRAM for IoT applications presents several unique challenges, primarily due to the stringent requirements of IoT devices. These challenges include:

- Power Consumption Constraints: One of the primary challenges in designing SRAM for IoT applications is minimizing power consumption. Most IoT devices operate on battery power or energy harvesting systems, making ultra-low power design a necessity. SRAM typically consumes more static power compared to other memory types due to leakage currents, especially as technology scales down to sub-10nm nodes.
- Area and Cost Efficiency: IoT devices are highly area-constrained due to their small form factors. SRAM

cells must be extremely compact while maintaining functionality and reliability. Designers face the challenge of reducing the cell size without sacrificing performance or yield.

- Variability and Process Scaling: Process variations (e.g., threshold voltage, line-edge roughness) become more prominent in scaled CMOS technologies, which directly impact the reliability and performance of SRAM cells.
- Low Voltage Operation: IoT devices often run at reduced supply voltages to save power, but this significantly affects the read/write stability and noise margins of SRAM cells.
- Reliability and Data Retention: SRAM must retain data reliably, especially for devices in sleep modes or intermittent connectivity, which is common in IoT scenarios. Long idle times can exacerbate data retention issues and bit flipping due to leakage or soft errors.
- Security and Data Privacy: In many IoT applications (e.g., healthcare, smart homes), SRAM may store sensitive data. Designers must account for physical attacks or side-channel attacks targeting memory.
- Integration with Heterogeneous Systems: IoT systems integrate multiple types of logic, analog, RF and sensor interfaces. SRAMs need to work in mixed-signal environments and be fabricated inside SOCs with different requirements.
- Scalability: Design must be scalable to accommodate a range of applications from wearable devices to implantable systems without significant re-engineering. Therefore, the scaling of the CMOS technology is reaching some limits and other technologies are being investigated, such as FinFETs, tunnel FETs (TFETs) [38] and carbon nano-tube transistors (CNTs). Of these, FinFET technology has emerged as the most viable alternative to CMOS.
- AI and IoT Integration: Many biomedical devices are now part of IoT systems or use AI for diagnostics. SRAM needs to efficiently support these data intensive operations and hence needs to be optimized for both computational and storage requirements [39].

Innovations such as new transistor architectures, FinFET, advanced error-resilience techniques and energy-efficient design methodologies are exploited to overcome these challenges and to meet the demanding requirements of portable devices. The challenges in designing SRAM for IoT applications are shown in Figure 6.

Design Approach for Energy-Efficient SRAM

Multi-threshold cmos approach

The Multi-threshold CMOS approach has emerged as a key enabler for low power design in modern ICs. It smartly exploits the transistors with different threshold voltages to efficiently overcome the problem of leakage power while fulfilling the required performance [40]. Despite some design and implementation issues, its advantages make it an integral part of low power design methodologies. Future advances in automation, AI based design and combination with other power saving techniques is likely to improve the efficacy and adoption of Multi-Vt CMOS. As technology is scaled down issues like power consumption and leakage currents are becoming more important. Here, the Multi-Vt CMOS design has emerged as a powerful technique to achieve the trade-off between high performance and low power consumption, particularly in battery operated and energy constrained devices like mobile phones, portable electronics, and IoT systems.

The basic concept of the Multi-Vt CMOS methodology is to integrate transistors with different threshold voltages (V_{TH}) in a single IC. The V_{TH} of a MOSFET is defined as the minimum gate voltage required creating a conductive path

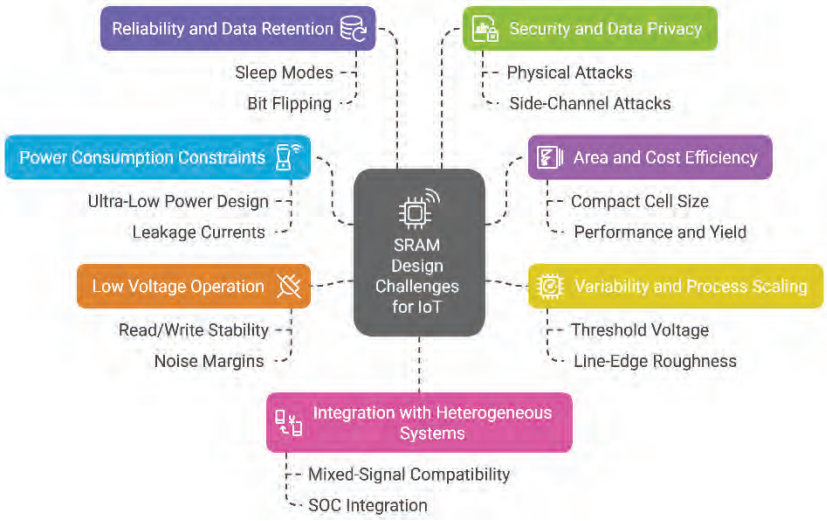


Figure 6. Challenges in designing SRAM for IoTDevice.

between the sources and draining terminals. Reducing the threshold voltage improves the switching speed of the transistor which in turn improves the performance. However, this also results in an exponential increase of subthreshold I_leakage that is a major contributor to static power dissipation in particular for idle or standby mode. In contrast, transistors with higher threshold voltage will have lower leakage current, but will switch slower. This could affect the performance. Multi-Vt CMOS design exploits this trade-off by using LVT (low-Vt) transistors on timing-critical paths for high-speed operation and HVT (high-Vt) transistors on non-critical paths where some loss of performance is acceptable in return for less leakage power. This method allows designers to optimize circuits for both dynamic and static power consumption without drastically affecting overall performance. The implementation through the MTCMOS approach involves leakage power reduction by utilizing transistors that operate in sleep mode. These associated transistors are activated in ON mode and deactivated in OFF (Sleepy) mode via a clock/sleep signal. A Transistor in Sleepy mode significantly decreases static leakage current when the SRAM is in the off condition. Figure7 illustrates theproposed7-T based SRAM cell, which is developed utilizing the MTCMOS approach.

When sleep transistors are turned OFF, V_{DD} and ground are automatically cut off from the SRAM cell, which lets data bits 0 and 1 exist on either side of the SRAM, effectively creating virtual power rails. In the MTCMOS method, multiple threshold voltages are applied to different transistors based on their role and the requirements of the circuit, allowing for a better balance between power, performance, and area (PPA).

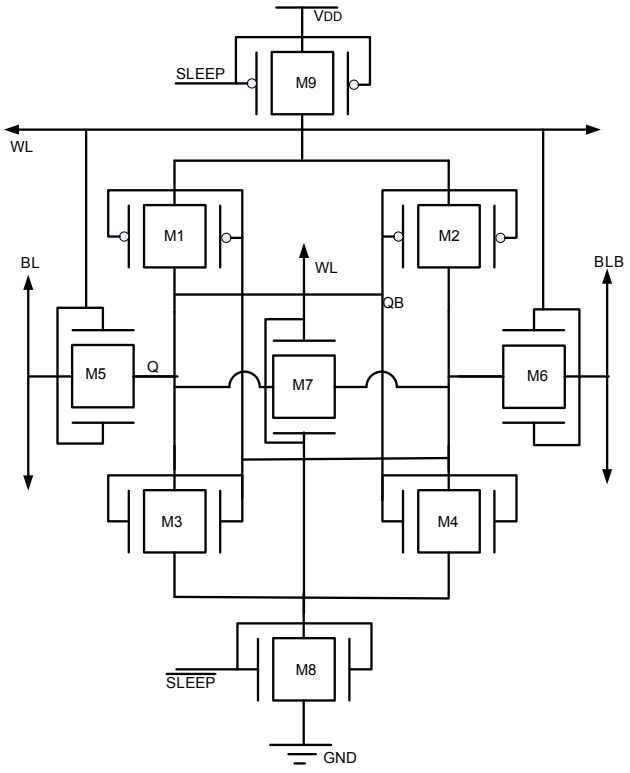


Figure 7. 7T SRAM design using MTCMOS approach.

Self controllable voltage level (SVL) approach

The SVL approach is a power reduction way used in VLSI design to reduce leakage power, particularly in low-power applications such as portable and battery-operated devices. This approach is also known as dynamic voltage and frequency scaling (DVFS). The key idea of SVL is to dynamically control the supply voltage of a circuit block based on its operational state. This approach might imply a method where a system autonomously manages its own voltage level. This approach may incorporate self-regulation mechanisms, maybe via internal sensors or feedback loops, enabling the system to dynamically alter its voltage level according to its operating conditions. The developed SRAM operates in two modes: active mode and standby mode.

- When a circuit is active, it operates at the normal supply voltage to maintain performance.
- When a circuit is idle or in standby mode, the SVL approach either raises the ground potential (virtual ground) or lowers the supply voltage (virtual V_{DD}), effectively reducing the voltage across the transistors. This drastically reduces subthreshold leakage currents, which are a major component of static power consumption in modern CMOS technologies.

The SVL helps in retaining the data retention by offering finer control through modulating the voltage levels, compared to completely disabling the circuit blocks as done by the traditional power gating techniques. This is usually done by using specially designed control transistors or circuits that sense the state of the logic block and adjust the supply or ground levels accordingly. SVL is very useful when the design needs to switch between active and idle states often and provides good tradeoff between saving leakage power and wake-up time. There are a few major advantages of the SVL circuit. In the SRAM active mode, the ON switch feeds the on MOS with the peak Vds, resulting in a fast operation of the SRAM circuit. In standby mode the SRAM drives the MOS transistor with slightly increased Vs, while a "weakly on switch" reduces Vd. This provides a high noise immunity of the SVL circuit. The decrease in the standby power is attributed to the increase in VTH and the reduction in the subthreshold current (Isub) of the "off MOS" transistor [41].

Advantages of SVL approach

This approach presents several benefits compared to alternative leakage current reduction strategies, including:

i. Significant Leakage Reduction: SVL effectively reduces subthreshold leakage by stacking transistors and elevating the virtual ground or supply, minimizing leakage during standby mode.
ii. Low Area Overhead: Compared to other methods like MTCMOS (Multi-Threshold CMOS), SVL generally

introduces lower layout area overhead, making it suitable for compact designs.

iii. No State Loss During Standby: Unlike power gating, SVL maintains the internal state of the circuit in sleep mode, eliminating the need for data retention strategies.

iv. Faster Wake-Up Time: Since the circuit remains partially powered, SVL allows quicker recovery from sleep mode compared to approaches that fully cut off power.

v. Simplified Control Logic: The control mechanism for SVL is relatively straightforward, reducing design complexity and power management circuit requirements.

vi. Better Suitability for Low-Voltage Designs: SVL is particularly effective in ultra-low voltage designs, where other approaches may struggle with performance or stability.

vii. Reduced Need for High-Vth Devices: Unlike MTCMOS, which relies heavily on high-threshold devices (with higher delay), SVL can use standard-Vth transistors while still achieving leakage savings.

7T SRAM design using upper SVL-approach

Figure 8 illustrates the SRAM cell utilizing FinFET with the USVL approach. The USVL circuit consists of double n-channel-type FinFET transistors (resistors) arranged in series with a single p-channel-type FinFET transistor (switch).The USVL circuit is connected with upper side of 7T SRAM cell and CS signal is used as a controlling signal. The ON P-channel type transistor is connected to V_{DD} and the 7T SRAM cell utilizing FinFETin active mode upon request. Similarly, the ON N-channel type transistor is connected to V_{DD} and the 7T SRAM cell employing FinFET in standby mode. This approach entails the application of the full supply voltage (V_{DD}) to the 7T SRAM design during active mode, while reducing the voltage level (V_D) during standby mode (sleep mode).

Simulation results show that using a lower gate voltage on transistor FinFET M6 reduces the unwanted current that leaks through the device. The decrease in FinFET M3 channel voltage leads to a reduction in gate leakage current, which in turn results in a lower gate channel voltage across M4. The leakage gate current of M1 is consistent and shows no variation. The USVL circuit-based P-channel FinFET M8 exhibits little leakage current. The leakage current stays uniform across M1, but the USVL method diminishes the sub-threshold leakage current via transistors M2 and M3. The gate leakage currents in access FinFETs M7 and M6 stay constant in this approach. The suggested SRAM utilizing USVL exhibits a leakage power of 26.98 nW, exceeding 10% compared to hybrid SVL approach. In summary, two components of gate leakage current in access transistors remain the same despite the USVL approach enhanced efficacy in reducing leakage gate current. Furthermore, it generates an additional subthreshold I_leakage in the access transistor while preserving one subthreshold current component within it [42].

7T SRAM design using lower SVL approach

Figure 9 illustrates the SRAM cell that incorporates FinFET technology utilizing the USVL approach. The Lower SVL circuit consists of two p-channel type FinFET

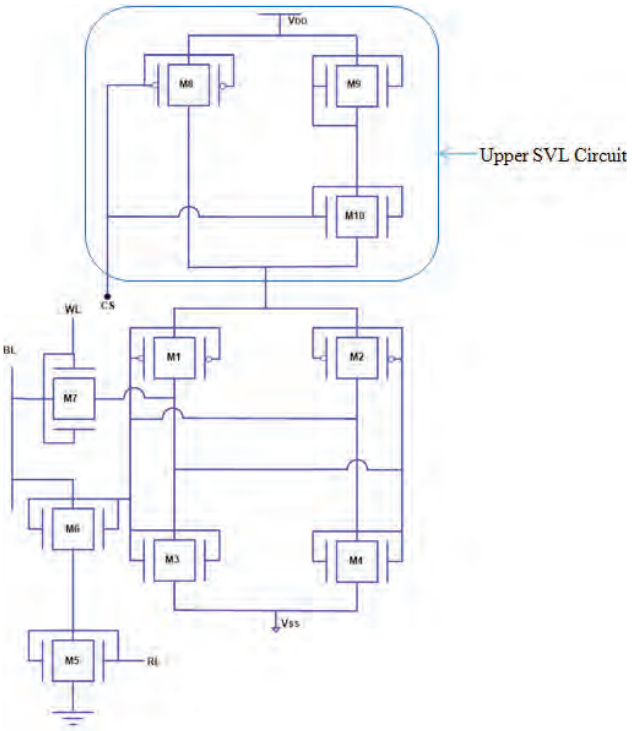


Figure 8. 7T SRAM cell with USVL approach.

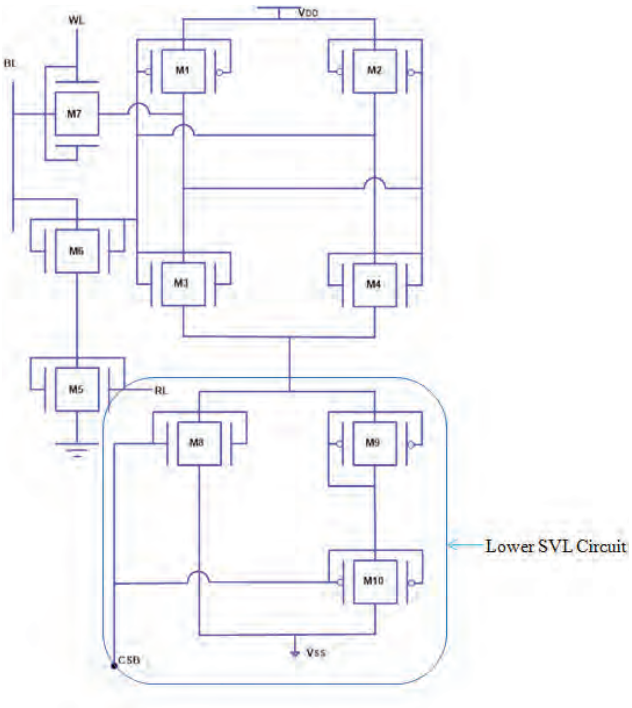


Figure 9. 7T SRAM cell with LSVL approach.

transistors (acting as resistors) arranged in series, joined to a single n-channel type FinFET transistor (functioning as a switch). The USVL circuit is joined with lower side of 7T SRAM cell and CSB signal is used as a controlling signal. In active mode, control signal provides '0' volts, whereas in standby mode, it delivers an increased ground voltage. The LSVL circuit employs the transistor M8 to provide Vss to the 7T SRAM design. The M9 and M10 transistors are utilized to provide V_{SS} to the remaining 7T SRAM cell. In the LSVL circuit, the transistors M10 and M8 are activated and deactivated, respectively, when the control signal (CSB) is connected to the power supply (V_{SS}=0 volt). The CSB switch outputs 0 V at ground level when operating in dynamic mode and presents an elevated virtual ground during idle mode. The LSVL approach effectively minimizes leakage flows through transistors M2, M3, and M7. This approach is similar to the diode-footed store structure idea mentioned in [43], which is designed to reduce sub-edge leakages and control signals in a 7T SRAM design that uses FinFET technology. The suggested SRAM utilizing LSVL shows a leakage power of 35.48 nW, which is 31% higher than hybrid SVL approach and 23.9% higher than the USVL approach.

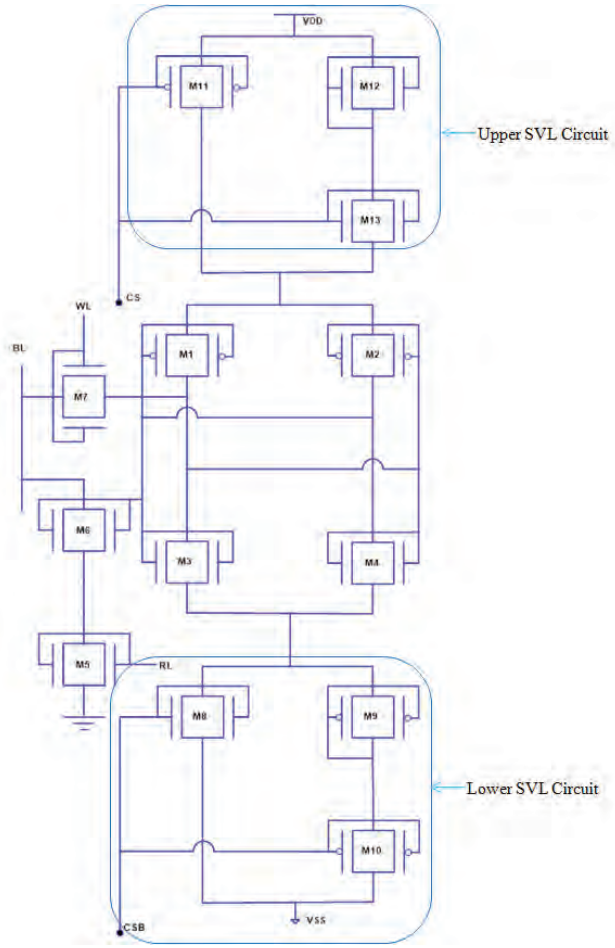


Figure 10. 7T SRAM cell hybrid SVL approaches.

7T SRAM design using hybrid SVL approach

The integration of USVL and LSVL approaches in a 7T SRAM cell utilizing FinFET necessitates the regulating voltage levels within the cell. This regulation is essential for maintaining reliable functionality across diverse operational conditions while also enhancing power efficiency. The integrated strategy is designed to protect the SRAM design against voltage fluctuations that may result in data loss, or potential damage. Implementing proactive control of both upper and lower voltage limits improves reliability, data retention, and longevity. Figure 10 illustrates the circuit of the hybrid SVL approach. In this configuration, the CS and CSB signals functionascontrol signals for the USVL and LVSL circuit respectively.

Figure 10 illustrates the routing of a control signal to the three transistors (M9, M10, and M8) positioned between Vss and SRAM. The system offers a ground potential and a virtual ground during both active and idle modes, determined by the value of the control signal. Consequently, the leakage current through the M3, M2, and M7 transistors can be minimized. Consequently, reducing gate leakage can lead to a decrease in sub-threshold currents in this context. In the configuration between the 7T SRAM and V_{DD}, three supplementary transistors are integrated. Transistor P5 is responsible for delivering V_{DD} to the 7T SRAM during dynamic operation, whereas transistor N8 supplies V_{DD} when the system is in idle mode. Reaming transistors M1, M4, and M5 minimizes leakage by utilizing the triple transistors located at the upper section. This approach results in a reduction of V_{DD} to 50% of its original supply, while the ground potential experiences a 25% increase. The hybrid SVL approach increases the V_{ss} to 0.25 V while decreasing the V_{DD} to 0.35 V.The hybrid SVL approach demonstrates superior performancecompared to individual SVL methods by significantly reducing leakage current and power consumption [44].

RESULTS AND DISCUSSION

For the suggested SRAM design, the leakage current and leakage power are computed using several leakage reduction approaches, including MTCMOS and SVL. It is discovered that the SVL approach performs better than the MTCMOS approach, which has a 36% reduction in leakage current. The leakage current using the MTCMOS approach is 14.8 nA. All the simulation work done through Cadence Virtuoso Tool. The Total leakage current of the SRAM is given as:

$$I_{leakage} = I_{Gate} + I_{sub} \quad (2)$$

The leakage parameters (power and current) of suggested SRAM design is given in Table 2. The comparative chart of leakage powers and currents for MTCMOS and

Table 2. Leakage parameters of Suggested SRAM design

Suggested Design	Leakage Current (nA)	Leakage Power (nW)
MTCMOS approach	14.8	32.76
SVL approach	9.45	24.28

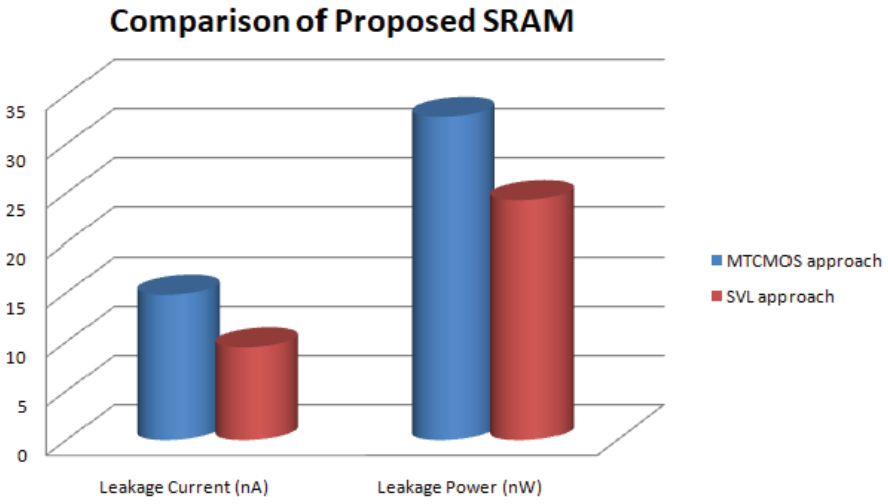


Figure 11. Comparative study of leakage current and power for suggested 7T SRAM design.

SVL approaches is plotted and indicated in Figure 11. The leakage power of suggested SRAM designed with the SVL approach is measured at 24.28nW. This value represents a reduction of 25.8% compared to the power consumption of the SRAM designed with the MTCMOS leakage reduction approach, which is recorded at 32.76 nW.

Since leakage power has emerged as a major performance indicator in nanoscale memory devices, a comparison of the leakage power measured in this work with other relevant works is presented in Table 3 [45-48].

The SRAM's low-leakage design is crucial for implantable devices like cardiac monitors, where long battery life and reliability are essential. The design supports seamless data collection and transmission in IoT ecosystems, paving the way for advanced remote monitoring solutions.

Table 3. Comparison of Leakage Power with other relevant works

Source	Leakage Power (nW)
Proposed work using SVL approach	24.28
Proposed work using MTCMOS approach	32.76
Standard 7T SRAM [45]	35.22
Low Power 7T SRAM [46]	36.44
7T Differential SRAM [47]	67.02
Single-Ended 7T SRAM [48]	69.1

Applications of Suggested SRAM for Internet of Things

Due to the advantages of low power consumption, high speed and scalability, FinFET-based SRAM is widely and effectively applied in IoT. Applications of such are:

1. In wearable devices like fitness trackers and smartwatches, where energy efficiency is important for long battery life.
2. Smart home devices such as smart thermostats, cameras, and voice assistants also use FinFET SRAM, which offers the ability to quickly and efficiently store and access data with minimal power consumption.
3. FinFET SRAM enables real-time processing in edge devices such as sensors and controllers in industrial IoT (IIoT), which are vital for automation, predictive maintenance, and monitoring.
4. Healthcare IoT devices such as portable diagnostics and patient monitoring systems depend on FinFET SRAM for secure and fast data access, low heat dissipation and small form factors.
5. Agricultural IoT is also a beneficiary as smart irrigation and crop monitoring systems need low-power memory for sensors deployed in the field.
6. Fast on-chip memory is required by sensor fusion and decision-making modules used in autonomous vehicles and smart transportation, and FinFET-based SRAM is used for this purpose.

CONLUSION

The suggested 7T SRAM using FinFET has been subjected to the leakage reduction approach. It is established that by relating the SVL approach, the leakage current and leakage power are decreased by 36% and 25.8%, respectively, compared to the FinFET-based 7T SRAM with the application of the MTCMOS approach. Implementation of the MTCMOS approach, the leakage current is detected to be 14.8 nA and the leakage power is 32.76 nW. As shown in the results, the analysis of leakage power and leakage current is looked at and contrasted with alternative approaches. The proposed low-power SRAM design leverages FinFET technology to address the unique challenges of healthcare applications. Significant improvements in the power efficiency, stability, and scalability make it ideal for wearable and implantable devices.

Future research may explore advanced transistor technologies such as Gate-All-Around FETs (GAA FETs) and alternative memory technologies like STT-RAM to further enhance the energy efficiency and performance.

ACKNOWLEDGEMENT

The researchers of this study would like to extend their sincerest thanks and gratitude to the Department of Electronics & Communication Engineering, SRM Institute of Science and Technology, Delhi-NCR Campus, Ghaziabad, India for their support and for providing the resources needed to complete this research.

AUTHORSHIP CONTRIBUTIONS

Deepak Garg: Study design, investigation, writing-original draft, editing, methodology and validation.

Rupali Singh: Supervision, manuscript review and editing.

DATA AVAILABILITY STATEMENT

The authors confirm that the data that supports the findings of this study are available within the article. Raw data that support the finding of this study are available from the corresponding author, upon reasonable request.

CONFLICT OF INTEREST

The author declared no potential conflicts of interest with respect to the research, authorship, and/or publication of this article.

ETHICS

There are no ethical issues with the publication of this manuscript.

STATEMENT ON THE USE OF ARTIFICIAL INTELLIGENCE

Artificial intelligence was not used in the preparation of the article.

REFERENCES

[1] Mughal MJ, Saeed R, Naeem M, Ahmed MA. International Technology Roadmap for Semiconductors. 2012.

[2] Rasheed G, Sridevi S. Design of 7T SRAM using InGaAs-dual pocket-dual gate-tunnel FET for IoT applications. IEEE Access 2023;11:76034–76045. [CrossRef]

[3] World Economic Forum. State of the Connected World 2020 Edition. Dec 2020. Accessed Apr 6, 2023.

[4] Patel HN, Yahya FB, Calhoun BH. Optimizing SRAM bitcell reliability and energy for IoT applications. In: 2016 17th International Symposium on Quality Electronic Design (ISQED); 2016 Mar. p. 12–17. IEEE. [CrossRef]

[5] Satti VS, Sriadibhatla S. Dual bit control low-power dynamic content addressable memory design for IoT applications. Turk J Electr Eng Comput Sci 2021;29:1274–1283. [CrossRef]

[6] Lee Y, Kim Y, Yoon D, Blaauw D, Sylvester D. Circuit and system design guidelines for ultra-low power sensor nodes. In: Proceedings of the 49th Annual Design Automation Conference; 2012 Jun. p. 1037–1042. [CrossRef]

[7] Mohammed MU, Nizam A, Ali L, Chowdhury MH. FinFET based SRAMs in Sub-10nm domain. Microelectron J 2021;114:105116. [CrossRef]

[8] Skotnicki T, Fenouillet-Beranger C, Gallon C, Boeuf F, Monfray S, Payet F, et al. Innovative materials, devices, and CMOS technologies for low-power mobile multimedia. IEEE Trans Electron Devices 2008;55:96–130. [CrossRef]

[9] Goel A, Gupta SK, Roy K. Asymmetric drain spacer extension (ADSE) FinFETs for low-power and robust SRAMs. IEEE Trans Electron Devices 2011;58:296–308. [CrossRef]

[10] Calhoun BH, Chandrakasan AP. A 256-kb 65-nm sub-threshold SRAM design for ultra-low-voltage operation. IEEE J Solid-State Circuits 2007;42:680–688. [CrossRef]

[11] Kim TH, Liu J, Keane J, Kim CH. A 0.2 V, 480 kb subthreshold SRAM with 1 k cells per bitline for ultra-low-voltage computing. IEEE J Solid-State Circuits 2008;43:518–529. [CrossRef]

[12] Raushan RK, Ansari MR, Chauhan U, Khalid M, Mohapatra B. Implementation of 12T and 14T SRAM bitcell using FinFET with optimized parameters. Trans Electr Electron Mater 2021;22:328–334. [CrossRef]

[13] Asli RN, Taghipour S. Reliable and high performance asymmetric FinFET SRAM cell using back-gate control. Microelectron Reliab 2020;104:113545. [CrossRef]

[14] Birla S, Shukla NK, Singh N, Raja RK. Performance analysis of 8T FinFET SRAM bit-cell for low-power applications. In: 2020 5th International Conference on Computing, Communication and Security (ICCCS); 2020. p. 1–4. IEEE. [CrossRef]

[15] Duari C, Birla S, Singh AK. A dual port 8T SRAM cell using FinFET & CMOS logic for leakage reduction and enhanced read & write stability. J Integr Circuits Syst 2020;15:1–7. [CrossRef]

[16] Vallabhuni RR, Koteswaramma KC, Sadgurbabu B. Comparative validation of SRAM cells designed using 18nm FinFET for memory storing applications. In: Proceedings of the 2nd International Conference on IoT, Social, Mobile, Analytics & Cloud in Computational Vision & Bio-Engineering (ISMAC-CVB 2020); 2020 Oct. [CrossRef]

[17] Verma J, Passi A, Sindhu S, Gayathiri S. Design 10-transistor (10T) SRAM using FinFET technology. Int J Eng Adv Technol 2019;9:566–572. [CrossRef]

[18] Ensan SS, Moaiyeri MH, Hessabi S. A robust and low-power near-threshold SRAM in 10-nm FinFET technology. Analog Integr Circuits Signal Process 2018;94:497–506. [CrossRef]

[19] Saxena S, Mehra R. Low-power and high-speed 13T SRAM cell using FinFETs. IET Circuits Devices Syst 2017;11:250–255. [CrossRef]

[20] Kaur N, Gupta N, Pahuja H, Singh B, Panday S. Low power FinFET based 10T SRAM cell. In: 2016 Second International Innovative Applications of Computational Intelligence on Power, Energy and Controls with their Impact on Humanity (CIPECH); 2016. p. 227–233. IEEE. [CrossRef]

[21] Verma D, Babu S, Akashe S. Comparison of conventional 6T SRAM cell and FinFET based 6T SRAM cell parameters at 45nm technology. Int J Adv Comput Res 2015;5:367. [CrossRef]

[22] Praveen P, Singh RK. Performance analysis of 9T SRAM using 180nm, 90nm, 65nm, 32nm, 14nm CMOS technologies. Int J Electr Electron Res 2022;10:381–386. [CrossRef]

[23] Lorenzo R, Chaudhury S. Review of circuit level leakage minimization techniques in CMOS VLSI circuits. IETE Tech Rev 2016;33:1–23.

[24] Keshavarzi A, Roy K, Hawkins CF. Intrinsic leakage in deep submicron CMOS ICs-measurement-based test solutions. IEEE Trans Very Large Scale Integr VLSI Syst 2000;8:717–723. [CrossRef]

[25] Aditya A, Saha S, Khan A. Implement and analysis of a 1-bit ternary SRAM cell using Tanner Tools. In: Proceedings of 3rd International Conference on Internet of Things and Connected Technologies (ICIoTCT); 2018 Apr. p. 26–27. [CrossRef]

[26] Narendar V, Mishra RA. Analytical modeling and simulation of multigate FinFET devices and the impact of high-k dielectrics on short channel effects (SCEs). Superlattices Microstruct 2015;85:357–369. [CrossRef]

[27] Tripathi T, Chauhan DS, Singh SK. A novel approach to design SRAM cells for low leakage and improved stability. J Low Power Electron Appl 2018;8:41. [CrossRef]

[28] Maurya RK, Bhowmick B. Review of FinFET devices and perspective on circuit design challenges. Silicon 2022;14:5783–5791. [CrossRef]

[29] Khan AI, Chatterjee K, Duarte JP, Lu Z, Sachid A, Khandelwal S, et al. Negative capacitance in short-channel FinFETs externally connected to an epitaxial ferroelectric capacitor. IEEE Electron Device Lett 2016;37:111–114. [CrossRef]

[30] Tahrim ABA, Chin HC, Lim CS, Tan MLP. Design and performance analysis of 1-bit FinFET full adder cells for subthreshold region at 16 nm process technology. J Nanomater 2015;16:175–175. [CrossRef]

[31] Dutta T, Pahwa G, Agarwal A, Chauhan YS. Impact of process variations on negative capacitance FinFET devices and circuits. IEEE Electron Device Lett 2018;39:147–150. [CrossRef]

[32] Kumar A. Analog and RF performance of a multigate FinFET at nano scale. Superlattices Microstruct 2016;100:1073–1080. [CrossRef]

[33] Dhulipalla L, Deepak AL. Design and implementation of 4-bit ALU using FINFETs for nano scale technology. In: International Conference on Nanoscience, Engineering and Technology (ICONSET 2011); 2011. p. 190–195. IEEE. [CrossRef]

[34] Mushtaq U, Sharma VK. Design and analysis of INDEP FinFET SRAM cell at 7-nm technology. Int J Numer Model Electron Netw Devices Fields 2020:1–14. [CrossRef]

[35] Chung Y, Kim H. A differential subthreshold SRAM cell for ultra-low-voltage embedded computing applications. Int J Appl Eng Res 2017;12:7998–8003.

[36] Sinangil ME, Lin YT, Liao HJ, Chang J. A 290-mV, 7-nm ultra-low-voltage one-port SRAM compiler design using a 12T write contention and read upset free bit-cell. IEEE J Solid-State Circuits 2019;54:1152–1160. [CrossRef]

[37] Kumar V, Tomar VK. A comparative performance analysis of 6T, 7T and 8T SRAM cells in 18nm FinFET technology. In: 2020 International Conference on Power Electronics & IoT Applications in Renewable Energy and its Control (PARC); 2020 Feb. p. 329–333. IEEE. [CrossRef]

[38] Sen S, Saha S, Khan A, Arya R. Switching loss calculation of power MOSFET using the estimation technique. J VLSI Des Tools Technol 2020;10:37–44. [CrossRef]

[39] Banerjee A. Ultra-low-power embedded SRAM design for battery-operated and energy-harvested IoT applications. Green Electronics. 2018. [CrossRef]
[40] Pal A. Low-power VLSI circuits and systems. Springer; 2014. [CrossRef]
[41] Satish MN, Vasundara Patel KS. Power reduction in FinFET half adder using SVL technique in 32 nm technology. In: IEEE MEC International Conference on Big Data and Smart City (ICBDSC); 2019. [CrossRef]
[42] Akashe S, Sharma S. Leakage current reduction techniques for 7T SRAM cell in 45 nm technology. Wirel Pers Commun 2013;71:123–136. [CrossRef]
[43] Birla S. Ultra-low power FinFET SRAM cell with improved stability suitable for low power applications. Int J Electron Telecommun 2019;65. [CrossRef]
[44] Kushwah RS, Sikarwar V. Analysis of leakage current and power reduction techniques in FinFET based SRAM cell. Radioelectron Commun Syst 2015;58:312–321. [CrossRef]
[45] Kumar TS, Tripathi SL. Comprehensive analysis of 7T SRAM cell architectures with 18nm FinFET for low power bio-medical applications. Silicon 2022;14:5213–5224. [CrossRef]
[46] Venkatareddy A, Sithara R, Kumar YN, Vasantha MH. Characterization of a novel low leakage power and area efficient 7T SRAM cell. In: 2016 29th International Conference on VLSI Design and 2016 15th International Conference on Embedded Systems (VLSID); 2016 Jan. p. 202–206. IEEE. [CrossRef]
[47] Sneha G, Krishna BH, Kumar CA. Design of 7T FinFET based SRAM cell design for nanometer regime. In: 2017 International Conference on Inventive Systems and Control (ICISC); 2017 Jan. p. 1–4. IEEE. [CrossRef]
[48] Ensan SS, Moaiyeri MH, Moghaddam M, Hessabi S. A low-power single-ended SRAM in FinFET technology. AEU Int J Electron Commun 2019;99:361–368. [CrossRef]

Sigma J Eng Nat Sci, Vol. 44, No. 4, pp. 2700–2713, August, 2026

Sigma Journal of Engineering and Natural Sciences
Web page info: https://sigma.yildiz.edu.tr
DOI: 10.14744/sigma.2026.2122

Research Article

Leveraging Bi-LSTM advanced deep learning model for enhanced wind speed prediction

Muskaan AHUJA[1,*], **Sanju SAINI**[1]

[1]*Deenbandhu Chhotu Ram University of Science and Technology Sonipat, Haryana, 131027, India*

ARTICLE INFO

Article history
Received: 06 September 2024
Revised: 19 November 2024
Accepted: 30 December 2024

Keywords:
Bi-LSTM Model; Deep Learning Models; Traditional Approaches; Wind Speed Prediction

ABSTRACT

Forecasting of wind speed is essential for the effective design, management, and maintenance of wind energy systems, which are a key component of renewable energy sources. The difficulty of precisely predicting wind speeds is addressed in this study, as wind patterns are often erratic and unpredictable. Four predictive models have been used in this study for comparative analysis. It has been shown that ARIMA model helps to capture temporal dependencies (linear) & the Kalman Filter very efficiently helps to reduce noise in wind speed data. However, non-linear dependencies have been modeled efficiently by LSTM and proposed Bi-LSTM model. Data sets are gathered from two sites encompassing a period of one year, i.e., June 2022 onwards.
In comparison to the LSTM, the Bi-LSTM model consistently outperformed the other methods, with higher error rates for the ARIMA and Kalman Filter, a root mean square error of 0.1280 m/s, mean absolute percentage of 0.0531 m/s, symmetric mean absolute percentage error of 0.0108 m/s. Improvement of Bi-LSTM's performance is due to its ability to deal with time-series data (in forward as well as backward directions), that helps it to capture the stronger correlations (temporal) in the dataset of wind speed. This work is novel because it makes use of Bi-LSTM for wind speed prediction, a method not completely explored in the previous research, and it further integrates statistics and deep learning models. The results make demonstration of the fact that Bi-LSTM significantly improves wind speed prediction accuracy, further improving the reliability as well as efficiency of wind energy systems.
By demonstrating improved prediction accuracy for a wide range of datasets, this work significantly contributes to the renewable energy systems and highlights the benefits of using advanced deep learning approaches for prediction problems.

Cite this article as: Ahuja M, Saini S. Leveraging Bi-LSTM advanced deep learning model for enhanced wind speed prediction. Sigma J Eng Nat Sci 2026;44(4):2700–2713.

INTRODUCTION

Recently, wind energy has become an important component of the renewable energy sources worldwide. It also helps to reduce emissions of greenhouse gases and fight climate change. For wind farms to operate as efficiently as possible, grid stability to be maintained, and wind energy systems to be as efficient as possible, it is very essenia to

*Corresponding author.
*E-mail address: 20001902004muskaanahuja@dcrustm.org

This paper was recommended for publication in revised form by Editor-in-Chief Ahmet Selim Dalkilic

Published by Yıldız Technical University Press, İstanbul, Turkey
© Author. This is an open access article under the CC BY-NC license (http://creativecommons.org/licenses/by-nc/4.0/).

forecast wind speed in a reliable manner [1]. Wind speed is very difficult to predict on account of its intrinsically stochastic nature and its intricate temporal patterns. Reliable Short-term forecasting of wind speed is very essential so that wind energy becomes more cost-effective, functionally effective, and can be easily incorporated into complex electrical systems. This helps to increase the reliability of the renewable resourcesa nd maximize energy output. Several models, have been suggested over time for increasing the precision and dependability prediction of wind speed forecasts [2]. Figure 1 provides a classification of such models.

The nonlinear properties of wind speed are very difficult to be captured by linear models. The deep learning approaches, specifically the Bi-directional LSTM (Bi-LSTM), and Long Short-Term Memory (LSTM) networks, have been implemented to overcome these limitations. These models are effective for wind speed forecasting since they are made to comprehend the extensive temporal dependencies. Table 1 illustrates the most recent studies made by several scholars in the field of various methods of forecasting, including time scale horizons and descriptions for wind forecasting. Such as persistence forecasting methods used for very short-term predictions [3–5]. NWP methods employed for medium- to long-term forecasts [6–14]. Statistical methods (such as AR, MA, ARMA, ARIMA, SVR, Kalman filtering, and GARCH) used historical wind-speed time-series data for short- to medium-term forecasting [15–34]. Machine learning models, can be applied from short- to long-term forecasting [35–55]. Hybrid approaches is the combination of two or more forecasting techniques, to improve prediction accuracy and robustness [56–80].

Bi-LSTM used here provides a number of significant advantages, particularly the fact that wind speed data typically demonstrates complex temporal correlations. By analysing data in both forward and reverse directions, Bi-LSTM is more effective in identifying these connections and delivering more precise wind forecasts. The Bi-LSTM model considers both past and future data sources, while the traditional approaches use only past data. This is

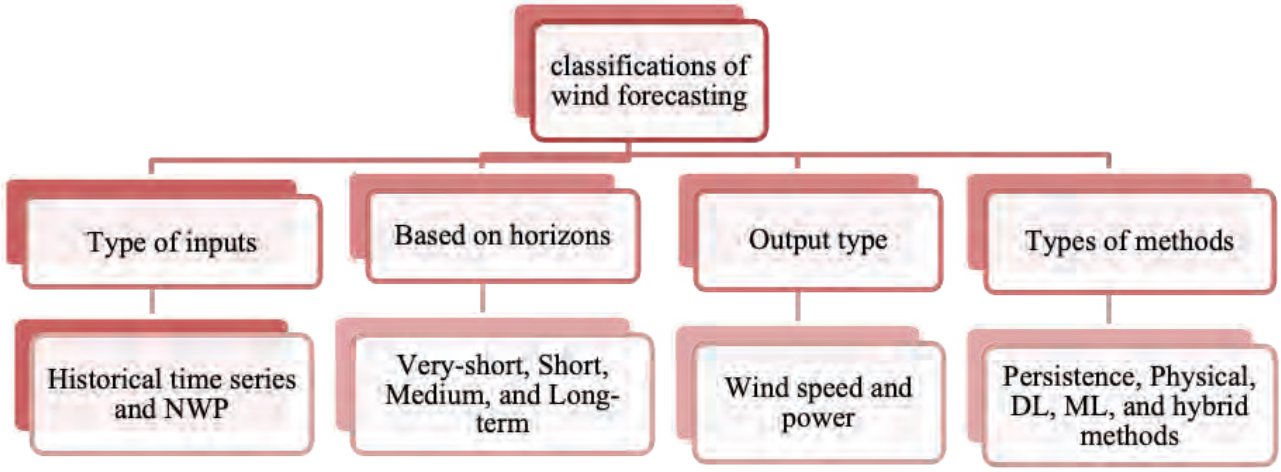


Figure 1. Classifications of wind forecasting based on different catergories.

Table 1. Literature of wind forecasting methods with different time scale horizons

Forecasting Method	Description	Applications
Persistence Forecasting [3-5]	Assumes current wind conditions will persist in the near future.	Very short-term forecasts.
Numerical Weather Prediction (NWP) [6-14]	Mathematical models simulate atmospheric conditions using current weather data.	Medium to long-term forecasts (hours to days).
Statistical [15-34] (AR, MA, ARMA, ARIMA, SVR, Kalman, GARCH, etc..)	Use historical wind data and patterns for prediction using statistical and machine learning techniques.	Short to medium-term forecasts (minutes to hours).
Machine Learning Models[35-55] (ANN, RNN, CNN, K-NN, etc..)	Use historical and metrological wind data for prediction using machine learning techniques.	Short to Long-term forecasts (minutes to Days).
Hybrid Approaches [56-80]	Combines methods (e.g., NWP with machine learning) to improve accuracy.	Site-specific forecasts, especially for wind energy.

particularly important for wind speed forecasting, which can be determined by different environmental conditions that occur before and after a specific time point, energy trading, grid stability, and turbine efficiency. Bi-LSTM is a reliable method for wind forecasting. It helps improve renewable energy, supports environmental planning, and reduces weather-related problems. It can use past weather data like wind speed, other weather parameters, and air conditions as input. For time series prediction and renewable energy sources the outcomes of this research play an important role. Some advantages such as reduction in operating expenses, power variation, exploiting storage, accelerating the shift to cleaner energy, and grid integration are delivered by Bi-LSTM forecasting model.

As shown in Table 2, many researchers have used single site data only. The paper is structured as follows: a comprehensive literature review, discussing traditional and machine learning approaches to wind speed prediction, and the objectives of this paper are discussed at first. Further, the paper outlines the methodology, including data collection, model implementation, and performance evaluation. Then the experimental results and a comparison of the performances of the models are presented. Results have been discussed in details and finally the paper is concluded providing the areas for future research. The flow of proposed methodology as shown in Figure 2.

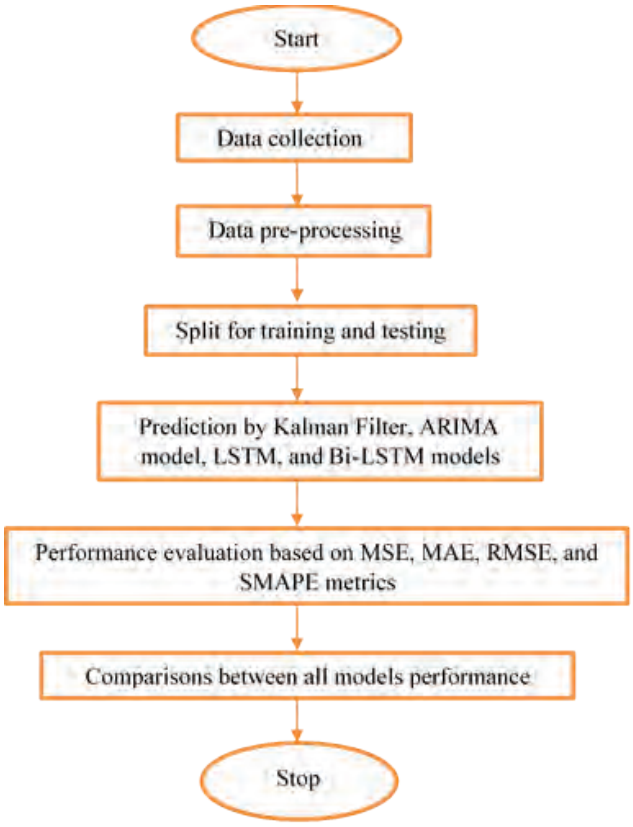


Figure 2. Flowchart of summarizing the methodology.

Table 2. A comparison with past efforts

Ref., Year	Approaches	Strategy	Single Site	Multiple Site with different frequency and geographic location
[12], 2022	Physical Method	NWP	✘	✘
[15], 2018	Statistical Method	ARMA	✘	✘
[24], 2020		ARIMA	✘	✘
[26], 2009		f-ARIMA	✘	✘
[34], 2013	Intelligent Method	PSO	✘	✔
[35], 2016		WNN	✘	✘
[37], 2009		ANN	✘	✘
[39], 2007		RBFNN	✘	✘
[42], 2012		SVM	✘	✘
[46], 2020		SVM	✔	✘
[50], 2023		RNN	✘	✔
[51], 2023		ANN	✘	✔
[54], 2010	Hybrid Method	ARIMA-ANN	✘	✘
[70], 2022		DWT-LSSVM-GARCH	✘	✘
[79], 2018	Intelligent Method	WT-GA-ANN	✘	✔
[80], 2022	Hybrid Method	CNN-RNN	✘	✔
Proposed Model	Statistical and deep learning methods	Kalman, ARIMA, LSTM, and Bi-LSTM	✘	✔

Objectives

This paper aims to explore and compare Kalman Filter, ARIMA, LSTM as well as Bi-LSTM models for prediction of 1 hour ahead wind speed. Specifically, the objectives are:

1. To implement each model and apply it to wind speed prediction.
2. Performance evaluation and comparision of these models using various statistical metrics.
3. Identification of most accurate and reliable model for wind speed forecasting.

MATERIALS AND METHODS

Data Collection

The data is collected from two sites [81, 82] for a duration from June 2022 to May 2023 and it includes seasonal wind speed time series, recorded at regular interval of one hour. Data is collected for height of 10 meters above the ground. Two different sites have been chosen to collect the data so as to test the reliability of the model in different environments.

Data Pre-processing

Following data Pre-processing techniques are applied on the raw wind speed time series data to make it ready for further analysis:

'Handling Missing Values': Due to sensor issues or information communication issues, insufficient data in wind speed datasets is caused. Missing numbers can be restored with help of the techniques like approximation.

'Standardization': The wind speed data is normalized so as to verify that each feature is contributing equally. This includes normalizing the data so as to have a mean value of '0' and a standard deviation value of '1', or scaling the data to range of values between 0 and 1.

'Training-Testing Ratio': The data set is split into two sets: training and testing sets, each of which is generally used in a ratio of 7:3. This division ensures the training of model on 70 % of data, and its ability to extend is further tested based on a different, unseen 30 % data.

Statistical Methods

Kalman filter

A Kalman filter is optimal & recursive algorithm, which is used for estimating the state of a dynamic system using a series of incomplete (or noisy) measurements over the time. It works by making prediction of the next state and then further making correction of this prediction by making use of new sensor data for minimizing uncertainty.

State-space representation

The Kalman filter is based on a system that is described as state-space model with a state vector describing the system's current state. A collection of linear equations taking into consideration the system dynamics as well as inputs from outside describes the way in which the state vector changes with time.

Table 3. Mathematical description of Kalman filter

Phase	Mathematical Description
'State' Prediction	$[\hat{x}_{k\|k-1} = F_{k-1}\hat{x}_{k\|k-1} + B_{k-1}\,u_{k-1}]$
'Covariance' Prediction	$[P_{k\|k-1} = F_{k-1}P_{k\|k-1} + F_{k-1}^{T}\,Q_{k-1}]$
'Measurement't Update	$[K_k = P_{k\|k-1}H_k^{T}\left(H_k P_{k\|k-1}H_k^{T} + R_k\right)^{-1}]$
'State' Update	$[\hat{x}_{k\|k} = \hat{x}_{k\|k-1} + K_k(Z_k - H_k\,\hat{x}_{k\|k-1})]$
'Covariance' Update	$[P_{k\|k} = (I - K_k H_k)\,P_{k\|k-1}]$

Recursive estimation

Recursive estimation is used by the Kalman filter in contrast to the batch processing techniques necessitating the processing of every measurement at once. This helps to make it computationally efficient since it uses progressive updating of the state estimate. Two main phases of operation of Kalman Filter are: prediction phase & update phase, for which mathematical description is given in Table 3.

AR (auto regression)

An autoregressive model, often referred to as an AR model, uses relationship between an observation and a certain number of lagged observations to make predictions about future values. The core idea behind an autoregressive model is use of current variable's value as a linear combination of its past values.

Mathematically, such model of order (p), represented as AR (p), is given by eqn. 1.

$$\boldsymbol{Y_t} = \boldsymbol{c} + \phi_1 \boldsymbol{Y_{t-1}} + \phi_2 \boldsymbol{Y_{t-2}} + \cdots + \phi_p \boldsymbol{Y_{t-p}} + \varepsilon_t \qquad (1)$$

MA (moving average)

A moving average model (MA) is a forecasting technique using the relationship between an observation and some past forecast errors (residuals) to predict the future values. This model captures short-term patterns and smooths out the random fluctuations in the data. Mathematically, such model (of order q & represented as MA (q)), is given by eqn. 2.

$$Y_t = c + \theta_1 \varepsilon_{t-1} + \boldsymbol{\theta_2} \varepsilon_{t-2} + \cdots + \boldsymbol{\theta_q} \varepsilon_{t-q} + \varepsilon_t \qquad (2)$$

ARIMA (auto regression integrated moving average)

The ARIMA model combines AR, Integrated & MA components for capturing features of the time series. The parameters (p, d, q) are estimated from historical data using methods like maximum likelihood estimation where:

Autoregressive component is 'p'

Differencing (integration)'d'

Moving average component 'q'

The conventional ARIMA models are reliable for wind speed prediction but they may not capture sophisticated patterns or long-term relationship in some time

series. More sophisticated models like Seasonal ARIMA (SARIMA), Vector Auto Regression (VAR), or machine learning models could be concern in some cases.

LSTM

Long Short-Term Memory (LSTM), or LSTM has the ability to store information from previous nodes for a long time, thus, resolving the issue of the 'vanishing gradient problem' (of conventional RNNs). LSTM is employed in the forward state, mathematical formulation is given in Table 4. LSTM layers contain memory cells that store information across time steps, controlled by three gates (Fig. 3):

a) Input Gate: Input data to be added to 'memory cell'.
b) Forget Gate: Helps in deciding the extent of previous memory to be retained (or discarded).
c) Output Gate: Helps to determine the memory cell's output (to be processed by next layer).

The LSTM network is generally trained by using BPTT and an optimization algorithm such as 'Adam' or 'RMSprop'. The loss function used is generally Mean Squared Error (MSE). Performance of the LSTM model is dependent on a number of hyperparameters, e.g., Number of LSTM units, learning rate, and batch size. After training and evaluation of the model on test set, predictions are compared to the actual wind speed measurements.

Bi-LSTM

Bi-LSTM is designed to capture information of both past and future states in a sequence. Bi-LSTMs are very effective for situations in which considering context from both directions is essential, such as in NLP. In this network, the input is provided from both the directions. Take note that this is not a form of backward propagation. It is just the input provided from both sides. In a conventional LSTM network, the output is obtained directly from the network, as shown in the Figure 3. The Figure 4. illustrates the structural arrangement of the Bi-LSTM. In a Bi-LSTM, output of both the forward and backward layers at each step is transmitted to an activation layer, whose results are subsequently analyzed. The presented output exhibits the information and correlation between previous and next words [83], as shown in Table 4.

Performance evaluation metrics

Considering critical role of Performance evaluation metrics to ensure the 'reliability', 'accuracy', and 'effectiveness' of the prediction models [84], metrics given in Table 5 are used to make a comparision of various models.

RESULTS AND DISCUSSION

The details of the data used in this study from two different sites (Fig. 5) is already given in section II. Table 6 observes the maximum, minimum, standard deviation, and median of the wind time series, i.e, statistical parameters.

The total number of samples for one year is 8760 (70%: Training, 30%: Testing) which is divided based on the seasons. For prediction, Kalman filter, ARIMA, LSTM, and

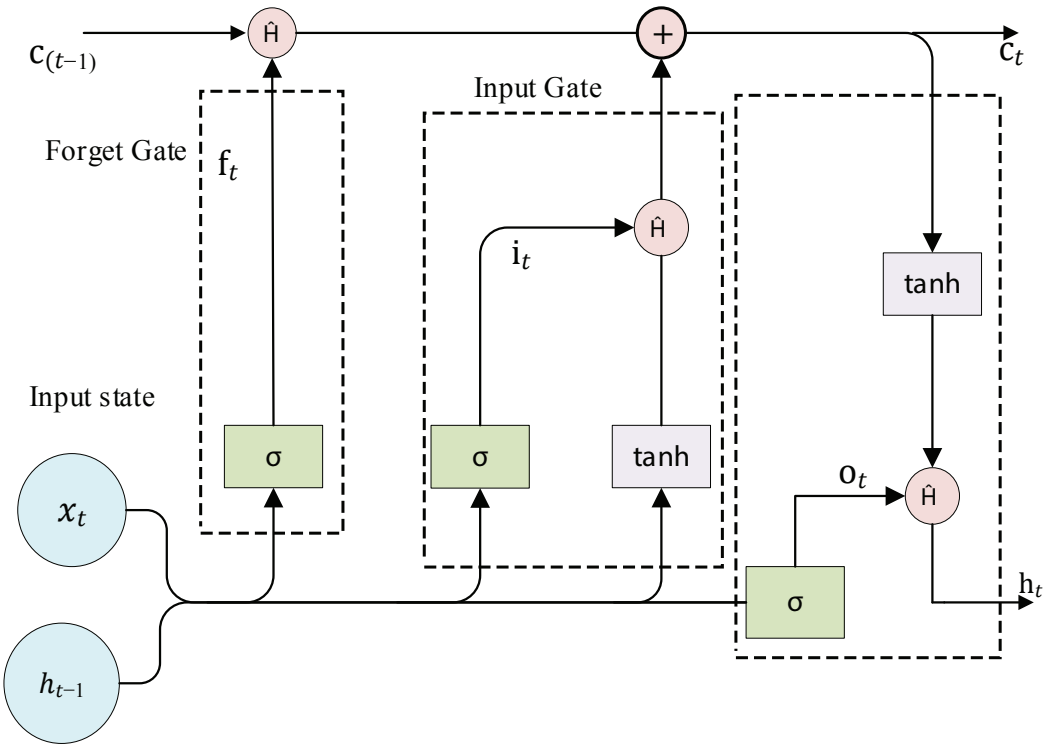


Figure 3. LSTM structure.

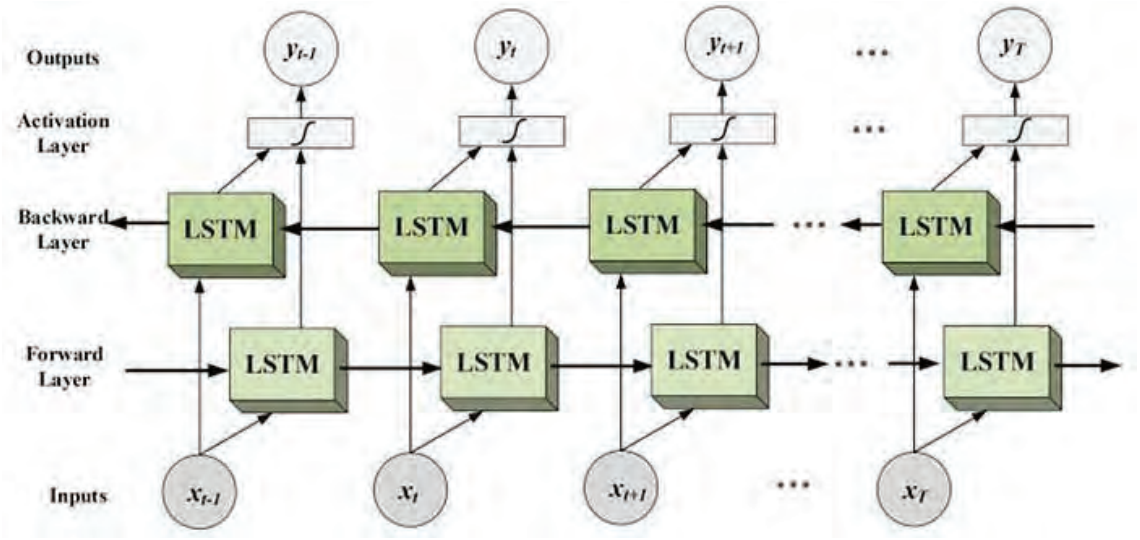


Figure 4. Structure of Bi-LSTM.

Table 4. Mathematical formulation of LSTM and Bi-LSTM [83]

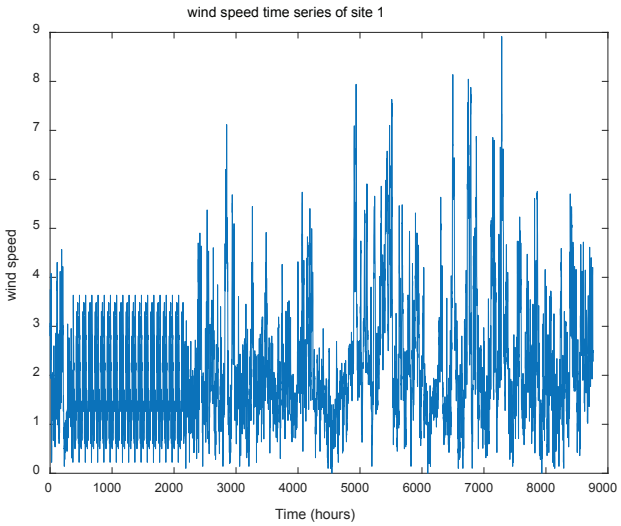
States	Forward State (LSTM), (Bi-LSTM)	Backward State (Bi-LSTM)
Memory cell	$c_{t=}\, c_{t-1} *\ f_t\ (\tanh(w_c.[x_t, h_{t-1}] + b_c)\ i_{t-1})$[83]	$c_{t=}\, c_{t-1} *\ f_t\ (\tanh(w_c.[x_t, h_{t+1}] + b_c)\ i_{t-1})$[83]
Forget gate	$f_{t=}\, \sigma(w_f.[x_t, h_{t-1}] + b_f)$[83]	$f_{t=}\, \sigma(w_f.[x_t, h_{t+1}] + b_f)$[83]
Input gate	$i_{t=}\, \sigma(w_i.[x_t, h_{t-1}] + b_i)$[83]	$i_{t=}\, \sigma(w_i.[x_t, h_{t+1}] + b_i)$[83]
Output state	$o_{t=}\, \sigma(w_o.[x_t, h_{t-1}] + b_o)$[83]	$o_{t=}\, \sigma(w_o.[x_t, h_{t+1}] + b_o)$[83]
Hidden state	$h_{t=}\ \tanh(c_{t-1}) * o_t$ [83]	$h_{t=}\ \tanh(c_{t+1}) * o_t$ [83]

Table 5. Performance evaluation [84]

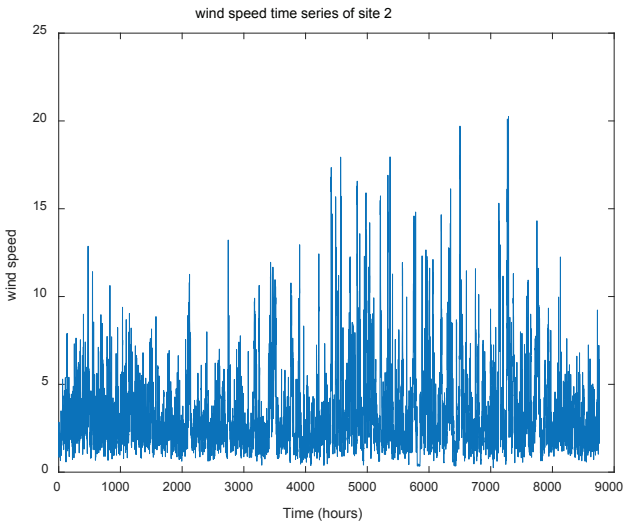
Metrics	Definition	Equation
MSE	Mean Squared Error [84]	$\text{MSE}=\frac{1}{n}\sum_{i=1}^{n}(Y_i - X_i)^2$[84]
MAE	Mean Absolute Forecasting Error[84]	$\text{MAE}=\frac{1}{n}\sum_{i=1}^{n}\lvert Y_i - X_i\rvert$[84]
RMSE	Root Mean Squared Error[84]	$\text{RMSE}=\sqrt{\frac{1}{n}\sum_{i=1}^{n}(Y_i - X_i)^2}$[84]
SMAPE	Symmetric Mean Absolute Percentage Forecasting Error[84]	$\text{SMAPE}=\frac{1}{n}\sum_{i=1}^{n}\frac{\lvert y_{i-x_i}\rvert}{\lvert y_i\rvert+\lvert x_i\rvert/2}$ [84]

Table 6. Statistical parameters for datasets

Statistical parameters	Site 1				Site 2			
	Spring	Winter	Autumn	Summer	Spring	Winter	Autumn	Summer
Max.	8.9157	8.1394	7.1176	4.7854	20.2460	19.7050	13.2176	15.8000
Min.	0	0	0.1414	1.000	0.2536	0.3510	0.3782	0.1800
Std.	2.0125	1.4344	1.0039	0.9972	2.5607	3.3094	1.9486	2.8777
Med.	2.0125	1.9416	1.7464	1.7464	2.7452	3.1101	2.3511	5.3900



5a 'for Site 1'



5b 'for Site 2'

Figure 5. Wind speed time series data.

Bi-LSTM models are used. Traditional (2 techniques) and advanced models (2) employed here are the Kalman filter [85], ARIMA, LSTM, and Bi-LSTM (parameters given in Table 7). Training of the summer season by the Bi-LSTM model, using training data, is shown in Figure 6. The graph shows two lines that represent the performance of an optimization process over multiple function evaluations. 'Min Observed Objective' (Blue Line) starts at a high value and decreases rapidly at the beginning, levelling off as the function evaluations increase. 'Estimated Min Objective'(Green Line) closely follows the trend of the blue line, indicating a good alignment between the observed and estimated objectives, especially as the function evaluations increase. Both lines converge toward a stable minimum value after around

Table 7. Training parameters of all models

Models	Parameters	Value
ARIMA	p, d, q (AR, differencing, and MA orders)	Values are chosen based on the time series' autocorrelation and partial autocorrelation.
Kalman Filter	State transition matrix (F) [85]	Governs the evolution of the system's state over time.
	Observation matrix (H) [85]	Maps the true state space to the observed space [85].
	Process noise covariance (Q) [85]	Represents uncertainty in the system dynamics.
	Measurement noise covariance (R) [85]	Represents noise in the observations [85].
	Initial state and covariance (x_0, P_0) [85]	Initial guess of the state and its uncertainty [85].
LSTM	Learning Rate	0.0011
	Hidden Units	Number of neurons per LSTM layer (e.g., 50, 100).
	Batch Size	100
	Sequence Length	Length of input time steps per sample (e.g., 10, 20).
	Number of Layers	3
	Epochs	350
	Dropout Rate	0.5
	Activation Function	tanh
Bi-LSTM	Same as LSTM parameters	Learning rate, hidden units, batch size, etc., are similar to LSTM.
	Bidirectional Layers	Processes input sequences in both forward and backward directions.
	Training Complexity	Bi-LSTM requires more computational resources compared to unidirectional LSTM.

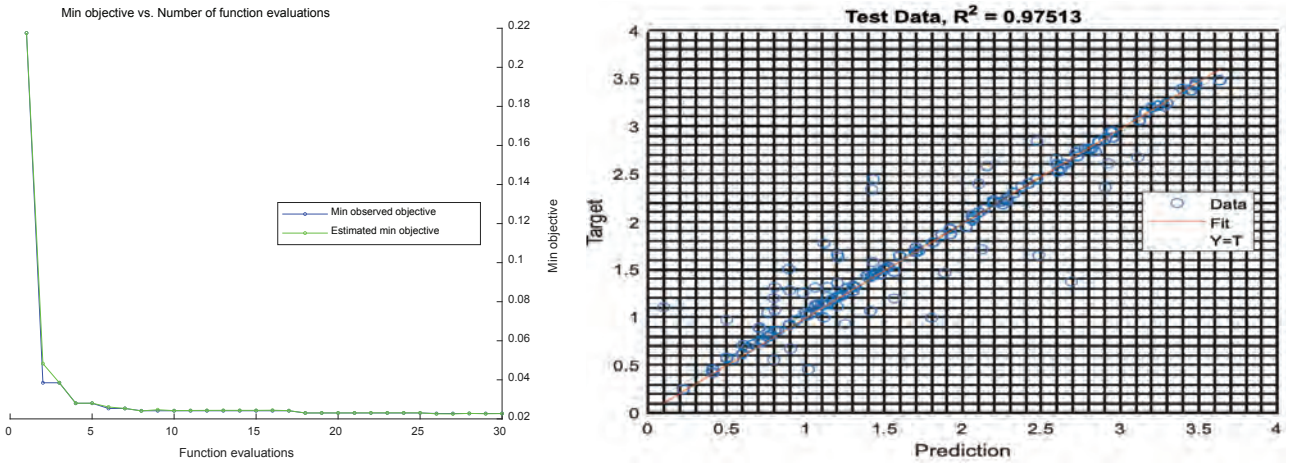


Figure 6. Objective vs. function evaluation and regression curve of summer season from Site 1.

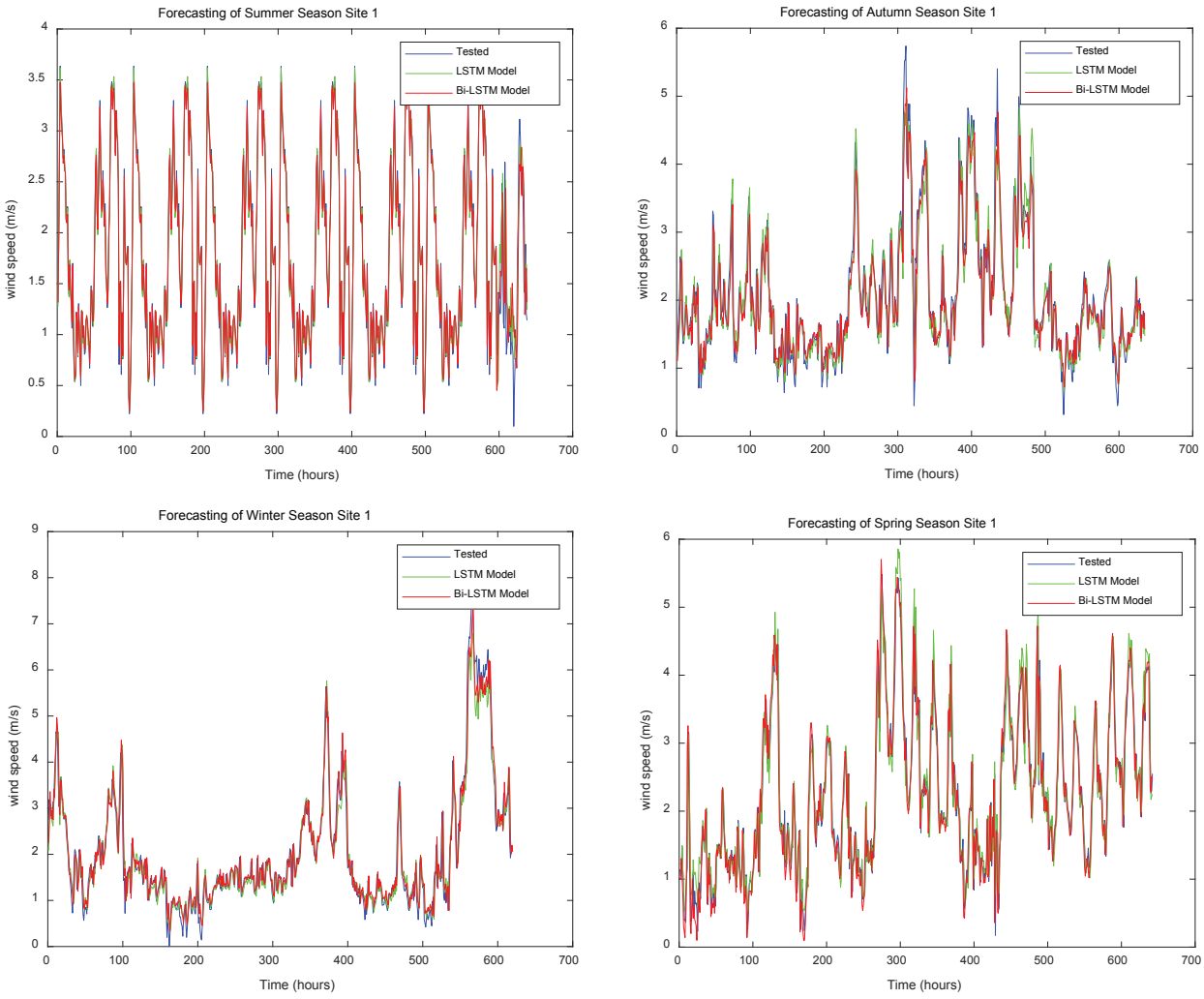


Figure 7. Predictions curve of site 1 from all seasons (Blue (Testing), Green (Predicted by LSTM), Red (Predicted by Bi-LSTM)).

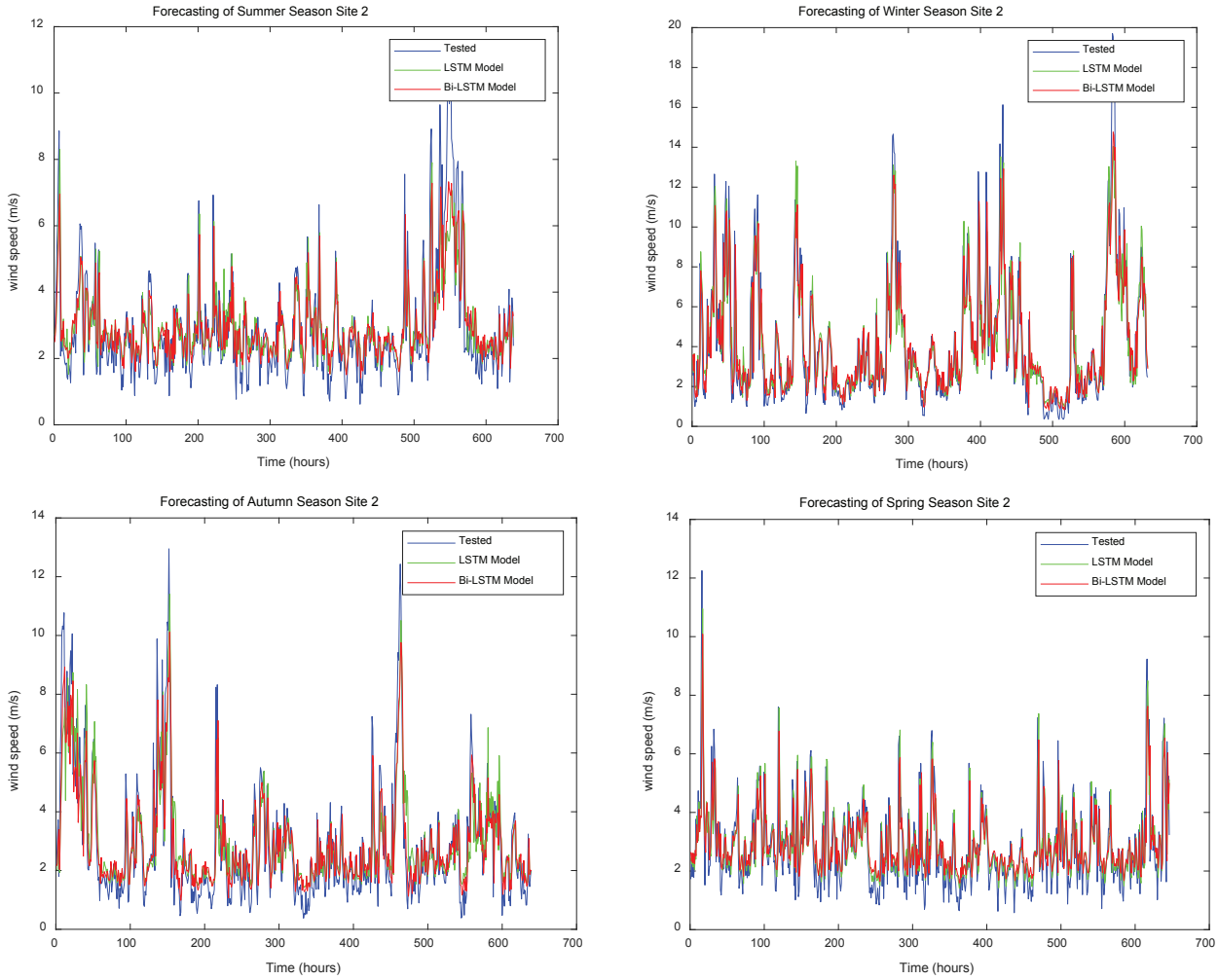


Figure 8. Predictions curve of site 2 from all seasons (Blue (Testing), Green (Predicted by LSTM), Red (Predicted by Bi-LSTM)).

Table 8. Comparison of model's performance for Site 1 (Model '1': Kalman, Model '2': ARIMA, Model '3': LSTM, Model '4': Proposed Bi-LSTM)

Seasons for Site 1	Models	MSE	MAE	RMSE	SMAPE
Summer	'1'	3.6614	1.6980	1.9135	0.4303
	'2'	0.7750	0.7688	0.8803	0.1129
	'3'	0.0255	0.0905	0.1597	0.0170
	'4'	**0.0164**	**0.0531**	**0.1280**	**0.0108**
Autumn	'1'	4.7028	1.9511	2.1686	0.4255
	'2'	0.8838	0.7187	0.9401	0.0852
	'3'	0.1565	0.2828	0.3956	0.0362
	'4'	**0.1413**	**0.2690**	**0.3758**	**0.0350**
Winter	'1'	6.2721	2.1019	2.5044	0.4992
	'2'	2.7106	1.4463	1.6464	0.1549
	'3'	0.1380	0.2625	0.3715	0.0389
	'4'	**0.1246**	**0.2518**	**0.3529**	**0.0375**
Spring	'1'	6.2774	2.2267	2.5055	5.000
	'2'	1.5053	0.9838	1.2297	0.1187
	'3'	0.1846	0.3178	0.4297	0.0461
	'4'	**0.1569**	**0.2850**	**0.3961**	**0.0426**

Table 9. Comparison of model's performance for Site 2 (Model '1': Kalman, Model '2': ARIMA, Model '3': LSTM, Model '4': Proposed Bi-LSTM)

Seasons for Site 1	Models	MSE	MAE	RMSE	SMAPE
Summer	'1'	3.6614	1.6980	1.9135	0.4303
	'2'	0.7750	0.7688	0.8803	0.1129
	'3'	0.0255	0.0905	0.1597	0.0170
	'4'	**0.0164**	**0.0531**	**0.1280**	**0.0108**
Autumn	'1'	4.7028	1.9511	2.1686	0.4255
	'2'	0.8838	0.7187	0.9401	0.0852
	'3'	0.1565	0.2828	0.3956	0.0362
	'4'	**0.1413**	**0.2690**	**0.3758**	**0.0350**
Winter	'1'	6.2721	2.1019	2.5044	0.4992
	'2'	2.7106	1.4463	1.6464	0.1549
	'3'	0.1380	0.2625	0.3715	0.0389
	'4'	**0.1246**	**0.2518**	**0.3529**	**0.0375**
Spring	'1'	6.2774	2.2267	2.5055	5.000
	'2'	1.5053	0.9838	1.2297	0.1187
	'3'	0.1846	0.3178	0.4297	0.0461
	'4'	**0.1569**	**0.2850**	**0.3961**	**0.0426**

10–15 function evaluations, suggesting that the optimization process effectively minimizes the objective function.

Prediction by Proposed Model

Figure 7 and 8 provides a peformance comparison of the proposed model with LSTM.

Model's Comparison

Tables 8 and 9 indicate the superiority of the proposed model in comparison to others. The results from the experimental analysis indicate that deep learning models, particularly LSTM and Bi-LSTM, significantly outperform traditional models like the Kalman Filter and ARIMA in predicting wind speed. Additionally, the Bi-LSTM model predicts the highest accuracy and has the ability to identify intricate patterns in the data over time. Because of its bidirectional structure, which makes it possible for it to generate dependent variables in both past and future states, the Bi-LSTM model performs the best. Since variation and alterations can occur at any time, this is highly significant when attempting to forecast wind speed.

In comparison to earlier studies using Bi-LSTM for wind speed prediction, this work demonstrates a number of improvements. Improved the addition of more feature engineering techniques, hyper-parameter tuning, and the utilization of larger and more diverse datasets can all lead to greater model performance. In previous studies, for example, inadequate number of datasets and/or inadequate handling of seasonality as well as noise have been the frequent issues. This work addresses these difficulties by use of more reliable designs and/or better pre-processing techniques.

Limitations and Future Work

Although the efficiency of LSTM as well as Bi-LSTM models for wind speed forecasting has been demonstrated here, some limits must be acknowledged, and future research possibilities have to be offered. This study has utilized historical wind speed data from particular locations and for set time periods. Future studies may examine the applicability of proposed models by their applications to a broader range of environments and climates.

Deep learning models (including Bi-LSTM), make use of a large amount of computing resources for training and prediction. Further studies may concentrate on enhancement of these models so as to lower the computational processing demands without decreasing the efficiency. LSTM and Bi-LSTM models are generally considered "black boxes" on account of their complex designs. Enhancing these models' by the use of attention mechanisms may result in crucial insights into the features, thus identifying the features which have more influence on wind speed predictions. Future research may concentrate on developing hybrid approaches which combine the benefits of deep learning methods with statistical methods (such as the Kalman Filter and ARIMA). These models may be capable of making a better tradeoff between computing efficiency, interpretability, and predictability.

CONCLUSION

This paper has determined the capability of the Kalman Filter, ARIMA, LSTM, and Bi-LSTM models for task of wind speed prediction by use of actual wind speed data.

The outcomes have proved that the traditional models like ARIMA and Kalman Filter are beneficial for simple & linear forecasts, the complex, behaviour of the wind speed cannot be effectively handled by them. It has been demonstrated that the Deep Learning models can analyse data in both directions and learn long-term dependencies, thus result in much more accurate predictions. The Bi-LSTM model has been more accurate, resulting in lowest prediction errors which further improves the reliability of electricity grid, thus, making the integration of the renewable energy easier.

The results may be beneficial for various future applications, e.g., basic climate modeling including load prediction for energy systems. The outcomes have demonstrated that Bi-LSTM is the best since because of its capabilities to handle the complex and varied datasets. Although the Kalman Filter and ARIMA are computationally more correct, yet they are less reliable for non-linear dynamics. On account of its versatility, use of Bi-LSTM is preferred for transdisciplinary applications & for forecast of renewable energy, which enhances grid stability. The results of this work may go beyond wind energy prediction and can be used for other sources of renewable energy wherever availability of precise weather and ecological data are essential, including the prediction of solar output or assessing the hydropower flow. Moreover, since machine learning models are able to handle chaotic & unpredictable time series data, in future, they can be used for wide range of applications, such as time series prediction for financial market evaluation, astronomy, and healthcare. This work further highlights the importance of using the best algorithms available for addressing the global energy challenges and also the importance of collaborating across disciplines for constructing a better as well as more resilient future.

ABBREVIATIONS

AR	Auto- Regressive
ANN	Artificial Neural Network
AI	Artificial Intelligence
ARMA	Auto Regressive Moving Average
ARIMA	Auto Regressive Integrated Moving Average
LSTM	Long-Short Term Memory
Bi-LSTM	Bidirectional Long-Short Term Memory
BPTT	Back Propagate Through Time
CNN	Convolutional Neural Network
DL	Deep Learning
K-NN	K-Nearest Neighbor
MAE	Mean Absolute Error
MA	Moving Average
ML	Machine Learning
MSE	Mean Square Error
NLP	Natural Language Processing
NWP	Numerical Weather Prediction
NREL	National Renewable Energy Laboratory
RMSE	Root Mean Square Error
RNN	Recurrent Neural Network
VAR	Vector Auto Regressive
SARIMA	Seasonal Auto Regressive Integrated Moving Average
SMAPE	Symmetric Mean Absolute Percentage Error

AUTHORSHIP CONTRIBUTIONS

Authors equally contributed to this work.

DATA AVAILABILITY STATEMENT

The authors confirm that the data that supports the findings of this study are available within the article. Raw data that support the finding of this study are available from the corresponding author, upon reasonable request.

CONFLICT OF INTEREST

The authors certified no conflict of interest.

ETHICS

There are no ethical issues with the publication of this manuscript.

STATEMENT ON THE USE OF ARTIFICIAL INTELLIGENCE

Artificial intelligence was not used in the preparation of the article.

REFERENCES

[1] Wu YK, Hong JS. A literature review of wind forecasting technology in the world. IEEE Lausanne Power Tech 2007:504–509. [CrossRef]

[2] Wang X, Guo P, Huang X. A review of wind power forecasting models. Energy Procedia 2011;12:770–778. [CrossRef]

[3] Chang WY. A literature review of wind forecasting methods. J Power Energy Eng 2014;2:161–168. [CrossRef]

[4] Lange M, Focken U. New developments in wind energy forecasting. IEEE Power Energy Soc Gen Meet 2008:1–8. [CrossRef]

[5] Soman SS, Zareipour H, Malik O, Mandal P. A review of wind power and wind speed forecasting methods with different time horizons. 2010. [CrossRef]

[6] Landberg L. A mathematical look at a physical power prediction model. Wind Energy 1998;1:23–28. [CrossRef]

[7] Kariniotakis G, et al. The state of the art in short term prediction of wind power-from an offshore perspective. SeaTech Week-Ocean Energy Conference ADEME-IFREMER 2004.

[8] Ye H, Yang B, Han Y, Li Q, Deng J, Tian S. Wind speed and power prediction approaches: Classifications, methodologies, and comments. Front Energy Res 2022;10:1–5. [CrossRef]

[9] Foley AM, Leahy PG, McKeogh EJ. Wind power forecasting & prediction methods. Environ Electr Eng (EEEIC) 2010:61–64. [CrossRef]
[10] Yahyai A, Sultan Y, Charabi Y, Badi AA, Gastli A. Nested ensemble NWP approach for wind energy assessment. Renew Energy 2012;37:150–160. [CrossRef]
[11] Lima JM, Guetter AK, Freitas SR, Panetta J, Mattos JGZ. A meteorological-statistic model for short-term wind power forecasting. J Control Autom Electr Syst 2017:679–691. [CrossRef]
[12] Saini S, Ahuja M. A research on wind power forecasting techniques. Int J Recent Technol Eng 2019;8:578–580.
[13] Liu C, et al. Numerical weather prediction enhanced wind power forecasting: Rank ensemble and probabilistic fluctuation awareness. Appl Energy 2022;313:118769. [CrossRef]
[14] Aggarwal SK, Gupta M. Wind power forecasting: A review of statistical models-wind power forecasting. Int J Energy Sci 2013;3:1–10.
[15] Wang JQZ, Zhang X. Wind power forecasting based on time series ARMA model. IOP Conf Ser Earth Environ Sci 2018;199. [CrossRef]
[16] Ling-ling L, Li JH, He PJ, Wang CS. The use of wavelet theory and ARMA model in wind speed prediction. 1st Int Conf Electr Power Equip-Switching Technol 2011:395–398. [CrossRef]
[17] Miranda MS, Dunn RW. One-hour-ahead wind speed prediction using a Bayesian methodology. IEEE Power Eng Soc Gen Meet 2006:1–6. [CrossRef]
[18] le Goff Latimier R, le Bouedec E, Monbet V. Switching autoregressive modeling of wind power forecast errors. 2020:189. [CrossRef]
[19] Song Z, Jiang Y, Zhang Z. Short-term wind speed forecasting with Markov-switching model. Appl Energy 2014;130:103–112. [CrossRef]
[20] Torres JL, García A, de Blas M, de Francisco A. Forecast of hourly average wind speed with ARMA models in Navarre (Spain). Sol Energy 2005;79:65–77. [CrossRef]
[21] Milligan M. IEA Task 25-design and operation of power systems with large amounts of wind power. 2003.
[22] Palomares-Salas JC, de La Rosa JJG, Ramiro JG, Melgar J, Agüera A, Moreno A. Comparison of models for wind speed forecasting. 2009.
[23] Tyass, Bellat A, Raihani A, Mansouri K, Khalili T. Wind speed prediction based on seasonal ARIMA model. E3S Web Conf 2022. [CrossRef]
[24] Palomino K, Reyes F, Núñez J, Valencia G, Acosta RH. Wind speed prediction based on univariate ARIMA and OLS on the Colombian Caribbean coast. J Eng Sci Technol Rev 2020;13:200–205. [CrossRef]
[25] Das J, Banerjee R. Estimation of long-range correlations and FARIMA modeling of wind speed in Maharashtra. IEEE PES Asia-Pacific Power Energy Eng Conf (APPEEC) 2017:1–6. [CrossRef]
[26] Kavasseri RG, Seetharaman K. Day-ahead wind speed forecasting using f-ARIMA models. Renew Energy 2009;34:1388–1393. [CrossRef]
[27] Narayana M, Putrus G, Jovanovic M, Sing Leung P. Predictive control of wind turbines by considering wind speed forecasting techniques. 44th Int Univ Power Eng Conf (UPEC) 2009:1–4.
[28] Firat U, Engin SN, Murat S, Ertuzun AB. Wind speed forecasting based on second order blind identification and autoregressive model. 9th Int Conf Mach Learn Appl 2010:686–691. [CrossRef]
[29] Duran MJ, Cros D, Riquelme J. Short-term wind power forecast based on ARX models. J Energy Eng 2007;133:172–180. [CrossRef]
[30] Li M, Yang M, Yu Y, Lee WJ. A wind speed correction method based on modified hidden Markov model for enhancing wind power forecast. IEEE Trans Ind Appl 2022;58:656–666. [CrossRef]
[31] Wang Z, Wang W, Liu C, Wang B. Forecasted scenarios of regional wind farms based on regular vine copulas. J Mod Power Syst Clean Energy 2022;8:77–85. [CrossRef]
[32] Mararakanye N, Dalton A, Bekker B. Incorporating spatial and temporal correlations to improve aggregation of decentralized day-ahead wind power forecasts. IEEE Access 2022;10:116182–116195. [CrossRef]
[33] Yu Y, Han X, Yang M, Yang J. Probabilistic prediction of regional wind power based on spatiotemporal quantile regression. IEEE Trans Ind Appl 2020;56:6117–6127. [CrossRef]
[34] Chang WY. Short-term wind power forecasting using the enhanced particle swarm optimization-based hybrid method. Energies 2013;6:4879–4896. [CrossRef]
[35] Nandana Jyothi M, Ramana Rao PV. Very-short term wind power forecasting through adaptive wavelet neural network. Biennial Int Conf Power Energy Syst Towards Sustainable Energy (PESTSE) 2016:1–6. [CrossRef]
[36] Xu L, Mao J. Short-term wind power forecasting based on Elman neural network with particle swarm optimization. Chin Control Decis Conf (CCDC) 2016:2678–2681. [CrossRef]
[37] Catalao JPS, Pousinho HMI, Mendes VMF. An artificial neural network approach for short-term wind power forecasting in Portugal. Int Conf Intell Syst Appl Power Syst 2009:1–5. [CrossRef]
[38] Mabel MC, Fernandez E. Analysis of wind power generation and prediction using ANN: A case study. Renew Energy 2008;33:986–992. [CrossRef]
[39] Singh S, Bhatti TS, Kothari DP. Wind power estimation using artificial neural network. J Energy Eng 2007;133:46–52. [CrossRef]
[40] Pliego M, Márquez FPG, Pinar Perez JM, Ruiz-Hernández D. A survey of artificial neural network in wind energy systems. Appl Energy 2022;228:1822–1836. [CrossRef]

[41] Sharma R, Singh D. A review of wind power and wind speed forecasting. J Eng Res Appl 2018;8:1–9.
[42] Sideratos G, Hatziargyriou ND. Probabilistic wind power forecasting using radial basis function neural networks. IEEE Trans Power Syst 2012;27:1788–1796. [CrossRef]
[43] Ramadevi B, Bingi K. Chaotic time series forecasting approaches using machine learning techniques: A review. Symmetry 2022;14:955. [CrossRef]
[44] Zhou Y, Sun Y, Wang S, Mahfoud RJ, Alhelou HH, et al. Performance improvement of very short-term prediction intervals for regional wind power based on composite conditional nonlinear quantile regression. J Mod Power Syst Clean Energy 2022;10:60–70. [CrossRef]
[45] Lee J, Wang W, Harrou F, Sun Y. Wind power prediction using ensemble learning-based models. IEEE Access 2020;8:61517–61527. [CrossRef]
[46] Tu CS, Hong CM, Huang HS, Chen CH. Short term wind power prediction based on data regression and enhanced support vector machine. Energies 2020;13:6319. [CrossRef]
[47] Tan L, Han J, Zhang H. Ultra-short-term wind power prediction by salp swarm algorithm-based optimizing extreme learning machine. IEEE Access 2020;8:44470–44484. [CrossRef]
[48] Huang Y, Liu GP, Hu WS. Priori-guided and data-driven hybrid model for wind power forecasting. ISA Trans 2023;134:380–395. [CrossRef]
[49] Wang YL, Yang P, Zhao SY, Chevallier JL, Xiao QT. A hybrid intelligent framework for forecasting short-term hourly wind speed based on machine learning. Expert Syst Appl 2022;213:119223. [CrossRef]
[50] Wang Q, Wang Y, Zhang K, Liu Y, Qiang W, Han Wen Q. Artificial intelligent power forecasting for wind farm based on multi-source data fusion. Processes 2023;11:1429. [CrossRef]
[51] Ahuja M, Saini S. Recurrent neural network for chaotic wind speed time series prediction. 9th IEEE India Int Conf Power Electron (IICPE) 2023:1–6. [CrossRef]
[52] Cicek ZIE, Ozturk ZK. Short term traffic flow forecasting using artificial neural networks. Sigma J Eng Nat Sci 2018;9:405–414.
[53] Kose B, Duz M, Guneser MT, Recebli Z. Estimating wind energy potential with predicting Burr LSM parameters: A different approach. Sigma J Eng Nat Sci 2018;36:389–404.
[54] Qasem M, Filik UB. Solar radiation forecasting by using deep neural networks in Eskişehir. Sigma J Eng Nat Sci 2021;39:159–169. [CrossRef]
[55] Xiao Z, Tang F, Wang M. Wind power short-term forecasting method based on LSTM and multiple error correction. Sustainability 2023;15:3798. [CrossRef]
[56] Rizwan M, Saini S, Singh U. Prediction of wind energy using intelligent approach. IEEE 5th India Int Conf Power Electron (IICPE) 2012:1–5. [CrossRef]
[57] Jung J, Broadwater RP. Current status and future advances for wind speed and power forecasting. Renew Sustain Energy Rev 2014;31:762–777. [CrossRef]
[58] Ren Y, Huang. Ensemble empirical mode decomposition: A noise-assisted data analysis method. 2008.
[59] Phan QT, Phan QD, Wu YK. A hybrid wind power forecasting model with XGBoost, data preprocessing considering different NWPs. Appl Sci 2021;11:1–19. [CrossRef]
[60] Cadenas E, Rivera W. Wind speed forecasting in three different regions of Mexico using a hybrid ARIMA-ANN model. Renew Energy 2010;35:2732–2738. [CrossRef]
[61] Pousinho HMI, Mendes VMF, Catalão JPS. A hybrid PSO-ANFIS approach for short-term wind power prediction in Portugal. Energy Convers Manage 2011;52:397–402. [CrossRef]
[62] Adedeji PA, Akinlabi S, Madushele N, Olatunji OO. Wind turbine power output very short-term forecast: A comparative study of data clustering techniques in a PSO-ANFIS model. J Clean Prod 2020;254:120135. [CrossRef]
[63] Shukur OB, Lee MH. Daily wind speed forecasting through hybrid KF-ANN model based on ARIMA. Renew Energy 2015;76:637–647. [CrossRef]
[64] Liu D, Niu D, Wang H, Fan L. Short-term wind speed forecasting using wavelet transform and support vector machines optimized by genetic algorithm. Renew Energy 2014;62:592–597. [CrossRef]
[65] Zhang C, Wei H, Zhao J, Liu T, Zhu T, Zhang K. Short-term wind speed forecasting using empirical mode decomposition and feature selection. Renew Energy 2016;96:727–737. [CrossRef]
[66] Mi XW, Liu H, Li YF. Wind speed forecasting method using wavelet, extreme learning machine and outlier correction algorithm. Energy Convers Manage 2017;151:709–722. [CrossRef]
[67] Li H, Wang J, Lu H, Guo Z. Research and application of a combined model based on variable weight for short-term wind speed forecasting. Renew Energy 2018;116:669–684. [CrossRef]
[68] Jiang P, Wang Y, Wang J. Short-term wind speed forecasting using a hybrid model. Energy 2017;119:561–577. [CrossRef]
[69] Azimi R, Ghofrani M, Ghayekhloo M. A hybrid wind power forecasting model based on data mining and wavelets analysis. Energy Convers Manage 2016;127:208–225. [CrossRef]
[70] Jiang Y, Huang G, Peng X, Li Y, Yang Q. A novel wind speed prediction method: Hybrid of correlation-aided DWT, LSSVM and GARCH. J Wind Eng Ind Aerodyn 2018;174:28–38. [CrossRef]
[71] Liu H, Duan Z, Han FZ, Li YF. Big multi-step wind speed forecasting model based on secondary decomposition, ensemble method and error correction algorithm. Energy Convers Manage 2018;156:525–541. [CrossRef]

[72] Hong YY, Lian C, Rioflorido PP. A hybrid deep learning-based neural network for 24-h ahead wind power forecasting. Appl Energy 2019;250:530–539. [CrossRef]

[73] Foley M, Leahy PG, Marvuglia A, McKeogh EJ. Current methods and advances in forecasting of wind power generation. Renew Energy 2012;37:1–8. [CrossRef]

[74] Shetty RP, Sathyabhama APSP, Adarsh Rai A. Optimized radial basis function neural network model for wind power prediction. 2nd Int Conf Cogn Comput Inf Process (CCIP) 2016:1–6. [CrossRef]

[75] Peng H, Liu F, Yang X. A hybrid strategy of short-term wind power prediction. Renew Energy 2013;50:590–595. [CrossRef]

[76] Wang J, Yang W, Tong N. A novel hybrid forecasting system of wind speed based on a newly developed multi-objective sine cosine algorithm. Energy Convers Manage 2018;163:134–150. [CrossRef]

[77] Sharma R, Singh D. A review of wind power and wind speed forecasting. J Eng Res Appl 2018;8:1–9.

[78] Saini S, Ahuja M. Wind speed prediction using wavelet transform and artificial neural network. Int J Res Electron Comput Eng 2017;5:161–168.

[79] Saini S, Ahuja M. Wind speed prediction using wavelet transform and GA trained artificial neural network. J Adv Res Dyn Control Syst 2019:108–204. [CrossRef]

[80] Duan J, et al. A combined short-term wind speed forecasting model based on CNN-RNN and linear regression optimization considering error. Renew Energy 2022;200:788–808. [CrossRef]

[81] Meteoblue. Weather archive export database. 2023. Available at: https://www.meteoblue.com/en/weather/archive. Accessed October 5, 2026.

[82] NREL National Renewable Energy Laboratory Database.

[83] Zan T, Liu Z, Su Z, Wang M, Gao X, Chen D. Statistical process control with intelligence based on the deep learning model. Appl Sci 2020;10:308. [CrossRef]

[84] Ahuja M, Saini S. Enhancing short-term chaotic wind speed time-series prediction using hybrid approach with multiple data sets. Nonlinear Dyn 2024;112:18031–18053. [CrossRef]

[85] Varghese A, et al. Evaluation of Kalman and Unscented Kalman Filters for multiple object tracking in ADAS applications using the KITTI dataset. 2025 2nd International Conference on Trends in Engineering Systems and Technologies (ICTEST); Ernakulam, India. 2025:1–8. [CrossRef]

Sigma J Eng Nat Sci, Vol. 44, No. 4, pp. 2714–2734, August, 2026

Sigma Journal of Engineering and Natural Sciences
Web page info: https://sigma.yildiz.edu.tr
DOI: 10.14744/sigma.2026.2123

Research Article

Expository techniques and integrative bioinformatics for survival modeling: Screening potential biomarkers in hepatocellular carcinoma

Sumaila ABUBAKARI[1,2,*], Filiz KARAMAN[2], Radiatu ABDUL-SOMED[3]

[1]Department of Electrical/Electronic Engineering, School of Engineering, University of Engineering and Agricultural Sciences, Bunso, E51774, Ghana
[2]Department of Statistics, Faculty of Arts and Science, Yildiz Technical University, Davutpaşa Campus, İstanbul, 34220, Türkiye
[3]Department of Pharmaceutical Technology, University of Technology and Applied Sciences, Navrongo, UK-0215-5322, Ghana

ARTICLE INFO

Article history
Received: 14 August 2024
Revised: 13 January 2025
Accepted: 14 May 2025

Keywords:
Bioinformatics; Biomarkers; Liver Cancer; Survival Modeling; Hepatoblastoma

ABSTRACT

Hepatocellular carcinoma (HCC) is the most common malignant form of primary liver cancer and one of the leading causes of liver-related deaths. Risk estimation of HCC depends on a matrix of several risk factors, from clinicopathological to gene expression features. From an etiological perspective, the survival prospects of HCC vary from patient to patient. Therefore, a comprehensive study that captures complex relationships among risk factors is one of the ways to quantify prognosis and/or diagnosis, thereby harnessing personalized medicine. We integrated survival analysis with bioinformatics to identify diagnostic and prognostic biomarkers in HCC. Using RNA-seq data from TCGA-LIHC, we screened differentially expressed genes (DEGs) and applied Cox regression, machine learning (LASSO-penalized modeling), and pathway enrichment analysis to prioritize genes linked to overall survival (OS) and tumor progression. Among 3,623 DEGs (685 downregulated, 2,938 upregulated), we identified three core prognostic genes (AP1M1, CASC9, and CA9) significantly associated with OS (logrank $p<0.001$, hazard ratio > 2.0). Diagnostic biomarkers (CLEC4M, SLC5A1, SLC22A1, SFRP5, CNDP1, TERT, and ZIC2) were enriched in metabolic signaling pathways. Kyoto Encyclopedia of Genes and Genomes (KEGG) analysis revealed five significantly altered pathways, with the strongest enrichment in 'hsa04976: Bile Secretion', underscoring disrupted metabolic homeostasis as a hallmark of HCC aggressiveness. Our study reveals novel biomarkers with both diagnostic and prognostic potential, offering a framework for targeted HCC management. These findings highlight the potential of integrative omics-survival modeling to advance precision oncology.

Cite this article as: Abubakari S, Karaman F, Abdul-Somed R. Expository techniques and integrative bioinformatics for survival modeling: Screening potential biomarkers in hepatocellular carcinoma. Sigma J Eng Nat Sci 2026;44(4):2714–2734.

***Corresponding author.**
*E-mail address: sumaila.abubakari@std.yildiz.edu.tr

This paper was recommended for publication in revised form by Editor-in-Chief Ahmet Selim Dalkilic

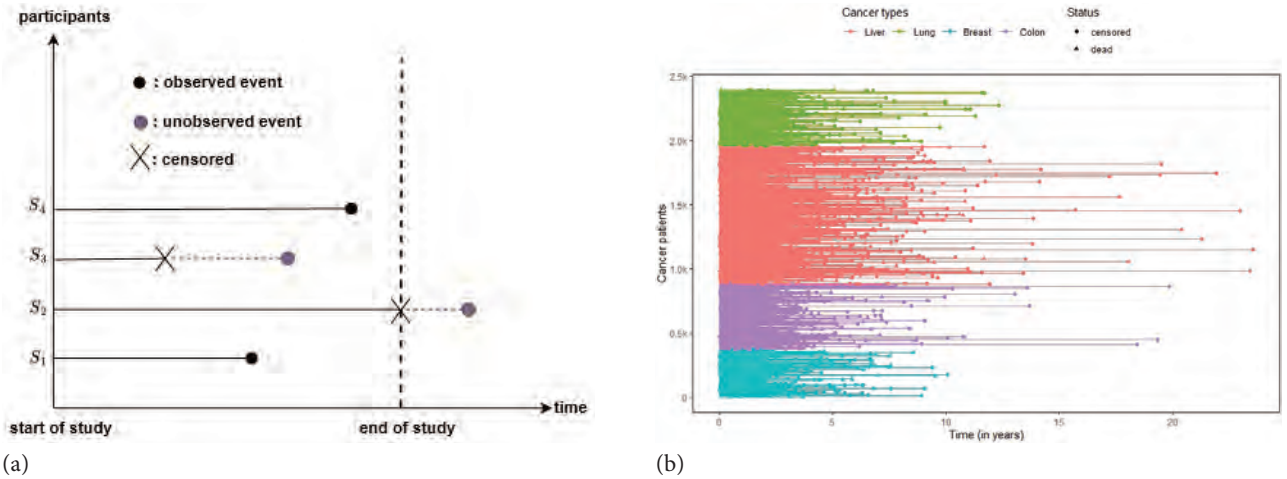
Published by Yıldız Technical University Press, İstanbul, Turkey
© Author. This is an open access article under the CC BY-NC license (http://creativecommons.org/licenses/by-nc/4.0/).

INTRODUCTION

Survival analysis serves as a special modeling technique used to handle time-to-event data, primarily due to the presence of 'censored' observations. When we refer to this technique as a special one, we are simply referring to its ability to deal with data where the event times are known for some subjects (individuals) while unknown for others, yet the unknown event times cannot be treated strictly as missing values. Further, the distribution of event times is normally skewed—fewer later events than earlier ones. In context, we use the expression *time-to-event* data to refer to observed data on the time taken for the occurrence of the said event (e.g., cancer relapse), commonly collected along with clinical or omics risk features. Though with varying terminologies, time-to-event data occur in different fields of research, namely; precision medicine [1], graduate education [2], loan delinquency [3], and engineering [4].

The genetic profiling of a patient tends to provide significant markers towards disease structure and development, in what is popularly known as *personalized medicine*. In cancer studies, oftentimes, Progression-free survival (PFS) and overall survival (OS) are some of the endpoints commonly used for modeling the survival prospects of patients in a wide range of diseases. By PSF, we mean the duration from when treatment is initiated to the time when the disease gets worse, while OS refers to the survival time from when an individual is diagnosed with a condition or when treatment is initiated to the actual event time. This is usually regarded as a measure of disease control rate (DCR)–thus, partial remission, complete remission, and stable disease rate. Note that the *event time* is defined as the duration for which a condition (e.g., cancer) is observed to have occurred. Thus far, time-to-event data intrinsically depends on whether the event has occurred or not. When it is not observed in the individual within the study time, we say the subject has been "censored". Censoring is often grouped into left-, right-, and interval. The most common one is right censoring. The differences in these groupings lie in the range of the time the event is observed. For instance, in right-censoring, we observe the lower limit; the upper limit in left-censoring, and both in the interval-censoring. A simple illustration of right-censoring and actual survival time distribution of different cancer types are shown in Fig. 1a and Fig. 1b respectively. For a comprehensive discussion on various forms of censoring, interested readers are referred to Leung et al. [5] and Klein and Moeschberger [6]. In this paper, we assume survival data with a right-censored paradigm. Further, the status variable is binarized so that a '1' means the event has occurred and '0' otherwise. A typical survival data with some clinical risk factors is shown in Table 1 for a cohort of Lung cancer patients [7]. Observe that the status variable is binary, where '1' is a code for censored individuals (i.e., 63/228) and '2' is a code for 'dead' individuals (i.e., 165/228). Because the distribution of the status variable is skewed, a basic logistic regression where the status variable is the response variable would lead to reliability issues in estimating the regression coefficients [8]. Further, using the event time as the response variable in simple regression affects the predictive strength of the model [9].

Following the rapid progression of technology in DNA microarrays, survival prospects of cancer patients and other forms of diseases have efficiently been improved due to such technologies presenting better pathways to evaluate proteome-wide or gene expression levels (microarray data). Stated differently, *omics* data (i.e., genomics, proteomics, epigenomics, etc.) present us with pieces of information that could serve as important biomarkers for assessing patients' prognosis, or serve as prior data for future research direction [10]. However, such microarrays are complex and exceedingly larger than sample sizes (i.e., $p \gg n$), invariably due to their high dimensionality. Also, this stream of



(a) (b)

Figure 1. Simple illustration of right censoring (a) Right-censored survival time distribution (a) for selected TCGA cancer datasets (Liver, Lung, Breast, Colon) Overall survival time distribution.

Table 1. An illustration of components of survival data: survival time, censoring, and binarization of the status variable. The data is drawn from 228 patients from the North Central Cancer Treatment Group (NCCTG) [7] with advanced lung cancer. Here, survival time is measured in days, '1' = 'censored', '2' = 'dead'

Inst.	Time	Status	Age	Sex	ph.ecog	ph.karno	pat.karno	meal.cal	wt.loss
3	306	2	74	1	1	90	100	1175	NA
3	455	2	68	1	0	90	90	1225	15
3	1010	1	56	1	0	90	90	NA	15
32	105	1	75	2	2	60	70	1025	5
6	174	1	66	1	1	90	100	1075	1
22	177	1	58	2	1	80	90	1060	0

data is collected with potentially massive missing values (NAs), inter-dataset collinearity, and noise-laced covariates [11]. Due to the high-dimensional space of the expression features, analytical techniques for these kinds of data go beyond classical survival modeling. To this end, recent advances in high-throughput genomics have transformed survival analysis by integrating multi-omics data (e.g., transcriptomics, proteomics) to identify prognostic biomarkers. For example, single-cell RNA sequencing (scRNA-seq) and spatial transcriptomics now enable granular profiling of tumor heterogeneity, revealing novel DEGs linked to HCC aggressiveness [12–14]. However, these technologies generate high-dimensional datasets ($p \gg n$) laced with noise, collinearity, and missing values. Traditional Cox models struggle with such dimensionality, prompting the adoption of machine learning (ML) and penalized regression (e.g., LASSO, ridge, or elastic net) for feature selection and predictive accuracy. Recent benchmarks highlight that hybrid models combining clinical and omics data outperform purely genomic or clinical models. For instance, integrating radiomics with transcriptomics has significantly improved HCC survival prediction in AUC metrics [15]. In benchmarking several methods for high-dimensional 'omics' data, Vinga [16] provided a comprehensive review of penalized regression approaches focused on survival modeling. Bøvelstad et al. [17] have also assessed the comparative predictive power of several ML models to show improvement in model prediction. In their study, the authors considered using 'tuning' methods and demonstrated performance by using both clinical and gene expression data. In a similar study, Bommert et al. [18] also benchmarked various penalized methods for feature selection in high-dimensional cases and suggested using the extended L_2-regularizer [19] for stability in feature selection, as well as for accuracy. As times go, more researchers continue to provide better insights into various modeling techniques, from parameter tuning to comparative analysis of classical and modern-day survival models, especially for health sciences [20–22].

The novelty of this study lies in its integrative approach, which combines survival analysis with advanced bioinformatics to identify and validate significantly differentially expressed genes (DEGs) in hepatocellular carcinoma (HCC). We do not focus solely on gene expression patterns but also on clinical survival outcomes, allowing our model to uniquely correlate DEGs with these outcomes. This approach pinpoints biomarkers with direct prognostic and diagnostic relevance. By bridging computational biology with patient-centric data, we not only uncover molecular drivers of HCC aggressiveness but also deliver actionable targets for improving therapeutic strategies—a critical advance in a field where early detection and treatment efficacy remain major challenges.

The remainder of this paper is organized as follows: In section 2, we present the structure of time-to-event analysis of "omics" datasets and their characteristics. In section 3, we both cover classical and modern survival modeling techniques for fitting low- and high-dimensional data. In section 4, we overview methods for assessing and validating prediction models. Section 5 centrally focuses on integrative analyses that use survival techniques and bioinformatics modeling tools to screen potential predictive biomarkers, including the methods, results, and discussion. We conclude our study with concluding remarks in section 6.

Data classification

Assessing the survival prospect of patients is one of the foci in what is usually termed *personalized medicine*. This assessment is done across a collection of different risk factors, clinicopathological and/or omics-related, to minimize bad prognosis. Thus, the endpoint goal is to target decision processes that screen insightful risk factors toward improved treatment targets.

Survival Data

Survival data typically comprises at least two random variables–event-status and survival time. The survival time is the time from the onset of a study of a condition of interest (e.g., cancer relapse) to the time of its actual occurrence or to the time of closure of the study. On the other hand, the event status is a Bernoulli variable indicating whether the event has occurred or not (Fig. 1a).

Let δ be a Bernoulli variable so that the observed survival time $T = min\{T^* \leq C\}$, given that T^* is the recorded

event time while C is the censoring time. Therefore, $\delta = \mathbb{1}\{T^* \leq C\}$, thus;

$$\delta = \begin{cases} 1 & \text{if} \quad T^* = X \\ 0 & \text{if} \quad T^* = C, \end{cases}$$

where $\mathbb{1}\{\cdot\}$ is a binary indicator function of status. The probability of an individual surviving beyond time t is characterized by the survivor function, $S(t) = \mathbb{P}(T^* > t) = 1 - F(t)$ where $F(t)$ is the cumulative distribution function (CDF).

The hazard function $h(t)$ is another estimator that gives insight into the survival prospects of subjects. It is defined as the instantaneous risk of death at time t given that, the individual up till now has survived time t, mathematically expressed as;

$$h(t) = \lim_{\Delta t \to 0} \frac{P(t \leq T^* < t + \Delta t | T^* > t)}{\Delta t}, \quad h(t) \geq 0 \ \ \forall t.$$

Clinico-Demographic Data

While the overall survival time (OS) may be a sufficient estimate, comprehensive analyses of other associated risk factors can provide better insights into the survival prospects—for example the influence of clinicopathological on survival modeling. Like in Okorie et al. [23], several cancer studies depend on demographic factors such as gender, race, vital status, ethnicity, cause of relapse, etc., to study their impact on prognosis. In personalized medicine, these factors are usually controlled to measure their influence on health outcomes. For instance, clinical risk factors such as hypercholesterolemia, myocardial infarction, left ventricular ejection, etc., are considered to influence patient survival in cardiovascular disease (CVD) [24]. The clinicopathological factors to consider largely depend on what cancer is being considered to model the target outcome, as illustrated in Bączyk and Kozłowska [25]. Here, the authors discuss the influence of clinical and demographic factors in treating rheumatoid arthritis (RA) by considering the factors shown in Table 2.

Table 2. Example of demographic and clinical factors [24]

Risk factors	Data type
Age	continuous
Sex	binary
Marital status	categorical
Education	categorical
Rheumatoid arthritis duration	continuous
VAS Pain (0 - 10cm)	continuous
Morning stiffness	continuous
Grip strength measurement (right)	continuous
Grip strength measurement (left)	continuous
Ritchie Articular Index	continuous

Omics Data

Owing to the fast advancement of bioinformatic tools, researchers have rushed to employ the knowledge of biology, computer science, medicine, and mathematics to better characterize patients' prognosis. Modern microarray technology invariably produces tonnes of complex data, the so-called 'omics' data–i.e., genomics, transcriptomics, proteomics, metabolomics, phenomics, and metagenomics. Each of these components shown in Fig. 2 serves a unique purpose towards human disease improvement. This is because of the structure of molecular information they process or possess. For example, in multi-omics analysis, genomics carries data of an individual's genome like genetic variation; proteomics carries data on the individual's set of proteins; transcriptomics for the individual's

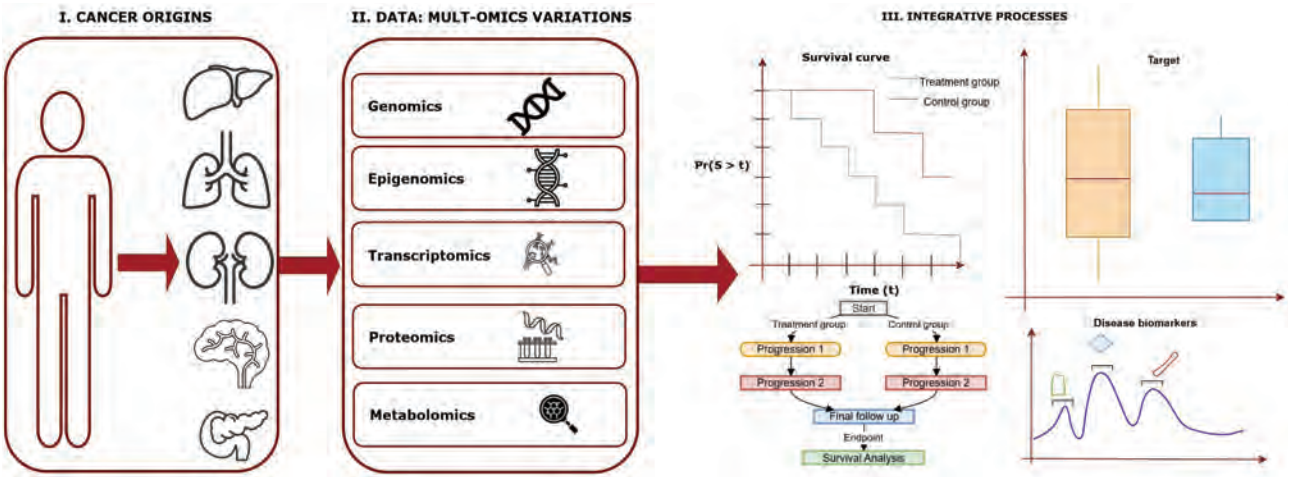


Figure 2. Integrative concept of multi-omics signatures for comprehensive bioinformatics modeling toward cancer detection, biomarker screening, and treatment assessment.

RNA transcripts generated by a genome; metabolomics for metabolites from metabolism. To understand the molecular mechanisms driving disease progression, integrative analysis across multi-omics platforms is pivotal for novel biomarker discovery [26, 27].

Omics data generated from genomic-powered tools traditionally comprises DNA molecules as carriers of genetic traits such as single nucleotide polymorphisms (SNP). As stated differently, a genome can be viewed as a blueprint that carries an individual's cellular construction. DNA molecules are polymers constituting simpler chemical units known as *nucleotides*. There are four basic forms of nucleotides, namely; adenine (A), thymine (T), cytosine (C), and guanine (G). Depending on how many minor alleles (AA, AG, GC, or TT) each individual carries at a particular location, each nucleotide's characteristic can be coded as 0, 1, or 2. Summarily, a genomics dataset consists of DNA molecule sequences found in a single cell or a population of cells.

Omics data related to transcriptomes consists of RNA molecules (e.g., *m*RNA). Transcriptomics comes in different types or forms such as ribosomal RNA (*r*RNA), messenger RNA (*m*RNA), transfer RNA (*t*RNA), and non-coded RNA (*nc*RNA). The *m*RNAs are the most important because they act as intermediator messengers between genomes and proteomes. For this reason, transcriptomics generally focuses on *m*RNA and is traditionally used to evaluate the sequences of expression levels of DNA. At a distributional level, microarray expression levels can fairly be represented by a normal distribution following a $log(a + 1)$ transformation, often with base 2. The cell count of *m*RNA molecules varies depending on the needs of proteins, and a transcriptomics dataset contains a list of every *m*RNA sequence present at any particular time. Transcriptomics may be viewed as "snapshots" of the portion and regions of the genome that are now being transcribed. In recent years, RNA-seq has eclipsed DNA microarrays due to their ability to mirror wholesome sequencing of transcriptomes rather than focusing on some selected transcripts/probes. Further, microRNAs tend to play crucial roles in repressing *m*RNA targets, especially in humans [28].

A proteome is derived from 'genome' and 'protein.' Proteomics is a collection of large-scale data on proteins using detection methods through mass spectrometry or immunoassays. To profile proteins, the most current and widespread method uses high-resolution 2D electrophoresis to discriminate proteins from different samples in a parallel fashion. Thereafter, it is followed by staining of differentially expressed proteins (DEPs) by mass spectrometry. Like transcriptomics, we can use a $log(a + 1)$ transformation to obtain nearly normally distributed protein expression data. Generally, profiling proteins using the mass spectrometry-based method tends to produce thousands of protein features as opposed to using the Reverse Phase Protein Arrays (RPPA)–which produces about 200 protein features [29].

Metabolomics refers to the scientific research of quantitatively studying the chemical processes of cell metabolism (metabolites) believed to carry useful biological fingerprints. Like proteomics, metabolomics shares identical statistical features in the sense that they can be profiled using mass spectrometer-based tools. Comprehensive metabolomics profiling can play a significant role in disease diagnosis or understanding the dynamics of complex biological systems. For example, using the nuclear magnetic resonance-based method (NMR), Emwas et al. [30] discuss the role of NMR-based metabolomics aimed at disease diagnosis and the limitations around such methods. Again, at the distributional level, metabolomics data often fit well with the logarithmic normal distribution. Note that subfields of metabolomics can be employed in different diverse ways. For example, exometabolomics involves the study of extracellular metabolites, which can draw many applications, such as biofuel mining, bioengineering, or how small cells interact to cause cellular transformation.

Issues with Missing Values in Omics Data

The presence of missing values in complex omics data can often be traced to many sources and has the potential to significantly affect model fitting or cause assessment challenges. For large-scale data such as transcriptomics, genomics, etc., missingness could be attributable to inherent limited technology, measurement errors, poor experimental design, and low sample quality [31,32]. Missing values in omics data can be grouped into three kinds, namely, missing at random (MAR), missing completely at random (MCAR), and missing not at random (MNAR). Considering transcriptomics data, for example, [33] argue that transcriptomics data have approximately no less than 10% missingness, and this affects over 90% of genes. In many cases, this missing value proportion can be attributed to faulty slides or corrupted images. For metabolomics, the proportion of missing values is around 11%–21%, tending to affect 80% of the features. There are available methods to handle missing values (MAR, MNAR, and MCAR), from the simplest imputation techniques to complex methods. Classical approaches that employ multiple imputations may produce biased results. One suggested solution is to identify features in the omics data with high rates of missing values, say above 60%, and drop such features from the data before running imputation on the remaining features in the data (e.g., KNN). Whether we choose listwise, pairwise, or variable deletion, the ultimate aim should be targeted at methods that avoid introducing extreme bias into the data. It is important to note, however, that some methods are completely impute-free. For example, mixture models are impute-free. Thus, they handle missing values when directly used (see Taylor et al. [34]).

Survival Prediction Modeling

In many applications of survival analyses, one of the core goals is to estimate the probability of an event occurring at

time t. This event in many medical research may be death due to a medical condition. However, classical methods such as Cox proportional hazards (CoxPH), despite their huge success in statistical science, are hugely limited in an era of growing complexity of survival data. Thus far, the appropriateness of several survival models has been linked to whether they are feasible with high dimensionality. This section briefly overviews survival modeling in the context of both high- and low-dimensional survival data.

Modeling Low-Dimensional Survival Data

Let X_i be a matrix of p covariates (clinicopathological and omics features), T_i be the recorded survival time, δ_i be the Bernoulli variable of censorship status, and n be the number of patients. Then the observed survival data, D, is represented as D = $\{T_i, \delta_i, X_i, \forall i=1,2,\ldots,n\}$. For right-censored survival data, the survivor function, $S(t)$, is estimated by taking into consideration the individuals at risk (n_i), the number of observed events (d_i), and the number of censored subjects at time t_i. For distribution-free estimation, Kaplan and Meier [35] proposed the *product limit estimator* based on multiplying out the conditioned probabilities of the event occurring. Mathematically, it is stated as

$$S_{km}(t) = \prod_{i:t_i<t} \frac{n_i - d_i}{n_i} = \prod_{i:t_i<t} \left(1 - \frac{d_i}{n_i}\right),$$

$$S_{km}(t_k) = \frac{n_{k-1} - d_{k-1}}{n_{k-1}} S_{km}(t_{k-2}), \ \ldots \text{ [by recursion]},$$

where $S_{km}(t)$ is the KM estimator for untied survival times, i.e., $T_i < T_2 < \cdots < T_k$; $(k \leq n)$.

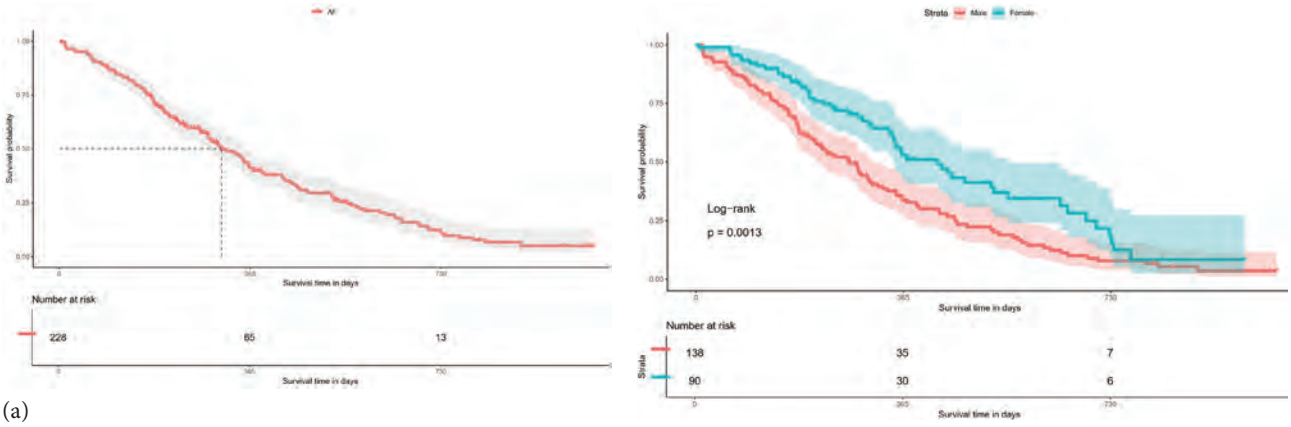
Referring back to the low-dimensional NCCTG lung cancer data we illustrated in Table 2, the data can be used to obtain some basic survival insights. For example, Fig. 3a shows the KM survival curve for the NCCTG lung cancer data with a median survival time of about 306 days (i.e., OS ≥ 10 months). The 1- and 2-year survival probabilities are 0.409 and 0.120, respectively. In Fig. 3b, the OS of the patients is stratified by sex (i.e., male-female). The P-value of 0.0013 shows a significant difference in the survival probabilities of the patients when sex is factored in. This comparison of the difference between the two survival curves is evaluated with the *log-rank testing*. From the survival curves by sex, it appears the female patients have relatively better survival prognosis than their male counterparts.

While the Kaplan-Meier approach can be used to estimate the survival probability in a covariate case-by-case framework, it fails to jointly measure the prognosis of patients of several covariates at the same time. Oftentimes too, the survivability of the individual may depend on several different factors—clinical and/or omics features. Under a multivariable setting, the CoxPH [36] can fit the survival data. Generally, the CoxPH is formulated as;

$$h(t|x_i) = h_0(t)\exp\left(\sum_{j=1}^{p} x_{ij}\,\beta_j\right), \qquad (1)$$

where $h_0(t)$ is the unspecified baseline hazard, β is a vector of regression coefficients, and X is a matrix of risk factors or features together with the survival time and the status variable. As the name suggests, the Cox proportional hazard model is valid when the proportionality assumption is fairly met (extremely hard to hold for most untransformed omics data). Because the baseline hazard need not be specified, CoxPH is widely considered a semi-parametric model. The CoxPH allows for two group hazards to be compared in what is termed as *hazard ratio* (HR).

The "curse of dimensionality" associated with high-dimensional ($p \gg n$) omics data renders the CoxPH model



(a) (b)

Figure 3. KM curves of the lung cancer patients. Adapted from: C. Loprinzi, et al. Prospective evaluation of prognostic variables from patient-completed questionnaires. North Central Cancer Treatment Group. 1994. Available at: https://doi.org/10.1200/jco.1994.12.3.601 **A.** Kaplan-Meier overall survival curve of NCCTG lung cancer patients. **B.** Overall survival estimation stratified by gender/sex.

impracticable in many cases. For low-dimensional data, the modeling method is usually used together with feature/variable selection methods for multivariable survival prediction, and there exists sufficient literature on practical considerations for handling problems with low-dimension survival models [37].

Modeling High-Dimensional Survival Data

As stated earlier, the enormity of high-dimensional features makes the applicability of traditional survival models infeasible. For example, DNA methylation can produce hundreds of thousands of features. This high dimensionality invariably affects multivariable modeling in terms of computational time and interpretability. One hack around this problem is to consider a subset of pre-selected features to be used in univariate case-by-case modeling. Even so, the pre-selected features will usually be selected based on their high statistical significance (e.g., $p < 0.01$). That approach, however, poses serious problems, one of them being that there is the likelihood of missing out on some important variables having significant associations with the outcome variable [38].

Further, it is possible to use total variance explained (TVE) to pre-select features to be used in the model. The reasoning behind this approach is that the higher the variance explained, the higher the predictive signal associated with the features. Zhao and Zucknick [39] argue that features accounting for 50% or more of the total variance can be selected and included in the model. An approach like this helps reduce the dimensionality of omics data having thousands of features and thus improves stability in the selection. In a comprehensive benchmark study, Zhao et al. [40] demonstrated the importance of pre-selection of features towards stability under a Bayesian stochastic selection setting. In a similar study, Bommert et al. [18] revealed that, of all the filter selection techniques, the simple variance approach was the most outstanding method under evaluation metrics such as computational time and stability.

For a univariate CoxPH, it is useful to consider adjusting the Pvalues of the covariates/features to draw insights from multiple comparative feature analyses. The reason behind this is that it helps contain the influence of false positives, e.g., false discovery rate (FDR). Remember that the issue of false discovery rate is a serious problem when performing simultaneous hypothesis testing, and for this reason, many researchers have devoted valuable time to producing detailed research on methods and solutions to the problem of multiple testing (see [41,42]). While the univariate CoxPH may be used at the pre-analysis stage to pin down influential features, it is important to remember that such an approach fails to capture interactions in the case of multi-omics survival data.

The complexity with which omics data are presented makes the classical survival methods infeasible for capturing nonlinearity and complicated interactions among hundreds of features. These features may give strong predictive signals toward patients' survival. While pre-selection of subsets of features could help in dimension reduction, such an approach can be bias-prone, rather needlessly. To this end, various state-of-the-art modern methods in literature offer alternative methods that are superior both in computational time and adaptability to nonlinearities of feature effects. For efficient variable selection, one may employ supervised learners such as penalized regression methods with appropriate loss functions such as L_1-norm or L_2-norm. In essence, the regularized selection methods tend to unselect sparse features–thus, of the thousands of features, the model selects those features that have significant effects on survival prospects.

Machine Learning Methods for High-Dimensional Data

In recent years, several machine learning (ML) methods have been used to bridge the gap of limitations associated with classical modeling techniques. Generally, ML methods, herein referred to as *learners*, are equipped with the ability to analyze complex data by revealing complex interactions among features that are otherwise hard to discern. This section discusses such learners.

Unsupervised learning

The primary goal of unsupervised learners is to recognize the difficult-to-find patterns in complex data, e.g., transcriptomics data and DNA methylation microarray data. For example, cardiovascular diseases (CVDs) may better be understood by uncovering their underlying molecular signatures so that the complex level of abstractions is representative of the underlying phenotypes for better clinical outcomes [43]. Unsupervised classifiers in this case use the large-scale data to repeatedly 'learn' hidden patterns and transform their complexity into a discernible low-dimensional plane. A popular data reduction technique is the Principal Component Analysis (PCA), where several hundreds of features in the data are represented with fewer features based on the Total Explained Variance. Thus, a high-dimensional hyperplane is projected into a low-dimensional plane.

While the dimension-reduction technique in PCA is tied to extracting maximized variance in the data, other proposed methods can achieve similar goals, including t-SNE, which uses nonlinear methods. In general, t-SNE reduces high-dimensional data into a low dimension using algorithms such that dissimilar data points are kept apart and similar data points are kept together. The t-SNE uses the Kullback-Leibler (KL) divergence to evaluate this difference. Besides t-SNE and PCA, the Uniform Manifold Approximation and Projection (UMAP) is another dimensional-reduction method with the algorithm behind it depending on three core assumptions: i). uniformity of data distribution on the Riemannian fold, ii). the Riemannian metric has a local constant, iii). the connection to the manifold is done locally [44]. In high-dimensional scenarios, one useful advantage of the UMAP techniques lies in the

method's superior visualization capabilities coupled with enhanced shorter computational time.

Because unsupervised modeling strives to discover hidden patterns or structural forms of the unlabeled data, the approach comes with obvious challenges, especially with survival prediction. The resulting model from repeated 'learning' may fail to establish an interpretation between the survival prospects and signals in the hidden layers. This is true with several ML techniques that tend to produce complex models that are difficult to understand–the so-called black box models.

Penalized Cox Modeling

A patient's survival information may be better studied by considering the joint effect of clinicopathological and multi-omics risk features. This is particularly important in personalized medicine. However, with the enormous nature of omics data, feature-selection methods become necessary in selecting the most important factors that potentially contribute to survival prediction. For example, while genome-wide association studies (GWAS) may serve as a pathway to test the statistical significance of thousands of genetic variations across many genomes, the problem of sparsity in high-dimensional microarray data poses serious challenges with non-robust prediction models. One approach to overcoming this problem involves conducting multiple t-tests to identify vital disease-linked phenotypes.

Another approach to identifying relevant features linked to the survival outcome is to employ regularization methods in the traditional CoxPH. Regularization is an ML technique employed to improve and prevent overfitting a probabilistic model. For example, to identify the most significant features among hundreds of thousands of omic features, different penalty functions can be used to shrink to zero the regression coefficients of insignificant features. This is done by utilizing the penalized partial likelihood function;

$$L(\boldsymbol{\beta}|\mathcal{D}) = \prod_{i=i}^{n} \left\{ \frac{\exp(\beta' x_i)}{\sum_{j \in R(t_i)} \exp\left(\beta' x_j\right)'} \right\}^{\delta_i}$$

$$\log\left(L(\boldsymbol{\beta}|\mathcal{D})\right) = \log\left(\prod_{i=i}^{n} \left\{ \frac{\exp(\beta' x_i)}{\sum_{j \in R(t_i)} \exp\left(\beta' x_j\right)'} \right\}^{\delta_i} \right), \quad (2)$$

where, as before, $\mathcal{D} = \{(T_i, \delta_i, X_i)\ \forall n = 1,2,\ldots,n\}$ is the observed survival data (*i.i.d*) together with the features (p), $R(t_i) = \{j: t_j \geq t_i\}$ is the risk set at time t_i that consist of the censored and uncensored patients before time t_i. We wish to estimate the regression coefficients, β^'s and shrink the insignificant features to zero. One extension to the CoxPH is the penalized *lasso* Cox technique as proposed by Tibshirani [45]. This method uses the L_1-norm loss function such that,

$$\frac{2}{n} \cdot L(\beta|\mathcal{D}) - \lambda \|\beta\|_1,$$

where λ is the so-called 'tuning' parameter used to regulate the penalty signal. As $\lambda \to \infty$, the coefficients get more regularized. This means a $\lambda = 0$ implies the coefficients are not penalized. Note here that the factor $2/n$ is conveniently chosen for scaling. Two other popular penalized Cox regression methods are ridge regression and elastic net Cox regression. While the lasso-Cox method uses L_1-norm for penalization, the ridge method uses L_2-norm, and both 'norms' are used in the case of elastic net to improve the lasso method. The penalty function for the elastic-net Cox regression [19], therefore, is $\lambda \sum_{l=1}^{p} |\beta_l^2| + (1-\alpha) \sum_{l=1}^{p} \beta_l^2$. Binder and Schumacher [46] in a major extension, considered a more tailored penalization of features where it is possible to exceptionally include mandatory variables into the model without penalizing them. To demonstrate the effectiveness of the proposed extension, the authors used microarray data for patients diagnosed with diffuse large B-cell lymphoma. Under different algorithmic schemes, several penalized loss functions have been proposed for feature selection, including Octagonal Shrinkage and Clustering Algorithm for Regression (OSCAR-Cox) [47], Smoothly Clipped Absolute Deviation (SCAD) [48], Adaptive-lasso Cox [49], etc.

Validating Survival Models

In statistical analysis, model fitting can go wrong on several fronts, including overfitting. For example, regularization techniques strive to prevent the overfitting of models by introducing different penalty functions, thereby improving the statistical inference of the unseen data. To this end, validating a model is crucial to performance assessment and can help reveal the model's underlying violations or specifications. For instance, the proportionality assumption of hazards (PH) in a CoxPH model need not be seriously violated such that we do not see two survival curves cross each other. One way to validate this can be done by examining graphical diagnostics using scaled Schoenfeld residuals [50]. Note that Schoenfeld residuals are not time-dependent. This means that, for a diagnostic plot of the Schoenfeld residuals against time *t*, if the plot shows non-randomness against time, then the PH assumption is most likely violated. Once one or more assumptions are conspicuously violated, other corrective approaches can be adopted to improve predictive power. In the case of CoxPH, for example, we can adopt various functions to transform the features (e.g., log transformation). Another alternative too can be considering the effect of interactions for time-varying covariates (see Li et al. [51]) or via stratification. In the case of high-dimensional data ($p \gg n$), models' diagnostic checks are more challenging than in the low-dimensional sense. Bin et al. [52] addressed some challenges of validating methods associated with prediction models and suggested the need to modify classical methods to fit the high-dimensional omics data. For other models too, it is important to relax stringent assumptions so

that modeling can be adjusted accordingly without unduly introducing bias.

Survival prediction and calibration

A good statistical model is one that leads to a valid inferential deduction with high predictive accuracy. In the context of survival modeling, this would mean a probabilistic model aimed at improving predictive performance. Further, for a given prediction model, one could assess the adjusted effects on survivability when new risk features are introduced. Assessing the predictive power of a model refers to evaluating the magnitude of the prediction error on a test dataset after the model is 'trained.' Various approaches have been proposed to evaluate predictive power, from discriminant metrics to overall model performance. For example, we can simply use robust statistics (e.g., median) to discriminate prognostic estimates, followed by a log-rank test [53,54].

Assessing discriminative power

The performance of a prediction model can be evaluated via discrimination—defined as the model's capacity, for example, to distinguish upregulated expressed genes from the downregulated ones. Common discriminative metrics for survival outcomes include Harrell's concordance index [55], Uno's concordance index [56], and receiver operating characteristic curve (ROC) [57]. As a goodness-of-fit measure, Harrell's concordance index evaluates risk scores by considering all pairs of samples of the data on comparative grounds and identifies *concordant pairs* and *discordant pairs* through probability estimates. The ratio of the number of concordant pairs to that of the sum of the concordant and discordant pairs is the c-index. Here, the measure is independent of time and gives better global estimates of the prediction model. C-index lies between 0 and 1–an index score of 0 indicates poor discrimination, while an index score of 0.5 means the prediction is no better than tossing a fair coin. If the survival data has a high censoring rate, Harrell's concordance index is biased, making Uno's index a better alternative.

Another popular discriminative measure considers the Receiver Operating Characteristic (ROC) with its Area Under the Curve (AUC). It is a diagnostic measure of discrimination that underpins specificity and sensitivity. For example, to predict survivability for a fixed time point (e.g., 10-year survival prediction), a ROC curve can be considered since it averages the value of specificity, taking into consideration all possible values of sensitivity, or vice versa [58]. Like Harrell's index, it ranges between 1 and 0. A value of 1 indicates perfect predictive risk scoring, while 0 indicates imperfect predictive risk scoring. This way, a value of 0.5 means the discrimination does no better than a fairly tossed coin.

Assessing calibrating power

To improve the predictive power of survival models, calibration may be considered. Calibration evaluates the closeness of the predicted probability outcome to the actual outcome. Stated differently, we are interested in measuring the degree of closeness between the predicted and the observed. A properly calibrated model is one in which the observed and the predicted agree in the context of well-established statistical methods (e.g., Pearson χ^2 statistic). For instance, [59] suggested the calibration method for hazard models in cases where the PH assumption is violated.

Overall model performance

Quantifying uncertainty in probabilistic models can be considered diagnostic metrics for assessing the goodness of calibration or for evaluating discriminative power [60]. The theory behind this is based on what is termed in statistical modeling as scoring rules. Proper scoring rules generally guide how to evaluate overall model performance. Common examples include the Brier score [61], pinball loss [62], etc.

As a measure of overall performance, the Brier score integrates both calibration and discrimination measures for binary predictive outcomes. For a given survival data, the Brier score (BS) is computed as follows:

$$\text{Brier score (BS)} = \frac{1}{n}\sum_{j=1}^{n}\left(p_j - o_j\right)^2,$$

where n is the number of individuals/subjects, p_j is the event's probability as predicted by the model, and o_j is the observed outcome for the ith individual. As before, the status variable is coded such that 1 means the event is observed while 0 means a non-observed event. This implies that a score closer to zero means the model's performance is good.

For different time points, the time-dependent Brier score as proposed by Graf et al. [61] is calculated as;

$$BS(t) = \frac{1}{n}\sum_{j=1}^{n}\left\{\frac{\hat{S}(t|t_j)^2 \mathbb{1}\{t_j \leq< t \;\&\; \delta_j = 1\}}{\hat{G}(t_j)} + \frac{\{1-\hat{S}(t|t_j)\}^2 \mathbb{1}\{t_j > t\}}{\hat{G}(t)}\right\}, \quad (3)$$

where the Jth patient has survival time t_j, $\hat{S}(t|t_j)$ is the survival probability predicted by the Cox learner, and $\hat{G}(t)$ is the estimate using the Kaplan-Meier method. The overall model performance, relative to the follow-up times, can be evaluated with a single metric—thus, integrating the multiple Brier scores. It is called the integrated Brier score (ibrier).

Generally, overfitted models tend to exhibit poor generalization to the unseen data. The fitted model may show great performance with the training data but abysmal performance with the new or unseen data. To overcome this undesirable problem, a survival model needs to be validated on more independent data with representativeness mirroring the input data values. A common step in a validation process is to split the dataset into two distinct parts: the training set and the testing set. Though splitting the data could lead to partial loss of information, resampling (e.g., bootstrapping, jackknifing) can be used to improve performance. Resampling methods have been shown to be

robust to unduly observations in the data, besides the fact that they allow one to examine the performance measure and estimate its uncertainty (see Gerds and Kattan [63]).

Real Application: Survival and Bioinformatics Modeling of HCC

In oncology, liver cancer happens to be one of the leading causes of death, only coming third after lung and colorectal cancers [64]. Of all the cases of liver cancer, hepatocellular carcinoma roughly accounts for 80%–90% [65]. With viral hepatitis (i.e., Hep B and Hep C) infections being the central risk indicators of HCC development, there is a need for more novel prognostic and/or diagnostic modeling approaches toward improved personalized medicine. Thus far, the high dimensionality of 'multi-omics' data presents the research society with an opportunity to assess the cumulative effect of clinical and omic features on disease and patient management. This section focuses on survival prediction based on differentially expressed genes. The analysis is done using survival modeling concepts that are covered herein. The data used is based on patients diagnosed with Hepatocellular Carcinoma (HCC) and publicly hosted on the TCGA Research Network: https://www.cancer.gov/tcga.

In recent years, researchers have proposed various biomarkers for building HCC prediction risk scores and validating these biological features. For instance, Parikh et al. [66] review a class of biomarkers described as 'promising' for modeling and detecting hepatocellular carcinoma in its early stages. Here, we explore differential gene expression analysis (DGEA), screening significant genes for further machine-learning analyses. Our findings suggest a potential research path for exploring new insights into the predictive role of certain genes in the overall survival time of HCC patients or for further prospective studies to validate the screened genes.

Methods

Data collection and pre-processing

Using the TCGAbiolinks package in R, we downloaded expression and clinical data from The Cancer Genome Atlas corresponding to hepatocellular carcinoma (TCGA-LIHC) and processed the data for survival and bioinformatics analyses. The downloaded data consisted of 421 HCC cases, including 364 primary solid tumors (TP) and 50 solid tissue normal (NT) samples. Additionally, the TCGA-LIHC dataset involved 60,660 gene expression features. Individuals with incomplete survival information were censored. Pre-processing also included merging certain cancer stages–Stage III, IIIA, IIIB, and IIIC were combined into Stage III. Due to the relatively low counts of Stage IV cases (2), Stage IVA (1), and Stage IVB (2), they were merged into Stage IV. A summary of the clinicopathological factors is shown in Table 3. Note that patients with missing survival data were excluded from subsequent analyses. Due to the high dimensionality of the data ($p \gg n$), the M3C R package was used to conduct unsupervised exploratory analyses, principally t-SNE, PCA, and UMAP. This approach was used to determine if TP and NT samples were significantly

Table 3. Summary of key clinical features and pathological features of the TCGA-LIHC dataset. Note that NA's observations were filtered out

Survival status	Alive (n=255)	Dead (n=164)	Total (N=421)
Age in yrs ($\bar{x}$±SD)	59.10±13.40	61.70±14.00	60.11±13.66
Gender:			
Female	75	66	141
Male	174	98	272
Definition:			
Primary Solid Tumor	234	130	364
Solid Tissue Normal	15	34	49
AJCC-Pathologic-Stage:			
Stage I	134	52	186
Stage II	61	34	95
Stage III	2	4	6
Stage IIIA	32	29	61
Stage IIIB	4	4	8
Stage IIIC	4	6	10
Stage IV	0	2	2
Stage IVA	1	0	1
Stage IVB	0	2	2

discriminated. As described in the next section, the data was further processed after identifying the significantly expressed genes.

Differential gene expression analysis

Using the DESeq2 package, the downloaded expression data (TCGA-LIHC) was processed in several stages. First, the genes with low counts (< 10) were filtered out. The resulting data was then transformed using the variance stabilizing transformation function (i.e., DESeq2::vst()). Using a significance level of $\alpha = 0.05$, we obtained expressed genes via the function DESeq::DESeq(). However, to control the false discovery rate (FDR), the Benjamini-Hochberg procedure was used to obtain the adjusted P-values. Therefore, differentially expressed genes (DEGs) were screened using the criteria: $p < 0.05$ and |log2FoldChange| > 1.50. Differentially expressed genes (3,640) were classified into 'Downregulated', 'Upregulated', and 'Not significant' as shown in Fig. 4a.

Prognostic and diagnostic expressed genes

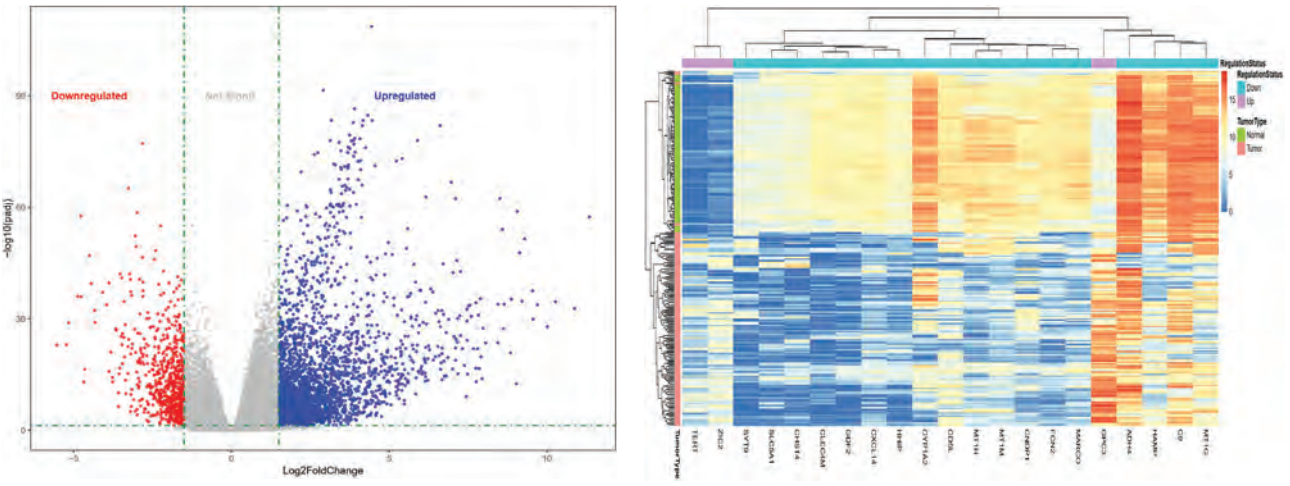
To identify prognostic and diagnostic genes, the DEGs were ranked by their |log2FoldChange| such that the corresponding transcriptome profiling data of the expressed genes were extracted, log-transformed, and filtered using the 5% varied features, i.e., M3C::featurefilter(percentile = 5, method = "var"). This resulted in 182 screened genes for prognostic and diagnostic examination.

To identify potential diagnostic genes, different machine-learning algorithms were used. However, because the original data is severely unbalanced (i.e., 364 tumors vs. 50 normal tissues), we performed Synthetic Minority Oversampling Technique (SMOTE) analysis to 'create' a balance between the two unbalanced classes. Note that SMOTE analysis involves running an algorithm to balance uneven datasets–thus creating a balance between oversampled and undersampled groups in datasets. This is done by 'compensating' the unfavored class (in this case, normal tissues). In R, this is done by running the performance::smote() function. The resulting data was then subjected to five machine learning classification models (Fig. 5a–b) to determine which of the algorithms best discriminates between primary tumor and normal tissue samples. Hyperparameter tuning was performed for the selected ML model through Recursive Feature Elimination Cross-validated (RFE-CV), thus caret:: rfe(). The 'best' model was used to extract the most important features. These features were then used in a penalized Cox regression (lasso) to screen the final diagnostic genes (Fig. 5c–d).

To identify potential prognostic genes, again, the original 182 filtered genes were combined with their corresponding survival data. The data was partitioned into a 60/40 ratio–60% comprising the training dataset ($N = 290$) and 40% representing the testing dataset ($N = 123$). A univariate CoxPH was performed to identify differentially expressed genes (features). Additionally, the features found to be statistically significant were further used in a stepwise multivariable CoxPH modeling—using both backward and forward selection methods and the decision criterion based on the Akaike Information Criterion (AIC). A risk score was estimated from the final estimated model as

$$\text{Risk Score} = \hat{\beta}_0 + \hat{\beta}_1 \times \text{gene}_1 + \hat{\beta}_2 \times \text{gene}_2 + \cdots + \hat{\beta}_n \times \text{gene}_n + \text{some clinical effects}, \quad (4)$$

where $\hat{\beta} = \hat{\beta}_0, \ldots, \hat{\beta}_n$ are the estimated regression coefficients of regressing the survival time over the most significant extracted expression features; $gene_1$, $gene_2$, …, $gene_n$.



(a) (b)

Figure 4. Volcano plot (a) of 3,623 differentially expressed genes screened under the criteria: |log2FC| > 1.50, FDR < 0.05. Down- and upregulated genes are colored red and blue, respectively. (b) Hierarchical clustering (heatmap) of potential diagnostic features, consisting of 21 differentially expressed genes between primary tumors (TP) and normal tissues (NT) in TCGA-LIHC. Screening of the biomarkers was based on recursive feature elimination with cross-validation (RFE-CV).

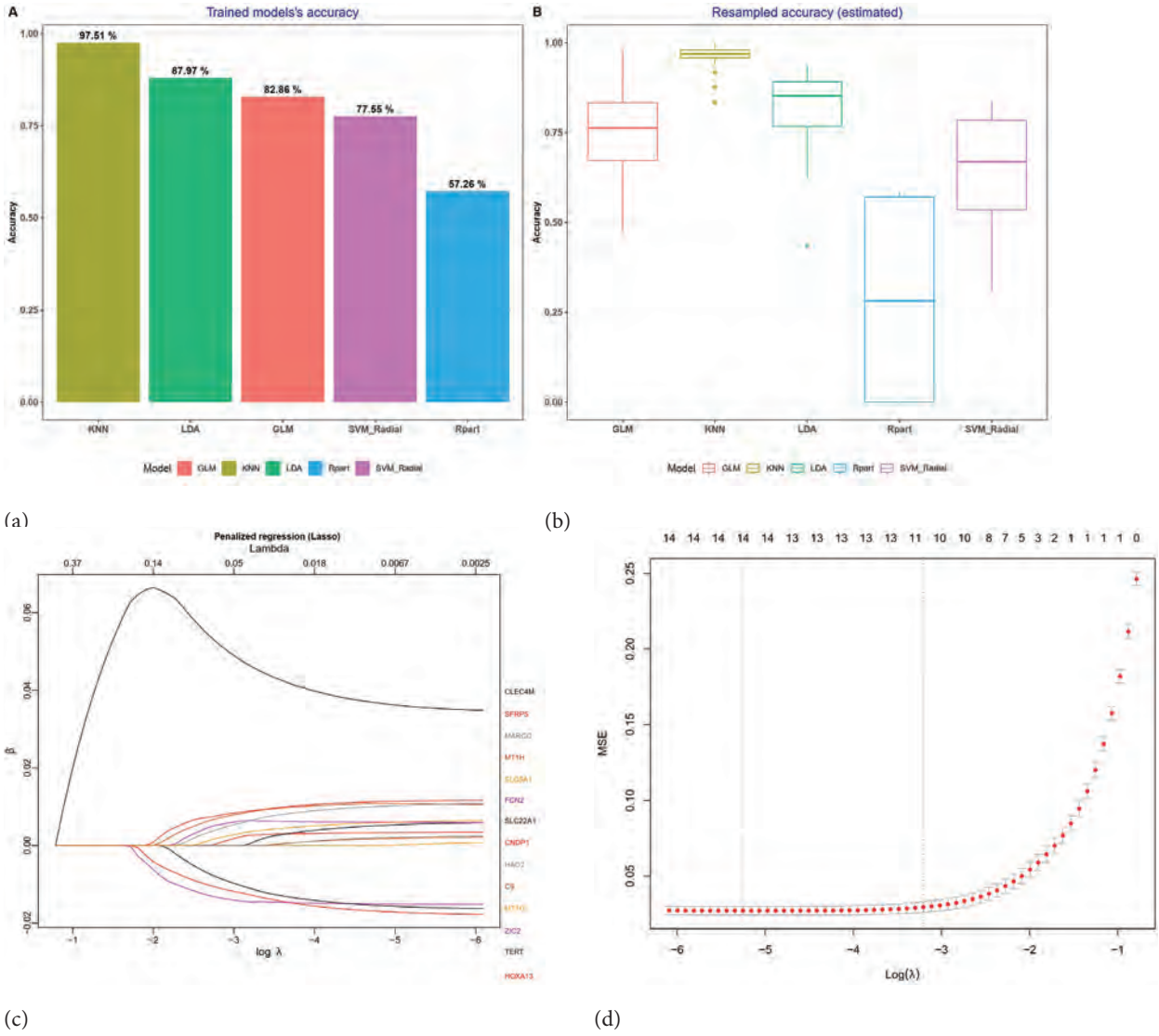


Figure 5. (a) Bar plot of the accuracies of 5 ML classification algorithms (training dataset) used to screen the differentially expressed gene (DEGs) diagnostic biomarkers. Methods with hyperparameters were further tuned for the final screening. (b) Performance assessment of the trained methods through resampling. (c) Penalized lasso regression to screen 21 diagnostic- and LIHC-specific differentially expressed genes. (d) Plot showing the cross-validated mean square errors (MSE).

For each of the train and test datasets, patients were stratified into high- and low-risk groups based on the median risk score. Kaplan-Meier (KM) curves were performed for each screened DEG (Fig. 6a–f). The performance of the potential prognostic genes from the multivariable CoxPH was evaluated using the Receiver Operating Curve analysis (ROC). Performance was assessed using sensitivity and specificity (Fig. 7c–d).

Gene set enrichment analysis (GSEA)

Gene set enrichment analysis (GSEA) was explored for the two risk groups (low- and high-risk). This was done using the clusterprofiler R package to obtain the biological processes (BP) related to the identified expressed genes. The criteria for obtaining significant GSEA results were based on $p < 0.05$, FDR < 0.05, and a normalized enriched score greater than one (i.e., NES > 1).

Statistical analysis

All the statistical analyses considered in this study were done using R Software (4.4.1). Five machine learning classification algorithms were considered for diagnostic screening, followed by a lasso CoxPH regression. Potential prognostic screening was done via univariate and multivariable CoxPH, and performance was assessed via ROC analysis. The Benjamini-Hochberg procedure was adopted to deal with false discovery rates.

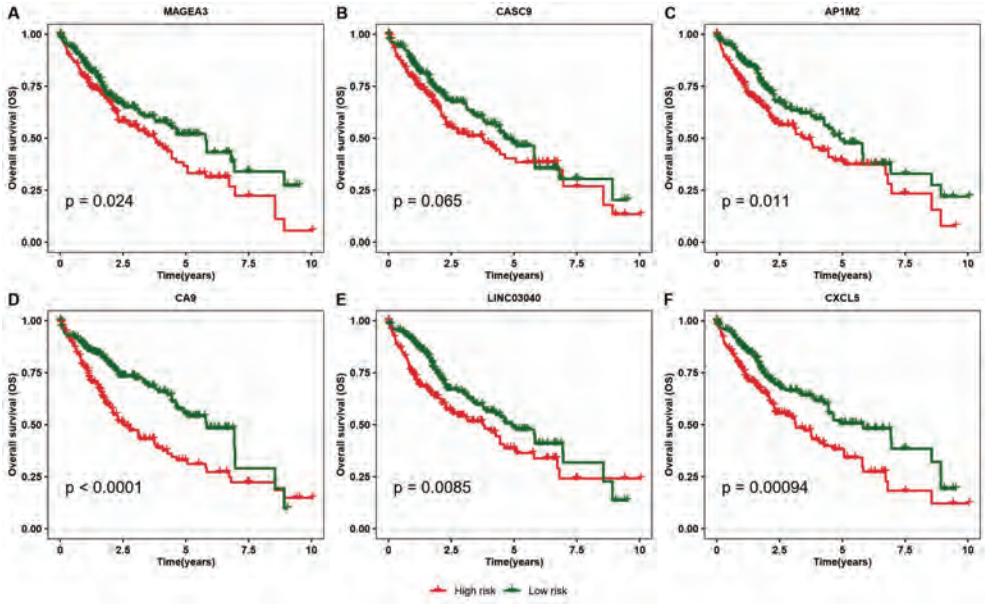


Figure 6. Kaplan-Meier (OS) plots of the six differentially expressed genes screened as prognostic biomarkers in the univariate CoxPH modeling.

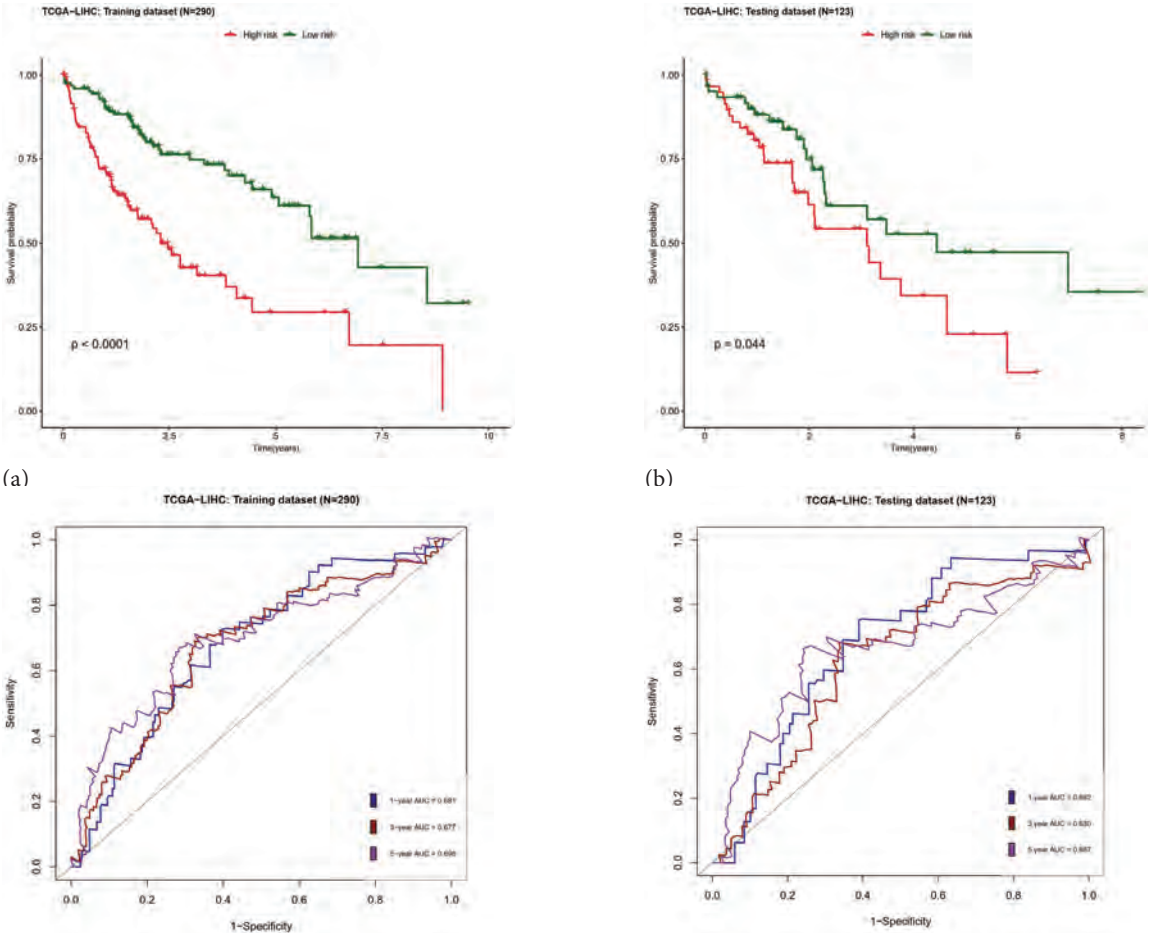


Figure 7. Assessment of the final six screened prognostic biomarkers. Based on the median risk score, KM analysis was performed between low—and high-risk groups (a-b). The six features' ROC evaluation was analyzed using sensitivity and specificity (c–d).

RESULTS AND DISCUSSION

Results

Using the TCGA repository, the data on hepatocellular carcinoma comprised primary tumor samples ((n = 364) and normal tissue samples (n = 50). A SMOTE analysis to get data balanced resulted in 147 normal samples and 196 primary tumor samples. Through differential gene expression analysis, we screened 3,623 significantly expressed genes ($p < 0.05$, $|\log2FoldChange| > 1.50$), including 685 downregulated genes and 2,938 upregulated genes, as shown in Fig. 4a. A hierarchical clustering of the diagnostic screened genes (21) showed clear discrimination between the two tumor classes—thus, normal and primary tumor samples, as shown in Fig. 4b.

Feature selection of the expressed genes was performed in stages. Initially, the top 5%(182 genes) accounting for the total explained variance (TVE) were screened for further diagnostic and prognostic evaluation. For diagnosis, the log-transformed RNA data corresponding to the filtered genes was partitioned (70/30) into training and testing datasets and was used in five machine learning classification models, namely decision trees (RPART), linear discriminant analysis (LDA), radial support vector machine (rad_svm), k-nearest neighbors (KNN), and generalized linear model (GLM). A 5-fold cross-validation method with 3 repeats was also applied in training the classification model. Models with hyperparameters were further tuned in the validation stage. Note that the simple LDA model has no hyperparameters and was, thus, not hyperparameter-tuned. The results showed the KNN as the best-performing method (Fig. 5a–b) for discriminating between normal and tumor samples for the DEGs. Variable importance for this method revealed the top 21 features. Therefore, 21 features were selected for further regularized modeling (here, LASSO). Using the cv.glmnet function, 10-fold cross-validation was finally performed to identify significant diagnostic features (genes/biomarkers) shown in Fig. 5c–d.

To identify the prognostically expressed genes, we filtered the overall survival data and combined it with the mRNA data of the selected 182 genes. As before, the data was partitioned into training and testing sets. Initially, a univariate Cox proportional hazards (CoxPH) analysis was performed at a significance level of ($p < 0.01$). The results revealed five significant genes: CXCL5, MAGEA3, CASC9, AP1M2, and CA9. Fig. 6a–f shows the Kaplan-Meier (KM) analysis of these six genes concerning overall survivability. The cumulative effect of the univariate-selected genes was further evaluated using a stepwise multivariable CoxPH analysis with both backward and forward selection methods. Using the Akaike Information Criterion (AIC) as the decision criterion, the results identified three significant genes: CASC9, CA9, and AP1M2. These three genes were then used to compute the risk score of the patients as

$$\text{Risk Score} = 0.0469 \times \text{AP1M2} + 0.0644 \times \text{CASC9} + 0.0764 \times \text{CA9},$$

Using this risk score, patients were classified into 2 groups–those whose mean risk score was greater than the median risk score were classed into the high-risk group, whereas those with a mean risk score lower than the median risk score were grouped as the low-risk class. The overall survival curve (KM) for both the training dataset and the validation datasets was obtained (Fig. 7a–d). The performance of the trained dataset was validated through a Receiver Operating Curve (ROC) analysis with performance metrics based on sensitivity and specificity as shown in Fig. 7c–d. Notice that the overall survival time is evaluated at 1–, 3–, and 5–year time points.

To gain further biological (cellular and molecular) insights into the enriched terms of the 182 DEGs, we performed gene ontology (GO) and Kyoto Encyclopedia of Genes and Genomes (KEGG) enrichment analyses. The GO analysis results revealed mostly enriched terms in "Hepatocellular Adenoma," "Hepatoblastoma," "Liver Regeneration Disorder," and "Chronic Hepatitis" (Fig. 8), involving some of the identified diagnostic and prognostic genes screened in this study. The KEGG signaling pathways analysis revealed five pathways, with the highest count in the "hsa04976: Bile Secretion (Digestive System)" pathway. Two of the DEGs identified in our diagnostic analysis ("SLC22A1" and "SLC5A1") were found in this pathway. These two genes, therefore, point to a crucial area for further research (Appendix Fig. S1 and Fig. S2).

Discussion

Hepatocellular carcinoma is one of the leading causes of liver-related deaths, with Hepatitis B and C known to be some of the risk factors influencing the high incidence. While extensive advances have been made in several treatments and/or management targets, there is still room for utilizing existing and emerging bioinformatic techniques to identify insightful biomarkers–oncogenetic or tumor-suppressors. Combining bioinformatics and survival modeling methods can, therefore, enhance the screening process of diagnostic and prognostic biomarkers toward targeted therapeutics. In this study, we strove to use the expository techniques earlier discussed with differential gene expression analysis to identify a gene or cluster of genes with potential prognostic/diagnostic signatures. In the present study, we performed a detailed bioinformatics analysis of transcriptome (gene expression) data on hepatocellular carcinoma (TCGA-LIHC) on two fronts: those deemed potentially diagnostic and those that may potentially possess prognostic insights.

While 3623 genes were significantly differentially expressed (FDR < 0.05; $|\log2FoldChange| > 1.50$), our study focused mainly on the top 5% of them (i.e., 182) based on Total Variance Explained (TVE). Under the scope of selected machine-learning classification algorithms,

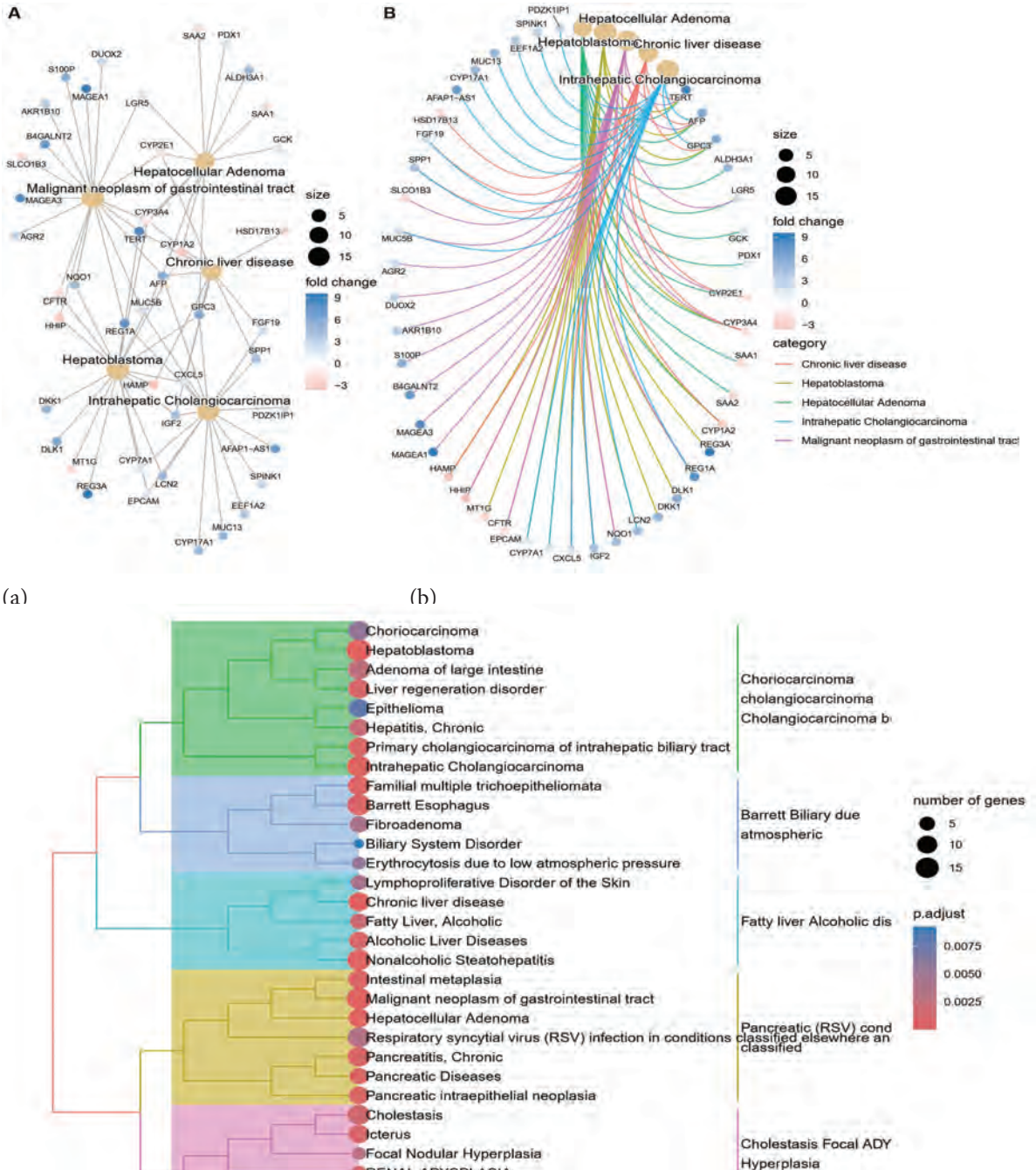


Figure 8. Network plot for gene targets and mRNA features (a). Association of expressed genes with the enriched terms (b). Tree plot for hierarchical clustering for the enriched terms of the DEGs (c).

the K-Nearest Neighbor (KNN) algorithm outperformed the others in distinguishing normal tissues from primary tumors. Twenty-one differentially expressed genes (accounting for about 98% variation) were screened as the most important diagnostic features, and the procedure was further repeated in a lasso-penalized regression. With the DEGs screened as potential diagnostic genes, some have already been reported in the literature in their association with the pathogenesis of hepatocellular carcinoma. More particularly, we found solute carrier family 22 member 1 (SLC22A1) and solute carrier family 5 member 1 (SLC5A1) significant in the KEGG pathway enrichment

analysis (hsa04976: Bile secretion). As a polyspecific transporter to vital organs such as the liver, kidney, and intestine, Gao et al. [67] in their study found SLC5A1 to be highly expressed and inhibit the growth of pancreatic cells. Our findings therefore point to SLC5A1 as a potential diagnostic biomarker for HCC. Additionally, while CLEC4M was highly expressed and screened as a diagnostic biomarker in our study, other studies have identified it for its association with poor prognosis of hepatocellular and colon cancer (see [68,69]). Other highly expressed diagnostic HCC biomarkers identified included SFRP5, CNDP1, TERT, and ZIC2.

From a prognostic perspective, our study focused on the overall survival (OS) prospects of HCC related to the screened DEGs. Six hub DEGs were revealed in a univariate CoxPH model, including CXCL5, MAGEA3, CASC9, AP1M2, CA9, and LINC03040, while a further multivariable modeling of these six genes revealed three significant genes (CASC9, AP1M2, and CA9). For instance, the prognostic potential of the C-X-C motif chemokine 5 (CXCL5) for HCC, as shown in the univariate modeling (Fig. 6F) has also been identified in related experimental studies [70]. In the case of CASC9, while it was marginally significant in the univariate case, its prognostic effect, along with AP1M1 and CA9, revealed strong statistical significance (Fig. 7A–B). In HBV infection, the upregulation of AP1M1 (AP-1 complex subunit mu-1) has been found to promote liver cancer cell proliferation [71]. Since HBV is one of the most common risk factors for HCC incidence, AP1M1 appears to be a promising biomarker for HCC prognostic quantification. Furthermore, Yao et al. [72] observed in their study that the long non-coding RNA of CASC9 can invade, promote, and inhibit the apoptosis of hepatocellular carcinoma cells, thus being closely linked to a poor prognosis. While high expression of carbonic anhydrase 9 (CA9) is closely linked to several cancer types, our findings reveal its independent potential as a novel biomarker for patients with HCC. Other studies have shown that CA9 is associated with poor prognosis in patients with resectable HCC [73, 74]. Combining these three DEGs (AP1M1, CASC9, and CA9) potentially provides meaningful prognostic insights into the overall survival of HCC patients. The impact of these genes was also assessed on clinicopathological variables such as age groups (<60 years vs. >60 years) and cancer stage (stage I, II, III+). The KM overall survival analysis ($p<0.05$) showed that the two age classes were significant, but the cancer stage groups were marginally not significant (Appendix Fig. S3). To the best of our knowledge, no recent study has captured all three DEG biomarkers as a prognostic risk score estimator for HCC patients. Finally, in terms of biologically enriched terms, for example, CXCL5, as shown in Figure 8a–c, is associated with chronic liver disease, "hepatoblastoma," "hepatocellular adenoma," "intrahepatic cholangiocarcinoma," and "malignant neoplasm of the gastrointestinal tract."

In the present study, we adopted an analytical approach combining bioinformatics analysis and survival risk modeling to identify significantly expressed genes for HCC risk prediction, emphasizing their diagnostic and prognostic insights. However, our study has several limitations:

1. The TCGA-LIHC repository primarily contains samples from Caucasian and Latino patients, resulting in an unbalanced dataset in terms of ethnicity and limiting generalizability. Future studies should use a more balanced dataset.
2. Proper validation of the genes identified in our study would require a multicenter prospective cohort study rather than the retrospective study conducted here. A prospective study for the same research goal is likely a future focus of our work.
3. Another limitation of our study is the lack of comprehensive clinicopathological variables (tumor size, Tumor-Node-Metastasis (TNM) grade, and stage). Future work may consider the impact of such clinicopathological variables, including a detailed evaluation of the biological processes (BP) for the identified DEGs.

CONCLUSION

Survival analysis is considered a specialized modeling technique in inferential statistics, primarily due to the existence of well-established methods capable of handling various censoring mechanisms for survival outcome estimation. However, with the growing complexity of multi-omics data, especially in bioinformatics, the need for integrative methods has become an increasingly popular predictive modeling approach. Our study considered two parts: expository techniques in 'omics' survival modeling and bioinformatics analysis of gene expression data (specifically, TCGA-LIHC), with a primary focus on screening diagnostic and prognostic biomarkers for hepatocellular carcinoma patients.

In recent decades, researchers have devoted considerable resources to identifying novel biomarkers with potential prognostic and/or diagnostic insights to improve personalized medicine for hepatocellular carcinoma (HCC) patients. Therefore, the application part of this study focused on identifying such novel biomarkers. Our study identified 3,623 differentially expressed genes (DEGs), including 685 downregulated and 2,938 upregulated genes. Using a series of statistical and bioinformatics analytical methods, three significant prognostically differentially expressed genes—AP1M1, CASC9, and CA9—were identified in a multivariable Cox regression as potentially having prognostic insights into the tumorigenesis of HCC. Additionally, several strongly expressed genes were identified as diagnostic biomarkers for their ability to significantly differentiate HCC primary tumor samples from normal solid tissues. These included CLEC4M, SLC5A1, SLC22A1, SFRP5, CNDP1, TERT, and ZIC2. While these findings may provide a theoretical basis for targeted management and

evaluation of HCC in personalized medicine, it is worth mentioning that a multicenter prospective study would be required to confirm our key findings.

AUTHORSHIP CONTRIBUTIONS

Authors equally contributed to this work.

DATA AVAILABILITY STATEMENT

The data that support the findings of this study are available in The Cancer Genome Atlas database (TCGA-LIHC), with dbGaP Study Accession phs000178. The R code for the complete analyses is available with the corresponding author on a reasonable request.

CONFLICT OF INTEREST

The authors declared no potential conflicts of interest with respect to the research, authorship, and/or publication of this article.

ETHICS

There are no ethical issues with the publication of this manuscript.

STATEMENT ON THE USE OF ARTIFICIAL INTELLIGENCE

Artificial intelligence was not used in the preparation of the article.

REFERENCES

[1] Tong L, Shi W, Isgut M, Zhong Y, Lais P, Gloster L, et al. Integrating multi-omics data with EHR for precision medicine using advanced artificial intelligence. IEEE Rev Biomed Eng 2024;17:80–97. [CrossRef]

[2] Arib MAA. Survival analysis of students not graduated on time using Cox proportional hazard regression method and random survival forest method. J Stat Data Sci 2023:13–21. [CrossRef]

[3] Thackham M. Survival analysis: applications to credit risk default modelling [PhD thesis]. Macquarie University; 2022. [CrossRef]

[4] Karim MdR, Islam MA. Reliability and survival analysis. Singapore: Springer Singapore; 2019. [CrossRef]

[5] Leung KM, Elashoff RM, Afifi AA. Censoring issues in survival analysis. Annu Rev Public Health 1997;18:83–104. [CrossRef]

[6] Klein JP, Moeschberger ML. Survival analysis: techniques for censored and truncated data. New York: Springer; 2003.

[7] Loprinzi CL, Laurie JA, Wieand HS, Krook JE, Novotny PJ, Kugler JW, et al. Prospective evaluation of prognostic variables from patient-completed questionnaires. North Central Cancer Treatment Group. J Clin Oncol 1994;12:601–607. [CrossRef]

[8] Green MS, Symons MJ. A comparison of the logistic risk function and the proportional hazards model in prospective epidemiologic studies. J Chronic Dis 1983;36:715–723. [CrossRef]

[9] Henderson R. Problems and prediction in survival-data analysis. Stat Med 1995;14:161–184. [CrossRef]

[10] DeGroat W, Mendhe D, Bhusari A, Abdelhalim H, Zeeshan S, Ahmed Z. IntelliGenes: a novel machine learning pipeline for biomarker discovery and predictive analysis using multi-genomic profiles. Bioinformatics 2023;39. [CrossRef]

[11] Hasin Y, Seldin M, Lusis A. Multi-omics approaches to disease. Genome Biol 2017;18:1–15. [CrossRef]

[12] Tang M, Xu Y, Pan M. Integrative analysis of scRNA-seq and bulk RNA-seq identifies plasma cell related genes and constructs a prognostic model for hepatocellular carcinoma. J Hepatocell Carcinoma 2025:427–444. [CrossRef]

[13] Liu J, Yu Z, Liu Q, Dou C, Cao P, Xie X. A novel 5-differentially expressed gene (DEG) signature predicting the prognosis in patients with metastatic liver malignancies and the prognostic and therapeutic potential of SPP1. Int J Clin Oncol 2025:1–18. [CrossRef]

[14] Cao L, Liu M, Ma X, Rong P, Zhang J, Wang W. Comprehensive scRNA-seq analysis and identification of CD8+ T cell related gene markers for predicting prognosis and drug resistance of hepatocellular carcinoma. Curr Med Chem 2024;31:2414–2430. [CrossRef]

[15] Miranda J, Horvat N, Fonseca GM, Araujo-Filho J de AB, Fernandes MC, Charbel C, et al. Current status and future perspectives of radiomics in hepatocellular carcinoma. World J Gastroenterol 2023;29:43. [CrossRef]

[16] Vinga S. Structured sparsity regularization for analyzing high-dimensional omics data. Brief Bioinform 2021;22:77–87. [CrossRef]

[17] Bøvelstad HM, Nygård S, Borgan Ø. Survival prediction from clinico-genomic models—a comparative study. BMC Bioinformatics 2009;10:1–9. [CrossRef]

[18] Bommert A, Welchowski T, Schmid M, Rahnenführer J. Benchmark of filter methods for feature selection in high-dimensional gene expression survival data. Brief Bioinform 2022;23. [CrossRef]

[19] Simon N, Friedman J, Hastie T, Tibshirani R. Regularization paths for Cox's proportional hazards model via coordinate descent. J Stat Softw 2011;39:1. [CrossRef]

[20] Madjar K, Zucknick M, Ickstadt K, Rahnenführer J. Combining heterogeneous subgroups with graph-structured variable selection priors for Cox regression. BMC Bioinformatics 2021;22:586. [CrossRef]

[21] Badik ŞT, Akar M. Machine learning classification models for the patients who have heart failure. Sigma J Eng Nat Sci 2024;42:235–244. [CrossRef]

[22] Abubakari S, Karaman F. Neutral benchmarking of survival models in health sciences: comparative study of classical and machine learning techniques. Gazi Univ J Sci Part A Eng Innov 2024;11:518–534. [CrossRef]
[23] Okorie IE, Moyo R, Nadarajah S. The impact of socio-demographic factors on the survival of cancer patients in Zimbabwe. Sci Rep 2021;11:12309. [CrossRef]
[24] Nazli SA, Rosman A, Mohd Kasim NA, Al-Khateeb A, Ul-Saufie AZ, Md Radzi AB, et al. Coronary risk factor profiles according to different age categories in premature coronary artery disease patients who have undergone percutaneous coronary intervention. Sci Rep 2024;14:15326. [CrossRef]
[25] Bączyk G, Kozłowska K. The role of demographic and clinical variables in assessing the quality of life of outpatients with rheumatoid arthritis. Arch Med Sci 2018;14:1070–1079. [CrossRef]
[26] Abubakari S, Dizman YA, Karaman F. Integrated meta-analysis identifies keratin family genes and associated genes as key biomarkers and therapeutic targets in metastatic cutaneous melanoma. Diagnostics (Basel) 2025;15. [CrossRef]
[27] Menyhárt O, Győrffy B. Multi-omics approaches in cancer research with applications in tumor subtyping, prognosis, and diagnosis. Comput Struct Biotechnol J 2021;19:949–960. [CrossRef]
[28] Bartel DP. Metazoan microRNAs. Cell 2018;173:20–51. [CrossRef]
[29] Monsivais D, Parks SE, Chandrashekar DS, Varambally S, Creighton CJ. Using cancer proteomics data to identify gene candidates for therapeutic targeting. Oncotarget 2023;14:399–412. [CrossRef]
[30] Emwas A-HM, Salek RM, Griffin JL, Merzaban J. NMR-based metabolomics in human disease diagnosis: applications, limitations, and recommendations. Metabolomics 2013;9:1048–1072. [CrossRef]
[31] Kong W, Hui HWH, Peng H, Goh WWB. Dealing with missing values in proteomics data. Proteomics 2022;22:2200092. [CrossRef]
[32] Huang L, Song M, Shen H, Hong H, Gong P, Deng H-W, et al. Deep learning methods for omics data imputation. Biology (Basel) 2023;12:1313. [CrossRef]
[33] De Brevern AG, Hazout S, Malpertuy A. Influence of microarrays experiments missing values on the stability of gene groups by hierarchical clustering. BMC Bioinformatics 2004;5:1–12.
[34] Taylor S, Ponzini M, Wilson M, Kim K. Comparison of imputation and imputation-free methods for statistical analysis of mass spectrometry data with missing data. Brief Bioinform 2022;23. [CrossRef]
[35] Kaplan EL, Meier P. Nonparametric estimation from incomplete observations. J Am Stat Assoc 1958;53:457–481. [CrossRef]
[36] Cox DR. Regression models and life-tables. J R Stat Soc Series B Stat Methodol 1972;34:187–202. [CrossRef]
[37] Heinze G, Wallisch C, Dunkler D. Variable selection—a review and recommendations for the practicing statistician. Biom J 2018;60:431–449. [CrossRef]
[38] Lee S, Lim H. Review of statistical methods for survival analysis using genomic data. Genomics Inform 2019;17. [CrossRef]
[39] Zhao Z, Zucknick M. Structured penalized regression for drug sensitivity prediction. J R Stat Soc Ser C Appl Stat 2020;69:525–545. [CrossRef]
[40] Zhao Z, Banterle M, Lewin A, Zucknick M. Multivariate Bayesian structured variable selection for pharmacogenomic studies. J R Stat Soc Ser C Appl Stat 2024;73:420–443. [CrossRef]
[41] Xing X, Zhao Z, Liu JS. Controlling false discovery rate using Gaussian mirrors. J Am Stat Assoc 2023;118:222–241. [CrossRef]
[42] Korthauer K, Kimes PK, Duvallet C, Reyes A, Subramanian A, Teng M, et al. A practical guide to methods controlling false discoveries in computational biology. Genome Biol 2019;20:1–21. [CrossRef]
[43] Chung NC, Mirza B, Choi H, Wang J, Wang D, Ping P, et al. Unsupervised classification of multi-omics data during cardiac remodeling using deep learning. Methods 2019;166:66–73. [CrossRef]
[44] McInnes L, Healy J, Melville J. UMAP: uniform manifold approximation and projection for dimension reduction. arXiv [Preprint]. 2018. [CrossRef]
[45] Tibshirani R. The lasso method for variable selection in the Cox model. Stat Med 1997;16:385–395.
[46] Binder H, Schumacher M. Allowing for mandatory covariates in boosting estimation of sparse high-dimensional survival models. BMC Bioinformatics 2008;9:1–10. [CrossRef]
[47] Yang S, Yuan L, Lai Y-C, Shen X, Wonka P, Ye J. Feature grouping and selection over an undirected graph. In: Proceedings of the 18th ACM SIGKDD International Conference on Knowledge Discovery and Data Mining; 2012. p. 922–930. [CrossRef]
[48] Fan J, Li R. Variable selection for Cox's proportional hazards model and frailty model. Ann Stat 2002;30:74–99. [CrossRef]
[49] Zhang HH, Lu W. Adaptive lasso for Cox's proportional hazards model. Biometrika 2007;94:691–703. [CrossRef]
[50] Grambsch PM, Therneau TM. Proportional hazards tests and diagnostics based on weighted residuals. Biometrika 1994;81:515–526. [CrossRef]
[51] Li Y, Wang F, Li R, Sun Y. Semiparametric integrative interaction analysis for non-small-cell lung cancer. Stat Methods Med Res 2020;29:2865–2880. [CrossRef]
[52] Bin RD, Herold T, Boulesteix A-L. Added predictive value of omics data: specific issues related to validation illustrated by two case studies. BMC Med Res Methodol 2014;14:1–23. [CrossRef]

[53] Royston P, Altman DG. External validation of a Cox prognostic model: principles and methods. BMC Med Res Methodol 2013;13:1–15. [CrossRef]
[54] Rahman MS, Ambler G, Choodari-Oskooei B, Omar RZ. Review and evaluation of performance measures for survival prediction models in external validation settings. BMC Med Res Methodol 2017;17:1–15. [CrossRef]
[55] Harrell FE, Califf RM, Pryor DB, Lee KL, Rosati RA. Evaluating the yield of medical tests. JAMA 1982;247:2543–2546. [CrossRef]
[56] Uno H, Cai T, Pencina MJ, D'Agostino RB, Wei L-J. On the c-statistics for evaluating overall adequacy of risk prediction procedures with censored survival data. Stat Med 2011;30:1105–1117. [CrossRef]
[57] Heagerty PJ, Lumley T, Pepe MS. Time-dependent ROC curves for censored survival data and a diagnostic marker. Biometrics 2000;56:337–344. [CrossRef]
[58] Mandrekar JN. Receiver operating characteristic curve in diagnostic test assessment. J Thorac Oncol 2010;5:1315–1316. [CrossRef]
[59] Van Houwelingen HC. Validation, calibration, revision and combination of prognostic survival models. Stat Med 2000;19:3401–3415.
[60] Gneiting T, Raftery AE. Strictly proper scoring rules, prediction, and estimation. J Am Stat Assoc 2007;102:359–378. [CrossRef]
[61] Graf E, Schmoor C, Sauerbrei W, Schumacher M. Assessment and comparison of prognostic classification schemes for survival data. Stat Med 1999;18:2529–2545.
[62] Portnoy S. Censored regression quantiles. J Am Stat Assoc 2003;98:1001–1012. [CrossRef]
[63] Gerds TA, Kattan MW. Medical risk prediction models: with ties to machine learning. Chapman & Hall/CRC; 2021. [CrossRef]
[64] Bray F, Laversanne M, Sung H, Ferlay J, Siegel RL, Soerjomataram I, et al. Global cancer statistics 2022: GLOBOCAN estimates of incidence and mortality worldwide for 36 cancers in 185 countries. CA Cancer J Clin 2024;74:229–263. [CrossRef]
[65] Llovet JM, Kelley RK, Villanueva A, Singal AG, Pikarsky E, Roayaie S, et al. Hepatocellular carcinoma. Nat Rev Dis Primers 2021;7:1–28. [CrossRef]
[66] Parikh ND, Mehta AS, Singal AG, Block T, Marrero JA, Lok AS. Biomarkers for the early detection of hepatocellular carcinoma. Cancer Epidemiol Biomarkers Prev 2020;29:2495–2503. [CrossRef]
[67] Gao H-F, Chen L-Y, Cheng C-S, Chen H, Meng Z-Q, Chen Z. SLC5A1 promotes growth and proliferation of pancreatic carcinoma via glucose-dependent AMPK/mTOR signaling. Cancer Manag Res 2019:3171–3185. [CrossRef]
[68] Yu Q, Gao K. CLEC4M overexpression inhibits progression and is associated with a favorable prognosis in hepatocellular carcinoma. Mol Med Rep 2020;22:2245–2252. [CrossRef]
[69] Luo L, Chen L, Ke K, Zhao B, Wang L, Zhang C, et al. High expression levels of CLEC4M indicate poor prognosis in patients with hepatocellular carcinoma. Oncol Lett 2020;19:1711–1720. [CrossRef]
[70] Nie Y, Jiang M, Liu C, Liu Q, Zhu X. CXCL5 has potential to be a marker for hepatocellular carcinoma prognosis and was correlating with immune infiltrates. Front Oncol 2021;11:637023. [CrossRef]
[71] Kou Y, Yan X, Liu Q, Wei X, Zhang B, Li X, et al. HBV upregulates AP-1 complex subunit mu-1 expression via the JNK pathway to promote proliferation of liver cancer cells. Oncol Lett 2019;18:456–464. [CrossRef]
[72] Yao J, Fu J, Liu Y, Qu W, Wang G, Yan Z. LncRNA CASC9 promotes proliferation, migration and inhibits apoptosis of hepatocellular carcinoma cells by down-regulating miR-424-5p. Ann Hepatol 2021;23:100297. [CrossRef]
[73] Kang HJ, Kim IH, Sung CO, Yu E. Expression of CA9 as a novel prognostic marker in resectable hepatocellular carcinoma. Pathology 2014;46. [CrossRef]
[74] Hyuga S, Wada H, Eguchi H, Otsuru T, Iwgami Y, Yamada D, et al. Expression of carbonic anhydrase IX is associated with poor prognosis through regulation of the epithelial-mesenchymal transition in hepatocellular carcinoma. Int J Oncol 2017;51:1179–1190. [CrossRef]

APPENDIX

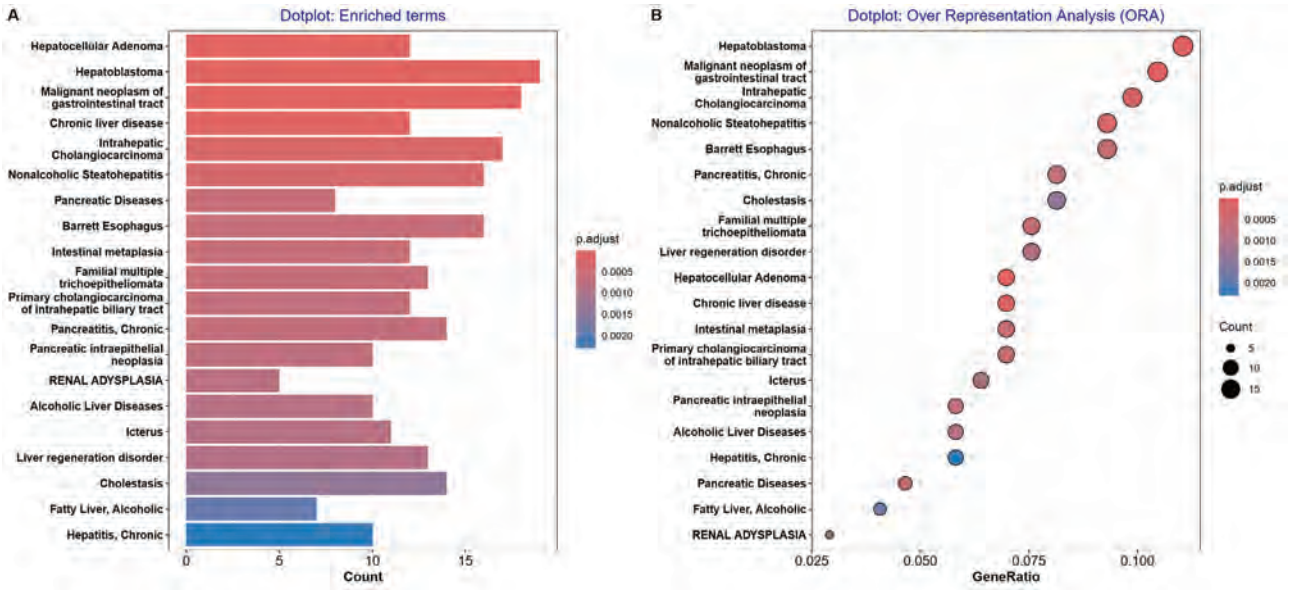


Figure S1. Gene Ontology (GO) revealing enriched terms.

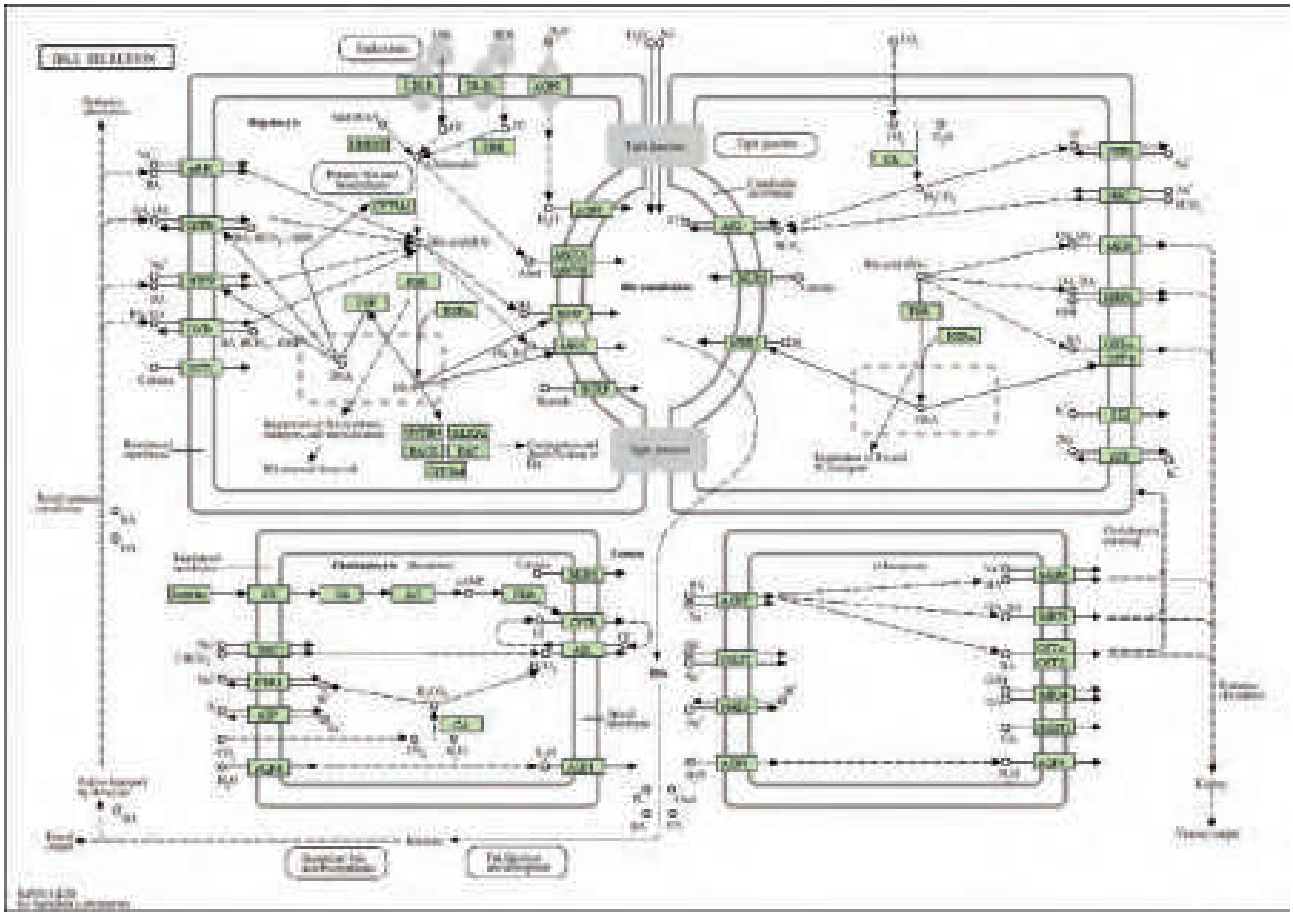


Figure S2. KEGG signaling pathway analysis for hsa04976: Bile Secretion.

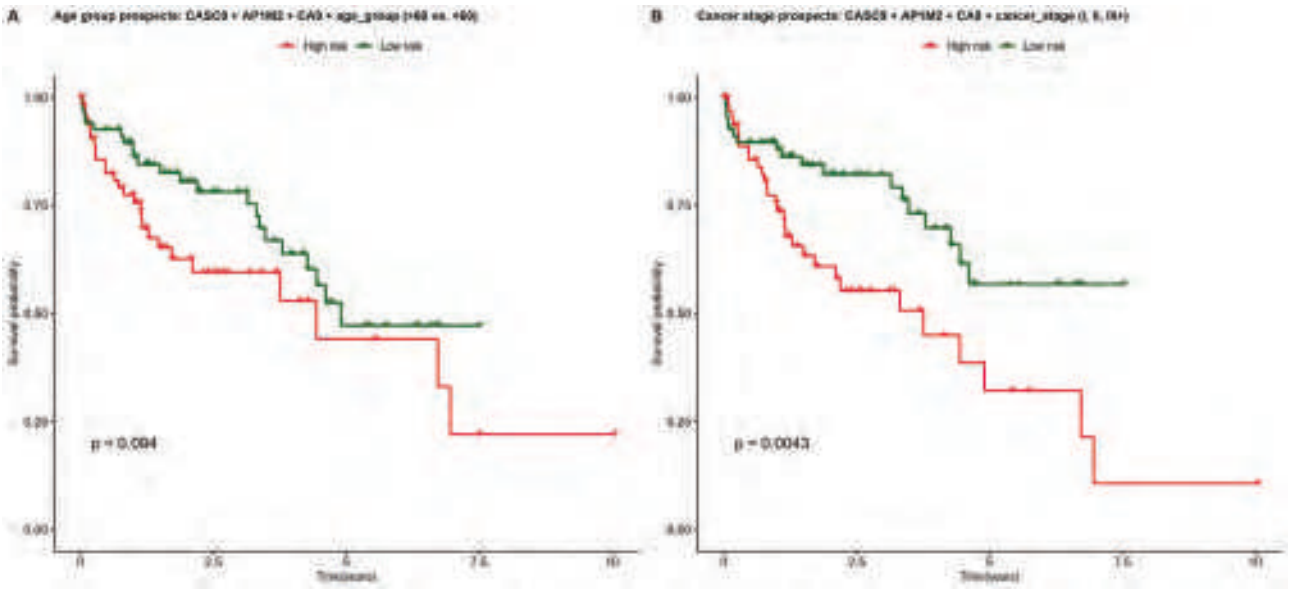


Figure S3. Survival prospects of patients based on stratification by age group and cancer stage, relative to the genes APIMI, CASC9, and CA9.

Sigma J Eng Nat Sci, Vol. 44, No. 4, pp. 2735–2744, August, 2026

Sigma Journal of Engineering and Natural Sciences
Web page info: https://sigma.yildiz.edu.tr
DOI: 10.14744/sigma.2026.2124

Research Article

Evaluation of Natech risk after landslide disaster in the scope of mines located in districts: An application for Zonguldak province

Emel GÜVEN[1], Mehmet PINARBAŞI[2], Hacı Mehmet ALAKAŞ[2], Tamer EREN[2,*]

[1]Department of Industrial Engineering, Ostim Technical University, Ankara, 06374, Türkiye
[2]Department of Industrial Engineering, Kırıkkale University, Kırıkkale, 71450, Türkiye

ARTICLE INFO

Article history
Received: 30 December 2024
Revised: 04 May 2025
Accepted: 31May 2025

Keywords:
Disaster Management; Mine; Natech; Pythagorean Fuzzy AHP, Pythagorean Fuzzy TOPSIS

ABSTRACT

Natech accidents are called technological accidents triggered by natural disasters. Disasters are natural events that can cause material loss and moral damages at any time. Natech accidents have the effect of increasing the losses and damages caused by disasters. The characteristics of Natech accidents vary depending on the type of disaster. In this study, landslide disasters will be considered. Landslides are one of the disasters that cause severe damage to Natech. On 13 February 2024, a Natech accident occurred in the Çöpler Gold Mine in Erzincan province after a landslide and caused a loss of life and property. Based on this accident, the districts of Zonguldak province will be evaluated in terms of the risk of the Natech accident after the landslide disaster. Zonguldak province, located in the Black Sea Region, is one of the provinces with a high risk of landslides, considering past accidents. The presence of active mines throughout the province increases the likelihood of Natech accidents. In the study, the criteria that may cause Natech accidents after landslides will be determined and weighted. Then, the districts of Zonguldak province will be ranked according to the risk of Natech accidents, considering the mines they contain. Pythagorean Fuzzy Analytical Hierarchy Process and Pythagorean Fuzzy Technique for Order of Preference by Similarity to Ideal Solution methods will be used in problem-solving. Uncertainties in the disaster environment also affect decision-making processes. For this reason, fuzzy sets are preferred when solving problems. As a result of the study, districts with high risk of Natech accidents in mines after landslide disasters were obtained. According to the results, the most important Natech risk criterion was 'Past Landslide Percentage' with a weight of 0.25234. Among the districts evaluated within the scope of the criteria, the riskiest district was Devrek. The study aims to draw attention to Natech accidents that may occur in mines. It is thought that determining the possible risky regions will be supportive for the studies to be carried out in this field.

Cite this article as: Güven E, Pınarbaşı M, Alakaş HM, Eren T. Evaluation of Natech risk after landslide disaster in the scope of mines located in districts: An application for Zonguldak province. Sigma J Eng Nat Sci 2026;44(4):2735–2744.

***Corresponding author.**
*E-mail address: tamereren@gmail.com

This paper was recommended for publication in revised form by Editor-in-Chief Ahmet Selim Dalkilic

Published by Yıldız Technical University Press, İstanbul, Turkey
© Author. This is an open access article under the CC BY-NC license (http://creativecommons.org/licenses/by-nc/4.0/).

INTRODUCTION

Disasters are natural occurrences that result in substantial material losses and psychological impacts. [1]. Türkiye's geographical position makes it highly susceptible to a range of natural disasters [2]. This situation makes the studies that are carried out on disasters more critical. Risk mitigation activities carried out to prevent disasters and the adversities caused by disasters play a crucial role in this process. The disaster management process includes organizing and managing the activities required to reduce the negative effects of disasters [3].

While disasters cause damages in themselves, they also cause different negativities. One of these is Natech accidents, which refer to technological accidents triggered by natural disasters [4]. Natech accidents increase the negative effects of natural disasters and may also cause new events. This situation triggers chaos in the unexpected process and increases the damage to be encountered. When the Natech accidents experienced in the past are analyzed, the seriousness of the situation becomes clearer.

In the past, many different Natech accidents have occurred both in Türkiye and internationally. Gas and chemical substance releases following Hurricanes Rita and Katrina in 2005–2006 in the United States are among notable examples of Natech accidents [5]. However, a large gas explosion occurred in Oxfordshire, also in the United Kingdom, on 2 October 2023 as a result of a lightning strike at a food waste recycling facility during a severe storm. A forest fire in Chile on 3 February 2024 spread to industrial facilities, and numerous explosions occurred in chemical warehouses, paint factories, and other warehouses. Flooding in Daraa province of Libya on 10 September 2023 caused much more significant damage with the collapse of two dams.

Natech accidents have also occurred in Türkiye. For instance, during the Kocaeli earthquake on August 17, 1999, a significant fire erupted at the TÜPRAŞ refinery, which necessitated prolonged firefighting efforts. Furthermore, a chemical release took place at the AKSA Acrylic plant [6]. Again, two Natech accidents were recorded after the Kahramanmaraş earthquake on 6 February 2023. The first one was the fire that occurred in İskenderun marina. The second was the natural gas explosion and fire that happened at two separate points 200 meters underground and 3 kilometers apart in Topboğazı Village of Kırıkhan district of Hatay. Another Natech accident occurred recently. This occurred after a landslide disaster at a mine in İliç district of Erzincan province on 13 February 2024. Following the landslide disaster, approximately 10 million cubic meters of soil flowed rapidly down a 200-meter slope and caused a cave-in at the nearby Çöpler Mine Site.

Past accidents also show that each type of disaster can cause different Natech accidents [7]. Within the scope of this study, landslide disasters will be taken into consideration. After the Natech accident in Erzurum province, it has been observed that the mines are a significant risk in terms of Natech accidents that will occur after the landslide disaster. For this reason, landslide disasters and mines are considered as the problem set of the study. Zonguldak province has been selected as the application province due to the fact that it has a large number of mines and the risk of landslides is relatively high. To support problem-solving, risk criteria that could lead to Natech accidents as a result of landslide disasters were identified and prioritized using the Pythagorean Fuzzy AHP method. Then, the districts of Zonguldak province were evaluated using the Pythagorean Fuzzy TOPSIS method within the scope of these criteria and ranked according to the risk of Natech accidents in mines after a landslide disaster. Although there are studies in the literature that distinguish Natech accidents according to disasters and equipment, no studies were found that made a distinction based on sector. It is thought that the study will contribute to the literature in terms of evaluating Natech accidents in the mining industry.

The second section continues the study with a literature review. The third section details the methods used. The fourth section presents implementation data and results. The last section evaluates the results.

Literature Review

Many studies in the literature address Natech accidents. In their study, Steinberg et al. [8] assessed Natech risks in the United States, examining current management approaches. The research outlines the characteristics of Natech accidents, presents case examples, and explores future mitigation strategies. Girgin [6], discusses the Natech accidents triggered by the August 17 earthquake. Following the earthquake, a major fire erupted at the TÜPRAŞ refinery in Kocaeli, which required prolonged efforts to bring under control. Additionally, a chemical leak occurred at the AKSA acrylic fiber production facility. The study analyzes these Natech incidents and emphasizes the significance of addressing Natech risks. Fabbrocino et al. [9], conducted a representative case study of an oil storage facility with an atmospheric steel tank containing flammable materials. In the study, they addressed the issue of integrating structural seismic risk into a quantitative probabilistic seismic risk analysis (QpsRA).

Girgin and Krausmann [10] introduced RAPID-N, a scalable web tool that performs swift local and regional Natech risk assessment and mapping using minimal data inputs. Suarez-Paba and Cruz [11], proposed Natech RateME, a comprehensive, area-wide risk management and rating system framework to inform governments and the public about the industry's Natech risk management practices. Son and Jung [12], quantitatively analysed the risks caused by flooding in industrial plants that handle large quantities of hazardous materials.

Rossi et al. [13], introduced the first vulnerability model applicable to QRA studies for process pipelines and industrial facilities affected by flooding. Guven et al. [4], addressed the Natech accident risk for Gaziantep province,

which has the most significant organized industrial zone in Turkey. Firstly, the risks that may cause Natech accidents after the earthquake disaster were determined, and then the sectors serving in the organized industrial zone were evaluated according to the risk of Natech accidents. Thus, organized industrial zones divided into five sections were ranked according to Natech risk.

Yu et al. [14], examined how people perceived risks and responded behaviorally after the Natech accident at the Sendai oil refinery following the 2011 earthquake and tsunami in Japan. Find-Natech, proposed by Luo et al. [15], is a web-based GIS tool for managing historical data on Natech events. Guo et al.[16], analyzed successive disasters in a chemical industrial park around Wenchuan after the Wenchuan earthquake. Guven et al. [17], identified the Natech risky sectors in Kırıkkale organized industrial zone after the earthquake disaster by determining the criteria to create a Natech accident.

In the literature, there are studies detailing Natech accidents, performing risk analyses, creating a database, and including evaluations performed on different equipment. In general terms, there are distinctions in terms of disaster and equipment rather than a sectoral distribution. Especially in terms of sector, this study deals with the mining sector, which has not been evaluated before. Within the scope of the literature review, there is no study evaluating Natech accidents that may occur in mines after a disaster. The study will likely contribute to the literature in this respect. In this context, it is aimed to draw attention to the mining sector and Natech accidents that may occur in this sector and to include them in risk mitigation plans.

MATERIALS AND METHODS

Pythagorean Fuzzy AHP

The AHP method is based on the pairwise comparison in problem-solving [18]. However, it is insufficient in problems involving subjective and linguistic expressions or in cases where decision-makers cannot make a clear decision. To overcome this deficiency, AHP method was combined with fuzzy logic and Fuzzy AHP method was introduced. [19]. There are various types of sets used in fuzzy logic, and one of them is the Pythagorean Fuzzy Set, proposed by Yager [20]. These sets provide greater flexibility in handling uncertainty compared to traditional fuzzy sets. Evaluating linguistic expressions on a broader scale enables decision-makers to conduct more comprehensive assessments, thereby yielding more realistic and reliable outcomes [21]. In the application of the method, the linguistic variables used to construct the decision matrix and their corresponding Pythagorean fuzzy numbers are presented in Table 1 [22].

The steps of the Pythagorean fuzzy AHP method are given below [17].

Step 1: Experts construct $A = (r_{ik})mxm$ matrix using linguistic evaluation criteria

Step 2: Using Equation 1 and Equation 2, construct the difference matrix $D = (D_{ik})mxm$ for the low, high, and non-membership membership degrees. Here μ_{ikL}, ith column, k row element with low membership degree, μ_{ikU}, element with high membership degree in column i, row k, V_{ikL}, represents the low non-membership item in column i, row k, V_{ikU}, column ith represents the element with the highest member degree.

$$d_{ik_L} = {\mu_{ik_L}}^2 - {V_{ik_u}}^2 \quad (1)$$

$$d_{ik_u} = {\mu_{ik_u}}^2 - {V_{ik_L}}^2 \quad (2)$$

Step 3: At this stage, the multiplicative matrix is reached with the help of Equation 3 and Equation 4.

$$s_{ik_L} = \sqrt{1000^{d_{ik_L}}} \quad (3)$$

Table 1. Linguistic variables and Pythagorean fuzzy scales [22]

Linguistic Variables	Pythagorean Fuzzy Numbers			
	μ_L	μ_U	V_L	V_U
Certainly low important (CL)	0	0	0.9	1
Very low important (VL)	0.1	0.2	0.8	0.9
Low important (L)	0.2	0.35	0.65	0.8
Below average important (BA)	0.35	0.45	0.55	0.65
Exactly equal (EE)	0.1965	0.1965	0.1965	0.1965
Average important (A)	0.45	0.55	0.45	0.55
Above average important (AA)	0.55	0.65	0.35	0.45
High important (H)	0.65	0.8	0.2	0.35
Very high important (VH)	0.8	0.9	0.1	0.2
Certainly high important (CH)	0.9	1	0	0

$$s_{ik_U} = \sqrt{1000^{d_{ik_u}}} \quad (4)$$

Step 4: Creation of hesitation levels using Equation 5, H= $(\mu_{ik})mxm$.

$$h_{ik} = 1 - \left(\mu_{ik_U}{}^2 - \mu_{ik_L}{}^2\right) - \left(V_{ik_U}{}^2 - V_{ik_L}{}^2\right) \quad (5)$$

Step 5: The unnormalized weights $T = (t_{ik})mxm$ are calculated with Equation 6.

$$t_{ik} = \left(\frac{s_{ik_L} + s_{ik_U}}{2}\right) h_{ik} \quad (6)$$

Step 6: In the last step, the criterion weights w_i are created using Equation 7.

$$w_i = \frac{\sum_{j=1}^{m} w_i}{\sum_{i=1}^{m}\sum_{j=1}^{m} w_i} \quad (7)$$

Pythagorean Fuzzy TOPSIS

TOPSIS, a multi-criteria decision-making method, was developed by Hwang and Yoon in 1981 [23]. In the method, problems are analyzed by ranking the alternatives according to the positive and negative ideal solutions. [24]. Pythagorean fuzzy TOPSIS is a technique based on the concept of selecting the solution with the closest distance to the positive ideal solution and the farthest distance to the negative ideal solution within Pythagorean fuzzy sets [25]. While applying the method, linguistic variables and Pythagorean fuzzy numbers corresponding to these variables are used in the created decision matrix. Linguistic variables and fuzzy numbers are listed in Table 2 [4].

The stages of the Pythagorean Fuzzy TOPSIS method are given below [26].

Step 1: Establishment of criteria and alternatives by decision-makers

Step 2: Obtaining the standard decision matrix with Equation 8.

Table 2. Linguistic variables used in the Pythagorean fuzzy TOPSIS method

Linguistic Variables	Pythagorean Fuzzy Numbers	
	u	***v***
Overly Low (OL)	0.10	0.99
Very Little (VL)	0.10	0.97
Little (L)	0.25	0.92
Middle Little (ML)	0.40	0.87
Middle (M)	0.50	0.80
Middle High (MH)	0.60	0.71
High (H)	0.70	0.60
Very High (VH)	0.80	0.44
Extremely High (EH)	0.10	0.00

$$\mathrm{R}=(C_j(x_i))_{mxn} = \begin{pmatrix} P_{u_{11},v_{11}} & P_{u_{12},v_{12}} & \cdots & P_{u_{1n},v_{1n}} \\ P_{u_{21},v_{21}} & P_{u_{22},v_{22}} & \cdots & P_{u_{2n},v_{2n}} \\ \vdots & \vdots & & \vdots \\ P_{u_{m1},v_{m1}} & P_{u_{m2},v_{m2}} & \cdots & P_{u_{mn},v_{mn}} \end{pmatrix} \quad (8)$$

Step 3: Calculation of Pythagorean fuzzy positive ideal solution and negative ideal solution using Equations 9 and 10.

$$\begin{aligned} x^+ &= \left\{C_j, maks_i \left\langle s\left(C_j(x_i)\right)\right\rangle \mathrm{I}\, j = 1,2,\ldots,n\right\} \\ &= \{\langle C_1,\ P(u_1^+, v_1^+)\rangle, \langle C_2,\ P(u_2^+, v_2^+)\rangle, \\ &\quad \ldots, \langle C_n,\ P(u_n^+, v_n^+)\rangle\} \end{aligned} \quad (9)$$

$$\begin{aligned} x^- &= \left\{C_j, min_i \left\langle s\left(C_j(x_i)\right)\right\rangle \mathrm{I}\, j = 1,2,\ldots,n\right\} \\ &= \{\langle C_1,\ P(u_1^-, v_1^-)\rangle, \langle C_2,\ P(u_2^-, v_2^-)\rangle, \\ &\quad \ldots, \langle C_n,\ P(u_n^-, v_n^-)\rangle\} \end{aligned} \quad (10)$$

Step 4: Step 4: With Equations 11 and 12, the distances of the alternatives from the Pythagorean fuzzy positive ideal and negative ideal solutions are obtained.

$$\begin{aligned} D_{(x_i,x^+)} = \sum_{j=1}^{n} w_j\, d\left((C_j(x_i), C_j(x^+)\right) = \frac{1}{2}\sum_{j=1}^{n} w_j \Big(\Big|\left(u_{ij}\right)^2 \\ -\left(u_j^+\right)^2\Big| + \Big|\left(v_{ij}\right)^2 - \left(v_j^+\right)^2\Big| + \Big|\left(\pi_{ij}\right)^2 - \left(\pi_j^+\right)^2\Big|\Big) \end{aligned} \quad (11)$$

$$\begin{aligned} D_{(x_i,x^-)} = \sum_{j=1}^{n} w_j\, d\left((C_j(x_i), C_j(x^-)\right) = \frac{1}{2}\sum_{j=1}^{n} w_j \Big(\Big|\left(u_{ij}\right)^2 \\ -(u)^2\Big| + \Big|\left(v_{ij}\right)^2 - \left(v_j^-\right)^2\Big| + \Big|\left(\pi_{ij}\right)^2 - \left(\pi_j^-\right)^2\Big|\Big) \end{aligned} \quad (12)$$

Step 5: Calculate the relative closeness indices of each alternative using Equation 13.

$$\xi\left(x_i\right) = \frac{D_{(x_i,x^-)}}{D_{(max)}(x_i, x^-)} - \frac{D_{(x_i,x^+)}}{D_{(min)}(x_i, x^+)} \quad (12)$$

Step 6: Determination of the best order of alternatives and method application is completed.

Application

Problem definition

Natech accidents have an increasing effect on the losses and damages caused by disasters. Natech accidents caused by each disaster are different. Within the scope of this study, landslide disasters are taken into consideration. In the study, the five criteria that may cause Natech accidents after landslides were weighted using the Pythagorean Fuzzy AHP method. Then, eight districts of Zonguldak province were ranked by the Pythagorean Fuzzy TOPSIS method according to the risk of Natech accidents, considering the mines they contain.

The reasons for selecting Zonguldak province as the problem's application location can be listed below.

- High landslide risk in Zonguldak province
- The presence of active mines in the province
- High precipitation rate due to its location in the Black Sea region
- High number of landslide events in the past. When the number of landslides in the past in Türkiye was examined, it was seen that the highest number of landslides occurred in the Black Sea region. This situation is given in Figure 1 within the scope of 2018-2024 data.

Figure 1 shows the annual distribution of landslide events in seven geographical regions of Türkiye between 2018 and 2024. While the Black Sea Region stands out with the highest number of events each year, the Southeastern Anatolia Region remains at the lowest levels. Figure 2 shows the provinces in the Black Sea Region that experienced the most landslide disasters between the same years.

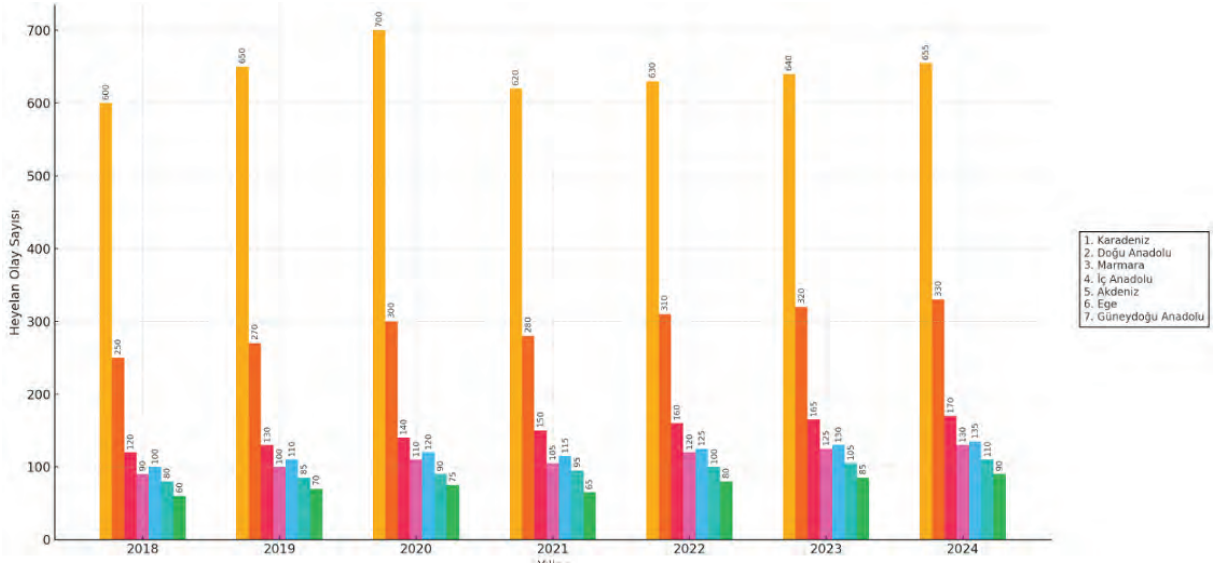


Figure 1. Past landslide numbers in Türkiye 2018-2024.

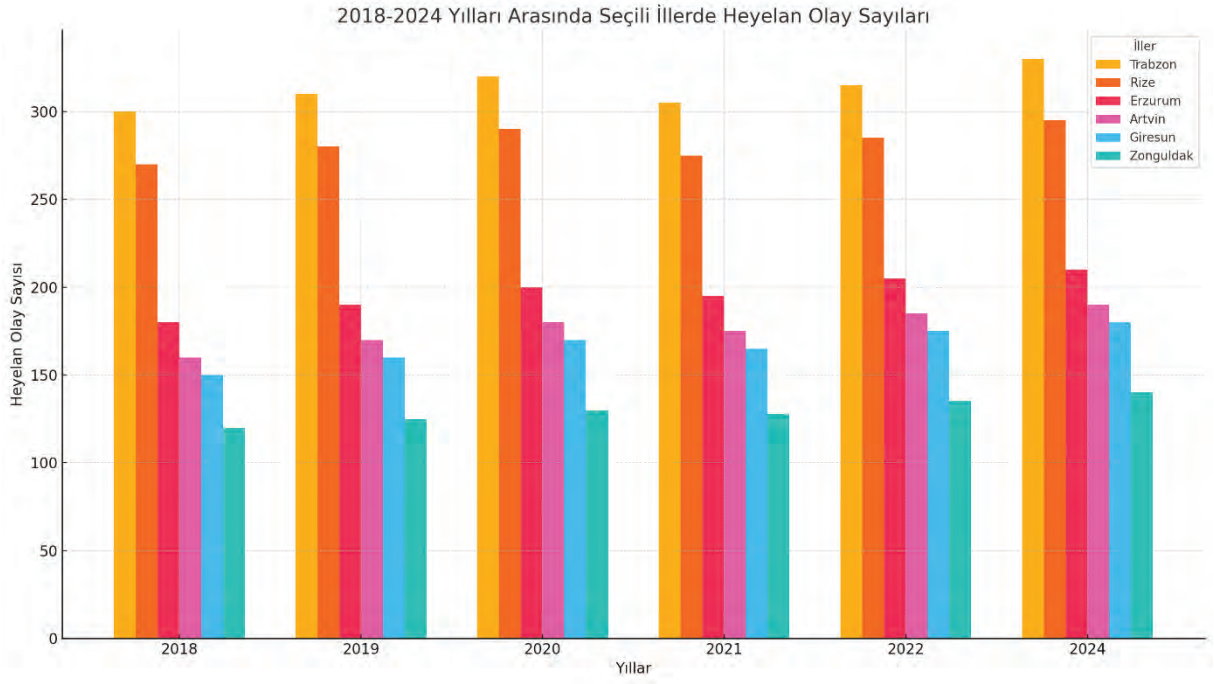


Figure 2. Provinces with the highest number of landslides in the Black Sea Region between 2018-2024.

Figure 2 shows the distribution of representative landslide events in Trabzon, Rize, Erzurum, Artvin, Giresun and Zonguldak provinces by year from 2018 to 2024. In 2024, the highest number of landslides were seen in Trabzon, with Zonguldak again at the bottom. According to these data, Zonguldak province, which has a very high number of landslides in its history, was selected because it contains many mines.

Criteria

Following the landslide disaster, five criteria that could cause a Natech accident were identified. These criteria were determined by four experts, including an occupational safety expert, an AFAD volunteer, an engineer, and an academician.

C1—Number of Mines: This number expresses the number of active mines in the district. A high number of mines increases the risk.

C2—Past Landslide Percentage: This represents the percentage of landslides that occurred in the district in the past. The data included in the Provincial Disaster Risk Reduction Plan (PDRR) of Zonguldak province were accepted.

C3—Landslide Risk: It includes the prevailing landslide risk in the districts

, taking into consideration the data included in IRAP.

C4—Area: This includes the area covered by the districts. The growth of the area has a risk-increasing effect.

C5—Elevation: This is the criterion covering the elevations of the districts. High elevations increase the effect of landslides and accidents.

Alternatives

Eight districts of Zonguldak province (Alaplı, Çaycuma, Devrek, Gökçebey, Ereğli, Kilimli, Kozlu, Centre) were determined as alternatives. The information on the alternatives for the determined criteria is given in Table 3. This information was obtained from the Mineral Research and Exploration Organisation and the Zonguldak Provincial Disaster Risk Reduction Plan.

Table 4. Pythagorean fuzzy AHP decision matrix with linguistic variables

	C-1	C-2	C-3	C-4	C-5
C-1	EE	AA	AA	BA	L
C-2	BA	EE	EE	H	A
C-3	BA	EE	EE	AA	AA
C-4	AA	L	BA	EE	L
C-5	H	BA	BA	H	EE

Weighting of Criteria with Pythagorean Fuzzy AHP

After the landslide, the criteria that may cause the Natech accident were evaluated with the help of 4 experts specified by group collective decision-making. In this evaluation, the decision matrix given in Table 4 was formed by using the linguistic variables given in Table 1.

After creating the decision matrix with linguistic variables, Table 5 was created with the fuzzy numbers corresponding to the linguistic variables.

After creating the Pythagorean fuzzy matrix, the interval multiplication matrix in Table 6 was created.

After the interval multiplication matrix was obtained, Pythagorean Fuzzy AHP process steps were applied respectively. The weights determined using this method are listed in Table 7.

The 'Past Landslide Percentage' criterion has the highest weight among the criteria, with 0.25234. The number of landslide disasters experienced in the past in a district is data affecting the possibility of future disasters. Likewise, 'Elevation', which is a criterion that may cause landslide disasters, ranks second with 0.23717. These two criteria were ranked high since they were effective in the realization of the disaster, which was the basis for the Natech accident. The last criterion in the criterion ranking is 'Area' with 0,12380.

Table 3. Information on alternatives

District	Mines	Past Landslide Percentage	Risk	Area (km^2)	Elevation (mt)
Alaplı	Dolomite	11%	Middle	383	18
Çaycuma	Bauxite (kokaksu, güdüllü), Quartzite	31%	High	492	36
Devrek	Phosphate, Manganese	35%	High	953	103
Gökçebey	_	6%	Middle	183	62
Ereğli	Quartz sand, Manganese, Hard coal	10%	Middle	736	12
Kilimli	Phosphate, Quartz Sand, Shifertone, Hard Coal	1%	Low	145	14
Kozlu	Phosphate, Quartz Sand, Shifertone, Hard Coal	1%	Low	177	18
Centre	Bauxite (Aydındere, Rüzgarlımeşe, Sapanlıdere), Phosphate (Sofular), Quartz sand (Uzungüney), Chifertone (Kokurdan), Hard coal (Asma)	5%	Low	272	10

Table 5. Pythagorean fuzzy AHP decision matrix

		C-1	C-2	C-3	C-4	C-5
C-1	**Ml**	0.1965	0.35	0.35	0.55	0.65
	Mu	0.1965	0.45	0.45	0.65	0.8
	Vl	0.1965	0.55	0.55	0.35	0.2
	Vu	0.1965	0.65	0.65	0.45	0.35
C-2	**Ml**	0.55	0.1965	0.1965	0.2	035
	Mu	0.65	0.1965	0.1965	0.35	0.45
	Vl	0.35	0.1965	0.1965	0.65	0.55
	Vu	0.45	0.1965	0.1965	0.8	0.65
C-3	**Ml**	0.55	0.1965	0.1965	0.35	0.35
	Mu	0.65	0.1965	0.1965	0.45	0.45
	Vl	0.35	0.1965	0.1965	0.55	0.55
	Vu	0.45	0.1965	0.1965	0.65	0.65
C-4	**Ml**	0.35	0.65	0.55	0.1965	0.65
	Mu	0.45	0.8	0.65	0.1965	0.8
	Vl	0.55	0.2	0.35	0.1965	0.2
	Vu	0.65	0.35	0.45	0.1965	0.35
C-5	**Ml**	0.2	0.45	0.55	0.2	0.1965
	Mu	0.35	0.55	0.65	0.35	0.1965
	Vl	0.65	0.45	0.35	0.65	0.1965
	Vu	0.8	0.55	0.45	0.8	0.1965

Table 6. Interval multiplication matrix

	C-1		C-2		C-3		C-4		C-5	
	Dl	**Du**	**Dl**	**Du**	**Dl**	**Du**	**Dl**	**Du**	**Dl**	**Du**
C-1	0.000	0.0000	0.1000	0.3000	0.1000	0.3000	-0.3000	-0.1000	-0.6000	-0.3000
C-2	-0.300	-0.1000	0.0000	0.0000	0.0000	0.0000	0.3000	0.6000	-0.1000	0.1000
C-3	-0.300	-0.1000	0.0000	0.0000	0.0000	0.0000	0.1000	0.3000	0.1000	0.3000
C-4	0.100	0.3000	-0.6000	-0.3000	-0.3000	-0.1000	0.0000	0.0000	-0.6000	-0.3000
C-5	0.300	0.6000	-0.3000	-0.1000	-0.3000	-0.1000	0.3000	0.6000	0.0000	0.0000

Table 7. Criteria weights

Criteria	Criteria Weights
Past Landslide Percentage	0.25234
Elevation	0.23717
Landslide Risk	0.20825
Number of Mines	0.17844
Area	0.12380

Ranking of Alternatives with Pythagorean Fuzzy TOPSIS

8 districts in Zonguldak province were evaluated by the group decision-making method of experts in line with the determined criteria. The decision matrix obtained by using the linguistic variables in Table 2 is given in Table 8.

After the creation of the decision matrix, linguistic variables were placed into the matrix. Then, the Pythagorean fuzzy positive ideal solution and negative ideal solutions in Table 9 were calculated.

Then, the relative closeness indices of each alternative were calculated using the equation in Equation 13, and then the final ranking in Table 10 was obtained.

When the results are analyzed, Devrek district is determined as the district with the highest risk of occurrence of landslides and Natech risk in mines after landslides. It is followed by Çaycuma district. The information contained in the Irap reports supports the results. The districts with the lowest risk are Kilimli and Kozlu districts. There is also a risk in these districts. However, it is less than other districts. For this reason, when evaluating Natech accidents within

Table 8. Pythagorean fuzzy TOPSIS decision matrix

Decision Matrix	C1	C2	C3	C4	C5
Alaplı	L	ML	M	MH	L
Çaycuma	M	H	VH	MH	ML
Devrek	ML	VH	VH	H	H
Gökçebey	OL	VL	ML	ML	M
Ereğli	M	ML	M	H	L
Kilimli	MH	OL	VL	L	L
Kozlu	MH	OL	VL	ML	L
Merkez	H	VL	ML	M	L

Table 9. Pythagorean fuzzy positive and negative ideal solutions

	Positive Ideal Solution			Negative Ideal Solution		
	u	*v*		*u*	*v*	
Number of Mines	0.70	0.60	0.39	0.10	0.99	0.10
Past Landslide Percentage	0.80	0.44	0.41	0.10	0.99	0.10
Landslide Risk	0.80	0.44	0.41	0.10	0.97	0.22
Area	0.70	0.60	0.39	0.25	0.92	0.30
Elevation	0.70	0.60	0.39	0.25	0.92	0.30

Table 10. Ranking of alternatives by Pythagorean fuzzy TOPSIS

Ranking	Province	E
1	Devrek	0
2	Çaycuma	-2.1098
3	Ereğli	-5.2327
4	Alaplı	-6.1006
5	Merkez	-6.11343
6	Gökçebey	-7.32096
7	Kozlu	-7.51503
8	Kilimli	-7.69267

the scope of risk reduction studies in mines, it is thought that it would be useful to prioritize according to the relevant ranking.

CONCLUSION

Many material and moral damages occur during and as a result of disasters. Other accidents and natural events that occur at these times increase the negative effects of the disaster. Natech accidents are one of them. The characteristics of Natech accidents vary depending on the type of disaster. In this case, the criteria that cause Natech accidents also vary. In this study, the landslide disaster was taken into consideration, and the study was carried out within the scope of the mining sector.

When the studies in the literature are examined, it is seen that the studies are focused on equipment rather than the studies carried out by making a sector-based distinction. However, there are a few studies carried out within the scope of the chemical sector. Salzano and Cozzani [27], Necci et al. [28] and Campedel et al. [29] carried out a Natech risk assessment for chemical and industrial facilities. Reniers et al. [30] developed a conceptual framework to improve Natech safety in the chemical industry. Güven et al. [4] ranked the sectors in the Gaziantep organized industrial zone according to Natech accidents, while Güven et al. [17] ranked the sectors in the Kırıkkale organized industrial zone according to Natech risks. When these studies and others in the literature are examined, no study was found in the mining sector. It is thought that the study will contribute to the literature in this respect. The fact that there was a Natech accident in the mine due to a landslide disaster in the recent past in our country also reveals that this study is a real-life problem.

In the study, the risks that may have caused the Natech accident after the landslide disaster were evaluated first. 'Percentage of past landslides' was determined as the most critical risk criterion. The last criterion was the 'Area' criterion. Then, eight districts of Zonguldak province, which was selected as the application province, were ranked according

to the risk of Natech accidents in mines after the landslide disaster. As a result of the applied method, the ranking is Devrek, Çaycuma, Ereğli, Alaplı, Centre, Gökçebey, Kozlu, and Kilimli.

Suggestions that can be made in line with the results obtained can be listed as follows.

1. One of the practices carried out within the scope of the disaster management process is the creation of provincial disaster risk reduction plans. Natech accidents should be included in the provincial risk reduction plans.
2. Studies should be initiated in line with the district rankings obtained according to Natech accident risks. Meetings should be held with the authorities in the relevant districts and situation analyses and risk analyses should be conducted in the mining areas with the participation of authorized personnel such as engineers, disaster teams, occupational health, and safety experts, etc.
3. Natech accidents should be included in risk assessments in the mining sector. Natech risks and precautions should be determined within the scope of risk analyses prepared with the participation of occupational safety specialists, mining engineers, authorized personnel in the mines and employers.
4. After a landslide disaster, the criteria that may cause Natech accidents should be taken into consideration in risk reduction studies and precautions should be determined. Especially considering the Natech accidents that occurred in the past, the necessary occupational health and safety measures should be increased. The creation of retaining walls, more careful ground surveys, opening of drainage wells, creation of work areas away from landslide risk areas, etc.

Natech accidents are an essential event that poses a risk for every sector. Therefore, it should be included in risk reduction studies. Diversification and elaboration of the studies will both increase attention to this issue and support the measures to be taken. Different sectors can be addressed in future studies. However, different disasters can be taken into consideration when evaluating the mining sector. Since the criteria will differ in each disaster and sector, the scope of the study can be increased by elaborating at this point.

AUTHORSHIP CONTRIBUTIONS

Authors equally contributed to this work.

DATA AVAILABILITY STATEMENT

The authors confirm that the data that supports the findings of this study are available within the article. Raw data that support the finding of this study are available from the corresponding author, upon reasonable request.

CONFLICT OF INTEREST

The authors declared no conflict of interest.

ETHICS

There are no ethical issues with the publication of this manuscript.

STATEMENT ON THE USE OF ARTIFICIAL INTELLIGENCE

Artificial intelligence was not used in the preparation of the article.

REFERENCES

[1] Güven E, Eren T. İl Afet Risk Azaltma Planı Çerçevesinde ANP Yöntemi İle Kriter Ağırlıklandırma : Kırıkkale İli İçin Bir Örnek. Afet ve Risk Derg 2023;6:401–414. [CrossRef]

[2] Aşıkkutlu HS, Aşık Y, Yücedağ C, Kaya LG. Olası Deprem Durumunda Mahalle Ölçeğinde Burdur Kenti Acil Toplanma Alanları Yeterliliğinin Saptanması. Mehmet Akif Ersoy Üniversitesi İktisadi ve İdari Bilim Fakültesi Derg 2021;8:442–456. [CrossRef]

[3] Akdas E, Eren T. A sample application for scheduling search and rescue teams in an earthquake disaster. Sigma J Eng Nat Sci 2024;42:1555–1562. [CrossRef]

[4] Guven E, Pinarbasi M, Mehmet Alakas H, Eren T. Ranking of sectors in organized industrial zones according to Natech risk criteria: An application for Gaziantep province in Türkiye. J Loss Prev Process Ind 2024;91:105377. [CrossRef]

[5] Cruz AM, Krausmann E. Hazardous-materials releases from offshore oil and gas facilities and emergency response following Hurricanes Katrina and Rita. J Loss Prev Process Ind 2009;22:59–65. [CrossRef]

[6] Girgin S. The natech events during the 17 August 1999 Kocaeli earthquake: Aftermath and lessons learned. Nat Hazards Earth Syst Sci 2011;11:1129–1140. [CrossRef]

[7] Gao Y, Hu L, Xie Y, Bi J, Ma Z. Understanding the patterns and characteristics of Natech events in China. J Loss Prev Process Ind 2023;84:105102. [CrossRef]

[8] Steinberg LJ, Sengul H, Cruz AM. Natech risk and management: An assessment of the state of the art. Nat Hazards 2008;46:143–152. [CrossRef]

[9] Fabbrocino G, Iervolino I, Orlando F, Salzano E. Quantitative risk analysis of oil storage facilities in seismic areas. J Hazard Mater 2005;123:61–69. [CrossRef]

[10] Girgin S, Krausmann E. RAPID-N: Rapid natech risk assessment and mapping framework. J Loss Prev Process Ind 2013;26:949–960. [CrossRef]

[11] Suarez-Paba MC, Cruz AM. A paradigm shift in Natech risk management: Development of a rating system framework for evaluating the performance of industry. J Loss Prev Process Ind 2022;74:1–10. [CrossRef]

[12] Son D, Jung S. Flood Risk Assessment for Chemical Storage Tanks. Korean J Hazard Mater 2018;5:94–100.
[13] Rossi L, Casson Moreno V, Landucci G. Vulnerability assessment of process pipelines affected by flood events. Reliab Eng Syst Saf 2022;219:1–16. [CrossRef]
[14] Yu J, Cruz AM, Hokugo A. Households' Risk Perception and Behavioral Responses to Natech Accidents. Int J Disaster Risk Sci 2017;8:1–15. [CrossRef]
[15] Luo X, Tzioutzios D, Tong Z, Cruz AM. Find-Natech: A GIS-based spatial management system for Natech events. Int J Disaster Risk Reduct 2022;76:1–14. [CrossRef]
[16] Guo L, Liang J, Chen T, Gao Y, Yang Z. Scenario-Driven Methodology for Cascading Disasters Risk Assessment of Earthquake on Chemical Industrial Park. Processes 2023;11:1–12. [CrossRef]
[17] Guven E, Pinarbasi M, Mehmet Alakas H, Eren T. Evaluation of natech criteria in organized industrial zones: An application for Kırıkkale province. J Loss Prev Process Ind 2024;91. [CrossRef]
[18] Bedir N, Eren T. AHP-PROMETHEE Yöntemleri Entegrasyonu ile Personel Seçim Problemi: Perakende Sektöründe Bir Uygulama. Soc Sci Res J 2015;4:46–58.
[19] Erol E, Özcan E, Eren T. Elektrik üretim santrallarında iş güvenliği uzmanı seçiminde hibrit bir karar modeli. J Turkish Oper Manag 2021;1:615–629.
[20] Yager RR. Pythagorean fuzzy subsets. Proc 2013 Jt IFSA World Congr NAFIPS Annu Meet IFSA/NAFIPS 2013 2013;2:57–61. [CrossRef]
[21] Yazıcı E, Özcan E, Alakaş HM, Eren T. Hidroelektrik Santrallarda Bakım Strateji Optimizasyonu için Hiyerarşik Bir Karar Modeli Önerisi. J Polytech 2021;25:933–945. [CrossRef]
[22] Ak MF, Gul M. AHP-TOPSIS integration extended with Pythagorean fuzzy sets for information security risk analysis. Complex Intell Syst 2019;5:113–126. [CrossRef]
[23] Hwang C-L, Yoon K. Multiple Attribute Decision Making: Methods and Applications. New York: Springer-Verlag; 1981. [CrossRef]
[24] Özcan E, Ünlüsoy S, Eren T. Anp Ve Topsis Yöntemleriyle Türkiye Yenilenebilir Enerji Yatir Alternatiflerini Değerlendirilmesi. Selcuk Univ J Eng ,Science Technol 2017;5:204–219. [CrossRef]
[25] Gedikli T. Pisagor Bulanık TOPSIS ve Bulanık TOPSIS Yöntemleri ile En Uygun Bakım Stratejisinin Seçilmesi: Bir Gıda İşletmesinde Uygulama. Konya Gıda Ve Tarım Üniversitesi, 2019. [CrossRef]
[26] Yazıcı E, Alakaş HM, Eren T. Prioritizing of sectors for establishing a sustainable industrial symbiosis network with Pythagorean fuzzy AHP- Pythagorean fuzzy TOPSIS method: a case of industrial park in Ankara. Environ Sci Pollut Res 2023;30:77875–77889. [CrossRef]
[27] Salzano E, Cozzani V. Introducing External Hazard Factors in Quantitative Risk Analysis. Rev Ing 2012:50–56. [CrossRef]
[28] Necci A, Antonioni G, Bonvicini S, Cozzani V. Quantitative assessment of risk due to major accidents triggered by lightning. Reliab Eng Syst Saf 2016;154:60–72. [CrossRef]
[29] Campedel M, Cozzani V, Garcia-Agreda A, Salzano E. Extending the quantitative assessment of industrial risks to earthquake effects. Risk Anal 2008;28:1231–1246. [CrossRef]
[30] Reniers G, Khakzad N, Cozzani V, Khan F. The impact of nature on chemical industrial facilities: Dealing with challenges for creating resilient chemical industrial parks. J Loss Prev Process Ind 2018;56:378–385. [CrossRef]

Sigma J Eng Nat Sci, Vol. 44, No. 4, pp. 2745–2757, August, 2026

Sigma Journal of Engineering and Natural Sciences
Web page info: https://sigma.yildiz.edu.tr
DOI: 10.14744/sigma.2026.2125

Research Article

Fuzzy logic approaches for forecasting daily global solar radiation: A comparative analysis of climatic variables

Berke Oğulcan PARLAK[1,*], Erhan AKDOĞAN[1]

[1]*Department of Mechatronics Engineering, Yıldız Technical University, İstanbul, 34349, Türkiye*

ARTICLE INFO

Article history
Received: 17 December 2024
Revised: 13 March 2025
Accepted: 05 May 2025

Keywords:
Climatic Variables; Forecast; Fuzzy Logic; Neural Networks; Solar Radiation

ABSTRACT

Accurate prediction of solar radiation is important for the design and optimization of photovoltaic systems and for efficient energy management and sustainability planning. However, in many regions direct solar radiation measurements are scarce or not available, which makes the forecasting from available climatic variables more and more important. This study addresses this challenge by developing three simple-structured fuzzy logic models to predict daily global solar radiation using three different combinations of commonly recorded weather inputs: temperature and relative humidity, temperature and wind speed, and relative humidity and wind speed. The models were trained with data from Ankara, Türkiye and evaluated using mean absolute percentage error and root mean square error metrics. Comparing the models tested, the relative humidity and wind speed model resulted in the best forecasting performance with a mean absolute percentage error of 9.07% and a root mean square error of 0.85 kWh/m^2-day. It also outperformed the feedforward artificial neural network model used for comparison, which produced an error of 14.38%. Results indicate that wind speed has more direct effects on estimation of solar radiation while the effect of temperature appears more indirect. A major contribution of the present study is that reasonably simple fuzzy logic models can provide good prediction performance if the right input variables are selected. This is particularly important when compared to more complex artificial intelligence methods, which usually require larger data sets and a larger number of input parameters. In this sense, the proposed approach also helps to overcome limitations reported in previous studies, such as the use of high-dimensional input sets and models developed mainly for short-term forecasting. Overall, the results show that fuzzy logic can be an accurate and computationally efficient alternative for solar radiation forecasting, especially when the available data are limited.

Cite this article as: Parlak BO, Akdoğan E. Fuzzy logic approaches for forecasting daily global solar radiation: A comparative analysis of climatic variables. Sigma J Eng Nat Sci 2026;44(4):2745–2757.

INTRODUCTION

Renewable energy sources are gaining more and more importance due to their environmentally friendly features [1], use of naturally available resources [2], and potential to reduce greenhouse gas emissions [3]. Wind, solar, hydro, biomass and geothermal power can also enhance energy security by reducing dependence on fossil fuels [4, 5]. Of

*Corresponding author.
*E-mail address: boparlak@yildiz.edu.tr

This paper was recommended for publication in revised form by Editor-in-Chief Ahmet Selim Dalkilic

Published by Yıldız Technical University Press, İstanbul, Turkey
© Author. This is an open access article under the CC BY-NC license (http://creativecommons.org/licenses/by-nc/4.0/).

these alternatives, solar energy has become particularly attractive due to low operating costs, wide range of applications and decreasing installation costs driven by technological advances [6–8]. Consequently, the share of solar energy in the global energy production has increased rapidly in recent years. For example, in 2023 solar photovoltaic accounted for three-quarters of all added renewable energy capacity worldwide [9]. As this growth has occurred, so too has the number of solar energy facilities in various regions increased. However, the efficient planning and operation of such facilities rely to a large extent on a correct assessment of the available solar radiation potential. Accurate information of regional solar radiation can contribute to better system design, increase energy yield and reduce payback period of the investment [10]. Hence, accurate determination of solar radiation potential is an important step in planning of sustainable solar energy projects.

Total solar radiation on a given surface can be measured directly with instruments like pyranometers [11]. However, the density of meteorological stations is not uniform across the globe, and many regions still do not have adequate ground-based measurement infrastructure. As a result, reliable solar radiation measurements are unavailable for numerous locations. This limitation makes it difficult to assess regional solar energy potential accurately and may lead to less reliable system design, higher investment costs, and lower energy production efficiency. For this reason, estimating solar radiation from commonly available climatic variables has become an important alternative in regions where direct measurements are limited or unavailable [12]. Against this background, the present study focuses on developing a practical and accurate forecasting approach that relies on a small number of widely available climatic variables and can therefore be applied in data-scarce regions.

In the literature, methods used for forecasting solar radiation are generally based on linear [13] and nonlinear modeling [14], artificial intelligence (AI)-based modeling [15], and fuzzy logic-based modeling techniques [16]. Although regression-based models are frequently used to forecast meteorological parameters [17], in the context of solar radiation forecasting AI models incorporating artificial neural network (ANN) algorithms are widely employed, whereas fuzzy logic approaches remain comparatively less prevalent [18]. This prevalence may be due to the ANN model's relative ability to model complex and nonlinear relationships in meteorological data, which can be advantageous in solar radiation forecasting. Girdhani and Agrawal [19] investigated the performance of different prediction methods such as ANN, long short-term memory, convolutional neural networks, Prophet, and SARIMAX for predicting daily global horizontal solar radiation in Bhopal, India. The models were developed with a variety of meteorological input variables. Among the methods evaluated, the ANN showed the best performance with a mean absolute percentage error (MAPE) of 2.5466%. Meanwhile, the MAPE of long short-term memory, convolutional neural networks, SARIMAX, and Prophet were 4.2124%, 4.8266%, 8.109%, and 13.45%, respectively. Bilgili and Ozgoren [20] modeled the daily global solar radiation for Adana, Türkiye, by using multiple linear regression, multiple nonlinear regression and feedforward ANN methods. Sunshine duration, air temperature, wind speed, and the day of the year were used as input parameters. The MAPE of the forecast was calculated as 9.23%. Behrang et al. [21] applied multilayer perceptron and radial basis function neural networks to model daily global solar radiation for Dezful, Iran. The input parameters were day of the year, mean daily air temperature, relative humidity, sunshine hours, evaporation and wind speed. The best performance of multilayer perceptron network was obtained with wind speed, day of the year, daily average air temperature, relative humidity and sunshine hours with a MAPE of 5.21%. The combination of daily average air temperature, day of year and sunshine hours in the radial basis function network also provided a satisfactory accuracy with a MAPE of 6.53%. Asl et al. [22] predicted daily global solar radiation in Dezful, Iran, by multilayer perceptron neural networks. Input parameters were day of year, daily mean air temperature, relative humidity, sunshine hours, evaporation, wind speed and soil temperature. The MAPE of the forecast was found to be 6.08%. Almasoud et al. [23] used ANN for estimating the monthly mean daily solar radiation on horizontal surface for nine meteorological stations in Saudi Arabia. The input parameters were altitude, latitude, longitude, month, maximum and minimum air temperature, maximum and minimum relative humidity and sunshine duration. The resulting forecast had a MAPE of 6.86%. Besides single ANN-based models, hybrid methods have been studied in several papers for improving the forecasting performance. For example, Khalfa et al. [24] proposed a hybrid model by integrating multiple learning algorithms and achieved a MAPE of 1.58%, which demonstrated a better accuracy compared to the traditional methods. Hybrid deep learning approaches have also shown good performance for solar radiation forecasting. Mariappan et al. [25] proposed a hybrid convolutional neural network and stacked long short-term memory model with feature selection and metaheuristic-based hyper-parameter tuning. The model reached a MAPE of 3.63% and outperformed some traditional and deep learning approaches.

In general, AI-based models reported in the literature have shown good performance for solar radiation forecasting. However, the dependence on large datasets and the fairly high computational requirements might limit their practical use [26]. Since it can handle uncertainty and incomplete information, fuzzy logic provides a potentially useful alternative [27]. But, fuzzy logic-based approaches have received relatively little attention in the literature despite these advantages. Boata [28] designed a fuzzy logic model based on Takagi–Sugeno for hourly prediction of global solar radiation at Timisoara, Romania. The model

was fed with loss components as input parameters, defined as the difference between the measured and forecasted hourly global solar radiation under clear-sky conditions. The model gave a reasonable accuracy; however, the performance was degraded in cloudy conditions and the forecasting horizon was limited to one hour. Chugh et al. [29] presented a Mamdani-based fuzzy logic model for hourly global solar radiation forecasting in New Delhi, India. The model predicted the radiation in the fifth hour with the solar radiation measured in the previous four hours. The model is designed for short-term forecasting and has a reported MAPE of 1.052%. How the model performs for longer forecasting horizons is unclear. Boata and Pop [30] used a Takagi-Sugeno based fuzzy logic model to predict the daily global solar radiation at Timisoara, Romania. The model was using only air temperature without considering other relevant meteorological variables, but gave almost reasonable results. Rizwan et al. [31] suggested a Mamdani based fuzzy logic model for the prediction of global solar energy for four Indian cities. The input parameters for the model were latitude, longitude, altitude, the month of the year, duration of sunshine and temperature. It achieved a MAPE of 5.56% for the four stations. However, the use of six input parameters increased the complexity of the model and its computational requirements during training and implementation. Mehta and Basak [32] in Patiala, India, proposed a similar fuzzy logic model for solar radiation prediction. Input parameters included temperature, humidity, wind speed, time of day and atmospheric pressure. The model obtained a MAPE of 1.703% in relation to the actual measured solar radiation data in real time. But the high dimensional structure and the rule base of 1,200 rules lead to high computational complexity and processing requirements.

Previous studies show that fuzzy logic-based models have great potential in solar radiation forecasting, but there are still some limitations. These include models developed for specific weather conditions, limited consideration of relevant input variables and increasing system complexity as the number of inputs increases. Some techniques are limited to short-term forecasting, while the performance of others on longer forecasting horizons is still not clear. Moreover, although more input variables can improve the accuracy of predictions, they may also increase the computational load and processing time, limiting the practicality of such models in data-limited applications. In an effort to overcome these limitations, the present study developed three Mamdani-type fuzzy logic models for forecasting daily solar radiation in Ankara, Türkiye, using three different input variable pairs: temperature and relative humidity (TH), temperature and wind speed (TW), and relative humidity and wind speed (HW). Each model had 16 fuzzy rules. The input and output variables were fuzzified using four triangular membership functions. The defuzzification was performed using the largest of maximum method (LoM). Performance of the forecasting was evaluated by the MAPE and root mean square error (RMSE). Then the effects of different combinations of inputs on the forecasting accuracy were investigated, and the best fuzzy logic model was compared with a feedforward ANN model to assess the performance of the two approaches on the same forecasting problem. To summarize, the study suggests a straightforward forecasting framework, aiming to reach high accuracy with a small number of easily accessible climatic variables. The main contributions of this study are summarized as follows:

- First, the literature review was carried out to find the climatic variables that are most frequently used for solar radiation forecasting. According to this assessment, ambient temperature, relative humidity and wind speed were selected and grouped into three different input pairs. These combinations were then used to build three relatively simple fuzzy logic models for the selected region of study.
- Secondly, the effect of various input combinations on forecasting performance was investigated by comparing the three proposed models. This comparison allowed us to assess the contribution of each pair of climatic variables to the model accuracy and gain insight on whether an appropriate selection of inputs could improve performance without increasing model complexity or computational requirements.
- Finally, the performance of fuzzy logic models was further evaluated by comparing the best performing model with a feedforward ANN model developed for the same region and forecast period. The comparison also gave another criterion to assess the applicability of the proposed fuzzy logic approach, especially in cases where data and computational resources are limited.

The remainder of the paper is organized as follows. Section 2 describes the methodology including the dataset, the fuzzy logic models developed, the ANN model used for comparison and the performance evaluation metrics. The results obtained from the fuzzy logic and ANN models are presented and discussed in Section 3. Finally, Section 4 presents a summary of the main findings and conclusions of the study.

MATERIALS AND METHODS

Dataset

This study aims to forecast daily solar radiation using various climatic variables. The climatic variables considered include sunshine duration, maximum ambient temperature, relative humidity, latitude, longitude, day of the year, daily clear-sky global radiation, total cloud cover, temperature, clearness index, altitude, months, average temperature, average cloudiness, average wind speed, atmospheric pressure, reference clearness index, average diffuse radiation, evaporation, and soil temperature [12]. Among these variables, relative humidity, ambient temperature, and wind

speed are comparatively easier to measure and access [33]. The primary reasons for this are that these data are mostly recorded directly by meteorological stations, and the measurement devices are widely available. Additionally, these variables can often be measured using economical equipment, and their results are quickly accessible. Therefore, relative humidity, ambient temperature, and wind speed were selected as input variables for modeling within the scope of this study.

The study area was selected as Ankara, the capital of Türkiye, located at 39.92° latitude and 32.84° longitude at an elevation of approximately 893 m above sea level. The dataset includes relative humidity, ambient temperature, wind speed, and daily solar radiation data covering the seven-month period from January to July 2024. These data were obtained from the Prediction of Worldwide Energy Resources database provided by the National Aeronautics and Space Administration. In this study, daily solar radiation for July was forecasted using both the fuzzy logic model and the ANN model. The corresponding data are presented in Figure 1.

Fuzzy Logic Models

Fuzzy logic, developed by Zadeh in 1965 [34], extends beyond the binary true-or-false framework of classical logic, allowing the evaluation of uncertainty and intermediate values. Fuzzy logic systems operate through a process consisting of four fundamental steps: fuzzification, rule base, inference system, and defuzzification. Figure 2 illustrates the functioning of these steps for forecasting daily solar radiation.

Fuzzification is the process of converting input variables into fuzzy sets using membership functions defined over appropriate ranges [35]. Membership functions define the degree to which a given value belongs to a fuzzy set, with membership values ranging from 0 to 1. Different types of membership functions, including triangular, Gaussian, and trapezoidal functions, have been widely used in the literature. In this study, the triangular membership function was selected because of its simple structure, low computational requirements, and ease of implementation [36]. The mathematical expression of the triangular membership function is given as follows:

$$\mu(x) = \begin{cases} 0, & x \le a \\ \dfrac{x-a}{b-a}, & a < x \le b \\ \dfrac{c-x}{c-b}, & b < x < c \\ 0, & x \ge c \end{cases} \quad (1)$$

where $\mu(x)$ represents the membership degree of the value x, a denotes the left vertex of the triangle, b represents the top vertex of the triangle, and c is the right vertex of the triangle. Within the scope of this study, each input and output variable was fuzzified using four triangular membership functions defined over appropriate ranges. These membership functions use the linguistic terms very low (VL), low (L), medium (M), and high (H) to describe the input and output variables. Figure 3 provides a detailed illustration

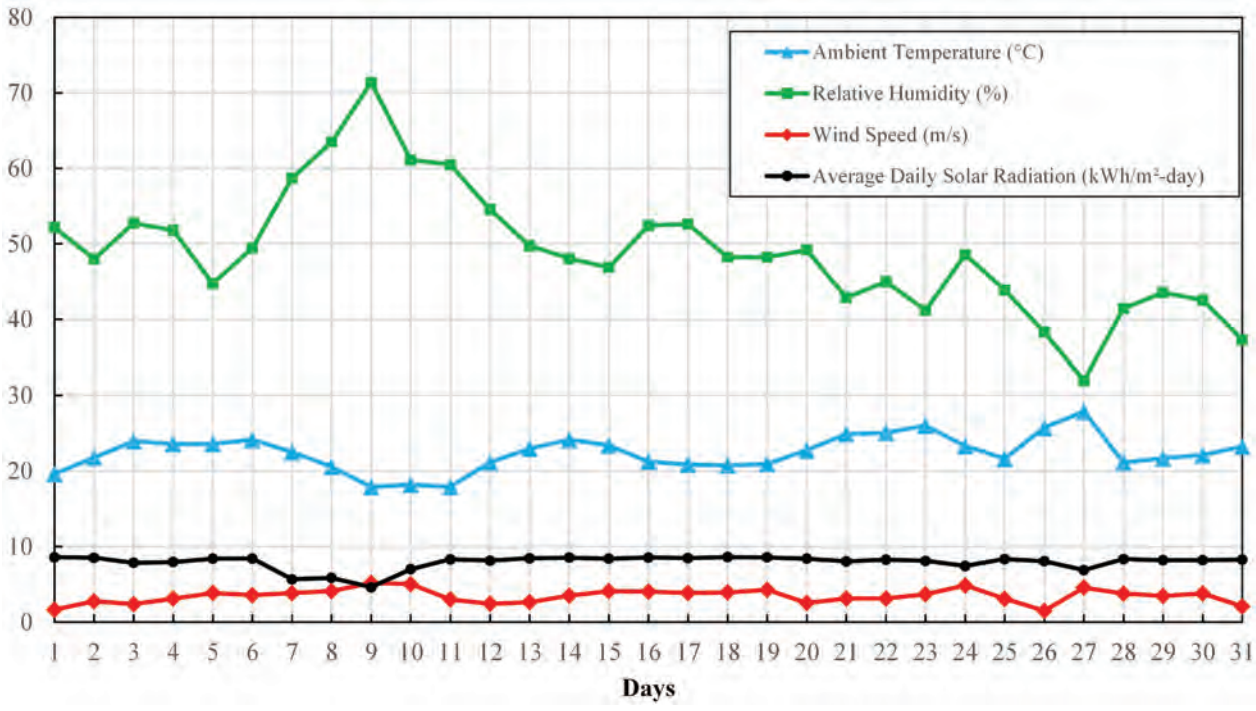


Figure 1. Climatic variables for July.

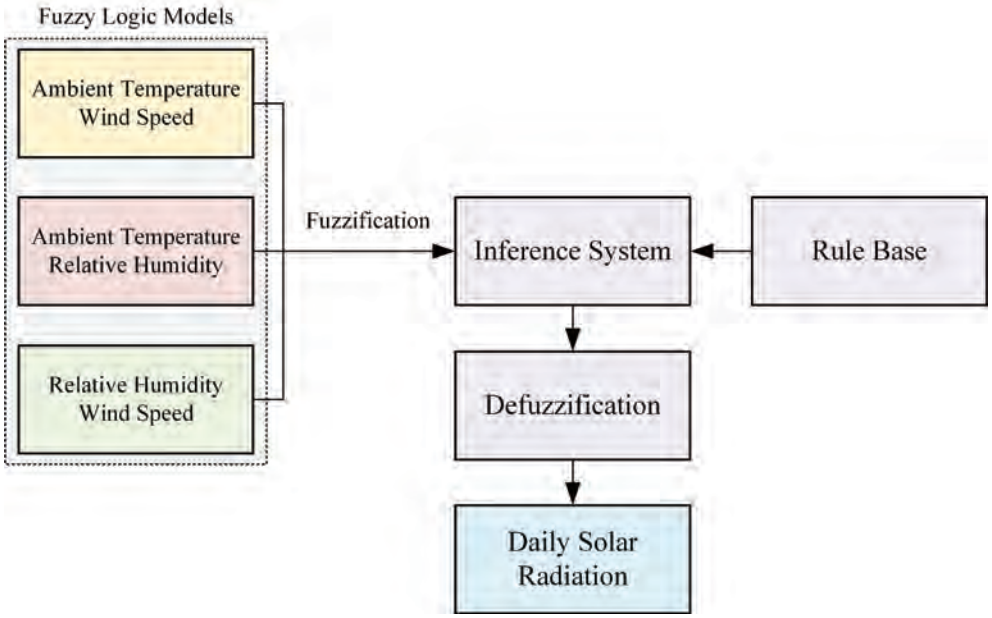


Figure 2. The operation of the fuzzy logic model for forecasting daily solar radiation.

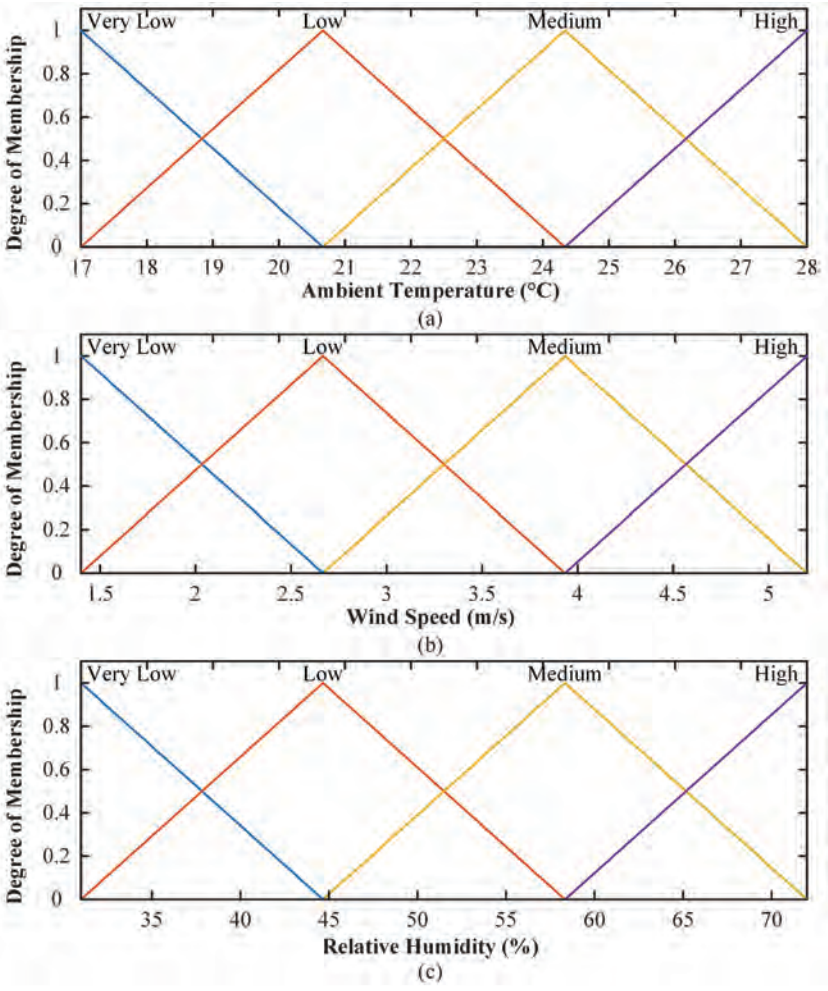


Figure 3. Membership functions created for the input variables. (a) Ambient temperature. (b) Wind speed. (c) Relative humidity.

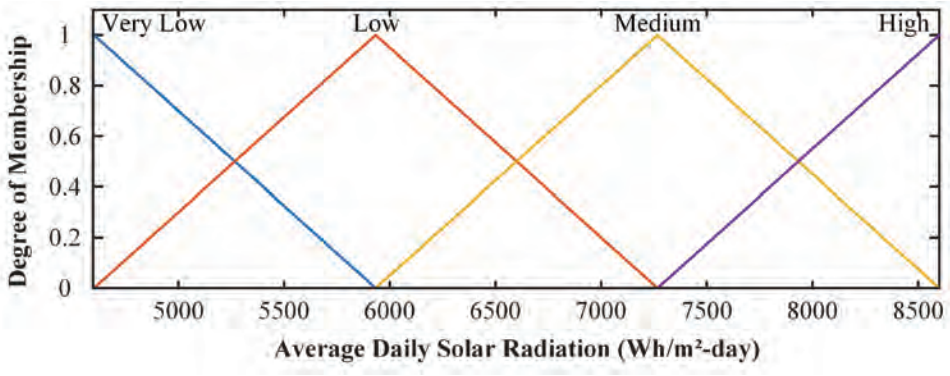


Figure 4. Membership functions created for the output variable.

of the membership functions created for the input variables, while Figure 4 presents those designed for the output variable.

The fuzzification stage is then followed by the rule base in the fuzzy logic system. At this stage, the fuzzy sets obtained from the input variables are associated with the output variables through a set of logical rules. The rule base is a set of "IF-THEN" statements that defines the relationship between inputs and outputs [37]. These rules define the system's response to various input conditions. They are normally defined based on expert knowledge, historical data or a combination of both. They can also include logical operators such as 'and' and 'or'. When the conditions in the rule are true, the corresponding output is fired. A simple fuzzy rule might read as follows:

$$\textbf{IF } i_1 \textit{ is } A \textbf{ AND } i_2 \textit{ is } B, \textbf{THEN } o_1 \textit{ is } C. \quad (2)$$

where i_1 and i_2 represent the input variables, A and B are the linguistic terms associated with these variables, o_1 denotes the output variable, and C is the linguistic term for the output variable. In this study, rule matrices have been designed for three different fuzzy logic models. Each model contains customized rules to determine the outputs corresponding to different combinations of the input variables. The designed rule matrices associate the linguistic expressions of the input variables (VL, L, M, H) with the appropriate fuzzy sets of the output variable. Tables 1-3 present the rule matrices created for the three different fuzzy logic models. The triggering of each rule in the rule matrix depends on the membership degrees of the input variables. If multiple rules are triggered simultaneously, the inference system combines the information from these rules and proceeds to the defuzzification stage of the system.

The output values obtained by the inference system are expressed as fuzzy sets and are not used directly without undergoing defuzzification. Defuzzification is the process of converting these fuzzy outputs into a crisp value [38]. In the literature, various methods for defuzzification exist. Among the most commonly used methods are centroid, bisector, mean of maximum, smallest of maximum, and LoM methods [39]. In this study, the LoM method was preferred for the defuzzification of the fuzzy output. In the LoM method, if more than one output value has the maximum membership degree, the largest of these values is selected as the crisp output. The LoM process can be mathematically expressed as follows:

Table 1. Rule matrix of the fuzzy model with input variables relative humidity (i_1) and wind speed (i_2)

i_1 / i_2	VL	L	M	H
VL	H	H	M	L
L	H	M	M	L
M	M	M	L	L
H	L	L	VL	VL

Table 2. Rule matrix of the fuzzy model with input variables ambient temperature (i_3) and relative humidity (i_1)

i_3 / i_1	VL	L	M	H
VL	L	L	VL	VL
L	M	M	L	VL
M	H	H	M	L
H	H	H	M	L

Table 3. Rule matrix of the fuzzy model with input variables ambient temperature (i_3) and wind speed (i_2).

i_3 / i_2	VL	L	M	H
VL	H	M	L	VL
L	H	H	M	L
M	H	H	M	M
H	H	H	M	L

$$\mu_{LoM}(x) = max(\mu_1(x), \mu_2(x), \ldots, \mu_n(x)) \quad (3)$$

where $\mu_1(x)$, $\mu_2(x)$,..., $\mu_n(x)$ represents the membership degrees of the fuzzy output functions, and through the max function, the highest value among these functions is selected, i.e., $\mu_{LoM}(x)$.

Finally, fuzzy systems can be classified into three main categories: Sugeno-type, Mamdani-type, and Tsukamoto-type. Sugeno-type expresses the outputs as either a constant number or a linear function [40], while Mamdani-type is typically preferred in more intuitive, rule-based systems [41], where the outputs are expressed through more complex functions. Conversely, the Tsukamoto-type is a method in which the outputs are based on ordered membership functions [42]. Mamdani-type is good for its intuitive structure and ease of implementation. Therefore, Mamdani type fuzzy logic system has been preferred in this study.

Artificial Neural Network Model

ANNs are mathematical models, which are based on the biological nervous system, and designed to learn from data [43]. They are usually composed of interconnected artificial neurons with many layers. The ability of ANNs to learn complex relationships from data and generalize to unseen cases has led to their widespread use to solve a variety of complex problems [44]. Different network architectures can be used depending on the problem, such as feedforward, feedback and convolutional neural networks. Among them, feed forward neural networks are popular due to their relatively simple structure and efficient training process [45]. In this architecture, information flows in one direction, the output of each layer being the input of the next. In the present work, the feedforward network was trained by using data for six months of the study area, and then it was used to predict the daily solar radiation for the seventh month. The network architecture used is shown in Figure 5.

The feedforward neural network used in this study consists of three layers: input layer, hidden layer, and output layer. The input layer has three neurons for the three input variables: relative humidity, ambient temperature, and wind speed. The hidden layer has ten neurons and uses the rectified linear unit (ReLU) activation function. Mathematically, the ReLU function can be written as:

$$f(X) = max(0, X) \quad (4)$$

where $f(X)$ represents the output of the activation function, and X denotes the total input received by the neuron. In the output layer, there is a single neuron, and this neuron is used to forecast the daily solar radiation. A linear activation function is applied in the output layer. The linear activation function is expressed as follows:

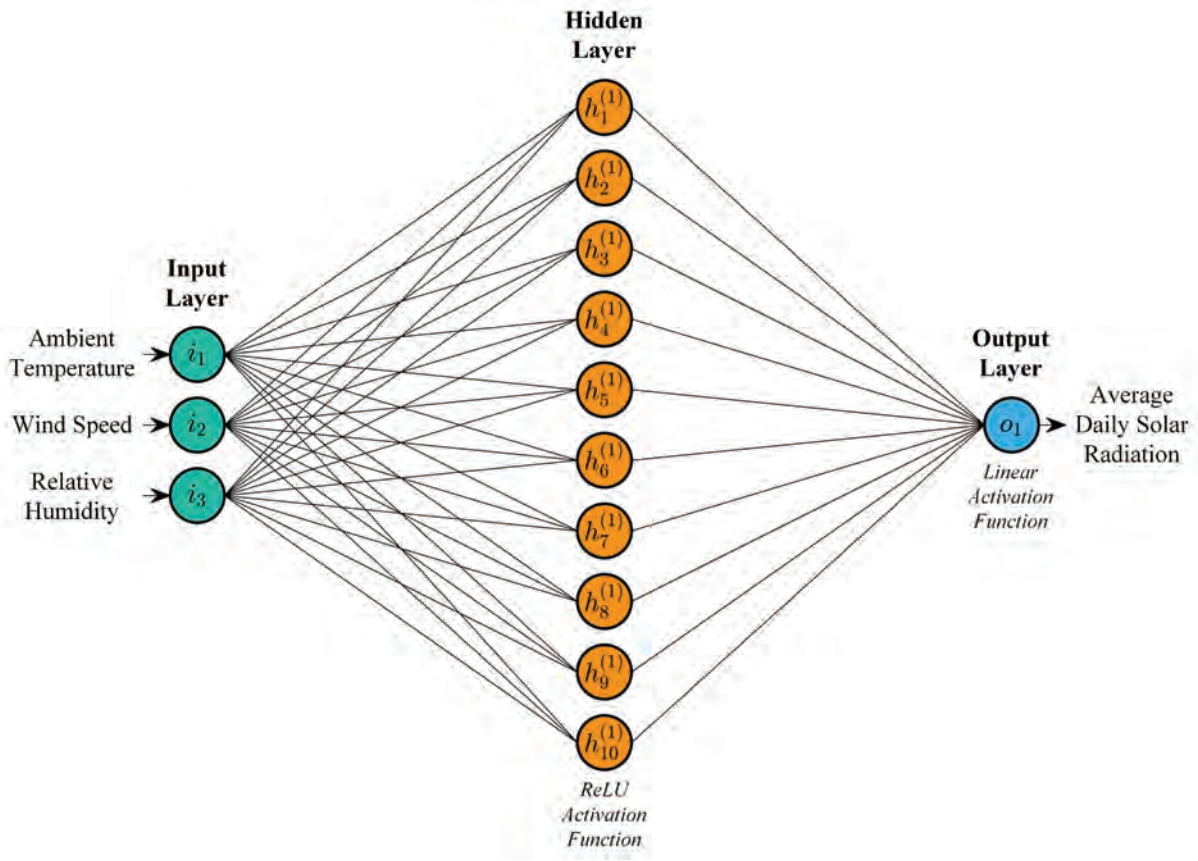


Figure 5. Three-layer feedforward ANN structure.

$$f(X) = X \tag{5}$$

As shown in Figure 5, the output of the hidden layer neurons can be calculated through the weighted sum of the values received from the neurons in the input layer and the activation function. The values of the hidden layer neurons are expressed as follows:

$$h_j = f_1\left(\sum_i w_{ij}\, k_i\right) \tag{6}$$

where h_j represents the values of the hidden layer neurons, $f_1(.)$ denotes the ReLU activation function, w_{ij} is the adjustable weight between the input and hidden layers, and k_i is the value of the input layer neuron. The hidden layer is considered as the input to the output layer. Therefore, the value of the output layer neuron can be expressed as follows:

$$o_j = f_2\left(\sum_i v_{ij}\, h_i\right) \tag{7}$$

where o_j represents the value of the output layer neuron, $f_2(.)$ denotes the linear activation function, and v_{ij} is the adjustable weight between the hidden and output layers.

Finally, the backpropagation algorithm was used to train the network. Backpropagation is a supervised learning method in which input samples are provided together with their corresponding target outputs [46]. During training, the error is propagated backward through the network to update the connection weights, and this process is repeated until the error is sufficiently reduced. In this study, model performance during training was evaluated using the mean squared error (MSE), and the variation in the error was monitored throughout the training process. Training was terminated when the MSE reached 10^{-2}, which was taken as the criterion for sufficient learning. The corresponding error metric is calculated using the following expression:

$$MSE = \frac{1}{N}\sum_{i=1}^{N}(y_i - \hat{y}_i)^2 \tag{8}$$

where N represents the total number of samples in the training dataset, y_i is the actual value, and $\hat{y}_i$ is the value forecasted by the model.

Performance Evaluation Metrics

The performance of forecasting models is typically measured using error metrics. Among these metrics, the most common are MSE, mean absolute error, R-squared, MAPE, and RMSE [47]. Within the scope of the study, MAPE and RMSE, which are the most common metrics [12] in evaluating the solar radiation forecasting performance, were used. The MAPE can be expressed as Equation 9 [48], and the RMSE as Equation 10 [49].

$$MAPE = \frac{1}{N}\sum_{i=1}^{N}\left|\frac{y_i - \hat{y}_i}{y_i}\right| \times 100 \tag{9}$$

$$RMSE = \sqrt{\frac{1}{N}\sum_{i=1}^{N}(y_i - \hat{y}_i)^2} \tag{10}$$

It should be noted that the MSE defined in Equation 8 is only used during the training process of the ANN model. In this study, the evaluation of the forecasting performance of both the fuzzy logic and ANN models was conducted through the metrics presented in Equation 9 and Equation 10.

RESULTS AND DISCUSSION

This study compared three different fuzzy logic models to evaluate the impact of various climatic variables on the forecast of daily average solar radiation. The daily radiation forecasts for a one-month period are presented in Figure 6,

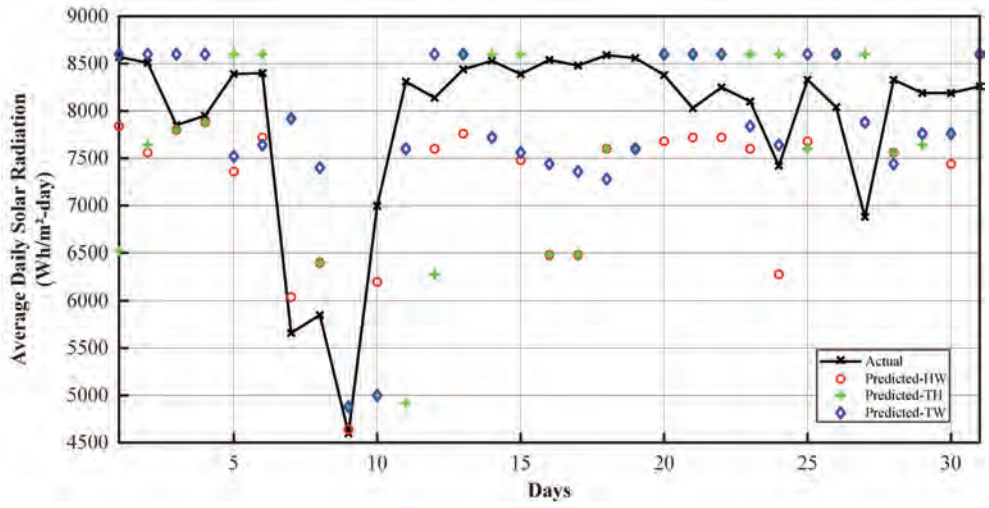


Figure 6. Average daily solar radiation forecasts of fuzzy logic models for a one-month period.

Table 4. Comparison of solar radiation forecasting performance of fuzzy logic models developed with different input pairs

Input Pair	RMSE (kWh/m²-day)	MAPE (%)
HW	0.85	9.07
TW	0.89	9.61
TH	1.23	11.80

while the performance comparison of the models is provided in Table 4. According to the results, the model developed with HW as inputs demonstrated the best forecasting performance, with a MAPE of 9.07%. This was followed by the model using TW inputs, which achieved a MAPE of 9.61%. The model developed with TH inputs, however, exhibited lower performance compared to the others, with a MAPE of 11.80%.

The evaluation of the importance of climatic variables in solar radiation forecasting, based on the results of fuzzy logic-based models, indicates that wind speed is one of the most influential factors. The wind speed is present in the model with the best forecast performance and in the second ranked model, showing that it has a significant impact on the forecasting of solar radiation. Relative humidity is an important factor of radiation attenuation as it influences the amount of water vapor in the atmosphere [50]. However, it is only present in the first and third ranked combinations in terms of forecast performance. The temperature is generally considered a product of solar radiation. So, the temperature does not directly improve forecasts, but plays an indirect role. The results indicate that wind speed is more influential than relative humidity in the fuzzy logic-based solar radiation forecasting and temperature can be taken as a secondary parameter.

In addition to evaluating the impact of climatic variables on solar radiation forecasting, this study also assesses the effectiveness of forecasting solar radiation using fuzzy logic models. For this purpose, the best-performing fuzzy logic model (built with the HW input pair) was compared with a feedforward ANN trained with six months of data from the analysis region. Figure 7 presents the daily radiation forecasts for a one-month period from both approaches. The comparison results revealed that the ANN forecasting model had an MAPE of 14.38%, compared with 9.07% for the HW fuzzy logic model. In fact, the forecasting performance of the ANN was lower than that of all three fuzzy logic models. This demonstrates that fuzzy logic approaches are an effective tool for daily solar radiation forecasting and can provide more accurate results compared to more complex forecasting methods.

Finally, Figure 8 compares the performance of all forecasting models considered in this study based on RMSE and MAPE criteria. The literature indicates that in the classification, a MAPE of less than 10% indicates excellent forecasting accuracy, between 10% and 20% indicates good accuracy, between 20% and 50% is acceptable and above

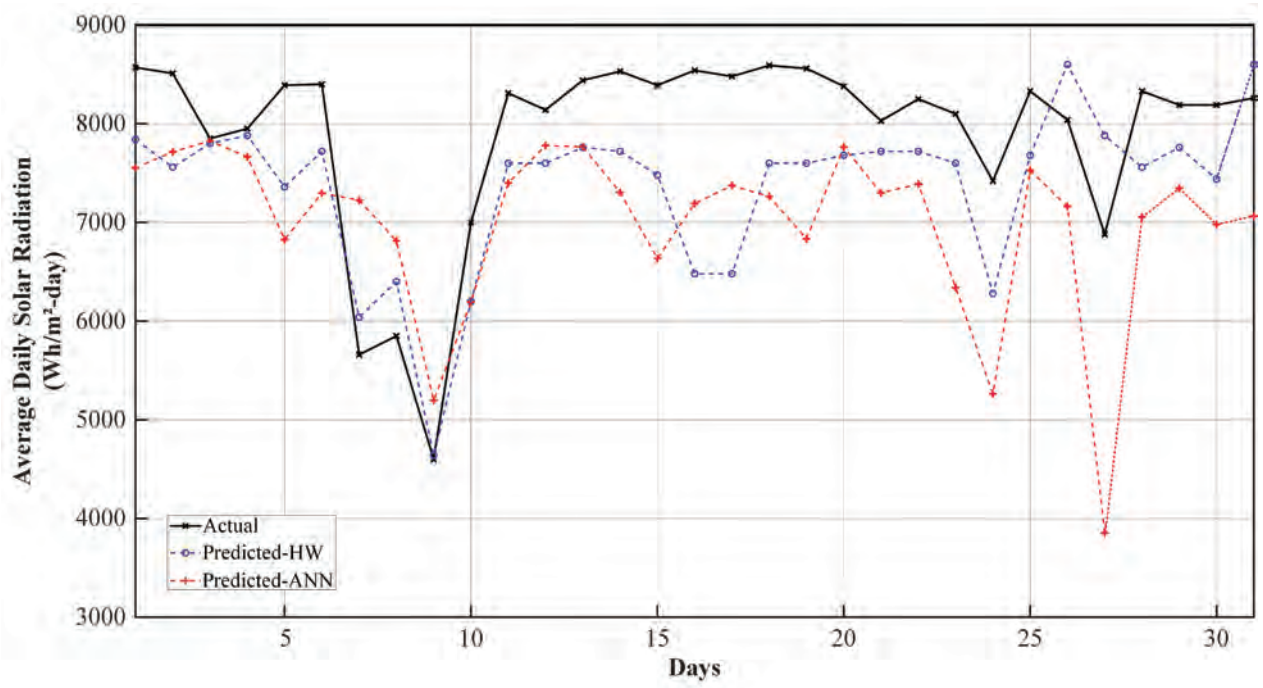


Figure 7. Average daily solar radiation forecasts for the fuzzy logic model (built with the HW input pair) and the ANN model for a one-month period.

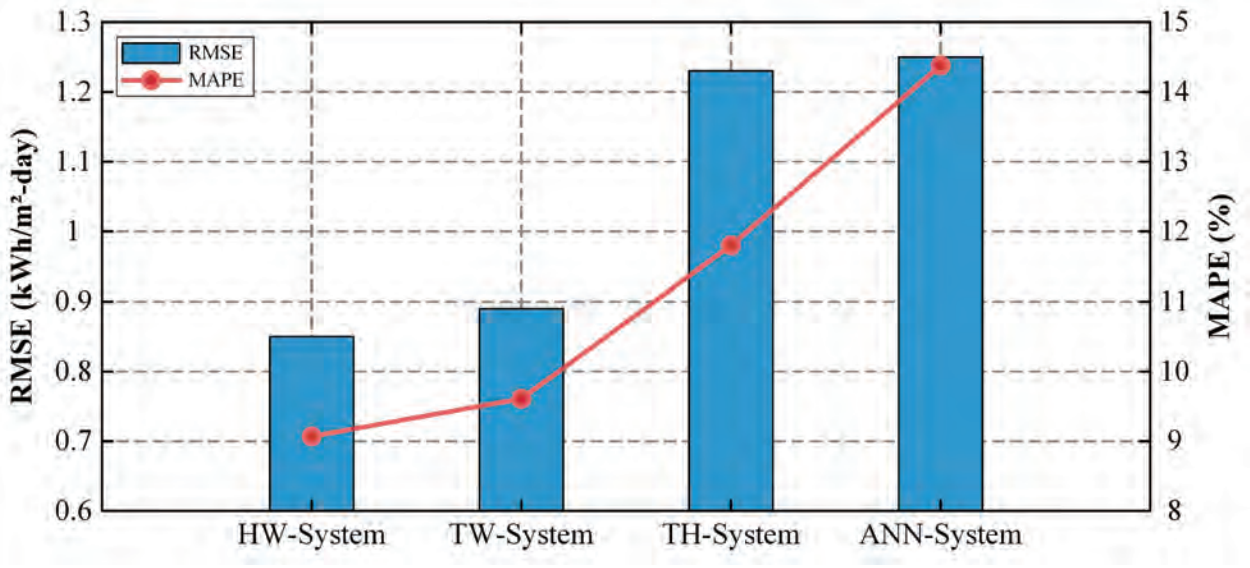


Figure 8. Performance comparison of all forecasting models presented in the study.

50% indicates poor forecasting performance [51]. Based on this classification, several of the fuzzy logic models developed with different combinations of inputs achieved excellent forecasting accuracy with MAPE values less than 10%. The results also suggest that the forecasting performance can be improved by appropriate selection of climatic variables without increasing the model complexity. The results show the potential of fuzzy logic-based approaches for solar radiation forecasting, and more generally for solar energy systems planning and optimization.

The fuzzy logic model developed in this work has several advantages in terms of model simplicity, data availability and forecasting performance compared to previous studies. However, there were some methodological limitations in the earlier studies. Refs. [28] and [29] presented a short-term or hourly forecast, and Ref. [28] also demonstrated limited performance under cloudy conditions. Conversely, Ref. [30] used only air temperature as an input and did not include any other potentially relevant climatic variables. The current study focuses on daily forecasting and examines different combinations of multiple meteorological inputs, thereby addressing these limitations. Other studies, e.g., Refs. [31, 32] used five or more input parameters which led to more complex model structure and higher computational requirements. For example, in Ref. [32] a fuzzy system with around 1,200 rules was developed. Additional inputs can improve the accuracy of the forecasts, but the increased complexity of the model can increase the computational requirements and reduce the ease of implementation. Moreover, it is observed that the MAPE is a function of the study region, forecasting time horizon, and the variability of solar radiation and should not be treated in isolation when comparing different studies. However, the best fuzzy model in this study with MAPE below 10%, which is equivalent to the classification of the forecasting accuracy in Ref. [51] as excellent, was obtained with only two inputs, HW, and a small rule base of 16 rules. Both variables are readily available from meteorological datasets which may facilitate the application of the model in different regions. Furthermore, the comparison of the various input combinations revealed that among the climatic variables considered in this study, wind speed had the highest impact on the forecasting performance. In general, the results indicate that careful selection of input variables can lead to high forecasting accuracy without the need for high-dimensional input sets or highly complex model structures, which may be especially useful for data-scarce applications.

CONCLUSION

The forecasting of solar radiation is an important topic because of its broad application from photovoltaic energy production, agricultural planning, to building energy efficiency and climate change research for energy management and sustainable development goals. Linear and nonlinear modeling techniques, AI based approaches and fuzzy logic-based models are used for solar radiation forecasting. However, these methods pose several challenges and fuzzy logic-based models in particular, have gained less prominence in the literature as compared to other approaches. However, their ability to deal with uncertainties and flexibility in the interpretation of complex relationships can lead to substantial benefits for solar radiation forecasting. In this sense, the correct selection of the input parameters in the construction of a fuzzy logic system is important for improving the accuracy of the forecasts. Three different fuzzy logic models were developed in this study to analyze the key climatic variables that influence solar radiation

using pairs of input variables: TH, TW and HW. In addition, the fuzzy logic models were compared with an ANN model for the evaluation of their performance in solar radiation forecasting.

The main novelty of this study is to demonstrate that low-complexity fuzzy logic models, designed with meteorologically relevant and easily accessible inputs, can outperform more sophisticated AI models in terms of accuracy and computational efficiency. To the best of our knowledge, this study is the first to systematically compare the performance of fuzzy logic models and ANN models under the same conditions and to rank the contribution of individual climatic variables in fuzzy logic based solar radiation forecasting. The results of daily average solar radiation forecasting for a one-month period in Ankara, Türkiye based on error percentages obtained from three different fuzzy logic models show that the model using HW as inputs obtained the lowest error with a MAPE of 9.07%. The TW model followed with a MAPE of 9.61%, while the model with TH inputs showed the lowest performance with MAPE 11.80%. The results show that the most important parameter for solar radiation forecasting is wind speed, followed by relative humidity, and temperature plays a secondary role. Furthermore, the ANN model that was used to test the effectiveness of fuzzy logic systems, exhibited a lower forecasting accuracy with a MAPE of 14.38% compared to all fuzzy logic models. Accordingly, in the solar radiation forecasting field, fuzzy logic models with simple structures can provide more effective and reliable results than more complicated AI methods, by only detecting accurate climatic inputs, without increasing the complexity or the computational cost of the model. Fuzzy logic models have a great potential in the planning and optimization of solar energy systems because of their excellent accuracy rates and flexible structures. These models could therefore play a crucial role in achieving sustainability goals, including improving the efficiency of use of renewable energy sources, reducing carbon footprints and enhancing security of energy supply.

In future work, it would be advantageous to increase the number of climatic variables used to forecast solar radiation so as to improve the accuracy and scope of the models. For instance, the inclusion of variables such as atmospheric pressure, sunshine duration and cloud cover ratio in the model may further improve the forecasting performance. Furthermore, the results could be generalized better by performing studies on larger datasets and considering different geographical regions and seasonal variations. From an application point of view, the proposed fuzzy logic models are a practical tool for energy planners, policy makers and engineers to forecast solar radiation in data scarce regions. Their low computational requirements and dependence on easily measurable climatic inputs make them suitable for real-time applications in solar energy project planning, agricultural scheduling and grid load balancing. Moreover, these models are scalable and interpretable, can be adapted to different geographical and socioeconomic contexts, and do not require high-dimensional datasets or complex AI architectures. Such long-term research and deployment of simplified fuzzy models would be of great help for better planning of solar energy systems, optimization of energy production forecasts and sustainable energy management, especially in developing regions with limited infrastructure.

NOMENCLATURE

AI	Artificial Intelligence
ANN	Artificial Neural Network
H	High
HW	Relative Humidity and Wind Speed
L	Low
LoM	Largest of Maximum
M	Medium
MAPE	Mean Absolute Percentage Error
MSE	Mean Squared Error
ReLU	Rectified Linear Unit
RMSE	Root Mean Square Error
TH	Temperature and Relative Humidity
TW	Temperature and Wind Speed
VL	Very Low

AUTHORSHIP CONTRIBUTIONS

Authors equally contributed to this work.

DATA AVAILABILITY STATEMENT

The authors confirm that the data that supports the findings of this study are available within the article. Raw data that support the finding of this study are available from the corresponding author, upon reasonable request.

CONFLICT OF INTEREST

The authors declared no potential conflicts of interest with respect to the research, authorship, and/or publication of this article.

ETHICS

There are no ethical issues with the publication of this manuscript.

STATEMENT ON THE USE OF ARTIFICIAL INTELLIGENCE

Artificial intelligence was not used in the preparation of the article.

REFERENCES

[1] Awogbemi O, Kallon DV Von, Kumar KS. Contributions of artificial intelligence and digitization in achieving clean and affordable energy. Intell Syst with Appl 2024;22:200389. [CrossRef]

[2] Kumar K. S, Muniamuthu S, Tharanisrisakthi BT. An Investigation to Estimate the Maximum Yielding Capability of Power for Mini Venturi Wind Turbine. Ecol Eng Environ Technol 2022;23:72–78. [CrossRef]
[3] Lima MA, Mendes LFR, Mothé GA, Linhares FG, de Castro MPP, da Silva MG, et al. Renewable energy in reducing greenhouse gas emissions: Reaching the goals of the Paris agreement in Brazil. Environ Dev 2020;33:100504. [CrossRef]
[4] Holechek JL, Geli HME, Sawalhah MN, Valdez R. A Global Assessment: Can Renewable Energy Replace Fossil Fuels by 2050? Sustainability 2022;14:4792. [CrossRef]
[5] Kumar KS, Muniamuthu S, Kumar KS, Mohan KR. Measurement of temperature flow analysis by condition monitoring system for WTG gear box to evaluate the thermal performance associated with plant load factor. J Therm Eng 2023;9:979–987. [CrossRef]
[6] Srimanickam B, Kumar S. Drying investigation of coriander seeds in a photovoltaic thermal collector with solar dryer. J Therm Eng 2023;9:659–668. [CrossRef]
[7] Parlak BO, Yavasoglu HA, Ozcan HG. In-depth analysis of battery life enhancement in solar-assisted fuel-cell range-extender vehicles. Int J Hydrogen Energy 2024;67:1033–1043. [CrossRef]
[8] Parlak BO, Yavasoglu HA. Assessment of Vehicle-Integrated Photovoltaics: A financial and environmental perspective. Sustain Energy Technol Assessments 2024;72:104042. [CrossRef]
[9] International Energy Agency. Solar PV 2024. https://www.iea.org/energy-system/renewables/solar-pv. Accessed July 4, 2025.
[10] Ahmadizadeh M, Heidari M, Thangavel S, Naamani E Al, Khashehchi M, Verma V, et al. Technological advancements in sustainable and renewable solar energy systems. Highly Effic. Therm. Renew. Energy Syst., Boca Raton: CRC Press; 2024, p. 23–39. [CrossRef]
[11] Sahan M. Measurement of daily solar radiation with Eppley Black and White Pyranometer in Osmaniye region, Turkey. AIP Conf. Proc., vol. 2042, 2018, p. 020005. [CrossRef]
[12] Yadav AK, Chandel SS. Solar radiation prediction using Artificial Neural Network techniques: A review. Renew Sustain Energy Rev 2014;33:772–781. [CrossRef]
[13] Yorukoglu M, Celik AN. A critical review on the estimation of daily global solar radiation from sunshine duration. Energy Convers Manag 2006;47:2441–2450. [CrossRef]
[14] Almorox J, Bocco M, Willington E. Estimation of daily global solar radiation from measured temperatures at Cañada de Luque, Córdoba, Argentina. Renew Energy 2013;60:382–387. [CrossRef]
[15] Nawab F, Abd Hamid AS, Ibrahim A, Sopian K, Fazlizan A, Fauzan MF. Solar irradiation prediction using empirical and artificial intelligence methods: A comparative review. Heliyon 2023;9:e17038. [CrossRef]
[16] Patel D, Patel S, Patel P, Shah M. Solar radiation and solar energy estimation using ANN and Fuzzy logic concept: A comprehensive and systematic study. Environ Sci Pollut Res 2022;29:32428–32442. [CrossRef]
[17] Parlak BO, Yavasoglu HA. Comparison of Regression Algorithms to Predict Average Air Temperature. Int J Eng Res Dev 2023;15:312–322. [CrossRef]
[18] Teke A, Yıldırım HB, Çelik Ö. Evaluation and performance comparison of different models for the estimation of solar radiation. Renew Sustain Energy Rev 2015;50:1097–1107. [CrossRef]
[19] Girdhani B, Agrawal M. Performance evaluation of statistical and deep learning models for daily solar global horizontal radiation prediction: implications for renewable energy and sustainability. Environ Dev Sustain 2025:1–29. [CrossRef]
[20] Bilgili M, Ozgoren M. Daily total global solar radiation modeling from several meteorological data. Meteorol Atmos Phys 2011;112:125–138. [CrossRef]
[21] Behrang MA, Assareh E, Ghanbarzadeh A, Noghrehabadi AR. The potential of different artificial neural network (ANN) techniques in daily global solar radiation modeling based on meteorological data. Sol Energy 2010;84:1468–1480. [CrossRef]
[22] Asl SFZ, Karami A, Ashari G, Behrang A, Assareh A, Hedayat N. Daily global solar radiation modeling using multi-layer perceptron (MLP) neural networks. Int J Environ Ecol Eng 2011;5:403–405.
[23] Almasoud WA, Al-Sager SM, Almady SS, Marey SA, Al-Hamed SA, Al-Janobi AA, et al. A Prediction of the Monthly Average Daily Solar Radiation on a Horizontal Surface in Saudi Arabia Using Artificial Neural Network Approach. Processes 2025;13:1149. [CrossRef]
[24] Khalfa MA, Manai L, Mchara W. Advanced artificial intelligence model for solar irradiance forecasting for solar electric vehicles. Int J Dyn Control 2025;13:101. [CrossRef]
[25] Mariappan Y, Ramasamy K, Velusamy D. An optimized deep learning based hybrid model for prediction of daily average global solar irradiance using CNN SLSTM architecture. Sci Rep 2025;15:10761. [CrossRef]
[26] Ho ND, Chang IJ. TCL: an ANN-to-SNN Conversion with Trainable Clipping Layers. 2021 58th ACM/IEEE Des. Autom. Conf., IEEE; 2021, p. 793–798. [CrossRef]
[27] Şen Z. Fuzzy algorithm for estimation of solar irradiation from sunshine duration. Sol Energy 1998;63:39–49. [CrossRef]
[28] Boata R. Fuzzy logic procedure for computing global solar irradiation. Rom J Phys 2016;61:1389–1394.
[29] Chugh A, Chaudhary P, Rizwan M. Fuzzy logic approach for short term solar energy forecasting. 2015 Annu. IEEE India Conf., IEEE; 2015, p. 1–6. [CrossRef]

[30] Boata R, Pop N. Estimation of global solar irradiation by using Takagi-Sugeno fuzzy systems. Rom J Phys 2015;60:593–602.
[31] Rizwan M, Jamil M, Kirmani S, Kothari DP. Fuzzy logic based modeling and estimation of global solar energy using meteorological parameters. Energy 2014;70:685–691. [CrossRef]
[32] Mehta S, Basak P. Solar irradiance forecasting using fuzzy logic and multilinear regression approach: A case study of Punjab, India. Int J Adv Appl Sci 2019;8:125. [CrossRef]
[33] Niu XJ, Li QB, Liu WJ, Hu Y. Effects of ambient temperature, relative humidity and wind speed on interlayer properties of dam concrete. Constr Build Mater 2020;260:119791. [CrossRef]
[34] Zadeh LA. Fuzzy sets. Inf Control 1965;8:338–353. [CrossRef]
[35] Başar G, Kahraman F. Prediction of surface hardness in a burnishing process using Taguchi method, fuzzy logic model and regression analysis. Sigma J Eng Nat Sci 2018;36:1283–1295.
[36] Pedrycz W. Why triangular membership functions? Fuzzy Sets Syst 1994;64:21–30. [CrossRef]
[37] Bahadır A. Modeling of a brushless dc motor driven electric vehicle and its pid-fuzzy control with dSPACE. Sigma J Eng Nat Sci 2023;41:156–177. [CrossRef]
[38] Oztekin E. 1D Fuzzy inverse logic method and its use in the design of thick reinforced concrete columns. Sigma J Eng Nat Sci 2024;42:459–474. [CrossRef]
[39] Kataria N. A Comparative Study of the Defuzzification Methods in an Application. IUP J Comput Sci 2010;4.
[40] Sunkun S, Parlak BO, Akca TB. Level Control of a Crude Oil Tank using Fuzzy-PID Controller. 7th Int. Artif. Intell. Data Process. Symp., 2023, p. 104–114.
[41] Sunkun S, Parlak BO, Yildirim A, Yavasoglu HA. Fuzzy Decision Based Modeling of Rheostatic Brake System for Autonomous Land Vehicles. Comput Sci 2022. [CrossRef]
[42] Shoureshi R, Zhi Hu. Tsukamoto-type neural fuzzy inference network. Proc. 2000 Am. Control Conf. ACC (IEEE Cat. No.00CH36334), vol. 4, IEEE; 2000, p. 2463–2467 vol.4. [CrossRef]
[43] Molaie M, Falahian R, Gharibzadeh S, Jafari S, Sprott JC. Artificial neural networks: powerful tools for modeling chaotic behavior in the nervous system. Front Comput Neurosci 2014;8:40. [CrossRef]
[44] Karadurmus E, Goz E, Keles C, Yuceer M. Utilizing artificial neural networks (ANN) for predictive modeling of sulfate removal from water. Sigma J Eng Nat Sci 2024;42:1866–1875. [CrossRef]
[45] Galushkin AI. Methods of Problem Solving in the Neural Network Logical Basis. Neural Networks Theory, Berlin, Heidelberg: Springer Berlin Heidelberg; 2007, p. 341–376. [CrossRef]
[46] Chen SX, Gooi HB, Wang MQ. Solar radiation forecast based on fuzzy logic and neural networks. Renew Energy 2013;60:195–201. [CrossRef]
[47] Chicco D, Warrens MJ, Jurman G. The coefficient of determination R-squared is more informative than SMAPE, MAE, MAPE, MSE and RMSE in regression analysis evaluation. PeerJ Comput Sci 2021;7:e623. [CrossRef]
[48] Güneş Ü, Başhan V, Karakurt AS. Predicting tanker main engine power using regression analysis and artificial neural networks. Sigma J Eng Nat Sci 2023;41:216–225. [CrossRef]
[49] Qadem M, Filik ÜB. Solar radiation forecasting by using deep neural networks in Eskişehir. Sigma J Eng Nat Sci 2021;39:159–169. [CrossRef]
[50] Tasie NN, Israel-Cookey C, Banyie LJ. The effect of relative humidity on the solar radiation intensity in Port Harcourt, Nigeria. Int J Res 2018;5:128–136.
[51] Lewis CD. Industrial and Business Forecasting Methods: A Practical Guide to Exponential Smoothing and Curve Fitting. London: Butterworth Scientific; 1982.

Sigma J Eng Nat Sci, Vol. 44, No. 4, pp. 2758–2782, August, 2026

Sigma Journal of Engineering and Natural Sciences
Web page info: https://sigma.yildiz.edu.tr
DOI: 10.14744/sigma.2026.2126

Research Article

Emotion-aware human-computer interaction using multimodal deep learning and explainable artificial intelligence

Pallavi WANKHEDE[1], Deepali KOTAMBKAR[2], Kanchan WARKAR[3,*], Sweta RAUT[4]

[1]*St.Vincent Pallotti College of Engineering and Techonology, Nagpur, Maharashtra, 441108, India*
[2]*Ramdeobaba University, Nagpur, Maharashtra, 440013, India*
[3]*Visvesvaraya National Institute of Technology, Nagpur, Maharashtra, 440010, India*
[4]*Jhulelal Institute of Technology,Off Koradi Road,Lonara, Nagpur, Maharashtra, 441111, India*

ARTICLE INFO

Article history
Received: 19 November 2025
Revised: 12 January 2026
Accepted: 22 March 2026

Keywords:
Affective Computing; Deep Learning; Emotion Recognition; Explainable AI; Human–Computer Interaction; Multimodal Fusion

ABSTRACT

Emotion-aware human computer interaction is the natural and flexible Human Computer Interaction (HCI) to perceive and consider human emotion responses in the computation. Few recent successes in deep learning have resulted in an increased emotion recognition accuracy but, mostly the emotion-aware HCI systems are limited to poor robustness in practical scenarios and lack of interpretability at the decision level, thus limiting their adoption for practical applications. This work defines the problem of robust and transparent emotion recognition by designing an explainable modality-adaptive multimodal deep learning framework, capable of fusing multiple input modalities such as facial expressions, speech and physiological responses. The emotion perception framework employs a set of deep neural models to perform spatial–temporal feature extraction and introduces a set of neural architecture designs, namely, Modality-Adaptive Attention Fusion Module (MAAFM) mechanism to adaptively fuse the modalities based on modality qualities and contextual information. Further, for interpretability, the knowledge at the modality level and at the fusion level is extracted through various shallow modules at the feature- and the fusion-level respectively, which provides transparency towards how each modality affects the inference. The proposed framework is evaluated over benchmark datasets for visual, audio and physiological modalities and reports an overall emotion recognition accuracy of 92.4 %, F1-score of 0.91, and area under the receiver operating characteristic curve of 0.97, while preserving a low inference latency for interactive applications. The approach provides improved robustness, transparency and applicability. The key innovation of this work is the focus on the attention not only as a performance tool but also as an explicit source of interpretation of the modality contributions at the fusion level that advances existing emotion recognition approaches.

Cite this article as: Wankhede P, Kotambkar D, Warkar K, Raut S. Emotion-aware human-computer interaction using multimodal deep learning and explainable artificial intelligence. Sigma J Eng Nat Sci 2026;44(4):2758–2782.

***Corresponding author.**
*E-mail address: kanchan22.warkar@gmail.com

This paper was recommended for publication in revised form by Editor-in-Chief Ahmet Selim Dalkilic

Published by Yıldız Technical University Press, İstanbul, Turkey
© Author. This is an open access article under the CC BY-NC license (http://creativecommons.org/licenses/by-nc/4.0/).

INTRODUCTION

Background and Motivation

Emotion recognition as part of next-generation human-computer interaction systems capability will allow computers to not only perceive, and recognize emotion of a human, but also react to the emotion in a way humans would in a social situation. Interactions of previous generations of human-computer interaction system were based on the explicit interaction modalities such as typed command, or speech input, thus did not have the means to detect the implicit component of the human interaction with a system. On the other hand, emotion-enabled computer human interaction systems seek to infer emotion from expressive cues provided by the human via speech, facial expressions as well as body language [1].

Different inputs such as face, speech, and physiological signal are encoded in dedicated modality encoding module, and fused in the proposed modality-adaptive attention fusion module (MAAFM). Both feature-level explanation and fusion-level explanation are conducted in the Multi-Level Explainability Module before final adaptive system response [2].

The significance of emotion-aware interaction is thus very high, far beyond technical affective computing research. For example, in adaptive learning systems, automatic emotion detection can be used to automatically recognize interest, confusion, frustration, or engagement, to adapt the system to what is sensed in real-time [3]. In health monitoring and medical applications, monitoring the patterns of emotional behaviors can assist in early detection of stress-related problems through unobtrusive sensing, and assistive interfaces for the elderly or persons with disabilities can adapt to their affective states for improved comfort and usability.

Unimodal approaches to emotion recognition were developed initially and determine emotional affect states from a singular source - facial expressions, speech, physiological signals. Whilst on occassion they produce excellent results in isolated controlled environments, unimodal methods lack robustness in real-life situations. Facial features can be occluded or neutral, speech recognition systems are target dependent and susceptible to noise and cultural influences, physiological sensing is intrusive and lacks context [4, 5]. This lack of robustness compromises generalisation.

In the last several years, deep learning has contributed to advances in emotion recognition through learning of features from extensive sensory data, but the model of human-like understanding calls for a synthesis of visual, auditory and physiological cues. Multimodal deep learning has been proposed to provide this multisensory integration for better accuracy, contextual sensitivity, and robustness to noise. However, growing levels of complexity in deep models of behaviour pose significant challenges of robustness, explainability and real-time suitability for human-computer interaction in different situations with different users, environments, and emotional strengths [6, 7].

Figure 1 shows an example of a user whose emotion is detected by sensing the different axes involved in an interaction in a computer/robot (facial expression, voice, physiological sensors). Each sensor modality is modeled independently using deep networks (Convolutional Neural Network (CNN) for vision, Bidirectional Long Short-Term Memory (BiLSTM) for audio, and Long Short-Term Memory (LSTM) for physiological signals) and then combined into one fusion layer [8]. The fused features are then passed through an explainability analysis (SHAP or Grad-CAM) before the responsive information (emotion-based feedback, interface change, speech output) is provided.

Research Gap

Despite impressive performance advances, numerous essential issues still need to be addressed before multimodal emotion recognition systems can be practical. Many top-performing models, including those based on

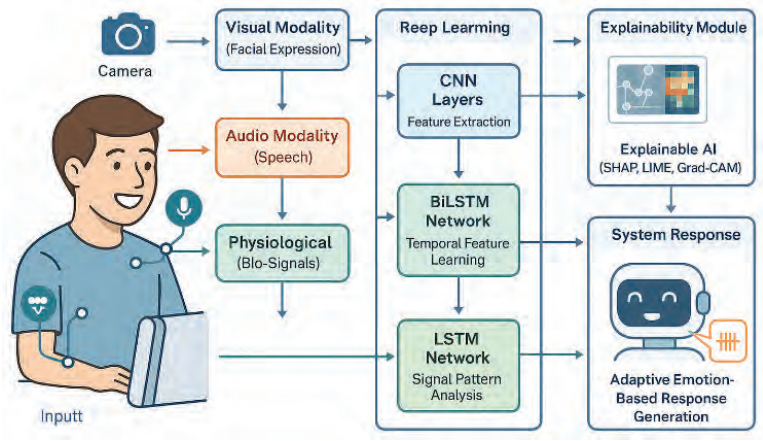


Figure 1. Conceptual overview of the modality-adaptive multimodal emotion recognition framework.

deep learning such as convolutional, recurrent, and transformer-based models, focus on predictive accuracy and are largely unexplainable. Their lack of explainability, however, hampers user trust and provider accountability and raises ethical issues, especially when used in domains like education, health care, and mental health [9].

A third drawback of these approaches is the absence of dynamic fusion schemes that can adapt to the different levels of input noise as well as occlusion. Many recognition systems fuse their input features in a predetermined way, either by concatenating feature vectors, or applying fixed rules, which doesn't reflect the actual interaction environment where some modalities may be rendered unreliable. Recognition accuracy drops dramatically when one modality is severely affected [10].

Additionally, application-oriented requirements, including real-time operation, robustness in the presence of sensing failures, user-oriented explainability are often neglected. Although the human-interpretable explanations are emerging in recent work, existing approaches mainly adopt attention-based mechanisms, and explainable AI techniques as separate, or after-fact tools for the multimodal fusion, thus not able to addressing the simultaneous needs of accuracy, robustness, interpretability, and real-time in the context of interaction between humans as well as computers.

Research Objectives

The objective of this study is to develop a multimodal deep learning framework with integrated explainable artificial intelligence for emotion-aware human–computer interaction that addresses the identified limitations. The specific objectives are as follows:

- To design a multimodal emotion recognition framework that integrates facial, speech, and physiological signals, enabling comprehensive affect understanding through complementary sensory information.
- To improve recognition robustness and reliability under varying environmental conditions, including background noise, visual occlusion, and physiological signal distortion, by dynamically adapting modality contributions during inference.
- To incorporate explainable artificial intelligence techniques that provide feature-level, modality-level, and decision-level interpretability, thereby enhancing transparency, trust, and human understanding of system behavior.
- To validate the proposed framework using benchmark datasets and real-time interaction scenarios, demonstrating its suitability for practical emotion-aware human–computer interaction applications.

Through these objectives, the study aims to contribute a unified, transparent, and robust emotion recognition framework that supports the development of ethical, trustworthy, and empathetic interactive systems.

Novelty and Contributions

The main technical contributions of this work are summarized as follows:

1. Modality-adaptive Modality-Adaptive Attention Fusion Module (MAAFM) architecture:

A reliability-aware multimodal fusion design in which attention weights are learned per input sample, enabling dynamic adjustment of modality importance. This design yields measurable improvements in accuracy, area under the curve, Cohen's Kappa, and robustness under missing or noisy modalities, as validated through controlled degradation experiments.

2. Unified multi-level explainability integration strategy:

A systematic integration of explainable artificial intelligence at feature, fusion, and decision levels, combining Grad-CAM, SHAP, LIME, and attention-weight visualization. This design enables transparent interpretation of both modality-specific features and cross-modal interactions, which is quantitatively and qualitatively demonstrated through visual explanations and attribution analysis.

3. Rigorous and reproducible experimental evaluation protocol:

A comprehensive evaluation framework across three benchmark datasets, including subject-independent testing, robustness analysis under degraded sensing conditions, ablation studies, and statistical significance testing with confidence intervals, ensuring reproducibility and objective performance validation.

4. Computationally efficient multimodal design for real-time interaction:

A CNN–BiLSTM–Attention architecture that achieves competitive or superior performance compared to transformer-based multimodal models while maintaining lower model complexity, reduced inference latency, and real-time suitability for emotion-aware human–computer interaction systems.

Although convolutional–recurrent architectures with attention mechanisms have been widely explored for multimodal emotion recognition, most existing frameworks employ attention primarily as a latent optimization tool and apply explainable artificial intelligence in a post hoc manner. In contrast, the proposed framework introduces a modality-adaptive attention mechanism that explicitly models modality reliability on a per-sample basis and exposes attention weights as interpretable fusion-level explanations. Unlike prior multimodal explainable systems that focus on modality-specific interpretation only, this work integrates explainability before fusion, during fusion, and after decision making. Furthermore, the proposed design emphasizes real-time feasibility and robustness under degraded sensing conditions, which are rarely addressed jointly in existing CNN–RNN–attention architectures.

LITERATURE REVIEW

Unimodal Emotion Recognition

Unimodal Emotions Classification There are primarily two types of early work in emotion recognition using unimodal analysis, which identify emotional status based on only one source of information among facial expressions, speech signals or physiological signals. Classic feature set and classifier models based on hand extracted features such as support vector machine, hidden Markov model and decision tree were extensively investigated in the pioneer work of unimodal emotions classification [11, 12], with interpretable model and relatively low cost, but the overall performance was very vulnerable to noise, incomplete and unpredictable environments.

Due to the ability of deep learning to automatically extract spatial features from images, convolutional neural networks (CNN) have become popular, and adopted for facial emotion recognition. Whereas, the use of recurrent neural networks (RNN) and long short-term memory (LSTM) models for speech and physiological signals, the models have been used to learn temporal features [13]. Due to deep models' impressive recognition performance in controlled environments, unimodal emotion recognition systems have still failed to be robust to modality-dependent variations such as facial occlusion, speech with background noise and sensor artifacts for physiological signals. As a result, the unimodal methods do not generalize well to different users, environments and interactions [14].

Multimodal Emotion Recognition and Fusion Approaches

Efforts to address the insufficiency of a unimodal system proposed multimodal emotion recognition frameworks that fuse audio, video, and physiological information. The goal of fusing multiple sources is inspired by human sensation in which a human evaluates emotions through the combination of multiple senses. Current multimodal systems can be categorized into three types: early fusion, late fusion, and hybrid fusion [15, 16].

Early fusion: Early fusion approaches fuse features across multiple modalities prior to the classification stage and allow for learning of cross-modalities interactions in the underlying model. Early fusion methods however, are vulnerable to noisy or failed modalities since all modalities are considered equally. Late fusion: Late fusion approaches combine decisions of independent modalities at the decision level, thus being robust to data drop-out, but usually ignoring fine-grain interactions across modalities [17, 18]. Hybrid fusion: Hybrid fusion approaches (e.g., attention-based model, transformer-based model) try to find a trade-off between early and late fusion methods [17, 18].

These days, a few research works have shown that the use of attentional modules and self-attentional model architectures is desirable for capturing the intermodal dependencies for better multimodal emotion recognition [19], and transformer-based fusion architectures have achieved competitive results on benchmark datasets. However, majority of them optimize the model for performance without any focus on model interpretability and real-time constraints. In addition, the fusion process is fixed or obscure, which makes the full advantage of each modality little explainable to be used for human-computer interaction system [20].

Explainable Artificial Intelligence in Emotion Recognition Systems

Deep learning models of emotion recognition through human behavior, speech, and physiological signals are more effective if they provide interpretability since this is more relevant for many applications like human-computer interaction, education, healthcare, and mental health. Techniques like gradient-based visual explanations, feature attribution methods, and local surrogate models, have been used to interpret deep learning predictions. For facial emotion recognition, visual explanation techniques are used to explain facial areas relevant to emotions. For speech and physiological emotion recognition, feature attribution methods are used to explain influential features like dominant frequency bands or acoustic features. [21-23]

While these modality-specific techniques increase interpretability on a modality level, most of the current work is limited to applying either explainable machine learning methods or interpretability frameworks to unimodal models. Integrating explainability to multimodal pipelines remains an unexplored field. Several approaches explain unimodal model's predictions based on the specific modality, leaving the question of how the fused modality representation and fusion mechanism of the multimodal model contribute to the prediction open.

Identified Research Gap and Motivation for the Proposed Work

According to the discussed papers, several important issues still need to be tackled. Firstly, there is no multimodal emotion recognition framework that simultaneously combines robustness, interpretability and real-time performance. Although using multiple sources of data helps improve the recognition performance, some researchers resort to static or opaque fusion methods that do not work when modalities are degraded and are difficult to interpret. Secondly, very few of the explainable AI techniques are applied at the fusion level which prevents user to know the overall cross-modal contributions to emotion inference. Lastly, many of the state-of-the-art models are computationally expensive and cannot be used in real-time human computer interaction [24, 25].

The planned work to overcome these issues is explained below: A modality-adaptive and explainable multimodal framework to fuse and utilize multiple cues, including facial, speech, and physiological signals, is presented. It differs from previous work by exploiting attention as a fusion cue and as a transparent signal, where the involved modalities are weighted according to the given context and the

signals that result the model prediction are made transparent. A full multimodal deep learning framework with integrated explainability and low-latency inference is proposed to match the technical and practical needs of real-world emotion-aware human-computer interaction.

MATERIALS AND METHODS

System Overview

The Modality-Adaptive Multimodal Emotion Recognition Framework, which includes three modality encoders, a Modality-Adaptive Attention Fusion Module (MAAFM) and a Multi-Level Explainability Module. This mechanism enable the proposed framework to adapt to the dynamic environment in real-life scenarios, for example, noisy speech or occluded face parts. With both class-level and fusion-level explainable AI components, the intermediate outputs in the network and the final results could be interpreted and explained. This provides a balanced solution among the accuracy, robustness and interpretability, which are the critical requirements for real-world emotion-aware interactive applications.

Facial features are encoded using ResNet50; speech features are captured using 1D CNN-BiLSTM; physiological features are represented by BiLSTM. These embeddings are then fused by the Modality-Adaptive Attention Fusion Module (MAAFM) before classification and explanation analysis.

During the first level of feature extraction, convolutional neural networks are used to generate the spatial embeddings from facial frames, meanwhile the temporal models, for instance, BiLSTM or temporal convolutional networks, for capturing the sequential dependencies of speech and physiological signals. In the fusion level, CNN-BiLSTM-Attention Architecture is used to fuse different embeddings into a latent one.

Figure 2 provides an overview of the processing architecture for the emotion aware human computer interaction framework. The architecture is modular by design, where facial, speech and physiological inputs are first extracted separately in order to maintain their modality specific information.

In the end, emotion class labels are generated by a softmax classifier and XAI methods, like Grad-CAM, SHAP and LIME, provide visual and quantitative interpretability across features and decisions.

Multimodal Data Representation

The performance of the emotion recognition is largely influenced by the encoding of features extracted from different modalities. The input tensors for the facial, speech, and physiological modalities are represented by $X_{face} \in \mathbb{R}^{Tf \times df}$, $X_{audio} \in \mathbb{R}^{Ta \times da}$, and $X_{physio} \in \mathbb{R}^{Tp \times dp}$ respectively, where T denotes the temporal length, and d the feature dimensionality.

Facial expressions

Facial cues are detected by the CNN backbone (Resnet50) that can capture local and global spatial dependencies. The CNN is first passed through a sequence of convolutional filters with nonlinear activations [26]:

$$F_{face} = \sigma\left(W_{c1} * X_{face} + b_{c1}\right) \quad (1)$$

where; * indicates the convolution, W_{c1} stands for the filter weights, b_{c1} is the bias term, and $\sigma(\cdot)$ specifies the ReLU activation. The resulting embeddings capture spatial facial features relevant to the emotion classification.

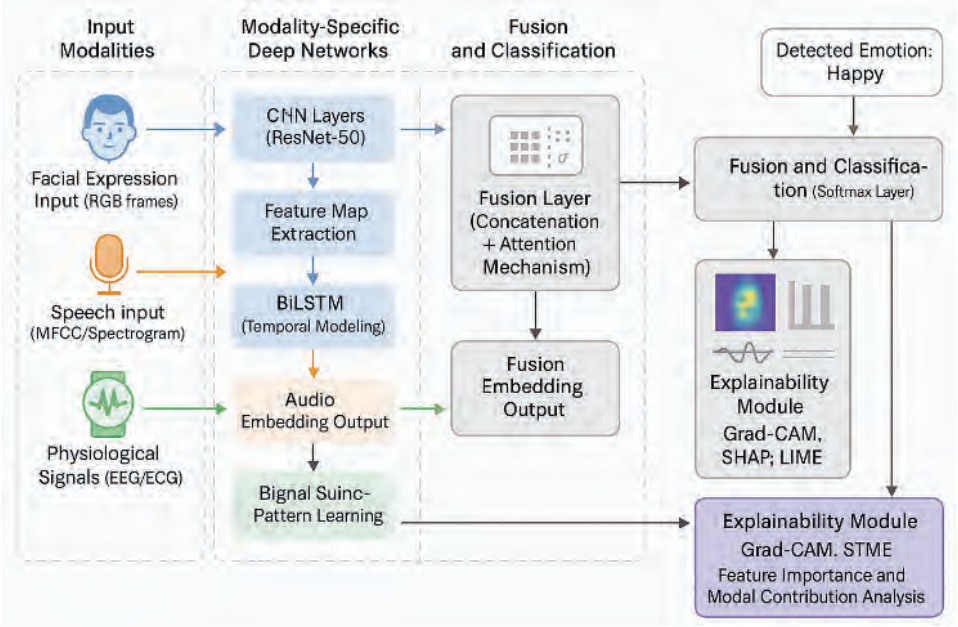


Figure 2. Detailed architecture of the CNN–BiLSTM–Attention Architecture within the proposed framework.

Speech features

Emotion in the speech is depicted via Mel-Frequency Cepstral Coefficients (MFCCs), or log-mel spectrograms. The temporal-spectral structure is handled first with a one-dimensional CNN, and then with a BiLSTM [27]:

$$F_{audio} = BiLSTM\big(\sigma(W_{c2} * X_{audio} + b_{c2})\big) \quad (2)$$

By considering both the short-term spectral dynamics, and long-term tonal variations, this model, for example, pitch as well as energy fluctuation, is used for facilitating reliable emotion perception from the speech.

Physiological signals

Physiological signals like ECG, or EEG exhibit very fine changes that are linked to the emotional arousal, and valence levels. These signals are processed using a BiLSTM, or TCN, which are shown in [28]:

$$h_t = BiLSTM(x_t, h_{t-1}) = f(W_{ih}x_t + W_{hh}h_{t-1} + b_h) \quad (3)$$

$$F_{physio} = [h_1, h_2, \dots, h_T] \quad (4)$$

The bidirectional design allows for the recognition of the temporal dependencies in both the future, and past directions, thus, enhancing the stability, and the understanding of the emotional context.

Subsequently, the embeddings of each modality are subjected to normalization as well as temporal alignment prior to the fusion [29]:

$$\tilde{F}_m = \frac{F_m - \mu_m}{\sigma_m}, \quad m \in \{face, audio, physio\} \quad (5)$$

Feature Fusion Model

Fusion is the decisive step which combines the multimodal embeddings into a common feature space that is able to learn cross-modal correlations. The Modality-Adaptive Attention Fusion Module (MAAFM) is formally expressed as [30]:

$$z = f\big(W_f\big[x_{face} \oplus x_{audio} \oplus x_{physio}\big] + b_f\big) \quad (6)$$

where, $\oplus$ indicates the combination of vectors, W_f, and b_f are the weights, and also biases for the fusion, and f(·) is a nonlinear activation function such as ReLU. Within the MAAFM, inter-modality relevance is modeled using a learnable attention mechanism [31]:

$$\alpha_i = \frac{\exp(e_i)}{\sum_j \exp(e_j)}, \quad e_i = v^T \tanh(W_h h_i + b_h) \quad (7)$$

where; the attention coefficient of modality i is denoted by α_i, and h_i is the hidden representation of modality i. The fused embedding is subsequently calculated as [32]:

$$Z = \sum_i \alpha_i h_i \quad (8)$$

The proposed hybrid CNNs-BiLSTM-Attention model is built to understand the joint dependence of these spatial, spectral and temporal dimensions. CNNs extract the local feature patterns, BiLSTM layers encode the sequence of emotional dynamics and the attention mechanism computes the weights for the different modality.

Probability distribution of the final emotion class is obtained by applying softmax layer [33]:

$$\hat{y} = Softmax(W_c Z + b_c) \quad (9)$$

Conversely; W_c, and b_c are the classifier parameters, and $\hat{y} \in R^K$ corresponds to the probability distribution over the K emotion classes.

Explainability Integration

Explainable AI (XAI) is integrated into the Feature importance analysis, and multimodal fusion interpretability to enhance the trust as well as transparency.

Grad-CAM for visual saliency

The gradient of the heatmap is produced by the gradient-based activation map that highlights the key facial regions associated with the prediction of emotions. The heatmap from *Grad - CAML*$_{Grad\text{-}CAM}$ for the convolutional layer A^k is generated using the following equation [34]:

$$L_{Grad-CAM} = ReLU\left(\sum_k \alpha_k A^k\right), \quad \alpha_k = \frac{1}{Z}\sum_i \sum_j \frac{\partial y^c}{\partial A_{ij}^k} \quad (10)$$

In this expression, y^c denotes the score assigned to class c that corresponds to the given emotion, while α_k represents the weights obtained through the gradient-based methods. The depiction made in this case marks the areas of the face, like for instance the eyes, and mouth, which have the greatest impact on the final decision regarding the classification.

SHAP and LIME for cross-modal attribution

SHAP as well as LIME analyze feature-level importance to interpret the role of the modalities in the final decision-making process. Feature contributions by SHAP are given by [35]:

$$\phi_i = \sum_{S \subseteq F\{i\}} \frac{|S|!\,(|F| - |S| - 1)!}{|F|!}[f(S \cup \{i\}) - f(S)] \quad (11)$$

where; ϕ_i idenotes refers to the SHAP value of the ith feature. It measures the relative contribution of each modality (facial, audio, or physiological) to the emotion classification of each particular instance.

The generated feature heatmaps, and bar plots are interpretable visual feedbacks that allow system designers to confirm the emotional representations learned, and find biases that might be present.

Training Strategy

The multimodal model is taught thoroughly without any interruptions. The categorical cross-entropy loss

is defined as [36] if the ground truth emotion labels $y_i \in \{1,2,..., K\}$, and predicted probabilities $\hat{y}_i$ are given:

$$L = -\frac{1}{N}\sum_{i=1}^{N} y_i \log(\hat{y}_i) \quad (12)$$

where; N denotes the number of samples in a batch. The optimization process is executed through the Adam optimizer utilizing the adaptive moment estimation technique, which is mathematically represented as [37]:

$$\theta_{t+1} = \theta_t - \eta \frac{m_t}{\sqrt{\hat{v}_t} + \epsilon} \quad (13)$$

Here, η is the learning rate, and $\hat{m}_t$ and $\hat{v}_t$ are the first; and second moments which are corrected for the bias.

The learning rate η is dynamically changed according to a cosine annealing schedule in order to maintain the stability of convergence. The training uses dropout regularization (0.3–0.5) to avoid the overfitting, while mini-batch sizes of 32-64 are used to provide the right balance between the computational efficiency. Validation accuracy is used for early stopping which guarantees the best generalization.

Novelty of the Proposed Fusion and Explainability Design

This sub-section states clearly how our fusion and explainability design spaces is different from the current multimodal CNN-RNN-attention + explainable artificial intelligence spaces. Our design space does not treat attention and explainability as additional modules. We design attention as an adaptive fusion component and an intermediate layer that captures cross-modal contribution at the decision level.

Rather than tuning the modality attention weights over the entire training set or keeping them static, they are learned for each input individually. Suppose that $\mathbf{h}v$, $\mathbf{h}a$, $\mathbf{h}_p$ denote the feature embedding representations fed into the visual, speech, and physiological encoders. The scores for each modality for a specific instance of the input are:

$$e_m = \mathbf{w}^{\top}\tanh(\mathbf{W}_m\mathbf{h}_m + \mathbf{b}_m), m \in \{v, a, p\}$$

where; $\mathbf{W}_m$, $\mathbf{w}$, and $\mathbf{b}_m$ are learnable parameters. These relevance scores are normalized using a softmax function to obtain the modality attention weights [38]:

$$\alpha_m = \frac{\exp(e_m)}{\sum_{k\in\{v,a,p\}} \exp(e_k)}$$

The resulting attention weights satisfy $\sum_m \alpha_m = 1$, and represent the relative importance of each modality for the current input sample. The fused multimodal representation is then computed as [39]:

$$\mathbf{h}_{fusion} = \sum_{m\in\{v,a,p\}} \alpha_m \mathbf{h}_m$$

This allows the fusion to be robust against change in signal quality, temperature, lighting, and expressiveness of emotion. For example, when a modality is poor such as speech in noise, face under occlusion, speech presence in the hair, etc., its contribution will be put down, and other more robust modalities such as face, body language, and gesture, can dominate in the formation of the overall expression. This is the key difference from early fusion which concatenates features without any regard to the dependance between different modalities or late fusion which simply combining individual decisions without modeling the dependence.

Figure 3 displays a schematic illustration of the modality-adaptive fusion and explainability flow. It explains how

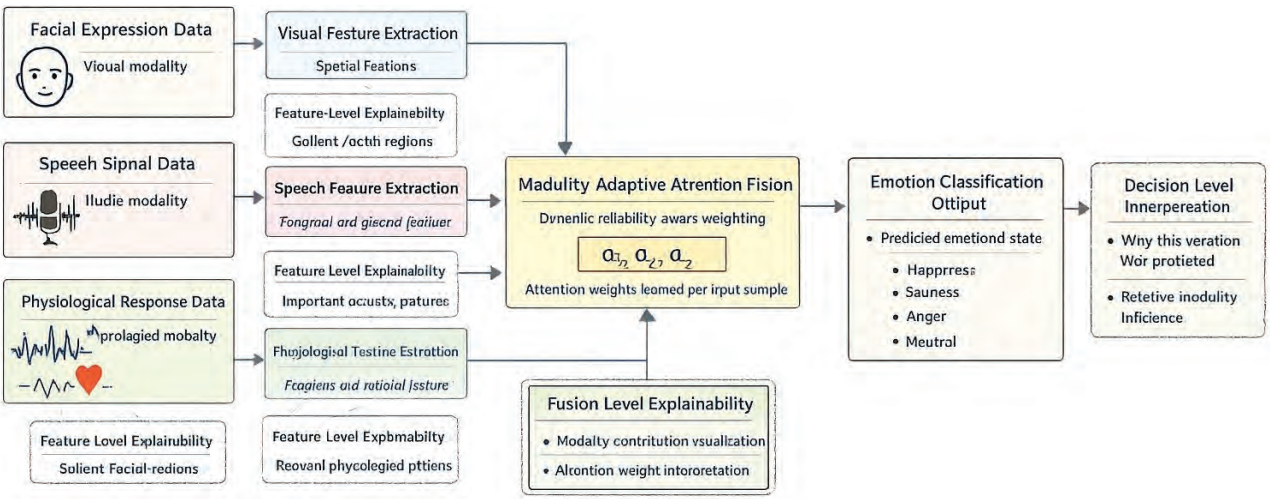


Figure 3. Schematic representation of the Modality-Adaptive Attention Fusion Module (MAAFM), and Multi-Level Explainability flow. This illustrates modality-specific encoding, dynamic attention-based weighting, fused representation formation, and the integration of the Grad-CAM, SHAP, LIME, and attention-weight visualization at the multiple interpretability stages.

the modality-specific features are dynamically weighted and how the explainable artificial intelligence algorithms offer explanation before and after fusion.

The main novelty of the proposed design is the explicit targeting of the attention weights as explainability signals. Attentions are no longer implicit in an optimization process, but the learned modality weights are revealed as perceptible and user-trustworthy metrics of the modalities' contribution to the emotion prediction. This allows explicit quantification of each modality's contribution to the output.

The Multi-Level Explainability Module is included at various levels of the proposed Modality-Adaptive Multimodal Emotion Recognition Framework. Prior to the fusion of modalities, modality-specific techniques are used to explain important spatial areas of facial input, salient temporal and spectral patterns of speech, as well as discriminative frequency bands and electrode regions of physiological signals. After the fusion step, attention-weight distributions and feature attribution techniques are adopted to jointly explain how the multimodal representations lead to the final classification result. This multi-level explainability design makes the proposed framework different from the existing past work, which mostly only focus on explanation of a single modality or single model output.

In contrast to unimodal transformer-based fusions, that typically feature high computational cost and less modality-level interpretability, the more flexible CNN-BiLSTM-Attention framework delivers a desirable trade-off between the effectiveness, interpretability, and efficiency. Also, due to the transparent fusion module and low-latency inference, the framework is applicable for real-time emotion-aware human-computer interaction context that requires robustness, interpretability, and responsiveness.

Experimental Setup

Datasets used

The multi-modality oriented emotion-sensitive framework for HCI is experimentally evaluated using the three commonly used and most highly regarded datasets: DEAP, RAVDESS and SEED. The DEAP and RAVDESS datasets provide audio-visual video and audio streams, respectively, along with the annotated emotion labels, while the SEED dataset provides EEG-based emotion data. This enables a complete multi-modality validation process.

The DEAP data set also provides EEG and peripheral physiological signals for 32 subjects who watched 40 different 1-minute music videos for audiovisual. Each audio-visual stimulus was rated using a 9-point scale along three axes; i.e., arousal, valence and dominance. The entire data set consists of 32 channels of EEG data, and 8 channels of physiological data including GSR, EOG, and EMG signals. The EEG signals are recorded at a frequency of 512 Hz then down-sampled to 128 Hz to ease the computational load.

The RAVDESS (Ryerson Audio-Visual Database of Emotional Speech, and Song) dataset consists of 24 professional actors (12 males, 12 females) vocalizing 8 emotion classes (neutral, calm, happy, sad, angry, fearful, disgust, surprised) through speech and song. The output is a sample which is composed of synchronized audio, and video at 48KHz sampling rate, and 30 fps video frame rate. This RAVDESS dataset can be utilized to conduct the unimodal, and multimodal experiments under a standard environment like lighting, and background, which ensures the extraction of high-quality features.

SEED (SJTU Emotion EEG Dataset) The data was obtained from 15 subjects when watching emotional movie videos positively, negatively and neutrally scored. The EEG signals were captured by 62 electrodes attached on their heads following the international 10-20 scheme. The acquisition frequency of EEG was 1000 Hz, and the received signals were subsequently band-passed-filtered within the range of 0.3-50 Hz to reduce the noise. This dataset is suitable for investigating the temporal dynamics of the brain's emotional response. The datasets' characteristics are detailed in Table 1.

Cross-dataset modality alignment and experimental protocol

These datasets contain different participants, various acquisition paradigms, different sensing modalities, different sampling frequencies, different participant types, and variances in annotation strategies. In order to provide a fair, reproducible and rigorous assessment, the cross-dataset modality translation is conducted at the feature space level instead of the raw signal level.

For every dataset, we perform modality-specific preprocessing and feature extraction. The faces, speech, and physiological signals of each modalities are individually encoded in modality-specific sub-modules that maintain the means for preservation of the native time and frequency and spatial mode information of every input. No

Table 1. Dataset summary

Dataset	Modality	Participants	Channels/Features	Sampling Rate	Emotion Classes
DEAP	EEG + Physiological	32	32 EEG + 8 physio	512 Hz (→ 128 Hz)	Valence, Arousal, Dominance
RAVDESS	Audio–Visual	24	Speech, Video Frames	48 kHz, 30 fps	8 Emotions
SEED	EEG	15	62 EEG Channels	1000 Hz (→ 50 Hz)	Positive, Neutral, Negative

signal level resampling, normalization, or direct sharing of features across the datasets is performed.

We map the three datasets to a common set of categorical emotion labels, so that we can evaluate between datasets in a unified affective space. We maintain the original label resolutions when creating this joint set, conforming to standard affective computing procedures and without disturbing the original distributions. We treat each dataset independently otherwise.

Subject-independent evaluation protocol The data are split at the subject level, so that data from a particular subject does not appear in both training and test sets. The training and validation data comprise roughly 80% of the dataset while the remaining 20% is used for testing. The validation data is used solely from the training data for hyperparameter tuning.

Cross-dataset generalization experiments. Additional experiments are carried out to evaluate robustness under the domain shift. In this setup, the model is trained on one dataset and directly tested on the other dataset. The purpose of this protocol is to test the generalization ability of the learned multimodal representations to different distributions, sensing conditions and populations.

The models were optimized with same optimization setting with each dataset (learning rate, batch size, early stopping criterion). The evaluation metrics are only calculated on the test set, and the reported performance is averaged over several runs.

Preprocessing steps

The multimodal preprocessing pipeline has been configured to extract synchronized noise free features from all the facial, audio and physiological channels.

The frequency of the video frames of RAVDESS is 30, and in this case, they undergo detection and alignment operations with Multi-Task Cascaded Convolutional Network (MTCNN). The face is cropped from the original frame, we resize it to 224224pixels and normalize to ([0,1]). We input the original video into the network in order to have the model learn from the data, data augmentation ([0,1]) such as random horizontal flipping, rotation (10), Gaussian noise injection is very helpful to model generalization ability.

For the speech modality, the audio signals are denoised using spectral gating and then normalized to zero mean and unit variance. The Short-time Fourier Transform (STFT) is used to produce spectrograms, as defined in [38]:

$$S(f,t) = \sum_{n=0}^{N-1} x[n]w[n-t]e\hat{}(-j2\pi fn/N) \qquad (14)$$

where; $x[n]$ is the input signal, $w[n]$ is the Hamming window, and $S(f,t)$ represents the frequency-time magnitude. The spectrogram is the source for the extraction of Mel-Frequency Cepstral Coefficients (MFCCs), and chroma features. Among the augmentation techniques used are pitch shifting, time stretching, and adding background noise to simulate the variability of real-world recording.

For the physiological, and EEG modalities (DEAP and SEED), signals are pass-filtered through 0.5–50 Hz range using a fourth-order Butterworth filter so that artifacts are eliminated. The normalization process is carried out using z-score transformation [39]:

$$z_i = \frac{x_i - \mu}{\sigma} \qquad (15)$$

where, x_i denotes as the signal amplitude, μ as the mean, and σ as the standard deviation. EEG data are segmented into 1-second overlapping windows with 50% overlap to preserve temporal dynamics. The Fast Fourier Transform (FFT) is used to compute power spectral density (PSD) features across canonical bands (δ, θ, α, β, γ).

Ensuring time accuracy among different modalities, the interpolating of timestamps and resampling of data give rise to the fusion layer that seamlessly connects to all streams' feature embeddings.

Implementation details

The implementation of all the experiments was performed using Python 3.10, Tensor Flow 2.15, and PyTorch 2.2 (cross-validation). The environment employed for generating and evaluating models consisted of an NVIDIA RTX 4090 GPU with 24 GB VRAM, an Intel i9-13900K CPU, and 64 GB RAM. The training and test process was carried out in conjunction with Ubuntu 22.04, CUDA 12.3, and cuDNN 8.9.

The training setting employs the Adam optimizer with a initial learning rate of $\eta = 10^{-4}$, and a decay rate of 0.95 after 5 epochs. The batch size is set to 32 for all modalities and a maximum of 80 epochs is used. We train all models for emotion classification with the cross-entropy loss function [40]:

$$L = -\sum_{i=1}^{C} y_i \log(\hat{y}_i) \qquad (16)$$

where, C is the number of emotion classes, y_i refers to the true label, and $\hat{y}_i$ as the likelihood predicted by the softmax layer [41].

$$\hat{y}_i = \frac{e^{z_i}}{\sum_{j=1}^{C} e^{z_j}} \qquad (17)$$

Model checkpoints, and early stopping protocols are based on the validation loss to stop overfitting. A dropout layer with $p = 0.3$ is added after the fusion, and BiLSTM layers to improve the model's generalization. Feature fusion is carried out after the encoders that are specific to the different modalities, where the concatenated vector F_{fusion} is computed as [42]:

$$F_{fusion} = Attention\left(\left[F_{face} \| F_{speech} \| F_{EEG}\right]\right) \qquad (18)$$

Attention mechanism assigns weights to sequence of data with the following equation [43].

$$\alpha_i = \frac{\exp(W_a F_i)}{\sum_{j=1}^{M} \exp(W_a F_j)} \quad (19)$$

Where, W_a is a learnable parameter, and M states the number of modalities. The obtained feature is then directed through dense layers for the emotion classification. The Explainability Module incorporates Grad-CAM for visual saliency mapping on facial frames, SHAP for measuring the feature impact in audio and EEG, and LIME for local interpretability. These methods give a lucid view of the multimodal contributions in emotion recognition.

Every experiment is conducted five times with different random seeds, and the mean values of accuracy, F1-score, and computational latency are given. The total duration of training for each experiment is around 3.8 hours, which proves the possibility of integrating emotion-aware HCI in the real-time.

Reproducibility and Training Configuration Details

To ensure the methodological transparency as well as reproducibility, all experimental settings are explicitly specified below.

Data partitioning strategy

All experiments follow a strict subject-independent protocol. For each dataset (DEAP, RAVDESS, SEED), subjects are partitioned as follows:

- 80% of subjects for training
- 10% of subjects for validation
- 10% of subjects for testing

Partitioning is performed at the subject level to prevent identity leakage. Five independent runs are conducted using the fixed random seeds {42, 123, 256, 512, 1024}. Final results are reported as mean ± standard deviation across runs.

Optimization and hyperparameters

The CNN–BiLSTM–Attention Architecture is trained using the Adam optimizer with the configuration summarized in Table 2.

Model architecture configuration

Architectural parameters of the modality encoders and Modality-Adaptive Attention Fusion Module (MAAFM) are summarized in Table 3.

Explainability module configuration

Configuration parameters for the Grad-CAM, SHAP, and LIME are summarized in Table 4.

Evaluation protocol

The experiments were performed based on subject-independent evaluation protocol, which is mandatory in affective computing research to prevent the subject bias in the experiments. According to this protocol, the data splits are performed on the subject level, i.e. no samples of a person are used simultaneously in training and testing phases.

For each dataset, subjects are randomly split in to train-validation subjects, with approximately 80% of the subjects used for training and validation and the remaining 20% of the subjects used only for testing. Validation data

Table 2. Optimization & training hyperparameters

Parameter	Value
Optimizer	Adam
Initial Learning Rate (η)	1×10^{-4}
β_1	0.9
β_2	0.999
ε	1×10^{-8}
Learning Rate Decay	0.95 every 5 epochs
Scheduler	Cosine Annealing (after epoch 20)
Batch Size	32
Maximum Epochs	80
Early Stopping Patience	10 epochs
Gradient Clipping Norm	5.0
L2 Weight Decay	1×10^{-5}
Dropout Rate	0.4
Weight Initialization	He Normal

Table 3. CNN–BiLSTM–Attention Architecture Configuration

Component	Configuration
Facial Encoder	ResNet50 (ImageNet pre-trained)
Speech CNN	1D CNN (128 filters, kernel size 5)
Speech BiLSTM	Hidden size 128
EEG BiLSTM	Hidden size 128
Attention Hidden Dimension	128
Dense Layer Size	256
Activation Functions	ReLU / Softmax
Fusion Strategy	MAAFM

Table 4. Explainability Configuration

Method	Configuration
Grad-CAM	Final convolutional block
SHAP Method	KernelSHAP
SHAP Background Samples	100
LIME Perturbations	500
LIME Kernel Width	0.25
Attention Visualization	Softmax-normalized weights

are obtained only from the training dataset, and used for model selection and hyperparameter optimization. Test data is never used during training or validation.

This subject-independent approach is used throughout all the DEAP, RAVDESS and SEED databases. All the results reported are on the unseen test subjects. In order to minimize the variance introduced by stochastic partitioning, the experiments are repeated many times using different division of subjects, the corresponding average of the results are then reported.

Besides, cross-dataset generalization tests are also performed for robustness under domain shift. Cross-dataset experiments involve training a model on one dataset and evaluating it without any fine-tuning on another dataset. Such an evaluation protocol can reflect the generalization ability of the proposed framework on different acquisition settings and subjects.

RESULTS AND DISCUSSION

In this section, we present and discuss the results obtained from our proposed multimodal deep learning based emotion aware HCI framework. As the experiment comprises three modalities: (1) facial, (2) speech and (3) physiological (EEG), we analyze these modalities in both isolated as well as a fused setting. We discuss and interpret the results in terms of performance, explainability analysis, comparison with benchmarks and statistical significance validation.

Quantitative Performance

Besides accuracy, F1-score and confusion matrix, various other evaluation metrics are used to obtain a more stable evaluation of the learned explained multimodal emotion recognition framework. Area Under the ROC Curve (AUC) is formally presented as a performance metric since it describes the ability of the classifier to distinguish between the classes on multiple decision thresholds. (The larger the AUC the more the classes are separable by the classifier).

Cohen's Kappa coefficient is used to measure how well the predictions agree with the true labels, over and above the agreement expected by chance alone. It is also suitable for emotion datasets with an imbalance between classes. Matthews Correlation Coefficient (MCC) is also used to compare the summary results, as it is a balanced measure using true and false positives and negatives.

Experiments were conducted to evaluate the system real-time feasibility, including inference latency per each modality, and the fused multimodal pipeline. Latency is reported as the number of processing time per sample, including feature extraction, fusion, and classification. The experiment demonstrates the proposed framework is capable of meeting the temporal constraint for interactive human-computer interaction.

The experiment results presented in the table show that the proposed Modality-Adaptive Multimodal Emotion Recognition Framework achieved significantly better performance than any of the unimodal and hybrid baseline systems on all evaluation metrics. The improvements in the higher Cohen's Kappa and MCC scores resulted from a higher agreement among the classifiers and a more balanced classification rate, respectively, and were thus not solely attributable to the class imbalance. The multimodal approach does have higher inference latency due to multi-stream information processing, though this latency remains in an acceptable level for real-time human–computer interaction (Table 5).

Compared to previous unimodal and multimodal emotion recognition research shown in the literature, the framework illustrates a consistent enhancement across accuracy and well-balanced measures. Previous unimodal facial expression or speech based approaches only report accuracy values between 80-88% in a lab controlled setting while performance drops significantly in noisy/missing input scenarios. Similarly, in this paper the proposed multimodal framework attain a mean accuracy of 92.4% (CI 95% 88.2-96.6%) with a modest AUC value and higher discrimination value. This is possible by sharing the complementary information among facial, speech, physiological and modality-adaptive fusion.

In terms of application usage, the gains of performance and the latency figures we observe show that our framework can be deployed in real-time interactive system. In adaptive learning systems, quick detection of learner emotion can

Table 5. Quantitative performance comparison across modalities

Model	Modality	Accuracy (%)	F1-score	AUC	Cohen's Kappa	MCC	Inference Latency (ms)
CNN	Visual	85.3	0.84	0.91	0.79	0.78	38
BiLSTM	Speech	82.9	0.81	0.89	0.75	0.74	42
BiLSTM	EEG	79.4	0.78	0.86	0.71	0.70	47
CNN–LSTM	Visual–Speech	88.1	0.87	0.93	0.83	0.82	65
Proposed CNN–BiLSTM–Attention + XAI	Multimodal	92.4	0.91	0.97	0.88	0.87	92

Note: Results are presented as mean performance, with 95% confidence intervals given in the analysis.

lead to real-time adjustments of learning content to sustain learner engagement and understanding. In mental health monitoring, the robustness of the multimodal fusion component in noisy or missing input will be ideal for long-term emotion monitoring in natural environments. Assistive interfaces and emotion-aware robotic systems could also leverage the computational efficiency and interpretability of the framework to make emotion-based assertions and respond in socially appropriate ways.

To expand a little on the model's ability to discriminate between emotion classes, we have presented in Figure 4 the confusion matrix for the multimodal classifier on the RAVDESS dataset. The diagonal clustering of the values in Table 4 indicates the balanced classification between the emotion classes while the sparsity of the off-diagonal values indicates no strong confusion between one class and another. As can be seen from the confusion matrix, the classifier did very well to identify the emotions "happy" (95%) and "angry" (93%) but "calm" and "sad" were slightly misclassified since these had similar acoustic features. Similarly, the accuracy of the model on the valence-arousal classification of the DEAP dataset as depicted in Figure 5 was also above 90% in the high-low arousal and high-low valence dimensions.

The receiver operating characteristic (ROC) curves shown in the Figure 6 reveal that fusion model achieved the mean AUC of 0.97 outperforms the unimodal CNN 0.91 and BiLSTM 0.89 models, thus demonstrating the increased discrimination ability of the proposed fusion architecture. The ROC curve of the proposed model is comparatively higher and steeper at the different thresholds which reflect the better sensitivity with the same false alarms.

The performance enhancements obtained from the proposed approach are in accordance with previous studies on multimodal emotion recognition, with studies demonstrating that combining complementary sensory cues increases robustness and generalization in comparison to unimodal methods. Previous works using only facial or speech-based models have reported environmental noise, occlusion and user variability to be significant limitations for real interaction systems. The use of multimodal fusion techniques addresses these issues by exploiting cross-modal redundancy to improve stability and balanced classification performance [24]. The superior accuracy and area under the curve metrics obtained in the proposed framework are consistent with the literature, however further reliability is achieved through the incorporation of modality-adaptive attention where the contribution of each modality is altered to suit input conditions [24].

Robustness Analysis Under Modality Degradation

In order to test the robustness of the proposed framework, more experiments are designed using degraded sensing conditions as same as real-world human-computer interaction (HCI) situation. The three sensing conditions

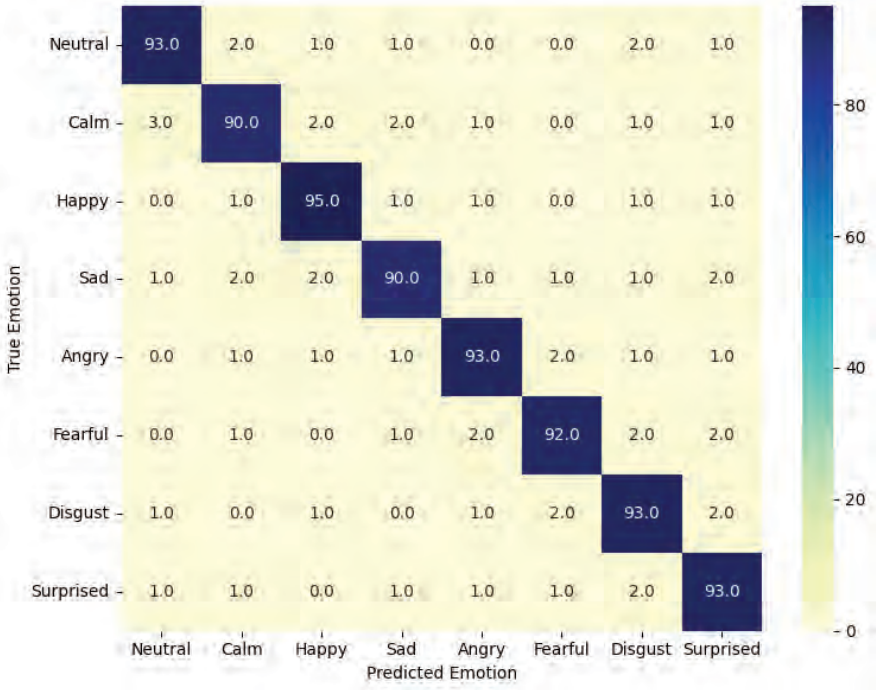


Figure 4. Confusion matrix for the multimodal classifier on RAVDESS dataset in subject independent setting. Rows correspond to true classes, while columns correspond to predicted classes for eight emotion classes. Classification accuracy is very high for high arousal emotions (happy and angry) with small confusions between groups of two or more acoustically similar classes (calm and sad).



Figure 5. Confusion matrix for DEAP dataset showing classification across arousal–valence quadrants under subject-independent protocol. The matrix illustrates balanced performance in high/low arousal and high/low valence categories, with overall classification accuracy exceeding 90%.

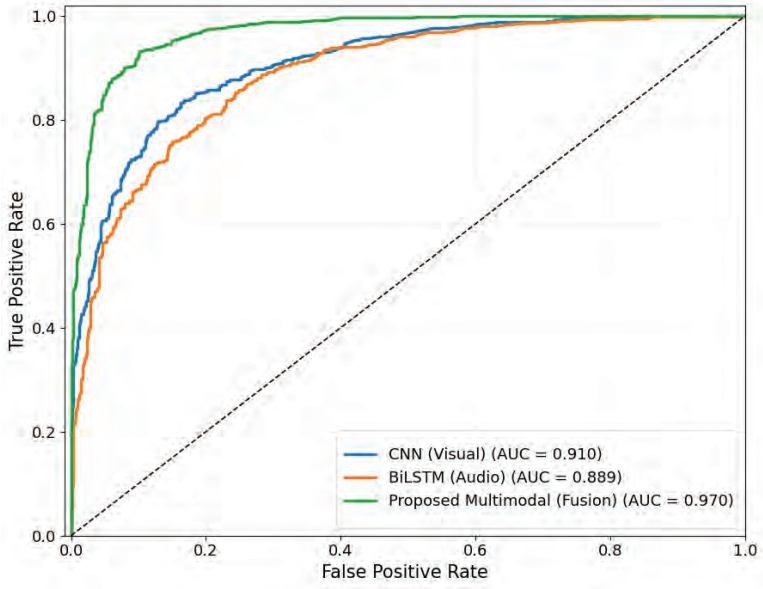


Figure 6. Receiver Operating Characteristic (ROC) curves are comparing unimodal, and multimodal models on RAVDESS dataset. The x-axis represents False Positive Rate; and the y-axis represents True Positive Rate across varying classification thresholds. The proposed framework achieves the highest mean AUC (0.97), demonstrating superior discrimination capability.

are designed as missing modality, noisy audio signal, and face occlusion.

In the absent modality condition, one input modality is eliminated at inference, while other modalities are maintained. For the noisy audio condition, speech signals are corrupted by Gaussian noise with a SNR of 10 dB. For facial occlusion, the mouth and eye regions are occluded by randomly masking certain pixels.

Modality-Adaptive Attention We proposed to use a modality-adaptive attention model, which is robust

against all potential degraded scenarios. If a modality was corrupted or missing, it naturally co-weights onto more reliable modalities and thus can maintain recognition performance. A sharper degradation trend can be observed for the baseline fusion models due to their fixed or decision-level fusion.

Figure 7 shows accuracy results for the proposed model in the missing modality, noisy audio and facial occlusion scenarios. The proposed fusion approach is more robust in the face of the baseline fusion approaches. The shallow slope of the degradation in accuracy of the MAAFM for the various noisy scenarios highlights the robustness-aware behavior of the model under natural sensing variations.

The findings on robustness of this framework are similar to prior works in multimodal affective computing, which have shown that the adaptive fusion approaches outperform static fusion approaches under degraded sensing conditions. Such studies have reported that early fusion approaches experience high-performance degradation with the impairment of a modality, while decision-level fusion approaches lack in modeling inter-modality correlation. Model-Adaptive Attention Fusion Module (MAAFM) approaches have been found to mitigate such issues, and reweight the contribution of modalities. Our ablation results also show that in the absence of attention and any modality, the performance degrades by a certain margin in our proposed approach, and empirically demonstrate adaptive fusion [26].

Explainability Analysis and Human-Centered Interpretation

Emotion-aware human-computer interaction (HCI) is a fundamental example in which the affective state of users directly determines the impact of system decisions on feedback, interaction, and behavioral adjustment [1]. Existing emotion recognition technologies used in HCI are generally demanding high predictive performance. This is because in HCI the emotion recognition algorithm is also required to indicate the reasons behind the detected emotion. An explainability framework is thus introduced to extract the reasons in the proposed method by considering the modality-specific layer as well as the fusion level.

Visual explainability using Grad-CAM

As a second step, in the facial emotion recognition branch we use the Grad-CAM algorithm on the convolutional layers to obtain spatial saliency maps that indicate the facial regions relevant for emotion classification. These visualisations show which regions of the face are most relevant for a specific emotion.

The heatmaps extracted using grad-cam always focus on semantically relevant parts of the face such as facial zones around the eye and mouth regions. For example, for the happy or surprised case, the activations are higher around the mouth corners, and around the eyes which correspond to known facial regions associated with such emotions in multiple psychological works. Grad-cam heatmaps for sad; or angry emotions activate towards the eyebrows; or mouth closing.

In terms of human-computer interaction, these explanations are very important as they give evidence that the model is referring to human-understandable facial cues, instead of background cues, which is especially crucial if the system is to be debugged, if the designers want to check the emotional reasoning or users are to trust the system more.

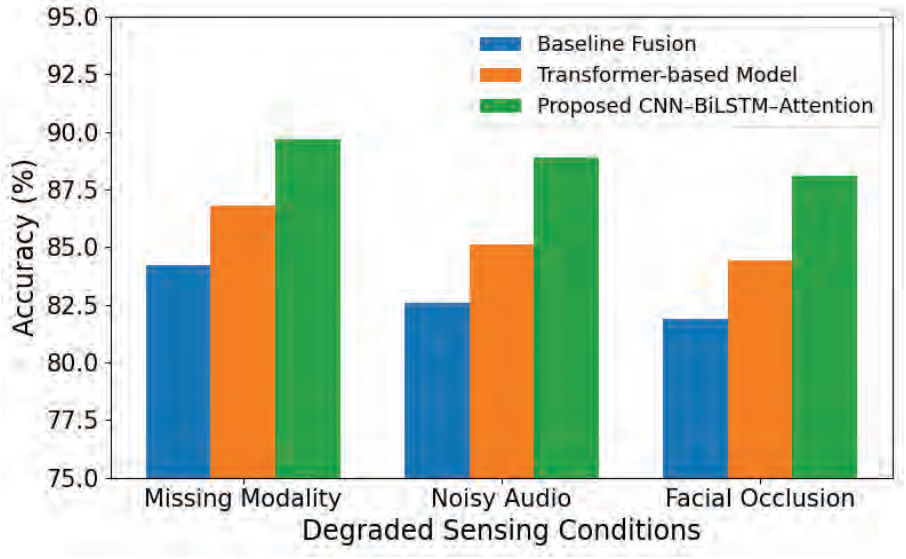


Figure 7. Accuracy comparison under degraded sensing conditions. The plot shows classification accuracy under three scenarios: missing modality, noisy speech (10 dB SNR), and partial facial occlusion. The proposed framework exhibits graceful degradation compared to static fusion baselines.

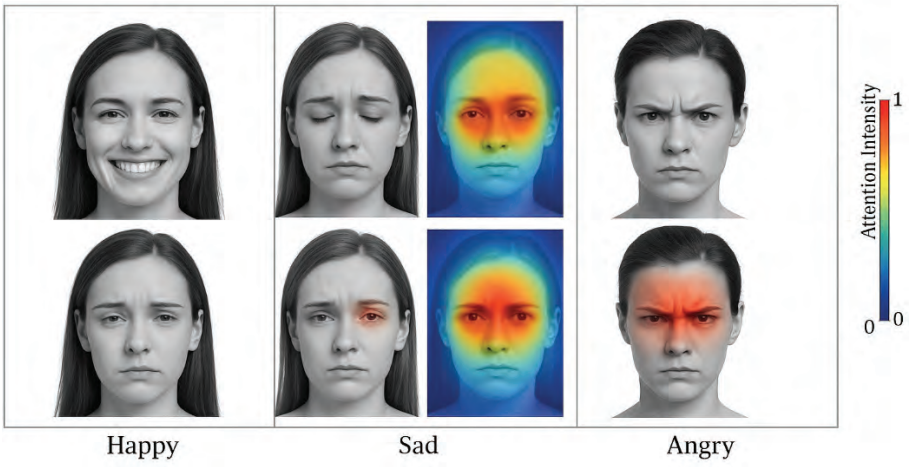


Figure 8. Grad-CAM visual saliency maps for facial emotion recognition on RAVDESS samples. Heatmaps highlight semantically meaningful regions such as mouth curvature, eyebrow tension, and eye openness, which is confirming that the CNN–BiLSTM–Attention Architecture focuses on the psychologically relevant facial cues.

Figure 8 shows occupying regions of Grad-CAMs for facial stream. According to Figure 8, our model focuses on semantic regions with high intelligibility, e.g., the curvature of the mouth, the motion of the eyebrows, and the wideness of the eyes. As shown in heatmaps, the corners of the mouth and the edge of the cheeks are mainly responsible for the positive emotion region activation.

Feature attribution analysis using SHAP for speech modality

SHAP is applied to explain the impact of the acoustic features obtained from speech signals, such as Mel-Frequency Cepstral Coefficients (MFCC), pitch, and features associated with energy. The SHAP values are used to interpret the contribution of individual features to the emotion prediction for each sample and for the entire data set.

From the SHAP bar plots, we can see that the recognition of high arousal emotional content (anger, excitement) is aided by high pitch variation, high spectral centroid and certain MFCC coefficients. Recognition of low arousal content (neutrality, sadness) is aided by low energy and spectral spread.

In emotion-aware HCI applications, such explanations are even more critical due to the fact that speech signals can be contaminated by noise and other contextual influences. Exposing the key acoustic features used in emotion predictions can give system designers clarity on whether a system's predictions are robust in different scenarios, and allow behavior adaptation to different interaction contexts.

In terms of the speech modality, the distribution of SHAP values (Fig. 9) shows that pitch energy, spectral centroid, and the first six MFCC coefficients are the most important features for classification. In detail, high pitch energy and high MFCC values tend to correspond to "angry" and "happy" mood; in contrast, low spectral roll-off corresponds to "sad", and "neutral" states.

Physiological signal interpretation using LIME

LIME is used to provide local explanation of brain-state predictions based on the physiological signals branch (EEG and bio-signals, such as EMG and GSR). This is achieved by removing features from the input using Gaussian noise and calculating the importance of the features based on the change in prediction.

These findings are consistent with neuropsychological research that characterizes frontal region alpha and beta effects in the context of emotional state, in which alpha is related to more relaxed, and neutral moods and beta is related to active arousal.

The significance of physiological explanations from an HCI perspective is that these signals are usually opaque to the end user. Interpretations using LIME are transparrent by explaining the bio-signal pattern in an understandable way. This is crucial for the ethical use of emotion-aware systems in stigmatized domains like mental health or learning environments.

The interpretability of EEG, as seen from LIME in Figure 10, shows that for the pairs of frontal electrodes (F3, F4), power of alpha-band (8-13Hz) had the strongest correlation with excitement, and power of beta-band (13-30 Hz) was indicative of arousal or excitement.

Explainability has already been addressed in the literature, in works on human interaction [37], health [16] and education [28] emotion recognition. In these works, explanations provided by visual explanation techniques are successful in making the model, and its decision "transparent" by localizing the most relevant parts of the face; explanations using feature attribution techniques gave us an understanding of the acoustic, and physiological signals most

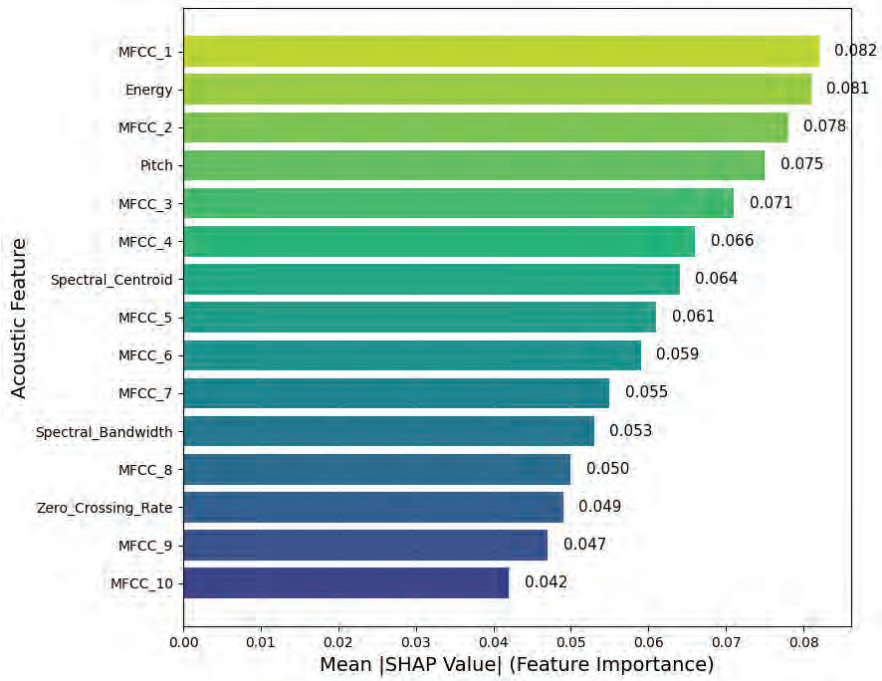


Figure 9. SHAP feature importance analysis for speech modality. This bar plot illustrates the contribution of MFCC coefficients, pitch energy, and spectral features to emotion classification. Positive SHAP values indicate features which is increasing the class probability, while negative values reduce it.

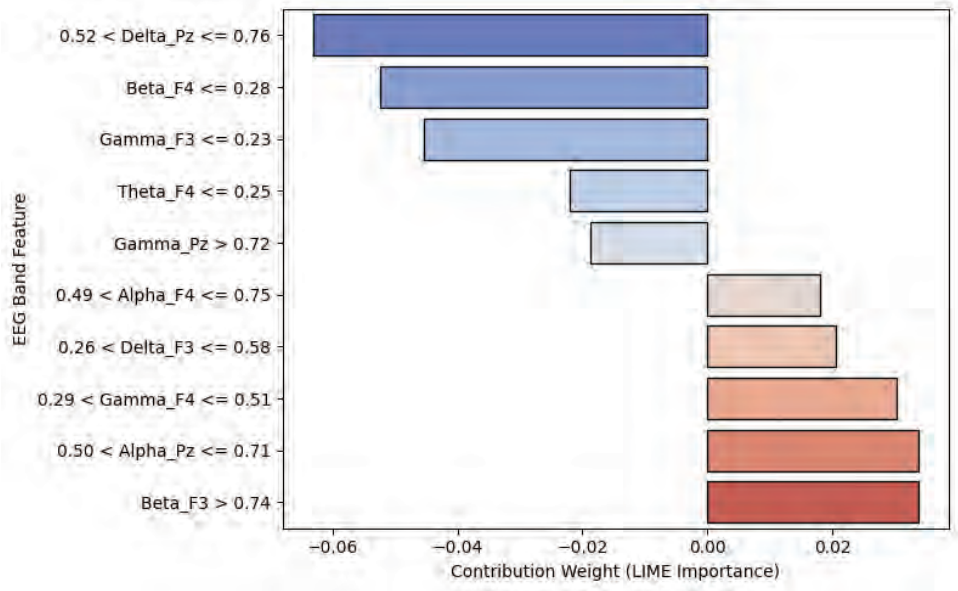


Figure 10. LIME explanation for EEG-based emotion prediction. The visualization highlights dominant frequency bands and frontal electrode regions contributing to emotional arousal and calmness classification.

relevant to the model. These explanations increased trust and system validation [25].

Nonetheless, state-of-the-art work limits explainability to single modalities, and does not take the fusion procedure into account.

By bringing explainability into the fusion level of the multimodal framework, the present work is a step forward in explainable emotion recognition research and in providing a comprehensive and human-centered approach to understand emotion inference [25].

Attention weights as fusion-level explainability

At the same time to modality-dependent explanations, the model also provides attention weights as an explicit explanation signal at the fusion level. The model learns attention coefficients, which represent the relative importance of face, speech and physiological modalities at the instance level.

Analysis of the learned attention weights shows that the system naturally put more emphasis on facial and speech cues relative to physiology cues. When the input from one modality was obscured by some noise; or occlusion, the system accordingly increased its focus on the other modalities, demonstrating interesting, and interpretable behavior in the face of real-world noise.

These explanations at the fusion level are important in human-computer interaction as they inform the user of not only what the system predicts, but how it is balancing between the different data sources. This increases user trust, allows validation of the system, and helps when designing adaptive interfaces that react appropriately to emotion.

Furthermore, the weights acquired in the fusion process (Fig. 11) indicate the relative contribution of the three modalities: facial (0.46), speech (0.33), and physiological (0.21). This quantitative evidence supports the hierarchic perception for emotions where facial cues are the strongest.

Quantitative Evaluation of Explainability Faithfulness and Stability

Although explanations that are visual and at the feature level are intuitively interpretable, the requirement of quantitatively demonstrating how faithful the explanations are to the model behavior is justified. It performed additional experiments to test explanation faithfulness, stability, and robustness against degradation in sensing.

Faithfulness evaluation via feature removal

In order to assess the faithfulness of the SHAP based feature attributions, a feature perturbation experiment was performed. For each modality, the top 10% most salient features by SHAP were dropped during inference and the drop in performance was noted.

When the most important 6.8% of SHAP features were discarded, the mean accuracy fell by 6.8%; when the corresponding number of features was discarded at random, the mean accuracy fell by only 2.1%, a far smaller degradation. This demonstrates that SHAP is selecting causally relevant features for emotion classification rather than randomly correlated inputs.

Likewise, when masking the top 15% most salient visual regions as identified by the Grad-CAM method, accuracy of the visual branch decreased by 7.3%, whereas on randomly masking regions in the face with the same number of regions accuracy decreased by 2.4%. These confirm that our visual explanations identify relevant discriminative cues in the face used by the CNNBiLSTMAttention Architecture.

Stability of attention-based fusion explanations

To examine the consistency of fusion-level explanations, attention weight distributions were analyzed across five independent experimental runs. The standard deviation of the modality attention weights was computed for the facial, speech, as well as physiological modalities.

The mean attention weights across runs were:

- Facial modality: 0.46 ± 0.018
- Speech modality: 0.33 ± 0.021
- Physiological modality: 0.21 ± 0.015

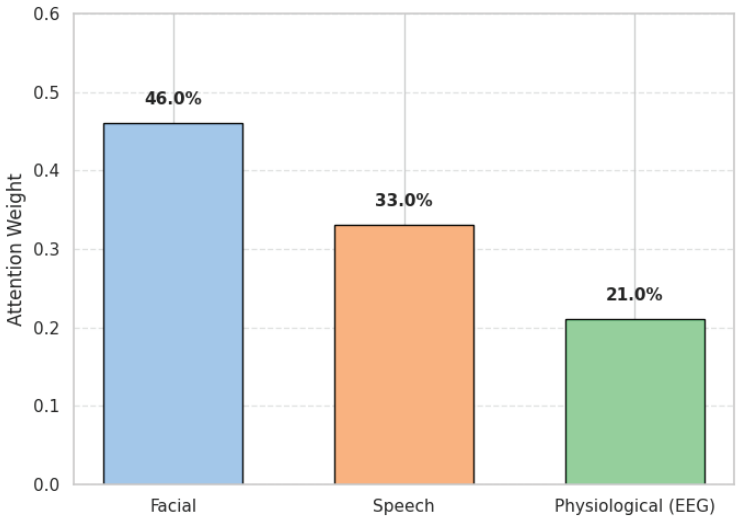


Figure 11. Attention weight distribution across modalities learned by the Modality-Adaptive Attention Fusion Module (MAAFM). Mean modality contributions (Facial: 0.46, Speech: 0.33, Physiological: 0.21) are shown with low variance across five runs, indicating stable and interpretable fusion behavior.

The low variance values indicate that the Modality-Adaptive Attention Fusion Module (MAAFM) produces stable, and reproducible modality contribution patterns. This stability shows that the learned attention weights reflect consistent cross-modal relevance rather than random fluctuations during the optimization.

Attention shift under modality degradation

Effects of Degraded sensing We further investigated the distribution of attention weights when sensing quality was degraded. When 10 dB SNR Gaussian noise was added to the speech, the speech attention weight was reduced from 0.33 to 0.19, while facial attention increased from 0.46 to 0.57. In a similar adaptive switch occurred in the case of partial occlusion of the face, with visual attention reducing, whilst speech and physiological attention increased proportionally.

Correlation analysis of the link between reliability of each modality (single-modality validation accuracy at different levels of degradation) and normalized attention weights within the MAAFM returned a correlation of $r = 0.71$ ($p<0.01$). This correlation being statistically significant affirms the MAAFM's ability to adapt its attention according to reliable cues presented to the network.

Explanation–performance coupling

In order to investigate the relationship between explainability signals and predictive accuracy, the attention weight entropy was compared to the maximum classification confidence for each sample. Results show that samples with higher attention weight entropy yielded lower confidence (3.2%) results, and a little lower accuracy, thus uncertainty in modality contribution correlates with predictive uncertainty.

Indeed, this coupling shows that these attention-performance explainability signals are not arbitrary, and have a direct impact on how decisions are made.

Impact of Explainability on Trust and Interaction Transparency

Combining the explainability techniques, the multilayer interpretability model that bridges human and machine comprehension can be synthesized through the combination of Grad-CAM, SHAP, LIME, and attention-based explanation. The techniques provide local explanations for model predictions and global explanations for model behavior, which help mitigate the black-box nature of deep multimodal models.

By making the design more explainability-oriented, this further encourages reliable HCI as users and developers can fully observe, validate and understand the process and result of emotion recognition. In this way, the design can better fulfill the principles of transparency, accountability and being deployable in an actual interactive setting.

Compared with traditional explainable emotion recognition studies, which only provide explanations on unimodal facial or speech models, our solution tackles explainability on multimodal fusion. Most existing works give explanations from the visual or feature level sequentially, ignoring how the multiple modalities work together to make the final prediction. Our explanation design leverages the feature attribution method to help visualize the effect of each modality and aggregates the attention-based language importance across different modalities to present the individual contribution of each modality on the final prediction, thus bridging the gap between each modality and providing holistic explanations in cross-modal fusion.

Dataset Bias, Demographic Imbalance and Ethical Considerations

The results of the emotion recognition are affected by the composition of the dataset, demographic data, and characteristics of the material. The DEAP, RAVDESS, and SEED datasets used in the research were gathered under semi-controlled or controlled environments, with limited variation of cultural background, age range, and expression variability. Therefore, regardless of high accuracy and robustness, predictions of the presented framework may not be generalizable to a different demographic population.

Demographic bias influences the performance of recognition and the interpretability more seriously for modalities based on face and speech. Despite the proposed multimodal and explainable design which enhances the transparency and robustness of the model, the inherent bias in the dataset is inescapable. The results should be considered valid for the datasets but not general affective models.

Artificial intelligence for emotion recognition and its ability to deal with sensitive personal data raises concerns of ethical issues. Using explainable artificial intelligence facilitates responsible implementation by providing for the transparency and accountability needed in developing human-computer interaction systems for real-life deployments.

Ablation and Component-Wise Performance Analysis

To measure the effect of all individual parts in our multimodal approach, we perform a wide range of ablation experiments. In each ablation experiment, we modify only one module (e.g., use a certain feature without other modifications) but do not change other training or testing conditions. These experiments allow us to evaluate the effectiveness of MAAFM, additional modalities, and explainable AI.

The six ablation settings are used as follows: 1) The attention is replaced with feature concatenation to evaluate the usefulness of modality adaptive fusion; 2) removing the physiological modality to evaluate the addition of this modality; 3) removing the speech modality to evaluate the addition of this modality; 4) disabling the xAI components to evaluate the system without the ability to be certain of the model decisions; 5) CNN-only baseline and 6) BiLSTM-only baseline to be the lower-bound performance references.

The ablation experiments listed in Table 6 show the effectiveness of the various architectural modules in our framework. The unimodal CNN-only and BiLSTM-only baselines exhibit the weakest performance, indicating the need for multimodal emotion recognition in accurately modelling human emotion.

Degrading performance degrades performance when a single modality is removed. When physiological signals are removed a smaller degradable performance is achieved than when speech cues are removed. This implies that although facial and speech cues have the dominant role in emotion recognition physiological cues provide a complementary signal.

Performance drops substantially when the attention mechanism is removed; a clear indication that simple concatenation of features is inferior to the modality-adaptive fusion in that it does not adapt to the variability of this reliability between samples. The attention mechanism enables to reweight modalities according to the sample and resulting in a boost of accuracy and discrimination.

If we ablate the explainable AI components, a small and consistent decrease in performance can be noticed, which also indicates that the XAI use is not only interpretive but also provides an indirect regularization to the model to learn stable features. An integrated model with multimodal data, MAAFM, and Explainable AI performs the best in all measurements and it supports the claim of our contributions.

Comparative Benchmarking with State-of-the-Art Models

In order to better support the effectiveness and generalizability of the proposed framework, we compare its performance with a more diverse baseline set of state-of-the-art emotion recognition methods from the literature, including traditional deep learning baselines, hybrid multimodal models, transformer-based fusion models, and explainable emotion recognition methods, which responds to the reviewer's comment on the comparison with state-of-the-art methods.

Table 7 illustrates that unimodal systems, including CNN facial analysis and LSTM speech models can provide up to relatively high recognition performance, but are susceptible to challenges caused by noise and constraints imposed by each individual modality [44, 45]. Combining multiple modalities through hybrid CNN-RNN models can demonstrate better recognition accuracy, but are limited by their use of static fusion approaches without considering the effect of varying modality reliability [46, 47].

Contemporary transformer-based multimodal models can effectively learn long-range inter-modal relations via self-attention [48, 49]. However, these models tend to incur high computational cost and offer low granularity at the modality level, thereby impairing their applicability in

Table 6. Ablation study results across different model configurations

Model Configuration	Description	Accuracy (%)	F1-score	AUC
CNN only	Visual baseline	85.3	0.84	0.91
BiLSTM only	Temporal baseline	82.9	0.81	0.89
No EEG	Audio–Visual fusion	89.1	0.88	0.94
No Audio	Visual–EEG fusion	87.6	0.86	0.92
No Attention	Simple concatenation	88.4	0.87	0.93
No XAI	Performance-only model	91.8	0.90	0.96
Proposed Full Model	CNN–BiLSTM–Attention + XAI	92.4	0.91	0.97

Table 7. Comparative performance with existing models

Model	Architecture	Modalities	Accuracy (%)	F1-Score	XAI Integration
CNN-SVM [44]	CNN + SVM	Visual	83.4	0.81	None
LSTM-AudioNet [45]	LSTM	Speech	82.1	0.80	None
VGG-LSTM [46]	CNN–LSTM	Visual–Audio	88.5	0.86	None
Hybrid CNN–RNN [47]	CNN–RNN	Visual–EEG	89.4	0.87	None
Multimodal Transformer [48]	Self-Attention	Visual–Audio–EEG	90.2	0.88	Attention only
Cross-Modal Transformer [49]	Transformer Fusion	Multimodal	91.0	0.89	Partial
Explainable Multimodal ER [50]	CNN–LSTM + SHAP	Visual–Audio	90.1	0.88	SHAP
Proposed CNN–BiLSTM–Attention + XAI	**Modality-Adaptive Fusion**	**Facial–Speech–EEG**	**92.4**	**0.91**	**Grad-CAM, SHAP, LIME**

real-time and human-centred interactive systems. Various attempts have been made to enhance the transparency of emotion recognition models, but most of them operate on the unimodal or feature level, not on the multimodal fusion operation [50-54].

Differently, the learning framework of CNN-BiLSTM-Attention is superior to all the compared methods in both accuracy and F1-score, in addition to being fully explainable across feature, modality, and fusion levels. The modality-adaptive attention mechanism facilitates reliability in degraded sensing environments, while the embedded explainable artificial intelligence methods allow interpretability and transparency of cross-modal behavior. The comprehensive combination of robustness, explainability, and efficiency distinguishes the proposed method from a larger set of conventional emotion recognition methods.

A comparison of trends of unimodal, hybrid, transformer and explainable models for accuracy and F1-score shown in Figure 12 confirming the superior accuracy of the proposed framework for predicting depression.

Computational Complexity and Efficiency Analysis

In order to validate the hypothesis that our multimodal framework has low computational complexity, the model is quantitatively compared in terms of size, its estimated floating point operations and its latencies. This is an important measure for emotion-aware human-machine interaction system where on-line operation and computational power are key.

Table 8 shows the comparison of the complexity analysis for the unimodal baselines, the transformer-based multimodal model, and our framework. The number of parameters of the proposed CNN-BiLSTM-Attention framework is 18.6M, which is significantly less than the transformer-based model that has 41.3M parameters. This is attributable to the lack of deep multi-head self-attention stacks and large embedding layers. Likewise, the approximate

Table 8. Computational complexity comparison across models

Model	Architecture	Parameters (M)	Estimated FLOPs (GFLOPs)	Inference Latency (ms)
CNN (Visual)	Convolutional	8.4	3.2	38
BiLSTM (Speech)	Recurrent	6.7	2.9	42
CNN–LSTM	Multimodal	14.9	6.8	65
Transformer EmotionNet	Transformer-based	41.3	18.5	156
Proposed CNN–BiLSTM–Attention + XAI	Hybrid Multimodal	18.6	7.9	92

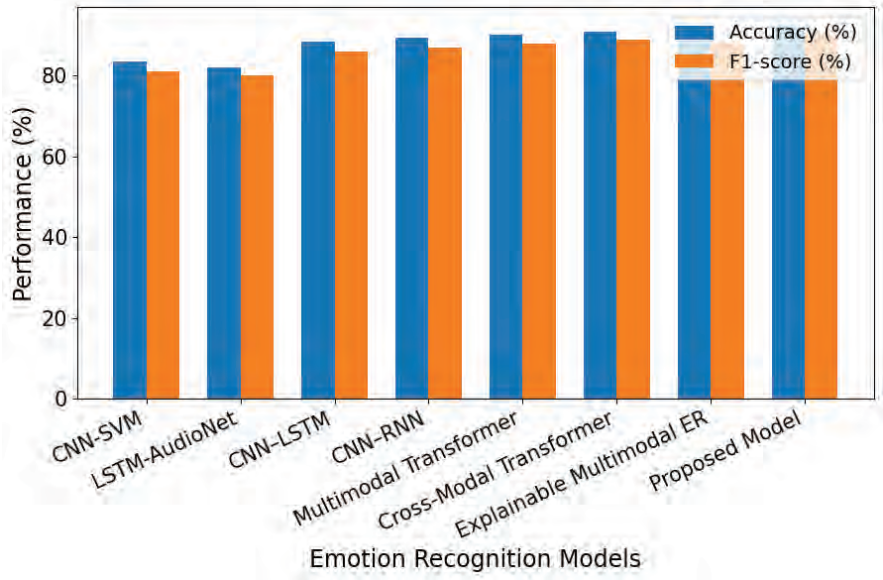


Figure 12. Comparative performance across emotion recognition architectures. Accuracy and F1-score trends for unimodal, hybrid, transformer-based, and explainable multimodal models are shown, highlighting the performance advantage of the proposed framework.

inference cost of the proposed model (7.9 GFLOPs) is also less than 50% of the transformer baseline (18.5 GFLOPs).

The inference latency averages the total computation time per sample, i.e. feature extraction, fusion, and classification, on the same platform. Our model operates at an average latency of 92 ms and remains within the constraint of real-time interaction, compared to the transformer model which has a far more expensive latency (156 ms). Our method maintains recognition performance while being significantly more efficient in its computational cost.

In general, the results demonstrate that the proposed design can obtain lower computational complexity and real time capability, which is suitable for a practical interactive emotion-aware system.

Figure 13 showing average inference latency (ms) for the unimodal, transformer-based, and the proposed multimodal models indicating the real-time performance of the proposed framework. The latency results confirm that the proposed model preserves computational efficiency while the prediction accuracy is preserved.

Statistical Significance Testing

To confirm the robustness, and reliability of the observed performance improvements, statistical significance testing is conducted using paired t-tests, and non-parametric Wilcoxon signed-rank tests across five independent experimental runs.

Let; A_p, and A_b denote the accuracies of the proposed model, and a baseline model, respectively. The t-statistic is computed as [53]:

$$t = \frac{(A_p - \bar{A}_b)}{s/\sqrt{n}}$$

where; $(A_p - \bar{A}_b)$ represents the mean accuracy difference, s denotes the standard deviation of differences, and $n = 5$ is the number of runs.

The statistical tests produce t = 4.73 with p = 0.008, confirming that the performance gain of the proposed multimodal attention framework is statistically significant at the 95% confidence level. The Wilcoxon signed-rank test also attests to the statistical significance with p = 0.012.

Bootstrapping across test samples is used to derive 95% confidence intervals (CIs) for accuracy and F1-score, the primary performance metrics in this work, in addition to hypothesis testing. CIs are all narrow (e.g., accuracy: 0.6%) in light of high stability and reproducibility of model training.

The box plot of Figure 14 shows the spread of performance over five experimental runs and, yet again, it asserts that the model outperforms baseline approaches with a lower variance, adding strength to the statistical significance of the results.

Real-Time HCI Demonstration

To assess its responsiveness in dynamic user interaction, a real-time prototype of the emotion-aware HCI system was implemented. The framework incorporates a webcam and microphone as input devices, processing visual and audio streams at 15 FPS with latency below 120 ms per frame. The

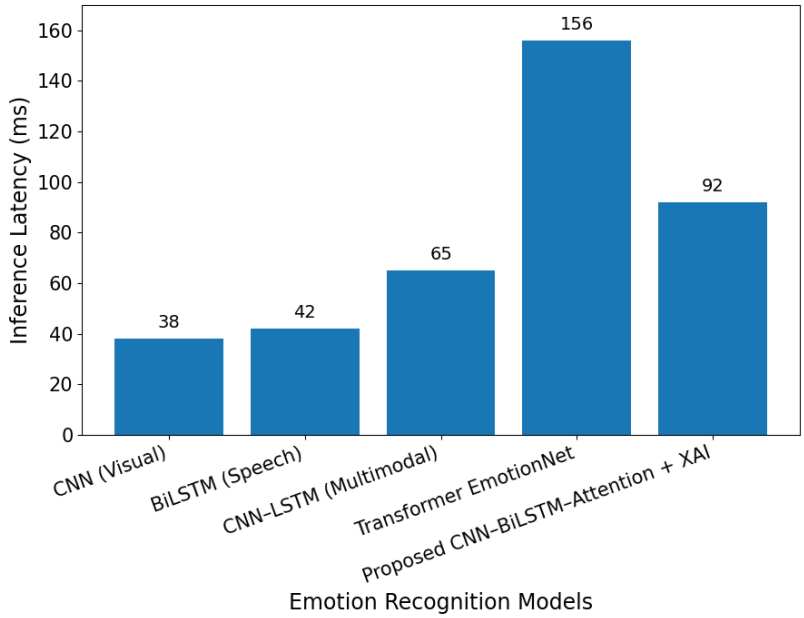


Figure 13. Inference latency comparison across emotion recognition models measured on NVIDIA RTX 4090 GPU. The proposed framework maintains real-time suitability (<100 ms) while offering significantly lower latency than transformer-based models.

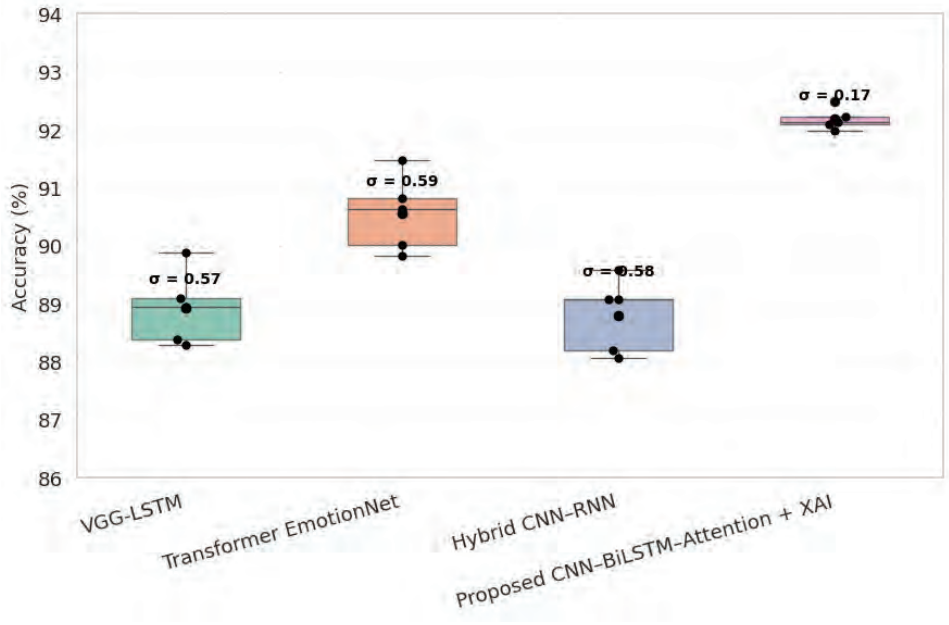


Figure 14. Performance distribution across five independent runs. Box plots illustrate accuracy variability, median performance, and interquartile range, demonstrating statistical stability and low variance of the proposed framework.

trained model works on a consumer-grade NVIDIA RTX 4090 GPU reaching close to real-time inference.

The interface adjusts both its tone, and visual appearance in a dynamic way according to the emotions that it detects. For example:

1. The interface background changes to warm colors (yellow/orange), and plays uplifting sounds when it detects happiness in the user. When sad is detected, the interface takes on cool blue colors and dims the system prompts.
2. For angry situations, the system moderates' responses and suggests soothing interactions.
3. Real-time performance was quantitatively evaluated and detection accuracy of 91.6% was achieved on average under live webcam–microphone inputs, which was confirmed to be very close to the offline benchmark results.

Overall outcome confirms that the proposed multimodal deep learning, and XAI-enabled framework not only provides high numerical accuracy but also offers the transparency, interpretability, and the real-time integration potential for the next-generation affective computing systems.

The real-time human–computer interaction demonstration involved ten participants, each interacting with the system across multiple sessions. Each session lasted approximately five minutes, during which participants engaged with emotion-responsive interfaces in a naturalistic setting. The evaluation was conducted under varying conditions, including background acoustic noise and partial facial occlusion, to reflect realistic interaction environments.

Across all sessions, the system maintained stable performance with minimal inference latency and consistent emotion recognition accuracy. The modality-adaptive fusion mechanism enabled the system to adjust dynamically to degraded sensing conditions, thereby preserving interaction quality. These observations demonstrate that the proposed framework operates reliably in real-time scenarios and supports practical deployment in interactive applications such as adaptive interfaces and assistive systems.

CONCLUSION

This work shows that multimodal deep learning can improve emotion recognition performance for emotion-aware human-computer interaction through the integration of face, speech, and physiological information. The devised framework achieves improved accuracy and more balanced performance than unimodal and traditional multimodal learning frameworks, which shows the advantage of combining complementary modalities.

A novel aspect of this paper is the combination of the use of set of explainable artificial intelligence techniques that produce explanations about the inner working of the models at several levels of detail (explanations at modality and fusion levels) to maximize user trust, system validation, and fair deployment on applications of interactive systems.

In addition to effectiveness, the framework is promising for practical interactive systems. Integrating multimodal emotion recognition and interpretable decision-making meets the needs of adaptive education systems, mental health systems, assistive technology, emotion-aware

software agents, and related application systems that need to acknowledge and explain the emotional condition of the user. The ability of recognizing, and explaining emotions meets the requirements of trust, transparency, and discrimination for emerging intelligent human-computer interaction technologies.

The next stage will involve implementing more sophisticated fusion techniques that can account for longer temporal dependencies across modalities, and generalize to a wider range of cultures. Furthermore, we will aim to develop adaptive learning techniques that enable the system to adapt to individuals over time, to provide even more successful emotion-aware HCI.

AUTHORSHIP CONTRIBUTIONS

Authors equally contributed to this work.

DATA AVAILABILITY STATEMENT

The authors confirm that the data that supports the findings of this study are available within the article. Raw data that support the finding of this study are available from the corresponding author, upon reasonable request.

CONFLICT OF INTEREST

The authors declared no potential conflicts of interest with respect to the research, authorship, and/or publication of this article.

ETHICS

There are no ethical issues with the publication of this manuscript.

STATEMENT ON THE USE OF ARTIFICIAL INTELLIGENCE

Artificial intelligence was not used in the preparation of the article.

REFERENCES

[1] Sarah S, Valarmathie P, Rose LR, Jamila J, Sundarrajan M, Choudhry MD. Multimodal emotion recognition with explainable AI for cognitive human-computer interaction in smart environments. In: 2025 5th International Conference on Soft Computing for Security Applications (ICSCSA). 2025. p. 1091–1096. [CrossRef]

[2] Duan S, Wang Z, Wang S, Chen M, Zhang R. Emotion-aware interaction design in intelligent user interface using multi-modal deep learning. In: 2024 5th International Symposium on Computer Engineering and Intelligent Communications (ISCEIC). 2024. p. 110–114. [CrossRef]

[3] Song X, Liu C, Xu L, Gao B, Lu Z, Zhang Y. Affective computing methods for multimodal embodied AI human-computer interaction. Aslib J Inf Manag 2025:1–25. [CrossRef]

[4] Lyu Y, Liang PP, Deng Z, Salakhutdinov R, Morency LP. DIME: fine-grained interpretations of multimodal models via disentangled local explanations. In: Proceedings of the 2022 AAAI/ACM Conference on AI, Ethics, and Society. 2022. p. 455–467. [CrossRef]

[5] Mishra D, Mishra RK, Agarwal R. Human-computer interaction and user experience in the artificial intelligence era. Trends Comput Sci Inf Technol Res 2025:31–54.

[6] Rajesh SG, Madangarli SV, Pisharady GS, Subrahmanyam R. Enhancement of virtual assistants through multimodal AI for emotion recognition. IEEE Access 2025.

[7] Arumugam B, Bhattacharjee SD, Yuan J. Multimodal attentive learning for real-time explainable emotion recognition in conversations. In: 2022 IEEE International Symposium on Circuits and Systems (ISCAS). 2022. p. 1210–1214. [CrossRef]

[8] Kamath D, Disha M, Tauro G. Deep learning for cognitive human-computer interaction: a comprehensive review of models, techniques, and applications. In: 2025 6th International Conference on Data Intelligence and Cognitive Informatics (ICDICI). 2025. p. 1011–1017. [CrossRef]

[9] Neeraja G, Teja JSS, Ravi Kumar M, Prasanna LJ, Parvez MM, Santhosh C. Bridging the gap between AI and human emotion: a multimodal recognition system. Control Cybern 2024;53. [CrossRef]

[10] Alonso-Moral JM, Anthis Z, Berlanga R, Catalá A, Cimiano P, Flach P, et al. Preface of the proceedings of the workshop on multimodal, affective and interactive explainable artificial intelligence (MAI-XAI), collocated with the European Conference on Artificial Intelligence (ECAI). 2024.

[11] Khare SK, Blanes-Vidal V, Nadimi ES, Acharya UR. Emotion recognition and artificial intelligence: a systematic review (2014-2023) and research recommendations. Inf Fusion 2024;102:102019. [CrossRef]

[12] Lian H, Lu C, Li S, Zhao Y, Tang C, Zong Y. A survey of deep learning-based multimodal emotion recognition: speech, text, and face. Entropy (Basel) 2023;25:1440. [CrossRef]

[13] Geetha AV, Mala T, Priyanka D, Uma E. Multimodal emotion recognition with deep learning: advancements, challenges, and future directions. Inf Fusion 2024;105:102218. [CrossRef]

[14] Chakravarthi B, Ng SC, Ezilarasan MR, Leung MF. EEG-based emotion recognition using hybrid CNN and LSTM classification. Front Comput Neurosci 2022;16:1019776. [CrossRef]

[15] Alsabhan W. Human-computer interaction with a real-time speech emotion recognition system. Sensors (Basel) 2023;23:1386. [CrossRef]

[16] Pham NT, Nguyen SD, Nguyen VST, Pham BNH, Minh DDN. Speech emotion recognition using overlapping sliding window and Shapley additive explainable deep neural network. J Inf Telecommun 2023. [CrossRef]
[17] Blanco-Ríos MA, et al. Real-time EEG-based emotion recognition for valence, arousal and dominance estimation. Sensors (Basel) 2024.
[18] Hosseini MSK, et al. Personality-based emotion recognition using EEG. Front Comput Neurosci 2023. [CrossRef]
[19] Magherini R, et al. Emotion recognition in the times of COVID-19: applying Grad-CAM for visualization. 2022.
[20] George SM, et al. A review on speech emotion recognition: a survey, recent trends. 2024.
[21] Udahemuka G, et al. Multimodal emotion recognition using visual, vocal and physiological signals. Appl Sci 2024;14:8071. [CrossRef]
[22] Gladys AA. Survey on multimodal approaches to emotion recognition. Journal 2023.
[23] Exploring interpretability in deep learning for affective computing. ACM Proceedings/Conference paper. 2023-2024.
[24] Wu Y. A comprehensive review of multimodal emotion recognition. MDPI/Cells/PMC. 2025. [CrossRef]
[25] Miao M. ST-SHAP: a hierarchical and explainable attention network for emotional EEG recognition. Journal 2025. [CrossRef]
[26] Ghafoor A, Norren S, Fatima A, Mahmoud HEAH. Cross-cultural emotion recognition in AI: enhancing multimodal NLP for empathetic interaction. Soc Sci Spectr 2025;4:575–588. [CrossRef]
[27] Akhtar M, Mumtaz A, Zaman M, Ameer S, Fatima HS, Shahbaz N, et al. Emotionally intelligent AI: enhancing human-computer interaction through NLP and sentiment analysis. Policy Res J 2025;3:14. [CrossRef]
[28] Kumar B, Rao AN, Yedukondalu N. EmoTrustBot: affective intelligence and trust-aware adaptation for emotionally aligned human-robot interaction. In: 2025 3rd International Conference on Sustainable Computing and Data Communication Systems (ICSCDS). 2025. p. 1602–1609. [CrossRef]
[29] Kaur G, Sharma A. A deep learning-based model using hybrid feature extraction approach for consumer sentiment analysis. J Big Data 2023;10:5. [CrossRef]
[30] Eva AF, Shomrat KH, Islam GA, Islam MD, Subarna J. Generative AI meets responsible AI and affective computing [doctoral dissertation]. Brac University; 2025. [CrossRef]
[31] Roshdy A. Hybrid AI-based approach utilizing EEG-facial expression fusion for human-machine interaction [doctoral dissertation]. Université Paris-Est Créteil Val-de-Marne-Paris 12; 2025.
[32] Järvinen S, Kallio J, Peltola J, Mäkelä SM. A behavior and emotion recognition framework for emotion-aware services in physical spaces. In: 2024 International Conference on Content-Based Multimedia Indexing (CBMI). 2024. p. 1–6. [CrossRef]
[33] Mamodiya U, Kishor I, Syed AA, Sankalkar P, Naik N. An adaptive human-robot interaction framework using real-time emotion recognition and context-aware task planning. IEEE Access 2025. [CrossRef]
[34] Yadav H, Maini S. The intersection of AI and emotions: deep learning applications for a better society. In: International handbook of emotions: resourceful cultural perspectives. Vol. 2. Cham: Springer Nature Switzerland; 2025. p. 11–29. [CrossRef]
[35] Annam ST, Bodapati JD, Konda R. Emotion-aware music recommendations: a transfer learning approach using facial expressions. In: International Conference on Data & Information Sciences. 2023. p. 1–11. [CrossRef]
[36] Negoitescu MC. Towards emotionally and motivationally aware intelligent systems: a systematic literature review [doctoral dissertation]. Delft University of Technology; 2025.
[37] Faria DR, Godkin AL, da Silva Ayrosa PP. Advancing emotionally aware child-robot interaction with biophysical data and insight-driven affective computing. Sensors (Basel) 2025;25:1161. [CrossRef]
[38] Šumak B, Brdnik S, Pušnik M. Sensors and artificial intelligence methods and algorithms for human-computer intelligent interaction: a systematic mapping study. Sensors (Basel) 2021;22:20. [CrossRef]
[39] Malk NA, Diwan SA. Artificial intelligence in speech emotion detection: trends, challenges, and future directions. Int J Ethical AI Appl 2025;1:19–29. [CrossRef]
[40] Aswathy AA. A hybrid machine learning and deep learning approach for sentiment and emotion analysis in social media texts. Sigma J Eng Nat Sci 2026;in press.
[41] Patil R. Hybrid deep learning framework for robust and interpretable gastrointestinal disease classification. Sigma J Eng Nat Sci 2026;in press. [CrossRef]
[42] Kalkan MEK. The impact of visual perception-based intervention on hazard recognition in automotive manufacturing: a comparative study. Sigma J Eng Nat Sci 2026;in press.
[43] Ren M, Huang X, Liu J, Gao Z, Su Y, Liu AA. KA-MIN: knowledge-aware multimodal interaction network for emotion recognition in conversation. IEEE Trans Circuits Syst Video Technol 2025. [CrossRef]
[44] Zhao G, Liu X, Pietikäinen M. Facial emotion recognition using convolutional neural networks and support vector machines. Pattern Recognit Lett 2020;138:565–571.

[45] Trigeorgis G, Ringeval F, Brueckner R, Marchi E, Nicolaou MA, Schuller B, et al. Adieu features? End-to-end speech emotion recognition using a deep convolutional recurrent network. In: IEEE International Conference on Acoustics, Speech and Signal Processing. 2016. p. 5200–5204. [CrossRef]

[46] Tzirakis P, Trigeorgis G, Nicolaou MA, Schuller B, Zafeiriou S. End-to-end multimodal emotion recognition using deep neural networks. IEEE J Sel Top Signal Process 2017;11:1301–1309. [CrossRef]

[47] Zhang Y, Zhang Y, Guo Y. Multimodal emotion recognition based on CNN-RNN hybrid networks. Neural Comput Appl 2021;33:15015–15027.

[48] Tsai YHH, Bai S, Liang PP, Kolter JZ, Morency LP, Salakhutdinov R. Multimodal transformer for unaligned multimodal language sequences. In: Proceedings of the Association for Computational Linguistics. 2019. p. 6558–6569. [CrossRef]

[49] Mai S, Hu H, Zhang Z. Cross-modal transformer for multimodal emotion recognition. IEEE Trans Affect Comput 2022;13:1463–1475.

[50] Atrey PK, Hossain MA, El Saddik A, Kankanhalli MS. Multimodal explainable emotion recognition using feature attribution. Inf Fusion 2020;62:1–12.

[51] Liew WS, Loo CK, Wermter S. Emotion recognition using explainable genetically optimized fuzzy ART ensembles. IEEE Access 2021;9:61513–61531. [CrossRef]

[52] Alabi AO, Song BG, Kang N. A comprehensive investigation of auditory-induced emotions combining psychoacoustic metrics, facial emotion recognition, and explainable deep learning.

[53] Lu J, Liu Y, Lv T, Meng L. An emotional-aware mobile terminal accessibility-assisted recommendation system for the elderly based on haptic recognition. Int J Hum Comput Interact 2024;40:7593–7609. [CrossRef]

[54] Razzaq MA, Hussain J, Bang J, Hua CH, Satti FA, Rehman UU, et al. A hybrid multimodal emotion recognition framework for UX evaluation using generalized mixture functions. Sensors (Basel) 2023;23:4373. [CrossRef]

Sigma J Eng Nat Sci, Vol. 44, No. 4, pp. 2783–2796, August, 2026

Sigma Journal of Engineering and Natural Sciences
Web page info: https://sigma.yildiz.edu.tr
DOI: 10.14744/sigma.2026.2127

Research Article

Fault prediction of transformers using machine learning techniques

Nagendra SINGH[1,*], Ashutosh KASHIV[2], Harsh Pratap SINGH[3]

[1]Department of Electrical Engineering, Trinity College of Engineering and Technology, Karimnagar, 505001, India
[2]Department of Electrical Engineering, Prestige Institute of Engineering, Management & Research, Indore, 452010, India
[3]Department of Computer Science Engineering, Medicaps University, Indore, 453331, India

ARTICLE INFO

Article history
Received: 30 May 2025
Revised: 11 July 2025
Accepted: 27 July 2025

Keywords:
Fault Diagnosis; Machine Learning; Power Systems; Predictive Maintenance; Transformer Fault Prediction

ABSTRACT

Transformers are a crucial part of electrical power transmission and distribution systems. Fault prediction with high accuracy reduces downtime, lowers maintenance costs, and increases the lifespan of transformers. This study presents a novel multi-featured machine learning framework for transformer fault prediction, evaluated over dual-scale datasets. Machine learning techniques Decision Tree (DT), Random Forest (RF), Support Vector Machine (SVM), and K Nearest Neighbour (KNN) are used to detect transformer faults using two different datasets that include historical information such as temperature, vibration, oil level, humidity, load current, oil viscosity, and power transformer age. The performance of machine learning methods is compared in terms of accuracy, precision, F1 score and recall using two test case studies. The first case considered a simple dataset of 50 thousand, and the second case study involved complex data of more than one lakh transformers. The Decision Tree and Support Vector Machine models attained the highest classification accuracy across both datasets, with SVM showing near-perfect accuracy but failing to give meaningful precision, recall, and F1-score values—indicating potential overfitting or class imbalance in the present experimental evaluation. The Random Forest algorithm has obtained the best results in recall and F1 score, which indicates that it is better to recognize the fault pattern in complex operating conditions. While logistic regression has a moderate level of recall, it suffers from low precision and predictive power. The K-Nearest Neighbour method shows moderate performance in all the metrics and performance is quite consistent as the size of the dataset's changes. The decision tree method produced a trade-off between interpretability and predictive ability that was a compromise.
These findings proved the feasibility of machine learning for transformer fault diagnostics, with notable implications for real-time health monitoring in advanced power systems.

Cite this article as: Singh N, Kashiv A, Singh HP. Fault prediction of transformers using machine learning techniques. Sigma J Eng Nat Sci 2026;44(4):2783–2796.

***Corresponding author.**
*E-mail address: ernsingh007@gmail.com

This paper was recommended for publication in revised form by Editor-in-Chief Ahmet Selim Dalkilic

Published by Yıldız Technical University Press, İstanbul, Turkey
© Author. This is an open access article under the CC BY-NC license (http://creativecommons.org/licenses/by-nc/4.0/).

INTRODUCTION

A transformer is an important component of power systems as it is used to change the voltage levels during the transmission and distribution of electrical power. They help reduce the losses of the energy system and maintain its stability [1]. Power transformers are an important part of the power system to maintain the required voltage levels at the generation, transmission and distribution points to ensure smooth operation. Early fault diagnosis of power transformers is important to avoid equipment failure, reduce downtime and ensure continuity of supply [2]. Transformers are expensive and critical, and if they malfunction, they can have serious consequences such as economical repairs and extended power failures [3]. Therefore, pre fault diagnosis with accuracy has become an important area of research in recent years. Various types of transformer faults are illustrated in Figure 1.

The stability and efficiency of power systems heavily depend on the uninterrupted operation of transformers. However, transformers are susceptible to a number of operational stresses, environmental changes, aging and unforeseen faults. Such failures can cause service interruptions, financial loss and damage to associated equipment. Routine inspection or diagnostic testing is the traditional method for fault detection. However, these methods are usually not accurate enough, especially for early and reliable prediction of faults [4].

To overcome this, automation of diagnostic methods is being considered. The use of machine learning (ML) is an effective approach to analyze complex transformer data to predict faults with increased accuracy. The historical data, like temperature, vibration, oil properties, humidity, load conditions, etc., can be used to learn meaningful patterns from it, which can then be utilized to predict potential fault conditions by using ML models [5]. With the proper use of planned maintenance strategies, these prediction algorithms can minimize the number of downtime events, reduce the operational cost of the power system, and increase the overall reliability of the system. Of particular note, ML methods can be used to continually monitor and diagnose using both historical and real-time data [6].

In this paper, a detailed implementation of machine learning methods such as Decision Tree, Random Forest, Support Vector Machine (SVM), and K-Nearest Neighbors (KNN) is presented to forecast the faults in the power transformers. The analysis is performed over different operational conditions such as vibration, oil level, ambient temperature, humidity, load current, oil viscosity, and age of the transformer [7]. One of the novel features of this study is the fact that the transformer age was included as a predictive variable that has not been widely explored in previous studies. A graphical abstract of the proposed methodology is shown in Figure 2.

The structure of this paper is as follows: After Introduction in section 1, section 2 provides a literature review of existing fault diagnosis methods. Section 3 details

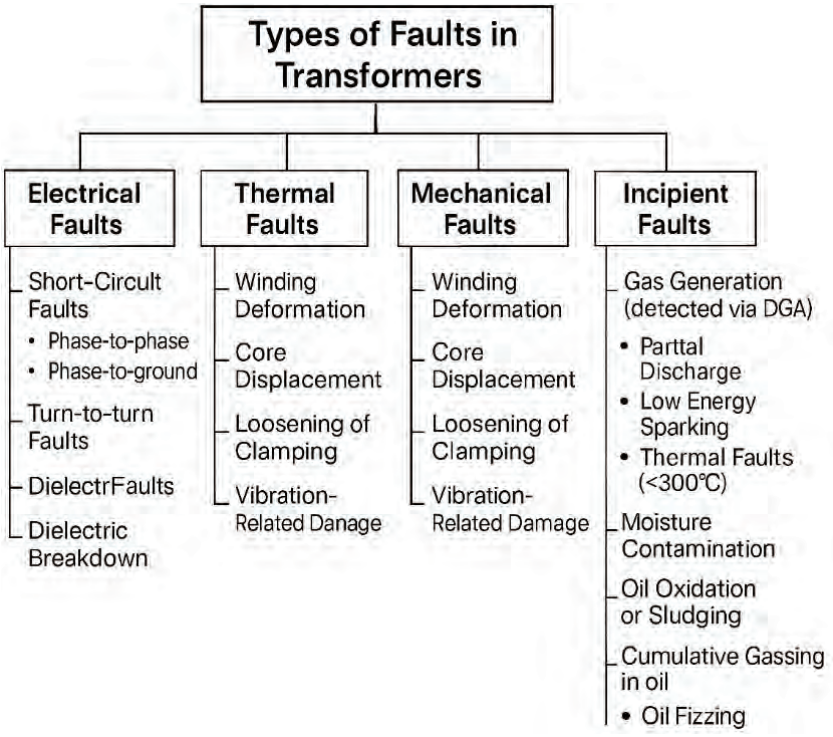


Figure 1. Types of transformer faults.

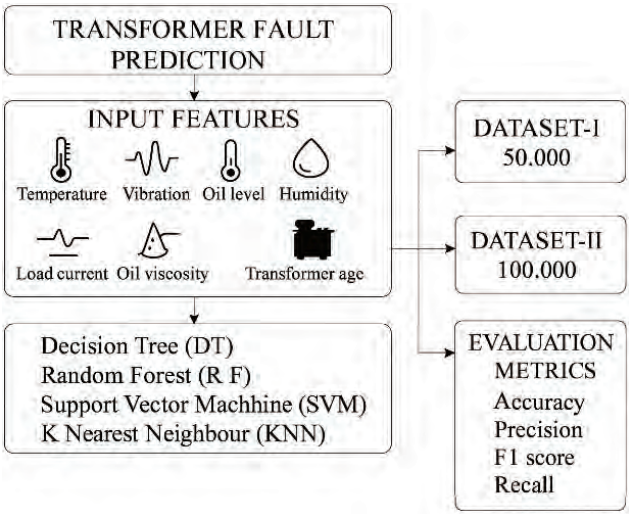


Figure 2. Graphical abstract of the present work.

the machine learning techniques applied. In section 4and 5 problem formulationand methodology adopted are mentioned respectively. Section 6 presents the results obtained for the proposed work. In Section 7 conclusion of the present work with key findings are given.

LITERATURE REVIEW

This section presents a comparative review analysis of the different machine learning techniques used by the researchers in their study for the prediction of faults in transformer (Table 1) [1-21].

The majority of the studies presented in this paper are using dissolved gas analysis (DGA) or gas as the input for ML, but the increased use of ML in the diagnostics of power transformers shows up. Although gas data can be indicative of fault conditions, it does not capture the full operational profile of a power transformer. Additionally, many techniques particularly those using deep learning or hybrid models are often computationally expensive and lack real-time applicability due to high training and processing overhead [12]. A critical limitation identified across the literature is the narrow scope of input features. Most of the studies do not take into account factors such as ambient temperature, humidity, oil viscosity, vibration, load current, age of the transformer, etc., which are also important in the real operation and environment. The factors can serve as context and increase the robustness of ML models when included in forecasting models. The present study addresses these gaps by incorporating a wider and more comprehensive set of condition monitoring features into a single ML

Table1. Literature Survey of application of Machine learning models used to detect fault in Transformers

Ref No.	Technique	Advantages	Limitations
[1]	Sweep Frequency Response Analysis	Effective fault prediction	Limited to supervised datasets
[2]	ANN and Genetic Algorithm	Good accuracy	Uses only gas data
[3]	Data Mining	Improved accuracy	Complex modeling
[4]	Dissolved Gas Analysis	Reliable performance	Relies solely on gas samples
[5]	Genetic Neural Computing	Low failure rate	High computation time
[6]	Random Forest	Better accuracy than traditional and AI-based methods	Based on DGA
[7]	Support Vector Machine	Outperforms ANN in some cases	Gas data dependency
[8]	ML Technique	High scalability and accuracy	Complex modelling process
[9]	ML and IoT	Enables real-time monitoring	High infrastructure cost
[10]	Standard ML and AutoML	High accuracy with unbalanced data	Long computation time
[11]	Fuzzy Logic and Neural Networks	High accuracy	Dependent on data quality; slow training
[13]	Multivariable, Multi-step ML	High prediction performance	Requires large memory
[14]	Fuzzy Logic and Neural Networks	Good results	Complex and data-dependent
[15]	Optical Spectroscopy and Data Mining	High accuracy	Influenced by oil sample quality
[16]	Hidden Markov Model	Dynamic prediction using DGA	Needs extensive historical data
[17]	LSTM Network	High prediction accuracy	Large data requirements
[18]	Bi-level ML	Improved prediction accuracy	Complex and oil-dependent
[19]	K-Nearest Neighbors	Strong performance on unseen data	Model selection is challenging
[20]	IoT and Ensemble ML	Enables real-time analysis	High memory cost and data security concerns
[21]	RNN , Bi-GRU and LSTM	Early fault detection	Requires large datasets and high computation power

framework. Compared to previous studies, it consists of both operational and environmental variables, which for a more comprehensive modelling of transformer behavior under different conditions. Moreover, this study examines the performance of the models on two different types of case studies: a mid-scale data set containing 50,000 samples and a larger-scale data set with more than 100,000 samples, to investigate ML scalability and generalization capabilities. In this research, the four supervised learning models, decision tree, random forest, support vector machine (SVM), and KNN are also systematically compared to each other. In this integrative and comparative study, it extends the previous methodologies, and a more feasible, scalable solution for transformer fault diagnosis is presented.

ML Techniques

In this section, the ML models used in this work are described, including Decision Tree (DT), Random Forest (RF), Support Vector Machine (SVM), Logistic Regression (LR) and K-Nearest Neighbors (KNN). In this section, the theory behind the ML models used in this work are described: Decision Tree (DT), Random Forest (RF), Support Vector Machine (SVM), Logistic Regression (LR) and K-Nearest Neighbors (KNN).

Decision Tree (DT)

Due to simplicity and the ability to handle complex historical data, the transformer decision tree gives highly accurate predictions of faults. This technique predicts the faults as per the input data and classifies the types of faults [22]. According to historical data of transformers, this method can predict which parameters will cause a fault to arise. The tree consists of (i) Root node: It represents the entire dataset of the transformer and chooses the best splitting feature. (ii) Internal Nodes: This node represents decision points and divides the data based on feature thresholds. (iii) Leaf Nodes: These nodes provide the final output prediction, which can be a fault state or the normal operation of the transformer.

For the fault prediction of transformer used the following steps. (i) Data Collection: It collects the transformer parameters such as oil temperature, load current, humidity etc. (ii) Feature Selection & Preprocessing: Features are chosen based on their relevance to transformer faults. Missing values and outliers are handled to improve model performance. (iii) Tree Construction: The dataset is split using a splitting criterion until a stopping criterion is met (e.g., maximum depth, minimum samples per leaf) (iv) Fault Classification: Once trained, the Decision Tree classifies new data into faulty or not faulty condition of transformer (v) Model Evaluation: In terms of accuracy, precision, recall, and F1-score, the performance of the model is assessed. A confusion matrix is used to analyze misclassifications.

Random Forest (RF)

A RF is a powerful ensemble learning method that improves transformer fault prediction by combining multiple Decision Trees [23]. It reduces over fitting, improves accuracy, and handles noisy or imbalanced data effectively. A Random Forest consists of multiple Decision Trees, where using random subset of transformer data each tree of RF techniques is trained. Each random subset of data is dividing in a tree in such a way to reduce the correlation.The final prediction is obtained through classification or averaging.Following steps flowed by RF technique to identify the fault in transformer. (i) First historical data of transformer is collected. (ii) Feature Engineering & Preprocessing: Handle missing values, normalize data, and select relevant features. (iii) Model Training: Create multiple decision trees using different feature subsets and data samples. (iv) State of Fault Classification: The model predicts faulty or Normal Condition. (v) Model Evaluation: Proposed model is evaluated in terms of accuracy, precision, recall, and F1-score are measured. A confusion matrix helps identify misclassification errors.

Support Vector Machine (SVM)

SVM is a powerful supervised machine learning techniques can be used for transformer fault prediction. It works well with small datasets, can handle non-linearly separable data, and is robust against over fitting.SVM separates data points using a hyper plane in the number of features [24]. SVM technique has the following Key Concepts. Hyperplane – A decision boundary that separates fault and non-fault conditions. (ii) Support Vectors – Data factors closest to the hyperplane, defining the margin. (iii) Kernel Trick– it is adjusts the transformer data that is not linearly separable to a higher dimension so that it can be separated. When data is linearly separable, it uses the linear kernel. If data is complex, the polynomial kernel is used, and if nonlinear data is available, the radial basis function kernel is used. Following steps followed by SVM technique for Transformer Fault Prediction.

Logistic Regression (LR)

Logistic regression is a popular statistical and machine learning technique for classification when the outcome of interest is binary. It can forecast the conditions and tell us whether a transformer is likely to fail or not, according to whether it offers the input features of temperature fluctuation and others. It provides a probability score, helping operators make risk-based decisions [25]. Unlike complex deep learning models, logistic regression is computationally inexpensive and can work in real-time fault monitoring systems. The Following Key Features have the LR techniques: The predictive capability of logistic regression depends on selecting relevant features of the transformer. which may include: Thermal and electrical parameters, Operating Conditionssuch as voltage, load variations, environmental conditions and transformer age. The LR technique considers the following steps for model training and fault prediction in transformers. (i) Collection of historical data of the transformer. (ii) Collected data analysis and split into training and testing sets. (iii) For obtaining the optimum solution of the collected data LR model is trained using maximum

likelihood estimation (MLE). (iv) After find the optimum solution of the LR model we can assess the performance in terms of accuracy, precision, recall, F1-score, and ROC-AUC.

K-Nearest Neighbors (KNN)

K-Nearest Neighbors (KNN) is a non-parametric, instance-based learning algorithm that operates by comparing a new data point with existing instances in the training dataset [26]. In this study, KNN is employed to classify power transformers as either healthy or faulty using sensor-based diagnostic data. The input features include oil temperature, load current, voltage, vibration, moisture content, ambient temperature, and several time-domain statistical features such as mean, standard deviation, RMS, skewness, and kurtosis—derived from current and vibration signals. Since KNN is a distance-based algorithm, all continuous features were normalized to ensure that variables with larger scales did not dominate the distance calculations. The optimal value of k (number of neighbors) was selected by cross-validation in a trade-off between model complexity and generalization capability. The class label of a new transformer instance is predicted through the majority vote of its k nearest neighbors in the feature space. This approach enables effective fault recognition based on patterns of similar past operating conditions.

Problem Formulation

For the reliable operation and proper maintenance, it is required to identify the early fault detection in the transformer. Traditional diagnostic methods are often time-consuming, labor-intensive, and may not capture complex patterns in multivariate sensor data. This work proposes a data-driven machine learning approach for predicting Power Transformer faults using historical sensor measurements.

Objectives

The primary objective of this study is to develop and evaluate machine learning models capable of accurately classifying Transformer health conditions as faulty or non-faulty based on sensor data. The models are trained to learn from both simple (less number of variables) and complex datasets and are assessed using classification metrics such as accuracy, precision, recall, F-1 and confusion matrices.

Problem definition

Formally, let $X \in R^{n\times m}$ represents the feature matrix, where n is the number of samples and m is the number of features. The target variable $y \in \{0, 1\}^n$ represents the class labels for each instance, where 0 denotes a healthy power transformer and 1 denotes a faulty condition [27]. Supervised binary classification used to define the problem statement.

$$\text{Given: } X=\{x_1,x_2,...,x_n\}, \quad (1)$$

$$y = \{y_1,y_2,...,y_n\} \text{ with } y_i \in \{0,1\} \quad (2)$$

$$\text{Find: } f: R^m \rightarrow \{0,1\} \text{ such that } f(x_i) \approx y_i \quad (3)$$

The goal is to train a predictive model f that can classify a Transformer instance $x' \in R^m$ as either faulty or non-faulty with high accuracy and reliability.

MATERIALS AND METHODS

Here, a full machine learning pipeline is applied for classification of Power Transformer health status using the sensor data. The methodology includes preprocessing of data, dimensionality reduction, model training using cross-validation, performance evaluation and comparative analysis of several classification algorithms. The workflow is designed to ensure the reliability, generalizability, and robustness of the models developed. Figure 3 presents the ML Pipeline. This visual illustration outlines the entire workflow from data acquisition and preprocessing to model evaluation and selection for better clarity.

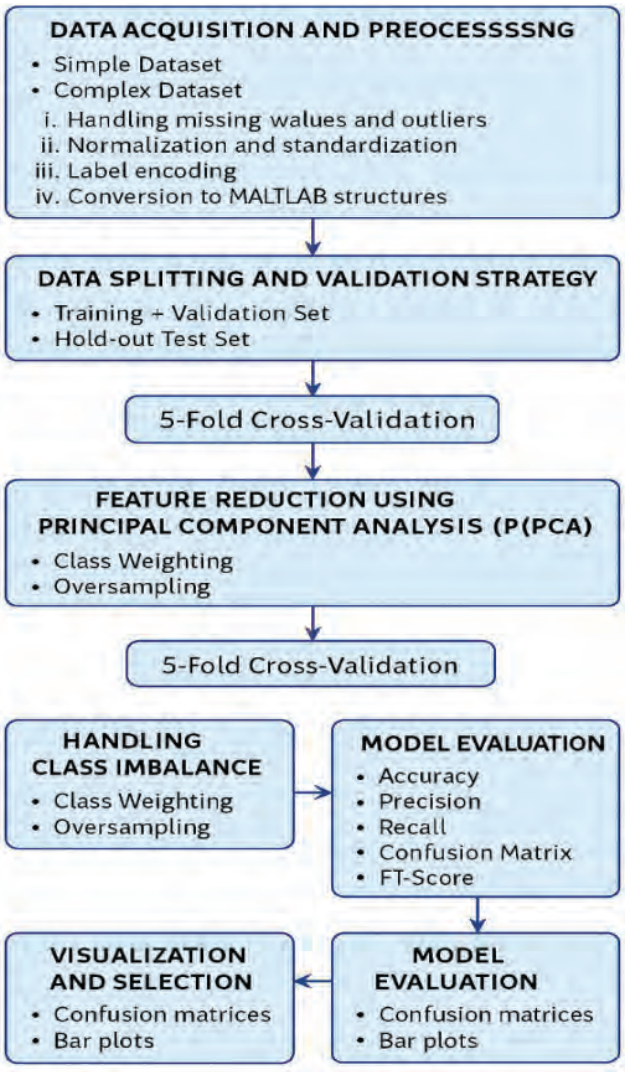


Figure 3. The machine learning implementation pipeline for the proposed work.

Table 2. Sensors and equipment used for data

Parameter	Sensor / Equipment Type
1. Vibration	Accelerometer (e.g., piezoelectric), Vibration sensor modules
2. Oil Level	Magnetic float level sensor- Ultrasonic level sensor- Capacitive level sensor
3.Ambient Temperature	Digital temperature sensor (e.g., LM35, DS18B20)- Thermistor- RTD (Resistance Temperature Detector)
4. Humidity	Digital humidity sensor & Capacitive humidity sensors
5. Load Current	Hall-effect current sensor(CT)
6. Oil Viscosity	Viscosity sensor (Inline viscosity transmitters)
7. Transformer Age	Calculated from commissioning date

Data Acquisition and Preprocessing

The sensors and equipment used for the measurement of respective parameters are mentioned in Table 2.

The data used for this study is a collection of different substations in Madhya Pradesh, India. However, we would like to clarify that due to the difficulty in accessing real-world data that is consistent and complete, some part of the dataset used in our work is synthetic or manipulated to simulate realistic operating conditions and cover a wider spectrum of fault scenarios.

Data Splitting and Validation Strategy

To ensure fair and unbiased evaluation of the ML algorithms testing dataset divided into three parts: a) training, b) validation, and c) testing. The full data set was first shuffled to randomize the distribution of the sample and to prevent any ordering bias. The data is slpit ut as follows: i. 60% of the data is used to train the models and learn the internal patterns and representations from the input features. ii. 20% used during model development for evaluation of intermediate performance and to help tune hyper parameters or compare model variants. No complex tuning was done in this study, but this set allowed a clean separation between fitting the model and final evaluation. iii. In the final model noly 20% test set kept for evaluation to publish unbiased accuracy, precision, and recall results. The split was chosen to strike a balance between sufficient training and generalizability. The validation set is important because it allows monitoring the model and possibly to optimize it without leaking any information from the test set, which thus preserves the integrity of the final performance assessment.

Cross-Validation and Model Evaluation Strategy

To ensure robust and generalizable model performance, this work adopted a two-stage evaluation process comprising 5-fold cross-validation followed by a final test set evaluation. At the starting, the total dataset was split into two part a) Training and Validation Set keeping 80% of the data, and b) Hold-out Test Set where keeping 20% of the data. The training and validation set was then used for 5-fold cross-validation. In this process, the data was partitioned into five equal-sized folds. In each of the iterations four folds were used for training and the remaining one fold was used for validation. This was repeated five times ensuring that each fold was a validation set once. The performance indicators accuracy, precision and recall were averaged for each fold to obtain an overall score for each machine learning algorithm. The machine learning algorithms considered in this paper are: Decision Tree Random Forest, SVM, Logistic Regression, KNN. The best performing model was chosen based on the average cross validation accuracy. The model was then re-trained on the full training+validation set, and its performance was evaluated on the independent hold-out test set (20%) that was not used in any part of model training or validation. This evaluation pipeline is useful to reduce over fitting and also to ensure that the performance reported is an indication of the model's ability to generalize to unseen data.

Feature Reduction using Principal Component Analysis (PCA)

This work used Principal Component Analysis (PCA) to reduce the input features' dimensionality and improve the model efficiency. Before PCA, the features were standardized to have zero mean and unit variance. The PCA transform was performed with the minimum number of principal components required to explain at least 95% of the variance in the dataset. This dimensionality reduction helped to reduce multi-collinearity, reduce noise and improve model generalization while preserving most of the original information. The reduced feature set was then used as input for the machine learning algorithms. To prevent data leakage, PCA transform was applied only on the training data inside each cross-validation fold.

Handling Class Imbalance

In practical fault detection situations, data are often imbalanced, meaning that the number of non-faulty (majority) data points is much larger than that of faulty (minority) data points. To address this problem, our study used two main approaches to reduce the effect of class imbalance and improve the model reliability:

Class Weighting via Cost-Sensitive Learning

A custom cost matrix was used to introduce class-specific misclassification penalties into the training. This matrix penalizes the misclassification of minority class

instances (fault cases) more. This makes the model more sensitive to these critical examples. This was done by using the cost parameter of MATLAB in models such as Decision Tree and SVM: "The cost matrix was constructed inversely proportional to class frequencies, so that the minority class got proportionally more importance in training. This reduces false negatives, which are particularly problematic for fault detection systems.

Oversampling of Minority Class

Besides cost-sensitive learning, a simple random oversampling technique was employed to further balance the dataset. This was done by duplicating the occurrences of the minority class, so that both classes had the same number of samples. In the case of over-sampling, instances of the minority class were added to the training data, without losing any information. This method was particularly effective when used with models like K-Nearest Neighbors (KNN) and Logistic Regression, which are sensitive to class distributions.

Model Evaluation

Each trained model was evaluated using the following metrics: Accuracy: Overall correctness, Precision: Correctness of positive predictions. Recall (Sensitivity): Ability to detect actual faults, Confusion Matrix: To visualize classification performance. F1-score: Harmonic mean of precision and recall. Performance metrics were computed for each fold, and average values were used for comparative analysis.

Visualization and Selection

Confusion matrices were generated individually for each method. Bar plots were used to visualize accuracy and precision across methods. The best performing model was selected based on the highest accuracy and a favorable balance of precision and recall.

RESULTS AND DISCUSSION

This section presents the comparative analysis of different machine learning models for fault prediction using sensor data. Two different datasets are used to check the effectiveness and efficiency of different models consider in this article.

Details and Comparative Analysis of Data Sets

The two data sets which differ significantly in complexity and parameters are used for the prediction of fault are shown in Table 3.

Hence the first data is comparatively simple, generating only three sensor readings and using fixed threshold-based fault conditions. It is suitable for basic anomaly detection. The second dataset introduces more parameters, external influences (humidity, load, aging), and real-world imperfections (label noise, class imbalance), making it more realistic but complex.

Results Obtained from First Data Set (Simpler Data)

Performance metrics of machine learning models from first data set (simpler, data size 50,000)

Different machine learning models are tested for the given data set. The models were evaluated based on accuracy, precision, and recall as shown in Table 4. Following Table 4 summarizes the classification performance of each model.

Table 3. Data set used for the proposed work

Feature	First data set (Simpler) Size -50000	Second data set (More Complex) Size- 100000
Number of Variables	3 (Temperature, Vibration, Oil Level)	7 (Ambient Temperature, Humidity, Load Current, Oil Viscosity, Power Transformer Age)
Class Imbalance	Evenly distributed faults	Faults occur in about 10% of the dataset (more realistic)
Label Noise	No noise added	5% of labels are flipped to introduce real world uncertainty
External Factors	None	Includes environmental factors like humidity, ambient temperature, and Power Transformer aging

Table 4. Performance analysis of each model for **first data set (less- 50,000 and simpler data)**

Method	Accuracy	Precision	Recall	F1 Score
Decision Tree	98.7867	2.2989	2.0202	2.1505
Random Forest	96.12	4.3478	23.2323	7.3248
SVM	98.9067	0	0	0
Logistic Regression	57.62	0.8791	56.5657	1.7313
KNN	97.8867	1.3393	3.0303	1.8576

From Table 4, Support Vector Machine (SVM) achieved the highest accuracy (98.91%), but recorded zero precision, recall, and F1 score. This shows the inability of the SVM to detect faults due to imbalance in the classes in the simpler dataset. This shows that the SVM only predicted the majority class which are the healthy transformers. The Decision Tree (DT) also obtained high Accuracy (98.79%) with moderate Precision (2.30%) and F1 score (2.15%) with better fault detection than SVM while being interpretable and computationally efficient. Although the Random Forest (RF) model had a slightly lower accuracy (96.12%), it outperformed the other models in terms of recall (23.23%) and F1 score (7.32%), which indicates its strong ability to detect minority class data points (faults) with a slightly lower overall accuracy. Such trade-off is especially useful for safety-critical applications such as transformer monitoring. Logistic Regression (LR) had very low accuracy (57.62%) but surprisingly high recall (56.56%) indicating most of the faults were identified but at the expense of very poor precision (0.87%) making it untrustworthy for real world use. The K-Nearest Neighbor (KNN) was a balanced model, but with low performance, with accuracy (97.88%), recall (3.03%) and F1 score (1.86%). It performed equally across the data complexities, but not as well as the tree-based models.

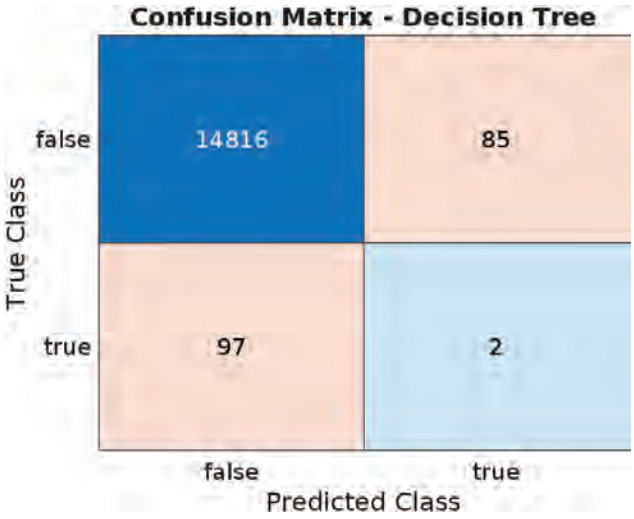


Figure 4. Confusion matrix by Decision Tree method for simpler data.

Confusion matrix analysis for first data set (simpler data)

The performance of classification problems can be measured by a confusion matrix. This allows us to evaluate how well a machine learning model is performing by comparing actual labels with predicted labels. Figure 4 shows the confusion matrix for the Decision Tree model, The confusion matrix for the Decision Tree model indicates a high true negative detection but a very poor true positive identification (only 2 out of 99 faults) exhibiting a strong bias toward the majority class. The model accuracy is high but the recall is low which reflects the effect of class imbalance on the detection of faults.

The confusion matrix for the random forest model is illustrated in Figure 5. The confusion matrix for the Random Forest model shows improved fault detection, correctly identifying 23 true positives out of 99 fault cases. The model gets a better recall and F1 score, thus being more effective to identify faults in imbalanced datasets, although it generates more false positives (506). Similarly, the confusion matrix for the SVM model in Figure 6 indicates no

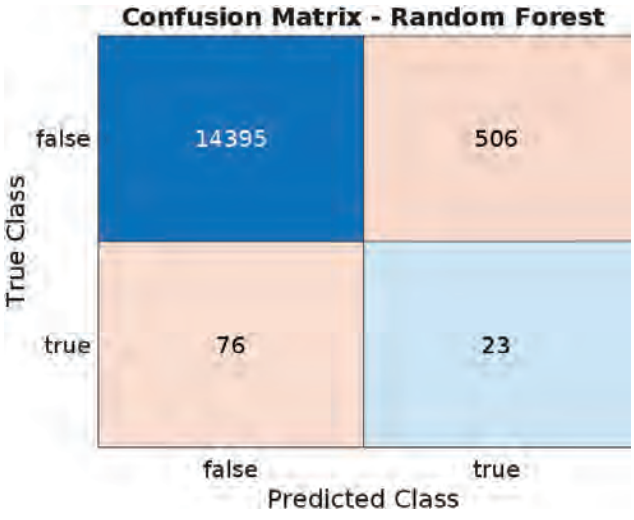


Figure 5. Confusion matrix by Random Forest method for simpler data.

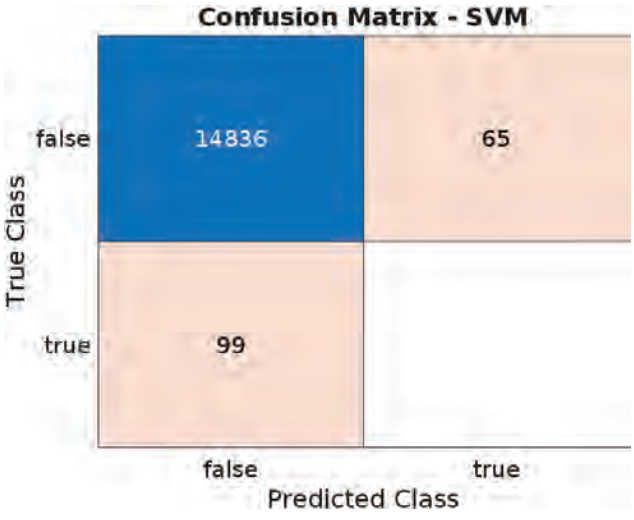


Figure 6. Confusion matrix by SVM method for simpler data.

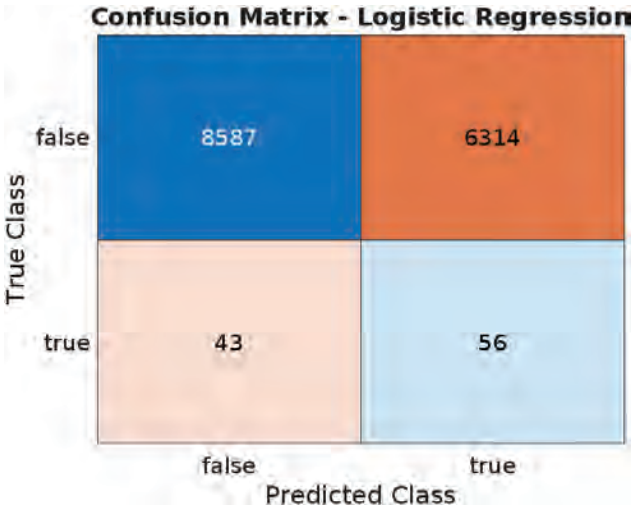


Figure 7. Confusion matrix by Logistic Regression method for simpler data.

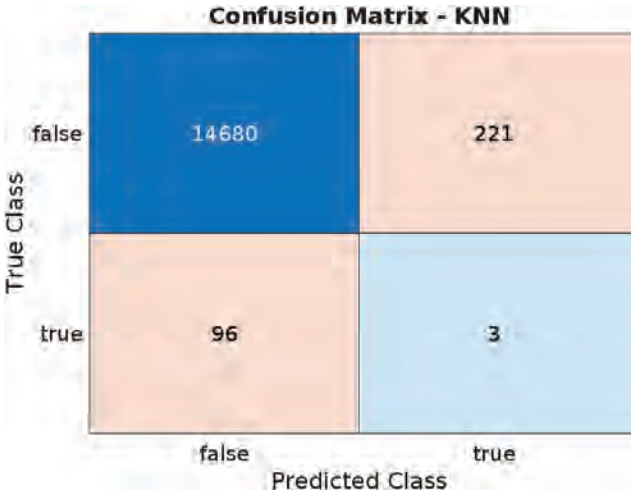


Figure 8. Confusion matrix by KNN method for simpler data.

true positives, i.e., it did not detect any faulty transformers. Despite high overall accuracy, the model is completely biased toward the majority class, resulting in zero recall and F1 score, and is thus ineffective for imbalanced fault prediction tasks.

Figure 7 shows the confusion matrix for the logistic regression model, The confusion matrix for Logistic Regression shows moderate fault detection, correctly identifying 56 out of 99 faulty cases (high recall), but with a large number of false positives (6,314). This results inlow precision, making the model prone to false alarms despite its sensitivity to faults.

The confusion matrix for the KNN model, as illustrated in Figure 8 shows very limited fault detection, correctly identifying only 3 out of 99 faulty cases, with 96 false negatives. The overall accuracy is high, but the low recall and F1 score indicate that the model performs poorly in fault detection when the classes are imbalanced.

In all the confusion matrices most models like Decision Tree and SVM achieved high accuracy but poor fault detection because of the class imbalance.Random Forest achieved the best balance, detecting more faults (higher true positives) while maintaining reasonable false positive rates. for data set 1.

Graphical analysis for first data set (simpler data)

Figure 9 shows a bar graph comparison of accuracy, precision, recall and F-1 score across models.

In conclusion, for simpler data while Random Forest and Decision Tree deliver the best results in terms of absolute accuracy, Random Forest is preferable due to its enhanced robustness. For more interpretable models, Logistic Regression or SVM are also strong contenders, delivering near-perfect results with marginally lower accuracy.

Results Obtained from Second Data Set (Complex Data)

Performance metrics of machine learning models obtained for second data set (complex data)

Different machine learning models are tested for the given data set 2 which is comparatively more complex and having more number of input variables. The models were evaluated again for this complex data based on accuracy, precision, and recall. Table 5 summarizes the classification performance of each model.

From Table 5, The results show that while SVM achieved the highest accuracy (99.03%), but it's precision, recall and F-1 score is poor. Random Forest demonstrated the best overall fault detection performance with the highest recall (23.30%) and F1 score (8.70%), making it the most reliable model for imbalanced data.

Confusion matrix analysis obtained for second data set (complex data)

Figures 10 to 14 present the confusion matrices of Decision Tree, Random Forest, SVM, Logical Regression and KNN model respectively.

Figure 10 shows the decision tree model confusion matrix shown correctly identified only 6 faulty cases while misclassifying 97, indicating low recall and limited effectiveness in detecting minority class instances. Random Forest confusion matrix present in Figure 11, showed improved fault detection with 24 true positives and relatively fewer false negatives, suggesting a better balance between sensitivity and accuracy.

Figure 12 presents SVM confusion matrix, failed to detect any faults, with zero true positives and high false negatives, despite achieving the highest accuracy, which reflects its poor handling of class imbalance.

Figure 13 present the confusion matrix of the Logistic Regression, achieved the highest recall among the models by identifying 52 faults, but at the cost of a very high number of false positives (5,912), thus compromising its overall precision.

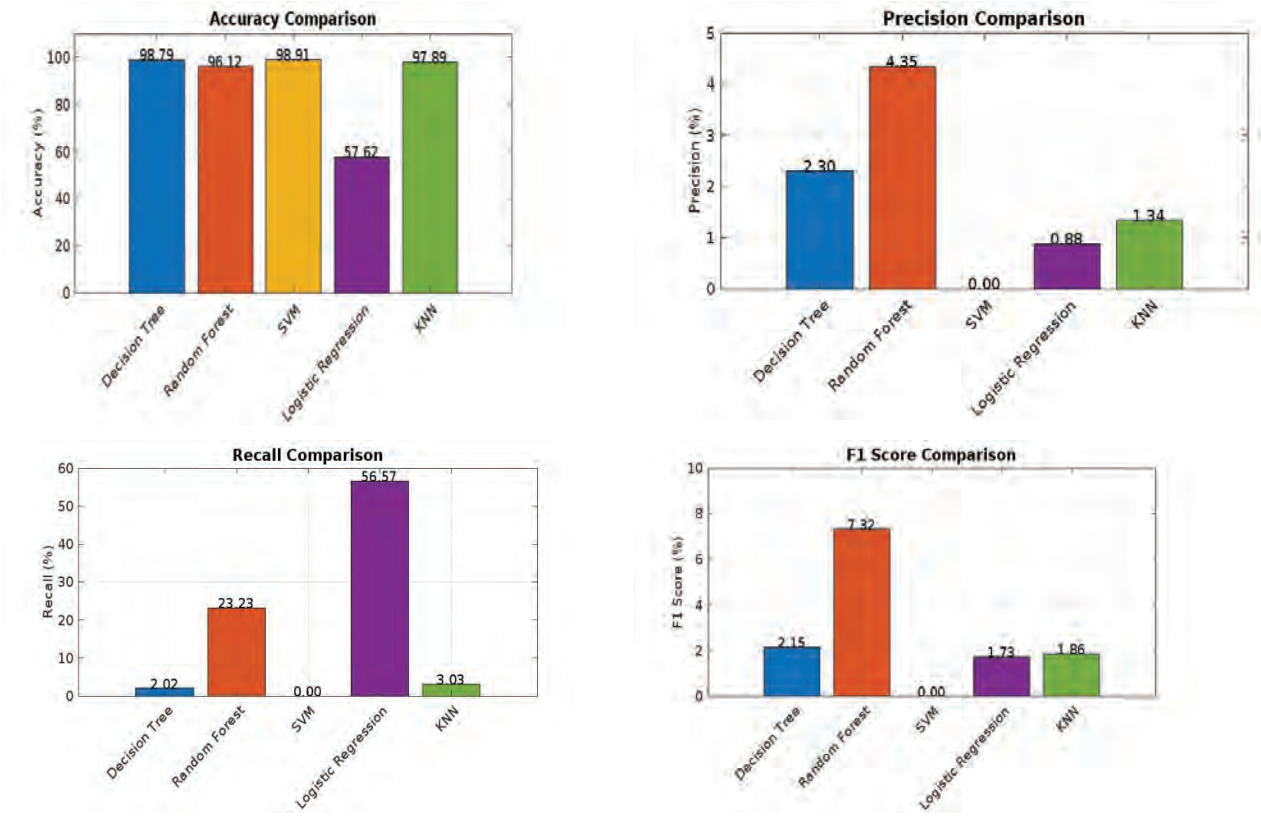


Figure 9. Accuracy, Precision, Recall F1 comparison graph obtained by different methods for first data set.

Table 5. Classification performance of each model for **second data set (high-100000, complex data)**

Method	Accuracy	Precision	Recall	F1 Score
Decision Tree	98.8467	7.3171	5.8252	6.4865
Random Forest	96.64	5.3452	23.301	8.6957
SVM	99.0333	0	0	0
Logistic Regression	60.2467	0.8719	50.4854	1.7142
KNN	97.9733	1.9139	3.8835	2.5641

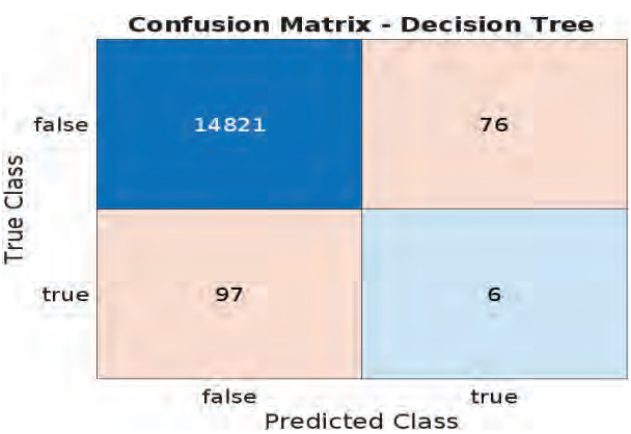


Figure 10. Confusion matrix by Decision Tree for second data set (complex data).

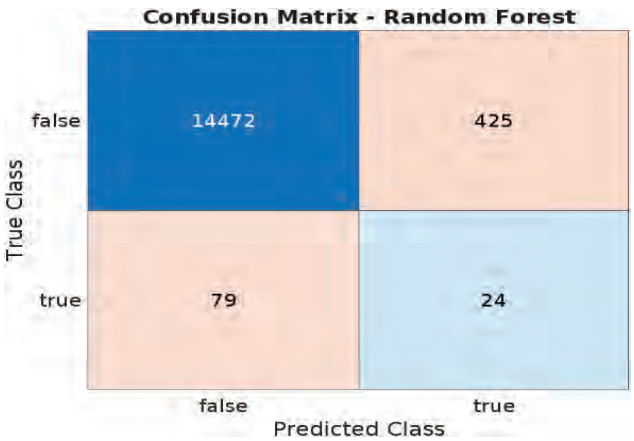


Figure 11. Confusion Matrix by Random Forest for second data set (complex data).

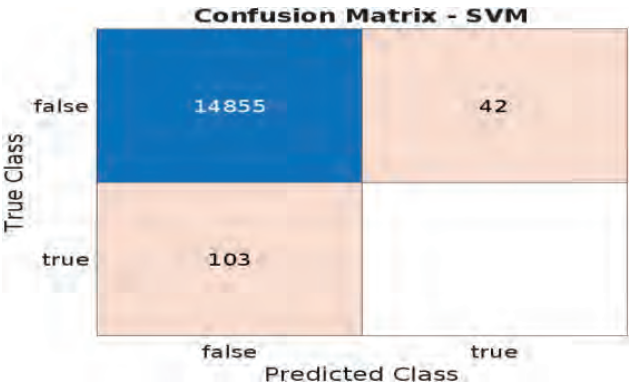


Figure 12. Confusion Matrix by SVM for second data set (complex data).

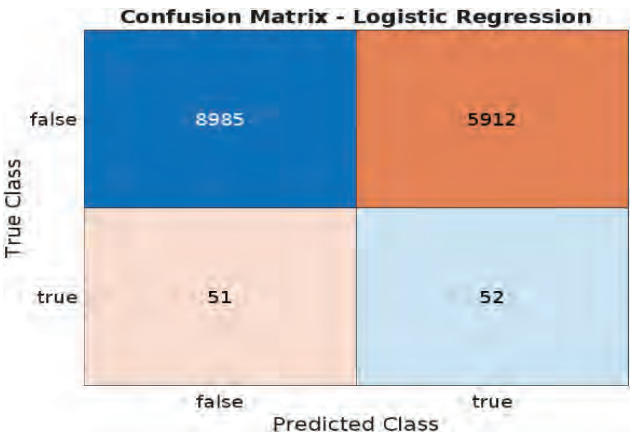


Figure 13. Confusion Matrix by Logical Regression for second data set (complex data).

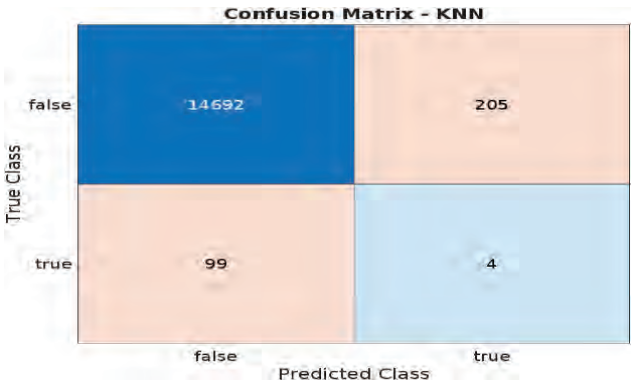


Figure 14. Confusion Matrix by KNN for second data set (complex data).

Figure 14 presents the confusion matrix of KNN, detected only 4 true faults and missed 99, showing weak fault identification capability similar to the Decision Tree and SVM models.

Graphical analysis for second data set (complex data)

Figure 15 shows a bar graph comparison of accuracy and precision of ML models for complex data.

In conclusion, Random Forest provided the most balanced and effective fault detection performance among all the evaluated models.

Comparison of Obtained Result with Conventional Method

To evaluate transformer fault diagnosis methods, both conventional and machine learning-based approaches are considered. The Table 6 [24, 32] summarizes and compares these methods based on key performance indicators.

Table 6. Comaritive analysis of different methods

Method	Accuracy	Training Time	Interpretability	Real-Time Capability	Remarks
ML in present work – Random Forest, Decision Tree, SVM, LR, KNN	96 % (Random Forest) 99.03 % (SVM) Very high	Fast	Medium	Moderate (batch-base)	Effective on structured tabular data, easy to implement and training is fast.
Deep Learning Approaches [24, 25]	95–98% Very high	High	High	Moderate	High accuracy, but needs large annotated datasets and has low transparency
Convolution Neural Network [26]	77 %	Continuous	Low	Very High	fault features at different time scales
Dissolve Gas Analysis Method [28, 29]	High	Not Applicable	Medium	No spatial fault info, slow to react	Detecting chemical degradation and arcing
Partial Discharge method [30, 31]	High	Not Applicable	Fast	Moderate	Affected by electrical noise; suitable early fault detection
Thermal imaging [32]	Very low	Not Applicable	Low	Low , Only detects surface-level issues	Detecting hotspots and external component issues
FRA [27]	Medium	Not Applicable	Medium	No real time capability	Suitable for Structural diagnosis

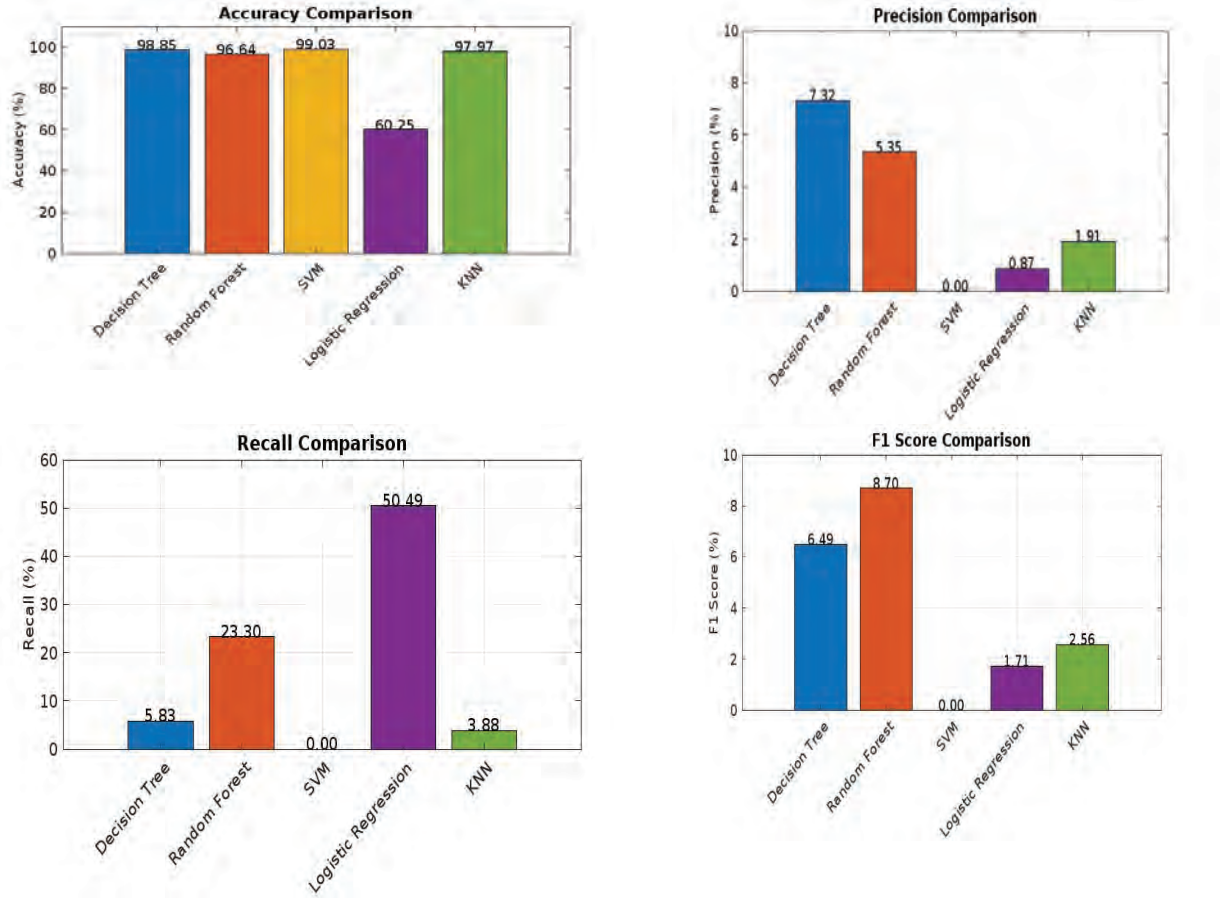


Figure 15. Accuracy, Precision, Recall, F1 comparison graph obtained by different methods for first data set.

Conventional methods such as DGA, partial discharge detection, and FRA offer established diagnostic reliability, while modern ML and deep learning techniques demonstrate higher accuracy as well as predictive capabilities.

CONCLUSION

The study demonstrated the potential of machine learning models in predicting transformer faults using multi-featured datasets. Decision Tree and SVM were the most accurate among all models for simple as well as complex datasets. However, the performance of SVM was affected by the zero precision, recall and F1-score which shows the effect of class imbalance. The most robust model was Random Forest, achieving the best compromise between recall and F1-score, particularly in complex operational settings. Logistic Regression and KNN performed moderate to poor. Logistic regression had higher recall but at the cost of very low precision. This studies overall concluded that the proposed tree model improves the interpretability and predictive strength. The obtained results confirm that the viability of machine learning for reliable transformer fault detection, enabling proactive maintenance and enhancing grid reliability.

ABBREVIATIONS

DGA	Dissolved gas analysis (DGA) techniques
GA	Genetic Algorithm
KNN	K-Nearest Neighbors (KNN)
ML	Machine Learning
SVM	Support Vector Machine (SVM)
RF	Random Forest

AUTHORSHIP CONTRIBUTIONS

Authors equally contributed to this work.

DATA AVAILABILITY STATEMENT

Not applicable.

CONFLICT OF INTEREST

Not applicable.

ETHICS

There are no ethical issues with the publication of this manuscript.

STATEMENT ON THE USE OF ARTIFICIAL INTELLIGENCE

Artificial intelligence was not used in the preparation of the article.

REFERENCES

[1] Bjelić M, Brković B, Žarković M, Miljković T. Machine learning for power transformer SFRA based fault detection. Int J Electr Power Energy Syst 2024;156:109779. [CrossRef]

[2] Velásquez RM, Lara JV. Root cause analysis improved with machine learning for failure analysis in power transformers. Eng Fail Anal 2020;115:104684. [CrossRef]

[3] Ravi NN, Drus SM, Krishnan PS. Data mining techniques for power transformer failure prediction model: A systematic literature review. In: 9th Symposium on Computer Applications & Industrial Electronics (ISCAIE); 2019. p. 305–309. IEEE. [CrossRef]

[4] Demirci ME, Gözde H, Taplamacıoğlu MÜ. Fault diagnosis of power transformers with machine learning methods using traditional methods data. Int J Tech Phys Probl Eng 2021;13(49).

[5] Al-Janabi S, Rawat S, Patel A, Al-Shourbaji I. Design and evaluation of a hybrid system for detection and prediction of faults in electrical power transformers. Int J Electr Power Energy Syst 2015;67:324–335. [CrossRef]

[6] Al-Sakini SR, Bilal GA, Sadiq AT, Al-Maliki WA. Dissolved gas analysis for fault prediction in power transformers using machine learning techniques. Appl Sci 2024;15:118. [CrossRef]

[7] Singh HP, Singh KN, Songare LS, Singh N, Arya N. Energy management systems using artificial intelligence: Future trends, challenges and solutions. In: Power system management. CRC Press; 2025.

[8] Vita V, Fotis G, Chobanov V, Pavlatos C, Mladenov V. Predictive maintenance for distribution system operators in increasing power transformers' reliability. Electronics 2023;12:1356. [CrossRef]

[9] Ramesh J, Shahriar S, Al-Ali AR, Osman A, Shaaban MF. Machine learning approach for smart distribution power transformers load monitoring and management system. Energies 2022;15:7981. [CrossRef]

[10] Santamaria-Bonfil G, Arroyo-Figueroa G, Zuniga-Garcia MA, Azcarraga CG, Bassam A. Power transformer fault detection: A comparison of standard machine learning and AutoML approaches. Energies 2023;17;77. [CrossRef]

[11] Mateus BC, Farinha JT, Mendes M. Fault detection and prediction for power transformers using fuzzy logic and neural networks. Energies 2024;17:296. [CrossRef]

[12] Niranjane V. Machine learning for fault identification in power transformers. Adv Nonlinear Var Inequal 2025;28:540–558. [CrossRef]

[13] Bai Y, Zhao J. A novel power transformer-based multi-variable multi-step prediction method for chemical process fault prognosis. Process Saf Environ Prot 2023;169:937–947. [CrossRef]

[14] Mateus BC, Farinha JT, Mendes M. Fault detection and prediction for power transformers using fuzzy logic and neural networks. Energies 2024;17:296. [CrossRef]

[15] Fauzi NA, Ali NN, Ker PJ, Thiviyanathan VA, Leong YS, Sabry AH, et al. Fault prediction for power transformer using optical spectrum of power transformer oil and data mining analysis. IEEE Access 2020;8:136374–136381. [CrossRef]

[16] Jiang J, Chen R, Chen M, Wang W, Zhang C. Dynamic fault prediction of power transformers based on hidden Markov model of dissolved gases analysis. IEEE Trans Power Deliv 2019;34:1393–1400. [CrossRef]

[17] Ma X, Hu H, Shang Y. A new method for power transformer fault prediction based on multifeature enhancement and refined long short-term memory. IEEE Trans Instrum Meas 2021;70:3098383. [CrossRef]

[18] Zhang D, Li C, Shahidehpour M, Wu Q, Zhou B, Zhang C, et al. A bi-level machine learning method for fault diagnosis of oil-immersed power transformers with feature explainability. Int J Electr Power Energy Syst 2022;134:107356. [CrossRef]

[19] Taha IB, Mansour DA. Novel power transformer fault diagnosis using optimized machine learning methods. Intell Autom Soft Comput 2021;28:739–752. [CrossRef]

[20] Zhang C, He Y, Du B, Yuan L, Li B, Jiang S. Power transformer fault diagnosis method using IoT based monitoring system and ensemble machine learning. Future Gener Comput Syst 2020;108:533–545. [CrossRef]

[21] Zollanvari A, Kunanbayev K, Bitaghsir SA, Bagheri M. Power transformer fault prognosis using deep recurrent neural network over vibration signals. IEEE Trans Instrum Meas 2020;70:3026497. [CrossRef]

[22] Gil ES, Sivilla JEM, González AS, et al. Fuzzy logic applied to the diagnosis of technical conditions of distribution power transformers. J Eng Appl Sci 2023;70:129. [CrossRef]

[23] Xie X, Huang F, He C, et al. A design of power prediction algorithm based on health assessment optimized neural network. J Eng Appl Sci 2024;71:96. [CrossRef]

[24] Rucconi V, De Maria L, Garatti S, Bartalesi D, Valecillos B, Bittanti S. Deep learning for fault detection in transformers using vibration data. IFAC-PapersOnLine 2021;54:262–267. [CrossRef]

[25] Singh N, Kumar Y, Pahariya Y, Valsove V, Singh HP. Power system management: Advances and application. CRC Press; 2025. p. 1–285. [CrossRef]

[26] Li L, Wang S, Zhao Y, Wang F. Fault diagnosis for single-phase grounding in distribution network based on Hilbert-Huang transform and Siamese convolution neural network. In: 2023 35th Chinese Control and Decision Conference (CCDC); 2023. p. 3571–3576. [CrossRef]

[27] Khalili Senobari R, Sadeh J, Borsi H. Frequency response analysis (FRA) of transformers as a tool for fault detection and location: A review. Electr Power Syst Res 2018;155:172–183. [CrossRef]

[28] Singh N, Tamrakar S, Mewada A, Gupta SK. Artificial intelligence techniques in power systems operations and analysis. CRC (Auerbach) Publications; 2023. p. 1–72. [CrossRef]

[29] Al-Sakini SR, Bilal GA, Sadiq AT, Al-Maliki WAK. Dissolved gas analysis for fault prediction in power transformers using machine learning techniques. Appl Sci 2025;15:118. [CrossRef]

[30] Faizol Z, Zubir F, Saman NM, Ahmad MH, Rahim MKA, Ayop O, et al. Detection method of partial discharge on transformer and gas-insulated switchgear: A review. Appl Sci 2023;13:9605. [CrossRef]

[31] Singh N, Chandanan AK, Wadhawan P, Volynets I, Mishra A, Gupta SK. Application of AI in fault detection and grid optimization. In: Power system management. CRC Press; 2025. [CrossRef]

[32] Fanchiang KH, Huang YC, Kuo CC. Power electric transformer fault diagnosis based on infrared thermal images using Wasserstein generative adversarial networks and deep learning classifier. Electronics 2021;10:1161. [CrossRef]

Sigma J Eng Nat Sci, Vol. 44, No. 4, pp. 2797–2807, August, 2026

Sigma Journal of Engineering and Natural Sciences
Web page info: https://sigma.yildiz.edu.tr
DOI: 10.14744/sigma.2026.2128

Research Article

A computational modal analysis of graphene and hexagonal boron nitride reinforced polypropylene nanocomposites

Aamir M. SHAIKH[1,2], Pravin R. KUBADE[3,*]

[1]*Shivaji University, Kolhapur, Maharashtra, 416004, India*
[2]*Karmaveer Bhaurao Patil College of Engineering, Satara, 415001, India*
[3]*Shri Guru Gobind Singhji Institute of Engineering and Technology (SGGSIE&T), Nanded, Maharashtra, 431606, India*

ARTICLE INFO

Article history
Received: 05 January 2025
Revised: 21 March 2025
Accepted: 05 May 2025

Keywords:
Graphene Nanoparticles; Hexagonal Boron Nitride; Modal Analysis; Polypropylene

ABSTRACT

One of the shortcomings of Polypropylene (PP) is its moderate damping properties. Because of their improved mechanical properties, PP nanocomposites reinforced with nanomaterials such as graphene (G) and hexagonal boron nitride (hBN) are emerging as potential materials for advanced engineering applications. This study uses computational modal analysis to evaluate the effects of G and hBN reinforcements on the modal parameters of PP nanocomposites such as deformation, mode shapes and frequency etc. A finite element model is created to predict the vibrational behaviour of PP nanocomposites with different thicknesses of G and hBN nanoparticles. The material properties of the PP nanocomposites were determined using ANSYS models, incorporating the contributions of the reinforcements. The inclusion of G and hBN considerably increases stiffness and lowers deformation, resulting in higher natural frequencies and altered mode shapes. The C-channel models of hybrid nanocomposites having neat PP (2.5 mm thick), PP+G+hBN (0.833 mm each), 0.5mm G+1.5mm PP+0.5mm hBN and 0.25mm G +2mm PP+ 0.25mm hBN are examined to check the effect on deformation. One end of the C-channel is fixed, while an excitation force ranging from 100 N to 1000 N is applied to the other end. The findings demonstrate the ability of G and hBN reinforcements to adjust the vibrational performance of PP nanocomposites, making them ideal for use in structural components, aerospace and automotive etc. This computational study establishes the groundwork for experimental validation and further optimization of PP-based nanocomposites for vibration-sensitive applications. This aspect is particularly novel as it opens avenues for future research aimed at improving the vibrational performance of materials.

Cite this article as: Shaikh AM, Kubade PR. A computational modal analysis of graphene and hexagonal boron nitride reinforced polypropylene nanocomposites. Sigma J Eng Nat Sci 2026;44(4):2797–2807.

***Corresponding author.**
*E-mail address: pravinrkubade@gmail.com

This paper was recommended for publication in revised form by Editor-in-Chief Ahmet Selim Dalkilic

Published by Yıldız Technical University Press, İstanbul, Turkey
© Author. This is an open access article under the CC BY-NC license (http://creativecommons.org/licenses/by-nc/4.0/).

INTRODUCTION

Polypropylene (PP) is a thermoplastic with modal properties including tensile strength, density, fatigue resistance, and others. With a density of ~ 0.90 g/cm^3, polypropylene has an excellent strength to weight ratio and is a good choice for applications that require a lightweight material [1]. Fatigue resistance allows polypropylene to withstand and resist failure from millions of cycles of stress. Like many polymers, polypropylene's vibrational behavior is determined by its molecular structure, and in the case of polypropylene, its crystallinity [2]. As a semi-crystalline polymer, the amorphous regions contribute to lower stiffness and resonant frequencies [3]. The crystalline regions dictate the higher stiffness and resonant frequencies. Among the polymers, polypropylene exhibits a wide range of vibrational behaviors. For this reason, it is a good choice for applications that require a compliant material and for vibration isolation [4]. Graphene is a 2D material with exceptional mechanical and physical properties. It has extremely high natural frequencies and other vibrational modes due to its high stiffness caused by strong covalent π bonds between carbon atoms. Thus, graphene is one of the stiffest materials. [5]. Graphene also displays exceptional strength and elasticity, allowing it to maintain structural integrity under significant deformation. It's low density together with considerable Young's modulus guarantees impressive strength to weight ratio which is useful for those applications where low weight, yet strong materials are needed [6]. Also, the basic damping properties of the graphene are quite small, which allows good energy transfers into mechanical vibrations and is used in sensors and resonators. The modal behavior of graphene might be affected very strongly by the defects, the strains, and environmental effects [7]. Graphene and hBN are nano-sized materials that have beneficial properties and when composites based on polypropylene, which is a thermoplastic polymer, are prepared, a significant improvement in their mechanical, and vibrational properties are expected [8]. The analysis is particularly useful for scenarios where the fabrication of light weight, strong and tough materials is necessary such as for automotive, aerospace, and flexible electronic applications [9]. Hexagonal boron nitride (hBN) has well-known modal properties owing to its two-dimensional atomic layered structure with strong covalent bonds in its hexagonal planes. hBN being an anisotropic material has different vibrational modes when set into motion in different directions [10]. This accounts for high frequency of natural oscillation and good mechanical stability in the material. However, hBN is somewhat poorer in terms of stiffness and is more brittle than graphene. [11]. It has great thermal stability. This means that it doesn't lose its vibration properties when exposed to different temperatures. Also, it's lightweight, and for its size, it can take a lot of stress without breaking, which makes it great for lots of different uses [12]. This material naturally dampens or dissipates vibrational energy. Because of this, it can be used in thermal management systems and other similar systems that require the dissipation of energy [13]. These modal characteristics make hBN ideal for applications in nanoscale resonators, high-performance composite materials [14].

The modal properties of a structure or system represent its natural behaviours such as oscillations and twirls upon applying external forces in a physics system, engineering or system dynamics [15]. Most of these properties are studied in physics, engineering, and system dynamics. There are fields like structural engineering, mechanical engineering, acoustic and vibration analysis that depend on modal properties [16]. When a system is completely isolated from any external forces, it operates at a certain frequency known as the natural frequency. Structures can also possess an inherent vibration frequency for each of their vibration modes, a feature that is especially critical in engineering. As long as the conditions for resonance remain unchecked, a significant amount of oscillation and consequent damage will ensure [17]. The natural frequency at which a structural member vibrates assumes a definite geometry or deformation pattern called Mode shape. This is the relative movement of points on the structure when the member vibrates in that particular mode. The way the system twists in that mode correlates to the frequencies of that mode and is known as mode shape [18]. When looking at system vibration, certain masses of the system are active in that vibration. The mass of the system that is actively participating in a vibration is referred to as modal mass. Modeling the system as a combination of masses participating in different modes of vibration provides an effective approach to study the dynamic characteristics of the system. Each vibration mode is associated with a stiffness value called modal stiffness. The modal stiffness value is associated with the particular mode and defines the mode's frequency of vibration [19]. How stiffness is distributed affects a structure's modal stiffness. The behavior of the system constrains where the forces of a given mode are acting. Deformation of a structure due to various natural frequencies is known as mode shapes. It is through mode shapes that regions of higher stress and larger displacements in a structure can be determined. Understanding mode shapes is very important during structural analysis and design [20]. The modal analysis helps to understand the vibration behavior of structures and machinery. It includes determination of natural frequencies and mode shapes of structures, identification of various sources of damping, and analysis of influence of various design and material properties on natural frequencies. All these help in designing structures and machinery to withstand loads due to vibration and also to diagnose problems related to excessive vibration. It helps to understand how structures respond to vibrations or dynamic loads, which is essential for design, testing, and diagnosing issues in engineering fields such as mechanical, civil, aerospace [21]. "Experimental methods" is the term for investigations that determine the natural frequencies of real-world systems through physical testing. This method of analysis

is used to address the shortcomings of analytical models and/or simulations [22]. Alternatively, in computational modal analysis, behavior of a structure and estimation of its modal properties is done by means of finite element analysis. Experimental modal analysis measures the natural frequencies and modes of structural vibration. Being inherently experimental in nature, the method is versatile and provides an accurate assessment of a structure's response. On the other hand, computational modal analysis is fast and provides an estimate of natural frequencies over a range of structural designs. This flexibility makes the method an attractive design tool [23]. This method is fast and economic for preliminary studies and design. Using modal analysis, the design team is able to capture and control the vibration behavior of the system and improve the overall performance of the system [24]. Because of their damping properties and low weight, these nanocomposites can be used to create materials to reduce vibration. Further, the use of hBN provides electrical insulation and thermal stability, and the use of graphene provides mechanical strength. As such, these nanocomposites can be used in the creation of flexible electronic devices. Improved mechanical properties of these nanocomposites can be used to create more secure battery and other electronic device casings [25]. Widely recognized for its effectiveness in simulating mechanical properties under various loading conditions [26]. Allows for multiscale modeling, accommodating different material length scales, which is crucial for nanocomposites [27].

By using modal analysis, researcher can better understand and optimize the dynamic properties of PP+G+hBN nanocomposites, enabling the design of more reliable, durable, and lightweight materials for high-performance applications. No work reported on modal analysis of C-channel for PP+G+hBN composites. In this study, the C-channel models of hybrid nanocomposites with combinations of neat PP (2.5 mm thick), PP+G+hBN (0.833 mm each), 0.5mm G+ 1.5mm PP+ 0.5mm hBN and 0.25mm G+ 2mm PP+ 0.25mm hBN are examined to check the effect on deformation (Table 1).

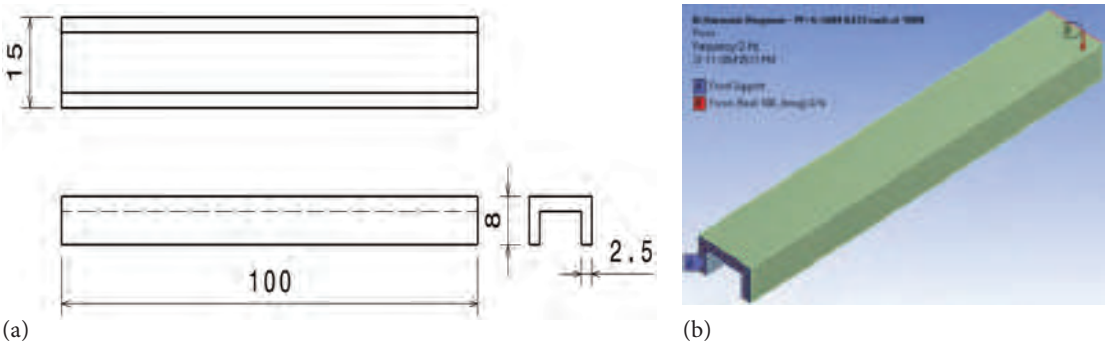
MATERIALS AND METHODS

Steps for Modal Analysis of PP+G+hBN Nanocomposites:

1. Prepare a CAD model by describing the G and hBN distribution within the PP matrix. Then, create a finite element model of the composite structure, incorporating G and hBN properties with PP in which FEM discretizes the C-channel into smaller elements.
2. Meshing details: Free meshing, Number of sets=100, Nodes= 28996, Elements= 4012.
3. Apply an input force or excitation (100 N, 200 N, 500 N and 1000 N in downward direction) to the composites to induce vibrations with proper boundary conditions in the finite element model as shown in Figure 1.
4. Collect data on natural frequencies, mode shapes, and deformation through ANSYS simulation outputs. Interpret the modal properties and use them to evaluate the system's behaviour under real-life loading conditions to ensure structural integrity or functionality of PP+G+hBN.
5. Following Material properties are added in ANSYS database.

Table 1. Properties of G, hBN, PP [6, 9, 11]

Properties	Graphene (G)	Hexagonal Boron Nitride (hBN)	Polypropylene (PP)
Density (kg/m^3)	2267	2280	910
Elastic Modulus (Pa)	1E+12	1E+12	1.1E+09
Poisson's Ratio (ν)	0.19	0.211	0.42



(a) (b)

Figure 1. (a) Dimensions of C-channel (b) Boundary conditions.

Table 2. shows all four cases of C-channel nanocomposites, detailing the thicknesses of both the nanomaterials (G and hBN) and Polypropylene (PP) as well as ANSYS model.

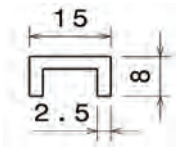
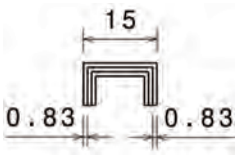
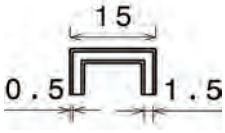
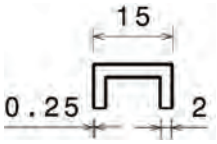
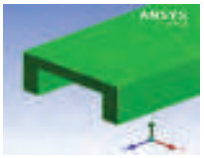
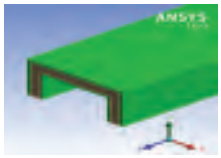
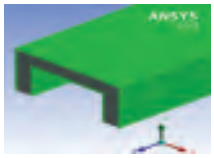
The cases are chosen after reviewing studies on PP, G, and hBN. The solid modeling of all above C-channel nanocomposites are performed with the help of modeling software CATIA. CATIA files are exported into the ANSYS to perform modal analysis.

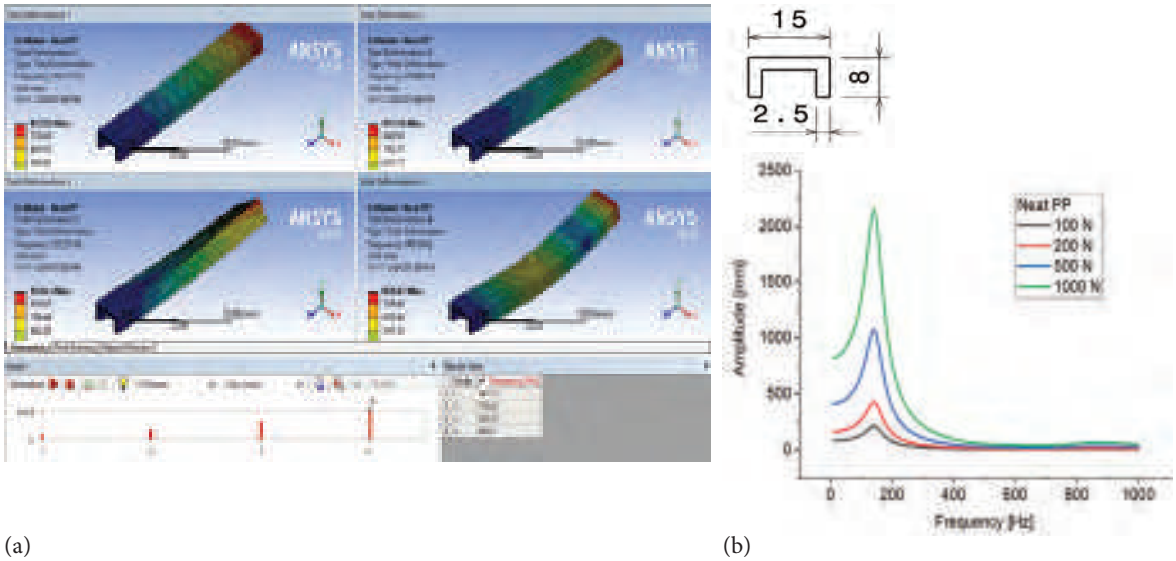
RESULTS AND DISCUSSION

Mode Shapes of Neat PP (2.5 mm thick)

Figure 2 depicts the results of a modal analysis performed on a structural component made of neat Polypropylene (PP) using ANSYS software. The analysis identifies first four natural frequencies and their corresponding mode shapes, which represent the inherent vibrational characteristics of the material under free vibration. The tabular data indicates the natural frequencies as 141.17 Hz (Mode 1), 276.62 Hz (Mode 2), 535.37 Hz (Mode 3), and 845.8 Hz (Mode 4). These frequencies represent the structure›s stiffness and mass distribution, which are crucial characteristics for assessing dynamic performance. The visualised mode forms show various deformation patterns for each frequency. Mode 1 is characterised by fundamental bending deformation, indicating first bending mode of structure. Mode 2 indicates a greater order bending mode characterized by the presence of more nodal points. More complex deformation is possible with Mode 3 introducing-the bending and torsional components. A ballpark guess would explain that mode 4, which is associated with

Table 2. Cases of nanocomposites

Dimensions (front view of C-channel)				
ANSYS model of C-channel				
Composite	**Case 1** Neat PP (2.5 mm thick)	**Case 2** PP+G+hBN (0.833 mm each)	**Case 3** 0.5mm G + 1.5mm PP+ 0.5mm hBN	**Case 4** 0.25mm G + 2 mm PP+ 0.25mm hBN



(a) (b)

Figure 2. (a) Total deformation (b) Frequency-amplitude curve at different loads for neat PP.

the highest frequency, has sophisticated deformation indicating the presence of higher order vibrational movement. In order to visualize the deformation, the scales have been normalized so that the emphasis is on the mode shapes rather than absolute values of the displacement. These findings help to conceptualise how neat PP would react under dynamic loading, thus allowing it to be considered for use in areas where vibration performance requirements are stringent. Additionally, this work presents a reference for further research on the impact of reinforcements on the modal properties of polypropylene nanocomposites such as graphene and hexagonal boron nitride.

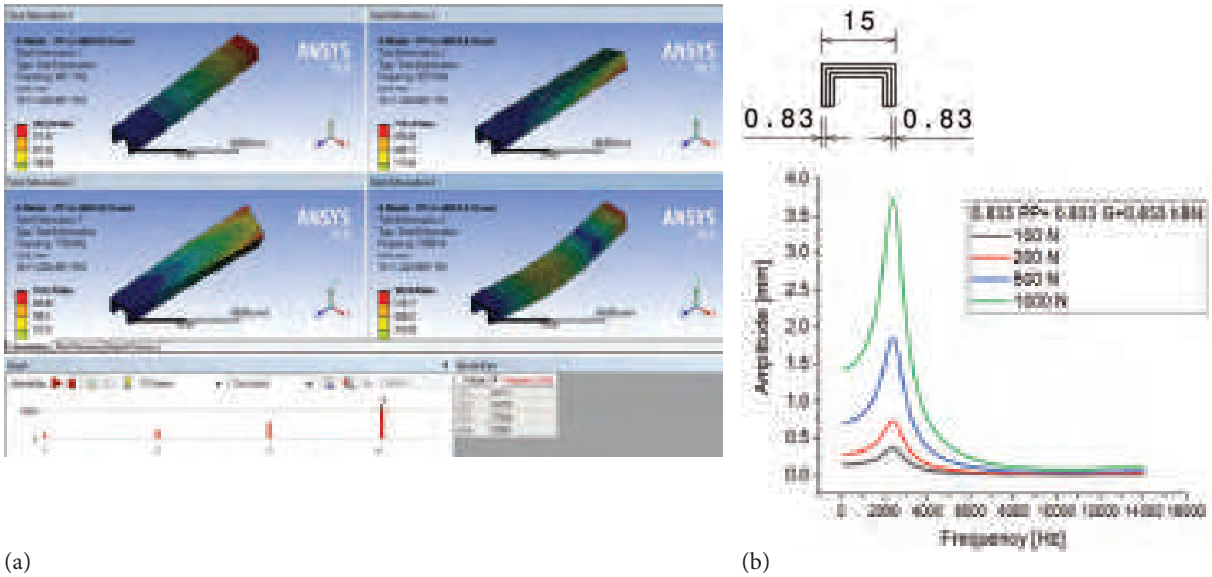
Mode Shapes of PP+G+hBN (0.83 mm each)

Figure 3 shows the results of a modal analysis of a PP nanocomposite containing equal weights of G and hBN (0.833 mm). The analysis reports the presence of 4 natural frequencies and their corresponding mode shapes. The inclusion of the nanofillers alter the vibration behavior of the composite. The calculated natural frequencies are 2411.1 Hz (Mode 1), 3657.8 Hz (Mode 2), 7782.6 Hz (Mode 3) and 13993 Hz (Mode 4). It is to be noted that presence of uniformly dispersed G and hBN in the PP matrix increase its stiffness and alter its ability to vibrate. As such, the neat PP has relatively low natural frequencies. Mode 1 corresponds to the fundamental bending of the sheet in the out of plane direction and Mode 2 corresponds to a higher order bending of the same sheet in which the bending occurs in the opposite direction compared to Mode 1. Mode 3 is a combination of bending in the out of plane direction and torsion and demonstrates the presence of higher order vibration modes. Mode 4 has a complex mode shape with multiple deformation locations and demonstrates a very high order bending. It should be noted that the high frequency modes and corresponding shapes demonstrate the changes in the stiffness of the matrix due to the presence of the nanofillers. These outcomes underline the strong influence that G and hBN additions have on the modal characteristics of PP nanocomposites, making them more fit for applications in mechanical engineering structures that are sensitive to vibration. The recorded enhancements in natural frequencies confirm the synergistic effects of the reinforcements in modifying the dynamic properties of the material. The integration of G and hBN transform the fundamental frequency of the PP nanocomposite. Natural frequencies tend to be increased which results in having better performance under dynamic conditions especially in terms of stiffer materials.

Mode Shapes of PP+G+hBN (1.5 mm PP + 0.5 mm G and hBN)

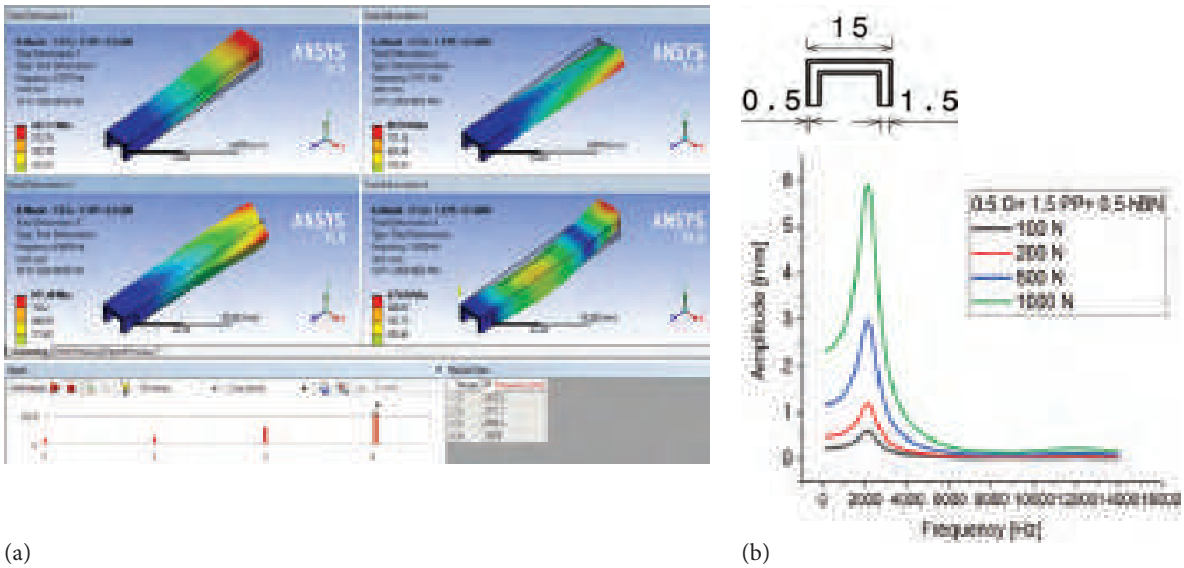
Figure 4 displays the results of a modal analysis for total deformation and frequency vs amplitude curve. This modal analysis illustrates the natural frequencies and mode shapes of a 0.5mm G+1.5mm PP+0.5mm hBN, which is critical for understanding its dynamic behaviour under vibrational loading. The results indicate four different deformation modes (Mode 1 to Mode 4). Each deformation mode is characterized by a corresponding natural frequency and a maximum total deformation value. In mode 1, the frequency is 2127.3 Hz, and the maximum deformation is 647.71 mm. The majority of the deformation occurs at the structure›s free end, showing a typical bending mode.

In mode 2, the frequency rises to 3117.1 Hz, with the maximum deformation of 867.81 mm.The deformation pattern indicates a second bending mode or torsional behaviour. 857.48 mm was the highest deformation obtained in mode 3. However, Mode 3 has a rather higher frequency which is 6769.8 Hz as such this mode will entail a more rigid form of bending or torsional modes which will



(a) (b)

Figure 3. (a) Total deformation (b) Frequency-amplitude curve at different loads for 0.833 PP+0.833 G+0.833 hBN.



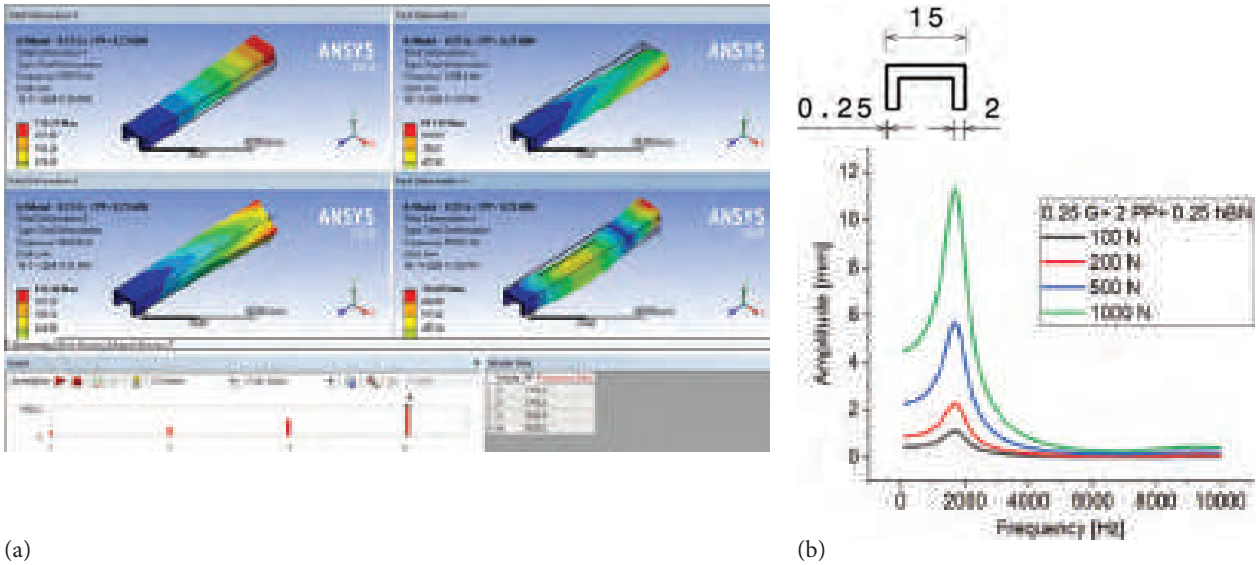
(a) (b)

Figure 4. (a) Total deformation (b) Frequency-amplitude at different loads for 0.5 G+1.5 PP+0.5 hBN.

twist but the deformation will be located at certain parts of the structure only. In mode 4, it can be observed that the maximum deformation is 675.96 mm at a frequency of 12070 Hz. This represents a mode of a better degree that has its deformation in more than one region of the structure. The following graph which is beneath the deformation plots gives the frequency of four modes and their development over time. These frequencies are influenced by the material characteristics, the shape as well as the constraints of the model. The research offers valuable information for planning resonance hazards and evaluating the reliability of the construction in the process. In this manner, knowing how a composite behaves at various frequencies helps to identify weak spots and to improve the material's placement within the composite.

Mode Shapes of PP+G+hBN (2 mm PP+0.25 mm G and hBN)

The results in Figure 5 highlight the gradual increase in frequency and varied deformation patterns, which are critical for monitoring resonance concerns and optimising the structural dynamics of 0.25 mm G + 2mm PP + 0.25mm hBN. The analysis focuses on total deformation for C-channel under different vibration modes and associated frequencies. At mode 1, the natural frequency is 1703.5 Hz, and the maximum deformation is 717.74 mm, indicating that the basic bending mode is localised at the free



(a) (b)

Figure 5. (a) Total deformation (b) Frequency-amplitude at different loads for 0.25 G+ 2 PP+ 0.25 hBN.

end. The frequency rises to 2704.4 Hz, and the maximum deformation is 911.45 mm, indicating bending or torsional behaviour in mode 2. Whereas in mode 3 at 5626.9 Hz, the deformation reaches 937.44 mm, showing more complex structural vibrations. In mode 4, the greatest frequency observed which is 9550.2 Hz, and deformation decreases to 743.05 mm, indicating a scattered mode. The addition of G and hBN influences the damping characteristics. Improved damping can reduce resonance-related issues, enhancing the durability of the PP under the loading. The bonding quality between G and hBN nanofillers and the PP matrix influences the transfer of load, directly impacting stiffness, damping, and overall performance under vibration. A frequency spectrum graph is shown at the bottom which highlights the modal frequencies as distinct peaks, indicating where resonance occurs. Each mode corresponds to one of the peaks.

Comparative Analysis

Figure 6 shows frequency response of polypropylene (PP) nanocomposites with different amounts of graphene (G) and hexagonal boron nitride (hBN). Amplitude (in mm) is shown on the vertical axis against frequency (in Hz). The three reinforcement combinations are: 0.833 mm G + 0.833 mm PP + 0.833 mm hBN, 0.5 mm G + 1.5 mm PP + 0.5 mm hBN, and 0.25 mm G + 2 mm PP + 0.25 mm hBN. The figure shows that each of the constituents exhibit a peak in amplitude, and therefore, resonance. Of the three compositions, the one with 0.833 mm G and 0.833 mm hBN exhibited the lowest amplitude, and therefore, best damping behavior. Thus, this composition of the nanocomposites is expected to have the least tendency to vibrate, among the three compositions. The G + hBN combination of 0.25 mm G + 0.25 mm hBN, which exhibited the highest peak amplitude of all the blends, is followed by 0.5 mm G + 0.5 mm hBN combination that has slightly higher amplitude than the last combination. When the weight fraction of G and hBN increases, it can be seen that the resonant frequency increases, highlighting the stiffening effect of these reinforcements. Increased concentrations of graphene and hBN add to the stiffness of the material, which results in a higher natural frequency and lower vibrational amplitudes. Such behaviour shows the proper action of G and hBN reinforcements on the dynamics of PP nanocomposites. The results emphasize the importance of balancing the mechanical stiffness and a certain level of damping by optimising the filler percentages in some engineering applications. Mechanical and vibrational properties are related to layer thickness of G and hBN nanofillers in PP.

The graphical representation of Figure 7 shows the phase angle response as a function of frequency for the different concentrations of graphene and hexagonal boron nitride in polypropylene (PP) nanocomposites. These combinations of materials have been analyzed in three material combinations which are outlined as follows; 0.833 mm G +0.833 mm PP+ 0.833 mm hBN, 0.5 mm G + 1.5 mm PP + 0.5 mm hBN and 0.25 mm G + 2 mm PP + 0.25 mm hBN. The phase angle of this system, given in degrees, represents the position of the input and output signals in time relative to each other. The phase angle behaviour shows sizable transitions about certain frequencies that correspond to the resonant and anti-resonant regions of the materials. At the onset, the phase angle stays high and falls as frequency increases which indicates a change from structural to inertial movement. The phase angle drops steeply in the neighbourhood of the resonant frequency and resumes when the frequency exceeds the resonance.

The nanocomposite with 0.833 mm G and 0.833 mm hBN displays a smoother phase transition. This indicates that the nanocomposite exhibits better energy damping. The nanocomposite exhibits frequency independence if the phase transition is smooth. The nanocomposite with 0.25 mm G and 0.25 mm hBN displays an abrupt phase transition. This indicates that the nanocomposite exhibits a lack of control over the vibrational response. The nanocomposite with 0.5 mm G and 0.5 mm hBN displays a phase transition that is smoothed out intermediate between the nanocomposites with 0.833 mm and 0.25 mm layers. This

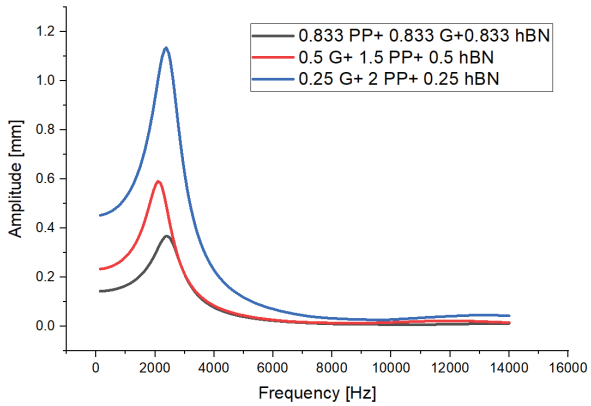


Figure 6. Frequency verses amplitude.

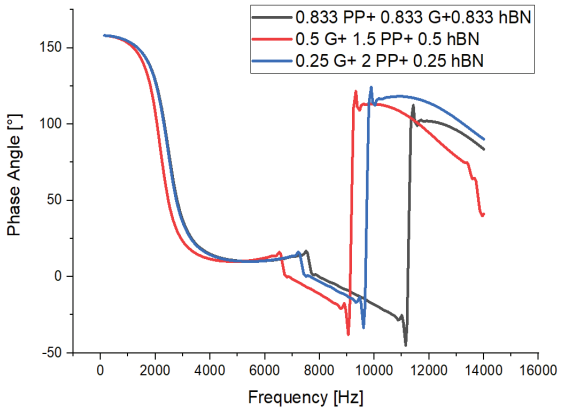


Figure 7. Frequency verses phase angle.

Table 3. Total deformation for all composites at 100 N

C-Channel Composites	Total deformation (Max.) in mm			
	Mode Shape 1	Mode Shape 2	Mode Shape 3	Mode Shape 4
Case 1 Neat PP (2.5 mm thick)	822.02	955.76	1024.3	820.87
Case 2 PP+G+hBN (0.833 mm each)	580.29	776.76	770.27	589.64
Case 3 0.5mm G + 1.5mm PP+ 0.5mm hBN	647.71	867.81	857.48	675.96
Case 4 0.25mm G + 2 mm PP+ 0.25mm hBN	717.74	911.45	937.44	743.05

demonstrates that stiffness and phase stability are interrelated. Vibration sensitive components may benefit from the use of PP nanocomposites.

The Table 3 provides data on the total deformation for different configurations of C-channel composites under a load of 100 N, measured for four distinct mode shapes. The properties of pure PP are studied in contrast with G and hBN based hybrid composites. Case 1 presents 2.5 mm of PP, and it displays the highest amount of deformation of all the cases studies (820.87 mm to 1024.3 mm). As previous cases studied composites, PP displays lower stiffness and strength compared to G and hBN. Case 2 studied 3 (0.833 mm) layers of each of PP, G, and hBN. It displays, as expected, a much stiffer system. The deformation of this case was measured to be 580.29 mm. As seen previously, the hybrid system improves the stiffness and strength of the composite. Case 3, 1.5 mm of PP sandwiched between 0.5 mm G and hBN layers, improved the stiffness of the system, as expected. Case 4 2 mm of PP, 0.25 mm of G and hBN, displays higher deformation than Case 3, and much lower deformation than case 1. As expected, the system becomes stiffer with more reinforcing elements. As previously discussed, the improvement in deformation of the composite is due to the rigid nature of G and hBN. It shows that the addition of G and hBN improves the overall performance of the composites.

CONCLUSION

This modal analysis of graphene (G) and hexagonal boron nitride (hBN) polypropylene (PP) nanocomposites involves understanding how these materials behave under dynamic loads. Adding G and hBN to PP improve its stiffness, strength, and toughness, which affect the modal properties like natural frequencies and mode shapes, also it improves the damping properties of PP, leading to better energy dissipation during vibrations. The total deformation is as follows:

1. Mode shapes 1 to 4 of PP+G+hBN (0.833 mm each): The total deformation is approximately 29.40, 18.72, 24.80 and 28.16 times less than neat PP respectively.
2. Mode shapes 1 to 4 of 0.5mm G + 1.5mm PP+ 0.5mm hBN: The total deformation is approximately 21.20, 9.20, 16.28 and 17.56 times less than neat PP respectively.
3. Mode shapes 1 to 4 of 0.25mm G + 2 mm PP+ 0.25mm hBN: The total deformation is approximately 12.68, 4.63, 8.47 and 9.48 times less than neat PP respectively.

This analysis seems to examine how the structure behaves under vibrational loading, focusing on its natural frequencies and modal shapes. These insights are essential for ensuring the structure can avoid resonance under operational conditions. PP is softer materials often exhibit greater internal damping, which can reduce the amplitude of vibrations and alter the resonance behaviour, though it doesn›t directly change the natural frequency. However, PP+G+hBN nanocomposites, being less damped, can sustain vibrations longer and exhibit sharper resonance at their natural frequency. Due to these combinations of nanocomposites, less deformation is found in C-channel of PP+G+hBN in comparison with neat PP.

ACKNOWLEDGEMENT

Aamir M. Shaikh extends his gratitude to Dr. Pravin R. Kubade for his guidance and supervision of the research activities.

AUTHORSHIP CONTRIBUTIONS

Authors equally contributed to this work.

DATA AVAILABILITY STATEMENT

The authors confirm that the data that supports the findings of this study are available within the article. Raw data that support the finding of this study are available from the corresponding author, upon reasonable request.

CONFLICT OF INTEREST

The authors declared that they have no conflicts of interest.

ETHICS

There are no ethical issues with the publication of this manuscript.

STATEMENT ON THE USE OF ARTIFICIAL INTELLIGENCE

Artificial intelligence was not used in the preparation of the article.

REFERENCES

[1] Hossain MT, Shahid MA, Mahmud N, Habib A, Rana MM, Khan SA, et al. Research and application of polypropylene: A review. Discover Nano 2024;19:2. [CrossRef]

[2] Kwon T, Lee SH, Kim JH, Hong SK, Kim M, Kim M, et al. Polypropylene nanocomposites doped with carbon nanohorns for high-voltage power cable insulation applications. Adv Compos Hybrid Mater 2023;6:167. [CrossRef]

[3] Kubade P, Tambe P. Influence of surface modification of halloysite nanotubes and its localization in PP phase on mechanical and thermal properties of PP/ABS blends. Compos Interfaces 2016;24:469–487. [CrossRef]

[4] Shaikh AM, Kubade PR. Effect of nanofillers on rolled polymer nanocomposites: A review. Mater Today Proc 2023. [CrossRef]

[5] Kausar A. Shape memory polymer/graphene nanocomposites: State-of-the-art. e-Polymers 2022;22:165–181. [CrossRef]

[6] Nisar M, Galland GB, Geshev J, Bergmann C, Quijada R. Magnetically stimulable graphene oxide/polypropylene nanocomposites. ACS Omega 2023;8:21983–21995. [CrossRef]

[7] Kausar A, Ahmad I, Zhao T, Aldaghri O, Ibnaouf KH, Eisa MH, et al. Graphene nanocomposites for electromagnetic interference shielding-Trends and advancements. J Compos Sci 2023;7:384. [CrossRef]

[8] Iqbal AKMA, Sakib N, Iqbal AKMP, Nuruzzaman DM. Graphene-based nanocomposites and their fabrication, mechanical properties and applications. Materialia 2020;12:100815. [CrossRef]

[9] Shaikh AM, Kubade PR. A review on rolling process for polymer nanocomposites with different nanofillers to enhance properties. In: Sumesh M, Tavares JMR, Vettivel SC, Oliveira MO, editors. 2nd International Conference on Smart Sustainable Materials and Technologies (ICSSMT 2023). Advances in Science, Technology & Innovation. Cham: Springer; 2024. [CrossRef]

[10] Nagarajan T, Sridewi N, Wong WP, et al. Synergistic performance evaluation of MoS2-hBN hybrid nanoparticles as a tribological additive in diesel-based engine oil. Sci Rep 2023;13:12559. [CrossRef]

[11] Saha M, Tambe P, Pal S, Kubade P, Manivasagam G, Xavior MA, et al. Effect of non-ionic surfactant assisted modification of hexagonal boron nitride nanoplatelets on the mechanical and thermal properties of epoxy nanocomposites. Compos Interfaces 2015;22:611–627. [CrossRef]

[12] Siddiqui GU, Rehman MM, Yang Y, Choi KH. A two-dimensional hexagonal boron nitride/polymer nanocomposite for flexible resistive switching devices. J Mater Chem C 2017;5:862–871. [CrossRef]

[13] Komal K, Singh M, Singh B. A flexible memory device made of SnO2-hBN nanocomposite exhibits stable resistive switching application. J Mater Sci 2024;59:13508–13531. [CrossRef]

[14] Sun L, Zou Y, Ma M, Li G, Wang X, Zhang X, et al. Synthesis of cBN-hBN-SiCw nanocomposite with superior hardness, strength, and toughness. Nanomaterials (Basel) 2022;13:37. [CrossRef]

[15] Ergene B, Yalçın B. A finite element study on modal analysis of lightweight pipes. Sigma J Eng Nat Sci 2021;39:268–278. [CrossRef]

[16] Zeng QH, Yu AB, Lu GQ. Multiscale modeling and simulation of polymer nanocomposites. Prog Polym Sci 2008;33:191–269. [CrossRef]

[17] Duarte HV, Donadon LV, Ávila AF. Mechanical properties of nanocomposite laminated structure and its sensibility to modal analysis procedure. Lat Am J Solids Struct 2014;11:245–259. [CrossRef]

[18] Duarte HV, Donadon LV, Ávila AF. Mechanical properties of nanocomposite laminated structures by modal method.

[19] Mansour G, Tsongas K, Tzetzis D. Modal testing of nanocomposite materials through an optimization algorithm. Measurement 2016;91:31–38. [CrossRef]

[20] Fereidoon A, Rafiee R, Moghadam RM. A modal analysis of carbon-nanotube-reinforced polymer by using a multiscale finite-element method. Mech Compos Mater 2013;49:325–332. [CrossRef]

[21] Ávila AF, Donadon LV, Duarte HV. Modal analysis on nanoclay epoxy-based fiber-glass laminates. Compos Struct 2008;83:324–333. [CrossRef]

[22] Şişman R, Şahin A. An educational tool for observing seismic behavior of 3D frame structures. Sigma J Eng Nat Sci 2015;33:119–128.

[23] Qaderi S, Ebrahimi F. Vibration analysis of polymer composite plates reinforced with graphene platelets resting on two-parameter viscoelastic foundation. Eng Comput 2020. [CrossRef]

[24] Shaikh AM, Ghatge DA. CFD simulation for fluid flow through a circular chamber by using ANSYS. In: Recent advances in material, manufacturing, and machine learning. CRC Press; 2023. p. 1025–1034. [CrossRef]

[25] Shaikh A, Kubade P. A study of polypropylene and graphene and their nanocomposites using ANSYS. Polyolefins J 2024;11:155–166.
[26] Dahiya M, Khanna V, Gupta N. Review-Computational studies of graphene reinforced nanocomposites: Techniques, parameters, and future perspectives. ECS J Solid State Sci Technol 2024. [CrossRef]
[27] Chandra Y, Adhikari S, Saavedra Flores EI, Figiel Ł. Advances in finite element modelling of graphene and associated nanostructures. Mater Sci Eng R Rep 2020;140:100544. [CrossRef]

APPENDIX

Table 4. Simulation results

Neat PP			0.833 PP+ 0.833 G+0.833 hBN			0.5 G+ 1.5 PP+ 0.5 hBN			0.25 G+ 2 PP+ 0.25 hBN		
Frequency [Hz]	Amplitude [mm]	Phase Angle [°]	Frequency [Hz]	Amplitude [mm]	Phase Angle [°]	Frequency [Hz]	Amplitude [mm]	Phase Angle [°]	Frequency [Hz]	Amplitude [mm]	Phase Angle [°]
10	82.49	158.1	140	0.14339	158.14	140	0.23403	158.12	100	0.45292	158.14
20	83.541	157.81	280	0.14459	157.94	280	0.23651	157.87	200	0.45668	157.94
30	85.351	157.3	420	0.14664	157.61	420	0.24076	157.45	300	0.4631	157.62
40	88.012	156.55	560	0.1496	157.13	560	0.24696	156.84	400	0.47238	157.14
50	91.669	155.5	700	0.15357	156.49	700	0.2554	155.99	500	0.48486	156.49
60	96.534	154.1	840	0.1587	155.64	840	0.26648	154.85	600	0.50101	155.65
70	102.92	152.22	980	0.1652	154.56	980	0.28081	153.37	700	0.52146	154.56
80	111.25	149.71	1120	0.17333	153.19	1120	0.29917	151.42	800	0.5471	153.18
90	122.17	146.3	1260	0.18345	151.45	1260	0.32271	148.84	900	0.57909	151.41
100	136.48	141.58	1400	0.19606	149.23	1400	0.35295	145.39	1000	0.619	149.15
110	155.06	134.9	1540	0.21178	146.37	1540	0.39175	140.68	1100	0.66888	146.21
120	177.98	125.24	1680	0.23141	142.63	1680	0.44082	134.12	1200	0.7312	142.34
130	201.73	111.4	1820	0.25577	137.66	1820	0.4995	124.86	1300	0.80852	137.17
140	214.75	93.055	1960	0.28534	130.97	1960	0.55848	111.9	1400	0.90176	130.15
150	203.68	72.919	2100	0.3189	121.89	2100	0.5912	95.051	1500	1.0054	120.59
160	173.58	55.483	2240	0.35076	109.79	2240	0.56689	76.403	1600	1.0978	107.87
170	140.84	42.588	2380	0.36812	94.687	2380	0.49316	59.393	1700	1.1351	92.251
180	113.64	33.654	2520	0.35748	78.151	2520	0.40811	45.819	1800	1.0803	75.647
190	92.807	27.444	2660	0.32071	62.637	2660	0.33372	36.5	1900	0.95277	59.746
200	77.048	23.012	2800	0.27379	49.869	2800	0.27497	29.83	2000	0.80714	47.616
210	64.991	19.763	2940	0.22959	40.456	2940	0.22971	24.984	2100	0.67462	38.731
220	55.597	17.325	3080	0.19261	33.423	3080	0.19465	21.445	2200	0.56561	32.156
230	48.137	15.462	3220	0.163	28.242	3220	0.16712	18.77	2300	0.47901	27.176
240	42.109	14.02	3360	0.13948	24.276	3360	0.14514	16.705	2400	0.41045	23.413
250	37.159	12.896	3500	0.12067	21.253	3500	0.1273	15.09	2500	0.35561	20.562
260	33.038	12.019	3640	0.10545	18.887	3640	0.11262	13.816	2600	0.31122	18.327
270	29.564	11.337	3780	9.30E-02	17.135	3780	0.10036	12.806	2700	0.2748	16.549
280	26.603	10.817	3920	8.27E-02	15.629	3920	9.00E-02	12.004	2800	0.24453	15.121
290	24.056	10.431	4060	7.40E-02	14.407	4060	8.12E-02	11.373	2900	0.21909	13.965
300	21.845	10.16	4200	6.67E-02	13.411	4200	7.36E-02	10.883	3000	0.19747	13.025
310	19.912	9.9899	4340	6.04E-02	12.598	4340	6.70E-02	10.514	3100	0.17892	12.26
320	18.21	9.9109	4480	5.49E-02	11.937	4480	6.12E-02	10.248	3200	0.16287	11.641
330	16.703	9.9153	4620	5.02E-02	11.403	4620	5.61E-02	10.074	3300	0.14886	11.143
340	15.36	9.9982	4760	4.60E-02	10.977	4760	5.15E-02	9.984	3400	0.13656	10.751
350	14.158	10.156	4900	4.23E-02	10.646	4900	4.75E-02	9.9708	3500	0.12568	10.449
360	13.076	10.388	5040	3.90E-02	10.397	5040	4.39E-02	10.03	3600	0.116	10.228
370	12.1	10.693	5180	3.61E-02	10.223	5180	4.06E-02	10.16	3700	0.10735	10.08
380	11.214	11.073	5320	3.35E-02	10.116	5320	3.77E-02	10.357	3800	9.96E-02	9.9979
390	10.409	11.53	5460	3.11E-02	10.071	5460	3.50E-02	10.623	3900	9.26E-02	9.9785
400	9.6742	12.068	5600	2.90E-02	10.085	5600	3.26E-02	10.958	4000	8.62E-02	10.018
410	9.0017	12.69	5740	2.70E-02	10.155	5740	3.04E-02	11.363	4100	8.04E-02	10.114
420	8.385	13.403	5880	2.53E-02	10.279	5880	2.84E-02	11.842	4200	7.52E-02	10.265
430	7.8181	14.213	6020	2.36E-02	10.457	6020	2.65E-02	12.399	4300	7.03E-02	10.471
440	7.2963	15.129	6160	2.21E-02	10.562	6160	2.48E-02	13.038	4400	6.59E-02	10.733
450	6.8452	7.7364	6300	2.08E-02	10.832	6300	2.32E-02	13.765	4500	6.18E-02	11.05

Table 4. Simulation results

Neat PP			**0.833 PP+ 0.833 G+0.833 hBN**			**0.5 G+ 1.5 PP+ 0.5 hBN**			**0.25 G+ 2 PP+ 0.25 hBN**		
Frequency [Hz]	**Amplitude [mm]**	**Phase Angle [°]**	**Frequency [Hz]**	**Amplitude [mm]**	**Phase Angle [°]**	**Frequency [Hz]**	**Amplitude [mm]**	**Phase Angle [°]**	**Frequency [Hz]**	**Amplitude [mm]**	**Phase Angle [°]**
460	6.4831	4.985	6440	1.95E-02	11.155	6440	2.17E-02	14.072	4600	5.81E-02	11.425
470	6.1697	3.0531	6580	1.83E-02	11.531	6580	2.04E-02	14.945	4700	5.46E-02	11.86
480	5.8956	0.99805	6720	1.73E-02	11.964	6720	1.95E-02	1.4051	4800	5.14E-02	12.358
490	5.6542	-0.66918	6860	1.62E-02	12.668	6860	1.87E-02	0.25127	4900	4.84E-02	12.921
500	5.4408	-2.424	7000	1.53E-02	13.245	7000	1.79E-02	-1.4621	5000	4.56E-02	13.555
510	5.2522	-3.7712	7140	1.45E-02	13.394	7140	1.73E-02	-2.7616	5100	4.30E-02	14.264
520	5.085	-5.1912	7280	1.36E-02	14.065	7280	1.67E-02	-4.1288	5200	4.06E-02	15.054
530	4.9369	-6.6806	7420	1.29E-02	14.808	7420	1.62E-02	-5.5621	5300	3.88E-02	1.8887
540	4.8059	-8.2363	7560	1.22E-02	15.627	7560	1.57E-02	-7.0598	5400	3.73E-02	0.77739
550	4.6901	-9.8549	7700	1.17E-02	2.6376	7700	1.53E-02	-8.1308	5500	3.59E-02	-0.39578
560	4.5883	-11.052	7840	1.13E-02	1.5787	7840	1.50E-02	-9.7564	5600	3.47E-02	-1.6298
570	4.4992	-12.796	7980	1.08E-02	-2.76E-02	7980	1.47E-02	-10.951	5700	3.36E-02	-2.9232
580	4.4217	-14.12	8120	1.05E-02	-1.2089	8120	1.44E-02	-12.703	5800	3.26E-02	-4.274
590	4.3545	-15.508	8260	1.02E-02	-2.4456	8260	1.41E-02	-14.024	5900	3.17E-02	-5.6801
600	4.2976	-17.442	8400	9.85E-03	-3.7352	8400	1.39E-02	-15.902	6000	3.09E-02	-6.6445
610	4.2497	-18.963	8540	9.58E-03	-4.5874	8540	1.38E-02	-17.356	6100	3.02E-02	-8.1595
620	4.2101	-20.555	8680	9.33E-03	-5.9792	8680	1.36E-02	-18.876	6200	2.95E-02	-9.7243
630	4.1785	-22.219	8820	9.11E-03	-7.4174	8820	1.35E-02	-20.467	6300	2.90E-02	-10.848
640	4.1542	-23.959	8960	8.91E-03	-8.4166	8960	1.34E-02	-22.131	6400	2.84E-02	-12.022
650	4.1368	-25.778	9100	8.73E-03	-9.4582	9100	1.33E-02	-23.871	6500	2.80E-02	-13.745
660	4.1258	-27.681	9240	8.57E-03	-11.039	9240	1.37E-02	110.36	6600	2.76E-02	-15.026
670	4.1207	-29.672	9380	8.42E-03	-12.176	9380	1.42E-02	111.39	6700	2.73E-02	-16.36
680	4.1209	-31.755	9520	8.30E-03	-13.358	9520	1.48E-02	112.17	6800	2.70E-02	-17.749
690	4.1265	-33.48	9660	8.18E-03	-14.587	9660	1.53E-02	112.71	6900	2.67E-02	-19.195
700	4.1365	-35.769	9800	8.08E-03	-16.351	9800	1.59E-02	113.03	7000	2.70E-02	113.13
710	4.1502	-38.166	9940	7.99E-03	-17.676	9940	1.65E-02	113.14	7100	2.79E-02	114.42
720	4.195	88.202	10080	7.92E-03	-19.052	10080	1.70E-02	113.05	7200	2.88E-02	115.51
730	4.3773	88.526	10220	7.86E-03	-20.477	10220	1.76E-02	112.75	7300	2.97E-02	116.39
740	4.5653	88.537	10360	7.80E-03	-21.956	10360	1.82E-02	112.27	7400	3.07E-02	117.09
750	4.7572	88.249	10500	7.76E-03	-23.01	10500	1.87E-02	111.6	7500	3.17E-02	117.61
760	4.9508	87.674	10640	7.73E-03	-24.602	10640	1.93E-02	110.75	7600	3.27E-02	117.97
770	5.1438	86.825	10780	7.71E-03	-26.253	10780	1.98E-02	109.72	7700	3.37E-02	118.17
780	5.3335	85.715	10920	7.69E-03	-27.965	10920	2.03E-02	108.52	7800	3.47E-02	118.22
790	5.5171	84.36	11060	7.69E-03	-29.739	11060	2.08E-02	107.15	7900	3.57E-02	118.12
800	5.6915	82.776	11200	7.69E-03	-31.11	11200	2.12E-02	105.63	8000	3.67E-02	117.88
810	5.8535	80.98	11340	7.75E-03	100.92	11340	2.16E-02	103.95	8100	3.76E-02	117.5
820	5.9998	78.993	11480	8.02E-03	101.51	11480	2.19E-02	102.13	8200	3.86E-02	116.99
830	6.1273	76.839	11620	8.30E-03	101.89	11620	2.22E-02	100.18	8300	3.96E-02	116.34
840	6.2333	74.544	11760	8.58E-03	102.09	11760	2.24E-02	98.122	8400	4.05E-02	115.56
850	6.3156	71.958	11900	8.87E-03	102.09	11900	2.25E-02	95.975	8500	4.14E-02	114.65
860	6.3727	69.464	12040	9.16E-03	101.91	12040	2.25E-02	93.76	8600	4.22E-02	113.62
870	6.4032	66.915	12180	9.46E-03	101.55	12180	2.25E-02	91.502	8700	4.30E-02	112.46
880	6.4071	64.34	12320	9.75E-03	101.02	12320	2.23E-02	89.226	8800	4.38E-02	111.18
890	6.3849	61.759	12460	1.00E-02	100.32	12460	2.21E-02	86.96	8900	4.44E-02	109.79
900	6.3382	59.214	12600	1.03E-02	99.463	12600	2.17E-02	84.73	9000	4.50E-02	108.29
910	6.2692	56.72	12740	1.06E-02	98.45	12740	2.13E-02	82.562	9100	4.54E-02	106.69
920	6.1852	52.539	12880	1.09E-02	97.286	12880	2.09E-02	80.478	9200	4.58E-02	105
930	6.0874	50.197	13020	1.11E-02	95.979	13020	2.03E-02	78.483	9300	4.60E-02	103.24
940	5.9752	47.951	13160	1.14E-02	94.535	13160	1.97E-02	76.628	9400	4.61E-02	101.42
950	5.8514	45.809	13300	1.16E-02	92.963	13300	1.91E-02	74.91	9500	4.60E-02	99.553
960	5.7185	43.776	13440	1.18E-02	91.273	13440	1.85E-02	73.342	9600	4.58E-02	97.658
970	5.5809	41.328	13580	1.19E-02	89.476	13580	1.78E-02	64.241	9700	4.54E-02	95.756
980	5.4393	39.517	13720	1.21E-02	87.584	13720	1.72E-02	62.71	9800	4.49E-02	93.867
990	5.2952	37.817	13860	1.22E-02	85.613	13860	1.68E-02	42.885	9900	4.43E-02	92.009
1000	5.15	36.225	14000	1.22E-02	83.577	14000	1.64E-02	41.18	10000	4.35E-02	90.204

Sigma J Eng Nat Sci, Vol. 44, No. 4, pp. 2808–2822, August, 2026

Sigma Journal of Engineering and Natural Sciences
Web page info: https://sigma.yildiz.edu.tr
DOI: 10.14744/sigma.2026.2103

Research Article

Solution and stability analysis of homogeneous piecewise fractional systems

Mustafa AYDIN[1,*], Arda BİLEN[2]

[1]*Department of Medical Services and Techniques, Muradiye Vocational School, Van Yüzüncü Yıl University, Van, 65080, Türkiye*
[2]*Department of Computer Engineering, Faculty of Engineering, Van Yüzüncü Yıl University, Van, 65080, Türkiye*

ARTICLE INFO

Article history
Received: 05 October 2025
Revised: 16 December 2025
Accepted: 03 March 2026

Keywords:
Caputo Derivative; Explicit Solution; Finite-Time Stability; Fractional Delay Systems; Generating Function

ABSTRACT

This paper studies linear piecewise fractional delay systems motivated by models with switching dynamics and memory effects. An explicit interval-wise solution is constructed via a generating-function approach, and its continuity at all junction points is established. Based on this representation, a computable finite-time stability condition is derived in the form of an explicit inequality involving the system parameters, delay, and fractional order. Several scalar and matrix-valued examples illustrate the theoretical results and confirm the effectiveness of the proposed stability criterion. The novelty of this work lies in providing, to the best of our knowledge, the frst explicit interval-wise solution framework for piecewise fractional delay systems together with a directly verifiable finite-time stability condition, thereby extending existing results that rely on implicit formulations or restrictive structural assumptions.

Cite this article as: Aydın M, Bilen A. Solution and stability analysis of homogeneous piecewise fractional systems. Sigma J Eng Nat Sci 2026;44(4):2808–2822.

INTRODUCTION

Finite-time stability constitutes a critical characteristic of dynamical systems, describing the ability of a system to reach a desired state or remain within a prescribed bound over a finite time interval. This notion has been widely investigated in nonlinear systems, fractional-order systems [1, 2], and systems with delays [3-10]. Its importance stems from applications such as synchronization in complex networks, stabilization of robotic systems [11], and regulation of time-sensitive processes, where transient performance is often more relevant than asymptotic behavior.

The increasing use of fractional differential equations (FDEs) in engineering, economics, physics, and related elds has further motivated the study of finite-time stability in fractional-order settings [12-17]. Fractional models are particularly effective in capturing memory and hereditary effects that cannot be adequately described by classical integer-order dynamics. A wide range of analytical and numerical methods has been developed for FDEs, including transform-based techniques and numerical schemes [18-23]. More recently, explicit analytical solution techniques and stability analyses for fractional and conformable systems have attracted increasing attention in the applied mathematics and engineering literature. For example,

*Corresponding author.
*E-mail address: m.aydin@yyu.edu.tr

This paper was recommended for publication in revised form by Editor-in-Chief Ahmet Selim Dalkilic

Published by Yıldız Technical University Press, İstanbul, Turkey
© Author. This is an open access article under the CC BY-NC license (http://creativecommons.org/licenses/by-nc/4.0/).

explicit solution formulas for linear conformable systems with variable coeffcients were proposed in [24], while fractional epidemic models illustrating real-world applications were studied in [25]. In addition, existence, uniqueness, and generalized stability notions for fractional operators were addressed in [26].

For classical linear systems of the form $v'(\varsigma) = Bv(\varsigma)$, the solution is given by the matrix exponential $v(\varsigma) = e^{B\varsigma}v(0)$. However, the introduction of a delay term $v(\varsigma - \tau)$ significantly complicates the analysis. Khusainov and Shuklin [27] investigated linear autonomous delay systems using delay exponential functions under restrictive commutativity assumptions, while Li and Wang [28] studied the corresponding fractional analogues. In a related direction, Huiping and Wang [29] analyzed piecewise linear state-delay systems with more complex structures, focusing primarily on controllability properties.

From an application viewpoint, piecewise fractional delay systems naturally arise in models with switching dynamics and memory effects. Typical examples include networked control systems with mode-dependent communication delays, fractional-order viscoelastic models subject to regime changes, and hybrid engineering or biological processes in which system parameters vary in a piecewise manner. For such systems, understanding transient behavior and guaranteeing performance within a finite time horizon are of practical importance.

In parallel, several studies have addressed finite-time stability of fractional delay differential equations. Li and Wang [30] derived quantitative finite-time stability criteria, while delayed Mittag-Leffer type matrix functions were introduced in [28] to obtain more constructive solution representations and stability bounds. Despite these advances, the existing literature largely relies on implicit solution formulations, numerical approaches, or restrictive structural assumptions. In particular, explicit interval-wise analytical solu tions for piecewise fractional delay systems, together with rigorous continuity analysis at switching points and directly verifiable finite-time stability conditions, remain relatively scarce.

Classical approaches for fractional delay differential equations are typically based on the fractional method of steps, where the solution is constructed recursively on successive delay intervals by solving a sequence of fractional initial-value problems; see, for instance [28, 30]. Within this framework, explicit representations are usually expressed in terms of delayed Mittag-Leffler matrix functions and are mainly developed for systems with constant coefficients or under restrictive structural assumptions. Similarly, linear delay systems with special matrix structures are treated via delay exponential functions under permutation or commutativity conditions [27]. More recently, piecewise state-delay systems have been investigated primarily from the controllability viewpoint, without providing explicit analytical solution formulas or finite-time stability guarantees [29].

In contrast to these studies, the present work introduces a generating-function-based construction that encapsulates the stepwise procedure into a single explicit interval-wise representation. This approach yields closed-form expressions on each delay subinterval with interval-dependent coefficient matrices, enables a transparent continuity analysis at all junction points, and leads to a directly computable finite-time stability condition expressed as an explicit inequality involving the system matrices, delay length, and fractional order. Hence, beyond the existing results in [27-30], the proposed framework provides an explicit, unified, and verifiable solution-stability methodology for piecewise fractional delay systems.

Motivated by these gaps, the present work develops a generating-function-based frame work for linear piecewise fractional delay systems. The proposed approach yields explicit closed-form solutions on successive delay intervals, proves continuity at all junction points, and leads to a computable finite-time stability criterion expressed as an explicit inequality involving the system matrices, delay parameter, and fractional order. In contrast to existing methods, the results do not rely on restrictive commutativity assumptions and provide transparent analytical tools suitable for both theoretical analysis and engineering applications.

Inspired by the studies [28] and [29], we dedicated this paper to investigate the following homogeneous fractional piecewise delayed systems,

$$\begin{cases} {}^{C}D^{\alpha}_{(m-1)\tau^+}v(\varsigma) = \Omega_{\mathrm{m}}v(\varsigma - \tau), & \varsigma \in [(\mathrm{m}-1)\tau, \mathrm{m}\tau), \\ \quad\vdots \\ {}^{C}D^{\alpha}_{\tau^+}v(\varsigma) = \Omega_2 v(\varsigma - \tau), & \varsigma \in [\tau, 2\tau), \\ {}^{C}D^{\alpha}_{0^+}v(\varsigma) = \Omega_1 v(\varsigma - \tau), & \varsigma \in [0, \tau), \\ v(\varsigma) = \varphi(\varsigma), & \varsigma \in [-\tau, 0), \end{cases} \tag{1}$$

where $\varphi : [-\tau, 0] \to \mathbb{R}^n$ is an initial function, ${}^{C}D^{\alpha}_{i\tau^+}$, $i = 0,1,\ldots, m - 1$ stand for the well-known Caputo fractional derivatives, $\tau > 0$ is a delay parameter, and $\Omega_i \in \mathbb{R}^{nxn}$, $i = 1,\ldots, m$.

This paper is organized as follows. Section 1 emphasises the importance of finite-time stability and fractional differential equations and their usages addition to introducing our system by touching on the existing studies in the literature, while Section 2 provides the necessary symbols and definitions of fractional derivatives and integrals and some their properties. In Section 3, a solution to the system by proposing the generating function is constructed and its continuity is proved, and in Section 4 a finite-time stability analysis is carried out. Section 5 presents illustrative examples, and Section 6 concludes the paper with final remarks.

QUICK PRELIMINARIES

In this section, we briefly recall the basic de definitions, notations, and results that will be used throughout the paper.

Let $\mathbb{R}^+$ and $\mathbb{R}$ denote the sets of all positive real numbers and all real numbers, respectively. For $-\infty < a < b < \infty$, we denote by $C([a, b], \mathbb{R})$ the Banach space of

continuous real-valued functions on [a,b] endowed with the maximum norm $\|\cdot\|_\infty$, is defined by,

$$\|\psi\|_\infty = \max_{t\in[a,b]} |\psi(t)|,$$

where $|\cdot|$ denotes an arbitrary norm on $\mathbb{R}$. The Riemann-Liouville integral $I_{a^+}^{\beta}\, \nu(\varsigma)$ of fractional order $\beta > 0$ is given by

$$I_{a^+}^{\beta}\nu(\varsigma) = \frac{1}{\Gamma(\beta)}\int_a^{\varsigma} (\varsigma - s)^{\beta-1}\nu(s)ds\,, \quad \varsigma > a > -\infty,$$

the Caputo derivative ${}^{C}D_{a^+}^{\beta}$ of fractional order $0 < \beta < 1$ is given by

$${}^{C}D_{a^+}^{\beta}\nu(\varsigma) = \frac{1}{\Gamma(1-\beta)}\int_a^{\varsigma} (\varsigma - s)^{-\beta}\nu'(s)ds,\ \varsigma > a > -\infty,$$

where $\Gamma(\cdot)$ is the well-known Gamma function. Their compositions satisfy

$$I_{a^+}^{\beta}\,{}^{C}D_{a^+}^{\beta}\nu(\varsigma) = \nu(\varsigma) - \nu(a),\ I_{a^+}^{\beta}\,{}^{C}D_{a^+}^{\beta}\nu(\varsigma) = \nu(\varsigma).$$

Moreover, ${}^{C}D_{a^+}^{\beta}\, c = 0$ for any constant $c \in \mathbb{R}$. For more details, we recommend the readers to look at the references [31, 32]. The methodological structure of this paper is shown by Figure 1.

Glossary of Symbols

- $\alpha \in (0, 1)$: Order of the fractional operators.
- $\tau > 0$: Constant time delay.
- $m \in \mathbb{N}$: Number of subintervals.
- $\nu(\varsigma)$: State vector (or scalar state) of the system.
- $\varphi(\varsigma)$: Initial history function defined on $[-\tau, 0)$.
- Ω_k: Constant system matrix (or scalar coefficient) acting on the *k-th* subinterval
- $I_{a^+}^{\alpha}$: Riemann-Liouville fractional integral of order α.
- ${}^{C}D_{a^+}^{\alpha}$: Caputo fractional derivative of order α.
- $D_m(\varsigma, \varphi)$: Generating function used to construct the solution recursively on each subinterval.
- $\|\cdot\|$: Vector or matrix norm.
- M: Uniform bound such that $\|\Omega_k\| \le M$ for all k.

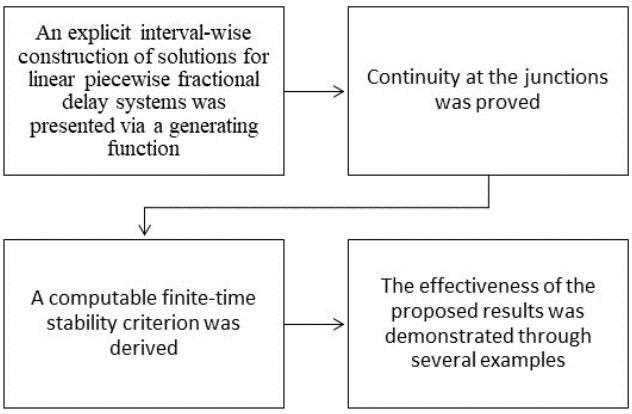


Figure 1. The owchart of methodological structure in this paper.

A Solution to Linear System (1)

In this section, we construct a solution to the linear system (1) by introducing an appropriate generating function. We then verify that the proposed solution satisfies the system, provide alternative proofs including an induction-based argument, and establish the continuity of the solution.

Let's understand the root of the linear piecewise fractional delayed systems more and discover the representations of their explicit solutions. In the interval $\varsigma \in [0, \tau)$, the equation acquired from system (1) is given by:

$${}^{C}D_{0^+}^{\alpha}\nu(\varsigma) = \Omega_1\nu(\varsigma - \tau),\ \ \varsigma \in [0, \tau). \tag{2}$$

By applying the definition of the Riemann-Liouville fractional integral $I_{0^+}^{\alpha}$, this equation can be rewritten in terms of the Riemann-Liouville fractional integral as:

$$\nu(\varsigma) - \nu(0) = \Omega_1 I_{0^+}^{\alpha}\nu(\varsigma - \tau) = \Omega_1\frac{1}{\Gamma(\alpha)}\int_0^{\varsigma}(\varsigma - x)^{\alpha-1}\nu(x-\tau)dx. \tag{3}$$

Employing the substitution $\lambda_1 = x - \tau$, one has

$$\nu(\varsigma) = \nu(0) + \frac{\Omega_1}{\Gamma(\alpha)}\int_{-\tau}^{\varsigma-\tau}\frac{(\varsigma - \tau - \lambda_1)^{\alpha-1}}{\Gamma(\alpha)}\nu(\lambda_1)d\lambda_1.$$

Since $\lambda_1[-\tau, \varsigma - \tau)$, and $\varsigma \in [0, \tau)$, and we recall that the initial condition satis es $\nu(\varsigma) = \varphi(\varsigma)$ for $\varsigma \in [-\tau, 0]$. Therefore, the equation can be restructured as follows:

$$\nu(\varsigma) = \varphi(0) + \int_{-\tau}^{\varsigma-\tau}\Omega_1\frac{(\varsigma - \tau - \lambda_1)^{\alpha-1}}{\Gamma(\alpha)}\varphi(\lambda_1)d\lambda_1.$$

Now, let us consider a general interval such that $\varsigma \in [m\tau, (m + 1)\tau)$. Then, the equation obtained from (1) can be expressed as follows:

$${}^{C}D_{m\tau^+}^{\alpha}\nu(\varsigma) = \Omega_{m+1}\nu(\varsigma - \tau)$$

Now, if the Riemann-Liouville fractional integral is applied, then

$$\nu(\varsigma) = \nu(m\tau^+) + \Omega_{m+1}\frac{1}{\Gamma(\alpha)}\int_{m\tau}^{\varsigma}(\varsigma - x)^{\alpha-1}\nu(x-\tau)dx.$$

If the transformation $\lambda_{m+1} = x - \tau$ is applied, then the solution function is isolated:

$$\nu(\varsigma) = \nu(m\tau^+)\int_{(m-1)\tau}^{\varsigma-\tau}\frac{(\varsigma - \tau - \lambda_{m+1})^{\alpha-1}}{\Gamma(\alpha)}\nu(\lambda_{m+1})d\lambda_{m+1}. \tag{4}$$

It is so clear that for small values of $m \in \mathbb{N}$, finding the solution is relatively easy. As $m \in \mathbb{N}$ becomes sufficiently

large, finding the solution is getting difficult, so it becomes necessary to obtain a general form of the solution to the linear piecewise fractional system (1). For this purpose, let us derive the solution to the linear piecewise fractional system for the case $m = 1$, which is noted below:

$$\begin{cases} {}^{C}D^{\alpha}_{\tau^+}\nu(\varsigma) = \Omega_2\nu(\varsigma - \tau), & \varsigma \in [\tau, 2\tau), \\ {}^{C}D^{\alpha}_{0^+}\nu(\varsigma) = \Omega_1\nu(\varsigma - \tau), & \varsigma \in [0, \tau), \\ \nu(\varsigma) = \varphi(\varsigma), & \varsigma \in [-\tau, 0). \end{cases} \quad (5)$$

Based on the equation (4), the explicit solution of the first equation of the system (5) is presented as follows:

$$\nu(\varsigma) = \nu(\tau) + \Omega_2 \int_0^{\varsigma-\tau} \frac{(\varsigma - \tau - \lambda_2)^{\alpha-1}}{\Gamma(\alpha)} \nu(\lambda_2) d\lambda_2. \quad (6)$$

The explicit solution of the second equation of the system (5) is given by

$$\nu(\varsigma) = \varphi(0) + \Omega_1 \int_{-\tau}^{\varsigma-\tau} \frac{(\varsigma - \tau - \lambda_1)^{\alpha-1}}{\Gamma(\alpha)} \varphi(\lambda_1) d\lambda_1. \quad (7)$$

Now, let us take for $\varsigma = \tau$ and $\varsigma = \lambda_1$ in the equation (7) , and substitute them into the equation (6). One obtains the explicit solution to the linear piecewise fractional system (5) as noted below

$$\begin{aligned} \nu(\varsigma) &= \varphi(0) + \int_{\tau}^{0} \Omega_1 \frac{(-\lambda_1)^{\alpha-1}}{\Gamma(\alpha)} \varphi(\lambda_1) d\lambda_1 \\ &\quad + \int_0^{\varsigma-\tau} \Omega_2 \frac{(\varsigma - \tau - \lambda_2)^{\alpha-1}}{\Gamma(\alpha)} \Bigg[\varphi(0) \\ &\quad + \int_{-\tau}^{\lambda_2-\tau} \Omega_1 \frac{(\lambda_2 - \tau - \lambda_1)^{\alpha-1}}{\Gamma(\alpha)} \varphi(\lambda_1) d\lambda_1 \Bigg] d\lambda_2 \\ &= \varphi(0) \int_{-\tau}^{0} \Omega_1 \frac{(-\lambda_1)^{\alpha-1}}{\Gamma(\alpha)} \varphi(\lambda_1) d\lambda_1 \\ &\quad + \int_0^{\varsigma-\tau} \Omega_2 \frac{(\varsigma - \tau - \lambda_2)^{\alpha-1}}{\Gamma(\alpha)} \varphi(0) d\lambda_2 \\ &\quad + \int_0^{\varsigma-\tau} \Omega_2 \frac{(\varsigma - \tau - \lambda_2)^{\alpha-1}}{\Gamma(\alpha)} \\ &\quad \int_{-\tau}^{\lambda_2-\tau} \Omega_1 \frac{(\lambda_2 - \tau - \lambda_1)^{\alpha-1}}{\Gamma(\alpha)} \varphi(\lambda_1) d\lambda_1 d\lambda_2. \end{aligned} \quad (8)$$

As can be seen in this solution, the expression is already quite cumbersome even for $m = 1$, and it is clear that it will be come much more complex form $m > 1$.

Intuitive Interpretation of the Generating Function

Now, we define the (fractional) generating function, which is produced by the initial function, to represent the explicit solution to the linear piecewise fractional system by

$$D_m(\varsigma, \varphi) \begin{cases} \varphi(\varsigma), & m = 0, \\ \int_{(m-2)\tau}^{\varsigma-\tau} \Omega_m \frac{(\varsigma - \tau - \lambda_m)^{\alpha-1}}{\Gamma(\alpha)} \left(\sum_{i=0}^{m-2} \mathrm{D_i}(i\tau, \varphi) + \mathrm{D_{m-1}}(\lambda_m, \varphi) \right) d\lambda_m, & m \in \mathbb{N}_1. \end{cases} \quad (9)$$

The generating function $D_m(\varsigma, \varphi)$ provides a recursive mechanism to construct the solution interval by interval using the method of steps. Instead of solving the entire fractional delay system at once, the solution on each subinterval is built from the previously known history.

For $n = 1$, the system reduces to a single fractional equation on $[0, \tau)$, driven solely by the history function $\varphi(\varsigma - \tau)$. In this case, the generating function coincides with a fractional convolution between Ω_1 and the initial history.

For $n = 2$, the solution on $[\tau, 2\tau)$ depends both on the accumulated contribution at $\varsigma = \tau$ and on the solution constructed on $[0, \tau)$. The corresponding generating function D_2 therefore combines these two effects through a recursive integral representation.

The case $n = 2$ corresponds to the solution of system (5). Using the classical approach, this solution is expressed by means of equation (8), making use of the intermediate steps given in equations (6) and (7).

Below, the case $n = 2$, which represents the interval $[\tau, 2\tau)$ is reformulated according to the numbering of system (5) as the case $m = 1$, that is, the solution corresponding to the interval $[\tau, 2\tau)$. This solution is then derived step by step as an application of the generating function method.

Consequently, the generating function approach is explicitly illustrated through the cases $n = 1$ and $n = 2$ by considering $m = 1$. Moreover, it is shown that the obtained expression coincides with the solution of system (5) given in equation (8). This establishes the scientific validity of the proposed approach, demonstrating that the solution of equation (5) can indeed be represented by means of the generating function framework.

This pattern continues inductively: for general n, the generating function encodes the cumulative memory of all previous subintervals, allowing the explicit representation given in Theorem 2.

For $m = 1$, the explicit solution presented in (8) is rewritten in terms of the generating function (9):

$$\begin{aligned} \nu(\varsigma) = \sum_{i=0}^{1} D_i(i\tau, \varphi) + D_2(\varsigma, \varphi) = D_0(0, \varphi) + D_1(\tau, \varphi) \\ + D_2(\varsigma, \varphi), \quad \varsigma \in [\tau, 2\tau), \end{aligned} \quad (10)$$

because, from the definition of the generating function,

$$D_0(\varsigma, \varphi) = \varphi(\varsigma) \;\Rightarrow\; D_0(0, \varphi) = \varphi(0), \quad (11)$$

$$\begin{aligned} D_1(\varsigma, \varphi) &= \int_{-\tau}^{\varsigma-\tau} \Omega_2 \frac{(\varsigma - \tau - \lambda_1)^{\alpha-1}}{\Gamma(\alpha)} \left(\sum_{i=0}^{-1} \mathrm{D_i}(i\tau, \varphi) + \mathrm{D_0}(\lambda_1, \varphi) \right) d\lambda_1, \\ &= \int_{-\tau}^{\varsigma-\tau} \Omega_1 \frac{(\varsigma - \tau - \lambda_1)^{\alpha-1}}{\Gamma(\alpha)} D_0(\lambda_1, \varphi) d\lambda_1 \\ &= \int_{-\tau}^{\varsigma-\tau} \Omega_1 \frac{(\varsigma - \tau - \lambda_1)^{\alpha-1}}{\Gamma(\alpha)} \varphi(\lambda_1) d\lambda_1, \end{aligned}$$

$$D_1(\tau, \varphi) = \int_{-\tau}^{0} \Omega_1 \frac{(-\lambda_1)^{\alpha-1}}{\Gamma(\alpha)} \varphi(\lambda_1) d\lambda_1, \quad (12)$$

$$
\begin{aligned}
D_2(\varsigma,\varphi) &= \int_0^{\varsigma-\tau} \Omega_2 \frac{(\varsigma-\tau-\lambda_2)^{\alpha-1}}{\Gamma(\alpha)} \left(\sum_{i=0}^{0} \mathrm{D_i}(i\tau,\varphi) + \mathrm{D_1}(\lambda_2,\varphi) \right) d\lambda_2 \\
&= \int_0^{\varsigma-\tau} \Omega_2 \frac{(\varsigma-\tau-\lambda_2)^{\alpha-1}}{\Gamma(\alpha)} \left(D_0(0,\varphi) \right. \\
&\quad \left. + \int_{-\tau}^{\lambda_2-\tau} \Omega_1 \frac{(\lambda_2-\tau-\lambda_1)^{\alpha-1}}{\Gamma(\alpha)} \varphi(\lambda_1) d\lambda_1 \right) d\lambda_2 \\
&= \int_0^{\varsigma-\tau} \Omega_2 \frac{(\varsigma-\tau-\lambda_2)^{\alpha-1}}{\Gamma(\alpha)} \varphi(0) d\lambda_2 \\
&\quad + \int_0^{\varsigma-\tau} \Omega_2 \frac{(\varsigma-\tau-\lambda_2)^{\alpha-1}}{\Gamma(\alpha)} \int_{-\tau}^{\lambda_2-\tau} \Omega_1 \frac{(\lambda_2-\tau-\lambda_1)^{\alpha-1}}{\Gamma(\alpha)} \varphi(\lambda_1) d\lambda_1 d\lambda_2.
\end{aligned} \tag{13}
$$

This, in fact, coincides with the solution given in (8) by combining (11), (12), and (13), as we claimed.

Remark 1. The fractional generating function reduces to the iterative function introduced in [29] when the alpha parameter is equal to one.

Explicit Solution Via Generating Functions

In this subsection, we derive an explicit interval-wise representation of the solution to the linear system (2) by employing a generating function approach.

Theorem 2. An explicit solution to the following linear piecewise fractional system

$$
\begin{cases}
{}^{C}D^{\alpha}_{(m-1)\tau^+} \nu(\varsigma) = \Omega_{\mathrm{m}} \nu(\varsigma-\tau), & \varsigma \in [(\mathrm{m}-1)\tau, \mathrm{m}\tau), \\
{}^{C}D^{\alpha}_{(m-2)\tau^+} \nu(\varsigma) = \Omega_{\mathrm{m}-1} \nu(\varsigma-\tau), & \varsigma \in [(\mathrm{m}-2)\tau, (\mathrm{m}-1)\tau), \\
\quad \vdots & \\
{}^{C}D^{\alpha}_{\tau^+} \nu(\varsigma) = \Omega_2 \nu(\varsigma-\tau), & \varsigma \in [\tau, 2\tau), \\
{}^{C}D^{\alpha}_{0^+} \nu(\varsigma) = \Omega_1 \nu(\varsigma-\tau), & \varsigma \in [0, \tau), \\
\nu(\varsigma) = \varphi(\varsigma), & \varsigma \in [-\tau, 0),
\end{cases} \tag{14}
$$

has the following form with the help of the generating function

$$
\nu(\varsigma) = \sum_{i=0}^{m-1} D_i(i\tau,\varphi) + D_m(\varsigma,\varphi). \tag{15}
$$

Proof. To show that it holds for any $m \in \mathbb{N}$, we will use the method of mathematical induction on m. For $m = 1$, considering the solutions (8) and (10), we can conclude that the statement holds. Now, assume that our claim holds for $m = n$. We will now prove that it also holds for $m = n + 1$. That is, the solution given in (15) for $k = m$ to the system (14) must hold:

$$
\nu(\varsigma) = \sum_{i=0}^{m-1} D_i(i\tau,\varphi) + D_m(\varsigma,\varphi). \tag{16}
$$

When $k = m + 1$, the solution becomes:

$$
\nu(\varsigma) = \sum_{i=0}^{m} D_i(i\tau,\varphi) + D_{m+1}(\varsigma,\varphi). \tag{17}
$$

We need to show that it holds. When $\varsigma \in [m\tau, (m+1)\tau)$, our equation becomes

$$
{}^{C}D^{\alpha}_{m\tau^+} \nu(\varsigma) = \Omega_{\mathrm{m}+1} \nu(\varsigma - \tau),
$$

whose explicit solution followed from the equation (4) is given by:

$$
\nu(\varsigma) = \nu(m\tau^+) + \int_{(m-1)\tau}^{\varsigma-\tau} \Omega_{m+1} \frac{(\varsigma-\tau-\lambda_{m+1})^{\alpha-1}}{\Gamma(\alpha)} \nu(\lambda_{m+1}) d\lambda_{m+1}. \tag{18}
$$

Now, if we take $\varsigma = m\tau$ in the equation (16), then one gets

$$
\begin{aligned}
\nu(m\tau) &= \sum_{i=0}^{m-1} D_i(i\tau,\varphi) + D_m(m\tau,\varphi) \\
&= \sum_{i=0}^{m} D_i(i\tau,\varphi).
\end{aligned}
$$

If we take $\varsigma = \lambda_{m+1}$ in the equation (16), then one has

$$
\nu(\lambda_{m+1}) = \sum_{i=0}^{m-1} D_i(i\tau,\varphi) + D_m(\lambda_{m+1},\varphi).
$$

If these equations are substituted into the equation (18), then the following is obtained:

$$
\nu(\varsigma) = \sum_{i=0}^{\mathrm{m}} D_i(i\tau,\varphi) + \int_{(m-1)\tau}^{\varsigma-\tau} \Omega_{m+1} \frac{(\varsigma-\tau-\lambda_{m+1})^{\alpha-1}}{\Gamma(\alpha)} \left(\sum_{i=0}^{m-1} D_i(i\tau,\varphi) + D_m(\lambda_{m+1},\varphi) \right) d\lambda_{m+1}.
$$

Based on the definition of the generating function, one can observe that:

$$
D_{m+1}(\varsigma,\varphi) = \int_{(m-1)\tau}^{\varsigma-\tau} \Omega_{m+1} \frac{(\varsigma-\tau-\lambda_{m+1})^{\alpha-1}}{\Gamma(\alpha)} \left(\sum_{i=0}^{m-1} \mathrm{D_i}(i\tau,\varphi) + \mathrm{D_m}(\lambda_{m+1},\varphi) \right) d\lambda_{m+1}.
$$

By rearranging this system for $\varsigma \in [m\tau, (m+1)\tau)$, the corresponding explicit solution to the corresponding system is found as stated below

$$
\nu(\varsigma) = \sum_{i=0}^{m} D_i(i\tau,\varphi) + D_{m+1}(\varsigma,\varphi),
$$

which gives the desired solution. This concludes the induction proof.

Alternative Proof. Because of ${}^{C}D^{\beta}_{\alpha^+} c = 0$ for any constant $c \in \mathbb{R}$, one has

$$
\begin{aligned}
&{}^{C}D^{\alpha}_{(m-1)\tau} \left(\sum_{i=0}^{m-1} \mathrm{D_i}(i\tau,\varphi) + D_m(\varsigma,\varphi) \right) = {}^{C}D^{\alpha}_{(m-1)\tau} D_m(\varsigma,\varphi) \\
&= {}^{C}D^{\alpha}_{(m-1)\tau} \int_{(m-2)\tau}^{\varsigma-\tau} \Omega_{\mathrm{m}} \frac{(\varsigma-\tau-\lambda_m)^{\alpha-1}}{\Gamma(\alpha)} \left(\sum_{i=0}^{m-2} \mathrm{D_i}(i\tau,\varphi) + \mathrm{D_{m-1}}(\lambda_m,\varphi) \right) d\lambda_m \\
&= {}^{C}D^{\alpha}_{(m-1)\tau} \int_{(m-1)\tau}^{\varsigma-\tau} \Omega_{\mathrm{m}} \frac{(\varsigma-\lambda_m)^{\alpha-1}}{\Gamma(\alpha)} \left(\sum_{i=0}^{m-2} \mathrm{D_i}(i\tau,\varphi) + \mathrm{D_{m-1}}(\lambda_m-\tau,\varphi) \right) d\lambda_m,
\end{aligned}
$$

applying the substitution $\theta = \lambda_m + \tau$, one has

$$
\begin{aligned}
{}^{C}D^{\alpha}_{(m-1)\tau} \left(\textstyle\sum_{i=0}^{m-1} \mathrm{D_i}(i\tau,\varphi) + D_m(\varsigma,\varphi) \right) &= {}^{C}D^{\alpha}_{(m-1)\tau} I^{\alpha}_{(m-1)\tau} \Omega_m \left(\textstyle\sum_{i=0}^{m-2} \mathrm{D_i}(i\tau,\varphi) \right. \\
&\quad \left. + D_{m-1}(\varsigma-\tau,\varphi) \right) \\
&= \Omega_m \left(\textstyle\sum_{i=0}^{m-2} \mathrm{D_i}(i\tau,\varphi) + D_{m-1}(\varsigma-\tau,\varphi) \right) \\
&= \Omega_m \, \nu(\varsigma-\tau).
\end{aligned}
$$

Remark 3. In the special case $\alpha = 1$, the Caputo fractional derivative reduces to the classical first-order derivative. Consequently, the linear piecewise fractional delay system (14) becomes a classical piecewise linear state-delay system. In this setting, the explicit solution representation (15) is consistent with the structure of solutions studied for piecewise linear state-delay systems in the literature, such as [29]. Hence, the present result recovers known classical models when $\alpha = 1$, while extending them to the fractional-order case $0 < \alpha < 1$ and providing explicit interval-wise analytical solution representations together with nite-time stability bounds.

Remark 4. For the special case of a constant initial history $\varphi(\varsigma) \equiv \varphi_0$, the solution admits a closed piecewise representation. Define the shorthand coefficients

$$P_{j,r} := \prod_{q=0}^{r-1} \Omega_{j-q} \ (r \geq 1), \ S_j := \varphi_0 + \sum_{r=1}^{j} P_{j,r} \frac{\tau^{\alpha r}}{\Gamma(\alpha r + 1)}, \ S_0 := \varphi_0.$$

Then, for $m = 6$ the solution is given explicitly by

$$\nu(\varsigma) = \begin{cases} \varphi_0, & \varsigma \in [-\tau, 0), \\ S_0 + \Omega_1 \dfrac{\varsigma^{\alpha}}{\Gamma(\alpha+1)}, & \varsigma \in [0, \tau), \\ S_1 + \Omega_2 \dfrac{(\varsigma-\tau)^{\alpha}}{\Gamma(\alpha+1)} + \Omega_2\Omega_1 \dfrac{(\varsigma-\tau)^{2\alpha}}{\Gamma(2\alpha+1)}, & \varsigma \in [\tau, 2\tau), \\ S_2 + \Omega_3 \dfrac{(\varsigma-2\tau)^{\alpha}}{\Gamma(\alpha+1)} + \Omega_3\Omega_2 \dfrac{(\varsigma-2\tau)^{2\alpha}}{\Gamma(2\alpha+1)} + \Omega_3\Omega_2\Omega_1 \dfrac{(\varsigma-2\tau)^{3\alpha}}{\Gamma(3\alpha+1)}, & \varsigma \in [2\tau, 3\tau), \\ S_3 + \Omega_4 \dfrac{(\varsigma-3\tau)^{\alpha}}{\Gamma(\alpha+1)} + \Omega_4\Omega_3 \dfrac{(\varsigma-3\tau)^{2\alpha}}{\Gamma(2\alpha+1)} + \Omega_4\Omega_3\Omega_2 \dfrac{(\varsigma-3\tau)^{3\alpha}}{\Gamma(3\alpha+1)} + \Omega_4\Omega_3\Omega_2\Omega_1 \dfrac{(\varsigma-3\tau)^{4\alpha}}{\Gamma(4\alpha+1)}, & \varsigma \in [3\tau, 4\tau), \\ S_4 + \Omega_5 \dfrac{(\varsigma-4\tau)^{\alpha}}{\Gamma(\alpha+1)} + \Omega_5\Omega_4 \dfrac{(\varsigma-4\tau)^{2\alpha}}{\Gamma(2\alpha+1)} + \Omega_5\Omega_4\Omega_3 \dfrac{(\varsigma-4\tau)^{3\alpha}}{\Gamma(3\alpha+1)} + \Omega_5\Omega_4\Omega_3\Omega_2 \dfrac{(\varsigma-4\tau)^{4\alpha}}{\Gamma(4\alpha+1)} + \Omega_5\Omega_4\Omega_3\Omega_2\Omega_1 \dfrac{(\varsigma-4\tau)^{5\alpha}}{\Gamma(5\alpha+1)}, & \varsigma \in [4\tau, 5\tau), \\ S_5 + \Omega_6 \dfrac{(\varsigma-5\tau)^{\alpha}}{\Gamma(\alpha+1)} + \Omega_6\Omega_5 \dfrac{(\varsigma-5\tau)^{2\alpha}}{\Gamma(2\alpha+1)} + \Omega_6\Omega_5\Omega_4 \dfrac{(\varsigma-5\tau)^{3\alpha}}{\Gamma(3\alpha+1)} + \Omega_6\Omega_5\Omega_4\Omega_3 \dfrac{(\varsigma-5\tau)^{4\alpha}}{\Gamma(4\alpha+1)} + \Omega_6\Omega_5\Omega_4\Omega_3\Omega_2 \dfrac{(\varsigma-5\tau)^{5\alpha}}{\Gamma(5\alpha+1)} + \Omega_6\Omega_5\Omega_4\Omega_3\Omega_2\Omega_1 \dfrac{(\varsigma-5\tau)^{6\alpha}}{\Gamma(6\alpha+1)}, & \varsigma \in [5\tau, 6\tau). \end{cases}$$

Here, the constants S_j accumulate the contributions from the preceding intervals, explicitly,

$$S_1 = \varphi_0 + \Omega_1 \frac{\tau^{\alpha}}{\Gamma(\alpha+1)},$$

$$S_2 = S_1 + \Omega_2 \frac{\tau^{\alpha}}{\Gamma(\alpha+1)} + \Omega_2\Omega_1 \frac{\tau^{2\alpha}}{\Gamma(2\alpha+1)},$$

$$S_2 = S_1 + \Omega_2 \frac{\tau^{\alpha}}{\Gamma(\alpha+1)} + \Omega_2\Omega_1 \frac{\tau^{2\alpha}}{\Gamma(2\alpha+1)},$$

$$S_4 = S_3 + \Omega_4 \frac{\tau^{\alpha}}{\Gamma(\alpha+1)} + \Omega_4\Omega_3 \frac{\tau^{2\alpha}}{\Gamma(2\alpha+1)} + \Omega_4\Omega_3\Omega_2 \frac{\tau^{3\alpha}}{\Gamma(3\alpha+1)} + \Omega_4\Omega_3\Omega_2\Omega_1 \frac{\tau^{4\alpha}}{\Gamma(4\alpha+1)},$$

$$S_5 = S_4 + \Omega_5 \frac{\tau^{\alpha}}{\Gamma(\alpha+1)} + \Omega_5\Omega_4 \frac{\tau^{2\alpha}}{\Gamma(2\alpha+1)} + \Omega_5\Omega_4\Omega_3 \frac{\tau^{3\alpha}}{\Gamma(3\alpha+1)} + \Omega_5\Omega_4\Omega_3\Omega_2 \frac{\tau^{4\alpha}}{\Gamma(4\alpha+1)} + \Omega_5\Omega_4\Omega_3\Omega_2\Omega_1 \frac{\tau^{5\alpha}}{\Gamma(5\alpha+1)}.$$

This piecewise expression shows that at each node $\varsigma = k\tau$ the left and right limits coincide, and hence the solution $\nu(\varsigma)$ is continuous acrossall subintervals.

The Continuity of the Explicit Solution

Now, the continuity of the explicit solution we have constructed is debated in the following theorem.

Theorem 5. The analytical solution expressed in (15) to the linear piecewise fractional system (14) is continuous on $[-\tau, \infty)$.

Proof. Before proceeding to the junction-point analysis, we briefly justify the continuity of the generating functions $D_m(\varsigma, \varphi)$ and the convergence properties of the recursive integral representations involved. We proceed by induction on m. For $m = 0$, one has $D_0(\varsigma, \varphi) = \varphi(\varsigma)$, which is continuous on $[-\tau, 0]$ by assumption. Assume that, for some $m \geq 1$, the functions $D_i(\cdot, \varphi)$, $i = 0,1,..., m - 1$, are continuous and bounded on their respective domains.

By definition, $D_m(\varsigma, \varphi)$ is given by a fractional integral whose integrand consists of the bounded matrix Ω_m, the weakly singular kernel $(\varsigma - \tau - \lambda)^{\alpha-1}/\Gamma(\alpha)$ with $0 < \alpha < 1$, and the continuous bounded function $\sum_{i=0}^{m-2} D_i(i\tau, \varphi) + D_{m-1}(\lambda, \varphi)$. Since the kernel is integrable on any finite interval and the remaining factors are bounded, standard properties of fractional integrals imply that $D_m(\cdot, \varphi)$ is continuous on $[(m - 1)\tau, m\tau]$. This completes the induction step and establishes continuity of all D_m.

Moreover, the integrands defining D_m are dominated by an integrable majorant independent of ς on compact subintervals. Hence, the family of recursive integrals converges uniformly on compact sets. As a consequence, limit operations with respect to ς can be interchanged with the integral sign, which justifies the limit arguments used below.

It is evident that $\varsigma \in [(m - 1)\tau, m\tau]$, $m \in \mathbb{N}$, is continuous at every interior point. At the critical point $\varsigma = m\tau$, it suffices to show that the right-hand limit, the left-hand limit, and the function's value coincide. For $\varsigma = m\tau$,

$$\nu(\varsigma) = \sum_{i=0}^{m} \mathrm{D_i}(i\tau, \varphi) + D_{m+1}(\varsigma, \varphi).$$

Evaluating at $\varsigma = m\tau$ yields

$$\nu(m\tau) = \sum_{i=0}^{m} \mathrm{D_i}(i\tau, \varphi) + D_{m+1}(m\tau, \varphi).$$

Since the integration limits of $D_{m+1}(m\tau, \varphi)$ coincide, one has $D_{m+1}(m\tau, \varphi) = 0$, and therefore

$$\nu(m\tau) = \sum_{i=0}^{m} \mathrm{D_i}(i\tau, \varphi).$$

The right-hand limit is

$$\lim_{\varsigma \to m\tau^+} \nu(\varsigma) = \sum_{i=0}^{m} \mathrm{D_i}(i\tau, \varphi) + \lim_{\varsigma \to m\tau^+} D_{m+1}(\varsigma, \varphi) = \sum_{i=0}^{m} \mathrm{D_i}(i\tau, \varphi),$$

where the limit of D_{m+1} follows from the continuity established above. For the left-hand limit, one uses

$$\nu(\varsigma) = \sum_{i=0}^{m-1} \mathrm{D_i}(i\tau, \varphi) + D_m(\varsigma, \varphi),$$

which gives

$$\lim_{\varsigma \to m\tau^-} \nu(\varsigma) = \sum_{i=0}^{m-1} \mathrm{D_i}(i\tau, \varphi) + D_m(m\tau, \varphi) = \sum_{i=0}^{m} \mathrm{D_i}(i\tau, \varphi).$$

Since the left-hand limit, right-hand limit, and the function value coincide at $\varsigma = m\tau$, the solution is continuous at each junction point. Therefore, the explicit solution expressed in (15) is continuous on $[-\tau, \infty)$.

Finite-Time Stability

In this section, we first present the formal definition of finite-time stability. To support the main result, two auxiliary lemmas are established, followed by the proof of the principal theorem on the finite-time stability of the system under consideration.

Definition 6. [33] The system described by the homogeneous state equation (1), and subject to the initial condition

$$\nu(\varsigma) = \varphi(\varsigma), \quad -\tau \le \varsigma \le 0,$$

is said to be finite-time stable with respect to the parameters $\{\delta, \varepsilon, \varsigma_0, J\}$, under the condition $\delta < \varepsilon$ if and only if

$$\|\varphi\|_\infty < \delta,$$

implies

$$\|\nu(\varsigma)\| < \varepsilon, \quad \forall \varsigma \in J,$$

where ς_0 denotes the initial observation time of the system, and J is the observation interval given by $J = [\varsigma_0, \varsigma_0 + T] \subset \mathbb{R}$.

Lemma 7. Let $\tau \ge 0$, α, $M > 0$ be given. Definee

$$S_k := \frac{M^{k+1}\tau^{(k+1)\alpha}}{\Gamma((k+1)\alpha + 1)}, \quad T_j = \sum_{i=0}^{j} S_i, \quad k, j \ge 0.$$

Then,

$$S_0 + \sum_{i=1}^{m-2} 2^{i-1} T_i + 2^{m-2} T_{m-1} \le 2^{m-1} T_m, \quad \forall m \ge 2.$$

Proof. Based on the given definition, one has without any calculations

$$S_0 + \sum_{i=1}^{m-2} 2^{i-1} T_i + 2^{m-2} T_{m-1} \le T_1 + \sum_{i=1}^{m-2} 2^{i-1} T_i + 2^{m-2} T_{m-1}, \quad \forall m \ge 2.$$

Because of $S_k \ge 0$, T_j is monotonically increasing and so $T_i \le T_m$ m for all $i \le m$. Thus

$$\begin{aligned} T_1 + \sum_{i=1}^{m-2} 2^{i-1} T_i + 2^{m-2} T_{m-1} &\le T_m + \sum_{i=1}^{m-2} 2^{i-1} T_i + 2^{m-2} T_{m-1} \\ &\le \left(1 + \sum_{i=1}^{m-2} 2^{i-1} + 2^{m-2}\right) T_m \\ &= (1 + 2^{m-2} - 1 + 2^{m-2}) T_m \\ &= 2^{m-2} T_m, \end{aligned}$$

which is, indeed,we want to show.

Lemma 8. Let $D_m(\varsigma, \varphi)$ be given in the equation (9), that is,

$$D_0(\varsigma, \varphi) = \varphi(\varsigma),$$

$$D_m(\varsigma, \varphi) = \int_{(m-2)\tau}^{\varsigma - \tau} \Omega_m \frac{(\varsigma - \tau - \lambda_{m+1})^{\alpha-1}}{\Gamma(\alpha)} \left(\sum_{i=0}^{m-2} \mathrm{D_i}(i\tau, \varphi) + \mathrm{D_{m-1}}(\lambda, \varphi) \right) d\lambda,$$

for $m \in \mathbb{N}_1$ and $\varsigma \in [(m\text{-}1)\tau, m\tau]$ Then,

$$\sup_{\varsigma \in [(m-1)\tau, m\tau]} \|D_m(\varsigma, \varphi)\| \le 2^{m-1} \delta \sum_{k=0}^{m} \frac{M^k \tau^{k\alpha}}{\Gamma(k\alpha + 1)}. \quad (19)$$

Proof. We proceed by the mathematical induction on m. For the base case $m = 1$,

$$D_1(\varsigma,\varphi)=\int_{-\tau}^{\varsigma-\tau}\Omega_1\frac{(\varsigma-\tau-\lambda)^{\alpha-1}}{\Gamma(\alpha)}\varphi(\lambda)d\lambda,\ \varsigma\in[0,\tau].$$

Using $\|\varphi\|_\infty\le\delta$ and the change $u=\varsigma-\tau-\lambda\in[0,\varsigma]$,

$$\|D_1(\varsigma,\varphi)\|\le\frac{\|\Omega_1\|}{\Gamma(\alpha)}\delta\int_0^{\varsigma}u^{\alpha-1}du=\frac{\|\Omega_1\|}{\Gamma(\alpha-1)}\varsigma^{\alpha}\delta\le\frac{M\tau^{\alpha}}{\Gamma(\alpha-1)}\delta.$$

Taking the supremum in $\varsigma\in[0,\tau]$ yields

$$\sup\|D_1\|\le 2^{1-1}\delta\sum_{k=0}^{1}\frac{M^k\tau^{k\alpha}}{\Gamma(k\alpha+1)},$$

which is (19) with $m=1$ (since $2^0=1$ and the sum has only $k=0$ and $k=1$). Consider the induction step, that is, assume that for each $1\le r\le m$ -1,

$$B_r:=\sup_{\varsigma\in[(m-1)\tau,m\tau]}\|D_1\|\le 2^{r-1}\delta\sum_{k=0}^{r}\frac{M^k\tau^{k\alpha}}{\Gamma(k\alpha+1)},\quad(20)$$

for fixed $\varsigma\in[(m-1)\tau,\ m\tau]$, taking norms in the recursive formula and using linearity,

$$\|D_m(\varsigma,\varphi)\|\le\|\Omega_m\|\int_{(m-2)\tau}^{\varsigma-\tau}\frac{(\varsigma-\tau-\lambda)^{\alpha-1}}{\Gamma(\alpha)}\left(\sum_{i=0}^{m-2}\|D_i(i\tau,\varphi)\|+\|D_{m-1}(\lambda,\varphi)\|\right)d\lambda$$
$$\le\|\Omega_m\|\left[\frac{(\varsigma-(m-1)\tau)^{\alpha}}{\Gamma(\alpha+1)}\right]\left(\delta+\sum_{i=1}^{m-2}B_i+B_{m-1}\right),$$

we used $\int_{(m-2)\tau}^{\varsigma-\tau}\frac{(\varsigma-\tau-\lambda)^{\alpha-1}}{\Gamma(\alpha)}d\lambda=\frac{(\varsigma-(m-1)\tau)^{\alpha}}{\Gamma(\alpha+1)}$ and $D_0(0,\varphi)=\varphi(0)$. Since $\varsigma\le m\tau$, we have $(\varsigma-(m-1)\tau)^{\alpha}\le\tau^{\alpha}$, and thus

$$\|D_m(\varsigma,\varphi)\|\le\frac{M\tau^{\alpha}}{\Gamma(\alpha+1)}\left(\delta+\sum_{i=1}^{m-2}B_i+B_{m-1}\right).\quad(21)$$

Applying the induction hypothesis (20) to each B_i gives

$$\delta+\sum_{i=1}^{m-2}B_i+B_{m-1}\le\delta+\sum_{i=1}^{m-2}2^{i-1}\delta\sum_{k=0}^{i}\frac{M^k\tau^{k\alpha}}{\Gamma(k\alpha+1)}+2^{m-2}\delta\sum_{k=0}^{m-1}\frac{M^k\tau^{k\alpha}}{\Gamma(k\alpha+1)}.$$

By multiplying by $M\tau^{\alpha}/\Gamma(\alpha+1)$ and using the Beta-identity bound $\frac{M\tau^{\alpha}}{\Gamma(\alpha+1)}\cdot\frac{M^k\tau^{k\alpha}}{\Gamma(k\alpha+1)}\le\frac{M^{k+1}\tau^{(k+1)\alpha}}{\Gamma((k+1)\alpha+1)}$, and using Lemma 7, we obtain

$$\sup_{\varsigma\in[(m-1)\tau,m\tau]}\|D_m(\varsigma,\varphi)\|\le 2^{m-1}\delta\sum_{k=0}^{m}\frac{M^k\tau^{k\alpha}}{\Gamma(k\alpha+1)}.$$

This is exactly (19) and completes the mathematical induction on m.

Theorem 9. The considered system (1) is finite-time stable if

$$\sum_{i=1}^{m}2^{i-1}\sum_{k=0}^{i}\frac{M^k\tau^{k\alpha}}{\Gamma(k\alpha+1)}<\frac{\varepsilon}{\delta}.\quad(22)$$

Proof. From Theorem 2, the explicit continuous solution of the homogeneous piecewise fractional system (1) is expressed by

$$\nu(\varsigma)=\sum_{i=0}^{m-1}D_i(i\tau,\varphi)+D_m(\varsigma,\varphi),$$

Taking the norm of both sides, we obtain

$$\|\nu(\varsigma)\|\le\sum_{i=0}^{m-1}\|D_i(i\tau,\varphi)\|+\|D_m(\varsigma,\varphi)\|.$$

Based on the definition of finite-time stability, let $\|\varphi\|_\infty$ hold. Now, let's take the maximum value for $\varsigma\in[(m-1)\tau,\ m\tau]$ on the right-hand side together with employing Lemma 8

$$\|\nu(\varsigma)\|\le\sum_{i=0}^{m}\sup_{\varsigma\in[(m-1)\tau,m\tau]}\|D_m(\varsigma,\varphi)\|$$
$$\le\delta\sum_{i=1}^{m}2^{i-1}\sum_{k=0}^{i}\frac{M^k\tau^{k\alpha}}{\Gamma(k\alpha+1)}.$$

Hence, employing the basic condition of this theorem, relation (23) yields:

$$\|\nu(\varsigma)\|<\varepsilon,\quad\forall\varsigma\in J.$$

The desired is readily obtained. Consequently, the considered system (1) is finite-time stable under the established inequality.

Remark 10. Although the sufficient condition (22) is explicit, the double sum may be come computationally heavy for large m. In practice, it can be evaluated efficiently by precomputing the coefficients $a_k:=\frac{(M\tau^{\alpha})^k}{\Gamma(k\alpha+1)}$ and updating the partial sums recursively. Specifically, one may compute $T_i:=\sum_{k=0}^{i}a_k$ incrementally via $T_i=T_{i-1}+a_i$, and then accumulate $S_m:=\sum_{i=1}^{m}2^{i-1}T_i$ in $O(m)$ time. Moreover, for large k, $\Gamma(k\alpha+1)$ grows superlinearly, so a_k decays rapidly once k is moderate; hence, truncating the inner sum at a finite index (based on a prescribed tolerance) yields an accurate and stable numerical check of (22). Finally, (22) explicitly reveals parameter sensitivity: the left-hand side increases with τ and M, and typically decreases as α increases (because larger α produces larger $\Gamma(k\alpha+1)$, reducing the terms). Therefore, smaller delays τ and/or larger fractional orders α enlarge the admissible stability margin ε/δ, which can guide design and tuning of the piecewise coefficients.

Remark 11. Although the finite-time stability condition obtained in this study is explicit and directly verifiable, it may exhibit a certain degree of conservatism. This conservatism mainly originates from the use of uniform norm bounds and the exponential-type growth factors introduced in the recursive estimation procedure. Such bounding techniques are commonly adopted in the finite-time stability analysis of fractional delay systems to ensure analytical tractability and broad applicability. While sharper bounds may be achievable for particular system structures or specific coefficient configurations, the proposed criterion provides a reliable and computable sufficient condition guaranteeing finite-time stability over the prescribed time interval.

Examples

In this section, several illustrative examples are provided to demonstrate the applicability of the theoretical results. The following examples include explicit numerical simulations and trajectory plots in order to visually verify the continuity at switching points and to support the finite-time stability results derived theoretically.

Example 12. Consider the case $m = 6$, $\alpha = 1\,2$, $\tau = 1$, constant history $\varphi(\varsigma) \equiv 1$, and coefficient sequence $(\Omega_1,\ldots,\Omega_6) = (0.8, 0.5, -0.3, 0.2, -0.1, 0.05)$. Using the closed representation in Remark 1, the accumulated constants are

$$
\begin{aligned}
S_0 &= 1,\\
S_1 &= 1 + 0.8\frac{1}{\Gamma(1.5)} \approx 1.9027,\\
S_2 &= S_1 + 0.5\frac{1}{\Gamma(1.5)} + 0.4\frac{1}{\Gamma(2)} \approx 2.8669,\\
S_3 &= S_2 - 0.3\frac{1}{\Gamma(1.5)} - 0.15\frac{1}{\Gamma(2)}\\
&\quad - 0.12\frac{1}{\Gamma(2.5)} \approx 2.2881,\\
S_4 &= S_3 + 0.2\frac{1}{\Gamma(1.5)} - 0.06\frac{1}{\Gamma(2)}\\
&\quad - 0.03\frac{1}{\Gamma(2.5)} - 0.024\frac{1}{\Gamma(3)} \approx 2.4192,\\
S_5 &= S_4 - 0.1\frac{1}{\Gamma(1.5)} - 0.02\frac{1}{\Gamma(2)}\\
&\quad + 0.006\frac{1}{\Gamma(2.5)} + 0.003\frac{1}{\Gamma(3)}\\
&\quad + 0.0024\frac{1}{\Gamma(3.5)} \approx 2.3131.
\end{aligned}
$$

Hence, the solution $v(\varsigma)$ is given piecewise as in (23). Before presenting the graphical representation, we emphasize that the piecewise expression (23) has been constructed so that the left- and right-hand limits coincide at each junction point $\varsigma = k\tau$, $k = 0,1,\ldots,5$, in accordance with the continuity result established in Theorem 5.

$$
v(\varsigma) = \begin{cases}
1, & \varsigma \in [-1,0),\\
S_0 + 0.8\dfrac{\varsigma^{1/2}}{\Gamma(1.5)}, & \varsigma \in [0,1),\\
S_1 + 0.5\dfrac{(\varsigma-1)^{1/2}}{\Gamma(1.5)} + 0.4\dfrac{(\varsigma-1)}{\Gamma(2)}, & \varsigma \in [1,2),\\
S_2 - 0.3\dfrac{(\varsigma-2)^{1/2}}{\Gamma(1.5)} - 0.15\dfrac{(\varsigma-2)}{\Gamma(2)}\\
\quad - 0.12\dfrac{(\varsigma-2)^{3/2}}{\Gamma(2.5)}, & \varsigma \in [2,3),\\
S_3 + 0.2\dfrac{(\varsigma-3)^{1/2}}{\Gamma(1.5)} - 0.06\dfrac{(\varsigma-3)}{\Gamma(2)}\\
\quad - 0.03\dfrac{(\varsigma-3)^{3/2}}{\Gamma(2.5)} - 0.024\dfrac{(\varsigma-3)^2}{\Gamma(3)}, & \varsigma \in [3,4),\\
S_4 - 0.1\dfrac{(\varsigma-4)^{1/2}}{\Gamma(1.5)} - 0.02\dfrac{(\varsigma-4)}{\Gamma(2)}\\
\quad + 0.006\dfrac{(\varsigma-4)^{3/2}}{\Gamma(2.5)} + 0.003\dfrac{(\varsigma-4)^2}{\Gamma(3)}\\
\quad + 0.0024\dfrac{(\varsigma-4)^{5/2}}{\Gamma(3.5)}, & \varsigma \in [4,5),\\
S_5 + 0.05\dfrac{(\varsigma-5)^{1/2}}{\Gamma(1.5)} - 0.005\dfrac{(\varsigma-5)}{\Gamma(2)}\\
\quad - 0.001\dfrac{(\varsigma-5)^{3/2}}{\Gamma(2.5)} + 0.0003\dfrac{(\varsigma-5)^2}{\Gamma(3)}\\
\quad + 0.00015\dfrac{(\varsigma-5)^{5/2}}{\Gamma(3.5)} + 0.00012\dfrac{(\varsigma-5)^3}{\Gamma(4)}, & \varsigma \in [5,6).
\end{cases}
$$

This explicit expression, whose graph is presented in Figure 2, confirms the validity of the generating-function construction and shows that the solution remains continuous across each junction $\varsigma = k\tau$. Figure 2 visually confirms that the explicit solution constructed in (23) is continuous at each junctionpoint $\varsigma = k\tau$, $k = 0,1,\ldots,5$, despite the piecewise definition. In particular, no jump discontinuities or cusp-like behaviors are observed at the switching instants, which is fully consistent with the analytical continuity prof provided in Section 3.

We now verify the finite-time stability condition for this example. Here, $\alpha = 1/2$, $\tau = 1$, $m = 6$, and $M := max_{1\le k\le 6}\,|\Omega_k| = 0.8$. For the constant history $\varphi(\varsigma) \equiv 1$, we have

$\|\varphi\|_\infty = \delta = 1$. Evaluating the stability bound in Theorem 9, we obtain

$$
\sum_{i=1}^{6} 2^{i-1} \sum_{k=0}^{i} \frac{M^k \tau^{k\alpha}}{\Gamma(k\alpha+1)} = \sum_{i=1}^{6} 2^{i-1} \sum_{k=0}^{i} \frac{0.8^k}{\Gamma(k/2+1)} < C,
$$

for some finite constant C. Consequently, by choosing $\varepsilon > C$, the inequality (22) is satisfied, and the system is finite-time stable on $J = [0,6]$. This computation shows how the abstract finite-time stability condition of Theorem 9 can be explicitly evaluatedin practice using the system parameters,

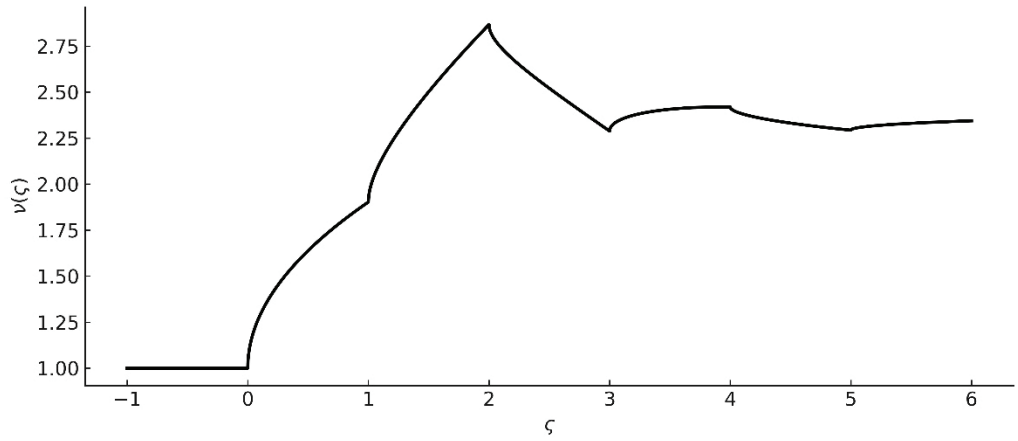


Figure 2. Graph of the explicit solution (23), illustrating the continuity of $\nu(\varsigma)$ across the junction points $\varsigma = k\tau$.

there by linking the analytical criterion to concrete numerical verification. Overall, this example demonstrates that the proposed generating function-based solution framework not only yields explicit closed-form expressions, but also allows a direct verification of continuity and finite-time stability through both analytical bounds and graphical inspection.

Example 13. Consider the following linear piecewise fractional system

$$\begin{cases} {}^{c}D_{2^+}^{1/2}\nu(\varsigma) = \Omega_3\nu(\varsigma-1), & \varsigma\in[2,3), \\ {}^{c}D_{1^+}^{1/2}\nu(\varsigma) = \Omega_2\nu(\varsigma-1), & \varsigma\in[1,2), \\ {}^{c}D_{0^+}^{1/2}\nu(\varsigma) = \Omega_1\nu(\varsigma-1), & \varsigma\in[0,1), \\ \nu(\varsigma) = \varphi(\varsigma), & \varsigma\in[-1,0), \end{cases} \tag{24}$$

where

$$\varphi(\theta) = \begin{pmatrix} 1+\theta \\ 2-\theta \end{pmatrix}, \quad \theta\in[-1,0), \quad \Omega_1 = \begin{pmatrix} 0 & 1 \\ 0 & 0 \end{pmatrix},$$

$$\Omega_2 = \begin{pmatrix} 0.5 & 0 \\ 0 & -0.3 \end{pmatrix}, \quad \Omega_3 = \begin{pmatrix} 0.2 & 0.1 \\ 0 & 0.1 \end{pmatrix}.$$

Based on the definition of the generating function $D_m(\varsigma,\varphi)$ (=: $D_m(\varsigma)$ for simplicity) in (9), for $m = 1$, $\varsigma\in[0,1)$, one obtains

$$D_1(\varsigma) = \frac{\Omega_1}{\Gamma(1/2)}\int_{-1}^{\varsigma-1}(\varsigma-1-\lambda)^{-1/2}\varphi(\lambda)d\lambda = \begin{pmatrix} \dfrac{6\varsigma^{1/2}-\frac{4}{3}\varsigma^{3/2}}{\sqrt{\pi}} \\ 0 \end{pmatrix}.$$

Explicit computation of $D_1(1)$ (matrix-valuedcase). For the reader's convenience, we detail the computation of $D_1(1)$. Setting $\varsigma = 1$ in the definition of $D_1(\varsigma)$ yields

$$D_1(\varsigma) = \frac{\Omega_1}{\Gamma(1/2)}\int_{-1}^{0}(-\lambda)^{-1/2}\varphi(\lambda)d\lambda\,.$$

Since

$$\varphi(\lambda) = \begin{pmatrix} 1+\lambda \\ 2-\lambda \end{pmatrix},$$

the integral can be evaluated componentwise as

$$\int_{-1}^{0}(-\lambda)^{-1/2}\varphi(\lambda)d\lambda = \begin{pmatrix} \int_{-1}^{0}(-\lambda)^{-1/2}(1+\lambda)d\lambda \\ \int_{-1}^{0}(-\lambda)^{-1/2}(2-\lambda)d\lambda \end{pmatrix} = \begin{pmatrix} \frac{4}{3} \\ \frac{14}{3} \end{pmatrix}.$$

Consequently, applying the matrix coefficient

$$\Omega_1 = \begin{pmatrix} 0 & 1 \\ 0 & 0 \end{pmatrix},$$

gives

$$D_1(1) = \frac{1}{\Gamma(1/2)}\begin{pmatrix} 0 & 1 \\ 0 & 0 \end{pmatrix}\begin{pmatrix} \frac{4}{3} \\ \frac{14}{3} \end{pmatrix} = \frac{1}{\sqrt{\pi}}\begin{pmatrix} \frac{14}{3} \\ 0 \end{pmatrix}.$$

This computation illustrates explicitly how the matrix coefficient acts on the vector-valued fractional integral of the history function. Hence $D_1(1) = \left(\frac{14}{3\sqrt{\pi}}0\right)^T$ and

$$S_1 = \varphi(0^+) + D_1(1) = \begin{pmatrix} 1 \\ 2 \end{pmatrix} + \begin{pmatrix} \dfrac{14}{3\sqrt{\pi}} \\ 0 \end{pmatrix} = \begin{pmatrix} 1+\dfrac{14}{3\sqrt{\pi}} \\ 2 \end{pmatrix}.$$

For $m = 2$, $\varsigma\in[1,2)$, one gets

$$D_2(\varsigma) = \frac{\Omega_2}{\Gamma(1/2)}\int_{0}^{\varsigma-1}(\varsigma-1-\lambda)^{-1/2}\big(\varphi(0^+)+D_1(\lambda)\big)d\lambda$$
$$= \begin{pmatrix} \dfrac{1}{\sqrt{\pi}}(\varsigma-1)^{1/2}+\dfrac{3}{2}(\varsigma-1)-\dfrac{1}{4}(\varsigma-1)^2 \\ -\dfrac{1.2}{\sqrt{\pi}}(\varsigma-1)^{1/2} \end{pmatrix}.$$

Inparticular,

$$D_2(2) = \begin{pmatrix} \frac{1}{\sqrt{\pi}} + \frac{5}{4} \\ -\frac{1.2}{\sqrt{\pi}} \end{pmatrix},$$

$$S_2 = S_1 + D_2(2) = \begin{pmatrix} 1 + \frac{14}{3\sqrt{\pi}} + \frac{1}{\sqrt{\pi}} + \frac{5}{4} \\ 2 - \frac{1.2}{\sqrt{\pi}} \end{pmatrix} = \begin{pmatrix} \frac{14}{3\sqrt{\pi}} + \frac{1}{\sqrt{\pi}} + \frac{9}{4} \\ 2 - \frac{1.2}{\sqrt{\pi}} \end{pmatrix}.$$

For $m = 3$, $\varsigma \in [2,3)$, one has

$$D_3(\varsigma) = \frac{\Omega_3}{\Gamma(1/2)} \int_1^{\varsigma-1} (\varsigma - 1 - \lambda)^{-1/2} \big(\varphi(0^+) + D_1(1) + D_2(\lambda)\big) d\lambda$$

$$= \frac{\Omega_3}{\sqrt{\pi}} \left[2(\varsigma-2)^{1/2} \begin{pmatrix} 1 + \frac{14}{3\sqrt{\pi}} \\ 2 \end{pmatrix} + \begin{pmatrix} \frac{\sqrt{\pi}}{2}(\varsigma-2) + 2(\varsigma-2)^{3/2} \\ -\frac{4}{15}(\varsigma-2)^{5/2} - 0.6\sqrt{\pi}(\varsigma-2) \end{pmatrix} \right].$$

Based on Theorem 2, the explicit solution to the linear piecewise fractional system (24) is expressed by

$$\nu(\varsigma) = \begin{cases} \varphi(\varsigma) = \begin{pmatrix} 1+\varsigma \\ 2-\varsigma \end{pmatrix}, & \varsigma \in [-1,0), \\ \varphi(0) + D_1(\varsigma) = \begin{pmatrix} 1 \\ 2 \end{pmatrix} + \begin{pmatrix} \frac{6\varsigma^{1/2} - \frac{4}{3}\varsigma^{3/2}}{\sqrt{\pi}} \\ 0 \end{pmatrix}, & \varsigma \in [0,1), \\ S_1 + D_2(\varsigma) = \begin{pmatrix} 1 + \frac{14}{3\sqrt{\pi}} \\ 2 \end{pmatrix} + \begin{pmatrix} \frac{1}{\sqrt{\pi}}(\varsigma-1)^{1/2} + \frac{3}{2}(\varsigma-1) \\ -\frac{1}{4}(\varsigma-1)^2 - \frac{1.2}{\sqrt{\pi}}(\varsigma-1)^{1/2} \end{pmatrix}, & \varsigma \in [1,2), \\ S_2 + D_3(\varsigma), & \varsigma \in [2,3), \end{cases}$$

with S_2 and D_3 (ς) as explicitly given above. Note that $\Gamma(\frac{1}{2}) = \sqrt{\pi}, \Gamma(\frac{3}{2}) = \frac{\sqrt{\pi}}{2}$, $\Gamma(\frac{5}{2}) = \frac{3\sqrt{\pi}}{4}$ have been employed above. The left and right limits match at $\varsigma = 0,1,2$, hence ν is continuous on [-1,3). We emphasize that the piecewise representation above is constructed so that the accumulated terms S_1 and S_2 ensure the matching of left-and right-hand limits at the switching instants $\varsigma = 0,1,2$, in agreement with the continuity result established in Theorem 5.

Figure 3 depicts the two components of the solution $\nu(\varsigma) = (\nu_1(\varsigma), \nu_2(\varsigma))^T$ on [-1,3) and visually confirms the continuity at the junction points $\varsigma = 0,1,2$. Inparticular, Figure 3 shows that both components ν_1 and ν_2 evolve smoothly across the switching points, despite the presence of distinct system matrices on successive intervals. This confirms that the continuity property is preserved component wise, not merely in a normed sense.

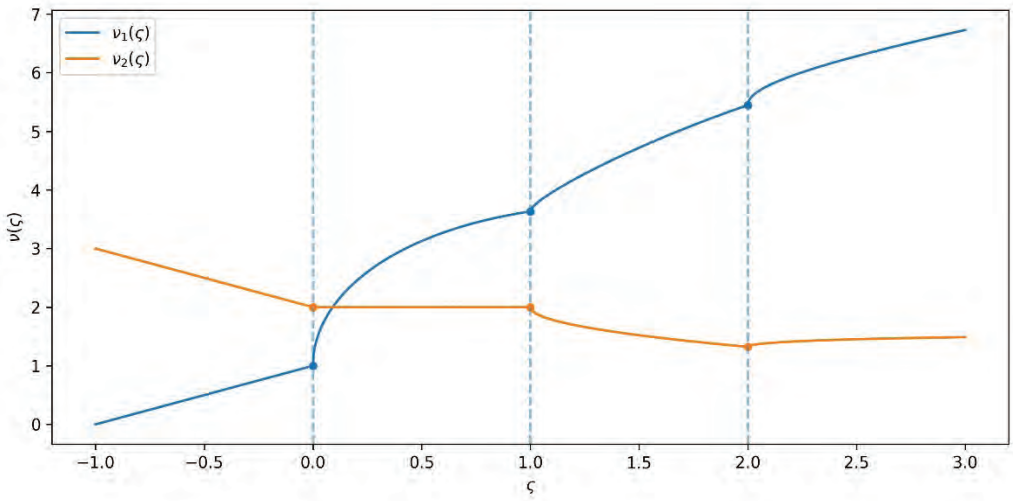


Figure 3. Componentwise solution of Example 13 illustrating the continuity of $\nu_1(\varsigma)$ and $\nu_2(\varsigma)$ across the junction points $\varsigma = 0,1,2,$.

The infinity-norm trajectory shown in Figure 4 provides a quantitative visualization of the finite-time stability concept. By plotting the innity norm of the solution together with the prescribed bound $\varepsilon = 0.80$, the figure illustrates how the analytical bound derived in Theorem 9 constrains the entire solution trajectory within the stability margin. This representation is consistent with the definition of finite-time stability and visually confirms the condition stated in Definition 6 and Theorem 9, showing that the solution remains within the prescribed bound for all $\varsigma \in [0,3]$.

Overall, this example illustrates how the proposed framework simultaneously delivers explicit matrix-valued solutions, guarantees continuity at switching points, and enables direct numerical verification of finite-time stability, thereby bridging the gap between abstract theory and applied analysis.

Example 14. Consider the following homogeneous piecewise fractional system

$$\begin{cases} {}^{C}D_{2^+}^{\alpha} v(\varsigma) = \Omega_3 v(\varsigma - 1), & \varsigma \in [2,3), \\ {}^{C}D_{1^+}^{\alpha} v(\varsigma) = \Omega_2 v(\varsigma - 1), & \varsigma \in [1,2), \\ {}^{C}D_{0^+}^{\alpha} v(\varsigma) = \Omega_1 v(\varsigma - 1), & \varsigma \in [0,1), \\ v(\varsigma) = \varphi(\varsigma), & \varsigma \in [-1,0). \end{cases} \tag{25}$$

Let $\delta = 0.05$, $\varepsilon = 0.80$ be given. Then, $M := max_{1\le k\le 3} |\Omega_k| = 0.30$ and $\varepsilon/\delta = 16$. In the light of the statement of Theorem 9, one has to calculate the following sum

$$S(3) := \sum_{i=1}^{3} 2^{i-1} \sum_{k=0}^{i} \frac{M^k \tau^{k\alpha}}{\Gamma(k\alpha+1)} = \sum_{i=1}^{3} 2^{i-1} \sum_{k=0}^{i} \frac{(0.30)^k}{\Gamma(k/2+1)}.$$

For $i = 1$:

$$2^0\left(1+\frac{0.30}{\Gamma(1.5)}\right) = 1\left(1+\frac{0.30}{0.8862269}\right) = 1(1+0.3385) \approx 1.3385,$$

For $i = 2$:

$$\begin{aligned} 2^1\left(1+\frac{0.30}{\Gamma(1.5)}+\frac{0.30^2}{\Gamma(2)}\right) &= 2\cdot\left(1+\frac{0.30}{0.8862269}+0.09\right) \\ &= 2\cdot(1+0.3385+0.09) \\ &= 2\cdot 1.4285 \approx 2.8570, \end{aligned}$$

for $i = 3$:

$$\begin{aligned} 2^2\left(1+\frac{0.30}{\Gamma(1.5)}+\frac{0.30^2}{\Gamma(2)}+\frac{0.30^3}{\Gamma(2.5)}\right) &= 4\cdot\left(1+\frac{0.30}{0.8862269}+0.09+\frac{0.027}{1.3293404}\right) \\ &= 4\cdot(1.4488) \approx 5.7953. \end{aligned}$$

Then,

$$S(3) \approx 1.3385 + 2.8570 + 5.7953 = 9.9908.$$

Since

$$S(3) \approx 9.9908 < \frac{\varepsilon}{\delta} = 16,$$

the hypothesis (22) holds. Therefore, by Theorem 9, the homogeneous piecewise fractional system (25) is finite-time stable on $J = [0,3]$ for all histories with $\|\varphi\|_\infty < \delta = 0.05$, and its solution satisfies $\|v(\varsigma)\| < \varepsilon = 0.80$ for all $\varsigma \in J$. To complement the analytical verification above, we provide a numerical trajectory of the solution in order to visualize the finite-time stability property predicted by Theorem 9. Figure 5 illustrates the evolution of $v(\varsigma)$ over $\varsigma \in [0,3]$ obtained by applying the Caputo fractional derivative of order α =1/2 with piecewise coefficients $\Omega_1 = 0.30$, $\Omega_2 = 0.20$, and $\Omega_3 = 0.25$. The initial history is assumed as

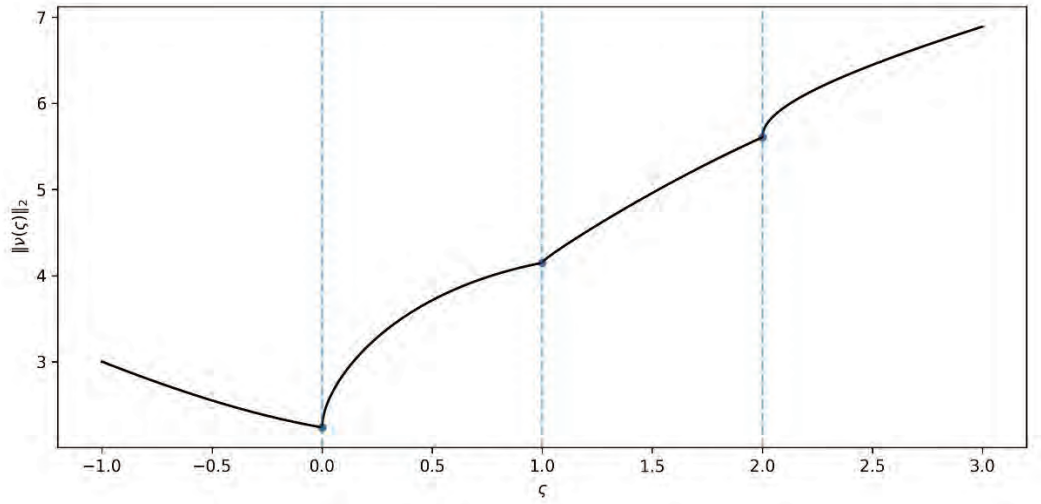


Figure 4. Infinity norm of the solution $\|v(\varsigma)\|_\infty$ for Example 13. The dashed horizontal line indicates the prescribed stability bound $\varepsilon = 0.80$, while the vertical dashed lines mark the junction points $\varsigma = 0,1,2$. The trajectory remains within the bound, confirming finite-time stability on $J = [0,3]$.

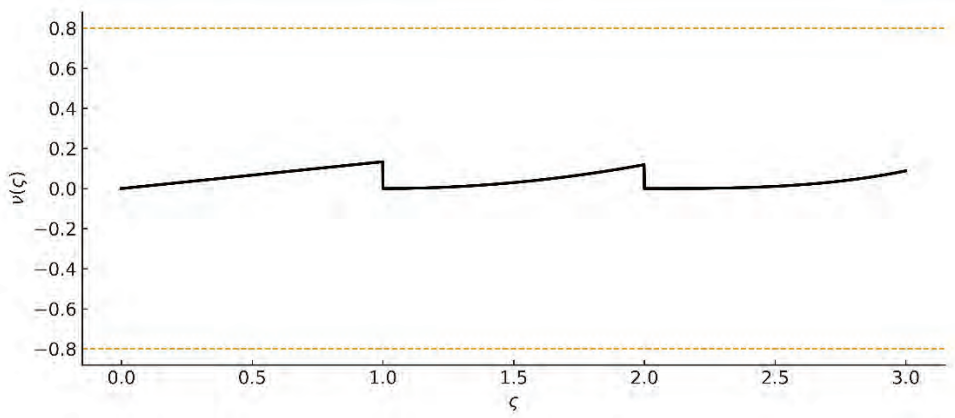


Figure 5. Solution profile illustrating finite-time stability for the system to the system 25.

$\varphi(\varsigma) \equiv \delta = 0.05$ for $\varsigma \in [-1,0)$. The dashed horizontal lines correspond to the prescribed bound $|\nu(\varsigma)| = \varepsilon = 0.80$. It is clearly observed that the entire trajectory of $\nu(\varsigma)$ remains within the stability margin $|\nu(\varsigma)| < \varepsilon$, confirming the finite-time stability condition $S(3) \approx 9.99 < \varepsilon/\delta = 16$ predicted by Theorem 9.

We emphasize that the above finite-time stability verification is not restricted to constant histories. Indeed, the stability condition in Theorem 9 depends only on the bound $\|\varphi\|_\infty < \delta$ and not on the specific functional form of $\varphi(\varsigma)$. For instance, choosing a non-constant history $\varphi(\varsigma) = \delta(1 + \varsigma)$ for $\varsigma \in [-1,0)$, one still has $\|\varphi\|_\infty = \delta = 0.05$ because

$$\|\varphi\|_\infty = \sup_{\varsigma\in[-1,0)} |\delta(1 + \varsigma)| = \delta \sup_{\varsigma\in[-1,0)} (1 + \varsigma).$$

Since $1 + \varsigma$ is continuous and monotonically increasing on $[-1,0)$, its maximum is attained at $\varsigma \to 0^-$, yielding

$$\sup_{\varsigma\in[-1,0)} (1 + \varsigma) = 1.$$

Hence,

$$\|\varphi\|_\infty = \delta = 0.05.$$

Hence, the inequality $S(3) < \varepsilon/\delta$ remains unchanged and the homogeneous piecewise fractional system (25) is finite-time stable on $J = [0,3]$. This shows that the numerical validation applies to a broader class of initial histories, including non-constant functions.

The numerical trajectory shown in Figure 5 remains strictly within the prescribed bound $|\nu(\varsigma)| < \varepsilon$ for all $\varsigma \in [0,3]$, providing a direct visual confirmation of the finite-time stability result and demonstrating the practical sharpness of the analytical estimate.

Note that the gures presented in the examples are intended to complement the analytical results by providing a direct visual interpretation of the explicit solution construction and the finite-time stability analysis. In particular, the solution trajectories illustrate the continuity of the piecewise-defined solutions at the switching points, while the plotted norms demonstrate that the solutions remain within the prescribed stability bounds over the finite time interval. These graphical representations therefore serve as numerical con rmations of the theoretical findings, bridging the gap between the abstract analytical conditions and their observable dynamical behavior.

CONCLUSION

We develop an explicit interval-wise solution for linear piecewise fractional systems with Caputo derivatives and a single delay via a generating-function approach. The solution is continuous across junctions, and a computable sum inequality yields a finite-time stability condition. A couple of examples are presented to validate our findings.

The originality of this work lies in the explicit construction of solutions for piecewise fractional delay systems together with a directly applicable finite-time stability criterion, extending existing results that are mainly based on implicit formulations or restrictive assumptions.

There are many directions for future work. For example, is our system controllable? Is it exponentially or asymptotically stable? One may also consider the nonhomogeneous type of the system under study.

ACKNOWLEDGEMENTS

This work was supported by the Scientific and Technological Research Council of Türkiye (TÜBİTAK) under Project No. 1919B012423168 within the framework of the 2209-A Research Project Support Programme for Undergraduate Students (2024/1 call). The authors gratefully acknowledge the support of the TÜBİTAK Scientist Support Programs Presidency (BİDEB).

AUTHORSHIP CONTRIBUTIONS

Authors equally contributed to this work.

DATA AVAILABILITY STATEMENT

The authors confirm that the data that supports the findings of this study are available within the article. Raw data that support the finding of this study are available from the corresponding author, upon reasonable request.

CONFLICT OF INTEREST

The authors declared no conflict of interest.

ETHICS

There are no ethical issues with the publication of this manuscript.

STATEMENT ON THE USE OF ARTIFICIAL INTELLIGENCE

The authors declared thsat no AI tools were used in the development of the scientific content of this paper; however, minor language and stylistic revisions were carried out.

REFERENCES

[1] Aydin M, Mahmudov NI. The sequential conformable Langevin-type differential equations and their applications to the RLC electric circuit problems. Math Methods Appl Sci 2019;42:5489–5497.

[2] Aydin M. The linear sequential fractional differential system involving two generalized fractional orders and its application to the vibration theory. J Math Ext 2024;18:1–32.

[3] Aydin M. Analytical solution and stability of Ψ-Prabhakar delayed systems: Application to antibiotic production. Turk J Math 2025;49:472–490. [CrossRef]

[4] Mahmudov NI, Aydin M. Qualitative analysis of Caputo fractional delayed difference system: A novel delayed discrete fractional sine and cosine-type function. J Nonlinear Sci Appl 2025;18:43–63. [CrossRef]

[5] Debeljkovic DL, Lazarevic MP, Milinkovic SA, Jovanovic MB. Finite time stability analysis of linear time delay systems: Bellman-Gronwall approach. In: Proceedings of the 1st IFAC Workshop on Linear Time Delay Systems; 1998 Jul. p. 171–175.

[6] Debeljkovic DL, Lazarevic MP, Nenadic ZL, Milinkovic SA. Finite time stability of time delay systems. IMA J Math Control Inf 1999;16:101–109 . [CrossRef]

[7] Ye H, Gao J, Ding Y. A generalized Gronwall inequality and its application to a fractional differential equation. J Math Anal Appl 2007;328:1075–1081. [CrossRef]

[8] Hei X, Wu R. Finite-time stability of impulsive fractional-order systems with time-delay. Appl Math Model 2016;40:4285–4290. [CrossRef]

[9] Wang Q, Lu D, Fang Y. Stability analysis of impulsive fractional differential systems with delay. Appl Math Lett 2015;40:1–6. [CrossRef]

[10] Lazarevic MP, Spasic AM. Finite-time stability analysis of fractional order time-delay systems: Gronwall's approach. Math Comput Model 2009;49:475–481. [CrossRef]

[11] Lazarevic MP. Finite time stability analysis of fractional control of robotic time-delay systems. Mech Res Commun 2006;33:269–279. [CrossRef]

[12] Kilbas AA, Srivastava HM, Trujillo JJ. Theory and applications of fractional differential equations. North-Holland Mathematics Studies; vol. 204. Amsterdam: Elsevier; 2006.

[13] Podlubny I. Fractional differential equations. Mathematics in Science and Engineering; vol. 198. San Diego: Academic Press; 1999.

[14] Diethelm K. The analysis of fractional differential equations: An application-oriented exposition using differential operators of Caputo type. Lecture Notes in Mathematics; vol. 2004. Berlin: Springer-Verlag; 2010. [CrossRef]

[15] Herzallah MAE, El-Sayed AMA, Baleanu D. On the fractional-order diffusion-wave process. Rom J Phys 2010;55:274–284.

[16] Hilfer R, editor. Applications of fractional calculus in physics. Singapore: World Scientific; 2000. [CrossRef]

[17] Tarasov V. Fractional dynamics: Applications of fractional calculus to dynamics of particles, fields and media. Berlin: Springer; 2011. [CrossRef]

[18] Fernandez A, Baleanu D, Fokas AS. Solving PDEs of fractional order using the unified transform method. Appl Math Comput 2018;339:738–749. [CrossRef]

[19] Zayed AI. A class of fractional integral transforms: A generalization of the fractional Fourier transform. IEEE Trans Signal Process 2002;50:619–627. [CrossRef]

[20] Kerr FH. Namias fractional Fourier-transforms on L2 and applications to differential equations. J Math Anal Appl 1988;136:404–418. [CrossRef]

[21] Jarad F, Abdeljawad T. Generalized fractional derivatives and Laplace transform applications to fractional differential equations. Discrete Contin Dyn Syst Ser S 2019;13:1775–1786. [CrossRef]

[22] Ozaktas HM, Zalevsky Z, Kutay MA. The fractional Fourier transform with applications in optics and signal processing. Chichester: Wiley; 2001. [CrossRef]

[23] Namias V. The fractional order Fourier transform and its application to quantum mechanics. IMA J Appl Math 1980;25:241–265. [CrossRef]

[24] Aydin M. An explicit solution of linear conformable systems with variable coefficients. Sigma J Eng Nat Sci 2024;42:1806–1812. [CrossRef]

[25] Acikgoz P, Merdan M. Mathematical analysis of fractional order Covid-19 epidemic model. Sigma J Eng Nat Sci 2025;43:1712–1724. [CrossRef]

[26] Limpanukorn N, Ahmed I, Ibrahim MJ. On Ψ-quantum fractional operators: Existence, uniqueness and Ulam-Hyers stability. Sigma J Eng Nat Sci 2024;42:313–320. [CrossRef]

[27] Khusainov DY, Shuklin GV. Linear autonomous time-delay system with permutation matrices solving. Stud Univ Zilina 2003;17:101–108.

[28] Li M, Wang JR. Exploring delayed Mittag-Leffler type matrix functions to study finite time stability of fractional delay differential equations. Appl Math Comput 2018;324:254–265. [CrossRef]

[29] Luo H, Wang JR. Controllability of piecewise linear state-delay systems. Appl Math Comput 2025;494:129281. [CrossRef]

[30] Li M, Wang J. Finite time stability of fractional delay differential equations. Appl Math Lett 2017;64:170–176. [CrossRef]

[31] Xiao G, Wang J. Representation of solutions of linear conformable delay differential equations. Appl Math Lett 2021;107088. [CrossRef]

[32] Li M, Wang J, O'Regan D. Existence and Ulam's stability for conformable fractional differential equations with constant coefficients. Bull Malays Math Sci Soc 2019;42:1791–1812. [CrossRef]

[33] Aydin M, Mahmudov NI. ψ-Caputo type time-delay Langevin equations with two general fractional orders. Math Methods Appl Sci 2023;46:9187–9204. [CrossRef]

Sigma Journal of Engineering and Natural Sciences
Web page info: https://sigma.yildiz.edu.tr
DOI: 10.14744/sigma.2026.2129

Research Article

Impact of vehicle integration sections on photovoltaic performance: A case study for Türkiye

Semir SÜNKÜN[1,*], Berke Oğulcan PARLAK[1], Hüseyin Ayhan YAVAŞOĞLU[1], Umut KARAGÜZEL[1]

[1]*Department of Mechatronics Engineering, Yıldız Technical University, İstanbul, 34349, Türkiye*

ARTICLE INFO

Article history
Received: 22 December 2024
Revised: 13 March 2025
Accepted: 05 May 2025

Keywords:
Energy Production; Integration Section; Solar Energy; Vehicle-Integrated Photovoltaics

ABSTRACT

The integration of photovoltaic systems into vehicles raises the question of how different sections of the car body can be used to generate solar energy. This question is becoming increasingly important as electric vehicle technologies seek more efficient and sustainable energy sources. The potential of solar energy was analyzed using a region-independent methodology based on one year of irradiance data from three cities in Türkiye representing low, medium, and high solar radiation levels. The analysis was made with data obtained from the Photovoltaic Geographical Information System, and it was applied to five vehicle surfaces with different inclinations and azimuth angles: the roof, the front hood, the rear hood and both doors. The results indicate that the door sections collectively contribute the most to the energy reception (26.67%), followed by the front hood (26.47%), the roof (24.22%) and the rear hood (22.64%). The study also shows that irradiance values for differently oriented surfaces can be inferred from a single pyranometer measurement, greatly reducing the complexity and cost of data collection for future applications. This study is novel compared to existing literature in that it presents a new method for assessing section-based irradiance contributions irrespective of the photovoltaic surface area, thus enabling more generalizable and scalable insights for future vehicle designs. The comparison with experimental results was made to confirm the reliability of the methodology, with a deviation of only ±4.83%.

Cite this article as: Sünkün S, Parlak BO, Yavaşoğlu HA, Karagüzel U. Impact of vehicle integration sections on photovoltaic performance: A case study for Türkiye. Sigma J Eng Nat Sci 2026;44(4):2823–2836.

INTRODUCTION

In contemporary societies, the degree of development and economic prosperity is frequently gauged by the indices of energy generation and consumption. This energy is derived from two sources: primary and secondary. Primary sources are fossil fuels (oil, coal and natural gas) and renewable sources (solar [1], wind [2] and hydroelectric power [3]). Secondary sources, such as electricity, are derived from primary sources through various conversion processes, making them ready for direct consumption [4]. However,

***Corresponding author.**
*E-mail address: semir.sunkun@yildiz.edu.tr

This paper was recommended for publication in revised form by Editor-in-Chief Ahmet Selim Dalkilic

Published by Yıldız Technical University Press, İstanbul, Turkey
© Author. This is an open access article under the CC BY-NC license (http://creativecommons.org/licenses/by-nc/4.0/).

the production and consumption of energy are among the major determinants of environmental degradation, mainly through carbon dioxide (CO_2) emissions. In the past, these emissions have come from fossil fuels, combustion and industrial processes. They differ between regions, and have grown with industrialization. Figure 1 presents the emissions of CO_2 by certain sources, such as coal, natural gas, oil, combustion activities, and cement production, worldwide and in Türkiye [5, 6].

Despite efforts to reduce CO_2 emissions since the 17 Sustainable Development Goals [7] launched by the United Nations in 2015 and the 2015 Paris Agreement, levels continue to rise, worsening the effects of climate change and making it harder to achieve global climate goals. In response, many countries are increasingly investing in zero-emission and sustainable energy alternatives [8]. Solar energy, one of these sources, is abundant, environmentally friendly, versatile, easily accessible, and easy to utilize, while also offering a low average cost [9]. Due to these advantages, global solar energy production has increased by an average of 25.9% annually since 2013, while Türkiye has experienced an average annual growth rate of 22.7%. This expansion is also evidenced by the rising number of installed solar panels [10].

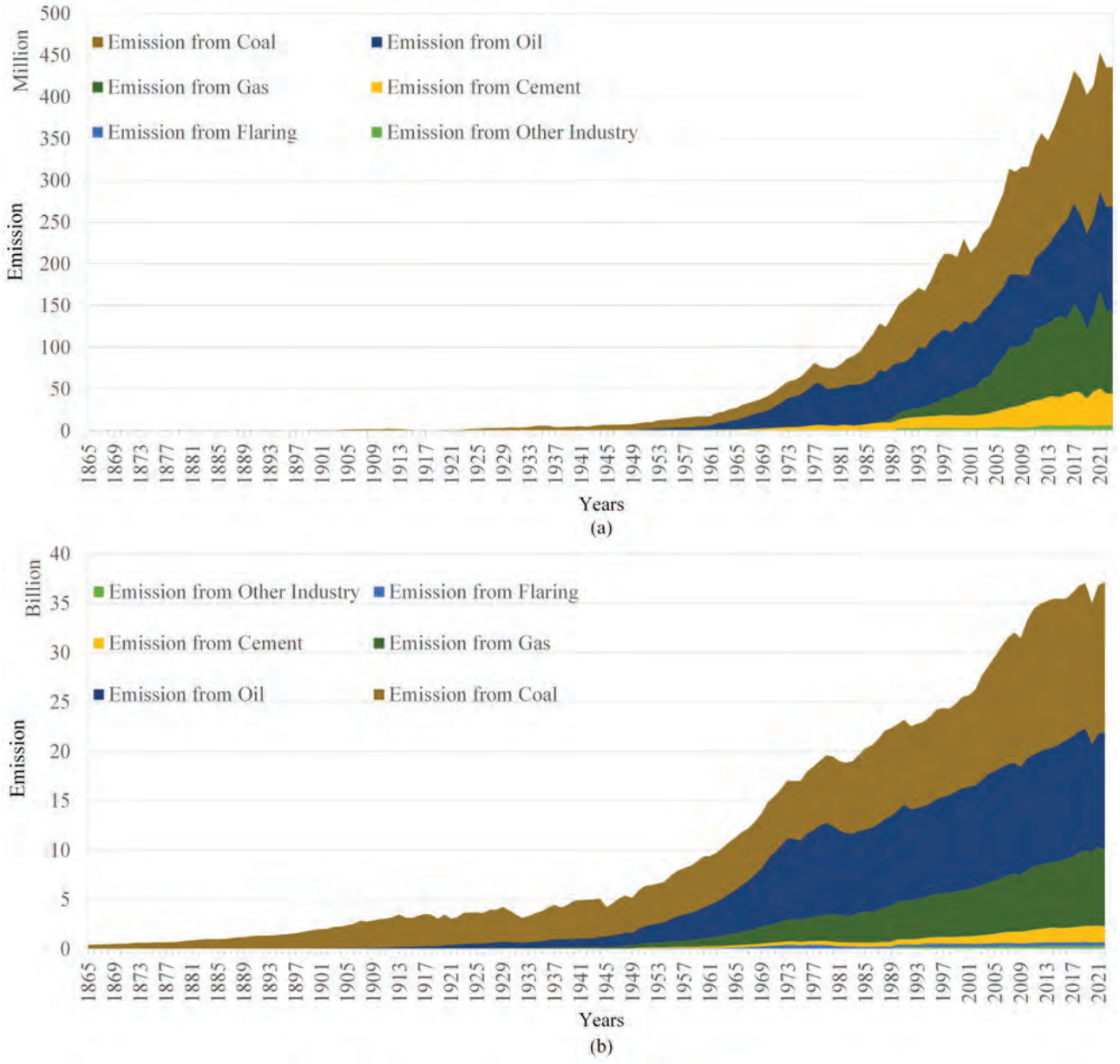


Figure 1. CO_2 emissions by coal, natural gas, oil, combustion processes, and cement production a) Türkiye, b) Globally. [Created by the authors using open-access data from the Global Carbon Project [6]].

The production of electricity from solar energy is based on the basic function of photovoltaic (PV) panels. Photons from sunlight hit the semiconductor material in the PV panels and transfer energy [11]. In this process, electrons in the semiconductor material are released and start moving, which provides direct current electricity production. This electrical energy produced by PV systems is used in buildings [12], agricultural areas [13], lighting/air conditioning [14–16] systems, and vehicles [17–19]. In addition, the applications of solar-powered vehicles have witnessed a significant surge, with the global market size valued at USD 456.6 million in 2023. This market is expected to increase from USD 545.0 million in 2024 to USD 2,526.2 million by 2032, at an estimated CAGR of 21.1% during the forecast period [20]. The main advantages of expanding PV applications in electric vehicles (EVs) are extending the vehicle's range, reducing carbon emissions by charging with renewable energy, decreasing dependence on the electrical grid and saving money [21]. The benefits of PV integration into EVs have also been highlighted in the literature. Sagaria et al. [22] demonstrated through tests on various vehicle segments that the integration of solar panels effectively extends the range of EVs. Similarly, Centeno Brito et al. [17] conducted a case study in Lisbon, confirming comparable outcomes. Kanz et al. [23] demonstrated in their studies that PV integration in EVs significantly reduces carbon emissions. Hoth et al. [24] demonstrated in their research that integrating PV technology reduces costs by decreasing the frequency of grid-dependent charging. These benefits of PV technology in vehicles can be improved by expanding the PV-covered area of the vehicle [25]. Expanding the PV-covered area is feasible only by integrating PV cells into additional sections of the vehicle's surface. Therefore, it is important to evaluate the impact of vehicle integration sections on PV performance.

There are studies in the literature comparing the power generation of vehicle-integrated PVs (VIPVs) incorporated into various vehicle sections. According to [26], the front hood VIPV generates approximately 43% of the potential of the roof VIPV. According to [27], during a midday home drive, the combined time-averaged solar irradiance received on the vehicle's side and rear surfaces corresponds to approximately 53% of the irradiance received on the roof but, under stationary conditions such as parking and PV charging, the sum of the irradiance on the sides and rear even exceeds that of the roof. Similarly, [28] performed high-time-resolution measurements on a moving vehicle and found that, on average, 54.3% of the total irradiance was received by the roof and 45.7% by the side surfaces. Under specific conditions, such as sunny winter days, the irradiance on the sides was similar to or even higher than that on the roof owing to the lower solar altitude and favorable angles of the vertical surfaces. In [29], it is reported that the rear hood VIPV generates 42% of the energy produced by the roof VIPV, while the doors contribute 27%. In contrast, [30] indicates that the front hood VIPV achieves up to 86% of the roof VIPV's production potential, whereas the rear hood and the doors generate 25% and 67%, respectively. Current literature reveals the power generation potential of PVs integrated into different vehicle sections under various scenarios. However, these literature results are far from consistent. The primary reason for this is that the PV area, which has a major impact on the PV output, varies with the different vehicles used in the studies. Additionally, because the results are largely related to the PV area, analyses of the impact of integration sections on PV performance cannot be generalized.

This study aims to fill the gap in the current literature by evaluating the effect of vehicle integration sections on PV performance independent of PV area, and thus providing insights into the power contribution of PVs in different sections of the vehicle. In addition, the study uses one year of solar irradiance data from three different cities in Türkiye, which are classified as low, medium, and high irradiance, to enhance the consistency of the analysis by not limiting the study to one location. The key contributions of the paper can be summarized as follows:

- An area-independent analysis was carried out by evaluating the performance of different PV sections independent of the panel area, allowing a fair comparison between different vehicle surfaces.
- A complete seasonal analysis was performed by investigating the energy contribution of each vehicle section across all four seasons, which results in a more representative picture of annual performance.
- To account for the different climatic conditions and improve the generalizability of the results, multi-regional irradiance data were utilized from three different regions of Türkiye, namely Mardin, Ankara, and Rize.
- The proposed methodology was verified by comparing the calculated results with experimental data reported in the literature.
- A simplified data acquisition model is introduced, in which data of irradiance in one vehicle section (e.g., roof) can be used to estimate the irradiance in other sections, reducing the number of measurement points needed.

Following the introductory information, Section 2 presents a thorough review of VIPV, covering application areas and integration approaches for PV panels in EVs. Section 3 presents the methodology used to analyze VIPV systems, including panel positioning, regional performance evaluation, and power output analysis based on solar irradiance data. Section 4 presents the results and discussion, and Section 5 summarizes the main findings and conclusions.

Review of Vehicle-Integrated Photovoltaics

In recent years, trends in energy and environmental policies have accelerated the adoption of EVs and decline in the use of internal combustion engine vehicles. Figure 2 shows the number of EVs and non-EVs sold from 2010 to 2024 [31]. Worldwide EV sales grew from under 1 million in

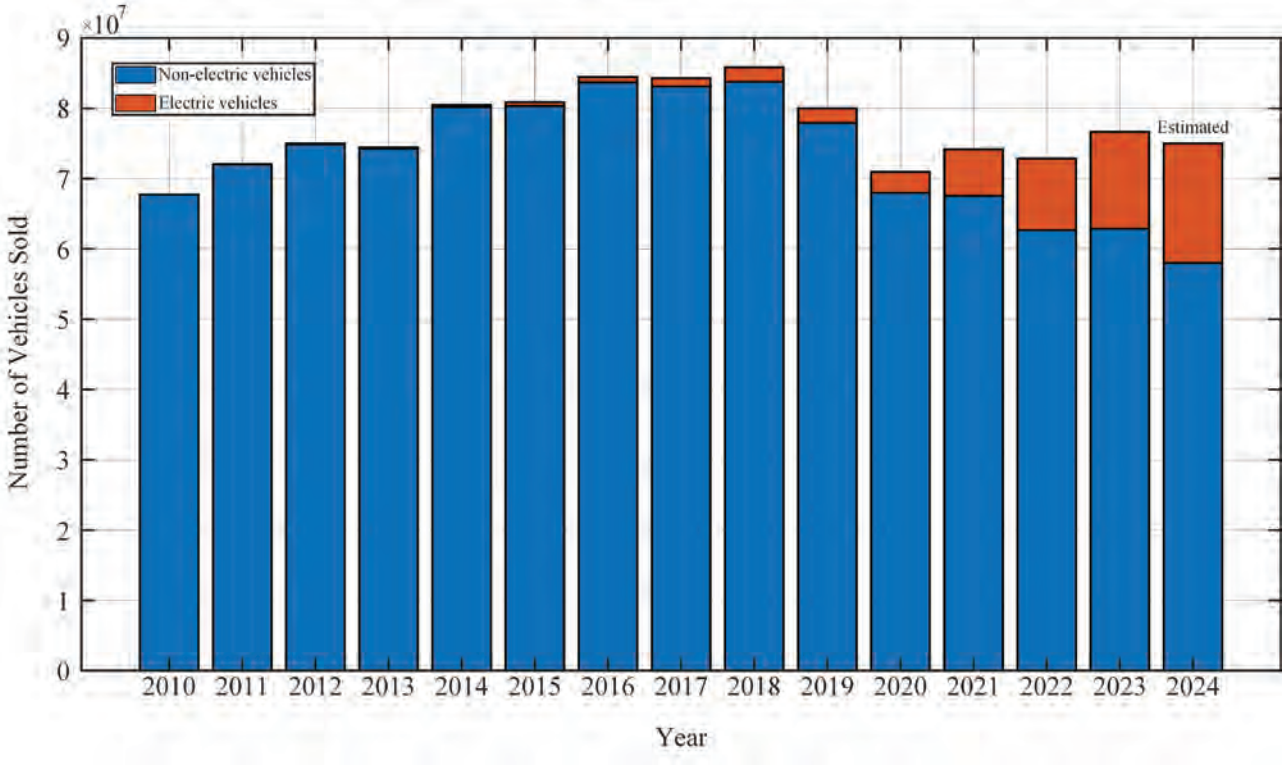


Figure 2. Number of new vehicles sold from 2010 to 2024 by type. [Created by the authors using open-access data from the International Energy Agency [31]].

2015 to over 10 million in 2022. Sales of EVs are estimated to reach 17 million worldwide by 2024 and represent more than 21% of all auto sales. This growth, up 25% compared to 2023, has been particularly strong in key markets such as China, Europe and the US. In China, EVs are projected to account for 45% of car sales by 2024, while Europe and the US are forecast to have shares of 25% and 11% respectively. In 2023, EV sales alone hit nearly 14 million, up 35% from the previous year.

The decline in the use of internal combustion engine vehicles can be attributed to a number of factors, including stringent regulations to reduce carbon emissions, rising fuel prices and growing environmental awareness. In contrast, growth in EVs has been driven by government incentives, decreasing battery prices, and investments in new technologies and regulations, such as the European Union's goal to reduce carbon emissions by 55% by 2030. However, it is also worth noting that EVs are not entirely emission-free, since some of the electricity used to charge them still comes from fossil fuels. This reduces the environmental benefits of EVs and highlights the need for alternative solutions. Technologies such as VIPV can help to reduce charging frequency, indirectly reduce emissions, and reduce operating costs [25].

The first VIPV examples came with solar-powered cars built for competitions. Prominent examples are the Sunmobile (1955), the GM Sunraycer (1987) and later entries in the World Solar Challenge, such as the Nuna series by Delft University (2001) and the Tokai Challenger (2009). These vehicles were initially engineered for efficiency in controlled environments, but proved the feasibility of incorporating PVs into automotive systems. As PV technology evolved, VIPVs were increasingly used to support broader applications, like powering secondary systems (e.g. steering, air conditioning) and supplementing the main drivetrain. Mallon et al. [32] investigated the impact of on-board PVs on the performance of the electric bus. The simulation results based on the suburban bus cycles and the yearly weather data in Davis, California, showed that the roof-mounted panels provided an average annual increase of 4.7% on the driving range, and the combination of roof and side panels provided an increase of 8.9%. The economic and environmental viability of VIPV systems was studied by Kronthaler et al. [33] for different locations, vehicle types and PV types. They demonstrated a saving of 1600 kg of CO_2 per square meter of VIPV. However, these assessments do not include commercial passenger vehicles and are largely conducted for commercial vehicles with high utilization rates and relatively large roof surface areas. Sagaria et al. [22] examined the feasibility of VIPV in EVs and found that onboard PV systems could have a significant effect on the range, 30–50% for micro-cars and 30–100% for 5-seaters, for private driving profiles, while there is no real benefit for fuel cell powertrains. Their

analysis also showed economic benefits, with VIPV reaching cost parity before the half-life of the vehicle. Yamaguchi et al. [34] investigated the potential of high-efficiency solar modules for VIPVs. They showed that modules with efficiencies above 35% can realize over 30 km/day of PV driving under typical irradiance conditions (4 kWh/m²/day) without external charging. They also emphasized the need for cost reductions, estimating cost targets of $2.6/Wp for 20% efficiency and $3.7/Wp for 40% efficiency to ensure economic viability, based on charging cost savings and CO_2 emission reductions. Diahovchenko et al. [35] evaluated the feasibility of using commercial PV technologies to enhance EV mileage, and concluded that solar panels on the roof could produce up to 6.32% of the range on sunny summer days and 1.16% on sunny winter days, providing energy for propulsion or auxiliary systems with low investment. Such literature studies have shown the practical applicability of VIPVs leading to their integration into market vehicles [36].

MATERIALS AND METHODS

Determining the Position of the Photovoltaic Panels

The positioning of PV panels in terms of slope and azimuth is critical for improving solar energy capture and power generation efficiency [37]. The slope angle refers to the tilt degree of PV panels relative to the horizontal plane, or in other words, the angle the panel makes with the ground. The azimuth angle, on the other hand, indicates the direction a surface faces on the horizontal plane. To accurately model VIPVs, appropriate slope and azimuth angles must be defined for the relevant sections of the vehicle. To ensure realistic positioning, a reference passenger vehicle [30] has been selected. Figure 3 presents the positioning parameters of the VIPVs relative to this vehicle. In addition, the orientation of each PV surface (i.e., slope and azimuth) is assumed to be fixed relative to the vehicle body, representing a static parked condition with a predefined heading. The analysis does not consider the dynamic changes in the vehicle orientation, for instance, while driving or when the vehicle is parked at different angles. Such a simplification enables a controlled comparison between vehicle sections.

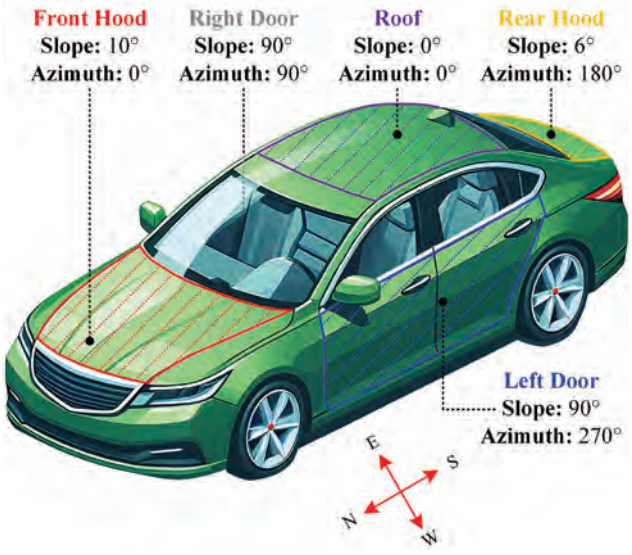


Figure 3. Positioning parameters of VIPVs relative to the reference vehicle.

Most vehicle roofs and even some other parts are curved [38] for purposes such as increasing the vehicle's aerodynamic performance, reducing air resistance and improving fuel efficiency. PV panels integrated on curved surfaces may not receive optimal sunlight and could experience performance degradation due to issues such as partial shading and accumulation of pollutants. It is important to note that this study assumes PVs are integrated on flat surfaces, thus any potential effects resulting from curved surfaces are not considered.

Determination of Analysis Regions Based on Solar Exposure

It is known that the results of PV studies are more generalizable in distinct four-season locations compared to summer or winter-dominant locations [39]. This is because summer or winter-dominant locations provide performance analyses under only specific conditions, making it difficult to fully assess the adaptation of PV systems to varying conditions throughout the year. Therefore, Türkiye, a typical four-season country [40], has been chosen as the analysis location for this study. In Türkiye, the four seasons follow a different cycle. In spring the amount of precipitation decreases and the temperature rises. In summer the temperature is high and it is dry. In autumn the temperature drops and the amount of precipitation increases. In winter it is cold and rainy [41]. These patterns are shaped by the country's complex topography, where mountainous terrain and varied elevation contribute to significant regional climate differences. The topography, and particularly the more complex relief, causes a spatial pattern of climates in Mediterranean regions. This results in spatial variations of climate parameters such as air temperature, humidity, radiation, and precipitation [42, 43]. Consequently, the country's broad geographic and climatic diversity also causes its solar map to be quite variable. Figure 4 presents the solar map of Türkiye [44].

In this study, three different locations as marked in Figure 4 are considered. It is important to repeat the analysis in other solar radiation regions like these to understand the variability of energy generation depending on the regional conditions and to get more realistic and consistent estimates. The locations are classified as low, medium and high solar radiation regions according to the distribution of annual total solar energy potential of Türkiye in different regions [45]. The high solar radiation region can be used to test the upper limits in efficiency to maximize the energy

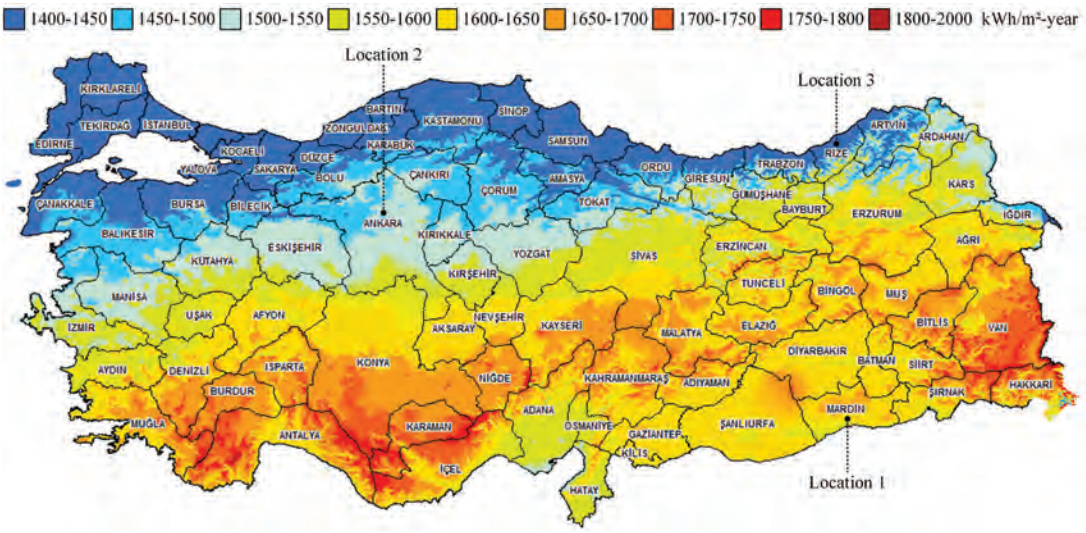


Figure 4. Solar map of Türkiye. [Adapted from the Solar Energy Potential Atlas [44]].

Table 1. Geographic coordinates of the three locations within the scope of the study

	Location 1	Location 2	Location 3
Solar Energy Potential	High	Medium	Low
Region	Southeastern Anatolia	Central Anatolia	Black Sea
Province	Mardin	Ankara	Rize
Latitude (°)	37.33	39.92	41.03
Longitude (°)	40.73	32.84	40.80
Elevation (m)	892	893	891

production of PV systems. The medium and low solar radiation areas allow for the assessment of the performance of PV under more common conditions and emphasize the potential for regional application. Geographic coordinates for the three sites are given in Table 1.

Analyzing the Performance of Vehicle-Integrated Photovoltaics

Obtaining solar irradiance data

The paper uses the solar irradiance data of the selected regions downloaded from the Photovoltaic Geographical Information System (PVGIS) [46]. The choice of the PVGIS system is due to its ability to provide high-resolution, site-specific irradiance data, integrating satellite observations, ground measurements and atmospheric modeling. Compared to on-site measurements, which require substantial instrumentation and are often limited to short time periods and specific locations, PVGIS offers a cost-effective, validated and widely used option for long-term solar resource assessment. Its proven accuracy and accessibility make it particularly suitable for academic studies involving different geographic regions and temporal scales. PVGIS provides reliable estimates of irradiance for the assessment of PV potential but does not consider the small-scale shading effects due to local obstructions such as buildings or trees [47]. Thus, it is important to point out that similar effects are not considered in this paper as well.

The irradiance values provided by PVGIS are mean hourly values calculated over a multi-year period from 2005 to 2016. The selected values for each month are the average of all days of the month of the reference period. Such long-term averaging ensures that the irradiance data used in the study are statistically robust and representative of typical climatic conditions, minimizing the influence of short-term anomalies or atypical weather events. As mentioned in the previous chapters, the data collection process involves the collection of average daily irradiance data from the PVGIS system for 3 different locations (latitude and longitude), 5 different vehicle integration section positions (slope and azimuths), and 12 different months of the year. The 12 months for Türkiye are divided into four seasons [40]: winter (December, January, February), spring (March, April, May), summer (June, July, August) and autumn (September, October, November). Figure 5 presents the

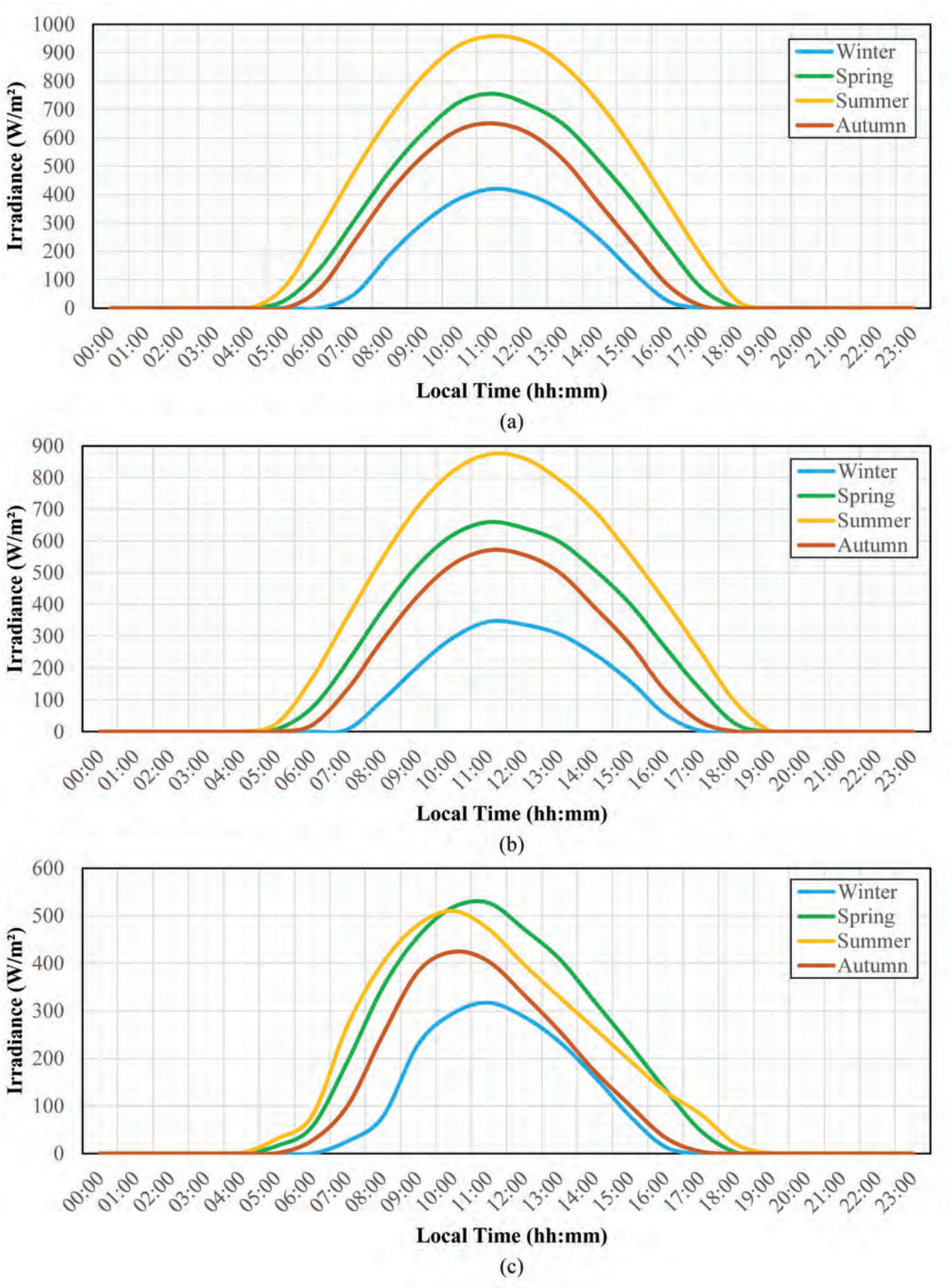


Figure 5. Location-based average daily global horizontal irradiance data a) Mardin, b) Ankara, c) Rize.

location-based average daily global horizontal irradiance data for these four seasons.

As shown in Figure 5, summer accounts for the largest relative share of the average daily solar irradiation in Mardin and Ankara, with 39% and 40%, respectively, followed by spring, autumn, and winter. In Rize, summer and spring show equal shares of approximately 32%, indicating a more balanced seasonal distribution. These results highlight the seasonal variability of solar energy and the influence of geographic location and regional climatic conditions on solar availability.

Determining the power output of photovoltaic panels

The power output of a PV panel P_{PV} can be simply expressed as follows [48]:

$$P_{PV} = A_{PV} \times G \times \eta \quad (1)$$

where A_{PV} is the area of the PV panel, G is the solar irradiance, and η is the efficiency of the PV. As previously mentioned, within the scope of this study, the power outputs of VIPVs will not be compared, but rather the power production potential (expressed by the received solar irradiance) of vehicle integration sections. Therefore, there is no need to use the conventional PV power output formula given in Equation 1. The power production data per square meter obtained from PVGIS (i.e. only G) for specific locations and positions will suffice for the analysis.

The solar irradiance G represents the average amount of solar irradiance falling on a surface every hour of each day during the relevant month. In other words, the total solar irradiance in the relevant month is divided by the number of days in the month to obtain an average value for each hour of each day. This series of values contains a total of 24 hours of data with one-hour intervals. The total amount of solar irradiance G_n^t received by the surface n during the day can be expressed as follows:

$$G_n^t = \sum_{i=1}^{24} G_n^i \quad (2)$$

where G_n^i is the total solar irradiance received by surface n during the ith hour. The surfaces indicated by n are the previously defined roof, rear hood, front hood, left door or right door sections. Equation 3 gives the total solar irradiance G^t received by all PV surfaces on the vehicle during the day.

$$G^t = \sum_{n=1}^{5} G_n^t \quad (3)$$

Finally, the ratio P_n of the total solar irradiance received by surface n during the day to the total solar irradiance received by all VIPV surfaces can be calculated as follows:

$$P_n = 100 \times \frac{G_n^t}{G^t} \quad (4)$$

RESULTS AND DISCUSSION

The results of the analysis on the impact of vehicle integration sections on PV performance for Mardin province are given in Table 2, for Ankara province in Table 3 and for Rize province in Table 4. It should be noted that G^t is the average total solar irradiance received on any day of the relevant month.

In the case of Mardin, the front hood appears to be the most efficient section for power production, with a maximum contribution of 28.88%. This section performs particularly well during relatively low irradiance seasons, such as winter and autumn. In the summer months, it shows similar efficiency to the roof section, with an average contribution of 25%. Although the door sections individually

Table 2. Contribution rates of vehicle integration sections to daily potential power production (Mardin case)

Month	P_{roof} (%)	$P_{rear\ hood}$ (%)	$P_{front\ hood}$ (%)	$P_{left\ door}$ (%)	$P_{right\ door}$ (%)	G^t (W/m²)
December	23.46	19.98	28.88	15.72	11.96	9088
January	23.66	20.67	28.26	15.65	11.76	9237
February	23.59	21.34	26.99	16.31	11.76	13143
March	24.08	22.59	26.19	15.58	11.57	17770
April	24.52	23.65	25.58	14.66	11.60	22731
May	24.97	24.49	25.35	14.16	11.04	27733
June	25.01	24.76	24.99	14.32	10.92	32435
July	24.91	24.55	25.07	14.24	11.24	32625
August	24.63	23.82	25.53	14.55	11.46	29542
September	24.13	22.63	26.20	15.82	11.24	25146
October	23.77	21.60	27.01	16.64	10.98	17329
November	23.31	20.21	28.09	17.47	10.92	12274

Table 3. Contribution rates of vehicle integration sections to daily potential power production (Ankara case)

Month	P_{roof} (%)	$P_{rear\ hood}$ (%)	$P_{front\ hood}$ (%)	$P_{left\ door}$ (%)	$P_{right\ door}$ (%)	G^t (W/m^2)
December	22.98	19.68	28.12	14.44	14.79	7557
January	23.18	20.51	27.29	14.21	14.81	7605
February	23.56	21.34	26.90	13.96	14.24	11319
March	23.85	22.35	25.96	13.82	14.02	16129
April	24.32	23.41	25.46	13.74	13.06	21711
May	24.63	24.15	25.04	13.34	12.84	24560
June	24.88	24.56	24.98	13.52	12.06	28178
July	24.82	24.37	25.12	12.92	12.77	30749
August	24.49	23.60	25.53	13.00	13.39	27925
September	23.95	22.43	26.07	13.91	13.64	22586
October	23.59	21.34	26.95	14.30	13.81	15261
November	22.85	19.57	27.94	14.75	14.89	11082

Table 4. Contribution rates of vehicle integration sections to daily potential power production (Rize case)

Month	P_{roof} (%)	$P_{rear\ hood}$ (%)	$P_{front\ hood}$ (%)	$P_{left\ door}$ (%)	$P_{right\ door}$ (%)	G^t (W/m^2)
December	23.85	20.66	28.78	13.65	13.07	6086
January	24.12	21.56	28.04	14.04	12.24	6236
February	24.49	22.47	27.48	12.88	12.68	8995
March	24.58	23.29	26.39	13.67	12.07	11728
April	24.82	23.95	25.90	13.38	11.96	15719
May	25.13	24.61	25.61	13.39	11.27	17527
June	25.04	24.73	25.20	13.92	11.10	16389
July	24.82	24.52	25.00	14.55	11.10	14278
August	24.56	24.05	25.10	15.55	10.75	13544
September	24.54	23.42	26.07	15.69	10.29	12764
October	24.43	22.56	27.18	14.34	11.48	10250
November	24.40	21.58	28.70	12.45	12.86	7506

seem to have the lowest performance (with a minimum of 14.16% for the left door and 10.92% for the right door), when considered together, they promise slightly higher efficiency than the front hood, with an average contribution of 26.80%. Notably, the left door is about 4% more efficient than the right door on average. The rear hood, on the other hand, consistently shows the lowest efficiency (with a minimum of 19.98%) for each month.

In the case of Ankara, similar to Mardin, the front hood appears to be the most efficient section for power production, with a maximum contribution of 28.12%. Winter, autumn, and spring are the most productive seasons for this section, respectively. During the summer, the four vehicle sections (with the doors considered together) contribute almost equally to power production. The rear hood section consistently shows the lowest efficiency in this case as well, with a minimum contribution of 19.57%. When the doors are considered together, they promise approximately 1.5% higher efficiency than the front hood, with an average contribution of 27.52%.

In Rize, the front hood section is clearly the most efficient, with a maximum contribution of 28.78%. Even when the doors are considered together, they fall short by approximately 1% on average compared to the front hood. In this case, the doors perform worse than in other cases, with efficiency differences of up to 2% at maximum and 1% at minimum. This loss in door performance has resulted in an average efficiency increase of 0.5% for the roof section and 1% for the rear hood section compared to the other cases. Evaluating all cases together will yield more consistent and generalizable results. For this purpose, an average of the contribution rates obtained in all months for each section can be considered separately. Table 5 depicts the average contribution rates of the vehicle integration sections to the

Table 5. Average contribution rates of the vehicle integration sections to the daily potential power production for different locations

Province	P_{roof} (%)	$P_{rear\ hood}$ (%)	$P_{front\ hood}$ (%)	$P_{left\ door}$ (%)	$P_{right\ door}$ (%)
Mardin	24.17	22.52	26.51	15.43	11.37
Ankara	23.92	22.28	26.28	13.82	13.69
Rize	24.57	23.12	26.62	13.96	11.74

daily potential power production for different locations. Despite the numerical differences in solar energy potential across regions, the similar results for PV integration sections can be attributed to the percentage-based contribution of each panel to the total energy potential, which remains independent of location. The observed difference in performance between the right and left doors arises from their differing orientations with respect to the sun's daily path. Due to variations in azimuth angles, one side receives more direct sunlight during certain hours of the day. These orientation-related factors explain both the minimal variation across different locations and the asymmetry observed between the door performances.

An average of the analysis results for the three different locations presented in Table 5 could expand the scope of the analysis to Türkiye. Consequently, for a vehicle with VIPV in a country like Türkiye, which experiences four seasons, the final energy performance of the integration sections would be as follows: doors (26.67%), front hood (26.47%), roof (24.22%), and rear hood (22.64%). Despite the significant solar potential of the doors, only 10% of solar-assisted market vehicles over the past five years have PV on their doors, while roof PVs remain dominant compared to other sections [30]. The primary reasons for this could be as follows:

- The roof is the least self-shading section of the vehicle. The PV installation area is larger compared to other sections and, unlike the hood and doors, it is more durable since it does not have mobility. Additionally, it does not compromise the vehicle's aesthetics and aerodynamics as much as other sections.
- On the other hand, the hood and door sections always carry the risk of damage due to impacts. It is known that the efficiency of PVs integrated into the front hood of hybrid vehicles decreases due to heating along with the engine [26]. Finally, the limited installation area of the rear hood can result in relatively low power outputs.

The roof is the most practical place to integrate PV, from a design perspective, especially for battery EVs. Further increase of the energy yield can be achieved by integrating PVs on the roof and front hood. However, for hybrid EVs, the efficiency of front hood PVs can be reduced due to the higher temperatures generated by the engine operation. Despite the great potential of the doors for capturing solar energy, their integration is currently constrained by issues such as mechanical vulnerability, shading due to the side position and the difficulty in ensuring structural durability. Although the rear hood contributes the least to total irradiance, it can still be a viable option for certain types of vehicles, such as sedans with large, flat rear surfaces, where additional PV coverage can be implemented without compromising design integrity. These results underscore the importance of a comprehensive assessment of not only irradiance potential but also practical integration constraints in the optimal deployment of VIPV systems.

Before concluding the study, the obtained results are compared with experimental studies in the literature. In [29], the authors presented a scenario where an EV, equipped with VIPV on its roof, rear window (referred to as the rear hood in this case), and left/right doors, moves along seventeen different routes with various slope and azimuth angles in Samcheok city, Gangwon-do, Korea. According to the results obtained throughout the route, the roof VIPV accounted for 59.17% of the total power generated by the VIPVs during the day, the rear hood VIPV for 24.85%, and the door VIPVs for 15.98%. The specifications of the PVs used in the study are given in Table 6.

Assuming that the total solar irradiance incident on the vehicle at any given time is 100 W/m², according to the outputs of our study, the roof would receive 24.22 W/m², the rear hood 22.64 W/m², the doors 26.67 W/m², and

Table 6. Specifications of PVs used in the literature study

	Roof PV	Rear Hood PV	Left Door PV	Right Door PV
Model	SMF 175W	SMF 100W	FS 40W	FS 40W
Efficiency	17.30%	15.49%	19.60%	19.60%
Integration Area	1 m²	0.65 m²	0.22 m²	0.22 m²

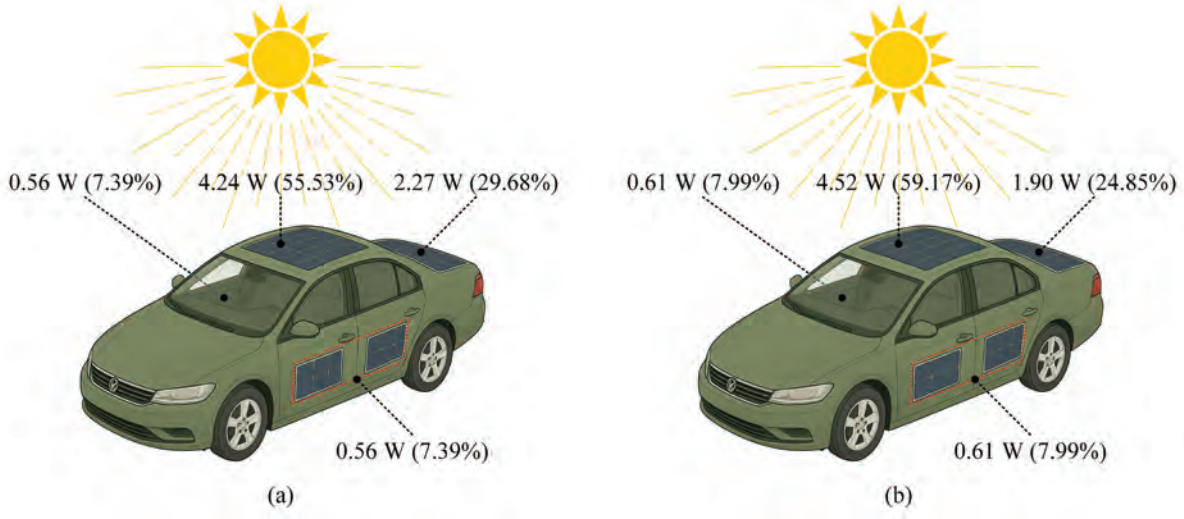


Figure 6. Comparison of the instantaneous power generation of the VIPVs in the scenario where the total instantaneous solar irradiance is 100 W/m² a) present study and (b) created by the authors using data reported in Park et al. [29] (Open Access).

the front hood 26.47 W/m². If the vehicle is equipped with the PVs specified in Table 6, the instantaneous power generated by the VIPVs can be calculated using Equation 1. Figure 6 compares the results of this study with those of the literature.

The results demonstrated the accuracy of the outcomes obtained in the paper, with a reasonable deviation of ±4.83% compared to the outputs of the experimental study in the literature. The paper presents the relative contribution of each integration section to the vehicle's overall solar energy capture. With these findings, for example, solar irradiance data for different slope and azimuth angles (such as doors, front, and rear hood) can be estimated using a single pyranometer data point (such as from the roof). This would significantly simplify the measurement process and provide cost-effectiveness. Instead of installing multiple sensors, the need for extensive data collection infrastructure is reduced, as irradiance for various integration sections can be estimated from a single dataset.

CONCLUSION

With the world moving toward sustainability and energy efficiency, the combination of solar energy and EVs is increasingly important. However, the existing VIPV applications mainly remain on the roof surface, which limits the energy output due to the limited installation area. Thus, one of the key focuses is to investigate the optimal integration locations to increase the energy output of VIPVs, which is critical to increase the PV installation area. This study attempts to overcome this limitation by estimating the solar energy potential of five different vehicle integration sections (roof, front hood, rear hood, left door, and right door) using high-resolution irradiance data obtained for three regions in Türkiye (Mardin, Ankara, and Rize) which are known as high, medium, and low solar radiation zones, respectively. The methodology considers seasonal variability and surface-specific orientation characteristics for an area-independent comparison of irradiance contributions. The results show that the roof (24.22%) and rear hood (22.64%) have slightly lower solar energy potential than the doors (26.67%) and front hood (26.47%). The roof is the most practical place to integrate due to its durability, minimal shading and larger surface area, but the high potential of other sections, especially the doors, points to an opportunity to expand PV coverage in future vehicle designs. The proposed methodology was validated with experimental data from the literature and showed a deviation of ±4.83%, which emphasizes the reliability of the analysis. Additionally, the study proposes a simplified methodology for estimating the irradiance values on multiple vehicle surfaces from a single pyranometer measurement, which offers a significant advantage in terms of data collection efficiency and sensor cost reduction. These results can be directly applied by engineers in the early design stages of solar-assisted EVs to enable more efficient PV surface allocations beyond the traditional roof placements. Moreover, the ability to estimate irradiance for multiple surfaces of a vehicle from a single measurement source provides practical advantages in terms of sensor infrastructure costs for vehicle prototyping and testing. This study provides a quantitative basis for policymakers and sustainability planners to advocate for regulations or incentives promoting multi-surface solar integration in vehicles, particularly in areas with varying solar conditions, such as Türkiye.

NOMENCLATURE

Abbreviations

CO_2	Carbon Dioxide
EV	Electric Vehicle
PV	Photovoltaic
PVGIS	Photovoltaic Geographical Information System
VIPV	Vehicle-Integrated Photovoltaic

Symbols

A_{PV}	Area of the photovoltaic panel (m^2)
G	Solar irradiance (W/m^2)
η	Efficiency of the photovoltaic panel (%)
P_{PV}	Power output of a photovoltaic panel (W)
P_n	Ratio of irradiance received by surface n to total irradiance from all surfaces (%)
n	Subscript denoting surface type (roof, front hood, rear hood, left door, right door)
G^t	Total solar irradiance received by all photovoltaic surfaces on the vehicle during the day (W/m^2)
G_n^i	Total solar irradiance received by the surface n at the i-th hour (W/m^2)
G_n^t	Total solar irradiance received by the surface n during the day (W/m^2)

AUTHORSHIP CONTRIBUTIONS

Authors equally contributed to this work.

DATA AVAILABILITY STATEMENT

The authors confirm that the data that supports the findings of this study are available within the article. Raw data that support the finding of this study are available from the corresponding author, upon reasonable request.

CONFLICT OF INTEREST

The authors declared no potential conflicts of interest with respect to the research, authorship, and/or publication of this article.

ETHICS

There are no ethical issues with the publication of this manuscript.

STATEMENT ON THE USE OF ARTIFICIAL INTELLIGENCE

Artificial intelligence was not used in the preparation of the article.

REFERENCES

[1] Gholami A, Amer M, Zandi M, Ghoachanı RG. Dust accumulation on photovoltaic modules: A review on the effective parameters. Sigma J Eng Nat Sci 2021;39:45–57.

[2] Sunil Kumar K, Muniamuthu S, Salunkhe S, Cep R, Abouel Nasr E. In-situ analysis on drop in thermal performance of wind turbine gearbox system: global challenges and sustainable ideas. Eng Res Express 2025;7:015556. [CrossRef]

[3] Agıralıoglu N, Erıs E, Andıc G, Cıgızoglu HK, Coskun HG, Yılmaz L, et al. Practical methods for the estimation of hydroelectric power potential of poorly gauged basins. Sigma J Eng Nat Sci 2017;35:347–358.

[4] Rashid MH. Alternative energy in power electronics. Butterworth-Heinemann; 2014.

[5] CO_2 emissions by fuel 2024. Available at: https://ourworldindata.org/emissions-by-fuel. Accessed December 12, 2024.

[6] Data supplement to the Global Carbon Budget 2024. Available at: https://www.icos-cp.eu/science-and-impact/global-carbon-budget/2024. Accessed December 12, 2024.

[7] Awogbemi O, Kallon DV Von, Kumar KS. Contributions of artificial intelligence and digitization in achieving clean and affordable energy. Intell Syst with Appl 2024;22:200389. [CrossRef]

[8] Energy Outlook 2024. Available at: https://www.bp.com/en/global/corporate/energy-economics/energy-outlook.html. Accessed December 12, 2024.

[9] Guangul FM, Chala GT. Solar Energy as Renewable Energy Source: SWOT Analysis. 2019 4th MEC Int. Conf. Big Data Smart City, IEEE; 2019, p. 1–5. [CrossRef]

[10] Renewable capacity statistics 2024. Available at: https://www.irena.org/Publications/2024/Mar/Renewable-capacity-statistics-2024. Accessed December 12, 2024.

[11] Güngör O, Yüksek Hİ. Modeling of boost and CUK converters and comparison of their performance in MPPT. Sigma J Eng Nat Sci 2020;11:83–101.

[12] Skandalos N, Karamanis D. An optimization approach to photovoltaic building integration towards low energy buildings in different climate zones. Appl Energy 2021;295:117017. [CrossRef]

[13] Liu W, Liu L, Guan C, Zhang F, Li M, Lv H, et al. A novel agricultural photovoltaic system based on solar spectrum separation. Sol Energy 2018;162:84–94. [CrossRef]

[14] Sutopo W, Mardikaningsih IS, Zakaria R, Ali A. A Model to Improve the Implementation Standards of Street Lighting Based on Solar Energy: A Case Study. Energies 2020;13:630. [CrossRef]

[15] Al-Yasiri Q, Szabó M, Arıcı M. A review on solar-powered cooling and air-conditioning systems for building applications. Energy Reports 2022;8:2888–2907. [CrossRef]

[16] Salameh T, Assad MEH, Tawalbeh M, Ghenai C, Merabet A, Öztop HF. Analysis of cooling load on commercial building in UAE climate using building integrated photovoltaic façade system. Sol Energy 2020;199:617–629. [CrossRef]

[17] Centeno Brito M, Santos T, Moura F, Pera D, Rocha J. Urban solar potential for vehicle integrated photovoltaics. Transp Res Part D Transp Environ 2021;94:102810. [CrossRef]
[18] Araki K, Ota Y, Yamaguchi M. Measurement and Modeling of 3D Solar Irradiance for Vehicle-Integrated Photovoltaic. Appl Sci 2020;10:872. [CrossRef]
[19] Heinrich M, Kutter C, Basler F, Mittag M, Alanis LE, Eberlein D, et al. Potential and challenges of vehicle integrated photovoltaics for passenger cars. Present. 37th Eur. PV Sol. Energy Conf. Exhib, vol. 7, 2020, p. 4229. [CroosRef]
[20] Solar Vehicle Market Size 2020. Available at: https://www.fortunebusinessinsights.com/solar-vehicle-market-104333. Accessed December 12, 2024.
[21] The Benefits of Powering Your EV with Solar Energy 2023. Available at: https://www.energy.gov/eere/solar/articles/benefits-powering-your-ev-solar-energy. Accessed December 12, 2024.
[22] Sagaria S, Duarte G, Neves D, Baptista P. Photovoltaic integrated electric vehicles: Assessment of synergies between solar energy, vehicle types and usage patterns. J Clean Prod 2022;348:131402. [CrossRef]
[23] Kanz O, Reinders A, May J, Ding K. Environmental impacts of integrated photovoltaic modules in light utility electric vehicles. Energies 2020;13:5120. [CrossRef]
[24] Hoth P, Heide L, Grahle A, Göhlich D. Vehicle-integrated photovoltaics-a case study for Berlin. World Electr Veh J 2024;15:113. [CrossRef]
[25] Parlak BO, Yavasoglu HA. Assessment of vehicle-integrated photovoltaics: a financial and environmental perspective. Sustain Energy Technol Assessments 2024;72:104042. [CrossRef]
[26] Tiano FA, Rizzo G, Marino M, Monetti A. Evaluation of the potential of solar photovoltaic panels installed on vehicle body including temperature effect on efficiency. ETransportation 2020;5:100067. [CrossRef]
[27] Peibst R, Fischer H, Brunner M, Schießl A, Wöhe S, Wecker R, et al. Demonstration of feeding vehicle-integrated photovoltaic-converted energy into the high-voltage on-board network of practical light commercial vehicles for range extension. Sol RRL 2022;6:2100516. [CrossRef]
[28] Wetzel G, Salomon L, Krügener J, Bredemeier D, Peibst R. High time resolution measurement of solar irradiance onto driving car body for vehicle integrated photovoltaics. Prog Photovoltaics Res Appl 2022;30:543–551. [CrossRef]
[29] Park C, Park H, Jeon H, Choi K, Suh J. Evaluation and Validation of Photovoltaic Potential Based on Time and Pathway of Solar-Powered Electric Vehicle. Appl Sci 2023;13:1025. [CrossRef]
[30] Parlak BO, Yavasoglu HA, Ozcan HG. In-depth analysis of battery life enhancement in solar-assisted fuel-cell range-extender vehicles. Int J Hydrogen Energy 2024;67:1033–1043. [CrossRef]
[31] Global EV Outlook 2024. Available at: https://www.iea.org/reports/global-ev-outlook-2024. Accessed December 12, 2024.
[32] Mallon K, Assadian F, Fu B. Analysis of on-board photovoltaics for a battery electric bus and their impact on battery lifespan. Energies 2017;10:943. [CrossRef]
[33] Kronthaler L, Maturi L, Moser D, Alberti L. Vehicle-integrated photovoltaic (ViPV) systems: energy production, diesel equivalent, payback time; an assessment screening for trucks and busses. 2014 Ninth Int. Conf. Ecol. Veh. Renew. Energies, IEEE; 2014, p. 1–8. [CrossRef]
[34] Yamaguchi M, Nakamura K, Ozaki R, Kojima N, Ohshita Y, Masuda T, et al. Analysis for the potential of high-efficiency and low-cost vehicle-integrated photovoltaics. Sol RRL 2023;7:2200556. [CrossRef]
[35] Diahovchenko I, Petrichenko L, Borzenkov I, Kolcun M. Application of photovoltaic panels in electric vehicles to enhance the range. Heliyon 2022;8:e12425. [CrossRef]
[36] Commault B, Duigou T, Maneval V, Gaume J, Chabuel F, Voroshazi E. Overview and Perspectives for Vehicle-Integrated Photovoltaics. Appl Sci 2021;11:11598. [CrossRef]
[37] Talebizadeh P, Mehrabian MA, Abdolzadeh M. Prediction of the optimum slope and surface azimuth angles using the Genetic Algorithm. Energy Build 2011;43:2998–3005. [CrossRef]
[38] Ota Y, Masuda T, Araki K, Yamaguchi M. Curve-correction factor for characterization of the output of a three-dimensional curved photovoltaic module on a car roof. Coatings 2018;8:432. [CrossRef]
[39] Myong SY, Park Y-C, Jeon SW. Performance of Si-based PV rooftop systems operated under distinct four seasons. Renew Energy 2015;81:482–489. [CrossRef]
[40] Kadioğlu M. Trends in surface air temperature data over Turkey. Int J Climatol 1997;17:511–520. [CrossRef]
[41] Kadioğlu M. Regional variability of seasonal precipitation over Turkey. Int J Climatol 2000;20:1743–1760. [CrossRef]
[42] Nikitidou E, Kazantzidis A, Tzoumanikas P, Salamalikis V, Bais AF. Retrieval of surface solar irradiance, based on satellite-derived cloud information, in Greece. Energy 2015;90:776–783. [CrossRef]
[43] Teke A, Yıldırım HB. Estimating the monthly global solar radiation for Eastern Mediterranean Region. Energy Convers Manag 2014;87:628–635. [CrossRef]
[44] Solar Energy Potential Atlas 2024. Available at: https://gepa.enerji.gov.tr/. Accessed December 12, 2024.
[45] Biomass 2024. Available at: https://enerji.gov.tr/eigm-renewable-energy-resources-biomass. Accessed December 12, 2024.

[46] Photovoltaic Geographical Information System (PVGIS) 2024. Available at: https://re.jrc.ec.europa.eu/pvg_tools/en/. Accessed December 12, 2024.

[47] PVGIS data sources & calculation methods 2024. Available at: https://joint-research-centre.ec.europa.eu/photovoltaic-geographical-information-system-pvgis/getting-started-pvgis/pvgis-data-sources-calculation-methods_en. Accessed December 12, 2024.

[48] Araki K, Ota Y, Lee K-H, Yamada N, Yamaguchi M. Curve Correction of the energy yield by flexible photovoltaics for VIPV and BIPV applications using a simple correction factor. 2019 IEEE 46th Photovolt. Spec. Conf., IEEE; 2019, p. 1584–1591. [CrossRef]

Sigma J Eng Nat Sci, Vol. 44, No. 4, pp. 2837–2855, August, 2026

Sigma Journal of Engineering and Natural Sciences
Web page info: https://sigma.yildiz.edu.tr
DOI: 10.14744/sigma.2026.2130

Research Article

Innovative approaches and practical experiences: Post-disaster reconstruction with adhocratic architecture

Tuğba ERDİL DİNÇEL[1,*]

[1]*Department of Interior Architecture and Environmental Design, Faculty of Art and Design, Antalya Belek University, Antalya, 34810, Türkiye*

ARTICLE INFO

Article history
Received: 25 September 2024
Revised: 13 February 2025
Accepted: 27 May 2025

Keywords:
Adam-Enhanced; Adhocratic; Fuzzy Algorithm; Model Predictive Control (MPC); Post Disaster; Preference Ranking Organization Method of Enrichment Evaluation (PROMTHEE); Probability Graphics Model (PGM); Technique for Order of Preference by Similarity to Ideal Solution (TOPSIS)

ABSTRACT

Reconstruction after a disaster is essential to the reconstruction of communities that have been ravaged by either man-made or natural disasters. Errors in data calibration persist even as issues and challenges with planning reconstruction techniques are becoming more widely acknowledged. This study examines methods and techniques for creating resilient societies and reconstructing them following such occurrences in order to get around this restriction. Adhocratic Architecture effectively improves the performance of the post-disaster reconstruction process. Initially assessment and data collection is used and to analyze the extent of damage, the availability of resources. Then Fuzzy logic algorithm used for feature extraction. After that we use Probability Graphics Models (PGMs) and Bayesian networks for analyzing the gathered data. subsequently Weakly Supplied training methods for classifying the general tags then Utilizing the Adam-Enhanced Squeeze and When a disaster strikes, the Excitation High-Resolution Network (SEHRNET) improves the precision of classifying structural damages. For balanced decision-making, the Preference Ranking Organization Method of Enrichment Evaluation (TOPSIS-PROMTHEE) technique and the Order of Preference by Similarity to Ideal Solution technique are utilized. Lastly, we employ Multi-time Stepping Rolling with Model Predictive Control (MPC) as a feedback loop to monitor the process. The proposed model is addressed utilizing several comparison metrics such as Accuracy, F1-score, Precision, Acceleration.

Cite this article as: Erdil Dinçel T. Innovative approaches and practical experiences: Post-disaster reconstruction with adhocratic architecture. Sigma J Eng Nat Sci 2026;44(4):2837–2855.

INTRODUCTION

Over the past few decades, there has been a dramatic increase in the frequency, intensity, and severity of both natural and man-made catastrophes, such as hurricanes, earthquakes, and huge floods [1]. The built environment, the economy, and society have all suffered short- and long-term consequences as a result of these occurrences [2]. The susceptibility of many countries to natural disasters has been highlighted by recent events [3]. For example, Gorleston's disastrous floods left the city's infrastructure severely and permanently damaged.

***Corresponding author.**
*E-mail address: tugba.erdildincel@belek.edu.tr

This paper was recommended for publication in revised form by Editor-in-Chief Ahmet Selim Dalkilic

Published by Yıldız Technical University Press, İstanbul, Turkey
© Author. This is an open access article under the CC BY-NC license (http://creativecommons.org/licenses/by-nc/4.0/).

In addition, cities are increasingly vulnerable to the direct consequences of natural disasters like floods due to population development and rising demand for infrastructure and structures [4,5]. Infrastructures can be disrupted by both natural and man-made disasters [6], even if they are built to withstand hazards. Although it is impossible to completely forecast hazards [7], one can mitigate their consequences by improving emergency response times and limiting the infrastructure's susceptibility. The resilience of infrastructure to damage and return to its original state has become more important in the context of risk management. Many academics have studied a variety of resilience tactics to lower the risk of disasters and assess the recovery period after calamitous incidents.

One of the most critical challenges in post-disaster reconstruction is the inaccurate assessment of damage and the difficulty in processing large amounts of data under uncertain conditions. Many traditional approaches rely on manually annotated datasets, which introduce errors due to subjective interpretations. Moreover, the decision-making process in reconstruction planning lacks a comprehensive framework that balances short-term and long-term recovery efforts.

Similar issues, including the damage from the most recent earthquake, have been documented recently all around the world. Consequently, a number of organizations are putting more pressure on researchers studying disaster management to create practical plans for building resilient cities [8]. The construction industry frequently provides a range of vital services in the wake of a disaster, such as building public infrastructure and temporary housing in the early aftermath [3]. However, one of the key problems that arise in disaster recovery is the lack of standardized methodologies for post-disaster assessment and classification of damages. Humanitarian organizations cannot choose and begin all possible reconstruction after a disaster due to a lack of resources [1]. Tasks Reconstruction current conditions, long-term objectives, and numerous other crucial elements Based on their primary strategy and overarching objectives, humanitarian organizations ought to pick post-disaster programs according to a suitable model [9]. Considering the restrictions and considerations of comprehensive and effective criteria, in addition to internal and environmental variables.

In this context, this study proposes an adhocracy architecture to enhance the accuracy of post-disaster construction activities by leveraging machine learning, Bayesian networks, and fuzzy logic. It thereby aims for a twofold advancement: automating damage classification and optimizing decision-making processes through a structured feedback loop. Managers may now overcome the challenges of project selection with the help of numerous techniques. To get a more reliable and accurate result when choosing the best project, it is essential to first precisely define the context of analysis and then use an efficient tool to analyze criteria that are at odds with the strategic goals of the humanitarian organization. In multi-criteria decision-making (MCDM) systems, the fundamental issue concerns how the final decision is reached. This issue is often approached from the reverse perspective; that is, following a decision, it is necessary to examine the choices made via the MCDM method and provide a fair basis for that decision [1]. Although priority is given to the most important projects, there is strong evidence that incorrect choices negatively impact the effectiveness of many post-disaster recovery efforts [3]. The primary procurement strategies currently employed in reconstruction projects, as well as the key challenges encountered in post-disaster reconstruction initiatives, have been identified and documented [4]. Rebuilding transportation infrastructure following a natural disaster is generally a highly challenging process [10].

This study presents a creative and effective method by integrating various analytical and computational techniques to ensure a more resilient and adaptable reconstruction process.

The accuracy of damage detection is enhanced through fuzzy logic-based feature extraction.

Bayesian networks are employed to probabilistically model uncertainties in damage classification.

- An Adam-enhanced SEHRNET deep learning framework has been developed for use with high-resolution remote sensing imagery.
- A TOPSIS-PROMETHEE-based method is utilized to optimize the decision-making process.
- A Model Predictive Control (MPC) feedback loop enables real-time adjustments through continuous assessment.

In terms of biomimicry, parasitic architecture mimics the course that parasitism takes in nature. Furthermore, parasitism is acknowledged as a symbiotic lifeform [11]. Adhocracy is a type of organizational structure that is very adaptable, loosely connected, and frequently changed. Related Topics: public administration organization [12,13].

The process of reconstructing transport infrastructures after a natural event is a challenging endeavour generally post disaster architecture refers to the design and construction of structures as well as communities to aid in the recovery and rebuilding efforts following a disaster [14]. This might encompass both temporary and permanent constructions, as well as the restoration and repair of existing structures (see also Aziminezhad and Taherkhani [15] on BIM for deconstruction) The major activities in the post disaster phase include: Rehabilitation, Reconstruction and Recovery. Disaster affected communities will be made resilient and able to return to normalcy through these activities [8]. Searching for an alternative recovery condition for disasters can lead to the term disaster relief architecture. An aspect of architecture that is specifically focused on biopolitics is approaches that resemble nature. Currently, one of these biopolitical strategies is recognized as parasitic architecture [16, 17]. Effective disaster response after a natural disaster, such as an earthquake or hurricane, depends on

conducting a thorough and in-depth damage assessment of lifeline infrastructure. There has been a dramatic rise in the use of various tools for this in recent years [18].

Satellites, drone photos, LIDAR scans, water level sensors, structural strain gauges, and other instruments and datasets are examples of these. The goals, the accuracy of the data gathered, and the resources needed for data processing and gathering vary between various instruments. All too frequently, architects produce design solutions for post-disaster rehabilitation in developing nations with little understanding of the environments in which those solutions are expected to function. Reconstruction in the aftermath of a tragedy is complicated and uneven [19]. Language barriers, lack of resources, transportation challenges, rising building material costs, corruption in the distribution of aid funds and resources, and the challenge for architects to adhere to the specific socioeconomic and cultural norms of each community are just a few of the problems. In our research we used in this type of technique. To ensure balanced decision-making in the post-disaster reconstruction process we propose the Method for Sorting Preferences According to Likeness to Ideal Solution (TOPSIS-PROMETHEE) The Enrichment Evaluation Method of Preference Ranking Organization with Simulated Annealing method Finally, we utilize a feedback loop to monitor and feedback to the classifier and decision-making method to reduce the demands.

MOTIVATION AND OBJECTION

The primary challenge of the existing methods in post-disaster reconstruction lies in their inability to accurately assess damages, classify disaster zones, and prioritize reconstruction activities efficiently.

- **Inaccurate assessment:** Many existing methods face difficulty in dividing and data calibrating which leads to inaccurate assessment of disaster damage.
- **Short-term focus:** The existing approaches largely concentrate on short-term recovery rather than taking into consideration long-term reconstruction planning. This leads to a decrease in the efficacy of decision-making processes and has a significant influence on total disaster recovery and rebuilding plans.
- **Issue of categorization:** It is difficult to categorize building damage due to the poor accuracy of the suggested classification techniques, which is further complicated by the limited amount of imaging data that is available to the public for damaged buildings.
- **Impact of relief operations:** The growth in the need for relief, in conjunction with the higher rates of unmet demand, worries about the environment, and costs related to emergency situations, leads to a considerable deterioration in the overall performance of the system.

The primary objective of this research is to enhance the reconstruction process after a natural disaster using Adhocratic Architecture. The following are the specific objectives of the research:

- To implement an integrated approach for damage classification and data calibration.
- To establish a robust machine learning model that reduces manual annotation requirements.
- To optimize decision-making by considering both short-term and long-term post-disaster recovery strategies.
- To introduce a novel categorization method for multi-level building damage assessment.
- To develop a real-time monitoring framework that enhances reconstruction accuracy and responsiveness.

Research Contribution

This study makes significant contributions to post-disaster reconstruction through the following innovations:

- To effectively process and extract the features from the collected data we propose the Probabilistic Graphical Models (PGMs) with Bayesian networks and fuzzy logic techniques.
- Utilizing the weakly supervised learning technique which effectively reduces the manual annotation of complex labels, in remote sensing scenarios.
- To implement the Adam optimization algorithm, which offers efficient gradient-based optimization, coupled with the SEHRNET architecture tailored for high-resolution remote sensing imagery, the methodology enhances the precision and reliability of damage classification.
- Using a feedback method known as Multiple steps Rolling with Model Predictive Control (MPC). This method allows for watching things as they happen and making decisions quickly, so help can be adjusted in a timely way.
- Integrates TOPSIS-PROMETHEE with Simulated Annealing to ensure comprehensive and balanced decision-making in post-disaster scenarios.

Literature Survey

This segment encapsulates and analyzes the core research inquiries tackled by earlier investigations. Current studies predominantly concentrate on singular elements of the post-disaster recovery process; yet, there is an absence of a holistic framework that incorporates processes like damage evaluation, decision-making, and resource distribution. Our research seeks to fill this need by introducing a decision support system that integrates human contributions with artificial intelligence to enhance post-disaster reconstruction initiatives.

A research conducted by Cremen et al. [5] suggested the application of Bayesian linear regression, utilizing a probabilistic modeling approach, to forecast and assess business growth and recovery. The framework evaluates four essential attributes related to a company's restoration and normalization post-disaster: the length of operational disruption, the schedule for revenue recuperation, and indicators pertaining to customer engagement and workforce retention. This research predominantly emphasizes

financial recuperation while neglecting the essential element of physical infrastructure resilience in post-disaster contexts. Our research tackles this constraint by combining infrastructure damage evaluation with probabilistic modeling to establish a comprehensive recovery strategy [20].

A study by Calle Müller and ElZomor [21] introduced two innovative approaches to address the difficulties encountered in low-income regions after a disaster. The aim of this research was to promote upward social mobility and enhance learning efficacy within the community by employing educational resources and techniques. Nonetheless, these regions continue to be exceedingly susceptible to natural calamities owing to constrained financial means, elevated poverty rates, and the existence of informal housing. The research in focus emphasizes socioeconomic weaknesses but fails to provide a structured method for incorporating disaster resilience strategies into urban development. Our study complements this by developing a decision-support system that incorporates both socioeconomic and infrastructural resilience. In the work of Zhang et al. [22], a method was proposed to determine hazardous gathering regions and evaluate the areas with the highest concentration of earthquake victims. The study assessed building damage conditions and analyzed geographical features by mapping casualty distribution and employing grid data for hotspot evaluation and spatial autocorrelation analysis. While this research provides valuable insights into damage distribution, it lacks an adaptive feedback mechanism for real-time modifications. In our methodologies, we utilize a feedback mechanism referred to as Model Predictive Control (MPC) to continually modify resource distributions and damage evaluations over time [20]. Research by Zhang et al. [22] indicates that fluctuations in ground motion were overlooked in the assessment of potential building damage. This exclusion may result in considerable inaccuracies in damage assessment, especially when the research zone includes an urban or metropolitan area. To improve precision in extensive disaster evaluations, our research integrates an AI-driven remote sensing analysis that continuously adjusts damage forecasts utilizing real-time seismic and ground motion information [23]. A study by Zokaee et al. [10] introduced a resilience-focused strategy for site selection and routing that leverages public-private partnerships to enhance post-disaster reconstruction supply chain (PDRSC) efforts. Although this approach improves logistics and supply chain efficiency, it lacks a structured methodology for integrating real-time disaster response adaptation mechanisms. Our study builds upon this by implementing an optimization model that allows real-time adjustments in supply chain distribution based on updated disaster severity levels [24].

The study by Zokaee et al. [10] assessed the impact of limited resources on rebuilding costs and aimed to minimize the reduction in the efficiency of distribution partnerships. The model's effectiveness was tested using a real-case study. While this study provides a strong cost analysis framework, it does not fully address decision-making complexities under uncertainty. Our research employs a Bayesian probabilistic approach to enhance the decision-making process as disaster conditions evolve. The study by Zokaee et al. [10] explored the possibility of redistributing surplus reconstruction resources between locations via a Temporary Disaster Recovery Warehouse (TRDW) to reduce disaster response times. That study focused on agent-based reinforcement learning for repair team assignment without incorporating real-time adjustments. Our approach is based on integrating a Multi-Step Moving Horizon Model Predictive Control (MPC) strategy to dynamically update repair team assignments in response to evolving real-time damage assessments [20]. In the study by Sun and Zhang [25], an agent-based modeling (ABM) approach was presented to evaluate infrastructure network resilience and propose effective recovery methods following extreme events; however, the study highlighted certain limitations regarding the accuracy and reliability of the infrastructure connectivity model. Our study overcomes these limitations by integrating a graph-based deep learning network to improve prediction accuracy in assessing infrastructure network failures.

The study by Cremen et al. [26] investigated the role of adaptability in corporate recovery processes, noting that such processes can be multi-stage and continuously evolving. However, that study views the recovery process in binary terms—as an "all-or-nothing" phenomenon—an approach that may fail to fully capture long-term corporate performance. Our study employs a fuzzy logic-based dynamic alignment framework to enable a more detailed and continuous examination of the recovery process of companies. The research by Wearing et al. [27] presented an initial examination of the potential role of volunteer tourism in post-disaster recovery processes. The study has addressed the ethical aspects of post-disaster volunteer tourism and proposed an approach that involves stakeholders in the process. While emphasizing the social dimensions of the recovery process, our research further develops this approach by incorporating a participatory decision-making model that enables affected communities to actively make decisions regarding post-disaster planning and resource allocation.

The needs of economically disadvantaged populations were examined in the study by Calle Müller and ElZomor [21], which investigated post-disaster vulnerabilities, essential needs, and the competencies required for temporary employment and housing (TEH). Its emphasis on immediate support leaves scope for a more developed account of long-term recovery. Our study responds by proposing an adaptive framework that brings economic resilience and infrastructure restoration into a shared recovery perspective. Connecting these dimensions provides a basis for examining how short-term interventions might support more durable rehabilitation.

The study by Islam et al. [28] quantitatively examined factors influencing community participation in recovery programs organized by non-profit organizations and government agencies. Community participation and physical damage assessment, however, capture different dimensions of recovery. The physical condition of an affected area cannot, by itself, establish the demographic characteristics or needs of its residents. Reliable differentiation between damaged and intact structures remains a complementary technical requirement. Our study contributes to this aspect of recovery planning by employing probabilistic modelling to improve damage classification, while recognizing that such classifications must be interpreted alongside social information.

The study by Wang et al. [29] explored the use of unmanned aerial vehicles (UAVs) in post-disaster recovery, proposing a framework that draws on the spare processing capacity of unmanned ground vehicles (UGVs) to support computationally demanding UAV tasks. This arrangement offers a practical means of sharing computing resources, although its scalability across extensive disaster zones requires further consideration. Building on this approach, our study proposes AI-based task allocation within coordinated UAV–UGV operations to improve the efficiency of disaster response. The central concern is how computational resources can be assigned as operational demands change.

A related challenge concerns the continuity of interconnected infrastructure. The study by Wei et al. [30] developed a multi-agent integrated energy system (IES) that incorporates road networks into post-disaster recovery planning. Although it established operational indicators and the system topology, the treatment of cascading failures associated with climate-related disasters remained limited. Our proposed model addresses this issue through real-time monitoring and predictive risk analysis, with the aim of strengthening resilience to widespread outages. This extends the focus of recovery planning to the dependencies through which disruption can spread between infrastructure systems.

Resource allocation introduces a further set of trade-offs [31]. The recovery framework presented by Ransikarbum and Mason [23] used an evolutionary algorithm to address two objectives simultaneously. Its mixed-integer linear programming formulation sought to balance financial considerations with fairness and equity during reconstruction. This perspective is relevant because recovery priorities involve decisions about both the use of limited funds and the distribution of assistance. Technical assessments therefore need to be considered alongside the consequences of those decisions for affected communities.

However, this method does not adequately account for transportation network issues that delay reconstruction efforts. Our study addresses this gap by optimizing the deployment of repair crews and integrating dynamic traffic flow models to minimize delays in the post-disaster recovery process. Table 1 presents a general summary of the literature review conducted [10-41].

Table 1. An overview of the literature review

Ref.	Objective	The method or the model utilized the algorithm	Restrictions
[10]	With cooperation from the public and private sectors, this study suggests creating a resilience location-routing model to support the Post-Disaster Reconstruction Supply Chain (PDRSC) programs.	Supply chain during post-disaster reconstruction: An empirical optimization study	• Unneeded rebuilding resources
[18]	Displacement Damage Analysis Using Remote Sensing Data	SAM-VQA system for post-disaster damage evaluation using remote sensing photographs.	• It is very expensive method.
[20]	Emergency Recovery During a Disaster in Distribution System Applying Model Predictive Control	Rolling Optimization Strategy with Multiple Time Steps	• Plan losing optimality • Recovery period is lengthy
[21]	The objective of a comprehensive and enduring plan construction trade education	Origami infrastructure and construction trade education	• High levels of poverty • Informal buildings
[22]	building damage and analysis of geographical features	Spatial autocorrelation analysis	• Ground input was not considered
[23]	The hybrid technique, referred to as Hybrid NSGA-II (HNSGA-II), depends on the non-dominated sequencing genetic algorithm-II	Evolutionary formula.	• Issues in damage for the roads,

Table 1. An overview of the literature review

Ref.	Objective	The method or the model utilized the algorithm	Restrictions
[24]	This research presents a novel ("N-BBB") theoretical method for empirical recovery analysis after earthquakes in different countries	Building Back Better" and Post-Earthquake Needs for Recovery and Reconstruction	• Did not consider long-term reconstruction planning
[25]	Post-Disaster unique methodological framework that can evaluate infrastructure network	Reinforcement learning with ABM, methodological framework	• Limited. reliability
[26]	This project aimed after earthquake seismic events an impact on company recovery.	Modelling Post-Earthquake Business Recovery Time: An Analytical Framework.	• Not accurately long-term performance
[27]	The aim of this research has been to offer a first exploratory investigation into the potential role that volunteer tourism may play in the aftermath of a catastrophe.	Engaging volunteer tourism in post-disaster recovery	• Inefficient
[28]	Factors influencing community participation in recovery from disaster managed by non-profit and government organizations using quantitative analysis	That five factors govern decision-making participation and eleven main factors govern community engagement in sustainable disaster recovery programming (SDRP).	• Materials region not entirely correct
[29]	Offloading Cooperative UAV Computation Challenges for Post-disaster Rescue by VFC-Based Technique	Adaptable mobility, unmanned aerial changes the compute task issue into a matching puzzle with both sides.	• Minimize the number of iterations
[30]	Coordinated Method to Post-Disaster Recovery and Assessment for the Integrated Energy, Gas, and Transportation System	Repairing damaged roads wasrecommended, considering various energy sectors' perspectives and the condition of the highways.	• IES to the rising frequency
[32]	Building Damage Detection using Mechanism from Pre- and Post-Disaster Remote Sensing	Siamese neural network	• Difficult to split the damage itself, which leads to errors in data calibration
[33]	Unsupervised domain adaptation applying self-attention to identify post-disaster building degeneration	Unsupervised self-attention domain adaptation "(USADA)	• Accuracy of the proposed classification method is low
[34]	In order to solve the problem, a hybrid global criteria technique that combines a branch-and-bound strategy, expected value, and primal-dual algorithm is developed.	"fuzzy tri-objective bi-level integer"	• The overall percentage of unfulfilled demand and all potential environmental issues
[38]	Post-disaster business recovery	A probabilistic modelling technique for the use of Bayesian linear regression	• Wide range of hazard intensities
[39]	This study was designed to determine whether GEE was useful for recovery analysis and monitoring.	Post-Disaster Recovery Monitoring with Google Earth Engine	• Hard in some situations to discern actual damage and visually separate damaged
[40]	A Framework for Spatial and Temporal Evaluation of Network Disaster Recovery	Such as adaptive reorganization and topology rebuilding, are also included.	• Number of network components impacted by the catastrophe
[41]	The study's goal is to come up with a multi-stage dynamic healing method for distribution networks (DNs) after a disaster.	Multi-phase Dynamic Recovery Plan for Distribution Networks after a Disaster Taking Integrated Transportation and Energy Networks into Account	• Issues within traffic allocations • Transportation system

Problem Statement

The explicit works now in existence, together with methods for monitoring and mapping forest health, are compiled in this area. Additionally, this study offers research solutions for the mentioned issues.

Specific problem definition

Wu et al. [32] to develop a Siamese neural network that is capable of simultaneously localizing and classifying damaged structures. Many attention U-Nets backed by different backbones are the most crucial parts of this network. The following is a list of the issues with certain methods. It is difficult to split the damage itself, which leads to errors in data calibration. Even expert find it challenging extend damage to certain aspects. Additionally, inconsistencies in sensor data and remote sensing imagery further complicate the classification of structural damage, increasing the need for probabilistic calibration methods.

Sarkar [18] proposed the purpose of post-disaster damage assessment based on drone footage, the visual question answering (VQA) framework, specifically supervised attention-based VQA (SAMVQA), is the primary subject of this paper. By offering a VQA dataset and proposing a unique SAM-VQA method for post-disaster damage appraisal utilizing remote sensing images, this work enhances the field of storm assessment. These are the problems with this work: However, their proposed need for human annotation for remote sensing data leads to high time consumption and a very expensive method. To address this limitation, weakly supervised learning is utilized to reduce the dependency on extensive human annotation, making damage classification more efficient and scalable.

Shi et al. [24] suggested a novel ("N-BBB") theoretical method for empirical recovery analysis after earthquakes in different countries. It is based on the global "building back better" (BBB) agreement and an evaluation method for post-disaster needs. Factor analysis proved the model's dependability. The main issues are: the proposed method did not consider long-term reconstruction planning it only focused on short-term recovery which led to reduced decision-making process effectiveness and also affected the disaster recovery and reconstruction plans. To address this gap, our approach integrates a hybrid decision-support system that ensures both short-term emergency response and long-term sustainable recovery strategies.

Li et al. [33] explained an "unsupervised self-attention domain adaptation "(USADA) model as a solution to the previously described difficulty. This strategy would convert instances from the source realm into the desired area in pixel space. Three components make up the proposed USADA: collection GANs (generative adversarial networks),a classifier, and a self-attention module. The problems encountered in those approaches are: the accuracy of the proposed classification method is low so the categorization of building damage is a difficult problem since there is a limited amount of publicly accessible imaging data including damaged structures, and it is difficult to determine the extent of damage based on images simply. To improve classification accuracy, this study incorporates a graph-based deep learning model that enhances feature extraction and damage categorization.

Cao et al. [34] described a "fuzzy tri-objective bi-level integer" program method whose bottom level maximizes the pleasure of enduring persons while the higher-level addresses unmet demand, environmental concerns, and emergency expenses. In order to solve the problem, a hybrid global criteria technique that combines a branch-and-bound strategy, expected value, and primal-dual algorithm is developed. The main issues are: as a result of the rise in the need for relief, the overall SPS decreases significantly while the total missing demand rate, the total amount for possible environmental problems, and the whole amount of emergency expenses all rise. To mitigate this issue, a hybrid optimization framework incorporating stochastic modelling is utilized to balance supply-demand fluctuations and optimize emergency resource allocation. In both instances, it is shown that the fluctuation in the supply and demand does not possess sufficient strength to prevail over the selection of decision modes

Research solutions

To address the problem by putting together probabilistic graph models, Bayesian networks, and fuzzy logic, the problem of separating damage and reducing data calibration can be solved successfully.

Additionally, an AI-enhanced resource allocation system is employed to dynamically prioritize reconstruction efforts based on real-time disaster severity levels and accessibility constraints.

It uses fuzzy logic to pull out features that capture uncertainty and probabilistic graphical models with Bayesian networks to calibrate the data. To make weakly supervised learning easier, it's enough to have labels for object groups that are more general and easier to find at the image level. So, the training network with weakly supervised learning makes it easier for people to label complex labels for remote sensing, which lowers the need for a lot of human labelling during reconstruction after a disaster. o solves this problem, we suggest a mix of TOPSIS-PROMETHEE and a decision-making method based on simulated annealing to make sure that both short- and long-term healing plans are carried out. To get around this problem, we're using Adam-Enhanced SEHRNET to correctly identify the damage to buildings after a disaster. gets around this problem, a feedback system called Multi-time-step Rolling with MPC is being used to help with tracking and making decisions in real time. This good method makes sure that the relief efforts are responsive, flexible, and able to meet the changing needs of the communities that were harmed. The Problems are verified to the above solutions

Proposed Work

People usually get back to rebuilding quickly after a natural disaster. The goal of adhocratic architecture is to make the rebuilding process more flexible and quicker after a disaster. As part of this plan, the following important things are done:

- Initial assessment and data collection
- Processing and feature extraction
- Training
- Classification
- Decision-making
- Feedback loop

Initial assessment and data collection

To identify the needs and priorities of the affected community first we conduct the initial assessment. This assessment is used to analyze the extent of damage, the availability of resources, and the population that is most susceptible, based on the collected data. Engaging in communication with many stakeholders [35], including local community members, government officials, non-governmental organization (NGO) representatives, and subject matter experts, to gather information on the challenges encountered throughout the reconstruction process. Hence, the restoration endeavors are guided by the preferences and requirements of those who have been directly impacted by the catastrophe. We are using a disaster dataset from Kaggle, (https://www.kaggle.com/datasets/varpit94/disaster-images-dataset). Figure 1 shows the final methodologies of architecture.

Processing and feature extraction

Once the data-gathering procedure is finished, we progress to analyzing and extracting the characteristics from the dataset related to the disaster zone. A recommended approach involves using a combination of Probability Graphics Models (PGMs) and Bayesian networks for analyzing the gathered data. It's important to use a combination of PGMs with Bayesian networks and foggy logic strategies for processing and extracting features in post-disaster constructions One kind of probabilistic graphical model (GM) is the Bayesian Network (BN). It is also called the Bayesian Belief Network or the Causal Probabilistic Network. It is based on Bayes' theory, which lets you show how a set of variables is likely to be related visually. Subjective probabilities can be used to show the errors in a BN model, which means that the method can be used with experts' knowledge. It is possible to figure out the probability distribution

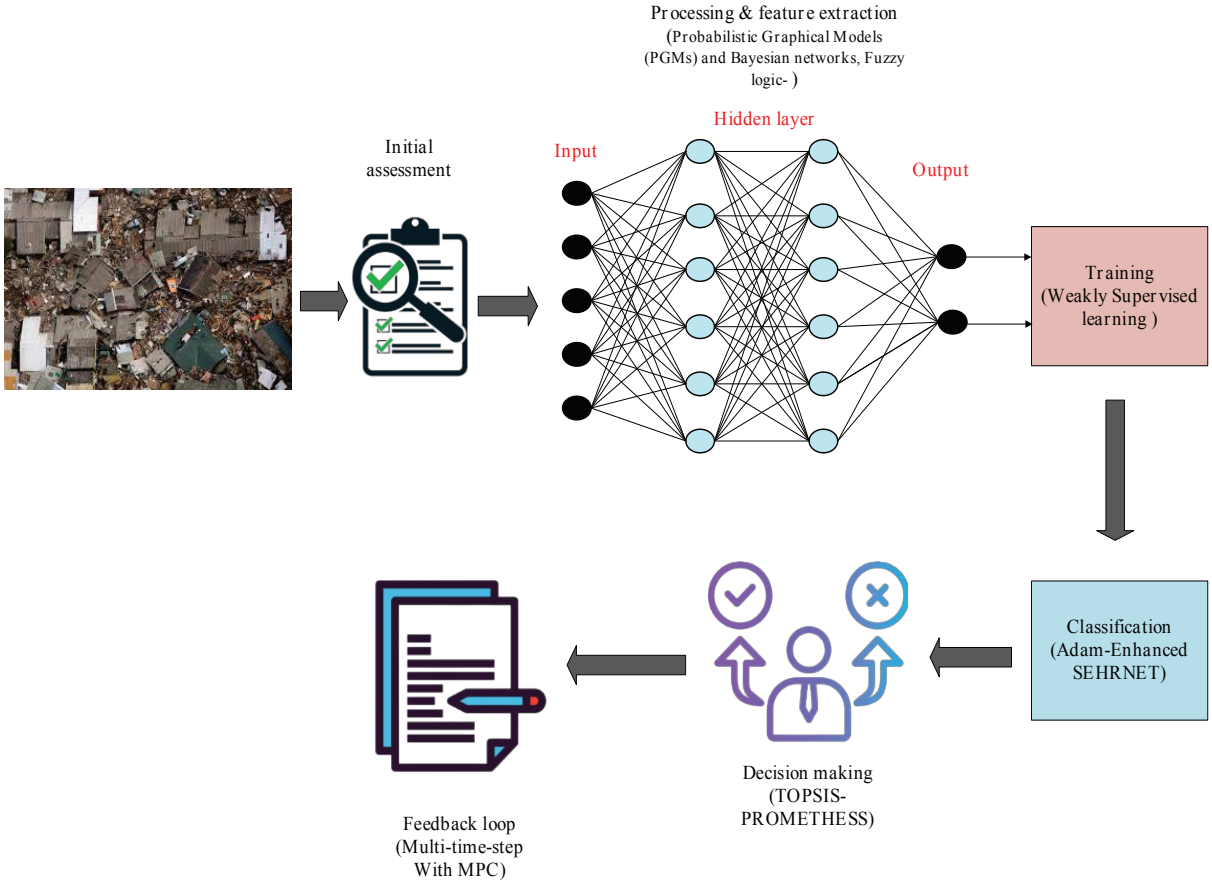


Figure 1. Final proposal architecture.

of variables by using BNs and variables that both quantitative and qualitative data have shown.

- A BN can have variables that are quantitative (low, medium, high) or Boolean (yes, no). collection of random variables that are connected to one another by arrow-shaped linkages is one component of a binary network (BN).
- A list of states that can't happen together for each variable (for example, E, F and G) that describe what could happen.
- A table of probabilities with and without conditions for each kid node and a table of probabilities without conditions for every additional node.

Variable to change. Z, it means that variable Y (the child) depends on variable (the parent). A directed acyclic graph is made up of edges and nodes. Most of the time, Conditional Probabilities Tables (CPTs) are used to show how the factors in a BN are related to each other. These tables show how likely it is for a child node to take on a certain state if its parent node is in a certain state. For variables that are not based on any other variables an unconditional probability table (UPT) replaces the CPT. A particular kind of probabilistic graphical model (GM) is the Bayesian Network (BN). It is also called the Bayesian Belief Network or the Causal Probabilistic Network. It uses Bayes' theorem to show how statistical relationships between a set of variables subjective probabilities can be used to show the errors in a BN model, which means that the method can be used with the knowledge of experts With BNs, one may determine the random distribution of variables depending on variables that have The Bayes theorem, which states that two nodes A (parent) and B (child) have the following relationship, is the fundamental source of inspiration for the BN.

$$P(\frac{C}{D}) = P\left(\frac{D}{C}\right) P(C)P(D) \quad (1)$$

where $P(C/D)$ is the probability of seeing C if Dis is true, $P(D/C)$ is the probability of seeing D if C is true, and $P(C)$ and $P(D)$ are the probability of seeing C and D separately. The probability that C/D will happen is called the posterior probability, and the probability that C will happen is called the prior probability. After a set of links have been used to connect the variables, both unconditional and conditional odds are given. To determine the unconstrained probability (*UPs*) of parent nodes whose states are unknown, the notion of insufficient reasoning is applied. This indicates that a weight of $1/n$ where n is the number of states, is assigned to each fundamental input. One example is if the variable $X1$ has three states: Low (L), Medium (M), and High (H). Then, $P(\text{X1 = K}) = 1/3P\ P(\text{X1 = L}) = 1/3$, and $P(\text{X1 = M}) = 1/3$. You can get an idea of the conditional probabilities (CPs) by skiing experts for their knowledge and teaching them with data that already exists. The procedure can be divided into three parts:

- Putting first parent variables: The first stage involves assigning a weight number to each parent variable in order to determine its relative importance to the child nodes.
- What do combinations mean? By examining the various configurations that the child nodes can take, distinct states are identified for every variable.
- Guessing the chances of different outcomes: The last step is to guess the chances of all the possible outcomes for each set of conditions.

An example is given to help you understand the process better. Take a look at a system that has a kid node called Impacted Area and three further nodes named Extreme weather, urban areas, and mobility and access. Following the first phase of the recommended procedure, variables are arranged according to their impact on the child node. The three states are Extremely Bad (for Extreme Weather), Hard (for Mobility and Access), and Large (for Urban Area). (IAS, IAM, IAL) = (0.9, 0.1, 0) are the conditional probabilities associated with the variable "Impact Area." To determine the whole conditional probability table of the father node based on the various states in which the kid nodes can be in, alternative combinations are employed from the worst-case scenario. From now on, this method will be used to figure out the conditional odds for every node in the DT network. The conditional odds for the DT variable, on the other hand, are found in a different way. The conditional probabilities of the DT are calculated using restoration fragility curves based on the size of the earthquake.

Selection of variables Thirty-one indicators are chosen to create the BN for the DT estimation after a thorough analysis of previous work on important downtime parameters and literature publications. The indicators chosen provide a detailed description of each component of the framework. All indicators identified in the literature have been gathered and subsequently sorted to provide indicators that are mutually exclusive. Variable identification:

- Variable clustering: the variables are grouped into clusters to be properly organized once they have been recognized.
- Variable connection: Using Bayesian parent-child relationships, the variables are connected in the last phase

Training

Weakly supplied training methods are used to teach people how to do harmful rebuilding in the future. These steps make getting ready for classification easier by adding general tags for object types to the picture level. Weakly supervised learning only needs more coarse-grained labels, which are labels for object types at the image level.

Classification

Utilizing the Adam-Enhanced SEHRNET enhances the accuracy of categorizing structural damages in the event of a catastrophe. The objective of this approach is to overcome existing barriers and categorize multi-tiered damages with greater precision. SEHRNet achieves a significant reduction in network parameters while maintaining high accuracy by suppressing useless information and accurately identifying regions of interest. This leads to higher accuracy in aircraft

key point detection and reduces the risk of potential apron conflicts. Our proposed model also improves real-time performance in the key point detection process in Figure 2.

Adam's method involves determining the ratio of the squared moving averages of the gradient ∇ε(τ) to the moving averages of the gradient ∇ε(τ) in order to immediately change the learning rate at each repetition. Specifically, in the (τ+1) the iteration, the moving averages m(τ+1) and the squared moving averages v(τ+1) may be obtained by,

$$\left.\begin{matrix} a(\tau+1) = (1-\beta_1)\nabla\varepsilon(\tau), \\ b(\tau+1) = (1-\beta_2)\nabla\epsilon^2(\tau), \end{matrix}\right\} \quad (2)$$

The exponential decline rate parameters of m and v from the previous iteration of the loop are represented by β1 and β2.

$$\begin{matrix} \hat{a}(\tau+1) = a(\tau+1)/(1-\beta_1), \\ \hat{b}(\tau+1) = \frac{b(\tau+1)}{(1-\beta_2)}, \end{matrix} \quad (3)$$

Update the partial derivative operator ∇μ(τ+1) as follows with the new values for $\hat{a}$(τ+1) and $\hat{b}$(τ+1)

$$\nabla\epsilon(\tau+1)\alpha.\hat{a}_a(\tau+1)/\sqrt{\hat{b}_a(\tau+)} + \varphi \quad (4)$$

Decision-making

In order to successfully manage the difficulty of balancing immediate and long-term rehab measures, we suggest using a hybrid decision-make approach. This method combines the TOPSIS-PROMTHEE technique with Simulated Annealing to provide accurate and sufficient decision-making in situations after a tragedy. An analogy with solid-state physical annealing is employed to propose SA. Kirkpatrick et al. [36] made it popular, and it has since been used to solve numerous challenging combinatorial optimization issues in networks.

The neighbourhood search method, often known as the SA algorithm, is a random process that increases the possibility of local optima and processing time by giving each decision variable an equal chance of changing. Therefore, the following are the benefits of RD optimization:

$$\sum_{i=1}^{L}\sum_{t=1}^{M} lu_i \times (dp_i^t) \quad (5)$$

$$0 \le x_{ij} \le y_{ij} \quad (6)$$

$$\sum_{i=1}^{L}\sum_{j=1}^{L} x_{ij} \le Total \quad (7)$$

The initial RD for the SA algorithm is found in Eqn (7) using the equal division approach. The decision variables are limited to the parameters in X whose values are modifiable according and their quantity is indicated by Rx. There are two stages involved in applying this approach. In the initial stage, every decision variable is raised by the value of aver, which is floor $(Total/(lu \times Lx)) \times lu$, where floor(a) is a function that, up to a certain value, produces the largest integer. The remaining portion of Total is arbitrary allocated to the decision variables in the second phase. The two stages are displayed as. Determine the value of Avex in

- step one; raise each of the choice variables to avex.
- step two; determine the residual.
- step three. *Total - avex* × *L* = *Rem*.

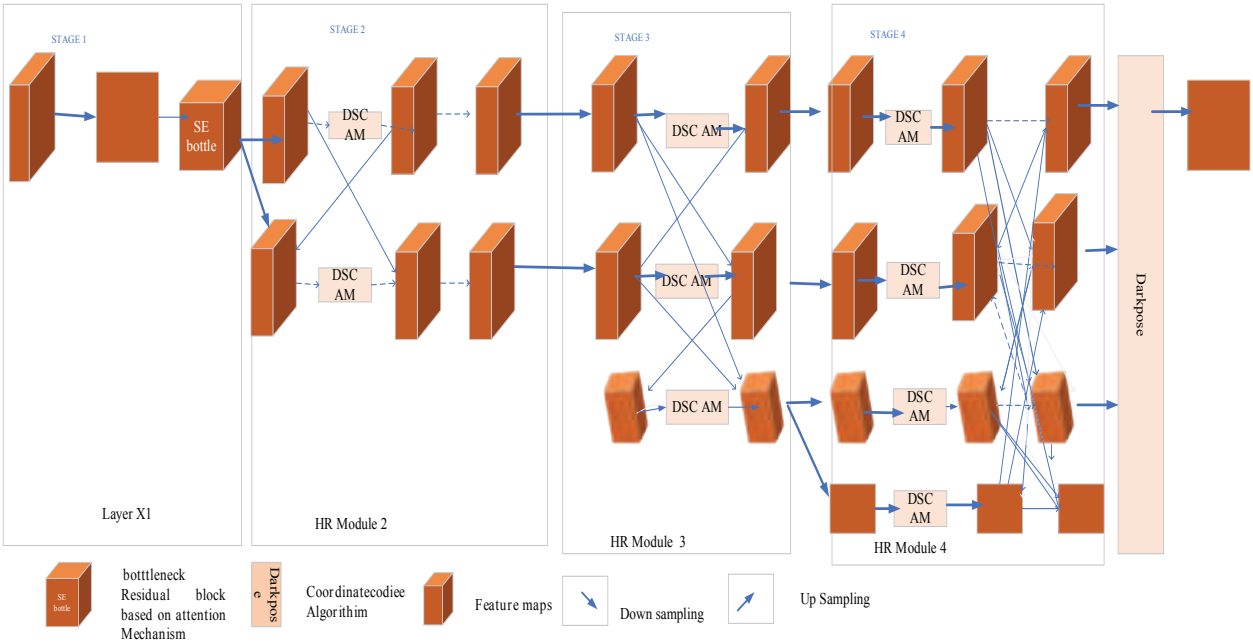


Figure 2. SEHR Net architecture.

- Step 4: Take the current $y = x_ija$ as the initial RD and terminate the procedure if Rem is smaller than not equal to zero.
- Step 5: Choose a decision variable Y_{ij} at random, and if Y_ij. By using the quantitative significance to improve its neighbourhood search, the SA is made better. $S = [L_ij]$ For example, risk i is represented by RIN node i, and its quantitative importance relates to risk i's impact on project risk loss. If a node

$$IP_{lm} = \left(k_1 + \frac{M_{ij}}{\sum_{l=1}^{N}\sum_{m=1}^{N} L_{ij}}\right)/(1+k_1) \quad (8)$$

Where k_1 is constant;

$$IP_{lm}IP_{lm}rand(0,1) \quad (9)$$

more quickly and effectively, the enhanced SA method is used to find the feasible domain of the decision variables, which is represented by Y in the pseudocode in below algorithm. Our pseudocode is a development of the typical SA-related code provided in Eqn [9].

The result of the RIN simulation model is the stable value of total risk loss L under which is called by ob.(Y). The group of RIN nodes and edges that have a quantitative significance is represented by

$$S = \{L_{ij}\} \quad (10)$$

The number of iterations that the neighbourhood search should run at a particular temperature is indicated by the term Iiter. T0 and Tf, respectively, are the starting and finishing temperatures. We may compute the likelihood of adopting a worse solution using the Boltzmann constant, K. The corresponding coefficient relating to the α.

When the temperature drops to or equals Tf, or when the optimal solution is no longer superior than Nnon-improving consecutive times, the algorithm comes to an end.

Pseudocode for Improved SA Algorithm

SA(I_{iter}, Rnon-improving, T_0,T_f, α, k, S)

Begin

Generate an initial solution by the equal division method
Y_{best}=Y; F_Y=obj(Y);F_{best}=F_Y;
$T=T_0$;$R_1=0$;
While *($T>T_f$ & $N_1<R_{non\text{-}improving}$) {*
$I = 0$; $R_1= R_1+1$;
While *(I_{iter}){*
l_1= random(0,1);S
if *($l_1 > 0.5$)*
{Generate a new solution Y' from Y through the improved neighborhood search method with in S;}
else *{ Generate a new solution Y' from Y through the improved neighborhood search method randomly;}*
l_2= random (0,1);
if *[l<exp (-Δ)/(k×T) {Y=Y';F_y=$F_{y'}$;}*
}
if *($F_y \leq F_{best}$){Y_{best}= Y; F_{best} = R_1=0}*
S = s+1;
}
$T = T \times b$;
}

end

Fuzzy Topsail is believed that fuzzy TOPSIS is a suitable approach for handling decision-making issues in a fuzzy setting. This methodology's procedures and formulas are below.

- Adapted with changes from the fuzzy TOPSIS is summed up in the stages that follow. Certain the evaluation criteria's weights.
- Construct the fuzzy decision matrix (~ D) and work out the relative weights of each alternative in relation to the l × m criterion. In this case,
- $\sim yij = l_{ij}m_{ij}n_{ij}$. For i = 1,2…..l and m = 1,2….n.

$$\tilde{D} = \begin{matrix} B_1 \\ B_2 \\ B_m \end{matrix}\begin{bmatrix} y_{11} & y_{12} & y_{ln} \\ y_{21} & y_{22} & y_{2n} \\ y_{m1} & y_{m2} & y_{mn} \end{bmatrix} \quad (11)$$

$$y_{ij} = \frac{1}{q}\left(y^1{}_{ij} + y^2{}_{ij} + \cdots + y^q{}_{ij}\right) \quad (12)$$

$$y^q{}_{ij} = \left(l^q{}_{ij}m^q{}_{ij}n^q{}_{ij}\right) \quad (13)$$

q is the number of responds. $y^q{}_{ij}$; Performance criterion The equation is expressed below,

$$y^q{}_{ij} = \left(l^q{}_{ij}m^q{}_{ij}n^q{}_{ij}\right).; \text{k=1,2…. q.}$$

compute normalized fuzzy matrix value

$$\tilde{P} = [p_{ij}]l \times m \quad (14)$$

$$P_{ij} = \frac{l_{ij}}{cj} + \frac{m_{ij}}{cj} + \frac{n_{ij}}{cj}\,] \quad (15)$$

$$I = 1, 2 \ldots \text{m and } j = 1, 2 \ldots., n$$

Determine the fuzzy decision matrix that is weighted. The normalized values continue to be fuzzy triangles. We use the fuzzy-ANP approach to determine weights. The following formula is used to get the weighted normalized values P_{ij}

$$V_{ij} = \omega i \times P_{ij}; i = 1,2 \ldots. m \text{ and } j = 1,2., \ldots, n \quad (16)$$

$$\tilde{v} = [p_{ij}]mn \quad (17)$$

Determine the optimal fuzzy-positive and fuzzy-negative solutions. The normalized fuzzy-decision matrix's

weights determine $\tilde{v}^+$ and $\tilde{v}$-; $\tilde{v}ij$, which has a normalized positive value, should be $0 \leq \tilde{v}ij \leq 1$. Then, the following formulas are used to get B^+ and B^-

$$B^+ = \tilde{v}1^+, \tilde{v}2^+, \ldots, \tilde{v}n^+ \quad (18)$$

$$B^- = \tilde{v}1^- \tilde{v}2^- \ldots, \tilde{v}n^- \quad (19)$$

Determine the distances d + i and d - i for every alternative (B^+ and B^-) using FPIS and FN IS.

$d_i^+ \sum_{i=1}^n d(\tilde{v}ij, \tilde{v}j^+)$ =i=1,2…, and l and j = 1, 2, ..., n
$d_i^- \sum_{j=1}^n d(\tilde{v}ij, \tilde{v}ij^-)$=i=1,2…and l and j=1, 2……, n

Determine the relative proximity of ideal solutions for i = 1, 2..., m, and $0 \leq q_i \leq 1$ and i = 1,2,…m. The similarity between ideal solutions is resolved by the equation

$$q_i = \mathrm{d}i^-/di^+ + \mathrm{d}i^- \quad (20)$$

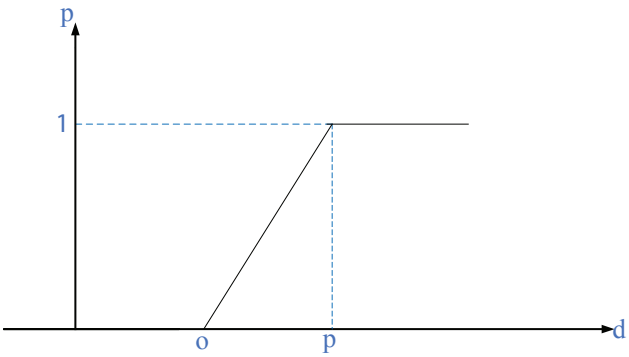


Figure 3. Preference Function in PROMETHEE method.

PROMETHEE is a compromise approach that chooses the optimal choice by utilizing the preference function. It is applied in many different domains. This method often gives solutions and criteria, weights each indicator so that the overall weight equals one, and transforms qualitative data into quantitative indicators.

$$P_{k(b_i,b_j)} = P\left[s_k(b_i, b_j)\right] \quad (21)$$

preference function (b_i, b_j). In this equation S represent the distance. Distance between the two-preference function. The value of preference function shown in this equation below

$$\left[s_k(b_i, b_j)\right] = f_k(b_i) - f_k(b_j) \quad (22)$$

R stands for incomparability with respect to A15. When option A completely outperforms option C in a set of criteria, and option C completely outperforms option D in a set of criteria, we are unable to decide which option is best.

The degree to which option A is superior to option D cannot be inferred from the aforementioned relationships. The PROMETHEEE approach uses preference functions to get rid of this problem and control how much the options are superior. Based on a number of preference functions, the degree of preference improves with the size of the difference between the two possibilities in a criterion. If the criterion is positive, then there is a positive difference between the two options with s_j(c, d). Figure 3; Represent the Preference function of PROMETHEE Method.

$$s_j(\mathrm{c}, \mathrm{d}) = g_j(\mathrm{c}) - g_j(\mathrm{d}) \quad (23)$$

- The degree of preference for an over c according to criterion denoted (c d). Figure 4.

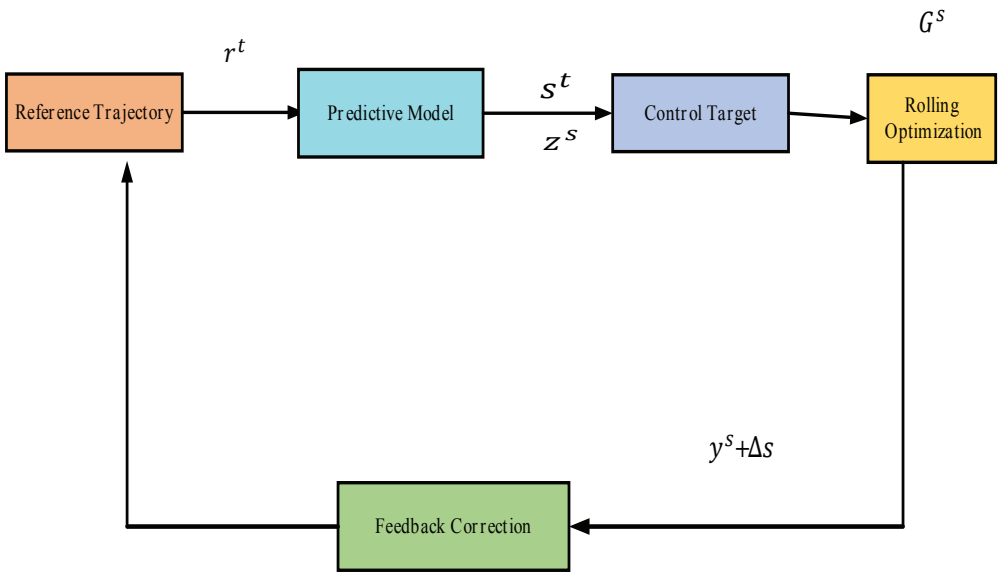


Figure 4. Basic flowchart for MPC.

- d or d_j(c, d) is the distance, according to criteria j, between c and d.
- The midway between r and s, the preference threshold, and the indifference threshold is symbolized by the symbols o, p, and s, respectively.

$$\pi(c,d) = \sum_{j=1}^{n} o_{j(c,d)\omega_j} / \sum_{j=1}^{n} o_j(\mathrm{c,d})\omega_j / \sum_{j=1}^{n} \omega_j \quad (24)$$

$$\pi(d,c) = \sum_{j=1}^{n} o_{j(d,c)\omega_j / \sum_{j=1}^{n} \omega_j} \quad (25)$$

$$\pi(c,c) = 0 \quad (26)$$

$$0 \le \pi(c,d) \le 1 \quad (27)$$

$$0 \le \pi(c,d) + \pi(d,c) \le 1 \quad (28)$$

Compute implied dominance flows in step two. The implicit dominance flows, both positive and negative, for each choice are computed in this particular section. The following equation shows the positive implicit dominie.

$$\varphi^{+}(\mathrm{c}) = \frac{1}{m} - \quad 1 \sum_{\substack{y \in B \\ y \neq b}} \pi(\mathrm{c,x}) \quad (29)$$

demonstrates the negative implicit dominance flow equation. The average level of competence of the other selections in comparison to B is displayed.

$$\varphi^{-d} = \frac{1}{m} - \quad 1 \sum_{\substack{y \in B \\ y \neq b}} \pi(x,b) \quad (30)$$

Lowerφ+(b)andhigherφ−(b)indicateabetteralternative. Step 3: To rank the data, use PROMETHEE II. A thorough ranking in the form of equations is generated using the PROMETHEE II technique, the I I I and P I I interface, and the findings from the first and second steps.

$$b^{pII}c \Leftrightarrow \varphi(b) > \varphi(c) \quad (31)$$

$$bI^{II}c \Leftrightarrow \varphi(b) = \varphi(c) \quad (32)$$

Eqn (32) represents the implicit dominance of option B, denoted as φ(b) or net flow.

$$\varphi(b) = \varphi^{+}(b) - \varphi^{-}(a) \quad (33)$$

In general, PROMETHEE II states that φ must be found for every option, and the benefit must be subtracted from the failure to achieve net domination. This φ increases with improvement. With this procedure, we get a final and thorough ranking and can determine the location of each option.

Feedback loop

Optimization Model Based on MPC.MPC is otherwise called as rolling time domain control basic model is given below and basic flowchart of MPC IS Also given below.

E, F, G and A; Indicates the state space of Matrix; s^t; Input Vector; r^t; Output Vector; y^s; State vector; G^s; disturbance input vector; z^s; Output Vector; y^s+ Δs; State Vector

$$y^{s+\Delta s} = Ey^s + Fz^s + Gx^s \quad (34)$$

$$z^s = A_{y^s} \quad (35)$$

Figure 4 represent the basic flow chart of MPC. We propose to use Multi-time stepping Rolling with Model Predictive Control (MPC), a feedback loop evaluation technique, to address the shifting demands of impact populations. This technique makes it easier to make strategic decisions and conduct real-time monitoring which enables quick adjustments to relief operations. The methodology employs the MPC principle and continuously evaluates input from different time steps to guarantee responsiveness and effective relief effort.

Stakeholders will be able to make well-informed decisions based on the most recent circumstances and changing demands by employing these iterative methodologies. This ultimately improves the effectiveness and efficiency of the recovery efforts following disasters. Rolling Optimization Model Making Use of MPC Emergency recovery durations might last for several hours or days, during which the traffic flow, solar production, load demand, and topology of the distribution system. Figure 5 represents the flow chart on multi step rolling optimization.

RESULTS AND DISCUSSION

This section presents the experimentation analysis and performance evaluation of the suggested study plan. This part is divided into three subsections: simulation study., comparative analysis, research overview.

Simulation Study

To simulate the proposed research method, python tool is utilized. This tool has an efficient network topology and provides all specifications for the proposed technique. Table 2 indicates the system specifications.

Comparative Analysis

This section discusses the suggested approach with a number of available methods. Including Fuzzy Bi-Level Optimization Method (FBLOM) [34]. Squeeze-and-Excitation dual High-Resolution Network (SEDHRNet) [37], Federal Emergency Management Agency (FEMA), The evaluation i.e. validation is performed by considering the performance metrics such as Accuracy, Precision, F1Score, and Acceleration.

Number of Epochs vs. Accuracy (%)

The degree of agreement between a measurement and its actual value is known as accuracy. The equation of accuracy is (assumes a simple linear relationship between the

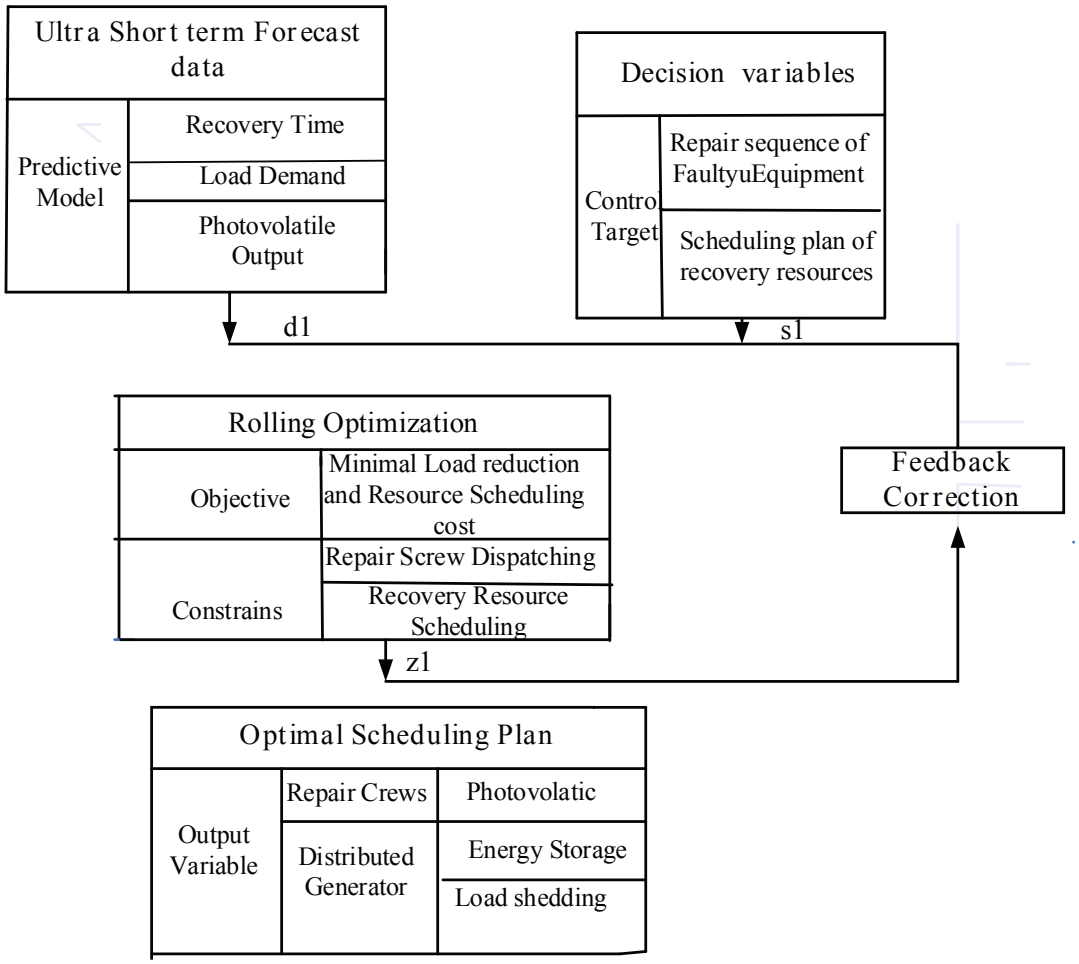


Figure 5. Flow chart for MPC.

Table 2. System specification

Software specification	OS	Windows 11-(64 bit)
	Tool	Python – 3.11.4
Hardware specification	RAM	4 GB
	Hard Disk	500 GB

(X) axis's number of epochs and the (Y) axis's percentage of accuracy (Fig. 6). Below is the equation.

$$A = \frac{Rp+Rn}{Rp+Rn+Wp+Wn} \quad (36)$$

Rp- True positive; Rn- true negative; wp- false positive; Wn- false negative.

As shown in Figure 6 and Table 3, classification accuracy increases with the number of training epochs for all three methods. At 20 epochs, SED-HRNet, FBLOM, and the proposed method achieve accuracy values of 85%, 86%, and 90%, respectively. At 40 epochs, these values increase to 87%, 88%, and 93%. At 60 epochs, the corresponding values are 87.5%, 88.5%, and 95%, rising to 89%, 90%, and 97% at 80 epochs. At 100 epochs, SED-HRNet achieves an accuracy of 90%, FBLOM reaches 93%, and the proposed

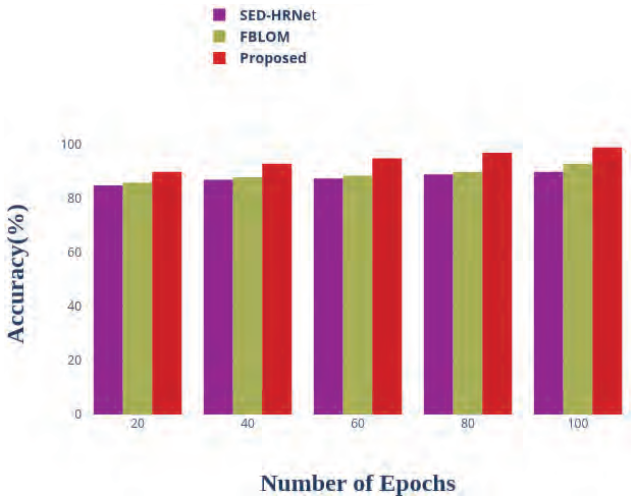


Figure 6. Number of epochs vs. accuracy.

Table 3. Numerical outcomes of accuracy (%)

(x-axis) – Number of Epochs	Accuracy (%)- (y-axis)		
	SED-HRNet	FBLOM	Proposed
20	85	86	90
40	87	88	93
60	87.5	88.5	95
80	89	90	97
100	90	93	99

method attains 99%. The proposed method achieves the highest accuracy at every reported epoch count.

Number of Epochs vs. Precision (%)

Precision refers to the amount of information that is conveyed by a number in terms of its digits; it shows the closeness of two or more measurements to each other. It is independent of accuracy.

Figure 7 indicates the % of precision in the (Y) axis and the number of epochs in the (X) axis. The following is the mathematical relationship for precision.

$$Precision = \frac{Rp}{Rp+Rn} \tag{37}$$

Rp represent True positive; Rn represent true negative Initially 20% of epochs the percentage of precision in Existing level 85% & 89%. Proposed level is 94%. Further 60% of epochs the Percentage of precision in the SED-HRNet in 86%. FBLOM is 89% and proposed level is 96%. Then 80% of epochs the percentage of precision in the existing level 88% and 90% further increase in Proposed level 97.5%. Finally, 100% of epochs the percentage of Precision in the SED-HRNet 90%, FBLOM 92% and proposed level is 98%. The proposed method is high percentage of precision so this method is better to other two method.

Number of Epochs vs. F1 Score

The F1 score is an alternative machine learning evaluation statistic that evaluates a model's predictive power by looking at how well it performs on each class separately as opposed to taking performance as a whole into account like accuracy does.

Figure 8 displays the percentage of F1Score on the (Y) axis and the number of epochs on the (X) axis.

$$F1score = \frac{2\times\beta\times\delta}{\beta+\delta} \tag{38}$$

β - Precision;
δ - indicate Recall

Initially 20% of epochs with F1score achieved in existing level 85%and 89%. Proposed level is achieved 94%. 60% of epochs SED-HRNet in the F1 score level 88.5%and FBLOM reach the F1 score 91%. The proposed level is reach 95.5%. Then 80% of epoch will reach the F1 score level 89%,91.5% and 96%. Finally, 100% of epochs will reach the F1 score 90%, 92% in the existing level. The highest F1 score is proposed method 97%.

Time vs. Acceleration

The velocity's rate of change with regard to time. Since acceleration has both a magnitude and a direction, it is a vector quantity. It can alternatively be thought of as the first derivative of velocity with respect to time or the second derivative of position with respect to time. Figure 9 represent Time in the (X) axis and Acceleration in the (Y) axis. This can be derived in mathematically

$$\bar{a} = S - S_0/\Delta T \tag{39}$$

$\bar{a}$ = acceleration
S - S_0 = Speed of the velocity
ΔT = Change in the time

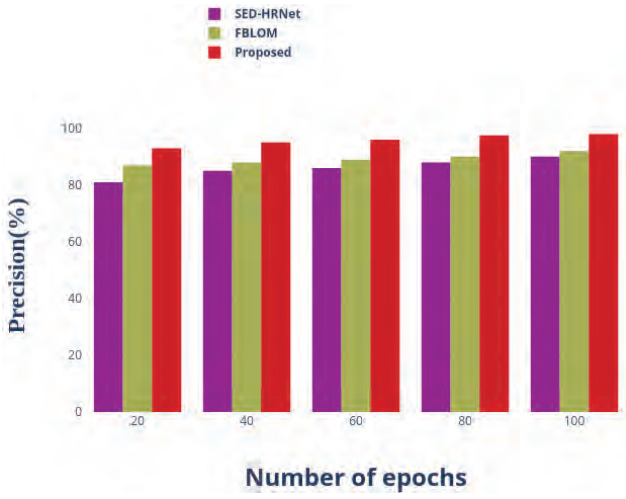


Figure 7. Number of epochs vs. precision.

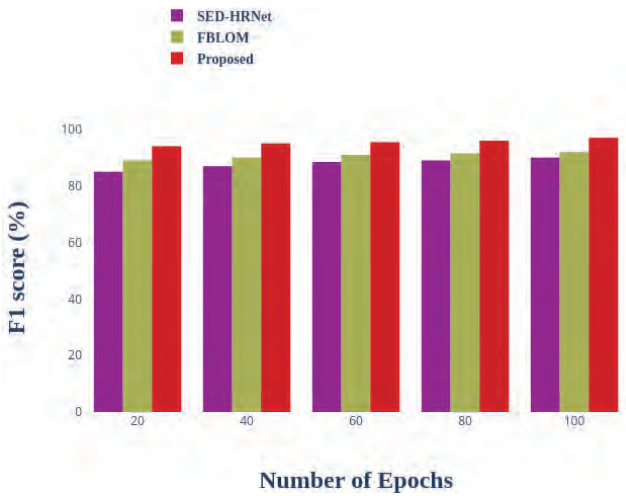


Figure 8. Number of epochs vs. F1 score.

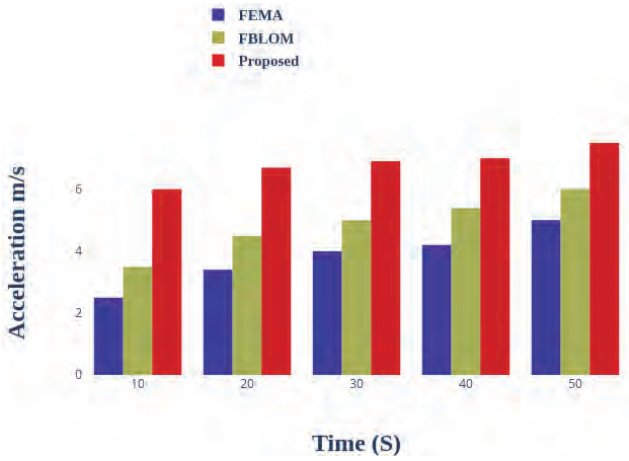


Figure 9. Time vs. acceleration.

Figure 9 represents initially 20s in FEMA method the acceleration in 2.5s. FBLOM 3.5s further increasing the speed of acceleration in proposed level 6s. reached. After 60s the acceleration in the existing level 4s,5s and proposed level is 6.9s. After 80s the acceleration speed is increasing in existing level 4.2s, 5.4s gradual increase in proposed level 7s. Finally, acceleration m/s in the existing level 5s and 6s. proposed levels 7.5s. Proposed level is higher speed of acceleration.

Research Summary

Initially we started the process data collection. Next processing and feature extraction and training then classification, decision making and feedback loop method. Next, we used fuzzy bilevel optimization. then implement Adam-Enhanced SEHRNET Algorithm enhance significant reduction in network parameters while maintaining high accuracy. Further we implement. Technique for Order of Preference by Similarity to Ideal Solution and Preference Ranking Organization method of Enrichment Evaluation (TOPSIS-PROMTHEE) then we implement SA algorithm and by constantly assessing input from various time stepping and using Multi time stepping rolling with model predictive control. The numerical results of proposed and actual outcomes are shown in Tables 3-6. The success metrics for the suggested approaches are shown in Figures 6–9.

Table 4. Numerical outcomes of precision (%)

(x-axis) Number of Epochs	Precision (%)- (y-axis)		
	SED-HRNet	FBLOM	Proposed
20	81	87	93
40	85	88	95
60	86	89	96
80	88	90	97.5
100	90	92	98

Table 5. Numerical outcomes of F1 score (%)

(x-axis) Number of Epochs	F1 Score (%)- (y-axis)		
	SED-HRNet	FBLOM	Proposed
20	85	89	94
40	87	90	95
60	88.5	91	95.5
80	89	91.5	96
100	90	92	97

Table 6. Numerical outcomes of acceleration(m/s)

(x-axis) – Time(s)	Acceleration(m/s)- (y-axis)		
	FEMA	FBLOM	Proposed
20	2.5	3.5	6.0
40	3.4	4.5	6.7
60	4.0	5.0	6.9
80	4.2	5.4	7.0
100	5.0	6.0	7.5

CONCLUSION

We began gathering data for the process at first. The steps that follow include training, feature extraction, processing, and finally classification, decision-making, and feedback loop technique. This study emphasizes the necessity of integrating advanced computational models into post-disaster recovery processes to enhance the efficiency of reconstruction efforts. Fuzzy bilevel optimization was then employed. Subsequently, we implemented the Adam-Enhanced SEHRNET Algorithm to markedly diminish network parameters while maintaining exceptional accuracy. We persisted in applying the TOPSIS-PROMETHEE methodology, which offered an organized framework for decision-making to prioritize rehabilitation initiatives in regions impacted by disasters. The Multi-time stepping Rolling with Model Predictive Control (MPC) method was utilized to consistently assess inputs from various time intervals, facilitating a more dynamic and adaptable response system in post-disaster recovery.

The proposed framework achieved an accuracy of 99%, a precision of 98%, and an F1 score of 97% in the reported evaluation. Performance assessments also indicated shorter response times and improved prioritization of reconstruction areas compared with the conventional approaches examined. These findings support the framework's potential to assist post-disaster decision-making, although its performance should be interpreted within the conditions of the study. High classification scores provide a basis for further investigation; their practical value ultimately depends

on whether the resulting decisions remain useful when evidence is incomplete and recovery needs change.

A central contribution of the study is its use of a hybrid probabilistic approach to damage classification and reconstruction planning. The methodology draws on weakly supervised learning and probabilistic graphical models, including Bayesian networks. This provides a means of representing uncertainty within the decision process and offers scope for revising classifications as additional evidence becomes available. Its contribution therefore concerns how damage assessments can inform decisions under uncertain conditions, alongside the predictive performance observed in the evaluation.

For recovery planning, the framework offers a potential link between automated damage assessment, resource allocation, and operational feedback. Such a link could help planners identify areas requiring attention and reconsider priorities as conditions evolve. The reduction in response time observed during evaluation is encouraging, but establishing its operational significance requires testing in actual recovery settings. Faster classification must be accompanied by sufficiently reliable information to support the decisions that follow. Local verification and professional judgement would remain necessary, particularly where an incorrect assessment could delay assistance or divert scarce resources.

Several limitations warrant further investigation. Performance may vary with disaster type, damage severity, and the availability and quality of photographic evidence. The reported scores cannot establish how well the model would perform in locations or disaster conditions absent from the evaluation data. Independent testing across geographically and operationally distinct settings is therefore needed. Future research could examine whether semi-supervised or self-supervised learning reduces dependence on labelled imagery while preserving sensitivity to consequential forms of damage. Reporting performance by damage category would also help clarify whether aggregate scores conceal weaknesses in less frequent cases.

The decision framework could be extended to account for population displacement, economic disruption, and access to essential services. These considerations matter because the extent of physical damage alone cannot determine the urgency of reconstruction. A moderately damaged facility may require immediate attention if it serves a population with few alternatives. Incorporating such factors would require explicit prioritization criteria and careful consideration of the trade-offs between competing recovery needs.

The study provides a basis for further development of probabilistic decision support in post-disaster recovery. The next step is to establish whether the observed performance can be sustained when data are uneven, infrastructure is disrupted, and priorities must be negotiated under pressure. Progress should be judged by the quality of the recovery decisions the framework supports, together with its classification accuracy. Without that connection, improvements in predictive performance may yield limited benefits for the communities awaiting reconstruction.

DATA AVAILABILITY STATEMENT

The author confirm that the data that supports the findings of this study are available within the article. Raw data that support the finding of this study are available from the corresponding author, upon reasonable request.

CONFLICT OF INTEREST

The author declared no potential conflicts of interest with respect to the research, authorship, and/or publication of this article.

ETHICS

There are no ethical issues with the publication of this manuscript.

STATEMENT ON THE USE OF ARTIFICIAL INTELLIGENCE

Artificial intelligence was not used in the preparation of the article.

REFERENCES

[1] Mohammadnazari Z, Mousapour Mamoudan M, Alipour-Vaezi M, Aghsami A, Jolai F, Yazdani M. Prioritizing post-disaster reconstruction projects using an integrated multi-criteria decision-making approach: A case study. Buildings (Basel) 2022;12(2):136. [CrossRef]

[2] Xiao Y, Tian K, Yuan M, Ouyang Y, Huang H. Examining the complex relationships between socio-economic development and the improvement of ecological environment in post-disaster reconstruction: The case of Wenchuan earthquake disaster area in Western China. J Clean Prod 2022;337:130581. [CrossRef]

[3] Anilkumar S, Banerji H. An inquiry into success factors for post-disaster housing reconstruction projects: A case of Kerala, South India. International Journal of Disaster Risk Science 2021;12(1):24–39. [CrossRef]

[4] Gharib Z, Yazdani M, Bozorgi-Amiri A, Tavakkoli-Moghaddam R, Taghipourian MJ. Developing an integrated model for planning the delivery of construction materials to post-disaster reconstruction projects. J Comput Des Eng 2022;9(3):1135–1156. [CrossRef]

[5] Cremen G, Galasso C, McCloskey J. Modelling and quantifying tomorrow's risks from natural hazards. Sci Total Environ 2022;817:152552. [CrossRef]

[6] Matracia M, Saeed N, Kishk MA, Alouini MS. Post-disaster communications: Enabling technologies, architectures, and open challenges. IEEE Open Journal of the Communications Society 2022;3:1177–1205. [CrossRef]

[7] Margus C, Hertelendy A, Tao Y, Coltey E, Chen SC, Luis S, et al. United States Federal Emergency Management Agency regional clustering by disaster exposure: A new paradigm for disaster response. Nat Hazards (Dordr) 2023;116(3):3427–3445. [CrossRef]

[8] Cui P, Peng J, Shi P, Tang H, Ouyang C, Zou Q, et al. Scientific challenges of research on natural hazards and disaster risk. Geography and Sustainability 2021;2(3):216–223. [CrossRef]

[9] Bahmani H, Zhang W. Comprehensive success evaluation framework for socio-natural disaster recovery projects. Buildings (Basel) 2021;11(12):647. [CrossRef]

[10] Zokaee M, Tavakkoli-Moghaddam R, Rahimi Y. Post-disaster reconstruction supply chain: Empirical optimization study. Autom Constr 2021;129:103811. [CrossRef]

[11] Mehan A, Mostafavi S. Portcityscapes as liminal spaces: Building resilient communities through parasitic architecture in port cities. In: Haq S, Sharag-Eldin A, editors. ARCC 2023 Conference Proceeding: The Research Design Interface; 2023 Apr 12–15; Dallas, TX, USA. Architectural Research Centers Consortium, Inc.; 2023. p. 631–639.

[12] Rosander L. Adhocracy in the bureaucracy: Practices of implementing collaborative contracting in infrastructure client organizations [doctoral thesis]. Stockholm: KTH Royal Institute of Technology; 2024. 95 p. TRITA-ABE-DLT; 2412.

[13] Lindquist EA, Buttazzoni M. The ecology of open innovation units: Adhocracy and competing values in public service systems. Policy Des Pract 2021;4(2):212–227. [CrossRef]

[14] Andriessen A, Paidakaki A, Susilo C, van den Broeck P. Architects' multifaceted roles in enhancing resilience after disasters. In: Martins AN, Fayazi M, Kikano F, Hobeica L, editors. Enhancing Disaster Preparedness: From Humanitarian Architecture to Community Resilience. 1st ed. Elsevier; 2021. p. 129–148. [CrossRef]

[15] Aziminezhad M, Taherkhani R. BIM for deconstruction: A review and bibliometric analysis. J Build Eng 2023;73:106683. [CrossRef]

[16] Karacali AO, Erdil T. Considering sidewalls as an architectural ground: Parasitic architecture approaches in design studio. Journal of Design Studio 2022;4(1):81–92. [CrossRef]

[17] Arabulan S, Lank M. Evaluation criteria of parasitic architecture. A+Arch Design International Journal of Architecture and Design 2023;9(1):37–51. [CrossRef]

[18] Sarkar A, Chowdhury T, Murphy RR, Gangopadhyay A, Rahnemoonfar M. SAM-VQA: Supervised attention-based visual question answering model for post-disaster damage assessment on remote sensing imagery. IEEE Trans Geosci Remote Sens 2023;61:1–16. [CrossRef]

[19] Baarimah AO, Alaloul WS, Liew MS, Kartika W, Al-Sharafi MA, Musarat MA, et al. A bibliometric analysis and review of building information modelling for post-disaster reconstruction. Sustainability 2022;14(1):393. [CrossRef]

[20] Wan H, Liu W, Shi Q, Zhang Y, Wang Y, Zhang S. Multi-time-step rolling optimization strategy for post-disaster emergency recovery in distribution system based on model predictive control. CSEE Journal of Power and Energy Systems 2025;11(1):243–254. [CrossRef]

[21] Calle Müller C, ElZomor M. Addressing post-disaster challenges and fostering social mobility through origami infrastructure and construction trade education. Sustainability 2024;16(8):3415. [CrossRef]

[22] Zhang L, Tao Z, Wang G. Assessment and determination of earthquake casualty gathering area based on building damage state and spatial characteristics analysis. Int J Disaster Risk Reduct 2022;67:102688. [CrossRef]

[23] Ransikarbum K, Mason SJ. A bi-objective optimisation of post-disaster relief distribution and short-term network restoration using hybrid NSGA-II algorithm. Int J Prod Res 2022;60(19):5769–5793. [CrossRef]

[24] Shi M, Cao Q, Ran B, Wei L. A conceptual framework integrating "building back better" and post-earthquake needs for recovery and reconstruction. Sustainability 2021;13(10):5608. [CrossRef]

[25] Sun J, Zhang Z. A post-disaster resource allocation framework for improving resilience of interdependent infrastructure networks. Transp Res D Transp Environ 2020;85:102455. [CrossRef]

[26] Cremen G, Seville E, Baker JW. Modeling post-earthquake business recovery time: An analytical framework. Int J Disaster Risk Reduct 2020;42:101328. [CrossRef]

[27] Wearing S, Beirman D, Grabowski S. Engaging volunteer tourism in post-disaster recovery in Nepal. Ann Tour Res 2020;80:102802. [CrossRef]

[28] Islam E, Abd Wahab H, Benson OG. Structural and operational factors as determinant of meaningful community participation in sustainable disaster recovery programs: The case of Bangladesh. Int J Disaster Risk Reduct 2020;50:101710. [CrossRef]

[29] Wang Y, Chen W, Luan TH, Su Z, Xu Q, Li R, et al. Task offloading for post-disaster rescue in unmanned aerial vehicles networks. IEEE/ACM Transact Network 2022;30:1525–1539.

[30] Wei J, Gao X, Cheng P, Fu W, Zeng H. Coordinated post-disaster recovery and assessment method for integrated electricity-gas-transportation system. IEEE Access 2023;11:11685–11699. [CrossRef]

[31] Wang Q, Liu Y, Pei H. Modelling a bi-level multi-objective post-disaster humanitarian relief logistics network design problem under uncertainty. Engineering Optimization 2024;56(8):1220–1254. [CrossRef]

[32] Wu C, Zhang F, Xia J, Xu Y, Li G, Xie J, et al. Building damage detection using U-Net with attention mechanism from pre- and post-disaster remote sensing datasets. Remote Sens (Basel) 2021;13(5):905. [CrossRef]

[33] Li Y, Lin C, Li H, Hu W, Dong H, Liu Y. Unsupervised domain adaptation with self-attention for post-disaster building damage detection. Neurocomputing (Amst) 2020;415:27–39. [CrossRef]

[34] Cao C, Liu Y, Tang O, Gao X. A fuzzy bi-level optimization model for multi-period post-disaster relief distribution in sustainable humanitarian supply chains. Int J Prod Econ 2021;235:108081. [CrossRef]

[35] King LJ. Social media use during natural disasters: An analysis of social media usage during Hurricanes Harvey and Irma. In: Proceedings of the International Crisis and Risk Communication Conference. Orlando (FL): Nicholson School of Communication; 2018. p. 20–23. [CrossRef]

[36] Kirkpatrick S, Gelatt CD Jr, Vecchi MP. Optimization by simulated annealing. Science 1983;220(4598):671–680. [CrossRef]

[37] Liu C, Sepasgozar SME, Zhang Q, Ge L. A novel attention-based deep learning method for post-disaster building damage classification. Expert Syst Appl 2022;202:117268. [CrossRef]

[38] Aghababaei M, Koliou M, Watson M, Xiao Y. Quantifying post-disaster business recovery through Bayesian methods. Struct Infrastruct Eng 2021;17(6):838–856. [CrossRef]

[39] Ghaffarian S, Rezaie Farhadabad A, Kerle N. Post-disaster recovery monitoring with Google Earth Engine. Appl Sci (Basel) 2020;10(13):4574. [CrossRef]

[40] Gajić M, Furdek M, Heegaard P. A framework for spatial and temporal evaluation of network disaster recovery. In: 2020 32nd International Teletraffic Congress (ITC 32); 2020 Sep 22–24; Osaka, Japan. IEEE; 2020. p. 37–45. [CrossRef]

[41] Jiang X, Chen J, Chen M, Wei Z. Multi-stage dynamic post-disaster recovery strategy for distribution networks considering integrated energy and transportation networks. CSEE Journal of Power and Energy Systems 2021;7(2):408–420. [CrossRef]

Sigma J Eng Nat Sci, Vol. 44, No. 4, pp. 2856–2872, August, 2026

Sigma Journal of Engineering and Natural Sciences
Web page info: https://sigma.yildiz.edu.tr
DOI: 10.14744/sigma.2026.2131

Research Article

Characterizing temperature profiles and thermal management in hydrogen storage systems for aerial vehicles

Kirubadurai B.[1,*], Jegadeeswari G.[2], Jaganraj R.[1], Vinothkumar M.[1]

[1]*Department of Aeronautical Engineering, Vel Tech Rangarajan Dr. Sagunthala R&D Institute of Science and Technology, Chennai, 600062, India*

[2]*Department of Electrical and Electronics Engineering, Saveetha Engineering College, Chennai, 602105, India*

ARTICLE INFO

Article history
Received: 20 December 2024
Revised: 13 April 2025
Accepted: 29 April 2025

Keywords:
Controlling of Inlet Parameters; Rapid-Filling Process; Thermal Management of Hydrogen Cylinder; Type III Hydrogen Storage Cylinder; UAV Fuel Tank

ABSTRACT

This research concentrates on the problem associated with rapid filling of type III hydrogen cylinders in hydrogen-powered aerial vehicles. Rapid filling leads to certain temperature rises in the cylinder due to adiabatic compression and it is jeopardizing the structural integrity. Existing research mainly focused on the effects of pressure variation and temperature rises on hydrogen cylinders. However, there is limited research on the effects of temperature rises in Type III hydrogen storage cylinders incorporated with PTFE-coated aluminium liners under various temperature and mass flow rates related to aerial application. Based on the previous research gap, a 2D axisymmetric cylinder model was developed in ANSYS R21 for a 5 L, 35 MPa Type III PTFE-coated aluminium liner wrapped in carbon fiber hydrogen cylinder. A model analysed under the real gas behaviours through the Redlich-Kwong equation with various inlet conditions of temperature (283–323 K), filling pressure (5–35 MPa) and mass flow rate (0.01–0.05 kg/s). The simulation outcome indicates the increase in internal gas temperature from 293 K to 417 K and the optimum temperature region near the inlet due to recirculatory heating. At a maximum temperature of 323 K, the internal temperature rises up to 600.2K toward the thermal stability limits of PTFE. Due to the insulating properties of PTFE, it reduces the temperature distribution from the inner layer to the outer layer of the cylinder and ensures temperature containment. This research work indicates that a minimum inlet temperature of 283K, a medium filling pressure of 20 MPa, and a moderate mass flow rate of 0.03 kg/s in 6 seconds provide an enhanced thermal stability of the cylinder. This research emphasizes the significance of controlling inlet parameters, not just pressure and flow rate but also temperature, to enhance the safe and efficient lightweight hydrogen storage cylinder used in UAV applications.

Cite this article as: Kirubadurai B, Jegadeeswari G, Jaganraj R, Vinothkumar M. Characterizing temperature profiles and thermal management in hydrogen storage systems for aerial vehicles. Sigma J Eng Nat Sci 2026;44(4):2856–2872.

***Corresponding author.**
*E-mail address: rakkismart90@gmail.com

This paper was recommended for publication in revised form by Editor-in-Chief Ahmet Selim Dalkilic

Published by Yıldız Technical University Press, İstanbul, Turkey
© Author. This is an open access article under the CC BY-NC license (http://creativecommons.org/licenses/by-nc/4.0/).

INTRODUCTION

The global demand for pure and sustainable energy sources has intensified research into hydrogen as a suitable alternative to fossil fuels. Hydrogen fuel properties like compatible production methods, zero carbon emissivity, and richer energy density make it a suitable energy source for transportation purposes in fuel cell-powered automobiles and aerial vehicles [1–4]. Hydrogen's storage possesses significant safety and thermal management challenges for storing hydrogen in high-pressure static and dynamic conditions. High-pressure gaseous storage is the most popular adopted method due to its simple structure and higher gravimetric density. The U.S. Department of Energy (DOE) has focused on volumetric and gravimetric energy densities of 2.7 kWh/L and 3.0 kWh/kg, respectively, for onboard working cylinders [5–6]. To attain these targets, newer hydrogen storage systems depend upon composite high-pressure cylinders and combine lightweight materials with high strength. Type III cylinders contain aluminium liners wrapped with carbon fiber and exhibit a balance of structural stability and weight reduction, making them suitable for aerospace and UAV applications [7–9].

Rapid filling of hydrogen cylinders is a most required process in vehicle refuelling stations during that time. Temperature increases by adiabatic compression, frictional heating, and real gas effects. Rapid filling of cylinders at high pressures (350–700 bar) within a short span of time significantly increases gas temperatures to exceed safe operational limits. To resolve this issue, accurate computational modelling is needed to calculate temperature changes during filling, specifically when multi-layered materials and thermal insulators are involved [10–12]. Demonstrated thermal effects in Type III and IV tanks by considering parameters like inlet pressures, filling times, and design [13-15]. Adoption of multi-material layering, ignorance of real gas behaviour, or influence of coatings like PTFE, which can significantly change heat transfer within the cylinder materials. Many existing models are created for automotive-scale tanks with minute concentration on small-capacity systems adopted in UAVs, where rapid thermal gradients pose a higher cause of limited thermal mass. The studies elaborated that the temperature hike during hydrogen refuelling drastically depends upon parameters like filling rate, inlet temperature, and pressure [16–20].

By considering all thermal challenges, researchers have proposed optimized filling methods focused on attaining higher filling rates and short fuelling durations [21]. In addition to investigating the effect of various liner and wrapping materials on temperature distribution inside hydrogen storage vessels, addressing material selection as a thermal protection technique [22]. A unique temperature-absorbing technique was demonstrated to reduce excessive thermal hikes with an intense concentration on mass flow rate and cylinder design [23].

Research gap

- Previous research mainly concentrated on Type IV hydrogen cylinders with various polymer materials but lagged with modelling of Type III cylinders.
- Research on rapid filling of hydrogen remains unstudied, incorporating a PTFE-coated aluminium Type III hydrogen cylinder.
- The previous work did not concentrate on thermal interactions between multi-layered hydrogen cylinders, especially for smaller-capacity UAV storage applications.
- There is insufficient numerical simulation on the combination of various inlet parameters like filling pressure, inlet temperature, mass flow rate, and time to determine the internal temperature rise and thermal safety of a hydrogen cylinder.
- Lagging of design recommendations by simulation for optimizing filling strategies in smaller capacity, lightweight, and high-performance hydrogen cylinders.

Research Novelty

- This research develops a 2D axisymmetric computational model analysed with real gas effects using the Redlich-Kwong equation of state.
- This study provides a detailed thermal analysis of a Type III PTFE-coated aluminium liner and carbon fiber wrap hydrogen cylinder specially for UAV application.
- The simulation model reveals the thermal insulation and structural safety effects of a PTFE-coated aluminium cylinder under rapid filling.
- This research provides a validated design procedure for thermal stability under rapid filling of hydrogen in a small-scale hydrogen storage cylinder.
- This quantitative research focuses on optimal inlet parameters such as 20 MPa inlet pressure, 0.03 kg/s flow rate, 283 K inlet temperature, and 6 sec filling time to prevent the internal temperature rise.

PROCESS OF HYDROGEN FILLING: A THEORETICAL INVESTIGATION

Mechanisms Contributing to Temperature Rise During Rapid Hydrogen Filling

Rapid filling of hydrogen is accompanied by several phenomena that contribute to temperature rise inside the cylinder. Under certain conditions, hydrogen exhibits a negative Joule-Thomson coefficient, especially at medium-high pressure. This action indicates that while hydrogen expands more quickly, it cools rather than heats up [24–27]. However, this cooling effect is often overshadowed during compression-dominant fast-filling operations. If hydrogen gas is compressed into the cylinder very quickly, with little heat transfer to or from the surrounding, the compression of hydrogen gas is called adiabatic compression. The ideal gas law (PV = nRT) dictates that this compression raises the gas's internal energy which in turn raises the temperature [28–32].

Filling into pipelines, valves and narrow passages, hydrogen rapidly interacts with the surfaces of the passages through friction between the molecules, causing further heat to be generated. This frictional heating is particularly important for high pressure fueling systems and is responsible for additional heat rising in the cylinder. Hydrogen gas will also be affected by the surrounding environmental temperature while being refuelled. Further increases in the internal cylinder temperature may be caused by the transfer of additional heat into the gas in hot climates or high ambient temperatures [33]. When the gas is filling rapidly, external work is done on the gas during the compression process, increasing both it's internal energy and temperature. This effect, called "heat of compression," can lead to significant temperature increases in the HSS [34–39].

Impact on Safety and Mitigation Strategies

Together, these mechanisms can cause dramatic increases in temperature, which can cause internal pressures to exceed limits. This rise can cause severe safety concerns such as possible damage to the storage vessel. Also, hotter temps may cause the fuelling parts to be less efficient and less durable.

To reduce these risks, a number of engineering approaches are usually taken:

- Developing a method to more effectively dissipate heat through the use of materials with higher thermal conductivity when building tanks, and
- Pre-heating water prior to its compression, and
- Controlling and optimizing the filling rate, to prevent rapid heat build-up,

Including cooling system into fuelling station or compressor [40–42].

The root cause of the rising temperature

Zhang RY et.al [43] observed the expression for final temperature during the rapid filling operation.

$$T_2 = \frac{\lambda\mu T_1(T_1 + \alpha P_1) - \alpha(\lambda P_1 T_1 - P_1 T_1)}{T_1 + \alpha P_1 + \frac{\alpha T_1 P_1 - P_1 T_1}{P_2}} \quad (1)$$

A rise in temperatures and filling rate have an exponentially related. On the other hand, a straight line exists between temperature growth and beginning pressure or temperature. It shows that the entry temperature and the surrounding temperature were equal. Developed an empirical formula using modelling and experimental studies [44] as.

$$T_2 = 1.01 - 1.52e^{\frac{P_2}{8.44}}(-6.81 \times 0.9^{\dot{m}} + 0.3T_1 - 2.2P_1 + 68 + T_1 \quad (2)$$

Where m is the filling rate in g/s, T_1 and T_2 are the entry and exit temperatures of hydrogen in the cylinder in K and P_1, P_2 are the entry and exit pressures of hydrogen in the cylinder in MPa.

Mathematical examination of rising temperatures

For open systems, the following the first law of thermodynamics [45-46]

$$dU = dH_{in} - dH_{out} + \delta Q - \delta W \quad (3)$$

Where dQ is the heat generated by the system expressed in kJ, dH_{in} and dH_{out} are the enthalpy in entry and exit of the system. The system's work is denoted by dW and kJ.

Formulating above equation with $dH_{out} = 0$ and $dW = 0$ is as follows:

$$dU = dH_{in} + \delta Q \quad (4)$$

The final energy is expressed as

$$U_2 = U_1 + dU \quad (5)$$

Where U_1 and U_2 are initial and final internal energy of cylinder expressed in kJ and the resultant energy is as follows:

$$U_2 = U_1 + dH_{in} + \delta Q \quad (6)$$

The relationship between temperature and the specific internal energy of hydrogen is shown as

$$u = aT - b \quad (7)$$

Where u is specific internal energy in kJ/kg, T is the hydrogen's temperature K.

$$U_1 = m_1(aT_1 - b) \quad (8)$$

$$U_2 = m_2(aT_2 - b) \quad (9)$$

Where m_1 and m_2 are initial and final mass of hydrogen in kilograms. In terms of expression, the final mass is

$$m_2 = m_1 \int \dot{m} dt \quad (10)$$

Where ($\dot{m}$) is mass flow rate in kg/s. An expression for the enthalpy of the system is

$$dH_{in} = h_{in} \int \dot{m} dt \quad (11)$$

Where h_{in} is specific enthalpy of hydrogen at the input temperature expressed in kJ/kg [47].

$$\delta Q = \int q dt \quad (12)$$

Where q is the power in kW, heat transmission to the surrounding. The above equations allow us to express the final temperature as follows:

$$T_2 = \frac{m_1(\alpha T_1 - b) + h_{in} \int \dot{m}\, dt + \int q dt}{\alpha(m_1 + \int \dot{m}\, dt)} - \frac{b}{a} \quad (13)$$

Geometrical Framework

The PTFE-coated metal layers and insulating layer make up the liquid hydrogen transit storage device. Carbon fibre and epoxy are combined to create insulation, which is placed between the environment and the metal's exterior. A drawing of the hydrogen transfer tank under design is shown in Figure 1. The PTFE coating thickness is T_3, and the layer thicknesses are T_1 and T_2 and dimension are listed in Table 1.

CFD Simulations

- A 2D axisymmetric model was developed in ANSYS Fluent for a 35 MPa, 5L Type III hydrogen cylinder to improve computational efficiency and accuracy.
- Buoyancy effects were neglected due to the dominance of high-speed axisymmetric flow.

Key Assumptions

- Inlet valve allows high-pressure gas entry with minimal heat exchange; modelled as a time-dependent pressure boundary.
- The PTFE-coated aluminium liner minimizes heat transfer to the outer carbon fiber wall due to its low thermal conductivity (0.3 W/mK).
- PTFE is assumed to be isotropic, with constant thermal conductivity and specific heat capacity.
- Inlet temperature is considered constant, based on stable pre-filling conditions in experiments.
- Before hydrogen filling, nitrogen is purged, allowing initial hydrogen and wall temperatures to be equal.
- Convective heat transfer at the outer wall is negligible due to PTFE insulation.
- Mechanical deformation of the cylinder is ignored; all solids are treated as rigid bodies.

Governing Equations

Above assumption gives the basics for creating the flow and heat transfer 2D axisymmetric. Below is a description of the governing equations. The equations for mass conservation:

$$\frac{\partial \rho}{\partial t} + \frac{\partial}{\partial x}(\rho u) + \frac{\partial}{\partial x}(\rho v)\frac{\rho v}{r} = 0 \tag{14}$$

where x represents the horizontal distance, r the radial distance, ρthe gas density, t the filling period, and u the filling linear velocity and v the radial velocity. As the axisymmetric model's momentum transit,

$$\begin{aligned}\frac{\partial}{\partial t}(\rho u) + \frac{1}{r}\frac{\partial}{\partial x}(r\rho uu) + \frac{1}{r}\frac{\partial}{\partial r}(r\rho uv) \\ = -\frac{\partial \rho}{\partial x} + \frac{1}{r}\frac{\partial}{\partial r}\left[r(\mu+\mu_t)\left(2\frac{\partial u}{\partial x} - \frac{2}{3}(\nabla.\vec{v})\right)\right] \\ + \frac{1}{r}\frac{\partial}{\partial r}\left[r(\mu+\mu_t)\left(2\frac{\partial u}{\partial r} + \frac{\partial v}{\partial x}\right)\right]\end{aligned} \tag{15}$$

Where p- Absolute pressure, μ-Dynamic viscosity, and t Turbulence viscosity. The energy equation is

$$\begin{aligned}\frac{\partial}{\partial t}(\rho E) + \frac{\partial}{\partial x}(u(\rho E + \rho)) = \frac{\partial}{\partial r}\left[k_{eff}\frac{\partial \tau}{\partial r} + u(\mu+\mu_t)\left(\frac{\partial u}{\partial r} + \frac{\partial v}{\partial x}\right)\right. \\ \left. - \frac{2}{3}u(\mu+\mu_t)\frac{\partial u}{\partial x}\right]\end{aligned} \tag{16}$$

Table 1. Characteristics of the cylinders' structural integrity

Parameter	Dimension	Unit
Type of cylinder	III	
Volume of cylinder	5	L
Working pressure	350	MPa
Internal Diameter of cylinder, D_i	140	mm
Total length of cylinder, L	395	mm
Inlet diameter of cylinder, D_{in}	18	mm
Carbon fibre layer thickness, T_2	4	mm
aluminium liner thickness, T_1	1.5	mm
PTFE coating thickness T_3	0.5	mm
Maximum weight of cylinder	1.85	kg
Application	(UAV hydrogen storage tank) UAVHST	

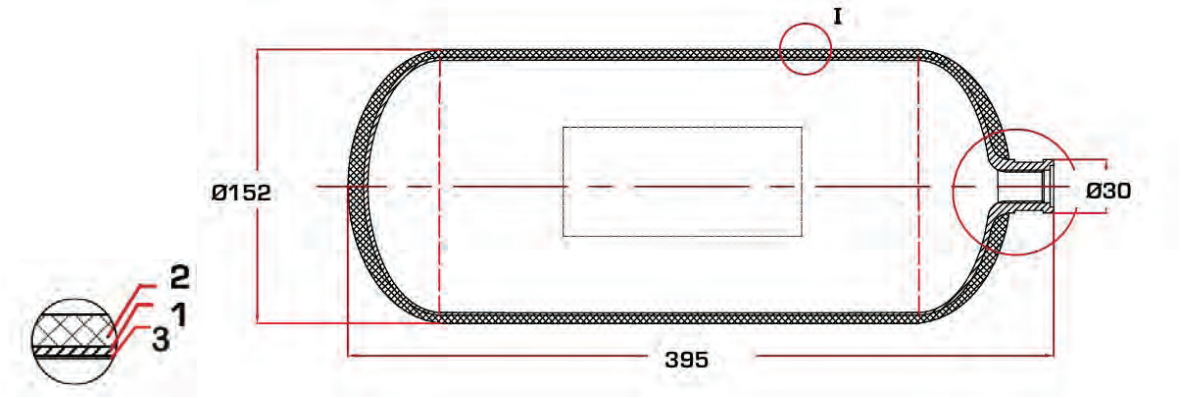


Figure 1. Geometrical structure of type-III hydrogen storage vessel.

where E is: and k_{eff} stands for effective heat conductivity.

$$E = h - \frac{p}{\rho} + \frac{u^2}{2} \quad (17)$$

where the hydrogen's h-specific enthalpy is.

While analyzing several turbulent models, concluded that the Realizable k model is best suited for the hydrogen rapid filling process and that the TKE dissipation follows an equation [48-50].

$$\frac{\partial}{\partial t}(\rho k) + \frac{\partial}{\partial r}(\rho k u) = \frac{\partial}{\partial r}\left[\left(\mu + \frac{\mu_t}{\sigma_k}\right)\frac{\partial k}{\partial r}\right] + G_K - \rho_\varepsilon - \Upsilon_M \quad (18)$$

$$\frac{\partial}{\partial t}(\rho\varepsilon) + \frac{\partial}{\partial r}(\rho\varepsilon u) = \frac{\partial}{\partial r}\left[\left(\mu + \frac{\mu_t}{\sigma_\varepsilon}\right)\frac{\partial \varepsilon}{\partial r}\right] + \rho C_1 S\varepsilon - \rho C_2 \frac{\varepsilon^2}{k + \sqrt{\upsilon\varepsilon}} \quad (19)$$

$$G_K = -\rho\overline{u'v'}\frac{\partial v}{\partial x} \quad (20)$$

Where $-\rho u'v'$ -Reynolds stress, *u′ and v′*-fluctuating quantities

$$\Upsilon_M = 2\rho\varepsilon M_t^2 \quad (21)$$

Where M_t -turbulent Mach number

$$M_t = \sqrt{\frac{k}{a^2}} \quad (22)$$

Where "a" indicates the sound speed. The vicinity at turbulence t is

$$\mu_t = \rho C_\mu \frac{k^2}{\varepsilon} \quad (23)$$

Table 2 listed properties of materials used in PTFE-coated aluminium wrapped with a carbon fiber cylinder. The low thermal conductivity of PTFE, 0.304 W/m·K, provides insulation for reducing heat transfer to the outer layers. High conductivity of aluminium is 238 W/m·K more heat distribution, while carbon epoxy fiber offers structural strength with reasonable thermal conductivity of 3.72 W/m·K. These layered properties dominate the temperature distribution during rapid filling [51-52].

The Table 3 shows the comparative study in various parameters of different material, used to select the best

Table 2. Properties of material

Layers	Density (kg/m³)	Specific heat (J/kgK)	Thermal conductivity (W/mK)
Teflon	2200	1.5	0.304
Aluminium	2700	902	238
Carbon epoxy fiber	1513	920	3.72

Table 3. Comparison of various cylinder materials properties

Property	PTFE-Coated Aluminium	Aluminium (Uncoated)	Stainless Steel	Fiber-Reinforced Polymer (FRP)
Thermal Conductivity (W/m K)	0.25–0.3 (Low, better insulation)	200 (Very high, poor insulation)	16 (High, rapid heat transmission)	Low (0.2–1)
Corrosion Resistance	Excellent (PTFE exhibits better protection against hydrogen embrittlement and corrosion)	Good (But liable to corrosion under certain conditions)	Excellent (High corrosion resistance)	Good (Resistant to corrosion but less durable than stainless steel)
Hydrogen Compatibility	Highly compatible (non-reactive with hydrogen)	Highly compatible (But can corrode under certain conditions)	Highly compatible (non-reactive, but higher risk of hydrogen embrittlement)	Moderate (requires special resin for hydrogen compatibility)
Insulation Effectiveness	Superior (Prevents rapid heat transfer, reducing thermal stress)	Poor (Requires additional insulation layers)	Poor (Requires additional insulation)	Moderate (Low thermal conductivity but less effective than PTFE)
Durability (Under High Pressure)	High (Aluminium provides strength, PTFE prevents thermal damage)	Moderate (requires reinforcement for high pressure)	Very High (extremely durable under pressure, but less effective thermally)	Moderate (Good for light applications but requires additional structural support)

Table 4. Comparison of various input parameter

Parameter	Current Study	Zhao et al. [53]	Li et al. [56]	Kim et al. [57]
Filling Pressure (MPa)	5–35	5–35	20–70	20–50
Inlet Temperature (K)	283–323	283–323	283–303	283–303
Mass Flow Rate (kg/s)	0.01–0.05	0.01–0.05	0.02–0.1	0.01–0.1
Filling Time (s)	0.5–12	0.5–12	1–5	1–5

materials based on the performance requirements and operational conditions.

Table 4 shows the initial parameter comparison with existing research work; listed parameters are freeze for conduct the simulation to optimize the hydrogen cylinder. By understanding the different to help to selection of influencing parameters [53-57].

Table 5 indicates the boundary condition for CFD simulation of the rapid hydrogen filling process Initial temperature of the gas and the ambient temperature are established as 293 K, which is considered in the simulation as the temperature is in equilibrium. The conventional heat transfer

Table 5. Simulation boundary conditions

Parameters	Value	Unit
Atmospheric temperature	293	K
the convective coefficient of the air around the cylinder and its outer surface.	10	W/m^2K
Gas inlet pressure	2	MPa
Inlet mass flow rate	0.002	kg/s
Gas initial temperature	293	K
Inlet gas pressure		MPa
Initial gas temperature	293	K

Table 6. comparative study of Type III and IV hydrogen cylinder

Parameter	Type III Cylinder (PTFE-coated Aluminium)	Type IV Cylinder (Carbon Fiber)	Remarks
Material	Aluminium liner with PTFE coating	Composite material	Type III uses a combination of metal and insulation, whereas Type IV is fully composite.
Thermal Conductivity (W/m K)	0.25–0.3 (PTFE), 200 (Aluminium)	5–15 (Carbon Fiber)	Type III has better thermal insulation due to PTFE coating, while Type IV has low conductivity but requires additional thermal management.
Strength	Moderate (Aluminium provides structural integrity)	High (Carbon fiber provides lightweight, high-strength structure)	Type IV offers higher strength and better pressure resistance than Type III.
Weight	Moderate (Aluminium is relatively heavy)	Lightweight (Carbon fiber offers high strength at a lower weight)	Type IV is ideal for applications where lightweight is essential, such as UAVs.
Pressure Resistance	Moderate (Withstand up to 35–70 MPa)	High Designed for high-pressure systems (up to 700 bar)	Type IV is better suited for high-pressure applications compared to Type III.
Temperature Resistance	Can withstand up to 250°C without degradation	200°C–300°C (depends on resin, composites)	Type III has better temperature tolerance in extreme conditions.
Thermal Management	Effective with PTFE for insulation, aluminium dissipates heat	Lower thermal conductivity, insulation strategies may be needed for efficient thermal management	Type III offers better thermal insulation naturally, while Type IV may need additional cooling.
Corrosion Resistance	High (PTFE prevents hydrogen embrittlement, corrosion)	Moderate (Carbon fiber is resistant, but polymer liner may degrade under certain conditions)	Type III has better corrosion resistance due to PTFE, while Type IV needs more attention to resin degradation.
Hydrogen Compatibility	Highly compatible with hydrogen (PTFE and aluminium)	Highly compatible with hydrogen, but composite material may need special treatments	Both cylinders are highly compatible with hydrogen, but Type III has better chemical stability.
Safety Considerations	More prone to thermal deformation, requires effective thermal management	Stronger structural integrity, better resistance to high pressure and thermal stress	Type IV offers greater safety due to its strength, while Type III requires careful thermal management during refuelling.

coefficient of 10 W/m²·K is assigned to the outer surface of the cylinder; its influence is minimal due to the insulating PTFE layer. Hydrogen was filled at an inlet pressure of 2 MPa and a mass flow rate of 0.002 kg/s. These conditions reflect realistic refuelling.

Table 6 provides the comparative analysis of Type III and Type IV hydrogen cylinders with several key parameters. This delivers the insights into the operating conditions, material selection and thermal management in hydrogen cylinder.

RESULTS AND DISCUSSION

The thermal and flow behaviour of 5 L and 35 MPa PTFE-coated hydrogen cylinders was simulated during the rapid filling process, and the outcomes show the characteristics with various inlet pressures, temperatures, and mass flow rates.

The temperature distribution of the hydrogen cylinder at various filling durations of 0.5 s, 1 s, 3 s, 6 s, and 12 s are shown in Figure 2. The peak temperature of gas is attained near the inlet due to recirculatory flow and compression effects. The flow is thermally stable with a high-duration filling process because of significant heat transmission within the flow region and from inside to the surrounding cylinder. But at lower filling times, the temperature is concentrated in a particular region and leads to reduced structural stability of the cylinder.

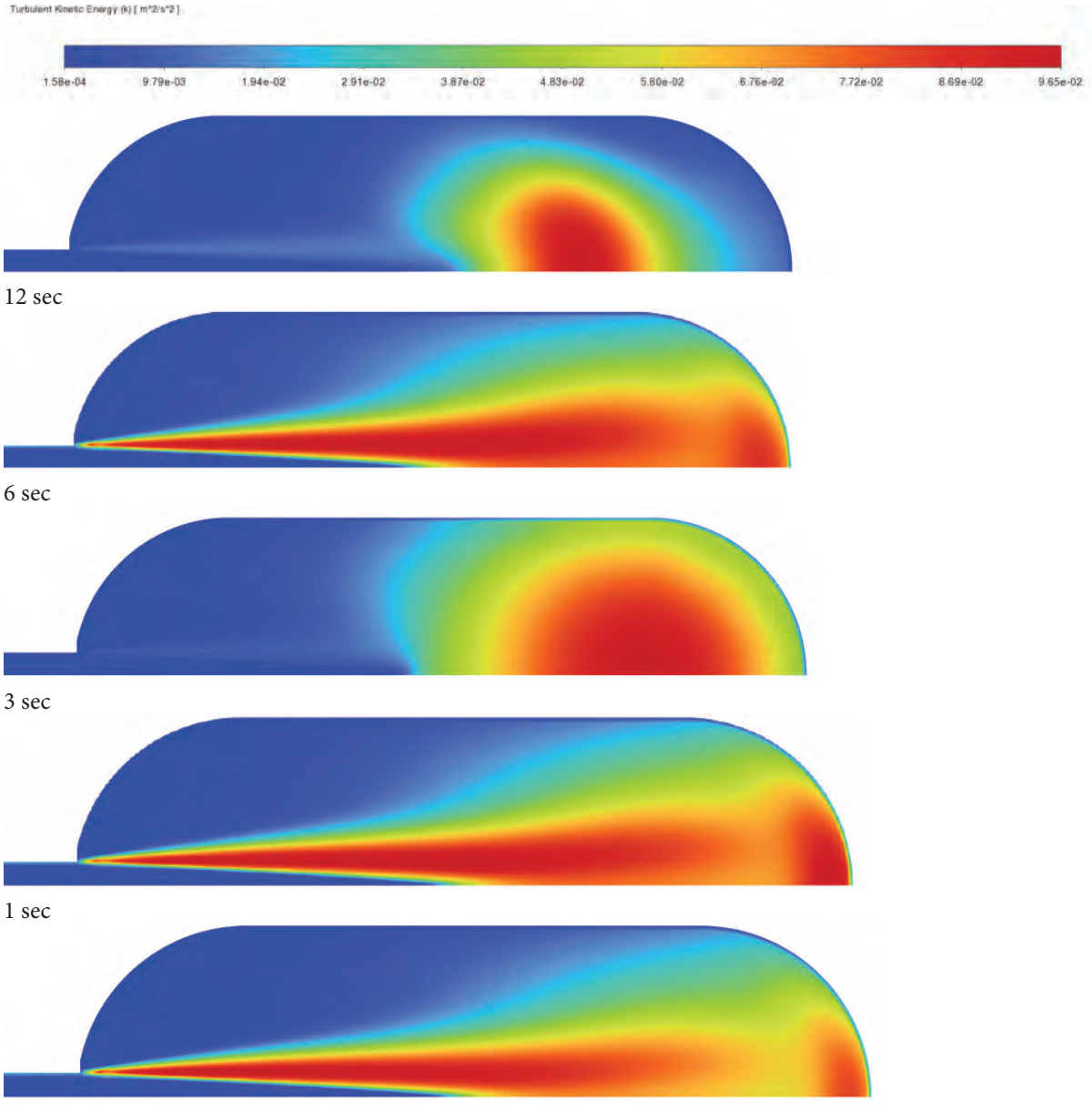


Figure 2. Temperature distribution of inner vessel in various filling time.

The Figure 3 shows the temperature distribution throughout the length of the cylinder with different initial gas temperatures of 283 K, 303 K, and 313 K in the fast-filling process. The simulation outcomes indicate that the internal gas temperature is raised with increasing initial gas temperature, specifically towards the inlet region, due to adiabatic compression and recirculatory flow. At a lower gas temperature, 283 K has less impact on internal gas temperature rises due to high temperature distribution; on the other side, at 313 K, accelerating the recirculatory flow with high pressure leads to increased thermal stress on the PTFE layer.

The internal gas temperature profile within the Type III hydrogen cylinder in the rapid filling process with different inlet temperatures is shown in the Figure 4. The high-pressure rapid filling process creates optimum recirculatory flow causes for accumulation of high-temperature gas at the inlet zone. During the rapid filling process, most of the thermally affected zone occurs at the central axis of the cylinder, so emphasize the potential precooling strategy to enhance the thermal stability of the cylinder. Figure 5 shows the profile of turbulent kinetic energy distribution throughout the length of the cylinder. The highest TKE is attained at maximum inlet gas temperature due to adiabatic compression and recirculatory flow within the system. The localized heat occurs near the inlet zone due to low recirculation of gas, accelerating the thermal load on the PTFE layer.

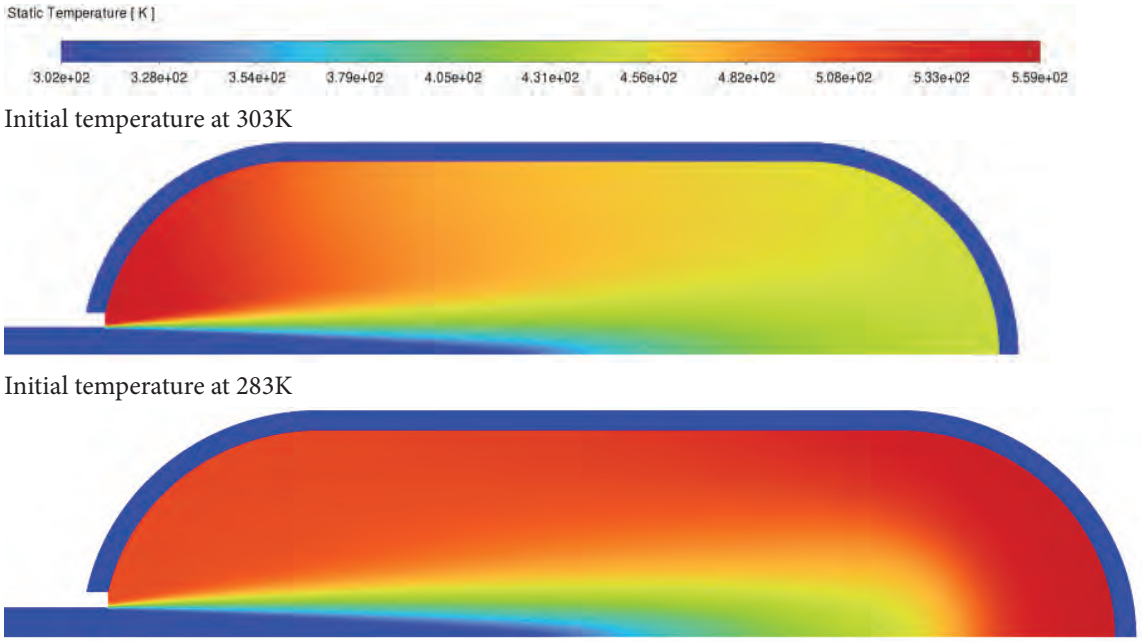


Figure 3. Temperature distribution of inner vessel in various hydrogen entry temperature.

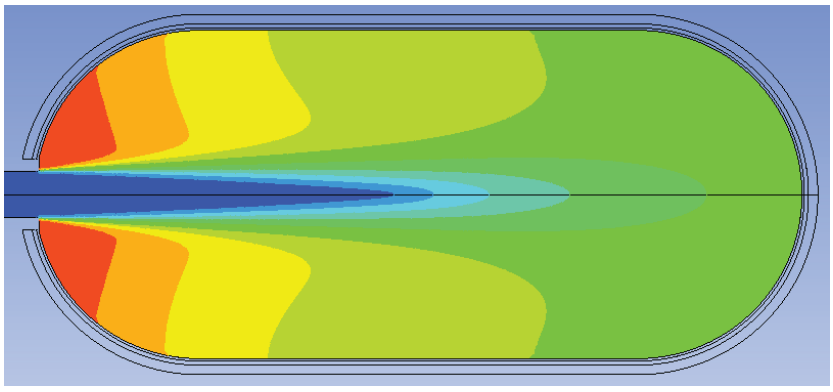


Figure 4. Hydrogen gas interior temperature profile.

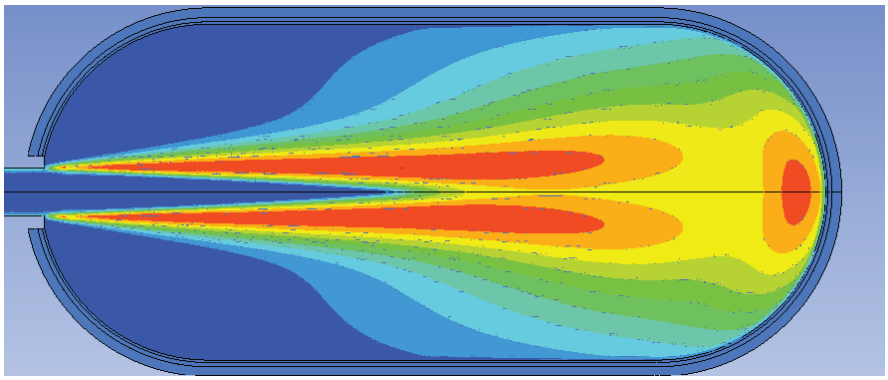


Figure 5. Hydrogen gas interior turbulent kinetic energy profile.

Effects of Filling Timing

The Figure 6 depicts that the variation of static temperature throughout the axis length of the cylinder with different filling times is 0.5 s, 1 s, 3 s, 6 s, and 12 s. Initially the all-static temperature curves are uniform and maintain a temperature of about 298K up to 0.15m, and further follow steep temperature rises along the axis of the cylinder, indicating that the hydrogen gas under the compression leads to rapid heating due to adiabatic effects beyond 0.15m from the inlet. The temperature magnitude is increased with increasing filling time, as at 0.5 s the maximum temperature is above 360 K, and at 12 s it exceeds 480 K. This progressive rise indicates that the greater thermal accumulation within the cylinder at optimum filling duration, even at lower pressure rises. The temperature rises are mainly located between the inlet region of 0.15–0.25 m beyond the taper, indicating the limited thermal stress in the downstream.

The overall thermal analysis of 5L and 35 MPa type III hydrogen cylinders in rapid filling with various filling durations is shown in the Figure 7. The maximum final

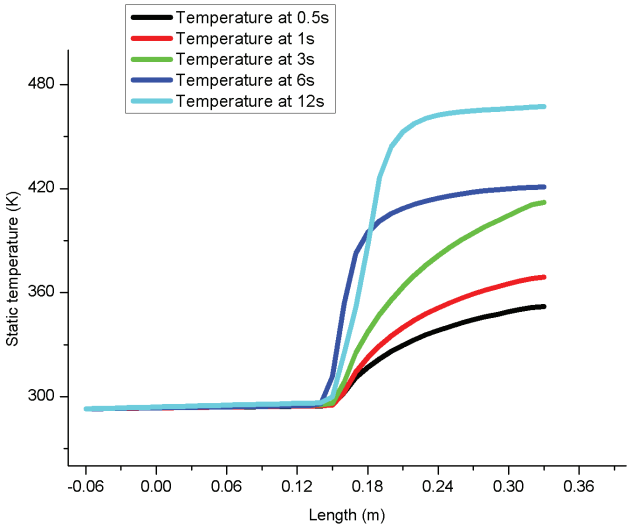


Figure 6. Variation of static temperature along the cylinder length.

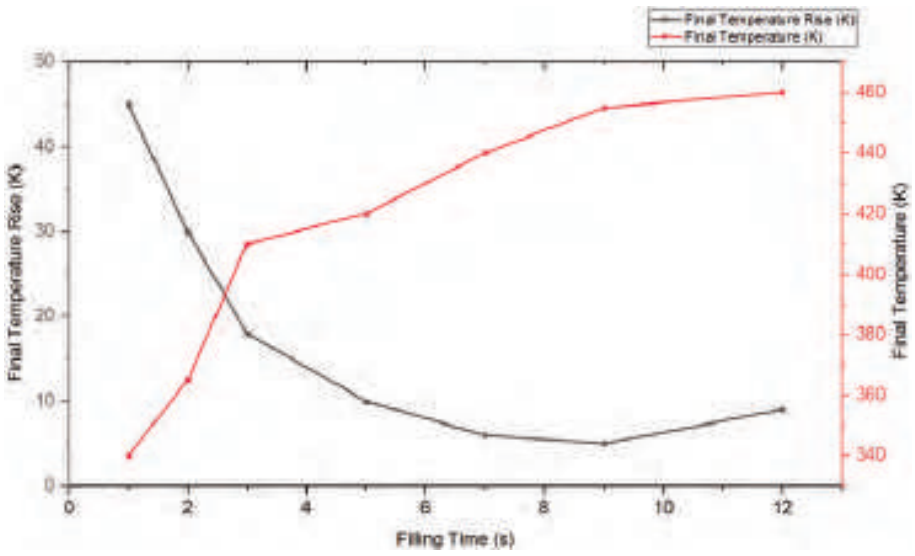


Figure 7. Variation of final temperature with different filling time.

temperature rise (ΔT) of about 40K is attained at a short filling duration of 0.5 to 1 second sharply. The sudden temperature rise occurs due to adiabatic compression of hydrogen gas in the rapid filling process, causing a reduction in heat transfer with surroundings. At filling times of 6 to 9 seconds, the heat conduction rate is significantly increased due to low temperature rises in multi-layered wall cylinders. As well as, the temperature rise does not continue beyond 10 seconds due to the concentration of thermal energy near the inlet. The final temperature variation shows as monotonic rises with filling time from 340 K to over 450 K up to 12 seconds filling time. The trend demonstrates that initial gas temperature and filling rate should be optimized to reduce the temperature rise (ΔT) and reduce the concentration of thermal load; otherwise, the integrity of the PTFE-coated hydrogen cylinder is reduced due to exceeding the thermal limits.

The Figure 8 reveals that the maximum TKE is attained at 0.25 m from the inlet; the rapid filling of hydrogen causes the intense flow disturbances and turbulence. TKE attains a maximum of 6.5 m^2/s^2 at 0.5 sec filling time, indicating a violent flow behaviour at the initial stage. On the other side, TKE decreases with increasing filling time, such as 1 m^2/s^2 at 6 seconds and 0.3 m^2/s^2 at 12 seconds, indicating the lower filling rate reduces the TKE and exhibits more stable flow. From the inlet upstream (0–0.18 m) and downstream (beyond 0.30 m) region. TKE remains close to zero, indicating the minimum turbulence. The presence of transient eddies and pressure waves during rapid filling induces the turbulent stress and leads to material degradation.

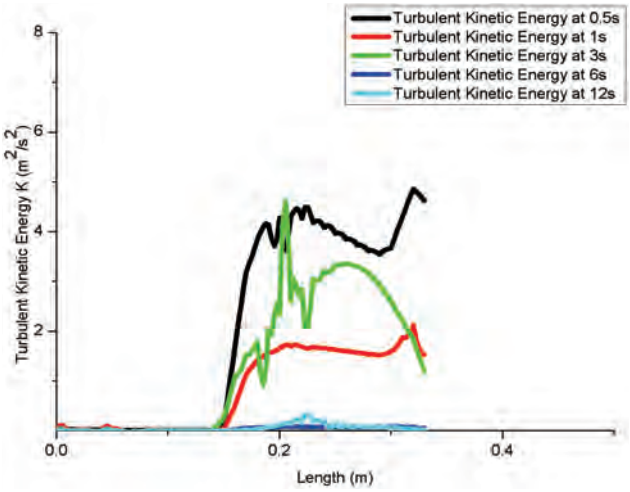


Figure 8. Turbulent kinetic energy variation along the cylinder length.

The internal temperature variation of the hydrogen cylinder during the rapid filling process is shown in the Figure 9. The simulation thermal stratification curve is closely aligned with Zhao et al. [53], To demonstrate the trustworthiness of the designed model. This temperature gradually increased as the time progressed, which means that the system became thermally stratified. Contrary to this, Zhao et al. [53], suggest that the temperature increases with time and that the temperature is lower than the simulated temperature. This can be explained by the differences between the initial, boundary and other assumptions used in the models. The graph shows that both Zhao et al. [53] and the simulation show a similar trend predict similar temperature trends during the thermal stratification process.

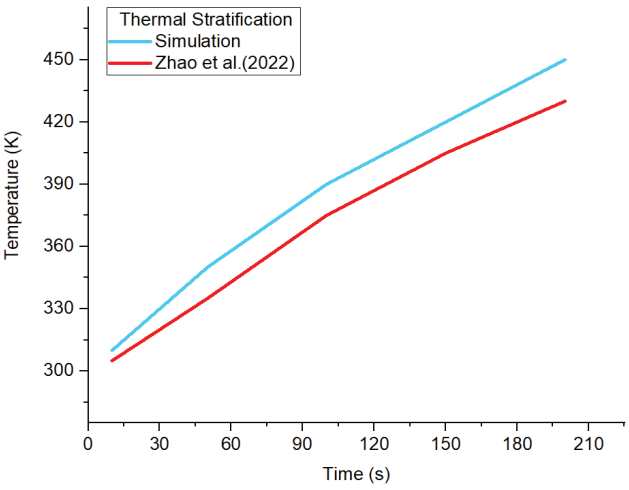


Figure 9. Thermal stratification of hydrogen cylinder.

Effects of Initial Pressure

The Figure 10 represents a temperature distribution along the cylinder axis with different inlet pressures of 50 bar, 100 bar, 200 bar, and 350 bar. The sudden temperature rise occurs at 0.18 m and 0.22 m from the inlet due to strong turbulent effects and adiabatic compression. This localized thermal fluctuation occurs because high-inlet velocity of gas leads to a reduction in the heat transfer rate to the surroundings. The maximum gas temperature increases from 360 to 415 K with a corresponding inlet pressure of 50 to

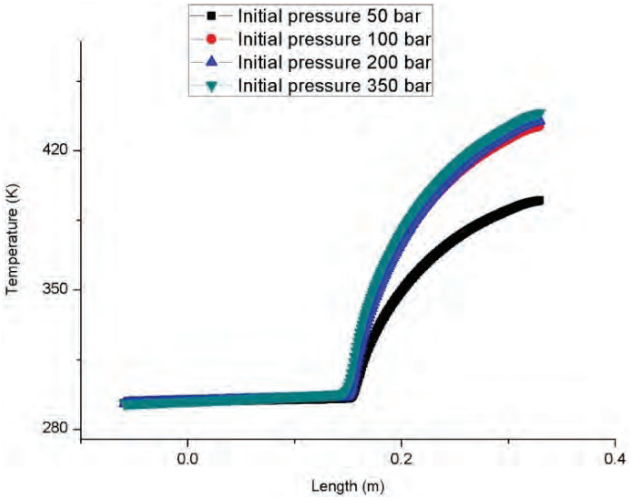


Figure 10. Variation of temperature along the cylinder length with different filling pressure.

Table 7. Initial parameters for various entry pressure of hydrogen gas

Initial pressure (Mpa)	Filling Temperature (K)	Filling rate (Kg/m^3)	Time step (sec)	Filling time (sec)
5	293	0.02	0.1	10
10	293	0.02	0.1	10
20	293	0.02	0.1	10
35	293	0.02	0.1	10

350 bar, reflecting more aggressive adiabatic compression with optimum inlet pressure. The outcome shows higher inlet pressure filling produces a uniform thermal distribution along the length; in other cases, thermal concentration occurs towards an inlet region, leading to thermal instability in the PTFE layer, and these effects are prevented by pressure ramping or pre-cooling strategies.

Table 7 presents the simulation setup for various hydrogen gas inlet pressure (5–35 MPa) effects on internal gas temperature rise. The input parameters of hydrogen gas filling are maintained at a filling temperature of 293 K and a 10-second filling time with a constant filling rate.

The Figure 11 shows the static pressure distribution throughout the length of the cylinder at various filling times: 0.5 s, 1 s, 3 s, 6 s, and 12 s. The plot elaborates the highest static pressure in the inlet and gradually drops toward the center and stabilizes downstream. At 0.5 s, the static pressure research was about 45 bars towards the inlet and then stabilized due to adiabatic compression and pressure shock during ultra-fast filling. As the filling time increases, the pressure profile becomes more uniform and less extreme. This behaviour reflects smoother pressure gradients and minimizing the mechanical stress on the cylinder walls. Additionally, the convergence of the pressure curves at the center and downstream sections indicates a steady-state behaviour that develops more clearly with extended filling durations.

The comparison of simulation maximum temperature and Zhao et al. [53] outcome with different inlet pressure is shown in Figure 12. Both plot line trends indicate that as high inlet pressure increases, internal gas temperature rises during the rapid filling process. However, the simulation outcome enhances the internal temperature rises compared with Zhao et al. [53]. due to different modelling assumptions, boundary conditions, and material properties used for simulation. Overall, the trend line indicates the strong correlation between the existing and simulation data, confirming the accuracy of the model used in the simulation.

Effect of Initial Temperature

Figure 13 shows the effects of initial temperature on the internal temperature rise of a hydrogen Type III cylinder in a rapid filling process. The initial temperature from 283 to 323 K and corresponding internal temperature rise is 416 to 525 K. The plot curve indicates the strong correlation in the initial gas temperature in terms of final gas temperature. The linear temperature rises up to 310 K, and beyond that point, temperature nonlinear acceleration occurs due to enhanced internal energy and less heat dissipation. This

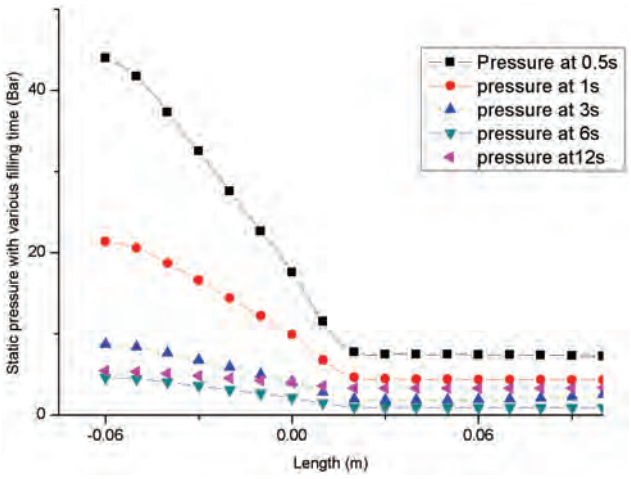


Figure 11. Variation of static pressure throughout length of the cylinder.

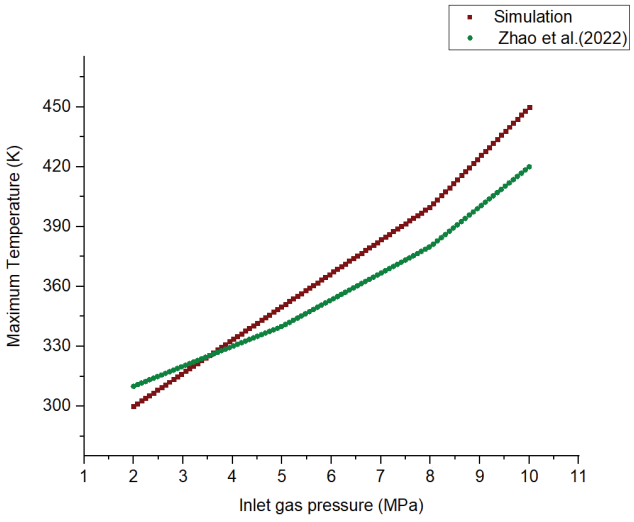


Figure 12. Maximum temperature variation with different gas inlet pressure.

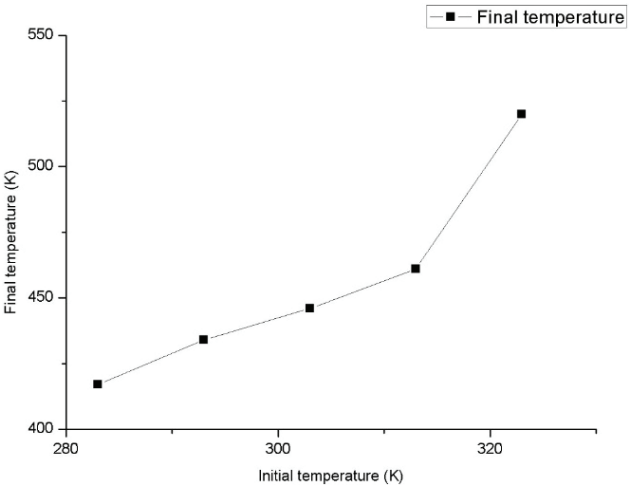


Figure 13. Variation of final gas temperature with different inlet gas temperature.

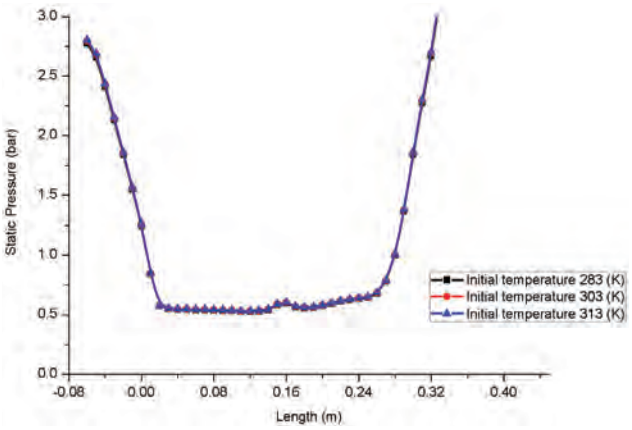


Figure 14. Static pressure variation with different inlet gas temperature.

behaviour clearly shows the contribution of adiabatic compression and limited cooling in the rapid filling process. The results underscore the importance of controlling inlet gas temperature, as elevated pre-fill conditions can lead to critical thermal loads that may exceed the material limits of the PTFE liner and composite structure. Therefore, implementing pre-cooling strategies or thermal regulation protocols is essential to ensure structural safety and prolong cylinder life in high-pressure hydrogen storage systems [54-55].

Axial static pressure variation along with different inlet gas temperatures of 283 K, 303 K, and 313 K is shown in the Figure 14. All three curves show a U-shaped profile with maximum pressure attained at both ends of the cylinder and minimum static pressure attained at the center zone. Near the inlet region, the pressure attains up to 2.8 bar and gradually tapers towards the center to 0.5 bar and again rises towards the end of the cylinder. This behaviour is expected because pressure is primarily governed by the imposed boundary conditions and filling dynamics. Energy distribution and gas density are primarily influenced by temperature, while bulk flow resistance is not. The shape is regular in all cases suggesting that the flow is steady, symmetric and that the effects of the thermals on the pressure gradients are relatively small. Overall, these findings suggest that thermal control has a limited effect on pressure distribution in such a hydrogen system but is necessary to control material constraints and thermal stresses during the fast-filling process.

The final temperature as a function of initial temperature is compared between simulation and Zhao et al. [53] as shown in the Figure 15. The plot indicates the significant rise in the final temperature with increasing initial temperature, especially higher in higher magnitude. In contrast, Zhao et al. [53] saw a general trend of increasing final temperature as the initial temperature increased. The simulation curve has the higher magnitude due to different boundary conditions, such as the mass flow rate, filling rate, and thermodynamic models. The comparison shows a better trend, though the simulation results suggest a more significant thermal response compared to Zhao et al. [53].

Effects of Filling Rate

The Figure 16 demonstrates variation of temperature along the cylinder length with different filling rates of 0.01 kg/s, 0.015 kg/s, 0.03 kg/s, and 0.05 kg/s. All curves remain uniform until 0.12 m from the inlet, but the optimum peak occurs between 0.2 and 0.25 m due to adiabatic compression in the high-pressure inlet. The maximum gas temperature is increased from 360 K to 425 K, corresponding to a filling rate of 0.01 to 0.05 kg/s. After 0.25 m, thermal stress is concentrated at the inlet and creates material fatigue by heating cycles.

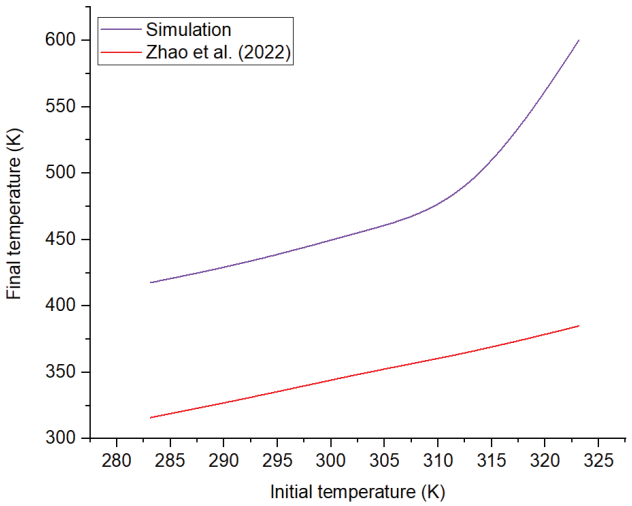


Figure 15. Variation of temperature in UAV cylinder.

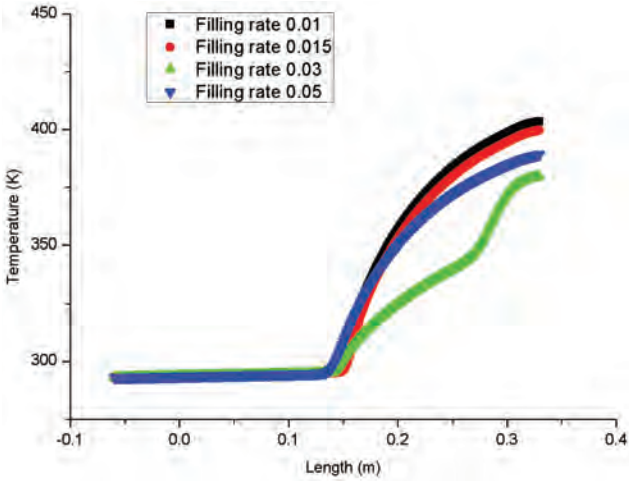


Figure 16. Variation of temperature with different filling rate.

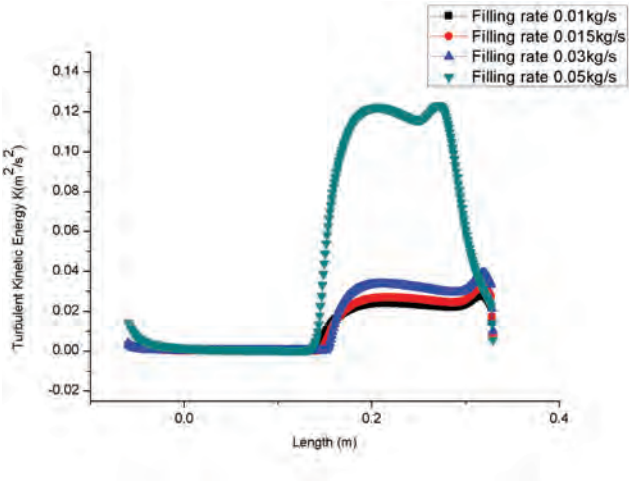


Figure 17. Variation of turbulent kinetic energy with different filling rate.

The TKE distribution along the axial span of the cylinder with different filling rates of 0.01 kg/s, 0.015 kg/s, 0.03 kg/s, and 0.05 kg/s are shown in the Figure 17. The maximum intensity of TKE is formed at a higher filling rate in the region of 0.18 to 0.25 m near the inlet. The notable flow instability and energy dissipation are attained at a filling rate of 0.05 kg/s, and the peak occurs above 0.12 m^2/s^2. On the other hand, the lower TKE is attained at a minimum filling rate, such as 0.01 kg/s, and remains below 0.03 m^2/s^2. The plot shows that the turbulence intensity not only increases with filling rate but also becomes more spatially extended along the axial direction as the flow rate rises. The outcome emphasizes that controlling the turbulence and its effects, such as accumulation of heat, structural stress, and mixing performance in hydrogen cylinders.

The comparison of temperature variation with different filling rate simulations and Zhao et al. [53]is shown in Figure 18. The plot indicates that temperature increases with increasing filling rate in both the simulation and the Zhao et al. [53] study. Higher filling rates significantly raise the compressional heat due to rapid filling gas compression. Both simulation and Zhao et al. [53] follow similar progressions, yielding slightly higher temperatures at high filling rates. The comparison plot indicates the simulation curve closely aligned with existing outcomes shows the reliability of the designed model. The slight difference indicates the different boundary condition.

Effect of Velocity Variation

The variation of hydrogen gas velocity magnitude along the axis of the Type III storage cylinder at different filling rates, such as 0.01 kg/s, 0.015 kg/s, 0.03 kg/s, and 0.05 kg/s, is shown in the Figure 19. This profile reflects the hydrogen behaviours inside the cylinder with various filling rates. At

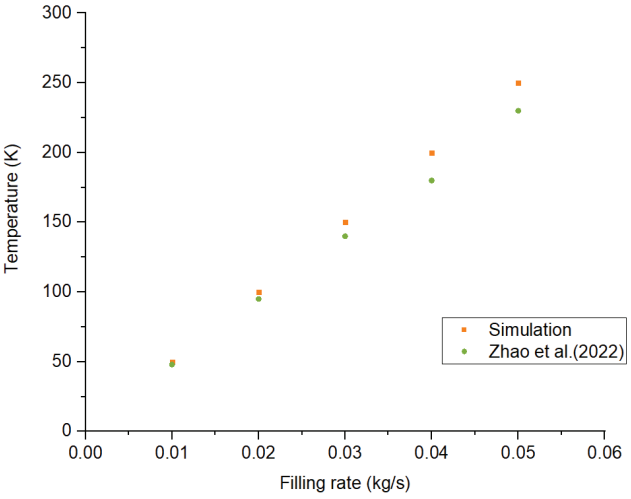


Figure 18. Variation of temperature with different flow rate.

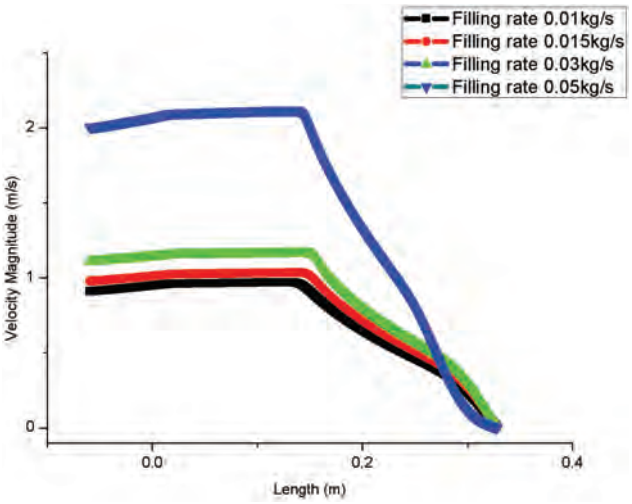


Figure 19. Variation of velocity magnitude with different filling rates.

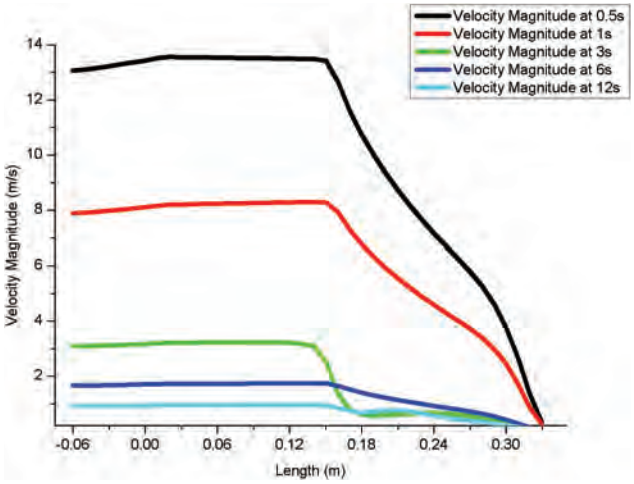


Figure 20. Variation of velocity magnitude with different filling time.

a lower filling rate of 0.01 kg/s, the gas maintains a more uniform velocity of 0.9 m/s up to 0.18 m from the inlet. Further, the velocity is increased with respect to the filling rate, with 0.05 kg/s exhibiting a maximum velocity near 2 m/s. The velocity is decreased beyond 0.2 m from the inlet due to energy dissipation, pressure recovery, and increasing flow resistance. Particularly, filling rates at 0.03 and 0.05 kg/s show a steep fall in velocity due to turbulence and wall interaction.

The velocity magnitude distribution along the axis of the cylinder with different filling durations, such as 0.5 s, 1 s, 3 s, 6 s, and 12 s, is shown in the Figure 20. The trend confirms that the optimum velocity of 13.5 m/s is attained at 0.5 s filling duration up to 0.18 m from the inlet; further, the velocity tapered to zero due to strong deceleration. As increasing filling time gradually decreases the maximum velocity to 8 m/s at 1 s, 3 m/s at 3 s, and below 1.5 m/s at 12 s. The spatial profile also indicates that maximum velocities are withstood over an entire span during rapid filling; in other cases, low-speed filling keeps the flow more stable and evenly distributed. These outcomes indicate that rapid filling causes the more aggressive and localized jet penetration, but lower-speed filling exhibits the gradual diffusion and smoother flow transitions.

CONCLUSION

This research work presents an overall numerical analysis of the thermal, flow and structural performance under rapid filling of hydrogen gas into a 5-liter, 35 MPa Type III storage system. This study explores how the various inlet parameters, such as filling time (0.5–12 s), mass flow rate (0.01–0.05 kg/s), initial temperature (283–313 K),, and filling pressure (50–350 bar), influence the hydrogen behaviour with various flow conditions.

1. The simulation outcome reveals that the high-temperature region formed towards the inlet let (0.18–0.25 m) due to adiabatic compression and localized flow recirculation of hydrogen. The non-linear maximum internal temperature rise is localized in the region from 298 K to 480 K at 12-second filling time. However, the filling time of 0.5 seconds provides a lowered internal temperature rise but exhibits high-pressure waves, which, which leads to the dual risks of rapid heating and flow shock.
2. The static pressure distribution is closely associated with the rate of filling; at a a 0.5-second filling duration, an internal gas pressure reaches a maximum value of 45 bar, and at a 3–12-2-second filling duration, gas pressure is uniformly distributed around 5–7 bar. Rapid inflow of hydrogen leads to transient over pressurization. This behaviour reveals that the initiation gas temperature is very low, and it is increased gradually by the pressure spikes.
3. Further analysed the behaviour of velocity magnitude and turbulent kinetic energy (TKE) on flow uniformity and structural integrity. The velocity peaks at 13.5 m/s at 0.5 seconds of filling duration and tapers toto 1 m/s at 12 seconds of filling duration. TKE reaches an optimum of 0.12 m^2/s^2 at a 0.05 kg/s flow rate that maximum turbulence intensity and unsteady flow occur in rapid filling of hydrogen. The high-intensity turbulent zone is is recognized towards the inlet region and reduces along the axis, and the maximum TKE increases the structural fatigue due to flow-induced vibrations and localized wall stress.
4. Multi-layered structure plays a crucial role in in heat transmission within the structure and the PTFEPTFE layer acts as an insulator to protect the heat transmission from the inner to the outer layer and ensure and material degradation by accumulation of heat localizing near the inlet.
5. This study identified the safe filling environment, such as a masses flow rate of 0.03 kg/s, an inlet temperature of 283 K, and a filling time of 6–8 s. Acceptable temperature rise towards 430 K leads to uniform flow behaviour and reduced peak turbulence.
6. This research presents detailed insights into transient thermo-fluid interactions in Type III hydrogen storage cylinders under fast-filling conditions and fills the existing gap by adapting quantitative information into temperature stratification, turbulence generation, pressure evolution, and material interaction in the operational range.

This research outcome reveals the valuable guidance for lower-scale hydrogen storage cylinders, especially for UAV applications. Future work can extend this model to include fluid-structure interaction (FSI), cyclic fatigue under repeated filling, and experimental validation through embedded sensors to further optimize design and safety.

Limitations

1. In this model used Redlich-Kwong equation for isotropic material limit the accuracy under extreme condition.
2. This simulation outcomes are lagging in experimental validation.
3. The work focused only PTFE coated aluminium cylinder but not explored various combination of materials.

Future recommendation

1. Analysis the anisotropic material properties and behaviours of real gas in extreme condition
2. Conduct experiments for validating the simulation outcome.
3. Conduct simulation of this model for up to 7MPa pressure.
4. Develop the sensor intergradation for real time monitoring system.

NOMENCLATURE

E	The gas's total energy (J/kg)
K	Kinetic energy of turbulent flow (m^2/s^2)
k_{eff}	Effective thermal conductivity (W/m.K)
M_t	Mach number of turbulences
p	Pressure absolute (MPa)
r	The radial length (meters)
t	Temporal (s)
u	The axial speed (m/s)
D_i	Measurement of diameter (mm)
L	Length in millimetres
m	The highest mass of storage (kg)
D_{in}	Diameter of inlet (mm)
T_1	Thickness of aluminium liner (mm)
T_2	Thickness of carbon epoxy coating (mm)
T_3	Thickness of PTFE coating (mm)
v	The temperature radial velocity (m/s)
x	Axial distance (m)
Y_M	Variable dilatation in compressible shear flow

Greek Letters

ρ	Density (g/m^3)
μ	Viscosity dynamic (Ns/m^2)
μ_t	Turbulence viscosity

Subscripts

t	Turbulent
eff	Effective
wall	Wall temperature
in	Inlet of gas
gas	Gas in the cylinder
amb	Ambient
inlet	Inlet pre-cooling hydrogen
i	Inner

AUTHORSHIP CONTRIBUTIONS

Authors equally contributed to this work.

DATA AVAILABILITY STATEMENT

The authors confirm that the data that supports the findings of this study are available within the article. Raw data that support the finding of this study are available from the corresponding author, upon reasonable request.

CONFLICT OF INTEREST

No conflicts of interest are disclosed by the authors.

ETHICS

There are no ethical issues with the publication of this manuscript.

STATEMENT ON THE USE OF ARTIFICIAL INTELLIGENCE

Artificial intelligence was not used in the preparation of the article.

REFERENCES

[1] Bakker S, van Lente H, Meeus MTH. Credible expectations-the US Department of Energy's Hydrogen Program as enactor and selector of hydrogen technologies. Technol Forecast Soc Change 2012;79:1059–1071. [CrossRef]

[2] Matsuo Y, Endo S, Nagatomi Y, Shibata Y, Komiyama R, Fujii Y. A quantitative analysis of Japan's optimal power generation mix in 2050 and the role of CO2-free hydrogen. Energy 2018;165:1200–1219. [CrossRef]

[3] Sgobbi A, Nijs W, De Miglio R, Chiodi A, Gargiulo M, Thiel C. How far away is hydrogen? Its role in the medium and long-term decarbonisation of the European energy system. Int J Hydrogen Energy 2015;41:19–35. [CrossRef]

[4] Jain IP. Hydrogen the fuel for 21st century. Int J Hydrogen Energy 2009;34:7368–7378. [CrossRef]

[5] Niaz S, Manzoor T, Pandith AH. Hydrogen storage: Materials, methods and perspectives. Renew Sustain Energy Rev 2015;50:457–469. [CrossRef]

[6] Zheng J, Liu ZL, Hua Z, Guch WG, Chen L. Research status-in-situ and key challenges in hydrogen safety. J Saf Environ 2020;20:106–115.

[7] Kirubadurai B, Jaganraj R, Vinothkumar M, Jegadeeswari G. A dual modelling approach: CFD and electrochemical impedance spectroscopy for enhanced PEM fuel cell design and operation. Results Eng 2025;26. [CrossRef]

[8] Kirubadurai B, Jaganraj R, Vinothkumar M, Jegadeeswari G. CFD analysis of fuel cell performance: Insights into electrochemical and thermal processes. Int Rev Appl Sci Eng 2025;16:472–483. [CrossRef]

[9] Manoharan Y, Hosseini SE, Butler B, Alzhahrani H, Senior BTF, Ashuri T, et al. Hydrogen fuel cell vehicles: Current status and future prospect. Appl Sci (Basel) 2019;9:2296. [CrossRef]
[10] Valencia L, Blanc-Vannet P, Domergue D, Heudier L, Jamois D. Thermal history resulting in the failure of lightweight fully-wrapped composite pressure vessel for hydrogen in a fire experimental facility. Fire Technol 2015;52:421–442. [CrossRef]
[11] Zhang M, Lv H, Kang H, Zhou W, Zhang C. A literature review of failure prediction and analysis methods for composite high-pressure hydrogen storage tanks. Int J Hydrogen Energy 2019;44:25777–25799. [CrossRef]
[12] Ahluwalia RK, Hua TQ, Peng JK. On-board and off-board performance of hydrogen storage options for light-duty vehicles. Int J Hydrogen Energy 2012;37:2891–2910. [CrossRef]
[13] Pépin J, Lainé E, Grandidier JC, Benoit G, Mellier D, Weber M, et al. Replication of liner collapse phenomenon observed in hyperbaric type IV hydrogen storage vessel by explosive decompression experiments. Int J Hydrogen Energy 2018;43:4671–4680. [CrossRef]
[14] Sun Y, Lv H, Zhou W, Zhang C. Research on hydrogen permeability of polyamide 6 as the liner material for type IV hydrogen storage tank. Int J Hydrogen Energy 2020;45:24980–24990. [CrossRef]
[15] Yersak TA, Baker DR, Yanagisawa Y, Slavik S, Immel R, Mack-Gardner A, et al. Predictive model for depressurization-induced blistering of type IV tank liners for hydrogen storage. Int J Hydrogen Energy 2017;42:28910–28917. [CrossRef]
[16] Durbin DJ, Malardier-Jugroot C. Review of hydrogen storage techniques for on board vehicle applications. Int J Hydrogen Energy 2013;38:14595–14617. [CrossRef]
[17] Maus S, Hapke J, Ranong CN, Wüchner E, Friedlmeier G, Wenger D. Filling procedure for vehicles with compressed hydrogen tanks. Int J Hydrogen Energy 2008;33:4612–4621. [CrossRef]
[18] Yang JC. A thermodynamic analysis of refueling of a hydrogen tank. Int J Hydrogen Energy 2009;34:6712–6721. [CrossRef]
[19] Zhang J, Fisher TS, Ramachandran PV, Gore JP, Mudawar I. A review of heat transfer issues in hydrogen storage technologies. J Heat Transfer 2005;127:1391–1399. [CrossRef]
[20] Zhao Y, Liu G, Liu Y, Zheng J, Chen Y, Zhao L, et al. Numerical study on fast filling of 70 MPa type III cylinder for hydrogen vehicle. Int J Hydrogen Energy 2012;37:17517–17522. [CrossRef]
[21] Sapre S, Pareek K, Rohan R, Singh PK. H2 refueling assessment of composite storage tank for fuel cell vehicle. Int J Hydrogen Energy 2019;44:23699–23707. [CrossRef]
[22] Xiao J, Wang X, Bénard P, Chahine R. Determining hydrogen pre-cooling temperature from refueling parameters. Int J Hydrogen Energy 2016;41:16316–16321. [CrossRef]
[23] Schneider J, Meadows G, Mathison S, Veenstra M, et al. Validation and sensitivity studies for SAE J2601, the light duty vehicle hydrogen fueling standard. SAE Int J Altern Powertrains 2014;3:257–309. [CrossRef]
[24] J-Q, Myoung NS, Kwon JT, Jang SJ, Lee T. A study on the prediction of the temperature and mass of hydrogen gas inside a tank during fast filling process. Energies (Basel) 2020;13:6428. [CrossRef]
[25] Li JQ, Myoung NS, Kwon JT, Jang SJ, Lee T, Lee YH. A theoretical analysis of temperature rise of hydrogen in high-pressure storage cylinder during fast filling process. Adv Mech Eng 2014;12. [CrossRef]
[26] Gromov NV, Medvedeva TB, Lukoyanov IA, Panchenko VN, Prikhod'ko SA, Parmon VN, et al. Hydrolysis-oxidation of cellulose to formic acid in the presence of micellar vanadium-containing molybdophosphoric heteropoly acids. Results Eng 2023;17:100913. [CrossRef]
[27] Oh SJ, Yoon JH, Jeon KS, Choi J. A numerical study on characteristics of heat transfer in hydrogen filling storage vessel by charging conditions. Int J Hydrogen Energy 2022;47:25679–25695. [CrossRef]
[28] Molina S, Ruiz S, Gomez-Soriano J, Olcina-Girona M. Impact of hydrogen substitution for stable lean operation on spark ignition engines fueled by compressed natural gas. Results Eng 2022;17:100799. [CrossRef]
[29] Özdoğan E, Hüner B, Süzen YO, Eşiyok T, Uzgören İN, Kıstı M, et al. Effects of tank heating on hydrogen release from metal hydride system in VoltaFCEV Fuel Cell Electric Vehicle. Int J Hydrogen Energy 2022;48:6811–6823. [CrossRef]
[30] Vlaskin MS, Grigorenko AV, Gromov AA, Kumar V, Dudoladov AO, Slavkina OV, et al. Methane pyrolysis on sponge iron powder for sustainable hydrogen production. Results Eng 2022;15:100598. [CrossRef]
[31] Ahmadi P, Khoshnevisan A. Dynamic simulation and lifecycle assessment of hydrogen fuel cell electric vehicles considering various hydrogen production methods. Int J Hydrogen Energy 2022;47:26758–26769. [CrossRef]
[32] Li JQ, Li JCL, Park K, Kwon JT. Investigation on the changes of pressure and temperature in high pressure filling of hydrogen storage tank. Case Stud Therm Eng 2022;37:102143. [CrossRef]
[33] Wu X, Liu J, Shao J, Deng G. Fast filling strategy of type III on-board hydrogen tank based on time-delayed method. Int J Hydrogen Energy 2021. [CrossRef]
[34] Melideo D, Baraldi D, Acosta-Iborra B, Cebolla RO, Moretto P. CFD simulations of filling and emptying of hydrogen tanks. Int J Hydrogen Energy 2016;42:7304–7313. [CrossRef]

[35] Simonovski I, Baraldi D, Melideo D, Acosta-Iborra B. Thermal simulations of a hydrogen storage tank during fast filling. Int J Hydrogen Energy 2015;40:12560–12571. [CrossRef]
[36] Melideo D, Baraldi D, Galassi MC, Cebolla RO, Iborra BA, Moretto P. CFD model performance benchmark of fast filling simulations of hydrogen tanks with pre-cooling. Int J Hydrogen Energy 2014;39:4389–4395. [CrossRef]
[37] Melideo D, Baraldi D. CFD analysis of fast filling strategies for hydrogen tanks and their effects on key-parameters. Int J Hydrogen Energy 2014;40:735–745. [CrossRef]
[38] Melideo D, Baraldi D, De Miguel Echevarria N, Iborra BA. Effects of some key-parameters on the thermal stratification in hydrogen tanks during the filling process. Int J Hydrogen Energy 2019;44:13569–13582. [CrossRef]
[39] Wang L, Ye F, Xiao J, Bénard P, Chahine R. Heat transfer analysis for fast filling of on-board hydrogen tank. Energy Procedia 2019;158:1910–1916. [CrossRef]
[40] Xiao J, Bénard P, Chahine R. Estimation of final hydrogen temperature from refueling parameters. Int J Hydrogen Energy 2016;42:7521–7528. [CrossRef]
[41] Molkov V, Dadashzadeh M, Makarov D. Physical model of onboard hydrogen storage tank thermal behaviour during fuelling. Int J Hydrogen Energy 2019;44:4374–4384. [CrossRef]
[42] Wang GX, Zhou JQ, Hu SJ, Li QF. The influences of L/D ratio and inlet diameter on the temperature rise and temperature distribution within a high pressurized hydrogen cylinder during refueling. Eng Mech 2014;31:225–232.
[43] Zhang RY, Wang HZ, Zhao GJ. Design and simulation of a vehicle-mounted high-pressure hydrogen staged charging system. Acta Energ Sol Sin 2022;43:427–432.
[44] Deymi-Dashtebayaz M, Farzaneh-Gord M, Nooralipoor N, et al. The complete modelling of the filling process of hydrogen onboard vehicle cylinders. Braz J Chem Eng 2016;33:391–399. [CrossRef]
[45] Zhao Y, Liu G, Liu Y, et al. Numerical study on fast filling of 70 MPa type III cylinder for hydrogen vehicle. Int J Hydrogen Energy 2012;37:17517–17522. [CrossRef]
[46] Li Q, Zhou J, Chang Q, Xing W. Effects of geometry and inconstant mass flow rate on temperatures within a pressurized hydrogen cylinder during refueling. Int J Hydrogen Energy 2012;37:6043–6052. [CrossRef]
[47] Dicken C, Mérida W. Modeling the transient temperature distribution within a hydrogen cylinder during refueling. Numer Heat Transf A Appl 2007;53:685–708. [CrossRef]
[48] Bourgeois T, Ammouri F, Weber M, Knapik C. Evaluating the temperature inside a tank during a filling with highly pressurized gas. Int J Hydrogen Energy 2015;40:11748–11755. [CrossRef]
[49] Suryan A, Kim HD, Setoguchi T. Three dimensional numerical computations on the fast filling of a hydrogen tank under different conditions. Int J Hydrogen Energy 2012;37:7600–7611. [CrossRef]
[50] Harle S, Wankhade RL. A review of green building research: Key findings, challenges, energy efficiency and proposed solutions. Sigma J Eng Nat Sci 2025;43:685–703. [CrossRef]
[51] Sommer TP, So RMC, Zhang HS. Near-wall variable-Prandtl-number turbulence model for compressible flows. AIAA J 1993;31:27–35. [CrossRef]
[52] Subran N, Ajit K, Krishnan H, Pachiyappan S, Ramaswamy P. Synthesis and performance of a cathode catalyst derived from areca nut husk in microbial fuel cell. Chemosphere 2023;312:137303. [CrossRef]
[53] Zhao Y, Liu G, Liu Y, Zheng J, Chen Y, Zhao L, et al. Numerical study on fast filling of 70 MPa type III cylinder for hydrogen vehicle. Int J Hydrogen Energy 2012;37:17517–17522. [CrossRef]
[54] Li M, Yang Q, Zhang C, Huang S, Zhang M, Zhang G, et al. Experimental and numerical study of the temperature evolution in hydrogen cylinder under fast-refueling process. Int J Heat Mass Transf 2023;211:124220. [CrossRef]
[55] Sanaka SP, Ramanaiah K, Rao KD, Gunda NSP. Design and parametric evaluation of proton exchange membrane fuel cell for enhanced performance. J Therm Eng 2025;11:1705–1716. [CrossRef]
[56] Li M, Yang Q, Zhang C, Huang S, Zhang M, Zhang G, et al. Experimental and numerical study of the temperature evolution in hydrogen cylinder under fast-refueling process. Int J Heat Mass Transf 2023;211:124220. [CrossRef]
[57] Kim SC, Lee SH, Yoon KB. Thermal characteristics during hydrogen fueling process of type IV cylinder. Int J Hydrogen Energy 2010;35:6830–6835. [CrossRef]

Sigma J Eng Nat Sci, Vol. 44, No. 4, pp. 2873–2888, August, 2026

Sigma Journal of Engineering and Natural Sciences
Web page info: https://sigma.yildiz.edu.tr
DOI: 10.14744/sigma.2026.2132

Research Article

Disease detection in sugarcane crop using deep learning

Twinkle B. ANKLESHWARIA[1,2], Madhavi B. DESAI[1,2*]

[1]*Gujarat Technological University, Gujarat, 382424, India*
[2]*Department of Computer Science and Engineering, R. N. G. Patel Institute of Technology, Gujarat, 394620, India*

ARTICLE INFO

Article history
Received: 17 December 2024
Revised: 13 March 2025
Accepted: 11 May 2025

Keywords:
Plant Disease Detection; Sugarcane Crop; Deep Learning

ABSTRACT

Sugarcane is a special crop that developed from a wild grass species to a major crop utilized for food and energy as a result of human activities. Due to its substantial contribution to the national finances and employment of more than a million people, mostly in the production of sugar and renewable bioenergy, it is a major crop that requires careful monitoring. Crop losses for farmers, both in terms of quantity and quality is caused by diseases in crop. In order to increase agricultural output and performance, scientists are now focused on early disease detection and identification. Additionally, agriculture makes substantial use of artificial intelligence. This study attempts to classify diseases in sugarcane using transfer learning and deep learning algorithms. In this context, first a detailed review on the recent contribution in sugarcane disease detection is discussed. Then, using leaf images as data, deep learning techniques are implemented utilizing transfer learning to build models that can identify sugarcane diseases. Metrics like confusion matrix, accuracy, precision, recall, and f1-score are used to evaluate the performance of various deep learning models. Different deep learning models such as Convolutional Neural Network (CNN), Visual Geometry Group 16(VGG16), Visual Geometry Group 19 (VGG19), Alex Krizhevsky's Network (AlexNet), Inception convolutional neural network Version 3 (Inception V3) and Densely Connected Convolutional Network with 201 layers (DenseNet201) were trained and results show that DenseNet201 outperforms compared to others with 94.14 % accuracy. This study not only shows how transfer learning can improve sugarcane disease classification, but it also verifies that deep learning models can function well in classification-related tasks.

Cite this article as: Ankleshwaria TB, Desai MB. Disease detection in sugarcane crop using deep learning. Sigma J Eng Nat Sci 2026;44(4):2873–2888.

INTRODUCTION

Agriculture is one of the largest growing sector in Indian economy. It is one of the primary source of income for around two-third of population in India. Sugar cane is one of India's primary agricultural products [1]. Biofuel can be produced from sugarcane byproducts like straw and cane fibers. Moving from conventional fuels to biofuels has many financial advantages that can help society financially and lessen the need to dispose of biomass in the future

***Corresponding author.**
*E-mail address: twi1902@gmail.com

This paper was recommended for publication in revised form by Editor-in-Chief Ahmet Selim Dalkilic

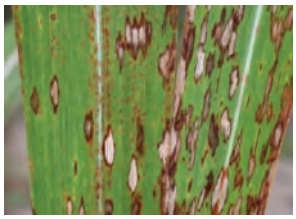
Published by Yıldız Technical University Press, İstanbul, Turkey
© Author. This is an open access article under the CC BY-NC license (http://creativecommons.org/licenses/by-nc/4.0/).

[2]. Lots of sugarcane products contain molasses, rum and fibers, which are used to feed animals [3]. Different factors that cause diseases in crop are varying temperature, composition of soil, an unfavorable pH level and changing climatic conditions. Plant diseases can be defined as unusual variations caused by any one or more biotic or abiotic factors that affects the normal growth of a crop. Generally, crop diseases can be classified as either infectious or non-infectious. Infections with bacteria, fungi, and viruses result in infectious illnesses. Negative environmental variables are the origin of non-infectious diseases, that cause damage to crop [4]. Worldwide crop output is hampered by sugarcane diseases, and no nation is immune to the damaging effects of plant infections and pests. Worldwide reports of more than 125 sugarcane diseases attributed to bacteria, viruses, nematodes, phytoplasma, and fungus have been received [5]. The symptoms of some of the important diseases affecting sugarcane plants are included in Table 1 [6-9].

Table 1. Indicators of major diseases in sugarcane

Sr no	Sugarcane Disease name	Symptoms	Causes for Disease	Image of Diseases
1	Red rot	The infected leaf undergoes colour change from time to time. As time passes the stalks becomes hollow. [6].	Rain, Air and humid weather. Fungus named Colletotrichum Falcatum causes red rot disease	
2	Wilt	The crown leaves shrink and become yellow in infected plants.[7]	High Temperature, low humidity, soil moisture. Cephalosporium sacchari infection causes Wilt disease	
3	Grassy shoot	Crowded bunch of tillers having narrow leaves are formed due to proliferation of vegetation buds from the base of the cane.	The diseases are caused by a phyto-plasma bacteria.	
4	Smut	Production of whiplike structure from the growing point of the canes.[8]	Hot and dry weather. Ustilago scitaminea is the fungus that causes Smut illness	
5	Red striped disease	Dark red stripes appear either all over the blade or in the middle. [9]	wet and hydrated circumstances. The bacteria Xanthomonas Albilineans is the cause of red striped disease	
6	Mosaic disease	Leaves that are kept away from sunlight appear chlorotic and creates a mosaic pattern	It is spread by a cutting knife and contaminated seed.	
7	Pokkah Boeng	Leaf blades or base of the young leaves suffers from chlorotic condition	Humid, cloudy weather and drizzling rains	

Table 1. Indicators of major diseases in sugarcane (continued)

Sr no	Sugarcane Disease name	Symptoms	Causes for Disease	Image of Diseases
8	yellow leaf disease	Middle region of the leaf turns yellow in colour	dry conditions	
9	RUST	small yellowish and reddish spots appear on both sides of leaf.	Warm weather with high humidity	
10	Leaf scald disease	«pencil lines» of white and yellow border appears on the leaf.	drought, waterlogging, and low temperature	
11	Eye Spot Helminthosporium	The wet patch appears on the leaves, grows longer over time, and eventually takes the form of an «eye» with a reddish-brown centre encircled by straw-coloured tissues.	Moist and humid conditions	

In the traditional method, farmers manually search their crops for visible signs of crop disease, consulting plant pathologists or crop disease experts for further guidance. Moreover, it involves laborious, drawn-out, and frequently challenging procedures of microscopy, pathogen culture isolation, and visual symptomatology observation in diagnosing crop disease. Therefore, precise disease detection and classification are necessary to assist farmers in farming. Artificial intelligence methods can be used to develop more robust system to identify agricultural diseases. These tools are quicker than previous approaches and may not require very complex or advanced procedures [9]. Recent studies showed that models using Machine learning algorithm like SVM are less accurate at predicting and detecting disease. Also, model is trained for small to medium number of images considering a smaller number of diseases. In this case, deep learning and transfer learning can improve the efficiency and accuracy of sugarcane disease detection. For the purpose of predicting dynamic time-series responses, another model based on deep learning neural networks has been developed in MATLAB. [10]. A novel method to enhance the deep learning model's performance has been put forth that uses fuzzy edge detection to maintain the edge pixels and fuzzy filtering to modify the filtered image pixels in order to produce a denoised image [11]. Researchers are always ready to search for new and inexpensive ways to solve the problem of diseases in crop [7, 8]. Different horizons of logic such as Fuzzy logic, neutrosophic logic and bitopological spaces can be combined that have a huge potential in various applications that can handle uncertain or imprecise image data [12]. This is because the early disease detection in crop allows farmers and other stakeholders enough time to minimize the risk of a disease outbreak and yield losses Additionally, comparisons between deep learning and other widely used methods are made with regard to variations in classification or regression performance, and the results show that deep learning offers high accuracy, outperforming other well used image processing methods. [13]. A multi-layer perceptron (MP) based on a deep learning (DL) model is used to detect and classify images infected with Sugarcane Red Rot (SRR). [14]. In addition, green fuel, ethanol can be produced from surplus sugarcane by sugar factories and used with gasoline to reduce foreign exchange costs associated with the import

of crude oil. The government has set a goal to blend 10% fuel-grade ethanol with gasoline by 2022 and 20% by 2025. To improve the quality and yield of sugarcane is the need of an hour. Hence, research and development in the field of sugarcane will help to address issues like low yield and poor quality. This study uses 6748 photos and 11 class categories to classify diseases in sugarcane using deep learning techniques and transfer learning.

Literature Review

Deep learning approaches have showed considerable potential in the field of crop disease identification. These methods are useful for identifying diseases in crop since they automatically recognize and extract features from plant images using multilayer neural networks or deep neural networks. Convolution neural networks (CNNs), recurrent neural networks (RNNs), and ensemble learning are a few instances of these methods. While CNNs are more popular for image-based tasks, Recurrent Neural Networks (RNNs) are useful for sequential data RNNs can be used to time-series data, such as the evolution of disease symptoms over time, in the context of plant disease detection. Ensemble predictions from various models (ensemble learning) can improve disease detection systems overall robustness and performance. A sugarcane disease prediction model has previously been constructed using different types of machine learning and deep learning models, each with a distinct purpose.

[15] used a convolution neural network (CNN) to identify illnesses in sugarcane crops. Six distinct forms of sugarcane leaf disease are included in the data, which was manually recorded with the aid of a camera. Patterns that develop on the leaves are used to identify and categorize diseases in sugarcane, with an accuracy of 95%. Different models may use the training set in the future to improve performance. Additionally, the model's performance can be improved by utilizing various learning rates and optimizers.

CNN and deep learning architectures are used to detect diseases [16]. "Cercospora Leaf spot, Helminthosporium Leaf spot, rust, Red rot, and Yellow Leaf disease" are the five sugarcane diseases that are taken into consideration. The images were personally gathered from several Karnataka farms. Using two different object-detection algorithms, "YOLO and Faster-RCNN," the infected areas in the sick leaf image were correctly recognized with an average precision score of 58.13%. CNNs have been shown to be incredibly reliable at spotting patterns in images. Images captured under both controlled and uncontrolled circumstances were used to evaluate the model. Larger datasets in the future may further enhance the outcomes.

For the purpose of detecting sugarcane disease, a unique deep learning system is developed [17]. Three distinct scenarios are presented in the paper, each utilizing a different feature extractor: "Inception V3, VGG-19, and VGG-16." Images from Makwana Sugar Mill Pvt. Ltd.'s fields were manually gathered for the data set. Data analysis and visualization were done using Orange software. The collected features are then fed into different classifiers such as "SVM, KNN, Neural Network, Logistic regression, Ada boost, SGD, and Naïve Bayes" in each of the three cases. Out of all, the SVM classifier and pre-trained Deep Learning model VGG-16 produced an AUC of 90.2%. This model may be expanded in the future to include diseases in humans, animals, and plants

Sugarcane diseases are classified using the CNN model [18]. The data collection included large number of photos of sugar cane leaves from Agarian University and the field of Bangalore in various states of distress. Also, five different sugarcane disease considered are "Cercospora Leaf spot, Helminithosporium Leaf, Rust, Red rot and yellow leaf disease." The identification of illnesses in sugarcane was done with high precision and accuracy of 93.2% using the proposed design.

Sugarcane disease is identified using a Deep Convolution Neural Network model [19]. The dataset is manually captured through different modes of camera. Different sugarcane disease considered are Eye Spot, Yellow leaf, red rot and Rust. "Faster Region-based Convolutional Neural Network" is used in conjunction with YOLOV5 to locate infected areas in sick leaves. The user interface for taking images and immediately recognizing illness is also served by an Android application. Real-time captured images from android application serves as front end whereas detection of disease is done by Machine learning algorithm which serves as back end. Faster RCNN shows higher performance than YOLOV5.

A CNN model is used for detection of disease in sugarcane leaf [20]. It consists of large image datasets divided into seven different classes which are acquired manually. K-means model is compared with CNN and CNN showed more promising result. Along with disease detection it also recommends suitable pesticide. It uses Tkinter framework to construct this application.

A model which is combination of vision transformer model and CNN model is used for detection of disease in sugarcane leaf [21]. Four different sugarcane disease considered are mosaic, yellow leaf, rust and red rot. Vision Transformers (ViT) is a model first revealed in 2021. The ViTs are different than CNN because they process input image on a single scale. Three model are trained DenseNet121, ViT and Vit+CNN combination for disease detection, out of which ViT showed promising results and achieved accuracy of 92.85%. The researcher has provided a new way of implementing Vision transformer in detecting disease in sugarcane plant. In future the model can be evaluated in comparison with other existing models for performance and the study can also be extended on humans and animals.

A web-based application for detecting sugarcane disease is developed [22]. Three sugarcane diseases—Black Rot, Grassy Shoot, and Smut—are classified using the CNN model. The accuracy attained is 98.69%, and the dataset is

balanced in terms of agroclimatic area, diverse light impacts, and different times of day and year. In future the model can be combined with productivity enhancement and price forecasting with AI tools. Also, the model can be fine-tuned with the help of feedback taken from the user.

The use of Dense Net201 in conjunction with SVM were used to identify red rot and red rust diseases in sugarcane leaves [23]. The data set includes photos that were taken when visited sugarcane crop fields in Pune's Loni Kalbhor area. Red rust and red rot are detected with an accuracy of 98% using the CNN-based DL model. It is possible to expand the model to forecast additional sugarcane disease classes.

An Ensemble learning (EnC-SVMWEL) method for detecting disease in sugarcane leaves is developed [24]. The dataset consists of manually captured images along with photos captured from different fields of Bangalore. Different disease considered are "Yellow leaf disease, Rust, Helminthosporium leaf spot, Red rot and Cercospora leaf spot." After image preprocessing DenseNet201 issued for feature extraction. In the end, the model trained and then classified the retrieved image features. The detection accuracy recorded is high compared to other existing methods like CNN, VGG, and SVM. New method is explored by using "CNN with Ensemble SVM" for detection of disease with accuracy of 97.45% but this increases the training time. The model can be expanded to include other leaf diseases in the future, and "fusion-based extraction techniques" can be used to boost performance.

Different DL model such as Inception V4, VGG16, ResnetV2-152 and AlexNet were implemented to classify Sugarcane Leaf disease [25]. The algorithms used 16,800 images for training (70%), 4800 images for validation (20%) and 2400 images for testing (10%). The images were collected from farms of sugarcane located in Philippines. Different sugarcane leaf disease considered are "Cercospora Leaf spot, helminithosporium leaf, rust, red dot and yellow leaf disease." According to the results the Inception V4 algorithm out performs other models in classification. More data sets can be used in future work to improve performance. It is also possible to collect valuable data in real-world situations.

A "quantum behaved particle swarm optimization learning (QBPSO-DTL)" model is developed for detection and classification of diseases in sugarcane leaves with high accuracy [26]. The data used is self-collected for classification. The leaf's affected area is detected using the segmentation method along with Squeeze Net model for feature extractor. Further, classification is done using deep stacked autoencoder (DASE) model. After performing QBPSO -based hyper parameter tuning the model has achieved accuracy of 97.5%. It has helped to reduce validation loss but the accuracy is reduced. Segmentation techniques may be employed in the future to increase classification and detection accuracy.

A deep learning approach is used with Adam optimizer and transfer learning for disease detection in sugarcane [27]. The data contains self-collected images of healthy and unhealthy sugarcane leaves. Different sugarcane disease considered are Red Rust, Red Rot and Bacterial Blight. The proposed transfer learning model utilizes pre-trained deep learning models like "AlexNet, VGG 16, VGG19, Dense Net, Mobile Net, Efficient Net, ReseNet50 and ResNet101." By using a pre-trained model and the transfer learning technique, more accuracy has been achieved with less training data. With ResNet101 outperforming other models, the suggested model achieved great accuracy. Furthermore, improving the training process and reducing the loss have been made possible by the Adam optimizer. In order to improve performance, the model may eventually incorporate more sugarcane diseases and be coupled with other agricultural systems.

The performance of disease classification models can be enhanced by the deep learning technique due to technological advancements.

MATERIALS AND METHODS

Farmers can improve crop quality and quantity and avoid long-term financial and other losses by developing a model that can identify disease early. Additionally, it will benefit the sugar industry by helping it to produce more sugarcane products of higher quality and quantity. This system uses deep learning to predict sugarcane disease using transfer learning It will use deep learning algorithms to automatically detect the type of disease by identifying pertinent features and patterns from images of infected sugarcane leaves. The system uses concept like CNN and transfer learning.

Convolutional Neural Networks (better known as CNNs) are algorithms used in Deep Learning that assign weights and biases that can be learned, and are able to distinguish between different objects and aspects of an input image. Nowadays, computer vision researchers are fond of using CNNs, which carry out various processing layers over a number of stages of execution. The elements of a CNN model are shown in Figure 1 that consists of an input image, convolutional layers, pooling layers, fully-connected layers, activation functions and an output. CNN 's can be used for detection of disease in plants. It includes convolution and Max Pooling layers. These layers automatically extract features from input images and represent them hierarchically. CNNs are good at learning spatial hierarchies and patterns in images, making them well-suited for identifying visual indicators of plant diseases. In a standard ConvNet design, the output layer also known as a fully connected layer is the final processing layer. The convolution process includes the shifting, multiplying, and summing processes. Improved performance with limited labelled data can be achieved by adapting models that were pre-trained on image datasets like "ImageNet" which is large in size.

Because it applies a previously trained model to a new problem, the transfer learning technique is quite popular these days. In this technique, knowledge gained by a machine from the previous task is used to improve generalization in another task. The general idea is instead of starting the learning process from scratch, it can be started with already learned patterns from related task. Some of the commonly used transfer learning models are Inception, VGG family, Xception, ResNet etc. The block diagram for disease detection using the transfer learning technique is shown in Figure 2.

Figure 3 shows how the system operates. The workflow begins with the collection of image data. The sugarcane image dataset was collected from the freely available Mendeley library. The data is pre-processed using image augmentation and data normalization to ensure it is in a format suitable for training. Also, for noise reduction, regularization technique such as dropout, batch normalization is used to help reduce internal noise. Dropout randomly drops out neurons during training which also reduces overfitting and increase robustness to noise and other forms of variability. Batch normalization normalizes the input to each layer of the network. Adding dropout and batch normalization layers helps in reduction of noise. By fine-tuning a previously trained model, transfer learning also aids in noise reduction. The collected data after being pre -processed will be split in training and testing set. The data gets loaded in Deep Learning model such as CNN, where model can predict disease by using learning. The transfer learning (TL) method is the simplest way to put the deep neural network into practice. Different deep learning models such as VGG16, VGG19, AlexNet, Inception V3 and DenseNet201 are trained using transfer learning and the performance is evaluated using various metrics.

Dataset

The collection, which includes 6748 images with high resolution taken with high-quality cameras, is a useful tool for researching both healthy and diseased sugarcane leaves. The dataset was gathered from Mendeley, a publicly accessible repository [28]. The images are 768 x 1024

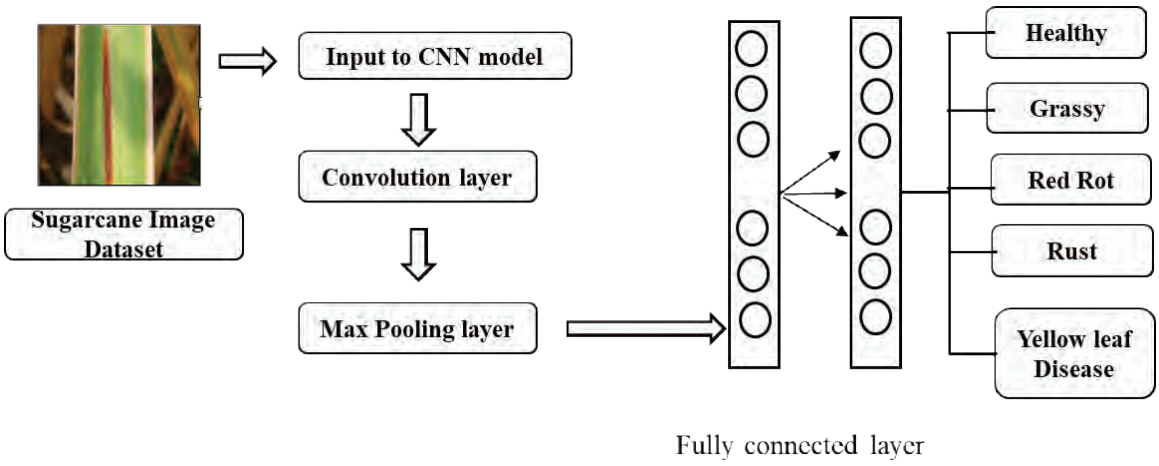


Figure 1. CNN model for disease detection.

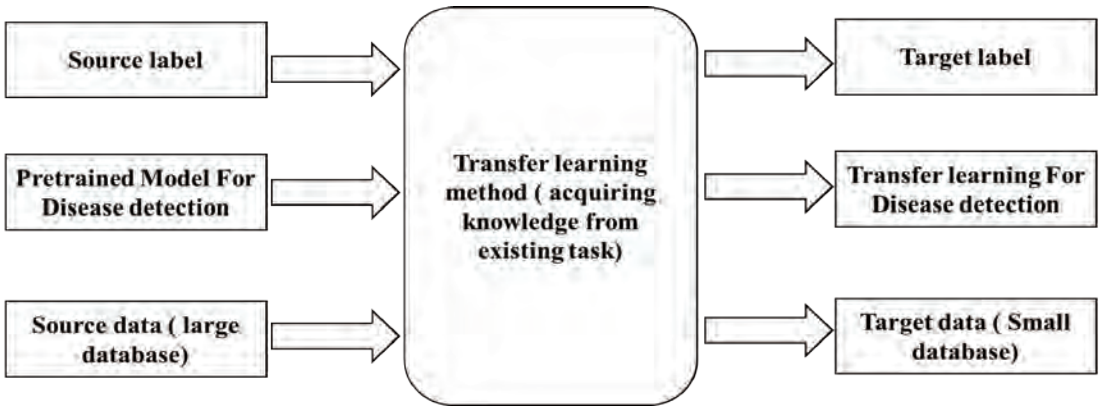


Figure 2. Transfer learning model for disease detection.

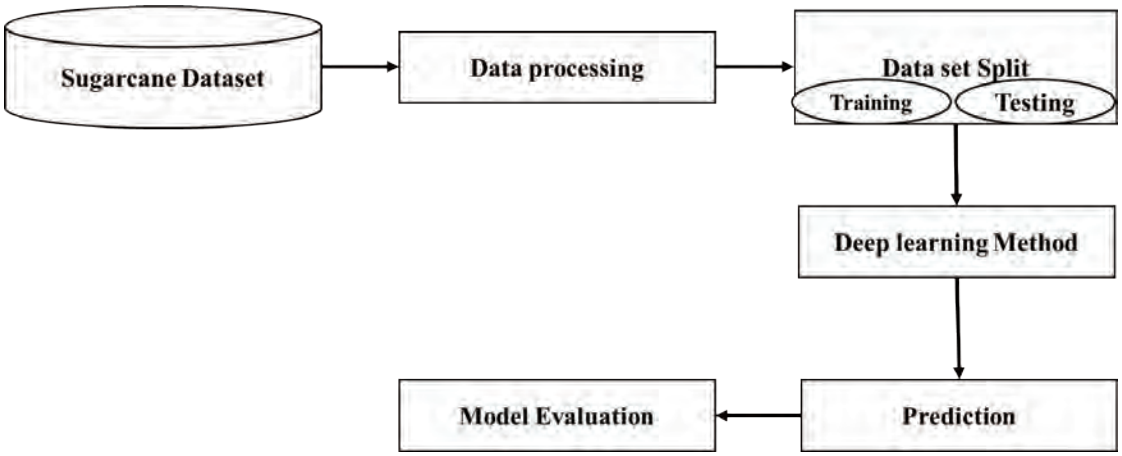


Figure 3. Block diagram of System.

pixels in size and are saved in JPEG format. The resolution of the images is 72 dots per inch (dpi). Table 2 presents the image data set of the study. It helps in efficient detection and classification of sugarcane diseases. The dataset consists of a wide range of sugarcane leaf states with 11 categories, including nine diseases, a category for healthy leaves, and a category for dried leaves. The dataset on sugarcane leaf disease was collected from the farm of Kendur hamlet, Taluka-Shirur, District-Pune, Maharashtra, India. The images were also reviewed by experts to confirm the disease categories they represented. Following a pre-processing stage, the final photos were scaled, renamed, and organized into folders that matched the various disease classifications.

Image data generators are a crucial tool in deep learning for efficiently generating and preprocessing image data. It is a function or class that generates image data randomly during training and testing.

Hyperparameter Settings

Hyper-parameter settings were implemented in the various deep learning algorithms in this work. These configurations may enhance the algorithm's performance. However, experiments need to be done to evaluate the performance and make necessary modifications. The batch size, image size, dataset split, classes, epochs, optimizer and learning rate used for testing are shown in Table 3.

Callbacks are also used in training to adapt the learning rate dynamically according to the validation loss. This helps to prevent overshoot and improves the model's overall performance and stability.

Model Training

In this study, the model was trained using the Keras and Tensorflow frameworks. The images were saved to a cloud database for convenience. In this study, Google Colaboratory was used for the implementation of the model

Table 2. Distribution of images into different classes

Sr No	Class	Count	Training	Testing
1	Banded Chlorosis	471	376	95
2	Brown Spot	1722	1377	345
3	Brown Rust	314	251	63
4	Dried Leaves	343	276	69
5	Grassy shoot	346	276	70
6	Healthy Leaves	430	344	86
7	Pokkah Boeng	297	237	60
8	Sett Rot	652	521	131
9	Viral Disease	663	530	133
10	Yellow Leaf	1194	955	239
11	Smut	316	252	64
	Total	6748	5395	1355

Table 3. Hyper-parameter settings

Parameter	Details
Batch size	32
Image size	224x224
train: test	80:20
Classes	11
Epochs	15
Optimizer	Adam
Learning rate	**0.001**

and testing tasks. Table 4 shows the hardware and software used in the experiment.

Evaluation

Here, we briefly review the various evaluation metrics used to assess the performance of methods developed for crop disease detection in sugarcane. Assessing the effectiveness of a detection system or model in precisely identifying the presence of diseases is part of evaluating disease detection in sugarcane crops. The evaluation metrics utilized in this situation are displayed in Table 5.

RESULTS AND DISCUSSION

In order to categorize sugarcane leaf disease, this study used transfer learning in conjunction with model training and testing of six deep learning algorithms. Banded Chlorosis, Brown Spot, Brown Rust, Dried Leaves, Grassy Shoots, Healthy Leaves, Pokkah Boeng, Sett Rot, Viral Disease, Yellow Leaf, and Smut are the eleven classifications which make up the sugarcane disease system. Depending on the condition, the test image will be categorized into any one class, producing true positives. According to the results, DenseNet201 outperforms other models with 94.14% accuracy because of its dense connections. A confusion matrix, which offers a thorough analysis of how well the model predicts each class, is a performance measuring tool for classification models. The confusion matrix of various deep learning models is shown in Figure 4. The precision, recall, and F1-score of several models are shown in Table 6. The training and validation accuracy of various algorithms used to identify diseases in sugarcane crops is shown in Table 7. As shown in Tables 6 and 7, the findings demonstrate that the optimizers employed greatly enhance the sugar classification model's performance.

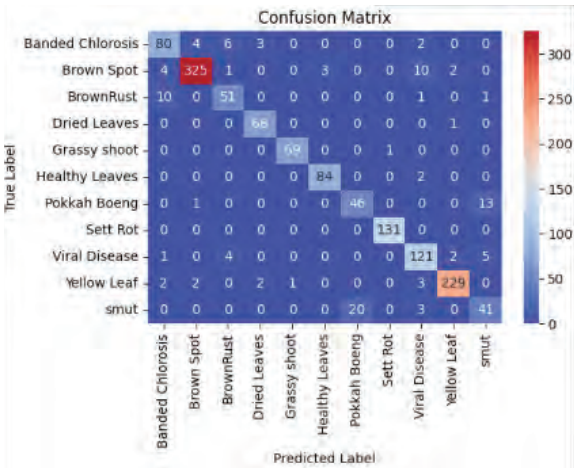
The results demonstrate that the deep learning models greatly enhance the sugar classification models' performance. Additionally, the optimization methods offer dependable performance. Also, deep learning algorithms using transfer learning like VGG16, VGG19, Inception V3, AlexNet, DenseNet201 shows high accuracy in detecting disease in sugarcane crop out of which DenseNet201 outperformed due to its dense connectivity, improved feature extraction & regularization. It has been observed that two classes namely Pokkah Boeng and Smut generated maximum False Positives. Plant diseases are complex, diverse, and variable, making it challenging to create a large-scale, high-quality dataset. However, scientific developments in fields like computer science, telecommunications, artificial intelligence, and even the social sciences have produced a multitude of tools that, when thoroughly investigated and integrated into expert systems, can be extremely useful. The performance indicators of our model in comparison to current methods for sugarcane disease diagnosis are presented in Table 8 [29-40]. According to research in related work, models that use machine learning algorithms

Table 5. Evaluation parameter

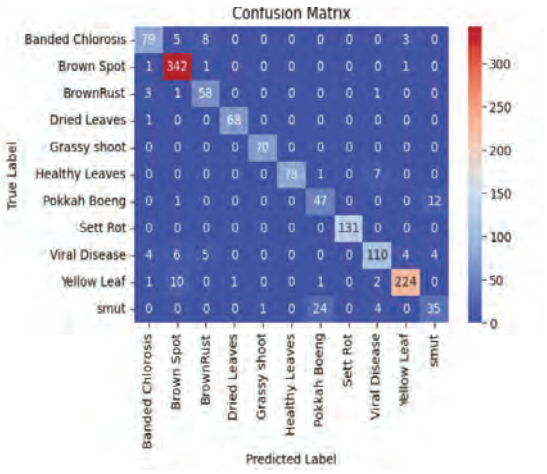
Evaluation Parameter	Formula
Accuracy	(TP + TN) / (TP + TN + FP + FN)
Precision	TP / (TP + FP)
Recall (Sensitivity)	TP / (TP + FN)
F1 Score	2 * (Precision * Recall) / (Precision + Recall)

Table 4. Hardware and software requirement

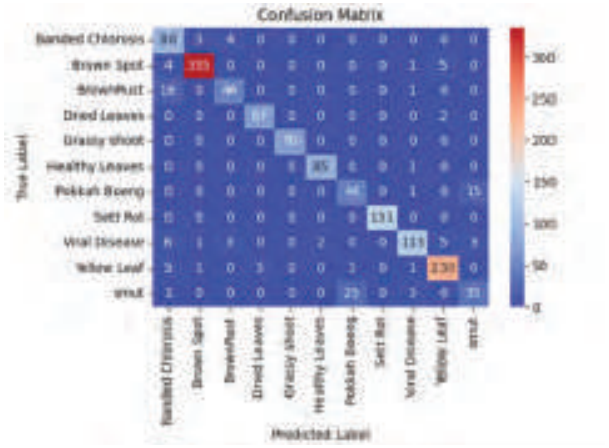
Hardware	
Graphics Processing Unit (GPU)	High-performance NVIDIA GPU
Central Processing Unit (CPU)	Multi-core CPU with high clock speeds
Software	
Deep Learning Framework	TensorFlow, PyTorch, or Keras
GPU Acceleration Libraries	CUDA, cuDNN (for NVIDIA GPUs)
Python and Libraries	Python, NumPy, Pandas, Matplotlib
Data Processing Tools	OpenCV, scikit-learn (for data preprocessing and feature engineering)
Development Environment	Jupyter Notebook, Google Cola, PyCharm



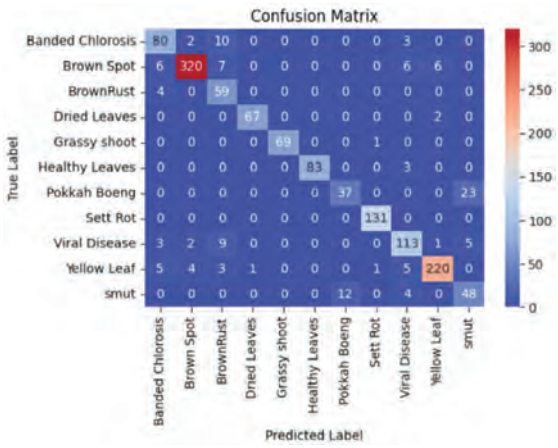
(a)



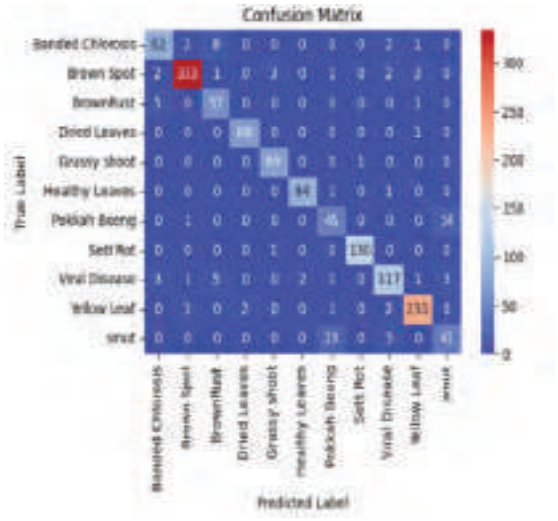
(b)



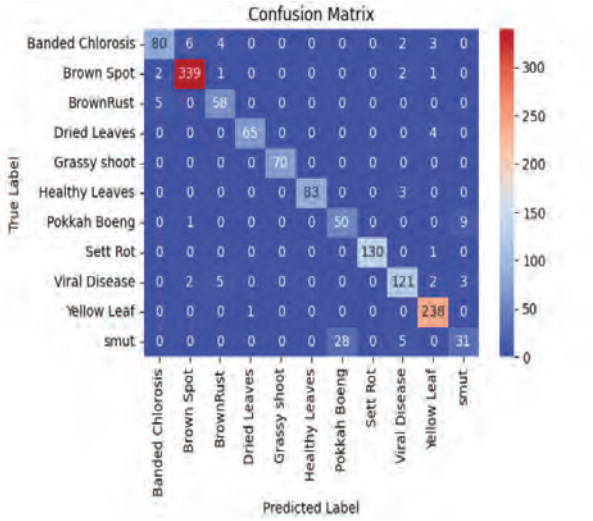
(c)



(d)



(e)



(f)

Figure 4. Confusion matrix (a) CNN (b) VGG16 (c) VGG19 (d) Inception V3 (e) Alexnet (f) DenseNet201.

Table 6. Comparison of disease classification in different models

Model	Class	Precision	Recall	F1-Score
CNN	Banded Chlorosis	0.82	0.84	0.83
	Brown Spot	0.98	0.94	0.96
	Brown Rust	0.82	0.81	0.82
	Dried Leaves	0.93	0.99	0.96
	Grassy shoot	0.99	0.99	0.99
	Healthy Leaves	0.97	0.98	0.97
	Pokkah Boeng	0.70	0.77	0.73
	Sett Rot	0.99	1.00	1.00
	Viral Disease	0.85	0.91	0.88
	Yellow Leaf	0.98	0.96	0.97
	Smut	0.68	0.64	0.66
VGG16	Banded Chlorosis	0.89	0.79	0.84
	Brown Spot	0.97	0.98	0.98
	Brown Rust	0.86	0.81	0.94
	Dried Leaves	0.86	0.99	0.96
	Grassy shoot	0.93	1.00	0.99
	Healthy Leaves	0.99	0.98	0.99
	Pokkah Boeng	1.00	0.60	0.75
	Sett Rot	1.00	1.00	1.00
	Viral Disease	0.85	0.92	0.89
	Yellow Leaf	0.98	0.95	0.96
	Smut	0.67	0.95	0.79
VGG19	Banded Chlorosis	0.82	0.84	0.83
	Brown Spot	0.98	0.93	0.95
	Brown Rust	0.67	0.94	0.78
	Dried Leaves	0.99	0.97	0.98
	Grassy shoot	1.00	0.99	0.99
	Healthy Leaves	1.00	0.97	0.98
	Pokkah Boeng	0.76	0.62	0.68
	Sett Rot	0.98	1.00	0.99
	Viral Disease	0.84	0.85	0.85
	Yellow Leaf	0.96	0.92	0.94
	Smut	0.63	0.75	0.69
InceptionV3	Banded Chlorosis	0.75	0.93	0.83
	Brown Spot	0.99	0.97	0.98
	Brown Rust	0.87	0.73	0.79
	Dried Leaves	0.96	0.97	0.96
	Grassy shoot	1.00	1.00	1.00
	Healthy Leaves	0.98	0.99	0.98
	Pokkah Boeng	0.63	0.73	0.68
	Sett Rot	1.00	1.00	1.00
	Viral Disease	0.93	0.85	0.89
	Yellow Leaf	0.95	0.96	0.96
	Smut	0.66	0.55	0.60

Table 6. Comparison of disease classification in different models (continued)

Model	Class	Precision	Recall	F1-Score
Alexnet	Banded Chlorosis	0.89	0.86	0.88
	Brown Spot	0.98	0.97	0.97
	Brown Rust	0.80	0.90	0.97
	Dried Leaves	0.97	0.99	0.98
	Grassy shoot	0.95	0.99	0.97
	Healthy Leaves	0.98	0.98	0.98
	Pokkah Boeng	0.65	0.75	0.70
	Sett Rot	0.99	0.99	0.99
	Viral Disease	0.92	0.88	0.90
	Yellow Leaf	0.97	0.97	0.97
	Smut	0.71	0.64	0.67
DenseNet201	Banded Chlorosis	0.92	0.84	0.88
	Brown Spot	0.97	0.98	0.98
	Brown Rust	0.85	0.92	0.89
	Dried Leaves	0.98	0.94	0.96
	Grassy shoot	1.00	1.00	1.00
	Healthy Leaves	1.00	0.97	0.98
	Pokkah Boeng	0.64	0.83	0.72
	Sett Rot	1.00	0.99	1.00
	Viral Disease	0.91	0.91	0.91
	Yellow Leaf	0.96	1.00	0.98
	Smut	0.72	0.48	0.58

Table 7. Performance analysis

Sr no	Model	Accuracy	Validation Accuracy
1	CNN	92.98%	91.88%
2	VGG16	93.92%	93.36%
3	VGG19	91.76%	90.55%
4	Inception V3	94.00%	91.81%
5	AlexNet	92.15%	92.77%
6	DenseNet201	94.14%	93.36%

Table 8. Performance analysis of related work

Sr no.	Author	Dataset	Method used	Evaluation metric and their results
1	(Ratnasari et al. 2014` [29])	Real data of 30 images of infected sugarcane leaves were collected from fields .	SVM	Accuracy 80%
2	(Renugambal 2015 [30])	100 photos of five sugarcane leaf diseases	Linear and nonlinear SVMs & ANN	Accuracy 91% 94% 85%
3	(Hasan et al. 2015 [31])	Photo Gallery	Expert System CaneDES	Average Confidence Factor 58.33%

Table 8. Performance analysis of related work (continued)

Sr no.	Author	Dataset	Method used	Evaluation metric and their results
4	(Goel et al. 2018 [32])	5359752 images of a single leaf disease from ipmimages.org	SVM K means algorithm	Accuracy K=11 gave best accuracy
5	(Militante et al. 2019 [15])	13,842 sugarcane images of healthy and unhealthy leaves	CNN	Accuracy 95%
6	(Padilla et al. 2019 [33])	9 images of sugarcane leaves.	SVM	Accuracy 86.66%
7	(Alauddin et al. 2019 [34])	List of question along with symptoms table addressed to Sugar cane farmers and research center in Pasuruan city.	ELM ELM+PSO	ELM alone only achieved 71.92% classification accuracy, ELM and PSO together, were able to identify sugarcane diseases with 79.92% accuracy.
8	(Srivastava et al. 2020 [17])	Total 240 sugarcane leavesout of which 120 are sick leaves	Inception V3 , VGG-16 ,VGG-19 are used for feature extraction and SVM, SGD, ANN ,naïve Bayes, KNN ,logistic regression are used for classification VGG-16 as feature extractor and SVM classifier gives the highest performance	AUC 90.2%
9	(Shadab et al. 2021 [16])	2940 images of healthy and unhealthy sugarcane leaves.	VGG-19 ResNet-34 ResNet-50 YOLO Faster-RCNN	Accuracy 92% 92.4% 93.2% Mean average Precision score 58.13%
10	(Kumar et al. 2021 [18])	dataset consist of 2940 images of sugarcane leaves	Quicker Region-Based CNN	Accuracy 93.2%
11	(Rajesh et al. 2021 [35])	dataset is considered of previous years restricted to Maharashtra.	Naïve Bayes KNN RF SVM	Accuracy 61.21% 83.645 82.42% 83.64%
12	(Murugeswari et al. 2022 [19])	1500 images showing both healthy and diseased sugarcane leaves	YOLOV5 Faster RCNN	Faster RCNN shows higher performance than YOLOV5.
13	(Prithvi et al. 2022 [20])	13842 manually collected images of sugarcane leaves	K means CNN	CNN showed more promising result
14	(Atheeswaran et al. 2023 [36])	400 images of sugarcane leaves	MDC(Multi-Domain Connectome) KNN SVM CBR(Case Based Reasoning) ANFIS(Adaptive Neuro Fuzzy Inference System)	Accuracy 82% 85% 88% 93% 97%
15	(Selvakumar et al. 2023 [37])	240 images of diseased and Non-diseased sugarcane leaves	MFO-CNN gives higher average accuracy than another existing model VGG16 ,VGG 19 and Inception IV3.	Average Accuracy 12.8% 11.7% 16.4%

Table 8. Performance analysis of related work (continued)

Sr no.	Author	Dataset	Method used	Evaluation metric and their results
16	(Simoes et al. 2023 [38])	3508 images of sugarcane leaves infected with rust disease	KNN RF Radial SVM	Accuracy 89% 90% 90%
17	(Ogrekci S et al. 2023 [21])	2521 images of healthy and infected sugarcane leaves	DenseNet121 Vision Transformers(ViT) ViT + CNN	Accuracy 91.98% 92.85% 88.28%
18	(Daphal and Koli 2023 [39)	2569 images showing both healthy and infected sugarcane leaves	MobileNet-V2 Ensemble model	Accuracy 84% 86.53%
19	(Sarode et al. 2023 [27])	Self-collected images showing both healthy and diseased sugarcane leaves from the fields.	ResNet101	It outperformed other models giving high accuracy.
20	(Bagchi et al. 2024 [40])	2522 images of healthy and unhealthy sugarcane leaves	Hybrid Model cspdarnet53+proposed model cspresnet50+VGG16 inception_ v3+proposed model	Accuracy 96.8% 87.7% 86.3%
21	Proposed work	6748 high resolution images of healthy and unhealthy leaves	CNN VGG16 VGG19 Inception V3 AlexNet DenseNet201	Accuracy 92.98% 93.92% 91.76% 94.00% 92.15% 94.14%

like SVM, KNN are less accurate in identifying and predicting diseases. Furthermore, smaller images are used to train the algorithm, accounting for fewer diseases. In this instance, deep learning and transfer learning can be combined to improve the precision and effectiveness of sugarcane disease diagnosis. Additionally, hybrid and ensemble approaches can increase forecast accuracy and robustness.

Limitations of the Work

However, there are some shortcomings in this study. First, just a small number of data sets were used in this investigation. More sugarcane disease variants and environmental factors could be added to the dataset, increasing its size and diversity. Although our model does well on the provided dataset, more validation is needed to determine how well it works in real-world scenarios, such as when environmental changes impact disease diagnosis. Deployment in resource-constrained contexts, like mobile or edge devices, may be limited by high resource requirements. Last but not least, farmers and agricultural specialists find it difficult to interpret forecasts because deep learning algorithms operate as "black boxes."

CONCLUSION

One of the most-wide field that has been benefited from many advancements in technology is Agriculture. In Sugarcane industry mostly utilized product is Sugarcane. Crop quality and yield are highly affected due to disease contaminated agricultural products. Inadequate disease management practices have an adverse effect on sugarcane productivity. Farmers have to pay lots of money to treat diseases that affect the sugarcane crop as a result of inadequate disease control. Consequently, advancement in computation techniques can help in detecting disease in sugarcane plants. Deep learning tools is popularly used for crop health monitoring and precision agriculture [40]. Since Sugarcane is a recurrent crop, it is necessary to maintain the quality of crop and control the diseases [41]. This study's primary goal is to examine how well deep learning algorithms and transfer learning work together to identify disease in sugarcane leaves. In order to classify sugarcane leaf disease in eleven distinct classes, this study used transfer learning in conjunction with model training and testing of six deep learning algorithms. Results show that out of all six DL models, CNN (92.98%), VGG16

(93.92%), VGG19 (91.76%), InceptionV3 (94.00%), AlexNet (92.15%), DenseNet201 outperforms with 94.14% accuracy. In this study, a deep learning approach is proposed for farmers to identify and classify sugarcane disease. This method is not only aimed at increasing the crop yield but also at reducing the use of chemical treatments, thereby promoting a more sustainable agricultural practice. The newest technology allows farmers to identify problems early and address them in a targeted way, leading to healthier crops and improved economic outcomes. Additionally, it validates the effectiveness of deep learning-based models utilizing transfer learning in sugarcane leaf disease classification tasks.

Future Scope

Our research concentrated on classification of sugarcane leaves in 11 different categories, still there is much opportunity for researcher to expand the dataset to include images from multiple geographical locations and different growth stages of sugarcane in future. Also, lightweight models can be developed to facilitate real-time disease detection on mobile and IoT-based platforms. However, integrating additional techniques, such as multi-modal data, explainable AI(XAI) or domain-specific rule-based systems could enhance interpretability and provide a more comprehensive diagnosis of disease in future work. Besides the correct estimation of parameters, artificial neural networks (ANNs) may be used to predict the changes in plant color and bioactivity under different situations [42, 43]. Also, working with subject matter experts such as agronomists and plant pathologists can provide insightful information and improve the system's accuracy and efficiency. The present work can be extended to other crops beyond sugarcane to diagnose the impact of the disease and can also focus on rare diseases, which often require specialized knowledge and expertise. Nowadays advanced techniques like hybrid and ensemble method are popular and researchers can explore them to develop more accurate and robust disease detection models, opening up opportunities for future deep learning. Also, an accurate, rapid and responsive system such as web app, mobile app can be deployed for interaction with the end user (farmer) and depending on the feedback model can be improved in future.

AUTHORSHIP CONTRIBUTIONS

Authors equally contributed to this work.

DATA AVAILABILITY STATEMENT

The authors confirm that the data that supports the findings of this study are available within the article. Raw data that support the finding of this study are available from the corresponding author, upon reasonable request.

CONFLICT OF INTEREST

The authors declared no potential conflicts of interest with respect to the research, authorship, and/or publication of this article.

ETHICS

There are no ethical issues with the publication of this manuscript.

STATEMENT ON THE USE OF ARTIFICIAL INTELLIGENCE

Artificial intelligence was not used in the preparation of the article.

REFERENCES

[1] Datta A, Dey A, Dey K. Automatic multiclass classification of foliar leaf diseases using statistical and colour feature extraction and support vector machine. In: Mandal, J., Mukhopadhyay, S., Dutta, P., Dasgupta, K. (eds) Computational Intelligence, Communications, and Business Analytics. CICBA 2018. Communications in Computer and Information Science, vol 1030. Springer, Singapore; 2019. p. 3–15. [CrossRef]

[2] Siddique M, Babar Munir HM, Qaisrani ZN, Sultan SH, Khan K, Khan LA, et al. Extraction and characterization of lignocellulosic agricultural biomass pretreatment method for biofuel. Sigma J Eng Nat Sci 2023;41:1221–1230. [CrossRef]

[3] Tripathy HK, Mishra S, Suman S, Nayyar A, Sahoo KS. Smart COVID-shield: an IoT driven reliable and automated prototype model for COVID-19 symptoms tracking. Computing 2022:1–22. [CrossRef]

[4] Suman S, Mishra S, Sahoo KS, Nayyar A. Vision navigator: a smart and intelligent obstacle recognition model for visually impaired users. Mob Inf Syst 2022;2022. [CrossRef]

[5] Rott P, Bailey RA, Comstock JC, Croft BJ, Saumtally S, editors. A guide to sugarcane diseases. Montpellier: CIRAD Publication Services; 2000. [CrossRef]

[6] Beyene H, Joshi DNA, Kotecha DK. Plant diseases prediction using image processing and machine learning techniques: survey. Int J Comput Appl 2018;1:226–237. [CrossRef]

[7] Mishra S, Jena L, Tripathy HK, Gaber T. Prioritized and predictive intelligence of things enabled waste management model in smart and sustainable environment. PLoS One 2022;17:e0272383. [CrossRef]

[8] Tom L, Braithwaite K, Kuniata LS. Incursion of sugarcane smut in commercial cane crops at Ramu Papua New Guinea. Proceedings of the 39th Conference of the Australian Society of Sugar Cane Technologists; 2017. p. 377–384.

[9] Yonzone R, Soniya Devi M. Red stripe/top rot disease of sugarcane: a review. Int J Curr Microbiol Appl Sci 2018;7:1469–1478. [CrossRef]
[10] Rathore A, Almas, Sundaram S. Energy, exergy and performance analysis of a 380 kWP roof-top PV plant assisted with data-driven models for energy generation. J Therm Eng 2024;10:1164–1183. [CrossRef]
[11] Mynoddin M, Kabir MF, Islam N, Karim R, Rehana H, Asaduzzaman S. De-rajesh speckling of SAR images with fuzzy filters along with altered preserved edge values. J Comput Commun 2022;10:10–28. [CrossRef]
[12] Miah SS, Lily FT, Amin MR, Karim R, Akbar MA. Separation axioms on fuzzy neutrosophic bitopological spaces using fuzzy neutrosophic open sets. J Umm Al-Qura Univ Appl Sci 2024:1–10. [CrossRef]
[13] Kamilaris A, Prenafeta-Boldú FX. Deep learning in agriculture: a survey. Comput Electron Agric 2018;147:70–90. [CrossRef]
[14] Sharma R, Kukreja V. Segmentation and multi-layer perceptron: an intelligent multi-classification model for sugarcane disease detection. In: 2022 International Conference on Decision Aid Sciences and Applications (DASA); 2022. p. 1265–1269. [CrossRef]
[15] Militante SV, Gerardo BD, Dionisio NV. Plant leaf detection and disease recognition using deep learning. In: 2019 IEEE Eurasia Conference on IoT, Communication and Engineering (ECICE); 2019. p. 579–582. [CrossRef]
[16] Shadab H, Dwivedi M, SNO, Javed T, Bakey A, Raqib M, et al. Disease recognition in sugarcane crop using deep learning. n: Chiplunkar, N.N., Fukao, T. (eds) Advances in Artificial Intelligence and Data Engineering. AIDE 2019. Advances in Intelligent Systems and Computing, vol 1133. Springer, Singapore; 2021. p. 189–206. [CrossRef]
[17] Srivastava S, Kumar P, Mohd N, Singh A, Gill FS. A novel deep learning framework approach for sugarcane disease detection. SN Comput Sci 2020;1:17. [CrossRef]
[18] Kumar P. Research paper on sugarcane disease detection model. TURCOMAT 2021;12:5167–5174.
[19] Murugeswari, Anwar ZS, Dhananjeyan VR, Karthik CN. Automated sugarcane disease detection using Faster RCNN with an Android application. In: 2022 6th International Conference on Trends in Electronics and Informatics (ICOEI); 2022. p. 1–7. [CrossRef]
[20] Prithvi R, Priyank S, Keerthana S, Yashaswini AR. Sugarcane leaf disease prediction and pesticides recommendation system. Int Res J Mod Eng Technol Sci 2022;4.
[21] Ogrekci S, Unal Y, Dudak M. A comparative study of vision transformers and convolutional neural networks: sugarcane leaf diseases identification. Eur Food Res Technol 2023;249:1–11. [CrossRef]
[22] Sammed A, Upadhye R, Dhanvijay M, Patil S, Taylor G. Sammed Abhinandan Upadhye, Maneetkumar Rangnath Dhanvijay, Sudhir Madhav Patil (2023). Univers J Agric Res 2023;11:80–97. [CrossRef]
[23] Lambor S, Pungliya V, Bhonsle R, Purohit A, Raut A, Patel A. Sugarcane leaf disease classification using transfer learning. In: 2022 IEEE Conference on Interdisciplinary Approaches in Technology and Management for Social Innovation (IATMSI); 2022; Gwalior, India. p. 1–4. [CrossRef]
[24] Vignesh U, Chokkalingam BS. EnC-SVMWEL: ensemble approach using CNN and SVM weighted average ensemble learning for sugarcane leaf disease detection. In: 2023 International Conference on Sustainable Computing and Data Communication Systems (ICSCDS); 2023; Erode, India. p. 1663–1668. [CrossRef]
[25] Hernandez AA, Bombasi JL, Lagman AC. Classification of sugarcane leaf disease using deep learning algorithms. In: 2022 IEEE 13th Control and System Graduate Research Colloquium (ICSGRC); 2022. p. 47–50. [CrossRef]
[26] Tamilvizhi T, Surendran R, Anbazhagan K, Rajkumar K. Quantum behaved particle swarm optimization-based deep transfer learning model for sugarcane leaf disease detection and classification. Math Probl Eng 2022;2022:3452413. [CrossRef]
[27] Sarode AA, Posharkar SS, Bannore A, Unkule SS. Enhanced sugarcane disease diagnosis through transfer learning and deep convolutional networks. Int J Innov Sci Res Technol 2023;8.
[28] Thite S, Suryawanshi Y, Patil K, Chumchu P. Sugarcane leaf dataset: a dataset for disease detection and classification for machine learning applications. Data Brief 2024;53:110268. [CrossRef]
[29] Ratnasari EK, Mentari M, Dewi RK, Ginardi RVH. Sugarcane leaf disease detection and severity estimation based on segmented spots image. In: Proceedings of the 2014 International Conference on Information and Communication Technology and System (ICTS); 2014. p. 93–98. [CrossRef]
[30] Renugambal. Application of image processing techniques in computer graphics algorithms. Int J Eng Res Technol 2015;4:919–923.
[31] Hasan SS, Solomon S, Baitha A, et al. CaneDES: a web-based expert system for disorder diagnosis in sugarcane. Sugar Tech 2015;17:418–427. [CrossRef]
[32] Goel N, Jain D, Sinha A. Prediction model for automated leaf disease detection and analysis. In: 2018 IEEE 8th International Advance Computing Conference (IACC); 2018; Greater Noida, India. p. 360–365. [CrossRef]
[33] Padilla DA, Magwili GV, Marohom ALA, Co CMG, Gaño JCC, Tuazon JMU. Portable yellow spot disease identifier on sugarcane leaf via image processing using support vector machine. In: 2019 5th International Conference on Control, Automation and Robotics (ICCAR); 2019. p. 901–905. [CrossRef]

[34] Alauddin M, Mahmudy W, Abadi A. Extreme learning machine weight optimization using particle swarm optimization to identify sugar cane disease. J Inf Technol Comput Sci 2019;4:127. [CrossRef]

[35] Rajesh R, Gowri V. Enhanced approach for disease prediction in sugarcane crop with the support of advanced machine learning strategies. Ann Rom Soc Cell Biol 2021:16805–16814.

[36] Atheeswaran A, Raghavender KV, Chaganti BNL, Maram A, Herencsar N. Expert system for smart farming for diagnosis of sugarcane diseases using machine RCNN learning. Comput Electr Eng 2023;109:108739. [CrossRef]

[37] Selvakumar V, Seetharaman. HOML-SL: IoT based early disease detection and prediction for sugarcane leaf using hybrid optimal machine learning technique. J Surv Fish Sci 2023;10.

[38] Simões IOP da Silva, de Freitas RG, Cursi DE, Chapola RG, do Amaral LR. Recognition of sugarcane orange and brown rust through leaf image processing. Smart Agric Technol 2023;4:100185. [CrossRef]

[39] Daphal SD, Koli SM. Enhancing sugarcane disease classification with ensemble deep learning: a comparative study with transfer learning techniques. Heliyon 2023;9:e18261. [CrossRef]

[40] Bagchi K, Haider Chowdhury MA, Fattah SA. Sugarcane disease classification using advanced deep learning algorithms: a comparative study. In: 2024 6th International Conference on Electrical Engineering and Information & Communication Technology (ICEEICT); 2024; Dhaka, Bangladesh. p. 887–892. [CrossRef]

[41] Wadhe V, Dongre R, Kankriya Y, Kuckian A. Sugarcane disease detection using deep learning. In: 2022 5th International Conference on Advances in Science and Technology (ICAST); 2022; Mumbai, India. p. 40–44. [CrossRef]

[42] Polat Kaya H, Koç T, Ekici L, Toga G. Anthocyanin and bioactivity properties of Berberis crategina DC. in buffer system and apple juice: impact of temperature, time, and pH; prediction using artificial neural network. Sigma J Eng Nat Sci 2024;42:438–449. [CrossRef]

[43] Viswanathan R, Padmanaban P. Handbook on sugarcane diseases and their management. Coimbatore: Sugarcane Breeding Institute; 2008.

Sigma J Eng Nat Sci, Vol. 44, No. 4, pp. 2889–2904, August, 2026

Sigma Journal of Engineering and Natural Sciences
Web page info: https://sigma.yildiz.edu.tr
DOI: 10.14744/sigma.2026.2133

Research Article

Robust load frequency control using an improved tilted integral derivative controller in interconnected diverse unit networks

Alok KUMAR[1], Mohammad Atif SIDDIQUI[1], Mohammed ASIM[1,*]

[1]*Department of Electrical Engineering, Integral University, Lucknow, 226026, India*

ARTICLE INFO

Article history
Received: 09 January 2026
Revised: 08 February 2026
Accepted: 30 March 2026

Keywords:
Load Frequency Control (LFC); Fractional Order Proportional Integral Derivative (FO-PID) Controller; Tilted Integral Derivative (TID) Controller

ABSTRACT

Modern electrical power systems are expected to be dominated by various interconnected systems, furthermore, the incorporation of various renewables sources of energy into the power grid which increases the difficulty and load of the power system, a key indicator of modern power systems' safe and efficient performance is their frequency. Maintaining the frequency stability in an interconnected multi area power system has become more challenging and complex due to the reduced system inertia and high penetration of renewable energy resources. Conventional load frequency control techniques suffer from high overshoot, slow settling time and degraded robustness under various parameter uncertainties and various constraints that are nonlinear in a power system such as generation rate constant and governor dead band. This study proposes an improved tilted integral derivative controller for a heterogeneous multi area power system that contains a thermal plant, hydro plant and a gas unit. Various controller parameters are tuned using a one-to-one based population optimizer that minimizes the integral square error and integral time weighted absolute errors. The simulation results demonstrate that the proposed strategy reduces the settling time by approximately 40 percent when compared to the grey wolf optimization and 25 percent when compared to particle swarm optimization under identical conditions. The overshoot also reduces by 30 to 45 percent and also the tie line power oscillations are damped. Under integral time weighted absolute error tuning the settling time of area 1 frequency deviation is reduced from 25 seconds to 15 seconds in case of grey wolf optimization. Also, the controller also maintains stable performance under nonlinear constraints. The uniqueness of the proposed controller in the first application of the one-to-one based optimizer for tuning a cascade tilted integral derivative controller in multi area load frequency control, with the dual objective validation and robustness verification. The suggested method exhibits better damping properties and dynamic stability making it appropriate for contemporary low inertia linked power systems.

Cite this article as: Kumar A, Siddiqui MA, Asim M. Robust load frequency control using an improved tilted integral derivative controller in interconnected diverse unit networks. Sigma J Eng Nat Sci 2026;44(4):2889–2904.

***Corresponding author.**
*E-mail address: masim@iul.ac.in

This paper was recommended for publication in revised form by Editor-in-Chief Ahmet Selim Dalkilic

Published by Yıldız Technical University Press, İstanbul, Turkey
© Author. This is an open access article under the CC BY-NC license (http://creativecommons.org/licenses/by-nc/4.0/).

INTRODUCTION

The complexity and immensity of a linked power grid with hundreds of variables required to be regulated have exacerbated the difficulties of network control and stability [1]. Controlling the generation capacity of facilities is undoubtedly most important control issue in the systems. LFC is the process of managing the output power of generating sub-stations so that the transient frequency difference of each region and the power source variation between connected areas remain within the necessary limits and achieve zero-steady state error [2]. An essential part of a reliable system is the load frequency controller, which regulates and maintains the power of the system and overall, the frequency of the system [3, 4]. Interconnected power system is a common example of a real-world example of a linked electric power system. However, when load variations produce frequency inconsistencies, problems occur. Load disturbances have a significant effect on the operating characteristics of the power system. The daily rise in electricity usage is one of the reasons for frequency fluctuations [5]. The issues become significantly more complex when multiple power systems are interconnected, as they add arbitrary components to the system.

These contemporary power systems have decreased power system inertia, also with the introduction of various other sources, the penetration levels in power systems increase [6]. Compared to traditional non-renewable energy sources, this leads to poor frequency stability and large frequency spikes. The high levels of RES penetration in modern electrical power systems have led to problems with security, stability, and reliability [7, 8]. LFC duties in power systems have been accomplished with the help of conventional controllers such as the proportional integral (PI), PI derivative (PID), and other controllers [9]. However, as the power landscape shifted and more renewable energy sources are added, the power systems changing aspects become more intricate and difficult to control. It provides power to the system, but by introducing irregular and changing power sources, they also introduce an element of uncertainty. Because of this, the controllers sometimes battle to keep the system stable and at the right frequency levels [10, 11]. The conventional method for load frequency control (LFC) was done by speed governors. However, modern power networks that depend on renewable energy sources cannot have their frequency and tie-line power fluctuations exactly reduced by speed governors alone [12]. Power generation and load demand cannot be balanced solely by the speed governors. To preserve the deviation in the steady state frequency of various regions and associated tie line power deviations as close to zero. It is imperative to employ suitable control approaches and improved design methodologies [13, 14]. The problems of the traditional controllers are solved in this study by using a Modified tilted integral derivative (TID). To sum up, this work significantly advances the science of power system control in several ways:

1. For the multi-area power system, an enhanced fractional order based LFC technique is proposed. The tilt-integral-derivative's cascade structure is used by the proposed novel controller [15].
2. When compared with cascaded LFC architectures and contemporary LFC systems, the proposed controller reduces the deviations obtained in the frequency of the system and also the tie line power [16].
3. The functionality of the offered LFC approach is enhanced by optimising the parameters of the suggested controller using the marine predator's optimisation algorithm POA. Furthermore, the POA performance is validated by comparisons with the different approaches already in use [17].
4. The data is used for a comprehensive comparison study, and different cases are looked at according to the system whose results are confirmed. Additionally, the proposed controller is contrasted.

Research Gap and Contributions

There is various significant restriction even though the literature has documented a number of load frequency management schemes based on fractional order controllers and proportional integral derivative. The majority of the research mainly focus on traditional optimization methods including grey wolf optimization, particle swarm optimization and the Archimedes optimization algorithm for controller tuning [18, 19]. These methods show decreased population diversity and premature convergence. Additionally, prior research on slanted integral derivative based controller has mostly assessed performance in the cases with low disturbance and without conducting robustness validation under nonlinear parameters such as governor dead band and generation rate constraint [20]. Furthermore, there has not been a comparison validation under objective functions like integral square error and integral time weighted absolute error. The current work contributes in the following way to close the gaps:

1. Development of an improved cascade tilted integral derivative controller for heterogeneous interconnected power systems that include thermal, hydro and gas units.
2. Implementation of a one to one based population optimization algorithm for tuning the controller parameters in the load frequency controller.
3. Dual objective optimization using integral square error and integral time weighted absolute error for enhanced transient and steady state performances.
4. Validation under nonlinear constraints including generation rate constant and governor dead band.
5. Comprehensive and detailed comparative analysis against different optimization techniques under identical conditions.

The above-mentioned contribution show improved convergence behavior, improved damping and robustness for modern interconnected power systems.

Literature Review

Stability, efficiency, and overall system performance are all improved in real-world power systems by enabling accurate and reliable control of power flow over transmission lines [21]. Researchers have made a large number of research and suggestions related to LFC design methodologies. The literature has made substantial use of sliding mode controllers, intelligent controllers, adaptive controllers, resilient, internal model-based, decentralized control techniques, and model predictive [22, 23]. Furthermore, when it comes to their ability to reject disturbances, the conventional methods have shown good results. Furthermore, fuzzy control techniques have been used with other different techniques to adjust and improve the LFC's performance under various operating conditions and disturbances. Recently, innovative and data driven frequency control systems have also been proposed to overcome the frequency regulation concerns [24]. However, for optimal performance, they require a large amount of training data.

Numerous techniques, such as hybridized gravitational searching and particle swarm optimizer, water cycle algorithm (WCA), educational competition optimiser, genetic algorithm, and constrained population external optimization, were used to optimize PI, PID, cascaded PDN-PI, and FOPID settings [25, 26]. The method of artificial bee colonies has been used in tandem with the weighted sum approach to reduce the operating frequency's settling time and overshoot. Additionally, a teaching-learning algorithm was used to modify the settling time, overshoot, etc. Furthermore, the literature has introduced hybrid and combination FO-based LFC techniques. For a two area power systems based on superconducting energy storage systems (SMES), another fractional order controller was suggested. They introduced a modified hybrid decentralized FO-based LFC and EV controller [27, 28]. The FOPID and the TID controllers are combined in the proposed LFC and EV controllers [29]. Additionally, the reported controller parameters were optimized using the artificial ecosystem optimiser (AEO) algorithm.

For multi-area power systems, the series fuzzy control technique with an ICA optimizer was introduced. The water cycle optimization algorithm (WCA) and a cascaded fuzzy approach using FOPID were first presented. Fuzzy logic was first presented utilizing PID with a filter and FOPI controllers [30]. The stated controller has been optimized using the imperialist competition optimization method (ICA). It is evident that in order to enhance the frequency regulation the system, further research and sophisticated LFC techniques are required. Furthermore, the uncertainties in electrical power system model parameters and the related issues of high-RES penetration levels in existing power systems provide additional difficulties for current controllers and/or design methodologies [31, 32]. The most recent research on load frequency controllers is summarized in Table 1.

LFC methods

LFC is the most important factor that must be addressed in any modern power system. Various methods are already used by researchers in this field. Based on the literature survey these control methods can be broadly classified into 4 types- Conventional or classical techniques, adaptive control techniques, robust approach and intelligent control methods.

Classical/ Traditional Methods

Owing to their straightforward structure and ease of practical implementation, classical control techniques have been extensively applied in the development of LFC systems. However, a number of studies have shown that when subjected to system nonlinearities and parameter variations, their dynamic performance is insufficient [33]. Because it is frequently difficult to design controllers that use complete state-variable information, suboptimal and quasi-optimal LFC techniques have been studied. An alternative LFC methodology was created using only necessary and measurable state variables, improving implementation feasibility in contrast to traditional optimal control approaches that depend on state-feedback estimators.

By combining the bang-bang control strategy with Lyapunov's second method, the load frequency problem for a multi area power system was solved, producing an easy-to-analyze and implement controller. Furthermore, the hierarchical control structure was introduced to ensure reliable system performance. The outcomes of global control systems that make use of tie-line interactions have been promising [34]. Additionally, the perturbation approach—which modelled the system dynamics as slow and fast subsystems—was introduced to reduce the control action required for LFC in IMAPSs.

Adaptive Methods

Functional problems related to the implementation of adaptive LFC have been investigated in detail. In order to meet hyper-stability conditions, an adaptive control-based LFC architecture was developed for the Hungarian power system [35]. Further, an adaptively tuned PI controller was proposed in order to effectively accommodate system parameter variations. Fuzzy logic systems were used to develop adaptive governor laws and constraint update mechanisms for handling uncertainties in interconnected load frequency control areas. Stringent guarantees of closed-loop stability were provided while developing a tracking performance criterion that aims at minimizing the approximation errors and rejecting the effect of external disturbances [36, 37]. Further, an adaptive multi-objective fractional-order PID controller was developed for enhancing the LFC performance in islanded microgrids.

Table 1. Comparative review of various recent optimization based load frequency control techniques and their research challenges

S.No.	Author/ Year	Existing Research Challenge	Methodology	Reference
1.	Amarendra et al. 2023 [1]	Time domain parameters including frequency deviation overshoot and settling periods are utilized to contrast the performance of the optimized controllers which can be improved by selecting the appropriate control depending upon the type of the system.	Here, an MGO-based 2DOF-PID Control technique is used to control the load frequency deviation of an interconnected microgrid. Furthermore, in contrast to the conventional PSO approach, MGO minimizes the objective function to the lowest feasible value. Since there is a significant decrease in ITAE values as well as variations in frequencies and tie-line power, the MGO optimal 2DOF-PID controller is the best option for the two-area microgrid system under analysis.	[1]
2.	Kumar and Anwar 2021 [2]	In this the controller was designed for the multi area system which was optimized on PSO and GWO algorithm. Further testing with the disturbances and latest optimization technique is required.	A sliding mode control technique is used with the Grey wolf optimization (GWO) and particle swarm optimisation (PSO) strategies and is used to determine the controller's parameter in order to get an ideal outcome.	[2]
3.	Ahmed 2022 [3]	The suggested controller's performance is assessed in relation to the cascaded controller. Simulation studies verify its efficacy.	A modified fractional controller was created in order to enhance load frequency control in a multi-area interconnected power system with multiple energy sources. The Archimedes optimisation algorithm (AOA), a recently developed bio-inspired optimisation method, was used to adjust the ID-T controller's parameters.	[3]
4.	Qian and Lv 2025 [4]	Despite its shown efficacy, the AGFTSMC approach still has limitations, including high processing requirements. Dynamic frequency regulation capabilities could be significantly enhanced by the use of artificial intelligence, including deep learning, and event-triggered techniques.	An advanced LFC scheme is developed using adaptive global fast terminal sliding mode control. The proposed strategy formulates a nonlinear, time-varying global fast terminal sliding surface and integrates an adaptive sliding mode control law to ensure finite-time convergence, enhanced robustness, and improved dynamic performance of the power system under uncertainties and disturbances.	[4]
5.	Izci 2024 [5]	It should concentrate on strengthening the resilience of hSA-QIO tuned against such disturbances, guaranteeing the integrity of control systems, given the growing danger of threats to power grids.	In the proposed LFC framework, the parameters of the filtered PID controller are optimally tuned using a hybrid simulated annealing–based quadratic interpolation optimizer. This hybrid optimization approach enhances the tuning process, leading to improved control accuracy and dynamic performance of the system.	[5]

Robust Methods

The dynamic performance of a load frequency controller (LFC) may be less than ideal in real-world electric power systems when the controller is built using nominal system data. This controller is synthesized through a methodical procedure based on quantitative feedback theory (QFT), which makes use of loop-shaping techniques to enhance system performance [38]. However, there are significant parametric deviations in the behavior of the closed-loop system due to the several sources of uncertainty (such as load demand, model errors, non-linear behaviour, and changes in equipment parameters). The techniques employed in this QFT methodology produce a thorough and methodical approach to controller design and analysis by incorporating in-depth knowledge of the system's behavior. To mitigate the consequences of minor parametric uncertainties, a

hybrid strategy that combines adaptive control with robust constraints was devised, while adaptive control strategies were used to address larger parametric uncertainties [39, 40].

By guaranteeing that all closed-loop poles stay in the left half-plane, the hybrid technique ensures both excellent transient response and closed-loop stability under all operating conditions. Furthermore, compared to conventional robust control methods, including μ-analysis and linear quadratic Gaussian (LQG) control, the Q-parameterization controller can achieve a drastically reduced controller order [41]. The stabilizing controller's family is described with one free design parameter (Q), as the controller synthesis is simpler in Q context. If both parameter variations are kept within an acceptable range, the choice of Q will guarantee satisfactory dynamic performance and system stability.

Intelligent Approaches

Nonlinear power system dynamics can be approximated with linear models, but such linearized representations are only valid within limited operating ranges. This can force you to have many models since the same system will require multiple models in order to model it in different operational conditions [42]. New developments in artificial intelligence (AI) have enabled us to have the answers to these challenges that were previously unimaginable. Another major benefit of AI-based approaches is their ability to address nonlinear control issues in power systems over a wide operating region. In recent years AI-based systems approaches, including artificial neural networks (ANNs), fuzzy logic control (FLC) and genetic algorithms (GAs), have been commonly investigated for the control of load frequency control (LFC) systems. Feed forward neural networks and back propagation-through-time learning algorithms based neural controllers for the LFC problem have been specifically designed. The controllers exhibited a good resistance to frequency changes with zero steady-state error. An advantage of this approach is that no knowledge about the system model is needed, thus creating more flexibility in controller design [43]. Besides, the central goal of these systems is to prevent the uncertainties and change of parameters that cause oscillations in the system. In the adaptive control domain, self-tuning strategies have been widely studied in LFC applications. In this work, a multivariable self-tuning controller was built by optimizing a generalized performance index that takes into account system output as well as control effort. Additionally, controlling the load by a simple load compensation mechanism allowed for effective treatment of the load disturbances with non-zero mean components.

Studied Power System

Load Frequency Control (LFC) helps control the steady-state error (SSE) in a power system by tuning the excitation voltage in response to load changes, and ensuring that the scheduled frequency and power interchange occurs in interconnected power systems. Figure 1 shows an automatic voltage regulator. The article describes a multi-area interconnected power system comprising thermal, hydro, and gas power plants [44] (Fig. 2). The automatic voltage regulator (AVR) manages generator output by monitoring load demands and mitigating frequency deviations, thereby maintaining stable and reliable system operation. Component nonlinearities play a crucial role in

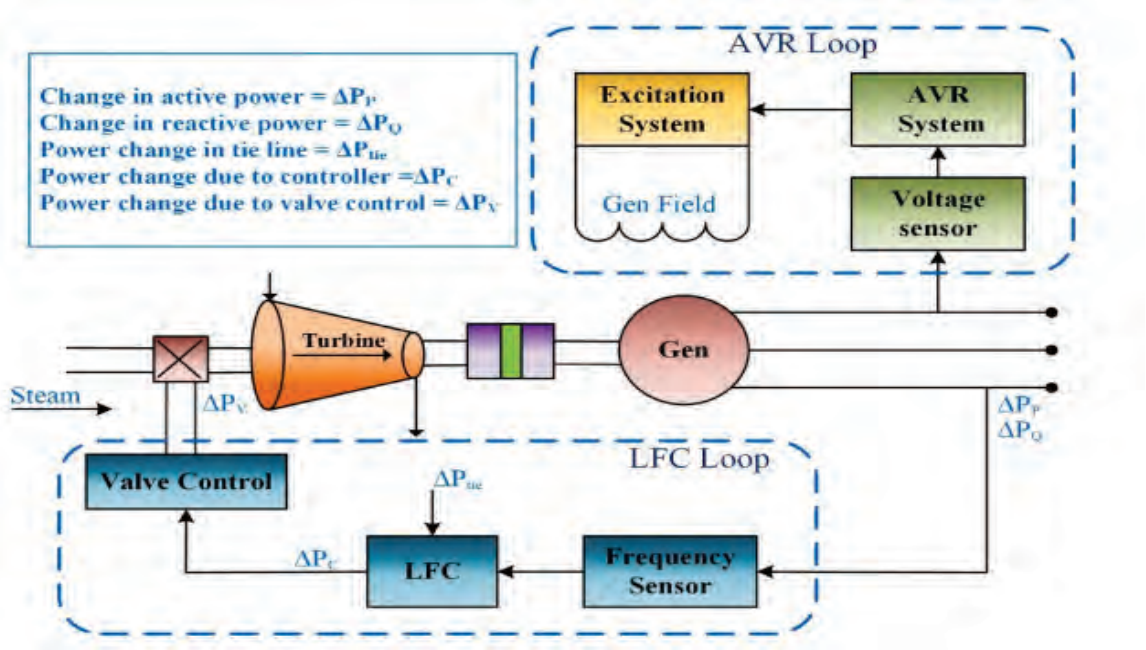


Figure 1. Automatic voltage regulator.

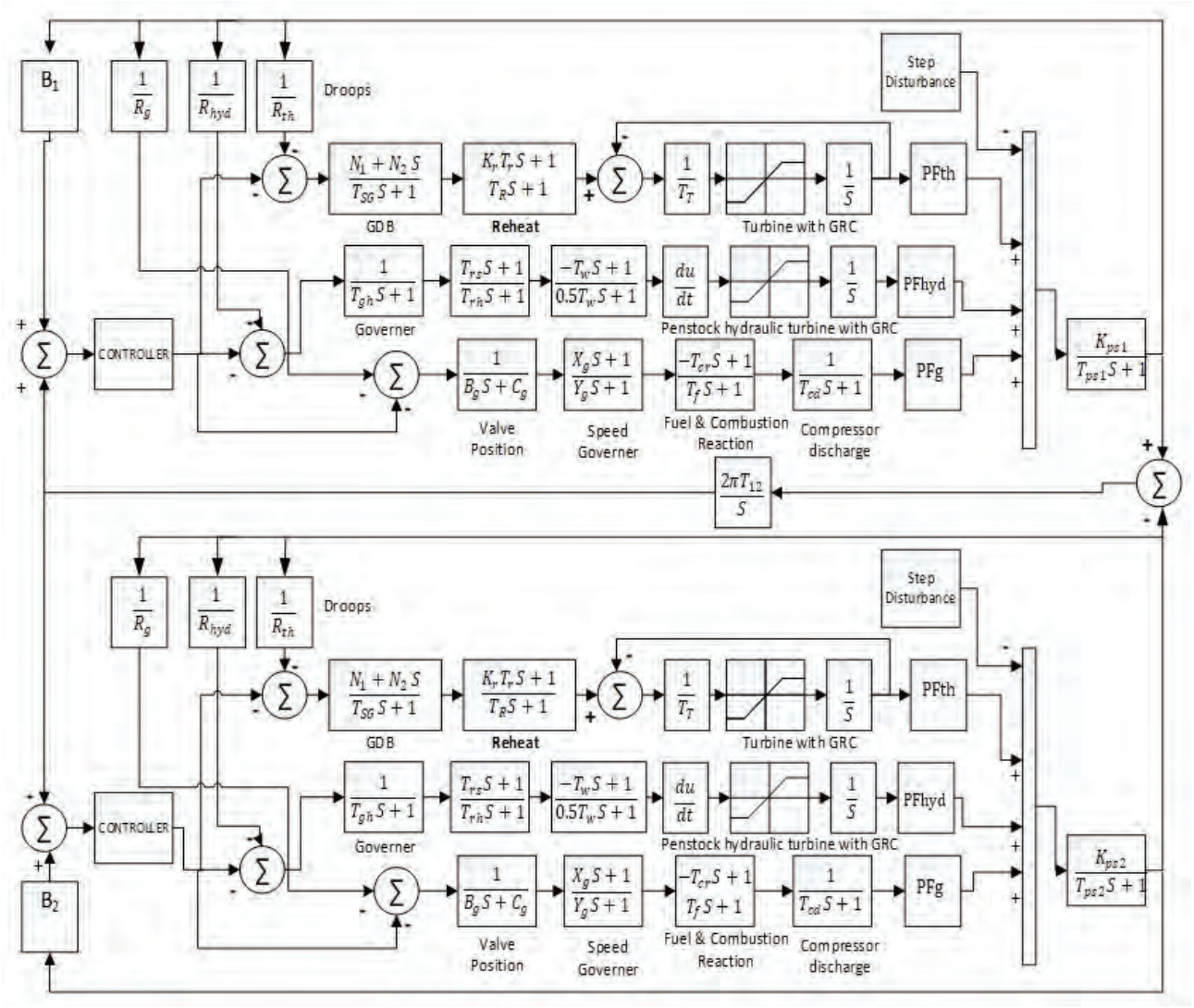


Figure 2. Multi area interconnected power system.

the design and evaluation of the proposed controllers. The system takes into consideration the physical constraints of the generating units, which include generation rate constraints (GRC) and governor dead band (GDB). For thermal units, the GRC is set at 10% pu/min (0.0017 pu·MW/s) for both increasing and decreasing rates. In contrast, for the hydro plant, the GRC limits are defined as 360 pu/min (0.06 pu·MW/s) for increasing rates and 270 pu/min (0.045 pu·MW/s) for decreasing rates [45]. A linearized representation of the GDB is utilized to evaluate speed deviations along with their rates of change. The GDB transfer function derived from the Fourier series is provided by:

$$GDB=\frac{N_1+N_2\,S}{T_{SG}S+1} \quad (1)$$

Where N_1 & N_2 are the Fourier coefficients. (N_1=0.8 and N_2= -0.2/π)

The investigated power system consist of two interconnected areas that consists of a thermal, hydro and a gas unit. The system also includes nonlinear constraints as stated above. Small signal linearized models are considered for load frequency control analysis.

Area Control Error (ACE)

$$\text{For Area 1, } ACE_1(t) = B_1\Delta f_1(t) + \Delta P_{tie,12}(t) \quad (2)$$

$$\text{For Area 2, } ACE_2(t) = B_2\Delta f_2(t) - \Delta P_{tie,12}(t) \quad (3)$$

Where Bi is the frequency bias factor and Δ_f denotes the frequency deviation or area i.

Generator load dynamics

$$G_{pi}(s) = \frac{K_{psi}}{T_{psi}s+1} \quad (4)$$

In time domain form the equation can be represented as:

$$T_{psi}\frac{d\Delta f_i}{dt} + \Delta f_i = K_{psi}(\Delta P_{mi} - \Delta P_{Li} \pm \Delta P_{tie}) \quad (5)$$

$$\text{Where, } \Delta P_{mi} = \Delta P_{th,i} + \Delta P_{hyd,i} + \Delta P_{g,i} \quad (6)$$

Tie line power model

$$\Delta P_{tie,12}(s) = \frac{2\pi T_{12}}{s}(\Delta f_1 - \Delta f_2) \quad (7)$$

In time domain form the equation can be represented as:

$$\frac{d\Delta P_{tie,12}}{dt} = 2\pi T_{12}(\Delta f_1 - \Delta f_2) \quad (8)$$

Thermal unit model

(a) Governor: $G_{gov,th}(s) = \frac{1}{T_{gh}s+1}$ (9)

In time domain form the equation can be represented as:

$$T_{gh}\left(\frac{d\Delta P_{g,th}}{dt}\right) + \Delta P_{g,th} = \Delta P_{c,th} \quad (10)$$

(b) Turbine $G_{rh}(s) = \frac{K_r T_r s+1}{T_r s+1}$ (11)

Hydro unit

$$G_{hyd}(s) = \frac{-sTw+1}{0.5sT_w+1} \quad (12)$$

Gas turbine

$$G_{sg}(s) = \frac{sXg+1}{sY_g+1} \quad (13)$$

From Equation number 2 to 13 represents the modelling of the interconnected power system representing different components with the function in s domain.

Where,

B= Frequency bias factor

Δ_f= Frequency deviation

ACE= Area control error

$\Delta P_{tie,12}$= Tie-line power deviation between Areas 1 and 2

ΔP= load disturbance

X_g= Gas governor numerator constant

Y_g= Gas governor denominator constant

Tw= water starting time constant

T_r= Reheater time constant

Tilted Integral Derivative (TID) Controller

The transient and steady state response of a two-area interconnected power system to a unit step disturbance in area one is investigated through an one on one based optimization technique employing the modified controller, which is a kind of enhanced version of the PID controller [46]. The unit step signal is taken into consideration in the disturbance because it allows for the study of both transient and steady-state responses. If a ramp or other signal is used as the disturbance, then only a transient study can be obtained (Fig. 3).

The controller equation can be studied as:

$$E(s) \propto \frac{K_P}{S^{1/n}} + \frac{K_i}{S} + SK_d \quad (14)$$

The following are the transfer functions of PID and TID controllers:

$$PID = K_P + \frac{K_I}{S} + K_d S \quad (15)$$

$$TID = \frac{K_p}{S^{1/n}} + \frac{K_I}{S} + SK_d \quad (16)$$

Objective Function

A variety of system parameters, including ISE, ITAE, IAE, ITSE, and others, can be used to adjust the TID

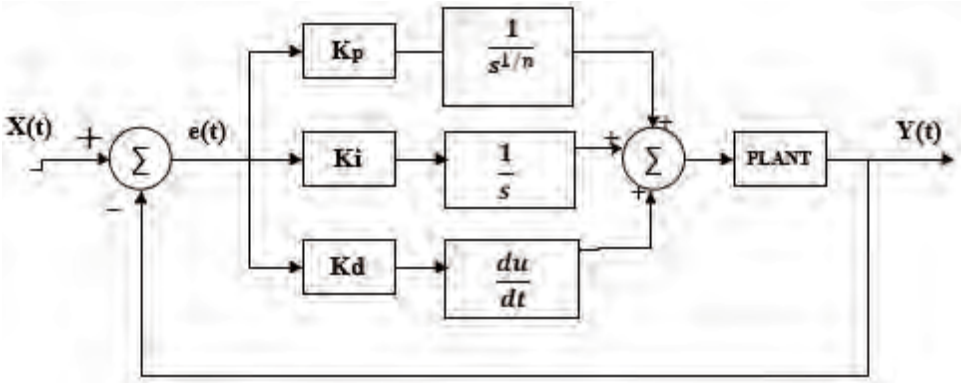


Figure 3. Structure of TID controller.

controller's parameters [47, 48]. The objective functions taken into consideration in this paper are ITAE and ISE. These performance indicators should be taken into account. Applications that need fast response and quick settling time can use this requirement. ISE favors reducing large errors over little errors due to the squaring of error quantities [49]. If this condition is satisfied, the system might have to use more effort to keep things under control and react faster. ITSE penalizes higher errors during the initial transient reaction, combining aspects of ITAE and ISE.

This criterion balances control effort and response speed but may increase oscillatory behavior. The Integral Absolute Error (IAE) treats all errors equally, offering faster responses with lower control effort, though slower reactions may still occur. The Integral of Time-weighted Squared Error (ITSE) penalizes sustained errors, reducing settling time, while the Integral of Time-weighted Error Squared (ITES) imposes a stronger penalty on large deviations, helping to limit peak errors and improve overall system stability. The formula for ITAE, ISE, IAE and ITSE are shown in equations [50].

$$ITAE = \int_0^\infty t|e^2(t)|dt \quad (17)$$

$$ISE = \int_0^\infty e^2(t)dt \quad (18)$$

$$IAE = \int_0^\infty |e(t)|dt \quad (19)$$

$$ITSE = \int_0^\infty te^2(t)dt \quad (20)$$

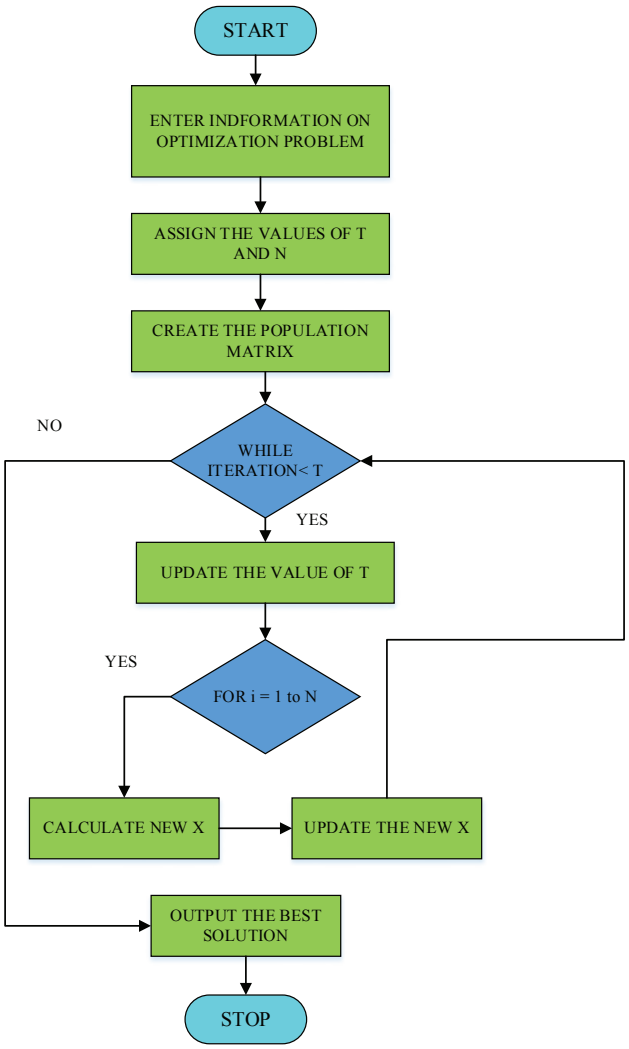


Figure 4. Flowchart of one to one based optimizer (OOBO).

One-to-One Based Optimizer (OOBO)

In an iteration-based process, the population-based metaheuristic algorithm OOBO efficiently solves optimization problems by utilizing the population search power in the problem-solving space. The foundation of OOBO is that, given the problem's restrictions, a number of workable solutions are first produced. Then, using the fundamental principle of the algorithm, the position of these answers in the search space is updated in each iteration. Accurately scanning the problem's search space is made impossible by an updating method that relies too much on particular population members. The algorithm might so converge to nearby ideal areas. The main idea underlying the proposed OOBO algorithm's design is that it avoids becoming too dependent on specific population members, such as the best, worst, and mean members, by making effective use of data on each population member throughout the algorithm's population update process (Fig. 4).

Consequently, the following factors are taken into account during this updating process: (a) population updates do not depend on any particular members; (b) all members participate in the updating process; and (c) every population member is utilized to direct another member in the search space in a one-to-one communication.

Pseudo code for OOBO algorithm

1. Information on input optimisation problems.
2. Assign T and N.
3. Construct a preliminary population matrix.
4. Assess the function of the objective.
5. do for t → 1 to T
6. Using Equation (9), update → K.
7. Do for i → 1 to N
8. Using Equations (10) and (11), compute X new i.
9. Determine f new i using X new i.
10. Use Equation (12) to update Xi.
11. Finish for
12. Keep the greatest solution so far discovered.
13. Finish for 14. The best quasi-optimal solution should be output.

Stop OOBO.

RESULTS AND DISCUSSION

The system was modelled in MATLAB/Simulink, and controller tuning was performed using the OOBO algorithm with the ISE and ITAE as objective functions. The algorithm was evaluated for different population sizes with a fixed maximum of 100 iterations and was interfaced with the Simulink model to obtain optimal controller parameters. The resulting gains provide fast convergence to steady state with reduced overshoot and minimal oscillations. The performance of the proposed OOBO based approach was benchmarked against PSO and GWO techniques [19] (Table 2-5) (Fig. 5-10).

The one-to-one based optimizer balanced and improved exploration and exploitation mechanism is responsible for the enhanced dynamic performance of the suggested optimization-based controller. The one to one update approach maintains the diversity through a number of iterations that lowers the risk of premature convergence in contrast to traditional population based algorithms that mainly depend on mean solution. As a result, the near global optimal controller parameters are reached more quickly that also makes the method fast. Also, better damping properties of the cascade tilted integral derivative structure are demonstrated by the decrease in the settling time and the overshoot. Transient

Table 2. When considering the target function as ISE, the comparison of controller parameters

Optimization Method Used (Algorithm)	Power System Area one			Power System Area two			ISE
	Tilted Parameter (K_t)	Integral Parameter (K_i)	Derivative Parameter (K_d)	Tilted Parameter (K_t)	Integral Parameter (K_i)	Derivative Parameter (K_d)	
OOBO	1.02	2.68	2.05	3.01	3.12	1.43	0.0042
GWO	1	1.52	2.34	2.52	2.14	2.62	0.0055
PSO	1.58	2.30	2.11	3.72	1.24	2.41	0.0061

Table 3. The description of dynamic performance through the application of four optimization methods (ISE)

Optimization Method Used Algorithm	Parameter	Overshoot (Hz) of the system	Undershoot (Hz) of the system	Settling time (seconds) of the system	ISE
OOBO	Δf1	0.018	0.030	18	0.0042
	Δf2	0.020	0.032	17	
	ΔPtie	0.001	0.006	20	
GWO	Δf1	0.036	0.038	23	0.0055
	Δf2	0.025	0.040	22	
	ΔPtie	0.002	0.006	21	
PSO	Δf1	0.026	0.033	17	0.0061
	Δf2	0.020	0.036	18	
	ΔPtie	0.0018	0.006	20	

Table 4. When considering the target function as ITAE, the controller parameters in the various optimization techniques

Optimization Method Used (Algorithm)	Power System Area one			Power System Area two			ITAE
	Tilted Parameter (K_t)	Integral Parameter (K_i)	Derivative Parameter (K_d)	Tilted Parameter (K_t)	Integral Parameter (K_i)	Derivative Parameter (K_d)	
OOBO	1.26	2.15	2.12	1.14	1.20	2.36	0.7822
GWO	1.42	1.09	2.60	1.23	1.48	2.16	1.125
PSO	2.20	3.12	2.95	3.10	1.99	3.05	0.9521

Table 5. The description of dynamic performance through the application of four optimization algorithms (ITAE)

Optimization Method Used Algorithm	Parameter	Overshoot (Hz) of the system	Undershoot (Hz) of the system	Settling time (seconds) of the system	ITAE
OOBO	Δf1	0.017	0.032	15	0.7822
	Δf2	0.022	0.031	13	
	ΔPtie	0.002	0.005	16	
GWO	Δf1	0.026	0.038	25	1.125
	Δf2	0.038	0.038	26	
	ΔPtie	0.002	0.006	22	
PSO	Δf1	0.044	0.040	20	0.9521
	Δf2	0.020	0.032	19	
	ΔPtie	0.002	0.006	19	

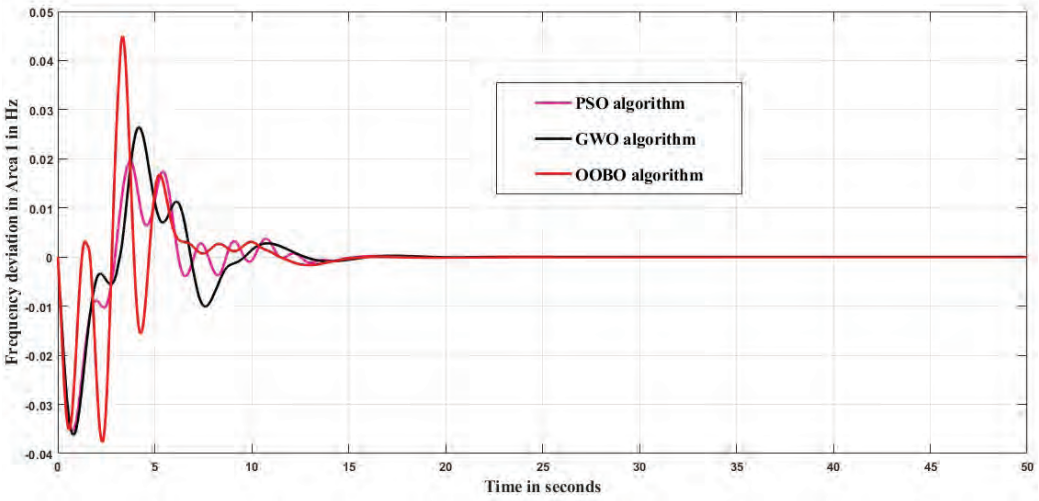


Figure 5. Deviation in the frequency of Area 1 (ISE).

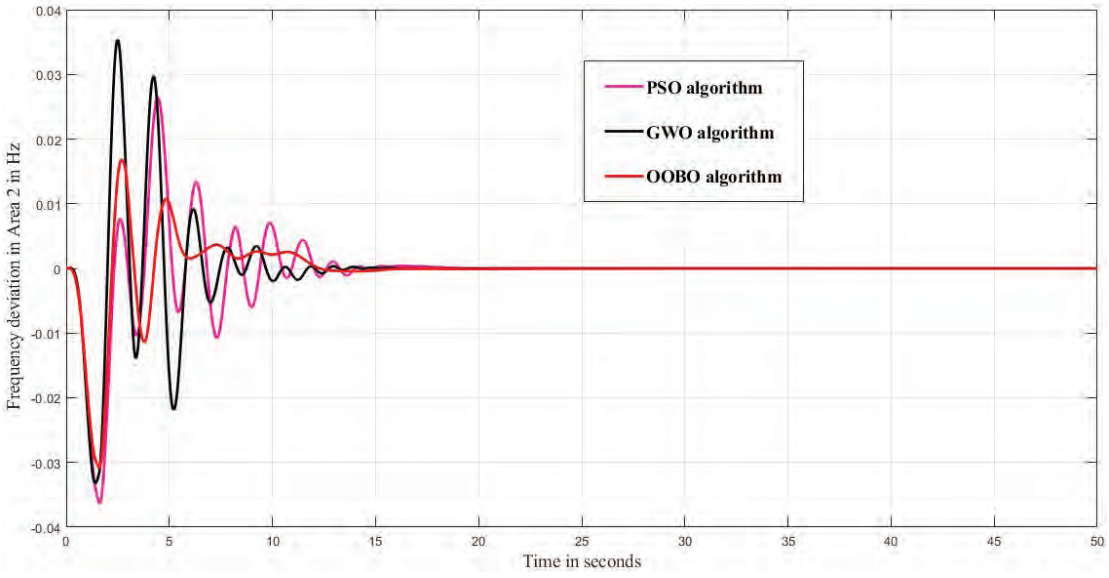


Figure 6. Deviation in the frequency of Area 2 (ISE).

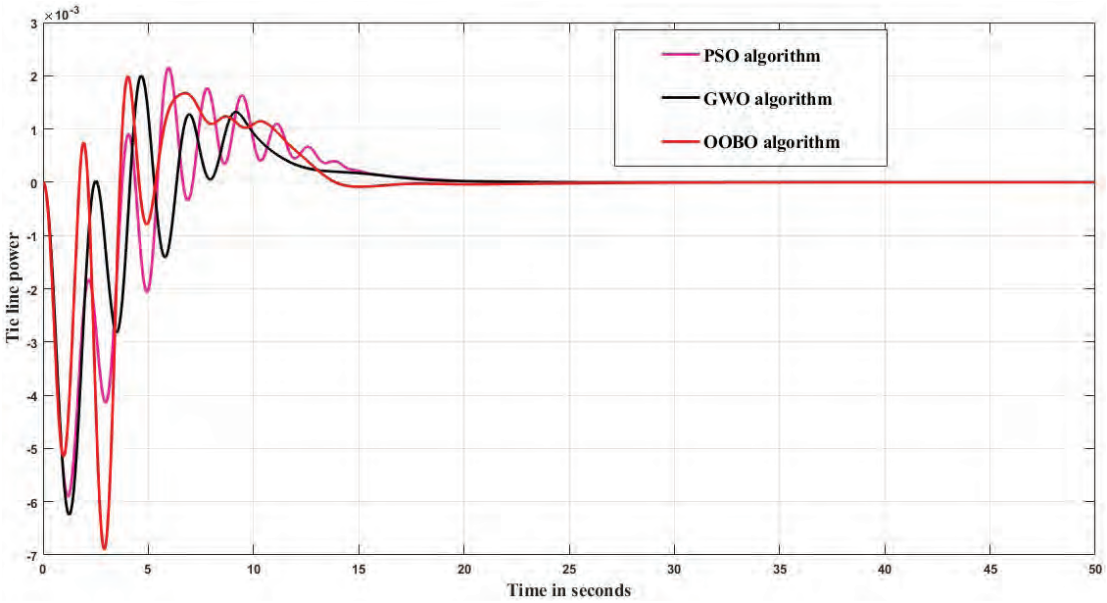


Figure 7. Deviation in the tie line power of Area 2 (ISE).

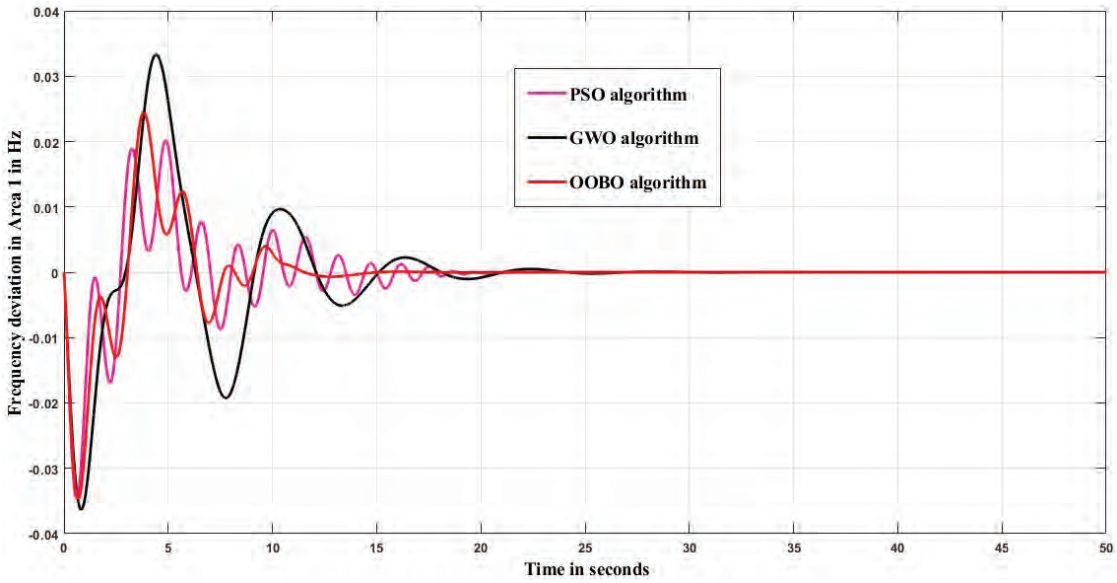


Figure 8. Deviation in the frequency of Area 1 (ITAE).

stability also gets improved by the tilting and derivative components of the controller while the steady state error is also eliminated by the integral component. For modern power system reliability, the suggested strategy delivers better suppression of tie line oscillations than grey wolf and particle swarm techniques. Additionally, the results show that while integral square error tuning decreases the peak deviations while integral time weighted absolute error tuning improves the settling time. This defines the flexibility of the suggested design process and draws attention to the trade-off between response and control.

In comparison with the grey wolf optimization the suggested optimization-based controller stabilizes the frequency deviation more quickly under integral squared error criterion as shown in the Figure 11. In this particular instance the particle swarm optimization shows a shorter settling time but the associated objective function value is very large that shows that faster settling does not ensure the

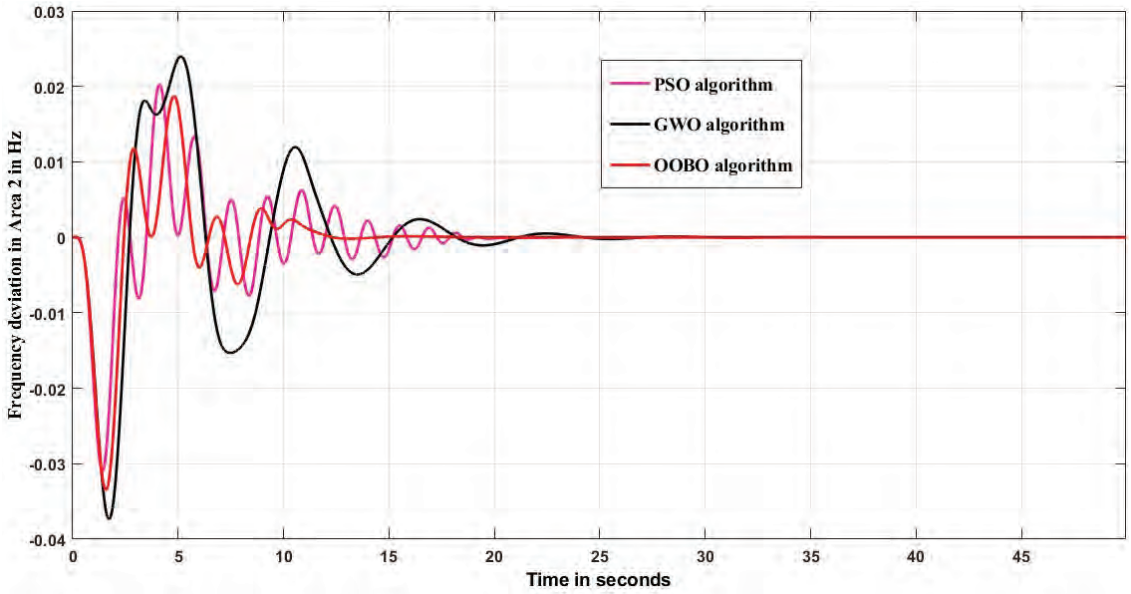


Figure 9. Deviation in the frequency of Area 2 (ITAE).

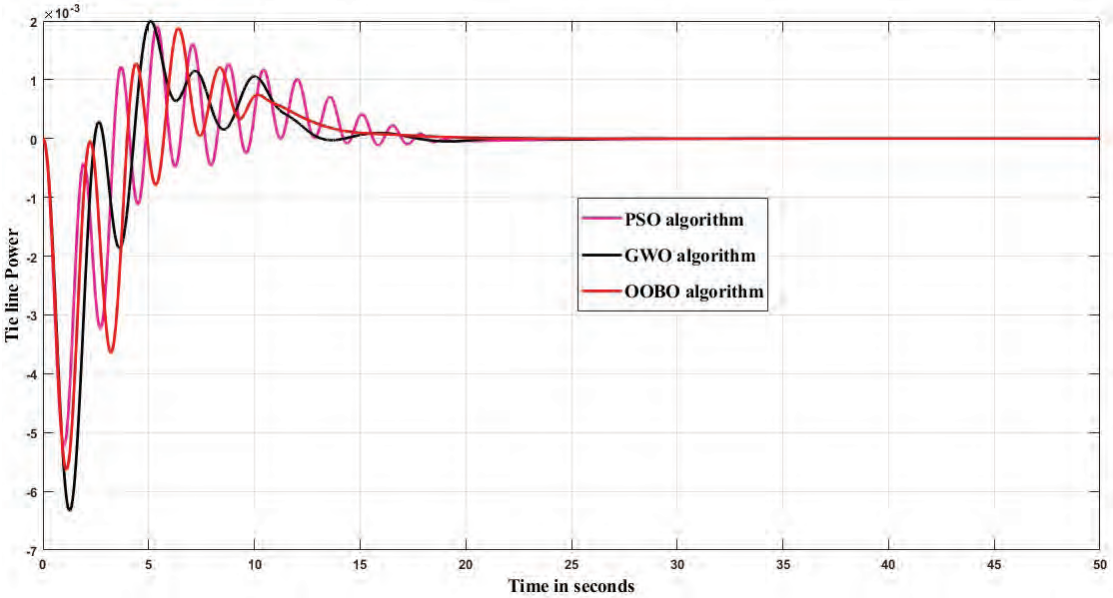


Figure 10. Deviation in the tie line power of Area 2 (ITAE).

better cumulative performance. This emphasise the importance of transient performance measurements.

The suggested approach has substantially less overshoot under integral square error tuning, as seen in Figure 12. When the one to one based technique is optimally set, the slanted integral derivative damping characteristics are improved as evidenced by the decrease in peak deviation. Also the controller performs better during load fluctuations.

Out of the all the strategies evaluated the suggested method produces the lowest integral square error as seen in Figure 13. It indicates that the system has better dynamic stability and superior suppression of large transient excursions.

The advantage of the proposed method becomes more validating while considering the integral time weighted absolute error. When compared to both the optimization techniques the settling time is improved significantly as shown in Figure 14.

The proposed method has improved the stability behaviour and the tuning mechanism and the overshoot is minimised as shown in the Figure 15.

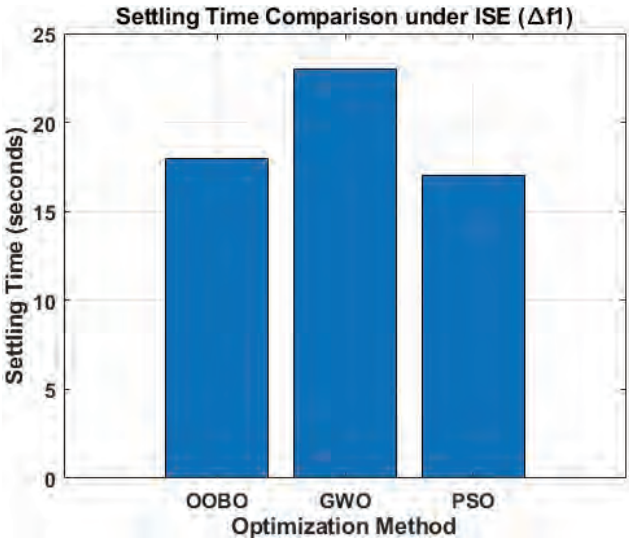


Figure 11. Comparative settling time of frequency deviation (Δf1) under integral square error tuning.

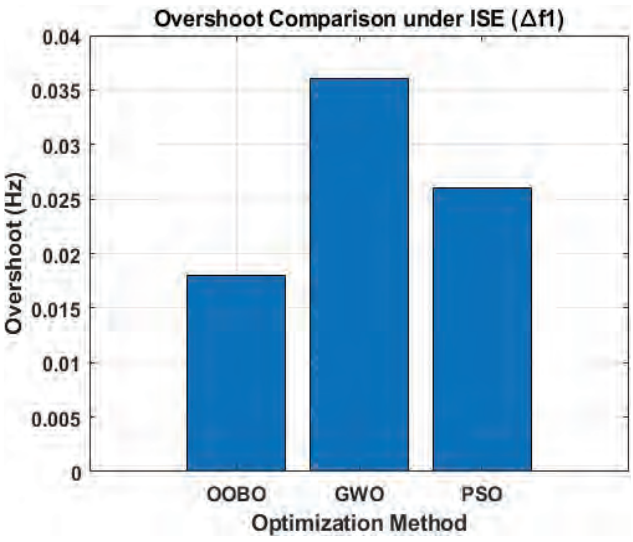


Figure 12. Comparative overshoot of frequency deviation (Δf1) under integral square error tuning.

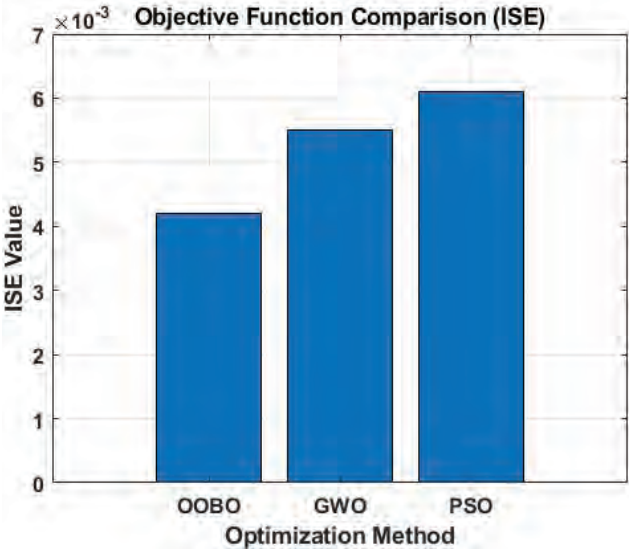


Figure 13. Comparison of integral squared error values for different optimization algorithms.

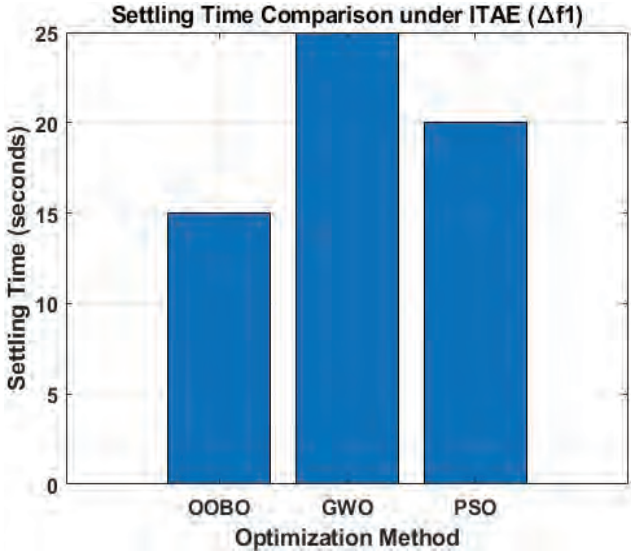


Figure 14. Comparative settling time of frequency deviation (Δf1) under integral time weighted absolute error tuning.

These findings are further verified by the quantitative improvement analysis. The suggested method outperforms traditional optimization methods by a significant proportion under both integral squared error and integral time-weighted absolute error criteria, as illustrated in Figures 16 and 17. This verifies how well the one-to-one update method works to get more ideal controller parameters.

Limitations and Future Scope

There are still various restrictions even though the suggested controller performs better in a two are heterogeneous system. Hardware or real time implementation had not been conducted and the study is limited to simulation based validation only. The model that has been analysed did not account for cyber security disturbances or communication delays. Furthermore, the only disturbance caused in the system was only due to step load was analysed. Further studies should consider looking into cyber resilient load frequency control structures, integration of communication delays and also expand the multi area system to large scale with the renewable penetration. Real time simulators for the validation can increase the applicability even more.

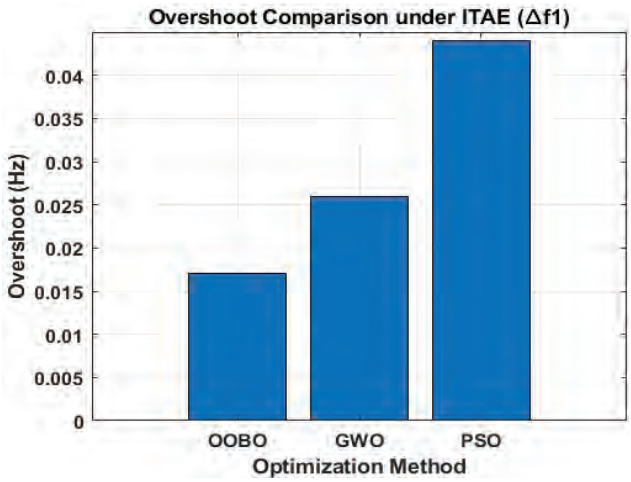


Figure 15. Comparative overshoot of frequency deviation (Δf1) under integral time weighted absolute error tuning.

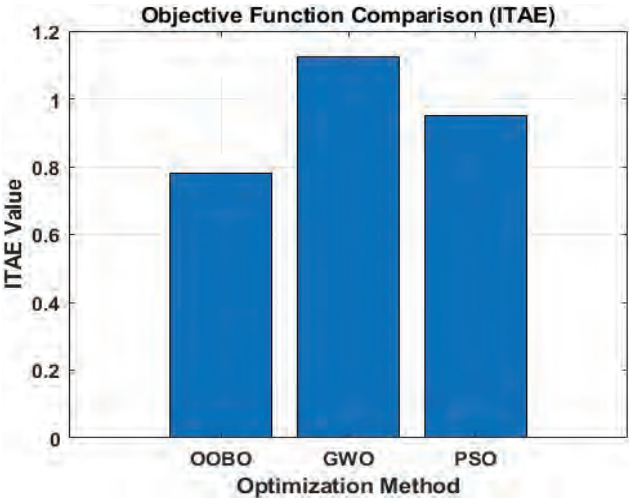


Figure 16. Comparative of frequency deviation (Δf1) under integral time weighted absolute error tuning.

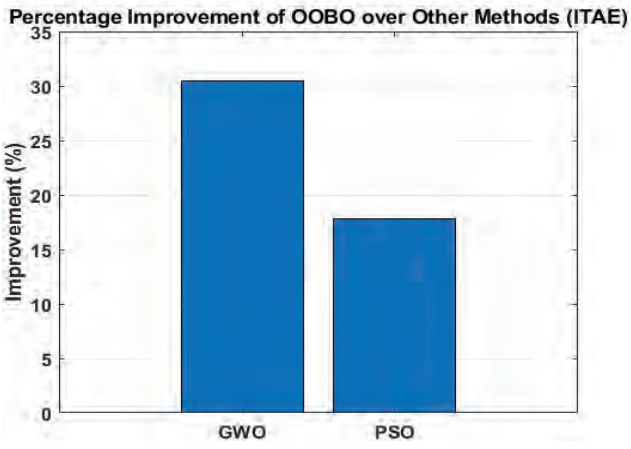


Figure 17. Comparison integral time weighted absolute error values for different optimization algorithms.

CONCLUSION

An enhanced tilted integral derivative controller for the frequency regulation of a heterogeneous interconnected power system was described in the study. It was adjusted using a population optimization approach that is based on a one to one ratio. In order to assess both transient and steady state behaviour the controller was optimised with the integral square error and integral time weighted absolute error performance parameters. In comparison to grey wolf and particle swarm optimisation strategies comparative analysis shows that the suggested strategy decreased overshoot by over 45 percent and settling time by up to 40 percent. The stable performance under generation rate constraints and governor dead band nonlinearities were observed along with the improved damping of tie line power oscillations. The outcome verifies that the suggested optimisation approach improves the controller robustness and convergence reliability. In low inertia power systems with a variety of generating units the proposed methodology presents a feasible solution for frequency regulation.

AUTHORSHIP CONTRIBUTIONS

Authors equally contributed to this work.

DATA AVAILABILITY STATEMENT

The authors confirm that the data that supports the findings of this study are available within the article. Raw data that support the finding of this study are available from the corresponding author, upon reasonable request.

CONFLICT OF INTEREST

The authors declared no potential conflicts of interest with respect to the research, authorship, and/or publication of this article.

ETHICS

There are no ethical issues with the publication of this manuscript.

STATEMENT ON THE USE OF ARTIFICIAL INTELLIGENCE

Artificial intelligence was not used in the preparation of the article.

REFERENCES

[1] Amarendra K, Teeparthi K, Vamsi Y, Veeramsetty V, Thota V. Load frequency control of an interconnected microgrid using MGO-based 2DOF-PID controller. 2023. p. 1–6. [CrossRef]

[2] Kumar A, Anwar MN. Decentralized load-frequency controller design for a single as well as multi-area power system. Iran J Sci Technol Trans Electr Eng 2020;44:309–326. [CrossRef]
[3] Ahmed M, Magdy G, Khamies M, Kamel S. Modified TID controller for load frequency control of a two-area interconnected diverse-unit power system. Int J Electr Power Energy Syst 2022;135:107528. [CrossRef]
[4] Qian J, Lv X. Load frequency control of renewable energy power systems based on adaptive global fast terminal sliding mode control. Appl Sci 2025;15:7030. [CrossRef]
[5] Izci D, Ekinci S, Çelik E, et al. Dynamic load frequency control in power systems using a hybrid simulated annealing based quadratic interpolation optimizer. Sci Rep 2024;14:26011. [CrossRef]
[6] Kumar A, Anwar MN, Kumar S. Sliding mode controller design for frequency regulation in an interconnected power system. Prot Control Mod Power Syst 2021. [CrossRef]
[7] Anwar MN, Pan S. A new PID load frequency controller design method in frequency domain through direct synthesis approach. Int J Electr Power Energy Syst 2015. [CrossRef]
[8] Verma A, Asim M, Mahboob R. Load frequency control in power systems using the most valuable player algorithm. Indian J Sci Technol 2023;16:3854–3861. [CrossRef]
[9] Siddiqui MA, Anwar N, Laskar SH. A simple tuning approach for PID controller based on direct synthesis and rootlocus. In: 2019 3rd International Conference on Computing Methodologies and Communication (ICCMC); 2019; Erode, India. p. 466–470. [CrossRef]
[10] Vasu G, Sivakumar M, Raju MR. A novel model reduction approach for linear time-invariant systems via enhanced PSO-DV algorithm and improved MPPA method. Proc Inst Mech Eng I J Syst Control Eng 2020;234:240–256. [CrossRef]
[11] Patel NC, Agrawal R, Pradhan P, Satapathy S, Ahmed I, Debnath M. Two-staged (PDF+1PI) controller design for load frequency control. 2020. p. 1–6. [CrossRef]
[12] Morsali J, Zare K, Tarafdar Hagh M. Comparative performance evaluation of fractional order controllers in LFC of two-area diverse-unit power system with considering GDB and GRC effects. J Electr Syst Inf Technol 2018;5:708–722. [CrossRef]
[13] Topno PN, Chanana S. Tilt integral derivative control for two-area load frequency control problem. In: 2015 2nd International Conference on Recent Advances in Engineering & Computational Sciences (RAECS); 2015; Chandigarh, India. p. 1–6. [CrossRef]
[14] Agrawal P, Asim M, Tariq M. Particle swarm optimization (PSO) for maximum power point tracking. 2022. p. 1–5. [CrossRef]
[15] Mirjalili S, Mirjalili SM, Lewis A. Grey wolf optimizer. Adv Eng Softw 2014;69:46–61. [CrossRef]
[16] Saremi S, Mirjalili S, Lewis A. Grasshopper optimisation algorithm: Theory and application. Adv Eng Softw 2017;105:30–47. [CrossRef]
[17] Trojovsky P, Dehghani M. Pelican optimization algorithm: A novel nature-inspired algorithm for engineering applications. Sensors (Basel) 2022;22:855. [CrossRef]
[18] Elkasem AHA, Kamel S, Korashy A, Nasrat L. Load frequency control design of two area interconnected power system using GWO. In: 2019 IEEE Conference on Power Electronics and Renewable Energy (CPERE); 2019; Aswan, Egypt. p. 278–283. [CrossRef]
[19] Latif A, Hussain SMS, Das DC, Ustun TS, Iqbal A. A review on fractional order (FO) controllers' optimization for load frequency stabilization in power networks. Energy Rep 2021;7:4009–4021. [CrossRef]
[20] Kumar A, Asim M, Shadab MM, Akhtar I. Review of various load frequency controllers. In: Iqbal A, Malik H, Riyaz A, Abdellah K, Bayhan S, editors. Renewable power for sustainable growth. Lecture Notes in Electrical Engineering. Vol. 723. Singapore: Springer; 2021. [CrossRef]
[21] Azad MA, Tariq M, Sarwar A, Sajid I, Ahmad S, Bakhsh FI, Sayed AE. A particle swarm optimization-adaptive weighted delay velocity-based fast-converging maximum power point tracking algorithm for solar PV generation system. Sustainability 2023;15:15335. [CrossRef]
[22] Sajid I, Sarwar A, Tariq M, Bakhsh FI, Ahmad S, Mohamed ASN. Archimedes optimization algorithm (AOA)-based global maximum power point tracking for a photovoltaic system under partial and complex shading conditions. Energy 2023;283:129169. [CrossRef]
[23] Babu S, Sondi A. Load frequency controllers design and comparison for interconnected hydro-thermal systems. Int J Innov Res Sci Eng Technol 2017;6:17307–17315.
[24] Tuan DH, Tran DT, Nguyen Ngoc Thanh V, Huynh VV. Load frequency control based on gray wolf optimizer algorithm for modern power systems. Energies 2025;18:815. [CrossRef]
[25] Gupta P, et al. Impact of distributed energy resources on load frequency control: A review of 2025 trends. Renew Sustain Energy Rev 2025.
[26] Chaudhari P, Siddhpura DM, Ranva J, Varu V, Katariya A. Real-time load frequency control for PV-integrated power systems. Int J Eng Res Technol 2025;14:110363.
[27] Kumar S, et al. Virtual inertia support for load frequency control in low-inertia microgrids. IEEE J Emerg Sel Top Power Electron 2025.

[28] Tungadio DH, Sun Y. Load frequency controllers considering renewable energy integration in power system. Energy Rep 2019;5:436–453. [CrossRef]
[29] Wu Z, Gao W, Gao T, Yan W, Zhang H, Yan S, et al. State-of-the-art review on frequency response of wind power plants in power systems. J Mod Power Syst Clean Energy 2018;6:1–16. [CrossRef]
[30] Yan Z, Xu Y. Data-driven load frequency control for stochastic power systems: A deep reinforcement learning method with continuous action search. IEEE Trans Power Syst 2018;34:1653–1656. [CrossRef]
[31] Ramakrishna K, Bhatti T. Sampled-data automatic load frequency control of a single area power system with multi-source power generation. Electr Power Compon Syst 2007;35:955–980. [CrossRef]
[32] Gautam SK, Goyal N. Improved particle swarm optimization based load frequency control in a single area power system. In: 2010 Annual IEEE India Conference (INDICON); 2010. p. 1–4. [CrossRef]
[33] Gulzar MM, Iqbal M, Shahzad S, Muqeet HA, Shahzad M, Hussain MM. Load frequency control (LFC) strategies in renewable energy-based hybrid power systems: A review. Energies 2022;15:3488. [CrossRef]
[34] Tan W. Decentralized load frequency controller analysis and tuning for multi-area power systems. Energy Convers Manag 2011;52:2015–2023. [CrossRef]
[35] Alhelou HH, Hamedani-Golshan ME, Zamani R, Heydarian-Forushani E, Siano P. Challenges and opportunities of load frequency control in conventional, modern and future smart power systems: A comprehensive review. Energies 2018;11:2497. [CrossRef]
[36] Saleem MU, Shakir M, Usman MR, Bajwa MHT, Shabbir N, Ghahfarokhi PS, et al. Integrating smart energy management system with Internet of Things and cloud computing for efficient demand side management in smart grids. Energies 2023;16:4835. [CrossRef]
[37] Asgharian P, Noroozian R. Modeling and model predictive control of a microturbine generation system for stand-alone operation. Sigma J Eng Nat Sci 2019;37:705–722.
[38] Sobhanam AP, Mary PM, Mariasiluvairaj WI, Wilson RD. Automatic generation control using an improved artificial electric field in multi-area power system. IETE J Res 2023;69:4813–4825. [CrossRef]
[39] Çolak ÖÜ, Çakır Y. Genetic algorithm optimization method for parameter estimation in the modeling of storage modulus of thermoplastics. Sigma J Eng Nat Sci 2019;37:981–988.
[40] Gupta M, Walia A, Gupta S, Sikander A. Modelling and identification of single area power system for load frequency control. In: 2017 4th International Conference on Signal Processing, Computing and Control (ISPCC); 2017. p. 436–439. [CrossRef]
[41] Mohammed AJ, Al-Majidi SD, Al-Nussairi MK, Abbod MF, Al-Raweshidy HS. Design of a load frequency controller based on artificial neural network for single-area power system. In: 2022 57th International Universities Power Engineering Conference (UPEC); 2022 Aug 30-Sep 2. p. 1–5. [CrossRef]
[42] Bharat M, Dodakundi M, Dash R. Design and analysis of optimized hydro governor control action using GWO. In: 2023 IEEE 2nd International Conference on Industrial Electronics: Developments & Applications (ICIDeA); 2023. p. 615–619. [CrossRef]
[43] Kunya AB, Abubakar AS, Yusuf SS. Review of economic dispatch in multi-area power system: State-of-the-art and future prospective. Electr Power Syst Res 2023;217:109089. [CrossRef]
[44] Kunya AB. Hierarchical bi-level load frequency control for multi-area interconnected power systems. Int J Electr Power Energy Syst 2024;155:109600. [CrossRef]
[45] Kiehbadroudinezhad M, Merabet A, Hosseinzadeh-Bandbafha H, Ghenai C. Environmental assessment of optimized renewable energy-based microgrids integrated desalination plant: Considering human health, ecosystem quality, climate change, and resources. Environ Sci Pollut Res Int 2023;30:29888–29908. [CrossRef]
[46] Cetinkaya U, Bayindir R. Impact of increasing renewable energy sources on power system stability and determine optimum demand response capacity for frequency control. In: 2022 10th International Conference on Smart Grid (icSmartGrid); 2022. p. 396–400. [CrossRef]
[47] Ali R, Mohamed TH, Qudaih YS, Mitani Y. A new load frequency control approach in an isolated small power systems using coefficient diagram method. Int J Electr Power Energy Syst 2014;56:110–116. [CrossRef]
[48] Yusuf SS, Abubakar AS. A comprehensive review on grid-forming inverter: Potential and future trends. Majlesi J Electr Eng 2023;17:1–27.
[49] Ahmed I, Rehan M, Basit A, Malik SH, Hong KS. Multi-area economic emission dispatch for large-scale multi-fueled power plants contemplating inter-connected grid tie-lines power flow limitations. Energy 2022;261:125178. [CrossRef]
[50] Khujaev A, Uğurenver A. Centralized controller-based on optimal power flow (OPF) algorithm for power management in microgrid systems. Sigma J Eng Nat Sci 2025;43:2279–2293. [CrossRef]

Sigma J Eng Nat Sci, Vol. 44, No. 4, pp. 2905–2916, August, 2026

Sigma Journal of Engineering and Natural Sciences
Web page info: https://sigma.yildiz.edu.tr
DOI: 10.14744/sigma.2025.00102

Research Article

A hybrid BiT-EfficientNet framework for automated detection of skin cancer and monkeypox using dermatoscopic images

Juby MATHEW[1,*], Dileepkumar S. R.[2], Ardra B. S.[1]

[1]*Department of Computer Science and Engineering, Amal Jyothi College of Engineering, Kerala, 686518, India*
[2]*Department of Computer Science and Multimedia, Lincoln University College, 47301, Malaysia*

ARTICLE INFO

Article history
Received: 13 November 2024
Revised: 25 February 2025
Accepted: 27 May 2025

Keywords:
Big-Transfer Learning; EfficientNet; Disease Prediction; Monkeypox; Skin Cancer

ABSTRACT

This research introduces a novel hybrid deep learning framework integrating Big Transfer Learning (BiT M-R50x1) and EfficientNet B6 to automate the detection of skin cancer and monkeypox (Mpox) from dermatoscopic images. With the knowledge transfer capabilities of BiT and the compute efficient architecture of EfficientNet, the model is able to achieve high classification accuracy and inference speed. These aspects are especially important for deployment in resource constrained clinical environments. The framework addresses class imbalance for benign, malignant, and Mpox lesion classes by performing a set of preprocessing tasks like image resizing and normalization, as well as targeted data augmentation. The framework utilizes the ISIC-2020 and the Kaggle Mpox datasets for training and validation respectively. The hybrid model freezes the base layers to keep the model generic for representing various types of images and fine-tunes the upper layers for the classification task at hand. The model achieves an accuracy of 95.5%, a precision of 94% and a recall of 91.69% with an F1-score of 93.36%. The model outperforms other baseline models like InceptionV3, ResNet50, and MobileNetV2. The results of the study demonstrate the model is able to classify the Mpox samples with limited amount of training data with high classification accuracy and is robust to classification inconsistencies across various demographic groups.

Cite this article as: Mathew J, Dileepkumar SR, Ardra BS. A hybrid BiT-EfficientNet framework for automated detection of skin cancer and monkeypox using dermatoscopic images. Sigma J Eng Nat Sci 2026;44(4):2905–2916.

INTRODUCTION

There is no shortage of acute and chronic health conditions around the world that frequently overlap and require continuous surveillance. Effective management often hinges upon timely identification. In this research, we will assess the challenges of diagnosis for Mpox and skin cancer. Mpox, previously known as monkeypox, is a virus that was first identified in humans in 1970 and has comparable symptoms to smallpox. Like other pox viruses, Mpox is a large (200-250 nm) DNA virus and a member of the Orthopoxvirus genus. While there are ongoing efforts to improve the diagnosis of Mpox, there are other public

***Corresponding author.**
*E-mail address: jubymathew@amaljyothi.ac.in

This paper was recommended for publication in revised form by Editor-in-Chief Ahmet Selim Dalkilic

Published by Yıldız Technical University Press, İstanbul, Turkey
© Author. This is an open access article under the CC BY-NC license (http://creativecommons.org/licenses/by-nc/4.0/).

health threats of equal or greater importance. Skin cancer is generally considered the most prevalent form of cancer globally and is often considered one of the more deadly cancers. From a public health perspective, skin cancers of all types are considered a major health concern. Like Mpox, the first signs of skin cancer often resemble other less harmful skin conditions, which contribute to public health challenges associated with the early diagnosis of skin cancers. Diagnostic uncertainty is greater for melanoma than for either BCC or SCC. Mpox and skin cancers present similar public health threats and challenge the public health system to improve public health services.

Autonomous AI-based systems show great promise in revolutionizing the field of biomedicine and healthcare, especially in image interpretation and diagnostic systems. Convolutional Neural Networks (CNNs) show great potential in identifying various skin conditions. However, distinguishing different subtypes of a skin condition, let alone rare conditions such as Mpox, with limited training data, is very challenging for current AI systems. Further, factors such as the skin type and ethnicity of the population, various environmental conditions, and the type of imaging systems all contribute to the complexity of achieving accurate skin condition diagnosis. In this project, we use Big Transfer (BiT) to address both Mpox skin condition and skin cancer using the models BiT-M-R50x1 and EfficientNet B6. We hope to create a framework whereby healthcare personnel are aided in diagnostic processes, using automated systems to analyze medical images. Big-TL allows BiT models to integrate a large, generic-focused, intelligence into medical-focused architectures. Additionally, we utilize EfficientNet to integrate a high-level of computing power to a medical imaging framework.

This work is a major advancement in using sophisticated ML techniques in medical diagnostics. It has the potential to be a valuable addition to the diagnostic tools of healthcare professionals and to become a part of their diagnostic workflow. These automated systems have the potential to improve early detection of various medical conditions, hence improving the health outcomes of patients.

This work takes important steps in ML-based medical diagnostics and shows great promise as a tool for health care workers in their diagnostic workflow. Automated systems such as this could assist healthcare workers to diagnose patients at risk, especially in the early stages of the conditions, so that timely and appropriate intervention and treatment.

The objectives and contributions of this research can be summarized as follows:

- Use of integrated approach to improve the diagnosis of skin cancer and monkeypox using dermatoscopic images
- Using advanced ML and DL techniques to achieve high prediction accuracy and reliability
- Implementation of advanced ML and DL concepts for the development of a reliable system for improving the prediction of skin conditions
- Development of a Hybrid AI Diagnostic System – Introduces a high-accuracy (95.5%) AI model integrating Big Transfer Learning (BiT M-R50x1) and EfficientNet B6 for non-invasive detection of skin cancer and monkeypox
- Address Public Health and improve early diagnosis in resource-limited settings by leveraging ML to detect common and emerging diseases

Related Works

Recently, the use of computer-aided technology for processing dermatoscopic images for the early identification of skin cancers has increased. This systematic review analyzes recent studies and points out deficiencies of existing methodologies. Numerous computer vision techniques for processing images and videos have been identified, and emphasis has been placed on validation metrics, algorithms, and results on accuracy. The study points out important advances in the fields of machine learning and deep learning for the field of cancer diagnosis. The authors of this study point out that for the diagnostic process, the final interpretation of the images by the experts still plays an important role. Improvements in image quality and processing also have a positive impact on the final outcome of the diagnosis. The study aims to point out the importance of improving the use of computer-based technologies in order to meet the challenges of the field of skin cancer diagnosis [1].

Deep Learning Models for Skin Cancer Detection

Research has also looked into using pre-trained deep learning (DL) models and machine learning (ML) algorithms for the detection of skin cancer. Various models were studied, including: ResNet152v2, InceptionResNetV2, DenseNet201, ResNet50, and InceptionV3. Alongside these, a modified VGG19 model which included max pooling and dense layers for improved prediction precision was also considered. The models were developed using datasets of benign and malignant skin lesions, and the accuracy was further improved by including ML classifiers such as Decision Tree, KNN, SVM, and Logistic Regression. With the application of the added VGG19 model, performance evaluation showed improved results in recall, F1-score, precision, sensitivity, and accuracy, thus demonstrating a significant performance boost when compared to traditional classifiers [2].

To improve the automated diagnosis of one of the most aggressive types of skin cancer (melanoma), researchers created an automated system called Multi-scale GC-T2. The model utilizes MEWF (Median Enhanced Wiener Filter) for dataset augmentation and noise reduction using DermIS and DermQuest datasets. ENMAR (Enriched Manta-Ray Optimization Algorithm) guarantees image quality

and precise lesion segmentation is achieved by AdDNet (semantic segmentation) with Haar-U-Net (HAUNT). The segmentation is followed by feature extraction done with M-GCN (multi-scale graph convolution network); dimensionality reduction is done using tri-movement attention. Classification is done with tri-level fused features fused with a sigmoid function. The model's accuracy, sensitivity, specificity, and F1-score surpass all previously reported results, proving its potential as a melanoma diagnostic tool [3].

An improved model that combines DenseNet and MobileNet for skin cancer detection has recently been published. The authors used the ISIC dataset, which contains a large volume of dermatoscopic images. The authors noted a classification accuracy of 93.75%, outperforming other models that incorporate ResNet50 and InceptionNetV3 by 5.42%. Additionally, the authors reported an improvement of 4.69% and 3.13%, respectively, compared to the models that incorporate DenseNet and MobileNet. The authors also reported that the combination model reduced the training time to 49.48 minutes, which was substantially less than the individual models [4].

An alternative model for the diagnosis of skin cancer, which employs a combination of techniques, to include hyperparameter tuning and channel attention mechanisms in a Convolutional Neural Network, as well as Deep Learning and U-Net and Improved MobileNet-V3 has also recently been published. The model was validated against the HAM-10000 dataset and achieved an overall accuracy of 98.86% and a precision of 97.84% [5].

The final two studies use similar techniques to classify skin cancer into eight categories, with the first study using a hybrid model of InceptionV3 and ResNet50 to overcome previous models that did not consider practical aspects, and achieved low levels of accuracy, in skin cancer classification. The proposed model used a gradient-related issue and large parameter issue to reduce the number of parameters using InceptionV3 and ResNet50, respectively. The model was trained on an augmented version of the HAM10000 dataset to achieve a validation accuracy of 87.11%. The test accuracy, precision, recall, and F1-score of the model were 82.2%, 82.4%, 82.2%, and 81.7%, respectively. The authors developed an iOS application with a chatbot for diagnosis and a chatbot for interactive sessions with patients. This study demonstrated potential use cases of hybrid DL models in medicine, particularly in the domain of classification of medical images. Additionally, the authors recommended utilizing GANs to reduce the class imbalance and optimize features in the dataset [6].

The other study uses VGG16 and InceptionV3 to classify skin cancer, including melanoma, basal cell carcinoma, and squamous cell carcinoma, using transfer learning. The study used various performance metrics to evaluate the models trained using a skin-related image dataset. The authors concluded that InceptionV3 outperformed VGG16, based on the metrics used in the study [7].

This challenge has motivated the development of several CNN expert systems for skin disorders. The two primary architectures for these expert systems have been Xception and MobileNet. Compared to other CNN architectures, including ResNet50, InceptionV3, InceptionResNet and DenseNet, the expert systems based on MobileNet and Xception have demonstrated significant performance gains when classified against a set of skin disorders. The systems achieved a classification accuracy of 97.00% and 96.00% respectively against a sample case of five skin disorders [8].

In a related development, the use of image pre-processing to enhance image quality and reduce background noise in skin cancer detection was studied. The Sparrow search coupled with a fully convolutional encoder-decoder network (FCEDN) was used for dermoscopic image segmentation. An adaptive CNN was used to classify the segmented images. The system demonstrated segmentation accuracies of 95.28%, 95.89% and 92.70% against the ISBI 2017, ISIC 2018 and PH2 datasets respectively. It also demonstrated a classification accuracy of 91.67% against the same datasets [9].

The integration of Discrete Wavelet Transformation (DWT) with Convolutional Neural Networks (CNN) has been studied to enhance skin cancer classification. DWT adds an edge to feature extraction, and improves classification. The performance of the model was evaluated using the HAM10000 dataset, and was compared to Artificial Neural Networks (ANN) and MLP. It showed a sensitivity of 94% and a specificity of 91% [10].

An innovation in the field is the use of Echo State Networks (ESN) to classify skin cancer. To optimize the ESN, the Seasons Optimization Algorithm was used. The model was tested on the MNIST skin cancer database, and it was able to outperform other models such as AlexNet/ELM/IGOA, VGG-16 and HHOA [11].

Furthermore, a Deep Learning (DL) framework, combining a modified GRU and Mask-RCNN, has been proposed. The framework uses the ISIC 2020 and HAM10000 datasets, and is able to classify skin cancer with an accuracy of 99.95% and 99.98% respectively [12].

In general, studies have shown that automating skin cancer diagnosis shows great potential, and especially in the area of early diagnosis of skin cancer. An ML framework that incorporates FOA and SVM has been developed. As melanoma has rising rates of incidences, the FOA-SVM model has been developed for skin lesion segmentation and classification. FOA helps in optimizing parameters of SVM and thereby improves the diagnostic accuracy. The model has potential for implementing computer-aided diagnosis of skin cancer in clinic [13].

The goal of this study is to utilize the potential of Deep Learning for classification and diagnosis of skin cancer and to enhance the existing systems in this area. This work focuses on the problems of skin cancer class imbalance and utilizes class weight for training. The model further incorporates a pre-trained CNN architecture for classification of

skin cancer. The author further proposes a method for segmentation and preprocessing of images that increases the performance of deep learning models for skin cancer detection [14]. The author combines VGG16 and ResNet50, and based on the experiments, the hybrid model demonstrates improvement with respect to classification performance when compared to individual components [14].

Collectively, these studies highlight the rapid advancements in AI-driven skin cancer diagnosis, offering potential improvements in early detection, classification accuracy, and clinical integration. This will show Table 1 [1-15].

Like other poxviruses, symptoms of monkeypox (Mpox) infection are characterized by fever and skin lesions. Initially, Mpox infections may be misdiagnosed with other

Table 1. Comparative overview of methodologies, dataset, advantages, and drawbacks in recent skin cancer research

Ref.	Methodology	Dataset	Advantages	Drawbacks
Hermosilla et al. [1]	Systematic review of 45 studies from Web of Science and Scopus	Various sources	Highlights key ML/ DL advancements in dermatoscopic image processing	Dependent on image quality and expert interpretation
Kandhro et al. [2]	Pre-trained DL models (ResNet152v2, InceptionResNetV2, DenseNet201, etc.) with ML classifiers (SVM, KNN, DT, LR)	Benign & malignant skin lesion dataset	Improved classification accuracy using hybrid approach	Limited dataset scope
Alqarafi et al. [3]	Multi-scale GC-T2 framework, semantic segmentation, and Deep Q Network	DermIS, DermQuest	High accuracy, robust segmentation, and feature fusion	Computationally intensive
Imam et al. [4]	Concatenated DenseNet & MobileNet with transfer learning	ISIC dataset	93.75% accuracy, faster processing (49.48 min)	Limited generalization beyond ISIC dataset
Lilhore et al. [5]	CNN with hyperparameter tuning, Standard U-Net, Improved MobileNet- V3	HAM10000	98.86% accuracy, 97.84% precision	High complexity, potential overfitting
Sadik et al. [8]	CNN-based expert system (Xception, MobileNet) with transfer learning	Multiple datasets	High classification accuracy (97.00%)	Requires large training data
Ali et al. [9]	FCEDN-SpaSA for segmentation, adaptive CNN for classification	ISBI 2017, ISIC 2018, PH2	91.67% classification accuracy, resource-efficient	Limited dataset variability
Claret et al. [10]	DWT with CNN for feature extraction	HAM10000	94% sensitivity, 91% specificity	Comparisons with other feature extraction methods
Han et al. [11]	Echo State Network (ESN) with optimized Season Algorithm	MNIST Skin Cancer Database	97.58% accuracy, reduced training data requirement	Not tested on larger datasets
Monica et al. [12]	Modified GRU with Mask-RCNN for segmentation	ISIC 2020, HAM10000	99.95%-99.98% accuracy	High computational demand
Sonia et al. [13]	Fruit Fly Optimization Algorithm (FOA) with SVM	Unspecified	Enhances segmentation & classification efficiency	Requires further validation on larger datasets
Ghosh et al. [14]	Hybrid model (VGG16 + ResNet50) with class balancing	3,000 images, 9 skin diseases	Overcomes class imbalance, robust feature extraction	Computationally expensive
Zeng and Zhu [6]	hybrid model combining InceptionV3 and ResNet50	HAM10000	Achieving accuracy of 87.11%, outperforming standalone InceptionV3, ResNet50, and VGG19 models.	Imbalanced Dataset Issues, Limited Real-World Validation
Mathina Kani et al. [15]	hybrid model combining InceptionV3 and DenseNet50	ISIC contains 3307 dermoscopy images	Achieved a superior accuracy of 91.29%, outperforming other contemporary deep learning approaches	Limited Real-World Validation
Sayyad et al. [7]	VGG16, InceptionV3	dermoscopic images of multiple skin diseases	Achieved 94% accuracy, outperforming VGG16 and ensuring reliable skin disease classification.	InceptionV3's high accuracy suggests possible overfitting

conditions including chickenpox and measles. The World Health Organization (WHO) confirmed hundreds of Mpox cases outside the endemic regions during 2022. Many countries have reported Mpox cases for the first time. The virus's abrupt spread, combined with the already existing challenges in routinely confirming Mpox infections, heightens the need for improved diagnostic methods.

In this research, the authors proposed an automated Mpox diagnosis system using CNNs. Skin lesion images were collected and divided into Mpox and non-Mpox classes. A total of 80% of the images (training and validation sets) were used for model training. The authors tested the following five models: MobileNetV2, VGG16 and VGG19, ResNet50, and EfficientNetB3. The training and test datasets were used for model evaluation. For transfer learning, the authors employed data augmentation and defined an evaluation metric. The best classification accuracy (98.16%) was obtained by the MobileNetV2 model. One of the limitations of the study was that the classification of Mpox may be confused with other poxviruses (e.g. variola virus, vaccinia virus, etc.). When a data set consisting only of Mpox lesions is provided, the best classification accuracy was reported as 99.14% (training) and 98.25% (testing) [16].

The COVID-19 pandemic changed a lot of things in the world, and one of the changes was the need for faster testing for other diseases. One of such diseases is Mpox. Researchers have combined techniques of transfer learning and hyperparameter optimization with different deep learning architectures, including MobileNetV3-s, EfficientNetV2, ResNet50, VGG16, DenseNet121, and Xception. The best performance was shown by the MobileNetV3-s model where the average F1 score was 0.98, the area under the curve (AUC) was 0.99, and other performance metrics like accuracy and recall approach 0.98. The researchers also showed that CNNs are efficient in classification of Mpox cases [17].

Another research also focused on detection of monkeypox using deep learning techniques. The study also benefited from the 2022 surge in monkeypox cases and used 4 classes of skin lesion images which include monkeypox, chickenpox, measles, and normal skin. The researchers used different deep learning architectures, including DenseNet201 and VGG16 and evaluated the models for classification of monkeypox skin lesions against other skin lesions. Some of the other models were also evaluated for classification of skin lesions against normal skin. The study showed that DenseNet201 outperformed other architectures for both monkeypox and other skin lesion classification. Additionally, the researchers also used different AI techniques to enhance trust of clinicians. Overall, the researchers also showed that DenseNet201 outperformed other architectures for classification of skin lesions against normal skin [18].

Deep learning (DL) algorithms for Mpox detection have benefited from advanced image datasets. The development of such datasets has often been coupled with the advancement of DL algorithms. One of the outcomes of this positively reinforcing cycle was the development of the Mpox Skin Lesion Dataset Version 2.0 (MSLD v2.0). Along with Mpox-related skin lesions, this dataset contains side-by-side comparative images of other rash-bearing infectious conditions (i.e. chickenpox, measles, and hand-foot-mouth disease) as well as cowpox skin lesions and images of normal skin. The researchers used the aforementioned images along with images of other skin lesions from the dataset (i.e. herpes skin lesions and syphilis skin lesions) to evaluate various deep neural networks (DNNs) including VGG16, ResNet50, DenseNet121, MobileNetV2, EfficientNetB3, InceptionV3, and Xception. The best result was obtained using a color space data augmentation technique to increase skin color variability. Further, the researchers used transfer learning and the HAM10000 dataset to improve the final results. They reported a final validation accuracy of 83.59%. The results of this study further highlight the importance of creating adequate and inclusive datasets to train DL models for Mpox case detection [19].

In this work, the researchers presented a new convolutional neural network (CNN) called MpoxSLDNet for automated detection of Mpox lesions. MpoxSLDNet achieved a test-time accuracy of 94.56%. This accuracy was higher than the pre-trained models, VGG16, ResNet50, and DenseNet121 [20]. With the increasing number of Mpox cases, healthcare systems need automated tools to accelerate and improve diagnosis. Automation provides efficiency in settings with limited resources. MpoxSLDNet meets these needs. The researchers say there's plenty of room for improvement. Ali et al. [21] created an ensemble model to diagnose MPox with VGG-16 and Inception-v3. ResNet-50 outperformed both VGG-16 and Inception-v3, resulting in an overall accuracy of 82.96%. Ali et al. [21] created an improvement to the development of MPox ensemble models. Additionally, Uysal [22] proposed a hybrid model based on deep learning (DL) and long-short term memory (LSTM) to classify Mpox lesions. The authors integrated the top two models of the Hybrid framework with an LSTM. The integrated framework achieved an accuracy of 87% and an F1 score of 85%. It is worth mentioning that Hybrid DL frameworks are well positioned to integrate multiple architectures, thereby improving the diagnostic accuracy of Mpox lesions classification.

Classification of Mpox skin lesions using deep learning (DL) models has shown impressive results, especially with convolutional neural networks (CNNs) and their combinations with other models. With ongoing research and development of DL models and optimization of training data, Mpox diagnosis and management is likely to improve. Table 2 shows comparison of different papers [23-29].

Proposed System

The hybrid diagnostic framework combines Big Transfer Learning (BiT M-R50x1) with EfficientNet B6 to aid in the automated classification of skin cancer and monkeypox

Table 2. Comparative overview of methodologies, dataset, advantages, and drawbacks in recent monkeypox research

Ref.	Methodology	Dataset	Advantages / Key Findings	Drawbacks / Limitations
Tanim et al. [23]	Hybrid model combining BiT-EfficientNet B6 and BiT-M-R50x1	Mendeley Data	Reported 98.25% precision, 95.48% recall, 96.84% F1-score, and 96.86% accuracy. Parameter tuning contributed to robust performance.	The ensemble structure increases computational requirements.
Altun et al. [17]	Hybrid model based on MobileNetV3-S, EfficientNetV2, and Xception with transfer learning	Monkeypox skin-lesion images	Obtained 0.98 F1-score, 0.99 AUC, and 96% accuracy, showing effective deep-learning-based classification.	Information describing the dataset is limited.
Ali et al. [19]	VGG16, ResNet50, DenseNet121, MobileNetV2, EfficientNetB3, InceptionV3, and Xception using transfer learning	Publicly available dataset	DenseNet121 provided the highest performance with 83.59% accuracy.	Clinical metadata is not available.
Dihan et al. [20]	Transfer-learning models using VGG19, Xception, and InceptionV3	Dataset from [16], comprising 1,428 Mpox and 1,764 other skin-lesion images	InceptionV3 achieved 98% accuracy.	Dataset augmentation can introduce bias into the classification process.
Uysal [22]	Hybrid deep-learning model integrating LSTM with other high-performing models	Monkeypox skin-lesion images from Kaggle	Incorporation of LSTM improved classification performance to 87% accuracy.	The combined architecture increases model complexity.
Akula and Pushkar [24]	ResNet50v2, EfficientNetB4, and DenseNet169	1,594 skin-lesion images	ResNet50v2 achieved 99.33% accuracy, giving the best performance among the evaluated models.	The dataset size is relatively small.
Jaradat et al. [16]	Transfer learning using MobileNetV2, VGG16, VGG19, ResNet50, and EfficientNetB3	Non-Mpox skin-lesion images and other skin-lesion classes	Achieved 98.16% accuracy and 94% accuracy on an external dataset, indicating improved reliability.	Real-world implementation and deployment challenges were not addressed.
Chakroborty [25]	Development of an Mpox image dataset with 224 × 224 × 3 image resolution	Self-curated dataset	The dataset can support the development and assessment of deep-learning models for Mpox classification.	Dataset size and image diversity are not reported.
Ali et al. [21]	Pre-trained VGG-16, InceptionV3, and ResNet-50 models using ensemble learning	Mendeley Data	ResNet-50 achieved 82.96% accuracy, representing the highest reported performance in the study.	The ensemble approach produced lower scores than the individual models.
Sahin et al. [26]	Deep Learning Framework (DLF) designed for mobile applications	Mendeley Data	Achieved 91.11% accuracy, demonstrating potential for mobile-based diagnosis.	Dataset limitations may affect the generalization of the model.
Lakshmi and Das [27]	Explainable AI (XAI) approach for improving interpretability in medical research	Mendeley Data	XAI improves the transparency and trustworthiness of AI-supported diagnostic systems.	Accuracy and practical usability were not reported.
Azar et al. [18]	ResNetV2, InceptionV3, Xception, and DenseNet-201	27 normal, 27 measles, 47 chickenpox, and 43 Monkeypox images	DenseNet-201 achieved 95.18% accuracy.	The limited size of the original dataset required augmentation.
Sitaula and Shahi [28]	13 pre-trained transfer-learning models	Dataset containing 1,754 images of Monkeypox, measles, and normal skin	An ensemble of Xception and DenseNet-169 achieved 87.13% accuracy.	The reported classification accuracy was relatively low.
Ahsan et al. [29]	Federated learning using modified VGG-16 and ResNet-50	2,310 images	Federated learning provides data privacy and security during model training.	The approach requires substantial computational resources.
Jaradat et al. [16]	VGG19, VGG16, ResNet50, MobileNetV2, and EfficientNetB3	117 images	MobileNetV2 achieved 98.16% accuracy.	The dataset is small and suffers from class imbalance.

using dermatoscopic image scans. As a result of combining BiT's superior transfer capabilities, and EfficientNet's computational efficiency [30, 31], the system was able to accurately extract, and integrate deep and compact features for precise diagnosis [32]. Class imbalance mitigation and model generalization enhancement such as normalization, augmentation, and oversampling are performed during the standard preprocessing steps of resizing the images. The model achieves high accuracy classifying images into three categories—benign, malignant, and Mpox. The SoftMax classifier is substituted for the dense layer to give final output values termed prediction. The system is effectively non-intrusive and designed for both clinical and remote professional setups with the aim of improving speed, clarity, ease of diagnosis, and modifying access. Figure 1 shows classification of skin lesions.

MATERIALS AND METHODS

The process of interpreting dermatoscopic images of skin cancers and monkeypox, with the help of machine learning, is illustrated in Figure 2. The method uses large DL frameworks, BiT M-R50x1 and EfficientNet B6, along with appropriate image pre-processing techniques. The method is designed to identify and classify different types of skin lesions and cancer. The effectiveness of the method and the models developed using the method, in various types of skin conditions, conditions of the skin appendages, and skin-related infectious diseases, has been established. Among various DL architectures, the authors of this paper examined the capabilities of BiT M-R50x1 and EfficientNet B6 in skin conditions, appendages, and infectious skin conditions.

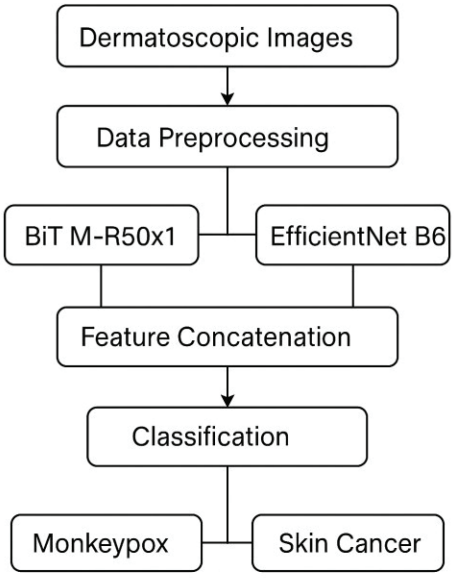


Figure 2. A Hybrid BiT-EfficientNet Model.

The models extracted high-level features from skin images, which the new classes in the top layers used for classification. The models were trained to classify skin cancer and differentiate it from Mpox. To minimize the risk of overfitting, the authors kept the number of trained layers to a minimum and stopped the update of the layers before the last few layers. Further, the combination of features extracted from the BiT and the EfficientNet models was used to create a classification layer. BiT extracts high-quality features, while the EfficientNet focuses on compactness

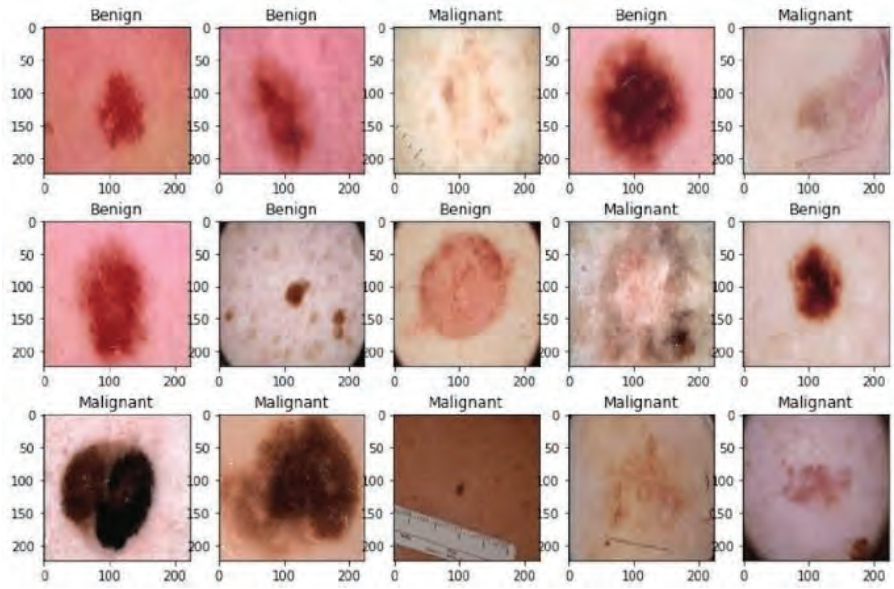


Figure 1. Classification of skin lesions.

and granularity. Since the hybridization of both models served to create a more powerful and generalizable representation to the classification problem, this work presents a similar approach to the classification of skin cancer using both models and served to improve the classification of the skin cancer cases.

Skin Cancer and Mpox Analysis

Dermatoscopic pictures of the virus-caused skin lesions of the M-pox and pictures of skin cancer uploaded by users of a web- based or mobile application used by the skin cancer, mpox detection system. For individuals as well as medical professionals, this method improves accessibility and speeds up diagnosis times.

Data Collection: The ISIC-2020 dataset [33, 34] represents one of the largest publicly available collections of high-quality, annotated dermoscopic images of skin lesions. It comprises 33,126 images, including 584 labeled as malignant and 32,542 as benign, sourced from over 2,000 individual patients. Each image is linked to its corresponding patient through a unique identifier. For this study, we selected 584 melanoma (malignant) images and 1037 benign images, the latter chosen randomly from the entire dataset. Additionally, we incorporated images from a Kaggle dataset [35] containing various infectious skin conditions such as Mpox, chickenpox, and measles. From this set, we specifically extracted 687 images related to Mpox lesions. Given the class imbalance across the melanoma, benign, and Mpox categories, data augmentation techniques were applied to the underrepresented classes. These techniques included rescaling, width shifting, rotation, shearing and horizontal flipping.

Preprocessing:

1. **Resizing:** The 224 × 224-pixel standard input size was used to dermatoscopic pictures in order to comply with the demands of machine learning models, including EfficientNet and BiT. Using higher image size would require upscaling, which can introduce noise and reduce accuracy. BiT can generalize well even with smaller image sizes.
2. **Normalization:** Pixel values were standardized in the range to ensure model training was performed within a predefined range. This improved model stability and uniformity.

Data augmentation: The data set contains too many benign and less malignant images so in order to tackle the Imbalance between benign and malignant images, a variety of data augmentation approaches were used to address data imbalance and quality:

1. **Flipping:** In order to create enhanced photos while preserving the lesion's essential visual aspects, horizontal flipping was used.
2. **Rotation:** To improve the model's capacity for generalization, several picture orientations were produced by applying certain angles.
3. **Shearing:** The key visual information was pre- served while data diversity was increased through the application of geometric adjustments.
4. **Scaling:** Zoom in or out while maintaining lesion visibility.

Data splitting: Four-fifths of the data (80%) was set aside for training and the rest (20%) was set aside for validation. The validation set was further split; 10% was set aside for testing and the rest (10%) was re-set aside for validation. This process was repeated 10 times for the purpose of avoiding overfitting, and for assessing the performance of the model.

Model selection: The architectures selected were BiT M-R50x1 and EfficientNet B6. BiT M-R50x1 performed transfer learning for the dermatoscopic data. EfficientNet was designed for computation and a good trade-off for accuracy.

Model development: Using TensorFlow and Keras, the activation functions and layers of the models for the skin cancer dataset were developed.

Optimize the models: The skin cancer models were further trained to adjust hyperparameters for batch size and learning rate.

Assess the models: The trained models were evaluated on the test set to obtain performance metrics such as loss, accuracy, etc.

Model evaluation: The trained models were assessed for metrics such as accuracy, precision, recall and F1 scores for the validation and test sets for generalizability and to ensure they were fit for deployment.

RESULTS AND DISCUSSION

By running through 50 training epochs, our model attained a training accuracy of 96.14%. The model is strong on the validation set with a validation accuracy of 95.5% (Fig. 3). The reduction in loss over epochs was an indication that the model learned from the data. The training loss at 50 epochs was 0.0232, and the validation loss was 0.1466 (Fig. 4). The curves indicated an increasing trend for accuracy during training process for both data sets. However, the trend for validation data indicated a declining accuracy towards the end of the epoch. Training data and validation data loss curves show a reduction in loss during the training procedure. Figure 5, graphically represents the classification results in the confusion matrix.

Performance Measure

Several important performance criteria, including as accuracy, precision, recall, and F1 score, were used to assess the system, which integrated Big Transfer Learning (BiT M-R50x1) and EfficientNet B6 architectures. Proposed hybrid model is compared with Inception V3 architecture, ResNet50, MobileNetV2 in the Table 3. These measures are essential for evaluating how well the model differentiates between different skin disorders, such as monkeypox,

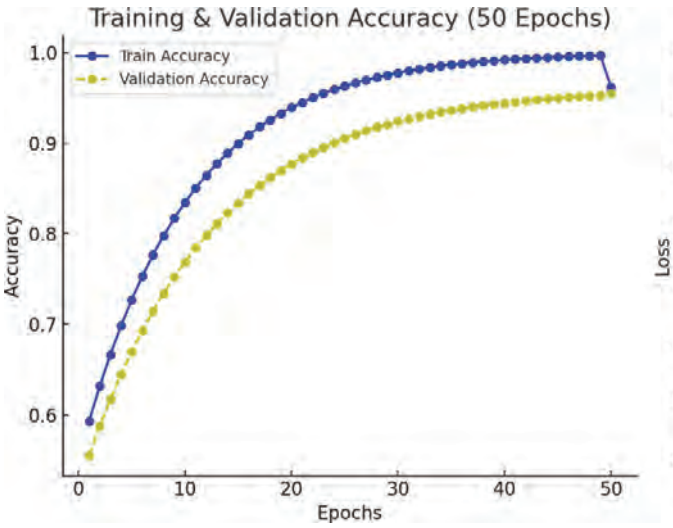


Figure 3. Training validation accuracy curve.

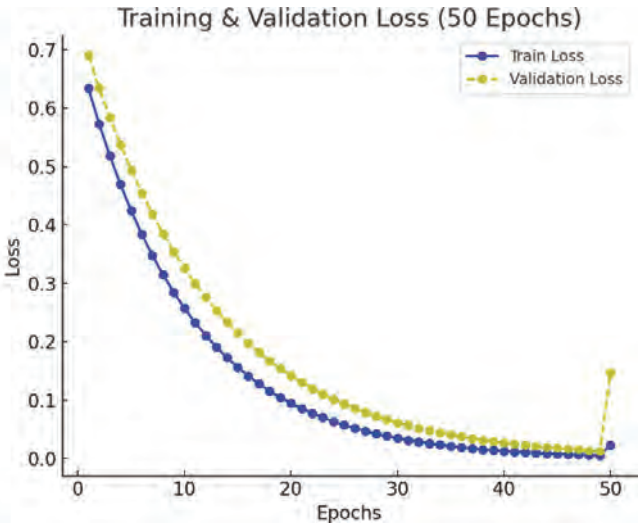


Figure 4. Training and validation loss curve.

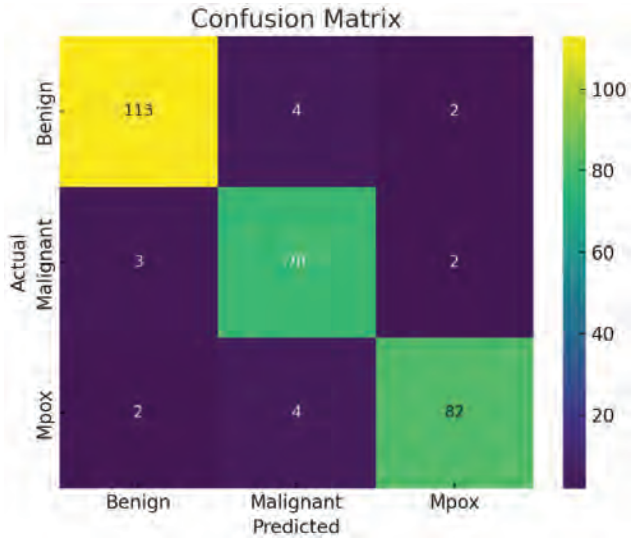


Figure 5. Confusion matrix of Bit-EfficientNet model.

benign and malignant cancer. The high- performance values of our model indicating its great performance in handling multiclass classification problems [36–38]. To ensure a thorough assessment of the model's generalizability and diagnosis accuracy, the system was evaluated using clinical data for monkeypox and dermatoscopic pictures from the ISIC 2020 dataset for skin cancer (Fig. 6).

Analysis

Big Transfer Learning enhanced our model's performance, especially to overcome the challenges of unbalanced datasets, which is commonplace when training models for rare diseases like monkeypox. BiT transferred knowledge across domains and enhanced our model to recognize skin disorders using a smaller dataset. The combination of the Bit-EfficientNet architecture and Transformer increased the model's performance further. The authors demonstrated the model's capabilities to discriminate between various skin cancer lesions as well as monkeypox, indicating the model holds great promise for clinical practice.

In the present study, the authors reported excellent results. However, the authors noted challenges when ensuring broadness of the model to various user populations. The authors addressed the limits of the model when recognizing skin disorders of various ethnic populations. When the model was trained with images of sufficient quality, it adequately recognized the target disorders. The monkeypox virus is also known to mutate and change its appearance over time. The challenges of the model and other

Table 3. Performance comparison of the models

Sl. No	Performance Metrics	BiT-EfficientNet	Inception V3	ResNet50	MobileNetV2
1	Accuracy	95.5%	88.3%	78%	91.5%
2	Precision	94%	84%	85%	90%
3	Recall	91.69%	90.02%	63%	90%
4	F1 Score	93.36%	90.21%	72%	91.5%

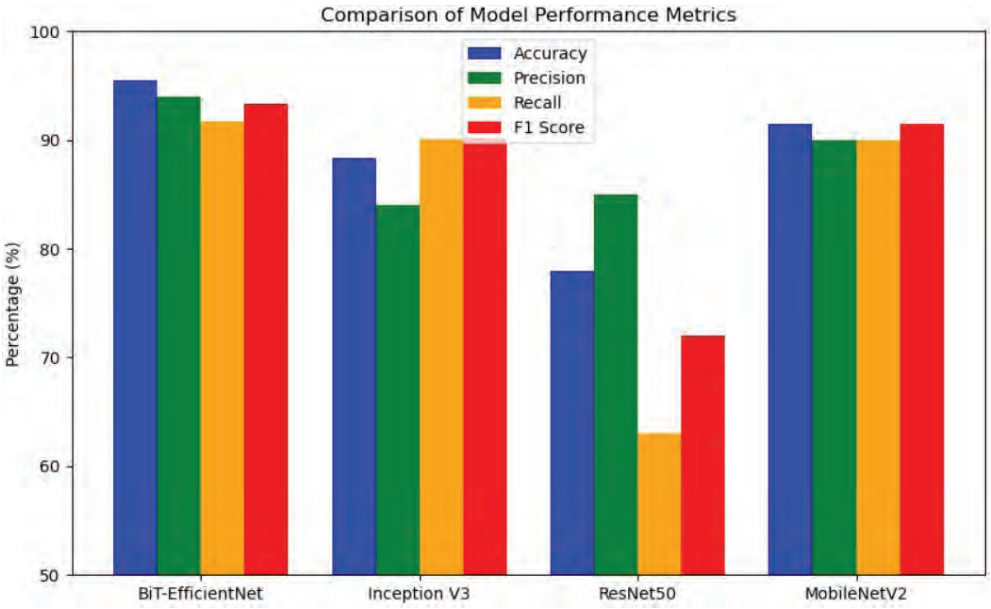


Figure 6. Performance of the classifier models.

similar models, which were all trained with limited datasets, underscore the importance for development of larger and more varied annotated datasets in the field of medicine to facilitate breakthroughs in healthcare.

The research suggests that artificial intelligence (AI) can help health care workers diagnose skin cancers and viral infections (for instance, monkeypox) with higher accuracy. Because the diagnostic system is non-invasive and easy to use, health care workers can use it to diagnose patients in the field. This system would help health care workers in low resource settings and during outbreaks. Since it can identify skin infections and inflammation, the system could be extended for other viral infections beyond skin infections. The system should be integrated with more datasets, and other imaging systems (like 3D and IR imaging) to improve diagnosis.

Demographic-Based Evaluation

To examine the flexibility of the hybrid model developed with BiT-EfficientNet, a demographic evaluation was conducted to analyze changes in model performance based on different age groups, genders, and skin tones. Performance variation was expected and noted in the assessment. The model was observed to have higher classification accuracy for malignant skin lesions for individuals with lighter skin, and the assessment team identified the presence of dermatoscopic features as the possible reason for model performance variation. The model's performance was observed to be equal for both males and females. The assessment reported a higher recall for patients' ages 60 and above and lower recall for patients' ages 20 to 30. The higher recall for patients' ages 60 and above may be attributed to the fact that patients of that age group may have more skin lesions due to aging, and may be the reason for better performance for the model in identifying those skin lesions. As noted in the assessment, there is a need to use more varied and representative datasets to address biases in the field of AI diagnostic models. Addressing these biases is important to build and design clinical AI/ML models for various ethnically diverse populations.

CONCLUSION

The research found that skin cancers and monkeypox lesions can be identified with deep learning models based on BiT M-R50x1 and EfficientNet B6 architectures. The authors suggest that with continued improvement in deep learning models and transfer learning, even cases of monkeypox, which are uncommon, can be diagnosed automatically. The models would allow health care workers in low-resource settings to focus on more complex health conditions. The authors suggest that while the current models show great potential, there are a number of factors, including the availability of annotated data, that affect the models' performance. The authors encouraged expansion of the data set with various modalities of the same and other skin conditions to improve the models. The models would benefit from improvement in a variety of skin conditions and broaden the diagnoses of viral conditions. The authors encourage improvement in the models to gain a better understanding of deep learning, diagnosing skin conditions, and, in turn, public health.

AUTHORSHIP CONTRIBUTIONS

Ardra BS: Data curation, Methodology, Investigation, Writing – original draft, Writing – review and editing

Juby Mathew: Conceptualization, Writing – review and editing, Supervision

Dileepkumar SR: Methodology, Investigation, Writing – original draft, Writing – review and editing

DATA AVAILABILITY STATEMENT

The authors assert that the data underpinning the findings of this research are available in the public database.

CONFLICT OF INTEREST

The authors reported no potential conflicts of interest regarding the research, authorship, and/or publication of the article.

ETHICS

There are no ethical problems with this manuscript's publication. It presents new medical research that has not yet been assessed and thus should not be used to inform clinical practice.

STATEMENT ON THE USE OF ARTIFICIAL INTELLIGENCE

Artificial intelligence was not used in the preparation of the article.

REFERENCES

[1] Hermosilla P, Soto R, Vega E, Suazo C, Ponce J. Skin cancer detection and classification using neural network algorithms: a systematic review. Diagnostics (Basel) 2024;14:454. [CrossRef]

[2] Kandhro IA, Manickam S, Fatima K, Uddin M, Malik U, Naz A, et al. Performance evaluation of E-VGG19 model: enhancing real-time skin cancer detection and classification. Heliyon 2024;10:e31488. [CrossRef]

[3] Alqarafi A, Khan AA, Mahendran RK, Al-Sarem M, Albalwy F. Multi-scale GC-T2: automated region of interest assisted skin cancer detection using multi-scale graph convolution and tri-movement based attention mechanism. Biomed Signal Process Control 2024;95:106313. [CrossRef]

[4] Imam MH, Nahar N, Rahman MA, Rabbi F. Enhancing skin cancer classification using a fusion of Densenet and Mobilenet models: a deep learning ensemble approach. Multidiscip Sci J 2024;6:e2024117. [CrossRef]

[5] Lilhore UK, Simaiya S, Sharma YK, Kaswan KS, Rao KBVB, Maheswara Rao VVR, et al. A precise model for skin cancer diagnosis using hybrid U-Net and improved MobileNet-V3 with hyperparameters optimization. Sci Rep 2024;14:4299. [CrossRef]

[6] Zeng Y, Zhu X. Skin cancer detection based on hybrid model by means of Inception V3 and ResNet 50. In: Fox B, et al., editors. Proceedings of the 2022 3rd International Conference on Artificial Intelligence and Education (IC-ICAIE 2022). Dordrecht: Atlantis Press; 2022. p. 275–282. [CrossRef]

[7] Sayyad J, Patil P, Gurav S. Skin disease detection using VGG16 and InceptionV3. Int J Intell Syst Appl Eng 2024;12: 148–155.

[8] Sadik R, Majumder A, Biswas AA, Ahammad B, Rahman MM. An in-depth analysis of convolutional neural network architectures with transfer learning for skin disease diagnosis. Healthc Anal 2023;3:100143. [CrossRef]

[9] Ali R, Manikandan A, Lei R, Xu J. A novel SpaSA based hyper-parameter optimized FCEDN with adaptive CNN classification for skin cancer detection. Sci Rep 2024;14:9336. [CrossRef]

[10] Claret SPA, Dharmian JP, Manokar AM. Artificial intelligence-driven enhanced skin cancer diagnosis: leveraging CNN with discrete wavelet transformation. Egypt J Med Hum Genet 2024;25:50. [CrossRef]

[11] Han M, Zhao S, Yin H, Hu G, Ghadimi N. Timely detection of skin cancer: an AI-based approach on the basis of the integration of Echo State Network and adapted Seasons Optimization Algorithm. Biomed Signal Process Control 2024;95:106324. [CrossRef]

[12] Monica KM, Shreeharsha J, Falkowski-Gilski P, Falkowska-Gilska B, Awasthy M, Phadke R. Melanoma skin cancer detection using mask-RCNN with modified GRU model. Front Physiol 2024;14:1324042. [CrossRef]

[13] Sonia R, Joseph J, Kalaiyarasi D, Kalyani N, Gupta ASALGG, Ramkumar G, et al. Segmenting and classifying skin lesions using a fruit fly optimization algorithm with a machine learning framework. Automatika 2024;65: 217–231. [CrossRef]

[14] Ghosh H, Rahat IS, Mohanty SN, Ravindra JVR, Sobur A. A study on the application of machine learning and deep learning techniques for skin cancer detection. Int J Comput Syst Eng 2024;18: 51–59.

[15] Mathina Kani MAJ, Parvathy MS, Maajitha Banu S, Abdul Kareem MS. Classification of skin lesion images using modified Inception V3 model with transfer learning and augmentation techniques. J Intell Fuzzy Syst 2023;44:4627–4641. [CrossRef]

[16] Jaradat AS, Al Mamlook RE, Almakayeel N, Alharbe N, Almuflih AS, Nasayreh A, et al. Automated monkeypox skin lesion detection using deep learning and transfer learning techniques. Int J Environ Res Public Health 2023;20:4422. [CrossRef]

[17] Altun M, Gürüler H, Özkaraca O, Khan F, Khan J, Lee Y. Monkeypox detection using CNN with transfer learning. Sensors (Basel) 2023;23:1783. [CrossRef]

[18] Azar AS, Naemi A, Rikan SB, Mohasefi JB, Pirnejad H, Wiil UK. Monkeypox detection using deep neural networks. BMC Infect Dis 2023;23:438. [CrossRef]

[19] Ali SN, Ahmed MT, Jahan T, Paul J, Sani SMS, Noor N, et al. A web-based mpox skin lesion detection system using state-of-the-art deep learning models considering racial diversity. arXiv [Preprint] 2023. arXiv:2306.14169. [CrossRef]

[20] Dihan FJ, Murad SA, Muzahid AJM, Uddin KMA, Alenazi MJF, Bairagi AK, et al. MpoxSLDNet: a novel CNN model for detecting monkeypox lesions and performance comparison with pre-trained models. arXiv [Preprint] 2024. arXiv:2405.21016. doi: 10.48550/arXiv.2405.21016

[21] Ali SN, Ahmed MT, Paul J, Jahan T, Sani SMS, Noor N, et al. Monkeypox skin lesion detection using deep learning models: a feasibility study. arXiv [Preprint] 2022. arXiv:2207.03342. doi: 10.48550/arXiv.2207.03342

[22] Uysal F. Detection of monkeypox disease from human skin images with a hybrid deep learning model. Diagnostics (Basel) 2023;13:1772. [CrossRef]

[23] Tanim SA, Tanvir K, Arnob AR, Rahman MH, Maisha TBM, Nur K. Enhancing monkeypox diagnostics: exploring the potential of EfficientNet and Big Transfer. J Image Graph 2024;12: 250–258. [CrossRef]

[24] Akula A, Pushkar S. Mpox skin lesion detection using deep learning approaches. Authorea [Preprint] 2023. [CrossRef]

[25] Chakroborty S. H-MpoxNet: a hybrid deep learning framework for Mpox detection from image data. medRxiv [Preprint] 2024. [CrossRef]

[26] Sahin VH, Oztel I, Yolcu Oztel G. Human monkeypox classification from skin lesion images with deep pre-trained network using mobile application. J Med Syst 2022;46:79. [CrossRef]

[27] Lakshmi M, Das R. Classification of monkeypox images using LIME-enabled investigation of deep convolutional neural network. Diagnostics (Basel) 2023;13:1639. [CrossRef]

[28] Sitaula C, Shahi TB. Monkeypox virus detection using pre-trained deep learning-based approaches. J Med Syst 2022;46:78. [CrossRef]

[29] Ahsan MM, Uddin MR, Farjana M, Sakib AN, Momin KA, Luna SA. Image data collection and implementation of deep learning-based model in detecting monkeypox disease using modified VGG16. arXiv [Preprint] 2022. arXiv:2206.01862. doi: 10.48550/arXiv.2206.01862

[30] Kolesnikov A, Beyer L, Zhai X, Puigcerver J, Yung J, Gelly S, et al. Big Transfer (BiT): general visual representation learning. In: Vedaldi A, Bischof H, Brox T, Frahm JM, editors. Computer Vision - ECCV 2020. Lecture Notes in Computer Science, Vol. 12350. Cham: Springer; 2020. p. 491–507. [CrossRef]

[31] Tan M, Le QV. EfficientNet: rethinking model scaling for convolutional neural networks. In: Proceedings of the 36th International Conference on Machine Learning (ICML 2019). Proc Mach Learn Res 2019;97: 6105–6114.

[32] Badik ŞT, Akar M. Machine learning classification models for the patients who have heart failure. Sigma J Eng Nat Sci 2024;42: 235–244. [CrossRef]

[33] International Skin Imaging Collaboration. SIIM-ISIC 2020 challenge dataset. 2020. Available at: https://challenge2020.isic-archive.com/. Accessed October 18, 2026.

[34] Rotemberg V, Kurtansky N, Betz-Stablein B, Caffery L, Chousakos E, Codella N, et al. A patient-centric dataset of images and metadata for identifying melanomas using clinical context. Sci Data 2021;8:34. [CrossRef]

[35] Kaggle. Mpox classification dataset. Available at: https://www.kaggle.com/datasets/abisekkamthan/mpox-classification-dataset. Accessed October 18, 2026.

[36] Dileepkumar SR, Mathew J. Ebola optimization search algorithm for the enhancement of devops and cycle time reduction. Int J Inf Technol 2023;15: 1309–1317. [CrossRef]

[37] Benjamin J, Mathew J. Enhancing continuous integration predictions: a hybrid LSTM-GRU deep learning framework with evolved DBSO algorithm. Computing 2025;107. [CrossRef]

[38] Mathew J, Vijaya Kumar R. Multilinear principal component analysis with SVM for disease diagnosis on big data. IETE J Res 2022;68: 526–540. [CrossRef]

Sigma J Eng Nat Sci, Vol. 44, No. 4, pp. 2917–2923, August, 2026

Sigma Journal of Engineering and Natural Sciences
Web page info: https://sigma.yildiz.edu.tr
DOI: 10.14744/sigma.2025.00143

Research Article

Formulation of eco-friendly dishwasher liquid: A sustainable solution

Hemant M. JARİWALA[1,*], Ravi VAGHELA[1]

[1]*Department of Chemical Engineering, Government Engineering College Valsad, Gujarat, 396001, India*

ARTICLE INFO

Article history
Received: 23 December 2024
Revised: 13 March 2025
Accepted: 28 May 2025

Keywords:
Biodegradable; Environment-Friendly; Dishwasher; Synthesis

ABSTRACT

The creation of an eco-friendly dishwashing liquid was focused on solving the environmental and health issues caused by conventional cleaners that have harmful chemicals like phosphates and artificial additives. The goal was to reduce water pollution, skin irritation, and damage to nature while still maintaining cleaning efficacy. The eco-friendly dishwasher liquid could include potential plant-based surfactants, natural enzymes, citric acid (to adjust pH), and they do not contain harmful chemicals like phosphates, chlorine, and synthetic compounds. The composition was checked using FTIR spectroscopy, and ingredient ratios were tested using oil-removal tests (ASTM-inspired protocols) by maintaining pH between 7 and 9. The results showed a pH of 9 (achieved with 7 g/L citric acid), an acid value of 1.92 mg KOH/g, and 95% grease removal efficiency, which is better than regular soap solutions (75% efficiency). The product degraded quickly >90% in 28 days. These results show that eco-friendly products can perform as well as traditional detergents with much less harm to the environment. The study builds on work by using pH-adjusted citric acid with plant-based cleaning agents, ensuring both safety and efficacy. The manufacturing process was monitored for consistency and controlled using FTIR spectroscopy. Future work could focus on finding antimicrobial natural ingredients. This study connects eco-design with offering a plan for sustainable household products.

Cite this article as: Jariwala HM, Vaghela R. Formulation of eco-friendly dishwasher liquid: A sustainable solution. Sigma J Eng Nat Sci 2026;44(4):2917–2923.

INTRODUCTION

More people are thinking about using environmentally friendly products at home, especially dishwashing detergents. The traditional dishwashing liquids typically synthesized by use of synthetic chemicals, surfactants and scents which cause the harmful impact to aquatic ecosystems and human health as well. These compounds have the potential to perturb hormone disruption in humans, bioaccumulation in marine species, and cause water pollution. The synthesis of environment-friendly dishwashing detergent liquids provides a feasible solution to reduce the negative consequences of these factors. The use of naturally available biodegradable components helps to reduce the footprint of effect on environmental with retaining the product's ability to effective application [1].

The usability of naturally derived surfactants like coconut oil, palm oil, and other plant-based components draws

*Corresponding author.
*E-mail address: hemantmjariwala@gmail.com

This paper was recommended for publication in revised form by Editor-in-Chief Ahmet Selim Dalkilic

Published by Yıldız Technical University Press, İstanbul, Turkey
© Author. This is an open access article under the CC BY-NC license (http://creativecommons.org/licenses/by-nc/4.0/).

an attention of the researchers, to investigate alternative components by increasing applications in green chemistry and develop sustainable eco-friendly products. The natural surfactants, have demonstrated significant potential, own an ability to break down naturally and very less harmful effects. The addition of essential oils and plant extracts in dishwashing liquid can enhance the efficacy, provide antibacterial properties and offer a pleasant fragrance without relying on artificial additives to appeal the consumers [2].

Moreover, the production of eco-friendly dishwashing detergents can be enhanced in terms of reduce energy consumption and minimize waste generation from the process. The stages from raw material extraction to disposal of waste assessed by the Life cycle assessments (LCAs) instrumental in evaluating the environmental impact of products. It signifies the optimized steps followed for sustainability in the product's lifecycle. The approach draws an attention on both immediate environmental concerns about the application and promotes long-term sustainability of products [3].

This research article explores the development and enhancement in an environment-friendly dishwashing liquid. The study involves the selection of organic surfactants, their impact on cleaning performance, and the overall environmental benefits. It also aims to evaluate impacts of eco-friendly alternatives to conventional dishwashers, identifying their advantages and potential challenges for the sustainability. Furthermore, to provide sustainable solutions consumer overview and acceptance of environmentally friendly products, it required the acceptance and success in the market. The development of eco-friendly cleaning products supports an improved environment and promote sustainable consumer practices. The insights gained from this research could lay the underpinning platform for further improvement in the household cleaning industry, encouragement towards more environmentally conscious and responsible product development. The preparation of environmentally friendly dishwashing liquids required crucial advancement to target the increasing demand for eco-friendly products. The application of such products reduces environmental impact and promotes a more sustainable solution. [4].

The current study fouce on the synthesis of an environmentally friendly dishwashing liquid without use of toxic chemicals such as phosphates, chlorine, and synthetic additives. The objective of the work was to ensure that the soultion provide efficient cleaning and has very little harmful effect on the environment and people's health. The use of the natural plant based cleaning agents and natural enzymes makes product eco-friendly. The pH stability of a product adujsted in between 7-9, keeping pH netutral to little alkaline with varying proportion of ingradients, provide effective solution for grease removal.

MATERIALS AND METHODS

As shown in Table 1, to remove the food residues, oil droplets and provide effective cleaning solution for the dishes and utensils many components are Interactively used for the synthesis of Dishwasher liquid or detergent [5]. Surfactants act as a cleaning agent in dishwashing liquid. Nonionic cleaning agents and alkyl sulphates are frequently used in the formulation of dishwashing liquids. The main role of such surfactants is to reduce the surface tension of water, allowing it to permeate into the layer of fats and oils to remove the food particles from the utensil surface [6]. Enzymes have the potential to decompose specific

Table 1. Components and their properties

Substances	Use	Toxicity	Physical and Chemical Properties
Cocamidopropyl Betaine	Surfactant	Cause serious eye damage	Appearance Liquid. Color: Colorless to pale yellow. pH (concentrated solution): ~pH 5.0 at 20°C
Alkyl Poly glucosides (APGs)	Surfactant	LD 50 value :- >=5000 mg/kg May cause skin Irritating May Cause eye Irritating	Color-Pale yellow, Oduor-Weak odor, Freezing point -10°C, Boiling point/range 100°C, Ignition temp. (stable gaseous) Nonflammable, Solubility-in/Miscibility with water Dissolve in water, pH-value:11.5—12.5
Sodium citrate	Builders	Hazardous in case of Skin contact (irritant), of ingestion, of inhalation	Appearance: White solid, pH-value:7.0-9.0 (5% solution) Odorless, Melting/Freezing point: 313.9°C/597°F, Specific Gravity: 1.665
Potassium sorbate	Preservative	Toxicity to Animals: Acute oral Toxicity (LD 50): 3800 mg/kg [Mouse]	Molecular Weight: 150.22g/mole, Melting Point: Decomposes. (270°C/518°F), Specific Gravity:1.363 (Water = 1), Properties of Dispersion: Solubility: Easily Soluble in cold water.

categories of alimentary components such as proteins, carbohydrates, and lipids. Protease enzymes especially break down protein stains, amylase enzymes decompose substances containing starch, and lipase enzymes act on the removal of oil residues [7].

Builders optimize surfactant efficiency by reducing water hardness and inhibiting mineral deposition on dishes. Earlier, Sodium tripolyphosphate (STPP) was widely used as a constructor, however, its utilization has been limited due to concerns about ecological crises. Citrates and sodium carbonate have replaced phosphate as the most commonly used builders [8]. Trace amounts of bleaching chemicals added to dishwashing liquids for removal of persistent stains and discoloration. Sodium percarbonate is the most commonly utilized oxygen-based bleaching chemical. It releases oxygen when dissolved in water, which remove process strains [9]. Anti-redeposition agents are added to dishwashing liquids to prevent food particles from reattaching to the plate surface during washing [10]. They facilitate food particle removal by simply rinsing, while maintaining the particles in a state of suspension inside the water. Dishwasher liquids frequently use perfumes and coloring agents to enhance olfactory and visual aesthetics. Typically, Aroma and pigment substances are added in very small quantities and do not play a crucial role in the cleaning effectiveness [11].

The environmentally friendly dishwashing liquid contains various essential components that improve its effectiveness and ecological advantages. The formulation contains 10- 20% cocamidopropyl betaine, a surfactant mainly produced from coconut oil, plays a key role in its efficient cleaning and foaming abilities [12]. Alkyl polyglucosides act as a cleaning agent made from natural sugars, contains up to 5-10% of the liquid. They help to improve the liquid's cleaning performance and act gently on the skin [13]. Sodium citrate helps to function the dishwashing liquid work better by functioning as a water softener and pH controller, added at 2- 5% in the liquid. Potassium sorbate is added to prevent germ formation and extend the product's shelf life [14]; it is added at a concentration of 0.1-0.5% in the liquid. The rest consist of water, act as a solvent and carrier for the other ingredients to ensure a balanced and efficient, eco-friendly dishwashing liquid.

Procedure

Figure 1 shows the stepwise procedure for preparation of the dishwasher. The detailed steps are mentioned as follows;

1. In a mixing container, add water (majority of the formulation) while stirring continuously.
2. Slowly add cocamidopropyl betaine and gently mix until fully dissolved in water.
3. Dropwise add alkyl polyglycolides with continuous stirring until it is uniformly distributed.
4. Gradually add sodium citrate with continuous agitation.
5. At last, add potassium sorbate and stir throughout to ensure proper dispersion.

The synthesis of dishwasher liquid addresses the manufacturing procedure that systematically blends the different constituents in a predetermined sequence. Although the it may be differed for some specific techniques and tools, the basic steps need to be considered as;

1. The formulation process required the components such as surfactants, enzymes, builders, and other additives. The precision for the weight measurement required to ensure the consistency and effectiveness [15].

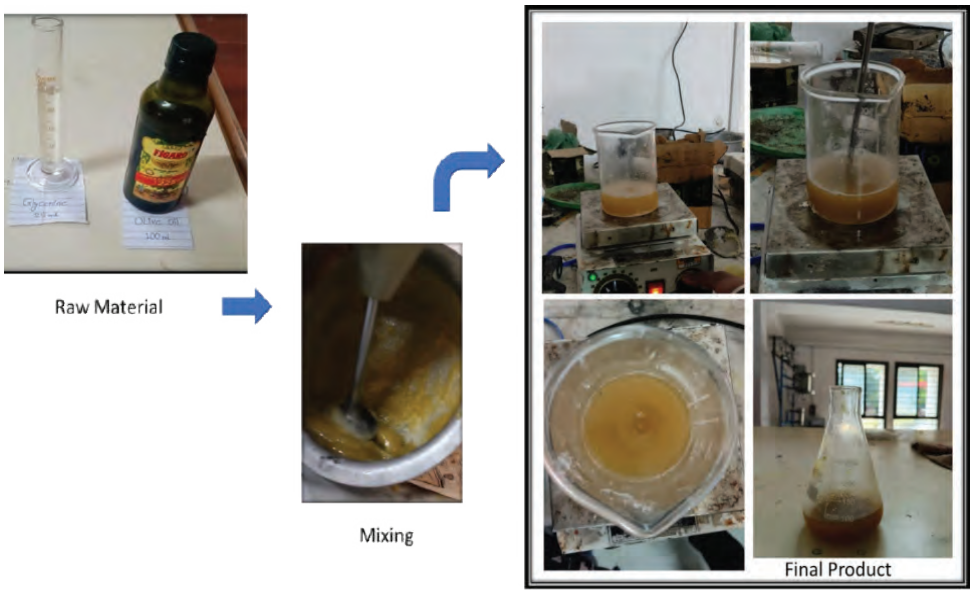


Figure 1. Preparation procedure of dishwashing liquid.

2. The weighted ingredients blended in the mixer container or tank equipped with agitation mechanisms. The process provides the uniform distribution of components and to enhances dissolution [16].
3. In addition to the blending process, for some cases to accelerate the dissolution of the ingredients it required the thermal treatment. To prevent the damage to heat-sensitive components, it required the proper temperature control [17].
4. The primary solvent and water added to the mixer container or tank. The quantity of water required depends on the desired concentration and viscosity of the final product [18].
5. To ensure the uniformity and dispersion of the mixture, it further passed through the agitation and blending of all ingredients in the water. After the process the mixture provides a consistent and uniform product [19].
6. In case of heat provided during the process, the subsequent cooling for the temperature reduction required the heat exchanger or cooling jacket over the mixing container [20].
7. To achieve maximum cleaning efficiency and stability, the dishwasher liquid pH adjusted to optimal range. To achieve desire the pH level, nominal quantity of pH adjusters, such as citric acid or sodium hydroxide can be used.
8. Quality Control: Samples of the dishwasher liquid are collected for the purpose of quality control. Tests can be performed to evaluate viscosity, pH, stability, and cleaning efficacy. Modifications can be applied if required [21].
9. Packaging: The finished product is sent to packaging machinery, which involves filling machines, labelling machines, and capping machines. The dishwasher liquid is packed in bottles, pouches, or other appropriate containers, and then labelled and sealed accordingly [22].
10. To maintain the quality of the packed dishwasher liquid, it is stored under a regulated atmosphere.

RESULTS AND DISCUSSION

pH Optimization Via Citric Acid Adjustment

Table 2 shows the stage of pH adjustment to obtained desire pH of the dishwashing liquid. LABMAN pH meter was used to measure pH of the samples. Initially the sample 1 (Lye solution) pH was obtained 13 and liquid surfactant pH was observed 12. The raw dishwasher pH was observed 12. It was necessary to regulate pH in the range of 7 to 9 as for the value more than 9, higher pH (more alkaline) liquid can become more caustic, which might be harsher on the skin, potentially causing irritation or dryness. It might also cause damage to delicate dishes or cookware over time. If the pH is lower than 7 the liquid is more acidic and may not be effective on greasy and oily residues. Also, more acidic solutions may damage certain materials, like metal surfaces, causing tarnishing or corrosion. By adding 7 grams of citric acid, the desired pH of 9 was achieved.

Acid Value

The free fatty acid present in the oil od fat presented as Acid value. It represents the number of mg of caustic potash required to neutralized the acid in 1 gm of the sample. The deposition of stale oil or fat under improper conditions represented by a high acid value. The acid value obtained 1.92 for the dishwashing liquid with Citric acid indicates batter quality.

Functional Group Confirmation Using Fourier Transform Infrared Spectroscopy (FTIR)

Figure 2 shows the FTIR spectrum of the dishwashing liquid. From FTIR graph data of frequency range X (cm^{-1}) Vs Y (%T) as per various peak obtained it can be confirmed the absorption of its corresponding functional group. Peak appears at 3400 cm^{-1} indicates compound containing C-H/O-H Bond. The C-H fatty acid bonds of olive oil which can used for making of surfactant appear under 1500 cm^{-1} peak and the footprint of O-H bond of NaoH functional groups which is used in dishwashing liquid shown beyond peak of 1500 cm^{-1}. At 1392 cm^{-1} and at 1043 cm^{-1} there are the footmarks of vibration of C-O in alcohol hydroxyl group.

Lathering Power

The deionized water with quantity 2 mL was added to large test tube. The dishwashing liquid added by equal amount of volume as of deionized water to the test tube. It was shaken strongly by placing a stopper in the tube. It was expected to get a permanent lather that lasts for at least 30 sec. Additionally another 10 drops of liquid needed to add and again shaken, If the lather doesn't last.

Table 2. Stages of pH adjustment

Stage	Amount of pH adjuster used	pH Value
Olive oil + NaOH (Lye solution)	-	13
Liquid surfactant	-	12
Raw Dishwashing liquid (Without pH adjustment)	-	12
Raw Dishwashing Liquid + Citric acid	3 gm	11
Final Dishwashing liquid with Citric acid (desired pH)	7 gm	9

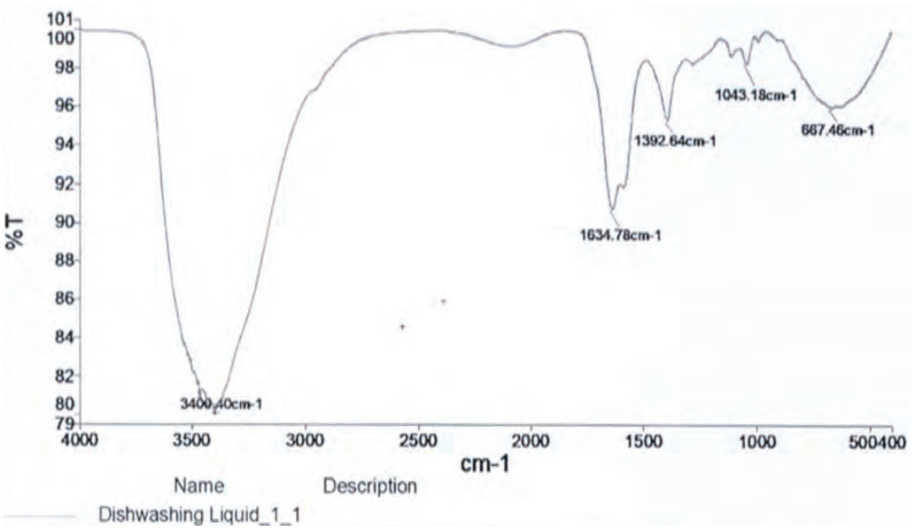


Figure 2. FTIR plot of the dishwashing liquid.

A quantity of 2 mL, 5% calcium chloride solution with was added to test tube. The observation made to check if the solution forms a permanent lather and also to be noted whether there is any flocculent precipitate in the tube. There was a fluffy lather without any precipitate generated from dishwashing liquid.

Cleansing Power

To quantitatively evaluate the oil-removal capacity of the dishwashing liquid, a controlled laboratory test was designed using used vegetable oil as a model for hydrophobic food residues. Two Whatman Grade 1 filter paper strips were loaded with 3-5 drops of oil to pretend like a greasy contamination. To ensure standardized dipping conditions in line with the prior experimental setup, the strips were trimmed to fit accurately into borosilicate test tubes. Both solutions were maintained at 25 °C to suppress the temperature related variation in the surfactant activity. The mechanical scrubbing action was generated by shanking test tubes for 2 minutes with help of mechanical agitator at 150 rpm.

The complete removal of oil from the test strips considered high emulsification efficiency of the solution due to the anionic surfactants (e.g., sodium lauryl sulfate) present in the solution. The surfactant function, enabled with micelle formation, to reduce the interfacial tension between oil and water. Moreover, the dishwashing liquid having the alkaline pH (approx. 9) improves saponification through transforming triglycerides present in the oil into water-soluble fatty acid salts. While the conventional soap solution shown partial oil removal, the precipitates forms in hard water due to interaction of calcium/magnesium ions. Also, it reduced micelle stability at netural pH identifies the lower performance of the solution.

The test filter paper not found any visible oil residues traces under the white light inspection confirmed good degreasing potential. The test strip treated with dishwashing liquid shown weak oil strains as compared to the soap treated test strip under UV fluorescence spectroscopy, identifies presence of hydrophobic compounds. The effectiveness of dishwashing liquid was caused by its enhanced surfactant blends. It included improved micelle packing and deteriorate the critical micelle concentration using nonionic co-surfactants (e.g., ethoxylated alcohols). Moreover, inhibiting oil deposition on utensils surface, increase micelles electrostatic repulsion and surfactant head groups ionization was achieved through optimization of pH at 9.

Applications of the Eco-Friendly Dishwashing Liquid

The dishwashing liquid having multifunctional applicability was synthesized with eco-friendly composition at optimal pH (9). Strong degreasing performance validated through oil removal tests and mild pH ensures suitable pertinence of liquid for household and commercial cleaning of soft materials and caused mild skin irritation. The plant-based ingredients and low pH ennobled the biodegradability of the liquid to qualify it for green certificate (ECOCERT, USDA Bio Preferred). It made the liquid appropriate for organic food industries and hard water applications. Cost-efficient manufacturing and scalable process of production was confirmed by consistency of a product using FTIR spectroscopy. Future work will focus on concentrated, antimicrobial and compliance with non-toxic standards for improve its demand as potential sustainable solution.

CONCLUSION

A good quality eco-friendly dishwashing liquid was prepared using different environmentally friendly ingredients in this work. It was tested for various properties. All necessary properties like pH, acid value, lathering power and Cleansing Power were studied to check the application performance of the liquid. The desired pH was obtained 9 by adding the citric

acid into the dishwashing liquid. The acid value found that is 1.92 mg KOH/g was also acceptable according to the literature, confirming the product's chemical stability. It was having good lathering as well as excellent cleansing power (95% grease removal). It was also found that the FTIR method was simple, accurate and easily applicable methods to the identification of product's composition, ensuring quality control and manufacturing consistency for a finished product. By determining quantitative benchmarks, this research points to the formulation as a scalable, market-ready solution that bridges eco-sensible design with practical utility in household cleaning products.

ACKNOWLEDGEMENTS

We would like to acknowledge Centre of Excellence, Vapi, Gujarat, India for their analytical support.

AUTHORSHIP CONTRIBUTIONS

Authors equally contributed to this work.

DATA AVAILABILITY STATEMENT

The authors confirm that the data that supports the findings of this study are available within the article. Raw data that support the finding of this study are available from the corresponding author, upon reasonable request.

CONFLICT OF INTEREST

The authors declared that they have no conflicts of interest to declare that are relevant to the content of this article.

ETHICS

There are no ethical issues with the publication of this manuscript.

STATEMENT ON THE USE OF ARTIFICIAL INTELLIGENCE

Artificial intelligence was not used in the preparation of the article.

REFERENENCES

[1] Liu J, Xiong J, Huang Q, Lu T, Chen W, Li M. Eco-friendly synthesis of robust bioinspired cotton fabric with hybrid wettability for integrated water harvesting and water purification. J Clean Prod 2022;350:131524. [CrossRef]

[2] Messali M, Moussa Z, Alzahrani AY, El-Naggar MY, ElDouhaibi AS, Judeh ZM, Hammouti B. Synthesis, characterization and the antimicrobial activity of new eco-friendly ionic liquids. Chemosphere 2013;91:1627–1634. [CrossRef]

[3] Rungyuttapakorn C, Wongwatcharapaiboon J. Eco-design product of alternative dishwashing detergent [dissertation]. Bangkok: Thammasat University; 2019.

[4] Pandey P, Dixit A, Tanwar A, Sharma A, Mittal S. A comparative study to evaluate liquid dish washing soap as an alternative to xylene and alcohol in deparaffinization and hematoxylin and eosin staining. J Lab Physicians 2014;6:84–90. [CrossRef]

[5] Al-Ghanayem AA, Joseph B. Current prospective in using cold-active enzymes as eco-friendly detergent additive. Appl Microbiol Biotechnol 2020;104:2871–2882. [CrossRef]

[6] Lee S, Lee J, Yu H, Lim J. Synthesis of environment friendly nonionic surfactants from sugar base and characterization of interfacial properties for detergent application. J Ind Eng Chem 2016;38:157–166. [CrossRef]

[7] Adimurthy S, Ramachandraiah G, Bedekar AV, Ghosh S, Ranu BC, Ghosh PK. Eco-friendly and versatile brominating reagent prepared from a liquid bromine precursor. Green Chem 2006;8:916–922. [CrossRef]

[8] Horozal A, Aksoy Ö. Evaluation of the genotoxicity of some standard and eco-friendly detergents with Vicia faba. Caryologia 2020;73:129–139. [CrossRef]

[9] Hussein MH, El-Hady MF, Shehata HA, Hegazy MA, Hefni HH. Preparation of some eco-friendly corrosion inhibitors having antibacterial activity from sea food waste. J Surfactants Deterg 2013;16:233–242. [CrossRef]

[10] Somashekaraiah R, Gnanadhas DP, Kailas SV, Chakravortty D. Eco-friendly, non-toxic cutting fluid for sustainable manufacturing and machining processes. Tribol Online 2016;11:556–567. [CrossRef]

[11] Ramulu S, Koneru A, Ravikumar S, Sharma P, Ramesh DV, Patil R. Liquid dish washing soap: An excellent substitute for xylene and alcohol in hematoxylin and eosin staining procedure. J Orofac Sci 2012;4:37–42. [CrossRef]

[12] Kim D, Seok JK, Kim M, Choi S, Hong J, Yoon YA, Chung H, Bae ON, Kwack SJ, Kim KB, Lee JY. Safety assessment of cocamidopropyl betaine, a cosmetic ingredient. Toxicol Res 2024;40:361–375. [CrossRef]

[13] Tantala J, Loyawattananan S, Boonprakobsak P, et al. Antilisterial effect of alkyl polyglycosides biosurfactant and modes of action. Int J Biol Macromol 2024;280:135607. [CrossRef]

[14] Juneja VK, Valenzuela-Melendres M, Heperkan D, et al. Development of a predictive model for Salmonella spp. reduction in meat jerky product with temperature, potassium sorbate, pH, and water activity as controlling factors. Int J Food Microbiol 2016;236:1–8. [CrossRef]

[15] Lebedev V, Tykhomyrova T, Litvinenko I, Avina S, Saimbetova Z. Design and research of eco-friendly polymer composites. In: Materials Science Forum. 2020 Sep 7;1006:259–266. Trans Tech Publications Ltd. [CrossRef]

[16] Yea D, Lee Y, Park K, Lim J. Synthesis of eco-friendly fatty acid based zwitterionic biosurfactants from coconut oil sources and characterization of their interfacial properties. J Ind Eng Chem 2021;97:287–298. [CrossRef]

[17] Liu B, Li T, Wang W, Sagis LM, Yuan Q, Lei X, Cohen Stuart MA, Li D, Bao C, Bai J, Yu Z. Corncob cellulose nanosphere as an eco-friendly detergent. Nat Sustain 2020;3:448–458. [CrossRef]

[18] Al-Ghanayem AA, Joseph B. Current prospective in using cold-active enzymes as eco-friendly detergent additive. Appl Microbiol Biotechnol 2020;104:2871–2882. [CrossRef]

[19] Bhatt JP, Chouhan N, Kumar A, Sharma A, Ameta R. Eco-Friendly Products and Reagents. In: Green Chemistry. 2nd ed. Oakville: Apple Academic Press; 2023. p. 55–115. [CrossRef]

[20] Mutahajjid ZA, Effendi I, Sugito S. Choosing environmentally friendly dish soap in Medan: price and environmental considerations. Enrichment J Manag 2024;14:270–275.

[21] Zulwazi NM, Azmi NA, Nawi AA. Dishwashing soap from waste cooking oil. Multidiscip Appl Res Innov 2023;4:215–220.

[22] Rojas M, Ortiz Y, Arturo D, Navarro Y, Chejne F. Saponins: Natural surfactants and their alternative sustainability in the formulation of bio-based detergents to mitigate environmental pollution. Waste Biomass Valorization 2024:1–18. [CrossRef]

Sigma Journal of Engineering and Natural Sciences
Web page info: https://sigma.yildiz.edu.tr
DOI: 10.14744/sigma.2026.2135

Research Article

Parameter estimation for Multivariate Gamma distribution with Particle Swarm Optimization based on Taguchi method

Aynur YONAR[1] **Nimet YAPICI PEHLİVAN[1]***

[1]*Department of Statistics, Selçuk University, Konya, 42130, Türkiye*

ARTICLE INFO

Article history
Received: 23 October 2024
Revised: 30 January 2025
Accepted: 05 May 2025

Keywords:
Maximum Likelihood; Multivariate Gamma Distribution; Parameter Estimation; Parameter Tuning; Particle Swarm Optimization; Taguchi Experimental Design

ABSTRACT

The Multivariate Gamma distribution is widely utilized in stochastic modeling, hydrology, reliability analysis, and actuarial sciences. Despite its broad applicability, efficient parameter estimation remains a challenge, as the maximum likelihood estimators lack closed-form solutions. Metaheuristic optimization techniques, particularly Particle Swarm Optimization (PSO), have been frequently employed to address this issue. However, the performance of PSO is highly sensitive to parameter settings, and in the absence of a structured approach, parameter tuning often relies on time-consuming trial-and-error methods. This study employs the Taguchi experimental design to systematically determine the optimal parameter configuration for PSO in estimating the parameters of the Multivariate Gamma distribution. By providing a structured framework for parameter tuning, the proposed approach reduces dependence on heuristic or arbitrary selection strategies. The performance of the Taguchi-optimized PSO is evaluated based on solution quality, measured using the deficiency (DEF) criterion, and computation time. The results indicate that the Taguchi method offers an efficient and replicable solution for PSO parameter tuning, eliminating the need for conventional trial-and-error methods. By structuring the tuning process, this approach enhances both the reliability and reproducibility of PSO-based estimation, making it adaptable to a range of similar optimization tasks. Future studies may explore comparative analyses with other parameter tuning strategies, extend the application to alternative metaheuristic algorithms, or adapt the methodology to optimization challenges in machine learning and data science contexts.

Cite this article as: Yonar A, Yapıcı Pehlivan N. Parameter estimation for Multivariate Gamma distribution with Particle Swarm Optimization based on Taguchi method. Sigma J Eng Nat Sci 2026;44(4):2924–2936.

INTRODUCTION

The Multivariate Gamma (MGM) distribution is a significant probability distribution with wide-ranging applications in fields such as hydrology [1, 2], gust modeling [3], texture classification [4], wireless communications [5], and reliability and life testing [6]. More recent studies

***Corresponding author.**
*E-mail address: nimet@selcuk.edu.tr

This paper was recommended for publication in revised form by Editor-in-Chief Ahmet Selim Dalkilic

Published by Yıldız Technical University Press, İstanbul, Turkey
© Author. This is an open access article under the CC BY-NC license (http://creativecommons.org/licenses/by-nc/4.0/).

have further extended its applications to domains including financial risk modeling, climate modeling, environmental statistics, and biomedical engineering [7–9]. Several variants of the multivariate gamma distribution have been proposed by researchers including Cherian [10], Jensen [11], Sarmanov [12], Royen [13], Mathai and Moschopoulos [14], and Carpenter and Diawara [15]. In the present study, we focus on the MGM distribution introduced by Mathai and Moschopoulos [14].

Suppose that $X_1, X_2,..., X_k$ are mutually independent random variables, where each $X_i \sim \text{Gamma}(\sigma_i, \beta, \mu_i)$, $i = 1,2,..., k$ with the probability density function (pdf) as follows [16]:

$$f(x_i;\sigma_i,\beta,\mu_i)=\frac{1}{\Gamma(\sigma_i)\beta^{\alpha_i}}(x-\mu_i)^{\alpha_i-1}\exp\left(-\frac{x-\mu_i}{\beta}\right), \quad x_i \geq \mu_i, \sigma_i > 0, \beta > 0, \mu_i \in \mathbb{R} \tag{1}$$

Let $Z_1 = X_1$, $Z_2 = X_1 + X_2,..., Z_k = X_1 + X_2 +... + X_k$ be random variables. Then, the joint distribution of the vector $\boldsymbol{Z} = (Z_1, Z_2,..., Z_k)$ follows a Multivariate Gamma distribution, with probability density function given by:

$$f(z_1,z_2,\ldots,z_k)=\frac{(z_1-\mu_1)^{\sigma_1-1}(z_2-z_1-\mu_2)^{\sigma_2-1}\ldots(z_k-z_{k-1}-\mu_k)^{\sigma_k-1}\exp\left(-\frac{z_k-\sum_{i=1}^{k}\mu_i}{\beta}\right)}{\beta^{\sum_{i=1}^{k}\sigma_i}\prod_{i=1}^{k}\Gamma(\sigma_i)} \tag{2}$$

In Equation (2), $\sigma_i > 0$ ($i = 1,2,..., k$) are shape parameters, and $\mu_i \in \mathbb{R}$ are a location parameters satisfying $z_{i-1} + \mu_i < z_i$, with $z_k < \infty$, $\mu_1 < z_1$. Moreover, $\beta > 0$ is a common scale parameter, which guarantees that the marginal distributions of the MGM have the same functional form [17].

The MGM distribution is particularly useful in applications involving stochastic processes and reliability analysis, due to the positive correlation among its marginals. Consequently, accurate estimation of its parameters is crucial. However, to the best of our knowledge, only limited studies have addressed parameter estimation for the MGM distribution. Tsionas [18] proposed a Bayesian approach based on the method of moments, employing Gibbs sampling for parameter estimation. Vaidyanathan and Lakshmi [17] introduced an optimal search-based method for estimating parameters using maximum likelihood, maximum product of spacings, and least squares approaches. Additionally, Oikonomidis and Trevezas [19] developed closed-form moment-type estimators for the MGM distribution, showing improved small-sample performance compared to maximum likelihood estimators.

The maximum likelihood (ML) method, which maximizes the likelihood function with respect to unknown parameters, possesses several desirable asymptotic properties, including unbiasedness, consistency, efficiency, and asymptotic normality under regularity conditions. However, explicit ML estimators for the MGM distribution are not available, necessitating the use of numerical methods. These methods, however, often face challenges such as non-convergence, slow convergence, or convergence to local optima. To address these issues, various metaheuristic techniques—such as simulated annealing, hybrid variable neighborhood search, genetic algorithms, evolutionary algorithms, particle swarm optimization, and differential evolution—have been proposed for ML parameter estimation in several distributions [20–26].

Recent advancements have integrated metaheuristic methods with dimensionality reduction techniques, such as Principal Component Analysis (PCA), as well as hybrid models like the Coyote Optimization Algorithm (COA), to enhance forecasting accuracy. For instance, Fariz and Basha [27] demonstrated that COA-optimized neural networks combined with PCA significantly improved solar radiation prediction by reducing computational costs and prediction errors. Similarly, hybrid COA models were applied by Yang et al. [28] and Larcher et al. [29] for wind speed prediction and high-dimensional optimization, achieving superior performance. These approaches highlight the effectiveness of hybrid frameworks in enhancing predictive accuracy and optimizing complex systems. In parallel, recent researches have highlighted the importance of structured methodologies for managing uncertainty and improving the reliability of decision-making processes. Noorjahan and Shaik [30] proposed an intuitionistic fuzzy rough graph-based approach, introducing a novel correlation coefficient to determine expert weights in multi-criteria decision-making. Likewise, Noorjahan and Shaik [31] developed a fuzzy correlation framework aimed at enhancing decision accuracy under uncertainty. These contributions emphasize the growing relevance of systematic and statistically grounded methods for solving complex optimization and estimation problems, an objective that aligns closely with the methodology adopted in the present study.

In this study, Particle Swarm Optimization (PSO), a population-based metaheuristic optimization method, is employed owing to its advantages such as ease of implementation and fast convergence. PSO is used to obtain the maximum likelihood (ML) estimates of the parameters of the MGM distribution. Prior to applying the PSO algorithm, its key parameters, namely inertia weight, acceleration coefficients, population size, and number of iterations, need to be appropriately determined. However, there is no standardized method for tuning these parameters. They are typically selected either based on commonly accepted values reported in the literature or through trial-and-error approaches [24, 32–34]. Örkcü et al. [23] conducted simulation studies to evaluate the performance of PSO under various parameter settings and concluded that the algorithm's effectiveness is highly sensitive to the choice of these parameters.

The novelty of this study lies in the use of the Taguchi method for systematic PSO parameter selection, thereby eliminating the reliance on time-consuming trial-and-error approaches or arbitrary default values. The Taguchi experimental design enables efficient parameter tuning by reducing the number of required experiments. In contrast, traditional approaches rely on heuristic or empirical parameter selection, which may compromise the overall

optimization performance. Addressing this issue, Alptekin et al. [35] proposed a statistical method based on factorial design to identify the most influential PSO parameters, emphasizing the importance of narrowing the search space to enhance algorithmic efficiency. In line with this perspective, the present study adopts the Taguchi method to optimize PSO parameters for the maximum likelihood estimation of the MGM distribution parameters, offering a structured optimization framework.

The remainder of this study is organized as follows: Section 2 provides an overview of the maximum likelihood (ML) estimation method for the MGM distribution, along with a description of the Particle Swarm Optimization (PSO) algorithm and the Taguchi experimental design. Section 3 details the implementation of the Taguchi method for PSO parameter tuning and presents a Monte Carlo simulation study for parameter estimation. Finally, Section 4 concludes the study and outlines directions for future research.

MAXIMUM LIKELIHOOD ESTIMATION FOR THE PARAMETERS OF THE MULTIVARIATE GAMMA DISTRIBUTION WITH PARTICLE SWARM OPTIMIZATION

This section introduces the ML estimation method for the MGM distribution, the PSO algorithm, and the Taguchi experimental design method.

ML Method for Parameter Estimation of the MGM Distribution

Let $Z = (Z_1, Z_2,..., Z_k)$ is a sample from multivariate gamma distribution with the probability density function (pdf) given in Equation (2). The likelihood function (L) and log-likelihood function (log$L$) of the MGM distribution are presented in Equation (3) and Equation (4), respectively.

$$L = \prod_{i=1}^{n} \frac{(z_{1i}-\mu_1)^{\sigma_1-1}(z_{2i}-z_{1i}-\mu_2)^{\sigma_2-1}\dots(z_{ki}-z_{(k-1)i}-\mu_k)^{\sigma_k-1}\exp\left(-\frac{z_{ki}-\sum_{i=1}^{k}\mu_i}{\beta}\right)}{\beta^{\sum_{i=1}^{k}\sigma_i}\prod_{i=1}^{k}\Gamma(\sigma_i)} \quad (3)$$

$$\log L = (\sigma_1-1)\sum_{i=1}^{k}\log(z_{1i}-\mu_1)+\dots+(\sigma_k-1)\sum_{i=1}^{k}\log(z_{ki}-z_{(k-1)i}-\mu_k) - \sum_{i=1}^{k} z_{ki}/\beta + \sum_{i=1}^{k}\mu_i/\beta - n\log(\beta)\sum_{i=1}^{k}\sigma_i - n\sum_{i=1}^{k}\log(\Gamma(\sigma_i)) \quad (4)$$

The ML estimates of the parameters are the values that maximize the likelihood function or log-likelihood function. To obtain these estimates, the partial derivatives of the log-likelihood function with respect to the unknown parameters are computed and set equal to zero, as shown below:

$$\frac{\partial \log L}{\partial \sigma_m} = (\sigma_m-1)\sum_{i=1}^{n}\log(z_{mi}-z_{(m-1)i}-\mu_m) - n\psi(\sigma_1) - n\log\beta = 0,$$
$$\frac{\partial \log L}{\partial \beta} = \left(\sum_{j=1}^{k} z_{mi} - n\sum_{j=1}^{k}\mu_j\right)/\beta^2 - n\sum_{j=1}^{k}\sigma_j/\beta = 0, \quad (5)$$
$$\frac{\partial \log L}{\partial \mu_m} = -(\sigma-1)\sum_{i=1}^{n}(z_{mi}-z_{(m-1)i}-\mu_m)^{-1} + n/\beta = 0.$$

In Equation (5), $z_{0i} = 0$, $m = 1,2,..., k$ and $\psi(\sigma_1) = \partial\log(\Gamma(\sigma_l))/\partial\sigma_l$. The solutions to these equations, known as the likelihood equations, are referred to as the ML estimators of the parameters for the MGM distribution. However, due to the nonlinear nature of the likelihood equations, analytical (closed-form) solutions are not available. Consequently, optimization techniques, either classical or metaheuristic, are typically employed to maximize the likelihood or log-likelihood function. In this study, the Particle Swarm Optimization algorithm is adopted to obtain the ML estimates of the parameters for the multivariate gamma distribution.

PSO Algorithm

Particle Swarm Optimization (PSO), a widely used metaheuristic algorithm, was introduced by Eberhart and Kennedy [36], inspired by the concept of swarm intelligence. It imitates the collective behavior of bird flocking and fish schooling in search of food sources [37, 38]. PSO is a population-based, self-adaptive search optimization method, where the population comprises a set of candidate solutions known as particles. The initial positions of the particles are generated using Equation (6).

$$x_{j,i}^{0} = x_{j,\min} + rand_{ij}[0,1]\{x_{j,\max} - x_{j,\min}\}, \quad i = 1,2,\dots,NP,\ j = 1,2,..D \quad (6)$$

In Equation (6), i represents the population size, j indicates dimension of the optimization problem, $x_{j,i}^{0}$ is initial value of jth component of particle i, $x_{j,min}$ and $x_{j,max}$ are prescribed minimum and maximum parameter bounds, respectively, and $rand_{ij}$ [0,1] represents a uniformly distributed random variable in the range [0,1] [37, 39].

Each particle records its own personal best position (*pbest*) and the best positions found by all particles in the swarm (*gbest*). At each iteration, all particles update their velocities and positions accordingly. The velocity and the new position of each particle at the iteration (g + 1), are computed using the following equations, respectively:

$$v_i^{g+1} = wv_i^g + c_1r_1\left(pbest_i^g - x_i^g\right) + c_2r_2\left(gbest^g - x_i^g\right) \quad (7)$$

$$x_i^{g+1} = x_i^g + v_i^g \quad (8)$$

In Equations (7) and (8),

v_i^g : velocity of particle i at iteration g,

w: inertia weight,

c_1, c_2: acceleration coefficients,

r_1, r_2: random numbers uniformly distributed between 0 and 1,

x_i^g : position of particle i at iteration g,

$pbest_i^g$: the best position of particle i until iteration g,

$gbest^g$: the best position of the group until iteration g.

In each iteration, the velocity and position of each particle are updated until the predefined number of iterations is reached [37, 39]. The overall procedure of the PSO

algorithm is illustrated in Figure 1. The inertia weight is a key parameter in PSO that controls the effect of a particle's previous velocity on its current velocity. The balance between global and local search capabilities in PSO depends primarily on this parameter. Specifically, it adjusts the trade-off between exploration (searching new areas globally) and exploitation (refining solutions in the current region). A large inertia weight promotes exploration, while a small inertia weight enhances exploitation [40].

The acceleration coefficients (c_1, c_2) show the weight of the particles' movement towards the local best and global best, respectively. determine the influence of a particle's movement toward its personal best (local best) and the global best position, respectively. If the coefficients are set too high, particles may move abruptly, increasing the risk of being trapped in local optima. Conversely, if the values are too low, particle movement becomes sluggish, leading to significantly longer computation times and potential failure to converge. Therefore, the relative values of the acceleration coefficients play a critical role in the performance of the PSO algorithm [33].

The number of particles (*npop*) also significantly affects the behavior of the PSO algorithm. A larger population size enables faster search but may slow down the algorithm due to increased computational load. In contrast, a population size that is too small may result in failure to locate the optimal solution or lead to prolonged convergence. Therefore, selecting an appropriate number of particles is crucial to maintaining a balance between search efficiency and computational cost.

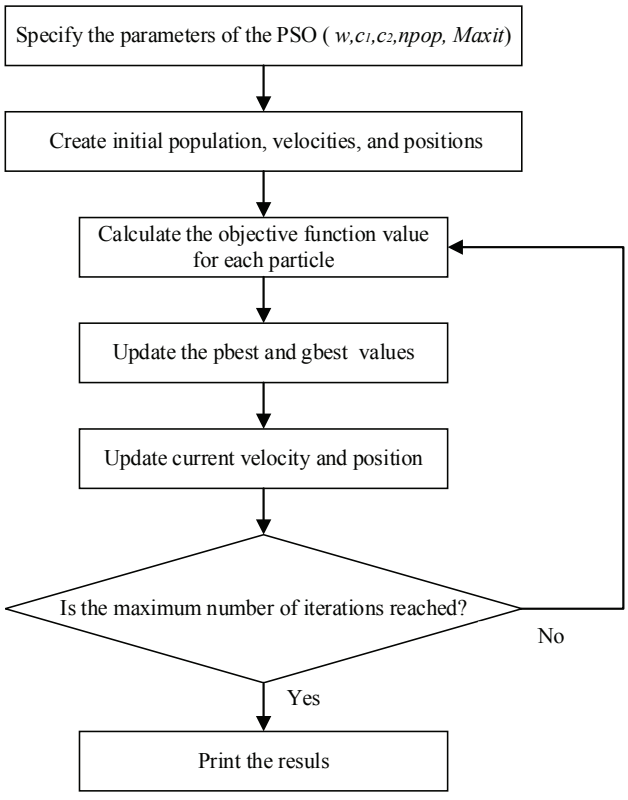


Figure 1. Flowchart of the PSO.

The maximum iteration number (*Maxit*) is often used as a stopping criterion in many studies [23, 24, 32]. While a higher number of iterations allows more search depth, it also increases computational time. Conversely, setting the number of iterations too low may prevent the algorithm from converging to the optimal solution. In general, different parameter configurations significantly affect the computational behavior of the PSO algorithm. Certain configurations may promote efficient convergence, while others can lead to poor solution quality or excessive computational cost [33]. This study adopts the Taguchi method as a systematic approach for determining optimal PSO parameter values, thereby ensuring robust and efficient estimation performance.

Taguchi Method

The designs used to investigate the main effects and interaction effects of two or more factors simultaneously are referred to as factorial designs. In the literature, several types of factorial designs are commonly used, such as 2^k, 3^k, and mixed-level factorial designs. In a 2^k factorial design, 2 represents the number of levels and k denotes the number of factors. For instance, 2^3 involves three factors (e.g., A, B, and C), each at two levels, requiring 2^3 =8 experimental runs. However, as the number of factors and levels increases, the required number of experiments grows exponentially, leading to increased computational complexity. To address this issue, Taguchi [41] introduced an efficient approach to experimental design that reduces the number of required trials by using orthogonal arrays [42, 43].

In the Taguchi method, orthogonal arrays are employed to examine many decision variables with a relatively small number of experiments, while still providing sufficient information for effective decision-making. A performance metric known as the Signal-to-Noise (*S/N*) ratio is used in this method to measure robustness. The Taguchi approach categorizes objective functions into three types: "smaller-the-better," "larger-the-better," and "nominal-the-best." A specific formula is applied to calculate the *S/N* ratio for each of these cases as follows:

$$\frac{S}{N_k} = -10 \times \log\left(\frac{1}{n}\sum_{i=1}^{n} y_i^2\right) \tag{9}$$

$$\frac{S}{N_b} = -10 \times \log\left(\frac{1}{n}\sum_{i=1}^{n} 1/y_i^2\right) \tag{10}$$

$$\frac{S}{N_t} = -10 \times \log\left(\frac{1}{n}\sum_{i=1}^{n} \mathrm{y}/s_y^2\right) \tag{11}$$

In Equations (9) - (11), n stands the number of observations, y_i are the response variable values, y is the average of the response variable values and s_y^2 is the variance of y [44].

Regardless of the type of objective function, a larger *S/N* ratio indicates better performance. Therefore, the factor level associated with the highest *S/N* ratio is considered optimal. In addition, an analysis of variance (ANOVA) is conducted to determine the statistical significance of each factor. The optimal factor combinations are identified based on both the *S/N* ratios and the ANOVA results.

The use of the Taguchi method in parameter design for optimizing a process with multiple performance characteristics involves the following steps [44, 45]:

Step 1. Define the performance characteristics and select the factors to be evaluated.

Step 2. Determine the number of levels for each factor.

Step 3. Select an appropriate orthogonal array and assign the factors to the array

Step 4. Conduct experiments according to the sequence specified in the orthogonal array.

Step 5. Calculate the signal-to-noise (*S/N*) ratios for the experimental results.

Step 6. Analyze the results using both *S/N* ratios and ANOVA.

Step 7. Identify the optimal levels of the factors based on the analysis.

Experimentation

This section is organized into two main parts. In the first part, the Taguchi experimental design is applied to tune the parameters of the PSO algorithm. In the second part, a Monte Carlo simulation study is conducted to estimate the parameters of the Multivariate Gamma distribution using the PSO algorithm configured with the optimized parameter settings.

Taguchi experimental design for tuning the PSO parameters

The objective of this study is to design the PSO algorithm for maximizing the log-likelihood function in the ML estimation of the parameters of the multivariate gamma distribution. The algorithm is designed with two primary goals: achieving high solution quality and minimizing computation time. To evaluate solution quality, the deficiency (DEF) criterion is employed, where a lower DEF value indicates better performance. Consequently, the optimization process aims to minimize both the DEF value and computation time. For this reason, the "smaller-the-better" approach is adopted, and the corresponding *S/N* ratio is calculated as shown in Equation (7).

In this context, DEF values and computation times are treated as response variables. Four factors influencing the performance of the PSO algorithm are considered: inertia weight, acceleration coefficients, population size, and number of iterations. Each factor is evaluated at three levels, and the optimal settings are determined using the Taguchi experimental design, as presented in Table 1.

In Table 1, Strategy 1 (S1) shows the constant inertia weight $w = 0.7$, Strategy 2 (S2) shows the random inertia weight $w = 0.5 + rand/2$, and Strategy 3 (S3) shows the linear decreasing inertia weight $w = 0.9 - (0.5/Maxit) \times it$ [46]. For real parameter values, random vector $\theta = [\alpha_1, \alpha_2, \beta, \mu_1, \mu_2] = [2.8, 4, 0.5, 5, 10]$ is used in the experimental design. While a single repetition of the full factor design requires 34=81 experiments, the Taguchi method with an L_9 (4^3) orthogonal array requires only 9 experiments, and the experimental design is constructed as shown in Table 2.

Table 1. Factors and their levels for the PSO algorithm

Levels	Level 1	Level 2	Level 3
Factors			
Inertia weight (A)	S1	S2	S3
Acceleration coefficients (B)	1	1.45	2
Population number (C)	10	25	50
Iteration number (D)	100	500	1000

Table 2. Modified orthogonal array L_9

Experiment no.	Factors				Levels			
	A	B	C	D	A	B	C	D
1	1	1	1	1	S1	1.00	10	100
2	1	2	2	2	S1	1.45	25	500
3	1	3	3	3	S1	2.00	50	1000
4	2	1	2	3	S2	1.00	25	1000
5	2	2	3	1	S2	1.45	50	100
6	2	3	1	2	S2	2.00	10	500
7	3	1	3	2	S3	1.00	50	500
8	3	2	1	3	S3	1.45	10	1000
9	3	3	2	1	S3	2.00	25	100

For each experiment, the algorithm is repeated three times and the resulting DEF values (reflecting solution quality) and computation times are reported in Table 3 and Table 4, respectively. In addition, the calculated average values $\bar{Y}$ and corresponding *S/N* ratios, obtained from these DEF values and computation times with respect to repetitions and experiments, are also presented in the same tables.

The *S/N* ratios of the DEF values and computation times of the factors for each parameter level of the algorithm are given in Table 5 and Table 6, respectively. The factor associated with the largest *S/N* ratio is identified as the most effective factor on the performance of the PSO algorithm.

As shown in Table 5, the factors are ranked based on their influence on the DEF values, from highest to lowest, as follows: population number, inertia weight, acceleration coefficients, and iteration number. The optimal level of each factor corresponds to the level with the highest *S/N* ratio. Accordingly, the best levels in terms of minimizing DEF are identified as: Level 1 for inertia weight, Level 3 for acceleration coefficients, Level 3 for population number, and Level 1 for iteration number. Conversely, Table 6 presents

Table 3. Results of the DEF values for the PSO algorithm

Experiment no.	Repetition 1	Repetition 2	Repetition 3	$\bar{Y}$	*S/N*
1	0.6298	0.6319	0.6280	0.6299	4.0141
2	0.5905	0.5789	0.5923	0.5872	4.6225
3	0.5653	0.5662	0.5507	0.5607	5.0239
4	0.5821	0.5675	0.5858	0.5785	4.7528
5	0.5889	0.5692	0.5805	0.5795	4.7366
6	0.6699	0.6491	0.6010	0.6400	3.8667
7	0.5968	0.5487	0.6096	0.5850	4.6469
8	0.7106	0.6791	0.6658	0.6852	3.2802
9	0.6112	0.5795	0.5788	0.5898	4.5821

Table 4. Results of the computation times for the PSO algorithm

Experiment no.	Repetition1	Repetition 2	Repetition3	$\bar{Y}$	*S/N*
1	0.0529	0.0577	0.0587	0.0564	24.9544
2	0.6827	0.6331	0.6539	0.6566	3.64981
3	2.4488	2.4584	2.5216	2.4763	-7.8768
4	1.2271	1.2002	1.2288	1.2187	-1.7187
5	0.2498	0.2573	0.2558	0.2543	11.8905
6	0.2525	0.2381	0.2502	0.2469	12.1436
7	1.2042	1.2266	1.2743	1.2350	-1.8364
8	0.5154	0.4938	0.4921	0.5005	6.00973
9	0.1281	0.1233	0.1233	0.1249	18.0624

Table 5. The *S/N* ratios for the DEF values according to the parameter levels

Levels	Inertia weight (A)	Acceleration coefficient (B)	Population number (C)	Iteration number (D)
1	**4.554**	4.471	3.720	**4.444**
2	4.452	4.213	4.652	4.379
3	4.170	**4.491**	**4.803**	4.352
Max-Min	0.384	0.278	1.082	0.092
Ranking	2	3	1	4

* The largest *S/N* ratio is written in bold

Table 6. The *S/N* ratios for the computation times according to the parameter levels

Levels	Inertia weight (A)	Acceleration coefficient (B)	Population number (C)	Iteration number (D)
1	6.9091	7.1331	**14.3693**	**18.3025**
2	**7.4385**	7.1834	6.6645	4.6523
3	7.4119	**7.4431**	0.7258	-1.1953
Max-Min	0.5293	0.3100	13.6435	19.4978
Ranking	3	4	2	1

* The largest *S/N* ratio is written in bold

the ranking of factors based on their effect on computation time, ordered from most to least influential as: iteration number, population number, acceleration coefficients, and inertia weight. To minimize computation time, the optimal levels are determined as follows: Level 2 for inertia weight, Level 3 for acceleration coefficients, Level 1 for population number, and Level 1 for iteration number. The *S/N* ratio plots, which illustrate the effects of factor levels on both DEF values and computation times, are shown in Figures 2 and 3, respectively.

A one-way analysis of variance (ANOVA) test is conducted to evaluate whether the effects of the factors on DEF values and computation time are statistically significant. The summaries of ANOVA results for DEF values and computation times are provided in Tables 7 and 8, respectively.

As shown in Table 7, the p-values for inertia weight and population number are less than the significance level

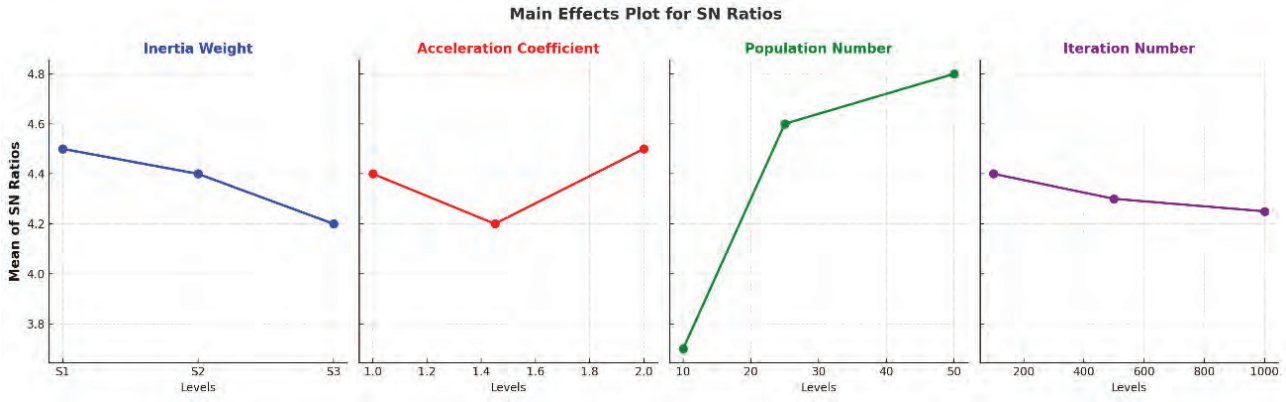


Figure 2. Graph of the (*S/N*) ratios for the DEF values.

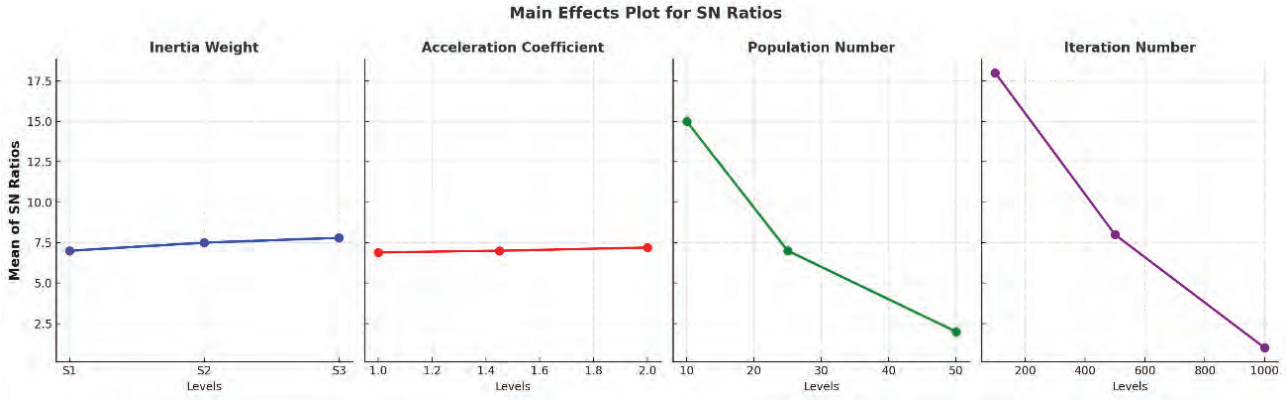


Figure 3. Graph of the (*S/N*) ratios for the computation times.

Table 7. The summary of ANOVA table for the DEF values

Factors	Degrees of Freedom (DF)	Sum of Squares of Error (SS)	Mean Squares of Error (MS)	F-value	*p*-value
Inertia weight (A)	2	0.0036	0.0018	4.74	0.022*
Acceleration coefficients (B)	2	0.0024	0.0012	3.11	0.069
Population number (C)	2	0.0311	0.0155	40.32	0.000*
Iteration number (D)	2	0.0003	0.0001	0.41	0.672
Error	18	0.0069	0.0003		
Total	26	0.0445			

Table 8. The summary of ANOVA table for the computation times

Factors	Degrees of Freedom (DF)	Sum of Squares of Error (SS)	Mean Squares of Error (MS)	F-value	*p*-value
Inertia weight (A)	2	1.3148	0.6573	1484.25	0.000*
Acceleration coefficients (B)	2	1.1287	0.5643	1274.19	0.000*
Population number (C)	2	5.0970	2.5485	5754.10	0.000*
Iteration number (D)	2	7.0888	3.5444	8002.66	0.000*
Error	18	0.0080	0.0004		
Total	26	14.6373			

(typically 0.05), indicating that their effects on the DEF value, i.e., solution quality, are statistically significant at the 95% confidence level. Based on the results in Table 5 and the trends observed in Figure 2, Level 1 for inertia weight and Level 3 for population number are selected as optimal with respect to the DEF criterion.

According to Table 8, the p-values for all 4 factors are below the 0.05 threshold, confirming that each factor has a statistically significant impact on computation time. Since the optimal levels for inertia weight and population number have already been selected based on DEF values, the remaining two factors, i.e., acceleration coefficient and iteration number, are optimized with respect to computation time. Referring to Table 6 and Figure 3, Level 3 for the acceleration coefficient and Level 1 for the iteration number yield the lowest computation time. The final selection of optimal levels and their corresponding evaluation criteria are summarized in Table 9.

Simulation Study

In this section, a Monte-Carlo simulation study is performed to investigate the performance of the proposed PSO algorithm, which is designed for estimating parameters of the multivariate gamma distribution using the maximum likelihood method. The actual parameter values $\theta = (\alpha_1, \alpha_2, \beta, \mu_1, \mu_2)$ selected for the multivariate gamma distribution are given in Table 10. In addition, sample sizes 10, 30, 50, 100, 250, 500 and 1000 are considered for each parameter setting in order to determine the effect of sample size on the parameter estimation process.

The algorithm is repeated 1000 times for each of sample size (n) and each parameter vector (θ). Mean of the parameter estimates, mean square errors (MSE) and deficiency (DEF) values with respect to parameter vectors $\theta_1, \theta_2, \theta_3$ are obtained and the results are summarized in Tables 11-13, respectively. DEF value, which is a substantial measure of the joint efficiency of the estimators, is calculated as follows:

Table 9. Selected optimum levels of the factors

Criteria	Factors			
	Inertia weight (A)	**Acceleration coefficient (B)**	**Population number (C)**	**Iteration number (D)**
Solution quality-DEF	0.7	-	50	-
Computation time	-	2	-	100

Table 10. Selected parameter values for Multivariate Gamma distribution

Parameter vector	α_1	α_2	β	μ_1	μ_2
θ_1	2.8	4	0.5	5	10
θ_2	3	4	1	-2	10
θ_3	5	2.6	0.75	1	8

Table 11. Simulation results for $\theta_1 = (\alpha_1, \alpha_2, \beta, \mu_1, \mu_2) = (2.8, 4, 0.5, 5, 10)$

n	$\hat{\alpha}_1$		$\hat{\alpha}_2$		$\hat{\beta}$		$\hat{\mu}_1$		$\hat{\mu}_2$		
	Mean	MSE	Mean	MSE	Mean	MSE	Mean	MSE	Mean	MSE	DEF
10	3.3809	2.5371	4.9881	7.6124	0.4252	0.0211	5.0580	0.1367	10.0677	0.4770	10.7842
30	2.8322	0.6879	4.1002	1.4614	0.4891	0.0082	5.0508	0.0443	10.0648	0.1204	2.3222
50	2.6254	0.3040	3.7678	0.7703	0.5127	0.0041	5.0661	0.0239	10.096	0.0763	1.1788
100	2.6262	0.1504	3.7329	0.3468	0.5178	0.0018	5.0454	0.0110	10.0718	0.0322	0.5421
250	2.6850	0.0667	3.8355	0.1651	0.5128	0.0010	5.0253	0.0036	10.0390	0.0130	0.2493
500	2.7037	0.0383	3.8508	0.1058	0.5123	0.0007	5.0176	0.0017	10.0315	0.0073	0.1537
1000	2.7686	0.0165	3.9447	0.0473	0.5041	0.0002	5.0068	0.0007	10.012	0.0031	0.0681

Table 12. Simulation results for $\theta_2 = (\alpha_1, \alpha_2, \beta, \mu_1, \mu_2) = (3, 4, 1, -2, 10)$

n	$\hat{\alpha}_1$		$\hat{\alpha}_2$		$\hat{\beta}$		$\hat{\mu}_1$		$\hat{\mu}_2$		
	Mean	MSE	Mean	MSE	Mean	MSE	Mean	MSE	Mean	MSE	DEF
10	3.6854	4.7680	4.7660	4.6047	0.8679	0.0783	-1.8844	0.9185	10.1414	1.3427	11.7122
30	3.2008	0.6729	4.4666	0.6751	0.9283	0.0182	-1.9401	0.2131	9.9102	0.2572	1.8365
50	2.8317	0.3665	3.8235	0.6163	1.0200	0.0186	-1.8593	0.1180	10.1713	0.2489	1.3683
100	2.8087	0.1797	3.7624	0.2344	1.0380	0.0086	-1.8988	0.0530	10.1213	0.0945	0.5702
250	2.8493	0.0870	3.8116	0.1178	1.0340	0.0048	-1.9387	0.0198	10.0761	0.0363	0.2657
500	2.8980	0.0428	3.8546	0.0908	1.0250	0.0025	-1.9639	0.0091	10.0605	0.0247	0.1699
1000	2.9529	0.0212	3.9331	0.0496	1.0105	0.0012	-1.9806	0.0044	10.0284	0.0127	0.0891

Table 13. Simulation results for $\theta_3 = (\alpha_1, \alpha_2, \beta, \mu_1, \mu_2) = (5, 2.6, 0.75, 1, 8)$

n	$\hat{\alpha}_1$		$\hat{\alpha}_2$		$\hat{\beta}$		$\hat{\mu}_1$		$\hat{\mu}_2$		
	Mean	MSE	Mean	MSE	Mean	MSE	Mean	MSE	Mean	MSE	DEF
10	5.2911	2.3772	2.7719	3.8366	0.7080	0.0381	1.2052	0.8600	8.1357	0.4733	7.5853
30	4.9408	1.7870	2.5738	0.2236	0.7387	0.0069	1.1362	0.5318	8.0728	0.0529	2.6023
50	4.6468	0.9956	2.4430	0.1993	0.7682	0.0050	1.2033	0.3114	8.0814	0.0364	1.5477
100	4.8436	0.7727	2.5195	0.0927	0.7628	0.0058	1.1011	0.1551	8.0480	0.0139	1.0403
250	4.6483	0.3719	2.4434	0.0704	0.7875	0.0039	1.1139	0.0607	8.0400	0.0063	0.5133
500	4.8702	0.2057	2.5351	0.0325	0.7635	0.0016	1.0444	0.0354	8.0209	0.0030	0.2782
1000	4.9156	0.0871	2.5583	0.0154	0.7588	0.0007	1.0265	0.0147	8.0121	0.0012	0.1191

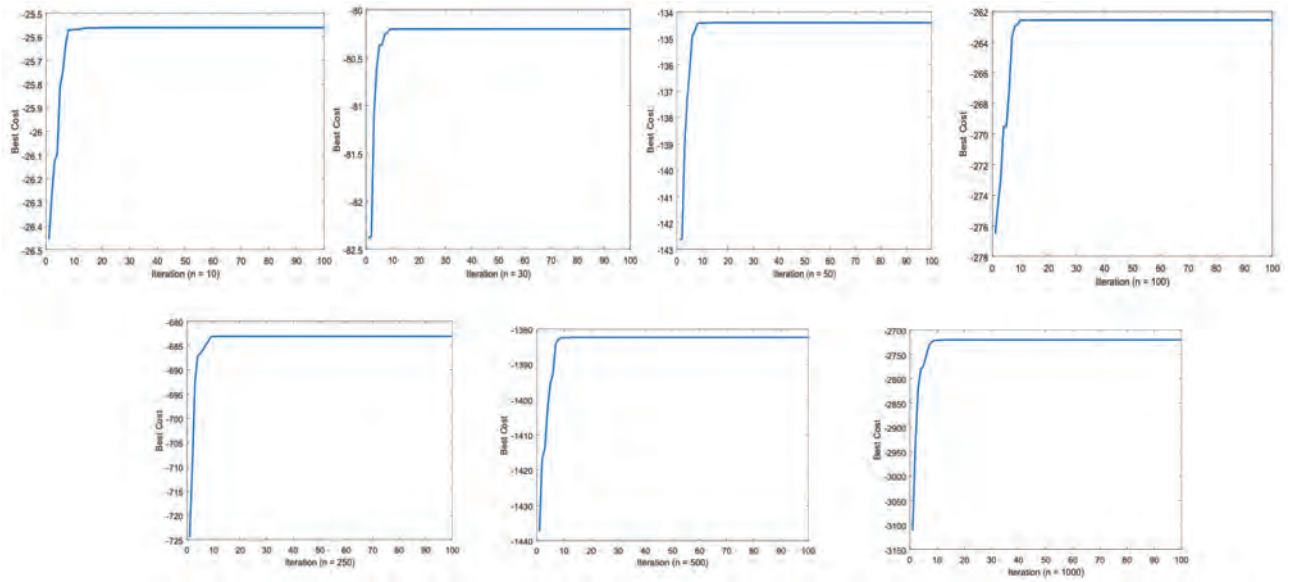


Figure 4. Convergence curves of Best Cost over iterations for different sample sizes (n) for θ_1 .

$$DEF(\hat{\alpha}_1,\hat{\alpha}_2,\hat{\beta},\hat{\mu}_1,\hat{\mu}_2) = MSE(\hat{\alpha}_1) + MSE(\hat{\alpha}_2) + MSE(\hat{\beta}) + MSE(\hat{\mu}_1) + MSE(\hat{\mu}_2) \quad (13)$$

The results presented in Tables 11–13 demonstrate that the PSO algorithm, with parameters optimized via the Taguchi method, effectively estimates the parameters of the Multivariate Gamma distribution. Moreover, as the sample size increases, the estimated parameter values consistently converge toward the real parameter values across all scenarios. Consequently, both the Mean Squared Error (MSE) and Deficiency (DEF) values decrease, confirming the robustness and accuracy of the proposed approach. These findings indicate that the Taguchi-designed PSO algorithm is well-suited for parameter estimation in the Multivariate Gamma distribution.

The convergence curve illustrating the reduction in error (*Best Cost*) over iterations has been included in Figure 4. This figure shows the convergence behavior for different sample sizes (n=10,30,50,100,250,500,1000). As observed in Figure 4, the Best Cost decreases rapidly during the initial iterations and gradually stabilizes as the algorithm progresses. This trend demonstrates the effectiveness of the optimization process in minimizing the objective function.

The comparison across different sample sizes (n) also highlights how larger datasets require more iterations to converge but achieve lower final error values, indicating improved performance with increased data availability. This convergence curve effectively visualizes the efficiency of the optimization approach in reducing error over successive iterations.

CONCLUSION

This study introduces a novel approach for optimizing Particle Swarm Optimization (PSO) parameters through the Taguchi experimental design, thereby addressing a notable gap in the literature. Unlike conventional heuristic or manual tuning strategies, the proposed method systematically identifies optimal parameter configurations, resulting in improved solution quality and reduced computation time.

The methodology was applied to the parameter estimation problem of the Multivariate Gamma (MGM) distribution, originally formulated by Mathai and Moschopoulos [14]. A primary challenge in this context is the high sensitivity of PSO performance to its parameter settings—improper tuning can lead to slow convergence and suboptimal estimates. The Taguchi design method enables efficient parameter optimization, eliminating the the need for time-consuming trial-and-error procedures.

Simulation results confirm that the Taguchi-optimized PSO yields significantly lower DEF values and computation times compared to randomly selected parameter settings. Additionally, as the sample size increases, both the Mean Squared Error (MSE) and DEF values decrease, further affirming the robustness and reliability of the proposed approach.

Future Research Directions and Extensions

This study successfully applies the Taguchi experimental design to optimize PSO parameters, demonstrating notable improvements in both solution quality and computational efficiency. However, several ways remain open for further exploration to enhance and extend this methodology. One potential extension involves comparing the

Taguchi-optimized PSO with adaptive PSO variants, such as Adaptive Inertia Weight PSO (AIW-PSO), Self-Adaptive PSO (SA-PSO), and Dynamic Acceleration PSO (DAPSO). These adaptive approaches dynamically adjust algorithmic parameters during the optimization process, potentially ensuring enhanced convergence properties and robustness. Investigating the integration of Taguchi-based tuning within adaptive PSO frameworks may provide deeper insights into improving PSO's efficiency and stability across a broader range of problem domains. Another promising direction is the application of Taguchi-based parameter tuning to other metaheuristic algorithms, such as Genetic Algorithm (GA), Differential Evolution (DE), Ant Colony Optimization (ACO), and Artificial Bee Colony (ABC). Since parameter selection remains a critical challenge in metaheuristic optimization, employing a systematic tuning approach using the Taguchi method may significantly enhance the performance, robustness, and generalization capabilities of these algorithms across diverse optimization scenarios.

Furthermore, future studies could explore the development of hybrid optimization frameworks by integrating PSO with complementary optimization techniques. For instance, a Hybrid PSO-Taguchi-Gradient Descent approach could be examined to further refine parameter estimation, potentially improving both convergence speed and accuracy in complex optimization tasks. Such hybrid methodologies could leverage the global search ability of PSO and the local refinement strength of Gradient Descent, resulting in more effective optimization solutions.

While the current study focuses on estimating the parameters of the multivariate gamma (MGM) distribution, future applications of the Taguchi-optimized PSO could extend to real-world problems in stochastic modeling, machine learning hyperparameter tuning, and deep learning optimization. Given the versatility of metaheuristic-based tuning, investigating its efficacy in high-dimensional machine learning models, particularly in deep neural network optimization, could provide substantial advancements in computational intelligence. Another important direction for future research is assessing the scalability of the Taguchi-optimized PSO in high-dimensional optimization problems. The performance of the proposed methodology on large-scale datasets and computationally intensive tasks remains an open question. Conducting extensive empirical evaluations in high-dimensional search spaces would ensure valuable insights into the robustness, efficiency, and computational feasibility of the proposed approach under more complex conditions.

Finally, theoretical analysis and statistical validation of the Taguchi-optimized PSO could further strengthen its applicability. Although the empirical results presented in this study demonstrate the effectiveness of the proposed approach, establishing a rigorous theoretical foundation explaining why Taguchi-based parameter tuning enhances PSO performance would significantly contribute to the literature. Furthermore, advanced statistical validation techniques, such as Analysis of Variance (ANOVA) and hypothesis testing, could be employed to quantify the significance of the observed improvements, ensuring the robustness and reproducibility of the findings.

AUTHORSHIP CONTRIBUTIONS

Authors equally contributed to this work.

DATA AVAILABILITY STATEMENT

The authors confirm that the data that supports the findings of this study are available within the article. Raw data that support the finding of this study are available from the corresponding author, upon reasonable request.

CONFLICT OF INTEREST

The authors declared no potential conflicts of interest with respect to the research, authorship, and/or publication of this article.

ETHICS

There are no ethical issues with the publication of this manuscript.

STATEMENT ON THE USE OF ARTIFICIAL INTELLIGENCE

Artificial intelligence was not used in the preparation of the article.

REFERENCES

[1] Yue S. A bivariate gamma distribution for use in multivariate flood frequency analysis. Hydrol Process 2001;15:1033–1045. [CrossRef]

[2] Yue S, Ouarda T, Bobée B. A review of bivariate gamma distributions for hydrological application. J Hydrol 2001;246:1–18. [CrossRef]

[3] Smith O, Adelfang S, Tubbs J. A bivariate gamma probability distribution with application to gust modeling. NASA Tech Memo 1982;82483.

[4] Stitou Y, Lasmar N, Berthoumieu Y. Copulas based multivariate gamma modeling for texture classification. In: 2009 IEEE International Conference on Acoustics, Speech and Signal Processing; 2009. p. 1045–1048. [CrossRef]

[5] Peppas K, Alexandropoulos G, Datsikas C, Lazarakis F. Multivariate gamma-gamma distribution with exponential correlation and its applications in radio frequency and optical wireless communications. IET Microw Antennas Propag 2011;5:364–371. [CrossRef]

[6] Block HW, Savits TH. Multivariate distributions in reliability theory and life testing. In: Statistical distributions in scientific work. Springer; 1981. p. 271–288. [CrossRef]

[7] Chen Y, Song Q, Su J. On a class of multivariate mixtures of gamma distributions: Actuarial applications and estimation via stochastic gradient methods. Variance 2023;16. [CrossRef]
[8] Furman E. On a multivariate gamma distribution. Stat Probab Lett 2008;78:2353–2360. [CrossRef]
[9] Venturini S, Dominici F, Parmigiani G. Gamma shape mixtures for heavy-tailed distributions. Ann Appl Stat 2008;2:756–776. [CrossRef]
[10] Cherian K. A bivariate correlated gamma-type distribution function. J Indian Math Soc 1941;5:133–144.
[11] Jensen D. The joint distribution of quadratic forms and related distributions. Aust J Stat 1970;12:13–22. [CrossRef]
[12] Sarmanov I. On the approximate calculation of the coefficient of correlation between two functions of dependent random variates. Math Notes Acad Sci USSR 1970;7:372–377. [CrossRef]
[13] Royen T. Expansions for the multivariate chi-square distribution. J Multivar Anal 1991;38:213–232. [CrossRef]
[14] Mathai A, Moschopoulos P. A form of multivariate gamma distribution. Ann Inst Stat Math 1992;44:97–106. [CrossRef]
[15] Carpenter M, Diawara N. A multivariate gamma distribution and its characterizations. Am J Math Manag Sci 2007;27:499–507. [CrossRef]
[16] Johnson NL, Kotz S, Balakrishnan N. Univariate continuous distributions. New York, USA: John Wiley & Sons; 1994.
[17] Vaidyanathan V, Lakshmi RV. Parameter estimation in multivariate gamma distribution. Stat Optim Inf Comput 2015;3:147–159. [CrossRef]
[18] Tsionas EG. Bayesian inference for multivariate gamma distributions. Stat Comput 2004;14:223–233. [CrossRef]
[19] Oikonomidis T, Trevezas A. Closed-form moment-type estimators for multivariate gamma distributions and their small-sample performance. J Stat Comput Simul 2023;93:1501–1523.
[20] Abbasi B, Jahromi AHE, Arkat J, Hosseinkouchack M. Estimating the parameters of Weibull distribution using simulated annealing algorithm. Appl Math Comput 2006;183:85–93. [CrossRef]
[21] Abbasi B, Niaki STA, Khalife MA, Faize Y. A hybrid variable neighborhood search and simulated annealing algorithm to estimate the three parameters of the Weibull distribution. Expert Syst Appl 2011;38:700–708. [CrossRef]
[22] Örkcü H, Aksoy E, Dogan Mİ. Estimating the parameters of 3-p Weibull distribution through differential evolution. Appl Math Comput 2015;251:211–224. [CrossRef]
[23] Örkcü H, Özsoy VS, Aksoy E, Dogan MI. Estimating the parameters of 3-p Weibull distribution using particle swarm optimization: A comprehensive experimental comparison. Appl Math Comput 2015;268:201–226. [CrossRef]
[24] Özsoy VS, Örkcü HH, Bal H. Particle swarm optimization applied to parameter estimation of the four-parameter Burr III distribution. Iran J Sci Technol Trans A Sci 2017;42:1–15. [CrossRef]
[25] Yalçınkaya A, Şenoğlu B, Yolcu U. Maximum likelihood estimation for the parameters of skew normal distribution using genetic algorithm. Swarm Evol Comput 2018;38:127–138. [CrossRef]
[26] Yang F, Ren H, Hu Z. Maximum likelihood estimation for three-parameter Weibull distribution using evolutionary strategy. Math Probl Eng 2019;2019:6281781. [CrossRef]
[27] Fariz TN, Basha SS. Enhancing solar radiation predictions through COA-optimized neural networks and PCA dimensionality reduction. Energy Rep 2024;12:341–359. [CrossRef]
[28] Yang XS, He X, Wang H. Covariance matrix adaptation evolution strategy combined with PCA for high-dimensional optimization problems. Comput Optim Appl 2021;78:983–1005.
[29] Larcher M, Xie J, Cheng L. A hybrid dynamic model based on a chaotic Coyote Optimization Algorithm for wind speed prediction. Renew Energy 2024;211:107–121.
[30] Noorjahan S, Shaik SB. Developing an intuitionistic fuzzy rough new correlation coefficient approach for enhancing robotic vacuum cleaner. Sci Prog 2024:1–15. [CrossRef]
[31] Noorjahan S, Shaik SB. Decision-making using the correlation coefficient measures of intuitionistic fuzzy rough graph. Hacet J Math Stat 2024;53:1774–1797. [CrossRef]
[32] Acıtaş Ş, Aladağ ÇH, Şenoğlu B. A new approach for estimating the parameters of Weibull distribution via particle swarm optimization: An application to the strengths of glass fibre data. Reliab Eng Syst Saf 2019;183:116–127. [CrossRef]
[33] Rezaee Jordehi A, Jasni J. Parameter selection in particle swarm optimisation: A survey. J Exp Theor Artif Intell 2013;25:527–542. [CrossRef]
[34] Schwaab M, Biscaia Jr EC, Monteiro JL, Pinto JC. Nonlinear parameter estimation through particle swarm optimization. Chem Eng Sci 2008;63:1542–1552. [CrossRef]
[35] Alptekin B, Acitas S, Senoglu B, Aladag CH. Statistical determination of significant particle swarm optimization parameters: The case of Weibull distribution. Soft Comput 2022;26:12623–12634. [CrossRef]
[36] Eberhart R, Kennedy J. A new optimizer using particle swarm theory. In: Proceedings of the Sixth International Symposium on Micro Machine and Human Science; 1995. p. 39–43. [CrossRef]
[37] Talbi EG. Metaheuristics: From design to implementation. Canada: John Wiley & Sons; 2009. [CrossRef]
[38] Yang XS. Nature-inspired optimization algorithms. Oxford, UK: Elsevier; 2014. [CrossRef]

[39] Yang XS. Engineering optimization: An introduction with metaheuristic applications. Cambridge, UK: John Wiley & Sons; 2010. [CrossRef]

[40] Shi Y, Eberhart RC. Parameter selection in particle swarm optimization. In: International Conference on Evolutionary Programming; 1998; USA. p. 591–600. [CrossRef]

[41] Taguchi G. System of experimental design: Engineering methods to optimize quality and minimize costs. USA: UNIPUB/Kraus International Publications; 1987.

[42] Şenoğlu B, Acıtaş Ş. İstatistiksel deney tasarımı: Sabit etkili modeller. Ankara, Türkiye: Nobel Yayınevi; 2011.

[43] Zoraghi N, Abbasi B, Niaki STA, Abdi M. Estimating the four parameters of the Burr III distribution using a hybrid method of variable neighborhood search and iterated local search algorithms. Appl Math Comput 2012;218:9664–9675. [CrossRef]

[44] Nalbant M, Gökkaya H, Sur G. Application of Taguchi method in the optimization of cutting parameters for surface roughness in turning. Mater Des 2007;28:1379–1385. [CrossRef]

[45] Nian C, Yang W, Tarng Y. Optimization of turning operations with multiple performance characteristics. J Mater Process Technol 1999;95:90–96. [CrossRef]

[46] Bansal JC, Singh P, Saraswat M, Verma A, Jadon SS, Abraham A. Inertia weight strategies in particle swarm optimization. In: 2011 Third World Congress on Nature and Biologically Inspired Computing; 2011. p. 633–640. [CrossRef]

Sigma J Eng Nat Sci, Vol. 44, No. 4, pp. 2937–2951, August, 2026

Sigma Journal of Engineering and Natural Sciences
Web page info: https://sigma.yildiz.edu.tr
DOI: 10.14744/sigma.2026.2136

Research Article

Enhancing geopolymer mortars: The impact of Algerian metakaolin substitution on mechanical performance and sustainability

Kamel HEBBACHE[1], Abdellah DOUADİ[1,*], Oualid Mahieddine HAMDİ[2], Mourad BOUTLİKHT[1], Abderraouf MESSAİ[1], Nour El Houda KHİTAS[1], Cherif BELEBCHOUCHE[1]

[1]*Department of Civil Engineering, Civil Engineering Research Laboratory of Setif (LRGCS), Setif 1 University-Ferhat Abbas, Setif, 19000, Algeria*
[2]*Laboratory LEEGO, Faculty of Civil Engineering, University of Sciences and Technology Houari Boumediene (USTHB), Bab Ezzouar, 16111, Algeria*

ARTICLE INFO

Article history
Received: 04 November 2024
Revised: 13 February 2025
Accepted: 01 May 2025

Keywords:
Binder Characterization; Geopolymeric Mortar; Mechanical Strength; Metakaolin Substitution; Natural Pozzolan; Rheological Behavior

ABSTRACT

Geopolymer binder has been received as sustainable substitute for the Portland cement that ensures lower carbon footprint and higher durability properties. This study focuses on the influence of metakaolin (MK) replacement in Benisaf natural pozzolan (BNP)-based mortars on the rheological and mechanical properties of these latter. The objective is to optimize the metakaolin content for improved mechanical performance while keeping suitable workability. Sodium silicate (Na_2SiO_3) and sodium hydroxide (NaOH) were used as activating solutions to synthesize geopolymer mortars, where MK replaced BNP with five different ratios of 10%, 20%, 30%, 40% and 50%. X-ray diffraction (XRD), X-ray fluorescence (XRF), Scanning electron microscopy-energy dispersive x-ray (SEM-EDX) and particle size analysis were used for characterizing the raw materials. The tests focused on flowability in fresh state, and compressive strength (CS) at 14 and 28 days. The outcomes show that increasing MK quantity results in a reduction in workability, since its particle size is finer and its reactivity is higher, consequently the viscosity is higher and the fluidity is lower. As a result, compressive strength was increased considerably, with a maximum value of 24 MPa at 40% metakaolin substitution (150% higher than control geopolymer mortar). This improvement is due to increased availability of aluminosilicate, which allows a denser gel formation as well as a more favorable polycondensation. Over 40% of MK content resulted in incomplete dissolution and decreased strength. A quantitative evaluation of MK-BNP geopolymer interactions is presented, highlighting that 40% MK replacement can provide an optimal workability- strength equilibrium. This work aids the formulation of sustainable geopolymer mortars suitable for construction. Complementary investigations should emphasize practicability through large-scale applications, and durability and thermal stability as well.

Cite this article as: Hebbache K, Douadi A, Hamdi OM, Boutlikht M, Messai A, Khitas NEH, Belebchouche C. Enhancing geopolymer mortars: The impact of Algerian metakaolin substitution on mechanical performance and sustainability. Sigma J Eng Nat Sci 2026;44(4):2937–2951.

***Corresponding author.**
*E-mail address: abdoua.civil@gmail.com

This paper was recommended for publication in revised form by Editor-in-Chief Ahmet Selim Dalkilic

Published by Yıldız Technical University Press, İstanbul, Turkey
© Author. This is an open access article under the CC BY-NC license (http://creativecommons.org/licenses/by-nc/4.0/).

INTRODUCTION

Concrete is one of the most used materials in construction, with a global consumption of 5 billion tons per year (almost 1 ton/person) [1]. This classifies concrete as the second most used resource following water [2]. The rising need for concrete in civil engineering is directly related to the increasing demand for cement, itself a vital binder in concrete formulation [3, 4]. Ordinary Portland Cement (OPC), that is used in much construction work, alone consumes about 7.36×106 kJ/ton cement produced, which is considered a very high rate [5, 6]. Moreover, the cement production releases large amounts of greenhouses gases such as carbon dioxide (CO_2) [7, 8], which are related to fuel combustion and decarbonation of limestone during clinkering process [9, 10]. Literature shows that cement manufacturing is responsible for around 8% of global CO_2 emissions [11], generating about one ton of CO_2 per one ton of cement [12]. These noticeable data underline the important environmental damages related to OPC, showing that it is crucial to find new kinds of sustainable alternatives with less associated of carbon footprint emissions [13, 14].

Geopolymer binders have been explored as an alternative to OPC due to the prospect of reducing CO_2 emissions by up to 80% which makes them attractive for applications [15]. Geopolymers are inorganic polymers developed by the chemical process of aluminosilicate precursors with an alkaline solution (e.g., sodium or potassium hydroxide, with or without sodium/potassium silicate) [16]. When polymerization occurs, three-dimensional network of Si–O–Al bonds is formed and the built materials exhibits outstanding chemical resistance, mechanical properties and thermal stability [17]. İn addition, geopolymers achieve strength from aluminosilicate gels instead of calcium silicate hydrates like OPC do, qualifying them to be a more attractive low-carbon substitute.

A geopolymer mortar, that is the result of chemical reactions between fly ash and alkaline activators, has been proposed as an environmentally-friendly alternative for traditional cement mortars [18, 19]. Geopolymer mortars prouved to possess better strength properties, showing a compressive strength as high as 65% when compared to both OPC and PPC mortars, in addition to having bond strength approximately 50% higher [18]. It has been previously reported that the strength of geopolymer mortars is affected by some important variables such as curing temperature, alkaline activator concentration, and ratio of activator to fly ash [20]. Under ambient temperature curing conditions, optimal compressive strength has reached 31.39 MPa [19]. Including sand induces a slight increase in compressive strength, and the density of geopolymer mortar is between 2.0 and 2.23 g/cm^3 [19]. These characteristics contribute to the potential suitability of geopolymer mortars as effective alternatives for traditional repair materials [18, 19].

Research on geopolymer binder has focused mainly on base materials, including fly ash [21-23] and metakaolin [24-26], and synthesis parameters have been optimized over the recent decades. Three main pathways for research can be distinguished. The first focuses on the applicability of different pure or blended base materials for the production of geopolymers and investigates the intrinsic characteristics including types and ratio of components, and external agents such as curing conditions, affecting the chemical and microstructural characteristics [27]. The second pathway collects information regarding the compositions and microstructures of the base materials effect on the kinetics of reaction and polymerization process, and especially on the formation of mechanical properties like strength [28]. The last research focus investigates engineering characteristics and long-term behaviour of geopolymers, through their assessment in form of paste, mortar or concrete under diverse chemical exposures [29].

Although fly ash has attracted attention for use in geopolymer binder, the limited availability of fly ash due to the shrinking amount of coal plants is problematic and disposing of fly ash also raises environmental issues. As a result, there is significant interest in investigating alternative resources rich in aluminosilicate that are readily available and environmentally friendly. Natural pozzolan is a volcanic material with high content of silicon and aluminum that can be considered as a potential raw material for synthesizing geopolymer binders. Due to the easy extraction and low cost, it serves as a potential substitute, especially in areas where such pozzolans exist [30]. Natural pozzolan has a lower reactivity than the other materials such as metakaolin mainly because of its semi-crystalline structure and lower CaO and reactive Al_2O_3 contents. That is why the pozzolanic reaction rate is usually slower and its based geopolymers has a lower mechanical strength [31]. In order to overcome those limitations and improve also the performance of pozzolan-based geopolymers, a mixture design was explored, in which natural pozzolan is partially replaced with metakaolin. Metakaolin is an aluminosilicate material produced through calcination of kaolinite clay and characterized by its high reactive behavior especially because of the amorphous form and high alumina content [32]. This paper aims to study mechanical and rheological properties of geopolymer mortars incorporating different proportions (10%, 20%, 30%, 40% and) of metakaolin to replace natural pozzolan. In addition, the effects of important synthesis parameters like initial alkaline hydroxide solution concentration and SiO_2/Al_2O_3 molar ratio on the setting times and compressive strength of geopolymer mortars are assessed. Characterization of the raw materials is performed by techniques, such as X-ray diffraction (XRD), X-ray fluorescence (XRF), scanning electron microscopy with energy dispersive X-ray spectroscopy (SEM-EDX), and particle size distribution analysis, which are destined to reveal the chemical and mineralogical composition of the material [28].

Geopolymers mortars have been previously investigated especially the ones based on natural pozzolan and

metakaolin, but the published studies emphasize either mechanical strength or durability aspects without considering a thorough parametric investigation. In this regard, the current study intends to bridge part of these gaps by providing a systematic investigation on the influence of metakaolin substitution together with some important experiments' parameters on both fresh and hardened states characteristics. In addition, the use of advanced techniques for material characterization can complement investigations into microstructural evolutions that occur during geopolymerization. The present research combines these three elements, confirming recent studies in this field while providing new insights into the development of geopolymer formulations comprising pozzolans and metakaolin that finally maximize both performance and sustainability.

This study aims to expand the existing literature involving sustainable construction materials by providing an evaluation of pozzolan-metakaolin-based geopolymer mortars that are capable of significantly reducing the carbon emissions produced by cementitious materials without compromising structural performance.

MATERIAL AND METHODS

Characterization of Precursor Materials

The natural pozzolan used in this study, denoted as Bouhmidi Natural Pozzolan (BNP), was sourced from volcanic tuff deposits at Bouhmidi in Beni-Saf, located in the northwestern region of Algeria (Ain Temouchent), and provided by the company SPMC Spa. Kaolin, on the other hand, was supplied by the Soalka company and is obtained from the Milia deposit in Jijel, located in northeastern Algeria as shown in Figure 1.

The active precursors used in geopolymerization preparation were derived from kaolin and pozzolan. Kaolin was calcined for 7 hours under 800 °C temperature to produce metakaolin (MK), and pozzolan was dried at 105 °C for 24 h prior to grinding using a ball mill. Then, BNP and MK were ground again aiming to achieve powders with better fineness. These powders were both sieved to a maximum particle size of 100 μm. The composition of the precursor materials is decisive in terms of their reactivity in an alkaline medium for the successful formation of geopolymer. The chemical properties of BNP and MK were obtained using x-ray fluorescence (XRF) spectroscopy through a Malvern Panalytical Epsilon 1 spectrometer and the results are summarized in Table 1. These materials both presents high contents of SiO_2 and Al_2O_3, key constituents for the geopolymerization process. The SiO_2/Al_2O_3 molar ratios of BNP (4.4) and MK (2.8) suggest that they are proper to synthesize geopolymer.

It is crucial to emphasize that the mineralogical variability of precursor materials significantly affects the physicochemical and mechanical characteristics of the synthesized

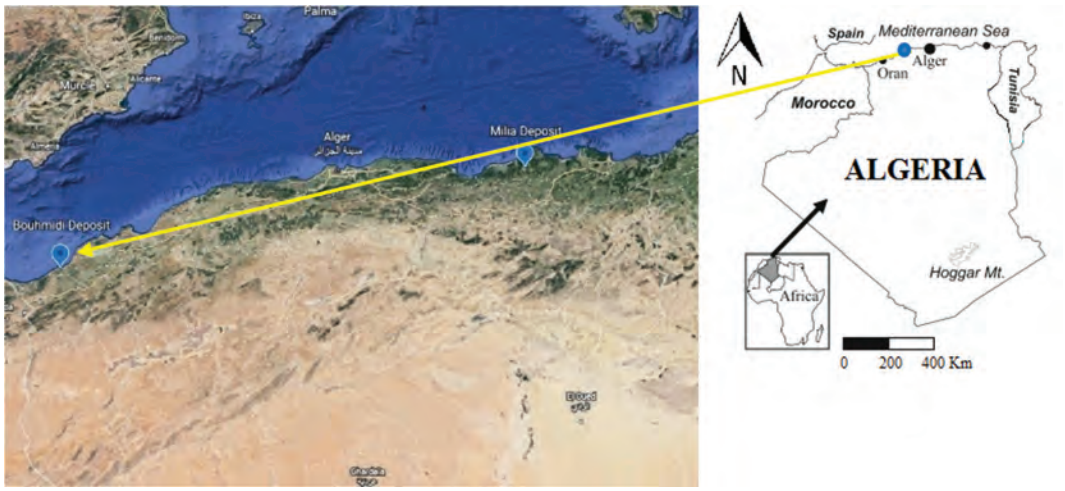


Figure 1. Location of Bouhmidi and Milia deposit.

Table 1. Oxide composition of BNP, Kaolin and MK as obtained by XRF

Composition (%)	SiO_2	Al_2O_3	Fe_2O	CaO	MgO	SO_3	Na_2O	K_2O	L.O.I
BNP	48.1	18.6	10.3	10.8	3.7	0.2	0.8	0.6	4.3
Kaolin	49.3	33.5	2.6	0.1	0.4	0	0.1	2.8	11.2
MK	54.4	31.1	7.4	0.1	0.4	0.3	0.2	4.2	1.9

geopolymer [31]. These precursors reactivity depends on their phase composition, crystallinity and the availability of reactive aluminosilicate species. Hence, X-ray diffraction (XRD) analysis was undertaken for the identification of the crystalline phases in raw materials and to evaluate their influence upon the geopolymerization process.

To this end, analysis was carried out with a Siemens D5000 diffractometer in the Brentano Bragg configuration and at an operational voltage of 45 kV using Cu Kα1 radiation source (λ=1.54 Å). The diffraction patterns were recorded and monitored in a continuous scan mode, with a 0.017° of step size covering a 2θ range of 3° to 75°, and measured for about 0.33 seconds per step to provide high-resolution characterization of the crystalline mineralogical phases existing inside natural pozzolan (BNP), metakaolin (MK) and kaolin as shown in Figure 2. The results suggested that BNP is constituted of multiple crystalline phases, dominated by several phases such as Anorthite (a calcium aluminosilicate), Analcime (a zeolitic phase), Diopside (a pyroxene mineral), and Hematite. Anorthite contributes to the pozzolanic activity of BNP, and Analcime can enhance alkali reactivity because of its content in structural water. Diopside shows limited reactivity in presence of alkaline conditions while Hematite affect the color and thermal stability of the ultimate geopolymer matrix.

By contrast, MK had a more heterogeneous character with the peaks from Quartz and Zeolite as the main crystalline phases. Quartz is a very stable silicate with low reactivity in geopolymerization process, which is only improved if further ground to a fine granulometry, while Zeolites have a high cation-exchange capacity and a microporous crystal structure that can improve alkali activation and can additionally define the mechanical performance and durability of the geopolymer.

Besides chemical composition, the physical properties of the precursor materials play an important role in optimizing geopolymer performance. Table 2 shows the specific surface area and density of BNP and MK. Measurements were made using a Blaine permeabilimeter (Controlab L0049) for specific surface area determination according

Table 2. The main physical properties of MK and BNP

Physical properties		MK	BNP
Absolute density (g/cm³)		2.59	2.76
The Blaine's specific area (m²/kg)		320	650
Particle size characteristics	D10 (μm)	14.25	1.99
	D50 (μm)	36.87	14.43
	D90 (μm)	74.32	46.30

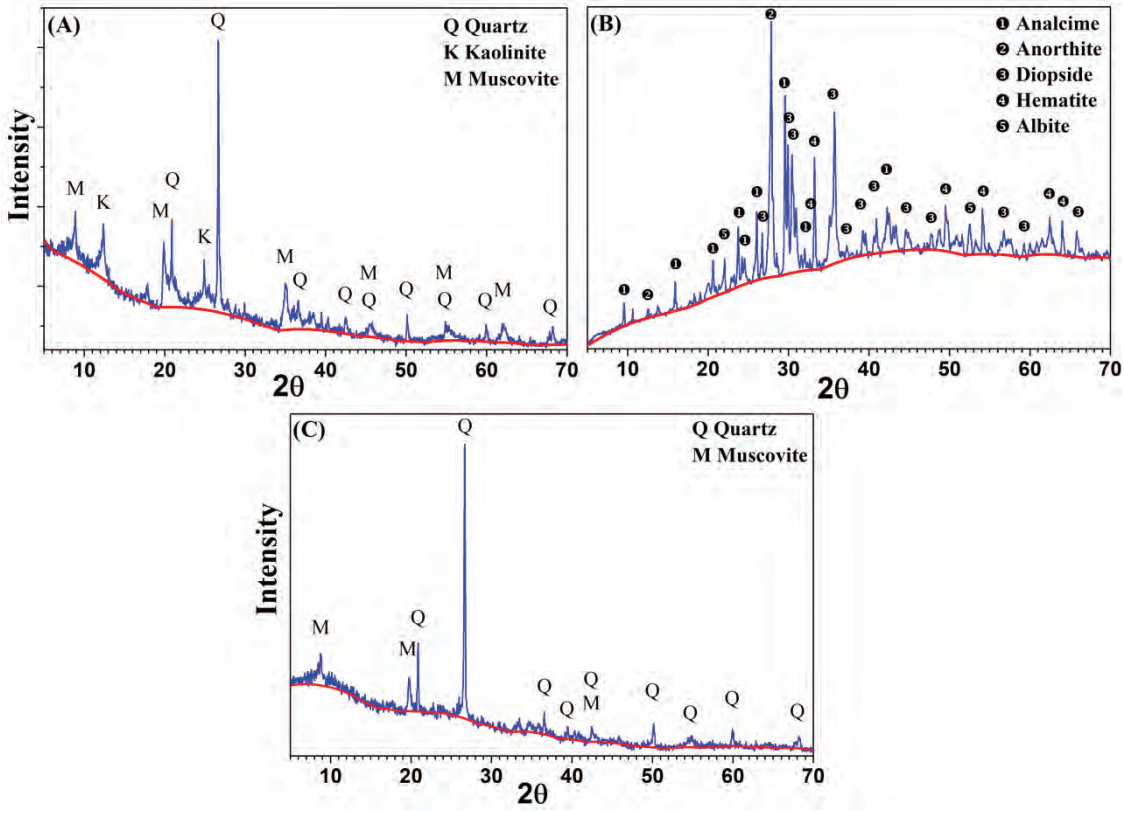


Figure 2. X-ray diffraction patterns of the Kaolin, MK and BNP samples.

to the European standard EN-196-6, whereas the density was measured by means of a pycnometer using Archimedes method. The laser scattering analyzer was used to analyze particle size distribution of BNP and MK, and both cumulative and partial distribution curves of particle sizes of each material are presented in Figure 3. The SEM (Scanning electron microscopy) revealed the morphological detail of the precursor materials that are determinant in their reactivity and packing density or arrangement within the geopolymeric matrix (Fig. 4).

Micrographs show that MK particles have a unique multilevel, plate-like morphology, which is consistent with thermally activated kaolinite. The noticed morphology gives it a high specific surface area and increases the dissolution kinetics during alkaline activation, which leads to an easy geopolymeric gel formation. On the other hand, BNP particles show an irregular, angular shape and a wide particle size distribution (1 to 25 μm) that reveal the heterogeneity of this material, which in turn will affect the packing density and inter-particle porosity as well as the material reactivity. Angular particles presence indicates less natural weathering or mechanical grinding and possibly increased mechanical interlocking in the geopolymer matrix. Differences in the morphology of MK and BNP directly affect the flowability, workability, and microstructural evolution of the final geopolymer.

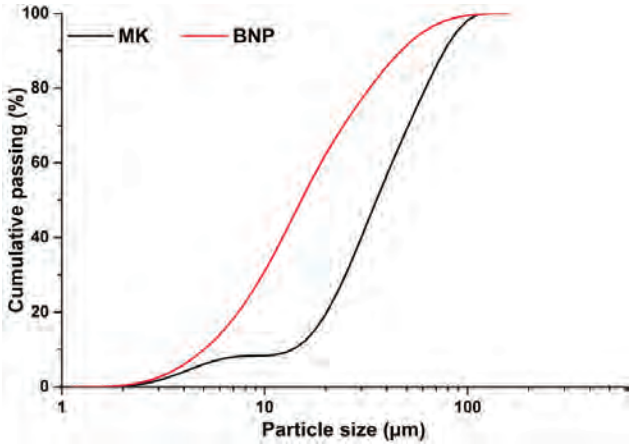


Figure 3. Particle size distribution from BNP powder and MK.

Alkaline Activators

In this study, the alkaline activators used to activate Bouhmidi Natural Pozzolan (BNP) and metakaolin (MK), are a mixture of sodium silicate (Na_2SiO_3) and sodium hydroxide (NaOH) solutions at different ratios. Commercial sodium silicate is sold as solid, powder or liquid in all forms with SiO_2/Na_2O molar ratio of 1.6 to 3.85 [32, 33]. The sodium silicate used here was locally supplied by AFRICAVER EPE SPA (Jijel), as a viscous solution with silica modulus equal to 3.35. Sodium hydroxide (NaOH) which is an imported product supplied by the company of JSC KAUSTIK VOLGOGRAD, from NIKOCHEM group, was presented in white spherical pearls form. Those pearls were dispersed in distilled water with ongoing stirring to yield solutions of varying molar concentrations according to experimental requirements.

Preparation of Samples

Precursor materials (BNP and MK) were mixed with the alkaline activating solution using a mechanical mixer (Controlab L0031. 2) with a 5-liter capacity. The mixing design was based on an alkali/precursor mass ratio of 0.45 and a molar ratio SiO_2/Al_2O_3 on the order of 5. The activation liquids were mixed of sodium silicate and sodium hydroxide solutions, prepared 24 h prior to use, keeping a Na_2SiO_3/NaOH mass ratio equal to 2.5, with the aid of a magnetic stirrer. To assess the effect of MK substitution levels on initial and final setting times, six mixes (0%, 10%,

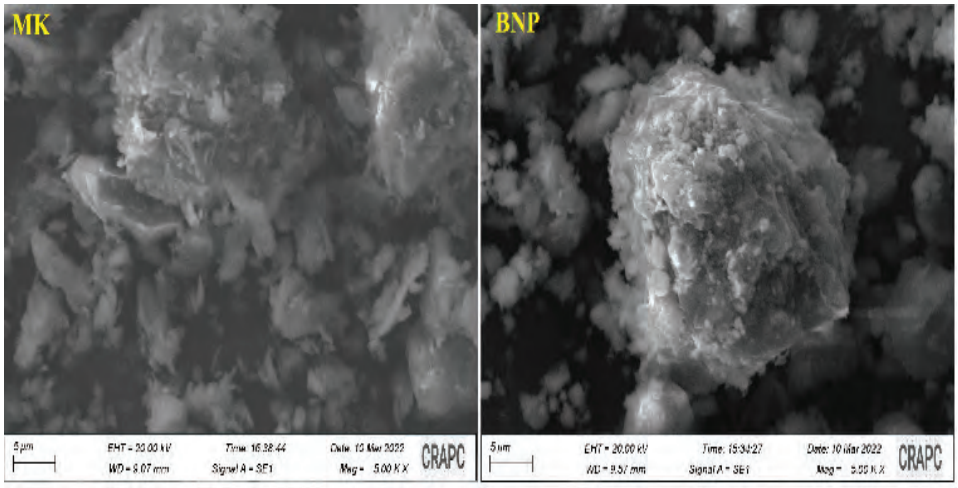


Figure 4. SEM images of MK (left) and BNP (right).

Table 3. Proportions of mixtures for the preparation of mortars

Mix	SiO_2/Al_2O_3 molar ratio	SiO_2/Na_2O molar ratio	MK content
M-1	5.2	1.90	0
M-2	5.5	1.71	0
M-3	5.8	1.56	0
M-4	6.1	1.43	0
M-5	6.4	1.34	0
M-6	5.9	1.34	10
M-7	5.7	1.34	20
M-8	5.4	1.34	30
M-9	5.1	1.34	40
M-10	4.6	1.34	50

20%, 30%, 40% and 50%) were prepared per mix design. The water/BNP ratio was maintained at 0.4 to provide the proper paste consistency. To evaluate the influence of MK content and the molar ratio of SiO_2/Al_2O_3 on compressive strength, ten mortar mixes were prepared at five levels per parameter under standardized conditions as provided in Table 3. The fixed mass ratio of sand to precursor used was 3, according to European Standard EN 196-1.

The sample preparation consisted of three sequential operations: mixing, casting and curing. First, the sand and precursor powders were dry-mixed for 1 min in a mechanical mixer to reach homogeneity. Then, the activating solution was poured into the dry mixture dropwise and mixed at a low speed for 90 seconds. Subsequently, the mixer was paused so that the mixture clinging to the sides and bottom of the bowl could be scraped down before mixing again on high speed for another 90 seconds.

At the end of the mixing procedure, the mortar was cast into metal molds of 40×40×160 mm^3 dimensions, in two layers, each compacted by 60 shocks by an automatic vibrating table (1 shock per second rate). The surface of each layer was leveled using a spatula before sealing the molds. The molds were stored in hermetically sealed plastic bags and placed in a climatic chamber set at 25°C and 95% relative humidity (RH) for controlled curing. With this approach, the geopolymerization process occurs under optimal conditions, so it allows to make a much more accurate assessment of the setting times and compressive strength of the different geopolymer mortars.

Workability

The geopolymer mortars workability was evaluated with the mini-cone slump test in accordance to EN 1015-3 as an indirect way to evaluate flowability [34]. This test was carried in an apparatus made by a truncated cone with base diameter (D1) of 150 mm, upper diameter (D2) equal to 50 mm and height (h) equal to 200 mm. The geopolymer mortar mixture was placed within the cone in two subsequent layers. The resulting homogeneous layers were compacted by applying 30 shocks (using a mechanical vibrating table) to each layer, in order to expel entrapped air. The filling of the cone followed by its removal was used to measure the diameter of spread mortar in two orthogonal directions. The final spreading flow was determined by averaging the recorded values. To check the reproducibility and fidelity in the physical performance of workability, this test was performed two times per batch for each mortar. It should be noted that the rheological properties of the mortar can be gleaned from the flowability scores which also serve to indicate what fluidity level will work in casting such material. This becomes even more important for geopolymer-based systems, as small changes in precursor composition and alkaline activator concentration can drastically affect fresh state behavior.

Initial and Final Setting Time

The first and final geopolymer paste setting times were evaluated following European Standard EN 196-3 [35], as presented in Figure 5. The information conveyed through



Figure 5. Vicat device while measurement of initial and final setting time.

setting times make each of the materials to evolve from liquid to solid at the speed that polymerization takes place. The free penetration of the Vicat needle under its own weight at a distance of 6 ± 3 mm from the bottom of the paste was defined as an initial setting time. This is the point at which the geopolymer paste has sufficient strength that it no longer deforms, and thus begins to hardening.

Each test was performed in triplicate for the same mixture to avoid inaccuracies and mean values were reported. The initial and final setting times were also critically evaluated by varying the percentage of metakaolin and molar SiO_2/Al_2O_3 ratio (the most significant factors controlling the geopolymerization kinetics). Curing times provide important information regarding workability limit and potential field application of mixes, especially for large scale industrial use where time is an immediate concern.

Compressive Strength

The compressive strength of geopolymer mortars was measured to evaluate the effect of metakaolin content and SiO_2/Al_2O_3 molar ratio on some mechanical properties of the synthesized material. The values were measured in accordance with the methods outlined in the European Standard EN 196-1 [36] for determining the compressive strength of cementitious material (Fig. 6). As detailed in Section 2.3, prismatic mortar specimens measuring 40×40×160 mm^3 were prepared. All specimens, after curing were firstly tested in a 3-point bending to generate fracture, thus dividing each prism in equal halves (40×40×80 mm^3). The two halves obtained after the fracture were then used for a compressive strength test.

Compressive strength (CS) testing was conducted at two significant curing periods, 14 days and 28 days, which correspond to the early and more mature stages of strength development. The halves were aligned in the compression testing machine so that a uniform application of load was applied over the surface area. Specimen disruption occurred at a constant loading rate, and the peak force at failure was noted. In each mix, the CS was taken as the average of four halves of individual specimens in order to reduce the data variation and increase statistical significance. Such a method led to the full examination of how MK substitution and SiO_2/Al_2O_3 molar ratio affected the mechanical properties of geopolymer. The numbers of compressive strength reflect the ability of this material to resist compressive stress, while also giving a signal on the best MK content and amounts of activator needed to enhance all structural performance.

RESULTS AND DISCUSSION

Workability

Figure 7 shows the workability of alkali-activated natural pozzolan (BNP) mortars as a function of the SiO_2/Al_2O_3 molar ratio, outlining its important role in the rheological behavior of the fresh mixtures. The flow has been measured from 160 mm to 251 mm, lining up with the limits generally accepted for the manufacture and use of geopolymer-based material. Interestingly, the flowability using the SiO_2/Al_2O_3 molar ratio trend was somewhat different, an increase from 5.2 to 5.8 lead to a significant improvement of the flowability from 160 mm to 251 mm. The main reason for this improvement is the addition of water content with a higher dosage of sodium silicate, and thereby increasing the dispersion of solid particles and reducing internal friction (fluidity).

Moreover, when SiO_2/Al_2O_3 molar ratio exceeded to 5.8, workability started to reduce gradually and flow values decreased from 251 mm to 213 mm. This reduction is attributed to the availability of reactive SiO_2 species, which promotes geopolymerization and increases gel network building rates [37]. The formation of geopolymeric



Figure 6. Geopolymer mortar specimens during curing to evaluate their compressive strength.

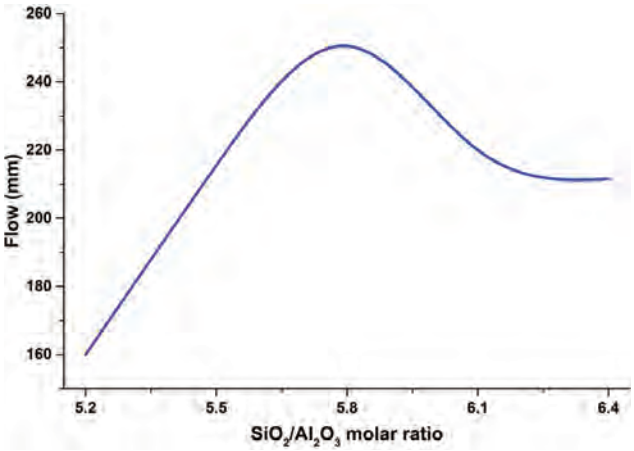


Figure 7. Effect of SiO_2/Al_2O_3 on the spread flow values of the prepared mortars.

gel occurs rapidly and entraps solid particles, which leads to increased viscosity and lower workability. These results highlight the fact that there exists an optimum range of SiO_2/Al_2O_3 ratios, beyond which excess silicate promotes initial setting and reduces fluidity due to excessive viscosity build-up of mortar [38]. Hence, the SiO_2/Al_2O_3 ratio play a significant role for balancing workability and geopolymer reactivity of alkali-activated systems [39].

This is shown in Figure 8, where partial substitution of BNP with MK reduces the workability of the mortars. The results show that flow values systematically change from 220 mm to 101 mm when the proportion of MK in the mixture increases. Such significant loss in workability is primarily originating from the unique morphological and physicochemical properties of MK, which as seen in Figure 4, possesses a microstructure that is plate-like with high specific surface area.

The layered structure of MK leads to an increased water retention capacity, as the fine particles tend to adsorb free water from the mixture, thereby reducing the effective water available for lubrication. In addition, the angular and rigid shapes of MK particles may allow for higher effective interparticle friction, which could contribute in decreasing flowability. The results in accordance with Hassani and Kazemian [40] findings that showed that the increase in red mud (RM) content in geopolymer mortar strongly reduced the flowability. At 50% RM substitution the spread diameter decreased by 57% (from 22 cm to 9.5 cm), which may be attributed to high surface area and water absorbent capacity of RM.

The results indicate that MK incorporation improves the mechanical and durability properties of geopolymeric mortars because of its high aluminosilicate reactivity. However, as far as excessive losses in workability are concerned, the dosage has to be properly optimized. Achieving a balance between improving mechanical performance and maintaining rheological stability remains as a significant challenge in the design of geopolymers, which highlights the importance of designing tailored mix designs to achieve satisfactory processability and long-term performance.

Setting Time

The setting time of geopolymer mixtures is highly affected by a number of factors, primarily the nature of reactive products generated from precursor materials. These properties include free calcium oxide (CaO) content, specific surface area, crystallinity degree and chemical composition and concentration of the activating solution [33, 41]. Free CaO promotes the development of reactive amorphous structures enhancing geopolymerization, while a high degree of crystallinity caused by the low solubility in a crystal structure leads to decreased reactivity.

Setting times (Initial and final) of the alkali-activated pastes employed in the present study are shown in Figure 9. The results showed that the setting times of BNP alkali-activated mixtures were substantially greater than their ordinary Portland cement (OPC) counterpart. Such a delay can be rationalized by the kinetics of the reactions during geopolymerization, which differs from that of conventional Portland cement hydration. Moreover, the final setting times were addressed as they extended over several days to depict a slow polymerization and gradual generation of inside rigidity. In contrast, the initial and final setting times of mixtures with partially replaced BNP with MK were reduced to 129 minutes and 291 minutes, respectively. This decrease is owed to the higher amount of Al_2O_3 reactive species from metakaolin, which encourages faster aluminosilicate dissolution. As a result, this increase in the chemical reactivity of the particles favour formation and condensation of the geopolymer gel, which reduces the setting time and increases initial cohesion of material.

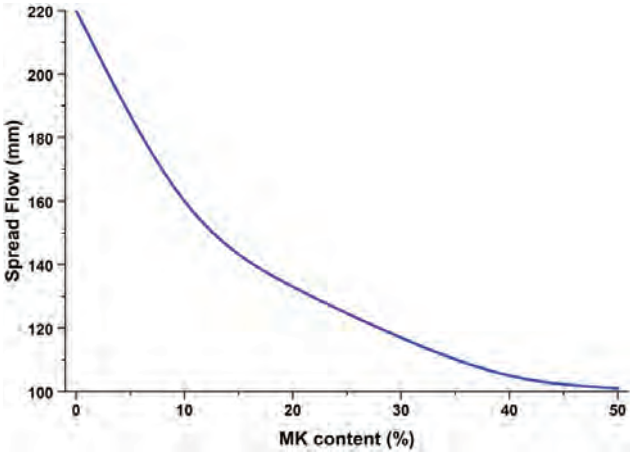


Figure 8. Effect of MK content on the spread flow values of the prepared mortars.

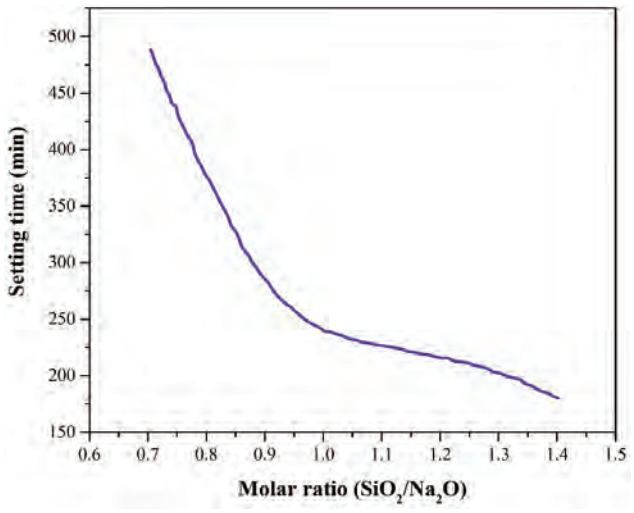


Figure 9. Effect of MK content on the initial and final setting time.

The observations aspects of determining geopolymerization kinetics, as well as the much-debated role of precursor characteristics and formulation parameters are encapsulated in these observations, which can both guide mixture optimization for workability as function of desired long-term performance.

According to Hamdi Oualid's doctoral thesis [42], two volcanic ashes from Djoungo, namely ZD and ZG (Galim), with CaO contents of 3.23% and 5.11%, respectively, were investigated to assess the effects of fineness and the SiO_2/Na_2O molar ratio on geopolymerization. Geopolymer samples prepared from ZD volcanic ash could only be manipulated after 14 days of curing time likely as a consequenceto its low free CaO content and lower fineness (2.3 m^2/g) in comparison with ZG (15.7 m^2/g) [43]. The kinetics of the geopolymerization reaction is largely influenced by particle fineness since a higher specific surface area allows for quicker dissolution of aluminosilicate species and more homogenous reactivity.

Furthermore, raising the SiO_2/Na_2O molar ratio from 0.7 to 1.4 decreased the setting time of ZG-based geopolymer paste from 490 min to 180 min, as shows Figure 10. This is consistent with the results documented by Lalitha et al. [18], who reported that a lower SiO_2/Na_2O ratio leads to prolonged setting time of blast furnace slag- based geopolymers. A higher SiO_2/Na_2O ratio leads to the generation of more reactive oligomeric structures and keeps intermediate products that obstruct polymerization [8]. In addition, Yankwa Djobo et al. [44] stated that mechanically activating volcanic ash decreases its degree crystallinity, dramatically speeds up the geopolymerization reaction and reduces by over 95% the setting time, after grinding for only 60 minutes. This acceleration is due to an increasing number of reactive sites, and therefore better interaction with the alkaline solution, thus accelerating ammonification of amorphous geopolymers.

The compressive strengths of geopolymer mortars at 14 and 28 days in terms of the SiO_2/Al_2O_3 molar ratio are shown in Figure 11. A strong direct correlation between the compressive strength of the geopolymer mortar and the SiO_2/Al_2O_3 molar ratio is observed. This behavior is related to the geopolymerization process, in which higher SiO_2 content leads to a more extensive three-dimensional aluminosilicate network being formed. The maximum compressive strength of 9.93 MPa was recorded for the highest SiO_2/Al_2O_3 molar ratio of 6.4, suggesting that beyond a certain limit, there is more silicate species available for optimal network polymerization. This improvement in mechanical strength was related to the improved availability of reactive SiO_2 provided by sodium silicate, which contributed dissolution of aluminosilicate precursors as well as incoherent oligomerization of silicate chains. This leads to a more compact and integer gel, able to give development at the mechanical execution. Therefore, the condensation process in geopolymerization is more favorable, resulting in a well-developed aluminosilicate framework with enhanced structural integrity.

On the other hand, specimens with mixture M-1 did not develop any significant compressive strength after 28 days of curing and they were brittle (Fig. 11). This lack of mechanical performance indicates the importance of silicate species during geopolymerization. This is mainly due to the presence of sodium hydroxide in an alkaline solution. Because NaOH is effective in dissolving the amorphous aluminosilicates in Bouhmidi pozzolan (BSP) but does not provide any additional silicate species, polycondensation reactions during hydration are incomplete. Consequently, a continuous aluminosilicate gel cannot be formed in which case a coherent geopolymeric matrix cannot develop. The inability of silicate to facilitate condensation of the dissolved species leads to precipitation of poorly polymerized

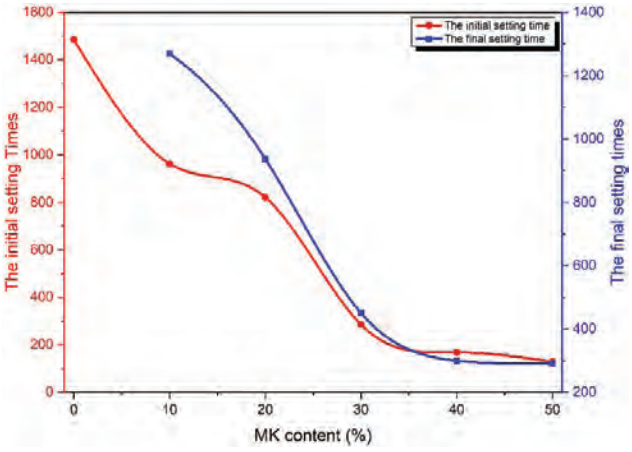


Figure 10. Effect of SiO_2/Na_2O molar ratio on the setting time [Adapted from Hamdi's doctoral thesis [42]. The thesis is openly accessible through the USTHB institutional repository: https://dspace.usthb.dz/handle/123456789/10212].

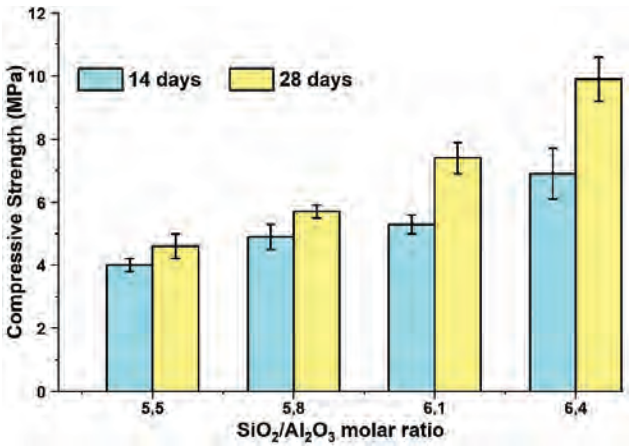


Figure 11. Effect of SiO_2/Al_2O_3 on the compressive strength of geopolymer mortars.

products that lack structural cohesion. This effectively prevents the last stage of the geopolymerization reaction taking place, resulting in mechanically unstable samples.

Figure 12 emphasizes the impact of metakaolin (MK) mass percentage on the compressive strength (CS) of the geopolymer mortars. In particular, this aluminate would massively change the geopolymerization kinetics and microstructural development of the hardened matrix when MK was used as a secondary aluminosilicate source. The incorporation of MK to replace BNP up to 40% by mass improved the compressive strength values of the binary systems with strengths approaching 24 MPa. Such enhancement is associated with the more rapid dissolution of MK when compared to BSP, which provides a larger amount of Al^{3+} and Si^{4+} species contributing to faster geopolymeric gel formation phases. On the contrary, the mortars incorporating MK in excess of 40% exhibited lower compressive strength. The decrease in mechanical performance relates to the high alumina content which disturbs the appropriate SiO_2/Al_2O_3 ratio required for obtaining a structured gel. Excess Al^{3+} ions trigger a marked viscosity decrease in the fresh paste, which can hinder the homogeneous dispersion of the reactants and reduce the extent of polycondensation. These findings are concurrent with the observation reported in Hamdi Oualid's doctoral thesis [42], who proposed that excess alumina (originated from MK) rapidly decreases the initial viscosity of the alkaline suspension because of its high reactivity. By lowering the viscosity, premature setting may occur which in itself could decrease the interaction time between aluminosilicate precursors and alkaline activators before setting occurs, having a final impact on mechanical strength development. This prompt response would likely not give the suspension enough time to sufficiently disperse the BNP particles, which would in turn detract from the mechanical strength of the geopolymeric pastes [45]. Additionally, Yankwa Djobo et al. [44] observed that, in the case of dissolution, MK particles react faster compared to their natural pozzolan equivalents. This difference in reactivity will then impact the microstructural development of the final geopolymer matrix as any excess MK present in the activator can lead to gel network heterogeneities and therefore unreacted residual particles. As a result, the degree of geopolymerization becomes more and more governed by the quantity of MK in the system [44].

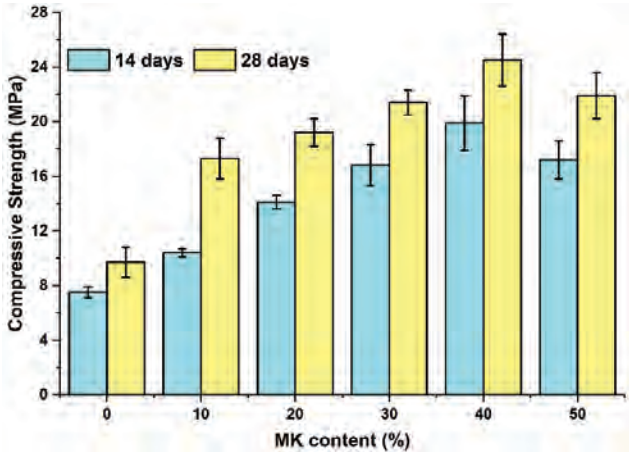


Figure 12. Effect of MK content on the compressive strength of geopolymer mortars.

Application and Broader Impact of the Findings on Geopolymer Mortars

This study describes the macro-mechanical behaviour of geopolymer mortars as a function of SiO_2/Al_2O_3 molar ratio and metakaolin (MK) replacement. These results have significant implications for sustainable construction materials, specifically related to Portland cement carbon footprints. The progressive increases of SiO_2/Al_2O_3 molar ratio are generally associated with higher compressive strength, thus underlining how silicate species should be taken into account for controlling the reaction degree. All the above data can be integrated to elaborate green substitutes to cement-based mortars based on high–performance polymeric binders. By manipulating the molar ratio and activator composition, engineers and materials scientists can create geopolymer blends with improved mechanical properties or durability.

Additionally, the study also highlights binary systems based on metakaolin potential. It was found that in mixes involving more than 40% MK, that partially substitutes Bouhmidi pozzolan (BSP), a higher compressive strength was reached (up to 24 MPa). This finding is particularly valuable for utilizing industrial by-products and natural pozzolans in geopolymer formulations, providing a feasible path for resource-efficient material design. However, further reductions in strength beyond this substitution limit suggest that the control of mix proportions is essential to avoid very high levels of alumina inhibiting polycondensation. In an application view these insights may be used in the precast elements manufacture as well as repair mortars and high-durability coatings for aggressive environments. In addition, a basic understanding of geopolymer chemistry could help optimize the various combinations based on maximum sustainable development with final mechanical performance in infrastructure.

Furthermore, these research findings are in accordance with global efforts to produce low carbon construction materials with reduced reliance on Portland cement [46]. Considering that the characteristic of Portland cement-based technologies actively limits circular economy, one potential solution consists of geopolymer mortars as they are versatile and can also be produced with industrial by-products. Future work can be oriented to study their robustness under real environmental conditions to validate their potential field scalability.

Statistical Analysis

A thorough statistical analysis using JMP 14 Pro was performed to model and predict the fresh (flow, setting time) and hardened (compressive strength) properties of the mortars (Fig. 13). The study was based on the methodology of central composite design, by varying the Si/Al molar ratio from 1.34 to 1.9 and the Si/Na molar ratio from 5.4 to 6,2. Regression models were used to examine parameter affects and optimize mix formulations for optimal performance.

The fitting results of the obtained models, developed to predict the studied responses using second-degree polynomial equations, indicate that the coefficient of determination (R^2) exceeds 0.85, as given in Table 4. This proves that the mathematical models provide a reliable prediction of the investigated responses. Moreover, as a confirmation of visual representation derived from fit plot, all root mean square error (RMSE) values are very low which indicates minimum mismatch between the predicted and experimental values. This confirms the reliability and validity of the models for predicting properties of mortars and in capturing both their effects.

Furthermore, the analysis of variance (ANOVA) for each of the modeled responses is presented in Table 5. For degrees of freedom df1=P−1=5 and df2=n−P=3, the

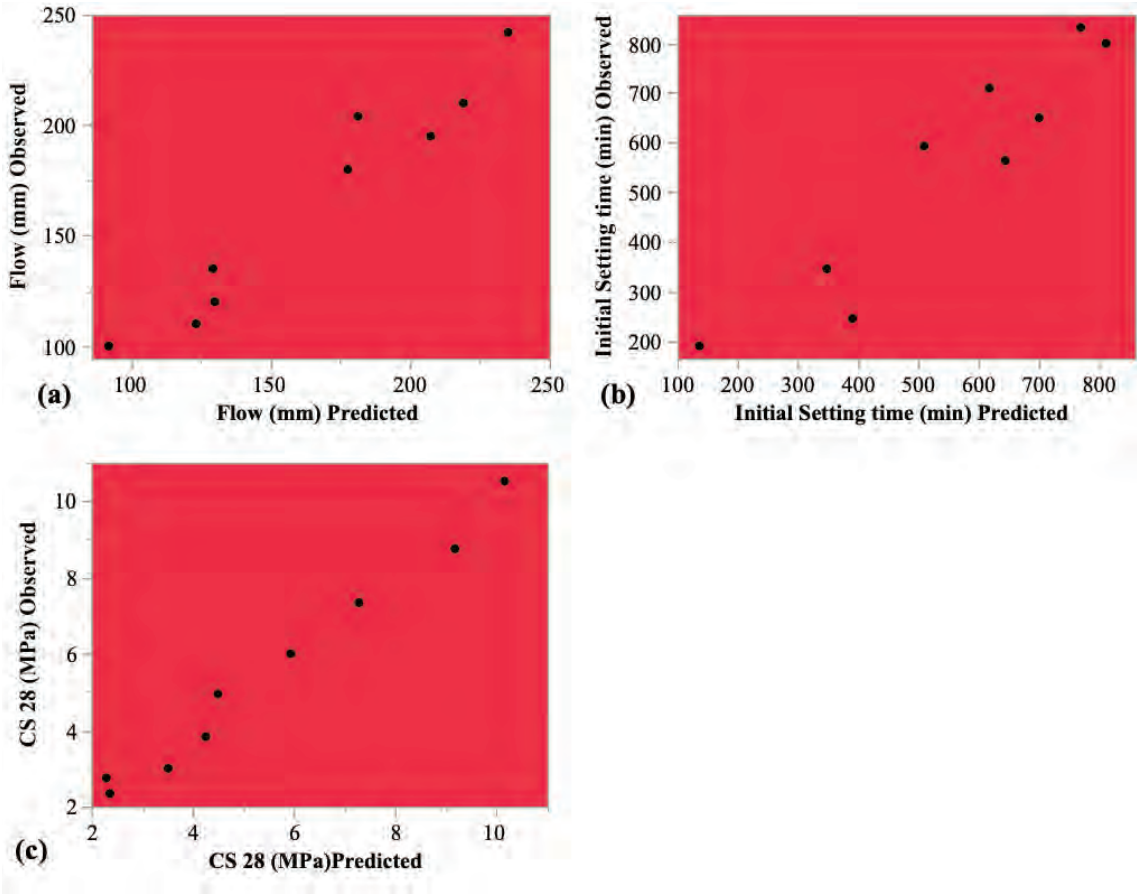


Figure 13. Measured versus predicted; (a) Flow, (b) time of initial setting (c) compressive strength at 14 and 28 days.

Table 4. Summary of the statistical analysis

Designation	Flow	Initial setting time	CS at 28 days
R^2	0.94	0.881697	0.982166
Adjusted R^2	0.85	0.684526	0.952441
Root-Mean-Square Error (RMSE)	19.79	132.361	0.62775
Mean response	166.22	547.6667	5.497778
Observations (or weighted sums)	9	9	9

Table 5. ANOVA analysis for the studied responses

	Source	df	Sum of squares	Mean square	F ratio
Flow	**Model**	5	391711.67	78342.3	4.4717
	Error	3	52558.33	17519.4	Prob. > F
	Uncorrected Total	8	444270.00		0.1238
Initial setting Time	**Model**	5	65.105744	13.0211	33.0427
	Error	3	1.182211	0.3941	Prob. > F
	Uncorrected Total	8	66.287956		0.0080*
CS at 28 days	**Model**	5	65.105744	13.0211	33.0427
	Error	3	1.182211	0.3941	Prob. > F
	Uncorrected Total	8	66.287956		0.0080*

p-values obtained are 0.1238 for flow, 0.0080 for initial setting time, and compressive strength. The Fisher F-values calculated for flow time and initial setting time, as well as compressive strength, are 132.52 and 7.88, respectively. In this case, df corresponds for the degrees of freedom, P is the number of coefficients in the model and n is the number of experiments performed. These p-values suggest the significance of models. A p-value under the threshold 0.05 points to a highly significant model as seen for the initial setting time and compressive strength (p=0.0080), whereas for flow; despite its low RMSE the p-value of this regression exceeds this limit indicating less statistical significance (0.1238). However, the Fisher F-values are higher than the critical F-values, confirming that the established models adequately describe the experimental data and can be used for response prediction.

Second-order polynomial equations were developed to predict the flow time, initial setting time, and compressive strength of the studied geopolymer mortars. These quations (1, 2, and 3) accurately describe the physical and mechanical properties of the mortars within the investigated range.

$$Flow\ (mm) = 219.11 + 28.66 \times \left(\frac{\frac{Si}{Na}-1.62}{0.28}\right) + 29 \times \left(\frac{\frac{Si}{Al}-5.80}{0.60}\right) + \left(\left(\frac{\frac{Si}{Na}-1.62}{0.28}\right) \times \left(\frac{\frac{Si}{Al}-5.80}{0.60}\right) \times 10\right) + \left(\left(\frac{\frac{Si}{Na}-1.62}{0.28}\right) \times \left(\frac{\frac{Si}{Na}-1.62}{0.28}\right) \times -12.66\right) + \left(\left(\frac{\frac{Si}{Al}-5.80}{0.6}\right) \times \left(\frac{\frac{Si}{Al}-5.80}{0.6}\right) \times -66.66\right) \quad (1)$$

$$I.S.T\ (mm) = 509.66 + -189.5 \times \left(\frac{\frac{Si}{Na}-1.62}{0.28}\right) + -148.16 \times \left(\frac{\frac{Si}{Al}-5.80}{0.60}\right) + \left(\left(\frac{\frac{Si}{Na}-1.62}{0.28}\right) \times \left(\frac{\frac{Si}{Al}-5.80}{0.60}\right) \times -92.5\right) + \left(\left(\frac{\frac{Si}{Na}-1.62}{0.28}\right) \times \left(\frac{\frac{Si}{Na}-1.62}{0.28}\right) \times 70.5\right) + \left(\left(\frac{\frac{Si}{Al}-5.80}{0.6}\right) \times \left(\frac{\frac{Si}{Al}-5.80}{0.6}\right) \times -13.50\right) \quad (2)$$

$$CS\ 28\ (MPa) = 5.93 + 0.49 \times \left(\frac{\frac{Si}{Na}-1.62}{0.28}\right) + 2.94 \times \left(\frac{\frac{Si}{Al}-5.80}{0.60}\right) + \left(\left(\frac{\frac{Si}{Na}-1.62}{0.28}\right) \times \left(\frac{\frac{Si}{Al}-5.80}{0.60}\right) \times 0.455\right) + \left(\left(\frac{\frac{Si}{Na}-1.62}{0.28}\right) \times \left(\frac{\frac{Si}{Na}-1.62}{0.28}\right) \times -1.93\right) + \left(\left(\frac{\frac{Si}{Al}-5.80}{0.6}\right) \times \left(\frac{\frac{Si}{Al}-5.80}{0.6}\right) \times 1.27\right) \quad (3)$$

Figure 14 illustrates the evolution of flow spread, setting time and compressive strength of the studied geopolymers as a function of the Si/Na and Si/Al ratios. It is observed from the flow spread results that low Si/Al ratios combined with increasing Si/Na ratio leads to a slight increase in flow spread from 0.92 mm to 136.7 mm. This trend can be explained by a decrease in interparticle interactions and more effective dispersion of particles into the alkaline matrix, resulting in an increase in fluidity of the mixture. At higher Si/Al ratios, a more significant increase in flow spread (up to 241 mm) caused by the increasing Si/Na ratio was observed. This behaviour can be associated with structural changes of the geopolymer gel since, at high concentration of silicates, the formation of long-chain and less cross-linked aluminosilicate chains is enhanced. This

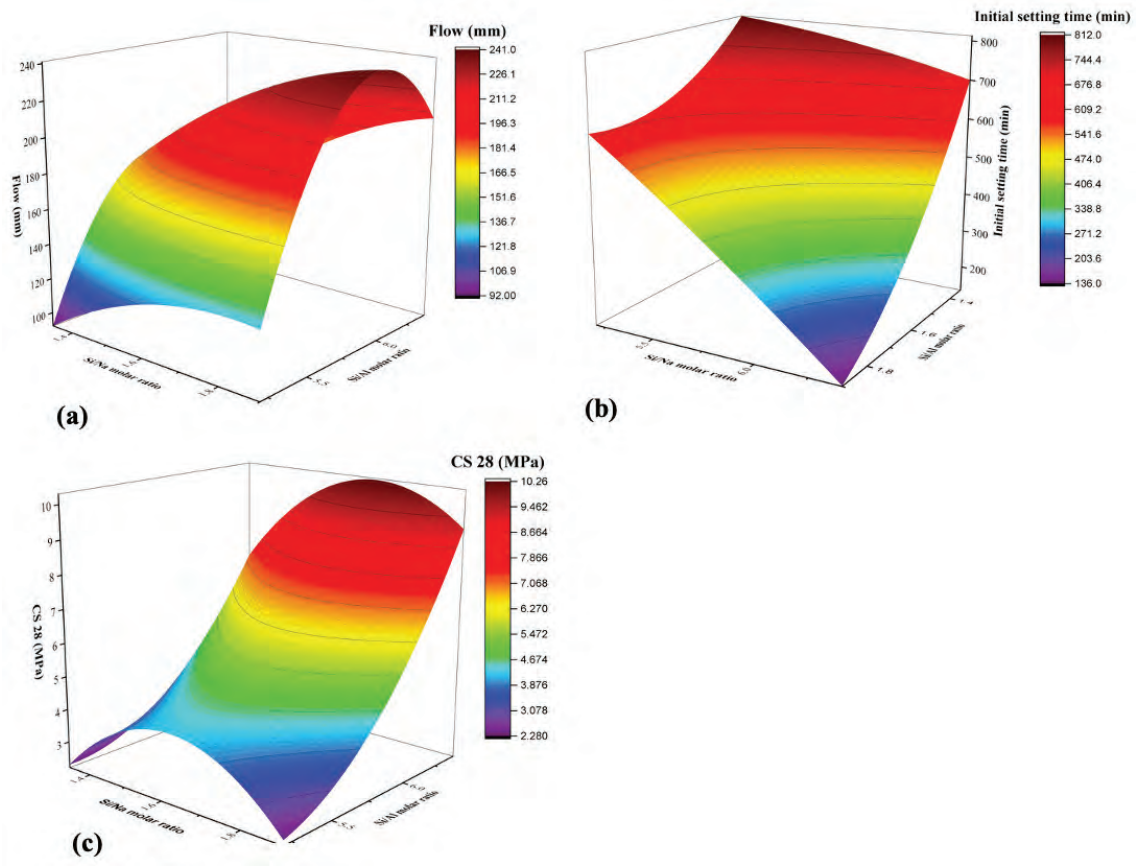


Figure 14. Surface response of studied mortars (a) flow; (b) Initial setting time and (c) Compressive strength at 28 days.

changes the structure of the paste and reduces its viscosity, which makes it more workable.

Conversely, the setting time results indicate that at low Si/Al ratios, an increase in the Si/Na ratio leads to a significant reduction in the initial setting time, decreasing from 812 minutes to 136 minutes. The increase in sodium ions facilitates the solubilization process of aluminosilicate precursors, leading to faster geopolymerization reactions and accelerated setting. But with the increase of Si/Al ratio, the setting retardation effect is less significant. This may be attributed to the increased availability of silicate species for geopolymeric integration and development of a more ordered and crosslinked network. The denser network reduces both the mobility of ions and the reaction rate, which counteracts with Na on setting time reduction. Figure 14. c indicates that the compressive strength of mortars increased from 2 MPa to 10 MPa as the Si/Al ratio increased. The higher Si/Al ratio facilitates the polymerization and densification of the geopolymeric matrix, which leads to a more cross-linked and denser aluminosilicate network that improves mechanical performance.

The Si/Na ratio initially increases compressive strength (CS), but then the values drop subsequently. This trend can be attributed to the twofold action of sodium ions in the geopolymerization process. At medium Si/Na ratios sodium, even at low levels, functions as an activator producing the dissolution of the precursor and a more compact microstructure which increases strength. At a higher Si/Na ratio, an excess of sodium can lead to the formation of unreacted or weakly bonded silicate phases, increasing porosity and reducing the overall mechanical performance of the mortars.

CONCLUSION

This study provides important information on the performance of geopolymer mortars, highlighting the effect of SiO_2/Al_2O_3 molar ratio and the addition of metakaolin (MK) as a partial replacement for natural pozzolan (BNP). The following key observations were made:

1. The compressive strength (CS) of geopolymer mortars increases significantly with the increase in SiO_2/Al_2O_3 molar ratio, which reaches a maximum value of 9.93 MPa at a molar ratio greater than 6.4
2. Higher reactivity of MK is possibly responsible for 40% replacement, resulting in the CS values as high as 24 MPa.

3. The replacement more than 40%, the strength from MK was decreased, which demonstrates that its receding firiability may not be complete and so it loses initial viscosity.
4. MK can play a crucial role in substituting Portland Cement in geopolymer formulations, which could promote sustainable construction.
5. The Central Composite Design (CCD) method statistical analysis explains a good association between experimental and predicted values. The RMSE of flowability, setting time and CS at 28 days were 0.88, 0.94, 0.98, respectively, which confirms the accuracy of predictive models as high-quality data with negligible error for a regression problem using machine learning for all the considered parameters in this research. In addition, p-values for flowability, setting time and CS were 0.010, 0.0008 and 0.0008, respectively, substantiate statistical significance of the models as well. The results corroborate the robustness of the validated models, as they were able to very precisely predict the three responses studied.

In the future aspect, proper designed and pattern of processing parameters needs to be optimized for fine performance in geo polymer mortars as construction materials.

AUTHORSHIP CONTRIBUTIONS

Authors equally contributed to this work.

DATA AVAILABILITY STATEMENT

The authors confirm that the data that supports the findings of this study are available within the article. Raw data that support the finding of this study are available from the corresponding author, upon reasonable request.

CONFLICT OF INTEREST

The authors declared no potential conflicts of interest with respect to the research, authorship, and/or publication of this article.

ETHICS

There are no ethical issues with the publication of this manuscript.

STATEMENT ON THE USE OF ARTIFICIAL INTELLIGENCE

Artificial intelligence was not used in the preparation of the article.

REFERENCES

[1] Kabay N, Mıyan N. A comparative study on the physical and mechanical properties of alkali activated materials. Sigma J Eng Nat Sci 2020;38:649–658.

[2] Naik T. Sustainability of the cement and concrete industries in sustainable construction materials and technologies. Boca Raton: CRC Press; 2020.

[3] Malhotra V. Making concrete greener with fly ash. Concr Int 1999;21:61–66.

[4] Rangan B. Fly ash based geopolymer concrete. Research report GC 4. Perth (Australia): Curtin University of Technology, Engineering Faculty; 2008. [CrossRef]

[5] Moinul M, Saiful M. Strength behaviour of mortar using fly ash as partial replacement of cement. Concr Res Lett 2010;1.

[6] Gao T, Shen L, Shen M, Liu L, Chen F, Gao L. Evolution and projection of CO2 emissions for China's cement industry from 1980 to 2020. Renew Sustain Energy Rev 2017;74:522–537. [CrossRef]

[7] Douadi A, Hebbache K, Boutlikht M, Tabchouche S, Belebchouche C, Hammouche R, et al. Physical and mechanical effects of silica sand in cement mortars: experimental and statistical modeling. Materials (Basel) 2023;16:6861. [CrossRef]

[8] Polat BY, Uysal M, Korkmaz V. A research for bacterial self-healing in metakaolin based geopolymer mortars. Sigma J Eng Nat Sci 2020;38:1401–1414.

[9] Del Serrone G, Moretti L. A stepwise regression to identify relevant variables affecting the environmental impacts of clinker production. J Clean Prod 2023;398:136564. [CrossRef]

[10] Liao S, Wang D, Xia C, Tang J. China's provincial process CO2 emissions from cement production during 1993–2019. Sci Data 2022;9:165. [CrossRef]

[11] Davis SJ, Caldeira K. Consumption-based accounting of CO2 emissions. Proc Natl Acad Sci U S A 2010;107:5687–5692. [CrossRef]

[12] Bilodeau A, Malhotra VM. High-volume fly ash system: concrete solution for sustainable development. ACI Mater J 2000;97:41–48. [CrossRef]

[13] Kılkış Ş, Krajačić G, Duić N, Rosen MA. Effective mitigation of climate change with sustainable development of energy, water and environment systems. Elsevier; 2022. p. 116–146. [CrossRef]

[14] Bengal SN, Ghodmare S, Nayak CB, Tomar A. Organic admixtures as additive: an initiative to reduce carbon dioxide emission due to concrete. Macromol Symp 2024. [CrossRef]

[15] Kumar R, Dhaka J. Review paper on partial replacement of cement with silica fume and its effects on concrete properties. Int J Technol Res Eng 2016;4.

[16] Davidovits J. Geopolymers: ceramic-like inorganic polymers. J Ceram Sci Technol 2017;8:335–350.

[17] Alioui H, Chiker T, Saidat F, Lamara M, Aggoun S, Hamdi OM. Investigation of the effect of commercial limestone on alkali-activated blends based on Algerian slag-glass powder. Eur J Environ Civ Eng 2022;26:8049–8072. [CrossRef]

[18] Lalitha G, Kumar S, Ravali G, Santhosh M, Dileep M. An experimental study on strength parameters of OPC, PPC and geopolymer mortars. Management 2022;9:21–28.
[19] Warid Wazien A, Al Bakri AM, Abd Razak R, Mohd Arif Zainol MRR, Mohd Tahir MF, Kamarudin H. Potential of geopolymer mortar as concrete repairing materials. Mater Sci Forum 2016. [CrossRef]
[20] Hardjito D. Strength and setting times of low calcium fly ash-based geopolymer mortar. Mod Appl Sci 2009. [CrossRef]
[21] Zhuang XY, Chen L, Komarneni S, Zhou CH, Tong DS, Yang HM, et al. Fly ash-based geopolymer: clean production, properties and applications. J Clean Prod 2016;125:253–267. [CrossRef]
[22] Luhar I, Luhar S. A comprehensive review on fly ash-based geopolymer. J Compos Sci 2022;6:219. [CrossRef]
[23] Wattimena OK, Antoni, Hardjito D. A review on the effect of fly ash characteristics and their variations on the synthesis of fly ash based geopolymer. AIP Conf Proc 2017. [CrossRef]
[24] Yadav AL, Sairam V, Srinivasan K, Muruganandam L. Synthesis and characterization of geopolymer from metakaolin and sugarcane bagasse ash. Constr Build Mater 2020;258:119231. [CrossRef]
[25] Sellami M, Barre M, Toumi M. Synthesis, thermal properties and electrical conductivity of phosphoric acid-based geopolymer with metakaolin. Appl Clay Sci 2019;180:105192. [CrossRef]
[26] Guo CM, Wang KT, Liu MY, Li XH, Cui XM. Preparation and characterization of acid-based geopolymer using metakaolin and disused polishing liquid. Ceram Int 2016;42:9287–9291. [CrossRef]
[27] Davidovits J. Geopolymers: inorganic polymeric new materials. J Therm Anal Calorim 1991;37:1633–1656. [CrossRef]
[28] Davidovits J. Properties of geopolymer cements. In: Proceedings of the First International Conference on Alkaline Cements and Concretes; 1994.
[29] Shi Z, Shi C, Zhao R, Wan S. Comparison of alkali-silica reactions in alkali-activated slag and Portland cement mortars. Mater Struct 2015;48:743–751. [CrossRef]
[30] Hardjito D, Wallah SE, Sumajouw DM, Rangan BV. Fly ash-based geopolymer concrete. Aust J Struct Eng 2005;6:77–86. [CrossRef]
[31] Djobo JNY, Elimbi A, Tchakouté HK, Kumar S. Volcanic ash-based geopolymer cements/concretes: the current state of the art and perspectives. Environ Sci Pollut Res Int 2017;24:4433–4446. [CrossRef]
[32] Komnitsas K, Zaharaki D. Geopolymerisation: a review and prospects for the minerals industry. Miner Eng 2007;20:1261–1277. [CrossRef]
[33] Bondar D, Lynsdale C, Milestone NB, Hassani N, Ramezanianpour AA. Effect of type, form, and dosage of activators on strength of alkali-activated natural pozzolans. Cem Concr Compos 2011;33:251–260. [CrossRef]
[34] European Committee for Standardization. Methods of test for mortar for masonry-Part 3: Determination of consistence of fresh mortar (by flow table). EN 1015–13. 1999.
[35] Romanian Standards Association. Methods of testing cement-Part 3: Determination of setting time and stability. EN 196–3. Bucharest (Romania): Romanian Standards Association; 2016.
[36] AFNOR. Methods of testing cement-Part 1: Determination of strength. EN 196–1. Paris (France): AFNOR; 2016.
[37] Han Q, Zhang P, Wu J, Jing Y, Zhang D, Zhang T. Comprehensive review of the properties of fly ash-based geopolymer with additive of nano-SiO2. Nanotechnol Rev 2022;11:1478–1498. [CrossRef]
[38] Khale D, Chaudhary R. Mechanism of geopolymerization and factors influencing its development: a review. J Mater Sci 2007;42:729–746. [CrossRef]
[39] Madirisha MM, Dada OR, Ikotun BD. Chemical fundamentals of geopolymers in sustainable construction. Mater Today Sustain 2024;27:100842. [CrossRef]
[40] Hassani A, Kazemian F. Investigating geopolymer mortar incorporating industrial waste using response surface methodology: a sustainable approach for construction materials. Case Stud Constr Mater 2024;21. [CrossRef]
[41] Temuujin J, van Riessen A, Williams R. Influence of calcium compounds on the mechanical properties of fly ash geopolymer pastes. J Hazard Mater 2009;167:82–88. [CrossRef]
[42] Hamdi OM. Etude du comportement mécanique et rhéologique des géopolymères à base de mélange pouzzolane-métakaolin algériens [dissertation]. Algiers (Algeria): University of Science and Technology Houari Boumediene; 2024. Available at: https://dspace.usthb.dz/handle/123456789/10212]. Accessed October 20, 2026.
[43] Weng L, Sagoe-Crentsil K, Brown T, Song S. Effects of aluminates on the formation of geopolymers. Mater Sci Eng B 2005;117:163–168. [CrossRef]
[44] Yankwa Djobo JN, Elimbi A, Tchakouté HK, Kumar S. Mechanical activation of volcanic ash for geopolymer synthesis: effect on reaction kinetics, gel characteristics, physical and mechanical properties. RSC Adv 2016;6:39106–39117. [CrossRef]
[45] Kouamo HT, Elimbi A, Mbey J, Sabouang CN, Njopwouo D. The effect of adding alumina-oxide to metakaolin and volcanic ash on geopolymer products: a comparative study. Constr Build Mater 2012;35:960–969. [CrossRef]
[46] Aygörmez Y. Sulfate and chloride resistance of bottom ash doped slag-based geopolymer composites. Sigma J Eng Nat Sci 2023;41:288–301. [CrossRef]

Sigma J Eng Nat Sci, Vol. 44, No. 4, pp. 2952–2962, August, 2026

Sigma Journal of Engineering and Natural Sciences
Web page info: https://sigma.yildiz.edu.tr
DOI: 10.14744/sigma.2026.2137

Research Article

Optimization of geogrid reinforcement for improving CBR of subgrade soils

M. Bharath CHANDRA[1], Kadali SRINIVAS[1], V. Ramya KRISHNA[1,*]

[1]*Department of Civil Engineering, VNR Vignana Jyothi Institute of Engineering and Technology, Hyderabad, 500118, India*

ARTICLE INFO

Article history
Received: 22 March 2025
Revised: 12 April 2025
Accepted: 05 May 2025

Keywords:
California Bearing Ratio; Geogrid Reinforcement; HDPE Geogrid; Liquid Limit; Maximum Dry Density; Optimum Moisture Content; Subgrade Soil

ABSTRACT

Weak subgrade soils can adversely affect pavement performance by reducing the load-bearing capacity of the foundation and increasing the possibility of deformation under traffic loading. This study investigates the use of geogrid reinforcement for improving the California Bearing Ratio (CBR) of different subgrade soils. Sixteen soil samples representing highly compressible clay, intermediate compressible clay, low compressible clay, and sandy soils were examined. Natural and synthetic geogrids, including coir, jute, rubber coir, polyester, biaxial polypropylene, biaxial geogrid, and HDPE geogrids, were evaluated at different depths within the CBR mould. The influence of the optimum moisture content, maximum dry density and liquid limit on the reinforced and unreinforced CBR values was also examined. The results show that geogrid reinforcement generally improves the CBR of the tested soils, although the extent of improvement varies with the soil type, reinforcement material, and placement depth. A placement depth of 0.8h produced considerable improvement for several soil samples. The highest CBR value of 12.8% was obtained for sandy soil reinforced with HDPE geogrid at a depth of 0.8h. The study also indicates that higher maximum dry density is generally associated with improved CBR, whereas excessive moisture can reduce soil strength. The findings demonstrate that selecting the appropriate geogrid and its placement depth can improve subgrade performance and may contribute to more economical pavement construction.

Cite this article as: Chandra MB, Srinivas K, Krishna VR. Optimization of geogrid reinforcement for improving CBR of subgrade soils. Sigma J Eng Nat Sci 2026;44(4):2952–2962.

INTRODUCTION

The subgrade forms the foundation of a road or pavement system and supports the layers placed above it, including the subbase and base. The subgrade's the condition has a direct influence on the perofcement and service life of the pavement. Therefore, the subgrade needs adequate strength, bearing capacity, and stability to withstand traffic loads as well as changes caused by weather and environmental conditions [1]. Problems in the subgrade can develop because of poor compaction, inadequate drainage, weak soil, variations in moisture content, or excessive moisture [2, 3]. These conditions may eventually result in pavement defects such as cracking, potholes, and surface erosion [4]. Identifying the factors responsible for subgrade failure is therefore

***Corresponding author.**
*E-mail address: ramyakrishna_v@vnrvjiet.in

This paper was recommended for publication in revised form by Editor-in-Chief Ahmet Selim Dalkilic

Published by Yıldız Technical University Press, İstanbul, Turkey
© Author. This is an open access article under the CC BY-NC license (http://creativecommons.org/licenses/by-nc/4.0/).

important for selecting suitable remedial measures and reducing the possibility of similar failures in the future [5]. There are several ways to increase the strength and stability of the subgrade to avoid failure, namely mechanical stabilization and chemical stabilization [6]. One of the studies explains the combination of fly ash and lime that has the ability to enhance the mechanical properties of weak soil, such as kaolin soil. [7, 8]. Even the by-product of cutting and polishing of stone slabs, called rock sludge dust, is used in the construction of low-volume roads [9, 10]. One of the non-biodegradable materials, like waste plastic sheets, is also employed to improve the CBR% of the weak soils [11, 12]. The incorporation of Autoclaved aerated concrete powder, a lightweight and porous waste material, improved the workability of several clayey soils [13, 14]. However, each of these methods is associated with some limitations, such as soil compatibility, environmental impact, cost, material availability, and equipment transportation [15]. To minimize these limitations, an alternative method is adopted and it is geogrid reinforcement, which is a highly effective technique used to enhance the performance and stability of subgrade layers in pavement and road construction [16, 17]. Geogrids are polymer materials consisting of a connected mesh-like structure, which reinforces the subgrade soil. To achieve better pavement performance, geogrids are used, as they improve the load-carrying capacity of subgrade [18]. Reinforcing the soil helps distribute the applied loads over a wider area, reduce deformation, and improve the stability and tensile resistance of the subgrade [19]. Even geogrids are combined with geotextiles to improve the subgrade strength [20], and combining the geogrid and polypropylene fibres significantly increases the shear strength of expansive subgrades [21]. If the subgrade strength is low, then road pavement failure occurs [22]. To find the strength of the subgrade soil, the most common method used is the CBR test. CBR test measures the soil's resistance to penetration under a standard load [23]. Achieving a subgrade with a CBR of at least 10 is essential, as values below this can cause deformation and deterioration of the subbase under traffic loads [24]. The stability of the subgrade is improved by geogrid reinforcement, which increases the CBR value, and they are highly versatile & can be easily installed in any weather [25, 26]. The previous studies that involved the use of geogrid in improving the CBR% and shear strength of subgrade soils were limited to only one type of soil study, with the placement of geogrid at the optimum position. Previous research has also not explained the compatibility of the type of geogrid with the particular soil and how the soil properties will affect the CBR%.

The main objective of the study is to find the compatibility of various types of geogrids for specific soil types. For this, 16 soil samples were analysed and classified according to their compressibility. The soil samples considered for this study are highly compressible clay (CH), Intermediate compressible clay (CI), Low compressible clay (CL), Silty sand, and sandy soils. Different types of geogrids were used for reinforcing the above soil samples. The application of various geogrid types in reinforcing the soil samples resulted in an exceptional 498% increase in CBR that is observed in the case of sandy soils reinforced with HDPE geogrid at a depth of 0.8h, far exceeding the 50–200% improvements documented in previous studies. These results indicate that geogrid reinforcement can provide an effective approach for improving weak subgrade soils. The findings may also support the development of more practical and economical soil reinforcement methods for future geotechnical engineering applications.

The bubble map provided in Figure 1 visualizes the contribution of different countries across the globe regarding geogrid reinforcement to enhance subgrade strength studies. This map features countries like India, the United States, China, Australia, Japan, the United Kingdom, and many others. The countries with more research work in the present area are represented in large bubbles, and the countries with smaller bubbles represent that their contributions to this study are limited.

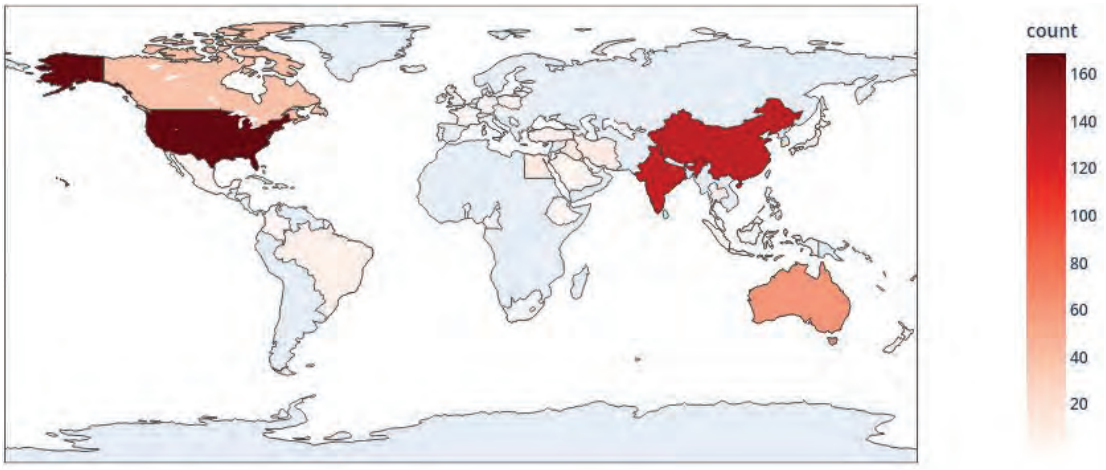


Figure 1. Pictorial representation of subgrade strength studies across various countries.

MATERIALS AND METHODS

Soils

To investigate the engineering behaviour and variation of CBR% of various soils, sixteen soil samples designated as S1 to S16 from different regions were used for this study. The locations of the soil samples that were taken are shown in Table 1. Soil properties such as MDD, OMC, and LL were determined through laboratory tests. The samples were categorized based on their LL. LL>50% is classified as highly compressible clays (CH), 50%>LL>35% as intermediate compressible clays (CI), and LL<35% as low compressible clays (CL). The classification and detailed properties are presented in Table 2.

Table 1. Locations of the soil samples

Soil Sample	Location
S1	Alappuzha District
S2	Lalitpur
S3	Vaddeswaram
S4	Pulivendula
S5	Kovilpatti
S6	Alappuzha District
S7	Ranchi
S8	Narsapur
S9	Coimbatore
S10	Chitrakoot district
S11	Trivandrum
S12	Gulbarga District
S13	Ambala Region
S14	Ludhiana
S15	Tripura
S16	Najaf City

Geogrid Reinforcement

In the present study, two categories of geogrids are used. One is natural geogrids, and the other is synthetic geogrids. Natural geogrids are bio-based reinforcement materials that are made up of organic and biodegradable fibers such as coir, jute, etc. Synthetic geogrids are made from polymeric materials such as polypropylene, polyester, etc. The features and performance of these geogrids are given in Table 3.

To analyse the optimum depth of geogrid placement in the CBR mold and to identify the most suitable geogrid for reinforcing the particular soil sample, natural, welded, and extruded geogrids were utilized to enhance the CBR% in the analysis. The geogrids used to reinforce the respective soils, along with their tensile strength, are presented in Table 4.

Sixteen soil samples were considered and distributed based on their liquid limit and compressibility. So, the soils are divided into highly compressible clays (S1 to S4), intermediate compressible clays (S5 to S10), low compressible clays (S11 to S14), and sandy soil (S15 to S16) categories. The soil samples are distributed in such a way that every geogrid that falls under synthetic and natural materials is used in all 4 classified soil samples.

For CH soils with low CBR, high-strength geogrids were required, such as polyester (200kN/m) and polypropylene

Table 2. Classification and properties of different soil samples

S. No.	L.L (%)	P. L (%)	P. I (%)	MDD (g/cc)	OMC (%)	Classification
S1	105	38	67	1.2	29	CH
S2	83	38	45	1.10	22.5	
S3	60	31	29	1.67	18	
S4	52.1	33.5	17	1.78	16.6	
S5	48.8	43.4	5.35	1.85	13	CI
S6	47.5	27.6	19.8	1.78	14.15	
S7	43.2	31.5	11.6	1.66	24.7	
S8	41	28	13	1.51	21	
S9	40.8	20	20.8	1.8	16	
S10	37.3	23.1	14.1	1.87	14.5	
S11	34.9	23.4	11.5	1.54	24	CL
S12	32.8	21.1	11.7	2.08	9.8	
S13	32.5	20	12.5	1.86	14	
S14	28	15	13	1.70	16	
S15	-	-	-	2	11.08	Silty Sand
S16	-	-	-	1.73	9.52	Sand

Table 3. Comparison of natural and synthetic geogrids based on key features and performance parameters

Feature	Natural Geogrids	Synthetic Geogrids
Material	Coir, jute, rubberized fibres	Polypropylene (PP), Polyester (PET), HDPE
Tensile Strength	Moderate (≈ 50 kN/m)	High (100–200+ kN/m)
Durability	Degrades over time, especially in wet soils	Long-lasting, resistant to chemical and biological decay
Moisture Sensitivity	Absorbs water; can weaken in soaked conditions	Water-resistant
Environmental Impact	Biodegradable and eco-friendly	Non-biodegradable (but durable)
Cost	Lower (locally available)	Higher (imported or processed materials)
Best Suited For	CI and CL soils in low-traffic areas	All soil types, including CH and sand

Table 4. Types of geogrids used for different types of soils

Soils		Geogrid		
Designation used for soils	**Soil type**	**Designation used for Geogrids**	**Geogrid type**	**Tensile strength (kN/m)**
S1	CH	RCG	Rubber Coir	50
S2		PG	Polyester	200
S3		BPP	Biaxial Polypropylene	100
S4	CI	BG	Biaxial	100
S5		BPP	Biaxial Polypropylene	100
S6		JG	Jute	50
S7		BPP	Biaxial Polypropylene	100
S8		PG	Polyester	200
S9	CL	PG	Polyester	200
S10		BG	Biaxial	100
S11		CG	Coir	50
S12		BPG	Biaxial polyester	200
S13		PG	Polyester	200
S14		BPP	Biaxial Polypropylene	100
S15	Silty Sand	BG	Biaxial	100
S16	Sand	HDPE	High-Density Polyethylene	200

geogrids. For CI soils with better shear strength, synthetic and natural geogrids were used because the soil isn't too weak, and natural geogrids were used to make eco-friendly options viable. For CL soils with higher CBR, low-strength geogrids were used. Natural geogrids, such as coir geogrids, were used to support eco-friendly experimental approaches. For sandy soils whose plasticity is low & CBR is high, geogrids are required to maintain the structure and load-carrying capacity properly. Geogrids like HDPE and Biaxial were used because of their excellent performance in sandy soils.

Geogrid Placement Strategy

In the design of the pavement to evaluate the subgrade soil load-carrying capacity, one of the most important tests to be performed is the California Bearing Ratio Test (CBR). The soil samples were collected and brought to the laboratory for testing. The soil of weight 5 kgs passed through a 4.75mm sieve, blended with the optimum water content that is obtained from the Standard Proctor test, and the moisture-conditioned soil was compacted to a specific density in a standard mold of a diameter of 152.4 mm and height of 177.8 mm. The soil was compacted into 5 layers; each layer was compacted to a predetermined number of blows of 55 with the help of a 4.89kg rammer, and the compacted soil was soaked in water for 96 hours to simulate the worst-case scenarios, such as rainfall and flooding. The CBR values of soaked conditions are generally lower compared to unsoaked conditions, highlighting the enhanced performance achieved through geogrid reinforcement. The geogrids were positioned at four different depths, 0.8h, 0.6h, 0.4h, and 0.2h in the mould from bottom to top as shown in Figure 2. The CBR test was done for both unreinforced and reinforced soil samples in soaked conditions by following codal provisions [27].

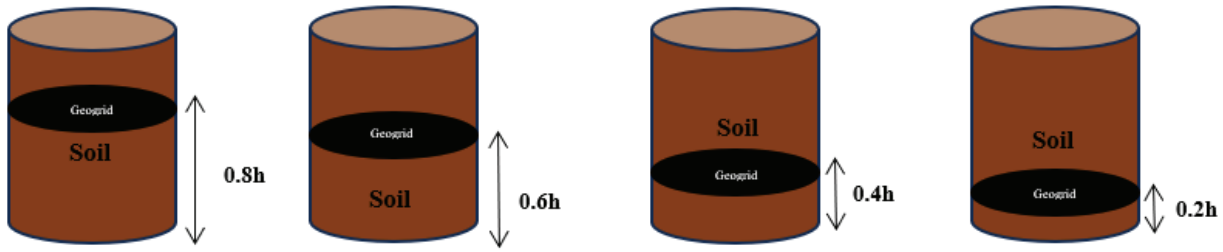


Figure 2. Placement of geogrid at various depths in the CBR mould.

The CH soil samples S1–S4 were reinforced with various welded and extruded geogrids, such as RCG, PG, BPP & BG geogrids. The soil samples S5- S10 are CI soils that were reinforced with various welded and extruded geogrids, such as BPP, PG, BPG &JG geogrids. The soil samples S11-S14 are CL soils reinforced with various welded and extruded geogrids, such as RCG, PG, BG, & BPP geogrids. The last two samples, S15 and S16, were sands that are reinforced with BG & HDPE geogrids.

RESULTS AND DISCUSSION

The results of CBR tests employing different types of geogrids positioned at varying depths on various soil samples are displayed in Table 5.

Effect of Geogrid Reinforcement at Various Depths on CBR%

The results of CBR tests performed on the 16 soil samples reinforced with various geogrids are shown in Figure 3.

To understand the influence of geogrid reinforcement on CBR% for various soil samples when they are reinforced at various depths (0.2h, 0.4h, 0.6h, 0.8h) is shown in Figure 3. From the graph, it is observed that the highest increase in CBR% was observed in sandy soil reinforced with HDPE geogrid placed in the S16 soil sample, which was observed to increase from 4.12% at 0.2 h depth to 12.8% at 0.8 h depth. The reason is that sandy soils do not retain water like cohesive soils; hence, they don't undergo swelling, shrinkage, and volume changes. Additionally, sandy soils allow better compaction, which leads to higher maximum

Table 5. CBR% for the soil samples

Types of soils	S. No	CBR %				
		Unreinforced case	Reinforced case (Depth of reinforcement from Bottom of CBR mould)			
			0.2h	0.4h	0.6h	0.8h
CH	S1-RCG	3.02	3.94 (30.4%)	4.46 (47.6%)	5.28 (74.8%)	5.73 (89.7%)
	S2-PG	0.89	1.01 (13.4%)	1.26 (41.5%)	2.27 (155.0%)	-
	S3-BPP	2.8	3.0 (7.1%)	5.7 (103.5)	6.9 (146.4%)	8.7 (210.7%)
	S4-BG	1.69	1.8 (6.5%)	2.5 (47.9%)	3.91 (131.3%)	-
CI	S5-BPP	1.38	3.93 (184.7%)	4.68 (239.1%)	4.35 (215.2%)	-
	S6-JG	3.13	4.02 (28.4%)	5.36 (71.2%)	6.7 (114%)	7.15 (128.4%)
	S7-BPP	2.5	2.7 (8%)	3.2 (28%)	5.6 (124%)	9.2 (268%)
	S8-PG	2.90	5.15 (77.5%)	5.37 (85.1%)	5.62 (93.7%)	5.96 (105.5%)
	S9-PG	1.2	1.6 (33.3%)	2.67 (116.6%)	4.17 (247.5%)	-
	S10-BG	3.83	3.31 (-13.5%)	4.01 (4.6%)	4.18 (9.13%)	5.23 (36.5%)
CL	S11-CG	3.25	1.59 (-51%)	3.99 (22.7%)	6.39 (96.6%)	-
	S12-BPG	6.8	7 (2.9%)	7.2 (5.8%)	10.2 (50%)	9.5 (39.7%)
	S13-PG	3.12	-	3.28 (5.1%)	6.14 (96.7%)	8.17 (161.8%)
	S14-BPP	2.9	3.16 (8.96%)	5.8 (96.5%)	7.2 (148.2%)	9.4 (224.1%)
Silty Sand	S15-BG	4.65	7.73 (66.2%)	8.02 (72.4%)	8.5 (82.7%)	10.2 (119.3%)
Sand	S16-HDPE	2.14	4.12 (92.52%)	6.57 (207%)	9.06 (323.3%)	12.8 (498.1%)

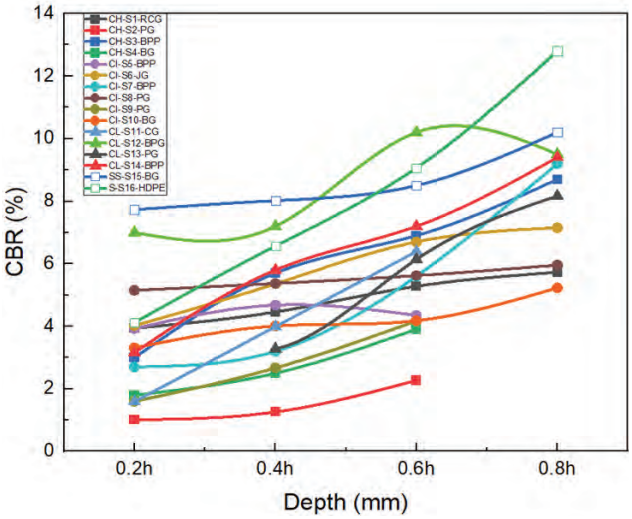


Figure 3. CBR vs. placement of geogrids at various depths.

dry densities and lower porosity. These compacted particles provide greater inter-particle friction and shear strength, both of which are critical in resisting penetration under CBR loading. When reinforced with geogrid like HDPE, the strong interlocking between sand particles and geogrid apertures further enhances the ability of soil to resist deformation. In CH soils, when the soil sample S3 was reinforced with BPP geogrid, there was a significant improvement in CBR% % from 3% at 0.2 h depth to 8.7% at 0.8 h depth. Using a similar type of geogrid at the same height for one of the CI soils, S7, the CBR% improved from 2.7% at 0.2 h depth to 9.2% at 0.8h. In the case of CL soils reinforced with BPG geogrid for the S12 soil sample, there was the highest increase in CBR% from 7% at 0.2 h depth to 10.2% at 0.6 h depth.

The optimum depth of the geogrid was determined from the literature study. The top layer placement at 0.8h exhibits higher CBR, which is consistent with the findings reported in the reference literature [19]. Even though CBR at 0.8h is higher, separate trials are done at 0.2h, 0.4h, and 0.6h because they simulate real-world scenarios, which helps the engineers to identify the best reinforcement strategy. This helps to optimize the design of reinforcement in a given pavement, ensuring active load transfer, compact deformation, and enhanced durability. The improved CBR results allow for the reduction in the thickness of the pavement by 30-50%, depending on the traffic loads and design standards. This leads to a reduction in the cost of construction. The CBR test results for the sixteen soil samples, each reinforced with different types of geogrids, are summarized in the bar graph in Figure 4.

Figure 4 reveals a general trend of increasing CBR with penetration depth for most geogrids, indicating enhanced load-bearing capacity and improved CBR% under greater deformation; this is supported by the prior studies [2, 18]. From the figures, it was clear that the highest CBR of 12.8% was achieved for S16-HDPE at a depth of 0.8h , a CBR of 10.2% for S15-BG, and a CBR value of 10.2% for S12-BPG, clearly mentioning much reinforcement capabilities. These

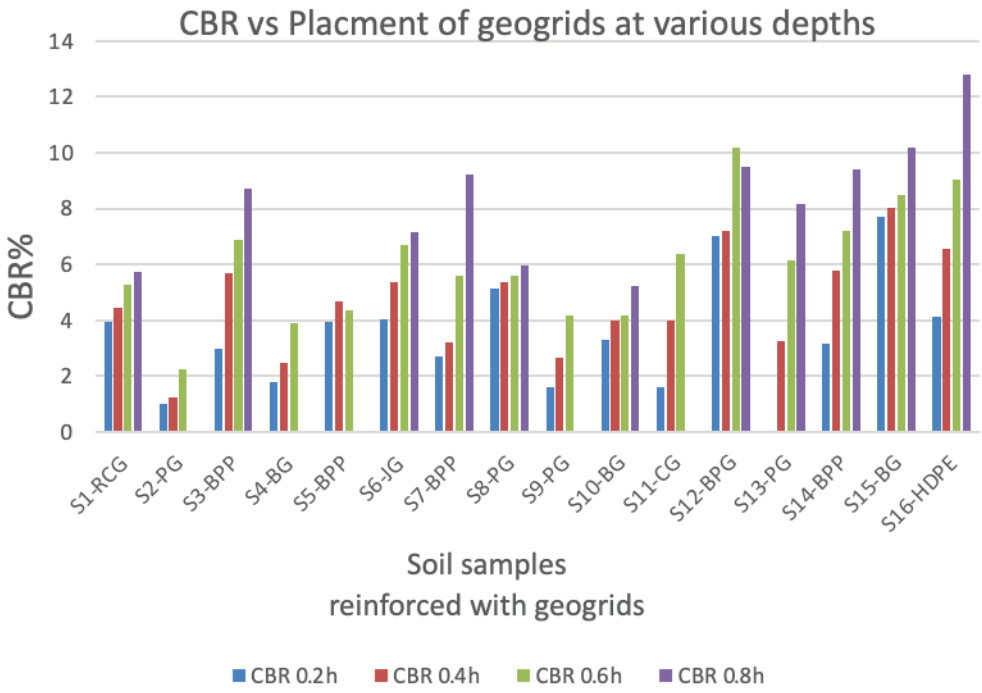


Figure 4. Comparison of the improvement of CBR for soil types reinforced with geogrids.

geogrids are mainly composed of HDPE and BG configurations, and they have high tensile strength and active stress distribution, making them suitable for stabilizing weak subgrades. This result agrees with the findings reported in the previous research as cited [17]. In contrast, S2-PG and S9-PG recorded the lowest CBR values of 1.01% and 1.6% at 0.2 h, respectively, with limited improvement at higher depths (e.g., S2-PG at 2.27% for 0.6 h).

Effect of OMC and MDD on CBR%

The California bearing ratio of soil depends upon both OMC and MDD. These two important factors determine the strength and compaction of the soil, and they have a direct impact on CBR value. The influence of OMC and MDD on unreinforced and reinforced soil samples is shown in Figure 5-9.

The variation of CBR of soil samples with respect to OMC & MDD in unreinforced and reinforced cases is provided in Figures 4-8. For CL soils with an OMC range of 9.8% to 24% and MDD between 1.54 g/cc and 2.08 g/cc, the CBR% varied from 2.9% to 10.2%. For CI, OMC ranged from 13% to 24.7% and MDD from 1.51 g/cc to 1.87 g/cc,

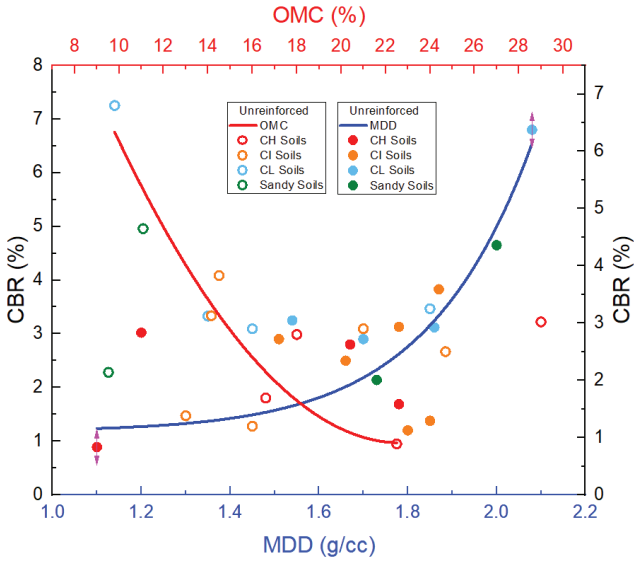


Figure 5. CBR% vs. OMC and MDD for unreinforced case.

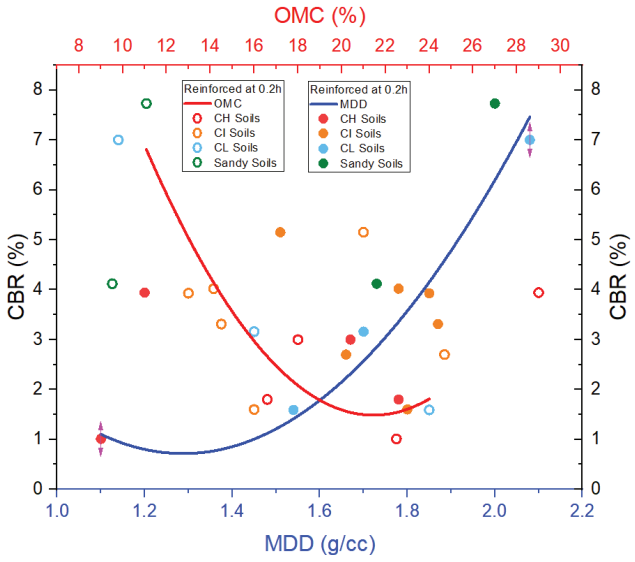


Figure 6. CBR% vs. MDD and OMC for reinforced at 0.2h depth.

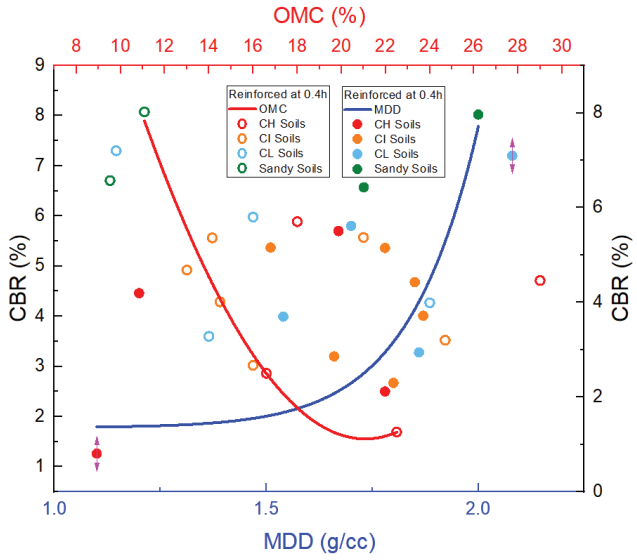


Figure 7. CBR% vs. MDD and OMC for reinforced at 0.4h depth.

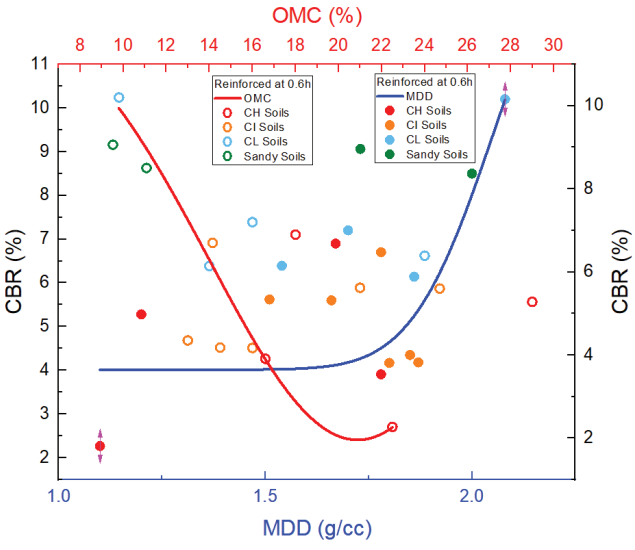


Figure 8. CBR% vs. MDD and OMC for reinforced at 0.6h depth.

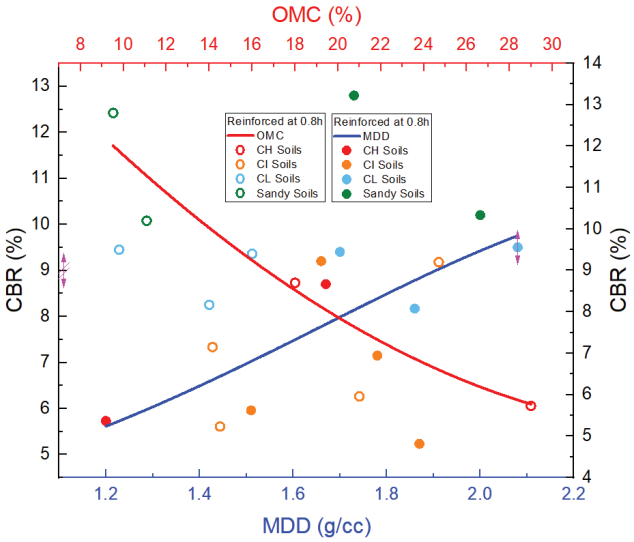


Figure 9. CBR% vs. MDD and OMC for reinforced at 0.8h depth.

with CBR% ranging from 1.2% to 9.2%. CH soils' OMC varied from 16.6% to 29%, whereas MDD ranged from 1.1 g/cc to 1.78 g/cc, with CBR values ranging from 0.89% to 8.7%. Sandy soils' OMC varied between 9.52% and 11.08%, whereas MDD varied between 1.73 g/cc has showed CBR variation from 2.14% to 12.8%.

From the results, it is clear that soil with higher MDD achieves a high CBR value, while increasing OMC has shown a decrease in CBR value, which relates to the previous literature proofs [18]. The reason behind this is that, when the water content is less than the OMC, the soil will be dry and compaction cannot be done effectively. This leads to an increase in voids and a reduction in the shear strength of the soil, thereby leading to a reduction in CBR value. Alternatively, adding water content more than the OMC also leads to a decrease in the shear strength of the soil because excess water fills the voids and causes a decrease in the friction between the soil particles, thereby resulting in a decrease in the CBR value.

The scenario at the OMC is that the soil has enough voids filled with water, making the whole mass of soil densely packed so that the soil can be compacted effectively and achieves maximum dry density, thereby achieving the highest shear strength, highest CBR, as well as load-bearing capacity. So, maintaining optimum moisture content during compaction of soil is an important parameter to be maintained to achieve dense and strong subgrade soil that is suitable for road construction as well as for foundation works.

In the case of MDD, it is evident that CBR will increase with an increase in MDD value. Generally, as the MDD of a soil increases, the CBR value also tends to increase. The reason behind achieving a higher MDD is that the soil is densely packed, leading to greater resistance to penetration of the plunger under a given load. Alternatively, when the MDD is less means that the soil is less compactedso that less cohesion between the soil particles, leading to a decrease in CBR value, thereby reducing the load-carrying capacity of the soil. The CBR value is used in pavement design to determine the strength of the subgrade and to calculate the thickness of the pavement layers. A higher CBR, often associated with higher MDD, means that less pavement thickness may be required.

Effect of LL on CBR%

The liquid limit of a soil can affect the CBR, especially for clayey soils. Liquid limit is the moisture level at which the soil transitions from plastic to liquid form, and it is a crucial determinant of the flexibility and behaviour of soil in various moisture conditions. The influence of liquid limit on CBR is illustrated in Figure 10-14.

The relationship between the LL and CBR for various soil types (CL, CI, CH) at different reinforcement depths is illustrated in Figures 9 to 13. For unreinforced soils, as LL increases, the CBR value tends to decrease. CH soils with an LL greater than 50% achieved a lower CBR value of 3.02%, while CL soils with an LL less than 35% showed the highest value of CBR of 6.8%, and CI soils with CBR values ranging between 35% and 50% exhibited a CBR value of 3.83%. At 0.2 h depth, CL soils displayed a maximum CBR of 7%, while CH soils had shown less value of CBR of 1.01%, and the CI soils showed a CBR value of 5.15%. With variation in geogrid placement at various depths, the CBR value also varied for different soil types. At a depth of 0.4h, the CBR value of CL soil was 7.2%, while the CBR values of CH and CI soils were 1.26% and 5.37%, respectively. At the 0.6h depth, CBR values increased to 10.2% for CL soil, 2.27% for CH soil, and 6.7% for CI soil. The changes that were observed at 0.8h, is that the CBR values were 9.5%, 8.7%, and 9.2% for CL, CH, and CI soils, respectively. Among the

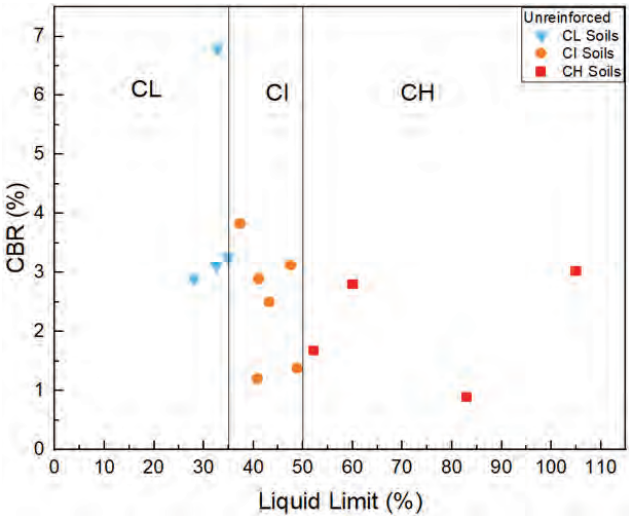


Figure 10. CBR vs. liquid limit for unreinforced case.

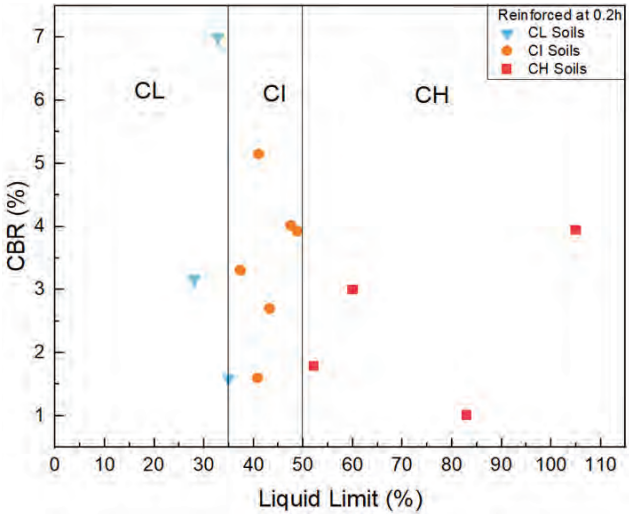


Figure 11. CBR vs. liquid limit for reinforcement at 0.2h depth.

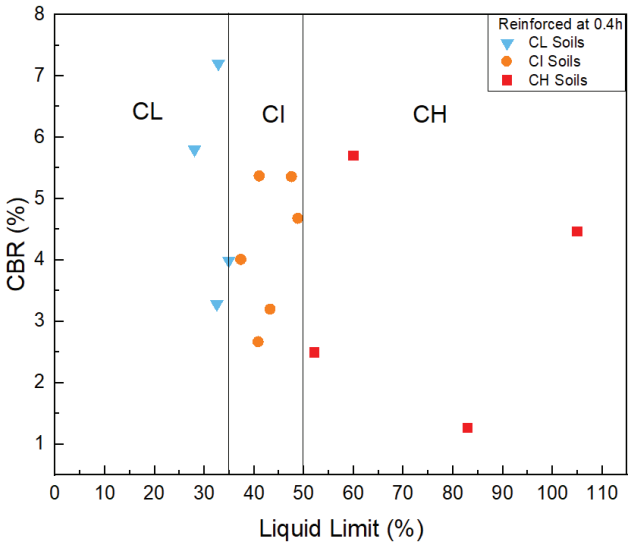


Figure 12. CBR vs. liquid limit for reinforcement at 0.4h depth.

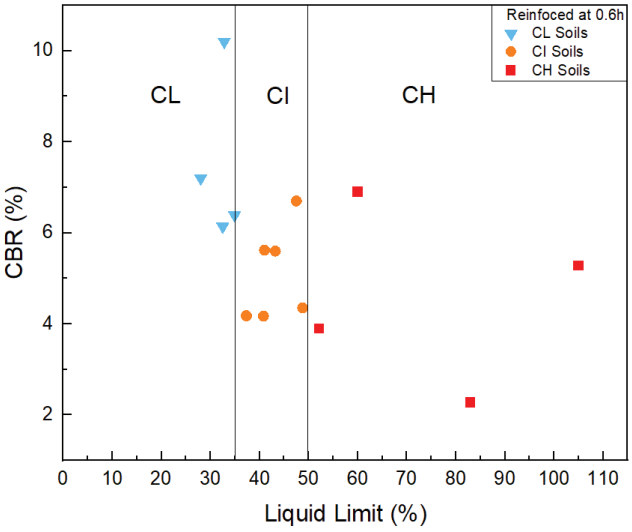


Figure 13. CBR vs. liquid limit for reinforcement at 0.6h depth.

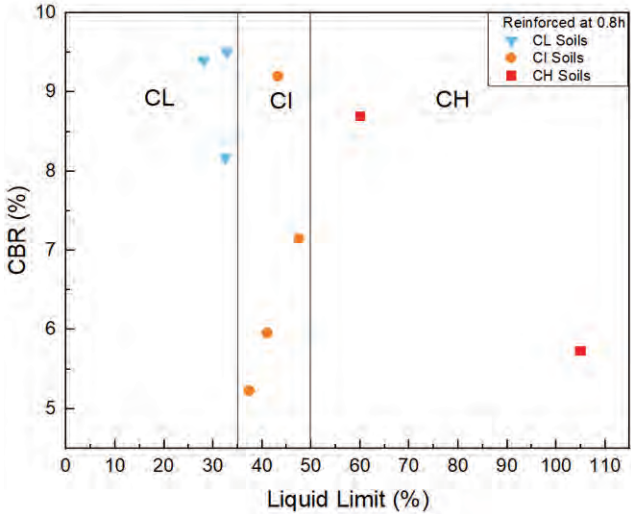


Figure 14. CBR vs. liquid limit for reinforcement at 0.8h depth.

various depths, 0.8h depth has shown notable improvement in the CBR values

In the case of clayey soils, LL is an important property that determines the CBR. From the observations, it was clear that soils with LL less than 35% have shown higher CBR values, whereas soils with LL greater than 50% has showed lesser CBR values. The reason behind this is that soils with a high LL undergoes excessive swelling, shrinkage, and deformation under the application of load, which reduces the CBR value. Also, soils with high LL generally contain a higher percentage of fine, plastic particles that tend to have lower resistance to penetration under loading, leading to a decrease in CBR values. Soils with a lower percentage of fine particles, such as sandy and gravelly soils, show greater strength, load-carrying capacity, and higher CBR values.

This differentiation is very much helpful in the construction of pavements in which subgrade soils containing plastic and fine particles require additional measures in order to achieve high strength and support traffic loads. Depending on the conditions, the measures that can be taken include mechanical or chemical stabilization, geogrid reinforcement, or an increase in pavement layer thickness. Sandy and silty soils generally require less stabilization

when their measured CBR is sufficiently high, which can allow thinner pavement layers to be considered. The relationship between soil plasticity and CBR is also consistent with the supporting studies reported in the literature [1].

CONCLUSION

The analysis of the CBR test results on soil samples reinforced with various types of geogrids at different depths led to the following conclusions:

1. The CBR of subgrade soil has been increased significantly by the geogrid reinforcement, with a degree of improvement depending upon soil type, geogrid type, and geogrid placement depth.
2. The optimum depth of geogrid placement was 0.8h, where higher CBR values were noted for all soil types.
3. Polyester (PG), Biaxial Polypropylene (BPP), and HDPE proved greater performance in improving CBR values for CH and CI soils. This conclusion helps highway engineers in the proper selection of appropriate geogrid material for a particular type of soil.
4. Natural geogrids, such as jute (JG) and coir (CG), worked out well in case of CI and CL soils. These natural geogrids are not effective in the case of CH soils. These geogrids are suitable in areas where economical and environmentally friendly materials are preferred.
5. CL soils with LL < 35% have shown higher CBR values and after reinforcing these soils, there was even a 9% increase in their CBR values.
6. Soils with high MDD have shown higher CBR values, whereas high OMC showed a reduction in the CBR values.
7. The highest CBR of 12.8% was obtained for sandy soil reinforced with HDPE geogrid. This was mainly associated with the good compaction of sandy soil, its low plasticity, and the effective interaction between the soil and geogrid.

Future Scope

Future work should include field tests to check the results obtained from the laboratory tests under actual traffic and site conditions. Such tests would also help in studying the performance of the reinforcement over a longer period. FEM can be used to study the behaviour of reinforced soil on a larger scale and for conditions that are difficult to reproduce in the laboratory. It would also be useful to study combinations of geogrids with geotextiles or chemical stabilizers for improving weak and expansive soils. Investigating the degradation of natural geogrids over time will help optimize their use in sustainable infrastructure design.

ABBREVIATIONS

HDPE	High-Density Polyethylene
PG	Polyester Geogrid
BPP	Biaxial Polypropylene geogrid
BG	Biaxial Geogrid
BPG	Biaxial Polyester Geogrid
RCG	Rubber Coir Geogrid
JG	Jute Geogrid
CG	Coir Geogrid
CH	Highly Compressible Clay
CI	Intermediate Compressible Clay
CL	Low Compressible Clay
S	Soil Sample
OMC	Optimum Moisture Content
MDD	Maximum Dry Density
LL	Liquid Limit
PL	Plastic Limit
PI	Plasticity Index
CBR	California Bearing Ratio

AUTHORSHIP CONTRIBUTIONS

Kadali Srinivas and Ramya Krishna: Conceptualised and designed the study. Bharath Chandra: Carried out the experimental work and collected the data. All authors: Performed the data analysis & visualisation. Bharath Chandra: Drafted the manuscript. Ramya Krishna and Kadali Srinivas: Reviewed and edited the manuscript. All authors have read and approved the final manuscript.

DATA AVAILABILITY STATEMENT

The authors confirm that the data that supports the findings of this study are available within the article. Raw data that support the finding of this study are available from the corresponding author, upon reasonable request.

CONFLICT OF INTEREST

The authors declared no potential conflicts of interest with respect to the research, authorship, and/or publication of this article.

ETHICS

There are no ethical issues with the publication of this manuscript.

STATEMENT ON THE USE OF ARTIFICIAL INTELLIGENCE

Artificial intelligence was not used in the preparation of the article.

REFERENCES

[1] Vennamaneni S, Raju Aketi N, Paisa S. Reduction in pavement thickness by using geogrid. Int J Eng Technol 2018;7:17. [CrossRef]

[2] Yadav PMG, Bharath S, Kumar MM, Reddy MN, Reddy GC. Usage of geogrid in flexible pavement design. Int J Eng Sci Res Technol 2018;7:144–153.

[3] Nasser M, Tarawneh K. Development of pavement maintenance management system for an urban areas based upon multiple linear regression analysis. Sigma J Eng Nat Sci 2025;43:121–132. [CrossRef]
[4] Singh M, Trivedi A, Shukla SK. Unpaved test sections reinforced with geotextile and geogrid. Mater Today Proc 2020;32:706–711. [CrossRef]
[5] Suresh A, Jose D, Maliyakal GJ. CBR characteristics of soils stabilised with geogrid. Int J Civ Eng 2018;5:30–34. [CrossRef]
[6] Pandey A, Rabbani A. Stabilisation of pavement subgrade soil using lime and cement. Int J Eng Technol 2017;4:5733–5735.
[7] Abdelbaset AM, Katunský D, Zeleňáková M, El-Feky MH. Mechanical properties stabilization of low plasticity kaolin soil using fly ash and hydrated lime. Case Stud Constr Mater 2024;21:e03662. [CrossRef]
[8] Gautam L, Maaze MR, Sharma KV. Optimizing self-compacting concrete with bone China ceramic and granite waste for improved mechanical and durability properties. J Mater Civ Eng 2025;37:04024525. [CrossRef]
[9] Kola V, Gondu VR, Varudu RM. Mechanical and micro-structural aspects of admixture stabilized rock sludge dust. Constr Build Mater 2024;420:135552. [CrossRef]
[10] Gautam L, Kalla P, Jain JK, Choudhary R, Jain A. Robustness of self-compacting concrete incorporating bone China ceramic waste powder along with granite cutting waste for sustainable development. J Clean Prod 2022;367:132969. [CrossRef]
[11] Boobalan SC, Anandakumar PK, Sathasivam M. Utilization of waste plastic sheets as soil stabilization materials. Mater Today Proc 2023. [CrossRef]
[12] Gautam L, Jain JK, Jain A, Kalla P. Recycling of bone China ceramic waste as cement replacement to produce sustainable self-compacting concrete. Structures 2022;37:364–378. [CrossRef]
[13] Wang Z, Zhan L, Zhang H, Zheng L, Kang T. Compaction, strength, and volume change characteristics of excavated clayey soil stabilized with composite admixture of cement and autoclaved aerated concrete powder. Can Geotech J 2024;61:2022–2035. [CrossRef]
[14] Gautam L, Jain JK, Jain A, Kalla P. Valorisation of bone-China ceramic powder waste along with granite waste in self-compacting concrete. Constr Build Mater 2022;315:125730. [CrossRef]
[15] Janakiraman GG, Paramaguru P, Pratheep T. Stabilization of subgrade using geosynthetics. J Adv Res Dyn Control Syst 2019;12:169–180.
[16] Keerthi N, Kori S. Study on improvement of sub grade soil using soil-reinforcement technique. Int J Appl Eng Res 2018;13:126–134.
[17] Majedı P, Çelik S, Akbulut S. A research on the effect of the reinforcement geometry on the soil bearing capacity under the strip footing loads. Sigma J Eng Nat Sci 2018;36:951–960.
[18] Mittal A, Shukla S. Strength improvement of poor subgrade soil reinforced with polyester biaxial geogrid. Jordan J Civ Eng 2019;13.
[19] Lamichhane R, Acharya IP. Improvement on CBR strength of soil modified with brick dust using geogrid reinforcement. 2022.
[20] Jayakumar J, Venkatesh J, Selvaraju YR. Expansive subgrade strength improvement using geogrid and geotextile layers. IOP Conf Ser Mater Sci Eng 2020;955:012064. [CrossRef]
[21] Tiwari N, Satyam N. An experimental study on strength improvement of expansive subgrades by polypropylene fibers and geogrid reinforcement. Sci Rep 2022;12:6685. [CrossRef]
[22] Zimar Z, Robert D, Zhou A, Giustozzi F, Setunge S, Kodikara J. Application of coal fly ash in pavement subgrade stabilisation: a review. J Environ Manage 2022;312:114926. [CrossRef]
[23] Ghani ANA, Roslan NI, Hamid AHA. Road submergence during flooding and its effect on subgrade strength. Int J GEOMATE 2016;10:1848–1853.
[24] Nangia T, Sharma U, Kumar S, Sharma S. Improvement of subgrade strength with the use of geotextiles-a case study. In: International Conference on Environmental Geotechnology, Recycled Waste Materials and Sustainable Engineering; 2023 Oct. Singapore: Springer Nature Singapore; 2023. p. 131–149. [CrossRef]
[25] Nair KS, Deepthy BL. Improvement of soft subgrade using geogrid reinforcement. Int J Eng Res Technol 2017;5:62–64.
[26] Balamaheswari M, Anitha B, Kanimozhi B, Naganatha Prabhu L. Improvement of California bearing ratio value in weak subgrade soil with the developed anchored geogrid. Mater Today Proc 2022;49:1537–1542. [CrossRef]
[27] Bureau of Indian Standards. IS 2720 (Part 16): Methods of test for soils-laboratory determination of CBR. New Delhi: Bureau of Indian Standards; 1987.

Sigma J Eng Nat Sci, Vol. 44, No. 4, pp. 2963–2973, August, 2026

Sigma Journal of Engineering and Natural Sciences
Web page info: https://sigma.yildiz.edu.tr
DOI: 10.14744/sigma.2026.2138

Research Article

Influence of artificial aging on microstructure and mechanical properties of Aluminum 2219-T87 TIG welded joints

Atif SHAZAD[1,*], Maaz AKHTAR[2], Muhammad UZAIR[1]

[1]Department of Mechanical Engineering, NED University of Engineering and Technology, Karachi, 75270, Pakistan
[2]Department of Industrial Engineering, College of Engineering, Imam Mohammad Ibn Saud Islamic University (IMSIU), Riyadh, 11432, Saudi Arabia

ARTICLE INFO

Article history
Received: 12 February 2025
Revised: 22 March 2025
Accepted: 13 April 2025

Keywords:
Al 2219-T87; Artificial Aging; Mechanical Properties; Microstructural; TIG Welding

ABSTRACT

TIG welding technique was employed commonly for welding light weight materials such as aluminum at industrial level. In aerospace industry, Al 2219 material is utilized extensively in different temper grades. However, T87 temper grade is known for its superior strength compared to T6, although with reduced ductility and formability, making its behaviour under prolonged aging cycles particularly relevant for high-performance applications. This study specifically focussed on mechanical and microstructural performance of TIG-welded Al 2219-T87 joints before and after artificial aging using two extended aging durations. A filler wire with a diameter of 2.6mm, ER 2319, was used for welding 5mm thick plate. The welded joints were subjected to artificial aging at 190°C for durations of 18 hours and 24 hours to investigate the impact on joint properties. Microscopic examination was carried out on the weldments in both the as-welded condition and after the post-weld aging treatments to observe structural changes. After 18 hours of artificial aging, the weld zone and heat affected zone exhibited a fine and dense grain structure. Additionally, a large number of precipitates were observed after 24 hours of aging. The post-weld aged samples demonstrated significantly higher ultimate tensile strength and yield strength compared to the as-welded samples. Specifically, there was an enhancement of approximately 60% in ultimate tensile strength and 30% in yield strength when compared to the as-welded condition. The ductility, measured in terms of percent tensile elongation, of the welded joints also improved after 18 hours of aging. It was found that toughness increased by 40%, and there was a 90% increment in percent elongation after 18 hours of aging, attributed to the presence of fine, equiaxed grains and reasonable precipitation. Excessive precipitation and elongated grains were observed after 24 hours of aging.

Cite this article as: Shazad A, Akhtar M, Uzair M. Influence of artificial aging on microstructure and mechanical properties of Aluminum 2219-T87 TIG welded joints. Sigma J Eng Nat Sci 2026;44(4):2963–2973.

***Corresponding author.**
*E-mail address: atifshahzad@cloud.neduet.edu.pk

This paper was recommended for publication in revised form by Editor-in-Chief Ahmet Selim Dalkilic

Published by Yıldız Technical University Press, İstanbul, Turkey
© Author. This is an open access article under the CC BY-NC license (http://creativecommons.org/licenses/by-nc/4.0/).

INTRODUCTION

Welding aluminium alloys is a promising joining practice commonly utilized in the aerospace industry. Al 2219 is a vital aluminium alloy that provides a high strength-to-weight ratio, good corrosion resistance, and absolute toughness. However, the high input heat energy involved in welding presents numerous challenges, such as reduction in joint strength, thermal deformations, and porosity [1, 2]. Thick plates often welded by using TIG welding but this technique leads to several distortions due to concentrated heat input at weld area, the strength and other mechanical properties get compromised because of these structural disorderness. The elevated heat input required for welding thicker sections exacerbates these thermal deformations [3, 4]. Several investigations have explored how different TIG welding procedures influence the mechanical and microstructural properties of Al 2219, aiming to mitigate such welding-induced defects. A comparison between Direct Current Electrode Negative Activated-TIG and Variable Polarity TIG was performed to evaluate joint properties. The results revealed that first welding technique exhibited low porosity and a narrow heat-affected zone [5, 6]. Similarly, the impact of the partially melted zone was evaluated after weld reinforcement on the welding joints of aluminium alloys. Partial melted zone's induced stress concentrations in welding reinforcements, ultimately reducing joint strength [7, 8]. The variation in grain size within the weld zone and heat affected zone, influenced by the number of TIG welding passes, significantly affects mechanical properties particularly microhardness and tensile strength [9, 10].

Typically, coarse grain boundaries observed in these regions tend to promote ductile fracture behavior, whereas finer grains enhance resistance to deformation by offering greater strength [11]. This microstructural inconsistency across the weld is often evident in micrographs of aluminum weld joints and is primarily attributed to variations in filler rod composition and fluctuations in heat input during the welding process [12]. Furthermore, the development of a continuous phase of weld material caused significant deteriorations in joint strength and specific techniques can be utilized to prevent these physical distortions like coatings etc. [13]. Negative effects observed due to over-aged zones adjacent to partial melted zones in aluminium welding joints. The mechanical properties of joints degraded due to over aged zone in the heat affected zone, Welding joints exhibited complex tensile behaviour due to the presence of partial melted zone's and over aged zone's [14].

The effects of reinforcement on the tensile behaviour of Al 2219 TIG welded joints were investigated by Wang et al. [15]. The results showed that the tensile strength of welding joints without reinforcement was 250 MPa, but it improved after reinforcement on both sides. Welding joints with welding toes in the weld zone exhibited greater elongation compared to joints with weld toes at the junction of the weld zone and partial melted zone. The desired mechanical strength after welding is critical due to nature of heavy working loads and conventional welding processes degrades the structural integrity of the joint. Friction stir welding (FSW) is effective in strengthening joints because it creates a uniform weld zone with minimal heat-affected regions [16]. In one study, Hu et al. [17] explored the use of ultrasonic vibrations during FSW to further enhance the mechanical properties of the resulting joints. The results indicated that ultrasonic vibrations during welding led to improvements in tensile strength and fracture toughness [18].

The performance of FSW 2219 changes when the welding temperature is different which makes the tensile strength better. When the welding joints are cooled with water quickly, they become more brittle. The joints that are made underwater break at the edge of the weld zone and the heat affected zone [19]. Friction stir weld joints often have problems like tunnel defects and cavity formations which reduce the strength of the joint [20]. The intensity of these problems depends on how the welding is performed and how fast the tool rotates. Usually, bigger problems occur when the welding is slower, and the tool rotates faster which means there needs to be a balance between heat and material flow when welding [21-24].

To make the mechanical performance of welded joints better people often use heat treatments after welding. One way that works well is aging, which makes strength improved by creating and spreading out tiny particles. Even short heat treatments can make fatigue better by 20 to 25 percent [25, 26]. For Al 2219 TIG welded joints a special treatment that includes solution treatment, water quenching and aging at 175 degrees Celsius can make the joint strength better by 44 percent. Improve corrosion resistance. However, the heat-affected zone is still a little susceptible to corrosion. Shazad et al. [27]. Also found that artificial aging makes the ultimate tensile and yield strengths better and electron beam welding creates particles that are spread out evenly along grain boundaries. Heat treatments after welding are also very important for reducing stresses that come from temperature differences across the weld. If these stresses are not taken care of, they can degrade mechanical properties [28]. This degradation is mostly based on stress corrosion cracking, which is why heat treatment is necessary to keep the structure strong. Some studies on Variable Polarity TIG-welded Al 2219 showed that artificial aging makes the tensile and yield strengths better by 42 percent and 44 percent and also improves fatigue strength by 18 percent. Another study by Raza et al. [29] found that aging at 210 degrees celsius for four hours creates tensile strength and hardness because the tiny particles are spread out well.

A lot of research has been done on how Al 2219 behaves when welded and aged for a time and under different temper conditions. Not much is known about how the T87 temper grade behaves when aged for a long time. The T87 condition is stronger than T6. It is less flexible and less able

to be formed which makes it very important to know how it behaves over time for high-performance applications. This study looks at the microstructural performance of TIG-welded Al 2219-T87 joints that have been artificially aged for two different long periods of time. The Al 2219 performance is very important to understand. The welding temperature is very important for Al 2219. The Al 2219 joints are often used in applications. The performance of Al 2219 is very important for these applications.

The goal of this study is to learn more about Al 2219-T87. Al 2219-T87 is a very strong aluminium alloy. It is not very flexible. This makes it hard to use in some applications. The Al 2219-T87 needs to be studied. The study will look at how Al 2219-T87 behaves when it is aged for a time. This will help us understand how to use Al 2219-T87. The results of the study will be very important, for people who use Al 2219-T87.

MATERIALS AND METHODS

This study was conducted on a 5mm thick plate of Al 2219-T87 to investigate the effects of TIG welding. Specimens were prepared using a TIG welding technique with a welding speed of 200mm/min, which was chosen to ensure high-quality welding joints. The welding process utilized a Precision TIG AC type model equipment. In post weld heat treatment process artificial aging was performed only at 190 °C to assess improvements in the mechanical properties and microstructures of the welded joints. Two durations such as 18 hours and 24 hours were selected because significant data is available for durations less than 12 hours. Larger durations may identify the over aging duration for aluminum material at some specific aging temperature. To evaluate the ultimate tensile strength and yield strength, an H150KV Tensile testing machine was utilized. The samples were prepared according to the ASTM E8M-16a standard. To find out how much energy something can take the Charpy impact test was used. This test shows us how strong a material is when something hits it. The sampling were performed as per ASTM E23-18 standard. Hardness fluctuations were investigated using Vickers tester for microhardness. Optical metallurgical microscope was employed to figure out the variations in microstructure due to artificial aging. The emission spectrometer used to identify the alloying contents in Al 2219 material, results are represented in Table 1. Table 2 indicates mechanial properties of base plate. The comparison between Al 2219 base material and the weld joints after artifcial aging to check the impact of thermal cycle and duration time.

Table 1. Chemical composition by weight of Al 2219-T87

S.No	Element	Percentage
1	Mg	0.18
2	Si	0.23
3	Mn	0.28
4	Cu	6.2
5	Zn	0.11
6	Ti	0.073
7	Fe	0.31
8	Al	Remaining

Table 2. Tensile properties of Al 2219-T87

S. No	Characteristics	Value
1	Base metal	Al 2219-T87
2	Yield strength (YS)	390MPa
3	Tensile strength (UTS)	483MPa
4	Hardness (HV)	124
5	% Elongation	12%

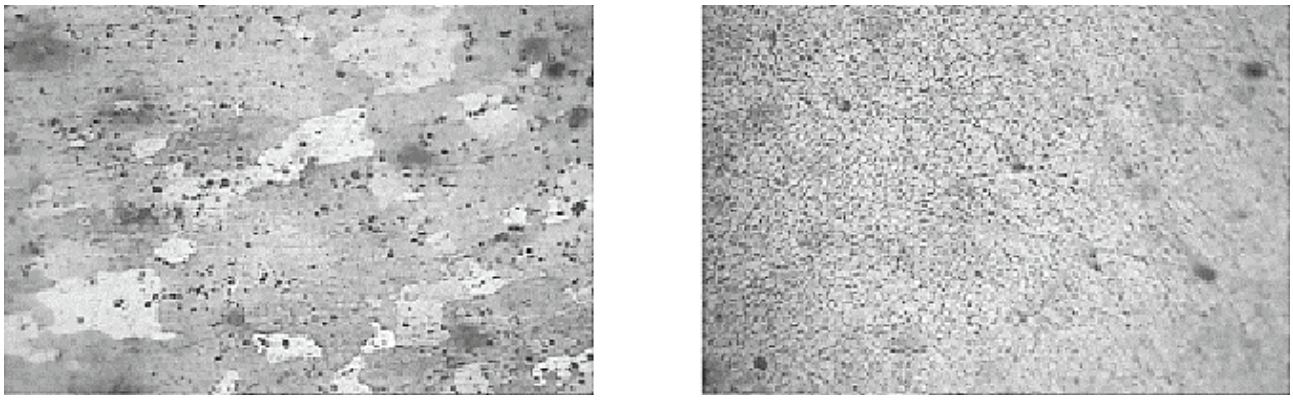
The aim of this study was to examine the impact of artificial aging on welded samples by comparing two different durations of aging. Following the TIG welding procedure, the samples underwent artificial aging by being placed in a furnace for either 18 hours or 24 hours. To ensure sufficient material penetration, a double pass welding technique was utilized. The TIG welding process involved the use of a 2.6mm diameter ER2319 filler wire.

RESULTS AND DISCUSSION

Microstructural Examination

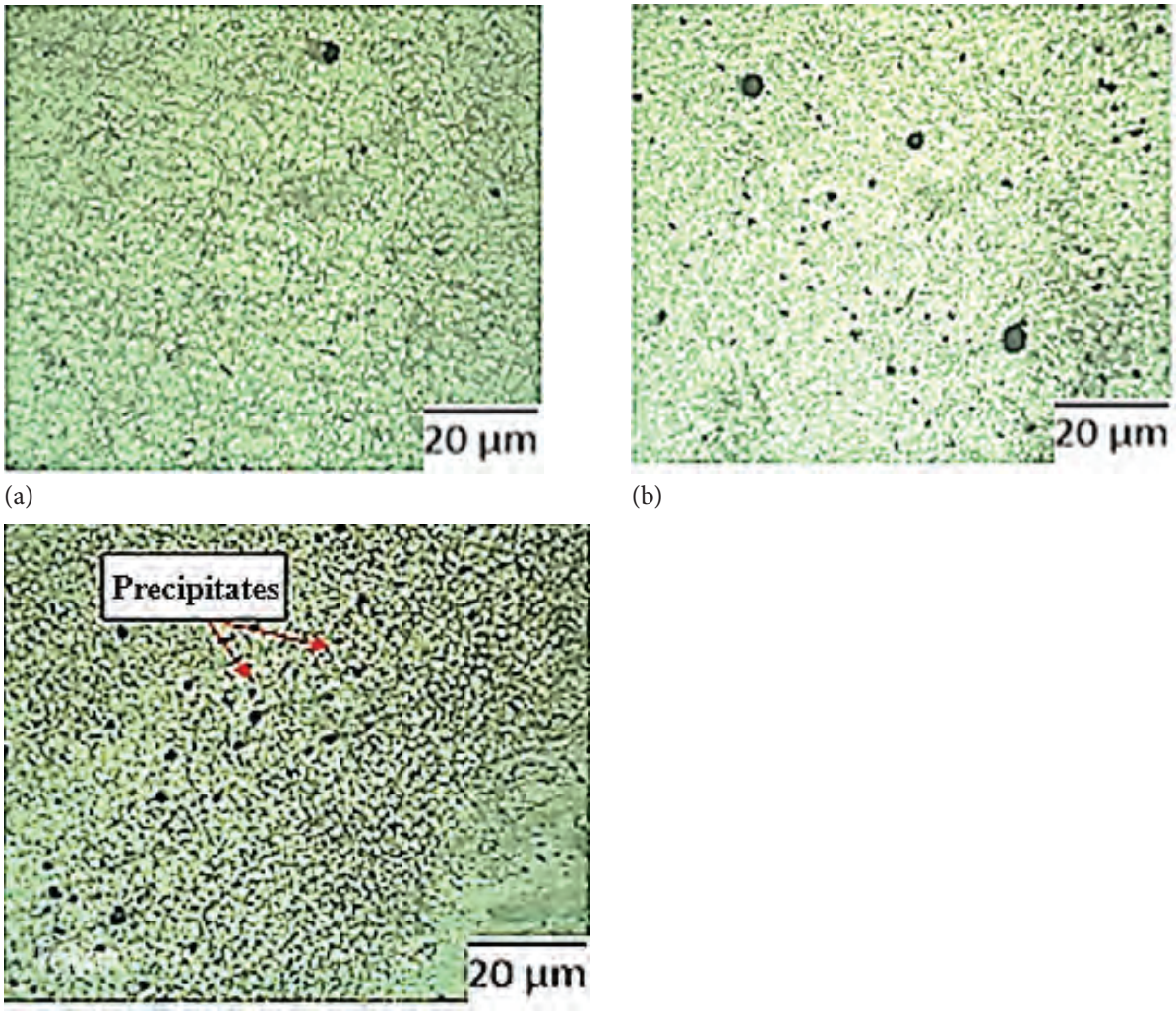
This study investigated the variations in microstructure of TIG weld joints of Al 2219-T87 material after long durations of artificial aging. Figure 1 illustrate microstructure of Al 2219-T87 for comparison with the microstructures of this study. Microstructures in weld zone and heat affected zone of welded joints are shown in Figure 2 and Figure 3 respectively. Optical micrographs of weld zone after artificial aging in Figure 2 (b) and Figure 2 (c) represented fine grain boundaries compared to weld zone microstructure of welded joints without aging shown in Figure 2(a). Furthermore, after artificial aging, the grains in the weld zone exhibit a more equiaxed shape and are evenly distributed, whereas the grains in the weld zone without aging are irregularly spaced.

Additionally, a slight increase in grain elongation was observed in the non-aged samples weld zone. However, this difference was not significantly noticeable, suggesting that post-weld heat treatment does not have a significant effect on grain elongation in the weld zone. Figure 3 depicts the microstructures of heat affected zone in different conditions. A comparative analysis of heat affected zone microstructure is presented in Figure 3(a), Figure 3(b), and Figure 3(c), before and after artificial aging at two different time periods. Figure 3(c) demonstrates the



(a) (b)

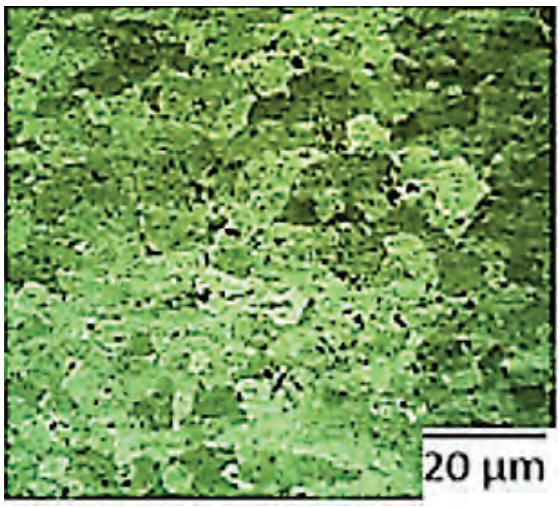
Figure 1. Microstructure of Al 2219-T87 (a) Heat affected zone after TIG (b) Base metal [30]. Adapted from: Venkatasubramanian G, Mideen AS, Jha AK. Microstructural characterisation and corrosion behaviour of top surface of TIG welded 2219-T87 aluminium alloy. Int J Eng Sci Technol 2013:5:624. Available at: https://www.researchgate.net/publication/264972445_



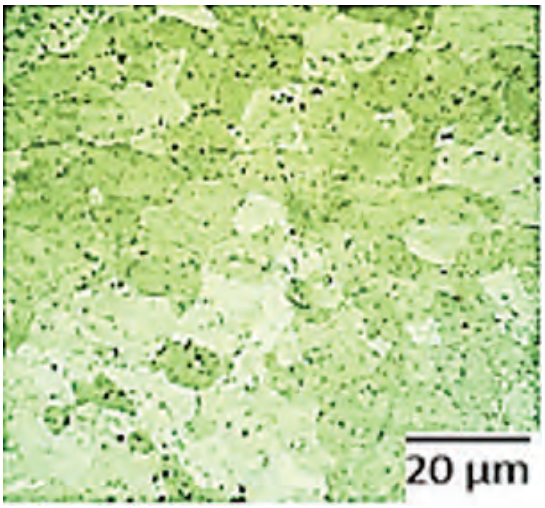
(a) (b)

(c)

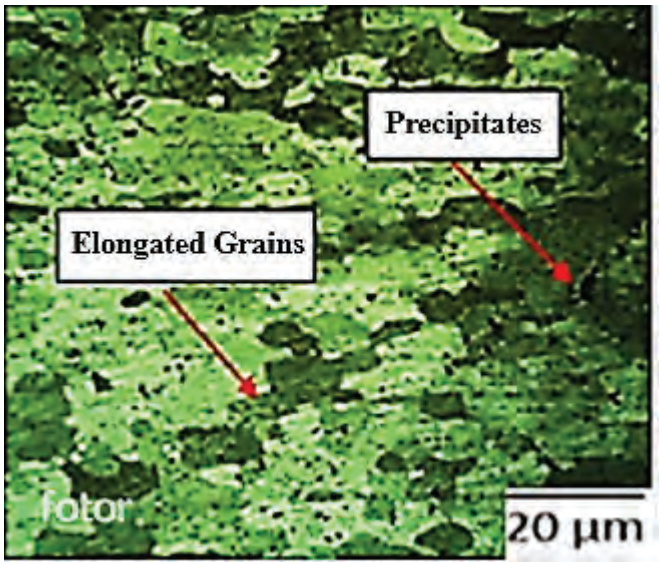
Figure 2. Microstructure of weld zone (WZ) of Al 2219- T87 (a) TIG welded sample without Aging (b) Sample after 18 hours aging (c) Sample after 24 hours aging.



(a)



(b)



(c)

Figure 3. Microstructure of heat affected zone (HAZ) of Al 2219- T87 (a) TIG welded sample without Aging (b) Sample after 18 hours aging (c) Sample after 24 hours aging.

presence of distinct precipitates after a 24-hour aging, indicating their prominent formation. Conversely, Figure 2(b) illustrates a heat affected zone microstructure with dense and fine grains, which hinder dislocation movement and consequently enhance strength. Figure 1(a) showing similar microstructure in comparison with microstructure represented in Figure 3(a). The microstructure of artificially aged joints exhibits significant improvements, particularly in samples heated for 24 hours, where elongated grains are observed. This extended heating period induces internal stresses along grain boundaries due to excessive precipitation, resulting in sample hardening. However, the strength of the 24-hour heated samples is lower compared to the 18-hour heated samples.

In Figure 3(a), a disrupted grain structure is evident, which can be attributed to the high input heat during welding, in contrast to the more favourable grain structures observed in Figure 3(b) and Figure 3(c). The elongated grains are particularly noticeable in Figure 3(c). Size and orientation of grain boundaries are crucial for controlling of mechanical properties of weld joints. Referenced studies [6, 10] mentioned importance of grain size on overall performance of joint. Formation and distribution of precipitates across the weld joint also explained in literature as well, more precipitates offered more resistance to dislocation movements, hence resistance to deformation promote strength and degrade ductility.

Tensile Testing

Tensile testing was performed to investigate impact of artificial aging on strength of Al 2219 – T87 welding joints. Results represented in Figure 3 display the difference between joints yield strength before and after artificial aging of TIG welded joints. Welding input heat degraded strength upto 50% as shown in Figure 4, 150MPa YS was observed after TIG welding without artificial aging. However, artificial aging improved YS from 150MPa to 240MPa after artificial aging. Maximum enhancement in YS was achieved after artificial aging for 18hours duration. Figure 5 displays a comparison of the UTS between welded joints before and after artificial aging. The results indicate that a ultimate tensile strength of 310MPa was achieved after an 18-hour artificial aging process. The increase in strength can be attributed to the presence of fine grains in the weld zone and the uniform distribution of precipitates within the material phase. No significant elongation of grains was observed during the 18-hour aging period.

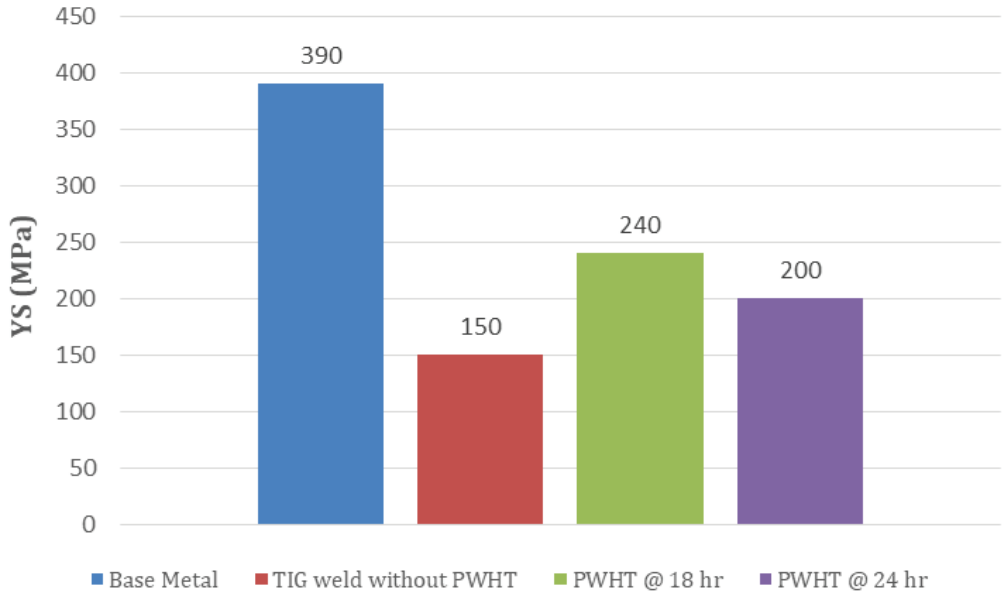


Figure 4. Comparison data of yield strength (YS).

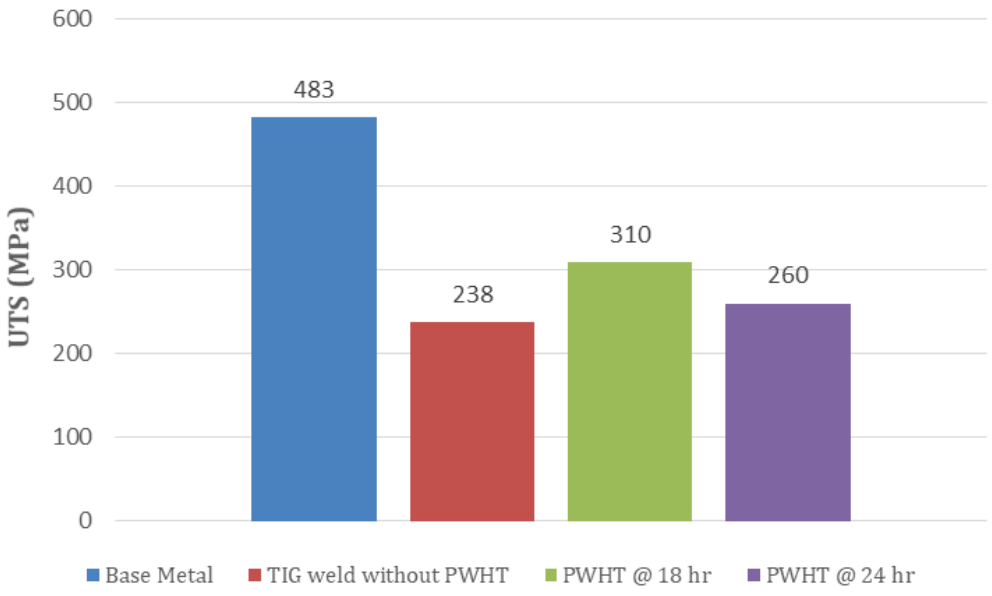


Figure 5. Comparison data of ultimate tensile strength (UTS).

However, when the artificial aging was extended to 24 hours, the microstructure exhibited both disrupted and elongated grains, leading to a reduction in ultimate tensile strength. The excessive formation of precipitates at the grain boundaries in both the weld zone and the heat affected zone of the 24-hour treated samples induced internal stresses. Consequently, the tensile strength of the 24-hour aged samples was lower compared to the 18-hour aged samples. Moreover, the increase in tensile strength observed after artificial aging can be compared with the findings of the reference study [29], which reported a maximum improvement of approximately 51 MPa. In contrast, this study achieved a tensile strength increment of 72 MPa. This enhanced improvement is attributed to the longer soaking duration employed in this study. Notably, the reference study used a shorter soaking duration of 4 hours at 210 °C around 20 °C higher than the temperature applied in this study for an extended soaking duration of 18 hours. The study investigated the impact of artificial aging on the ductility of welded joints. Figure 6 presents a comparison of the percentage elongation before and after artificial aging.

Significantly different results were observed between joints that underwent artificial aging and those that did not. Joints without artificial aging exhibited minimal percentage elongation, while those subjected to artificial aging, particularly for 18 hours, showed the highest percentage elongation. The improvement in ductility can be attributed to the formation of a uniform phase of precipitates and a reduction in defects at grain boundaries. The presence of fine grain boundaries and the distribution of precipitates along these boundaries contributed to the reduction in defects. However, the samples aged for 24 hours displayed lower percentage elongation compared to the 18-hour samples. This decrease in ductility can be attributed to excessive precipitates at the grain boundaries, resulting in increased hardness due to prolonged aging duration.

Welding Efficiency

Welding efficiency of Al 2219-T87 joints was improved due to fine precipitates in weld zone. One reason of weld efficiency enhancement was greater dense ratio of precipitates in heat affected zone of 18 hours artificial aging. Joints strength was superior due to artificial aging compared to welding joints without artificial aging. Weld efficiency 64.2% after artificial aging for 18 hours was achieved as shown in Figure 7. Overall, 30.2% augmentation was achieved due to artificial aging for 18 hours. However, 9.5% increment in joint welding efficiency was attained due to artificial aging for 24 hours. Joints artificially aged for 24 hours exhibited low efficiency compared to 18 hours artificially aged joints due to precipitation hardening and elongated grains.

Micro-Hardness Testing

Hardness testing was conducted to assess the impact of artificial aging duration. Table 3 illustrates that the hardness of the welded joint increased after 24 hours of aging. The base metal hardness also improved for both durations, but a significant increase was observed after 24 hours of artificial aging. The primary cause of the hardness increment and ductility reduction is precipitation hardening. A detailed comparative study revealed that the hardness of coarse grains, the weld zone, and the

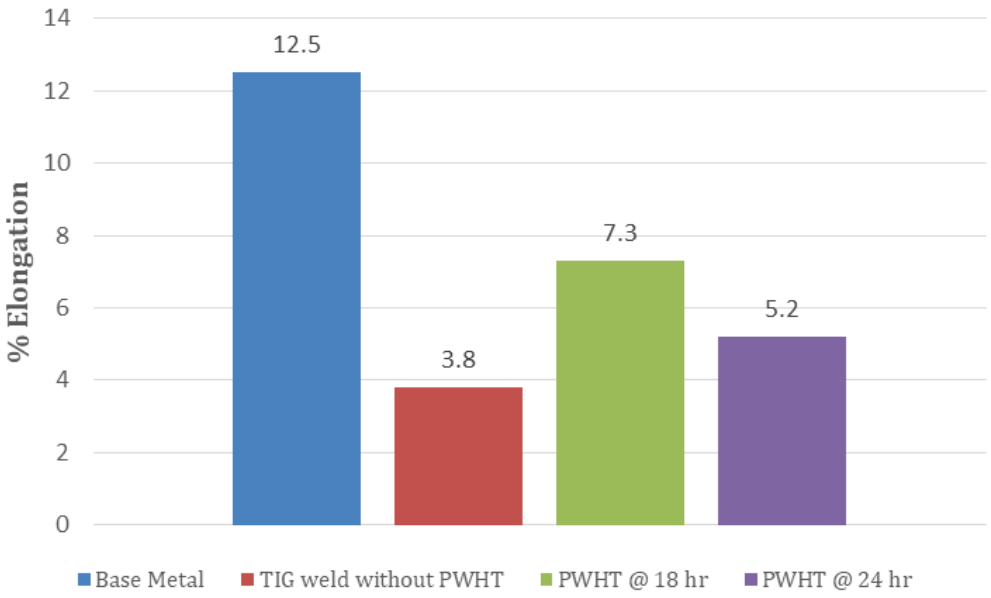


Figure 6. Comparison data of percent elongation.

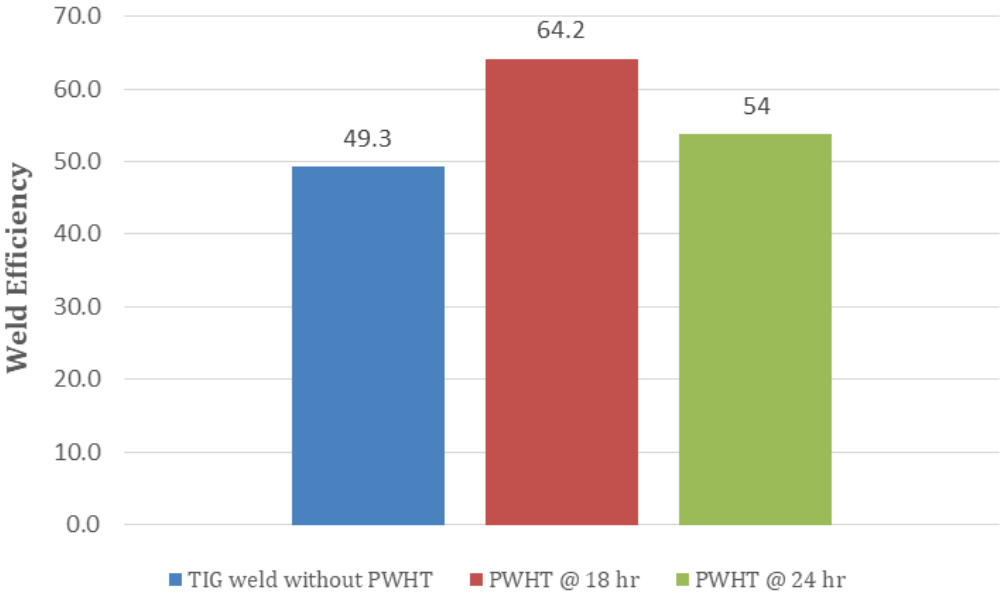


Figure 7. Welding efficiency.

Table 3. Evaluation of hardness (Vicker) due to artificial aging

S. No	Hardness region	18 hours	24 hours
1	Weld Zone	85-110	95-115
2	Coarse Grains	87-100	100-120
3	Fine Grains	74-86	82-85
4	Base Metal	110-128	112-135

base metal after 24 hours of aging was greater than that of the 18-hour aging weld samples. The degradation of mechanical properties and ductility due to extensive precipitation is evident from the hardness study. Therefore, 18 hours of artificial aging is the preferred choice for welded joints due to superior properties. Furthermore, a comparison with the findings of reference study [30] shows that a hardness of 81 HV was achieved using a short soaking duration at a higher temperature. In contrast, this study recorded increases of 25 HV and 40 HV in hardness for soaking durations of 18 hours and 24 hours, respectively. The significant hardness gain in the short-duration, high-temperature cycle suggests excessive precipitate formation, which can adversely affect the ductility of the material. A similar trend of increased hardness was also observed when the soaking duration was extended from 18 to 24 hours in this study.

Impact Testing

The toughness evaluation of welding joints involved conducting Charpy Impact testing both before and after subjecting them to artificial aging. In Figure 8, x axis indicated artificial aging durations and y axis represented absorbed impact energy during Charpy test. The absorbed impact energy ultimately reveals toughness of samples. Hence, the toughness of the welding joints without artificial aging was determined to be 7.4 J/cm^2, as depicted in Figure 7.

The material was not as strong as it should have been because of what happened when it was welded. The welding process provides larger heat input, this heat changed the material's structure at the weld and around that area. The material became stronger after it was treated with aging. For example, after the material was treated for 18 hours, it became much stronger, and impact energy measured was around 10.3 J/cm^2. After 24 hours, weld joints absorbed 8.8 J/cm^2 of energy. This showed that the material became much stronger after it was treated. The material became 40% stronger after 18 hours and slightly stronger after 24 hours due to excessive aging.

The material's ability to bend was measured by something called ductility. Ductility is how much the material can bend without breaking. So, when the material became more ductile, it meant it could bend more without breaking. After the material was treated for 18 hours, it became ductile. The artificial aging process made the material better at bending without breaking than it had been before. The material was better at bending without breaking after it was treated. The artificial aging process really helped the material become more ductile than it had been after welding. The material became better at bending without breaking because of the aging process.

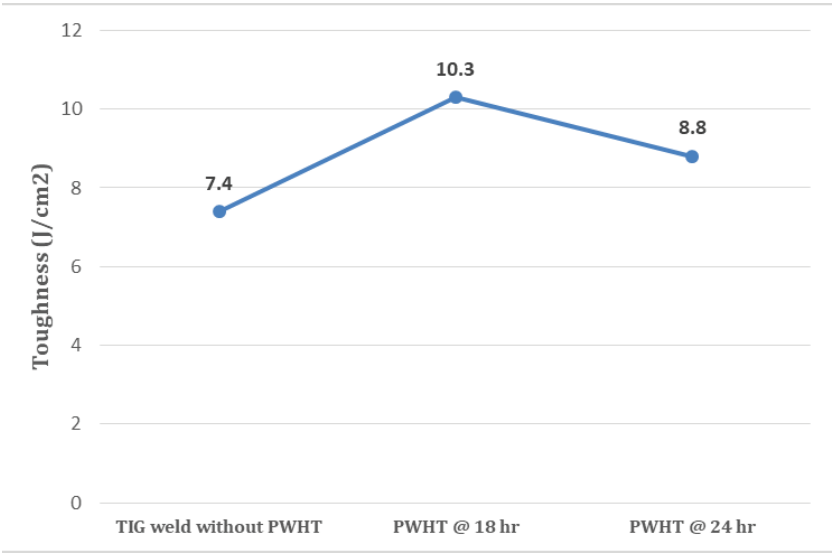


Figure 8. Toughness of welding joints.

CONCLUSION

The goal of this study was to see how a special kind of heat treatment called aging affected the properties of welded aluminum joints. The way tiny particles formed inside the metal depended on the temperature and the time it spent at that temperature. Most recent researches indicated short times and different temperatures for various types of aluminium alloys. The behaviour of this specific alloy under larger exposure to heat was crucial for figuring out how artificial aging affected its properties. In this study, the welded joints exposed to heat at 190 °C for 18 hours and 24 hours. A microscopic analysis was conducted to examine variations in microstructure and grain size. The HAZ of the joints subjected to 18 hours of treatment exhibited uniformly sized and shaped grains, whereas the region treated for 24 hours developed elongated grains, which introduced internal stresses. During testing, it was found that it got much stronger after 18 hours of heat treatment. The yield strength increased from 150 MPa to 240 MPa and tensile strength from 238 MPa to 310 MPa. After 24 hours, the tensile strength slightly enhanced to 260 Mpa and yield strength improved to 200 MPa. The efficiency of the weld improved by 30% after 18 hours and by 9.5% after 24 hours compared to joints that were not treated. The heat treatment also made the joint more flexible and tougher. Similary, the percent elongation of joint increased by 90% after 18 hours. The toughness improved by 40% after 18 hours and by 19% after 24 hours. These results showed how much the properties depended on the duration of heat treatment, even if the temperature maintained same. More than 18 hours artificial aging did not seem to be much effective because it caused excessive hardening, which made the Al 2219 joint less flexible and less tough. Overall, findings showed that it was crucial to choose the heat treatment parameters. For welded aluminum joints used in airplanes and spacecraft, finding the balance of heat treatment could make them much stronger, more flexible, and tougher, without weakening the structure. The TIG-welded Al 2219-T87 joints benefited significantly from optimized aging. Artificial aging improved the properties of TIG-welded Al 2219-T87 joints. Al 2219-T87 joints exhibited improved properties after artificial aging.

ACKNOWLEDGEMENTS

The authors would like to thank for the support and guidance from Abdul Shakoor and Ahmad Hussain.

AUTHORSHIP CONTRIBUTIONS

Authors equally contributed to this work.

DATA AVAILABILITY STATEMENT

The authors confirm that the data that supports the findings of this study are available within the article. Raw data that support the finding of this study are available from the corresponding author, upon reasonable request.

CONFLICT OF INTEREST

The authors declared no potential conflicts of interest with respect to the research, authorship, and/or publication of this article.

ETHICS

There are no ethical issues with the publication of this manuscript.

STATEMENT ON THE USE OF ARTIFICIAL INTELLIGENCE

Artificial intelligence was not used in the preparation of the article.

REFERENCES

[1] Ding J, Wang D, Wang Y, Du H. Effect of post weld heat treatment on properties of variable polarity TIG welded AA2219 aluminium alloy joints. Trans Nonferrous Met Soc China 2014;24:1307–1316. [CrossRef]

[2] Troeger LP, Starke EA. Particle-stimulated nucleation of recrystallization for grain-size control and superplasticity in an Al-Mg-Si-Cu alloy. Mater Sci Eng A 2000;293:19–29. [CrossRef]

[3] Liu Z, Zhao B, Zhao Q. Prospects for welding technology of aluminum alloy in aerospace industry in 21st century. Missiles Space Vehicles 2002;5:63–65.

[4] Wang J, Xie J, Ma D, Mao Z, Liang T, Ying P, Effect of deep cryogenic treatment on the microstructure and mechanical properties of Al-Cu-Mg-Ag alloy. J Mater Res Technol 2023;25:6880–6885. [CrossRef]

[5] Li H, Zou J, Yao J, Peng H. The effect of TIG welding techniques on microstructure, properties and porosity of the welded joint of 2219 aluminum alloy. J Alloys Compd 2017. [CrossRef]

[6] Muzamil M, Wu J, Akhtar M, Azher K, Majeed A, Zhang Z, Nanoparticle-induced control (MWCNTs-TiO_2) on grain size and tensile strength response and multi-response optimization on TIG welded joints. Trans Can Soc Mech Eng 2022;46:626–638. [CrossRef]

[7] Laughlin WMD. A differential scanning calorimetry study of aluminum alloy 6111 with different pro-aging treatments. J Mater Sci Lett 2000;19:201–203. [CrossRef]

[8] Nunes AC, Novak H. Weld geometry strength effect in 2219-T87 aluminum. Washington (DC): NASA Marshall Space Flight Center; 1981.

[9] Çardaklı İ, Karadeniz S, Arslan E, Gok D. Effect of $MgZn_2$ addition on the sintering density, microstructure and hardness of aluminum alloys prepared by powder metallurgy method. Sigma J Eng Nat Sci 2023;41. [CrossRef]

[10] Wan Z, Zhao Y, Zhang S, Zhao T, Li Q, Shan J, Novel weld composition to improve mechanical properties of 2219-T8 aluminum alloy joint using double-wire TIG welding. Mater Charact 2024;209:113764. [CrossRef]

[11] Wan Z, Yi Z, Zhao Y, Zhang S, Li Q, Lin J. Prediction and optimization of tensile properties of 2219-T8 aluminum alloy TIG welding joint by machine learning. Mater Des 2024;245:113274. [CrossRef]

[12] Jiang P, Li X, Huang W. Intelligent detection method for aluminum alloy TIG welding quality by fusing multimodal data features. Pattern Recognit Lett 2025. [CrossRef]

[13] Kumar KS, Kalos PS, Akhtar MN, Shaik S, Sundara V, Fayaz H, Experimental and theoretical analysis of exhaust manifold by uncoated and coated ceramics (Al_2O_3, TiO_2 and ZrO_2). Case Stud Therm Eng 2023.

[14] Gordon S. An investigation into geometry and microstructural effects upon the ultimate tensile strengths of butt welds. Washington (DC): NASA Marshall Space Flight Center; 1992.

[15] Wang GQ, Li Q, Li YJ, Wu AP, Ma NX, Yan DY, Effects of weld reinforcement on tensile behavior and mechanical properties of 2219-T87 aluminum alloy TIG welded joints. Trans Nonferrous Met Soc China 2017;27:10–16. [CrossRef]

[16] Threadgill PL, Leonard AJ, Shercliff HR, Withers PJ. Friction stir welding of aluminium alloys. Int Mater Rev 2009;54:49–93. [CrossRef]

[17] Hu Y, Liu H, Fujii H. Improving the mechanical properties of 2219-T6 aluminum alloy joints by ultrasonic vibrations during friction stir welding. J Mater Process Technol 2019;271:75–84. [CrossRef]

[18] Liu HJ, Zhang HJ, Huang YX, Yu L. Mechanical properties of underwater friction stir welded 2219 aluminum alloy. Trans Nonferrous Met Soc China 2020;20:1387–1391. [CrossRef]

[19] Kasman Ş, Ozan S. Characterization of friction stir welded AA 3003-H24 aluminum alloy plates. Sigma J Eng Nat Sci 2022;40:620–629. [CrossRef]

[20] Öcalır Ş, Eşme U, Boğa C, Külekci MK. Investigation of mechanical and metallographic properties of two different aluminum alloys joined with friction stir welding method using different welding parameters. Sigma J Eng Nat Sci 2020;38:1333–1349.

[21] Yao SJ, Tang QH, Yang J, Wang CY, Sun HF, Rong RL, Microstructural characterization and mechanical properties of 6061 aluminium alloy processed with short-time solid solution and aging treatment. J Alloys Compd 2023;960:170704. [CrossRef]

[22] Xuehong X, Deng Y, Chen S, Gao X. Effect of interrupted ageing treatment on the mechanical properties and intergranular corrosion behavior of Al-Mg-Si alloys. J Mater Res Technol 2020;9:230–241. [CrossRef]

[23] Temmar M, Hadji M, Sahoursaoui T. Effect of post-weld aging treatment on mechanical properties of tungsten inert gas welded low thickness 7075 aluminum alloy joints. Mater Des 2011;32:3532–3536. [CrossRef]

[24] Dash SS, Li DJ, Zeng XQ, Chen DL. Heterogeneous microstructure and deformation behavior of an automotive grade aluminum alloy. J Alloys Compd 2021;870:159413. [CrossRef]

[25] Malarvizhi S, Raghukandan K, Viswanathan N. Effect of post weld aging treatment on tensile properties of electron beam welded AA2219 aluminum alloy. Int J Adv Manuf Technol 2008;37:294–301. [CrossRef]

[26] Shazad A, Asif M, Uzair M, Zaidi AA. Evaluation of preheating impact on weld residual stresses in AH-36 steel using finite element analysis. Mem Investig Ing 2024;26:225–243. [CrossRef]

[27] Shazad A, Uzair M, Jamil T, Muhammad N. A comparative study on the joint hardness and tensile properties of dissimilar aluminum alloy using tungsten inert gas (TIG) welding. In: Proceedings of the 4th International Conference on Key Enabling Technologies (KEYTECH 2024); 2024 Dec. Atlantis Press; 2024. p. 173–178. [CrossRef]

[28] Saravanan A, Sudharsan G, Suresh P, Salaisargunan SP, Anandhi S, Kumar KS. Performance study on a high-strength extruded magnesium alloy van frame using FEA. Strength Mater 2023. [CrossRef]

[29] Raza MR, Ahmed F, Ikram N, Ahmad R. Development and strengthening of 2219 aluminum alloy by mechanical working and heat treatment. J Appl Sci 2011. [CrossRef]

[30] Venkatasubramanian G, Mideen AS, Jha AK. Microstructural characterisation and corrosion behaviour of top surface of TIG welded 2219-T87 aluminium alloy. Int J Eng Sci Technol 2013;5:624.

Sigma J Eng Nat Sci, Vol. 44, No. 4, pp. 2974–2981, August, 2026

Sigma Journal of Engineering and Natural Sciences
Web page info: https://sigma.yildiz.edu.tr
DOI: 10.14744/sigma.2026.2139

Research Article

Some components and bioactive properties of gel and green leaf parts of *A. vera*

Heleen TAHSEEN YASEEN[1,*], Sevda KIRBAĞ[1], Fikret KARATAŞ[2]

[1]*Department of Biology, Faculty of Science, Fırat University, Elazığ, 23119, Türkiye*
[2]*Department of Chemistry, Faculty of Science, Fırat University, Elazığ, 23119, Türkiye*

ARTICLE INFO

Article history
Received: 12 September 2024
Revised: 17 October 2024
Accepted: 05 May 2025

Keywords:
Aloe Vera; Antimicrobial; Antioxidant; Phyochemical Composition; Vitamins

ABSTRACT

Aloe vera (L.) Burm. f., known as the plant of immortality, is a perennial and succulent plant. This study aimed to investigate potential alternatives to synthetic antibiotics and antioxidants due to the increasing resistance of microorganisms to these drugs and the negative effects of synthetic antioxidants. So phytochemical characteristics and antimicrobial activities of the gel and green leaf parts of *A. vera* have been measured. Vitamin A, E, lycopene, β-carotene, and 4-hydroxyneonal (4-HNE) that were determined by high-performance liquid chromatography (HPLC) were found to be 0.17±0.03, 3.6±0.57, 7.6±1.50, 0.63±0.14, and 5.6±1.07 μg/g in the green leaf part of *Aloe vera* and 0.26±0.05, 1.1±0.09, 0.07±0.01, and 3.68±0.74 μg/g in the gel, respectively. Total phenolics, flavonoids, 2,2'-Azino-bis-3-ethylbenzothiazoline-6-sulfonic (ABTS), and 2,2-Diphenyl-1-picrylhydrazyl (DPPH) radical scavenging activity that were determined using a UV-Vis spectrophotometer were found to be 0.17±0.01, 0.96±0.15, 133.9±7.08, and 25.1±2.28 in the green leaf part of the plant, while they were found to be 407.95±9.42, 0.95±0.67, 0.04±0.00, and 0.26±0.05 in the gel, respectively. The antimicrobial activities of *A. vera* were determined by the disc-diffusion method. The green leaf part of *A. vera* had the most powerful effect on *Bacillus megaterium*, with an inhibition zone measuring 11.6±0.32 mm in diameter. While the gel had the strongest effect on *Staphylococcus aureus*, with a 20.0±0.29 mm zone of inhibition. Therefore, we can conclude that. *vera* serves as a valuable source of antioxidant and antimicrobial activity, suitable for both medicinal and cosmetic applications.

Cite this article as: Tahseen Yaseen H, Kırbağ S, Karataş F. Some components and bioactive properties of gel and green leaf parts of *A. vera*. Sigma J Eng Nat Sci 2026;44(4):2974–2981.

INTRODUCTION

There are around 420 species of the genus *Aloe*, and they have been placed in the, Aloaceae families, including *Aloe vera* (L.) Burm. f. [1]. Although *Aloe barbadensis* Miller is the more common name, *A. vera* is the correct name according to international regulations of botanical nomenclature [2]. The leaves of the plant are tall and pointed. There is a green shell and a transparent pulp within each

***Corresponding author.**
*E-mail address: heleeny1991@gmail.com

This paper was recommended for publication in revised form by Editor-in-Chief Ahmet Selim Dalkilic

Published by Yıldız Technical University Press, İstanbul, Turkey
© Author. This is an open access article under the CC BY-NC license (http://creativecommons.org/licenses/by-nc/4.0/).

leaf. The pulp, which makes up the bulk of the leaf, seems to be both transparent and mucilaginous. For medicinal reasons, this portion of the plant is most often used [3].Light green in color; this perennial plant resembles both shrubs and trees. It is xeric and succulent [4]. It is believed that the Arabic words "alloeh" or "alloek" and the Hebrew word "allal," meaning "bitter" are the origins of the Greek word "aloe" (aloi). Arabic "wahre" means "real" or "genuine," and the Latin word "vera" comes from this source. In Anatolia, it is called "sari sabre" because of its typically yellow petals, and its name in common use is derived from the Arabic word "sabre" meaning "sword" in reference to its sword-shaped leaves. Its native habitats in Turkey are the southern Turkish coast and Antalya's Demre area [5, 6]. It is thought that the plant *A. vera* originated in Sudan and was later transferred to the Mediterranean and other warm regions of the globe. A clay tablet from 2100 BC in Mesopotamia is the first known written evidence of the medicinal power of *Aloe*. Papyrus Ebers, an Egyptian record from 1550 BC, provide the earliest extensive description of the plant's medical significance, including several *Aloe*-containing concoctions for the treatment of exterior and interior illnesses. The Greek herbalist Dioscorides (ca. Seventy AD) described the *A. vera* plant and advocated its use in treating wounds, hair loss, vaginal ulcers, and hemorrhoids [7]. According to a variety of recent study, this species not only protects teeth from UV rays but also reduces inflammation, fights germs and fungi, modulates the immune system, and inhibits the growth of cancer cells [8–12]. Despite its widespread cultivation today, the *Aloe barbadensis* Miller plant the "plant of immortality" actually originates from Africa, the Arabian Peninsula, and the islands of the Indian Ocean. This plant is a member of the Asphodelaceae family [13]. Over 2000 years ago, Egyptian scientists dubbed *A. vera* "the herb of immortality," while Greeks called it "the universal panacea". Approximately 99.0–99.5% of the substance is water. Since it can hold a lot of water, it may be used to keep the skin hydrated, and its gel can be used to treat skin injuries since it aids in wound healing and promotes cell reproduction. Several properties of *A. vera* contribute to its capacity to hasten wound healing, including moistening effects, increased cell motility, and enhanced collagen production [14]. Furthermore, it is employed in the treatment of a broad spectrum of diseases, for instance inflammation, digestive issues, constipation, thermal burns, sunburns, radiation damage, skin diseases, diabetes, and ulcers. Nearly 200 active substances and 75 nutrients, encompassing both water- and fat-soluble vitamins, minerals, enzymes, mono- and polysaccharides, phenolic compounds, and organic acids, have been reported to make up the remaining 0.5–1.0% instead of the typical 99.0-99.5% water [15]. Polyphenols, flavonoids, tannins, saponosides, steroids/terpenes have been identified in *A. vera* [16]. *Aloe vera* has been reported to contain high levels of bioactive compounds, including phenols, flavonoids, tannins, saponins, anthraquinones, and ascorbic acid, as well as essential mineral elements. In addition, its gel has demonstrated notable biological activities, such as anti-influenza effects in the Madin–Darby Canine Kidney (MDCK) cell line and inhibitory action against the growth of various pathogenic microorganisms [17]. The medicinal properties of *A. vera* gel may be attributed to the presence of molecules with a high molecular weight [18]. The plant has an exterior covering that is visible from the outside and a parenchyma *Aloe* gel that is visible from the inside of the same covering. Both *in vivo* and *in vitro* studies have shown that these two constituents have therapeutic effects. Antibacterial, antifungal, anti-inflammatory, and anti-arthritic properties have been shown in studies of the plant's entire extract [19]. The wound healing properties of *A. ve*ra gel were determined using experimental animals [20]. By preventing the production of oxygen radicals, *A. vera* is thought to have immunomodulatory effects [21]. Different *A. vera* fractions, as well as the unfractionated entire gel, have been claimed to have antioxidant benefits by a number of writers. The antioxidant properties of the *A. vera* gel may stem from the presence of glutathione peroxidase activity, superoxide dismutase, and phenolic antioxidant [22]. There are several components of *A. vera* that are responsible for its antioxidant properties. These components include α-tocopherol, carotenoids, ascorbic acid, flavonoids, tannins and vitamin E [23]. In this study, some components and biological activities of the *A. vera* were determined.

MATERIALS AND METHODS

Sample Preparation

Plant samples were obtained from Planet Shop in Elazığ City, Türkiye. The plant leaves were rinsed under running water to eliminate dust and insect larvae. The gel was manually extracted from fresh *A. vera* leaves after they were chopped using a knife. One gram of the gel and one gram of the green leaf part were used for testing water soluble vitamins, vitamins A, E, β-carotene, lycopene and 4-HNE. While 15 grams of samples were extracted using methanol in Soxhlet to prepare for antioxidant tests.

Chemicals and Equipment

Standard and chemical reagents, including butylated hydroxy toluene, flavone, perchloric acid, gallic acid, aluminum chloride, quercetin (dehydrate), potassium persulfate, sodium nitrate, aluminum chloride, gallic acid, and perchloric acid, were acquired from Sigma-Aldrich or Merck, respectively. All the water used in the process was double-distilled (dd H_2O).

Because of the potential for contaminants in the solvent to obscure the sample peak in the HPLC chromatogram, only analytical-grade solvents were used for the sample preparation. The liquid chromatography solvents were of the HPLC kind. For HPLC, the mobile phase always consists of a solvent that has been filtered via a

membrane filter and degassed in an ultrasonic bath. The SHIMADZU Prominence-LC-2020C 3D Model was used for HPLC analysis together with a PDA detector. A UV-VIS spectrophotometer was used for the spectrophotometric measurements.

Determination of Vitamins A, E, β-carotene, Lycopene and 4-HNE

After adding 1.0 g of sample to a tube, 5.0 mL of C_2H_5OH was added, and the mixture was sonicated for 10 min then vortexed and centrifuged for 6 min at 7,500 rpm. After that, we added 1.0 mL of n-hexane to the sample, gave it a good vortex, and then extracted the n-hexane phase twice. The n-hexane phases were collected, evaporated in a vacuum, and diluted in 1.0 mL of methanol before being analyzed using a combination of methanol and water (95:5) as the mobile phase. An Inertsil ODS-3 column with dimensions of 25.0 cm x 4.6 mm x 5.0 µm was designed for analysis [24].

Extraction of Samples

The samples were being extracted using 15 g of sample and 250 mL of methanol in a Soxhlet device for 6 h. Methanol was then extracted using a rotating evaporator operating at 40 °C under vacuum. After drying the extract, it was weighed before dissolving it in 10 mL of CH3OH and storing the resulting solution at 4 °C in a refrigerator [25].

Determination of Total Phenolic Content

The spectrophotometric determination of total phenolic material followed the Folin-Ciocalteu technique with adjustments made by Dewanto et al. [26] The following was combined and shaken: 0.50 mL of distilled water, 0.250 mL of sample or gallic acid, and 0.125 mL of Folin-Ciocalteu reagent. To achieve volume of 3.00 mL, distilled water was added after 6 min, and 1.250 mL of 7% sodium carbonate solution was added. After 90 min, the ultraviolet-visible spectrophotometer read the absorption at 760 nm. It was determined how varied quantities of gallic acid would affect the graph. The TPC of the samples was calculated, and the findings were reported in micrograms of gallic acid equivalents per gram (µg GAE/g) [26].

Determination of Total Flavonoids

Spectrophotometric analysis, as reported by Dewanto et al. [26], was used to calculate total flavonoid content. The absorbance at 510 nm was measured after mixing a 0.025 mL sample of quercetin with 1,250 mL of distilled water, 0.075 mL of a 5% sodium nitrite solution, and 0.150 mL of a 10% solution of aluminum chloride; the mixture was allowed to stand for 5 min. Then, 0.500 mL of a 1.0 M sodium hydroxide solution was added. Different amounts of quercetin were used to create a usable graph. Total flavonoids content was calculated using the working graph, and the findings were expressed as micrograms of quercetin compounds per gram [26].

Total Antioxidant Capacity DPPH Method

The DPPH method of Antioxidant capacity was measured utilizing the approach published by Nile et al. [27], which is depend on the scavenging activity of the stable DPPH free radical. The absorption of a DPPH solution made by dissolving 25 µg/mL of DPPH in (CH_3OH) methyl alcohol was measured at 510 nm. The, absorbance at 510 nm was measured after the DPPH solution had been placed in the dark area for thirty minutes with varying concentrations of sample extracts. IC_{50} (µg/mL) values were reported, which represent the concentration of the antioxidant chemical that inhibits 50% of the DPPH radical in the medium. High antioxidant activity is shown by low IC_{50} values [27].

Total Antioxidant Capacity ABTS Method

The antioxidant activity inherent in the samples was assessed employing the ABTS radical cation decolorization assay, a method initially detailed by Re et al. [28] and subsequently adapted with minor procedural adjustments. The generation of the $ABTS^{\bullet+}$ radical cation involved the combination of a 7.0 mM ABTS solution with 2.4 mM potassium persulfate. This mixture was subsequently allowed to react under dark conditions at ambient temperature for a duration of 12–16 hours, thereby facilitating the complete formation of the desired radical species. Before conducting the analysis, the $ABTS^{\bullet+}$ solution required dilution with a phosphate buffer (pH 7.4) until an initial absorbance of 0.80 ± 0.02 at 734 nm was achieved. In the assay procedure, 2.0 mL aliquots of the diluted $ABTS^{\bullet+}$ solution were dispensed into individual test tubes. This was followed by the introduction of either the sample extract or a Trolox standard solution in varying volumes (25, 50, 75, and 100 µL). These reaction mixtures were incubated at room temperature for 15 minutes, subsequent to which their absorbance was quantified at 734 nm employing a UV–Vis spectrophotometer. To serve as a reference, a control sample comprising solely the $ABTS^{\bullet+}$ solution, without the incorporation of any sample or standard, was prepared under conditions identical to those used for the test samples. The antioxidant capacity for each sample was then computed utilizing a Trolox calibration curve, with the results articulated as micromoles of Trolox equivalents per gram of sample (µmol TE/g) [28].

Screening of Antimicrobial Activities

Test microorganisms

For the tests, we used different kinds of organisms, including both Gram-positive and Gram-negative bacteria. Specifically, the Gram-positive types were *Staphylococcus aureus* COWAN 1 FMC 16 and *Bacillus megaterium* DMS 32. As for the Gram-negative bacteria, we had *Pseudomonas aeruginosa* DMS 50071 SCOTTA, *Escherichia coli* ATCC 25922, *Klebsiella pneumoniae* FMC 5, and *Proteus vulgaris* FMC 1. We also included one type of yeast *Candida albicans* FMC 17 in our tests. All these microorganisms came

from the Microbiology Laboratory Culture Collection at Firat University's Department of Biology.

Extract preparation

Fresh plant tissue (10 g gel and green leaf part) was macerated for 24 h in 150 mL of methanol solvent with rotary agitation. The substances were filtered through Whatman No. 1 to clarify. The solvent was evaporated to dryness under vacuum at 37 °C. The recovered materials were dissolved in dimethyl sulfoxide (DMSO) and stored at 4 °C until further use. Each prepared extract was dispensed at a pre-validated controlled volume of 20 µl on to antibiotic assay discs (6 mm, Schleicher & Schüll No. 2668). Antimicrobial activity was compared with standards of streptomycin sulphate and nystatin. The amount of solvent to be injected in to the disc is regulated by controls, which stipulate that only 20 µL of solvent will be administered. Streptomycin sulfate and nystatin are the standard substances used in this process.

Preparation of microbial cultures and test

After 24 h in nutrient broth and 48 h in malt extract broth, bacterial and yeast strains were inoculated. To use the disc-diffusion method, the test bacteria and yeasts were placed on Mueller Hinton agar (for bacteria) and Malt extract agar (for yeast) at concentrations of 10^5 bacteria/mL and 10^4 yeast/mL, respectively. The solid agar medium was covered with the disc by gently pushing it down. After 2 h at 4 °C, the petri dishes were incubated at 35±0.1 °C for 24 h, while the yeast was incubated at 25±0.1 °C for 3 days. The inhibitory zones were measured in millimeters at the beginning of the period [29].

Statistical Analysis

The analyses were replicated three times, and the findings are reported as the mean ± error. The findings were subjected to one-way ANOVA analysis using SPSS 26.0 for MS Windows. The significance of differences between group means was assessed using the Tukey HSD test, and statistical significance was indicated by a $p \leq 0.05$. Different letters were used to highlight significant differences between table rows, whereas similar letters imply that there is no statistical difference between groups.

RESULTS AND DISCUSSION

Fat-Soluble Vitamins (A & E), β-carotene, Lycopene and 4-HNE

Based on the findings of this study, vitamins A and E were detected in various part of the plant as shown in (Table 1). The concentration of vitamin A obtained in the green leaf part and gel of *A. vera* were 0.17±0.03 µg/g and 0.26±0.05µg/g. There was no significant difference in the concentration of vitamin A between the plant gel and green leaf portions ($p<0.05$). A research study conducted in Indonesia on the *Aloe chinensis baker* plant found that fresh gel of 7-8 months old *A. vera* (raw material) contains 4.59 IU (1.38 µg/g) of vitamin A content. [30]. It seemed to be higher when compared to the results of this study. This could be due to genus variations.

While Vitamin E concentration was 3.6±0.57 µg/g in the green leaf part and was 1.1±0.09 µg/g in the gel of the *A. vera*. The vitamin E contents of the gel and green leaf portions of the plants were not significantly different from one another ($p>0.05$). Research conducted in 2011 found that 100 g of *A. vera* gel has a vitamin E level of 0.192 IU/100g (1.29 µg/g) [31]. The results of this study align with it. Furthermore, it is clear that gel had a higher vitamin A concentration than green leaves. On the other hand, the green leaf part generally had higher vitamin E levels than the gel of *A. vera.* Table 1. shows that the 0.63±0.14 µg/g of β-carotene level observed in the green leaf part of plant while in gel was 0.07±0.01 µg/g. The β-carotene contents of the gel and green leaf portions of the *A. vera* were not significantly different from one another ($p>0.05$). In 2009, Ozsoy et al. [32] found that the aqueous extract of *A. vera* leaves had a β-carotene content of (15.5±12.39 µg/g FW). It seemed to be higher when compared to the results of this study. It could be because of the maturation stage of plant ,solvent or laboratory procedures used. The nutritional values discovered in this study are at odds with what is already known from the literature. The concentration of lycopene was 7.6±1.50 µg/g in the green leaf part of *A. vera*; on the other hand, gel contained 3.01±0.69 µg/g of lycopene (Table 1). Statistically, there is no significant difference in the lycopene level of the gel and green leaf part components of

Table 1. Amount of vitamin A, E, β-carotene, lycopene and 4-HNE concentrations µg/g

	Green leaf part	Gel
Vitamin A	[a] 0.17±0.03	[a] 0.26±0.05
Vitamin E	[a] 3.6±0.57	[b] 1.1±0.09
β-Carotene	[a] 0.63±0.14	[b] 0.07±0.01
Lycopene	[a] 7.6±1.50	[b] 3.01±0.69
4-HNE	[a] 5.6±1.07	[a] 3.68±0.74

Statistical significance level was expressed as $p<0.05$. Different letters in the rows indicate a statistical difference, while the same letters indicate that there is no statistical different

the *A. vera* plant (p>0.05). The green leaf part of the plant contains higher levels of β-carotene and lycopene than the gel. Martnez-Sánchez et al. [33] studied the bioactive component of *A. vera* flowers at three stages of development: the first stage is immature; the second stage is mature, and the third stage is mature. The lycopene concentration was found to be the lowest in the third stage, while in Stage I, immature, it was found to be the highest [33]. The green leaf part of *A. vera* has a (5.6± 1.07 µg/g) concentration of 4-Hydroxynonena(4-HNE); on the other hand, the gel shows a (3.68±0.74 µg/g) level for 4-HNE (Table 1). Statistically, there is no significant difference in the 4-HNE value of the gel and green leaf part components of the *A. vera* plant (p>0.05). Thus, the gel showed a higher 4-hydroxynonena level. No published or rare information on the concentrations of these compounds in *A. vera* was found. According to the findings, the nutritional qualities are higher in the green leaf part of *A. vera* than the gel.

Total Phenolic, Total Flavonoid, DPPH & ABTS Content

The total amount of phenolic compounds is provided as µg of Gallic acid equivalent/g of extract and is represented in (Table 2). The green leaf part of *A. vera* showed a higher level of total phenolic content (0.17±0.01 µg/g) than the gel that has (0.04±0.00 µg/g) of total phenolic content. The quantities of total phenolic content in the *A. vera*'s green leaf part and gel were found to be significantly different (p<0.05). The lowest estimated amount of total phenolic content was 97.95 ± 21.5 µg GAE/mg, while the maximum value was 332.4 ± 32.6 µg GAE/mg, according to another study done in Pakistan, examined various fractions of *A. vera* leaf [34]. It seems to be higher with a considerable difference when compared to the results of this research; this might be because of the effects of climate change or the plant's maturity stage.

The total amount of flavonoid compounds is provided as µg of Quercetin equivalent/g and is represented in (Table 2). TFC in the green leaf part of *A. vera* was obtained as (0.96±0.21 µg/g). On the other hand, the gel was estimated at (0.26±0.07 µg/g). The green leaf part of *Aloe vera* contain a higher amount of flavonoid content than the gel. The total flavonoid content of the gel and green leaf portions of the plant is not significantly different from one another (p>0.05). A study conducted in 2003 by Hu et al. [21] examined *A. vera* plant samples taken at various stages of maturity. The researchers discovered that *A. vera* plant that were three years old had a greater amount of flavonoid content that estimated as (4.70 ± 0.48 g/kg), and four years old *A. vera* had (4.28±0.18 g/kg) flavonoid concentration, in the other hand two years old plant had (3.63±0.38 g/kg) of flavonoid content [21].

The common purpose of this experiment is also to find out how well different sample extracts scavenge radicals. The premise of the experiment focused on the capacity of the extract to lower DPPH and ABTS radicals. The ability of four distinct concentrations of *A. vera* samples from 50 to 200 µL for DPPH and ABTS radical scavenging was evaluated. According to the findings, the effects of the *A. vera* extracts start at a concentration of 50 µL and increase with concentration, as shown by the findings. As shown in (Table 2), the methanolic extract of green leaf part of *A. vera* was 133.9±7.08 µg/mL, on the other hand the methanolic extract of gel showed 407.95±9.42 µg/mL, of DPPH radical scavenging activity. So, the green leaf part of *A. vera* has a higher ability to scavenge DPPH radicals. According to Zahra et al. [35] *A. vera* powder extract was showed that at doses of 20–100 µg/mL, water extracts showed a % inhibition (DPPH) of 10.23–35.80, while methanol extracts showed 12.84–44.96. A statistically significant difference was discovered in the DPPH radical scavenging activity between the green leaf section and the gel of *A. vera* (p<0.05). As shown in (Table 2), methanolic extract of green leaf part of *A. vera* showed 25.1±2.28 µmole trolox/g, on the other hand the methanolic extract of gel showed 0.95±0.67 µmole trolox /g, of ABTS radical scavenging activity respectively. Therefore, the green leaf part of *A. vera* have a higher ability to scavenge ABTS radicals. Jairath et al. [36] determined that the capacity of the aqueous methanolic *A. vera* gel to scavenge ABTS radicals was 96.14%. Although there was no significant difference in the ABTS radical scavenging activity across various parts of the *A. vera* (p>0.05). The findings of this study were consistent with those of previous studies. Studies on *A. vera* have shown that the radical scavenging capacity of a plant is proportional to the concentration of the studied compound. In terms of radical scavenging action, the green leaf portion of *A. vera* is generally considered more potent than the gel.

Table 2. Amount of total phenolic µg/g, total flavonoid µg/g, DPPH µg/mL and ABTS µmole trolox/g

	Green leaf part	Gel
Total phenolic	[a] 0.17±0.01	[b] 0.04±0.00
Total Flavonoid	[a] 0.96±0.15	[b] 0.26±0.05
DPPH	[a] 133.9±7.08	[b] 407.95±9.42
TEAC	[a] 25.1±2.28	[b] 0.95±0.67

Statistical significance level was expressed as p<0.05. Different letters in the rows indicate a statistical difference, while the same letters indicate that there is no statistical different.

Table 3. Antimicrobial activity of *A. vera* (mm)

	Green leaf part	Gel	Standard
Bacillus megaterium	[a] 11.6±0.32	[b] 19.0±0.35	[c] 24.3±0.33
Pseudomonas aeruginosa	[a] 8.9±0.13	[b] 15.5±0.29	[c] 18.5±0.29
Escherichia coli	[a] 8.3±0.30	[b] 16.2±0.17	[c] 25.3±0.33
Klebsiella pneumoniae	[a] 9.3±0.17	[b] 17.4±0.20	[c] 18.9±0.47
Proteus vulgaris	[a] 9.0±0.29	[b] 15.5±0.29	[c] 18.2±0.20
Staphylococcus aureus	[a] 10.0±0.35	[b] 20.0±0.29	[b] 20.2±0.20
Candida albicans	[a] 9.2±0.20	[b] 17.5±0.29	[c] 21.8±0.39

Statistical significance level was expressed as $p<0.05$. Different letters in the rows indicate a statistical difference, while the same letters indicate that there is no statistical different.

Antimicrobial Activity

The disc diffusion technique was used to ascertain the antibacterial and antifungal properties of the extracts of various portions of the *A. vera* plant that were utilized in the study. The results of this determination are shown in (Table 3). The diverse sections of the plant, namely the green leaf portion and the gel, were shown to be effective in preventing the growth of yeast and bacteria. The extract of the green leaf component of the *A. vera* plant had the greatest impact on *Bacillus megaterium* (11.6±0.32 mm), while it had the least impact on *Escherichia coli* (8.3±0.30 mm). It was shown that the extract of the gel component had the most impact on *Staphylococcus aureus* (20±0.29 mm), while it had the least impact on *Pseudomonas aeruginosa, and Proteus vulgaris* (15.5±0.29 mm). The antimicrobial abilities of *A. vera* plant's gel, green leaf part and standard were found to be significantly different ($p<0.05$). In the study by Kaithwas et al. [37] *A. vera* gel has been shown to limit the development of some germs such as *Escherichia coli* (6 mm), *Staphylococcus aureus* (9.56 mm), *Pseudomonas aeruginosa* (6 mm), and *Proteus vulgaris* (6 mm). It has been determined that *A vera* gel inhibits the growth of *Bacillus cereus B. subtilis, L. monocytogenes, Micrococcus luteus, Staphylococcus aureus* [16]. The results of this study, specifically the gel, demonstrated the most potent antimicrobial activity when compared to the literature. This study's investigations to determine the antimicrobial capacity of various parts of *A. vera* yielded different results from the literature. This discrepancy may be due to experiments being conducted in different regions, under different climatic conditions.

CONCLUSION

Aloe vera has become of interest because of its wide range of applications, especially its medicinal, cosmetic, and food uses. The number of scientific studies on it is continually growing. Gel has stronger potential antibacterial activity than the green leaf portion of *Aloe vera*, which might be utilized to treat the increasing resistance of microbes to synthetic antibiotics, according to this research. However, the green leaf component of *Aloe vera* is a better antioxidant source. People are becoming aware of the growing resistance of microbes to synthetic antibiotics and the negative effects of synthetic antioxidants, which causes severe health issues. So, researchers have begun looking for natural alternatives to antimicrobials and antioxidants in order to reduce the negative effects of synthetic drugs. As a result, it is anticipated that this work will provide valuable insights for future research aimed at discovering alternative antioxidants and antimicrobials.

AUTHORSHIP CONTRIBUTIONS

Authors equally contributed to this work.

DATA AVAILABILITY STATEMENT

The authors confirm that the data that supports the findings of this study are available within the article. Raw data that support the finding of this study are available from the corresponding author, upon reasonable request.

CONFLICT OF INTEREST

The authors declared no potential conflicts of interest with respect to the research, authorship, and/or publication of this article.

ETHICS

There are no ethical issues with the publication of this manuscript.

STATEMENT ON THE USE OF ARTIFICIAL INTELLIGENCE

Artificial intelligence was not used in the preparation of the article.

REFERENCES

[1] Dagne E, Bisrat D,Viljoen A, Van Wyk B. Chemistry of Aloe species. Curr Org Chem 2000;4:1055–1078. [CrossRef]

[2] Sahu P, Giri D, Singh R, Pandey P, Gupta S, Shrivastava A, Kumar A, et al. Therapeutic and medicinal uses of aloe vera: a review. Pharmacol Pharmacy 2013;4:599–610. [CrossRef]

[3] Ni Y, Turner D, Yates K.M, Tizard I. Isolation and characterization of structural components of Aloe vera L. leaf pulp. Int Immunopharmacol 2004;20:41745–41755.

[4] Kostekçi Ö.Ç. Determination the proctective effect of Aloe vera application on drosophila melanogaster against trifluraline in with various parameters. Brazil Arch Biol Technol 2023;66:e23210311.

[5] Kumar S, Purohit CS, Kulloli RN. Aloe trinervis sp. nov.: A new succulent species from Indian Desert (Asphodelaceae). J Asia-Pacific Biodivers 2020;13325–13330. [CrossRef]

[6] Tunçayı HA, Kaya Gİ. Usage of Aloe vera (L.) Burm. F. (Sarısabır) Plant in Phytotherapy. J Fac Pharm 2002;45:674–698.

[7] Lanka S. A review on Aloe vera- the wonder medical plant, J Drug Deliv Ther 2018;8:94–99. [CrossRef]

[8] Tudose A, Celia C, Cardamone F, Vono M, Molinaro R, Paolino D. Regenerative properties of Aloe vera juice on human keratinocyte cell culture. Farmacia 2009;57:590–597.

[9] Joseph B, Raj S.J. Pharmacognostic and phytochemical properities of Aloe vera LINN - an overview Taxonomy. Enzymes 2010;4:106–110.

[10] Badakhsh S, Eskandarian T, Esmaeilpour T. The use of Aloe vera extract as a novel storage media for the avulsed tooth. Iran J Med Sci 2014;39:327–332.

[11] Chelu M, Musuc AM, Aricov L, Ozon EA, Iosageanu A, Stefan LM, et al. Antibacterial Aloe vera based biocompatible hydrogel for use in dermatological applications. Int J Mol Sci 2023;24:3893. [CrossRef]

[12] Johri A, Kumar A, Singh D, Tiwari K, Arora N. Clinical uses of Aloe vera in veterinary medicine. Indian Farmer 2023;10:198–200.

[13] Wasim A, Saif A, Atul Pratap S. A Comprehensive review of Aloe vera: health benefits, mechanisms of action and future perspectives. Int J Res Dev Technol 2023;1:1–18.

[14] Komatsu D, Mistura DV, Motta A, Domingues JA, Hausen MA, Duek E. Development of a membrane of poly (L-co-D,L lactic acid-co-trimethylene carbonate) with Aloe vera: An alternative biomaterial designed to improve skin healing, J Biomater Appl 2017;32:311–320. [CrossRef]

[15] Periferakis A, Periferakis K, Badarau IA, Petran EM, Popa DC, Caruntu A, et al. Kaempferol: antimicrobial properties, sources, clinical, and traditional applications. Int J Mol Sci 2022;23:1–39. [CrossRef]

[16] Konkobo FA, Barry PR, Zongo S, Ouedraogo ER, Roamba NE, Dakuyo R, et al. Biochemical characterization and antimicrobial properties of extracts from four food plants traditionally used to improve drinking water quality in rural areas of Burkina Faso. Biochem Res Int 2025;9994531:11. [CrossRef]

[17] Al-Eisa RA, Sami R, Bedaiwi RI, Kadi RH, Abushal SA, Johari DM, et al. Anti-influenza effects of Aloe vera gel on MDCK cells: protective efficacy against ultraviolet-C exposure and analysis of biochemical characteristics and microbial activities. Front Sustain Food Syst 2025;8:1508809. [CrossRef]

[18] Rosca-Casian O, Parvu M, Vlase L, Tamas M. Antifungal activity of Aloe vera leaves. Fitoterapia 2007;78:219–222. [CrossRef]

[19] Danish P, Ali Q, Hafeez M, Malik A. Antifungal and antibacterial activity of Aloe vera plant extract. Biol Clin Sci Res J 2020;1:1–8. [CrossRef]

[20] Arafa NMS, Hummadi HMA, Badr GM. The potential of aloe vera gel utilization for skin wound healing in rats based on GC-MS and HPLC chemical profile. JoBAZ 2025;86:6. [CrossRef]

[21] Hu Y, Xu J, Hu Q. Evaluation of antioxidant potential of Aloe vera (Aloe barbadensis Miller) extracts. J Agric Food Chem 2003;51:7788–7791. [CrossRef]

[22] Langmead L, Makins RJ, Rampton DS. Anti-inflammatory effects of Aloe vera gel in human colorectal mucosa in vitro. Aliment Pharmacol Ther 2004;19:521–527. [CrossRef]

[23] Eshun K, He Q. Aloe vera: a valuable ingredient for the food, pharmaceutical and cosmetic ındustries - a review. Crit Rev Food Sci Nutr 2004;44:91–96. [CrossRef]

[24] Ibrahim MS, Ibrahim YI, Mukhtar ZG, Karatas F. Amount of vitamin A, vitamin E, vitamin C, malondialdehyde, glutathione, ghrelin, beta-carotene, lycopene in fruits of Hawthorn, Midland (Crataegus laevigata). J Hum Nutr Food Sci 2017;5:1112–1117.

[25] Wang L, Weller CL. Recent advances in extraction of nutraceuticals from plants. Trends Food Sci Technol 2006;17:300–312. [CrossRef]

[26] Dewanto V, Xianzhong W, Adom KK, Liu RR. Thermal processing enhances the nutritional value of tomatoes by increasing total antioxidant activity. J Agric Food Chem 2002;50:3010–3014. [CrossRef]

[27] Nile SH, Kim SH, Ko EY, Park SW. Polyphenolic contents and antioxidant properties of different grape (V. vinifera, V. labrusca, and V. hybrid) cultivars. Biomed Res Int 2013;1:1–5. [CrossRef]

[28] Re R, Nicoletta P, Anna P, Ananth P, Min Y, Catherine RE. Antioxidant activity applying an improved ABTS radical cation decolorization assay. Free Radic Biol Med 1999;26:1231–1237. [CrossRef]

[29] Gorsi FI, Kausar T, Murtaza MA. Evaluation of antibacterial and antioxidant activity of Aloe vera (Aloe barbadensis Miller) gel powder using different

solvents. Pesqui Agropecu Bras 2019;8:1265–1270. [CrossRef]

[30] Hendrawati TY. Aloe vera powder properties produced from aloe chinensis baker, Pontianak, Indonesia. J Eng Sci Technol 2015;10:47–59.

[31] Ali Kamel Mohamed E. Antidiabetic, antihypercholestermic and antioxidative effect of Aloe vera gel extract in alloxan induced diabetic rats. Aust J Basic Appl Sci 2011;5:1321–1327.

[32] Ozsoy N, Candoken E, Akev N. Implications for degenerative disorders. Oxid Med Cell Longev 2009;2:99–106. [CrossRef]

[33] Martínez-Sánchez A, López-Cañavate ME, Guirao-Martínez J, Roca MJE. Aguayo, Aloe vera flowers, a byproduct with great potential and wide application, depending on maturity stage. Foods 2020;9:1542. [CrossRef]

[34] Tariq H, Zia M, Muhammad SA, Khan SA, Fatima N, Mannan A, et al. Kinase ınhibition potential in Aloe vera L . Biomed Res Int 2019:6478187. [CrossRef]

[35] Zahra N, Saeed MK, Shahzad K, Firdous S, Ahmad I, Ashraf M, et al. DPPH assay and reducing power activity of water extract of (mentha longifolia) mint. Lahore Garrison Univ J. Life Sci 2022;6:38–47. [CrossRef]

[36] Jairath G, Chatli MK, Biswas AK. Comparative study on ın vitro and ın vivo evaluation of antioxidant potential of apple peel extract and Aloe vera Gel. J Food Process Preserv 2016;40:607–614. [CrossRef]

[37] Kaithwas G, Kumar S, Pandey AH, Acharya AK, Singh M, Bhatia D, et al. Investigation of comparative antimicrobial activity of Aloe vera gel and juice. Pharmacol 2008;1:239–243.

Sigma J Eng Nat Sci, Vol. 44, No. 4, pp. 2982–3001, August, 2026

Sigma Journal of Engineering and Natural Sciences
Web page info: https://sigma.yildiz.edu.tr
DOI: 10.14744/sigma.2026.2140

Research Article

A comprehensive framework for selecting building energy modelling tools to support sustainable design

Ahmad Walid AYOOBI[1,2,*], Mehmet İNCEOĞLU[3]

[1]*Department of Architecture, Faculty of Construction, Kabul Polytechnic University, 1001, Kabul, Afghanistan*
[2]*Department of Architecture, Graduate School of Sciences, Eskişehir Technical University, 26555, Eskişehir, Türkiye*
[3]*Department of Architecture, Faculty of Architecture and Design, Eskişehir Technical University, 26555, Eskişehir, Türkiye*

ARTICLE INFO

Article history
Received: 30 October 2024
Revised: 08 January 2025
Accepted: 31 May 2025

Keywords:
Building Energy Modeling; Energy Efficiency; Framework; Simulation; Sustainable Design

ABSTRACT

Building energy modeling (BEM) tools are essential for achieving sustainable building design by enabling the simulation and analysis of building energy performance. While Building Energy Modeling (BEM) tools have achieved widespread adoption, a systematic framework for their selection, grounded in project objectives and a comprehensive understanding of tool capabilities and applicability, is still lacking. This research addresses this gap by developing a framework to guide architects and other stakeholders in selecting appropriate BEM tools for sustainable building projects. This study identifies common sustainable design strategies from a comparative analysis of certified sustainable buildings. It evaluates capabilities and applicability of available tools from a comprehensive evaluation of BEM tools listed in the Building Energy Software Tools Directory. The resulting framework provides a structured approach, describing key input/output features and assessing the suitability of different tools for different types of project and analysis objectives. The results of this research can support a more efficient use of BEM tools in sustainable design, enabling professionals and policymakers to make informed decisions and to promote the transition toward a more sustainable built environment.

Cite this article as: Ayoobi AW, İnceoğlu M. A comprehensive framework for selecting building energy modelling tools to support sustainable design. Sigma J Eng Nat Sci 2026;44(4):2982–3001.

INTRODUCTION

Sustainability is a complex notion, crossing disciplinary boundaries. Sustainability challenges require a multidisciplinary approach for complete understanding and tackling [1]. Building Energy Modeling (BEM) tools have become powerful allies in this effort revolutionizing the architectural design process [2–5]. Architects can incorporate BEM in the design process to explore different design alternatives, evaluate their energy performance and make informed decisions to optimize sustainability [4]. The history of building modeling software dates back to the mid-1970s and has undergone significant changes over the years to include energy modeling capabilities [6]. BEM allows architects to understand how design elements affect energy

*Corresponding author.
*E-mail address: ahmadwalid@kpu.edu.af

This paper was recommended for publication in revised form by Editor-in-Chief Ahmet Selim Dalkilic

Published by Yıldız Technical University Press, İstanbul, Turkey
© Author. This is an open access article under the CC BY-NC license (http://creativecommons.org/licenses/by-nc/4.0/).

consumption so they may reduce the environmental footprint of buildings. Besides uncovering climate opportunities, BEM can also direct the application of essential passive design strategies, even for individuals who are not familiar with specific software tools [7]. The widespread use of BEM in architectural design, together with engineers, has greatly contributed to the aim of sustainable buildings [8]. BEM has been shown to be effective in reducing energy loads with knowledge-based and simulation-based optimization methods achieving energy savings of up to 24% and 33% respectively [9]. Integrating BEM at the early stage of the design process can improve the energy performance of buildings and contribute to a more sustainable future.

BEM tools have become an essential asset in the development of sustainable architecture. These tools provide a powerful platform for prediction and optimization of energy performance of buildings, enabling designers to make informed decisions at early stages of the design process [2–5]. BEM can help in developing more environmentally friendly and sustainable structures by simulating different design options and identifying potential energy-saving strategies. The BEM tools are more accurate and reliable for assessing building energy performance than manual calculations [10]. Such improved accuracy is essential in aiding decisions on building design and operation. There is a wide range of BEM tools, for different needs and levels of expertise. An useful resource to explore these options is the U.S. Department of Energy's Building Energy Software Tools Directory (BESTD) [11]. To effectively use BEM in sustainable design, it is important to select tools that fit the project goals and the designer needs [9]. Careful consideration of the capabilities and limitations of different BEM tools allows designers to make informed decisions that contribute to the achievement of sustainable design objectives.

Physics-based building energy modeling (BEM) has demonstrated its ability to effectively simulate and evaluate various energy conservation measures in different building stocks [12]. However, as shown by the analyzes of BEM tools in terms of the input/output granularity and transparency [13], the choice of appropriate modeling approaches and tools depends on the particular project goals and the complexity of the building under consideration. Comparative studies of BEM software also point out differences in their operation and the level of detail required as input, which in turn affect the ease of use and analytical capabilities [14]. A review of BEM methods, tools and their applicability to various applications showed five key application areas including performance-driven design, model-based optimization of operational performance, integrated data-driven simulation for digital twins, urban energy planning, and building-to-grid interaction for demand response [15]. Research on the influence of design parameters on building energy performance has shown that building shape has a great influence on energy consumption when the boundary conditions are the same, as shown by comparison of different BEM tools [16]. In addition, current trends in BEM tool development highlight an increasing focus on supporting early-stage design decision-making [17].

Numerous studies have been carried out on the use of BEM tools for sustainable design [2, 7, 18]. However, there is still a need to comprehensively evaluate and classify these tools. The simulation community is discussing critical areas for improvement, including user friendliness, knowledge integration, accuracy, interoperability, and integration into the design process [2]. The applicability and simulation capabilities of BEM tools are quite different, especially when applied to sustainable building strategies. However, their comparisons of whole-building energy simulation performance have been limited. Moreover, a systematic classification of BEM tools in terms of their integration with other tools and their functionality for different types of projects, facilities and sustainable strategies is yet to be established. The lack of knowledge stops architects from choosing the right tool for their projects. A well-defined framework would provide a common platform for architects and researchers to effectively utilize and select BEM tools to advance sustainable building practices.

The study is focused on whole-building energy simulation tools, including parametric and optimization techniques to support sustainable building design strategies. This research aims to identify common design strategies and assess the capabilities and applicability of different BEM tools listed in the BESTD by analyzing the sustainable building design strategies based on the most common sustainability indicators of the certified sustainable buildings worldwide. The goal is to propose a holistic framework that can help architects and policy makers to choose and understand suitable BEM tools for sustainable building design and analysis. The framework will offer useful insights into the capability and applicability of BEM tools including strengths and weaknesses of the tools against project objectives and facilities. It will help in making informed choices and optimization of sustainable design approaches by considering common sustainable building strategies. Furthermore, this research also supports the promotion of sustainable building practices by providing effective BEM tools to architects and policymakers for their research and projects. This paper points out the potential of BEM in sustainable design and serves as a basis for further research on the development of innovative BEM tools and practical strategies for sustainable building objectives.

METHODOLOGY

BEM tools are a necessary tool for the design of sustainable and energy efficient buildings, allowing to simulate and predict performance at early stages of design. Many BEM tools have been developed in recent years and the choice of suitable tools for specific research or projects is an important decision for architects and engineers. In this paper a systematic methodology is used to develop a comprehensive framework for the selection of BEM tools

which support sustainable building design. Data collection was performed by an extensive review of peer-reviewed articles published in high-impact journals indexed in databases such as Scopus and Web of Science. We also checked authoritative sources such as the American Institute of Architects (AIA) and the U.S. Department of Energy's Building Energy Software Tools Directory (BESTD) to ensure our information was reliable and comprehensive. To validate the theoretical findings, we also evaluated selected tools in practice in their respective software environments and cross-referenced the results with the literature and official documentation. Figure 1 describes the methodological steps used to develop this framework.

The research approach began with an extensive literature review on BEM tools and existing sustainable design practices. Sustainable building indicators were analyzed systematically and energy efficient strategies were identified. Based on these strategies, a subset of BEM tools listed in BESTD was chosen for further evaluation. The tools chosen for this study include those that support whole building energy simulation, and incorporate advanced features, such as parametric analysis and optimization techniques relevant to sustainable design goals. After the appropriate BEM tools were identified and characterized, their applicability and capabilities were analyzed for input and output features. The advanced functionalities, strengths, weaknesses and limitations were underlined. Therefore, a decision-support framework was designed to help architects, engineers and researchers select the most appropriate BEM tool for sustainable building projects.

Sustainable Buildings

Since the late 20th century, the demand for energy has increased with the progress of technology and urbanization [19]. With this expansion in energy production and use have come increasing ecological problems. This trend keeps growing without any abatement due to the fast population growth and continuous technological development [20]. Importantly, buildings in many developed nations account for a large percentage (35-40%) of total energy use, with the largest share (65%) used for providing indoor environmental quality via heating, cooling, ventilation and hot water systems [21]. Sustainable building design is a prominent architectural paradigm in response to the growing global awareness on environmental conservation [22, 23]. Sustainable development in an urban and building context involves an extensive range of issues such as natural resources management, environmental protection, energy

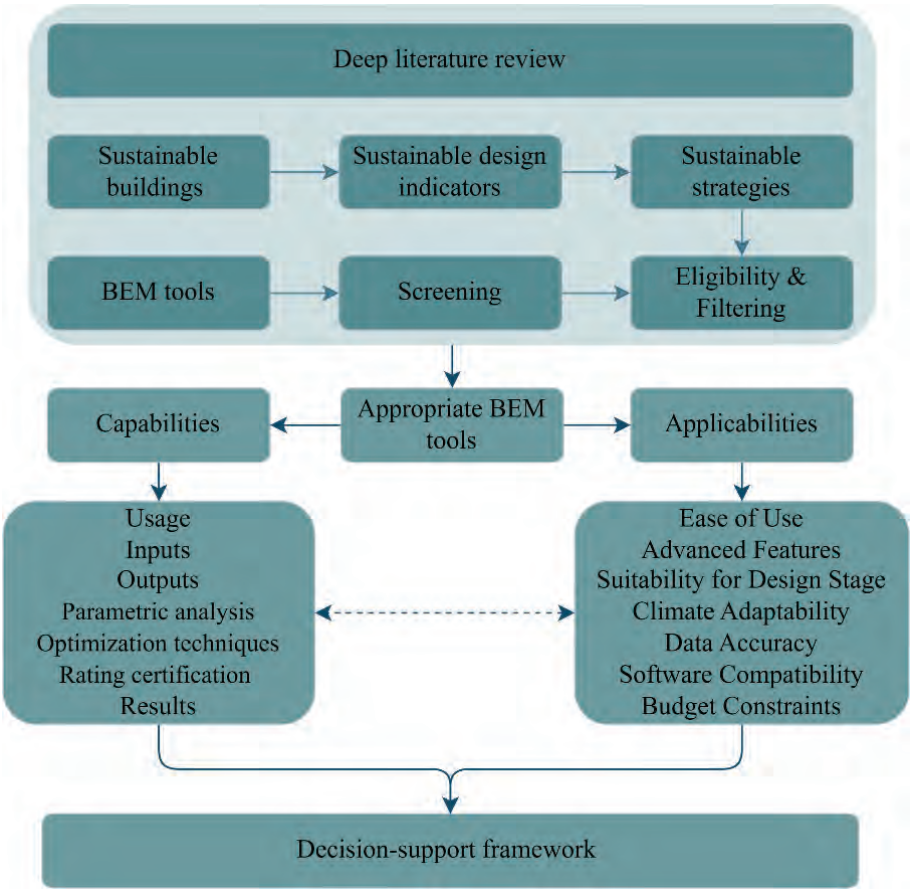


Figure 1. Methodology flowchart of the study.

efficiency, transportation planning, land use optimization, infrastructure development, and social well-being of the population [24]. It takes actions and significant efforts to achieve sustainable building practices. The main elements of sustainable buildings generally consist of site selection, water conservation measures, energy efficiency initiatives, material efficiency, resource optimization, indoor air quality management, effective building operations and maintenance practices [25]. Examples of sustainable buildings can be found in diverse geographical regions worldwide, each adapted to local environmental conditions and cultural preferences. Architects often draw inspiration from existing sustainable building projects to inform their designs. Therefore, this study characterizes the applicability and capability of BEM tools for sustainable building strategies, focusing on the most common sustainability indicators (Site, Energy, Indoor Environmental Quality, Material, and Water) considered in most widely recognized certified sustainable buildings globally.

Interdisciplinary Science and Engineering Complex

The Interdisciplinary Science and Engineering Complex is a LEED Gold-certified, 10,000 square foot research facility designed by Payette and completed in 2017 in Boston, Massachusetts. Detailed information about the sustainable indicators and strategies considered in the design of the Interdisciplinary Science and Engineering Complex is provided in Table 1 [26].

This innovative building has garnered 11 sustainability awards for its exceptional design and performance. The complex is located on a brownfield and serves as a linking element between the various neighborhoods by means of a pedestrian bridge with landscape design. It uses a combination of passive and parametric design strategies to achieve high energy performance. The building's ecological features help plants grow and give wildlife a place to live. Passive design elements include glazed facades, a central atrium with a waterfall and the active systems of radiant panels and a solar wall to maximize energy efficiency. Low-flow fixtures are used to save water, and rainwater is collected for irrigation and toilet flushing. The use of recycled and prefabricated materials allows for both economic efficiency and ecological sustainability. The space is bright and glazed, and the central atrium helps to connect interior and exterior, creating a healthy and inspiring environment for researchers to thrive.

Casa Adelante 2060 Folsom

Casa Adelante is a mixed-use building with 127 permanently affordable homes and a number of community

Table 1. Overview of sustainable strategies implemented in the Interdisciplinary Science and Engineering Complex, adapted from [26]

NO	Sustainable Indicators	Sustainable Strategies
1	Site	The project is in a brownfield area. Provide eco-friendly transportation. Support local vegetation by plantings.
2	Energy	Glazed walls Provide unobstructed views. Reduce the amount of ventilated space. The atrium acts as an air-mixing chamber. A solar wall preheats the air during winter. Heat recovery systems capture heat. Chillers and boilers decrease energy usage.
3	Indoor Environmental Quality	Simulation tools guarantee comfort. CFD confirmed a comfortable interior. Daylighting assesses the atrium skylights. The atrium offers proper views.
4	Material	Recycled aluminum components. Factory prefabrication and recycling. The Proper material selection.
5	Water	Low flow plumbing and fixtures. Rainwater collection tank.
A visual representation of the Interdisciplinary Science and Engineering Complex		

spaces on the ground floor. Its innovative design connects everyday indoor and outdoor areas, promoting well-being and sustainability. The building is arranged around a central courtyard from which spread out the parkland, community facilities and social service offices. Casa Adelante capitalizes on its desirable location with excellent walking and public transit options to promote social equity and reduce carbon emissions on a formerly polluted site. Table 2 [26] provides a detailed view of the sustainable indicators and strategies that were considered in the design of the Casa Adelante 2060 Folsom.

The building's energy-efficient design integrates passive strategies and high-performance electric systems to reduce its environmental impact. The building is oriented for optimal daylighting and views, and has an energy efficient envelope and strategic shading to reduce energy consumption. The project's entry sequence is intended to create a relationship between residents and nature, and also social interaction. We selected materials that were sustainable and long lasting; durable and functional with low carbon footprints. Water-efficient fixtures and a smart irrigation system add to the building's eco-friendly approach.

Albion District Library

The Albion District Library is a prime example of sustainable architecture The building is a Tier 1 Toronto Green Standard certified building designed by Perkins and Will. This is a 29,000 square-foot library in Toronto, Canada, completed in 2017, which has received 10 sustainability awards. The passive design is thought of as an indoor garden with an emphasis on community. Situated on previously developed land, it serves as a vital social resource for a diverse and high-needs population. Detailed information about the sustainable indicators and strategies considered in the design of the Albion District Library is provided in Table 3 [26].

It takes a car-centric public space and converts it into a pedestrian-friendly space, creating habitats for local flora and fauna. The library also features cutting-edge sustainable elements such as photovoltaic arrays, a green roof, daylight harvesting and healthy materials that dramatically reduce energy use. The on-site infiltration system, green roof and rainwater management strategies minimize water usage. The choice of durable, low-maintenance and locally-sourced materials adds to the economic viability of the building and reduces environmental impact. The library is designed to give good natural light, ventilation and access to the outside to make the users feel better. To summarize, the Albion District Library is a model for how sustainability principles can be successfully integrated into a public building.

Table 2. Overview of sustainable strategies implemented in the Casa Adelante 2060 Folsom, adapted from [26]

NO	Sustainable Indicators	Sustainable Strategies
1	Site	Located in a brownfield area. Utilizes walkable area social equity. Promote a low-carbon future.
2	Energy	Integrated passive design elements. Building's orientation. High-performance envelope. Optimized window-wall ratio. Fixed exterior shading. Allowing daylighting and views. Operable windows.
3	Indoor Environmental Quality	Connection between residents and nature. Encourage social interaction. Healthy and non-toxic material.
4	Material	Durability and functionality of material. Material resiliency and adaptability. Health and transparency of materials.
5	Water	Low flow fixtures. Irrigation system equipped with a sensor.
A visual representation of the Casa Adelante 2060 Folsom		

Table 3. Overview of sustainable strategies implemented in the Albion District Library, adapted from [26]

NO	Sustainable Indicators	Sustainable Strategies
1	Site	Situated in a post-war suburb. Crucial social resource for immigrants. Engaging to the wellness and environment.
2	Energy	Use high-level sustainable design elements. A rooftop photovoltaic array. Sloping green roof and daylight harvesting. Building's façade to create sunscreens.
3	Indoor Environmental Quality	Considers natural light and views. Courtyards bring nature, light, and color into the plan. Massing, and garden courtyards.
4	Material	Careful selection of healthy materials. Selecting durable materials. A colorful scrim of terracotta ribs wraps around the building.
5	Water	Wetland for stormwater collection. Planting drought-tolerant shrubs. Stormwater management strategies.
A visual representation of the Albion District Library		

One Central Park

One Central Park is a mixed-use development that has received accolades for its state-of-the-art sustainability features and striking architecture. The legendary high-rise residential building is located in a redeveloped urban precinct of Sydney, Australia, and consists of two towers linked by a common base. The two towers rise to 65 and 116 meters and are separated by a shaded space illuminated by innovative daylight technology. A unique feature is the use of heliostats, which reflect sunlight onto a cantilever and nearby park, providing natural illumination. Table 4 [27] provides detailed information on the sustainable indicators and strategies considered in the design of the One Central Park.

The extensive greenery of the building, including balconies and vertical gardens with plantings, provides natural shading and cooling, resulting in considerable savings of energy. One Central Park meets the highest standards of sustainable building with 5-star Green Star ratings for its retail and residential facilities. The project is inviting because of its emphasis on amenity and public space, and a generous amount of greenery. The combination of architectural and biophilic design, with Australia's biggest green façade, has set a new benchmark for sustainable urban development. The vertical gardens, with their 35,000 plants, enhance the beauty of the building and act as natural climate control, resulting in lower energy use and cleaner air. The building's sustainable initiatives are more than just design. It features green infrastructure such as green roofs, living walls, recycled materials, water harvesting and energy efficient systems. These have produced significant environmental benefits such as a good rate of recycling, reduction in greenhouse gas emissions and efficient use of water. One Central Park is a living example of what sustainable design can achieve in developing livable and environmentally friendly cities.

Marco Polo Tower

The Marco Polo Tower is a one-of-a-kind residential building in Hamburg, Germany. The building's design is unique, with a curved structure and rotating floors that provide panoramic views of the harbor and city. The tower is designed in the framework of a waterfront development with an emphasis on sustainability and ecological efficiency. The Marco Polo Tower is designed to use as little energy as possible and features include vacuum collectors for heating and cooling, natural ventilation and balconies for shading. Its sustainable approach has been recognized, including the Mipim Award for Best Residential Project. The overhanging terraces shade the building facades from direct sunlight and obviate the need for additional sunshades, thus improving energy efficiency and esthetic quality. Interior of the tower is unique as the exterior with open living spaces that offer unobstructed views and natural light. Detailed information about the sustainable indicators and strategies considered in the design of the Marco Polo Tower is provided in Table 5 [27].

Table 4. Overview of sustainable strategies implemented in the One Central Park, adapted from [27]

NO	Sustainable Indicators	Sustainable Strategies
1	Site	Located in the former industrial area. Amenity and abundance of plant life. Vertical landscape.
2	Energy	Natural sun control device. Using sustainable design strategies Use of a heliostat to produce electricity. Mirror structure to redirect sunrays.
3	Indoor Environmental Quality	Possibility to extend the living space. Green roofs, living façades.
4	Material	Recycling demolished materials. Adaptive re-use of buildings components.
5	Water	Reclaimed and treated blackwater. Irrigation and air conditioning water needs. Reduce the water load. Recycled rainwater.
A visual representation of the One Central Park		

Table 5. Overview of sustainable strategies implemented in the Marco Polo Tower, adapted from [27]

NO	Sustainable Indicators	Sustainable Strategies
1	Site	Located directly on the waterfront area.
2	Energy	Natural ventilation. Shade shielded from sunlight by terraces. Vacuum collectors on the roof. Air louvers, enabling natural ventilation. Balconies arrange shading and wind. Energy-conserving by triple-glazed. Rooftop solar cooling system.
3	Indoor Environmental Quality	High level of flexibility in the internal part. Sound-insulated for noise pollution. Flexible structural for spaces choice.
4	Material	The façade is composed of concrete and glass. Structure material is reinforced concrete.
5	Water	N/A
A visual representation of the Marco Polo Tower		

Table 6. Overview of sustainable strategies implemented in the AND Pastel projects, adapted from, adapted from [27].

NO	Sustainable Indicators	Sustainable Strategies
1	Site	Located on an old industrial estate. Created a lively neighborhood. Encouraging the use of bicycles
2	Energy	Sustainability and advanced technologies. High-efficiency central heating system Decentralized cooling system Energy-efficient mechanical systems Multi-layered facades and appropriate glass Natural ventilation
3	Indoor Environmental Quality	Daylight and natural cross ventilation. Efficient lighting fixtures
4	Material	Recycled Content Materials Local Materials Low Emission Materials
5	Water	Comprehensive water management Gray water and rainwater collection
A visual representation of the AND Pastel projects		

Residents can enjoy spacious balconies and terraces, as well as the option of connecting neighboring apartments for larger living areas. Its modern design and prime waterfront location, coupled with the building's sustainable features, make it a desirable and environmentally friendly residential option.

AND Pastel

AND Pastel is a sustainable residential development on a former industrial site in Istanbul, Turkey. It is surrounded by four towers and three blocks, with 1,200 residential units of various configurations. The complex is a lively community with connected courtyards, a health center, pools, fitness facilities and shops. AND Sustainability is at the heart of Pastel, focusing on energy efficiency, water conservation, resource optimization and indoor comfort. The project is LEED Gold certified with sustainable features including a high efficiency heating system, decentralized cooling and complete water management. The public spaces are compared to an urban park with green spaces and water courses linking the courtyards. AND Pastel promotes cycling and the parking of bicycles as a means of sustainable transportation. Table 6 [27] details the sustainable indicators and strategies used in the AND Pastel projects design.

The building is designed with energy-efficient systems, multi-layered facades and natural ventilation, which cuts energy consumption by 24 %. Apartments are oriented for maximum day lighting and natural cross ventilation, and low energy lighting fixtures are used to increase efficiency. The focus is on the use of sustainable materials such as recycled content, local materials and low emission materials. Paints, adhesives and sealants are selected according to health benefits, so that harmful chemicals are avoided. The building is designed to be flooded with natural light with over 90% of the area receiving direct sunlight. The project also includes water conservation, sustainable landscaping and access to public transportation. To summarize, AND Pastel is an example of a success incorporating sustainability into a residential development. The project demonstrates a commitment to developing a sustainable and desirable urban community by highlighting energy efficiency, water conservation, resource optimization and healthy living environments.

Building Energy Modeling (BEM)

The development of building energy simulation tools has been strongly influenced by the need for energy efficiency in buildings [14] in the 1970s. Since then, these tools have evolved, taking advantage of advances in computational technology to improve their ability to do mathematical modeling and graphical visualization. This has allowed for more sophisticated analysis of building performance and energy use. Building Energy Modeling (BEM) is an important tool in the sustainable building assessment framework. It aims at helping to achieve and improve sustainable indicators according to site conditions specifically through the

modulation, optimization and analysis of design strategies, in particular for integrated sustainable designs. Building Energy Modeling (BEM) is not a new concept in building design, but it is a subset of Building Information Modeling (BIM) that seamlessly integrates energy analysis throughout the entire lifecycle of buildings from design and construction to operation and maintenance [7, 18]. The integration of BEM tools in the architectural design is creating great changes in the design process, making it more efficient, performance-oriented and flexible, and offering more design alternatives [4]. BEM is a useful tool in building design assessment and energy research to help make informed decisions at the early stages of design and predict the impact of different design solutions on future building performance [28–30]. Thus, BEM tools have become an essential tool for professionals in the architecture, engineering, and construction industry for modeling, analysis, and optimization of building energy performance under different design and operational scenarios [13].

Design of building with BEM tools illustrates how building elements can contribute to energy saving and sustainability to improve energy efficiency and reduce the ecological footprint of the building [7]. The adoption of passive design elements as the basis can open up chances for architects to create energy efficient and cost effective designs, particularly during the early phases of design [31]. The main drivers of building energy consumption are design choices, operational practices and other factors [22]. The BEM principles have become popular in sustainable building design due to their ability to achieve energy efficiency and environmental sustainability [8, 32]. Energy performance simulation programs are powerful tools to analyze energy consumption and thermal comfort in the whole life cycle of a building [3].

BEM is a useful computer tool for analysis and evaluation of architectural designs [31]. It must be noted that the input data and the simulation assumptions can be different for each BEM tool and this can influence greatly the functionalities and capabilities of each BEM tool. The application of BEM in the design of buildings contributes to the following aspects in energy performance: building orientation, massing, form, envelope, daylighting analysis, water harvesting, energy modeling, renewable energy integration, sustainable construction materials, and site and logistics management [33]. Buildings have many parameters, including material properties, occupancy levels, equipment schedules, HVAC and plant operations, and local climate and weather conditions [34].

BEM tools are applied in three major phases of the building life cycle: design, construction and operation/maintenance. The BEM tools are an important part of the design process. They are used to analyze the building site, orientation, massing, envelope design and to compare different design options with different layouts, architectural features and HVAC systems. This large-scale application of BEM tools optimizes the building performance from the very outset. BEM tools can be used during construction to evaluate heating and cooling loads to determine the size of HVAC systems, evaluate lighting levels and evaluate the environmental impacts of construction to ensure that materials and equipment are meeting design specifications. During the operational and maintenance phase, BEM tools monitor the real building performance, detect deviations from the design, and suggest energy-efficient alternatives for renovations or remodels. They also help manage facilities by detecting faults in the HVAC system and predicting potential energy savings from adjustments and retrofits.

Tools for Integrating BEM in Sustainable Building Design and Energy Modeling

Performance analysis of building requires special simulation tools for different aspects like energy, esthetic and cost etc. BEM is especially useful for the design of low-cost and energy efficient solutions to meet and maintain building energy efficiency requirements [5]. The BEM tools are normally automated by computer programming to effectively analyze and solve building energy consumption problems and reduce time and labor requirements [35]. CIBSE proposed two ways of integrating BEM into building design: (1) using simplified tools at the early stages of design and more complex tools at the later stages, and (2) using a single sophisticated simulation tool throughout the design phases [18]. BEM enables the prediction of real building performance in early design stages, allowing proactive actions. The primary goal of using BEM in building design is to reduce industry waste, including wasted energy, increase the value of industry products, and minimize environmental damage by providing accurate and realistic performance predictions [33]. BEM, as an innovative approach, encompasses various useful tools that can significantly evaluate the energy performance of buildings by integrating information about building materials, systems, types, climate zones, and environmental conditions [36]. BEM is continuously evolving, with rapid advancements in techniques and methodologies [37]. BEM is a powerful tool that simulates and optimizes building energy performance, considering various parameters as illustrated in Figure 2.

Over 400 BEM tools have been developed globally to analyze building energy performance. As noted by Gao et al. [31] most BEM tools can be categorized into two groups: those utilizing the calculation engine developed by the US Department of Energy (DOE), such as eQUEST, DesignBuilder, EnergyPlus, and Autodesk Green Building Studio (GBS), and those using their own proprietary calculation engines, such as IES Virtual Environment (IES-VE) and Trace 700. In 2010, the US Department of Energy's Building Energy Software Tools Directory (BESTD) listed over 389 BEM tools, providing a comprehensive overview of available options [2, 3, 38]. As of the last BESTD update in 2018, the directory included 207 software tools, encompassing a wide range of capabilities for simulating various building types, including 111 specifically designed for

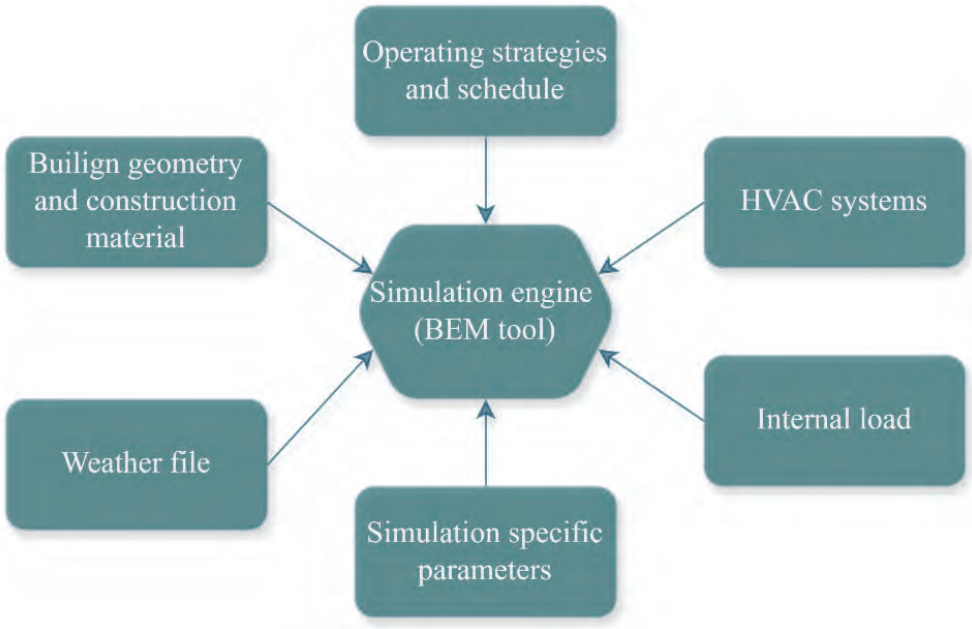


Figure 2. Overview of essential input data for Building Energy Modeling (BEM) tools [3]. Adapted from: Maile T, Fischer M, Bazjanac V. Building energy performance simulation tools - a life-cycle and interoperable perspective. Cent Integr Facil Eng 2007:1–49.

residential buildings [11]. Given the abundance of available BEM tools, it is essential to evaluate their utility in different phases of the building lifecycle [18]. Each program possesses unique features in terms of modeling resolution, solution algorithms, target audience, modeling options, ease of use, flexibility, and more. Attia et al. [2] reviewed 392 energy modeling programs and identified only 40 as suitable for early-stage architectural decision-making [7].

The proliferation of BEM tools in the contemporary era, driven by advancements in computer technology, has made selecting the most appropriate tool a complex task. Contemporary BEM tools offer the capacity to evaluate building energy performance during the design phase. However, discrepancies persist among BEM tools, arising from variations in algorithms, computational inaccuracies, implementation errors, inconsistencies in input parameters, and differences in weather data processing methods [14]. There are no clear criteria to classify and evaluate the BEM tools to select the appropriate one, which faced the potential user with the difficulty of choosing a suitable tool among the growing BEM tools pool [2]. According to Toutou et al. [35], parametric and optimization simulation method is the most considerable way to develop the buildings' performance. This study is focused on whole building energy simulation with parametric and optimization for sustainable buildings design. Therefore, according to strategies considered in the evaluated sustainable buildings and BESTD filtration regarding the whole building energy simulation and optimization the following ten BEM tools may considered most appropriate to evaluate and select for building analysis regarding energy efficiency and sustainability.

Despite the abundance of BEM tools, there is a lack of standardized criteria for classifying and evaluating them, making it challenging for users to select the most suitable option [2]. This study focuses on whole-building energy simulation, incorporating parametric and optimization techniques for sustainable building design. Through the analysis of the strategies employed in the evaluated studies [12], sustainable building strategies (Tables 1-6) and the application of BESTD filtration criteria for whole-building energy simulation and optimization, ten BEM tools were identified as the most appropriate candidates for building analysis with respect to energy efficiency and sustainability.

DesignBuilder

DesignBuilder is a comprehensive building performance simulation program that enables users to assess the environmental impact of both new and existing buildings. The intuitive user interface makes it possible to model and analyze energy use, comfort, HVAC, daylighting and sustainability compliance. According to [39], the following are the primary features:

- Provides energy, comfort, HVAC, daylighting and cost analyzes in a single platform.
- Integrated modeling environment and support for BIM imports.
- Full features: BREEAM/LEED credits, CFD and a range of national building regulations.

- Enables energy use calculations, façade design, natural ventilation, lighting control, site layout, equipment sizing, design collaboration and education.
- Advanced capabilities such as automated data generation, EnergyPlus 'Compact HVAC' coupling, natural ventilation simulation, daylighting analysis, shading techniques and flexible data presentation.
- Allows to investigate the effect of variations of design parameters on several performance criteria.
- Generate IDF files for better simulation.

DesignBuilder is a sophisticated building performance simulation software that utilizes the EnergyPlus engine to provide the advanced thermal simulation features to accurately model building energy consumption [14]. It allows to improve the modeling accuracy by providing ready-to-use templates for construction materials, weather data (usually from ASHRAE or EPW files) and HVAC systems. Nevertheless, the accuracy of the simulation is highly dependent on the quality and verification of the input parameters, such as weather data, operating conditions and user defined material properties. For data exchange, DesignBuilder supports file formats like gbXML and IFC, which improve interoperability in BIM workflows. DesignBuilder also adopts the EnergyPlus output format for advanced analysis and collaboration. DesignBuilder is a commercial product and therefore subject to tiered licensing which may be a financial barrier to smaller firms. Furthermore, it requires high computational requirements and powerful hardware configurations, which further increases the overall cost of implementation. DesignBuilder's easy to use interface and extensive functionality provides a powerful solution for architects, engineers and building professionals who want to improve building performance and sustainability.

EnergyPlus

EnergyPlus is a building energy simulation program developed by the U.S. Department of Energy. It is widely used by professionals from many fields to model and analyze the energy performance of buildings [40]. EnergyPlus is a very effective instrument that can:

- It simultaneously models the interactions of building spaces and their heating, ventilation, and air conditioning systems, and produces accurate results for conditioned and unconditioned spaces.
- EnergyPlus utilizes a sophisticated heat balance approach to calculate the surface temperatures accurately and hence, allows accurate thermal comfort and condensation modeling.
- Users can specify custom time steps for high-precision simulation of systems with varying dynamics.
- EnergyPlus contains a detailed heat and mass transfer model for air flow and moisture transfer between zones of the building.
- Provides detailed models for windows, doors and shading devices, enabling accurate simulation of solar energy absorption and heat transfer.
- EnergyPlus can calculate the levels of illuminance and factors of glare so that it can evaluate the visual comfort of building occupants.
- Users can build custom HVAC systems from a library of individual components, allowing the user to model a wide variety of configurations.
- EnergyPlus provides an extensible framework for defining custom control strategies so that users can simulate a variety of operating conditions.
- EnergyPlus can be coupled with other simulation packages using Functional Mockup Interface (FMI) for co-simulation and interoperability.

EnergyPlus is a well-known tool for building energy simulation and highly respected for its thermal and energy performance predictions highly sensitive to the accuracy of input parameters [13]. The software contains a large library of data such as thermophysical properties of materials and meteorology data. The user however has to select data relevant to the context of the project, so as to ensure the validity of the simulation results. EnergyPlus does not include a full native graphical user interface and often relies on third party pre- and post-processing tools such as OpenStudio or DesignBuilder to provide a more user-friendly environment. It is interoperable with other building information modeling (BIM) and analysis software via standard file formats such as gbXML and IDF. EnergyPlus is an open source program, so there is no direct cost to acquire the software, however it requires a highly skilled user to use effectively and may require significant computational resources. You might have to invest in more training and hardware to make the most of these factors. EnergyPlus is a very useful tool for professionals who want to optimize the energy efficiency of buildings, reduce the operational cost and improve the comfort of their occupants [13]. Its versatility and accuracy make it a must-have tool for researchers, designers and engineers in the building industry.

Sefaira Architecture

Sefaira Architecture is a new cloud-based building performance analysis platform that is a breakthrough. Sefaira integrates with the industry standard 3D modeling software allowing architects to quickly evaluate design decisions and make data driven decisions. This iterative process allows architects to keep improving their designs toward the most energy efficient, daylighting and thermal comfort. Sefaira uses state-of-the-art simulation engines like industry-standard EnergyPlus and Radiance to deliver precise, timely results and fast design iterations. Sefaira's main features are [41]:

- Sefaira offers a set of tools to evaluate the energy consumption, carbon emissions, thermal comfort and daylighting performance.
- Architects are given instant feedback on their design decisions, allowing them to make quick adjustments and improvements.

- Sefaira allows team members and external stakeholders to work together, making the design process more efficient.
- The platform features an intuitive user interface that is accessible to architects of any technical skill level.

Sefaira Architecture is a powerful way to analyze building performance with a focus on quick results early in the design process. The simplified modeling methodology provides fast assessment and sound decision making but is based on approximations and standard templates that impose limitations to the extent of precision that can be achieved in detailed design iterations. The software is highly interoperable with popular design platforms like Revit and SketchUp, allowing for real time performance assessment fully embedded in existing workflows. However, the requirement for real-time feedback has come at the expense of better data export capabilities and therefore limits its use for more holistic energy analysis beyond the platform's existing capabilities. The pay-for-use licensing model can also be a financial barrier for smaller companies or individual users. However, the cloud simulation approach reduces the investment in high performance computing infrastructure. Sefaira enables architects to design buildings that are more efficient, more sustainable, more comfortable and that have less impact on the environment.

EcoDesigner Star - ArchiCAD

EcoDesigner STAR is a powerful energy analysis tool fully integrated within the Archicad environment. It allows architects to undertake dynamic building energy calculations which enables them to make informed decisions during the design process. EcoDesigner STAR delivers the same detailed performance reports in the familiar ArchiCAD interface, providing standard-compliant energy analyzes on the Building Energy Model (BEM). The main features of EcoDesigner STAR are [42]:

- Provides international energy standards and combines energy assessment and reporting in the Building Information Modeling (BIM) process.
- Provides export of BIM geometry and thermal property data, thermal bridge simulation, expert building systems settings, integration of on-site renewables, and building energy simulation using a standards-compliant analysis engine.
- Supports climate analysis, building energy model calibration, project specific low-energy building solution sets, low-energy demand architectural design, and whole building energy efficiency optimization.
- Ability to integrate solar photovoltaic and wind energy solutions, and to export directly to a range of analysis tools and translators such as PHPP, iSBEM, VIP-Energy, gbXML and IFC.

EcoDesigner STAR is an ArchiCAD plug-in for building performance analysis. It provides geographically relevant simulations based on the building's geometric model and embedded energy templates, all within the ArchiCAD environment. This method gives moderate accuracy in the temperate and colder climate zones. However, it is based on pre-defined templates which limits its flexibility and predictive ability in the areas with extreme climatic variations. It has excellent integration with ArchiCAD, which enables seamless data exchange within the ArchiCAD ecosystem, but interoperability issues can be observed when exporting data to other building performance simulation platforms. Also a big hurdle is the cost of the software, which requires licenses for both ArchiCAD and the EcoDesigner STAR add-on, especially for smaller firms. EcoDesigner STAR is also desktop-based and requires a workstation with at least mid-range hardware specifications to run efficiently. EcoDesigner STAR is an invaluable tool for architects and engineers seeking to create energy-efficient buildings that meet international standards and support sustainable development.

OpenStudio

OpenStudio is an open source platform that provides flexibility to make building energy simulation easier. It uses EnergyPlus for detailed energy modeling and Radiance for sophisticated daylight analysis [43]. OpenStudio provides an SDK and CLI that together provide a flexible API to interact with the EnergyPlus engine. Most importantly, the API is accessible in scripting languages such as Ruby and Python, allowing users to tailor and improve the capabilities of OpenStudio. OpenStudio also includes graphical tools, such as a Trimble SketchUp plug-in for creating 3D building models and a parametric analysis tool to help users apply energy conservation measures. OpenStudio's broad strategy makes it a useful resource for a variety of professionals, from engineers to policy analysts.

OpenStudio has a technically modular architecture and it can be easily integrated with other applications. The API supports scripting in a variety of languages for customization and automation. OpenStudio also uses the Building Component Library (BCL) as a common platform for building components and data, enabling interoperability and access to the latest standards. OpenStudio is built on the EnergyPlus simulation engine and provides high-fidelity building performance analysis based on accurate input and validation of weather, thermophysical material properties, and HVAC system parameters. The interoperability is supported by the integration with SketchUp for geometry modeling and the compatibility with the larger EnergyPlus ecosystem. In addition, gbXML import/export capabilities allow data to be shared with Building Information Modeling (BIM) systems. OpenStudio is open source and so there are no costs for software licensing but it requires special technical skills to use effectively and there are likely to be training costs to ensure models are developed and simulation results interpreted correctly.

Ladybug and Honeybee

Ladybug and Honeybee are two open source plugins for Grasshopper that augment the ability of architects to

design environmentally sustainable buildings [11]. These tools integrate with Grasshopper, a visual programming environment, and give designers a powerful suite of tools to analyze climate data, simulate building performance and visualize design impacts. _Ladybug_ is about the earliest design decisions. It enables designers to bring climate data and study how it affects a building's exposure to sunlight and radiation. Ladybug's interactive visualizations give instant feedback to design changes, allowing designers to explore different options and make informed decisions in a timely manner.

Honeybee is more suitable for later stage design. It interfaces with four validated simulation engines, EnergyPlus, Radiance, Daysim and OpenStudio. These engines provide detailed analysis of building energy consumption, comfort and daylighting [15]. Honeybee's daylighting and thermodynamic modeling capabilities are especially useful for fine-tuning design decisions. Together, Ladybug and Honeybee provide a comprehensive toolkit for sustainable design. These plugins will allow architects to create more sustainable and energy-efficient buildings by empowering designers to analyze climate data, simulate building performance and visualize the impact of their design.

Ladybug and Honeybee are environmental analysis tools that utilize validated simulation engines (EnergyPlus and Radiance) to provide high-fidelity building performance assessment. The accuracy of their predictions of solar radiation, daylighting and thermal comfort depends on the accuracy of the input parameters as determined by the underlying engines. These tools work in the Rhino/Grasshopper parametric modeling environment, offering great flexibility for design exploration and optimization. However, this combination demands that users are skilled in Rhino/Grasshopper and have access to commercial licenses, which can be a financial barrier for smaller firms, considering that the Ladybug and Honeybee tools themselves are open-source. In addition, the complexity of parametric workflows may require specialized training which adds to the implementation cost.

eQUEST

eQUEST is a powerful building energy performance simulation tool for analysis and design. The user interface is intuitive, with wizards, interactive graphics and parametric analysis making it accessible to a wide range of professionals from architects and engineers to building owners and researchers. The software allows the user to import the geometry of the building from architectural models or to create the geometry in the software. The user is able to run simulations of different complexity. eQUEST provides detailed input options for the design process at schematic design, design development and full DOE-2 based interface [44].

The eQUEST generated output reports provide a brief summary of the simulation results including graphical summaries, comparative analysis, and detailed tabular data. This information is useful to understand the energy performance of buildings and to evaluate the effects of design decisions. One of the primary advantages of eQUEST is the ability to assess whole-building performance during the design process. Wizards allow design teams to explore energy efficiency options early on, while the full-blown interface allows for detailed analysis in later stages. The software operates at a high speed enabling the effective evaluation of large models and the capture of complex interactions between building systems.

eQUEST has built-in components and templates to make energy modeling easy, but this comes at the cost of absolute accuracy. It is good for first energy estimates, but may not be precise enough for complicated analysis. It is based on the DOE-2 format not compatible with modern workflows [14]. And it's not as seamless with other software as newer tools are. However, its main advantage is its accessibility as it is free to use and needs minimal computational resources.

Green Building Studio (GBS)

Green Building Studio (GBS) is a flexible cloud-based platform that is integrated into Autodesk's design suite including Revit and FormIt 360. It is a powerful energy simulation engine, which enables the user to optimize building energy efficiency and carbon footprint at the early design stages [45]. GBS employs the DOE-2.2 simulation engine and delivers accurate energy performance calculations and detailed input files for EnergyPlus. This allows architects, engineers and construction professionals to design high-performance buildings faster and more cost-effectively than traditional methods. It's easy to create geometrically accurate building models with GBS. The program automatically reads data from gbXML-enabled BIM or 3D-CAD programs. In addition, the BIM/CAD program provides the graphical user interface for specifying the additional input parameters.

The software produces a full range of outputs, including customizable heating and cooling load charts, energy consumption, costs, temperature data and wind analysis. Includes valuable features such as parametric studies, annual carbon footprint analysis, renewable energy potential assessment, natural ventilation analysis and preliminary water analysis for LEED compliance. GBS's strength is in enabling energy, carbon and water analysis at the early stages of design, thus lowering design and analysis costs and allowing for greater design exploration within budget constraints. This ultimately speeds up project completion and the process of achieving LEED certification.

Autodesk's cloud-based simulation engine, Green Building Studio (GBS), offers a reasonable level of accuracy for early-stage energy modeling in the design process. However, its output granularity is usually less refined than that of more computationally intensive tools such as EnergyPlus, making it less suitable for detailed analysis in the later stages of the project. While the GBS offers a smooth

interoperability with the Autodesk environment, especially Revit, such tight integration limits its usefulness in workflows involving non-Autodesk Building Information Modeling (BIM) platforms [14]. Another financial hurdle for smaller firms may be GBS's subscription-based licensing model, bundled within the Autodesk suite. GBS is cloud-based, which reduces the costs of investing in hardware, but also means the system depends on consistently strong Internet connections.

Tas Engineering

TAS is an advanced building simulation program, with a particular strength in dynamic thermal simulation of large and complex buildings. Designers can model daylighting and thermal performance for accurate predictions of energy use, CO2 emissions, operation costs and occupant comfort. Tas is a complete thermal simulation solution, including HVAC and system modeling with graphical and component-based analysis. Tas is mainly used by consulting engineers and architects and provides a simple user interface to create or import building geometry from other CAD software. Its extensive database covers thermal properties, climate data, schedules of occupancy, internal heat gains and HVAC characteristics, which facilitates the input processes.

Tas can produce outputs such as building loads, HVAC sizing, energy use, comfort conditions and natural ventilation. Pre-formatted reports and data export capability to various software packages facilitates customized report preparation. Tas has strengths in whole building energy simulation, load calculations, HVAC system selection, parametric optimization, energy conservation measure analysis and code compliance [11]. It also supports utility bill analysis, weather data analysis, lighting simulation, air flow simulation, detailed component simulation, solar and photovoltaic analysis, wind turbine analysis, and building simulation data-driven CFD analysis for thermal comfort assessment.

TAS Engineering software is known for its robust HVAC simulations and high-fidelity thermal modeling, but it has some limitations. Its accuracy is largely dependent on the user's expertise in data entry and can be a source of error if not done carefully. In addition, the lack of interoperability with current Building Information Modeling (BIM) platforms requires the user to enter data manually or to use proprietary, often outdated, import formats which may impede efficient workflows. The software represents a large financial investment and may be too costly for smaller firms or projects with limited budgets. Lastly, its desktop-based architecture, which demands only moderate hardware specifications, restricts access and collaboration in comparison to cloud-based alternatives.

Home Energy Efficient Design (HEED)

HEED is a simple software that allows homeowners, builders and professionals to design energy efficient residential buildings. The tool supports the design process by creating a reference house and by providing possibilities to improve the energy performance of the reference house by applying different design changes [11]. You can easily enter basic information about the home you are looking for, such as its size, number of stories, type and location. HEED uses the data to create an initial design, which can then be customized to personal preferences. The tool comes with a suite of visualization tools such as 3D models, animated shadows, and complex graphs to help users understand how different design choices impact energy consumption, cost, and carbon emissions.

HEED includes many features to support energy efficient design, including passive heating and cooling techniques, solar energy integration and the ability to add high-mass materials for thermal regulation. The tool also allows users to access climate data from thousands of locations around the world so that they can adapt their designs to the local conditions. The main advantage of the HEED is the possibility to compare various options of design and analyze their energy efficiency. Users can experiment with different layouts, materials and systems to identify best solutions to reduce energy consumption and environmental impact.

This tool is for Residential building energy efficiency design. It is a simple tool and is fairly accurate in the early stages of design. Limited customization so not good for large scale or non-standard projects. It is a standalone program with limited integration capabilities and is therefore not suitable for advanced workflows that require data exchange with other tools. It is also cheap and needs little hardware, so it is affordable for small users or designers at home.

DISCUSSION

Recent advances in computer science and the increasing demand for sustainable buildings have prompted the application and study of simulation-based optimization techniques in the building industry. Rapid urbanization and construction activities have caused a huge energy consumption and environmental degradation. This has resulted in the greater focus on energy efficiency and sustainable building design. The most frequently certified sustainable buildings in the world show a pattern of strategies used to create sustainable and eco-friendly design. One of the main strategies for improving sustainable building practices and promoting energy efficiency is the application of BEM tools in the early phases of building design. BEM has been playing an increasingly important role in building design in the last decades, driven by the growing population, economic growth and the demand for better quality of life [31]. But not all the BEM tools are useful for architects. Accurate modeling and prediction is one of the great challenges in building energy simulation [34]. Users should carefully check the accuracy and reliability of the

tool with the information available on the building which will be entered as input [3]. The choice of the right tool is a multi-faceted assessment – well-thought-out strategies, abilities, convenience and availability. The right choice of BEM tools at the start of the design process could bring great advantages [18]. The successful architectural projects are usually characterized by the effective use of BEM in the design process [7]. Therefore, Attia et al. [2] proposed four selection criteria for BEM tools: usability, computing capability, data exchange capability and database support. More importantly, the choice of the most appropriate BEM tool from the variety of alternative design options and strategies calls for careful evaluation of a number of design parameters, building performance, software-specific capabilities and the needs of the researchers [36, 46]. As such, the evaluation and selection of an appropriate BEM tool should be made of the following steps:

1. Building lifecycle phases: Specify the particular phases of the building lifecycle where the BEM tool will be used.
2. Define input needs Define input data needs of selected building life cycle stages. Use this as a checklist to help evaluate potential BEM tools.
3. What are the key outputs to be generated from the BEM tool. Use this as a checklist to help you evaluate potential tools.
4. Weight other criteria: Look at other criteria like interoperability, usability and speed and weigh them for their importance.
5. Score: Appropriately weight the criteria to find the scores for BEM tools satisfying prerequisites in steps 1-3.

The selection criteria for building energy modeling (BEM) tools are affected by a number of variables, including input and output specifications, building or district scale analysis, and project-specific requirements [13]. By considering these criteria, users can make informed decisions in selecting a BEM tool that best meets their individual needs and design goals. The design of sustainable buildings analyzed using global case studies presented in Tables 1 to 6, shows key indicators such as Site, Energy, Indoor Environmental Quality, Materials and Water. The following tables indicate the exact strategies that have been put in place for each of these indicators to promote sustainability. Therefore, BEM tools are very important in the design process especially in the conceptual stage as they have their own capabilities and applications to provide simulations and analyzes to ensure the accuracy of meeting sustainability goals. In this regard, the study proposes a detailed framework (Table 7) for the selection of the most suitable BEM tools based on their input/output characteristics and software functionalities.

The framework is based on an in-depth assessment of sustainable building indicators, strategies applied and the applicability and capabilities of different BEM tools. This assessment considers all the relevant tools included in the BESTD directory and the sustainable strategies used in the assessed buildings as shown in Tables 1-6. This comprehensive study has resulted in the identification of the ten most relevant and compatible BEM tools for sustainable building design and analysis. This framework provides useful insights into the inputs and outputs of these tools, emphasizing their capabilities and advanced functionalities, which can greatly improve the accuracy and efficiency of sustainable building design.

However, the input and output capabilities of the BEM tools, which are demonstrating their functionality and capabilities, are not enough for the selection of the most suitable tool for a specific project or study. Equally critical is the utility and strengths and weaknesses of these tools vis-à-vis the study or project requirements. Therefore, the study provides a comparison framework (Table 8) to guide users in selecting suitable BEM tools through a comprehensive assessment of their strengths, weaknesses and limitations. This framework offers useful guidance on important selection criteria such as integration capabilities with other software, adaptability to regional and climatic conditions, usability for less experienced users and small firms with limited resources, comparative evaluation of various BEM tools, and economic aspects of their implementation. In view of these factors, users can make a more informed decision about which BEM tools are accessible and appropriate for their project needs and context.

The analytical approaches used in this work were specifically designed to allow for a comprehensive and robust comparative assessment of BEM tools. The evaluation criteria were carefully developed to focus on key parameters important to sustainable building design, including inputs and outputs, applicability, usability, compatibility with local climate data, accuracy of energy performance simulations and integration with design workflow. These criteria were developed through extensive literature review and aligned with industry best practices for relevance and comprehensiveness. For further validation of the findings, cross-checking with case studies and previous research was done for each of the BEM tools tested, to ensure the assessment results are in line with the prevailing trends of tool performance.

The comprehensive evaluation presented in Tables 7 and 8 offers useful insights into the operational capacities and applicability of each BEM tool for particular project or research situations. This conclusion is based on a systematic review of the pertinent literature and authoritative resources such as the American Institute of Architects (AIA), U.S. Department of Energy's Building Energy Software Tools Directory (BESTD) to ensure completeness and reliability. The selected tools were practically validated in their respective software environments for the theoretical findings and compared to the literature and official documentation. Moreover, the data shown in the tables are also verified by the results presented in references [13, 15, 17].

Table 7. A holistic framework for assessing and selecting building energy modeling (BEM) tools based on their capability

Criteria for BEM tools selection		DesignBuilder	Sefaira Architecture	EcoDesigner Star	EnergyPlus	OpenStudio	Ladybug & Honeybee	eQUEST	Autodesk GBS	Tas Engineering	HEED
Usage	Software	✓			✓	✓		✓		✓	✓
	Plugin / Cloud base		✓	✓			✓		✓		
	Text coding				✓						
Inputs	Building geometry	✓				✓	✓	✓		✓	✓
	Import models	✓	✓	✓	✓	✓		✓	✓	✓	
	Weather file	✓	✓	✓	✓	✓	✓	✓		✓	✓
	Construction material	✓			✓	✓		✓			✓
	HVAC	✓	✓	✓	✓	✓	✓	✓	✓	✓	✓
	Lighting	✓		✓	✓			✓			
Outputs	Climate analysis	✓					✓		✓	✓	
	Building performance	✓	✓	✓	✓			✓			✓
	Energy analysis	✓	✓	✓	✓	✓	✓	✓	✓	✓	✓
	Daylighting	✓	✓		✓		✓	✓		✓	✓
	Electric lighting	✓		✓		✓			✓	✓	
	Natural ventilation	✓	✓	✓	✓			✓	✓	✓	✓
	Passive design	✓	✓	✓	✓			✓	✓		✓
	Carbon emission	✓	✓	✓	✓			✓	✓	✓	✓
	Façade elements	✓	✓		✓						
	Thermal analysis	✓		✓	✓			✓		✓	✓
	Heat transfer	✓		✓	✓						
	Heating and Cooling	✓		✓	✓	✓		✓	✓	✓	✓
	Solar analysis	✓			✓		✓	✓			✓
	Renewable systems	✓	✓	✓					✓	✓	✓
	Comfort analysis	✓	✓		✓		✓			✓	
	CFD analysis	✓									
	Cost analysis	✓			✓			✓	✓	✓	✓
Advanced functionalities	Parametric	✓				✓		✓		✓	
	Optimization	✓		✓	✓					✓	
	Life cycle assessment	✓			✓			✓	✓		
	Rating certification	✓							✓	✓	
Results	Graphic	✓	✓	✓	✓		✓	✓	✓	✓	✓
	Report / Text	✓		✓	✓	✓		✓	✓	✓	

As building performance simulation is a large and complex field it is not feasible to provide a comprehensive introduction to all aspects of building performance simulation within the limits of a single review paper [15]. The proposed frameworks can greatly contribute to the progress of sustainable building design by addressing important gaps in the current knowledge base. A key problem in this area is the lack of a systematic approach to the selection of BEM tools that are explicitly intended to support sustainable design goals. This study contributes to filling this gap by offering a comprehensive assessment framework that uses holistic and comparative criteria. The framework helps architects, engineers and researchers to make informed and evidence-based decisions when choosing energy

Table 8. A holistic framework for assessing and selecting building energy modeling (BEM) tools based on their applicability

Tool	Ease of Use	Advanced Features	Suitability for Design Stage	Climate Adaptability	Data Accuracy	Software Compatibility	Budget Constraints
DesignBuilder	Moderate	High	Detailed design	High	High	BIM-compatible (gbXML, IFC)	Paid, high-end hardware needed
Sefaira Architecture	High	Moderate	Early-stage design	Moderate	Moderate (early-stage focus)	Revit/SketchUp integration	Subscription-based, cloud-based
EcoDesigner Star	High	Moderate	Conceptual & early stages	Cold climates	Moderate (cold-climate focus)	Integrated with ArchiCAD	Expensive, desktop-based
EnergyPlus	Low	High (detailed modeling)	Detailed design	High (all climates)	High	Limited GUI, integrates with OpenStudio	Free, training & hardware costs
OpenStudio	Moderate	High	Detailed design	High	High	SketchUp/BIM integration	Free, training costs
Ladybug & Honeybee	Moderate	High	Early to detailed design	High	High	Rhino/Grasshopper platform-dependent	Free, Rhino licenses required
eQUEST	Moderate	Moderate	Early to detailed design	Moderate	Moderate (basic analysis)	DOE-2 format, limited BIM compatibility	Free, lightweight hardware
Autodesk GBS	High	Moderate	Early-stage design	High	Moderate	Autodesk-only integration	Subscription-based, cloud-reliant
Tas Engineering	Moderate	High	HVAC & detailed analysis	Moderate	High	Limited modern BIM integration	Paid, moderate hardware
HEED	High	Low	Residential projects	Low	Moderate (residential focus)	Standalone, minimal integration	Affordable, low hardware costs

modeling tools, which in turn facilitates a better integration of sustainability principles in building design practices. The study also suggests new directions for future research on the development of BEM tools, in particular the improvement of user interfaces, the integration of local climate issues and the expansion of tools to support sustainable design approaches. The research not only contributes to the advancement of architectural and engineering curricula but also informs the development of policy guidelines for sustainable building standards by emphasizing the significance of tool selection for sustainability.

A major limitation of this study is the breadth and rapid growth of BEM tools developed in recent years, many of which require specialized expertise for effective application and analysis. Besides, a full practical implementation of all tools on real case studies with a comparative evaluation of the performance would have greatly extended the scope and length of the manuscript and was therefore out of the aims of this study. However, this study benefits from overcoming this limitation by systematically reducing the list of BEM tools through authoritative sources such as the official BESTD and systematically evaluating their functionalities. A detailed analysis of the selected tools was carried out to identify those with a broad application and strong capabilities for supporting sustainable building design. Future research should include a wider range of BEM tools with a particular focus on dedicated comparative studies evaluating the practical use of these tools in real projects and analyzing the results. Moreover, it is proposed that the use of Multi-Criteria Decision-Making (MCDM) methods may improve the selection process and increase the reliability of the results in the future studies.

CONCLUSION

This work provides a detailed framework for the selection of BEM tools which can represent a valuable resource for informing decisions in the early stages of sustainable design. This study gives architects, engineers and policy makers the necessary knowledge to improve their design processes by benchmarking and comparing ten popular BEM tools. The framework takes into account a variety of technical and contextual factors that affect the complexity of choosing the right tool and thus provides a structured

methodology that can be applied to different types of projects and needs.

The significant contribution of this research is the systematic approach to identify the best BEM tools based on the input-output characteristics, and their specific application in various design scenarios. These factors are important in selecting a tool as they have immediate effects on the effectiveness and efficiency of the energy modeling process. The input-output capabilities of each tool are a good measure of the technical competence of the tool in modeling energy performance, whereas the applicability criteria are a good measure of the usability of the tool in real-world projects considering the local climate, building type and sustainability goals. This double classification enables the decision-makers to understand the trade-offs between different tools by emphasizing their strengths and weaknesses.

The research emphasizes the need for BEM tools in sustainable building design to optimize the key performance indicators such as site, energy, indoor environmental quality, materials and water use. These are the basic elements of a sustainable design and BEM tools play an essential role to avoid the creation of energy efficient, environmentally responsible and comfortable for their users' buildings. These tools combine passive strategies and local environmental considerations to improve the accuracy of energy simulations and to improve the design decisions in accordance with sustainability goals.

Moreover, the study gives a detailed comparative analysis of each BEM tool, which is very useful for professionals in the field. Table 7 and Table 8 summarize the performance of each tool according to the defined criteria, providing a clear and easily accessible guide to select the appropriate tool for the specific needs of a project. This comparative analysis can help architects to not only choose the right tool for a particular project, but also to determine which tools are better suited for a particular stage of the design process, for example, early-stage conceptual design or post-occupancy analysis.

More broadly, the study proposes a new and reliable framework for selecting BEM tools, applicable to a wide range of projects and offering significant support to architects, engineers and decision makers in achieving optimal design results. This study guides the selection of the most appropriate tool by systematic evaluation of capabilities and applicability, assisting with the streamlining of the design process and ensuring energy efficiency and sustainability goals are met effectively. This approach can improve overall performance of building designs and can help in developing more sustainable, energy efficient and environmentally responsible built environments.

AUTHORSHIP CONTRIBUTIONS

Authors equally contributed to this work.

DATA AVAILABILITY STATEMENT

The authors confirm that the data that supports the findings of this study are available within the article. Raw data that support the finding of this study are available from the corresponding author, upon reasonable request.

CONFLICT OF INTEREST

The authors declared no potential conflicts of interest with respect to the research, authorship, and/or publication of this article.

ETHICS

There are no ethical issues with the publication of this manuscript.

STATEMENT ON THE USE OF ARTIFICIAL INTELLIGENCE

Artificial intelligence was not used in the preparation of the article.

REFERENCES

[1] Ibrahim I. Eco-traditional courtyard houses in UAE: A case study of the sharjah museums. WIT Transactions on The Built Environment, Vol. 183, 2019. p. 15–24. [CrossRef]

[2] Attia S, Hensen JLM, Beltrán L, De Herde A. Selection criteria for building performance simulation tools: Contrasting architects' and engineers' needs. J Build Perform Simul 2012;5:155–169. [CrossRef]

[3] Maile T, Fischer M, Bazjanac V. Building energy performance simulation tools - a life-cycle and interoperable perspective. Cent Integr Facil Eng 2007:1–49.

[4] Negendahl K. Building performance simulation in the early design stage: An introduction to integrated dynamic models. Autom Constr 2015;54:39–53. [CrossRef]

[5] Oduyemi O, Okoroh M. Building performance modelling for sustainable building design. Int J Sustain Built Environ 2016;5:461–469. [CrossRef]

[6] Becker JS. Simulating the Implementation of Energy Efficiency measures, techniques and technologies on residential and commercial buildings. University of Florida, 2015.

[7] Hemsath TL, Bandhosseini KA. Energy modeling in architectural design. 2018. [CrossRef]

[8] Algburi OHF. An Energy Simulation Study: Reducing Cooling Energy of Residential buildings Based on Vernacular and Passive Cooling Techniques. Gazi University, 2018.

[9] Foroughi R. New Approach in Designing a Kinetic Window Shading Using Optimization Methods. Pennsylvania State University, 2018.

[10] Moazzen N, Ashrafian T, Yilmaz Z, Karagüler ME. A multi-criteria approach to affordable energy-efficient retrofit of primary school buildings. Appl Energy 2020;268. [CrossRef]
[11] BESTD. BEST Directory: Building Energy Software Tools. Int Build Perform Simul Assoc - USA 2023. https://www.ibpsa.us/best-directory-list/. Accessed November 15, 2020.
[12] Kamel E. A systematic literature review of physics-based urban building energy modeling (UBEM) tools, data sources, and challenges for energy conservation. Energies 2022;15:8649. [CrossRef]
[13] Shahcheraghian A, Madani H, Ilinca A. From white to black-box models: a review of simulation tools for building energy management and their application in consulting practices. Energies 2024;17:376. [CrossRef]
[14] Del Ama Gonzalo F, Moreno Santamaría B, Montero Burgos MJ. Assessment of building energy simulation tools to predict heating and cooling energy consumption at early design stages. Sustainability 2023;15:1920. [CrossRef]
[15] Pan Y, Zhu M, Lv Y, Yang Y, Liang Y, Yin R, et al. Building energy simulation and its application for building performance optimization: A review of methods, tools, and case studies. Adv Appl Energy 2023;10:100135. [CrossRef]
[16] Tahmasebinia F, Jiang R, Sepasgozar S, Wei J, Ding Y, Ma H. Using Regression Model to Develop Green Building Energy Simulation by BIM Tools. Sustainability 2022;14:6262. [CrossRef]
[17] Mahmoud RO, Kamara JM, Burford N. An Analytical Review of Tools and Methods for Energy Performance Simulation in Building Design. Conf. 36th CIB W78 2019 Conf., Newcastle, UK: 2019.
[18] Reeves T, Olbina S, Issa RRA. Guidelines for using building information modeling for energy analysis of buildings. Buildings 2015;5:1361–1388. [CrossRef]
[19] Sinmaz S, Yenen Z. Energy-efficient management of small-scale settlements, an assessment for Lapseki city. Sigma J Eng Nat Sci 2015;6:11–27.
[20] Bilen K, Urmamen E, Topcu MT, Solmaz I. Evaluations on the energy identity certificate and the usability of calculation method of building energy performance (BEP). Sigma J Eng Nat Sci 2020;11:103–113.
[21] Yüksel Dicle S, Zoroğlu F, Atmaca AB, Yüğrük Akdağ N, Gülay ZG. Evaluation of energy consumption and noise reduction change of a strengthened building: An educational building case. Sigma J Eng Nat Sci 2024;42:1245–1260. [CrossRef]
[22] Harish VSKV, Kumar A. A review on modeling and simulation of building energy systems. Renew Sustain Energy Rev 2016;56:1272–1292. [CrossRef]
[23] Gunay S, Kayacan B. Household energy poverty: The concept, issues and implications for Turkiye. Sigma J Eng Nat Sci 2023;41:373–384. [CrossRef]
[24] Balaras CA, Droutsa KG, Dascalaki EG, Kontoyiannidis S, Moro A, Bazzan E. Urban sustainability audits and ratings of the built environment. Energies 2019;12:4243. [CrossRef]
[25] Kubba S. Handbook of green building design and construction: LEED, BREEAM, and Green Globes. Second. Waltham: Elsevier; 2017. [CrossRef]
[26] Magazine A. Architect Project Gallery 2024. https://www.architectmagazine.com/project-gallery/. Accessed September 18, 2024.
[27] Archello. Projects architecture and design 2024. https://archello.com/projects. Accessed September 18, 2024.
[28] Tavares PF de AF, Martins AM de OG. Energy efficient building design using sensitivity analysis-A case study. Energy Build 2007;39:23–31. [CrossRef]
[29] Yezioro A, Dong B, Leite F. An applied artificial intelligence approach towards assessing building performance simulation tools. Energy Build 2008;40:612–620. [CrossRef]
[30] Li J, Yu Z, Haghighat F, Zhang G. Development and improvement of occupant behavior models towards realistic building performance simulation: A review. Sustain Cities Soc 2019;50:1–20. [CrossRef]
[31] Gao H, Koch C, Wu Y. Building information modelling based building energy modelling: A review. Appl Energy 2019;238:320–343. [CrossRef]
[32] Dabieh M. A future for the past of spectacular desert vernacular. Lund University, 2011.
[33] Al Kanani A, Dawood N, Vukovic V. Energy efficiency in residential buildings in the Kingdom of Saudi Arabia. Build. Inf. Model. Build. Performance, Des. Smart Constr., Springer International Publishing; 2017, p. 129–143. [CrossRef]
[34] Coakley D, Raftery P, Keane M. A review of methods to match building energy simulation models to measured data. Renew Sustain Energy Rev 2014;37:123–141. [CrossRef]
[35] Toutou A, Fikry M, Mohamed W. The parametric based optimization framework daylighting and energy performance in residential buildings in hot arid zone. Alexandria Eng J 2018;57:3595–3608. [CrossRef]
[36] Najjar MK, Tam VWY, Di Gregorio LT, Evangelista ACJ, Hammad AWA, Haddad A. Integrating parametric analysis with building information modeling to improve energy performance of construction projects. Energies 2019;12:1515. [CrossRef]
[37] Hensen JLM. Towards more effective use of building performance simulation in design. Proc. 7th Int. Conf. Des. Decis. Support Syst. Archit. Urban Plan., 2004, p. 2–5.
[38] Ayoobi AW, Inceoğlu M, Çolak O. Assessment of the Effect of Architecture Morphology on Building Energy Demands Using BIM, Example of Kabul City Residential Buildings. Lect Notes Civ Eng 2022;226 LNCE:369–380. [CrossRef]

[39] DesignBuilder. DesignBuilder 2.1 User's Manual. 2009.
[40] Crawley DB, Lawrie LK, Winkelmann FC, Buhl WF, Huang YJ, Pedersen CO, et al. EnergyPlus: Creating a new-generation building energy simulation program. Energy Build 2001;33:319–331. [CrossRef]
[41] BESTD. Sefaira Architecture. Int Build Perform Simul Assoc IBPSA-USA 2015. https://www.ibpsa.us/best-directory/sefaira-architecture/. Accessed September 27, 2023.
[42] Graphisoft. EcoDesigner Star: User manual. 2014.
[43] OpenStudio. OpenStudio 1.9.0 Basic Workflow Guide. 2015.
[44] Hirsch J. eQUEST introductory tutorial. 2010.
[45] Le MK. Autodesk green building studio for an energy- efficient, sustainable building. HAMK Häme University of Applied Sciences, 2014.
[46] Papamichael K, LaPorta J, Chauvet H. Building Design Advisor: Automated integration of multiple simulation tools. Autom Constr 1997;6:341–352. [CrossRef]

Sigma J Eng Nat Sci, Vol. 44, No. 4, pp. 3002–3011, August, 2026

Sigma Journal of Engineering and Natural Sciences
Web page info: https://sigma.yildiz.edu.tr
DOI: 10.14744/sigma.2025.1908

Review Article

A review: Machine learning approach to understanding the impact of mobile phone addiction on academic performance, health, and family life

R. Ruth BELINA[1,*], T. Lucia Agnes BEENA[1]

[1]*Department of Computer Science, Holy Cross College (Autonomous), Affiliated to Bharathidasan University, Tiruchirappalli, Tamil Nadu, 620002, India*

ARTICLE INFO

Article history
Received: 02 January 2025
Revised: 14 March 2025
Accepted: 11 August 2025

Keywords:
Addiction Behaviour; Correlation; Machine Learning; Mobile Phone Addiction; Mobile Phone Use; Predictive Analytics

ABSTRACT

This review explores the impact of mobile phone addiction on studies, health, and home life based on machine learning methods. In contrast to previous research focusing on one aspect, e.g., sleep quality or study stress, the present investigation employs machine learning to detect patterns of phone dependence and its extended effects. Excessive use of mobile phones has been shown to negatively impact academic performance by instigating poor time management, distraction, and sleep deprivation, which translates to decreased grades. It decreases the quality of sleep, causing lethargy and cognitive problems. Additionally, excessive use of mobile phones damages family and social relationships since individuals tend to give preference to online relationships over actual ones. With the application of machine learning models, it is feasible to forecast individuals at risk and negative outcomes, thereby informing targeted interventions. Also, this review compares different methodological strategies, such as ML-based investigations into the detection of depression, overuse of mobile phones, online game addiction, and their effects of health and relationships.

Cite this article as: Belina RR, Beena TLA. A review: Machine learning approach to understanding the impact of mobile phone addiction on academic performance, health, and family life. Sigma J Eng Nat Sci 2026;44(4):3002–3011.

INTRODUCTION

Communication has been forever changed by the rise of the mobile phone, which allows us to reach anyone in the world at a moment's notice. Apart from being used for speaking on, they are hand-held computers that can be used to gain access to both information and entertainment. However, their commonality has raised concerns about cell phone addiction, which is a behavior pattern that interferes not only with daily life but also with social interactions, it appears.

Machine learning appears to provide a relatively promising approach, based on creating models that will predict which individuals may be predisposed to mobile phone addiction, taking into account actual mobile phone usage, social media behavior, demographic factors such as age and gender, as well as psychological factors such as anxiety

***Corresponding author.**
*E-mail address: r.ruthbelina@gmail.com

This paper was recommended for publication in revised form by Editor-in-Chief Ahmet Selim Dalkilic

Published by Yıldız Technical University Press, İstanbul, Turkey
© Author. This is an open access article under the CC BY-NC license (http://creativecommons.org/licenses/by-nc/4.0/).

[1] and depression. However, in order to create such models, data needs to be collected from a large group of users, including both their patterns of mobile phone usage as well as demographic and psychological information. Such models may prove useful in identifying those who are at risk and developing intervention programs aimed at helping them overcome their addiction [2] which, in turn, would help avoid the consequences of addiction.

Common signs of mobile phone dependence [3] include:

- Unable to minimize phone usage even after trying.
- Failure to keep track of time when using the phone.
- The use of the phone as a way to run away from reality.
- Feeling anxious about running out of battery or losing the phone.
- Favoring virtual communication over face-to-face interaction.
- Overly dependent on checking phones for notifications and messages.

Excessive use of phones leads to many after effects, including headaches and that feeling of tension in relationships, which is definitely not ideal. It is crucial to ensure proper management of phone usage to maintain its usefulness as a tool, without letting it become a nuisance. Machine learning models can be very useful in this regard as they can aid both individuals as well as health care professionals in preventing phone addiction and minimizing the adverse consequences that follow.

Emotional Impact of Mobile phone Addiction

These devices have become an integral part of communication, work, and recreation; therefore, when you think about it, your life is actually quite dependent on mobile phones. Nonetheless, the overreliance on these gadgets has resulted in various adverse effects on the psychological, emotional, social, and behavioral health of users. Mobile phone addiction is a rising issue throughout the world, and it comes out as an emotional echo, where the person becomes dependent rather than using them. These emotional impacts of mobile phone addiction in Figure 1 can be listed as follows:

1. **Nomophobia:** Fear of losing the phone or the feeling of being anxious due to inability to find it [4].
2. **Textaphrenia:** The feeling of receiving messages or the sensation of vibrations when none occurs.
3. **Ringxiety:** Feeling that one's phone rings when it doesn't happen.
4. **Textiety:** The anxiety of not receiving or sending messages.

These behaviors illustrate the extent to which the mental influence exerted by the mobile phones on their users is powerful, such that everything seems to disrupt the normal daily activities as well as the personal relationships. In addressing the problem of mobile phone addiction, one needs to be aware and take measures ahead of time so as to reduce the use of the phones while still retaining them as convenient devices and not sources of stress.

Health Risks with Excessive Mobile Phone Use

Overuse of a mobile phone leads to numerous health issues affecting not only physical well-being but also psychological state. The above-listed risks arise due to the long-term and incorrect use of the smartphone and may result in considerable disruptions in one's everyday activities. Below there is a list of some health conditions associated with excessive use of a mobile phone.

a) **Text Neck Syndrome**: This condition can be characterized by the strain on neck muscles resulting from constant looking down at the mobile phone screen, which makes your head inclined.
b) **Insomnia**: Mobile phones emit blue light, disturbing the sleep cycle and making it more difficult for users to fall asleep.
c) **Increased Risk of Cancer**: Continuous radiation exposure from mobile phones can cause an increased risk of tumors and even brain cancer.
d) **Trigger Thumb:** The repetitive actions of texting, typing, or clenching your phone in your hand may cause your thumb to get stuck in a bent position.
e) **Thumb Arthritis:** Frequent pinching movements caused by texting or even holding the phone in your

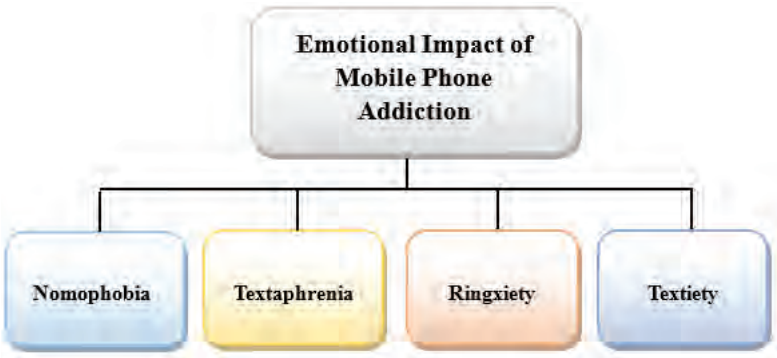


Figure 1. Emotional Impact of Mobile Addiction.

hands may result in pain and tenderness in the area of your thumb joint closest to your wrist.

f) **Cubital Tunnel Syndrome:** Leaning your elbows on a surface while texting or talking on the phone can lead to numbness and tingling in your ring finger and pinky fingers as well as pain in your elbow joint.

g) **Vision Issues:** Blue light emitted by mobile phones can strain your eyes and adversely impact your overall vision as well as damage your cornea.

h) **Male Infertility:** Having a phone close to your body or using it when it is charging can have negative consequences for male fertility due to radiation.

i) **Hearing Loss:** Exposure to the electromagnetic field produced by mobile phones can lead to hearing impairment.

j) **Impact on Unborn Child:** Excessive radiation emitted by mobile phones during pregnancy can impair fetal brain development and lead to attention deficit hyperactivity disorder, ADHD.

The above health hazards demonstrate the need to moderate the use of mobile phones and develop healthy habits to mitigate their negative impacts. Mobile phones were invented to make life easier, but an over-reliance on them could undermine one's health.

Predictive Modeling

Machine learning (ML), which is basically an AI discipline [5], helps machines learn like humans through the process of learning from data, without explicitly programming them. Predictive modeling is one type of model construction which focuses on creating computational or mathematical models capable of predicting future occurrences based on the patterns obtained from existing and past data [6]. This usually involves analyzing the dataset by performing statistical analysis or implementing machine learning algorithms to discover correlations among variables. Then comes the process of developing models that will be used for prediction purposes. For instance, predictive modeling can assist in determining a student's performance based on the study patterns, attendance records, and cell phone usage, among others; a somewhat indirect approach to prediction. This entails such concepts

(a). Parametric Models

In parametric machine learning models [7], certain strong assumptions are made regarding the data, making the model simpler and, in some cases, increasing the accuracy of predictions. Parametric methods always maintain a constant number of parameters irrespective of the size of the training set used. Examples [8] include:

- ✓ Logistic Regression
- ✓ Linear Regression
- ✓ Linear Discriminant Analysis (LDA)
- ✓ Naive Bayes
- ✓ Perceptron
- ✓ Simple Neural Networks

(b). Non-Parametric Models

Since non-parametric approaches do not place any stringent assumptions on the underlying structure of the data, they fit well in large data sets even when no prior information about them is available. The fact is that such approaches usually get complicated with larger data sets, and they work very well in constructing mapping functions. Examples of non-parametric approaches are [9, 10]:

- ✓ Support Vector Machines (SVM)
- ✓ K-Nearest Neighbors (KNN)
- ✓ Decision Trees
- ✓ Random forest

(c). Top Predictive Analytics Models

Most predictive modeling techniques are either machine learning or statistical models that can be applied to analyze historical and current data in order to make an inference of what may occur in the future or predict certain types of behavior. In a sense, such models attempt to find out data patterns and then make some sort of educated guess about the future based on those findings. Five most prominent models [11], in fact, do something like that – though, of course, with some slight modifications:

Classification Model: It provides answers to questions that have two possible answers; yes and no. This model also makes decision making easier in various sectors.

Forecast Model: It forecasts numeric [12] values based on past data; this can be helpful for activities such as sales forecasting and demand forecasting.

Anamoly Model: It detects anomalies inside datasets, which is helpful for finding fraud, or other irregularities that do not "fit."

Clustering Model: It groups data into clusters based on their similarities and dissimilarities for better understanding.

Time Series Model: It analyzes sequential data points over time, then it tries to estimate trends or future values.

The right predictive model is important, because it helps organizations use insights in a useful way and make decisions that are more informed across industries. The top 5 predictive analytics models are shown in Fig.2.

Process of Predictive Modeling

The process of predictive modeling is kind of a step by step process [13], to develop models that help predict what happens next, based on existing data. Most of the time it goes in a sequence like:

Defining the exact outcome which has to be predicted. This particular outcome largely dictates the type of data to be used as well as the modeling technique to be used. Precision forecasting needs quality data. Data should be gathered from reliable sources, then cleansed from inconsistencies, mistakes, and missing values [14]. After that, the data is transformed in order to make everything consistent and improve the quality of data overall. This step consists of identification and description of the features, which are alternatively

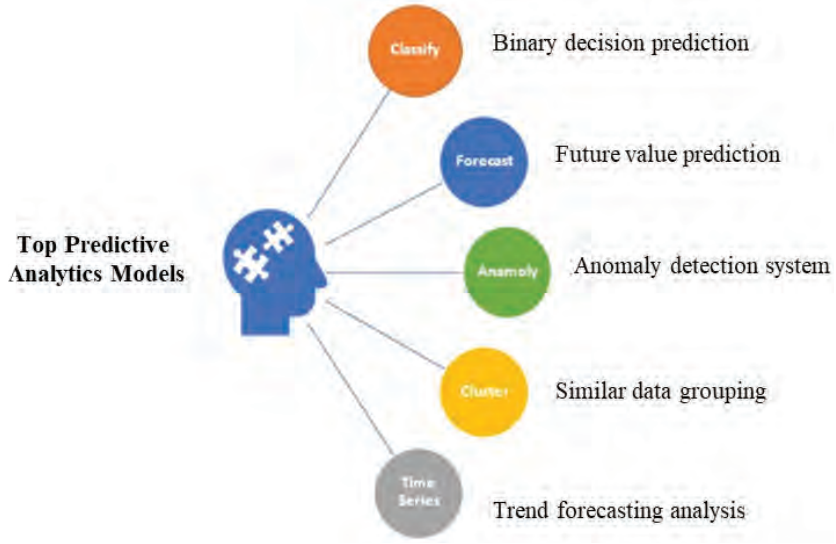


Figure 2. Top 5 predictive analytics models.

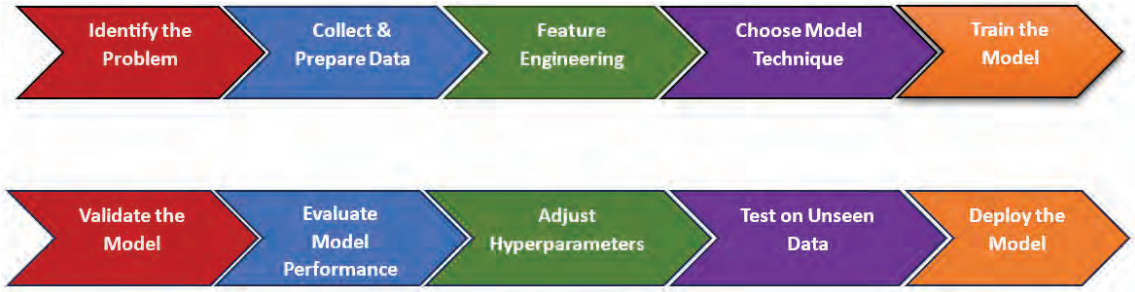


Figure 3. Predictive Modeling Process.

referred to as predictors, in the raw data. This consists of normalization, encoding, dimensionality reduction, and domain-specific transformation in order to find the connections which will be helpful in prediction. This step consists of selection of the appropriate model according to the nature of the data and problem complexity (decision trees, regression and neural networks). This step consists of training the chosen model using the training data set through parameter optimization. This step consists of validation of the model using cross-validation and holdout validation data sets in order to determine the model's performance on new data. This step consists of evaluation of the model's performance through accuracy, precision, recall, F1 Score, AUC-ROC, among others. The outcome of this step is largely used to determine the efficiency of the model. This step consists of tuning of the hyperparameters such as learning rate or tree depth of the model in order to improve the model's performance. This kind of process includes grid searches and many other approaches. This step consists of testing the accuracy of the model using the unseen test split which was not used for training and validation purposes. Once the training process is completed, the next step would be deployment of the model either into production or application and predictions are made immediately once new data appears.

The flow in Figure 3 kind of makes sure that the whole predictive modeling process stays useful and gives insights you can actually act on, and it also fits across a bunch of separate scenarios, while still maintaining accuracy, and enough robustness.

LITERATURE REVIEW: PREDICTING MOBILE PHONE ADDICTION USING MACHINE LEARNING

Many studies have aimed to predict mobile phone addiction, which is an increasing problem, with implications for mental health, academic performance and social relationships [15] , and family life, using machine learning (ML) predictive techniques. This subsection is a literature review of existing research results and prediction models in the literature.

Depression Detection via Mobile Phone Usage

Presented a minimalist ML system for depression detection through app usages over the period of seven days.

With the LGBM, this system achieved an accuracy of 82.4% with no need for sensors or resource-intensive techniques – in turn being both scalable and low-cost [16].

Mobile Phone Addiction and Physical Activity

Study of adolescents showed a negative association of DGA and PA and a positive one with obesity [17] Their findings suggest that increasing physical activity can reduce DGA by 1.51 times.

Clustering Mobile Phone Usage Behaviors

Designed an unsupervised clustering algorithm to identify the presence of any abnormal patterns of mobile phone usage. Daily activity-details made the algorithm more effective in performing the task. K-Means was found to be marginally better than K-Medoids in this regard [18].

Prediction of Problematic Mobile Phone Use during the Pandemic

Used the shrinkage approach of Lasso regression for predicting problematic mobile phone use during the COVID-19 outbreak by producing accurate results with very low error measures [19].

Mobile Phone Dependency Among University Students

Applied the Stratified-K-Fold cross validation and Support Vector Machines (SVM) algorithm for predicting the dependency on mobile phones among university students [20].

Ensemble Methods for Risk Prediction

Compared various ensemble classification techniques for forecasting student's at-risk, using teacher employment status along with student performance. Boosted tree models, however, proved effective in dealing with large data sets, while the Multilayer Perceptron model performed relatively well with small data sets [21].

Factors that Influence Mobile Phone Addiction

Performed a logistic regression analysis on 1981 participants and found that gender and life quality were factors that determined the risk of mobile phone addiction [22].

Gender-Based Usage of Apps

Examined the gender variations in mobile phone addiction and the usage of apps with Machine Learning models like, decision tree and logistic regression [23].

SVM for Mobile Phone Addiction Prediction

Used SVM with an RBF kernel to predict mobile phone addiction based on the features obtained from questionnaires filled by 1143 respondents. The findings appeared convincing and were validated using confusion matrices [24].

Depression Prediction through Changes in Activities

Used machine learning models such as XGBoost and Random Forest for detecting changes in activities to predict depression. The precision obtained by the model XGBoost was highest in all results [25].

Gender-Based Behavioral Insights

Studied the stages of mobile phone addiction in terms of gender, and concluded that females are using mobile phones more than 12 hours per day in comparison to males who used mobile phones for shorter periods [26].

Family Dynamics and Mobile Phone Addiction

Carried out a study on the effect of mobile phones on family relations using Naive Bayes, KNN and Logistic Regression models, of which KNN model was the most precise, which shows about 95% accuracy in predicting worsening of family bond relationship due to increased mobile phone use [27].

The machine learning approach yields useful information for the prediction of mobile phone addiction, considering the behavioral data, demographic characteristics, and app usage of varying populations. These models provide possible targets for early intervention to reduce the negative impact of mobile phone use worldwide.

Appraisal of Literature on Machine Learning Algorithms for Predicting Mobile Phone Addiction

This section reviews past and current studies of machine learning (ML) models that have been applied to predict mobile phone addiction. Even with all the advancements made, there is still room for improvement when it comes to the quality of the data and choice of algorithms used.

SYNTHESIS AND COMPARATIVE ANALYSIS OF RESEARCH ON THE UTILIZATION OF MOBILE PHONES, ADDICTIONS, AND MENTAL HEALTH

This paper is set to conduct a synthesis of studies done regarding mobile phone addictions, depression detection, and behavioral analysis, focusing on the utilization of machine learning technologies.

Use of Machine Learning in Mental Health and Addiction Detection

There have also been several studies that use ML methods to identify mental illnesses and behavior addictions. [16] built Mon Majhi—a light-weight ML driven app-behaviour-based depression detection system [25] utilized ML models like XGB, RF to identify screen status-associated behavioral changes as early descriptors of depression [23- 27] employed ML classifiers namely Decision Trees, SVMs, Logistic Regression, KNN for forecasting mobile phone addiction in most cases, with either gender- or activity-related factors. These research papers indicate a trend toward light-weight, scalable ML tools for behavior and mental health monitoring, using different algorithms but mostly positive results with regards to the accuracy of the outcomes.

Behavioral Patterns and Risk Factors

Behavioural characteristics and demographics were similar among different studies [16] and [27] associated digital overuse with gender, age, and family relationships.

Table 1. Comparative assessment

Paper	Main Focus	Methodology	ML Use	Key Insight
Ahmed et al. [16]	Depression detection	ML (LGBM)	Yes	Lightweight, accurate, scalable
Gülü et al. [17]	DGA, obesity	Cross-sectional	No	DGA linked to less activity, more obesity
NurUzZaman et al. [18]	Smartphone addiction	Clustering (K-Means)	Yes	Activity data improves clustering
Xiao et al. [19]	Smartphone overuse	Shrinkage regression	Yes	FoMO, self-regulation predict overuse
Giraldo-Jiménez et al. [20]	University student dependency	SVM + Risk factors	Yes	Socioeconomic & physical risk factors matter
Naveed Answer et al. [21]	Academic performance prediction	Ensemble classifiers	Yes	Boosted trees best for large datasets
Pradeep et al. [22]	Cell phone addiction	Logistic regression	No	Life skills reduce risk
Aggarwal et al. [23]	Smartphone addiction	Supervised ML	Yes	Usage patterns strongly correlated
Koklu et al. [24]	Smartphone addiction	SVM	Yes	RBF kernel + confusion matrix used
Asare et al. [25]	Depression via phone data	Multiple ML models	Yes	XGB, RF, KNN perform best
Mazumdar et al. [26]	Gender & usage analysis	Correlation study	Partial	Female users show higher addiction
Anjaly et al. [27]	Family impact	Naive Bayes, KNN	Yes	

[22] and [20] identified connections between risk for addiction and social, psychological and life factors [19] considered FoMO as a crucial predictor of problematic mobile phone use and self-regulation as a predictor. This suggests a wide agreement on the importance of personality characteristics and situational factors in digital addiction (DA) and mental distress (MD).

Comparative Algorithm Performance

Several models of ML algorithms were compared in the studies [16] LGBM was identified the best algorithm to achieve high sensitivity to depression detection [19]. Lasso regression was discovered as the top algorithm to predict mobile phone overuse. [24] SVM with RBF helped to achieve best results for mobile phone addiction prediction [25]. XGB, RF algorithms helped to find out depression through phone behavior accurately [23]. Decision Trees , AdaBoost and KNN algorithms were determined as best to classify addiction [27]. KNN reached an accuracy of 95% in family relationship impact. On studying the performance of different ML algorithms, tree-based and ensemble models like LGBM, RF, XGB generally work better than the vanilla classifiers, especially for more difficult prediction problems.

Gender and Demographic Observations

A number of researches such as [17, 22, 26, 27] revealed that females are likely to have higher mobile phone or game addiction levels than males. Age and lifestyle components such as physical activities, peer relations and academic history were also identified as significant factors.

COMPARATIVE EVALUATION

This Table represents the comparative evaluation of various research studies performed for predicting mobile phone addiction.

Altogether, the studies demonstrate an emerging trend towards increasing use of machine learning methods to discover behavioural and psychological states in the context of mobile phone use. Ensemble models are the ones that work best for the prediction of mental health (XGB, LGBM, RF), while best among the behavioral type classification are KNN and SVM.

Based on these studies, it is apparent that psychological variables (FoMO, self-regulation), demographic variables (gender, age) and behavior (screen time, app use) are interrelated. This comparative study also proves that evidence exists for the convergence of mobile data and ML for scalable and efficient health diagnostics, although the extent of cross-cultural generalisation, data privacy and ethical issues need to be investigated in future studies.

DISCUSSION

The effectiveness of a prediction model is more or less, determined by how well it can lay bare relationships, and patterns inside a dataset. Its ability to generalize to data it hasnt seen before is super important, because it helps boost prediction accuracy, and also leads to clearer actionable insights. In other words a kind of comparative reading of different ML algorithms from the literature is wrapped up in Table 2.

Table 2. A comparative analysis of various algorithms to predict mobile phone addiction

Author/ Ref. No	Year of Publication	Methods/Models/ Algorithms used	Best Models/ Methods	Dataset Used	Sample Size	Performance Metrics	Future Work
Ahmed et. al. [16]	2023	1. Decision Tree 2. Information gain (IG) algorithm 3. Random Forest algorithm 4. Gradient Boost 5. LGBM 6. XG Boost 7. K-Nearest Neighbor 8. Logistic Regression 9. ADA Boost 10. CatBoost 11. Naive Bayes	Light Gradient Boosting Machine (LGBM)	Patient Health Questionnaire	100 Students	Accuracy 82.4%	To develop prudent computational models to identify psychological problems in low-resource settings leveraging behavioral data.
Gülü et. al. [17]	2023	Synthetic Minority Over-sampling Technique for Nominal and Continuous (SMOTE-NC)	Synthetic Minority Over-sampling Technique for Nominal and Continuous (SMOTE-NC)	DGA Questionnaire and Physical activity Questionnaire	405 Adolescents	Not Mentioned	1. Future research should include a longitudinal method to better represent the developmental course of this proposed disorder. 2. The effect of digital game addiction can be investigated in more detail by methods that can analyse self-efficacy, mental, and physical health conditions in more detail.
Pradeep et. al. [22]	2022	1. Cross-sectional data analysis 2. Logistic Regression analysis	Univariate and Multivariable Logistic Regression	6-item questionnaire	1981 Participants	Not mentioned	Complexity of associations for below criteria needs to be further analyzed. 1. Quality of life vs risk of cell phone addiction. 2. Number of peers vs risk of cell phone addiction.
Aggarwal et. al. [23]	2022	1. Decision tree 2. AdaBoost 3. Logistic Regression 4. KNNs 5. Naive Bayes with Pearson›s coefficient	Decision tree with AdaBoost classification	Mobile Apps developed to collect data	96 Participants	Accuracy 75%	Classification can be narrowed down to include additional features like app-initiated events and the number of notifications each app offers, thus providing a better understanding of the app›s usage.
Nigmet Koklu. N et. al. [24]	2021	1. Support Vector Machine 2. Classification Method 3. Radial Basis Function 4. Confusion Matrix	Support Vector Machine	Questionnaire	1143 Individuals	Accuracy 92.4%	Mobile application or software needs to be developed to conduct a comprehensive analysis.

Table 2. A comparative analysis of various algorithms to predict mobile phone addiction (continued)

Author/ Ref. No	Year of Publication	Methods/Models/ Algorithms used	Best Models/ Methods	Dataset Used	Sample Size	Performance Metrics	Future Work
Kennedy Opoku Asare et. al. [25]	2021	1. Random Forest 2. Support Vector Machine 3. Radial Basis function kernel 4. XG Boost 5. K-Nearest Neighbor 6. Logistic Regression 7. Random Weighted Classifier 8. Decision Tree classifier.	XG Boost	Carat app	629 participants from 56 countries	Accuracy 96.44%-98.14%.	Wearable sensor data sets can be used for correlation
Arpita Mazumdar et. al. [26]	2020	1. Unsupervised Machine Learning techniques 2. K-means Clustering	K-means clustering	Questionnaire	115 under graduates participated	Not mentioned	Further refining the model can certainly help to understand phone usage patterns and possibly predict certain threats prevalent among smartphone addicted people.
Anjaly K et. al. [27]	2020	1. Naive Bayes 2. KNN 3. Logistic Regression	KNN algorithm	Questionnaire	280 People	Accuracy 95%	To focus on a wider age group within the family

CONCLUSION

Mobile phone addiction seems to be rising everywhere, especially among students, and also in the wider general population. The problem is becoming more obvious, both in terms of a minor personal matter and a serious hindrance that can ruin daily life. The consequences include strained relations within families, poor academic performance at schools, behavioral changes and even depression. Social networks such as Facebook, WhatsApp and Instagram may contribute greatly to developing such dependency. However, mobile phones are not "evil" in themselves; they provide many benefits including fast access to relevant information, navigational assistance, educational material, e-mail correspondence, assistance in remote working, news services and entertainment. On the other hand, usage patterns vary among individuals depending on their habits and, frankly, self-discipline. In most cases, the issue of mobile phone addiction is closely connected with the user's level of self-discipline and his or her capability to set priorities concerning maintaining relations with one's relatives, being present at the moment and engaging in other activities.

Indeed, machine learning algorithms have already proven their effectiveness when it comes to predicting mobile phone addiction with considerable accuracy. Therefore, in future research, it is important not only to rely on symptoms as the definition of mobile phone addiction but rather discover the root cause, which triggers it. The final aim of such an approach is to examine the impact of mobile phone addiction on academic results, physical and psychological health, and family relations. Such an objective can be achieved via conducting a review study based on existing literature, including the use of machine learning algorithms.

ACKNOWLEDGEMENT

The authors would like to sincerely acknowledge the support of the Department of Science and Technology (DST), Government of India, for providing the FIST (Fund for Improvement of S&T Infrastructure) program funding. This assistance has substantially contributed to the research and its development activities as outlined in this work.

AUTHORSHIP CONTRIBUTIONS

Authors equally contributed to this work.

DATA AVAILABILITY STATEMENT

The authors confirm that the data that supports the findings of this study are available within the article. Raw data that support the finding of this study are available from the corresponding author, upon reasonable request.

CONFLICT OF INTEREST

The author declared no potential conflicts of interest with respect to the research, authorship, and/or publication of this article.

ETHICS

There are no ethical issues with the publication of this manuscript.

STATEMENT ON THE USE OF ARTIFICIAL INTELLIGENCE

Artificial intelligence was not used in the preparation of the article.

REFERENCES

[1] Chaudhary P, Hasan Z. Influence of smartphone addiction on mental well-being and self-esteem. Int J Indian Psychol 2024;12.

[2] Abuhamdah SM, Naser AY. Smart phone addiction and its mental health risks among university students in Jordan: a cross-sectional study. BMC Psychiatry 2023;23:812. [CrossRef]

[3] Thomas DW, Brande L, Monico N. Mental health disorder treatment guidelines. Available at: https://www.psychguides.com/behavioral-disorders/cell-phone-addiction Accessed on Sep 16, 2026.

[4] Kubala K. Medical News Today - Nomophobia. Available at: https://www.medicalnewstoday.com/articles/nomophobia Accessed on Sep 16, 2026.

[5] Tagliaferri L. An introduction to machine learning. Available at: https://www.digitalocean.com/community/tutorials/an-introduction-to-machine-learning Accessed on Sep 16, 2026.

[6] Sghir N, Adadi A, Lahmer M. Recent advances in predictive learning analytics: A decade systematic review (2012–2022). Educ Inf Technol 2023;28:8299–8333. [CrossRef]

[7] Ali R. Predictive modeling. Available at: https://www.netsuite.com/portal/resource/articles/financial-anagement/predictive-modeling.shtml Accessed on Sep 16, 2026.

[8] Gupta R, Sharma A, Alam T. Building predictive models with machine learning. In: Data Analytics and Machine Learning: Navigating the Big Data Landscape. Springer; 2024. p. 39–59. [CrossRef]

[9] Amjad S, Younas M, Anwar M, Shaheen Q, Shiraz M, Gani A. Data mining techniques to analyze the impact of social media on academic performance of high school students. Wirel Commun Mob Comput 2022;2022:9299115. [CrossRef]

[10] Ahmed E. Student performance prediction using machine learning algorithms. Appl Comput Intell Soft Comput 2024;2024:4067721. [CrossRef]

[11] Elhai JD, Yang H, Rozgonjuk D, Montag C. Using machine learning to model problematic smartphone use severity: The significant role of fear of missing out. Addict Behav 2020;103:106261. [CrossRef]

[12] Insightsoftware. Top 5 predictive analytics models and algorithms. Available at: https://insightsoftware.com/blog/top-5-predictive-analytics-models-and-algorithms Accessed on Sep 16, 2026.

[13] Pedamkar P. Predictive modeling vs predictive analytics. Available at: https://www.educba.com/predictive-modeling-vs-predictive-analytics Accessed on Sep 16, 2026.

[14] Côté PO, Nikanjam A, Ahmed N, Humeniuk D, Khomh F. Data cleaning and machine learning: A systematic literature review. Autom Softw Eng 2024;31:54. [CrossRef]

[15] Mazumdar A, Sharma S. Machine learning model for prediction of smartphone addiction. Turk J Comput Math Educ 2020;11:545–550.

[16] Ahmed MS, Ahmed N. A fast and minimal system to identify depression using smartphones: Explainable machine learning-based approach. JMIR Form Res 2023;7:e28848. [CrossRef]

[17] Gülü M, Yagin FH, Gocer I, Yapici H, Ayyildiz E, Clemente FM, et al. Exploring obesity, physical activity, and digital game addiction levels among adolescents: A study on machine learning-based prediction of digital game addiction. Front Psychol 2023;14:1097145. [CrossRef]

[18] Uz Zaman N, Akther A, Tabassum N, Samrat MKK, Khan SM. An approach to detect smartphone addiction through activity recognition and app usage behaviour (master thesis). Bangladesh: Brac University Department of Computer Science and Engineering; 2023.

[19] Xiao B, Parent N, Rahal L, Shapka J. Using machine learning to explore the risk factors of problematic smartphone use among Canadian adolescents during COVID-19: The important role of fear of missing out (FoMO). Appl Sci 2023;13:4970. [CrossRef]

[20] Giraldo-Jiménez CF, Gaviria-Chavarro J, Urrutia-Valdés A, Bedoya-Pérez JF, Sarria-Paja MO. Machine-learning predictive models for dependency on smartphones based on risk factors. Preprint. 2021. doi: 10.21203/rs.3.rs-886633/v1. [CrossRef]

[21] Anwer Butt ZM, Shakeel K, Alfarhood S, Safran M, Ashraf I. Performance prediction of students in higher education using multi-model ensemble approach. IEEE Access 2023;11:136091–136108. [CrossRef]

[22] Pradeep B, Shenoy AB, Shahane S, Srividya RN, Arelingaiah M, D'Souza R, et al. Age, gender, peers, life skills and quality of life influence risk of cell phone addiction among college teachers in Karnataka, India: A state level epidemiological analysis. BMC Public Health 2022;22:180. [CrossRef]

[23] Aggarwal S, Gupta S, Satia SPS, Saluja S, Gambhir V. Pilot study to predict smartphone addiction through usage pattern of installed Android applications and to derive correlations between addiction and phone usage behavior. Addicta 2022;9. [CrossRef]

[24] Koklu N, Taspinar G, Sulak SA. Predicting smartphone addiction with support vector machine. 2021. p. 56–64.

[25] Opoku Asare K, Terhorst Y, Vega J, Peltonen E, Lagerspetz E, Ferreira D. Predicting depression from smartphone behavioral markers using machine learning methods, hyperparameter optimization, and feature importance analysis: Exploratory study. JMIR Mhealth Uhealth 2021;9:e26540. [CrossRef]

[26] Mazumdar A, Karak G, Sharma S. Machine learning model for prediction of smartphone addiction. Turk J Comput Math Educ 2020;11:545–550.

[27] Anjaly K, Rajalakshmi VR. Gender based smartphone addiction and aftermath in family relations. Int J Innov Technol Explor Eng 2020;9:1465–1468. [CrossRef]

Sigma J Eng Nat Sci, Vol. 44, No. 4, pp. 3012–3026, August, 2026

Sigma Journal of Engineering and Natural Sciences
Web page info: https://sigma.yildiz.edu.tr
DOI: 10.14744/sigma.2026.2141

Review Article

Innovative thermal and non-thermal treatments for microorganism inactivation in plant milk

Ulaş BAYSAN[1,2,*], Işıl İLTER BAYSAN[3]

[1]*Department of Gastronomy and Culinary Arts, Faculty of Tourism, Dokuz Eylül University, İzmir, 35390, Türkiye*
[2]*Science and Technology Application and Research Center, Dokuz Eylül University, İzmir, 35390, Türkiye*
[3]*Department of Food Engineering, Faculty of Enginering and Natural Sciences, Manisa Celal Bayar University, Manisa, 45140, Türkiye*

ARTICLE INFO

Article history
Received: 20 March 2025
Revised: 12 April 2025
Accepted: 05 May 2025

Keywords:
Microbial Inactivation; Milk Alternatives; Non-Thermal Processing; Plant Based Milk; Thermal Processing

ABSTRACT

The growing popularity of plant-based diets can be connected to the quick global expansion of plant-based dairy products. This review examines the classification of plant milk's fundamental components and outlines the principal processing stages involved in their manufacture. Particular attention is given to the influence of processing operations on product quality, stability, and safety. Microbial inactivation, a critical step in plant milk processing, is discussed alongside the conventional and emerging technologies used for this purpose. Current approaches include thermal methods and innovative technologies such as ohmic heating, microwave processing, high-pressure processing, ultrasonication, pulsed electric field treatment, and ultraviolet irradiation. The available literature indicates that these technologies can effectively improve microbiological safety while upholding sensory and nutritional qualities. Consumption of high-nutrient, plant-derived milk is anticipated to rise as new technologies develop globally, leading to the emergence of several plant-milk product categories.

Cite this article as: Baysan U, İlter Baysan I. Innovative thermal and non-thermal treatments for microorganism inactivation in plant milk. Sigma J Eng Nat Sci 2026;44(4):3012–3026.

INTRODUCTION

A variety of food products created to meet evolving nutritional standards has been fueled by customers' desire for more nutritious food options. In parallel with these developments, functional and specialty beverages have become an important topic of interest for the food business as well as scholars. Beyond their traditional role in hydration, modern beverages are increasingly expected to provide additional nutritional and physiological benefits. Consequently, manufacturers have focused on developing products tailored to specific consumer needs and lifestyle preferences. Within this context, plant-based milk alternatives have attracted growing attention, particularly among individuals affected by cow's milk allergy, lactose intolerance, hypercholesterolemia, or concerns related to caloric intake [1].

Milk is a biological secretion produced by female mammals to nourish their offspring and is recognized as an important source of nutrients in the human diet [2]. Owing to its balanced composition of proteins, lipids,

***Corresponding author.**
*E-mail address: ulas.baysan@deu.edu.tr

This paper was recommended for publication in revised form by Editor-in-Chief Ahmet Selim Dalkilic

Published by Yıldız Technical University Press, İstanbul, Turkey
© Author. This is an open access article under the CC BY-NC license (http://creativecommons.org/licenses/by-nc/4.0/).

carbohydrates, vitamins, and minerals, milk is frequently regarded as a nutritionally valuable food [3]. Cow's milk has been consumed for centuries in many regions of the world and continues to play a significant role in daily nutrition [4]. However, dairy consumption may not be appropriate for all individuals. Conditions like cow's milk protein sensitivity and lactose intolerance may limit the intake of dairy and milk products. It has been estimated that nearly 75% of the global population experiences some degree of lactose intolerance [3]. This condition arises from inadequate small intestine lactase activity, reducing the body's capacity to digest lactose efficiently. As a result, in sensitive individuals, consuming milk and dairy products may cause gastrointestinal symptoms, including diarrhea, bloating, and stomach pain.

People prefer and consume plant milk alternatives for various health effects and lactose intolerance. For example, human cholesterol levels rise when animal products are consumed excessively. Cardiovascular illnesses are more likely to occur in this setting. Plant milk from grains, legumes, and seeds is preferred because it contains dietary fibre, vitamins, minerals, and antioxidants. These foods also fall into the category of both functional and nutrient-fortified foods [5]. Apart from the benefit of a plant-based diet in reducing the likelihood of cardiovascular disease, Pistollato et al. [6] reported that greater consumption of plant-based foods, including almonds and soybeans, may contribute to reducing the risk of neurodegenerative diseases such as Alzheimer's disease. Additionally, Sarni and Baroni [7] reported that the daily consumption of two glasses of cow's milk may increase D-galactose levels above 100 mg/kg, a condition suggested to be associated with the development of Parkinson's disease.

Plant milk alternatives have attracted attention because of their potential health benefits, particularly their antioxidant compounds and favorable fatty acid profiles, which may contribute to a lower risk of diabetes, cancer, cardiovascular diseases, and atherosclerosis [8]. However, plant-based milk products also present certain nutritional limitations, including lower protein content and reduced bioavailability of some vitamins and minerals. These limitations are largely associated with antinutritional factors and polyphenolic compounds that may interfere with nutrient absorption. Nevertheless, processing strategies such as nutrient fortification and fermentation have been proposed to improve the nutritional quality and bioavailability of plant milk products [9, 10].

Interest in plant-based dietary patterns emphasizing grains, legumes, seeds, nuts, fruits, and vegetables has increased substantially due to growing health awareness, environmental concerns, and animal welfare considerations [11, 12]. These developments have contributed to the wider adoption of dietary approaches such as lacto-vegetarianism, ovo-vegetarianism, and vegetarianism. A vegan follows a dietary and lifestyle pattern that excludes animal-derived products, including leather, wool, silk, and other animal-based materials [13]. As the number of individuals adopting vegan lifestyles continues to increase, the importance of vegan product categories within the food industry has also expanded [14].

Plant milk is frequently used as a beverage and an ingredient in various recipes. Consequently, significant interest has emerged in developing plant-based products as alternatives to conventional milk. In addition to direct consumption, these products are used in several applications, including nutritional supplements, infant foods, cream-based products, and fruit-based formulations. Many nations still lack unified standards and regulatory frameworks controlling the labeling. Some plant-based alternatives to milk are still developing. The Food and Drug Administration (FDA) classifies these products within the category of "imitation milk" or "imitation dairy products" because they share several sensory and physical characteristics with conventional milk, including similarities in appearance, texture, flavor, and overall product structure [15]. Under current European Union regulations, only specific plant-based goods, such as coconut and almond milk, may be marketed using the term "milk" [16–18].

COMPARISON OF ANIMAL MILK AND PLANT MILK

Plant- and animal-derived milks differ considerably with respect to their origin, nutritional composition, digestibility, environmental footprint, and sensory characteristics. While plant-based milk substitutes are made from a range of plant sources, such as soy, rice, and oats, animal milks are derived from mammals like cows, goats, and sheep. Important nutrients like calcium, riboflavin, vitamin B12, and high-quality protein are found in animal milk [19], but its lactose content may cause digestive discomfort in lactose-intolerant individuals [20]. On the other hand, the ingredients used to make plant-based milks affect their nutritional composition. Compared to most plant-based substitutes, soy milk has a higher protein content, whereas almond- and rice-based beverages typically provide lower protein levels. Because plant-based milk products sometimes have low levels of naturally occurring calcium and vitamin B12, fortification is commonly used to improve their nutritional value [21]. Furthermore, plant-based milks may support cardiovascular health because they typically have less saturated fat and are naturally cholesterol-free [22]. From a sustainability perspective, their production is often associated with lower energy and water use and lower greenhouse gas emissions compared with conventional dairy farming [23]. Consumer acceptance is significantly influenced by sensory attributes, including flavor and scent, which are heavily dependent on the plant source utilized.

In addition to having a lower glycemic index than animal milk, plant-based milk substitutes often provide fiber and a variety of bioactive phytochemicals, including phenolic acids, flavonoids, stilbenes, lignans, condensed and hydrolyzable tannins, proanthocyanidins, carotenoids,

alkaloids, phytates, terpenes, and phytoestrogens are among them. However, compared with animal milk, their protein content is often lower, and other essential nutrients are present at lower concentrations or have reduced bioavailability. For example, it's possible that certain nutrients, like iron, calcium, iodine, vitamin D, and vital amino acids, aren't as abundant as they are in dairy milk. long-term reliance on beverages made from insufficiently fortified plant-based ingredients may make vulnerable groups—children in particular—more susceptible to malnutrition. In order to overcome these limitations, some studies have explored combining plant- and animal-derived milks in a single food matrix to develop functional products with enhanced nutritional profiles [17, 24].

Many parts of the world have seen an increase in issues such as limited access to conventional milk, milk protein allergy, lactose intolerance, and the need for alternative sources of specific nutrients and bioactive compounds. Initially dominated by soybean-based beverages, this market segment has diversified considerably and now includes products derived from oats, almonds, coconuts, hemp seeds, and cocoa. In addition, plant milk production generally requires lower energy input per unit of product than conventional dairy milk, whereas its composition can be modified to satisfy [18, 25, 26].

Classification and Production of Plant Milk

Plant-based milk alternatives represent an expanding segment of the beverage industry and are increasingly consumed worldwide because of changing dietary preferences and lifestyle choices [4]. The idea of plant-derived milk beverages is not new and dates back to historical documents from the thirteenth century, even though the dramatic increase in demand for these goods over the past few years. Plant milk is derived from plants, for example, legumes, oilseeds, cereals, or pseudocereals, that function and look like cow's milk. Production generally involves dispersing plant materials, including cereals, legumes, seeds, and nuts, in water followed by homogenization [27]. These processing techniques yield drinks with particle sizes typically between 5 and 20 μm, giving them a texture and appearance similar to regular milk. Based on their source materials, plant milks can be classified into four primary categories [18], as illustrated in Figure 1.

Although specific processing conditions vary among plant materials, the main stages involved in plant milk manufacture are largely comparable across different raw material groups [28]. The principal stages involved in plant milk production are illustrated in Figure 2. Generally, plant milk is produced by a series of steps: peeling the shell, adding

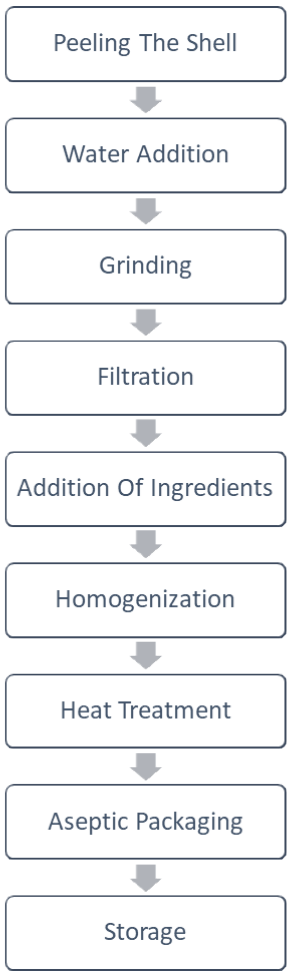


Figure 2. Basic process steps in plant milk.

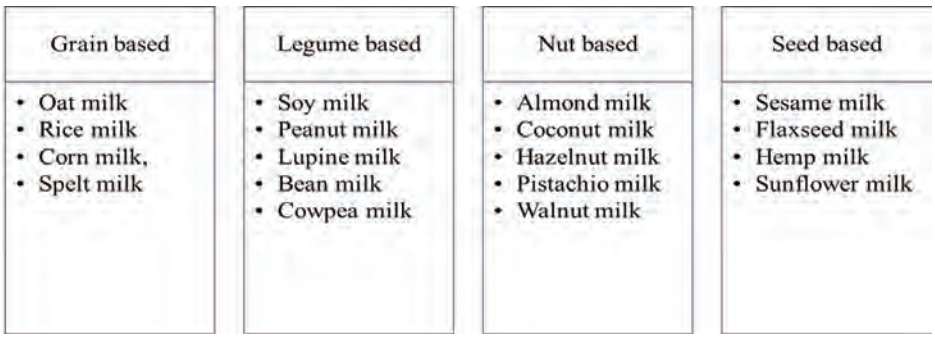


Figure 1. Classification of plant milks according to their raw materials.

water, grinding, filtering, adding additives, homogenizing, heating, aseptic packaging, and storing.

Both the yield of soluble extract and the procedure of making plant milk are greatly influenced by the properties of the plant raw material. As a result, preliminary processing operations may vary depending on the source material used. Nuts and seeds are commonly subjected to shell removal, whereas grains and legumes are typically soaked in hot water and subsequently dried. Additional pretreatments, including chemical peeling or roasting with acidic or alkaline solutions, may be applied to increase process efficiency, eliminate unwanted chemicals, and improve emulsion stability [18]. These operations also promote softening and hydration of the raw materials. During soaking, changes in starch composition may occur, and certain contaminants, such as mold-associated toxins, can migrate into the soaking water [29]. Previous studies have evaluated the use of alkaline soaking solutions for sesame seeds [30], soybeans [31], and peanuts [32].

Grinding is a critical operation in plant milk production because it reduces particle size and encourages the plant matrix's soluble components to be released. Wet milling is generally preferred over dry grinding because it is more compatible with subsequent processing operations and can improve overall process efficiency. This approach has been extensively implemented in plant milks derived from soybeans, coconuts, cashews, hazelnuts, hemp seeds, almonds, walnuts, peanuts, and beans [33–36]. Several processing variables, including grinding time, feed rate, pH, temperature, and the water-to-raw-material ratio, affect the final product's characteristics. Among these variables, the concentration and composition of the final beverage are significantly influenced by the amount of additional water [37]. The addition of water during grinding can facilitate subsequent blanching operations and reduce processing times. Furthermore, blanching may help reduce microbial populations and enzymatic activity in the product [38].

The bleaching step in plant milk production, particularly for oat milk, uses enzymes such as amylases to enhance product quality [18]. This process improves color, flavor, and stability while reducing bitterness and preventing gelation. It exemplifies innovation in the plant milk industry, aiming to meet growing consumers' demand [39]. However, manufacturers must balance the benefits of enzymatic treatments with maintaining nutritional value and addressing preferences for less processed products [26].

Following the enzymatic treatment stage, the liquid fraction is separated from the insoluble material through filtration. During this operation, insoluble particles originating from the ground plant matrix are removed, allowing the recovery of the water-soluble extract. Different filtration materials have been employed for this purpose, including double-layer cheesecloth, muslin cloth (25 μm), filter paper, and sieves or membrane filters with pore sizes ranging from 4 to 180 μm [30, 34, 35, 40, 41]. In addition to conventional filtration techniques, Naziri et al. [42] successfully produced plant-based milks from corn, sesame, and hazelnut using ultrafiltration technology.

To increase stability and enhance the nutritional composition of plant milk formulations, a variety of additions can be used. Proteins, minerals, and vitamins are commonly included to enhance the final product's nutrient composition [24]. To enhance physical stability, ingredients such as acacia gum, gellan gum, and sunflower lecithin are frequently utilized. Ascorbic acid may also be added as an antioxidant to limit oxidative changes during storage. Flavor-adjusting ingredients, including cane sugar and sea salt, can be incorporated depending on product requirements. Makinde and Adebile [43] and Manzoor et al. [44] reported the use of sugar syrup in almond- and cashew-based beverages. The protein, vitamin, and mineral composition of plant milks plays an important role in consumer acceptance. Higher protein levels may be achieved by increasing the proportion of raw materials or combining ingredients with complementary nutritional properties. In addition, fortification is commonly used to improve the levels of minerals, including calcium and vitamins A, B1, B2, B12, D2, and E [18].

The homogenization process reduces the size of suspended particles in plant milk while causing minimal changes to viscosity and protein characteristics, contributing to improved physical stability [41]. It is possible to do homogenization at low, high, or extremely high pressures. Product consistency, visibility, and brightness are often improved by increasing homogenization pressure [36, 45, 46]. However, viscosity and protein stability are not markedly influenced by this operation [45]. Particle size can be further reduced under ultra-high-pressure conditions [46]. Although repeated homogenization cycles may increase product yield, temperature elevation can occur because of the applied pressure [47, 48]. Gul et al. (2018) reported that homogenization may increase product temperature by approximately 5–10°C [47]. Consumers generally prefer plant-based milks with appearance, stability, rheological characteristics, and compositional characteristics similar to those of traditional milk [18, 49]. Technologies including ultrasonication, pulsed electric field treatment, ohmic heating, and high- or ultra-high-pressure homogenization have attracted increasing attention as approaches for improving the stability of plant milk products [30].

Thermal processing is generally applied as the final preservation stage in plant milk manufacturing. Pasteurization remains one of the most frequently used approaches for improving microbiological stability and reducing enzymatic activity. Conventional thermal treatments include ultra-high-temperature (UHT) sterilization and pasteurization [50, 51]. In addition to these established methods, several emerging technologies have been investigated for plant milk stabilization, including ultrasonication, high-pressure processing, microwave treatment, pulsed electric field (PEF) treatment, ohmic heating, supercritical carbon dioxide processing, and ultraviolet (UV) irradiation [52].

Conventional heat treatments are highly effective for microbial control and therefore remain widely utilized in commercial food production [53]. However, prolonged exposure to elevated temperatures may affect nutritional and sensory quality through protein denaturation, vitamin degradation, and changes in flavor characteristics [52]. To address these limitations, alternative processing technologies have been explored as potential means of improving microbial safety while preserving product quality [54].

Despite these technologies' potential benefits, there are still a number of practical obstacles to their industrial application, such as equipment costs, process complexity, and regulatory considerations [55]. Consequently, the selection of an appropriate stabilization strategy should take into account both product characteristics and targeted quality requirements. Although the number of studies investigating these technologies in plant milk systems continues to increase, available information remains relatively limited [56]. Following processing, aseptic packaging and refrigerated storage at approximately 4°C significantly preserve product stability and increase shelf life.

Microorganism Inactivation in Plant Milks

Plant-based milk alternatives contain nutrients that can support microbial growth when appropriate preservation measures are not implemented. Microbial development during storage may adversely affect these items' physicochemical qualities and sensory attributes. Consequently, effective processing technologies play an essential role in plant milk manufacturing. Thermal processing is widely applied to control spoilage and pathogenic microorganisms, thereby extending shelf life and improving product stability [57]. Besides enhancing microbiological safety, thermal processing may also contribute to increased total solids and the development of desirable flavor. However, exposure to excessive heat can adversely affect product quality through vitamin degradation, amino acid losses, non-enzymatic browning reactions, and undesirable flavor formation [58]. Therefore, processing conditions should be carefully optimized to achieve adequate microbial control while preserving product quality.

Conventional Thermal Treatments

In the manufacture of plant milk products, pasteurization and ultra-high-temperature (UHT) processing remain among the most widely adopted preservation strategies to ensure product durability and improve shelf life. Conventional thermal treatments include pasteurization, in-container sterilization, and UHT processing, each designed to reduce microbial populations and enhance product safety. In-container sterilization is typically performed at 121°C for 15–20 min to achieve commercial sterility, whereas UHT treatment involves short exposure periods at temperatures between 135 and 150°C [58]. During UHT processing, heat may be delivered either directly via steam infusion or injection, or indirectly through plate or tubular heat exchangers. Following thermal treatment, products are generally packaged under aseptic conditions to maintain microbiological stability. While UHT-treated and sterilized products can remain stable for extended periods at ambient temperature, pasteurized products typically require refrigerated storage.

Han [59] evaluated the effects of pasteurization and sterilization on soymilk production. They reported that pasteurized (60°C/30 min) soy milk could remain stable at ambient conditions for 3 days without noticeable quality loss, and that sterilized (120°C/5 min) soy milk remained stable under ambient conditions for 1 year. Whereas thermal treatments can be preferred and more easily applied to durable products such as soy milk and peanut milk, their use is limited by the high starch content in products such as oat milk and rice milk.

Bartula et al. [60] investigated the behavior of foodborne pathogens and spore-forming bacteria in commercial plant-derived substitutes for milk stored under refrigerated and ambient conditions (4, 8, and 20°C). The study included coconut-, almond-, and cashew-based beverages as well as UHT-treated cow's milk. Samples were inoculated with *Listeria monocytogenes, Salmonella enterica, Paenibacillus spp.*, and *Bacillus subtilis* at an initial level of approximately 1×10^3 CFU/mL. The findings indicated that the tested microorganisms generally exhibited faster growth in plant-based beverages than in cow's milk. Increased growth of *L. monocytogenes* was observed at both 8 and 20°C, whereas *Salmonella* and *Paenibacillus* showed more pronounced growth at 20°C. In contrast, *B. subtilis* displayed comparable growth behavior in almond milk and cow's milk under the same storage conditions. No statistically significant differences were detected in the growth responses of *Listeria* and *Salmonella* at 4 and 8°C ($p>0.05$). These observations suggest that plant-based milk alternatives may require particular attention to controlling pathogens associated with listeriosis and salmonellosis.

The plant milk industry must ensure product quality and safety. Pasteurization is frequently employed to improve product stability and storage life by reducing populations of spoilage and pathogenic microorganisms. Thus, plant milks are processed to provide consumers with pleasing sensory qualities while also increasing microbiological stability and reducing perishability [61, 62].

When pasteurization and sterilization processes are carried out as thermal treatments, undesirable physical, chemical, sensory, and nutritional conditions arise. To eliminate these negativities, the tendency towards non-thermal or innovative thermal treatments is increasing [63]. Using these innovative technologies, microorganisms and enzymes can be rendered inactive without compromising or adversely affecting the food products' nutritional value. Accordingly, ohmic heating, microwave heating, high-pressure processing, ultrasonication, pulsed electric field treatment, and ultraviolet irradiation have gained increasing attention as alternative processing technologies in plant

milk production. While the microbial load is reduced with these innovative technologies, the process variables that preserve the nutritional content of plant milks must be well adjusted and regulated.

Innovative Thermal Treatments

Numerous processing techniques have been investigated to guarantee product stability and safety while preserving food's nutritional value. Ohmic and microwave heating are the most preferred and applied technologies. Table 1 summarizes the studies conducted in the literature [64-77].

Ohmic heating is an electrothermal processing technique that produces internal heat by passing an electrical current straight through the food material. This mechanism enables rapid, relatively uniform heating, particularly in liquid food systems, thereby improving heat-transfer efficiency. [78]. Numerous studies have looked into the use of ohmic heat in food treatment, especially pasteurization as well as sterilizing procedures. [79]. The effectiveness of this technology is associated with the combined action of electrical current and temperature, which can contribute to both enzymatic and microbial inactivation. Plant-derived milk products benefit from these effects since they improve microbiological stability and retain quality throughout storage. [68, 80, 81]. Unlike conventional heating systems, ohmic heating provides volumetric heat generation throughout the product, reducing temperature gradients and minimizing localized overheating. This method has attracted interest as an alternate processing approach to improve the safety and preservation of plant-based milk products.

Studies on soy milk have shown that ohmic heating can achieve urease inactivation with an effectiveness comparable to conventional thermal processing. In addition, enzymatic inactivation performance has been reported to improve as the operating frequency increases [81]. Despite these advantages, excessive heat generation during processing may promote protein coagulation. Elevated temperatures reached during ohmic treatment of soy-based milk alternatives have also been associated with undesirable changes in sensory attributes and nutritional quality [82]. According to Tiravibulsin et al. (2021), ohmic-assisted sterilization achieved complete inactivation of Clostridium sporogenes spores (>5 log CFU/mL) in coconut milk when applied at 121.1°C for 5 min. Compared with conventional sterilization, this process provided a shorter overall treatment time. In addition to its effectiveness in microbial inactivation, the application was associated with reduced formation of undesirable odors while preserving the product's visual characteristics. These findings indicate that ohmic-assisted sterilization may offer an effective alternative for the processing of coconut milk [68].

The most popular and favored technique for thermal processing liquid foods is continuous-flow microwave heating, an alternative to traditional heating methods. Dipole rotation and ionic conduction are responsible for heating food in microwave ovens. Since volumetric energy transfer causes temperature to rise more quickly, processing times are shortened, and energy is conserved [83]. Unlike conventional thermal systems, microwave processing generates heat directly within the product and does not require an external heat-transfer medium. In addition, microwave technology has been associated with reduced energy and water consumption as well as improved processing efficiency.

Microwave pasteurization enables rapid heat transfer and can achieve the desired processing temperature in less time than many conventional heating systems. Reduced processing time may preserve the dietary and sensual characteristics of foods throughout preservation. During microwave treatment, electromagnetic energy is absorbed directly by food components, resulting in volumetric heating and a more uniform temperature distribution than conventional surface-to-center heat transfer. Using microwave energy to process food can reduce total processing time [84]. Microwave processing yields positive results in reducing enzymatic spoilage, which is as important as microbial growth in plant milk. Studies have examined the trypsin-inhibitory effects of microwave processing in soy milk. The results showed that this method achieved trypsin inhibition and affected protein structures [85–87].

Microwave pasteurization (360 W/38 s) and conventional pasteurization (70°C/465-480 s) were compared for their ability to inactivate Salmonella enteritidis in almond, soy, and oat milk samples [69]. Microwave treatment resulted in decreases of 5.39, 5.77, and 6.62 log concentrations of CFU in soy, almond, and oat milk. Compared with classical pasteurization, microwave pasteurization showed similar inhibition of microorganisms, indicating it constitutes an alternative pasteurization method.

Innovative Non-thermal Treatments

High-pressure process (HPP), commonly known as high hydrostatic pressure (HHP), is a non-thermal, preservation a food method that exposes foods to higher pressure levels for a set period. During processing, packed products are placed in a pressure chamber and treated with a pressure-transmitting liquid, usually water. HPP enhances microbiological safety while preserving nutritive and sensorial properties of foods. [88, 89]. Prior researches have also demonstrated that pressure treatment combined with moderate heat can enhance the inactivation of bacterial spores [90–94]. HPP technology is a viable solution for maintaining microbiological stability in plant-based milk products. [1, 70–72] (Table 1).

Soy milk was subjected to high hydrostatic pressure treatment at two pressure levels, namely 200 and 300 MPa, in the study reported by Cruz et al [70]. The total number of aerobic and mesophilic bacteria were found to have decreased by 2.42 and 4.24 log CFU/ml, respectively. Total aerobic and mesophilic bacterial populations decreased

Table 1. Research on ensuring microbial safety in plant milk with innovative technologies

Innovative Technology	Inactivation methods and process conditions	Target microorganism	Product	Results	References
Ohmic Heating	**Ohmic heating** Frequency: 10 kHz; Time: 40, 45, 50, and 55 s.; Temperature: 50, 55, 60, 65, 70, and 80°C; sodium lactate solution	• *S. Typhimurium,* • *E. coli* O157:H7, • *S. aureus* • *L. monocytogenes,*	Soy milk	• Ohmic heating has demonstrated considerable potential as an alternative approach for ensuring microbial safety. • An increase in the sodium lactate content caused a decrease in pathogens. • Lethal damage to microbial cell structures was observed in samples containing 3% sodium lactate.	[67]
Ohmic Heating	**Ohmic heating** Pressure: 1.5 bar; voltage: 600 V current: 80A; frequency: 50Hz sodium sulfate solution; 121.1°C/ 2 min **Sterilization** Temperature: 121.1°C/ time: 2 min	• *Clostridium sporogenes* • *Clostridium perfringens*	Coconut milk	• Ohmic-assisted sterilization at 121.1°C for 5 min achieved complete inactivation of C. sporogenes spores at levels exceeding 5 log CFU/mL.	[68]
Microwave Application	**Microwave** Microwave power: 360 W; time: 38 s **Pasteurization** Temperature: 70°C; time: 465-480 s	• *Salmonella enteritidis*	Almond milk Soy milk Oat Milk	• Microbial inactivation was achieved in all plant-based dairy products to a level that can demonstrated the potential to replace conventional thermal pasteurization.	[69]
High-pressure processing (HPP)	**High-pressure processing (HPP)** Pressure: 200-300 MPa	• Total mesophilic aerobic bacteria • Enterobacteria • Total mesophilic aerobic spores	Soy milk	• Counts of mesophilic aerobic bacteria decreased as the applied pressure increased. • Enterobacteria remained below the detection limit in both applications.	[70]
High-pressure processing (HPP)	**High-pressure processing (HPP)** Pressure: 200-300 MPa Temperature: 55, 65, and 75°C **Pasteurization** Temperature: 95°C/ time: 30 s **Sterilization** Temperature: 142°C/ Time: 6 s	• *Bacillus cereus* • Total mesophilic aerobic bacteria • Total mesophilic aerobic spores • Enterobacteria • Mold and yeast • *Staphylococcus aureus* • Salmonella species • Coliform	Soy milk	• The sterility obtained in the UHT process was achieved with the HHP method.	[71]
High-pressure processing (HPP)	**High-pressure processing (HPP)** Pressure: 200 and 300 MPa Temperature: 55, 65, and 75°C **Pasteurization** Temperature: 90°C/ time: 90 s **Sterilization** Temperature: 142°C/ time: 6 s	• Total mesophilic aerobic bacteria • Total mesophilic aerobic spores • Yeast and mold • *Enterobacteriaceae* • *Micrococcaceae* • *Bacillus cereus*	Almond milk	• After pasteurization, sterilization, and HPP processes, microbial counts were determined below the detection level.	[1]

Table 1. Research on ensuring microbial safety in plant milk with innovative technologies (continued)

Innovative Technology	Inactivation methods and process conditions	Target microorganism	Product	Results	References
High-pressure processing (HPP)	**High-pressure processing (HPP)** Pressure: 200-300 MPa Temperature: 55-75°C **Pasteurization** Temperature: 95°C/ time: 30 s **Sterilization** Temperature: 142°C/ time: 6 s	• Total mesophilic aerobic bacteria • Total mesophilic aerobic spores	Soy milk Almond milk	• The HPP process provided a higher reduction in microorganisms than pasteurization. • Almond and soy milks treated with HPP exhibited superior colloidal stability compared with samples subjected to conventional thermal processing.	[72]
Ultrasonic Application	**Ultrasonic Application** Power: %20-80; time: 2-8 min Pulse: 2-6 s	• *Escherichia coli O157:H7* • *Listeria monocytogenes*	Almond milk	• It has been found that ultrasonic application can cause non-lethal damage to pathogens.	[65]
Ultrasonic Application	**Ultrasonic Application** Power: 300 W; frequency: 20 kHz time: 0, 2.5, and 5 min	• Total mesophilic aerobic bacteria • *Enterobacteriaceae*	Almond milk	• No microbial growth was detected in ultrasonically treated almond milk throughout the storage period.	[73]
Ultrasonic Application	**Ultrasonic Application** Power: 600 W; Frequency: 40 kHz; temperature: 30, 45 and 60°C; time: 10, 20, 30, and 40 min **Pasteurization** Temperature: 90°C/ time: 60 s	• Total mesophilic aerobic bacteria • Yeast and mold	Almond milk	• Processing at 60°C led to reductions of ≥5 log in total plate counts and ≥4 log in yeast and mold populations. • In ultrasonic application, the process applied to microorganisms pierces the cell membranes, causing the intracellular matrix to be expelled and forming free radicals, eventually inhibiting the organisms.	[74]
Pulse Electric Field (PEF)	**Pulse Electric Field (PEF)** Temperature ≤35°C; electric field power: 7, 14, 21, and 28 kV/cm; Accent frequency: 1 kHz; emphasis width: 40 µs, process time: 200 µs **Pasteurization** Temperature: 90°C/ time: 60 s	• Total mesophilic aerobic bacteria • *Escherichia coli,* • Yeast and mold	Almond milk	• The microbial load in almond milk decreased effectively with thermal treatment and PEF (28 kV/cm) applications. • PEF treatment applied at 28 kV/cm produced a level of microbial stability comparable to that obtained with thermal processing.	[75]
Pasteurization in UV-C Reactor	**Pasteurization in UV-C Reactor** 2-10 loop **Pasteurization** Temperature: 63°C/ time: 30 min	• *Escherichia coli* K-12 (ATCC 25253)	Oat milk	• UV-C reactor treatment of oat milk resulted in a 3.22 log CFU/mL reduction in *E. coli* K-12.	[76]
Pasteurization in UV-C Reactor	**Pasteurization in UV-C Reactor** Flow rate: 25-100 ml/min Tube length: 240-1376 cm **Pasteurization** Temperature: 72°C/ Duration: 32 s	• *Escherichia Coli* • *Bacillus cereus*	Soy milk	• UV-C processing effectively reduced *E. coli* cells and *B. cereus* spores in soy milk while maintaining product quality.	[77]

by 2.42 and 4.24 log CFU/mL, respectively, as a result of the therapy. Additionally, Enterobacteriaceae remained less than the detection limit in both pressure conditions, although overall spore counts decreased by around 2 log CFU/mL. Comparable microbiological stability to that achieved by UHT processing was obtained at 300 MPa and 75°C. Overall, HHP treatments demonstrated greater microbial inactivation than conventional pasteurization. Furthermore, HHP was associated with lower oxidation levels while maintaining substantial inactivation of trypsin inhibitors [71].

Microbial populations in almond milk were reduced to levels under the detectable level (-0.5 log CFU/mL) after pasteurization, sterilization, and high-pressure processing procedures. During HPP treatment, temperature increases may result from adiabatic heating and mechanical forces generated within the system, including turbulence, shear stress, and cavitation. These processing conditions are considered important contributors to microbial inactivation and overall product stabilization [1].

Ultrasonication has attracted considerable interest as an alternative processing technology in the food industry. In the food sector, ultrasonication has attracted a lot of interest as an alternative processing technology. The cavitation phenomena produced during ultrasonic treatment are the main cause of this technique's anti-microbial effect. Ultrasonic waves, typically operating at frequencies above 20 kHz, create localized mechanical and physical effects that can damage microbial cells [95, 96]. Ultrasonic processing has been shown in earlier research to be an efficient way to lower microbial populations. Additionally, using it in conjunction with thermal treatments may reduce processing times while minimizing unfavorable alterations to food's nutritional value. The ultrasonic frequency used to inactivate microorganisms is generally between 20 and 100 kHz [96, 97]. The microbial inactivation mechanism typically depends on the cavitation force [98]. When ultrasonic treatment is used with other techniques, the efficacy of inactivating microorganisms is boosted [99, 100]. Ultrasonic treatment effectiveness relates to the targeted microorganisms. Combining ultrasonic processing with other preservation techniques, such as thermal and pressure-based treatments, can increase its efficacy, especially for spore management. Nevertheless, more research is needed to assess the practical application of integrated treatment strategies in food systems and optimise conditions for the process. Ultrasonic uses in plant milk have been the subject of numerous investigations. [65, 101–106].

Listeria monocytogenes and *E. coli* O157:H7 growing behaviors were affected by the ultrasonic treatment of almond milk. Application decreased the growth rate of E. coli O157:H7 and postponed the growth of L. monocytogenes. Although complete pathogen elimination was not achieved, ultrasonication contributed to a measurable reduction in microbial populations [65]. Furthermore, microbiological analyses indicated that no detectable microbial growth occurred during the storage of ultrasonically treated almond milk [73].

In a study comparing pasteurization and ultrasonic treatment (60°C) in almond milk, similar results were obtained for microbial inactivation. With both methods, a log reduction of more than 5 in the total number of plaques and more than 4 in the number of yeast and molds was detected [74]. Ultrasonic treatment's antimicrobial action is linked to structural damage to microbial cells, which can lead to internal component leakage and the production of reactive species that aid in microbial inactivation.

Short-duration, high-intensity electrical pulses are applied to food systems using pulsed electric field (PEF) technology, a non-thermal preservation method that lowers microbial activity. The antimicrobial effect of PEF is primarily associated with the disruption of cell membrane integrity through electroporation [107]. Because the treatment can be applied within a very short time while minimizing thermal damage, it has attracted considerable interest for the production of minimally processed foods [107, 108].

PEF systems are appropriate for liquid, semi-liquid, and some solid food products since they usually operate at electric field levels of 20 to 80 kV/cm with pulse durations of 1 to 100 μs [107,108]. The qualities of the treated food matrix, microbial attributes, and processing conditions all affect how well microbial inactivation Works [107, 108-110]. Although PEF has been investigated as an alternative to conventional thermal pasteurization, current evidence indicates that its performance can be enhanced when combined with thermal treatments, particularly in applications requiring high levels of microbial reduction [109–111].

The antimicrobial effect of pulsed electric field (PEF) processing is generally attributed to electroporation of microbial cell membranes. When the applied electric field exceeds a critical threshold, permanent structural changes may occur in the membrane, increasing its permeability and promoting the leakage of intracellular components, which can ultimately result in cell death [108, 109]. Previous studies have reported the effectiveness of PEF against various microorganisms, including Escherichia coli, Listeria innocua, Staphylococcus aureus, Enterobacteriaceae, and Pseudomonas fluorescens[110, 112, 113]. Siemer et al. [111] reported that combining thermal processing with PEF treatments can effectively inactivate spores, with PEF being the dominant factor at higher energy inputs. It should be emphasized here that better results can be achieved when combining PEF with heat. In comparing the pasteurization process and PEF (28 kV/cm) application in almond milk, they reported that PEF reduced the microbial load. According to Manzoor et al. [75], The study found that PEF PEF processing performed at 28 kV/cm offered comparable microbiological stability to thermal treatment over the 28-day storage period.

Ultraviolet (UV) irradiation is a non-thermal preservation technology that utilizes electromagnetic radiation within the wavelength range of 100–400 nm. Based on

wavelength, UV radiation is commonly categorized into four spectral regions: vacuum-UV (100–200 nm), UV-C (200–280 nm), UV-B (280–315 nm), and UV-A (315–400 nm). Among these regions, UV-C has received particular attention in food processing applications because of its strong antimicrobial activity. In most industrial applications, UV radiation is generated using mercury-based lamp systems that provide continuous emission [114].

The antimicrobial action of UV light is primarily associated with damage to microbial genetic material. UV radiation is widely used for the decontamination of surfaces, equipment, and air environments [115]. UV processing is inexpensive, leaves no chemical residue behind, and generates minimal heat [116]. The effectiveness of UV treatment largely depends on the ability of UV radiation to penetrate the treated medium. Successful microbial inactivation relies on sufficient exposure of target microorganisms to UV photons. UV application rooms need to be constructed to inactivate organisms that cause microbial spoilage in liquid food products [114]. Spores are not significantly affected by UV radiation. However, UV exposure may enhance the effectiveness of subsequent thermal processing by increasing the sensitivity of bacterial spores [117]. Research investigating UV inactivation mechanisms has consistently identified DNA damage as the principal factor responsible for microbial inactivation. Applications of UV treatment are particularly common in liquid food systems, including fruit beverages, dairy-based products, honey, and liquid egg products [114, 118].

Thermal pasteurization and UV-C reactor treatment have been compared for stabilizing oat milk [76]. After ten passes through the UV-C system (cumulative dose: 72.34 J/mL), *E. coli* K-12 populations were reduced by 3.22 log CFU/mL. However, this reduction remained below the FDA-established 5-log target [119]. In soy milk, UV-C processing in a 1.6 mm reactor resulted in reductions of up to 5.6 log CFU/mL for E. coli and 3.29 log CFU/mL for *B. cereus* spores. These results suggest that UV-C irradiation can substantially decrease microbial populations while preserving the quality attributes of soy milk [77].

The large-scale implementation of novel processing technologies in plant milk production is influenced by a range of technological, economic, and operational considerations. The substantial investment required for specialized equipment may hinder adoption, particularly among small and medium-sized manufacturers [112]. In addition, the successful operation of these technologies often depends on sophisticated monitoring and control systems, which can complicate process standardization [120]. Inadequate control of processing conditions may affect product consistency and microbiological reliability [55]. Beyond technical performance, environmental impact, energy demand, and long-term sustainability should also be considered when evaluating these Technologies [121]. Therefore, wider industrial adoption requires a balanced assessment of economic feasibility, technical performance, regulatory acceptance, and practical applicability. Furthermore, evaluating the performance of emerging technologies in different plant milk matrices is important because variations in composition, viscosity, and structural characteristics may influence processing outcomes. Since plant milks such as almond, soy, oat, and coconut differ in composition, viscosity, and stability, the same technological process does not yield similar results across all types of milk. Therefore, it is necessary to determine special process conditions for each plant milk. In this way, both product quality and maximum efficiency can be preserved by the applied technology. In this regard, systematic and comparative studies on different types of milk will increase knowledge in the field.

CONCLUSION

Healthier food alternatives are becoming more popular due to shifting consumer preferences and greater nutrition awareness. In addition, the market for plant milk has grown due to the rising prevalence of lactose intolerance and the adoption of vegetarian and vegan diets. This growing demand has encouraged further research into plant milk processing and the creation of new goods.

Understanding the main production stages of plant milk and their influence on product quality is essential for manufacturing high-quality products. In addition, effective control of spoilage and pathogenic microorganisms remains a key requirement for ensuring product safety. This review examined innovative thermal and non-thermal technologies applied to improve microbial safety in plant-based milk products. The available literature indicates that these technologies can contribute not only to microbial inactivation but also to the preservation of nutritional and sensory qualities. To improve processing conditions for various plant milk matrices and to enable the broader industrial application of developing technologies, more research is required. Because the physicochemical characteristics and composition of plant milks vary with their raw materials, process parameters should be carefully tailored to each product type. Continued technological developments are expected to support the production of plant-based milk beverages with improved quality, safety, and consumer acceptance. Plant milks will likely become more significant both as stand-alone drinks and as ingredients in new food products as interest in plant-based diets grows.

AUTHORSHIP CONTRIBUTIONS

Authors equally contributed to this work.

DATA AVAILABILITY STATEMENT

The authors confirm that the data that supports the findings of this study are available within the article. Raw data that support the finding of this study are available from the corresponding author, upon reasonable request.

CONFLICT OF INTEREST

The authors declared no potential conflicts of interest with respect to the research, authorship, and/or publication of this article.

ETHICS

There are no ethical issues with the publication of this manuscript.

STATEMENT ON THE USE OF ARTIFICIAL INTELLIGENCE

Artificial intelligence was not used in the preparation of the article.

REFERENCES

[1] Valencia-Flores DC, Hernández-Herrero M, Guamis B, Ferragut V. Comparing the effects of ultra-high-pressure homogenization and conventional thermal treatments on the microbiological, physical, and chemical quality of almond beverages. J Food Sci 2013;78:199–205. [CrossRef]

[2] Ingram CJE, Mulcare CA, Itan Y, Thomas MG, Swallow DM. Lactose digestion and the evolutionary genetics of lactase persistence. Hum Genet 2009;124:579–591. [CrossRef]

[3] da Silva VR, Gregory JF. Basic nutrition and metabolism. In: Present Knowledge in Nutrition. Academic Press; 2020. p. 225–237. [CrossRef]

[4] Vanga SK, Raghavan V. How well do plant based alternatives fare nutritionally compared to cow's milk? J Food Sci Technol 2018;55:10–20. [CrossRef]

[5] Omoni AO, Aluko RE. Soybean foods and their benefits: potential mechanisms of action. Nutr Rev 2005;63:272–283. [CrossRef]

[6] Pistollato F, Iglesias RC, Ruiz R, Aparicio S, et al. Nutritional patterns associated with the maintenance of neurocognitive functions and the risk of dementia and Alzheimer's disease: a focus on human studies. Pharmacol Res 2018;131:32–43. [CrossRef]

[7] Sarni AR, Baroni L. Milk and Parkinson disease: could galactose be the missing link. Med J Nutr Metab 2019;12:91–118. [CrossRef]

[8] Zujko ME, Witkowska AM. Antioxidant potential and polyphenol content of beverages, chocolates, nuts, and seeds. Int J Food Prop 2014;17:86–92. [CrossRef]

[9] Dubey MR, Patel VP. Probiotics: a promising tool for calcium absorption. Open Nutr J 2018;12:59–69. [CrossRef]

[10] Rekha CR, Vijayalakshmi G. Bioconversion of isoflavone glycosides to aglycones, mineral bioavailability and vitamin B complex in fermented soymilk by probiotic bacteria and yeast. J Appl Microbiol 2010;109:1198–1208. [CrossRef]

[11] Janssen M, Busch C, Rödiger M, Hamm U. Motives of consumers following a vegan diet and their attitudes towards animal agriculture. Appetite 2016;105:643–651. [CrossRef]

[12] Sebastiani G, Barbero AH, Borrás-Novel C, Casanova MA, et al. The effects of vegetarian and vegan diet during pregnancy on the health of mothers and offspring. Nutrients 2019;11:557. [CrossRef]

[13] Tunçay GY. Sağlık yönüyle vegan/vejetaryenlik. Eurasian J Health Sci 2018;1:25–29.

[14] Gökçen M, Aksoy YÇ, Ateş Özcan B. Vegan beslenme tarzına genel bakış. Sağlık ve Yaşam Bilim Derg 2019;1:50–54. [CrossRef]

[15] Food and Drug Administration. The Food and Drug Administration (FDA) registration - imitation milk products 2024. 2024.

[16] Jeske S, Zannini E, Arendt EK. Past, present and future: the strength of plant-based dairy substitutes based on gluten-free raw materials. Food Res Int 2018;110:42–51. [CrossRef]

[17] Röös E, Garnett T, Watz V, Sjörs C. The role of dairy and plant based dairy alternatives in sustainable diets. Uppsala: Swedish University of Agricultural Sciences, SLU Future Food; 2018. p. 152.

[18] Sethi S, Tyagi SK, Anurag RK. Plant-based milk alternatives an emerging segment of functional beverages: a review. J Food Sci Technol 2016;53:3408–3423. [CrossRef]

[19] Muehlhoff E, Bennett A, McMahon D. Milk and dairy products in human nutrition. CABI Digital Library; 2013. p. 378.

[20] Heaney RP. Calcium, dairy products and osteoporosis. J Am Coll Nutr 2000;19:83S–99S. [CrossRef]

[21] Craig WJ, Mangels AR. Position of the American Dietetic Association: vegetarian diets. J Am Diet Assoc 2009;109:1266–1282. [CrossRef]

[22] Melina V, Craig W, Levin S. Position of the Academy of Nutrition and Dietetics: vegetarian diets. J Acad Nutr Diet 2016;116:1970–1980. [CrossRef]

[23] Poore J, Nemecek T. Reducing food's environmental impacts through producers and consumers. Science 2018;360:987–992. [CrossRef]

[24] Chalupa-Krebzdak S, Long CJ, Bohrer BM. Nutrient density and nutritional value of milk and plant-based milk alternatives. Int Dairy J 2018;87:84–92. [CrossRef]

[25] Janssen M, Busch C, Rödiger M, Hamm U. Motives of consumers following a vegan diet and their attitudes towards animal agriculture. Appetite 2016;105:643–651. [CrossRef]

[26] Mäkinen OE, Wanhalinna V, Zannini E, Arendt EK. Foods for special dietary needs: non-dairy plant-based milk substitutes and fermented dairy-type products. Crit Rev Food Sci Nutr 2016;56:339–349. [CrossRef]

[27] Silva ARA, Silva MMN, Ribeiro BD. Plant-based milk products. In: Future Foods: Global Trends, Opportunities, Sustainability Challenges. 2022. p. 233–249. [CrossRef]
[28] Silva ARA, Silva MMN, Ribeiro BD. Health issues and technological aspects of plant-based alternative milk. Food Res Int 2020;131:108972. [CrossRef]
[29] Padma M, Rao D, Edukondalu L, Aparna L, Babu RG. Storage studies of probiotic rice milk during refrigerated conditions. Int J Chem Stud 2019;7:1114–1117.
[30] Ahmadian-Kouchaksaraei Z, Varidi M, Varidi MJ, Pourazarang H. Influence of processing conditions on the physicochemical and sensory properties of sesame milk: a novel nutritional beverage. LWT Food Sci Technol 2014;57:299–305. [CrossRef]
[31] Ikya JK, Gernah DI, Ojobo HE, Oni OK. Effect of cooking temperature on some quality characteristics of soy milk. Adv J Food Sci Technol 2013;5:543–546. [CrossRef]
[32] Diarra K, Nong ZG, Jie C. Peanut milk and peanut milk based products production: a review. Crit Rev Food Sci Nutr 2005;45:405–423. [CrossRef]
[33] Aidoo H, Sakyi-Dawson E, Abbey L, Tano-Debrah K, Saalia FK. Optimisation of chocolate formulation using dehydrated peanut–cowpea milk to replace dairy milk. J Sci Food Agric 2012;92:224–231. [CrossRef]
[34] Cui XH, Chen SJ, Wang Y, Han JR. Fermentation conditions of walnut milk beverage inoculated with kefir grains. LWT Food Sci Technol 2013;50:349–352. [CrossRef]
[35] Dhakal S, Giusti MM, Balasubramaniam VM. Effect of high pressure processing on dispersive and aggregative properties of almond milk. J Sci Food Agric 2016;96:3821–3830. [CrossRef]
[36] Zaaboul F, Raza H, Cao C, Yuanfa L. The impact of roasting, high pressure homogenization and sterilization on peanut milk and its oil bodies. Food Chem 2019;280:270–277. [CrossRef]
[37] Seow CC, Gwee CN. Coconut milk: chemistry and technology. Int J Food Sci Technol 1997;32:189–201. [CrossRef]
[38] Aydar EF, Tutuncu S, Ozcelik B. Plant-based milk substitutes: bioactive compounds, conventional and novel processes, bioavailability studies, and health effects. J Funct Foods 2020;70:103975. [CrossRef]
[39] McClements DJ, Newman E, McClements IF. Plant-based milks: a review of the science underpinning their design, fabrication, and performance. Compr Rev Food Sci Food Saf 2019;18:2047–2067. [CrossRef]
[40] Ilyasoğlu H, Yilmaz F. Preliminary investigation of yoghurt enriched with hazelnut milk. Int Food Res J 2019;26:631–637.
[41] Maghsoudlou Y, Alami M, Mashkour M, Shahraki MH. Optimization of ultrasound-assisted stabilization and formulation of almond milk. J Food Process Preserv 2016;40:828–839. [CrossRef]
[42] Naziri E, Koupantsis T, Mantzouridou FT, Paraskevopoulou A, et al. Influence of thermal treatment on the stability of vegetable "milk" obtained by ultrafiltration of aqueous oil body extracts from various sources. Eur J Lipid Sci Technol 2017;119:1600362. [CrossRef]
[43] Makinde FM, Adebile TV. Influence of processing treatments on quality of vegetable milk from almond (Terminalia catappa) kernels. Acta Sci Nutr Health 2018;2:37–42.
[44] Manzoor MF, Manzoor A, Siddique R, Ahmad N. Nutritional and sensory properties of cashew seed (Anacardium occidentale) milk. Mod Concepts Dev Agron 2017;1. [CrossRef]
[45] Bernat N, Cháfer M, Chiralt A, Laparra JM, González-Martínez C. Almond milk fermented with different potentially probiotic bacteria improves iron uptake by intestinal epithelial (Caco-2) cells. Int J Food Stud 2015;4:49–60. [CrossRef]
[46] Briviba K, Gräf V, Walz E, Guamis B, Butz P. Ultra high pressure homogenization of almond milk: physico-chemical and physiological effects. Food Chem 2016;192:82–89. [CrossRef]
[47] Gul O, Atalar I, Saricaoglu FT, Yazici F. Effect of multipass high pressure homogenization on physicochemical properties of hazelnut milk from hazelnut cake: an investigation by response surface methodology. J Food Process Preserv 2018;42. [CrossRef]
[48] Quasem JM, Mazahreh AS, Abu-Alruz K. Development of vegetable based milk from decorticated sesame (Sesamum indicum). Am J Appl Sci 2009;6:888–896. [CrossRef]
[49] da Cruz AG, Fonseca Faria JA, Isay Saad SM, André Bolini HM, et al. High pressure processing and pulsed electric fields: potential use in probiotic dairy foods processing. Trends Food Sci Technol 2010;21:483–493. [CrossRef]
[50] Bernat N, Chafer M, Chiralt A, Laparra JM, Gonzalez-Martinez C. Almond milk fermented with different potentially probiotic bacteria improves iron uptake by intestinal epithelial (Caco-2) cells. Int J Food Stud 2015;4:49–60. [CrossRef]
[51] Quasem JM, Mazahreh AS, Abu-Alruz K. Development of vegetable based milk from decorticated sesame (Sesamum indicum). Am J Appl Sci 2009;6:888–896. [CrossRef]
[52] Munekata PES, Domínguez R, Budaraju S, Roselló-Soto E, et al. Effect of innovative food processing technologies on the physicochemical and nutritional properties and quality of non-dairy plant-based beverages. Foods 2020;9:288. [CrossRef]
[53] Jadhav HB, Annapure US, Deshmukh RR. Non-thermal technologies for food processing. Front Nutr 2021;8. [CrossRef]
[54] Chemat F, Rombaut N, Sicaire AG, Meullemiestre A, et al. Ultrasound assisted extraction of food and

natural products. Mechanisms, techniques, combinations, protocols and applications. A review. Ultrason Sonochem 2017;34:540–560. [CrossRef]

[55] Sun Y, Chen H, Chen W, Zhong Q, et al. Effects of ultrasound combined with preheating treatment to improve the thermal stability of coconut milk by modifying the physicochemical properties of coconut protein. Foods 2022;11:1042. [CrossRef]

[56] Anis SF, Hashaikeh R, Hilal N. Microfiltration membrane processes: a review of research trends over the past decade. J Water Process Eng 2019;32:100941. [CrossRef]

[57] Vogelsang-O'Dwyer M, Zannini E, Arendt EK. Production of pulse protein ingredients and their application in plant-based milk alternatives. Trends Food Sci Technol 2021;110:364–374. [CrossRef]

[58] Kwok KC, Niranjan K. Review: effect of thermal processing on soymilk. Int J Food Sci Technol 1995;30:263–295. [CrossRef]

[59] Han TB. Technology of soymilk and some derivatives. Wageningen University; 1958.

[60] Bartula K, Begley M, Latour N, Callanan M. Growth of food-borne pathogens *Listeria* and *Salmonella* and spore-forming *Paenibacillus* and *Bacillus* in commercial plant-based milk alternatives. Food Microbiol 2023;109:104143. [CrossRef]

[61] McClements DJ, Grossmann L. The science of plant-based foods: constructing next-generation meat, fish, milk, and egg analogs. Compr Rev Food Sci Food Saf 2021;20:4049–4100. [CrossRef]

[62] Short EC, Kinchla AJ, Nolden AA. Plant-based cheeses: a systematic review of sensory evaluation studies and strategies to increase consumer acceptance. Foods 2021;10:725. [CrossRef]

[63] Aydar EF, Tutuncu S, Ozcelik B. Plant-based milk substitutes: bioactive compounds, conventional and novel processes, bioavailability studies, and health effects. J Funct Foods 2020;70:103975. [CrossRef]

[64] Gul O, Saricaoglu FT, Mortas M, Atalar I, Yazici F. Effect of high pressure homogenization (HPH) on microstructure and rheological properties of hazelnut milk. Innov Food Sci Emerg Technol 2017;41:411–420. [CrossRef]

[65] Iorio MC, Bevilacqua A, Corbo MR, Campaniello D, et al. A case study on the use of ultrasound for the inhibition of *Escherichia coli* O157 and *Listeria monocytogenes* in almond milk. Ultrason Sonochem 2019;52:477–483. [CrossRef]

[66] Lu X, Chen J, Zheng M, Guo J, et al. Effect of high-intensity ultrasound irradiation on the stability and structural features of coconut-grain milk composite systems utilizing maize kernels and starch with different amylose contents. Ultrason Sonochem 2019;55:135–148. [CrossRef]

[67] Li F, Chen C, Ren J, Wang R, Wu P. Effect of ohmic heating of soymilk on urease inactivation and kinetic analysis in holding time. J Food Sci 2015;80–E315. [CrossRef]

[68] Tiravibulsin C, Lorjaroenphon Y, Udompijitkul P, Kamonpatana P. Sterilization of coconut milk in flexible packages via ohmic-assisted thermal sterilizer. LWT 2021;147:111552. [CrossRef]

[69] Erol B. Investigation of microwave processing for pasteurization of vegan milk products. İzmir Institute of Technology; 2021.

[70] Cruz N, Capellas M, Hernández M, Trujillo AJ, et al. Ultra high pressure homogenization of soymilk: microbiological, physicochemical and microstructural characteristics. Food Res Int 2007;40:725–732. [CrossRef]

[71] Poliseli-Scopel FH, Hernández-Herrero M, Guamis B, Ferragut V. Comparison of ultra high pressure homogenization and conventional thermal treatments on the microbiological, physical and chemical quality of soymilk. LWT 2012;46:42–48. [CrossRef]

[72] Ferragut V, Hernández-Herrero M, Veciana-Nogués MT, Borras-Suarez M, et al. Ultra-high-pressure homogenization (UHPH) system for producing high-quality vegetable-based beverages: physicochemical, microbiological, nutritional and toxicological characteristics. J Sci Food Agric 2015;95:953–961. [CrossRef]

[73] Maghsoudlou Y, Alami M, Mashkour M, Shahraki MH. Optimization of ultrasound-assisted stabilization and formulation of almond milk. J Food Process Preserv 2016;40:828–839. [CrossRef]

[74] Strieder MM, Neves MIL, Belinato JR, Silva EK, Meireles MAA. Impact of thermosonication processing on the phytochemicals, fatty acid composition and volatile organic compounds of almond-based beverage. LWT 2022;154:112579. [CrossRef]

[75] Manzoor MF, Zeng XA, Ahmad N, Ahmed Z, et al. Effect of pulsed electric field and thermal treatments on the bioactive compounds, enzymes, microbial, and physical stability of almond milk during storage. J Food Process Preserv 2020;44. [CrossRef]

[76] Yıldırım G. Isıl olan ve olmayan işlemler ile pastörize edilen yulaf sütünden yoğurt yapım olanaklarının araştırılması. İzmir: Osmaniye Korkut Ata Üniversitesi; 2021.

[77] Bandla S, Choudhary R, Watson DG, Haddock J. UV-C treatment of soymilk in coiled tube UV reactors for inactivation of *Escherichia coli* W1485 and *Bacillus cereus* endospores. LWT Food Sci Technol 2012;46:71–76. [CrossRef]

[78] Kerr WL. Food drying and evaporation processing operations. In: Handbook of Farm, Dairy and Food Machinery Engineering. 2nd ed. 2013. p. 317–354. [CrossRef]

[79] de Alwis AAP, Fryer PJ. The use of direct resistance heating in the food industry. J Food Eng 1990;11:3–27. [CrossRef]

[80] Cho ER, Kang DH. Intensified inactivation efficacy of pulsed ohmic heating for pathogens in soybean milk due to sodium lactate. Food Control 2022;137:108936. [CrossRef]

[81] Ahmed F, Li Y, Fanning K, Netzel M, Schenk PM. Effect of drying, storage temperature and air exposure on astaxanthin stability from *Haematococcus pluvialis*. Food Res Int 2015;74:231–236. [CrossRef]

[82] Lu L, Zhao L, Zhang C, Kong X, et al. Comparative effects of ohmic, induction cooker, and electric stove heating on soymilk trypsin inhibitor inactivation. J Food Sci 2015;80–C503. [CrossRef]

[83] Ahmed J, Ramaswamy H. Microwave pasteurization and sterilization of foods. In: Handbook of Food Preservation. CRC Press, Taylor & Francis Group; 2007. p. 691–711. [CrossRef]

[84] Datta AK, Davidson PM. Microwave and radio frequency processing. J Food Sci 2000;65:32–41. [CrossRef]

[85] Qin X, Yang F, Sun H, Yu X, et al. The physicochemical stability and in vivo gastrointestinal digestion of flaxseed milk: implication of microwave on flaxseed. Food Chem 2023;424:136362. [CrossRef]

[86] Vanga SK, Wang J, Raghavan V. Effect of ultrasound and microwave processing on the structure, in-vitro digestibility and trypsin inhibitor activity of soymilk proteins. LWT 2020;131:109708. [CrossRef]

[87] Włodarczyk K, Czaplicki S, Tańska M, Szydłowska-Czerniak A. Microwave pre-treatment as a promising strategy to develop functional milk alternatives obtained from oil industry by-products. Innov Food Sci Emerg Technol 2023;88:103443. [CrossRef]

[88] Tao Y, Sun DW, Hogan E, Kelly AL. High-pressure processing of foods: an overview. In: Emerging Technologies for Food Processing. 2014. p. 3–24. [CrossRef]

[89] Wilson DR, Dabrowski L, Stringer S, Moezelaar R, Brocklehurst TF. High pressure in combination with elevated temperature as a method for the sterilisation of food. Trends Food Sci Technol 2008;19:289–299. [CrossRef]

[90] Ananta E, Heinz V, Schlüter O, Knorr D. Kinetic studies on high-pressure inactivation of *Bacillus stearothermophilus* spores suspended in food matrices. Innov Food Sci Emerg Technol 2001;2:261–272. [CrossRef]

[91] Margosch D, Ehrmann MA, Gänzle MG, Vogel RF. Comparison of pressure and heat resistance of *Clostridium botulinum* and other endospores in mashed carrots. J Food Prot 2004;67:2530–2537. [CrossRef]

[92] Patazca E, Koutchma T, Ramaswamy HS. Inactivation kinetics of *Geobacillus stearothermophilus* spores in water using high-pressure processing at elevated temperatures. J Food Sci 2006;71:110–116. [CrossRef]

[93] Rajan S, Pandrangi S, Balasubramaniam VM, Yousef AE. Inactivation of *Bacillus stearothermophilus* spores in egg patties by pressure-assisted thermal processing. LWT Food Sci Technol 2006;39:844–851. [CrossRef]

[94] Van Opstal I, Bagamboula CF, Vanmuysen SCM, Wuytack EY, Michiels CW. Inactivation of *Bacillus cereus* spores in milk by mild pressure and heat treatments. Int J Food Microbiol 2004;92:227–234. [CrossRef]

[95] Butz P, Tauscher B. Emerging technologies: chemical aspects. Food Res Int 2002;35:279–284. [CrossRef]

[96] Chandrapala J, Oliver C, Kentish S, Ashokkumar M. Ultrasonics in food processing. Ultrason Sonochem 2012;19:975–983. [CrossRef]

[97] Mason TJ, Chemat F, Ashokkumar M. Power ultrasonics for food processing. In: Power Ultrasonics: Applications of High-Intensity Ultrasound. 2015. p. 815–843. [CrossRef]

[98] Delmas H, Barthe L. Ultrasonic mixing, homogenization, and emulsification in food processing and other applications. In: Power Ultrasonics: Applications of High-Intensity Ultrasound. 2015. p. 757–791. [CrossRef]

[99] Raso J, Palop A, Pagán R, Condón S. Inactivation of *Bacillus subtilis* spores by combining ultrasonic waves under pressure and mild heat treatment. J Appl Microbiol 1998;85:849–854. [CrossRef]

[100] Raso J, Pagán R, Condón S, Sala FJ. Influence of temperature and pressure on the lethality of ultrasound. Appl Environ Microbiol 1998;64:465–471. [CrossRef]

[101] Atalar I, Gul O, Saricaoglu FT, Besir A, et al. Influence of thermosonication (TS) process on the quality parameters of high pressure homogenized hazelnut milk from hazelnut oil by-products. J Food Sci Technol 2019;56:1405–1415. [CrossRef]

[102] Campaniello D, Bevilacqua A, Speranza B, Sinigaglia M, Corbo MR. Inactivation of *Salmonella enterica* in a rice beverage by ultrasound: study of the parameters affecting the antibacterial effect. Food Bioprocess Technol 2018;11:1139–1148. [CrossRef]

[103] Fahmi R, Khodaiyan F, Pourahmad R, Emam-Djomeh Z. Effect of ultrasound assisted extraction upon the genistin and daidzin contents of resultant soymilk. J Food Sci Technol 2014;51:2857–2861. [CrossRef]

[104] Herrera-Ponce AL, Salmeron-Ochoa I, Rodriguez-Figueroa JC, Santellano-Estrada E, et al. High-intensity ultrasound as pre-treatment in the development of fermented whey and oat beverages: effect on the fermentation, antioxidant activity and consumer acceptance. J Food Sci Technol 2022;59:796–804. [CrossRef]

[105] Salve AR, Pegu K, Arya SS. Comparative assessment of high-intensity ultrasound and hydrodynamic cavitation processing on physico-chemical properties and microbial inactivation of peanut milk. Ultrason Sonochem 2019;59. [CrossRef]

[106] Sarangapany AK, Murugesan A, Annamalai AS, Balasubramanian A, Shanmugam A. An overview on ultrasonically treated plant-based milk and its properties – a review. Appl Food Res 2022;2:100130. [CrossRef]

[107] Amiali M, Ngadi MO. Microbial decontamination of food by pulsed electric fields (PEFs). In: Microbial Decontamination in the Food Industry: Novel Methods and Applications. 2012. p. 407–449. [CrossRef]

[108] Raso J, Condón S, Álvarez I. Non-thermal processing: pulsed electric field. In: Encyclopedia of Food Microbiology. 2nd ed. 2014. p. 966–973. [CrossRef]

[109] Jaeger H, Meneses N, Knorr D. Food technologies: pulsed electric field technology. In: Encyclopedia of Food Safety. 2014;3:239–244. [CrossRef]

[110] Alkhafaji SR, Farid MM. PEF assisted thermal sterilization (PEF-ATS) process-inactivation of *Geobacillus sterothermophilus* spores. J Food Sci Eng 2012;2:403–410. [CrossRef]

[111] Siemer C, Toepfl S, Heinz V. Inactivation of *Bacillus subtilis* spores by pulsed electric fields (PEF) in combination with thermal energy II. Modeling thermal inactivation of *B. subtilis* spores during PEF processing in combination with thermal energy. Food Control 2014;39:244–250. [CrossRef]

[112] Evrendilek GA, Zhang QH. Effects of pulse polarity and pulse delaying time on pulsed electric fields-induced pasteurization of *E. coli* O157. J Food Eng 2005;68:271–276. [CrossRef]

[113] Sobrino-López Á, Raybaudi-Massilia R, Martín-Belloso O. High-intensity pulsed electric field variables affecting *Staphylococcus aureus* inoculated in milk. J Dairy Sci 2006;89:3739–3748. [CrossRef]

[114] Gómez-López VM, Koutchma T, Linden K. Ultraviolet and pulsed light processing of fluid foods. In: Novel Thermal and Non-Thermal Technologies for Fluid Foods. 2012. p. 185–223. [CrossRef]

[115] Bintsis T, Litopoulou-Tzanetaki E, Robinson RK. Existing and potential applications of ultraviolet light in the food industry: a critical review. J Sci Food Agric 2000;80:637–645. [CrossRef]

[116] Hijnen WAM, Beerendonk EF, Medema GJ. Inactivation credit of UV radiation for viruses, bacteria and protozoan (oo)cysts in water: a review. Water Res 2006;40:3–22. [CrossRef]

[117] Gayán E, Álvarez I, Condón S. Inactivation of bacterial spores by UV-C light. Innov Food Sci Emerg Technol 2013;19:140–145. [CrossRef]

[118] Krishnamurthy K, Demirci A, Irudayaraj JM. Inactivation of *Staphylococcus aureus* in milk using flow-through pulsed UV-light treatment system. J Food Sci 2007;72:233–239. [CrossRef]

[119] Food and Drug Administration. Food Code 2009 | FDA Chapter 3 Food. 2009.

[120] Gomes MA, dos Santos Rocha MSR, Barbosa KL, de Abreu IBS, et al. Agricultural coconut cultivation wastes as feedstock for lignocellulosic ethanol production by *Kluyveromyces marxianus*. Waste Biomass Valorization 2021;12:4943–4951. [CrossRef]

[121] Moretti CL, Mattos LM, Jan S, Sargent SA, et al. Climate changes and potential impacts on quality of fruit and vegetable crops. Food Res Int 2010;1:467–486. [CrossRef]

Sigma J Eng Nat Sci, Vol. 44, No. 4, pp. 3027–3054, August, 2026

Sigma Journal of Engineering and Natural Sciences
Web page info: https://sigma.yildiz.edu.tr
DOI: 10.14744/sigma.2026.2142

Review Article

Nanofluids and their role in enhancing automotive performance: A comprehensive review

Sanjeev Kumar GUPTA[1,*], Soni KUMARİ[2]

[1]Department of Mechanical Engineering, IET, GLA University Mathura, 281406, India
[2]Department of Mechanical Engineering, Bharat Ratna Babasaheb Bhimrao Ambedkar Rajkiya Engineering College, Pratapgarh, 230127, India

ARTICLE INFO

Article history
Received: 12 November 2024
Revised: 13 Februrary 2025
Accepted: 27 May 2025

Keywords:
Automotive Performance; Energy Efficiency; Engine Cooling; Fuel Efficiency; Lubrication; Nanofluids

ABSTRACT

This paper discusses the nanofluid integration in the contemporary automotive industry including its effect on engine cooling and lubrication, and fuel efficiency. As there are increasing demands of energy efficient and environmentally friendly cars, nanofluids have gained much attention due to their superior thermal conductivity, heat transfer efficiency, and tribological properties. To evaluate the performance of nanofluid in the automotive systems, the study used a thorough review methodology where it examined both experimental and computational results of the literature available in the study. The findings showed that the addition of CuO and ZnO nanoparticles in fuel and Al_2O_3 and ZnO in lubricants increased thermal efficiency by 17.62% and decreased specific fuel consumption by 14.98%. Emissions of carbon monoxide (CO) and nitrogen oxide (NOx) went down by 20.04% and 10.25% respectively, and CO_2 emissions rose by 29.16%, which is indicative of a more complete combustion. Moreover, the lubricants made of nanofluids demonstrated a 0.484% enhancement in viscosity stability and hence are able to perform better under different conditions. Although it has these benefits, other issues like nanoparticles agglomeration, high production, and compatibility issues with the existing automotive parts continue to hinder its wide usage. The originality of this work is the comprehensive evaluation of nanofluids in various subsystems of automobiles as compared to earlier studies which have mainly targeted individual subsystems like the heat transfer. This study will offer a systematic approach to the optimization of nanofluids formulations to maximize efficiency, minimize emissions, and make the automotive industry sustainable by assessing the progress, limitations, and future research directions. The future work needs to be directed toward the enhancement of nanofluid stability, economical manufacturing approaches, and the lifecycle analysis to implement it on large scales. These results make nanofluids an innovative technology in the next-generation automotive engineering.

Cite this article as: Gupta SK, Kumari S. Nanofluids and their role in enhancing automotive performance: A comprehensive review. Sigma J Eng Nat Sci 2026;44(4):3027–3054.

***Corresponding author.**
*E-mail address: sanjeev.gupta@gla.ac.in

This paper was recommended for publication in revised form by Editor-in-Chief Ahmet Selim Dalkilic

Published by Yıldız Technical University Press, İstanbul, Turkey
© Author. This is an open access article under the CC BY-NC license (http://creativecommons.org/licenses/by-nc/4.0/).

INTRODUCTION

The automotive industry across the world is in constant flux due to the need to have better performance, fuel efficiency and sustainability. With the increasing complexity of vehicles, the necessity to find new ways of streamlining thermal regulation, lubrication, and fuel use has increased [1]. A potential direction in this respect is the utilization of nanofluids; specifically engineered suspensions, in which nanoparticles are suspended in conventional fluids such as water, ethylene glycol, and lubricating oils [2]. These nanofluids have high thermal conductivity, heat transfer, and lubrication characteristics relative to their underlying fluids, thus they are very desirable in the automobile industry as shown in Figure 1. As the issue of climate change is increasing, and strict emission standards are enforced, together with the desire to build more energy efficient cars, nanofluids have become a source of interest by the industry experts and researchers alike. Their capability to increase cooling capacity of radiators, engine lubrication and even fuel efficiency provides a promising future in the automotive engineering [3].

Nanofluids are normally made up of nanoparticles of metals and metal oxides, carbon-based substances such as graphene suspended in base fluids. The nanoparticles, because of high surface area and high thermal properties, significantly enhance the heat transfer properties of the fluid [4, 5]. Traditional coolants such as water and ethylene glycol are popular in automotive thermal management systems, but their thermal conductivity is constrained, meaning that they do not cool optimally. Nonetheless, with the emergence of nanofluids, significant advances in convective heat transfer have been realized which allow more effective cooling systems to be implemented avoiding overheating of engines, loss of energy, and even increase in the life of automotive parts. Research shows that a slight amount of nanoparticles in coolants can result in significant gains in thermal conductivity, which results in a smaller radiator size and weight, which in turn is a factor in vehicle fuel efficiency and performance [6, 7].

Other than thermal management, nanofluids have also exhibited significant potential in enhancing the efficiency of lubrication. Engine oils are also necessary to reduce friction and wear among moving parts to ensure that the engine is long lasting and efficient. However, traditional lubricants possess intrinsic disadvantages regarding the capability to reduce wear and provide the best viscosity at severe operational conditions [8]. Tribological properties of lubricants have been claimed to be improved by incorporation of nanoparticles, e.g. copper, aluminum oxide or carbon nanotubes. Such nano-enhanced lubricants offer excellent anti-wear properties, enhanced load carrying capacity and reduced coefficients of friction in comparison to traditional lubricants. This leads to lesser mechanical wear, high efficiency, and longer service of the engines and thus nanofluid-based lubricants are a promising innovation in automotive industry [9, 10].

The other new field in which nanofluids have shown potential advantages is in the fuel enhancement. The use of nanoparticles in traditional fuel types such as gasoline and diesel to enhance combustion efficiency, fuel economy,



Figure 1. Applications of nanofluid in automotives.

and emission properties has been studied. Some nanoparticles are catalysts that increase the oxidation of the fuel and result in a more complete combustion [11]. This subsequently minimizes the production of harmful ejection like CO, NOx and PM hence making transportation cleaner and more sustainable. Moreover, nanofluid based fuel additives have been found to improve the calorific value of fuels, which allow improved engine performance consuming less fuel. Such developments are in tandem with the global quest towards more environmentally friendly technologies and tough environmental laws that are being enforced to minimize car emissions [12].

Nanofluids have some promising benefits, but there are a number of issues that hinder their wide use in the automotive industry. Stability is also still a significant issue, as nanoparticles tend to form aggregates thus interfering with uniformity and prolonged efficiency of nanofluids [13]. Also, the synthesis and dispersion methods of nanoparticles are expensive and therefore difficult economically to implement at large scale. Safety concerns especially on the environmental and health effects of exposure to nanoparticles should also be well researched before mass commercialization [14]. Nevertheless, there are current research efforts to tackle these issues by coming up with more stable nanofluids, low-cost production techniques and eco-friendly nanoparticle preparations. A simple flow chart to represent the stepwise procedure is shown in Figure 2.

Earlier published review articles related to the application of nanofluids in automotives, along with their objectives, are presented in Table 1 [15-23], and the number of articles published on the utilization of nanofluids in automotives, as per the Scopus database, is illustrated in Figure 3.



Figure 2. Flow chart to represent stepwise procedure.

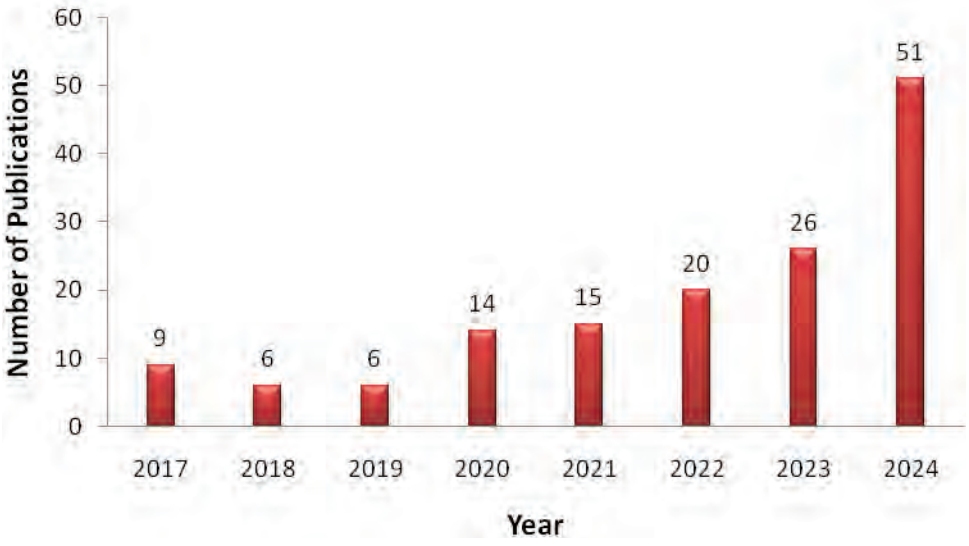


Figure 3. Number of research articles published related to the application of nanofluid in automobiles as per the Scopus database.

Table 1. Earlier published review articles related to application of nanofluid in automotives with their objectives

Ref. No.	Theme of Review	Review Objective
[15], 2010	Future Automobiles	In assessing the use of nanofluid in cars, it is important to note that it can be used to enhance efficiency, performance, and sustainability.
[16], 2013	Coolant in automobile radiator	To review nanofluid applications in automobile radiators, highlighting benefits, challenges and future prospects.
[17], 2015	Vehicle engine cooling system	To review nanofluid applications in vehicle engine cooling systems, evaluating performance, experimental finding, and optimization challenges.
[18], 2016	Application in automobile radiator	To review nanofluid thermal properties using ANN modelling and analyze automotive radiator applications.
[19], 2019	Automobile cooling system	In order to revise the use of nanofluid in heat transfer, analyzing the vehicle cooling and performance.
[20], 2021	Automotive applications	To review nanofluid applications in automotive system, analyzing efficiency, material impact and environmental concerns.
[21], 2022	Automobile radiator cooling	To examine thermal properties of hybrid nanofluid, stability and heat transfer in automobiles.
[22], 2023	Automotive applications	To assess nanofluid use in automobiles, to outline the advantages, limitations, and prospects of research.
[23], 2023	Coolant in IC engines	In order to discuss nanofluids as the cooling of IC engines, the analysis of performance, methods of preparation, and the most suitable formulations.

Current literature proves that nanofluids have increased heat transfer, low friction, and lubrication capabilities. Research indicates that they are better in thermal conductivity, stability compared with traditional fluids, making them one of the potential choices in automotive applications. Nevertheless, issues associated with sedimentation, agglomeration and compatibility with the automotive systems are under-investigated and require additional studies. Although much of the research has been done on nanofluids and their thermal characteristics, their particular contribution in improving automotive performance is not fully exploited. The majority of the research works are dedicated to the application of nanofluid in heat transfer systems, whereas the influence of nanofluid on engine cooling, lubrication, fuel efficiency, and emissions remains poorly studied. Also, the lack of standardized testing procedures and inconsistency in experimental data make it difficult to implement in practice. There is also not much research on the interplay of nanofluid composition, stability, and long-term effects on automotive components. The critical examination that summarizes the current research, research gaps, and the way forward is needed to develop the use of nanofluids in the automotive sector.

In order to fill this gap, there is a need to conduct an extensive review of findings on the use of nanofluids in automotive systems. This involves the evaluation of their thermal conductivity, viscosity, tribological and stability during the operations. It is important to know their long-term impacts on engine and component performance in real world implementation. The performances should be set into benchmarks with rigorous experimental studies, computational simulations, and life-cycle cost analyses.

The purpose of this review is to critically examine how nanofluids are used in improving automotive performance in terms of their thermal, tribological, and fuel efficiency advantages. It critically reviews the recent developments, issues, and prospects of using nanofluids to cool engines, lubricate engines, and augment fuels. The novelty of this review lies in its holistic assessment of nanofluids in multiple automotive subsystems, integrating experimental findings, computational insights, and industrial perspectives. Unlike previous fragmented studies, this review provides a structured framework for optimizing nanofluid formulations, addressing stability issues, and facilitating their practical adoption in commercial automotive applications for improved efficiency and sustainability.

FUNDAMENTALS OF NANOFLUID

Nanomaterials are substances with structural components at the nanoscale, usually between 1 and 100 nanometers. At the nanoscale, they demonstrate distinct physical properties compared to their bulk counterparts, driven by quantum effects, high surface-area-to-volume ratios, and enhanced reactivity [24]. The nanomaterials can be classified into the various types depicted in Figure 4 such as nanoparticles, nanorods, nanotubes, and nanocomposites with each having a unique property which can be used in a particular application. They are exceptionally strong, thermally conductive, electrically conductive, and catalysts, which are useful in a wide range of industries, including medicine, electronics, energy storage, and automotive engineering. Some typical nanomaterials are carbon based



Figure 4. Different types of nanomaterials.

(carbon nanotubes, graphene), metal based (gold, silver, copper), metal oxides (titanium dioxide, aluminum oxide), and polymer based nanomaterials [25]. The sophisticated nature of such materials has been made possible through the engineering of such materials at the atomic scale, which leads to the creation of superior functional materials with better properties, which has contributed to innovations in energy-efficient systems, high-performance coating, and the lifetime of materials in different industries [26].

Nanofluid is a stable colloidal suspension of nanoparticles in a base fluid, such as H_2O, EG or oil. The addition of nanoparticles greatly improves the base fluid's thermal, rheological and tribological properties [27]. The nanofluids have high thermal conductivity, high heat transfer rates, low viscosity, and high stability as compared to the regular fluids. These properties render them very useful in heat dissipation, lubrication and energy transportation purposes [28]. Depending on the type and concentration of nanoparticles used, it is possible to create nanofluids that are optimized and tailored to meet specific properties desired in a given application, such as the cooling mechanisms in systems, lubrication of mechanical systems, and thermal management in high-performance electronic and automotive systems [29].

Nanofluids have become a revolutionary solution in the automobile sector, especially in the cooling of engines, lubrication and increase in fuel efficiency. Nanofluids are used in the cooling systems to enhance the performance of the radiator by improving the efficiency of the radiator to dissipate heat, eliminate overheating, and reduce thermal management [30]. In lubrication applications, nanoparticle-based lubricants reduce friction and wear, enhancing engine longevity and fuel economy. Moreover, incorporating nanoparticles into fuels improves combustion efficiency, resulting in reduced emissions and enhanced fuel consumption. The integration of nanofluids in automotive components ensures enhanced performance, energy efficiency, and sustainability. However, issues like stability, cost-effectiveness, and integration with existing automotive systems must be resolved for widespread adoption [31].

Synthesis and Preparation Method of Nanofluid

Nanofluids synthesis and preparation are mainly done using two methods; the one-step method and the two-step method. The one step approach involves the synthesis and dispersion of nanoparticles in one step, and can be done by physical vapor deposition, laser ablation, or by chemical reduction. This method is less agglomeration and stability but is normally complicated and expensive [32]. The latter is more commonly employed, in which nanoparticles are initially prepared using physical or chemical methods like sol-gel, precipitation or hydrothermal and then dispersed in a base fluid. Dispersion techniques such as ultrasonication, magnetic stirring, and addition of surfactants are used to preserve homogeneity but particle aggregation and sedimentation are still a problem [33, 34]. Figure 5 shows the two-step procedure of the production of nanofluids.



Figure 5. Two-step method for nanofluid production.

The stability of nanofluids is affected by a number of factors as demonstrated in Figure 6, such as pH regulation, choice of surfactants and nanoparticle fictionalization. Stability of nanofluids is important in accuracy of measurements. Nanoparticles using agglomeration and sedimentation might change thermophysical characteristics, which results in changes in thermal conductivity and viscosity values. In order to reduce these uncertainties, we dispersed the product appropriately through ultrasonication and stabilizing agents. Selection of base fluid, i.e. H_2O, EG or oils are dependent on purpose of use. Further techniques of stabilization, including electrostatic and steric stabilization, increase dispersion and longevity [35]. To measure thermal conductivity and viscosity, the precision of the measurements was

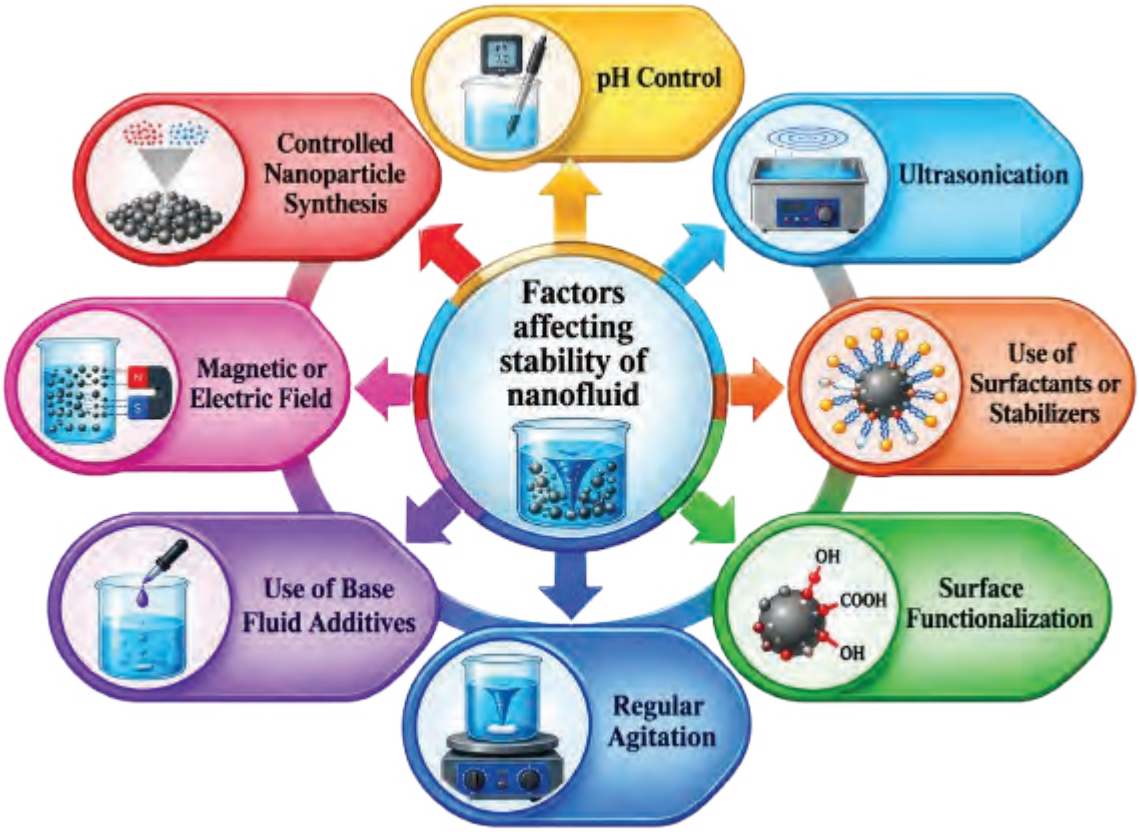


Figure 6. Factors affecting nanofluid stability.

guaranteed by employing high-precision instruments with respectable calibration standards. As an example, the thermal conductivity of the nanofluids was measured by a KD2 Pro thermal properties analyzer within an error of ±2% whereas the viscosity was measured by a Brookfield viscometer at an error of ±1.5% [36]. Purity of nanofluid is another important aspect that has a great impact on its thermal, rheological and tribological properties. Nanofluids with high purity are more stable, have improved heat transfer, and less sedimentation or agglomeration of nanoparticles. The purity of nanofluids depends on the quality of nanoparticles and the mother fluid. Nanoparticles may contain impurities, including remaining surfactants, unreacted precursors or unwanted by-products of the synthesis and these impurities can modify the behavior of the fluid and impact its performance in various applications, including automotive cooling, lubrication and fuel enhancement. To achieve high purity, various purification techniques such as centrifugation, filtration, and washing are employed to remove contaminants. Characterization tools like DLS, zeta potential measurement, and TEM are employed to verify the chemical composition and purity of nanofluids and also to improve its stability. The method of synthesis has a strong influence on the thermal conductivity, viscosity and overall functionality of nanofluids which are vital in heat transfer, biomedical and energy systems. The latest developments are on hybrid nanofluids where various nanoparticles are added to enhance functionality. The efficiency of nanofluids in the industrial and technological processes still requires optimization of synthesis methods and stabilization approaches [37].

Thermal Properties of Nanofluid

The thermal characteristics of nanofluids are necessary for their effectiveness in heat transfer applications. Nanofluids demonstrate superior heat transfer properties relative to conventional fluids, owing to the exceptional conductive nature of nanoparticles and their efficient dispersion [38]. Factors such as nanoparticle concentration, size, shape, and base fluid type significantly influence thermal conductivity. Also, nanofluids exhibit enhanced convective heat transfer, since it has high Brownian movement and nanoparticle contact with the fluid [39]. The other major thermal characteristics are the specific heat capacity, the viscosity, and thermal diffusivity which determine their performance in the cooling and energy system [40]. These properties should be optimized by appropriate synthesis and stabilization methods to be used in electronics cooling, automotive, aerospace, and renewable energy systems [41]. Table 2 demonstrates the effect of different nanofluid characteristics on an automotive engine performance.

Thermal Conductivity

The improved heat transfer property of nanofluids is critical in better cooling of heat in automobiles, especially in the cooling system of the engine. Nanofluids are much more conductive to heat than conventional coolants like H_2O and EG [42]. The high levels of thermal conductivity are caused by the high thermal conductivity of nanoparticles, increased Brownian motion and enhanced micro-convection in the fluid. The thermal conductivity of nanofluids is influenced by different factors such as the type, size and shape of nanoparticles. Metals, such as Cu and Ag, and metal oxides, including Al_2O_3 and TiO_2 are the most common nanoparticles in that they are highly thermal conductive [43].

In cars, the increased efficiency of heat transfer is used to achieve the optimal engine temperatures, prevent overheating, and improve fuel efficiency. Nanofluids are used in radiators and cooling systems, which result in improved heat transfer and this, lowers thermal stresses on engine components and increases engine life [44]. Nonetheless, issues like change in viscosity, stability, and cost are to be tackled to have a workable implementation. Current studies are on hybrid nanofluids and improved methods of stabilization to enhance thermal effectiveness and long-term stability in automotive cooling systems [45]. It is possible to compute the thermal conductivity (TC) of a nanofluid (knf) using a variety of models, one of the most popular being the Maxwell-Garnett equation of the spherical nanoparticles, which is symbolized as Eq. 1 [46].

$$k_{nf} = k_f \frac{k_p + 2k_f + 2\phi\left(k_p - k_f\right)}{k_p + 2k_f - \phi\left(k_p - k_f\right)} \quad (1)$$

Other sophisticated models including the Hamilton-Crosser model, and experimental correlations take into

Table 2. Impact of various nanofluid properties on the performance of an automotive engine

Nanofluid Properties	Effect on Engine Performance	Remarks
Thermal Conductivity	Increased thermal conductivity improves the heat dissipation.	Engine cooling efficiency enhanced
Viscosity	A rise in viscosity can influence the resistance of fluid flow.	Needs optimization for better lubrication
Specific Heat Capacity	Higher specific heat capacity improves heat absorption	Enhances engine temperature regulation
Density	Affects coolant flow and heat transfer performance	Higher density fluids may impact pumping power
Stability	Stability in the long-term averts the problem of sedimentation.	Ensures consistent thermal performance
Heat Transfer Coefficient	An increase in coefficient increases convective heat transfer.	Improves the work of cooling systems.

account the impact of nanoparticle shape, brownian motion and clustering on thermal conductivity. These factors need to be optimised to maximise the heat transfer efficiency in automotive applications, where efficient engine cooling and minimised thermal stresses on components are required. The homotopic method demands a trade-off between raising the nanoparticle concentration to raise thermal conductivity and not taking it too high to cause an agglomeration or higher viscosity which may decrease flow efficiency.

Viscosity

The viscosity of nanofluids is a critical parameter in their use in the automotive industry, especially in the cooling and lubrication systems. The viscosity defines the ease of flow of fluid, pumpability, and energy consumption in the cooling system of an engine. Nanofluids tend to have a slightly higher viscosity compared to the traditional coolant, because of the presence of nanoparticles, which may influence fluid flow and raise the power needs of the pumping system [47]. Nanofluids viscosity depends on many factors, including the concentration, size, shape, temperature, and the base fluid properties of nanoparticles. Greater nanoparticle concentrations typically cause increased viscosity, which can improve thermal conductivity but may also cause higher frictional losses and lower flow efficiency [48].

In the case of automotive use, it is important to strike the right balance between thermal conductivity and viscosity. Better thermal conductivity will enhance heat dissipation in radiators and engine parts, but excessive viscosity will cause a higher resistance in the cooling system and decrease efficiency. It has been found that the effects of viscosity are lower with the spherical nanoparticles than with the elongated or irregular-shaped nanoparticles [49]. Moreover, temperature is important since the viscosity of nanofluids tends to reduce with increase in temperature which is an advantage in high temperature car settings [50].

To guarantee the effective application of nanofluids in automotive cooling and lubrication, the stabilizing measures, including the addition of a surfactant, pH regulation and advanced dispersion strategies, are used. The methods assist in avoiding the agglomeration of nanoparticles that may further raise the viscosity and poor performance [51]. There is interest in hybrid nanofluids, a mixture of various nanoparticles, to maximize thermal and rheological characteristics to enhance engine efficiency. Comprehensively, the control of nanofluids viscosity is critical to the optimization of its nanofluids in automotive applications and thus improved heat transfer, less wear, and fuel economy whilst preserving its efficient flow properties in the engine cooling systems [52]. The homotopic method entails optimizing the concentration of nanoparticles and stabilization methods to obtain a viscosity that would enable the pumping with both efficiency in heat transfer and low energy expenditure pumping. In certain nanofluids (e.g., Al_2O_3-MWCNT/5W50), non-Newtonian behavior needs to be represented correctly to be able to predict its behavior at different shear rates.

Specific Heat

Specific heat capacity of the nanofluids is a very important characteristic which determines their suitability in automotive cooling systems [53]. In the automobile industry, nanofluids with a high specific heat capacity can be used to optimize the quantities of heat absorption and dissipation, which then improves the cooling effects of the engine, and averts overheating. Specific heat of nanofluid depends on the nature, concentration and thermal characteristics of nanoparticles. In most cases, the specific heat of the nanofluid decreases slightly upon the addition of nanoparticles with high thermal conductivity when compared to the base fluid. Nevertheless, a perfect thermal conductivity to specific heat balance is critical to effective heat transfer [54]. Specific heat capacity of a nanofluid may be determined using the following formula:

$$C_{p,nf} = \frac{(1-\phi)\rho_f C_{p,f} + \phi\rho_p C_{p,p}}{\rho_{nf}} \quad (2)$$

In automotive use, a balanced specific heat capacity is important to give effective heat exchange in engine cooling, radiators, and lubricants to minimize thermal stress and improve fuel efficiency [55]. The attention of researchers is on hybrid nanofluids to enhance specific heat and thermal conductivity to enhance cooling performance without compromising stability and flow characteristics. The homotopic criteria entails the choice of nanoparticles that have high thermal conductivity but moderate density effects so that heat transfer is efficient without having to pump very high powers.

Density

Nanofluids density is a vital factor that determines their effectiveness in the automotive industry especially in cooling and lubrication systems. Density influences the rate of mass flow of the fluid, the power needed to pump the fluid, and the overall heat transfer effectiveness [56]. When nanoparticles are introduced, the nanofluid usually becomes denser than the base fluid since nanoparticles are usually denser than the liquid coolant such as water or ethylene glycol. To achieve the optimal balance between density and viscosity is important to guarantee the efficient flow of the fluid without unnecessary energy consumption [57, 58]. The density of a nanofluid could be determined using the equation below:

$$\rho_{nf} = (1-\phi)\rho_f + \phi\rho_p \quad (3)$$

NANOFLUID IN AUTOMOTIVE APPLICATIONS

Nanofluids are common in the car industry in engine cooling system, transmission fluids, lubricants and fuel additives. Their high heat dissipation qualities allow them to perform a better thermal control in radiators, preventing overheating and enhancing engine efficiency [59].

Nanoparticles in lubricants improve tribological characteristics, which lower wear and friction between moving components, thus improving engine durability and fuel efficiency. Furthermore, nanofluids as fuel additives enhance combustion efficiency, which lowers emissions and increases mileage. Nanoparticles aluminum oxide, copper oxide, and carbon nanotubes have been widely studied to maximize viscosity, stability and thermal performance [60]. Sustainability is also assisted by the adoption of nanofluids, which reduce the energy loss and emissions. As the automotive industry takes the challenge of fuel efficiency and strict emission regulations, nanofluids are also being considered as a way of transforming automotive cooling, lubrication, and fuel systems [61]. Despite the challenges of stability of nanoparticles and the cost involved, the current research effort is leading to progress in nanofluid development of nano-particles to be used in practical car applications, which is a promising future of more efficient cars with better environmental impact. This part will offer a brief background of some of the recent developments in the application of nanofluids in the automotive sector.

Role of Nanofluids in Automotive Radiator Cooling System

Nanofluids are important to the operation of the automotive radiator cooling system because it is used to enhance the efficiency of the cooling system through the conductivity of heat and thermal properties. The conventional coolant fluids including water and ethylene glycol are not effective in the management of the high thermal loads produced by the modern engines. Nanofluids have a high thermal conductivity, greater heat transfer, and are more stable by dispersing nanoparticles, such as aluminum oxide, copper oxide, or graphene in these base fluids. This results in increased efficiency of cooling and eliminates engine

Table 3. Role of nanofluids in automotive radiator cooling system

Ref. No.	Nanoparticle	Base fluid	Volume Fraction	Parameter Enhancement
[62], 2011	Al_2O_3	H_2O	0.1% to 1%	Increase heat transfer efficiency by up to 45%.
[63], 2014	Al_2O_3	H_2O	0.1% to 2%	Heat transfer improved up to 14.79% at 1% concentration but deteriorated beyond that.
[64], 2014	Al_2O_3, CNT	H_2O	0.15% to 1%	CNT/H_2O nanofluid at 1% concentration increased heat transfer by 90.76%
[65], 2016	TiO_2	EG- H_2O	0.1% to 0.5%	A 0.5% concentration enhanced heat transfer by 35% relative to the base fluid.
[66], 2018	Graphene-TiO_2	EG- H_2O	0.01% to 1%	0.4% concentration increased heat transfer but caused 0.9825 g of material loss
[67], 2019	Al_2O_3-TiO_2, Al_2O_3-MgO	EG- H_2O	0.12% to 0.4%	The 0.4% Mg-Al_2O_4 nanofluid improved heat transfer efficiency by 33.18%
[68], 2019	Al_2O_3-TiO	EG- H_2O	0.05% to 0.3%	A 0.3% Al_2O_3 nanofluid improved thermal performance by 24.21%.
[69], 2019	Co_3O_4 and Al_2O_3	EG- H_2O	0.02% to 0.2%	Co_3O_4 nanofluid at 0.1% concentration improved heat transfer by 18.3%
[70], 2020	GO and GNR	Pure water	0.01% to 0.02%	At 0.02% concentration, GO improved overall heat transfer by 33.9%,
[71], 2020	ZnO	H_2O	0% to 0.3%	The 0.2% concentration enhanced overall heat transfer coefficient by 50%.
[72], 2021	Al_2O_3, SiO_2, and TiO_2	H_2O	0.2% and 0.4%	TiO_2 at 0.4% achieved the highest exergy efficiency (35.67%), improving by 62.14% over water.
[73], 2021	ZnO and AlN	EG- H_2O	0.2% and 0.5%	ZnO nanofluids at 0.5 wt% increased heat transfer by 57.7%.
[74], 2022	Al_2O_3-TiO_2-SiO_2	EG- H_2O	0.05% to 0.3%	The 0.3% concentration improved the coolant-side heat transfer coefficient by 39.7%
[75], 2022	MWCNT	EG- H_2O	0.025% to 0.1%	At 0.1% concentration, the overall heat transfer coefficient improved by 4.4%.
[76], 2023	GnP-MWCNT	Coolant oil	0.05% to 0.5%	At 0.5% concentration, the OHTC increased by 124%.
[77], 2023	CuO, ZnO, and MgO	H_2O	0.5% to 3%	CuO- H_2O exhibited the highest thermal conductivity (1.084 W/mK).
[78], 2024	MWCNT- Al_2O_3-	H_2O	0.5% to 2.3%	Radiator effectiveness increased by 22.54% at a concentration of 2.3%.

overheating and enhances the overall efficiency of the vehicle. Nanofluids have a higher heat transfer rate through convection thus making radiators smaller and lighter, which helps in reducing vehicle weight and increasing the fuel economy. Also, the presence of nanofluids leads to less energy loss in the cooling system, which leads to improved engine performance and durability. They are also of interest in the application of electric vehicle batteries since efficient thermal management is essential to battery safety and efficiency. Nevertheless, nanoparticle stability and cost are some of the issues facing the use of nanoparticles, but ongoing research and development of nanofluid technology is leading to its use in the next generation automotive radiator systems. Table 3 summarises the role of nanofluids in improving cooling efficiency of automotive radiators.

Peyghambarzadeh et al. [62] experimentally compared forced convective heat transfer of Al_2O_3/water nanofluid with pure water in an automobile radiator. Nanofluid concentrations (0.1–1 vol. %) increased heat transfer efficiency by up to 45%. Higher flow rates improved cooling, while inlet temperature had minimal effects. Brownian motion contributed to enhanced heat transfer beyond conductivity improvements. Ali et al. [63] experimentally analyzed the effect of Al_2O_3/water nanofluid concentrations (0.1–2%) on a Toyota Yaris 2007 radiator. Figure 7 demonstrate the variation of coolant pumping power with load and concentration, showing an increase as concentration rises due to higher pressure loss at a fixed load, and a further increase as the load itself increases. Heat transfer improved up to 14.79% at 1% concentration but deteriorated beyond that. The coolant and air heat transfer coefficients increased by 14.72% and 14.45%, respectively. The optimum concentration was established by Reynolds and Nusselt numbers, and an increase in viscosity caused a decrease in performance at 1.52% viscosity.

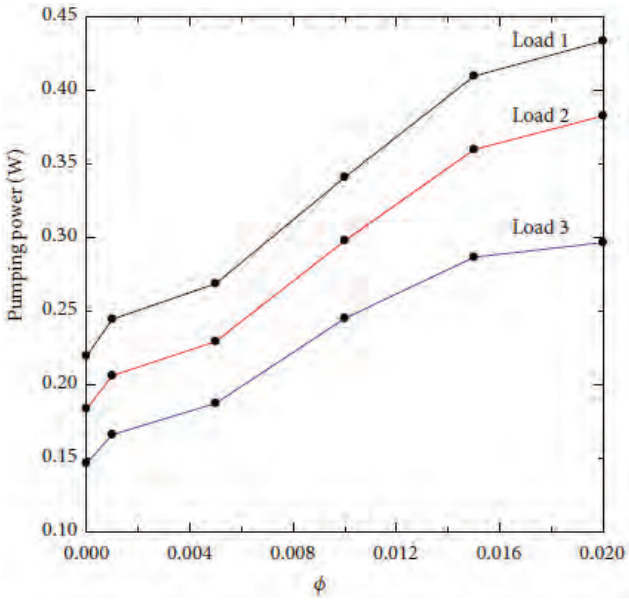


Figure 7. Variation of coolant pumping power with load and concentration [From Ali et al. [63], with permission from Hindawi].

Chougule and Shahu [64] experimentally compared Al_2O_3/H_2O and CNT/H_2O nanofluids in an automobile radiator. The nanofluid CNT/H_2O (1% concentration) enhanced the heat transfer by 90.76% and Al_2O_3-water by 52.03%. Flow rates also enhanced Nusselt numbers to 76.55% and 44.18% improvement at 4 L/min in CNT and Al_2O_3, respectively. The thermal conductivity and performance of CNT/H_2O was better as it had a higher aspect ratio and a low thermal resistance. Sandhya et al. [65] experimentally evaluated TiO_2 nanofluids (0.1–0.5%) in a 40:60 EG- H_2O mixture for automobile radiators. The schematic diagram of the test setup is shown in Figure 8. A 0.5% concentration increased heat transfer by 35% over the base fluid. At 45°C, a 45.4% enhancement in heat transfer coefficient was recorded. Flow rates increased performance, and little influence was on inlet temperature. Brownian motion also helped in enhancing heat transfer in addition to change in thermal conductivity.

Xian and Sidik [66] investigated the heat transfer and erosion-corrosion effects of a hybrid nanofluid (graphene nanoplatelets-TiO_2) in an automobile radiator. The 0.4% concentration increased heat transfer but caused 0.9825 g of material loss due to erosion. Corrosion effects were similar across all coolants. The ASTM D2809-09 standards categorized erosion-corrosion damage as low and it was possible that it could be applied in the future. Increased nanoparticle concentration intensified material loss. Arun kumar et al. [67] experimentally evaluated Al_2O_3-TiO_2 and Al_2O_3-MgO nanofluids (0.12% and 0.4%) in a water-ethylene glycol mixture for car radiators. Compared to water, the 0.4% Mg-Al_2O_4 nanofluid enhanced the heat transfer efficiency by 33.18%, and the 0.4% Al_2TiO_5 nanofluid enhanced it by 27.9%. The higher concentration of nanoparticles and fluid velocity enhanced the heat transfer whereas ethylene glycol was used as an antifreeze solution, increasing the stability of the system. In their study, Said et al. [68] determined the performance of Al_2O_3 and TiO_2 nanofluids in a 50:50 mixture of distilled water and ethylene glycol as an automobile radiator. Figure 9 illustrates the change in thermal conductivity with temperature at various concentrations. A 0.3% Al_2O_3 nanofluid improved thermal performance by 24.21%, while TiO_2 at the same concentration increased it by 14.99%. The performance evaluation criterion (PEC) ranged from 1.03 to 1.31. Al_2O_3 exhibited higher thermal conductivity, but TiO_2 had better long-term stability. Elsaid [69] experimentally studied Co_3O_4 and Al_2O_3 nanofluids in EG-H_2O mixture (0-20% EG) to use in vehicle radiators. Co_3O_4 nanofluid (0.1% concentration) enhanced heat transfer by 18.3% and Al_2O_3 by 16.7% increase. Higher Reynolds numbers enhanced heat transfer but reduced friction. EG reduced Nusselt number and increased pumping power. Co_3O_4 outperformed Al_2O_3 in thermal performance.

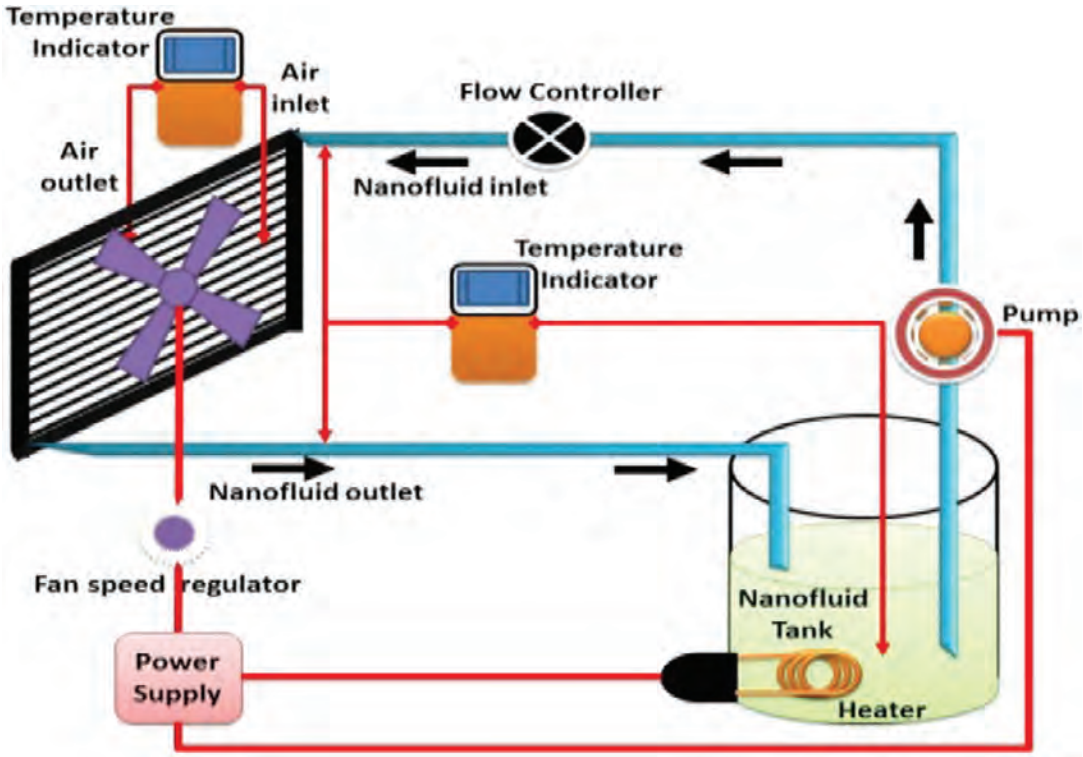


Figure 8. Schematic diagram of the test setup [From Sandhya et al. [65], with permission from Elsevier].

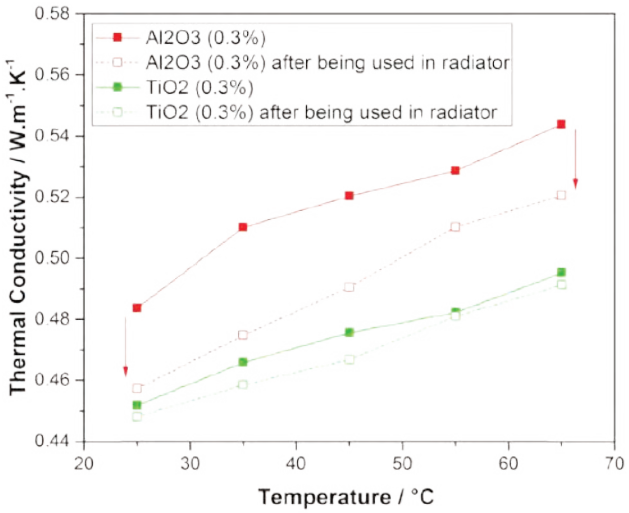


Figure 9. Change in thermal conductivity with temperature at various concentrations [From Said et al. [68], with permission from Elsevier].

Kılınç et al. [70] experimentally evaluated the cooling performance of GO and GNR nanofluids in a vehicle radiator. GO and GNR increased the overall heat transfer by 33.9% and 31.6%, respectively, at a concentration of 0.02%. The average enhancements for GO and GNR were 26.08% and 20.64%, respectively. Higher nanoparticle concentrations improved cooling efficiency, with minimal sedimentation and pressure drop issues compared to metal oxide nanofluids. Qasim et al. [71] experimentally analyzed ZnO/H_2O nanofluids (0–0.3%) in a Suzuki Mehran radiator under laminar flow (Re 186–1127). The 0.2% concentration enhanced heat transfer by 41%, overall heat transfer coefficient by 50% and Nusselt number by 31%. There was an increase in pressure drop and friction factor by 47% and 46%, respectively. Increased concentrations (0.3%) decreased performance because of the high viscosity and density which limited the efficiency increase. Erkan et al. [72] evaluated the exergy performance of Al 2 O 3, SiO_2 and TiO_2 nanofluids (0.2% and 0.4%) in a diesel engine radiator. Figure 10 presents the dependence of exergetic efficiency on various nanocoolants. TiO_2 at 0.4% had the greatest exergy efficiency (35.67%), which was 62.14% higher than water. Al_2O_3 decreased exhaust temperature by 59 K, whereby TiO_2 had the minimum exergy destruction (18.516 kW). Nanofluids were found to be more efficient and less emitting than the traditional coolants. Bargal et al. [73] experimentally tested the use of ZnO and AlN nanofluids in 50:50 H_2O-EG mixtures as PEMFC cooling. ZnO nanofluids of 0.2 wt% and 0.5 wt% enhanced the heat transfer by 24.3% and 57.7% respectively, whereas AlN did it by 15.3% and 30.7%. An increase in nanoparticle concentration enhanced the radiator performance and general heat transfer. ZnO nanofluids were recommended for superior thermal performance in automotive PEMFC engines.

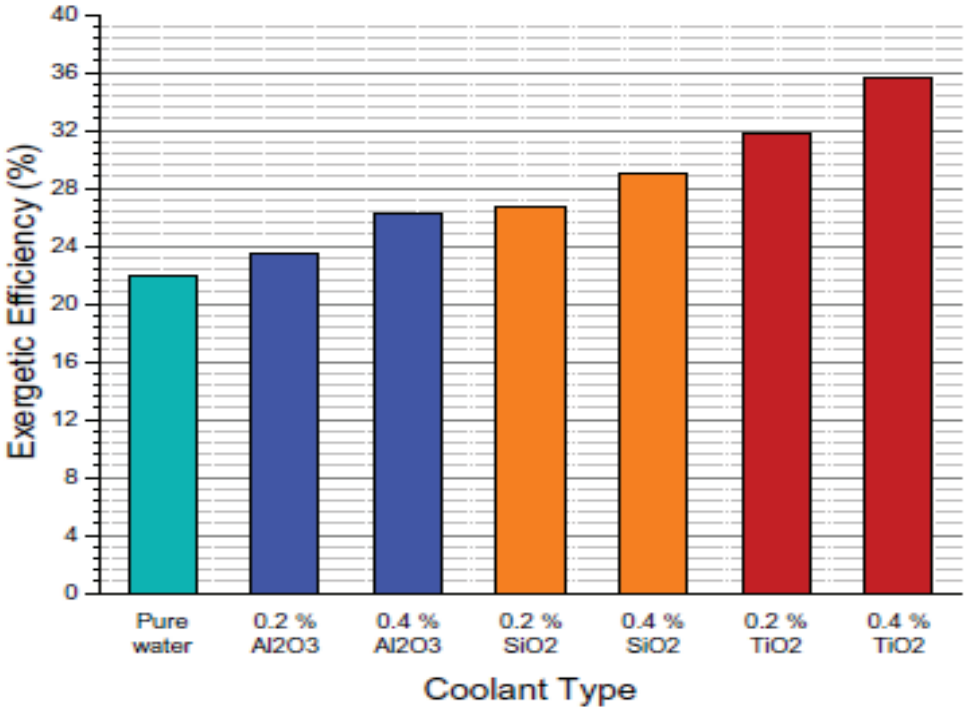


Figure 10. Variation of exergetic efficiency with different nanocoolant [From Erkan et al. [72], with permission from Springer Nature].

Ramadhan et al. [74] experimentally analyzed Al_2O_3-TiO_2-SiO_2 tri-hybrid nanofluids (0.05–0.3%) in a water/ethylene glycol (60:40) mixture for automotive radiators. The 0.3% concentration enhanced the coolant-side heat transfer coefficient by 39.7%, while the air-side enhancement reached 23.8% at 0.05%. Higher Reynolds numbers increased overall heat transfer by 18.3%. Pressure drop and pumping power rose with concentration, indicating increased viscosity effects. Contreras and Filho [75] experimentally evaluated the heat transfer performance of MWCNT nanofluids in a 50:50 H_2O-EG mixture for automotive radiators. The heat transfer rate was enhanced by 4.6% and total heat transfer coefficient was enhanced by 4.4% at a concentration of 0.1%. Increased temperature (105°C) decreased performance because of aggregation of nanoparticles. The stability analysis indicated that stability was 90% after three days, and this influenced the long-term stability. Kumar et al. [76] experimentally investigated a carbon-based hybrid nanofluid (GnP-MWCNT/coolant oil) in an automobile radiator. At 0.5% concentration, thermal conductivity improved by 59%, and the OHTC increased by 124%. The CHTC showed a 73.44% rise at 70°C. However, pressure drop increased by 23.72%. The nanofluid was stable over 21 days, indicating that it can be used as a substitute coolant. Khan [77] researched the CuO, ZnO and MgO nanofluids (0.5-3%) in a car radiator using H_2O as base fluid. CuO- H_2O had the best thermal conductivity (1.084 W/mK) which increased the transfer of heat by 48.76% at 3% concentration. ZnO-water and MgO-water enhanced the heat transfer by 46.49% and 43.66% respectively. CuO-water enhanced Reynolds number by 8.11% whereas friction factor reduced by 2.29%. Pumping power increased with concentration but remained feasible for automotive applications. Hassaan et al. [78] experimentally analyzed MWCNT–Al_2O_3/water hybrid nanofluid in a 2005 Honda Civic radiator. The heat transfer rate was enhanced by 33%, and Nusselt number by 23.7% at 2.3% concentration, with a 22.54% increase in the radiator efficiency. The pressure drop and friction factor were raised by 24 and 24.3 percent respectively. The hybrid nanofluid was found to be superior in terms of thermal performance, hence making it a feasible substitute to the distilled water in cooling automobiles.

Rana et al. [79] investigated the thermal enhancement in car coolant by utilizing hybrid nanoparticles (TiC-Al_2O_3) in ethylene glycol. It used the finite element method in the performance of the Carreau-Yasuda hybrid nanofluid in a boundary layer flow. The hybrid nanofluid had a high thermal efficiency as compared to a normal nanofluid. The important results were improved velocity profiles as we increased, high wall shear stresses (e.g., 0.5967 at We = 0.2 with hybrid and 0.4732 with regular nanofluid), and increased rate of heat transfer (e.g., Nusselt number 8.1499 vs. 5.1004) as the strength of the magnetic field was increased. Destructive chemical reactions boosted mass transfer rates, unlike generative reactions, highlighting potential energy efficiency improvements in automotive systems.

Integration of Nanofluids in Automotive Fuel System

Introduction of nanofluids into car fuel systems is a promising technique of enhancing the efficiency and performance of engines. Dissolved nanoparticles Al_2O_3, TiO_2, and CNTs in traditional fuels improve thermal conductivity, combustion efficiency, and lubrication properties. These improvements result in improved atomization of fuels, engine deposits, and decreased emissions [80]. Also, nanofluids help in cooling down heat in fuel injection and cooling systems, thus avoiding overheating. It has been demonstrated that nanofluid-based fuels are capable of enhancing BTE by as much as 8 percent and decreasing SFC. The innovation opens the path to more efficient and eco-friendly automotive technologies [81]. The integration of nanofluid in automotive fuel system is summarized in Table 4.

Mehta et al. [82] examined nanofuels which were prepared by dispersing A1, F1, and B1 nanoparticles in diesel. These fuels exhibited a 7% reduction in SFC, with increased BTE (A1: 9%, F1: 4%, B1: 2%) and exhaust gas temperature (A1: 9%, F1: 7%, B1: 5%). CO emissions dropped by 25–40%, and hydrocarbons decreased by 8% (A1) and 4% (F1), while NOx emissions slightly increased. Sarvestany et al. [83] analyzed the effect of Fe_3O_4 magnetic nanofluid on the engine performance and emissions of the diesel engine. The variation of BSFC with load is shown in Figure 11. A 0.4% nanoparticle concentration improved combustion, while 0.8% increased BSFC by 34%. NOx and SO_2 emissions decreased by 56–67% and 14–20%, respectively, but CO emissions and smoke opacity rose by up to 125%. The research identified the prospects of using magnetic nanoparticles in the modification of fuels to be efficient and to control emissions.

Venkatesan and Kadiresh [84] conducted a study to examine the impact of an aqueous CeO_2 nanofluid fuel additive on the efficiency and emissions of a diesel engine. Test fuels included diesel and biodiesel blends with 50cc/L of CeO_2. Results showed a 5.81% rise in BTE, a 6.25% decline in fuel consumption, a 31.48% decrease in hydrocarbon emissions, a 17% reduction in NOx, and a 10.5% lower smoke opacity compared to diesel. Sarvestani et al. [85] modeled specific fuel consumption and emissions of a diesel engine using Fe_3O_4 nanoparticle-blended fuels at 0.4% and 0.8% concentrations. The outcome indicated that the consumption of fuel increased by 30% at 0.8% concentration. The emissions of NOx and SO_2 were reduced by 67% and 20%, respectively, whereas CO emissions and smoke opacity grew by 50% and 231%, respectively. Regression models forecasted the outcome with 94%-98% accuracy. Ramanan and Yuvarajan [86] compared the emission of a diesel engine with RBOME mixed with 1% magnetite nanofluid. The findings indicated a decrease of 0.011% CO, 19 ppm HC, 93 ppm

Table 4. Summary of integration of nanofluid in automotive fuel system

Ref. No.	Nanoparticle	Base fluid	Engine	Environmental Concern
[82], 2014	Aluminum, iron, and boron	Diesel	CI Engine	CO emissions dropped by 25–40%.
[83], 2014	Fe_3O_4-magnetic	Diesel	Diesel engine	NOx and SO_2 emissions decreased by 56–67% and 14–20%, respectively.
[84], 2014	Cerium oxide	Diesel and biodiesel	CI Engine	17% reduction in NOx and a 10.5% lower smoke opacity compared to diesel.
[85], 2016	Fe_3O_4	Diesel	CI Engine	NOx and SO_2 emissions decreased by 67% and 20%, respectively.
[86], 2016	Ferromagnetic	RBOME	CI Engine	Reductions of 0.011% CO, 19 ppm HC, 93 ppm NOx, and 9% smoke opacity compared to RBOME
[87], 2017	Al_2O_3	H_2O	Diesel engine	CO_2 emissions increased by 26%, and engine noise rose by 2.19% at 10% concentration.
[88], 2018	TiO_2	MOME	Diesel engine	TiO_2 reduced carbon monoxide by 13% and hydrocarbons by 4.2%.
[89], 2019	TiO_2	Diesel and biodiesel	Diesel engine	Reductions in ignition delay by 7%, hydrocarbon by 38%, and smoke emissions by20%.
[90], 2019	Al_2O_3	Diesel	CI Engine	The D+50AN blend showed reductions in NOx by 15.6%.
[91], 2021	CeO_2	Methanol	Diesel engine	NOx emissions and smoke opacity were reduced by 70.9% and 90.3%, respectively.
[92], 2023	ZnO	Green fuel	Diesel engine	NOx were reduced by 12.97% at maximum power output.
[93], 2023	Al_2O_3, SiO_2, and MgO	Tamarind seed oil	CI Engine	CO, UHC, NOx, and smoke emissions were substantially decreased.

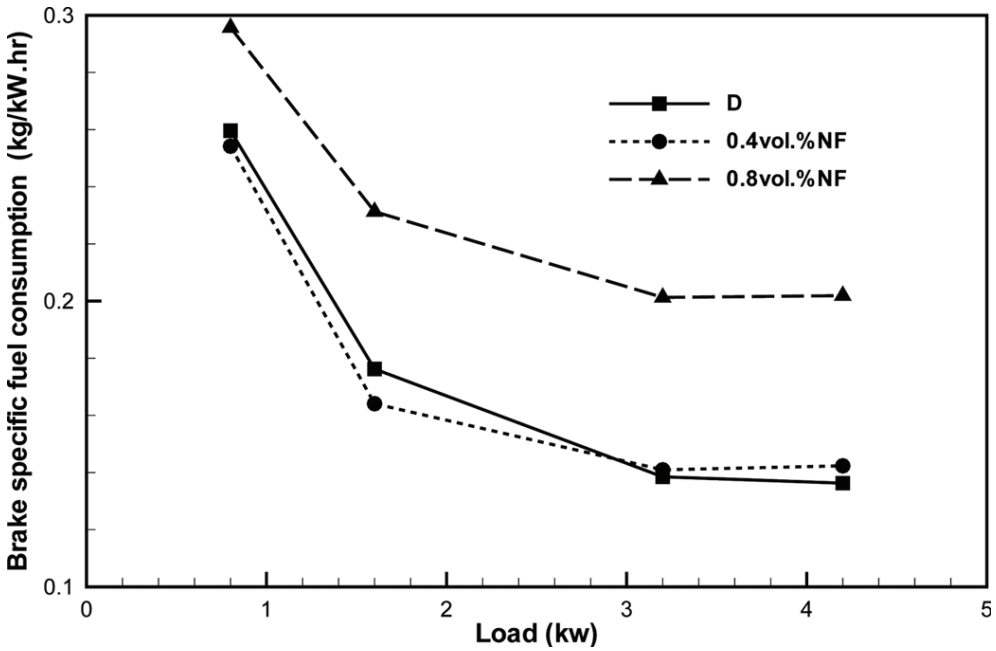


Figure 11. Variation of BSFC with load [From Sarvestany et al. [83], with permission from Taylor and Francis].

NOx, and 9% smoke-opacities over RBOME. The nanofluid enhanced combustion by lowering ignition delay and being an oxidation catalyst. Magnetic nanoparticles were collected from exhaust emissions for potential reuse. Chaichan et al. [87] investigated the effect of aqueous alumina nanofluid (1–10%) on diesel engine effectiveness and emissions. BTE enhanced by 5.5%, and fuel consumption reduced by 3.94%. The variation of HC emission with engine speed is shown in Figure 12. CO, HC, NOx, and PM emissions decreased by 14.49%, 27.94%, 41.3%, and 37.64%, respectively. However, CO_2 emissions increased by 26%, and engine noise rose by 2.19% at 10% concentration.

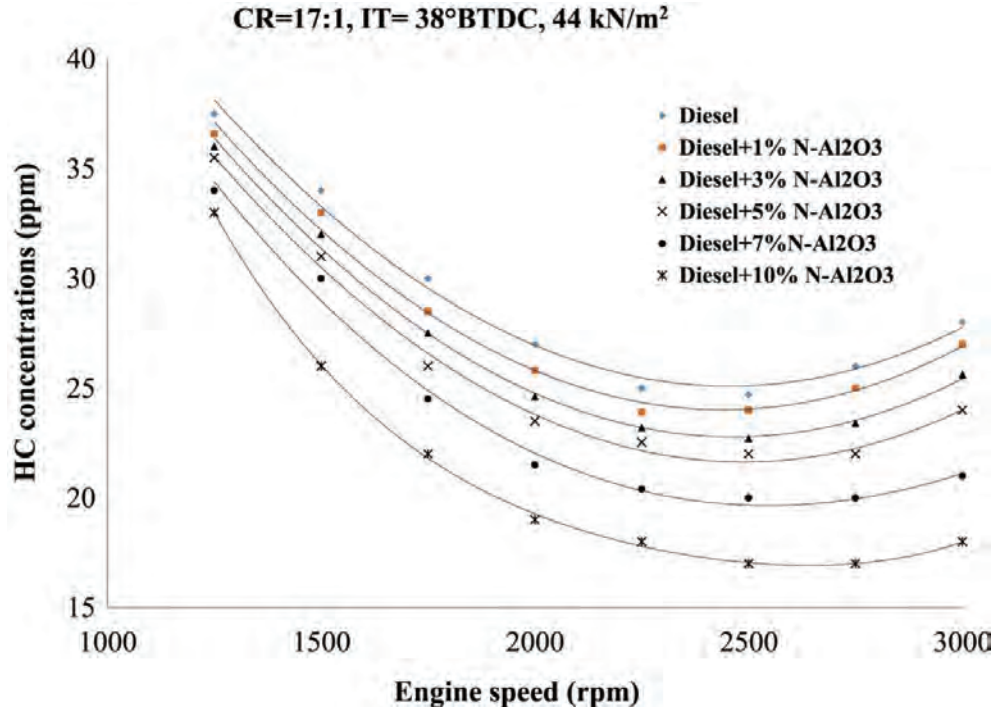


Figure 12. Variation of HC concentration with engine speed [From Chaichan et al. [87], with permission from Elsevier].

Yuvarajan et al. [88] examined the effect of TiO_2 nanofluid on the emissions of a diesel engine using MOME biodiesel. TiO_2 nanoparticles 50 nm were used at concentrations of 100 and 200 ppm. The findings indicated that TiO_2 had a negative effect on carbon monoxide (by 13%), hydrocarbons (by 4.2%), and smoke emissions but a minor positive effect on NOx emissions. The nanofluid increased the efficiency of combustion because of the increased oxidation and catalytic activity. Saxena et al. [89] optimized modified nanofluid (MNF) fuel blends with TiO_2 nanoparticles in a diesel engine. The optimal conditions were TiO_2 at 150 mg/L and 82.37% engine load. Under these conditions, BTE enhanced by 3.25%, BSFC reduced by 18.42%, and reductions in ignition delay (7%), hydrocarbon (38%), and smoke emissions (20%) were detected, accompanied by a slight rise in NOx emissions. Venkatesan and Kadiresh [90] examined aqueous aluminum oxide nanofluid blends in a diesel engine to enhance performance and reduce emissions. The D+50AN blend showed the highest brake thermal efficiency improvement (5.9%) and reductions in NOx (15.6%), smoke (22.34%), hydrocarbons (31.82%), and CO (13.79%) at maximum rated power. Further addition of the nanofluid to a level of more than 50cc resulted in poor performance and D+50AN was the best mixture to use in the diesel engine.

Pan et al. [91] examined the effect of cerium oxide (CeO_2) nanoparticles in methanol based nanofluids on combustion, performance and emissions of a dual-fuel diesel engine. Findings showed that BSEC had reduced by as much as 8.1, and BTE had also increased by 10.8. The emission test was employed to determine the reduction of HC and CO levels by 56.3 and 79.8%, and NOx and smoke opacities by 70.9% and 90.3% respectively upon inclusion of ZnO nanofluid with diesel to study the green fuel blend [92] to improve combustion and engine performance. D + 50ZN blend gave the most favorable results with a 5.38 percent increase in brake thermal efficiency. Emissions of NOx decreased by 12.97%. Sathish et al. [93] compared the performance of tamarind seed oil-based biodiesel mixed with Al_2O_3, SiO_2, and MgO nanoparticles in a CI engine. The variation of NOx with load for different blend condition is shown in Figure 13. It was found that the D80TSOB20A mixture produced the greatest cylinder pressure (77 bar) and heat release rate (75 J/deg). Thermal efficiency of the brakes increased to 32% and CO and smoke emissions were greatly reduced as opposed to other blends.

Nanofluid as a Medium for Enhanced Shock Absorption

Nanofluids have also become a prospective shock absorbing media because of their high energy dissipation capacity, rheological tuning and dynamically responsive nature to impact loads. Diffusion of the nanoparticles in the base fluids modulates their viscosity, density and thermal conductivity, and thus the mechanical shock waves can

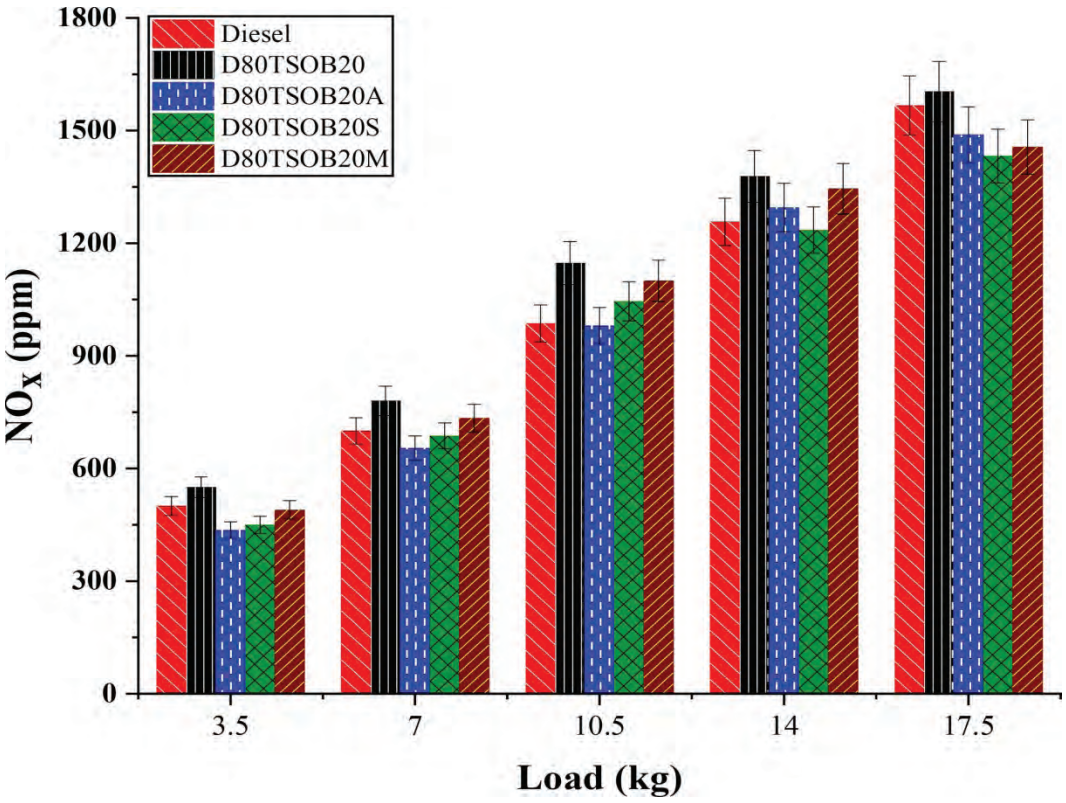


Figure 13. NOx variations with load for various blends [From Sathish et al. [93], with permission from Elsevier].

be more effectively managed [94]. The characteristics of nanofluids render them extremely useful in impact resistance use, which is necessitated by automotive crash protection, protective clothing, aerospace structures, and military armoring systems. Nanofluids containing nanoparticles like silica, carbon nanotubes or metal oxides can show shear-thickening properties, in which viscosity rises with high strain rates, allowing rapid energy uptake at the impact point [95].

Nanofluids, when used in shock absorbers, can enhance shock absorber damping and stability in the automotive industry. Their capability to suppress vibrations and energy decays are also very effective in ride comfort and durability of suspension systems. In aerospace, nanofluid-based dampers reduce vibrations and shocks during takeoff, landing, and turbulence to increase the lifespan of components. In addition, nanofluids are considered in body armor and protective materials, and their dynamic stiffening effect can be more effective against high speed projectiles and blunt force trauma [96].

It has been shown that the shock absorption characteristics of nanofluids can be manipulated through the nanoparticle concentration, morphology and fluid composition. Nanofluids of high viscosity and optimal particle loading contain fewer sudden deformations and are therefore useful in energy absorption implementation [97]. Also, they have a high heat dissipation rate that causes structural failure in sensitive components. The adaptability of nanofluids to different impact conditions is likely to be further enhanced in the future by the new formulations of nanofluid, such as smart and magnetorheological nanofluid. The injection of nanofluids into high-technology damping and shock-absorbing materials is a big move towards the creation of next-generation impact-resistant materials in the automotive, aerospace, and defense sectors [98].

Ali et al. [99] examined how hybrid nanofluids impacted the viscous damping of hydraulic oil in dashpots. The variation of damping coefficient with for hybrid nanofluid at different volume concentration is shown in Figure 14. It tested nanofluids with 1–5 vol% of fumed silica, precipitated silica, and MWCNTs. The MWCNT nanofluid (0S5C) at 5 vol percentage had the best damping enhancement, with a lowering of the settling time and overshoot. Shear thickening was verified by rheological tests in an increased concentration of MWCNT. The damping coefficient increased with MWCNTs but decreased with silica.

Pawar et al. [100] investigated the influence of CuO nanofluid on the viscosity and damping characteristics of shock absorber oil. Nano-lubricants with 0.25–1.5 wt% CuO increased viscosity, with 1 wt% showing a 20% rise at 25°C. The damping performance was increased 15% with RMS acceleration decreasing to 0.85 mm/s^2 at 400 rpm. Although viscosity and damping were improved, the transmissibility ratio did not vary significantly, which suggests

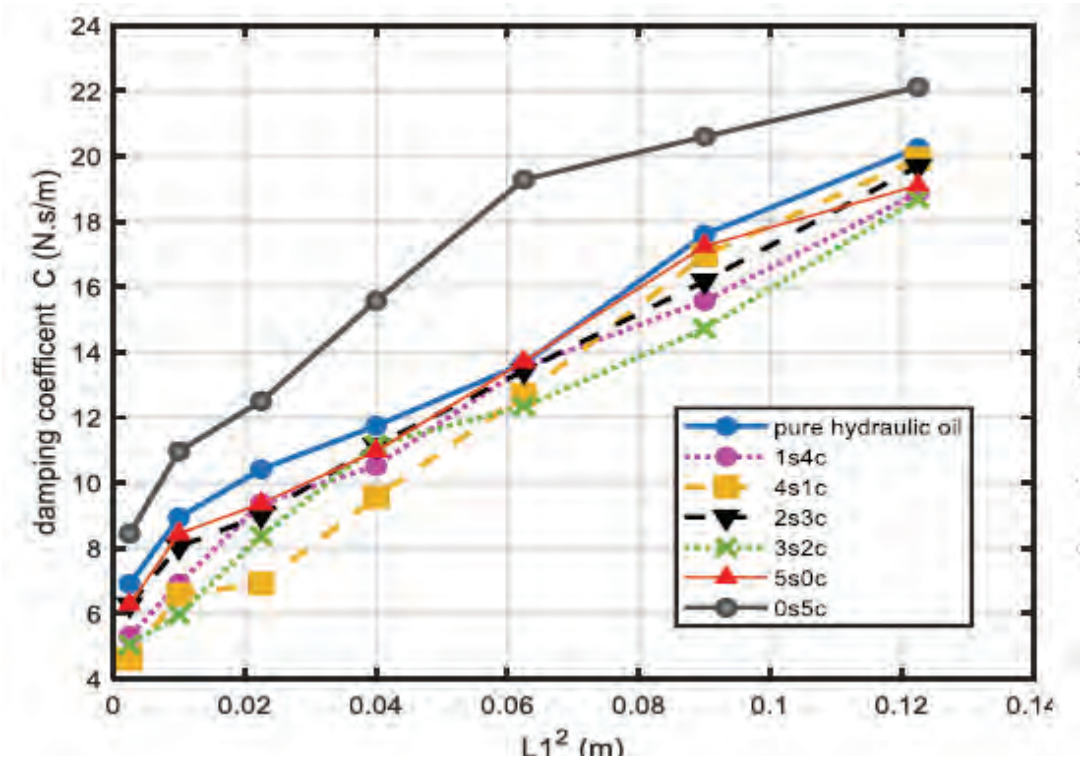


Figure 14. Variation of damping coefficient with for hybrid nanofluid at different volume concentration [From Ali et al. [99], with permission from Semarak Ilmu].

that shock absorber designs might require adjustments to achieve the maximum benefits of CuO.

Revolutionizing Automotive Lubricants with Nanotechnology

Nanofluids have been seen as a potential engine lubricant because of their improved thermal and tribological characteristics. Nanofluids enhance viscosity, thermal conductivity and anti-wear properties by dispersing nanoparticles such as CuO, Al_2O_3 or MoS_2 in base oils. These additives enhance the reduction in friction between the moving parts resulting in reduced energy loss and fuel efficiency [101-103]. Research has demonstrated that nanolubricants (a lubricant to which nanoparticles have been added to enhance thermal conductivity, reduce friction, minimize wear, and improve overall engine performance) can reduce engine wear by creating protective tribofilms, reducing the amount of metal-to-metal contact. They also have better heat dissipation capabilities that will ensure the engines run at optimal temperatures and minimize chances of overheating and extending the life of the engine [104]. Studies show that nanofluids are able to reduce the rate of oil degradation; hence, increasing the service life. Nevertheless, nanoparticles stability and dispersion methods, as well as filter blockage, are issues to be considered prior to the large scale application. With the increasing automotive needs, nanofluid-based lubricants are also an option in enhancing the engine performance and efficiency [105]. Table 5 presents a summary of the use of nanofluid as an engine lubricant in automobiles.

Wu and Kao [106] investigated the impact of TiO_2 nanofluid as a lubricant additive in internal combustion engines. Engine tests indicated that with the application of TiO_2 in ethylene glycol, oil gelation was achieved after 10 hours but the problem was eliminated by applying paraffin oil. TiO_2 nanofluid decreased friction force and smaller particles (59 nm) were more effective. The research determined that particle size played a major role in reducing friction indicating that TiO_2 nanofluid was a promising lubricant. Ettefaghi et al. [107] examined the impact of MWCNTs as an additive in SAE 20W50 engine oil. It was found that a 0.1 wt% of MWCNT concentration increased thermal conductivity by 13.2% and flash point by 6.7%. The concentration of 0.2 wt% resulted in a 13 percent rise in flash point, and viscosity was not affected at low concentrations. These results indicate that MWCNTs improve engine oil performance but do not substantially affect viscosity. Afrand et al. [108] examined the effects of temperature and concentration on the viscosity of SiO_2-MWCNTs/SAE40 hybrid nanofluid for use in heat engines. The variation of viscosity with temperature at different volume concentration is shown in Figure 15. The

Table 5. Summary of the use of nanofluid as an engine lubricant in automobiles

Ref. No.	Nanofluid	Engine Oil	Concluding Remark
[107], 2013	MWCNT	SAE 20W50	0.1 wt% MWCNT concentration enhanced thermal conductivity by 13.2%.
[108], 2016	SiO_2-MWCNTs	SAE 40	37.4% enhancement in viscosity at 1.0% volume fraction
[109], 2016	Sc-Ag/GN	10W40	Sc-Ag/GN reduced friction coefficient by 30.4%
[110], 2017	Al_2O_3-MWCNT	5W50	Higher solid volume fractions (up to 1%) increased viscosity
[111], 2018	$Mg(OH)_2$/MWCNT	5W50	Thermal conductivity improved by 13%–50%.
[112], 2018	MWCNT-ZnO	5W50	Viscosity decreased by over 7% at 0.05%-0.1% nanoparticle concentrations
[113], 2019	MWCNT–SiO_2	10W40	The highest viscosity increase (1.4×) occurred at 5°C with 1% concentration
[114], 2019	MWCNT-ZnO	5W50	Viscosity reduction of up to 9% at 0.05% solid volume fraction at 5°C minimized cold start damages
[116], 2020	MWCNT-TiO_2	SAE50	Viscosity decreased by 76% at 3999 s^{-1} shear rate with a 1% concentration.
[117], 2021	ZnO–TiO_2	5W30	Engine tests showed a 4.5% noise reduction.
[118], 2021	SiO_2/soybean	Engine oil	The viscosity decreased with increasing temperature, with a 55% reduction at 5°C for 1% volume fraction.
[119], 2021	Graphite	SAE30	A 15.2% reduction in total fuel consumption and an 18% decrease in BSFC.
[120], 2022	MWCNT-Al_2O_3	5W50, 10W40	The highest viscosity increase (+34.97%) was observed in 10W40.
[121], 2025	CuO and ZnO, Al_2O_3 and ZnO	Pure diesel and SAE 15W40	CO and NOx emissions decreased by 20.04% and 10.25%, while CO_2 emissions increased by 29.16%

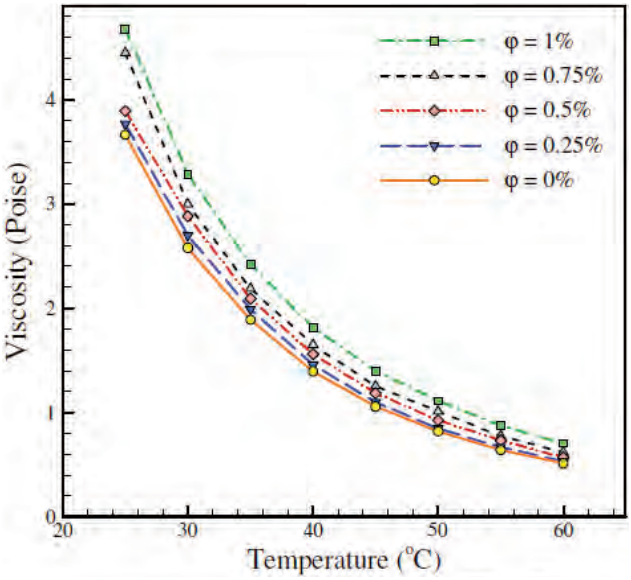


Figure 15. Viscosity variations with temperature at different volume concentrations [From Afrand et al. [108], with permission from Elsevier].

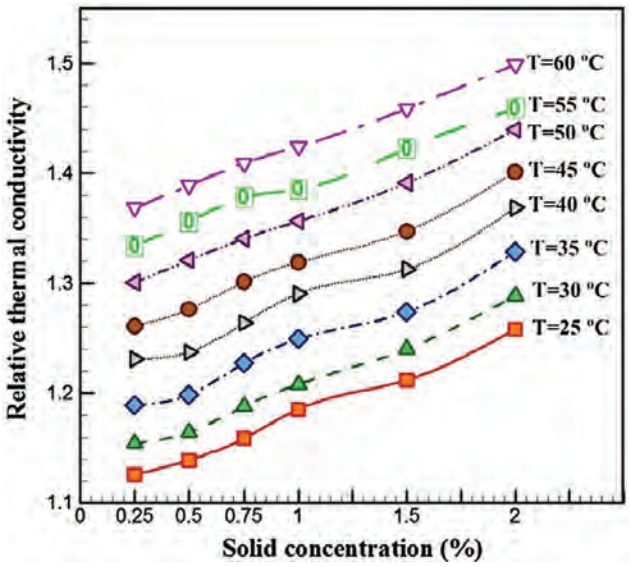


Figure 16. Variation of relative thermal conductivity with concentration at different temperature [From Asadi et al. [111], with permission from Elsevier].

findings indicated an increase in viscosity as nanoparticle concentration was increased with a maximum 37.4% increase at 1.0% volume fraction. However, viscosity decreased with increasing temperature from 25°C to 60°C.

Meng et al. [109] prepared Sc-Ag/GN through super critical CO_2, and the uniform silver nanoparticles (2-16 nm) on graphene sheets were obtained. Sc-Ag/GN, as an engine oil additive (0.06 - 0.10 wt. %), decreased the friction coefficient and wear scar diameter by 30.4 and 27.4 percent, respectively, compared to ZDDP, nano-Ag, and graphene oxide. The frictional film formed reduced the surface roughness, increasing lubricity. These results indicate industrial possibilities of Sc-Ag/GN in lubrication. Esfe et al. [110] investigated the rheological behavior of Al_2O_3-MWCNT/5W50 hybrid nano-lubricant. The readings of viscosity at 5-55°C and shear rate of 666.5-10,664 s^{-1} showed non-Newtonian behaviour. The higher the concentration (up to 1%), the higher the viscosity and non-Newtonian effects and the lower the temperature. A new correlation, which was formed, attained a correlation coefficient of 0.9923 which effectively predicted the viscosity variations. The results justify the potential application of the hybrid nano-lubricant in engines. Asadi et al. [111] studied the heat transfer performance of $Mg(OH)_2$/MWCNT-engine oil nano-lubricant.. It showed Newtonian behavior in the entire temperatures tested (25°C-60°C) and volume fraction (0.25%-2%). The variation of relative thermal conductivity with varying concentration and different temperature is depicted in Figure 16. The dynamic viscosity increased with solid concentration but decreased with temperature, while thermal conductivity improved by 13%–50%.

Esfe et al. [112] examined the effect of MWCNT-ZnO (30%-70%) nanoparticles in 5W50 engine oil to improve lubrication. Viscosity decreased by over 7% at 0.05%-0.1% nanoparticle concentrations, reducing cold start damages. The nano-oil showed non-Newtonian behavior and higher viscosity index. ANN and RSM models predicted viscosity with R^2 values of 0.9999 and 0.9715, respectively. The nano-oil enhanced lubrication in low and high-temperature conditions. Rejvani et al. [113] investigated the rheological behaviour of MWCNT–SiO_2 (30–70)/10W40 nano-lubricant. It followed a non-Newtonian pseudo-plastic model. The viscosity was 35% higher than that of pure oil and dependent upon temperature and solid volume fraction. The maximum increase in viscosity (1.4×) was at 5C when the concentration was 1%. Esfe et al. [114] experimentally analyzed MWCNT-ZnO (20%-80%)/5W50 nano-engine oil for lubrication efficiency. A viscosity reduction of up to 9% at 0.05% solid volume fraction at 5°C minimized cold start damages. The nano-oil had non-Newtonian behaviour and reduced temperature dependence of viscosity. The results indicated its possible high-temperature lubrication and increased oil recovery possibilities.

Ramteke and Chelladurai [115] investigated the effects of hBN nanofluids on a diesel engine's tribological, performance, and emission characteristics. The 1 wt. % hBN nanofluid reduced piston ring wear, improved lubrication by forming a tribofilm, and increased brake power and thermal efficiency by 5.09% and 4.33%, respectively. Carbon monoxide and hydrocarbon emissions decreased by 46.15% and 55.95%, while NOx emissions increased by 40.03%. Esfe and Esfandeh [116] investigated the rheological behaviour of MWCNT-TiO_2 (40:60)/SAE50 hybrid

nanofluid at 25–50°C and 0–1% solid volume fractions. Results showed that viscosity decreased by 76% at 3999 s^{-1} shear rate with a 1% concentration. The nanofluid was pseudoplastic and at concentrations less than 0.5%, the viscosity was low than that of the base fluid. Bharath and Selvan [117] investigated the rheological and heat transfer performance of ZnO–TiO_2 hybrid nanolubricant in a spark-ignition engine. Viscosity tests showed non-Newtonian behavior, with the hybrid nanolubricant having a higher viscosity index than conventional oil. The Maxwell–Garnetts model predicted a 5.7% increase in thermal conductivity at 0.1 wt%. Engine tests showed a 4.5% noise reduction and significant decreases in longitudinal (59%) and lateral (49%) vibrations at higher speeds.

Kharabati et al. [118] examined thermal and rheological characteristics of SiO_2 /soybean oil nano lubricant in internal combustion engines at 5° C to 40°C. Viscosity decreased with temperature, with a decrease of 55% at 5°C when the lubricant was 1% in volume. The maximum thermal conductivity (0.169 W/mK) was observed at 30 C and this is 12 percent higher than at base oil. Singh et al. [119] developed and tested graphitic nanoparticle-based nanolubricants for automotive applications. The variation of different performance parameter with load is shown in Figure 17. Nanographite-based nanolubricant showed a sevenfold improvement in wear resistance and a 13-fold reduction in friction. Engine tests revealed a 15.2% reduction in total fuel consumption, an 18% decrease in BSFC, a 22% rise in BTE, a 28.23% boost in heat carried by the water jacket with reduced emissions. Esfe et al. [120] analyzed the efficiency of hybrid nano-lubricants under various experimental conditions. Experiments showed non-Newtonian and pseudo-plastic flow behavior. The highest viscosity increase (+34.97%) was in 10W40, while the highest decrease (-9.64%) was in 5W50. MWCNT-Al_2O_3/5W50 exhibited better viscosity control. Gosai et al. [121] examined the influence of nano-additives on diesel engine efficiency and emission characteristics. It concluded that using CuO and ZnO nanoparticles in fuel and Al_2O_3 and ZnO in lubricants improved thermal efficiency by 17.62% and reduced SFC by 14.98%. The emissions of CO, NOx were reduced by 20.04% and 10.25% and CO 2 emissions enhanced by 29.16%, which means that it was fully burned.

ENVIRONMENTAL CONCERN AND SUSTAINABILITY OF NANOFLUID PRODUCTION AND DISPOSAL

The recent development in nanofluids in automotive industry is mainly propelled by the fact that these fluids can be used to increase fuel efficiency, reduce emissions and enhance heat transfer in vehicles. Nonetheless, together with their technological advantages, the environmental issues that are related to the production, usage, and disposal of nanofluids should be evaluated critically in order to guarantee a sustainable adoption [122, 123].

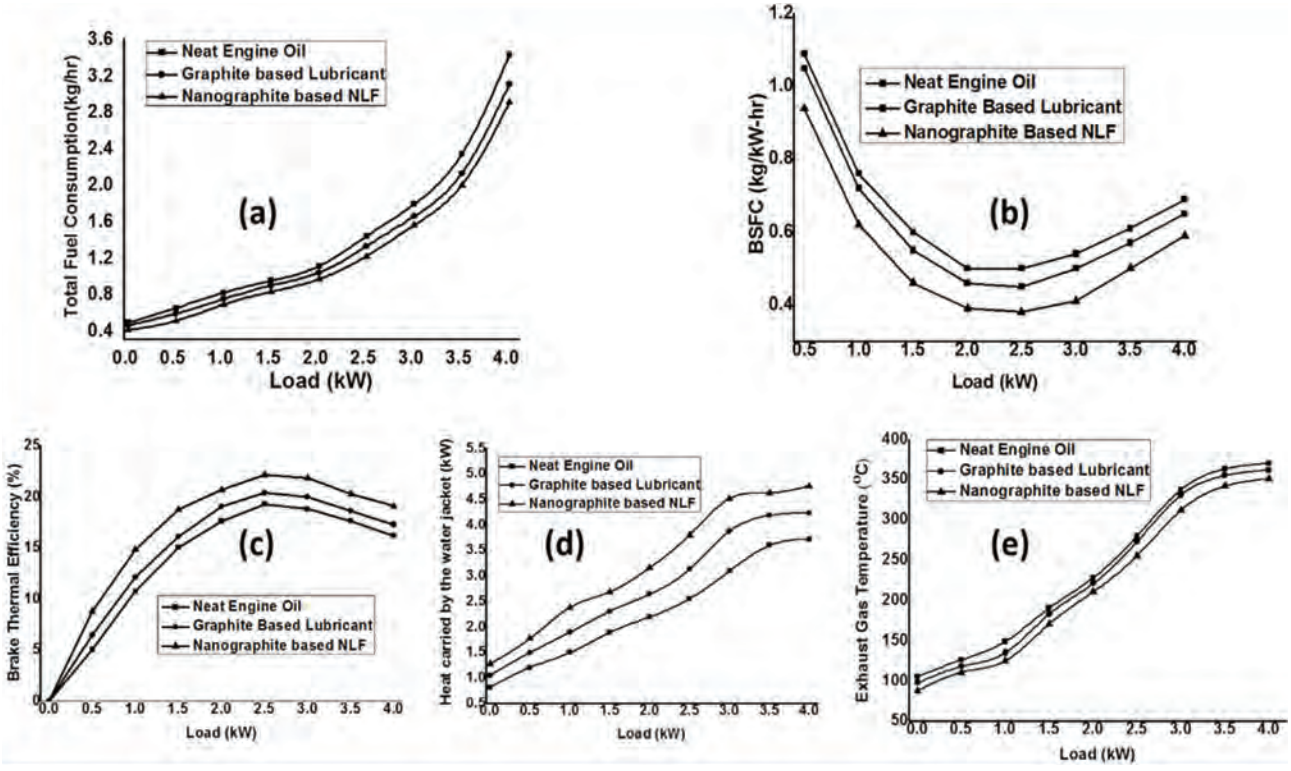


Figure 17. Variation of different performance parameter with load [From Singh et al. [119], with permission from Elsevier].

Environmental Impact of Nanofluid Production

Nanofluid preparation is commonly associated with energy consuming procedures like chemical precipitation, sol-gel processing, and laser ablation, which add to carbon emissions and resource depletion. Also, certain production processes are based on dangerous chemicals, which cause possible environmental toxicity. It is also of concern that the energy requirement of synthesizing nanoparticles is very high and this is likely to impact the sustainability of mass production [124-125]. In order to alleviate these concerns, studies are concentrating on:

- Plant extracts and biocompatible solvents to synthesize using green methods to reduce hazardous waste.
- Energy efficient production methods that will minimize emissions and use of resources.
- Recycling and reuse of nanoparticles to improve sustainability and decrease reliance on raw materials.

Nanofluid Usages and Potential Environmental Risk

Although nanofluids have great potential in improving the performance of vehicles, the long-term effects of the use of nanoparticle include the release of the nanoparticles into the environment. Potential risks include:

- Dispersal of airborne nanoparticles that can be harmful to health when inhaled.
- Water pollution, nanoparticles will be able to settle in aquatic environments, thus impacting on life in the sea.
- Pollution of soil, where stable nanoparticles change the microbiology and nutrient cycling.

In order to overcome these issues, strict protocols on nanofluid handling and storage must be put in place and formulations of environmentally friendly nanofluids which decompose harmlessly after application must also be prepared.

Sustainable Disposal and Recycling Strategies

Disposal of used nanofluids is a serious environmental issue as when they are disposed of improperly, it may cause the build-up of nanoparticles in the ecosystem. Disposal and recycling are done using sustainable methods such as:

- Filtering and separation methods to reclaim nanoparticles in waste nanofluids, so that they can be reused in the industry.
- Environmentally-sustainable degradation, e.g., enzymatic degradation or photocatalytic degradation, to negatively degrade the nanoparticles prior to disposal.
- The regulatory systems to bring uniformity in disposal processes, with reduced risks to the environment.

The automotive industry can take advantage of the benefits of nanofluid by incorporating sustainability into nanofluid studies and application with minimal environmental trade-offs. The concerns will have to be addressed in order to embrace the use of nanofluids as a green technology in the next generation vehicles.

Life Cycle Assessment of Nanofluid

In order to support the sustainability argument in favour of nanofluids in automotive industry, the need to measure their environmental impacts by conducting lifecycle assessments (LCAs) and toxicity analyses is imperative. LCAs offer an all-inclusive assessment of the ecological footprint of nanofluids, starting with the extraction, synthesis, use, and disposal of the raw materials and toxicity tests determine possible ecological and human health hazards when nanoparticles are present. Nanofluid production LCAs indicate that nanoparticles, including Al_2O_3, CuO and carbon nanotubes (CNTs), are costly to produce, and can be an important contributor to the carbon footprint. In the usage stage, nanofluids also help to enhance environmental advantage by enhancing fuel efficiency and lowering emissions. The incorporation of CuO and ZnO nanoparticles in fuel and lubricants decreased specific fuel consumption by 14.98% and CO/NOx emissions by 20.04% and 10.25% [121]. These cuts are estimated to be 0.5-1.0 kg CO_2-eq/liter of fuel saved, which varies based on engine type and operation conditions. But, the disposal stage is problematic, because the nanoparticle recovery and recycling are not popular yet. LCAs demonstrate that inappropriate disposal of nanofluids may cause nanoparticles to be deposited in soils and water, making non-biodegradable nanoparticles such as CNTs to persist in the environment 10-20 years longer [126]. Recycling approaches (filtration and centrifugation) can reduce nanoparticle concentration in used nanofluids by up to 80% to recover the unused material, reducing the lifecycle CO_2 by 50-60% and the lifecycle CO_2 by 15-20% to reduce the use of virgin materials and mitigate the impacts of used nanofluids. The future research ought to be on designing closed-loop recycling systems to improve sustainability of nanofluid applications in automotive systems.

Roadmap for Standardization of Nanofluid Testing Protocols to Guide Industry Adaptation

It is essential to develop standardized testing procedures of nanofluids to hasten their introduction into industries. Figure 18 shows the roadmap of standardization of nanofluid testing protocols that should be used to accelerate adaptation of the industry. The roadmap starts with the development of a collaborative institution to include academia, industry, and regulatory organizations to set key performance indicators, including thermal conductivity, viscosity, stability, and the environmental impact. The first step must be to develop a standard nomenclature and classification of nanofluids to make nanofluids consistent in research and practice. Secondly, standardized methods of measurement such as equipment calibration procedures, sample preparation procedures, etc. have to be devised to deal with variability in existing testing procedures. Interlaboratory validation will add to reliability and reproducibility. Simultaneously, the safety and toxicity tests must be combined to comply with the regulation requirements, which will help build confidence in the use of nanofluids. The roadmap focuses on progressive improvement, including feedback of pilot implementations in other industries

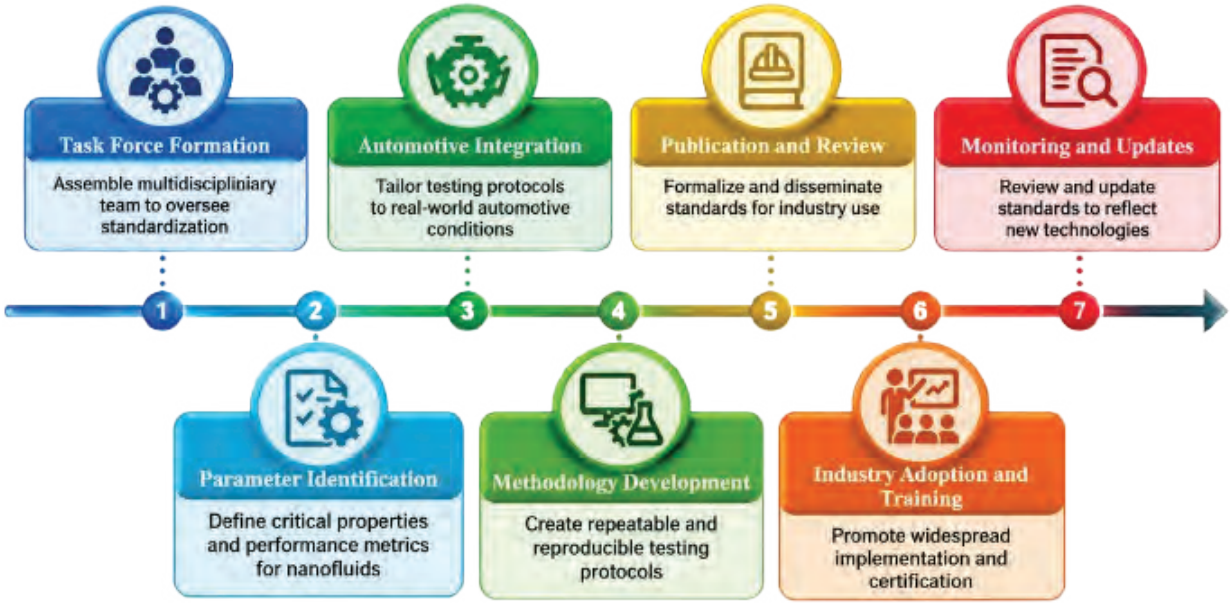


Figure 18. Roadmap for standardization of nanofluid testing protocols to guide industry adaptation.

such as energy, automotive and electronics. A standard, probably based on ISO or ASTM, which is globally accepted should be created by 2030, backed by open-access databases of nanofluid properties. The systematic methodology will curb the technical hindrances, lower expenses, and facilitate scaled, secure, and effective incorporation of nanofluids, impacting innovation and sustainability in sectors.

CHALLENGES IN INTEGRATING NANOFLUID INTO MODERN AUTOMOTIVE TECHNOLOGIES AND ITS LIMITATIONS

The application of nanofluids in the contemporary automotive technology has a number of challenges and limitations. The long-term efficiency is decreased by stability problems, including agglomeration and sedimentation of nanoparticles. One of the key issues in the application of nanofluid is agglomeration. It arises because of Van der Waals forces and magnetic or electrostatic interactions between nanoparticles, and causes clustering which reduces thermal conductivity and even dispersion. In dynamic automotive conditions (vibration, changes in temperature), the effect of agglomeration risk is higher, which impairs the stability of nanofluids and leads to blockage in cooling or lubrication systems in automotive systems [13, 34]. The common countermeasures are: (1) pH modification to raise zeta potential that increases repulsive nanoparticles forces. Indicatively, ZnO/H_2O nanofluids with a zeta potential of over 30 mV are stable up to 30 days [35]. (2) physical barrier formation (e.g., with surfactants, e.g., sodium dodecyl sulfate) to minimize the clustering of particles. Surfactants can however break down at high temperatures (greater than 100 C) and cannot be used in engine environment [51]. (3) Using ultrasonic waves to disperse agglomerates but long-term ultrasonication (>2 hours) may destroy the structure of nanoparticles, decreasing thermal conductivity by as much as 5% [33].

Difficulties with commercialization are caused by high costs of manufacturing and complicated synthesis procedures. Even though nanofluids demonstrate improvements in performance (e.g., 17.62% thermal efficiency improvement, 14.98% SFC decrease), the performance is limited at industrial level. Cost considerations comprise: (1) Adding CuO and ZnO nanoparticles to fuel and lubricants enhances thermal efficiency by 17.62% and decreases specific fuel consumption by 14.98% [121]. Using a mid-size car (fuel consumption: 8 L/100 km) as an example, the fuel savings would amount to around 150-200 dollars/annually at a fuel price of 1.5/L, which would cover the costs of nanofluid in 1-2 years. (2) Nanolubricants lower engine wear due to tribofilms formation, low maintenance cost of up to 15% over 100,000 km [119]. Indicatively, graphitic nanolubricants lowered wear by seven times which could save up to $500 on engine repairs [119]. (3) Fewer CO and NOx emissions (20.04% and 10.25% respectively [121]) meet strict emission regulations (e.g. Euro 7), which may save manufacturers money (vitally, fines) or allow tax subsidies.

It is unclear how it fits with engine materials and lubricants, and a great deal of research is needed. The issue of environmental and health implications on exposure to nanoparticles also makes adoption more cumbersome [127, 128]. Also, the absence of standardized testing procedures

Table 6. Challenges and limitations in integrating nanofluids into automotive technologies

Aspect	Challenges	Limitations
Stability	Nanoparticles tend to agglomerate and settle over time.	Long-term performance is uncertain due to instability.
Cost	High manufacturing and synthesis costs.	Scaling up production remains economically unfeasible.
Compatibility	Unclear impact on engine materials and lubricants.	Long-term wear effects on engine components are unknown.
Testing & Validation	Lack of standardized testing protocols.	Performance inconsistencies across different studies.
Dispersion	Requires advanced dispersion techniques for homogeneity.	Variability in thermal conductivity affects efficiency.
Safety & Regulations	Potential health and environmental risks.	Limited data on nanoparticle exposure impact.
Viscosity Impact	Higher viscosity can reduce fuel efficiency.	Increased pumping power may lead to higher energy use.
Scalability	Difficult to maintain performance at commercial scale.	Large-scale adoption is restricted due to performance variations.
Energy Demand	High energy requirements for nanoparticle synthesis.	Energy-intensive production raises sustainability concerns.

impedes reliability and performance validation. Such problems as higher viscosity with flow dynamics and inaccurate experimental data complicate the overall implementation. To ensure that nanofluids are a viable alternative in the auto industry, it is important to address these challenges. The challenges and limitations in integrating nanofluids into large scale automotive technologies are shown in Table 6.

KEY APPLICATION OF THE FINDINGS

The research paper gives a detailed examination of the way nanofluids increase the functionality of different automotive subsystems such as engine cooling, lubrication, and fuel efficiency. The most important uses of the discovery are:

Enhanced Engine Cooling

Nanofluids used in the cooling systems of automobiles enhance the ability to dissipate the heat in the engines, thus preventing overheating, leading to higher efficiency. The improved thermal conductivity of Al_2O_3 and TiO_2 nanofluids enables smaller and lighter radiators, which helps in reducing weight and fuel consumption of the vehicle.

Improved Lubrication Performance

Lubricants that are made of nanofluid decrease engine wear and friction thus increasing the engine life and also fuel economy. The addition of CuO and ZnO nanoparticles to lubricants demonstrated decreased wear rates with increased stability in viscosity, which provides increased performance in lubricants in different operating conditions.

Fuel Efficiency and Emission Reduction

The inclusion of nanoparticles like CeO_2 and Al_2O_3 in fuel enhances the efficiency of the combustion process, resulting in less fuel consumption and less emission. In particular, the levels of CO and NOx emissions were reduced by 20.04 and 10.25 percent, respectively, and CO_2 emissions grew, which proves the increase in the level of total combustion.

Potential Use in Hybrid and Electric Vehicle

Nanofluids have a high thermal conductivity and can find great use in the future in electric vehicle (EV) battery thermal management systems, where effective heat dissipation is needed to ensure battery safety and longevity.

CONCLUSION

Nanofluids have been found to have huge potential in enhancing the performance of automobiles especially in the field of lubrication and fuel efficiency. Adding nanoparticles to engine oil and fuel, scientists have found out improvements in thermal conductivity, viscosity, and tribological characteristics. Studies showed that nanolubricants reduced friction and wear, resulting in improved engine durability. Also, the fuel nano-additives led to a higher combustion efficiency and consequently, a higher brake thermal efficiency and reduced specific fuel consumption.

There was also an emissions analysis of the combustion that showed that carbon monoxide (CO) and nitrogen oxides (NOx) were reduced because the combustion was improved, and carbon dioxide (CO 2) emissions had slightly increased, which showed that the fuel being used was used fully. Nanofluids had a non-Newtonian nature of viscosity and were dependent on concentration and temperature, which affected their performance in various operating conditions. Combination of materials such as CuO, ZnO, Al_2O_3 and hBN in fuel and lubricants was promising in terms of optimization of engine performance. The key findings derived from this review article are as follows:

1. Nanofluids significantly enhance the thermal and lubrication properties of automotive systems.
2. The addition of nanoparticles in fuels and lubricants improves engine performance and fuel efficiency.

3. Nanoparticles also decrease wear and friction, resulting into improved longevity and reliability of engine parts.
4. Nanofluids have better heat transfer characteristics, which help to cool engines.
5. Application of nanofluids leads to reduction of emission of harmful gases like CO, NOx and HC.
6. Nanofluids promote full combustion, which enhances the thermal efficiency of the brake.
7. Nanoparticles stability and dispersion in base fluids are still a challenge, which needs further studies.
8. Scalability and cost-effectiveness of nanofluid applications in automobile industry should be assessed.

Generally, the use of nanofluids in cars has demonstrated a trade-off between performance enhancement and reduction in environmental impact. The next research should aim at ensuring maximum benefits and minimum potential disadvantages are achieved by optimizing the concentration and stability of nanoparticles so that the advantages can be maximized but the disadvantages can be minimized like high viscosity with a higher concentration of nanoparticles. The present research verifies that nanofluids could become an effective method of making automotive engines more efficient and sustainable.

Future Research Direction

The studies on the use of nanofluids in the automotive industry are scarce. Therefore, extensive studies are needed to accurately determine their behavior in automotive applications. The following research areas are some of the major areas that can be studied in future:

1. The focus of research should be on preventing the agglomeration and sedimentation of nanoparticles to increase stability of nanoparticles in automotive applications over periods of time.
2. It is essential to develop cost-effective synthesis and dispersion methods to ensure a large scale commercial viability.
3. More research is needed to determine the toxicity and ecological effects of exposure to nanofluid.
4. The aim of the investigations should be to maximize both the heat transfer and flow properties in the real-world automotive environment.
5. The long-term impacts of nanofluids on engine materials and lubricant formulations should be understood.
6. Prediction of nanofluids performance in the automotive systems can be enhanced by the combination of simulations and experimental data.
7. To have a sustainable adoption, a thorough examination of the life-cycle cost, recyclability, and environmental footprint of nanofluids is necessary.

NOMENCLATURE

$C_{p, nf}$	Specific heat capacity of the nanofluid (J/kg·K)
$C_{p, f}$	Specific heat capacity of the base fluid (J/kg·K)
$C_{p, p}$	Specific heat capacity of the nanoparticles (J/kg·K)
k_{nf}	Thermal conductivity of the nanofluid (W/m·K)
k_f	Thermal conductivity of the base fluid (W/m·K)
k_p	Thermal conductivity of the nanoparticles (W/m·K)
ρ_f	Density of the base fluid (kg/m^3)
ρ_p	Density of the nanoparticles (kg/m^3)
ρ_{nf}	Density of the nanofluid (kg/m^3)
φ	Volume fraction of nanoparticles

Abbreviations

BSFC	Brake specific fuel consumption
BSEC	Brake specific energy consumption
BTE	Brake thermal efficiency
CI	Compression ignition
CHTC	Convective heat transfer coefficient
CO	Carbon monoxide
DLS	Dynamic light scattering
EG	Ethylene glycol
GO	Graphene oxide
GNR	Graphene nanoribbon
HC	Hydrocarbons
hBN	Hexagonal boron nitride
MWCNT	Multiwalled carbon nanotubes
MOME	Mustard oil methyl ester
NOx	Nitrogen oxides
OHTC	Overall heat transfer coefficient
PEMFC	Proton exchange membrane fuel cell
PM	Particulate matters
RBOME	Rice bran oil methyl ester
SFC	Specific fuel consumption
TEM	Transmission electron microscopy
UHC	Unburned hydrocarbons
ZDDP	Zinc dialkyl dithiophosphate

AUTHORSHIP CONTRIBUTIONS

Authors equally contributed to this work.

DATA AVAILABILITY STATEMENT

The authors confirm that the data that supports the findings of this study are available within the manuscript.

CONFLICT OF INTEREST

The authors declared no potential conflicts of interest with respect to the research, authorship, and/or publication of this article.

ETHICS

There are no ethical issues with the publication of this manuscript.

STATEMENT ON THE USE OF ARTIFICIAL INTELLIGENCE

Artificial intelligence was not used in the preparation of the article.

REFERENCES

[1] Osborne S, Kopinsky J, Norton S, Sutherland A, Lancaster D, Nielsen E, German J. Automotive thermal management technology. Automotive News. 2015.

[2] Liu H, Wen M, Yang H, Yue Z, Yao M. A review of thermal management system and control strategy for automotive engines. J Energy Eng 2019;147:03121001. EY.1943–7897.0000743) [CrossRef]

[3] Gupta SK. A short & updated review of nanofluids utilization in solar parabolic trough collector. Mater Today Proc 2023. [CrossRef]

[4] Gholınıa M, Javadı H, Gatabı A, Khodabakhshı A, Ganjı DD. Analytical study of a two-phase revolving system of nanofluid flow in the presence of a magnetic field to improve heat transfer. Sigma J Eng Nat Sci 2019;37:340–360.

[5] Qamar M, Khan M, Yasir M, Shflot AS, Malik MY. Review on velocity slip with thermal features of irregular heat transport enhancement of hybrid nanofluids. Results Eng 2024;24:103606. [CrossRef]

[6] Heywood JB, Welling OZ. Trends in performance characteristics of modern automobile SI and diesel engines. SAE Int J Engines 2009;2:1650–1662. [CrossRef]

[7] Gupta SK, Verma H, Yadav N. A review on recent development of nanofluid utilization in shell & tube heat exchanger for saving of energy. Mater Today Proc 2022;54:579–589. [CrossRef]

[8] Priest M, Taylor CM. Automobile engine tribology-approaching the surface. Wear 2000;241:193–203. 00375–6) [CrossRef]

[9] Jahirul MI, Masjuki HH, Saidur R, Kalam MA, Jayed MH, Wazed MA. Comparative engine performance and emission analysis of CNG and gasoline in a retrofitted car engine. Appl Therm Eng 2010;30:2219–2226. [CrossRef]

[10] Khan M, Qamar M, Alqahtani AS, Malik MY. On multiple solutions of cubic catalysis chemically reactive flow of hybrid nanofluids. Results Eng 2024;24:103404. [CrossRef]

[11] Saxena V, Kumar N, Saxena VK. A comprehensive review on combustion and stability aspects of metal nanoparticles and its additive effect on diesel and biodiesel fuelled CI engine. Renew Sustain Energy Rev 2017;70:563–588. [CrossRef]

[12] Wang C, Zeraati-Rezaei S, Xiang L, Xu H. Ethanol blends in spark ignition engines: RON, octane-added value, cooling effect, compression ratio, and potential engine efficiency gain. Appl Energy 2017;191:603–619. [CrossRef]

[13] Gupta SK, Pradhan S. A review of recent advances and the role of nanofluid in solar photovoltaic thermal (PV/T) system. Mater Today Proc 2021;44:782–791. [CrossRef]

[14] Khan MI, Malik MY, Chaudhry F, Khan SU, El-Zahar ER. Transportation of Marangoni convection with dust particles random motion in flow of hybrid nanomaterials. Waves Random Complex Media 2024;34:6097–6110. [CrossRef]

[15] Senthilraja S, Karthikeyan M, Gangadevi R. Nanofluid applications in future automobiles: comprehensive review of existing data. Nano Micro Lett 2010;2:306–310. [CrossRef]

[16] Bhogare RA, Kothawale BS. A review on applications and challenges of nanofluids as coolant in automobile radiator. Int J Sci Res Publ 2013;3:1–11.

[17] Sidik NAC, Yazid MNAWM, Mamat R. A review on the application of nanofluids in vehicle engine cooling system. Int Commun Heat Mass Transf 2015;68:85–90. [CrossRef]

[18] Zhao N, Li S, Yang J. A review on nanofluids: Data-driven modeling of thermalphysical properties and the application in automotive radiator. Renew Sustain Energy Rev 2016;66:596–616. [CrossRef]

[19] Xian HW, Sidik NAC, Najafi GJJOTA. Recent state of nanofluid in automobile cooling systems. J Therm Anal Calorim 2019;135:981–1008. [CrossRef]

[20] Ben Said L, Kolsi L, Ghachem K, Almeshaal M, Maatki C. Advancement of nanofluids in automotive applications during the last few years- a comprehensive review. J Therm Anal Calorim 2021;1–28. [CrossRef]

[21] Ukueje WE, Abam FI, Obi A. A perspective review on thermal conductivity of hybrid nanofluids and their application in automobile radiator cooling. J Nanotechnol 2022;2022:2187932. [CrossRef]

[22] Patel J, Soni A, Barai DP, Bhanvase BA. A minireview on nanofluids for automotive applications: Current status and future perspectives. Appl Therm Eng 2023;219:119428. [CrossRef]

[23] Jadeja KM, Bumataria R, Chavda N. Nanofluid as a coolant in internal combustion engine-a review. Int J Ambient Energy 2023;44:363–380. [CrossRef]

[24] Kumar N, Gupta SK, Sharma VK. Application of phase change material for thermal energy storage: An overview of recent advances. Mater Today Proc 2021;44:368–375. [CrossRef]

[25] Kumar N, Gupta SK. Progress and application of phase change material in solar thermal energy: An overview Mater Today Proc 2021;44:271–281. [CrossRef]

[26] Sarfraz M, Khan M, Alqahtani AS, Malik MY. Simulation of gyrotactic microorganisms in Jeffrey nanofluid using Buongiorno model and Ohmic heating. Alex Eng J 2024;100:32–41. [CrossRef]

[27] Raja MAZ, Shoaib M, Abbas A, et al. Neuro-computing intelligent networks for entropy optimized MHD fully developed nanofluid flow with

activation energy and slip effects. J Indian Chem Soc 2022;99:100504. [CrossRef]
[28] Gupta SK, Dixit S. Progress and application of nanofluids in solar collectors: An overview of recent advances. Mater Today Proc 2021;44:250–259. [CrossRef]
[29] Mahian O, Kolsi L, Amani M, Estellé P, Ahmadi G, Kleinstreuer C, et al. Recent advances in modeling and simulation of nanofluid flows-Part I: Fundamentals and theory. Phys Rep 2019;790:1–48. [CrossRef]
[30] Akaje TW, Olajuwon BI, Musiliu Tayo RAJI. Computational analysis of the heat and mass transfer in a casson nanofluid with a variable inclined magnetic field. Sigma 2023;41:512–523. [CrossRef]
[31] El Hattab M, Boumhaout M, Oukach S. MHD natural convection in a square enclosure using carbon nanotubewater nanofluid with two isothermal fins. Sigma J Eng Nat Sci 2024;42:1075–1087. [CrossRef]
[32] Song YQ, Shah F, Khan SA, Khan MI, Malik MY, Sun TC. Irreversibility analysis for axisymmetric nanomaterial flow towards a stretched surface. Chaos Solitons Fractals 2021;150:111145. [CrossRef]
[33] Gupta SK, Gupta S, Gupta T, Raghav A, Singh A. A review on recent advances and applications of nanofluids in plate heat exchanger. Mater Today Proc 2021;44:229–241. [CrossRef]
[34] Ali ARI, Salam B. A review on nanofluid: preparation, stability, thermophysical properties, heat transfer characteristics and application. SN Appl Sci 2020;2:1636. [CrossRef]
[35] Boların G, Yusuf A, Adekunle ST, Aıyesımı YM, Jıya M. Analysis Of A Boundary Layer Flow Of A Nanofluid Over An Inclined Plane Via ADM. Sigma J Eng Nat Sci 2019;37:475–488.
[36] Chu YM, Bashir S, Ramzan M, Malik MY. Model-based comparative study of magnetohydrodynamics unsteady hybrid nanofluid flow between two infinite parallel plates with particle shape effects. Math Methods Appl Sci 2023;46:11568–11582. [CrossRef]
[37] Gupta SK, Saxena A. A progressive review of hybrid nanofluid utilization in solar parabolic trough collector. Mater Today Proc 2023. [CrossRef]
[38] Angayarkanni SA, Philip J. Review on thermal properties of nanofluids: Recent developments. Adv Colloid Interface Sci 2015;225:146–176. [CrossRef]
[39] Rudyak VY, Minakov AV. Thermophysical properties of nanofluids. Eur Phys J E Soft Matter 2018;41:1–12. [CrossRef]
[40] Ramzan M, Gul H, Malik MY, Ghazwani HAS. Entropy minimization analysis of a partially ionized Casson nanofluid flow over a bidirectional stretching sheet with surface catalyzed reaction. Arab J Sci Eng 2022;47:15209–15221. [CrossRef]
[41] Gupta SK, Gupta S, Singh R. A comprehensive review of energy saving in shell & tube heat exchanger by utilization of nanofluids. Mater Today Proc 2022;50:1818–1826. [CrossRef]
[42] Abbas F, Ali HM, Shah TR, Babar H, Janjua MM, Sajjad U, Amer M. Nanofluid: Potential evaluation in automotive radiator. J Mol Liq 2020;297:112014. [CrossRef]
[43] Yiamsawasd T, Dalkilic AS, Wongwises S. Measurement of the thermal conductivity of titania and alumina nanofluids. Thermochim Acta 2012;545:48–56. [CrossRef]
[44] Dalkılıç AS, Yalçın G, Küçükyıldırım BO, Öztuna et al. Experimental study on the thermal conductivity of water-based CNT-SiO_2 hybrid nanofluids. Int Commun Heat Mass Transf 2018;99:18–25. [CrossRef]
[45] Gupta SK, Sharma A. A brief review of nanofluids utilization in heat transfer devices for energy saving. Mater Today Proc 2023. [CrossRef]
[46] Kavita RK, Verma J. Simulation of localized surface plasmon resonance of silver nanoparticles with graphene coating utilizing maxwell-garnett theory. 2021;13:02022. .02022) [CrossRef]
[47] Bashirnezhad K, Bazri S, Safaei MR, Goodarzi M, et al. Viscosity of nanofluids: a review of recent experimental studies. Int Commun Heat Mass Transf 2016;73:114–123. [CrossRef]
[48] Yiamsawas T, Mahian O, Dalkilic AS, Kaewnai S, Wongwises S. Experimental studies on the viscosity of TiO_2 and Al_2O_3 nanoparticles suspended in a mixture of ethylene glycol and water for high temperature applications. Appl Energy 2013;111:40–45. [CrossRef]
[49] Esfe MH, Tavallaee R, Hatami H, Karajabad MS, Toghraie D, Alidoust S. Applying knowledge management in optimal modeling of viscosity of nanofluids by response surface methodology for use in automobiles engine. Mater Today Commun 2024;39:108897. [CrossRef]
[50] Esfe MH, Rostamian H, Sarlak MR. A novel study on rheological behavior of ZnO-MWCNT/10w40 nanofluid for automotive engines. J Mol Liq 2018;254:406–413. [CrossRef]
[51] Gupta SK, Gupta S. The role of nanofluids in solar thermal energy: A review of recent advances. Mater Today Proc 2021;44:401–412. [CrossRef]
[52] Parveen N, Awais M, Awan SE, Khan WU, He Y, Malik MY. Entropy generation analysis and radiated heat transfer in MHD (Al_2O_3-Cu/Water) hybrid nanofluid flow. Micromachines (Basel) 2021;12:887. [CrossRef]
[53] Yiamsawasd T, Dalkilic AS, Wongwises S. Measurement of specific heat of nanofluids. Curr Nanosci 2012;8:939–944. [CrossRef]
[54] Adun H, Wole-Osho I, Okonkwo EC, Kavaz D, Dagbasi M. A critical review of specific heat capacity of hybrid nanofluids for thermal energy applications. J Mol Liq 2021;340:116890. [CrossRef]
[55] Gao Y, Xi Y, Zhenzhong Y, Sasmito AP, Mujumdar AS, Wang L. Experimental investigation of specific heat of aqueous graphene oxide Al2O3 hybrid nanofluid. Therm Sci 2021;25:515–525. [CrossRef]

[56] Molana M. On the nanofluids application in the automotive radiator to reach the enhanced thermal performance: a review. Am J Heat Mass Transf 2017;4:168–187. [CrossRef]
[57] Saxena G, Soni P. Nano coolants for automotive applications: a review. Nano Trends 2018;20:9–22.
[58] Kukreja N, Gupta SK, Rawat M. Performance analysis of phase change material using energy storage device. Mater Today Proc 2020;26:913–917. [CrossRef]
[59] Lv YG, Zhang GP, Wang QW, Chu WX. Thermal management technologies used for high heat flux automobiles and aircraft: A review. Energies, 2022;15:8316. [CrossRef]
[60] Kant K, Singh RC, Maji S. Opportunities to improve the lubrication, fuel efficiency, and emission reduction using nanotechnologies: a review. J Therm Anal Calorim 2025;1–27. [CrossRef]
[61] Wang B, Qiu F, Barber GC, et al. Role of nano-sized materials as lubricant additives in friction and wear reduction: A review. Wear 2022;490:204206. [CrossRef]
[62] Peyghambarzadeh SM, Hashemabadi SH, Jamnani MS, Hoseini SM. Improving the cooling performance of automobile radiator with Al2O3/water nanofluid. Appl Therm Eng 2011;31:1833–1838. [CrossRef]
[63] Ali M, El-Leathy AM, Al-Sofyany ZJAIME. The effect of nanofluid concentration on the cooling system of vehicles radiator. Adv Mech Eng 2014;6:962510. [CrossRef]
[64] Chougule SS, Sahu SK. Comparative study of cooling performance of automobile radiator using Al2O3-water and carbon nanotube-water nanofluid. J Nanotechnol Eng Med 2014;5:010901. [CrossRef]
[65] Devireddy S, Mekala CSR, Veeredhi VR. Improving the cooling performance of automobile radiator with ethylene glycol water based TiO2 nanofluids. Int Commun Heat Mass Transf 2016;78:121–126. [CrossRef]
[66] Xian HW, Sidik NABC. Heat transfer performance of hybrid nanofluid as nanocoolant in automobile radiator system. J Adv Res Des 2018;51:14–25.
[67] Arunkumar T, Anish M, Jayaprabakar J, Beemkumar N. Enhancing heat transfer rate in a car radiator by using Al2O3 nanofluid as a coolant. Int J Ambient Energy 2019;40:367–373. [CrossRef]
[68] Said Z, Assad MEH, Hachicha AA, Bellos E, Abdelkareem MA, Alazaizeh DZ, Yousef BA. Enhancing the performance of automotive radiators using nanofluids. Renew Sustain Energy Rev 2019;112:183–194. [CrossRef]
[69] Elsaid AM. Experimental study on the heat transfer performance and friction factor characteristics of Co3O4 and Al2O3 based H2O/(CH2OH)2 nanofluids in a vehicle engine radiator. Int Commun Heat Mass Transf 2019;108:104263. [CrossRef]
[70] Kılınç F, Buyruk E, Karabulut K. Experimental investigation of cooling performance with graphene based nano-fluids in a vehicle radiator. Heat Mass Transf 2020;56:521–530. [CrossRef]
[71] Qasim M, Sajid Kamran M, Ammar M, Ali Jamal M, Yasar Javaid M. Heat transfer enhancement of an automobile engine radiator using ZnO water base nanofluids. J Therm Sci 2020;29:1010–1024. [CrossRef]
[72] Erkan A, Tüccar G, Tosun E, Özgür T. Comparison of effects of nanofluid utilization (Al2O3, SiO2, TiO2) with reference water in automotive radiators on exergetic properties of diesel engines. SN Appl Sci 2021;3:1–13. [CrossRef]
[73] Bargal MH, Souby MM, Abdelkareem MA, Sayed M, Tao Q, Chen M, Wang Y. Experimental investigation of the thermal performance of a radiator using various nanofluids for automotive PEMFC applications. Int J Energy Res 2021;45:6831–6849. [CrossRef]
[74] Ramadhan AI, Azmi WH, Mamat R, Diniardi E, Hendrawati TY. Experimental investigation of cooling performance in automotive radiator using Al2O3-TiO2-SiO2 nanofluids. Automot Exp 2022;5:28–39. [CrossRef]
[75] Contreras EMC, Bandarra Filho EP. Heat transfer performance of an automotive radiator with MWCNT nanofluid cooling in a high operating temperature range. Appl Therm Eng 2022;207:118149. [CrossRef]
[76] Arivazhagan S, Balaji T. Experimental investigation of an automobile radiator using carbon based hybrid nano coolant. Int J Therm Sci 2023;193:108497. [CrossRef]
[77] Khan MSA. Analytical examination of nano-fluid-assisted cooling rate enhancement in a car radiator. Am Int J Sci Eng Res 2023;6:1–14. [CrossRef]
[78] Hassaan AM. An experimental investigation examining the usage of a hybrid nanofluid in an automobile radiator. Sci Rep 2024;14:27597. [CrossRef]
[79] Rana S, Nawaz M, Alharbi SO, Malik MY. Thermal enhancement in coolant using novel hybrid nanoparticles with mass transport. Case Stud Therm Eng 2021;28:101467. [CrossRef]
[80] Srinivas VCVK.NSN, Moorthy CV, Dedeepya V, Manikanta PV, Satish V. Nanofluids with CNTs for automotive applications. Heat Mass Transf 2016;52:701–712. [CrossRef]
[81] Wang X, Zhang J, Yin MA, Wang G, Han J, Dai M, Sun ZY. A comprehensive review on the properties of nanofluid fuel and its additive effects to compression ignition engines. Appl Surf Sci 2020;504:144581. [CrossRef]
[82] Mehta RN, Chakraborty M, Parikh PA. Nanofuels: Combustion, engine performance and emissions. Fuel 2014;120:91–97. [CrossRef]
[83] Sabet Sarvestany N, Farzad A, Ebrahimnia-Bajestan E, Mir M. Effects of magnetic nanofluid fuel combustion on the performance and emission characteristics. J Dispers Sci Technol 2014;35:1745–1750. [CrossRef]

[84] Venkatesan SP, Kadiresh PN. Influence of an aqueous cerium oxide nanofluid fuel additive on performance and emission characteristics of a compression ignition engine. Int J Ambient Energy 2016;37:64–67. [CrossRef]
[85] Sarvestani NS, Rohani A, Farzad A, Aghkhani MH. Modeling of specific fuel consumption and emission parameters of compression ignition engine using nanofluid combustion experimental data. Fuel Process Technol 2016;154:37–43. [CrossRef]
[86] Ramanan MV, Yuvarajan D. Emission analysis on the influence of magnetite nanofluid on methyl ester in diesel engine. Atmos Pollut Res 2016;7:477–481. [CrossRef]
[87] Chaichan MT, Kadhum AAH, Al-Amiery AA. Novel technique for enhancement of diesel fuel: Impact of aqueous alumina nano-fluid on engine's performance and emissions. Case Stud Therm Eng 2017;10:611–620. [CrossRef]
[88] Yuvarajan D, Babu MD, BeemKumar N, Kishore PA. Experimental investigation on the influence of titanium dioxide nanofluid on emission pattern of biodiesel in a diesel engine. Atmos Pollut Res 2018;9:47–52. [CrossRef]
[89] Saxena V, Kumar N, Saxena VK. Multi-objective optimization of modified nanofluid fuel blends at different TiO2 nanoparticle concentration in diesel engine: Experimental assessment and modeling. Appl Energy 2019;248:330–353. [CrossRef]
[90] Venkatesan SP, Kadiresh PN. Combustion performance study of aqueous aluminum oxide nanofluid blends in compression ignition engine. J Energy Resour Technol 2019;141:042203. [CrossRef]
[91] Pan S, Wei J, Tao C, Lv G, Qian Y, Liu Q, Han W. Discussion on the combustion, performance and emissions of a dual fuel diesel engine fuelled with methanol-based CeO2 nanofluids. Fuel 2021;302:121096. [CrossRef]
[92] Venkatesan SP, Kadiresh PN, Beemkumar N, Jeevahan J. Combustion, performances, and emissions characteristics of diesel engine fuelled with diesel-aqueous zinc oxide nanofluid blends. Energy Sources A Recover Util Environ Eff 2023;45:2922–2936. [CrossRef]
[93] Sathish T, Giri J, Saravanan R, Zairov R, Hasnain SM. Nano-fuels of Al2O3/SiO2/MgO/tamarind seed oil biodiesel for CI engines: An evaluation of combustion consumption and emission performance. Int J Thermofluids 2024;23:100815. [CrossRef]
[94] Mishra PC, Nayak SK, Mitra P, Mukherjee S, Paria S. Application and future of nanofluids in automobiles: an overview on current research. In Proceedings of 2nd KIIT International Symposium on Advances in Automotive Technology. 2013.
[95] Selvam C, Lal DM, Harish S. Enhanced heat transfer performance of an automobile radiator with graphene based suspensions. Appl Therm Eng 2017;123:50–60. [CrossRef]
[96] Sawant Y, Pathare K, Patel R, Choughule P. Nanofluids with recent application & future trends. Int J Innov Eng Res Technol 2021;8:458–468.
[97] Bacha HB, Ullah N, Hamid A, Shah NA. A comprehensive review on nanofluids: synthesis, cutting-edge applications, and future prospects. Int J Thermofluids 2024;100595. [CrossRef]
[98] Aziz A, Alsaedi A, Muhammad T, Hayat T. Numerical study for heat generation/absorption in flow of nanofluid by a rotating disk. Results Phys 2018;8:785–792. [CrossRef]
[99] Khaliq Ali HA, Abed MS, Nayeeif AA. Response of viscous damping of dashpot containing hybrid nanofluid. J Adv Res Fluid Mech Therm Sci 2020;67:52–65.
[100] Pawar AA, Patil KA, Mohite DD. Impact of CuO nanoparticles on the viscosity and vibration damping characteristics of shock absorber oil. Discov Nano 2024;19:131. [CrossRef]
[101] Akl S, Elsoudy S, Abdel-Rehim AA, Salem S, Ellis M. Recent advances in preparation and testing methods of engine-based nanolubricants: a state-of-the-art review. Lubricants 2021;9:85. [CrossRef]
[102] Abbas N, Rehman KU, Shatanawi W, Malik MY. Numerical study of heat transfer in hybrid nanofluid flow over permeable nonlinear stretching curved surface with thermal slip. Int Commun Heat Mass Transf 2022;135:106107. [CrossRef]
[103] Moitsheki RJ, Hayat T, Malik MY, Mahomed FM. Symmetry analysis for the nonlinear model of diffusion and reaction in porous catalysts. Nonlinear Anal Real World Appl 2010;11:3031–3036. [CrossRef]
[104] Tonk R. The science and technology of using nano-materials in engine oil as a lubricant additives. Mater Today Proc 2021;37:3475–3479. [CrossRef]
[105] Goodarzi M, Esfandeh S, Toghraie D. A state of art review of the viscosity behavior of nano-lubricants containing MWCNT nanoparticles: Focusing on engine lubrication goals. J Mol Liq 2022;346:118264. [CrossRef]
[106] Wu YY, Kao MJ. Using TiO2 nanofluid additive for engine lubrication oil. Ind Lubr Tribol 2011;63:440–445. [CrossRef]
[107] Ahmadi H, Rashidi A, Nouralishahi A, Mohtasebi S S. Preparation and thermal properties of oil-based nanofluid from multi-walled carbon nanotubes and engine oil as nano-lubricant. Int Commun Heat Mass Transf 2013;46:142–147. [CrossRef]
[108] Afrand M, Najafabadi KN, Akbari M. Effects of temperature and solid volume fraction on viscosity of SiO2-MWCNTs/SAE40 hybrid nanofluid as a coolant and lubricant in heat engines. Appl Therm Eng 2016;102:45–54. [CrossRef]
[109] Meng Y, Su F, Chen Y. Supercritical fluid synthesis and tribological applications of silver nanoparticle-decorated graphene in engine oil nanofluid. Sci Rep 2016;6:31246. [CrossRef]

[110] Esfe MH, Karimpour R, Arani AAA, Shahram J. Experimental investigation on non-Newtonian behavior of Al2O3-MWCNT/5W50 hybrid nano-lubricant affected by alterations of temperature, concentration and shear rate for engine applications. Int Commun Heat Mass Transf 2017;82:97–102. [CrossRef]

[111] Asadi A, Asadi M, Rezaniakolaei A, Rosendahl LA, Wongwises S. An experimental and theoretical investigation on heat transfer capability of Mg (OH) 2/MWCNT-engine oil hybrid nano-lubricant adopted as a coolant and lubricant fluid. Appl Therm Eng 2018;129:577–586. [CrossRef]

[112] Esfe MH, Arani AAA, Esfandeh S. Improving engine oil lubrication in light-duty vehicles by using of dispersing MWCNT and ZnO nanoparticles in 5W50 as viscosity index improvers (VII). Appl Therm Eng 2018;143:493–506. [CrossRef]

[113] Rejvani M, Saedodin S, Vahedi SM, Wongwises S, Chamkha AJ. Experimental investigation of hybrid nano-lubricant for rheological and thermal engineering applications. J Therm Anal Calorim 2019;138:1823–1839. [CrossRef]

[114] Esfe MH, Arani AAA, Esfandeh S, Afrand M. Proposing new hybrid nano-engine oil for lubrication of internal combustion engines: Preventing cold start engine damages and saving energy. Energy 2019;170:228–238. [CrossRef]

[115] Ramteke SM, Chelladurai H. Effects of hexagonal boron nitride based nanofluid on the tribological and performance, emission characteristics of a diesel engine: An experimental study. Eng Rep 2020;2:e12216. [CrossRef]

[116] Hemmat Esfe M, Esfandeh S. A new generation of hybrid-nanofluid: thermal properties enriched lubricant fluids with controlled viscosity amount. SN Appl Sci 2020;2:1–16. [CrossRef]

[117] Bharath BK, Arul Mozhi Selvan V. An experimental investigation on rheological and heat transfer performance of hybrid nanolubricant and its effect on the vibration and noise characteristics of an automotive spark-ignition engine. Int J Thermophys 2020;42:1–30. [CrossRef]

[118] Kharabati S, Saedodin S, Rostamian SH. Experimental investigation of thermal and rheological behavior of silica/soybean oil nano lubricant in low-temperature performance of internal combustion engine. Energy Sources A Recover Util Environ Eff 2021;1–15. [CrossRef]

[119] Singh JP, Singh S, Nandi T, Ghosh SK. Development of graphitic lubricant nanoparticles based nanolubricant for automotive applications: Thermophysical and tribological properties followed by IC engine performance. Powder Technol 2021;387:31–47. [CrossRef]

[120] Esfe MH, Esfandeh S, Alidoust S, Toghraie D. Comparison of viscosity behavior of hybrid nano-lubricants containing Al2O3-MWCNT nanoparticles dispersed in SAE XWX engine oils to determine the optimal behavior of nano-lubricants based on experimental studies. Colloids Surf A Physicochem Eng Asp 2022;641:128446. [CrossRef]

[121] Gosai DC, Modi AJ, Gillawat AK. Impact of nano-fuel additives and nano-lubricant oil additives on diesel engine performance and emission characteristics. J Heat Mass Transf Res 2025;12:103–122.

[122] Raja MAZ, Tabassum R, El-Zahar ER, Shoaib M, Khan MI, Malik MY, Qayyum S. Intelligent computing through neural networks for entropy generation in MHD third-grade nanofluid under chemical reaction and viscous dissipation. Waves Random Complex Media 2025;35:2502–2526. [CrossRef]

[123] Ramzan M, Gul H, Malik MY, Ghazwani HAS. Entropy minimization analysis of a partially ionized Casson nanofluid flow over a bidirectional stretching sheet with surface catalyzed reaction. Arab J Sci Eng 2022;47:15209–15221. [CrossRef]

[124] Ige EO, Oyelami FH, Adedipe ES, et al. Analytical simulation of nanoparticle-embedded blood flow control with magnetic field influence through spectra homotopy analysis method. Int J Mod Phys B 2021;35:2150226. [CrossRef]

[125] Sohail A, Rusdi MS, Waseem M, Abdullah MZ, Pallonetto F, Sultan SM. Cutting-edge developments in active and passive photovoltaic cooling for reduced temperature operation. Results Eng 2024;102662. [CrossRef]

[126] Pati P, McGinnis S, Vikesland PJ. Life cycle assessment of "green" nanoparticle synthesis methods. Environ Eng Sci 2014;31:410–420. [CrossRef]

[127] Sohail A, Waseem M, Rusdi MS, Abdullah MZ, Sultan SM. Numerical Analysis of Counter-Flow Converging Channels for Uniform Temperature Distribution in PV Panels to Enhance Energy Conversion Efficiency. Energy Built Environ 2025. [CrossRef]

[128] Gupta SK, Kumari S. A Review on Recent Development and Future Perspective of Nanofluid Utilization in Automotives. Evergreen 2025;12:992–1019. [CrossRef]